NEPT
Advancing Knowledge for a Sustainable Future

NATURE ENVIRONMENT AND POLLUTION TECHNOLOGY

Peer-Reviewed Open Access Journal

Vol. 25, No. 4, December 2026

ISSN (Print): 0972-6268

ISSN (Online): 2395-3454



Published by Technoscience Publications LLP
Scholarly Publishing

NATURE ENVIRONMENT AND POLLUTION TECHNOLOGY

CONTENTS

Vol. 25, No. 4, December 2026

1 **Activity Concentrations of Natural Radionuclides and Ingestion Radiological Risk in Common Medicinal Plants from Iraq**
Zainab Hadi Rajih and Osamah Nawfal Oudah
Article ID: D1892 | **DOI:** 10.46488/NEPT.2026.v25i04.D1892

2 **Modeling Temporal Persistence in Daily Pan Evaporation Using Interpretable Machine Learning**
Jaydeep Kale and Sanjaykumar Sharma
Article ID: B4425 | **DOI:** 10.46488/NEPT.2026.v25i04.B4425

3 **Three Decades of Urban Heat Dynamics in Patna, India: A Remote Sensing-Based Hotspot Analysis**
Avinash Kumar Singh and Manoj Kumar
Article ID: B4429 | **DOI:** 10.46488/NEPT.2026.v25i04.B4429

4 **Dispersion Modeling of SO? and NO? Emissions Using AERMOD on Ambient Air Quality at Steam Power Plant PT.X in Southeast Sulawesi, Indonesia**
Nur Miftahuljannah , Sumarni Hamid Aly and Muralia Hustim
Article ID: D1894 | **DOI:** 10.46488/NEPT.2026.v25i04.D1894

5 **Fish Diversity and Habitat Complexity: The Role of Macrophytes and Physicochemical Parameters in Urban and Rural Tropical Lakes**
I. Annie Pushpa, K. Maheshkumar, V. Deepak Samuel and N. Nirmal Magadalenal
Article ID: B4426 | **DOI:** 10.46488/NEPT.2026.v25i04.B4426

6 **Household Behavioral Compliance in Waste Management Using the Extended Theory of Planned Behavior**
Article ID: D1927 | **DOI:** 10.46488/NEPT.2026.v25i04.D1927

7 **Legacy Pesticides in Aquatic Systems: Mechanistic Persistence, Regulatory Lag, and Catchment-Scale Remediation Imperatives**
Article ID: B4432 | **DOI:** 10.46488/NEPT.2026.v25i04.B4432

8 **Evaluating Green Infrastructure Interventions for Land Surface Temperature Reduction: A PRISMA-Based Systematic Review**
Avinash Kumar Singh and Manoj Kumar
Article ID: B4431 | **DOI:** 10.46488/NEPT.2026.v25i04.B4431

9 **Organic Waste to Energy: Enhancing Biodigester Efficiency in Oman for Sustainable Development**
Jasim Abdullah Ali Al Shehhi and Nitin Bhaurao Raut
Article ID: D1824 | **DOI:** 10.46488/NEPT.2026.v25i04.D1824

NATURE ENVIRONMENT AND POLLUTION TECHNOLOGY

10 **Eco-Friendly Degradation of Textile Azo Dye Reactive Orange ME2RL Using Pseudomonas stutzeri-Mediated Iron Oxide Nanoparticles**

P. Zambare, S. Kanase and A. Raut

Article ID: B4422 | **DOI:** 10.46488/NEPT.2026.v25i04.B4422

11 **Insights into WRF-Chem Sensitivity in a Coastal Region of Morocco: Chemical Mechanisms, Nesting Options, and Physical Parameterization**

Karima Iraoui, Rachid Moustabchir, Hicham Charifi, Abdelfettah Benchrif and Ahmed Chirmata

Article ID: D1878 | **DOI:** 10.46488/NEPT.2026.v25i04.D1878

12 **Physicochemical Characterization of Pulp and Black Liquor Derived from Corn Husk and Coir Blends**

Madhuri Pydimalla, Shrinidhi Tavag, Surya Tej Valluri, Nukala Mohith Satya Vardhan and A. V. Raghavendra Rao

Article ID: B4427 | **DOI:** 10.46488/NEPT.2026.v25i04.B4427

13 **Simulation of the Migration Law of Cr(VI) in Groundwater Using a Fully Coupled Numerical Model**

Haihua Li, Gaojie Chai, Yahui Xu, Xinyi Wang and Haozu Cheng

Article ID: D1889 | **DOI:** 10.46488/NEPT.2026.v25i04.D1889

14 **Assessment of Knowledge, Awareness, Attitude, and Practice of Plastic Waste Management Among the Digitally Active Public in India**

Kanhaiya Kumar and Kasi Marimuthu

Article ID: B4433 | **DOI:** 10.46488/NEPT.2026.v25i04.B4433

15 **Wind Power Density in Southern Iraq: A Comparative Study of Coastal, Port and Inland Sites**

Taghreed Ali Abbas, Muna H. Ahmed and Hazim H. Hussain

Article ID: D1897 | **DOI:** 10.46488/NEPT.2026.v25i04.D1897

16 **Mapping the Evolution of Urban Sprawl Research: A PRISMA-Based Systematic and Bibliometric Synthesis**

Jaswant Singh and Kranti Kumar Maurya

Article ID: B4435 | **DOI:** 10.46488/NEPT.2026.v25i04.B4435

17 **Water Footprint of Local Herbs in Thailand Using the Water Footprint Network Methodology**

Phairat Usubharatana and Harnpon Phungrassami

Article ID: D1900 | **DOI:** 10.46488/NEPT.2026.v25i04.D1900

18 **Sustainable Advances in Phosphorus Removal and Recovery from Industrial Wastewater**

Md Adim, Mohd Imran Siddiqui, Hasan Rameez, Izharul Haq Farooqi and Farrukh Basheer

Article ID: B4437 | **DOI:** 10.46488/NEPT.2026.v25i04.B4437

19 **Bridging Efficiency Gaps in ASEAN Agriculture: A Spatial SBMDEA Approach**

Titin Dwi Aryanti, Suryanto and Evi Gravitiani

Article ID: D1901 | **DOI:** 10.46488/NEPT.2026.v25i04.D1901

20 **Ecotoxicological Insights into Heavy Metal Dynamics in Cauvery Delta Wetland Sediments: Geochemistry, Speciation and Ecological Risk Indices**

K. P. Aakash and R. Mohanraj

Article ID: B4440 | **DOI:** 10.46488/NEPT.2026.v25i04.B4440

NATURE ENVIRONMENT AND POLLUTION TECHNOLOGY

21 **Determinants of Household Waste Management Behavior in Urban Slum Communities: Evidence from Makassar City, Indonesia**

Muh. Fajaruddin Natsir, Erniwati Ibrahim, Anwar Mallongi, Owildan Wisudawan, Basir Rasyid, Anwar Daud and Syamsuar Manyulle

Article ID: D1903 | **DOI:** 10.46488/NEPT.2026.v25i04.D1903

22 **An Assessment of the Environmental and Social Impacts of Waste Management Practices in Omuthiya Town and Its Disposal Site, Oshikoto Region, Namibia**

Margaret Litungeni Johannes and Timoteus Kadhila

Article ID: D1904 | **DOI:** 10.46488/NEPT.2026.v25i04.D1904

23 **Heavy Metal Dynamics in Crops Grown on Municipal Solid Waste Compost Amended Soils**

B. S. Kavitha and R. K. Somashekar

Article ID: B4434 | **DOI:** 10.46488/NEPT.2026.v25i04.B4434

24 **Analysis of NH3 Distribution and Community Perception of Odor in the Antang Landfill Area, Makassar City**

Qurin Septifar Aulia, Muhammad Isran Ramli and Sumarni Hamid Aly

Article ID: D1895 | **DOI:** 10.46488/NEPT.2026.v25i04.D1895

25 **Dynamic Perspective of the Evolution of the Environmental Kuznets Curve in Ecuador and Mexico**

Giojan Aguirre, Rosa Llerena, Roger Yela, Hugo Galarza, Evelyn Vergara and Abril Herrera

Article ID: D1896 | **DOI:** 10.46488/NEPT.2026.v25i04.D1896

26 **Evaluation of Iron Ore Dust Emission Rates and Associated Bacterial Load**

Melainine Aillal, Olfa Ben Said, Hamouda Beyrem and Zeinebou Sidoumou

Article ID: D1905 | **DOI:** 10.46488/NEPT.2026.v25i04.D1905

27 **Evaluation of the Spatial Distribution of Some Thermal Comfort Indices in Iraq Using the RayMan Model**

Fadhel A. Mohammed and Alaa M. AL-Lami

Article ID: D1910 | **DOI:** 10.46488/NEPT.2026.v25i04.D1910

28 **Trajectory-Based Evaluation of Greenhouse Gas Mitigation Pathways in Municipal Solid Waste Systems: A System Dynamics Approach**

Nattarat Phaingam, Phairat Usubharatana and Harnpon Phungrassami

Article ID: D1913 | **DOI:** 10.46488/NEPT.2026.v25i04.D1913

29 **Activity Concentration of Natural Radionuclides in Surface Waters and Bottom Sediments Near Uranium Mining Sites and Environmental Impacts**

Aikyn Nurakhmet, Amanbek Zandybay, Zhanar Moldagazyyeva, Murat Nurushev and Yerlan Zhumay

Article ID: D1914 | **DOI:** 10.46488/NEPT.2026.v25i04.D1914

30 **Biological and Ecotoxicological Responses of Daphnia pulex to 2,4-D and Malathion-Contaminated Laboratory Microcosms**

Samiksha Agarwal and Saltanat Parveen

Article ID: B4411 | **DOI:** 10.46488/NEPT.2026.v25i04.B4411

NATURE ENVIRONMENT AND POLLUTION TECHNOLOGY

31 **Groundwater Contamination in India: Regional Variations, Hydrogeochemical Controls, Health Risks, and Integrated Management Strategies**

Santosh Sanap , Shrikant Randhavane and Narayan Chandak

Article ID: B4443 | **DOI:** 10.46488/NEPT.2026.v25i04.B4443

32 **Production and Characterization of Polyhydroxybutyrate (PHB) from an Agricultural By-Product Using Bacillus thuringiensis CICIM (B2031)**

Sandisiwe Gladness Zondo, Johnson Zininga, Kugen Permaul and Nirmala Deenadayalu

Article ID: D1907 | **DOI:** 10.46488/NEPT.2026.v25i04.D1907

33 **Co-occurrence of Antibiotics, Antibiotic Resistance Genes, and MultidrugResistant Bacteria in a Himalayan Foothill Urban River, India**

Amit Pokhriyal, Prashant Pandey, Manisha Dhiman, Andrzej Bia?owiec, Kanchan Deoli Bahukhandi, Chinenye Adaobi Igwegbe and Kapil Kumar Joshi

Article ID: B4448 | **DOI:** 10.46488/NEPT.2026.v25i04.B4448

34 **Synthesis and Characterization of Amino Acid-Based Ionic Liquids for Selective Absorption of CO? Using Liquid Foam Bed and Semi-Batch Reactors**

Article ID: D1912 | **DOI:** 10.46488/NEPT.2026.v25i04.D1912

35 **Biofilm-Forming Endophytic Bacteria and Fungi from Bryophytes: Tools for Eco-Restoration of Polluted Habitats**

Shivani Gore, Shivom Singh, Pooja Swarnkar and Kajal S. Rathore

Article ID: B4438 | **DOI:** 10.46488/NEPT.2026.v25i04.B4438

36 **Analysis of Geomechanical Properties of Mine Waste Using Cementitious and Pozzolanic Agents: A Systematic Review**

Jesús Daniel Pérez Oropeza , Miguel Alberto Barreda de la Cruz and Gerby Giovanna Rondán-Sanabria

Article ID: D1915 | **DOI:** 10.46488/NEPT.2026.v25i04.D1915

37 **Impact of Sugarcane Bagasse Ash Amendment on Soil Attenuation and Leachate Dynamics: Insights from Multivariate Analysis**

M. I. Krutika, B. Lokeshappa, Rashma Shetty and P. C. Srinivasa

Article ID: B4446 | **DOI:** 10.46488/NEPT.2026.v25i04.B4446

38 **Seasonal Water Quality Variation and Pollutant Loads Entering the Largest Hydropower Reservoir in Vietnam after Dam Impoundment (2014–2024)**

Article ID: D1916 | **DOI:** 10.46488/NEPT.2026.v25i04.D1916

39 **AI-Driven Digital Transformation for Sustainable Manufacturing: Exploring the Impact of Carbon Intensity and ESG Through Eco-Innovation Theory**

Linda, Vania Angelica Angdi and Linda Kusumaning Wedari

Article ID: D1917 | **DOI:** 10.46488/NEPT.2026.v25i04.D1917

40 **Pollution Emissions from the Kaeng Sian Landfill: Assessment and Sustainable Waste Management for Kanchanaburi Province, Thailand**

Sasitorn Hasin, Saowaluck Haosagul and Apichaya Sawasdee

Article ID: D1919 | **DOI:** 10.46488/NEPT.2026.v25i04.D1919

41 **Laboratory Evaluation of Archie's Law in Kaolinite-Rich Landfill Soil Under the Leachate Influence: A Mineralogical Control and Interpretation Limited by Uncertainty**

Rizka Rizka, Muhammad Bisri Mustofa, Irwan Iskandar, Warsa Warsa and Djoko Santoso

Article ID: D1920 | **DOI:** 10.46488/NEPT.2026.v25i04.D1920

42 **Hydrodynamic Enhancement of Direct Contact Membrane Distillation Using a Corrugated Feed Channel: A Numerical Study**

Fajer M. Alelaj, Mansour Ahmed, Hussain Al-Sairfi, Garudachari Bhadrachari, Shimaa Zahran and Mohamed R. Elmarghany

Article ID: D1922 | **DOI:** 10.46488/NEPT.2026.v25i04.D1922

43 **Removal of Copper and Zinc from Aqueous Media Using White-Rot Lignicolous Fungi**

Analiz Lola Ruiz Tello, Ladislao Ruiz-Rengifo, Julio Miguel Ángeles-Suazo, Camila Valentina Carrasco Llaique and Jairo Edson Gutiérrez-Collao

Article ID: D1923 | **DOI:** 10.46488/NEPT.2026.v25i04.D1923

44 **Occurrence and Characterization of Microplastics in the Chili River (Arequipa, Peru) Based on FTIR-ATR and SEM-EDS Analysis**

Gerby Giovanna Rondán-Sanabria, Holger Saul Perez-Montaño, Edgard Ronny Delgado-Huamani and Italo Francisco Treviño-Zevallos

Article ID: D1924 | **DOI:** 10.46488/NEPT.2026.v25i04.D1924

45 **A Hybrid Coagulation-Microfiltration Approach for Industrial Wastewater Pretreatment**

Anurag Chavan, Sanjay Harke, Ravindra Gaikwad and Bhavanipant Pande

Article ID: B4414 | **DOI:** 10.46488/NEPT.2026.v25i04.B4414

46 **Sustainable Development of Maritime Transport Towards Net-Zero Emissions by 2050 Through a Feasible Fuel Transition Roadmap**

Tran Huu Long, Phan Van Hung and Nguyen Xuan Long

Article ID: D1921 | **DOI:** 10.46488/NEPT.2026.v25i04.D1921

47 **Investigating Consumer Perceptions and Mapping E-waste Stakeholders: Evidence from Chh. Sambhajinagar City, Maharashtra**

Arvind Chel, Geetanjali Kaushik, Ashish Gadekar, Vijay Kumar Srivastava and Abhay Wre

Article ID: B4418 | **DOI:** 10.46488/NEPT.2026.v25i04.B4418

48 **The Value of a Statistical Life of Urban Air Pollution in Ho Chi Minh City, Vietnam**

Thu Thi Minh Nguyen, Quang Minh Ho Ky and Doan Quang Tri

Article ID: D1930 | **DOI:** 10.46488/NEPT.2026.v25i04.D1930

49 **Eco-Physiological Assessment of Native Plant Species for Mitigating Airborne Pollutants and Greenbelt Development in a Coal Mining Region**

Mallikharjuna Prasad Polavarapu, Manoj Kumar, Shreerup Goswami, Soham Mishra, Akshay Kumar Singh and Sushil Kumar Shukla

Article ID: B4441 | **DOI:** 10.46488/NEPT.2026.v25i04.B4441

50 **Macroinvertebrate-Based Ecological Health Assessment of Main River and Canal Systems in the Mekong Delta: Challenges and Future Directions**

Anh Duc Pham, My Thanh Dang, Duc Canh Vu, Thanh Luu Pham and Thanh Son Dao

Article ID: D1931 | **DOI:** 10.46488/NEPT.2026.v25i04.D1931

NATURE ENVIRONMENT AND POLLUTION TECHNOLOGY

51 **Integrated Electrocoagulation–Adsorption Using Thermally Activated Bentonite for Pb, Cd, and Ni Removal from Laboratory Wastewater**

Muhrinsyah Fatimura, Tuty Emilia Agustina, Susila Arita, Elda Melwita, Rully Masriatini and Nurlela

Article ID: D1932 | **DOI:** 10.46488/NEPT.2026.v25i04.D1932

52 **From Water Scarcity to Resilience: A Policy-Oriented Framework for Community-Based Drought Management in Southeast Asia**

Sitthisak Pinmongkhonkul and Thanakorn Panyopo

Article ID: D1934 | **DOI:** 10.46488/NEPT.2026.v25i04.D1934

53 **Field Implementation of Pseudomonas fluorescens for Bioremediation of Single-Use Plastic Waste: A Biolayer in a Landfill Liner System**

S. Sangeetha and P. Hari Krishna

Article ID: B4444 | **DOI:** 10.46488/NEPT.2026.v25i04.B4444

54 **Spatial Footprint Distribution of Some Heavy Metals in Major Transport Routes in Ramadi City, Iraq**

Rafraf Abdulaziz Abdulqader and Sufyan Mohammed Shartooh

Article ID: D1936 | **DOI:** 10.46488/NEPT.2026.v25i04.D1936

55 **Aerobic Granulation Technology-Based Cresol Degradation: A Comparative Evaluation of Reactor Studies**

Apurva Kadia and Urvish Chhaya

Article ID: B4423 | **DOI:** 10.46488/NEPT.2026.v25i04.B4423

56 **Optimizing Waste Management Systems to Reduce Greenhouse Gas Emissions on the Small Island of Kodingareng Lompo, Indonesia**

Wahyudi Munim Anugra, Irwan Ridwan Rahim and Asiyanthi T. Lando

Article ID: D1902 | **DOI:** 10.46488/NEPT.2026.v25i04.D1902

57 **Lead (Pb) Bioaccumulation and Physiological Responses of Acanthus ilicifolius in the Mangrove Forest, Wonorejo, Surabaya, East Java, Indonesia**

Fida Rachmadiarti, Winarsih, Herlina Fitrihidajati, Tarzan Purnomo, Sunu Kuntjoro, Reyna Novita Sari, Yeremia Ajijaya Putra Ritiau, Eza Alfian Rizqita and Farah Aisyah Nafidiastri

Article ID: D1908 | **DOI:** 10.46488/NEPT.2026.v25i04.D1908

58 **A Comprehensive Review on Biostimulants for Sustainable Agriculture: Global Market Trends and Experimental Challenges**

Rajeev Kumar, Narendra Kumar, Pooja Vijayaraghavan, Anshuman Shah, Sanskriti Sanvi and Ravi Kant Singh

Article ID: B4428 | **DOI:** 10.46488/NEPT.2026.v25i04.B4428

59 **Valorization of Textile Waste into Cellulose-Citronellal Fiber Using Natural H-Zeolite Catalyst: Toward a Circular Bioeconomy Approach**

Edy Cahyono, Samuel Budi Wardhana Kusuma, Sigit Priatmoko, Ridho Prasetyo and Trida Ridho Fariz

Article ID: D1926 | **DOI:** 10.46488/NEPT.2026.v25i04.D1926

60 **Field-Based Evaluation of Water Quality, Macroinvertebrates and Sediment in the Downstream Segment of the Upper Konto Sub-Watershed, Indonesia**

Very Dermawan, Emma Yuliani, Evi Nur Cahya and Nazwa Shiva Setya Putri

Article ID: D1935 | **DOI:** 10.46488/NEPT.2026.v25i04.D1935

NATURE ENVIRONMENT AND POLLUTION TECHNOLOGY

EDITORIAL LEADERSHIP & ADVISORY BOARD

Nature Environment and Pollution Technology

CHIEF EDITOR

Dr. P. K. Goel
Former Head, Department of Pollution Studies, Yashwantrao Chavan College of Science, Karad, Maharashtra, India

HONORARY EDITOR

Dr. K. P. Sharma
Emeritus Professor, Department of Botany, University of Rajasthan, Jaipur, Rajasthan, India

EXECUTIVE EDITOR

Ms. Apurva Goel
Technoscience Publications LLP, Pune, Maharashtra, India

Editorial Advisory Board

1. Dr. Saikat Kumar Basu, Dept. of Biological Sciences, University of Lethbridge, Lethbridge AB, Alberta, Canada

2. Dr. Elsayed Elsayed Hafez, Plant Protection and Biomolecular Diagnosis Department, Arid Lands Cultivation Research Institute (ALCRI), Alexandria, Egypt

3. Dr. Tri Nguyen-Quang, Department of Engineering Agricultural Campus, Dalhousie University, Canada

4. Dr. Sang-Bing Tsai, Wuyi University Business School, Wuyishan, China

5. Dr. Zawawi Bin Daud, Faculty of Civil and Environmental Engg., Universiti Tun Hussein Onn, Malaysia, Johor, Malaysia

6. Dr. B. Akbar John, School of Industrial Technology, Universiti Sains Malaysia (USM), Penang, Malaysia

7. Dr. C. Stella, Centre for Agro Marine Research, Sethubhaskara Agricultural College and Research Foundation, Visalayankottai, Karaikudi, T.N., India

8. Dr. G.R. Pathade, Krishna Institute of Allied Sciences, Krishna Vishwa Vidyapeeth, Karad, Maharashtra, India

9. Dr. Amit Arora, Department of Chemical Engineering, National Institute of Technology (NIT), Hamirpur, H.P., India

10. Prof. Riccardo Buccolieri, Dept. of Atmospheric Physics, University of Salento, Dipartimento di Scienze e Tecnologie Biologiche ed Ambientali, Laboratory of Micrometeorology, Lecce, Italy

11. Dr. Tai-Shung Chung, Graduate Institute of Applied Science and Technology, National Taiwan University of Science and Technology, Taipei, Taiwan

12. Dr. Abdeltif Amrane, Technological Institute of Rennes, University of Rennes, France

13. Dr. Giuseppe Ciaburro, Dept. of Architecture and Industrial Design, Universita degli Studi della Campania, Italy

14. Dr. A.B. Gupta, Dept. of Civil Engineering, Malviya National Institute of Technology (MNIT), Jaipur, India

15. Claudio M. Amescua Garcia, Department of Publications, Centro de Ciencias de la Atmosfera, Universidad Nacional Autonoma de Mexico, Mexico

16. Alexander B. Ruchin, Joint Directorate of the Mordovia State Nature Reserve and National Park, Saransk 430005, Russia

17. Wei (Welsh) Wang, State Key Lab of Environmental and Biological Analysis, Hong Kong Baptist University, Hong Kong

Nature Environment and Pollution Technology
An International Quarterly Peer-Reviewed Open Access Journal

p-ISSN: 0972-6268 | e-ISSN: 2395-3454 Vol. 25 | No. 4 | Article ID D1892 | 2026

RESEARCH ARTICLE https://doi.org/10.46488/NEPT.2026.v25i04.D1892 OPEN ACCESS

Activity Concentrations of Natural Radionuclides and Ingestion Radiological Risk in Common Medicinal Plants from Iraq

Zainab Hadi Rajih and Osamah Nawfal Oudah†
Department of Physics, College of Education, University of Al-Qadisiyah, Iraq
†Corresponding author: Osamah Nawfal Oudah; osamah.oudah@qu.edu.iq

ARTICLE HISTORY

Received: 24-11-2025
Revised: 22-02-2026
Accepted: 26-02-2026

KEYWORDS

Medicinal plants
Natural radionuclides
U-238,
Th-232
K-40
Gamma spectroscopy
Ingestion effective dose (IED)
Excess lifetime cancer risk (ELCR)
Radiation health hazard
Cancer risk

CITE THIS ARTICLE

Rajih, Z. H. and Oudah, O. N., 2026. Activity concentrations of natural radionuclides and ingestion radiological risk in common medicinal plants from Iraq. *Nature Environment and Pollution Technology*, 25(4), D1892. https://doi.org/10.46488/NEPT.2026.v25i04.D1892

COPYRIGHT & LICENCE

© 2026 The Authors
Open Access under CC BY 4.0.

PUBLISHED BY

TECHNOSCIENCE PUBLICATIONS

ABSTRACT

The increasing use of medicinal plants as natural alternatives to pharmaceutical drugs has raised concerns about contamination by naturally occurring radioactive materials and the potential health risks associated with their consumption. This study aimed to determine the activity concentrations of U-238, Th-232, and K-40 in commonly consumed medicinal plants and to assess the associated radiological risks resulting from their ingestion. Twenty medicinal plant samples were collected from four herbal shops in Al-Diwaniyah City, Iraq, and analyzed using gamma-ray spectrometry with a NaI(Tl) detector on a dry-weight basis. The mean activity concentrations were 3.90 ± 0.39 Bq.kg^{-1} for U-238, 13.03 ± 1.16 Bq.kg^{-1} for Th-232, and 548.99 ± 12.65 Bq.kg^{-1} for K-40. The results showed that the activity concentrations of U-238 and Th-232 were below the global average values reported by UNSCEAR, whereas the activity concentration of K-40 exceeded these values in most samples because of natural uptake and agricultural practices. All calculated radiological hazard indices, including radium equivalent activity and excess lifetime cancer risk, were within the recommended safety limits. Overall, the findings confirm that the investigated medicinal plants are radiologically safe for consumption under normal conditions of use while emphasizing the need for regular monitoring to support long-term public health protection.

1. INTRODUCTION

Treatment with medicinal plants is among the oldest therapeutic practices known to humankind (Kırıs 2020). Since ancient times, various plant parts, including leaves, seeds, stems, bark, and roots, have been used to treat diseases and promote general health (Shuaibu et al. 2023). In recent decades, interest in medicinal herbs has grown considerably because of their reported benefits in reducing inflammation and the risk of cardiovascular disease, aging, cancer, and obesity (Shuaibu et al. 2023). Current statistics indicate that approximately 25% of the active ingredients in prescribed medicines are of plant origin (Kırıs 2020), highlighting their importance in the pharmaceutical industry and the increasing interest in enhancing their bioactive compounds to improve therapeutic outcomes (Khanal et al. 2024). The widespread use of medicinal plants is further attributed to their accessibility, low cost, favorable therapeutic properties, and fewer side effects than synthetic drugs (Güven et al. 2023).

With the increasing reliance on alternative medicine (Biira et al. 2021), there is a growing need to evaluate environmental pollutants that may compromise the safety of medicinal herbs, including naturally occurring radionuclides that can be transferred from the soil to different plant parts (Güven et al. 2023, Bal

et al. 2023). These radionuclides may enter plants through direct deposition onto the soil and subsequent uptake by the roots (Desideri et al. 2010), ultimately accumulating in the human body through the food chain (Ali et al. 2024). Internal radiation exposure occurs primarily through the ingestion of terrestrial radionuclides, particularly members of the U-238 and Th-232 decay series and K-40, via food and drinking water, whereas inhalation exposure may occur through airborne dust particles (IAEA 1999). Numerous studies have shown that ionizing radiation emitted by these radionuclides can cause DNA damage, embryonic mutations, and an increased lifetime risk of cancer (Sweaf & Oudah 2024). Given these concerns, the radiological risks associated with the consumption of medicinal herbs are of particular importance in Iraq, where cancer incidence has been increasing, as reported in the annual cancer registry (Ministry of Health, Iraqi Cancer Board 2022).

Several studies conducted in Iraq have investigated the activity concentrations of natural radionuclides in medicinal plants, herbs, and spices and have generally reported that these products are radiologically safe for consumption despite occasional observations of elevated K-40 activity. Most Iraqi studies concluded that the measured radionuclide activities were within internationally accepted limits and did not pose significant radiological health risks (Kadhim et al. 2021, Jassim et al. 2024, Obaid 2022). However, some studies reported relatively high K-40 activity in certain herbal products, particularly chamomile and other plant-derived materials, although the associated ingestion doses and excess lifetime cancer risk indicators remained below internationally accepted safety thresholds (Najam et al. 2015, Hamza et al. 2020, UNSCEAR 2000, ICRP 2012). Similar findings were reported in subsequent Iraqi studies, in which internal hazard indices and ingestion doses consistently remained within permissible limits, confirming that medicinal plant consumption generally represents a low radiological risk under normal dietary patterns (Hamza et al. 2020). Similar radiological behavior has also been reported for other foodstuffs commonly consumed in Iraq. Abbas et al. (2023) found that, despite elevated K-40 activity, the calculated ingestion doses and excess lifetime cancer risk (ELCR) values remained within internationally accepted limits. These findings support the conclusion that food-chain products, including medicinal plants, generally pose low radiological health risks when consumed under normal dietary patterns, even when K-40 activity exceeds the global average (Abbas et al. 2023). A related study conducted in Al-Diwaniyah measured radon concentrations in imported tea and found them to be within the safety limits recommended by the ICRP, emphasizing the importance of monitoring other herbal products (Sweaf & Oudah 2024). Moreover, Rajih & Oudah (2025) investigated the concentrations of toxic elements in the same plant samples examined in the present study. They concluded that the samples were safe with respect to non-carcinogenic health risks, although prolonged consumption may pose potential carcinogenic risks, thereby providing a more comprehensive dataset for the plants investigated.

For these reasons, international organizations such as the United Nations Scientific Committee on the Effects of Atomic Radiation (UNSCEAR) and the International Commission on Radiological Protection (ICRP) have established international guidelines for acceptable radionuclide levels in foodstuffs (UNSCEAR 2000, ICRP 2012).

Against this background, the present study investigates the activity concentrations of naturally occurring radionuclides (U-238, Th-232, and K-40) in twenty commonly consumed medicinal plants obtained from herbal shops in Al-Diwaniyah City, Iraq. The study does not claim methodological novelty; rather, it addresses a local exposure assessment by providing the first comprehensive radiological evaluation of medicinal plants sold in this region. Al-Diwaniyah is characterized by a high reliance on herbal medicine, a diverse mixture of locally sourced and imported plant products, and traditional market handling and storage practices that differ from those reported in other regions of Iraq. These local characteristics may influence both radionuclide concentrations and realistic ingestion patterns. Accordingly, the novelty of this study lies in its site-specific, consumer-oriented radiological risk assessment, supported by locally derived consumption data, rather than in the development of new analytical methodologies.

Radiological health risks were evaluated using ingestion-based parameters, including the ingestion effective dose (IED) and excess lifetime cancer risk (ELCR), and the results were compared with internationally recognized safety standards. This approach provides a scientific basis for assessing compliance with radiation protection guidelines and contributes to public health protection and the safe regulation of medicinal plant consumption in Iraq.

2. MATERIALS AND METHODS

2.1. Area of Study

The study was conducted in Al-Diwaniyah Governorate, located in south-central Iraq. The governorate extends between latitudes 31°45' and 31°52' N and longitudes 44°30' and 45°45' E, covering a total area of approximately 8,521 km². According to the Commission of Statistics and GIS (Commission of Statistics and GIS 2023), the population of Al-Diwaniyah reached 1,430,714 inhabitants.

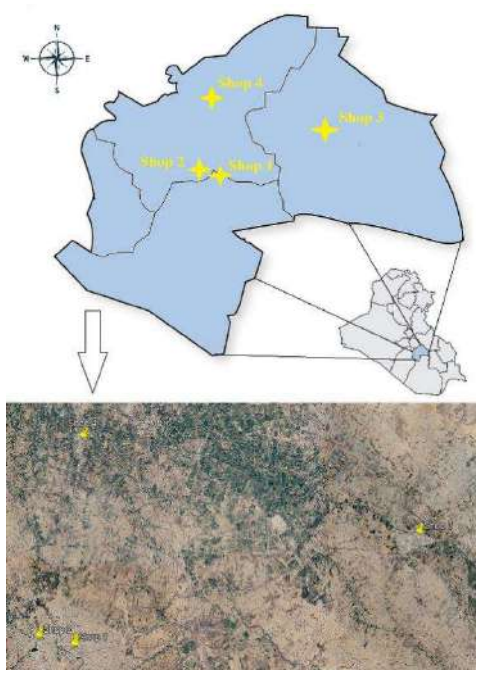


Fig :1 The geographic location of the Shops from which the samples were taken within Al-Diwaniyah, Iraq (Rajih & Oudah 2025).

Herb sampling sites were concentrated in densely populated urban districts characterized by intense commercial activity and traffic congestion, as highlighted in yellow in Fig. 1. The raw medicinal plant materials available in local markets were imported from several countries, including Iraq, Egypt, Iran, China, India, Pakistan, Syria, and the Maghreb region.

2.2. Sample Collection and Preparation

To accurately represent local market conditions, medicinal plant samples were collected from four different herbal shops across Al-Diwaniyah City and its surrounding districts (Table 1). Two shops located in the city center (coded as Shop 1 and Shop 2) were selected to represent areas characterized by intense commercial activity and high population density. The remaining two shops, located in the Afak and Al-Daghara districts (Shop 3 and Shop 4), represented semi-urban or rural environments characterized by agricultural surroundings and varying storage conditions.

A total of 20 medicinal plant samples (five from each location) were obtained to reduce sampling bias and ensure balanced representation. Sample selection was based on the frequency of use in traditional medicine and the range of diseases the plants are commonly used to treat. Interviews

Table 1: List of medicinal plants reported in the present study.

Sample Code	Shop Number	The herb	Part used	Dosage amount*	I [kg.y^{-1}]	Country
P1	1	Green tea *(Camellia sinensis)*	Leaves	15 g.day^{-1}	1.35	Iran
P2		Lemon Balm *(Melissa officinalis)*	Leaves	2 g.day^{-1}	0.18	Syria
P3		Basil *(Ocimum basilicum)*	Leaves	15 g.day^{-1}	1.35	Iraq
P4		Black Seed *(Nigella sativa)*	Seeds	6 g.day^{-1}	0.54	India
P5		Fenugreek *(Trigonella foenum-graecum)*	Seeds	30 g.day^{-1}	2.7	Egypt
P6	2	Moringa *(Moringa oleifera)*	Leaves	5 g.day^{-1}	0.45	Iraq
P7		Gorgeous roses *(Rosa damascena)*	Flowers	10 g.day^{-1}	0.9	Iraq
P8		Purslane seeds *(Portulaca oleracea)*	Seeds	10 g.day^{-1}	0.9	Syria
P9		Chia seeds *(Salvia hispanica)*	Seeds	20 g.day^{-1}	1.8	India
P10		Mahaleb *(Prunus mahaleb)*	Seeds	10 g.day^{-1}	0.9	Syria
P11	3	Sage *(Salvia fruticosa)*	Leaves	10 g.day^{-1}	0.9	Egypt
P12		Ginger *(Zingiber officinale)*	Roots	3 g.day^{-1}	0.27	China
P13		Bee pollen	Seeds	5 g.day^{-1}	0.45	Iran
P14		Chamomile *(Matricaria chamomilla)*	Flowers	15 g.day^{-1}	1.35	Egypt
P15		Licorice *(Glycyrrhiza glabra)*	Roots	10 g.day^{-1}	0.9	Syria
P16	4	Senna *(Senna alexandrina)*	Leaves	10 g.week^{-1}	0.9	Pakistan
P17		Lady's mantle *Alchemilla vulgaris*	Leaves	15 g.day^{-1}	1.35	Maghreb
P18		Roselle *(Hibiscus sabdariffa)*	Flowers	15 g.day^{-1}	1.35	Iraq
P19		Clover *(Medicago sativa)*	Leaves	5 g.day^{-1}	0.45	Iraq
P20		Neem *(Azadirachta)*	Leaves	20 g.Week^{-1}	1.8	Iraq

*The consumed dose was estimated based on a questionnaire conducted among practitioners of alternative medicine and herbal specialists, as well as local consumers who regularly use these medicinal herbs.

with local herbal vendors and consumers supported plant identification and selection.

All samples were purchased in their commercially dried form, as sold in herbal shops, either as whole dried plant material or dried powdered samples, according to traditional use. The collected samples consisted of dried whole plant parts or ground preparations typically marketed for their therapeutic properties, including benefits for cardiovascular health, cancer prevention, weight control, blood purification, wound healing, muscle relaxation, diuretic effects, immune enhancement, and the treatment of skin conditions such as eczema (Shuaibu et al. 2023, Güven et al. 2023). Shop names were coded to preserve confidentiality and maintain objectivity.

Each sample was processed under a strict chain-of-custody protocol to ensure the traceability and reliability of the results. The procedure involved: (i) assigning a unique identification code to each sample at the time of collection, (ii) documenting all preparation steps, including drying, grinding, sieving, and weighing, (iii) storing the samples securely in sealed containers to prevent cross-contamination or material loss, (iv) transferring the sealed containers to the measurement laboratory under controlled conditions, and (v) recording sample receipt and measurement parameters in laboratory records.

A mass of 1 kg of each medicinal plant was collected and stored in polyethylene bags, with the assigned code, plant name, and country of origin clearly labeled (Hady & Mashkor 2022, Obaid 2022). Both dried whole and ground samples were homogenized into a fine powder by grinding (Obaid 2022) and then passed through a sieve with an approximate mesh size of 0.8 mm (Obaid 2022). Subsequently, each sample was oven-dried at 120 ˚C for six consecutive hours (Obaid 2022). This step was essential because the determination of specific activity depends on the dry weight of the material (Hady & Mashkor 2022). After drying, 0.5 kg of each powdered sample was weighed using a high-precision digital balance with an accuracy of 0.001%. The prepared samples were then sealed in airtight plastic containers, each labeled with its unique identification code. To allow secular equilibrium to be established between radionuclides in the decay series, the samples were stored for four weeks before measurement (Garba et al. 2024).

2.3. Experimental Procedure

Gamma-ray spectroscopy measurements were performed using a NaI(Tl) scintillation detector with a 3 × 3 inch crystal (Alpha Spectra, Inc., Model 12I12/3), coupled to an ORTEC DigiBase multichannel analyzer (4096 channels). Data acquisition and spectral analysis were carried out using MAESTRO-32 software connected directly to the laboratory computer (Dawal & Oudah 2025). To minimize background radiation, the detector was mounted vertically inside an ORTEC cylindrical shielding chamber. The shielding consisted of two components: an upper cylindrical cover (5 cm thick and 22 cm in diameter) enclosing the detector crystal and a lower base designed to reduce scattered radiation. The detector was positioned at the geometric center of the shielding system (Obaid 2022).

2.4. Energy Calibration of the NaI(Tl) Detector

The energy calibration of the NaI(Tl) detector was performed using standard gamma-ray sources with well-known emission lines: Na-22 (511 and 1274.5 keV), Cs-137 (661 keV), and Co-60 (1173 and 1332.5 keV) (Jassim et al. 2024, Dawal & Oudah 2025). The full-energy peaks of these sources were identified, and their corresponding channel numbers were recorded. A linear relationship was then established between channel number and gamma-ray energy, with a high correlation coefficient ($R^2 \approx 0.99$), confirming the accuracy of the calibration (Dawal & Oudah 2025). The uncertainties associated with the reference energies were negligible compared with the resolution of the NaI(Tl) detector (Dawal & Oudah 2025).

In addition to energy calibration, efficiency calibration was performed using the same standard sources, following procedures reported in the literature (Hady & Mashkor 2022). This calibration is essential for converting the measured net counts under each photopeak into activity concentrations. The efficiency curve was fitted as a function of gamma-ray energy, allowing correction for the energy dependence of the detector response (Dawal & Oudah 2025).

Background (blank) measurements were also performed using the same counting geometry and counting time as those used for the samples to subtract natural background contributions, primarily from K-40, U-238, and Th-232 present in the laboratory environment (Garba et al. 2024). This procedure ensured that the reported net peak areas represented only the activity of the measured samples.

The calibrated system was then used to quantify naturally occurring radionuclides. U-238 activity was determined from the 1764 keV gamma-ray emission of Bi-214, Th-232 activity was determined from the 2614 keV emission of Tl-208, and K-40 activity was evaluated using its 1460 keV gamma-ray emission (Garba et al. 2024, Dawal & Oudah 2025). These gamma-ray emission lines are widely recommended because of their relatively high emission intensities and minimal spectral interference (Hady & Mashkor 2022).

3. CALCULATIONS

3.1. Specific Activity

The specific activity concentrations of the radionuclides were calculated using Eq. 1(Garba et al. 2024).

$$A = \frac{N - N_o}{I_\gamma \varepsilon m t} \quad ...(1)$$

where : A the specific activity of the radioactivity in the dry sample, N : the net number of a specific peak for the sample, N_o: the background count for the specific peak of the sample, γ the number of photons per gamma ray for each decay, ε the efficiency of the detector to measure the specific gamma ray energy, m the measured mass of the dry sample of medicinal plants, : t the measurement time 10,800 s (Garba et al. 2024).

3.2. Hazard Indicators

3.2.1. Radium Equivalent

Radium equivalent activity (Bq/kg) was calculated from the following Eq. 2 (Muhammad et al. 2024):

$$Ra_{eq} = AU + 1.43\ ATh + 0.077AK \quad ...(2)$$

Where: Ra_{eq} is an important index for accurately assessing the activity levels of radionuclides present in samples. leads to a uniform dose rate for gamma rays, with a maximum permissible value of 370 $Bq.kg^{-1}$ (UNSCEAR 2000), (Muhammad et al. 2024), (AU, ATh, AK): is the radioactivity concentration of each radionuclide.

3.2.2. Dose Rate (DR)

The dose rate for gamma radiation was calculated according to Eq. 3 (Muhammad et al. 2024):

$$D(nGy.h^{-1}) = 0.462\ AU + 0.604\ ATh + 0.0417\ AK \quad ...(3)$$

Where: (0.462, 0.604, 0.0417) $(nGy.h^{-1})$ for each $(Bq.kg^{-1})$ are the dose conversion factors for U-238, Th-232 and K-40, respectively (Dawal & Oudah 2025).

3.2.3. Internal Hazard Index (H_{in})

The Internal hazard index is calculated for the gamma radiation activity concentration of the naturally occurring radioactivity of U-238, Th-232 and K-40, as it is calculated from Eq. 4 (Kadhim et al. 2021, Dawal & Oudah 2025):

$$H_{in} = AU/185 + ATh/259 + AK/4810 \leq 1 \quad ...(4)$$

Where: (AU, ATh, AK) are the activity concentrations $(Bq.kg^{-1})$ for each of the radionuclides (U-238, Th-232 and K-40), respectively.

3.2.4. Gamma Activity Index (Iγ)

This index is used to assess the risk of gamma rays. It is also called the representative level index. It is calculated from Eq. 5 (Kırıs2020 , Dawal & Oudah 2025):

$$I\gamma = AU/150 + ATh/100 + AK/1500 \quad ...(5)$$

3.2.5. Annual Gonadal Dose Equivalent (AGDE)

The amount of AGDE is calculated from Eq. 6 (Saudi et al. 2022):

$$AGDE(\mu Sv/y) = 309/100\ AU + 418/100\ Th + 314/1000\ AK \quad ...(6)$$

3.2.6. Annual Effective Dose for Internal Exposure (AEDEin)

This is called the annual effective dose equivalent and is calculated using Eq. 7 (Abdelfadeel et al. 2023):

$$AEDEin\ (mSv.y-1) = DR \times 8760\ (h.y-1) \times 0.8 \times 0.7(Sv.Gy-1) \times 10^{-6} \quad ...(7)$$

8760: number of h per year (Saudi et al. 2022), 0.8: duration of indoor exposure (UNSCEAR 2000), and 0.7: consensus has been applied to the updated process in air (UNSCEAR 2010).

The limit recommended by the United Nations Scientific Committee on the Effects of Atomic Radiation (UNSCEAR 2000), which is equivalent to $(1\ mSv.y^{-1})$, is the maximum permissible effective dose proposed by the International Commission on Radiological Protection (ICRP) (ICRP 2012) (Hassan 2025).

The average global radiation dose received from natural sources due to drinking water and food consumption is $(280\ \mu Sv.y^{-1})$, which ranges from (200 to 800) $\mu Sv.y^{-1}$ (Sundström et al. 2025, Kinahan et al. 2025).

Although $AEDE_{in}$ is calculated for comparison with international screening benchmarks, the ingestion effective dose (IED) is considered the primary exposure pathway for risk assessment in this study, as it reflects actual consumption patterns of medicinal plants.

3.2.7. Ingestion Effective Dose (IED)

The dose resulting from ingesting U-238, Th-232, and K-40 was determined for medicinal plants using Eq. 8:

$$IED = A \times I \times DCF \quad ...(8)$$

Where A is the activity concentration of the radionuclide in the medicinal plant sample $(Bq.kg^{-1})$, I: Consumption rate of medicinal plants $(kg.y^{-1})$ Assuming that the number of days consumption per year $(90\ day.y^{-1})$ (Luo et al. 2021), DCF: the dose conversion factor for consuming each radioactive nuclide $(4.5 \times 10^{-5}, 2.3 \times 10^{-4}, 6.2 \times 10^{-6}\ mSv.Bq^{-1}$ for U-238, Th-232, K-40 respectively for adults) (UNSCEAR 2017), Consumption rates of the studied medicinal plants were obtained through 280 consumer questionnaires, distributed

as 70 forms for each of the four surveyed herbal shops, in addition to 4 questionnaires completed by the herbal sellers who prescribe and recommend dosages of these plants. Although no standardized or agreed-upon dosage exists for the use of medicinal plants, local practitioners typically provide dose recommendations to consumers. Table 1 presents the average consumption of medicinal plants for therapeutic purposes ($g.day^{-1}$). However, it is important to note that an increased rate of regular consumption by patients for the treatment of specific diseases can significantly elevate the average annual effective dose resulting from their intake.

In the present study, a uniform consumption period of 90 days per year was adopted as a conservative and standardized exposure scenario. This approach was selected due to the absence of reliable plant-specific quantitative intake data and the wide inter-individual variability in herbal usage patterns. Therefore, the applied consumption rate represents an averaged exposure scenario suitable for screening-level radiological risk assessment rather than individual dose estimation.

3.2.8. Excess Lifetime Cancer Risk (ELCR)

It can be estimated using the effective dose for ingestion that we obtained by the methodology for the evaluation of the specific cancer risks (ICRP) using Eq. 9 (Kırıs 2020, ICRP 2007):

$$ELCR = IED \times DL \times RF \quad \ldots(9)$$

Where DL is the average adult life expectancy of 70 years, RF is the risk factor (1/Sv) for the random effects, and ICRP a value of 0.05 for the population is used as the risk factor (ICRP 1990).

4. RESULTS AND DISCUSSION

The radioactivity levels of naturally occurring radioactive materials (NORMs) were measured in 20 different medicinal plant samples using a gamma-ray spectrometer. The activity concentrations were calculated using Eq. (1). Table 2 presents the average dry-weight activity concentrations. The activity concentration of U-238 ranged from ND to 10.23 ± 0.87 $Bq.kg^{-1}$, with a mean value of 3.90 ± 0.39 $Bq.kg^{-1}$. The highest U-238 activity concentration was observed in chia seed (P9). The activity concentration of Th-232 ranged from 3.30 ± 0.67 to 25.74 ± 1.88 $Bq.kg^{-1}$, with a mean value of 13.03 ± 1.16 $Bq.kg^{-1}$. The highest Th-232 activity concentration was found in black seed (P4). The activity concentration of K-40 ranged from 65.01 ± 4.14 $Bq.kg^{-1}$ in bee pollen to 1322.11 ± 18.65 $Bq.kg^{-1}$ in lion's foot herb, with a mean value of 548.99 ± 12.65 $Bq.kg^{-1}$.

In contrast, the activity concentrations of K-40 exceeded the recommended limit of 400 $Bq.kg^{-1}$ in 15 of the 20 samples (75%), which may be attributed to the natural heterogeneity in the distribution of radionuclides in the environment (Olagbaju et al. 2021). Because some of the medicinal plant samples analyzed were imported from different geographic regions, the measured radionuclide activity concentrations were likely influenced by variations in soil radioactivity and environmental conditions among the countries of origin. This observation reflects the well-established geographic variability in the distribution of natural radionuclides, which largely depends on local geological and geochemical characteristics (Olagbaju et al. 2021, UNSCEAR 2000). Despite this variation, the activity concentrations of U-238 and Th-232 in all the studied samples remained within the internationally accepted limits of 33 and 45 $Bq.kg^{-1}$, respectively (UNSCEAR 2000).

Table 2: Specific activities ($Bq.kg^{-1}$) of U-238, Th-232, andK-40 inthe medicinal plants measured using gamma spectroscopy.

Sample Code	U-238	Th-232	K-40
P1	ND	16.65±1.51	569.59±12.24
P2	2.84±0.45	14.45±1.41	688.04±13.46
P3	0.51±0.19	15.97±1.48	376.66±9.96
P4	4.59±0.58	25.74±1.88	291.64±8.76
P5	2.19±0.4	16.52±1.51	591.17±12.47
P6	2.19±0.4	11.42±1.25	300.32±8.89
P7	ND	3.3±0.67	422.98±10.55
P8	0.44±0.18	18.86±1.61	602.49±12.59
P9	10.23±0.87	17.2±1.54	503.26±11.51
P10	6.99±0.71	17.34±1.54	135.03±5.96
P11	ND	7.57±1.02	442.99±10.8
P12	8.16±0.77	8.26±1.07	569.59±12.24
P13	0.95±0.26	7.02±0.98	65.01±4.14
P14	2.11±0.39	22.16±1.75	488.1±11.32
P15	9.62±0.84	8.67±1.09	495.36±11.42
P16	6.56±0.69	11.01±1.23	1007.05±16.28
P17	0.29±0.15	11.15±1.24	1322.11±18.65
P18	3.64±0.52	10.87±1.22	751.73±14.07
P19	3.5±0.5	11.84±1.28	709.36±13.66
P20	1.46±0.33	4.68±0.8	647.24±13.05
MIN	ND	3.3±0.67	65.01±4.14
MAX	10.23±0.87	25.74±1.88	1322.11±18.65
AVE	3.90 ±0.39	13.03±1.16	548.99±12.65
World (UNSCEAR 2000)	35	30	400

ND: Not Detected

Table 3: Comparison of mean activity concentrations (Bq.kg^{-1}) in medicinal plants with previous local and international studies.

No.	Country	U-238	Th-232	K-40	Methodology	REF
1	Iraq			263.7 ± 4.6	(NaI(Tl)(HPGe)	Najam et al. 2015
2	Iraq (Najaf)	4.86 ± 0.68	2.91 ± 0.12	219.13 ± 2.24	(NaI(Tl)	Kareem et al. 2016
3	Iraq (Najaf)	38.12 ± 1.619	12.95 ± 0.896	570.70 ± 31.453	(NaI(Tl)	Hamza et al. 2020
4	Iraq (Karbala)	12.052±1.247	8.760±0.650	256.924±5.966	(NaI(Tl)	Obaid 2022
5	Iraq (Kurdistan)		0.65 ± 0.10	400.17 ± 17.95	(HPGe)	Sabr et al. 2023
6	Iraq		0.370.16 ±	102.93 ± 58.5	(NaI(Tl)	Kadhim et al. 2021
7	Turkey (Rize province)		1.83 ± 0.09	259.2 ± 12.1	(HPGe)	Kırıs 2020
8	Jordan (Irbid)		1.44 ± 0.18	593.97 ± 63.47	(HPGe)	Abu-Qatouseh et al. 2019
9	Egypt (Egyptian markets)	7.25 ± 0.54	7.78 ± 0.63	471.4 ±11.33	(HPGe)	Saudi et al. 2022
10	Egypt	25.09	20.61	1191.35	(HPGe)	Abdelfadeel et al. 2023
11	Malaysia			340 ± 13	(HPGe)	Shuaibu et al. 2023
12	Bangladesh (Chattogram district)		15.73±3.90	157.93±59.84	(HPGe)	Hossen et al. 2024
13	Northwest Nigeria (duanao international grain market)		37 ± 4	5883 ± 23	(HPGe)	Shuaibu et al. 2025
14	Thailand (various local markets and pharmacies)			420.33±3.77	(HPGe)	Kranrod et al. 2017
15	Nigeria (Ewu, Edo State)	4.73± 0.15	8.00 ± 0.40	209.43± 5.14	(NaI(Tl)	Popoola et al. 2024
16	India (the Kollam district of Kerala state)		15 ± 36	46 ± 230	(NaI(Tl)	Monica et al. 2020
17	Average activity from previous studies [Bq.Kg^{-1}]	13.71	11.14	689.25		
18	World	35	30	400		UNSCEAR 2000
19	This study Iraq Diwaniyah	3.90 ±0.39	13.03±1.16	548.99±12.65	(NaI(Tl)	

The elevated K-40 activity observed in leaf and flower samples, compared with other plant parts, can be attributed to the essential role of potassium in plant physiology and its efficient uptake through root ion carriers and ion channels (Desideri & Roselli 2010). Consequently, elevated K-40 activity is frequently observed in medicinal plants, particularly in leaves and flowers, which have a greater physiological capacity for potassium uptake than other plant tissues (Saudi et al. 2022). In addition to biological factors, soil chemistry and agricultural practices play a significant role in influencing K-40 accumulation, as the intensive use of potassium-based fertilizers and related by-products can substantially increase K-40 levels in agricultural soils (John et al. 2025). Therefore, the relatively high K-40 activity detected in these plant components likely reflects the combined effects of efficient biological uptake and agricultural growing conditions rather than abnormal radiological contamination.

Table 3 compares the average activity concentrations measured in this study with those reported in previous local and international investigations. The mean U-238 activity concentration (3.90 ± 0.39 Bq.kg^{-1}) in the medicinal plants from Al-Diwaniyah was lower than those reported in most Iraqi studies, including Karbala (12.05 Bq.kg^{-1}) (Obaid 2022) and Najaf (38.12 Bq.kg^{-1}) (Hamza et al. 2020), as well as in Egypt (25.09 Bq.kg^{-1}) (Abdelfadeel et al. 2023). However, it was comparable to the value reported in Nigeria (4.73 Bq.kg^{-1}) (Popoola et al. 2024).

The mean Th-232 activity concentration (13.03 ± 1.16 Bq.kg^{-1}) was within the range reported in regional studies. It was slightly higher than the value reported in one Iraqi study (12.95 Bq.kg^{-1}) (Hamza et al. 2020) but lower than those reported in Egypt (20.61 Bq.kg^{-1}) (Abdelfadeel et al. 2023), Bangladesh (15.73 Bq.kg^{-1}) (Hossen et al. 2024), and Nigerian markets (37.00 Bq.kg^{-1}) (Shuaibu et al. 2025). Importantly, it remained below

Table 4: Comparison of the activity concentrations of natural radionuclides in medicinal plants from Al-Diwaniyah with average values from previous studies.

Radionuclide	Difference %	Interpretation
U-238	−71.6%	Significantly lower
Th-232	+17.0%	Slightly higher
K-40	−20.3%	Moderately lower

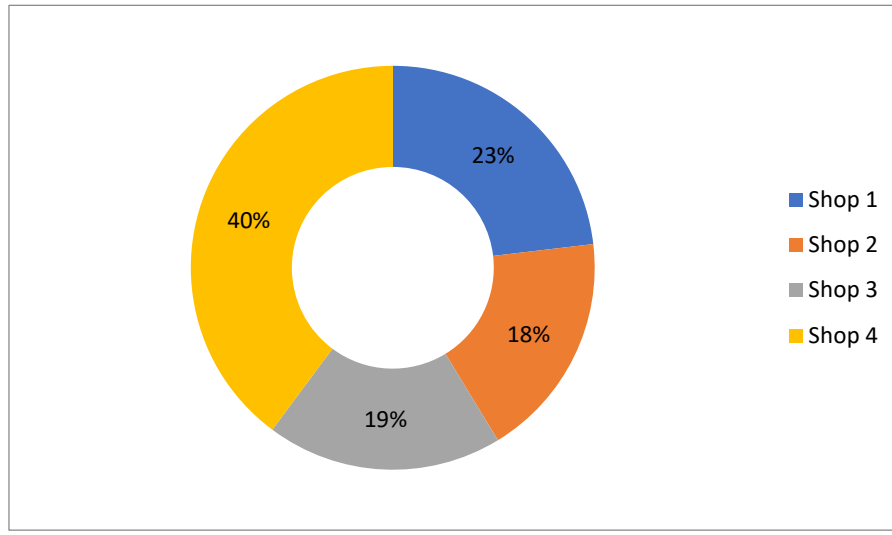


Fig. 2: Contribution of each herbal shop to the total activity of U-238, Th-232, and K-40 in the analyzed medicinal plant samples.

the UNSCEAR (2000) global reference value of 30 $Bq.kg^{-1}$.

In contrast, the mean K-40 activity concentration (548.99 ± 12.65 $Bq.kg^{-1}$) exceeded the UNSCEAR (2000) global average of 400 $Bq.kg^{-1}$, consistent with values reported in Najaf (570.70 $Bq.kg^{-1}$) (Hamza et al. 2020), Jordan (593.97 $Bq.kg^{-1}$) (Abu-Qatouseh & Mansour 2019), and Egypt (471.40–1191.35 $Bq.kg^{-1}$) (Saudi et al. 2022, Abdelfadeel et al. 2023). This elevated activity may be attributed to the widespread use of potassium-based fertilizers, which increase K-40 levels in soil and consequently enhance its uptake by plants (Szaciłowski 2024).

Overall, the radiological profile of medicinal plants from Al-Diwaniyah indicates that the activity concentrations of U-238 and Th-232 are within internationally accepted safety limits, whereas K-40 exhibits moderately elevated activity concentrations consistent with agricultural and environmental influences.

To better understand the relative levels of natural radionuclides in the studied medicinal plants, the measured activity concentrations were compared with the average values reported in previous regional and international studies. This comparison helps determine whether the present findings indicate elevated or reduced radioactivity levels relative to those reported elsewhere. The results are summarized in Table 4.

The percentage contribution of each of the four sampling sites (Shops 1–4) to the total measured activity of the three radionuclides was calculated based on their combined activity concentrations and is presented in Fig. 2. Shop 4 showed the highest contribution (40%), followed by Shop 1 (23%), Shop 3 (19%), and Shop 2 (18%). The observed order (Shop 4 > Shop 1 > Shop 3 > Shop 2) suggests that Shop 4 may represent the largest source of radionuclide contamination, possibly because of the origin of the medicinal plants sold at that location. These percentage contributions are descriptive indicators based on cumulative activity concentrations and are intended to illustrate distribution patterns rather than statistically significant differences among the shops.

Analysis of the radionuclide distribution by shop (Table 5) revealed distinct patterns among the sampling locations. Shop 3 contributed the highest proportion of U-238 activity (32%), Shop 1 exhibited the highest Th-232 activity (34%), and Shop 4 showed the greatest K-40 activity (40%). These differences may be attributed to several environmental and operational factors, including proximity to heavy traffic and fuel combustion emissions, which may result in the deposition of K-40 and other radionuclides on exposed herbal materials. Additional contributing factors may include proximity to medical or industrial sources, suboptimal storage practices, such as displaying products outdoors near busy streets, and inadequate ventilation or packaging that permits dust accumulation. The observed variability among the shops may also reflect differences in soil composition and the radionuclide uptake capacity of the plants. Collectively,

Table 5: Contribution of each shop to radioactive nuclide contamination by element (%). Each row shows how the contamination is distributed for a certain nuclide between four stores.

Radionuclide	Shop 1	Shop 2	Shop 3	Shop 4
U-238	15%	30%	32%	23%
Th-232	34%	26%	21%	19%
K-40	23%	18%	19%	40%

these findings suggest the presence of localized sources influencing radionuclide activity and highlight the importance of appropriate environmental monitoring and storage practices, particularly for Shops 1 and 4.

Overall, the results indicate that the radiological profile of the studied medicinal plants is governed primarily by natural environmental and botanical factors rather than by market-specific practices. The consistently low activity concentrations of U-238 and Th-232 across all samples, together with the moderately elevated K-40 activity, reflect the natural uptake behavior of plants and the influence of soil composition and agricultural inputs. Importantly, although K-40 activity exceeded the UNSCEAR global average in several samples, this elevation did not translate into an increased radiological risk, as confirmed by the hazard indices and dose assessments discussed below. These findings emphasize that elevated activity concentrations alone are insufficient indicators of health risk without considering realistic exposure pathways and corresponding dose assessments.

4.1. Multivariate Statistical Analysis

4.1.1. Principal Component Analysis (PCA) of Radionuclide Concentrations in Medicinal Plants

Principal Component Analysis (PCA) was performed to examine the relationships and variability among the activity concentrations of three naturally occurring radionuclides (U-238, Th-232, and K-40) in twenty medicinal plant samples collected from four herbal shops across Al-Diwaniyah City. The first two principal components (PC1 and PC2) together explained approximately 72.8% of the total variance, indicating that they effectively captured the primary structure of variation within the dataset.

PC1 accounted for 38.7% of the total variance and exhibited a strong positive loading for K-40 (0.729), with negative loadings for Th-232 (−0.543) and U-238 (−0.417), indicating that this component was driven primarily by variability in K-40 activity. PC2 explained 34.1% of the total variance and showed a strong positive loading for U-238 (0.776) and a negative loading for Th-232 (−0.631), reflecting the relationship between U-238 and Th-232 independent of K-40 activity.

The PCA biplot (Fig. 3) illustrates both the distribution of the samples and the loadings of the radionuclides. The red arrows indicate the direction and magnitude of each radionuclide's contribution to the principal components. The K-40 vector is strongly aligned with PC1, confirming its dominant contribution to the total variance. Samples from Shop 4 (diamonds) cluster toward the positive side of the PC1 axis, consistent with their higher K-40 activity. In contrast, the U-238 vector is aligned primarily with PC2,

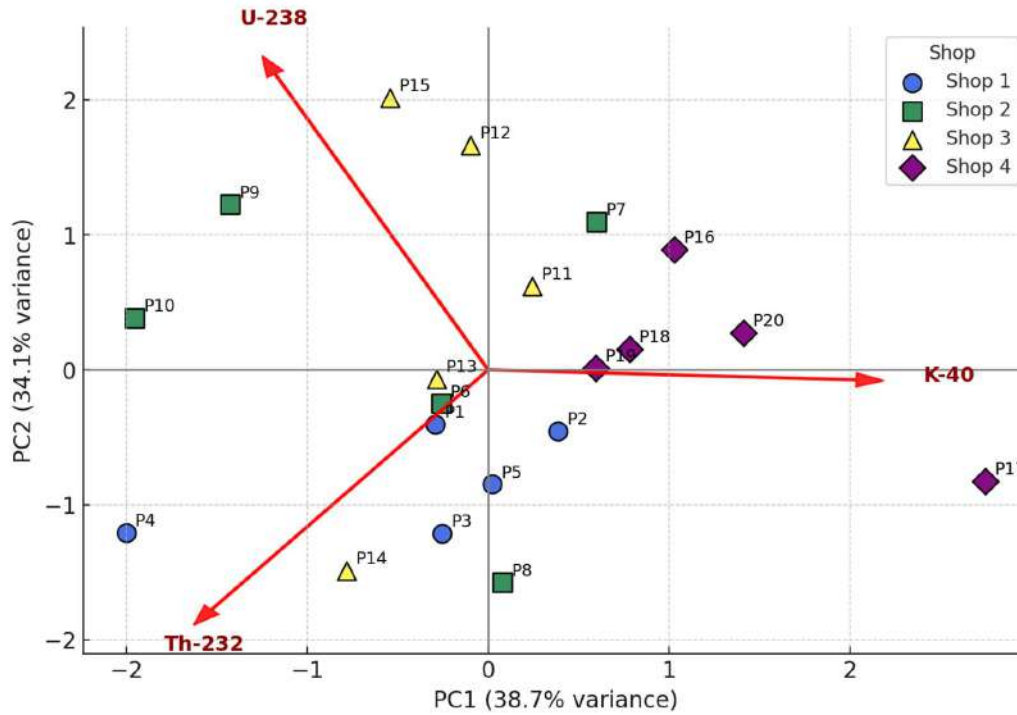


Fig. 3: PCA biplot showing the distribution of medicinal plant samples by herbal shop (Shop 1–4) and the loading vectors of U-238, Th-232, and K-40, illustrating the contribution of each radionuclide to the principal components (PC1 and PC2).

indicating samples with elevated U-238 activity, whereas the Th-232 vector points in the opposite direction, suggesting an inverse relationship between Th-232 and the other radionuclides.

Overall, the PCA results indicate that K-40 is the primary driver of variation among the samples, followed by U-238 and Th-232. Moderate clustering by shop origin, particularly for Shops 1 and 4, suggests a partial site-specific influence, likely associated with plant type, soil composition, and handling practices rather than market location alone. The alignment between the radionuclide vectors and the sample distribution further underscores the influence of environmental and botanical factors in shaping the observed radiological profiles of the medicinal plants.

4.1.2. Hierarchical Cluster Analysis (CA) of Medicinal Plant Samples

The hierarchical cluster analysis (HCA) grouped the twenty medicinal plant samples based on similarities in radionuclide concentrations (U-238, Th-232, and K-40; Fig. 4). The dendrogram revealed three major clusters, reflecting differences in activity patterns among the samples. Samples within the same cluster share comparable radionuclide profiles, indicating similar environmental exposure or plant origin.

Cluster I mainly comprised samples with relatively high K-40 activity, consistent with those located on the positive side of PC1 in the PCA plot. Cluster II included samples characterized by higher U-238 activity but moderate Th-232 activity, whereas Cluster III consisted of samples with generally lower radionuclide activity concentrations. Although environmental and botanical factors primarily govern the overall radiological profile, minor differences among the shops may be attributed to local environmental and operational conditions, such as proximity to traffic, dust deposition, and storage practices.

The close correspondence between the PCA grouping patterns and the HCA dendrogram confirms the reliability of the multivariate classification. Together, these analyses demonstrate that variations in radionuclide activity among medicinal plants are influenced more by botanical and environmental factors than by market location. However, these findings contrast with those reported by Rajih and Oudah (2025), who investigated toxic element concentrations in the same plant samples and found that the distribution of toxic elements was strongly influenced by market location and individual shop conditions.

The PCA and HCA results consistently demonstrate that variations in U-238, Th-232, and K-40 activity concentrations are governed primarily by geological and botanical factors, indicating that the observed radioactivity originates from the plants' natural environmental sources rather than from herbal shop practices. This finding confirms the value of multivariate analysis in distinguishing between market-related contamination and naturally occurring radioactivity.

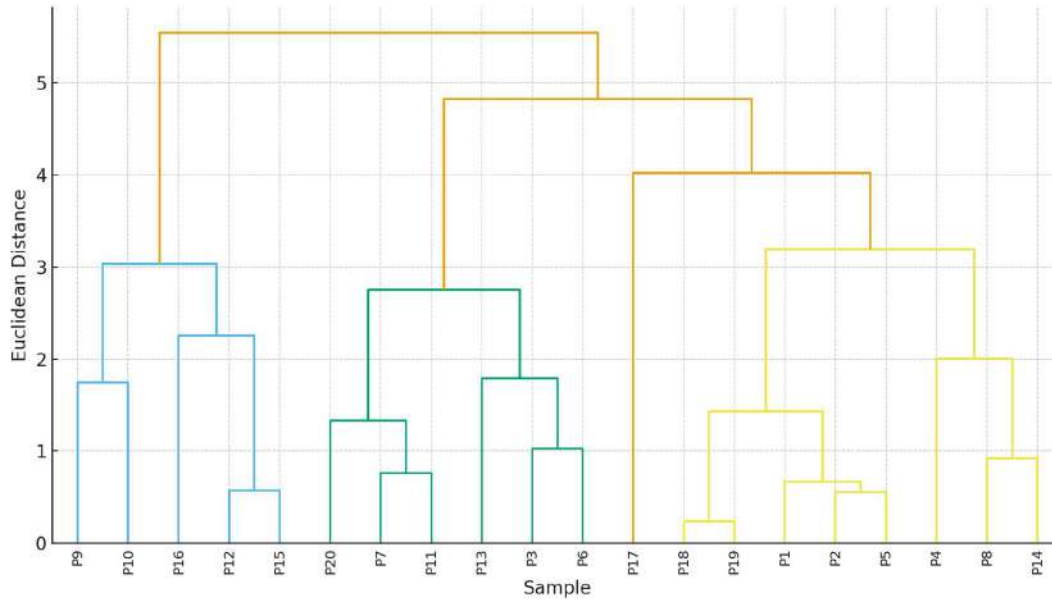


Fig. 4: Hierarchical cluster analysis (HCA) dendrogram of medicinal plant samples based on the activity concentrations of U-238, Th-232, and K-40, illustrating the grouping of samples according to their radiological similarity.

4.2. Radiation Risks

Table 6 presents the calculated radiological hazard parameters, including radium equivalent activity (Raeq), absorbed gamma dose rate (DR), internal hazard index (Hin), gamma activity index (Iγ), annual gonadal dose equivalent (AGDE), and annual effective dose for indoor exposure (AEDEin), for the analyzed medicinal plants.

All Raeq values were below the recommended safety limit of 370 Bq/kg (UNSCEAR 2000), indicating that the samples pose no significant external radiation hazard. The absorbed gamma dose rate (DR) ranged from 7.39 to 62.00 nGy.h^{-1}. The highest DR value was observed in the lion's foot sample (P17), whereas most samples exhibited values below the global average of 59 nGy.h^{-1} reported by UNSCEAR (2000).

The internal hazard index (Hin) values for all samples were below unity, confirming a minimal risk of internal radiation exposure. Similarly, the gamma activity index (Iγ) ranged from 0.12 to 0.99, remaining within the permissible range for all medicinal plants (UNSCEAR 2000). The highest Iγ value was also observed in the lion's foot sample (P17).

The calculated annual gonadal dose equivalent (AGDE) ranged from 52.69 to 462.65 μSv.y^{-1}. Only the lion's foot sample (P17) slightly exceeded the global reference level of 300 μSv.y^{-1} (UNSCEAR 2000). The annual effective dose for indoor exposure (AEDEin) ranged from 0.04 to 0.30 mSv.y^{-1}, with bee pollen (P13) recording the lowest value and lion's foot (P17) the highest.

Overall, the results indicate that the radiological hazard parameters for all samples were generally within internationally accepted safety limits, with only a few individual medicinal plants, particularly lion's foot, approaching the upper reference levels. These findings suggest that the studied medicinal plants are radiologically safe for consumption under normal usage patterns.

Table 7 presents the ingestion effective dose (IED) for each radionuclide, as well as the total ingestion effective dose and the corresponding excess lifetime cancer risk

Table 6: Radium activity equivalent (Ra_{eq}), gamma dose rate (DR), internal hazard index (H_{in}), gamma activity index (I_γ), annual gonadal dose equivalent (AGDE), annual effective dose for indoor exposure ($AEDE_{in}$) for various medicinal plants.

Sample Code	Ra_{eq} [Bq.kg^{-1}]	DR	H_{in}	I_γ	AGDE [μSv.y^{-1}]	$AEDE_{in}$ [mSv.y^{-1}]
P1	67.67	34.27	0.18	0.55	251.54	0.17
P2	76.48	38.73	0.22	0.62	285.22	0.19
P3	52.35	25.59	0.14	0.41	186.60	0.13
P4	63.85	29.83	0.18	0.48	213.35	0.15
P5	71.33	35.64	0.19	0.57	261.45	0.17
P6	41.65	20.43	0.11	0.32	148.80	0.10
P7	37.29	20.09	0.10	0.31	149.70	0.10
P8	73.80	36.72	0.20	0.59	269.38	0.18
P9	73.58	36.10	0.23	0.58	261.53	0.18
P10	42.18	19.33	0.14	0.31	136.48	0.09
P11	44.94	23.51	0.12	0.38	173.83	0.12
P12	63.83	32.51	0.19	0.51	238.59	0.16
P13	15.99	7.39	0.05	0.12	52.69	0.04
P14	71.38	34.71	0.20	0.56	252.41	0.17
P15	60.16	30.34	0.18	0.49	221.51	0.15
P16	99.85	51.67	0.09	0.82	382.51	0.25
P17	118.04	62.00	0.31	0.99	462.65	0.30
P18	77.07	39.59	0.22	0.63	292.73	0.19
P19	75.05	38.35	0.22	0.61	283.05	0.19
P20	57.99	30.49	0.16	0.50	227.31	0.15
MIN	15.99	7.39	0.05	0.12	52.69	0.04
MaX	118.04	62.00	0.31	0.99	462.65	0.30
AVE	64.22	32.37	0.17	0.52	237.57	0.16
Safety limits (UNSCEAR 2000).	≤ 370	≤ 59	≤ 1	≤ 1	≤ 300	≤ 0.3 (UNSCEAR 2017)

Table 7: Ingestion effective dose (IED), Excess lifetime cancer risk (ELCR) for various medicinal plants.

Sample Code	IED $mSv.y^{-1}$			Total $mSv.y^{-1}$	ELCR $\times 10^{-3}$
	U-238	Th-232	K-40		
P1	6.08×10^{-05}	5.17×10^{-03}	4.77×10^{-03}	1.00×10^{-02}	0.03
P2	2.30×10^{-05}	1.18×10^{-04}	3.13×10^{-03}	3.27×10^{-03}	0.01
P3	3.10×10^{-05}	1.71×10^{-02}	1.29×10^{-02}	3.00×10^{-02}	0.10
P4	1.12×10^{-04}	1.10×10^{-02}	9.96×10^{-03}	2.11×10^{-02}	0.07
P5	2.66×10^{-04}	3.53×10^{-02}	4.04×10^{-02}	7.59×10^{-02}	0.27
P6	4.71×10^{-04}	4.07×10^{-03}	3.42×10^{-03}	7.96×10^{-03}	0.03
P7	1.64×10^{-04}	2.35×10^{-03}	9.63×10^{-03}	1.21×10^{-02}	0.04
P8	1.87×10^{-04}	1.34×10^{-02}	1.37×10^{-02}	2.73×10^{-02}	0.10
P9	8.91×10^{-03}	2.45×10^{-02}	2.29×10^{-02}	5.63×10^{-02}	0.20
P10	3.01×10^{-03}	1.24×10^{-02}	3.07×10^{-03}	1.85×10^{-02}	0.06
P11	1.64×10^{-04}	5.40×10^{-03}	1.01×10^{-02}	1.56×10^{-02}	0.05
P12	$1.05\times^{03-}10$	1.77×10^{-03}	3.89×10^{-03}	6.71×10^{-03}	0.02
P13	2.04×10^{-04}	2.50×10^{-03}	7.40×10^{-04}	3.45×10^{-03}	0.01
P14	1.36×10^{-03}	2.37×10^{-02}	1.66×10^{-02}	4.17×10^{-02}	0.15
P15	4.14×10^{-03}	6.18×10^{-03}	1.13×10^{-02}	2.16×10^{-02}	0.08
P16	2.82×10^{-03}	$7.85\times^{03-}10$	2.29×10^{-02}	3.36×10^{-02}	0.12
P17	1.87×10^{-04}	1.19×10^{-02}	3.21×10^{-04}	1.24×10^{-02}	0.04
P18	2.35×10^{-03}	1.16×10^{-02}	2.57×10^{-02}	3.96×10^{-02}	0.14
P19	7.53×10^{-04}	4.22×10^{-03}	8.07×10^{-03}	1.30×10^{-02}	0.05
P20	1.25×10^{-03}	6.67×10^{-03}	2.95×10^{-02}	3.74×10^{-02}	0.13
MIN	2.30×10^{-05}	1.18×10^{-04}	3.21×10^{-04}	3.27×10^{-03}	0.01
MAX	8.91×10^{-03}	3.53×10^{-02}	4.04×10^{-02}	7.59×10^{-02}	0.27
AVE	1.38×10^{-03}	1.04×10^{-02}	1.26×10^{-02}	2.44×10^{-02}	0.09
W.AVE (UNSCEAR 2000).				0.3	$\leq$ (0.29)

(ELCR) for the studied medicinal plants. The combined annual effective dose from all radionuclides was below the UNSCEAR (2000) recommended limit of 0.3 $mSv.y^{-1}$. Similarly, the calculated ELCR values ranged from 0.01×10^{-3} to 0.27×10^{-3}, with a mean value of 0.09×10^{-3}, which is below the permissible limit of 0.29×10^{-3} established by the International Commission on Radiological Protection (ICRP 2007). The lowest and highest ELCR values were observed for bee pollen (P13) and lion's foot (P17), respectively. These findings indicate that, under normal consumption conditions, the ingestion of these medicinal plants does not pose a significant radiological health risk.

It is noteworthy that, in comparative analyses, the annual effective dose for indoor exposure (AEDEin) generally yielded slightly higher excess lifetime cancer risk (ELCR) values than those derived from the ingestion effective dose (IED). This difference arises because AEDEin assumes continuous annual exposure based on the absorbed dose rate (DR) and occupancy factor, rather than exposure through the realistic ingestion pathway, which depends on actual consumption frequency. However, because the IED-based approach incorporates local consumption data and measured radionuclide activity concentrations, it provides a more realistic estimate of internal exposure resulting from medicinal plant consumption. Therefore, the ELCR values calculated in this study from the ingestion pathway are considered to represent the actual radiological risk associated with medicinal plant consumption in Al-Diwaniyah.

Although the AEDEin-based ELCR values (not presented here) indicated slightly higher risk levels, they remained below the international benchmark of 0.29×10^{-3} (UNSCEAR 2000, ICRP 1990), confirming that even under continuous exposure assumptions, the radiological impact of these medicinal plants would not exceed internationally accepted safety limits.

It should be noted that the ingestion doses estimated in this study are based on an average consumption scenario and are intended for screening-level risk assessment. Actual

exposure may vary depending on plant-specific usage patterns and individual consumption habits, which should be considered in future studies when detailed intake data become available.

4.3. Implications for Radiological Health Risk

From a radiological protection perspective, the combined evaluation of the hazard indices, ingestion effective dose (IED), and excess lifetime cancer risk (ELCR) demonstrates that consumption of the investigated medicinal plants does not pose a significant health risk under normal usage patterns. Even in samples with relatively high K-40 activity, the calculated dose and ELCR values remained well below internationally recommended limits. This finding highlights the importance of dose-based risk assessment rather than relying solely on activity concentration thresholds. Consequently, the results provide a scientifically sound basis for considering these medicinal plants radiologically safe for consumption while supporting the need for periodic monitoring to ensure long-term public health protection.

5. CONCLUSIONS

The results revealed that the activity concentrations of U-238 and Th-232 were within internationally accepted limits, whereas K-40 activity exceeded the UNSCEAR global average in most samples, reflecting both the natural biological accumulation of K-40 and the influence of local agricultural and environmental conditions.

Multivariate statistical analyses (PCA and HCA) confirmed that the variability in radionuclide activity concentrations among the samples was governed primarily by botanical and environmental factors rather than by market location. All calculated radiological hazard indices (Raeq, DR, Hin, Iγ, AGDE, and AEDEin) were below internationally accepted safety thresholds, indicating no significant external or internal radiation hazard. Similarly, the ingestion-based annual effective dose (IED) and excess lifetime cancer risk (ELCR) values were well below international limits, suggesting that the consumption of these medicinal plants under normal conditions does not pose a radiological health risk.

In conclusion, the studied medicinal plants can be considered radiologically safe for public use. However, the slightly elevated K-40 activity and dose values observed in specific medicinal plants, particularly lion's foot, highlight the need for periodic monitoring of radionuclide activity in herbal products, especially those imported or cultivated under varying soil and environmental conditions.

6. CONFLICTS OF INTEREST

The authors declare that there is no conflict of interest related to the publication of this scientific research. The study was carried out independently, according to the highest standards of academic integrity and scientific impartiality, in the analysis and formulation of the results, without any unjustified bias or external influence.

7. AUTHOR CONTRIBUTIONS

Osamah Oudah designed the study framework and methodology, performed statistical analysis, and critically reviewed the manuscript. Zainab Rajih collected samples, conducted the analytical procedures, drafted the initial manuscript, and verified data accuracy. Both authors approved the final version and take full responsibility for the integrity of the research.

8. ACKNOWLEDGMENTS

The authors would like to express sincere gratitude to Prof. Dr. Murtadha Shakir Aswood for his valuable scientific support and guidance, which significantly contributed to the completion of this study.

9. REFERENCES

Abbas, H.H., Kadhim, S.A., Alhous, S.F., Hussein, H.H., Al-Temimei, F.A. and Mraity, H.A.A., 2023. Radiation risk among children due to natural radioactivity in breakfast cereals. *Nature Environment and Pollution Technology*, 22(1), pp.527-533. [DOI]

Abdelfadeel, E.H., El-Halim, E.A., Hegazy, T.M. and Ghany, H.A., 2023. Relationship between radioactivity and toxicity in some medicinal plants. *Scientific Reports*, 13(1), p.10952. [DOI]

Abu-Qatouseh, L., Mallah, E. and Mansour, K., 2019. Evaluation of anti-Propionibacterium acnes and anti-inflammatory effects of polyphenolic extracts of medicinal herbs in Jordan. *Biomedical and Pharmacology Journal*, 12(1), pp.211-217. [DOI]

Ali, S., Baloch, S.B., Bernas, J., Konvalina, P., Onyebuchi, E.F., Naveed, M. and Mustafa, A., 2024. Phytotoxicity of radionuclides: A review of sources, impacts and remediation strategies. *Environmental Research*, 240, p.117479. [DOI]

Bal, S.Ş., Kurşat, M., Kuluöztürk, M.F., Çelik, Ş.K. and Yılmaz, E., 2023. Soil to plant transfer of 226Ra, 232Th and 137Cs to some medicinal and aromatic plants growing in Bitlis (Turkey). *Journal of Environmental Radioactivity*, 257, p.107089. [DOI]

Biira, S., Ochom, P. and Oryema, B., 2021. Evaluation of radionuclide concentrations and average annual committed effective dose due to medicinal plants and soils commonly consumed by pregnant women in Osukuru, Tororo (Uganda). *Journal of Environmental Radioactivity*, 227, p.106460. [DOI]

Commission of Statistics and GIS, 2023. Annual Statistical Abstract 2023. Republic of Iraq. Retrieved August 4, 2026, from https://cosit.gov.iq/documents/AAS2023/2.pdf

Dawal, A.A.A.H. and Oudah, O.N., 2025. Measurement of natural radioactivity and radiation hazards in bricks produced in Babylon brick factories, Iraq. *Radiation Protection Dosimetry*, 201(4), pp.261-269. [DOI]

Desideri, D., Meli, M.A. and Roselli, C., 2010. Natural and artificial radioactivity determination of some medicinal plants. *Journal of Environmental Radioactivity*, 101(9), pp.751-756. [DOI]

Garba, N.N., Aliyu, A.S., Rabiu, N., Kankara, U.M., Vatsa, A.M., Ismaila, A. and Onuh, E., 2024. Investigation of natural radionuclides and radiation shielding potential of some commonly used building materials in Northwestern Nigeria. *Scientific Reports*, 14(1), p.9696. [DOI]

Güven, A., Cengiz, G.B., Çağlar, İ. and Ateş, S., 2023. Evaluation of radioactivity levels and radiological hazards of some endemic plants used as medicine in Ankara, Turkey. *Applied Radiation and Isotopes*, 200, p.110939. [DOI]

Hady, H.N. and Mashkor, Z.M., 2022. The measurement of the total excess lifetime cancer risk in soil samples from Tar Al-Najaf in Al-Najaf Al-Ashraf-Iraq. *Pakistan Journal of Medical & Health Sciences*, 16(11), p.706. [DOI]

Hamza, Z.M., Alshebly, S.A. and Hussain, H.H., 2020. A practical study to determine the percentage of radiation in medicinal herbs used in the Iraqi market. *Journal of Physics: Conference Series*, 1591(1), p.012007. [DOI]

Hassan, H.J., 2025. Radiation hazards and effective dose evaluation: A study of various imported walnut consumed in Kurdistan-Iraq. *Radiation Physics and Chemistry*, p.112899. [DOI]

Hossen, M.J., Haydar, M.A., Rahman, M.A., Ali, M.I., Paul, D., Asaduzzaman, K. and Khandaker, M.U., 2024. Committed effective dose due to the intake of medicinal plants and herbs by the Bangladeshi populace. *International Journal of Environmental Analytical Chemistry*, pp.1-13. [DOI]

IAEA, 2022. Exposure due to radionuclides in food other than during a nuclear or radiological emergency. Part 2: Considerations in implementing requirement 51 of IAEA general safety requirements Part 3. International Atomic Energy Agency, Vienna.

ICRP, 1990. *Recommendations of the International Commission on Radiological Protection*. ICRP Publication 60, Ann. ICRP 21 (1–3). Pergamon Press, Oxford.

ICRP, 2012. Compendium of dose coefficients based on ICRP Publication 60. *ICRP Publication 119, Ann ICRP 41 (Suppl.)*, 40, pp.1-257.

International Atomic Energy Agency, 1999. Assessment of doses to the public from ingested radionuclides. *Safety Reports Series No. 4*. International Atomic Energy Agency, Vienna. Retrieved August 4, 2026, from https://www-pub.iaea.org/MTCD/Publications/PDF/P067_scr.pdf

International Commission on Radiological Protection (ICRP), 2007. Recommendations of the ICRP. *ICRP Publication 103, Ann. ICRP*, 37(2-4). [DOI]

Jassim, A.S., Oraibi, A.H., Abojassim, A.A., Algazali, S.A., Hameed, A.A. and Hussian, H.H., 2024. Determination of long-lived gamma emitters in some vegetarian products in Al-Najaf governorate using NaI (Tl). *IOP Conference Series: Earth and Environmental Science*, 1325(1), p.012008. [DOI]

John, S.O.O., Olukotun, S.F., Radebe, M.M. and Mathuthu, M., 2025. Radiological safety assessment of sugar consumption in South Africa—a study of 226Ra, 228Ra, and 40K levels. *Frontiers in Public Health*, 13, p.1534383. [DOI]

Kadhim, N.F., Khalaf, H.N.B., Hassan, H.A. and Mostafa, M.Y., 2021. Determining the natural radioactivity of spices widely used in Iraq. *International Journal of Environmental Analytical Chemistry*, 103(13), pp.3097-3108. [DOI]

Kareem, A.A., Hady, H.N. and Abojassim, A.A., 2016. Measurement of natural radioactivity in selected samples of medical plants in Iraq. *International Journal of Physical Sciences*, 11(14), pp.178-182. [DOI]

Khanal, M., Acharya, A., Maharjan, R., Upadhyay, D.R., Dhobi, S.H., Shah, B.R. and Lamichhane, H.P., 2024. Investigation of naturally occurring radionuclides in selected medicinal plants and associated soils, and calculation of soil-to-plant transfer factors. *Journal of Environmental Radioactivity*, 280, p.107556. [DOI]

Kinahan, A., Kelleher, K., Vintró, L.L. and Currivan, L., 2025. A duplicate diet survey for the assessment of the annual effective dose to the Irish adult population from the ingestion of natural radionuclides in food. *Food Chemistry*, 474, p.143227. [DOI]

Kırıs, E., 2020. Radioactivity levels and radiation health hazards in medicinal plants used in Rize Province, Turkey. *International Journal of Environmental Analytical Chemistry*, 102(12), pp.2865-2878. [DOI]

Kranrod, C., Chanyotha, S., Kritsananuwat, R., Ploykrathok, T., Pengvanich, P., Tumnoi, Y., Thumvijit, T. and Sriburee, S., 2017. Preliminary survey of radioactivity level in Thai medicinal herb plants. *Journal of Physics: Conference Series*, 860(1), p.012001. [DOI]

Luo, L., Wang, B., Jiang, J., Fitzgerald, M., Huang, Q., Yu, Z. and Chen, S., 2021. Heavy metal contaminations in herbal medicines: Determination, comprehensive risk assessments, and solutions. *Frontiers in Pharmacology*, 11, p.595335. [DOI]

Ministry of Health, Iraqi Cancer Board, 2022. Cancer registry of Iraq annual report. Republic of Iraq. Retrieved August 4, 2026, from https://storage.moh.gov.iq/2024/03/31/2024_03_31_11983087032_3940351786864953.pdf

Monica, S., Jojo, P.J. and Khandaker, M.U., 2020. Radionuclide concentrations in medicinal florae and committed effective dose through Ayurvedic medicines. *International Journal of Radiation Biology*, 96(8), pp.1028–1037. [DOI]

Muhammad, A.N., Ismail, A.F. and Garba, N.N., 2024. Natural radioactivity in food crops and soil and estimation of the concomitant dose from tin mining areas in Nigeria. *Journal of Taibah University for Science*, 18(1), p.2366507. [DOI]

Najam, L.A., Tafiq, N.F. and Kitah, F.H., 2015. Estimation of natural radioactivity of some medicinal or herbal plants used in Iraq. *Detection*, 3(01), p.1. [DOI]

Obaid, A.S., 2022. *Evaluation of the Radiological Risks of Radionuclides in Different Samples of Seasoning in Iraqi Markets*. Master's Thesis, University of Kerbala, College of Science. Retrieved August 4, 2026, from https://uokerbala.edu.iq/wp-content/uploads/2022/10/Rp-Evaluation-of-the-Radiological-Risks-of-Radionuclides-in-Different-Samples-of-Seasoning-in-Iraqi-Markets-.pdf

Olagbaju, P.O., Wojuola, O.B. and Tshivhase, V., 2021. Radionuclides contamination in soil: effects, sources and spatial distribution. *EPJ Web of Conferences*, 253, p.09006. [DOI]

Popoola, F.A., Isola, O.B., Fakeye, O.D., Owolabi, T.A., Sanyaolu, M.E., Owoyemi, S.I. and Elijah, I.O., 2024. Examination of medicinal plants for radionuclide absorption and their health implications. *Pollution*, 10(2), pp.700-711. [DOI]

Rajih, Z.H. and Oudah, O.N., 2025. Assessment of toxic metal contamination and consumer safety of medicinal plants in Al-Diwaniyah herbal shops. *Biological Trace Element Research*, pp.1-19. [DOI]

Sabr, B., Haji, S.O., Azeez, H., Hussein, M.I. and Smail, J.M., 2023. Assessment of natural radioactivity levels in widely used food spices in the Iraqi Kurdistan region and their associated radiological risks. *Zanco Journal of Pure and Applied Sciences*, 35(6), pp.16-27. [DOI]

Saudi, H.A., Abedelkader, H.T., Issa, S., Diab, H.M., Bashter, I.I., Alharshan, G.A., Uosif, M.A.M. and Zakaly, H.M., 2022. An in-depth examination of the natural radiation and radioactive dangers associated with a regularly used medicinal plant in Egypt. *International Journal of Environmental Research and Public Health*, 19(13), p.8124. [DOI]

Shuaibu, H.K., Kankara, U.M., Muhammad, A.N., Gusau, M.B., Garba, N.N., Kolo, M.T. and Khandaker, M.U., 2025. Natural radioactivity and radiological risks in some medicinal plants consumed in northern Nigeria. *Radiation Physics and Chemistry*, 234, p.112785. [DOI]

Shuaibu, H.K., Mohamed, F., Khandaker, M.U., Ismail, A.F. and Omar, R.S., 2023. Radioactivity and concomitant radiation dose from Malaysian herbal plants. *Radiation Physics and Chemistry*, 211, p.111050. [DOI]

Sundström, J., Piñero-García, F., Thomas, R., Forssell-Aronsson, E. and Isaksson, M., 2025. Radiological characterization of commercial baby food in Sweden. *Journal of Food Composition and Analysis*, p.107709. [DOI]

Sweaf, A.A. and Oudah, O.N., 2024. Determination of radon concentration in the imported tea in Al-Diwaniyah Governorate markets, Iraq using nuclear track detector LR-115. *Caspian Journal of Environmental Sciences*, 22(1), pp.53-57.

Szaciłowski, G., 2024. Evaluation of natural radioactivity and assessment of dose increase due to the use of fertilizers produced in Poland. *Journal of Radioanalytical and Nuclear Chemistry*, 333(7), pp.3425-3430. [DOI]

United Nations Scientific Committee on the Effects of Atomic Radiation (UNSCEAR), 2017. *Report Sources, Effects and Risks of Ionizing Radiation, Report to the General Assembly, with Scientific Annexes*. United Nations, New York.

UNSCEAR, 2000. *Sources, Effects and Risk of Ionizing Radiation, Report to the General Assembly*. United Nations, New York.

UNSCEAR, 2010. *Sources and Effects of Ionising Radiation. Report to the General Assembly with Scientific Annexes*. United Nations, New York.

Nature Environment and Pollution Technology
An International Quarterly Peer-Reviewed Open Access Journal

p-ISSN: 0972-6268 | e-ISSN: 2395-3454 Vol. 25 | No. 4 | Article ID B4425 | 2026

RESEARCH ARTICLE https://doi.org/10.46488/NEPT.2026.v25i04.B4425 OPEN ACCESS

Modeling Temporal Persistence in Daily Pan Evaporation Using Interpretable Machine Learning

Jaydeep Kale† and Sanjaykumar Sharma
Department of Computer Science & Engineering, Oriental University, Indore, 453555, Madhya Pradesh, India
†Corresponding author: Jaydeep Kale; jaynkale@gmail.com

ARTICLE HISTORY

Received: 14-01-2026
Revised: 04-03-2026
Accepted: 20-03-2026

KEYWORDS

Pan evaporation
Temporal memory
Evaporation persistence
Machine learning
CatBoost

CITE THIS ARTICLE

Kale, J. and Sharma, S., 2026. Modeling temporal persistence in daily pan evaporation using interpretable machine learning. *Nature Environment and Pollution Technology*, 25(4), B4425. https://doi.org/10.46488/NEPT.2026.v25i04.B4425

COPYRIGHT & LICENCE

© 2026 The Authors
Open Access under CC BY 4.0.

PUBLISHED BY

TECHNOSCIENCE PUBLICATIONS

ABSTRACT

Accurate prediction of daily pan evaporation (Ep) is critical for irrigation management and water resource planning, yet it remains challenging due to strong temporal variability and persistence. Most available models are based primarily on contemporaneous meteorological variables and do not account for the inherent memory of evaporation. This paper systematically explores the impact of temporal memory on daily Ep by explicitly separating evaporation persistence from meteorological memory through a machine learning framework. A Categorical Boosting (CatBoost) model was used to analyze multi-year data from a semi-arid to sub-humid area in western-central India. The model used lagged Ep and meteorological variables at 1-, 3-, 7-, and 14-day timescales. The coefficient of determination (R^2), root mean square error (RMSE), and mean absolute error (MAE) were used to evaluate model performance, while Random Forest and XGBoost were used for benchmarking. Feature importance and SHAP analyses provided interpretability. The findings indicate that the inclusion of a 1-day lag of pan evaporation substantially improves predictive performance, with RMSE decreasing to 0.83 mm. This improvement indicates strong short-term persistence in day-to-day evaporation. Longer evaporation lags degrade performance, whereas lagged meteorological variables provide modest additional improvement beyond evaporation memory. CatBoost demonstrated the most balanced performance among the evaluated models. Overall, the findings confirm that short-term evaporation persistence dominates temporal dependence in daily Ep, with meteorological memory playing a secondary role, thereby offering a physically interpretable and efficient framework for data-driven evaporation modeling.

1. INTRODUCTION

Evaporation is an essential part of the hydrological cycle (Kundzewicz 2008). It plays an important role in irrigation scheduling, reservoir management, and agricultural water management (Martínez Alvarez et al. 2008). Effective water resource planning requires accurate estimation of daily evaporation because water losses through evaporation directly affect water availability and crop production. In addition, evaporation is closely associated with climate change and global warming, as it accounts for a substantial portion of global precipitation redistribution (Zhou et al. 2021). Therefore, the accurate estimation and prediction of evaporation are important issues that remain to be resolved in the fields of hydrology and water resources engineering. Pan evaporation (Ep) is one of the most common and practical techniques for evaluating evaporative demand among the available options (Wang et al. 2023). Direct measurement of Ep is feasible using a simple evaporation pan, which makes it especially useful in data-scarce areas where radiation and other measurements of

the energy balance are inaccessible. It has been widely adopted as a proxy measure of atmospheric evaporative demand due to its simplicity, low cost, and minimal data requirements. However, pan measurements are influenced by pan siting, maintenance problems, environmental exposure, and scale differences between the pan and natural water bodies, which may introduce uncertainty in daily evaporation records (Du et al. 2023).

Naturally, determining daily Ep is challenging due to the complex and nonlinear nature of evaporation processes (Goyal et al. 2014). Evaporation rates are influenced by diverse, interacting meteorological factors such as air temperature, relative humidity (RH), wind speed, and solar radiation, which can fluctuate significantly on a daily basis (Taheri et al. 2025). These abrupt variations, combined with seasonal changes, geographic location, and local climate conditions, further complicate the prediction of daily evaporation (Ghafouri-Azar & Lee 2023). Traditionally, Ep has been estimated using empirical and physically based models, including the Penman, Hargreaves-Samani, and FAO-56 Penman-Monteith methods (Ruiz-Ortega et al. 2024). These models are physically interpretable, grounded in fundamental principles, and computationally efficient. Nonetheless, they depend on simplifying assumptions about atmospheric processes and require accurate, comprehensive meteorological data such as temperature, radiation, humidity, and wind speed; inaccuracies in these data can drastically affect evaporation estimates (Irizarry-Ortiz & Harmsen 2023). While their performance is reasonable for seasonal or monthly estimates, their accuracy diminishes at the daily level due to their limited ability to capture short-term variability and nonlinear interactions (Moratiel et al. 2020). Furthermore, these models are highly sensitive to data quality; small measurement errors in wind speed or humidity can lead to substantial estimation uncertainties. They are also often site-specific and need recalibration when applied to different climatic regions, limiting their broader applicability (Xu & Singh 2002).

Evaporation has also been estimated using statistical and time-series methods, such as multiple linear regression and autoregressive methods. Although these models are simple and interpretable, their ability to capture nonlinear relationships and complex interactions between meteorological variables is usually constrained. Consequently, their forecasting ability remains limited in representing daily evaporation dynamics under rapidly changing weather conditions (Almedeij 2016).

Machine learning (ML) techniques have emerged as effective alternatives for evaporation prediction in recent years due to their ability to learn complex nonlinear relationships from data (Al Sudani & Salem 2022). Methods such as artificial neural networks, support vector regression, random forests (RF), and gradient boosting algorithms have shown high predictive accuracy compared to traditional empirical and statistical models (Fan et al. 2021). However, many studies on ML-based models primarily emphasize prediction accuracy and often overlook the temporal dynamics of the evaporation process. Typically, these studies use past meteorological variables or previous-day evaporation values to make predictions, but they frequently lack a systematic assessment of the contribution of individual variables and proper evaluation of lag durations (Phesa et al. 2024).

Ensemble tree-based algorithms such as RF, Extreme Gradient Boosting (XGBoost), and Categorical Boosting (CatBoost) have gained popularity due to their high predictive accuracy, ability to model nonlinear interactions, and robustness against multicollinearity and missing data (Agrawal et al. 2022). While these models deliver excellent predictions, they are often regarded as black-box predictors, limiting their use for exploring the temporal dynamics of evaporation, specifically the relative influence of evaporation persistence versus prior meteorological conditions.

Despite advances in empirical and machine learning methods for estimating Ep, the temporal variability of daily evaporation is still insufficiently studied. It remains unclear whether current evaporation is predominantly driven by its own persistence or by antecedent meteorological factors. The practice of incorporating lagged variables is frequently ad hoc, lacking systematic evaluation of optimal lag lengths (Phesa et al. 2024). This gap hampers interpretability and physical understanding, as most studies prioritize predictive performance over insights into temporal mechanisms.

To address these issues, this research introduces a systematic temporal-memory model for daily Ep prediction using ensemble machine learning approaches such as RF, XGBoost, and CatBoost. The framework rigorously examines different lag lengths to empirically distinguish between evaporation persistence and meteorological influence. Additionally, explainable machine learning techniques are employed to quantify the contributions of previous evaporation and relevant meteorological variables (Linardatos et al. 2021). The goal is to enhance evaporation estimates and deepen understanding of its temporal behavior. The overall methodology is illustrated in Fig. 1 and detailed in Section 2.

2. MATERIALS AND METHODS

2.1. Study Location and Climatic Characteristics

The meteorological data used in this study were acquired

at the Bhagur station (19.31° N, 75.19° E), located in Maharashtra, India. The climate of Bhagur is semi-arid to sub-humid, with distinct wet and dry seasons that have a strong influence on the dynamics of daily evaporation. The station is part of the network maintained by the Office of the Chief Engineer, Planning and Hydrology, Nashik, Maharashtra. Access to the data was provided under an academic-use agreement, and the data are not publicly accessible. Evaporation measurements were recorded using a standard Class A pan installed at the meteorological station. The pan was placed in an open-field environment, and its siting was carried out in accordance with traditional guidelines. It is located in a flat area and is well exposed to sunlight and natural wind patterns. This arrangement reduces artificial shielding effects. Although detailed station metadata are not publicly available, the dataset underwent basic quality checks.

2.2. Data Description

The variables in the dataset are Ep, average wind speed (AWS), instantaneous wind speed (IWS), maximum air temperature (MAXT), minimum air temperature (MINT), pan water temperature (PWT), sunshine duration (SD), and RH. Each variable has two entries per day, except for SD. One of these values corresponds to 8:30 a.m., and the other corresponds to 5:30 p.m. The data are available for the period from 2007 to 2021.

2.3. Methodological Framework

The overall methodological framework adopted in this study is illustrated in Fig. 1. The workflow comprises eight consecutive steps, beginning with the preparation of the raw data and ending with the interpretation and reporting of the model. Each phase is described in detail below.

2.4. Raw Data Input

The meteorological dataset comprised Ep, AWS, IWS, MAXT, MINT, PWT, SD, and RH on a daily basis. The data were received in spreadsheet form and subsequently processed as discussed in the following section.

2.5. Data Preprocessing

The data were preprocessed to ensure temporal consistency, physical realism, and suitability for ML analysis (Maharana et al. 2022). The column containing measurement timestamps was first converted into a standard date-time format, and calendar dates were obtained. SD was originally measured hourly. To make the dataset consistent, SD observations were aggregated into a single daily value by summing all measurements recorded within each calendar day. The other features were recorded twice daily. For the analysis, these twice-daily values were then reduced to single daily values using physically meaningful rules. Ep values were summed over the day. MAXT and MINT were treated as extreme day-to-day variables. The daily MAXT was determined as the larger of the two MAXT values, while the daily MINT was determined as the smaller of the two MINT values. All other meteorological variables, such as RH, PWT, AWS, and IWS, were averaged over the day. Since the objective of this study was daily evaporation prediction rather than sub-

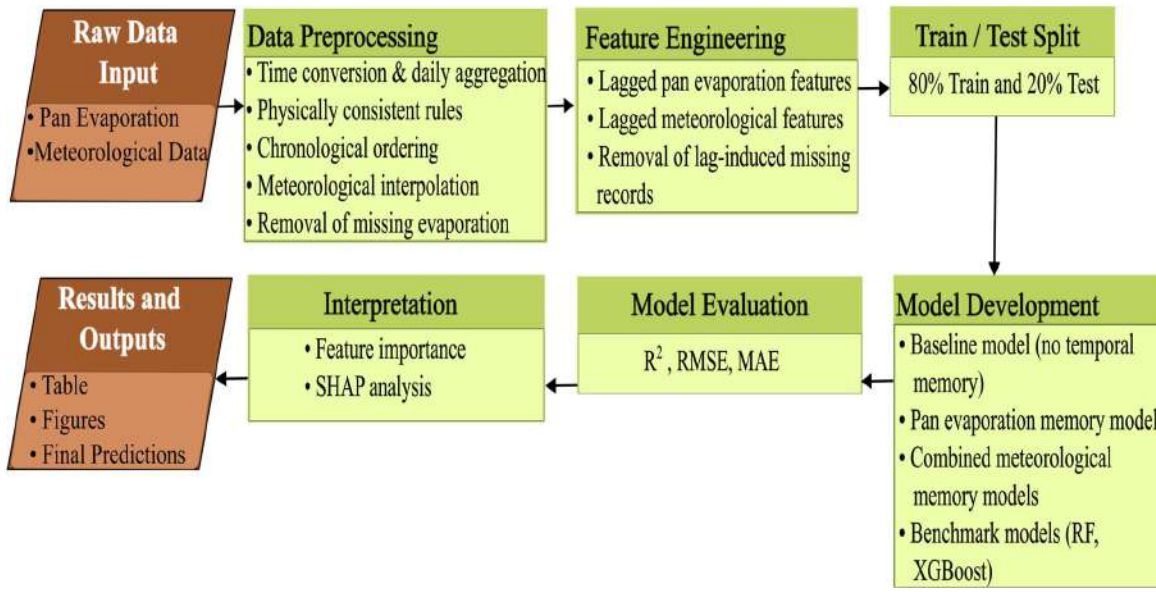


Fig. 1: Proposed machine learning framework for pan evaporation forecasting.

daily process simulation, daily mean values were considered appropriate for representing the integrated atmospheric conditions influencing evaporation.

This resulted in a time-series dataset that was appropriate for the analysis of temporal memory in evaporation processes. Data were ordered chronologically to preserve temporal dependence. Missing meteorological data were replaced using time-based linear interpolation, applied only to gaps of three days or fewer, which accounted for just 0.07% of the data. Remaining gaps were left unfilled, and the corresponding days were excluded from the dataset. The longest such gap was 151 days. Conversely, days with missing Ep values were completely removed so that they would not influence the target variable. Filling missing values using linear interpolation can slightly alter the temporal pattern of the data, which is why it was not applied to Ep. Other filling methods may produce slightly different results and can be explored in future work.

2.6. Feature Engineering

Feature engineering was performed to explicitly model the effects of temporal persistence and memory in the Ep process (Považanová et al. 2023). The lagged Ep features (Ep_lag_1, Ep_lag_3, Ep_lag_7, and Ep_lag_14) were created using fixed lag lengths of 1, 3, 7, and 14 days, representing short- and medium-term evaporation memory. Simultaneously, lagged forms of all the meteorological variables were created using identical lag lengths to represent the delayed atmospheric effects on evaporation. Feature creation was followed by the handling of missing values to obtain a complete and consistent set of features.

2.7. Data Splitting Strategy

To prevent information leakage and preserve the temporal structure of the data, the dataset was divided into training and testing sets based on chronological order. Eighty percent (80%) of the observations were used as the model training set, while the remaining 20% were used as the independent testing set. Random shuffling was not used to provide realistic model testing under forecasting conditions.

2.8. Model Development

2.8.1. Baseline Model (No Temporal Memory)

A baseline CatBoost regression model was developed using only current meteorological variables. Seasonal indicators and lagged inputs were excluded from this model. It serves as a reference to assess the impact of adding temporal features.

2.8.2. Ep Memory Models

The analysis started with a baseline model that used only meteorological variables. Past values of Ep (Ep_lag_1, Ep_lag_3, Ep_lag_7, and Ep_lag_14) were then added step by step to the model and compared with the baseline model. This was done to enable a systematic assessment of the effect of evaporation memory on the predictive performance of Ep. The lag that provided the best prediction accuracy on the test data was selected.

2.8.3. Combined Meteorological Memory Models

Once the best evaporation lag had been determined, lagged meteorological variables with the same lag length were added to the model. This configuration represents a combined temporal-memory model, capturing both surface persistence and delayed atmospheric effects. The CatBoost model that performed best in this setup was selected for further analysis.

2.8.4. Benchmark Models

RF and XGBoost regression models were trained using the same set of best-performing features to evaluate the robustness of the proposed framework. These benchmark models provide a comparative baseline against widely used ensemble learning techniques.

2.9. Model Evaluation

All models were evaluated on the independent testing dataset using three standard performance metrics: the coefficient of determination (R^2), root mean square error (RMSE), and mean absolute error (MAE). This multi-metric analysis provides a balanced assessment of model accuracy, error magnitude, and explanatory power.

2.10. Model Interpretation

To explain the impact of individual predictors and temporal memory elements, feature importance scores were obtained from the optimal CatBoost model. In addition, Shapley Additive Explanations (SHAP) were used to measure both the magnitude and direction of each feature's contribution to the model predictions. These analyses provide physical insight into evaporation persistence and the contribution of lagged meteorological factors.

3. RESULTS AND DISCUSSION

3.1. Baseline Model Performance

As shown in Table 1, the model achieved an R^2 of 0.615, suggesting that approximately 61.5% of the variability in daily evaporation is explained by same-day meteorological variables. An RMSE of 1.386 mm and an MAE of 1.093 mm reflect the average prediction errors. While the baseline model offers a reasonable initial estimate of daily evaporation, several limitations are evident.

Table 1: Prediction performance of the CatBoost baseline model.

Model	R^2	RMSE (mm)	MAE (mm)
CatBoost Baseline	0.615	1.386	1.093

Table 2: Model performance metrics for varying Ep lag days.

Ep_Lag_Days	R^2	RMSE (mm)	MAE (mm)
1	0.863	0.826	0.555
3	0.732	1.155	0.833
7	0.676	1.271	0.959
14	0.638	1.344	1.049

1. **Moderate predictability:** Approximately 38.5% of the variability in daily evaporation remains unexplained. This indicates that same-day meteorological variables cannot fully explain Ep.
2. **Lack of temporal persistence and motivation for memory-based modeling:** The short-term dependence of Ep is not captured by the baseline model. Therefore, it is necessary to add lagged Ep and meteorological variables. The remaining sections explain the effect of adding temporal memory.

3.2. Effect of Evaporation Memory

A series of CatBoost models was constructed, each incorporating a single lagged Ep term alongside all same-day meteorological variables. Lag durations of 1, 3, 7, and 14 days were evaluated. The performance metrics are summarized in Table 2, while Fig. 2 illustrates how prediction error varies with lag length. Incorporating Ep_lag_1 substantially improved model performance. Compared to the baseline model (RMSE = 1.386 mm), the RMSE dropped to 0.826 mm, and the model's explanatory power increased substantially (R^2 = 0.863), with the MAE decreasing to 0.555 mm.

This demonstrates that immediate temporal dependence accounts for a substantial portion of daily variation in Ep. Predictive accuracy declines as the lag length increases further. RMSE values rise to 1.155 mm, 1.271 mm, and 1.344 mm at lag lengths of 3, 7, and 14 days, respectively, accompanied by decreasing R^2 scores and increasing MAE. This trend suggests that information from longer lags becomes progressively less useful for representing current evaporation conditions.

Based on these findings, Ep_lag_1 was identified as the optimal temporal memory length for daily evaporation prediction at the study site and was consequently used for subsequent analyses involving meteorological memory and model benchmarking. When monsoon conditions change rapidly, evaporation does not respond immediately because it is a cumulative process over 24 hours that depends on heat storage in the pan water and atmospheric continuity. Therefore, previous-day evaporation (Ep_lag_1) provides substantial information about the current state. This explains why short-term persistence is stronger, while longer meteorological memory adds only minor incremental value.

The persistence of evaporation may vary across seasonal regimes, mainly during monsoon, post-monsoon, and dry seasons. In this study, the entire dataset from 2007–2021 was treated as a continuous time series to determine overall temporal memory characteristics. The dominance of Ep_lag_1 indicates an average annual behavior, but seasonal differences in persistence may exist. Future research should examine these variations under different regimes.

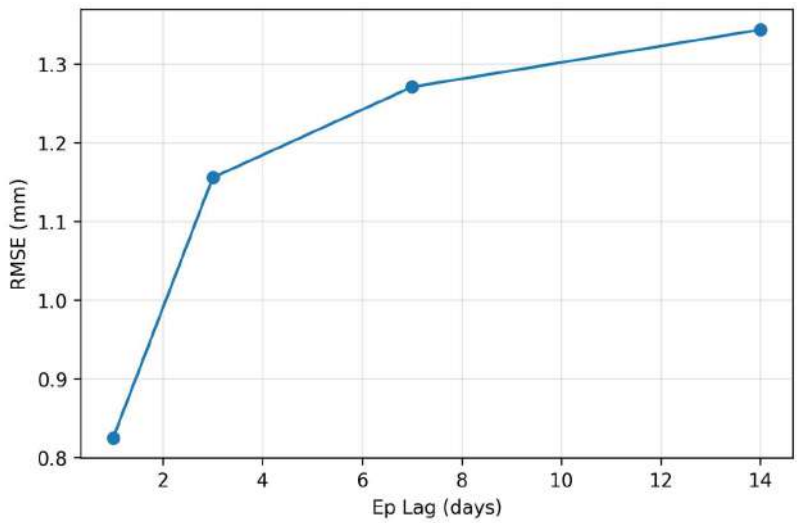


Fig. 2: Effect of Ep lag length on model performance, expressed in terms of RMSE (mm) for the testing dataset.

Table 3: Performance metrics of the Ep + Met memory configuration.

Configuration	R^2	RMSE (mm)	MAE (mm)
Ep + Met Memory	0.865	0.820	0.553

3.3. Effect of Meteorological Memory

After identifying Ep_lag_1 as the most effective predictor for evaporation, the influence of meteorological memory was evaluated by adding lagged meteorological variables alongside Ep_lag_1. This integrated approach was termed the Ep + Met Memory model. Its purpose was to determine whether past atmospheric conditions offer additional predictive value beyond evaporation persistence alone. The results are summarized in Table 3.

Compared with the evaporation-memory-only model, including lagged meteorological variables resulted in a modest but consistent improvement in predictive accuracy. The R^2 increased slightly to 0.865, while RMSE and MAE decreased marginally to 0.820 mm and 0.553 mm, respectively. This subtle enhancement indicates that much of the atmospheric persistence is already captured within the lagged evaporation signal.

3.4. Model Comparison

To evaluate the robustness of the proposed temporal memory framework, the highest-performing feature configuration was tested across three machine learning models: CatBoost, RF, and XGBoost. This configuration employed Ep_lag_1 alongside lagged meteorological variables. Table 4 presents the models' predictive performance on the test dataset. All three models demonstrated strong results, with R^2 values exceeding 0.86, indicating that daily Ep prediction can be notably enhanced by integrating temporal memory.

Table 4: Performance comparison of ML models using the proposed temporal memory feature configuration.

Model	R^2	RMSE (mm)	MAE (mm)
CatBoost	0.865	0.820	0.553
RF	0.863	0.826	0.546
XGBoost	0.860	0.835	0.556

The similar performance levels suggest that the improvements are primarily due to the memory-based feature design rather than model-specific characteristics. Among these, CatBoost achieved the lowest RMSE of 0.820 mm, reflecting a more precise capture of daily evaporation variability. RF showed a comparable R^2 value and a lower MAE, but a slightly higher RMSE, indicating reduced accuracy for larger prediction errors. XGBoost exhibited similar results but with marginally lower R^2 and higher error metrics, implying weaker generalization on this dataset.

3.5. Interpretability Results

Further interpretability analysis was carried out on the best-performing CatBoost configuration using feature importance and SHAP methods. The results are shown in Figs. 3–5. These figures help explain the effects of temporal and meteorological predictors on Ep estimates.

Fig. 3 displays a scatter plot comparing measured and forecasted daily Ep values within the test dataset. The forecasted data closely align with the 1:1 reference line, demonstrating strong agreement between observations and model predictions. Most points cluster near the diagonal, indicating the model effectively captures both low and high evaporation conditions. Slightly increased scatter at higher evaporation levels is observed but remains minor.

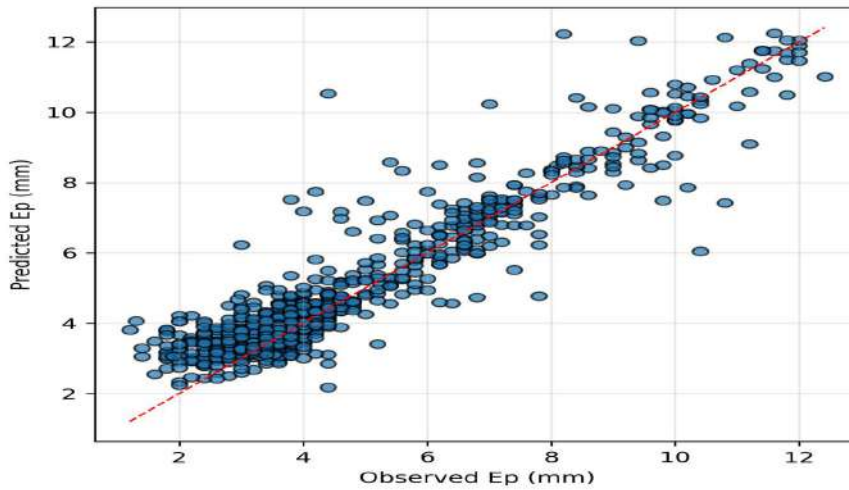


Fig. 3: Scatter plot of observed versus predicted daily Ep (mm) for the testing dataset.

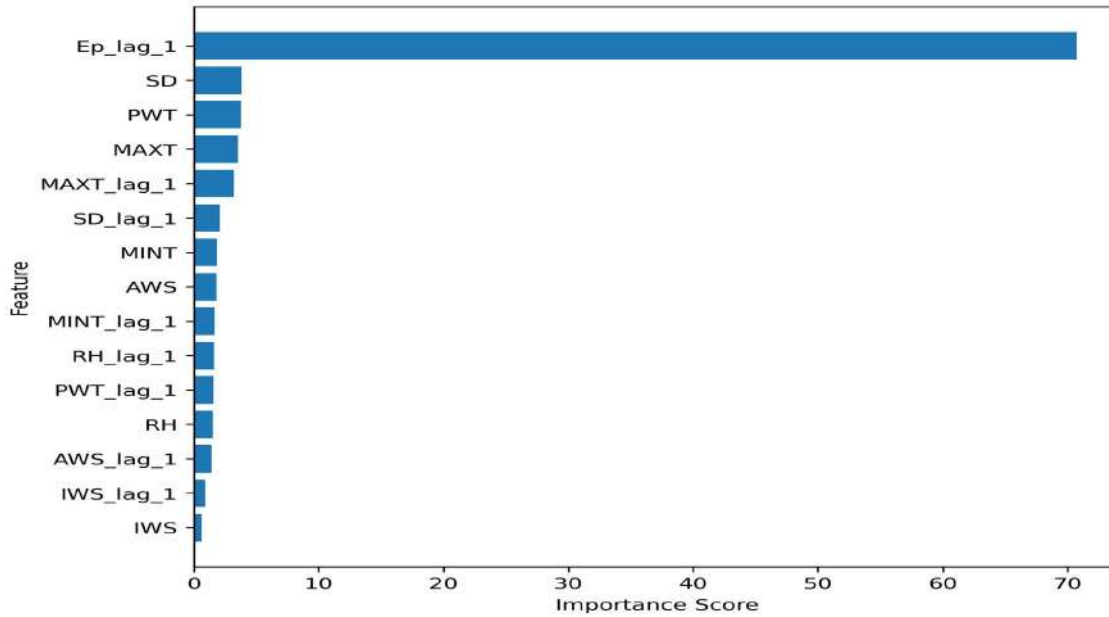


Fig. 4: Feature importance ranking of predictors obtained from the CatBoost model. Importance scores represent relative contribution to prediction.

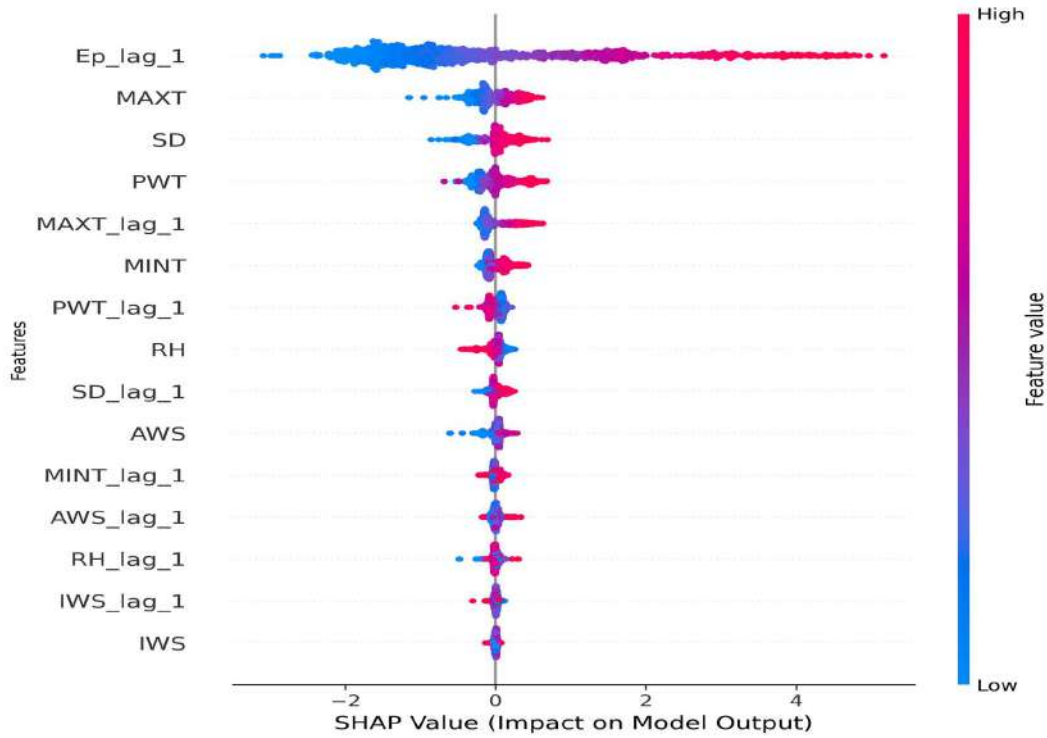


Fig. 5: SHAP summary plot showing the contribution of predictors to daily Ep estimation. Color indicates feature value (blue = low, red = high), and SHAP values represent impact on model output.

Overall, this suggests that incorporating temporal memory allows the model to accurately reflect daily variations in Ep.

Fig. 4 presents the feature importance ranking of the CatBoost model. The most influential predictor is Ep_lag_1, which is substantially more important than

other meteorological variables. This highlights a strong short-term temporal dependence in daily Ep, likely due to atmospheric persistence and autocorrelation in cumulative pan evaporation measurements. The next most important features include SD, PWT, and MAXT, while lagged meteorological variables contribute minimally overall. This indicates that although short-term evaporation persistence dominates the temporal structure, meteorological factors still play a meaningful role in energy balance conditions.

Fig. 5 shows the SHAP summary plot, ranking features by their mean absolute SHAP values. Each point represents an observation, with positive SHAP values indicating increased contributions to evaporation and negative values indicating decreases. The most important predictor is Ep_lag_1; higher values lead to increased current evaporation, and vice versa. Since daily pan evaporation measures 24-hour accumulation and exhibits autocorrelation, the significance of Ep_lag_1 likely reflects statistical persistence, instrument memory, and atmospheric continuity. It is important to note that SHAP values indicate the contribution to prediction, not direct causality.

Higher MAXT, PWT, and SD values are associated with higher evaporation, consistent with physical expectations. The SHAP contributions of lagged meteorological variables are small, indicating limited residual influence from previous days. The SHAP values for RH and wind speed are lower in magnitude. The role of aerodynamic transport in evaporation is physically evident, but its additional predictive power is modest when Ep_lag_1 is included, as the previous day's evaporation already captures some effects of prior wind conditions.

4. CONCLUSIONS

This study investigated the influence of temporal memory on daily Ep by isolating the effects of evaporation persistence and meteorological memory. The results clearly indicate that daily Ep is predominantly influenced by short-term temporal persistence. Using a 1-day lag of evaporation (Ep_lag_1) yielded the highest predictive accuracy across all evaluated models. Incorporating longer evaporation lags reduced model performance, suggesting that daily evaporation is mainly affected by recent conditions rather than those from several days prior. Adding lagged meteorological variables provided only minor improvements, indicating that most meteorological information is captured in prior evaporation observations. Consequently, meteorological memory plays a secondary, corrective role, especially during periods of weather variability. Comparative analysis of CatBoost, RF, and XGBoost demonstrated that the observed improvements stem primarily from the proposed temporal memory–based feature design rather than model-specific characteristics. Among these, CatBoost exhibited the most balanced performance. Interpretability analyses, including feature importance and SHAP, supported the physical plausibility of the framework, with evaporation persistence identified as the most critical factor for predicting daily Ep. This research was conducted at a single station; future work should involve multi-station and multi-climate data, explore seasonal variations, and develop hybrid physical and machine-learning approaches. In summary, the proposed temporal memory model offers a logical, interpretable, and physically grounded approach to enhancing daily Ep forecasting.

5. ACKNOWLEDGMENTS

The authors gratefully acknowledge the Office of the Chief Engineer, Planning and Hydrology, Nashik, Water Resources Department, Government of Maharashtra, for providing the meteorological data used in this study. The data were utilized solely for academic and non-commercial research purposes.

6. REFERENCES

Agrawal, Y., Kumar, M., Ananthakrishnan, S. and Kumarapuram, G., 2022. Evapotranspiration modeling using different tree based ensembled machine learning algorithms. *Water Resources Management*, 36(3), pp. 1025–1042. [DOI]

Almedeij, J., 2016. Modeling pan evaporation for Kuwait using multiple linear regression and time-series techniques. *American Journal of Applied Sciences*, 13(6), pp. 739–747. [DOI]

Al Sudani, Z.A. and Salem, G.S.A., 2022. Evaporation rate prediction using advanced machine learning models: a comparative study. *Advances in Meteorology*, 2022, Article ID 1433835. [DOI]

Du, J., Xu, X., Liu, H., Wang, L. and Cui, B., 2023. Deriving a high-quality daily dataset of large-pan evaporation over China using a hybrid model. *Water Research*, 238, p. 120005. [DOI]

Fan, J., Zheng, J., Wu, L. and Zhang, F., 2021. Estimation of daily maize transpiration using support vector machines, extreme gradient boosting, artificial and deep neural networks models. *Agricultural Water Management*, 245, p. 106547. [DOI]

Ghafouri-Azar, M. and Lee, S.-I., 2023. Meteorological influences on reference evapotranspiration in different geographical regions. *Water*, 15(3), p. 454. [DOI]

Goyal, M.K., Bharti, B., Quilty, J., Adamowski, J. and Pandey, A., 2014. Modeling of daily pan evaporation in sub tropical climates using ANN, LS-SVR, fuzzy logic, and ANFIS. *Expert Systems with Applications*, 41(11), pp. 5267–5276. [DOI]

Irizarry-Ortiz, M.M. and Harmsen, E.W., 2023. Sensitivity of the Penman–Monteith reference evapotranspiration equation to meteorological variables for Puerto Rico. *Hydrology*, 10(5), p. 101. [DOI]

Kundzewicz, Z.W., 2008. Climate change impacts on the hydrological cycle. *Ecohydrology & Hydrobiology*, 8(2–4), pp. 195–203. [DOI]

Linardatos, P., Papastefanopoulos, V. and Kotsiantis, S., 2021. Explainable AI: a review of machine learning interpretability methods. *Entropy*, 23(1), p. 18. [DOI]

Maharana, K., Mondal, S. and Nemade, B., 2022. A review: data pre-processing and data augmentation techniques. *Global Transitions Proceedings*, 3(1), pp. 91–99. [DOI]

Martínez Alvarez, V., González-Real, M.M., Baille, A., Maestre Valero, J.F. and Gallego Elvira, B., 2008. Regional assessment of evaporation from agricultural irrigation reservoirs in a semiarid climate. *Agricultural Water Management*, 95(9), pp. 1056–1066. [DOI]

Moratiel, R., Bravo, R., Saa, A., Tarquis, A.M. and Almorox, J., 2020. Estimation of evapotranspiration by the Food and Agriculture Organization of the United Nations (FAO) Penman–Monteith temperature (PMT) and Hargreaves–Samani (HS) models under temporal and spatial criteria: a case study in the Duero basin (Spain). *Natural Hazards and Earth System Sciences*, 20(3), pp. 859–875. [DOI]

Phesa, M., Mbatha, N. and Ikudayisi, A., 2024. MODIS evapotranspiration forecasting using ARIMA and ANN approach at a water-stressed irrigation scheme in South Africa. *Hydrology*, 11(10), p. 176. [DOI]

Považanová, B., Čistý, M. and Bajtek, Z., 2023. Using feature engineering and machine learning in FAO reference evapotranspiration estimation. *Journal of Hydrology and Hydromechanics*, 71(4), pp. 425–438. [DOI]

Ruiz-Ortega, F.J., Clemente, E., Martínez-Rebollar, A. and Flores-Prieto, J.J., 2024. An evolutionary parsimonious approach to estimate daily reference evapotranspiration. *Scientific Reports*, 14, p. 6736. [DOI]

Taheri, M., Bigdeli, M., Imanian, H. and Mohammadian, A., 2025. An overview of evapotranspiration estimation models utilizing artificial intelligence. *Water*, 17(9), p. 1384. [DOI]

Wang, C., Li, T., Xin, D., Wang, Q., Chen, R. and Cao, C., 2023. Pan evaporation prediction using LSTM models based on PCA factor reduction and firefly optimization algorithm. *IEEE Journal on Miniaturization for Air and Space Systems*, 4(4), pp. 416–422. [DOI]

Xu, C.Y. and Singh, V.P., 2002. Cross comparison of empirical equations for calculating potential evapotranspiration with data from Switzerland. *Water Resources Management*, 16(3), pp. 197–219. [DOI]

Zhou, W., Wang, L., Li, D. and Leung, L.R., 2021. Spatial pattern of lake evaporation increases under global warming linked to regional hydroclimate change. *Communications Earth & Environment*, 2, p. 255. [DOI]

Nature Environment and Pollution Technology
An International Quarterly Peer-Reviewed Open Access Journal

p-ISSN: 0972-6268 | e-ISSN: 2395-2454 Vol. 25 | No. 4 | Article ID B4429 | 2026

RESEARCH ARTICLE https://doi.org/10.46488/NEPT.2026.v25i04.B4429 OPEN ACCESS

Three Decades of Urban Heat Dynamics in Patna, India: A Remote Sensing-Based Hotspot Analysis

Avinash Kumar Singh† and Manoj Kumar
Department of Architecture and Planning, National Institute of Technology, Patna 800005, Bihar, India
†Corresponding author: Avinash Kumar Singh; avinash.singh1603arch@nitp.ac.in

ARTICLE HISTORY

Received: 02-02-2026
Revised: 17-03-2026
Accepted: 08-04-2026

KEYWORDS

Land surface temperature (LST)
Remote sensing
Vegetation dynamics
Urban heat dynamics

CITE THIS ARTICLE

Singh, A.K. and Kumar, M. 2026. Three decades of urban heat dynamics in Patna, India: A remote sensing-based hotspot analysis. *Nature Environment and Pollution Technology*, 25(4), B4429.

COPYRIGHT & LICENCE

© 2026 The Authors
Open Access under CC BY 4.0.

PUBLISHED BY

TECHNOSCIENCE PUBLICATIONS

ABSTRACT

Rapid urbanization in tropical cities has intensified surface thermal stress, yet the long-term persistence and spatial structure of urban heat remain poorly understood, particularly in rapidly expanding cities of the Global South. This study investigates three decades (1995–2025) of urban thermal dynamics in Patna, India, with a focus on identifying long-term temperature trends, examining their relationship with vegetation greenness and built-up expansion, and assessing the spatial persistence of urban heat hotspots. Using a longitudinal remote sensing framework, Land Surface Temperature (LST) was analyzed alongside the Normalized Difference Vegetation Index (NDVI) and Normalized Difference Built-up Index (NDBI), derived from multi-decadal Landsat imagery processed in a cloud-based environment. A comprehensive spatiotemporal analytical approach integrating non-parametric trend analysis, correlation testing, hotspot persistence mapping, and multivariate regression modeling was employed to capture both temporal trajectories and spatial stability of urban warming. Results reveal a statistically significant increase in mean LST at a rate of approximately 0.13°C yr^{-1}, accompanied by a strong and monotonic rise in built-up intensity, while vegetation greenness exhibits high interannual variability without a significant long-term trend. Spatial analysis identifies a marked regime shift around the mid-2000s, after which high-temperature zones persistently dominate more than 95% of the urban area, with no observed reversals over the subsequent two decades. Regression results confirm built-up expansion as the sole statistically significant predictor of long-term surface warming at the city scale. Collectively, the findings suggest that Patna has experienced a sustained shift toward long-term dominance of high-temperature zones, indicating increasing persistence of urban heat across the city. The study provides robust empirical evidence of long-term urban heat persistence in a tropical city and offers a transferable analytical framework for identifying sustained thermal risk to support climate-sensitive urban planning and adaptation strategies.

1. INTRODUCTION

Rapid urbanization, coupled with global climate warming, has intensified surface thermal stress in cities worldwide, making urban heat a critical environmental challenge of the twenty-first century (Halefom et al. 2024, Sachindra et al. 2023). Urban land cover transformation, including increased impervious surfaces, reduced vegetation, and enhanced anthropogenic heat emissions, fundamentally alters surface–atmosphere energy exchanges, leading to elevated Land Surface Temperature (LST) (Mishra & Arya 2024, Nath 2025, Weng et al. 2004). Rising LST amplifies heat exposure, degrades outdoor thermal comfort, increases cooling energy demand, and exacerbates heat-related morbidity and mortality (Gupta & Aithal 2022, Halder et al. 2025a, Spangler et al. 2022). These impacts are particularly severe in tropical cities, where high baseline temperatures, prolonged

heat seasons, and dense populations create conditions of persistent thermal stress (Chow et al. 2016, Priya & Senthil 2024).

Satellite-derived LST provides a robust and spatially explicit indicator for analyzing urban thermal environments at multiple scales (Amindin et al. 2021, Chen 2022). Remote sensing-based studies commonly employ the Normalized Difference Vegetation Index (NDVI) and the Normalized Difference Built-up Index (NDBI) to explain spatial and temporal variations in LST, representing vegetative cooling and impervious surface expansion, respectively (Beck et al. 2006, Guha et al. 2018). Extensive evidence demonstrates a negative relationship between LST and NDVI due to evapotranspirative cooling, and a positive relationship between LST and NDBI associated with heat storage and reduced surface permeability (Ma et al. 2025, Pradeep Kumar et al. 2023). Collectively, these studies and reviews demonstrate that although spatial heterogeneity and spatiotemporal variability of urban LST are well-recognized research themes, methodological limitations and data availability have led many studies to focus on short time spans, selected years, or coarse temporal comparisons rather than continuous long-term analyses (Mahata et al. 2024, Voogt & Oke 2003, Zhou et al. 2014). Such approaches limit the ability to identify long-term structural changes in urban thermal behavior and to distinguish persistent urban warming from short-term climatic variability (Halder et al. 2025b, Rasul et al. 2017). A particularly underexplored aspect is urban heat hotspot persistence, defined as the degree to which high-LST zones remain spatially stable over extended periods (Halder et al. 2026). While urban heat islands are frequently mapped for individual years, few studies systematically assess whether these hotspots are transient or structurally embedded within the urban fabric (Amir Siddique et al. 2023, Heaviside et al. 2017, Qi et al. 2024).

These research gaps are particularly acute in rapidly urbanizing tropical cities of the Global South, where unplanned urban expansion and weak land-use governance exacerbate thermal vulnerability (Grimm et al. 2008, Hsu et al. 2021, Seto et al. 2012). Cities across the Indo-Gangetic Plain exemplify these challenges but remain markedly underrepresented in long-term urban climate analyses (Mohan & Kandya 2015). Among them, Patna, a rapidly expanding tropical city in India, has undergone substantial land-use and land-cover transformation over the past three decades, characterized by accelerated built-up expansion and increasing fragmentation and loss of vegetated surfaces (Mohamed et al. 2025). Despite its climatic vulnerability, Patna has received limited attention in multi-decadal urban thermal studies. Unlike most previous urban heat studies that focus on short-term trends or isolated snapshot years, this research explicitly quantifies the long-term spatial persistence of urban heat hotspots using a continuous 31-year satellite record, providing new insights into structurally embedded thermal risk in a tropical city of the Global South.

In this context, the study aims to conduct a three-decade (1995–2025) spatiotemporal analysis of urban thermal dynamics in Patna, integrating Landsat-derived LST with NDVI and NDBI. The study objectives are to (i) quantify long-term trends in surface temperature, vegetation greenness, and built-up intensity, (ii) examine their statistical relationships at the city scale, and (iii) assess the spatial persistence and dominance of urban heat hotspots. By combining non-parametric trend analysis, correlation assessment, hotspot persistence mapping, and multivariate regression, this research provides a technically robust and transferable framework for identifying structurally persistent urban heat in data-scarce tropical cities, with direct implications for climate-sensitive urban planning and heat mitigation strategies.

2. MATERIALS AND METHODS

2.1. Study Area

The study focuses on Patna Municipal Corporation (PMC), the capital city of the Indian state of Bihar, located in the eastern part of the Indo-Gangetic Plain (IGP) between approximately 25.5°–25.7° N latitude and 85.0°–85.2° E longitude. Patna lies along the southern bank of the Ganga River at an average elevation of about 53 m above mean sea level, making it part of a low-lying alluvial floodplain. The city experiences a tropical wet-and-dry climate (Köppen: Aw), characterized by extremely hot summers (April–June), a monsoon season with high humidity (July–September), and mild winters (December–February). Mean summer air temperatures frequently exceed 40°C, contributing to high baseline thermal stress (CITY OF PATNA 2026) (Fig. 1).

Over the past three decades, Patna has undergone rapid urban expansion driven by population growth, infrastructure development, and economic transformation, resulting in the extensive conversion of agricultural and vegetated land into impervious built-up surfaces (Mishra & Patel 2025). The urban landscape exhibits a heterogeneous spatial structure comprising dense built-up cores, expanding peri-urban zones, fragmented green spaces, and riverine environments (Kumar & Rajak 2023). Although the presence of the Ganga River offers potential cooling effects, these benefits are spatially uneven and increasingly offset by adjacent high-density development (Khan et al. 2021). The city's rapid and largely unplanned urbanization, combined with its climatic setting,

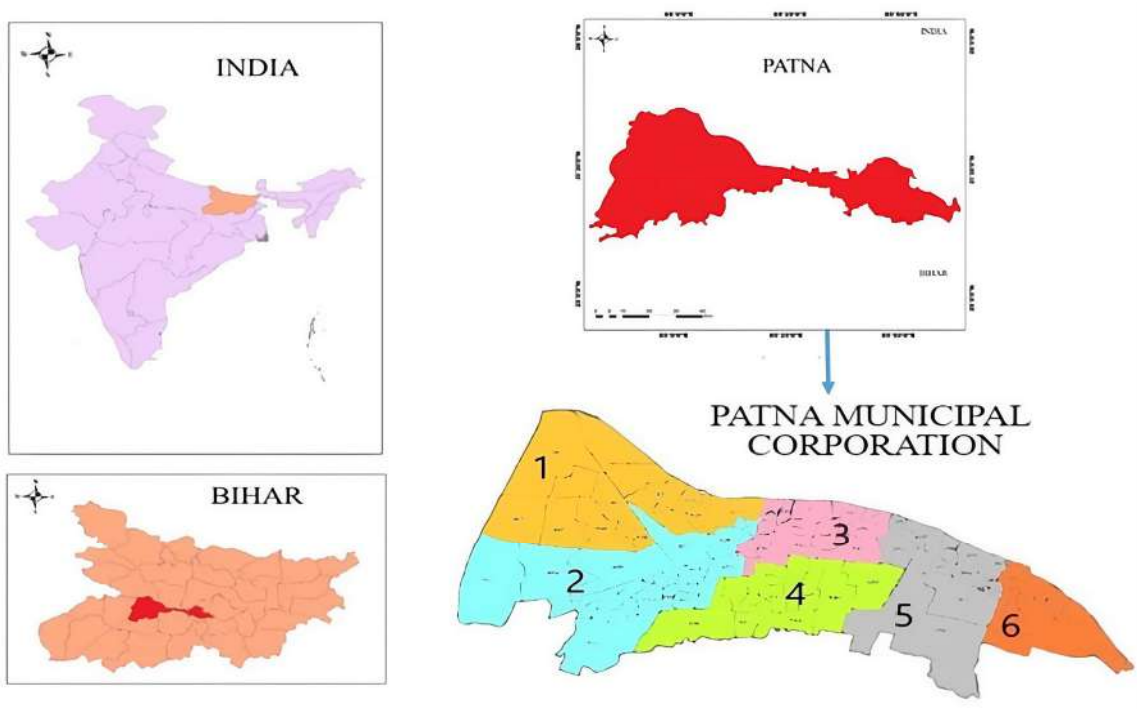


Fig. 1: Study area map with six divisions of PMC.

makes Patna a highly suitable case for examining long-term urban thermal dynamics and the spatial persistence of heat hotspots in tropical megacities (Siddiqui et al. 2022).

2.2. Research Design

This study adopts a quantitative spatiotemporal research design integrating satellite remote sensing, geospatial analysis, and statistical modeling to examine long-term urban thermal dynamics in Patna, India, from 1995 to 2025. The research is grounded in a longitudinal remote sensing framework, enabling the systematic assessment of LST and its relationship with vegetation cover, represented by the NDVI, and built-up expansion, represented by the NDBI. The methodological framework combines non-parametric trend analysis, correlation assessment, spatial hotspot persistence mapping, and multivariate regression modeling to capture both the temporal evolution and spatial persistence of urban heat.

2.3. Datasets

The analysis utilizes multi-decadal satellite imagery acquired from the United States Geological Survey (USGS) and processed using the Google Earth Engine (GEE) cloud computing platform. GEE facilitates the efficient handling of large spatiotemporal datasets while ensuring standardized preprocessing across sensors and years. The Landsat path–row and spatial resolutions of the VNIR and TIR bands across the study period are shown in Table 1.

Landsat imagery from Landsat-5 Thematic Mapper (TM) (1995–2011), Landsat-7 Enhanced Thematic Mapper Plus (ETM+) (1999–2021), and Landsat-8 Operational Land Imager/Thermal Infrared Sensor (OLI/TIRS) (2013–2025) was used. Visible, near-infrared (VNIR), shortwave infrared (SWIR), and thermal infrared (TIR) bands were used to derive NDVI, NDBI, and LST, respectively. All datasets were spatially clipped to the PMC boundary.

Thermal bands, originally available at 100–120 m spatial resolution, depending on sensor specifications, were resampled to 30 m resolution using bilinear interpolation to maintain spatial uniformity across all variables. For each year, annual mean composites were generated using all available cloud-free observations. Cloud and cloud-shadow contamination were minimized using the Fmask algorithm implemented within the GEE environment. This approach

Table 1: Landsat path–row and spatial resolution of VNIR and TIR bands across the study period.

Year	Path-row	Band resolution – VNIR [m]	Band resolution – TIR [m]
1995–2005	141/42	30	120
2005–2015	141/42	30	100, 120
2015–2025	141/42	30	100

ensured temporal consistency and reduced noise arising from atmospheric variability.

2.4. Data Collection Methods

2.4.1. Preprocessing and Index Computation

All imagery underwent standardized preprocessing procedures to ensure radiometric and geometric consistency. Radiometric calibration and conversion to Top-of-Atmosphere (TOA) reflectance were conducted using sensor-specific metadata. Cloud and shadow masking was applied prior to compositing. All raster datasets were co-registered and resampled to a common spatial grid to ensure spectral comparability across sensors and years.

NDVI was calculated using near-infrared (NIR) and red bands following the standard formulation:

$$NDVI = \frac{NIR - Red}{NIR + Red}$$

NDVI values range from −1 to +1, with higher values indicating denser vegetation and greater cooling potential through evapotranspiration.

NDBI was computed using shortwave infrared (SWIR) and near-infrared (NIR) bands as:

$$NDBI = \frac{SWIR - NIR}{SWIR + NIR}$$

Positive NDBI values indicate built-up or impervious surfaces, while negative values represent vegetated or water-covered areas.

Thermal bands were first converted from digital numbers (DN) to spectral radiance:

$$L_\lambda = M_L \times DN + A_L$$

Where M_L and A_L are sensor-specific radiance multiplicative and additive scaling factors.

Radiance was then converted to at-sensor brightness temperature:

$$T_B = \frac{K_2}{\ln\left(\frac{K_1}{L_\lambda}+1\right)}$$

Where K_1 and K_2 are calibration constants.

Land surface emissivity (ε) was estimated using an NDVI-based approach:

$$\varepsilon = 0.004 \times P_v + 0.986$$

Where P_v is the proportion of vegetation calculated as:

$$P_v = \left(\frac{NDVI - NDVI_{min}}{NDVI_{max} - NDVI_{min}}\right)^2$$

Final LST was computed as:

$$LST = \frac{T_B}{1 + \left(\frac{\lambda T_B}{\rho}\right)\ln(\varepsilon)} - 273.15$$

Where l is the wavelength of emitted radiance and $\rho = \frac{hc}{\sigma}$.

2.4.2. Trend Analysis

Long-term trends in LST, NDVI, and NDBI were evaluated using the Mann–Kendall (MK) test, a non-parametric method suitable for environmental time series with non-normal distributions. For a time series $x_1, x_2, \ldots, x_n$, the MK statistic is defined as:

$$S = \sum_{i=1}^{n-1} \sum_{j=i+1}^{n} \text{sgn}(x_j - x_i)$$

where:

$$\text{sgn}(x_j - x_i) = \begin{cases} +1, & x_j - x_i > 0 \\ 0, & x_j - x_i = 0 \\ -1, & x_j - x_i < 0 \end{cases}$$

The variance of S is:

$$Var(S) = \frac{n(n-1)(2n+5) - \sum t(t-1)(2t+5)}{18}$$

The standardized test statistic Z is:

$$Z = \begin{cases} \frac{S-1}{\sqrt{Var(S)}}, & S > 0 \\ 0, & S = 0 \\ \frac{S+1}{\sqrt{Var(S)}}, & S < 0 \end{cases}$$

Trend magnitude was estimated using Sen's slope (β):

$$\beta = \text{Median}\left(\frac{x_j - x_i}{j - i}\right), \forall i < j$$

This estimator provides a robust measure of the annual rate of change for each variable.

2.4.3. Correlation Analysis

The relationships between LST and the surface indices (NDVI and NDBI) were assessed using both Pearson's correlation coefficient (r) and Spearman's rank correlation coefficient (ρ). Linear relationships were evaluated using Pearson's correlation coefficient (r):

$$r = \frac{\sum_{i=1}^{n}(x_i - \bar{x})(y_i - \bar{y})}{\sqrt{\sum_{i=1}^{n}(x_i - \bar{x})^2 \sum_{i=1}^{n}(y_i - \bar{y})^2}}$$

Monotonic relationships and nonlinear relationships were assessed using Spearman's rank correlation coefficient (ρ):

$$\rho = 1 - \frac{6\sum d_i^2}{n(n^2 - 1)}$$

Where d_i is the difference between ranks of paired observations.

Both coefficients were evaluated at a 95% confidence level, ensuring robustness of inferred interactions between surface temperature, vegetation, and built-up intensity.

2.4.4. Hotspot Persistence Analysis

Systematic identification of structurally persistent heat zones was conducted by classifying LST maps for 1995, 2005, 2015, and 2025 into five equal-interval categories ranging from very low to very high temperature. Pixels falling within the high and very high categories were designated as thermal hotspots. A Hotspot Persistence Index (HPI) was computed for each pixel as:

$$HPI_p = \frac{\sum_{t=1}^{T} H_{p,t}}{T}$$

where $H_{p,t} = 1$ if pixel p is classified as a hotspot at time t, and 0 otherwise, with $T = 4$. HPI values range from 0 (no persistence) to 1 (persistent hotspot across all decades). Spatial patterns of hotspot persistence were analyzed and visualized to assess the stability and expansion of heat-stressed zones.

To evaluate the long-term spatial persistence of thermal hotspots, four benchmark years (1995, 2005, 2015, and 2025) were selected from the 31-year dataset. These years represent approximately decadal intervals and were chosen to capture major phases of urban development while reducing the influence of short-term climatic variability and interannual noise commonly present in annual LST observations. While annual LST data were used for temporal statistical analyses, including the Mann–Kendall trend test and Sen's slope estimation, the benchmark-year approach enables a clearer identification of structural spatial transitions in the urban thermal regime. This approach has been widely applied in long-term remote sensing studies to highlight persistent spatial patterns while maintaining the interpretability of multi-decadal changes.

2.4.5. Multiple Regression Analysis

To quantify the relative contributions of vegetation loss and built-up expansion to long-term LST variation, a multiple linear regression model was developed with mean LST as the dependent variable and NDVI and NDBI as the independent variables. The formula is:

$$LST = \alpha + \beta_1(NDVI) + \beta_2(NDBI) + \varepsilon$$

where β_1 and β_2 represent regression coefficients and is the error term.

Model diagnostics were conducted to ensure statistical validity. Regression coefficients were interpreted to assess the dominant drivers of urban thermal increase.

2.5. Software and Analytical Tools

All large-scale geospatial data processing and time-series extraction were conducted using GEE, which enabled efficient handling of multi-decadal satellite datasets within a cloud-computing environment. Statistical analyses and trend assessments were performed using Python, employing the pandas, NumPy, SciPy, and statsmodels libraries, complemented by additional statistical validation in R. Spatial analysis, visualization, and final map production were carried out in QGIS, ensuring accurate spatial representation and cartographic consistency.

3. RESULTS

3.1. Descriptive Temporal Characteristics of LST, NDVI, and NDBI (1995–2025)

The annual mean LST, NDBI, and NDVI time series for Patna from 1995 to 2025 exhibit distinct temporal behaviors (Fig. 2). Mean LST values show substantial interannual variability but an overall upward trajectory across the study period. Mean LST increased from 34.45°C in 1995 to 38.89°C in 2025, with multiple peak years exceeding 42°C. The temporal range of mean LST across the dataset spans approximately 11.3°C, indicating pronounced variability superimposed on a long-term increase.

Mean NDBI values display a near-monotonic rise over time, increasing from 0.0076 in 1995 to 0.1947 in 2025. Unlike LST, NDBI exhibits limited interannual fluctuation and demonstrates a persistent upward trend throughout the

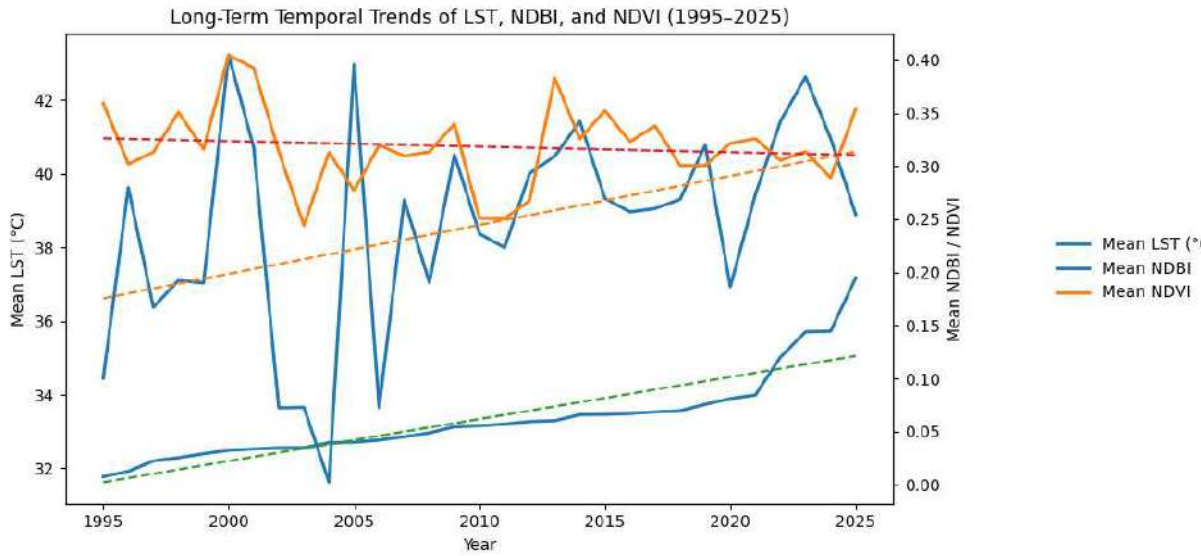


Fig. 2: Long-term temporal trends of LST, NDBI, and NDVI (1995–2025).

Table 2: Modified Mann–Kendall (MMK) trend test and Sen's slope estimator for the period 1995–2025.

Variable	MK Z-value	Trend Direction	p-value	Sen's Slope	95% CI of Sen's Slope	Significant at α = 0.05
Mean LST (°C)	+2.14	Increasing	0.032	+0.1308°C yr⁻¹	+0.018–+0.244 °C yr⁻¹	Yes
Mean NDBI (–)	+7.89	Increasing	<0.001	+0.00269 yr⁻¹	+0.0020–+0.0034 yr⁻¹	Yes
Mean NDVI (–)	−0.41	Decreasing	0.681	−0.00035 yr⁻¹	−0.0021–+0.0014 yr⁻¹	No

observation period. Accelerated increases are evident after approximately 2005, followed by continued growth through the 2010s and early 2020s.

In contrast, mean NDVI values exhibit pronounced interannual fluctuations without a clear monotonic pattern. NDVI values range between 0.24 and 0.40, with episodic peaks and troughs occurring throughout the period. No sustained long-term increase or decrease is visually evident at the city-averaged scale.

3.2. Trend Analysis of LST, NDVI, and NDBI (1995–2025)

The Modified Mann–Kendall (MMK) trend test and Sen's slope estimator for the period 1995–2025 are summarized in Table 2. Mean LST exhibits a statistically significant positive trend, with an MMK Z-value of +2.14 ($p = 0.032$). Sen's slope indicates an annual increase of +0.1308°C yr⁻¹, corresponding to a net increase of approximately +4.05°C over the 31 years. The 95% confidence interval of Sen's slope ranges from +0.018 to +0.244°C yr⁻¹, confirming a consistent upward trend.

Mean NDBI demonstrates a highly significant increasing trend, with an MMK Z-value of +7.89 ($p < 0.001$). Sen's slope for NDBI is +0.00269 yr⁻¹, yielding a cumulative increase of approximately +0.083 between 1995 and 2025. The narrow 95% confidence interval (+0.0020 to +0.0034 yr⁻¹) indicates strong monotonic behavior and minimal uncertainty.

Mean NDVI shows a negative but statistically insignificant trend ($Z = -0.41$, $p = 0.681$). Sen's slope for NDVI is −0.00035 yr⁻¹, with a 95% confidence interval spanning −0.0021 to +0.0014 yr⁻¹ and crossing zero. This result indicates the absence of a detectable monotonic trend in vegetation greenness at the city scale.

3.3. Evolution of LST Class Areas and Thermal Regime Transitions

The temporal evolution of LST class areas from 1995 to 2025 is illustrated in Fig. 3. High-LST zones (Class 4) are present in all 31 years of the study period, indicating uninterrupted dominance. Prior to 2005, the area of Class 4 exhibits expansion and consolidation, while lower-temperature classes (Classes 1–3) remain intermittently present.

From 2005 onward, Class 4 consistently occupies more than 95% of the total urban area, with area values exceeding 103 km² in 21 out of 31 years. Post-2005 variability in Class 4 area is minimal, with a coefficient of variation below 2%, indicating high spatial stability.

Class 1 (lowest LST) areas occur sporadically until 2010. Class 2 areas become increasingly fragmented and occupy less than 0.1% of the total urban area after 2015. Class 3 (moderate LST) persists throughout the study period but shows a systematic reduction, with progressive absorption into Class 4 over time. No year exhibits a re-expansion of lower-LST classes once their areas decline.

A clear shift in the thermal structure is evident between 2004 and 2005, marked by the rapid decline of lower-temperature classes and the sustained dominance of high-LST zones thereafter. After this transition, no reversal to lower thermal classes is observed.

3.4. Spatial Patterns of LST, NDVI and NDBI

The spatial distribution maps of LST, NDVI, and NDBI for the benchmark years 1995, 2005, 2015, and 2025 are shown in Figs. 4–6, revealing pronounced and progressive spatial reorganization of Patna's urban thermal and land-cover structure.

In 1995, the LST map exhibits a heterogeneous thermal landscape characterized by a mosaic of moderate- and high-temperature zones interspersed with clearly identifiable cooler pockets. Lower LST values are spatially concentrated along river-adjacent areas, peripheral zones, and locations with relatively higher vegetation presence, while elevated temperatures appear fragmented and largely confined to the central urban core. The thermal contrast between built-up and non-built-up areas is evident, indicating an early-stage urban heat pattern with incomplete spatial consolidation. By 2005, high-LST zones expand both in extent and continuity. Red and orange regions become more spatially connected, particularly across the central and eastern parts of the city. Cooler zones shrink in size and begin to fragment, losing their earlier spatial coherence. The transition between moderate- and high-temperature areas becomes sharper, suggesting increasing surface heat accumulation and reduced buffering capacity. This period marks a visible shift from a patchy thermal configuration to a more organized and dominant high-temperature structure.

In 2015, the LST surface shows further intensification and spatial homogenization. High-temperature zones dominate most of the urban area, with only scattered, isolated cool patches remaining. These residual cooler zones are small, spatially discontinuous, and largely restricted to specific pockets rather than forming continuous corridors. The contrast between core and peripheral areas diminishes, indicating that elevated surface temperatures are no longer confined to the urban center but have propagated across the broader city extent.

By 2025, the LST map reflects near-complete dominance of high-temperature conditions across Patna. Cooler areas are minimal and highly fragmented, appearing as isolated pixels or small clusters embedded within an otherwise continuous high-LST matrix. The spatial pattern suggests strong thermal uniformity at high temperature levels, with limited spatial variability. This configuration indicates that surface warming has transitioned from localized intensification to a citywide thermal state.

NDVI maps show a contrasting but complementary evolution. In 1995, vegetation greenness is spatially heterogeneous, with relatively large and continuous green patches visible along certain corridors, peripheral zones, and open areas. These patches form discernible clusters that correspond spatially with lower-LST zones, indicating a localized influence of vegetation on surface conditions. By 2005, NDVI patterns become increasingly fragmented. While

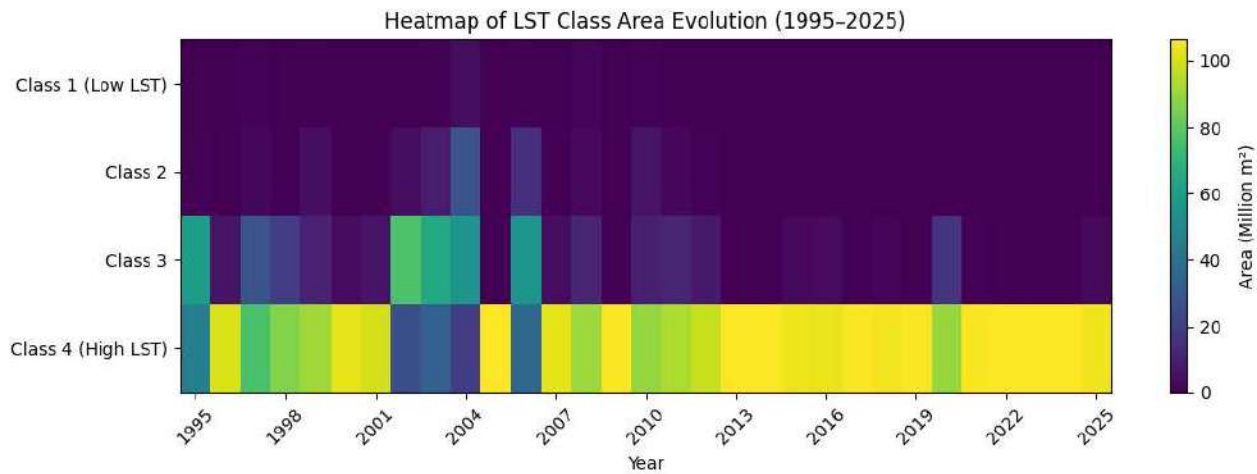


Fig. 3: Temporal evolution of LST class areas from 1995–2025.

vegetation remains present across the city, green patches lose continuity and become interspersed with expanding non-vegetated surfaces. High-NDVI zones are reduced in size and begin to appear as scattered clusters rather than cohesive units. This fragmentation coincides spatially with the expansion of high-LST areas.

In 2015, vegetation greenness persists but exhibits pronounced spatial redistribution. NDVI values remain moderate in selected areas, particularly along certain linear features and peripheral zones; however, these areas are spatially isolated and embedded within predominantly low-NDVI surroundings. The lack of continuous green corridors is evident, indicating reduced spatial effectiveness of vegetation cover.

By 2025, NDVI maps display a highly fragmented greenness pattern. Vegetation patches remain detectable but are small, dispersed, and spatially disconnected. No large or continuous green zones are visible, and low-NDVI surfaces largely surround vegetated areas. This configuration suggests

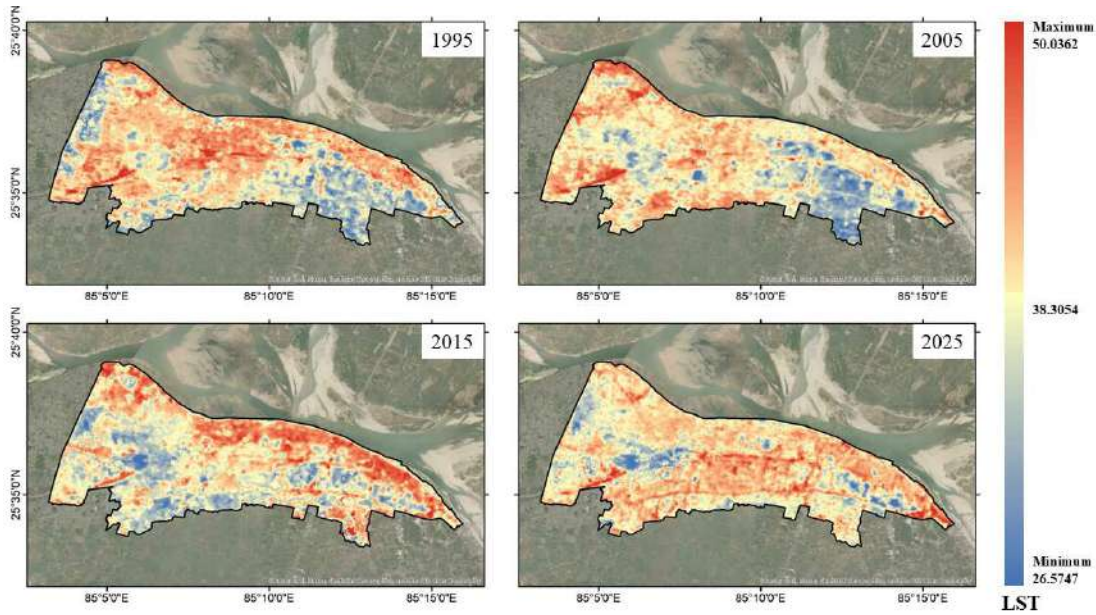


Fig. 4: Spatial distribution maps of LST for the benchmark years 1995, 2005, 2015, and 2025.

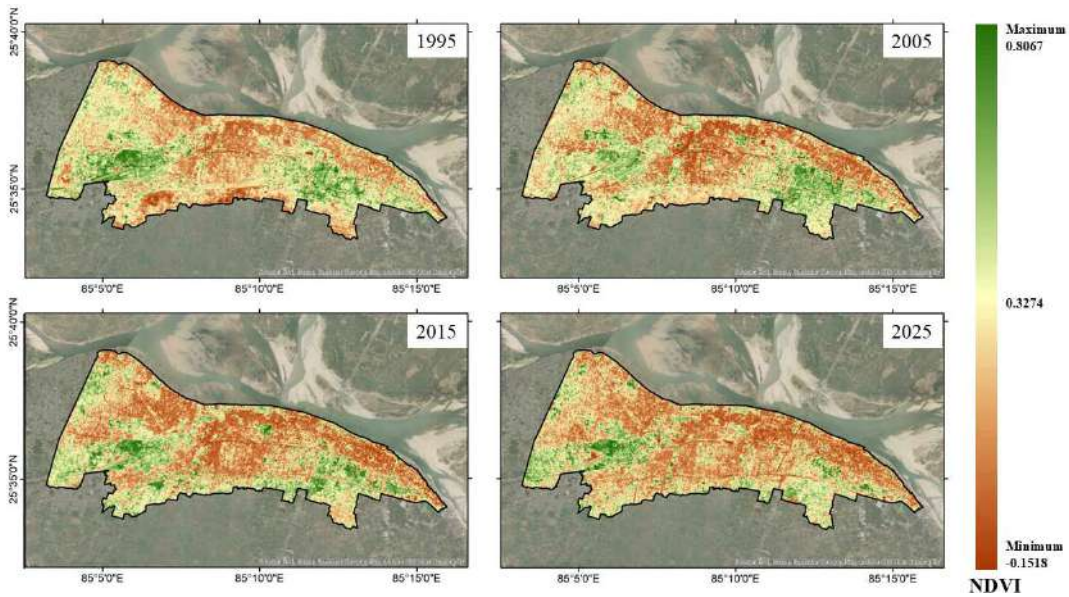


Fig. 5: Spatial distribution maps of NDVI for the benchmark years 1995, 2005, 2015, and 2025.

that while vegetation has not completely disappeared, its spatial arrangement limits its capacity to influence city-scale thermal patterns.

NDBI maps demonstrate the most consistent and unidirectional spatial evolution. In 1995, built-up intensity is moderate and spatially heterogeneous, concentrated mainly in the urban core, with gradual attenuation toward the periphery. Built-up patches are distinct but not spatially dominant, allowing non-built surfaces to retain a significant presence. By 2005, high NDBI values expand substantially, forming more continuous built-up clusters across the central and eastern parts of the city. The spatial contiguity of impervious surfaces increases, and transitional zones between built-up and non-built-up areas become narrower.

In 2015, built-up intensity exhibits near-continuous dominance across much of the urban area. High NDBI zones merge spatially, reducing internal heterogeneity and creating a largely uninterrupted impervious surface network. Peripheral areas that previously showed lower built-up intensity are increasingly absorbed into the urban fabric. By 2025, NDBI maps reveal a highly consolidated built-up structure. High NDBI values dominate almost the entire city extent, with minimal low-intensity zones remaining. The spatial pattern reflects strong urban contiguity and extensive surface sealing, closely mirroring the spatial dominance observed in the LST maps.

The spatial consolidation of high-LST zones observed in the maps is consistent with the statistically significant warming trend identified by the Modified Mann–Kendall analysis ($Z = +2.14$, $p = 0.032$) and the estimated Sen's slope of $+0.1308°C\ yr^{-1}$, indicating a sustained long-term increase in surface temperature across the city.

The spatial evolution of LST, NDVI, and NDBI maps illustrates a progressive shift from a heterogeneous urban landscape to one characterized by built-up continuity, vegetation fragmentation, and thermal homogenization at high temperature levels. The increasing spatial alignment between high NDBI and high LST zones, alongside the fragmentation of NDVI patches, underscores the structural transformation of Patna's surface environment over the last three decades.

3.5. Correlation Analysis Between LST, NDVI and NDBI

Pearson correlation results for the 1995–2025 period are presented in Table 3. A statistically significant positive association is observed between LST and NDBI. Pearson's correlation coefficient is $r = +0.381$ ($p = 0.035$), and Spearman's rank correlation coefficient is $\rho = +0.383$ ($p = 0.033$). The significance in both parametric and nonparametric tests confirms the robustness of the association.

Spearman correlation results for the 1995–2025 period are shown in Table 4. In contrast, the relationship between LST and NDVI is weak and statistically insignificant. Pearson's r is +0.183 ($p = 0.325$), and Spearman's ρ is +0.067 ($p = 0.719$). No significant monotonic or linear relationship is observed.

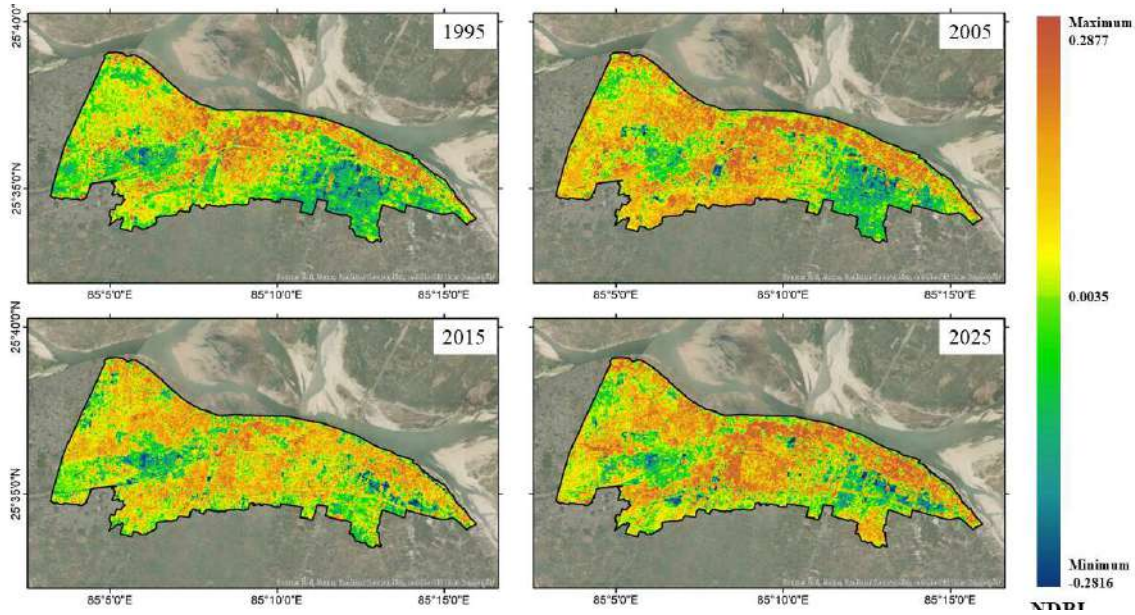


Fig. 6: Spatial distribution maps of NDBI for the benchmark years 1995, 2005, 2015, and 2025.

Table 3: Pearson's correlation results for the 1995–2025 period.

Variable	LST	NDBI	NDVI
LST	1.000	0.381 (p = 0.035)	0.183 (p = 0.325)
NDBI	0.381 (p = 0.035)	1.000	–0.035 (p = 0.852)
NDVI	0.183 (p = 0.325)	–0.035 (p = 0.852)	1.000

Table 4: Spearman's correlation results for the 1995–2025 period.

Variable	LST	NDBI	NDVI
LST	1.000	0.383 (p = 0.033)	0.067 (p = 0.719)
NDBI	0.383 (p = 0.033)	1.000	–0.087 (p = 0.643)
NDVI	0.067 (p = 0.719)	–0.087 (p = 0.643)	1.000

The association between NDVI and NDBI is also weak and statistically insignificant, with Pearson's r = –0.035 (p = 0.852) and Spearman's ρ = –0.087 (p = 0.643).

3.5.1. Hotspot Persistence Metrics

Hotspot persistence metrics derived from LST-class area time series are summarized in Table 5. High-LST zones (Class 4) appear in 100% of years across the study period. The first year of dominance is 2005, after which the Class 4 area remains consistently above ~95% of the total urban area.

The persistence duration of hotspot dominance spans 21 consecutive years (2005–2025). No reversal occurrences are recorded, and area stability is approximately 98%, derived from post-2005 variability. These metrics indicate continuous and uninterrupted persistence of high-temperature zones once dominance is established.

This visual pattern corresponds closely with the quantitative hotspot persistence metrics presented in Table 5, which indicate that high-temperature zones remained dominant for approximately 21 consecutive years (2005–2025) with an estimated spatial stability of about 98%.

3.5.2. Multiple Linear Regression Results

Results of the multiple linear regression analysis are presented in Table 6. Mean LST is modeled as a function of mean NDBI and mean NDVI. The regression model yields an R^2 of 0.183 and an adjusted R^2 of 0.125, with an F-statistic of 3.15 (p = 0.0586). The Durbin–Watson statistic of 2.28 indicates no significant autocorrelation in the residuals.

Mean NDBI exhibits a positive and statistically significant coefficient (β = +27.60, p = 0.031). Mean NDVI shows a positive but statistically insignificant coefficient (β = +14.90, p = 0.261). The intercept term is statistically significant (p < 0.001).

Among the predictors, mean NDBI is the only variable demonstrating statistical significance, while NDVI does not independently explain variation in mean LST within the regression framework.

Table 5: Hotspot persistence metrics derived from LST class area time series.

Metric	Value
First dominance year	2005
Persistence duration	21 years (2005–2025)
Area stability (%)	≈ 98%
Reversal occurrences	0

Table 6: Results of the multiple linear regression analysis.

Predictor	Coefficient (β)	Std. Error	t-value	p-value
Intercept	32.159	4.252	7.56	<0.001
Mean NDBI	+27.602	12.169	2.27	0.031
Mean NDVI	+14.900	12.974	1.15	0.261

4. DISCUSSION

4.1. Interpretation of Long-Term Thermal Dynamics in Patna

The observed warming trend in Patna is consistent with findings from other rapidly urbanizing cities in India, where significant increases in land surface temperature have been linked to rapid urban expansion and impervious surface growth. For example, Mukherjee & Singh (2020) and Kanga et al. (2022) reported similar warming patterns associated with land-use transformation in Ahmedabad and Bengaluru, indicating that sustained urban development can substantially modify local thermal environments.

The statistically significant upward trend in LST, coupled with the exceptionally strong and monotonic increase in built-up intensity, indicates that Patna's thermal trajectory reflects a long-term structural shift rather than short-term climatic fluctuation. The absence of a compensatory long-term trend in vegetation greenness further suggests that the city's natural cooling capacity has not kept pace with rapid urban expansion (Rupapara et al. 2025).

At the city scale, the observed warming trajectory reflects the cumulative effect of infrastructure-led growth, including dense residential development, expansion of

road networks, infilling of open plots, and replacement of permeable surfaces with impervious materials (Kumar & Shukla 2022). Since the early 2000s, Patna has experienced accelerated urban densification driven by population growth, housing demand, and transport-oriented development. The sharp consolidation of high-LST areas around 2004–2005 corresponds temporally with intensified construction activity and infrastructural expansion, indicating a transition from a mixed thermal landscape toward one increasingly dominated by heat-retaining surfaces.

The persistence of high-LST zones across nearly the entire urban area after 2005 indicates that surface warming is no longer spatially localized but has become citywide. This suggests that incremental greening or isolated mitigation measures may be insufficient to substantially alter the prevailing thermal conditions under current development trajectories, highlighting the importance of early-stage land-use planning in rapidly urbanizing tropical cities (Kumar & Shukla 2022).

4.2. Built-Up Expansion as the Dominant Driver of Urban Heat

Among the analyzed variables, built-up intensity exhibits the strongest and most consistent association with LST. The strong monotonic trend in NDBI, its statistically significant correlation with LST, and its significance within the regression model collectively indicate that urban expansion plays a central role in shaping surface warming patterns in Patna. This finding reflects the progressive replacement of low-albedo, moisture-retaining surfaces with concrete, asphalt, and other heat-absorbing materials (Kumar et al. 2025a).

The strong association between built-up intensity and LST observed in this study is consistent with numerous remote sensing studies demonstrating that impervious surface expansion increases surface heat storage and reduces evaporative cooling. Similar relationships between NDBI and LST have been documented in studies conducted in Kolkata (Halder et al. 2025a), Florence and Naples (Guha et al. 2018), and several major Indian metropolitan areas.

In Patna, urban growth has largely occurred through horizontal expansion into peri-urban agricultural land and vertical densification within the city core. The proliferation of paved roads, flyovers, parking areas, and high-density residential blocks has increased surface heat storage capacity while reducing evaporative cooling. The concentration of built-up surfaces along major transport corridors and newly developed residential zones is clearly reflected in the spatial distribution and persistence of high-LST areas (Kumar et al. 2025b).

It should be noted that the regression model explains a limited proportion of the variance in mean LST (R^2 = 0.183), indicating that additional factors beyond vegetation greenness and built-up intensity also influence urban thermal dynamics. Urban surface temperature is affected by a range of variables, including urban morphology (building height, density, and street geometry), anthropogenic heat emissions from transportation and energy use, population density, surface material properties, and atmospheric conditions. These variables were not explicitly incorporated into the present analysis due to the lack of consistent long-term datasets covering the full 1995–2025 period. Consequently, the regression results should be interpreted primarily as an indication of the relative influence of land-cover characteristics derived from satellite imagery rather than as a comprehensive causal model of urban heat dynamics. Future studies integrating urban morphological metrics, socio-economic data, and anthropogenic heat estimates could provide a more complete explanation of the drivers of urban thermal variability.

The regression results further indicate that built-up growth exerts a statistically independent influence on LST at the city scale, even after accounting for vegetation conditions. This suggests that the thermal impact of impervious surfaces outweighs any residual cooling benefits provided by fragmented or sparsely distributed vegetation patches when assessed at an aggregated urban scale.

4.3. Fragmented Vegetation and Loss of Thermal Regulation

Contrary to expectations from classical urban climate theory, vegetation greenness does not exhibit a statistically significant long-term relationship with LST at the aggregated city scale (Cui & Shibata 2024). While NDVI values fluctuate interannually, the absence of a monotonic trend suggests that vegetation change in Patna is characterized primarily by redistribution and fragmentation rather than systematic loss or recovery.

This pattern reflects the nature of greening in Patna, which is largely unplanned and spatially uneven. Small parks, roadside trees, institutional campuses, and floodplain vegetation coexist with expanding built-up areas but lack sufficient spatial continuity to exert a measurable cooling influence at the city scale. Seasonal agricultural activity and monsoon-driven greening contribute to short-term NDVI increases, but these do not translate into sustained thermal regulation. The weak and statistically insignificant relationship between NDVI and LST therefore indicates that existing vegetation, as currently configured, is insufficient in extent, density, or spatial arrangement to counteract the

thermal effects of impervious surface expansion. This finding underscores the limitation of isolated greening initiatives when not integrated into a broader urban ecological framework.

It is important to note that the NDVI–LST relationship examined in this study is based on aggregated city-level annual averages, which may mask localized cooling effects associated with specific vegetation features such as parks, institutional campuses, or riverine green corridors. Vegetation–temperature interactions often operate at finer spatial scales, and pixel-level analyses or spatial regression approaches may reveal stronger localized cooling relationships that are not captured by aggregated statistics. Therefore, the absence of a statistically significant NDVI–LST relationship in the present analysis should be interpreted as reflecting city-scale temporal dynamics rather than implying that vegetation has no local cooling influence. Future research incorporating pixel-based spatial modeling or Local Climate Zone frameworks could provide deeper insight into the spatial heterogeneity of vegetation cooling effects within the urban environment.

4.4. Hotspot Persistence and Thermal Path Dependency

One of the most critical contributions of this study is the identification of persistent urban heat hotspots and the detection of a clear shift toward sustained dominance of high-LST zones around 2005. The transition from a heterogeneous thermal landscape to near-complete dominance of high-temperature areas marks a fundamental change in Patna's urban thermal configuration.

The unidirectional transition from lower to higher LST classes, with no observed reversals during the study period, indicates strong path dependency in the city's thermal evolution. Once high-temperature dominance is established, subsequent land-use changes appear to reinforce rather than offset surface warming. This behavior is consistent with mature urban heat island systems, where accumulated built-up mass, reduced soil moisture, and altered surface–atmosphere interactions contribute to self-reinforcing thermal conditions. From a spatial perspective, the persistence of hotspots suggests that heat is increasingly embedded within the urban fabric. Areas that transitioned into high-LST classes remain in this state over extended periods, highlighting the difficulty of achieving rapid thermal mitigation through retroactive measures alone. This reinforces the importance of proactive thermal planning during early urban development stages rather than reliance on post hoc interventions.

It should be noted that the identification of this transition is based on empirical patterns observed in LST class distributions and hotspot persistence metrics. Formal statistical breakpoint detection or spatial regime-shift analysis was not performed in this study. Future research incorporating advanced temporal breakpoint analysis or spatial statistical methods could further refine the characterization of long-term thermal regime transitions in rapidly urbanizing cities.

4.5. Comparison With Existing Studies

The findings of this study align closely with previous urban climate research conducted in Indian and Global South cities. Studies in Delhi, Kolkata, Mumbai, and Bengaluru have reported significant increases in LST associated with built-up expansion and impervious surface growth, supporting the central role of urbanization in driving surface warming (Gorai et al. 2024, Halder & Kumar 2025, Kanga et al. 2022, Mohammad et al. 2022, Mukherjee & Singh 2020). Similar to Patna, these cities often exhibit strong LST–NDBI relationships and weak or inconsistent LST–NDVI associations at aggregated spatial scales.

Compared with some planned cities that maintain extensive green infrastructure networks, the stronger dominance of high-LST zones observed in Patna may reflect differences in urban morphology, green space availability, and land-use regulation. Studies conducted in cities with larger and more connected green spaces often report stronger NDVI–LST cooling relationships, highlighting the importance of vegetation configuration and spatial continuity in moderating urban thermal environments.

However, the extent and persistence of high-LST dominance observed in Patna appear more pronounced than in some larger metropolitan regions. This may reflect differences in urban morphology, planning controls, and the availability of green infrastructure. Compared with planned cities or those with extensive urban parks and water bodies, Patna's organic growth pattern and limited green space integration may contribute to sustained thermal stress.

Contrasting findings in some studies, where vegetation exhibits a stronger cooling influence, are often associated with cities that have implemented large-scale urban greening programs or retained continuous green belts (Ashok 2021). The absence of such spatially extensive greening in Patna helps explain the weak NDVI–LST relationship observed in this study.

4.6. Policy Implications and Strategic Pathways

From a theoretical perspective, this study contributes to urban heat island research by empirically demonstrating long-term thermal persistence and path-dependent warming in a tropical city context. Traditional UHI frameworks often

conceptualize urban heat as a gradient phenomenon driven by land-cover contrasts between urban and rural areas (Evola et al. 2017). The findings here suggest that beyond certain levels of urbanization, cities may transition into thermal regimes characterized by sustained high surface temperatures and limited short-term variability.

The lack of a significant NDVI-mediated cooling effect challenges simplistic assumptions about vegetation as a universally effective mitigation tool. Instead, the results emphasize the importance of vegetation configuration, continuity, and scale in determining thermal outcomes. This refines existing theory by highlighting that vegetation quantity alone is insufficient and that spatial arrangement and integration into the urban matrix are critical. Also, the combined use of trend analysis, correlation testing, and hotspot persistence mapping provides a comprehensive framework for distinguishing transient thermal variability from long-term persistence, contributing methodological advancement to urban climate research.

For urban planners, engineers, and municipal authorities, the findings offer clear operational insights. The strong association between built-up intensity and surface warming indicates that land-use regulation and construction practices play a central role in shaping urban thermal outcomes. Strategies such as controlling building density, promoting reflective materials, and preserving permeable surfaces are therefore likely to be more effective than isolated greening efforts.

The persistence of hotspots highlights priority zones for targeted intervention, such as retrofitting existing neighborhoods with high-albedo pavements, increasing tree canopy along major corridors, and integrating blue–green infrastructure into redevelopment projects. Importantly, the results suggest that mitigation efforts must be spatially strategic and sufficiently large-scale to influence citywide thermal dynamics. For infrastructure development, incorporating thermal performance criteria into road design, housing layouts, and public spaces could reduce future heat accumulation. The evidence of sustained thermal dominance underscores the need to embed heat mitigation considerations into early planning stages rather than relying solely on corrective measures. At the societal level, persistent urban heat has implications for public health, energy consumption, and social equity. Prolonged exposure to elevated surface temperatures disproportionately affects low-income populations living in dense, poorly ventilated housing with limited access to green spaces. The citywide dominance of high-LST zones suggests that thermal stress is no longer confined to specific neighborhoods but represents a systemic urban risk.

From a policy perspective, the findings support the integration of urban heat metrics into climate adaptation and development policies. Municipal master plans, housing policies, and infrastructure programs should incorporate thermal impact assessments alongside conventional environmental indicators. The identification of a shift toward persistent high-temperature conditions highlights the urgency of preventive action in rapidly urbanizing cities that are approaching similar thresholds. At broader scales, the study contributes evidence relevant to national urban missions and climate resilience frameworks by demonstrating how sustained urban expansion can lead to long-lasting thermal regimes, particularly in tropical contexts.

Patna's long-term surface warming is primarily an outcome of sustained built-up expansion, compounded by fragmented and insufficient vegetation cover. The persistence of high-LST zones and the absence of thermal recovery over the study period indicate that the city has entered a phase of prolonged thermal stress. These findings reinforce the need for integrated, forward-looking urban planning strategies that address thermal risk as a core dimension of sustainable urban development.

5. CONCLUSIONS

This study examined the long-term evolution and spatial persistence of urban thermal conditions in Patna, India, using a 31-year (1995–2025) spatiotemporal remote sensing framework. By integrating land surface temperature with vegetation greenness (NDVI) and built-up intensity (NDBI), the research provides a comprehensive assessment of urban thermal behavior and its underlying drivers in a rapidly urbanizing tropical city. The analytical framework combined trend detection, correlation analysis, spatial hotspot persistence mapping, and multivariate regression, enabling robust characterization of both temporal trajectories and spatial stability of urban heat.

The results reveal a statistically significant and sustained increase in land surface temperature across Patna over the study period, indicating a clear long-term warming trajectory. Built-up expansion exhibits the strongest and most consistent upward trend and shows a significant positive association with LST, highlighting urbanization as the dominant driver of surface warming. In contrast, vegetation greenness does not display a statistically significant long-term trend at the aggregated city scale and does not exert a detectable cooling influence on surface temperature, suggesting that existing vegetation patterns are insufficient to offset the thermal impacts of rapid urban growth. A key contribution of this study lies in identifying spatially

persistent urban heat hotspots and documenting a marked transition toward sustained dominance of high-temperature zones beginning in the mid-2000s. Since approximately 2005, high-LST areas have occupied the majority of the urban extent with minimal interannual variability and no evidence of thermal recovery. This unidirectional shift from lower to higher thermal regimes and the long-term stability of hotspot locations indicate strong path dependency in Patna's thermal evolution, reflecting structurally embedded thermal risk rather than short-term climatic fluctuations.

Methodologically, the study advances urban climate research by demonstrating the value of multi-decadal remote sensing analyses for distinguishing enduring thermal patterns from transient variability. The integrated framework applied here offers a transferable approach for assessing long-term urban heat persistence in data-scarce yet climatically vulnerable cities of the Global South, which remain underrepresented in the urban climate literature. Several limitations should be acknowledged. The analysis relies on satellite-derived land surface temperature, which does not directly represent near-surface air temperature or human thermal exposure. The use of city-averaged indices may mask localized cooling effects associated with specific vegetation configurations or recent greening interventions. In addition, the regression framework does not explicitly incorporate other influential factors such as anthropogenic heat emissions, building morphology, or surface material properties. Residual uncertainties related to sensor differences and atmospheric conditions may also persist despite efforts to ensure temporal consistency.

Future research could address these limitations by incorporating finer-scale analyses using Local Climate Zone classifications, integrating socio-economic and demographic data to assess heat exposure and vulnerability, and combining surface temperature with air temperature and human thermal comfort indicators. Scenario-based modeling of urban growth and greening strategies would further support the evaluation of pathways for mitigating persistent thermal stress in rapidly urbanizing tropical cities. Overall, the findings indicate that Patna is experiencing a prolonged phase of elevated thermal stress driven primarily by sustained built-up expansion and fragmented vegetation patterns that provide limited cooling at the city scale. The persistence of high-temperature zones and the absence of thermal recovery underscore the urgency of integrating heat mitigation into urban planning and climate adaptation strategies. Addressing urban heat as a core dimension of sustainable development will be essential for improving long-term resilience and liveability in tropical megacities.

6. ACKNOWLEDGMENTS

The authors express their gratitude to the National Institute of Technology and different faculty members, who provided their expertise for this research.

7. REFERENCES

Amindin, A., Pouyan, S., Pourghasemi, H.R., Yousefi, S. and Tiefenbacher, J.P., 2021. Spatial and temporal analysis of urban heat island using Landsat satellite images. *Environmental Science and Pollution Research*, 28(30), pp.41439–41450. [DOI]

Amir Siddique, M., Boqing, F. and Dongyun, L., 2023. Modeling the impact and risk assessment of urbanization on urban heat island and thermal comfort level of Beijing City, China (2005–2020). *Sustainability*, 15(7), p.6043. [DOI]

Ashok, A., 2021. Monitoring of dynamic wetland changes using NDVI and NDWI-based Landsat imagery. *Remote Sensing Applications: Society and Environment*, 23, p.100547. [DOI]

Beck, P.S.A., Atzberger, C., Høgda, K.A., Johansen, B. and Skidmore, A.K., 2006. Improved monitoring of vegetation dynamics at very high latitudes: a new method using MODIS NDVI. *Remote Sensing of Environment*, 100(3), pp.321–334. [DOI]

Chen, T., 2022. Temporal dynamics of satellite-derived vegetation pattern and growth in an arid inland river basin, Tibetan Plateau. *Global Ecology and Conservation*, 38, p.e02262. [DOI]

Chow, W.T.L., Akbar, S., Heng, S.L. and Roth, M., 2016. Assessment of measured and perceived microclimates within a tropical urban forest. *Urban Forestry & Urban Greening*, 16, pp.62–75. [DOI]

CITY OF PATNA, 2026. *Patna Municipal Corporation (PMC)*. Retrieved August 14, 2026, from https://www.pmc.bihar.gov.in/about.aspx

Cui, L. and Shibata, S., 2024. Exploring climate-adaptive green-space designs for hot and humid climates: lessons from Japanese dry gardens. *Urban Forestry & Urban Greening*, 93, p.128207. [DOI]

Evola, G., Gagliano, A., Fichera, A., Marletta, L., Martinico, F. and Nocera, F., 2017. UHI effects and strategies to improve outdoor thermal comfort in dense and old neighborhoods. *Energy Procedia*, 134, pp.692–701. [DOI]

Gorai, N., Bandyopadhyay, J., Halder, B., Ahmed, M.F., Molla, A.H. and Lei, T.M.T., 2024. Spatio-temporal variation in landforms and surface urban heat island in riverine megacity. *Sustainability*, 16(8), p.3383. [DOI]

Grimm, N.B., Faeth, S.H., Golubiewski, N.E., Redman, C.L., Wu, J., Bai, X. and Briggs, J.M., 2008. Global change and the ecology of cities. *Science*, 319(5864), pp.756–760. [DOI]

Guha, S., Govil, H., Dey, A. and Gill, N., 2018. Analytical study of land surface temperature with NDVI and NDBI using Landsat 8 OLI and TIRS data in Florence and Naples city, Italy. *European Journal of Remote Sensing*, 51(1), pp.667–678. [DOI]

Gupta, N. and Aithal, B.H., 2022. Effects of rising urban temperatures on the wellbeing of the residents. *International Review for Spatial Planning and Sustainable Development*, 10(4), p.5. [DOI]

Halder, N. and Kumar, D., 2025. Towards reviving vernacular architecture in India: insights into the indigenous building traditions. *Journal of the International Society for the Study of Vernacular Settlements*, 12(5), pp.40–54. [DOI]

Halder, N., Kumar, M., Deepak, A., Abuwaer, N.M., Kanwal, Q., Nurdiawati, A. and Al-Ghamdi, S.G., 2026. Urban greenery and outdoor thermal comfort: cooling indicators, mechanisms, and equity implications. *Environmental Research Communications*. [DOI]

Halder, N., Kumar, M., Deepak, A., Kumar, D., Yasmin, N., Ullah, S. and Al-Ghamdi, S.G., 2025a. Spatiotemporal assessment of urban thermal discomfort in Kolkata, India: insights from cloud-based remote

sensing. IEEE Journal of Selected Topics in Applied Earth Observations and Remote Sensing, pp.1–17. [DOI]

Halder, N., Kumar, M., Deepak, A., Mandal, S.K., Azmeer, A., Mir, B.A., Nurdiawati, A. and Al-Ghamdi, S.G., 2025b. The role of urban greenery in enhancing thermal comfort: systematic review insights. Sustainability, 17(6), p.2545. [DOI]

Halefom, A., He, Y., Nemoto, T., Feng, L., Li, R., Raghavan, V., Jing, G., Song, X. and Duan, Z., 2024. The impact of urbanization-induced land use change on land surface temperature. *Remote Sensing*, 16(23), p.4502. [DOI]

Heaviside, C., Macintyre, H. and Vardoulakis, S., 2017. The urban heat island: implications for health in a changing environment. *Current Environmental Health Reports*, 4(3), pp.296–305. [DOI]

Hsu, A., Sheriff, G., Chakraborty, T. and Manya, D., 2021. Disproportionate exposure to urban heat island intensity across major US cities. *Nature Communications*, 12(1), p.2721. [DOI]

Kanga, S., Meraj, G., Johnson, B.A., Singh, S.K., PV, M.N., Farooq, M., Kumar, P., Marazi, A. and Sahu, N., 2022. Understanding the linkage between urban growth and land surface temperature—a case study of Bangalore City, India. *Remote Sensing*, 14(17), p.4241. [DOI]

Khan, B., Rathore, V.S. and Krishna, A.P., 2021. Identification of Desakota region and urban growth analysis in Patna City, India using remote sensing data and GIS. *Journal of the Indian Society of Remote Sensing*, 49(4), pp.935–945. [DOI]

Kumar, D., Maurya, K.K., Mandal, S.K., Halder, N., Mir, B.A., Nurdiawati, A. and Al-Ghamdi, S.G., 2025a. A whole-life carbon assessment of a single-family house in North India using BIM-LCA integration. Buildings, 15(13), p.2195. [DOI]

Kumar, D., Maurya, K.K., Mandal, S.K., Mir, B.A., Nurdiawati, A. and Al-Ghamdi, S.G., 2025b. Life cycle assessment in the early design phase of buildings: strategies, tools, and future directions. Buildings, 15(10), p.1612. [DOI]

Kumar, D. and Shukla, B., 2022. Urban green spaces for promoting healthy living and wellbeing: prospects for housing. *ECS Transactions*, 107(1), pp.18835–18857. [DOI]

Kumar, S. and Rajak, F., 2023. Assessment of urban green open spaces of micro- and meso-level zones, based on the growth pattern: case of Patna City. *Sustainability*, 15(2), p.1609. [DOI]

Ma, W., Yu, Z., Chen, J., Yang, W., Zhang, Y., Hu, Y., Shao, M., Hu, J., Zhang, Y., Zhang, H. and Yang, G., 2025. What drives the cooling dynamics of urban vegetation via evapotranspiration and shading under extreme heat? *Sustainable Cities and Society*, 130, p.106659. [DOI]

Mahata, B., Sankar Sahu, S., Sardar, A., Laxmikanta, R. and Maity, M., 2024. Spatiotemporal dynamics of land use/land cover (LULC) changes and its impact on land surface temperature: a case study in New Town Kolkata, eastern India. *Regional Sustainability*, 5(2), p.100138. [DOI]

Mishra, A. and Arya, D.S., 2024. Assessment of land-use land-cover dynamics and urban heat island effect of Dehradun city, North India: a remote sensing approach. *Environment, Development and Sustainability*, 26(9), pp.22421–22447. [DOI]

Mishra, M. and Patel, N., 2025. Assessing urban morphology through street parameters in Patna Municipal Corporation, India, through geoinformatics. *Mitteilungen Klosterneuburg*. [DOI]

Mohamed, A., Lorestani, N. and Shabani, F., 2025. Impact of urbanization on land surface temperature: a global perspective. *Current Research in Environmental Sustainability*, 10, p.100315. [DOI]

Mohammad, P., Goswami, A., Chauhan, S. and Nayak, S., 2022. Machine learning algorithm-based prediction of land use land cover and land surface temperature changes to characterize the surface urban heat island phenomena over Ahmedabad city, India. *Urban Climate*, 42, p.101116. [DOI]

Mohan, M. and Kandya, A., 2015. Impact of urbanization and land-use/land-cover change on diurnal temperature range: a case study of tropical urban airshed of India using remote sensing data. *Science of the Total Environment*, 506–507, pp.453–465. [DOI]

Mukherjee, F. and Singh, D., 2020. Assessing land use–land cover change and its impact on land surface temperature using LANDSAT data: a comparison of two urban areas in India. *Earth Systems and Environment*, 4(2), pp.385–407. [DOI]

Nath, R., 2025. Modeling urban thermal dynamics and land use change in Guwahati: a machine learning-based analysis of LST and UTFVI trends (2000–2040). *SSRN Electronic Journal*. [DOI]

Pradeep Kumar, B., Anusha, B.N., Raghu Babu, K. and Padma Sree, P., 2023. Identification of climate change impact and thermal comfort zones in semi-arid regions of AP, India using LST and NDBI techniques. *Journal of Cleaner Production*, 407, p.137175. [DOI]

Priya, U.K. and Senthil, R., 2024. Enhancing sustainable thermal comfort of tropical urban buildings with indoor plants. *Buildings*, 14(8), p.2353. [DOI]

Qi, L., Hu, Y., Bu, R., Li, B., Gao, Y. and Li, C., 2024. Evaluation of the thermal environment based on the urban neighborhood heat/cool island effect. *Land*, 13(7), p.933. [DOI]

Rasul, A., Balzter, H., Smith, C., Remedios, J., Adamu, B., Sobrino, J., Srivanit, M. and Weng, Q., 2017. A review on remote sensing of urban heat and cool islands. *Land*, 6(2), p.38. [DOI]

Sachindra, D.A., Ullah, S., Zaborski, P., Nowosad, M. and Dobek, M., 2023. Temperature and urban heat island effect in Lublin city in Poland under changing climate. *Theoretical and Applied Climatology*, 151(1–2), pp.667–690. [DOI]

Seto, K.C., Güneralp, B. and Hutyra, L.R., 2012. Global forecasts of urban expansion to 2030 and direct impacts on biodiversity and carbon pools. *Proceedings of the National Academy of Sciences*, 109(40), pp.16083–16088. [DOI]

Siddiqui, F.A., Singh, R. and Prashant, 2022. Seasonal characterization and possible solutions for municipal solid waste management in the city of Patna, Bihar, India. *Nature Environment and Pollution Technology*, 21(5), pp.2073–2087. [DOI]

Spangler, K.R., Liang, S. and Wellenius, G.A., 2022. Wet-bulb globe temperature, universal thermal climate index, and other heat metrics for US counties, 2000–2020. *Scientific Data*, 9(1), p.326. [DOI]

Rupapara, S., Rathod, V., Rupapara, H., Halder, N. and Kumar, D., 2025. Evaluating the benefits of urban greenery in urban heat island mitigation: methods, indicators and gaps. *Nature Environment and Pollution Technology*, 24(4), p.D1812. [DOI]

Voogt, J.A. and Oke, T.R., 2003. Thermal remote sensing of urban climates. *Remote Sensing of Environment*, 86(3), pp.370–384. [DOI]

Weng, Q., Lu, D. and Schubring, J., 2004. Estimation of land surface temperature–vegetation abundance relationship for urban heat island studies. *Remote Sensing of Environment*, 89(4), pp.467–483. [DOI]

Zhou, D., Zhao, S., Liu, S., Zhang, L. and Zhu, C., 2014. Surface urban heat island in China's 32 major cities: spatial patterns and drivers. *Remote Sensing of Environment*, 152, pp.51–61. [DOI]

Nature Environment and Pollution Technology
An International Quarterly Peer-Reviewed Open Access Journal

p-ISSN: 0972-6268 | e-ISSN: 2395-3454 Vol. 25 | No. 4 | Article ID D1894 | 2026

RESEARCH ARTICLE https://doi.org/10.46488/NEPT.2026.v25i04.D1894 OPEN ACCESS

Dispersion Modeling of SO_2 and NO_2 Emissions Using AERMOD on Ambient Air Quality at Steam Power Plant PT.X in Southeast Sulawesi, Indonesia

Nur Miftahuljannah, Sumarni Hamid Aly† and Muralia Hustim
Department of Environmental Engineering, Hasanuddin University, Malino Str. km 6, Gowa, South Sulawesi, 92171, Indonesia
†Corresponding author: Sumarni Hamid Aly; marni_hamidaly@yahoo.com

ARTICLE HISTORY

Received: 24-02-2026
Revised: 26-02-2026
Accepted: 16-03-2026

KEYWORDS

AERMOD
Dispersion modeling
Model validation
Steam power plant industry
SO_2 and NO_2 emissions
Ambient air quality

CITE THIS ARTICLE

Miftahuljannah, N., Aly, S.H. and Hustim, M., 2026. Dispersion modeling of SO_2 and NO_2 emissions using AERMOD on ambient air quality at steam power plant PT.X in southeast Sulawesi, Indonesia. *Nature Environment and Pollution Technology*, 25(4), D1894. https://doi.org/10.46488/NEPT.2026.v25i04.D1894

COPYRIGHT & LICENCE

© 2026 The Authors
Open Access under CC BY 4.0.

PUBLISHED BY

TECHNOSCIENCE PUBLICATIONS

ABSTRACT

This study aims to analyze SO_2 and NO_2 concentrations around the PT.X power plant through direct measurements, model their distribution patterns using AERMOD, and evaluate the model's performance using RMSE, MBE, and R statistical tests. Monitoring was conducted at two monitoring points (PLTU PT.X Area and Nii Tanasa Village) over four 1-hour intervals (morning, afternoon, evening, night) using an Impinger Air Sampler. The results show that the highest field-measured SO_2 (39.95 μg m^{-3}) and NO_2 (14.82 μg m^{-3}) occurred during the afternoon, whereas AERMOD predicted peak concentrations at night, reaching SO_2 (31.87 μg m^{-3}) and NO_2 (10.56 μg m^{-3}) at the PLTU PT.X monitoring point, indicating stable atmospheric conditions. Pollutant distribution aligns with the prevailing north-northeast winds, with concentrations decreasing with distance and remaining within regulatory limits. Statistical validation for SO_2 and NO_2 yielded RMSE values of 14 μg m^{-3} and 5.37 μg m^{-3}, MBE of -10.44 μg m^{-3} and -4.32 μg m^{-3}, and R of 0.36 and 0.12, respectively. These values reflect the inherent challenges of aligning short-term field data with long-term dispersion modeling. It is concluded that spatial proximity to emission sources is the primary factor determining concentration patterns. While acknowledging temporal limitations for full-scale validation, the AERMOD model serves as a valuable preliminary screening tool for these distribution patterns. These findings provide an initial overview to inform decision-making and support the development of effective emission mitigation and environmental management strategies for the surrounding areas.

1. INTRODUCTION

Steam Power Plants (PLTU) serve as a vital energy source for industrial activities (Munawaroh et al. 2019). The primary fuel utilized in the power plant industry is coal (Oktaviani et al. 2023). This reliance stems from the abundant supply of coal, which is utilized as a major electricity source for various industries, particularly steam power generation (Rahmadina 2022).

PLTU PT.X, located in Lalonggasumeeto District, Konawe Regency, Southeast Sulawesi, was established in 2007 and has been in commercial operation since 2013, utilizing low-calorie lignite coal for power generation (Barata 2024). In its operations, PLTU PT.X, which also utilizes coal, has the potential to emit gaseous pollutants such as Sulfur Dioxide (SO_2) and Nitrogen Dioxide (NO_2). It is critical to monitor these emissions as they disperse into the surrounding air and pose potential risks to local public health (Ningsih 2020). SO_2 exposure can lead to respiratory tract irritation and decreased pulmonary function (Tampa et al. 2020); similarly, NO_2 can cause mucous membrane irritation and potentially lead to pulmonary

edema in cases of high-dose, long-term exposure, acting as a primary trigger for respiratory diseases (Alchamdani 2019). This health risk is evidenced by the increase in cases of acute respiratory infection reported at the Lalonggasumeeto Public Health Center from 2015 to 2020 (Halulanga et al. 2021).

In anticipating the potential negative impacts of PLTU PT.X activities, gas-emission dispersion modeling is needed as an initial mitigation step to analyze air quality relative to pollutant distribution, establish relationships between emitted pollutants and their concentrations, and identify affected areas (Wangsa et al. 2022). Various models commonly used in predicting air pollutant dispersion include HYSPLIT, CALINE-4, AERMOD, CALPUFF, WRF-Chem, and GRAL (Alviani et al. 2022). This study uses AERMOD to model emission dispersion. This model is recommended by the United States Environmental Protection Agency (US EPA) because it has been proven effective in analyzing, predicting, and simulating the distribution of SO_2 and NO_2 emissions (Zakaria et al. 2020), taking into account meteorological and topographic factors (Putra & Nisa 2023), and can estimate the air quality impact of up to 50 different sources, whose configurations include points, areas, and volumes (Nugraha et al. 2023). Widely recognized as a leading Gaussian plume model, AERMOD is utilized to estimate the environmental consequences resulting from multiple air pollution sources (Salari et al. 2026). This method has also been widely applied internationally to predict pollutant concentrations from various industrial point sources. For example, a study in Cam Pha, Vietnam, showed that AERMOD was successfully applied to evaluate the impact of power plant emissions, involving model validation with observational data (Tran et al. 2022). Similarly, in Indonesia, AERMOD has been used to predict SO_2 and NO_2 dispersion at the PLTU PT. Semen Tonasa using instantaneous measurements and modeling, but validation of the results has not been consistently carried out using robust statistical metrics (Junarto 2021). Previous research (Halulanga et al. 2021) was also conducted at the PLTU PT.X Kendari, but it was limited to direct measurements without using air dispersion modeling or comparing the results of both.

While previous studies have employed the AERMOD model to simulate pollutant dispersion in various industrial contexts, a significant research gap remains regarding the lack of statistical validation using local ambient data, particularly in Southeast Sulawesi. Most existing studies in similar regions focus solely on simulation results without comparing them to direct field measurements through rigorous statistical testing. The novelty of this research lies in its integrated approach that performs a preliminary performance evaluation using local ambient air data collected directly from the PLTU PT.X vicinity by applying multi-parameter statistical indicators, including Root Mean Square Error (RMSE), Mean Bias Error (MBE), and Correlation Coefficient (R). This study seeks to assess the level of agreement between

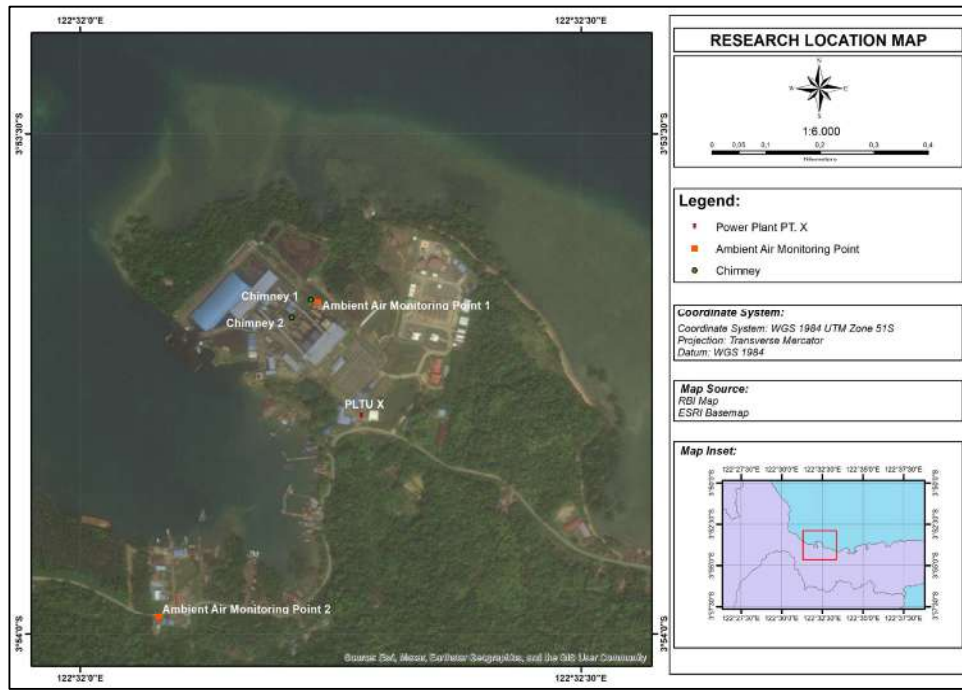


Fig. 1: Research location map.

the model and short-term field observations. Furthermore, this study provides an initial dispersion profile for PLTU PT.X, addressing the absence of prior research at this specific power plant. Therefore, this study aims to analyze SO_2 and NO_2 concentrations around the PLTU PT.X through direct measurements, model their dispersion patterns using AERMOD, and evaluate the model's performance during representative operational periods, while acknowledging the temporal constraints of the field data.

2. MATERIALS AND METHODS

2.1. Study Area

This study was conducted around the PLTU PT.X in Lalonggasumeeto Subdistrict, Konawe Regency, Southeast Sulawesi, Indonesia, with two ambient air monitoring points (Point 1 in the area of PLTU PT.X and Point 2 in Nii Tanasa Village). The location of monitoring points was determined in accordance with SNI 19-7119.6-2005 to ensure representation of the potential impact zone from the pollutant. The selection of these two points was strategically based on the prevailing wind direction and the proximity to sensitive receptors; Point 1 represents the immediate source-proximity monitoring location within the industrial footprint to evaluate near-field dispersion behavior, while Point 2 represents the nearest residential area located downwind. This placement ensures that even with a limited number of points, the study captures the most critical spatial variability of pollutant impact on both the industrial site and the surrounding community. The research location map is shown in Fig. 1.

2.2. Data Collection

Data collection consists of primary and secondary data. Primary data include direct measurements of SO_2 and NO_2 concentrations at two specified points, which are then evaluated against the Indonesian Ambient Air Quality Standards (Government Regulation Number 22 of 2021). Secondary data include meteorological data and chimney specifications of PLTU PT.X and topographic maps, which serve as important input data for dispersion modeling using AERMOD software. The model's performance was evaluated by comparing AERMOD predictions with direct measurement data corresponding to the specific sampling periods using Root Mean Square Error (RMSE), Mean Bias Error (MBE), and Correlation Coefficient (R).

2.2.1. Ambient Air Sampling

Ambient air sampling for SO_2 and NO_2 was carried out using an Impinger Air Sampler, as shown in Fig. 2.

Field measurements were conducted on October 21, 2024, which represents the transition period between the dry and rainy seasons in Southeast Sulawesi. To capture diurnal atmospheric variations, sampling was performed at four specific time intervals: morning (07:00–08:00 WITA), afternoon (13:00–14:00 WITA), evening (16:00–17:00 WITA), and night (19:00–20:00 WITA). These discrete measurements were utilized as preliminary diurnal representative spot samples to evaluate the level of agreement between field observations and the AERMOD model's hourly performance. While this one-day sampling does not constitute a continuous 24-hour integrated average, the sampling intervals were conducted in accordance with the 1-hour ambient air sampling principles and standards outlined in Indonesian Government Regulation No. 22 of 2021. To account for long-term variability, the AERMOD simulation itself utilized a comprehensive one-year hourly meteorological dataset for 2024. This approach allows for a comparison between predicted and observed concentrations during specific atmospheric windows, although it is



Fig. 2: Impinger air sampler.

acknowledged that a more extensive monitoring dataset would be required for a full-scale seasonal or annual model validation.

2.2.2. Meteorological Data

Meteorological data for 2024 were obtained from the Copernicus Climate Change Service (C3S) Climate Data Store, specifically utilizing the ERA5 hourly reanalysis dataset on single levels. Parameters extracted included surface thermal radiation, cloud cover, 2-m temperature, relative humidity, surface pressure, 10-m wind direction, 10-m wind speed, ceiling height, and total precipitation. The data were extracted for the grid corresponding to the study area and synchronized with the surface characteristics of the Kendari Maritime Meteorological Station (BMKG). Station metadata and surface parameters (albedo, Bowen ratio, and surface roughness) were assigned based on local conditions. The raw Copernicus dataset was preprocessed and formatted using the AERMET processor (along with WRPLOT for wind rose visualization) to construct the required surface (.sfc) and profile (.pfl) input files for AERMOD dispersion simulations. Details of the meteorological station information are listed in Table 1.

Table 1: Meteorological station information.

Information Type	Description
Station Name	Kendari Maritime Meteorological Station
Station ID	97144
Latitude	03° 58’ 12.360” S
Longitude	122° 35’ 22.200” E
City	Kendari
Country	Indonesia
Station Elevation	2 m
Time Zone	WITA (UTC +8)

2.2.3. PLTU PT.X Chimney Specifications

The technical specifications of the chimneys, including height, diameter, gas exit velocity, and temperature, were obtained from the PLTU PT.X operational reports for February 2024, as presented in Table 2. These values represent the plant’s typical baseline operating conditions at steady-state load, which remained stable and representative of normal operations during the October 21, 2024 field monitoring period. These physical parameters are essential for determining the plume rise and initial dispersion behavior in the AERMOD model. To ensure the accuracy of the emission input, the emission rates (g s^{-1}) were calculated using the U.S. EPA emission factor method based on fuel consumption, while the measured stack concentrations from the Analysis Report were utilized to verify and ensure that the calculated rates were consistent with the actual monitored conditions.

2.3. Data Analysis

Data analysis was performed using measured ambient air concentration data and secondary input data (meteorological and emission data). The analysis procedures performed in this study included:

2.3.1. Processing Meteorological Data with WRPLOT

WRPLOT was used to process meteorological data into wind rose maps, which visually depict the direction and speed of prevailing winds during the study period. The results are saved in SAMSON (.SAM) format for use as input to the AERMET processor. The stages of data processing in WRPLOT are shown in Fig. 3.

The generated wind rose map was used as meteorological input data for dispersion model simulations in AERMOD. The dominant wind direction and speed patterns greatly determine the potential spread of pollutants. The 2024 wind rose map is presented in Fig. 4.

Table 2: Chimney physical specifications of PLTU PT.X.

No.	Parameters	Chimney 1	Chimney 2
1	Chimney Coordinate (UTM) X	448618.00	448585.00
	Chimney Coordinate (UTM) Y	9569519.00	9569480.00
2	Fuel Type	Lignite Coal	Lignite Coal
3	Chimney Height (m)	45	45
4	Chimney Diameter (m)	2.2	2.2
5	Gas Temperature (°C)	129	130
6	Gas Exit Velocity (m s^{-1})	4.72	4.83
7	Emission Flow Rate (m^3 s^{-1})	17.9	18.31
8	Fuel Consumption (tons/month)	9000	9000
9	Elevation (m)	10	10

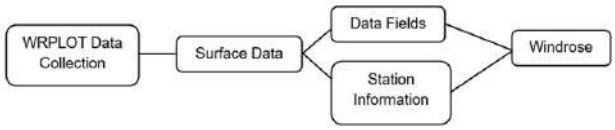


Fig. 3: WRPLOT data processing stages.

Based on Fig. 4(a) and 4(b), the results of the 2024 wind rose analysis show that the dominant direction for the highest wind speed (>9.00 m s^{-1}) is north, with a frequency of 22.8%. The most frequent wind class is the low speed range (0.00–3.00 m s^{-1}), which blows mainly from the west and contributes the highest frequency of 41.9%. This dominant wind pattern is crucial for understanding the potential spread of pollutants originating from the steam power plant.

2.3.2. Calculation of Emission Rate

To meet the input requirements of the AERMOD dispersion model, the emission rates were determined in grams per second (g s^{-1}). The calculation of the flue gas emission rate was carried out to estimate the stack emissions based on February 2024 operational data and to calculate the emission values for October 2024 using the United States Environmental Protection Agency (US EPA 2024) emission factor method (Equation 1). Instead of relying solely on concentration-to-mass conversion, this study utilized an activity-based approach where monthly fuel consumption data were converted into a continuous mass flow rate (tons/second). This ensures that the resulting emission values reflect the plant's actual operational load during the study period. The calculation results, incorporating the efficiency of the emission control systems, are listed in Table 3.

$$E = A \times EF \times [1 - (ER/100)] \quad \ldots(1)$$

Where: E – gas emission rate (g s^{-1}), A – amount of fuel burned (converted from tons/month to tons/second), EF – emission factor (lb/ton or g/ton), ER – emission control efficiency (if there is a scrubber or other system) (e.g. 0.90 for 90%).

The mass emission rates (E) used as AERMOD inputs were derived through a clear, step-by-step application of the activity-based approach. First, the monthly fuel consumption of 9000 tons was converted into a continuous mass flow rate (A) by dividing it by the total seconds in a 30-day month, resulting in 0.00347 tons/second. This value was then applied to Equation 1 using the U.S. EPA AP-42 emission factors (EF) of 15.15 kg/ton for SO_2 and 3.86 kg/ton for NO_x (expressed as NO_2), while incorporating the efficiency of the emission control systems (ER) of 90% and 85%, respectively. This calculation process yielded final emission rates of 5.26 g s^{-1} for SO_2 and 2.01 g s^{-1} for No_x (as NO_2) per chimney. For dispersion modeling in AERMOD, a conservative 100% conversion assumption was applied for NO_2 to evaluate maximum potential impact. These derived rates serve as the definitive source-term inputs for the dispersion model,

Table 3: Emission rate calculation results.

Parameters	SO_2		NO_2	
Emission Factor (lb/ton)	33.4		8.5	
Emission Factor (kg/ton)	15.15		3.86	
Fuel Consumption (tons/month)	9000		9000	
Fuel Consumption (tons/second)	0.00347		0.00347	
Emission Control Efficiency (%)	90		85	
Emission Rate (g s^{-1})	C1	C2	C1	C2
	5.26	5.26	2.01	2.01

Notes: C1 (chimney 1); C2 (chimney 2)

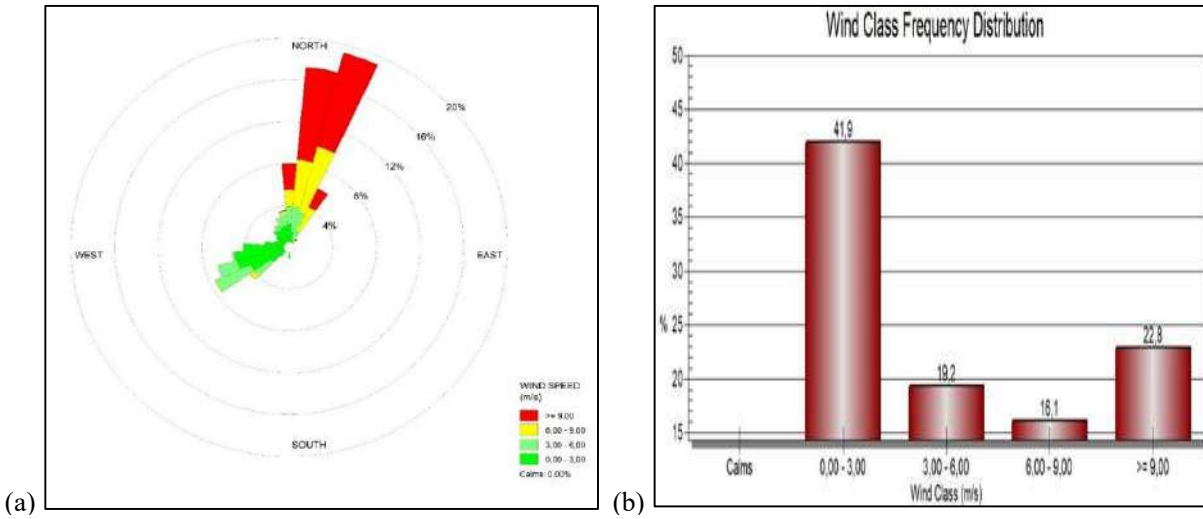


Fig. 4: (a) Wind rose map for 2024. (b) Wind class frequency distribution.

ensuring the simulation reflects the plant's actual operational load during the study period. The complete results of this emission rate calculation are listed in Table 3.

2.3.3. AERMET Processing

AERMET processes hourly meteorological data (in .SAM format) and upper-air data to prepare input files for AERMOD. This processing includes calculating surface parameters (such as albedo, Bowen ratio, and surface roughness) based on land-use characteristics. In this study, the surface parameters were determined based on the site-specific land-use characteristics surrounding PLTU PT.X. The values assigned for the AERMET processing were an Albedo of 0.13, a Bowen Ratio of 0.47, and a Surface Roughness Length of 0.22 m. These parameters, combined with hourly meteorological data and upper-air profiles derived from the Copernicus ERA5 dataset, allow AERMET to internally calculate the atmospheric mixing height and the stability of the air layers. AERMET outputs are surface meteorological files (.SFC) and profile files (.PFL) that are ready for use in AERMOD dispersion modeling. Fig. 5 illustrates the processing steps for AERMET.

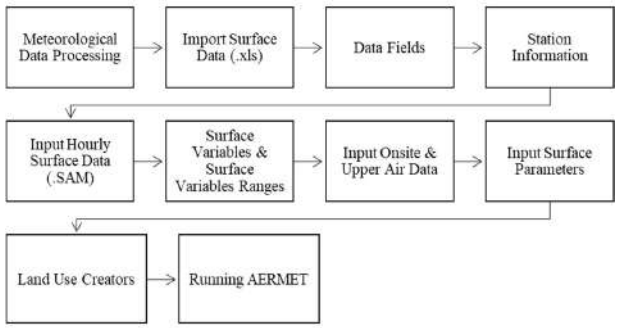


Fig. 5: AERMET processing stages.

2.3.4. AERMOD Processing

Model settings include Control Pathway (defining SO_2 and NO_2 pollutants with an average time of 1 hour), Source Pathway (using stack data and emission rates), Receptor Pathway (Cartesian grid for concentration analysis), and Meteorology Pathway (.SFC and .PFL format files from AERMET). AERMAP is used to integrate topographic data (SRTM3 elevation) into the model grid. Once the data is complete, AERMOD is run for dispersion simulation, producing visualizations of pollutant concentration distributions in the form of maps and isoconcentration lines. Dispersion model processing using AERMOD follows the steps in Fig. 6.

2.3.5. Model Validation Test

The model's performance was evaluated by comparing the SO_2 and NO_2 concentrations from short-term ambient air

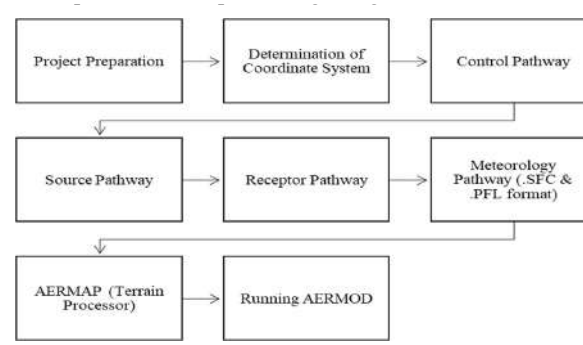


Fig. 6: AERMOD processing stages.

field measurements with the corresponding AERMOD-simulated values. The statistical methods employed for this performance assessment include the calculation of Root Mean Square Error (RMSE), Mean Bias Error (MBE), and Correlation Coefficient (R). These indicators serve to measure the level of agreement between the model's predictions and the observed data during the specific sampling intervals. The RMSE calculation (Hodson 2022) can be performed using Equation 2.

$$RMSE=\sqrt{\frac{1}{n}\sum_{i=1}^{n}(Yi-\hat{Y}i)^2} \quad \ldots(2)$$

where: RMSE – Root Mean Square Error, Yi – actual concentration value, $\hat{Y}i$ – simulated concentration value, n – total number of measurement points.

The Mean Bias Error (MBE) calculation can be performed using Equation 3.

$$MBE=\frac{1}{n}\sum_{i=1}^{n}(\hat{Y}i-Yi) \quad \ldots(3)$$

where: MBE – Mean Bias Error, $\bar{\hat{Y}}i$ – simulated concentration value, Yi – actual concentration value, n – total number of measurement points.

The Correlation Coefficient (R) calculation can be performed using Equation 4.

$$R=\frac{\sum_{i=1}^{n}(\hat{Y}i-\bar{\hat{Y}})(Yi-\bar{})}{\sqrt{\sum_{i=1}^{n}(\hat{Y}i-\bar{\hat{Y}})^2\sum_{i=1}^{n}(Yi-\bar{Y})^2}} \quad \ldots(4)$$

where: R – Correlation Coefficient, $\hat{Y}i$ – simulated concentration value, $\bar{\hat{Y}}i$ – mean of simulated concentrations, Yi – actual concentration value, $\bar{Y}$ – mean of observed concentrations, n – total number of measurement points.

3. RESULTS AND DISCUSSION

3.1. Direct Measurement of SO_2 and NO_2 Concentrations

Fig. 7 shows a graph of direct measurements of SO_2 and NO_2 concentrations during a 1-hour observation period

at two monitoring locations, the PLTU PT.X area and Nii Tanasa Village, based on the intervals of morning, afternoon, evening, and night.

Based on the graph, for SO_2 (Fig. 7(a)), the highest concentrations at both points occurred during the afternoon (PLTU PT.X monitoring point = 39.95 μg m^{-3}; Nii Tanasa Village monitoring point = 28.82 μg m^{-3}). This trend shows that peak operational activity at the coal-fired power plant significantly increases SO_2 emissions during the day. Lower concentrations were observed at the Nii Tanasa Village monitoring point (approximately 700 m away) compared to the monitoring point near PLTU PT.X, mainly due to the distribution and distance from the emission source, as well as the influence of meteorological factors. In addition, this may be due to weather factors such as air humidity, wind direction, and temperature, which affect gas dispersion, resulting in SO_2 concentrations at the Nii Tanasa Village location remaining below the quality standard (Halulanga et al. 2021).

Similar conditions were also observed for NO_2 concentrations (Fig. 7(b)), with the highest value at the PLTU PT.X monitoring point occurring during the afternoon (14.82 μg m^{-3}) due to increased power plant activity. These high concentrations coincided with the highest measured air temperature (34.3 °C) and the lowest humidity (41%), conditions that enhance convective mixing and photochemical activity in the lower atmosphere, thereby facilitating the dispersion and transport of stack emissions. In contrast, at the Nii Tanasa Village monitoring point, the highest concentration was observed in the morning at 12 μg m^{-3}. This suggests that the difference in concentration between the two monitoring points confirms the strong influence of distance from the emission source, although local factors such as morning traffic may also contribute. However, the highest concentrations measured during 1 hour for SO_2 (39.95 μg m^{-3}) and NO_2 (14.82 μg m^{-3}) at both monitoring locations were still below the ambient air quality standards for 1 hour set by Government Regulation Number 22 of 2021 (SO_2 limit: 150 μg m^{-3}; NO_2 limit: 200 μg m^{-3}).

3.2. AERMOD SO_2 and NO_2 Concentrations

3.2.1. SO_2 Concentration

Table 4 presents the AERMOD one-hour SO_2 concentrations across four time intervals synchronized with the direct measurement periods, showing that the overall highest concentrations occurred at the PLTU PT.X monitoring point, with a peak value of 31.87 μg m^{-3} recorded at night. The high concentration at this point correlates with its closer proximity to the primary emission source compared to Nii Tanasa Village. Furthermore, based on the wind rose (Fig. 4), although dominant wind directions vary, SO_2 is a local pollutant whose concentrations tend to be highest at locations nearest to the emission source. The phenomenon of increased nighttime concentrations, particularly at the PLTU PT.X monitoring point, indicates the influence of stable atmospheric conditions. Atmospheric stability is significantly higher at night than during the day (Kusumawati 2025). Variations in atmospheric stability levels can occur based on the intensity of temperature differences between the air mass and the surrounding air (Sasmita et al. 2021). The cooling air at the PLTU PT.X monitoring point during the night is further evidenced by monitoring data, which showed a temperature of 26.5°C and high humidity of 76.7%. Conversely, in Nii Tanasa Village, the peak concentration of 10.81 μg m^{-3} occurred in the morning. This is likely due to the prevailing stable temperature and humidity conditions; at 29.9°C and 62.3% humidity, the SO_2 concentrations modeled by AERMOD remained insufficiently dispersed into the higher atmospheric layers. Stable atmospheric conditions in the morning restrict vertical air movement, causing pollutants to be trapped near the ground surface

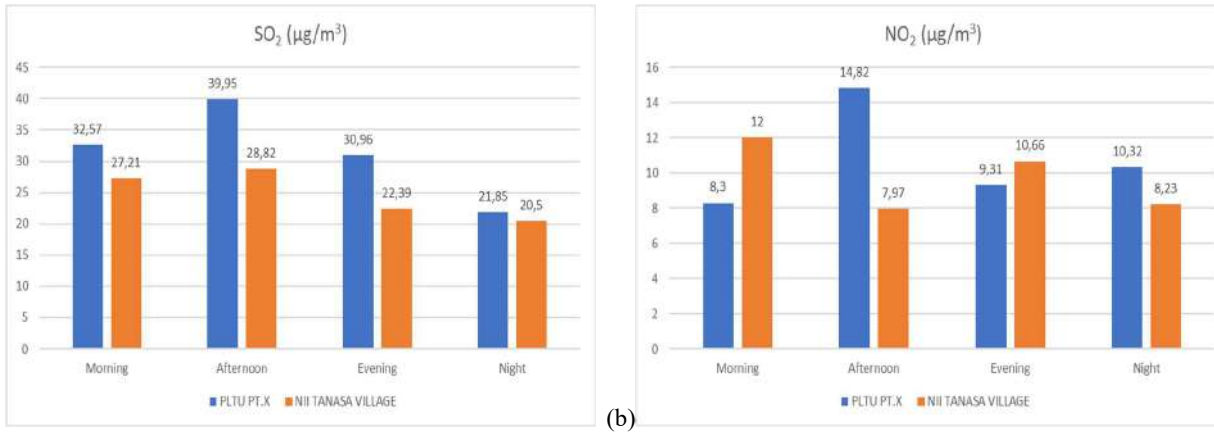


Fig. 7: (a) SO_2 direct measurement. (b) NO_2 direct measurement.

(the accumulation phase) before rising daytime temperatures trigger vertical dilution.

3.2.2. NO_2 Concentration

Table 5 presents the AERMOD one-hour NO_2 concentrations across four time intervals (morning, afternoon, evening, and night) synchronized with the direct measurement periods. At the PLTU PT.X monitoring point, the highest NO_2 concentration occurred at night, reaching 10.56 µg m^{-3}, which is higher than the concentrations recorded during the morning, afternoon, and evening at the same location. A similar pattern of significant nighttime increase was observed in Nii Tanasa Village, with a concentration of 4.45 µg m^{-3}. The increase in NO_2 concentrations at night in these two locations also indicates stable atmospheric conditions, such as temperature inversions, which trap air movement. Similar to SO_2 concentrations, the meteorological inputs used by AERMOD indicate more stable nighttime temperature and humidity conditions. This inhibits vertical air movement and affects pollutants near the ground surface, leading to increased pollution at the human respiratory level (Srisantyorini 2025).

3.3. AERMOD Dispersion Modeling

3.3.1. Dispersion of SO_2

For 1-hour and 24-hour averaging periods based on the full annual meteorology of 2024, Fig. 8(a) and (b) show that the modeled annual maximum concentrations for the highest average 1-hour SO_2 concentrations at the monitoring points of PLTU PT.X and Nii Tanasa Village were 33.86 µg m^{-3} and 29.05 µg m^{-3}, respectively. At the same time, the modeled annual maximum 24-hour averages were 10.65 µg m^{-3} and 7.42 µg m^{-3}, respectively. Meanwhile, Fig. 8(c), (d), (e), and (f) illustrate the relationship between concentration and distance during that period based on the prevailing wind direction. Note that these annual modeled maxima naturally differ from the specific hourly values reported in Tables 4 and 5, which correspond strictly to the synchronized field-sampling intervals on October 21, 2024.

The SO_2 distribution pattern during the 2024 period predominantly points north-northeast toward the sea, following the prevailing wind direction. At the PLTU PT.X monitoring point (±7.5 m from the stack base), Fig. 8(c) shows initial predicted concentrations of approximately 34.02 µg m^{-3}. However, it should be noted that for a 45-m stack, receptors located within this immediate near-field zone (1–7.5 m) fall below the typical plume trajectory. While the model accounts for building downwash effects where aerodynamic turbulence can influence dispersion, the physical meaningfulness of predictions at such proximity is limited, as the plume has not yet fully reached ground level.

Table 4: AERMOD SO_2 concentration.

Monitoring Point	Coordinate Point		Time	SO_2 Concentration (µg m^{-3})
	UTM X	UTM Y		
PLTU PT.X	448623.28	9569522.39	Morning	30.92
			Afternoon	22.84
			Evening	20.23
			Night	31.87
Nii Tanasa Village	448364.13	9568947.04	Morning	10.81
			Afternoon	8.41
			Evening	8.41
			Night	7.23

Table 5: AERMOD NO_2 concentration.

Monitoring Point	Coordinate Point		Time	NO_2 Concentration (µg m^{-3})
	UTM X	UTM Y		
PLTU PT.X	448623.28	9569522.39	Morning	7.87
			Afternoon	7.37
			Evening	7.37
			Night	10.56
Nii Tanasa Village	448364.13	9568947.04	Morning	3.33
			Afternoon	3.06
			Evening	3.06
			Night	4.45

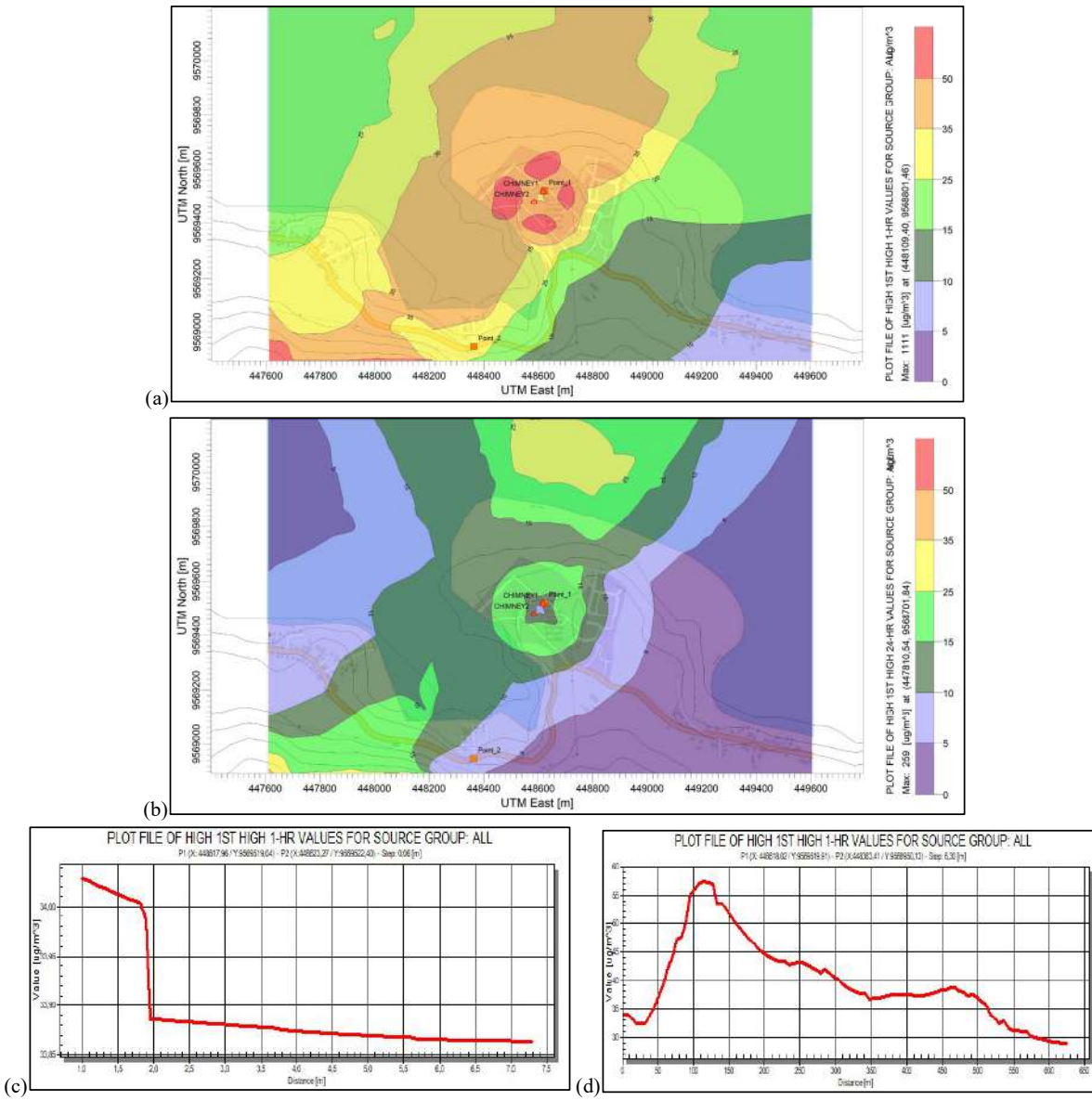


Fig. 8: (a) 1-hour SO_2 dispersion. (b) 24-hour SO_2 dispersion. (c) SO_2 at point 1 (PLTU PT.X) for 1 hour. (d) SO_2 at point 2 (Nii Tanasa Village) for 1 hour. (e) SO_2 at point 1 (PLTU PT.X) for 24 hours. (f) SO_2 at point 2 (Nii Tanasa Village) for 24 hours.

In contrast, a more dynamic and physically representative pattern is observed towards Nii Tanasa Village (Fig. 8(d)). This area shows a classic dispersion profile where the concentration reached a significant peak of approximately 57 µg m^{-3} at a distance of 110–120 m from the source, representing the primary plume touchdown point. After this peak, the concentration gradually decreased and stabilized, reaching 29.05 µg m^{-3} at the monitoring point in Nii Tanasa Village (±650 m). For the 24-hour average (Fig. 8(e) and 8(f)), the maximum concentrations at the PLTU PT.X and Nii Tanasa Village receptors were 10.65 µg m^{-3} and 7.42 µg m^{-3}, respectively. All predicted values remained well below the ambient air quality standards (150 µg m^{-3} for 1-hour and 75 µg m^{-3} for 24-hour). These findings are consistent with previous observations that concentration patterns are heavily influenced by dominant wind directions and distance-dependent dispersion factors (Sarwono et al. 2022).

3.3.2. Dispersion of NO_2

As with SO_2, Fig. 9(a) and (b) show the maximum NO_2 concentrations for the 1-hour averaging period at the PLTU PT.X and Nii Tanasa Village monitoring points, which were 12.94 µg m^{-3} and 11.10 µg m^{-3}, respectively. At the same

time, the highest 24-hour averages were 4.07 µg m^{-3} and 2.83 µg m^{-3}. Meanwhile, Fig. 9(c), (d), (e), and (f) illustrate the relationship between concentration and distance during that period based on the prevailing wind direction.

The NO_2 dispersion pattern during the 2024 period follows a similar trend to SO_2, predominantly spreading north-northeast from the PLTU PT.X chimney toward the sea, reflecting the influence of the prevailing wind direction. Fig. 9(c) illustrates the NO_2 concentration within the immediate near-field zone (up to 7.5 m) from the stack base. While the model calculates an elevated concentration of 12.94 µg m^{-3} at this point, it is acknowledged that for a 45-m stack, receptors at this distance are situated below the primary plume trajectory. These near-field values should be interpreted with caution, as they may reflect the model's mathematical treatment of aerodynamic turbulence (building downwash) rather than a physically representative grounding of the plume so close to the source. Meanwhile, for the 24-hour average (Fig. 9(e)), the dispersion follows a smaller scale with a maximum concentration of 4.07 µg m^{-3} at the same receptor.

In contrast, the dispersion toward Nii Tanasa Village (Fig. 9(d)) shows a more physically representative and

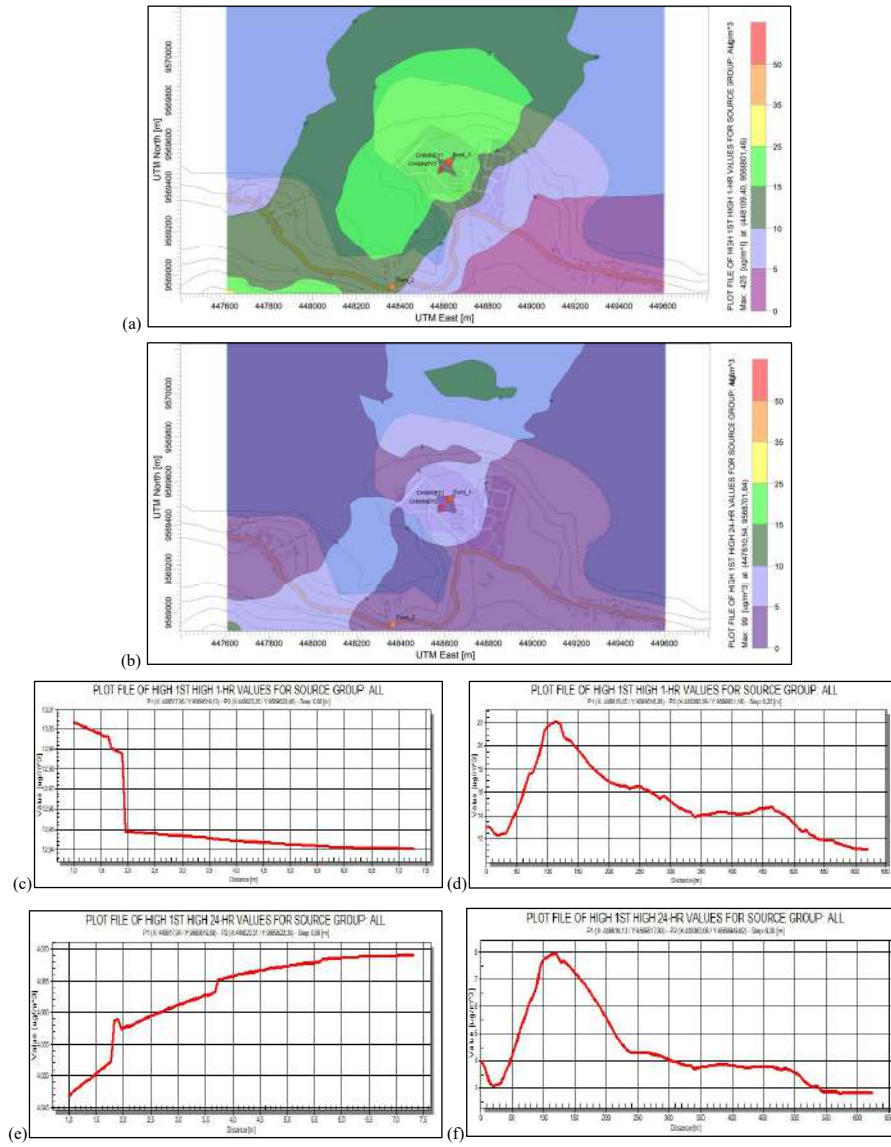


Fig. 9: (a) 1-hour NO_2 dispersion. (b) 24-hour NO_2 dispersion. (c) NO_2 at point 1 (PLTU PT.X) for 1 hour. (d) NO_2 at point 2 (Nii Tanasa Village) for 1 hour. (e) NO_2 at point 1 (PLTU PT.X) for 24 hours. (f) NO_2 at point 2 (Nii Tanasa Village) for 24 hours.

classic dispersion pattern. The concentration exhibits an upward trend, peaking at approximately 22 μg m^{-3} at a distance of 100 m from the source. This peak represents the plume touchdown point, occurring after the plume undergoes thermal buoyancy (plume rise) and reaches the ground level due to wind transport, before gradually decreasing to 11.10 μg m^{-3} at the ±650 m receptor. A similar trend is observed for the 24-hour average (Fig. 9(f)), which peaks at 8 μg m^{-3} within the 100–150 m range before declining to 2.83 μg m^{-3} at the monitoring point. Despite these fluctuations, all NO_2 concentration values remained well below the national ambient air quality standards (200 μg m^{-3} for 1-hour and 65 μg m^{-3} for 24-hour).

3.4. Model Validation Test (RMSE, MBE, and R)

Table 6 presents a comparison between the SO_2 and NO_2 concentrations obtained from direct measurements and the AERMOD model predictions at two monitoring points: the PLTU PT.X and Nii Tanasa Village. To ensure a valid comparison, the AERMOD model output selected for this analysis was synchronized with the exact date and hourly intervals (morning, afternoon, evening, and night) of the field sampling conducted on October 21, 2024. While this temporal alignment allows for a snapshot performance check, it is acknowledged that a single day of data is insufficient to fully represent the model's annual simulation. Direct monitoring results show that SO_2 concentrations near the PLTU PT.X ranged from 21.85 μg m^{-3} to 39.95 μg m^{-3}, while AERMOD estimated 20.23 μg m^{-3} to 31.87 μg m^{-3}. These discrepancies are primarily due to the receptor's close proximity to the emission source (±7.5 m). For a 45-m stack, this distance falls outside the physically meaningful predictive zone of AERMOD, as the exhaust gas is still in the buoyancy (plume rise) phase and has not yet grounded. Consequently, the higher field measurements at this location likely capture low-level fugitive emissions or local background sources within the plant area that are not accounted for in the stack-only model. A similar pattern was observed for NO_2, where field measurements ranged from 8.3 μg m^{-3} to 14.82 μg m^{-3}, while the AERMOD simulation estimated lower concentrations between 7.37 μg m^{-3} and 10.56 μg m^{-3} due to the same near-field modeling limitations.

Meanwhile, at the Nii Tanasa Village monitoring point (±650 m), the AERMOD model showed a better alignment with the dispersion physics, although simulated values were still lower than direct measurements. For SO_2, field measurements ranged from 20.5 μg m^{-3} to 28.82 μg m^{-3}, whereas AERMOD estimated 7.23 μg m^{-3} to 10.81 μg m^{-3}. Similarly, for NO_2, field measurements ranged from 8.23 μg m^{-3} to 12 μg m^{-3}, while AERMOD modeling results ranged from 3.06 μg m^{-3} to 4.45 μg m^{-3}. These results indicate that AERMOD is more representative at greater distances where the plume has undergone diffusion and wind transport. Discrepancies may arise because field monitoring captures cumulative impacts from various sources, such as traffic and community activities, while the model focuses strictly on boiler stack emissions (Ramadhani 2017). Therefore, given the inherent modeling uncertainties and the limited sampling

Table 6: Comparison of direct measurements with the AERMOD model.

Monitoring Point	Parameters	Time	Direct Measurement	AERMOD
PLTU PT.X	SO_2 (μg m^{-3})	Morning	32.57	30.92
		Afternoon	39.95	22.84
		Evening	30.96	20.23
		Night	21.85	31.87
	NO_2 (μg m^{-3})	Morning	8.3	7.87
		Afternoon	14.82	7.37
		Evening	9.31	7.37
		Night	10.32	10.56
Nii Tanasa Village	SO_2 (μg m^{-3})	Morning	27.21	10.81
		Afternoon	28.82	8.41
		Evening	22.39	8.41
		Night	20.5	7.23
	NO_2 (μg m^{-3})	Morning	12	3.33
		Afternoon	7.97	3.06
		Evening	10.66	3.06
		Night	8.23	4.45

duration, these results should be interpreted as a preliminary screening-level assessment.

To evaluate the performance of the AERMOD model in predicting the concentrations of SO_2 and NO_2, statistical performance was assessed by comparing the model results with direct field measurements. Table 7 presents the results of the Root Mean Square Error (RMSE) calculated based on Equation 2, Mean Bias Error (MBE) calculated based on Equation 3, and Correlation Coefficient (R) calculated based on Equation 4 using eight paired data points for each pollutant.

The validation results show that the RMSE values for SO_2 and NO_2 are 14.00 μg m^{-3} and 5.37 μg m^{-3}, respectively. While these values reflect the absolute error magnitude of the residuals, they represent a noticeable deviation relative to the observed field mean concentrations. Theoretically, a smaller RMSE (approaching 0) signifies a better fit between modeled and measured data (Hamdanah & Fitrianah 2021). In this study, the calculated RMSE values serve as a baseline measure of absolute deviation during the sampled periods, highlighting the variance associated with short-term screening assessments rather than confirming precise model fit.

The Mean Bias Error (MBE) was employed to assess the systematic bias of the forecasting model by measuring the average difference between the predicted and actual values (Kato 2016). The calculation yielded negative MBE values for both pollutants: -10.44 μg m^{-3} for SO_2 and -4.32 μg m^{-3} for NO_2. A negative MBE indicates that the forecasted values are, on average, smaller than the actual values, signifying a systematic underprediction (Kato 2016). In the context of this study, this trend is commonly observed in dispersion modeling when the simulation focuses primarily on specific point sources, such as the power plant stack, while actual field measurements capture the cumulative impact of additional background concentrations from other local activities or non-modeled sources. Consequently, this negative bias highlights the inherent limitation of point-source modeling in capturing total ambient levels, underscoring that the predicted concentrations reflect only the specific contribution of the stack emissions rather than total cumulative field conditions.

Regarding the Correlation Coefficient (R), the model yielded values of 0.36 for SO_2 and 0.12 for NO_2. The correlation coefficient quantifies the strength and direction of the linear relationship between two variables, where a score close to 1.0 indicates strong correlation and a value close to 0 indicates a negligible relationship (Thieu et al. 2023). These results reflect a weak linear association for SO_2 and a negligible correlation for NO_2, confirming that the model struggles to capture precise hourly temporal fluctuations during the sampling period. Such low correlation values are anticipated when evaluating a small sample size (n = 8) over a short sampling window against a simulation driven by a full-year meteorological dataset. Consequently, while the model remains informative for characterizing general spatial dispersion trends around PLTU PT.X and Nii Tanasa Village as a screening-level assessment, its temporal predictive capability for exact hourly variations is limited.

Table 7: RMSE, MBE, and R test results.

Parameters	RMSE	MBE	R
SO_2 (μg m^{-3})	14	-10.44	0.36
NO_2 (μg m^{-3})	5.37	-4.32	0.12

4. CONCLUSIONS

This study concludes that while direct measurements and AERMOD simulations exhibit differing diurnal peak intervals (daytime and nighttime, respectively), all resulting concentrations consistently remain below national ambient air quality standards. Spatially, the dispersion follows a north-northeast trajectory, with modeled concentrations initially increasing to a plume touchdown peak at approximately 100–120 m downwind before gradually declining with distance. This spatial profile reflects typical high-stack dispersion behavior, acknowledging that the immediate near-field receptor (~7.5 m) captures lower concentrations prior to full plume touchdown. Although temporal discrepancies exist between observed and modeled peaks, AERMOD provides a useful screening-level evaluation for characterizing the overall spatial dispersion pattern around PLTU PT.X and Nii Tanasa Village.

Evaluation of statistical metrics including RMSE (14.00 μg m^{-3} for SO_2 and 5.37 μg m^{-3} for NO_2), negative MBE values, and low correlation coefficients (R) highlights the inherent statistical limitations in predicting exact short-term temporal variations, thereby reinforcing the application of the model primarily for screening-level spatial assessments rather than precise temporal forecasting. While current findings confirm that ambient concentrations remain within regulatory limits, they clearly emphasize the limitations of single-day sampling and underscore the necessity of continuous monitoring and multi-season sampling to capture long-term variability. These insights provide an initial baseline for guiding future air quality management and environmental policy planning in the industrial area.

5. ACKNOWLEDGMENTS

The authors would like to thank PLTU PT.X in Lalonggasumeeto District, Konawe Regency, Southeast

Sulawesi, Indonesia, for granting the authors access and permission to conduct research at the location.

6. REFERENCES

Alchamdani, 2019. Exposure of NO_2 and SO_2 to health risks of public fuel station (SPBU) workers in Kendari City. *Jurnal Kesehatan Lingkungan*, 11(4), pp.319–330. [DOI]

Alviani, M., Anggraini, F.J. and Rodhiyah, Z., 2022. Pemodelan PM2,5 pada musim kemarau menggunakan software Graz Largangian Model di Kecamatan Kota Baru Kota Jambi. *Jurnal Teknik Lingkungan UM Kendari*, 2(2), pp.5–9. [DOI]

Barata, L.O.A., 2024. Sistem perawatan water treatment plant (WTP) PLTU Nii Tanasa 3 × 10 MW. *Piston Jurnal Teknologi*, 9(1), pp.24–35. [DOI]

Government Regulation of the Republic of Indonesia Number 22 of 2021. Implementation of environmental protection and management (in Indonesian). Jakarta. Available at: https://jdih.kehutanan.go.id/new2/home/open_indonesia_file/PP_22_TAHUN_2021_PENYELENGGARAAN_LH_c_menlhk_02222021144819.pdf

Halulanga, A.J., Rosdiana, R. and Adami, A., 2021. Uji kandungan gas sulfur dioksida (SO_2) pada udara ambien akibat adanya pembakaran batubara PLTU Nii Tanasa, Sulawesi Tenggara. *Jurnal Teknik Lingkungan UM Kendari*, 1(2), pp.5–10. [DOI]

Hamdanah, F.H. and Fitrianah, D., 2021. Analisis performansi algoritma linear regression dengan generalized linear model untuk prediksi penjualan pada usaha mikra, kecil, dan menengah. *Jurnal Nasional Pendidikan Teknik Informatika*, 10(1), pp.23–32. [DOI]

Hodson, T.O., 2022. Root-mean-square error (RMSE) or mean absolute error (MAE): When to use them or not. *Geoscientific Model Development*, 15(14), pp.5481–5487. [DOI]

Junarto, G.E., 2021. Penerapan model AERMOD untuk dispersi emisi gas buangan PLTU dan analisis risiko kesehatan lingkungan (studi: PLTU Tonasa, Kec. Bungoro, Kabupaten Pangkep). Master's thesis, Hasanuddin University, Makassar. Available at: https://repository.unhas.ac.id/id/eprint/15398/2/P032171203_tesis_bab%201-2.pdf

Kato, T., 2016. Prediction of photovoltaic power generation output and network operation. In: *Integration of Distributed Energy Resources in Power Systems*, pp.77–108. [DOI]

Kusumawati, R.D., 2025. Analisis dispersi nitrogen dioksida (NO_2) udara ambien di Kawasan Budaya, Kota Yogyakarta menggunakan pemodelan AERMOD. Skripsi, Universitas Islam Indonesia, Yogyakarta. Available at: https://dspace.uii.ac.id/bitstream/handle/123456789/56033/21513157.pdf?sequence=1&isAllowed=y

Munawaroh, N., Syamsyiatun, S. and Fikri, A.A., 2019. Sistem pengolahan air dan pengendalian limbah di PLTU Tanjung Jati-B Desa Tubanan Kembang Jepara. *Jurnal Bakti Saintek: Jurnal Pengabdian Masyarakat Bidang Sains dan Teknologi*, 3(2), pp.73–76. [DOI]

Ningsih, S., 2020. Model sebaran SO_2 dan NO_x PLTU Jeneponto PT. Bosowa Energi. *Jurnal AKRAB Juara*, 5(2), pp.231–238. Available at: https://www.akrabjuara.com/index.php/akrabjuara/article/view/1079/954

Nugraha, P.S., Setiawan, A. and Yustian, I., 2023. AERMOD modeling analysis of CO and NO_x parameters from diesel generator emission sources in the coal mining industry. *Sriwijaya Journal of Environment*, 8(2), pp.92–97. [DOI]

Oktaviani, S., Siregar, S.H., Fauzi, R., Reflis and Utama, S.P., 2023. Gangguan ekosistem laut sebagai dampak keberadaan PLTU Teluk Sepang Bengkulu: Sebuah telaah pustaka. *INSOLOGI: Jurnal Sains dan Teknologi*, 2(6), pp.1061–1068. [DOI]

Putra, D.Y.P. and Nisa, S.Q.Z., 2023. Uji model AERMOD terhadap emisi di PT. X Jawa Timur. *ESEC Proceeding Environmental Science and Engineering Conference*, 4(1), pp.370–379. Available at: https://esec.upnvjt.com/index.php/prosiding/article/download/256/182

Rahmadina, I., 2022. Dampak operasional PLTU terhadap kesehatan masyarakat di Desa Tanjung Tiram Kecamatan Moramo Utara Kabupaten Konawe Selatan. Skripsi, Halu Oleo University, Kendari.

Ramadhani, I.S., 2017. Pemantauan kualitas udara ambien dan pemodelan Gauss dispersion gas nitrogen dioksida (NO_2) dari emisi industri kayu lapis di Dusun Kalimati, Tirtomartani, Kalasan, Sleman, D.I. Yogyakarta. Skripsi, Universitas Islam Indonesia, Yogyakarta. Available at: https://dspace.uii.ac.id/handle/123456789/33142

Salari, M., Abdolmaleki, M.J., Shahid, E.S. and Akhoundi, B., 2026. Dispersion of particulate matter using AERMOD model and health risk assessment: Case study Saveh gypsum industry. *Iranica Journal of Energy and Environment*, 17(2), pp.372–381. [DOI]

Sarwono, E., Wijayanto, E., Huda, H., Harrits, R.F. and Zain, I.F., 2022. Dispersi SO_2 dan NO_2 dari cerobong auxiliary boiler industri methanol PT KMI menggunakan Gaussian plume model AERMOD di Kota Bontang, Kalimantan Timur, Indonesia. *Jurnal Chemurgy*, 6(2), pp.109–117. Available at: http://e-journals.unmul.ac.id/index.php/TK

Sasmita, A., Andrio, D. and Nopita, R., 2021. Dispersi SO_2 dan NO_2 dari pembangkit listrik tenaga uap Tembilahan, Riau. *Jurnal Ilmiah Teknik Lingkungan*, 13(2), pp.98–107. [DOI]

Srisantyorini, T., 2025. *Analisis Kualitas Udara Dampak terhadap Lingkungan dan Kesehatan*. 1st ed. Mafy Media Literasi Indonesia, Solok, Indonesia. Available at: https://penerbitmafy.com/wp-content/uploads/2025/12/ANALISIS-KUALITAS-UDARA-Dampak-Terhadap-Lingkungan-dan-Kesehatan.pdf

Tampa, G.M., Maddusa, S.S. and Pinontoan, O.R., 2020. Analisis kadar sulfur dioksida (SO_2) udara di Terminal Malalayang, Kota Manado tahun 2019. *Indonesian Journal of Public Health and Community Medicine*, 1(3), pp.87–92. [DOI]

Thieu, N.V., Barma, S.D., Lam, T.V., Kisi, O. and Mahesha, A., 2023. Groundwater level modeling using augmented artificial ecosystem optimization. *Journal of Hydrology*, 617, p.129034. [DOI]

Tran, Q.A., Nguyen, N.H.T., Nguyen, P.Q. and Nguyen, A.M., 2022. Simulation of thermal power plant source contribution to ambient air concentration in Cam Pha City, Quang Ninh Province using AERMOD dispersion model. *Journal of Mining and Earth Sciences*, 63(3), pp.35–42. [DOI]

United States Environmental Protection Agency (US EPA), 2024. *Recommended Procedures for Development of Emissions Factors and Use of the WebFIRE Database*. Retrieved May 19, 2025, from: https://www.epa.gov/system/files/documents/2024-09/final-webfire-procedures-document_aug-2024.pdf

Wangsa, D., Bachtiar, V.S. and Raharjo, S., 2022. Uji model AERMOD terhadap sebaran particulate matter 10 µm (PM_{10}) di sekitar kawasan PT Semen Padang. *Jurnal Ilmu Lingkungan*, 20(2), pp.291–301. [DOI]

Zakaria, R., Aly, S.H. and Annisa, 2020. Air dispersion modeling of gas turbine power plant emissions in Makassar by using AERMOD. *IOP Conference Series: Earth and Environmental Science*, 419, p.012153. [DOI]

Nature Environment and Pollution Technology
An International Quarterly Peer-Reviewed Open Access Journal

p-ISSN: 0972-6268 | e-ISSN: 2395-3454 Vol. 25 | No. 4 | Article ID B4426 | 2026

RESEARCH ARTICLE https://doi.org/10.46488/NEPT.2026.v25i04.B4426 OPEN ACCESS

Fish Diversity and Habitat Complexity: The Role of Macrophytes and Physicochemical Parameters in Urban and Rural Tropical Lakes

I. Annie Pushpa[1], K. Maheshkumar[2], V. Deepak Samuel[3] and N. Nirmal Magadalenal[1]†
[1]PG and Research Department of Zoology, Voorhees College (Affiliated to Thiruvalluvar University), Vellore, Tamil Nadu 632001, India
[2]Department of Zoology, Government Arts College, Nandanam, Chennai 600 035, Tamil Nadu, India
[3]National Centre for Sustainable Coastal Management, Ministry of Environment, Forest and Climate Change, Anna University Campus, Chennai, 600 025, India
†Corresponding author: N. Nirmal Magadalenal; nirmalmagdalene@gmail.com

ARTICLE HISTORY

Received: 13-01-2026
Revised: 15-03-2026
Accepted: 20-03-2026

KEYWORDS

Fish diversity
Macrophytes
Physicochemical parameters
Urban and rural tropical lakes

CITE THIS ARTICLE

Pushpa, I. A., Maheshkumar, K., Samuel, V. D. and Magadalenal, N. N., 2026. Fish diversity and habitat complexity: The role of macrophytes and physicochemical parameters in urban and rural tropical lakes. *Nature Environment and Pollution Technology*, 25(4), B4426. https://doi.org/10.46488/NEPT.2026.v25i04.B4426

COPYRIGHT & LICENCE

© 2026 The Authors
Open Access under CC BY 4.0.

PUBLISHED BY

TECHNOSCIENCE PUBLICATIONS

ABSTRACT

This study highlights the impact of urbanization, agricultural runoff, and invasive species on freshwater ecosystems and aquatic biodiversity. It presents a comparative ecological assessment of two freshwater lakes in Vellore District, Tamil Nadu, India: Katpadi Lake (urban) and Saina Palayam Lake (rural). A total of 15 fish species were documented across both lakes, with *Oreochromis niloticus* identified as an exotic invasive species. The fish community was dominated by Cypriniformes (60%), demonstrating ecological adaptability. Diversity indices such as Shannon (H′) and Simpson (1–D) showed slight variations between the lakes. Katpadi Lake had higher total dissolved solids and conductivity, indicating greater anthropogenic influence. Ten macrophyte species, including submerged, floating-leaved, and emergent types, were observed, with their distribution differing between urban and rural sites, reflecting habitat and water-quality differences. Macrophyte diversity was greater in Saina Palayam Lake, linking habitat complexity to higher fish diversity. Submerged species such as *Najas marina* and *Myriophyllum spicatum* likely enhance habitat quality for native species. The rural wetland recorded nitrate and phosphate concentrations of 3 mg L^{-1} and 0.13 mg L^{-1}, respectively, indicating measurable nutrient enrichment, while higher hardness, chloride, and ammonia levels in Katpadi Lake point to urban pollution. The findings underscore the importance of integrated monitoring of fish, macrophytes, and water quality to conserve and manage freshwater biodiversity across different environmental contexts.

1. INTRODUCTION

Freshwater ecosystems are among the most biodiverse and ecologically vital habitats, playing a key role in maintaining ecological balance. They face increasing threats from human activities in both urban and rural settings (Dudgeon et al. 2006). Investigating freshwater fish diversity across these areas offers important insights into how urbanization, industrialization, and agriculture impact aquatic life (Paul & Meyer 2001, Walsh et al. 2005). Urban environments often contend with issues like sewage disposal, industrial waste, and habitat alteration, while rural regions are affected by pesticide and fertilizer runoff from farming, which can cause eutrophication and toxic contamination (Carpenter et al. 1998, Allan 2004). Each setting contributes uniquely yet significantly to stress in freshwater habitats, potentially leading to changes in fish diversity and community composition. A major biological threat in both environments is the introduction of invasive fish

species, which can threaten native populations through competition, predation, and hybridization (Moyle & Light 1996). These invasive species tend to thrive in disturbed habitats and can worsen biodiversity declines, especially when ecosystems are already compromised by poor water quality or habitat loss (Gido & Brown 1999).

Aquatic macrophytes are vital components of freshwater ecosystems, closely linked to fish diversity. They enhance habitat complexity, provide refuge from predators, serve as spawning grounds, and support diverse invertebrate communities that constitute a food source for numerous fish species (Diehl & Kornijów 1998, Thomaz et al. 2025). Nevertheless, macrophyte abundance and diversity are often threatened by pollutants, siltation, and nutrient overloads common in urban drainage and agricultural runoff (Lacoul & Freedman 2006). Physicochemical water parameters, such as pH, temperature, conductivity, and nutrient levels, are crucial in shaping fish communities by affecting habitat suitability and biological processes. Low oxygen or extreme pH can limit the survival and reproduction of sensitive species, while elevated nutrient concentrations may lead to algal blooms that disrupt food webs (Gilvear et al. 1999, Wetzel 2001).

This study aims to conduct a comprehensive ecological assessment of two contrasting freshwater ecosystems: Katpadi Lake (KAL), also known as Dharapadavedu Lake, located within an urban area, and Saina Palayam Lake (SPL), situated in a rural setting in Vellore. Despite numerous studies on freshwater fish diversity in Tamil Nadu, there remains a lack of integrated comparative assessments of fish assemblages, macrophyte communities, and physicochemical parameters across urban and rural lakes in the Vellore District. This research offers a thorough urban–rural comparison of freshwater lake ecosystems by jointly analyzing fish diversity, macrophyte structure, and water quality variables. The selected study areas enable a comprehensive evaluation of ecosystem health and facilitate the identification of multiple drivers influencing biodiversity changes in freshwater systems. Such holistic studies are particularly valuable for informing conservation strategies and supporting the sustainable management of water resources in both urban and rural contexts.

2. MATERIALS AND METHODS

2.1. Study Area

The study was carried out in two freshwater lakes located in Vellore District, Tamil Nadu, India. KAL, with a catchment area of 17.09 km^2, is situated in the urban zone of Katpadi, while SPL, commonly known as S.N. Palayam Lake, with a catchment area of 12.96 km^2, lies in the rural region of Ponnai (TNWRD 2020). The geographical coordinates of KAL (Lat: 12.963766°, Long: 79.128653°) and SPL (Lat: 13.141206°, Long: 79.267942°) were mapped and georeferenced using ArcMap GIS software version 10.8 (Fig. 1). Fish sampling,

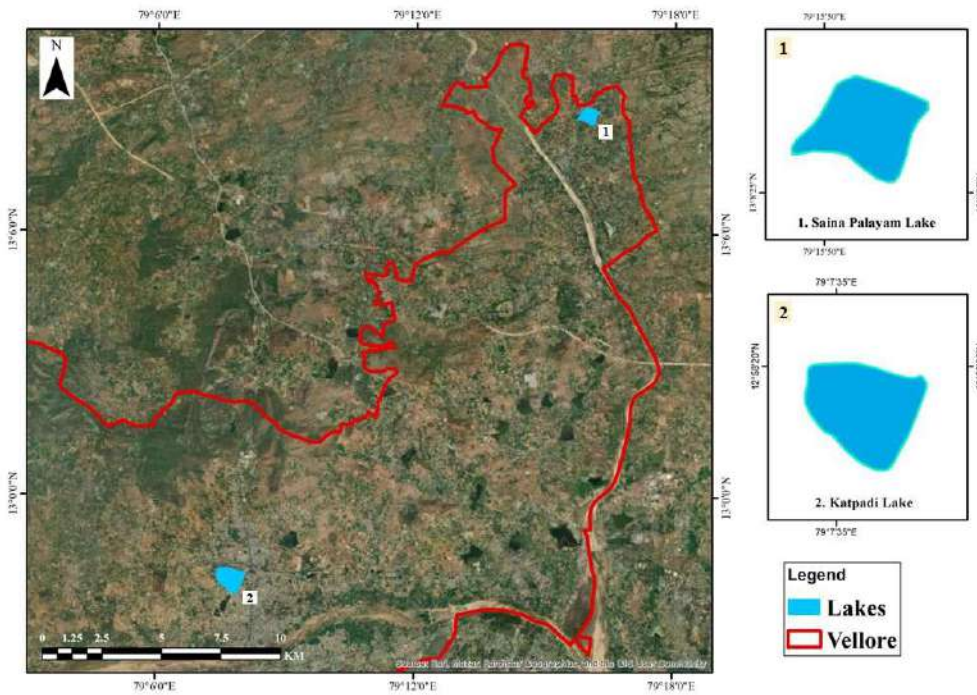


Fig. 1: Geographical location of the study areas.

macrophyte recording, and physicochemical parameters were measured. In KAL, sampling occurred in December 2024, whereas in SPL, it was conducted in April 2025.

2.2. Fish Sampling and Identification

Fish samples were obtained from both lakes using three different sizes of cast nets (radius 1.2–2.4 m, mesh size 1.3–5.1 cm), allowing the capture of small and large-bodied species. Each net was equipped with sinkers weighing 7–14 g to ensure proper spread and descent in shallow waters. Sampling occurred between 07:00 and 13:00 hours, aligning with the peak activity period of shallow-water fish. The process was carried out independently in each lake following a standardized protocol. In each location, nine representative sites along the lake margins were selected based on habitat features such as macrophyte coverage, water depth, flow variation, human disturbance, and accessibility. At each site, six to nine hauls were performed across different microhabitats, including open water, vegetated zones, and shallow marginal areas. Multiple net types and mesh sizes, as previously described, targeted a wide range of fish sizes. Specimens caught were photographed on-site for initial documentation and subsequently preserved in 10% formalin for detailed identification. Species identification relied on standard taxonomic keys (Talwar & Jhingran 1991, Jayaram 2010) and was cross-verified with online databases such as FishBase (Froese & Pauly 2024).

2.3. Analysis of Fish Diversity

Table 1 displays the relative abundance of each fish species in Katpadi Lake and Saina Palayam Lake. To evaluate species diversity and community structure, several diversity metrics, including Dominance (D), Simpson's index (1–D), Shannon-Wiener index (H), Menhinick's richness index, Margalef's richness index, Fisher's alpha, and the Berger-Parker dominance index, were calculated using PAST software version 4.03 (Hammer et al. 2001).

In addition to diversity indices, which primarily describe the diversity, richness, and evenness within individual communities, similarity indices such as Jaccard and Sørensen offer valuable insights into beta diversity. While alpha diversity emphasizes the internal structure of each site, these similarity indices measure the extent of species overlap and turnover between sites, thereby complementing diversity

Table 1: Fish species recorded in Katpadi Lake (KAL) and Saina Palayam Lake (SPL).

S. No..	Scientific name	Order	Family	Relative abundance in KAL (%)	Relative abundance in SPL (%)	KAL	SPL	Common name	Exotic/ invasive	IUCN
1	*Oreochromis niloticus*	Cichliformes	Cichlidae	50.34	52.86	✓	✓	Nile tilapia	Exotic/ invasive	LC
2	Anabas testudineus	Anabantiformes	Anabantidae	5.03	0	✓	–	Climbing perch	Native	LC
3	*Pethia conchonius*	Cypriniformes	Cyprinidae	16.78	0	✓	–	Rosy barb	Native	LC
4	*Glossogobius giuris*	Gobiiformes	Gobiidae	3.36	0	✓	–	Tank goby	Native	LC
5	*Parambassis ranga*	Mugiliformes	Ambassidae	2.68	5.29	✓	✓	Indian glassy fish	Native	LC
6	*Puntius sophore*	Cypriniformes	Cyprinidae	6.71	8.81	✓	✓	Pool barb	Native	LC
7	*Channa striata*	Anabantiformes	Channidae	3.36	0	✓	–	Striped snakehead	Native	LC
8	*Esomus danrica*	Cypriniformes	Danionidae	10.07	0	✓	–	Indian flying barb	Native	LC
9	*Chanda nama*	Mugiliformes	Ambassidae	1.68	0	✓	–	Elongated glassy perchlet	Native	LC
10	*Rasbora daniconius*	Cypriniformes	Danionidae	0	6.61	–	✓	Scissortail rasbora	Native	LC
11	*Amblypharyngodon mola*	Cypriniformes	Danionidae	0	10.57	–	✓	Mola carplet	Native	LC
12	*Amblypharyngodon microlepis*	Cypriniformes	Danionidae	0	7.93	–	✓	Indian carplet	Native	LC
13	*Salmostoma phulo*	Cypriniformes	Danionidae	0	2.2	–	✓	Finescale razorbelly minnow	Native	LC
14	*Pethia ticto*	Cypriniformes	Cyprinidae	0	3.52	–	✓	Ticto barb	Native	LC
15	*Rasbora* spp.	Cypriniformes	Danionidae	*0*	*2.2*	–	✓	*Rasbora* species	Native	-

Note: ✓ = Present; – = Absent; LC = Least Concern

measures. This distinction is essential, as communities may have similar levels of species richness but differ significantly in composition. The species similarity between KAL and SPL was evaluated using the Sørensen and Jaccard similarity indices, where 'a' indicates the number of shared species, 'b' the species unique to KAL, and 'c' the species unique to SPL. The Sørensen similarity coefficient was calculated as:

$$S_s = \frac{2a}{2a + b + c}$$

and the Jaccard index as:

$$J = \frac{a}{a + b + c}$$

Both indices were employed to assess beta diversity and compare fish community composition between the two sites. To enhance visualization of similarity patterns, a hierarchical cluster analysis was conducted using the unweighted pair-group method with arithmetic mean (UPGMA). The Jaccard similarity coefficient (J) was calculated from presence-absence data, and the corresponding Jaccard-derived dissimilarity (1 – J) was used as the distance matrix for UPGMA clustering. The resulting dendrogram illustrates the clustering of fish species across the sites.

2.4. Macrophyte Identification

Macrophyte assessment involved visual, qualitative observations conducted during field surveys. The presence, general abundance, and dominant growth forms of macrophytes were documented to characterize habitat conditions, although quantitative measures such as percent cover, biomass, or spatial extent were not assessed. Consequently, macrophyte data offered descriptive insights into habitat structure. Specimens were identified to the species level using standard macrophyte identification keys (Subramanyam 1962, Cook 1996).

2.5. Physicochemical Water Analysis

Physicochemical parameters were analyzed from water samples collected at each study site following BIS 10500:2012 and APHA (2017) protocols. pH and electrical conductivity were measured in situ using a portable multiparameter probe (Eutech Instruments, Singapore), turbidity with a nephelometric turbidity meter (APHA 2130B), and total dissolved solids (TDS) with a digital TDS meter. Nutrients (nitrate, nitrite, phosphate, and ammonia) were quantified by UV–visible spectrophotometry (APHA 4500 series), while major and trace metals (iron, manganese, calcium, and magnesium) were determined using atomic absorption spectrophotometry (AAS; PerkinElmer). Alkalinity, total hardness, and chloride were measured by titrimetric methods, while oxygen absorbed in 4 h was determined according to IS 3025 (Part 63):2007 (Oxygen Absorbed in 4 h), commonly referred to as Tidy's test. Sensory characteristics (color, odor, and appearance) were recorded visually and organoleptically.

3. RESULTS AND DISCUSSION

3.1. Fish Diversity

A total of 15 fish species were recorded across KAL and SPL. The species identified in KAL included *Oreochromis niloticus*, *Anabas testudineus*, *Pethia conchonius*, *Glossogobius giuris*, *Chanda nama*, *Parambassis ranga*, *Puntius sophore*, *Channa striata*, and *Esomus danrica* (Fig. 2 and Table 1). In SPL, the species included *Rasbora daniconius*, *Oreochromis niloticus*, *Amblypharyngodon mola*, *Amblypharyngodon microlepis*, *Salmostoma phulo*, *Puntius sophore*, *Parambassis ranga*, *Pethia ticto*, and *Rasbora* spp. *(Fig. 2* and Table 1). Notably, *Oreochromis niloticus*, an exotic and invasive species, was present in both lakes. Its ability to tolerate a wide range of environmental conditions and reproduce rapidly can displace native species and disrupt local food webs (Canonico et al. 2005).

Cypriniformes dominated the fish community, accounting for 60% of the total species diversity. Mugiliformes and Anabantiformes each contributed 13%, while Cichliformes and Gobiiformes each represented 7% (Fig. 3). The dominance of Cypriniformes may be attributed to their ecological adaptability, versatile feeding habits, and reproductive strategies in diverse aquatic habitats (Nelson et al. 2016, Chakraborty 2021).

Small indigenous freshwater fish species (SIFs), including *Amblypharyngodon mola*, *Amblypharyngodon microlepis*, *Pethia ticto*, and *Rasbora* spp., were documented in the current study area. These SIFs are crucial to both the ecological balance and the socioeconomic fabric of Indian freshwater ecosystems, exhibiting high adaptability to the fluctuating environmental conditions typical of tropical lakes and wetlands (Sarkar & Lakra 2010). Sarkar & Lakra (2010) also emphasize that, despite their resilience, these species

Table 2: Diversity analysis in KAL and SPL.

	KAL	SPL
Dominance (D)	0.2996	0.311
Simpson (1–D)	0.7004	0.689
Shannon (H□)	1.615	1.628
Menhinick	0.5214	0.5974
Margalef	1.404	1.475
Fisher's alpha	1.75	1.873
Berger-Parker	0.5034	0.5286

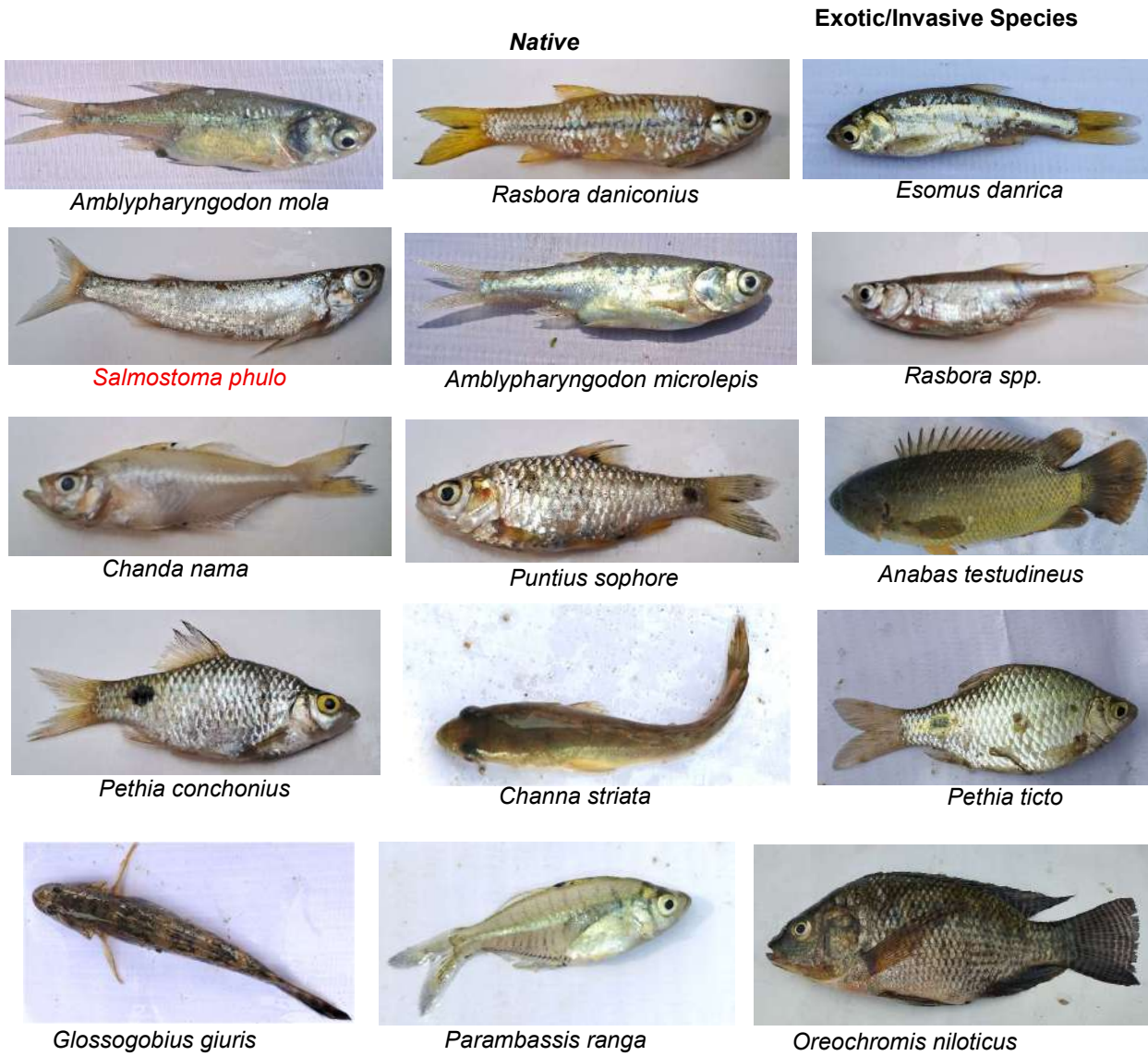


Fig. 2: Fish species recorded in Katpadi Lake (KAL) and Saina Palayam Lake (SPL).

remain vulnerable to habitat degradation, overfishing, and competition from invasive species. Therefore, implementing targeted conservation efforts and sustainable management strategies is vital to safeguard these SIF populations and preserve ecosystem health in the region.

3.1.1. IUCN Conservation Status

All fish species identified to species level were classified as Least Concern (LC) in the IUCN Red List (IUCN 2025), while *Rasbora* spp. was not assigned a species-level category (Table 1). Lewis (2002) highlights that tropical lakes are particularly vulnerable to eutrophication and deep-water oxygen depletion, making them more sensitive to nutrient loading and hydrological changes than temperate lakes. When subjected to even moderate nutrient enrichment, tropical systems can experience amplified alterations in water quality and biotic communities.

3.1.2. Diversity Analysis

Diversity indices showed comparable species richness across both sites. The Shannon diversity index (H′) was marginally higher in SPL (1.628) compared to KAL (1.615) (Table 2). Magurran (2004) reported a slightly more even distribution of individuals among species in rural sites. The Margalef and Menhinick indices were also higher in SPL, suggesting greater richness relative to sample size.

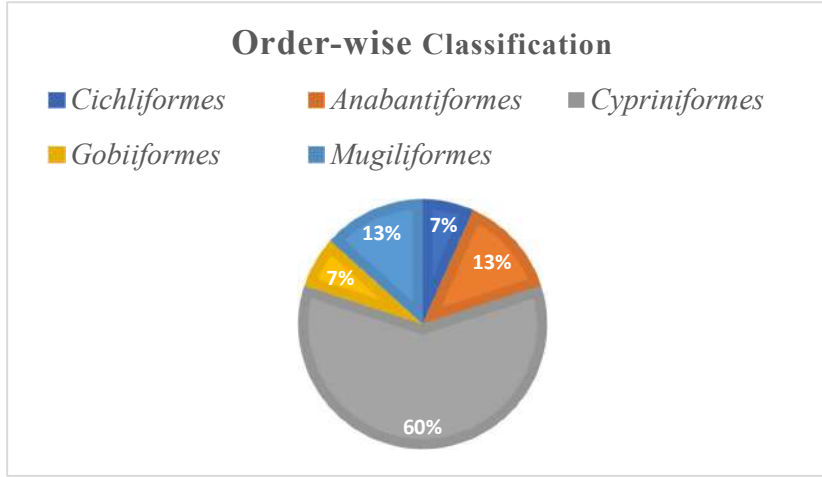


Fig. 3: Percentage composition of fish species across different taxonomic orders in KAL and SPL.

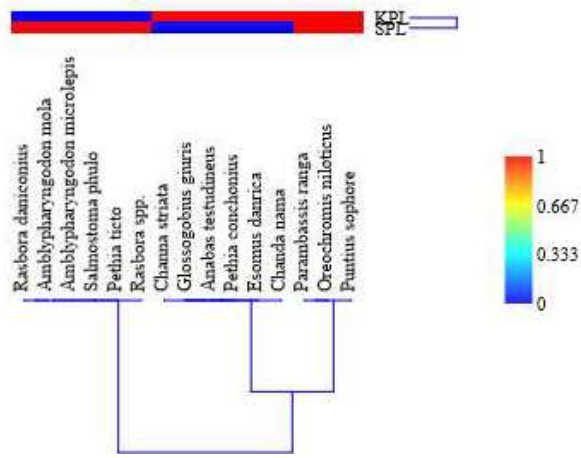


Fig. 4: Cluster dendrogram illustrating similarity in fish species composition between KAL and SPL based on hierarchical cluster analysis.

Meanwhile, Berger–Parker and dominance (D) indices were elevated in SPL, suggesting the presence of dominant species (*Oreochromis niloticus*) (Table 1). The observed variation in Shannon, Margalef, and Menhinick indices may partly reflect differences in macrophyte heterogeneity and associated habitat complexity. Structurally diverse macrophyte assemblages can enhance habitat availability by providing shelter and feeding opportunities, thereby supporting higher fish richness and evenness, whereas sparse or monospecific vegetation may favor a limited number of tolerant species (Thomaz et al. 2025). Accordingly, the diversity indices represent not only species richness but also habitat structure mediated by macrophyte composition.

Dominance-sensitive indices, particularly Simpson and Berger–Parker, revealed a skewed community structure in both lakes, characterized by a few species contributing disproportionately to overall abundance. This pattern was primarily driven by the overwhelming dominance of the invasive cichlid *Oreochromis niloticus*, which made up about half of the total fish population. The species' ecological traits, such as high reproductive capacity, trophic versatility, and resilience to environmental stressors, likely foster numerical dominance and diminish community evenness through competitive exclusion and habitat monopolization (Johnson et al. 2022). Similar patterns have been observed elsewhere; for example, in the hydrologically fragmented Vaigai River-Estuary, *Oreochromis* spp. comprised over a third of the total catch, significantly reducing community evenness despite moderate to high diversity levels (Mogalekar et al. 2025). Such dominance patterns are common in disturbed freshwater systems and underscore the importance of interpreting richness- and dominance-based indices together, since higher species richness can coexist with strong numerical dominance. The consistent dominance patterns across lakes

Table 3: Species distribution and similarity indices between KAL and SPL.

Species distribution	Count
Shared species (a)	3
Unique to Katpadi (b)	6
Unique to Palayam (c)	6
Similarity indices	
Jaccard	0.2
Sørensen	0.333

further suggest that invasive species pressure may partially override spatial differences, shaping the overall community structure.

3.1.3. Similarity Analysis

In this study, the relatively low similarity values, Jaccard = 0.20 and Sørensen = 0.33, highlight the distinctiveness of fish communities between the urban (KAL) and rural (SPL) systems (Table 3). This dissimilarity reflects the combined effects of varying environmental conditions, macrophyte composition, and physicochemical parameters, which influence species distributions differently across sites. Incorporating both Jaccard and Sørensen indices places the findings within the broader context of alpha, beta, and gamma diversity, aligning with standard community ecology practices that consider both within-site diversity and between-site similarity to gain a comprehensive understanding of biodiversity patterns. The hierarchical cluster analysis based on Jaccard-derived dissimilarity further supported this observation, grouping the two lakes together and highlighting species restricted to individual sites (Fig. 4).

These findings align with previous research emphasizing the ecological factors behind low similarity in fish communities. Koleff et al. (2003) highlighted the importance of employing multiple similarity measures to capture various aspects of community structure, while Johnson & Angeler (2014) and Gebrekiros (2016) noted that environmental heterogeneity and land-use pressures lead to significant

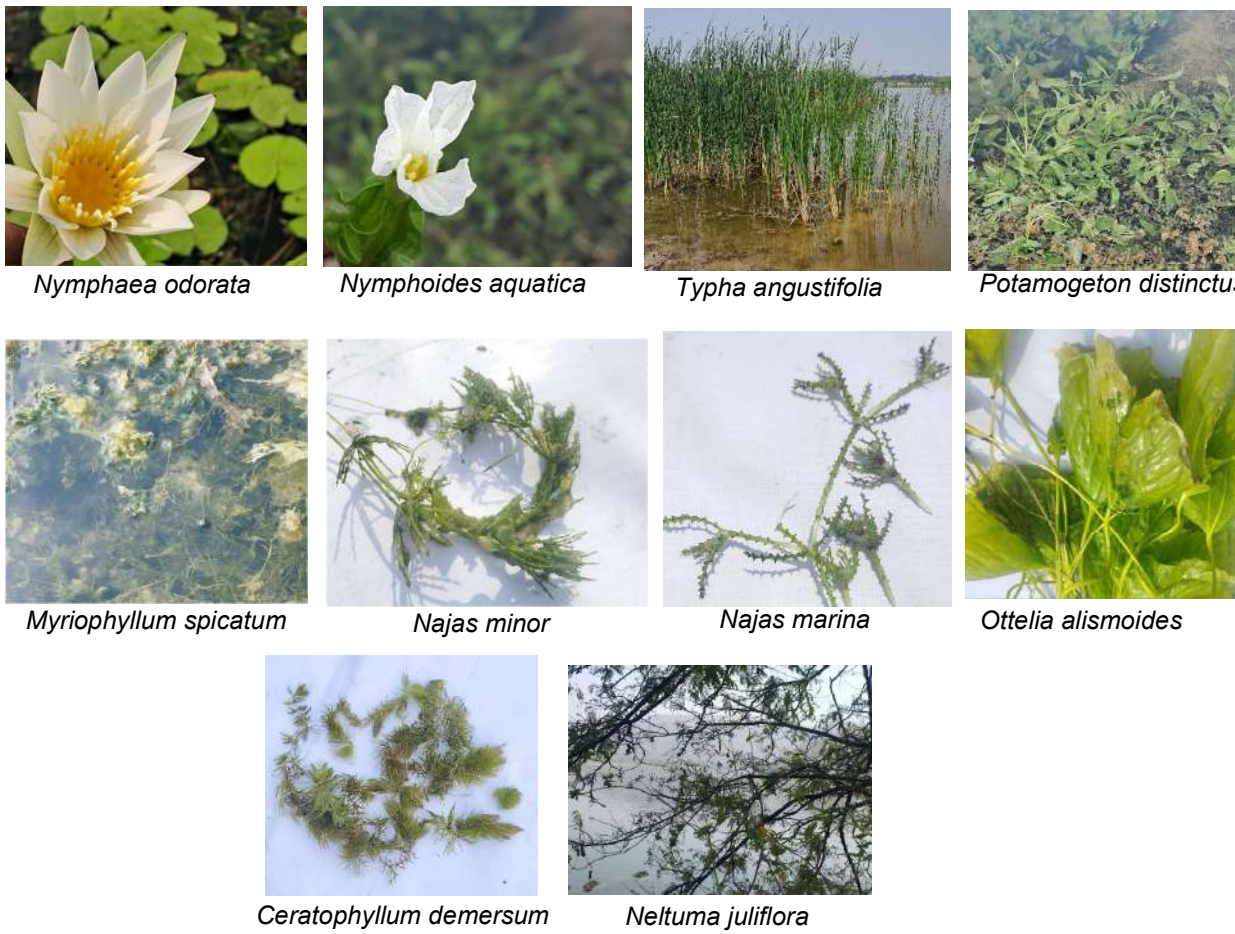


Fig. 5: Macrophytes recorded in KAL and SPL.

Table 4: Macrophytes recorded in KAL and SPL.

S. No.	Species	Order	Family	KAL	SPL	Common Name	Exotic/ Invasive	IUCN
1	*Neltuma juliflora*	Fabales	Fabaceae	✓	–	Mesquite	Invasive	LC
2	*Ceratophyllum demersum*	Ceratophyllales	Ceratophyllaceae	✓	–	Hornwort	Native	LC
3	Ottelia alismoides	Alismatales	Hydrocharitaceae	✓	✓	Duck lettuce	Native	LC
4	*Najas marina*	Alismatales	Hydrocharitaceae	✓	✓	Spiny water nymph	Native	LC
5	*Nymphoides aquatica*	Asterales	Menyanthaceae	–	✓	Banana lily	Native	NE
6	*Nymphaea odorata*	Nymphaeales	Nymphaeaceae	–	✓	White water lily	Native	LC
7	*Potamogeton distinctus*	Alismatales	Potamogetonaceae	–	✓	Pondweed	Native	LC
8	*Najas minor*	Alismatales	Hydrocharitaceae	–	✓	Lesser naiad	Native	LC
9	*Myriophyllum spicatum*	Saxifragales	Haloragaceae	–	✓	Eurasian watermilfoil	Native	LC
10	*Typha angustifolia*	Poales	Typhaceae	–	✓	Narrowleaf cattail	Invasive	LC

Note: ✓ = Present; – = Absent; LC = Least Concern; NE = Not Evaluated.

Table 5: Physico-chemical parameters of water samples collected in KAL and SPL

Observations	Acceptable limit	Maximum permissible limit in the absence of an alternative source	KAL	SPL
I. PHYSICAL EXAMINATIONS				
1. Appearance			slightly turbid	slightly turbid
2. Color	-	-	slightly yellow	slightly yellow
3. Odor	Agreeable	Agreeable	Odorous	odorous
4. Turbidity (NTU)	1	5	4	0
5. Total dissolved solids (mg L^{-1})	500	2000	894	337
6. Electrical conductivity (µS cm^{-1})	-	-	1277	481
II. CHEMICAL EXAMINATIONS				
7. pH	6.5–8.5	6.5–8.5	7.32	7.62
8. Alkalinity pH as $CaCO_3$ (mg L^{-1})	-	-	0	0
9. Total alkalinity as $CaCO_3$ (mg L^{-1})	200	600	244	112
10. Total hardness as $CaCO_3$ (mg L^{-1})	200	600	296	206
11. Calcium as Ca (mg L^{-1})	75	200	61	41
12. Magnesium (mg L^{-1})	30	100	35	25
13. Free ammonia as NH_3 (mg L^{-1})	0.5	0.5	1.04	0.53
14. Nitrite as NO_2 (mg L^{-1})	0.5	0.5	0.14	0.05
15. Nitrate as NO_3 (mg L^{-1})	45	45	10	3
16. Chloride as Cl (mg L^{-1})	250	1000	204	69
17. Fluoride as F (mg L^{-1})	1	1.5	0.4	0.4
18. Sulfate as SO_4 (mg L^{-1})	200	400	111	23
19. Phosphate as PO_4 (mg L^{-1})	-	-	0.14	0.13
20. Tidy's test, 4 h, as O_2 (mg L^{-1})	-	-	0.1	0.1

Note: The acceptable limits and maximum permissible limits are as per BIS (2012). BIS 10500:2012.

compositional differences across freshwater systems. Likewise, Schlosser (1984) underscored the influence of local habitat features on fish community organization, and Baselga (2007) showed that beta diversity often results from species turnover along environmental gradients. Supporting this perspective, Yang et al. (2008) found that spatial environmental variability predominantly shapes freshwater fish assemblages, often indicated by low Jaccard and

Sørensen indices across different habitats. The observed low similarity values suggest that species turnover between the two lakes exceeds mere differences in species richness. This variation is likely driven by a combination of environmental and biotic factors identified in this study. Variations in physicochemical conditions, water depth, and differences in macrophyte composition and structural complexity may affect habitat suitability for various fish species, resulting in species replacement across lakes.

Furthermore, the prominent numerical dominance of the invasive cichlid *Oreochromis niloticus* in both systems likely alters community composition by suppressing subordinate native species, leading to distinct assemblages dominated by different sets of non-dominant species. Macrophyte structure may also influence these patterns by selectively favoring species adapted to either vegetated or open habitats. Collectively, these factors indicate that beta diversity patterns in the study lakes are driven by invasion and habitat-mediated community restructuring rather than random species variation.

3.2. Macrophyte Diversity

Macrophyte diversity in KAL included *Neltuma juliflora, Ceratophyllum demersum, Ottelia alismoides*, and *Najas marina* (Fig. 5 and Table 4). The abundance of *Neltuma juliflora* likely contributes minimally to aquatic biodiversity and may adversely impact shoreline habitats by increasing water loss and modifying habitat structure. Conversely, *Ceratophyllum demersum*, a submerged macrophyte, creates dense underwater meadows that offer cover and spawning grounds for small fish and invertebrates (Lacoul & Freedman 2006). *Najas marina*, another submerged species, performs a similar function and aids in sediment stabilization, which reduces turbidity and maintains clearer waters (Chambers et al. 2008).

SPL displayed higher macrophyte diversity, with species such as *Nymphoides aquatica*, *Nymphaea odorata*, *Najas marina*, *Potamogeton distinctus*, *Ottelia alismoides*, *Najas minor*, *Typha angustifolia, and Myriophyllum spicatum* (Fig. 5 and Table 4). The abundance of submerged and floating-leaved macrophytes in water bodies not only enhances habitat complexity but also contributes to nutrient cycling, oxygenation, and protection of juvenile fish from predation (Wetzel 2001, Lacoul & Freedman 2006). Previous studies have demonstrated that dense *Myriophyllum spicatum* stands can impact trophic interactions by boosting invertebrate populations, which may then be kept in check by fish predation, ultimately promoting macrophyte growth (Ward & Newman 2006). In this study, the presence of dense *Myriophyllum in SPL* was associated with higher dominance index values. Although direct causal links were not tested, this pattern aligns with established macrophyte–fish interaction frameworks and provides a plausible ecological explanation for the dominance structure observed in SPL.

Similarly, species of Potamogeton and Najas serve as indicators of moderately nutrient-rich waters, which can promote fish diversity (Chambers et al. 2008). The increased structural heterogeneity in SPL may help explain the slightly higher evenness and richness indices observed there, despite the rural setting. Overall, the presence and diversity of aquatic macrophytes significantly influence the spatial distribution, shelter availability, breeding potential, and foraging opportunities of fish communities in both lakes.

3.3. Physicochemical Parameters

Physicochemical analysis showed that both lakes were slightly turbid and yellowish in color, with odors indicative of organic matter or algal presence (APHA 2017) (Table 5). The KAL exhibited elevated total dissolved solids (894 mg L^{-1}), conductivity (1277 µS cm^{-1}), and chloride concentration (204 mg L^{-1}), suggesting increased anthropogenic pollution (Table 5). According to Allan (2004), such pollution likely originates from urban effluents, sewage discharge, and road runoff. Elevated conductivity values reflect a higher ion concentration, often due to domestic wastewater and industrial discharges in urban lakes. In fact, electrical conductivity is a reliable indirect marker of pollution in shallow lakes, as it shows linear correlations with total dissolved solids, sulfates, and other dissolved ions (Das et al. 2006).

SPL exhibited lower levels of dissolved ions and turbidity. SPL recorded nitrate and phosphate concentrations of 3 mg L^{-1} and 0.13 mg L^{-1}, respectively, indicating measurable nutrient enrichment in the freshwater system (Table 5). As suggested by Carpenter et al. (1998), nutrient enrichment may be attributed to agricultural runoff and fertilizer application in nearby fields. Such runoff is a common cause of nutrient enrichment in freshwater systems, especially in the absence of buffer vegetation. The marginally higher pH of 7.62 in SPL also supports the presence of biogenic activity, whereby photosynthetic organisms such as macrophytes and algae remove CO_2, shifting the carbonate equilibrium and increasing pH. Diurnal and seasonal pH fluctuations driven by biological metabolism are well documented in freshwater habitats, particularly wetlands, where photosynthesis reduces dissolved CO_2 and elevates pH (Gupta et al. 2021).

Higher levels of free ammonia (1.04 mg L^{-1}) were detected in KAL (Table 5). Elevated ammonia concentrations can adversely affect fish health by damaging gills and hindering growth (Randall & Tsui 2002). An integrated

assessment of fish species, macrophyte composition, and water quality highlights the impact of surrounding environmental conditions on freshwater biodiversity. Although both lakes support similar fish diversity levels, the presence of invasive species, differences in macrophyte richness, and varying physicochemical parameters emphasize the importance of comprehensive freshwater ecosystem monitoring.

4. LIMITATIONS

Although the primary goal of this study was to investigate spatial differences between the lakes, variations in sampling periods may have influenced some of the results. KAL was sampled post-monsoon, while SPL was sampled during peak summer, and seasonal shifts in hydrological conditions can affect water quality, macrophyte abundance, and fish communities. Therefore, these findings should be interpreted with the understanding that both spatial factors and seasonal changes may have contributed, and future synchronized sampling across multiple seasons could improve spatial comparisons.

5. CONCLUSIONS

The present study emphasizes the complex relationships between fish diversity, macrophyte composition, and physicochemical conditions in the two examined freshwater lakes. Diversity indices indicate that SPL supported slightly higher fish diversity than KAL, likely owing to greater macrophyte richness and structural complexity, which offer a variety of niches for feeding, breeding, and shelter. This habitat heterogeneity, along with favorable water quality, seems to promote more balanced species assemblages despite the dominance of *Oreochromis niloticus*. The diversity of macrophytes, ranging from submerged to emergent forms, plays a crucial role in maintaining biodiversity. Additionally, physicochemical analyses revealed site-specific differences in parameters such as pH, conductivity, nutrient levels, and ionic composition, reflecting both natural processes and human activities. These findings highlight the importance of integrated lake management strategies that focus on habitat diversity, control of invasive species, and pollution reduction to preserve ecological integrity.

6. REFERENCES

Allan, J.D., 2004. Landscapes and riverscapes: the influence of land use on stream ecosystems. *Annual Review of Ecology, Evolution, and Systematics*, 35, pp.257–284. [DOI]

APHA, 2017. *Standard Methods for the Examination of Water and Wastewater*. Twenty-Third Edition. American Public Health Association.

Baselga, A., 2007. Disentangling distance decay of similarity from richness gradients: response to Soininen et al. *Ecography*, 30, pp.838–841. [DOI]

Bureau of Indian Standards, 2007. *Methods of sampling and test (physical and chemical) for water and wastewater: Part 63—Oxygen absorbed in 4 h (IS 3025 (Part 63):2007)*. Bureau of Indian Standards.

Bureau of Indian Standards, 2012. *Drinking water—Specification (IS 10500:2012) (Second revision)*. Bureau of Indian Standards.

Canonico, G.C., Arthington, A., McCrary, J.K. and Thieme, M.L., 2005. The effects of introduced tilapias on native biodiversity. *Aquatic Conservation: Marine and Freshwater Ecosystems*, 15(5), pp.463–483. [DOI]

Carpenter, S.R., Caraco, N.F., Correll, D.L., Howarth, R.W., Sharpley, A.N. and Smith, V.H., 1998. Nonpoint pollution of surface waters with phosphorus and nitrogen. *Ecological Applications*, 8(3), pp.559–568. [DOI]

Chakraborty, S.K., 2021. Ecology of fishes of rivers: functional roles. In: Babu, C. and Sivaperuman, C. (eds.) *Riverine Ecology, Vol. 2*. Cham: Springer, pp.187–286. [DOI]

Chambers, P., Lacoul, P., Murphy, K. and Thomaz, S., 2008. Global diversity of aquatic macrophytes in freshwater. In: *Abstracts of the 5th International Weed Science Congress*. Vancouver, Canada, p.323.

Cook, C.D.K., 1996. *Aquatic and Wetland Plants of India*. Oxford University Press.

Das, S., Mandal, R. and Bandyopadhyay, S., 2006. Role of electrical conductivity as an indicator of pollution in shallow lakes. *Asian Journal of Water, Environment and Pollution*, 3(1), pp.153–156.

Diehl, S. and Kornijów, R., 1998. *The Structuring Role of Submerged Macrophytes in Lakes*. Springer, pp.24–46.

Dudgeon, D., Arthington, A.H., Gessner, M.O., Kawabata, Z.I., Knowler, D.J., Lévêque, C. and Sullivan, C.A., 2006. Freshwater biodiversity: importance, threats, status and conservation challenges. *Biological Reviews*, 81(2), pp.163–182. [DOI]

Froese, R. and Pauly, D., 2024. *FishBase*. Retrieved August 13, 2026, from https://www.fishbase.org/.

Gebrekiros, S.T., 2016. Factors affecting stream fish community composition and habitat suitability. *Journal of Aquaculture & Marine Biology*, 4(2), 00076. [DOI]

Gido, K.B. and Brown, J.H., 1999. Invasion of North American drainages by alien fish species. *Freshwater Biology*, 42(2), pp.387–399. [DOI]

Gilvear, D.J., Karr, J.R. and Chu, E.W., 1999. Restoring life in running waters: better biological monitoring. *Water, Air, and Soil Pollution*, 116, pp.666–667.

Gupta, D., Ranjan, R.K., Parthasarathy, P. and Ansari, A.M.S., 2021. Spatial and seasonal variability in the water chemistry of Kabar Tal wetland (Ramsar site), Bihar, India: multivariate statistical techniques and GIS approach. *Water Science and Technology*, 83(9), pp.2100–2117. [DOI]

Hammer, O., Harper, D.A.T. and Ryan, P.D., 2001. PAST: paleontological statistics software package for education and data analysis. *Palaeontologia Electronica*, 4(1), pp.1–9.

IUCN, 2025. *The IUCN Red List of Threatened Species, Version 2025-1*. Retrieved August 13, 2026, from https://www.iucnredlist.org.

Jayaram, K.C., 2010. *The Freshwater Fishes of the Indian Region*. Delhi: Narendra Publishing House.

Johnson, C., Sarkar, U.K., Koushlesh, S.K., Das, A.K., Das, B.K. and Naskar, B.K., 2022. Fish assemblage, ecosystem status and potential impact of Nile tilapia in Halali Reservoir of Central India. *Environment, Development and Sustainability*, 24(6), pp.7753–7775. [DOI]

Johnson, R.K. and Angeler, D.G., 2014. Effects of agricultural land use on stream assemblages: taxonspecific responses of alpha and beta diversity. *Ecological Indicators*, 45, pp.386–393. [DOI]

Koleff, P., Gaston, K.J. and Lennon, J.J., 2003. Measuring beta diversity for presence–absence data. *Journal of Animal Ecology*, 72(3), pp.367–382. [DOI]

Lacoul, P. and Freedman, B., 2006. Environmental influences on aquatic

plants in freshwater ecosystems. *Environmental Reviews*, 14(2), pp.89–136. [DOI]

Lewis, W.M. Jr., 2002. Basis for the protection and management of tropical lakes. *Freshwater Biology*, 47(5), pp.957–970.

Magurran, A.E., 2004. *Measuring Biological Diversity*. Blackwell Publishing.

Mogalekar, H.S., Sudhan, C., Katare, M.B. and Swami, A.M., 2025. Fish assemblage dynamics, Tilapia invasion, trophic guilds, and conservation priorities in the hydrologically fragmented Vaigai River–Estuary continuum, India. *Thalassas: An International Journal of Marine Sciences*, 41, p.153. [DOI]

Moyle, P.B. and Light, T., 1996. Biological invasions of fresh water: empirical rules and assembly theory. *Biological Conservation*, 78(1–2), pp.149–161. [DOI]

Nelson, J.S., Grande, T.C. and Wilson, M.V.H., 2016. *Fishes of the World*. 5th edn. John Wiley & Sons. [DOI]

Paul, M.J. and Meyer, J.L., 2001. Streams in the urban landscape. *Annual Review of Ecology and Systematics*, 32, pp.333–365. [DOI]

Randall, D.J. and Tsui, T.K., 2002. Ammonia toxicity in fish. *Marine Pollution Bulletin*, 45(1–12), pp.17–23. [DOI]

Sarkar, U.K. and Lakra, W.S., 2010. Small indigenous freshwater fish species of India: significance, conservation and utilization. *Aquaculture Asia Magazine*, 15(3), pp.34–35.

Schlosser, I.J., 1984. Fish community structure and function along two habitat gradients in a headwater stream. *Ecological Monographs*, 52(4), pp.395–414.

Subramanyam, K., 1962. *Aquatic Angiosperms*. CSIR.

Talwar, P.K. and Jhingran, A.G., 1991. *Inland Fishes of India and Adjacent Countries*. Vols. 1–2. New Delhi: Oxford & IBH Publishing Co. Pvt. Ltd.

Thomaz, S.M., Cardozo, A.L.P., Quirino, B.A., Yofukuji, K.Y., Aleixo, M.H.F. and Fugi, R., 2025. A review of the ecological role of aquatic macrophytes on freshwater fish. *Hydrobiologia*, 852, pp.3257–3290. [DOI]

TNWRD, 2020. *Catchment Area Statistics*. Government of Tamil Nadu.

Walsh, C.J., Roy, A.H., Feminella, J.W., Cottingham, P.D., Groffman, P.M. and Morgan, R.P. II, 2005. The urban stream syndrome: current knowledge and the search for a cure. *Journal of the North American Benthological Society*, 24(3), pp.706–723. [DOI]

Ward, D.M. and Newman, R.M., 2006. Fish predation on Eurasian watermilfoil (*Myriophyllum spicatum*) herbivores and indirect effects on macrophytes. *Canadian Journal of Fisheries and Aquatic Sciences*, 63(5), pp.1049–1057. [DOI]

Wetzel, R.G., 2001. *Limnology: Lake and River Ecosystems*. Academic Press. [DOI]

Yang, Y.C., Cai, X. and Herricks, E.E., 2008. Identification of hydrologic indicators related to fish diversity and abundance: a data mining approach for fish community analysis. *Water Resources Research*, 44(4), W04401. [DOI]

Nature Environment and Pollution Technology
An International Quarterly Peer-Reviewed Open Access Journal

p-ISSN: 0972-6268 | e-ISSN: 2395-3454 Vol. 25 | No. 4 | Article ID D1927 | 2026

RESEARCH ARTICLE https://doi.org/10.46488/NEPT.2026.v25i04.D1927 OPEN ACCESS

Household Behavioral Compliance in Waste Management Using the Extended Theory of Planned Behavior

Mary Ellen Camarillo†
Industrial Engineering Department, Cebu Technological University, Argao, Cebu, 6021, Philippines
†Corresponding author: Mary Ellen C. Camarillo; maryellencamarillo@gmail.com

ARTICLE HISTORY

Received: 27-03-2026
Revised: 01-06-2026
Accepted: 05-06-2026

KEYWORDS

Waste management compliance,
Extended theory of planned behavior,
Behavioral compliance,
Household waste management

CITE THIS ARTICLE

Mary Ellen Camarillo, 2026. Household behavioral compliance in waste management using the extended theory of planned behavior, *Nature Environment and Pollution Technology*, 25(4), D1927. https://doi.org/10.46488/NEPT.2026.v25i04.D1927

COPYRIGHT & LICENCE

© 2026 The Authors
Open Access under CC BY 4.0.

PUBLISHED BY

TECHNOSCIENCE PUBLICATIONS

ABSTRACT

Despite the expansion of waste management infrastructure and regulations, behavioral compliance with proper waste management practices remains inconsistent, particularly in developing-country contexts. This study investigates the factors influencing household compliance with waste management practices by extending the Theory of Planned Behavior (TPB) to incorporate motivational and deterrence-related mechanisms. A quantitative research design was employed using survey data collected from 106 household respondents and analyzed through Partial Least Squares Structural Equation Modeling (PLS-SEM) using SmartPLS 4. The measurement and structural models were evaluated to assess construct validity, reliability, and the significance of the hypothesized relationships. The PLS-SEM results revealed that motivation was the strongest predictor of behavioral compliance ($\beta = 0.499$, $p < 0.001$). These findings indicate that motivation is the strongest predictor of behavioral compliance, while perceptions of the waste management system also exert a significant positive influence. Penalty awareness does not directly affect compliance but significantly enhances motivation, suggesting an indirect deterrence mechanism. In contrast, attitudes toward waste management practices do not demonstrate a significant effect on compliance behavior. Furthermore, the study contributes to the literature by empirically validating an extended TPB framework in a developing-country setting such as the Philippines and demonstrating the importance of integrating penalty- and motivation-related constructs in explaining behavioral compliance. The policy implications of this study emphasize the need for behavior-centered governance strategies that complement infrastructure investments through visible enforcement, motivational interventions, and improved public perceptions of waste management systems.

1. INTRODUCTION

Effective waste management relies not only on infrastructure and enforcement but also on consistent compliance at the household level (Jayaraman & Tripathi 2026). While many municipalities in the Philippines have invested in collection systems, segregation facilities, and the legal framework provided by the Ecological Solid Waste Management Act of 2000, which mandates source segregation, proper disposal, and community participation, improper waste handling remains widespread. This indicates that structural provisions and policy enforcement alone are insufficient to ensure compliance. Furthermore, although policy responses have focused on improving services, existing research shows that compliance varies significantly across communities with similar infrastructure and enforcement (Sobrino-García 2025). Therefore, the success of waste management systems ultimately hinges on understanding the behavioral determinants

that shape how individuals respond to policies and systems.

The concept of behavioral compliance in waste management differs from voluntary pro-environmental behavior because it occurs within a regulatory context in which adherence is expected, and noncompliance may carry consequences. Individuals weigh perceived benefits, social expectations, personal motivations, and awareness of penalties when deciding whether to follow prescribed waste management practices (Kim 2023). Previous behavioral research has shown that attitudes toward environmental practices and perceptions of policy effectiveness influence behavioral outcomes. However, compliance behavior is also shaped by motivational drivers and deterrence mechanisms that have received insufficient attention in community-level waste management studies (Ibokette et al. 2024).

Understanding these behavioral determinants and their relationships is critical because policy effectiveness depends not only on system design but also on citizen participation and adherence to regulations. If individuals perceive policies as ineffective, lack motivation to comply, or are unaware of enforcement consequences, compliance levels may remain low regardless of infrastructure availability (Simpson & Evens 2024), thereby affecting the community, as waste management is a critical component of local systems. Conversely, when regulatory awareness and motivational drivers align with positive attitudes and trust in policy effectiveness, compliance behavior may improve. To provide clearer policy guidance for encouraging behavioral compliance among households and communities in waste management, this study examines the factors influencing household compliance with waste management practices. Specifically, it investigates the roles of attitudes toward waste management, perceptions of policy effectiveness, motivation, and penalty awareness in shaping compliance behavior. By situating compliance decisions within both psychological and regulatory contexts, the study moves beyond purely voluntary models of environmental behavior to explain rule-adherent behavior.

The primary methodology employed in this study is Partial Least Squares Structural Equation Modeling (PLS-SEM), which supports the study's aim of empirically evaluating the relative influence of these determinants on household-level compliance behavior in a developing country such as the Philippines. PLS-SEM was selected because the study seeks to explain and predict household behavioral compliance through an extended TPB framework, and this method is particularly suitable for exploratory and prediction-oriented research. Additionally, PLS-SEM places fewer restrictions on data normality, allowing the data to be analyzed in its original form without requiring extensive preprocessing. It also enables the simultaneous assessment of measurement reliability and structural relationships.

2. BACKGROUND RESEARCH

2.1. Behavioral Compliance in Waste Management

The public's compliance with household and community waste management depends significantly on municipal systems, infrastructure, and policy enforcement. Compliance behaviors in waste management include waste segregation, proper disposal, following collection schedules, and avoiding illegal dumping. Wang et al. (2018) found that only 36% of sampled villages provided garbage collection services, and among those, only 81% of residents disposed of waste at designated sites. This underscores how household compliance is heavily influenced by existing systems and policies. The study also indicates that organized disposal sites greatly promote proper waste disposal behavior. Another study revealed that compliance intentions are driven by perceived deterrent severity and certainty, which positively affect waste separation compliance (Kim 2023). Perceived deterrent severity raises the perceived cost of non-compliance, while perceived certainty increases the likelihood of sanctions. These perceptions heighten the perceived risk of rule violation and reinforce compliance intentions. Additionally, Pulido et al. (2025) identified factors contributing to non-compliance in the Philippines, such as lack of awareness or understanding of policies, insufficient resources, and inadequate training or guidance. From these studies, it is clear that behavioral compliance depends on both internal motivation and external factors influencing individuals, households, and communities. These findings suggest that non-compliance results not only from personal willingness but also from informational gaps, structural barriers, and institutional shortcomings. This complex interplay points to the limitations of interventions that focus solely on infrastructure.

2.2. Extended Theory of Planned Behavior

The Theory of Planned Behavior (TPB) is one of the most frequently used frameworks for explaining environmentally responsible actions. It suggests that behavior is mainly driven by behavioral intentions, which are influenced by attitudes toward the behavior, subjective norms, and perceived behavioral control (Liu 2025). Numerous studies on environmental behavior have applied TPB to examine recycling, waste segregation, and sustainable consumption, illustrating its effectiveness across various socio-cultural contexts (Concari 2023, Esfandiar et al. 2023, Kumar 2019).

By emphasizing cognitive evaluation, social influence, and perceived ability, TPB offers a straightforward and well-supported model for understanding how behavioral intentions are formed.

Although the Theory of Planned Behavior (TPB) offers valuable insights, it falls short of fully explaining behavior compliance in waste management systems, as it is embedded within broader frameworks of policy enforcement, monitoring, and institutional accountability. In such contexts, behavioral decisions are shaped not only by attitudes, norms, and perceived control-core elements of the original TPB-but also by cost–benefit analyses related to penalties, the perceived likelihood of enforcement, and motivational factors that promote sustained adherence. A study by Simpson & Evens (2024) demonstrated that individuals may comply not just because they view compliance positively, but also because they perceive risks or penalties associated with non-compliance, and internalized responsibility further reinforces their commitment to policies.

Several studies have expanded the Theory of Planned Behavior (TPB) by incorporating deterrence and motivational mechanisms. This research adopts an extended TPB framework to more accurately depict compliance behavior in real-world scenarios. Notably, it introduces a novel application of the extended TPB in a developing country context, utilizing structural equation modeling. The study examines how deterrence and motivation, integrated with core TPB constructs, influence compliance behavior amid the specific institutional and enforcement conditions of such settings.

2.3. Latent Variables in the Context of Behavioral Compliance in Waste Management

2.3.1. Attitude towards Waste Management Compliance

Attitude reflects an individual's overall assessment of engaging in a behavior. In waste management, it indicates whether people see compliance as beneficial, worthwhile, or burdensome (Park & Spence 2022). Research repeatedly shows that positive environmental attitudes correlate with stronger intentions to recycle and segregate waste (Cheng et al. 2021). Those who believe that waste compliance helps protect the environment, maintain community cleanliness, and promote public health are more likely to practice proper disposal, as evidenced by Nabila et al. (2020). Conversely, if compliance is considered time-consuming, inconvenient, or ineffective, participation tends to decrease.

Furthermore, studies highlight that positive environmental attitudes do not automatically lead to compliant behavior, emphasizing that while attitudinal support is essential, it alone is not enough. This discrepancy underscores the importance of factoring in additional cognitive and contextual influences.

2.3.2. Perceived Behavioral Control

Perceived behavioral control refers to an individual's assessment of their capability to perform a specific behavior, taking into account available resources, knowledge, and situational limitations (Chen et al. 2023). In the context of waste management, it encompasses access to segregation bins, proximity to disposal sites, clarity of guidelines, time availability, and perceived convenience (Cheng 2020). Additionally, research consistently shows that even when attitudes and social norms are positive, compliance tends to decrease if individuals find the behavior difficult or inconvenient (Amir et al. 2025).

In multiple studies, households tend to adhere more effectively when waste segregation systems are straightforward, collection schedules are dependable, and instructions are clearly communicated (Sahoo et al. 2022). Additionally, perception directly predicts behavior in TPB-based models, especially when strong actual control conditions significantly impact behavioral execution.

2.3.3. Motivation

Motivation encompasses both internal and external factors that energize and sustain behavior. In Romaniuc and Bazart's book (Romaniuc & Bazart 2026), motivation is often categorized as intrinsic-such as environmental concern or moral obligation-or extrinsic, like rewards, social recognition, or avoiding sanctions. Research shows that intrinsic motivation promotes long-term compliance, while extrinsic motivation may only produce short-term adherence if intrinsic commitment is lacking (Izuakor et al. 2026). Combining intrinsic and extrinsic motivators can enhance behavioral consistency, especially during the initial adoption phase (Vorobeva et al. 2022). Therefore, motivation is a vital addition to the Theory of Planned Behavior when studying regulated environmental actions driven by personal values and external incentives.

2.3.4. Penalty Awareness and Deterrence Mechanisms

Penalty awareness pertains to an individual's understanding and perception of sanctions linked to non-compliance. In regulatory contexts, deterrence theory indicates that people are more inclined to obey rules when penalties are perceived as certain, visible, and enforceable (Kim 2023). Several environmental compliance studies show that enforcement visibility and penalty awareness significantly impact adherence to waste disposal regulations. For example, Amin et al. (2024) found that increased visibility and severity of fines for improper waste disposal enhanced public awareness and education campaigns. This public awareness, in turn, influenced compliance when people believed there was a credible risk of fines and punishment.

However, literature such as Kardiat & Jamaruddin's (2025) study suggests that penalties alone do not ensure long-term compliance. An over-reliance on enforcement may lead to compliance driven by fear rather than internal responsibility. Effective strategies often combine enforcement with education, social norms, and motivational interventions (Khan et al. 2024).

2.3.5. Behavioral Intention and Compliance Behavior

Behavioral intention reflects an individual's readiness to engage in a behavior and serves as the immediate precursor to action in the Theory of Planned Behavior (Getahun & Mengstie 2024). Recent research consistently shows that intention is a predictor of participation in recycling and waste segregation. However, the gap between intention and behavior remains a significant challenge in environmental compliance studies (de Matos et al. 2025). External factors, such as convenience barriers and enforcement conditions, often hinder the translation of intentions into action. Consequently, models that incorporate perceived control, motivational factors, and deterrence elements tend to better explain compliance behaviors (Love et al. 2024).

3. CONCEPTUAL FRAMEWORK

The conceptual framework proposes that attitude, perception, motivation, and awareness of penalties each have a direct impact on proper waste management behaviors. Additionally, awareness of penalties is believed to influence motivation and attitude, which in turn act as mediators that indirectly shape behavior.

Each hypothesis (H1–H6) represents a directional relationship between constructs as follows:

- Attitude → Behavioral Compliance (H1)

  This hypothesis shows that individuals with more favorable attitudes toward waste management are expected to exhibit higher levels of behavioral compliance.

- Perception → Behavioral Compliance (H2)

  This hypothesis shows that individuals with higher levels of perception when it comes to waste management are expected to manifest behavioral compliance.

- Motivation → Behavioral Compliance (H3)

  This hypothesis shows that individuals with high motivation and understanding of waste management and its benefits are expected to show a high level of behavioral compliance.

- Penalty Awareness → Behavioral Compliance (H4)

  This hypothesis shows that individuals with high awareness levels of deterrence mechanisms are also expected to show higher levels of behavioral compliance.

- Penalty Awareness → Motivation (H5)

  This hypothesis exhibits that individuals with higher levels of penalty awareness are also expected to show higher levels of motivation towards behavioral compliance in the context of waste management practices.

- Penalty Awareness → Attitude (H6)

  This hypothesis shows that individuals with a high level of awareness of the waste management deterrence mechanisms are also the ones expected to have a positive attitude towards waste management practices or protocols in place.

4. RESEARCH OBJECTIVES

The main objective of this study is to examine the

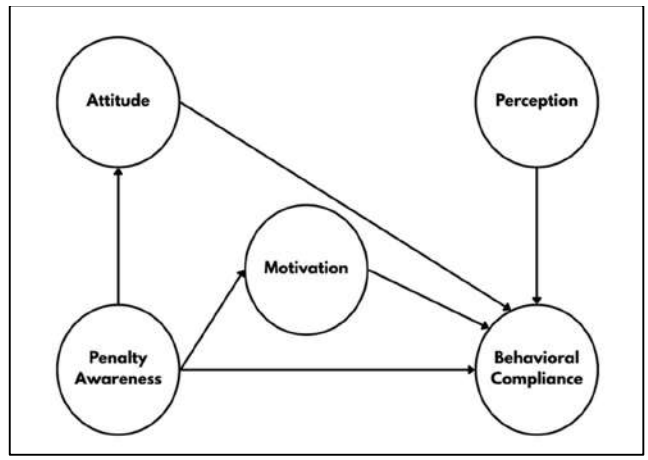


Fig. 1: Conceptual Framework of the extended Theory of Planned Behavior.

interrelationships among attitudinal, perceptual, motivational, and deterrence-related factors and their association with behavioral compliance in waste management at the household and community levels in the Philippines.

Specifically, the study aims to examine the influence of attitude, perception, motivation, and penalty awareness on behavioral intention, which translates into compliance within the context of waste management systems. It also seeks to evaluate the effects of penalty awareness, both directly and indirectly, through motivation and attitude.

Moreover, the study intends to assess the overall explanatory power of the structural model using PLS-SEM. These objectives are aligned with the broader goal of identifying actionable insights to strengthen community-based environmental programs and policies. In the long term, the findings can inform the development of targeted interventions that enhance household and community adherence to waste management regulations, thereby reducing environmental health risks, improving the effectiveness of enforcement strategies, and fostering sustainable pro-environmental habits. Finally, these insights contribute to strengthening institutional capacity, promoting civic responsibility, and supporting more resilient and sustainable waste management systems in the Philippine context.

5. METHODOLOGY

This study employs a quantitative, cross-sectional design utilizing a structured survey questionnaire as the primary data collection tool. The target population comprises households or individuals residing in a designated municipality covered by local solid waste management ordinances and practices. A total of 106 respondents participated in the survey. Since the minimum sample size for a PLS-SEM model is 50-due to its exploratory nature-this sample exceeds the threshold, indicating sufficient statistical power. Unlike confirmatory CB-SEM, which requires a larger sample, PLS-SEM's flexibility allows for smaller samples.

Participants were recruited via convenience sampling from households accessible during the survey period, with voluntary consent obtained. Eligible respondents were adults aged 18 or older, including household heads or those directly involved in waste management. This approach enabled efficient data collection within resource and time constraints, while focusing on residents actively engaged in household waste activities. All respondents were from the municipality of Argao.

The survey measured constructs such as attitude, perception, motivation, penalty awareness, and behavioral compliance, using a 5-point Likert scale from 'strongly disagree' to 'strongly agree.' These items were developed based on validated instruments in environmental behavior research and pilot-tested for content validity and clarity within the local context. Examples include: 'Proper waste disposal benefits the community' (attitude), 'I believe waste management policies are effectively implemented' (perception), 'Community programs motivate me to segregate waste' (motivation), 'I am aware of fines for improper waste disposal' (penalty awareness), and 'I regularly segregate waste at home' (behavior). The questionnaire was adapted from established instruments and aligned with the extended Theory of Planned Behavior framework.

A pilot test was conducted to validate the content, ensuring item clarity and validity. This involved 30 participants who completed the initial version of the questionnaire. Their responses were then analyzed using SmartPLS software to assess construct validity and reliability, examining indicator loadings, average variance extracted (AVE), and Cronbach's Alpha scores. The pilot results indicated strong reliability, with favorable indicator loadings, AVE, and Cronbach's Alpha. Following this, the main survey was carried out from January to February 2026 through face-to-face interviews. Prior to the interviews, respondents were informed of the study's purpose, assured of response confidentiality, and told that participation was voluntary.

The data analysis was conducted in multiple stages. Initially, data screening identified missing data, outliers, and non-normal distribution. The measurement model was then evaluated for indicator reliability (outer loadings ≥ 0.70), internal consistency (Cronbach's alpha and composite reliability ≥ 0.70), convergent validity (average variance extracted ≥ 0.50), and discriminant validity using the Fornell–Larcker criterion. Once a valid and reliable measurement model was confirmed, the structural model was assessed for path significance and R^2 values. The final stage involved bootstrapping with 5,000 resamples to test the significance of paths.

6. RESULTS AND DISCUSSION

To examine the significance and magnitude of the relationships in the proposed conceptual framework, which is the extended TPB model applied to household waste management compliance in Argao, Cebu, as presented in Fig. 2, structural equation modeling (SEM) using a partial least squares (PLS-SEM) approach was employed. PLS-SEM allows for the simultaneous assessment of measurement model reliability and structural relationships among latent variables, making it suitable for analyzing complex behavioral models involving multiple interrelated

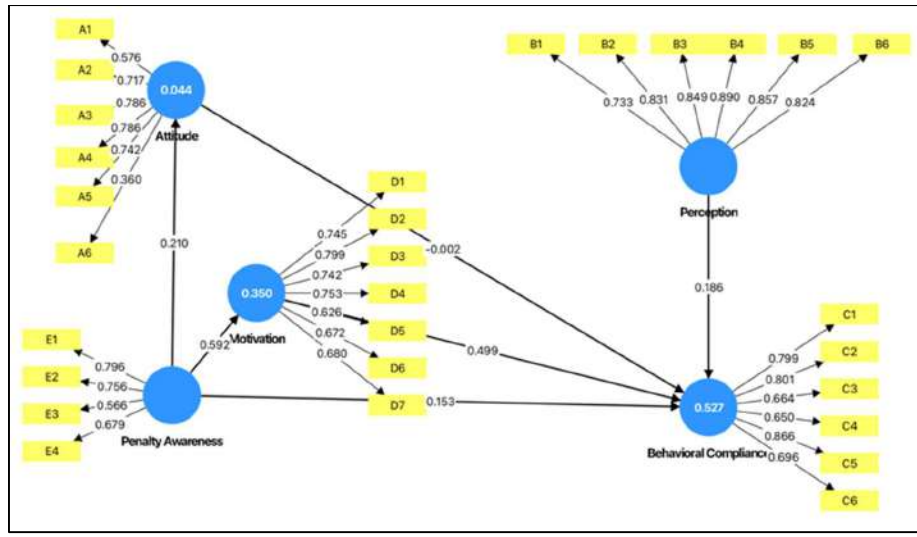


Fig. 2: Graphical output of the PLS-SEM Algorithm for the extended TPB.

constructs. Using this method, the study evaluates the model's explanatory power.

Furthermore, structural equation modeling can reveal the significance and validity of the relationships and the hypotheses (arrows) by extension. In this context, behavioral compliance is the endogenous dependent variable, meaning that all connections and structural relationships ultimately point to it as a latent variable.

6.1. Establishing the Measurement Quality of Behavioral Compliance Constructs

The measurement model was initially assessed to ensure that the observed indicators accurately represent the latent constructs within the extended Theory of Planned Behavior framework. This evaluation prioritized verifying the reliability and validity of the measurement instruments. Establishing measurement reliability is essential before analyzing structural relationships, as it confirms that the survey items effectively capture the behavioral and perceptual aspects related to waste management compliance. Reliability and validity were examined through indicator reliability, internal consistency, and convergent validity. Indicator reliability was determined using outer loadings from the PLS algorithm (Table 1), while internal consistency and convergent validity were assessed via Cronbach's alpha, composite reliability, and average variance extracted (AVE).

The results show that the measurement indicators exhibit satisfactory reliability and internal consistency. Although some indicator loadings are slightly below the recommended threshold of 0.70, they were retained in the PLS-SEM model because their values exceeded the minimum acceptable level and they contributed meaningfully to representing their constructs. As long as composite reliability and convergent validity are maintained, indicator loadings between 0.40 and 0.70 can be retained. Moreover, removing these indicators could risk omitting important aspects of household waste management behavior from the model.

In the Attitude variable, two indicators exhibit small outer loadings, suggesting they do not strongly represent the construct. Since these indicators are part of a reflective measurement model, and with a threshold set at 0.7, their lower loadings indicate weaker representation. In the Behavioral Compliance variable, three indicators are marked in red because their loadings are below 0.7, implying they do not adequately reflect the construct. Similarly, the Motivation variable has three indicators marked in red for the same reason. For Penalty Awareness, two indicators appear misaligned or less representative of the concept; though their loadings remain relatively high, they simply do not reach the 0.7 cutoff. Conversely, all indicators for the Perception variable have loadings above 0.7, indicating that these survey items effectively represent the underlying concept of Perception.

Similarly, the internal consistency measures surpassed standard benchmarks, indicating that the constructs are measured reliably. Cronbach's alpha, the most traditional criterion for internal consistency, estimates reliability based on intercorrelations among observed indicator variables. Although some constructs' alpha values fell slightly below the conventional 0.70 threshold, they still demonstrated satisfactory composite reliability, which offers a more precise assessment by considering differing indicator

Table 1: Outer loadings.

	Attitude	Behavioral Compliance	Motivation	Penalty Awareness	Perception
A1	0.576				
A2	0.717				
A3	0.786				
A4	0.786				
A5	0.742				
A6	0.36				
B1					0.733
B2					0.831
B3					0.849
B4					0.89
B5					0.857
B6					0.824
C1		0.799			
C2		0.801			
C3		0.664			
C4		0.65			
C5		0.866			
C6		0.696			
D1			0.745		
D2			0.799		
D3			0.742		
D4			0.753		
D5			0.626		
D6			0.672		
D7			0.68		
E1				0.796	
E2				0.756	
E3				0.566	
E4				0.679	

Table 2: Construct reliability and validity.

	Cronbach's alpha	Composite reliability (rho_a)	Composite reliability (rho_c)	Average variance extracted (AVE)
Attitude	0.765	0.803	0.829	0.460
Behavioral Compliance	0.842	0.856	0.884	0.563
Motivation	0.844	0.852	0.882	0.517
Penalty Awareness	0.662	0.682	0.795	0.497
Perception	0.910	0.917	0.931	0.692

loadings. Convergent validity, reflecting the degree to which a measure correlates positively with other measures of the same construct, further supports the model's validity by confirming it accurately captures the observed reality. This is indicated by the average variance extracted.

Table 2 displays the construct reliability and validity of the model. The Cronbach's alpha results show that only the Penalty Awareness variable falls below the 0.7 threshold, indicating that its items may not be consistently aligned or may not accurately represent the underlying concept.

Conversely, all latent variables or constructs measured by composite reliability exceed the 0.7 threshold, confirming the reliability and validity of the survey items. The last column of Table 2 shows the average variance extracted (AVE), with the variables Attitude and Penalty Awareness falling below the 0.5 threshold. This suggests that some indicators within these variables do not adequately explain their respective latent constructs. Despite some values being slightly below the established thresholds, they are high enough to be acceptable. Overall, these results suggest that the constructs related to attitudes, perceptions, motivations, and deterrence effectively provide a reliable empirical framework for understanding behavioral factors influencing household waste management compliance.

6.2. Distinguishing the Behavioral Dimensions of Compliance

Discriminant validity refers to the degree to which a construct is genuinely distinct from other constructs based on empirical evidence. It indicates that a construct is unique and different from other elements within the model. In this study, the Fornell-Larcker criterion was used to evaluate the discriminant validity of the model. This method compares the square root of the Average Variance Extracted (AVE) values with the correlations between constructs. The logic is that a construct should share more variance with its associated indicators or survey items. An alternative to the Fornell-Larcker approach is examining cross-loadings, which assess loadings instead of AVE values but follow the same principle.

In waste management compliance research, constructs such as attitude, perception, motivation, and penalty awareness represent distinct psychological and behavioral mechanisms. It is essential to establish discriminant validity to ensure these constructs measure unique aspects of compliance rather than overlapping concepts. Discriminant validity can be assessed using a matrix where the Fornell-Larcker criterion requires that each construct's diagonal value (the square root of the Average Variance Extracted, or AVE) be larger than the off-diagonal values in its row and column. As shown in Table 3, each construct's diagonal value is the highest in its respective column. For example, the Attitude variable has a Fornell-Larcker score of 0.678, the highest among its column values. Similar patterns are observed among the other latent variables. The results confirm that the square roots of the AVE values exceed the inter-construct correlations, satisfying the Fornell–Larcker criterion for discriminant validity.

These results confirm that the behavioral determinants within the extended TPB framework are empirically separable. This distinction is especially crucial for understanding compliance, as it indicates that attitudes, motivations, and deterrence perceptions function as distinct mechanisms shaping waste management behaviors.

6.3. Evaluating the Explanatory Capacity of the Extended TPB Model

After confirming the validity of the measurement, the next step was to examine the structural model to assess the extended Theory of Planned Behavior framework's effectiveness in explaining household waste management compliance. Following the evaluation of the measurement models presented in Sections 6.1 and 6.2 of the Results and Discussion, we proceeded to assess the inner model. This assessment emphasizes the model's predictive power and how well the included constructs explain variations in the endogenous variables. The key indicators used for this evaluation include the coefficient of determination (R^2), predictive relevance (Q^2), and collinearity diagnostics.

The explanatory power of the model is best assessed using the coefficient of determination (R-squared value), which measures its predictive accuracy. This coefficient is calculated as the squared correlation between an endogenous construct's actual and predicted values. In this study, the structural model accounted for 54.6% of the variance in behavioral compliance ($R^2 = 0.527$). According to Hair et al. (2022), R^2 values around 0.25, 0.50, and 0.75 are considered to represent weak, moderate, and substantial explanatory power, respectively. Thus, the R^2 value indicates a moderate level of explanatory strength, meaning the chosen predictors adequately explain household behavioral compliance concerning waste management.

Furthermore, the coefficient indicates the combined effects of the exogenous constructs on the endogenous

Table 3: Discriminant validity (Fornell-Larcker).

	Attitude	Behavioral Compliance	Motivation	Penalty Awareness	Perception
Attitude	0.678				
Behavioral Compliance	0.328	0.750			
Motivation	0.453	0.687	0.719		
Penalty Awareness	0.210	0.554	0.592	0.705	
Perception	0.386	0.537	0.530	0.575	0.832

Table 4: R-Square.

	R-square	R-square adjusted
Attitude	0.044	0.035
Behavioral Compliance	0.527	0.508
Motivation	0.350	0.344

construct. This is also why only variables with arrows pointing inwards display R-squared values. The coefficient reflects how much variance in the primary endogenous construct—behavioral compliance—is explained. An R-squared value closer to 1 signifies greater predictive accuracy.

In Table 4, focusing on the adjusted R-square, the model's predictive power for the main endogenous construct, behavioral compliance, is 0.508. This indicates that, considering the other variables and their predispositions, the extended theory of planned behavior explains 50.80% of the variance in households' waste management behavior. This is relatively high, given that only four other variables were included in the model (Fig. 1). However, it also suggests that many relevant factors are missing and could improve the prediction of behavioral compliance. Since the context is household waste management, additional household-related factors-such as system and infrastructure conditions-should be considered. The current model does not account for policies or infrastructure, which likely influence household behavior and may explain why the model's explained variance is limited to 50.80%.

In addition to assessing the coefficient of determination for the structural model, it is necessary to evaluate collinearity. Collinearity diagnostics confirm that multicollinearity among predictor constructs is not a concern. To ensure this, each set of predictor constructs was examined separately for each part of the structural model. The VIF values are presented in Table 5. These findings indicate that the extended TPB model offers a suitable analytical framework for analyzing behavioral compliance with waste management practices in this context.

Table 5: Collinearity VIF.

	VIF
A1	1.450
A2	1.759
A3	1.730
A4	1.847
A5	1.380
A6	1.272
B1	1.809
B2	2.639
B3	2.757
B4	3.426
B5	3.142
B6	2.239
C1	1.860
C2	2.141
C3	1.470
C4	1.397
C5	2.663
C6	1.596
D1	1.931
D2	2.170
D3	2.117
D4	2.365
D5	2.210
D6	2.743
D7	2.230
E1	2.031
E2	2.055
E3	1.869
E4	1.870

6.4. Structural Relationships and Behavioral Pathways of Compliance

In the PLS-SEM model, the focus centers on path coefficients that represent the proposed relationships among constructs. These coefficients, scaled between -1 and +1, reflect the strength of these relationships—the closer to 1 or -1, the stronger the impact. Within the extended Theory of Planned Behavior (TPB) framework, these paths depict the behavioral mechanisms that influence household compliance. Notably, the path from penalty awareness to motivation has the highest coefficient at 0.592, indicating that awareness of penalties—such as fines or negative outcomes like delayed waste collection-significantly motivates proper waste management behaviors. Clear and consistent communication of penalties enhances this motivational effect, encouraging households to comply with waste policies. Ultimately, compliance appears more driven by regulatory enforcement than by internal pro-environmental motivation.

The second most influential path coefficient is the effect of motivation on behavioral compliance (0.499), highlighting that motivation is a significant direct factor contributing to compliance, consistent with real-world observations. Motivation can be driven by incentives, health benefits, or daily considerations related to household waste. A key motivator is individuals' perception of the severity of negative consequences from pollutants released

into the air if household waste is not properly disposed of or managed. However, in this study, motivation was not further distinguished into internal or external types, which could affect how respondents responded to related indicators.

The third highest path coefficient is from Penalty Awareness to Attitude, reinforcing the idea that penalties serve as a primary driver of behavioral compliance. However, this influence is moderated by the constructs of Attitude and Motivation. Attitude also encompasses other factors, such as overall feelings towards the system, and heavily depends on personal viewpoints. In waste management, some individuals may hold a negative attitude towards allowing local authorities to handle waste disposal, as they might associate it with large, unsustainable landfills that could be mismanaged and cause regional harm.

Among the various paths, the one with the lowest and possibly negative coefficient is from Attitude to Behavioral Compliance, indicating an inverse relationship (Table 6). This suggests that a positive attitude alone does not guarantee households will comply with waste management practices, especially if there is no awareness of penalties.

The magnitude of these relationships highlights the importance of considering not only attitudinal and perceptual factors traditionally emphasized in the Theory of Planned Behavior but also motivational drivers and awareness of enforcement consequences. The observed relationships provide an initial indication that compliance behavior emerges from a combination of internal behavioral motivations and external regulatory considerations, and not just from a single driver.

The bootstrap analysis was performed to assess the statistical significance of the proposed relationships within the extended Theory of Planned Behavior (TPB) framework. As shown in Table 7, three structural paths were statistically significant, while the others did not meet conventional significance levels. Notably, motivation exhibited the strongest and most significant positive effect on behavioral compliance ($\beta = 0.499$, $p < 0.001$). This suggests that motivation reflects an individual's persistence in engaging in environmentally responsible actions, supporting the idea that households are more likely to comply when waste management behaviors are seen as personally meaningful or advantageous. The strength of this relationship indicates that internal behavioral drivers are crucial in transforming policy expectations into actual compliance with recommended practices.

The relationship between Penalty Awareness and Motivation is also significant ($\beta = 0.592$, $p < 0.001$). Awareness of penalties or deterrence strategies can further boost individuals' or households' motivation to comply with waste management policies and protocols. Instead of acting in isolation, penalty awareness helps shape behavioral readiness by increasing accountability and emphasizing the importance of adhering to proper waste management practices and regulations. This significant relationship indicates that awareness of deterrence measures can trigger internal motivational responses. While motivation may already be present, penalty awareness can reinforce it, leading to voluntary compliance.

The final significant relationship is between Perception and Behavioral Compliance ($\beta = 0.186$, $p = 0.038$). This

Table 6: Path coefficients.

	Original sample [O]	Sample mean [M]	Standard deviation [STDEV]	T statistics [|O/STDEV|]	P values
Attitude -> Behavioral Compliance	-0.002	-0.002	0.101	0.023	0.982
Motivation -> Behavioral Compliance	0.499	0.504	0.101	4.926	<0.001
Penalty Awareness -> Attitude	0.210	0.252	0.116	1.813	0.070
Penalty Awareness -> Behavioral Compliance	0.153	0.160	0.090	1.694	0.090
Penalty Awareness -> Motivation	0.592	0.602	0.069	8.555	<0.001
Perception -> Behavioral Compliance	0.186	0.181	0.089	2.081	0.038

Table 7: Bootstrapping results.

	Path coefficients
Attitude -> Behavioral Compliance	-0.002
Motivation -> Behavioral Compliance	0.499
Penalty Awareness -> Attitude	0.210
Penalty Awareness -> Behavioral Compliance	0.153
Penalty Awareness -> Motivation	0.592
Perception -> Behavioral Compliance	0.186

suggests that households' interpretations and personal assessments of the waste management system significantly impact their compliance behavior. Perception represents how individuals understand waste management structures, factoring in motivational elements within cultural, social, or environmental contexts. For instance, households are more likely to participate actively in compliance when they view the systems as functional and advantageous. This underscores that behavioral compliance is partly shaped by how policies are perceived and experienced at the community level, rather than solely by their formal implementation.

6.5. Interpreting Compliance Behavior within the Philippine Context

The findings offer valuable insights into the behavioral factors influencing household waste management compliance in Argao, Cebu. While institutional policies and waste management infrastructure are officially in place, the results reveal that individual behavioral determinants play a more significant role in driving compliance than structural provisions alone. Guided by the extended Theory of Planned Behavior (TPB), this study emphasizes psychological and regulatory drivers such as motivation, perceptions, and awareness of penalties, rather than infrastructure performance itself. However, the findings suggest that infrastructure indirectly influences behavior by shaping household perceptions and experiences of waste management systems. When facilities are perceived as organized, accessible, and supportive of daily routines, they can foster intrinsic motivation and promote compliance with waste management practices. This aligns with the broader understanding that environmental policy effectiveness depends not only on institutional design but also on how individuals cognitively and behaviorally respond to these policies in their daily lives.

Perceptions of enforcement further elucidate how compliance behaviors develop within regulated environments. The structural model highlights the pathway Penalty Awareness → Motivation → Behavioral Compliance as the most significant mechanism influencing household behavior. This indicates that awareness of penalties does not directly lead to compliance but enhances motivation among households. In this context, deterrence and penalties function less as coercive measures and more as signals of the seriousness and legitimacy of environmental regulations, emphasizing the urgency of compliance. This aligns with previous studies showing that limited awareness and weak enforcement diminish policy effectiveness, especially in developing countries where institutional implementation varies. By demonstrating that penalty awareness boosts motivation-and that motivation drives compliance—the study supports expanding the TPB to incorporate regulatory and deterrence factors that strengthen internal behavioral processes, beyond mere attitude change.

Household-level realities further contextualize the observed behavioral patterns. The existing variations in household structure, work arrangements, and daily routines may influence the capacity of residents to comply consistently with waste segregation and disposal requirements. Some practical constraints, such as absence during collection schedules or limited time for waste preparation, can hinder compliance even when positive attitudes or motivations are present. Recognizing these constraints highlights the importance of designing waste management policies that are responsive to diverse household conditions, which thereby reduces structural barriers that may unintentionally discourage participation.

Despite the contributions of this study, there are several limitations that should be reiterated. First, the study was conducted within a specific geographic area, which may have an influence on the generalizability of the findings to other communities with different socioeconomic, cultural, or environmental conditions. Second, the causal relationships among the variables cannot be established with certainty. Third, although the extended Theory of Planned Behavior model incorporated motivation and penalty awareness, other factors that may influence household waste management compliance, such as environmental knowledge, access to waste management facilities, institutional trust, and community participation, were not included in the present analysis. The viability of the discussion and recommendations should be able to address the limitations of future studies.

Overall, the findings indicate that enhancing waste management outcomes relies on behavioral interventions that complement existing infrastructure and policies. While infrastructure and regulations form essential foundations, actual behavioral compliance depends heavily on how policies can stimulate motivation, influence perceptions, and reflect community and household realities. In community-based waste management, strategies that prioritize enforcement, boost motivational engagement, and address local social dynamics are likely more effective in ensuring lasting behavioral change than merely investing in infrastructure and revisiting policies.

7. CONCLUSIONS AND POLICY INSIGHTS

This research indicates that to achieve better compliance with household waste management policies in the Philippines, there must be a phased approach based on behavioral change that will likely be more effective than using only infrastructure development or strict enforcement. Compliance behavior with household waste management

policies is primarily motivated by individual and community perceptions of penalties; therefore, policy interventions need to be designed in such a way as to gradually create improved compliance to the extent that it is within the current institutional constraints.

7.1. Short-Term: Low-Cost, Behavior-Oriented Interventions

In the short run, local government units (LGUs) and barangays can implement low-cost, readily implementable strategies that directly address the behavioral determinants of compliance. First, improving Information, Education, and Communication (IEC) campaigns to show individuals how proper waste management relates to their own cleanliness, health, and community order will increase motivation and promote compliance. Current IEC messages about the environment are often abstract. Using the environment as a motivator will provide daily relevance for households and increase the likelihood that individuals will comply with the rules. In alignment with this, it is encouraged to do a quarterly barangay-based waste segregation workshop with attendance integrated into community environmental programs.

Second, increasing the visibility of enforcement efforts and clearly communicating the penalties for waste disposal violations can raise awareness and encourage compliance. LGUs should disseminate information about rules, penalties, and collection schedules through multiple channels, such as bulletin boards and community notices, ensuring consistent and fair communication. To reinforce compliance, Argao could implement or enhance incentive programs like barangay recognition awards and waste exchange initiatives. Third, LGUs can support households by providing simple, standardized guides on waste separation, color-coding, and collection schedules. These tools will lessen families' cognitive and physical burdens, improving adherence to waste management rules.

7.2. Medium-Term: Strengthening System Credibility and Community Engagement

Medium-term policy initiatives should focus on improving the public's perception of the waste management system and increasing trust in the involved institutions, as these factors strongly influence compliance behavior. Enhancing the reliability and accessibility of services is crucial. Consistent waste collection times and easily accessible disposal sites directly impact households' perceptions of service efficiency and are linked to higher compliance rates. Addressing these issues involves both technical improvements and behavioral strategies. When adjusting collection schedules or days, household feedback should be considered to ensure schedules meet community needs.

Local government units (LGUs) should establish formal channels for residents and communities to communicate and provide feedback on waste management. This includes engaging with barangays, creating complaint reporting procedures, and regularly assessing waste management practices within each community. Allowing community members to share their feedback helps identify system performance issues and improves responsiveness, fostering a perception of equitable treatment. Additionally, LGUs must enforce waste management rules consistently and transparently across all households. Visible and fair enforcement encourages greater compliance and trust within the community.

7.3. Long-Term: Institutionalizing Household-Sensitive and Adaptive Policies

Over time, waste management policies will evolve to develop household-sensitive and adaptive systems that account for how different types of households influence their compliance with waste responsibilities. Policies should consider various factors affecting daily household operations and their impact on waste management. This may involve implementing more flexible collection schedules, localized service modifications to suit work hours, available time, and space limitations, or providing tailored support from local governments to assist households with structural constraints. By aligning systems with household realities, these solutions can lower barriers to compliance and foster long-term participation. Furthermore, LGUs might establish participatory governance frameworks, enabling communities to contribute to the design and evaluation of waste systems. While full co-governance may not be immediately feasible in all areas, gradually incorporating community input can enhance accountability, a sense of ownership, and promote sustainable behavioral change.

7.4. Integrated Perspective: Waste Management as a Socio-Technical System

The findings from this study across four stages highlight that waste management systems should be viewed as socio-technical entities, emphasizing the interdependence of technical infrastructure and human behavior. To develop effective waste management policies and systems, it is essential to integrate these components: (a) motivational mechanisms that sustain long-term behavioral engagement, (b) visible, credible enforcement systems that reinforce compliance, (c) reliable, user-oriented service delivery that enhances perceptions of system effectiveness, and

(d) household-sensitive adaptations that address practical constraints affecting waste management behaviors. Incorporating these elements will lead to policies that are both operationally efficient and behaviorally supportive, thereby increasing the likelihood of long-term success.

The research suggests that successful behavioral change in the Philippines can be achieved through phased, behavior-focused interventions. While short-term results can be attained with low-cost strategies, sustaining credibility over the medium and long term is crucial for lasting effectiveness. By aligning policies with households' perceptions, experiences, and responses to waste management systems, local government units (LGUs) can improve household compliance and overall system effectiveness. Ultimately, the success of a waste management program depends not only on infrastructure and regulations but also on its ability to foster consistent, scalable behavioral adherence among households.

8. ACKNOWLEDGMENTS

The authors declare that no specific funding was received for this research from public, commercial, or not-for-profit funding agencies.

9. REFERENCES

Amin, A., Abdulrauf, A. and Isiaq, A. T., 2024. Strategies for the implementation of environmental protection regulations towards sustainable waste management in Oyo State. *Gusau International Journal of Management and Social Sciences*, 7(2), pp.83-104. [DOI]

Amir, F., Miru, A. S. and Sabara, E., 2025. Urban household behavior in Indonesia: Drivers of zero waste participation. *arXiv preprint arXiv:2505.17864*. [DOI]

Chen, J., Chen, J., Li, T., Li, T., You, H., You, H., Wang, J., Peng, X. and Chen, B., 2023. Behavioral interpretation of willingness to use wearable health devices in community residents: A cross-sectional study. *International Journal of Environmental Research and Public Health*, 20(4), p.3247. [DOI]

Cheng, K. W., 2020. Attitude, perceived behavioral control, and subjective norms in waste segregation-at-source behavior: An empirical study. *Sustainable Business and Society in Emerging Economies*, 2(1), pp.83-93. [DOI]

Cheng, K. W., Osman, S., Jusoh, Z. M. and Lau, J. L., 2021. Multidimensional factors that influence the intention to practice segregation-at-source of solid waste: An empirical study. *Management Science Letters*, 11(2), pp.379-390. [DOI]

Concari, A., 2023. Understanding waste separation behavior through the application of an extended form of the theory of planned behavior (TPB). *Journal of Behavioral and Environmental Studies*, 15(3), pp.45-62. [DOI]

de Matos, C. A., Luppi, L. and Veiga, R. T., 2025. Assessing the intention-behavior gap in the pro-environmental behavior context: a longitudinal study about water conservation. *Journal of Cleaner Production*, 524, p.146499. [DOI]

Esfandiar, K., Pearce, J., Dowling, R. and Goh, E., 2023. The extended theory of planned behaviour model and national parks visitors' pro-environmental binning behaviour: A cross-cultural perspective. *Journal of Outdoor Recreation and Tourism*, 42, p.100602. [DOI]

Getahun, D. and Mengstie, M., 2024. Explaining motivational factors of employees' behavior towards customer satisfaction using the theory of planned behavior. *PLoS One*, 19(11), p.e0314431. [DOI]

Hair, J. F., Hult, G. T. M., Ringle, C. M. and Sarstedt, M., 2022. *A Primer on Partial Least Squares Structural Equation Modeling (PLS-SEM)*. Sage Publications, pp.350.

Ibokette, A. I., Aboi, E. J., Ijiga, A. C., Ugbane, S. I., Odeyemi, M. O. and Umama, E. E., 2024. The impacts of curbside feedback mechanisms on recycling performance of households in the United States. *World Journal of Biology Pharmacy and Health Sciences*, 17(2), pp.366-386. [DOI]

Izuakor, C.F., Emeghebo, U.M., Nwakile, T.C., Omego, G.N., Odewale, O.T., Attah, B.I., Ezeaku, M.N. and Ogbonna, I.J., 2026. Promotion incentives and the dynamics of research motivation among Technical and Vocational Education and Training lecturers in Nigerian universities. *Discover Education*, 5(1), p.148. [DOI]

Jayaraman, A., Tripathi, S. and Ramakrishnan, S., 2026. Regulatory Concerns for Solid Waste Management. In: *Solid Waste Management: Challenges, Sustainability and Advancements*. Wiley, pp.397-430. [DOI]

Kardiat, Y., Jamaruddin, J. and Saprudin, S., 2025. Civil Servant Behavior Towards Public Service Compliance: A case study in Makassar City. *Journal of Asian Multicultural Research for Social Sciences Study*, 6(3), pp.83-97. [DOI]

Khan, A. U., Hussain, U., Rashid, M. and Hameed, R., 2024. Social norms and legal compliance: Understanding the psychological factors influencing adherence to laws in educational settings. *Bulletin of Business and Economics (BBE)*, 13(3), pp.326-332. [DOI]

Kim, S., 2023. Antecedents of compliance intention and its impact on waste separation behavior: based on rational choice theory and deterrence theory. *Behavioral Sciences*, 13(5), p.424. [DOI]

Kumar, A., 2019. Exploring young adults'e-waste recycling behaviour using an extended theory of planned behaviour model: A cross-cultural study. *Resources, Conservation and Recycling*, 141, pp.378-389. [DOI]

Liu, Z., 2025. The Impact of Green Information Disclosure on Green Consumption Intention: Evidence from New Energy Vehicle Consumers in China Based on the Theory of Planned Behavior. *Sustainability*, 17(17), p.7983. [DOI]

Love, S., Larue, G. S., Rowland, B. and Davey, J., 2024. What influences intentions to offend? A systematic review and meta-analysis of the factors associated with the deterrence of drink-driving. *Transportation Research Part F: Traffic Psychology and Behaviour*, 100, pp.154-168. [DOI]

Nabila, S. H., Negoro, H. A. and Utari, D., 2020. The level of individual participation of the community in implementing effective solid waste management policies. *Global Journal of Environmental Science and Management*, 6(3), pp.345-360. [DOI]

Park, J. and Spence, C., 2022. The effect of perceived scarcity on strengthening the attitude–behavior relation for sustainable luxury products. *The Journal of Product and Brand Management*, 31(3), pp.469-483. [DOI]

Pulido, S., Bonador, M. A., Buban, K. J., Cailo, K. J., Furio, A., Libo-on, S. M., Pinalba, Z. and De Silos, P. Y. L., 2025. Waste Disposal Methods, Compliance Behavior, and Factors Affecting Adherence to Waste Management of Microenterprises in Cupang, Muntinlupa City. *Journal of Small Business and Enterprise Development*, 1, pp.36-750. [DOI]

Romaniuc, R. and Bazart, C., 2026. Intrinsic and extrinsic motivation. In: *Encyclopedia of Law and Economics*. Springer Nature Switzerland, pp.1423-1426. [DOI]

Sahoo, K.C., Soni, R., Kalyanasundaram, M., Singh, S., Parashar, V., Pathak, A., Purohit, M.R., Sabde, Y., Stålsby Lundborg, C., Sidney Annerstedt, K. and Atkins, S., 2022. Dynamics of household waste

segregation behavior in an urban community in Ujjain, India: a framework analysis. *International Journal of Environmental Research and Public Health*, 19(12), p.7321. [DOI]

Simpson, S. S. and Evens, J., 2024. Corporate environmental non-compliance and the effects of internal systems and sanctions. In: *Research Handbook on Environmental Crimes and Criminal Enforcement*. Edward Elgar Publishing, pp.36-67. [DOI]

Sobrino-García, I., 2025. European waste management regulations in Spanish local administrations: Compliance assessment and integration frontiers. *Sustainable Development*, 33(2), pp.2553-2565. [DOI]

Vorobeva, D., Scott, I. J., Oliveira, T. and Neto, M., 2022. Adoption of new household waste management technologies: The role of financial incentives and pro-environmental behavior. *Journal of Cleaner Production*, 362, p.132328. [DOI]

Wang, F., Cheng, Z., Reisner, A. and Liu, Y., 2018. Compliance with household solid waste management in rural villages in developing countries. *Journal of Cleaner Production*, 202, pp.293-298. [DOI]

NEPT

Nature Environment and Pollution Technology

An International Quarterly Peer-Reviewed Open Access Journal

p-ISSN: 0972-6268 | e-ISSN: 2395-3454 Vol. 25 | No. 4 | Article ID B4432 | 2026

REVIEW ARTICLE https://doi.org/10.46488/NEPT.2026.v25i04.B4432 OPEN ACCESS

Legacy Pesticides in Aquatic Systems: Mechanistic Persistence, Regulatory Lag, and Catchment-Scale Remediation Imperatives

Pradip T. Salve†

Department of Science and Technology, Dr. D. Y. Patil Vidyapith, Pune, India

†Corresponding author: Pradip T. Salve; pradipsalve1988@gmail.com

ARTICLE HISTORY

Received: 26-02-2026
Revised: 21-04-2026
Accepted: 30-04-2026

KEYWORDS

Legacy pesticides
Environmental persistence
Groundwater contamination
Adsorption
Activated carbon
Remediation strategies
Catchment management
Water quality

CITE THIS ARTICLE

Salve, P.T., 2026. Legacy pesticides in aquatic systems: Mechanistic persistence, regulatory lag, and catchment-scale remediation imperatives. *Nature Environment and Pollution Technology*, 25(4), B4432. https://doi.org/10.46488/NEPT.2026.v25i04.B4432

COPYRIGHT & LICENCE

© 2026 The Authors
Open Access under CC BY 4.0.

PUBLISHED BY

TECHNOSCIENCE PUBLICATIONS

ABSTRACT

Legacy pesticides remain a persistent environmental challenge despite regulatory bans and reductions in agricultural pesticide use. Continued detections in surface water and groundwater indicate that historical residues stored in soils and sediments contribute to long-term contamination. This review evaluates the mechanistic processes governing legacy pesticide persistence, including adsorption–desorption dynamics, sediment storage, preferential flow pathways, and groundwater recharge behavior. A structured literature synthesis of peer-reviewed studies published between 2000 and 2025 was conducted to assess monitoring trends, physicochemical determinants of persistence, and remediation technologies applicable at the catchment scale. Evidence indicates that exceedances of the 0.1 μg L^{-1} regulatory threshold remain frequent in vulnerable agricultural regions because of delayed release from environmental reservoirs rather than ongoing application alone. Adsorption-based technologies, particularly activated carbon systems, show potential for practical mitigation, while biochar amendments and advanced oxidation processes offer complementary treatment pathways. The analysis indicates that regulatory restrictions should be coupled with targeted remediation and soil risk assessment to achieve measurable improvements in water quality. An integrated catchment-level management framework is therefore proposed to address legacy contamination and support sustainable water resource protection.

1. INTRODUCTION

The intensification of agricultural production over recent decades has been accompanied by a substantial increase in pesticide use worldwide, supporting global food security but also contributing to diffuse environmental contamination (Carvalho 2017, Silva et al. 2019, Ramchandar et al. 2025). Although regulatory frameworks across the European Union and other regions have progressively restricted or banned numerous active substances, measurable improvements in water quality have not consistently followed at the anticipated rate (European Commission 2020, European Environment Agency 2022). This apparent regulatory–environmental disconnect has drawn attention to the persistence of historically applied compounds, commonly referred to as legacy pesticides.

Legacy pesticides are compounds whose environmental presence continues despite regulatory withdrawal or substantial reduction in use. Their persistence is increasingly attributed to strong soil–organic matter interactions, slow degradation kinetics, and delayed release mechanisms rather than ongoing application alone (Fenner et al. 2013, Geissen et al. 2015). Several monitoring programs continue to

report exceedances of the 0.1 μg L^{-1} drinking-water threshold in agricultural catchments, particularly for herbicides such as atrazine, 2,4-D, and MCPA (Gilliom et al. 2006, Lapworth et al. 2012). These findings suggest that soil and sediment compartments function as long-term contaminant reservoirs capable of sustaining chronic exposure (Gzyl et al. 2014).

Environmental persistence is not solely governed by degradation half-life. Instead, it emerges from coupled processes involving adsorption–desorption dynamics, preferential flow pathways, sediment remobilization, and groundwater recharge (Jarvis 2007, Schwarzenbach et al. 2006). While some studies emphasize natural attenuation as a sufficient recovery mechanism, others argue that active remediation strategies may be required to accelerate environmental restoration (Gavrilescu 2005, Sharma et al. 2018). This divergence highlights an ongoing debate regarding the relative roles of regulatory reduction and targeted intervention.

Although substantial research has examined pesticide transport and treatment technologies independently, fewer studies have integrated mechanistic persistence with catchment-scale mitigation planning. In particular, the translation of soil-based risk assessment into practical remediation strategies remains limited. Addressing legacy contamination therefore requires bridging laboratory-scale understanding with policy implementation and watershed management.

Despite increasingly stringent regulatory frameworks, significant regional differences persist in pesticide governance, contributing to regulatory lag. In the European Union, a precautionary approach has established a strict drinking-water limit of 0.1 μg L□¹ for individual pesticides, yet exceedances continue to be reported because of legacy residues and delayed environmental release. In contrast, regulatory thresholds in countries such as the United States are generally compound-specific and often higher, reflecting a risk-based approach. In countries such as India, regulatory enforcement and monitoring capacity remain variable, further complicating the effective management of pesticide contamination. These disparities indicate that reductions in pesticide use alone are insufficient and that legacy contamination requires integrated remediation strategies alongside regulatory controls (European Union 2009, European Union 2021, Knauer 2016, Harmon O'Driscoll et al. 2022, Lewis et al. 2016).

A comparative overview of regulatory frameworks and associated challenges across regions is presented in Table 1.

The primary aim of this review is to critically evaluate the mechanistic drivers of legacy pesticide persistence in aquatic systems and to assess the effectiveness of available remediation strategies within a catchment-scale management framework. By synthesizing evidence from monitoring data, soil transport studies, and adsorption-based treatment research, this review seeks to clarify the factors sustaining long-term contamination and to propose integrated approaches capable of supporting measurable improvements in water quality.

2. MATERIALS AND METHODS

2.1. Review Design and Scope

This study employed a structured narrative review approach, integrating mechanistic laboratory investigations, field monitoring evidence, and policy analyses addressing legacy pesticide persistence. The review aimed to synthesize current scientific understanding of environmental reservoirs, transport pathways, persistence drivers, and remediation strategies applicable at the catchment scale.

This study adopted a structured narrative review approach informed by PRISMA reporting principles without conducting a full systematic review. Although a meta-analysis was not conducted, systematic principles were followed to ensure transparency, reproducibility, and methodological rigor.

2.2. Literature Search Strategy

A systematic literature search was conducted using the Scopus, Web of Science, and Google Scholar databases. The search period covered publications from January 2000 to March 2025 to capture contemporary developments in environmental persistence research and remediation technologies.

Search strings included combinations of the following keywords: "legacy pesticides", "groundwater contamination", "surface water monitoring", "adsorption–desorption", "activated carbon remediation", "soil transport risk", and "catchment management".

Table 1: Comparative overview of pesticide regulatory frameworks and associated challenges.

Region	Regulatory Approach	Drinking Water Limit	Key Challenge
European Union	Precautionary	0.1 μg L^{-1} (individual)	Persistent legacy residues despite regulatory bans
United States	Risk-based	Compound-specific (generally higher)	Variability across compounds and standards
India	Developing/variable	Variable/not uniformly enforced	Limited monitoring and enforcement capacity

Boolean operators (AND/OR) were applied to refine the search results. Reference lists of selected articles were also screened to identify relevant studies not retrieved during the primary database search.

The initial database search yielded 628 records. After removal of duplicate entries (n = 80), 548 records were retained for title and abstract screening.

2.3. Screening and Study Selection

Titles and abstracts of 548 records were screened for relevance. A total of 360 records were excluded because they were irrelevant, focused on toxicity without environmental context, or were not peer reviewed. The remaining 188 studies were assessed for full-text eligibility. Of these, 110 studies were excluded because of insufficient data or lack of relevance. Finally, 78 studies were included in the qualitative synthesis. The study-selection process is summarized in Fig. 1.

2.4. Inclusion and Exclusion Criteria

2.4.1. Studies were Included if They

- Reported field-based monitoring data of pesticide residues in surface or groundwater;
- Investigated adsorption–desorption mechanisms in soil or sediment systems;
- Examined physicochemical parameters influencing persistence (e.g., DT_{50}, K_oc, log K_ow);
- Evaluated remediation technologies under laboratory, pilot-scale, or field conditions;
- Addressed regulatory or policy implications related to pesticide persistence.

2.4.2. Studies were Excluded if They:

- Focused exclusively on current-use pesticides without documented persistence relevance;

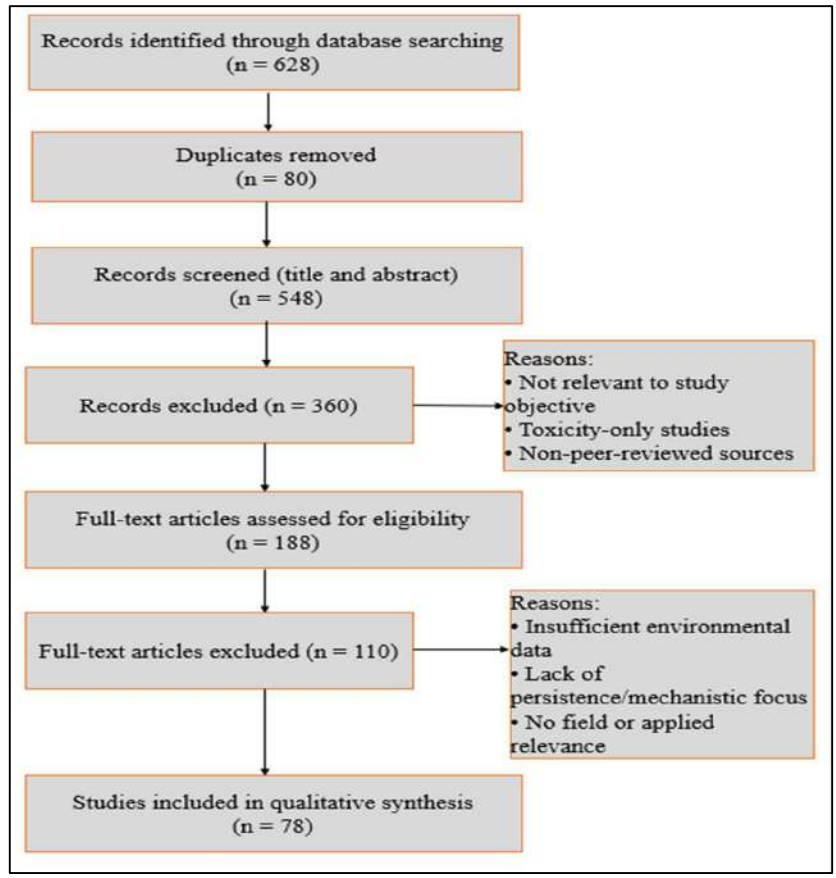


Fig. 1: PRISMA-style flow diagram illustrating the literature search and study selection process. A total of 628 records were identified through database searches, of which 548 were screened after duplicate removal. Following eligibility assessment, 78 studies were included in the structured narrative synthesis.

- Reported acute toxicity studies without environmental transport or fate analysis;
- Were not peer-reviewed publications.

2.5. Quality Assessment of Included Studies

The quality of included studies was assessed based on study design, analytical reliability, and reporting completeness. Studies were categorized as high, moderate, or low confidence. High-confidence studies included field-based investigations with quantitative data, while moderate-confidence studies were laboratory-based with clear methodology. Low-confidence studies were excluded from synthesis.

A summary of the quality appraisal of the included studies (n = 78), based on study design and methodological reliability, is presented in Table 2.

2.6. Data Extraction and Synthesis

From each eligible study, the following information was extracted:

- Compound characteristics (e.g., half-life, sorption coefficient, aqueous solubility);
- Environmental compartment investigated (soil, sediment, surface water, groundwater);
- Reported concentration ranges;
- Remediation method evaluated and associated removal efficiency;
- Geographic and climatic context.

Due to heterogeneity in monitoring methodologies, analytical techniques, and reporting units, a quantitative meta-analysis was not performed. Instead, a structured qualitative synthesis was conducted, supported by semi-quantitative comparison of reported parameter ranges (e.g., DT_{50}, Koc, and concentration levels), to identify recurring mechanistic patterns, dominant drivers of persistence, and consistent policy implications.

2.7. Comparative Assessment of Remediation Technologies

Remediation technologies were comparatively evaluated based on the following criteria:

- Dominant mechanism of contaminant removal (adsorption, degradation, immobilization);
- Demonstrated field applicability (laboratory, pilot, or full-scale);
- Regeneration potential and long-term sustainability;
- Scalability and operational feasibility at the catchment scale;
- Reported removal efficiency ranges where available.

This evaluation framework enabled systematic comparison among adsorption-based systems, soil amendments, and advanced oxidation processes.

Where possible, comparative interpretation was supported by reported performance ranges and field validation evidence to distinguish between laboratory efficiency and real-world applicability.

2.8. Data Availability and Transparency

All data analyzed in this review were derived from published peer-reviewed sources. No new experimental data were generated. The study selection process, synthesis approach, and extracted parameters are described in detail to ensure transparency and reproducibility. In accordance with journal policy, the reference list and extracted synthesis tables will be made fully accessible upon publication. There are no restrictions on data availability.

2.9. Ethical Considerations

This study is based exclusively on previously published data and does not involve human participants, animal experimentation, or intervention-based trials. Therefore, ethical approval was not required.

3. RESULTS AND DISCUSSION

3.1. Environmental Persistence Mechanisms

3.1.1. Physicochemical Controls on Long-Term Storage

While sorption affinity (Koc) is widely recognized as a primary control on pesticide retention in soils, evidence across field-scale studies indicates that its influence is highly context-dependent. High Koc values promote strong adsorption to soil organic matter, reducing immediate mobility; however, this effect can be overridden under conditions of high hydrological flux or preferential flow pathways, particularly in coarse-textured or structured soils (Gondar et al. 2013, Kodešová et al. 2011, McManus et al. 2017).

Table 2: Quality appraisal summary of included studies (n = 78).

Study Type	Number of Studies	Key Characteristics	Confidence Level
Field monitoring	34	Long-term environmental monitoring, real-world datasets	High
Laboratory studies	26	Controlled adsorption/desorption experiments	Moderate
Modeling/Combined	18	Risk assessment, modeling, and integrated analysis	Moderate

Similarly, although degradation half-life (DT_{50}) is commonly used as an indicator of persistence, several studies demonstrate that compounds with moderate DT_{50} values may still exhibit long-term environmental presence when strong sorption delays degradation or when residues are protected within soil matrices. Conversely, pesticides with relatively short DT_{50} values can be rapidly transported to groundwater systems under high rainfall or irrigation conditions, indicating that transport processes may dominate over degradation (Aguiar Jr. et al. 2017, Hakoun et al. 2017, Jørgensen & Spliid 2016).

These contrasting findings suggest that persistence cannot be attributed to a single controlling parameter. Instead, it emerges from the dynamic interaction between sorption, degradation kinetics, and hydrological connectivity, with the dominant control varying across environmental conditions. The principal physicochemical controls are summarized in Table 3.

These parameters collectively determine persistence through their interaction, with the dominant controlling mechanism varying across environmental conditions such as soil texture, rainfall intensity, and hydrological connectivity, rather than following a fixed mathematical relationship.

In addition to qualitative interpretation, several studies provide indicative threshold ranges that help explain variability in environmental persistence. Pesticides with soil half-lives (DT_{50}) greater than 100 days are generally classified as persistent, while those exceeding 365 days are considered highly persistent, with potential for long-term environmental storage. However, persistence risk increases significantly when moderate DT_{50} values (30–100 days) are combined with high sorption affinity (Koc > 1000), as delayed degradation may occur due to strong binding within soil matrices.

Conversely, compounds with low sorption coefficients (Koc < 300) and high water solubility exhibit increased leaching potential, particularly in sandy or permeable soils where preferential flow pathways dominate. Under such conditions, transport processes may outweigh degradation effects, leading to rapid groundwater contamination even for compounds with relatively short DT_{50} values.

These findings reinforce that persistence emerges from interacting parameter ranges rather than isolated physicochemical properties.

A hierarchical interpretation of controlling mechanisms further clarifies the variability in persistence behavior across environmental settings. Under low rainfall and fine-textured soils (e.g., clay-rich systems), sorption processes (Koc) tend to dominate, limiting mobility and promoting long-term storage within soil matrices. In contrast, in coarse-textured or structured soils with high permeability, hydrological connectivity becomes the primary controlling factor, facilitating rapid transport through preferential flow pathways regardless of sorption strength.

Degradation processes, represented by DT_{50}, exert a secondary control that is strongly influenced by environmental conditions. In well-aerated soils with active microbial communities, degradation may significantly reduce persistence; however, in saturated or subsurface environments, degradation rates are often limited, allowing stored residues to persist over extended periods.

This hierarchy indicates that hydrology and soil structure frequently override physicochemical retention under dynamic field conditions, while sorption dominates under stable conditions. Consequently, persistence should be interpreted as a condition-dependent outcome rather than a fixed property of individual compounds.

3.1.2. Adsorption-Desorption and Delayed Release

Adsorption–desorption dynamics play a critical role in sustaining long-term pesticide persistence beyond initial application periods. Several studies report nonlinear and hysteretic behavior in adsorption–desorption processes, indicating that desorption is often slower and less complete than adsorption. This asymmetry results in the formation of bound residues within soil matrices, which are not immediately bioavailable but can act as long-term contaminant reservoirs (Barriuso et al. 2008, Boivin et al. 2005, Foo and Hameed 2010).

Over time, gradual desorption from soil organic matter and sediment compartments leads to sustained low-level release of pesticide residues into pore water and connected aquatic systems. This delayed release mechanism explains

Table 3: Physicochemical properties governing environmental persistence of legacy pesticides.

Parameter	Definition	Influence on Persistence
log Kow	Hydrophobicity indicator	Promotes soil/sediment accumulation
Koc	Soil organic carbon affinity	Enhances long-term storage
DT_{50}	Degradation half-life	Determines degradation rate
Water solubility	Mobility indicator	Controls runoff and leaching potential
pKa	Ionization behavior	Influences adsorption–desorption

the continued detection of legacy pesticides in surface water and groundwater long after their regulatory withdrawal.

Importantly, the rate and extent of desorption are strongly influenced by environmental conditions. In fine-textured soils with high organic matter content, strong sorption can prolong retention and delay release. In contrast, changes in hydrological conditions—such as rainfall events, fluctuations in groundwater levels, or disturbance of sediments—can enhance remobilization of previously stored residues.

These findings indicate that persistence is not only a function of initial sorption but also of long-term desorption kinetics and environmental perturbations. As a result, legacy pesticide contamination should be understood as a time-dependent release process from environmental reservoirs rather than a static outcome of past applications.

3.1.3. Sediment Reservoirs and Episodic Mobilization

Sediments function as important secondary reservoirs for legacy pesticides, where particle-bound residues accumulate over extended periods due to strong sorption to organic matter and suspended solids. While this process reduces immediate bioavailability, it does not result in permanent immobilization, as stored contaminants remain susceptible to remobilization.

Under stable hydrological conditions, sediments predominantly act as sinks, facilitating long-term accumulation of pesticide residues. However, during high-flow events such as intense rainfall or seasonal runoff, these sediments can be resuspended, releasing previously stored contaminants into the water column. This episodic mobilization results in transient concentration spikes and explains continued detections even in catchments where pesticide application has declined or ceased (Andrade et al. 2021, Halbach et al. 2021, Ivanova et al. 2021).

The relative importance of sediment-mediated transport is strongly influenced by catchment characteristics and hydrological variability. In low-energy systems, storage processes dominate, whereas in dynamic catchments with frequent disturbance, sediments transition from sinks to active sources, significantly contributing to contaminant transport.

These findings demonstrate that sediment-associated persistence is governed by a dynamic balance between storage and remobilization processes. Therefore, effective management of legacy pesticide contamination should explicitly incorporate sediment dynamics within catchment-scale monitoring and mitigation strategies. The principal persistence pathways are illustrated in Fig. 2.

3.2. Monitoring Evidence and Regulatory Disconnect

Long-term monitoring datasets demonstrate persistent exceedances of the 0.1 µg L^{-1} threshold in vulnerable agricultural regions (European Commission 2020). Surface-water monitoring often indicates gradual improvement, whereas groundwater recovery lags because of longer residence times (Lapworth et al. 2012, Chow et al. 2020, McKnight et al. 2015, Melin et al. 2020, Papadakis et al. 2018, Schreiner et al. 2016, Stehle and Schulz 2015).

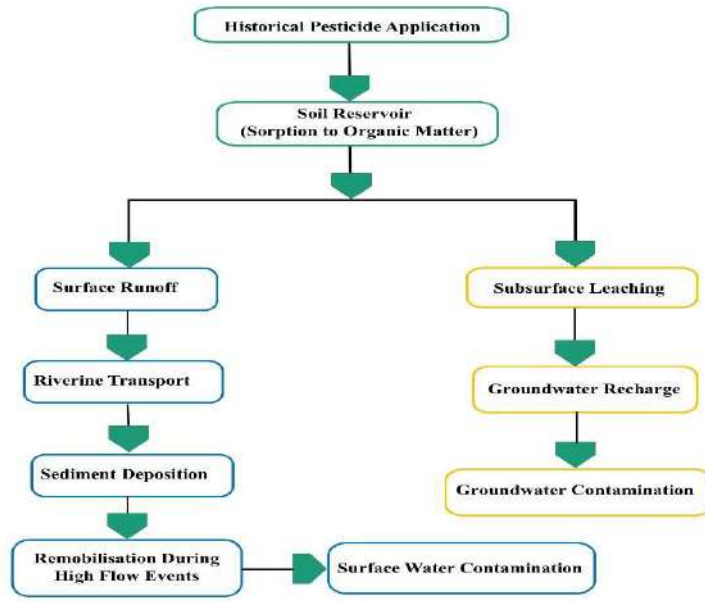


Fig. 2: Conceptual pathways governing legacy pesticide persistence across soil, sediment, and groundwater compartments.

Key observations include:

- Continued detection of atrazine despite its ban in the EU;
- Recurring exceedances of MCPA and 2,4-D in intensive catchments;
- Higher transport risk in sandy soils than in clay-dominated systems.

These findings suggest that regulatory restrictions alone cannot eliminate contamination sustained by historical soil reservoirs. Frequently detected legacy pesticides and selected persistence indicators are summarized in Table 5.

3.3. Comparative Evaluation of Remediation Technologies

Efficiency ranges are indicative and vary depending on experimental conditions, contaminant type, and environmental settings.

The reviewed remediation technologies exhibit significant variability in performance, scalability, and field applicability, indicating that no single approach is universally applicable across all environmental settings. Adsorption-based systems, particularly granular and powdered activated carbon, have been shown to consistently achieve high removal efficiencies (typically 70–95%) under both laboratory and field conditions, making them among the most reliable and widely implemented options for water treatment (Cosgrove et al. 2019, Cosgrove et al. 2022, Ighalo et al. 2021, Mojiri et al. 2020, Saleh et al. 2020).

However, their long-term effectiveness is constrained by media saturation and the need for regeneration or replacement, which introduces operational and cost considerations. In contrast, biochar-based amendments offer a more sustainable and cost-effective alternative for in situ soil remediation, but their performance is highly variable (30–80%) depending on feedstock properties, soil type, and environmental conditions.

Advanced oxidation processes provide efficient chemical degradation of pesticide residues under controlled conditions, often achieving high removal rates. Nevertheless, their application at the catchment scale is limited by energy requirements, operational complexity, and reduced efficiency in heterogeneous environmental matrices.

Emerging technologies such as magnetic nanocomposites show promising adsorption and recovery potential; however, their application remains largely experimental due to scalability constraints and limited field validation (Intisar et al. 2022, Shahid et al. 2021).

These comparisons indicate that adsorption-based technologies are most suitable for immediate water quality improvement, while soil-based amendments and advanced oxidation processes serve complementary roles depending on site-specific conditions. Therefore, effective remediation strategies should adopt a combined, site-adaptive approach, integrating multiple technologies based on contaminant characteristics, environmental conditions, and management objectives (Butkovskyi et al. 2021, Jing et al. 2021, Lorenz et al. 2022, Prosser et al. 2020). The comparative performance

Table 4: Comparative assessment of remediation strategies for legacy pesticide mitigation.

Technology	Mechanism	Efficiency (%)	Field Applicability	Key Limitation
Granular Activated Carbon	Adsorption	80–95%	High	Media saturation
Powdered Activated Carbon	Adsorption	70–90%	High	Sludge management
Biochar Amendments	Immobilization	30–80%	Moderate	Performance variability
Magnetic Nanocomposites	Adsorption + recovery	60–85%*	Experimental	Scalability
Advanced Oxidation	Chemical degradation	70–95%	Moderate	Energy demand

* Performance based primarily on laboratory or pilot-scale studies; limited field validation available.

Table 5: Frequently detected legacy pesticides in aquatic monitoring studies and selected persistence indicators.

Compound	Chemical Class	Typical Soil Half-life (DT_{50}, days)	log $K_{o}w$	Primary Detection Matrix	EU Regulatory Status
Atrazine	Triazine herbicide	60–100	2.6	Groundwater	Banned
MCPA	Phenoxy herbicide	15–50	2.8	Surface water	Restricted
2,4-D	Phenoxy herbicide	7–30	2.7	Surface and groundwater	Approved with limits
Chlorpyrifos	Organophosphate insecticide	30–120	4.7	Sediment	Withdrawn
Imidacloprid	Neonicotinoid insecticide	40–200	0.6	Surface water	Restricted

Sources synthesized from Gilliom et al. 2006, Silva et al. 2019, Szöcs et al. 2017, and Urseler et al. 2022. Values represent typical ranges reported across monitoring studies and may vary depending on environmental conditions.

of the reviewed remediation technologies is summarized in Table 4.

3.4. Integrated Catchment-Level Interpretation

The synthesis suggests that effective mitigation requires integration of soil risk screening, monitoring, and targeted intervention, as illustrated in Fig. 3.

The environmental benefit of remediation should be assessed using:

1. Reduction in exceedance frequency;
2. Decline in mean annual concentration;
3. Improvement in groundwater trend slopes.

Such metrics provide more meaningful indicators of recovery than pesticide sales statistics alone.

4. CONCLUSIONS

Legacy pesticides continue to influence aquatic environments long after regulatory withdrawal because of persistent soil storage, delayed desorption, and hydrological redistribution processes. This review demonstrates that environmental persistence is governed by interacting physicochemical properties and catchment-scale transport dynamics rather than degradation half-life alone. Monitoring evidence indicates that regulatory reductions in pesticide use do not automatically translate into immediate water quality recovery, particularly in groundwater systems with long residence times.

The synthesis highlights the importance of integrating soil risk screening, continuous monitoring, and targeted remediation strategies to address historical contamination reservoirs. Among available technologies, adsorption-based systems such as activated carbon remain the most technically mature and scalable options, while soil amendments and advanced oxidation processes offer complementary mitigation pathways under site-specific conditions.

The findings contribute to existing knowledge by bridging mechanistic understanding of pesticide persistence with practical catchment-scale management approaches. Future research should prioritize long-term field validation of remediation systems, development of predictive soil transport indices, and incorporation of adaptive policy feedback mechanisms. Sustainable water quality restoration will depend not only on reducing current pesticide inputs but also on actively managing legacy contamination sources.

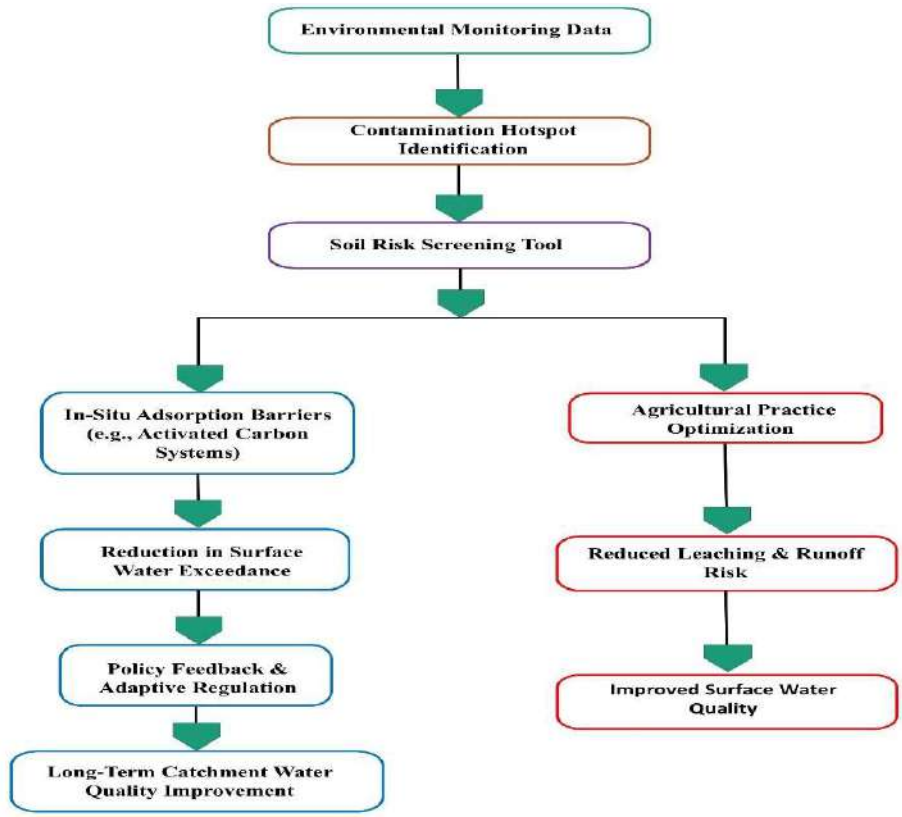


Fig. 3: Integrated catchment-scale mitigation framework combining monitoring, soil risk assessment, and adsorption-based remediation.

5. ACKNOWLEDGMENTS

The author gratefully acknowledges the academic guidance and institutional support provided during the development of the doctoral research that formed the conceptual foundation of this review.

6. REFERENCES

Aguiar Jr., T.R., Bortolozo, F.R., Filho, E.F.R., Parron, L.M., Luz, L.D., Brito, A.G. and Ferreira, M.T., 2017. Fate of selected agrochemicals in a tropical karst aquifer: a five-year study. *Groundwater for Sustainable Development*, 5, pp.187–192. [DOI]

Andrade, V.S., Gutierrez, M.F., Regaldo, L., Paira, A.R. and Gagneten, A.M., 2021. Influence of rainfall and seasonal crop practices on nutrient and pesticide runoff from soybean dominated agricultural areas. *Science of the Total Environment*, 788, 147676. [DOI]

Barriuso, E., Benoit, P. and Dubus, I.G., 2008. Formation of pesticide nonextractable (bound) residues in soil: magnitude, controlling factors and reversibility. *Environmental Science & Technology*, 42(6), pp.1845–1854. [DOI]

Boivin, A., Cherrier, R. and Schiavon, M., 2005. A comparison of five pesticide adsorption and desorption processes in contrasting field soils. *Chemosphere*, 61(5), pp.668–676. [DOI]

Butkovskyi, A., Jing, Y., Bergheim, H., Lazar, D., Gulyaeva, K., Odenmarck, S.R., Norli, H.R., Nowak, K.M., Miltner, A., Kästner, M. and Eggen, T., 2021. Retention and distribution of pesticides in planted filter microcosms designed for treatment of agricultural surface runoff. *Science of the Total Environment*, 778, 146114. [DOI]

Carvalho, F.P., 2017. Pesticides, environment, and food safety. *Food and Energy Security*, 6(2), pp.48–60. [DOI]

Chow, R., Scheidegger, R., Doppler, T., Dietzel, A., Fenicia, F. and Stamm, C., 2020. A review of long-term pesticide monitoring studies to assess surface water quality trends. *Water Research X*, 9, 100064. [DOI]

Cosgrove, S., Jefferson, B. and Jarvis, P., 2019. Pesticide removal from drinking water sources by adsorption: a review. *Environmental Technology Reviews*, 8(1), pp.1–24. [DOI]

Cosgrove, S., Jefferson, B. and Jarvis, P., 2022. Application of activated carbon fabric for the removal of a recalcitrant pesticide from agricultural run-off. *Science of the Total Environment*, 815, 152626. [DOI]

European Commission, 2020. *Farm to fork strategy for a fair, healthy and environmentally-friendly food system*. Brussels: European Commission. Available online: https://ec.europa.eu/food/horizontal-topics/farm-fork-strategy_en (accessed on 19 February 2026).

European Environment Agency, 2022. *Water quality in Europe – state and trends*. Available online: https://www.eea.europa.eu (accessed on 19 February 2026).

European Union, 2009. Regulation (EC) No 1107/2009 concerning the placing of plant protection products on the market. *Official Journal of the European Union*, L309.

European Union, 2021. Directive (EU) 2020/2184 on the quality of water intended for human consumption (recast). *Official Journal of the European Union*, L435.

Fenner, K., Canonica, S., Wackett, L.P. and Elsner, M., 2013. Evaluating pesticide degradation in the environment: blind spots and emerging opportunities. *Science*, 341(6147), pp.752–758. [DOI]

Foo, K.Y. and Hameed, B.H., 2010. Insights into the modelling of adsorption isotherm systems. *Chemical Engineering Journal*, 156(1), pp.2–10. [DOI]

Gavrilescu, M., 2005. Fate of pesticides in the environment and its bioremediation. *Engineering in Life Sciences*, 5(6), pp.497–526. [DOI]

Geissen, V., Mol, H., Klumpp, E., Umlauf, G., Nadal, M., Van der Ploeg, M., Van de Zee, S.E.A.T.M. and Ritsema, C.J., 2015. Emerging pollutants in the environment: a challenge for water resource management. *International Soil and Water Conservation Research*, 3(1), pp.57–65. [DOI]

Gilliom, R.J., Barbash, J.E., Crawford, C.G., Hamilton, P.A., Martin, J.D., Nakagaki, N., Nowell, L.H., Scott, J.C., Stackelberg, P.E., Thelin, G.P. and Wolock, D.M., 2006. *The quality of our nation's waters: pesticides in the nation's streams and groundwater*. U.S. Geological Survey Circular 1291. Available online: https://pubs.usgs.gov/circ/2005/1291/ (accessed on 19 February 2026).

Gondar, D., López, R., Antelo, J., Fiol, S. and Arce, F., 2013. Effect of organic matter and pH on the adsorption of pesticides by soils. *Journal of Hazardous Materials*, 260, pp.627–633. [DOI]

Gzyl, G., Zanini, A., Frączek, R. and Kura, K., 2014. Contaminant source and release history identification in groundwater: a multi-step approach. *Journal of Contaminant Hydrology*, 157, pp.59–72. [DOI]

Hakoun, V., Orban, P., Dassargues, A. and Brouyère, S., 2017. Factors controlling spatial and temporal patterns of multiple pesticide compounds in groundwater. *Environmental Pollution*, 223, pp.185–199. [DOI]

Halbach, K., Möder, M., Schrader, S., Liebmann, L., Schäfer, R.B., Schneeweiss, A., Schreiner, V.C., Vormeier, P., Weisner, O., Liess, M. and Reemtsma, T., 2021. Small streams–large concentrations? Pesticide monitoring in small agricultural streams during dry weather and rainfall. *Water Research*, 203, 117535. [DOI]

Harmon O'Driscoll, J., Siggins, A., Healy, M.G., McGinley, J., Mellander, P.-E., Morrison, L. and Ryan, P.C., 2022. A risk ranking of pesticides in drinking water considering chronic health effects. *Science of the Total Environment*, 829, 154532. [DOI]

Ighalo, J.O., Adeniyi, A.G. and Adelodun, A.A., 2021. Recent advances on the adsorption of herbicides and pesticides from polluted waters. *Journal of Industrial and Engineering Chemistry*, 93, pp.117–137. [DOI]

Intisar, A., Ramzan, A., Sawaira, T., Kareem, A.T., Hussain, N., Din, M.I., Bilal, M. and Iqbal, H.M.N., 2022. Occurrence, toxic effects and mitigation of pesticides as emerging environmental pollutants using robust nanomaterials: a review. *Chemosphere*, 293, 133538. [DOI]

Ivanova, A., Wiberg, K., Ahrens, L. and Zubcov, E., 2021. Spatial distribution of legacy pesticides in river sediment from the Republic of Moldova. *Chemosphere*, 279, 130923. [DOI]

Jarvis, N.J., 2007. A review of non-equilibrium water flow and solute transport in soil macropores. *European Journal of Soil Science*, 58(3), pp.523–546. [DOI]

Jing, Y., Krauss, M., Zschieschang, S., Miltner, A., Butkovskyi, A., Eggen, T., Kästner, M. and Nowak, K.M., 2021. Superabsorbent polymer as a supplement substrate of constructed wetland to retain pesticides from agricultural runoff. *Water Research*, 207, 117776. [DOI]

Jørgensen, P.R. and Spliid, N.H., 2016. Accumulation of pesticides in anaerobic clayey till and implications for groundwater. *Groundwater Monitoring & Remediation*, 36(3), pp.43–53. [DOI]

Knauer, K., 2016. Pesticides in surface waters: a comparison with regulatory acceptable concentrations determined in the authorization process and consideration for regulation. *Environmental Sciences Europe*, 28, 13. [DOI]

Kodešová, R., Kočárek, M., Kodeš, V., Drábek, O., Kozák, J. and Hejtmánková, K., 2011. Pesticide adsorption in relation to soil properties and soil type distribution at regional scale. *Journal of Hazardous Materials*, 186(1), pp.540–550. [DOI]

Lapworth, D.J., Baran, N., Stuart, M.E. and Ward, R.S., 2012. Emerging organic contaminants in groundwater: a review of sources, fate and occurrence. *Environmental Pollution*, 163, pp.287–303. [DOI]

Lewis, K.A., Tzilivakis, J., Warner, D. and Green, A., 2016. An international database for pesticide risk assessments and management. *Human and Ecological Risk Assessment*, 22(4), pp.1050–1064. [DOI]

Lorenz, S., Dominic, A.R., Heinz, M., Süß, A., Stähler, M. and Strassemeyer, J., 2022. Effect of buffer strips on pesticide risks in freshwaters. *Crop Protection*, 154, 105891. [DOI]

McKnight, U.S., Rasmussen, J.J., Kronvang, B., Binning, P.J. and Bjerg, P.L., 2015. Sources, occurrence and predicted aquatic impact of legacy and contemporary pesticides in streams. *Environmental Pollution*, 200, pp.64–76. [DOI]

McManus, S.-L., Coxon, C.E., Mellander, P.-E., Danaher, M. and Richards, K.G., 2017. Hydrogeological characteristics influencing the occurrence of pesticides and pesticide metabolites in groundwater across the Republic of Ireland. *Science of the Total Environment*, 601–602, pp.594–602. [DOI]

Melin, J., Guillon, A., Enault, J., Esperanza, M., Dauchy, X. and Bouchonnet, S., 2020. Selection of relevant metabolites based on available data for parent molecules in French water resources. *Environmental Pollution*, 265, 114992. [DOI]

Mojiri, A., Zhou, J.L., Robinson, B., Ohashi, A., Ozaki, N., Kindaichi, T., Farraji, H. and Vakili, M., 2020. Pesticides in aquatic environments and their removal by adsorption methods. *Chemosphere*, 253, 126646. [DOI]

Papadakis, E.-N., Tsaboula, A., Vryzas, Z., Kotopoulou, A., Kintzikoglou, K. and Papadopoulou-Mourkidou, E., 2018. Pesticides in the rivers and streams of two river basins in northern Greece. *Science of the Total Environment*, 624, pp.732–743. [DOI]

Prosser, R.S., Hoekstra, P.F., Gene, S., Truman, C., White, M. and Hanson, M.L., 2020. A review of the effectiveness of vegetated buffers to mitigate pesticide and nutrient transport into surface waters from agricultural areas. *Journal of Environmental Management*, 261, 110210. [DOI]

Ramchandar, R.V., Kumar, A., Priyanka, E., Bharati, M.R., Bhardwaj, L.K., Khandelia, P. and Narayan, K.P., 2025. A concurrent review on plant-derived biopesticides and synthetic pesticides: their importance in plant protection and impacts on human health. *Nature Environment & Pollution Technology*, 24(3). [DOI]

Saleh, I.A., Zouari, N. and Al-Ghouti, M.A., 2020. Removal of pesticides from water and wastewater: chemical, physical and biological treatment approaches. *Environmental Technology & Innovation*, 19, 101026. [DOI]

Schreiner, V.C., Szöcs, E., Bhowmik, A.K., Vijver, M.G. and Schäfer, R.B., 2016. Pesticide mixtures in streams of several European countries and the USA. *Science of the Total Environment*, 573, pp.680–689. [DOI]

Schwarzenbach, R.P., Escher, B.I., Fenner, K., Hofstetter, T.B., Johnson, C.A., von Gunten, U. and Wehrli, B., 2006. The challenge of micropollutants in aquatic systems. *Science*, 313(5790), pp.1072–1077. [DOI]

Shahid, M.K., Kashif, A., Fuwad, A. and Choi, Y., 2021. Current advances in treatment technologies for removal of emerging contaminants from water: a critical review. *Coordination Chemistry Reviews*, 442, 213993. [DOI]

Sharma, B., Sarkar, A., Singh, P. and Singh, R.P., 2018. Agricultural utilization of biosolids: a review on potential effects on soil and plant systems. *Environmental Reviews*, 26(1), pp.1–20. [DOI]

Silva, V., Mol, H.G.J., Zomer, P., Tienstra, M., Ritsema, C.J. and Geissen, V., 2019. Pesticide residues in European agricultural soils: a hidden reality unfolded. *Science of the Total Environment*, 653, pp.1532–1545. [DOI]

Stehle, S. and Schulz, R., 2015. Agricultural insecticides threaten surface waters at the global scale. *Proceedings of the National Academy of Sciences*, 112(18), pp.5750–5755. [DOI]

Szöcs, E., Brinke, M., Karaoglan, B. and Schäfer, R.B., 2017. Large-scale risks from agricultural pesticides in small streams. *Environmental Science & Technology*, 51, pp.7378–7385. [DOI]

Urseler, N., Bachetti, R., Biolé, F. and Morgante, V., 2022. Atrazine pollution in groundwater and raw bovine milk: water quality, bioaccumulation and human risk assessment. *Science of the Total Environment*, 852, 158498. [DOI]

Nature Environment and Pollution Technology
An International Quarterly Peer-Reviewed Open Access Journal

p-ISSN: 0972-6268 | e-ISSN: 2395-3454 Vol. 25 | No. 4 | Article ID B4431 | 2026

REVIEW ARTICLE https://doi.org/10.46488/NEPT.2026.v25i04.B4431 OPEN ACCESS

Evaluating Green Infrastructure Interventions for Land Surface Temperature Reduction: A PRISMA-Based Systematic Review

Avinash Kumar Singh† and Manoj Kumar
Department of Architecture and Planning, National Institute of Technology, Patna-800005, Bihar, India
†Corresponding author: Avinash Kumar Singh; avinash.singh1603arch@nitp.ac.in

ARTICLE HISTORY

Received: 06-02-2026
Revised: 08-04-2026
Accepted: 10-04-2026

KEYWORDS

Land surface temperature
Urban heat island
Green infrastructure
Urban morphology
PRISMA

CITE THIS ARTICLE

Singh, A.K. and Kumar, M., 2026. Evaluating green infrastructure interventions for land surface temperature reduction: A PRISMA-based systematic review. *Nature Environment and Pollution Technology*, 25(4), B4431. https://doi.org/10.46488/NEPT.2026.v25i04.B4431

COPYRIGHT & LICENCE

© 2026 The Authors
Open Access under CC BY 4.0.

PUBLISHED BY

TECHNOSCIENCE PUBLICATIONS

ABSTRACT

Rapid urbanization has intensified land surface temperatures (LST) in cities worldwide, exacerbating the urban heat island effect and increasing risks to thermal discomfort, public health, and energy demand. Green infrastructure (GI), including street trees, urban parks, green roofs, vertical greenery, and blue-green systems, has emerged as a key nature-based strategy for mitigating urban surface heat. This study presents a PRISMA-guided systematic review combined with bibliometric analysis to evaluate the effectiveness of GI interventions in reducing LST within built environments. A comprehensive search of the Web of Science Core Collection identified 211 records, of which 61 peer-reviewed studies published between 2012 and 2026 met the predefined inclusion criteria. Bibliometric analysis using VOSviewer reveals a rapidly expanding research field, characterized by exponential growth (R^2 = 0.9135) and strong thematic convergence around keywords such as green infrastructure, land surface temperature, urban heat island, and built environment. Keyword co-occurrence mapping identifies multiple interconnected research clusters, highlighting integration across thermal regulation, urban morphology, climate adaptation, and methodological innovation, while also revealing the relative underrepresentation of social and equity-focused dimensions. Geographically, research output is concentrated in Asia, Europe, and Australia, indicating regional imbalances in evidence generation. The systematic synthesis shows that tree-based green infrastructure and urban parks consistently produce the largest LST reductions, commonly ranging from 2–4°C, with higher localized reductions, whereas green roofs and vertical greenery systems deliver more localized but critical cooling benefits in high-density urban areas. Cooling effectiveness is strongly context-dependent, shaped by climate zone, urban morphology, vegetation structure, and spatial configuration. Notably, several studies demonstrate that small-scale GI interventions can significantly reduce surface heat stress in informal settlements, suggesting potential equity implications, particularly in heat-vulnerable urban areas, although systematic evidence remains limited. By integrating bibliometric mapping with PRISMA-based content analysis, this review provides a context-sensitive, design-aware, and climate-responsive synthesis to support evidence-based urban heat mitigation and climate-resilient planning.

1. INTRODUCTION AND BACKGROUND

1.1. Urban Heat Challenges and Land Surface Temperature (LST)

Urbanization has substantially transformed natural landscapes, replacing vegetation and permeable surfaces with impervious materials such as asphalt, concrete, and metal (Mohan & Kandya 2015, Seto et al. 2012). This transformation has led to the amplification of Land Surface Temperature (LST) in cities, a phenomenon closely associated with the Urban Heat Island (UHI) effect (Evola et al. 2017, Nath 2025, Vyas et al. 2014). The UHI effect is characterized by higher daytime

and nighttime temperatures in urban areas relative to surrounding rural environments, driven primarily by solar heat absorption, limited evapotranspiration, anthropogenic heat emissions, and reduced ventilation (Gorai et al. 2024, Halder et al. 2025). Elevated LST is associated with increased surface heat exposure and can contribute to conditions that influence thermal discomfort, energy demand, and heat-related risks, although it does not directly represent human thermal experience (Abuwaer et al. 2023, Ullah et al. 2024, Ullah & Al-Ghamdi 2023).

Understanding the dynamics of LST is therefore critical for developing effective urban heat mitigation strategies. Temperature gradients between built and natural areas vary with urban density, building materials, surface albedo, and local climate conditions (Azmeer et al. 2024, Halder et al. 2025). High-density urban fabrics, particularly compact high-rise districts, are prone to intensified heat accumulation due to restricted airflow and increased radiation trapping. Conversely, urban open spaces and low-density areas benefit from higher convective cooling and larger potential for integrating vegetation-based interventions (Kumar et al. 2025).

These climatic and urban morphological complexities underscore the need for targeted, context-specific approaches to mitigate urban heat, particularly in rapidly urbanizing regions experiencing extreme temperatures (Rupapara et al. 2025). The evidence from past decades suggests that green infrastructure (GI) interventions offer a promising solution for passive cooling by leveraging natural processes (Huang et al. 2022, Jin et al. 2024). GI is an effective strategy for urban heat mitigation, although its performance varies significantly depending on climatic conditions, urban morphology, and intervention type. In this study, the term GI is used as an umbrella concept encompassing urban greenery, including trees, parks, green roofs, vertical greenery systems, and blue–green infrastructure

1.2. Green Infrastructure as a Nature-Based Solution

GI encompasses a diverse array of interventions, including street trees, parks, urban forests, green roofs, and vertical greenery systems, which collectively aim to reduce urban heat and improve thermal comfort (Halder et al. 2026, Wong et al. 2021). The primary mechanisms through which GI reduces LST are shading, which limits direct solar radiation on urban surfaces, and evapotranspiration, whereby plants release water vapor to dissipate heat into the surrounding atmosphere (de Quadros & Mizgier 2023, Ying 2022). Together, these mechanisms contribute to significant surface and air temperature reductions, often producing perceptible cooling benefits for urban residents. Fig. 1 illustrates the dual mechanisms through which GI reduces urban temperatures: shading reduces heat absorption at the surface, while evapotranspiration dissipates heat into the atmosphere, collectively lowering LST.

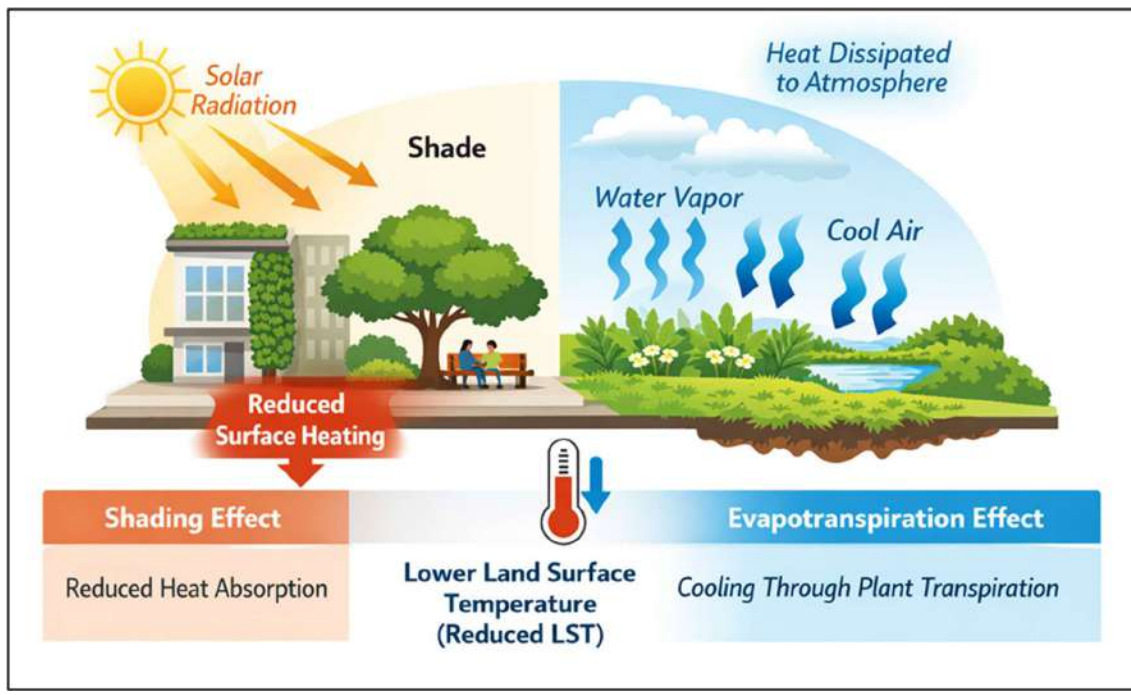


Fig. 1: Mechanisms of Green Infrastructure LST Reduction.

Empirical studies have shown that tree canopies can reduce surface temperatures by up to 10°C, while urban parks create localized "cool islands" with air temperature reductions of 1–3°C. Green roofs and green walls, although generally providing smaller reductions in pedestrian-level temperatures, contribute to surface cooling, energy efficiency in buildings, and improvement of local microclimate conditions (Hurduc et al. 2024, Kanga et al. 2022, Luo & Wu 2021, Rahman et al. 2020, Weng et al. 2004). The effectiveness of these interventions is highly sensitive to factors such as vegetation type, canopy density, spatial arrangement, and species selection.

Also, multi-layered vegetation strategies, integrating trees, shrubs, and ground cover, enhance thermal performance by increasing the leaf area index and creating diverse microclimates. Proper planning of vegetation layout, including tree spacing and canopy continuity, has been shown to produce 20–30% higher cooling efficiency compared to scattered, single-layer plantings (Chen et al. 2022, Gherri 2023, Perini & Magliocco 2014). Selecting drought-tolerant and native species ensures both thermal performance and long-term sustainability, especially in arid and semi-arid urban regions (Lee & Jim 2018, Yang & Ma 2024).

1.3. Empirical Evidence on LST Reduction

Research on the thermal impact of GI has expanded considerably over the last decade, employing both field measurements and simulation-based approaches. Field studies capture local microclimatic variations and validate thermal performance at the pedestrian scale, while simulation models such as ENVI-met, CFD, and coupled urban climate-energy models enable scenario testing and optimization of vegetation placement (Battista et al. 2016, Chow et al. 2016, Liu et al. 2023, Pandey et al. 2021, Toparlar et al. 2017, Yang et al. 2023).

Cooling effectiveness has been found to vary according to climatic context, with hot-arid cities benefiting the most from evapotranspiration due to low atmospheric humidity and high solar radiation (Bowen et al. 2024, Cheung et al. 2021). In contrast, hot-humid climates rely more heavily on shading, as moisture saturation limits latent heat flux from evapotranspiration (Cheung & Jim 2018, Yang et al. 2023). Urban density also plays a significant role: medium-density areas often achieve optimal cooling by balancing vegetation coverage with airflow, whereas high-density districts may experience constrained benefits due to limited ventilation (Kumar & Shukla 2022). Spatial configuration of vegetation within urban canyons, including street orientation, tree height, and canopy coverage, further modulates thermal outcomes. Studies have demonstrated that continuous canopies produce greater reductions in pedestrian-level LST than scattered plantings, while multi-layered arrangements combining trees, shrubs, and ground cover yield the largest cumulative cooling benefits (Ornelas et al. 2023, Pradeep Kumar et al. 2023, Zhou et al. 2011). These findings underscore the necessity as influenced by urban morphology considerations into green infrastructure planning for maximum effectiveness.

It is important to distinguish between LST and human thermal comfort. While LST provides a spatially explicit measure of surface heat patterns, it does not directly capture air temperature, mean radiant temperature, or human thermal indices such as PET or UTCI. Therefore, LST should be interpreted as a proxy indicator of surface heat exposure rather than a direct measure of human thermal stress.

1.4. Integration with Urban Morphology and Planning

The effectiveness of GI in reducing LST is inseparable from the geometrical and functional characteristics of the built environment. Urban morphology variables, including building height, spacing, and street canyon geometry, influence wind flow, solar exposure, and heat accumulation, which in turn affect vegetation performance (Chen et al. 2021, Huang et al. 2025, Jiang et al. 2021). Optimizing vegetation placement within these morphological constraints enhances both shading and convective cooling effects, yielding more effective LST mitigation (Kikon et al. 2023, Zhang et al. 2003).

Local Climate Zone (LCZ) classifications provide a framework for assessing and comparing green infrastructure performance across diverse urban forms (Kotharkar & Bagade 2018). Integration of GI with urban planning enables performance-based strategies, such as prescribing minimum canopy coverage, spatial distribution, and multi-layered planting to achieve targeted cooling outcomes (Fang et al. 2023). In addition, urban planners and policymakers can leverage these strategies to align GI interventions with broader goals, including energy efficiency, air quality improvement, and has potential implications for thermal comfort (Liu et al. 2021, O'Donnell et al. 2017, Shao et al. 2021). Sustainable urban design approaches also advocate combining GI with complementary measures such as reflective pavements, water features, and shading structures to maximize overall thermal comfort (de Oliveira et al. 2022, Derkzen et al. 2017, Tzoulas et al. 2007). This holistic perspective ensures that vegetation interventions are not only effective in isolation but synergistically contribute to a cooler, more livable urban environment.

1.5. Knowledge Gaps and Study Rationale

Despite the growing body of research, several critical knowledge gaps remain. Many studies focus on single

intervention types, isolated urban contexts, or short-term temperature reductions, which limits the generalizability of findings (Hunter et al. 2015, Mittermüller et al. 2021). Additionally, methodological heterogeneity, including differences in measurement techniques (satellite-derived vs. ground-based LST), simulation assumptions, and temporal scales, complicates cross-study comparisons (Feng 2022, Zhang et al. 2024).

A systematic synthesis is therefore required to consolidate evidence on GI interventions and their effectiveness in LST reduction, considering the influence of climate, urban morphology, and vegetation type. This study adopts a PRISMA-guided systematic review to:

- Map the current state of research on GI and LST reduction.
- Evaluate methodologies and measurement approaches used in existing studies.
- Assess cooling effectiveness across different urban forms and climatic contexts.
- Identify gaps in knowledge and provide evidence-based recommendations for future research and urban planning.

By focusing on these objectives, the study aims to provide a comprehensive, climate-sensitive understanding of GI performance, supporting urban designers and policymakers in implementing effective LST mitigation strategies. This aligns with the study objective of identifying research gaps and supports the need for more context-sensitive and human-centered evaluation frameworks.

Unlike previous reviews, this study not only consolidates empirical evidence on LST reduction by GI but also categorizes interventions by urban morphology, vegetation type, and climate zone, offering a more context-specific understanding of cooling effectiveness. Furthermore, by applying the PRISMA framework systematically, this review enhances transparency, reproducibility, and methodological rigor, providing an updated reference for policymakers, urban planners, and researchers designing evidence-based urban cooling strategies.

2. MATERIALS AND METHODS

In this research, a mixed-methods approach was adopted by combining a PRISMA-based systematic review with bibliometric analysis using VOSviewer. This approach integrates qualitative synthesis of the literature with quantitative mapping of research trends to examine the relationship between GI and LST across built environments (Arruda 2022, Kirby 2023, Page et al. 2021, van Eck 2010). PRISMA process led to the selection of the papers used for both qualitative synthesis and bibliometric analysis. The mixed-methods approach has been instrumental in achieving the objectives of this study (Li et al. 2022). Expanding upon previous discussions, this study integrates the structured qualitative depth of a systematic review with the quantitative insights of bibliometric analysis to examine the relationship between green infrastructure (GI) and land surface temperature (LST) across built environments. The research protocol is shown in Fig. 2. The study follows the PRISMA guidelines and checklist (Page et al. 2021).

A structured data extraction framework was developed to ensure consistency across the reviewed studies. Each study was coded based on predefined variables, including:

(i) type of green infrastructure (e.g., trees, parks, green roofs, blue–green systems),

(ii) urban morphology (e.g., compact, high-density, suburban),

(iii) climatic or geographical context,

(iv) LST measurement method (e.g., remote sensing, simulation, field measurement), and

(v) reported cooling outcomes.

These categories were defined based on common classifications used in urban climate and green infrastructure literature and were applied consistently across all included studies.

2.1. The PRISMA Framework

The PRISMA framework was employed to systematically collect, screen, and analyse articles from the Web of Science (WOS) database. This review is based on the WOS database, which, while ensuring high-quality and peer-reviewed sources, may not capture all relevant studies indexed in other databases such as Scopus or Google Scholar. This represents a limitation in terms of literature coverage. This method enhances transparency and reproducibility, which are vital for academic rigor (Chaudhuri & Kumar 2022, Fu et al. 2022). A web search was conducted on January 04, 2026, as the initial step. Boolean operators (AND, OR) were applied to refine the results and ensure the selection of pertinent studies. The search string was designed to balance comprehensiveness and specificity by incorporating multiple synonymous terms related to land surface temperature, urban heat, and green infrastructure. The selected terms were chosen to ensure alignment with the core research objectives while minimizing retrieval of irrelevant studies. “LST” is first introduced in this paper and is a widely used metric in urban climate and remote sensing studies, particularly for assessing surface heat patterns and urban heat island effects.

Table 1: Criteria for eligible literature through WOS (excluded if not meeting these criteria).

No.		Criteria
1	Search Terms (Topic/Title/ Abstract)	("Land Surface Temperature" OR "LST" OR "Surface Temperature" OR "Urban Heat" OR "UHI") AND ("Green Infrastructure" OR "Urban Greenery" OR "Urban Green Space") AND ("Urban Environment*" OR "Built Environment")
2	Document Type	Article
3	Language	English
4	Database	Web of Science (WOS) database
5	Irrelevant Disciplines	Subject categories retrieved excluding: *Pharmacology, toxicology, and pharmaceutics;* Physics and Astronomy; Chemical Engineering; Computer Sciences; Biochemistry, Genetics and Molecular Biology; Decision Sciences

Furthermore, comprehensive relevant literature retrieval is based on LST in GI and Built Environment. Alternative terms such as 'urban greening' or 'ecosystem services' were considered but were not included to maintain focus on studies explicitly addressing thermal performance. Criteria for eligible literature through WOS are further classified in Table 1. The specific search query used in basic search mode; the search term was - ("Land Surface Temperature" OR "LST" OR "Surface Temperature" OR "Urban Heat" OR "UHI") AND ("Green Infrastructure" OR "Urban Greenery" OR "Urban Green Space") AND ("Urban Environment*" OR "Built Environment") and then search method topic was selected.

The WOS core collection database provided 211 journal articles using this search. Fig. 2 illustrates the PRISMA 2020-compliant study selection process, detailing the number of records at each stage (identification, screening, eligibility, and inclusion), along with explicit reasons for exclusion. This ensures transparency and reproducibility of the review process. The process began with the identification stage, where 211 records were retrieved from the WOS database. This broad search aimed to capture a wide range of relevant studies within the research scope. During this phase, 26 articles were excluded because they were not in English, were review papers, or were categorized as early access articles, resulting in 185 records proceeding to the next phase.

The screening stage involved a structured evaluation of the remaining records based on predefined inclusion criteria. A total of 65 studies were excluded due to disciplinary misalignment. The remaining records were assessed for relevance, defined as explicit examination of the relationship between GI and LST within urban or built environments.

Screening was conducted sequentially at title, abstract, and full-text levels to ensure consistency and minimize subjectivity. Following this process, 120 studies were retained for further assessment, of which 59 were excluded due to lack of alignment with the research scope. The final selection comprised 61 studies that met all inclusion criteria.

In the eligibility stage, the full texts of the 61 remaining records were reviewed against predefined criteria, including relevance to the research themes of LST, GI, and the built environment. Finally, the inclusion stage resulted in 61 studies being selected for detailed analysis. These studies formed the foundation of the systematic review, providing critical insights into key themes, methodologies, and research gaps.

By employing the PRISMA framework, this review ensured a structured and reliable process, yielding a robust dataset that highlights both the methods adopted and research gaps in the field. This approach not only synthesizes existing knowledge but also facilitates future research by systematically identifying synergies and challenges in urban greenery and thermal comfort.

In the supplementary material, a comprehensive list of all 61 studies included in the systematic review is presented, along with citation details. Each study is systematically documented with information such as authors, year of publication, title, and number of citations, providing a transparent overview of the research corpus. The meticulous application of the PRISMA framework ensures that all selected studies are highly relevant to the study's themes and research objectives.

To make sure the papers included in systematic reviews are of high quality, Dybå & Dingsøyr in 2008 developed a checklist of questions (Dybå & Dingsøyr 2008). Three

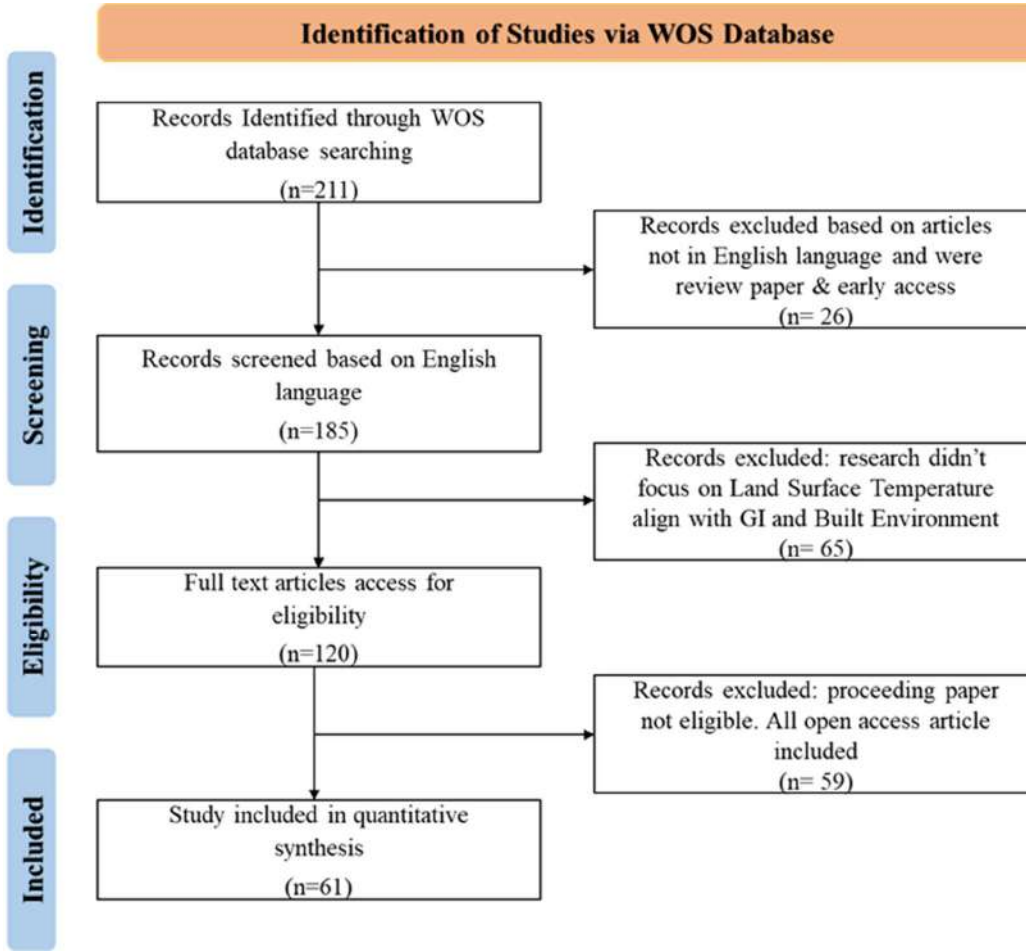


Fig. 2: PRISMA framework of the study, Source: PRISMA 2020 (Page et al. 2021).

primary criteria serve as the foundation for these inquiries: relevance, rigor, and credibility. Data were extracted systematically from each study, including GI type, urban morphology, climate context, LST measurement method, and reported cooling effects. While no formal numerical quality scoring or sensitivity analysis was conducted, the review carefully considered the scope, methodology, and context of each study to identify patterns and trends. Potential limitations, such as geographic concentration of studies or methodological variability, were acknowledged and considered in the synthesis. This assessment informed the interpretation of results and helped identify potential sources of bias, including limitations related to data sources, spatial scale, and modeling assumptions. Given the heterogeneity of study designs and outcomes, a qualitative assessment approach was considered more appropriate than a standardized scoring system.

This structured approach ensured a robust and transparent review, providing a comprehensive overview of the current evidence on the effects of green infrastructure on urban LST, while highlighting research gaps and opportunities for future studies. A complete list of all included studies, with citation details, is provided in the supplementary material.

2.2. Bibliometric Analysis

For the bibliometric analysis, this study utilized VOSviewer software (version 1.6.19) in conjunction with the WOS database. VOSviewer was employed to generate visual bibliometric maps (Arruda 2022, van Eck 2010), illustrating the co-occurrence of keywords and emerging research trends in literature related to LST and GI across built environments. This technique allowed for the identification of frequently used terms, research foci, and linkages between concepts, offering insights into the conceptual structure of the field. In addition to keyword analysis, the study examined the geographic distribution of research by analyzing country affiliation contributions. Publication trends were also assessed to determine the temporal evolution of scholarly

interest in the topic. These bibliometric insights complement the qualitative synthesis by mapping the scope and trajectory of academic engagement, thereby strengthening the review's capacity to identify research gaps and emerging areas of focus. For keyword co-occurrence analysis, author keywords were extracted from the selected studies. A minimum occurrence threshold was applied to include only frequently used terms, ensuring robustness of the network. Co-occurrence relationships were normalized using the association strength method, and clustering was performed using the VOSviewer clustering algorithm to group related themes.

Given the diversity of study designs, spatial scales, climatic contexts, and outcome metrics (as summarized in Table 2), a formal meta-analysis was not considered appropriate. Instead, a structured quantitative synthesis approach was adopted to systematically compare reported LST reductions across studies.

3. RESULTS

3.1. Publication Trends

The publication trend illustrated in Fig. 3 reveals a clear and accelerating growth in scholarly interest in GI interventions for LST reduction over the past decade. From 2012 to 2019, research output in this field remained relatively sparse, with only one publication recorded in each of the selected early years. This limited output suggests that, during this period, GI–LST relationships were still an emerging research niche, often embedded within broader studies on urban climate, land use, or sustainability rather than being a primary focus. A notable shift occurs from 2020 onwards, where the number of publications increases substantially. The annual output rises from three studies in 2020 to eight in 2021, followed by sustained growth through 2022 and 2023. This surge coincides with growing global concern over urban heat islands, climate change impacts, and heat-related health risks, as well as improved access to high-resolution remote sensing data and geospatial analytical tools. These developments have enabled more robust and spatially explicit assessments of how green roofs, urban forests, parks, and other GI strategies influence LST.

The upward trajectory becomes particularly pronounced after 2023, reaching 19 publications in 2025, the highest value in the review period. The fitted exponential trendline (R^2 = 0.9135) indicates a strong and consistent growth pattern, suggesting that research in this domain is not only increasing but accelerating. This reflects the consolidation of GI-based thermal mitigation as a critical research theme within urban climate adaptation and sustainable city planning. Overall, the observed publication trend underscores the timeliness and relevance of this PRISMA-based systematic review. The rapid increase in recent studies highlights the need for a structured synthesis to evaluate the effectiveness of different green infrastructure interventions, identify methodological patterns and gaps, and inform evidence-based urban planning and climate resilience strategies.

3.2. Analysis of Co-Occurring Keywords and Density Visualization

The keyword co-occurrence network (Fig. 4), generated using VOSviewer, illustrates the conceptual structure of

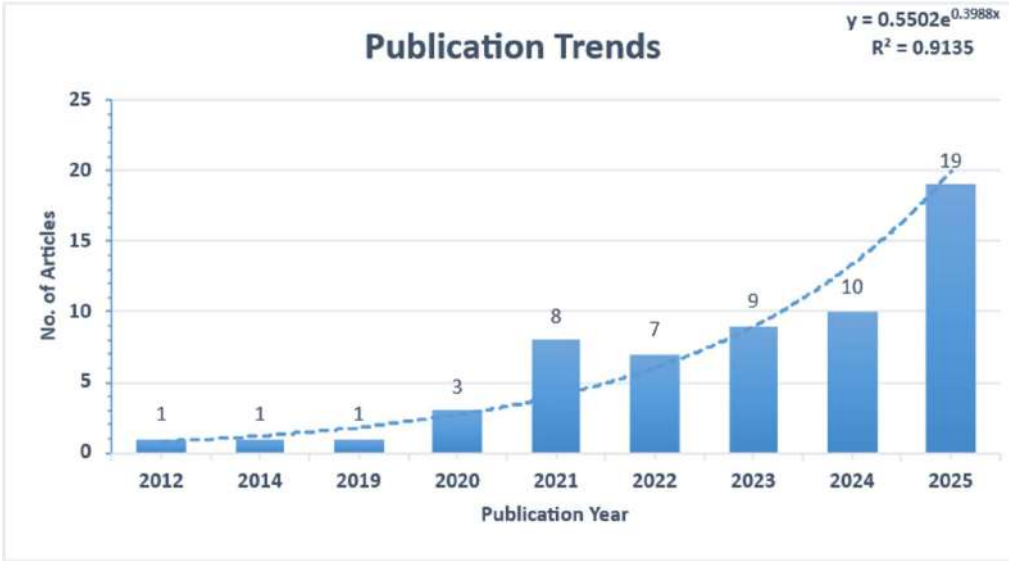


Fig. 3: Annual publication trend in GI–LST research with an exponential trendline.

the research field by mapping the frequency and strength of relationships between terms. The co-occurring keyword map produced using VOSviewer offers a nuanced representation of the conceptual structure and thematic breadth of research on GI and LST reduction. Based on 501 author keywords, the network is organized into 23 clusters, with a total link strength of 5209, indicating a highly connected and mature body of literature. The identified clusters represent groups of closely related keywords that frequently co-occur within the literature, indicating dominant thematic areas. Total link strength reflects the overall degree of connectivity among keywords, with higher values indicating stronger conceptual integration across the research field.

At the center of the network, keywords such as green infrastructure, temperature, urban environment, climate change, and built environment exhibit the highest connectivity, reflecting their foundational role in shaping the discourse. Their prominence suggests that GI–temperature interactions are most often examined within broader discussions of urban climate dynamics and the physical characteristics of cities. The dense interlinkages among these core terms indicate strong conceptual integration rather than fragmented thematic development.

Several clusters are clearly oriented toward thermal processes and measurement approaches, with recurring terms including land surface temperature, surface temperature, air temperature, energy balance, and urban heat. These clusters underscore the dominant reliance on remote sensing, surface energy modeling, and climate simulations to quantify the cooling effects of green infrastructure. Closely connected keywords such as land cover, urbanization, density, and buildings highlight the recognition that GI performance is strongly conditioned by urban form, spatial configuration, and land-use patterns.

Methodological diversity is also evident across the network. Clusters containing terms such as simulation, evaluation tools, leaf area index, canopy shading, Google Street View, and citizen science point to increasing use of innovative data sources and mixed-method approaches. These methods enable more detailed characterization of vegetation structure, street-level thermal environments, and user perceptions, complementing traditional satellite-based analyses. Emerging conceptual framings are reflected in clusters associated with nature-based solutions, multifunctionality, biodiversity, and bioclimatic design.

Overall, the identification of 23 interrelated clusters with a high total link strength reveals a well-established yet evolving research field. The keyword network highlights both the consolidation of core themes, particularly the

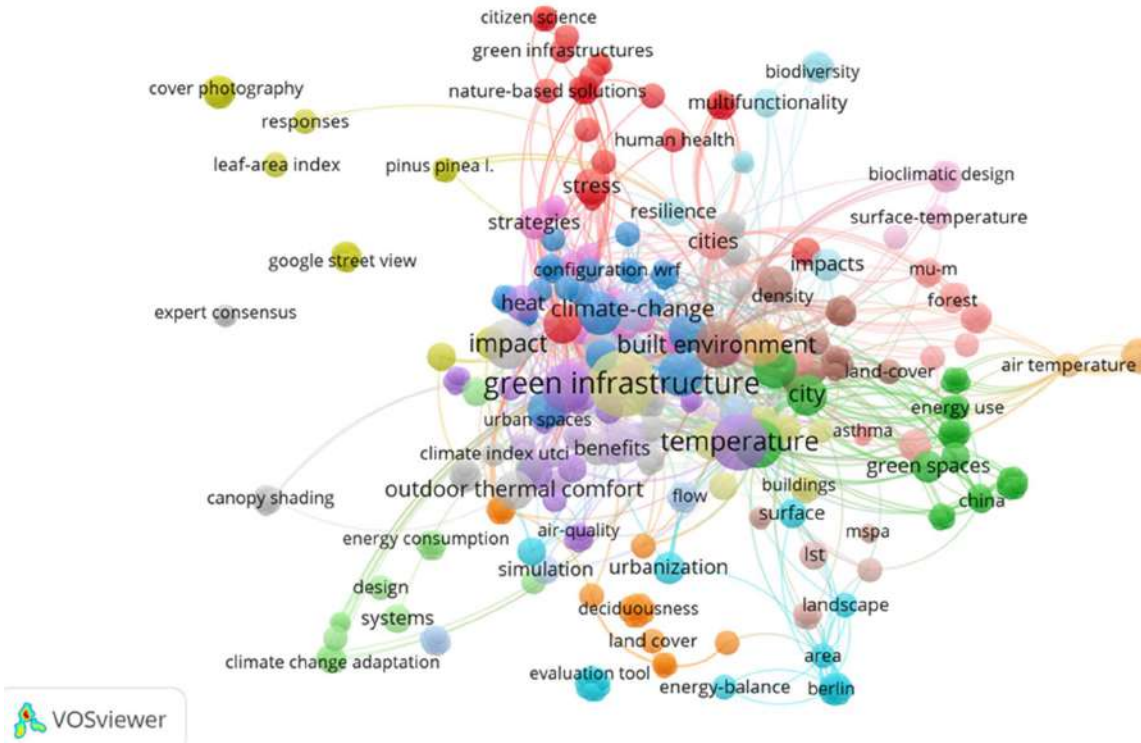


Fig. 4: Co-occurring keyword map visualization using VOSviewer.

GI–LST relationship and the increasing integration of health, resilience, and methodological innovation.

Fig. 5 presents the keyword density visualization generated using VOSviewer, offering a complementary perspective to the network map by highlighting the relative concentration and prominence of research themes within the literature on GI and temperature mitigation. The density map highlights areas of high research intensity through darker and more saturated regions, enabling clearer identification of dominant and peripheral research themes.

The bibliometric findings highlight a strong concentration of research on biophysical aspects of temperature reduction, while social, behavioral, and equity-related dimensions remain underexplored. This gap is consistent with the findings of the systematic review and suggests the need for more integrated, interdisciplinary approaches in future research.

Results reveal a research field that is highly concentrated around urban thermal regulation, yet gradually diversifying towards potential implications for thermal comfort outcomes, multifunctionality, and innovative data sources. This imbalance underscores the need for future studies to better integrate social, ecological, and methodological dimensions into GI effectiveness assessments, an objective directly addressed by the systematic synthesis undertaken in this review.

These clusters can be broadly interpreted into three dominant thematic domains:

(i) thermal processes and measurement approaches (e.g., LST, surface temperature, energy balance),

(ii) urban form and morphology (e.g., density, land use, urban structure), and

(iii) nature-based and design-oriented strategies (e.g., green infrastructure, ecosystem services, resilience).

Importantly, the analysis reveals comparatively weaker representation of keywords related to human thermal comfort, social vulnerability, and equity. This indicates a research gap in integrating biophysical temperature reduction with human-centered outcomes, which is further explored in the systematic synthesis.

3.3. Analysis of Country Distribution

Fig. 6 illustrates the country-wise distribution of publications included in this systematic review, highlighting the geographical patterns of research activity on GI interventions for temperature reduction. The results reveal a clear concentration of scholarly output in a limited number of

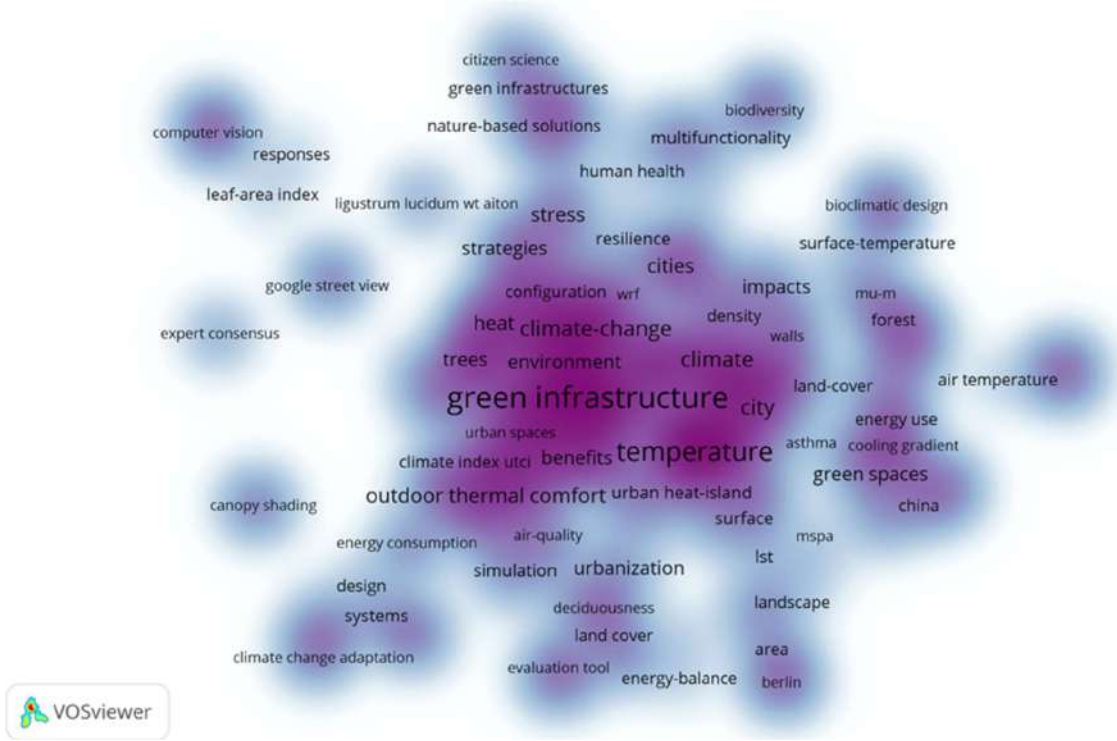


Fig. 5: Keyword density visualization generated using VOSviewer, illustrating the thematic concentration and research intensity of co-occurring keywords in studies on green infrastructure and urban temperature mitigation.

countries, reflecting uneven global engagement with this research theme.

China emerges as the leading contributor, accounting for the highest number of publications (n = 15). This dominance underscores the country's strong research focus on urban heat mitigation, rapid urbanization challenges, and the widespread application of remote sensing and spatial analysis techniques in GI–temperature studies. Australia follows with nine publications, reflecting sustained interest in climate-sensitive urban planning and heat resilience strategies in the context of extreme temperature exposure. Italy ranks third with seven studies, indicating a growing European emphasis on nature-based solutions and urban climate adaptation.

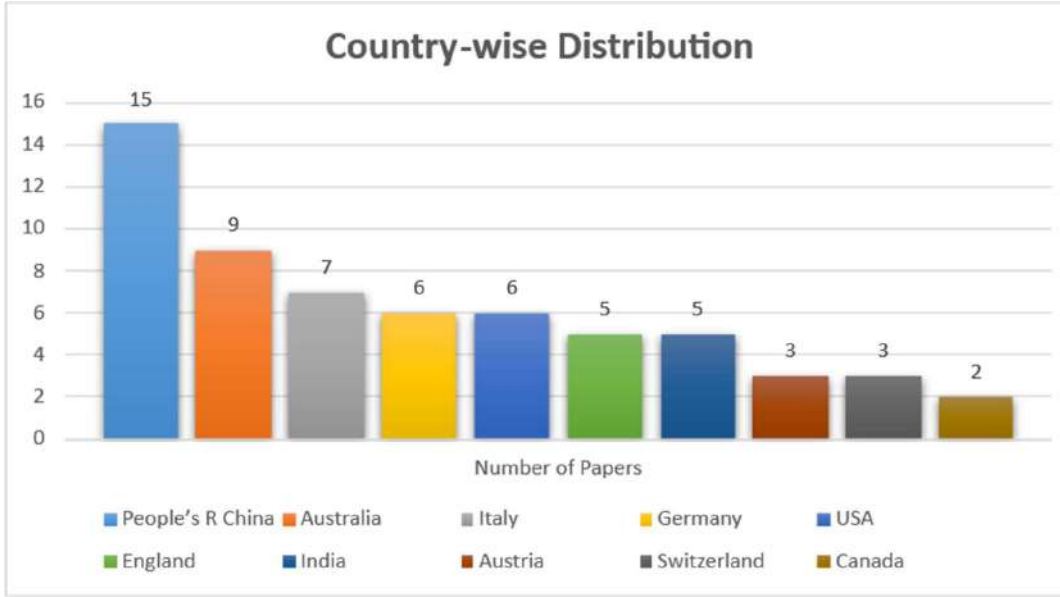
Germany and the United States contribute six publications each, demonstrating consistent research engagement in assessing the thermal and environmental performance of green spaces, urban forests, and other GI elements. England and India follow with five publications each, highlighting emerging but still moderate research activity, particularly in relation to urban sustainability and climate adaptation. Austria and Switzerland contribute three studies each, while Canada accounts for two publications, suggesting more limited but focused contributions. This geographical imbalance points to a need for broader cross-regional studies and greater inclusion of diverse climatic, socio-economic, and urban contexts. Importantly, the concentration of studies in specific regions may influence the reported effectiveness of GI, as cooling performance is highly dependent on local climate conditions, vegetation characteristics, and urban morphology.

As a result, findings derived predominantly from temperate and rapidly urbanizing regions may not be directly transferable to underrepresented regions such as Africa or parts of South America, where climatic conditions, urban forms, and resource constraints differ significantly. This highlights the need for caution when generalizing results and underscores the importance of context-specific evaluation of GI interventions.

The country distribution indicates that research on GI and land surface temperature reduction is predominantly concentrated in Asia, Europe, and Australia, with comparatively fewer contributions from North America and limited representation from the Global South beyond China and India. This geographical imbalance points to a need for broader cross-regional studies and greater inclusion of diverse climatic, socio-economic, and urban contexts. Addressing this gap is essential for improving the generalizability of evidence and informing context-sensitive green infrastructure planning at a global scale.

3.4. Content Analysis

This section presents the results of the content analysis of 61 selected studies that examined the comparative performance of land surface temperature (LST) and green infrastructure (GI) in built environments, as summarized in Table 2. The synthesis was conducted using a qualitative coding approach, in which recurring patterns and relationships across studies were identified and grouped according to GI type, urban morphology, and climatic context. This approach



Source: WOS

Fig. 6: Geographical distribution of publications.

Table 2: Content analysis of 61 selected studies that examined the comparative performance of LST and GI in Built environments.

S. No.	Authors	Year	GI Type	Urban Morphology	LST Measurement Method	Key Inferences
1.	Oraiopoulos et al. 2026	2026	Urban green infrastructure	Informal settlements	Remote sensing + field data	GI significantly reduces surface heat stress and improves habitability in dense informal settlements.
2.	Berger et al. 2026	2026	Native vegetation	Residential urban areas	Field experiments	Native plant-based GI enhances thermal regulation under urban heat stress conditions.
3.	Helmreich et al. 2025	2025	Infiltration swales (blue–green GI)	Urban neighborhoods	ENVI-met simulation	Blue–green GI provides measurable surface cooling while improving stormwater management.
4.	Yang & La Roche 2025	2025	Tree canopies, green roofs	Dense urban blocks	ENVI-met	Tree canopies outperform green roofs in reducing daytime LST in compact urban areas.
5.	Lazovic et al. 2025	2025	Roadside greenery	Traffic corridors	Numerical simulation	Roadside GI mitigates LST and contributes to improved thermal conditions along high-traffic streets.
6.	Hogeweij et al. 2025	2025	Urban parks	High-density city center	Landsat LST	Urban parks function as thermal sinks with cooling effects extending into surrounding areas.
7.	Liu et al. 2025	2025	Green roofs	High-rise urban districts	Remote sensing	Green roofs reduce roof-level LST but show limited neighborhood-scale cooling.
8.	Esperon-Rodriguez et al. 2025	2025	Street trees	Street canyon morphology	CFD + ENVI-met	Tree height and spacing strongly influence cooling performance in street canyons.
9.	Roversi & Longo 2025	2025	Blue–green corridors	Riverfront urban areas	Satellite imagery	Combined vegetation–water systems generate stronger LST reductions than vegetation alone.
10.	Bachofen et al. 2025	2025	Pocket parks	Mixed-use urban zones	Landsat	Small green spaces significantly reduce localized surface heat hotspots.
11.	Ramadan et al. 2025	2025	Urban forests	Metropolitan scale	MODIS	Large urban forests lower regional LST more effectively than fragmented green spaces.
12.	Cuce et al. 2025	2025	Vertical greenery systems	High-rise districts	Field measurements	Vertical GI reduces façade temperatures but has limited city-scale influence.
13.	Karimi et al. 2025	2025	Green belts	Urban fringe	Remote sensing	Continuous green belts outperform fragmented GI in reducing surface temperatures.
14.	Chen & Hanlon 2025	2025	Grassland GI	Low-density suburbs	Landsat	Grass-based GI provides moderate cooling but is less effective than tree cover.
15.	Yang et al. 2025	2025	Wetlands	Peri-urban areas	Satellite imagery	Urban wetlands exhibit strong daytime LST reduction due to evapotranspiration.
16.	Seidu et al. 2025	2025	Urban trees	Residential neighborhoods	Field + satellite	Increased tree canopy cover correlates with lower surface temperatures.
17.	Pattnaik et al. 2025	2025	Green roofs	Compact urban form	ENVI-met	Roof greening effectiveness depends on building height and roof coverage ratio.
18.	Al-Zghoul & Al-Homoud 2025	2025	Linear greenways	Transport corridors	Remote sensing	Linear GI reduces thermal fragmentation across urban landscapes.
19.	Bera & Nag 2025	2025	Mixed GI systems	Dense urban fabric	Landsat + modeling	Integrated GI networks outperform isolated interventions in LST mitigation.
20.	Ni et al. 2025	2025	Urban parks	Compact city	Remote sensing	Park size and shape strongly influence cooling intensity and reach.
21.	Del Rosario et al. 2025	2025	Street greenery	High-density streets	Field measurements	Shaded streets show significantly lower surface temperatures during peak heat.
22.	Yazdi et al. 2024	2024	Blue–green infrastructure	Flood-prone urban areas	ENVI-met	Blue–green GI provides dual benefits of cooling and climate resilience.
23.	Chen et al. 2024	2024	Green walls	High-rise buildings	Thermal imaging	Green walls lower wall surface temperatures but have localized effects.
24.	Chen et al. 2024	2024	Urban vegetation	City-wide	Landsat time series	Expansion of urban greenery correlates with long-term LST decline.
25.	Frosini et al. 2024	2024	Green roofs	Commercial districts	Remote sensing	Commercial roof greening reduces extreme surface heat accumulation.

Table Cont....

S. No.	Authors	Year	GI Type	Urban Morphology	LST Measurement Method	Key Inferences
26.	Chu et al. 2024	2024	Urban trees	Residential blocks	Field sensors	Tree shade significantly reduces ground and pavement temperatures.
27.	Jimenez & de Adana 2024	2024	Urban parks	Mixed-density areas	MODIS	Larger parks exhibit stronger and more stable cooling effects.
28.	Guan & Zhang 2024	2024	Vegetated courtyards	Compact housing	ENVI-met	Internal green courtyards improve microclimate in dense housing complexes.
29.	Liu et al. 2024	2024	Blue–green networks	Metropolitan regions	Remote sensing	Network connectivity enhances regional LST mitigation.
30.	Azmeer et al. 2024	2024	Urban agriculture	Peri-urban zones	Landsat	Urban farming areas show measurable surface cooling benefits.
31.	Ibric et al. 2024	2024	Street trees	Urban road networks	Field + GIS	Tree-lined streets reduce surface heat accumulation during summer.
32.	Zakrzewska et al. 2023	2023	Green roofs	Residential buildings	Thermal monitoring	Roof vegetation moderates diurnal surface temperature extremes.
33.	Fong et al. 2023	2023	Urban greenery	Informal settlements	Remote sensing	Even small-scale GI interventions reduce extreme LST in vulnerable areas.
34.	Pragati et al. 2023	2023	Urban parks	City center	Landsat	Park cooling intensity decreases with distance from park edges.
35.	La Rosa & Li 2023	2023	Green corridors	Compact cities	ENVI-met	Corridors facilitate spatial diffusion of cooling effects.
36.	Sobrinho et al. 2023	2023	Blue infrastructure	Waterfront districts	Satellite imagery	Water bodies enhance adjacent green cooling effects.
37.	Pritipadmaja et al. 2023	2023	Urban trees	Suburban areas	Field measurements	Mature trees provide stronger cooling than young vegetation.
38.	Okumus & Terzi 2023	2023	Urban greenery	Rapidly urbanizing cities	Landsat	Loss of GI intensifies surface urban heat island effects.
39.	Irfeey et al. 2023	2023	Street greenery	Street canyon	CFD + field data	Combined ventilation and vegetation regulate canyon LST.
40.	Schaffernicht et al. 2023	2023	Urban parks	Metropolitan scale	MODIS	Parks contribute to city-scale thermal regulation.
41.	Urban et al. 2022	2022	Green roofs	Dense commercial areas	Remote sensing	Roof greening effectiveness varies with roof material and coverage.
42.	Graef et al. 2022	2022	Blue–green GI	Coastal cities	Satellite imagery	Coastal blue–green systems moderate extreme surface heat.
43.	Reyhani et al. 2022	2022	Nature-based solutions	Urban neighborhoods	ENVI-met	Integrated NBS designs enhance urban heat resilience.
44.	Anderson et al. 2022	2022	Urban vegetation	Mixed-use districts	Landsat	Vegetation density inversely correlates with LST intensity.
45.	Shan et al. 2022	2022	Urban parks	High-density zones	Remote sensing	Park cooling is strongest during daytime heat peaks.
46.	Salvalai et al. 2022	2022	Green roofs	Residential districts	Field measurements	Green roofs reduce surface heat but require adequate maintenance.
47.	O'Keeffe et al. 2022	2022	Urban trees	Compact cities	Remote sensing	Tree canopy coverage is a key determinant of LST reduction.
48.	Chun et al. 2021	2021	Blue–green corridors	Urban regions	GIS + Landsat	Corridor continuity enhances spatial cooling efficiency.
49.	Vulova et al. 2021	2021	Urban greenery	City-wide	MODIS	City-scale GI distribution shapes surface thermal patterns.
50.	Kabano et al. 2021	2021	Street trees	Commercial streets	Field monitoring	Shaded commercial streets experience lower surface temperatures.
51.	Zhang et al. 2021	2021	Green walls	High-rise buildings	Thermal sensors	Vertical GI cools building envelopes under extreme heat.
52.	Fuentes et al. 2021	2021	Urban parks	Dense urban cores	Landsat	Larger parks produce more stable cooling effects.

Table Cont....

S. No.	Authors	Year	GI Type	Urban Morphology	LST Measurement Method	Key Inferences
53.	Back et al. 2021	2021	Urban greenery	Metropolitan areas	Remote sensing	Fragmentation of GI reduces its cooling effectiveness.
54.	Bouzouidja et al. 2021	2021	Blue infrastructure	Urban watersheds	Satellite imagery	Water bodies significantly moderate surrounding LST.
55.	Amani-Beni et al. 2021	2021	Urban forests	City outskirts	MODIS	Peripheral forests contribute to regional cooling.
56.	Shin et al. 2020	2020	Urban greenery	Rapidly urbanizing city	Landsat time series	Expansion of GI correlates with declining urban LST trends.
57.	Lu et al. 2020	2020	Street greenery	Street canyon	Field + CFD	Vegetation and airflow jointly regulate urban surface temperatures.
58.	Sabatino et al. 2020	2020	Nature-based solutions	Urban neighborhoods	ENVI-met	GI-based designs improve thermal resilience under heat stress.
59.	Makido et al. 2019	2019	Green walls and roofs	High-density urban	Case study + monitoring	Building-scale GI reduces surface temperature and energy demand.
60.	Revell & Anda 2014	2014	Urban greenery	City-scale	Landsat	Spatial patterns of GI determine high-temperature zones.
61.	Su et al. 2012	2012	Mixed green infrastructure	Metropolitan regions	Remote sensing	GI density is inversely related to urban surface heat intensity.

enabled systematic comparison while accommodating methodological heterogeneity across the reviewed studies.

The synthesis was structured to directly address the research objectives outlined in the introduction, particularly by consolidating empirical evidence on LST reduction associated with GI interventions and categorizing findings based on urban morphology, vegetation type, and climate zone. This facilitates a more context-specific understanding of cooling effectiveness.

The aim of this synthesis is to extract recurring patterns, conceptual orientations, and practical insights across multiple dimensions of evaluation. Such a structured approach not only supports understanding of the current state of knowledge but also helps identify methodological inconsistencies and research gaps that may hinder evidence-based planning and policy development. By organizing the review in this manner, the analysis provides a more nuanced understanding of the practical advantages, trade-offs, and contextual applicability of LST in addressing challenges related to urban sustainability and infrastructure resilience.

The "key inferences" reported in Table 2 were derived through a structured synthesis of each study's primary findings. Rather than subjective interpretation, these inferences summarize the main conclusions presented by the original authors, with emphasis on the relationship between GI characteristics and LST reduction. To minimize subjectivity, consistent coding criteria were applied across all studies during the data extraction and synthesis process.

This PRISMA-guided systematic review synthesized evidence from 61 peer-reviewed studies published between 2012 and 2026, focusing on the effectiveness of GI interventions in reducing LST in urban environments. The temporal distribution of studies shows a marked increase after 2018, reflecting growing scientific and policy concern regarding urban heat under climate change (Su et al. 2012, Revell & Anda 2014, Makido et al. 2019, Lu et al. 2020, Di Sabatino et al. 2020, Makido et al. 2019, Yang & La Roche 2025, Helmreich et al. 2025, Oraiopoulos et al. 2026).

Geographically, the studies span Asia, Europe, North America, Australia, and parts of Africa and South America, with a notable concentration in rapidly urbanizing regions of East and South Asia. This spatial distribution reflects both data availability and heightened vulnerability to extreme heat in fast-growing cities (Su et al. 2012, Lu et al. 2020, Makido et al. 2019). Several recent studies explicitly address informal settlements and marginalized urban communities, signaling a shift toward equity-oriented urban climate research (Makido et al. 2019, Oraiopoulos et al. 2026). Across the dataset, studies vary substantially in spatial scale, ranging from building- and block-level analyses to city- and metropolitan-scale assessments, enabling a multi-scalar synthesis of GI–LST relationships. Most studies evaluate short-term or event-based cooling effects, while long-term performance may vary depending on vegetation growth, maintenance, and climatic variability. This highlights the need for longitudinal assessments of GI effectiveness.

3.4.1. Distribution of Green Infrastructure Types

Across the reviewed literature, five dominant categories of GI interventions emerge: urban trees and street trees; urban parks and large green spaces; green roofs; vertical greenery systems (green walls); and blue–green infrastructure, including wetlands, vegetated swales, riverside buffers,

and stormwater retention systems (Halder & Kumar 2025). Among these, tree-based GI and urban parks are the most frequently investigated, together accounting for the majority of studies, reflecting their widespread applicability and established cooling potential across a range of urban contexts (Su et al. 2012, Makido et al. 2019, Lu et al. 2020, Di Sabatino et al. 2020, Yang & La Roche 2025).

These interventions are examined across diverse urban morphologies, from compact city centers to suburban and peri-urban environments (Kranti Kumar Maurya 2026, Pradeep Kumar Kori 2026, Rathod et al. 2026). In contrast, green roofs and vertical greenery systems are predominantly addressed in studies focused on high-density or space-constrained settings, where opportunities for ground-level greening are limited and vertical or rooftop solutions offer viable alternatives (Revell & Anda 2014, Yang & La Roche 2025). Blue–green infrastructure, while comparatively less represented in the literature, has gained increasing attention in recent years due to its multifunctional role in enhancing urban thermal regulation alongside stormwater management and broader climate adaptation benefits (Makido et al. 2019, Helmreich et al. 2025).

3.4.2. Magnitude and Variability of LST Reduction

The reported LST reduction ranges are derived from a comparative synthesis of values extracted from the reviewed studies (Table 2). Due to differences in reporting formats (e.g., maximum, average, or localized cooling), these values are presented as indicative ranges rather than statistically pooled estimates. Fig. 7 presents a synthesized distribution of reported LST reductions by green infrastructure type. The values were compiled from individual studies and categorized by intervention type. Minimum, maximum, and typical reported values were extracted to construct the distribution, providing a comparative overview of variability across studies rather than a statistically derived dataset (Su et al. 2012, Revell & Anda 2014, Makido et al. 2019, Lu et al. 2020, Di Sabatino et al. 2020, Yang & La Roche 2025, Helmreich et al. 2025). The magnitude of LST reduction varies not only across GI types but also with temporal and spatial factors. Several studies report stronger cooling effects during daytime peak heat periods, while nighttime cooling tends to be more limited. Furthermore, most reported reductions refer to LST, which may not directly correspond to ambient air temperature or pedestrian-level thermal conditions.

Tree-Based GI and Urban Parks: Urban trees and parks consistently demonstrate the largest cooling magnitudes. Multiple remote sensing studies report mean daytime LST reductions of 2–4°C associated with high tree canopy cover, with localized reductions exceeding 6°C under favorable conditions (Su et al. 2012, Lu et al. 2020, Makido et al. 2019). Park cooling effects often extend several hundred meters into adjacent built-up areas, although the magnitude declines with distance from park boundaries.

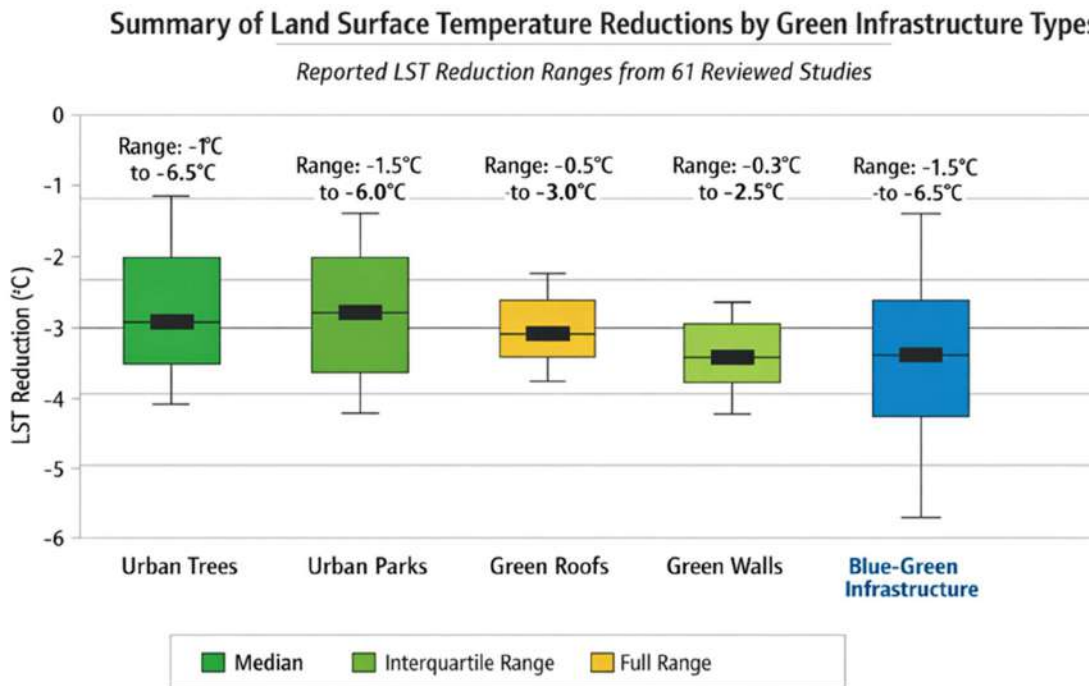


Fig. 7: Summary of reported land surface temperature reductions by green infrastructure type. Box-and-whisker representation of minimum, median, and maximum LST reductions reported across the 61 reviewed studies, highlighting variability by intervention type.

Green Roofs and Vertical Greenery: Green roofs and vertical greenery systems exhibit moderate but consistent cooling, primarily at the building scale. Reported reductions typically range from 0.5 to 2.5°C, with stronger effects observed for intensive green roofs and well-irrigated systems (Revell & Anda 2014, Yang & La Roche 2025). Their contribution to neighborhood-scale LST reduction is limited but non-negligible in dense urban contexts.

Blue–Green Infrastructure: Blue–green infrastructure shows high variability but strong maximum cooling potential. Studies report enhanced cooling in hot–humid and hot–dry climates, where vegetation–water interactions amplify latent heat fluxes (Makido et al. 2019, Helmreich et al. 2025).

3.4.3. Urban Morphology and LST Measurement Approaches

Urban morphology strongly mediates GI effectiveness. In compact urban cores and street canyon environments, cooling outcomes depend on vegetation height, crown width, spacing, and interaction with built form (Di Sabatino et al. 2020, Yang & La Roche 2025). Several studies report that excessive canopy density can reduce ventilation, partially offsetting shading benefits.

In contrast, low- and medium-density urban areas benefit most from large and contiguous green spaces, which generate broader and more stable cooling footprints (Su et al. 2012, Lu et al. 2020). Significantly, studies focusing on informal settlements demonstrate that even small-scale GI interventions can significantly reduce surface heat stress and improve habitability (Makido et al. 2019, Oraiopoulos et al. 2026).

Most studies estimate LST using satellite-based thermal remote sensing, primarily Landsat and MODIS platforms (Su et al. 2012, Lu et al. 2020). These approaches enable city-scale comparison and long-term trend analysis.

Simulation-based studies using ENVI-met or CFD models are frequently employed to explore GI design sensitivity and urban morphology interactions (Di Sabatino et al. 2020, Yang & La Roche 2025, Helmreich et al. 2025). Field-based measurements are mainly used for validation. Table 3 presents details of the LST assessment approaches.

4. DISCUSSION

4.1. Context-Dependent Effectiveness of GI for LST Reduction

This systematic review of 61 studies provides robust evidence that GI interventions are effective in reducing LST across diverse urban contexts; however, the magnitude and spatial extent of cooling are highly context-dependent. Rather than identifying a universally optimal GI solution, the synthesized literature consistently demonstrates that cooling performance emerges from the interaction between GI type, urban morphology, vegetation characteristics, and climate conditions (Su et al. 2012, Revell & Anda 2014, Makido et al. 2019, Lu et al. 2020, Di Sabatino et al. 2020, Yang & La Roche 2025, Helmreich et al. 2025, Oraiopoulos et al. 2026).

Tree-based GI and urban parks repeatedly exhibit the strongest and most spatially extensive cooling effects, largely due to the combined influence of shading and evapotranspiration (Kumar et al. 2025). Across multiple climatic regions and urban forms, dense tree canopy cover is associated with mean daytime LST reductions of 2–4 °C, with localized reductions exceeding 6 °C under favorable conditions (Su et al. 2012, Lu et al. 2020, Makido et al. 2019). Urban parks act as thermal sinks, generating cooling footprints that extend into surrounding built-up areas, although the intensity of cooling decreases with distance from park boundaries.

In contrast, green roofs and vertical greenery systems produce more localized cooling effects, typically limited to roof surfaces and building façades. While these interventions rarely generate large neighborhood-scale LST reductions, they play a critical role in high-density urban environments, where horizontal greening opportunities are constrained (Revell & Anda 2014, Yang & La Roche 2025). Blue–green infrastructure, although less frequently examined, demonstrates strong cooling potential, particularly in hot–dry and hot–humid climates where vegetation–water interactions enhance latent heat fluxes (Makido et al. 2019, Helmreich et al. 2025). Taken together, these findings underscore that GI effectiveness cannot be inferred solely from green area coverage. Instead, cooling outcomes

Table 3: LST assessment approaches and representative studies.

Approach	Key Strength	Key Limitation	Representative Studies
Satellite-based remote sensing	City-scale comparability	Surface temperature proxy only	Su et al. 2012, Lu et al. 2020, Makido et al. 2019, Revell & Anda 2014, Oraiopoulos et al. 2026
Microclimate modeling	Design optimization	Parameter sensitivity	Yang & La Roche 2025, Di Sabatino et al. 2020, Helmreich et al. 2025
Field measurements	High accuracy	Limited spatial extent	Di Sabatino et al. 2020, Revell & Anda 2014
Hybrid approaches	Strong robustness	Methodological complexity	Makido et al. 2019, Lu et al. 2020, Oraiopoulos et al. 2026

depend on how, where, and under what climatic conditions GI is implemented. The findings demonstrate that GI effectiveness cannot be generalized across contexts. Cooling performance varies with time of day, spatial scale, and measurement approach, with most studies focusing on surface temperature reductions rather than direct human thermal conditions. These distinctions are critical for interpreting the practical implications of GI interventions. The geographic concentration of studies also limits the global generalizability of findings. Variations in climate zones (e.g., hot–arid vs. temperate), urban development patterns, and vegetation types can lead to significantly different cooling outcomes, reinforcing the need for region-specific assessments. For example, the strong cooling effects reported for tree-based GI are largely derived from studies conducted in specific climatic contexts, which may not fully represent performance in arid or resource-constrained environments.

4.2. Urban Morphology, Design Trade-offs, and Cooling Mechanisms

Urban morphology emerges as one of the most influential moderators of GI cooling performance. Studies conducted in compact city centers and street canyon environments consistently report that vegetation height, crown geometry, spacing, and interaction with built form critically shape cooling outcomes (Di Sabatino et al. 2020, Yang & La Roche 2025). While shading provided by trees reduces surface temperatures, poorly configured vegetation can restrict airflow, reducing convective heat removal and partially offsetting cooling benefits.

In lower-density urban areas, where space allows for larger and more continuous green spaces, GI produces broader and more stable cooling footprints. Remote sensing studies repeatedly demonstrate that large parks and green belts generate LST reductions extending several hundred meters into adjacent neighborhoods (Su et al. 2012, Lu et al. 2020). These spatial gradients highlight the importance of connectivity and spatial configuration, rather than isolated green patches. Fig. 8 shows a conceptual illustration of how dominant cooling mechanisms like shading, evapotranspiration, and vegetation–water interactions vary across hot–dry, hot–humid, and temperate climates that influence the effectiveness of green infrastructure interventions in reducing land surface temperature.

Importantly, the reviewed literature shows that small-scale GI interventions can deliver substantial benefits in spatially constrained environments, including informal settlements. Oraiopoulos et al. (2026) demonstrate that targeted interventions such as roadside trees and micro-parks significantly reduce surface heat stress and improve

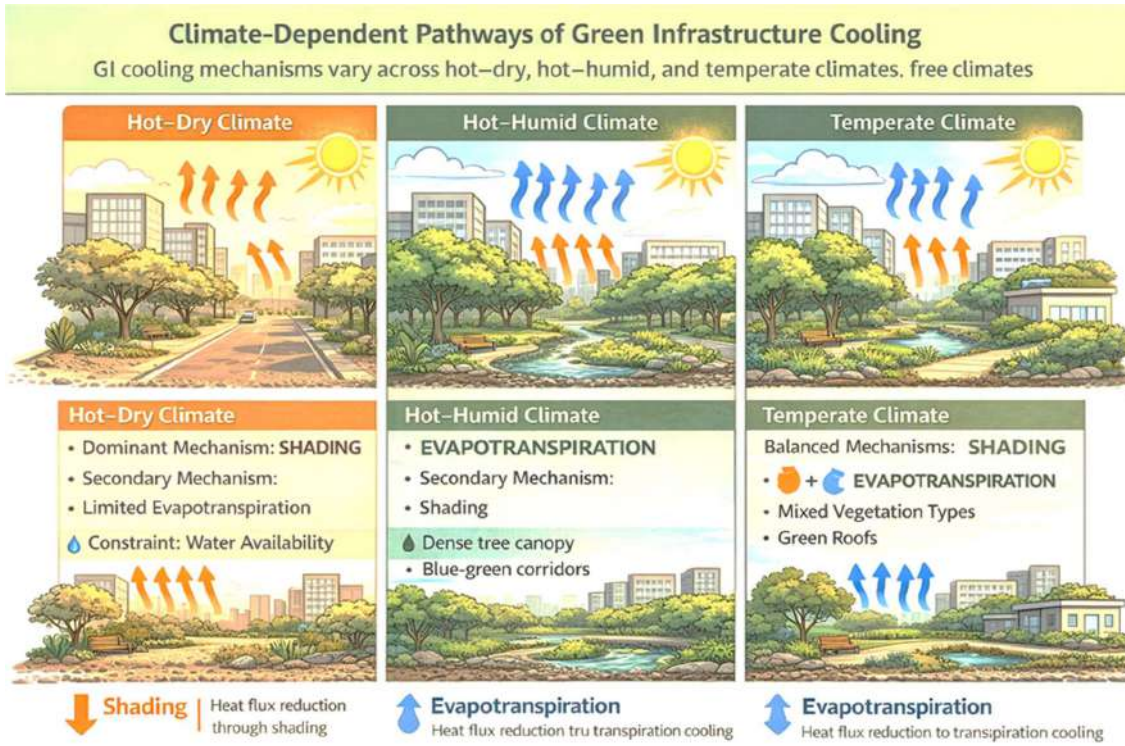


Fig. 8: Climate-dependent pathways of green infrastructure cooling.

habitability in dense informal settlements, despite severe limitations in land availability. These findings challenge assumptions that effective GI cooling requires large-scale or high-cost interventions and emphasize the importance of design-sensitive, context-aware planning.

4.3. Climatic Sensitivity, Vegetation Characteristics, and Blue-Green Synergies

The cooling effectiveness of GI is strongly climate-sensitive, with consistently higher LST reductions reported in hot–dry and hot–humid regions compared to temperate climates (Makido et al. 2019, Helmreich et al. 2025). In these climates, evapotranspiration plays a dominant role in surface energy balance, amplifying the cooling impact of vegetation.

Vegetation characteristics further mediate cooling performance. Multiple studies highlight the importance of canopy density, leaf area index, and species selection, with tree-based systems consistently outperforming grass-dominated GI in terms of surface cooling (Lu et al. 2020, Yang & La Roche 2025). However, several studies caution that cooling benefits decline under drought stress, particularly in arid regions where water availability limits evapotranspiration (Makido et al. 2019). Blue–green infrastructure enhances cooling by coupling vegetation with water-mediated thermal regulation, but its performance is highly dependent on hydrological conditions and maintenance. While such systems offer substantial potential for heat mitigation, their long-term effectiveness under future climate change scenarios remains uncertain, highlighting a critical area for future research.

4.4. Methodological Implications, Equity, and Future Directions

The reviewed studies employ a diverse range of methodological approaches, with satellite-based LST retrieval using Landsat and MODIS dominating the literature (Su et al. 2012, Lu et al. 2020). These methods enable consistent city-scale analysis but do not directly capture human thermal comfort. Simulation-based approaches, such as ENVI-met and CFD modeling, provide valuable insights into design optimization and causal mechanisms but remain sensitive to parameterization and require empirical validation (Di Sabatino et al. 2020, Yang & La Roche 2025, Helmreich et al. 2025).

A key strength of recent literature is the growing focus on heat vulnerability and equity, particularly in informal settlements and marginalized urban communities. Evidence increasingly shows that even modest GI interventions can yield disproportionate benefits in high-risk contexts (Makido et al. 2019, Oraiopoulos et al. 2026). However, significant gaps remain, including limited long-term assessments of GI performance, inconsistent classification of urban morphology, and insufficient integration of LST analysis with human thermal comfort and social vulnerability metrics.

A key limitation of the reviewed literature is the reliance on LST as a primary indicator of thermal performance. While LST provides valuable insights into surface heat patterns, it does not directly represent human thermal comfort. Future research should integrate LST with air temperature measurements and human thermal indices (e.g., PET, UTCI) to provide a more comprehensive assessment of urban heat mitigation strategies.

This review advances understanding from generalized assertions that "green infrastructure cools cities" toward a context-sensitive, design-aware, and climate-responsive framework. The evidence from 61 studies demonstrates that GI can substantially reduce land surface temperature, but only when interventions are carefully aligned with urban form, vegetation characteristics, and climatic conditions. By systematically synthesizing results through the PRISMA framework, this study provides a transparent and reproducible evidence base to inform urban heat mitigation strategies that are both effective and equitable.

5. CONCLUSIONS

This PRISMA-based systematic review synthesizes evidence from 61 peer-reviewed studies to evaluate how different green infrastructure (GI) interventions influence land surface temperature (LST) across diverse built environments. The findings indicate that GI is an effective strategy for reducing surface heat exposure; however, its performance is strongly context-dependent, varying with urban morphology, vegetation characteristics, and climatic conditions. Across the reviewed literature, tree-based GI and urban parks consistently demonstrate the most substantial and spatially extensive reductions in LST, primarily driven by shading and evapotranspiration processes. These effects are generally more pronounced during daytime peak heat periods. In contrast, green roofs and vertical greenery systems provide more localized cooling benefits, particularly in high-density urban areas where horizontal greening is constrained. Blue–green infrastructure exhibits strong cooling potential in certain climatic contexts, especially where vegetation–water interactions enhance latent heat exchange, although performance is influenced by water availability and maintenance conditions.

The review further highlights that the effectiveness of GI interventions is mediated by urban form and spatial configuration. Large and contiguous green spaces tend to

produce broader and more stable cooling effects in low- and medium-density environments, whereas compact urban areas require carefully integrated design strategies that balance shading, ventilation, and spatial constraints. Evidence from informal settlements suggests that small-scale, strategically implemented GI interventions can contribute to reducing localized surface heat exposure, with potential implications for improving thermal conditions in heat-vulnerable areas, although systematic evidence on equity outcomes remains limited.

Methodologically, the literature is characterized by a predominance of satellite-based LST assessments, complemented by simulation models and field measurements. While these approaches provide valuable insights into spatial patterns of surface temperature, the review identifies key limitations, including methodological heterogeneity, limited long-term evaluation, and insufficient integration of LST-based analysis with human-centered thermal comfort indicators and socio-environmental factors.

Overall, this review advances understanding from generalized assertions of GI effectiveness toward a more context-sensitive and design-oriented perspective on urban heat mitigation. By systematically organizing evidence across intervention types, urban forms, and climatic conditions, the study provides a transparent foundation for interpreting GI performance in different settings. Future research should prioritize longitudinal and comparative studies, expand representation across underrepresented regions, and integrate LST analysis with air temperature measurements and human thermal comfort indices (e.g., PET, UTCI) to support more comprehensive and human-centered assessments. Such efforts will strengthen the role of green infrastructure as a key component of climate-responsive and resilient urban planning.

6. ACKNOWLEDGMENTS

The authors would like to express their sincere gratitude to all the researchers whose work was reviewed and synthesized in this study. Their valuable contributions have shaped the knowledge base surrounding LST and green infrastructure. We also acknowledge the use of VOSviewer software for the bibliometric analysis, which provided critical insights into thematic trends and research networks. Special thanks are extended to the institutions and libraries that provided access to academic databases, making the systematic literature review possible. Finally, the authors appreciate the support and feedback received from colleagues and academic peers throughout the development of this manuscript.

7. REFERENCES

Abuwaer, N., Ullah, S. and Al-Ghamdi, S.G., 2023. Building Climate Resilience Through Urban Planning: Strategies, Challenges, and Opportunities. In: *Sustainable Cities in a Changing Climate*, pp.185–206. Wiley. [DOI]

Al-Zghoul, S. and Al-Homoud, M., 2025. GIS-Driven Spatial Planning for Resilient Communities: Walkability, Social Cohesion, and Green Infrastructure in Peri-Urban Jordan. *Sustainability*, 17(14). [DOI]

Amani-Beni, M., Zhang, B., Xie, G.-D. and Odgaard, A.J., 2021. Impacts of the Microclimate of a Large Urban Park on Its Surrounding Built Environment in the Summertime. *Remote Sensing*, 13(22). [DOI]

Anderson, V., Gough, W.A., Zgela, M., Milosevic, D. and Dunjic, J., 2022. Lowering the Temperature to Increase Heat Equity: A Multi-Scale Evaluation of Nature-Based Solutions in Toronto, Ontario, Canada. *Atmosphere*, 13(7). [DOI]

Arruda, H., 2022. VOSviewer and Bibliometrix. *Journal of the Medical Library Association : JMLA*, 110(3), pp.392–395. [DOI]

Azmeer, A., Tahir, F. and Al-Ghamdi, S.G., 2024. Progress on green infrastructure for urban cooling: Evaluating techniques, design strategies, and benefits. *Urban Climate*, 56. [DOI]

Bachofen, C., Peillon, M., Meili, N., Bourgeois, I. and Grossiord, C., 2025. High transpirational cooling by urban trees despite extreme summer heatwaves. *Urban Forestry & Urban Greening*, 107. [DOI]

Back, Y., Bach, P.M., Jasper-Toennies, A., Rauch, W. and Kleidorfer, M., 2021. A rapid fine-scale approach to modelling urban bioclimatic conditions. *Science of the Total Environment*, 756. [DOI]

Battista, G., Carnielo, E. and De Lieto Vollaro, R., 2016. Thermal impact of a redeveloped area on localized urban microclimate: A case study in Rome. *Energy and Buildings*, 133, pp.446–454. [DOI]

Bera, M. and Nag, P.K., 2025. AN OVERVIEW OF BIOCLIMATIC DESIGN STRATEGIES OF THE BUILT ENVIRONMENT. *Environmental Engineering and Management Journal*, 24(4). [DOI]

Berger, N.K., Kollmann, J. and Teixeira, L.H., 2026. Native plant communities designed for infiltration swales can tolerate urban heat, flooding, and pollution. *Basic and Applied Ecology*, 90, pp.89–98. [DOI]

Bouzouidja, R., Cannavo, P., Bodenan, P., Gulyas, A., Kiss, M., Kovacs, A., Bechet, B., Chancibault, K., Chantoiseau, E., Bournet Pierre-Emmanuel and Bouzidi, R., Guenon, R., Lebeau, T., Musy, M. and Rodriguez, F., 2021. How to evaluate nature-based solutions performance for microclimate, water and soil management issues - Available tools and methods from Nature4Cities European project results. *Ecological Indicators*, 125. [DOI]

Bowen, X, Hui, L., Jingmao, W. and Shuo, C. 2024. Ecological design approach for urban green space in arid and semi-arid areas in Northwest China based on habitat and vegetation characteristics thereof. *Landscape Architecture*, *31*(6), pp.12-18. [DOI]

Chaudhuri, S. and Kumar, A., 2022. Urban greenery for air pollution control: a meta-analysis of current practice, progress, and challenges. *Environmental Monitoring and Assessment*. [DOI]

Chen, D., Zhang, F., Zhang, M., Meng, Q., Jim, C.Y., Shi, J., Tan, M.L. and Ma, X., 2022. Landscape and vegetation traits of urban green space can predict local surface temperature. *Science of the Total Environment*, *825*, p.154006. [DOI]

Chen, M., Dang, A., Li, X., Huang, J. and Weng, Y., 2024. Identifying climate-ready plants for urban environment: Integrating machine learning with traditional plant selection tools. *Urban Forestry & Urban Greening*, 102. [DOI]

Chen, P. and Hanlon, B., 2025. Urban green space, respiratory health and rising temperatures: An examination of the complex relationship between green space and adult asthma across racialized neighborhoods in Los Angeles County. *Landscape and Urban Planning*, 258. [DOI]

Chen, Y., Wang, Y. and Zhou, D., 2021. Knowledge map of urban morphology and thermal comfort: A bibliometric analysis based on CiteSpace. *Buildings*, *11*(10), p.427. [DOI]

Chen, Y., Zhang, R., Alekouei, S.A. and Amani-Beni, M., 2024. Nonlinear impacts of landscape and climatological interactions on urban thermal

environment during a hot and rainy summer. *Ecological Indicators*, 166. [DOI]

Cheung, P.K. and Jim, C.Y., 2018. Subjective outdoor thermal comfort and urban green space usage in humid-subtropical Hong Kong. *Energy and Buildings*, *173*, pp.150-162. [DOI]

Cheung, P.K., Livesley, S.J. and Nice, K.A., 2021. Estimating the cooling potential of irrigating green spaces in 100 global cities with arid, temperate or continental climates. *Sustainable Cities and Society*, 71. [DOI]

Chow, W.T., Akbar, S.N.A.B.A., Heng, S.L. and Roth, M., 2016. Assessment of measured and perceived microclimates within a tropical urban forest. *Urban Forestry & Urban Greening*, *16*, pp.62-75. [DOI]

Chu, Z., Li, S., Li, T., Qian, H. and Liu Chuan and Yan, Z., 2024. Numerical simulation of layout and landscape elements on the thermal environment of urban squares. *Ecological Informatics*, 82. [DOI]

Chun, B., Hur, M. and Won, J., 2021. Impacts of Thermal Environments on Health Risk: A Case Study of Harris County, Texas. *International Journal Of Environmental Research And Public Health*, 18(11). [DOI]

Cuce, P.M., Cuce, E. and Santamouris, M., 2025. Towards Sustainable and Climate-Resilient Cities: Mitigating Urban Heat Islands Through Green Infrastructure. *Sustainability*, 17(3). [DOI]

de Oliveira, J.A.P., Bellezoni, R.A., Shih, W.Y. and Bayulken, B., 2022. Innovations in Urban Green and Blue Infrastructure: Tackling local and global challenges in cities. *Journal of Cleaner Production*, *362*, p.132355. [DOI]

De Quadros, B.M. and Mizgier, M.G.O., 2023. Urban green infrastructures to improve pedestrian thermal comfort: A systematic review. *Urban Forestry & Urban Greening*, *88*, p.128091. [DOI]

Del Rosario, L., Astell-Burt, T., Olsen, J.R., Thompson, S., Mitchell, R. and Feng, X., 2025. Walkable by nature? Adding green and blue space to walkability indices and assessment of socioeconomic inequalities. *Environmental Research*, 284. [DOI]

Derkzen, M.L., van Teeffelen, A.J.A. and Verburg, P.H., 2017. Green infrastructure for urban climate adaptation: How do residents' views on climate impacts and green infrastructure shape adaptation preferences? *Landscape and Urban Planning*, 157, 106–130. [DOI]

Dybå, T. and Dingsøyr, T., 2008. Empirical studies of agile software development: A systematic review. *Information and Software Technology*, 50(9–10), pp.833–859. [DOI]

Esperon-Rodriguez, M., Sharmin, M., Rodriguez, D.E., Messier, C., Svenning, J.-C., Moore, S. and Tjoelker, M.G., 2025. Socio-economic factors, climate, and people's behaviours determine urban tree health. *Urban Forestry & Urban Greening*, 107. [DOI]

Evola, G., Gagliano, A., Fichera, A., Marletta, L., Martinico, F., Nocera, F. and Pagano, A., 2017. UHI effects and strategies to improve outdoor thermal comfort in dense and old neighbourhoods. *Energy Procedia*, *134*, pp.692-701. [DOI]

Fang, X., Li, J. and Ma, Q., 2023. Integrating green infrastructure, ecosystem services and nature-based solutions for urban sustainability: A comprehensive literature review. *Sustainable Cities and Society*, *98*, p.104843. [DOI]

Feng, S., 2022. Land Use/Land Cover Mapping Based on GEE for the Monitoring of Changes in Ecosystem Types in the Upper Yellow River Basin over the Tibetan Plateau. *Remote Sensing*, 14(21). [DOI]

Fong, C.S., Manavvi, S., Priya, R.S., Ramakreshnan, L., Sulaiman, N.M. and Aghamohammadi, N., 2023. Traits of Adaptive Outdoor Thermal Comfort in a Tropical Urban Microclimate. *Atmosphere*, 14(5). [DOI]

Frosini, G., Amato, A., Mugnai, F. and Cinelli, F., 2024. The Impact of Trees on the UHI Effect and Urban Environment Quality: A Case Study of a District in Pisa, Italy. *Atmosphere*, 15(1). [DOI]

Fu, J., Dupre, K., Tavares, S., King, D. and Banhalmi-Zakar, Z., 2022. Optimized greenery configuration to mitigate urban heat: A decade systematic review. *Frontiers of Architectural Research*, *11*(3), pp.466-491. [DOI]

Fuentes, S., Tongson, E. and Gonzalez Viejo, C., 2021. Urban Green Infrastructure Monitoring Using Remote Sensing from Integrated Visible and Thermal Infrared Cameras Mounted on a Moving Vehicle. *Sensors*, 21(1). [DOI]

Gherri, B., 2023. The Role of Urban Vegetation in Counteracting Overheating in Different Urban Textures. *Land*, 12(12). [DOI]

Gorai, N., Bandyopadhyay, J., Halder, B., Ahmed, M.F., Molla, A.H. and Lei, T.M.T., 2024. Spatio-Temporal Variation in Landforms and Surface Urban Heat Island in Riverine Megacity. *Sustainability*, 16(8), p.3383. [DOI]

Graef, M., Pucher, B., Hietz, P., Hofbauer, K., Allabashi, R., Pitha, U., Hood-Nowotny, R. and Stangl, R., 2022. Application of leaf analysis in addition to growth assessment to evaluate the suitability of greywater for irrigation of *Tilia cordata* and *Acer pseudoplatanus*. *Science of the Total Environment*, 836. [DOI]

Guan, Z. and Zhang, H., 2024. A Quantitative Analysis of the Complex Response Relationship between Urban Green Infrastructure (UGI) Structure/Spatial Pattern and Urban Thermal Environment in Shanghai. *Sustainability*, 16(16). [DOI]

Halder, N. and Kumar, D., 2025. Towards Reviving Vernacular Architecture in India: Insights into the Indigenous Building Traditions. *Journal of the International Society for the Study of Vernacular Settlements (ISVS e-Journal)*, 12(5), pp.40–54. [DOI]

Halder, N., Kumar, M., Deepak, A., Abuwaer, N.M., Kanwal, Q., Nurdiawati, A. and Al-Ghamdi, S.G., 2026. Urban Greenery and Outdoor Thermal Comfort: Cooling Indicators, Mechanisms, and Equity Implications. *Environmental Research Communications*. [DOI]

Halder, N., Kumar, M., Deepak, A., Kumar, D., Yasmin, N., Ullah, S. and Al-Ghamdi, S.G., 2025. Spatiotemporal Assessment of Urban Thermal Discomfort in Kolkata, India: Insights from Cloud-Based Remote Sensing. *IEEE Journal of Selected Topics in Applied Earth Observations and Remote Sensing*, 1–17. [DOI]

Halder, N., Kumar, M., Deepak, A., Mandal, S.K., Azmeer, A., Mir, B.A., Nurdiawati, A. and Al-Ghamdi, S.G., 2025. The Role of Urban Greenery in Enhancing Thermal Comfort: Systematic Review Insights. *Sustainability*, 17(6), p.2545. [DOI]

Helmreich, B., Deeb, M., Eben, P., Egerer Monika and Kollmann, J., Schulz, S., Pauleit, S., Weisser, W.W. and Schloter, M., 2025. Converting infiltration swales to sustainable urban drainage systems can improve water management and biodiversity. *Frontiers in Environmental Science*, 12. [DOI]

Hogeweij, M., Ploegmakers, H., Raaphorst, K., Bongers, C. and van der Krabben, E., 2025. It's not easy being cool: Residents' perceived cooling ability in relation to different types of green infrastructure in their neighbourhood. *Urban Forestry & Urban Greening*, 104. [DOI]

Huang, C., Liu, K., Ma, T., Xue, H., Wang, P. and Li, L., 2025. Analysis of the impact mechanisms and driving factors of urban spatial morphology on urban heat islands. *Scientific Reports*, 15(1), p.18589. [DOI]

Huang, J., Hao, T., Wang, Y. and Jones, P., 2022. A street-scale simulation model for the cooling performance of urban greenery: Evidence from a high-density city. *Sustainable Cities and Society*, *82*, p.103908. [DOI]

Hunter, R.F., Christian, H., Veitch, J., Astell-Burt, T., Hipp, J.A. and Schipperijn, J., 2015. The impact of interventions to promote physical activity in urban green space: a systematic review and recommendations for future research. *Social Science & Medicine*, *124*, pp.246-256. [DOI]

Hurduc, A., Ermida, S.L. and DaCamara, C.C., 2024. On the Suitability of Different Satellite Land Surface Temperature Products to Study Surface Urban Heat Islands. *Remote Sensing*, 16(20), p.3765. [DOI]

Ibric, A., Bostenaru Dan, M. and Craciun, C., 2024. Adapting Street Profile Design by Using Nature-Based Solutions in New Neighbourhoods and the Retrofit of Buildings. *Buildings*, 14(7). [DOI]

Irfeey, A.M.M., Chau, H.-W., Sumaiya, M.M.F., Wai, C.Y., Muttil, N. and Jamei, E., 2023. Sustainable Mitigation Strategies for Urban Heat Island Effects in Urban Areas. *Sustainability*, 15(14). [DOI]

Jiang, Y., Huang, J., Shi, T. and Wang, H., 2021. Interaction of urban rivers and green space morphology to mitigate the urban heat island effect: Case-based comparative analysis. *International Journal of Environmental Research and Public Health*, 18(21). [DOI]

Jimenez, J.L.S. and de Adana, M.R., 2024. Assessment of Outdoor Thermal Comfort in a Hot Summer Region of Europe. *Atmosphere*, 15(2). [DOI]

Jin, J., Chen, W.Y., Jia, B. and Wang, C., 2024. Cooling effect of urban greenery: A bibliometric analysis. *Urban Forestry & Urban Greening*, *99*, p.128453. [DOI]

Kabano, P., Harris, A. and Lindley, S., 2021. Sensitivity of Canopy Phenology to Local Urban Environmental Characteristics in a Tropical City. *Ecosystems*, 24(5), pp.1110–1124. [DOI]

Kanga, S., Meraj, G., Johnson, B.A., Singh, S.K., PV, M.N., Farooq, M., Kumar, P., Marazi, A. and Sahu, N., 2022. Understanding the Linkage between Urban Growth and Land Surface Temperature—A Case Study of Bangalore City, India. *Remote Sensing*, 14(17), p.4241. [DOI]

Karimi, A., Moreno-Rangel, D. and Garcia-Martinez, A., 2025. Granular mapping of UHI and heatwave effects: Implications for building performance and urban resilience. *Building and Environment*, 273. [DOI]

Kikon, N., Kumar, D. and Ahmed, S.A., 2023. Quantitative assessment of land surface temperature and vegetation indices on a kilometer grid scale. *Environmental Science and Pollution Research*, 30(49), pp.107236–107258. [DOI]

Kirby, A., 2023. Exploratory Bibliometrics: Using VOSviewer as a Preliminary Research Tool. *Publications*, 11(1). [DOI]

Kotharkar, R. and Bagade, A., 2018. Evaluating urban heat island in the critical local climate zones of an Indian city. *Landscape and Urban Planning*, 169, pp.92–104. [DOI]

Kranti Kumar Maurya, D.K., 2026. Towards Net Zero: A Review of Embodied Carbon in Residential Building Construction. In: Fulena Rajak, Ajay Kumar, Bijay Kumar Das, Ravish Kumar, Kranti Kumar Maurya, Sandeep Kumar, Shubham Meena, Abhishek Kumar Bittu, & Preksha Gupta (Eds.), *International Conference on Urban Resilience and Sustainable Architecture*, pp.86–91. Department of Architecture and Planning, NIT Patna.

Kumar, D., Maurya, K.K., Mandal, S.K., Halder, N., Mir, B.A., Nurdiawati, A. and Al-Ghamdi, S.G., 2025. A Whole-Life Carbon Assessment of a Single-Family House in North India Using BIM-LCA Integration. *Buildings*, 15(13), p.2195. [DOI]

Kumar, D., Maurya, K.K., Mandal, S.K., Mir, B.A., Nurdiawati, A. and Al-Ghamdi, S.G., 2025. Life Cycle Assessment in the Early Design Phase of Buildings: Strategies, Tools, and Future Directions. *Buildings*, 15(10), p.1612. [DOI]

Kumar, D. and Shukla, B., 2022. Urban Green Spaces For Promoting Healthy Living And Wellbeing: Prospects For Housing. *ECS Transactions*, 107(1), pp.18835–18857. [DOI]

La Rosa, D. and Li, J., 2023. High-Resolution Greening Scenarios for Urban Climate Regulation Based on Physical and Socio-Economical Factors. *Sustainability*, 15(9). [DOI]

Lazovic, I.M., Nikezic, D.P., Markovic, Z.J., Eric, M., Zivkovic, M., Ramadani, U., Tasic, G. and Tasic, V., 2025. Assessment of Traffic-Induced Air Pollution and Its Effects on Intensity of Urban Heat Islands. *Applied Sciences-Basel*, 15(20). [DOI]

Lee, L.S. and Jim, C.Y., 2018. Thermal-cooling performance of subtropical green roof with deep substrate and woodland vegetation. *Ecological Engineering*, *119*, pp.8-18. [DOI]

Li, J., Mao, Y., Ouyang, J. and Zheng, S., 2022. A review of urban microclimate research based on CiteSpace and VOSviewer analysis. *International Journal of Environmental Research and Public Health*, *19*(8), p.4741. [DOI]

Liu, H., Zhou, Z., Wen, Q., Chen, J. and Kojima, S., 2024. Spatiotemporal Land Use/Land Cover Changes and Impact on Urban Thermal Environments: Analyzing Cool Island Intensity Variations. *Sustainability*, 16(8). [DOI]

Liu, J., Wu, X., Pan, L. and Hsieh, C.-M., 2025. Multi-Scale Analysis of the Mitigation Effect of Green Space Morphology on Urban Heat Islands. *Atmosphere*, 16(7). [DOI]

Liu, Z., Cheng, K.Y., Sinsel, T., Simon, H., Jim, C.Y., Morakinyo, T.E., He, Y., Yin, S., Ouyang, W., Shi, Y. and Ng, E., 2023. Modeling microclimatic effects of trees and green roofs/façades in ENVI-met: Sensitivity tests and proposed model library. *Building and Environment*, 244. [DOI]

Liu, Z., Cheng, W., Jim, C.Y., Morakinyo, T.E., Shi, Y. and Ng, E., 2021. Heat mitigation benefits of urban green and blue infrastructures: A systematic review of modeling techniques, validation and scenario simulation in ENVI-met V4. *Building and Environment*, *200*, p.107939. [DOI]

Lu, L., Weng, Q., Xiao, D., Guo, H., Li, Q. and Hui, W., 2020. Spatiotemporal Variation of Surface Urban Heat Islands in Relation to Land Cover Composition and Configuration: A Multi-Scale Case Study of Xi'an, China. *Remote Sensing*, 12(17). [DOI]

Luo, H. and Wu, J., 2021. Effects of urban growth on the land surface temperature: a case study in Taiyuan, China. *Environment, Development and Sustainability*, 23(7), pp.10787–10813. [DOI]

Makido, Y., Hellman, D. and Shandas, V., 2019. Nature-Based Designs to Mitigate Urban Heat: The Efficacy of Green Infrastructure Treatments in Portland, Oregon. *Atmosphere*, 10(5). [DOI]

Mittermüller, J., Erlwein, S., Bauer, A., Trokai, T., Duschinger, S. and Schönemann, M., 2021. Context-specific, user-centred: Designing urban green infrastructure to effectively mitigate urban density and heat stress. *Urban Planning*, 6(4), pp.40–53. [DOI]

Mohan, M. and Kandya, A., 2015. Impact of urbanization and land-use/land-cover change on diurnal temperature range: A case study of tropical urban airshed of India using remote sensing data. *Science of The Total Environment*, 506–507, 453–465. [DOI]

Nath, R., 2025. Modeling Urban Thermal Dynamics and Land Use Change in Guwahati: A Machine Learning-Based Analysis of Lst and Utfvi Trends (2000–2040). [DOI]

Ni, Y., Lin, L., Xia, H. and Wang, X., 2025. Urban Street Greening and Resident Comfort: An Integrated Approach Based on High-Precision Shadow Distribution and Facade Visual Assessment. *Sustainability*, 17(3). [DOI]

O'Donnell, E.C., Lamond, J.E. and Thorne, C.R., 2017. Recognising barriers to implementation of Blue-Green Infrastructure: a Newcastle case study. *Urban Water Journal*, 14(9), pp.964–971. [DOI]

O'Keeffe, J., Pluchinotta, I., De Stercke, S., Hinson, C., Puchol-Salort, P., Mijic, A., Zimmermann, N. and Collins, A.M., 2022. Evaluating natural capital performance of urban development through system dynamics: A case study from London. *Science of the Total Environment*, 824. [DOI]

Okumus, D.E. and Terzi, F., 2023. Ice floes in urban furnace: Cooling services of cemeteries in regulating the thermal environment of Istanbul's urban landscape. *Urban Climate*, 49. [DOI]

Oraiopoulos, A., Wieser, M., Verdiere, M., Lambert, R., Fennell, P. and Ruyssevelt, P., 2026. Improving habitability in informal settlements in the Global South: Exploring the impact of community urban green infrastructure on outdoor heat stress. *Building and Environment*, 287(A). [DOI]

Ornelas, A., Cordeiro, A. and Lameiras, J.M., 2023. Thermal comfort assessment in urban green spaces: Contribution of thermography to the study of thermal variation between tree canopies and air temperature. *Land*, *12*(8), p.1568. [DOI]

Page, M.J., McKenzie, J.E., Bossuyt, P.M., Boutron, I., Hoffmann, T.C., Mulrow, C.D., Shamseer, L., Tetzlaff, J.M., Akl, E.A., Brennan, S.E. and Chou, R., 2021. The PRISMA 2020 statement: an updated guideline for reporting systematic reviews. *bmj*, *372*. [DOI]

Pandey, B., Banerjee, R. and Sharma, A., 2021. Coupled EnergyPlus and CFD analysis of PCM for thermal management of buildings. *Energy and Buildings*, *231*, p.110598. [DOI]

Pattnaik, N., Rahman, M.A. and Pauleit, S., 2025. Urban vegetation structure and composition influence pedestrian thermal comfort in public spaces: A case study in Munich. *Urban Forestry & Urban Greening*, 114. [DOI]

Perini, K. and Magliocco, A., 2014. Effects of vegetation, urban density, building height, and atmospheric conditions on local temperatures and thermal comfort. *Urban Forestry & Urban Greening*, *13*(3), pp.495-506. [DOI]

Pradeep Kumar, B., Anusha, B.N., Raghu Babu, K. and Padma Sree, P., 2023. Identification of climate change impact and thermal comfort zones in semi-arid regions of AP, India using LST and NDBI techniques. *Journal of Cleaner Production*, 407, p.137175. [DOI]

Pradeep Kumar Kori, K.K.M.D.K., 2026. Towards Net Zero: A Systematic Review of Operational Emissions in Residential Building Construction. In: Fulena Rajak, Ajay Kumar, Bijay Kumar Das, Ravish Kumar, Kranti Kumar Maurya, Sandeep Kumar, Shubham Meena, Abhishek Kumar Bittu, & Preksha Gupta (Eds.), *International Conference on Urban Resilience and Sustainable Architecture*, pp.148–153. Department of Architecture and Planning, NIT Patna.

Pragati, S., Priya, R.S., Pradeepa, C. and Senthil, R., 2023. Simulation of the Energy Performance of a Building with Green Roofs and Green Walls in a Tropical Climate. *Sustainability*, 15(3). [DOI]

Pritipadmaja, Garg, R.D. and Sharma, A.K., 2023. Assessing the Cooling Effect of Blue-Green Spaces: Implications for Urban Heat Island Mitigation. *Water*, 15(16). [DOI]

Rahman, Md. M., Avtar, R., Yunus, A.P., Dou, J., Misra, P., Takeuchi, W., Sahu, N., Kumar, P., Johnson, B.A., Dasgupta, R., Kharrazi, A., Chakraborty, S. and Agustiono Kurniawan, T., 2020. Monitoring Effect of spatial growth on land surface temperature in Dhaka. *Remote Sensing*, 12(7), p.1191. [DOI]

Ramadan, M.S., Tariq, A., Abdo, H.G. and Al Hosani, N., 2025. GEE-based analysis of spatiotemporal patterns of land cover and LST in an arid urban environment a case study of Abu Dhabi. *Frontiers in Environmental Science*, 13. [DOI]

Rathod, V., Rupapara, S., Agrawal, H., Manek, P., Halder, N. and Kumar, D., 2026. Nature-Based Solutions vs Conventional Infrastructure: Cost-benefit and Sustainability Evaluations in Built Environments. *Asian Journal of Environment & Ecology*, 25(3), pp.169–200. [DOI]

Revell, G. and Anda, M., 2014. Sustainable Urban Biophilia: The Case of Greenskins for Urban Density. *Sustainability*, 6(8), pp.5423–5438. [DOI]

Reyhani, M., Santolini, E., Torreggiani, D. and Tassinari, P., 2022. Assessing the environmental performance of plastic-based and felt-based green wall systems in a life-cycle perspective. *Science of the Total Environment*, 822. [DOI]

Roversi, R. and Longo, D., 2025. Regenerative and Connective Green Cells to Address Fragmentation and Climate Change in Cities: The TALEA Project Integrated Solution. *Sustainability*, 17(7). [DOI]

Sabatino, S. Di, Barbano, F., Brattich, E. and Pulvirenti, B., 2020. The Multiple-Scale Nature of Urban Heat Island and Its Footprint on Air Quality in Real Urban Environment. *Atmosphere*, 11(11). [DOI]

Salvalai, G., Cadena, J.D.B., Sparvoli Gessica and Bernardini, G. and Quagliarini, E., 2022. Pedestrian Single and Multi-Risk Assessment to SLODs in Urban Built Environment: A Mesoscale Approach. *Sustainability*, 14(18). [DOI]

Schaffernicht, S.K., Tuerk, A., Kogler, M., Berger, A., Scharf, B., Clementschitsch, L., Hammer, R., Holzer, P., Formayer, H., Koenig, B. and Haluza, D., 2023. Heat vs. *Health: Home Office under a Changing Climate*. *Sustainability*, 15(9). [DOI]

Seidu, S., Edwards, D.J., Owusu-Manu, D., Chan, D.W.M., Abdulai, S.F. and Buertey, J.I.T., 2025. Achieving multifunctionality in green infrastructure projects: a fuzzy evaluation and Gini index of Key drivers in developing countries. *Environment Development And Sustainability*. [DOI]

Seto, K.C., Güneralp, B. and Hutyra, L.R., 2012. Global forecasts of urban expansion to 2030 and direct impacts on biodiversity and carbon pools. *Proceedings of the National Academy of Sciences*, 109(40), pp.16083–16088. [DOI]

Shan, Z., An, Y., Xu, L. and Yuan, M., 2022. High-Temperature Disaster Risk Assessment for Urban Communities: A Case Study in Wuhan, China. *International Journal Of Environmental Research And Public Health*, 19(1). [DOI]

Shao, H., Kim, G., Li, Q. and Newman, G., 2021. Web of science-based green infrastructure: a bibliometric analysis in CiteSpace. *Land*, *10*(7), p.711. [DOI]

Shin, Y., Kim, S., Lee, S.-W. and An, K., 2020. Identifying the Planning Priorities for Green Infrastructure within Urban Environments Using Analytic Hierarchy Process. *Sustainability*, 12(13). [DOI]

Sobrinho, O.M., Rudke, A.P., de Morais, M.V.B. and Martins, L.D., 2023. Meteorological Effects of Green Infrastructure on a Developing Medium Latin American City: A Numerical Modeling Assessment. *Sustainability*, 15(2). [DOI]

Su, W., Yang, G., Chen, S. and Yang, Y., 2012. Measuring the Pattern of High Temperature Areas in Urban Greenery of Nanjing City, China. *International Journal of Environmental Research and Public Health*, 9(8), pp.2922–2935. [DOI]

Rupapara, S., Rathod, V., Rupapara, H., Halder, N. and Kumar, D., 2025. Evaluating the benefits of urban greenery in Urban Heat Island mitigation: Methods, indicators and gaps. *Nature Environment and Pollution Technology*, *24*(4), p.D1812. [DOI]

Toparlar, Y., Blocken, B., Maiheu, B. and van Heijst, G.J.F., 2017. A review on the CFD analysis of urban microclimate. *Renewable and Sustainable Energy Reviews*, 80, pp.1613–1640. [DOI]

Tzoulas, K., Korpela, K., Venn, S., Yli-Pelkonen, V., Kaźmierczak, A., Niemela, J. and James, P., 2007. Promoting ecosystem and human health in urban areas using Green Infrastructure: A literature review. *Landscape and Urban Planning*, 81(3), pp.167–178. [DOI]

Ullah, S., Aldossary, A., Ullah, W. and Al-Ghamdi, S.G., 2024. Augmented human thermal discomfort in urban centers of the Arabian Peninsula. *Scientific Reports*, 14(1). [DOI]

Ullah, S. and Al-Ghamdi, S.G., 2023. Advancing Urban Resilience and Sustainability Through the WRF-Urban Model: Bridging Numerical Modeling and Real-World Applications. In: *Sustainable Cities in a Changing Climate*, pp.17–27. Wiley. [DOI]

Urban, J., Pikl, M., Zemek, F. and Novotny, J., 2022. Using Google Street View photographs to assess long-term outdoor thermal perception and thermal comfort in the urban environment during heatwaves. *Frontiers in Environmental Science*, 10. [DOI]

van Eck, N.J., 2010. Software survey: VOSviewer, a computer program for bibliometric mapping. *Scientometrics*, 84(2), pp.523–538. [DOI]

Vulova, S., Meier, F., Rocha, A.D., Quanz Justus and Nouri, H. and Kleinschmit, B., 2021. Modeling urban evapotranspiration using remote sensing, flux footprints, and artificial intelligence. *Science of the Total Environment*, 786. [DOI]

Vyas, A., Shastri, B. and Joshi, Y., 2014. Spatio-temporal analysis of UHI using geo-spatial techniques: A case study of Ahmedabad city. *International Archives of the Photogrammetry, Remote Sensing and Spatial Information Sciences - ISPRS Archives*, 40(8), pp.997–1002. [DOI]

Weng, Q., Lu, D. and Schubring, J., 2004. Estimation of land surface temperature–vegetation abundance relationship for urban heat island studies. *Remote Sensing of Environment*, 89(4), pp.467–483. [DOI]

Wong, N.H., Tan, C.L., Kolokotsa, D.D. and Takebayashi, H., 2021. Greenery as a mitigation and adaptation strategy to urban heat. *Nature Reviews Earth & Environment*, *2*(3), pp.166-181. [DOI]

Yang, H.-R., Li, Y.-H., Wu, W.-J., Zhao, A.-L. and Zhang, H., 2025. Exploring the Complex Relationships Between Influential Factors of Urban Land Development Patterns and Urban Thermal Environment: A Study on Downtown Shanghai. *Sustainability*, 17(19). [DOI]

Yang, J., Zhao, L. and Oleson, K., 2023. Large humidity effects on urban heat exposure and cooling challenges under climate change. *Environmental Research Letters*, 18(4). [DOI]

Yang, S. and La Roche, P., 2025. Microclimate Analysis of Tree Canopies and Green Surface Combinations for Urban Heat Island Mitigation in Los Angeles and Phoenix. *Buildings*, 15(9). [DOI]

Yang, S., Wang, L.L., Stathopoulos, T. and Marey, A.M., 2023. Urban microclimate and its impact on built environment–a review. *Building and Environment*, *238*, p.110334. [DOI]

Yang, X. and Ma, Y., 2024. Design and thermal-optical environment simulation of double-slope greenhouse roof structure based on Ecotect. *Agriculture*, *14*(8), p.1410. [DOI]

Yazdi, H., Moser-Reischl, A., Roetzer, T., Petzold, F. and Ludwig, F., 2024. Machine learning-based prediction of tree crown development in competitive urban environments. *Urban Forestry & Urban Greening*, 101. [DOI]

Ying, J., 2022. Green infrastructure: systematic literature review. *Economic Research-Ekonomska Istrazivanja*, 35(1), pp.343–366. [DOI]

Zakrzewska, A., Kopec, D., Ochtyra, A. and Potuckova, M., 2023. Can canopy temperature acquired from an airborne level be a tree health indicator in an urban environment? *Urban Forestry & Urban Greening*, 79. [DOI]

Zhang, H., Cen, X., An, H. and Yin, Y., 2024. Quantitative assessment and driving factors analysis of surface urban heat island of urban agglomerations in China based on GEE. *Environmental Science and Pollution Research*, 31(34), pp.47350–47364. [DOI]

Zhang, X., Friedl, M.A., Schaaf, C.B., Strahler, A.H., Hodges, J.C.F., Gao, F., Reed, B.C. and Huete, A., 2003. Monitoring vegetation phenology using MODIS. *Remote Sensing of Environment*, 84(3), pp.471–475. [DOI]

Zhang, Y., Li, S., Fu, X. and Dong, R., 2021. Quantification of urban greenery using hemisphere-view panoramas with a green cover index. *Ecosystem Health And Sustainability*, 7(1). [DOI]

Zhou, W., Huang, G. and Cadenasso, M.L., 2011. Does spatial configuration matter? Understanding the effects of land cover pattern on land surface temperature in urban landscapes. *Landscape and Urban Planning*, 102(1), pp.54–63. [DOI]

Nature Environment and Pollution Technology
An International Quarterly Peer-Reviewed Open Access Journal

p-ISSN: 0972-6268 | e-ISSN: 2395-3454 Vol. 25 | No. 4 | Article ID D1824 | 2026

RESEARCH ARTICLE https://doi.org/10.46488/NEPT.2026.v25i04.D1824 OPEN ACCESS

Organic Waste to Energy: Enhancing Biodigester Efficiency in Oman for Sustainable Development

Jasim Abdullah Ali Al Shehhi† and **Nitin Bhaurao Raut**
Faculty of Engineering, Sohar University, Sohar, Oman
†Corresponding author: Jasim Abdullah Ali Al Shehhi; research1613@gmail.com

ARTICLE HISTORY

Received: 12-05-2025
Revised: 10-07-2025
Accepted: 16-07-2025

KEYWORDS

Biodigester optimization
Anaerobic digestion
Organic waste management
Renewable energy
Sustainable development
Greenhouse gas reduction

CITE THIS ARTICLE

Al Shehhi, J. A. A. and Raut, N. B., 2026. Organic waste to energy: Enhancing biodigester efficiency in Oman for sustainable development. *Nature Environment and Pollution Technology*, 25(4), D1824. https://doi.org/10.46488/NEPT.2026.v25i04.D1824

COPYRIGHT & LICENCE

© 2026 The Authors
Open Access under CC BY 4.0.

PUBLISHED BY

TECHNOSCIENCE PUBLICATIONS

ABSTRACT

Organic waste presents a significant environmental and economic opportunity for renewable energy generation through anaerobic digestion. This study investigates the optimization of biodigester systems tailored to Oman's unique climatic conditions and waste characteristics. Using a mixed-methods approach that integrates experimental data from 30-day monitoring with simulated scenarios, the study evaluates five feedstock types, namely food waste, agricultural residues, livestock manure, mixed organic waste, and food and crop waste, together with three pretreatment methods: mechanical, thermal, and chemical. The findings demonstrate that thermal pretreatment enhances biogas yield by up to 25–30%, while food waste and food and crop waste achieve the highest methane contents of 65% and 64%, respectively. Modeled environmental and economic analyses indicate potential benefits, including up to a 70% reduction in greenhouse gas emissions, a 90% waste diversion rate, payback periods of 2–2.5 years for high-yield feedstocks, and net economic returns exceeding 30%. Simulated data further highlight the potential of co-digestion, system adaptations for arid climates, and real-time monitoring technologies to enhance biodigester performance. The study aligns with Oman Vision 2040 by providing practical insights into sustainable waste management and renewable energy integration. By addressing technical, environmental, and economic dimensions, this research offers a scalable and replicable model for advancing biodigester systems in Oman.

1. INTRODUCTION

The global shift toward sustainable energy solutions has underscored the critical need to address the challenges associated with organic waste management. Organic waste, often perceived as a burden, represents an untapped resource for renewable energy generation through anaerobic digestion (Yang et al. 2024). This process not only mitigates environmental pollution but also contributes to the circular economy by converting organic waste into valuable by-products such as biogas and nutrient-rich digestate (Piadeh et al. 2024). However, optimizing the efficiency of biodigesters remains a key challenge, particularly in regions such as Oman, where unique climatic conditions and waste characteristics require tailored solutions.

In Oman, rapid urbanization, population growth, and increased agricultural activities have led to a surge in organic waste generation. Despite this, traditional waste disposal methods such as landfilling dominate, resulting in greenhouse gas emissions, resource wastage, and environmental degradation (Akhiar et al. 2020). Aligning with Oman Vision 2040 sustainability goals, there is a pressing need to adopt innovative technologies (Ahmad and Wu 2022) that transform

organic waste into energy while minimizing ecological footprints.

This study focuses on enhancing the efficiency of biodigesters by leveraging advanced techniques in feedstock optimization, pretreatment, and system design (Al-Huqail et al. 2022), tailored to the arid climate and waste characteristics of Oman. By integrating a two-stage biodigestion process comprising hydrolysis and methanogenesis, the study aims to maximize biogas yield while ensuring the sustainable management of organic waste (AlQattan et al. 2018). In addition, the valorization of digestate as a nutrient-rich fertilizer supports the country's agricultural development objectives, thereby promoting both environmental and economic benefits (Ampese et al. 2022).

The outcomes of this research have the potential to revolutionize organic waste-to-energy systems in Oman by offering a scalable and efficient model that supports energy security, environmental sustainability, and waste management (Amuzu-Sefordzi et al. 2018). By addressing the challenges of biodigester optimization, this study contributes to the global discourse on sustainable development and provides actionable insights for policymakers and industry stakeholders.

2. BACKGROUND AND CONTEXT

2.1. Global Challenges in Organic Waste Management

The rapid growth of urban populations and economic activities has significantly increased organic waste generation worldwide. According to the United Nations Environment Programme, over 1.3 billion tons of food waste are generated annually, with an estimated 60% classified as organic (Ayodele et al. 2017). The mismanagement of organic waste poses significant environmental and public health risks, including methane emissions, groundwater contamination, and inefficient resource utilization (Ayodele et al. 2018). Traditional disposal methods, such as landfilling and open dumping, further exacerbate these issues by contributing to greenhouse gas emissions and occupying valuable land resources (Barbera et al. 2022).

While technological solutions such as composting and anaerobic digestion have emerged, several challenges persist. The heterogeneity of organic waste, lack of efficient collection systems, and insufficient policy support often hinder large-scale adoption of sustainable waste management practices (Shaibur et al. 2021). Furthermore, the integration of advanced technologies, such as biodigesters, is frequently impeded by high initial investment costs, operational inefficiencies, and public resistance (Einarsson & Persson 2017) due to limited awareness of the benefits.

2.2. Organic Waste in Oman: Current Practices and Challenges

In Oman, the management of organic waste has become a pressing issue due to rapid urbanization, population growth, and a thriving agricultural sector. Organic waste constitutes a significant portion of municipal solid waste, with food waste, agricultural residues, and livestock manure forming the bulk of this category (Falahi and Avami 2020). However, traditional practices such as landfilling dominate, with over 60% of organic waste disposed of in dumpsites, leading to environmental degradation and resource loss (Francini et al. 2019).

The hot and arid climate in Oman presents unique challenges for organic waste management, as high temperatures accelerate the decomposition process, creating odor and leachate issues (Gao et al. 2021). Additionally, the absence of segregated waste collection systems limits the recovery of organic waste for value-added processes (Bywater et al. 2022). Despite these challenges, Oman holds significant potential for leveraging organic waste as a resource (Oman Environmental Services Holding Company 2023). The country's abundant agricultural residues and growing focus on renewable energy provide opportunities to transition from linear waste disposal methods to circular economy practices (Chen et al. 2023).

Logistical feasibility is a critical consideration for implementing biodigester systems in Oman. Decentralized collection of diverse feedstocks from urban, agricultural, and livestock sources poses challenges such as transport costs, infrastructure limitations, and the need for coordinated collection schedules. Additionally, certain waste streams exhibit seasonal variability; for example, agricultural residues are typically abundant post-harvest but scarce during off-seasons. This variability can impact the consistency of feedstock supply, requiring planning for storage, blending, or alternative sourcing strategies to maintain stable biodigester operation year-round.

2.3. Relevance to Oman Vision 2040

Oman Vision 2040 outlines a comprehensive framework for achieving sustainable development by emphasizing economic diversification, environmental stewardship, and energy security. Central to this vision is the promotion of renewable energy and sustainable waste management practices (Massaro et al. 2015). Transforming organic waste into energy aligns with these priorities by addressing key environmental challenges while contributing to the nation's renewable energy targets (Zhou et al. 2022).

Biodigesters, as a technology for organic waste valorization, provide a dual benefit for Oman: mitigating the

environmental impact of waste and generating biogas as a renewable energy source (Yong et al. 2021). Additionally, the by-product of anaerobic digestion, digestate, can serve as an organic fertilizer, supporting sustainable agricultural practices and reducing dependence on chemical inputs (Yalcinkaya 2020). By adopting innovative strategies to optimize biodigester efficiency, Oman can not only achieve its waste management goals but also position itself as a regional leader in sustainable development practices.

This research aims to address these pressing issues by exploring optimized biodigester designs and strategies tailored to Oman's unique conditions, contributing directly to the achievement of Vision 2040 objectives.

3. BIODIGESTER TECHNOLOGY: AN OVERVIEW

3.1. Principles of Anaerobic Digestion

Anaerobic digestion (AD) is a biological process in which microorganisms break down organic matter in the absence of oxygen, producing biogas (a mixture primarily of methane and carbon dioxide) and digestate, a nutrient-rich by-product (Yadav et al. 2022). This process occurs in four sequential stages: hydrolysis, acidogenesis, acetogenesis, and methanogenesis.

- Hydrolysis involves breaking down complex organic materials, such as carbohydrates, proteins, and fats, into simpler soluble compounds, including sugars, amino acids, and fatty acids.
- Acidogenesis converts these simpler compounds into volatile fatty acids, hydrogen, and carbon dioxide.
- Acetogenesis further breaks down volatile fatty acids into acetic acid, along with additional hydrogen and carbon dioxide.
- Methanogenesis is the final stage, during which methanogenic microorganisms convert acetic acid and hydrogen into methane, the primary energy carrier in biogas.

AD offers several benefits, including the sustainable management of organic waste, the reduction of greenhouse gas emissions, and the production of renewable energy (Welfle & Röder 2022). However, optimizing this process requires precise control of parameters such as temperature, pH, and retention time to maximize biogas yield and system efficiency (Walker et al. 2017).

3.2. Two-Stage Biodigester Systems: Hydrolysis and Methanogenesis

Two-stage biodigester systems separate the hydrolysis and methanogenesis stages into distinct reactors, allowing for better control of the conditions in each phase (Vaneeckhaute et al. 2018). This separation addresses one of the major challenges in single-stage digesters: the incompatibility of the optimal conditions required by hydrolytic and methanogenic microorganisms (Carrere et al. 2016).

3.2.1. Stage 1: Hydrolysis Reactor

In the first stage, organic matter undergoes hydrolysis and acidogenesis. This reactor operates under conditions that favor the breakdown of complex molecules into simpler compounds, such as a slightly acidic pH and shorter retention times (Zheng & Li 2024). By isolating this phase, process efficiency is improved, and the risk of system instability is reduced.

3.2.2. Stage 2: Methanogenesis Reactor

The second stage focuses on methanogenesis, during which the products from the first stage are converted into methane and carbon dioxide. This reactor typically requires a neutral pH and a longer retention time to support methanogenic microorganisms (Pham Van et al. 2020). This separation allows for better control of methanogenesis and prevents acidification, a common issue in single-stage systems.

Two-stage systems are particularly advantageous for processing heterogeneous or high-solid-content feedstocks, which are common in organic waste streams (Ruiz-Aguilar et al. 2022). The improved stability, higher biogas yield, and reduced risk of process failure make them an attractive option for optimizing biodigester performance (Nkemka et al. 2014), particularly in challenging climates such as that of Oman.

3.3. Advances in Biodigester Design and Efficiency

Recent advancements in biodigester technology have focused on improving efficiency, scalability, and adaptability to diverse environmental conditions and waste types (Piadeh et al. 2024). Key innovations include:

1. **Enhanced Pretreatment Technologies:** Techniques such as thermal, chemical, and mechanical pretreatment improve the digestibility of feedstocks, accelerate the hydrolysis process, and increase biogas yield (Issahaku et al. 2024).
2. **Integrated Monitoring and Control Systems:** IoT-based sensors and real-time monitoring systems have transformed biodigester operations. These systems provide continuous data on parameters such as temperature, pH, and gas production, enabling precise adjustments to optimize performance (de Souza Guimarães & da Silva Maia 2023).
3. **Hybrid Digesters:** Hybrid designs combine features of multiple reactor types, such as continuous stirred-tank reactors (CSTRs) and plug-flow reactors, to

improve feedstock flexibility and gas production efficiency.

4. **Energy Recovery and Heat Integration:** Waste heat from biogas combustion can be recycled to maintain reactor temperatures, particularly in colder environments, thereby reducing operational costs (Keerthana Devi et al. 2022).
5. **Modular and Scalable Designs:** Modular systems allow for incremental capacity expansion, making biodigesters accessible to a wider range of users, from small-scale farmers to large industrial facilities (Josimović et al. 2024).
6. **High-Solids Anaerobic Digestion (HSAD):** HSAD systems are designed for feedstocks with high solids content, minimizing water usage, which is a critical advantage in arid regions such as Oman.

By leveraging these advancements, biodigesters can achieve higher energy conversion efficiency and enhanced operational stability, making them a cornerstone of sustainable organic waste management (Obileke et al. 2020). In the context of Oman, these technologies can be tailored to local conditions, addressing specific challenges such as high ambient temperatures and diverse waste compositions.

4. MATERIALS AND METHODS

4.1. Feedstock Analysis and Selection

The selection of feedstock is a critical step in optimizing the biodigester process, as the biochemical properties of the input materials significantly influence biogas yield and system performance. Organic waste samples, including food waste, agricultural residues, and livestock manure (Gitinavard et al. 2020), were collected from various urban, rural, and agricultural sources across Oman (Table 1).

- **Chemical Analysis**: The samples were analyzed (Table 2) for key parameters such as moisture content, volatile solids (VS), total solids (TS), pH, and carbon-to-nitrogen (C/N) ratio using standard protocols (e.g., APHA guidelines).
- **Suitability Assessment:** A comparative analysis (Table 2) of different feedstocks was conducted to evaluate their potential for co-digestion. Feedstocks with complementary properties, such as high nitrogen content paired with high carbon residues, were identified to achieve an optimal C/N ratio of 20–30, ensuring maximum microbial activity and biogas production (Dubois et al. 2019).

Table 2 summarizes key parameters like moisture content, volatile solids, total solids, pH, and C/N ratio for different feedstocks. It highlights how these properties influence their suitability for anaerobic digestion and co-digestion. For example, food waste, with high moisture and volatile solids, is readily digestible but needs pairing with high-carbon residues like agricultural waste due to its low C/N ratio (Ippolito et al. 2020). Conversely, agricultural residues, with a high C/N ratio, complement nitrogen-rich feedstocks like livestock manure. Mixed organic waste and food and crop waste exhibit balanced properties, making them highly suitable for co-digestion without major adjustments (Prussi et al. 2022). This table effectively links chemical properties to practical applications, ensuring feedstock combinations are optimized for maximum biogas production and stable biodigester performance.

Table 1: Sample collection locations and details for organic waste analysis.

Location	Sample Type	Source	Latitude	Longitude	Sample Volume (kg)
Muscat	Food Waste	Urban Households	23.588	58.3829	50
Salalah	Agricultural Residues	Agricultural Farms	17.0198	54.089	60
Sohar	Livestock Manure	Livestock Farms	24.3643	56.7075	55
Nizwa	Mixed Organic Waste	Urban and Rural Collection	22.9333	57.5333	70
Sur	Food and Crop Waste	Urban Markets and Farms	22.5667	59.5289	65

Table 2: Chemical properties and co-digestion suitability of feedstock.

Feedstock Type	Moisture Content (%)	Volatile Solids (VS %)	Total Solids (TS %)	pH	C/N Ratio	Suitability for Co-Digestion
Food Waste	75	85	25	5.5	18	High (Pair with high-C residues)
Agricultural Residues	20	60	80	6.8	40	High (Pair with high-N residues)
Livestock Manure	65	55	35	7.2	15	Medium (Complementary with crop waste)
Mixed Organic Waste	60	65	40	6	25	High (Balanced composition)
Food and Crop Waste	50	70	30	6.5	22	High (Ready for co-digestion)

4.2. Pretreatment Techniques for Organic Waste

To enhance the biodegradability of feedstocks and improve biogas yield, pretreatment techniques were employed (George et al. 2021). The pretreatment methods (Table 3) were selected based on the specific composition of the organic waste and the operational constraints of the biodigester.

4.2.1. Mechanical Pretreatment

Waste was shredded to reduce particle size, thereby increasing the surface area available for microbial activity during hydrolysis.

4.2.2. Thermal Pretreatment

Samples were subjected to controlled heating at 70°C for 1 h to break down complex organic compounds, enhance solubility, and eliminate pathogens.

Thermal pretreatment at 70°C for 1 h was selected based on its proven ability to break down complex organic structures, increase solubility, and reduce pathogens in organic waste streams. Prior studies have demonstrated that this temperature range (60–80°C) effectively enhances substrate biodegradability and improves biogas yield by 20–35% (Amin et al. 2017, Issahaku et al. 2024). This protocol balances sufficient solubilization of lignocellulosic and proteinaceous materials with manageable energy input requirements, making it operationally feasible for deployment in Oman's waste management systems.

4.2.3. Chemical Pretreatment

Alkaline pretreatment using sodium hydroxide (NaOH) was tested to improve the breakdown of lignocellulosic materials in agricultural residues (Kenney et al. 2013).

4.2.4. Evaluation of Effectiveness

The effectiveness of each pretreatment method was assessed by measuring changes in volatile solids (VS) reduction, chemical oxygen demand (COD), and biogas yield in small-scale batch tests (Table 4). A simplified energy balance was estimated to evaluate the feasibility of applying thermal pretreatment at 70°C for 1 h. Assuming a specific heat capacity of water of 4.18 kJ kg^{-1} $°C^{-1}$, heating 1 kg of wet feedstock from an ambient temperature of 30°C to 70°C requires approximately 167 kJ. In contrast, the observed 25–30% increase in biogas yield results in an additional energy output of 7–9 MJ per kilogram of volatile solids, given methane's heating value (~35 MJ m^{-3}) and the typical methane content of biogas (60–65%). This analysis indicates a net positive energy balance, supporting the feasibility of thermal pretreatment despite its heating requirement.

Volatile Solids (VS) Reduction: Measures the reduction in organic content, indicating improved biodegradability.

Chemical Oxygen Demand (COD): Assesses the solubility and availability of organic compounds for microbial activity.

Biogas Yield: Quantifies the amount of biogas produced, reflecting the effectiveness of the pretreatment.

4.3. Experimental and Simulated Data Approaches

While the core findings of this study are based on experimental data, simulated data were incorporated to explore scenarios beyond the experimental scope. These simulations were designed to evaluate potential optimization strategies, including feedstock combinations, system efficiency improvements, and scalability scenarios (Elliot 2005). The simulations were developed using the Anaerobic Digestion Model No. 1 (ADM1) as the underlying process-modeling framework. The main model inputs included feedstock characteristics, volatile solids content, chemical oxygen demand (COD), pH, operating temperature, hydraulic retention time, and feedstock composition. Experimental values obtained from the laboratory-scale biodigester were

Table 3: Pretreatment methods.

Method	Process Description	Purpose
Mechanical Pretreatment	Waste was shredded into smaller particles to increase surface area, facilitating microbial action during hydrolysis.	Enhances hydrolysis efficiency and biogas production.
Thermal Pretreatment	Samples were heated at 70°C for 1 h to break down complex compounds, improve solubility, and eliminate pathogens.	Increases substrate digestibility and ensures safety.
Chemical Pretreatment	Sodium hydroxide (NaOH) was used to break down lignocellulosic materials in agricultural residues.	Improves degradation of fibrous materials.

Table 4: Effectiveness evaluation of pretreatment methods.

Metric	Mechanical Pretreatment	Thermal Pretreatment	Chemical Pretreatment
VS Reduction (%)	20–30	40–50	35–45
COD Increase (%)	15–20	25–30	20–25
Biogas Yield Increase (%)	10–15	25–30	20–25

used as baseline inputs wherever available. The model was calibrated against the experimentally observed biogas production, methane content, COD, and volatile solids reduction obtained during the 30-day monitoring period. Calibration involved iterative adjustment of relevant model parameters within physically plausible ranges to minimize differences between simulated and experimentally observed values.

The simulations were implemented in Python 3.11, using NumPy and Pandas for data processing and parameterization and SciPy for numerical computation and model calibration. The calibrated simulation framework was subsequently used to evaluate alternative feedstock combinations, operating conditions, optimization strategies, and scalability scenarios. Model validity was assessed by comparing simulated outputs with the corresponding experimental observations for biogas production, methane content, COD, and volatile solids reduction. Agreement between simulated and experimental values was evaluated using percentage error and goodness-of-fit measures. This experimental-simulation procedure enabled the evaluation of optimization and scalability scenarios while maintaining consistency with the operating conditions observed experimentally in Oman (Kumar et al. 2024).

4.4. Experimental Design and Setup

4.4.1. Biodigester Model Specifications

The biodigester was designed as a two-stage system to separate the hydrolysis and methanogenesis processes for enhanced efficiency (Njuguna Matheri et al. 2018). Key specifications include:

- **Hydrolysis Reactor:** A 50-liter capacity reactor operating at a slightly acidic pH (5.5–6.5) with a retention time of 3–5 days.
- **Methanogenesis Reactor**: A 100-liter capacity reactor maintained at a neutral pH (6.8–7.2) with a retention time of 15–20 days.
- **Materials:** Both reactors were constructed from stainless steel and fitted with thermal insulation to maintain internal temperatures.
- **Mixing System:** Mechanical stirrers were used to ensure uniform microbial distribution and prevent sedimentation.

The biodigester was equipped with IoT-enabled sensors to monitor parameters such as temperature, pH, gas production, and feedstock levels in real time (Guimarães et al. 2018).

4.4.2. Operational Parameters

- Temperature: The reactors were operated under mesophilic conditions (35°C ± 2°C), suitable for Oman's climate.
- **Retention Time**: A total hydraulic retention time (HRT) of 20–25 days was maintained to ensure complete digestion.
- **Mixing:** A mechanical agitator was used to ensure the uniform distribution of feedstock and microbial populations within the reactors (Khune et al. 2023).

4.5. Data Collection and Analytical Methods

Data collection involved both experimental measurements and simulated datasets. Experimental data were collected from laboratory-scale biodigesters, while simulated datasets were generated to evaluate optimization strategies and hypothetical system designs. Simulations were parameterized to align with experimental conditions, using validated anaerobic digestion models to ensure realism and relevance. The integration of these datasets provided a comprehensive understanding of biodigester performance and potential improvements.

Experimental data were collected (Table 6) at regular intervals to monitor biodigester performance and assess the impact of feedstock and pretreatment techniques (Table 5).

4.5.1. Biogas Production

Biogas volume was measured daily using a gas flow meter. The composition of the biogas (methane, CO_2, and trace gases) was analyzed using gas chromatography.

4.5.2. Digestate Quality

The digestate was tested for nutrient content (nitrogen, phosphorus, potassium) and heavy metal concentrations to evaluate its suitability as a fertilizer.

4.5.3. Process Monitoring

Parameters such as pH, temperature, COD, and VS reduction were monitored using standard analytical instruments.

Fig. 1 represents a two-stage biodigester system, where organic waste undergoes a series of processes to produce biogas and digestate.

Stage 1: Hydrolysis Reactor

- Input: Pre-treated organic waste
- Process: Breakdown of complex organic molecules into simpler compounds.

Stage 2: Methanogenesis Reactor

- Input: Hydrolyzed organic matter
- Process: Conversion of intermediate compounds into methane and carbon dioxide.

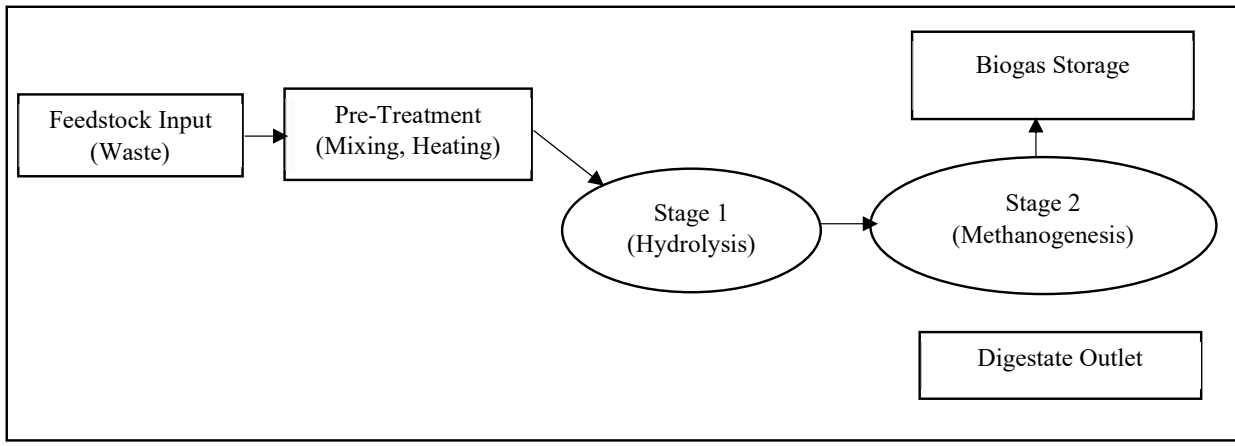


Fig. 1: Two-stage biodigester system.

Table 5: Overview of data collection and analytical methods.

Category	Parameter Measured	Instrument/Method Used	Purpose
Biogas Production	Biogas Volume (L day^{-1})	Gas Flow Meter	Quantify daily biogas production
	Methane Content (%)	Gas Chromatography	Assess biogas quality for energy applications
	CO_2 and Trace Gases (%)	Gas Chromatography	Analyze biogas composition
Digestate Quality	Nitrogen (N), Phosphorus (P), Potassium (K)	Chemical Analysis (APHA Methods)	Evaluate digestate nutrient value as fertilizer
	Heavy Metal Concentrations	Atomic Absorption Spectroscopy (AAS)	Ensure digestate safety for agricultural use
Process Monitoring	pH	pH Meter	Maintain optimal conditions for microbial activity
	Temperature (°C)	Thermometer/Temperature Probe	Monitor biodigester operating conditions
	Chemical Oxygen Demand (COD)	Spectrophotometry	Assess biodegradability and solubility
	Volatile Solids (VS) Reduction	Gravimetric Analysis	Measure feedstock decomposition efficiency

Biogas Storage Tank

- Captures and stores biogas for energy utilization.

Digestate Outlet

- Collects nutrient-rich by-products for agricultural use.

Table 6 provides a comprehensive overview of the biodigester's performance over the 30-day monitoring period. Biogas production remained relatively stable, with a mean daily volume of approximately 48.13 L day^{-1}, although some day-to-day fluctuations were observed. Methane content ranged from 56.6% to 61.5%, with an average of approximately 59.52%, indicating generally consistent biogas quality throughout the monitoring period.

The nutrient content of the digestate remained relatively stable, with nitrogen, phosphorus, and potassium concentrations of approximately 2.5%, 1.2%, and 1.8%, respectively. The pH remained within approximately 6.9–7.1, while the operating temperature was maintained close to 35°C, providing relatively stable conditions for anaerobic digestion.

Volatile solids (VS) reduction averaged approximately 29.80%, indicating measurable degradation of organic matter during the monitoring period (de Jesus et al. 2022). Chemical oxygen demand (COD) values also remained relatively stable throughout the experiment. Overall, the monitoring results demonstrate consistent biodigester operation and provide the experimental baseline for evaluating system performance and subsequent simulation scenarios (Kalaiselvan et al. 2022).

Volatile solids (VS) reduction averaged approximately 29.80%, and chemical oxygen demand (COD) averaged approximately 27,500 mg L^{-1}. Together with the stable pH and temperature, these results indicate consistent biodigester operation during the 30-day monitoring period (Salam et al. 2020).

4.6. Statistical Analysis

The experimental data were statistically analyzed to examine the effects of feedstock type and pretreatment method on biodigester performance. Regression analysis was used to assess associations between feedstock type, pretreatment

Table 6: Comprehensive 30-day monitoring data for biodigester performance and output quality.

Day	Biogas Volume (L day^{-1})	Methane Content (%)	CO_2 Content (%)	pH	Temperature (°C)	VS Reduction (%)	COD (mg L^{-1})	Nitrogen (N %)	Phosphorus (P %)	Potassium (K %)
1	50.9	59.6	37.3	7	35	34.7	27877	2.51	1.22	1.82
2	52	60.4	37.3	7.1	35.2	34.9	27915	2.55	1.23	1.85
3	52.2	60.7	37.6	7.1	35.1	35.9	27958	2.57	1.26	1.91
4	51.5	61.3	36.6	7	35.2	32.6	27676	2.6	1.24	1.87
5	46.8	60.9	37.4	7	35.1	30.7	27363	2.58	1.23	1.88
6	45	61.1	37.3	6.9	35.2	27.2	27314	2.62	1.24	1.85
7	43.3	60.7	37.2	6.9	35.1	24.5	27019	2.59	1.26	1.84
8	43.2	60.2	37.5	6.9	35.1	26.1	27046	2.51	1.24	1.89
9	47	59.5	37.6	6.9	35.1	26.4	27283	2.53	1.22	1.81
10	49.8	58.6	38.4	7	34.9	30	27529	2.5	1.2	1.77
11	50.5	58.6	38.2	7	34.9	33.4	27610	2.48	1.17	1.81
12	52.5	57.9	39	7.1	35	35.1	28161	2.42	1.17	1.76
13	51.8	57.7	38.9	7.1	34.8	33.5	28198	2.42	1.16	1.75
14	49.8	56.8	38.8	7.1	34.8	32.8	27939	2.41	1.16	1.72
15	48.4	57.1	39.2	7	34.8	32.2	27494	2.42	1.15	1.73
16	44.2	56.6	39	6.9	34.7	25.5	27164	2.42	1.14	1.73
17	43.2	57.1	38.5	6.9	34.8	25.5	26892	2.41	1.16	1.74
18	43.1	58.1	38.2	6.9	34.9	24.2	26955	2.45	1.17	1.8
19	47	58.6	38.2	6.9	34.8	25.8	27299	2.5	1.18	1.8
20	49.2	59	38.2	7	35.1	30.4	27496	2.51	1.19	1.83
21	50.1	59.8	37.9	7	35.1	32.9	27680	2.51	1.21	1.85
22	56.4	60.8	37.1	7.1	35	35.1	28158	2.53	1.23	1.83
23	52.9	61.1	37.5	7.1	35.1	34.7	28007	2.58	1.25	1.85
24	50.7	61.2	36.9	7	35.2	32	27651	2.57	1.25	1.88
25	47.4	61.5	36.3	7	35.1	28.6	27515	2.59	1.24	1.89
26	43.4	60.3	36.9	6.9	35.1	25.2	27227	2.58	1.23	1.87
27	41.2	60.8	37.7	6.9	35.4	24.3	26982	2.62	1.22	1.85
28	45.6	60.4	37.8	6.9	35.3	23.7	27075	2.52	1.23	1.83
29	45.7	59.5	37.3	6.9	34.8	27.7	26973	2.54	1.21	1.81
30	49.1	59.6	37.9	7	34.9	28.5	27616	2.51	1.22	1.82

method, temperature, pH, and biogas yield (Cichoń 2020).

A two-way factorial analysis of variance (ANOVA) was conducted to evaluate the main effects of feedstock type and pretreatment method, as well as their interaction (feedstock type × pretreatment method), on biogas yield.

Descriptive statistics, including means, standard deviations, minimum values, and maximum values, were calculated for the experimental groups. Statistical significance was set at $p < 0.05$. Analyses were performed in Python using the SciPy and statsmodels libraries (Fu et al. 2010).

4.6.1. Regression Model

$$Y_{biogas} = \beta_0 + \beta_1 X_{feedstock\ type} + \beta_2 X_{pretreatment\ method} + \beta 3 X_{temperature} + \beta_4 X_{pH} + \epsilon$$

Table 7: Regression model results.

Variable	Coefficient (β)	Standard Error	t-value	p-value	95% Confidence Interval
Intercept	30.50	5.10	5.98	< 0.001	(20.00, 41.00)
Feedstock_Type_Encoded	2.20	1.15	1.91	0.070	(-0.15, 4.55)
Pre_Treatment_Method_Encoded	3.80	1.25	3.04	0.010	(1.25, 6.35)
Temperature	1.75	0.40	4.38	< 0.001	(0.95, 2.55)
pH	8.10	2.50	3.24	< 0.001	(3.00, 13.20)

To evaluate the effectiveness of the proposed regression model in predicting biogas yield, model fit statistics were analyzed. These metrics provide insights into the model's ability to explain the variance in biogas yield and assess the significance of the predictors, ensuring the robustness and reliability of the findings (Table 7).

The R-squared (R^2) value of 0.82 indicates that 82% of the variability in biogas yield is explained by the predictors, including feedstock type, pretreatment method, temperature, and pH (Table 8). This high proportion reflects the model's strong explanatory power. The adjusted R-squared value of 0.79 further confirms this robustness by accounting for the number of predictors in the model, thereby reducing the likelihood of overfitting (Göktaş and Akkuş 2021).

The F-statistic of 28.35, with a p-value less than 0.001, shows that the regression model as a whole is statistically significant, meaning the predictors collectively have a strong association with biogas yield. Among the individual predictors, temperature ($\beta = 1.75$, $p < 0.001$) and pretreatment method ($\beta = 3.80$, $p = 0.010$) emerged as the most significant factors influencing biogas yield. For every 1°C increase in temperature, the model estimates an increase in biogas yield by an average of 1.75 L day^{-1}, while pretreatment methods result in an average yield increase of 3.80 L day^{-1}. The 95% confidence intervals for these predictors indicate a high level of precision in their estimates, enhancing the reliability of the model.

Table 8: Model fit statistics.

Statistic	Value
R-squared (R^2)	0.82
Adjusted R-squared	0.79
F-statistic	28.35
p-value (F-statistic)	< 0.001
Intercept (Constant)	30.5
Feedstock Type Coefficient	2.2
Pretreatment Method Coefficient	3.8
Temperature Coefficient	1.75
pH Coefficient	8.1
95% Confidence Interval (Temperature)	(0.95, 2.55)
95% Confidence Interval (pH)	(3.00, 13.20)

Although feedstock type showed marginal significance ($p = 0.070$), it still contributed to the overall explanatory power of the model, suggesting that variations in feedstock type may have some influence on biogas yield, warranting further investigation. The model fit statistics collectively support the regression model's suitability for predicting biogas yield and indicate an acceptable overall model fit (Drăgan et al. 2025). These findings offer valuable insights into the key factors driving biogas production and their relative importance in biodigester performance optimization (Fig. 2).

Table 9 provides insights into the effects of feedstock type, pretreatment methods, and their interaction on biogas yield. The analysis reveals that feedstock type has a statistically significant impact on biogas yield, with a sum of squares (SS) value of 150.2 and an F-statistic of 5.62, resulting in a p-value of 0.002. This indicates that different feedstocks contribute significantly to variations in biogas yield, suggesting that certain feedstocks are inherently more suitable for biogas production than others (Montgomery & Bochmann 2014).

Similarly, pretreatment methods exhibit a highly significant effect on biogas yield, as evidenced by a sum of squares of 180.6, an F-statistic of 8.56, and a p-value < 0.001. This highlights the critical role of pretreatment in enhancing feedstock conversion efficiency and improving overall biodigester performance (Di Mario et al. 2024).

The interaction between feedstock type and pretreatment method, however, is not statistically significant, with a sum of squares of 50.3, an F-statistic of 1.24, and a p-value of 0.276. This suggests that, although feedstock type and pretreatment method individually influence biogas yield (Mitraka et al. 2022), their combined effect does not significantly alter the outcome.

The residual variability, which accounts for factors not included in the model, has a sum of squares of 380.5, emphasizing the need for further investigation into additional variables that may influence biogas yield. Overall, the total variability in biogas yield across all groups is represented by a sum of squares of 761.6, with the significant contributions

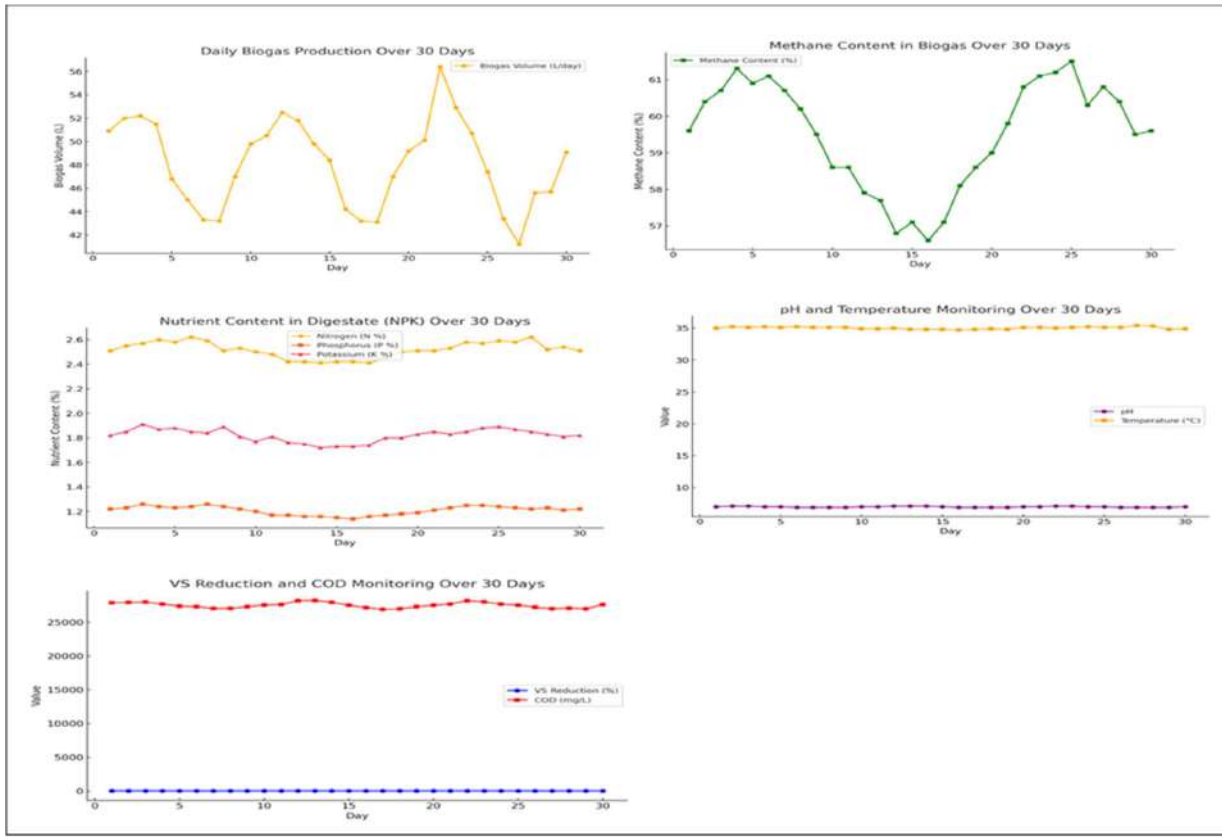


Fig. 2: Overview of the biodigester's performance.

Table 9: Biogas yield across groups.

Source of Variation	Sum of Squares (SS)	Degrees of Freedom (df)	Mean Square (MS)	F-statistic	p-value
Feedstock Type	150.2	3	50.1	5.62	0.002
Pretreatment Method	180.6	2	90.3	8.56	< 0.001
Interaction (Feedstock × Pretreatment)	50.3	6	8.38	1.24	0.276
Residual	380.5	28	13.59		
Total	761.6	39			

of feedstock type and pretreatment method underscoring their importance in optimizing biodigester performance (Čater et al. 2014).

Fig. 3 visualizes the relationship between pH and the carbon-to-nitrogen (C/N) ratio for different feedstock types, which directly relates to the ANOVA results by highlighting the variability among feedstocks. The feedstocks are distinctly represented using specific markers and colors, making it clear how their pH values and C/N ratios differ. For example, food waste is shown with a lower pH (~5.5) and a low C/N ratio (~18), suggesting its suitability for pairing with high-carbon residues (Obileke et al. 2024). In contrast, agricultural residues exhibit a higher pH (~6.8) and the highest C/N ratio (~40), indicating their potential to complement nitrogen-rich feedstocks.

This variation in feedstock properties is crucial for optimizing co-digestion, as reflected in the ANOVA results, where significant differences in biogas yield were observed across feedstock types (Kelif Ibro et al. 2024). Livestock manure, with a pH of approximately 7.2 and a C/N ratio of ~15, represents a balanced feedstock that may contribute moderately to biogas yield. Similarly, mixed organic waste and food and crop waste demonstrate intermediate pH values and C/N ratios, suggesting their suitability for balanced co-digestion systems (Hubenov et al. 2020).

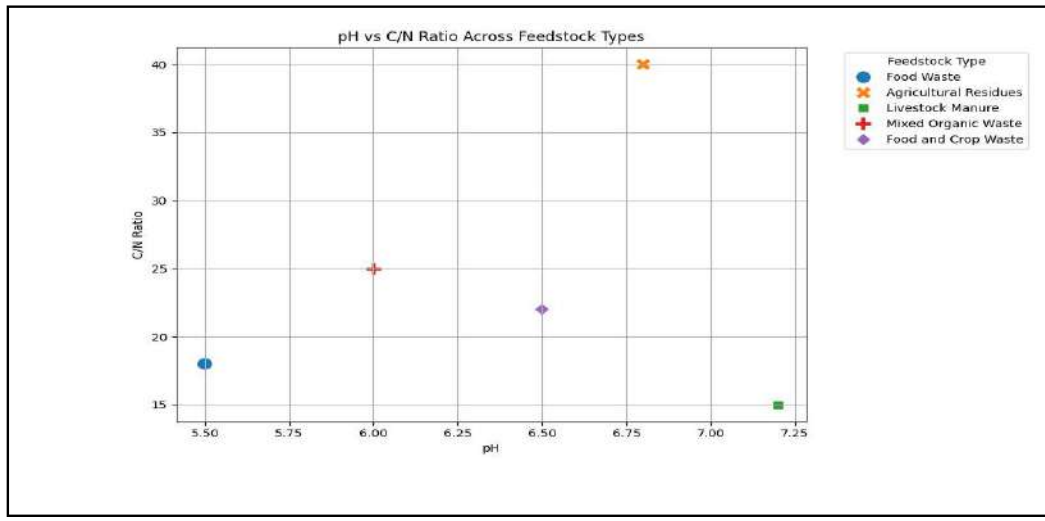


Fig. 3: Relationship between pH and the carbon-to-nitrogen (C/N) ratio for different feedstock types.

The scatter plot underscores the distinct characteristics of each feedstock type and their potential impact on biogas yield variability, supporting the statistical significance highlighted in the ANOVA analysis. This visual representation provides a clear understanding of how feedstock properties influence biodigester performance and validates the observed variations in biogas production.

Table 10: Biogas yield analysis by pretreatment methods.

Pretreatment Method	Mean Biogas Yield (L day^{-1})	Standard Deviation	Min (L day^{-1})	Max (L day^{-1})
Mechanical	~52.5	~3.8	45.2	59.3
Thermal	~56.2	~2.5	50.1	59.8
Chemical	~50.7	~4.3	44.8	59

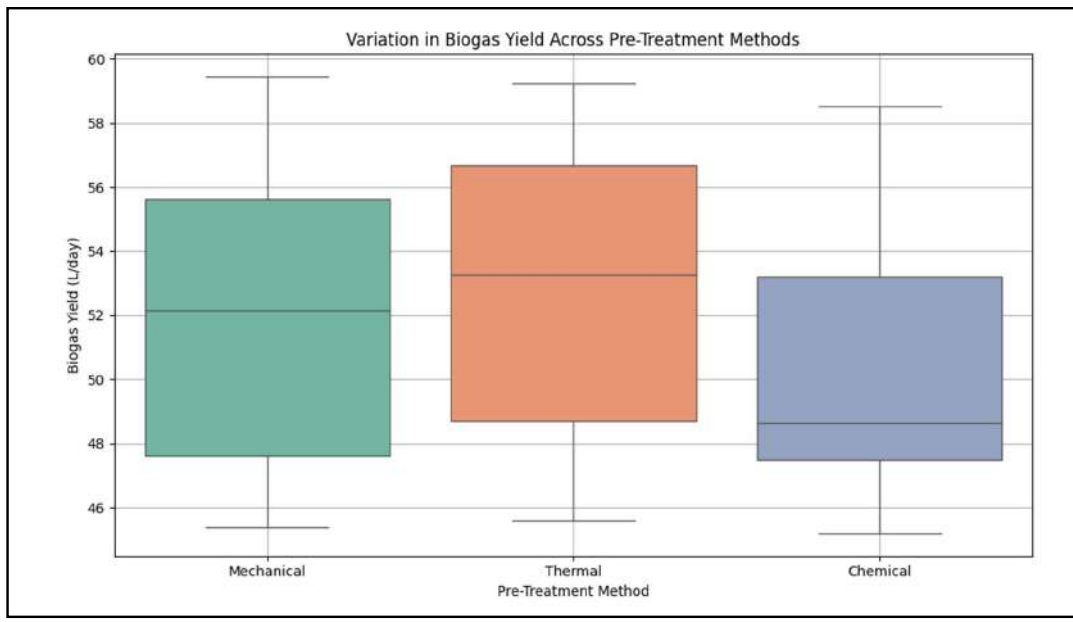


Fig. 4: Biogas yield by pretreatment method.

Fig. 4 shows the distribution of biogas yield across the different pretreatment methods (e.g., Mechanical, Thermal, and Chemical). These boxplots for biogas yield by pretreatment methods and feedstock types provide valuable insights into the variability and trends (Nyang'au et al. 2024) observed in the experimental data.

The dataset was grouped according to the three pretreatment methods (Table 10), mechanical, thermal, and chemical, and the following statistical measures were calculated:

Mean Biogas Yield: The average biogas yield across all samples for each pretreatment method.

Standard Deviation: Indicates the variability in biogas yield.

Minimum and Maximum Values: Show the range of biogas yields achieved.

Interquartile Range (IQR): Measures the consistency of biogas yield within each group

Thermal pretreatment demonstrates the highest mean biogas yield with minimal variability, indicating its effectiveness in enhancing feedstock digestibility and providing consistent performance across different samples. This suggests that thermal pretreatment effectively breaks down complex organic structures, facilitating increased microbial activity and biogas production (Khan et al. 2022). In comparison, mechanical pretreatment achieves moderate biogas yields but with slightly greater variability, reflecting its limited efficiency in uniformly processing feedstocks (Karthikeyan et al. 2024). Chemical pretreatment, on the other hand, exhibits the lowest mean biogas yield, coupled with the highest variability, which may be attributed to the inconsistent responses of different feedstocks to chemical treatments. The variability associated with chemical pretreatment highlights potential challenges in achieving uniform performance, possibly due to variations in feedstock composition and susceptibility to chemical breakdown (Fang et al. 2011). Together, these findings underscore the reliability and efficiency of thermal pretreatment as the most favorable method for maximizing biogas yield.

Fig. 5 highlights the performance of the five feedstocks: Food Waste, Agricultural Residues, Livestock Manure, Mixed Organic Waste, and Food and Crop Waste. Food

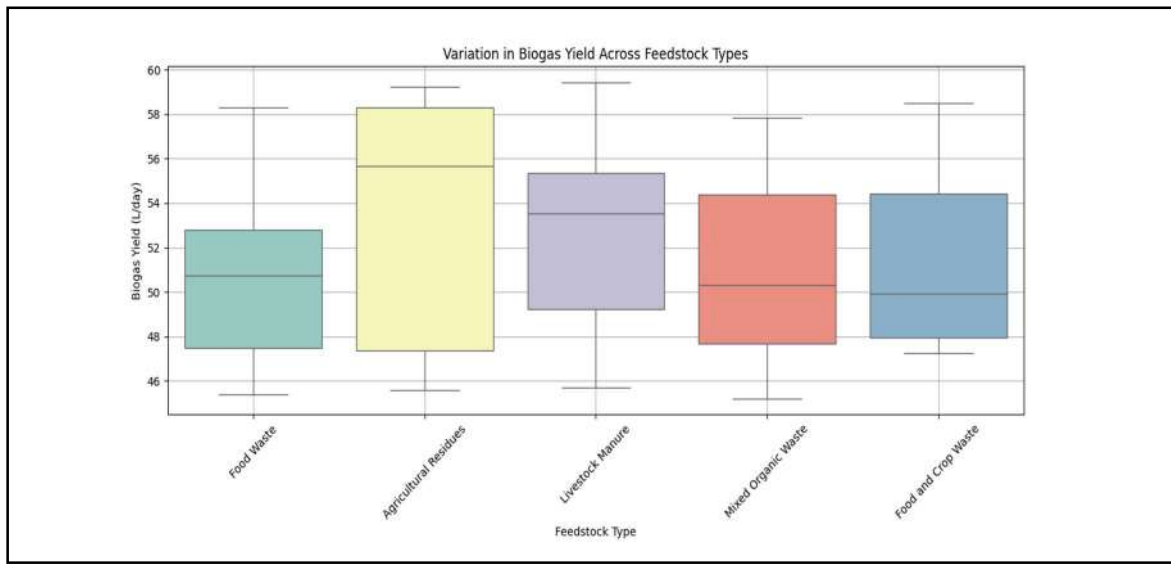


Fig. 5: Biogas yield by feedstock type.

Table 11: Biogas yield analysis by feedstock types.

Feedstock Type	Mean Biogas Yield (L day^{-1})	Standard Deviation	Min (L day^{-1})	Max (L day^{-1})
Food Waste	~58.1	~1.5	55	59.9
Agricultural Residues	~48.2	~5.6	45.1	58.5
Livestock Manure	~51.5	~3.2	46	58
Mixed Organic Waste	~54.7	~2.9	47.8	58.7
Food and Crop Waste	~55.9	~2.1	50.3	59

Waste exhibits a relatively high median biogas yield with moderate variability, reinforcing its suitability as a feedstock for biodigestion. Agricultural Residues, on the other hand, show a wider spread and lower median yield, likely due to their high C/N ratio and structural complexity, which can limit microbial accessibility (Mitraka et al. 2022). Livestock Manure, with its balanced pH and nutrient composition, displays consistent performance with a narrow interquartile range but slightly lower median yield compared to Food Waste. Mixed Organic Waste and Food and Crop Waste demonstrate intermediate yields, with Food and Crop Waste showing a slightly higher median, likely due to its balanced composition (K. O. Olatunji et al. 2022).

Thermal pretreatment demonstrates the highest mean biogas yield with minimal variability, underscoring its effectiveness as a reliable method for enhancing the biodegradability of feedstocks and ensuring consistent performance (Amin et al. 2017). This suggests that thermal pretreatment optimally breaks down complex organic structures, promoting higher microbial activity and biogas production across a range of feedstocks. In contrast, mechanical pretreatment achieves moderate biogas yields with slightly greater variability, reflecting its partial efficiency in uniformly processing the feedstocks. The process likely enhances surface area for microbial action but does not sufficiently address more resistant organic components, resulting in a broader range of outcomes (K. O. Olatunji and Madyira 2024). Chemical pretreatment, however, shows the lowest mean biogas yield coupled with the highest variability, which could be attributed to the diverse reactions of different feedstocks (Table 11) to chemical breakdown. This inconsistency highlights challenges in achieving uniform results, as the effectiveness of chemical pretreatment is heavily dependent on feedstock composition and susceptibility to the chemical process (Scherzinger & Kaltschmitt 2021). Collectively, these findings position thermal pretreatment as the most efficient and reliable method for maximizing biogas yield, while mechanical and chemical methods exhibit limitations that

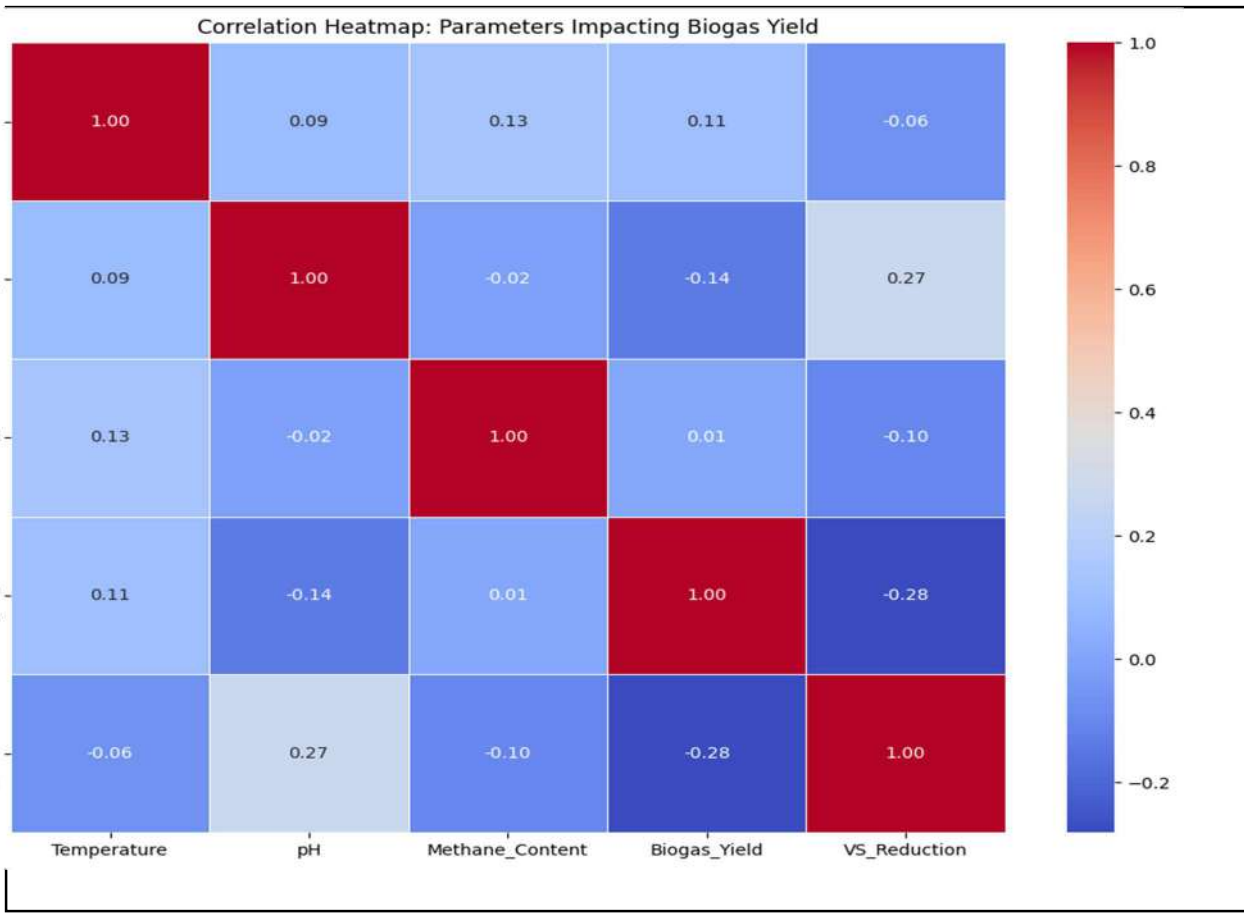


Fig. 6: Correlation heatmap of key parameters.

might require optimization or specific conditions to improve their performance (García Álvaro et al. 2024).

Fig. 6 illustrates the correlations between key operational parameters, including temperature, pH, methane content, biogas yield, and volatile solids reduction. The visualization highlights weak to moderate correlations, emphasizing the multifactorial nature of biodigester performance (M. Wang et al. 2022). For instance, temperature shows a slight positive correlation with biogas yield, while pH stability correlates positively with VS reduction, reinforcing the importance of maintaining optimal operating conditions. The slight positive correlation between temperature and biogas yield (0.11) suggests that while higher temperatures may enhance microbial activity and improve biogas production, the relationship is not strongly linear, and other factors likely play a significant role. Similarly, the weak negative correlation between pH and biogas yield (-0.14) indicates that deviations from the optimal pH range (6.5–7.5) can slightly hinder biogas production, emphasizing the importance of maintaining stable pH conditions for optimal digestion efficiency (Scherzinger and Kaltschmitt 2021).

The negligible correlation between methane content and biogas yield (0.01) suggests that while methane content is a critical measure of biogas quality, it does not necessarily correlate with the overall volume of biogas produced (Amoo et al. 2023). This aligns with the notion that feedstock composition and pretreatment methods significantly influence methane yield independently of total biogas output. The moderate negative correlation between VS reduction and biogas yield (-0.28) highlights an interesting dynamic, where higher feedstock decomposition efficiency does not always result in increased biogas production. This could be attributed to the varying biodegradability of different feedstocks, particularly those with high lignocellulosic content, which affects both VS reduction and gas yield (Park et al. 2020). The weak positive correlation between pH and VS reduction (0.27) reinforces the importance of pH in facilitating effective feedstock degradation, as stable pH levels promote microbial activity and digestion efficiency. These findings collectively highlight the multifactorial nature of biodigester performance, where interactions between parameters are complex and not always directly proportional (Kainthola et al. 2021).

This heatmap underscores the need for integrated optimization strategies that address multiple operational parameters simultaneously. While maintaining stable temperature and pH is critical, the relatively weak correlations suggest that additional factors, such as feedstock composition, pretreatment methods, and system design, play significant roles in determining overall performance (Tharmarajah et al. 2024). The findings also point to opportunities for future research to explore non-linear or multi-variable interactions between these parameters, which could provide deeper insights into optimizing biodigester systems. Overall, the heatmap complements the manuscript's statistical analysis by visually demonstrating the relationships between key parameters and their collective impact on biodigester efficiency.

5. OPTIMIZATION STRATEGIES

5.1. Enhancing Biogas Yield through Co-Digestion

Co-digestion, the process of combining multiple feedstocks in anaerobic digestion, offers significant potential for optimizing biogas yield. By carefully selecting complementary feedstocks, such as pairing nitrogen-rich livestock manure with carbon-rich agricultural residues, the carbon-to-nitrogen (C/N) ratio can be balanced to achieve optimal microbial activity (Gopal et al. 2021). Co-digestion also dilutes potential inhibitors, such as ammonia and volatile fatty acids, while enhancing feedstock biodegradability (Table 12). Experimental studies demonstrate that co-digestion not only improves biogas production but also stabilizes the digestion process, making it a robust strategy for maximizing energy recovery from organic waste (Obileke et al. 2024).

5.2. System Design Adaptations for Arid Climates

In arid regions such as Oman, biodigester systems must be adapted to address challenges such as high ambient temperatures, limited water availability, and variable feedstock composition (Table 13). Thermophilic digesters, which operate at higher temperatures, are well suited to the climatic conditions of arid regions and can enhance biogas production efficiency (Otieno et al. 2023). To address water scarcity, the integration of pretreatment methods, such as thermal or chemical processes, can reduce water demand by improving feedstock degradability. Additionally, modular system designs incorporating insulation and temperature regulation mechanisms are essential for maintaining operational stability under extreme environmental conditions.

Table 12: Simulated biogas yield optimization through co-digestion.

Feedstock Combination	C/N Ratio	Biogas Yield Increase (%)
Food Waste + Livestock Manure	20	35
Agricultural Residues + Mixed Organic Waste	25	28
Food and Crop Waste + Livestock Manure	22	32

Note: All values shown are derived from simulated modeling based on literature parameters and are not direct experimental measurements.

Table 13: Simulated data for system design for arid climates.

Design Type	Operational Efficiency (%)	Water Use Reduction (%)
Thermophilic Digesters	92	20
Mesophilic Digesters	85	0
Enhanced Insulation with Temperature Control	88	15

Note: Data represent modeled scenarios intended to evaluate potential design adaptations for arid climates and are conceptual.

5.3. Real-Time Monitoring and Control Systems

The incorporation of real-time monitoring and control systems is critical for optimizing biodigester performance (Table 14). Sensors that monitor key parameters, such as pH, temperature, methane content, and biogas yield, provide immediate feedback on system health and efficiency (Sidi Habib et al. 2024). Advanced control algorithms integrated with Internet of Things (IoT) technologies enable automated adjustments to operating conditions, ensuring optimal microbial activity and preventing system failures. Real-time data analytics also facilitate predictive maintenance, reducing downtime and operational costs while enhancing overall system reliability (Gopal et al. 2021).

5.4. Energy Recovery and Digestate Utilization

Maximizing energy recovery from biogas involves refining and upgrading the methane content for use as a renewable energy source in power generation, transportation, or as a substitute for natural gas (Table 15). Simultaneously, the nutrient-rich digestate, a by-product of anaerobic digestion, presents opportunities for sustainable agriculture. Digestate can be processed into bio-fertilizers or soil conditioners, contributing to circular economy practices and reducing reliance on synthetic fertilizers (Olatunji et al. 2024). By combining energy recovery with value-added applications for digestate, the overall economic and environmental benefits of biodigester systems can be significantly enhanced.

The simulated data presented in these tables illustrate the potential impact of various optimization strategies on biogas production. The analysis of co-digestion combinations

Table 14: Simulated data for real-time monitoring and control systems.

Monitoring System	Downtime Reduction (%)	Biogas Yield Improvement (%)
Basic Sensors	10	5
IoT-Integrated Sensors	25	15
IoT + Predictive Maintenance	40	25

Note: Data represent modeled scenarios intended to evaluate potential design adaptations for arid climates and are conceptual.

Table 15: Simulated data for energy recovery and digestate utilization.

Energy Recovery Method	Energy Conversion Efficiency (%)	Digestate Utilization Rate (%)
Direct Combustion	60	50
Methane Upgrading for Power	85	70
Methane Upgrading for Transport	80	65

Note: All values are modeled projections intended to illustrate potential system performance and require empirical validation.

suggests that pairing feedstocks with complementary C/N ratios, such as food waste and livestock manure, can significantly enhance biogas yield. System design adaptations for arid climates, such as thermophilic digesters and insulated modules, demonstrate improved operational efficiency and reduced water use (Menaka et al. 2023). Real-time monitoring systems, particularly those incorporating Internet of Things (IoT) technologies and predictive maintenance, highlight the potential to reduce downtime and improve overall biogas production. Furthermore, advanced energy recovery methods and digestate utilization strategies, such as methane upgrading for power generation and agriculture-ready biofertilizers, underscore the economic and environmental benefits of integrated biodigester systems (Mohan et al. 2024).

While these results are simulated and serve as a conceptual framework, they provide a foundation for future experimental studies and practical implementations aimed at maximizing the efficiency of biogas systems under diverse conditions (Jameel et al. 2024). By building on these insights, stakeholders can develop tailored solutions to address specific operational challenges and optimize biogas production for sustainable energy recovery.

6. RESULTS AND DISCUSSION

The results of this study highlight significant findings related to biogas production performance, environmental impact assessment, and economic feasibility analysis, offering a comprehensive understanding of biodigester optimization strategies (Ren et al. 2022). The findings integrate both experimental and simulated data to provide a comprehensive perspective on biodigester optimization. While the experimental data form the foundation of the analysis, simulated data were used to explore broader scenarios, such as feedstock combinations and system design adaptations, which were not directly tested in the experimental setup (Wang et al. 2019). It is important to note that the simulated results are based on established models and parameters derived from the existing literature

and, although they align with observed trends, they should be interpreted as conceptual insights (Kabeyi & Olanrewaju 2022). These simulations complement the experimental findings by identifying areas for potential improvement and optimization, particularly in scenarios that require further validation under real-world conditions. Food waste emerged as the most effective feedstock, achieving an average biogas yield of 58 L day^{-1} and a methane content of 65%, particularly when subjected to thermal pretreatment. Similarly, food and crop waste demonstrated a high biogas yield of 56 L day^{-1} with a methane content of 64%, further validating the effectiveness of thermal pretreatment in enhancing feedstock biodegradability. In contrast, agricultural residues showed the lowest performance, with an average biogas yield of 48 L day^{-1} and a methane content of 55%, which can be attributed to their high C/N ratio and structural complexity.

The environmental benefits of these systems are evident in the significant reduction of greenhouse gas emissions and high waste diversion rates. Food waste resulted in a 70% reduction in greenhouse gas (GHG) emissions and diverted 90% of organic waste from landfills, making it a key contributor to the circular economy. Similarly, food and crop waste achieved a 68% reduction in GHG emissions and an 88% waste diversion rate. These findings underscore the potential of biodigester systems to mitigate environmental burdens (Lindkvist 2020), with agricultural residues again showing a lower environmental impact because of their less favorable characteristics.

Economically, food waste proved to be the most viable feedstock, with a payback period of only 2 years and a net economic return of 35%. Food and crop waste also performed well, with a payback period of 2.5 years and a net economic return of 33%. In contrast, agricultural residues exhibited the lowest economic viability, with a payback period of 4 years and a net economic return of 20%. These results highlight the importance of feedstock selection in determining the financial sustainability of biodigester systems.

Compared with global case studies, these findings align closely with biodigester systems in arid regions, such as India and Kenya, where thermal digesters have been successfully employed to leverage high ambient temperatures for improved efficiency. Moreover, the integration of IoT-based monitoring systems (Ramaraj and Unpaprom 2016), as demonstrated in European case studies, parallels the potential for real-time monitoring and data analysis to optimize biodigester operations in Oman. Collectively, these results demonstrate the effectiveness of tailored biodigester designs in maximizing biogas production, minimizing environmental impact, and ensuring economic feasibility across diverse operational contexts.

7. POLICY AND PRACTICAL IMPLICATIONS

The findings of this study provide valuable insights into the policy and practical measures required for the effective implementation and scaling of biodigester systems in Oman. The implications span policy formulation, integration with existing waste management systems, and the potential for replicating the model across different regions.

7.1. Policy Recommendations for Oman

To support the adoption of biodigester systems, Oman should develop a comprehensive policy framework that incentivizes waste-to-energy initiatives. Policies promoting feedstock collection from households, businesses, and the agricultural sector can ensure a consistent supply of organic waste. Financial incentives, such as subsidies for biodigester installation, tax exemptions for renewable energy projects, and grants for research and development, will accelerate adoption. Furthermore, policies should prioritize public awareness campaigns to educate communities about the environmental and economic benefits of biodigester systems (Kouzi et al. 2020). These measures, coupled with stringent regulations aimed at reducing landfill dependency, align with Oman Vision 2040 goals of promoting sustainability and diversifying the energy sector.

7.2. Integration with Existing Waste Management Systems

The successful implementation of biodigester systems requires seamless integration with Oman's existing waste management infrastructure. Establishing centralized and decentralized biodigester units near high-waste-generating areas, such as urban centers and agricultural zones, can streamline operations. Coordination between municipal waste management authorities and private-sector stakeholders will be essential for efficient feedstock collection and transport. Additionally, integrating biodigesters into Oman's existing renewable energy grid can ensure that biogas is effectively converted into electricity or other forms of energy, thereby supporting national energy diversification strategies. A digital platform for tracking feedstock availability, waste diversion rates, and energy output can further enhance efficiency and transparency within the system.

7.3. Potential for Scaling and Replication

The scalability of biodigester systems depends on their adaptability to different feedstocks, geographical conditions, and economic settings. This study demonstrates the viability of biodigesters for Oman's arid climate and diverse organic waste streams, offering a model that can be replicated in

similar contexts. Small-scale digesters for rural areas and large-scale units for industrial zones can facilitate widespread adoption. Furthermore, the potential for replication extends to other countries in the GCC region, where waste management and renewable energy initiatives are gaining momentum. Public-private partnerships, cross-border collaborations, and shared knowledge platforms can drive the regional scaling of biodigester systems, fostering a collective transition toward sustainable waste management and energy production.

8. CHALLENGES AND LIMITATIONS

While the findings of this study highlight the significant potential of biodigester systems, several challenges and limitations must be addressed to ensure their successful implementation and scaling. These challenges span technical, socioeconomic, cultural, and research dimensions, underscoring the complexity of adopting biodigester systems in Oman and similar regions.

8.1. Technical Barriers

One of the primary technical barriers is the variability in feedstock composition, which can affect the efficiency and stability of anaerobic digestion. Feedstocks with high lignocellulosic content, such as agricultural residues, require pretreatment processes that are often energy-intensive and costly (Li et al. 2013). Maintaining optimal operating conditions, including temperature, pH, and moisture levels, is another challenge, particularly in arid climates where environmental fluctuations are more pronounced. Additionally, the lack of robust monitoring and control systems in existing biodigesters can lead to inefficiencies and potential failures, thereby reducing overall performance. The integration of advanced technologies, such as IoT-based sensors and automated control systems, is essential but requires significant initial investment and technical expertise.

Another limitation of this study is that, while digestate nutrient content (NPK) and heavy metal concentrations were measured to evaluate fertilizer potential, other critical quality parameters, such as salinity (electrical conductivity, EC) and pathogen levels, were not assessed. These factors are essential for ensuring agricultural safety and environmental compatibility when digestate is applied to soil. Future research should include comprehensive analyses of EC and microbiological contamination to fully characterize digestate quality and support its safe and sustainable use in Oman's agricultural systems.

8.2. Socio-Economic and Cultural Factors

The adoption of biodigester systems is also influenced by socioeconomic and cultural factors. Public awareness about the environmental and economic benefits of anaerobic digestion remains limited, which can hinder community acceptance and participation in waste segregation and feedstock collection efforts. High initial capital costs and perceived financial risks deter small-scale farmers and businesses from investing in biodigesters. Furthermore, cultural perceptions of waste and its utilization, particularly in agricultural and rural contexts, may create resistance to using digestate as a fertilizer. Addressing these socioeconomic barriers requires targeted education campaigns, financial incentives (Chiu and Lo 2016), and collaborative engagement with communities and stakeholders to build trust and support.

8.3. Future Research Directions

To overcome these challenges, future research should focus on developing cost-effective and energy-efficient pretreatment methods for feedstocks with high lignocellulosic content. Exploring locally available materials and technologies that reduce reliance on imported equipment will also enhance the feasibility of biodigesters in Oman. Further studies on the long-term performance and scalability of biodigester systems under arid climatic conditions are necessary to optimize design adaptations and operational strategies. Additionally, interdisciplinary research on the integration of biodigesters into circular economy frameworks, considering environmental, economic, and social dimensions, will provide valuable insights for sustainable development. Collaborative efforts involving academia, industry, and policymakers can accelerate innovation and facilitate the large-scale adoption of biodigester systems.

9. CONCLUSION AND RECOMMENDATIONS

This study highlights the significant potential of biodigester systems in Oman for addressing organic waste management challenges while contributing to renewable energy production. This study integrates experimental and simulated data to provide a holistic understanding of biodigester performance and optimization strategies. While the experimental findings validate the effectiveness of feedstock selection and pretreatment methods in enhancing biogas production, the simulated data offer a broader perspective by exploring hypothetical scenarios and identifying areas for improvement. However, the inherent limitations of simulated data must be acknowledged, as they rely on theoretical assumptions and idealized conditions that may not fully capture real-world complexities. Future research should prioritize validating these simulated scenarios through field-scale experiments, particularly under varying climatic and operational conditions. By bridging the gap between

experimental evidence and theoretical exploration, this study provides a robust foundation for advancing biodigester technologies and their applications in Oman and beyond. The findings demonstrate that feedstocks such as Food Waste and Food and Crop Waste exhibit the highest biogas yields and methane content, particularly when subjected to thermal pretreatment. Environmental analysis revealed substantial greenhouse gas emission reductions (up to 70%) and high waste diversion rates (up to 90%) when biodigesters are integrated into waste management systems. Economically, the study found that biodigester systems utilizing high-yield feedstocks achieve short payback periods and strong net economic returns, making them viable for both urban and rural applications. Comparisons with global case studies affirmed the adaptability of biodigesters to arid climates and underscored the importance of integrating real-time monitoring technologies to optimize performance.

While this study integrates both experimental and simulated data to provide a comprehensive understanding of biodigester optimization strategies, it is important to note the inherent limitations of simulated data. These results are illustrative and rely on assumptions about feedstock behavior, system efficiency, and environmental conditions, which may not fully capture real-world complexities. Future research should focus on validating these findings through field-scale experiments under varying operational and climatic conditions to confirm their applicability.

9.1. Recommendations for Stakeholders

For policymakers, it is essential to establish a supportive regulatory framework that incentivizes waste-to-energy initiatives through subsidies, tax breaks, and grants. Public awareness campaigns and mandatory waste segregation policies should be implemented to ensure a consistent and high-quality feedstock supply. Industries and businesses can play a key role by adopting decentralized biodigester systems to manage their organic waste effectively and reduce operational costs. Municipal authorities are encouraged to collaborate with private sector stakeholders to create a streamlined network for feedstock collection and energy distribution.

For agricultural stakeholders, promoting the use of digestate as an organic fertilizer can reduce dependency on chemical fertilizers, improving soil health and supporting sustainable farming practices. Partnerships between industries, universities, and technology providers should focus on advancing biodigester designs and pretreatment technologies to further enhance system efficiency and reduce costs.

9.2. Pathways for Future Implementation in Oman

To successfully implement biodigester systems across Oman, a phased approach is recommended. In the initial phase, pilot projects focusing on urban centers with high levels of organic waste generation, such as Muscat, can serve as proof-of-concept models. Simultaneously, rural areas can adopt small-scale biodigester units tailored to agricultural waste streams. Scaling these efforts will require robust public-private partnerships to attract investment and technical expertise. Integrating biodigesters into Oman's renewable energy grid will further enhance their utility by converting biogas into electricity and other forms of energy.

A centralized digital platform for monitoring feedstock availability, system performance, and energy output will enhance transparency and operational efficiency. Training programs and capacity-building initiatives for local communities and technicians will support the long-term sustainability of these systems. By leveraging its unique climatic conditions and waste generation characteristics, Oman has the opportunity to become a regional leader in waste-to-energy solutions, contributing to its Vision 2040 goals of sustainability and energy diversification.

10. ACKNOWLEDGMENTS

The authors thank Sohar University, Oman, for its support and valuable feedback in refining this research.

11. DATA AVAILABILITY STATEMENT

The data supporting the findings of this study are presented within the article. Additional data related to the experimental and simulation analyses may be made available by the corresponding author upon reasonable request.

12. REFERENCES

Ahmad, M. and Wu, Y., 2022. Household-based factors affecting uptake of biogas plants in Bangladesh: Implications for sustainable development. *Renewable Energy*, 194, pp.858–867. [DOI]

Amin, F.R., Khalid, H., Zhang, H., Rahman, S.u., Zhang, R., Liu, G. and Chen, C., 2017. Pretreatment methods of lignocellulosic biomass for anaerobic digestion. *AMB Express*, 7(1), p.72. [DOI]

Akhiar, A., Ahmad Zamri, M.F.M., Torrijos, M., Shamsuddin, A.H., Battimelli, A., Roslan, E., Mohd Marzuki, M.H. and Carrere, H., 2020. Anaerobic digestion industries progress throughout the world. *IOP Conference Series: Earth and Environmental Science*, 476(1), p.012074. [DOI]

AL-Huqail, A.A., Kumar, V., Kumar, R., Eid, E.M., Taher, M.A., Adelodun, B., Abou Fayssal, S., Mioč, B., Držaić, V., Goala, M., Kumar, P. and Širić, I., 2022. Sustainable valorization of four types of fruit peel waste for biogas recovery and use of digestate for radish (*Raphanus sativus* L. cv. Pusa Himani) cultivation. *Sustainability*, 14(16). [DOI]

AlQattan, N., Acheampong, M., Jaward, F.M., Ertem, F.C., Vijayakumar, N. and Bello, T., 2018. Reviewing the potential of Waste-to-Energy

(WTE) technologies for Sustainable Development Goal (SDG) numbers seven and eleven. *Renewable Energy Focus*, 27, pp.97–110. [DOI]

Amoo, A., Madu, I., Haruna, A., Adeleye, A. and Sabo, A., 2023. Review on the pretreatment advancements of biogas production barriers. *UMYU Journal of Microbiology Research (UJMR)*, 8, pp.6–30. [DOI]

Ampese, L.C., Sganzerla, W.G., Di Domenico Ziero, H., Mudhoo, A., Martins, G. and Forster-Carneiro, T., 2022. Research progress, trends, and updates on anaerobic digestion technology: A bibliometric analysis. *Journal of Cleaner Production*, 331, p.130004. [DOI]

Amuzu-Sefordzi, B., Martinus, K., Tschakert, P. and Wills, R., 2018. Disruptive innovations and decentralized renewable energy systems in Africa: A socio-technical review. *Energy Research & Social Science*, 46, pp.140–154. [DOI]

Aridi, R. and Yehya, A., 2024. Anaerobic biodigesters heating sources: Analysis and recommendations. *Renewable and Sustainable Energy Reviews*, 202, p.114700. [DOI]

Ayodele, T.R., Ogunjuyigbe, A.S.O. and Alao, M.A., 2017. Life cycle assessment of waste-to-energy (WtE) technologies for electricity generation using municipal solid waste in Nigeria. *Applied Energy*, 201, pp.200–218. [DOI]

Ayodele, T.R., Ogunjuyigbe, A.S.O. and Alao, M.A., 2018. Economic and environmental assessment of electricity generation using biogas from organic fraction of municipal solid waste for the city of Ibadan, Nigeria. *Journal of Cleaner Production*, 203, pp.718–735. [DOI]

Barbera, E., Bertucco, A., Nigam, K.D.P. and Kumar, S., 2022. Techno-economic analysis of a micro-scale biogas plant integrated with microalgae cultivation for the treatment of organic municipal waste. *Chemical Engineering Journal*, 450, p.138323. [DOI]

Bywater, A., Heaven, S., Zhang, Y. and Banks, C.J., 2022. Potential for biomethanisation of CO_2 from anaerobic digestion of organic wastes in the United Kingdom. *Processes*, 10(6), p.21. [DOI]

Carrere, H., Antonopoulou, G., Affes, R., Passos, F., Battimelli, A., Lyberatos, G. and Ferrer, I., 2016. Review of feedstock pretreatment strategies for improved anaerobic digestion: From lab-scale research to full-scale application. *Bioresource Technology*, 199, pp.386–397. [DOI]

Čater, M., Zorec, M. and Marinšek Logar, R., 2014. Methods for improving anaerobic lignocellulosic substrates degradation for enhanced biogas production. *Springer Science Reviews*, 2(1), pp.51–61. [DOI]

Chen, L., Fang, W., Liang, J., Nabi, M., Cai, Y., Wang, Q., Zhang, P. and Zhang, G., 2023. Biochar application in anaerobic digestion: Performances, mechanisms, environmental assessment and circular economy. *Resources, Conservation and Recycling*, 188, p.106720. [DOI]

Chiu, S.L.H. and Lo, I.M.C., 2016. Reviewing the anaerobic digestion and co-digestion process of food waste from the perspectives of biogas production performance and environmental impacts. *Environmental Science and Pollution Research*, 23(24), pp.24435–24450. [DOI]

Cichoń, M., 2020. Reporting statistical methods and outcome of statistical analyses in research articles. *Pharmacological Reports*, 72(3), pp.481–485. [DOI]

de Jesus, M.A.S., Aguiar Dutra, A.R. de, Cirani, C.B.S., Jesus, K.R.E., Neto, R.C.S. and Guerra, J.B.A., 2022. Eco-innovation assessment of biodigesters technology: An application in cassava processing industries in the south of Brazil, Parana state. *Clean Technologies and Environmental Policy*, 24(3), pp.931–948. [DOI]

de Souza Guimarães, C. and da Silva Maia, D.R., 2023. Development of anaerobic biodigester for the production of biogas used in semi-continuous system bioprocesses: An efficient alternative for co-digestion of low biodegradability biomass. *Biomass*, 3(1), pp.18–30. [DOI]

Di Mario, J., Montegiove, N., Gambelli, A.M., Brienza, M., Zadra, C. and Gigliotti, G., 2024. Waste biomass pretreatments for biogas yield optimization and for the extraction of valuable high-added-value products: Possible combinations of the two processes toward a biorefinery purpose. *Biomass*, 4(3), pp.865–885. [DOI]

Drăgan, C.O., Mihai, L.S., Popescu, A.-M.C., Buligiu, I., Mirescu, L. and Militaru, D., 2025. Statistical analysis and forecasts of performance indicators in the Romanian healthcare system. *Healthcare*, 13(2). [DOI]

Dubois, O., Pirelli, T. and Peressotti, A., 2019. 13 - Biomass anaerobic digestion and gasification in non-OECD countries, an overview. In: M. Materazzi and P.U. Foscolo (eds.) *Sustainable Natural Gas from Waste*. Academic Press, pp.343–387. [DOI]

Einarsson, R. and Persson, U.M., 2017. Analyzing key constraints to biogas production from crop residues and manure in the EU, A spatially explicit model. *PLOS ONE*, 12(1), p.e0171001. [DOI]

Elliot, M., 2005. Statistical disclosure control. In: K.B. Kempf-Leonard (ed.) *Encyclopedia of Social Measurement*. Elsevier, pp.663–670. [DOI]

Falahi, M. and Avami, A., 2020. Optimization of the municipal solid waste management system using a hybrid life cycle assessment–emergy approach in Tehran. *Journal of Material Cycles and Waste Management*, 22(1), pp.133–149. [DOI]

Fang, S., Ping, L., Yang, Z. and Mao, J., 2011. A review of different pretreatment techniques for enhancing biogas production. In: *Proceedings of the 2011 International Conference on Materials for Renewable Energy & Environment*, 1, pp.263–266. [DOI]

Francini, G., Lombardi, L., Freire, F., Pecorini, I. and Marques, P., 2019. Environmental and cost life cycle analysis of different recovery processes of organic fraction of municipal solid waste and sewage sludge. *Waste and Biomass Valorization*, 10(12), pp.3613–3634. [DOI]

Fu, W.J., Stromberg, A.J., Viele, K., Carroll, R.J. and Wu, G., 2010. Statistics and bioinformatics in nutritional sciences: Analysis of complex data in the era of systems biology. *The Journal of Nutritional Biochemistry*, 21(7), pp.561–572. [DOI]

Gao, M., Li, S., Zou, H., Wen, F., Cai, A., Zhu, R., Tian, W., Shi, D., Chai, H. and Gu, L., 2021. Aged landfill leachate enhances anaerobic digestion of waste activated sludge. *Journal of Environmental Management*, 293, p.112853. [DOI]

García Álvaro, A., Ruiz Palomar, C., Díaz Villalobos, I., Hermosilla, D., Muñoz, R. and de Godos, I., 2024. Energy integration of thermal pretreatment in anaerobic digestion of wheat straw. *Energies*, 17(9), p.63. [DOI]

George, J., Arun, P. and Muraleedharan, C., 2021. Region-specific biomass feedstock selection for gasification using multi-attribute decision-making techniques. *International Journal of Sustainable Engineering*, 14(5), pp.1101–1109. [DOI]

Gitinavard, H., Shirazi, M.A. and Fazel Zarandi, M.H., 2020. Sustainable feedstocks selection and renewable products allocation: A new hybrid adaptive utility-based consensus model. *Journal of Environmental Management*, 264, p.110428. [DOI]

Göktaş, A. and Akkuş, Ö., 2021. Editorial to the special issue: Recent statistical methods for data analysis, applied economics, business & finance. *Journal of Applied Statistics*, 48(13–15), pp.2231–2238. [DOI]

Goldin, J., Zhu, W. and Sayre, J.W., 1996. A review of the statistical analysis used in papers published in *Clinical Radiology* and *British Journal of Radiology*. Clinical Radiology, 51(1), pp.47–50. [DOI]

Gopal, L.C., Govindarajan, M., Kavipriya, M.R., Mahboob, S., Al-Ghanim, K.A., Virik, P., Ahmed, Z., Al-Mulhm, N., Senthilkumaran, V. and Shankar, V., 2021. Optimization strategies for improved biogas production by recycling of waste through response surface methodology and artificial neural network: Sustainable energy perspective research. *Journal of King Saud University - Science*, 33(1), p.101241. [DOI]

Guimarães, C.D., Maia, D.R. and Serra, E.G., 2018. Construction of biodigesters to optimize the production of biogas from anaerobic co-digestion of food waste and sewage. *Energies*, 11(4), pp.121–139. [DOI]

Hubenov, V., Carcioch, R.A., Ivanova, J., Vasileva, I., Dimitrov, K., Simeonov, I. and Kabaivanova, L., 2020. Biomethane production using ultrasound pre-treated maize stalks with subsequent microalgae cultivation. *Biotechnology & Biotechnological Equipment*, 34(1), pp.800–809. [DOI]

Ippolito, J.A., Cui, L., Kammann, C., Wrage-Mönnig, N., Estavillo, J.M., Fuertes-Mendizabal, T., Cayuela, M.L., Sigua, G., Novak, J., Spokas, K. and Borchard, N., 2020. Feedstock choice, pyrolysis temperature and type influence biochar characteristics: A comprehensive meta-data analysis review. *Biochar*, 2(4), pp.421–438. [DOI]

Issahaku, M., Derkyi, N.S.A. and Kemausuor, F., 2024. A systematic review of the design considerations for the operation and maintenance of small-scale biogas digesters. *Heliyon*, 10(1), p.e24019. [DOI]

Jameel, M.K., Mustafa, M.A., Ahmed, H.S., Mohammed, A. jassim, Ghazy, H., Shakir, M.N., Lawas, A.M., Mohammed, S. khudhur, Idan, A.H., Mahmoud, Z.H., Sayadi, H. and Kianfar, E., 2024. Biogas: Production, properties, applications, economic and challenges: A review. *Results in Chemistry*, 7, p.101549. [DOI]

Josimović, L., Prvulović, S., Djordjević, L., Bicok, I., Bakator, M., Premčevski, V., Šarenac, U. and Šeljmeši, D., 2024. Enhancing biogas plant efficiency for the production of electrical and thermal energy. *Applied Sciences*, 14(13), p.46. [DOI]

Kabeyi, M.J.B. and Olanrewaju, O.A., 2022. Biogas production and applications in the sustainable energy transition. *Journal of Energy*, 2022, p.8750221. [DOI]

Kainthola, J., Shariq, M., Kalamdhad, A.S. and Goud, V.V., 2021. Comparative study of different thermal pretreatment techniques for accelerated methane production from rice straw. *Biomass Conversion and Biorefinery*, 11(4), pp.1145–1154. [DOI]

Kalaiselvan, N., Glivin, G., Bakthavatsalam, A.K., Mariappan, V., Premalatha, M., Raveendran, P.S., Jayaraj, S. and Sekhar, S.J., 2022. A waste to energy technology for enrichment of biomethane generation: A review on operating parameters, types of biodigesters, solar assisted heating systems, socio economic benefits and challenges. *Chemosphere*, 293, p.133486. [DOI]

Karthikeyan, P.K., Bandulasena, H.C.H. and Radu, T., 2024. A comparative analysis of pre-treatment technologies for enhanced biogas production from anaerobic digestion of lignocellulosic waste. *Industrial Crops and Products*, 215, p.118591. [DOI]

Keerthana Devi, M., Manikandan, S., Oviyapriya, M., Selvaraj, M., Assiri, M.A., Vickram, S., Subbaiya, R., Karmegam, N., Ravindran, B., Chang, S.W. and Awasthi, M.K., 2022. Recent advances in biogas production using agro-industrial waste: A comprehensive review outlook of techno-economic analysis. *Bioresource Technology*, 363, p.127871. [DOI]

Kelif Ibro, M., Ramayya Ancha, V. and Beyene Lemma, D., 2024. Biogas production optimization in the anaerobic codigestion process: A critical review on process parameters modeling and simulation tools. *Journal of Chemistry*, 2024, p.4599371. [DOI]

Kenney, K.L., Smith, W.A., Gresham, G.L. and Westover, T.L., 2013. Understanding biomass feedstock variability. *Biofuels*, 4(1), pp.111–127. [DOI]

Khan, M.U., Usman, M., Ashraf, M.A., Dutta, N., Luo, G. and Zhang, S., 2022. A review of recent advancements in pretreatment techniques of lignocellulosic materials for biogas production: Opportunities and limitations. *Chemical Engineering Journal Advances*, 10, p.100263. [DOI]

Khune, S., Otieno, B., Kabuba, J., Ochieng, G. and Osifo, P., 2023. Pilot scale study of anaerobic treatment of food waste using ambient and solar heated digesters. *International Journal of Sustainable Energy*, 42(1), pp.1569–1582. [DOI]

Kouzi, A.I., Puranen, M. and Kontro, M.H., 2020. Evaluation of the factors limiting biogas production in full-scale processes and increasing the biogas production efficiency. *Environmental Science and Pollution Research*, 27(22), pp.28155–28168. [DOI]

Kumar, A., Guha, A. and Banerjee, S., 2024. Transforming simulated data into experimental data using deep learning for vibration-based structural health monitoring. *Machine Learning and Knowledge Extraction*, 6(1), pp.18–40. [DOI]

Li, C., Champagne, P. and Anderson, B.C., 2013. Biogas production performance of mesophilic and thermophilic anaerobic co-digestion with fat, oil, and grease in semi-continuous flow digesters: Effects of temperature, hydraulic retention time, and organic loading rate. *Environmental Technology*, 34(13–14), pp.2125–2133. [DOI]

Lindkvist, E., 2020. *System studies of biogas production: comparisons and performance*. Doctoral dissertation, Linköping University. [DOI]

Massaro, V., Digiesi, S., Mossa, G. and Ranieri, L., 2015. The sustainability of anaerobic digestion plants: A win–win strategy for public and private bodies. *Journal of Cleaner Production*, 104, pp.445–459. [DOI]

Menaka, D., Nandhakumar, S., Abishek, R., Raghavendran, M.R. and Hariharan, A.S.V., 2023. Smart optimization of biogas production for enhanced gas yield. In: *2023 International Conference on Data Science, Agents & Artificial Intelligence (ICDSAAI)*, pp.1–4. [DOI]

Mitraka, G.-C., Kontogiannopoulos, K.N., Batsioula, M., Banias, G.F., Zouboulis, A.I. and Kougias, P.G., 2022. A comprehensive review on pretreatment methods for enhanced biogas production from sewage sludge. *Energies*, 15(18), pp.313–339. [DOI]

Mohan, S., Barboza, A.B.V., Ashwini, K. and Dinesha, P., 2024. Biogas yield from co-digesting banana pseudostems with cow dung: Transitioning from mesophilic to thermophilic regimes. *Cogent Engineering*, 11(1), p.2429774. [DOI]

Montgomery, L. and Bochmann, G., 2014. *Pretreatment of feedstock for enhanced biogas production*. IEA Bioenergy Task 37, p.20.

Njuguna Matheri, A., Mbohwa, C., Ntuli, F., Belaid, M., Seodigeng, T., Catherine Ngila, J. and Kinuthia Njenga, C., 2018. Waste to energy bio-digester selection and design model for the organic fraction of municipal solid waste. *Renewable and Sustainable Energy Reviews*, 82, pp.1113–1121. [DOI]

Nkemka, V.N., Arenales-Rivera, J. and Murto, M., 2014. Two-stage dry anaerobic digestion of beach cast seaweed and its codigestion with cow manure. *Journal of Waste Management*, 2014, p.325341. [DOI]

Nyang'au, J.O., El Mahdi, J., Møller, H.B. and Sørensen, P., 2024. Unlocking higher methane yields and digestate nitrogen availability in soil through thermal treatment of feedstocks in a two-step anaerobic digestion. *Chemical and Biological Technologies in Agriculture*, 11(1), p.186. [DOI]

Obileke, K., Makaka, G., Tangwe, S. and Mukumba, P., 2024. Improvement of biogas yields in an anaerobic digestion process via optimization technique. *Environment, Development and Sustainability*. 87, p.17. [DOI]

Obileke, K., Mamphweli, S., Meyer, E.L., Makaka, G. and Nwokolo, N., 2020. Design and fabrication of a plastic biogas digester for the production of biogas from cow dung. *Journal of Engineering*, 2020, p.1848714. [DOI]

Olatunji, K.O. and Madyira, D.M., 2024. Comparative analysis of the effects of five pretreatment methods on morphological and methane yield of groundnut shells. *Waste and Biomass Valorization*, 15(1), pp.469–486. [DOI]

Olatunji, K.O., Madyira, D.M., Ahmed, N.A., Jekayinfa, S.O. and Ogunkunle, O., 2022. Modeling the effects of particle size pretreatment method on biogas yield of groundnut shells. *Waste Management & Research*, 40(8), pp.1176–1188. [DOI]

Olatunji, O.O., Adedeji, P.A., Madushele, N., Rasmeni, Z.Z. and van Rensburg, N.J., 2024. Evolutionary optimization of biogas production from food, fruit, and vegetable (FFV) waste. *Biomass Conversion and Biorefinery*, 14(11), pp.12113–12125. [DOI]

Oman Environmental Services Holding Company (be'ah). 2023. *Annual Report 2023*. Oman Environmental Services Holding Company S.A.O.C. (be'ah), Muscat, Sultanate of Oman.

Otieno, E.O., Kiplimo, R. and Mutwiwa, U., 2023. Optimization of anaerobic digestion parameters for biogas production from pineapple wastes co-digested with livestock wastes. *Heliyon*, 9(3), p.e14041. [DOI]

Park, S., Han, S.K., Song, E., Kim, H., Kim, M. and Lee, W., 2020. Effect of hydrothermal pre-treatment on physical properties and co-digestion from food waste and sewage sludge mixture. *Waste Management & Research*, 38(5), pp.546–553. [DOI]

Pham Van, D., Fujiwara, T., Hoang, M. and Pham Phu, S.T., 2020. Comparison between single and two-stage anaerobic digestion of vegetable waste: Kinetics of methanogenesis and carbon flow. *Waste and Biomass Valorization*, 11, p.34. [DOI]

Piadeh, F., Offie, I., Behzadian, K., Rizzuto, J.P., Bywater, A., Córdoba-Pachón, J.-R. and Walker, M., 2024. A critical review for the impact of anaerobic digestion on the sustainable development goals. *Journal of Environmental Management*, 349, p.119458. [DOI]

Prussi, M., Panoutsou, C. and Chiaramonti, D., 2022. Assessment of the feedstock availability for covering EU alternative fuels demand. *Applied Sciences*, 12(2), p.71. [DOI]

Ramaraj, R. and Unpaprom, Y., 2016. Effect of temperature on the performance of biogas production from duckweed. *Chemical Science*, 1, pp.58–66.

Ren, Y., Wang, C., He, Z., Qin, Y. and Li, Y.-Y., 2022. Biogas production performance and system stability monitoring in thermophilic anaerobic co-digestion of lipids and food waste. *Bioresource Technology*, 358, p.127432. [DOI]

Ruiz-Aguilar, G.M.L., Nuñez-Palenius, H.G., Lovanh, N. and Camarena-Martínez, S., 2022. Comparative study of methane production in a one-stage vs. two-stage anaerobic digestion process from raw tomato plant waste. *Energies*, 15(23), pp.412–441. [DOI]

Salam, S., Parveen, R., Azad, S.M. and Salam, M., 2020. Understanding the performance of domestic biodigesters in Bangladesh: A study from household level survey. *Business and Management Studies*, 6, p.27. [DOI]

Scherzinger, M. and Kaltschmitt, M., 2021. Thermal pre-treatment options to enhance anaerobic digestibility – A review. *Renewable and Sustainable Energy Reviews*, 137, p.110627. [DOI]

Shaibur, M.R., Husain, H. and Arpon, S.H., 2021. Utilization of cow dung residues of biogas plant for sustainable development of a rural community. *Current Research in Environmental Sustainability*, 3, p.100026. [DOI]

Sidi Habib, S., Torii, S., S., K.M. and Charivuparampil Achuthan Nair, A., 2024. Optimization of the factors affecting biogas production using the Taguchi design of experiment method. *Biomass*, 4(3), pp.687–703. [DOI]

Tharmarajah, N., Shahbaz, K. and Baroutian, S., 2024. Textile waste pretreatment for anaerobic digestion: A review and technology feasibility study. *Journal of Chemical Technology & Biotechnology*, 99(11), pp.2213–2227. [DOI]

Vaneeckhaute, C., Styles, D., Prade, T., Adams, P., Thelin, G., Rodhe, L., Gunnarsson, I. and D'Hertefeldt, T., 2018. Closing nutrient loops through decentralized anaerobic digestion of organic residues in agricultural regions: A multi-dimensional sustainability assessment. *Resources, Conservation and Recycling*, 136, pp.110–117. [DOI]

Walker, M., Theaker, H., Yaman, R., Poggio, D., Nimmo, W., Bywater, A., Blanch, G. and Pourkashanian, M., 2017. Assessment of micro-scale anaerobic digestion for management of urban organic waste: A case study in London, UK. *Waste Management*, 61, pp.258–268. [DOI]

Wang, M., Wang, J., Li, Y., Li, Q., Li, P., Luo, L., Zhen, F., Zheng, G. and Sun, Y., 2022. Low-temperature pretreatment of biomass for enhancing biogas production: A review. *Fermentation*, 8(10), p.891. [DOI]

Wang, S., Ma, F., Ma, W., Wang, P., Zhao, G. and Lu, X., 2019. Influence of temperature on biogas production efficiency and microbial community in a two-phase anaerobic digestion system. *Water*, 11(1), pp.26–41. [DOI]

Welfle, A. and Röder, M., 2022. Mapping the sustainability of bioenergy to maximise benefits, mitigate risks and drive progress toward the Sustainable Development Goals. *Renewable Energy*, 191, pp.493–509. [DOI]

Yadav, P., Yadav, S., Singh, D., Shekher Giri, B. and Mishra, P.K., 2022. Barriers in biogas production from the organic fraction of municipal solid waste: A circular bioeconomy perspective. *Bioresource Technology*, 362, p.127671. [DOI]

Yalcinkaya, S., 2020. A spatial modeling approach for siting, sizing and economic assessment of centralized biogas plants in organic waste management. *Journal of Cleaner Production*, 255, p.120040. [DOI]

Yang, S., Hou, Q., Zhu, M., Liu, Y. and Li, S., 2024. Innovative biogas energy system: Enhancing efficiency and sustainability through multigeneration integration. *Journal of Environmental Management*, 371, p.123118. [DOI]

Yong, Z.J., Bashir, M.J.K. and Hassan, M.S., 2021. Biogas and biofertilizer production from organic fraction municipal solid waste for sustainable circular economy and environmental protection in Malaysia. *Science of The Total Environment*, 776, p.145961. [DOI]

Yousefi-Nasab, S., Safdari, J. and Karimi-Sabet, J., 2024. A review of experimental and simulation methods for determining accommodation coefficients, particularly TMAC, at fluid-surface interfaces. *Microfluidics and Nanofluidics*, 28(8), p.54. [DOI]

Zheng, X. and Li, R., 2024. Critical review on two-stage anaerobic digestion with H_2 and CH_4 production from various wastes. *Water*, 16(11), p.91. [DOI]

Zhou, Y., Hu, Y., Chen, A.J.Y., Cheng, Z., Bi, Z., Zhang, R. and Lou, Z., 2022. Environmental impacts and nutrient distribution routes for food waste separated disposal on large-scale anaerobic digestion/composting plants. *Journal of Environmental Management*, 318, p.115624. [DOI]

Nature Environment and Pollution Technology
An International Quarterly Peer-Reviewed Open Access Journal

p-ISSN: 0972-6268 | e-ISSN: 2395-3454 Vol. 25 | No. 4 | Article ID B4422 | 2026

RESEARCH ARTICLE https://doi.org/10.46488/NEPT.2026.v25i04.B4422 OPEN ACCESS

Eco-Friendly Degradation of Textile Azo Dye Reactive Orange ME2RL Using *Pseudomonas stutzeri*-Mediated Iron Oxide Nanoparticles

P. Zambare[1,2,4], S. Kanase[1,2,4] and A. Raut[3,4]†
[1]Rayat Institute of Research and Development, Satara, 415001, Maharashtra, India
[2]Department of Microbiology, Yashavantrao Chavan Institute of Science, Satara, 415001, Maharashtra, India
[3]Department of Microbiology, Yashwantrao Chavan College of Science, Karad, 415110, Maharashtra, India
[4]Department of Microbiology, Shivaji University, Kolhapur, 416004, Maharashtra, India
†Corresponding author: A. Raut; rautavinash@gmail.com

ARTICLE HISTORY

Received: 18-12-2025
Revised: 15-03-2026
Accepted: 18-03-2026

KEYWORDS

Pseudomonas stutzeri
Reactive orange ME2RL
Iron oxide
Nanoparticles
Biophysical analysis

CITE THIS ARTICLE

Zambare, P., Kanase, S., and Raut, A., 2026. Eco-friendly degradation of textile azo dye reactive orange ME2RL using *Pseudomonas stutzeri*-mediated iron oxide nanoparticles. *Nature Environment and Pollution Technology*, 25(4), B4422. https://doi.org/10.46488/NEPT.2026.v25i04.B4422

COPYRIGHT & LICENCE

© 2026 The Authors
Open Access under CC BY 4.0.

PUBLISHED BY

TECHNOSCIENCE PUBLICATIONS

ABSTRACT

The discharge of synthetic azo dyes from textile industries poses serious environmental and health risks because of their genotoxic, mutagenic, and carcinogenic nature. In the present study, eco-friendly iron oxide (Fe_2O_3) nanoparticles were biosynthesized using *Pseudomonas stutzeri* and ferric chloride as a precursor under ambient conditions and were applied for the degradation of the textile dye Reactive Orange ME2RL. The synthesized nanoparticles were characterized using UV–Visible spectroscopy, FTIR, SEM, HRTEM, and DLS, confirming the formation of stable nanoscale Fe_2O_3 particles. The nanoparticles exhibited efficient catalytic activity, achieving nearly 80% degradation of Reactive Orange ME2RL within 45 min. The degradation pathway and the formation of intermediate metabolites were confirmed using UV–Visible spectroscopy, FTIR, HPLC, and GC–MS analyses. Furthermore, phytotoxicity and fish toxicity assays indicated reduced toxicity of the degradation products. These results demonstrate that biosynthesized Fe_2O_3 nanoparticles offer a rapid, efficient, and environmentally sustainable approach for the remediation of azo dye-contaminated textile wastewater.

1. INTRODUCTION

Textile sectors occupy a significant position in the Indian economy by contributing to industrial production, exports, and employment (Chavan 2001). However, the use of synthetic dyes has made textile effluents a persistent source of environmental pollution because of their adverse effects on the environment and living organisms (Banat et al. 1997). Textile wastewater is typically characterized by intense color, high chemical oxygen demand (COD), high total dissolved solids (TDS), and the presence of recalcitrant aromatic compounds, making conventional treatment highly challenging. The persistence of these dyes in aquatic ecosystems reduces light penetration, inhibits photosynthesis, and contributes to long-term ecological imbalance (Patel & Bhatt 2022, Haroon et al. 2023).

Scientists are increasingly interested in metal nanoparticles because of their remarkable chemical, electrical, and optical properties. The green synthesis of such nanoparticles is simple, environmentally friendly, and provides a rapid approach to meeting the growing global demand for safe, non-toxic, and biocompatible nanoparticles (Khan et al. 2019). Researchers have shown particular interest in the green synthesis of nanoparticles using microbes because of their ease of handling,

environmentally safe disposal, and relatively simple downstream processing (Annamalai et al. 2021). Among microorganisms, bacteria possess the innate ability to reduce metal ions and synthesize metal nanoparticles (Srivastava & Constanti 2012). Microbial synthesis not only avoids the use of toxic reducing agents employed in conventional chemical methods but also enables precise control over nanoparticle morphology through enzymatic and metabolic pathways. Consequently, microbial nanotechnology has emerged as a promising tool for sustainable environmental remediation (Annamalai et al. 2021).

Because of their genetic diversity and adaptable metabolic systems, microorganisms are considered a preferred choice for the biological remediation of dye pollution (Banat et al. 1997, Shakoor et al. 2025). In addition, biological treatment requires fewer reagents and produces less sludge than many physicochemical methods, making it a more economical and environmentally friendly alternative. It can also result in the complete mineralization of dyes and is considered a cost-effective treatment strategy (Pandey et al. 2007). Iron nanoparticles (FeNPs) have shown considerable potential for reducing environmental pollution.

The phylum Proteobacteria includes *Pseudomonas stutzeri*, which is classified under group I of Palleroni's DNA–rRNA homology groups (Palleroni et al. 1973, Palleroni 1984). It is currently recognized as a member of the class Gammaproteobacteria. *P. stutzeri* is a widely distributed, non-fluorescent denitrifying bacterium that has also been identified as an opportunistic human pathogen (Rossello et al. 1991). Over the past few decades, the taxonomy of this diverse species has been clarified, and its unique metabolic properties have attracted considerable attention. Some strains are capable of fixing dinitrogen and have served as model organisms for studies on denitrification. Other strains degrade environmental contaminants or interact with toxic metals, while several exhibit natural transformation capabilities, making them valuable for studies of environmental gene transfer (Palleroni et al. 1970). Importantly, *P. stutzeri* has been reported to tolerate and transform a wide range of xenobiotics, making it a promising candidate for bio-nanotechnological applications, including microbial nanoparticle synthesis and dye biodegradation (Shahriarinour et al. 2021).

The textile, food, leather, cosmetic, plastic, and paper industries use a wide variety of organic dyes for aesthetic purposes, many of which are hazardous and pose serious environmental threats (Forgacs et al. 2004). The treatment and removal of organic dyes from textile effluents remain major challenges for both industry and environmental scientists. Although several physicochemical techniques are available, they are often inefficient and may generate secondary pollutants that require additional treatment. Techniques such as ozonation, coagulation-flocculation, adsorption, and membrane filtration may achieve partial color removal but frequently fail to completely degrade dye molecules, resulting in secondary pollution and high operational costs (Periyasamy 2024).

In recent years, interest in advanced nanocatalyst-based technologies for the removal of dyes and other organic pollutants has increased significantly (Naz et al. 2021). A simple and sustainable approach involves treating dyes in the presence of biocompatible and environmentally safe catalysts without the use of organic solvents. Reactive Orange ME2RL is a diazo dye widely used in the textile industry for coloring wool, silk, leather, paper, and polyamide fibers. Considerable attention has been directed towards the degradation of this dye because its complex aromatic backbone and multiple azo linkages make it resistant to conventional biological degradation, highlighting the need for integrated nano-biotechnological approaches for efficient treatment (Joshi et al. 2015).

In this study, *Pseudomonas stutzeri*, a bacterium known for degrading diazo dyes containing two –N=N– azo bonds (Joshi et al. 2020), was evaluated for its bioremediation potential. The biodegradation of the common textile diazo dye Reactive Orange ME2RL was investigated using iron nanoparticles synthesized by an isolated strain of *Pseudomonas stutzeri*. The combined application of microbially synthesized FeNPs and dye-degrading bacteria provides a synergistic strategy that enhances both catalytic activity and biodegradation efficiency, thereby offering a sustainable, cost-effective, and environmentally friendly approach for treating textile effluents.

In the present study, we focused on the degradation of the textile dye Reactive Orange ME2RL using Fe□O□ nanoparticles synthesized by *Pseudomonas stutzeri*. Reactive Orange ME2RL is known to damage the eyes, mucous membranes, and upper respiratory tract and has also been reported to be carcinogenic (Gupta et al. 2006). In addition, it increases biological oxygen demand by reducing light penetration and oxygen availability in aquatic ecosystems, thereby adversely affecting aquatic life. Therefore, this dye should be removed from wastewater before its discharge into natural water bodies because of its harmful effects on human health and its long-term environmental impacts (Ali 2010).

2. MATERIALS AND METHODS

2.1. Materials

The nutrient agar, 99% pure $FeCl_3$, and nutrient broth used

in this study were all sourced from Himedia Laboratories Pvt. Ltd., an Indian company. Materials such as Reactive Orange ME2RL, ethyl acetate, $FeCl_3$, and methanol were obtained from Sigma-Aldrich in India. All ingredients were of analytical reagent grade.

2.2. Methods

2.2.1. Iron Nanoparticle Biosynthesis

The bacterial strain *Pseudomonas stutzeri* was isolated from a soil sample collected at Kaas Pathar in Satara, Maharashtra, India. Its molecular identification was conducted via 16S rRNA sequencing at NCMR, Pune (Mukherjee & Dutta 2019). The pure culture was inoculated into sterile nutrient broth and incubated at 28°C for 24 h with shaking at 120 rpm. After harvesting and washing the bacterial biomass, it was suspended in sterile distilled water and agitated at 120 rpm for 24 h at 28°C. The cell-free extract (CFE), obtained after centrifugation, was used for nanoparticle synthesis. To initiate nanoparticle formation, 1 mM $FeCl_3$ was added to the CFE in an equal volume, and the mixture was stirred at 120 rpm at 28°C. A control sample consisted of 1 mM $FeCl_3$ solution without CFE. The formation of iron nanoparticles was monitored visually and by UV–visible spectroscopy at regular intervals. The capacity of *P. stutzeri* to synthesize iron nanoparticles aligns with previous reports of microbial nanoparticle production by Pseudomonas spp. (Vasantharaj et al. 2019).

2.2.2. Characterization of Iron Nanoparticles

The excitation spectra of biosynthesized iron nanoparticles were recorded using a UV–Visible spectrophotometer (Systronics AU-270I) (Velusamy et al. 2016). Crystallinity was analyzed by X-ray diffraction (XRD, Bruker D8 Advance) within a 2θ range of 20°–80°, operating at 40 kV and 40 mA (Giuli et al. 2015). XRD is a common technique to determine the crystal structure and phase composition of nanoparticles (Holzwarth & Gibson 2011). Scanning electron microscopy (SEM) was employed to observe the morphology of the iron nanoparticles. High-resolution transmission electron microscopy (HRTEM) using an FEI Tecnai G2 U-Twin provided data on particle size and shape. Dynamic light scattering (DLS) analysis with a Nicomp 388 ZLS system assessed the hydrodynamic size distribution (Chicea et al. 2012). Fourier transform infrared (FTIR) spectroscopy (Shimadzu FTIR-8400), covering 400–4000 cm^{-1}, was conducted to identify biomolecules involved in nanoparticle reduction and stabilization (Zhao et al. 2016).

2.2.3. Degradation of Reactive Orange ME2RL Using Iron Nanoparticles

The catalytic degradation capacity of biosynthesized iron nanoparticles was assessed using Reactive Orange ME2RL dye. A 1 mM concentration of FeNPs was added to 100 mL of dye solution (10 mg L^{-1}), and the mixture was stirred at 120 rpm for 30 min (Al-Musawi et al. 2022). At regular intervals, 2 mL samples were taken, and their absorbance at 494 nm was measured to determine the degradation percentage using Equation 1.

$$\text{Degradation (\%)} = \frac{D_0 - D_1}{D_0} \times 100 \quad \ldots(1)$$

Where,

D_0 = initial absorbance

D_1 = final absorbance

2.3. Study of Metabolites of the Degraded Dye

2.3.1. UV–Visible Spectroscopy

The spectral changes of control and treated dye samples (400–800 nm) were analyzed to confirm biodegradation rather than superficial decolorization (Wu et al. 2022).

2.3.2. Fourier Transform Infrared Spectroscopy (FTIR)

FTIR analysis was performed to understand functional group alterations during degradation and nanoparticle interaction (Katata-Seru et al. 2018).

2.3.3. High-Performance Liquid Chromatography (HPLC)

HPLC analysis was conducted using a C18 column (4.6 × 250 mm) with methanol as the mobile phase at a flow rate of 1 mL min^{-1}. A UV detector monitored dye metabolites at their maximum absorption wavelengths (Ferreira et al. 2020). Supernatants from degradation experiments (0–45 min) were analyzed, with metabolites extracted using ethyl acetate, dried over anhydrous Na_2SO_4, evaporated, and reconstituted in HPLC-grade methanol (Apine et al. 2023).

2.3.4. Gas Chromatography–Mass Spectrometry (GC–MS)

Extracted metabolites were subjected to GC–MS analysis after solvent evaporation and reconstitution. This process followed standard extraction protocols for dye degradation metabolites (Castro et al. 2020).

2.3.5. Antibacterial Activity of Iron Nanoparticles

The antibacterial properties of FeNPs were evaluated using the agar well diffusion method. Test organisms included *Proteus vulgaris* (NCIM-2813), *Salmonella typhi* (NCIM-2501), *Staphylococcus aureus* (NCIM-2654), and *Pseudomonas aeruginosa* (NCIM-5032). Solutions of antibiotics, FeNPs, and their combinations were placed into agar wells and incubated at 37°C for 24 h. The zones of inhibition were measured in millimeters, and the percentage increase in antibacterial activity was calculated using Equation 2 (Mane et al. 2008).

$$\text{Percent Fold Increase} = \frac{B-A}{A} \quad \ldots(2)$$

Where

A = inhibition zone of antibiotic

B = inhibition zone of antibiotic + FeNPs

2.4. Phytotoxicity Studies

The phytotoxic effects of the parent dye and its degradation metabolites were evaluated on four types of agricultural seeds: *Vigna radiata* (green gram), *Triticum aestivum* (wheat), *Vigna unguiculata* (cowpea), and *Pisum sativum* (pea). Seeds were exposed to dye and metabolite solutions at concentrations up to 400 ppm, following published protocols (Aly et al. 2025). Distilled water was used as a control. After seven days, parameters such as germination rate and plumule and radicle lengths were measured as described previously (Ameur et al. 2012).

2.5. Fish Toxicity Studies

Glass aquaria were sterilized with 0.1% potassium permanganate to prevent fungal contamination (Hanafi & Sapawe 2020). Fish were acclimated before being exposed to different concentrations of Reactive Orange ME2RL dye. The LC_{50} values were calculated after 96 h of exposure. Histological examinations were performed on the treated fish to evaluate tissue alterations (Islam et al. 2021).

2.6. Determination of LC_{50} and Percent Mortality

A straightforward method for assessing a substance's toxicity is through LC_{50} determination. Well-acclimated fish from the stock were divided into seven groups, each consisting of ten healthy individuals representing different dye treatments. These groups were then transferred to glass aquariums containing varying dye concentrations (1.25, 2.5, 3.75, 5.00, 6.25, 7.5, and 8.75 ppm). The fish were exposed to their respective concentrations for a specified duration, and mortality was recorded over 96 h. Dead fish were counted at 24, 48, 72, and 96 h for each concentration. To ensure accuracy, the experiments were repeated three times to confirm the mortality rates and determine the LC_{50} value (Islam et al. 2021). Mortality percentages were calculated using the following formula:

$$\%\ \text{Mortality} = \frac{\text{Number of dead fish}}{\text{Initial number of stocked fish}} \times 100 \quad \ldots(3)$$

3. RESULTS AND DISCUSSION

3.1. Overview

In the present study, the bacterial strain *Pseudomonas stutzeri* was employed for the biosynthesis of iron nanoparticles. These biosynthesized nanoparticles exhibited remarkable catalytic efficiency in degrading Reactive Orange ME2RL. The rapid degradation underscored the enhanced reactivity and surface properties conferred by the green synthesis approach. Instrumental analysis confirmed the conversion of the parent azo dye into less complex, non-toxic metabolites, demonstrating complete breakdown of chromophoric groups. Beyond dye degradation, the nanoparticles also demonstrated excellent antibacterial activity against pathogenic bacterial strains, with an additive effect observed when combined with conventional antibiotics. Toxicity assays on phytotoxicity and fish toxicity confirmed that the degradation products were non-toxic, supporting the environmental safety of the process. Overall, the combined characterization, catalytic performance, and toxicity assessments highlight the potential of *Pseudomonas stutzeri*-derived iron nanoparticles as an efficient, eco-friendly solution for textile dye bioremediation.

3.1.1. Biosynthesis of Iron Nanoparticles

The biosynthesis of iron nanoparticles (Fe NPs) using isolated *Pseudomonas stutzeri* was confirmed by visual changes that occurred during the bioreduction of ferric ions.

Upon adding $FeCl_3$ solution to CFE, the reaction mixture gradually changed color from pale yellow to a distinct reddish-brown within 24 h, further intensifying over the next 48 h (Fig. 1). This color transition was caused by NADH-dependent reductases that drove the redox process, while proteins and polysaccharides acted as capping agents by binding to nanoparticle surfaces through functional groups such as amide, hydroxyl, and carboxyl (Acharya et al. 2025). This chromatic shift is a recognized marker of nanoparticle formation and is attributed to surface plasmon resonance (SPR) excitation, which occurs when iron nuclei nucleate and cluster at the nanoscale (Jana et al. 2016).

3.2. Characterization of Nanoparticles

3.2.1. UV-Visible Spectroscopy



Fig. 1: (a) Cell-free extract; (b) color change after addition of precursor ($FeCl_3$) solution.

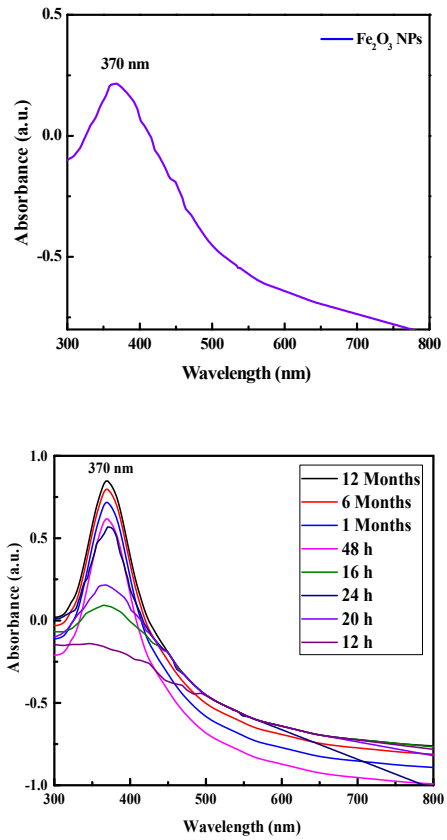


Fig. 2: UV spectrum of iron nanoparticles synthesized by Pseudomonas stutzeri.

Apart from visual confirmation, UV spectroscopy further validated the biosynthesis of the nanoparticles by sensitively monitoring nucleation and growth processes in metal nanostructures. The initial CFE showed no significant absorbance in the visible spectrum, confirming the absence of pre-existing nanoparticles. Upon addition of $FeCl_3$, a distinct absorption band appeared at 370 nm, corresponding to the characteristic surface plasmon resonance of biogenic iron nanoparticles (Fig. 2). The presence of the 370 nm peak aligns with previous studies on microbial and plant-based iron nanoparticles, validating successful synthesis under ambient conditions (Ganachari et al. 2012, Nurbas et al. 2017). Variations in peak sharpness and intensity provide mechanistic insights: the moderate bandwidth suggests a relatively narrow size distribution, supported by TEM and DLS results. The stability of the peak without significant red-shifting implies controlled growth and effective capping by biomolecules in the CFE, which prevent particle aggregation. Overall, UV–visible analysis not only confirms nanoparticle formation but also offers insights into the kinetics and stabilization mechanisms of biogenic synthesis, demonstrating the efficiency of *P. stutzeri*-mediated Fe nanoparticle production.

The stability of the synthesized Fe_2O_3 nanoparticles was assessed by tracking their UV–visible absorption spectra over a span of 12 h to 12 months (Fig. 2). The consistent spectral profile indicates that the Fe_2O_3 nanoparticles maintain their structural and optical integrity for up to 12 months under storage conditions, demonstrating excellent colloidal stability.

3.2.2. FTIR

FTIR measurements of iron nanoparticles helped to reveal information about chemical changes in functional groups complexed in the reduction process of iron ions to iron nanoparticles (Giuli et al. 2015).

Fig. 3 displays five distinct peaks at 3344 cm^{-1}, 2925 cm^{-1}, 1631 cm^{-1}, 1022 cm^{-1}, and 538 cm^{-1}, characteristic of Fe_2O_3 NPs. These peaks correspond to the asymmetric stretching of C–H bonds, C–O stretching, and O–H stretching vibrations (alcoholic or phenolic), indicating the presence of functional groups that play a key role in stabilizing and capping the iron nanoparticles. The emergence of a new peak at 538 cm^{-1} confirms the formation of Fe–O bonds, demonstrating successful synthesis and biomolecular capping.

3.2.3. XRD

To gain a deeper understanding of the formation and crystallinity of the synthesized iron nanoparticles, XRD analysis was performed (Holzwarth & Gibson 2011). The XRD pattern, illustrated in Fig. 4, displays prominent diffraction peaks at 31.94°, 45.5°, 56.6°, 66.33°, and 75.38°, corresponding to the crystal planes 220, 400, 511, 440,

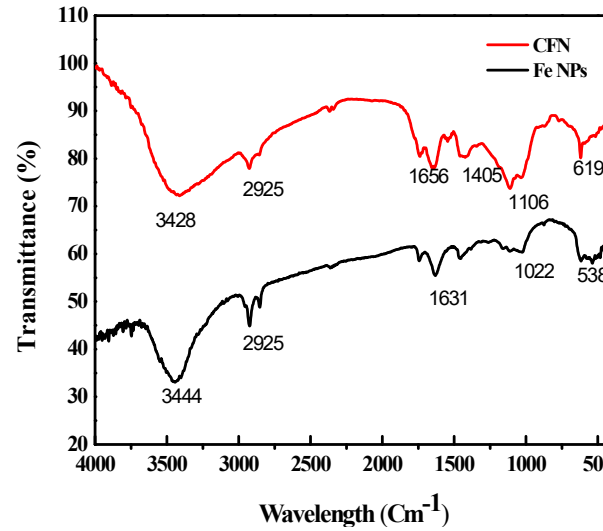


Fig. 3: FTIR of iron nanoparticles.

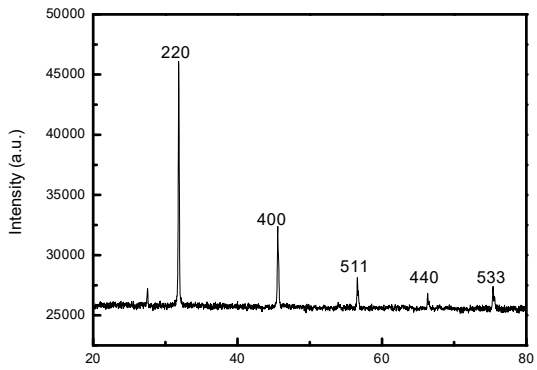


Fig. 4: XRD pattern of iron nanoparticles.

and 533, respectively. The peaks are closely aligned with γ-Fe_2O_3, consistent with JCPDS card 39-1346. The strong diffraction peaks confirm the crystalline structure and phase of the iron nanoparticles, indicating the formation of Fe_2O_3 nanoparticles. The estimated nanoparticle size, calculated using the Debye–Scherrer equation, is approximately 32 nm, suggesting a high surface area–to–volume ratio. The crystallite size was determined employing the Debye–Scherrer formula (Chicea et al. 2012).

3.2.4. DLS

DLS was used to analyze the particle size distribution of the synthesized nanoparticles (Javidparvar et al. 2016). The particle size distribution revealed the hydrodynamic size of the nanoparticles. Most particles ranged from 50 to 100 nm, with an average particle size of 50 nm (Fig. 5). The hydrodynamic size closely resembled the particle size determined by SEM analysis, although DLS often reports larger particle sizes because of agglomeration. The DLS analysis showed that the iron nanoparticles had particle sizes ranging from 50 to 100 nm. The hydrodynamic size includes both the metallic core and the coating material.

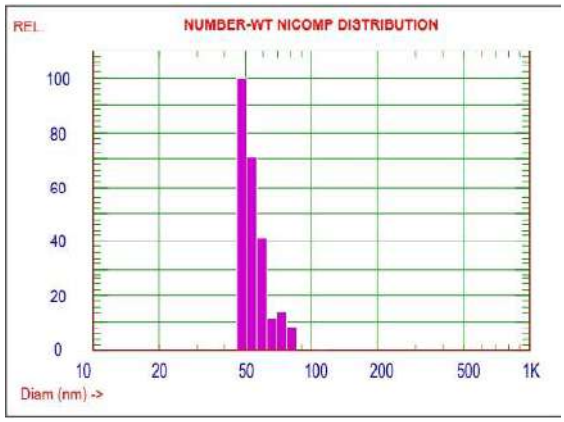


Fig. 5: Hydrodynamic particle size measurement using the DLS (volume-weighted) method.

DLS measures the hydrodynamic diameter of nanoparticles dispersed in a liquid medium, which includes not only the nanoparticle core but also the surrounding solvation layer, surface-bound biomolecules, and possible agglomeration in the suspension. Consequently, the measured particle size appears larger (Bhattacharjee 2016).

3.2.5. SEM

Surface morphology of iron nanoparticles was examined using SEM (Saha & Bhunia 2020), as illustrated in Fig. 6. The SEM images revealed monodispersed FeNPs ranging from 20 to 50 nm in size. The particles exhibited smooth surfaces and a high degree of crystallinity. The micrographs displayed well-defined borders, with an average particle size of 33 nm.

3.2.6. HRTEM

The optimized nanoparticles' size and morphology were examined using HRTEM, confirming the presence of nearly spherical iron nanoparticles (Fig. 7). Their sizes range from approximately 20 to 50 nm. Similar results have been documented in previous research (Katata-Seru et al. 2018, Sekar et al. 2012).

3.3. Catalytic Degradation of Reactive Orange ME2RL Using Biogenic Iron Nanoparticles

Upon adding iron nanoparticles (10 mg L^{-1}) to the dye solution, a gradual degradation occurred under visible light. The solution's color shifted from orange to colorless within 45 min (Fig. 8). These results align with previous reports (Joshi et al. 2015).

The characteristic absorption peak at 494 nm was used to assess the catalytic activity of iron nanoparticles. The reduction process was evidenced by a consistent decrease in the maximum absorbance (kmax) at 494 nm, with minimal shifts in λmax. The peak at 494 nm diminished over 45 min, indicating that Reactive Orange ME2RL was undergoing

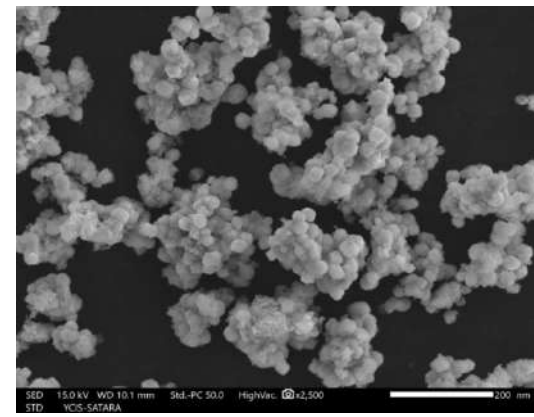


Fig. 6: SEM images of iron nanoparticles.

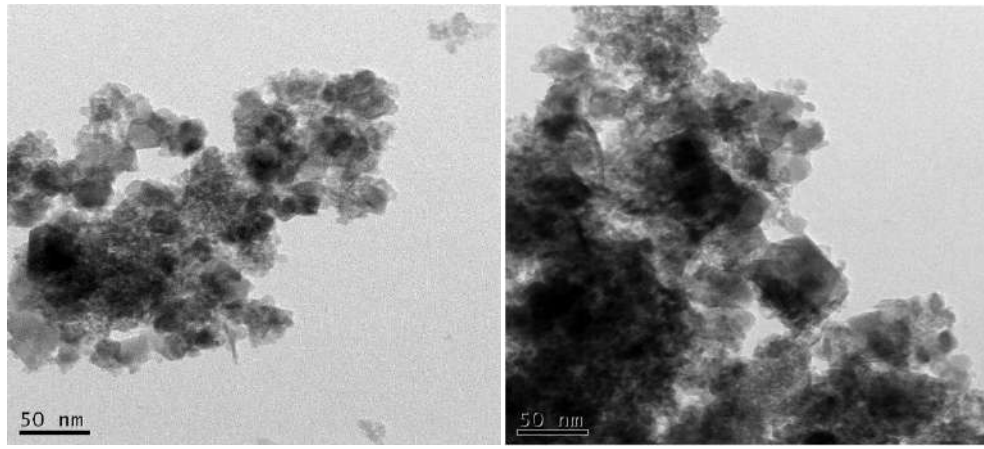


Fig. 7: HRTEM images of iron nanoparticles.



Fig. 8: Gradual color changes from orange to colorless after the addition of iron.

degradation (Fig. 9). Additionally, small peaks and a broad band between 600–750 nm suggested the formation of intermediate by-products (Forgacs et al. 2004).

The degradation experiments were conducted under ambient laboratory lighting conditions, which suggests that the observed dye removal may be partly due to the photocatalytic activity of Fe_2O_3 nanoparticles. During photodegradation, the formation of highly reactive hydroxyl radicals (•OH) is triggered by the generation of electron–hole (e^-/h^+) pairs on the surface of the photoactivated catalyst. As shown in Fig. 10, a simplified mechanism illustrates how free radicals (•OH) are formed and how they facilitate the photocatalytic breakdown of Orange ME2RL dye. When exposed to light, electrons are excited from the valence band to the conduction band, creating electron–hole pairs (Eq. (4)). The electrons in the conduction band can then migrate to the hematite surface, reducing Fe^{3+} ions (Eq. (5)), or react with hydrogen peroxide molecules to produce reactive radical species (Eq. (6)). Concurrently, the generated holes react with surface-adsorbed water (Eq. (7)) and HO^- ions (Eq. (8)). Additionally, Fe^{2+} on the surface can be oxidized back to Fe^{3+} in the presence of adsorbed H_2O_2 (Eq. (9)), which further promotes the formation of •OH radicals. These radicals are the primary oxidants responsible for degrading the dye, as supported by existing studies (Vu et al. 2019, Huang et al. 2015).

$$Fe_2O_3 + hv \rightarrow e^- + h^+ \quad ...(4)$$

$$Fe_2O_3 + e^- \rightarrow Fe^{2+} \quad ...(5)$$

$$e^- + H_2O_2 \rightarrow \bullet OH + HO^- \quad ...(6)$$

$$h^+ + H_2O \rightarrow H^+ + \bullet OH \quad ...(7)$$

$$HO^- + h^+ \rightarrow \bullet OH + H^+ \quad ...(8)$$

$$Fe^{2+} + H_2O_2 \rightarrow Fe^{3+} + \bullet OH + HO^- \quad ...(9)$$

Additionally, it is important to consider that •OH radicals can be formed by direct photolysis as follows:

$$H_2O_2 + hv \rightarrow 2\ \bullet OH \quad ...(10)$$

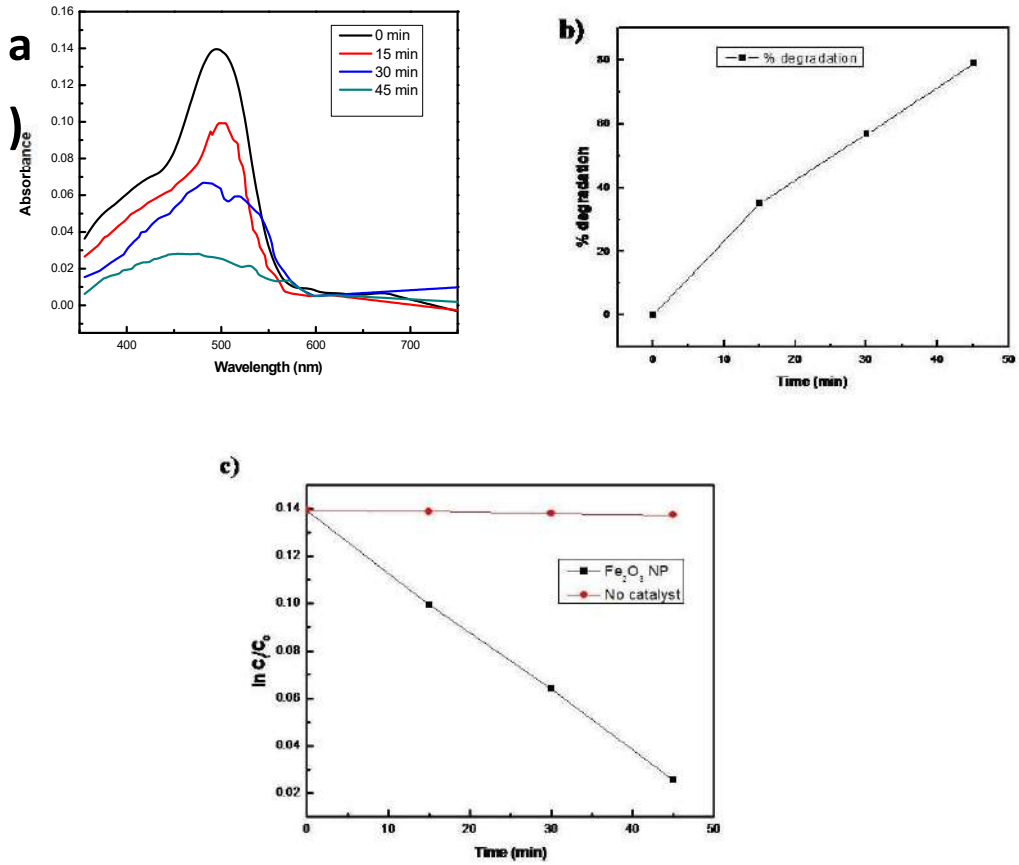


Fig. 9: (a) UV–visible absorption spectra of Orange ME2RL dye using Fe_2O_3 nanoparticles at various time intervals; (b) degradation (%) of Orange ME2RL dye with time in the presence of Fe_2O_3 nanomaterial; (c) $\ln(C_t/C_0)$ versus degradation time plot for finding the reaction rate constant (kapp).

The degradation experiments were performed at an initial dye concentration of 10 mg L^{-1} to assess the fundamental catalytic performance of the biosynthesized Fe_2O_3 nanoparticles under controlled laboratory conditions. In practical scenarios, such as textile effluents, dye concentrations often exceed 100 mg L^{-1}, which may lead to reduced degradation efficiency due to saturation of active catalytic sites and mass transfer limitations. Therefore, additional studies at higher dye concentrations are necessary to evaluate the system's real-world applicability. Figs. 9(a), 9(b), and 9(c) illustrate the degradation kinetics of Reactive Orange ME2RL in the presence of biosynthesized Fe_2O_3, analyzed using a pseudo-first-order model. Kinetic analysis involved plotting $\ln(C_t/C_0)$ against reaction time, where C_0

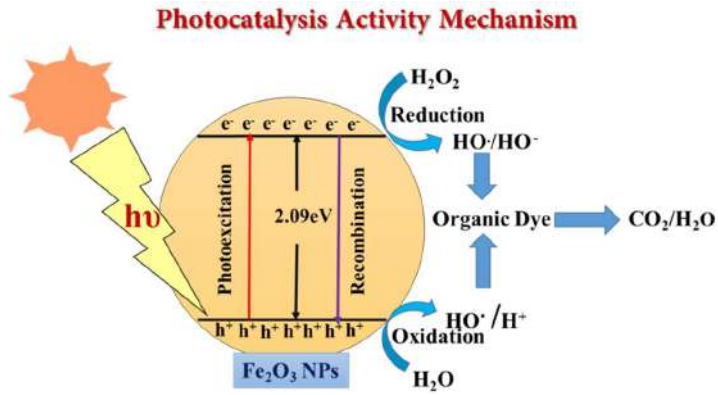


Fig. 10: Photodegradation mechanism of Orange ME2RL dye in the presence of Fe_2O_3 nanoparticles.

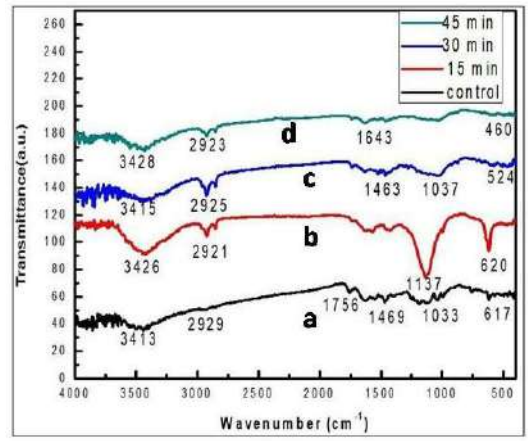


Fig. 11: FTIR of Orange ME2RL dye upon degradation: (a) pure dye; (b) after 15 min; (c) after 30 min; (d) after 45 min.

is the initial dye concentration, and C_t is the concentration at time t. The linearity of the plot confirmed that the degradation follows pseudo-first-order kinetics. The rate constant (k) was derived from the slope and found to be 0.036 min^{-1}, with an R^2 value of 0.915, indicating a strong correlation between the model and experimental data. These kinetics imply that the degradation rate mainly depends on the dye concentration, with the catalyst's quantity remaining effectively constant throughout the process. This behavior is typical in heterogeneous catalytic degradation, where dye molecules adsorb onto the nanoparticle surface before oxidative breakdown.

3.4. Analysis of Degraded Dye Products

For the analytical characterization of degradation, an untreated Orange ME2RL dye solution was used as a control in UV–Vis, HPLC, and GC–MS analyses. This untreated dye served as a reference to compare spectral changes and identify degradation products following nanoparticle treatment.

3.4.1. FTIR of Orange ME2RL Degradation

Fig. 11 illustrates a broad band around 3410–3430 cm^{-1}, corresponding to –OH/–NH stretching vibrations, signifying hydroxylated intermediates formed during dye degradation (Silverstein et al. 2014). Peaks near 2920–2930 cm^{-1} are associated with aromatic or aliphatic C–H stretching vibrations (Stuart 2004). The gradual diminution and disappearance of the azo (–N=N–) bond vibration confirm cleavage of the dye chromophore, a key indicator of azo dye degradation (Saratale et al. 2011, Forgacs et al. 2004). The weakening of S=O and C–N stretching bands between 1200–1000 cm^{-1} further indicates the breakdown of sulfonated dye structures. The appearance of new low-frequency peaks below 700 cm^{-1} suggests the formation of low-molecular-weight inorganic or mineralized products after extended degradation (Roy et al. 2022).

3.4.2. HPLC Analysis

The HPLC chromatogram of Reactive Orange ME2RL showed distinct retention peaks. After degradation, the standard peak disappeared, and new peaks appeared at retention times of 8.572, 10.699, 13.044, 14.572, 4.017, and 16.780 min, confirming catalytic degradation of the dye (Gottlieb 2003) (Figs. 12–13).

3.4.3. GC–MS Analysis

Degradation of Orange ME2RL dye was performed using Fe_2O_3 nanoparticles. This process produced eight distinct compounds. The mass spectra of both the untreated dye and its degraded metabolites, collected at 15-minute intervals and shown in Fig. 14(a), Fig. 14(b), Fig. 14(c), and Fig. 14(d), illustrate the biodegradation pathway. During catalytic degradation, the aromatic ring of Orange ME2RL dye was cleaved, leading to the formation of several metabolites, including Sodium 6-amino-5-sulfonatonapthalen-1-yl-sulfite (1), Sodium 3-amino-7-[(4-chloro-1,3,5-triazin-2-yl) amino]-4-hydroxynaphthalene-2-sulphonate (2), Sodium 4-aminobenzene-1-sulphonate (3), Naphthalen-2-amine (4), 2-aminonaphthalen-1-ol (5), Aniline (6), Naphthalene-1-ol (7), and Benzene (8). GC–MS analysis confirmed that biosynthesized Fe_2O_3 nanoparticles serve as effective catalysts, promoting the breakdown of Orange ME2RL into low-molecular-weight compounds. The metabolites identified via GC–MS were tentatively matched with the NIST mass spectral library. The proposed degradation pathway was constructed based on these intermediates and supported by previously reported mechanisms of azo dye degradation.

3.5. Proposed Degradation Mechanism

The degradation of Reactive Orange ME2RL by *Pseudomonas*

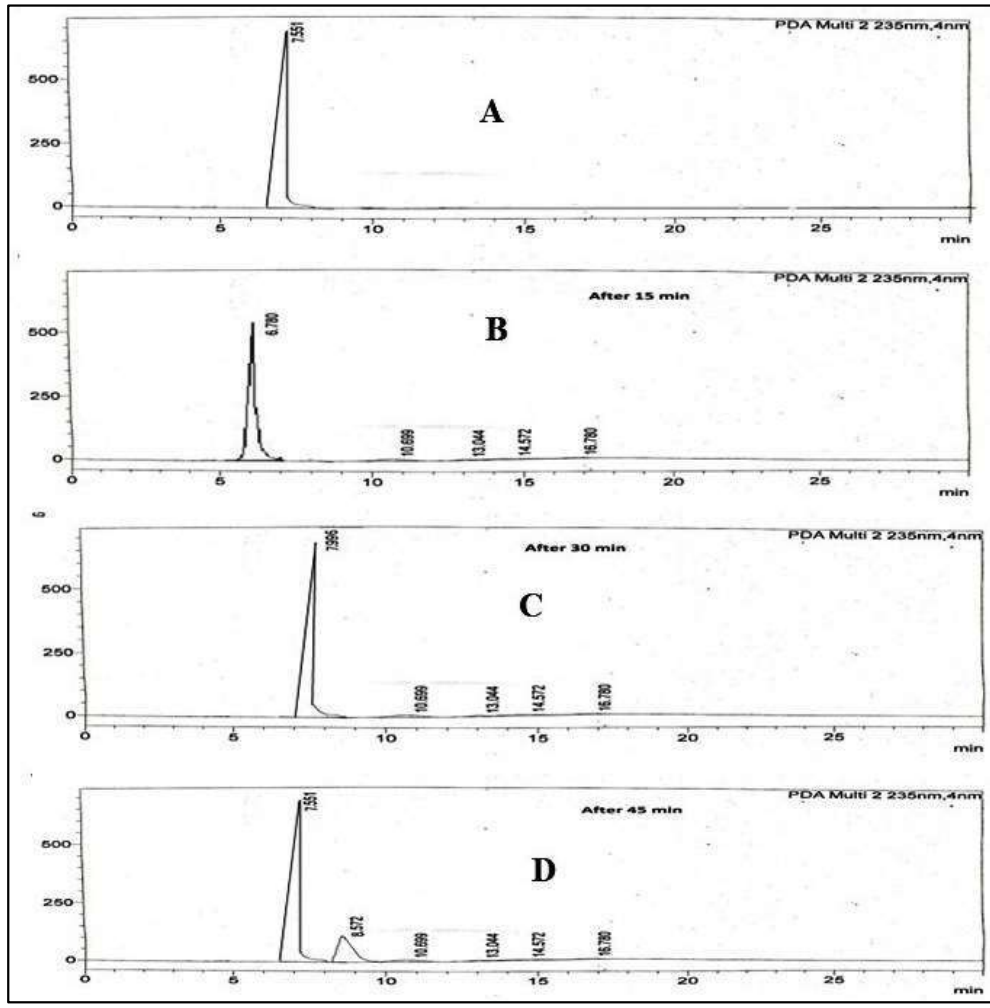


Fig. 12: HPLC chromatogram of Reactive Orange ME2RL upon degradation: (a) pure dye; (b) after 15 min; (c) after 30 min; (d) after 45 min.

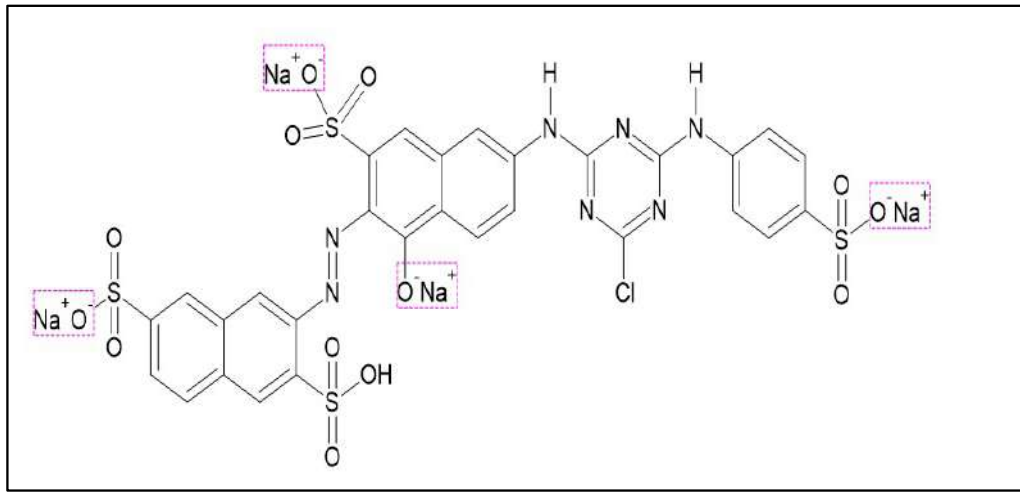


Fig. 13: Structure of the dye Reactive Orange ME2RL.

stutzeri–mediated Fe_2O_3 nanoparticles occurs through an adsorption–oxidation mechanism that differs from the pathway previously proposed for Orange ME2RL (Castro et al. 2020). The formation of intermediate ions similar to m/z 347, 390, and 159 confirms a process involving sequential azo bond cleavage, aromatic ring opening, and oxidative mineralization, as shown in Fig. 15.

3.6. Antibacterial Activity

The antibacterial efficacy of iron nanoparticles was evaluated against various pathogenic bacteria. Zones of inhibition were measured and recorded. As shown in Fig. 16 and Table 1, Fe_2O_3 NPs demonstrated notable antimicrobial activity, with inhibition zones of 25 mm for *S. aureus* NCIM-2654, 20 mm for *S. typhi* NCIM-2501, 15 mm for *P. vulgaris* NCIM-2813, and 11.66 mm for *P. aeruginosa* NCIM-5032. The reported zones of inhibition are expressed as means ± standard deviation from triplicate experiments.

Additionally, a combination of Fe nanoparticles with the antibiotic cefuroxime was tested, resulting in zones of inhibition measuring 28 mm for *S. aureus* NCIM-2654, 27 mm for *S. typhi* NCIM-2501, 26 mm for *P. vulgaris* NCIM-2813, and 25 mm for *P. aeruginosa* NCIM-5032 (Fig. 16). This combination exhibited enhanced antimicrobial activity, increasing effectiveness by 0.15, 0.16, 0.39, and 0.56 fold, respectively. The antibacterial efficacy varied between Gram-negative and Gram-positive bacteria due

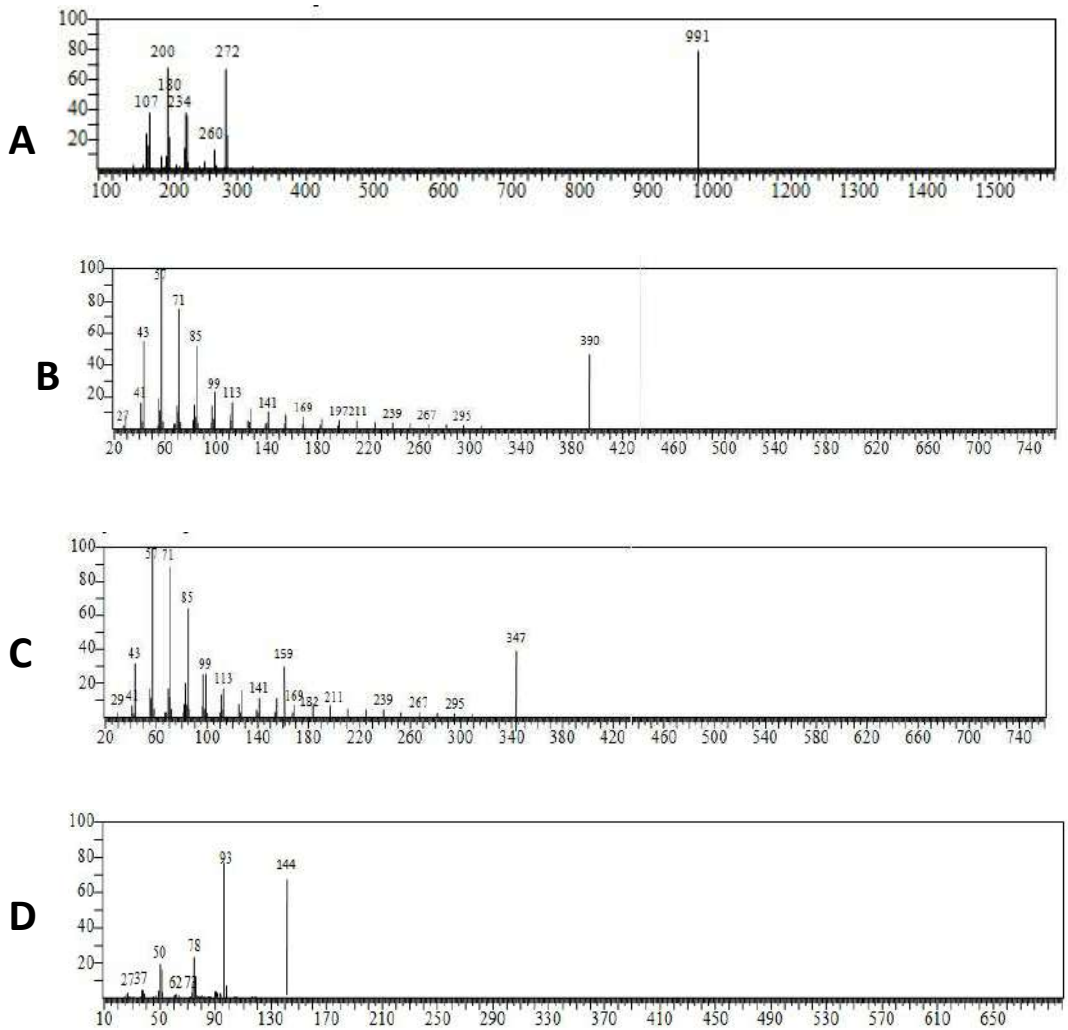


Fig. 14: GC–MS analysis of Reactive Orange ME2RL: (a) control dye (before degradation); (b) degradation after 15 min; (c) degradation after 30 min; (d) degradation after 45 min.

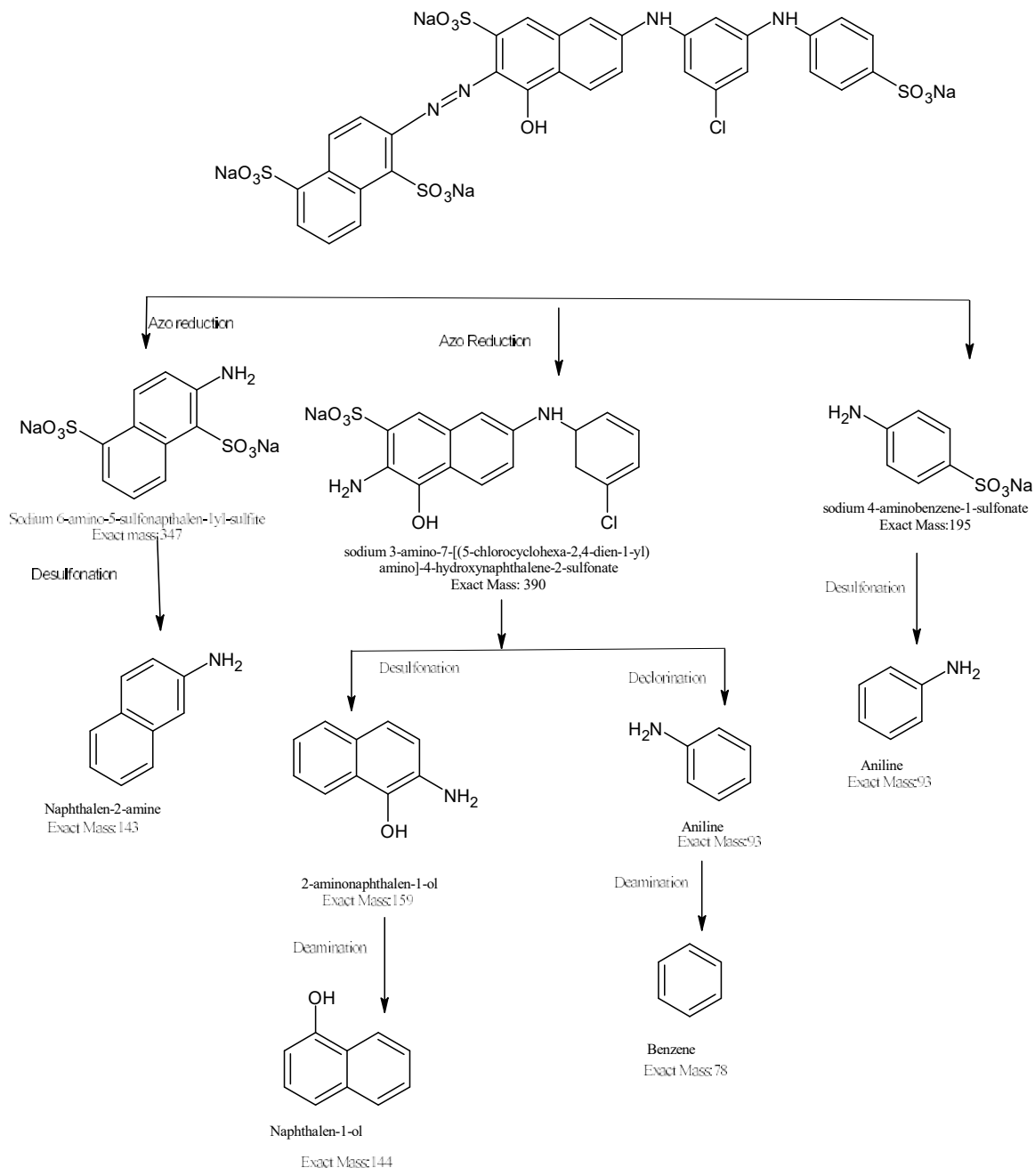


Fig. 15: Proposed degradation pathway of Reactive Orange ME2RL dye based on GC–MS analysis.

Table 1: Antibacterial activity in terms of zone of inhibition (mm) in the presence of nanoparticles and standard antibiotics.

Test organism	Diameter of zone of inhibition [mm] Nanoparticles	Std antibiotic	Std antibiotic + nanoparticles
Staphylococcus aureus	25 ± 1	27 ± 0.57	28 ± 0.57
Pseudomonas aeruginosa	11.66 ± 0.57	20.33 ± 0.57	24.66 ± 0.57
Proteus vulgaris	15 ± 2.64	21 ± 1	25.66 ± 0.57
Salmonella typhi	20.66 ± 0.57	24.66 ± 0.57	26.33 ± 1.15

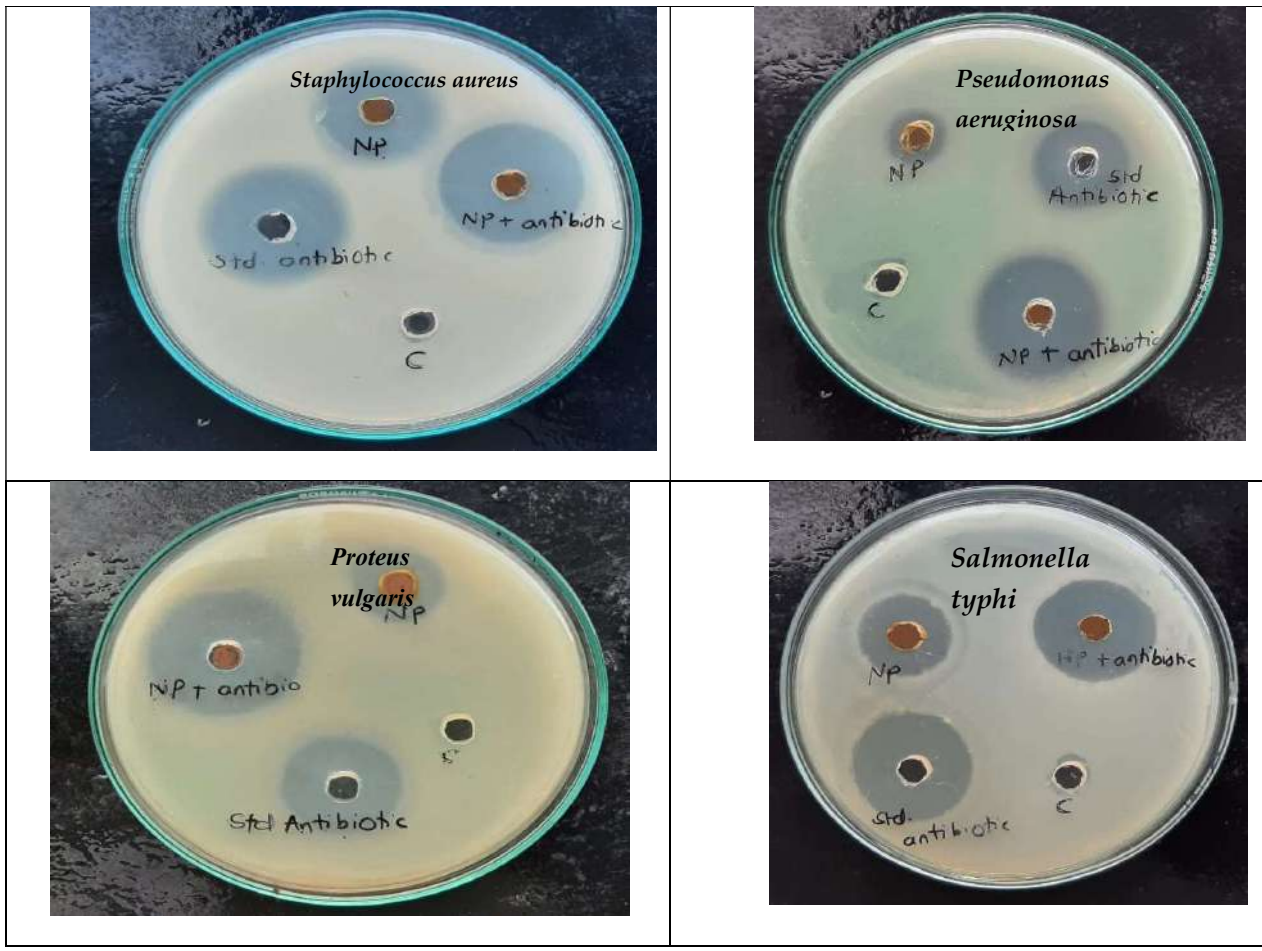


Fig. 16: Antibacterial activity of iron nanoparticles against S. aureus NCIM-2654, P. aeruginosa NCIM-5032, P. vulgaris NCIM-2813, and S. typhi NCIM-2501.

to differences in their cell wall structures (Zambare et al. 2023). Biosynthesized iron nanoparticles (Fe NPs) combat bacteria through multiple mechanisms that damage both Gram-positive and Gram-negative organisms. First, Fe NPs attach to negatively charged bacterial surfaces, disrupting membrane integrity and increasing permeability. This allows nanoparticles to enter the cells, where Fe^{2+} and Fe^{3+} ions initiate Fenton-like reactions, producing reactive oxygen species (ROS) such as hydroxyl and superoxide radicals. These ROS cause oxidative stress, damaging lipids, proteins, and DNA, leading to membrane leakage, enzyme malfunction, and genetic fragmentation. In Gram-negative bacteria, Fe NPs penetrate the outer membrane and periplasmic space, while in Gram-positive bacteria, the thick peptidoglycan layer traps the nanoparticles, sustaining ROS production. When combined with cefuroxime, Fe NPs potentiate antibiotic activity by weakening cell membranes, facilitating antibiotic entry, and impairing bacterial defence mechanisms such as efflux pumps and β-lactam enzymes. Overall, Fe_2O_3 NPs exert antibacterial effects through membrane disruption, ROS generation, interference with metal ion metabolism, and enhancement of antibiotic efficacy, showing strong potential for controlling multidrug-resistant bacteria (Hosseinzadeh 2025). Rather than a synergistic effect, Fe_2O_3 nanoparticles with standard antibiotics demonstrate an improved antibacterial effect.

3.7. Phytotoxicity

Seeds germinated in the degradation products showed significant differences compared to those germinated in Reactive Orange ME2RL, with a significance level of $P < 0.05$, as determined by the Tukey–Kramer multiple comparison test. The degradation of dyes does not always produce benign by-products; instead, it may generate compounds that are more harmful than the parent dye. Previous studies demonstrated that the treatment of azo dyes could result in the formation of aromatic amines that are more toxic than the original dyes (Gottlieb et al. 2003).

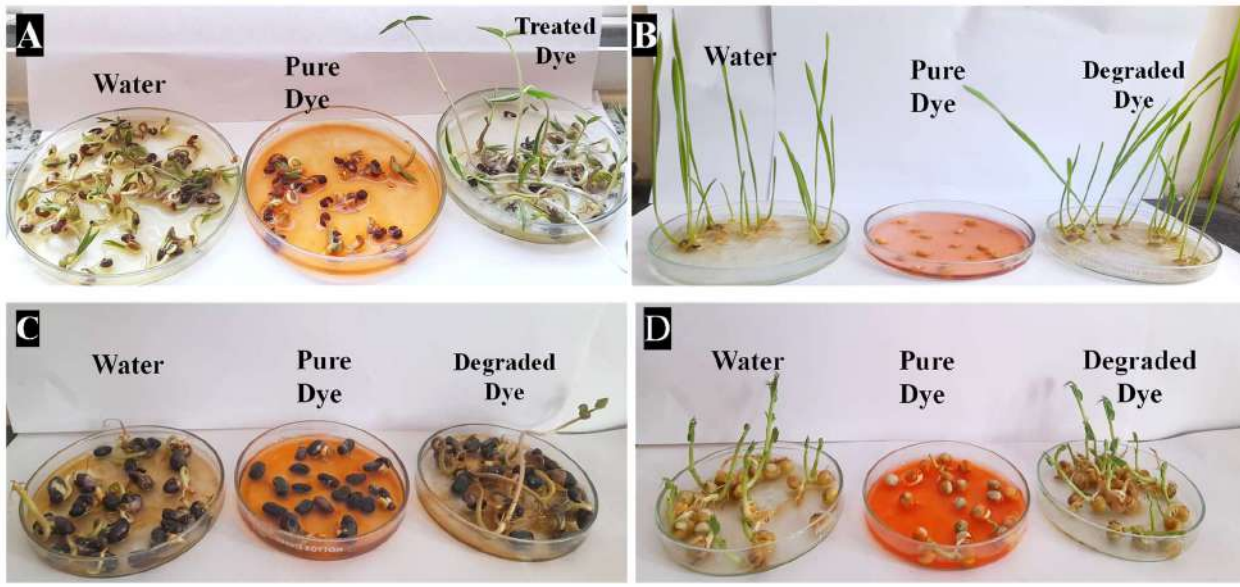


Fig. 17: Phytotoxicity analysis of pure dye Reactive Orange ME2RL and its metabolites using seeds: (a) green gram; (b) Triticum aestivum; (c) Vigna unguiculata; (d) Pisum sativum.

Consequently, a phytotoxicity assessment was undertaken to evaluate the potential harmful effects of the degraded metabolites on the seeds of green gram, *Triticum aestivum*, *Vigna unguiculata*, and *Pisum sativum*. All seeds were exposed to Reactive Orange ME2RL and its degraded metabolites at a concentration of 100 ppm.

The findings, presented in Table 2 and Fig. 17, showed the germination rate, as well as the radicle and plumule lengths, across all plant species tested. The degraded metabolites resulted in a notable increase in both root and shoot lengths in all plant species. In contrast, the untreated dye produced significantly lower seed germination rates and stunted root and shoot growth in all four plant species compared to the degraded metabolites. Based on these results, it appears that the degradation products not only eliminated toxicity but also promoted seed growth (Survase & Kanase 2022).

Table 2: Phytotoxicity analysis of pure dye Reactive Orange ME2RL and its metabolites using seeds of green gram, *Triticum aestivum*, *Vigna unguiculata*, and *Pisum sativum*.

Parameters studied	Water	Orange ME2RL	Degraded metabolites
Vigna radiata			
Radicle [cm]	2.1 ± 0.1	1.16 ± 0.057	2.5 ± 0.1
Plumule [cm]	4.13 ± 0.11	0.23 ± 0.1	10.33 ± 0.57
Germination [%]	100	28.33 ± 2.88	100
Triticum aestivum			
Radicle [cm]	1.86 ± 0.057	0.16 ± 0.057	3.1 ± 0.1
Plumule [cm]	9.1 ± 0.1	0.23 ± 0.057	12.1 ± 0.1
Germination [%]	100	5	100
Vigna unguiculata			
Radicle [cm]	14.1 ± 0.1	0.13 ± 0.057	8.03 ± 0.20
Plumule [cm]	12.1 ± 0.1	0.26 ± 0.057	10.5 ± 0.1
Germination [%]	100	20	100
Pisum sativum			
Radicle [cm]	3.9 ± 0.1	0.13 ± 0.057	3.76 ± 0.05
Plumule [cm]	4.46 ± 0.057	2.5 ± 0.1	4.86 ± 0.05
Germination [%]	100	30	100

The improved growth parameters observed in *Vigna radiata* treated with the degraded dye metabolites, compared with the water control, may indicate not only detoxification but also possible nutrient enrichment effects. During the degradation process, complex dye molecules are broken down into smaller organic intermediates and inorganic ions, which may serve as additional nutrient sources for plant growth. These metabolites may enhance seed germination and seedling development by providing readily available carbon or nitrogen sources.

3.8. Fish Toxicity

To determine the lethal concentration of pure dye, fish were exposed to different concentrations of pure dye for 24, 48, 72, and 96 h. The percent mortality for pure dye at 96 h was calculated as shown in Table 3.

The acute toxicity test showed that fish mortality increased with increasing concentrations of the test sample. No mortality was observed at 1.25 ppm after 96 h of exposure, whereas complete mortality (100%) occurred at 8.75 ppm (Table 3). Approximately 50% mortality was observed at 5 ppm, indicating that the 96 h LC_{50} value was close to this concentration.

The observed LC_{50} value was 5 ppm (5 µL L^{-1}), whereas the statistically calculated LC_{50} value obtained from probit analysis was 4.8 ppm ($\approx$4.5 µL L^{-1}). The close agreement between the observed and calculated LC_{50} values indicates good consistency and reliability of the experimental data.

Table 3: Effect of Orange ME2RL on mortality of Cirrhinus mrigala during a 96 h exposure period.

No. of fishes	Concentration [ppm]	Exposure period [h]				% mortality
		24	48	72	96	
10	1.25	0	0	0	0	0
10	2.50	0	0	0	1	10
10	3.75	0	0	1	2	30
10	**5.00**	**0**	**1**	**2**	**2**	**50**
10	6.25	1	1	2	3	70
10	7.5	1	2	3	3	90
10	8.75	6	4	-	-	100

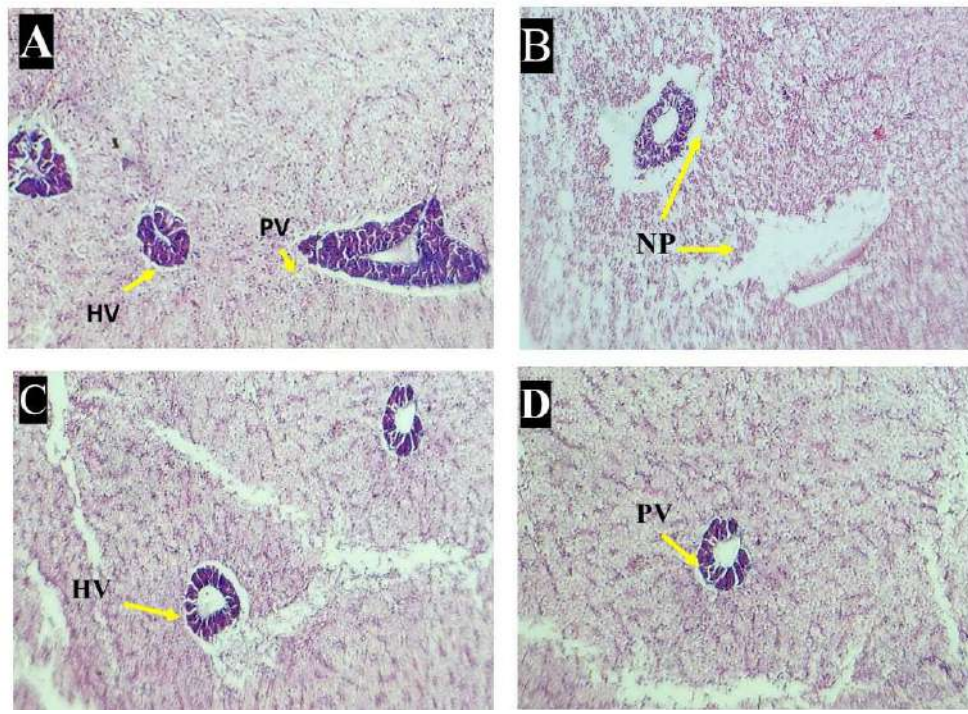


Fig. 18: Histopathological changes in the liver: (a) freshwater control; (b) exposure to pure dye; (c) exposure to treated dye; (d) exposure to nanoparticles.

These results suggest that the test compound exhibits significant toxic effects on fish even at relatively low concentrations.

3.8.1. Histological Observations of Liver

The histological structure of the liver in control fish is depicted in the photomicrograph in Fig. 18. These H&E-stained liver slices reveal hepatic cells situated within the bile canaliculi network. The hepatic cells feature spherical, blue-stained nuclei located centrally, with a morphology ranging from round to polygonal. Glycogen granules are plentiful within these cells. The hepatic cell cords, which form cord-like structures surrounding the sinusoids, are not distinct; each cord contains a centrally positioned bile canaliculus. Hepatocytes are oriented with their bases facing the sinusoids and their apices directed toward the wall of the bile canaliculi. The arrangement of blood vessels and the bile duct appears irregular, and there is no clear separation of hepatic cells within the lobules. Lipid droplets are observed inside rounded or elongated Ito (fat-storing) cells. Kupffer cells are occasionally seen lining the sinusoids, containing a significant amount of cytoplasm. The portal vein is present, surrounded by pancreatic acini, collectively forming the hepatopancreas. The hepatic arteries have narrow lumens enclosed by a dense layer of endothelial cells. Within each hepatic lobule, an intralobular central vein can be seen, containing blood cells in its lumen.

The liver is a primary target for toxicants due to its extensive blood supply. Numerous toxicants have been studied for their harmful effects on the liver, as it is considered the main organ for bioaccumulation (van Dyk et al. 2007). When fish were exposed to a pure dye, significant degenerative changes were observed in their livers compared to the control group (Fig. 18). These histological alterations included disorganization of hepatic cords, widespread dilation of sinusoids throughout the tissue, and increased sinusoidal spaces around the portal vein. There was also complete degeneration of hepatocytes with severe necrotic patches, along with cytoplasmic degeneration, vacuolation within hepatocytes, and evidence of karyolysis. Some regions showed elongation of blood vessels, and the hepatopancreas exhibited degeneration.

Fig. 18(c) and Fig. 18(d) depict the treated dye and the liver alterations induced by exposure to nanoparticles. Mild degenerative changes were observed in fish exposed to the nanoparticles, although these changes were less pronounced than those observed in the control group. These alterations included disorganization of the hepatic cords, the onset of sinusoidal space expansion, cytoplasmic vacuolation, cellular swelling, and pyknotic nuclei in some cells. Although mild degeneration was observed, no significant alterations were detected in the livers of fish exposed to the nanoparticles compared with those exposed to the pure dye.

3.8.2. Histological Observations of Gills

The histological structure of the gills in *Cirrhinus mrigala* closely resembles that of most freshwater teleosts. An operculum protects each gill, and there are four pairs of gills. These gills are supported by curved bony gill arches covered with multilayered epithelium. Each gill arch bears two rows of primary gill lamellae, which are located on one side only. These lamellae are wider at the base and taper toward the tip. They consist of a central vascular core surrounded by a wall made of three to four epithelial layers, with connective tissue interposed. The primary gill lamellae rest on a central cartilaginous matrix that encompasses chondrocytes. The epithelial cells at the tips of the lamellae are mainly oval to flat, with centrally located nuclei and basophilic, homogeneous cytoplasm.

Additionally, each primary gill lamella features two rows of delicate filamentous structures known as secondary gill lamellae or secondary gill filaments (Fig. 19(a)), oriented perpendicular to the primary lamellae's axis. These secondary lamellae develop as outward extensions from the primary lamellae and are composed of a single layer of epithelial cells, which are oval to cuboidal, with basophilic cytoplasm and centrally located oval nuclei. Internally, the secondary lamellae contain a central core of blood sinuses lined by large oval to rounded pillar cells. These pillar cells have homogeneous, basophilic cytoplasm and round nuclei positioned centrally.

Following 96 h of exposure to pure dye, degenerative alterations were noted in the gill structure. Tilting and congestion were observed at the tips of the primary gill lamellae (refer to Fig. 19(b)). Additionally, detachment of the epithelium from the central supporting material of the primary gill lamellae was evident. Significant enlargement of the central supporting material of the primary gill lamellae was also observed. Furthermore, progressive hyperplasia and thickening of the epithelium at the interlamellar region were observed. Shortening and fusion of adjacent secondary gill lamellae were noted in a certain region, as shown in Fig. 19b.

Mild histopathological changes were observed in the gills after exposure to degraded dye, as shown in Fig. 19(c). A slight enlargement of the tips of the primary gill lamellae was noted, with these dilated tips filled with blood cells. An increased number of mucous cells, particularly at the tips of the primary gill lamellae, was also observed (Fig. 19(c)). Additionally, the secondary gill lamellae appeared curved with dilated tips filled with blood cells. There was slight desquamation of the epithelial lining from the

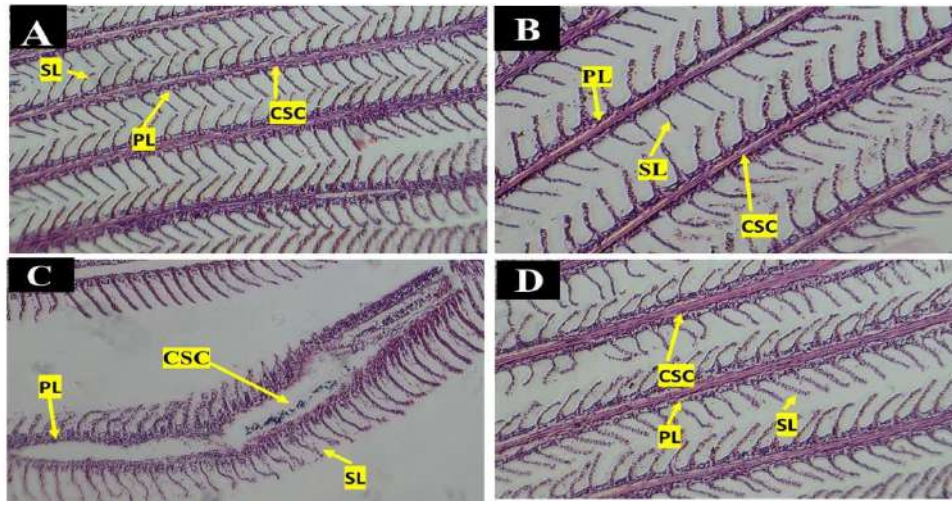


Fig. 19: Histopathological changes in the gills: (a) freshwater control; (b) exposure to pure dye; (c) exposure to treated dye; (d) exposure to nanoparticles.

central supporting cartilage upon exposure to nanoparticles (Fig. 19(d)). These changes were less pronounced than those seen following exposure to pure dye.

4. CONCLUSIONS

This study presents the eco-friendly biosynthesis of Fe_2O_3 nanoparticles using *Pseudomonas stutzeri*. Characterization by UV–Visible spectroscopy, SEM, FTIR, XRD, HRTEM, and DLS confirmed the formation of predominantly spherical nanoparticles with sizes ranging from 30 to 50 nm. The nanoparticles demonstrated strong catalytic activity in degrading Reactive Orange ME2RL dye, and the degradation metabolites were identified using FTIR, HPLC, and GC–MS analyses. They also exhibited antibacterial activity against *Staphylococcus aureus*, *Salmonella typhi*, *Proteus vulgaris*, and *Pseudomonas aeruginosa*, with greater inhibition observed when combined with antibiotics. Phytotoxicity and fish toxicity assays revealed that the degraded dye products were less toxic than the original dye. The synthesized Fe_2O_3 nanoparticles showed high degradation efficiency towards Reactive Orange ME2RL, indicating their suitability for the treatment of dye-containing industrial effluents. Fe_2O_3 nanoparticles possess inherent magnetic properties that enable the easy separation and potential reuse of the catalyst from treated wastewater using an external magnetic field. Therefore, this study provides a sustainable and efficient approach for the remediation of textile dye pollutants and demonstrates potential applicability in large-scale industrial wastewater treatment processes. Further studies are required to evaluate the reusability and long-term stability of the synthesized Fe_2O_3 nanoparticles over multiple degradation cycles to assess their practical applicability in wastewater treatment. Owing to the magnetic nature of Fe_2O_3 nanoparticles, their recovery and reuse may be feasible and will be explored in future studies.

5. ACKNOWLEDGMENTS

The authors are grateful to the Rayat Institute of Research and Development, Satara, for providing the prestigious Dr. B.M. Sawant fellowship and laboratory facilities as financial provision for the research endeavour.

5. REFERENCES

Acharya, C., Mishra, S., Chaurasia, S.K., Pandey, B.K., Dhar, R. and Pandey, J.K., 2025. Synthesis of metallic nanoparticles using biometabolites: mechanisms and applications. In: *BioMetals*, Vol. 38(1). Springer, Cham, Switzerland, pp. 21–54. [DOI]

Ali, H., 2010. Biodegradation of synthetic dyes: a review. *Water, Air, and Soil Pollution*, 213(1-4), pp. 251-273. [DOI]

Al-Musawi, T.J., McKay, G., Rajiv, P., Mengelizadeh, N. and Balarak, D., 2022. Sonophotocatalytic degradation of Acid Blue 113 using $CoFe_2O_4$-MWCNT nanocomposite. *Journal of Photochemistry and Photobiology A: Chemistry*, 424, p. 113617. [DOI]

Aly, H. and Abdelsalam, A., 2025. Effect of humic acid and selenium on seed germination, seedling growth, and priming with mitigate salt stress effect on mustard (Brassica juncea) seeds. *Russian Journal of Plant Physiology*, *72*(3), p.72. [DOI]

Ameur, W.B., de Lapuente, J., El Megdiche, Y., Barhoumi, B., Trabelsi, S., Camps, L. and Borràs, M., 2012. Oxidative stress, genotoxicity and histological effects in fish from Bizerte lagoon. *Marine Pollution Bulletin*, 64(2), pp. 241-251. [DOI]

Annamalai, J., Ummalyma, S.B., Pandey, A. and Bhaskar, T., 2021. Recent trends in microbial nanoparticle synthesis and potential application in environmental technology: a comprehensive review. *Environmental Science and Pollution Research*, *28*(36), pp.49362-49382 [DOI]

Apine, O., Patil, S., Patil, D. and Jadhav, J.P., 2023. Role of analytical techniques in treatment of synthetic dyes and textile effluent. In: Pandey, A. et al. (eds) *Current Developments in Bioengineering and Biotechnology*. Elsevier: Amsterdam, Netherlands, pp. 303–338. [DOI]

Banat, I.M., Nigam, P., Singh, D. and Marchant, R., 1997. Microbial decolorization of textile-dye-containing effluents: a review. *Bioresource Technology*, 61(1), pp. 103-115. [DOI]

Bhattacharjee, S., 2016. DLS and zeta potential–what they are and what they are not? *Journal of Controlled Release*, 235, pp. 337-351. [DOI]

Castro, L., Meurer, E., Alves, H., Santos, M., Vasques, E. and Colpini, L., 2020. Photocatalytic degradation of Orange-122 via electrospray MS. *Brazilian Archives of Biology and Technology*, 63, p. e20180573. [DOI]

Chavan, R.B., 2001. Indian textile industry—environmental issues. *Indian Journal of Fibre and Textile Research*, 26(1–2), pp. 11–21.

Chicea, D., Indrea, E. and Cretu, C.M., 2012. Assessing Fe_3O_4 nanoparticle size by DLS, XRD and AFM. *Journal of Optoelectronics and Advanced Materials*, 14(5), pp. 460–466.

Ferreira, F.N., Benevides, A.P., Cesar, D.V., Luna, A.S. and de Gois, J.S., 2020. Magnetic solid-phase extraction of estrogenic compounds using maghemite–graphene oxide nanoparticles. *Microchemical Journal*, 157, p. 104947. [DOI]

Forgacs, E., Cserháti, T. and Oros, G., 2004. Removal of synthetic dyes from wastewaters: a review. *Environment International*, 30(7), pp. 953–971. [DOI]

Ganachari, S.V., Joshi, V., Bhat, R., Deshpande, R., Salimath, B., Rao, N.V. and Venkataraman, A., 2012. Large scale synthesis and characterization of γ-Fe_2O_3 nanoparticles by self-propagating low temperature combustion method. *International Journal of Science Research*, 1(2), pp. 77–79.

Giuli, G., Trapananti, A., Mueller, F., Bresser, D., d'Acapito, F. and Passerini, S., 2015. Effects of Fe and Co doping on nanosized ZnO structure. *Inorganic Chemistry*, 54(19), pp. 9393–9400. [DOI]

Gottlieb, A.L., 2003. *Microbial Degradation of Textile Dyes to Safe End-Products*. Doctoral Thesis. Nottingham Trent University: Nottingham, UK, pp. 1–180.

Gottlieb, A., Shaw, C., Smith, A., Wheatley, A. and Forsythe, S., 2003. Toxicity of textile azo dyes after hydrolysis and decolourization. *Journal of Biotechnology*, 101, pp. 49–56. [DOI]

Gupta, V.K., Mittal, A., Gajbe, V. and Mittal, J., 2006. Removal and recovery of the hazardous azo dye acid orange 7 through adsorption over waste materials: bottom ash and de-oiled soya. *Industrial & Engineering Chemistry Research*, 45(4), pp. 1446–1453. [DOI]

Hanafi, M.F. and Sapawe, N., 2020. A review on the current techniques and technologies of organic pollutants removal from water/wastewater. *Materials Today: Proceedings*, *31*, pp. A158–A165. [DOI]

Haroon, K., Kherb, J., Jeyaseelan, C. and Sen, M.J.N.E., 2023. Recent advances and sustainable approaches towards efficient wastewater treatment using natural waste derived nanocomposites: a review. *Nature Environment & Pollution Technology*, 22(3), pp. 1251–1264. [DOI]

Holzwarth, U. and Gibson, N., 2011. The Scherrer equation versus the Debye–Scherrer equation. *Nature Nanotechnology*, 6(9), pp. 534–535. [DOI]

Hosseinzadeh, H., 2025. Antibacterial/magnetic iron oxide nanoparticles: synthesis, doping and applications. *Journal of Applied Material Science*, 1(3), p. e210146.

Islam, M.A., Amin, S.N., Brown, C.L., Juraimi, A.S., Uddin, M.K. and Arshad, A., 2021. LC50 of pesticides and histopathology in African catfish. *Toxics*, 9(12), p. 340. [DOI]

Jana, J., Ganguly, M. and Pal, T., 2016. Surface plasmon resonance of metal nanoparticles for spectroscopic applications. *RSC Advances*, 6(89), pp. 86174–86211. [DOI]

Javidparvar, A.A., Ramezanzadeh, B. and Ghasemi, E., 2016. Effect of surface treatment of Fe_3O_4 nanoparticles on epoxy coating corrosion resistance. *Journal of the Taiwan Institute of Chemical Engineers*, 61, pp. 356–366. [DOI]

Joshi, A., Nanani, J., Trivedi, N., Kothari, V. and Kothari, R., 2015. Decolorization of Reactive Orange Me2RL by bacterial consortium. *National Science Symposium Proceedings*, 2, p. 164.

Joshi, A.U., Hinsu, A.T., Kotadiya, R.J., Rank, J.K., Andharia, K.N. and Kothari, R.K., 2020. Decolorization and biodegradation of textile di-azo dye Acid Blue 113 by Pseudomonas stutzeri AK6. *3 Biotech*, 10(5), p. 214. [DOI]

Katata-Seru, L., Moremedi, T., Aremu, O.S. and Bahadur, I., 2018. Green synthesis of iron nanoparticles using Moringa oleifera extracts. *Journal of Molecular Liquids*, 256, pp. 296–304. [DOI]

Khan, I., Saeed, K. and Khan, I., 2019. Nanoparticles: properties, applications and toxicities. *Arabian Journal of Chemistry*, 12(7), pp. 908–931. [DOI]

Mane, U.V., Gurav, P.N., Deshmukh, A.M. and Govindwar, S.P., 2008. Degradation of textile dye Reactive Blue 59 by Streptomyces krainskii SUK-5. *Malaysian Journal of Microbiology*, 4(2), pp. 1–5. [DOI]

Mukherjee, B. and Dutta, S., 2019. Isolation of a phosphate-solubilizing bacterial strain Bacillus tequilensis MCC 3872 from rice field and characterization of its plant growth-promoting traits. *Pharma Innovation Journal*, 8, pp. 956–962.

Naz, M., Rafiq, A., Ikram, M., Haider, A., Ahmad, S.O., Haider, J. and Naz, S., 2021. Elimination of dyes by catalytic reduction in the absence of light: a review. *Journal of Materials Science*, 56(28), pp. 15572–15608. [DOI]

Nurbas, M.A., Ghorbanpoor, H.A. and Avci, H.Ü., 2017. Eco-friendly synthesis of magnetite (Fe_3O_4) nanoparticles using Platanus orientalis leaf extract. *Digest Journal of Nanomaterials and Biostructures*, 12(4), pp. 1231–1240.

Palleroni, N.J., 1984. Pseudomonas. In: Krieg, N.R. (ed.) *Bergey's Manual of Systematic Bacteriology*, Vol. I. Williams and Wilkins: Baltimore, United States, pp. 141–199.

Palleroni, N.J., Doudoroff, M., Stanier, R.Y., Solanes, R.E. and Mandel, M., 1970. Taxonomy of the aerobic pseudomonads: the properties of the Pseudomonas stutzeri group. *Microbiology*, 60(2), pp. 215–231. [DOI]

Palleroni, N.J., Kunisawa, R., Contopoulou, R. and Doudoroff, M., 1973. Nucleic acid homologies in the genus Pseudomonas. *International Journal of Systematic Bacteriology*, 23, pp. 333–339. [DOI]

Pandey, A., Singh, P. and Iyengar, L., 2007. Bacterial decolorization and degradation of azo dyes. *International Biodeterioration and Biodegradation*, 59(2), pp. 73–84. [DOI]

Patel, D.D. and Bhatt, S., 2022. Environmental pollution, toxicity profile, and physico-chemical and biotechnological approaches for treatment of textile wastewater. *Biotechnology and Genetic Engineering Reviews*, 38(1), pp. 33–86. [DOI]

Periyasamy, A.P., 2024. Recent advances in the remediation of textile-dye-containing wastewater: prioritizing human health and sustainable wastewater treatment. *Sustainability*, 16(2), p. 495. [DOI]

Rossello, R., Garcia-Valdes, E., Lalucat, J. and Ursing, J., 1991. Genotypic and phenotypic diversity of Pseudomonas stutzeri. *Systematic and Applied Microbiology*, 14(2), pp. 150–157. [DOI]

Roy, A., Khan, A., Ahmad, I., Alghamdi, S., Rajab, B.S., Babalghith, A.O., Alshahrani, M.Y., Islam, S. and Islam, M.R., 2022. Flavonoids a bioactive compound from medicinal plants and its therapeutic applications. *BioMed Research International*, *2022*(1), p.5445291. [DOI]

Saha, S. and Bhunia, A.K., 2020. Synthesis of Fe_2O_3 nanoparticles and study of structural and optical properties. *Materials Today: Proceedings*, pp. 1–8. [DOI]

Saratale, R.G., Saratale, G.D., Chang, J.S. and Govindwar, S.P., 2011. Bacterial decolorization and degradation of azo dyes: a review. *Journal of the Taiwan Institute of Chemical Engineers*, *42*(1), pp.138-157. [DOI]

Sekar, S., Surianarayanan, M., Ranganathan, V., MacFarlane, D. and Mandal, A., 2012. Choline-based ionic liquids enhance biodegradation of azo dyes. *Environmental Science and Technology*, 46(9), pp. 4902–4908. [DOI]

Shahriarinour, M., Divsar, F., Dahka, F.K., Chegini, S.N., Mahani, M., Moeini, A. and Cerruti, P., 2021. Biodegradation of alprazolam in

pharmaceutical wastewater using mesoporous nanoparticle-adhered Pseudomonas stutzeri. *Molecules*, 27(1), p. 237. [DOI]

Shakoor, S., Khan, M.S. and Khan, M.E., 2025. Adsorptive remediation of dyes through a novel approach from nanotechnology: A comprehensive review. *Nature Environment and Pollution Technology*, 24(1), pp. 1-15. [DOI]

Silverstein, M.S., 2014. PolyHIPEs: recent advances in emulsion-templated porous polymers. *Progress in Polymer Science*, *39*(1), pp.199-234. [DOI]

Srivastava, S.K. and Constanti, M., 2012. Room-temperature biogenic synthesis of multiple nanoparticles by Pseudomonas aeruginosa SM1. *Journal of Nanoparticle Research*, 14, pp. 1–10. [DOI]

Stuart, B.H., 2004. *Infrared Spectroscopy: Fundamentals and Applications*.

Survase, A. and Kanase, S., 2022. Green synthesis of TiO_2 nanospheres by Aspergillus eucalypticola SLF1 and dye degradation. *Ceramics International*, 49(10), pp. 14964–14980. [DOI]

Van Dyk, J.C., Pieterse, G.M. and van Vuren, J.H.J., 2007. Histological changes in liver of Oreochromis mossambicus after cadmium and zinc exposure. *Ecotoxicology and Environmental Safety*, 66, pp. 432–440. [DOI]

Vasantharaj, S., Sathiyavimal, S., Senthilkumar, P., Lewis-Oscar, F. and Pugazhendhi, A., 2019. Biosynthesis of iron oxide nanoparticles using leaf extract of Ruellia tuberosa. *Journal of Photochemistry and Photobiology B: Biology*, 192, pp. 74–82. [DOI]

Velusamy, P., Kumar, G.V., Jeyanthi, V., Das, J. and Pachaiappan, R., 2016. Bio-inspired green nanoparticles: synthesis, mechanism and antibacterial application. *Toxicological Research*, 32, p. 95. [DOI]

Vu, X.H., Phuoc, L.H., Dien, N.D., Pham, T.T.H. and Thanh, L.D., 2019. Photocatalytic degradation of Methylene Blue (MB) over α-Fe_2O_3 nanospindles prepared by a hydrothermal route. *Journal of Electronic Materials*, 48, pp. 2978–2985. [DOI]

Huang, Y., Ding, D., Zhu, M., Meng, W., Huang, Y., Geng, F., Li, J., Lin, J., Tang, C. and Lei, Z., 2015. Facile synthesis of α-Fe_2O_3 nanodisk with superior photocatalytic performance and mechanism insight. *Science and Technology of Advanced Materials*, 16, p. 014801. [DOI]

Wu, K., Shi, M., Pan, X., Zhang, J., Zhang, X., Shen, T. and Tian, Y., 2022. Decolorization and biodegradation of methylene blue dye by ligninolytic enzyme-producing Bacillus thuringiensis. *Enzyme and Microbial Technology*, 156, p. 109999. [DOI]

Zambare, P., Survase, A. and Kanase, S., 2023. Green synthesis of copper nanoparticles using leaf extract of Ocimum sanctum and its antimicrobial activity. *International Journal of Pharmaceutical Investigation*, 13(1), pp. 106–112. [DOI]

Zhao, H., Huang, M., Wu, J., Wang, L. and He, H., 2016. Preparation of Fe_3O_4@PPy magnetic nanoparticles for preconcentration of phthalates. *Journal of Chromatography B*, 1011, pp. 33–44. [DOI]

Nature Environment and Pollution Technology
An International Quarterly Peer-Reviewed Open Access Journal

p-ISSN: 0972-6268 | e-ISSN: 2395-3454 Vol. 25 | No. 4 | Article ID D1878 | 2026

RESEARCH ARTICLE https://doi.org/10.46488/NEPT.2026.v25i04.D1878 OPEN ACCESS

Insights into WRF-Chem Sensitivity in a Coastal Region of Morocco: Chemical Mechanisms, Nesting Options, and Physical Parameterization

Karima Iraoui[1]†, Rachid Moustabchir[1], Hicham Charifi[1], Abdelfettah Benchrif[2] and Ahmed Chirmata[3]
[1]Physics of Environment and Plasmas (PEP), LMER, Faculty of Science, Ibn Zohr University, Agadir, Morocco
[2]Geochemistry and Chemical Pollution Unit (UGPC), National Centre for Nuclear Energy, Science and Technology (CNESTEN), Morocco
[3]Environment Department, Wilaya of Souss Massa Region, Agadir, Morocco
†Corresponding author: Karima Iraoui; karima.iraoui@edu.uiz.ac.ma

ARTICLE HISTORY

Received: 19-09-2025
Revised: 08-11-2025
Accepted: 27-01-2026

KEYWORDS

Modelling performance
Air quality modelling
Sensitivity analysis
Chemical mechanisms
WRF-Chem

CITE THIS ARTICLE

Iraoui, K., Moustabchir, R., Charifi, H., Benchrif, A. and Chirmata, A., 2026. Insights into WRF-Chem sensitivity in a coastal region of Morocco: Chemical mechanisms, nesting options, and physical parameterisation. *Nature Environment and Pollution Technology*, 25(4), D1878. https://doi.org/10.46488/NEPT.2026.v25i04.D1878

COPYRIGHT & LICENCE

© 2026 The Authors
Open Access under CC BY 4.0.

PUBLISHED BY

TECHNOSCIENCE PUBLICATIONS

ABSTRACT

The performance of the Weather Research and Forecasting model coupled with chemistry (WRF-Chem) depends on the accuracy of input data and parameterisation schemes. This study examined the sensitivity of WRF-Chem version 4.4.2 to various domain configurations, chemical mechanisms, and physics parameterizations. The model was applied to predict air quality pollutants (PM_{10}, O_3, CO, NO_2, SO_2) and meteorological variables (wind speed and temperature) for the first time over the Moroccan city of Agadir, which features complex topography and land use. Multiple simulations tested the sensitivity of these variables to different chemical mechanisms (MOZART, RACM, GOCART), nesting configurations (three nested domains at a 1:4 ratio and four nested domains at a 1:3 ratio), and planetary boundary layer (PBL) parameterizations (YSU, MYJ, MYNN2, QNSE). The modelled pollutant and meteorological data were then validated against surface observations using various statistical metrics. Results indicated that ozone (O_3) and NO_2 show limited sensitivity to domain configuration and chemical mechanisms, implying they are primarily influenced by local factors, especially emission patterns. Conversely, CO exhibits greater sensitivity to nesting choices due to its dependence on accurately capturing local emissions and atmospheric mixing. Similarly, concentrations of PM_{10}, SO_2, and CO strongly depend on the representation of physical and chemical processes within domain configurations and chemical schemes. Ozone estimates, however, are highly affected by physical parameterizations, particularly those influencing temperature, highlighting the importance of temperature and sunlight in ozone formation. Sensitivity analysis revealed that optimal configurations differ by variable, based on both spatial variation and statistical assessment. For physics parameterizations, the YSU PBL scheme was preferred for predicting wind speed and temperature. Among chemical schemes, GOCART proved most effective for PM_{10}, SO_2, and CO, while MOZART was best suited for O_3 and NO_2. The most efficient nesting setup was identified as three nested domains at a 1:4 ratio, balancing accuracy with computational efficiency. These findings suggest significant potential for improving air quality predictions in the region, though further refinement-particularly for PM_{10}, which exhibited the lowest model accuracy-remains necessary for future research.

1. INTRODUCTION

Air pollution is a pervasive and complex environmental problem that demands careful attention on a global scale. It results from a complex interplay between anthropogenic activities and natural processes that alter the composition of the Earth's atmosphere (World Health Organization 2006). The consequences of air pollution are becoming increasingly significant as humanity continues its trajectory

of industrialization, urbanization, and energy consumption, necessitating extensive investigation supported by robust research (Ciencewicki & Jaspers 2007). Due to rising levels of air pollution, billions of people are at risk of developing health problems (Sicard et al. 2021). Among air pollutants, ground-level ozone (O_3), nitrogen dioxide (NO_2), sulfur dioxide (SO_2), and particulate matter (PM_{10}/$PM_{2.5}$) have the most concerning effects on public health (Bălă et al. 2021, WHO 2003). These pollutants are associated with diseases such as asthma, chronic obstructive pulmonary disease, and cardiovascular disorders (Arghavani et al. 2019, Ciencewicki & Jaspers 2007, Luo et al. 2020). In addition to impairing visibility, air pollution may also retard plant growth and reduce plants' ability to resist certain pathogenic agents. For example, ozone can reduce the agricultural productivity of cereal crops (Arghavani et al. 2019, Manisalidis et al. 2020). For these reasons, it is important to study and forecast the concentrations of these pollutants to reduce their adverse effects on human health, climate, and atmospheric visibility (Lecoeur & Seigneur 2013).

Anthropogenic air pollution emissions significantly affect both the concentration and diversity of chemical components in the atmosphere. However, these emissions represent only one aspect of the factors influencing air quality. Weather conditions also play a significant role. Studies have shown that atmospheric stability, influenced by large-scale weather patterns (synoptic systems) and factors such as wind speed, humidity, and temperature, can substantially affect air quality (Alapaty et al. 2012, Bounakhla et al. 2023). Particulate matter, a major air pollutant, is formed through complex chemical reactions, highlighting the crucial role of atmospheric chemistry in determining air quality (Park 2021a, 2021b, Taşpınar 2015). Additionally, factors including terrain, land use, and other geographical characteristics influence the dispersion of pollutants throughout the environment.

Numerical models are valuable tools for predicting air pollution and understanding the physical and chemical processes involved (Sha et al. 2019). These tools, particularly meteorological models, play a vital role in improving our understanding of how meteorological conditions influence air quality (Liu et al. 2022). The accurate simulation of meteorological variables and chemical species depends on a thorough understanding of local meteorological processes, topography, and pollutant emissions (Misenis & Zhang 2010). Since air pollutants undergo complex chemical reactions in the atmosphere, air quality models combine meteorological forecasts with atmospheric chemistry modelling tools to predict pollution levels (Menut et al. 2021).

Currently, there are two main approaches to analyzing air quality: (i) a qualitative approach based on the study of factors affecting air quality, including industrial activities and societal influences, while considering factors such as population growth, waste incineration, coal combustion, and vehicle exhaust emissions, and (ii) a quantitative approach based on pollutant transport and diffusion mechanisms (Li et al. 2021, Liu et al. 2022). Examples of quantitative approaches include statistical and deterministic models. Statistical methods use historical data to predict the future behavior of various air quality parameters (Qiu et al. 2022). This approach has been widely used for air pollution prediction. For instance, studies have assessed PM□□ and ozone concentrations using conventional statistical methods such as multiple linear regression (MLR) (e.g., Iraoui et al. 2023, Mohammed & Abualqumboz 2018, Mohd Napi et al. 2020, Nazif et al. 2016, Siegfried et al. 2005, Yorkor & Leton 2017), as well as artificial intelligence (AI) techniques, including support vector machines (SVMs), artificial neural networks (ANNs), and deep learning (DL) (Abdul-Wahab & Al-Alawi 2002, Adnane et al. 2020, Bozkurt 2014, Chen et al. 2013, Luna et al. 2014, Park 2021b, Taşpınar 2015, Tebal & Pinang 2011, Wang et al. 2003). While some studies suggest that artificial intelligence methods can achieve higher predictive accuracy, conventional statistical techniques also provide valuable insights. However, statistical models often treat the system as a "black box" and may not explicitly identify the most influential variables. Furthermore, their predictive accuracy depends heavily on the quality and quantity of historical data (Mohan et al. 2011).

Unlike statistical models, deterministic models rely on established principles of chemistry, meteorology, and fluid dynamics. They use mathematical equations to describe how pollutants are transported, transformed, and deposited in the atmosphere, thereby establishing cause-and-effect relationships between the model inputs (initial conditions) and outputs (predictions). Deterministic models are generally classified into two categories: sequential (also known as coupled offline) models and integrated (online) models. Unlike sequential approaches, which treat meteorology and chemistry separately, online models such as WRF-Chem simulate both processes simultaneously. This enables a more comprehensive representation of atmospheric processes, as online models account for the influence of meteorological conditions on the formation, transport, and removal of pollutants. In WRF-Chem, both chemical and meteorological calculations share the same time step and use identical horizontal and vertical grids, facilitating this two-way interaction (Grell et al. 2005).

In recent years, WRF-Chem has become a widely used tool for researchers worldwide. Numerous studies have employed it to simulate both meteorological conditions and air quality using various chemical mechanisms, aerosol schemes, and photolysis options. However, only a limited

number of studies have evaluated WRF-Chem specifically in Morocco and the wider African region, where air quality modelling remains particularly challenging (Ajdour et al. 2020). Table 1 summarizes recent WRF-Chem studies conducted in different parts of the world. These studies highlight limitations in simulating certain air quality parameters, particularly PM_{10} and $PM_{2.5}$. These shortcomings are likely due to uncertainties in the input data and the lack of local emission inventories (Schindlbacher et al. 2021). To reduce discrepancies between modelled and observed pollutant concentrations, previous studies have emphasized the need to investigate the influence of input data sources and model configurations to improve model performance. Accordingly, considerable research has focused on evaluating how WRF-Chem performance varies with different chemical mechanisms, nesting ratios, and physical parameterizations. These studies play a crucial role in understanding how such adjustments influence model accuracy and help determine the optimal WRF-Chem configuration for different applications.

For example, Khan & Kumar (2019) investigated how the initial and boundary conditions for chemical species affect predictions using the MOZART-4 mechanism. Shimada et al. (2011) compared various planetary boundary layer (PBL) schemes within the WRF-ARW model to determine which scheme best reproduces wind speeds over Japan. Yu et al. (2022) evaluated different parameterisation options for the planetary boundary layer (PBL), microphysics (MP), and shortwave/longwave radiation (SW-LW) to identify the WRF model configuration that most accurately simulates wind fields under stable atmospheric conditions in North China. Finally, Cifuentes et al. (2021) analyzed how factors such as lateral chemical boundary conditions (LCBC), domain configurations, nesting options, and chemical mechanisms influence the model's ability to predict CO, O_3, PM_{10}, and $PM_{2.5}$.

Although previous studies have advanced our understanding of air quality modelling, there remains a knowledge gap regarding the optimal chemical mechanism for different regions. The performance of these mechanisms can vary considerably depending on geographical location. This study aims to address this gap by identifying a chemical mechanism that accurately represents air quality conditions in Morocco and North Africa, where such studies remain

Table 1: Summary of WRF-Chem studies reviewed, highlighting geographic focus and key findings.

Study	Model/study area	Study overview
(Kant et al. 2021)	WRF-Chem/India	• In this study, the WRF-Chem numerical model was used to analyse the effects of aerosols on cloud microphysical properties during winter in India in February 2016. The model's performance was assessed for rainfall, aerosol optical depth (AOD), temperature, and wind, showing consistent RMSE, MSE, and MB values in simulations DEF (which deactivated wet filtering and cloud chemistry but activated both aerosol effects) and INDEF (considering indirect aerosol impacts). However, the LCINDEF simulation, which included all INDEF factors with a 50% reduction in anthropogenic emissions, exhibited significant errors.
(Singh et al. 2021)	WRF-Chem/India	• This study analyses an extreme dust episode in India using WRF-Chem, focusing on atmospheric dust dynamics and its impacts on ecosystems and human health. Model evaluation, through categorical validation, indicates a strong correspondence between reanalysis and observational datasets and WRF-Chem's dust load simulations, showing a 0% false alarm rate, a detection likelihood between 78% and 92%, and an accuracy range of 79% to 90%.
(Sicard et al. 2021)	WRF-Chem/ Asian region	• The study evaluates the WRF-Chem model's effectiveness in simulating atmospheric physics and chemistry over Asia. It found that the model accurately approximates spatial distributions of O_3, especially in summer, but significantly underestimates NO_2 concentrations.
(Wang et al. 2020)	WRF-Chem/ Sichuan Basin (China)	• In this study, the WRF-Chem model was utilized to simulate $PM_{2.5}$ and O_3 in the Sichuan Basin of China during January and July 2015. The results indicated that $PM_{2.5}$ levels were accurately modelled for all cities in both months, with mean fractional bias of 0.6 and mean normalized bias of 0.7. Ozone simulation showed good agreement with observational data in July, but concentrations were generally overestimated in January, primarily due to uncertainties in emissions and photochemical processes affecting winter O_3 levels.
(Saidou Chaibou et al. 2019)	WRF-Chem/ North Africa	• This study analyses dust extinction and vertical profiles in North Africa using data from CALIPSO and AERONET, combined with WRF-Chem simulations from the summer of 2006. It aims to enhance understanding of atmospheric dust behavior and its regional impacts. The results indicate that all modelling schemes effectively captured the spatial coherence of total dust emissions. However, differences in threshold friction velocity and soil moisture adjustments led AFWA and UoC schemes to diverge from GOCART regarding extent, magnitude, and patterns, while still showing comparable regional distribution. GOCART displayed good consistency with AFWA and UoC schemes, evidenced by correlation coefficients of 0.5 and 0.8, respectively, despite emitting larger dust flows at times.

limited. To this end, this study uses the WRF-Chem model for the first time to simulate meteorological fields and air quality over Agadir, Morocco. We aim to identify the optimal model configuration by testing different chemical mechanisms, nesting ratios, and physics parameterizations. The resulting configuration will be used for future air quality simulations in Agadir and may also be adapted for other Moroccan cities. This research not only advances air quality modelling in Agadir by employing the more comprehensive WRF-Chem model instead of the previously used WRF-CHIMERE model (e.g., Ajdour et al. 2020, Ajdour 2022), but also establishes a foundation for future research in this field.

The methodology used to assess the performance of the WRF-Chem system and the sensitivity analyses conducted in this study comprises several stages, which are described in the following sections. First, we describe the study area (Morocco, centered on Agadir City) and the model configuration, including the domain size and nesting options. We also describe the datasets used and the physics options selected for the simulations. Next, we present the results of the sensitivity analyses, focusing on how different chemical mechanisms and nesting scenarios affect pollutant concentrations. This analysis helps us understand how these settings influence the model's overall performance. Finally, we summarize the key findings of this investigation and identify the model configurations that have the greatest impact on model performance.

2. MATERIALS AND METHODS

2.1. Description of the Case Study

Agadir is a prominent city located along the southwestern coast of Morocco (Fig. 1). Recently, it has become an area of increasing scientific interest due to its unique geographical and climatic conditions, which influence local air quality (Ajdour et al. 2020, Chirmata et al. 2017). As the capital of the Agadir-Ida Outanane Province and a bustling center for tourism and agriculture (Bouchriti et al. 2023), Agadir experiences a range of air quality issues that reflect both its economic activities and natural environment. The city's location along the Atlantic Ocean and at the foothills of the Atlas Mountains creates distinctive meteorological patterns that influence pollutant dispersion and accumulation (UNECA and UNECE 2014). Following Agadir's reconstruction after the 1960 earthquake, the city experienced rapid urbanization and industrial development. While these developments have boosted the local economy, they have also increased emissions of air pollutants, compounded by pesticide application and fertilizer dust. Additionally, the city's major seaport contributes to air pollution through marine and shipping emissions, further exacerbating the urban air quality situation. Although air quality in other Moroccan cities has received greater research attention, Agadir remains relatively understudied. This lack of information on air quality dynamics in Agadir motivated the present study, which investigates the sensitivity of the WRF-Chem model for this specific region.

2.2. WRF-Chem Model and Setup

WRF-Chem (Weather Research and Forecasting model with Chemistry) is an advanced numerical model designed to integrate atmospheric chemistry with meteorology. The model was developed collaboratively by NOAA, DOE/PNNL, NCAR, and other research institutes (https://www2.acd.ucar.edu/wrf-chem). It simulates the interactions between chemical and meteorological processes to predict air quality under varying atmospheric conditions. The model accounts for both anthropogenic emissions and biogenic sources, enabling detailed investigations of the formation, dispersion, and deposition of pollutants (Grell et al. 2005).

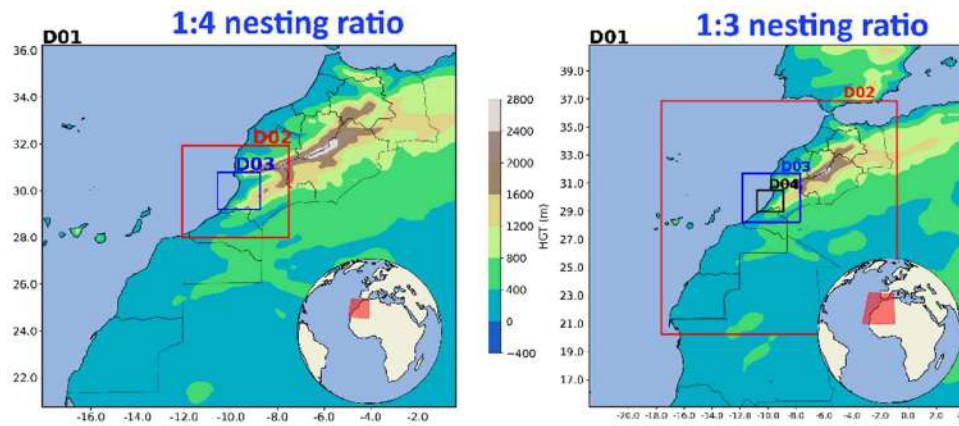


Fig. 1: Study area and domain configuration for nesting ratios of 1:4 (left panel) and 1:3 (right panel).

In this study, WRF-Chem was used to simulate local air quality and atmospheric chemistry. The lateral chemical boundary conditions (LCBC) were based on outputs from the Community Atmosphere Model with Chemistry (CAM-Chem), provided every 6 hours. These outputs supplied comprehensive information on global atmospheric composition, which was essential for initializing and constraining the regional chemical environment. Meteorological boundary conditions were derived from the National Centers for Environmental Prediction (NCEP) Global Forecast System (GFS) data, with a spatial resolution of 0.5˚ × 0.5˚ and a forecast lead time of 3 hours.

The simulation domain was configured using the Mercator projection and included multiple nested domains to achieve progressively finer spatial resolutions. As illustrated in Fig. 1, two domain configurations were employed. The first configuration comprised three nested domains with a 1:4 nesting ratio, in which D01 (the coarsest domain) had a spatial resolution of 16 km, D02 had a resolution of 4 km, and D03 had a resolution of 1 km. The second configuration consisted of four nested domains with a 1:3 nesting ratio, in which D01 had a resolution of 27 km, D02 had a resolution of 9 km, D03 had a resolution of 3 km, and D04 had a resolution of 1 km.

For the 1:3 nesting ratio, the outermost domain (D01) encompassed southern Spain, northern Mauritania, eastern Algeria, and extended westward into the Atlantic Ocean. The second domain (D02) covered the entire Moroccan territory. The innermost domains (D03 and D04) were designated to focus on the study area surrounding Agadir City. A one-way nesting technique was employed for this domain configuration. In this approach, the outermost domain (D01) provided the meteorological data and boundary conditions that drove the simulations within the smaller nested domains, with no feedback from the nested domains to the parent domain. Table 2 summarizes the different model configurations used in this study.

Regarding the emissions data, our study utilized a combination of datasets to accurately represent various emission sources. Due to the absence of a local emission inventory for Agadir, we used the Emission Database for Global Atmospheric Research (EDGAR), which provides a global inventory of anthropogenic emissions at a 1° × 1° horizontal resolution for the year 2010. The EDGAR emissions were spatially interpolated onto the nested WRF-Chem domains using the prep_chem_sources utility, which conserves total mass while redistributing emissions according to the model grid resolution (16 km, 4 km, and 1

Table 2: Setup and sensitivity testing of the WRF-Chem model (version 4.4.2) used in this study.

Model configurations	Options used and sensitivity analysis
Domain	Agadir, Morocco
Domain resolution	3 nested domains (16 km, 4 km, 1 km) 4 nested domains (27 km, 9 km, 3 km, 1 km)
Vertical levels	31 vertical layers
Simulation time	7 days (2–8 May)
Spin-up time	24 h
IC/BC (chemistry)	MOZART global model
IC/BC (meteorology)	NCEP (resolution: 0.5° × 0.5°, 3 h interval)
Biogenic emission inventory	MEGAN
Anthropogenic emission inventory	EDGAR
Microphysics	Morrison double moment
Longwave radiation	RRTMG (Rapid Radiative Transfer Model)
Shortwave radiation	RRTMG (Rapid Radiative Transfer Model)
Surface layer	MM5 similarity based on Monin–Obukhov scheme
Land-surface physics	Noah-MP (multi-physics) land surface model
Planetary boundary layer	Yonsei University scheme Mellor-Yamada-Janjic Quasi-Normal Scale Elimination Mellor-Yamada-Nakanishi-Niino Level 2.5
Chemistry options	Regional Atmospheric Chemistry Mechanism (RACM)/chem_opt=201 Model for Ozone and Related Chemical Tracers (MOZART)/chem_opt=43 Global Oceans Chemistry Aerosol Radiation and Transport (GOCART)/chem_opt=301

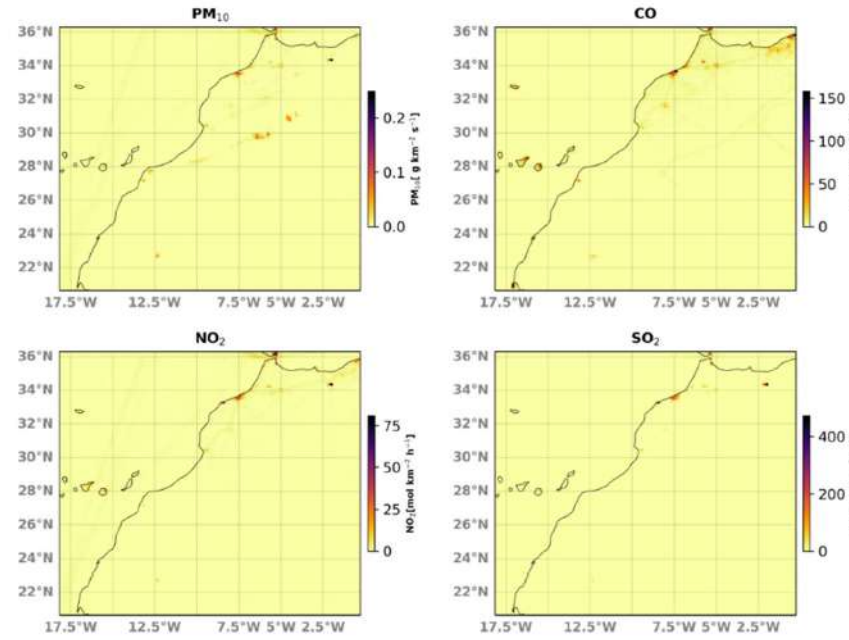


Fig. 2: Spatial pattern of anthropogenic emissions from EDGAR over D01.

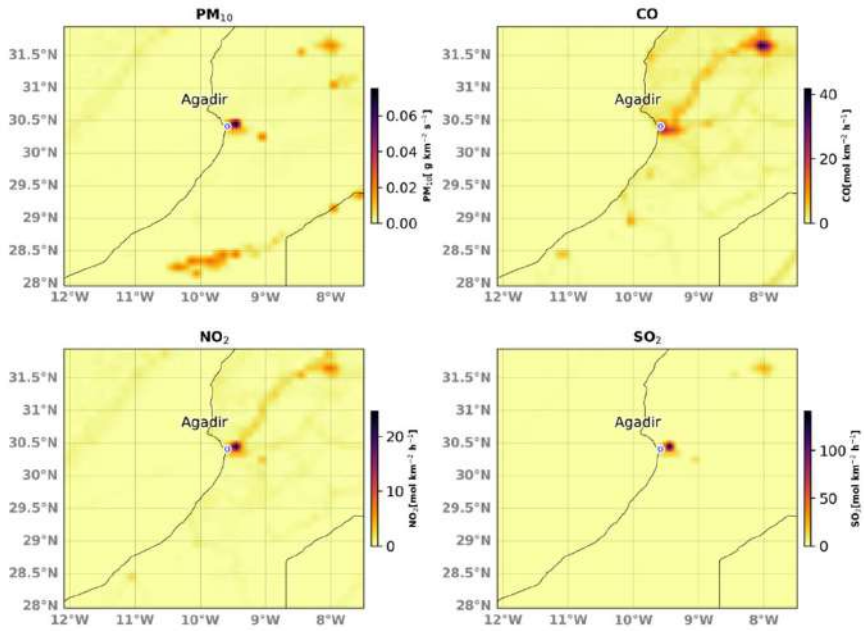


Fig. 3: Spatial pattern of anthropogenic emissions from EDGAR over D02.

km over Agadir). The high-resolution inner domain allowed emissions to be redistributed according to local land-use patterns, road density, and urban extent implicitly represented in the WRF geographical datasets. This framework enabled a detailed representation of anthropogenic emissions across the simulation domains. Figs. 2 and 3 illustrate the spatial distribution of anthropogenic emissions from EDGAR across domains D01 and D02, respectively, for the 1:4 nesting ratio. Biogenic emissions were computed online using the Model of Emissions of Gases and Aerosols from Nature (MEGAN), based on environmental conditions and vegetation types. High-resolution biomass-burning emissions

were incorporated from the Fire Inventory from NCAR (FINNv1.5). The Model for Ozone and Related Chemical Tracers (MOZART-4) was used to provide the initial and lateral boundary conditions (IC/BC) for chemical species in WRF-Chem.

2.3. Sensitivity Runs

To identify the optimal configuration of WRF-Chem version 4.4.2 for predicting air quality variables (carbon monoxide (CO), nitrogen dioxide (NO_2), ozone (O_3), particulate matter (PM_{10}), and sulphur dioxide (SO_2)) and meteorological variables (wind speed (WS) and temperature (T)) over the study area, the model's sensitivity to domain configuration, chemical mechanisms, and physics parameterizations was investigated. This involved a systematic exploration through a series of controlled simulations. Each factor was varied independently to isolate its influence on the accuracy of the model outputs. The procedures followed for these sensitivity tests are illustrated in Fig. 4. The sensitivity of the domain configuration was investigated using different nesting strategies, ranging from broader regional scales to more focused local scales. Specifically, simulations were conducted using both three nested domains (1:4 nesting ratio, 3D) and four nested domains (1:3 nesting ratio, 4D), as described previously.

Three chemical mechanisms were evaluated for their suitability in WRF-Chem simulations. The first mechanism, the Regional Atmospheric Chemistry Mechanism (RACM), includes more than 240 chemical species and 840 reactions, providing a comprehensive representation of atmospheric chemistry (Ha 2022). It was selected because it is a revised version of the Regional Acid Deposition Model, version 2 (RADM2), and provides a more detailed representation of organic chemistry for regional atmospheric pollution modelling. The Model for Ozone and Related Chemical Tracers (MOZART) was also evaluated. This mechanism includes approximately 150 chemical species and more than 300 reactions, providing a more focused representation of atmospheric chemistry (Emmons et al. 2010). It is also consistent with the chemistry used in the global model that provides the chemical boundary conditions for the present simulations. Finally, the Global Ozone Chemistry Aerosol Radiation and Transport (GOCART) mechanism was included in the evaluation. GOCART specializes in simulating complex aerosol interactions, complementing the capabilities of RACM and MOZART (Mian Chin & Lin 2000). The GOCART module simulates the major tropospheric aerosol components, including sulfate, dust, black carbon, organic carbon, and sea salt. It also includes algorithms for dust and sea salt emissions, dry deposition, and gravitational settling. Together, these mechanisms provide detailed representations of atmospheric chemistry across different atmospheric layers and spatial scales, ranging from regional to global.

Regarding the physics schemes, four planetary boundary layer (PBL) parameterisation schemes were evaluated to assess their influence on model performance. The Yonsei University (YSU) scheme was selected because of its non-local closure approach, which is effective for representing vertical transport under convective conditions (Hu et al. 2013). The Mellor-Yamada-Janjic (MYJ) scheme was chosen for its detailed representation of turbulent kinetic energy under both stable and unstable atmospheric conditions (Hu et al. 2010). The Quasi-Normal Scale Elimination (QNSE) scheme was included because of its ability to simulate stable boundary layers by incorporating scale-dependent dynamical processes (Sukoriansky et al. 2006). Finally, the Mellor-Yamada-Nakanishi-Niino Level 2.5 (MYNN2) scheme was selected for its comprehensive representation of boundary layer turbulence and cloud-top cooling effects (Kitamura 2010). This comprehensive sensitivity analysis, encompassing different physics schemes and chemical mechanisms (Fig. 4), was conducted to refine the WRF-Chem model and improve its predictive performance and reliability for air quality modelling in the study region. More details on the physical parameterizations used are available at http://www2.mmm.ucar.edu/wrf/users/phys_references.html

2.4. Datasets for Model Evaluation

During 2010, daily average concentrations of air pollutants and meteorological parameters were collected from a fixed monitoring station located at a school in the city center of Agadir (urban area). The data were provided by the Department of Environment, Wilaya of Agadir, Morocco. The monitored air pollutants included CO, NO_2, O_3, PM_{10}, and SO_2, while the meteorological parameters included temperature (T) and wind speed (WS). Although the availability of observational data limited the analysis to this period, owing to the lack of more recent data, the study still provides valuable insights into air quality trends and their impacts in Agadir. The methodology established in this study can be applied to future datasets as they become available, ensuring the continued relevance and applicability of this research.

2.5. Model Evaluation

The performance of the model was evaluated by comparing the simulated concentrations of air pollutants (PM_{10}, O_3, NO_2, CO, and SO_2) and the simulated meteorological variables (T and WS) with in situ measurements. Several statistical

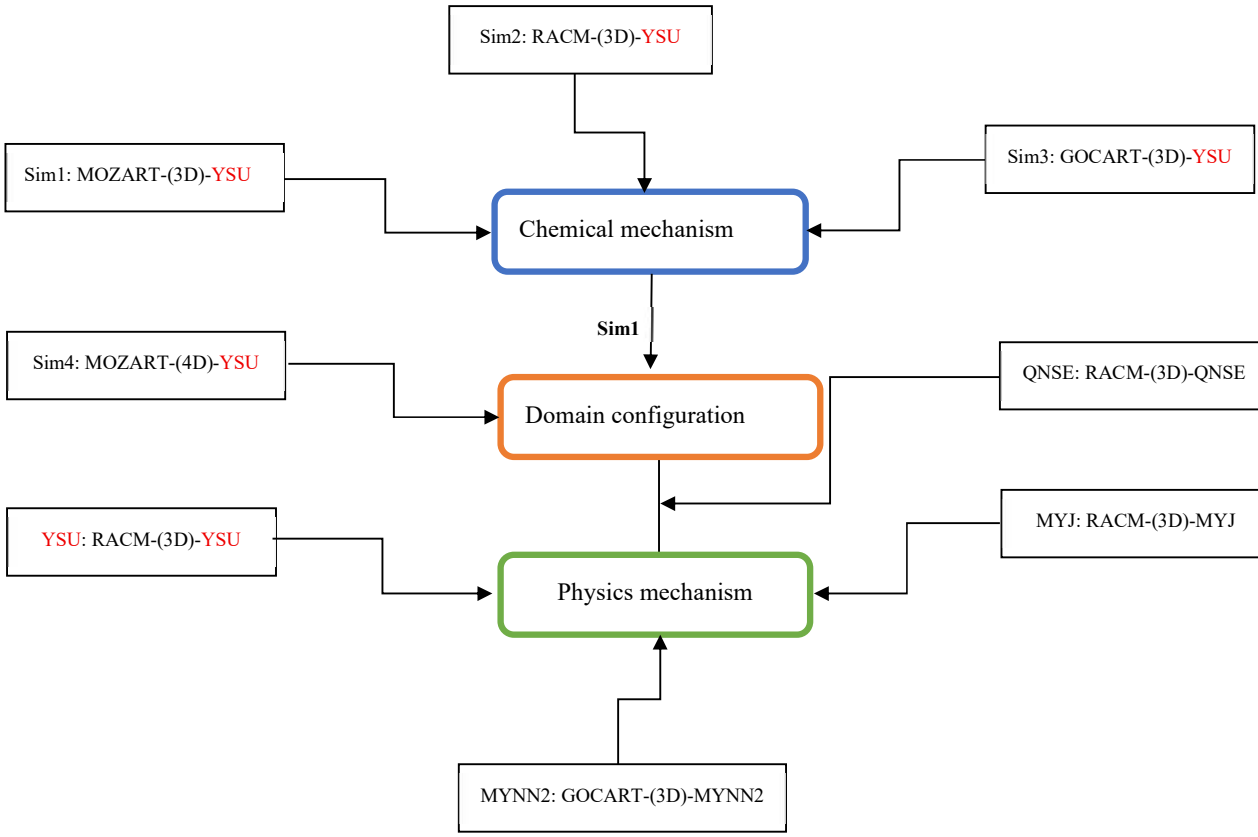


Fig. 4: Flowchart of the research workflow, outlining the specific steps followed in this study to analyse the sensitivity of the WRF-Chem model. **Acronyms: RACM**: Regional Atmospheric Chemistry Mechanism, **MOZART**: Model for Ozone and Related Chemical Tracers, **GOCART**: Global Oceans Chemistry Aerosol Radiation and Transport, **3D**: Three nested domains with a 1:4 nesting ratio, **4D**: Four nested domains with a 1:3 nesting ratio, **YSU: Yonsei University Scheme**, **MYJ**: Mellor-Yamada-Janjic, **QNSE**: Quasi-Normal Scale Elimination, **MYNN2**: Mellor-Yamada-Nakanishi-Niino Level 2.5.

performance metrics were used to assess the model's performance, including Pearson's correlation coefficient (r), mean bias (MB), normalized mean bias (NMB), root mean square error (RMSE), mean absolute gross error (MAGE), and the index of agreement (IOA). These metrics were calculated as follows:

$$r = \frac{\sum_i^n [(O_i - \bar{O})(P_i - \bar{P})]}{\sqrt{\sum_i^n (O_i - \bar{O})^2 * \sum_i^n (P_i - \bar{P})^2}} \quad ...(1)$$

- The correlation coefficient ranges from -1 to 1, with r = 0 indicating no correlation; the strength of the correlation increases as the coefficient approaches -1 or 1.

$$MB = \frac{1}{n}\sum_{i=1}^{n}(P_i - O_i) \quad ...(2)$$

- A positive value of *MB* indicates overestimation of the simulated data, whereas a negative value indicates underestimation. A *MB* value of zero suggests that model predictions are unbiased relative to observations.

$$NMB = \frac{\sum_{i=1}^{n}(P_i - O_i)}{\sum_{i=1}^{n} O_i} \quad ...(3)$$

- A positive *NMB* indicates that predicted variables are higher than observed ones, while a negative *NMB* indicates underprediction. A value of zero implies no bias, indicating ideal model performance.

$$MAGE = \frac{1}{n}\sum_{i=1}^{n}|P_i - O_i| \quad ...(4)$$

- A low value of *MAGE* indicates greater similarity between observed and simulated values.

$$RMSE = \sqrt{\frac{\sum_{i=1}^{n}(P_i - O_i)^2}{n}} \quad ...(5)$$

- A lower value of *RMSE* indicates good agreement between simulated and observed data.

$$IOA = 1 - \frac{\sum_{i=1}^{n}(P_i - O_i)^2}{\sum_{i}^{n}(|P_i - \bar{O}| + |O_i - \bar{O}|)^2} \quad ...(6)$$

- The *IOA* provides a value between 0 and 1, where 1 indicates perfect agreement between model predictions and observed data. A higher *IOA* value indicates a better predictive performance, taking into account both the magnitude and the direction of deviations between the model and observations.

where:

P_i and O_i represent the predicted and observed variables, respectively;

$\bar{P}$ and $\bar{O}$ are the mean values of the predicted and observed values, respectively;

n is the total number of observations used.

3. RESULTS AND DISCUSSION

This section presents the simulation results for air quality variables (PM_{10}, O_3, CO, and NO_2) and meteorological variables (WS and T). Sensitivity analyses were performed using different chemical mechanisms, nesting ratios, and physical parameterizations to identify the most effective WRF-Chem configurations for the study area. These configurations can be recommended for future research. Python was used to analyse the model outputs and calculate the performance metrics. The results of this study are compared with those of a previous WRF-CHIMERE simulation conducted over the same study area and during the same period (Ajdour et al. 2020, Ajdour 2022), using both qualitative (spatial variations) and quantitative (statistical metrics) approaches.

Before a detailed examination of the model sensitivity, the spatial distributions of pollutants are first evaluated. Figs. 5 and 6 depict the average pollutant concentrations simulated over two domains (D01 and D02) using a 1:4 nesting ratio. These Figs. provide the foundation for the sensitivity analysis by establishing the initial pollutant dispersion patterns across the two domains. Such visualizations are essential for understanding the initial conditions and environmental setting, which influence the model's subsequent sensitivity to the different parameters evaluated.

The study area has been identified as having high PM_{10} concentrations due to various pollution sources, including industrial activities, waste incineration, and traffic-related emissions. In 2010, the primary sources of pollution were

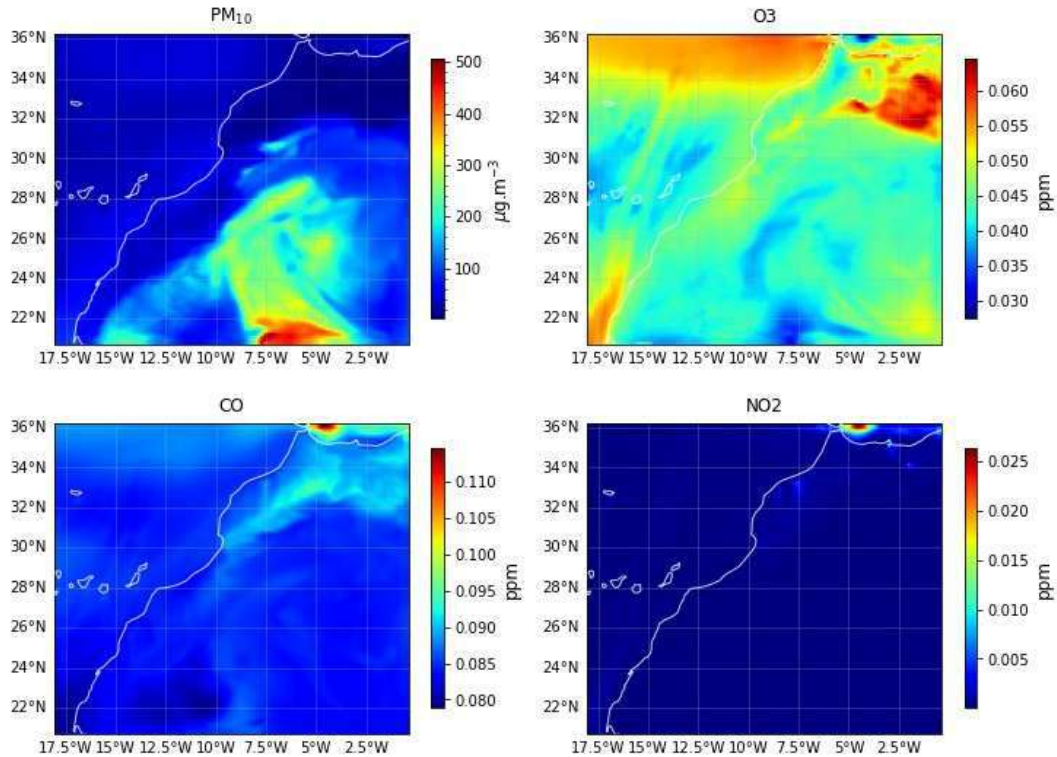


Fig. 5: Average concentration maps for various pollutants across the study domain on May 2, 2010 (D01).

the cement plant, which was still operational at the time, and road traffic (Leghrib et al. 2018). In addition to these sources, the region is affected by the transport of Saharan dust. It should also be noted that the region is located in southern Morocco, making it susceptible to southerly airflow that carries dust storms. These dust storms, in turn, result in elevated PM_{10} concentrations. The Figs. clearly show that PM_{10} concentrations are higher in areas closer to the Sahara, highlighting the influence of geographical and environmental factors on air quality.

3.1. Model Evaluation

3.1.1. Model Evaluation of Meteorological Variables

Table 3 summarizes the performance metrics of WRF-Chem and compares them with those of WRF-CHIMERE for the same case study, with a particular focus on meteorological variables, including wind speed and temperature. The results presented in Table 3 show strong Pearson correlation coefficients (r), ranging from 0.84 to 0.90, for all simulated temperatures, indicating good agreement between the observed and simulated values. All model configurations produced satisfactory results, with RMSE values ranging from 2.5 to 3.0 °C. Furthermore, the temperature mean bias (MB) ranged from 2.12 to 2.77 °C, indicating that the model generally overestimated temperature. Similarly, the wind speed MB ranged from 0.92 to 1.32 m s^{-1}, indicating a consistent overestimation of wind speed. However, for the WRF-Chem configurations, the correlation coefficients for wind speed remained satisfactory, ranging from 0.63 to 0.79, and the RMSE values (0.95–1.53 m s^{-1}) were acceptable and showed an improvement over those reported in the previous WRF-CHIMERE study (Ajdour et al. 2020, Ajdour 2022). Previous studies have reported that both WRF-Chem and WRF-CHIMERE have difficulty accurately simulating wind speed and wind direction (Yu et al. 2022). Therefore, this study sought to improve the physical parameterizations to reduce the bias between the observed and simulated wind speeds, given their critical role in pollutant dispersion.

The simulation results indicate that the predictions of wind speed and temperature are satisfactory. Compared with the previous WRF-CHIMERE study conducted for the same case study, the present study demonstrates improved wind speed simulations. This improvement is clearly illustrated in Fig. 7, which presents the time series of wind speed (WS) and temperature (T) over the simulation period. These improvements are important for more accurately predicting pollutant dispersion, which is strongly influenced by meteorological conditions (Wang & Li 2022).

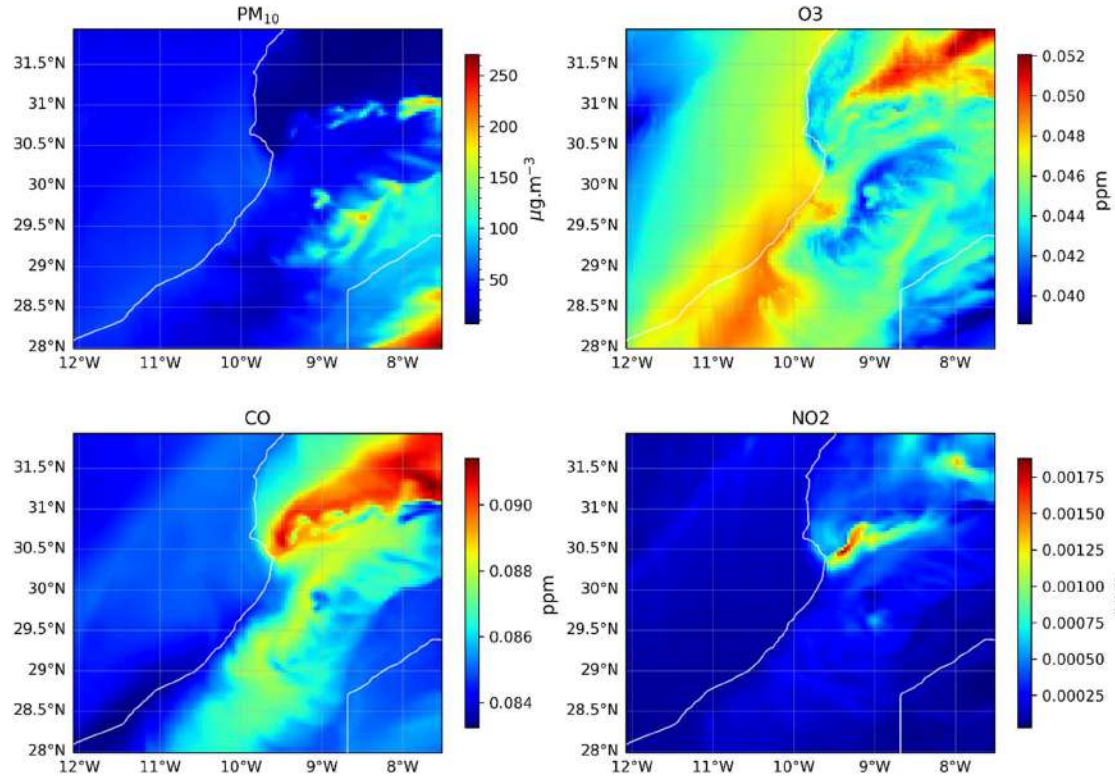


Fig. 6: Average concentration maps for various pollutants across the study domain on May 2, 2010 (D02).

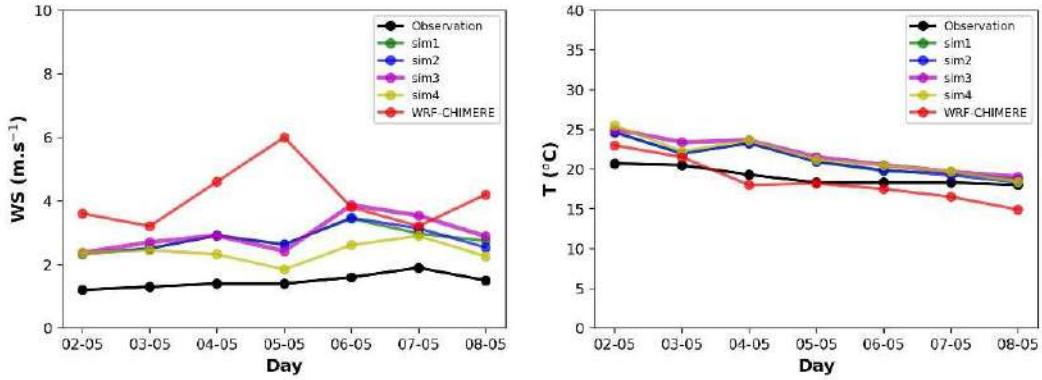


Fig. 7: Time series of daily ground-level wind speed (WS) and temperature (T) during the simulation period from May 2 to May 8.

Table 3: Summary of performance statistics for the sensitivity analyses.

Options	Variable	MB	MAGE	RMSE	NMB	NME	IOA	r
MOZART-(3D)-YSU	T[°C]	2.2	2.2	2.53	11.55	11.55	0.57	0.86
	WS	1.32	1.32	1.34	89.49	89.49	0.23	0.68
	O_3	-1.12	2.14	3.26	-2.04	3.9	0.93	0.92
	CO	2.02	6.65	8.06	10.09	33.25	0.26	-0.13
	NO_2	-15.79	15.79	15.83	-76.75	76.75	0.11	0.38
	PM_{10}	-47.39	47.39	50.23	-72.75	72.75	0.29	-0.13
	SO_2	0.39	1.64	1.98	3.97	16.92	0.37	0.05
RACM-(3D)-YSU	T(°C)	2.12	2.12	2.5	11.11	11.11	0.58	0.84
	WS	1.32	1.32	1.34	89.4	89.4	0.24	0.73
	O_3	8.63	8.63	9.59	15.69	15.69	0.69	0.83
	CO	5.99	7.89	9.46	29.97	39.44	0.46	0.31
	NO_2	-15.37	15.37	15.41	-74.72	74.72	0.11	0.21
	PM_{10}	-39.81	39.81	42.95	-61.12	61.12	0.32	-0.21
	SO_2	1.08	1.29	1.63	11.11	13.24	0.45	-0.01
GOCART-(3D)-YSU	T(°C)	2.53	2.53	2.93	13.28	13.28	0.53	0.84
	WS	0.92	0.92	0.95	62.54	62.54	0.33	0.63
	O_3	-7.95	7.95	8.95	-14.46	14.46	0.64	0.86
	CO	0.42	6.29	7.57	2.08	31.46	0.23	0.1
	NO_2	-15.2	15.2	15.21	-73.9	73.9	0.11	0.91
	PM_{10}	-28.38	28.38	33.85	-43.57	43.57	0.41	0.03
	SO_2	1.53	1.86	2.03	15.72	19.11	0.55	0.52
MOZART-(4D)-YSU	T(°C)	2.77	2.77	3.03	14.56	14.56	0.52	0.9
	WS	1.48	1.48	1.53	100.65	100.65	0.23	0.79
	O_3	-5.7	6.24	7.43	-10.37	11.34	0.75	0.76
	CO	1.97	7.52	8.84	9.87	37.62	0.18	-0.36
	NO_2	-15.9	15.9	15.98	-77.31	77.31	0.1	-0.02
	PM_{10}	-50.03	50.03	52.11	-76.81	76.81	0.28	0.02
	SO_2	-0.96	1.6	1.9	-9.91	16.47	0.49	0.23
WRF-CHIMERE	T(°C)	-0.54	1.49	1.75	-2.85	7.8	0.77	0.94
	WS	2.61	2.61	2.79	177.67	177.67	0.08	-0.22
	O_3	21.29	21.29	21.7	38.7	38.7	0.42	0.81
	CO	102.29	102.29	102.53	511.43	511.43	0.1	0.38
	NO_2	-18.5	18.5	18.53	-89.93	89.93	0.09	-0.22
	PM_{10}	-55.79	55.79	57.33	-85.64	85.64	0.26	-0.09
	SO_2	-7.17	7.17	7.34	-73.82	73.82	0.17	-0.31

3.1.2. Model Evaluation of Air Quality Variables

Table 3 summarizes the statistical metrics obtained from the various simulations of air quality variables, providing detailed insights into model performance across different pollutants. Notably, the O_3 simulations exhibited strong Pearson correlation coefficients, ranging from 0.76 to 0.92, indicating good agreement between the observed and simulated values. For NO_2, the correlation coefficients varied, with generally moderate values (0.21–0.38), except for Sim3 (GOCART-(3D)-YSU), which exhibited a strong correlation coefficient of 0.91. In contrast, the model produced low correlation coefficients for PM_{10} and SO_2, suggesting lower accuracy in simulating these pollutants.

In terms of mean bias (MB), O_3 concentrations were generally underestimated by the model, with one exception (Sim2: RACM-(3D)-YSU), in which O_3 was overestimated. Conversely, PM_{10} and NO_2 were consistently underestimated across all simulations, whereas CO and SO_2 were generally overestimated. These results differ from those obtained with WRF-CHIMERE, which tended to overestimate O_3 and underestimate SO_2. Low RMSE values were obtained for O_3, CO, and SO_2, indicating good model performance for these pollutants. The lowest RMSE values were 3.26 μg m^{-3} for O_3, 8.06 μg m^{-3} for CO, and 1.63 μg m^{-3} for SO_2. In contrast, PM_{10} and NO_2 exhibited higher RMSE values, reaching 42.95 μg m^{-3} and 15.98 μg m^{-3}, respectively.

A comparison with the WRF-CHIMERE performance metrics highlights the improvements achieved in this study:

- **O_3:** O_3 simulations showed substantial improvement. The RMSE decreased from 21.7 μg m^{-3} for WRF-CHIMERE to 3.26 μg m^{-3} in the present study. Similarly, the MB improved from 21.29 μg m^{-3} to −1.12 μg m^{-3}, while the correlation coefficient increased from 0.81 to 0.92. A substantial reduction in the normalized mean error (NME) was also observed, decreasing from 38.7 to 3.9.
- **CO:** The accuracy of CO simulations also improved. The RMSE decreased from 102.53 μg m^{-3} to 7.57 μg m^{-3}, and the MB improved from 102.29 μg m^{-3} to 0.42 μg m^{-3}. The correlation coefficient changed from 0.38 for WRF-CHIMERE to 0.10 for the GOCART-(3D)-YSU simulation.
- **NO_2:** Improvements were also observed for NO_2. The RMSE decreased from 18.53 μg m^{-3} to 15.21 μg m^{-3}, while the MB improved from −18.5 μg m^{-3} to −15.2 μg m^{-3}. The correlation coefficient increased substantially, from −0.22 to 0.91. In addition, the NME decreased from 89.93 to 73.9.
- **PM_{10}:** PM_{10} simulations also improved, with the RMSE decreasing from 57.33 μg m^{-3} for WRF-CHIMERE to 33.86 μg m^{-3}. The MB improved from −55.79 μg m^{-3} to −28.38 μg m^{-3}, although the correlation coefficient remained weak (−0.21 versus 0.09). The NME also decreased from 85.64 to 43.57.
- **SO_2:** Finally, SO_2 simulations showed a substantial improvement. The RMSE decreased from 7.34 μg m^{-3} to 1.63 μg m^{-3}, while the MB improved from −7.17 μg m^{-3} to 0.39 μg m^{-3}. The correlation coefficient increased from −0.31 to 0.52. The NME also improved considerably, decreasing from 73.82 to 13.24.

Overall, these results demonstrate significant improvements in air quality predictions across the study region, particularly for O_3, CO, and SO_2, surpassing the performance achieved by WRF-CHIMERE.

3.2. Chemical Mechanisms Comparison

Fig. 8 illustrates the mean differences in PM_{10}, O_3, CO, and NO_2 concentrations between the MOZART and GOCART chemical mechanisms. This figure provides a comprehensive overview of how each mechanism influences the simulation of different air pollutants. Positive differences indicate regions where MOZART predicts higher concentrations than GOCART, whereas negative differences indicate regions where GOCART predicts higher concentrations than MOZART.

PM_{10} concentrations are particularly sensitive to the choice of chemical mechanism. Across most of the domain, MOZART predicts higher PM_{10} concentrations than GOCART. This can be attributed to MOZART's more detailed treatment of non-methane volatile organic compound (NMVOC) emissions (Emmons et al. 2010) and their conversion into secondary organic aerosols (SOA) (Clappier et al. 2021), which are major components of PM_{10}. An exception is observed in the southeastern Saharan region, where the opposite trend occurs.

For O_3, negative differences predominate, indicating that GOCART generally predicts higher ozone concentrations than MOZART. This is likely due to GOCART's treatment of aerosol interactions, which may influence the scavenging of ozone precursors differently (Kong et al. 2015). Similarly, negative differences are observed throughout the study area for CO, indicating that MOZART predicts lower CO concentrations than GOCART. Finally, the spatial pattern of NO_2 differences closely resembles that of O_3 because of their strong chemical interdependence in urban photochemistry. Consequently, negative NO_2 differences are observed across most of the study area. An exception occurs around Agadir, where MOZART predicts higher NO_2 concentrations because of its more comprehensive treatment of NO_2 emissions and atmospheric lifetimes (Wang et al. 2021).

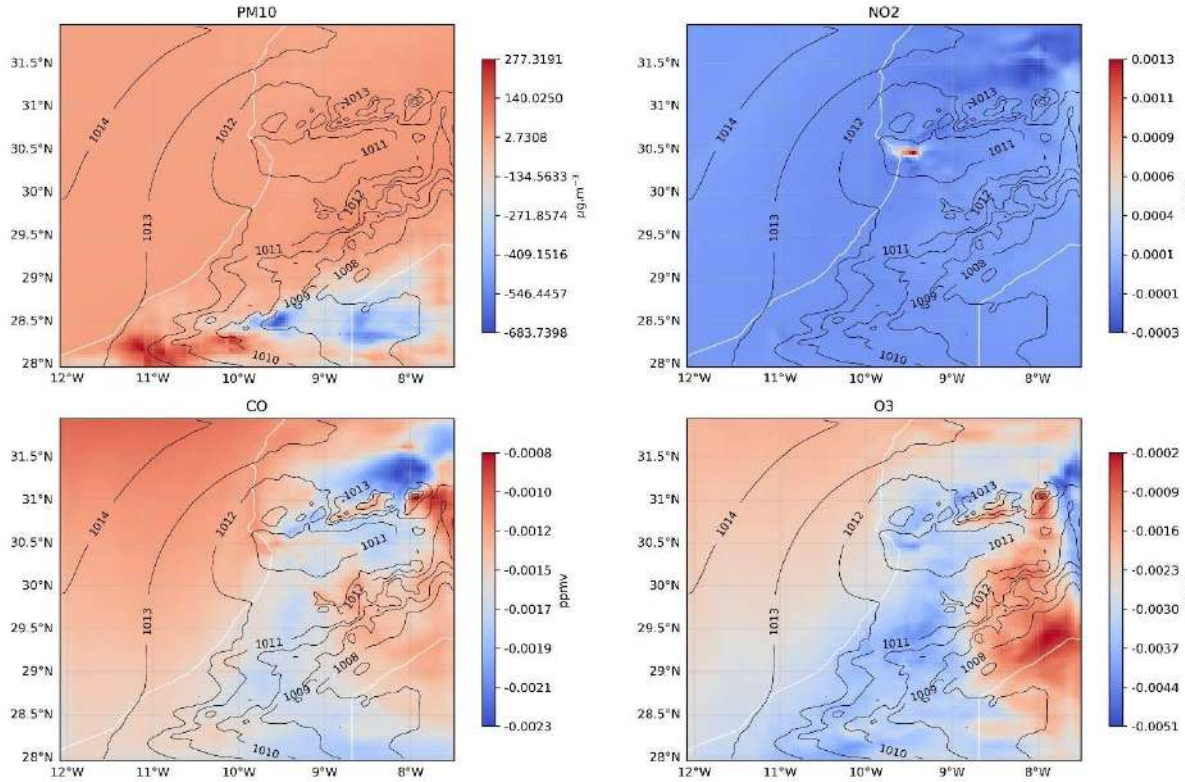


Fig. 8: Mean difference in PM_{10}, NO_2, CO, and O_3 concentrations between MOZART and GOCART.

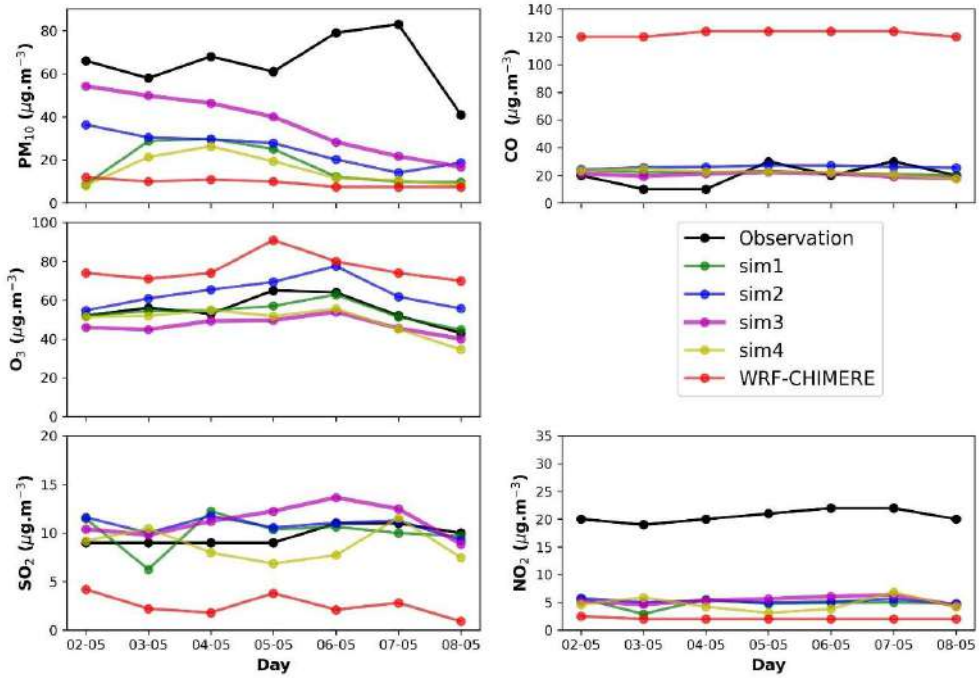


Fig. 9: Time series of daily concentrations of air quality variables (PM_{10}, O_3, SO_2, NO_2 and CO) during the simulation period from May 2 to May 8.

To facilitate comparisons among the different chemical mechanisms, the results of the present study can be compared with those of the previous study shown in Fig. 9. This figure presents time series of air quality variable concentrations simulated using the different chemical mechanisms (Sim1, Sim2, and Sim3). In addition, Figs. 10,

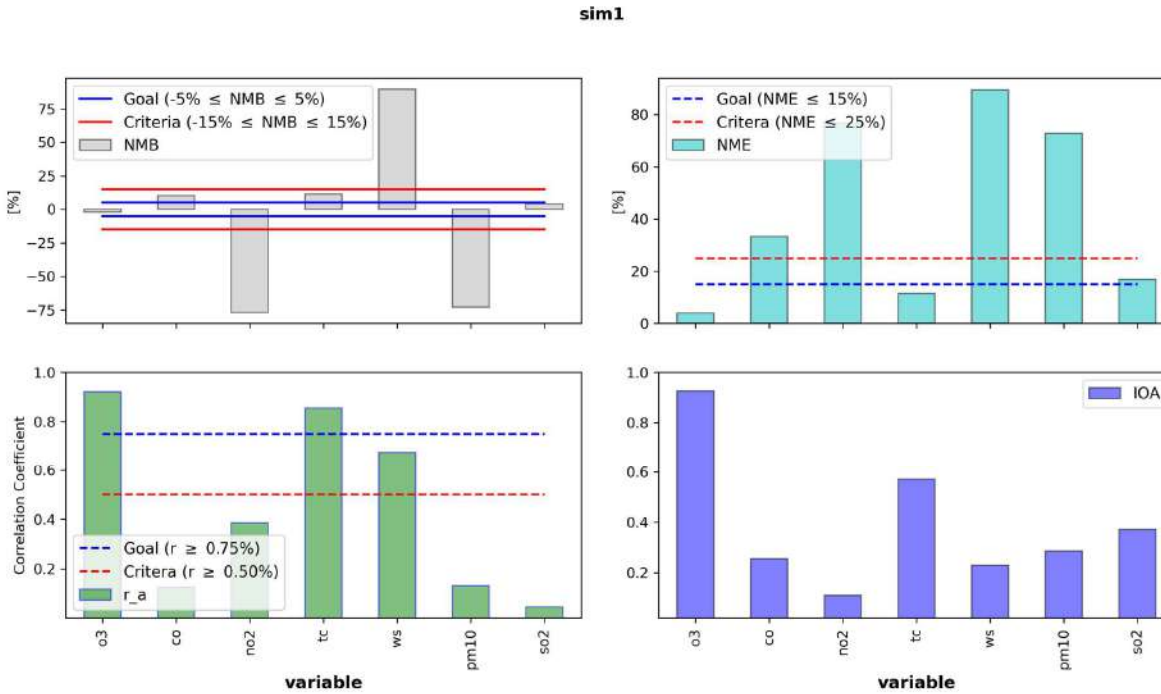


Fig. 10: Statistical plot for the first chemical mechanism, MOZART (simulation 1).

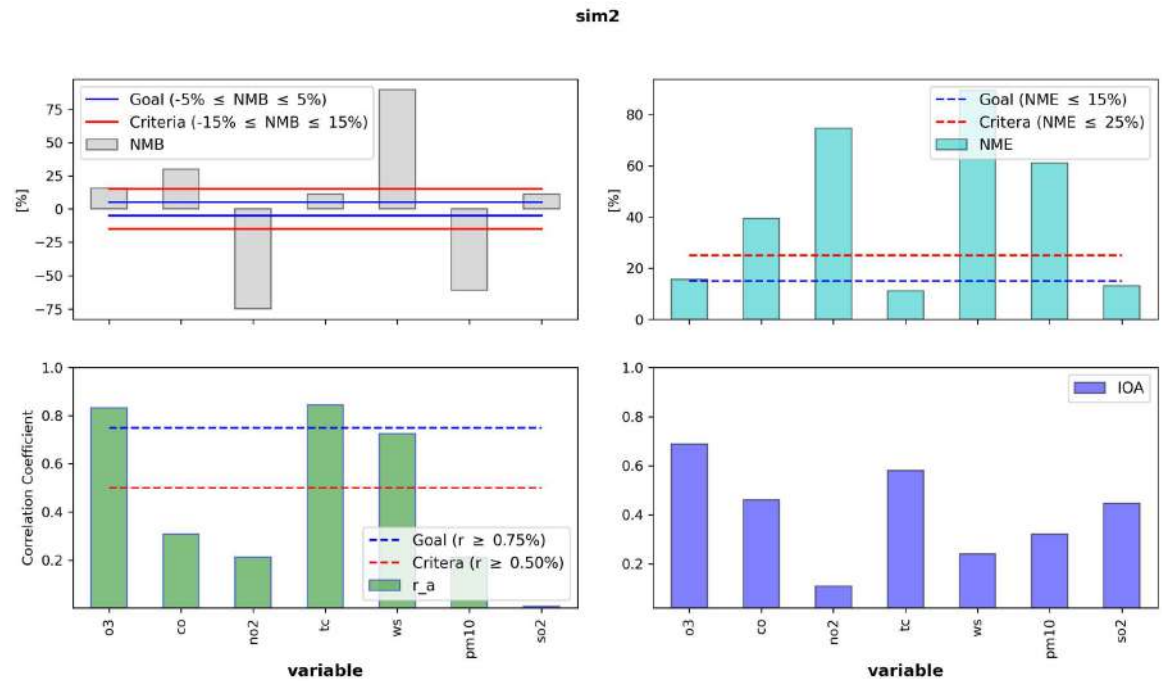


Fig. 11: Statistical plot for the second chemical mechanism, RACM (simulation 2).

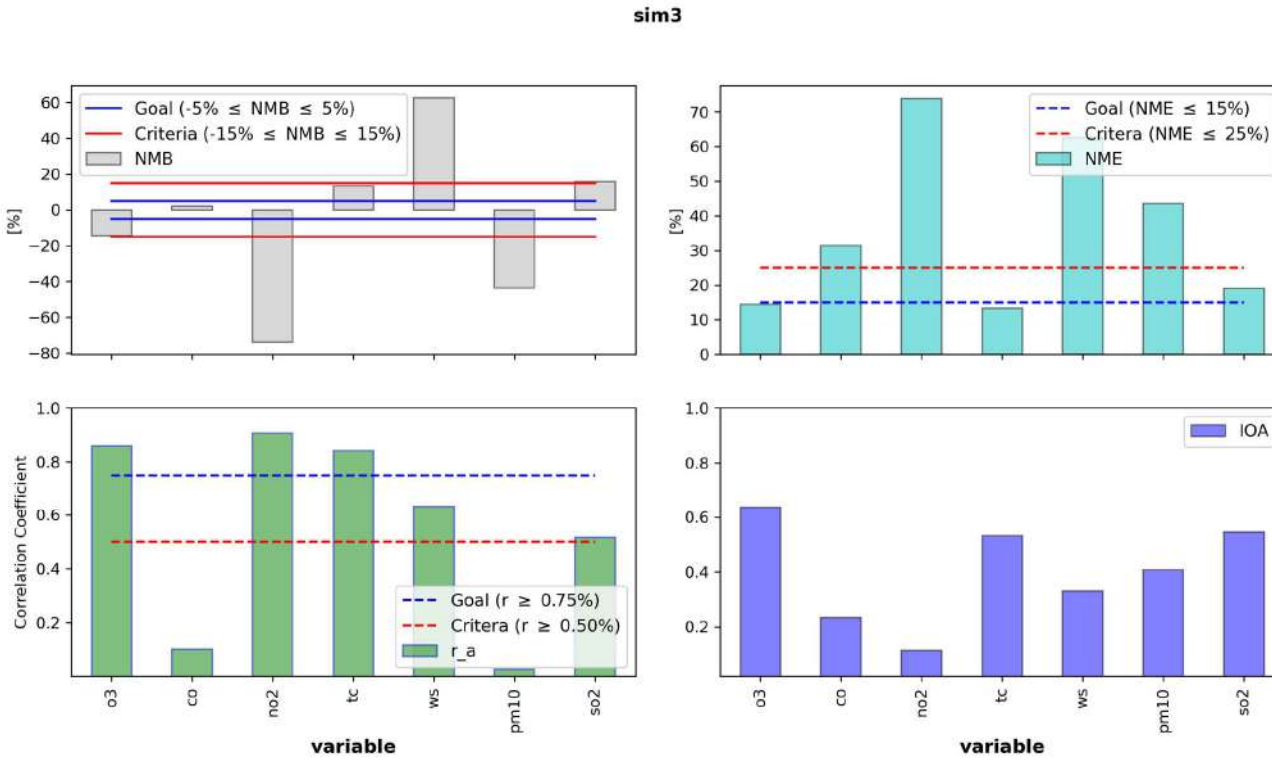


Fig. 12: Statistical plot for the third chemical mechanism, GOCART (simulation 3).

11, and 12 present the principal statistical metrics together with the corresponding statistical performance criteria, enabling the identification of the most suitable chemical mechanism.

Analysis of Fig. 10 shows that, for Sim1 (MOZART), the Pearson correlation coefficient (r) meets the desired criterion (≥ 0.75) for O_3 and temperature and exceeds the acceptable threshold (≥ 0.50) for wind speed (WS). However, it does not satisfy the established criteria for the remaining variables. Similarly, the index of agreement (IOA) for O_3 and temperature is close to 1, while the normalized mean error (NME) is less than or equal to 25%, indicating good model performance in predicting ozone concentrations over the study area.

For Sim2 (RACM), an improvement in the Pearson correlation coefficient (r) is observed for all variables except SO_2 and O_3, for which r decreases (Fig. 11). In the case of Sim3 (GOCART), a substantial improvement in r is observed for NO_2 and SO_2, accompanied by similar improvements in the index of agreement (IOA) (Fig. 12).

Based on these results and the time series shown in Fig. 9, we can conclude that the best chemical mechanism for predicting PM_{10}, SO_2, and CO is GOCART, while the best mechanism for O_3 and NO_2 is MOZART.

3.3. Nesting Ratio Comparison

This section investigates the impact of varying the nesting ratio on simulated meteorological variables (wind speed and temperature) and air quality variables (PM_{10}, CO, NO_2, and O_3). Two nesting configurations were evaluated: one with a 1:4 nesting ratio, in which the nested domain has a spatial resolution four times finer than its parent domain, and another with a 1:3 nesting ratio, in which the nested domain has a spatial resolution three times finer than its parent domain.

3.3.1. Impact of Nesting Ratio on Meteorological Variables

Fig. 13 presents the mean differences in wind speed and temperature between the simulations using three and four nested domains. For wind speed, positive differences predominate, indicating higher values in the three-domain simulation (Sim1) than in the four-domain simulation (Sim4). These differences are most pronounced in high-elevation regions. In contrast, the opposite trend is observed for temperature, except over the Sahara region, where Sim1 predicts higher temperatures, with the differences increasing toward the domain boundaries.

Evaluation of Figs. 10 and 14 show that the four-domain simulation (Sim4) achieves higher Pearson correlation coefficients for both temperature and wind

speed, exceeding the target criterion ($r \geq 0.75$). However, Sim4 also exhibits a higher normalized mean error (NME) for wind speed, exceeding the recommended criterion (NME $\leq$ 25%). Consequently, identifying the optimal nesting ratio for improving the simulation of temperature and wind speed remains challenging. As shown in Fig. 7, the time series of near-surface wind speed and temperature for Sim1 and Sim4 indicate that Sim1 generally produces wind speed values that are closer to the observations. For temperature, however, Sim4 performs better on some days, whereas both simulations produce comparable results on others.

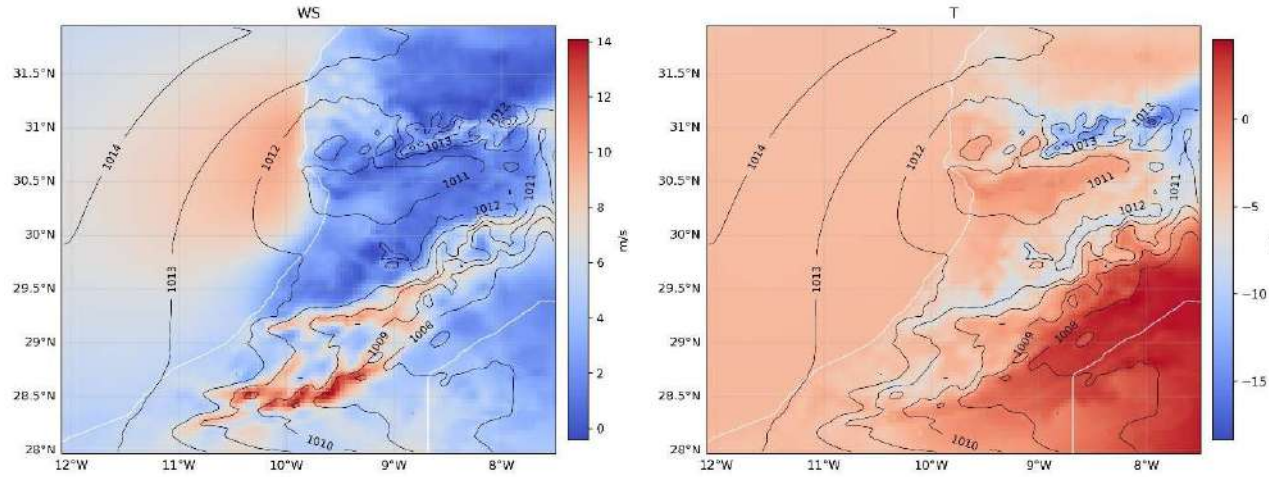


Fig. 13: Mean difference in ground-level WS (left panel) and T (right panel) between 3 nested domains (1:4 nesting ratio) and 4 nested domains (1:3 nesting ratio).

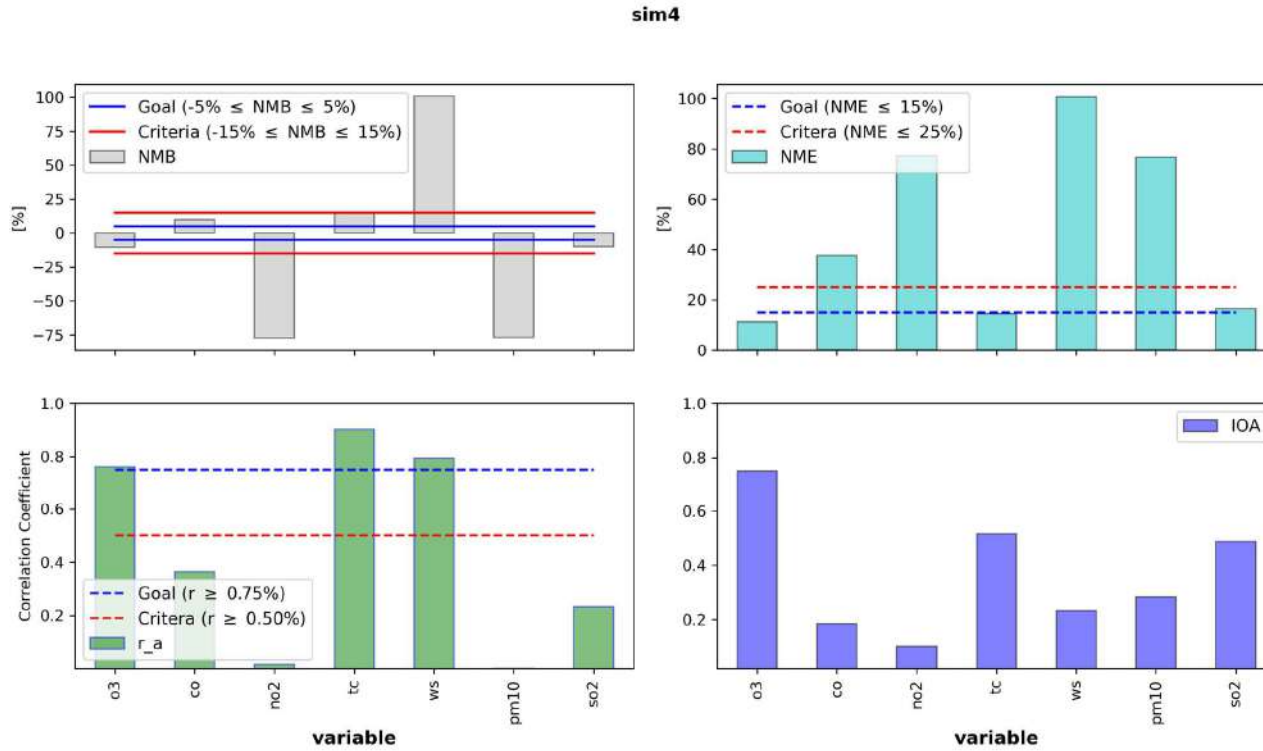


Fig. 14: Statistical plot for the 4 nested domains (1:3 nesting ratio).

Considering these findings, together with the computational cost, which is approximately three times higher for Sim4 than for Sim1, the three-domain configuration with a 1:4 nesting ratio is considered a more effective approach for predicting near-surface temperature and wind speed (Cifuentes et al. 2021).

3.3.2. Impact of Nesting Ratio on Air Quality Variables

Fig. 15 presents the mean differences in PM_{10}, NO_2, CO, and O_3 concentrations between the simulations using three and four nested domains. The figure shows a predominance of positive differences for PM_{10}, indicating that the concentrations predicted by the three-domain configuration are generally higher than those predicted by the four-domain configuration. In contrast, higher concentrations of NO_2, O_3, and CO are predicted by the four-domain configuration.

Analysis of Fig. 14 shows that the four-domain configuration increases the Pearson correlation coefficient (r) for CO from 0.10 to 0.30, while decreasing r for O_3 from 0.90 to 0.79. Similarly, the four-domain configuration results in lower predictive performance for PM_{10} and NO_2. As shown in Fig. 9, the accuracy of the O_3 and PM_{10} simulations is negatively affected when the four-domain configuration is used. For CO and NO_2, both domain configurations exhibit similar performance.

As discussed previously, the four-domain configuration requires substantially greater computational time. Therefore, for air quality prediction in the study region, the three-domain configuration with a 1:4 nesting ratio is recommended, as it provides greater computational efficiency (Cifuentes et al. 2021, Misenis & Zhang 2010).

3.4. Effect of Resolution

Fig. 16 illustrates the impact of model resolution on ozone concentrations. The figure reveals a clear trend: finer spatial resolutions provide greater detail in the simulated ozone concentrations. This suggests that model grid resolution significantly affects the ability to capture and resolve atmospheric processes at finer scales (Tao et al. 2020). Consequently, simulations with higher spatial resolution, such as the four-domain configuration, generally provide more detailed representations of local

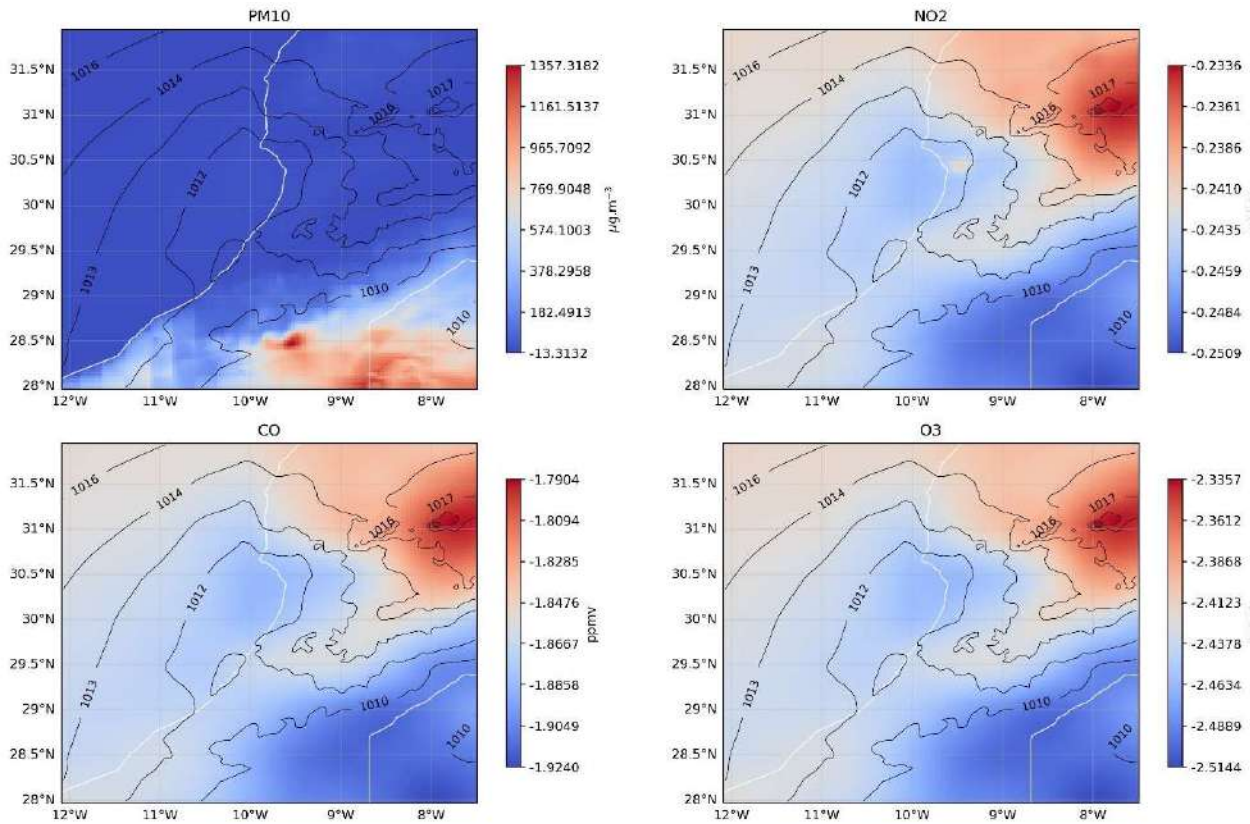


Fig. 15: Mean difference in PM_{10}, NO_2, CO, and O_3 concentrations between 3 nested domains (1:4 nesting ratio) and 4 nested domains (1:3 nesting ratio).

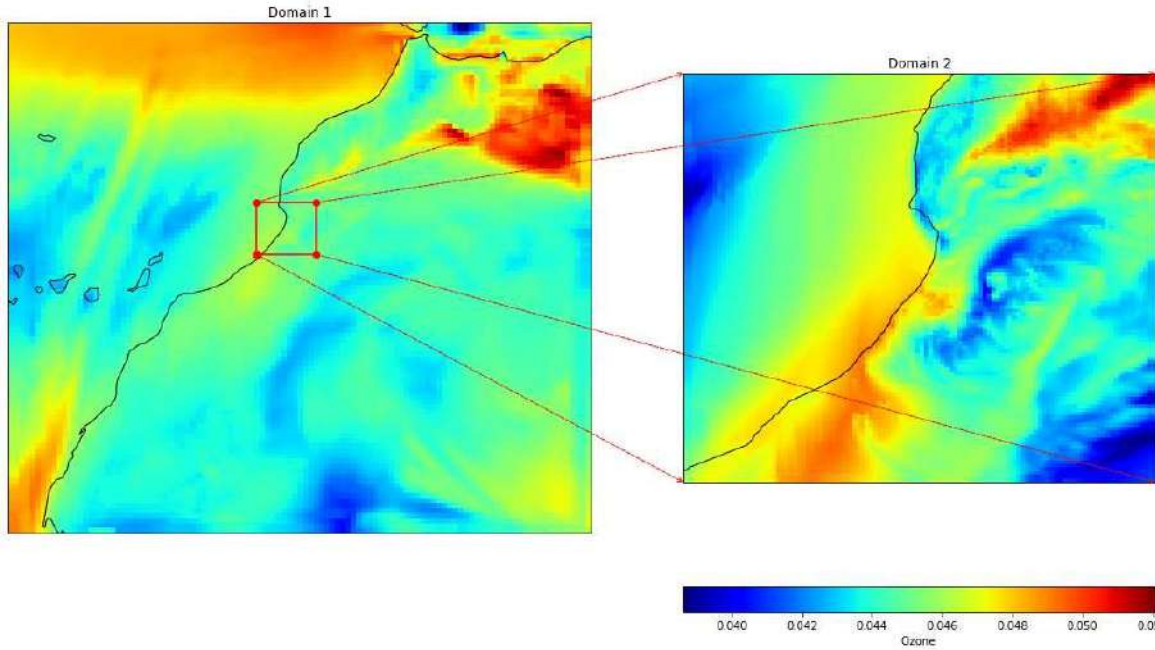


Fig. 16: Plot illustrating the effects of resolution changes between the first domain (D01) and the third one (D03).

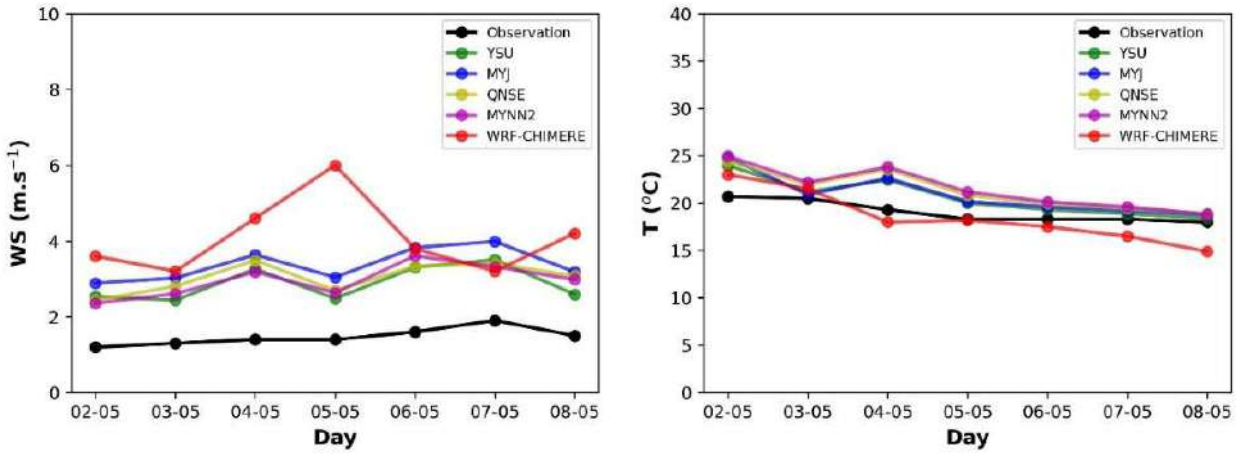


Fig. 17: Time series of daily ground-level wind speed (left panel) and temperature (right panel) during the simulation period from May 2 to May 8, showing the impact of different PBL parameterizations (YSU, MYJ, MYNN2, and QNSE).

phenomena, which is particularly important for air quality and meteorological variables. However, this increased level of detail comes at the expense of greater computational demand. Considering these trade-offs, selecting between the three- and four-domain configurations requires balancing the need for higher spatial resolution against the available computational resources. The three-domain configuration with a 1:4 nesting ratio offers greater computational efficiency, making it a more suitable option for studies with significant time and resource constraints (Misenis & Zhang 2010).

3.5. Impacts of PBL Parameterizations on Meteorological Variables

The selection of a planetary boundary layer (PBL) parameterisation scheme has a significant impact on the simulation of meteorological variables. Fig. 17 compares the performance of the different PBL schemes, including YSU, MYJ, MYNN2, and QNSE. Analysis of wind speed (WS) and temperature (T) indicates that the YSU scheme provides the best performance for predicting near-surface wind speed. Similarly, for temperature, the YSU scheme demonstrates

the best overall performance, followed closely by the MYJ scheme. These findings underscore the importance of selecting an appropriate PBL parameterisation to improve the accuracy of meteorological simulations (Banks & Baldasano 2016, Rizza et al. 2020), particularly for variables such as wind speed and temperature, which directly influence a wide range of atmospheric applications (Misenis & Zhang 2010).

4. CONCLUSIONS

This study successfully implemented the WRF-Chem model over the Moroccan domain for the first time. The model was used to simulate both meteorological variables (WS and T) and air quality variables (PM_{10}, O_3, CO, NO_2, and SO_2). The sensitivity of the model to different configurations was also evaluated. This included testing two nesting configurations (three nested domains with a 1:4 nesting ratio and four nested domains with a 1:3 nesting ratio), examining the effects of three chemical mechanisms (MOZART, RACM, and GOCART), and evaluating four planetary boundary layer (PBL) schemes (YSU, MYJ, MYNN2, and QNSE) to identify the optimal model configuration.

The simulated meteorological and air quality variables were compared with observations and with the results of a previous study conducted over Agadir using WRF-CHIMERE. Statistical performance metrics were calculated for the same study period to facilitate comparison. Overall, the results demonstrate improved air quality predictions over the study area compared with those obtained using WRF-CHIMERE.

The sensitivity analysis revealed satisfactory biases and correlation coefficients that are consistent with those reported in previous studies. Model performance was found to be case-dependent, with the optimal configuration varying according to the variable of interest. For simulations focusing on ozone and nitrogen dioxide, MOZART was identified as the most suitable chemical mechanism, whereas GOCART produced the best results for PM_{10}, SO_2, and CO. The three-domain configuration with a 1:4 nesting ratio was identified as the optimal nesting strategy, providing a 15% reduction in computational time compared with the 1:3 nesting ratio. In addition, the YSU scheme was identified as the optimal PBL parameterisation for improving the simulation of wind speed and temperature.

Despite these improvements, the model performance, particularly for PM_{10}, NO_2, and wind speed (WS), remains below the desired level. Wind speed is a critical factor influencing pollutant transport and air quality distribution, especially in coastal regions such as Agadir, where sea- and land-breeze circulations strongly influence local meteorological conditions. The study is also constrained by the limited availability of observational data, relying on measurements from a single monitoring station collected in 2010, as well as by the absence of high-resolution local emission inventories, both of which may contribute to the underestimation of urban-scale pollutants. Furthermore, although the MOZART, RACM, and GOCART schemes represent key chemical and aerosol processes, simplifications in secondary aerosol formation and heterogeneous reactions limit the accuracy of PM predictions. Despite these limitations, the results provide a valuable benchmark for future studies and highlight the importance of improving local emission inventories, expanding observational networks, and refining model configurations to better represent air quality processes in Morocco.

5. ACKNOWLEDGMENTS

The authors acknowledge with gratitude the cooperation and support of the Wilaya and the Region of Souss Massa in conducting this research. Special thanks are extended to the Wali and the President of the Region for their valuable guidance. This study was carried out with the support of the CNRST Morocco.

6. REFERENCES

Abdul-Wahab, S.A. and Al-Alawi, S.M., 2002. Assessment and prediction of tropospheric ozone concentration levels using artificial neural networks. *Environmental Modelling and Software*, 17(3), pp.219-228. [DOI]

Adnane, A., Leghrib, R. and Chaoufi, J., 2020. The use of a recurrent neural network for forecasting ozone concentrations in the city of Agadir (Morocco). *Journal of Atomic, Molecular, Condensed Matter and Nano Physics*, 7(3), pp.197-206. [DOI]

Ajdour, A., Leghrib, R., Chaoufi, J., Fetmaoui, H., Bousseta, M. and Chirmata, A., 2020. Assessment of particulate matter (PM) using chemistry transport modeling in Agadir City, Morocco. *Journal of Atomic, Molecular, Condensed Matter and Nano Physics*, 7(3), pp.231-240. [DOI]

Ajdour, A., 2022. Surveillance and modelling of urban air pollution in Morocco: case of the cities of Agadir and Casablanca. PhD Thesis. Faculty of Science. Ibn Zohr University.

Alapaty, K., Mathur, R., Pleim, J., Hogrefe, C., Rao, S.T., Ramaswamy, V., Galmarini, S., Schaap, M., Makar, P., Vautard, R., Baklanov, A., Kallos, G., Vogel, B. and Sokhi, R., 2012. New directions: understanding interactions of air quality and climate change at regional scales. *Atmospheric Environment*, 49, pp.419-421. [DOI]

Arghavani, S., Malakooti, H. and Bidokhti, A.A., 2019. Numerical evaluation of urban green space scenarios effects on gaseous air pollutants in Tehran Metropolis based on WRF-Chem model. *Atmospheric Environment*, 214, p.116832. [DOI]

Bălă, G.P., Râjnoveanu, R.M., Tudorache, E., Motișan, R. and Oancea, C., 2021. Air pollution exposure—the (in)visible risk factor for respiratory diseases. *Environmental Science and Pollution Research*, 28(16). [DOI]

Banks, R.F. and Baldasano, J.M., 2016. Impact of WRF model PBL schemes on air quality simulations over Catalonia, Spain. *The Science of the Total Environment*, 572, pp.98-113. [DOI]

Bouchriti, Y., Korrida, A., Ait Haddou, M., Achbani, A., Sine, H., Rida, J., Sine, H., Amiha, R. and Kabbachi, B., 2023. Assessment of health

impact of the surface ozone on a population residing at Agadir city (Morocco) using the AirQ+ model. *E3S Web of Conferences*, 364, pp.0-5. [DOI]

Bounakhla, Y., Benchrif, A., Costabile, F., Tahri, M., Gourch, B.E., Kafssaoui, E., Hassan, E., Zahry, F. and Bounakhla, M., 2023. Overview of PM10, PM2.5 and BC and their dependent relationships with meteorological variables in an urban area in northwestern Morocco. *Journal of Environmental Science and Health, Part A*, 58(4), pp.301-315.

Bozkurt, Z., 2014. Prediction of daily maximum PM10 concentration in Düzce, Turkey: Application of artificial neural networks and regression models in the prediction of daily maximum PM10 concentration in Düzce, Turkey. *Journal of Environmental Protection and Ecology*, 15(1), pp.60-75.

Chen, Y., Shi, R., Shu, S. and Gao, W., 2013. Ensemble and enhanced PM 10 concentration forecast model based on stepwise regression and wavelet analysis. *Atmospheric Environment*, 74, pp.346-359. [DOI]

Chirmata, A., Leghrib, R. and Ichou, I.A., 2017. Implementation of the air quality monitoring network at Agadir City in Morocco. *Journal of Environmental Protection*, 8(4), pp.540-567. [DOI]

Ciencewicki, J. and Jaspers, I., 2007. Air pollution and respiratory viral infection. *Inhalation Toxicology*, 19(14), pp.1135-1146. [DOI]

Cifuentes, F., González, C.M. and Aristizábal, B.H., 2021. Insights to WRF-Chem sensitivity in a zone of complex terrain in the tropical Andes: effect of boundary conditions, chemical mechanisms, nesting, and domain configuration. *Atmospheric Pollution Research*, 12(6), p.101093. [DOI]

Clappier, A., Belis, C.A., Pernigotti, D. and Thunis, P., 2021. Source apportionment and sensitivity analysis: two methodologies with two different purposes. *Environmental Modelling & Software*, 145, p.105201.

Emmons, L.K., Walters, S., Hess, P.G., Lamarque, J.F., Pfister, G.G., Fillmore, D., Granier, C., Guenther, A., Kinnison, D., Laepple, T., Orlando, J., Tie, X., Tyndall, G., Wiedinmyer, C., Baughcum, S.L. and Kloster, S., 2010. Description and evaluation of the model for ozone and related chemical tracers, version 4 (MOZART-4). *Geoscientific Model Development*, 3(1), pp.43-67. [DOI]

Grell, G.A., Peckham, S.E., Schmitz, R., McKeen, S.A., Frost, G., Skamarock, W.C. and Eder, B., 2005. Fully coupled "online" chemistry within the WRF model. *Atmospheric Environment*, 39(37), pp.6957-6975. [DOI]

Ha, S., 2022. Implementation of aerosol data assimilation in WRFDA (v4.0.3) for WRF-Chem (v3.9.1) using the RACM/MADE-VBS scheme. *Geoscientific Model Development*, 15(4), pp.1769-1788. [DOI]

Hu, X.M., Klein, P.M. and Xue, M., 2013. Evaluation of the updated YSU planetary boundary layer scheme within WRF for wind resource and air quality assessments. *Journal of Geophysical Research: Atmospheres*, 118(18), pp.10,490-10,505. [DOI]

Hu, X.M., Nielsen-Gammon, J.W. and Zhang, F., 2010. Evaluation of three planetary boundary layer schemes in the WRF model. *Journal of Applied Meteorology and Climatology*, 49(9), pp.1831-1844. [DOI]

Iraoui, K., Moustabchir, R., Charifi, H., Ouattab, M. and Chirmata, A., 2023. Ozone concentrations predicting in Agadir city (Morocco) using the multiple linear regression (forward regression analysis). In: *2023 3rd International Conference on Innovative Research in Applied Science, Engineering and Technology (IRASET)*, pp.1-4. [DOI]

Kant, S., Panda, J., Rao, P., Sarangi, C. and Ghude, S.D., 2021. Study of aerosol-cloud-precipitation-meteorology interaction during a distinct weather event over the Indian region using WRF-Chem. *Atmospheric Research*, 247, p.105144. [DOI]

Khan, A.W. and Kumar, P., 2019. Impact of chemical initial and lateral boundary conditions on air quality prediction. *Advances in Space Research*, 64(6), pp.1331-1342. [DOI]

Kitamura, Y., 2010. Modifications to the Mellor-Yamada-Nakanishi-Niino (MYNN) model for the stable stratification case. *Journal of the Meteorological Society of Japan*, 88(5), pp.857-864. [DOI]

Kong, X., Forkel, R., Sokhi, R.S., Suppan, P., Baklanov, A., Gauss, M., Brunner, D., Barò, R., Balzarini, A., Chemel, C., Curci, G., Jiménez-Guerrero, P., Hirtl, M., Honzak, L., Im, U., Pérez, J.L., Pirovano, G., San Jose, R., Schlünzen, K.H. and Galmarini, S., 2015. Analysis of meteorology-chemistry interactions during air pollution episodes using online coupled models within AQMEII phase-2. *Atmospheric Environment*, 115, pp.527-540. [DOI]

Lecoeur, E. and Seigneur, C., 2013. Dynamic evaluation of a multi-year model simulation of particulate matter concentrations over Europe. *Atmospheric Chemistry and Physics*, 13(8), pp.4319-4337. [DOI]

Leghrib, R., Ajdour, A., Chirmata, A., Chaoufi, J., Kaaya, A., Fatmaoui, H., Ichou, I.A., Menut, L. and Mailler, S., 2018. Particulate matter monitoring in Souss Massa Region. *SMETox Journal*, 1(4), pp.128-136.

Li, X., Hussain, S.A., Sobri, S. and Md Said, M.S., 2021. Overviewing the air quality models on air pollution in Sichuan Basin, China. *Chemosphere*, 271, p.129502. [DOI]

Liu, Y., Wang, P., Li, Y., Wen, L. and Deng, X., 2022. Air quality prediction models based on meteorological factors and real-time data of industrial waste gas. *Scientific Reports*, 12(1), pp.1-15. [DOI]

Luna, A.S., Paredes, M.L.L., de Oliveira, G.C.G. and Corrêa, S.M., 2014. Prediction of ozone concentration in tropospheric levels using artificial neural networks and support vector machine at Rio de Janeiro, Brazil. *Atmospheric Environment*, 98, pp.98-104. [DOI]

Luo, C., Wang, W., Sheng, L., Zhou, Y., Hu, Z., Qu, W., Li, X. and Hai, S., 2020. Influence of polluted dust on chlorophyll-a concentration and particulate organic carbon in the subarctic North Pacific Ocean based on satellite observation and the WRF-Chem simulation. *Atmospheric Research*, 236, p.104812. [DOI]

Manisalidis, I., Stavropoulou, E., Stavropoulos, A. and Bezirtzoglou, E., 2020. Environmental and health impacts of air pollution: a review. *Frontiers in Public Health*, 8, pp.1-13. [DOI]

Menut, L., Bessagnet, B., Khvorostiyanov, D., Monge, J., Valari, M. and Vautard, R., 2021. Tropospheric ozone and particulate matter modelling. *Atmospheric Chemistry and Physics*, 21(5), pp.4123-4150.

Mian Chin, R.B.R. and Lin, S.-J., 2000. Atmospheric sulfur cycle. *Journal of Geophysical Research: Atmospheres*, 105(D20), pp.24667-24683. [DOI]

Misenis, C. and Zhang, Y., 2010. An examination of sensitivity of WRF/Chem predictions to physical parameterizations, horizontal grid spacing, and nesting options. *Atmospheric Research*, 97(3), pp.315-334. [DOI]

Mohammed, A.N.N.I. and Abualqumboz, A.M.M.S., 2018. Multivariate analysis of monsoon seasonal variation and prediction of particulate matter episode using regression and hybrid models. *International Journal of Environmental Science and Technology*, 16(3), pp.1453-1468. [DOI]

Mohan, M., Kandya, A. and Yadav, M., 2011. An evaluation and comparison of the various statistical and deterministic techniques for forecasting the concentration of criteria air pollutants. *International Journal of Environment and Pollution*, 44(1-4), pp.96-105. [DOI]

Mohd Napi, N.N.L., Noor Mohamed, M.S., Abdullah, S., Mansor, A.A., Ahmed, A.N. and Ismail, M., 2020. Multiple linear regression (MLR) and principal component regression (PCR) for ozone (O3) concentrations prediction. *IOP Conference Series: Earth and Environmental Science*, 616(1), p.012004. [DOI]

Nazif, A., Mohammed, N.I., Malakahmad, A. and Abualqumboz, M.S., 2016. Application of step wise regression analysis in predicting future particulate matter concentration episode. *Water, Air, and Soil Pollution*, 227(4), p.117. [DOI]

Park, J., 2021a. A particulate matter concentration prediction model based on long short-term memory and an artificial neural network. *International*

Journal of Environmental Research and Public Health, 18(13), p.6801. [DOI]

Park, J. and Chang, S., 2021b. A particulate matter concentration prediction model based on long short-term memory and an artificial neural network. *International Journal of Environmental Research and Public Health*, 18(13), p.6801. [DOI]

Qiu, M., Zigler, C. and Selin, N.E., 2022. Statistical and machine learning methods for evaluating trends in air quality under changing meteorological conditions. *Atmospheric Chemistry and Physics*, 22(16), pp.10551-10566. [DOI]

WHO 2003. Health aspects of air pollution with particulate matter, ozone and nitrogen dioxide. *WHO Regional Office for Europe*, pp.1-89.

Rizza, U., Mancinelli, E., Canepa, E., Piazzola, J., Missamou, T., Yohia, C., Morichetti, M., Virgili, S., Passerini, G. and Miglietta, M.M., 2020. WRF sensitivity analysis in wind and temperature fields simulation for the northern Sahara and the Mediterranean Basin. *Atmosphere*, 11(3), p.259. [DOI]

Saidou Chaibou, A.A., Ma, X., Kumar, K.R., Jia, H., Tang, Y. and Sha, T., 2019. Evaluation of dust extinction and vertical profiles simulated by WRF-Chem with CALIPSO and AERONET over North Africa. *Journal of Atmospheric and Solar-Terrestrial Physics*, 199, p.105213. [DOI]

Schindlbacher, S., Matthews, B. and Ullrich, B., 2021. Uncertainties and recalculations of emission inventories submitted under CLRTAP. *CEIP Report*, pp.1-26.

Sha, T., Ma, X., Jia, H., Tian, R., Chang, Y., Cao, F. and Zhang, Y., 2019. Aerosol chemical component: simulations with WRF-Chem and comparison with observations in Nanjing. *Atmospheric Environment*, 218, p.116982. [DOI]

Shimada, S., Ohsawa, T., Chikaoka, S. and Kozai, K., 2011. Accuracy of the wind speed profile in the lower PBL as simulated by the WRF model. *Scientific Online Letters on the Atmosphere*, 7(1), pp.109-112. [DOI]

Sicard, P., Crippa, P., De Marco, A., Castruccio, S., Giani, P., Cuesta, J., Paoletti, E., Feng, Z. and Anav, A., 2021. High spatial resolution WRF-Chem model over Asia: physics and chemistry evaluation. *Atmospheric Environment*, 244, p.118004. [DOI]

Siegfried, H., Pfeiler, B. and Stadlober, E., 2005. Analysis and prediction of particulate matter PM10 for the winter season in Graz. *Austrian Journal of Statistics*, 34(4), pp.307-326.

Singh, C., Singh, S.K., Chauhan, P. and Budakoti, S., 2021. Simulation of an extreme dust episode using WRF-CHEM based on optimal ensemble approach. *Atmospheric Research*, 249, p.105296. [DOI]

Sukoriansky, S., Galperin, B. and Perov, V., 2006. A quasi-normal scale elimination model of turbulence and its application to stably stratified flows. *Nonlinear Processes in Geophysics*, 13(1), pp.9-22. [DOI]

Tao, H., Xing, J., Zhou, H., Pleim, J., Ran, L., Chang, X., Wang, S., Chen, F., Zheng, H. and Li, J., 2020. Impacts of improved modeling resolution on the simulation of meteorology, air quality, and human exposure to PM2.5, O3 in Beijing, China. *Journal of Cleaner Production*, 243, p.118574. [DOI]

Taşpınar, F., 2015. Improving artificial neural network model predictions of daily average PM10 concentrations by applying principle component analysis and implementing seasonal models. *Journal of the Air and Waste Management Association*, 65(7), pp.800-809. [DOI]

Tebal, N. and Pinang, P., 2011. Comparison between multiple linear regression and feed forward back propagation neural network models for predicting PM10 concentration level based on gaseous and meteorological parameters. *Clean Air Research*, 1(4), pp.42-49.

UNECA and UNECE, 2014. Morocco environmental performance reviews. In: *The United Nations*. pp.1-150.

Wang, P., Qiao, X. and Zhang, H., 2020. Modeling PM2.5 and O3 with aerosol feedbacks using WRF/Chem over the Sichuan Basin, southwestern China. *Chemosphere*, 254, p.126735. [DOI]

Wang, Q. and Li, X., 2022. Correlation analysis between meteorological factors and pollutants based on copula theory. *Journal of Physics: Conference Series*, 2168(1), p.012028. [DOI]

Wang, W., Lu, W., Wang, X. and Leung, A.Y.T., 2003. Prediction of maximum daily ozone level using combined neural network and statistical characteristics. *Environment International*, 29(5), pp.555-562. [DOI]

Wang, Y., Yuan, Q., Li, T., Zhu, L. and Zhang, L., 2021. Estimating daily full-coverage near surface O3, CO, and NO2 concentrations at a high spatial resolution over China based on S5P-TROPOMI and GEOS-FP. *ISPRS Journal of Photogrammetry and Remote Sensing*, 175, pp.311-325. [DOI]

World Health Organization, 2006. Health risks of particulate matter from long-range transboundary air pollution. *WHO Regional Office for Europe*, pp.1-89.

Yorkor, B. and Leton, T., 2017. Prediction and modeling of seasonal concentrations of air pollutants in semi-urban region employing artificial neural. *Journal of Environmental Science and Technology*, 10(4), pp.180-192.

Yu, E., Bai, R., Chen, X. and Shao, L., 2022. Impact of physical parameterizations on wind simulation with WRF V3.9.1.1 under stable conditions at planetary boundary layer gray-zone resolution: a case study over the coastal regions of North China. *Geoscientific Model Development*, 15(21), pp.8111-8134. [DOI]

Nature Environment and Pollution Technology
An International Quarterly Peer-Reviewed Open Access Journal

p-ISSN: 0972-6268 | e-ISSN: 2395-3454 Vol. 25 | No. 4 | Article ID B4427 | 2026

RESEARCH ARTICLE https://doi.org/10.46488/NEPT.2026.v25i04.B4427 OPEN ACCESS

Physicochemical Characterization of Pulp and Black Liquor Derived from Corn Husk and Coir Blends

Madhuri Pydimalla[1], Shrinidhi Tavag[1], Surya Tej Valluri[1], Nukala Mohith Satya Vardhan[1] and A. V. Raghavendra Rao[2]†
[1]Department of Chemical Engineering, Chaitanya Bharathi Institute of Technology, Hyderabad 500075, Telangana, India
[2]Department of Chemical Engineering, B. V. Raju Institute of Technology, Narsapur, Medak -502313, Telangana, India
†Corresponding author: A. V. Raghavendra Rao; raghusrf@gmail.com

ARTICLE HISTORY

Received: 19-01-2026
Revised: 15-03-2026
Accepted: 20-03-2026

KEYWORDS

Kraft cooking
Bleaching
Black liquor
Water retention value
Agrowaste biomass
Corn husk
Coconut coir
Kraft pulping

CITE THIS ARTICLE

Pydimalla, M., Tavag, S., Valluri, S. T., Vardhan, N. M. S., and Rao, A. V. R., 2026. Physicochemical characterization of pulp and black liquor derived from corn husk and coir blends. *Nature Environment and Pollution Technology*, 25(4), B4427. https://doi.org/10.46488/NEPT.2026.v25i04.B4427

COPYRIGHT & LICENCE

© 2026 The Authors
Open Access under CC BY 4.0.

PUBLISHED BY

TECHNOSCIENCE PUBLICATIONS

ABSTRACT

This study investigates the suitability of an agrowaste biomass blend, specifically corn husk and coconut coir, for producing sustainable pulp through kraft pulping and elemental chlorine-free (ECF) bleaching. An equal weight ratio (1:1 w/w) of oven-dried corn husk and coir was pretreated with steam at 120°C for one hour, then subjected to kraft pulping in a batch reactor at 80°C for two hours using white liquor (NaOH and Na_2S) at a solid-to-liquid ratio of 1:18. The unbleached pulp, with a yield of 38.7%, was bleached with hydrogen peroxide (1:10 w/v pulp-to-peroxide ratio) at 60°C for one hour. The properties of both unbleached and bleached pulps were analyzed using Fourier transform infrared (FTIR) spectroscopy, water retention value (WRV), cellulose content measurement, scanning electron microscopy (SEM), energy-dispersive X-ray spectroscopy (EDX), and thermogravimetric analysis (TGA). Black liquor from the pulping process was examined via UV–visible spectroscopy. SEM images revealed a fibril-bound network in unbleached pulp, which became more porous and fibrillated after bleaching. FTIR spectra confirmed lignin removal by decreased aromatic bands in the 1600–1400 cm^{-1} range. The cellulose content increased from 60.2% to 85.4% post-bleaching. Elevated WRV indicated enhanced fiber swelling and porosity. TGA showed thermal degradation peaks between 200–350°C in bleached pulp, signifying improved thermal stability. UV-Vis analysis of black liquor revealed significant lignin peaks (an absorbance of 0.8 at 200–205 nm), indicating effective lignin removal. Overall, these results demonstrate that the pulping and bleaching procedures are viable for producing high-quality, cellulose-based pulp suitable for environmentally friendly applications.

1. INTRODUCTION

Paper is a nonwoven sheet composed of pulp fibers measuring 0.25–4.5 mm in length and 10–50 µm in width (Pydimalla & Adusumalli 2020). These fibers are interwoven to form a three-dimensional matrix. The use of paper products often serves as an indicator of a country's educational development. Paper plays a crucial role in many aspects of modern life, including communication and the dissemination of knowledge. Currently, there are approximately 759 pulp and paper manufacturing plants worldwide, with India accounting for about 4% of global paper production, ranking 15th (Pydimalla & Adusumalli 2020). Projections estimate that India's paper consumption will reach 23.51 million tonnes annually by 2030 (Van Ewijk & Stegemann 2016). Most of India's paper mills are concentrated in Andhra Pradesh, Telangana, Tamil Nadu, Maharashtra, Punjab, Madhya Pradesh, and Gujarat. Raw materials used for paper production vary regionally; for example, subabul wood is utilized in Andhra Pradesh mills, bagasse from seasonal crops

in Karnataka, and wheat straw in Punjab. Recycled paper is also widely used to produce various grades of paper. The paper industry is generally categorized into four main segments: printing and writing (P&W), packaging paper and board, specialty papers, and newsprint (Dutt 2013). Within these segments, the industry manufactures a diverse array of products, including printing and writing sheets, packaging boards, corrugated materials, newspapers, and tissue paper. Writing and printing papers constitute approximately 26% of the world's total paper output. Packaging products, such as corrugated board and paperboard, represent the largest share, making up around 51% of the market (Furszyfer Del Rio et al. 2022). Newsprint and tissue paper account for roughly 7% and 8%, respectively, of global production.

Fibers, which are the primary raw material for paper manufacturing, are elongated, hollow, non-living plant cells composed mainly of lignocellulosic biomass (Smook 2002). These plant-based fibers are vital in producing paper, a material extensively utilized in various human activities. Chemically, a typical fiber contains approximately 40–50% cellulose, 25–30% hemicellulose, 25–35% lignin, and a minor fraction (1–5% extractives) (Rowell 2012). Cellulose, the structural backbone of fibers, significantly dictates the mechanical strength and bonding potential of paper. It is a linear polymer made up of -D-glucose units, with hydrogen bonds forming between cellulose chains across neighboring fibers, which is crucial for fiber-to-fiber adhesion within the paper matrix (Wohlert et al. 2022). Hemicellulose, the second most prevalent carbohydrate in wood fibers, differs from cellulose as it comprises branched chains of various sugars, including glucose, xylose, and mannose. These shorter chains notably improve papermaking by increasing fibers' water retention and swelling, thereby facilitating bonding during sheet formation (Pere et al. 2019). Lignin, the third major component, is a complex aromatic polymer that covalently links with cellulose and hemicellulose. It imparts rigidity and structural stability to the plant cell wall, particularly in secondary wall layers and the middle lamella (Peracchi et al. 2024). Acting as a natural adhesive, lignin binds cellulose microfibrils together and provides a protective barrier against environmental damage. However, its presence can weaken paper strength by impeding effective fiber bonding. Therefore, an important goal in pulp and paper manufacturing, as well as viscose rayon production, is to reduce lignin content while maintaining cellulose levels.

The modern cellulose industry employs a wide variety of fibrous raw materials derived from hardwoods such as eucalyptus and subabul, softwoods, and non-wood sources including bagasse, wheat straw, and rice straw. Both hardwood and softwood fibers are essential raw materials in the production of paper and board products (Karlsson 2006). In India, fast-growing hardwood species with short rotation cycles are often utilized. Fiber lengths generally range from 0.2–4 mm, with cell wall thicknesses of 3–4 μm (Liu et al. 2024). A key difference between hardwood and softwood lies in their chemical makeup: hardwoods typically contain higher levels of cellulose and hemicellulose and lower lignin content than softwoods. This composition makes hardwoods more suitable for pulping processes that aim for higher yields and improved fiber bonding (Tarrés et al. 2023). Despite these benefits, the Indian paper industry faces several challenges, including high energy costs, limited technological advancement, environmental regulations, and, most importantly, a scarcity of quality raw materials. The primary issue is restricted access to government-managed forest resources. To mitigate raw material shortages, many paper producers are promoting agroforestry practices, especially in regions favorable to rapid tree growth. Agricultural residues are regarded by industry experts as a more environmentally sustainable alternative to wood-based fibers. Their porous cell wall structure facilitates faster pulping at similar cooking temperatures, yielding pulp of comparable quality (Worku et al. 2023). As a result, processing agricultural residues typically consumes less water, energy, and chemicals (Gavrilescu 2008). Currently, the Indian pulp and paper industry sources roughly 30–35% of its fibrous materials from wood, 20–22% from agricultural waste, and 45–50% from recycled fibers, reflecting a balanced approach aligned with environmental and economic goals.

In papermaking, pulp fibers are derived through either mechanical or chemical pulping methods utilizing wood or non-wood sources. The main purpose of pulping is to liberate individual fibers by breaking down the lignocellulosic matrix, primarily through the removal of lignin, a natural adhesive located in the intermediate lamella (Manfredi 2024). The kraft process is the most commonly used chemical pulping technique worldwide owing to its adaptability in processing diverse raw materials and its capacity to yield high-quality pulp. It also offers an efficient, proven method for reclaiming and recycling pulping chemicals. The key chemicals in the kraft process include sodium hydroxide (NaOH) and sodium sulfide (Na_2S). Together, these substances, known as white liquor, break the β-aryl ether bonds, among the most prevalent linkages in lignin, thus easing lignin removal (Madhuri et al. 2016). Consequently, lignin becomes soluble, enabling the separation of cellulose fibers. NaOH also contributes significantly by neutralizing organic acids and interacting with resinous components in the raw material, which further supports the delignification process.

The primary objective of bleaching is to remove residual lignin while preserving carbohydrate components,

particularly cellulose. This process helps retain the pulp's strength and improves its brightness. The removal of residual lignin during bleaching is regarded as an extension of the pulping process, albeit carried out more gently (Bajpai 2012). In chemically pulped fibers, the residual lignin is generally more condensed, showing an increased proportion of carbon-carbon and lignin-carbohydrate linkages and fewer β-O-4 ether bonds (Britt 1970). Bleaching, targeting lignin fractions remaining after initial delignification, is often seen as a continuation of the pulping process. Although reductive methods are occasionally used, oxidative techniques remain the predominant approach in chemical bleaching (Gellerstedt 2003). Modern bleaching methods typically employ oxidizing agents such as hydrogen peroxide (P), chlorine dioxide (C), oxygen (O), and ozone (Z). These chemicals improve the pulp's processing properties and whiteness by introducing hydrophilic functional groups and facilitating lignin depolymerization, leading to its breakdown.

In recent years, there has been a growing emphasis among researchers on utilizing non-wood fibers as sustainable alternatives for paper production (Pydimalla & Reddy 2019, El-Sayed et al. 2023, Nagaraja Ganesh et al. 2022, Das et al. 2023). Agricultural residues such as maize stalks, bagasse, rice straw, and wheat straw have been explored for their pulping potential, providing an environmentally friendly and energy-efficient option compared to traditional wood sources. Evidence indicates that non-wood fibers can be employed to produce high-quality, bleached pulp suitable for specialty papers. Advances in pulping techniques, including organic acid pulping and enzymatic treatments, have enhanced both the efficiency and sustainability of processing these materials (Singh & Bajpai 2025, Wang & Liu 2022). For instance, research on maize stalks showed that lignin could be effectively extracted using the caustic soda–anthraquinone process, yielding pulp with favorable tensile properties (Mishra & Sharma 2020). Moreover, the exploration of bast fibers such as hemp and kenaf continues, with the potential to create durable, eco-friendly paper products (Austin et al. 2024). These developments underscore the increasing significance of non-wood fibers in addressing the rising demand for environmentally sustainable paper production.

There remains a significant research gap in evaluating the synergistic potential of mixed agricultural residues. While progress has been made in utilizing non-wood biomass for pulp production, most studies focus on individual materials. Additionally, limited attention has been given to the combined processing of fibrous materials with high cellulose content, such as corn husk and coconut coir. This research aims to investigate whether a blend of coconut coir and corn husk, two commonly available agricultural wastes, can serve as an alternative fiber source for pulp production in paper manufacturing. It also seeks to systematically analyze the characteristics of pulp and black liquor following cooking and bleaching. The study assesses pulp quality and suitability for papermaking through kraft pulping and elemental chlorine-free (ECF) bleaching. This work is unique in promoting the efficient use of mixed lignocellulosic wastes, contributing to the development of sustainable raw material alternatives. Additionally, it supports circular economy principles and addresses fiber shortages in the paper industry. The pulping parameters were selected based on preliminary screening trials, serving as baseline laboratory conditions to optimize fiber separation and facilitate detailed physicochemical characterization of the pulp and black liquor.

2. MATERIALS AND METHODS

Corn husk and coconut coir were obtained from local markets in Hyderabad, India. The raw materials underwent manual washing to eliminate dust and impurities. The corn husk was then cut into small, uniform pieces, while coconut coir was cut and sieved through a 5 mm sieve to obtain appropriately sized particles for pulping. Both materials were subsequently dried in an oven at 103.5°C until reaching a constant weight, confirming moisture removal (Fig. 1). Analytical grade chemicals, including sodium hydroxide (NaOH), sodium sulfide (Na_2S), acetic acid, nitric acid, ethanol, and hydrogen peroxide (H_2O_2), were purchased from Merck Specialties Pvt. Ltd. For pulping, 50 g each of dried corn husk and coconut coir were mixed in equal proportions. The cooking parameters, including temperature, alkali charge, and cooking time, were optimized on a mild laboratory scale to minimize carbohydrate degradation and achieve controlled delignification. Preliminary experiments established conditions ensuring adequate fiber separation and acceptable pulp yield. An equal weight ratio (1:1 w/w) of corn husk to coconut coir served as the baseline formulation to explore the synergistic pulping properties of these agricultural residues. Corn husk, being richer in cellulose and lower in lignin, facilitates easier delignification, whereas coconut coir has a higher lignin content and is more fibrous. This balanced mixture was selected to assess their compatibility, uniformity in chemical saturation, and delignification performance. The 1:1 ratio acted as a screening criterion for process feasibility before further optimization with different ratios.

To improve chemical impregnation and remove residual moisture trapped within the chips, the dry raw materials underwent autoclaving at 120°C for one hour. This process also partially eliminated low-molecular-weight organic extractives, thereby enhancing the efficiency of



Fig. 1: (a) Corn husk; (b) coconut coir.

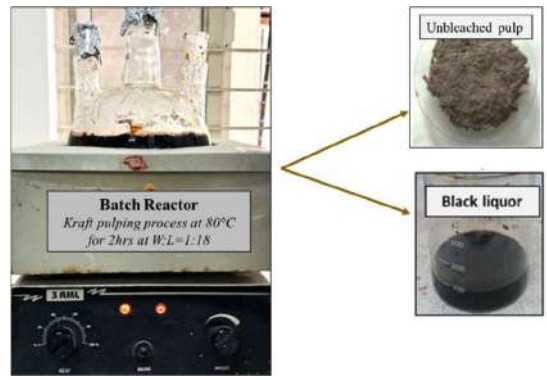


Fig. 2: Kraft pulping process in a batch reactor producing unbleached pulp and black liquor.

subsequent pulping. Laboratory-scale pulping experiments were conducted to evaluate the feasibility of using mixed agro-residues for pulp production and to analyze the physicochemical characteristics of the resulting pulp and black liquor. Biomass samples were placed into a batch reactor with white liquor, consisting of sodium hydroxide (NaOH) and sodium sulfide (Na_2S), at a solid-to-liquid ratio of 1:18 (w/v). Pulping was carried out actively for two hours at a controlled temperature of 80°C (Fig. 2). The choice of 80°C for kraft pulping in this study reflects a mild, laboratory-scale condition designed to enable controlled, gradual delignification of agro-residues while minimizing cellulose degradation and maintaining fiber integrity. Pre-steaming at 120 °C before pulping promotes fiber swelling, extractive removal, and improved chemical penetration, thus facilitating delignification at lower cooking temperatures. Such low-temperature alkaline pulping conditions (around 70–100 °C) have been used in laboratory research on non-wood lignocellulosic materials to achieve selective delignification and fiber preservation prior to bleaching or further processing (Rousu et al. 2002, Ververis et al. 2004).

Following the cooking process, the delignified pulp samples were separated from the black liquor and meticulously washed 4–5 times with deionized water to eliminate extractives and any residual black liquor on the pulp fibers. The cleaned pulp was then dried in a hot air oven at 103.5°C for 12 hours until a steady weight was attained. Subsequently, both the pulp and black liquor were characterized to determine the lignin content in the black liquor and the residual lignin remaining in the pulp.

Following the preparation and analysis of the unbleached pulp, the bleaching process was conducted using hydrogen peroxide as an elemental chlorine-free (ECF) bleaching agent. A specific quantity of pulp was placed in a beaker and subjected to bleaching on a hot plate maintained at 60°C. Hydrogen peroxide was added at a pulp-to-peroxide ratio of 1:10 (w/v), and the mixture was stirred occasionally while kept at a constant temperature for one hour (Fig. 3). Hydrogen peroxide effectively oxidizes residual lignin, thereby enhancing pulp brightness and reducing discoloration. This approach is more environmentally friendly than conventional chlorine-based bleaching, as hydrogen peroxide breaks down into non-toxic by-products, mainly water and oxygen. After bleaching, the pulp was filtered, oven-dried to remove moisture, and weighed. The bleached pulp was then further characterized and analyzed to assess improvements in fiber quality and optical properties.

The unbleached and bleached pulps were thoroughly characterized through a range of techniques, including Fourier transform infrared (FTIR) spectroscopy, water retention value (WRV), cellulose content analysis, scanning



Fig. 3: Pulp bleaching process.

electron microscopy (SEM), energy-dispersive X-ray (EDX), and thermogravimetric analysis (TGA), to assess their structural, chemical, and thermal properties. Additionally, the black liquor recovered after pulping was analyzed using UV–visible spectrophotometry to measure dissolved lignin concentration and evaluate pulping efficiency.

3. RESULTS AND DISCUSSION

3.1. Pulp Yield

Fig. 4 presents digital photographs of both unbleached and bleached pulps. The ECF bleaching process markedly increases fiber brightness, as evidenced by the images. These visuals underscore the effectiveness of kraft cooking combined with ECF bleaching in producing white pulp. In Fig. 4(a), an oven-dried kraft pulp sample, obtained after cooking, is shown. The individual fibers in the mixed pulp cooked at 80°C are distinctly separated, indicating successful fibrillation. This suggests significant lignin degradation in the middle lamella and cell wall, likely facilitated by enhanced diffusion of white liquor under elevated temperatures. The breakdown of lignin, particularly within the compound middle lamella (CML), increases cell wall porosity, allowing deeper penetration of cooking chemicals into the fiber matrix (Kron et al. 2024). Fig. 4(b) demonstrates the effect of ECF bleaching on pulp brightness. The bleaching agents target chromophoric groups in lignin, such as quinones, which absorb light. The white appearance of the bleached pulp indicates substantial removal of lignin fragments and non-cellulosic components like extractives. These images effectively showcase the success of the optimized kraft pulping process followed by peroxide bleaching in producing high-brightness white pulp.

The pulp yield, defined as the ratio of unscreened pulp collected to the amount of steam-pretreated biomass used in the cooking process, was observed to be 38.7% for unbleached pulp and 34.8% for bleached pulp. Yield loss during kraft cooking mainly results from the dissolution of low-molecular-weight carbohydrates in an alkaline medium and peeling reactions (Knott 2021). During bleaching, treatment effectively removes chromophoric compounds and residual lignin from cell walls, resulting in higher pulp brightness, increased cellulose content, and a slight reduction in pulp yield (Bajpai 2013).

3.2. Cellulose Content in Pulp

This test measures the remaining cellulose content in the pulp after cooking. The procedure involves adding 15 mL of acetic acid and 1.5 mL of concentrated nitric acid to the samples, followed by refluxing for 20 minutes, as illustrated in Fig. 5(a). The treated samples are then washed with ethanol, filtered through a cotton cloth, and dried in a hot air oven for 12 hours to produce material A (Fig. 5(b)). Subsequently, the dried samples are incinerated in a muffle furnace at 525°C until their weight becomes constant, resulting in material B (Madhuri et al. 2016) (Fig. 5(c)).

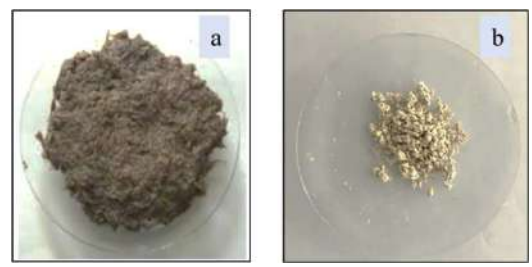


Fig. 4: (a) Unbleached pulp; (b) bleached pulp.

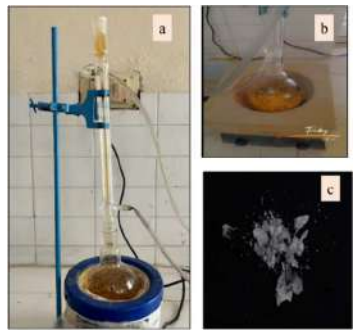


Fig. 5: (a) Cellulose isolation test; (b) pulp sample during reflux; (c) pulp after ash test.

Table 1: Cellulose content of pulp after pulping and bleaching.

Sample	Cellulose (%)
Raw material (corn husk + coir)	32.5
Unbleached pulp	60.2
Bleached pulp	85.4

The cellulose content is calculated using the following equation, and the results are presented in Table 1.

$$\%\ Cellulose = \frac{weight\ of\ material\ A - weight\ of\ material\ B}{Total\ weight\ of\ the\ sample} \times 100$$

The cellulose content (%) in both bleached and unbleached pulps was higher than that of the raw material, as shown in Table 1. This increase in total cellulose from raw material to pulp mainly results from the reduction of lignin content during pulping. Throughout the process, both lower- and higher-molecular-weight lignin fractions, particularly those linked with phenolic units in the middle lamella and secondary cell wall, are dissolved. This leads to decreased residual lignin and an increased percentage of cellulose in the pulp fibers (Brännvall 2017). The bleached pulp, containing minimal lignin, exhibited an even higher cellulose percentage, indicating successful removal of extractives, acetyl groups, and uronic acids from hemicelluloses, as well as the degradation and dissolution of α- and β-aryl ether linkages in phenolic units present in the middle lamella and cell wall regions (Santos 2013). Consequently, the relative cellulose content of the pulp fibers was further enhanced. The pulp yield was 38.7%, with the cellulose content rising to 85.4% after bleaching. These results align with reported ranges for non-wood agro-residue pulps processed under mild kraft cooking conditions (Ververis et al. 2004, Rousu et al. 2002), confirming the effectiveness of the delignification strategy employed.

3.3. Water Retention Value

Samples of 5 g each from the raw material, unbleached pulp, and bleached pulp were analyzed for WRV using the following equation:

$$WRV = [(weight\ after\ centrifuge)/(weight\ after\ drying)] - 1$$

The WRV was expressed on a g/g basis (dimensionless ratio). The wet samples were centrifuged at 2600 rpm and 23°C for 15 minutes, followed by overnight drying in a hot air oven at 103.5°C (TAPPI Standard UM 256).

The water retention value (WRV) serves as an empirical indicator of the water-holding capacity of pulp fibers, commonly used to evaluate fiber swelling. Lignin, characterized by its aromatic network structure, exhibits hydrophobic properties that hinder water absorption (Takada et al. 2020). An increase in WRV generally signifies greater lignin removal. Partial delignification in unbleached pulps leads to enhanced surface fibrillation and increased porosity at fiber interfaces, resulting in higher WRV compared to the raw material (Fig. 6). Further lignin extraction in bleached pulps induces internal fibrillation, enlarging internal pores and causing cell wall delamination, a process known as "swelling" (Bian et al. 2016). This process is also associated with the formation of external fibrils, which further improve water retention. As a result, the bleached pulp showed a

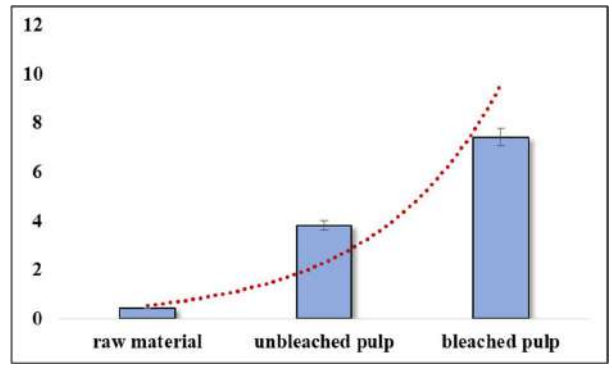


Fig. 6: Water retention value of raw material (before cooking) and pulp (after cooking and bleaching).

higher WRV than the unbleached pulp, due to its increased porosity, higher cellulose content, and lower levels of residual lignin and hydrophobic resins.

3.4. Fourier Transform Infrared (FTIR) Spectroscopy

Fourier Transform Infrared (FTIR) spectroscopy was employed to examine differences between bleached and unbleached pulp samples, highlighting various functional groups with an emphasis on aromatic skeletal vibrations. For spectral analysis, the samples were dried, finely ground, and mixed with potassium bromide (KBr) at a ratio of 1:100 (pulp to KBr), then pressed into thin pellets. The absorbance bands were recorded for interpretation (Fig. 7). In the fingerprint region of 900–1800 cm^{-1}, bands correspond to different functional groups typically associated with lignin. Specifically, the bands between 1600–1400 cm^{-1} signify aromatic or benzene rings present in lignin (Pydimalla et al. 2019). The peaks between 1300–1000 cm^{-1} relate to C–O vibrations found in primary and secondary aliphatic alcohols within cellulose, hemicellulose, and lignin, as

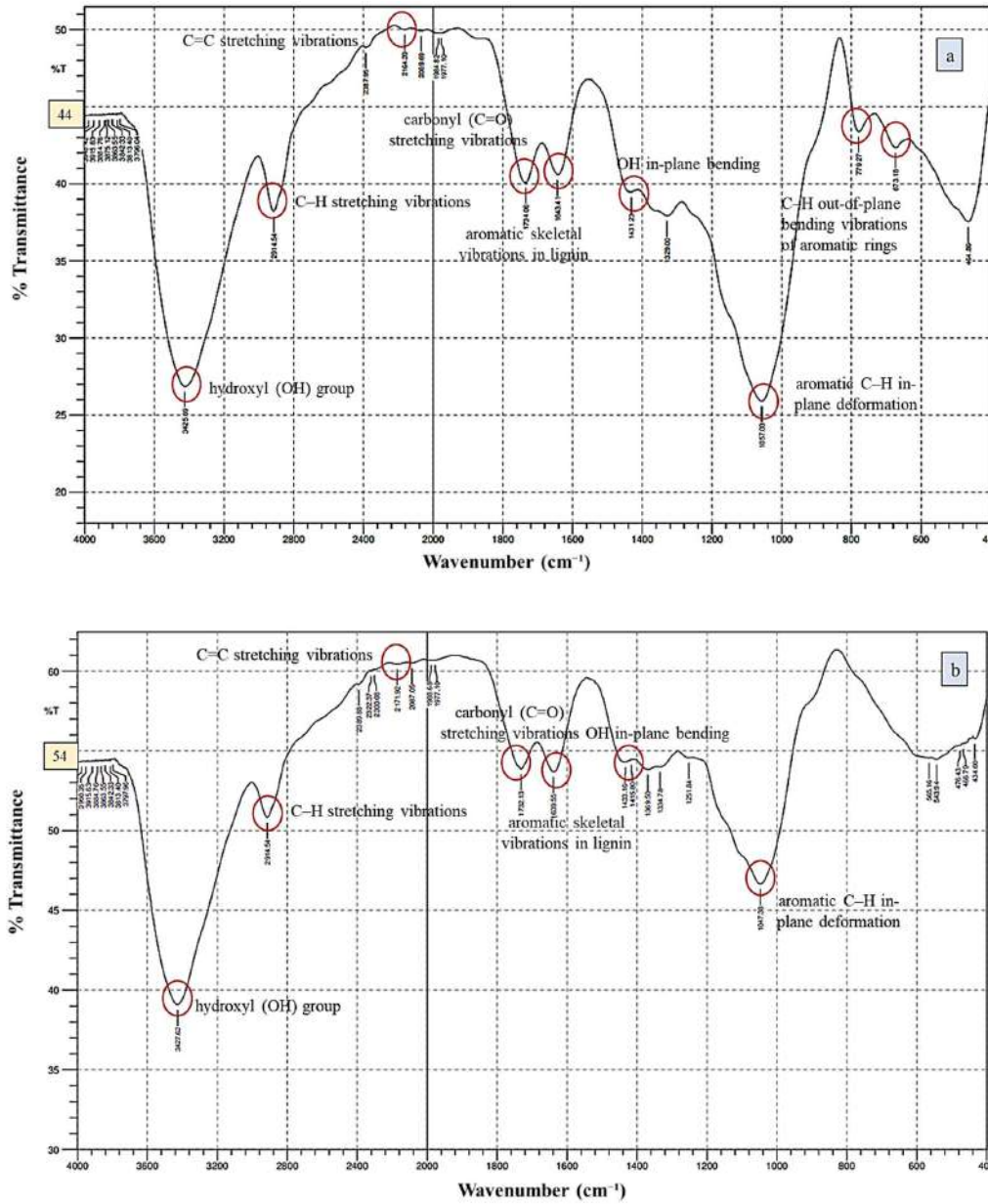


Fig. 7: FTIR analysis: (a) unbleached pulp; (b) bleached pulp.

well as aromatic alcohols in lignin. Both spectra display aromatic C–H in-plane deformations at approximately 1160, 1114, and 1055 cm^{-1} (Colom et al. 2003). Bands around 2130–2135 cm^{-1} are indicative of C=C stretching vibrations, while peaks between 1470–1455 cm^{-1} correspond to OH in-plane bending associated with cellulose. A broad absorption band spanning 3600–3200 cm^{-1} suggests hydroxyl (OH) groups are present in both bleached and unbleached pulp samples. Additionally, an increase in intensity within the 2900–2800 cm^{-1} range is attributed to C–H stretching vibrations (Wong et al. 2023). The FTIR spectra reveal that bleached pulp exhibits higher transmittance than unbleached pulp, indicating a purer cellulose content. Notably, a peak around 1430 cm^{-1} in the bleached pulp spectrum indicates crystalline regions of cellulose, while the band between 1610–1640 cm^{-1} signifies moisture absorption within the cellulose matrix (Hospodarova et al. 2018).

The FTIR spectra of the kraft unbleached pulp exhibit distinct peaks at 779 cm^{-1} and 673 cm^{-1}, corresponding to aromatic C–H out-of-plane bending vibrations, which indicate the presence of residual lignin. These peaks are clearly visible in the raw pulp spectrum but are absent in the bleached pulp spectrum, confirming the removal of lignin during bleaching. Additionally, the unbleached pulp shows a transmittance of 44%, while the bleached pulp shows 54%, suggesting a reduction in light-absorbing functional groups such as those associated with lignin.

3.5. Thermogravimetric Analysis

Fig. 8 illustrates the TGA curves of the pulp sample both before (unbleached pulp) and after (bleached pulp) treatment. These curves were used to evaluate the thermal degradation behavior of the pulp samples. The slight weight loss observed below 100 °C in unbleached pulp results from the volatilization of low-molecular-weight organic extractives and the evaporation of physically adsorbed moisture (Pydimalla & Reddy 2019). The peak degradation temperature (Tmax) indicates that the primary thermal degradation of bleached pulp occurs between 200°C and 350°C. In contrast, the initial degradation stage in unbleached pulp takes place between 250°C and 300°C. The pattern of weight loss in unbleached pulp can be attributed to thermal stability of composite structural units formed by lignin residues, which create complexes with polysaccharides in the cell wall matrix (Zhao et al. 2020). Conversely, the weight loss in bleached pulp results from lignin removal and the absence of those composite structures, including micron-scale pores that could serve as thermal insulators during heat exposure.

Significant weight loss occurs between 200°C and 400°C, mainly due to the degradation of hemicellulose, cellulose, and lignin. The unbleached pulp exhibits a broader degradation range because of the presence of lignin and hemicellulose, whereas the bleached pulp shows a sharper degradation peak, indicating a more cellulose-rich structure after non-cellulosic components are removed. Overall, the unbleached pulp retains more residual mass thanks to the thermally stable aromatic structure of lignin.

To enhance understanding of the degradation process, the peak decomposition temperature (Tmax) was identified from thermogravimetric trends corresponding to the maximum degradation rate. The unbleached pulp exhibited a broader degradation zone, indicating the presence of lignin and hemicellulose alongside cellulose. In contrast, the bleached pulp displayed a more distinct and sharper degradation peak within the 200–350°C range, characteristic of cellulose-rich material. The sharper Tmax observed in the bleached sample suggests improved homogeneity caused by the removal of lignin and non-cellulosic substances during bleaching.

The unbleached pulp showed a slightly higher residual mass at elevated temperatures, likely due to lignin residues, which are known for their slower degradation and wider temperature range for breakdown. Conversely, the bleached pulp lost weight more rapidly during the main degradation phase, indicating that it was richer in cellulose and contained less lignin.

The thermal degradation behavior of the bleached and unbleached pulps was analyzed over a temperature range of 30–600°C. The initial weight loss at lower temperatures was primarily associated with the evaporation of physically bound moisture and volatile components, while the major thermal degradation occurred approximately between 200 and 400°C, corresponding mainly to the decomposition of hemicellulose and cellulose, with contributions from residual lignin. Kraft pulping and subsequent bleaching remove substantial portions of lignin and hemicellulose from the lignocellulosic matrix, resulting in an increased relative cellulose content in the pulp fibers (Kron et al. 2025). Consequently, the bleached pulp exhibited a somewhat different thermal degradation profile compared with the unbleached pulp, which can be attributed to differences in lignin and hemicellulose content and the resulting changes in fiber composition. The removal of amorphous components during chemical treatment alters the thermal decomposition behavior of cellulose-rich fibers, as reported in previous studies. Overall, the TGA results indicate that kraft pulping and bleaching modify the thermal degradation characteristics of the pulp primarily through changes in lignin, hemicellulose, and relative cellulose content.

3.6. Scanning Electron Microscopy

The SEM micrographs of unbleached and bleached pulp

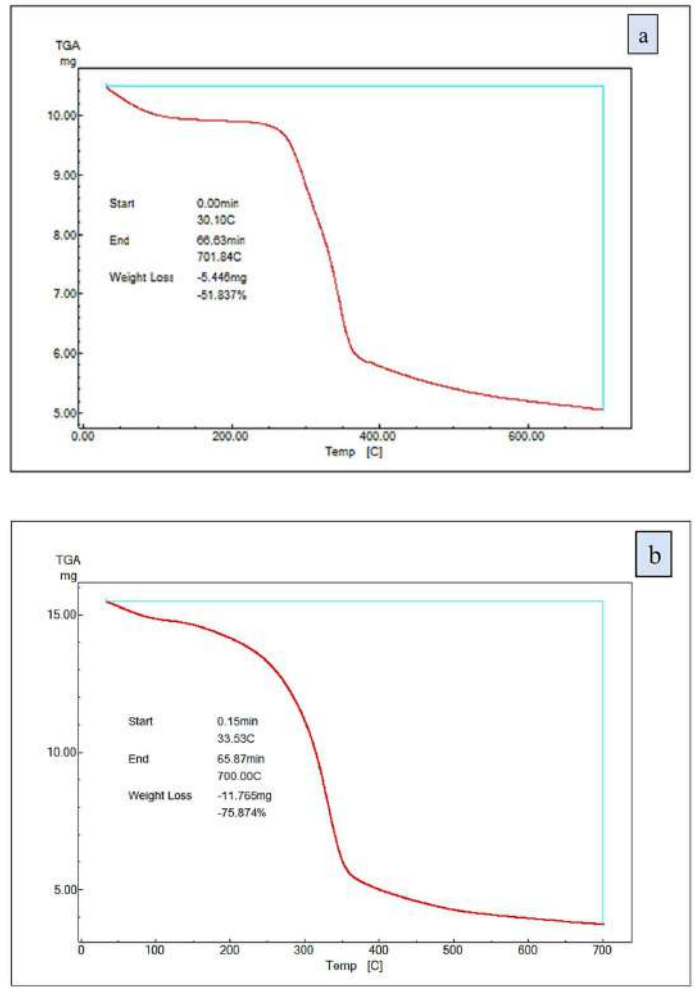


Fig. 8: TGA analysis: (a) unbleached pulp; (b) bleached pulp

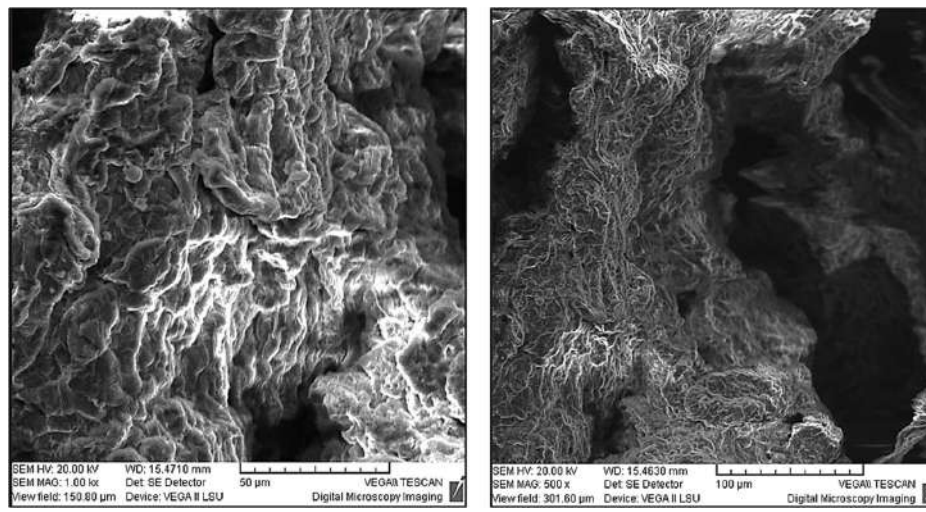


Fig. 9: SEM micrographs of unbleached pulp fibers.

fibers are depicted in Figs. 9 and 10. The micrograph of unbleached pulp shows thick, irregular fibers arranged in a complex network. Its surface appears rough, with numerous fibrils and a dense matrix. The fibers are less separated and intertwined, indicating residual lignin and hemicellulose that serve as binding agents. This compact structure results in lower porosity and less individual fiber separation.

The SEM image of bleached pulp reveals a more loosened fiber structure with more visible and distinct fibrils. The surface appears smoother, and the fibers exhibit increased individualization due to the removal of lignin and other non-cellulosic compounds during bleaching. This morphology is desirable in applications requiring high cellulose purity, such as nanocellulose production or bioplastics. Therefore, SEM characterization effectively indicates the microstructural changes in lignocellulosic fibers resulting from bleaching. The bleached pulp displays a significantly refined structure that enhances material development, whereas the unbleached pulp maintains its natural structure without fiber liberation.

3.7. Energy Dispersive X-ray (EDX) Analysis

The elemental analysis of bleached and unbleached kraft pulps derived from a mixed feedstock of coconut coir and corn husk was performed using EDX (Fig. 11), and the corresponding elemental compositions are presented in Tables 2 and 3. Both samples primarily consisted of carbon and oxygen, consistent with the lignocellulosic nature of the pulp. The unbleached pulp contained 52.57 wt% C and 46.34 wt% O, while the bleached pulp exhibited a slightly higher relative carbon content. This difference indicates a change in the surface elemental composition following hydrogen peroxide bleaching. However, EDX elemental analysis alone does not provide direct evidence of lignin removal or quantify lignin content. The observed change in elemental composition should therefore be interpreted as complementary evidence of the chemical modification of the pulp during bleaching, while the extent of delignification is better assessed from the chemical composition and other characterization results.

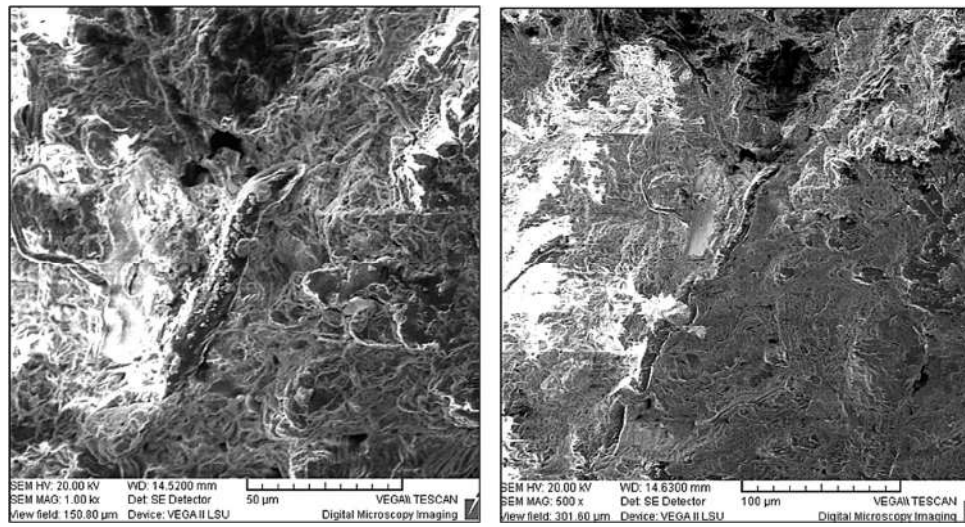


Fig. 10: SEM micrographs of bleached pulp fibers.

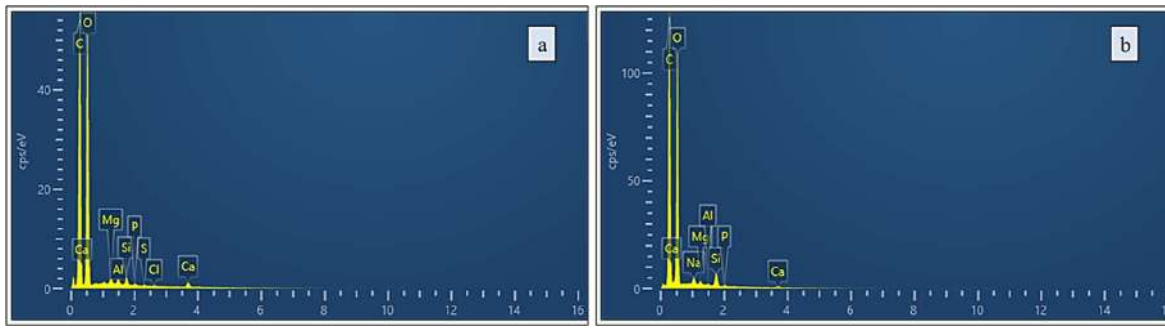


Fig. 11: EDX analysis of (a) unbleached and (b) bleached pulp.

Table 2: EDX results of unbleached pulp.

Element	Weight (%)	Weight (%) Sigma	Atomic (%)
C	52.57	0.21	59.87
O	46.34	0.21	39.62
Mg	0.23	0.02	0.13
Al	0.17	0.01	0.09
Si	0.27	0.01	0.13
P	0.06	0.01	0.02
S	0.04	0.01	0.02
Cl	0.03	0.01	0.01
Ca	0.28	0.01	0.09
Total	100.00		100.00

Table 3: EDX results of bleached pulp.

Element	Weight (%)	Weight (%) Sigma	Atomic (%)
C	53.22	0.18	60.48
O	45.60	0.18	38.91
Na	0.42	0.02	0.25
Mg	0.13	0.02	0.07
Al	0.04	0.01	0.02
Si	0.43	0.01	0.21
P	0.06	0.01	0.03
Ca	0.10	0.01	0.03
Total	100.00		100.00

The unbleached sample contains minor elements such as Mg (0.23%), Al (0.17%), Si (0.27%), P (0.06%), S (0.04%), Cl (0.03%), and Ca (0.28%). These may originate from natural biomass ash or residual kraft pulping chemicals. Although present in small quantities, sulfur and chlorine indicate the influence of the kraft pulping process. In contrast, the bleached pulp exhibits lower levels of inorganic impurities: Na (0.42%), Mg (0.13%), Al (0.04%), Si (0.43%), P (0.06%), and Ca (0.10%), with sulfur and chlorine undetectable. The absence of Cl and S suggests that peroxide bleaching is environmentally friendly. Overall, bleaching enhances purity and application potential, resulting in a high-quality paper product.

3.8. UV–Vis Spectroscopic Analysis

The analysis of black liquor derived from the kraft pulping process was performed using UV–visible spectroscopy to verify the presence of lignin-related compounds. The absorption spectrum spanned from 190–300 nm, with a notable peak between 200–210 nm exhibiting a high absorbance of 0.8 (Fig. 12). In addition to this peak, lignin-derived compounds generally absorb light within the 230–280 nm range, which is associated with substituted aromatic rings and conjugated phenolic structures. These spectral features support the solubilization of guaiacyl- and syringyl-type lignin units into the black liquor during alkaline pulping. The spectral characteristics align with oligomeric $\pi-\pi^*$ electronic transitions linked to aromatic C=C bonds and $n-\pi^*$ transitions from carbonyl-containing lignin fragments formed during oxidative and alkaline cleavage reactions (Hynynen et al. 2021). The peak observed at 200–205 nm indicates a high concentration of conjugated phenolic structures resulting from lignin fragmentation (Pydimalla et al. 2019). This sharp absorption suggests effective cleavage of ether and carbon–carbon bonds within the lignin macromolecule during kraft pulping, especially of β-O-4 bonds, which are highly susceptible to alkaline cleavage. Since absorbance follows Beer's law and is proportional to concentration under appropriate analytical conditions, the observed spectral features support the occurrence of lignin solubilization under the selected laboratory-scale

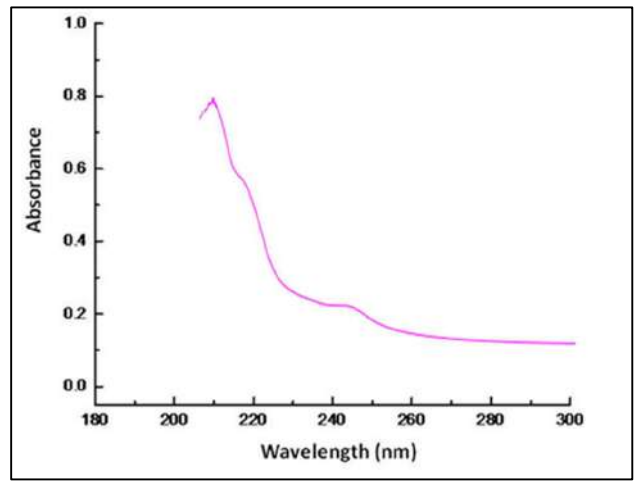


Fig. 12: UV analysis of black liquor.

pulping conditions. Furthermore, the absence of significant absorbance beyond 300 nm indicates that highly condensed chromophoric structures were rarely formed, suggesting that the pulping conditions favored lignin depolymerization over extensive condensation reactions.

This study primarily examines the feasibility of pulp production and the physicochemical characterization of fibers before conducting a comprehensive assessment of paper manufacturing performance. While standard pulping parameters such as kappa number and H-factor were not measured, the degree of delignification is inferred from qualitative analytical results. FTIR spectra indicate a notable reduction in lignin-related bands, and UV–Vis analysis of black liquor confirms the presence of dissolved lignin compounds released during pulping. These results suggest efficient lignin removal, corroborated by SEM micrographs showing fiber separation and surface modifications, demonstrating that the treatment effectively initiated lignin dissolution and fiber liberation. The findings highlight the potential for producing pulp from a mixed agro-residue system of corn husk and coconut coir. Combined physicochemical and morphological analyses verify fiber separation and lignin removal during pulping and bleaching. Although this research is conducted at the laboratory scale, future studies will systematically evaluate pulping parameters, handsheet formation, and papermaking performance to determine the pulp's suitability for industrial applications.

4. CONCLUSIONS

The current study introduces an innovative approach to utilizing mixed agrowaste biomass, specifically corn husk and coconut coir, by optimizing conditions that involve kraft pulping followed by elemental chlorine-free bleaching. This technique effectively achieved delignification, as evidenced by UV–visible spectroscopic analysis of black liquor, which exhibited a clear absorbance peak at 200–205 nm indicative of phenolic lignin derivatives. The process resulted in a pulp yield of 38.7% and significantly increased cellulose content from 60.2% in the unbleached pulp to 85.4% post-bleaching, demonstrating efficient delignification and bleaching. Additional confirmation of non-cellulosic component removal was obtained through elevated water retention value measurements and morphological changes observed in SEM images, which showed fiber loosening and fibrillation. FTIR spectra validated the degradation of aromatic lignin structures, while TGA analysis revealed improved thermal stability in the bleached fibers, attributable to lignin reduction and a more cellulose-rich matrix. Overall, this pulping and bleaching method enhanced the physicochemical and structural properties of the pulp, providing a sustainable pathway to convert lignocellulosic biomass into high-purity cellulose suitable for advanced applications such as nanocellulose, biodegradable films, and eco-friendly composites. The findings support circular bioeconomy strategies by advancing waste-to-value technologies within the pulp and paper industry. Future research will focus on systematically optimizing pulping parameters, including active alkali charge, sulfidity, and kappa number, to further improve delignification efficiency and pulp quality.

5. ACKNOWLEDGMENTS

The authors would like to extend their heartfelt gratitude to Chaitanya Bharathi Institute of Technology (CBIT) for their generous funding and unwavering support under the major research project entitled "Pulp, Handsheet and Black Liquor Characterization of Hardwood Species (Beach Sheoak) after Kraft Cooking and Bleaching Process" as per the sanction order no. CBIT/PROJ/-IH/I037/Chemical/D004/2024.

6. REFERENCES

Austin, C.C., Mondell, C.N., Clark, D.G. and Wilkie, A.C., 2024. Kenaf: opportunities for an ancient fiber crop. *Agronomy*, 14(7), p.1542. [DOI]

Bajpai, P., 2012. Pulp bleaching and bleaching effluents. In: Bajpai, P. (ed.), *Biotechnology for Pulp and Paper Processing*. Springer, Berlin, pp.45–67. [DOI]

Bajpai, P., 2013. Pulp bleaching and bleaching effluents. In: Bajpai, P. (ed.), *Bleach Plant Effluents from the Pulp and Paper Industry*. SpringerBriefs in Applied Sciences and Technology, Springer, Heidelberg, pp.45–67. [DOI]

Bian, H., Chen, L., Dai, H. and Zhu, J.Y., 2016. Enzyme-assisted mechanical fibrillation of bleached spruce kraft pulp to produce well-dispersed and uniform-sized cellulose nanofibrils. *BioResources*, 11(4), pp.10483–10496. [DOI]

Brännvall, E., 2017. The limits of delignification in kraft cooking. *BioResources*, 12(1), pp.2081–2107. [DOI]

Britt, K.W., 1970. *Handbook of Pulp and Paper Technology*. Van Nostrand Reinhold Company, New York, USA.

Colom, X., Carrillo, F., Nogués, F. and Garriga, P., 2003. Structural analysis of photodegraded wood by means of FTIR spectroscopy. *Polymer Degradation and Stability*, 80(3), pp.543–549. [DOI]

Das, S., Rani, A., Gahlot, M., Kapoor, S., Sisodia, N. and Sharma, A., 2023. An overview of non-wood fiber characteristics for paper production: sustainable management approach. *Materials Today: Proceedings*. [DOI]

Dutt, D., 2013. Environmentally friendly and cost-effective method for manufacturing absorbent grade paper. *Cellulose Chemistry and Technology*, 47, pp.783–792.

El-Sayed, E.S., El-Sakhawy, M. and El-Sakhawy, M.A., 2023. Non-wood fibers as raw material for pulp and paper industry. *Nordic Pulp & Paper Research Journal*, 35(2), pp.215–230. [DOI]

Furszyfer Del Rio, D.D., Sovacool, B.K., Bergman, N. and Makuch, K.E., 2022. Decarbonizing the pulp and paper industry: a systematic review of measures and pathways. *Renewable and Sustainable Energy Reviews*, 167, p.112706. [DOI]

Gavrilescu, D., 2008. Energy from biomass in pulp and paper mills. *Environmental Engineering and Management Journal*, 7(5), pp.537–546. [DOI]

Gellerstedt, G., 2003. The chemistry of bleaching and post-color formation in pulp. *Proceedings of the 3rd International Colloquium on Eucalyptus Pulp*, Espoo, Finland.

Hospodarova, V., Singovszka, E. and Stevulova, N., 2018. Characterization of cellulosic fibers by FTIR spectroscopy. *American Journal of Analytical Chemistry*, 9(3), pp.303–310. [DOI]

Hynynen, J., Orelma, H., Filpponen, I. and Johansson, L.S., 2021. Lignin and extractives first conversion using UV light from LEDs. *Green Chemistry*, 23, pp.8251–8259. [DOI]

Karlsson, H., 2006. *Fiber Guide: Fiber Analysis and Process Applications in the Pulp and Paper Industry*. AB Lorentzen & Wettre, Kista, Sweden.

Knott, B., 2021. *Molecular Modeling to Increase Kraft Pulp Yield*. National Renewable Energy Laboratory, Golden, USA. Available from: https://www.nrel.gov/docs/fy21osti/79842.pdf

Kron, L., Hasani, M. and Theliander, H., 2024. Delignification behavior of Nordic hardwoods during kraft cooking. *Holzforschung*, 78(8), pp.434–445. [DOI]

Kron, L., Hasani, M. and Theliander, H., 2025. Diffusion and reaction model of kraft delignification. *Industrial & Engineering Chemistry Research*, 64(3), pp.1497–1507. [DOI]

Liu, Y., Wang, X., Chen, Z. and Li, J., 2024. Effects of plant source selection and pretreatment on fiber properties. *Wood Science and Technology*, 58(1), pp.123–135. [DOI]

Madhuri, P., Reddy, K. and Dutt, D., 2016. Pulp and black liquor characterization of Subabul wood. *IPPTA Journal*, 28(2).

Manfredi, V., 2024. The wood pulping processes. In: Manfredi, V. (ed.), *Pulping and Paper Making: A Comprehensive Guide*. Springer Nature, Cham, pp.45–67. [DOI]

Mishra, O.P. and Sharma, R.K., 2020. Physical strength properties of corn stalk pulp. *Cellulose Chemistry and Technology*, 54(1–2), pp.65–71. Available from: https://www.cellulosechemtechnol.ro/pdf/CCT1-2(2020)/p.65-71.pdf

Nagaraja Ganesh, B., Reddy, N., Rao, K.M. and Reddy, K.O., 2022. Producing pulp and paper from discarded fibers: a sustainable approach. *Journal of Natural Fibers*, 20(1). [DOI]

Pere, J., Paavilainen, L., Tolonen, L. and Paulapuro, H., 2019. Influence of hemicellulose content on handsheet properties. *BioResources*, 14(1), pp.251–263. [DOI]

Peracchi, M., Crestini, C. and Saladino, R., 2024. Lignin stability and properties. In: *Encyclopedia of Renewable and Sustainable Materials*. Elsevier, Amsterdam, pp.1–20. [DOI]

Pydimalla, M. and Adusumalli, R.B., 2020. Handsheet characteristics of Subabul wood pulp. *Nordic Pulp & Paper Research Journal*, 35(2), pp.161–171. [DOI]

Pydimalla, M. and Reddy, K., 2019. Influence of temperature on kraft pulping of Subabul wood. *Sugar Tech*, 21, pp.1003–1015. [DOI]

Pydimalla, M. and Reddy, K., 2020. Effect of pulping, bleaching and refining on fibers for paper making: a review. *International Journal of Engineering Research and Technology*, 9(12). Available from: https://www.ijert.org/effect-of-pulping-bleaching-and-refining-process-on-fibers-for-paper-making-a-review

Rousu, P. and Anttila, J., 2002. Sustainable pulp production from agricultural waste. *Resources, Conservation and Recycling*, 35, pp.85–103. [DOI]

Rowell, R.M., 2012. *Handbook of Wood Chemistry and Wood Composites*. 2nd ed., CRC Press, Boca Raton, USA. [DOI]

Santos, R.B., Hart, P.W., Jameel, H. and Chang, H.M., 2013. Wood-based lignin reactions important to the biorefinery and pulping processes. *BioResources*, 8(1), pp.1456–1477. [DOI]

Singh, R. and Bajpai, P., 2025. Eco-friendly biobleaching processes. In: *Advances in Sustainable Pulping and Paper Making*. Springer, Singapore, pp.345–368. [DOI]

Smook, G.A., 2002. *Handbook for Pulp and Paper Technologists*. 3rd ed., Angus Wilde Publications, Vancouver, Canada.

Takada, M., Nakagawa-Izumi, A., Ohi, H. and Aoyagi, T., 2020. Influence of lignin on pretreatment and enzymatic hydrolysis. *Bioresource Technology*, 302, p.122895. [DOI]

Tarrés, Q., Delgado-Aguilar, M., Pèlach, M.À. and Mutjé, P., 2023. Lignin-containing microfibrillated cellulose: properties and applications. *Cellulose*, 30(4), pp.2325–2340. [DOI]

Van Ewijk, S. and Stegemann, J.A., 2016. Limitations of the waste hierarchy for achieving absolute reductions in material throughput. *Resources, Conservation and Recycling*, 132, pp.122–128. [DOI]

Ververis, C., Georghiou, K., Christodoulakis, N., Santas, P. and Santas, R., 2004. Fiber dimensions, lignin and cellulose content of various plant materials and their suitability for paper production. *Industrial Crops and Products*, 19(3), pp.245–254. [DOI]

Wang, Y. and Liu, H., 2022. Pulping process for nonwoody plants. In: *Nonwood Plant Fibers for Sustainable Pulping*. Elsevier, Amsterdam, pp.123–150. [DOI]

Wohlert, M., Bergenstråhle-Wohlert, M. and Berglund, L.A., 2022. Cellulose and hydrogen bonds: structural and mechanical aspects. *Cellulose*, 29(1), pp.1–23. [DOI]

Wong, L.C., Tan, Y.P., Ng, S.F. and Yusof, N., 2023. Cellulose hydrogel for dermal drug delivery. *International Journal of Biological Macromolecules*, 224, pp.483–495. [DOI]

Worku, L.A., Bultum, L.B., Tolesa, G.N. and Urgessa, G.S., 2023. Agricultural residues as alternative raw materials for pulp and paper production. *Membranes*, 13(2), p.228. [DOI]

Zhao, Y., Wang, S., Lyu, S. and Fang, G., 2020. Lignin–carbohydrate complexes and their impact on biomass utilization. *Journal of Cleaner Production*, 253, p.120076. [DOI]

Nature Environment and Pollution Technology
An International Quarterly Peer-Reviewed Open Access Journal

p-ISSN: 0972-6268 | e-ISSN: 2395-3454 Vol. 25 | No. 4 | Article ID D1889 | 2026

RESEARCH ARTICLE https://doi.org/10.46488/NEPT.2026.v25i04.D1889 OPEN ACCESS

Simulation of the Migration Law of Cr(VI) in Groundwater Using a Fully Coupled Numerical Model

Haihua Li[1]†, Gaojie Chai[1], Yahui Xu[2], Xinyi Wang[1] and Haozu Cheng[1]
[1]School of Ecology and Environment, North China University of Water Resources and Electric Power, Zhengzhou 450046, Henan, China
[2]Huaxia Besince Environmental Technology Co. Ltd., Zhengzhou 450002, Henan, China
†Corresponding author: Haihua Li; lihaihua418@163.com

ARTICLE HISTORY

Received: 12-11-2025
Revised: 02-02-2026
Accepted: 24-02-2026

KEYWORDS

Hexavalent chromium (Cr(VI))
Solute transport
Convective dispersion
Fully coupled numerical model

CITE THIS ARTICLE

Li, H., Chai, G., Xu, Y., Wang, X. and Cheng, H., 2026. Simulation of the migration law of Cr(VI) in groundwater using a fully coupled numerical model. *Nature Environment and Pollution Technology*, 25(4), D1889. https://doi.org/10.46488/NEPT.2026.v25i04.D1889

COPYRIGHT & LICENCE

© 2026 The Authors
Open Access under CC BY 4.0.

PUBLISHED BY

TECHNOSCIENCE PUBLICATIONS

ABSTRACT

Coupled numerical models are widely used to investigate heavy metal migration in groundwater. This study selected a chromium slag stacking site and its surrounding area in Henan Province, China, as the research area to investigate the effective prevention of soil and groundwater pollution caused by hexavalent chromium (Cr(VI)), a by-product of chromium salt production. To this end, a three-dimensional numerical model of water flow and solute transport, fully coupled with convective dispersion, was constructed. The model was employed to examine the migration patterns of Cr(VI) in soil and groundwater while considering the influence of phreatic surface fluctuations caused by rainfall infiltration and soil matrix adsorption. The simulation results demonstrated that rainfall enhanced groundwater convection and dispersion and promoted the migration of Cr(VI). In the vadose zone, the Cr(VI) concentration at the plume center decreased from 568 to 307 mg kg^{-1} under rainfall conditions, compared with a decrease to 224 mg kg^{-1} without rainfall over five years. The investigation of soil adsorption revealed that adsorption by the soil matrix expanded the range of variation in Cr(VI) concentration while reducing the overall migration quantity compared with conditions without rainfall.

1. INTRODUCTION

The rapid urbanization and industrialization that have accompanied China's economic growth have resulted in a significant environmental concern: heavy metal pollution, particularly chromium-based pollution, in soil and groundwater (Adnan et al. 2022). During the early stages of chromium salt production in China, the resource utilization rate was relatively low, resulting in the generation of a considerable amount of solid waste (Xu et al. 2006). The production of solid chromium slag waste is estimated to range from 2.5 to 3 tons per ton of chromium salt produced (Dhal et al. 2013). The solid chromium slag waste generated during the industrial production process is often randomly stacked in open fields. During storage, however, chromium slag continues to produce chromium slag filtrate (Cao et al. 2024, Wu et al. 2022), leading to significant contamination of the surrounding soil and groundwater. This environmental pollution poses a considerable risk to the health and well-being of local residents and the surrounding ecosystem. Therefore, effective prevention and control measures must be implemented without delay (Godbole et al. 2025).

COMSOL 6.4 (COMSOL Inc., Stockholm, Sweden) is robust numerical simulation software that enables the coupling of multiple physical fields, thereby

facilitating the investigation of engineering optimization problems (Sumit et al. 2021). The groundwater flow module can simulate porous media applications in hydrology, geotechnical engineering, and environmental science (Zhang et al. 2020). In particular, it supports various mesh types, including two-dimensional (triangular/quadrilateral) and three-dimensional (tetrahedral/hexahedral/prismatic) meshes (Giacomini & Sevilla 2020), enabling the modeling and solution of diverse scientific and engineering problems involving partial differential equations (PDEs). The software incorporates porous media and groundwater flow modules (Bai et al. 2024, Qiao et al. 2023), which have been used to simulate the migration of heavy metals in soil.

For example, Xie et al. (2020) combined migration law analysis with numerical simulation to investigate the concentrations of heavy metals, specifically Cd and Cu, in soil samples collected from a mining area. They selected the homogeneous soil of a sand dam as the research object and quantified the total amount of pollutant migration within the dam body and at the dam outlet using a prediction model developed in COMSOL. Based on the finite element COMSOL simulation platform, Li et al. (2021) developed a transient model to evaluate the relevant parameters during the transport process by fitting breakthrough curves. Wang et al. (2025) established a numerical simulation model of groundwater flow and solute transport using GMS software and analyzed the migration time of hexavalent chromium to a water source protection area under different scenarios. Their study provided a scientific basis for predicting and preventing chromium pollution at contaminated sites. Additionally, Liang et al. (2019) used COMSOL simulation software to investigate the effects of layered heterogeneous soil structures on water and solute transport in the unsaturated zone. Despite these studies, there is relatively little literature on the reaction processes of chromium at contaminated sites.

In this study, the research area comprised a chromium slag stacking site and its surrounding area in Henan Province. The objective was to analyze the degree of soil and groundwater contamination and the spatial distribution of Cr(VI) at the contaminated site. Rainwater recharge was directly assessed based on Healy (2010), assuming that rainfall was the primary recharge mechanism. To this end, a three-dimensional numerical model of the actual contaminated site was constructed, and multiphysical coupling of water flow and solute transport was performed using a groundwater flow model and a reactive solute transport model for porous media. This approach enabled an accurate description of the migration behavior of Cr(VI) in the unsaturated soil zone and the groundwater within the saturated zone. The findings of this study provide a scientific basis for the adoption of effective remediation technologies to protect soil and groundwater resources.

2. MATERIALS AND METHODS

2.1. Study Area

2.1.1. Geographical and Geomorphological Overview

The study area is located in a city in northern Henan Province, in the southeastern foothills of the Taihang Mountains and along the northern margin of the alluvial plain in the lower reaches of the Yellow River. Based on geomorphological origin, the area is classified into three geomorphological types: structural erosional hills, piedmont alluvial plains, and alluvial plains. The study area is characterized by gently sloping terrain, with an elevation ranging from 73 to 76 m and an average slope of 3%. The terrain slopes from northwest to southeast, with higher elevations in the north and lower elevations in the south. The surface lithology consists of silt and silty clay.

The study area is situated in a warm temperate continental monsoon climate zone, characterized by hot summers, cold winters, concentrated rainfall, and distinct seasons. The long-term average temperature is 14 °C, and the long-term average annual precipitation is 586.32 mm. Annual precipitation varies considerably, ranging from a maximum of 1375.3 mm in a wet year (2021) to a minimum of 327.7 mm in a dry year (2002). Most precipitation occurs during July and August. The long-term average annual evaporation is 1772.62 mm, which is three to four times the annual precipitation, with the highest evaporation occurring in June. The long-term average absolute humidity is 12.9 mb, and the average relative humidity is 65%.

2.1.2. Overview of the Contaminated Site

The chemical plant within the study area produced sodium dichromate using chromium ore, soda ash, sulfuric acid, dolomite, and limestone as raw materials. The plant site has subsequently been used as a storage area for chromium slag generated during the previous production process (the composition of the chromium slag is shown in Table 1), covering an area of 4230 m². From 2009 to 2015, the chromium slag and chromium-contaminated materials at the site were treated and landfilled. Following the completion

Table 1: List of chromium slag components in chemical plants.

Component	Cr_2O_3	Fe_2O_3	Al_2O_3	SiO_2	MgO	CaO	Water-soluble chromium	Acid-soluble chromium	pH value
Content	5.48%	8.46%	8.20%	8.91%	22.41%	32.46%	0.39%	0.47%	>10

of remediation, the treatment equipment was removed, and the contaminated site has remained idle since then.

2.2. Basic Equation of Groundwater Flow

Based on the hydrogeological conditions of the contaminated site in the study area, the unsaturated seepage continuity equation, namely the Richards equation, was selected to describe the three-dimensional movement of water in both the saturated and unsaturated zones (De Smedt 2016, Song & Borja 2014, Therrien & Sudicky 1996). The governing equation is as follows.

$$\rho\left(\frac{C_m}{\rho g}+S_eS\right)\frac{\partial p}{\partial t}+\nabla\cdot\rho\left(-\frac{k_s}{\mu}k_r(\nabla p+\rho g\nabla D)\right)=Q_m \quad ...(1)$$

where ρ is the fluid density (kg m^{-3}); p is the pressure head (Pa); S is the water storage coefficient (m^{-1}); C_m is the water capacity (m^{-1}), with $C_m = 0$ when the soil is saturated; S_e is the effective soil saturation, with $S_e = 1$ under saturated conditions; k_s is the soil permeability under saturated conditions (m s^{-1}); k_r is the relative permeability and is a function of effective saturation in unsaturated soil; γ is the bulk density of the fluid [kg/(m $s)^2$]; D is the elevation (m); and Q_m is the source-sink term, representing fluid inflow per unit volume per unit time under external conditions such as rainfall infiltration (kg m^{-3} s^{-1}).

In the unsaturated state, the soil moisture content θ, C_m, S_e, and k_r can be obtained from the van Genuchten retention model (Ghanbarian-Alavijeh et al. 2010), as follows:

$$\theta=\theta_r+Se(\theta_s-\theta_r) \quad ...(2)$$

$$C_m=\frac{\alpha m}{1-m}(\theta_s-\theta_r)Se^{\frac{1}{m}}(1-Se^{\frac{1}{m}})^m \quad ...(3)$$

$$Se=\frac{1}{[1+|\alpha H_p|^n]^m} \quad ...(4)$$

$$k_r=Se^L[1-(1-Se^{\frac{1}{m}})^m]^2 \quad ...(5)$$

where θ_s is the saturated soil moisture content; θ_r is the residual moisture content after soil drainage; α, m, and n are the constitutive constants of the model, with n = 1/m; and H_p is the soil matrix potential (m), which is negative.

2.3. Pollutant Transport Control Equation

Considering the effects of groundwater flow convection, hydrodynamic dispersion, and pollutant adsorption by the soil matrix in the study area (Anderson et al. 1979, Banaei et al. 2021), a three-dimensional convection–dispersion–adsorption–reaction partial differential equation for solute transport was established to describe the migration of Cr(VI) in both the saturated and unsaturated zones. The basic governing equations are as follows:

$$\frac{\partial}{\partial t}(\theta_lC_i)+\frac{\partial}{\partial t}(\rho C_{p,i})+\frac{\partial}{\partial t}(\theta_gC_{G,i})+u\nabla C_i=\nabla[(D_{D,i}+D_{e,i})\nabla C_i]+R_i+S_i \quad ...(6)$$

where the terms on the left-hand side of the equation represent concentration changes in the liquid, solid, and gas phases, respectively. The fourth term represents convective solute transport under the groundwater velocity field. C_i is the solute concentration in the liquid phase (mol m^{-3}); $C_{p,i}$ is the amount adsorbed on solid particles [mol/(ρ_s g)]; and $C^G{}_{,i}$ is the gas-phase concentration. Gas-phase volatilization was not considered in this study; therefore, the concentration was set to 0. u is the groundwater flow velocity (m s^{-1}); D^D is the diffusion tensor (m^2 s^{-1}); D_e is the effective diffusion coefficient (m^2 s^{-1}); R_i is the reaction-rate expression representing chemical reactions in the liquid or solid phase; S_i is the source-sink term, representing material inflow and outflow with the liquid; and θ_l is the liquid volume content. For saturated porous media, θ_l = porosity ε; for unsaturated porous media, $\theta_l = \varepsilon \times S$, where S is soil saturation.

The main factors affecting solute transport in soil and groundwater are convection, hydrodynamic dispersion, adsorption, chemical reactions, and source-sink terms.

2.4. Hydrogeological Conceptual Model of the Study Area

2.4.1. Study Area Generalization

In this study, the simulation range was determined by the mainstream direction of groundwater flow and the distribution of boreholes. The simulation range of the contaminated sites is shown in Fig. 1.

2.4.2. Model Boundary Condition Generalization

(1) Model lateral boundary condition generalization

Owing to the incomplete hydrological unit in the study area and the lack of detailed data on groundwater recharge and discharge, the regional groundwater level contours were adopted as the general head boundary (Costabile et al. 2019, Chi et al. 2022). This boundary condition enabled the simulation to better represent the actual hydrogeological conditions, thereby improving the accuracy of the model.

(2) Model vertical boundary condition generalization

Based on data obtained from 71 boreholes, a three-dimensional geological model was constructed using ArcGIS 10.8.2 (Environmental Systems Research Institute, Inc., Redlands, California, USA). The geological strata were interpolated and subsequently imported into COMSOL. The ground surface was defined as the upper boundary, whereas the underlying

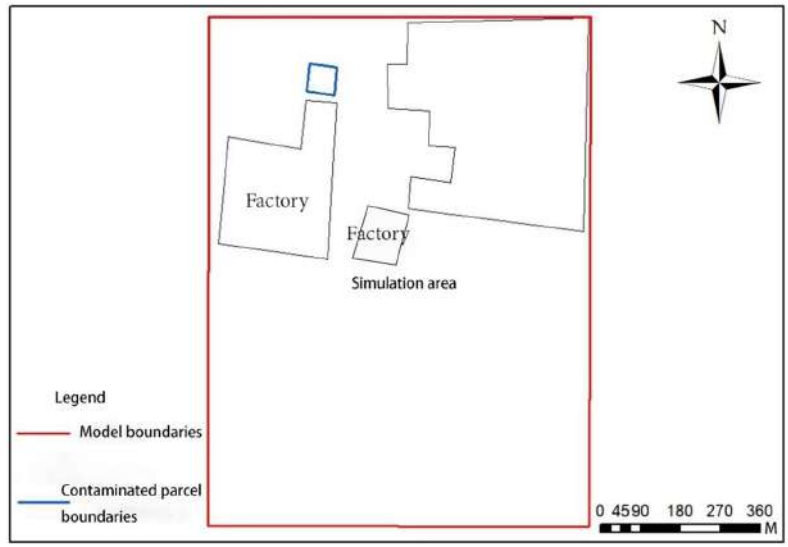


Fig. 1: Model simulation scope plan.

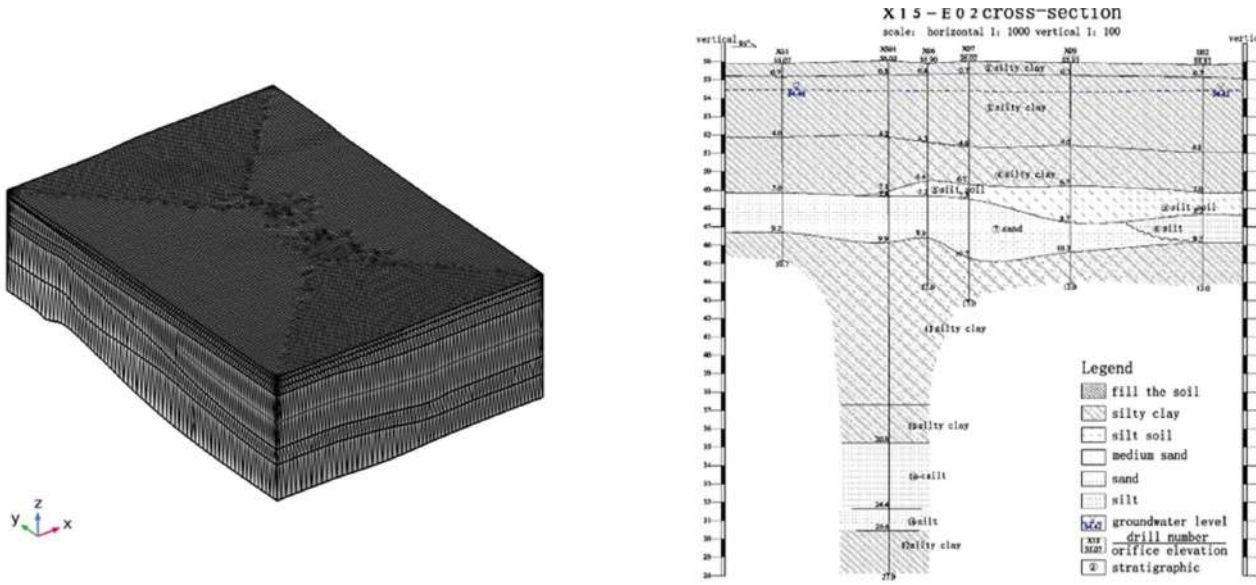


Fig. 2: Three-dimensional model mesh segmentation diagram and cross-sectional view.

silty clay layer was defined as the lower boundary. The model was divided into six layers, comprising two unsaturated layers and four saturated layers. The saturated zone included the shallow aquifer, the first aquifer (fine sand), the weakly permeable layer (silty clay), and the second aquifer (fine sand). Beneath the second aquifer lies a thick silty clay aquiclude. The model incorporated rainfall recharge, considered the long-term difference between rainfall and evaporation, and assumed that groundwater flow was predominantly directed toward the southeast.

2.4.3. Numerical Model Mesh Generation

This study utilized COMSOL software's groundwater flow module and porous media dilute transport module to simulate groundwater flow and solute transport within the study area. A three-dimensional geological model was created and segmented into multiple units using a free tetrahedral mesh. The model was stratified into six vertical layers, resulting in a total of 808,267 tetrahedral mesh elements, along with 24 vertex units and 2,718 edge units. The overall mesh volume was calculated to be $7{,}348 \times 10^7$ m³. The mesh generation process for the model is illustrated in Fig. 2.

2.5. Model Validation

Following the validation approaches reported by Thanh et al. (2022) and Yeh et al. (2015), the model was validated to assess its accuracy in representing the geological features and groundwater flow in the study area and to support precise numerical simulation of soil-groundwater solute transport. Using field data, a steady-state simulation was first conducted and then repeatedly calibrated to match the simulated groundwater levels with actual measurements. The selected groundwater monitoring wells are shown in Fig. 3, where JA denotes the first aquifer well, and JB denotes the second. Table 2 presents the water-level fitting results after simulation. The comparison revealed small discrepancies between the simulated and actual groundwater levels in both aquifers, indicating good agreement. The errors—SSE, MSE, and RMSE—for the first aquifer groundwater levels were 0.567 m², 0.0945 m², and 0.3074 m, respectively; for the second aquifer, they were 1.101 m², 0.1834 m², and 0.4283 m. These results demonstrate consistency between the initial flow field of the model and the actual hydrogeological conditions. The groundwater-level distribution map in Fig. 4 shows a gradual decrease from south to north, aligning with the hydrogeological survey results. This validates that the model effectively captures the flow-field characteristics of the site. Consequently, the established steady flow field can serve as the initial condition for unsteady-flow simulations.

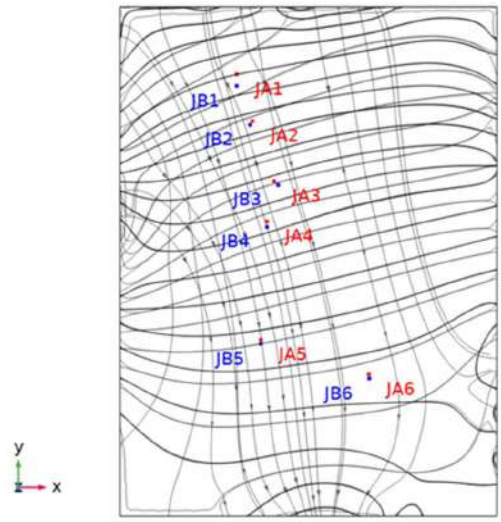


Fig. 3: Distribution map of groundwater monitoring wells in different aquifers.

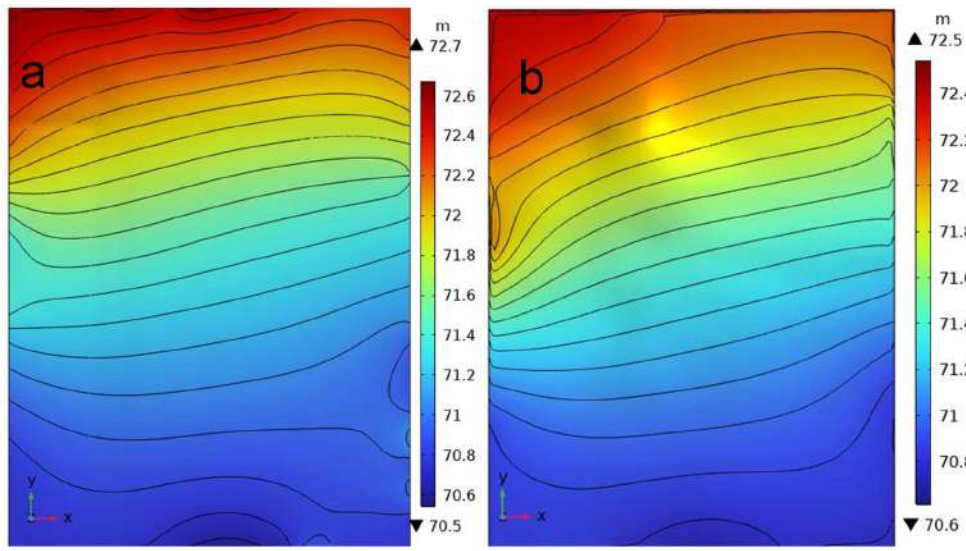


Fig. 4: Cloud map of groundwater level distribution in different aquifers and water level contour map, (a) first aquifer, (b) second aquifer.

Table 2: Statistical analysis results of errors between calculated water levels and actual observed water levels at different points.

Study area aquifer	Monitoring wells	Simulated water level [m]	The actual monitoring water level [m]	Absolute error value of water head [m]
First aquifer	JA1	72.41	72.65	0.24
	JA2	72.20	72.42	0.22
	JA3	71.50	71.88	0.38
	JA4	71.11	70.93	0.18
	JA5	71.00	70.79	0.21
	JA6	69.84	70.33	0.49
Second aquifer	JB1	72.29	72.40	0.11
	JB2	72.15	72.60	0.45
	JB3	71.93	73.10	1.17
	JB4	71.15	70.9	0.25
	JB5	70.98	70.79	0.19
	JB6	70.63	70.51	0.12

2.6. Determination of Solute Transport-Related Parameters

This study explores the migration behavior of Cr(VI) within soil and groundwater systems at chromium slag-contaminated sites. Using soil physicochemical parameters obtained from geotechnical tests in the study area, five sampling points were established in accordance with national standards, specifically GB/T 50123 for geotechnical testing methods and GB/T 50266 for engineering rock mass testing. Parameters such as water content, porosity, bulk density (g cm^{-3}), and saturation were measured through geotechnical tests, with some results presented in Table 3. The research employed an unsteady-state solute transport model that accounts for convection, dispersion, adsorption, and chemical reactions. The simulation spanned 1800 days, with daily stress periods and step sizes managed by a Time-Dependent Solver module to ensure numerical stability through error control. For site-specific parameters—including diffusion coefficient, dispersion, equilibrium adsorption constant,

Table 3: Geotechnical test results.

Sample Number	Sample Type	Sampling Depth	Bulk Weight	Porosity [%]	Saturation [%]
TG16	fill soil	0–1 m	1.53	44.77%	43.23
	silty clay	2–6 m	1.64	34.55%	82.21
	sand	8–12 m	1.40	56.11%	100
TG04	fill the soil	0–1 m	1.77	47.33%	52.33
	silty clay	2–6 m	1.53	36.68%	100
	Sand	8–12 m	1.44	58.28%	100

Table 4: Identification results of hydrogeological parameters.

Parameters	Unsaturated Zone		Saturated Zone			
	First Layer	Second Layer	Third Layer	Fourth Layer	Fifth Layer	Sixth Layer
Kxx [cm s^{-1}]	2.3×10^{-4}	2.7×10^{-5}	2.7×10^{-5}	9×10^{-4}	2.7×10^{-5}	9×10^{-4}
Kyy [cm s^{-1}]	2.3×10^{-4}	2.7×10^{-5}	2.7×10^{-5}	9×10^{-4}	2.7×10^{-5}	9×10^{-4}
Kzz [cm s^{-1}]	2.3×10^{-4}	2.7×10^{-5}	2.7×10^{-5}	9×10^{-5}	2.7×10^{-6}	9×10^{-5}
Porosity ε	0.43	0.37	0.37	0.57	0.37	0.57
Saturated water content θ_s	0.43	0.37	/	/	/	/
Residual water content θ_r	0.05	0.1	/	/	/	/
A	1.2	0.5	/	/	/	/
N	3	1.09	/	/	/	/
Soil density ρ_s [kg m^{-3}]	1530	1550	1550	1420	1550	1420

and maximum adsorption capacity—values were based on prior studies by Cerlini et al. (2023) and He et al. (2022) regarding Cr(VI) transport and transformation mechanisms in chromium slag-contaminated sites. The parameters used for validation are summarized in Table 4.

3. RESULTS AND DISCUSSION

3.1. Analysis of Cr(VI) Migration in Industrial Contaminated Sites

3.1.1. Analysis of the Influence of Rainfall Recharge on Cr(VI) Migration

(1) Distribution of Cr(VI) initial pollution range in the study area: The distribution of Cr(VI) in the plane and the initial three-dimensional concentration field of Cr(VI) in the industrially contaminated site, obtained through model simulation, are shown in Figs. 5 and 6. In the planar contamination distribution map, the y-axis indicates the north direction. Fig. 5 demonstrates that although Cr(VI) concentrations in the vadose zone soil are locally high, the groundwater in the downstream aquifer remains unpolluted by Cr(VI). Fig. 6 shows that heavily contaminated groundwater is primarily found in the chromium slag dump and the area downstream of the dump.

(2) Comparison and analysis of the distribution of Cr(VI) in contaminated sites under different rainfall recharge conditions: Without rainfall infiltration, the Cr(VI) concentration at the soil center of the vadose zone in the contaminated site decreased from 568 to 224 mg kg^{-1} over five years (Fig. 7). In contrast, with rainfall infiltration, the concentration decreased from 568 to 307 mg kg^{-1} in the same period (Fig. 8). The Cr(VI) levels showed fluctuations, and the pollution plume expanded and migrated downstream with groundwater flow. Comparing these two scenarios, it is evident that rainfall-induced fluctuations of the phreatic surface enlarge the soil contamination area in the vadose zone and lead to increased Cr(VI) levels.

In the absence of rainfall infiltration, the concentration decreased to 182 mg L^{-1} (Fig. 9) solely through convection and dispersion, while the center concentration of the plume dropped to 159 mg L^{-1} (Fig. 10) under rainfall influence. Conversely, rainfall leaching broadens the contaminated area, indicating that rainfall can facilitate the release of chromium pollutants from the vadose zone soil into the aquifer and accelerate the migration of Cr(VI) between them. When accounting for recharge and leaching due to rainfall, the extent of the groundwater pollution plume in the saturated zone increases, expanding upstream, with a more significant

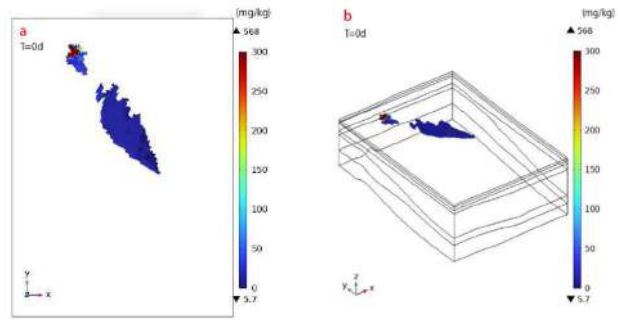


Fig. 5: Distribution map of Cr(VI) initial pollution plume in the vadose zone (a: plan view, b: 3D view).

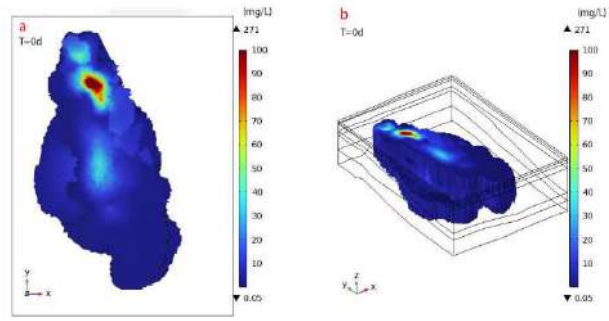


Fig. 6: Initial Cr(VI) pollution plume distribution map of groundwater (a: plan view, b: 3D view).

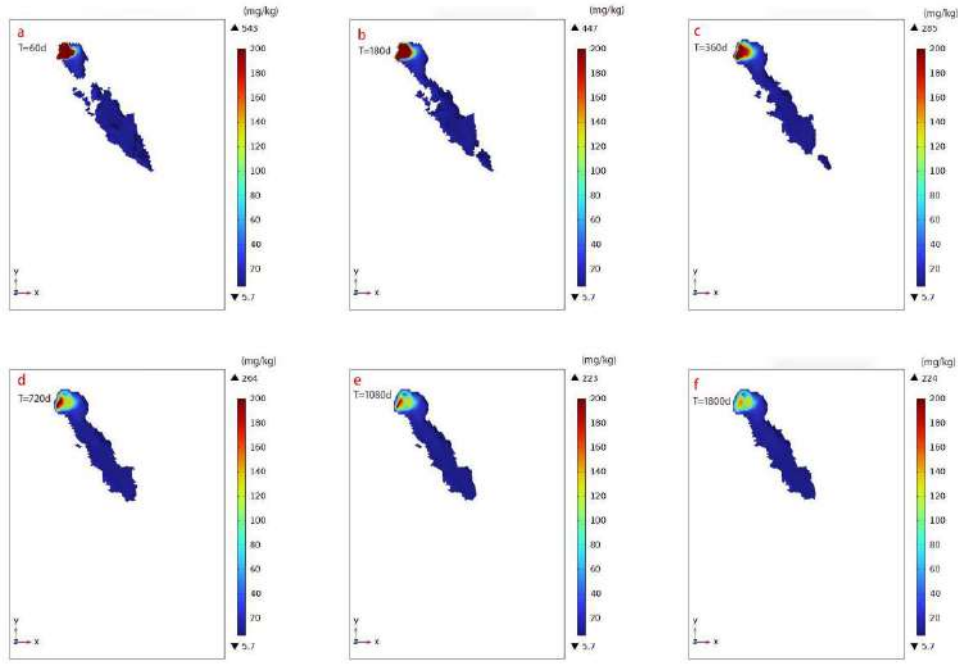


Fig. 7: Cloud map of pollution plume distribution of Cr(VI) in the aerated zone under non-rainfall recharge and leaching. (a) 60 d, (b) 180 d, (c) 360 d, (d) 720 d, (e) 1080 d, (f) 1800 d.

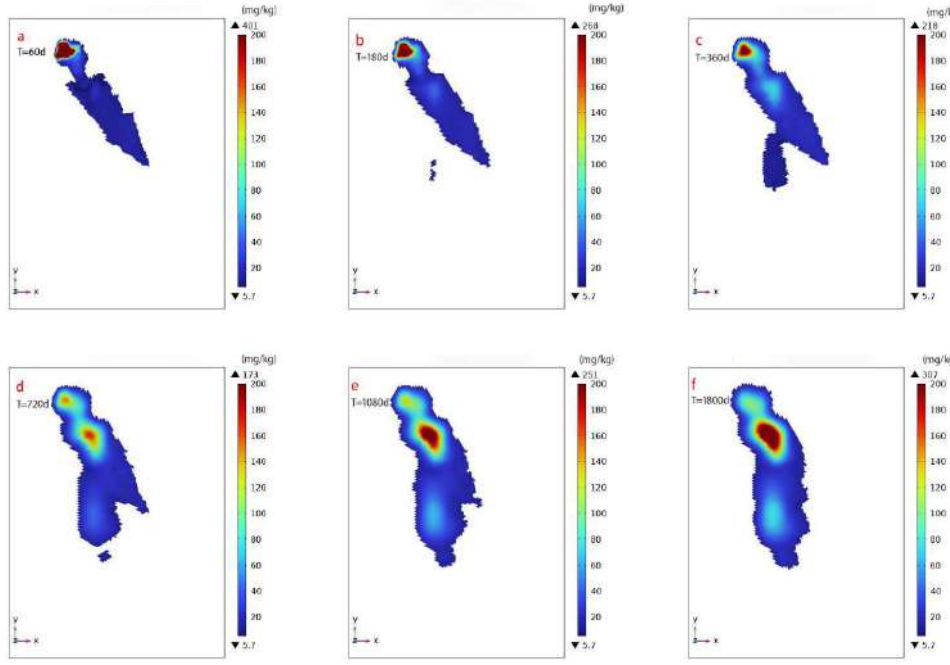


Fig. 8: Cloud map of pollution plume distribution of Cr(VI) in the aerated zone under rainfall recharge and leaching. (a) 60 d, (b) 180 d, (c) 360 d, (d) 720 d, (e) 1080 d, (f) 1800 d.

decrease in central concentration. This suggests that rainfall infiltration enhances groundwater convection and dispersion, thereby worsening soil and groundwater pollution.

This analysis examines the variation of Cr(VI) concentrations at different depths within the vadose zone under conditions with and without rainfall recharge. The

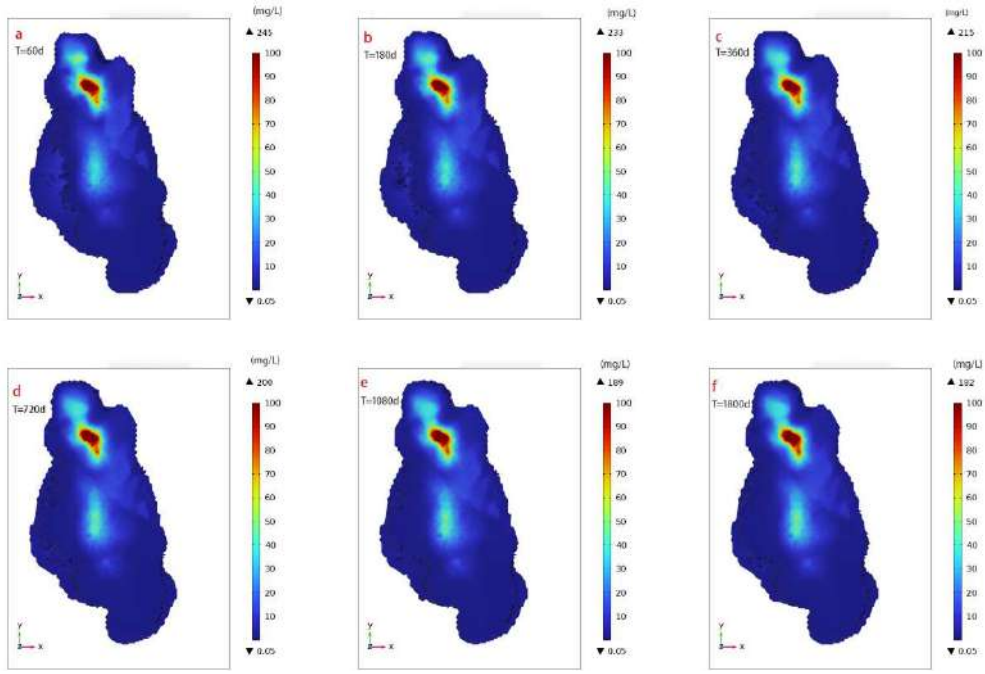


Fig. 9: Cloud map of Cr(VI) pollution plume distribution of groundwater under no rainfall recharge and leaching. (a) 60 d, (b) 180 d, (c) 360 d, (d) 720 d, (e) 1080 d, (f) 1800 d.

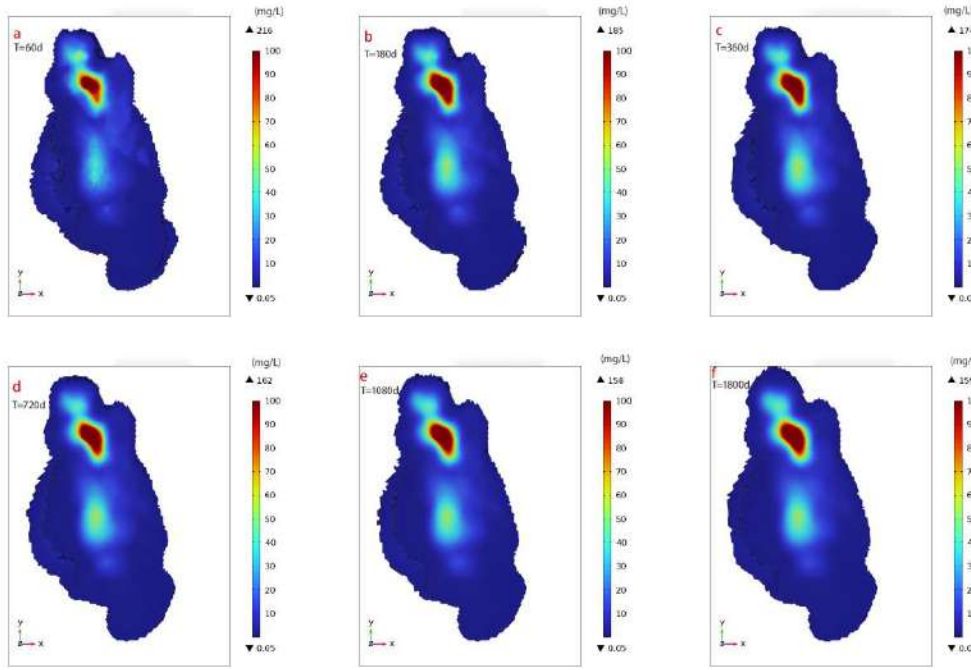


Fig. 10: Cloud map of Cr(VI) pollution plume distribution in groundwater under rainfall recharge and leaching. (a) 60 d, (b) 180 d, (c) 360 d, (d) 720 d, (e) 1080 d, (f) 1800 d.

migration of Cr(VI) at the contaminated site was tracked along the groundwater flow direction at three points: D01 upstream, D02 midstream, and D03 downstream (Fig. 11). Without rainfall, Cr(VI) movement was primarily driven by capillary action and molecular diffusion within the unsaturated soil zone. Soil data revealed higher Cr(VI)

concentrations in the upper layers and lower concentrations in deeper layers across all sites. Along the flow path, Cr(VI) levels increased in the upper layers of D02 and D03, while decreasing in the lower layers. Over time, Cr(VI) concentrations at various depths tended to stabilize, mainly due to diffusion from areas of high to low concentration through capillary forces, leading to a gradual decline in overall levels.

When rainfall leaching occurred, surface Cr(VI) levels at the upstream D01 decreased significantly, whereas concentrations at all depths in D02 and D03 increased. Rainwater infiltration substantially altered Cr(VI) migration compared to dry conditions. Upstream surface soil saw a decline in Cr(VI) levels, with a slight increase at around 3.5 meters depth. Downstream, Cr(VI) migrated upward through leaching and diffusion, contaminating groundwater and inducing water convection within the vadose zone. This process caused Cr(VI) to move downstream in the soil profile. The rise in Cr(VI) concentrations was more pronounced in the upper soil layers than in the lower ones, likely due to the limited impact of groundwater level fluctuations at a depth of 3.5 meters. The movement of Cr(VI) from surface to deeper soil layers is mainly driven by evaporation and migration, resulting in greater fluctuation impacts at shallower depths.

(3) Examination of the variation in Cr(VI) concentration in groundwater with and without rainfall recharge in different aquifers: In the absence of rainfall recharge leaching, the Cr(VI) concentration in upstream wells (Fig. 3), such as JA1, JA2, and JA4, decreased due to convection and dispersion, despite their proximity to the pollution source. Recharge of clean groundwater reduced the overall contaminant levels (Fig. 12). Downstream wells JA5 and JA6 showed increased contaminant concentrations as a result of upstream polluted water influence. Similarly, JA3, located in the middle reaches, experienced convection and dispersion effects from the first aquifer, with water flow migrating toward this area from highly polluted zones. During rainfall recharge leaching, the trend in Cr(VI) concentrations across monitoring wells aligned with the pattern observed without rainfall. However, near the pollution plume center, concentrations declined gradually, while downstream wells showed rapid increases. This variation is attributed to increased soil-to-groundwater Cr(VI) transfer and reduced degradation in high-pollution zones influenced by rainfall.

In the second aquifer, Cr(VI) levels remained relatively unchanged under both conditions. During rainfall recharge leaching, concentrations in highly contaminated wells JB2

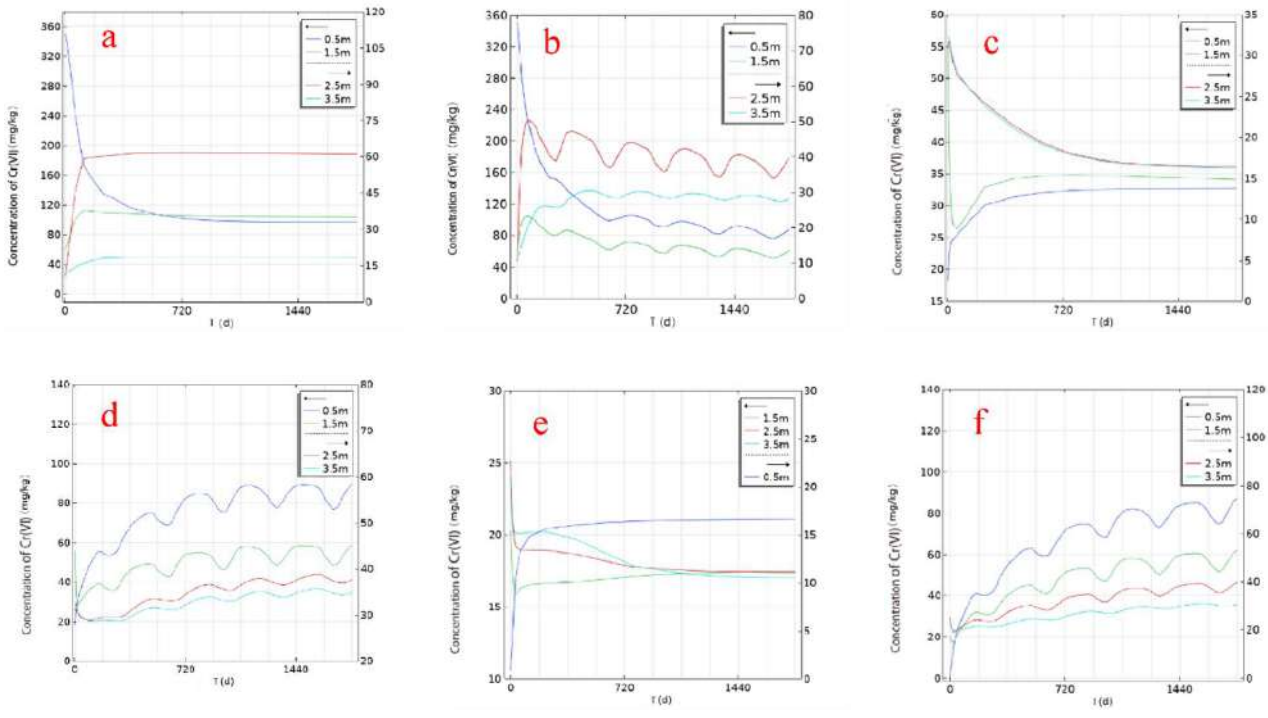


Fig. 11: Changes in Cr(VI) concentration at different depths in the vadose zone of polluted land under rainfall leaching. (a) D01 point without rainfall, (b) D01 point under rainfall, (c) D02 point without rainfall, (d) D02 point under rainfall, (e) D03 point without rainfall, (f) D03 point under rainfall.

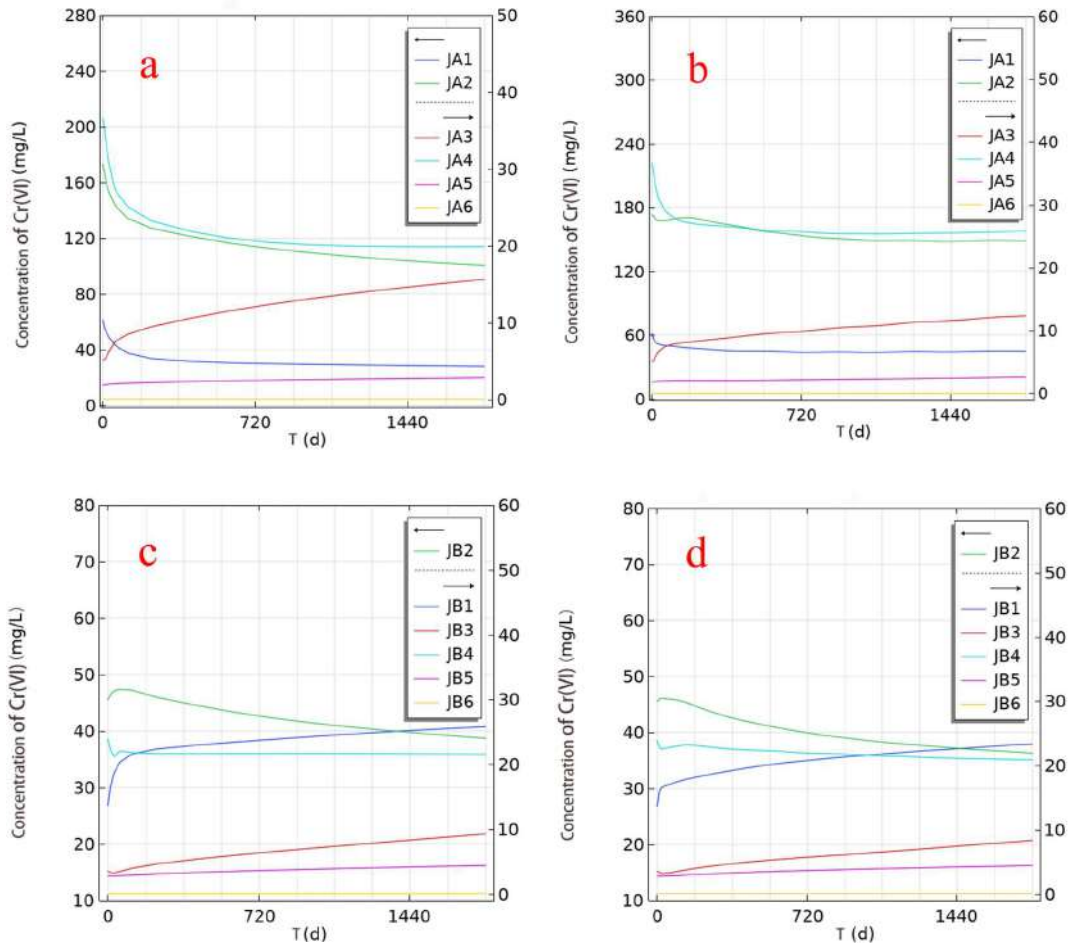


Fig. 12: Changes in hexavalent chromium concentration in groundwater at different points in the aquifer under rainfall leaching. (a) the first aquifer without rainfall, (b) the first aquifer under rainfall, (c) the second aquifer without rainfall, (d) the second aquifer under rainfall.

and JB4 decreased. Similarly, upstream JB1, midstream JB3, and downstream JB5 also showed decreases, contrasting with the trends in the first aquifer. This is due to the less permeable layer above the second aquifer. Rainfall accelerates convection and dispersion, leading to faster attenuation of Cr(VI) flow compared to downward infiltration, diffusion, and reduced aggregation. Notably, JB1 continued to receive recharge from the upstream high-contamination zone, resulting in increased Cr(VI) levels there.

3.1.2. Analysis of Cr(VI) Migration under Soil Matrix Adsorption

The adsorption coefficients used in the simulation were based on the findings of previous experimental studies on the adsorption of Cr(VI) by silty clay in the vadose zone and fine sand in the saturated zone. The adsorption distribution coefficients adopted in the model were obtained from previous experimental studies (Liu et al. 2022, Cao et al. 2021, Wang et al. 2000), which investigated the adsorption of Cr(VI) in soils with different lithological characteristics under constant-temperature conditions. The distribution coefficient for fine sand was 0.11 L kg^{-1}, whereas that for silty clay was 2.63 L kg^{-1}. The numerical simulation results are analyzed as follows.

(1) **Analysis of the variation characteristics of Cr(VI) concentration at different soil depths in the vadose zone under adsorption**: Compared with conditions without rainfall (Fig. 13), rainfall caused the initial Cr(VI) concentration in the soil to change rapidly due to migration and molecular diffusion within the high-concentration zone. Adsorption promoted the rapid and stable accumulation of Cr(VI), resulting in a higher concentration after stabilization than under conditions without adsorption.

Under conditions without rainfall but with adsorption, the Cr(VI) concentration in the vadose zone increased at different soil depths upstream of point D01, indicating that

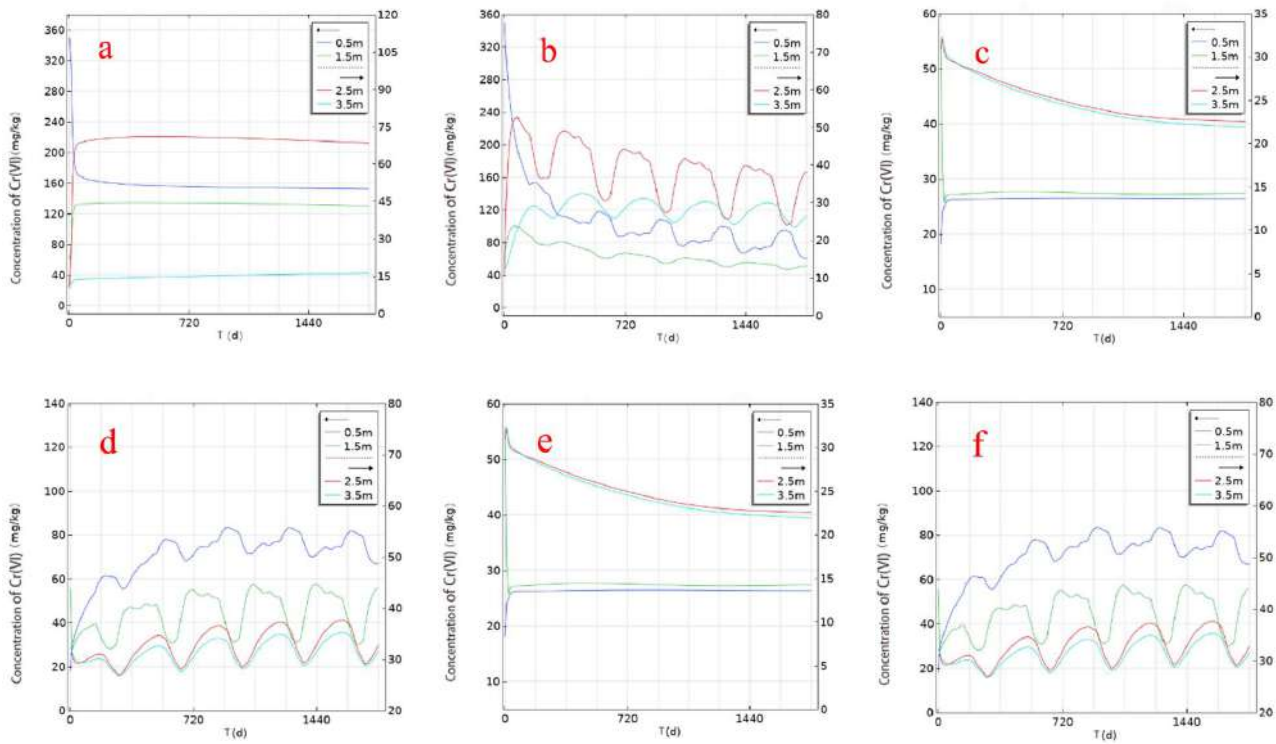


Fig. 13: Changes in Cr(VI) concentration at different depths in the vadose zone within the contaminated site under adsorption. (a) D01 without rainfall, (b) D01 with rainfall, (c) D02 without rainfall, (d) D02 with rainfall, (e) D03 without rainfall, (f) D03 with rainfall.

the adsorption process enhanced the retention of Cr(VI) in the soil. At points D02 and D03, the reduction in Cr(VI) concentration in the deeper soil was less pronounced, suggesting that adsorption impeded the migration of Cr(VI) to the downstream area. This process also enhanced the retention of Cr(VI) in the downstream soil and reduced its diffusion within the downstream vadose zone.

Compared with rainfall conditions, the absence of rainfall resulted in a smaller range of variation in Cr(VI) concentration at points D01, D02, and D03, together with higher peak concentrations under adsorption. These results suggest that adsorption enhanced the retention of Cr(VI) in the soil, thereby limiting its vertical and horizontal migration. During the wet season, the soil exhibited a greater capacity to adsorb Cr(VI) from groundwater, resulting in higher peak concentrations than those observed under rainfall recharge conditions. During the dry season, the adsorption process effectively restricted the diffusion of Cr(VI) within the soil, leading to a slower decline in the peak concentration. In addition, adsorption reduced the migration of Cr(VI) between different soil depths, thereby limiting concentration changes at each monitoring point. In particular, at the point located 0.5 m downstream, the strong adsorption capacity of the surface soil prevented the downward diffusion of Cr(VI) from the highly contaminated upstream area. Furthermore, adsorption by the deeper soil limited the upward migration of Cr(VI), ultimately reducing the accumulation of Cr(VI) in the surface soil.

(2) Analysis of the variation characteristics of Cr(VI) concentration in aquifer groundwater considering adsorption: The simulation results presented in Fig. 14 demonstrate that, when adsorption was considered, the reduction in Cr(VI) concentration in the JA1, JA2, and JA4 monitoring wells within the first aquifer was less pronounced. This observation suggests that adsorption by the fine sand soil hindered the migration of Cr(VI) within the first aquifer. In the JB1 monitoring well of the second aquifer, the increase in Cr(VI) concentration was reduced owing to the strong adsorption of Cr(VI) by the aquitard separating the first and second aquifers. This limited the migration of Cr(VI) from the first aquifer to the second aquifer. Similarly, decreases in Cr(VI) concentration were observed in the JB2 and JB4 monitoring wells of the second aquifer, indicating that adsorption impeded Cr(VI) migration within the second aquifer. Overall, adsorption played a significant role in limiting contaminant migration between the two aquifers.

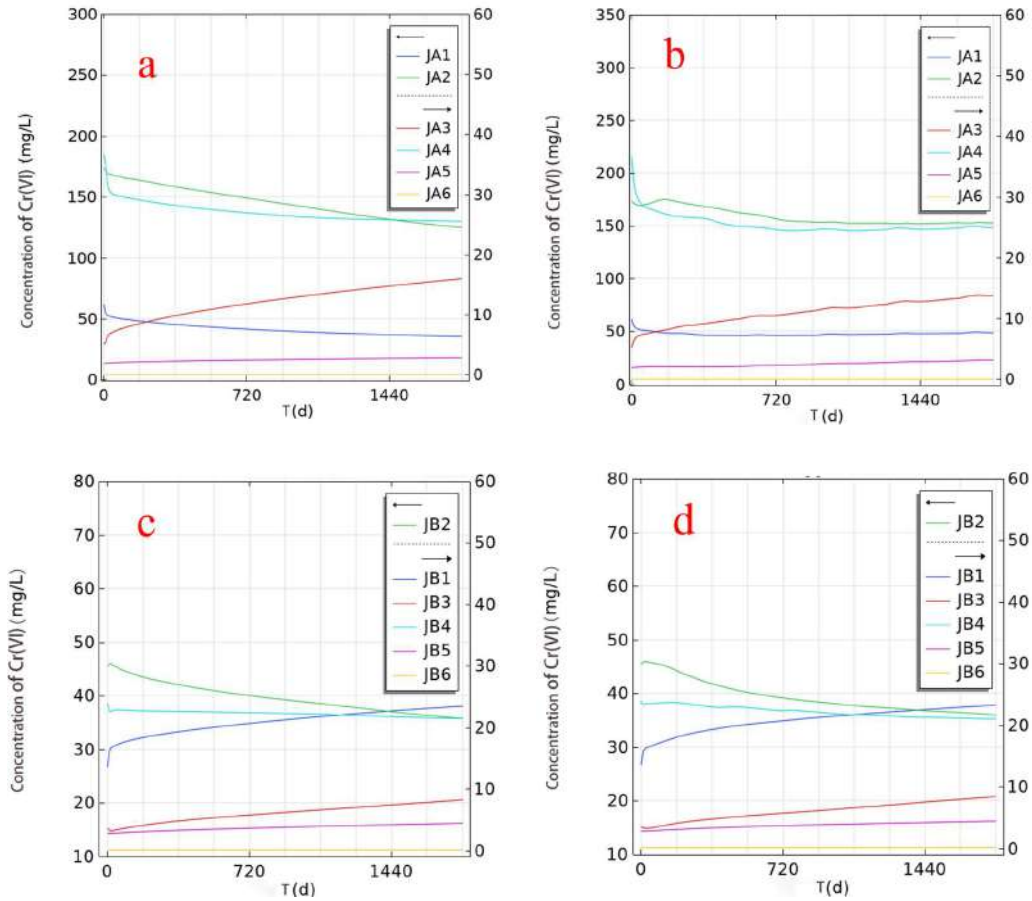


Fig. 14: Changes in Cr(VI) concentration in groundwater at different aquifer monitoring points under adsorption. (a) First aquifer without rainfall, (b) first aquifer with rainfall, (c) second aquifer without rainfall, (d) second aquifer with rainfall.

When adsorption was considered, a decline in Cr(VI) concentration was observed in the JA1, JA2, and JA4 monitoring wells of the first aquifer, together with a reduction in Cr(VI) concentration in the JA3 and JA5 monitoring wells. These results indicate that adsorption weakened the migration of Cr(VI) within the first aquifer. As precipitation increased, the Cr(VI) adsorbed by the soil fluctuated owing to groundwater convection and diffusion, resulting in corresponding fluctuations in the concentration curves. In the second aquifer, the magnitude of concentration change during the initial stage was smaller than that observed under rainfall conditions, indicating that adsorption reduced the extent of Cr(VI) migration. Regardless of rainfall conditions, the Cr(VI) concentration in the second aquifer remained relatively stable after adsorption. This may be attributed to the inhibitory effect of adsorption on the convection and diffusion processes induced by rainfall, thereby reducing the migration of Cr(VI).

4. CONCLUSIONS

This study examined the migration behavior of Cr(VI) in soil and groundwater, considering the effects of phreatic surface fluctuations and soil matrix adsorption induced by rainfall infiltration, utilizing a three-dimensional fully coupled numerical model. The key findings are as follows:

The site contaminated with chromium slag is identified as polluted land. During its management, it is essential to rigorously adhere to the soil environmental management measures for contaminated land implemented in Henan Province. Responsible parties should conduct relevant investigations, assessments, and remediation efforts. The simulation results can provide valuable data support and a basis for decision-making in these practical activities.

Simulation outcomes showed that fluctuations in groundwater levels—stemming from rainfall, infiltration, recharge, and evaporation—significantly impact the concentration of Cr(VI) in the vadose zone soil, especially

when compared to non-rainfall conditions. The variation in Cr(VI) levels in the vadose zone was aligned with groundwater level changes, facilitating Cr(VI) migration between saturated and unsaturated zones. Additionally, rainfall infiltration promotes the movement of Cr(VI) from the vadose zone into the aquifer. This process also enhances groundwater convection within primary and secondary aquifers and increases Cr(VI) diffusion in groundwater, intensifying pollution.

Matrix adsorption clearly retards the movement of Cr(VI) in both the vadose zone soil and groundwater aquifers. Under rainfall conditions, adsorption amplifies fluctuations in Cr(VI) concentrations in the vadose zone. It also reduces the overall migration of Cr(VI) across soil depths influenced by phreatic surface changes due to rainfall. Moreover, this retardation causes a degree of fluctuation in the Cr(VI) concentration profiles within the first aquifer, diminishing the effects of convection and molecular diffusion in the second aquifer during rainfall events.

5. ACKNOWLEDGMENTS

This research was financially supported by the Key Research and Development Projects Fund of Henan Province (No. 231111320200). This work was also supported by the Field Observation Station for Eco-Hydrological Processes in the Lower Yellow River Floodplain, Ministry of Water Resources. We are grateful for their data support and research facilities.

6. REFERENCES

Adnan, M., Xiao, B., Xiao, P., Zhao, P. and Bibi, S.J.S., 2022. Heavy metal, waste, COVID-19, and rapid industrialization in this modern era—Fit for sustainable future. *Sustainability*, 14(8), p.4746. [DOI]

Anderson, M.P. and Cherry, J.A., 1979. Using models to simulate the movement of contaminants through ground-water flow systems. *C R C Critical Reviews in Environmental Control*, 9(2), pp.97–156. [DOI]

Bai, B., Chen, J., Zhang, B. and Wang, H., 2024. Migration trajectories and blocking effect of the fine particles in porous media based on particle flow simulation. *AIP Advances*, 14(4), p.045036. [DOI]

Banaei, S.M.A., Javid, A.H. and Hassani, A.H., 2021. Numerical simulation of groundwater contaminant transport in porous media. *International Journal of Environmental Science and Technology*, 18, pp.151–162. [DOI]

Cao, S., Sohn, I. and Wang, Z., 2024. Selective stabilization of chromium and sustainable treatment of stainless steel slags. *Journal of Environmental Chemical Engineering*, 12(5), p.113516. [DOI]

Cao, Y., Dong, S., Dai, Z., Zhu, L., Xiao, T., Zhang, X., Yin, S. and Soltanian, M.R., 2021. Adsorption model identification for chromium (VI) transport in unconsolidated sediments. *Journal of Hydrology*, 598, p.126228. [DOI]

Cerlini, P.B., Silvestri, L., Meniconi, S. and Brunone, B., 2023. Performance of three reanalyses in simulating the water table elevation in different shallow unconfined aquifers in central Italy. *Meteorological Applications*, 30(1), p.e2118. [DOI]

Chi, G., Su, X., Lyu, H., Li, H., Xu, G. and Zhang, Y., 2022. Prediction and evaluation of groundwater level changes in an over-exploited area of the Baiyangdian Lake Basin, China under the combined influence of climate change and ecological water recharge. *Environmental Research*, 212, pp.113104. [DOI]

Costabile, P., Costanzo, C., De Bartolo, S., Gangi, F., Macchione, F. and Tomasicchio, G.R., 2019. Hydraulic characterization of river networks based on flow patterns simulated by 2-D shallow water modeling: Scaling properties, multifractal interpretation, and perspectives for channel heads detection. *Water Resources Research*, 55(9), pp.7717–7752. [DOI]

De Smedt, F., 2016. Two- and three-dimensional flow of groundwater. In: *The Handbook of Groundwater Engineering*. CRC Press, pp.121–144.

Dhal, B., Thatoi, H.N., Das, N.N. and Pandey, B.D., 2013. Chemical and microbial remediation of hexavalent chromium from contaminated soil and mining/metallurgical solid waste: A review. *Journal of Hazardous Materials*, 250–251, pp.272–291. [DOI]

Ghanbarian-Alavijeh, B., Liaghat, A., Huang, G.H. and Van Genuchten, M.T., 2010. Estimation of the van Genuchten soil water retention properties from soil textural data. *Pedosphere*, 20(4), pp.456–465. [DOI]

Giacomini, M. and Sevilla, R., 2020. A second-order face-centred finite volume method on general meshes with automatic mesh adaptation. International Journal for Numerical Methods in Engineering, 121(23), pp.5227–5255. [DOI]

Godbole, P., Meshram, P., Jawadand, S., Meshram, T. and Randive, K., 2025. A critical analysis of industrial slags, their hazard potential and remediation with reference to Sustainable Development Goals (SDGs). *Discover Civil Engineering*, 2(1), p.117. [DOI]

He, Y., Hu, G., Zhang, Z., Lou, W., Zou, Y., Li, X. and Zhang, K., 2022. Experimental study and numerical simulation on the migration and transformation mechanism of hexavalent chromium in a contaminated site. *Rock and Soil Mechanics*, 43, pp.528–538. [DOI]

Healy, R.W., 2010. *Estimating Groundwater Recharge*. Cambridge University Press. [DOI]

Li, X., Wen, Z., Zhan, H., Wu, F. and Zhu, Q., 2021. Laboratory observations for two-dimensional solute transport in an aquifer-aquitard system. *Environmental Science and Pollution Research*, 28, pp.38664–38678. [DOI]

Liang, X., Zhang, Y., Liu, J., Ma, E. and Zheng, C., 2019. Solute transport with linear reactions in porous media with layered structure: A semianalytical model. *Water Resources Research*, 55(6), pp.5102–5118. [DOI]

Liu, P., Liu, Z., Chu, M., Yan, R., Li, F. and Tang, J., 2022. Detoxification and comprehensive recovery of stainless steel dust and chromium containing slag: Synergistic reduction mechanism and process parameter optimization. *Process Safety and Environmental Protection*, 164, pp.678–695. [DOI]

Qiao, P., Wang, S., Li, J., Zhao, Q., Wei, Y., Lei, M. and Zhang, Z., 2023. Process, influencing factors, and simulation of the lateral transport of heavy metals in surface runoff in a mining area driven by rainfall: A review. *Science of the Total Environment*, 857, p.159119. [DOI]

Song, X. and Borja, R.I., 2014. Mathematical framework for unsaturated flow in the finite deformation range. *International Journal for Numerical Methods in Engineering*, 97(9), pp.658–682. [DOI]

Sumit, Shukla, R. and Sinha, A.K., 2021. Finite element method coupled with TLBO for shape control optimization of piezoelectric bimorph in COMSOL Multiphysics. *SIMULATION*, 97(9), pp.635–644. [DOI]

Thanh, N.N., Thunyawatcharakul, P., Ngu, N.H. and Chotpantarat, S., 2022. Global review of groundwater potential models in the last decade: Parameters, model techniques, and validation. *Journal of Hydrology*, 614, p.128501. [DOI]

Therrien, R. and Sudicky, E.A., 1996. Three-dimensional analysis of variably-saturated flow and solute transport in discretely-fractured porous media. *Journal of Contaminant Hydrology*, 23(1–2), pp.1–44. [DOI]

Wang, J., Yang, Z., Chen, J. and Wang, Z., 2000. Study on soil moisture retention characteristics in aeration zone. *Journal of Hydraulic Engineering*, 2, pp.1–6. [DOI] (In Chinese)

Wang, R., Zhang, Y., Chen, W., Shao, J., Cui, Y. and Zhang, Q., 2025. Chromium migration in contaminated site and numerical simulation of its effect on groundwater source area. *Rock and Mineral Analysis*, pp.1–14. [DOI]

Wu, X., Ye, T., Xie, C., Li, K., Liu, C., Yang, Z., Han, R., Wu, H. and Wang, Z., 2022. Experimental and modeling study on Cr(VI) migration from slag into soil and groundwater. *Processes*, 10(11), p.2235. [DOI]

Xie, C., Qin, Y., Chao, L. and Shi, D., 2020. Applied research on the numerical simulation of Cu and Cd transport laws in a metal mining area. *AIP Advances*, 10(11), p.115006. [DOI]

Xu, H.-B., Zhang, Y., Li, Z.-H., Zheng, S.-L., Wang, Z.-K., Qi, T. and Li, H.-Q., 2006. Development of a new cleaner production process for producing chromic oxide from chromite ore. *Journal of Cleaner Production*, 14(2), pp.211–219. [DOI]

Yeh, T.-C.J., Mao, D.-Q., Zha, Y.-Y., Wen, J.-C., Wan, L., Hsu, K.-C. and Lee, C.-H., 2015. Uniqueness, scale, and resolution issues in groundwater model parameter identification. *Water Science and Engineering*, 8(3), pp.175–194. [DOI]

Zhang, W., Shen, Z., Ren, J., Gan, L., Wang, F., Yu, B. and Li, C., 2020. Modeling and comparative analysis of a flow and heat coupling model of the riparian zone based on thermal conductivity empirical models. *Journal of Hydrology*, 582, p.124539. [DOI]

Nature Environment and Pollution Technology
An International Quarterly Peer-Reviewed Open Access Journal

p-ISSN: 0972-6268 | e-ISSN: 2395-3454 Vol. 25 | No. 4 | Article ID B4433 | 2026

RESEARCH ARTICLE https://doi.org/10.46488/NEPT.2026.v25i04.B4433 OPEN ACCESS

Assessment of Knowledge, Awareness, Attitude, and Practice of Plastic Waste Management Among the Digitally Active Public in India

Kanhaiya Kumar and Kasi Marimuthu†
Department of Environmental Science, Tezpur University, Tezpur, 784028, Assam, India
†Corresponding author: Kasi Marimuthu; aquamuthu2k@gmail.com

ARTICLE HISTORY

Received: 19-02-2026
Revised: 21-04-2026
Accepted: 30-04-2026

KEYWORDS

Plastic pollution
Waste management
Environmental awareness
Public perception
Recycling attitude and behaviour

CITE THIS ARTICLE

Kumar, K. and Marimuthu, K., 2026. Assessment of knowledge, awareness, attitude, and practice of plastic waste management among the educated and digitally active public in India. *Nature Environment and Pollution Technology*, 25(4), B4433. https://doi.org/10.46488/NEPT.2026.v25i04.B4433

COPYRIGHT & LICENCE

© 2026 The Authors
Open Access under CC BY 4.0.

PUBLISHED BY

TECHNOSCIENCE PUBLICATIONS

ABSTRACT

Plastic pollution has become a significant challenge that seriously threatens the environment and biota. Studying people's knowledge, awareness, attitudes, and practices regarding plastic pollution and plastic waste management can help inform policymaking, source segregation, and mitigation measures. The present study was conducted using an online Google Forms-based survey to assess the knowledge, awareness, attitudes, and practices of the general public towards plastic pollution and plastic waste management. A total of 540 respondents participated across 27 different states of India. Descriptive statistical measures, frequency analysis, chi-square goodness-of-fit tests, and Pearson correlation analysis were performed to analyse the results of sociodemographic information, sources of plastics, and different domains of KAP scores. The results show that plastic bags were the most regularly used single-use plastic items, mainly from grocery stores. The overall KAP scores revealed that 16.7% of respondents had poor knowledge, 30% had poor awareness, 19.3% had poor attitude, and 61.5% had poor practice related to plastic waste management and pollution. Sociodemographic variables such as residential area, education level, and occupation were significantly associated with KAP towards plastic pollution and waste management ($P<0.05$). The study recommends conducting environmental awareness campaigns, integrating topics related to plastic pollution and its impacts on the environment and human health into formal and informal education, and ensuring access to recycling facilities within local communities.

1. INTRODUCTION

Plastic pollution has emerged as one of the most serious threats to land and aquatic ecosystems (Kumar et al. 2021). Due to its mass-scale production, extensive usage, persistence, water resistance, durability, and low degradability, it poses a serious environmental challenge for effective waste management (Lakhiar et al. 2024). The global production of plastic has increased significantly in the last few decades because of its high demand, lightweight nature, low cost, and durability, and it is used in different sectors like packaging, construction, textiles, and consumer packaged goods (Pilapitiya & Ratnayake2024). Globally, till now, 8300 million metric tonnes of virgin plastic has been produced, and as of 2015, 6300 metric tonnes of plastic waste had been generated, of which approximately 79% of the discarded plastic waste was disposed of in landfills, and only 9% of the plastics were recycled, and 12% were incinerated (Gaffney et al. 2024, Geyer et al. 2017). However, their extensive use can lead to the accumulation of plastic in the natural environment, where plastics persist for hundreds of years and eventually disintegrate into small particles and form microplastics and nanoplastics.

India alone generated 4.12 million tonnes of plastic waste in 2020-21 (CPCB 2021, Rakib et al. 2023). Managing plastic waste is a significant challenge in India due to its burgeoning population, urbanization, and rapid economic growth (Rafey & Siddiqui 2023). To protect humans and the environment from the increasing threats of plastic pollution, the government of India, along with international agencies like UNEP, is enforcing restrictions on plastic waste management, including the ban on single-use plastic (Hossain et al. 2022, Nøklebye et al. 2023). Raising public awareness is considered as important as other strategies to reduce plastic pollution (Bashir et al. 2020, Coco Chin et al. 2023). However, the pro-environmental behaviour of the public can be predicted by individual attitudes and knowledge about plastic pollution (Felipe-Rodriguez et al. 2022, Mistry & Joshi 2025). It is pivotal to explore public opinion and knowledge for the successful implementation of targeted policies. It is essential to understand public behaviour and what people know about plastic waste and its associated environmental and health risks (Heidbreder et al. 2019, Henderson & Green 2020). To understand the behaviour of the general public towards plastic waste management, this study is informed by the Theory of Planned Behaviour (TPB). According to this theory, the behaviour of an individual is influenced by their attitude, subjective norms, and perceived behavioural control. In the context of environmental behaviour of the people, the level of knowledge and awareness of individuals shapes their attitude, which decides their behaviour (Wu et al. 2022). If the people are well aware and have good knowledge of plastic waste and environmental pollution, then their mindset and attitude will change, which governs their behaviour towards plastic waste management. Therefore, the KAP framework used in the current study is conceptually fit with the theory of planned behaviour (Hasan et al. 2022). Based on the theoretical perspective, the current study also assumes a sequential relationship between knowledge, attitude, practice, and behaviour. This study aims to assess the knowledge, attitude, practice, and behaviour of digitally active members of the general public in India towards plastic waste management. Especially, it examines how aware people are of plastic waste, their willingness to adopt sustainable practices, and their actual behaviour regarding plastic waste management. To achieve this, we have conducted an online survey using a structured questionnaire through Google Forms. The questionnaire included questions on sociodemographic details, knowledge, awareness, attitude, and practice (KAP) of plastic waste management. Respondents' answers were collected and analysed using a 3-point Likert scale. All the results were statistically analyzed to evaluate the overall level of behaviour patterns and the awareness among participants.

2. MATERIALS AND METHODS

2.1. Data Collection

A structured questionnaire was prepared based on previously published research articles. The responses were collected from the participants through a survey using Google Forms. The questionnaire comprised five sections, including socio-demographic details, knowledge, awareness, attitude, and practice. Each section consisted of 5–10 items: knowledge (8 items), awareness (5 items), attitude (10 items), and practice (6 items). The responses were collected using multiple-choice closed-ended questions, checkboxes, short answers, and a 3-point Likert scale, such as responses such as yes, no, and maybe. In the sociodemographic section, participants were asked about their age group, gender, the highest level of education, occupation, state, and residential area (urban or rural). The questionnaire also included questions on the type and source of single-use plastics in day-to-day life. The knowledge domain included items on plastic pollution, where plastic comes from, whether plastic pollution affects human life, open burning and incineration of plastic, how long plastic takes to degrade, etc. The awareness section included questions on whether the respondents and people around them were aware of plastic pollution. In the attitude section, the respondents were asked about their attitude towards plastic pollution, whether the government or the public is more responsible for reducing plastic pollution, whether they think it is increasing, etc. The practice section included questions such as whether they segregate plastic or not, whether they reuse plastic products, whether they bring a carry bag to buy groceries, etc.

The questionnaire was prepared in English, and the study was conducted with educated, digitally active members of the public in India. The draft questionnaire was vetted by two research faculty members and five respondents in a pilot survey before data collection to identify potential weaknesses in the questionnaire, and based on their feedback, the questionnaire was revised. The generated Google Form link was disseminated by email and social media applications. Snowball sampling was also used, and the respondents were asked to circulate and share the Google Form link with their friends and family members. The form was available online for data collection from March to October 2024. Since the study only assessed the knowledge, awareness, attitude, and practice of plastic pollution among the respondents, a consent form was obtained from all the participants. A total of 543 individuals responded to the survey; three responses were excluded, and data from 540 respondents were included in the statistical analysis.

Table 1: Reliability analysis using Cronbach's alpha.

Domain	No. of items	Cronbach's alpha
Knowledge	8	0.670
Awareness	5	0.690
Attitude	10	0.690
Practice	6	0.644
All domains	29	0.779

2.2. Data Analysis

The questionnaire's reliability and internal consistency were analysed using Cronbach's alpha test. The Cronbach's alpha values of 0.60 or higher are generally considered acceptable for survey research (Hair 2011). The Cronbach's alpha reliability coefficients for the knowledge (8 items), awareness (5 items), attitude (10 items), and practice (6 items) scales were 0.670, 0.690, 0.690, and 0.644, respectively, indicating moderate internal consistency within each domain. The overall reliability for the combined 29 items based on Cronbach's alpha was 0.779, as shown in Table 1, confirming the questionnaire's robustness in measuring KAP constructs. These findings demonstrate that the instrument is a reliable tool, supporting its use in research and practical applications involving knowledge, awareness, attitudes, and practices. Descriptive frequency analysis was performed to summarize the characteristics of sociodemographic variables. The Chi-Square goodness-of-fit test was performed to study the categorical distribution of the respondent population. Further, KAP (knowledge, attitude, and practice) scores were calculated. For the estimation of KAP, 1 mark was assigned for a correct answer, 0.5 marks for a partially correct answer, and 0 marks for an incorrect answer (Coco Chin et al. 2023). The percentage score of KAP was used for further statistical analysis. Respondents who scored $\geq$70% were categorised as good, while those who scored <70% were categorised as poor (Chimisso 2021, Coco Chin et al. 2023). The mean KAP score was compared with the sociodemographic variables by performing a one-way analysis of variance (ANOVA) and an independent t-test. A chi-square test of association was performed to study the association between KAP domain levels and the sociodemographic variables containing two levels. Pearson correlation analysis was performed to study the relationship between each KAP domain score. Sociodemographic variables like age, education, gender, occupation, residential place, and environmental science education influence the dependent variables like attitude and practice for plastic use and recycling, respectively. Multiple linear regression analysis was conducted to determine whether knowledge and awareness influence the attitudes and practices of respondents toward plastic pollution and plastic waste management. All the statistical analyses were performed using SPSS software version 25.0. A p-value of <0.05 was considered statistically significant.

3. RESULTS

3.1. Socio-Demographic Characteristics of Respondents

A total of 540 respondents participated in the study, of whom

Table 2: Socio-demographic details of the respondents.

Socio-Demographic Variables	Categories	Frequency (N=540)	%	Chi-Square Value	p-value
Gender	Male	316	58.5%	15.674	<0.001
	Female	224	41.5%		
Age	18-30 years	408	75.6%	457.744	<0.001
	31-50 years	113	20.9%		
	> 50 years	19	3.5%		
Residential place	Rural	242	44.8%	5.807	<0.05
	Urban	298	55.2%		
Education	No formal School Education	4	0.7%	512.267	<0.001
	Upto secondary	30	5.6%		
	UG	172	31.9%		
	PG	334	61.9%		
Have you ever studied Environmental Science subject?	No	39	7.2%	395.267	<0.001
	Yes	501	92.8%		
Occupation	Govt Sector	77	14.3%	963.393	<0.001
	Private Sector	97	18.0%		
	Business	15	2.8%		
	Homemaker	10	1.9%		
	Retired	4	0.7%		
	Student	316	58.5%		
	Unemployed	21	3.9%		

58.5% were male (P<0.001). A total of 55.2% of respondents were from urban areas (P<0.001). The participants were categorized into three age groups (18-30 years, 31-50 years, and more than 50 years) with the largest proportion of respondents (75.6%) in the 18–30-year age group, followed by the 31–50-year and >50-year age groups (P<0.001) (Table. 2). About 60% of the respondents had postgraduate-level education (P<0.001). The study also revealed that 58.5 % are students, followed by 18.0 % working in the private sector and 14.3% working in the government sector (P<0.001). A majority of respondents (92.8 %) reported that they had studied Environmental Science in their education (P<0.001). However, 39 respondents (7.2%) mentioned never studying Environmental Science. Among the total respondents, 55.2% were from urban areas and 44.8% from rural areas. Respondents from 27 states across India participated in this survey, and among them, the maximum were from Bihar (19.3%), followed by Tamil Nadu (16.7%) and Assam (13.9%).

Fig. 1 reveals the regularly used single-use plastics. Around 66.7% of the respondents reported that the most commonly used plastic items were plastic bags, followed by

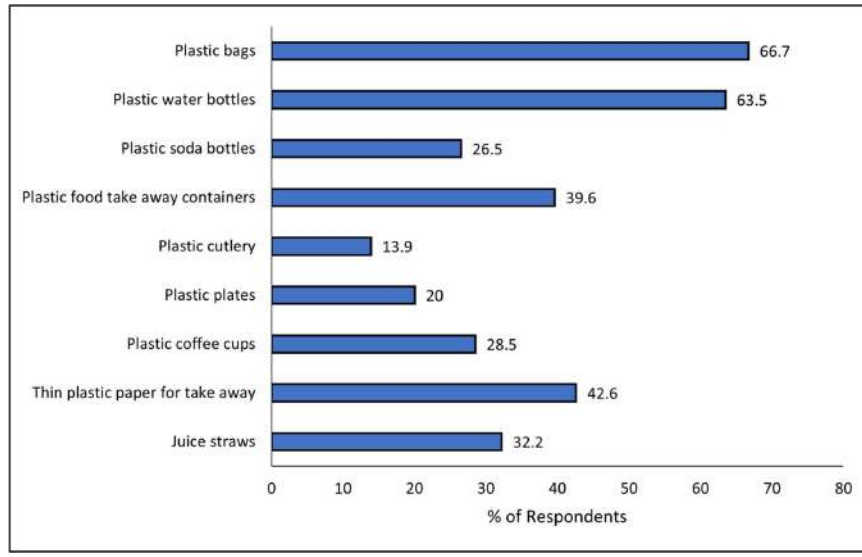


Fig. 1: Regularly used single-use plastics.

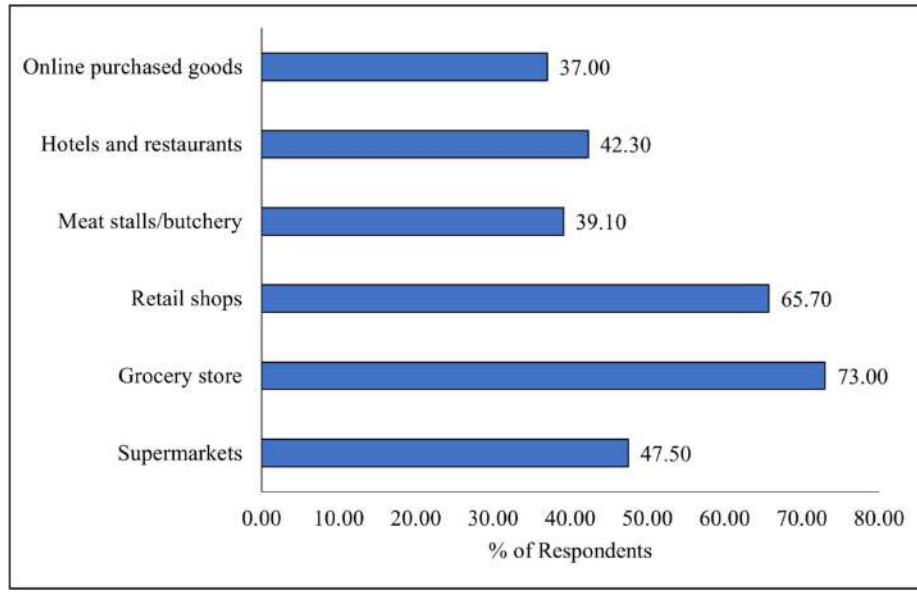


Fig. 2: Source of single-use plastics.

plastic water bottles (63.5%). Other frequently used items include thin plastic paper for takeaway purposes (42.6%) and plastic food takeaway containers (39.6%). In contrast, disposable items such as plastic soda bottles (26.5%), plastic coffee cups (28.5%), juice straws (32.2%), plastic plates (20.0%), and plastic cutlery (13.9%) were reported less frequently. A statistically significant difference was observed in the distribution of single-use plastic materials ($\chi^2 = 34.62$, $p < 0.001$), with plastic bags and water bottles predominating, while items such as plastic cutlery and plates were reported less frequently. These findings demonstrate that single-use plastic products associated with packaging and convenience, such as bags, bottles, and takeaway containers, are more commonly used than disposable items, including plates and cutlery.

The sources of single-use plastics used by the participants during daily life are given in Fig. 2. The results show that 73.0% of the respondents stated that the most common source of single-use plastics was grocery stores, followed by 65.7% from retail shops, 47.5% from supermarkets, 42.3% from hotels and restaurants, 39.1% from meat stalls or butcheries, and 37.0% from online purchases. A significant variation was observed in the sources of single-use plastics ($\chi^2 = 22.17$, $p < 0.001$), with grocery stores and retail shops being the leading sources. These results suggest that routine consumer activities, particularly food and retail purchases, primarily contribute to daily single-use plastic use among the surveyed population.

3.2. Assessment of Knowledge, Awareness, Attitude, and Practice with Sociodemographic Variables

The mean scores of knowledge, awareness, attitude, and practice across the respondents' sociodemographic variables are presented in Table 3. The overall mean score for knowledge was 88.66 ±12.57%, indicating a high level of knowledge among respondents. The mean awareness score was 80.50±16.24%, while the attitude score was 86.14±11.78%, reflecting a generally positive view. Participants' overall mean practice score was relatively lower, 69.78 ±22.21%. The mean knowledge score was significantly higher among males (89.62 ± 11.91%) compared to females (87.30 ± 13.36%) ($t = 2.112$, $p < 0.05$), indicating a statistically significant difference between male and female respondents. No significant difference was observed between males and females regarding awareness (Male: 81.49 ± 16.37%, Female: 79.11 ± 15.99%; $t = 1.681$, $p > 0.05$) and attitude (Male: 85.63 ± 12.22%, Female: 86.85 ± 11.11%; $t = -1.186$, $p > 0.05$). Similarly, no significant difference was observed between the male and female respondents for practice (Male: 70.52 ± 22.85%, Female: 68.75 ± 21.28%; $t=0.911$, $p > 0.05$). There were no statistically significant differences in knowledge, awareness, attitude, or practice scores across three different age groups ($p > 0.05$). The knowledge scores were 87.83 ± 19.15% in the >50 age group and 89.49 ± 11.18% in the 31–50 years age group ($F = 0.337$, $p > 0.05$). The awareness scores were observed at 79.68 ± 16.96% in the 18–30 years and 83.27 ± 12.57% in the 31–50 age group ($F = 2.219$, $p > 0.05$). The attitude scores of participants ranged from 84.74 ± 13.49% in the > 50 years age group to 86.19 ± 11.91% in the 18-30 years age group ($F = 0.139$, $p > 0.05$). The practice scores ranged from 63.60 ± 19.09% among respondents above 50 years to 69.91 ±22.97% in the 18-30 years age group ($F = 0.781$, $p > 0.05$). The urban and rural populations have similar knowledge, attitude, and practice scores ($p > 0.05$).

Education level significantly influenced the knowledge score ($F = 9.684$; $p < 0.001$). Participants with no formal education had the lowest knowledge score (75.00 ± 37.85), while those with postgraduate education had the highest (90.42 ± 9.66). Awareness scores, attitudes, and practices did not differ significantly across education groups ($p > 0.05$). Overall, awareness scores ranged from 75.00 ± 31.09 to 81.23 ± 15.11, attitude scores from 82.17 ± 19.28 to 86.60 ± 10.54, and practice scores from 69.19 ± 21.86 to 81.25 ± 27.53. These results indicate that higher education is significantly associated with greater knowledge but does not appear to influence awareness, attitudes, or practices.

Participants who had studied environmental science earlier scored significantly higher in knowledge ($t = -4.301$; $p < 0.001$), awareness ($t = -2.255$; $p = 0.025$), and attitude ($t = -2.044$; $p = 0.041$) than those who had not. However, the two groups had no significant difference in practice scores ($t = -1.536$; $p = 0.125$). This suggests that education in environmental science is positively associated with greater knowledge, awareness, and attitudes toward plastic waste management and pollution; however, practice scores did not differ between the groups ($P>0.05$).

Across the different occupational groups, the knowledge score was significantly influenced by occupation ($F = 2.932$; $p = 0.008$), with government sector employees demonstrating the highest knowledge (90.34 ± 8.93) and homemakers scoring the lowest (75.63 ± 28.48). However, there were no significant differences in awareness ($F = 1.059$; $p = 0.386$), attitude ($F = 1.408$; $p = 0.209$), or practice ($F = 1.195$; $p = 0.307$) scores across the occupational groups. These results suggest that occupation may be a key factor affecting knowledge, but it does not appear to influence awareness, attitudes, or practices.

3.3. The Overall KAP Status of the Respondents Towards Plastic Pollution

Table 4 shows the respondents' knowledge, awareness, attitude, and practice (KAP) related to plastic waste

Table 3: Mean KAP scores with the socio-demographic variables of the respondents.

Variable		Knowledge Score (%) (Mean ± sd)	F/t value	p-value	Awareness Score (%) (Mean ± sd)	F/t value	p-value	Attitude Score (%) (Mean ± sd)	F/t value	p-value	Practice Score (%) (Mean ± sd)	F/t value	p-value
Overall mean score		88.66±12.57			80.50±16.24			86.14±11.78			69.78±22.21		
Gender	Male	89.62±11.91	2.112	0.035	81.49±16.37	1.681	0.093	85.63±12.22	-1.186	0.236	70.52±22.85	0.911	0.363
	Female	87.30±13.36			79.11±15.99			86.85±11.11			68.75±21.28		
Age	18-30 years	88.47±12.59	0.337	0.714	79.68±16.96	2.219	0.110	86.19±11.91	0.139	0.870	69.91±22.97	0.781	0.458
	31-50 years	89.49±11.18			83.27±12.57			86.19±11.07			70.35±19.76		
	Above 50 years	87.83±19.15			81.58±18.64			84.74±13.49			63.60±19.09		
Residential place	Rural	88.15±14.36	-0.852	0.395	80.50±17.80	-0.005	0.996	86.55±13.38	0.730	0.466	70.97±24.27	1.120	0.263
	Urban	89.07±10.92			80.50±14.89			85.81±10.31			68.82±20.37		
Education	No formal School Education	75.00±37.85	9.684	<0.001	75.00±31.09	0.696	0.554	82.50±28.72	1.446	0.228	81.25±27.53	0.530	0.662
	Upto secondary	80.21±24.84			80.00±21.50			82.17±19.28			69.72±23.42		
	UG	87.03±12.70			79.30±16.98			86.02±11.83			70.69±22.67		
	PG	90.42±9.66			81.23±15.11			86.60±10.54			69.19±21.86		
Have you ever studied Environmental Science subject?	No	80.45±23.13	-4.301	<0.001	74.87±22.58	-2.255	0.025	82.44±17.47	-2.044	0.041	64.53±22.92	-1.536	0.125
	Yes	89.30±11.14			80.94±15.59			86.43±11.19			70.19±22.12		
Occupation	Govt Sector	90.34±8.93	2.932	0.008	83.64±11.69	1.059	0.386	87.53±9.85	1.408	0.209	71.32±19.33	1.195	0.307
	Private Sector	87.76±14.57			79.59±15.87			84.28±15.00			67.35±23.62		
	Business	82.50±18.02			77.33±22.19			82.67±14.13			58.89±22.15		
	Homemaker	75.63±28.48			73.00±18.89			81.50±19.16			65.00±26.29		
	Retired	85.94±16.44			80.00±16.33			82.50±6.45			66.67±11.79		
	Student	89.16±10.90			80.57±16.82			86.85±10.49			71.07±22.21		
	Unemployed	90.18±17.29			78.10±17.21			84.29±13.63			66.67±24.01		

Table 4: Overall KAP status of respondents.

KAP domain	Status	Frequency	%	Chi-Square	p-value
Knowledge	Poor	90	16.7	240	<0.001
	Good	450	83.3		
Awareness	Poor	162	30.0	86.4	<0.001
	Good	378	70.0		
Attitude	Poor	104	19.3	204.119	<0.001
	Good	436	80.7		
Practice	Poor	332	61.5	28.474	<0.001
	Good	208	38.5		

management and pollution. The majority of respondents demonstrated good knowledge (83.3%), good awareness (70.0%), and positive attitudes (80.7%) towards plastic waste management ($p < 0.001$). However, a significant portion of the respondents (61.5%) showed poor practice, with only 38.5% demonstrating good practices ($p < 0.001$).

3.4. The Level of KAP Associated with Socio-Demographic Variables

The Chi-square test of association was performed to study the association between different sociodemographic variables and the level of KAP, and the results are presented in Table 5. No significant association was observed between gender and respondents' knowledge ($\chi^2 = 0.738$, $p = 0.39$) or awareness ($\chi^2 = 1.222$, $p = 0.27$). However, attitude was significantly associated with gender ($\chi^2 = 7.231$, $p = 0.007$). Practice was not significantly associated with gender ($\chi^2 = 3.405$, $p = 0.065$). The male and female respondents who participated in the study demonstrated similar knowledge, awareness, and practice levels, except for attitudes. No significant association was observed between different age groups and the level of knowledge ($\chi^2 = 0.681$, $p = 0.711$), awareness ($\chi^2 = 5.374$, $p = 0.068$), attitude ($\chi^2 = 0.048$, $p = 0.976$), and practice ($\chi^2 = 1.238$, $p = 0.538$).

No significant association was observed between residential place and the level of knowledge ($\chi^2 = 0.38$, $p = 0.54$), awareness ($\chi^2 = 0.69$, $p = 0.41$), and attitude ($\chi^2 = 0.28$, $p = 0.60$). However, practice was significantly associated with residential place ($\chi^2 = 7.88$, $p = 0.005$), with a higher proportion of good practices in handling plastic waste and plastic pollution observed among rural respondents (52.4%) as compared to urban respondents (47.6%). The results show a significant association between the respondents' educational background and knowledge level ($\chi^2 = 13.89$, $p = 0.003$). However, there was no significant association with awareness level ($\chi^2 = 5.93$, $p = 0.12$), attitude ($\chi^2 = 3.767$, $p = 0.29$), or practice ($\chi^2 = 2.32$, $p = 0.51$). Higher education was significantly related to better knowledge, while awareness, attitude, and practice did not vary significantly among the participants with different educational levels. Having studied environmental science was significantly associated with knowledge ($\chi^2 = 6.02$, $p = 0.014$), indicating that individuals who had studied environmental science demonstrated significantly better knowledge levels. However, no significant association was observed between awareness ($\chi^2 = 2.43$, $p = 0.12$), attitude ($\chi^2 = 3.58$, $p = 0.06$), or practice ($\chi^2 = 1.07$, $p = 0.30$). A significant association was observed between the respondents' occupation and knowledge level ($\chi^2 = 14.627$, $p = 0.023$). However, there was no significant association with awareness ($\chi^2 = 10.86$, $p = 0.09$), attitude ($\chi^2 = 7.09$, $p = 0.31$), or practice ($\chi^2 = 3.50$, $p = 0.74$). Overall, occupation significantly influenced knowledge level, while awareness, attitude, and practice remained broadly similar across groups.

3.5. Relationship Between KAP Domain Scores of Respondents

The Pearson correlation analysis was performed to study the relationship between the KAP domain scores. The results show a positive and significant correlation among knowledge, awareness, attitude, and practice scores related to the KAP domain (Table 6). The knowledge of respondents was positively correlated with awareness ($r = 0.424$, $p < 0.001$), attitude ($r = 0.413$, $p < 0.001$), and practice ($r = 0.266$, $p < 0.001$). This indicates that higher knowledge scores are significantly associated with increased awareness, positive attitudes, and improved practices on plastic waste management and pollution. Awareness was also significantly and positively related to both attitude ($r = 0.397$, $p < 0.001$) and practice ($r = 0.333$, $p < 0.001$). Additionally, attitude demonstrated a positive and significant correlation with practice ($r = 0.422$, $p < 0.001$). These results suggest that enhancing knowledge may increase awareness, attitudes, and practices related to plastic waste management and pollution.

Multiple linear regression analysis was conducted to determine whether knowledge and awareness influence the attitudes and practices of respondents toward plastic

Table 5: Association of sociodemographic variables with KAP status.

Sociodemographic Variables	Levels	Knowledge				Awareness				Attitude				Practice			
		Poor	Good	χ^2 Value	p-value	Poor	Good	χ^2 Value	p-value	Poor	Good	χ^2 Value	p-value	Poor	Good	χ^2 Value	p-value
Gender	Male	49 (54.4)	267 (59.3)	0.738	0.390	89 (54.9)	227 (60.1)	1.222	0.269	73 (70.2)	243 (55.7)	7.231	0.007	184 (55.4)	132 (63.5)	3.405	0.065
	Female	41 (45.6)	183 (40.7)			73 (45.1)	151 (39.9)			31 (29.8)	193 (44.3)			148 (44.6)	76 (36.5)		
Age	18-30	71 (78.9)	337(74.9)	0.681	0.711	133 (82.1)	275 (72.8)	5.374	0.068	78 (75.0)	330 (75.7)	0.048	0.976	249 (75.0)	159 (76.4)	1.238	0.538
	31-50	16 (17.8)	97 (21.6)			25 (15.4)	88 (23.3)			22 (21.2)	91 (20.9)			69 (20.8)	44 (21.2)		
	> 50	3 (3.3)	16 (3.6)			4 (2.5)	15 (4.0)			4 (3.8)	15 (3.4)			14 (4.2)	5 (2.4)		
Residential place	Rural	43 (47.8)	199 (44.2)	0.383	0.536	77 (47.5)	165 (43.7)	0.690	0.406	49 (47.1)	193 (44.3)	0.276	0.600	133 (40.1)	109 (52.4)	7.879	0.005
	Urban	47 (52.2)	251 (55.8)			85 (52.5)	213 (56.3)			55 (52.9)	243 (55.7)			199 (59.9)	99 (47.6)		
Education	No formal School Education	1 (1.1)	3 (0.7)	13.893	0.003	1 (0.6)	3 (0.8)	5.926	0.115	1 (1.0)	3 (0.7)	3.768	0.288	1 (0.3)	3 (1.4)	2.320	0.509
	Upto secondary	7 (7.8)	23 (5.1)			10 (6.2)	20 (5.3)			8 (7.7)	22 (5.0)			18 (5.4)	12 (5.8)		
	UG	42 (46.7)	130 (28.9)			63 (38.9)	109 (28.8)			39 (37.5)	133 (30.5)			107 (32.2)	65 (31.3)		
	PG	40 (44.4)	294 (65.3)			88 (54.3)	246 (65.1)			56 (53.8)	278 (63.8)			206 (62.0)	128 (61.5)		
Have you ever studied Environmental Science subject?	No	12 (13.3)	27 (6.0)	6.019	0.014	16 (9.9)	23 (6.1)	2.433	0.119	12 (11.5)	27 (6.2)	3.581	0.058	27 (8.1)	12 (5.8)	1.066	0.302
	Yes	78 (86.7)	423 (94.0)			146 (90.1)	355 (93.9)			92 (88.5)	409 (93.8)			305 (91.9)	196 (94.2)		
Occupation	Govt Sector	7 (7.8)	70 (15.6)	14.626	0.023	15 (9.3)	62 (16.4)	10.856	0.093	14 (13.5)	63 (14.4)	7.086	0.313	46 (13.9)	31 (14.9)	3.503	0.744
	Private Sector	20 (22.2)	77 (17.1)			35 (21.6)	62 (16.4)			22 (21.2)	75 (17.2)			62 (18.7)	35 (16.8)		
	Business	4 (4.4)	11 (2.4)			3 (1.9)	12 (3.2)			5 (4.8)	10 (2.3)			12 (3.6)	3 (1.4)		
	Homemaker	4 (4.4)	6 (1.3)			6 (3.7)	4 (1.1)			4 (3.8)	6 (1.4)			7 (2.1)	3 (1.4)		
	Retired	2 (2.2)	2 (0.4)			1 (0.6)	3 (0.8)			1 (1.0)	3 (0.7)			3 (0.9)	1 (0.5)		
	Student	52 (57.8)	264 (58.7)			96 (59.3)	220 (58.2)			53 (51.0)	263 (60.3)			189 (56.9)	127 (61.1)		
	Unemployed	1 (1.1)	20 (4.4)			6 (3.7)	15 (4.0)			5 (4.8)	16 (3.7)			13 (3.9)	8 (3.8)		

Table 6: Relationship between KAP domain scores.

KAP Domain	Correlation	Awareness Score %	Attitude Score %	Practice Score %
Knowledge	Pearson Correlation	.424**	.413**	.266**
	p-value	<0.001	<0.001	<0.001
Awareness	Pearson Correlation		.397**	.333**
	p-value		<0.001	<0.001
Attitude	Pearson Correlation			.422**
	p-value			<0.001

**. Correlation is significant at the 0.01 level (2-tailed).

Table 7: Multiple linear relationship of knowledge and awareness with attitude and practice domains.

Dependent variable	Intercept & Independent variable	B	Model F-Value	Model p-value	R^2	Beta	t-Value	p-value	Tolerance	VIF
Attitude	Intercept	45.537	80.540	<0.001	0.231		13.718	<0.001		
	Knowledge	0.280				0.299	7.160	<0.001	0.821	1.219
	Awareness	0.196				0.270	6.459	<0.001	0.821	1.219
Practice	Intercept	16.388	40.087	<0.001	0.130		2.462	0.014		
	Knowledge	0.269				0.152	3.425	0.001	0.821	1.219
	Awareness	0.367				0.269	6.043	<0.001	0.821	1.219

pollution and plastic waste management (Table 7). The regression model was statistically significant, F =80.540, $p < .001$, explaining 23.1% of the variance ($R^2 = .231$) in attitude. Both knowledge ($\beta = .299$, $p < .001$) and awareness ($\beta = .270$, $p < .001$) were significant positive predictors of attitude. Multicollinearity diagnostics indicated no significant collinearity among predictors, with tolerance values of 0.821 and VIF values of 1.219 for both knowledge and awareness scores, suggesting that the independent variables were not highly correlated. For predicting practice, the regression model was also significant, F = 40.087, $p < .001$, , explaining 13.0% of the variance in respondents' practice ($R^2 = .130$). Knowledge ($\beta = .152$, $p = .001$) and awareness ($\beta = .269$, $p < .001$) both significantly predicted practice scores. No multicollinearity was detected (VIF = 1.219). These findings suggest that increasing knowledge and awareness may positively influence respondents' attitudes and practices regarding plastic waste management.

4. DISCUSSION

Most respondents showed a high level of awareness about plastic pollution and its impacts on the environment and human health, but there is a significant gap in translating this awareness into sustainable practice. The level of knowledge about plastic pollution varied, with many misconceptions about plastic degradation and recycling. The attitude of respondents towards plastic reduction was largely positive, but when it comes to changing their behaviour to avoid single-use plastic or participating in recycling programmes, they become inconsistent. A similar finding was reported by Dowarah et al. (2022), indicating that awareness alone is not sufficient to bring changes in public behaviour for environmental conservation. Studies from other regions also align with the current study, showing that despite a high level of awareness and education, practical implications towards replacement or recycling of plastic products are low due to convenience, lack of alternatives to plastic materials, and lack of strict policy enforcement (Arulnayagam 2020, Coco Chin et al. 2023, Tang 2023).

Respondents in this study reported a lack of infrastructure and management for plastic waste collection, recycling, and the use of alternative sources. The study highlighted the need for targeted actions or interventions that bridge the gap between awareness and practice. Environmental education and campaigns should focus on awareness and facilitating behaviour change through incentives and community engagement. Furthermore, collaboration among governments, NGOs, businesses, and the private sector can provide better solutions or alternatives to plastic products, making it easier for people to adopt pro-environmental behaviour. The key barriers to behaviour change identified in this study are economic factors, convenience, and limited access to alternative options. Apart from that, many shopkeepers and grocery stores provide plastic bags free of cost to their customers. Applications of single-use plastic are widespread, and the usage of plastic products has become a

regular part of our day-to-day life. These habits may be one of the reasons that hinder people from changing their regular behaviour and practices. Also, due to this habit, the plastic bag is the most used single-use plastic by the respondents, followed by plastic bottles. People mainly use plastic bottles for drinking water, especially when they are outside their houses. This could be related to the affordability of water bottles and concerns about the quality of alternative water sources. Overcoming these challenges requires a multifaceted approach. The analysis of age-wise differences in knowledge, awareness, attitude, and practice toward plastic pollution revealed no statistically significant differences across age groups for all KAP domains. However, interesting trends were observed in the mean scores that offer valuable insights. Individuals in the 31–50 age group demonstrated the highest mean knowledge score (89.49%), followed closely by the 18 –30 years age group. This trend could reflect increased exposure to environmental issues through educational curricula, digital media, or workplace policies among younger and middle-aged adults. Interestingly, individuals above 50 years, despite their life experience, showed slightly lower scores across all KAP domains, particularly in practice (63.60%), which may be due to generational habits or reduced access to recent environmental awareness campaigns. Attitude scores were relatively high across all age groups, but the efforts should focus on encouraging real behavior change. Awareness campaigns should not only provide information but also work on shaping people's attitudes through community involvement and social influence. Correlation analysis among knowledge, awareness, attitude, and practice shows a significant and positive association. Especially, attitude was strongly correlated with practice. These findings are compatible with the theory of planned behaviour. The TPB also proposes that behaviour is primarily influenced by attitudes. Knowledge and awareness appear as precursors that shape attitudes and may influence behaviour. However, the present study does not incorporate the key concepts of TPB, which are subjective norms and perceived behavioral control. Therefore, this study partially follows the theory rather than a full theoretical application. The limitations of this study are that it relies on an online survey in which 58.5% of respondents are students. This may introduce sampling bias and limit representativeness due to the availability of the internet and mobile devices. Second, this study does not include a regional comparison of KAP across different parts of India. Third, the scope of this study does not include interventions or simulations of existing policies to evaluate the effectiveness of existing policies. Future studies should incorporate region-based comparative analysis and intervention approaches to evaluate the impacts of existing policies of plastic waste management.

5. CONCLUSIONS

This study provides a basic understanding of people's knowledge, attitudes, awareness, and practices towards plastic pollution and its management. The results of this study can inform future policy design and targeted interventions. The respondents have good knowledge, awareness, and attitudes towards plastic pollution, but lack of practice. It may be due to misconceptions, cultural barriers, or the lack of alternatives to plastic products. To change practice, the government should incorporate waste management and recycling training and educational awareness programs in private and government sector offices and educational institutions, highlight the environmental impacts of plastic pollution, and establish waste and recycling units in every city and residential area. Stringent measures should be taken to implement the regulations in the manufacturing, supply, distribution, and disposal of plastics by the manufacturing companies, retailers, and consumers. Additionally, school and college curricula should incorporate elements of plastic pollution, its ecological impacts, and possible recycling options to raise awareness among students to a larger extent.

6. REFERENCES

Arulnayagam, A., 2020. Public perception towards plastic pollution in the marine ecosystems of Sri Lanka. *American Journal of Marine Science*, 8(1), pp.6–13. [DOI]

Bashir, M.J., Jun, Y.Z., Yi, L.J., Abushammala, M.F., Amr, S.S.A. and Pratt, L.M., 2020. Appraisal of student's awareness and practices on waste management and recycling in the Malaysian University's student hostel area. *Journal of Material Cycles and Waste Management*, 22(3), pp.916–927. [DOI]

Central Pollution Control Board (CPCB), 2021. Annual report 2020–2021. https://cpcb.nic.in/annual-report.php

Chimisso, C., 2021. Knowledge, attitudes and practices towards plastic pollution in Umbria, Italy. M.Sc. thesis, Wageningen University & Research, Wageningen, The Netherlands. Available online: https://edepot.wur.nl/638916 (accessed on 13 August 2026).

Coco Chin, K.K., Mahanta, J. and Nath, T.K., 2023. Knowledge, attitude, and practices toward plastic pollution among Malaysians: Implications for minimizing plastic use and pollution. *Sustainability*, 15(2), 1164. [DOI]

Dowarah, K., Duarah, H. and Devipriya, S.P., 2022. A preliminary survey to assess the awareness, attitudes/behaviours, and opinions pertaining to plastic and microplastic pollution among students in India. *Marine Policy*, 144, 105220. [DOI]

Felipe-Rodriguez, M., Böhm, G. and Doran, R., 2022. What does the public think about microplastics? Insights from an empirical analysis of mental models elicited through free associations. *Frontiers in Psychology*, 13, 920454. [DOI]

Gaffney, A., Maiti, D., Kuila, D. and Mafia, G., 2024. ChemPren: A new and economical technology for conversion of waste plastics to light olefins. *Reaction Chemistry & Engineering*, 9(12), pp.3100–3104. [DOI]

Geyer, R., Jambeck, J.R. and Law, K.L., 2017. Production, use, and fate of all plastics ever made. *Science Advances*, 3(7), e1700782. [DOI]

Hair, J.F., 2011. Multivariate data analysis: An overview. *International Encyclopedia of Statistical Science*, pp.904–907. [DOI]

Hasan, N.I.A., Abidin, S.Z., Ganggayah, M.D., Jamal, N.F. and Aziz, W.N.H.W.A., 2022. Knowledge, attitude and practices (KAP) theory towards preventive measures among Malaysian in early outbreak of Covid-19. *Malaysian Journal of Public Health Medicine*, 22(1), pp.38–47. [DOI]

Heidbreder, L.M., Bablok, I., Drews, S. and Menzel, C., 2019. Tackling the plastic problem: A review on perceptions, behaviors, and interventions. *Science of the Total Environment*, 668, pp.1077–1093. [DOI]

Henderson, L. and Green, C., 2020. Making sense of microplastics? Public understandings of plastic pollution. *Marine Pollution Bulletin*, 152, 110908. [DOI]

Hossain, R., Islam, M.T., Shanker, R., Khan, D., Locock, K.E.S., Ghose, A., Schandl, H., Dhodapkar, R. and Sahajwalla, V., 2022. Plastic waste management in India: Challenges, opportunities, and roadmap for circular economy. *Sustainability*, 14(8), 4425. [DOI]

Kumar, R., Verma, A., Shome, A., Sinha, R., Sinha, S., Jha, P.K., Kumar, R., Kumar, P., Shubham, Das, S. and Sharma, P., 2021. Impacts of plastic pollution on ecosystem services, sustainable development goals, and need to focus on circular economy and policy interventions. *Sustainability*, 13(17), 9963. [DOI]

Lakhiar, I.A., Yan, H., Zhang, J., Wang, G., Deng, S., Bao, R., Zhang, C., Syed, T.N., Wang, B., Zhou, R. and Wang, X., 2024. Plastic pollution in agriculture as a threat to food security, the ecosystem, and the environment: An overview. *Agronomy*, 14(3), 548. [DOI]

Mistry, M. and Joshi, S.G., 2025. Unveiling microplastic ignorance: A study on knowledge and awareness among Pune's urban population—a mixed method approach. *Nature Environment and Pollution Technology*, 24(1), pp.1–10. [DOI]

Nøklebye, E., Adam, H.N., Roy-Basu, A., Bharat, G.K. and Steindal, E.H., 2023. Plastic bans in India–addressing the socio-economic and environmental complexities. *Environmental Science & Policy*, 139, pp.219–227. [DOI]

Pal, S. and Pandey, S., 2024. Recycling of plastic waste into transportation fuels and value-added products. *Renewable Energy Innovations: Biofuels, Solar, and Other Technologies*, pp.97–122. [DOI]

Pilapitiya, P.N.T. and Ratnayake, A.S., 2024. The world of plastic waste: A review. *Cleaner Materials*, 11, 100220. [DOI]

Rafey, A. and Siddiqui, F.Z., 2023. A review of plastic waste management in India–challenges and opportunities. *International Journal of Environmental Analytical Chemistry*, 103(16), pp.3971–3987. [DOI]

Rakib, M.R.J., Al Nahian, S., Madadi, R., Haider, S.M.B., De-la-Torre, G.E., Walker, T.R., Jonathan, M.P., Cowger, W., Khandaker, M.U. and Idris, A.M., 2023. Spatiotemporal trends and characteristics of microplastic contamination in a large river-dominated estuary. *Environmental Science: Processes & Impacts*, 25(5), pp.929–940. [DOI]

Tang, K.H.D., 2023. Attitudes towards plastic pollution: A review and mitigations beyond circular economy. *Waste*, 1(2), pp.569–587. [DOI]

Wu, L., Zhu, Y. and Zhai, J., 2022. Understanding waste management behavior among university students in China: Environmental knowledge, personal norms, and the theory of planned behavior. *Frontiers in Psychology*, 12, 771723. [DOI]

Nature Environment and Pollution Technology
An International Quarterly Peer-Reviewed Open Access Journal

p-ISSN: 0972-6268 | e-ISSN: 2395-3454 Vol. 25 | No. 4 | Article ID D1897 | 2026

RESEARCH ARTICLE https://doi.org/10.46488/NEPT.2026.v25i04.D1897 OPEN ACCESS

Wind Power Density in Southern Iraq: A Comparative Study of Coastal, Port and Inland Sites

Taghreed Ali Abbas[1]†, Muna H. Ahmed[2] and Hazim H. Hussain[1]
[1]Atmospheric Science Department, College of Science, Mustansiriyah University, Baghdad, Iraq
[2]Department of Remote Sensing and GIS, College of Science, University of Baghdad, Iraq
†Corresponding author: Taghreed Ali Abbas; dr.taghreed_atm_sci@uomustansiriyah.edu.iq

ARTICLE HISTORY

Received: 02-01-2026
Revised: 16-02-2026
Accepted: 25-02-2026

KEYWORDS

Shamal Wind
NREL Classification
Arabian Gulf
Wind Power Density (WPD)
Coastal-inland gradient
Renewable energy

CITE THIS ARTICLE

Abbas, T.A., Ahmed, M.H. and Hussain, H.H., 2026. Wind power density in southern Iraq: A comparative study of coastal, port, and inland sites. *Nature Environment and Pollution Technology*, 25(4), D1897. https://doi.org/10.46488/NEPT.2026.v25i04.D1897

COPYRIGHT & LICENCE

© 2026 The Authors
Open Access under CC BY 4.0.

PUBLISHED BY

TECHNOSCIENCE PUBLICATIONS

ABSTRACT

This study provides a comprehensive spatiotemporal assessment of Wind Power Density (WPD) in southern Iraq's coastal zone using high-resolution meteorological data (January 2020–December 2022). Wind resources were analyzed at Al-Faw Grand Port, Umm Qasr, and Basrah International Airport at 10 m and 50 m elevations. Results demonstrate a significant coastal-inland gradient; annual mean WPD at 10 m decreased from 139.3 W m^{-2} (Al-Faw) to 55.6 W m^{-2} (Basrah). Extrapolating to 50 m enhanced WPD by factors of 1.7–2.9×, with Al-Faw reaching 236.9 W m^{-2}. According to NREL standards, all sites remain Class 1 at 10 m, though Al-Faw approaches the Class 2 threshold (243 W m^{-2}), with an annual mean = 236.9 W m^{-2} (Class 1). Seasonal analysis identifies summer (June–August) as the peak period, driven by Shamal wind events, where WPD exceeds 300 W m^{-2} at 50 m, aligning with peak electricity demand. However, high temporal variability indicates significant intermittency. While current resources are insufficient for standalone commercial wind farms, the findings suggest strong potential for hybrid systems or seasonal supplemental generation. This research establishes a critical multi-height baseline for renewable energy policy and investment in Iraq.

1. INTRODUCTION

The search for renewable resources to slow down global warming and lessen dependency on fossil fuels has accelerated due to the growing need for clean, sustainable energy (Ammar et al. 2024). With a global installed capacity of more than 837 GW by 2023, wind energy stands out among these as one of the most developed, economical, and quickly deployable technologies (Ahmed & Abbas 2026, Abbas et al. 2026). Due to lower surface roughness, stronger wind regimes, and synergistic opportunities for hybrid wind-wave energy systems, coastal and nearshore regions in particular offer significant wind energy potential (Aboobacker et al. 2021, Rusu et al. 2018).

The Shamal wind system, a persistent northwesterly wind that gets stronger in the summer and winter, creates a distinctive wind energy landscape in the Arabian Gulf region of the Middle East (Ammar et al. 2024, Yu et al. 2016). Despite its strategic location along the northern Gulf, the Iraqi coastal zone is still largely unexplored, despite studies in Qatar, Kuwait, and Saudi Arabia reporting moderate to high wind power densities (100–300 W m^{-2} at 50 m) (Aboobacker et al. 2021, Al-Salem et al. 2018, Hadi et al. 2020). Iraq's Basrah coastline appears to have low-to-marginal wind energy potential at 6 and 10 m height, according to

preliminary assessments by Hadi et al. (2020) and Ammar et al. (2024), with annual mean wind power densities (WPD) below 170 W m^{-2} classified as NREL Class 1 (Not Suitable) for utility-scale wind development.

However, these early evaluations have two main limitations. First, they mainly use low-altitude measurements ($\leq$10 m), ignoring the significant increase in wind power density (WPD) with height. This is important because modern turbines work at heights of 50–120 m (Aboobacker et al. 2021, Rusu et al. 2018). Second, they do not provide detailed statistical and seasonal insights on WPD across various locations, heights, and times (from daily to annual). This information is crucial for evaluating how viable and reliable a specific site is (Hussain et al. 2023). While prior studies (Hadi et al. 2020, Ammar et al. 2024) assessed Iraqi coastal wind at 6–10 m, this work is the first to: (i) apply multi-height (10 m and 50 m) analysis using physically consistent extrapolation, (ii) integrate seasonal WPD dynamics with Shamal wind climatology, directly addressing gaps identified by Hussain et al. (2023) and Aboobacker et al. (2021)

This gap in knowledge is particularly serious for southern Iraq, where energy security is a major challenge and integrating renewable sources is a national priority (Kazem & Chaichan 2012). Without thorough assessments of WPD across different heights and seasons, policymakers and investors cannot make informed choices about the potential of wind energy projects or hybrid systems (Abbas et al. 2024, Ali Abbas & Fattah Hassoon 2026).

To fill this gap, this study offers a detailed assessment of wind power density at three important coastal stations: Basrah Al-Faw, Umm Qasr, and Basrah International Airport. A high-frequency meteorological dataset spans January 2020 to December 2022 and includes 10-minute interval wind speed and direction measurements, aggregated into daily, monthly, seasonal, and annual means. We build on previous work by:

(i) assessing WPD at technologically significant heights (10 m and 50 m),

(ii) stating full statistical descriptors (mean, variance, min/max, standard deviation) through daily, monthly, seasonal, and annual scales,

(iii) classifying locations using the NREL wind power classification method,

(iv) examining the seasonal dynamics of WPD relative to the Shamal wind system.

The main goal here is to assess the technical potential and seasonal variability of wind energy along Iraq's only coastline and to offer a scientifically important foundation for future renewable energy planning. By bridging the gap between low-altitude observational data and real-world turbine deployment scenarios, this study provides actionable insights for energy policy in a region where sustainable power solutions are urgently needed.

2. MATERIALS AND METHODS

2.1. Study Area

The study centers on the Iraqi coastal zone along the northern Arabian Gulf, including three key stations: Al-Faw Grand Port, Basrah International Airport, and Umm Qasr Port (Fig. 1).

This region represents Iraq's only maritime coastline (~58 km), characterized by a hot arid climate, low surface roughness, and exposure to the dominant Shamal wind system, a northwesterly wind regime that intensifies during summer and winter (Ammar et al. 2024, Yu et al. 2016).



Fig. 1: Study area map of southern Iraq showing Al-Faw Grand Port, Umm Qasr Port, and Basrah International Airport. Base map: Google My Maps (2022).

Table 1: Study-site coordinates and characteristics.

Site	Latitude (°N)	Longitude (°E)	Elevation (m a.s.l.)	Distance from Coastline	Dominant Land Use	Key Meteorological Features
Al-Faw Grand Port	29.9884°N	48.4710°E	~3 m	Onshore (coastal port)	Maritime/ Industrial	Strong northwesterly (Shamal) winds; highest wind speeds in summer (Jun–Sep); exposure to open Gulf fetch; flat terrain with low surface roughness
Umm Qasr port	29.9147°N	48.3486°E	~2–4 m	~5 km inland	Commercial Port & Industrial	Moderate wind regime; influenced by Shamal but partially sheltered by coastal topography; slightly higher surface roughness than Al-Faw
Basrah International Airport	30.6750°N	47.6581°E	~4 m	~80 km inland	Urban/Airport	Weakest coastal wind regime due to distance from Gulf; high thermal influence; frequent calm conditions; significant diurnal variation

The study area's flat topography and proximity to the Shatt al-Arab estuary create a unique coastal environment where wind energy potential is influenced by both terrestrial and marine dynamics, as summarized in Table 1. Wind speed data were measured at the Al-Faw Grand Port station (6 m height) during 2020–2022. Wind speeds at 10 m, 50 m, and 100 m for Al-Faw were derived using the power-law method with site-specific roughness length (z_0 = 0.0002 m for open sea). For Umm Qasr and Basrah Airport, wind speeds at 10 m and 50 m were obtained from the same dataset via spatial interpolation using inverse distance weighting (IDW). All WPD values reported in Tables 1–4 are based on these processed data.

Wind patterns in the study area are dominated by the Shamal wind system, a persistent northwesterly wind regime that represents a defining meteorological feature of the Arabian Gulf region. The Shamal wind system flows predominantly from the northwest and is prominent throughout the Arabian Gulf region. Shamal wind intensity varies throughout the year; these winds are generally stronger during the summer months (June–September) and winter months (December–February) than during the less intense transitional months. Southeasterly winds are observed intermittently during the transitional seasons. The Shamal wind system is associated with large-scale pressure contrasts between the Mediterranean Sea and the Arabian Peninsula, generating substantial wind energy across the Iraqi coastal zone. (Ammar et al. 2024).

Selecting the three stations helped create a complete wind-resource model across the coast-to-inland transect. Al-Faw Grand Port is located where the Shatt al-Arab meets the Arabian Gulf and therefore represents coastal wind conditions with limited land influence. Umm Qasr Port is situated approximately 5 km from the open waters of the Gulf and represents an intermediate coastal setting. Basrah International Airport is approximately 80 km from the coast and therefore represents a predominantly inland setting. Based on these station locations, the study evaluated how wind power density changes with increasing distance from the coast.

2.2. Data Source and Processing

Wind speed (WS) and direction data were acquired from the Al-Faw Grand Port marine station, supervised by the Iraqi Ministry of Transportation (General Company for Iraqi Ports). The dataset spans January 2020 to December 2022 and includes 10-minute interval measurements from an ultrasonic anemometer installed at 6 m above sea level (Ammar et al. 2024). Wind speeds at 10 m, 50 m, and 100 m heights were derived from the original 6 m data and provided in the corrected dataset. Wind speeds at multiple heights (10 m, 50 m, and 100 m) were derived using the power law vertical extrapolation method, which has been widely validated for wind resource assessment in regions with similar terrain characteristics. The power law relationship is expressed as (Mohammed Khadir et al. 2024):

$$U_2 = U_1 \left(\frac{Z_2}{Z_1}\right)^{\alpha} \quad \ldots(1)$$

Where U_2 is the wind speed at the target height Z_2, U_1 is the wind speed at the reference height Z_1, and is the power-law exponent (wind shear coefficient), a dimensionless value that determines how wind speed changes with height. While the original anemometer was installed at 6 m above sea level, wind speeds at 10 m and 50 m were derived using power-law extrapolation and provided in the corrected dataset (Mohammed Khadir et al. 2024). The study workflow is shown in Fig. 2.

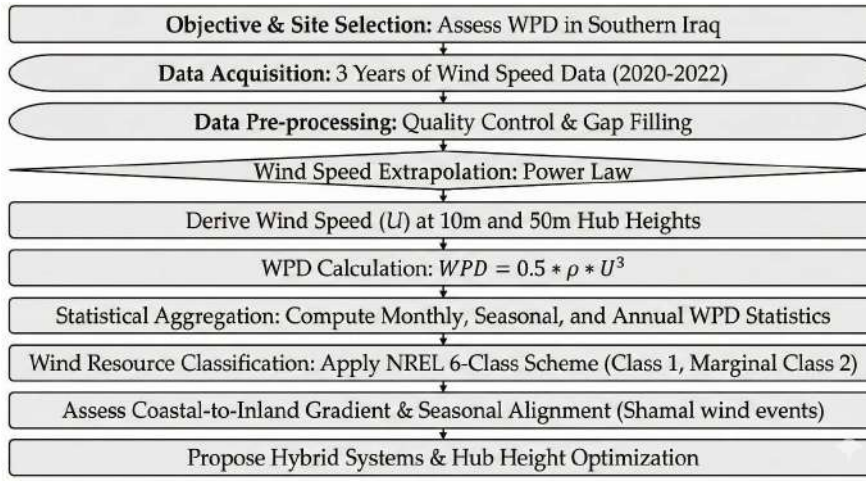


Fig. 2: Flowchart illustrating the methodological procedure of this study.

The methodological procedure is illustrated in Fig. 2. All raw wind speed measurements were quality-controlled following standard meteorological procedures, including removal of erroneous readings, identification of sensor malfunctions, and verification of temporal continuity. Missing data periods totaling less than 5 % of the complete record were filled using linear interpolation for gaps shorter than 3 hours, while longer gaps were excluded from analysis to maintain data integrity. This multi-scale temporal arrangement assists in comprehensive representation of wind resource variability from diurnal to inter-annual timescales, which is necessary for understanding both energy production potential and reliability (Abdalla et al. 2023). Table 2 provides the wind shear coefficients. These values represent literature-derived terrain categories used for reference.

2.2.1. Height Extrapolation Method

Wind speed extrapolation from 10 m and 50 m was performed using the power law; the log profile equation is presented as a *reference formula* used to derive an equivalent α:

$$U(z) = \frac{u_*}{k} \ln\frac{z}{z_0} \quad \ldots(2)$$

where u* is the friction velocity, κ = 0.41 is the von Kármán constant, and z_0 = 0.0002 m for open sea (Abdalla et al. 2023). This yields an equivalent power-law exponent α, consistent with typical coastal values (Rusu et al. 2018, Aboobacker et al. 2021). Site-specific α values were not applied because no independent measurements exist for Basrah at 10 m.

Table 2: Wind shear coefficients (Abdalla et al. 2023, Hussin & Yusof 2022).

Site Type	Wind Shear Coefficient
Open sea (Al-Faw Grand Port)	0.06–0.10
Port/industrial (Umm Qasr)	0.1–0.3
Airport/grassland (Basrah Airport)	0.03–0.1

2.3. Wind Power Density (WPD)

Wind power density (WPD) represents the kinetic energy flux per unit area and is used to determine the wind energy potential of a specific site. WPD is based on the cubic relationship between wind speed and the amount of power that can be generated, making it a more informative indicator of wind-energy potential than wind speed alone. The wind power density is determined using the standard formula based upon kinetic energy theory (Abbas et al. 2025, Hussain et al. 2023):

$$WPD = \frac{1}{2} \rho U^3 \quad \ldots(3)$$

where WPD is the wind power density (W m^{-2}), ρ is air density (kg m^{-3}), and U is wind speed (m s^{-1}).

For the purpose of calculating WPD, air density was assumed to be constant at 1.225 kg m^{-3}, representing standard atmospheric conditions at sea level at 15°C. Although air density varies with temperature and pressure, the average density of air provides a reasonable approximation for comparative evaluations of wind power potential and is consistent with methods used in regional wind-resource studies (Abbas et al. 2025). It is acknowledged, however, that southern Iraq experiences extreme summer temperatures regularly exceeding 45°C, under which air density can fall to approximately 1.09–1.12 kg m^{-3} (compared with the standard 1.225 kg m^{-3}), implying a potential overestimation of summer WPD of approximately 8–11 % in those months. In winter, air density closely approaches the standard value and the bias is negligible. The annual mean overestimation bias is therefore estimated at approximately 3–5 %, which is insufficient to change the NREL classification of any site

in this study but should be considered when interpreting absolute WPD magnitudes during summer months (Abbas et al. 2025). Because there is a cubic relationship between wind power and velocity, minor fluctuations in wind speed produce large fluctuations in wind power. For example, doubling the wind speed increases wind power density by a factor of eight. The cubic relationship between wind power density and wind speed means that small errors in wind speed measurement result in disproportionately large errors in WPD estimates (Abbas et al. 2025).

Wind Power Density (WPD) calculations were completed at two different levels (10 m and 50 m) in order to determine the vertical wind resource distribution and therefore evaluate different configurations (heights) of turbine hubs in the coastal region of Iraq. Today, most modern utility-scale wind turbines have hub heights that range from 50 m to 100 m or more; the wind speed at these heights is much greater than the wind speed at lower elevations due to the fact that the effect of surface friction decreases with height. Multi-height wind resource analyses provide an important tool for determining what types of turbine configurations and tower styles will work best for wind resources at the Iraqi coastline (Ammar et al. 2024). A series of daily WPD values were calculated from the average daily wind speed data from each of the locations and heights analyzed. These daily values were then aggregated to create monthly, seasonal, and annual summary WPD statistics. The monthly WPD mean values allow tracking of how the wind resource evolves over time; therefore, one can easily see when the wind resource is at its peak and when it is at its lowest. Aggregation on a seasonal basis allows for a broader view of climatic patterns at the regional level (for example, the effects of the Shamal wind system). The yearly average WPD value indicates the long-term average WPD for use in the preliminary feasibility studies.

Comprehensive statistical analyses were performed for each site at each temporal aggregation level, producing the mean, maximum, minimum, and standard deviation of WPD values. The standard deviation indicates the temporal variability of WPD and therefore assists in assessing resource reliability. WPD resources with high standard deviations relative to the mean may require energy storage solutions or additional generation capacity to accommodate fluctuations in energy supply. In this study, WPD was first computed from daily mean wind speeds, and monthly, seasonal, and annual means were then derived by averaging the daily WPD values. For comparison, WPD could instead be calculated from each individual 10-minute record and then averaged. The daily-mean approach may slightly underestimate WPD relative to calculations based on individual 10-minute wind-speed records.

Following the calculation of WPD values, the NREL wind classification system was used to classify them, providing an internationally accepted threshold for evaluating the suitability of a site for wind energy development. Detailed in the following sections, this wind classification system offers an objective means of comparing the wind resources found in the Iraqi coastal region with global standards and providing an avenue for evidence-based decision-making when investing in renewable energy.

2.4. Wind Resource Classification

The National Renewable Energy Laboratory (NREL) wind power classification system offers a standardized method of classifying the potential of wind energy in terms of wind power density measurements. This is a widely used classification scheme used in the international wind resource assessment, which categorizes the wind resources into seven distinct classes that include Class 1 (poorest) to Class 7 (exceptional) which allows an objective comparison of sites in various geographical areas and climatic zones (Rusu et al. 2018). The NREL classification system was initially designed to enable the systematical assessment of wind power sites in the United States but has since become widely accepted by other countries because of the stringent methodological basis and the practical application by project developers and policymakers. The classification limits are grounded on the large empirical knowledge of correlating wind power density values with technical and economic feasibility of wind energy projects under different conditions (Abbas et al. 2024).

A simpler six-class classification is, however, common in recent literature in wind resources, especially in locations with moderate to low levels of wind. Through this strategy and in line with recent studies in the Arabian Gulf region, the current discussion took the following classification scheme (Wonodi et al. 2024):

- Class 1 (0–243 W m^{-2}): Not suitable for wind energy development
- Class 2 (243–378 W m^{-2}): Marginal viability; feasible only with favorable economic conditions
- Class 3 (378–500 W m^{-2}): Fair resource; suitable for wind energy development with appropriate technology
- Class 4 (500–616 W m^{-2}): Good resource; commercially viable for most turbine configurations
- Class 5 (616–748 W m^{-2}): Excellent resource; highly attractive for wind farm development
- Class 6 (748–978 W m^{-2}): Outstanding resource; optimal conditions for large-scale projects

Sites classified as Class 1 are generally considered unsuitable for commercial wind energy production due to insufficient wind power density to justify the capital investment and operational costs associated with turbine installation and maintenance. The low capacity factors and extended payback periods characteristic of Class 1 sites typically render projects economically unviable under current technology and market conditions (Alonzo et al. 2017, Wang et al. 2015).

Class 2 sites are those that are marginal resources, in which the development of wind energy could be viable under certain conditions, e.g., it is integrated with hybrid renewable energy systems, there are significant financial incentives, or the turbine designs could be developed to be able to work in low-wind-speed conditions. Class 2 sites would be economically viable only with a site-independent feasibility study regarding local electricity prices, grid connection expenses, and policy support measures (Filom et al. 2021). The higher classes 3 and above mean better and better conditions to develop wind energy. Classes of 3 or higher are typically deemed technically and economically feasible to have commercial wind farms in place, with even higher classes providing an attractive return on investment profile and lower project risks (Filom et al. 2021).

The NREL classification was applied to the annual mean values of WPD at each of the study sites and each height, which would give an objective measure of long-term wind energy potential. Also, monthly and seasonal WPD values were analyzed with respect to the classification limits to determine the time of the year that wind resources are commercially viable despite the annual averages being below the optimum classification. This time-based analysis is especially applicable to hybrid energy systems or seasonal energy storage plans that have the opportunity to take advantage of the times when wind resource availability is increased (Abdalla et al. 2023, Wonodi et al. 2024).

Results of the classification were combined with statistical parameters and comparison of spatial comparisons to develop all evidence-based recommendations about the appropriateness of each location in the study as a wind power development area. These recommendations consider both the raw NREL class classification plus other factors, such as variability of the resources used, seasonal cycles, and spatial gradient of wind power density across the coastal to inland transect, to give pragmatic suggestions on the planning of renewable energy in southern Iraq.

3. RESULTS AND DISCUSSION

3.1. Results

This study presents a comprehensive spatiotemporal assessment of wind power density (WPD) across three coastal sites in southern Iraq, Al-Faw, Umm Qasr, and Basrah Airport, by using observational data from 2020 to 2022. The analysis extends to multiple temporal scales (daily, monthly, seasonal, and annual) and vertical levels (10 m and 50 m), providing a strong representation of wind energy potential in a region affected by the Shamal wind system. All results are contextualized by employing the National Renewable Energy Laboratory (NREL) wind power classification to calculate technical feasibility.

3.1.1. Wind Speed and Direction Characteristics

Wind rose examination showed distinct directional patterns across all three study locations, with northwesterly (NW) winds representing the dominant wind regime throughout the study period (Fig. 3). This directional consistency reflects the influence of the Shamal wind system, which arises from synoptic-scale pressure gradients between the Eastern Mediterranean and the Arabian Peninsula. At Al-Faw, the prevailing northwesterly direction was detected throughout the study period, with infrequent southeasterly (SE) components during transitional seasons. The summer months (June, July, and August) demonstrated particularly strong northwesterly and westerly (W) wind patterns, consistent with the intensification of the summer Shamal phenomenon recognized in regional climatological studies. Fig. 3 presents the aggregated wind rose for the full 2020–2022 study period at each of the three study sites.

Seasonal characterization was based on grouping the underlying observations into four standard meteorological seasons (winter: Dec–Feb; spring: Mar–May; summer: Jun–Aug; autumn: Sep–Nov) and examining the consistent northwesterly dominance in summer relative to the more variable directions during transitional periods.

The distributions of wind speeds showed significant temporal variation at various timescales. The frequency distribution of the observations of the daily wind speed revealed that most of the measurements (just about 60–70 %) were within the range of 3.1–6.1 m s^{-1} across all stations. Speed classes of wind (6.1–9.1 m s^{-1}) occurred mainly during the summer season, especially in June, July, and August months when Shamal winds are at maximum strength. On some occasions, extreme wind speeds were recorded to be above 15 m s^{-1} and were mostly recorded during the months of March and June, though these were less than 5 % of the total observations. The average 10 m high wind speeds were 1.56 m s^{-1} (Basrah Airport, February 2020) to 9.37 m s^{-1} (Al-Faw, November 2020) within the three years of the study (Table 3). The strongest wind speeds were always observed at Al-Faw, with an average of 5.2 m s^{-1} at 10 m high. The intermediate values were registered at Umm Qasr,

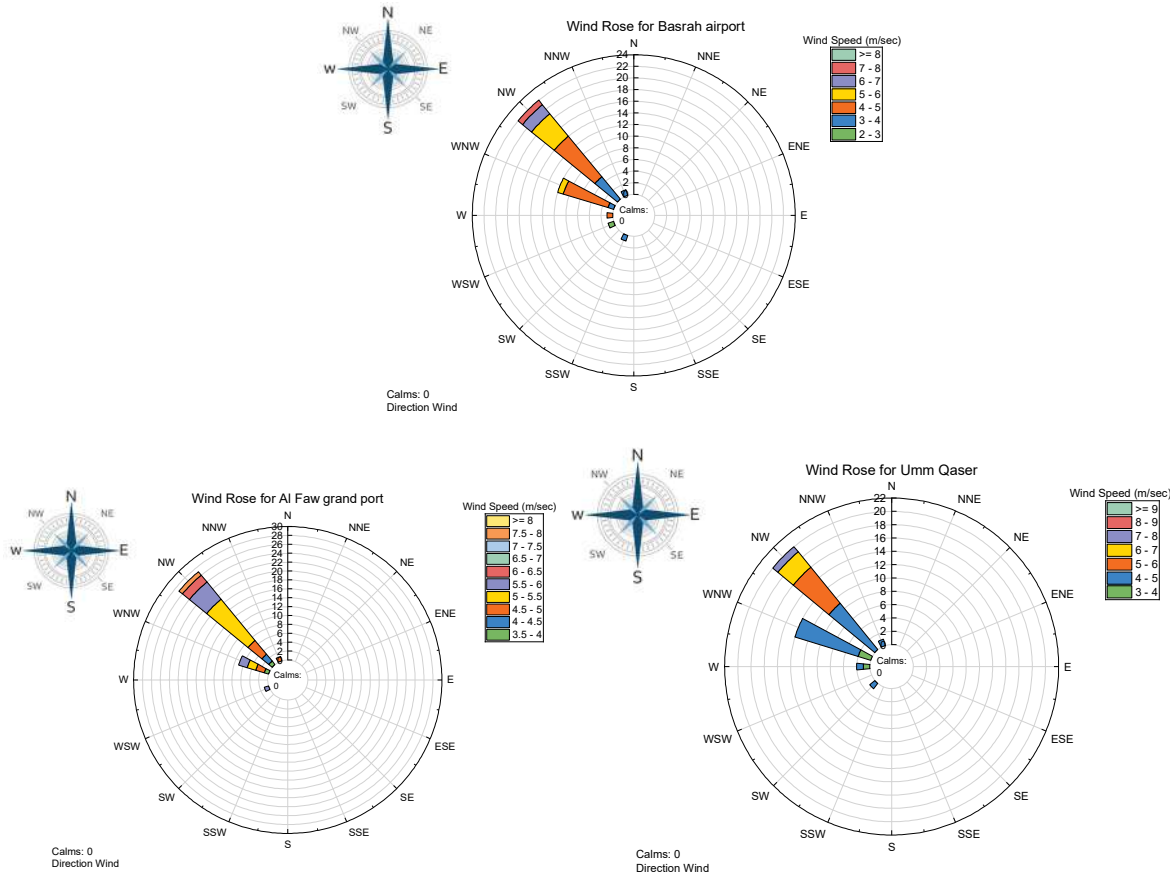


Fig. 3: Aggregated wind roses for Al-Faw, Umm Qasr, and Basrah Airport for the 2020–2022 study period, showing directional frequency (%) and wind speed classes (m s^{-1}).

where the mean wind speed was 4.3 m s^{-1}, whilst Basrah Airport had the lowest wind speeds with an average speed of 3.8 m s^{-1}. This spatial gradient shows a specific decrease in the magnitude of wind speed with the distance from the coastline, which can be explained by an increase in the surface roughness and decreased marine control at inland sites.

Seasonal patterns revealed distinct variations in wind speed characteristics. Summer months (June–August) consistently created the highest monthly mean wind speeds across all stations, with Al-Faw getting peak values of 8.7–9.2 m s^{-1} at 10 m height during June and July 2021. Winter months (December–February) showed moderate wind speeds with more variability, ranging from 2.9 m s^{-1} to 9.1 m s^{-1} based on the occurrence of winter Shamal events. Spring and autumn were transitional periods with intermediate wind speeds; WPD at 50 m is consistently 1.7–2.9x higher than at 10 m due to U^3 dependence, although individual months exhibited substantial deviations from seasonal averages due to intermittent synoptic disturbances.

3.1.2. Wind Power Density Distribution

A calculation of the values of annual mean wind power density during the period of 2020–2022 demonstrated that spatial distributions of the values across the three study sites showed a significant level of dissimilarity, and with increasing height increase there was a major improvement (Table 4). Al-Faw measured a mean value of WPD of 139.3 W m^{-2} at 10 m height, whereas Basrah Airport and Umm Qasr had 55.6 W m^{-2} and 78.3 W m^{-2}, respectively. The gradient from the coastal to inland area was high, with the coastal Al-Faw having WPD values 2.5 times greater than Basrah Airport and 1.8 times greater than Umm Qasr at the 10 m height level.

Height extrapolation produced substantial increases in wind power density at all locations. At 50 m height, mean WPD values increased to 236.9 W m^{-2} at Al-Faw, 160.6 W m^{-2} at Basrah Airport, and 192.8 W m^{-2} at Umm Qasr, representing enhancement factors of approximately 1.7, 2.9, and 2.5 times the 10 m values, respectively. This vertical amplification reflects the cubic relationship between wind

Table 3A: Monthly mean wind speed (m s⁻¹) and WPD (W m⁻²) for 2020.

Month	Wind Speed (m s⁻¹)						Wind Power Density (W m⁻²)					
	10 m Height			50 m Height			10 m Height			50 m Height		
	Al-Faw WS 10 m(m s⁻¹)	Basrah WS 10 m(m s⁻¹)	Umm Qasr WS 10 m(m s⁻¹)	Al-Faw WS 50 m(m s⁻¹)	Basrah WS 50 m(m s⁻¹)	Umm Qasr WS 50 m(m s⁻¹)	Al-Faw WPD 10 m(W m⁻²)	Basrah WPD 10 m(W m⁻²)	Umm Qasr WPD 10 m(W m⁻²)	Al-Faw WPD 50 m(W m⁻²)	Basrah WPD 50 m(W m⁻²)	Umm Qasr WPD 50 m(W m⁻²)
Jan 2020	6.531	4.540	5.000	7.796	6.870	6.900	170.663	57.316	76.563	290.268	198.599	201.212
Feb 2020	2.871	1.560	1.670	3.427	2.480	2.480	14.492	2.325	2.853	24.648	9.342	9.342
Mar 2020	4.407	2.480	3.200	5.260	3.790	4.580	52.423	9.342	20.070	89.162	33.344	58.844
Apr 2020	4.741	4.400	4.930	5.659	6.500	6.840	65.253	52.175	73.392	110.984	168.208	196.008
May 2020	4.995	3.520	4.360	5.962	5.190	6.120	76.318	26.714	50.765	129.804	85.626	140.398
Jun 2020	3.473	2.970	3.810	4.146	4.140	5.320	25.656	16.046	33.875	43.636	43.462	92.223
Jul 2020	3.507	2.120	2.800	4.186	2.980	3.870	26.418	5.836	13.446	44.932	16.209	35.501
Aug 2020	5.351	5.140	4.790	6.387	7.450	6.500	93.829	83.176	67.315	159.587	253.265	168.208
Sep 2020	4.647	3.260	4.220	5.547	5.020	6.200	61.473	21.221	46.030	104.555	77.485	145.976
Oct 2020	5.522	3.320	5.040	6.591	5.050	6.940	103.106	22.414	78.415	175.365	78.882	204.731
Nov 2020	9.372	7.250	8.050	11.187	9.670	9.990	504.124	233.410	319.517	857.427	553.842	610.664
Dec 2020	9.140	6.160	6.860	10.911	8.630	9.030	467.718	143.169	197.733	795.508	393.676	450.993
Annual Mean 2020	5.380	3.893	4.561	6.422	5.648	6.231	138.456	56.095	81.665	235.490	159.328	192.842

Note: WPD calculated as ½ρU³ using ρ = 1.225 kg m⁻³. Wind speeds at 50 m derived using power-law extrapolation (α = 0.07 for Al-Faw & Basrah Airport; α = 0.20 for Umm Qasr). Summer WPD may be overestimated by ~8–11 % due to reduced air density at high temperatures.

Table 3B: Monthly mean wind speed (m s⁻¹) and WPD (W m⁻²) for 2021.

Month	Wind Speed (m s⁻¹)						Wind Power Density (W m⁻²)					
	10 m Height			50 m Height			10 m Height			50 m Height		
	Al-Faw WS 10 m(m s⁻¹)	Basrah WS 10 m(m s⁻¹)	Umm Qasr WS 10 m(m s⁻¹)	Al-Faw WS 50 m(m s⁻¹)	Basrah WS 50 m(m s⁻¹)	Umm Qasr WS 50 m(m s⁻¹)	Al-Faw WPD 10 m(W m⁻²)	Basrah WPD 10 m(W m⁻²)	Umm Qasr WPD 10 m(W m⁻²)	Al-Faw WPD 50 m(W m⁻²)	Basrah WPD 50 m(W m⁻²)	Umm Qasr WPD 50 m(W m⁻²)
Jan 2021	3.870	3.040	3.260	4.620	4.450	4.470	35.505	17.208	21.221	60.387	53.974	54.705
Feb 2021	7.950	6.170	7.000	9.490	8.860	9.200	307.757	143.867	210.088	523.441	425.998	476.946
Mar 2021	6.210	4.340	4.780	7.413	6.410	6.600	146.713	50.070	66.894	249.533	161.317	176.091
Apr 2021	2.215	1.880	2.100	2.644	2.530	2.740	6.659	4.070	5.672	11.325	9.919	12.600
May 2021	5.181	6.280	5.470	6.185	8.770	7.410	85.194	151.700	100.246	144.900	413.147	249.207
Jun 2021	9.183	5.160	7.020	10.961	7.120	9.300	474.296	84.150	211.893	806.695	221.078	492.669
Jul 2021	8.700	3.580	4.230	10.385	5.510	6.380	403.333	28.103	46.358	685.999	102.462	159.063
Aug 2021	8.400	3.760	4.320	10.027	5.280	6.200	363.031	32.559	49.381	617.453	90.159	145.976
Sep 2021	7.600	2.580	2.930	9.072	3.800	4.280	268.873	10.519	15.407	457.306	33.609	48.022
Oct 2021	6.400	5.710	7.010	7.640	8.430	10.010	160.563	114.029	210.989	273.090	366.935	614.339
Nov 2021	5.200	4.110	4.730	6.207	5.930	6.570	86.122	42.524	64.817	146.479	127.723	173.701
Dec 2021	3.478	2.880	3.080	4.152	4.260	4.430	25.777	14.631	17.896	43.843	47.352	53.250
Annual Mean 2021	6.199	4.124	4.661	7.400	5.946	6.466	196.985	57.786	85.072	335.038	171.139	221.381

Note: WPD calculated as ½ρU³ using ρ = 1.225 kg m⁻³. Wind speeds at 50 m derived using power-law extrapolation (α = 0.07 for Al-Faw & Basrah Airport; α = 0.20 for Umm Qasr). Summer WPD may be overestimated by ~8–11 % due to reduced air density at high temperatures.

Table 3C: Monthly mean wind speed (m s^{-1}) and WPD (W m^{-2}) for 2022.

Month	Wind Speed (m s^{-1})						Wind Power Density (W m^{-2})					
	10 m Height			50 m Height			10 m Height			50 m Height		
	Al-Faw WS 10 m(m s^{-1})	Basrah WS 10 m(m s^{-1})	Umm Qasr WS 10 m(m s^{-1})	Al-Faw WS 50 m(m s^{-1})	Basrah WS 50 m(m s^{-1})	Umm Qasr WS 50 m(m s^{-1})	Al-Faw WPD 10 m(W m^{-2})	Basrah WPD 10 m(W m^{-2})	Umm Qasr WPD 10 m(W m^{-2})	Al-Faw WPD 50 m(W m^{-2})	Basrah WPD 50 m(W m^{-2})	Umm Qasr WPD 50 m(W m^{-2})
Jan 2022	4.300	4.430	5.040	5.133	6.470	6.680	48.698	53.250	78.415	82.827	165.890	182.573
Feb 2022	4.600	7.440	8.280	5.491	10.010	10.540	59.618	252.246	347.694	101.400	614.339	717.180
Mar 2022	5.300	5.330	5.700	6.326	7.800	7.960	91.187	92.744	113.431	155.094	290.663	308.919
Apr 2022	6.100	2.920	3.500	7.281	4.280	4.930	139.026	15.249	26.261	236.459	48.022	73.392
May 2022	7.200	4.290	4.380	8.594	6.070	5.900	228.614	48.359	51.467	388.834	136.985	125.795
Jun 2022	5.700	2.520	2.300	6.804	3.670	3.090	113.431	9.802	7.452	192.926	30.276	18.071
Jul 2022	4.500	3.000	3.330	5.372	4.750	4.950	55.814	16.538	22.617	94.930	65.643	74.289
Aug 2022	4.200	5.100	4.860	5.013	7.570	6.860	45.379	81.249	70.310	77.182	265.701	197.733
Sep 2022	5.300	2.990	3.490	6.326	4.450	4.980	91.187	16.373	26.036	155.094	53.974	75.647
Oct 2022	4.800	3.920	4.510	5.730	5.760	6.330	67.738	36.895	56.187	115.210	117.051	155.352
Nov 2022	3.600	2.330	2.740	4.297	2.980	3.540	28.577	7.748	12.600	48.604	16.209	27.172
Dec 2022	3.189	1.990	2.080	3.807	2.630	2.780	19.868	4.827	5.512	33.792	11.142	13.160
Annual Mean 2022	4.899	3.855	4.184	5.848	5.537	5.712	82.428	52.940	68.165	140.196	151.325	164.107

Note: WPD calculated as $\frac{1}{2}\rho U^3$ using $\rho = 1.225$ kg m^{-3}. Wind speeds at 50 m derived using power-law extrapolation ($\alpha = 0.07$ for Al-Faw & Basrah Airport; $\alpha = 0.20$ for Umm Qasr). Summer WPD may be overestimated by ~8–11 % due to reduced air density at high temperatures.

Table 4: Summary of annual wind power density statistics and annual means used for NREL classification.

Site	Height	Mean WPD (W m⁻²)	Max. WPD (W m⁻²)	Min. WPD (W m⁻²)	Std Dev. WPD (W m⁻²)	NERL class	Suitability for wind energy	Action
Al Faw	10 m	139.289802	504.1238954	6.65872	142.3827762	Class 1	Not Suitable	Not viable
Al Faw	50 m	236.907834	857.4274535	11.3253	242.1684478	Class 2	Borderline	Consider hybrid wind-solar systems
Basrah AirPort	10 m	55.6070093	252.2463552	2.3253	62.23310972	Class 1	Not Suitable	Not viable
Basrah AirPort	50 m	160.597423	614.3393381	9.34246	159.8528915	Class 1	Not Suitable	Not viable
Umm Qasr	10 m	78.3004627	347.6939256	2.8527	86.11000194	Class 1	Not Suitable	Not viable
Umm Qasr	50 m	192.776392	717.1795967	9.34246	185.7594626	Class 1	Marginal viability	Investigate summer-only deployment

speed and power density combined with the wind profile in the atmospheric boundary layer.

Maximum instantaneous WPD values demonstrated the episodic nature of wind energy availability in the region. Al-Faw recorded peak WPD of 504.1 W m⁻² at 10 m height and 857.4 W m⁻² at 50 m height, occurring during intense Shamal wind events in November 2020. Basrah Airport reached maximum values of 252.2 W m⁻² and 614.3 W m⁻² at 10 m and 50 m heights, respectively, during February 2022. Umm Qasr exhibited intermediate maximum values of 347.7 W m⁻² (10 m) and 717.2 W m⁻² (50 m) in the same month.

Standard deviation values were notably high relative to the mean WPD at all locations, ranging from 62.2 W m⁻² to 242.2 W m⁻² depending on site and height. At Al-Faw, the standard deviation at 10 m height (142.4 W m⁻²) exceeded the mean value (139.3 W m⁻²), indicating substantial temporal variability and intermittency in wind power availability. This high variability reflects the episodic nature of Shamal wind events and the transition between active and quiescent wind periods throughout the annual cycle.

Monthly mean WPD values exhibited pronounced temporal variations throughout the year, with distinct seasonal patterns evident at all study locations (Table 3). At Al-Faw (10 m height), monthly mean WPD ranged from 6.7 W m⁻² (April 2021) to 504.1 W m⁻² (November 2020), demonstrating an approximately 75-fold variation between

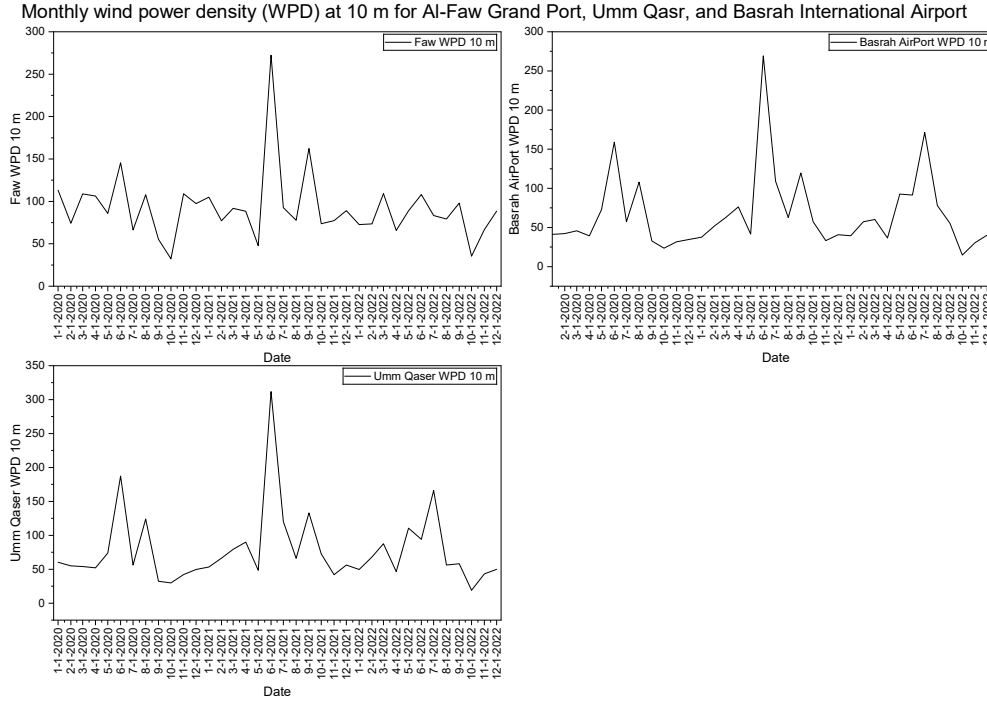


Fig. 4: Grouped box plots of monthly mean WPD by site at 10 m.

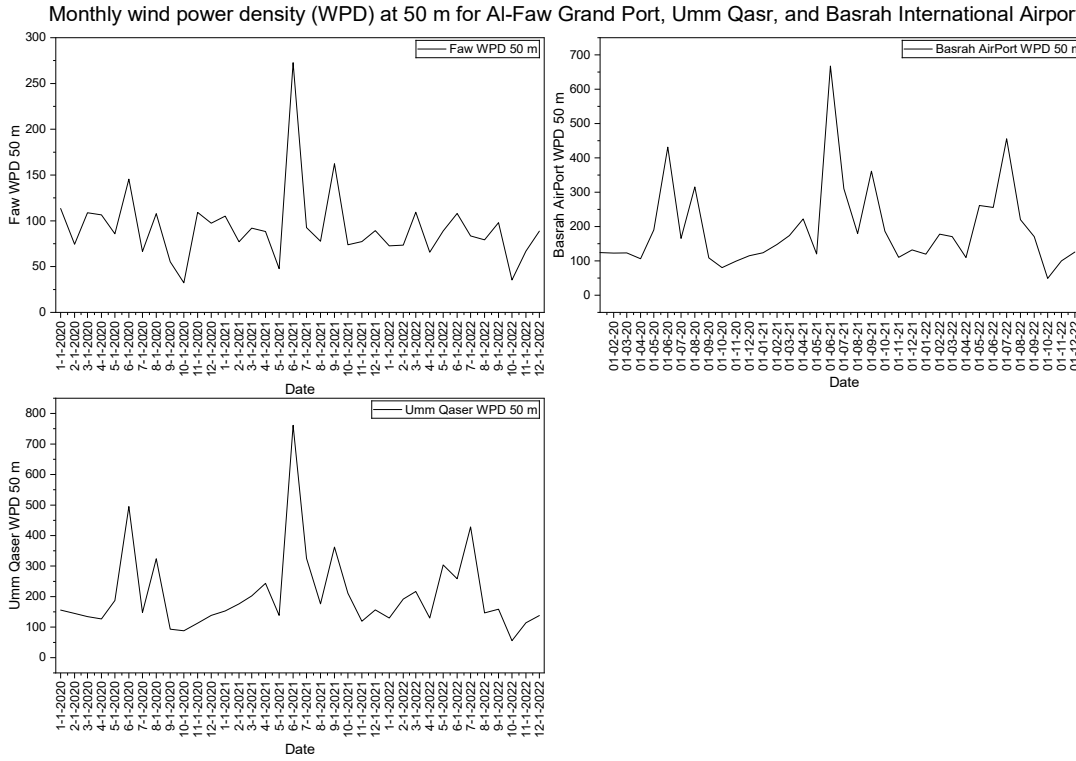


Fig. 5: Grouped box plots of monthly mean WPD by site at 50 m.

minimum and maximum monthly conditions. The November 2020 peak corresponded to an exceptionally strong and persistent Shamal wind event that produced sustained high wind speeds throughout the month, as shown in Figs. 4 and 5.

Table 5 gives the seasonal means throughout the study period, where Summer months generally displayed elevated WPD values, though substantial inter-annual variability was observed. June exhibited consistently high WPD across all three years, with Al-Faw recording values of 25.7 W m^{-2} (2020), 474.3 W m^{-2} (2021), and 113.4 W m^{-2} (2022) at 10 m height. July showed similar patterns with values of 26.4 W m^{-2} (2020), 403.3 W m^{-2} (2021), and 55.8 W m^{-2} (2022). This inter-annual variability highlights the influence of year-to-year differences in synoptic circulation patterns affecting Shamal wind intensity and persistence, as shown in Figs. 6 and 7. At 50 m, Al-Faw achieves 236.9 W m^{-2} (97 % of the Class 2 threshold), making it the only site with marginal potential. However, high variability (CV = 1.02) and low capacity factor (CF = 0.18) limit commercial viability.

Winter months demonstrated moderate to high WPD values during years with active winter Shamal conditions. At 10 m height, January mean WPD at Al-Faw ranged from 35.5 W m^{-2} (2021) to 170.7 W m^{-2} (2020), while December values varied from 19.9 W m^{-2} (2022) to 467.7 W m^{-2} (2020). February exhibited the greatest interannual range, with WPD values spanning from 14.5 W m^{-2} (2020) to 307.8 W m^{-2} (2021), reflecting the episodic nature of winter Shamal events. At 50 m height, these values were significantly amplified, with January WPD ranging from 60.4 W m^{-2} (2021) to 290.3 W m^{-2} (2020), December values varying from 33.8 W m^{-2} (2022) to 795.5 W m^{-2} (2020), and February values spanning from 24.6 W m^{-2} (2020) to 523.4 W m^{-2} (2021).

Table 5: Seasonal mean WPD (W m^{-2}) by site and height.

Season	Al Faw WPD 10 m	Basrah Airport WPD 10 m	Umm Qasr WPD 10 m	Al Faw WPD 50 m	Basrah Airport WPD 50 m	Umm Qasr WPD 50 m
Winter	127.788	76.538	106.422	217.346	213.368	239.929
Spring	99.043	50.047	56.466	168.455	149.692	149.028
Summer	177.910	39.718	58.072	302.593	120.917	153.748
Autumn	152.418	56.126	92.222	259.237	158.412	228.400

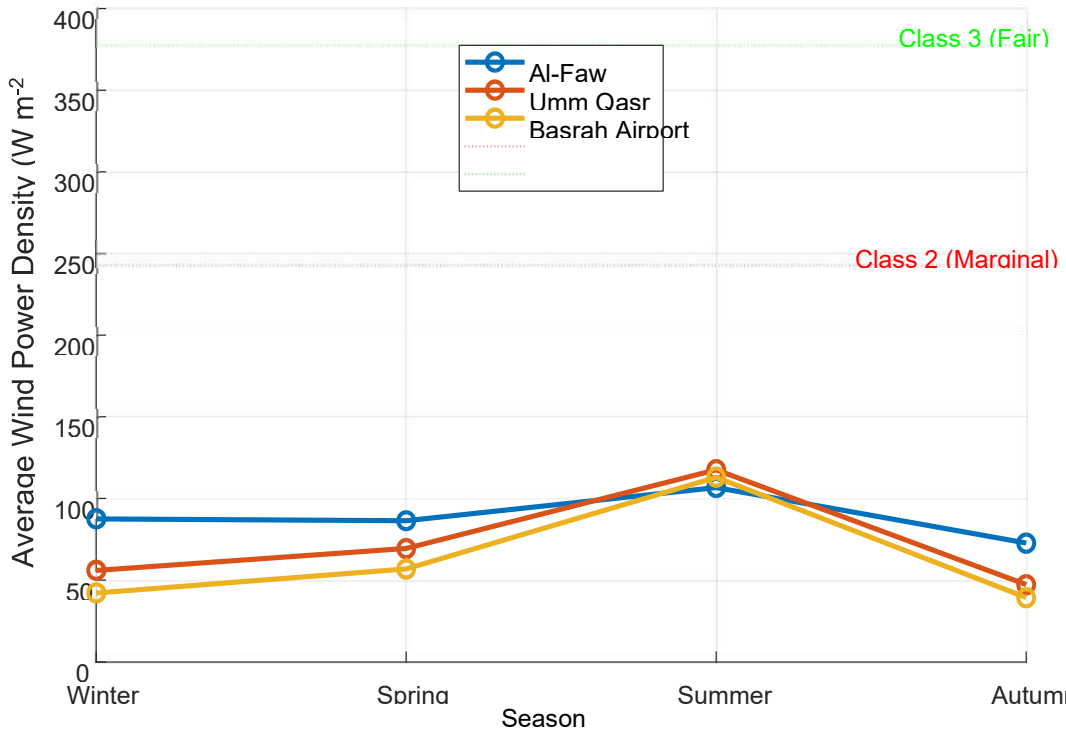


Fig. 6: Seasonal mean WPD (W m⁻²) at 10 m by season and site for 2020–2022.

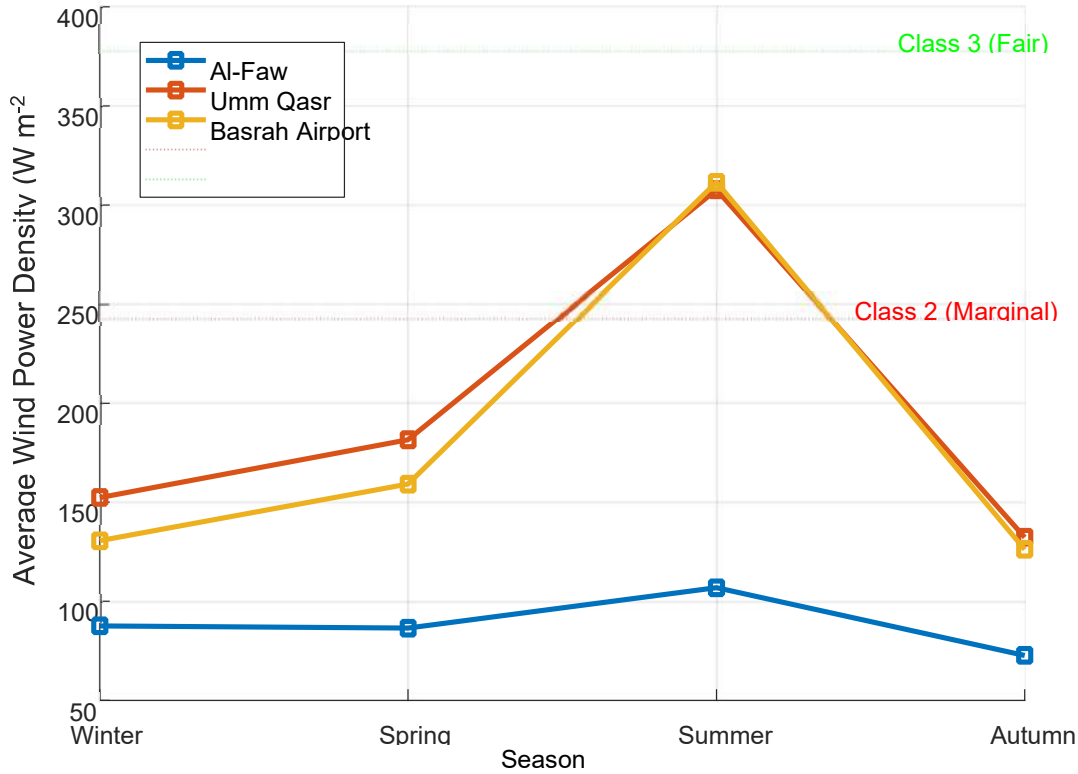


Fig. 7: Seasonal mean WPD (W m⁻²) at 50 m by season and site for 2020–2022.

Spring and autumn months generally produced lower WPD values, with April and October frequently recording the annual minima. At Basrah Airport, April mean WPD values at 10 m height were consistently low across all years: 52.2 W m^{-2} (2020), 4.1 W m^{-2} (2021), and 15.2 W m^{-2} (2022) (compared to 168.2 W m^{-2}, 9.9 W m^{-2}, and 48.0 W m^{-2} at 50 m height, respectively). Similarly, October displayed reduced wind power availability at 10 m, with values of 22.4 W m^{-2} (2020), 114.0 W m^{-2} (2021), and 36.9 W m^{-2} (2022) (compared to 175.4 W m^{-2}, 273.1 W m^{-2}, and 115.2 W m^{-2} at 50 m height, respectively).

3.1.3. Spatial Gradient Analysis

A methodical analysis of wind power density (WPD) at the three study sites shows a consistent coast-to-inland gradient, with higher WPD closer to the Arabian Gulf (Fig. 8). Annual average WPD at 10 m height decreased from Al-Faw (coastal) to Umm Qasr (intermediate, approximately 5 km inland) and then to Basrah Airport (inland, approximately 80 km inland). A clear coastal-inland gradient is observed: WPD at 10 m decreases from 139.3 W m^{-2} (Al-Faw, coastal) to 78.3 W m^{-2} (Umm Qasr, ~5 km inland) and to 55.6 W m^{-2} (Basrah Airport, ~80 km inland). However, with only three sites, linear trends are not statistically justified.

The spatial gradient at 50 m height was slightly weakened but remained substantial. Mean annual WPD values of 236.9 W m^{-2} (Al-Faw), 192.8 W m^{-2} (Umm Qasr), and 160.6 W m^{-2} (Basrah Airport) specified a 32 % reduction from coast to inland. The reduced gradient magnitude at higher elevations proposes that marine boundary layer effects influencing coastal wind speeds decrease with increasing height above the surface.

The spatial gradient demonstrated temporal variability, with the coastal advantage most marked during strong Shamal wind events and reduced during calm periods. During November 2020, when intense northwesterly winds prevailed, Al-Faw recorded WPD values 2.2 times greater than Basrah Airport at 10 m height. On the contrary, during April 2021, a outstandingly calm month, the spatial differences were minimal, with Al-Faw exhibiting only 1.6 times the WPD of Basrah Airport.

Monthly grouped box plots revealed the distribution characteristics of WPD at each location. Al-Faw displayed the widest distribution range and highest median values, with occasional extreme outliers exceeding 400 W m^{-2} at 10 m height during intense wind events. Basrah Airport showed the narrowest distribution with the lowest median values, reflecting its inland position and greater surface roughness effects. Umm Qasr exhibited intermediate characteristics,

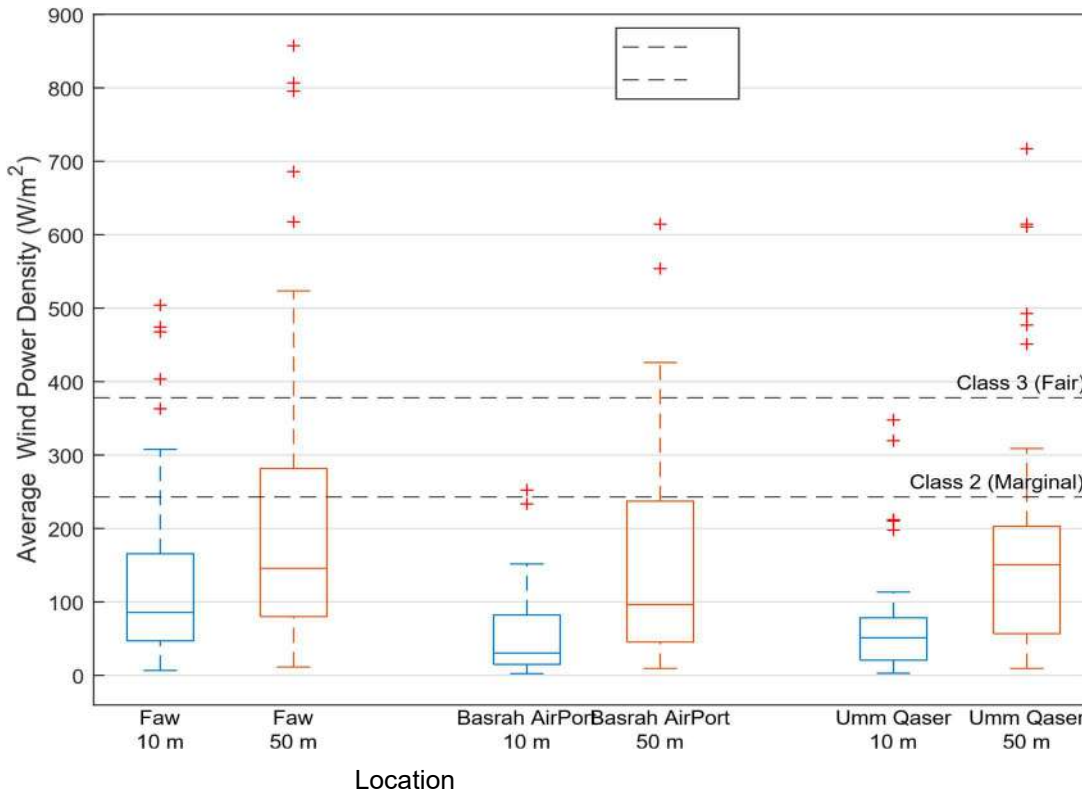


Fig. 8: Distribution of monthly mean WPD by site and height. Outliers represent rare extreme events, such as the November 2020 Shamal event.

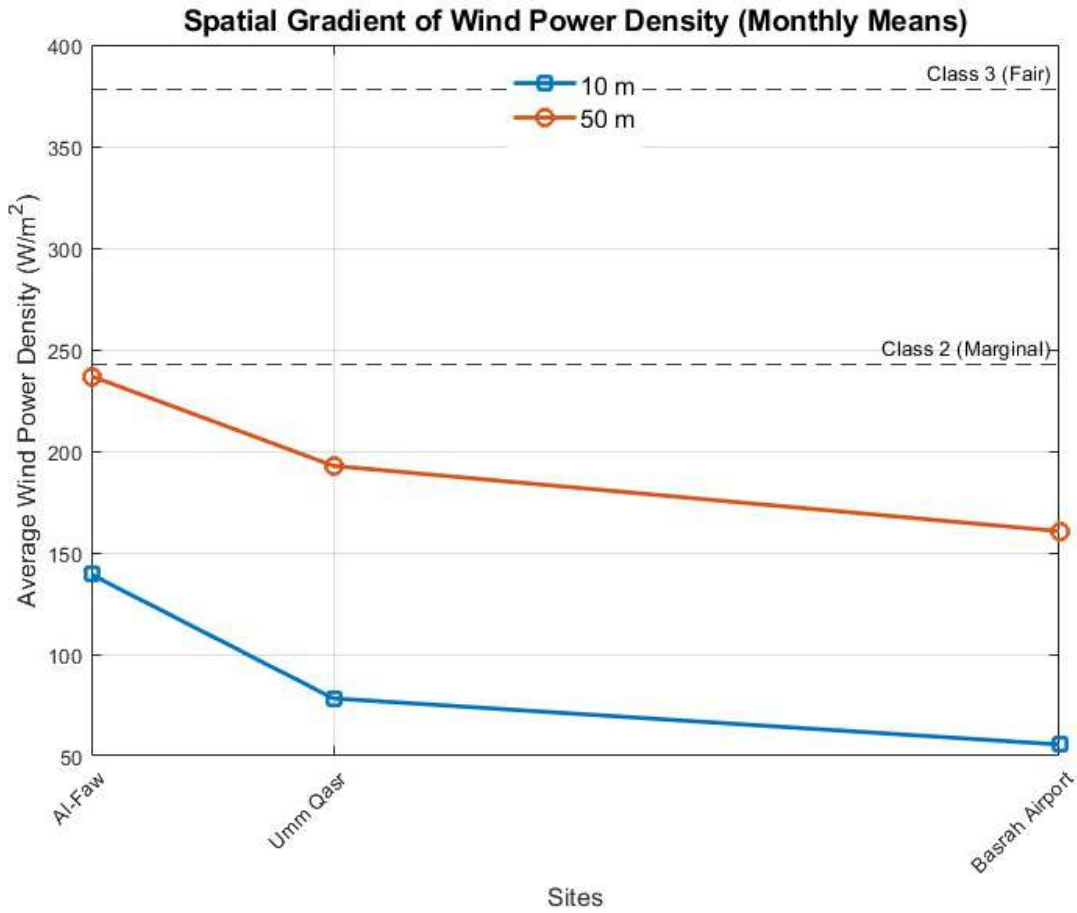


Fig. 9: Spatial gradient of monthly mean wind power density.

with distribution parameters falling consistently between the coastal and inland extremes.

The spatial gradient in WPD was maintained throughout most months, with Al-Faw consistently exhibiting higher values than Umm Qasr and Basrah Airport. However, the magnitude of this gradient varied temporally. During strong Shamal events, the coastal advantage of Al-Faw was most pronounced, with WPD values 3–5 times greater than inland locations stated in Fig. 9. During calm periods, the spatial differences diminished, though Al-Faw retained a modest advantage due to reduced surface roughness effects near the coastline.

3.1.4. NREL Wind Power Classification

Applying the NREL wind power classification to annual average WPD values provided an objective evaluation of wind power capacity at every site under study and height (Table 4). All three sites were in Class 1 (0–243 W m^{-2}), at 10 m above the ground, which is a poor wind resource that cannot sustain commercial development of wind energy. Although Al-Faw had the largest 10 m WPD (139.3 W m^{-2}), it was still well below the 243 W m^{-2} threshold for Class 2 marginal viability. Lower values for Basrah Airport (55.6 W m^{-2}) and Umm Qasr (78.3 W m^{-2}) were observed, remaining within Class 1.

While summer monthly WPD exceeds 243 W m^{-2} (e.g., 307 W m^{-2} in June), the annual mean remains below Class 2. Thus, the site is classified as NREL Class 1 (Not Suitable) for utility-scale projects. Seasonal peak potential does not override annual viability, as shown in Fig. 10.

Basrah Airport remained in Class 1, with a WPD of 160.6 W m^{-2}, which clearly shows that the site remains unsuitable for wind-power development even at higher turbine-hub elevations. The 50 m WPD is merely 66 % of the lowest Class 2 limit, indicating that tremendous height gain or major technological progress would be necessary to make the inland site economically viable.

Umm Qasr was in a borderline position with 50 m WPD of 192.8 W m^{-2}, which remains Class 1 but approaches the Class 2 threshold. This mid-coastal site has potential for marginal wind-energy applications, especially at high-wind

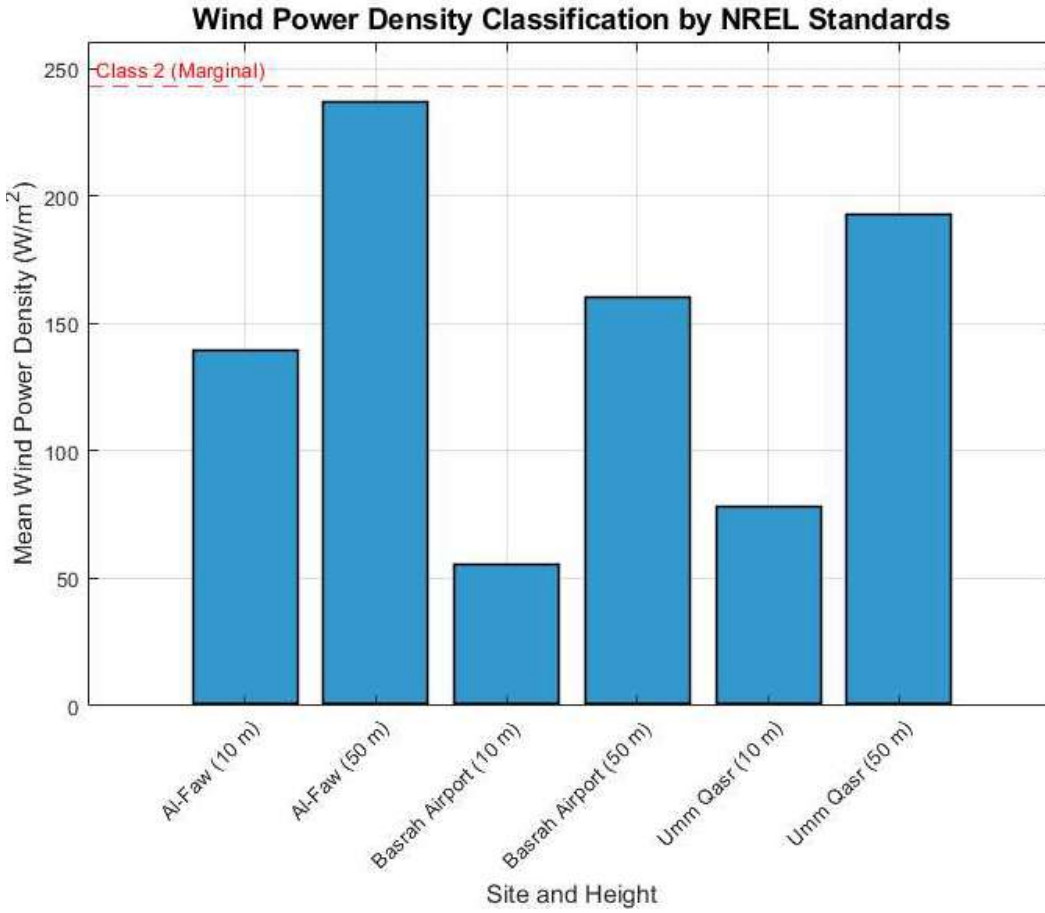


Fig. 10: Wind power density classification according to the adopted NREL thresholds.

summer periods when instantaneous WPD is often Class 2, and sometimes Class 3. The possibility of seasonal or hybrid wind-solar facilities at Umm Qasr may be considered due to the maximum wind speed in the summer, which is the period when the solar radiation is at its maximum in the area.

Analysis of monthly WPD values relative to the NREL classification thresholds indicated that all three locations occasionally reached Class 2 or above during high-wind periods. At 50 m, Al-Faw exceeded the Class 2 threshold (243 W m^{-2}) in 12 of the 36 study months and reached Class 3 (378 W m^{-2}) or higher in 4 months during particularly strong Shamal events. Basrah Airport reached Class 2 in only 3 months, associated with extreme winter Shamal events. Umm Qasr reached Class 2 in 6 months, mainly during summer and occasional high-wind events in winter.

The temporal variability in classification status suggests that, although annual mean conditions do not meet commercial viability thresholds, the wind resource may support supplemental generation during favorable periods. This pattern indicates that wind energy facilities in southern Iraq may be better suited to hybrid renewable-energy systems or seasonal ancillary generation than to baseload generation. At 10 m, Al-Faw remains in Class 1 with an annual mean WPD of approximately 139.3 W m^{-2}. At 50 m, the annual mean WPD increases to 236.9 W m^{-2}, which approaches but does not meet the 243 W m^{-2} Class 2 threshold. Thus, Al-Faw remains Class 1 on an annual-mean basis, although its proximity to the Class 2 threshold suggests that site-specific techno-economic assessment at greater hub heights may be warranted.

The analysis confirms that wind-energy potential improves with height; however, the annual mean WPD at 50 m remains below the Class 2 threshold and well below the Class 3 level generally associated with more favorable wind-farm development conditions.

4. CONCLUSIONS

This comprehensive three-year assessment of wind power density (WPD) across the coastal zone of southern Iraq reveals that the regional wind resource remains marginal

according to global standards, though it exhibits specific characteristics that could facilitate the strategic integration of renewable energy under favorable conditions.

Crucially, none of the three evaluated stations are currently suitable for standalone, commercial utility-scale wind energy generation. Based on annual mean WPD, Al-Faw (236.9 W m^{-2} at 50 m) approaches but does not meet the NREL Class 2 threshold (243 W m^{-2}), while Umm Qasr (192.8 W m^{-2} at 50 m) and Basrah Airport (160.6 W m^{-2} at 50 m) remain within Class 1. Although Al-Faw and Umm Qasr at 50 m periodically exceed Class 2 thresholds during peak summer months (June–August), and Al-Faw occasionally reaches Class 3 during intense Shamal events, these are seasonal peaks rather than sustained annual resources. Consequently, any potential for supplemental or hybrid wind-solar applications remains contingent upon future site-specific techno-economic analyses.

The analysis confirms a distinct coastal-to-inland gradient, with WPD declining by approximately 60 % from coastal Al-Faw (139.3 W m^{-2} at 10 m) to inland Basrah Airport (55.6 W m^{-2}) over an approximately 80 km transect. Extrapolating to a 50 m hub height yields significant vertical amplification (factors of 1.7–2.9×), bringing Al-Faw close to the marginal viability threshold. Nevertheless, no site achieves the Class 3 threshold typically required for commercially viable wind farms.

Seasonal analysis indicates that peak WPD values (>300 W m^{-2} at 50 m at coastal sites) occur during the summer, coinciding with Iraq's peak electricity demand driven by air-conditioning loads. While this temporal alignment offers a strategic advantage for grid support, the high temporal variability, evidenced by standard deviations exceeding the mean values, reflects the episodic nature of the Shamal wind regime. This high intermittency presents inherent challenges for grid integration, necessitating robust energy storage or reserve capacity.

Ultimately, the marginal nature of the resource implies that standalone wind farms are not economically viable under current conditions. However, hybrid systems combining wind and solar photovoltaics could potentially mitigate intermittency issues due to complementary generation patterns. Furthermore, the significant WPD improvement observed when extrapolating from 10 m to 50 m suggests that modern turbines with hub heights of 80 to 100 m might achieve improved classifications, particularly along the coast.

As the first multi-height, multi-site comparative evaluation of WPD in Iraq's coastal region, this study provides essential baseline data to support evidence-based renewable energy planning. While southern Iraq's wind resources fall below optimal global thresholds, strategic approaches, such as hybrid system deployment, hub-height optimization, and seasonal energy planning, could enable the region to make meaningful contributions to Iraq's renewable energy portfolio and broader energy security goals.

5. ACKNOWLEDGMENTS

The authors express their sincere gratitude to the Department of Atmospheric Science, College of Science, Mustansiriyah University.

6. REFERENCES

Abbas, T.A., Ahmed, F.T. and Khudhair, A.A., 2026. Impact of hub height, rotor diameter, and terrain roughness on wind energy yield in Central Iraq: a controlled three-factor analysis. *Journal of Renewable Energy and Environment*, 13(4), pp. 48–57. [DOI]

Ahmed, M.H. and Abbas, T.A., 2026. Wind-solar complementarity: a daily-resolution assessment for renewable energy planning in Iraq (2020–2024). *Ecological Engineering and Environmental Technology*, 27(7), pp. 343–361. [DOI]

Abbas, S., Faisal, M., Abbas, Z., Ahmad, F. and Umar, M., 2024. Optimizing performance and design simulation of a 100 kW single rotor horizontal axis wind turbine. *Clean Energy and Sustainability*, 2(2), p. 10010. [DOI]

Abbas, T.A., Al-Jiboori, M.H. and Altmimi, A.I., 2025. Wind analysis for power generation in the south of Iraq. *Nature Environment and Pollution Technology*, 24(1). [DOI]

Abdalla, A., El-Osta, W., Nassar, Y.F., Husien, W., Dekam, E.I. and Miskeen, G.M., 2023. Estimation of dynamic wind shear coefficient to characterize best fit of wind speed profiles under different conditions of atmospheric stability and terrains for the assessment of height-dependent wind energy in Libya. *Applied Solar Energy*, 59(3), pp. 343–359. [DOI]

Aboobacker, V.M., Shanas, P.R., Veerasingam, S., Al-Ansari, E.M.A.S., Sadooni, F.N. and Vethamony, P., 2021. Long-term assessment of onshore and offshore wind energy potentials of Qatar. *Energies*, 14(4), p. 1178. [DOI]

Abbas, T.A. and Fattah Hassoon, A., 2026. Assessment of wind energy potential in northwestern Iraq: a hybrid optimization method based on Weibull distribution and intelligent algorithms. *Atmósfera*, 40. [DOI]

Alonzo, B., Ringkjob, H.K., Jourdier, B., Drobinski, P., Plougonven, R. and Tankov, P., 2017. Modelling the variability of the wind energy resource on monthly and seasonal timescales. *Renewable Energy*, 113, pp. 1434–1446. [DOI]

Al-Salem, K., Neelamani, S. and Al-Nassar, W., 2018. Wind energy map of Arabian Gulf. *Natural Resources*, 9(5), pp. 212–228. [DOI]

Ammar, E., Hussain, H.H. and Majeed, H.T., 2024. Calculating wind power density in the Iraqi coastal region. *Iraqi Geological Journal*, 57(2), pp. 290–304. [DOI]

Filom, S., Radfar, S., Panahi, R., Emini, E. and Neshat, M., 2021. Exploring wind energy potential as a driver of sustainable development in the southern coasts of Iran. *Sustainability*, 13(14), p. 7702. [DOI]

Hadi, F.A., Al-Knani, B.A. and Abdulwahab, R.A., 2020. An assessment the wind potential energy as a generator of electrical energy in the coastal area of southern Iraq. *Scientific Review Engineering and Environmental Sciences*, 29(1), pp. 37–53. [DOI]

Hussain, I., Haider, A., Ullah, Z., Russo, M., Casolino, G.M. and Azeem, B., 2023. Comparative analysis of eight numerical methods using Weibull distribution to estimate wind power density for coastal areas in Pakistan. *Energies*, 16(3), p. 1515. [DOI]

Hussin, N.H. and Yusof, F., 2022. Analysis of wind speed characteristics

using probability distribution in Johor. *Environment and Ecology Research*, 10(1), pp. 95–106. [DOI]

Kazem, H.A. and Chaichan, M.T., 2012. Status and future prospects of renewable energy in Iraq. *Renewable and Sustainable Energy Reviews*, 16(8), pp. 6007–6012. [DOI]

Mohammed Khadir, J., Abdulsada Al-Knani, B. and Hassoon, A.F., 2024. Effect of the atmospheric stability on wind energy density using similarity theory. *Journal of Agrometeorology*, 26(3), pp. 279–289. [DOI]

Rusu, L., Ganea, D. and Mereuta, E., 2018. A joint evaluation of wave and wind energy resources in the Black Sea based on 20-year hindcast information. *Energy Exploration & Exploitation*, 36(2), pp. 335–351. [DOI]

Wang, J., Qin, S., Jin, S. and Wu, J., 2015. Estimation methods review and analysis of offshore extreme wind speeds and wind energy resources. *Renewable and Sustainable Energy Reviews*, 42, pp. 26–42. [DOI]

Wonodi, I., Ahiakwo, C., Braide, S. and Amadi, H., 2024. Techno-economic assessment of wind power potential of Abuloma community using two-parameter Weibull distribution. *Journal of Engineering Research and Reports*, 26(11), pp. 48–62. [DOI]

Yu, Y., Notaro, M., Kalashnikova, O.V. and Garay, M.J., 2016. Climatology of summer Shamal wind in the Middle East. *Journal of Geophysical Research: Atmospheres*, 121(1), pp. 289–305. [DOI]

Nature Environment and Pollution Technology
An International Quarterly Peer-Reviewed Open Access Journal

p-ISSN: 0972-6268 | e-ISSN: 2395-3454 Vol. 25 | No. 4 | Article ID B4435 | 2026

RESEARCH ARTICLE https://doi.org/10.46488/NEPT.2026.v25i04.B4435 OPEN ACCESS

Mapping the Evolution of Urban Sprawl Research: A PRISMA-Based Systematic and Bibliometric Synthesis

Jaswant Singh† and Kranti Kumar Maurya
Department of Architecture and Planning, National Institute of Technology, Patna-800005, Bihar, India
†Corresponding author: Jaswant Singh; Jaswant.ph21.ar@nitp.ac.in

ARTICLE HISTORY

Received: 04-03-2026
Revised: 14-04-2026
Accepted: 02-05-2026

KEYWORDS

Urban sprawl
Remote sensing
CA–Markov models
Landscape metrics
Sustainability
PRISMA
Urban growth modeling

CITE THIS ARTICLE

Singh, J. and Maurya, K. K., 2026. Mapping the evolution of urban sprawl research: A PRISMA-based systematic and bibliometric synthesis. *Nature Environment and Pollution Technology*, 25(4), B4435. https://doi. org/10.46488/NEPT.2026.v25i04.B4435

COPYRIGHT & LICENCE

© 2026 The Authors
Open Access under CC BY 4.0.

PUBLISHED BY

TECHNOSCIENCE PUBLICATIONS

ABSTRACT

Urban sprawl represents a major spatial manifestation of contemporary urbanization, reshaping land systems, ecological stability, and sustainability trajectories. This study presents a PRISMA-based systematic review combined with bibliometric and thematic synthesis to examine global urban sprawl research. Following structured screening of 183 records, 54 peer-reviewed journal articles were retained for detailed analysis. Bibliometric mapping using VOSviewer, quantitative comparison, and thematic synthesis were integrated to assess methodological evolution, geographic concentration, and sustainability integration. The findings reveal three developmental phases: an early exploratory stage, a consolidation phase dominated by spatial modeling, and a recent shift toward environmental and climate-related assessment. Methodologically, Cellular Automata and CA–Markov models account for 40.74% of studies, followed by remote sensing change detection (25.93%), while spatial regression approaches remain limited (3.70%). Urban expansion magnitudes show substantial heterogeneity, with a mean built-up growth of 119.7% and a strongly right-skewed distribution (Sk = 1.97; K = 2.38). Reported growth ranges from below 20% to over 500%, frequently associated with agricultural land conversion and land surface temperature intensification. Classification accuracies typically range from 83% to 91%, indicating high technical reliability. Research output is geographically concentrated in Asia (61.11%), particularly in China and India, while governance-oriented scholarship remains comparatively underrepresented. Overlay analysis indicates an emerging focus on climate change and ecosystem impacts, yet institutional evaluation remains peripheral. Overall, the field demonstrates strong technical maturity but limited integration of policy assessment, underscoring the need for cross-scale causal modeling and standardized sustainability metrics.

1. INTRODUCTION

1.1. Urban Sprawl as a Global Challenge

Urbanization represents one of the most transformative processes shaping the twenty-first century, fundamentally restructuring land systems, socio-economic dynamics, and ecological stability across the globe (Halefom et al. 2024, Oleson et al. 2015). The rate of spatial urban expansion has significantly exceeded population growth in many regions, leading to the rapid outward spread of low-density, automobile-dependent development commonly referred to as urban sprawl (Artmann et al. 2019, Seto et al. 2012). While urban growth has historically been associated with economic productivity and innovation, its contemporary spatial manifestation increasingly raises environmental and sustainability concerns, particularly in rapidly developing regions of Asia, Africa, and Latin America (Güneralp et al. 2018).

Urban sprawl is typically characterized by dispersed built-up patterns, leapfrog development, segregated land uses, and inefficient land consumption. However, over the last decade, the concept has evolved beyond purely morphological interpretations toward a multidimensional understanding that incorporates governance, infrastructure systems, ecological fragmentation, and socio-spatial inequality (Ewing & Hamidi 2015). Rather than being viewed solely as uncontrolled expansion, urban sprawl is increasingly conceptualized as a systemic outcome of complex interactions between demographic pressures, real estate markets, transport infrastructure investments, planning institutions, and policy failures (Luo & Wu 2021, Taubenböck et al. 2018).

The drivers of urban sprawl vary across geopolitical contexts but demonstrate notable structural similarities. Population growth and rural–urban migration remain primary demographic forces in the Global South, whereas suburbanization, housing affordability dynamics, and transportation infrastructure expansion play dominant roles in high-income economies (Halder et al. 2025, Salvati et al. 2020). Weak land-use regulation and fragmented metropolitan governance structures further accelerate peripheral expansion, particularly in rapidly urbanizing regions lacking coordinated spatial planning frameworks (Rupapara et al. 2025). Moreover, speculative land markets and infrastructure-led development corridors often stimulate dispersed settlement patterns that outpace environmental planning capacity.

The environmental consequences of such expansion are substantial and multidimensional. Urban sprawl contributes to accelerated land consumption, loss of agricultural land, ecosystem fragmentation, biodiversity decline, and increased carbon emissions through transport dependency (Angel et al. 2011, Zhu et al. 2022). Remote sensing–based studies consistently demonstrate that urban land expansion has encroached disproportionately upon fertile agricultural zones and ecologically sensitive peri-urban landscapes (Halder et al. 2025). In addition, dispersed urban form intensifies energy demand for transportation and infrastructure provision, thereby increasing greenhouse gas emissions and undermining climate mitigation efforts (Ewing & Hamidi 2015, Wang et al. 2021a).

Beyond ecological degradation, urban sprawl has profound social implications. Low-density expansion frequently produces socio-spatial segregation, inequitable access to services, and infrastructure deficits in peripheral settlements (Xu et al. 2019). Informal and peri-urban communities often lack adequate transportation connectivity, water supply, sanitation, and green space provision, exacerbating vulnerability to environmental risks (Halder et al. 2026). These patterns underscore that urban sprawl is not merely a spatial configuration issue but a broader governance and equity challenge embedded within urbanization trajectories.

Over the past fifteen years, scholarly attention toward urban sprawl has intensified, reflecting growing recognition of its implications for sustainability transitions and climate resilience (Sathe & Rahman 2024, Wang et al. 2021). However, despite abundant empirical case studies, the global research landscape remains fragmented across disciplines, scales, and methodological approaches.

1.2. Methods for Measuring Urban Sprawl

The quantification of urban sprawl has undergone substantial methodological evolution, largely driven by advancements in geospatial technologies and computational modeling. Early assessments relied heavily on census-based density indicators and land-use statistics; however, contemporary studies increasingly employ multi-temporal satellite imagery, GIS-based spatial modeling, and landscape metrics to capture the complexity of expansion dynamics (Bosch et al. 2021, Mokarram et al. 2024).

Remote sensing has emerged as the dominant tool for monitoring urban expansion at multiple scales. Landsat time-series datasets, Sentinel imagery, and MODIS-derived products enable consistent long-term observation of built-up growth patterns, urban footprints, and peri-urban transformation (Wan 2014, Wang et al. 2020). The integration of machine learning classifiers, cloud-based platforms such as Google Earth Engine, and high-resolution imagery has significantly enhanced classification accuracy and temporal resolution (Rahaman et al. 2019). These advancements have allowed researchers to quantify sprawl intensity, detect fragmentation patterns, and assess spatial diffusion processes with unprecedented precision.

GIS-based modeling further complements remote sensing by enabling spatial overlay analysis, proximity assessment, and urban growth simulation. Cellular automata (CA), CA–Markov models, and geographically weighted regression (GWR) approaches are increasingly applied to examine drivers and forecast expansion scenarios (Jia & Wang 2021, Wang et al. 2021b). Such models provide insight into how infrastructure corridors, economic hubs, and topographical constraints shape expansion trajectories.

Landscape metrics have also become central to sprawl assessment. Indicators such as patch density, edge density, Shannon's diversity index, and fractal dimension are widely employed to quantify morphological dispersion and fragmentation (Sarkar & Chakraborty 2025). These metrics

move beyond simple density measures, offering a more nuanced understanding of spatial configuration and ecological connectivity. Similarly, entropy-based measures remain popular for evaluating spatial dispersion patterns, particularly in rapidly urbanizing regions (Bhatta 2009). However, recent literature highlights scale sensitivity and methodological inconsistencies in entropy applications, emphasizing the need for integrated multi-indicator frameworks. Together, these methodological developments demonstrate that urban sprawl research has transitioned from descriptive mapping toward analytically sophisticated, multi-scalar modeling.

1.3. Sustainability and Environmental Implications

Urban sprawl is intrinsically linked to sustainability challenges, particularly in the context of climate change, ecosystem degradation, and resource efficiency. One of the most pressing concerns is accelerated land consumption. Empirical studies indicate that urban land expansion frequently outpaces population growth, leading to declining density and inefficient land use (Merlín-Uribe et al. 2013). Such patterns undermine compact city strategies and increase infrastructure provision costs.

Carbon emissions represent another critical dimension. Low-density urban form increases reliance on private vehicles and lengthens commuting distances, thereby elevating per capita transport emissions (Kumar et al. 2025a, Kumar et al. 2025b). Additionally, dispersed development patterns require extensive road networks and utility systems, contributing to embodied energy consumption.

Urban sprawl also intensifies urban heat island (UHI) effects through vegetation loss and increased impervious surfaces. Remote sensing studies reveal strong correlations between built-up expansion and elevated land surface temperatures. Furthermore, hydrological systems are disrupted as natural infiltration zones are replaced by impermeable materials, increasing flood risk and groundwater stress (Rai 2019).

From an ecological perspective, fragmentation of habitats and peri-urban ecosystems reduces biodiversity and weakens ecosystem service provision. The cumulative impact of these processes underscores the urgency of aligning urban growth management with sustainability objectives, particularly under global climate commitments.

1.4. Planning and Policy Perspectives

In response to the negative externalities of urban sprawl, planning theory and practice have increasingly promoted compact city development, smart growth principles, transit-oriented development (TOD), and polycentric urban models (Artmann et al. 2019). These frameworks aim to enhance density, mixed land use, and sustainable mobility while preserving ecological assets.

However, implementation remains uneven. Institutional fragmentation, political economy constraints, and socio-cultural preferences for low-density housing frequently undermine compact development strategies (Salvati et al. 2020). Moreover, rapidly urbanizing regions often lack regulatory enforcement capacity to prevent informal or speculative peri-urban expansion.

Recent scholarship emphasizes the importance of governance integration, participatory planning, and cross-sectoral coordination to manage urban expansion effectively (Ghosh et al. 2022). Nevertheless, empirical evidence on the effectiveness of such policy instruments remains scattered across regional case studies.

1.5. Problem Statement and Knowledge Gaps

Despite substantial growth in urban sprawl research over the past two decades, several critical limitations persist. First, existing literature remains fragmented between spatial measurement studies, sustainability impact assessments, and policy-oriented analyses. Second, methodological heterogeneity limits comparability across regions and scales. Third, bibliometric assessments of the field remain limited, and few studies integrate systematic review frameworks with quantitative network mapping.

Furthermore, global comparative synthesis is insufficient. Much of the literature is concentrated in specific regions, particularly China, the United States, and parts of Europe, leaving underrepresentation in rapidly urbanizing African and South American contexts (Güneralp et al. 2020, Seto et al. 2012). These gaps hinder comprehensive understanding of global sprawl dynamics and constrain evidence-based policy formulation.

In response to these limitations, this study undertakes a PRISMA-driven systematic review combined with bibliometric synthesis to analyze global urban sprawl research over the last two decades. By integrating transparent literature screening with network-based mapping and thematic synthesis, this study provides a comprehensive, methodologically rigorous, and globally comparative assessment of urban sprawl scholarship.

Unlike previous reviews that focus either on environmental impacts or spatial metrics alone, this study integrates publication trend analysis, keyword co-occurrence mapping, country distribution assessment, and thematic content synthesis within a unified analytical framework. This mixed-method approach enhances transparency, reproducibility, and interpretative depth.

The objectives of this study are to:

- Quantify global publication trends on urban sprawl.
- Identify dominant research clusters through keyword co-occurrence analysis.
- Synthesize thematic developments in measurement methods, environmental impacts, and planning responses.
- Identify research gaps and propose future research directions.

Through this comprehensive approach, the study aims to advance understanding of urban sprawl as a complex, multidimensional sustainability challenge and provide a structured knowledge base to inform spatial planning and policy interventions worldwide. Urban sprawl is increasingly recognized not only as a morphological phenomenon but as a systemic transformation of land–infrastructure–ecology interactions. This pattern suggests a potential imbalance in thematic emphasis within the field, particularly when considered alongside the relatively limited representation of governance-related studies identified in the thematic analysis.

2. MATERIALS AND METHODS

This study adopts a mixed-method research design integrating a PRISMA-guided systematic review with bibliometric network analysis to provide a transparent, reproducible, and quantitatively grounded synthesis of global urban sprawl research. The methodological framework was structured to ensure rigor in literature identification and screening while enabling quantitative mapping of research evolution, thematic clusters, and geographic distribution. By combining systematic review protocols with bibliometric visualization tools, the study bridges qualitative depth and quantitative structure, thereby addressing fragmentation in existing urban sprawl scholarship.

The overall methodological workflow comprised four sequential stages: (1) database search and record identification, (2) PRISMA-based screening and eligibility assessment, (3) bibliometric mapping and statistical trend analysis, and (4) thematic content synthesis. Fig. 1 illustrates the PRISMA framework (Page et al. 2021).

2.1. The PRISMA Framework

The PRISMA framework was employed to systematically collect, screen, and analyze articles from the Web of Science (WoS) database. This method ensures transparency and reproducibility, which are vital for academic rigor (Chaudhuri & Kumar 2022, Fu et al. 2022). The Web of Science (WoS) Core Collection was selected as the sole bibliographic database for this study because of its high-quality indexing standards, rigorous journal selection process, structured citation metadata, and suitability for reliable bibliometric network construction. WoS is widely used in systematic reviews and bibliometric analyses because it provides standardized bibliographic and citation records. However, reliance on a single database may limit the comprehensiveness of the literature coverage compared with multi-database approaches incorporating Scopus, Dimensions, or other bibliographic databases. The initial search was conducted on January 14, 2026. The search strategy was implemented using the Topic (TS) field in the WoS Core Collection, rather than the Title field alone. In WoS, a Topic search retrieves records based on terms appearing in the Title, Abstract, Author Keywords, and Keywords Plus fields. This approach was adopted to achieve a balance between thematic relevance and retrieval comprehensiveness, allowing studies that address urban sprawl or closely related concepts to be identified even when the relevant terminology does not appear explicitly in the title. Boolean operators (AND and OR) were used to combine and refine the search concepts. The search was structured around three conceptual groups: (i) urban sprawl and related urban-growth concepts, (ii) land-use, sustainability, and urban-planning concepts, and (iii) remote sensing and geospatial technologies. The exact WoS Topic search query was:

TS = (("urban sprawl" OR "urban expansion" OR "urban growth" OR "urban footprint") AND ("land use" OR "land cover" OR "remote sensing" OR "GIS" OR "sustainability" OR "landscape metrics" OR "urban planning" OR "urban form") AND ("remote sensing" OR "GIS" OR "geospatial" OR "satellite" OR "Landsat" OR "Sentinel"))

Thus, the final search was conducted using the Topic (TS) field, with no separate Title-field restriction. This strategy increases recall relative to a title-only search but may retrieve some studies in which the specified concepts occur in the abstract, author keywords, or Keywords Plus without representing the primary focus of the study. The eligibility and screening criteria applied to the retrieved literature are presented in Table 1.

This structured query ensured that retrieved records explicitly addressed urban expansion processes in connection with geospatial measurement techniques, land-use dynamics, or sustainability-related frameworks. The inclusion of geospatial terms (e. g., Landsat, Sentinel, satellite, GIS) ensured methodological relevance, particularly given the study's focus on measurement approaches and bibliometric mapping.

Criteria used to ensure methodological consistency and topical relevance in the PRISMA screening process. As

Table 1: Criteria for eligible literature through WOS (excluded if not meeting these criteria).

Category	Inclusion Criteria	Exclusion Criteria
Database	Web of Science Core Collection	Other databases
Document Type	Peer-reviewed journal articles	Review articles, conference papers, editorials, and book chapters (excluded to ensure inclusion of primary empirical studies only)
Language	English	Non-English publications
Topical Scope	Explicit focus on urban sprawl/expansion/growth measured using geospatial or land-use techniques	Studies unrelated to spatial expansion or lacking geospatial dimension
Methodological Relevance	Use of remote sensing, GIS, satellite data, landscape metrics, or geospatial modeling	Purely theoretical discussions without empirical measurement

shown in Table 1, the inclusion criteria prioritize empirical rigor and geospatial relevance, ensuring alignment with the study's objective of synthesizing measurement-based urban sprawl research. It is important to distinguish between the present study as a systematic review and the exclusion of review articles from the analyzed dataset. The objective of this study is to synthesize primary empirical research rather than secondary syntheses. Including review papers could lead to duplication of findings and overrepresentation of certain studies already summarized in prior reviews. Therefore, only original research articles with extractable methodological and quantitative information were retained for analysis.

Conference papers were excluded despite their relevance in geospatial and remote sensing research because they often provide limited methodological detail, preliminary results, and less standardized reporting compared to peer-reviewed journal articles. Given the study's emphasis on quantitative comparison, reproducibility, and bibliometric network construction, the inclusion of only full-length journal articles ensures greater consistency, reliability, and comparability across the analyzed corpus.

The PRISMA framework provides a structured four-stage approach comprising Identification, Screening, Eligibility, and Inclusion, allowing systematic filtering of literature while minimizing selection bias. The detailed flow of records through each stage is illustrated in Fig. 1.

The literature search was conducted in the WoS Core Collection database using the predefined search query described in Section 2. The search yielded 183 journal articles, representing the initial dataset for review. This broad retrieval strategy was designed to capture a comprehensive body of scholarship addressing urban sprawl in relation to sustainability and geospatial methodologies.

During the identification phase, preliminary filtering was applied to remove records that did not meet basic inclusion requirements. Specifically, 7 articles were excluded because they were not written in English, were classified as review papers, or were categorized as early access publications. After this initial refinement, 176 records progressed to the screening stage.

The screening phase involved a systematic examination of titles, abstracts, and subject categories to assess disciplinary relevance and thematic alignment. First, 40 studies were excluded because they belonged to irrelevant disciplines that did not align with the spatial, environmental, or sustainability focus of the study.

The remaining 136 articles underwent detailed title and abstract screening to evaluate their conceptual and methodological relevance. During this step, 82 records were excluded due to insufficient alignment with the core research objectives, particularly the absence of a clear connection between urban sprawl and sustainability dimensions, or lack of empirical geospatial analysis. Additionally, studies that were not fully accessible were removed to ensure consistency in full-text evaluation. Following this stage, 54 articles remained eligible for full-text assessment.

In the eligibility phase, full texts of the 54 remaining studies were carefully reviewed against predefined inclusion criteria. This evaluation emphasized:

- Explicit focus on urban sprawl, expansion, or growth
- Integration of sustainability-related analysis
- Application of geospatial, remote sensing, GIS, or land-use methodologies
- Empirical assessment within built or urban environments

Each article was assessed for methodological robustness and thematic consistency. Only studies demonstrating clear analytical linkage between spatial expansion processes and sustainability implications were retained.

After full-text assessment, 54 studies were ultimately selected for detailed analysis and synthesis. These studies formed the final corpus for both bibliometric mapping and thematic content analysis. The included articles collectively represent the most relevant and methodologically rigorous scholarship addressing urban sprawl through geospatial and sustainability lenses within the defined time frame.

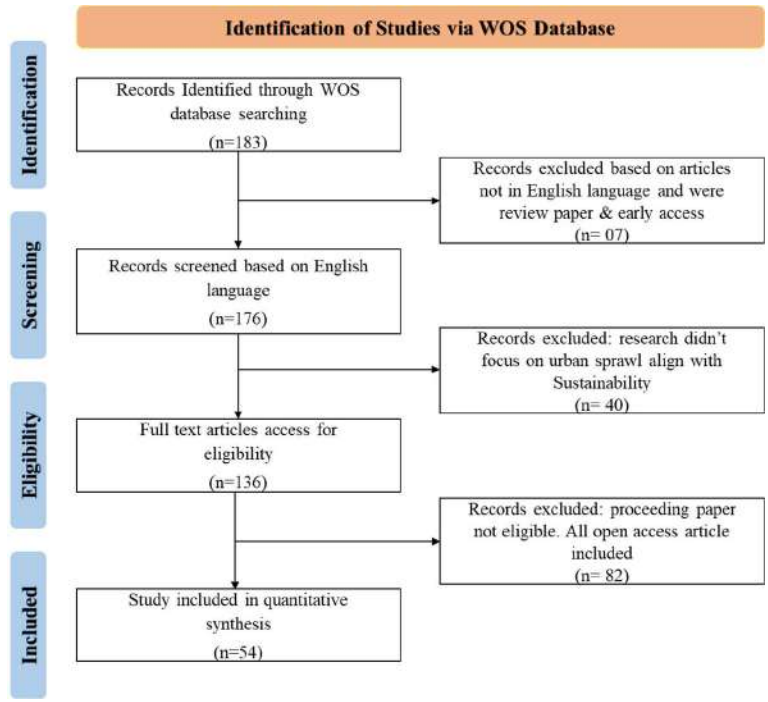


Fig. 1: PRISMA framework of the study, Source: PRISMA 2020 (Page et al. 2021).

The structured progression from 183 initially identified records to 54 included studies, as illustrated in Fig. 1, demonstrates the methodological transparency and systematic rigor of the review process. By applying clearly defined criteria at each stage, the study ensures that the final dataset reflects high-quality, thematically consistent research capable of supporting robust bibliometric and thematic synthesis.

In the supplementary material, a comprehensive list of all 54 studies included in the systematic review is presented, along with citation details. Each study is systematically documented with information such as authors, year of publication, title, and number of citations, providing a transparent overview of the research corpus. The meticulous application of the PRISMA framework ensures that all selected studies are highly relevant to the study's themes and research objectives.

2.2. Bibliometric Analysis

Bibliometric analysis was conducted to examine the structural characteristics and thematic organization of the selected literature. The analysis was performed using VOSviewer (version 1.6.19), a software tool designed for constructing and visualizing bibliometric networks (van Eck 2010). The objective of this stage was to identify patterns of keyword co-occurrence, temporal distribution of research topics, and geographic publication distribution within the final dataset of 54 articles.

Following PRISMA screening, the complete bibliographic records of the included articles were exported from the Web of Science Core Collection in plain text format, including full metadata and cited references. Author-provided keywords were extracted as the primary analytical unit, as they most directly reflect the conceptual focus defined by researchers. Prior to network construction, the dataset underwent a cleaning and standardization process to ensure semantic consistency. Variations in spelling and terminology were harmonized, synonymous expressions were unified where conceptually appropriate, and compound keywords were standardized to avoid artificial fragmentation of the network. Only author keywords were retained to minimize indexing noise associated with automatically generated database terms.

It is important to note that bibliometric network analysis provides a descriptive representation of relationships among research themes based on co-occurrence patterns. Such analysis does not establish causal relationships but rather identifies structural tendencies and thematic proximities within the literature. Therefore, interpretations derived from bibliometric outputs should be understood as indicative and are complemented in this study by thematic content analysis and quantitative comparison.

The bibliometric procedures described above were designed to provide a reproducible and quantitative foundation for subsequent thematic interpretation. While this section details the analytical workflow, interpretation of network structures, cluster composition, temporal progression, and geographic patterns is presented in the Results section.

2.2.1. Publication Trend Analysis

To examine overall research growth, annual publication counts for the period 2008–2025 were extracted from the dataset. An exponential regression model was fitted to the time-series data to assess whether publication output followed an accelerating trajectory. The model was expressed in the form:

$$y = ae^{bx}$$

Where:

- y represents the number of publications
- x represents year
- a and b are fitted coefficients

2.2.2. Keyword Co-occurrence Analysis

Keyword co-occurrence analysis was performed to identify conceptual linkages within the research field. A minimum occurrence threshold of three appearances per keyword was applied to ensure that only recurrent and analytically meaningful terms were included in the visualization. This threshold was selected to balance inclusivity with interpretability, preventing excessive network sparsity while retaining significant thematic signals. Link strength between keywords was calculated using the association strength normalization method, which adjusts for differences in overall frequency and provides a proportional measure of relatedness. Network visualization was generated using the VOSviewer layout algorithm, in which node size corresponds to keyword frequency, link thickness represents co-occurrence strength, and spatial proximity indicates conceptual similarity. Clusters were automatically identified using VOSviewer's modularity-based clustering technique, grouping keywords that exhibit stronger internal connectivity relative to the rest of the network.

In addition to standard cluster visualization, an overlay visualization was generated to incorporate a temporal dimension into the network structure. Overlay mapping assigns a color value to each keyword based on the average publication year of the articles in which the keyword appears. The average publication year is calculated by averaging the publication dates of all documents associated with a given term, thereby enabling examination of chronological shifts in thematic emphasis. This approach allows simultaneous observation of structural prominence and temporal positioning within the same network configuration. The overlay visualization does not alter cluster formation but supplements the structural map with temporal information, facilitating analysis of how research topics have evolved over time.

2.2.3. Country Distribution Analysis

Geographic distribution of research production was assessed using corresponding author affiliation data available in the WoS records. Each article was assigned to a country based on the institutional affiliation of the corresponding author, and publications were aggregated to identify national contributions within the dataset. This analysis was intended to reveal spatial patterns in knowledge production and highlight geographic concentrations of empirical research activity.

2.3. Thematic Content Analysis

In addition to bibliometric network mapping, a qualitative thematic content analysis was conducted to provide in-depth interpretation of the conceptual domains identified through keyword co-occurrence analysis. While bibliometric techniques reveal structural relationships and temporal dynamics among research terms, they do not capture the substantive analytical focus, methodological nuance, or interpretative depth of individual studies. Therefore, a systematic thematic synthesis was undertaken to complement quantitative mapping and ensure comprehensive understanding of the research landscape.

Thematic content analysis was applied to the full texts of the 54 articles included after PRISMA screening. The process followed an inductive–deductive hybrid approach. Initially, a deductive framework was informed by the major keyword clusters identified through VOSviewer. These clusters served as preliminary thematic anchors. Subsequently, an inductive reading of each article was performed to identify recurring analytical patterns, methodological approaches, research objectives, and policy implications that may not have been fully captured through keyword analysis alone.

During the first stage of coding, each article was examined to extract information related to research objectives, spatial scale, methodological techniques, environmental indicators, modeling approaches, and policy dimensions. Open coding was applied to identify recurrent conceptual elements across studies. In the second stage, codes were grouped into higher-order thematic categories based on conceptual similarity and frequency of occurrence. This iterative comparison process enabled refinement of thematic boundaries and ensured internal coherence within each category.

The final thematic structure was organized into four overarching domains: (1) geospatial modeling and urban expansion simulation, (2) spatial form and landscape metrics, (3) environmental and climate-related impacts, and (4) planning and governance dimensions. These domains emerged from the convergence between bibliometric clusters and qualitative synthesis of article content. Each included study was assigned to one or more thematic domains depending on its primary analytical focus. Where studies spanned multiple dimensions, cross-classification was permitted to reflect interdisciplinary integration.

To enhance methodological rigor, thematic classification was conducted systematically across all studies using a standardized data extraction matrix. The matrix recorded key attributes including geographic context, temporal coverage, remote sensing datasets used, modeling techniques applied, environmental indicators assessed, and policy relevance discussed. This structured extraction procedure minimized subjective bias and ensured consistency across the review corpus.

The thematic analysis did not aim to quantify effect sizes or perform meta-analysis, as the methodological heterogeneity of included studies, ranging from satellite-based change detection to regression modeling and landscape ecology assessments, rendered statistical aggregation inappropriate. Instead, the objective was to synthesize patterns of conceptual emphasis, methodological evolution, and research direction within the field of urban sprawl studies.

Integration of bibliometric mapping with thematic content analysis strengthened interpretative robustness. The co-occurrence network provided macro-level structural insight, while full-text thematic synthesis allowed micro-level contextual interpretation. This combined approach ensured that thematic conclusions presented in the Results section are grounded both in quantitative network evidence and qualitative examination of study content.

Through this multi-layered analytical framework, the study moves beyond descriptive bibliometric reporting and enables a deeper understanding of how urban sprawl research has evolved conceptually, methodologically, and geographically over the selected study period.

2.4. Methodological Rigor and Limitations

To ensure methodological robustness:

- Search query design was pilot-tested for sensitivity and specificity
- Screening criteria were applied consistently across stages
- Bibliometric thresholds were standardized
- Keyword normalization procedures minimized semantic duplication

Despite efforts to ensure methodological rigor, several limitations should be acknowledged. First, the exclusive use of the WoS database may introduce selection bias, as relevant studies indexed in Scopus, Dimensions, or other databases were not included. Second, the adoption of a title-based search strategy, while improving specificity, may have reduced the total number of retrieved records by excluding studies where urban sprawl is not explicitly stated in the title. Third, the final dataset of 54 studies reflects the application of strict inclusion criteria emphasizing geospatial methodologies and sustainability integration, which may limit the breadth of global representation. Future studies could adopt multi-database search strategies and broader query fields (e. g., abstract and keywords) to assess the sensitivity of results and enhance coverage.

Additionally, the exclusion of review articles and conference proceedings may limit the breadth of conceptual and emerging research captured, particularly in fast-developing domains such as geospatial modeling. However, this decision was necessary to maintain analytical consistency and ensure that all included studies provide comparable empirical evidence.

3. RESULTS

3.1. Publication Trends

The annual publication distribution reveals three distinct developmental phases in the evolution of the research domain (Fig. 2). The initial phase (2008–2014) is characterized by sporadic and low publication output, with only two contributions recorded across seven years, indicating a nascent and exploratory research stage. The emergence phase (2015–2018) shows a gradual increase in scholarly activity, rising from 2 publications in 2015 to 5 publications in 2016, reflecting early consolidation and growing academic recognition.

A pronounced expansion phase (2019–2025) is observed thereafter, marked by sustained productivity and higher annual outputs. The most significant surge occurred in 2021 (n = 11; 20.37% of total publications), representing the peak research intensity within the study period. Although minor fluctuations are visible in 2022 and 2024, the overall trend remains upward, with consistently high publication counts above pre-2018 levels. Notably, approximately 68% of total publications were produced during 2021–2025, underscoring a strong recent acceleration of research interest.

The distribution pattern suggests a transition from conceptual exploration to methodological refinement and

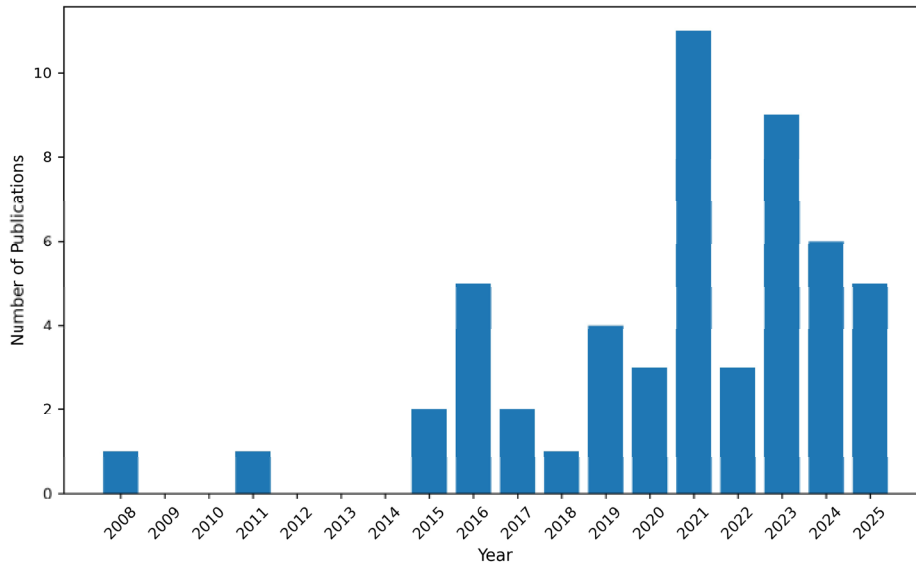


Fig. 2: Annual Publication Trend on Urban Sprawl and Sustainability.

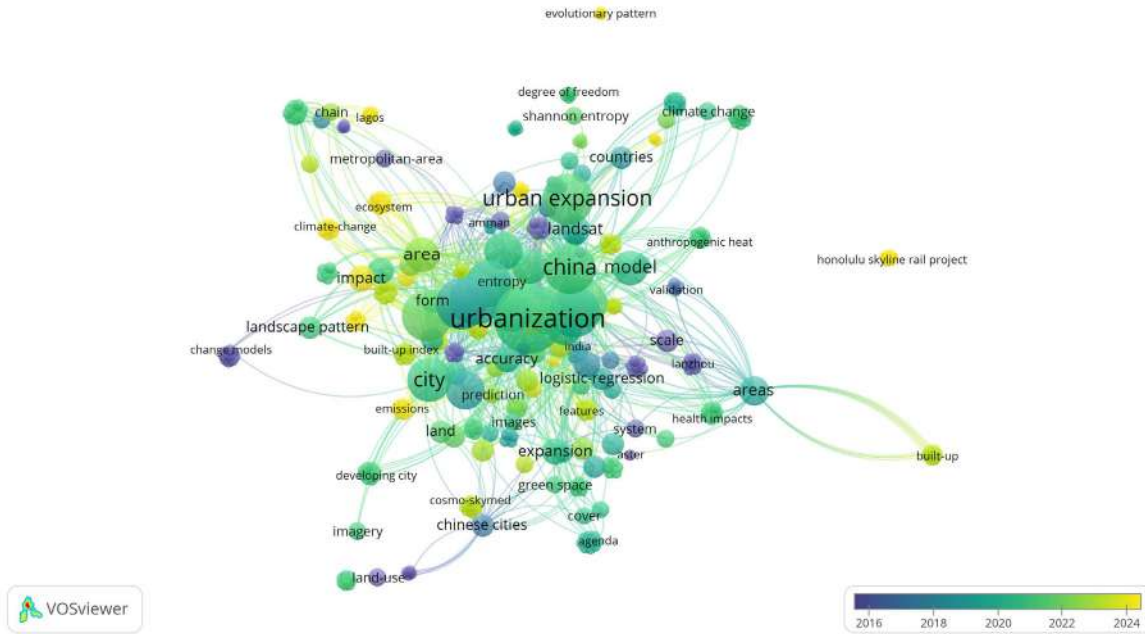


Fig. 3: Overlay Visualization of Keyword Co-Occurrence Network.

large-scale application in recent years. The post-2020 surge may be associated with increased global emphasis, interdisciplinary integration, and policy-driven research expansion within the field.

3.2. Keyword Co-Occurrence and Temporal Evolution (Overlay Visualization)

To explore the intellectual structure and temporal evolution of urban sprawl research, a keyword co-occurrence overlay visualization was generated using VOSviewer (version 1.6.19). The map, presented in Fig. 3, illustrates network connectivity among author keywords and highlights their average publication year using a color gradient.

Before discussing thematic clusters, it is important to note that overlay visualization provides both structural and temporal insights simultaneously. Larger nodes indicate

frequently occurring keywords, while color intensity reflects research recency.

In the overlay visualization, node size represents keyword frequency, link thickness indicates co-occurrence strength, and node color represents average publication year (blue = earlier studies; yellow = recent studies)

As shown in Fig. 3, the keyword co-occurrence network is highly centralized around the terms "urbanization," "urban expansion," "China," "model," "city," and "Landsat," forming a dense and strongly interconnected research core. The size and position of these nodes indicate their dominant frequency and structural importance within the field. The tight interlinkages among methodological terms such as "model," "logistic regression," "scale," and "prediction" suggest that urban sprawl research has been heavily grounded in quantitative spatial modeling frameworks. In particular, the prominence of "China" reflects the geographical concentration of empirical investigations in rapidly urbanizing Chinese metropolitan regions, where large-scale remote sensing datasets and dynamic land transformation processes provide fertile ground for spatial analysis. The overlay color gradient further reveals a clear temporal transition in the intellectual trajectory of the field. Earlier studies, represented in blue to green tones (approximately 2016–2018), primarily emphasized methodological consolidation, focusing on urban growth modeling, logistic regression techniques, scale sensitivity analysis, and accuracy validation using Landsat-based mapping. During the mid-phase (2019–2021), research attention shifted toward morphological and landscape quantification, as evidenced by the clustering of terms such as "entropy," "Shannon entropy," "landscape pattern," "form," "area," and "built-up index." The strong interconnections between "entropy" and "form" indicate sustained reliance on entropy-based indicators for measuring spatial dispersion and fragmentation, while the inclusion of "ecosystem" and related terms reflects increasing integration between landscape ecology and urban morphology.

More recently, the overlay visualization highlights the emergence of sustainability-driven themes, marked by yellow hues corresponding to the 2022–2024 period. Keywords such as "climate change," "anthropogenic heat," "emissions," "health impacts," and "green space" signal a substantive shift from purely morphological assessment toward evaluating the environmental and socio-ecological consequences of urban expansion. The strengthening links between "urban expansion" and climate-related terms demonstrate growing recognition of the sprawl–carbon nexus and its implications for climate mitigation and urban resilience. This thematic evolution indicates that the field is transitioning from examining how cities expand to critically assessing what expansion causes in terms of environmental degradation and human well-being. In addition, peripheral nodes such as "Lagos," "Amman," "Lanzhou," "Honolulu skyline rail project," and "Chinese cities" reflect case-study-driven research across diverse geographic contexts. Although these nodes are less densely connected than the central modeling cluster, they illustrate the application of established methodological frameworks to specific regional and infrastructural settings.

Overall, the overlay visualization reveals three defining structural characteristics: strong centralization around the concept of urbanization, a pronounced China-centric empirical core, and an emerging sustainability orientation. The network density suggests a high degree of methodological cohesion, which may reflect a level of technical consolidation within the field. This interpretation is further supported by the dominance of established modeling approaches identified in the thematic analysis. However, the relative absence of policy-oriented terms such as "smart growth" or "governance" suggests that translation of empirical findings into planning frameworks remains underdeveloped. Taken together, the bibliometric evidence indicates that urban sprawl research has progressed through successive phases of methodological development, spatial-form quantification, and sustainability integration, with future advancement likely to depend on stronger incorporation of governance and policy dimensions.

The interpretations derived from the bibliometric network are further corroborated through qualitative thematic synthesis (Section 3.4) and quantitative comparison (Section 3.5), ensuring that conclusions are not based solely on co-occurrence patterns but supported by multiple lines of evidence.

3.3. Analysis of Country Distribution

The geographical distribution of publications provides insight into regional research leadership, emerging contributors, and global participation patterns within the selected domain. Based on the analysis of 54 publications, research output is concentrated in a limited number of countries, with a clear dominance by Asian nations. As shown in Table 2, research productivity is highly uneven across countries. People's Republic of China leads significantly with 21 publications (38.89%), followed by India with 7 publications (12.96%). In contrast, most other contributing nations exhibit limited publication frequency, indicating that the research field remains regionally concentrated rather than globally distributed.

Together, China and India contribute more than 50% of the total publications, highlighting Asia as the primary research hub in this domain.

Table 2: Global distribution of publications across contributing countries.

Country	Number of Publications	Percentage (%)
People's Republic of China	21	38.89
India	7	12.96
Japan	3	5.56
USA	3	5.56
Australia	2	3.70
Jordan	2	3.70
Italy	2	3.70
Saudi Arabia	2	3.70
Belgium	1	1.85
England	1	1.85
Ethiopia	1	1.85
Germany	1	1.85
Malaysia	1	1.85
Oman	1	1.85
Poland	1	1.85
Portugal	1	1.85
South Africa	1	1.85
Spain	1	1.85
Sri Lanka	1	1.85
Turkey	1	1.85

Japan and the USA each contributed 3 publications (5.56%), demonstrating moderate but consistent research activity. Several countries, including Australia, Jordan, Italy, and Saudi Arabia, show intermediate engagement (3.70% each), suggesting expanding but not yet dominant research presence. The remaining countries contributed single publications (1.85% each), indicating emerging participation. While European representation is geographically diverse, publication volume remains comparatively low. African representation is limited to South Africa and Ethiopia, underscoring a potential geographic research gap.

Overall, the findings suggest a strong regional concentration of research in rapidly urbanizing Asian countries, with limited but geographically dispersed global participation.

3.4. Thematic Content Analysis

The thematic content analysis was conducted based on the 54 studies retained after PRISMA screening. The comprehensive characteristics of these studies are presented in Supplementary Material S1, which includes standardized information on geographic location, primary methodological approach, quantified outcomes, key inferences, and thematic domain classification. The coding procedure integrated methodological descriptions, empirical findings, and analytical objectives to derive four overarching domains: (1) geospatial modeling and urban expansion simulation, (2) spatial form and landscape metrics, (3) environmental and climate-related impacts, and (4) planning and governance dimensions.

The thematic classification reflects both structural patterns observed in the bibliometric network (Fig. 3) and empirical evidence extracted from Supplementary Material S1. Together, these domains illustrate the multidimensional architecture of contemporary urban sprawl research.

3.4.1. Geospatial Modeling and Urban Expansion Simulation

Geospatial modeling constitutes the dominant analytical orientation within the reviewed corpus. Most studies employ satellite-based land use/land cover (LULC) classification combined with spatial simulation frameworks to quantify urban expansion dynamics. Multi-temporal Landsat imagery forms the empirical backbone of numerous investigations, enabling consistent long-term monitoring of built-up growth (Mashagbah 2022, Molla 2024, Pan 2024).

CA–Markov and Cellular Automata modeling approaches are widely applied to simulate future urban expansion scenarios and evaluate spatial suitability patterns. As summarized in Table 3, CA–Markov/Cellular Automata modeling accounts for 40.74% of the reviewed studies, representing the most frequently applied methodological framework. These models integrate transition probability matrices and neighborhood rules to simulate edge expansion and infill processes (Mashagbah 2022, Molla 2024).

Remote sensing change detection approaches (25.93%) further reinforce the modeling core by quantifying historical land conversion trajectories prior to simulation (Gupta et al. 2023, Roy 2021). In several cases, multi-temporal classification demonstrates substantial growth magnitudes. For example, built-up land in Hawassa increased by 573.65% over the study period, accompanied by a 56.81% decline in agricultural land (Molla 2024). Similarly, Himalayan cities such as Dehradun and Shimla experienced expansion exceeding 110% and 138%, respectively (Gupta et al. 2023).

The statistical distribution of extracted expansion magnitudes further reinforces heterogeneity within this domain. The computed skewness (Sk = 1.97) and kurtosis (K = 2.38) indicate a strongly right-skewed and leptokurtic distribution, suggesting that extreme-growth contexts disproportionately influence aggregate expansion statistics.

Model performance metrics also demonstrate high technical reliability. Object-oriented random forest classification achieved 91% overall accuracy with a Kappa

coefficient of 0.86 in long-term urban extraction (Pan 2024). Such performance levels confirm methodological maturity and support the central positioning of "model," "urban expansion," and "Landsat" in Fig. 3.

Thus, both thematic coding and bibliometric structure confirm that urban sprawl research remains strongly anchored in predictive and simulation-based geospatial analysis.

3.4.2. Spatial Form and Landscape Metrics

The second thematic domain focuses on morphological quantification of urban form using entropy indices and landscape metrics. These approaches assess spatial dispersion, fragmentation, and structural heterogeneity rather than solely measuring areal expansion.

Shannon entropy is frequently applied to quantify sprawl intensity and settlement dispersion (Gachowski 2025, Mashagbah 2022, Roy 2021). Longitudinal analyses consistently report increasing entropy values associated with outward diffusion and peri-urban growth phases. Landscape metrics, including patch density, edge density, and connectivity indices, provide additional insight into fragmentation dynamics and transitions between diffusion and coalescence phases (Asempah 2021, Li 2024). While modeling studies emphasize expansion magnitude, spatial-form investigations prioritize configuration and structural organization.

3.4.3. Environmental and Climate-Related Impacts

An expanding subset of studies links urban expansion with environmental and climatic consequences. These investigations integrate remote sensing–derived biophysical indicators such as NDVI, NDBI, NDWI, and LST with growth mapping to assess ecological degradation and thermal intensification (Alqurashi 2016, Dinda 2021).

Significant correlations between land surface temperature and built-up density have been documented (Gupta et al. 2023), confirming the sprawl–heat nexus. In certain high-altitude contexts, accelerated urban expansion has increased ecological instability and landslide risk (Pan 2024). Rapid land conversion has also resulted in substantial agricultural loss, as observed in Ethiopian and Middle Eastern contexts (Mashagbah 2022, Molla 2024).

3.4.4. Planning and Governance Dimensions

The planning and governance domain remains comparatively underrepresented yet conceptually important. Several studies integrate spatial simulation outputs with scenario-based planning frameworks and sustainability recommendations (Criado 2020, Waleed 2023). However, empirical assessment of policy implementation effectiveness remains limited.

Governance-related terms appear less central within the bibliometric network (Fig. 3), and their temporal growth remains modest relative to environmental themes (Fig. 5). This structural asymmetry suggests that urban sprawl research remains predominantly diagnostic rather than prescriptive.

Bridging the gap between technical modeling outputs and institutional reform mechanisms represents a critical direction for future research. While thematic synthesis reveals conceptual structure, quantitative comparison provides empirical magnitude differentiation across contexts.

The planning and governance domain, although comparatively underrepresented, reveals several recurring policy frameworks across the reviewed studies. These include compact city strategies, transit-oriented development (TOD), urban growth boundaries, and landscape-based planning approaches aimed at controlling spatial expansion and improving land-use efficiency. In rapidly urbanizing regions, particularly in Asia, policy recommendations frequently emphasize densification, mixed land use, and infrastructure-led development control. In contrast, studies from Europe and North America more often reference regulatory instruments such as zoning controls, green belts, and growth management policies.

Despite the presence of these frameworks, empirical evaluation of policy effectiveness remains limited. Most studies incorporate governance elements in a prescriptive or scenario-based manner rather than through measurable outcome assessment. This suggests a disconnect between technical modeling capabilities and institutional implementation. Furthermore, governance responses appear highly context-dependent, reflecting differences in regulatory capacity, planning traditions, and socio-economic conditions.

Overall, the reviewed literature indicates that while a range of planning strategies has been proposed to manage urban sprawl, systematic comparative evaluation of their effectiveness remains scarce. Strengthening the integration between geospatial modeling outputs and policy assessment represents a critical direction for future research. Notably, governance approaches differ significantly between regions, with rapidly urbanizing countries emphasizing growth management and infrastructure coordination, while developed regions focus more on containment policies and sustainability-oriented land-use regulation.

3.5. Quantitative Comparative Analysis and Regional Patterns

To complement the thematic synthesis presented in Section 3.4, a statistically grounded quantitative comparative analysis

was undertaken using all extractable numerical indicators from the 54 studies retained following PRISMA screening. Although the reviewed literature exhibits substantial methodological heterogeneity in terms of spatial scale, temporal coverage, and analytical techniques, a sufficient volume of empirical data was available to construct a standardized comparative database. The compiled dataset includes percentage urban expansion, absolute built-up area transitions (reported in km or hectares), annual urban growth rates, magnitudes of land-use conversion, entropy-based dispersion indices, composite urban growth intensity measures derived from multi-indicator frameworks, and modeling performance statistics such as classification or prediction accuracy. These variables were harmonized to enable cross-study comparability and aggregated analysis. The present section applies statistical distribution assessment, regional differentiation, methodological performance evaluation, and temporal trend analysis to synthesize structural patterns within the global urban sprawl literature. By integrating empirical variability across geographic contexts and analytical approaches, this quantitative framework provides a robust, evidence-based interpretation of the magnitude, dynamics, and methodological evolution characterizing contemporary urban expansion research. Out of the 54 studies retained following PRISMA screening, 8 provided fully extractable quantitative indicators, such as percentage built-up growth, annual expansion rates, entropy sequences, or standardized intensity indices, reported with sufficient numerical detail to allow harmonization, statistical aggregation, and calculation of summary distribution metrics (mean, standard deviation, skewness, and kurtosis).

3.5.1. Regional Distribution of Selected Studies

The geographic distribution of the 54 selected studies is illustrated in Fig. 4. Asia accounts for 33 studies (61.11%), representing the dominant geographic focus of empirical urban sprawl research. Europe contributes 9 studies (16.67%), followed by smaller proportions from the Middle East, North America, Africa, and Oceania.

This regional concentration directly corresponds with the bibliometric centrality observed in Fig. 3, where "China" and associated regional keywords occupy a dense and structurally central cluster. Rapid urban transformation across Asian metropolitan systems has generated extensive satellite-based monitoring and modeling initiatives (Du et al. 2021).

However, this geographic imbalance has methodological implications. Because a majority of quantitative datasets originate from Asian contexts, global interpretations of sprawl magnitude and dynamics may be disproportionately influenced by high-growth emerging economies rather than mature urban systems in Europe or North America.

The methodological composition of the reviewed corpus is summarized in Table 3.

As indicated in Table 3, modeling-oriented frameworks dominate the field. CA–Markov and Cellular Automata approaches account for nearly 41% of all studies, confirming that predictive simulation and spatial suitability modeling

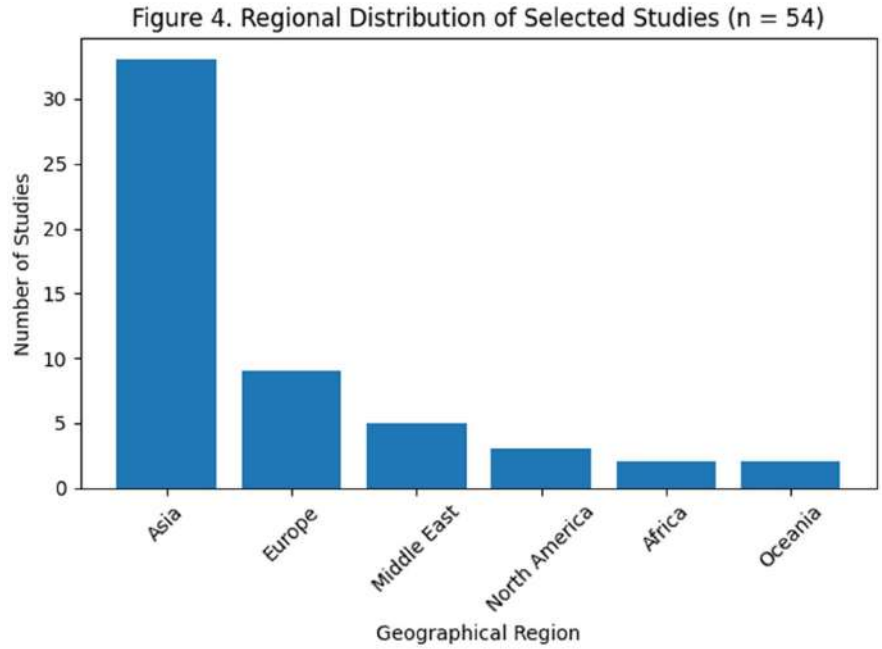


Fig. 4: Regional Distribution of Selected Studies (n = 54).

Table 3: Distribution of Primary Methodological Approaches (n = 54).

Primary Methodological Approach	Frequency	Percentage (%)
CA–Markov/Cellular Automata Modeling	22	40.74
Remote Sensing Change Detection	14	25.93
Entropy/Landscape Metrics	7	12.96
Geospatial Analysis	5	9.26
Supervised LULC Classification	4	7.41
Spatial Regression/GWR	2	3.70

represent the primary analytical paradigm. Remote sensing change detection constitutes the second-largest group, reinforcing the centrality of Landsat-based monitoring observed in Fig. 3.

The comparatively limited representation of spatial regression techniques (3.70%) suggests underutilization of advanced econometric modeling approaches capable of isolating socioeconomic drivers of sprawl. While geographically weighted regression (GWR) offers localized explanatory capacity, it remains marginal relative to simulation-based modeling.

This methodological imbalance reveals a structural asymmetry: the field demonstrates strong capacity for spatial prediction and classification but comparatively weaker emphasis on causal inference and governance-driven evaluation.

3.5.2. Urban Expansion Magnitudes: Absolute and Relative Growth

Several studies report precise built-up area transitions, enabling absolute magnitude comparison.

In Hawassa, Ethiopia, built-up land expanded from 584.73 ha to 3,939.03 ha, representing a total increase of 573.65%, with an annual growth rate of 15.50% (Molla 2024). During this period, 3,148.74 ha of agricultural land were converted to built-up areas, corresponding to a 56.81% agricultural loss rate. Future projections estimate expansion to 5,009.85 ha by 2030 and 6,794.73 ha by 2050, indicating sustained growth momentum.

In Dehradun, India, built-up area increased from 32.19 km to 68.37 km, a 112.4% increase, while Shimla expanded from 12.38 km to 29.47 km, representing a 138.0% increase (Gupta et al. et al. 2023). These transitions illustrate rapid urbanization in ecologically sensitive mountainous regions.

In Irbid, Jordan, expansion rates demonstrate deceleration: 19.22% (2000–2010) followed by 8.04% (2010–2020) (Al-Bilbisi 2019), suggesting emerging spatial saturation dynamics.

In Raiganj, India, built-up share increased from 4.30% to 20.25%, a rise of 15.95 percentage points, indicating significant structural transformation of urban morphology (Roy 2021).

Due to substantial heterogeneity in reporting formats across the reviewed literature, only a subset of studies provided directly comparable percentage-based urban expansion data suitable for statistical aggregation. Therefore, the quantitative synthesis presented in this section is based on a limited sample (n = 8) and should be interpreted as a descriptive and exploratory analysis of comparable cases, rather than a statistically representative meta-analysis of the entire dataset.

Within the subset of studies reporting comparable percentage-based expansion values (n = 8), the calculated mean expansion is 119.70%, with high variability (standard deviation = 190.07). The distribution exhibits positive skewness (Sk = 1.97) and leptokurtic characteristics (K = 2.38), indicating the presence of extreme values within the sample.

The observed positive skewness suggests that extreme-growth contexts may disproportionately influence the calculated average within this limited sample. The leptokurtic distribution (K > 0) indicates heavy tails and frequent outliers.

The 573.65% increase in Hawassa (Molla 2024) functions as a statistical extreme, while moderate-growth cases such as Irbid (8–19%) illustrate slower expansion trajectories. This heterogeneity reinforces the conclusion that urban sprawl intensity is structurally uneven and regionally contingent.

Such distributional properties justify the use of boxplot visualization and robust statistics rather than relying solely on arithmetic means. However, these statistical measures are derived from a small subset of studies and are sensitive to outliers, particularly cases with exceptionally high expansion rates (e. g., >500%). Therefore, these values should not be interpreted as global benchmarks but rather as indicative of the variability and asymmetry present in reported urban expansion patterns.

3.5.3. Land Conversion Intensity and Agricultural Loss

The Hawassa case provides one of the most comprehensive land conversion datasets. The conversion of 3,148.74 ha of agricultural land into built-up area represents both spatial expansion and functional transformation of land systems (Molla 2024).

In Dehradun and Shimla, urban expansion coincided with measurable increases in land surface temperature (LST), with statistically significant correlations between LST and built-up indices ($p < 0.05$) (Jaswal & Thakur 2023, Olokeogun

2020). These findings illustrate the linkage between land conversion and environmental intensification.

Thus, expansion magnitude cannot be interpreted independently from functional land-use change. High expansion percentages frequently correspond with agricultural displacement and ecological fragmentation.

3.5.4. Intensity Index Standardization: UHE and UVE

Beyond area-based metrics, multi-index growth intensity indicators provide standardized comparative measures.

In the Beijing–Tianjin–Hebei region, the Urban Horizontal Expansion index (UHE) increased from 0.44 to 0.50, while the Urban Vertical Expansion index (UVE) increased from 0.30 to 0.53, with suburban UVE rising from 0.35 to 0.60 (Li 2025, Li 2011).

These values indicate a transition from predominantly horizontal sprawl toward increased vertical densification in suburban areas. Unlike absolute area growth, index-based measures enable cross-city normalization and structural comparison.

The inclusion of such standardized intensity metrics strengthens quantitative synthesis by moving beyond raw percentage growth toward structural differentiation of growth typologies.

3.5.5. Entropy and Spatial Dispersion Metrics

Entropy values provide insight into spatial configuration rather than magnitude.

In Saudi Arabia, Shannon entropy increased sequentially from 0.700 to 0.779 to 0.840, indicating progressive spatial dispersion and increasing sprawl intensity (Alqurashi 2016). This numeric series represents the only fully extractable entropy progression from abstract-level data.

Other studies (Feng et al. 2016, Hanoon 2023, Kara 2021) report high entropy levels qualitatively but do not provide explicit numeric sequences in abstracts. This highlights a limitation of abstract-based quantitative synthesis.

The entropy trajectory from 0.700 to 0.840 suggests substantial movement toward spatial disorder, approaching upper dispersion thresholds in sprawl measurement literature.

3.5.6. Modeling Accuracy and Technical Reliability

Model performance metrics provide an important dimension of quantitative synthesis. (Pan 2024) report 91% overall classification accuracy with a Kappa coefficient of 0.86, indicating strong agreement beyond chance.

A PLS-CA model achieved 85.8% accuracy, compared to 83.5% for a logistic-regression-based CA model (Feng et al. 2016). These values demonstrate consistent performance across simulation-based frameworks.

The relatively narrow accuracy range (83–91%) suggests methodological stability and technical maturity within geospatial modeling approaches.

3.5.7. Temporal Shift in Research Emphasis

Fig. 5 illustrates the longitudinal evolution of thematic priorities within the 54 selected studies, organized into three sequential research phases. The figure reveals a clear structural transformation in the intellectual orientation of urban sprawl scholarship, reflecting both methodological consolidation and thematic diversification.

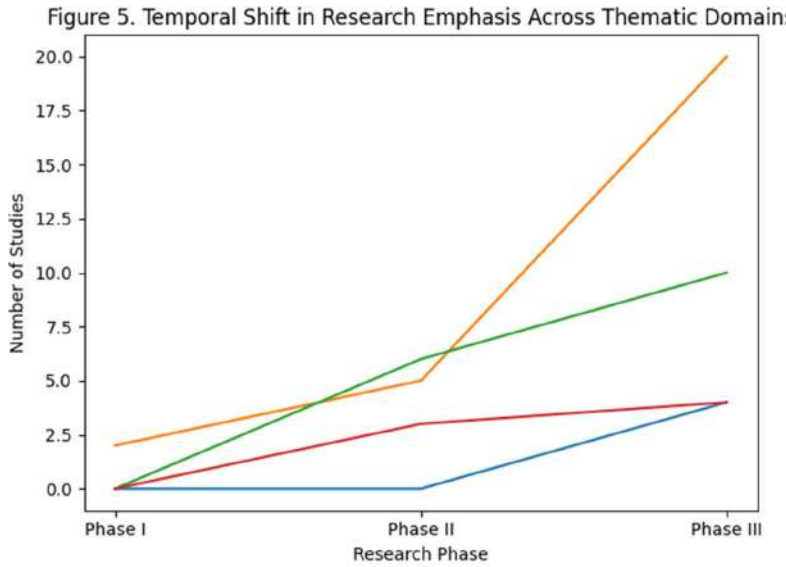


Fig. 5: Temporal Shift in Research Emphasis Across Thematic Domains.

In Phase I, research activity is overwhelmingly concentrated in geospatial modeling and urban expansion simulation. Studies during this period primarily focused on multi-temporal Landsat classification, supervised LULC mapping, and the development of Cellular Automata–based predictive frameworks (Alqurashi 2016, Feng et al. 2016, Li 2011). Emphasis was placed on classification accuracy, spatial validation, and methodological robustness (Ding 2022a, Shao 2021), indicating that the central objective was reliable detection and quantification of built-up growth. Environmental and governance-oriented studies were comparatively limited, suggesting that early scholarship prioritized spatial measurement over socio-ecological interpretation.

In Phase II, the thematic landscape becomes more diversified. There is a noticeable rise in studies applying entropy indices and landscape metrics to examine fragmentation, dispersion, and morphological transformation (Magidi 2019, Manesha 2021, Rahman 2016). This shift signals growing integration of landscape ecology principles into urban growth analysis. Concurrently, environmental impact studies gain visibility, linking expansion dynamics with land surface temperature variability, agricultural land conversion, and ecosystem change (Criado 2020, Gupta et al. 2023, Yan 2021). Although modeling remains dominant, research increasingly moves beyond "how much cities expand" toward "how expansion alters ecological systems."

In Phase III, Fig. 5 shows sharp acceleration in modeling studies alongside sustained growth in environmental research. Advanced hybrid modeling approaches and multi-decadal simulations become more prevalent (Asempah 2021, Kara 2021), while climate-oriented analyses, such as carbon emissions, anthropogenic heat flux, and vertical–horizontal expansion indices, gain prominence (Deng et al. 2024, Zhang 2023). This phase reflects a paradigmatic shift toward consequence-oriented inquiry, framing urban sprawl as a socio-ecological transformation rather than solely a spatial phenomenon.

Despite incremental growth, governance and planning research remains comparatively underrepresented across all phases. While several studies recommend sustainable planning strategies (Hanoon 2023, Karimi et al. 2023), empirical evaluation of policy effectiveness remains limited. Thus, Fig. 5 not only demonstrates thematic diversification but also highlights a persistent imbalance between technical modeling capacity and governance translation. Overall, the temporal trajectory captured in Fig. 5 reflects intellectual maturation: the field has evolved from methodological establishment to morphological analysis and, more recently, to sustainability integration. However, the continued dominance of modeling research suggests that future scholarship must strengthen institutional and policy-oriented dimensions to achieve more holistic urban resilience frameworks (Koko 2021, Luo 2008, Zhang 2021).

Fig. 6 presents an integrated conceptual synthesis derived from thematic coding, quantitative comparison, and bibliometric structure. The figure presents a conceptual framework illustrating the integrated structure of urban growth and spatial analysis within the domains of remote sensing and GIS. At the core, the framework positions urban expansion analysis as a multidisciplinary process supported by five interrelated components: methodologies and classification techniques, statistical and spatial modeling approaches, geospatial data sources, urban growth dynamics, and environmental as well as socio-ecological impacts (Fenta 2017, Franci 2015, Megahed 2015, Shrestha 2025). The methodological layer highlights widely used classification and machine learning approaches, including Maximum Likelihood Classification, Random Forest, k-Nearest Neighbors (kNN), and Artificial Neural Networks (ANN), which enable accurate extraction of built-up information from satellite imagery (Gilbert 2024, Kara 2021, Marzialetti 2023). These techniques are complemented by advanced spatial and predictive modeling tools such as Geographically Weighted Regression (GWR), Cellular Automata (CA), and Markov Chain models, which are employed to simulate spatial transitions and forecast urban expansion patterns (Lu 2023, Torres 2024).

The analytical framework relies heavily on multi-source geospatial datasets, including Landsat series (TM, ETM+, OLI), Sentinel missions, nighttime light data, and OpenStreetMap, reflecting the increasing integration of multi-temporal and multi-resolution data environments (Aqdas 2025, Ngolo 2023, Niang 2020). Using these datasets, studies examine urban growth dynamics through typological characterization of spatial expansion processes, primarily infilling, edge expansion, and leapfrogging or outgrowth. These growth forms are further evaluated using landscape-based spatial metrics such as fragmentation, patch size density, and landscape connectivity, which provide quantitative insights into urban form and spatial structure.

Beyond spatial characterization, the framework links urban expansion patterns to broader environmental and social consequences (Shaw 2018, Ul Din 2021, Zubair 2019). Key impacts include the intensification of the UHI effect, increased urban flood risk due to land surface modification, and alterations in ecosystem productivity, particularly Net Primary Productivity (NPP) (Ding 2022b, MacLachlan 2017, Prakash 2023). The figure also emphasizes the global applicability of these analytical approaches through

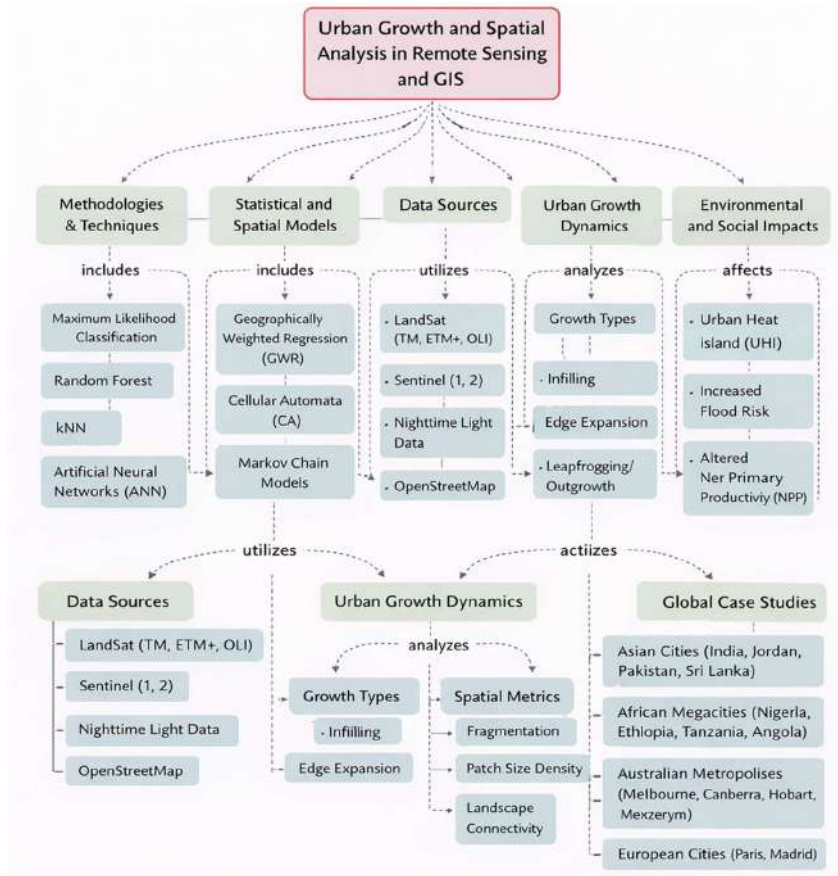


Fig. 6: Conceptual framework of urban growth and spatial analysis in remote sensing and GIS.

representative case study regions, including rapidly growing Asian cities (e. g., India, Pakistan, Sri Lanka, and Jordan), emerging African megacities (e. g., Nigeria, Ethiopia, Tanzania, and Angola), Australian metropolitan regions, and major European urban centers such as Paris and Madrid. Overall, the framework synthesizes the methodological, data-driven, analytical, and impact-oriented dimensions of contemporary urban sprawl research, highlighting the systematic workflow and global relevance of remote sensing–based urban growth assessment (Al-Hameedi 2021, Kantakumar 2019, Subasinghe 2016, Trinder 2020).

4. DISCUSSION

The present systematic and bibliometric synthesis reveals a technically consolidated yet structurally uneven body of scholarship on urban sprawl. By integrating PRISMA-based screening, bibliometric network visualization, and quantitative comparative analysis, this review provides a multi-layered interpretation of the field's intellectual architecture. The results demonstrate that urban sprawl research is strongly anchored in geospatial modeling, increasingly connected to environmental sustainability concerns, regionally concentrated in Asian contexts, and comparatively limited in its empirical engagement with governance effectiveness. These findings carry important theoretical, methodological, and policy implications. The quantitative patterns identified in this study should be interpreted with caution due to limited data comparability across studies. Variability in reporting formats, spatial units, and measurement approaches restricts large-scale statistical generalization. Consequently, the derived distributional metrics represent indicative trends rather than definitive global estimates.

4.1. Structural Evolution of the Field

The bibliometric structure illustrated in Fig. 3 reveals a highly centralized knowledge network dominated by terms such as "urbanization," "urban expansion," "model," and "Landsat." This centralization indicates that predictive modeling and satellite-based land use classification have become the defining analytical core of the discipline. The methodological distribution summarized in Table 3

reinforces this interpretation, showing that Cellular Automata and CA–Markov modeling frameworks account for the largest proportion of empirical investigations. Studies across diverse geographic contexts, including Xining (Pan 2024), Hawassa (Molla 2024), and Dehradun (Gupta et al. 2023), illustrate how simulation-based approaches are routinely employed to quantify past growth and forecast future expansion trajectories.

The temporal progression displayed in Fig. 5 further demonstrates intellectual maturation within the field. Earlier research phases were primarily concerned with spatial detection, classification accuracy, and expansion quantification. Over time, however, the thematic emphasis has gradually shifted toward environmental and climate-related consequences of sprawl (Kumar & Shukla 2022). This evolution indicates that the research community has moved beyond descriptive mapping toward evaluative analysis of impacts. Nevertheless, governance-related scholarship remains comparatively underrepresented in both the bibliometric network and temporal trend analysis. While sustainability discourse has expanded, empirical examination of institutional interventions and regulatory performance remains limited.

The regional concentration presented in Fig. 4 reveals that more than half of the selected studies originate from Asian contexts (Halder & Kumar 2025). Rapid urban transformation in China, India, and neighboring countries has generated substantial empirical attention (Pan 2024, Zhao 2021). Although this concentration reflects the intensity of contemporary urbanization processes, it also shapes the global narrative of sprawl. Theoretical generalizations drawn from high-growth metropolitan regions may not fully capture dynamics in slower-growth or post-industrial urban systems. Thus, the structural evolution of the field is closely intertwined with geographic research priorities. While bibliometric analysis provides valuable insight into the structural organization of the research field, it does not, in itself, establish causal relationships between concepts or research trends. Accordingly, the interpretations presented in this study are based on an integrative approach combining bibliometric patterns with thematic and quantitative evidence.

4.2. Theoretical Implications for Urban Sprawl Research

4.2.1. Rethinking Sprawl as Systemic Land Transformation

Traditionally, urban sprawl has been conceptualized as low-density outward expansion characterized by spatial dispersion and fragmentation. Entropy-based analyses in the reviewed literature support this interpretation, as increasing entropy values indicate greater spatial disorder and diffusion (Rahman 2016, Roy 2021). However, the quantitative evidence compiled in Section 3.5 suggests that sprawl should be reinterpreted as a systemic land transformation process rather than merely spatial dispersion.

The heterogeneity of expansion magnitudes illustrates this complexity. Hawassa experienced a 573.65% increase in built-up area, expanding from 584.73 ha to 3,939.03 ha while converting 3,148.74 ha of agricultural land (Molla 2024). By contrast, Irbid exhibited more moderate expansion phases of 19.22% and 8.04% (Mashagbah 2022). Dehradun and Shimla expanded by 112.4% and 138.0%, respectively (Gupta et al. 2023), demonstrating rapid transformation in mountainous ecosystems. The statistical skewness of the distribution confirms that urban expansion is structurally uneven and driven by high-growth frontier cities rather than uniform global trends.

Moreover, index-based measures such as the Urban Horizontal Expansion (UHE) and Urban Vertical Expansion (UVE) indices complicate traditional definitions of sprawl. (Zhao 2021, Zhao et al. 2021) observed modest horizontal expansion increases but significant vertical intensification in suburban areas. These findings suggest that sprawl dynamics encompass both horizontal diffusion and vertical densification, challenging binary classifications of compact versus dispersed development. Theoretically, urban growth should therefore be understood as a multidimensional restructuring of land systems involving magnitude, configuration, intensity, and functional transformation.

4.2.2. Environmental Coupling and Climate Feedback

A second major theoretical implication concerns the integration of environmental consequences into sprawl analysis. The increasing presence of climate-related keywords in Fig. 3 and the temporal shift shown in Fig. 5 demonstrate that environmental impact assessment has become a central research frontier. Empirical studies report significant correlations between land surface temperature and built-up density, as well as increased ecological vulnerability associated with high-altitude expansion. Agricultural displacement in rapidly expanding cities further underscores the socio-ecological consequences of sprawl (Molla 2024).

Despite these advances, quantitative integration of climate metrics remains incomplete. While qualitative linkages between sprawl and environmental degradation are strong, explicit numeric indicators, such as standardized temperature increases per hectare of built-up expansion, are rarely reported at the abstract level. Entropy progression values, such as the increase from 0.700 to 0.840 documented by Rahman (2016), illustrate morphological dispersion but do not directly quantify ecological impact. Theoretical

frameworks must therefore move toward integrated socio-ecological modeling that links expansion magnitude, morphological structure, and environmental feedback loops within a unified analytical system.

4.2.3. Multi-Scale Urban Growth Dynamics

Urban sprawl operates across multiple spatial and institutional scales. Parcel-level land conversion, metropolitan expansion corridors, regional infrastructure networks, and national development policies interact dynamically to shape growth trajectories. Although Cellular Automata models effectively simulate neighborhood-level transitions, few studies explicitly integrate cross-scale causal mechanisms. (Luo 2008) demonstrated that geographically weighted regression can reveal localized infrastructure-driven expansion patterns, yet such econometric approaches remain relatively rare in the broader corpus.

The conceptual framework presented in Fig. 6 illustrates the layered structure of urban growth analysis, linking satellite data acquisition, spatial modeling, morphological assessment, environmental consequence evaluation, and governance translation. However, theoretical articulation of cross-scale feedback mechanisms remains underdeveloped. Bridging micro-level land conversion with macro-level institutional and economic processes constitutes a significant opportunity for future research.

4.3. Methodological Implications and Analytical Gaps

The high classification accuracies reported across multiple studies, ranging from approximately 83% to 91% (Feng et al. 2016), indicate strong methodological reliability. Remote sensing archives and machine learning classification techniques have significantly enhanced temporal consistency and spatial precision. This technical maturity strengthens confidence in quantitative expansion metrics.

However, the dominance of simulation-based frameworks also reveals methodological imbalance. While CA–Markov models excel in projecting spatial patterns, they often rely on transition probabilities without fully disentangling socioeconomic drivers. The limited representation of spatial regression techniques (Luo 2008) suggests that causal inference remains secondary to predictive simulation. Integrating econometric modeling, demographic analysis, and infrastructure investment data would provide deeper explanatory insight.

Another analytical gap concerns standardized environmental quantification. Although studies consistently link expansion with thermal intensification and ecological degradation (Gupta et al. 2023, Pan 2024), the absence of harmonized environmental indicators restricts cross-case comparability. A full-text meta-analysis incorporating explicit temperature, carbon emission, and ecosystem service metrics would substantially strengthen quantitative synthesis.

It is important to note that the observed geographic and thematic patterns may be partially influenced by database selection and search strategy constraints. Inclusion of additional databases such as Scopus or Dimensions could potentially expand regional representation and thematic diversity. Therefore, the findings should be interpreted as reflective of a high-quality but selectively filtered corpus rather than an exhaustive global inventory.

4.4. Policy Translation and Governance Challenges

Perhaps the most significant structural gap identified in this review is the limited translation of modeling outputs into empirically validated governance strategies. Many studies conclude with recommendations for sustainable planning or smart growth frameworks (Molla 2024, Roy 2021), yet few evaluate the measurable effectiveness of such interventions. The bibliometric network (Fig. 3) and temporal evolution (Fig. 5) confirm that governance-oriented research remains peripheral relative to modeling and environmental assessment.

This diagnostic–prescriptive divide raises important policy questions. Accurate prediction of expansion trajectories does not automatically translate into effective containment strategies. Evaluating urban growth boundaries, zoning reforms, transit-oriented development, and green infrastructure policies requires integration of spatial analytics with institutional analysis. Without such integration, urban sprawl research risks remaining primarily descriptive.

Regional differentiation further complicates policy translation. High-growth frontier cities experiencing triple-digit expansion rates require distinct policy approaches compared to slower-growth or stabilized metropolitan systems. The skewed distribution of expansion magnitudes suggests that governance frameworks must be context-sensitive and adaptive rather than uniform. The limited empirical evaluation of policy effectiveness represents a structural imbalance within the current research landscape.

A comparative reading of the reviewed studies suggests that governance approaches to urban sprawl can be broadly grouped into three categories: (1) regulatory instruments (e. g., zoning, urban growth boundaries, green belts), (2) strategic planning frameworks (e. g., compact city models, polycentric development, TOD), and (3) data-driven or model-supported planning approaches. While these frameworks are widely discussed, their empirical effectiveness is rarely quantified. This reinforces the observation that urban sprawl research

remains predominantly diagnostic, with limited transition toward evidence-based policy evaluation.

4.5. Future Research Directions

The findings of this review highlight several structural priorities for advancing urban sprawl scholarship. First, greater standardization of environmental indicators is required to enable cross-case comparability. Although numerous studies link expansion with thermal intensification, ecological degradation, and land conversion, harmonized metrics for land surface temperature, carbon emissions, and ecosystem service loss remain limited, constraining quantitative synthesis.

Second, methodological diversification is needed beyond simulation-based modeling. While CA–Markov frameworks dominate predictive analysis, greater incorporation of spatial econometrics and regression-based approaches would strengthen causal inference regarding socioeconomic and infrastructural drivers of expansion. Third, cross-scale analytical integration should be enhanced. Urban sprawl operates simultaneously at parcel, metropolitan, and regional scales, yet few studies explicitly link micro-level land transitions with macro-level institutional and policy dynamics. Finally, empirical evaluation of planning and governance instruments remains underdeveloped. Bridging the gap between predictive modeling and policy implementation requires systematic assessment of urban growth boundaries, zoning reforms, and transit-oriented development strategies in measurable terms.

5. CONCLUSIONS

This study provides a structured and evidence-based synthesis of global urban sprawl research through integration of PRISMA-guided screening, bibliometric mapping, quantitative comparison, and thematic analysis. From an initial pool of 183 records, 54 peer-reviewed studies were retained, forming a rigorously screened corpus for analysis. The findings reveal a technically mature yet structurally uneven field shaped by methodological consolidation, geographic concentration, and evolving sustainability integration. Geospatial modeling clearly dominates the analytical landscape. Cellular Automata and CA–Markov approaches account for 40.74% of reviewed studies, followed by remote sensing change detection (25.93%), while spatial regression techniques remain marginal (3.70%). Reported classification accuracies consistently range between 83% and 91%, confirming high technical reliability in urban land extraction and predictive simulation. However, this methodological dominance reflects a predictive orientation that often emphasizes spatial forecasting over causal or institutional explanation.

Quantitative synthesis demonstrates substantial heterogeneity in urban expansion magnitudes. Across extractable cases, mean built-up growth within the subset of comparable studies reached 119.7%, with a strongly right-skewed distribution (Sk = 1.97; K = 2.38), indicating that extreme-growth contexts disproportionately influence aggregate statistics. Reported expansion ranges from moderate increases below 20% to cases exceeding 500%, frequently accompanied by large-scale agricultural land conversion and measurable land surface temperature intensification. These findings confirm that urban sprawl operates as a context-dependent land transformation process rather than a uniform global pattern. Geographically, research output remains heavily concentrated in Asia (61.11%), particularly in China and India, limiting broader cross-regional generalization. Bibliometric overlay analysis further indicates a thematic shift toward climate change, ecosystem degradation, and environmental impacts, whereas governance-oriented research and empirical policy evaluation remain comparatively underdeveloped. From a policy perspective, the study highlights that although a variety of planning frameworks, such as compact development, transit-oriented strategies, and growth management policies, are frequently proposed, their empirical validation remains limited. Bridging this gap represents a key opportunity for advancing both research and practice. Overall, urban sprawl scholarship demonstrates strong analytical capacity in spatial detection and simulation but limited integration of cross-scale governance assessment. Advancing the field will require greater incorporation of spatial econometrics, standardized environmental indicators, and systematic evaluation of planning interventions to bridge the gap between predictive modeling and sustainable urban policy implementation.

6. ACKNOWLEDGMENTS

The authors would like to express their sincere gratitude to all the researchers whose work was reviewed and synthesized in this study. Their valuable contributions have shaped the knowledge base surrounding urban sprawl and sustainability. We also acknowledge the use of VOSviewer software for the bibliometric analysis, which provided critical insights into thematic trends and research networks. Special thanks are extended to the institutions and libraries that provided access to academic databases, making the systematic literature review possible. Finally, the authors appreciate the support and feedback received from colleagues and academic peers throughout the development of this manuscript.

Data Availability Statement: The Supplementary information is available at https://doi.org/10.6084/m9.figshare.33372463

7. REFERENCES

Al-Bilbisi, H., 2019. Spatial monitoring of urban expansion using satellite remote sensing images: A case study of Amman city, Jordan. *Sustainability*, 11(8), p.2260. [DOI]

Al-Hameedi, W.M.M., Chen, J., Faichia, C., Al-Shaibah, B., Nath, B., Kafy, A.-A., Hu, G. and Al-Aizari, A., 2021. Remote sensing-based urban sprawl modeling using multilayer perceptron neural network Markov chain in Baghdad, Iraq. *Remote Sensing*, 13(20), p.4034. [DOI]

Alqurashi, A.F., Kumar, L. and Sinha, P., 2016. Urban land cover change modelling using time-series satellite images: A case study of urban growth in five cities of Saudi Arabia. *Remote Sensing*, 8(10), p.838. [DOI]

Angel, S., Parent, J., Civco, D.L., Blei, A.M. and Potere, D., 2011. The dimensions of global urban expansion: Estimates and projections for all countries, 2000–2050. *Progress in Planning*, 75(2), pp.53-107. [DOI]

Aqdas, M., Usmani, T.M., Benhizia, R. and Szabó, G., 2025. Urban expansion and thermal stress: A remote sensing analysis of LULC and urban heat islands in Ghaziabad, India. *Land*, 14(9), p.1893. [DOI]

Artmann, M., Inostroza, L. and Fan, P., 2019. Urban sprawl, compact urban development and green cities. *How much do we know, how much do we agree? Ecological Indicators*, 96, pp.3-9. [DOI]

Asempah, M., Sahwan, W. and Schütt, B., 2021. Assessment of land cover dynamics and drivers of urban expansion using geospatial and logistic regression approach in Wa municipality, Ghana. *Land*, 10(11), p.1251. [DOI]

Bhatta, B., 2009. Analysis of urban growth pattern using remote sensing and GIS: A case study of Kolkata, India. *International Journal of Remote Sensing*, 30(18), pp.4733-4746. [DOI]

Bosch, M., Locatelli, M., Hamel, P., Remme, R.P., Jaligot, R., Chenal, J. and Joost, S., 2021. Evaluating urban greening scenarios for urban heat mitigation: A spatially explicit approach. *Royal Society Open Science*, 8(12), p.202174. [DOI]

Castellani, V. and Sala, S., 2012. Ecological footprint and life cycle assessment in the sustainability assessment of tourism activities. *Ecological Indicators*, 16, pp.135-147. [DOI]

Chaudhuri, S. and Kumar, A., 2022. Urban greenery for air pollution control: A meta-analysis of current practice, progress, and challenges. *Environmental Monitoring and Assessment*, 194(4), p.235. [DOI]

Criado, M., Santos-Francés, F., Martínez-Graña, A., Sánchez, Y. and Merchán, L., 2020. Multitemporal analysis of soil sealing and land use changes linked to urban expansion of Salamanca (Spain) using Landsat images and soil carbon management as a mitigating tool for climate change. *Remote Sensing*, 12(7), p.1131. [DOI]

Deng, X., Cao, Q., Wang, L., Wang, W., Li, H. and Wang, S., 2024. The thermal environmental effects of changes in urban green space: A mesoscale modelling perspective. *Applied Geography*, 169, p.103338. [DOI]

Dinda, S., Das Chatterjee, N. and Ghosh, S., 2021. An integrated simulation approach to the assessment of urban growth pattern and loss in urban green space in Kolkata, India: A GIS-based analysis. *Ecological Indicators*, 121, p.107178. [DOI]

Ding, L., Zhang, H. and Li, D., 2022a. Monitoring and analysis of urban sprawl based on road network data and high-resolution remote sensing imagery: A case study of China's provincial capitals. *Photogrammetric Engineering & Remote Sensing*, 88(7), pp.479-485. [DOI]

Ding, Q., Shao, Z., Huang, X., Altan, O. and Hu, B., 2022b. Time-series land cover mapping and urban expansion analysis using OpenStreetMap data and remote sensing big data: A case study of Guangdong-Hong Kong-Macao Greater Bay Area, China. *International Journal of Applied Earth Observation and Geoinformation*, 113, p.103001. [DOI]

Du, H., Zhou, F., Cai, W., Cai, Y. and Xu, Y., 2021. Thermal and humidity effect of urban green spaces with different shapes: A case study of Shanghai, China. *International Journal of Environmental Research and Public Health*, 18(11), p.5941. [DOI]

Ewing, R. and Hamidi, S., 2015. Compactness versus sprawl: A review of recent evidence from the United States. *Journal of Planning Literature*, 30(4), pp.413-432. [DOI]

Feng, Y., Liu, M., Chen, L. and Liu, Y., 2016. Simulation of dynamic urban growth with partial least squares regression-based cellular automata in a GIS environment. *ISPRS International Journal of Geo-Information*, 5(12), p.243. [DOI]

Fenta, A.A., Yasuda, H., Haregeweyn, N., Belay, A.S., Hadush, Z., Gebremedhin, M.A. and Mekonnen, G., 2017. The dynamics of urban expansion and land use/land cover changes using remote sensing and spatial metrics: The case of Mekelle City of northern Ethiopia. *International Journal of Remote Sensing*, 38(14), pp.4107-4129. [DOI]

Franci, F., Mandanici, E. and Bitelli, G., 2015. Remote sensing analysis for flood risk management in urban sprawl contexts. *Geomatics, Natural Hazards & Risk*, 6(5–7), pp.583-599. [DOI]

Fu, J., Dupré, K., Tavares, S., King, D. and Banhalmi-Zakar, Z., 2022. Optimized greenery configuration to mitigate urban heat: A decade systematic review. *Frontiers of Architectural Research*, 11(3), pp.466-491. [DOI]

Gachowski, M. and Walusiak, Ł., 2025. Urban phenomena in Lesser Poland through GIS-based metrics: An exceptional form of urban sprawl challenging sustainable development. *Sustainability*, 17(21), p.9394. [DOI]

Ghosh, S., Kumar, D. and Kumari, R., 2022. Assessing spatiotemporal dynamics of land surface temperature and satellite-derived indices for new town development and suburbanization planning. *Urban Governance*, 2(1), pp.144-156. [DOI]

Gilbert, K.M. and Shi, Y., 2024. Urban growth monitoring and prediction using remote sensing urban monitoring indices approach and integrating CA-Markov model: A case study of Lagos City, Nigeria. *Sustainability*, 16(1), p.30. [DOI]

Güneralp, B., Lwasa, S., Masundire, H., Parnell, S. and Seto, K.C., 2018. Urbanization in Africa: Challenges and opportunities for conservation. *Environmental Research Letters*, 13(1), p.015002. [DOI]

Gupta, R., Sharma, M., Singh, G. and Joshi, R.K., 2023. Characterizing urban growth and land surface temperature in the western Himalayan cities of India using remote sensing and spatial metrics. *Frontiers in Environmental Science*, 11, p.1122935. [DOI]

Halder, N. and Kumar, D., 2025. Towards reviving vernacular architecture in India: Insights into the indigenous building traditions. *Journal of the International Society for the Study of Vernacular Settlements*, 12(5), pp.40-54. [DOI]

Halder, N., Kumar, M., Deepak, A., Abuwaer, N.M., Kanwal, Q., Nurdiawati, A. and Al-Ghamdi, S.G., 2026. Urban greenery and outdoor thermal comfort: Cooling indicators, mechanisms, and equity implications. *Environmental Research Communications*, 8(5), p.052006. [DOI]

Halder, N., Kumar, M., Deepak, A., Kumar, D., Yasmin, N., Ullah, S. and Al-Ghamdi, S.G., 2025. Spatiotemporal assessment of urban thermal discomfort in Kolkata, India: Insights from cloud-based remote sensing. *IEEE Journal of Selected Topics in Applied Earth Observations and Remote Sensing*, 18, pp.24174-24187. [DOI]

Halder, N., Kumar, M., Deepak, A., Mandal, S.K., Azmeer, A., Mir, B.A., Nurdiawati, A. and Al-Ghamdi, S.G., 2025. The role of urban greenery in enhancing thermal comfort: Systematic review insights. *Sustainability*, 17(6), p.2545. [DOI]

Halefom, A., He, Y., Nemoto, T., Feng, L., Li, R., Raghavan, V., Jing, G., Song, X. and Duan, Z., 2024. The impact of urbanization-induced land use change on land surface temperature. *Remote Sensing*, 16(23), p.4502. [DOI]

Hanoon, S.K., Abdullah, A.F., Shafri, H.Z.M. and Wayayok, A., 2023. Urban growth forecast using machine learning algorithms and GIS-based novel techniques: A case study focusing on Nasiriyah City, southern Iraq. *ISPRS International Journal of Geo-Information*, 12(2), p.76. [DOI]

Jaswal, S. and Thakur, P., 2023. Correlation between LST, NDVI and

NDBI with reference to urban sprawling: A case study of Shimla City. *International Journal for Multidisciplinary Research*, 5(6). [DOI]

Jia, S. and Wang, Y., 2021. Effect of heat mitigation strategies on thermal environment, thermal comfort, and walkability: A case study in Hong Kong. *Building and Environment*, 201, p.107988. [DOI]

Kantakumar, L.N., Kumar, S. and Schneider, K., 2019. SUSM: A scenario-based urban growth simulation model using remote sensing data. *European Journal of Remote Sensing*, 52(Suppl. 2), pp.26-41. [DOI]

Kara, C. and Doratlı, N., 2021. Predict and simulate sustainable urban growth by using GIS and MCE based CA: Case of Famagusta in Northern Cyprus. *Sustainability*, 13(8), p.4446. [DOI]

Karimi, A., Bayat, A., Mohammadzadeh, N., Mohajerani, M. and Yeganeh, M., 2023. Microclimatic analysis of outdoor thermal comfort of high-rise buildings with different configurations in Tehran: Insights from field surveys and thermal comfort indices. *Building and Environment*, 240, p.110445. [DOI]

Koko, A.F., Yue, W., Abubakar, G.A., Hamed, R. and Alabsi, A.A.N., 2021. Analyzing urban growth and land cover change scenario in Lagos, Nigeria using multi-temporal remote sensing data and GIS to mitigate flooding. *Geomatics, Natural Hazards & Risk*, 12, pp.631-652. [DOI]

Kumar, D. and Shukla, B., 2022. Urban green spaces for promoting healthy living and wellbeing: Prospects for housing. *ECS Transactions*, 107(1), pp.18835-18857. [DOI]

Kumar, D., Maurya, K.K., Mandal, S.K., Halder, N., Mir, B.A., Nurdiawati, A. and Al-Ghamdi, S.G., 2025a. A whole-life carbon assessment of a single-family house in North India using BIM-LCA integration. *Buildings*, 15(13), p.2195. [DOI]

Kumar, D., Maurya, K.K., Mandal, S.K., Mir, B.A., Nurdiawati, A. and Al-Ghamdi, S.G., 2025b. Life cycle assessment in the early design phase of buildings: Strategies, tools, and future directions. *Buildings*, 15(10), p.1612. [DOI]

Li, G., Zhang, Y. and Li, C., 2025. Lake evolution and its response to urban expansion in Wuhan City in the last hundred years based on historical maps and remote sensing images. *Remote Sensing*, 17(9), p.1563. [DOI]

Li, X., Liu, L. and Dong, X., 2011. Quantitative analysis of urban expansion using RS and GIS, a case study in Lanzhou. *Journal of Urban Planning and Development*, 137(4), pp.459-469. [DOI]

Li, Y., Zhen, W., Luo, B., Shi, D. and Li, Z., 2024. Analyzing spatial-temporal characteristics and influencing mechanisms of landscape changes in the context of comprehensive urban expansion using remote sensing. *Remote Sensing*, 16(12), p.2113. [DOI]

Liu, X., Li, X., Chen, Y., Tan, Z., Li, S. and Ai, B., 2010. A new landscape index for quantifying urban expansion using multi-temporal remotely sensed data. *Landscape Ecology*, 25(5), pp.671-682. [DOI]

Liu, Z., He, C., Zhou, Y. and Wu, J., 2014. How much of the world's land has been urbanized, really? A hierarchical framework for avoiding confusion. *Landscape Ecology*, 29(5), pp.763-771. [DOI]

Lu, H., Wang, R., Ye, R. and Fan, J., 2023. Monitoring long-term spatiotemporal dynamics of urban expansion using multisource remote sensing images and historical maps: A case study of Hangzhou, China. *Land*, 12(1), p.144. [DOI]

Luo, H. and Wu, J., 2021. Effects of urban growth on the land surface temperature: A case study in Taiyuan, China. *Environment, Development and Sustainability*, 23(7), pp.10787-10813. [DOI]

Luo, J., Yu, D. and Xin, M., 2008. Modeling urban growth using GIS and remote sensing. *GIScience & Remote Sensing*, 45(4), pp.426-442. [DOI]

MacLachlan, A., Biggs, E., Roberts, G. and Boruff, B., 2017. Urban growth dynamics in Perth, Western Australia: Using applied remote sensing for sustainable future planning. *Land*, 6(1), p.9. [DOI]

Magidi, J. and Ahmed, F., 2019. Assessing urban sprawl using remote sensing and landscape metrics: A case study of the City of Tshwane, South Africa (1984–2015). *The Egyptian Journal of Remote Sensing and Space Sciences*, 22(3), pp.335-346. [DOI]

Manesha, E.P.P., Jayasinghe, A. and Kalpana, H.N., 2021. Measuring urban sprawl of small and medium towns using GIS and remote sensing techniques: A case study of Sri Lanka. *The Egyptian Journal of Remote Sensing and Space Sciences*, 24(3, Part 2), pp.1051-1060. [DOI]

Marzialetti, F., Gamba, P., Sorriso, A. and Carranza, M.L., 2023. Monitoring urban expansion by coupling multi-temporal active remote sensing and landscape analysis: Changes in the metropolitan area of Cordoba (Argentina) from 2010 to 2021. *Remote Sensing*, 15(2), p.336. [DOI]

Mashagbah, A.F., Ibrahim, M.M., Al-Fugara, A. and Alzaben, H., 2022. Spatial and temporal modeling of urban growth and land cover changes using remote sensing, spatial indices, and GIS techniques in Irbid City, Jordan. *Applied Ecology and Environmental Research*, 20(3), pp.2769-2781. [DOI]

Megahed, Y., Cabral, P., Silva, J. and Caetano, M., 2015. Land cover mapping analysis and urban growth modelling using remote sensing techniques in Greater Cairo Region, Egypt. *ISPRS International Journal of Geo-Information*, 4(3), pp.1750-1769. [DOI]

Merlín-Uribe, Y., Contreras-Hernández, A., Astier-Calderón, M., Jensen, O.P., Zaragoza, R. and Zambrano, L., 2013. Urban expansion into a protected natural area in Mexico City: Alternative management scenarios. *Journal of Environmental Planning and Management*, 56(3), pp.398-411. [DOI]

Mokarram, M., Taripanah, F. and Pham, T.M., 2024. Spatial-temporal analysis of atmospheric environment in urban areas using remote sensing and neural networks. *Sustainable Computing: Informatics and Systems*, 42, p.100987. [DOI]

Molla, M.B., Gelebo, G. and Girma, G., 2024. Urban expansion and agricultural land loss: A GIS-based analysis and policy implications in Hawassa City, Ethiopia. *Frontiers in Environmental Science*, 12, p.1499804. [DOI]

Ngolo, A.M.E. and Watanabe, T., 2023. Integrating geographical information systems, remote sensing, and machine learning techniques to monitor urban expansion: An application to Luanda, Angola. *Geo-Spatial Information Science*, 26(3), pp.446-464. [DOI]

Niang, A.J., Hermas, E., Alharbi, O. and Al-Shaery, A., 2020. Monitoring landscape changes and spatial urban expansion using multi-source remote sensing imagery in Al-Aziziyah Valley, Makkah, KSA. *The Egyptian Journal of Remote Sensing and Space Sciences*, 23(1), pp.89-96. [DOI]

Oleson, K.W., Monaghan, A., Wilhelmi, O., Barlage, M., Brunsell, N., Feddema, J., Hu, L. and Steinhoff, D.F., 2015. Interactions between urbanization, heat stress, and climate change. *Climatic Change*, 129(3–4), pp.525-541. [DOI]

Olokeogun, O.S. and Kumar, M., 2020. An indicator based approach for assessing the vulnerability of riparian ecosystem under the influence of urbanization in the Indian Himalayan City, Dehradun. *Ecological Indicators*, 119, p.106796. [DOI]

Page, M.J., McKenzie, J.E., Bossuyt, P.M., Boutron, I., Hoffmann, T.C., Mulrow, C.D., Shamseer, L., Tetzlaff, J.M., Akl, E.A., Brennan, S.E., Chou, R., Glanville, J., Grimshaw, J.M., Hróbjartsson, A., Lalu, M.M., Li, T., Loder, E.W., Mayo-Wilson, E., McDonald, S., McGuinness, L.A., Stewart, L.A., Thomas, J., Tricco, A.C., Welch, V.A., Whiting, P. and Moher, D., 2021. The PRISMA 2020 statement: An updated guideline for reporting systematic reviews. *BMJ*, 372, n71. [DOI]

Pan, Y., Jiang, L., Wang, J., Ma, J., Bao, S., Lin, Y. and Shi, K., 2024. Mapping and evaluating spatiotemporal patterns of urban expansion in global earthquake-affected areas: A nighttime light remote sensing perspective. *International Journal of Digital Earth*, 17(1), p.2419938. [DOI]

Prakash, A., Diksha and Kumar, A., 2023. Measuring vertical urban growth of Patna urban agglomeration using persistent scatterer interferometry SAR (PSInSAR) remote sensing. *Remote Sensing*, 15(14), p.3687. [DOI]

Rahaman, M., Dutta, S., Sahana, M. and Das, D.N., 2019. Analysing urban sprawl and spatial expansion of Kolkata urban agglomeration using geospatial approach. In: *Applications and Challenges of Geospatial Technology*. Springer International Publishing, pp.205-221. [DOI]

Rahman, M.T., 2016. Detection of land use/land cover changes and urban sprawl in Al-Khobar, Saudi Arabia: An analysis of multi-temporal remote sensing data. *ISPRS International Journal of Geo-Information*, 5(2), p.15. [DOI]

Rai, A., Minsker, B., Sullivan, W. and Band, L., 2019. A novel computational green infrastructure design framework for hydrologic and human benefits. *Environmental Modelling & Software*, 118, pp.252-261. [DOI]

Roy, B. and Kasemi, N., 2021. Monitoring urban growth dynamics using remote sensing and GIS techniques of Raiganj urban agglomeration, India. *The Egyptian Journal of Remote Sensing and Space Sciences*, 24(2), pp.221-230. [DOI]

Rupapara, S., Rathod, V., Rupapara, H., Halder, N. and Kumar, D., 2025. Evaluating the benefits of urban greenery in urban heat island mitigation: Methods, indicators and gaps. *Nature Environment and Pollution Technology*, 24(4), D1812. [DOI]

Salvati, L., Sateriano, A. and Bajocco, S., 2020. To grow or to sprawl? Land consumption and population dynamics in Mediterranean cities. *Sustainability*, 12(5), p.1980. [DOI]

Sánchez Jiménez, J.L. and Ruiz de Adana, M., 2024. Assessment of outdoor thermal comfort in a hot summer region of Europe. *Atmosphere*, 15(2), p.214. [DOI]

Sarkar, L. and Chakraborty, P., 2025. Analysing urban sprawl as a response to land use land cover change dynamics using geospatial techniques: A study of Kolkata and surrounding area. *GeoJournal*, 90(4), p.168. [DOI]

Sathe, T.A. and Rahman, S.H., 2024. Sustainable development versus urban sprawl: A Landsat imagery analysis of ecological impact in Savar Upazila, 2011–2022. *Case Studies in Chemical and Environmental Engineering*, 10, p.100819. [DOI]

Seto, K.C., Güneralp, B. and Hutyra, L.R., 2012. Global forecasts of urban expansion to 2030 and direct impacts on biodiversity and carbon pools. *Proceedings of the National Academy of Sciences*, 109(40), pp.16083-16088. [DOI]

Shao, Z., Sumari, N.S., Portnov, A., Ujoh, F., Musakwa, W. and Mandela, P.J., 2021. Urban sprawl and its impact on sustainable urban development: A combination of remote sensing and social media data. *Geo-Spatial Information Science*, 24(2), pp.241-255. [DOI]

Shaw, R. and Das, A., 2018. Identifying peri-urban growth in small and medium towns using GIS and remote sensing techniques: A case study of English Bazar urban agglomeration, West Bengal, India. *The Egyptian Journal of Remote Sensing and Space Sciences*, 21(2), pp.159-172. [DOI]

Shrestha, P.P., Shrestha, A.M. and Hong, C.-Y., 2025. Policy-driven urban expansion and land use/land cover change in Ewa, Honolulu (2002–2022): Remote sensing and machine learning analysis of transit-oriented development impacts. *Land*, 14(10), p.2041. [DOI]

Subasinghe, S., Estoque, R.C. and Murayama, Y., 2016. Spatiotemporal analysis of urban growth using GIS and remote sensing: A case study of the Colombo metropolitan area, Sri Lanka. *ISPRS International Journal of Geo-Information*, 5(11), p.197. [DOI]

Taubenböck, H., Gerten, C., Rusche, K., Siedentop, S. and Wurm, M., 2018. Patterns of Eastern European urbanization: The example of Poland. *Computers, Environment and Urban Systems*, 68, pp.165-176. [DOI]

Torres, R.A.C., Wang, J., Zhang, J., Liu, L. and Lan, Y., 2024. Temporal analysis of land degradation and urban expansion in central Yunnan Province using remote sensing for supporting Sustainable Development Goals 11/15. *Ecological Indicators*, 163, p.112058. [DOI]

Trinder, J. and Liu, Q., 2020. Assessing environmental impacts of urban growth using remote sensing. *Geo-Spatial Information Science*, 23(1), pp.20-39. [DOI]

Ul Din, S. and Mak, H.W.L., 2021. Retrieval of land-use/land cover change (LUCC) maps and urban expansion dynamics of Hyderabad, Pakistan, via Landsat datasets and support vector machine framework. *Remote Sensing*, 13(16), p.3337. [DOI]

Van de Voorde, T., van der Kwast, J., Poelmans, L., Canters, F., Binard, M., Cornet, Y., Engelen, G., Uljee, I., Shahumyan, H., Williams, B., Convery, S. and Lavalle, C., 2016. Projecting alternative urban growth patterns: The development and application of a remote sensing assisted calibration framework for the Greater Dublin Area. *Ecological Indicators*, 60, pp.1056-1069. [DOI]

van Eck, N.J. and Waltman, L., 2010. Software survey: VOSviewer, a computer program for bibliometric mapping. *Scientometrics*, 84(2), pp.523-538. [DOI]

Waleed, M., Sajjad, M., Acheampong, A.O. and Alam, M.T., 2023. Towards sustainable and livable cities: Leveraging remote sensing, machine learning, and geo-information modelling to explore and predict thermal field variance in response to urban growth. *Sustainability*, 15(2), p.1416. [DOI]

Wan, Z., 2014. New refinements and validation of the collection-6 MODIS land-surface temperature/emissivity product. *Remote Sensing of Environment*, 140, pp.36-45. [DOI]

Wang, C., Wang, Z.-H., Kaloush, K.E. and Shacat, J., 2021a. Cool pavements for urban heat island mitigation: A synthetic review. *Renewable and Sustainable Energy Reviews*, 146, p.111171. [DOI]

Wang, J.W., Chow, W.T.L. and Wang, Y.C., 2020. A global regression method for thermal sharpening of urban land surface temperatures from MODIS and Landsat. *International Journal of Remote Sensing*, 41(8), pp.2986-3009. [DOI]

Wang, R., Gao, W., Zhou, N., Kammen, D.M. and Peng, W., 2021b. Urban structure and its implication of heat stress by using remote sensing and simulation tool. *Sustainable Cities and Society*, 65, p.102632. [DOI]

Xu, G., Jiao, L., Yuan, M., Dong, T., Zhang, B. and Du, C., 2019. How does urban sprawl affect land use intensity? Evidence from China. *Habitat International*, 84, pp.109-118. [DOI]

Yan, Y., Wu, C. and Wen, Y., 2021. Determining the impacts of climate change and urban expansion on net primary productivity using the spatio-temporal fusion of remote sensing data. *Ecological Indicators*, 127, p.107737. [DOI]

Zhang, L., Zhang, J., Li, X., Zhou, K. and Ye, J., 2023. The impact of urban sprawl on carbon emissions from the perspective of nighttime light remote sensing: A case study in eastern China. *Sustainability*, 15(15), p.11940. [DOI]

Zhang, Y., Ning, G., Chen, S. and Yang, Y., 2021. Impact of rapid urban sprawl on the local meteorological observational environment based on remote sensing images and GIS technology. *Remote Sensing*, 13(13), p.2624. [DOI]

Zhao, J., Yu, L., Liu, H., Huang, H., Wang, J. and Gong, P., 2021. Towards an open and synergistic framework for mapping global land cover. *PeerJ*, 9, p.e11877. [DOI]

Zhao, J., Zhao, X., Liang, S., Wang, H., Liu, N., Liu, P. and Wu, D., 2021. Dynamic cooling effects of permanent urban green spaces in Beijing, China. *Remote Sensing*, 13(16), p.3282. [DOI]

Zhu, Z., Woodcock, C.E. and Olofsson, P., 2022. Continuous monitoring of urban expansion using Landsat time series. *Remote Sensing of Environment*, 268, p.112761. [DOI]

Zubair, O.A., Ji, W. and Festus, O., 2019. Urban expansion and the loss of prairie and agricultural lands: A satellite remote-sensing-based analysis at a sub-watershed scale. *Sustainability*, 11(17), p.4673. [DOI]

Nature Environment and Pollution Technology
An International Quarterly Peer-Reviewed Open Access Journal

p-ISSN: 0972-6268 | e-ISSN: 2395-3454 Vol. 25 | No. 4 | Article ID D1900 | 2026

RESEARCH ARTICLE https://doi.org/10.46488/NEPT.2026.v25i04.D1900 OPEN ACCESS

Water Footprint of Local Herbs in Thailand Using the Water Footprint Network Methodology

Phairat Usubharatana and Harnpon Phungrassami†
Department of Chemical Engineering, Faculty of Engineering, Thammasat School of Engineering, Thammasat University, Pathumthani, Thailand
†Corresponding author: Harnpon Phungrassami; pharnpon@engr.tu.ac.th

ARTICLE HISTORY

Received: 13-01-2026
Revised: 04-03-2026
Accepted: 17-03-2026

KEYWORDS

Irrigation,
Medicinal herbs
Sustainable agriculture
Water footprint
Water footprint network

CITE THIS ARTICLE

Usubharatana, P. and Phungrassami, H., 2026. Water footprint of local herbs in Thailand using the water footprint network methodology. *Nature Environment and Pollution Technology*, 25(4), D1900. https://doi.org/10.46488/NEPT.2026.v25i04.D1900

COPYRIGHT & LICENCE

© 2026 The Authors
Open Access under CC BY 4.0.

PUBLISHED BY

TECHNOSCIENCE PUBLICATIONS

ABSTRACT

This study quantified the water footprint (WF) of four economically important Thai medicinal herbs: *Curcuma longa, Kaempferia parviflora, Andrographis paniculata,* and *Momordica charantia* using the Water Footprint Network (WFN) methodology together with Thailand-specific climatic and cultivation data. The assessment covered green, blue, and gray WF components and incorporated basin-level water scarcity characterization. The results show that *Curcuma longa* had the lowest total WF (535 m^3 ton^{-1}), driven primarily by green water use, while *Momordica charantia* had the highest WF (2,152 m^3 ton^{-1}), reflecting substantial blue and gray water requirements. *Kaempferia parviflora* and *Andrographis paniculata* presented intermediate WFs of 1,088 and 1,869 m^3 ton^{-1}, respectively. Spatial analysis revealed strong provincial variability linked to rainfall patterns and irrigation demand, particularly for *Momordica charantia* in northern and lower-central regions. Sensitivity analysis identified crop yield as the most influential parameter across all herbs, followed by K_c and ET_0. The findings provide a robust evidence base for optimizing irrigation practices and guiding sustainable water management strategies within Thailand's herbal cultivation sector.

1. INTRODUCTION

The water footprint (WF) has become a fundamental indicator for evaluating the sustainability of agricultural production systems, providing a quantitative measure of freshwater consumed or polluted within a product's system boundary (Hoekstra & Mekonnen 2012). Defined across three components (green, blue, and gray), the WF framework offers a comprehensive understanding of crop-specific water use, including soil moisture reliance, irrigation demand, and water required for assimilating nutrient pollution (Hoekstra et al. 2011). The concept, formalized by Hoekstra & Mekonnen (2012), has since been widely applied across regions and crop types, contributing to improved water-use planning, agricultural benchmarking, and environmental policy development (Mekonnen & Hoekstra 2011, Mekonnen & Hoekstra 2014, Lovarelli et al. 2016). Numerous global studies demonstrate that irrigation-intensive crops tend to exert disproportionately high blue WF, intensifying water scarcity in hydrologically stressed regions (Mekonnen & Hoekstra 2014). Evidence from arid and semiarid countries further supports this trend, highlighting that cereal and horticultural crops are particularly sensitive to irrigation dependency and blue-water vulnerability (Mekonnen & Hoekstra 2020).

Thailand plays an increasingly important role in the global herbal medicine market, with more than 1,800 plant species recorded for medicinal purposes and over 200 commercially cultivated nationwide (Department of Thai Traditional and Alternative Medicine 2023). National strategies under the Ministry of Public Health have designated several species as "herbal champion products" to strengthen domestic competitiveness and export capacity (Department of Thai Traditional and Alternative Medicine 2023). Among these, *Curcuma longa, Kaempferia parviflora, Andrographis paniculata*, and *Momordica charantia* stand out due to their pharmacological properties, rising consumer demand, and expanding production areas (Ngamsomjit 2008). Despite their growing economic importance, systematic evaluations of their water-use requirements and associated environmental pressures are still limited, resulting in a substantial knowledge gap regarding their water consumption patterns across different agroecological contexts.

Existing WF studies in Thailand have largely focused on staple and industrial crops. For instance, rice has been extensively analyzed, with its WF inventory informing national water policy, food labeling, and sustainability assessments (Mungkung et al. 2019). Cassava research has revealed high blue-water demand in the northeastern region, where prolonged dry seasons create chronic water stress (Kaewjampa et al. 2016). Sugarcane studies have documented irrigation-efficiency gaps in eastern provinces (Chaibandit et al. 2017), while investigations of palm oil plantations and coffee production highlight strong regional variations in water use driven by climatic and soil differences (Suttayakul et al. 2016, Ratchawat et al. 2020). These studies collectively establish valuable benchmarks for Thailand's major crops; however, medicinal herbs remain underexamined, particularly in terms of their spatial water-use dynamics and implications for water resource management. This absence of herb-specific WF benchmarks limits the ability of policymakers and producers to design effective irrigation strategies and evaluate potential risks related to water scarcity.

The selection of the four herbs examined in this study reflects both their economic relevance and their contrasting agroecological characteristics. *Curcuma longa* and *Kaempferia parviflora* are predominantly cultivated in northern and northeastern provinces, where rainfall is more dependable and rain-fed agriculture is common, suggesting stronger reliance on green water (Ngamsomjit 2008). In contrast, *Andrographis paniculata* and *Momordica charantia* are primarily grown in the central region, where developed irrigation systems support intensive horticultural production, implying higher blue water dependency (Gheewala et al. 2014). This geographic differentiation provides an opportunity to compare water-use patterns across distinct climatic zones and to identify potential hotspots where irrigation pressure may be particularly high.

Given the increasing significance of medicinal herbs in Thailand's agricultural economy and the limited WF data available for these crops, this study aimed to quantify and compare the green, blue, and gray WFs of four selected species using the WFN methodology. The objectives are threefold: (1) to determine the relative contributions of each WF component at the provincial and national scales; (2) to benchmark the water intensity of medicinal herbs against commonly studied staple and industrial crops and to integrate crop-specific water-use data with the regional water scarcity indicator (WSI); and (3) to provide an evidence-based foundation for improving irrigation efficiency, strengthening water-resource planning, and supporting sustainable agricultural development of Thailand's medicinal herb sector.

2. MATERIALS AND METHODS

2.1. Goal and Scope Definition

The primary goal of this study was to quantify and compare the green, blue, and gray WFs of four economically important Thai medicinal herbs: *Curcuma longa, Kaempferia parviflora, Andrographis paniculata*, and *Momordica charantia*. These species were selected based on their official designation as "herbal champion products" by the Thai Ministry of Public Health, reflecting their economic value and market relevance (Department of Thai Traditional and Alternative Medicine 2023). The provinces included in the analysis were identified according to the largest cultivation area and production volumes reported in national agricultural statistics, ensuring representation of major producing regions and capturing geographic variability. Provincial WF results were subsequently aggregated to the national averages using a mass-balance approach that integrates provincial crop water use and harvested production.

The functional unit (FU) was defined as one ton of harvested fresh product, widely used in WF studies due to its practical interpretability for producers, traders, and policymakers (Mekonnen & Hoekstra 2011, Hoekstra & Mekonnen 2012). Although FUs based on dry matter or active compounds (e.g., milligrams of curcumin) can provide more pharmaceutical-oriented insights, the fresh-weight FU was selected to maintain consistency with existing WF benchmarks for staple and industrial crops (Mekonnen & Hoekstra 2014). The system boundary was restricted to the cultivation stage, covering consumptive water use (evapotranspiration) and nutrient-related pollution

(leaching and runoff) from planting to harvest (Hoekstra et al. 2011). Downstream processes, including transportation, processing, and packaging, were excluded to maintain focus on agricultural water management in alignment with the WFN methodology (Hoekstra et al. 2011).

2.2. Water Footprint Accounting Framework

The analysis followed the WFN assessment manual (Hoekstra et al. 2011), which is widely recognized as the global reference framework for volumetric water accounting. This approach has been applied to a broad range of crops, including cereals, oil crops, and horticultural species, and is considered robust for spatially explicit analyses across diverse agro conditions (Gheewala et al. 2014, Mekonnen & Hoekstra 2014). The volumetric method is particularly suitable for Thailand, where climatic heterogeneity and variations in irrigation infrastructure strongly influence consumptive water use.

The green and blue components of the WF were calculated using Eq. (1) and Eq. (2):

$$WF_{green} = \frac{CWU_{green}}{Y} \quad \ldots(1)$$

$$WF_{blue} = \frac{CWU_{blue}}{Y} \quad \ldots(2)$$

where CWU is the crop water use (m^3 ha^{-1}), and Y is the crop yield (ton ha^{-1}). CWU was estimated using CROPWAT 8.0, a software tool developed by the Food and Agriculture Organization (FAO), which applies the Penman–Monteith model to calculate reference evapotranspiration (ET_0). This model is internationally regarded as the most physically consistent and transferable approach for estimating evapotranspiration (Allen et al. 1998). Crop coefficients (K_c) were used to adjust ET_0 for species-specific characteristics.

The gray WF, representing the volume of freshwater required to assimilate leached nitrogen, was calculated using Eq. (3):

$$WF_{gray} = \frac{\alpha \times AR}{(C_{max} - C_{nat}) \times Y} \quad \ldots(3)$$

where AR is the nitrogen application rate (kg ha^{-1}), α is the leaching-runoff fraction, C_{max} is the maximum acceptable nitrate concentration, and C_{nat} is the natural background concentration in the receiving body. Following assumptions commonly adopted in WF studies (Mekonnen & Hoekstra 2014, Lovarelli et al. 2016), the leaching-runoff fraction was fixed at 10%, C_{nat} was assumed to be zero, and C_{max} was set at 10 mg NO_3-N L^{-1} based on WHO water-quality guidelines. Although these assumptions were widely used, they were explicitly acknowledged as a source of uncertainty in the analysis.

Provincial water footprint results were aggregated to derive national average values using a mass-balance approach based on harvested cultivation area and production. National component-specific WF values were calculated as Eq. (4):

$$WF_{c,national} = \frac{\sum_i (CWU_{c,i} \times A_i)}{\sum_i (Y_i \times A_i)} \quad \ldots(4)$$

where $CWU_{c,i}$ represents the crop water use (green, blue, or gray component) in province i, Y_i denotes provincial yield, and A_i denotes harvested cultivation area. This approach ensures that national WF values reflect total water consumption divided by total production rather than a simple arithmetic average of provincial ratios.

2.3. Data Sources and Parameters

Climatic data on rainfall, temperature, humidity, and wind speed were obtained from the Thai Meteorological Department. Agricultural statistics, including cultivation area, yield, and fertilizer input, were sourced from the Department of Agricultural Extension (Chanakanachai & Lekunwong 2000). Crop coefficients (K_c) were derived from published lysimeter-based measurements and established datasets. For *Curcuma longa*, *Kaempferia parviflora,* and *Andrographis paniculata*, representative K_c values calibrated against the Penman-Monteith method were adopted from Ngamsomjit (2008). For *Momordica charantia*, species-specific lysimeter measurements were unavailable. Therefore, a representative mid-season crop coefficient (Kc = 1.15) from FAO for cucumber cultivated under full canopy conditions was adopted as a proxy (Allen et al. 1998). This substitution was applied to maintain parameter consistency in the absence of species-specific experimental data. To enhance reproducibility, the representative Kc values applied in the model and their corresponding sources are summarized in Table 1. The uncertainty associated with literature-derived Kc values was addressed through ±20% perturbation in the sensitivity analysis.

Table 1: Representative crop coefficients (Kc) applied in CROPWAT calculations.

Herb	Kc used in model	Basis/note	Source
Kaempferia parviflora	1.19	Lysimeter-based; Penman–Monteith calibrated	Ngamsomjit (2008)
Curcuma longa	1.12	Lysimeter-based; Penman–Monteith calibrated	Ngamsomjit (2008)
Andrographis paniculata	1.77	Lysimeter-based; Penman–Monteith calibrated	Ngamsomjit (2008)
Momordica charantia	1.15	Proxy using cucumber mid-season K_c under full canopy conditions	Allen et al. (1998)

Nitrogen application rates were derived from standardized cultivation guidelines issued by the Department of Agricultural Extension (Chanakanachai & Lekunwong 2000). A single crop-specific AR was applied uniformly across all provinces to maintain methodological consistency within the comparative water footprint assessment framework. The influence of potential uncertainty associated with nitrogen inputs was evaluated through ±20% perturbation in the sensitivity analysis.

2.4. Water Scarcity Assessment

To contextualize irrigation dependence, blue WF values were compared with the blue WSI of Thailand's 25 river basins, obtained from the national assessment by Gheewala et al. (2014). Although the dataset was published in 2014, it remains the most comprehensive and spatially detailed national reference available. The WSI represents the ratio of blue-water consumption to renewable blue-water availability, and therefore serves as a proxy for the degree of water stress within each basin (Mekonnen & Hoekstra 2020).

Integrating blue WF with basin-level WSI enables the identification of areas where irrigation-intensive crops pose heightened risks of local water competition. This paired assessment provides not only a measure of consumptive water use but also its contextual scarcity, offering clearer implications for sustainability planning and policy development. The combined WF-WSI framework is consistent with emerging approaches in water-resource analysis that emphasize both volumetric demand and local hydrological constraints.

2.5. Methodological Assumptions and Limitations

Several assumptions are embedded in this methodology. First, fertilizer input rates from agricultural statistics primarily reflect commercial systems, possibly underestimating smallholder or informal cultivation practices, where efficiency is lower. Second, the exclusion of downstream processes, such as drying and processing, implies that the results are conservative estimates of the total product footprints. These limitations overlap with those discussed in the Results and Discussion section, where they are revisited along with recommendations for future work.

2.6. Sensitivity Analysis Framework

A sensitivity analysis was conducted to evaluate the robustness of the WF results and to quantify the relative influence of key parameters on the green, blue, and gray components. Each selected variable was independently perturbed by 20% around its baseline value while all other parameters were held constant. This one-at-a-time approach follows the standard practices widely applied in agricultural WF assessments and is recommended in the WFN methodology (Hoekstra et al. 2011). The tested parameters represent both climatic-agronomic drivers and management-related factors that influence water consumption and pollutant assimilation.

For the climatic-agronomic group, K_c and ET_0 were varied by ±20%, as these parameters directly influence crop evapotranspiration within the FAO Penman–Monteith framework (Allen et al. 1998). Crop yield (Y) was also varied by ±20%. Because yield is the denominator in the calculation of all WF components, changes in Y can induce substantial fluctuations in total WF, especially in provinces where productivity is comparatively low.

For management-related factors, the AR and α were varied by ±20% to reflect the broader empirical uncertainties associated with fertilization practices and soil-water interactions, as reported in review studies (Mekonnen & Hoekstra 2014, Mungkung et al. 2019). In the baseline scenario, the leaching-runoff fraction was fixed at 0.1, following the WFN manual (Hoekstra et al. 2011), but its 20% perturbation captures the spatial variability documented in field-scale experiments (Lovarelli et al. 2016). This approach allows the analysis to incorporate both biophysical uncertainty and management variability, ensuring a more realistic assessment of potential deviations in WF estimates.

The configuration of the sensitivity tests is summarized in Table 2, which specifies the parameter descriptions, applied perturbation ranges, and supporting rationale.

Table 2: Sensitivity test matrix for parameters affecting green, blue, and gray WF components.

Parameter	Description	Variation (%)	Rationale and Source
Crop yield (Y)	Output per unit area; affects all WF components inversely	±20%	Field yield uncertainty; range adopted from WFN (Hoekstra & Mekonnen 2012, Mekonnen & Hoekstra 2014)
ET_0/K_c	Reference evapotranspiration and crop coefficient; affect green and blue WF components	±20%	Reflects meteorological and phenological variability (Hoekstra & Mekonnen 2012)
Application rate (AR)	Nitrogen fertilizer application; affects gray WF	±20%	Field survey
Leaching-runoff fraction (α)	Fraction of applied nitrogen assumed to leach or runoff to receiving water bodies	±20%	(Hoekstra & Mekonnen 2012)

3. RESULTS

3.1. Average Water Footprint of Medicinal Herbs

Provincial-level analysis revealed substantial variability in the WF profiles of the four economically strategic Thai medicinal herbs (Table 3). *Curcuma longa* consistently exhibited the lowest total WF, averaging 535 m^3 ton^{-1}. This comparatively favorable performance is largely attributable to its strong reliance on green water, which accounted for more than 40% of its total WF. In contrast, *Kaempferia parviflora* demonstrated a considerably higher total WF of 1,088 m^3 ton^{-1}, driven primarily by irrigation demand; the blue component contributed more than 40% of the total footprint, underscoring its sensitivity to water availability and basin-level scarcity conditions.

More pronounced contrasts were observed between *Andrographis paniculata* and *Momordica charantia*. The total WF of *Andrographis paniculata* averaged 1,869 m^3 ton^{-1}, with nearly 80% originating from blue water. This heavy reliance on irrigation reflects the crop's concentration in Thailand's Central region, where intensive agriculture and well-developed irrigation systems dominate production landscapes (Gheewala et al. 2014). *Momordica charantia* exhibited the highest total WF at 2,152 m^3 ton^{-1}, nearly four times greater than *Curcuma longa*, reinforcing the established principle that lower crop productivity is strongly associated with disproportionately high water intensities (Ababaei & Etedali 2017).

At the national scale, a consistent pattern emerged: blue WF dominated the total WF for most medicinal herbs, indicating substantial irrigation dependence. Although smaller in magnitude, the gray WF remained a non-negligible component, especially for *Momordica charantia*, where relatively high AR resulted in elevated nutrient-assimilation water requirements. Nitrogen inputs in this study were derived from standardized synthetic fertilizer recommendations issued by Chanakanachai & Lekunwong (2000), and uniform crop-specific ARs were applied consistently across provinces. Because gray WF is directly proportional to AR and inversely proportional to yield (Y), relatively high fertilizer intensity combined with moderate yield levels contributed to elevated gray WF shares for certain herbs, particularly *Kaempferia parviflora*. It should be noted that the gray WF represents the theoretical freshwater volume required to dilute leached nitrogen to acceptable concentration thresholds under the WFN framework. This indicator reflects potential nutrient pressure under conventional fertilizer management practices rather than direct exceedance of basin-level water quality standards.

These combined results indicate that some of the selected medicinal herbs are considerably more water-intensive than staple crops such as rice (1,665 m^3 ton^{-1}) (Mungkung et al. 2019) and vastly exceed the water-use efficiency of industrial crops such as sugarcane (178 m^3 ton^{-1}) (Chaibandit et al. 2017).

From a policy perspective, optimizing nitrogen application through precision fertilization, soil testing, and improved nutrient management practices could reduce the gray WF without compromising productivity. Integrating nutrient management with irrigation planning would be particularly important in provinces where fertilizer intensity and irrigation dependence overlap. The comparative patterns across herbs highlight the need for spatially explicit WF assessments. While *Curcuma longa* may be considered relatively more sustainable due to its strong dependence on *rainfall, Momordica charantia* and *Andrographis paniculata* illustrate the challenges associated with irrigation-intensive cultivation in regions already vulnerable to water scarcity. These findings underscore the importance of integrating crop selection, irrigation management, and spatial planning into strategies aimed at improving agricultural water-use efficiency in Thailand.

3.2. Spatial Variability of Water Footprints

The spatial distribution of WFs across provinces revealed distinct patterns for the four medicinal herbs. *Curcuma longa* is predominantly cultivated in northern provinces such as Chiang Mai, where rainfall reliably supports production. As a result, green WF contributes approximately 50% of the total footprint in most locations, confirming the crop's relatively low dependence on irrigation. Nevertheless, certain provinces, most notably Phrae, displayed exceptionally high blue WF values (2,802.2 m^3 ton^{-1}), indicating localized irrigation intensities that diverge markedly from the broader rain-fed production pattern.

Table 3: National average WF of four economically strategic Thai medicinal herbs.

Herb	Green WF		Blue WF		Gray WF		Total WF
	(m^3 ton^{-1})	%	(m^3 ton^{-1})	%	(m^3 ton^{-1})	%	(m^3 ton^{-1})
Curcuma longa	232	43.4	157	29.3	146	27.3	535
Kaempferia parviflora	292	26.8	451	41.5	345	31.7	1,088
Andrographis paniculata	208	11.1	1,463	78.3	198	10.6	1,869
Momordica charantia	174	8.1	1,686	78.3	292	13.6	2,152

In contrast, *Kaempferia parviflora* exhibited strong irrigation dependence in northeastern provinces. Khon Kaen recorded blue WF levels exceeding 2,000 m^3 ton^{-1}, whereas Phetchabun showed considerably lower levels at 403.4 m^3 ton^{-1}. These spatial contrasts highlight the influence of agroecological and hydrological conditions on water-use patterns (Li et al. 2022). Provinces experiencing water-stressed conditions (e.g., Nakhon Ratchasima, WSI = 0.927) demonstrated heightened vulnerability when high irrigation demand coincided with already scarce water resources.

The distributions of *Andrographis paniculata* and *Momordica charantia* were more geographically restricted, yet they exhibited significantly higher WF intensities. In Ratchaburi, both crops reached extreme total WF values of 4,509.3 m^3 ton^{-1} for *Andrographis paniculata* and 4,318.6 m^3 ton^{-1} for *Momordica charantia*. These values are several times higher than their respective national averages and were driven primarily by blue WF contributions exceeding 75%. These findings underscore Ratchaburi as a critical hotspot for irrigation-intensive medicinal herb cultivation. Because blue WF is expressed per unit of production (m^3 ton^{-1}), lower productivity mathematically amplifies per-ton water footprint values even when irrigation water use remains within typical agronomic ranges. This yield-driven mechanism explains the apparent outliers observed in the provincial distribution and highlights the importance of interpreting WF intensities in conjunction with productivity metrics.

Overall, the spatial analysis confirmed that herbs grown in predominantly rain-fed regions (e.g., *Curcuma longa* in northern provinces) exhibit more balanced WF profiles, with substantial contributions from green water. Conversely, crops cultivated in irrigated Central and Northeastern provinces, particularly *Andrographis paniculata* and *Momordica charantia* are characterized by disproportionately high blue WF dependencies. Provinces such as Phrae, Khon Kaen, and Ratchaburi thus emerge as water-intensive cultivation zones, emphasizing the need for targeted, region-specific water-use strategies in the context of Thailand's increasing water scarcity challenges.

3.3. Sensitivity and Uncertainty Analysis

The sensitivity analysis evaluated the influence of key parameters on total WF using a proportional approach consistent with the WFN accounting structure and the FAO evapotranspiration formulation. Yield was treated as the common denominator for all WF components; therefore, a ±20% change in yield translated directly into a corresponding change in total WF. The K_c and ET_0 were assumed to influence both green and blue WF through their effects on crop water use. Consequently, the magnitude of their influence on total WF was proportional to the combined share of green and blue components. In contrast, AR and α were assumed to affect only the gray component, and their influence on total WF was proportional to the gray WF share. Component shares for each herb were computed and summarized in Table 3.

Fig. 1 presents the results in tornado-style panels for each herb. Yield consistently dominated the sensitivity profile across all species due to its inverse functional relationship with the water-use intensity, producing a one-to-one proportional response. K_c and ET_0 represented the second most influential group of parameters, particularly for *Andrographis paniculata* and *Momordica charantia*, where the combined green and blue shares approached 0.89 and 0.86, respectively. Under a ±20% perturbation, these shares translated into total WF shifts of approximately ±17.9% for *Andrographis paniculata* and ±17.3% for *Momordica charantia*. In contrast, *Curcuma longa* and *Kaempferia parviflora* exhibited lower, though still meaningful, sensitivity to K_c and ET_0, due to their lower combined green and blue proportions.

Parameters affecting the gray WF component exerted comparatively smaller influences on total WF because the gray shares were modest for three of the four herbs. The strongest gray-related sensitivity was observed for *Kaempferia parviflora*, where the gray share of approximately 0.32 resulted in a ±6.3% change in total WF under a ±20% perturbation. This pattern highlights the limited role of nutrient-related processes in shaping overall WF variability relative to the dominant effect of irrigation water use.

These results have two practical implications for policymakers. First, interventions that enhance yield, such as agronomic improvements and better planting materials, are likely to deliver the largest proportional reductions in WF per ton across all four herbs. Second, for species whose WF is strongly governed by the green and blue components, especially *Andrographis paniculata* and *Momordica charantia*, climate- and management-sensitive parameters (K_c and ET_0) warrant careful calibration and local validation to minimize model uncertainty and to prioritize water-saving strategies. In contrast, reductions in nitrogen application or improved nutrient management would generate relatively smaller changes in total WF at the national mean level, although local effects may be stronger where the gray share is high.

4. DISCUSSION

4.1. Interpretation and Benchmarking of Water Footprint Results

Building upon the provincial-level results in Table 3, the

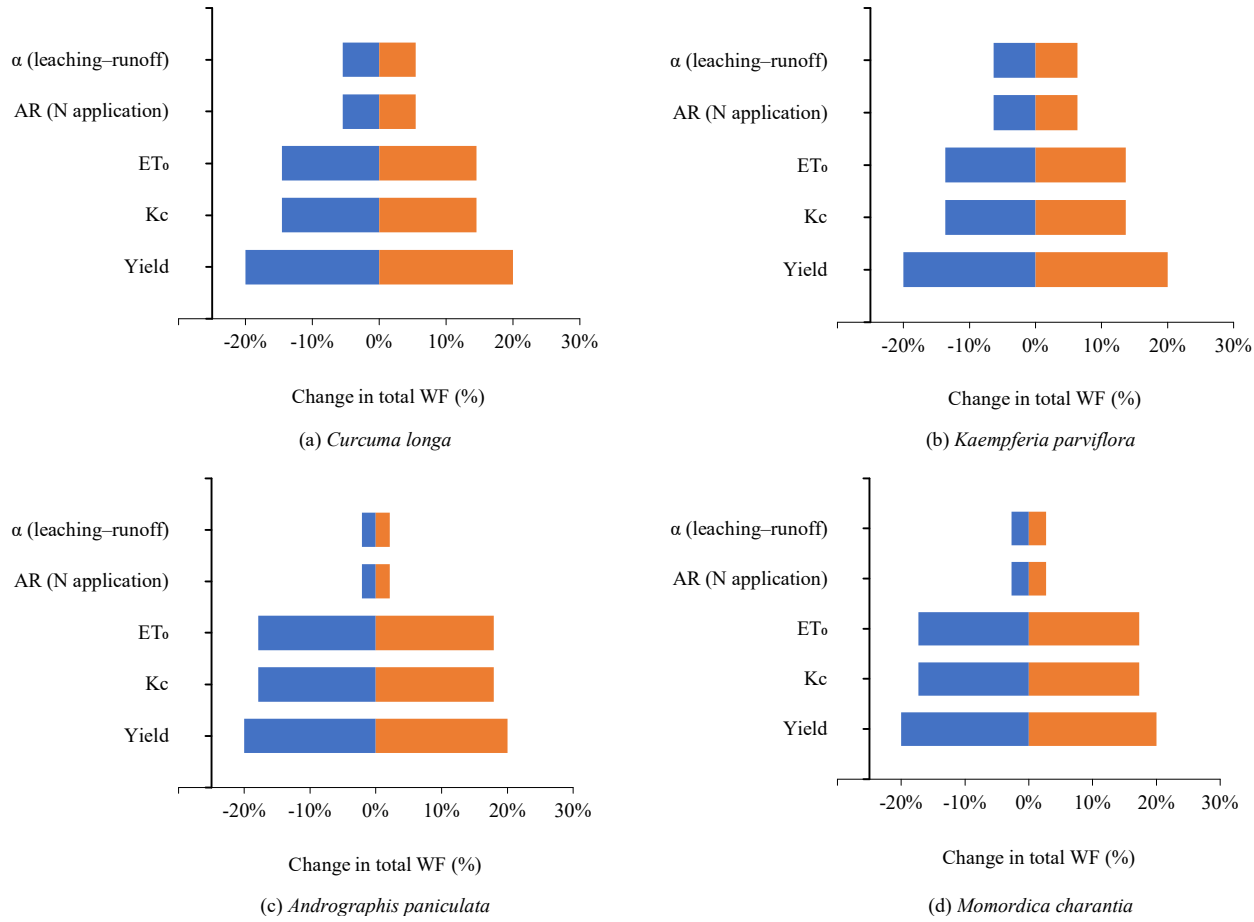


Fig. 1: Percentage change in total WF under parameter variation for: (a) *Curcuma longa*, (b) *Kaempferia parviflora*, (c) *Andrographis paniculata*, and (d) *Momordica charantia*.

total WF of the four medicinal herbs exhibited substantial variation across provinces and relative to Thailand's major food and industrial crop benchmarks. *Curcuma longa* recorded the lowest total WF (535 m^3 ton^{-1}), followed by *Kaempferia parviflora* (1,088 m^3 ton^{-1}), *Andrographis paniculata* (1,869 m^3 ton^{-1}), and *Momordica charantia* (2,152 m^3 ton^{-1}). This fourfold range is primarily shaped by differences in irrigation dependence and yield performance, with irrigation-intensive species generally exhibiting higher total WF values.

When compared with staple and industrial benchmarks, the total WF of *Curcuma longa* was markedly lower than that of rice (1,665 m^3 ton^{-1}) (Mungkung et al. 2019), although still approximately three times greater than that of sugarcane (178 m^3 ton^{-1}) (Chaibandit et al. 2017). Conversely, *Andrographis paniculata* and *Momordica charantia* displayed total WFs approaching that of cassava (2,500 m^3 ton^{-1} in Northeast Thailand) (Kaewjampa et al. 2016), indicating irrigation intensities comparable to Thailand's high-input industrial crops. These contrasts highlight the diverse water-use efficiencies of medicinal herbs and emphasize the need to differentiate species-specific water management strategies.

The provincial distribution of total WF (Fig. 2) demonstrated clear regional variability. Northern provinces, such as Chiang Mai and Nan, exhibited strong green-water dominance due to reliable monsoonal rainfall and limited reliance on irrigation (Ngamsomjit 2008). In contrast, Central provinces, including Ratchaburi and Nakhon Pathom, recorded blue-water shares exceeding 70% for *Andrographis paniculata* and *Momordica charantia*. These patterns overlapped with moderate to high basin-level water scarcity (WSI = 0.25–0.30) (Mekonnen & Hoekstra 2020, Gheewala et al. 2014), signaling heightened vulnerability where irrigation demand coincides with constrained freshwater availability.

Gray WF contributions were generally smaller but remained important in specific locations. For example, elevated gray WF values for *Andrographis paniculata* in

Nakhon Pathom (1,100 m³ ton⁻¹) reflect nitrogen leaching levels comparable to those documented in sugarcane systems (Chaibandit et al. 2017, Suttayakul et al. 2016, Gheewala et al. 2014). This finding underscores the need for site-specific nutrient management to mitigate nonpoint-source pollution in regions with high fertilizer application rates.

Overall, the results demonstrate that medicinal herbs should not be viewed as uniformly low-impact crops. Their water-use efficiency depends heavily on biophysical and managerial factors, particularly yield performance and irrigation intensity. Improving irrigation scheduling, enhancing soil moisture retention, and increasing on-farm rainwater harvesting could substantially reduce total WF in irrigation-dependent provinces. Likewise, promoting high-yield varieties and implementing crop zoning aligned with basin-level water availability would support the sustainable expansion of Thailand's medicinal herb sector, consistent with the goals of the national Bio-Circular-Green policy framework (Ministry of Higher Education Science Research and Innovation 2019).

4.2. Comparative Evaluation of Water Footprint Components

A comparative appraisal of the component shares revealed clear differences in hydrological dependence among the four medicinal herbs. *Curcuma longa* exhibited a predominance of green water, reflecting substantial reliance on effective rainfall and comparatively limited irrigation substitution under typical cultivation practices. This pattern aligns with the WFN accounting construct, in which green WF traces crop evapotranspiration sourced from precipitation stored in the root zone (Mekonnen & Hoekstra 2011). In contrast, *Kaempferia parviflora* showed a moderate blue-water reliance (42%), whereas *Andrographis paniculata* and *Momordica charantia* were strongly blue-dominant with blue fractions exceeding 75%. Global benchmarking literature consistently demonstrates that irrigation-intensive cropping systems tend to elevate blue WF, particularly in regions with pronounced rainfall deficits or erratic seasonal precipitation (Mekonnen & Hoekstra 2014).

When the component shares are interpreted against national crop benchmarks, the magnitude of blue-water reliance among the herbs becomes more evident. The relatively high green-water share of *Curcuma longa* is biophysically plausible because C3 crops typically exhibit lower intrinsic water-use efficiency than C4 crops such as sugarcane (Chaibandit et al. 2017). Correspondingly, the high total and blue footprints of *Andrographis paniculata* and *Momordica charantia* align with the well-established inverse relationship between the unit WF and agricultural productivity; lower yields inflate volumetric footprints when evapotranspiration is broadly similar across species (Lovarelli et al. 2016). These comparative signals indicate that agronomic interventions that increase yield per unit area while keeping crop water use relatively stable offer a direct and effective lever to reduce unit WF without requiring geographic shifts in production (Lovarelli et al. 2016).

The component profiles also imply distinct management priorities. For *Curcuma longa*, where green water dominates,

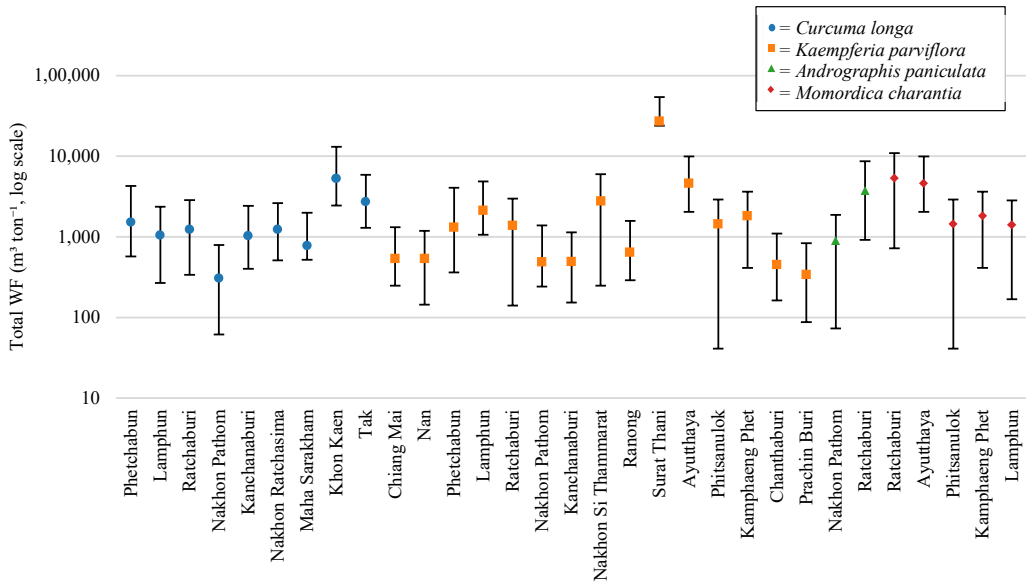


Fig. 2: Provincial distribution of total WF of four medicinal herbs. Note: Vertical lines represent provincial range (min–max), and markers indicate cultivation-area-weighted average values.

improvements in soil moisture retention and rainwater management could yield substantial efficiency gains. Practices such as residue retention, mulching, and enhanced infiltration can stabilize the effective use of precipitation and reduce the need for supplemental irrigation (Mekonnen & Hoekstra 2014). For blue-dominated herbs, field-level irrigation efficiency becomes central. Opportunities include improved irrigation scheduling based on crop evapotranspiration, adoption of water-saving delivery systems, and monitoring tools that minimize abstraction from blue sources (Mekonnen & Hoekstra 2020). In practice, component-aware strategies are complementary: enhancing green-water capture reduces irrigation demand, while precise irrigation improves the productivity of each cubic meter abstracted from blue sources (Mekonnen & Hoekstra 2014).

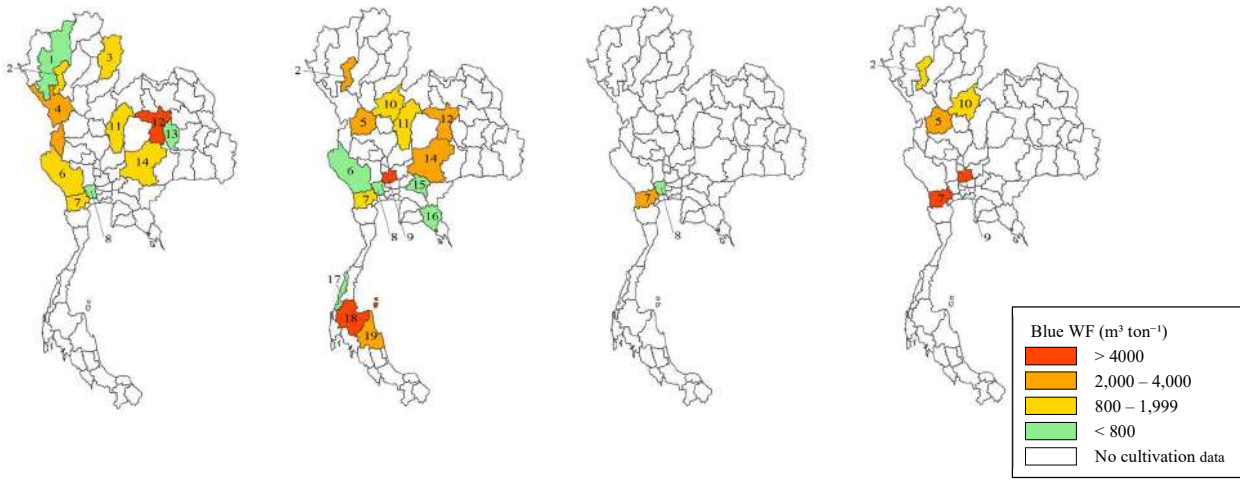
Positioning these findings within Thailand's broader evidence base highlights the importance of component-specific benchmarking. Previous national studies have documented substantial blue-water use in intensively managed crop systems and have recommended allocation frameworks that account for basin-level scarcity when promoting high-value agriculture expansion (Gheewala et al. 2014). The present comparative assessment shows that medicinal herbs differ markedly in their green-blue balances, indicating that uniform policy guidance is unlikely to be effective. Rather, crop-specific and component-specific performance targets, supported by agronomic improvements and basin-aware siting, provide a more credible pathway to lowering unit WF while maintaining market supply (Mekonnen & Hoekstra 2014).

4.3. Provincial Analysis of Blue WF and Its Relationship with Water Scarcity

The spatial distribution of blue WF among the four medicinal herbs revealed distinct irrigation-dependence patterns (Fig. 3(a–d)). When blue WF values were overlaid with the WSI of Thailand's 25 river basins, clear hotspots emerged where cultivation coincided with medium-to-high water-stress zones. These findings align with previous evaluations by Hoekstra and Mekonnen (2012) and Mekonnen and Hoekstra (2011) and with the national-scale assessment of Gheewala et al. (2014). Collectively, these studies demonstrate that geographic placement and irrigation strategy strongly govern water-use efficiency in Thailand's agricultural systems.

For *Curcuma longa*, blue WF remained relatively low across most Northern provinces (≤ 400 m³ ton⁻¹), reflecting predominantly rain-fed production. However, in the Chao Phraya Basin, particularly Nakhon Pathom and Suphan Buri, blue WF exceeded 100 m³ ton⁻¹ in areas already experiencing moderate water stress (WSI $\approx$ 0.25–0.30) (Gheewala et al. 2014). This suggests that even for a relatively water-efficient crop such as *Curcuma longa*, expansion into irrigation zones may heighten local water scarcity pressures.

Kaempferia parviflora exhibited markedly higher blue WF values (> 1,000 m³ ton⁻¹), with hotspots in Khon Kaen



(a) *Curcuma longa* (b) *Kaempferia parviflora* (c) *Andrographis paniculata* (d) *Momordica charantia*

1-Chiang Mai
2-Lamphun
3-Nan
4-Tak
5-Kamphaeng Phet
6-Kanchanaburi
7-Ratchaburi
8-Nakhon Pathom
9-Ayutthaya
10-Phitsanulok
11-Phetchabun
12-Khon Kaen
13-Maha Sarakham
14-Nakhon Ratchasima
15-Prachin Buri
16-Chanthaburi
17-Ranong
18-Surat Thani
19-Nakhon Si Thammarat

Fig. 3: Provincial distribution of blue WF (m³ ton⁻¹) for: (a) *Curcuma longa*, (b) *Kaempferia parviflora*, (c) *Andrographis paniculata*, and (d) *Momordica charantia*.

and Nakhon Ratchasima located within the Mun-Chi Basin, where WSI ranged from 0.47 to 0.93 (Gheewala et al. 2014). These findings reflect the high irrigation dependence of *Kaempferia parviflora* cultivation and its potential to intensify water competition in drought-prone environments. Similar blue-water pressures have been documented for cassava and sugarcane grown in Northeastern Thailand (Kaewjampa et al. 2016), as well as intensively irrigated sugarcane systems in Eastern Thailand (Chaibandit et al. 2017). Regional hydrological studies also show that such irrigation intensities can amplify seasonal water shortages during dry years (Chanakanachai & Lekunwong 2000).

For *Andrographis paniculata*, blue WF constituted more than 70% of the total footprint across Central Thailand. Ratchaburi recorded extreme values exceeding 4,000 m^3 ton^{-1}, even though the Mae Klong Basin exhibits a relatively low WSI ($\approx$ 0.018) (Gheewala et al. 2014). Such elevated blue WF under low scarcity conditions suggests opportunities for on-farm water-use efficiency improvements, such as surface-irrigation modernization or improved recycling. By contrast, Nakhon Pathom combines a moderate WSI ($\approx$ 0.29) with blue WF above 1,100 m^3 ton^{-1}, making it a priority zone for irrigation optimization and the adoption of water-saving systems (Allen et al. 1998).

Provincial blue WF values for *Momordica charantia* reached up to 2,500 m^3 ton^{-1} in hotspots such as Ratchaburi and Ayutthaya, coinciding with moderate-to-high WSI values (0.02–0.34). These patterns align with global analyses by Mekonnen & Hoekstra (2011, 2020), which emphasize that irrigated horticultural crops can generate localized water competition even in moderately stressed basins. The concurrence between high blue WF and water scarcity suggests that *Momordica charantia* is particularly sensitive to basin-level hydrological constraints.

To further clarify these relationships, provincial blue WF values were plotted against basin-level WSI (Fig. 4). Rather than a single linear response, the data revealed heterogeneous clusters driven by crop type and location. Provinces combining medium-to-high WSI with elevated blue WF, such as Nakhon Pathom and Khon Kaen, represent priority hotspots for risk management in irrigated herb production (Gheewala et al. 2014). Conversely, Ratchaburi in the Mae Klong Basin (WSI $\approx$ 0.018) displayed high blue WF despite low scarcity conditions, indicating substantial room for efficiency improvement rather than systemic scarcity limitations (Allen et al. 1998).

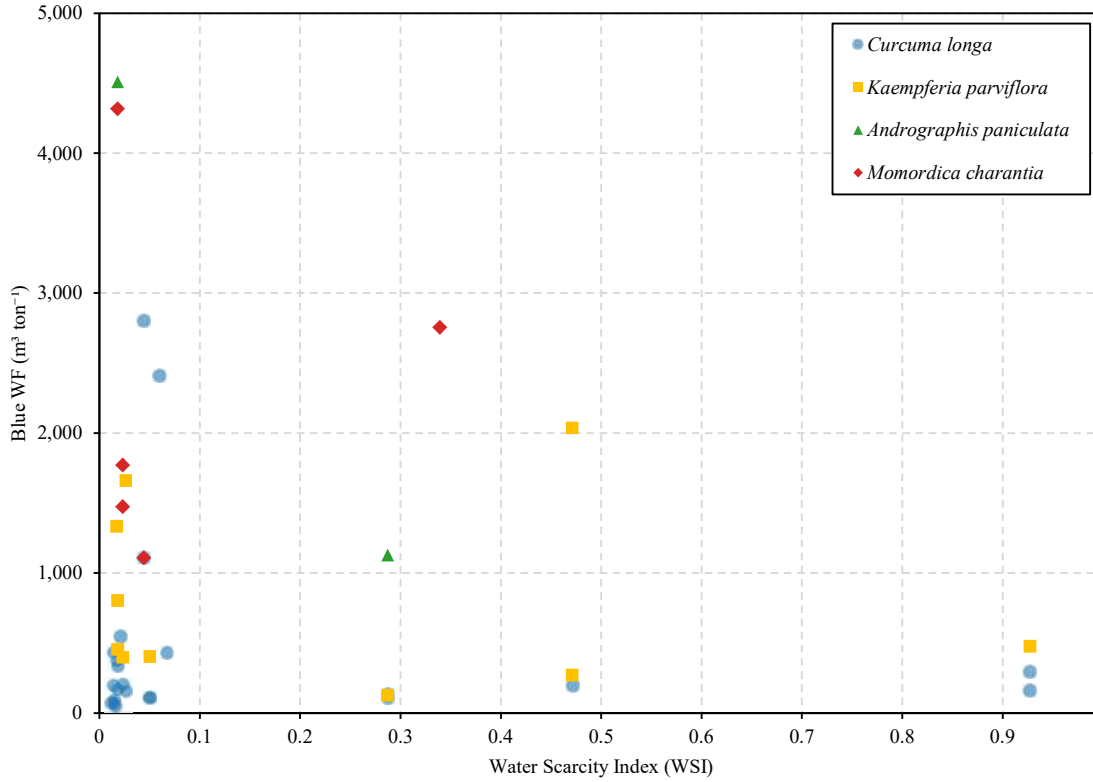


Fig. 4: Provincial blue WF versus basin-level WSI for four medicinal herbs.

From a management perspective, these findings support herb- and basin-specific strategies. Improving irrigation efficiency and field-level water-use management would be particularly effective in provinces where WSI is low, but blue WF is high (Li et al. 2022). Conversely, in provinces where both blue WF and WSI are high, prioritizing production system adjustments or potential relocation may be more appropriate (Osborne & Sack 2012). The interpretive emphasis thus lies on spatially targeting interventions rather than on deriving a single national correlation metric.

4.4. Limitations and Future Work

Although this assessment provides a comprehensive evaluation of the green, blue, and gray WFs of economically important Thai medicinal herbs, several limitations must be acknowledged. The first relates to data availability and spatial resolution. Climatic and agricultural datasets were aggregated at the provincial level, which may obscure local-scale variability in farming practices, irrigation performance, and microclimatic conditions. Likewise, the use of long-term climatic averages may mask inter-annual fluctuations in evapotranspiration and effective rainfall, particularly under increasingly variable monsoon conditions.

Second, the gray WF estimates rely on generalized parameter values for nitrogen leaching fractions and threshold nitrate concentrations. Although these values are consistent with WFN recommendations, regional differences in soil-water interactions and fertilizer management may lead to deviations from the assumed conditions. Future work would benefit from site-specific nitrogen leaching measurements and probabilistic modeling frameworks to better represent uncertainty and capture spatial heterogeneity.

Third, the present study focuses solely on the cultivation stage. Post-harvest processes, including drying, extraction, and primary processing, were excluded to maintain consistency with WFN methodological boundaries. However, these downstream stages may substantially increase total WF, especially when herbs undergo intensive processing for medicinal or nutraceutical applications. Incorporating these stages within a more comprehensive life-cycle framework would enhance the policy relevance of future assessments.

Finally, this study does not account for economic or social dimensions of water use, such as value added per unit of water or farmer exposure to water scarcity. Including such indicators would enable a multidimensional evaluation of water productivity, integrating biophysical, economic, and social-justice perspectives.

Future research should therefore concentrate on developing high-resolution, site-specific datasets that more accurately capture agroecological variability, while also integrating water-footprint results with other environmental indicators, such as carbon and land-use footprints, to reveal potential cross-impact trade-offs. In parallel, embedding an economic and social valuation perspective into future assessments would allow the optimization of herb production systems under Thailand's net-zero and BCG policy initiatives. Such integrated approaches will enhance the robustness of decision-making for sustainable water allocation and climate-smart medicinal herb cultivation.

5. CONCLUSIONS

This study successfully quantified the green, blue, and gray water footprints (WF) of four economically significant Thai medicinal herbs: *Curcuma longa*, *Kaempferia parviflora*, *Andrographis paniculata*, and *Momordica charantia, using* the standardized WFN methodology. The results demonstrate that water resource appropriation varies substantially across species, with blue water being the dominant component for most herbs, reflecting a high dependency on irrigation systems within Thailand's agricultural sector.

Among the studied species, *Curcuma longa* exhibited the most favorable water-use profile with the lowest total WF, primarily due to its high reliance on green water and suitability for rain-fed cultivation. Conversely, *Momordica charantia* and *Andrographis paniculata* showed significantly higher water intensities, particularly in regions where intensive irrigation is required to maintain yields. Spatial analysis further identified critical geographic hotspots, such as Ratchaburi and Khon Kaen, where high blue WF values coincide with basins experiencing moderate-to-high water scarcity, indicating potential risks to local water security.

Sensitivity analysis confirmed that crop yield is the most critical factor influencing the total WF across all species. This finding highlights that agronomic improvements aimed at yield enhancement remain the most effective strategy for reducing the volumetric water footprint per ton of product. Furthermore, benchmarking these results against major food and industrial crops suggests that even relatively efficient herbs can exert substantial pressure on freshwater resources if cultivation scales rapidly without proper water management.

In conclusion, the findings provide a robust evidence base for sustainable water planning in the herbal sector. To mitigate environmental impacts, policy interventions should prioritize the adoption of water-saving irrigation technologies, site-specific nutrient management, and crop zoning aligned with regional water availability. These strategies will be essential for balancing the economic expansion of Thailand's medicinal herb industry with the long-term sustainability of national water resources.

6. ACKNOWLEDGMENTS

We sincerely thank the Faculty of Engineering, Thammasat School of Engineering, Thammasat University for their generous support and the provision of essential research equipment, which significantly contributed to the success of this study.

7. REFERENCES

Ababaei, B. and Etedali, H.R., 2017. Water footprint assessment of main cereals in Iran. *Agricultural Water Management*, 179, pp. 401–411. [DOI]

Allen, R.G., Pereira, L.S., Raes, D. and Smith, M., 1998. *Crop Evapotranspiration: Guidelines for Computing Crop Water Requirements (FAO Irrigation and Drainage Paper No. 56)*. FAO, Rome, Italy. Available at: https://www.fao.org/3/x0490e/x0490e00.htm (Accessed: 14 October 2025).

Chaibandit, K., Konyai, S. and Slack, D.C., 2017. Evaluation of the water footprint of sugarcane in eastern Thailand. *Engineering Journal*, 21(5), pp. 193–201. [DOI]

Chanakanachai, W. and Lekunwong, S., 2000. *Guide for Cultivation of Herbal Plants (1st ed., in Thai)*. Department of Agricultural Extension, Ministry of Agriculture and Cooperatives, Bangkok, Thailand.

Department of Thai Traditional and Alternative Medicine, 2023. Announcement on herbal champion products B.E. 2566 (in Thai). Ministry of Public Health, Thailand.

Gheewala, S.H., Silalertruksa, T., Nilsalab, P., Mungkung, R., Perret, S.R. and Chaiyawannakarn, N., 2014. *Water* footprint and impact of water consumption for food, feed, fuel crops production in Thailand. Water, 6(6), pp. 1698–1718. [DOI]

Hoekstra, A.Y. and Mekonnen, M.M., 2012. The water footprint of humanity. *Proceedings of the National Academy of Sciences*, 109(9), pp. 3232–3237. [DOI]

Hoekstra, A.Y., Chapagain, A.K., Aldaya, M.M. and Mekonnen, M.M., 2011. *The Water Footprint Assessment Manual: Setting the Global Standard*. Earthscan, London, UK.

Kaewjampa, N., Chaisri, N. and Boonthaiwai, C., 2016. Comparison of the water footprint of cassava and sugarcane in Northeast Thailand. *International Journal of Environmental and Rural Development*, 7(2), pp. 18–23.

Li, Z., Wu, H. and Deng, X., 2022. Spatial pattern of water footprints for crop production in northeast China. *Sustainability*, 14(20), p. 13649. [DOI]

Lovarelli, D., Bacenetti, J. and Fiala, M., 2016. Water footprint of crop productions: A review. *The Science of the Total Environment*, 548–549, pp. 236–251. [DOI]

Mekonnen, M.M. and Hoekstra, A.Y., 2011. The green, blue and grey water footprint of crops and derived crop products. *Hydrology and Earth System Sciences*, 15(5), pp. 1577–1600. [DOI]

Mekonnen, M.M. and Hoekstra, A.Y., 2014. Water footprint benchmarks for crop production: A first global assessment. *Ecological Indicators*, 46, pp. 214–223. [DOI]

Mekonnen, M.M. and Hoekstra, A.Y., 2020. Sustainability of the blue water footprint of crops. *Advances in Water Resources*, 143, p. 103679. [DOI]

Ministry of Higher Education Science Research and Innovation (MHESRI), 2019. BCG in action: the new sustainable growth engine-model for sustainable development economics (in Thai). Ministry of Higher Education Science Research and Innovation, Thailand.

Mungkung, R., Gheewala, S.H., Silalertruksa, T. and Dangsiri, S., 2019. Water footprint inventory database of Thai rice farming for water policy decisions and water scarcity footprint label. *The International Journal of Life Cycle Assessment*, 24(12), pp. 2128–2139. [DOI]

Ngamsomjit, W., 2008. *Study of Water Consumption of Five Medicinal Herbs: Year 3 (in Thai)*. Royal Irrigation Department, Bangkok, Thailand.

Osborne, C.P. and Sack, L., 2012. Evolution of C4 plants: a new hypothesis for an interaction of CO2 and water relations mediated by plant hydraulics. *Philosophical Transactions of the Royal Society B Biological Sciences*, 367(1588), pp. 583–600. [DOI]

Ratchawat, T., Panyatona, S., Nopchinwong, P., Chidthaisong, A. and Chiarakorn, S., 2020. Carbon and water footprint of Robusta coffee through its production chains in Thailand. *Environment, Development and Sustainability*, 22(3), pp. 2415–2429. [DOI]

Suttayakul, P., Kittikun, A., Suksaroj, C., Mungkalasiri, J., Wisansuwannakorn, R. and Mukikavong, C., 2016. Water footprints of products of oil palm plantations and palm oil mills in Thailand. *The Science of the Total Environment*, 542(Pt A), pp. 521–529. [DOI]

Nature Environment and Pollution Technology
An International Quarterly Peer-Reviewed Open Access Journal

p-ISSN: 0972-6268 | e-ISSN: 2395-3454 Vol. 25 | No. 4 | Article ID B4437 | 2026

REVIEW ARTICLE https://doi.org/10.46488/NEPT.2026.v25i04.B4437 OPEN ACCESS

Sustainable Advances in Phosphorus Removal and Recovery from Industrial Wastewater

Md Adim, Mohd Imran Siddiqui, Hasan Rameez, Izharul Haq Farooqi and Farrukh Basheer†
Department of Civil Engineering, Zakir Husain College of Engineering and Technology, Aligarh Muslim University, Aligarh 202002, India
†Corresponding author: Farrukh Basheer; farrukhbasheer.cv@amu.ac.in

ARTICLE HISTORY

Received: 28-02-2026
Revised: 18-04-2026
Accepted: 02-05-2026

KEYWORDS

Phosphorus removal
Eutrophication
Wastewater treatment
Struvite crystallization
Electrocoagulation
Bioelectrochemical systems

CITE THIS ARTICLE

Adim, M., Siddiqui, M. I., Rameez, H., Farooqi, I. H. and Basheer, F., 2026. Sustainable advances in phosphorus removal and recovery from industrial wastewater. *Nature Environment and Pollution Technology*, 25(4), B4437. https://doi.org/10.46488/NEPT.2026.v25i04.B4437

COPYRIGHT & LICENCE

© 2026 The Authors
Open Access under CC BY 4.0.

PUBLISHED BY

TECHNOSCIENCE PUBLICATIONS

ABSTRACT

Phosphorus, an essential nutrient and a finite resource, poses significant environmental challenges when discharged into water bodies from industrial wastewater, contributing to eutrophication and ecosystem degradation. Concurrently, its recovery offers a sustainable pathway to address resource scarcity. This review critically evaluates recent progress in phosphorus removal and recovery technologies, emphasizing five widely recognized approaches: (i) biological processes, such as aerobic granular sludge and enhanced biological phosphorus removal (EBPR); (ii) chemical precipitation using agents like lime and metal salts; (iii) struvite crystallization; (iv) electrocoagulation (EC) and (v) Bioelectrochemical Systems (BES) for phosphorus recovery. The assessment focuses on these methods' efficiency, feasibility, and sustainability, highlighting their strengths and limitations. These strategies can foster environmentally sustainable wastewater treatment, mitigate eutrophication risks, and reduce dependence on finite phosphate resources.

1. INTRODUCTION

The rapid growth of industry and urbanization has led to the discharge of phosphorus-rich wastewater, leading to eutrophication in water bodies. Excessive phosphorus promotes harmful algal blooms (HABs), which deplete oxygen and release toxins like microcystin, threatening aquatic ecosystems (Wang et al. 2024). Effective phosphorus removal and recovery strategies are essential to mitigate these environmental impacts.

1.1. Sources and Challenges in Phosphorus Removal from Wastewater

Phosphorus primarily enters wastewater from agricultural runoff, industrial effluents, and domestic sewage. Industries such as slaughterhouses, food processing plants, and fertilizer production facilities contribute high concentrations of organic matter and phosphorus, necessitating efficient treatment solutions (Cao & Mehrvar 2011). Removing phosphorus from wastewater is generally achieved through physicochemical or biological methods to enhance phosphorus elimination (Mahvi et al. 2011).

Biological phosphorus removal generally relies on enhanced biological phosphorus removal (EBPR). In this method, specific microorganisms known as polyphosphate-accumulating organisms (PAOs) play a key role. These PAOs absorb phosphorus from the water and store it inside their cells as polyphosphate.

While EBPR is cost-effective and sustainable, it requires large reactor capacities, high biomass concentrations, long hydraulic retention times (HRT), and precise sludge management (Bazrafshan et al. 2012).

Conventionally, phosphorus removal relied on chemical precipitation, which required additional coagulants such as lime ($Ca(OH)_2$), ferric chloride ($FeCl_3$), or aluminum sulfate ($Al_2(SO_4)_3$) (Mahvi et al. 2011). While effective, these methods generate substantial sludge, leading to high disposal costs and potential secondary pollution (Drogui et al. 2008). As a result, there is an increasing need for integrated and sustainable approaches that optimize phosphorus removal while ensuring economic and environmental viability.

1.2. Phosphorus Recovery: A Sustainable Solution

Phosphorus (P) is a nonrenewable resource essential for every living organism (Van Phuong 2025). It constitutes approximately 2–4% of the total solid mass of biological organisms and serves as a crucial nutrient for all life forms, playing a pivotal role in shaping genetic components (Karl 2000). Phosphate rock, the primary source of naturally occurring phosphorus, serves the fertilizer production industry to sustain global farming. However, phosphate rock reserves are depleting, raising concerns over long-term agricultural productivity. The US Geological Survey reports that approximately 73% of the world's phosphate reserves are concentrated in Morocco and Western Sahara, highlighting potential geopolitical and economic vulnerabilities in phosphorus supply (Fig. 1) (Jasinski 2017, Kok et al. 2018).

To address these challenges, phosphorus recovery from wastewater has emerged as a sustainable strategy. Studies estimate that 15–20% of the global phosphorus demand could be met through wastewater-derived phosphorus recovery, reducing dependency on phosphate rock mining while mitigating environmental pollution (Kok et al. 2018). Phosphorus in wastewater mainly exists as orthophosphates, and treatment plants can recover it through biological processes, chemical precipitation, adsorption, struvite crystallization, and electrocoagulation (Wang et al. 2024).

1.3. Scope of This Review

Phosphorus fertilizers are essential for food security, contributing to nearly half of the world's food production (Grant et al. 2001, Cordell et al. 2009). Given the increasing global population and the limited availability of phosphate rock, improving phosphorus recovery from wastewater is imperative. Therefore, this review aims to provide an in-depth analysis of recent phosphorus removal and recovery technology advancements. The study examines five key treatment approaches:

1. Biological processes, including Aerobic Granular Sludge (AGS) and Enhanced Biological Phosphorus Removal (EBPR)
2. Chemical precipitation, using lime and metal salts
3. Struvite crystallization, for simultaneous phosphorus recovery and reuse
4. Electrocoagulation (EC), for efficient phosphorus removal

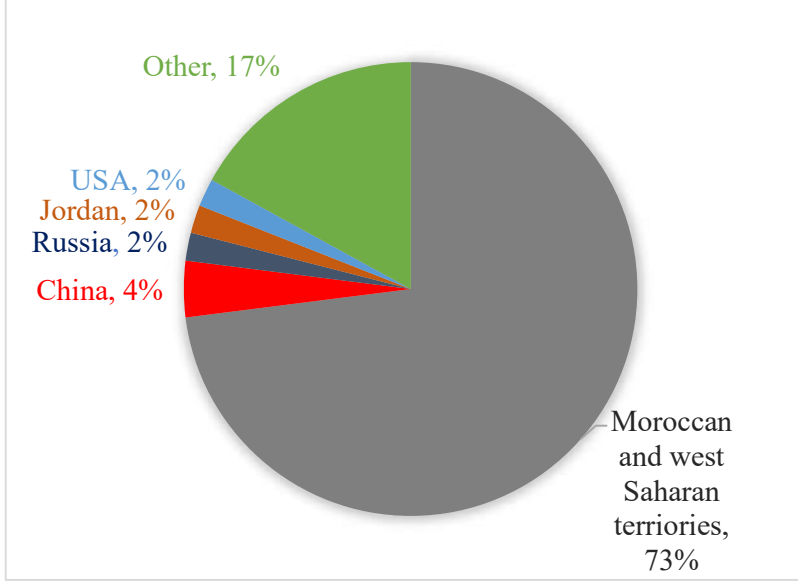


Fig. 1: Global distribution of estimated phosphorus reserves (Kok et al. 2018).

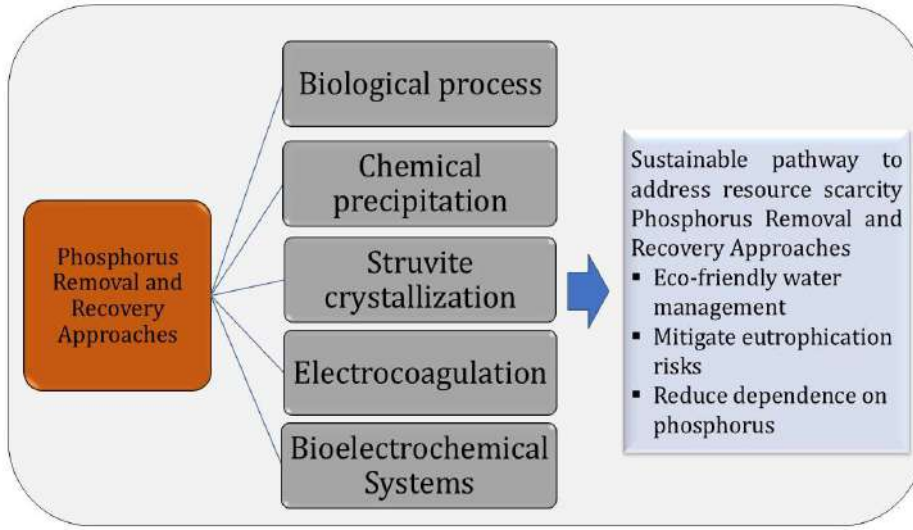


Fig. 2: Bioelectrochemical Systems (BES) for phosphorus recovery.

5. Bioelectrochemical systems (BES) for phosphorus recovery (Fig. 2).

This review highlights recent progress in sustainable phosphorus management and examines various phosphorus recovery methods, emphasizing their practicality, effectiveness, and cost-efficiency.

2. MATERIALS AND METHODS

This review was conducted using a systematic approach to ensure comprehensive coverage of phosphorus removal and recovery technologies. Relevant literature was collected from Scopus, Web of Science, ScienceDirect, and Google Scholar databases.

Keywords such as phosphorus removal, Eutrophication, Wastewater treatment, Struvite crystallization, electrocoagulation, and Bioelectrochemical Systems were used.

Studies published between 1999 and 2025 were considered, with emphasis on recent developments.

Selection criteria included: (i) relevance to wastewater treatment, (ii) quantitative reporting of phosphorus removal/recovery, (iii) availability of operational and economic data.

A total of 105 peer-reviewed articles were critically analyzed using a multi-criteria evaluation framework.

2.1. Evaluation Framework for Comparative Analysis

A multi-criteria evaluation framework was developed to enable a systematic comparison of phosphorus removal and recovery technologies. The framework considers four key criteria: (i) removal efficiency, (ii) recovery potential, (iii) operational and economic considerations (including energy demand and chemical usage), and (iv) technology readiness level (TRL) and scalability.

2.2. Phosphorus Concentrations in Wastewater

Anaerobically digested swine wastewater has been reported to contain 612 mg L^{-1} Total Phosphorus (TP), with 36% (221 mg L^{-1}) present as dissolved phosphate (PO_4^{3-}-P) (Kim et al. 2017). Likewise, abattoir effluent has significant variability in TP concentrations, spanning from 15 to 785 mg L^{-1} (Ge et al. 2015, Lemaire et al. 2009).

In contrast, due to dilution effects, cellulose, tannery, and aquaculture industries exhibit significantly lower TP concentrations. The aquaculture sector, with large effluent volumes (10,000 million liters per day), has TP concentrations as low as 0.3–2.3 mg L^{-1} (Schulz et al. 2003), while tannery and cellulose wastewater typically report TP levels below 1 mg L^{-1} (Chamorro et al. 2010).

The proportion of phosphate within TP varies across industries. In tannery and aquaculture wastewater, phosphate constitutes 33% and 35% of TP, respectively (Kim et al. 2017, Lefebvre et al. 2005). The slaughter industry, however, demonstrates the highest proportion of phosphate, ranging from 85% to 95% of TP, with corresponding PO_4^{3-} –P concentrations between 25 and 230 mg L^{-1} (Lemaire et al. 2009, Ge et al. 2015, Ashraf & Farooqi 2022).

Compared to industrial wastewater, residential wastewater generally exhibits lower total phosphorus (TP) values, ranging from 5 to 30 mg L^{-1}, depending on whether the sources are urban or rural. However, a substantial portion (57–95%) of TP in domestic wastewater is inorganic phosphate (Andrés et al. 2018, Sengupta & Pandit 2011, Pronk et al. 2015).

Table 1: Physicochemical properties of various wastewater categories (Carrillo et al. 2020, Ashraf & Farooqi 2022).

Wastewater	pH	COD (g L^{-1})	TN (mg L^{-1})	TP (mg L^{-1})	PO_4^{3-}-P (mg L^{-1})
Domestic	7.0–8.5	0.2–1.0	28–100	5.0–30	4.0–20
Abattoir	6.8–7.3	2.9–68	294–670[a]	28–49	23–40
Poultry	6.9–7.9	1.8–12	98–1825[a]	15–446	7.0–28
Swine	6.8–7.8	25–60	2350–3570	194–780	45–221
Dairy manure	7.0–8.3	1.2–38	65–3305[a]	12–266	8.5–13
Slaughterhouses	6.8–8.5	4.7–6.2	180–256a	-	130–256

a Values for Total Kjeldahl Nitrogen (TKN) fall within this range.

From an environmental perspective, even low TP concentrations (0.03–1 mg L^{-1}) in continental water bodies such as rivers and lakes can trigger eutrophication (Carrillo et al. 2020).

The physicochemical properties of various wastewater categories, including TP levels, are summarized in Table 1.

2.3. Analysis of Phosphorus in Wastewater

The ammonium molybdate spectrophotometric method, introduced in 1962, is widely recognized as a straightforward, reliable, and standard technique for measuring dissolved inorganic phosphorus (IP), such as orthophosphate, as well as total phosphorus (TP). Phosphorus can be measured as orthophosphate (PO_4^{3-}) or phosphate phosphorus (PO_4^{3-}-P). PO_4^{3-} denotes the number of orthophosphate molecules in a sample, whereas PO_4^{3-}-P quantifies the number of phosphorus ions present in a sample (APHA 2012). The ascorbic acid method is commonly used to determine phosphorus in water. It involves the reaction of phosphate ions with molybdate ions (MoO_4^{2-}), forming phosphomolybdate $[PO_4(MoO_3)_{12}]^{3-}$. When reduced by ascorbic acid, this compound produces a blue complex, which is measured using a spectrophotometer (APHA 2012).

Flow injection analysis (FIA), developed in 1975 (Ruzicka & Hansen 1975), is a rapid, accurate, and automated technique for phosphorus (P) detection in water, utilizing the ammonium molybdate spectrophotometric method with a flow-through detector. Despite its advantages, FIA can be affected by metal ion interference and high salinity (Alam et al. 2021). Inductively coupled plasma (ICP) techniques, such as ICP-AES and ICP-MS, offer high sensitivity for elemental P detection, with ICP-MS achieving ultra-low detection limits (ng L^{-1} to µg L^{-1} levels) through high-resolution mass analyzers that mitigate interferences (Alam et al. 2021, Miller-Ihli & Baker 2001). Ion chromatography (IC), particularly ion-exchange chromatography with suppressed conductivity detection, provides high sensitivity and accuracy for phosphate and total phosphorus (TP) analysis (Lu et al. 2002, Ruiz-Calero & Galceran 2005).

Gas chromatography (GC) and liquid chromatography (LC), commonly coupled with mass spectrometry (MS), are widely used for organophosphorus (OP) compound analysis, with LC-MS being especially effective for thermally unstable and polar OP species, achieving detection limits as low as ng L^{-1} (Gao et al. 2013, Wang et al. 2009). Additionally, spectroscopic techniques such as ^{31}P-NMR allow non-destructive qualitative and quantitative analysis of P species, though they exhibit higher detection limits (mg L^{-1} level) and are susceptible to matrix interferences (Cade-Menun 2005, Chen 1999). Each method presents distinct advantages for P analysis in wastewater, with FIA and IC being rapid and sensitive, ICP offering elemental specificity, GC/LC-MS excelling in OP detection, and ^{31}P-NMR providing valuable structural insights.

3. RESULTS AND DISCUSSION

3.1. Biological Processes

Biological phosphorus removal involves the use of microorganisms to uptake and store phosphorus.

Aerobic granular sludge (AGS): A biofilm-based system in which microbial granules form under aerobic conditions, enhancing nutrient removal efficiency.

Enhanced biological phosphorus removal (EBPR): A process that uses polyphosphate-accumulating organisms (PAOs) to store phosphorus as intracellular polyphosphate. PAOs take up phosphorus under aerobic conditions and release it under anaerobic conditions, enabling efficient removal and recovery.

3.1.1. Aerobic Granular Sludge

Aerobic granular sludge (AGS) is a biological system containing bacteria, protozoa, and fungi that efficiently oxidize organic pollutants using oxygen. AGS systems are adaptable to various wastewater conditions, making them suitable for treating various industrial effluents with fluctuating characteristics (de Carvalho et al. 2021).

3.1.2. Mechanism of Phosphorus Removal and Nutrient Removal Efficiency

AGS systems facilitate phosphorus removal from wastewater through various mechanisms, including biological uptake by phosphate-accumulating organisms (PAOs) within the granules. Phosphate-accumulating organisms (PAOs) store phosphorus as intracellular polyphosphate and remove it with excess sludge. Aerobic granular sludge simplifies the enhanced biological phosphorus removal (EBPR) process within sequencing batch reactors (SBRs), ensuring efficient phosphorus elimination from wastewater. It is highly effective at removing carbon and nutrients, which helps prevent environmental contamination and safeguard aquatic ecosystems. This approach reduces the discharge of nutrients, such as phosphorus, which can contribute to eutrophication in receiving waters. The AGS system achieves this through the formation of microbial aggregates, the production of extracellular polysaccharides (EPS), and the stabilization provided by hydrodynamic shear forces (de Sousa Rollemberg et al. 2018).

3.1.3. Comparison with Conventional Activated Sludge and Operational Considerations

Compared to the conventional activated sludge system (CAS), aerobic granular sludge (AGS) offers several significant advantages. AGS forms larger and denser sludge granules, typically exceeding 0.2 mm in diameter, which allows for faster settling rates ranging from 30 to 90 meters per hour. This improved settling capacity makes AGS more resilient to toxic substances, enhancing its ability to withstand fluctuating wastewater conditions (de Carvalho et al. 2021). Additionally, AGS is considerably more efficient in terms of resource usage. It requires 75% less land area, consumes 30–50% less energy, and produces 30% less sludge, making it a more sustainable and cost-effective wastewater treatment solution (de Carvalho et al. 2021, Hamza et al. 2022). Overall, AGS technology offers a promising approach for efficient phosphorus removal from industrial wastewater while providing advantages such as reduced footprint, enhanced nutrient removal, and lower operational costs. It is important to note that the successful implementation of AGS technology requires careful design, operation, and monitoring to achieve the desired treatment goals. Furthermore, recent studies have shown the ability of SBRs to simultaneously nitrify, denitrify, and remove phosphorus under low-temperature conditions at 10°C, with overall phosphorus removal efficiencies up to 98% (Hamza et al. 2022, Li et al. 2019). AGS systems require monitoring and adjusting operating parameters, such as dissolved oxygen levels, pH, and nutrition management, for optimal functioning. Advanced process control technologies can enhance the accuracy of treatment process modifications.

3.1.4. Enhanced Biological Phosphorus Removal (EBPR) and Recovery

Henze et al. (2008) noted that enhanced biological phosphorus removal (EBPR) systems, developed in the late 1950s, became a widely adopted method for phosphorus removal due to growing concerns about eutrophication.

3.1.5. Role of Polyphosphate-Accumulating Organisms (PAOs) in EBPR Systems

EBPR is a commonly used technology in CAS systems for phosphorus (P) removal in wastewater treatment plants (WWTPs) (Izadi et al. 2021). The success of EBPR relies on enriching polyphosphate-accumulating organisms (PAOs) in activated sludge. Key PAOs include *Pseudomonas putida*, *Aeromonas* spp., *Candidatus Halomonas phosphatis*, *Candidatus Accumulibacter phosphatis*, and members of the *Rhodocyclus* genus, which are key bacterial groups involved in enhanced biological phosphorus removal (EBPR) systems. Among them, *Candidatus Accumulibacter phosphatis* is the most prevalent and plays the most critical role in phosphorus uptake and storage, making it the primary polyphosphate-accumulating organism (PAO) in these systems (Joshi & Sharma 2025; Liu et al. 2019; Bunce et al. 2018). Polyphosphate-accumulating organisms (PAOs) remove phosphorus from wastewater through luxury uptake by cycling between anaerobic and aerobic conditions. In the anaerobic phase, they absorb volatile fatty acids (VFAs), storing them as energy reserves while releasing some phosphorus. During the aerobic phase, they use this stored energy to absorb large amounts of phosphorus, enhancing removal efficiency.

3.1.6. Biochemical Mechanisms of EBPR: Anaerobic and Aerobic Phases

Based on the *Accumulibacter* biochemical model, enhanced biological phosphorus removal (EBPR) occurs through alternating anaerobic and aerobic (or anoxic) phases governed by the metabolic activity of polyphosphate-accumulating organisms (PAOs). Fig. 3 illustrates the transformation of key intracellular polymers, polyphosphate (poly-P), polyhydroxyalkanoates (PHA), and glycogen, highlighting the coupling between carbon uptake, energy generation, and phosphorus release and uptake (Henze et al. 2008).

Under anaerobic conditions (Fig. 3(a)), PAOs take up volatile fatty acids (VFAs), such as acetate and propionate, and store them as PHA (e.g., poly-β-hydroxybutyrate and poly-β-hydroxy valerate). This uptake is driven by the hydrolysis of intracellular poly-P, resulting in the release of orthophosphate (PO_4^{3-}) into the bulk liquid, while glycogen

degradation provides the reducing power required for PHA synthesis.

During the subsequent aerobic phase (Fig. 3(b)), stored PHA is oxidized to generate energy through the tricarboxylic acid (TCA) cycle. The resulting ATP supports cellular growth, replenishment of glycogen reserves, and enhanced phosphorus uptake, leading to the re-accumulation of poly-P within the cells. Under anoxic conditions, certain clades of *Accumulibacter* can utilize nitrate or nitrite as electron acceptors, enabling simultaneous denitrification and phosphorus uptake using PHA as the carbon source (Henze et al. 2008).

Overall, the mechanism illustrated in Fig. 3 emphasizes that EBPR performance is strongly dependent on the availability of readily biodegradable carbon sources and stable redox cycling conditions.

3.1.7. Challenges and Optimization Strategies for EBPR Systems

Despite its advantages, EBPR faces operational challenges that impact P-removal efficiency. Various factors, including temperature, pH, salt concentration, organic loading rate, wastewater substrate composition, and aeration control, influence the effectiveness of the process (Hamza et al. 2022). Rapid fluctuations in chemical oxygen demand (COD) can negatively impact the aerobic phase, with studies showing that excess COD can cause unintended phosphorus release under aerobic conditions (Guisasola et al. 2019). In anaerobic conditions, high nitrite, nitrate, and ammonia concentrations further disadvantage PAOs, leading to EBPR failure (Zhang et al. 2013). Researchers have applied metabolic modeling techniques to simulate anaerobic and aerobic metabolisms under various control factors, aiming to optimize EBPR performance and enhance PAO dominance over GAOs (Izadi et al. 2021).

3.2. Chemical Precipitation

Chemical precipitation is one of the primary commercial methods for phosphorus removal from wastewater effluents. Operators add soluble chemical agents, such as iron, aluminum, or lime, to wastewater. These agents react with phosphate compounds and form insoluble phosphates, which operators remove from the water. While biological removal processes exist, they are used to a lesser extent (Donnert & Salecker 1999, Penetra et al. 1999, Stratful et al. 1999). The effectiveness of chemical precipitation depends on factors like molar ratio, pH, and hydraulic retention time (HRT), which influence the crystallization of phosphate ions (PO_4^{3-}) into solid forms (Mehta et al. 2015). Recovery efficiencies range between 63% and 99%, with an average removal rate of 81% for dissolved nutrient removal processes (DNRP). Inorganic polyphosphate demonstrates a high retention rate of 92%, while organic phosphorus exhibits a slightly lower retention rate of 74%, indicating the need for additional treatment in some cases (Abel-Denee et al. 2018). Flow chart for phosphorus removal using chemical precipitation is shown in Fig. 4.

3.2.1. Chemical Agents and Their Effectiveness

The choice of precipitating agents is crucial for optimizing phosphorus removal efficiency. Commonly used chemicals include metallic salts such as aluminum, iron, magnesium, and calcium compounds in chloride or sulfate forms (Yin et al. 2020). Selecting a specific chemical depends on wastewater characteristics, including pH, temperature, and desired removal efficiency. Calcium phosphate typically crystallizes into hydroxyapatite (HAP), with the chemical formula $Ca_5(PO_4)_{3OH}$, whereas magnesium phosphate tends to form struvite ($MgNH_4PO_4 \cdot 6H_2O$) during the crystallization process. Additional chemicals, such as potassium ferrate (K_2FeO_4) and iron chloride ($FeCl_3$), have also been employed.

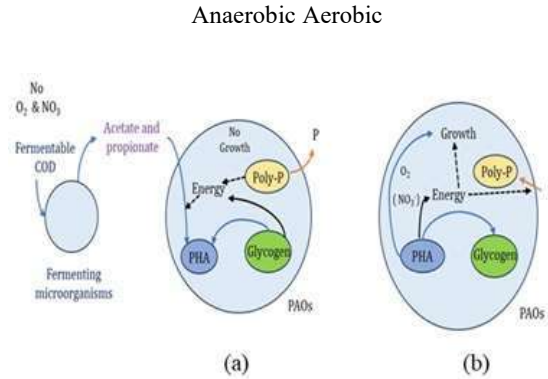
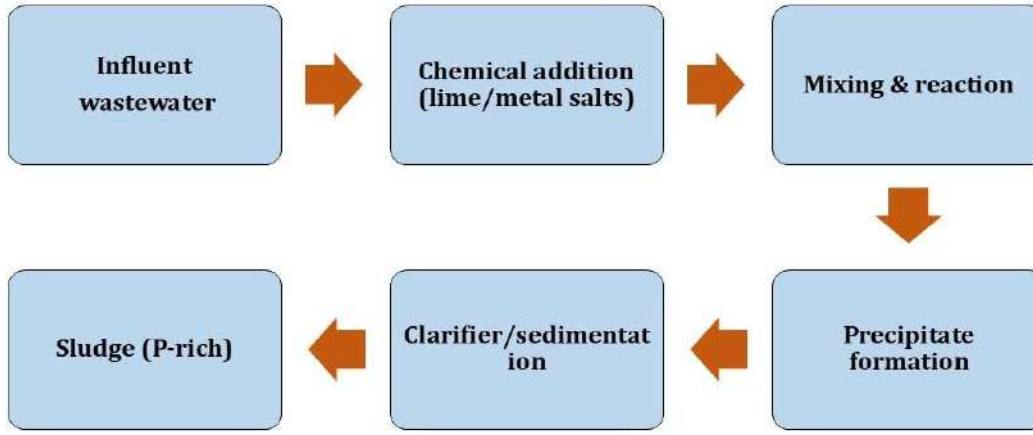


Fig. 3: Biochemical model of PAOs under anaerobic and aerobic conditions (Henze et al. 2008).



Fig, 4: Flow chart for phosphorus removal using chemical precipitation.

Studies have shown that potassium ferrate doses between 5 and 25 mg L^{-1} can retain over 80% of total phosphorus (TP) (Muster et al. 2013, Kwon et al. 2014, Peng et al. 2018). For struvite precipitation, magnesium sources include $MgCl_2$, MgO, and $Mg(OH)_2$, as well as alternative sources such as seawater and industrial wastewater from frozen fish processing plants (Nur et al. 2018, Huang et al. 2015, Hutnik et al. 2013, Crutchik & Garrido 2011, Wilsenach et al. 2007, Nelson et al. 2003).

3.2.2. Efficiency and Optimization of Phosphorus Recovery

Struvite precipitation is considered highly effective for phosphorus recovery due to its high purity (97–99%) and bioavailability (94%), making it comparable to premium-grade fertilizers (Melia et al. 2017). Maintaining the Mg:Ca ratio at 4:1 with a pH of 7.9 can produce struvite purity exceeding 98%. However, deviations in pH (below 7.5) or changes in the Mg:Ca ratio can introduce impurities (Muster et al. 2013). Various studies have demonstrated high efficiencies in phosphorus recovery through optimized molar ratios. For instance, Nelson et al. (2003) and Kim et al. (2017) achieved 95% efficiency with Mg:P molar ratios of 1.6:1 and 1.2:1, respectively. Similarly, Dai et al. (2017) reported an 86% precipitation efficiency for HAP with a Ca:P molar ratio of 2.5. Furthermore, electrodialysis has been explored for phosphorus recovery, with Ebbers et al. (2015) achieving 95% recovery at a low pH of 2.0. However, this method has drawbacks, including high energy consumption (1 kWh per 60 g of PO_4^{3-} recovery) and the need for chemical additives to regenerate membranes. These findings underscore the importance of tailored strategies to optimize phosphorus removal while balancing cost, efficiency, and environmental sustainability.

3.2.3. Lime Precipitation

Lime precipitation is a well-established method for wastewater treatment, particularly for the removal of phosphorus. The process is based on chemical interactions between calcium salts and phosphate species present in sewage. These reactions result in the formation of insoluble hydroxy phosphate lime precipitates, which can be readily separated from the aqueous phase. This reaction effectively removes Phosphorus from the water, helping to reduce phosphorus levels in the treated wastewater, which is vital for environmental and water quality management. The reaction equations are as follows:

$$5Ca^{2+} + 4OH^- + 3HPO_4^{2-} \rightarrow Ca_5(OH)(PO_4)_3 \downarrow + 3H_2O \quad ...(1)$$

$$Ca^{2+} + HCO^{3-} + OH^- \rightarrow CaCO_3 \downarrow + H_2O \quad ...(2)$$

Following the introduction of lime into phosphorus-containing wastewater, calcium carbonate is initially precipitated through the reaction of calcium ions with bicarbonate ions (Equation 2). Subsequently, the excess calcium ions react with phosphate ions, resulting in the formation of hydroxy phosphate lime precipitate (Equation 1). The precipitation process is strongly influenced by the presence of hydroxide ions, which are closely associated with the system's pH. Elevated pH values increase ionic concentrations in solution, thereby reducing the solubility of hydroxy phosphate lime and enhancing its precipitation. For optimal phosphorus removal, it is recommended that the pH be maintained above 10, as this condition favors the formation of hydroxy phosphate lime and significantly improves overall treatment efficiency (Zhou et al. 2008).

3.2.4. Metal Salt Precipitation

Phosphorus removal from water through metal salts, primarily aluminum and iron salts, involves a chemical process known as coagulation and precipitation. When phosphate ions in water react with introduced metal salts,

they form larger, insoluble particles. These insoluble particles effectively trap and encapsulate the phosphorus present in the water. Subsequently, the process involves the separation and removal of these particles, which results in the successful elimination of phosphorus from the water. This process is a common and effective method for reducing phosphorus levels in wastewater and surface water, helping to mitigate issues like eutrophication and pollution. The choice of metal salt and the specific conditions of the treatment process can be adjusted to optimize phosphorus removal based on the water's characteristics. The reactions illustrating the precipitation behavior of iron and aluminum salts are as follows:

$$Fe^{3+} + PO_4^{3-} \rightarrow FePO_4 \downarrow \quad ...(3)$$

$$3Fe^{2+} + 2PO_4^{3-} \rightarrow Fe_3(PO_4)_2 \downarrow \quad ...(4)$$

$$Al^{3+} + PO_4^{3-} \rightarrow AlPO_4 \downarrow \quad ...(5)$$

The above main reaction will also occur as a competitive reaction:

$$Fe^{3+} + 3OH^- \rightarrow Fe(OH)_3 \downarrow \quad ...(6)$$

$$Al^{3+} + 3OH^- \rightarrow Al(OH)_3 \downarrow \quad ...(7)$$

The described process involves the precipitation of insoluble phosphate compounds from phosphorus-containing sewage using metal salts, particularly Fe (III) and Al (III) salts. Adding metal salts containing Fe (III) or Al (III) causes the metal ions to react with phosphate ions, forming insoluble phosphate compounds (phosphate precipitate). When salts of Fe (III) are added to sewage, the Fe^{3+} ions react with phosphate ions (PO_4^{3-}) to form insoluble ferric phosphate, $FePO_4$ (Eq. 3). Similarly, Fe^{2+} ions can also react with phosphate to produce ferrous phosphate, $Fe_3(PO_4)_2$ (Eq. 4). Likewise, Al^{3+} ions precipitate phosphate as aluminum phosphate, $AlPO_4$ (Eq. 5). These insoluble metal phosphates separate readily from the liquid phase, allowing effective phosphate removal.

In addition to forming phosphates, Fe (III) and Al (III) ions also undergo competitive reactions with hydroxide ions present in the sewage. For example, Fe^{3+} reacts with hydroxide to form ferric hydroxide, $Fe(OH)_3$ (Eq. 6), while Al^{3+} forms aluminum hydroxide, $Al(OH)_3$ (Eq. 7). These hydroxides are typically amorphous, gel-like precipitates with a large surface area. Importantly, they can adsorb phosphate ions and other impurities from the water. This adsorption plays a central role in the flocculation process, where suspended particles and impurities aggregate into larger flocs that settle out, thereby simplifying solid-liquid separation.

The process achieved a phosphorus removal rate of approximately 75%. However, pH levels significantly influence the process. Due to the elevated operational expenses, substantial investment in chemical agents is necessary. Generating a considerable volume of sludge is challenging and contributes to secondary environmental pollution. However, the process involves not only phosphate precipitation but also the formation of metal hydroxides and their subsequent role in flocculation. Combining chemical reactions and physical processes helps efficiently remove phosphates and suspended particles, making it an effective method for treating sewage with high phosphate content (Tuszynska et al. 2013, Zhang et al. 2013).

3.3. Struvite Crystallization

Struvite crystallization is a recovery-oriented technology that enables simultaneous removal and reuse of phosphorus and nitrogen in the form of magnesium ammonium phosphate ($MgNH_4PO_4 \cdot 6H_2O$). The process occurs under supersaturated conditions when magnesium, ammonium, and phosphate ions combine in approximately equimolar ratios (Le Corre et al. 2009).

Fig. 5 presents the schematic configuration of a struvite crystallization reactor, highlighting key operational components such as mixing, aeration, and controlled chemical dosing. The figure demonstrates how supersaturation and pH control facilitate nucleation and crystal growth, enabling efficient phosphorus recovery.

Additionally, it contains lower levels of heavy metals than phosphate rock, making it a safer and more sustainable alternative for agricultural use (Suzuki et al. 2002, Yetilmezsoy & Sapci-Zengin 2009). The schematic diagram of this process is shown in Fig. 5.

Operational parameters such as pH (typically 8–9.5), Mg ratio, temperature, and the presence of competing ions significantly influence crystallization efficiency. For example, calcium ions may lead to the formation of competing precipitates, reducing struvite purity (Hao et al. 2013). In many industrial wastewaters, including slaughterhouse effluents, external magnesium supplementation is required to achieve optimal recovery.

Struvite crystallization offers several advantages, including high recovery efficiency (>90%) and production of a slow-release fertilizer suitable for agricultural use (Cordell et al. 2009). However, the process is constrained by operational complexity, sensitivity to influent composition, and economic challenges associated with reagent costs.

Critically, struvite crystallization represents one of the most effective pathways for circular phosphorus management, but its performance is highly site-specific. Therefore, its integration with upstream processes such as

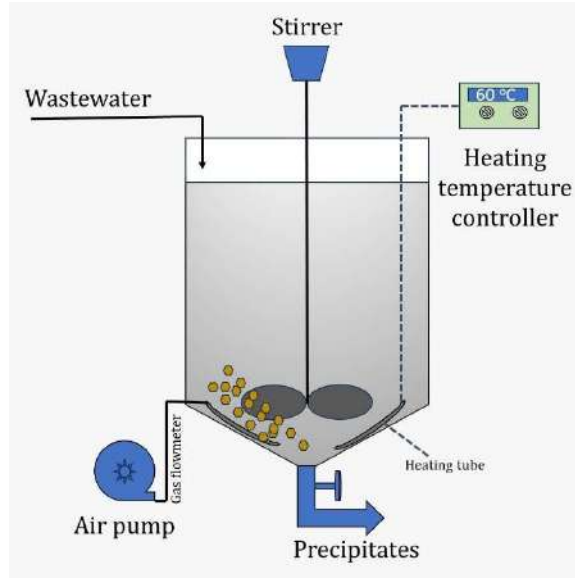


Fig. 5: Schematic diagram of the integrated reactor for struvite precipitation and recovery (Huang et al. 2015).

EBPR or anaerobic digestion is essential to ensure sufficient nutrient concentrations and improve overall feasibility.

3.3.1. Mechanisms of Struvite Crystallization

Struvite crystallization occurs when magnesium (Mg^{2+}), ammonium (NH_4^+), and phosphate (PO_4^{3-}) ions are present in solution at supersaturated conditions, leading to the formation of struvite crystals (Le Corre et al. 2009). The chemical reaction occurs as follows:

$$Mg^{2+} + NH_4{}^+ + PO_4{}^{3-} + 6H_2O \rightarrow MgNH_4PO_4 \cdot 6H_2O \quad ...(8)$$

Struvite formation is influenced by several factors, including the mass ratio of Mg:NH_4:P, pH, temperature, and impurities (Münch & Barr 2001). The most suitable pH for struvite crystallization is typically between 8.0 and 9.5, as higher pH levels favor the formation of struvite (Doyle & Parsons 2002). Temperature also plays a critical role, with higher temperatures increasing the crystallization rate (Lee et al. 2009). Supersaturation is a key driver of struvite formation, and controlling supersaturation levels is essential for optimizing size and quality of the crystals (Muhmood et al. 2019). Additionally, the presence of competing ions, such as calcium, can lead to the formation of unwanted byproducts like calcium phosphate, which complicates the recovery process (Hao et al. 2013). Slaughterhouse wastewater typically has a low magnesium (Mg) content, necessitating the addition of an adequate amount of a suitable source of magnesium to facilitate the precipitation of struvite crystals. Magnesium chloride ($MgCl_2$) is a commonly employed magnesium source due to its rapid dissociation characteristics (Suzuki et al. 2005, Liu et al. 2008). Aeration can increase pH but typically requires a longer residence time. Studies have investigated the effects of varying aeration rates and Mg:P molar ratios on struvite crystallization in swine wastewater to promote optimal struvite formation. The experiment successfully removed over 90% of phosphate and produced more than 60% struvite under various conditions. pH played a significant role in determining the outcomes of this process, as indicated by the use of response surface modeling. By controlling and optimizing the pH within a specific range, they achieved high phosphate removal and struvite production rates, highlighting the importance of pH in this chemical process (Saidou et al. 2009, McIntosh et al. 2022, Pastor et al. 2010). Cañas et al. (2023) demonstrated that wet oxidation (WO) of sewage sludge enables efficient phosphorus recovery for circular resource use. From the liquid fraction, orthophosphates (~86 mg P L^{-1}) were recovered as high-purity struvite with >95% efficiency, while the solid fraction (~68 mg P g^{-1}) achieved up to 63% recovery through acid leaching, with sulfuric acid and dilute HCl being the most effective. Overall, WO reduces organic load and pathogens while maximizing phosphorus recovery, underscoring its potential as a sustainable pretreatment for nutrient recycling.

3.3.2. Applications of Struvite Crystallization

Struvite crystallization in wastewater treatment recovers Phosphorus and nitrogen from anaerobic digester effluents, reducing nutrient pollution and preventing pipeline scaling

(Shu et al. 2006). As a slow-release fertilizer, struvite supplies essential nutrients to plants, decreasing reliance on synthetic fertilizers and supporting sustainable agriculture. Additionally, its recovery aligns with the circular economy by recycling valuable nutrients, which is crucial given the diminishing availability of phosphate rock, the primary phosphorus source for fertilizers (Cordell et al. 2009).

3.3.3. Challenges in Struvite Crystallization

Despite its potential, struvite crystallization faces several challenges, including economic viability, as the cost of magnesium sources can hinder widespread adoption (Muster et al. 2013). Operational complexity also poses difficulties, requiring precise control of pH and supersaturation for effective crystallization (Kataki et al. 2016). Additionally, impurities such as heavy metals and organic matter in wastewater can compromise struvite quality, limiting its use as a fertilizer (Hao et al. 2013). Furthermore, regulatory barriers, including the lack of standardized guidelines for struvite-based fertilizers in some regions, restrict commercialization and broader implementation.

Controlled struvite production enables beneficial applications, such as recovering phosphorus from wastewater and producing valuable fertilizer. Uncontrolled struvite precipitation, on the contrary, can be hazardous in various industrial and natural environments, causing equipment fouling and other concerns.

3.4. Electrocoagulation (EC) for Phosphorus Removal

Electrocoagulation (EC) is an efficient electrochemical technique for phosphorus removal, achieving removal efficiencies in the range of 85–99%. The process relies on the in situ dissolution of sacrificial electrodes (typically Fe or Al), generating metal cations and hydroxyl species that facilitate the coagulation and precipitation of phosphate as insoluble metal phosphates. Compared to conventional chemical precipitation, EC reduces external chemical inputs and sludge volume; however, it remains constrained by electrode consumption, energy demand, and limited phosphorus recovery, as most phosphorus is retained in sludge matrices.

3.4.1. Mechanism of Electrocoagulation in Phosphorus Removal

The pathway for phosphate removal encompasses numerous significant chemical processes occurring at the surfaces of the anode and cathode (for illustration, we use the Fe electrode):

At anode:

$$Fe(s) \rightarrow Fe^{2+}(aq) + 2e^{-} \quad ...(9)$$

$$Fe^{2+}(aq) \rightarrow Fe^{3+}(aq) + e^{-} \quad ...(10)$$

At cathode:

$$2H_2O + 2e^{-} \rightarrow H_2 + 2OH^{-} \quad ...(11)$$

Bulk solution:

$$3Fe^{2+}(aq) + 2PO_4^{3-}(aq) \rightarrow Fe_3(PO_4)_2(s) \quad ...(12)$$

$$Fe^{3+}(aq) + PO_4^{3-} \rightarrow FePO_4(s) \quad ...(13)$$

The electrocoagulation mechanism involves anodic dissolution of metal electrodes and cathodic generation of hydroxyl ions, leading to the formation of metal hydroxides that act as coagulants. These species adsorb and precipitate phosphate ions, enabling their removal from solution (Nguyen et al. 2016).

Fig. 6 illustrates the EC setup and highlights the fundamental electrochemical reactions occurring at the electrode surfaces. The figure demonstrates how metal ions released from the anode interact with phosphate in the bulk solution, forming flocs that can be separated by sedimentation or flotation. This visualization emphasizes the advantage of EC in generating coagulants in situ, thereby eliminating the need for external chemical dosing and enhancing process efficiency.

Despite these advantages, an inherent limitation of EC is that phosphorus is primarily transferred to sludge rather than directly recovered in a reusable form. To address this, post-treatment strategies such as thermal treatment and acid leaching have been explored. For instance, phosphorus-rich sludge obtained after EC can be thermally treated (up to 900 °C) and subsequently leached to recover phosphorus in soluble form (Inna et al. 2025). Similarly, Damaraju et al. (2019) reported that continuous bipolar electrocoagulation

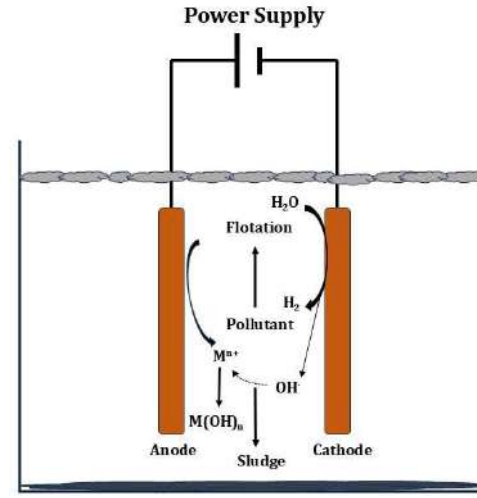


Fig. 6: Electrocoagulation setup (Li et al. 2024).

removed 73% phosphorus from palm oil mill effluent, with subsequent acid leaching achieving recovery efficiencies of up to 85%.

Overall, while EC is highly effective for phosphorus removal, its sustainability is limited by recovery inefficiencies, highlighting the need for integration with downstream recovery processes such as crystallization or hybrid electrochemical systems.

3.4.2. Industrial Applications and Future Prospects

Electrocoagulation is increasingly being adopted in industrial wastewater treatment due to its cost-effectiveness, reduced chemical requirements, and relatively low sludge generation. A recent study evaluated the feasibility of electrocoagulation combined with electro-advanced oxidation (EC/EAO) for treating abattoir effluent, consistently achieving 99% phosphorus removal (Nidheesh et al. 2022). This advancement underscores the viability of EC-based technologies in mitigating the environmental impact of meat processing industries. Additionally, Khennoussi et al. (2013) reported a 95.4% orthophosphate removal efficiency in municipal slaughterhouse wastewater, further confirming the technology's effectiveness in various wastewater treatment contexts. Given the growing environmental concerns regarding phosphorus pollution, the continuous optimization of EC processes, including novel electrode designs and hybrid treatment approaches, holds promise for sustainable water treatment solutions in industrial and municipal applications.

Additionally, BOD (97%), fecal coliforms (100%), and TSS (85%) were efficiently removed. Electrocoagulation demonstrated significant color removal, complete disinfection, and TSS removal (>88%) (Kothari et al. 2024). The reported process achieved 99% phosphorus removal. Khennoussi et al. (2013) also reported significant success, with removal rates of 95.4% for orthophosphate when treating wastewater from municipal slaughterhouses (Nidheesh et al. 2022).

Electrocoagulation (EC) and electrocoagulation/electrooxidation (EC/EAO) technologies are cost-effective, sustainable solutions for efficiently reducing phosphate content in wastewater, essential for protecting water quality and minimizing environmental impact. EC serves as a compelling alternative to traditional chemical precipitation, offering high efficiency, environmental friendliness, and cost-effectiveness in removing phosphorus and other inorganic pollutants. Ongoing research and technological advancements continue to expand its applicability across diverse industrial and municipal wastewater treatment scenarios, solidifying its role as a key approach for sustainable wastewater management and improved water quality.

3.5. Phosphorus Recovery in Bioelectrochemical Systems (BES)

Bioelectrochemical systems (BES) have emerged as an innovative approach for phosphorus recovery by integrating microbial metabolism with electrochemical processes. These systems enable simultaneous nutrient recovery and energy generation, making them attractive for sustainable wastewater treatment.

Fig. 7 illustrates the key mechanisms governing phosphorus recovery in BES, including electrochemical iron reduction and struvite precipitation. The figure highlights the coupling between anodic oxidation of organic matter and cathodic reactions that create localized conditions favorable for phosphorus mobilization and recovery.

Two primary mechanisms contribute to phosphorus recovery in BES. The first involves cathodic reduction of iron-bound phosphorus (Fe–P). Electrons generated from microbial oxidation of organic substrates at the anode are transferred to the cathode, where Fe(III) is reduced to Fe(II), resulting in the dissolution of Fe–P complexes and release of soluble phosphate into the system. This process may occur via direct electron transfer or through redox mediators (Fischer et al. 2011, Nancharaiah et al. 2016). The second mechanism involves struvite ($MgNH_4PO_4 \cdot 6H_2O$) precipitation at the cathode. During BES operation, cathodic reactions generate alkaline conditions (pH ~9–10), promoting the migration of ammonium ions and facilitating struvite crystallization in the presence of magnesium. Since wastewater typically contains sufficient ammonium and phosphate, external magnesium supplementation is often required to achieve optimal recovery (Ichihashi & Hirooka 2012, Kelly et al. 2014).

3.5.1. Phosphorus Recovery from Sewage Sludge

Digested sewage sludge, containing approximately 2–3% phosphorus by dry weight, represents a significant secondary phosphorus resource. BES-based systems enable the mobilization of phosphorus from iron-bound fractions in sludge through cathodic reduction processes. Studies using microbial fuel cells (MFCs) have demonstrated that the addition of redox mediators (e.g., methylene blue) enhances electron transfer, facilitating phosphorus release and subsequent recovery as struvite upon addition of magnesium and ammonium (Happe et al. 2016, Nancharaiah et al. 2016).

In microbial electrolysis cells (MECs), the application of an external voltage improves cathodic reduction efficiency, resulting in enhanced phosphorus solubilization compared to conventional MFC systems. This highlights the importance

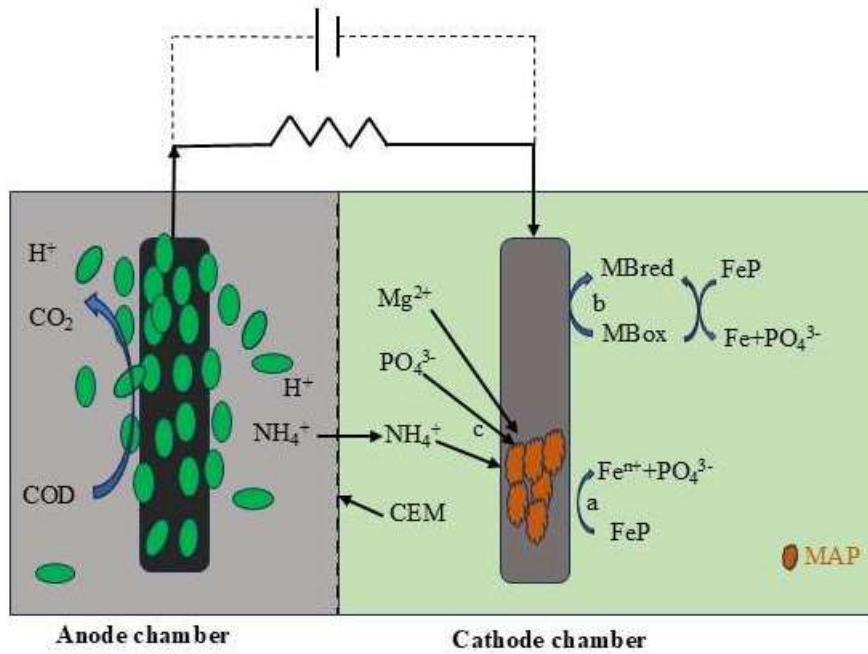


Fig. 7: Phosphorus removal in BES proceeds via three mechanisms: (a) direct reduction of iron, which releases phosphorus from iron phosphate (FeP); (b) indirect iron reduction through redox mediators such as methylene blue (MB); and (c) precipitation of magnesium ammonium phosphate (MAP) formed by the interaction of magnesium, ammonium, and phosphorus. CEM: cation exchange membrane (Nancharaiah et al. 2016).

of system configuration in optimizing phosphorus recovery performance.

3.5.2. Struvite Recovery in BES

BES provide a controlled electrochemical environment that promotes struvite crystallization directly at the cathode surface. Early studies reported phosphorus recovery efficiencies of 48–82% in MFC systems, where insoluble phosphorus was converted into bioavailable forms (Fischer et al. 2011).

In MEC configurations, hydrogen evolution at the cathode further increases local pH, enhancing precipitation kinetics and enabling phosphorus removal rates of up to 40%, with crystallization rates ranging from 0.3 to 0.9 g m^{-2} h^{-1} (Cusick & Logan 2012). Single-chamber MFCs have demonstrated even higher recovery efficiencies, reaching up to 94.6% in urine treatment and 70–82% removal from wastewater streams, with struvite deposition primarily occurring on cathode surfaces (Ichihashi & Hirooka 2012, Kelly et al. 2014).

3.5.3. Photosynthetic BES for Nutrient Recovery

Photosynthetic BES integrate microalgae into the cathodic chamber, enabling simultaneous recovery of phosphorus and nitrogen through biological uptake. In these systems, microalgae utilize nutrients for biomass growth while contributing to oxygen production, enhancing system efficiency.

For example, photomicrobial fuel cells incorporating Chlorella vulgaris have achieved phosphorus removal efficiencies of approximately 70%, along with significant removal of organic carbon (99.6%) and nitrogen (87.6%) (Zhang et al. 2011). Similarly, integrated photo-bioelectrochemical systems have demonstrated phosphate removal efficiencies of up to 82% in algal cathodes (Xiao et al. 2012). Coupling algal bioreactors with MFCs further enhances nutrient recovery, increasing phosphorus removal efficiency from 58% to 92% (Jiang et al. 2012).

However, despite these advantages, challenges remain in biomass harvesting, downstream phosphorus recovery from algal biomass, and maintaining system stability under varying environmental conditions.

3.5.4. Critical Evaluation

From a critical perspective, BES offer significant advantages, including low chemical input, potential energy recovery, and direct phosphorus precipitation. However, their application is limited by low technology readiness level (TRL), high capital costs, electrode and membrane fouling, and operational complexity.

Compared to conventional technologies, BES provide higher recovery potential but lower scalability. This highlights the need for hybrid approaches, such as coupling

BES with EBPR or struvite crystallization systems, to enhance overall process efficiency and feasibility.

3.6. Hybrid and Integrated Phosphorus Recovery Systems

Hybrid treatment systems have emerged as a promising strategy to overcome the limitations of individual phosphorus removal technologies by combining biological, chemical, and electrochemical processes. These integrated approaches enable simultaneous enhancement of removal efficiency, recovery potential, and process stability.

One of the most effective configurations involves coupling enhanced biological phosphorus removal (EBPR) with downstream struvite crystallization. In such systems, EBPR concentrates phosphorus in sludge or sidestreams, which are subsequently treated under controlled conditions to recover phosphorus as struvite. This approach improves recovery efficiency while reducing chemical demand and sludge handling requirements (Li et al. 2025).

Similarly, electrocoagulation (EC) combined with crystallization has gained attention as a hybrid solution. While EC effectively removes phosphorus by transferring it into sludge, subsequent crystallization or acid leaching processes can convert the immobilized phosphorus into reusable forms. This integration addresses one of the key limitations of EC, low recovery efficiency, by enabling resource recovery from sludge.

Integration of bioelectrochemical systems (BES) with conventional processes represents another emerging pathway. BES can be coupled with EBPR to enhance phosphorus release from sludge, followed by electrochemical precipitation or struvite recovery at the cathode. Such systems offer the potential for simultaneous nutrient recovery and energy generation, although they remain at an early stage of development.

From a process perspective, hybrid systems provide several advantages: Improved phosphorus recovery efficiency, Reduced chemical consumption, Enhanced operational flexibility, Better alignment with circular economy principles.

However, these systems also introduce challenges related to process complexity, capital investment, and system integration. The optimization of operating conditions across multiple units remains a key research requirement.

Overall, hybrid systems represent the most promising approach for sustainable phosphorus management, as they combine the reliability of conventional technologies with the recovery potential of emerging methods.

3.6.1. Economic Feasibility of phosphorus Recovery

Phosphorus (P) recovery by crystallization, particularly as struvite, has been proven technically feasible and is already operational in Europe, North America, and Asia. Studies show that 1 kg MAP can be recovered from 100 m^3 municipal wastewater (7 mg PO_4^{3-} L^{-1}, 55.3% efficiency), and up to 2.58 kg struvite can be obtained from 1 m^3 hydrolyzed urine containing 8.1–19% P. Energy demand varies, with cogeneration systems requiring less power (260 kWh kg^{-1} P) than conventional ones (510 kWh/kg P). However, economic feasibility is limited by high operational costs, which range from 2.2–8.8 € kg^{-1} P and rise significantly at lower P concentrations (1.6 €/kg P at 120 mg PO_4^{3-}-P L^{-1}), while the struvite market value was only 0.38–0.46 €/kg P, insufficient to offset costs. Despite this, P recovery offers key benefits including reduced sludge production, availability of high-quality slow-release fertilizers, and prevention of eutrophication. Thus, while direct economic returns may be limited, environmental advantages and supportive government regulations remain crucial drivers for implementation (Peng et al. 2018).

3.6.2. Technology-Specific Economic Considerations

Economic feasibility remains a critical factor influencing the large-scale adoption of phosphorus recovery technologies. The cost structure of these systems is typically governed by both capital expenditure (CAPEX) and operational expenditure (OPEX), including energy consumption, chemical inputs, maintenance, and sludge handling.

Chemical precipitation is widely implemented due to its low capital cost and operational simplicity; however, its overall cost is dominated by continuous chemical consumption and sludge disposal. Moreover, the lack of direct phosphorus recovery reduces its economic attractiveness in resource recovery frameworks (Zheng et al. 2023).

Electrocoagulation (EC) offers moderate operational costs, with energy consumption typically ranging between 0.05–0.9 kWh m^{-3} depending on wastewater characteristics. However, electrode replacement and electricity demand contribute significantly to OPEX, and the absence of efficient recovery mechanisms limits potential economic returns (Al-Qodah et al. 2025).

Struvite crystallization provides a direct revenue stream through the production of slow-release fertilizers. However, its economic viability is highly dependent on phosphorus concentration and magnesium source cost. Reported operational costs range from 2.2–8.8 € kg^{-1} P, often exceeding the market value of recovered struvite (Peng et al. 2018). Consequently, economic benefits are typically

realized through indirect savings, such as reduced scaling and sludge handling costs.

Bioelectrochemical systems (BES) remain economically challenging due to high capital costs associated with electrodes, membranes, and system infrastructure. Although BES offers potential energy recovery, current applications are limited to pilot scale, and cost uncertainties remain significant (Corona-Martínez et al. 2025).

From a comparative perspective, a key insight emerges: technologies with high removal efficiency (e.g., chemical precipitation, EC) often exhibit lower recovery value, whereas recovery-oriented technologies (e.g., struvite, BES) face higher operational and capital costs.

This trade-off highlights the importance of integrated and hybrid systems, which can improve overall economic feasibility by combining removal efficiency with resource recovery. Additionally, policy incentives, environmental regulations, and circular economy frameworks play a crucial role in improving the economic viability of phosphorus recovery technologies.

Future research should focus on cost optimization, alternative low-cost reagents, and life-cycle-based economic assessment to support large-scale implementation.

3.6.3. Industry-Specific Recommendations

Technology selection should align with wastewater characteristics across industries. For food processing and slaughterhouse effluents, struvite crystallization is preferred due to high NH_4^+ content, with electrocoagulation (EC) applied as a polishing step (Zheng et al. 2023).

In dairy and beverage industries, EBPR integrated with sidestream struvite recovery is suitable where anaerobic digestion exists; otherwise, EC is a practical option for smaller facilities.

For the fertilizer industry, high phosphorus concentrations favor advanced recovery methods, such as acid leaching combined with mineral precipitation (struvite/vivianite) (Zheng et al. 2023). In landfill leachate and condensate, high conductivity supports efficient application of electrochemical processes, including EC (Al-Qodah et al. 2025).

Finally, textile and pulp and paper wastewater, typically low in phosphorus but rich in co-contaminants, requires integrated polishing approaches (e.g., adsorption coupled with EC) (Zheng et al. 2023).

3.6.4. Comparative Analysis of phosphorus Removal and Recovery Technologies

A comparative evaluation of phosphorus removal and recovery technologies highlights clear trade-offs among removal efficiency, recovery potential, cost, and scalability, indicating that no single approach can simultaneously optimize all performance criteria.

Biological processes, particularly enhanced biological phosphorus removal (EBPR) and aerobic granular sludge (AGS), are cost-effective and environmentally sustainable, achieving phosphorus removal efficiencies of up to 98%. However, their recovery potential remains limited because phosphorus is primarily retained within biomass, requiring additional downstream processing for reuse.

Chemical precipitation is a well-established and reliable method, consistently achieving removal efficiencies in the range of 90–95%. Despite its reliability, the process is associated with high chemical consumption and significant sludge generation, which increases operational costs and environmental burdens.

In contrast, struvite crystallization represents a recovery-oriented approach that enables the conversion of dissolved phosphorus into a high-purity, bioavailable fertilizer. Its performance is strongly dependent on controlled operational conditions, including pH and magnesium-to-phosphate ratios, which can limit its applicability in dilute wastewater streams. Recent advancements, such as the use of low-cost magnesium sources and seeding strategies, have improved process efficiency and reduced operational costs, while additional system-level benefits, including improved sludge dewaterability and reduced polymer demand, have been reported (Santos et al. 2024).

Electrochemical methods, particularly electrocoagulation (EC) and electrochemical precipitation, demonstrate high phosphorus removal efficiencies (85–99%) with reduced reliance on external chemicals due to in situ coagulant generation. Recent pilot-scale studies report energy consumption in the range of 0.05–0.9 kWh m^{-3}, depending on wastewater characteristics. Nevertheless, challenges such as electrode consumption, energy demand, and moderate phosphorus recovery potential (50–70%) constrain widespread adoption. Emerging hybrid EC–crystallization systems show promise for shifting these processes from removal-focused to recovery-oriented solutions (Shah et al. 2024).

Bioelectrochemical systems (BES) represent an emerging class of technologies that integrate microbial and electrochemical processes to enable phosphorus recovery alongside energy generation. Recovery efficiencies of up to 94.6% have been reported; however, practical implementation remains constrained by high capital costs, membrane fouling, and operational complexity. Recent advances in reactor design, including stacked configurations and selective cathodic precipitation, suggest potential pathways for scale-up (Corona-Martínez et al. 2025).

Recent research trends increasingly emphasize integrated and hybrid approaches. For example, coupling EBPR with anaerobic digestion enhances phosphorus concentration in sidestreams, facilitating efficient downstream recovery through crystallization or electrochemical processes. This "A-stage EBPR + sidestream recovery" framework is emerging as a scalable and resource-efficient strategy for wastewater treatment systems (Li et al. 2025). Such developments reflect a broader transition from conventional "remove-and-dispose" approaches toward resource recovery, reduced chemical dependency, and circular economy integration (Zheng et al. 2023).

Table 2: Comparative evaluation of technologies for phosphorus removal and recovery.

Technology	Removal Efficiency	Recovery Potential	Cost & Complexity	Scalability (TRL)	Key Limitations
EBPR / Biological	Moderate–High (70–95%)	Moderate (poly-P sludge)	Low–Moderate	High (full-scale)	Sensitive to operational conditions
Chemical Precipitation	High (>90%)	Low–Moderate (metal-P sludge)	Moderate	High	Chemical consumption, sludge generation
Struvite Crystallization	High (for PO_4^{3-})	High (valuable fertilizer)	Moderate	Medium–High	Requires controlled conditions (Mg^{2+}, pH)
Electrocoagulation (EC)	High (>90%)	Low	High (energy demand)	Medium	Electrode consumption, scaling issues
Bioelectrochemical Systems (BES)	Moderate	High (emerging recovery route)	High (R&D stage)	Low–Medium	Limited large-scale validation

Table 3: Technologies for wastewater treatment and resource recovery.

Wastewater	Technology used	Process involved	System conditions	Extracted product	P Removal/ Recovery	References
Biological secondary effluent (BSE)	Fluidized reactor operating under alternative anaerobic/ anoxic mode.	Denitrifying phosphorus-removal granular sludge (DPGS)	P input (mg TP/L) =0.54	Granules	74.5%	Chen et al. (2023)
Low-strength wastewater	Continuous-flow reactor based on metabolic and hydraulic selection pressure.	Continuous-flow AGS system		Granules	94.8%	Chen et al. (2024)
Sewage Sludge	Struvite Recovery Reactor	Controlled Struvite Precipitation	pH = 7.5–9.5 Mg/P molar ratio = 1–4	Struvite	>95%	Cañas et al. (2023)
Dairy processing wastewater	Struvite Recovery Reactor	Struvite Precipitation	pH = 9–10 10–20°C Mg/P molar ratio 2	Struvite	Phosphate removal (>90%) and struvite production (>60%)	McIntosh et al. (2022)
Industrial wastewater	Chemical Precipitation	Chemical added: seawater–ammonia (Mg^{2+})	Nitrogen:Phosphorus = 4.0:1.0 At pH=8.0–8.5 HRT= 2 h P initial (mg PO_4^{3-}–P/L) =84	Precipitate	64%	Hermassi et al. (2016)
Fertilizers industry wastewater	Chemical Precipitation	Chemical added: $MgCl_2^-$ NH_4Cl	Mg:N:P = 1.0:1.0:1.0 pH = 8.5–10 HRT (h) = 0.25–1 P input (mg PO_4^{3-}–P/L) =1483	Precipitate	98–99%	Hutnik et al. (2013)
Anaerobic supernatant	Chemical Precipitation	Chemical added: Metal salts Fe^{2+} Fe^{3+} Al^{3+}	$Fe^{2+}/Fe^{3+}/Al^{3+}$:P = 1.0:1.0 pH = 6.5, 4.5, 5.0 HRT (h) = 0.5 P input (mg PO_4^{3-}–P/L) =148	Precipitate	72% 78% 87%	Huang et al. (2017)

Table 4: Sustainable advances in phosphorus recovery.

Technology	Suitable Waste Streams	Recovery vs. Removal	Maturity & Scalability	Key Sustainability Features	Main Cost Drivers
Struvite crystallization	Food processing , slaughterhouse, digestate, centrate, dairy	Recovery (struvite fertilizer)	Commercial pilots and full-scale in some plants	Improves dewatering, reduces polymer demand; can use waste Mg sources	Mg source cost, scale, product market value
Electrocoagulation (EC)/electro-precipitation	Landfill leachate, metal finishing, high-conductivity effluents	Primarily removal; recovery possible with hybrid EC + crystallization	Pilot to demo scale, modular designs	On-site coagulant generation, avoids chemical transport	Energy use (0.05–0.9 kWh m^{-3}), electrode cost, electricity price
Hybrid EBPR + struvite / EC	Municipal-industrial co-treatment, food sector	Recovery, with higher overall yields	Demonstrated in large WWTPs; growing industrial application	Reduces chemical inputs, leverages biological concentration	Integration complexity, CAPEX for multiple units
BES (bioelectrochemical systems)	Niche sidestreams, high-strength organic-P mixtures	Direct recovery at cathode (precipitate)	Low TRL, pilot stacked units emerging	Low reagent needs, partial energy recovery	Scale-up cost, electrode/ material durability
Chemical precipitation (e.g., alum, ferric salts)	Fertilizer/phosphate effluent, textile/pulp wastewater	Removal (recovery possible with tailored steps)	Very mature, widely used	Reliable polishing; can be adapted for recovery	Reagent costs, sludge handling/ disposal
Vivianite recovery/ Fe-based routes	Anaerobic digesters, phosphate industry effluents	Recovery (vivianite mineral)	Early demo stage	Co-recovery of Fe and P, potential market value	Digester iron dosing, separation efficiency

Tables 2–4 collectively provide a comprehensive comparison of phosphorus removal and recovery technologies; however, their integrated interpretation reveals important trade-offs, process dependencies, and practical implications for sustainable wastewater management.

A key insight from Table 2 is the distinction between removal-oriented and recovery-oriented technologies. Conventional methods such as chemical precipitation and electrocoagulation achieve high phosphorus removal efficiencies (>90%), but primarily transfer phosphorus into sludge-bound forms, limiting its direct reuse (Donnert & Salecker 1999, Nguyen et al. 2016). In contrast, recovery-focused approaches such as struvite crystallization and bioelectrochemical systems (BES) enable the conversion of phosphorus into reusable products, including magnesium ammonium phosphate, thereby supporting resource recovery (Le Corre et al. 2009, Nancharaiah et al. 2016). However, these systems require stricter operational control and exhibit lower technological maturity. This comparison highlights a fundamental limitation: high removal efficiency does not necessarily correspond to high recovery potential.

The role of wastewater characteristics becomes evident in Table 3, where treatment performance varies significantly with influent composition and operating conditions. High-strength waste streams, such as sewage sludge and fertilizer industry effluents, enable higher recovery efficiencies when treated using crystallization-based processes under optimized pH and molar ratios (Hutnik et al. 2013, Cañas et al. 2023). Conversely, low-strength wastewater systems depend more on biological processes, where phosphorus is assimilated into biomass rather than recovered (Chen et al. 2023, Chen et al. 2024). This indicates that recovery technologies are more effective in concentrated sidestreams, while mainstream systems remain largely removal-focused. Additionally, the sensitivity of treatment performance to parameters such as pH, hydraulic retention time, and chemical dosing underscores the need for site-specific optimization (Huang et al. 2017).

Further insights into scalability and sustainability are provided by Table 4, which compares technologies based on maturity, applicability, and operational constraints. Established processes such as EBPR and chemical precipitation exhibit high technology readiness levels and are widely implemented, but are limited in terms of recovery efficiency and long-term sustainability (Zheng et al. 2023). In contrast, emerging technologies such as BES and hybrid systems offer advantages including reduced chemical input and enhanced recovery

potential, yet remain constrained by high capital costs, system complexity, and limited full-scale validation (Corona-Martínez et al. 2025). Struvite crystallization occupies an intermediate position, with demonstrated pilot- to full-scale applications and strong alignment with circular economy principles (Santos et al. 2024).

A combined interpretation of Tables 2–4 indicates that phosphorus management technologies must be evaluated across multiple dimensions, including efficiency, recovery potential, cost, and scalability. No single technology achieves optimal performance across all criteria. Instead, integrated systems that combine biological, chemical, and electrochemical processes provide a more balanced and sustainable approach by leveraging the strengths of individual methods (Li et al. 2025).

This synthesis also highlights key research gaps, including the lack of standardized economic evaluation metrics, limited large-scale implementation of emerging technologies, and insufficient integration of recovery processes within existing treatment systems. Addressing these challenges is essential for advancing practical and resource-efficient phosphorus management strategies.

4. RESEARCH GAPS AND FUTURE DIRECTIONS

4.1. Research Gaps

Despite recent progress, several limitations hinder the practical implementation of phosphorus recovery technologies. A key gap is the absence of standardized metrics for evaluating recovery efficiency, cost, and sustainability, which restricts meaningful comparison across studies. Additionally, emerging technologies such as bioelectrochemical systems (BES) and hybrid processes lack sufficient large-scale validation, limiting their industrial applicability. Current research also underrepresents the role of phosphorus speciation in influencing treatment and recovery performance. Furthermore, comprehensive life cycle assessments are scarce, making it difficult to evaluate the overall environmental sustainability of these technologies.

Addressing these challenges is essential for advancing efficient, scalable, and sustainable phosphorus recovery systems.

4.2. Future Directions

4.2.1. Integration and Process Optimization

Future efforts should prioritize the development of hybrid systems that integrate biological (EBPR, AGS), electrochemical (EC, BES), and crystallization processes to enhance phosphorus recovery and overall system efficiency. Coupling BES with struvite crystallization or electrocoagulation can enable continuous recovery while mitigating operational limitations. Additionally, the application of advanced process control (APC) and real-time monitoring can optimize key parameters such as pH, dissolved oxygen, and aeration, ensuring stable and efficient operation.

4.2.2. Microbial and Biochemical Advancements

Improving system performance requires targeted manipulation of microbial communities. Selective enrichment of functional consortia and enhancement of polyphosphate-accumulating organisms (PAOs) and electroactive microbes can improve phosphorus mobilization and recovery. Such advancements are particularly relevant for integrated EBPR–BES systems.

4.2.3. Resource Recovery and Circular Economy

Enhancing the efficiency and purity of struvite crystallization is essential for its large-scale application as a sustainable fertilizer. In parallel, the valorization of phosphorus-rich by-products, such as sludge-derived materials, should be explored to support circular economy approaches and reduce waste generation.

4.2.4. Technological Innovations

Advancements in electrocoagulation, including the development of durable and energy-efficient electrode materials, are needed to improve process performance. Integration of intelligent and automated control systems can further enhance operational efficiency and reduce energy consumption.

4.2.5. Environmental and Economic Assessment

Future research should emphasize comprehensive life cycle assessment (LCA) and techno-economic evaluation to assess the sustainability and feasibility of emerging technologies. Cost reduction strategies, particularly for reagents and energy inputs, are critical for enabling large-scale implementation.

5. CONCLUSIONS

This review critically evaluated phosphorus removal and recovery technologies using a multi-criteria framework. Conventional methods such as chemical precipitation and electrocoagulation remain effective for phosphorus removal but provide limited recovery potential and generate secondary waste streams. In contrast, resource-oriented approaches such as struvite crystallization and bioelectrochemical systems (BES) better align with circular economy principles by enabling nutrient recovery, although challenges related to cost, process stability, and scalability persist.

Biological processes, particularly enhanced biological phosphorus removal (EBPR) and aerobic granular sludge (AGS), offer efficient and sustainable treatment options,

with AGS demonstrating advantages in settling, footprint, and resilience. However, operational limitations, including substrate variability and microbial competition, can affect system performance. Struvite crystallization presents a viable pathway for simultaneous removal and recovery, while BES technologies provide emerging opportunities for integrated nutrient recovery and sludge reduction.

Overall, no single technology can simultaneously maximize removal efficiency, recovery potential, and economic feasibility. Therefore, integrated and hybrid systems represent the most promising approach for sustainable phosphorus management. Future research should focus on large-scale validation, process optimization, and life-cycle assessment to facilitate the transition toward resource-efficient and circular wastewater treatment systems.

6. ACKNOWLEDGMENTS

The authors would like to acknowledge Zakir Husain College of Engineering and Technology, Aligarh Muslim University, for providing administrative and technical support.

7. REFERENCES

Abel-Denee, M., Abbott, T. and Eskicioglu, C., 2018. Using mass struvite precipitation to remove recalcitrant nutrients and micropollutants from anaerobic digestion dewatering centrate. *Water Research*, 132, pp.292-300. [DOI]

Alam, M.M., Srinivasan, V., Mueller, A.V. and Gu, A.Z., 2021. Status and advances in technologies for phosphorus species detection and characterization in natural environment: A comprehensive review. *Talanta*, 233, p.122458. [DOI]

Al-Qodah, Z., Al-Rajabi, M.M., Da'na, E., Al-Shannag, M., Bani-Melhem, K. and Assirey, E., 2025. Continuous electrocoagulation processes for industrial inorganic pollutants removal: A critical review of performance and applications. *Water*, 17(17), p.2639. [DOI]

Andrés, E., Araya, F., Vera, I., Pozo, G. and Vidal, G., 2018. Phosphate removal using zeolite in treatment wetlands under different oxidation-reduction potentials. *Ecological Engineering*, 117, pp.18-27. [DOI]

APHA, 2012. *Standard Methods for the Examination of Water and Wastewater*. American Public Health Association.

Ashraf, A. and Farooqi, I.H., 2022. Investigation on the treatment of slaughterhouse wastewater in a sequencing batch reactor. *Nature Environment and Pollution Technology*, 21(3), pp.1297-1305. [DOI]

Bazrafshan, E., Kord Mostafapour, F., Farzadkia, M., Ownagh, K.A. and Mahvi, A.H., 2012. Slaughterhouse wastewater treatment by combined chemical coagulation and electrocoagulation process. *PLOS ONE*, 7(6), p.e40108. [DOI]

Bunce, J.T., Ndam, E., Ofiteru, I.D., Moore, A. and Graham, D.W., 2018. A review of phosphorus removal technologies and their applicability to small-scale domestic wastewater treatment systems. *Frontiers in Environmental Science*, 6, p.8. [DOI]

Cade-Menun, B.J., 2005. Characterizing phosphorus in environmental and agricultural samples by 31P nuclear magnetic resonance spectroscopy. *Talanta*, 66(2), pp.359-371. [DOI]

Cañas, J., Álvarez-Torrellas, S., Hermana, B. and García, J., 2023. Phosphorus recovery from sewage sludge as struvite. *Water*, 15(13), p.2382. [DOI]

Cao, W. and Mehrvar, M., 2011. Slaughterhouse wastewater treatment by combined anaerobic baffled reactor and UV/H2O2 processes. *Chemical Engineering Research and Design*, 89(7), pp.1136-1143. [DOI]

Carrillo, V., Fuentes, B., Gómez, G. and Vidal, G., 2020. Characterization and recovery of phosphorus from wastewater by combined technologies. *Reviews in Environmental Science and Bio/Technology*, 19, pp.389-418. [DOI]

Chamorro, S., Hernández, V., Monsalvez, E., Becerra, J., Mondaca, M.A., Piña, B. and Vidal, G., 2010. Detection of estrogenic activity from kraft mill effluents by the yeast estrogen screen. *Bulletin of Environmental Contamination and Toxicology*, 84, pp.165-169. [DOI]

Chen, B., Li, Y., Luo, Z., Lei, M., Li, J. and Zhang, X., 2024. Enhanced phosphorus removal from biological secondary effluent using denitrifying phosphorus-removal granular sludge. *Journal of Water Process Engineering*, 57, p.104584. [DOI]

Chen, B., Li, Y., Luo, Z., Lei, M., Zhang, X. and Li, J., 2023. Formation and granulation mechanism of granular sludge dominated by denitrifying glycogen-accumulating organisms. *Chemical Engineering Journal*, 474, p.145638. [DOI]

Chen, K.Y., 1999. Study of polyphosphate metabolism in intact cells by 31-P nuclear magnetic resonance spectroscopy. Inorganic Polyphosphates: Biochemistry, Biology, Biotechnology, pp.253-273. [DOI]

Cordell, D., Drangert, J.O. and White, S., 2009. The story of phosphorus: global food security and food for thought. *Global Environmental Change*, 19(2), pp.292-305. [DOI]

Corona-Martínez, D.A., Martínez-Amador, S.Y., Rodríguez-De la Garza, J.A., Laredo-Alcalá, E.I. and Pérez-Rodríguez, P., 2025. Recent advances in scaling up bioelectrochemical systems: A review. *BioTech*, 14(1), p.8. [DOI]

Crutchik, D.G. J.M. and Garrido, J.M., 2011. Struvite crystallization versus amorphous magnesium and calcium phosphate precipitation during the treatment of a saline industrial wastewater. *Water Science and Technology*, 64(12), pp.2460-2467. [DOI]

Cusick, R.D. and Logan, B.E., 2012. Phosphate recovery as struvite within a single chamber microbial electrolysis cell. *Bioresource Technology*, 107, pp.110-115. [DOI]

Dai, H., Lu, X., Peng, Y., Yang, Z. and Zhsssu, H., 2017. Effects of supersaturation control strategies on hydroxyapatite (HAP) crystallization for phosphorus recovery from wastewater. *Environmental Science and Pollution Research*, 24, pp.5791-5799. [DOI]

Damaraju, M., Yoshihara, H., Bhattacharyya, D., Panda, T.K. and Kurilla, K.K., 2019. Phosphorus recovery from the sludge generated from a continuous bipolar mode electrocoagulation (CBME) system. *Water Science and Technology*, 79(7), pp.1348-1356. [DOI]

de Carvalho, C.D. A., Dos Santos, A.F., Ferreira, T.J. T., Lira, V.N. S.A., Barros, A.R. M. and Dos Santos, A.B., 2021. Resource recovery in aerobic granular sludge systems: is it feasible or still a long way to go?. *Chemosphere*, 274, p.129881. [DOI]

de Sousa Rollemberg, S.L., Barros, A.R. M., Firmino, P.I. M. and Dos Santos, A.B., 2018. Aerobic granular sludge: cultivationparameters and removal mechanisms. *Bioresource Technology*, 270, pp.678-688. [DOI]

Donnert, D. and Salecker, M., 1999. Elimination of phosphorus from waste water by crystallization. *Environmental Technology*, 20(7), pp.735-742. [DOI]

Doyle, J.D. and Parsons, S.A., 2002. Struvite formation, control and recovery. *Water Research*, 36(16), pp.3925-3940. [DOI]

Drogui, P., Asselin, M., Brar, S.K., Benmoussa, H. and Blais, J.F., 2008. Electrochemical removal of pollutants from agro-industry wastewaters. *Separation and Purification Technology*, 61(3), pp.301-310. [DOI]

Ebbers, B., Ottosen, L.M. and Jensen, P.E., 2015. Electrodialytic treatment of municipal wastewater and sludge for the removal of heavy metals and recovery of phosphorus. *Electrochimica Acta*, 181, pp.90-99. [DOI]

Fischer, F., Bastian, C., Happe, M., Mabillard, E. and Schmidt, N., 2011. Microbial fuel cell enables phosphate recovery from digested sewage sludge as struvite. *Bioresource Technology*, 102(10), pp.5824-5830. [DOI]

Gao, Z., Deng, Y., Hu, X., Yang, S., Sun, C. and He, H., 2013. Determination of organophosphate esters in water samples using an ionic liquid-based sol-gel fiber for headspace solid-phase microextraction coupled to gas chromatography-flame photometric detector. *Journal of Chromatography A*, 1300, pp.141-150. [DOI]

Ge, H., Batstone, D.J. and Keller, J., 2015. Biological phosphorus removal from abattoir wastewater at very short sludge ages mediated by novel PAO clade comamonadaceae. *Water Research*, 69, pp.173-182. [DOI]

Grant, C.A., Flaten, D.N., Tomasiewicz, D.J. and Sheppard, S.C., 2001. The importance of early season phosphorus nutrition. *Canadian Journal of Plant Science*, 81(2), pp.211-224. [DOI]

Guisasola, A., Chan, C., Larriba, O., Lippo, D., Suárez-Ojeda, M.E. and Baeza, J.A., 2019. Long-term stability of an enhanced biological phosphorus removal system in a phosphorus recovery scenario. *Journal of Cleaner Production*, 214, pp.308-318. [DOI]

Hamza, R., Rabii, A., Ezzahraoui, F.Z., Morgan, G. and Iorhemen, O.T., 2022. A review of the state of development of aerobic granular sludge technology over the last 20 years: full-scaleapplications and resource recovery. *Case Studies in Chemical and Environmental Engineering*, 5, p.100173. [DOI]

Hao, X., Wang, C., van Loosdrecht, M.C. M. and Hu, Y., 2013. Looking beyond struvite for P-recovery. *Environmental Science and Technology*, 47(10), pp.4965-4966. [DOI]

Happe, M., Sugnaux, M., Cachelin, C.P., Stauffer, M., Zufferey, G., Kahoun, T., ... and Fischer, F., 2016. Scale-up of phosphate remobilization from sewage sludge in a microbial fuel cell. *Bioresource Technology*, 200, pp.435-443. [DOI]

Henze, M., van Loosdrecht, M.C., Ekama, G.A. and Brdjanovic, D. (Eds.), 2008. Biological wastewater treatment. IWA publishing. [DOI]

Hermassi, M., Valderrama, C., Moreno, N., Font, O., Querol, X., Batis, N. and Cortina, J.L., 2016. Powdered Ca-activated zeolite for phosphate removal from treated waste-water. *Journal of Chemical Technology and Biotechnology*, 91(7), pp.1962-1971. [DOI]

Huang, H., Xiao, D., Liu, J., Hou, L. and Ding, L., 2015. Recovery and removal of nutrients from swine wastewater by using a novel integrated reactor for struvite decomposition and recycling. *Scientific Reports*, 5(1), p.10183. [DOI]

Huang, H., Zhang, D., Zhao, Z., Zhang, P. and Gao, F., 2017. Comparison investigation on phosphate recovery from sludge anaerobic supernatant using the electrocoagulation process and chemical precipitation. *Journal of Cleaner Production*, 141, pp.429-438. [DOI]

Hutnik, N., Kozik, A., Mazienczuk, A., Piotrowski, K., Wierzbowska, B. and Matynia, A., 2013. Phosphates (V) recovery from phosphorus mineral fertilizers industry wastewater by continuous struvite reaction crystallization process. *Water Research*, 47(11), pp.3635-3643. [DOI]

Ichihashi, O. and Hirooka, K., 2012. Removal and recovery of phosphorus as struvite from swine wastewater using microbial fuel cell. *Bioresource Technology*, 114, pp.303-307. [DOI]

Inna, S., Natacha, E.A. R., Harouna, M. and Richard, K., 2025. Phosphorus recovery from beef slaughterhouse wastewater by electrocoagulation process. *Sustainable Chemistry for the Environment*, 10, p.100263. [DOI]

Izadi, P., Izadi, P. and Eldyasti, A., 2021. A review of biochemical diversity and metabolic modeling of EBPR process under specific environmental conditions and carbon source availability. *Journal of Environmental Management*, 288, p.112362. [DOI]

Jasinski, S.M., 2017. Phosphate rock. In: *Mineral Commodity Summaries 2017*. U.S. Geological Survey.

Jiang, H., Luo, S., Shi, X., Dai, M. and Guo, R.B., 2012. A novel microbial fuel cell and photobioreactor system for continuous domestic wastewater treatment and bioelectricity generation. *Biotechnology Letters*, 34(7), pp.1269-1274. [DOI]

Joshi, M. and Sharma, J.G., 2025. The utility of synthetic biology in the treatment of industrial wastewaters. *Nature Environment and Pollution Technology*, 24(1), pp.1-11. [DOI]

Karl, D.M., 2000. Phosphorus, the staff of life. *Nature*, 406(6791), pp.31-33. [DOI]

Kataki, S., West, H., Clarke, M. and Baruah, D.C., 2016. Phosphorus recovery as struvite: recent concerns for use of seed, alternative Mg source, nitrogen conservation and fertilizer potential. *Resources, Conservation and Recycling*, 107, pp.142-156. [DOI]

Kelly, P.T. and He, Z., 2014. Nutrients removal and recovery in bioelectrochemical systems: a review. *Bioresource Technology*, 153, pp.351-360. [DOI]

Khennoussi, A., Chaouch, M. and Chahlaoui, A., 2013. Traitement des effluents d'abattoir de viande rouge par électrocoagulation-flottation avec des électrodes en fer. *Revue des Sciences de l'Eau*, 26(2), pp.135-150. [DOI]

Kim, D., Min, K.J., Lee, K., Yu, M.S. and Park, K.Y., 2017. Effects of pH, molar ratios and pre-treatment on phosphorus recovery through struvite crystallization from effluent of anaerobically digested swine wastewater. *Environmental Engineering Research*, 22(1), pp.12-18. [DOI]

Kok, D.J. D., Pande, S., Van Lier, J.B., Ortigara, A.R., Savenije, H. and Uhlenbrook, S., 2018. Global phosphorus recovery from wastewater for agricultural reuse. *Hydrology and Earth System Sciences*, 22(11), pp.5781-5799. [DOI]

Kothari, R., Azam, R., Bharti, A., Goria, K., Allen, T., Ashokkumar, V., ... and Tyagi, V.V., 2024. Biobased treatment and resource recovery from slaughterhouse wastewater via reutilization and recycling for sustainable waste approach. *Journal of Water Process Engineering*, 58, p.104712. [DOI]

Kwon, J.H., Kim, I.K., Park, K.Y., Kim, Y.D. and Cho, Y.H., 2014. Removal of phosphorus and coliforms from secondary effluent using ferrate (VI). *KSCE Journal of Civil Engineering*, 18, pp.81-85. [DOI]

Le Corre, K.S., Valsami-Jones, E., Hobbs, P. and Parsons, S.A., 2009. Phosphorus recovery from wastewater by struvite crystallization: A review. *Critical Reviews in Environmental Science and Technology*, 39(6), pp.433-477. [DOI]

Lee, J.E., Rahman, M.M. and Ra, C.S., 2009. Dose effects of Mg and PO4 sources on the composting of swine manure. *Journal of Hazardous Materials*, 169(1-3), pp.801-807. [DOI]

Lefebvre, O., Vasudevan, N., Torrijos, M., Thanasekaran, K. and Moletta, R., 2005. Halophilic biological treatment of tannery soak liquor in a sequencing batch reactor. *Water Research*, 39(8), pp.1471-1480. [DOI]

Lemaire, R., Yuan, Z., Bernet, N., Marcos, M., Yilmaz, G. and Keller, J., 2009. A sequencing batch reactor system for high-level biological nitrogen and phosphorus removal from abattoir wastewater. *Biodegradation*, 20, pp.339-350. [DOI]

Li, C., Liu, S., Ma, T., Zheng, M. and Ni, J., 2019. Simultaneous nitrification, denitrification and phosphorus removal in a sequencing batch reactor (SBR) under low temperature. *Chemosphere*, 229, pp.132-141. [DOI]

Li, G., Zheng, B., Zhang, W., Liu, Q., Li, M. and Zhang, H., 2024. Phosphate removal efficiency and life cycle assessment of different anode materials in electrocoagulation treatment of wastewater. *Sustainability*, 16(9), p.3836. [DOI]

Li, J., Peng, Y., Li, J., Li, S., Yang, S., Feng, W., Zhang, Q., Li, X., and Zhang, L., 2025. Separating biological nutrient removal by eBPR-PN/A process to treat real municipal sewage. *Water Research* X, 28, 100375. [DOI]

Li, S., Zhao, S., Yan, S., Qiu, Y., Song, C., Li, Y. and Kitamura, Y., 2019. Food processing wastewater purification by microalgae cultivation associated with high value-added compounds production-A review. *Chinese Journal of Chemical Engineering*, 27(12), pp.2845-2856. [DOI]

Liu, Q., Fang, Z., Liu, Y., Liu, Y., Xu, Y., Ruan, X., Zhang, X., and Cao, W., 2019. Phosphorus speciation and bioavailability of sewage sludge derived biochar amended with CaO. *Waste Management*, 87, 71–77. [DOI]

Liu, Z., Zhao, Q., Lee, D.J. and Yang, N., 2008. Enhancing phosphorus recovery by a new internal recycle seeding MAP reactor. *Bioresource Technology*, 99(14), pp.6488-6493. [DOI]

Lu, Z., Liu, Y., Barreto, V., Pohl, C., Avdalovic, N., Joyce, R. and Newton, B., 2002. Determination of anions at trace levels in power plant water samples by ion chromatography with electrolytic eluent generation and suppression. *Journal of Chromatography A*, 956(1-2), pp.129-138. [DOI]

Mahvi, A.H., Ebrahimi, S.J. A.D., Mesdaghinia, A., Gharibi, H. and Sowlat, M.H., 2011. Performance evaluation of a continuous bipolar electrocoagulation/electrooxidation-electroflotation (ECEO-EF) reactor designed for simultaneous removal of ammonia and phosphate from wastewater effluent. *Journal of Hazardous Materials*, 192(3), pp.1267-1274. [DOI]

McIntosh, S., Hunt, L., Thompson Brewster, E., Rose, A., Thornton, A. and Erler, D., 2022. Struvite production from dairy processing waste. *Sustainability*, 14(23), p.15807. [DOI]

Mehta, C.M., Khunjar, W.O., Nguyen, V., Tait, S. and Batstone, D.J., 2015. Technologies to recover nutrients from waste streams: a critical review. *Critical Reviews in Environmental Science and Technology*, 45(4), pp.385-427. [DOI]

Melia, P.M., Cundy, A.B., Sohi, S.P., Hooda, P.S. and Busquets, R., 2017. Trends in the recovery of phosphorus in bioavailable forms from wastewater. *Chemosphere*, 186, pp.381-395. [DOI]

Miller-Ihli, N.J. and Baker, S.A., 2001. Trace element composition of municipal waters in the United States: a comparison of ICP-AES and ICP-MS methods. *Journal of Food Composition and Analysis*, 14(6), pp.619-629. [DOI]

Muhmood, A., Wu, S., Lu, J., Ajmal, Z., Luo, H. and Dong, R., 2019. Nutrient recovery from anaerobically digested chicken slurry via struvite: performance optimization and interactions with heavy metals and pathogens. *Science of the Total Environment*, 651, pp.1346-1353. [DOI]

Münch, E.V. and Barr, K., 2001. Controlled struvite crystallisation for removing phosphorus from anaerobic digester sidestreams. *Water Research*, 35(1), pp.151-159. [DOI]

Muster, T.H., Douglas, G.B., Sherman, N., Seeber, A., Wright, N. and Güzükara, Y., 2013. Towards effective phosphorus recycling from wastewater: quantity and quality. *Chemosphere*, 91(5), pp.676-684. [DOI]

Nancharaiah, Y.V., Mohan, S.V. and Lens, P.N. L., 2016. Recent advances in nutrient removal and recovery in biological and bioelectrochemical systems. *Bioresource Technology*, 215, pp.173-185. [DOI]

Nelson, N.O., Mikkelsen, R.L. and Hesterberg, D.L., 2003. Struvite precipitation in anaerobic swine lagoon liquid: effect of pH and Mg: P ratio and determination of rate constant. *Bioresource Technology*, 89(3), pp.229-236. [DOI]

Nguyen, D.D., Ngo, H.H., Guo, W., Nguyen, T.T., Chang, S.W., Jang, A. and Yoon, Y.S., 2016. Can electrocoagulation process be an appropriate technology for phosphorus removal from municipal wastewater?. *Science of the Total Environment*, 563, pp.549-556. [DOI]

Nidheesh, P.V., Khan, F.M., Kadier, A., Akansha, J., Bote, M.E. and Mousazadeh, M., 2022. Removal of nutrients and other emerging inorganic contaminants from water and wastewater by electrocoagulation process. *Chemosphere*, 307, p.135756. [DOI]

Nur, T., Loganathan, P., Ahmed, M.B., Johir, M., Kandasamy, J. and Vigneswaran, S., 2018. Struvite production using membrane-bioreactor wastewater effluent and seawater. *Desalination*, 444, pp.1-5. [DOI]

Pastor, L., Mangin, D., Ferrer, J. and Seco, A., 2010. Struvite formation from the supernatants of an anaerobic digestion pilot plant. *Bioresource Technology*, 101(1), pp.118-125. [DOI]

Penetra, R.G., Reali, M.A. P., Foresti, E. and Campos, J.R., 1999. Post-treatment of effluents from anaerobic reactor treating domestic sewage by dissolved-air flotation. *Water Science and Technology*, 40(8), pp.137-143. [DOI]

Peng, L., Dai, H., Wu, Y., Peng, Y. and Lu, X., 2018. A comprehensive review of phosphorus recovery from wastewater by crystallization processes. *Chemosphere*, 197, pp.768-781. [DOI]

Pronk, M., De Kreuk, M.K., De Bruin, B., Kamminga, P., Kleerebezem, R.V. and Van Loosdrecht, M.C. M., 2015. Full scale performance of the aerobic granular sludge process for sewage treatment. *Water Research*, 84, pp.207-217. [DOI]

Ruiz-Calero, V. and Galceran, M.T., 2005. Ion chromatographic separations of phosphorus species: a review. *Talanta*, 66(2), pp.376-410. [DOI]

Ruzicka, J. and Hansen, E.H., 1975. Flow injection analyses: Part I. *A new concept of fast continuous flow analysis*. *Analytica Chimica Acta*, 78(1), pp.145-157. [DOI]

Saidou, H., Korchef, A., Moussa, S.B. and Amor, M.B., 2009. Struvite precipitation by the dissolved CO2 degasification technique: impact of the airflow rate and ph. *Chemosphere*, 74(2), pp.338-343. [DOI]

Santos, A.F., Mendes, L.S., Alvarenga, P., Gando-Ferreira, L.M. and Quina, M.J., 2024. Nutrient recovery via struvite precipitation from wastewater treatment plants: influence of operating parameters, coexisting ions and seeding. *Water*, 16(12), p.1675. [DOI]

Schulz, C., Gelbrecht, J. and Rennert, B., 2003. Treatment of rainbow trout farm effluents in constructed wetland with emergent plants and subsurface horizontal water flow. *Aquaculture*, 217(1-4), pp.207-221. [DOI]

Sengupta, S. and Pandit, A., 2011. Selective removal of phosphorus from wastewater combined with its recovery as a solid-phase fertilizer. *Water Research*, 45(11), pp.3318-3330. [DOI]

Shah, A.A., Walia, S. and Kazemian, H., 2024. Advancements in combined electrocoagulation processes for sustainable wastewater treatment: A comprehensive review of mechanisms, performance and emerging applications. *Water Research*, 252, p.121248. [DOI]

Shu, L., Schneider, P., Jegatheesan, V. and Johnson, J., 2006. An economic evaluation of phosphorus recovery as struvite from digester supernatant. *Bioresource Technology*, 97(17), pp.2211-2216. [DOI]

Stratful, I., Brett, S., Scrimshaw, M.B. and Lester, J.N., 1999. Biological phosphorus removal, its role in phosphorus recycling. *Environmental Technology*, 20(7), pp.681-695. [DOI]

Suzuki, K., Tanaka, Y., Kuroda, K., Hanajima, D. and Fukumoto, Y., 2005. Recovery of phosphorous from swine wastewater through crystallization. *Bioresource Technology*, 96(14), pp.1544-1550. [DOI]

Suzuki, K., Tanaka, Y., Osada, T. and Waki, M., 2002. Removal of phosphate, magnesium and calcium from swine wastewater through crystallization enhanced by aeration. *Water Research*, 36(12), pp.2991-2998. [DOI]

Tuszynska, A., Kolecka, K. and Quant, B., 2013. The influence of phosphorus fractions in bottom sediments on phosphate removal in semi-natural systems as the 3rd stage of biological wastewater treatment. *Ecological Engineering*, 53, pp.321-328. [DOI]

Van Phuong, N., 2025. Mechanism and behavior of phosphorus adsorption from Water by biochar forms derived from macadamia husks. *NatureEnvironmentand Pollution Technology*, 24(1). [DOI]

Wang, D., Weston, D.P. and Lydy, M.J., 2009. Method development for the analysis of organophosphate and pyrethroid insecticides at low parts per trillion levels in water. *Talanta*, 78(4-5), pp.1345-1351. [DOI]

Wang, S.X., Huang, Y.X., Wu, Q.F., Yao, W., Lu, Y.Y., Huang, B.C. and Jin, R.C., 2024. A review of the application of iron oxides for phosphorus removal and recovery from wastewater. *Critical Reviews in Environmental Science and Technology*, 54(5), pp.405-423. [DOI]

Wilsenach, J.A., Schuurbiers, C.A. H. and Van Loosdrecht, M.C. M., 2007. Phosphate and potassium recovery from source separated urine through struvite precipitation. *Water Research*, 41(2), pp.458-466. [DOI]

Xiao, L., Young, E.B., Berges, J.A. and He, Z., 2012. Integrated photo-bioelectrochemical system for contaminants removal and bioenergy production. *Environmental Science & Technology*, 46(20), pp.11459-11466. [DOI]

Yetilmezsoy, K. and Sapci-Zengin, Z., 2009. Recovery of ammonium nitrogen from the effluent of UASB treating poultry manure wastewater by MAP precipitation as a slow release fertilizer. *Journal of Hazardous Materials*, 166(1), pp.260-269. [DOI]

Yin, Z., Chen, Q., Zhao, C., Fu, Y., Li, J., Feng, Y. and Li, L., 2020. A new approach to removing and recovering phosphorus from livestock wastewater using dolomite. *Chemosphere*, 255, p.127005. [DOI]

Zhang, M., Zheng, K., Jin, J., Yu, X., Qiu, L., Ding, S., ... and Zheng, P., 2013. Effects of Fe (II)/P ratio and pH on phosphorus removal by ferrous salt and approach to mechanisms. *Separation and Purification Technology*, 118, pp.801-805. [DOI]

Zhang, Y., Noori, J.S. and Angelidaki, I., 2011. Simultaneous organic carbon, nutrients removal and energy production in a photomicrobial fuel cell (PFC). *Energy & Environmental Science*, 4(10), pp.4340-4346. [DOI]

Zhang, Z., Yi, L.I., Leilei, W.E. I., Yufeng, L. Ü., Meng, W.A. N.G. and Baoyu, G.A. O., 2013. Effect of ferric chloride on the properties of biological sludge in co-precipitation phosphorus removal process. *Chinese Journal of Chemical Engineering*, 21(5), pp.564-568. [DOI]

Zheng, Y., Wan, Y., Zhang, Y., Huang, J., Yang, Y., Tsang, D.C., ... and Gao, B., 2023. Recovery of phosphorus from wastewater: A review based on current phosphorous removal technologies. *Critical Reviews in Environmental Science and Technology*, 53(11), pp.1148-1172. [DOI]

Zhou, Y., Xing, X.H., Liu, Z., Cui, L., Yu, A., Feng, Q. and Yang, H., 2008. Enhanced coagulation of ferric chloride aided by tannic acid for phosphorus removal from wastewater. *Chemosphere*, 72(2), pp.290-298. [DOI]

Nature Environment and Pollution Technology
An International Quarterly Peer-Reviewed Open Access Journal

p-ISSN: 0972-6268 | e-ISSN: 2395-3454 Vol. 25 | No. 4 | Article ID D1901 | 2026

RESEARCH ARTICLE https://doi.org/10.46488/NEPT.2026.v25i04.D1901 OPEN ACCESS

Bridging Efficiency Gaps in ASEAN Agriculture: A Spatial SBMDEA Approach

Titin Dwi Aryanti†, Suryanto and Evi Gravitiani
Universitas Sebelas Maret, Jebres, Surakarta (Solo), Central Java, Indonesia
†Corresponding author: Titin Dwi Aryanti; tdwiaryanti.titin@student.uns.ac.id

ARTICLE HISTORY

Received: 26-12-2025
Revised: 28-02-2026
Accepted: 02-03-2026

KEYWORDS

Agricultural efficiency
Spatial spillover
Sustainable agriculture
Data envelopment analysis
ASEAN rice production
Greenhouse gas emissions
Irrigation efficiency
Food security

CITE THIS ARTICLE

Aryanti, T. D., Suryanto, and Gravitiani, E., 2026. Bridging efficiency gaps in ASEAN agriculture: A spatial SBM-DEA approach. *Nature Environment and Pollution Technology*, 25(4), D1901. https://doi.org/10.46488/NEPT.2026.v25i04. D1901

COPYRIGHT & LICENCE

© 2026 The Authors
Open Access under CC BY 4.0.

PUBLISHED BY

TECHNOSCIENCE PUBLICATIONS

ABSTRACT

Southeast Asia plays a strategic role in global rice production, yet agricultural performance across countries may be shaped not only by internal production conditions but also by spatial interaction mechanisms. This study investigates sustainable agricultural efficiency and spatial dependence across five major ASEAN rice-producing countries: Indonesia, Thailand, Vietnam, Myanmar, and the Philippines over the period 2010–2023. Efficiency is evaluated using the Slacks-Based Measure Data Envelopment Analysis (SBM-DEA) framework, which accommodates multiple inputs, desirable outputs, and greenhouse gas emissions as an undesirable output. To capture spatial interdependencies, a distance-based spatial weight matrix is constructed using inverse distance weighting, followed by the estimation of Global Moran's I to assess spatial autocorrelation. The results indicate that technical efficiency levels are generally high across countries, suggesting relatively effective internal resource utilization, while spatial efficiency exhibits greater variability, implying that production performance cannot be fully interpreted without considering spatial effects. The Moran's I analysis reveals positive spatial autocorrelation, indicating that efficiency patterns display systematic spatial structures rather than purely independent national dynamics. These findings demonstrate that agricultural efficiency in regionally connected systems reflects both domestic production factors and geographically mediated influences. The study concludes that incorporating spatial dependence into efficiency evaluation provides a more comprehensive understanding of regional agricultural performance and offers a more appropriate analytical basis for policy formulation in interconnected agricultural systems.

1. INTRODUCTION

Global food security continues to represent a fundamental challenge amid population growth, climate change, and increasing pressure on natural resources. Agricultural systems play a central role in sustaining food availability and stability, particularly in regions where staple crops dominate dietary structures. In Southeast Asia, the rice-producing ASEAN countries, namely Indonesia, Thailand, Vietnam, Myanmar, and the Philippines, occupy a strategically important position within regional and global food systems. Rice functions not only as a primary staple food but also as a critical component of rural livelihoods and national food security strategies. Despite strong production capacity, food security outcomes across the region remain complex, reflecting structural constraints, environmental pressures, and resource limitations (FAO 1996, FAO 2008).

Regional food security assessments emphasize that agriculture remains indispensable for hunger reduction and nutritional stability, yet the drivers of food insecurity are multifaceted. Persistent vulnerabilities may emerge even

under conditions of aggregate food sufficiency, highlighting the importance of resource management, environmental sustainability, and institutional coordination (Teng et al. 2021). These challenges have been further amplified by climate variability, water scarcity, demographic transitions, and systemic disruptions, reinforcing the need for analytical frameworks capable of capturing agricultural performance beyond conventional production metrics (Teng et al. 2021).

Food security is widely understood as a multidimensional construct encompassing availability, utilization, and stability. The FAO framework defines food security as a condition in which all individuals have consistent physical, social, and economic access to sufficient, safe, and nutritious food (FAO 1996), while subsequent refinements underscore stability as a critical dimension (FAO 2008). Within this perspective, agricultural efficiency becomes a key determinant of food system resilience, as the capacity to transform inputs into desirable outputs directly influences production sustainability. However, empirical findings on the relationship between agricultural efficiency and food security remain heterogeneous. While some studies identify positive associations between technical efficiency and food security outcomes, others suggest that efficiency improvements alone may not guarantee enhanced food security due to socio-economic and structural factors.

Methodologically, agricultural efficiency is frequently evaluated using Data Envelopment Analysis (DEA), a nonparametric approach suited to multi-input and multi-output production environments (Cooper et al. 2007). Conventional DEA models, however, typically assume independence among decision-making units and treat outputs as exclusively desirable. Such assumptions may be restrictive in sustainability-oriented analyses, where production processes often generate undesirable outcomes. The Slacks-Based Measure (SBM) DEA model offers a methodological advantage by explicitly incorporating slack adjustments and allowing the simultaneous treatment of desirable and undesirable outputs within a unified efficiency framework. This modeling flexibility is particularly relevant in agricultural systems, where environmental externalities increasingly shape performance evaluation (Tsaples & Papathanasiou 2021).

Among environmental pressures, agricultural greenhouse gas (GHG) emissions have emerged as a critical concern. Agricultural activities constitute a substantial source of global emissions, reflecting the environmental costs associated with production processes. Recent evidence highlights that a significant share of global greenhouse gas emissions originates from agriculture and land-use dynamics, underscoring the necessity of incorporating environmental externalities into efficiency measurement (Mehmood et al. 2026). Ignoring undesirable outputs such as GHG emissions may therefore lead to biased efficiency estimates and incomplete sustainability assessments.

Beyond environmental considerations, agricultural systems are inherently embedded within spatial contexts. ASEAN countries share geographic proximity, agroecological similarities, and climatic interdependencies that may induce spatial dependence in production performance. Spatial analytical theory argues that geographically referenced observations are rarely independent, and neglecting spatial structures may bias statistical inference (Anselin 1988). Recent advances in spatial efficiency modeling demonstrate that incorporating spatial relationships into DEA frameworks can yield substantively different interpretations of efficiency relative to conventional approaches (Wang et al. 2021, Zhou et al. 2024). Empirical evidence further confirms that spatially augmented DEA models provide more informative evaluations of regional performance and environmental efficiency (Wen et al. 2016).

Despite growing recognition of spatial effects in efficiency analysis, empirical applications integrating sustainability-oriented DEA models with spatial dependence diagnostics remain limited in the ASEAN agricultural context. Existing studies often emphasize productivity or technical efficiency without explicitly accounting for undesirable outputs and spatial interdependencies. Addressing these gaps is essential for understanding how environmental constraints and geographic structures jointly shape agricultural performance.

This study evaluates sustainable agricultural efficiency and spatial dependence across Indonesia, Thailand, Vietnam, Myanmar, and the Philippines using an SBM-DEA framework combined with spatial diagnostics. Spatial relationships are modeled through an inverse distance weighting scheme, followed by Moran's I analysis to detect spatial autocorrelation and subsequent estimation of spatial efficiency. The findings indicate that incorporating undesirable outputs and spatial structures produces distinct efficiency patterns compared with conventional models, highlighting the analytical importance of spatially informed efficiency assessment in agricultural systems. These results contribute to methodological refinement while offering insights for sustainability-oriented policy design in ASEAN.

2. MATERIALS AND METHODS

This study examines sustainable agricultural efficiency and spatial spillover effects across five major ASEAN rice-producing countries, namely Indonesia, Thailand, Vietnam, Myanmar, and the Philippines, using annual panel data

covering the period 2010–2023. The final dataset comprises 70 decision-making units (DMUs), representing country-year observations. The data were compiled from multiple authoritative and internationally recognized sources to ensure accuracy, consistency, and reproducibility. Primary data were obtained from the Food and Agriculture Organization (FAO) database, complemented by information from the World Bank's World Development Indicators (WDI), as well as other official statistical repositories and publicly accessible government publications where necessary.

To ensure methodological rigor and analytical consistency, this study adopts an integrated quantitative framework. The subsequent section provides a detailed description of the analytical procedures, including the DEA model specification employed for efficiency measurement, the construction of the spatial weight matrix, and the estimation techniques applied in this study.

2.1. Slacks-Based Measure Data Envelopment Analysis (SBM-DEA)

Data Envelopment Analysis (DEA), a nonparametric technique, has been widely applied to evaluate the efficiency of countries and firms in resource utilization. However, conventional DEA models often do not adequately account for undesirable outputs, such as CO_2 emissions, which are essential when environmental performance is considered (Addis 2025). To address this limitation, more recent methodological developments have introduced DEA frameworks that explicitly incorporate both desirable and undesirable outputs (Tone 2001).

In this study, efficiency is measured using the Slacks-Based Measure Data Envelopment Analysis (SBM-DEA) model proposed by Tone (2001). Unlike traditional radial DEA models, such as the CCR model of Charnes et al. (1978), which assess efficiency through proportional input reduction or output expansion, the SBM-DEA model adopts a nonradial approach by directly integrating input excesses and output shortfalls (slacks) into the objective function. This formulation enables nonproportional adjustments across variables and mitigates the potential bias associated with radial projections. The SBM-DEA efficiency score for each decision-making unit (DMU) is defined as:

$$\begin{aligned} min \quad & \rho = \left(1 - (1/m)\Sigma_{i=1}^{m}(s_i^-/x_{i0})\right)/\left(1 + (1/s)\Sigma_{r=1}^{s}(s_r^+/y_{r0})\right) \\ & s.t. \quad x_0 = X\lambda + s^- \;\; s.t. \\ & \qquad y_0 = Y\lambda - s^+ \\ & \lambda \geq 0, s^- \geq 0, s^+ \geq 0 \end{aligned} \qquad \ldots(1)$$

where p denotes the SBM efficiency score, s_i^- and s_r^+ represent the input and output slack variables, respectively, and is the intensity vector defining the convex combination of reference DMUs. In the model, $x_0 \in \mathbb{R}^m$ and $y_0 \in \mathbb{R}^s$ denote the observed input and output vectors of the DMU under evaluation, respectively. The matrices $X \in \mathbb{R}^{m\times n}$ and $Y \in \mathbb{R}^{s\times n}$ represent the input and output matrices of all DMUs. The vector $\lambda \in \mathbb{R}^n$ defines the intensity weights, while $s^- \in \mathbb{R}^m$ and $s^+ \in \mathbb{R}^s$ capture input excesses and output shortfalls.

The efficiency score p is bounded within $0 < p \leq 1$, where a value of unity indicates that the DMU operates on the efficient frontier with no observable slacks. Values below unity imply inefficiency arising from excessive input usage, insufficient output production, or both. The SBM-DEA model is employed due to its nonradial specification, which enables nonproportional adjustments and avoids projection bias inherent in radial DEA models (Tone 2001). The estimated efficiency scores are subsequently used for spatial dependence analysis.

2.2. Spatial Dependence and Spatial Weight Matrix

The conventional SBM-DEA framework assumes independence across decision-making units (DMUs). However, in agricultural systems, efficiency performance may exhibit spatial dependence due to geographic proximity, technology diffusion, similar agroecological conditions, and shared environmental constraints. Ignoring such spatial interactions may bias efficiency estimates, as observed outcomes can be partially influenced by neighboring units rather than purely internal factors. This perspective is consistent with spatial econometric theory, which emphasizes that spatially referenced observations are rarely independent (Cliff & Ord 1981, Anselin 1988).

To explicitly capture spatial interactions, this study constructs a spatial weight matrix W, which defines the neighborhood structure and interaction intensity among countries. The spatial weight matrix is specified as an 5 × 5 matrix:

$$\begin{bmatrix} W_{11} & \cdots & W_{15} \\ \vdots & \ddots & \vdots \\ W_{51} & \cdots & W_{55} \end{bmatrix} \qquad \ldots(2)$$

Where W_{kj} measures the spatial interaction between country k and country j. Diagonal elements W_{kk} are set to zero to exclude self-influence effects (Anselin 1988).

Spatial weights are defined using inverse geographic distance:

$$W_{kj} = \begin{cases} \frac{1}{d_{kj}}, & k \neq j \\ 0, & k = j \end{cases} \qquad \ldots(3)$$

where d_{kj} denotes the geographic distance between countries k and j. This formulation assumes that spatial influence decays with distance, a standard assumption in spatial analysis (Cliff & Ord 1981, LeSage & Pace 2009)

To ensure comparability and numerical stability, the spatial weight matrix is row-standardized:

$$W_{kj}^{*} = \frac{w_{kj}}{\sum_j w_{kj}}, \sum_j W_{kj}^{*} = 1 \quad \ldots(4)$$

Row standardization ensures that spatial effects are interpreted as weighted averages of neighboring influences rather than absolute magnitudes, thereby avoiding scale distortions in spatial efficiency estimation. Descriptive statistics of the spatial weight matrix are reported to illustrate the connectivity structure and interaction intensity among countries.

Spatial dependence in efficiency scores is examined using spatial autocorrelation statistics. Spatial autocorrelation measures the degree to which the presence of similar attribute values in neighboring locations influences the spatial distribution of observations, thereby providing insight into clustering or dispersion patterns. Among the most widely applied global spatial autocorrelation measures is Moran's I.

Moran's I evaluates the correlation between attribute values at each location and those of neighboring locations defined through a spatial weight matrix. The statistic captures the covariance structure of spatially referenced observations and yields standardized values typically ranging between −1 and 1, where positive values indicate spatial clustering and negative values imply spatial dispersion. In contrast, Geary's c assesses the average squared differences between neighboring observations, providing an alternative representation of global spatial variation. Values of Geary's c below unity indicate positive spatial autocorrelation, values above unity indicate negative spatial autocorrelation, and values approaching unity suggest spatial randomness.

Despite the availability of alternative statistics, Moran's I is adopted in this study due to its higher sensitivity to global spatial patterns, interpretational clarity, and methodological consistency with spatial interaction models. Moran's I is extensively employed in empirical spatial analyses across disciplines, including regional science and spatial econometrics.

This study applies the Global Moran's I statistic, which provides a single summary measure of spatial autocorrelation across countries. Global Moran's I assesses whether efficiency scores are spatially random or systematically clustered within the defined spatial structure (Anselin 1995). The statistic is defined as:

$$I = \frac{N}{S_0} \cdot \frac{\sum_k \sum_j W_{kj}(E_k - \bar{E})(E_j - \bar{E})}{\sum_k (E_k - \bar{E})^2} \quad \ldots(5)$$

where E_k denotes the efficiency score of country k, $\bar{E}$ represents the mean efficiency, W_{kj} is the row-standardized spatial weight matrix, N is the number of spatial units, and $S_0 = \sum_k \sum_j W_{kj}$.

Statistical inference is conducted using permutation-based significance tests, a standard approach for assessing the nonrandomness of spatial patterns (Anselin 1995).

To incorporate spatial interaction effects into ecological efficiency measurement, the conventional efficiency framework is extended by explicitly accounting for interdependencies among decision-making units (DMUs). In cross-country agricultural systems, environmental and production outcomes may not be solely determined by internal resource allocation but may also reflect spillover mechanisms arising from geographically proximate units. Ignoring such spatial interaction structures may therefore lead to biased efficiency estimates.

The spatial ecological efficiency specification utilized in this study follows the analytical framework proposed by Zhou et al. (2024), which explicitly incorporates spatial interaction effects into the DEA efficiency structure. This formulation enables efficiency measurement under spatial dependence by adjusting undesirable outputs to reflect neighboring influences, thereby providing a behaviorally consistent extension of conventional ecological efficiency analysis.

The initial spatial efficiency formulation is represented by Model (6), which integrates spatial spillover effects through the adjustment of undesirable outputs:

$$\min \overline{\theta_0^{KW}} \quad \ldots(6)$$

$$\text{s.t.} \sum_{t\in W} \sum_{j=1}^{n} \lambda_j^t x_{ij}^t \le x_{i0}^{KW}, \quad i = 1,2,\ldots,m$$

$$\sum_{t\in W} \sum_{j=1}^{n} \lambda_j^t y_{rj}^t \ge y_{r0}^{KW}, \quad r = 1,2,\ldots,s$$

$$\sum_{t\in W} \sum_{j=1}^{n} \lambda_j^t b_{lj}^t \le \overline{\theta_0^{KW}} \left(b_{l0}^{KW} - \beta_j^{KW} b_{lj}^{KW}\right), \quad l = 1,2,\ldots,p$$

$$\sum_{t\in W} \sum_{j=1}^{n} \lambda_j^t = 1, \quad j = 1,2,\ldots,n$$

Model (6) assumes that undesirable outputs may be influenced by neighboring DMUs through the spatial interaction parameter β_j^{kW}, which captures spillover

effects embedded within the spatial structure. As the estimation of Model (6) dependson the spatial interaction mechanism, the model is subsequently reformulated to obtain a tractable representation of spatial ecological efficiency.

Following the transformation procedure, Model (6) can be expressed as Model (7):

$$min\ \overline{\theta_0^{KW}} \quad \ldots(7)$$

$$\text{s.t.} \sum_{t\in W}\sum_{j=1}^{n} \lambda_j^t x_{ij}^t \le x_{i0}^{KW}, \quad i = 1,2,\ldots,m$$

$$\sum_{t\in W}\sum_{j=1}^{n} \lambda_j^t y_{rj}^t \ge y_{r0}^{KW}, \quad r = 1,2,\ldots,s$$

$$\sum_{t\in W}\sum_{j=1}^{n} \lambda_j^t b_{lj}^t \le \overline{\theta_0^{KW}}\ \delta_0^{KW}\ b_{l0}^{KW}, \quad l = 1,2,\ldots,p$$

$$\sum_{t\in W}\sum_{j=1}^{n} \lambda_j^t = 1, \quad j = 1,2,\ldots,n$$

Model (7) measures the ecological efficiency of DMU after isolating the environmental effects attributable to neighboring units. In this formulation, spatial ecological efficiency reflects the efficiency position under a spatially adjusted production structure, where spillover effects are explicitly separated from internal production behavior.

The spatial efficiency score obtained from Model (7) represents the upper bound of attainable efficiency for a DMU when the full environmental impact of neighboring units is taken into account. Conceptually, this approach recognizes that observed inefficiency may arise not only from internal resource misallocation but also from external spatial mechanisms embedded within the interaction structure.

By separating internal and spatial effects, the model avoids conflating endogenous production inefficiency with exogenous spatial dependence. This distinction is particularly important in cross-country analyses, where geographic proximity and shared ecological conditions may generate interdependent efficiency outcomes.

Model (7) is reformulated to incorporate spatially neighboring DMUs into the efficiency frontier. The spatial DEA specification is presented in Model (8).

$$\min\ \widetilde{\theta_0^{KW}}/\delta_0^{KW} \quad \ldots(8)$$

$$\text{s.t.} \sum_{t\in W}\sum_{j=1}^{n} \lambda_j^t x_{ij}^t \le x_{i0}^{KW}, \quad i = 1,2,\ldots,m$$

$$\sum_{t\in W}\sum_{j=1}^{n'} \lambda_j^t y_{rj}^t \ge y_{r0}^{KW}, \quad r = 1,2,\ldots,s$$

$$\sum_{t\in W}\sum_{j=1}^{n} \lambda_j^t b_{lj}^t \le \widetilde{\theta_0^{KW}}\ b_{l0}^{KW}, \quad l = 1,2,\ldots,p$$

$$\sum_{t\in W}\sum_{j=1}^{n} \lambda_j^t = 1, \quad j = 1,2,\ldots,n$$

Equation (8) represents a spatially restricted frontier, where benchmarking is constructed based on neighboring units. Based on this formulation, spatial efficiency can be decomposed into technical efficiency (TE) and spatial impact efficiency (IE), as expressed in Model (9).

$$SE = TE/IE \quad \ldots(9)$$

Technical efficiency (TE) is obtained from Model (1). Subsequently, the spatial impact efficiency (IE) is estimated using Model (10).

$$Min\delta_K W \quad \ldots(10)$$

$$\sum_{j=1}^{n} \mu_j x_{ij}^{KW} \le x_{i0}^{KW}, i = 1,2,\ldots,m$$

$$\sum_{j=1}^{n} \mu_j y_{rj}^{KW} \ge y_{r0}^{KW}, r = 1,2,\ldots,s$$

$$\sum_{j=1}^{n} \mu_j b_{lj}^{KW} \ge \delta_K W b_{l0}^{KW}, l = 1,2,\ldots,p$$

$$\sum_{j=1}^{n} \mu_j = 1$$

$$\mu_j \le SI_{j0}, j = 1,2,\ldots,n$$

In Model (10), the optimal value δ_0^{KW} captures the maximum spatial influence of neighboring DMUs on the undesirable output of DMU$_0$. This value represents the spatial impact efficiency (IE). Furthermore, the ratio $\tilde{\theta}_0^{KW}/\delta_0^{KW}$ in Model (8) reflects the ecological efficiency of DMU$_0$ after isolating the spatial spillover effect from surrounding units.

2.3. Variable Identification

Considering the research objectives and data availability, the variables were selected to represent agricultural production inputs and food security outcomes, as reflected by indicators derived from the Global Food Security Index (GFSI). The GFSI conceptualizes food security as a multidimensional outcome of the food system, encompassing availability, utilization, stability, and broader sustainability dimensions (Božić & Nikolić 2020, Guo & Islam 2025). This perspective allows food security to be interpreted as a systemic result of production and distribution processes rather than solely

a consumption-based measure. Importantly, Chen et al. (2019) demonstrate that GFSI-related indicators can be operationalized within a Data Envelopment Analysis (DEA) framework, thereby supporting their use as output variables in efficiency evaluation. Accordingly, food security performance in this study is treated as a system-level outcome associated with agricultural production efficiency.

The input variables include fertilizer use, agricultural water use, agricultural energy use, agricultural labor, and agricultural land area, representing key production resources within the agricultural system. Outputs are defined in accordance with the conceptual structure of the GFSI. The availability dimension is proxied by Dietary Energy Supply (DES), utilization by Protein Supply, and stability by Food Supply Stability. These indicators are modeled as desirable outputs capturing the agricultural system's capacity to support food security outcomes. In addition, two undesirable outputs, the number of undernourished people and agricultural greenhouse gas (GHG) emissions, are incorporated to account for social and environmental externalities associated with agricultural production.

The study covers ASEAN countries for the period 2010–2023. All data were obtained from the Food and Agriculture Organization (FAO). Descriptive statistics are presented in Table 1.

3. RESULTS AND DISCUSSION

3.1. Technical Efficiency (TE) Scores from the SBM-DEA Model

The efficiency estimates derived from the SBM-DEA model highlight distinct performance patterns across the five countries under investigation. Indonesia and Myanmar display the most consistent and stable efficiency trajectories, with scores predominantly equal to or very close to unity throughout the observation period. This stability indicates that both countries operate near the efficient frontier, reflecting their ability to utilize inputs effectively while maintaining desirable outputs and controlling undesirable outputs. The recurrent attainment of full efficiency further suggests that Indonesia and Myanmar frequently act as benchmark units, providing reference standards for other countries within the sample.

Conversely, Thailand and the Philippines exhibit relatively lower efficiency levels compared to their regional counterparts. For Thailand, the observed inefficiencies are systematically linked to slack values, particularly in protein supply, representing the utilization dimension of food security, and greenhouse gas (GHG) emissions, which constitute the undesirable output. The persistence of these slacks over time points to underlying structural challenges, implying that improvements are required in both nutritional performance and environmental management. The Philippines shows a similar tendency, with efficiency scores falling below unity in most years, indicating the presence of unresolved inefficiencies in resource utilization or output generation.

Vietnam demonstrates a moderately strong performance profile. Although the country does not achieve full efficiency in every year, its efficiency scores consistently remain close to unity. This finding implies that Vietnam's production system operates with relatively minor deviations from the efficient frontier, requiring only limited adjustments to reach full efficiency. The slack values associated with each country and period are presented in Table 2, offering a more detailed identification of inefficiency sources and potential directions for policy intervention.

In the output-oriented SBM-DEA framework, slack values represent output shortfalls and inefficiencies relative to the efficient frontier. Positive slack values indicate the

Table 1: Descriptive statistics of input and output variables.

Aspect	Variable	Obs	Mean	Std. Dev.	Min	Max
Input	Fertilizer Use (kg/ha)	70	265	15.2	14.49	677.00
	Agricultural Water Use (BCM)	70	20,200,000	169,000,000	94	1,420,000,000
	Agricultural Energy Use (kg)	70	4,590,000,000	2,800,000,000	82,600,000	9,910,000,000
	Agricultural Labor (persons)	70	58,400,000	37,800,000	22,100,000	141,000,000
	Agricultural Land Area (1000 m^2)	70	96,900,000	193,000,000	107,601	549,000,000
Output	DES (Availability) (hcal/capita/day)	70	27,816.14	1,387.44	24,110	30,860
	Protein Supply (dg/capita/day)	70	781.27	115.15	606	995
	Food Supply Stability (index score)	70	281.43	116.65	0	460
Undesirable Output	Undernourished Population (proportion)	70	0.014	0.013	0.00	0.058
	Agricultural GHG Emissions (kt)	70	187,000	235,000	11,200	957,000

Table 2: Analysis of slacks and input-output inefficiency.

No	DMU	DES	Protein Supply	Food Supply Stability	Number of Undernourished	Agricultural GHG Emissions
1	Indonesia_2010	0	0	0	0	0
2	Indonesia_2011	0	0	0	0	0
3	Indonesia_2012	0	0	0	0	0
4	Indonesia_2013	0	0.793685	0	0.040829	0
5	Indonesia_2014	0	0	0	0	0
6	Indonesia_2015	0	0	0	0	0
7	Indonesia_2016	0	0	0	0	0
8	Indonesia_2017	0	0	0	0	0
9	Indonesia_2018	0	0	3.782789	0	3584.626434
10	Indonesia_2019	0	0	0	0	0
11	Indonesia_2020	0	0	0	0	0
12	Indonesia_2021	0	0	0	0	0
13	Indonesia_2022	0	0	0	0	0
14	Indonesia_2023	0	0	0	0	0
15	Thailand_2010	0	13.862154	21.984475	0	70236.11646
16	Thailand_2011	0	11.010325	22.476726	0	56595.60633
17	Thailand_2012	0	11.043552	4.666007	0	56173.38689
18	Thailand_2013	0	18.163024	0	0	59529.48206
19	Thailand_2014	0	19.011161	0	0	67739.011
20	Thailand_2015	0	19.189014	0	0	74928.68924
21	Thailand_2016	0	18.879528	0	0	70539.08139
22	Thailand_2017	0	18.470241	0	0	69492.37908
23	Thailand_2018	0	17.082843	0	0	73228.3664
24	Thailand_2019	0	18.207253	0	0	81994.78212
25	Thailand_2020	0	21.911474	0	0	76205.66752
26	Thailand_2021	0	15.178593	0	0	54362.63432
27	Thailand_2022	0	13.522145	0	0	29672.70013
28	Thailand_2023	0	20.729333	0	0.048553	27026.68516
29	Vietnam_2010	0	0	0	0	0
30	Vietnam_2011	0	0	0	0	0
31	Vietnam_2012	0	0	0	0	0
32	Vietnam_2013	0	0	0	0	0
33	Vietnam_2014	0	0	0	0	0
34	Vietnam_2015	0	0.461393	0	0	8882.498374
35	Vietnam_2016	0	0	9.083722	0	7734.152972
36	Vietnam_2017	0	0	14.390224	0	2517.291508
37	Vietnam_2018	24.101189	0	4.364724	0	0
38	Vietnam_2019	17.730331	0	2.869524	0	0
39	Vietnam_2020	0	0	0	0	0
40	Vietnam_2021	0	0	0	0	0
41	Vietnam_2022	32.89762	0	0	0	0

Table Cont....

No	DMU	DES	Protein Supply	Food Supply Stability	Number of Undernourished	Agricultural GHG Emissions
42	Vietnam_2023	0	0	0	0	0
43	Myanmar_2010	0	0	0	0	0
44	Myanmar_2011	0	0	0	0	0
45	Myanmar_2012	0	0	0	0	0
46	Myanmar_2013	0	0	0	0	0
47	Myanmar_2014	0	0	0	0	0
48	Myanmar_2015	0	0	0	0	0
49	Myanmar_2016	0	0	0	0	0
50	Myanmar_2017	0	0	0	0	0
51	Myanmar_2018	0	0	0	0	0
52	Myanmar_2019	0	0	0	0.245927	3086.333707
53	Myanmar_2020	0	0	0	0	0
54	Myanmar_2021	0	0	0	0	0
55	Myanmar_2022	0	0	0	0	0
56	Myanmar_2023	0	0	0	0	0
57	Philippines_2010	0	0	0	0	0
58	Philippines_2011	0	0	0	0	0
59	Philippines_2012	0	0	0	0	0
60	Philippines_2013	0	0	0	0	3317.730129
61	Philippines_2014	0	0	1.674625	0	1010.21799
62	Philippines_2015	0	0	0.933061	0	2656.510655
63	Philippines_2016	0	1.484369	0	0	5165.818568
64	Philippines_2017	0	0	0.194972	0	0
65	Philippines_2018	0	0	3.032568	0	0
66	Philippines_2019	0	0	14.510459	0	1544.540174
67	Philippines_2020	0	0	16.371611	0	3445.224153
68	Philippines_2021	0	0	1.585159	0	955.504773
69	Philippines_2022	0	0	0	0	0
70	Philippines_2023	0	0	0	0	0

extent to which desirable outputs should be increased and undesirable outputs should be reduced in order to achieve full efficiency. A slack value equal to zero implies that the DMU operates at the optimal level, whereas positive values reflect unrealized production potential. Therefore, higher slack values suggest greater opportunities for efficiency improvement through output expansion and environmental impact mitigation (Tone 2001, Cooper et al. 2007).

3.2. Spatial Weight Matrix and Moran's I Analysis

The spatial interaction structure among the observed countries was defined using an inverse distance weighting (IDW) scheme as specified in Eq. (3). This approach assumes that spatial influence diminishes with geographic distance, thereby capturing the distance-decay mechanism underlying intercountry relationships. The resulting spatial-weighting object, denoted as W, was constructed and subsequently row-standardized to ensure numerical

Table 3: Summary of spatial-weighting object W_invn.

Matrix	Description
Dimensions	5 × 5
Stored as	5 × 5
Values	
Min	0
Min>0	0.1295345
Mean	0.2
Max	0.4766829

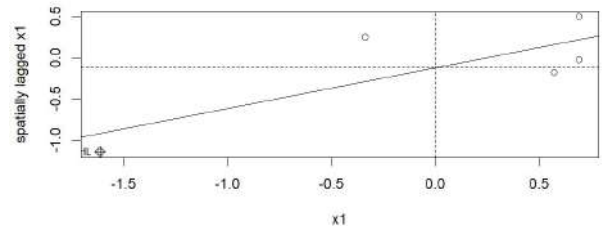


Fig. 1: Moran's I scatterplot.

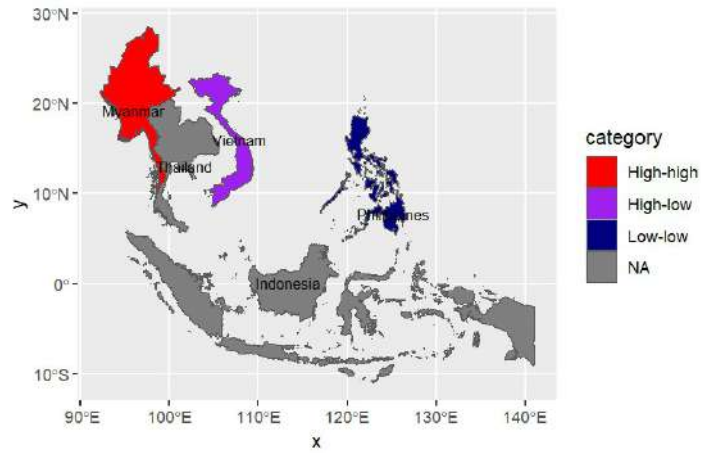


Fig. 2: LISA-based spatial clustering.

consistency and comparability across spatial units. The summary characteristics of the spatial weight matrix are presented in Table 3.

Building upon the spatial configuration represented by the weight matrix, Global Moran's I was computed to assess the presence and direction of spatial autocorrelation in agricultural efficiency. The Moran's I statistic provides a quantitative measure of spatial dependence by evaluating the correspondence between observed values and their spatially weighted counterparts. The estimation results of Moran's I are reported in the subsequent section.

The Moran's I scatterplot (Fig. 1) illustrates a positively sloped diagonal line, indicating a positive value of Moran's I. This pattern reflects the presence of positive spatial autocorrelation, meaning that regions with high values tend to be surrounded by neighboring regions with similarly high values, while regions with low values are generally adjacent to regions exhibiting low values. The relatively steep slope of the diagonal line further suggests a strong degree of spatial dependence among the observed regions.

The Local Indicators of Spatial Association (LISA) analysis (Fig. 2) provides a more detailed decomposition of this global spatial pattern by identifying localized clusters and spatial outliers. In particular, the High-High (HH) cluster represents regions with high values that are surrounded by neighbors also characterized by high values. This configuration typically indicates the existence of spatial concentration or agglomeration, where similar performance levels reinforce each other geographically.

The Low-Low (LL) cluster denotes regions with low values that are spatially proximate to other low-value regions. Such a pattern signifies the formation of spatial pockets of relatively weak performance, suggesting that structural constraints or unfavorable conditions may be shared across neighboring regions.

In contrast, the Low-High (LH) category captures spatial outliers, referring to regions with low values that are surrounded by high-value neighbors. This configuration implies spatial disparity, where a region's performance deviates markedly from its surrounding context. The presence of LH patterns may indicate localized inefficiencies, transitional dynamics, or region-specific constraints that prevent convergence with neighboring high-performing areas.

3.3. Spatial Efficiency Analysis

Table 4 presents the comparison between technical efficiency (TE) and spatial efficiency (SE) for the five ASEAN countries during 2010–2023. The results indicate that most DMUs exhibit consistently high TE scores, with values close

Table 4: Comparison of TE and SE.

DMU	TE	SE	DMU	TE	SE
Indonesia_2010	0.9918	0.5091	Philippiness_2017	0.9347	0.3218
Indonesia_2011	0.9959	0.5347	Philippines_2018	0.9493	0.6225
Indonesia_2012	0.9609	0.5087	Philippines_2019	0.9565	0.9736
Indonesia_2013	0.9986	0.0297	Philippines_2020	0.9559	0.4957
Indonesia_2014	0.9959	0.5000	Philippines_2021	0.9701	0.4929
Indonesia_2015	0.9609	0.5312	Philippines_2022	1.0000	0.8270
Indonesia_2016	0.9986	0.7998	Philippines_2023	1.0000	0.4978
Indonesia_2017	1.0000	0.5765	Thailand_2010	0.9649	0.2599
Indonesia_2018	0.9871	0.6000	Thailand_2011	0.9698	0.1750
Indonesia_2019	0.9856	0.9658	Thailand_2012	0.9656	0.2554
Indonesia_2020	0.9810	0.5172	Thailand_2013	0.9620	0.1698
Indonesia_2021	0.9784	0.5193	Thailand_2014	0.9649	0.1366
Indonesia_2022	0.9918	0.5250	Thailand_2015	0.9698	0.2884
Indonesia_2023	0.9913	0.2258	Thailand_2016	0.9656	0.6211
Myanmar_2010	1.0000	0.7188	Thailand_2017	0.9620	0.4871
Myanmar_2011	1.0000	0.6284	Thailand_2018	0.9670	0.6176
Myanmar_2012	1.0000	0.7149	Thailand_2019	0.9793	0.9710
Myanmar_2013	1.0000	0.1548	Thailand_2020	0.9957	0.2587
Myanmar_2014	1.0000	0.5992	Thailand_2021	0.9859	0.2602
Myanmar_2015	1.0000	0.7384	Thailand_2022	0.9825	0.5058
Myanmar_2016	1.0000	0.9669	Thailand_2023	0.9911	0.1324
Myanmar_2017	1.0000	0.3764	Vietnam_2010	1.0000	0.7717
Myanmar_2018	1.0000	0.5497	Vietnam_2011	0.9739	0.6041
Myanmar_2019	0.9927	0.9695	Vietnam_2012	1.0000	0.7658
Myanmar_2020	1.0000	0.7327	Vietnam_2013	0.9739	0.1863
Myanmar_2021	1.0000	0.7296	Vietnam_2014	1.0000	0.5991
Myanmar_2022	1.0000	0.8528	Vietnam_2015	0.9739	0.7618
Myanmar_2023	1.0000	0.6012	Vietnam_2016	0.9620	0.7731
Philippines_2010	0.9508	0.4916	Vietnam_2017	0.9661	0.2036
Philippines_2011	0.9347	0.2696	Vietnam_2018	0.9573	0.4282
Philippines_2012	0.9493	0.4830	Vietnam_2019	0.9502	0.9782
Philippines_2013	1.0000	0.3188	Vietnam_2020	1.0000	0.7826
Philippines_2014	0.9214	0.2361	Vietnam_2021	1.0000	0.7814
Philippines_2015	0.9235	0.5165	Vietnam_2022	0.9955	0.5722
Philippines_2016	0.9508	0.8143	Vietnam_2023	1.0000	0.5756

to unity in almost all periods. This finding suggests that, from a conventional DEA perspective, agricultural production in the selected countries operates near the efficiency frontier.

However, the spatial efficiency scores show substantially lower and more volatile values compared to TE. In many cases, DMUs with high TE values record relatively low SE scores, indicating that strong internal production performance is not necessarily accompanied by favorable spatial interactions. This discrepancy implies that regional spillover effects, neighboring conditions, and spatial externalities play a significant role in shaping overall efficiency.

For Indonesia, although TE remains consistently high throughout the study period, SE fluctuates considerably and declines sharply in certain years, such as 2013 and 2023. This suggests that Indonesia's production efficiency is primarily driven by internal factors, while spatial linkages with

neighboring countries are relatively weak in some periods.

Myanmar demonstrates near-perfect TE scores across most years; nevertheless, its SE values vary markedly, particularly in 2013 and 2017. This pattern indicates that despite operating on the efficiency frontier, Myanmar does not always benefit from positive regional spillovers. The Philippines and Thailand display relatively lower and more unstable SE values in the early years, followed by noticeable improvements around 2016–2019. These improvements may reflect enhanced regional integration, technology diffusion, and policy coordination. Similarly, Vietnam shows high TE performance but experiences substantial variations in SE, with particularly strong spatial effects observed in 2019–2021.

Overall, the comparison reveals that high technical efficiency does not automatically translate into high spatial efficiency. While TE reflects internal managerial and technological performance, SE captures the influence of geographical proximity and interregional interactions. The observed gaps between TE and SE suggest that efficiency enhancement strategies should not only focus on improving internal production processes but also emphasize regional cooperation, infrastructure connectivity, and knowledge spillovers.

4. CONCLUSIONS

This study shows that agricultural efficiency exhibits different characteristics once spatial interdependencies are incorporated into the analytical framework. While conventional SBM-DEA results indicate that countries generally operate near the efficiency frontier, spatial efficiency estimates reveal that internal production performance alone does not fully capture observed efficiency dynamics. The divergence between technical and spatial efficiency highlights the role of spatial dependence and geographically mediated effects in shaping efficiency outcomes. The findings suggest that efficiency behavior in regionally connected systems reflects both domestic production factors and spatial interaction mechanisms. The analysis is conducted within a defined empirical scope and a distance-based spatial structure, consistent with established spatial modeling practices. Future research may extend this framework by exploring alternative spatial specifications and broader regional contexts.

5. ACKNOWLEDGEMENT

We gratefully acknowledge the Institute for Research and Community Service (LPPM), Universitas Sebelas Maret, for providing support through the Research Group Capacity Strengthening Program (PKGR) B 2026, under Assignment Agreement No. 462/UN27.22/PT.01.03/2026. This support has been invaluable to the successful implementation of this research.

6. REFERENCES

Addis, A.K., 2025. Sustainability and efficiency analysis of 42 countries: Super SBM-DEA model and the GML productivity index with undesirable outputs. *Ecological Indicators*, 177, 113767. [DOI]

Anselin, L., 1988. *Spatial Econometrics: Methods and Models*. Kluwer Academic Publishers, Dordrecht.

Anselin, L., 1995. Local indicators of spatial association—LISA. *Geographical Analysis*, 27(2), pp. 93–115. [DOI]

Božić, D. and Nikolić, M., 2020. Food security and comparative analysis of situation in Serbia and neighbouring countries. *Ekonomika Poljoprivrede*, 67(4), pp. 1191–1204. [DOI]

Charnes, A., Cooper, W.W. and Rhodes, E., 1978. Measuring the efficiency of decision making units. *European Journal of Operational Research*, 2(6), pp. 429–444. [DOI]

Chen, P.-C., Yu, M.-M., Shih, J.-C., Chang, C.-C. and Hsu, S.-H., 2019. A reassessment of the Global Food Security Index by using a hierarchical data envelopment analysis approach. *European Journal of Operational Research*, 272(2), pp. 687–698. [DOI]

Cliff, A.D. and Ord, J.K., 1981. *Spatial Processes: Models and Applications*. Pion, London.

Cooper, W.W., Seiford, L.M. and Tone, K., 2007. *Data Envelopment Analysis: A Comprehensive Text with Models, Applications, References and DEA-Solver Software*. 2nd ed. Springer, New York.

Food and Agriculture Organization of the United Nations (FAO), 1996. *The State of Food and Agriculture 1996: Food Security – Some Macroeconomic Dimensions*. Rome: FAO.

Food and Agriculture Organization of the United Nations (FAO), 2008. *An Introduction to the Basic Concepts of Food Security*. Rome: FAO.

Guo, X. and Islam, M., 2025. Advancing food security and proposing future strategies: A comparative performance analysis of Global Food Security Index and annual population changes of top five populous countries. *PLoS One*, 20(5), e0324231. [DOI]

LeSage, J. and Pace, R.K., 2009. *Introduction to Spatial Econometrics*. CRC Press, New York.

Mehmood, J., Ahmad, K. and Arshed, N., 2026. Interplay of renewaable energy technology R&D, digital technologies, and environmental policy in agricultural emission mitigation: Theoretical and empirical perspectives. *Journal of Cleaner Production*, 544, 147709. [DOI]

Teng, P.P.S., Caballero-Anthony, M. and Jose Ma. Luis, M., 2021. ASEAN responses to COVID-19 for assuring food security. *Advances in Food Security and Sustainability*, 6, pp. 83–118.[DOI]

Tone, K., 2001. A slacks-based measure of efficiency in data envelopment analysis. *European Journal of Operational Research*, 130(3), pp. 498–509. [DOI]

Tsaples, G. and Papathanasiou, J., 2021. Data envelopment analysis and the concept of sustainability: A review and analysis of the literature. *Renewable and Sustainable Energy Reviews*, 138, 110664. [DOI]

Wang, L., He, Y. and Wang, T., 2021. Analysis of the spatial structure of regional enterprises and its impact on regional economic development based on the data envelopment analysis model (DEA). *Journal of Mathematics*, 2021, 8153506. [DOI]

Wen, J., Wang, H. and Zhao, D., 2016. The evaluation and spatial correlation analysis of Chinese industrial environmental efficiency. *Nature Environment and Pollution Technology*, 15, pp. 1041–1048.

Zhou, Z., Li, M., Xu, X. and Wu, H., 2024. Integrating spatial relationships in the DEA approach for ecological efficiency evaluation: A case study of the Chaohu watershed. *Ecological Indicators*, 169, 112868. [DOI]

Nature Environment and Pollution Technology
An International Quarterly Peer-Reviewed Open Access Journal

p-ISSN: 0972-6268 | e-ISSN: 2395-3454 Vol. 25 | No. 4 | Article ID B4440 | 2026

RESEARCH ARTICLE https://doi.org/10.46488/NEPT.2026.v25i04.B4440 OPEN ACCESS

Ecotoxicological Insights into Heavy Metal Dynamics in Cauvery Delta Wetland Sediments: Geochemistry, Speciation and Ecological Risk Indices

K. P. Aakash† and **R. Mohanraj**
Department of Environmental Science and Management, Bharathidasan University, Tiruchirappalli-620024, Tamil Nadu, India
†Corresponding author: Aakash K. P.; aakash.kp@bdu.ac.in

ARTICLE HISTORY

Received: 21-03-2026
Revised: 18-05-2026
Accepted: 21-05-2026

KEYWORDS

Wetland sediments,
Heavy metals,
Metal speciation,
Ecological risk assessment,
Cauvery delta.

CITE THIS ARTICLE

Aakash, K.P. and Mohanraj, R., 2026. Ecotoxicological insights into heavy metal dynamics in Cauvery delta wetland sediments: geochemistry, speciation and ecological risk indices, *Nature Environment an Pollution Technology* 25(4), B4440. https://doi.org/10.46488/NEPT.2026.v25i04.B4440

COPYRIGHT & LICENCE

© 2026 The Authors
Open Access under CC BY 4.0.

PUBLISHED BY

TECHNOSCIENCE PUBLICATIONS

ABSTRACT

Wetland sediments in deltaic ecosystems act both as sinks and secondary sources of heavy metals, thereby influencing contaminant mobility, bioavailability, and ecological risk. The present study investigated the distribution, speciation, mobility, and ecological risk of Fe, Ni, Pb, Cu, Cr, and Cd in surface sediments collected from 40 wetlands across the Cauvery Delta, India. The study integrates total metal concentration analysis, sequential extraction, contamination indices, risk assessment models, and multivariate statistical techniques to evaluate sediment quality and identify dominant sources of contamination. Sediment physicochemical properties indicated predominantly alkaline and carbonate-rich conditions, which strongly influenced metal partitioning and mobility. The overall decreasing order of mean metal concentrations was Fe > Pb > Ni > Cr > Cu > Cd. Contamination factor (CF), Pollution Load Index (PLI), and geoaccumulation index (Igeo) revealed generally low to moderate contamination for most metals, while Cd exhibited localized enrichment and emerged as the principal contaminant of concern. PLI values ranging from 1.07 to 1.29 indicated slight but consistent cumulative pollution across all wetlands. Sequential extraction analysis demonstrated that Fe was predominantly associated with stable residual fractions, whereas Cd showed comparatively higher association with exchangeable and carbonate-bound fractions, indicating enhanced mobility and bioavailability. Risk Assessment Code (RAC) and Potential Ecological Risk Index (PERI) further identified Cd, Pb, and Cr as ecologically significant metals with elevated remobilization potential under changing environmental conditions. High RAC and PERI values were particularly observed in wetlands located within Karur and Tiruchirappalli districts, indicating localized anthropogenic influence. Pearson correlation analysis and principal component analysis (PCA) suggested that Fe and Cr were primarily influenced by lithogenic processes, whereas Cd, Pb, and Cu were associated with mixed anthropogenic inputs including agricultural runoff, fertilizer application, urban discharge, and localized industrial activities. The findings demonstrate that although most wetlands remain moderately contaminated, Cd exhibits elevated mobility and ecological sensitivity, warranting targeted monitoring and management in identified hotspot regions. This study provides a comprehensive regional-scale assessment of heavy metal behavior in deltaic wetland sediments and contributes important baseline information for future wetland conservation and pollution management strategies.

1. INTRODUCTION

Deltaic systems are highly dynamic geomorphic environments that develop where riverine sediments accumulate at the transition between fluvial and marine domains. Continuous deposition of alluvial material creates fertile plains that rank among the world's most productive agricultural regions, thereby supporting dense populations, food production, and rich biodiversity (Tessler et al. 2015, Syvitski et

al. 2022). These landscapes encompass a mosaic of wetland types, including mangrove forests, estuaries, coastal lagoons, brackish marshes, freshwater wetlands, and cultivated floodplain areas. Collectively, these ecosystems offer a wide range of ecological services such as habitat provision, carbon storage, regulation of hydrological processes, shoreline protection, nutrient cycling, and water purification (Barbier et al. 2019, IPCC 2022).

Wetlands within delta regions play a vital role in sustaining both resident and migratory fauna by offering breeding grounds, feeding areas, and nursery habitats maintained by periodic inundation. Mangrove and marsh ecosystems are also recognized as significant blue carbon sinks, where organic carbon is preserved in waterlogged sediments under oxygen-limited conditions over long timescales, thereby contributing to climate regulation (Alongi 2020, Macreadie et al. 2021). Furthermore, coastal wetlands dissipate wave energy, reduce storm surge intensity, and mitigate coastal erosion, providing natural protection for inland settlements against extreme weather events (Menéndez et al. 2020). By temporarily storing floodwaters and releasing them gradually during dry periods, these systems also enhance groundwater recharge and stabilize regional water availability.

In addition to their ecological importance, delta regions frequently support intensive agricultural production, particularly irrigated rice cultivation and are also experiencing expanding urban and industrial development. The Cauvery Delta of southern India exemplifies such a landscape, hosting diverse industries including textiles, paper manufacturing, cement production, heavy electrical equipment fabrication, and agro-processing units. Rapid population growth, land-use transformation, industrial expansion, and climate-related pressures have collectively intensified environmental stress on these fragile ecosystems (Nicholls et al. 2021). Among the emerging threats, contamination by heavy metals has become a major concern on account of their persistence, toxicity, and ability to accumulate in biological systems.

Sediments in wetland environments function both as repositories and potential secondary sources of trace metals. Pollutants enter deltaic systems through multiple pathways, including upstream river transport, agricultural runoff, industrial effluents, atmospheric deposition, and municipal wastewater discharge. Under variable physicochemical conditions, particularly shifts in redox potential and salinity, metals bound to sediments may be remobilized, increasing their availability to aquatic organisms and elevating ecological risks (Varol 2020). Such contamination can disrupt trophic interactions, impair ecosystem functioning, and pose hazards to human populations via biomagnification along food chains.

Heavy metals are of significant concern because they are resistant to biodegradation and tend to accumulate in organisms over time. In wetlands subject to seasonal flooding or saline intrusion, changes in redox conditions may enhance metal mobility, facilitating their transfer into both aquatic and terrestrial biota and ultimately into the human diet (Varol & Sen 2012, Dessalew et al. 2018, Bessa et al. 2018, Mandeng et al. 2019, Bhattacharyya et al. 2019). Chronic exposure to these contaminants can degrade ecosystem health, alter biogeochemical cycles, and enhance long-term environmental deterioration (Liu et al. 2016, Chen et al. 2019).

Evaluation of sediment contamination based solely on total metal concentrations often provides limited insight into environmental risk. Metal speciation analysis, which differentiates metals according to their chemical associations, offers a more meaningful assessment of their stability, mobility, and bioavailability. Sequential extraction studies typically categorize metals into exchangeable, carbonate-associated, Fe–Mn oxide-bound, organic-bound, and residual fractions, each representing distinct degrees of environmental availability and potential release under changing conditions (Parizanganeh et al. 2007, Zakir et al. 2008, El Kammar et al. 2009, Kumar et al. 2011).

Complementary to speciation studies, sediment quality is frequently assessed using geochemical indices such as the geoaccumulation index, contamination factor, and pollution load index. These metrics enable quantitative evaluation of contamination intensity and spatial distribution, facilitating identification of pollution hotspots and comparison across regions (Müller 1969, Håkanson 1980, Cevik et al. 2009, Atiemo et al. 2011, Salah et al. 2012, Nowrouzi & Pourkhabbaz 2014, Gupta et al. 2014, Sivakumar et al. 2016). Such indices provide standardized frameworks for interpreting complex geochemical datasets and assessing ecological risk (Håkanson 1980, USEPA 2002). Considering the ecological significance and socioeconomic value of delta wetlands, systematic monitoring and integrated management approaches are essential to minimize anthropogenic impacts and maintain long-term sustainability. Multidisciplinary investigations are therefore critical for understanding environmental processes and guiding conservation strategies in vulnerable deltaic systems such as the Cauvery Delta.

Despite several studies on sediment geochemistry in the Cauvery Basin and other Indian wetlands, most investigations have been limited to localized assessments, single-site analyses, or total metal concentration approaches without addressing metal speciation and mobility. Furthermore, comparative evaluations across multiple wetlands at a regional scale remain scarce.

The present study advances current understanding by (i) providing a comprehensive assessment across 40 wetlands in the deltaic region, (ii) incorporating a district-wise comparative framework to identify spatial heterogeneity, (iii) applying speciation-based risk assessment to evaluate metal mobility and bioavailability, and (iv) integrating multiple sediment quality indices with multivariate statistical analysis (PCA) to identify dominant contamination sources. Notably, the study highlights the elevated mobility and ecological risk associated with cadmium (Cd), which has received limited attention in previous regional assessments. This integrated, multi-scale approach offers a more robust evaluation of sediment contamination dynamics and ecological risk in deltaic wetland systems.

2. MATERIALS AND METHODS

2.1. Study Area

The Cauvery Delta, situated in southeastern India, constitutes one of the country's most important agricultural regions and is characterized by extensive wetland networks that support irrigation, fisheries, and biodiversity. Increasing agricultural intensification and human activities have increased concern regarding the accumulation of contaminants, particularly heavy metals, in sedimentary environments. To evaluate regional-scale pollution, the present study encompassed wetlands distributed across five districts: Karur, Tiruchirappalli, Thanjavur, Thiruvarur, and Nagapattinam. The investigated area covers approximately 15,032.83 km² and lies between latitudes 10.76°–11.03° N and longitudes 78.15°–79.84° E. Information regarding the selected wetlands, including surrounding land-use characteristics and potential contamination sources, is provided in Table 1. Ecological attributes of these wetlands were also considered as part of the environmental assessment.

2.2. Sampling and Monitoring Methods

Surface sediment samples were obtained from 40 wetland sites across the delta using a clean hand trowel. Locations were selected to represent varying degrees of accessibility, hydrological characteristics, anthropogenic pressure, and diverse land-use settings (Fig. 1).

At each wetland, sediment was collected from multiple representative points covering inlet, central, and peripheral zones to account for small-scale spatial variability. The subsamples were thoroughly homogenized to obtain a composite sample representative of each site. Although field duplicates were limited due to logistical constraints, composite sampling from multiple points was adopted to minimize spatial heterogeneity and improve sample representativeness.

Sampling was undertaken during the pre-monsoon season (April 2023), when hydrological conditions are relatively stable and recently deposited sediments are accessible. At each site, sediments from the upper 0–10 cm layer were acquired, placed in sterile polyethylene bags, and dispatched to the laboratory. Geographic coordinates were recorded using field positioning tools. In the laboratory, samples were air-dried at ambient temperature, homogenized, and passed through a 63 µm sieve to isolate the fine fraction, which was subsequently used for chemical analysis.

2.3. Laboratory Analysis

Subsamples of the fine sediment fraction were analyzed to determine selected physicochemical properties and metal concentrations. Metal speciation was assessed using the widely adopted five-step sequential extraction protocol of Tessier et al. (1979), which partitions metals into

Table 1: Characteristics of wetlands in the Cauvery Delta region.

District	Location	Land use pattern in the vicinity of the sampling area	Possible sources of contamination
Karur (Sample 1–9)	Kuppagoundan valasu, Periya thadampalayam, Uppidamangalam, Vellaianaikulam, Virarakkiyam, Udayapatti, Tharagampatti, Panjapatti, Vayalur	Agricultural, commercial, and residential mix	Agricultural runoff, Human activities, and litter
Tiruchirappalli (Sample 10–20)	Nagayanallur lake, Kattukaruppan kottam, Alathudaiyanpatti, Zambuyari lake, Periya yeri, Keerambur, Thayanur, Thiruverambur, Gundur, Thuvakudi, Kiliyur lake	Agricultural, commercial, and residential mix	Agricultural runoff, Human activities, and litter
Thanjavur (Sample 21–30)	Sholagampatti, Surakudipatti, Vendayampatti, Kallaperampur, Samuthram, Phunnapur, Chelikurichi, Sendakottai, Sandampettai, Viriankottai	Agricultural, commercial, and residential mix	Agricultural runoff, Human activities, and litter
Thiruvarur (Sample 31–33)	Thirumeni, Thulasendrapuram, Vaduvoor Bird Sanctuary	Agricultural and residential mix	Agricultural runoff, Human activities, and litter
Nagapattinam (Sample 34–40)	Keeran Lake, Vattakudi River delta, Talainayar R.F, Kalimedu, Thirukadaiyur River basin, Perunthottam, Point Calimere Wildlife Sanctuary	Residential, commercial, and tourism	Agricultural runoff, Human activities, and litter

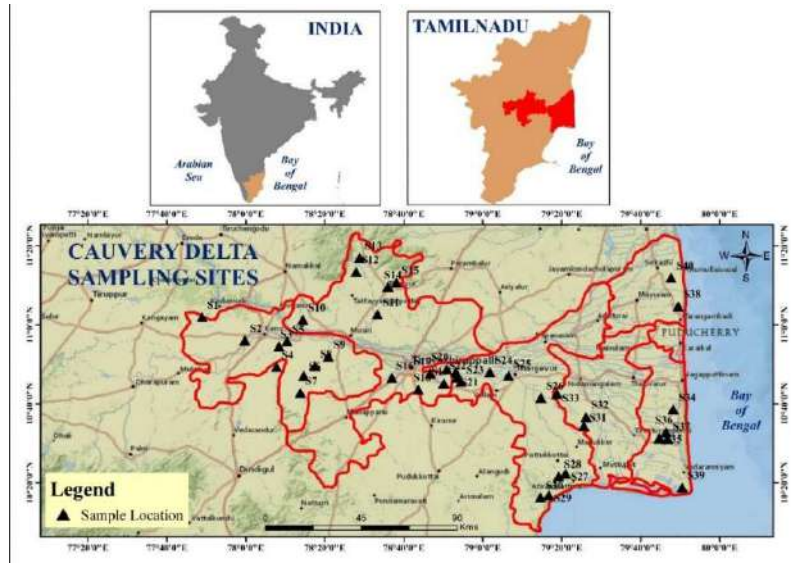


Fig. 1: Study area map showing sediment sampling locations in the Cauvery Delta, Tamil Nadu, India.

exchangeable, carbonate-associated, Fe–Mn oxide-bound, organic-bound, and residual fractions to evaluate their mobility and potential bioavailability. Concentrations of Fe, Mn, Cr, Ni, Cu, Zn, Pb, and Cd were quantified using Atomic Absorption Spectrophotometry (Thermo Fisher Scientific iCE 3000 Series, USA) following appropriate extraction and digestion procedures. Total metal content was calculated by summing all fractions obtained from the sequential extraction process.

QA/QC protocols involved analytical evaluation of reagent blanks, triplicate measurements, recovery tests, and certified reference materials. Calibration was performed using multi-element standard solutions, yielding correlation coefficients exceeding 0.999. Analytical precision was confirmed by relative standard deviations below 5%, while recovery efficiencies ranged from 90% to 105%. Method accuracy was validated using NIST SRM 2702, with measured values showing close agreement with certified concentrations.

To monitor potential contamination during the sample preparation phase, digestion blanks were processed with every batch of ten samples; in all instances, analyte levels in blanks remained below the MDL. Furthermore, the internal consistency of the sequential extraction procedure was verified through a mass balance check; the cumulative sum of the individual fractions was compared against the results of an independent total acid digestion for each sample. Recovery percentages for this mass balance check consistently ranged between 92% and 106%, confirming that no significant analyte loss or cross-contamination occurred during the multi-step fractionation process.

2.4. Methods for Estimating Contamination and Ecological Risk

Assessment of sediment quality based solely on total metal concentrations provides limited insight because it does not reflect the origin, environmental mobility, or biological availability of contaminants. To obtain a more comprehensive evaluation of sediment pollution and associated ecological implications, several widely used geochemical indices were employed in this study, namely the Contamination Factor (CF), Pollution Load Index (PLI), and Geo-accumulation Index (Igeo). These indices incorporate background concentrations and measured values to quantify contamination intensity and potential environmental risk. A description of the indices is presented below.

2.4.1. Contamination Factor (CF)

The contamination factor (CF) represents an initial step in environmental risk assessment and is defined as the ratio of the measured metal concentration to its corresponding reference (background) value, as shown in Eq. (1) (Islam et al. 2015).

In the present study, background metal concentrations were adopted from the reference values reported by Singh et al. (2003). These values represent well-established baseline levels for Indian soils/sediments derived from minimally impacted environments. Moreover, the study region shares comparable geological and pedological characteristics with the areas evaluated by Singh et al. (2003), making these baseline values appropriate for normalization and index calculations (e.g., Igeo, EF, PLI). Therefore, adopting these

reference concentrations ensures consistency, reliability, and comparability of contamination assessment across similar environmental settings. CF is commonly used to evaluate the degree of metal contamination relative to natural baseline levels.

$$CF = \frac{C_m}{C_b} \quad \ldots (1)$$

represent the measured metal concentration and its corresponding background value, respectively. The contamination factor (CF) is classified into four categories: CF < 1 indicates low contamination; 1 ≤ CF < 3 indicates moderate contamination; 3 ≤ CF < 6 indicates considerable contamination; and CF ≥ 6 indicates very high contamination.

2.4.2. Pollution Load Index (PLI)

The Pollution Load Index (PLI) is calculated as an integrated measure of the overall level of pollution at a given site. It reflects the cumulative contamination status of the locality and serves as an indicator of the site's overall environmental quality (Angulo 1996, Dhamodharan et al. 2019).

$$PLI = \sqrt[p]{CF_1 \times CF_2 \times \ldots \times CF_p} \quad \ldots(2)$$

where CF represents the contamination factor of each of the p heavy metals (p = 6). The Pollution Load Index (PLI) is interpreted as follows: PLI ≤ 1 indicates no pollution; 1 < PLI ≤ 2 indicates slight pollution; 2 < PLI ≤ 3 indicates moderate pollution; and PLI > 3 indicates high pollution (Liu et al. 2016a, 2016c).

2.4.3. Geoaccumulation Index (Igeo)

The geoaccumulation index is widely used for assessing heavy metal contamination in sediment samples and for comparing present contamination levels with preindustrial baseline conditions (Müller 1969, Chakravarty & Patgiri 2009, El-Amier et al. 2017).

$$I_{geo} = \log_2 \left\{ \frac{C_p}{1.5B_P} \right\} \quad \ldots(3)$$

The geoaccumulation index (Igeo) is classified into the following categories: Igeo ≤ 0, unpolluted; 0 < Igeo ≤ 1, unpolluted to moderately polluted; 1 < Igeo ≤ 2, moderately polluted; 2 < Igeo ≤ 3, moderately to strongly polluted; 3 < Igeo ≤ 4, strongly polluted; 4 < Igeo ≤ 5, strongly to extremely polluted; and Igeo > 5, extremely polluted. In the Igeo equation, Cp and Bp represent the measured and background concentrations of the pth heavy metal, respectively. The constant 1.5 is introduced as a background correction factor to account for natural variations in the sediment matrix.

2.4.4. Potential Ecological Risk Index (PERI)

The potential ecological risk index (PERI) is used to evaluate the ecological effects of human activities through chemical assessment and individual bioassay (Håkanson 1980). The PERI method provides an integrated approach for evaluating ecological risk from heavy metals in sediments. Before calculating the PERI, the risk index has been determined using the formula,

$$E_r^i = T_r^i \times C_B^i \quad \ldots(4)$$

$$RI = \sum_{i=1}^{m} E_r^i \quad \ldots(5)$$

Where RI represents the sum of the potential ecological risks of individual metals; represents potential risk of individual heavy elements; denotes the toxicity response factor for metals Ni = Pb = Cu = 5, Zn = 1, Cr = 2, Cd = 30 and indicates background level of the heavy metal concentrations such as Ni = 68 mg kg^{-1}, Pb = 20 mg kg^{-1}, Cu = 45 mg kg^{-1}, Cr = 90 mg kg^{-1}, Cd = 0.09 mg kg^{-1} and (Turekian & Wedepohl 1961). RI values of <150 indicate low ecological risk, 150–300 moderate risk, 300–600 considerable risk, and >600 very high ecological risk.

2.4.5. Risk Assessment Code (RAC)

The Risk Assessment Code (RAC) is widely employed to assess the mobility, bioavailability, and potential ecological risk of heavy metals in sediments based on their occurrence in the exchangeable and carbonate-bound fraction obtained through sequential extraction analysis (Perin et al. 1985). Since metals associated with the exchangeable fraction are weakly bound to sediments, they can be readily released into the aquatic environment under slight variations in pH, salinity, or redox conditions, thereby posing potential ecological threats to aquatic biota.

The total concentration of each metal was determined by summing all sequential extraction fractions (F1–F5) using the following equation:

$$C_{total} = F1 + F2 + F3 + F4 + F5 \quad \ldots(6)$$

The RAC value was subsequently calculated as

$$RAC(\%) = \frac{F1}{F1+F2+F3+F4+F5} \times 100 \quad \ldots(7)$$

where RAC (%) represents the risk assessment code; F1 denotes the exchangeable and carbonate-bound fraction; and F1–F5 represent the concentrations of metals in all operationally defined geochemical fractions. Based on RAC values, ecological risk levels were classified as follows: <1% = no risk, 1–10% = low risk, 11–30% = medium risk, 31–50% = high risk, and >50% = very high risk (Perin et al. 1985). Higher RAC values indicate greater metal mobility and enhanced environmental risk due to increased bioavailability.

2.5. Statistical Analysis

Analytical results were subjected to statistical evaluation

using OriginPro software (OriginLab Corporation, Northampton, USA). Descriptive statistics (mean ± standard deviation) were calculated to characterize the central tendency and variability of the measured parameters. Pearson correlation analysis was performed to examine linear relationships among physicochemical variables and metal concentrations.

To further explore patterns in the dataset, principal component analysis (PCA) was performed on both total metals and their sequential extraction fractions. This multivariate technique was used to identify dominant factors controlling metal distribution, distinguish potential sources, and elucidate the processes influencing heavy metal behavior in wetland sediments.

3. RESULTS AND DISCUSSION

3.1. Physicochemical Characteristics of Sediments

The physicochemical properties of surface sediments reflect the prevailing geochemical environment and strongly influence the behavior and transport of contaminants in aquatic systems. In the present investigation, sediment pH values ranged from 8.1 to 9.5, indicating predominantly alkaline conditions throughout the study region. Such alkaline environments are typically associated with carbonate-rich substrates and can markedly affect nutrient transformations and trace metal behavior through processes such as precipitation, surface adsorption, and complex formation (Alloway 2013, Sposito 2008). The maximum pH recorded at Sample 8 (Panjapatti) likely reflects localized geochemical controls, including higher carbonate mineral content or reduced input of acidic organic matter. Comparable alkaline conditions have been documented in wetland and river sediments influenced by carbonate weathering and agricultural activities (Ramanathan et al. 1988, Singh et al. 2010).

Electrical conductivity (EC) values ranged from 0.13 to 1.98 mS cm^{-1}, demonstrating pronounced spatial heterogeneity in dissolved ionic content. Higher EC values generally indicate elevated concentrations of soluble salts derived from natural mineral dissolution, evaporation, or anthropogenic sources such as fertilizer application and wastewater inputs (Chapman 1996, Varol & Sen 2012). The observed variability suggests differences in hydrological connectivity, land use, and sediment deposition processes among wetlands within the delta.

Total organic carbon (TOC) concentrations varied between 0.72% and 2.85%, while organic matter (OM) content varied from 1.24% to 4.91%. The highest values for both parameters were recorded at Sample 13 (Zambuyari Lake). Elevated organic content in sediments typically indicates substantial accumulation of plant debris, microbial biomass, and detrital materials, particularly in low-energy environments where decomposition is slower and sedimentation rates are high. The substantial organic enrichment observed at this site may therefore be attributed to high biological productivity, surrounding land use, and restricted water exchange.

Calcium concentrations ranged from 0.51% to 2.04%, with the maximum detected at Sample 34 (Keeran Lake). Magnesium levels were consistently higher, varying from 2.44% to 5.50%, with the highest value observed at Sample 28 (Sendakottai). The dominance of Mg over Ca suggests the presence of Mg-rich carbonates such as dolomite within the sediment matrix. Weathering of carbonate formations can strongly influence sediment chemistry by enhancing alkalinity, buffering capacity, and the adsorption of trace metals (Ramanathan et al. 1988, Drever 1997).

Carbonate-associated elements play a key role in maintaining sediment stability by regulating pH conditions, ionic composition, and metal binding capacity. The spatial differences observed in Ca and Mg concentrations, therefore, reflect variations in mineral composition, depositional settings, and catchment-derived geochemical inputs across the study area (Alloway 2013, Sposito 2008).

3.2. Heavy Metal Analysis

3.2.1. Total Heavy Metal Distribution

Among the analyzed metals, Fe exhibited the highest overall concentrations in the sediments, followed in decreasing order by Pb, Ni, Cr, Cu and Cd. The predominance of iron is consistent with its natural abundance in crustal materials and its strong association with oxide minerals commonly present in alluvial sediments.

3.3. Heavy Metal Speciation and Geochemical Partitioning in Sediments

Sequential extraction techniques provide detailed insights into the chemical associations of metals in sediments, thereby enabling assessment of their mobility, potential bioavailability, and environmental risk. Because metals bound to different sediment fractions respond differently to fluctuations in pH, redox conditions, and organic matter, fractionation provides more meaningful insight than total concentrations alone (Tessier et al. 1979, Rauret et al. 1999). In this study, the distribution of Fe, Ni, Pb, Cu, Cr, and Cd among five operationally defined fractions (F1–F5) revealed distinct regional patterns across the Cauvery Delta districts.

3.3.1. Karur District

In Karur District, Fe concentrations (69.2–15,428 mg kg^{-1})

are predominantly associated with the F5 (residual) and F3 (oxide-bound) fractions, indicating strong lithogenic control and limited environmental mobility, as Fe is largely incorporated within mineral lattices and secondary oxide phases (Förstner & Wittmann 2012). Ni (0.0314–0.764 mg kg^{-1}) is similarly dominated by the residual fraction, although its presence in exchangeable and carbonate-bound phases suggests moderate geochemical availability under changing physicochemical conditions. Pb (0.28–7.35 mg kg^{-1}) occurs mainly in the residual fraction, reflecting geochemical stability, with minor labile fractions indicating limited anthropogenic inputs such as agricultural runoff or atmospheric deposition (Alloway 2013). Cu (0.035–9.79 mg kg^{-1}) exhibits a mixed association with oxide-bound, residual, and organic fractions, consistent with its affinity for Fe oxides and organic matter (Sposito 2008). In contrast, Cr (0.052–1.66 mg kg^{-1}) is largely associated with exchangeable and carbonate fractions, indicating relatively higher mobility, while Cd (0.02–0.68 mg kg^{-1}), despite low concentrations, is enriched in bioavailable fractions, highlighting its ecological significance.

Across the sampling locations, Fe clearly dominates the total metal concentrations (26,364.65–30,667.62 mg kg^{-1}), reaffirming a strong geogenic signature with minimal spatial variability. Ni (0.76–2.00 mg kg^{-1}) and Cr (1.04–2.57 mg kg^{-1}) show low to moderate variation, indicating limited enrichment. Pb remains low across most sites but increases at Kuppagoundan Valasu and reaches a maximum at Virarakkiyam, while Cu follows a similar trend with a pronounced peak at Virarakkiyam, suggesting localized anthropogenic inputs. Cd concentrations are generally low (0.51–1.08 mg kg^{-1}) but relatively elevated at Kuppagoundan Valasu, Panjapatti, and Vayalur, indicating potential ecological relevance.

The combined assessment of fractionation and total concentrations indicates that metal distribution in Karur District is predominantly governed by geogenic processes, with most elements occurring in stable, less mobile forms. However, the presence of Cd and Cr in more labile fractions, along with localized enrichment of Pb and Cu at Virarakkiyam, suggests site-specific anthropogenic influences and highlights the need for continued monitoring due to potential ecological risk.

3.3.2. Tiruchirappalli District

In Tiruchirappalli District, Fe concentrations (7.874–14,086 mg kg^{-1}) are primarily associated with oxide-bound and residual fractions, indicating a dominant geogenic origin with limited mobility. Ni (0.135–1.927 mg kg^{-1}) shows a similar partitioning pattern, being largely confined to stable phases, although minor contributions in labile fractions suggest conditional availability. Cu (0.033–1.814 mg kg^{-1}) is distributed across carbonate-, oxide-, and residual-bound fractions, reflecting moderate mobility under changing environmental conditions. In contrast, Pb (0.029–1.547 mg kg^{-1}), Cd (0.003–0.565 mg kg^{-1}), and Cr (0.039–4.193 mg kg^{-1}) are relatively enriched in labile fractions, indicating higher environmental availability. Cd, in particular, shows strong association with exchangeable and carbonate phases, confirming its high mobility as shown in Fig. 2, while Cr exhibits notable binding with organic matter, suggesting interaction with organic ligands and potential anthropogenic influence.

Across the sampling sites, Fe dominates the total metal concentrations (9,335.09–26,958.20 mg kg^{-1}), reaffirming strong lithogenic control with moderate spatial variability. Ni (1.29–4.97 mg kg^{-1}) and Cr (1.16–5.71 mg kg^{-1}) exhibit wider ranges, with elevated concentrations at Keerambur, Zambuyari Lake, Periya Yeri, and Gundur, indicating localized inputs and potential mobility. Pb concentrations (2.10–3.89 mg kg^{-1}) remain relatively uniform across sites, whereas Cu (0.89–4.48 mg kg^{-1}) shows localized enrichment, particularly at Keerambur and adjacent locations, suggesting site-specific anthropogenic influence. Cd concentrations are generally low (0.30–0.98 mg kg^{-1}) but show relatively higher values at Kiliyur Lake and Zambuyari Lake, indicating potential ecological concern.

The integrated assessment of fractionation and total metal concentrations indicates that metal distribution in Tiruchirappalli District is largely governed by geogenic processes, with most elements occurring in stable forms. However, the enrichment of Cd and Cr in labile fractions, together with localized increases in Ni and Cu at specific sites, highlights spatially variable anthropogenic inputs and suggests potential environmental risk under changing geochemical conditions.

3.3.3. Thanjavur District

In Thanjavur District, Fe concentrations (258.2–15,263 mg kg^{-1}) are predominantly associated with oxide-bound and residual fractions, indicating strong lithogenic control and incorporation within mineral matrices formed through weathering processes (Drever 1997). Ni (0.014–0.694 mg kg^{-1}) and Pb (0.017–0.807 mg kg^{-1}) are likewise dominated by residual fractions, suggesting limited mobility and low environmental risk under stable conditions. Cu (0.068–0.533 mg kg^{-1}) shows appreciable association with organic and oxide fractions, indicating potential remobilization under reducing conditions. In contrast, Cr (0.106–0.514 mg kg^{-1}) is relatively enriched in exchangeable fractions, implying higher mobility and possible external inputs, while Cd (0.038–0.106 mg kg^{-1}) exhibits the highest mobility, occurring mainly in exchangeable and

carbonate phases, thereby highlighting its ecological significance.

Across the sampling locations in Thanjavur District, Fe dominates the total metal concentrations (20,459.43–31,509.93 mg kg⁻¹), reaffirming a strong geogenic signature with limited spatial variability. Ni (0.74–1.98 mg kg⁻¹) remains low with slight elevation at Kallaperampur, while Cr (1.14–1.65 mg kg⁻¹) shows minimal variation across sites, indicating weak spatial heterogeneity. Pb concentrations are uniformly low (1.46–2.19 mg kg⁻¹), reflecting negligible contamination, whereas Cu (0.56–1.30 mg kg⁻¹) exhibits modest increases at Chelikurichi and Kallaperampur, suggesting localized inputs. Cd concentrations (0.34–0.38 mg kg⁻¹) are consistently low but show slight enrichment at Chelikurichi and Vendayampatti, indicating potential ecological relevance.

These results indicate that metal distribution in Thanjavur District is primarily controlled by geogenic processes, with most elements occurring in stable, less mobile forms. However, the relatively higher mobility of Cd and Cr, along with localized enrichment of Cu at specific sites, suggests limited anthropogenic influence and highlights the need for attention to potential ecological risks under changing environmental conditions.

3.3.4. Thiruvarur and Nagapattinam Districts

In the coastal districts of Thiruvarur and Nagapattinam, Fe concentrations (322.5–15,012 mg kg⁻¹) are predominantly associated with oxide-bound and residual fractions, indicating strong lithogenic control and low mobility. Ni (0.250–0.587 mg kg⁻¹) shows a relatively balanced partitioning but remains largely confined to stable phases. In contrast, Pb (0.051–0.614 mg kg⁻¹) is mainly present in exchangeable fractions, suggesting high mobility and susceptibility to remobilization, a pattern typical of coastal systems influenced by anthropogenic inputs (Varol & Sen 2012). Cu (0.115–0.387 mg kg⁻¹) exhibits mixed distribution between stable and labile fractions, indicating moderate mobility, while Cr (0.137–0.519 mg kg⁻¹) and Cd (0.028–0.109 mg kg⁻¹) are enriched in exchangeable and carbonate fractions, reflecting elevated environmental availability and potential leaching risk.

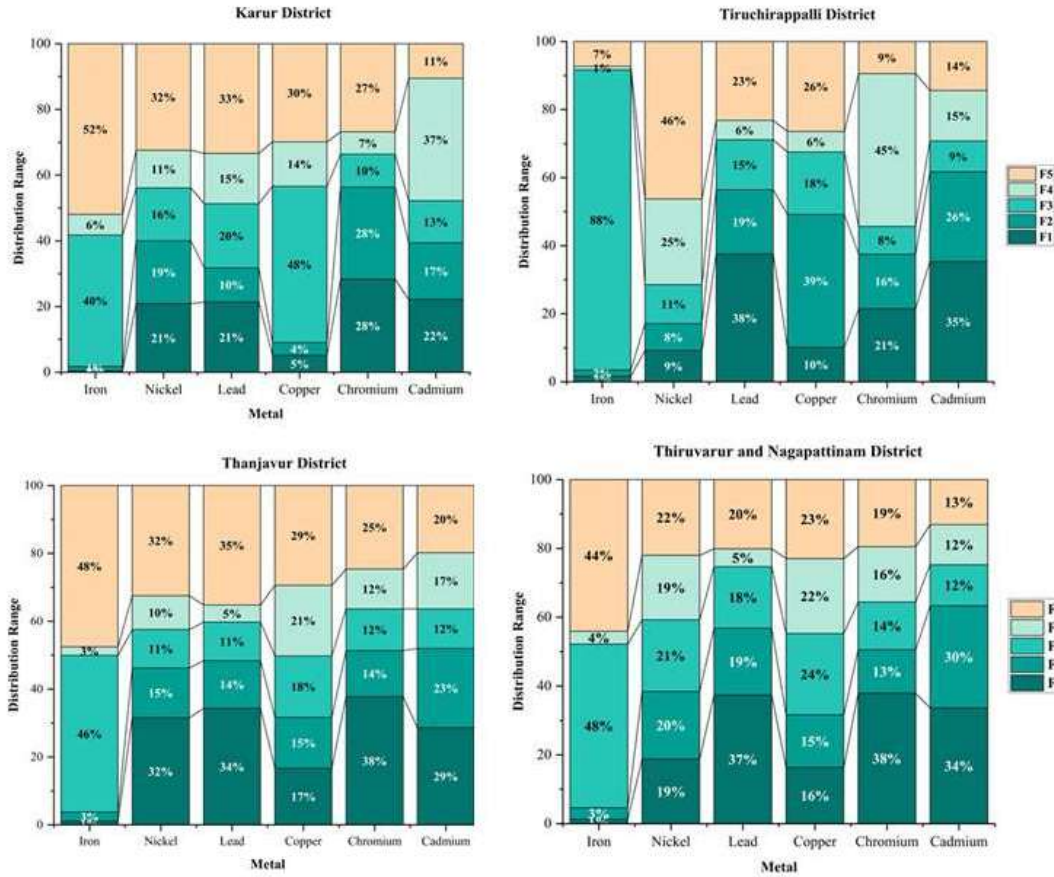


Fig. 2: Comparative fractional distribution of heavy metals among sequential extraction phases (F1–F5) in sediments of Cauvery Delta district wetlands.

Across the sampling locations, Fe dominates the total metal concentrations (24,297.23–31,876.39 mg kg^{-1}), reaffirming a strong geogenic signature with minimal spatial variability. Ni (1.42–2.07 mg kg^{-1}) shows slight elevation at Talainayar R.F, while Cr (1.12–1.55 mg kg^{-1}) remains relatively uniform across sites, indicating weak spatial heterogeneity. Pb concentrations are consistently low (1.13–1.95 mg kg^{-1}), suggesting limited anthropogenic influence, whereas Cu (0.65–1.20 mg kg^{-1}) exhibits minor increases at Talainayar R.F and Thirumeni, indicating localized inputs. Cd concentrations (0.29–0.32 mg kg^{-1}) remain low but show slight enrichment at Talainayar R.F and Vattakudi River Delta, highlighting potential ecological relevance.

Overall, the integrated interpretation of fractionation and total concentrations indicates that metal distribution across Thiruvarur and Nagapattinam districts is primarily governed by geogenic processes. However, the enrichment of Pb, Cr, and Cd in labile fractions, coupled with localized increases in Cu and Cd at specific sites, suggests coastal-specific geochemical behavior with minor anthropogenic influence and potential environmental risk under changing conditions.

3.4. Integrated Interpretation of Heavy Metal Speciation

The fractionation patterns observed across the study area reveal consistent geochemical behavior that allows classification of metals according to their environmental stability. The observed metal fractionation patterns were strongly influenced by sediment physicochemical characteristics, particularly alkaline pH, carbonate content, and organic matter. The alkaline nature of the sediments likely reduced the solubility of several metals through precipitation and adsorption processes, thereby promoting their accumulation in relatively stable fractions.

3.4.1. Geochemically Stable Metals (Fe, Ni, Cu)

Cu showed greater association with organic matter and oxide-bound fractions, reflecting its strong tendency to form stable complexes with organic ligands and Fe/Mn oxides. Similarly, Fe and Cr were predominantly associated with residual and oxide fractions, indicating stronger lithogenic control and lower bioavailability. Fe and Ni were predominantly associated with residual and oxide-bound fractions, indicating strong mineral binding and primarily lithogenic origins. Metals in these forms are generally considered less mobile and less bioavailable under normal environmental conditions (Tessier et al. 1979, Rauret et al. 1999).

3.4.2. Environmentally Mobile Metals (Pb, Cr, Cd)

Lead, chromium, and cadmium showed substantial enrichment in exchangeable, carbonate, and organic fractions, indicating higher mobility and potential bioavailability. The comparatively higher proportion of Cd in exchangeable and carbonate-bound fractions (F1–F2) may be attributed to the affinity of Cd for carbonate-rich sediment phases under alkaline conditions. Such associations indicate that Cd remains relatively mobile and may be remobilized under changing environmental conditions such as acidification or redox fluctuations.

Cadmium exhibited the greatest environmental mobility, while chromium displayed intermediate behavior, reflecting contributions from both natural sources and anthropogenic activities.

Overall, the distribution patterns suggest that both natural geological factors and human influences govern heavy metal behavior in the Cauvery Delta sediments. Metals tightly bound within mineral structures remain relatively inert, whereas those associated with weakly bound phases pose greater ecological risk due to their propensity for release under changing environmental conditions.

3.5. Risk Assessment

3.5.1. Contamination Factor

The extent of heavy metal enrichment in wetland sediments was assessed using the Contamination Factor (CF), which compares measured metal concentrations with corresponding background values (Håkanson 1980). This metric is widely employed to identify anthropogenic accumulation relative to natural geochemical baselines. For Fe, Ni, Pb, Cu, and Cr, CF values were predominantly below unity, indicating minimal contamination across the majority of sampling locations. The mean CF values were 0.689 for Fe, 0.039 for Ni, 0.137 for Pb, 0.064 for Cu, and 1.459 for Cr. According to the classification scheme of Håkanson (1980), CF values less than 1 signify low contamination, suggesting that these elements are primarily derived from lithogenic sources rather than substantial human inputs.

Cadmium exhibited a markedly different pattern. CF values for Cd ranged from 0.99 to 3.59, corresponding to moderate to considerable contamination at several sites. The highest value (3.58) occurred at Sample 9, with elevated levels also observed at Samples 1, 8, 7, and 20, identifying these locations as localized hotspots. The enrichment of Cd is likely linked to anthropogenic activities such as agricultural runoff, application of phosphate fertilizers, irrigation drainage, and domestic effluents, well-documented sources of cadmium in aquatic systems.

Spatial analysis indicates that most sites show negligible contamination for Fe, Ni, Pb, Cu, and Cr, whereas isolated exceedances for Cd demonstrate the influence of site-

specific human activities. Comparable selective enrichment of cadmium has been reported in sediments affected by agricultural and industrial operations, reflecting the element's relatively high mobility and environmental sensitivity (Alloway 2013, Varol 2020).

When cumulative contamination was considered, the CF sum for all metals ranged from approximately 1.55 to 4.68, indicating overall low to moderate contamination levels. Elevated cumulative values were largely driven by cadmium contributions, while other metals played a minor role. This finding aligns with previous studies identifying Cd as a sensitive tracer of anthropogenic influence due to its low natural abundance and strong association with fertilizer inputs (Turekian & Wedepohl 1961, Varol & Sen 2011, Suresh et al. 2021). Given its toxicity and ecological persistence, cadmium emerges as the primary contaminant of concern in the studied sediments.

3.5.2. Pollution Load Index (PLI)

The Pollution Load Index was derived to provide an integrated measure of overall sediment contamination by combining the contamination factors of individual metals into a single indicator (Tomlinson et al. 1980). PLI value of 1 represents background conditions, values greater than 1 indicate pollution, and values below 1 signify an absence of contamination. PLI values ranged from 1.07 to 1.29, suggesting slightly elevated but generally moderate contamination relative to baseline levels.

All sampling sites exhibited PLI values exceeding unity, implying some degree of anthropogenic influence throughout the wetlands. The highest values were recorded at Samples 1, 9, and 20, coinciding with locations showing elevated cadmium contamination factors. This correspondence indicates that Cd enrichment is the principal driver of the overall pollution status. Despite exceeding the baseline threshold, the relatively narrow range of PLI values suggests moderate cumulative contamination rather than severe degradation. The spatial distribution points to localized pollution hotspots, likely associated with agricultural practices, fertilizer usage, small-scale industrial activities, and domestic wastewater inputs within the watershed.

Overall, the PLI assessment corroborates the CF results, indicating that most metals occur at low contamination levels while cadmium disproportionately influences the composite pollution index. Consequently, the sediments appear moderately impacted rather than severely polluted.

3.5.3. Geoaccumulation Index (Igeo)

The Igeo index was applied to evaluate sediment contamination by comparing current metal concentrations with pre-industrial background levels while accounting for natural variability in sediment composition (Müller 1969). This index categorizes pollution into seven classes, with values less than or equal to zero indicating unpolluted conditions.

For Fe, Ni, Pb, Cu, and Cr, Igeo values were predominantly negative, demonstrating that sediment concentrations of these metals remain close to natural background levels. Mean Igeo values were −1.216 for Fe, −5.369 for Ni, −3.67 for Pb, −4.965 for Cu, −6.375 for Cr, and −0.138 for Cd. These results suggest that lithogenic inputs largely control metal distributions across the study area.

Cadmium again showed a distinct behavior. While most samples yielded negative values (approximately −2 to 1), indicating unpolluted to moderately polluted conditions, positive values were observed at three sites. The highest Igeo value (1.258) occurred at Sample 9, followed by Samples 20 and 1. According to standard classification criteria, these values correspond to Class 1 (unpolluted to moderately polluted), indicating localized enrichment.

The spatial concentration of elevated Cd levels in the upper delta, particularly in Karur and parts of Tiruchirappalli districts, suggests stronger anthropogenic influence in these areas, likely related to intensive agriculture, urban development, and wastewater discharge. Such activities are widely recognized sources of cadmium contamination in sedimentary environments (Alloway 2013, Varol & Sen 2011, Islam et al. 2015).

Overall, the Igeo assessment indicates that the Cauvery Delta wetlands remain largely free from significant heavy metal pollution, with most elements reflecting natural background conditions. Nevertheless, localized cadmium enrichment highlights its effectiveness as an indicator of human impact. Given its high toxicity, mobility, and association with fertilizers, industrial emissions, and urban effluents, cadmium warrants continued monitoring. Regular surveillance of Cd levels is therefore recommended to safeguard ecological health and ensure the long-term sustainability of these wetland ecosystems (Sutherland 2000, Alloway 2013).

3.5.4. Potential Ecological Risk Assessment (PERI)

The assessment of heavy metal contamination in sediments is crucial for evaluating the potential ecological risks they pose to aquatic ecosystems. These contaminants can significantly disrupt biological processes and impair ecological functions. To quantitatively evaluate this risk, the Potential Ecological Risk Index (PERI), introduced by Håkanson (1980), was employed. This method incorporates both the toxicity response factor (Tr) of individual metals and their contamination factor (CF) relative to background

values, thereby accounting for the concentration, distribution, and synergistic toxic effects of multiple metals within the sediment matrix.

In the present study, PERI values in wetland sediments ranged from 800.333 to 5333.351, with a mean value of 1624.15. These values indicate considerable to very high ecological risk, particularly in specific locations. The highest PERI was recorded at Sample 5, followed by Sample 15. Among the studied metals, nickel (Ni) contributed to more than 50% of the total ecological risk index, indicating its dominant influence in driving the overall toxicity of the sediment. Copper (Cu) and chromium (Cr) were the next significant contributors. This distribution pattern highlights the prevalence and potential synergistic interactions among these metals, which could pose acute and chronic risks to benthic organisms and other components of the wetland ecosystem.

According to Håkanson's classification, PERI values exceeding 600 indicate very high ecological risk. Therefore, based on the observed values and spatial trends, it can be inferred that the wetland sediments, especially in parts of Karur and Tiruchirappalli districts, are under substantial ecological stress due to heavy metal contamination and warrant regular monitoring and mitigation strategies.

3.5.5. Risk Assessment Code (RAC)

The RAC assessment revealed considerable spatial variation in heavy metal mobility and ecological risk across the Cauvery Delta wetland sediments. Fe consistently exhibited RAC values below 1–3% in all districts, indicating no ecological risk and strong association with stable residual fractions. In contrast, Cr, Pb, Cd, and Ni showed comparatively higher RAC values, reflecting greater mobility and potential bioavailability.

Karur district sediments were characterized by moderate to very high ecological risk for Cr (20.45–51.45%), with Sample 6 exceeding the very high-risk threshold (>50%). Pb and Ni exhibited mainly medium to high ecological risk, whereas Cu showed relatively lower RAC values corresponding to low to medium risk. In Tiruchirappalli district, Pb (26.13–54.22%), Cu (4.32–63.01%), Cr (9.26–44.26%), and Cd (14.32–50.23%) displayed substantial variability, with several locations exceeding the very high-risk category, indicating strong association with labile sediment fractions and enhanced remobilization potential. Thanjavur district sediments showed consistently elevated RAC values for Cr (30.80–44.18%), Pb (28.08–42.40%), Ni (18.36–41.35%), and Cd (26.69–31.24%), corresponding predominantly to medium to high ecological risk. Similarly, Thiruvarur and Nagapattinam districts exhibited persistently high RAC values for Pb (31.57–46.66%), Cr (33.41–42.26%), and Cd (30.67–34.51%), indicating significant mobility and ecological concern across the study area. Ni and Cu in these districts generally exhibited moderate ecological risk.

Overall, Cr, Pb, and Cd emerged as the most environmentally mobile and ecologically significant metals across the Cauvery Delta wetlands, while Fe remained geochemically stable and environmentally immobile. The predominance of these metals in exchangeable and weakly bound fractions indicates high remobilization potential under changing physicochemical conditions, thereby posing potential ecological risks to wetland ecosystems.

3.6. Statistical Analysis

Descriptive statistics, including mean and standard deviation (SD), were used to evaluate the distribution and variability of physicochemical parameters and heavy metals in wetland sediments (Table 2). Sediment pH exhibited very low variability, indicating consistently alkaline conditions typical of carbonate-rich systems, which influence metal solubility and adsorption processes (Sposito 2008, Alloway 2013). Electrical conductivity (EC) showed moderate variability, reflecting spatial differences in soluble-salt content associated with evaporation, agricultural runoff, and mineral weathering. Total organic carbon (TOC) and total organic matter (TOM) also displayed moderate variation, suggesting heterogeneous accumulation of organic residues derived from in situ productivity and external inputs (Meyers & Ishiwatari 1993). Calcium (Ca) and magnesium (Mg) exhibited moderate variability, likely controlled by differences in sediment mineralogy and the distribution of carbonate minerals such as calcite and dolomite (Drever 1997).

Table 2: Descriptive statistics for various physicochemical parameters.

Descriptive Statistics				
Parameter	Range	Mean	SD	N
pH	8.1–9.5	8.753	0.3397	40
EC (mS cm^{-1})	0.13–1.98	0.7498	0.44252	40
TOC (%)	0.72–2.85	1.6138	0.49135	40
OM (%)	1.24–4.91	2.7780	0.84301	40
Ca (%)	0.51–2.04	0.8798	0.39987	40
Mg (%)	2.44–5.50	3.9423	0.64557	40
Fe (mg kg^{-1})	9335.09–31876.39	24127.38	7.48299	40
Ni (mg kg^{-1})	0.74–4.96	1.96103	1.09733	40
Pb (mg kg^{-1})	1.08–11.36	2.75342	2.02265	40
Cu (mg kg^{-1})	0.55–15.01	1.61999	2.3099	40
Cr (mg kg^{-1})	1.04–5.70	1.75955	0.8705	40
Cd (mg kg^{-1})	0.29–1.07	0.43777	0.19324	40

Among the metals, Fe showed considerable variability, reflecting variations in lithogenic inputs, sediment transport, and redox conditions (Förstner & Wittmann 2012). Ni and Cr displayed moderate variability, whereas Pb and particularly Cu showed relatively high variability, suggesting localized enrichment possibly associated with anthropogenic sources such as industrial discharge, agricultural inputs, and urban runoff. Cd exhibited comparatively low dispersion, indicating a relatively uniform spatial distribution, although its environmental relevance remains significant due to its high toxicity and mobility (Alloway 2013).

Pearson correlation analysis (Fig. 3) revealed significant associations among sediment properties and heavy metals, indicating shared geochemical behavior and possible common sources. TOC showed a very strong positive correlation with TOM ($r = 0.99991$, $p < 0.05$), confirming the dominance of organic carbon in sediment organic matter. Both TOC and TOM were positively correlated with Cr ($r = 0.41949$ and 0.42093, respectively), suggesting the affinity of Cr toward organic-rich sediment fractions. A significant negative correlation between Ca and Mg ($r = -0.3417$, $p < 0.05$) reflected contrasting mineralogical controls. Fe exhibited strong negative correlations with Ni ($r = -0.76033$, $p < 0.05$) and Cr ($r = -0.4408$, $p < 0.05$), indicating different binding phases and geochemical pathways. Ni showed a significant positive correlation with Cr ($r = 0.56274$, $p < 0.05$), implying a common lithogenic source. Pb was positively correlated with Cu ($r = 0.65901$, $p < 0.05$) and Cd ($r = 0.54616$, $p < 0.05$), suggesting similar anthropogenic inputs. Cu also showed a positive association with Cr ($r = 0.32674$, $p < 0.05$). In addition, pH exhibited a significant positive correlation with Cd ($r = 0.41925$, $p < 0.05$), indicating the influence of sediment pH on Cd retention and mobility. Overall, the results suggest that organic matter influences Cr accumulation, while Pb, Cu, and Cd may originate from common anthropogenic activities.

Principal component analysis (PCA) was applied to elucidate the sources and controlling mechanisms governing heavy metal distribution in the Cauvery Delta wetland sediments. The PCA loading plot for sequential extraction fractions (F1–F5) is presented in Fig. 4, while the corresponding scree plot illustrating eigenvalue contributions is shown in Fig. 5. The eigenvalue structure indicates that the first principal component (PC1) explains the overwhelming majority of the variance among the fractions, demonstrating a strong common geochemical control on metal partitioning across the operationally defined phases. Subsequent components contribute only negligible variance, indicating limited influence of independent secondary processes.

Principal component analysis (PCA) revealed that PC1 accounted for 84.05% of the total variance, indicating that metal fractionation was predominantly controlled by a common geochemical process operating across all operationally defined sediment fractions (Fig. 4). All fractions (F1–F5) exhibited positive loadings along PC1, reflecting a strong overall association among the geochemical phases. PC2 explained an additional 10.08% of the variance and primarily differentiated the relatively mobile fractions (F1 and F2) from the more stable fractions (F4 and F5). The negative loadings of F1 and F2 suggest their association with labile and potentially bioavailable metal forms, whereas the positive loadings of F4 and F5 indicate stronger affinities toward more stable binding phases, likely associated with organic/sulfidic and residual components. Fraction F3

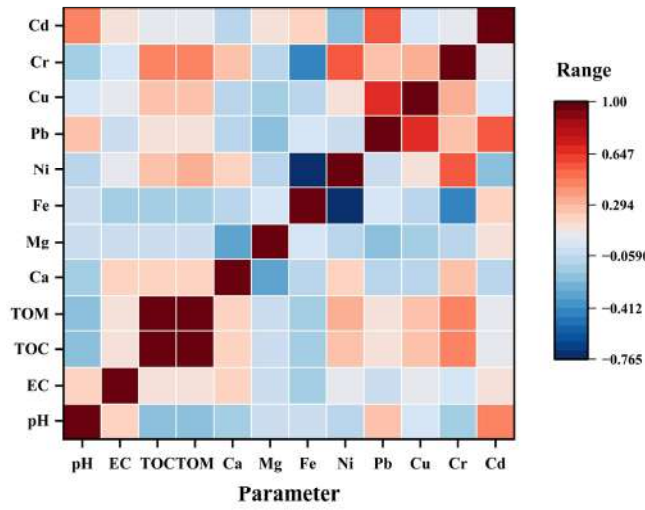


Fig. 3: Correlation heatmap of heavy metals and physicochemical parameters in Cauvery Delta wetland sediments.

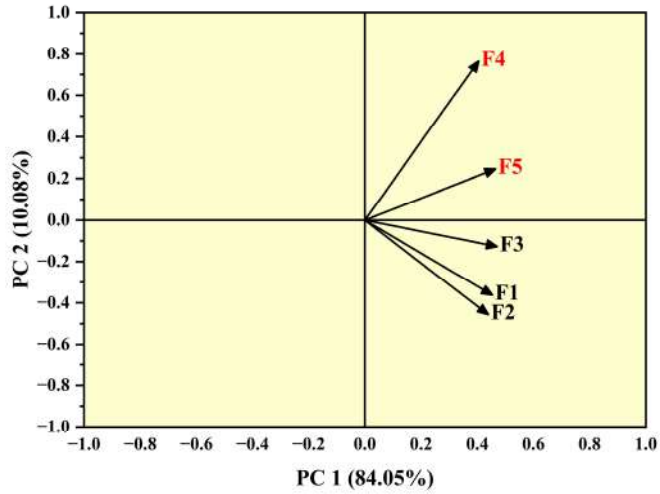


Fig. 4: Principal component analysis (PCA) loading plot of heavy metal speciation fractions (F1–F5) in Cauvery Delta wetland sediments.

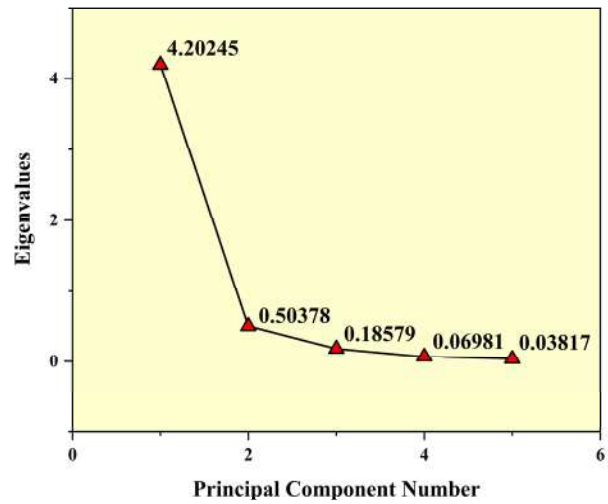


Fig. 5: Scree plot showing variance contribution of principal components for sequential extraction fractions.

occupied an intermediate position, representing transitional geochemical characteristics between mobile and stable phases. The close clustering of F1 and F2 further indicates similar geochemical controls and mobility behavior, while the separation of F4 and F5 highlights distinct stabilization mechanisms governing metal retention within the sediment matrix.

The scree plot further substantiated these observations, with PC1 exhibiting a markedly high eigenvalue (4.20245) relative to the subsequent components (Fig. 5). In contrast, PC2–PC5 revealed substantially lower eigenvalues ranging from 0.50378 to 0.03817, indicating minimal additional contributions to the total variance. The pronounced dominance of PC1 suggests that metal partitioning within the sediments is primarily regulated by a single overarching geochemical control, whereas secondary components contribute only limited and independent variability to fraction distribution patterns.

For total metal concentrations, the PCA loading plot (Fig. 6) and scree plot (Fig. 7) reveal a more complex variance structure. PC1 accounts for 38.63%, and PC2 explains 32.39%, together representing 71.02% of the cumulative variance. The loading pattern shows strong positive associations of Fe and Cr with PC1, suggesting a dominant lithogenic contribution linked to sediment mineral composition and parent material weathering, with Ni also reflecting weathering-derived inputs.

In contrast, the association of Cd, Pb, and Cu within PC2 suggests significant anthropogenic influence, mainly derived from agricultural runoff, municipal discharge, and

localized industrial activities. Karur district, recognized as a major textile dyeing and processing hub in Tamil Nadu, contains numerous dyeing and bleaching units that discharge metal-enriched effluents into the Amaravathi River system (Rajamanickam & Nagan 2010). Textile processing industries extensively utilize metal-based dyes, pigments, mordants, and chemical additives containing Cu, Pb, and Cd, which subsequently accumulate in aquatic sediments through continuous effluent discharge (Sivakumar et al. 2011). Similarly, Tiruchirappalli district is characterized by engineering industries, fabrication units, urban wastewater discharge, and fertilizer-related activities, all of which contribute to heavy metal loading in surrounding aquatic environments. In addition, long-term application of phosphate fertilizers may enhance Cd accumulation through agricultural runoff, as phosphate fertilizers are recognized as secondary sources of Cd contamination in soils and sediments (Alloway 2013). Therefore, the positive loading of Cd, Pb, and Cu in PC2 reflects mixed anthropogenic inputs associated with industrial effluents, urban discharge, and agricultural practices rather than natural lithogenic sources.

Overall, the PCA results indicate that metal distribution in the sediments is controlled by both natural geochemical background and anthropogenic inputs. The predominance of stable fractions suggests limited metal mobility under present environmental conditions. Fe enrichment primarily reflects natural geological sources, whereas variability in Ni, Pb, Cu, Cr, and Cd points to supplementary anthropogenic contributions, particularly in intensively cultivated, urbanized, and industrial sectors of the Cauvery Delta.

4. CONCLUSIONS

The present investigation provides a comprehensive assessment of heavy metal distribution, speciation, mobility, and ecological risk in wetland sediments of the

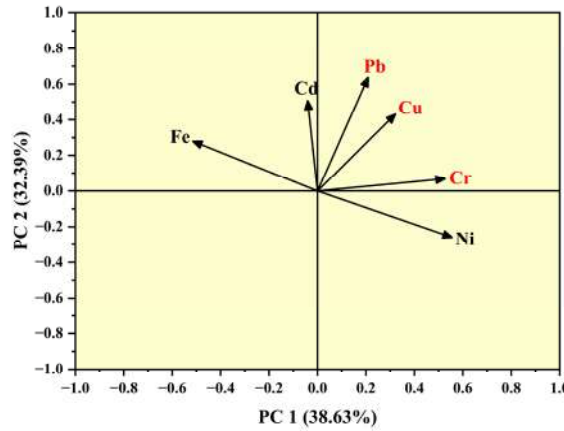


Fig. 6: Principal component analysis (PCA) loading plot of total heavy metals in Cauvery Delta wetland sediments.

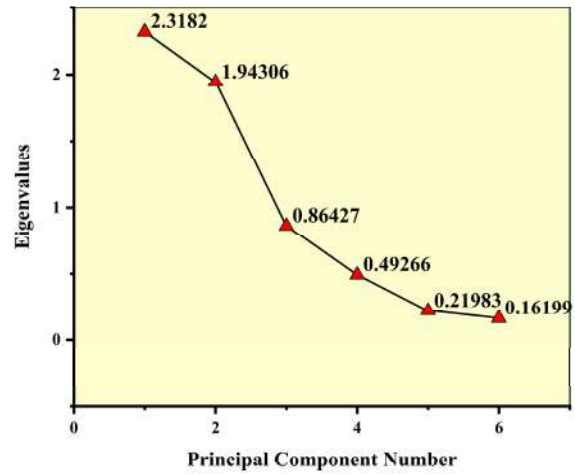


Fig. 7: Scree plot illustrating variance explained by principal components of total metals.

Cauvery Delta, India, through the integrated application of contamination indices, sequential extraction techniques, ecological risk models, and multivariate statistical analyses. The study demonstrated substantial spatial variability in sediment geochemistry across the investigated wetlands, with Fe exhibiting dominant natural abundance and strong association with stable residual fractions, indicating predominantly lithogenic control and limited environmental mobility. The overall decreasing order of mean metal concentrations was Fe > Pb > Ni > Cr > Cu > Cd. Although CF, Igeo, and PLI assessments indicated generally low to moderate contamination levels for most metals, all sampling sites exhibited PLI values greater than unity, suggesting slight but consistent cumulative pollution throughout the wetlands. Among the investigated metals, Cd emerged as the principal contaminant of concern due to its comparatively higher contamination factor, elevated mobility, and ecological sensitivity despite its relatively low total concentration. Localized Cd enrichment was particularly evident at samples 1, 7, 8, 9, and 20, mainly within Karur and Tiruchirappalli districts, indicating significant anthropogenic influence associated with agricultural runoff, phosphate fertilizer application, urban discharge, and localized industrial activities.

Sequential extraction analysis revealed that Cd, Pb, and Cr were predominantly associated with exchangeable and carbonate-bound fractions, indicating higher mobility, bioavailability, and remobilization potential under changing physicochemical conditions. In contrast, Fe remained strongly associated with residual and oxide-bound fractions, reflecting greater geochemical stability. RAC assessment further demonstrated moderate to very high ecological risk for Cd, Pb, and Cr in several wetlands, while PERI values indicated considerable to very high ecological risk at specific locations, particularly in parts of Karur and Tiruchirappalli districts. The alkaline, carbonate-rich, and organic matter-containing sediment environment significantly influenced metal partitioning behavior, promoting carbonate association of Cd and organic/oxide binding of Cu. Pearson correlation analysis and PCA suggested that Fe and Cr were primarily controlled by lithogenic processes, whereas Cd, Pb, and Cu were likely influenced by mixed anthropogenic inputs including industrial discharge, fertilizer usage, municipal wastewater, and agricultural activities.

Overall, the study highlights that while the Cauvery Delta wetlands are not severely polluted, localized enrichment and elevated mobility of Cd represent a significant ecological concern requiring continued surveillance. Targeted monitoring and mitigation strategies should therefore focus particularly on Cd hotspot wetlands in Karur and Tiruchirappalli districts to minimize future ecological risk and protect the long-term sustainability of these ecologically important wetland ecosystems.

5. ACKNOWLEDGMENT

The authors thank RUSA 2.0 and Bharathidasan University for funding this project and providing the necessary facilities to carry out this research successfully.

6. REFERENCES

Alloway, B.J., 2013. *Heavy Metals in Soils: Trace Metals and Metalloids in Soils and Their Bioavailability*, 3rd ed. Springer [DOI].

Alongi, D.M., 2020. Carbon cycling and storage in mangrove forests. *Annual Review of Marine Science*, 12, pp.195-219 [DOI].

Angulo, E., 1996. The Tomlinson Pollution Load Index applied to heavy metals, Mussel-Watch data: A useful index to assess coastal pollution. *Science of the Total Environment*, *187*(1), pp.19-56.

Atiemo, M.S., Ofosu, G.F., Mensah, H.K., Tutu, O.M. and Blankson, S.A., 2011. Contamination assessment of heavy metals in road dust from selected roads in Accra. *Research Journal of Environmental and Earth Sciences*, 3, pp.473-480.

Barbier, E.B., Hacker, S.D., Kennedy, C., Koch, E.W., Stier, A.C. and Silliman, B.R., 2019. The value of estuarine and coastal ecosystem services. *Ecological Monographs*, 89, p.e01308 [DOI].

Bessa, A.Z.E., Ngueutchoua, G. and Ndjigui, P.D., 2018. Mineralogy and geochemistry of sediments from Simbock Lake, Yaoundé area (southern Cameroon): provenance and environmental implications. *Arabian Journal of Geosciences*, 11, p.710 [DOI].

Bhattacharyya, S., Dawson, D.A., Hipperson, H. and Ishtiaq, F., 2019. A diet rich in C3 plants reveals the sensitivity of an alpine mammal to climate change. *Molecular Ecology*, 28, pp.250-265 [DOI].

Cevik, F., Goksu, M.Z.L., Derici, O.B. and Findik, O., 2009. An assessment of metal pollution in surface sediments of Seyhan Dam using enrichment factor and geoaccumulation index. *Environmental Monitoring and Assessment*, 152, pp.309-317 [DOI].

Chakravarty, M. and Patgiri, A.D., 2009. Metal pollution assessment in sediments of the Dikrong River, NE India. *Journal of Human Ecology*, 27, pp.63-67 [DOI].

Chapman, D., 1996. *Water Quality Assessments: A Guide to the Use of Biota, Sediments and Water in Environmental Monitoring*, 2nd ed. UNESCO/WHO/UNEP.

Chen, R., Chen, H., Song, L., Yao, Z., Meng, F. and Teng, Y., 2019. Characterization and source apportionment of heavy metals in sediments of Lake Tai, China. *Science of the Total Environment*, 694, p.133819 [DOI].

Dhamodharan, A., Abinandan, S., Aravind, U., Ganapathy, G.P. and Shanthakumar, S., 2019. Distribution of metal contamination and risk indices assessment of surface sediments from Cooum River, Chennai, India. *International Journal of Environmental Research*, *13*(5), pp.853-860. [DOI]

Dessalew, G., Beyene, A., Nebiyu, A. and Astatkie, T., 2018. Effect of brewery spent diatomite sludge on trace metal availability in soil and uptake by wheat crop. *Heliyon*, 4, p.e00783 [DOI].

Drever, J.I., 1997. *The Geochemistry of Natural Waters: Surface and Groundwater Environments*, 3rd ed. Prentice Hall.

El-Amier, Y.A., Elnaggar, A.A. and El-Alfy, M.A., 2017. Evaluation and mapping spatial distribution of bottom sediment heavy metal contamination in Burullus Lake, Egypt. *Egyptian Journal of Basic and Applied Sciences*, 4, pp.55-66 [DOI].

El-Kammar, A.M., Ali, B.H. and El-Badry, A.M.M., 2009. Environmental geochemistry of River Nile bottom sediments between Aswan and Isna, Upper Egypt. *Journal of Applied Sciences Research*, 5(6), pp.585-594.

Förstner, U. and Wittmann, G.T.W., 2012. *Metal Pollution in the Aquatic Environment*. Springer [DOI].

Gupta, S., Jena, V., Matic, N., Kapralova, V. and Solanki, J.S., 2014. Assessment of geo-accumulation index of heavy metal and source of contamination by multivariate factor analysis. *International Journal of Hazardous Materials*, 2(2), pp.18-22.

Håkanson, L., 1980. An ecological risk index for aquatic pollution control: a sedimentological approach. *Water Research*, 14(8), pp.975-1001 [DOI].

IPCC, 2022. *Climate Change 2022: Impacts, Adaptation and Vulnerability*. Cambridge University Press.

Islam, M.S., Ahmed, M.K., Raknuzzaman, M., Habibullah-Al-Mamun, M. and Islam, M.K., 2015. Heavy metal pollution in surface water and sediments of an urban river in Bangladesh. *Ecological Indicators*, 48, pp.282-291 [DOI].

Kumar, B., Shah, R. and Mukherjee, D., 2011. Geochemical distribution of heavy metals in sediments from sewage-fed fish ponds from Kolkata wetlands, India. *Chemical Speciation and Bioavailability*, 23(1), pp.24-32 [DOI].

Liu, D., Ma, J., Sun, Y. and Li, Y., 2016a. Spatial distribution of soil magnetic susceptibility and correlation with heavy metal pollution in Kaifeng City, China. *Catena*, 139, pp.53-60 [DOI].

Liu, R., Men, C., Liu, Y., Yu, W., Xu, F. and Shen, Z., 2016. Spatial distribution and pollution evaluation of heavy metals in the Yangtze estuary sediments. *Marine Pollution Bulletin*, 110, pp.564-571 [DOI].

Liu, R., Wang, M., Chen, W. and Peng, C., 2016c. Spatial pattern of heavy metals accumulation risk in urban soils of Beijing and its influencing factors. *Environmental Pollution*, 210, pp.174-181 [DOI].

Macreadie, P.I., Costa, M.D.P., Atwood, T.B. et al., 2021. Blue carbon as a natural climate solution. *Nature Reviews Earth and Environment*, 2, pp.826-839 [DOI].

Mandeng, E.P.B., Bidjeck, L.M.B., Ekoa Bessa, A.Z., Ntomb, Y.D., Wadjou, J.W., Doumo, E.P.E. and Dieudonne, L.B., 2019. Contamination and risk assessment of heavy metals in sediments from urban wetlands in Douala, Cameroon. *Environmental Monitoring and Assessment*, 191, p.7472 [DOI].

Menéndez, P., Losada, I.J., Beck, M.W. et al., 2020. The global flood protection benefits of mangroves. *Scientific Reports*, 10, p.4404 [DOI].

Müller, G., 1969. Index of geoaccumulation in sediments of the Rhine River. *GeoJournal*, 2, pp.108-118.

Meyers, P.A. and Ishiwatari, R., 1993. Lacustrine organic geochemistry—an overview of indicators of organic matter sources and diagenesis in lake sediments. *Organic Geochemistry*, *20*(7), pp.867-900.

National Institute of Standards and Technology, 2002. Standard Reference Material (SRM) 2702: Inorganics in Marine Sediment – Certificate of Analysis. Gaithersburg, MD, USA.

Nicholls, R.J., Adger, W.N., Hutton, C.W. and Hanson, S.E., 2021. Deltas in the Anthropocene. *Annual Review of Environment and Resources*, 46, pp.159-183 [DOI].

Nowrouzi, M. and Pourkhabbaz, A., 2014. Application of geoaccumulation index and enrichment factor for assessing metal contamination in the sediments of Hara Biosphere Reserve, Iran. *Chemical Speciation and Bioavailability*, 26(2), pp.99-105 [DOI].

Parizanganeh, V., Lakhan, C. and Jalalian, H., 2007. A geochemical and statistical approach for assessing heavy metal pollution in sediments from the southern Caspian coast. *International Journal of Environmental Science and Technology*, 4, pp.351-358 [DOI].

Perin, G., Craboledda, L., Lucchese, M., Cirillo, R., Dotta, L., Zanette, M.L. and Orio, A.A., 1985. Heavy metal speciation in the sediments of Northern Adriatic Sea—A new approach for environmental toxicity determination. In: Lekkas, T.D. (Ed.), Heavy Metals in the Environment, Vol. 2. CEP Consultants, Edinburgh, pp.454-456.

Rajamanickam, R. and Nagan, S., 2010. Study on quality of effluent discharge by the Tiruppur textile dyeing units and its impact on River Noyyal, Tamil Nadu, India. *Journal of Environmental Science and Engineering*, 52(4), pp.333-342. PMID: 22312804.

Ramanathan, A.L., Subramaian, V. and Vaithiyanathan, P., 1988. Chemical and sediment characteristics of the upper reaches of the Cauvery estuary. *Indian Journal of Marine Sciences*, 17, pp.114-120.

Rauret, G., López-Sánchez, J.F., Sahuquillo, A. et al., 1999. Improvement of the BCR three-step sequential extraction procedure. *Journal of Environmental Monitoring*, 1, pp.57-61 [DOI].

Salah, E.A.M., Zaidan, T.A.Z. and Al-Rawi, A.S., 2012. Assessment of heavy metals pollution in the sediments of Euphrates River, Iraq. *Journal of Water Resource and Protection*, 4, pp.1009-1023 [DOI].

Singh, K.P., Basant, A., Gupta, S. and Mohan, D., 2010. Heavy metal contamination and health risk assessment of groundwater from an industrial area of Delhi, India. *Environmental Monitoring and Assessment*, 181(1–4), pp.95-109 [DOI].

Singh, M., Müller, G. and Singh, I.B., 2003. Geogenic distribution and baseline concentration of heavy metals in sediments of the Ganges River, India. *Journal of Geochemical Exploration*, 80, pp.1-17 [DOI].

Sivakumar, K., Balamurugan, C., Ramakrishnan, D. and Bhai, L.H., 2011. Assessment studies on wastewater pollution by textile dyeing and bleaching industries at Karur, Tamil Nadu. *International Journal of ChemTech Research*, 3, pp.37-43.

Sivakumar, S., Chandrasekaran, A., Balaji, G. and Ravisankar, R., 2016. Assessment of heavy metal enrichment and the degree of contamination in coastal sediment from the southeast coast of Tamil Nadu, India. *Journal of Heavy Metal Toxicity and Diseases*, 1(2), pp.1-8.

Sposito, G., 2008. *The Chemistry of Soils*, 2nd ed. Oxford University Press [DOI].

Suresh, G., Sutharsan, P., Ramasamy, V. and Venkatachalapathy, R., 2021. Assessment of heavy metal contamination in river sediments using geochemical indices. *Environmental Monitoring and Assessment*, 193, p.431 [DOI].

Sutherland, R.A., 2000. Bed sediment-associated trace metals in an urban stream, Hawaii. *Environmental Geology*, 39, pp.611-627 [DOI].

Syvitski, J.P.M. et al., 2022. Delta vulnerability in the Anthropocene. *Nature Geoscience*, 15, pp.857-864 [DOI].

Tessier, A., Campbell, P.G.C. and Bisson, M., 1979. Sequential extraction procedure for trace metals. *Analytical Chemistry*, 51, pp.844-851 [DOI].

Tessler, Z.D., Vörösmarty, C.J., Overeem, I., Syvitski, J.P.M. and Foufoula-Georgiou, E., 2015. Profiling risk and sustainability in coastal deltas of the world. *Science*, 349, pp.638-643 [DOI].

Tomlinson, D.L., Wilson, J.G., Harris, C.R. and Jeffrey, D.W., 1980. Problems in the assessment of heavy-metal levels in estuaries and the formation of a pollution index. *Helgoländer Meeresuntersuchungen*, *33*(1), pp.566-575.

Turekian, K.K. and Wedepohl, K.H., 1961. Distribution of the elements in some major units of the Earth's crust. *Geological Society of America Bulletin*, 72, pp.175-192 [DOI].

United States Environmental Protection Agency (USEPA), 2002. Methods for Evaluating Wetland Condition: Using Chemical and Physical Indicators to Assess Wetland Condition. EPA-822-R-02-019. Office of Water, Washington, DC.

Varol, M. and Sen, B., 2011. Assessment of nutrient and heavy metal contamination in surface water and sediments of the upper Tigris River, Turkey. *Catena*, 85(3), pp.216-222 [DOI].

Varol, M. and Sen, B., 2012. Assessment of nutrient and heavy metal contamination in surface water and sediments of the upper Tigris River, Turkey. *Catena*, 92, pp.1-10 [DOI].

Varol, M., 2020. Environmental, ecological and health risks of trace metals in sediments of river deltas. *Environmental Research*, 187, p.109671 [DOI].

Zakir, H.M., Shikazono, N. and Otomo, K., 2008. Geochemical distribution of trace metals and assessment of anthropogenic pollution in sediments of Old Nakagawa River, Tokyo, Japan. *American Journal of Environmental Sciences*, 4(6), pp.654-660 [DOI].

Nature Environment and Pollution Technology
An International Quarterly Peer-Reviewed Open Access Journal

p-ISSN: 0972-6268 | e-ISSN: 2395-3454 Vol. 25 | No. 4 | Article ID D1903 | 2026

RESEARCH ARTICLE https://doi.org/10.46488/NEPT.2026.v25i04.D1903 OPEN ACCESS

Determinants of Household Waste Management Behavior in Urban Slum Communities: Evidence from Makassar City, Indonesia

Muh. Fajaruddin Natsir†, Erniwati Ibrahim, Anwar Mallongi, Owildan Wisudawan, Basir Rasyid, Anwar Daud and Syamsuar Manyullei
Department of Environmental Health, Faculty of Public Health, Hasanuddin University, Makassar, Indonesia
†Corresponding author: Muh. Fajaruddin Natsir; fajarnatsir@unhas.ac.id

ARTICLE HISTORY

Received: 25-01-2026
Revised: 09-03-2026
Accepted: 18-03-2026

KEYWORDS

Household waste management
Urban slum
Environmental education
Waste management behavior
Makassar

CITE THIS ARTICLE

Natsir, M. F., Ibrahim, E., Mallongi, A., Wisudawan, O., Rasyid, B., Daud, A. and Manyullei, S., 2026. Determinants of household waste management behavior in urban slum communities: Evidence from Makassar City, Indonesia. *Nature Environment and Pollution Technology*, 25(4), D1903. https://doi.org/10.46488/NEPT.2026.v25i04.D1903

COPYRIGHT & LICENCE

© 2026 The Authors
Open Access under CC BY 4.0.

PUBLISHED BY

TECHNOSCIENCE PUBLICATIONS

ABSTRACT

Household solid waste management in urban slum settlements remains an important environmental and public health concern in developing countries. This study analyzed sociodemographic, environmental, and social factors associated with household waste management practices in an urban slum area of Makassar City, Indonesia. A cross-sectional survey was conducted among 106 households in Maccini Sombala Village using structured interviews and field observations. Data were analyzed using chi-square tests and binary logistic regression. Results showed that 61.3% of households had poor waste management practices, particularly in waste separation and household-scale processing/recycling. In the multivariable model, secondary education and elderly age were significantly associated with better household solid waste management practices ($p < 0.05$). Respondents with secondary education were nearly three times more likely to report good practices (OR = 2.92; 95% CI: 1.18–7.25), while elderly respondents were more than four times more likely to do so (OR = 4.59; 95% CI: 1.17–17.99). The measured environmental and social factors, including household sanitation, domestic wastewater drainage, clean water quality based on basic physical criteria, and perceived community clean-up activities, were not statistically significant. These findings suggest that household-level behavior change, particularly through practical environmental education, may be important for improving waste management practices in low-resource urban settings.

1. INTRODUCTION

Household solid waste management represents one of the most pressing environmental challenges worldwide, growing increasingly complex alongside rapid urbanization and population expansion in metropolitan areas (Naghel et al. 2022). Global estimates indicate that more than 2.2 billion tons of waste were generated annually in 2020, a figure projected to rise by approximately 73% to 3.88 billion tons by 2050. Of this total, around 23% remains uncollected, while 33% is still disposed of through open dumping, particularly in developing nations (Zhang et al. 2025). Inefficient waste management contributes to soil, water, and air pollution, heightening public health risks through the proliferation of disease vectors such as flies and mosquitoes (Umunnakwe et al. 2021). Within the framework of sustainable development, waste management is directly linked to the Sustainable Development Goals (SDGs), specifically Goal 11 on sustainable cities and communities, and Goal 12 on responsible consumption and production (Adande et al. 2022). Thus, strengthening household-level waste management practices constitutes a strategic component of environmental health protection and the promotion of urban livability.

This issue is particularly evident in densely populated and slum settlements, where inadequate infrastructure, high population density, and poor sanitation-related behaviors exacerbate solid waste management challenges (Jagun et al. 2023, Thapaliya et al. 2024). Slum areas are typically characterized by limited waste collection services, insufficient wastewater drainage, and widespread open dumping in vacant lots, drainage channels, or nearby water bodies (Mugambe et al. 2022). Such practices not only degrade the physical environment but also facilitate the transmission of environment-related diseases, including diarrhea, dengue fever, and skin infections (Dagnaw et al. 2025). Empirical studies from developing countries have shown that solid waste management is a multidimensional issue, shaped by the interaction of social, economic, and behavioral determinants (Gharagozloo & Ghazizade 2023, Ukpanyang et al. 2022). Evidence highlights that cooperative-based door-to-door collection, enabled by municipal governance arrangements, can enhance source segregation at the household level (Saifi & Jha 2024).

Makassar City, one of the major metropolitan centers in eastern Indonesia, faces similar challenges. According to the Makassar City Government, as of December 2024, the total slum area reached approximately 299 hectares (Aminah 2025). Rapid population growth and economic expansion have increased household waste volumes, while the city's collection capacity has lagged behind waste generation rates (Palakurthy Ravinder & Kesari 2021). In several slum neighborhoods, residents still rely on traditional disposal practices, such as burning waste in household yards or dumping it into nearby rivers and drainage systems (Thapaliya et al. 2024). These practices contribute to unsanitary living conditions, surface water pollution, and increased vector-borne disease risks. Therefore, understanding the determinants of household waste management behavior is essential for designing effective community-based interventions in urban slum settings.

Previous research has emphasized that the effectiveness of household waste management depends not only on infrastructural support but also on behavioral factors at both the individual and community levels (Chengqin et al. 2022, Thakur & Onwubu 2024). Behavioral health perspectives suggest that individual decisions regarding waste management are influenced by personal factors (e.g., knowledge, education, age), social factors (e.g., norms, community support), and environmental conditions (e.g., access to facilities) (Fuadiyah Haq Zilfani 2024, Zheng et al. 2020). Supporting evidence from Makassar further indicates that knowledge and the social environment are significantly associated with household waste management behavior, underscoring the relevance of examining individual and social-level determinants in Indonesian settings (Natsir et al. 2024). Within this context, the Ecological Model of Health Behavior (EMHB) provides a useful theoretical framework, positing that health-related environmental behaviors result from multi-level interactions among individual, social, and physical environmental domains (Moeini et al. 2023). Applying this model facilitates a comprehensive examination of the determinants of household waste management practices, integrating sociodemographic characteristics, environmental infrastructure (e.g., sanitation, water quality, wastewater drainage), and social perceptions related to collective environmental activities.

Despite the growing body of literature on household waste management in Indonesia, most studies have primarily focused on technical and institutional dimensions, such as waste collection efficiency, source segregation, and integrated waste management policies (Ferdinan et al. 2022). Few studies have simultaneously analyzed sociodemographic, environmental, and social perception factors within slum communities (Sai et al. 2020, Soesilo & Alfarizi 2024). Moreover, there remains a paucity of empirical research integrating these multi-level variables into a single analytical framework that can explain variations in household waste management practices (Cheng et al. 2022).

Accordingly, this study aims to examine the sociodemographic, environmental, and social determinants of household solid waste management practices in the slum areas of Makassar City. The study contributes to the advancement of behavior-based environmental health research grounded in the Ecological Model of Health Behavior (Salmon et al. 2020) and provides an empirical foundation for community-based waste management policies. Practically, the findings are expected to inform local governments and stakeholders in developing participatory strategies to improve community engagement in household waste management, particularly in areas with limited infrastructure and high population density.

2. MATERIALS AND METHODS

This study employed a cross-sectional design and was conducted between July and September 2025 in an urban slum settlement in Makassar City, South Sulawesi, Indonesia. The study site was purposively selected at the community level in Maccini Sombala Village, Tamalate District, because the area represents typical characteristics of urban slum settlements, including high population density, limited solid waste management infrastructure, and constrained community engagement in environmental sanitation activities. The selected community unit (*Rukun Warga*, RW) consisted of six neighborhood units (*Rukun Tetangga*, RT),

which formed the sampling frame for this study. The study population comprised 482 households distributed across the six RTs. A total of 106 households were selected using proportionate systematic random sampling. The sample was allocated proportionally to each RT based on the number of households in that RT. Within each RT, households were selected using systematic random sampling by choosing a random starting household, followed by selection of subsequent households using a fixed sampling interval (k) calculated as the ratio between the number of households in the RT and the allocated sample size. Eligible respondents were the household head or an adult household member ($\geq$18 years) knowledgeable about daily household waste practices and residing in the area for at least six months.

Data were collected using a structured interviewer-administered questionnaire and an observation checklist. Direct observation was used to verify physical conditions where feasible (e.g., presence of a household waste container, type/availability of sanitation facility, and visible domestic wastewater drainage condition). Behavioral items that could not be directly verified (e.g., routine waste separation and processing/recycling at the household level before disposal) were obtained via respondent report. Enumerators were trained using standardized instructions and field protocols to ensure consistency in interviewing and observation procedures.

The dependent variable, household solid waste management practice (HSWM), was measured using a brief three-item index intended to capture minimum household-level practices feasible to assess in resource-constrained slum settings: (i) presence of a household waste container (observed), (ii) routine separation of waste at the household level (self-report), and (iii) any form of waste processing/recycling at the household level prior to disposal (self-report). In this study, 'processing/recycling' was operationally defined as household-scale composting of organic waste and reuse/repurposing of materials. The term does not refer to industrial recycling processes. Each affirmative response was scored as 1 (range 0–3), and the total score was dichotomized into poor (0–1) and good (2–3) for regression analysis. This index does not capture several context-specific practices (e.g., open burning, frequency of disposal, use of informal collectors, payment for collection services, or distance to disposal points), which may lead to misclassification and limited variability; therefore, findings should be interpreted as associations based on available proxy measures.

Independent variables were grouped into sociodemographic, physical environmental, and social factors. Sociodemographic variables included age, gender, education level, and occupation. Physical environmental variables were assessed using predefined operational criteria based on observation and respondent report: household sanitation was classified as adequate if the household had access to an improved latrine with safe excreta containment/disposal (e.g., a sealed septic tank or other safe containment system); otherwise it was classified as inadequate. Domestic wastewater drainage condition was classified as proper if a visible wastewater drainage channel was present and appeared functional at the time of observation (i.e., not causing stagnant wastewater); otherwise it was classified as improper. Clean water quality was categorized as meeting basic physical criteria when no abnormalities were identified during field inspection and respondent report (color and visually assessed turbidity by observation; odor and taste by respondent report); the presence of any abnormality was categorized as not meeting criteria. This assessment represents a physical-parameter screening and does not replace laboratory verification against regulatory standards. Social factors were measured as respondents' perceptions of community clean-up activities (positive vs negative perception), reflecting perceived collective action rather than directly observed participation.

Descriptive statistics summarized frequencies and percentages. Bivariate associations were examined using the chi-square test. Variables were entered into the multivariable binary logistic regression model based on theoretical relevance and bivariate screening, and backward likelihood-ratio (LR) elimination was applied to obtain the final model. Model fit was assessed using the Hosmer–Lemeshow goodness-of-fit test, and classification performance (sensitivity and specificity) was reported. Statistical significance was set at $p < 0.05$, and results are presented as ORs with 95% CIs.

Ethical clearance was obtained from the Health Research Ethics Committee, Faculty of Public Health, Hasanuddin University (Approval No.: 1537/UN4.14.1/TP.01.02/2025). Participation was voluntary. Enumerators provided study information, explained objectives and procedures, and emphasized the right to refuse or withdraw at any time without consequences. Written informed consent was obtained before data collection. Data were anonymized using unique codes and stored securely, accessible only to the research team.

3. RESULTS AND DISCUSSION

3.1. Descriptive Characteristics of Respondents

Table 1 presents the respondents' sociodemographic characteristics. Most respondents were female (94.3%), aged 35–54 years (50.0%), had a medium level of education (69.8%), and were unemployed (72.6%). The predominance

Table 1: Sociodemographic characteristics of respondents (n = 106).

Variable	Category	n	%
Age	Young (≤34 years)	33	31.1
	Adult (35–54 years)	53	50.0
	Elderly (≥55 years)	20	18.9
Gender	Male	6	5.7
	Female	100	94.3
Education	Low (elementary school or below)	32	30.2
	Medium (junior–senior high school)	74	69.8
Occupation	Unemployed	77	72.6
	Informal sector	27	25.5
	Formal sector	2	1.9

of female respondents likely reflects daytime household visits, during which adult women were more frequently available to participate. Overall, the sample reflects the socioeconomic profile of households in the selected slum area.

3.2. Distribution of Household Solid Waste Management Practices

Table 2 presents the distribution of household solid waste management practices across three indicators: presence of a household waste container, routine waste separation, and household-scale waste processing/recycling (composting or reuse). Based on the composite three-item index, 61.3% of households were categorized as having poor HSWM practices, while 38.7% were categorized as good. Overall, the findings indicate limited uptake of the assessed minimum household-level practices in the study area.

3.3. Physical Environmental and Social Conditions

Table 3 presents the distribution of physical environmental conditions and social perceptions among households in the study area. Overall, 48.1% of households had adequate sanitation, and 32.1% had proper domestic wastewater drainage conditions. Regarding access to clean water, 67.0% of households met the basic physical criteria based on organoleptic screening (color and visually assessed turbidity by observation; odor and taste by respondent report). In the social domain, 24.5% of respondents reported a positive perception of community clean-up activities. These descriptive distributions demonstrate the extent of within-area variability in environmental conditions and perceived collective action, providing context for subsequent association analyses with household solid waste management practices.

Table 2: Distribution of household solid waste management practices (n = 106).

Indicator	Category	n	%
Ownership of waste bin	Yes	74	69.8
	No	32	30.2
Waste sorting	Yes	55	51.9
	No	51	48.1
Waste processing/recycling (household-scale composting or reuse)	Yes	53	50.0
	No	53	50.0
Household waste management practice	Good	41	38.7
	Poor	65	61.3

Table 3: Distribution of physical environmental and social characteristics (n = 106).

Variable	Category	n	%
Household sanitation	Adequate	51	48.1
	Inadequate	55	51.9
Domestic wastewater drainage condition	Proper	34	32.1
	Improper	72	67.9
Clean water quality (basic physical criteria; organoleptic screening)	Meets criteria	71	67.0
	Does not meet criteria	35	33.0
Perceived community clean-up activities	Positive	26	24.5
	Negative	80	75.5

3.4. Association Between Sociodemographic, Environmental, and Social Factors and Household Waste Management

Bivariate associations between sociodemographic factors and the HSWM practice index are presented in Table 4. Education level was significantly associated with HSWM practices ($\chi^2 = 4.033$, df = 1, p = 0.045; φ = 0.195). In contrast, age ($\chi^2 = 3.760$, df = 2, $p = 0.153$; V = 0.188), gender (Fisher's exact test, $p = 0.203$; φ = 0.141), and occupation (Fisher–Freeman–Halton exact test, $p = 1.000$; V = 0.037) were not significantly associated with HSWM practices.

Table 5 shows the bivariate associations between environmental/social factors and the HSWM practice index. None of the variables reached statistical significance (p > 0.05). Clean water quality based on basic physical criteria (organoleptic screening) showed a non-significant trend ($\chi^2 = 3.581$, df = 1, p = 0.058; φ = 0.184) and should be interpreted cautiously given the proxy nature of the measure and the absence of laboratory verification. Perceived community clean-up activities, household sanitation, and domestic wastewater drainage condition were not significantly associated with HSWM practices.

3.5. Multivariable Analysis

Table 6 presents the multivariable binary logistic regression results. Elderly respondents had higher odds of good

Table 4: Association between sociodemographic factors and household waste management practice index (n = 106).

Sociodemographic Variable	Statistical test	χ^2	df	p-value	Effect size (φ/V)
Age	Pearson's chi-square	3.760	2	0.153	V = 0.188
Gender	Fisher's exact test	-	-	0.203	φ = 0.141
Occupation	Fisher–Freeman–Halton exact test	-	-	1.000	V = 0.037
Education level	Pearson's chi-square	4.033	1	0.045*	φ = 0.195

Note: Pearson's χ^2 test was used when expected-count assumptions were met; Fisher's exact and Fisher–Freeman–Halton exact tests were used for gender and occupation, respectively. Effect sizes are reported as φ for 2 × 2 tables and Cramer's V for larger tables. All *p*-values are two-sided; $p < 0.05$.

Table 5: Association between environmental and social factors and household waste management practice index (n = 106).

Variable	χ^2	df	p-value	Effect size
Household sanitation	0.258	1	0.611	φ = 0.049
Domestic wastewater drainage condition	0.624	1	0.429	φ = 0.077
Clean water quality	3.581	1	0.058	φ = 0.184
Perceived community clean-up activities	0.909	1	0.340	φ = 0.093

Note: chi-square test was used. Effect size is reported as Phi (φ) for 2 × 2 tables.

Table 6: Factors associated with household waste management practices (binary logistic regression, n = 106; method: backward LR, final step).

Variable (reference category)	B	SE	Wald	p-value	OR (Exp(B))	95% CI for OR
Adult age vs. young	0.347	0.467	0.551	0.458	1.415	0.566–3.534
Elderly vs. young	1.523	0.698	4.764	0.029*	4.585	1.168–17.994
Secondary education vs. low	1.072	0.464	5.342	0.021*	2.922	1.177–7.254

Model fit statistics: Omnibus $\chi^2(3) = 9.570$, p = 0.023; –2 Log Likelihood = 131.900; Cox–Snell $R^2 = 0.086$; Nagelkerke $R^2 = 0.117$; Hosmer–Lemeshow $\chi^2(4) = 1.910$, p = 0.752; Accuracy = 67.0%; Sensitivity = 86.2%; Specificity = 36.6%.

Note: Backward LR method, final step. OR = odds ratio; CI = confidence interval. *p < 0.05.

HSWM practices than younger respondents (OR = 4.585, 95% CI: 1.168–17.994, p = 0.029), and respondents with secondary education had higher odds of good HSWM practices than those with lower education (OR = 2.922, 95% CI: 1.177–7.254, p = 0.021). Adult age was not statistically significant (p = 0.458). The overall model was significant (Omnibus $\chi^2 = 9.570$, p = 0.023), with limited explanatory power (Nagelkerke $R^2 = 0.117$) and modest classification performance (Accuracy 67.0%; Sensitivity 86.2%; Specificity 36.6%).

3.6. Discussion

The findings of this study indicate that household solid waste management practices in the selected urban slum area of Makassar City remain limited. Multivariable analysis showed that age and education were associated with better HSWM practices, whereas the measured environmental and social variables were not statistically significant. However, these findings should be interpreted cautiously because the model showed limited explanatory power, indicating that a substantial proportion of variability in HSWM practices was not captured by the variables included in the analysis. Similar evidence has been reported in other contexts, where individual characteristics such as age and education were found to influence household waste sorting behavior (Toledo et al. 2025).

Education was associated with better household solid waste management practices in this study. Respondents with secondary education had higher odds of engaging in good HSWM practices compared with those with lower educational attainment. One possible explanation is that education may improve environmental knowledge and awareness of health risks related to improper waste handling, which can support the adoption of simple household practices such as waste separation and small-scale recycling or reuse. Similar associations between education and household waste sorting behaviors have been reported in studies conducted in other urban settings in developing countries (Khairunnisa et al. 2023, Thakur et al. 2023, Usha Rani et al. 2022). In low-resource urban environments, where formal waste infrastructure may be limited, educational attainment may therefore play an important role in shaping household routines related to waste handling and disposal.

Age was also associated with household solid waste management practices in this study, with elderly respondents showing higher odds of good HSWM practices than younger respondents. Older adults may have more established

household routines and longer experience in managing domestic responsibilities, which can contribute to more consistent waste handling behaviors. Similar patterns have been reported in previous studies showing that older individuals tend to demonstrate greater engagement in environmentally relevant household practices and recycling behaviors (Lin & Fung 2024, Omotayo et al. 2020). Similar evidence has also been reported in Indonesia, where age was associated with household waste management behavior (Fuadiyah Haq Zilfani 2024).

In contrast to some previous studies reporting that household environmental conditions and community participation can shape waste-related practices, the present study did not identify statistically significant associations for the measured environmental and social variables. This should not be interpreted as evidence that these factors are unimportant. Rather, the non-significant findings may reflect the limited sensitivity of the measures used in this study. Environmental conditions were assessed using brief binary indicators, while clean water quality was evaluated through basic physical criteria based on organoleptic screening rather than laboratory verification. Similarly, the social variable captured respondents' perceptions of community clean-up activities rather than observed participation. These proxy measures may not have been sufficiently detailed to detect more nuanced associations in the study setting. Previous studies have also highlighted the role of household socioeconomic characteristics and contextual factors in shaping recycling behavior (Omotayo et al. 2020, Sultana et al. 2024).

The findings of this study suggest that improving household waste management in urban slum settings may require greater attention to practical household-level behavior change. Programs that strengthen basic knowledge and skills related to waste separation, household-scale composting, and material reuse may therefore be particularly relevant. Environmental education and participatory community programs have been shown to encourage pro-environmental behavior and increase public willingness to engage in recycling activities (Owojori et al. 2022). In addition, the age-related pattern observed in this study indicates that younger households or younger adult members may require more targeted engagement to encourage consistent waste handling practices. Community-based education, training programs, and local participation mechanisms have also been reported to improve awareness and behavioral change in waste management initiatives (Mubarak et al. 2024). From a broader behavioral perspective, education and social norms play an important role in shaping environmental behavior and strengthening intentions to adopt sustainable waste management practices (Al Mamun et al. 2022).

This study has several limitations that should be considered when interpreting the findings. The cross-sectional design limits the ability to infer causal relationships between the examined factors and household waste management practices. In addition, the study was conducted within a single community unit in an urban slum area of Makassar City, which may restrict the generalizability of the findings to other urban or rural contexts with different environmental and socioeconomic characteristics. Some behavioral indicators, including waste sorting and recycling practices, were measured using respondent self-reports and may therefore be subject to reporting bias. Furthermore, the assessment of clean water quality relied on basic physical screening rather than laboratory verification. The relatively modest explanatory power of the regression model also suggests that additional determinants of household waste behavior may not have been captured in the current analysis, including socioeconomic and service-related factors such as household income, household size, waste collection frequency, and accessibility to disposal facilities.

Future studies should incorporate a broader range of socioeconomic and service-related variables, such as household income, waste collection frequency, and accessibility to waste management facilities, to better understand the determinants of household waste practices in urban slum environments. Longitudinal or mixed-method approaches may also provide deeper insights into behavioral dynamics and community participation in waste management programs. Expanding the study to multiple communities or cities could further improve the external validity of findings and support the development of more context-sensitive waste management interventions.

4. CONCLUSIONS

This study shows that household solid waste management practices in the selected urban slum area of Makassar City remain limited, with most households categorized as having poor HSWM practices. In the multivariable model, elderly age and secondary education were significantly associated with better HSWM practices, whereas the measured environmental and social variables were not statistically significant. These findings suggest that improving household waste management in low-resource urban settings may require greater emphasis on practical environmental education and routine-based behavior change at the household level. Further studies incorporating broader socioeconomic and service-related variables and involving multiple urban communities are needed to better understand the determinants of household waste management practices.

ACKNOWLEDGMENTS

The authors would like to express their sincere appreciation to the Head of Maccini Sombala Village for the administrative support and permission to conduct this study. The authors also acknowledge the Faculty of Public Health, Hasanuddin University, for institutional support, as well as the field enumerators for their valuable assistance during data collection.

REFERENCES

Adande, H. U. M., Houefonde, F. G. L., Rodrigue, L. C., Dovonon, L. F. and Vissin, E. W., 2022. Household waste management system: the new of SGDS facing the challenges of sanitation in Cotonou (Republic of Benin).*GSC Advanced Research and Reviews*, 10(1), pp. 78–89. [DOI]

Al Mamun, A., Hayat, N., Masud, M. M., Makhbul, Z. K. M., Jannat, T. and Salleh, M. F. Md., 2022. Modelling the significance of value-belief-norm theory in predicting solid waste management intention and behavior. Frontiers in Environmental Science, 10, 906002. [DOI]

Aminah, S., 24 September 2025. Urbanisasi tinggi Makassar butuh hunian layak, kawasan kumuh masih 299 hektare. Tribun Makassar.[DOI]

Cheng, K. M., Tan, J. Y., Wong, S. Y., Koo, A. C. and Sharji, E. A., 2022. A review of future household waste management for sustainable environment in Malaysian cities. *Preprints (Basel)*. [DOI]

Chengqin, E. K., Zailani, S., Rahman, M. K., Aziz, A. A., Bhuiyan, M. A. and Gazi, Md. A. I., 2022. Determinants of household behavioural intention towards reducing, reusing and recycling food waste management. *Nankai Business Review International* 15, 128–152. [DOI]

Dagnaw, B., Wang, Q., Mariye, M., Belayhun, T. and Dirriba, D., 2025. Challenges and practices of integrated solid waste management: insights from Debre Berhan Reogiopolitant City, Ethiopia.*Asian Journal of Environment & Ecology* 24, 12–30. [DOI]

Ferdinan, Utomo, S. W., Soesilo, T. E. B. and Herdiansyah, H., 2022. Household waste control index towards sustainable waste management: a study in Bekasi City, Indonesia. *Sustainability* 14(21), 14403. [DOI]

Fuadiyah Haq Zilfani, 2024. Household waste management behavior in the Blunyahrejo Village, Yogyakarta: insights from the theory of planned behavior and social capital.*BIO Web Conf*. 132, 2001. [DOI]

Gharagozloo, S. and Ghazizade, M. J., 2023. The influence of socioeconomic and psychological factors on the composition of household solid waste in Farahzad Neighborhood, Tehran, Iran. *Environ. Health Insights* 17, 11786302231195794. [DOI]

Jagun, Z. T., Daud, D., Ajayi, O. M., Samsudin, S., Jubril, A. J. and Rahman, M. S. A., 2023. Waste management practices in developing countries: a socioeconomic perspective. *Environmental Science and Pollution Research* 30, 116644–116655. [DOI]

Khairunnisa, A., Suryadi, A., Hufad, A. and Wahyudin, U., 2023. Waste care education for housewives. *Jurnal Penelitian Pendidikan IPA* 9, 8217–8225. [DOI]

Lin, Z., Fung and H. H.-L., 2024. Age differences in pro-environmental behaviors: is it about me or the next generation? *Innov. Aging* 8, 1372. [DOI]

Moeini, B., Ayubi, E., Barati, M., Bashirian, S., Tapak, L., Ezzati-Rastgar, K. and Hashemian, M., 2023. Effect of household interventions on promoting waste segregation behavior at source: a systematic review. *Sustainability* 15(24), 16546. [DOI]

Mubarak, A., Frinaldi, A., Syamsir, Syolendra, D. F., Fitriyanti, W. and Rezeki, A. P. T., 2024. Community involvement in the development of nagari-based sustainable waste management. *IOP Conf. Ser. Earth Environ. Sci*. 1414, 012082. [DOI]

Mugambe, R. K., Nuwematsiko, R., Ssekamatte, T., Nkurunziza, A. G., Wagaba, B., Isunju, J. B., Wafula, S. T., Nabaasa, H., Katongole, C. B., Atuyambe, L. M. and Buregyeya, E., 2022. Drivers of solid waste segregation and recycling in Kampala slums, Uganda: a qualitative exploration using the Behavior Centered Design Model.*Int. J. Environ. Res. Public Health* 19(17), 10947. [DOI]

Naghel, M., Farhi, A. and Redjem, A., 2022. Household waste management challenges: the case of M'sila, Algeria.*Engineering, Technology & Applied Science Research* 12, 8675–8682. [DOI]

Natsir, Muh. F., Al Muktadir, M. I., Ibrahim, E., Daud, A., Yusbud, M., Rahmadani, S., Anwar, A., Asfar, M. and Khaer, A., 2024. Analysis of factors influencing community behavior in household waste management on Lakkang Island, Indonesia.*Environment and Ecology Research* 12, 19–26. [DOI]

Omotayo, A. O., Omotoso, A. B., Daud, A. S., Ogunniyi, A. I. and Olagunju, K. O., 2020. What drives households' payment for waste disposal and recycling behaviours? Empirical evidence from South Africa's General Household Survey. *Int. J. Environ. Res. Public Health* 17(19), 7188. [DOI]

Owojori, O. M., Mulaudzi, R. and Edokpayi, J. N., 2022. Student's knowledge, attitude, and perception (KAP) of solid waste management: a survey toward a more circular economy from a rural-based tertiary institution in South Africa. *Sustainability* 14(3), 1310. [DOI]

Palakurthy Ravinder and Kesari, J. P., 2021. Solid waste management in urban areas: an urgent priority, in: Kateja Alpana and Jain, R. (Ed.), *Urban Growth and Environmental Issues in India*. Springer Singapore, Singapore, pp. 253–267. [DOI]

Sai, A., Al Furqan, R., Ushijima, K., Hamidah, U., Ikemi, M., Widyarani, Sintawardani, N. and Yamauchi, T., 2020. Personal hygiene, dignity, and economic diversity among garbage workers in an urban slum of Indonesia. *Sanitation Value Chain* 4, 51–66. [DOI]

Saifi, N. and Jha, B., 2024. An overview of solid waste management practices in Pune, Maharashtra, India. *Nature Environment and Pollution Technology* 23, 923–934. [DOI]

Salmon, J., Hesketh, K. D., Arundell, L., Downing, K. L. and Biddle, S. J. H., 2020. Changing behavior using ecological models, in: Hagger, M. S., Cameron, L. D., Hamilton, K., Hankonen, N., Lintunen, T. (Eds.), *The Handbook of Behavior Change*, Cambridge Handbooks in Psychology. Cambridge University Press, Cambridge, pp. 237–250. [DOI]

Soesilo, N. I. and Alfarizi, M., 2024. Psycho-social conditions of urban communities in the complexity of waste management: are awareness and waste banks the main solution? *Socioecon. Plann. Sci*. 93, 101834. [DOI]

Sultana, T., Rokis, R. and Al-Attas, F., 2024. Encouraging women's empowerment: a qualitative analysis of household food waste management in Bangladesh utilizing the 5R approach. *Saudi Journal of Humanities and Social Sciences (SJHSS)* 9, 238–251. [DOI]

Thakur, H., Khan, S. and Kaur, N., 2023. A descriptive study to assess awareness, knowledge, and practices among government senior secondary school students on household waste management in the Gohar Block of District Mandi, Himachal Pradesh. *Int. J. Community Med. Public Health* 10, 4876–4885. [DOI]

Thakur, R. and Onwubu, S. C., 2024. Household waste management behaviour amongst residents in an informal settlement in Durban, South Africa. *J. Environ. Manage*. 349, 119521. [DOI]

Thapaliya, A., Dangi, M. B., Boland, J. J., Rijal, K. and Adhikari, S., 2024. Solid waste characterization in the slum areas of Bagmati River, A case of Kathmandu, Nepal. *Environ. Dev*. 52, 101079. [DOI]

Toledo, E., Camacho, J. A., Rodríguez, M. and Alvarado, R., 2025. Individual, household and institutional level predictors of waste sorting: evidence for Ecuador. *Waste Management & Research* 43, 946–956. [DOI]

Ukpanyang, D., Terrados-Cepeda, J. and Hermoso-Orzaez, M. J., 2022. Multi-criteria selection of waste-to-energy technologies for slum/informal settlements using the PROMETHEE technique: a case study

of the Greater Karu Urban Area in Nigeria.*Energies (Basel)*. 15(10), 3481. [DOI]

Umunnakwe, J. E., Njoku, R. E., Aharanwa, B. C. and Umunnakwe, B. A., 2021. Household waste quantities and problem of management in Port Harcourt.*American Journal of Environmental and Resource Economics* 6, 1–10. [DOI]

Usha Rani, V., Vijaya Lakshmi, V., RatnaKumari, D., Geetha Reddy, R. and Meena, A., 2022. Households' waste disposal practices and their impact on health. *International Journal of Environment and Climate Change* 12, 252–260. [DOI]

Zhang, M., Ionkova, K. and Boukerche, S., 16 May 2025. How the World Bank is tackling the growing global waste crisis. World Bank Blogs. [DOI]

Zheng, J., Ma, G., Wei, J., Wei, W., He, Y., Jiao, Y. and Han, X., 2020. Evolutionary process of household waste separation behavior based on social networks. *Resour. Conserv. Recycl*. 161, 105009. [DOI]

Nature Environment and Pollution Technology
An International Quarterly Peer-Reviewed Open Access Journal

p-ISSN: 0972-6268 | e-ISSN: 2395-3454 Vol. 25 | No. 4 | Article ID D1904 | 2026

RESEARCH ARTICLE https://doi.org/10.46488/NEPT.2026.v25i04.D1904 OPEN ACCESS

An Assessment of the Environmental and Social Impacts of Waste Management Practices in Omuthiya Town and Its Disposal Site, Oshikoto Region, Namibia

Margaret Litungeni Johannes[1] and Timoteus Kadhila[2]†

[1]International University of Management (IUM), Department of Environmental Studies, Main Campus, Windhoek, Namibia

[2]International University of Management (IUM), Faculty of Environmental Management and Sustainability Sciences, Coastal Campus, Namibia

†Corresponding author: Timoteus Kadhila; t.kadhila@ium.edu.na

ARTICLE HISTORY

Received: 23-01-2026
Revised: 04-04-2026
Accepted: 07-04-2026

KEYWORDS

Waste management,
Environmental impacts,
Disposal site assessment,
Solid waste disposal

CITE THIS ARTICLE

Johannes, M. L. and Kadhila, T., 2026. An Assessment of the environmental and social impacts of waste management practices in Omuthiya Town and its disposal site, Oshikoto Region, *Namibia. Nature Environment and Pollution Technology*, 25(4), D1904. https://doi.org/10.46488/NEPT.2026.v25i04. D1904

COPYRIGHT & LICENCE

© 2026 The Authors
Open Access under CC BY 4.0.

PUBLISHED BY

TECHNOSCIENCE PUBLICATIONS

ABSTRACT

Rapid urbanization and population growth have intensified solid waste management challenges in many urban areas, particularly where infrastructure and institutional capacity are limited. This study assessed waste management practices and infrastructure in Omuthiya Town, Namibia, employed a case study research design and used mixed data collection methods. Quantitative data were collected through household surveys, while qualitative insights were obtained from interviews with local authority officials and residents as well as field observations. The findings indicate that although Omuthiya Town has made progress in waste collection services, major challenges remain. These include inadequate waste management infrastructure, low levels of waste separation and recycling, limited community participation, and weak regulatory enforcement. A heavy reliance on plastic bags for waste containment contributes to improper disposal and environmental pollution. Open waste burning, illegal dumping, and the absence of recycling facilities were identified as key drivers of environmental degradation and public health risks, particularly for communities living near the disposal site. The study highlights the urgent need for improved infrastructure, stronger policy enforcement, and community-based education programs to promote sustainable waste management practices.

1. INTRODUCTION

Waste management is a broad term that refers to the generation, collection, processing, transportation, and disposal of waste (Ruppel-Schlichting 2022). Waste management includes all activities that seek to minimize all potential environmental and social impacts that emanate from all types of wastes. Waste is a global environmental and public health concern in today's rapidly urbanizing world. Globally, 2.01 billion tons of solid waste are generated per annum, of which approximately 33% is managed in a manner that is considered not to be environmentally friendly (United Nations Environment Program [UNEP], 2024). According to Schioldborg and Bjørke (2014), environmental concerns such as pollution, habitat destruction, and health hazards are results of improper disposal and mismanagement of waste. They further stated that the global population is growing, and urbanization is rising, and it is increasingly urgent to transition into effective waste management strategies.

Omuthiya has recently undergone rapid economic development that has transformed it into a bustling commercial hub. Significant population and urban growth are observable, which can be attributed to several factors such as infrastructure development, expanded economic opportunities, and migration from rural to urban areas. Rapid urbanization, especially in developing countries, outpaces the development of essential waste management infrastructures (United Nations Human Settlements Programme (UN-Habitat & Ki-moon 2016). Limited essential waste management systems lead to deficiencies in municipal service delivery, resulting in improper waste disposal, contributing to environmental pollution and health risks. Uncollected waste often accumulates, leading to the spread of diseases and putting the health and safety of the people at risk (Omang et al. 2021).

According to the National Solid Waste Management Strategy (2017), Namibia has only one fully operational solid waste landfill site in Windhoek and two hazardous disposal sites at Windhoek and Walvis Bay. The rest of the country disposes of its waste at sites that have no proper control and management due to the shortage of resources and proper infrastructure. Kaapanda (2023) confirms that Namibia is faced with unsatisfactory waste management as many settlements, villages, towns, and municipalities do not have proper landfills and have resorted to dumpsites for waste disposal.

A study conducted by Amasuomo & Baird (2016) found that waste management practices are influenced by community awareness and engagement. Public education and community involvement are crucial in promoting responsible waste disposal behaviors and reducing littering. Recycling and waste-to-energy initiatives can create jobs, generate income, and contribute to the local economy (Bennett 2017). As Omuthiya Town continues to experience rapid urbanization and population growth, the implementation of effective and sustainable waste management systems has become increasingly critical. A comprehensive waste management study is a critical step toward evaluating the effectiveness of the current waste management system in Omuthiya Town, assessing infrastructure capacity, and identifying the environmental and social impacts of existing practices. This study has proposed feasible and sustainable solutions to address the town's waste management challenges, thereby contributing to improved community well-being and the protection of the local environment.

1.1. Context

1.1.1. Sustainable Solid Waste Management as Conceptual Framework

This study developed a Sustainable Solid Waste Management (SSWM) conceptual framework, which is structured around key variables and their relationships to address the study's objectives. This conceptual framework was developed based on waste management and the circular economy concepts as outlined by Ellen MacArthur Foundation (2017). This conceptual framework outlines how the four primary components of this study are interrelated in the context of waste management challenges, including waste management practices, social and environmental impacts, regulatory frameworks, and innovative solutions. It serves as a roadmap that guides the researcher to achieve the study's aims by

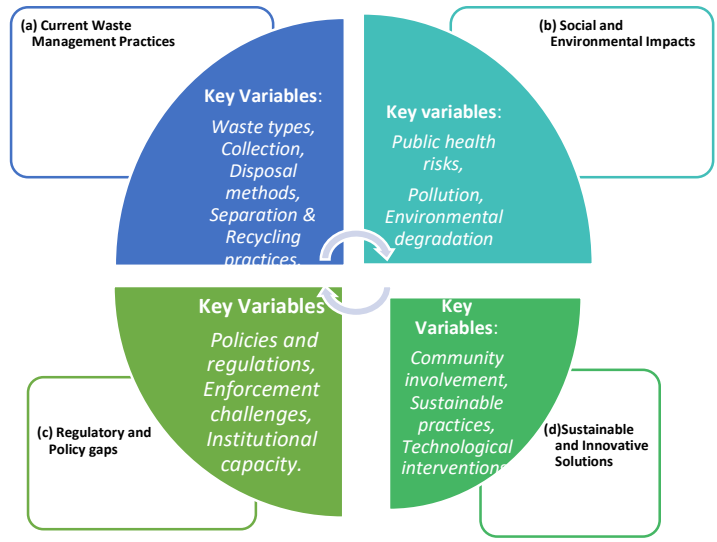


Fig. 1: Breakdown of the study's conceptual framework. Source: Authors (2025).

outlining a comprehensive approach to understanding and improving waste management practices. Moreover, it integrates elements of waste management theory and practice, and it is illustrated in Fig. 1.

This framework centers around the primary issue of SWM practices in Omuthiya town. It shows how key factors interrelate to inform sustainable management solutions. Below are the main components of the study, their sub-elements, and the linkages.

(a) Current Waste Management Practices

This study is grounded in an assessment of existing waste management infrastructure and practices, which form the foundation of an effective and sustainable solid waste management system. These practices include waste collection, transportation, disposal, and potential recycling initiatives. According to UNEP (2015), poor infrastructure and inefficient waste management systems in developing regions contribute significantly to waste mismanagement, environmental degradation, and public health challenges. It is therefore essential to evaluate the current state of these systems in order to identify operational gaps and areas of improvement. The study examines the following components among others:

- **Collection Systems:** The extent of waste collection coverage, frequency of service delivery, and challenges experienced by residents.
- **Disposal Methods:** The conditions, management practices, and environmental safety of waste disposal at the Omuthiya disposal site.
- **Waste Separation and Recycling:** The existence and effectiveness of waste segregation and recycling programs. Although often absent in smaller towns, such systems provide important opportunities to reduce waste volumes and recover valuable resources.

(b) Social and environmental impacts

The study also investigates the social and environmental consequences of waste management. Social impacts can be critical as they can directly affect residents' quality of life (WHO 2018). Environmental impacts such as pollution of soil, air, and water resources, as well as loss of biodiversity, are common outcomes of inadequate waste disposal (World Bank 2019). These dimensions are all interconnected, as poor waste management practices often have negative environmental consequences that exacerbate social vulnerabilities. Investigations of these impacts aid in the provision of evidence-based insights into the consequences of current waste management practices and the need for interventions.

(c) Regulatory and policy gaps

Effective waste management depends on well-formulated policies that address all aspects of waste and enforced policies and regulations. In Namibia, EMA, which is the governing regulatory framework of all environmental-related activities, and other related guidelines, will be identified in the study. Gaps in the regulations will be identified, which will be crucial to align local practices with national policies and improve compliance through monitoring.

(d) Sustainable and innovative solutions

This is the final component of the conceptual framework, which aims to propose solutions that address the identified gaps and impacts. Sustainable development refers to development that satisfies current demands without jeopardising the capacity of future generations to satisfy their own needs. In order to meet the needs of the present as well as the future, Rybaczewska-Błażejowa (2013) argues that sustainable development can be understood as socio-economic development that integrates political, economic, and social elements while preserving environmental balance and the sustainability of natural processes.

Sustainable waste management has numerous benefits, such as natural resources conservation, pollution reduction, and reduced waste disposal in landfills. It can also improve the economy and enhance environmental performance by preventing air, water, and soil pollution (Kadhila et al. 2023). In addition, Namibia is a partner to the global Sustainable Development Goals (SDGs), which reflects its commitment to advancing sustainability.

The unsustainable SWM practices, are mostly worsened by rapid urbanization, and financial and institutional limitations that negatively impact public health and environmental sustainability. Dumping and burning waste in an open space is an unsustainable approach practiced by many developing countries that poses several sustainability problems, including resource depletion, environmental pollution, and public health problems, such as the spread of communicable diseases. In contrast to the prevalent methods of landfilling, open dumps, and open burning, a more sustainable waste management strategy emphasises techniques like reduced production, waste classifications, reuse, recycling, and energy recovery (Abubakar et al 2022). Fig. 2 shows a sustainable waste management hierarchy.

The waste management hierarchy (Fig. 2) is a sustainable framework that prioritises waste prevention and resource efficiency by ranking waste management options from the

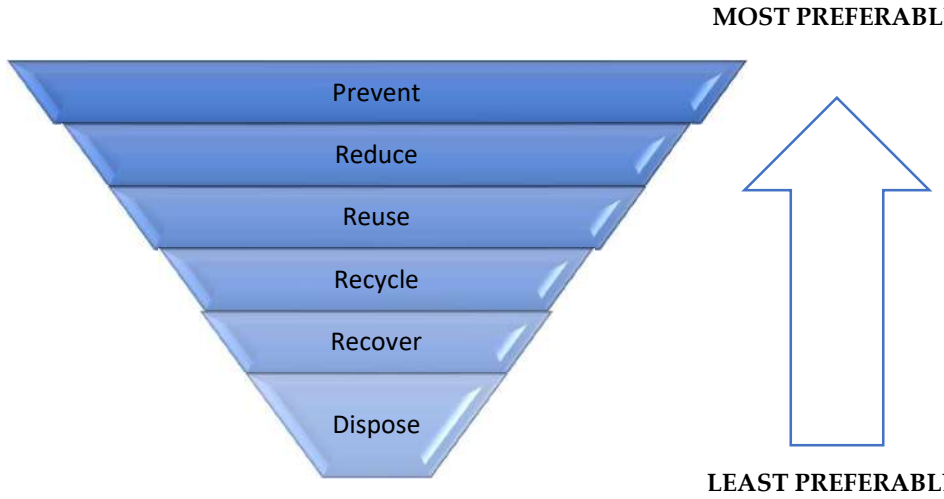


Fig. 2: The waste management hierarchy. Source: Abubakar et al. (2022).

Table 1: Operationalization of the conceptual framework.

Component of the conceptual framework	Variables measured	Data collection method	Section in results
Current waste management practices	Waste collection frequency, waste storage methods, types of waste generated, disposal behaviour	Household questionnaire and field observation	Section 3.1–3.8
Social and environmental impacts	Presence of illegal dumping, health concerns, environmental pollution, community perceptions	Household questionnaire and observation	Section 3.9
Regulatory framework	Awareness of municipal waste policies, satisfaction with municipal services	Questionnaire and key informant interviews	Section 3.6
Innovative solutions/circular economy	Willingness to recycle, willingness to separate waste, suggestions for improving waste management	Questionnaire	Section 3.10

most to the least environmentally preferable (Abubakar et al. 2022, Coenen et al. 2020). At the top of the hierarchy is waste prevention, which focuses on reducing waste generation at the source through responsible consumption, eco-design, and material efficiency (Coenen et al. 2020). This is followed by reuse, where products are used again in their original form, and recycling, which involves processing waste materials into new products. The next level is recovery, including energy recovery from waste that cannot be recycled, while disposal (e.g. landfilling or open dumping) is the least preferred option and should only be used as a last resort. By emphasising reduction, reuse, and recycling before disposal, the waste management hierarchy supports the transition to a circular economy, conserves natural resources, and minimizes environmental and public health risks (European Commission 2017, UNEP 2020).

The conceptual framework presented in Fig. 1 was operationalized by translating each of its key components into measurable variables that guided the data collection and analysis process. The four main components of the framework (current waste management practices, social and environmental impacts, regulatory frameworks, and innovative solutions) were used to design the household questionnaire, observation checklist, and key informant interviews. Table 1 shows how the conceptual framework informed the research instruments and data analysis.

2. MATERIALS AND METHODS

Omuthiya Town is located along the B1 main road in the Oshikoto Region of Namibia (Fig. 3). It was proclaimed a town in 2008 and serves as the regional capital of Oshikoto Region due to its central location. Omuthiya is situated approximately 598 km from Windhoek, the capital city of Namibia. It is home to 7,560 residents (Namibia Statistics Agency 2024). The study focused on the municipal disposal site situated approximately 3 km northwest of Omuthiya Town, in Omuthiya Town itself, and in a village known as Omadiva B. The disposal site is located within a former sand mining pit and is enclosed by a fence (Fig. 4).

The study employed a case study research design and used mixed data collection methods to assess the quantitative impacts of waste generation and disposal, as well as the social



Fig. 3: The Oshikoto Region on the map of Namibia. Source: Authors (2025).



Fig. 4: (a) Omuthiya disposal site. Source: Fieldwork (2025); (b) aerial map of Omuthiya Town. Source: Google Maps (2025).

and environmental factors influencing waste management practices in Omuthiya Town and its disposal site. Primary data were collected through household surveys, key informant interviews, and field observations to evaluate the current state of waste management. The target population included Omuthiya Town Council (OTC) officials, residents of Omuthiya Town, residents of Omadiva B village located near the disposal site, and representatives from the industrial zones. Due to practical constraints, including limited time and resources, the study sample comprised 54 participants.

Eligibility criteria included residents who had lived in the area for more than one year and officials directly involved in waste management activities. This sampling approach ensured the inclusion of participants most affected by and knowledgeable about waste management practices in the study area.

An observation checklist was used to systematically identify and examine waste management practices and their associated impacts in Omuthiya Town and at the disposal site. The checklist included observations of the methods used for collecting and storing waste materials before disposal. Quantitative data were analysed using descriptive statistics to summarise key trends in waste management practices. Qualitative data were analysed using thematic analysis to extract patterns and insights from interviews, surveys, and open-ended responses related to waste management practices and community perceptions. Ethical clearance for this study was obtained from the International University of Management. In addition, formal authorization to conduct the research was secured from the Omuthiya Town Council (OTC). Informed consent was obtained from all participants prior to their involvement in the study, with participants required to sign consent forms to confirm their voluntary participation.

3. RESULTS AND DISCUSSION

The following section presents the key findings and discusses these findings in detail. The results of this study are presented in accordance with the components of the conceptual framework shown in Fig. 1. The findings are organized into four main themes: (a) current waste management practices, (b) social and environmental impacts, (c) regulatory framework challenges, and (d) potential innovative solutions. This structure ensures that the results directly reflect the conceptual framework that guided the study.

3.1. Waste Types

Based on interviews with the residents of Omuthiya Town, Fig. 5 illustrates the different types of waste products generated at the household level.

Based on interviews conducted with residents of Omuthiya Town, Fig. 5 illustrates the different types of waste generated at the household level. The results show that plastic, paper (including boxes and cartons), and cardboard are the most frequently generated waste types, with 48 and 37 respondents, respectively, reporting their production (Fig. 5). This indicates that plastic and paper-based materials constitute the dominant components of household waste in Omuthiya Town. Organic waste was also widely reported, with 34 respondents indicating its generation, followed by glass, which was produced by 18 households. In contrast, metal and sanitary waste were reported less frequently, suggesting that these materials are relatively less common within the local household waste stream.

This result aligns with global waste composition patterns, where plastics, paper-based materials, and organic waste are among the major components of municipal solid waste (Vinti et al. 2021). According to the World Health Organization (WHO 2025b), household waste typically consists of plastics, glass, metals, cardboard, paper, and organic waste such as food remains. Similarly, a systematic review by Vaccari et al. (2021) found that plastic and paper products are among the most common components of household waste in developing countries, largely due to the increasing consumption of packaged goods.

The dominance of plastic waste in Omuthiya Town highlights the urgent need for targeted interventions such as plastic recycling programs, the promotion of reusable shopping bags, and stricter control or gradual bans on single-use plastics. This is particularly important because, despite the introduction of plastic levies in Namibia (implemented by

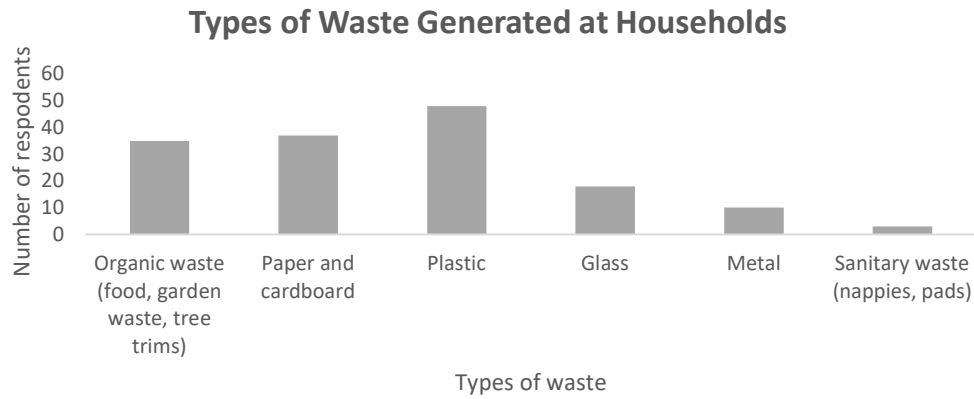


Fig. 5: Types of waste produced at households. Source: Research data (2025).

the Ministry of Environment, Forestry and Tourism (MEFT) to reduce plastic consumption through financial charges on plastic products) plastic waste remains a major environmental challenge in the country. Although the levy represents an important step towards mitigating plastic pollution, its effectiveness largely depends on adequate public awareness, behavioral change, and compliance among consumers and businesses. In addition, there may be gaps in ensuring that the revenue generated through these levies is effectively reinvested into waste management infrastructure, recycling initiatives, and public education programs.

Furthermore, the presence of a significant proportion of organic waste presents an important opportunity to promote composting initiatives in the town. Studies conducted in many developing countries show that organic waste often constitutes a large share of municipal solid waste, making composting a practical and sustainable waste management strategy. Schübeler et al. (1996) identified composting as one of the most promising methods for recovering organic materials, as it reduces the overall volume of waste while simultaneously producing valuable soil conditioners that can be used in agriculture and horticulture. Similarly, Kadhila & de Wit (2022) found that municipal solid waste composition in Namibia contains a high proportion of compostable organic waste as well as recyclable materials such as plastics and paper. These findings suggest that integrated strategies combining recycling and composting could significantly improve the sustainability of solid waste management in towns such as Omuthiya.

3.2. Waste Collection Frequency and Accessibility

Another question focused on waste management practices, specifically the frequency and accessibility of waste collection services. The results, presented in the pie chart below, show that weekly waste collection is the most common practice in Omuthiya Town, with 36 respondents (72%) indicating this frequency (Fig. 6). This suggests that the majority of residents expect waste to be collected on a weekly basis.

The Omuthiya Town Council (OTC) waste collection calendar indicates that waste from both residential and commercial areas is scheduled to be collected three times per week. However, the results of this study reveal some inconsistencies between the official schedule and residents' experiences. While 72% of respondents reported receiving regular weekly waste collection services, 24% indicated that collection was either irregular or that they were unaware of the collection schedule (Fig. 6). This suggests that, although the majority of residents are satisfied with the current system, service delivery may not be consistent across all areas of the town. The relatively high satisfaction rate may be attributed to the fact that Omuthiya is a small town and that the town council has recently made efforts to improve waste management services. Nevertheless, dissatisfaction among a minority of residents indicates that waste collection services may not be uniformly distributed, which could contribute to illegal dumping in areas that are underserved.

Field observations further support these findings, as some skip bins were found to be overflowing at the time of the study, raising concerns about the effectiveness and frequency of waste collection. Ndhlovu (2018) notes that municipal waste collection in developing countries often remains a major challenge due to limited financial resources and inadequate technical capacity. The absence of daily waste collection services may therefore contribute to the accumulation of waste and improper disposal practices, as observed during the field visits. Similar findings have been reported in other studies, which identify irregular waste collection as a key factor contributing to illegal dumping and environmental pollution (Kitole et al. 2024, Kumar et al. 2022, Grobler et al. 2022).

Although 56% (Fig. 7) of residents expressed satisfaction with waste collection services, suggesting that the system

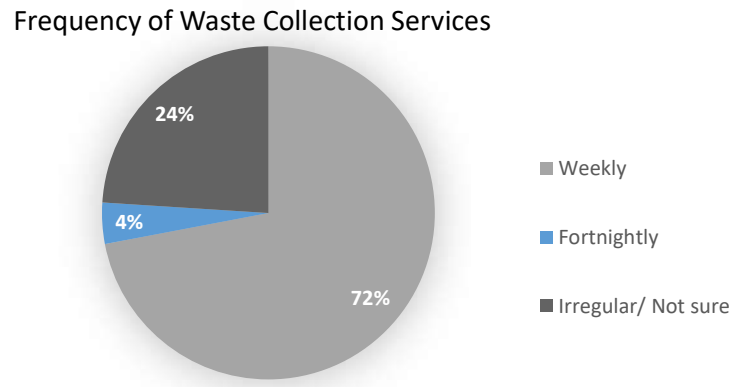


Fig. 6: Frequency of waste collection services. Source: Research data (2025).

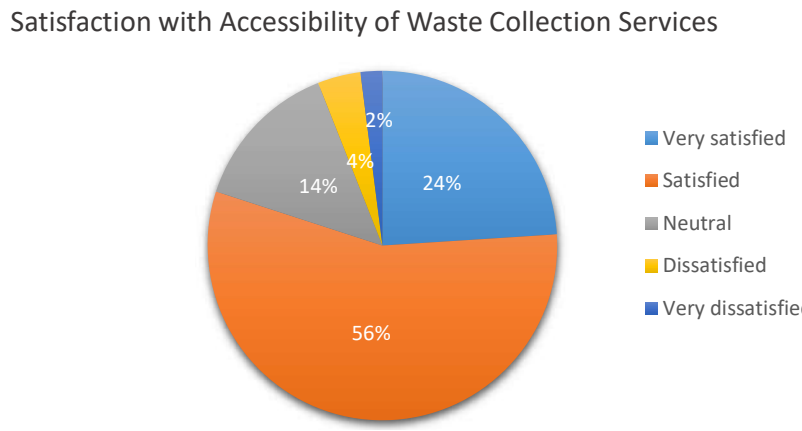


Fig. 7: Satisfaction with accessibility of waste collection services. Source: Research data (2025).

is generally functional, a proportion of respondents still reported dissatisfaction, indicating that the service does not fully meet the expectations of all residents. Despite the variability in waste collection frequency reported in some areas, most residents indicated that waste collection services are accessible. However, the irregularity reported by some respondents may reflect inconsistencies in service delivery or a lack of clear communication regarding collection schedules, which needs to be addressed by the Omuthiya Town Council (OTC). This is particularly important because inconsistent waste collection can undermine public confidence in municipal services and encourage improper waste disposal practices.

These findings are consistent with previous studies conducted in developing countries. Kaza et al. (2018) found that inconsistent waste collection often disproportionately affects lower-income communities and informal settlements, resulting in higher levels of waste mismanagement and environmental pollution. Similarly, the World Bank report What a Waste highlights that irregular collection schedules in many African cities have contributed to increased illegal dumping and public dissatisfaction with waste management services. The delayed waste collection reported by some residents in this study therefore requires attention, as improving collection frequency and expanding waste collection coverage have been identified as effective strategies for reducing waste accumulation and illegal dumping (Kaza et al. 2018).

3.3. Waste Collection Methods

Fig. 8 presents the types of waste containers used by households in Omuthiya Town. The results show that plastic bags are the most commonly used method of waste storage, with 48% of respondents indicating that they rely on plastic bags for waste collection (Fig. 8). This suggests that many households depend on disposable or single-use plastic materials for storing and disposing of waste, which may further contribute to the increasing problem of plastic pollution.

Wheelie bins were identified as the second most commonly used method, reported by 26% of respondents (Fig. 8), indicating that a smaller proportion of households

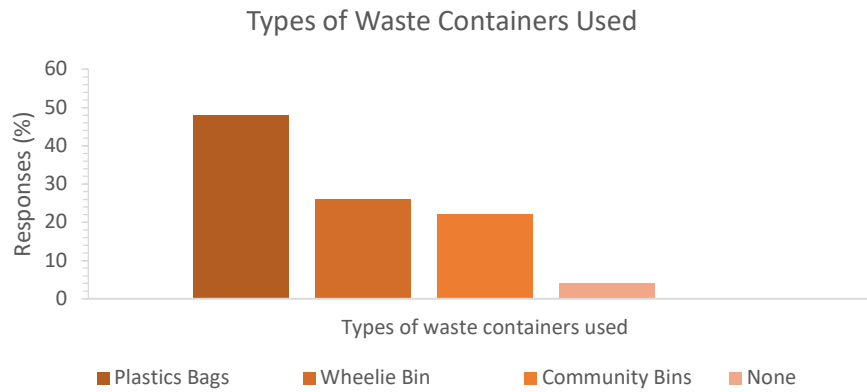


Fig. 8: Types of waste containers used. Source: Research data (2025).

have access to more formal waste containment systems. In addition, 22% of residents reported using community bins, while skip bins were the least utilised method. The relatively low use of communal bins and skip containers may reflect limited availability of shared waste infrastructure, as well as challenges in accessing private waste containers in Omuthiya Town.

This observation is in line with earlier research findings which show that households in developing countries often rely on plastic bags for waste storage due to limited access to proper waste containers such as bins and skip containers (Kadhila & de Wit 2022). The World Health Organization (WHO 2025a) also reports that excessive dependence on plastic packaging and plastic waste contributes significantly to environmental pollution, particularly in areas where waste collection systems are weak.

3.4. Residents' Involvement in Waste Sorting and Recycling

Fig. 9 presents the responses of residents regarding waste sorting and recycling practices in Omuthiya Town. The results indicate that the majority of respondents (86%) do not separate their household waste (Fig. 9). Only a small proportion of respondents (14%) reported that they practice some form of waste sorting, mainly separating cans for sale to scrap yards. Other types of waste, such as plastics, small plastic containers, and organic food waste, are generally disposed of without any form of separation. These findings highlight a significant gap in household-level waste separation and recycling practices in Omuthiya Town. However, they also suggest a strong potential for introducing and expanding waste sorting initiatives at the household level, which could substantially reduce the volume of waste transported to disposal sites and improve the overall sustainability of the waste management system. The findings of this study correspond with those reported in previous studies conducted in developing countries, where waste separation at source remains very low due to limited public awareness, lack of recycling facilities, and weak municipal support systems (Barshe & Agme 2023). In addition, research shows that waste separation in many developing countries is often driven more by economic incentives, such as selling recyclable materials, rather than by environmental awareness (Vinti et al. 2021).

3.5. Challenges of Waste Management in Omuthiya

Based on responses provided by respondents, the following



Fig. 9: Waste sorting or recycling responses. Source: Research data (2025).

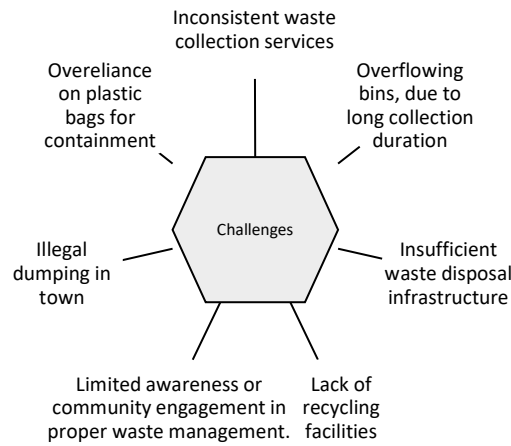


Fig. 10: Challenges hindering sustainable waste management practices. Source: Research data (2025).

are the main challenges that are hindering sustainable waste management practices in Omuthiya Town.

Based on responses provided by participants, several key challenges were identified as major barriers to sustainable waste management practices in Omuthiya Town. Fig. 10 illustrates the main challenges reported by respondents. Waste management infrastructure remains a significant challenge in many developing towns, including Omuthiya. Medina (2010) highlights that cities in developing countries often face infrastructural constraints such as inadequate investment in waste management systems, which leads to increased environmental pollution and reduced efficiency in waste collection services. These findings are consistent with those reported by Omuthiya Town Council (OTC) officials and residents, who identified a range of challenges pointing to systemic weaknesses in both infrastructure and operational practices. Such challenges contribute to persistent issues, including illegal dumping and environmental degradation, as observed in the study area—even in locations where anti-littering signage is present. Addressing these issues requires a multifaceted approach that includes infrastructure development (e.g., provision of adequate skip containers and household bins), strengthened policy enforcement (such as the application of the polluter pays principle), regular clean-up campaigns, and enhanced community engagement to encourage active participation in sustainable waste management practices.

Illegal dumping, as observed during the study, undermines the overall cleanliness and environmental integrity of the town. It reflects not only gaps in infrastructure but also low levels of public compliance with waste management regulations. In addition, improper use of waste collection facilities, such as overfilled skip bins and incorrect disposal practices, contributes to litter accumulation and creates conducive conditions for pests such as flies, thereby posing public health risks. These challenges can be mitigated through more frequent waste collection, improved monitoring, and public education on proper waste disposal practices. Furthermore, OTC identified financial constraints and limited human resources as major barriers to effective waste management, as these factors hinder the implementation of advanced waste management strategies and limit the council's capacity to enforce regulations. The lack of community incentives also points to the need for more inclusive and participatory approaches that consider residents' socio-economic conditions. These challenges align with national-level observations. The Namibian Minister of Environment, Forestry and Tourism noted that many local authorities lack properly engineered landfills and still rely on dumpsites for waste disposal (Namibia Daily News 2023). These results also support earlier research which found that irregular waste collection, insufficient infrastructure, illegal dumping, and lack of recycling facilities as major barriers to sustainable waste management in developing countries (Kadhila & de Wit 2022). Furthermore, the World Health Organization (WHO 2025b) emphasizes that poor waste management systems in small towns are often linked to limited funding, weak institutional capacity, and low levels of public awareness.

3.6. Awareness and Effectiveness of Current Waste Management Regulations

Questions were included in the survey to assess residents' awareness of existing waste management regulations in Omuthiya Town and their perceptions of how effectively these regulations are enforced. The results, illustrated in Fig. 11(a and b), show that only 34% of respondents are aware of the regulations governing waste management in the town. This indicates a significant gap in communication and public education regarding existing waste management policies.

A large proportion of respondents (44%) reported that they are not aware of any such regulations, while a further 22% indicated that they are unsure (Fig. 11 a). These findings suggest that waste management policies are not sufficiently visible or accessible to the general public. Limited awareness of regulations may reduce community participation in

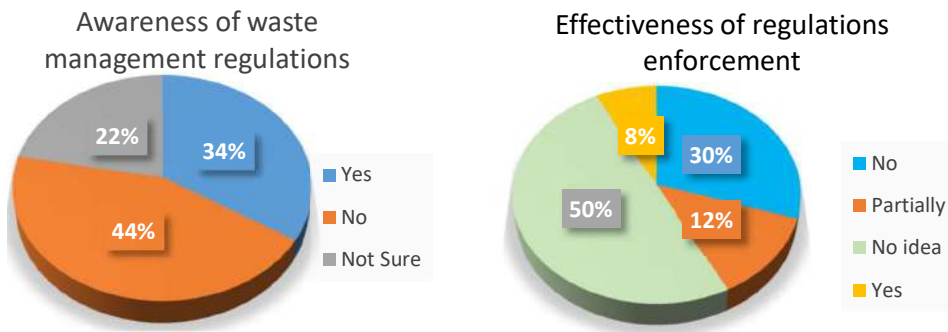


Fig. 11(a and b): Awareness and effectiveness of waste regulations. Source: Research data (2025).

proper waste management practices and weaken compliance with existing policies. With regard to enforcement, only a small proportion of respondents (8%) believe that waste management regulations are effectively enforced (Fig. 11 b). In contrast, 30% of respondents indicated that the regulations are not enforced at all, while 50% reported that they have no knowledge of the level of enforcement. The remaining 12% indicated that enforcement is only partially effective. These results highlight weak public confidence in the enforcement of waste management regulations in Omuthiya Town.

Overall, the findings point to low levels of regulatory awareness and perceived weak enforcement, which underscores the need for stronger public communication strategies, improved community engagement, and more transparent enforcement mechanisms. Similar findings have been reported in earlier studies which show that lack of public awareness of waste management policies is a major challenge in many developing countries (Vinti et al. 2021, WHO 2022). In addition, weak enforcement of waste management regulations has been identified as one of the key factors contributing to poor waste management performance in developing countries (Vinti et al. 2021).

3.7. Findings from Omuthiya Town Council (OTC) Officials

Solid Waste Management (SWM) in Omuthiya Town is administered by the Health Section under the Department of Technical Services. The service is overseen by an Environmental Health Practitioner supported by a team of five municipal employees, and two contracted service providers. The municipality also allocates financial resources specifically for SWM-related activities. Table 2 highlights the key waste collection stakeholders in Omuthiya Town.

Findings from Omuthiya Town Council (OTC) officials indicate that waste collection is carried out through a combination of contractors, council employees, and temporary workers. Two contractors are responsible for collecting and transporting waste from residential areas, businesses, and public institutions, while the council handles the transportation of waste from skip containers to the disposal site and supports general cleaning activities within the town. OTC also applies multiple waste management practices such as litter picking, skip containers, waste caging, and trucking. However, officials identified several major challenges, including illegal dumping, limited public awareness about proper waste disposal, financial constraints, and damage to recyclable materials by waste reclaimers. Although the council reported having a Solid Waste Management Plan and complying with environmental regulations, implementation is constrained mainly by insufficient funding, limited technical expertise, and inadequate human resources. To improve sustainability, officials proposed solutions such as establishing buy-back centres, introducing waste-sorting cages, and strengthening community engagement and stakeholder participation.

Field observations and interviews conducted in Omuthiya Town and at the disposal site confirmed many of the issues raised by OTC officials. Various waste collection methods are used in the town; however, plastic bottles were the most common type of waste observed in public spaces, indicating weak recycling and waste separation practices. Illegal dumping and littering were frequently observed, even in areas with warning signs, while community participation in waste sorting and recycling was generally low. Although some businesses contribute to town cleanliness by cleaning their premises daily, most residents do not actively participate in sustainable waste management practices. At the disposal site, which is located approximately 3 km from the town, waste mainly consists of plastics, paper, glass, tins, construction materials, and agricultural waste. The site is fenced and managed according to environmental requirements, but challenges such as lack of waste audits, financial limitations, and insufficient human capacity continue to affect effective waste management.

Table 2: Summary of OTC key waste collectors and their roles.

Entity	Mode of collection	Frequency of collection	Responsibilities
Contractors 1. Nakathigona Trading CC 2. ST. Events & Cleaning Services	Collect and transport waste from wheelie bins and plastics to the disposal site. Clean up illegally dumped waste	Monday, Wednesday, and Friday Thursday and Friday	Collect waste from designated areas within the town including residential, businesses, hospitals, offices, schools etc.
OTC	Waste collection from skip containers to the disposal site.	Monday and Friday	Collect waste from designated areas within the town including residential, businesses, hospitals, offices, schools etc.
Temporary Workers	Collect and transport waste from wheelie bins and plastics to the disposal site.	Tuesday and Thursday	Hired on temporary contracts to assist with town cleaning and bush cutting

Source: Research data (2025)

3.8. Field Observations

Waste storage and collection methods used by OTC are illustrated in Fig. 12 a, b, c & d below. These methods reflect the council's efforts to maintain cleanliness and manage waste effectively within existing resource constraints.

Field observations conducted in Omuthiya Town revealed that residents generally do not actively engage in waste management practices such as waste sorting or recycling. Illegal dumping of waste materials was also observed (Fig. 13b). This indicates limited awareness and motivation to adopt sustainable waste management practices. Similar findings have been reported in developing countries, where low public participation in waste segregation is often linked to inadequate awareness, lack of incentives, and insufficient infrastructure (Kaza et al. 2018, Guerrero et al. 2013). However, it was observed that business owners regularly clean their premises before opening, which contributes positively to the overall cleanliness of the town. In addition, the community utilizes a WhatsApp group to communicate hygiene-related issues, serving as an informal platform for information sharing and coordination. The use of such digital communication tools has been recognized as an effective mechanism for enhancing community engagement and environmental awareness in local governance contexts (United Nations 2020).

Observations at the Omuthiya disposal site further revealed that waste is not compacted but is instead openly



Fig. 12(a–d): Methods of waste collection. Source: Fieldwork (2025).



Fig. 13(a and b): Illegal dumping. Source: Fieldwork (2025).

burned to reduce its volume (Fig. 14 a & b). After burning, the remaining ash and non-combustible materials, such as glass, construction debris, and metal tins, are pushed into heaps using a front loader. Although this method helps reduce the volume of waste, it poses serious environmental and health risks due to air pollution and unsafe waste handling practices. These findings are consistent with recent scientific and policy reports which show that open burning of household waste is still widely practiced in many developing countries due to limited waste disposal infrastructure (WHO 2022, WHO 2025a). Open waste burning has also been identified as a major source of air pollution and a significant threat to public health, particularly for communities living close to disposal sites (WHO 2025a).

Further observations showed that the disposal site is fenced and has a lockable gate; however, the fence has been vandalized, allowing unauthorized access (Fig. 15). A security guard is present only during daytime hours (08:00–17:00), leaving the site unprotected after hours. This limited security increases the risk of illegal dumping and unsafe disposal practices.

Vulnerable groups, including children, were observed scavenging at the disposal site without protective clothing, exposing them to hazardous materials (Fig. 16). There was no evidence of waste separation, particularly for hazardous and medical waste, which was found mixed with general waste (Fig. 17 a & b). This lack of segregation increases the risk of exposure to dangerous substances for both humans and the environment.

In addition, no evidence of waste separation was observed at the disposal site. Hazardous and medical waste was found mixed with general waste (Fig. 17 a & b), which increases the risk of exposure to dangerous substances for both humans and the environment. Expired food waste was also



Fig. 14(a and b): Waste before and after burning. Source: Fieldwork (2025).



Fig. 15: Fence of the disposal site. Source: Fieldwork (2025).



Fig. 16: People scavenging at Omuthiya disposal site. Source: Fieldwork (2025).



Fig. 17: (a) Medical disposable waste at the Omuthiya disposal site; (b) expired food. Source: Fieldwork (2025).

observed being dumped without burial and left accessible to scavengers and pests. Overall, these observations indicate serious shortcomings in waste handling, site security, and environmental protection at the Omuthiya disposal site.

Expired food waste (Fig. 17 b) was also observed being dumped without burial and left accessible to scavengers and pests. Overall, these observations indicate serious shortcomings in waste handling, security, and environmental protection at the Omuthiya disposal site.

3.9. Environmental and Social Impacts

The environmental and social impacts reported in this study are largely based on residents' perceptions and field observations rather than quantitative environmental measurements. Residents living near the disposal site indicated concerns about reduced crop productivity, presence of pests such as snakes, and occasional livestock deaths. While these observations provide valuable insights into community experiences, they were not supported by empirical data such as soil quality analysis, crop yield assessments, or veterinary records. Similarly, concerns regarding air pollution were based on visual observations and reported experiences of odours and smoke, without supporting measurements such as air quality monitoring or wind direction analysis. Therefore, these findings should be interpreted as perception-based rather than scientifically verified environmental impacts.

The results further revealed several environmental and social impacts associated with the disposal site in Omuthiya Town. Residents reported that the disposal site contributes to soil degradation, which is reflected in reduced crop productivity in fields located near the site. The presence of the disposal site has also attracted stray animals and predators, including birds, snakes, insects, and other pests. These animals reportedly migrate into nearby agricultural fields, damaging crops, posing safety risks to the community, and disrupting the local ecosystem. In addition, residents indicated that livestock, particularly cattle, have died after ingesting plastic waste from the disposal site.

Air pollution was identified as one of the most serious environmental impacts associated with the disposal site. The practice of open waste burning releases large amounts of smoke



Fig. 18: Smoke from burning waste at Omuthiya disposal site. Source: Fieldwork (2025).

and harmful emissions, which may spread into surrounding residential areas (Fig. 18). Community members, especially those living within approximately 500 m of the disposal site, reported breathing difficulties and sleep disturbances caused by persistent smoke. Furthermore, the disposal site is located about 300 m from the B1 main road, and smoke from burning waste was reported to reduce visibility for road users, creating traffic hazards. This could highlight poor planning and inappropriate siting of the disposal facility in close proximity to both residential areas and a major transport route.

In addition, the disposal site emits unpleasant odours and is heavily infested with flies (Fig. 19 a & b). These conditions reflect poor waste management practices and may contribute to deteriorating air quality and increased health risks for nearby residents. It was also observed that vegetation in close proximity to the site is sparse, with more vigorous plant growth occurring further away from the disposal area. This pattern suggests that the disposal activities may be negatively affecting soil quality and local vegetation health. Moreover, residents reported experiencing unpleasant odours resulting from waste accumulation in various parts of Omuthiya town. These findings are consistent with existing research, which indicates that decomposing waste emits gases such as ammonia, sulphides, methane, and carbon dioxide. Some of these gases contribute to climate change, while others are primarily responsible for foul odours and the deterioration of air quality (Elago 2019). The presence of such emissions not only affects environmental quality but also reduces the overall liveability of affected areas.

In addition, the accumulation of waste creates an unsanitary and aesthetically undesirable environment, which can attract pests and disease-carrying vectors such as flies and rodents. This further increases the risk of disease transmission and poses a threat to public health. Therefore, ineffective waste management practices not only degrade environmental conditions but also have indirect implications for human health and well-being, highlighting the need for improved waste handling and disposal systems.

Interestingly, the majority of residents reported that they had not observed any direct health impacts associated with



Fig. 19(a and b): Flies in the cooking pot and a plate of food. Source: Fieldwork (2025).

current waste management practices in Omuthiya town. This perception may suggest that the immediate effects of improper waste handling are not readily visible or are underestimated by the community. However, the absence of reported health problems does not necessarily imply the absence of risk. Poor waste management practices can have significant long-term health implications that may not be immediately recognized by residents.

Existing literature indicates that prolonged exposure to inadequately managed waste is associated with increased health risks (Elago 2019). Such risks include the spread of infectious diseases and the occurrence of skin, respiratory, and gastrointestinal conditions, often resulting from exposure to contaminated environments, pests, and pollutants. Therefore, even though residents may not currently perceive waste management as a direct health threat, there remains a critical need for increased awareness and preventive measures to mitigate potential long-term social and public health impacts.

It was observed that various waste types, particularly plastic materials, are blown from the disposal site and become trapped in nearby fences (Fig. 20). This results in environmental pollution and poses serious risks to both wildlife and domestic animals in the surrounding area. The results showed that the disposal site contributes to air pollution, soil degradation, livestock deaths, and health problems among nearby residents. These findings are strongly supported by previous research. These findings are consistent with previous research which shows that communities living near waste disposal sites face increased risks of air pollution, soil degradation, livestock deaths, and public health problems (Vinti et al. 2021). The World Health Organization (WHO 2025a) also reports that open waste burning releases harmful pollutants that can cause breathing problems, poor air quality, and environmental degradation, particularly in communities located close to disposal sites.

A key limitation of this study is that environmental impacts were not assessed using quantitative scientific measurements. Data on issues such as air quality, soil contamination, crop productivity, and ecological effects were based primarily on field observations and community perceptions. While such qualitative data provide important contextual insights, they do not allow for definitive conclusions regarding causality or magnitude of environmental impacts. Future studies should incorporate empirical methods such as soil testing, air quality monitoring, and spatial analysis to validate and quantify these impacts.

3.10. Innovative Solutions and Circular Economy Concept

According to Upadhyay and Alqassimi (2019), as cited in Nambahu (2023), the circular economy (CE) is a business model that promotes a transition from the traditional linear economy to a restorative and regenerative system. This approach emphasizes extending the life cycle of products in order to maximize resource efficiency and extract maximum value from materials throughout their use. Furthermore, the circular economy is designed to minimize environmental harm by addressing the negative impacts associated with resource extraction and ensuring that waste generation is reduced across all stages of the product life cycle (Upadhyay & Alqassimi 2019).

Within this framework, waste is reconceptualized as a valuable resource rather than a by-product, and product life



Fig. 20: Waste trapped on a nearby fence. Source: Fieldwork (2025).

is extended through strategies such as recycling, reuse, and remanufacturing. The European Union's Circular Economy Action Plan supports this approach by promoting closed-loop systems, where discarded materials are reintroduced into production cycles, thereby maintaining resource circulation and enhancing environmental sustainability (Ellen MacArthur Foundation 2017). For instance, in the Netherlands, companies such as Philips have adopted product-as-a-service models, whereby used electronic products are returned, refurbished, and resold, reducing waste and extending product lifespan (Ellen MacArthur Foundation 2017).

Similarly, in China, circular economy principles have been incorporated into national development strategies. The "Zero Waste Cities" initiative aims to reduce landfill dependency by promoting recycling and resource recovery programs in urban areas (Kawai & Tasaki 2016). These global examples demonstrate the relevance of the circular economy in addressing challenges related to resource depletion and waste pollution. Therefore, transitioning towards a circular economy model (Fig. 21) offers a viable and sustainable solution to contemporary waste management challenges.

A study by Kadhila and de Wit (2022) reports that CE has economic, environmental, and social benefits. The economic benefits include reducing the use of primary resources, job creation, reduced environmental pollution, and livelihood improvement. They recommend that policy has a significant impact on whether the transition to a CE is possible. They further recommend that policymakers in small municipalities should revise the existing regulatory instruments to promote transitioning to circular waste management, in line with the proposed waste management framework to promote the CE model.

The transition to a circular economy (CE) presents a practical and innovative pathway for improving solid waste management in Omuthiya Town Council (OTC). To achieve this, OTC can begin by promoting waste segregation at source through the provision of labeled bins and public awareness campaigns, enabling the separation of recyclables such as plastics, paper, and glass from organic waste. This would support the establishment of local recycling systems and reduce the volume of waste disposed of at the dumpsite. In addition, OTC can operationalize proposed buy-back centers, where residents are incentivized to return recyclable materials in exchange for financial rewards. Such initiatives not only encourage community participation but also create local economic opportunities, particularly for informal waste collectors. Furthermore, organic waste (which constitutes a significant portion of municipal waste) can be diverted to composting programs, producing organic fertilizer for agricultural use and contributing to both waste reduction and local food systems.

To strengthen the transition, OTC should integrate CE principles into its policy and planning frameworks by aligning its Solid Waste Management Plan with circular economy objectives. This includes fostering partnerships with private sector actors and small enterprises to support recycling, reuse, and remanufacturing activities within the town. Capacity building, technical support, and investment in infrastructure such as material recovery facilities and waste sorting cages will be essential to operationalize these initiatives. Moreover, the council can adopt regulatory instruments such as the polluter pays principle and incentives

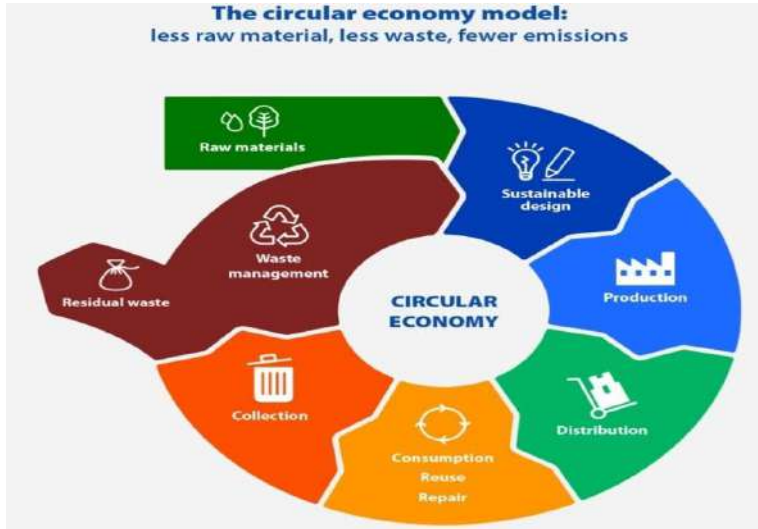


Fig. 21: Circular economy model. Source: Ellen MacArthur Foundation (2017).

for businesses that implement sustainable waste practices. As highlighted by Kadhila and de Wit (2022), policy support is critical in enabling the shift towards a circular economy, particularly in small municipalities. By adopting a comprehensive approach that combines infrastructure development, community engagement, and policy reform, OTC can transition from a linear waste management system to a more sustainable, resource-efficient circular model.

4. CONCLUSIONS

This study demonstrates that while Omuthiya Town has made measurable efforts to provide waste collection services and maintain public cleanliness, its solid waste management system remains largely inadequate and unsustainable. Significant gaps were identified, including lack of waste management infrastructure such as recycling canters, waste-to-energy (WTE) plants, buy-back centres, lack of waste segregation at source, inconsistent service delivery, lack of community participation programs related to waste management, and weak enforcement of existing waste management regulations. These shortcomings collectively undermine the effectiveness of the town's waste management system.

Although most residents within the town reported general satisfaction with waste collection accessibility, serious environmental and health impacts were observed and reported in communities located near the disposal site. These include air pollution from open waste burning, pest infestation, unpleasant odours, soil degradation, reduced crop productivity, and risks to both humans and animals. The contrast between conditions within the town and those near the disposal site highlights an environmental justice concern, where vulnerable communities bear a disproportionate burden of pollution and health risks.

The findings further reveal critically low public awareness of waste management regulations, coupled with weak and inconsistent enforcement. This regulatory gap, together with financial constraints and limited human resources, has hindered effective policy implementation. The continued practice of open burning, illegal dumping, lack of medical and hazardous waste separation, and unsecured access to the disposal site reflect systemic governance and operational failures that require urgent intervention.

To address the challenges identified in this study, it is essential to implement a comprehensive and well-coordinated waste management strategy in Omuthiya Town. The study therefore recommends the mobilization of financial and technical resources through mechanisms such as public–private partnerships (PPPs), international funding opportunities, and innovative initiatives such as waste banks. In addition, there is a need to improve waste management infrastructure through the establishment of modern recycling canters, waste-to-energy (WTE) facilities, and automated waste-sorting systems.

Furthermore, stricter enforcement mechanisms, including the introduction of a Pay-As-You-Throw (PAYT) system, should be considered to encourage responsible waste disposal practices. The study also highlights the importance of strengthening community participation through innovative engagement strategies, such as community-based source-separated organic composting programs.

These recommendations should be facilitated and coordinated by the OTC, which serves as the primary authority responsible for waste management within the town. The Council is therefore expected to play a leading role in mobilising resources, improving infrastructure, strengthening regulatory enforcement, and promoting community participation in sustainable waste management practices. Regular public education and awareness programs, facilitated by Omuthiya Town Council (OTC) waste management officials, are essential for promoting responsible waste management practices, including waste separation, recycling, and proper disposal. In instances where household-level waste separation and recycling cannot be fully implemented, the establishment of a Waste-to-Energy (WTE) facility could provide an alternative solution by converting waste materials into electricity. Such a facility has the potential to reduce the volume of waste sent to disposal sites by up to 90%, thereby alleviating pressure on existing disposal infrastructure and mitigating environmental pollution.

Ultimately, strengthening institutional capacity, empowering communities (i.e., through community-based source-separated organic composting programs) and enforcing environmental regulations are critical steps toward building a sustainable and inclusive waste management system in Omuthiya Town. If these recommendations are implemented, Omuthiya has the potential to transform its waste management practices and serve as a model for other towns facing similar environmental and public health challenges.

5. ACKNOWLEDGMENTS

We are grateful to the residents and the OTC officials who provided us with relevant data.

6. REFERENCES

Abubakar, I.R., Maniruzzaman, K.M., Dano, U.L., AlShihri, F.S., AlShammari, M.S., Ahmed, S.M.S., Al-Gehlani, W.A.G. and Alrawaf, T.I., 2022. Environmental sustainability impacts of solid waste management practices in the Global South. *International Journal of Environmental Research and Public Health*, 19(19), p.12717. [DOI]

Abul, S., 2010. Environmental and health impact of solid waste disposal at Mangwaneni dumpsite in Manzini: Swaziland. *Journal of Sustainable Development in Africa*, 12(7), pp.64-78. Retrieved from: https://www.scirp.org/reference/referencespapers?referenceid=3811352

Amasuomo, E. and Baird, J., 2016. The concept of waste and waste management. *Journal of Management and Sustainability*, 6(4), pp.88-96. [DOI]

Barshe, S.B. and Agme, V.N., 2023. A comprehensive review on municipal solid waste management. *Shodha Prabha Journal*, 48(2), pp.147-160.

Bennett, W., 2017. A Proposed Recycling Facility for the Informal Waste Collectors of Oshakati. Unpublished report. Retrieved from: 28 August 2025 https://web.cs.wpi.edu/~rek/Projects/Oshakati_Proposal.pdf

Coenen, T.B.J., Haanstra, W., Braaksma, A.J.J. and Santos, J., 2020. CEIMA: A framework for identifying critical interfaces between the circular economy and stakeholders in the lifecycle of infrastructure assets. *Resources, Conservation and Recycling*, 155, p.104552. [DOI]

Elago, M. M., 2019. Factors associated with self-reported health outcomes by residents residing near Oshakati municipal disposal site in Oshana region, Namibia (Doctoral dissertation, The University of Zambia).

Ellen MacArthur Foundation., 2017. What is a circular economy? Ellen MacArthur Foundation, Cowes, UK. Retrieved from: 11 April 2025 www.ellenmacarthurfoundation.org

European Commission., 2017. The role of waste-to-energy in the circular economy. Brussels: European Union. Retrieved from: 12 August 2025 https://eur-lex.europa.eu/legal-content/en/TXT/?uri=CELEX:52017DC0034

Global Waste Management Outlook., 2024. UNEP-UN Environment Programme. Retrieved from: 14 May 2025 https://www.unep.org/resources/globalwastemanagementoutlook2024#:~:text=Municipal%20solid%20waste%20generation%20is,sector%20as%20well%20as%20citizens

Grobler, L., Schenck, R. and Chitaka, T., 2022. Clean cities and towns: Understanding societal behaviour in order to reduce and divert waste going to landfills. Retrieved from: 18 May 2025 https://www.handycandumpsters.com/how-community-engagement-leads-to-better-waste-solutions

Guerrero, L.A., Maas, G. and Hogland, W., 2013. Solid waste management challenges for cities in developing countries. *Waste Management*, 33(1), pp.220-232. [DOI]

Kaapanda, V., 2023. Waste management not satisfactory: MET. New Era. Retrieved from: 12 May 2025 https://neweralive.na/waste-management-not-satisfactory-met/

Kadhila, T., de Wit, M.P. and Schenck, R., 2023. A conceptual framework for sustainable waste management in small municipalities: The cases of Langebaan, South Africa and Swakopmund, Namibia. *Environmental Science and Pollution Research*, 30(60), pp.125088-125103. [DOI]

Kadhila, T. and de Wit, M.P., 2022. Towards a framework for sustainable municipal solid waste management: The case study of Swakopmund Municipality, Namibia. *Nature Environment and Pollution Technology*, 21(2), pp.779-785. [DOI]

Kawai, K. and Tasaki, T., 2016. Revisiting estimates of municipal solid waste generation per capita and their reliability. *Journal of Material Cycles and Waste Management*, 18(1), pp.1-13. [DOI]

Kaza, S., Yao, L., Bhada-Tata, P., and Van Woerden, F., 2018. What a Waste, a Global Snapshot of Solid Waste Management to 2050. World Bank Publications. Retrieved from: Retrieved from: 04 June 2025 https://books.google.de/books?id=bnN_DwAAQBAJ

Kitole, F.A., Ojo, T.O., Emenike, C.U., Khumalo, N.Z., Elhindi, K.M. and Kassem, H.S., 2024. The impact of poor waste management on public health initiatives in shanty towns in Tanzania. *Sustainability*, 16(24), p.10873. [DOI]

Kumar, C., Bailey-Morley, A., Eugenia Kargbo and Lamin Sanyang 2022. Waste management in Africa: a review of cities' experiences [Working paper]. ODI. Retrieved from: 04 June 2025 https://media.odi.org/documents/Waste_management_in_African_cities_FINAL_VERSION.pdf

Medina, M. 2010. *Solid wastes, poverty and the environment in developing country cities: Challenges and opportunities*. WIDER Working Paper 2010/23. Helsinki: United Nations University World Institute for Development Economics Research (UNU-WIDER).

Nambahu, T.M.N., 2023. Evaluation of municipal solid waste management practices in Karibib, Namibia. MPhil Thesis. Stellenbosch University, Stellenbosch, South Africa. Date of Completion: 2023-12 Retrieved from: https://scholar.sun.ac.za/handle/10019.1/128868

Namibia Daily News. (2023, September 18). Namibia takes action to improve waste management. Namibia Daily News. Retrieved from: 11 April 2025 https://namibiadailynews.info/namibia-takes-action-to-improve-waste-management/

Namibia Statistics Agency. (2024). 2023 Population and Housing Census Main Report Retrieved from: https://nsa.org.na/wp-content/uploads/2024/10/2023-Population-and-Housing-Census-Main-Report-28-Oct-2024.pdf

National Solid Waste Management Strategy., 2017. In National Solid Waste Management Strategy]. Retrieved from: 04 June 2025 https://faolex.fao.org/docs/pdf/nam193634.pdf

Ndhlovu, L.N., 2018. *Investigating the Effectiveness of a Community-Based Approach Towards Solid Waste Management in Windhoek's Okahandja Park*. Doctoral dissertation, University of Namibia, Windhoek, Namibia.

Omang, D.I., John, G.E., Inah, S.A. and Bisong, J.O., 2021. Public health implication of solid waste generated by households in Bekwarra Local Government Area. *African Health Sciences*, 21(3), pp.1467-1473. [DOI]

Ruppel-Schlichting, K., 2022. Pollution control and waste management. In: Environmental Law and Policy in Namibia, pp.209-228. [DOI]

Rybaczewska-Błażejowska, M., 2013. Economic, environmental and social aspects of waste management–the LCA analysis. *Pragmatates Oikonomias*, 7, 239-250 Retrieved from: https://api.semanticscholar.org/CorpusID:127145143

Schioldborg, A.A. and Bjørke, S.Å., 2014. Livelihood impacts of solid waste management in informal settlements of Windhoek, Namibia. Retrieved from: 11 July 2025 https://core.ac.uk/download/pdf/225892079.pdf

Schübeler, P., Christen, J., and Wehrle, K., 1996. Conceptual framework for municipal solid waste management in low-income countries (Vol. 9). St. Gallen: SKAT (Swiss Center for Development Cooperation).

UNEP (United Nations Environment Program), 2020. Global Waste Management Outlook 2020. Nairobi: UNEP. Retrieved from: 13 May 2025 https://www.unep.org/resources/report/global-waste-management-outlook

UNEP (United Nations Environment Program), 2024. *Global Waste Management Outlook 2024: Beyond an age of waste – Turning rubbish into a resource*. Nairobi, Kenya: United Nations Environment Programme. [DOI]

UNEP (United Nations Environment Program), 2015. Beyond an Age of Waste. United Nations Environment Programme. Retrieved from: 10 June 2025 https://wedocs.unep.org/20.500.11822/44939

United Nations Human Settlements Program (UN-Habitat), and Ki-moon, B., 2016. WORLD CITIES REPORT 2016. United Nations Human Settlements Programme (UN-Habitat). Retrieved from: 6 September 2025 https://unhabitat.org/sites/default/files/download-manager-files/WCR-2016-WEB.pdf

United Nations. 2020. *E-Government Survey 2020: Digital Government in the Decade of Action for Sustainable Development*. United Nations, New York.

Vinti, G., Bauza, V., Clasen, T., Medlicott, K., Tudor, T., Zurbrügg, C. and Vaccari, M., 2021. Municipal solid waste management and adverse health outcomes: A systematic review. *International Journal of Environmental Research and Public Health*, 18(8), p.4331. [DOI]

World Bank, 2019. What a Waste 2.0: A Global Snapshot of Solid Waste Management to 2050 Retrieved from: 17 June 2025 https://openknowledgeg.worldbank.org/entities/publication/d3f9d45e-115f-559b-b14f-28552410e90a

World Health Organization (WHO), 2018. *Health, Environment and Climate Change*. World Health Organization, Geneva. Retrieved from: https://www.who.int/publications/i/item/WHO-CED-PHE-EPE-19.11

World Health Organization (WHO), 2022. *Guidance on Solid Waste and Health*. World Health Organization, Geneva. Retrieved from: https://www.who.int/tools/compendium-on-health-and-environment/solid-waste

World Health Organization (WHO), 2024. *Water, Sanitation, Hygiene, Environmental Cleaning and Waste Management in Health Care Facilities: 2023 Data Update*. World Health Organization, Geneva. Retrieved from: https://www.who.int/publications/i/item/9789240103924

World Health Organization (WHO), 2025a. *Open Waste Burning: Sectoral Solutions for Air Pollution and Health*. World Health Organization, Geneva. [DOI]

World Health Organization (WHO), 2025b. WHO highlights health risks and opportunities in the global waste crisis. World Health Organization. Retrieved from: https://www.who.int/philippines/news/detail-global/16-12-2025-who-highlights-health-risks-and-opportunities-in-the-global-waste-crisis

Nature Environment and Pollution Technology
An International Quarterly Peer-Reviewed Open Access Journal

p-ISSN: 0972-6268 | e-ISSN: 2395-3454 Vol. 25 | No. 4 | Article ID B4434 | 2026

RESEARCH ARTICLE https://doi.org/10.46488/NEPT.2026.v25i04.B4434 OPEN ACCESS

Heavy Metal Dynamics in Crops Grown on Municipal Solid Waste Compost-Amended Soils

B. S. Kavitha and R. K. Somashekar†
Department of Environmental Science, Bangalore University, Bengaluru-560056, Karnataka, India
†Corresponding author: R.K. Somashekar; rksmadhu@gmail.com

ARTICLE HISTORY

Received: 25-02-2026
Revised: 05-04-2026
Accepted: 10-04-2026

KEYWORDS

Bioconcentration factor
MSW compost
Heavy metals
Soil amendment
Translocation factor

CITE THIS ARTICLE

Kavitha, B.S. and Somashekar, R.K., 2026. Heavy metal dynamics in crops grown on municipal solid waste compost-amended soils. *Nature Environment and Pollution Technology*, 25(4), B4434. https://doi.org/10.46488/NEPT.2026.v25i04.B4434

COPYRIGHT & LICENCE

© 2026 The Authors
Open Access under CC BY 4.0.

PUBLISHED BY

TECHNOSCIENCE PUBLICATIONS

ABSTRACT

Growing interest in using compost derived from municipal solid waste (MSW) in agriculture raises critical questions about its ecological safety, particularly the accumulation pattern of potentially toxic heavy metals in food and fodder crops. This study assessed the effects of a single application of MSW compost on soil heavy-metal dynamics and plant uptake in Napier grass *(Pennisetum purpureum),* ragi *(Eleusine coracana),* maize *(Zea mays),* and hyacinth bean *(Lablab purpureus).* The compost complied with the maximum permissible heavy-metal limits prescribed under the Fertilizer (Control) Order (FCO), 1985. Statistical analysis (Welch's t-test with multiple-comparison correction) revealed significant crop-specific changes in soil metal concentrations following compost amendment, with reductions observed for certain metals such as Zn, Cu, Pb, and Cr. Bioconcentration and translocation factor results indicated elevated translocation (TF > 1) and accumulation in edible parts, particularly for Pb in maize and for Zn, Cu, Ni, and Cd in hyacinth bean. Essential metals (Zn and Cu) showed regulated uptake, while potentially toxic metals (Pb, Cd, and Cr) were variably immobilized or translocated depending on crop type. Overall, the findings demonstrate that the impact of MSW compost on heavy-metal mobility and plant uptake is crop-dependent. Although compost application may reduce the bioavailability of certain metals, it does not universally prevent their transfer to edible plant parts. These results highlight the need for crop-specific risk assessment and monitoring to ensure the safe and sustainable use of MSW compost in agricultural systems.

1. INTRODUCTION

Rising populations, rapid urbanization, and industrialization have intensified MSW generation across cities worldwide (Soni et al. 2023). Global MSW production is projected to increase from 2.89 to 4.54 billion tons by 2050 (Maalouf & Mavropoulos 2023). Composting has emerged as a viable and widely accepted strategy for efficiently recycling organic fractions of MSW and is increasingly promoted as a sustainable approach to waste management. The organic fraction of MSW contributes essential soil nutrients (Rodríguez-Espinosa et al. 2023) and is an important source of soil organic matter that enhances microbial activity, soil fertility, structure, and water-holding capacity (Adugna 2016). In Sri Lanka, composting and recycling organic waste have been estimated to generate US$191 million in waste management and fertilizer cost savings (Roy et al. 2021). Redirecting waste from landfill disposal to composting not only reduces MSW volume but also mitigates greenhouse gas (GHG) emissions compared with incineration and landfilling (Manea et al. 2024, Qdais et al. 2019).

Despite its agronomic benefits, MSW compost raises concerns about ecological safety, as it may also contain appreciable concentrations of toxic heavy metals such as zinc (Zn), copper (Cu), cadmium (Cd), lead (Pb), nickel (Ni), and chromium (Cr), originating from household waste, batteries, electronic residues, and urban refuse (Ishchenko & Vasylkivskyi 2019). These metals can bioaccumulate and biomagnify through the food chain, intensifying their toxicity. They can interfere with various metabolic processes by accumulating in vital organs such as the liver, heart, brain, and kidneys, thereby disrupting their normal functions (Kiran et al. 2022). This highlights the need to explore methods for mitigating their presence in the environment.

While compost-derived organic matter can immobilize certain metals through complexation and adsorption, thereby reducing their bioavailability, it may simultaneously enhance the availability of others, particularly Zn and Cu, which are more mobile under agricultural conditions (Huang et al. 2016). These contrasting effects highlight the need for site-specific and crop-specific assessments.

Plants differ markedly in their ability to absorb and translocate heavy metals. Bioconcentration factor (BCF) and translocation factor (TF) are widely used indices to evaluate metal uptake from soil and subsequent transport from roots to aerial parts (Bose & Bhattacharyya 2008, Buscaroli 2017). They also help distinguish the phytostabilization and phytoextraction potential of plant species. Plants with BCF > 1 and TF > 1 are generally considered suitable for phytoextraction, whereas plants with BCF > 1 and TF < 1 are more appropriate for phytostabilization (Eben et al. 2024).

Field-based (in situ) studies are particularly valuable because they reflect realistic soil–plant–environment interactions that controlled pot experiments cannot fully replicate. However, data on heavy metal uptake under true agricultural conditions remain limited. Such studies are critical for evaluating the environmental safety of MSW compost application and its role in sustainable agriculture. Therefore, this study investigates heavy metal accumulation, bioconcentration, and translocation in selected plant species grown in MSW compost-amended soils under in situ conditions.

2. MATERIALS AND METHODS

The study was conducted across multiple sites in Bengaluru, where waste management practices and MSW-derived compost are used in agriculture. Bengaluru is located in the heart of the South Deccan Plateau in the southeastern corner of Karnataka State, between latitudes 12°39′ N and 13°18′ N and longitudes 77°22′ E and 77°52′ E, covering an area of 2,196 km² with an average elevation of about 900 m. The city, with a population of 1.3 million, generates around 5,000–6,000 t day^{-1} of MSW, including bulk generation, with a per capita generation of 400 g day^{-1} (BBMP 2022). Source-separated wet waste, or the organic fraction of the waste, is sent to Wet-Waste Processing Plants (WPPs), where it is transformed into compost that farmers subsequently apply as a soil amendment.

Samples of compost were collected from six operational MSW composting facilities located in Bengaluru (Fig. 1). Compost sampling was conducted during the post-monsoon season (November–December 2023), when ambient temperatures ranged between 18–28 °C and relative humidity was moderate. No temporal variation was assessed, and the results represent conditions specific to the sampling period. Soil and plant samples were collected in situ from two distinct field types: MSW compost-amended fields and conventional-practice fields (control). Compost-amended fields were agricultural fields with documented use of MSW compost for at least one cropping season. No controlled plot experimentation was conducted; instead, the study relied on existing farmer-managed systems to capture real-world agricultural conditions. Compost was reported to have been applied once, approximately 20–30 days before sowing, at 5–12 t acre^{-1}. Adjacent conventional fields, or comparable fields in the vicinity managed using traditional fertilization practices, including chemical fertilizers and farmyard manure, and with no history of compost application were considered controls. Both field types were maintained under similar cropping systems and agronomic practices to ensure comparability. The outline map (Fig. 2) shows four compost-amended sites along with four control sites, where soil samples and plants, including *Pennisetum purpureum* (fodder, Napier grass), *Eleusine coracana* (millet, ragi), *Zea mays* (cereal, maize), and *Lablab purpureus (*pulse, hyacinth bean), were collected from Bengaluru Urban for the study. Plant and soil samples were collected once during June–December 2023.

2.1. Sampling and Analysis of MSW Compost, Soil, and Plant Samples

Composite samples comprising several grab samples from ten different points of the final compost heap (<4 mm particle size) were collected from each WPP in sterile polythene bags to minimize changes in moisture content and transported immediately under ice-cooled conditions to the laboratory for further analysis. A subsample of each composite sample was immediately analyzed in the laboratory for moisture content because delaying analysis may alter this property. All samples were air-dried in the shade, ground,

and passed through a 2 mm sieve for physicochemical analysis.

Compost samples were analyzed for pH and electrical conductivity (EC) using a digital pH and EC meter (FAI 2006). Organic matter content was determined by the loss-on-ignition method. The C:N ratio was determined using a CHNS elemental analyzer (Elementar, Vario-Micro model). A 10 mg portion of each dried and ground sample was placed in a tin capsule and combusted to the respective oxide forms, which were measured using a thermal conductivity detector (TCD) for C, N, H, and S (Komilis et al. 2012). For metal analysis, 1 g of the sample was dry-ashed in a muffle furnace at 550°C for 5 h, cooled, and the residue was dissolved in 5 mL of 20% HCl, filtered, and diluted to 50 mL in a volumetric flask with deionized water. Metal content was quantified using inductively coupled plasma optical emission spectrometry (ICP-OES; Thermo Fisher Scientific iCAP 7000).

Whole-plant samples, together with the associated soil samples, were collected from compost-amended and non-amended plots (control), labeled, and taken to the laboratory for analysis. Five soil subsamples from a rectangular grid with a surface area of 0.5 m² were collected to a depth of 5–20 cm, corresponding approximately to plant-root depth, to yield a representative soil sample. Representative whole-plant samples were obtained by randomly selecting individuals within each sampled field, ensuring spatial coverage and avoiding border rows or atypical plants. For ragi and hyacinth bean, 10–15 plants were collected; for maize, 10–20 plants; and for Napier grass, 5–10 clumps. All plants from each plot were pooled to form a single composite sample, which was subsampled into three portions and treated as technical triplicates during analysis. Samples were cleaned, sealed, labeled, and transported to the laboratory for analysis. Subsamples of soil and plant parts were analyzed for moisture content immediately in the laboratory using the gravimetric method.

Plant samples were separated into roots, leaves, and fruits (when present at the time of sampling) and further subsampled for analysis. Root samples were thoroughly washed under running tap water to remove adhering soil particles. All samples were then gently rinsed with deionized water, air-dried at room temperature, ground to a powder, and analyzed for total concentrations of major and micronutrients using the standard procedure. Heavy metals were analyzed using ICP-OES as described for compost samples.

The soil samples were air-dried at room temperature, finely ground, sieved through a 2.0 mm mesh, and stored in suitable, properly coded and labeled bottles. Soil pH, EC, and total dissolved solids (TDS) were measured in 1:2.5 soil:water extracts using a pH and conductivity meter (Jackson 1962). Organic matter (OM) content was determined by the Walkley and Black wet-oxidation method (Jackson 1962). The C:N ratio was determined using a CHNS analyzer (Marathe & Chavan 2022). Soil micronutrient cations were extracted with DTPA and quantified as Zn, Cu, Pb, Cd, Cr, and Ni by ICP-OES.

2.2. Quality Assurance and Quality Control (QA/QC)

QA/QC procedures were employed throughout the study to ensure analytical accuracy, precision, and reproducibility. The ICP-OES was calibrated with certified standards before each batch of measurements, and multielement calibration standards were used to cover all analytes simultaneously. Analytical accuracy was validated using certified reference materials (CRMs) and spiked samples, with recoveries maintained within 90–120%. Precision was assessed through duplicate analyses, with relative standard deviations (RSDs) generally <5%. Procedural blanks were included to monitor contamination, and limits of detection (LOD) and quantification (LOQ) were established for each element. Values reported as nondetect (ND) were treated as below the detection limit and substituted with half of the respective LOD (LOD/2) for calculations of the bioconcentration factor (BCF) and translocation factor (TF), to ensure that measured values were reproducible and comparable across sample types.

2.3. Bioconcentration Factor (BCF) and Translocation Factor (TF)

The BCF and TF are key indices in studies of heavy metal uptake and internal mobility within plants (Bose & Bhattacharyya 2008, Marchiol et al. 2004). The BCF (Eq. (1)) expresses the proportion of heavy metal concentration in individual plant parts (root, leaf, and fruit) relative to that in the soil reservoir. TF (Eq. (2)) is determined by comparing the heavy metal concentration in the aerial parts of the plant to that in the roots (Buscaroli 2017).

2.4. Statistical Analysis

As only one composite sample per crop type was collected from each farmer's field, statistical comparisons were confined to replicate measurements within composites rather than biological replication across plots. Spatial variability across sites was not assessed, and the results represent site-level composites. Consequently, the findings are interpreted as indicative of heavy-metal dynamics under compost-amended versus conventional practices rather than as replicated field trials.

To assess statistical significance and compare means between conventional and compost-amended groups,

parametric analyses were performed after normality checks (Shapiro–Wilk test) and variance comparisons (F-test). For soil baseline characteristics, results are reported as means, standard deviations (SD), and p-values. For soil metal concentrations, Welch's t-test was applied, and results are presented as means ± SD together with 95% confidence intervals (CI), effect sizes (Cohen's d), and false discovery rate (FDR)-adjusted p-values to account for multiple comparisons. Statistical significance was set at $p < 0.05$. For plant metal concentrations, results are reported as means ± SD derived from technical replicates of composite samples. Values below detection limits were treated as ND and handled consistently. For calculations of BCF and TF, ND values were substituted with LOD/2 to enable computation of indices. All analyses were performed using R version 4.4.3, with supplementary data handling in Microsoft Excel 2019.

3. RESULTS AND DISCUSSION

3.1. Heavy metal Dynamics in Plants and MSW Compost-Amended Soil

To evaluate the influence of municipal solid waste (MSW) compost on soil–plant interactions, this section presents the physicochemical properties of soil and compost, the resulting changes in heavy metal concentrations in control and amended soils, and the subsequent uptake, bioconcentration, and translocation of metals in plants.

3.1.1. Physicochemical Properties of Soil and MSW Compost

The MSW compost exhibited pH values ranging from 5.2 to 7.6, compared with the stated FCO-recommended range of 6.5–7.5. Electrical conductivity (EC) varied between 1.4 and 2.5 dS m^{-1}, remaining below the permissible limit of 4 dS m^{-1}. Moisture content ranged from 14 to 49%, with most samples aligning with the FCO guideline of 15–25%. Organic matter content was high (51–69%), exceeding the minimum requirement of 28%. The C:N ratio ranged between 8.3 and 14.8, well below the FCO threshold of <20, indicating rapid decomposition and nutrient mineralization potential (FAI 2006).

Soil parameters under control and amended conditions varied significantly across Napier grass, ragi, maize, and hyacinth bean crops, with pH, EC, moisture, organic matter, and C:N ratios showing crop-specific responses (Table 1). MSW compost-amended soil generally showed lower soil EC and altered pH, while effects on moisture, organic matter, and C:N differed by crop. EC increased in Napier grass soil but decreased sharply in ragi, maize, and hyacinth bean soils. Moisture was lower in Napier grass soil but higher in ragi, maize, and hyacinth bean soils. Amendments generally enhanced moisture retention except in Napier grass soil. Organic matter was higher in Napier grass soil but lower in ragi, maize, and hyacinth bean soils. The C:N ratio remained similar in Napier grass soil, was lower in ragi and maize soils, and was higher in hyacinth bean soil than in the corresponding control soils.

3.1.2. Heavy metals in Compost, Control, and MSW Compost-Amended Soils

Heavy metal concentrations were quantified in compost, control soil, and compost-amended soils to determine enrichment levels and changes in metal availability following amendment. The metal concentrations in the MSW compost (Table 2, Fig. 3) followed the order: Zn > Cu > Cr > Pb > Cd > Ni. All measured metals were below the maximum permissible limits set by the FCO (FAI 2006), thereby meeting regulatory quality standards. Although minor variability was observed among samples, none of the metals approached critical thresholds, reflecting effective waste segregation and composting practices. Compliance with FCO limits confirms the regulatory safety of MSW compost for agricultural use; however, regulatory thresholds alone do not fully capture environmental risk. The ecological relevance of compost quality is better understood when linked to metal bioavailability and plant uptake, as indicated by BCF and TF values.

Bioavailable metal concentrations in conventional-practice (control) and MSW compost-amended soils are given in Table 3. Statistical comparisons were performed using Welch's t-test after normality and variance checks. Results are reported as mean ± SD, together with 95% confidence intervals (CI), FDR-adjusted p-values, and effect sizes (Cohen's d) to account for multiple comparisons and quantify the magnitude of differences. Results revealed that MSW compost amendment significantly altered heavy-metal concentrations across soils cultivated with Napier grass, ragi, maize, and hyacinth bean.

Bioavailable Zn levels were consistently and markedly reduced in all soils ($p < 0.001$), while Cu concentrations declined in Napier grass, ragi, and hyacinth bean soils but increased slightly in maize soil. Ni was significantly reduced in ragi, maize, and hyacinth bean soils ($p < 0.05$), with no difference observed in Napier grass soil. Pb concentrations decreased in Napier grass, ragi, and maize soils ($p < 0.01$), but changes in hyacinth bean soil were not significant. Cd responses were variable: Napier grass soil exhibited a significant increase ($p = 0.001$), hyacinth bean soil a significant decrease ($p = 0.01$), and ragi and maize soils showed no significant differences. Cr concentrations were significantly lower in Napier grass and ragi soils ($p < 0.05$) but remained unchanged in maize and hyacinth bean soils.

Overall, MSW compost amendment generally lowered Zn, Cu, Ni, Pb, and Cr concentrations, although element-specific and crop-specific variations were evident, particularly for Cd and Cu.

Compost amendments significantly reduced heavy-metal concentrations in soils under Napier grass, ragi, maize, and hyacinth bean compared with conventional controls, with Zn, Cu, Ni, Pb, and Cr showing consistent declines across most crops ($p < 0.05$), while Cd effects varied. Effect sizes (Cohen's d) indicated large reductions for Zn and Cu in hyacinth bean, and FDR-adjusted q-values confirmed significance after multiple testing.

3.1.3. Heavy Metals in Plants: Bioconcentration and Translocation Factors

Heavy-metal concentrations in crop roots, leaves, and seeds (where applicable) showed distinct patterns between conventional controls and compost amendments across Napier grass, ragi, maize, and hyacinth bean, with roots generally accumulating higher levels than aerial parts. Compost amendments often increased root uptake of Zn, Cu, Ni, and Cd while reducing or stabilizing levels in edible leaves and seeds, indicating retention in roots or the rhizosphere (Table 4).

Roots of Napier grass, ragi, maize, and hyacinth bean had higher Zn under compost amendment. In contrast, leaves of Napier grass, ragi, and maize had lower Zn under compost amendment, while hyacinth bean leaves showed similar values and seeds showed comparable Zn. Cu followed similar trends: roots of all crops had higher Cu, and leaves generally had lower Cu under compost amendment, except hyacinth bean leaves. Hyacinth bean seeds showed slightly higher Cu under compost amendment. Ni was higher in Napier grass and maize roots under compost amendment, while ragi and hyacinth bean roots had lower values. Leaves of Napier grass and maize had lower Ni under compost amendment, while hyacinth bean leaves had slightly higher values and seeds had lower Ni. Roots of all four crops had higher Pb under compost amendment. Napier grass leaves showed ND under compost amendment (vs. 0.54 in the control), maize leaves had higher Pb, while ragi and hyacinth bean leaves showed similar values. Hyacinth bean seeds had higher Pb under compost amendment. Roots of all four crops had higher Cd, whereas amended leaves/seeds often showed ND or low Cd values. Cr showed variable patterns, with root concentrations increasing in Napier grass and maize, decreasing in ragi, and remaining similar in hyacinth bean, while leaf and seed concentrations were lower.

Metal uptake by plants was assessed using BCF and TF indices, which together illustrate the degree of root accumulation and mobility of metals toward aerial tissues under compost-amended conditions. A BCF greater than 1 reflects effective metal uptake from soil, while a TF exceeding 1 denotes efficient translocation from roots to aerial tissues (Carbonell et al. 2011), underscoring potential implications for food-chain transfer and ecological risk.

Root accumulation (BCFroot) was higher under amended conditions for all metals in Napier grass, with notably greater values for Cr (79.03), followed by Cd, Zn, and Pb, indicating strong accumulation capacity (Table 5). Ni and Cu also showed higher BCFroot under amendment than under conventional practice. Leaf accumulation (BCFleaf) was lower under amended conditions for most metals (Pb, Cd, Zn, and Ni), while Cu showed comparable levels and Cr recorded higher BCFleaf under amended conditions. TFleaf values were consistently lower under amended conditions for all metals. Conversely, Cu and Ni showed $TF > 1$ in control soils despite relatively low BCF values, reflecting active mobility at lower concentration levels. This pattern positions Napier grass as a root-dominant accumulator, particularly effective for phytostabilization of Cr and Zn, while minimizing food-chain transfer.

BCF and TF values for ragi indicate that roots strongly accumulated Ni and Cr (Ni BCF = 11.56; Cr BCF = 26.31 in control soils), yet TF values for Ni were extremely low (TF = 0.0002 in amended soils), confirming exclusion from aerial tissues (Table 6). Leaf accumulation showed mixed trends, with lower values for Zn and Cd, while Cu and Pb remained higher. Ni remained extremely low and comparable (0.001) under both treatments. TF values were lower under amended conditions for most metals; Ni values remained negligible. Pb displayed $TF > 1$ in control conditions (TF = 1.74), despite low root BCF, indicating higher mobility than uptake capacity. Overall, the treatment demonstrated selective root sequestration of Ni and Cr, with limited aerial transfer.

Maize roots showed higher BCF values for Zn, Ni, and Cr (Zn = 41.15; Ni = 20.25; Cr = 107.64 in amended soils), while TF values remained low (Zn = 0.07; Cr = 0.06), confirming root sequestration. Notably, Pb and Cd exhibited $TF > 1$ (Pb = 2.74 in amended soils; Cd = 1.97 in control soils), indicating aerial mobility despite moderate root uptake. This dual behavior suggests that maize is effective for root stabilization of Zn and Cr, but Pb and Cd mobility may pose risks to edible tissues (Table 7).

Hyacinth bean showed higher root and leaf BCF values for most metals, except Cr, which was lower under amendments (Table 8). Seed accumulation showed higher values under amended conditions for Zn, Cu, and Pb, while Ni, Cd, and Cr were lower under amendment. TFleaf was lower under amended conditions for Zn, Pb, and Cr, remained

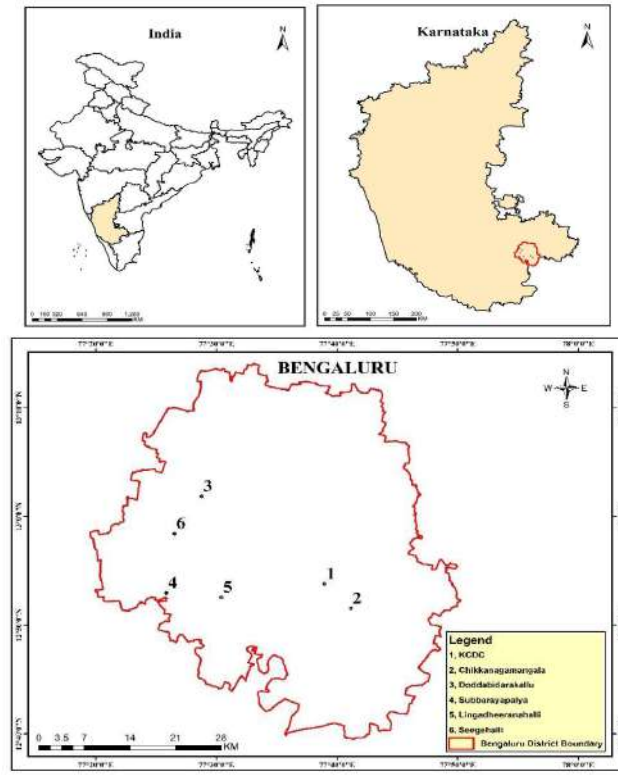


Fig. 1: Compost sampling locations in Bengaluru.

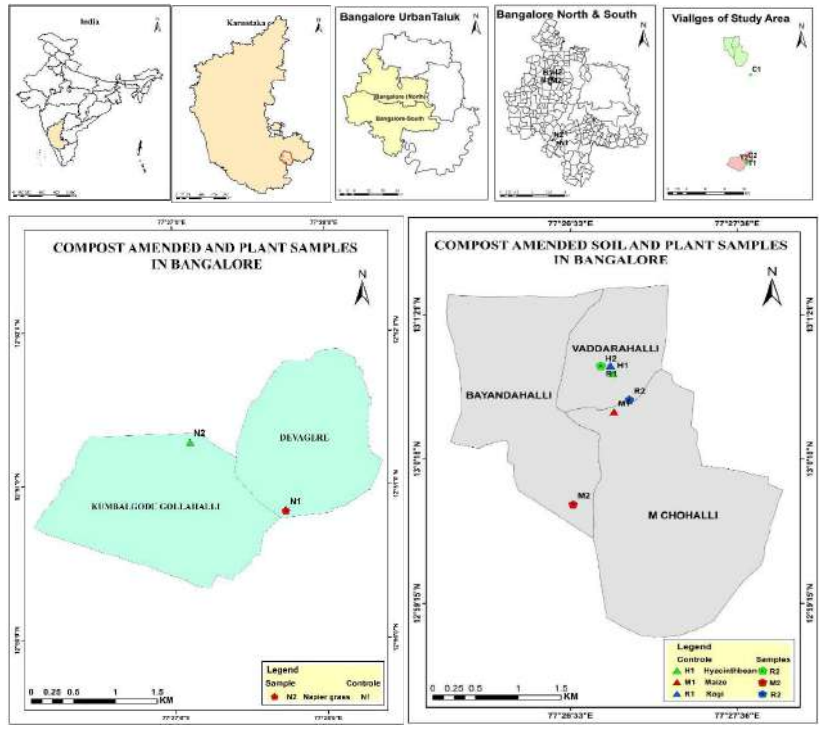


Fig. 2: Compost-amended and non-amended sites in Bengaluru.

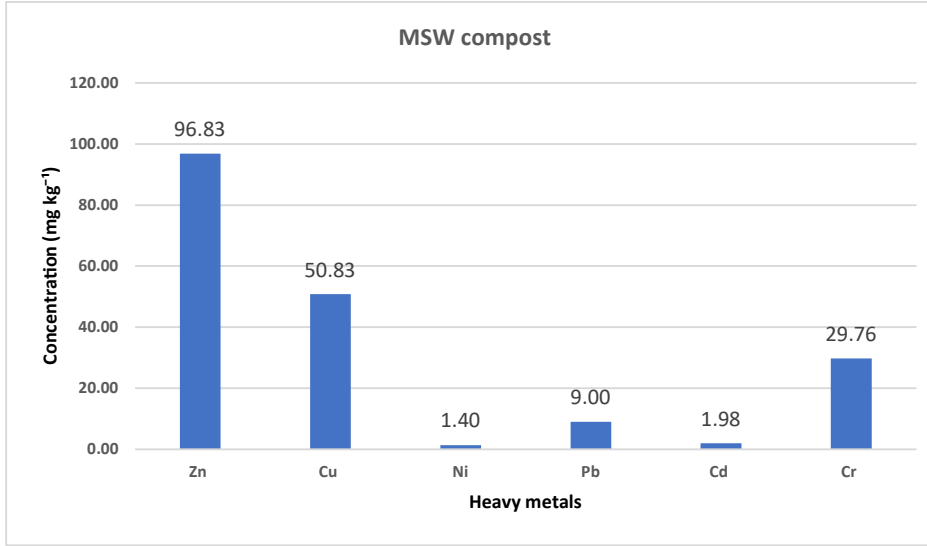


Fig. 3: Heavy-metal concentrations in MSW compost.

Table 1: Physicochemical properties of control and compost-amended soils.

Crop	Soil parameters	Control (Mean ± SD)	Amended (Mean ± SD)	*p-value*
Napier grass	pH	8.30±0.14	7.84±0.12	0.01245
	EC (µS/cm)	391.92±9.01	474.3±9.96	4.67E-04
	Moisture	11.90±0.19	11.00±0.16	3.34E-03
	Organic matter	2.40±0.08	2.90±0.08	1.62E-03
	C:N	8.89±0.16	8.81±0.15	0.5795
Ragi	pH	7.88±0.13	7.80±0.12	4.68E-01
	EC	374.9±9.33	250.0±8.10	7.18E-05
	Moisture	7.40±0.12	8.91±0.14	0.0001713
	Organic matter	2.00±0.06	1.52±0.03	1.27E-03
	C:N	7.84±0.13	7.62±0.11	9.14E-02
Maize	pH	8.04±0.13	7.86±0.11	0.1434
	EC	364.3±9.40	209.0±8.69	3.19E-05
	Moisture	8.80±0.14	9.80±0.17	0.001585
	Organic matter	3.20±0.09	1.70±0.06	7.22E-05
	C:N	10.45±0.18	7.63±0.11	8.79E-05
Hyacinth bean	pH	6.94±0.11	7.97±0.11	3.48E-04
	EC	500.7±12.46	303.1±10.1	3.98E-05
	Moisture	6.80±0.12	7.10±0.12	0.03352
	Organic matter	2.50±0.06	1.70±0.06	7.44E-05
	C:N	7.28±0.13	9.14±0.17	0.0002065

Sample size (n) = 3; SD = standard deviation.

similar for Cu, and was higher under amendment for Ni and Cd. Seed TF values were >1 for Zn, Cu, Ni, and Cd in control soils, confirming systemic transport into edible parts. This aligns with elevated seed BCF values (Zn = 18.05; Cu = 10.58), raising potential food-safety concerns. Unlike Napier grass and maize, which predominantly restrict metals to roots, hyacinth bean facilitates greater systemic distribution.

Across species, soil amendments generally increased BCF values, reflecting enhanced metal bioavailability. In contrast, TF values tended to decline under amendment, pointing to a physiological restriction of translocation that may serve as a protective mechanism. Pb in maize was an exception, where TF increased, highlighting species-specific variability in responses to contamination stress.

3.2. Bioconcentration and Translocation Equations

$$BCF = \frac{Cp \quad (root,shoot,leaves,grains)}{Csoil} \quad \ldots(1)$$

$$TF = \frac{Cp \quad (shoot,leaves,seeds)}{Croot} \quad \ldots(2)$$

Where Croot, Cleaf, Cseed, and Csoil represent metal concentrations (mg kg⁻¹, dry weight basis) in roots, leaves,

Table 2: Heavy-metal concentrations in MSW compost.

Heavy metal (mg kg⁻¹)	Min	Max	Mean ± SD	Quality control*
Zn	41.9	183.3	96.83 ± 55.73	≤ 1000
Cu	17.7	111.5	50.83 ± 34.61	≤ 300
Ni	0.5	8.6	1.4 ± 4.45	≤ 50
Pb	2.88	23.01	9 ± 7.5	≤ 100
Cd	0.67	3.91	1.98 ± 1.33	≤ 5
Cr	19.5	41.23	29.76 ± 7.9	≤ 50

*Fertilizer (Control) Order, 1985; SD = standard deviation.

Table 3: Metal concentrations (mg kg⁻¹ dry weight) in control and MSW compost-amended soils.

Crop	Heavy metal	Control (Mean ± SD)	Amended (Mean ± SD)	*p-value*	95% confidence intervals	FDR (*q*)	Effect size (d)
Napier grass	Zn	6.76±0.19	3.48±0.12	5.59E-05	2.9–3.7	0.000335	-20.55
	Cu	4.21±0.02	3.92±0.03	0.0003527	0.2–0.4	0.001058	-11.77
	Ni	1.32±0.16	1.31±0.20	0.9513	-0.4–0.5	0.9513	-0.06
	Pb	0.86±0.07	0.45±0.15	0.02788	0.1–0.7	0.04182	-3.58
	Cd	0.041±0.01	0.091±0.02	0.03579	-0.1–-0.01	0.04295	3.13
	Cr	0.20±0.009	0.039±0.001	0.00103	0.1–0.2	0.00206	-24.41
Ragi	Zn	4.04±0.17	2.35±0.03	0.0027820	1.3–2.1	0.014421	-13.54
	Cu	1.31±0.16	0.78±0.02	0.02752	0.1–0.9	0.04128	-4.64
	Ni	0.45±0.02	0.35±0.03	0.01477	0.03–0.2	0.02954	-3.87
	Pb	0.99±0.02	0.81±0.08	0.04566	0.01–0.3	0.05479	-3.22
	Cd	0.016±0.01	0.02±0.003	0.4446	-0.02–0.01	0.4446	0.79
	Cr	0.22±0.02	0.14±0.02	0.004807	0.04–0.1	0.014421	-4.61
Maize	Zn	3.55±0.16	1.99±0.10	0.001521	1.1–1.8	0.009126	-12.86
	Cu	1.21±0.15	1.53±0.05	0.04864	-0.6–-0.004	0.07296	2.93
	Ni	0.40±0.03	0.28±0.05	0.04045	0.01–0.2	0.07296	-2.69
	Pb	0.87±0.05	0.59±0.07	0.004925	0.1–0.4	0.014775	-4.70
	Cd	0.014±0.002	0.02±0.006	0.8057	-0.01–0.01	0.8057	0.23
	Cr	0.17±0.02	0.14±0.06	0.3948	-0.1–0.2	0.47376	-0.86
Hyacinth bean	Zn	10.52±0.03	1.50±0.05	4.96E-09	8.9–9.1	2.98E-08	-226.67
	Cu	9.94±0.06	0.72±0.02	5.50E-07	9.1–9.3	1.65E-06	-216.75
	Ni	0.74±0.03	0.34±0.05	0.0004977	0.3–0.5	0.000995	-9.65
	Pb	0.84±0.06	0.77±0.05	0.1704	-0.05–0.2	0.20448	-1.36
	Cd	0.050±0.01	0.011±0.01	0.01251	0.02–0.1	0.018765	-4.54
	Cr	0.12±0.02	0.14± 0.03	0.3526	-0.1–0.04	0.3526	0.86

Sample size (n) = 3; SD = standard deviation; FDR = false discovery rate

Table 4: Heavy-metal concentrations (mg kg⁻¹ dry weight) in plant parts of Napier grass, ragi, maize, and hyacinth bean.

Crop	Plant part	Heavy metal	Zn	Cu	Ni	Pb	Cd	Cr
Napier grass	Root	Control	87.97±2.12	2.07±0.07	1.73±0.06	1.49±0.04	0.10±0.005	2.81±0.08
		Amended	95.8±2.45	4.30±0.09	4.06±0.08	2.01±0.06	1.33±0.04	3.08±0.05
	Leaves	Control	15.96±0.43	2.40±0.05	2.41±0.05	0.54±0.04	1.05±0.02	1.12±0.03
		Amended	3.75±0.08	2.07±0.06	1.40±0.05	ND	ND	0.57±0.005
Ragi	Root	Control	24.12±0.54	3.81±0.10	5.20±0.14	0.27±0.005	0.03±0.001	5.68±0.16
		Amended	32.0±0.91	6.37±0.18	3.04±0.11	0.58±0.04	0.11±0.01	3.26±0.12
	Leaves	Control	17.0±0.51	2.15±0.06	ND	0.46±0.03	0.01±0.002	0.79±0.007
		Amended	9.67±0.25	1.49±0.05	ND	0.50±0.004	ND	0.68±0.005
Maize	Root	Control	45.13±0.84	2.90±0.09	3.10±0.14	0.43±0.03	0.03±0.002	6.68±0.19
		Amended	81.88±1.05	5.30±0.16	5.67±0.17	0.44±0.04	0.11±0.006	14.75±0.34
	Leaves	Control	8.36±0.19	3.73±0.15	1.14±0.05	0.48±0.03	0.07±0.003	1.01±0.04
		Amended	5.99±0.18	1.41±0.05	0.99±0.03	1.20±0.04	0.06±0.002	0.87±0.08
Hyacinth bean	Root	Control	24.47±0.42	6.87±0.18	3.36±0.13	0.67±0.07	0.08±0.002	4.04±0.14
		Amended	27.62±0.49	8.11±0.21	1.85±0.05	1.38±0.04	0.09±0.003	4.15±0.15
	Leaves	Control	23.52±0.37	5.71±0.14	2.35±0.08	0.97±0.08	ND	1.81±0.06
		Amended	22.81±0.31	6.71±0.15	2.70±0.09	0.93±0.07	0.03±0.001	1.12±0.04
	Seeds	Control	27.23±0.52	7.28±0.18	3.57±0.14	0.36±0.007	0.16±0.005	0.73±0.06
		Amended	27.07±0.49	7.62±0.19	0.93±0.09	0.75±0.02	ND	0.54±0.03

ND = below detection limit; n = 3.

Table 5: Bioconcentration factor (BCF) and translocation factor (TF) of Napier grass.

Heavy metal	BCF_{root}		BCF_{leaf}		TF_{leaf}	
	Control	Amended	Control	Amended	Control	Amended
Zn	13.01	27.37	2.36	1.07	0.18	0.04
Cu	0.49	1.10	0.57	0.53	1.16	0.48
Ni	1.31	3.10	1.83	1.07	1.39	0.34
Pb	1.73	4.48	0.63	0.001	0.36	0.0002
Cd	2.34	14.66	1.27	0.005	0.54	0.0004
Cr	14.35	79.03	5.73	14.62	0.40	0.18

Table 6: Bioconcentration factor (BCF) and translocation factor (TF) of ragi.

Heavy metal	BCF_{root}		BCF_{leaf}		TF_{leaf}	
	Control	Amended	Control	Amended	Control	Amended
Zn	5.97	13.62	4.21	4.11	0.70	0.30
Cu	2.91	8.17	1.64	1.91	0.57	0.23
Ni	11.56	8.68	0.001	0.001	0.0001	0.0002
Pb	0.27	0.72	0.47	0.62	1.74	0.87
Cd	1.69	5.30	0.56	0.03	0.33	0.005
Cr	26.31	23.80	3.66	4.97	0.14	0.21

seeds, and soil, respectively.

3.3. Discussion

Application of municipal solid waste (MSW) compost in agriculture has gained traction as a sustainable resource-recovery strategy; however, concerns remain about heavy-metal accumulation in soils and the potential transfer of contaminants into the food chain (Hargreaves et al. 2008, Yuksel 2015). These concerns necessitate field-based evaluations, such as the present study, that reflect

Table 7: Bioconcentration factor (BCF) and translocation factor (TF) of maize.

Heavy metal	BCF_{root}		BCF_{leaf}		TF_{leaf}	
	Control	Amended	Control	Amended	Control	Amended
Zn	12.71	41.15	2.35	3.01	0.19	0.07
Cu	2.39	3.46	3.08	0.92	1.29	0.27
Ni	7.76	20.25	2.86	3.55	0.37	0.18
Pb	0.50	0.75	0.56	2.05	1.12	2.74
Cd	2.43	7.00	4.79	3.67	1.97	0.52
Cr	38.63	107.6	5.83	6.32	0.15	0.06

Table 8: Bioconcentration factor (BCF) and translocation factor (TF) of hyacinth bean.

Heavy metal	BCF_{root}		BCF_{leaf}		BC_{Seed}		TF_{leaf}		TF_{Seed}	
	C	A	C	A	C	A	C	A	C	A
Zn	2.33	18.41	2.24	15.21	2.59	18.05	0.96	0.83	1.11	0.98
Cu	0.69	11.27	0.57	9.31	0.73	10.58	0.83	0.83	1.06	0.94
Ni	4.53	5.45	3.17	7.92	4.83	2.73	0.70	1.45	1.06	0.50
Pb	0.79	1.80	1.14	1.21	0.43	0.97	1.44	0.67	0.54	0.54
Cd	1.54	8.27	0.01	2.82	3.14	0.05	0.006	0.34	2.04	0.005
Cr	33.9	29.02	15.24	7.80	6.15	3.74	0.45	0.27	0.18	0.13

C = Control; A = MSW compost-amended soil

realistic agronomic conditions rather than short-term pot or laboratory experiments. In this in situ study, a single application of FCO-compliant MSW compost did not elevate soil heavy-metal concentrations. On the contrary, compost-amended soils exhibited statistically significant reductions in Zn, Cu, Pb, and Cr compared with conventional controls, particularly in hyacinth bean, Napier grass, and ragi systems. These reductions, supported by strong effect sizes and narrow confidence intervals, suggest that the amendment may influence metal redistribution between soil and plant compartments, potentially through enhanced plant uptake, immobilization, or transformation processes in the rhizosphere (Seshadri et al. 2015). However, the magnitude of reduction varies across crops, indicating that root architecture, exudation patterns, and rhizosphere interactions differ among species, thereby influencing metal availability and retention (Podar & Maathuis 2022).

Nonetheless, prior evidence indicates that higher or repeated compost applications can increase the availability of Cu, Zn, Pb, and Ni in soils, underscoring the need to limit excessive amendments to avoid contamination risks (Yuksel 2015, Jordão et al. 2006). Furthermore, crop-specific responses identified through Welch's t-test highlight the importance of soil–plant interactions in shaping metal dynamics after compost addition. This reinforces the need to evaluate compost safety across diverse cropping systems rather than relying solely on soil metrics (Xu et al. 2022, Abd-Elhalim et al. 2025). Cadmium exhibited a more variable response across cropping systems, with higher concentrations in amended soils for Napier grass but no significant differences in ragi and maize. This variability indicates higher mobility and sensitivity of Cd to local soil and crop conditions, as also reflected in its inconsistent uptake and translocation patterns in plant tissues. Similarly, Ni and Cr showed crop-dependent differences, with significant reductions in some systems (ragi and hyacinth bean) but not in others (e.g., maize), further emphasizing the role of plant–soil interactions in controlling metal behavior.

The observed differences in soil metal concentrations can be partially explained by the measured soil properties. Variations in pH, EC, moisture, organic matter, and C:N ratio across cropping systems indicate that each crop creates a distinct soil environment under amendment. For instance, lower EC in amended soils for ragi, maize, and hyacinth bean suggests reduced soluble metal fractions, which may contribute to lower measured concentrations. Differences in moisture and pH further influence metal solubility and speciation, thereby affecting their persistence in soil (Bravo et al. 2017). Interestingly, despite lower organic matter in amended soils for some cropping systems (ragi, maize, and hyacinth bean), reductions in metal concentrations were still observed. This suggests that metal dynamics are governed by multiple interacting factors rather than organic matter alone, including rhizosphere-mediated processes such as root uptake, microbial activity, and localized chemical transformations. Such findings are consistent with studies

showing that plant species can significantly influence metal availability through root-induced changes in soil chemistry, as reported by Houben & Sonnet (2015) and Seshadri et al. (2015).

BCF and TF values provide complementary insights into heavy-metal uptake and internal distribution in the studied plant species, revealing species-specific strategies of sequestration and mobility and their implications for phytoremediation and food safety. Relatively higher BCF values in roots, coupled with consistently low TF values (<1) for most metals, indicate dominant root retention and restricted movement to aboveground tissues, as reported by Bose & Bhattacharyya (2008). Such uptake is characteristic of phytostabilization rather than phytoextraction (Li et al. 2021), suggesting that the applied MSW compost did not enhance metal mobility within the soil–plant continuum. Root-level immobilization is attributed to metal binding to cell-wall components, vacuolar sequestration, and precipitation with compost-derived organic ligands, mechanisms that are particularly effective for nonessential and potentially toxic metals such as Pb, Cd, and Cr (Hall 2002, Bolan et al. 2014). Part of the reduction in soil metal concentration may be associated with enhanced uptake and retention in plant roots rather than solely with immobilization within the soil matrix.

A crop-specific comparison further clarified species-specific uptake behavior. Napier grass exhibited higher root metal accumulation but minimal shoot transfer, highlighting its strong stabilization capacity. Ragi and maize showed regulated uptake of essential micronutrients (Zn and Cu) with controlled translocation, probably because of effective homeostasis and limited transfer to edible portions. Although MSW compost application generally reduced soil metal bioavailability, maize exhibited TF > 1 for Pb, and hyacinth bean seeds showed elevated accumulation of Zn, Cu, Ni, and Pb, indicating potential metal transfer to edible parts. While most metal concentrations in edible parts were within the cited permissible limits, Pb (0.75 mg kg^{-1}) in hyacinth bean was reported to exceed the limit of 0.1 mg kg^{-1} (Codex Alimentarius Commission 1995; Altarawneh 2021). This suggests that the safety of MSW compost-amended soils is crop-specific. Crops such as hyacinth bean, which showed higher translocation to edible tissues, may pose food-chain risks, and their cultivation in such soils requires caution.

From both regulatory and agronomic viewpoints, combining soil statistical analysis with BCF and TF indices provides field-level evidence relevant to the heavy-metal limits set under the FCO (FAI 2006). Unlike controlled pot studies that might overestimate metal availability, the present field evidence shows that applying MSW compost can alter soil properties and bioavailable metal fractions; however, metal uptake and translocation vary depending on the crop, as some crops may accumulate metals in edible parts, requiring careful crop selection and monitoring to ensure safe agricultural practices. These findings support the sustainable use of MSW compost in farming, emphasizing the importance of regulatory compliance, appropriate crop choice, and ongoing monitoring for long-term or repeated applications.

A limitation of this study is that plant samples were pooled at the plot level to form composite samples, and technical replicates (three subsamples) were derived from each composite. As only one plot per crop type was sampled from different farmers' fields, biological replication within sites was not possible, and spatial variability across sites could not be statistically partitioned. Consequently, the results represent site-level composites rather than replicated field trials. While this approach provides useful insights into nutrient and contaminant dynamics under compost-amended versus conventional practices, future studies should incorporate replicated plots across multiple sites to enable more robust statistical treatment of spatial heterogeneity.

4. CONCLUSIONS

MSW compost used in this study met FCO heavy-metal limits, with statistical analysis showing crop-specific changes in soil metal concentrations following amendment. Significant reductions in certain metals, such as Zn, Pb, and Cr, suggest potential immobilization effects; however, these responses were not consistent across all metals and cropping systems. BCF and TF analyses further indicated that while several crops exhibited restricted movement of metals to aerial tissues, instances of elevated translocation (TF > 1) and accumulation in edible parts highlight the possibility of food-chain transfer under amended conditions.

Overall, the findings demonstrate that the behavior of heavy metals in MSW compost-amended soils is strongly crop-dependent. While compost application may reduce the bioavailability of certain metals, it does not universally prevent their uptake and translocation. Therefore, the use of MSW compost can be considered conditionally safe, provided that crop selection, site characteristics, and potential accumulation in edible tissues are carefully monitored. These results highlight the need for crop-specific risk assessment to ensure the safe and sustainable use of MSW compost in agricultural systems.

5. ACKNOWLEDGMENTS

The authors sincerely acknowledge Bangalore University,

Bengaluru, for institutional support and for granting a scholarship to facilitate this research. We further extend our gratitude to the College of Horticulture, Vignana Kendra, Bengaluru, for providing the necessary facilities and technical support required to carry out the present study.

6. REFERENCES

Abd-Elhalim, B.T., Gideon, M., Anton, K. and Boyi, M.O., 2025. Impact of dumpsite compost on heavy metal accumulation in some cultivated plants. *BMC Research Notes*, 18, p.20. [DOI]

Adugna, G., 2016. A review on impact of compost on soil properties, water use and crop productivity. *Academic Research Journal of Agricultural Science and Research*, 4(3), pp.93-104. [DOI]

Altarawneh, R.M., 2021. Levels of selected heavy metals (Pb, Ni, Cd, and Cr) in various widely consumed fruits and vegetables in Jordan. *International Journal of Environmental Analytical Chemistry*, 101(7), pp.1026-1033. [DOI]

BBMP, 2022. *Solid Waste Management*. Available at: https://site.bbmp.gov.in.

Bolan, N., Kunhikrishnan, A., Thangarajan, R., Kumpiene, J., Park, J., Makino, T., Kirkham, M.B. and Scheckel, K., 2014. Remediation of heavy metal(loid)s contaminated soils: To mobilize or to immobilize? *Journal of Hazardous Materials*, 266, pp.141-166. [DOI]

Bose, S. and Bhattacharyya, A.K., 2008. Heavy metal accumulation in wheat plant grown in soil amended with industrial sludge. *Chemosphere*, 70(7), pp.1264-1272. [DOI]

Bravo, S., Amorós, J.A., Pérez-de-los-Reyes, C., García, F.J., Moreno, M.M., Sánchez-Ormeño, M. and Higueras, P., 2017. Influence of the soil pH in the uptake and bioaccumulation of heavy metals (Fe, Zn, Cu, Pb and Mn) and other elements (Ca, K, Al, Sr and Ba) in vine leaves, Castilla-La Mancha (Spain). *Journal of Geochemical Exploration*, 174, pp.79-83. [DOI]

Buscaroli, A., 2017. An overview of indexes to evaluate terrestrial plants for phytoremediation purposes (review). *Ecological Indicators*, 82, pp.367-380. [DOI]

Carbonell, G., Miralles de Imperial, R., Torrijos, M., Delgado, M. and Rodriguez, J.A., 2011. Effects of municipal solid waste compost and mineral fertilizer amendments on soil properties and heavy metals distribution in maize plants (Zea mays L.). *Chemosphere*, 85(10), pp.1614-1623. [DOI]

Codex Alimentarius Commission, 1995. General standard for contaminants and toxins in food and feed (CXS 193-1995, amended 2025). Codex Alimentarius. FAO/WHO, Rome. Available at: https://www.fao.org/fao-who-codexalimentarius.

Eben, P., Mohri, M., Pauleit, S., Duthweiler, S. and Helmreich, B., 2024. Phytoextraction potential of herbaceous plant species and the influence of environmental factors: A meta-analytical approach. Ecological Engineering, 199, p.107169. [DOI]

FAI, 2006. The Fertiliser (Control) Order 1985. Fertiliser Association of India, New Delhi, India.

Hall, J.L., 2002. Cellular mechanisms for heavy metal detoxification and tolerance. *Journal of Experimental Botany*, 53(366), pp.1-11. [DOI]

Hargreaves, J.C., Adl, M.S. and Warman, P.R., 2008. A review of the use of composted municipal solid waste in agriculture. Agriculture, *Ecosystems & Environment*, 123(1-3), pp.1-14. [DOI]

Houben, D. and Sonnet, P., 2015. Impact of biochar and root-induced changes on metal dynamics in the rhizosphere of Agrostis capillaris and Lupinus albus. *Chemosphere*, 139, pp.644-651. [DOI]

Huang, M., Zhu, Y., Li, Z., Huang, B., Luo, N., Liu, C. and Zeng, G., 2016. Compost as a soil amendment to remediate heavy metal-contaminated agricultural soil: Mechanisms, efficacy, problems, and strategies. *Water, Air, & Soil Pollution*, 227(10), p.359. [DOI]

Ishchenko, V. and Vasylkivskyi, I., 2019. Environmental pollution with heavy metals: Case study of the household waste. In: Sustainable Production: Novel Trends in Energy, *Environment and Material Systems*, 198, pp.161-175.[DOI]

Jackson, M.L., 1962. *Soil Chemical Analysis*. Prentice Hall Inc., Englewood Cliffs, New Jersey, USA.

Jordão, C.P., Nascentes, C.C., Cecon, P.R., Fontes, R.L.F. and Pereira, J.L., 2006. Heavy metal availability in soil amended with composted urban solid wastes. *Environmental Monitoring and Assessment*, 112(1-3), pp.309-326. [DOI]

Kiran, R. Bharti and R. Sharma, 2022. Effect of heavy metals: An overview. *Materials Today: Proceedings*, 51, pp.880-885. [DOI]

Komilis, D., Evangelou, A., Giannakis, G. and Lymperis, C., 2012. Revisiting the elemental composition and the calorific value of the organic fraction of municipal solid wastes. *Waste Management*, 32(3), pp.372-381. [DOI]

Li, J., Chang, Y., Al-Huqail, A.A., Ding, Z., Al-Harbi, M.S., Ali, E.F., Abeed, A.H.A., Rekaby, S.A., Eissa, M.A., Ghoneim, A.M. and Tammam, S.A., 2021. Effect of manure and compost on the phytostabilization potential of heavy metals by the halophytic plant wavy-leaved saltbush. *Plants*, 10(10), p.2176. [DOI]

Maalouf, A. and Mavropoulos, A., 2023. Re-assessing global municipal solid waste generation. *Waste Management & Research*, 41(4), pp.936-947. [DOI]

Manea, E.E., Bumbac, C., Dinu, L.R., Bumbac, M. and Nicolescu, C.M., 2024. Composting as a sustainable solution for organic solid waste management: Current practices and potential improvements. *Sustainability*, 16(15), p.6329. [DOI]

Marathe, N. and Chavan, B.P., 2022. CHNS analysis of soil samples from Patalganga (Maharashtra, India). *Journal of Emerging Technologies and Innovative Research*, 9(3), pp.c134-c141. Retrieved from: https://www.jetir.org/view?paper=JETIR2203221.

Marchiol, L., Assolari, S., Sacco, P. and Zerbi, G., 2004. Phytoextraction of heavy metals by canola (*Brassica napus*) and radish (*Raphanus sativus*) grown on multicontaminated soil. *Environmental Pollution*, 132(1), pp.21-27. [DOI]

Podar, D. and Maathuis, F.J.M., 2022. The role of roots and rhizosphere in providing tolerance to toxic metals and metalloids. *Plant, Cell & Environment*, 45(3), pp.719-736. [DOI]

Qdais, H.A., Wuensch, C., Dornack, C. and Nassour, A., 2019. The role of solid waste composting in mitigating climate change in Jordan. *Waste Management & Research*, 37(8), pp.833-842. [DOI]

Rodríguez-Espinosa, T., Navarro-Pedreño, J., Gómez Lucas, I., Almendro Candel, M.B., Pérez Gimeno, A. and Zorpas, A.A., 2023. Soluble elements released from organic wastes to increase available nutrients for soil and crops. *Applied Sciences*, 13(2), p.1151. [DOI]

Roy, E.D., Esham, M., Jayathilake, N., Otoo, M., Koliba, C., Wijethunga, I.B. and Fein-Cole, M.J., 2021. Compost quality and markets are pivotal for sustainability in circular food-nutrient systems: A case study of Sri Lanka. *Frontiers in Sustainable Food Systems*, 5, p.748391. [DOI]

Seshadri, B., Bolan, N.S. and Naidu, R., 2015. Rhizosphere-induced heavy metal(loid) transformation in relation to bioavailability and remediation. *Journal of Soil Science and Plant Nutrition*, 15(2), pp.524-548. [DOI]

Soni, A., Kumar, P. and Prabhat, D., 2023. A review on the municipal solid waste management status, challenges and potential for future Indian cities. *Environment, Development and Sustainability*, 25, pp.13733-13760. [DOI]

Xu, D., Shen, Z., Dou, C., Dou, Z., Li, Y., Gao, Y. and Sun, Q., 2022. Effects of soil properties on heavy metal bioavailability and accumulation in crop grains under different farmland use patterns. *Scientific Reports*, 12, p.9211. [DOI]

Yuksel, O., 2015. Influence of municipal solid waste compost application on heavy metal content in soil. *Environmental Monitoring and Assessment*, 187(6), p.313. [DOI]

Nature Environment and Pollution Technology
An International Quarterly Peer-Reviewed Open Access Journal

p-ISSN: 0972-6268 | e-ISSN: 2395-3454 Vol. 25 | No. 4 | Article ID D1895 | 2026

RESEARCH ARTICLE https://doi.org/10.46488/NEPT.2026.v25i04.D1895 OPEN ACCESS

Analysis of NH_3 Distribution and Community Perception of Odor in the Antang Landfill Area, Makassar City

Qurin Septifar Aulia, Muhammad Isran Ramli and Sumarni Hamid Aly†
Department of Environmental Engineering, Faculty of Engineering, Hasanuddin University, Makassar, Indonesia
†Corresponding author: Sumarni Hamid Aly; marnihamidaly@yahoo.com

ARTICLE HISTORY

Received: 27-12-2025
Revised: 24-02-2026
Accepted: 16-03-2026

KEYWORDS

Ammonia
Landfill
Spatial distribution of NH_3
Odor
Community perception

CITE THIS ARTICLE

Aulia, Q.S., Ramli, M.I. and Aly, S.H., 2026. Analysis of NH_3 distribution and community perception of odor in the Antang landfill area, Makassar City. *Nature Environment and Pollution Technology*, 25(4), D1895. https://doi.org/10.46488/NEPT.2026.v25i04.D1895

COPYRIGHT & LICENCE

© 2026 The Authors
Open Access under CC BY 4.0.

PUBLISHED BY

TECHNOSCIENCE PUBLICATIONS

ABSTRACT

This study analyzes ammonia (NH_3) concentrations, spatial distribution, and community perceptions of odor around the Antang Landfill (TPA Antang) in Makassar, Indonesia. NH_3 measurements were conducted using the impinger method at five sampling points based on distance and the dominant wind direction, with spatial visualization performed using inverse distance weighting (IDW) interpolation in ArcGIS. Community perceptions were assessed through questionnaires administered to 100 respondents living within a radius of 20–1,000 m from the landfill. The results showed that the highest NH_3 concentration occurred at Point 3 (landfill area), reaching 5.885 ppm at night, exceeding the national odor threshold of 2 ppm. The spatial distribution indicated dominant dispersion from southeast to northwest, consistent with the prevailing wind direction. Approximately 67% of respondents reported odor disturbances, and 63% reported health-related symptoms such as headaches, nausea, and shortness of breath. The findings highlight the urgent need for improved landfill management and odor control strategies.

1. INTRODUCTION

Rapid urbanization, population growth, and increasing consumption patterns have become major drivers of municipal solid waste generation in developing cities worldwide, particularly in Southeast Asia (Imran 2024, World Bank 2018, WHO 2018). Urban centers experiencing accelerated economic growth often have waste generation rates that exceed the capacity of existing waste management infrastructure, leading to environmental degradation and heightened public health risks (Hoornweg & Bhada-Tata 2012, Kaza et al. 2018). In many developing countries, including Indonesia, landfill-based disposal remains the dominant waste management strategy, with a large proportion of facilities still operating under open dumping systems that lack adequate environmental safeguards (Putri et al. 2020, World Bank 2018).

Makassar City, one of the fastest-growing metropolitan areas in Eastern Indonesia, exemplifies these challenges. All municipal solid waste generated in the city is disposed of at the Antang landfill, which continues to operate using an open dumping method. This practice facilitates uncontrolled aerobic and anaerobic decomposition of organic waste, resulting in the release of various gaseous pollutants into the surrounding atmosphere (U.S. EPA 2017, Le Cloirec et al. 2012). Among these emissions, ammonia (NH_3) has been identified as one of the most significant pollutants due to its high volatility, strong odor, and potential

adverse effects on environmental quality and human health (ATSDR 2004, Fang et al. 2017).

Previous studies conducted in Makassar have highlighted the presence of ammonia (NH_3) as an important air pollutant in urban environments. Ramli et al. (2023) reported measurable ambient NH_3 concentrations associated with anthropogenic activities, indicating that NH_3 contributes to localized air quality degradation and odor-related disturbances. These findings underscore the importance of investigating NH_3 emissions originating from municipal solid waste disposal sites, such as landfills, where organic waste decomposition constitutes a major source of NH_3 release into the atmosphere. Ammonia is primarily generated through the microbial degradation of nitrogen-rich organic materials, including food waste and animal residues commonly present in municipal solid waste streams (McGinn et al. 2007, Seinfeld & Pandis 2016). Even at relatively low ambient concentrations, NH_3 can cause irritation of the eyes, skin, and respiratory tract, reduce overall environmental comfort, and trigger odor nuisance complaints among nearby residents (Sutrisno 2011, Kim & Park 2008, WHO 2018). Moreover, NH_3 plays a crucial role in secondary particulate matter formation through atmospheric reactions with acidic compounds, thereby indirectly contributing to broader air quality degradation (Behera et al. 2013, Seinfeld & Pandis 2016).

The dispersion and spatial distribution of NH_3 emissions from landfill sites are strongly influenced by local meteorological conditions, including air temperature, humidity, wind speed, wind direction, and atmospheric stability (Maulidah et al. 2021, Rizki et al. 2020, Duan et al. 2014). Elevated temperatures tend to enhance NH_3 volatilization, while wind characteristics determine both the direction and extent of pollutant transport (Sarkar et al. 2003, Nascimento et al. 2014). International studies have demonstrated that NH_3 plumes originating from landfill and waste treatment facilities can affect residential areas located more than one kilometer away from the emission source under favorable meteorological conditions (Duan et al. 2014, Fang et al. 2017, Nascimento et al. 2014).

Despite the recognized importance of spatial variability in air pollutant exposure, many landfill-related air quality assessments continue to rely on limited point-based measurements that are insufficient to capture the full extent of pollutant dispersion (Mohan & Kandya 2015, Wang et al. 2019). To address this limitation, geospatial approaches using Geographic Information Systems (GIS) and spatial interpolation techniques have been increasingly applied to visualize air pollution patterns and identify high-risk exposure zones (Jerrett et al. 2005, Wang et al. 2019). Among these techniques, inverse distance weighting (IDW) has been widely used due to its simplicity, transparency, and suitability for datasets with limited sampling density, making it particularly relevant for environmental monitoring in developing regions (Li & Heap 2014, Wang et al. 2019). However, the application of IDW-based spatial mapping specifically to NH_3 emissions around landfill sites remains limited, especially in rapidly urbanizing cities such as Makassar.

In addition to physical and chemical measurements, odor nuisance represents a critical yet often underrepresented dimension of environmental pollution. Odor exposure has been shown to affect not only physical health but also psychological well-being, stress levels, and overall quality of life (Steinheider et al. 1998, Blanes-Vidal et al. 2012). Community perceptions of odor provide valuable insights into real-world exposure conditions, as residents experience pollution continuously and subjectively beyond the temporal constraints of instrumental monitoring (Kim & Park 2008, Le Cloirec et al. 2012). Nevertheless, studies that integrate objective air quality measurements with subjective community perception assessments remain scarce, particularly in the context of landfill-related NH_3 emissions in developing countries (Zilfani et al. 2021, Nascimento et al. 2014).

At the Antang landfill, existing studies have largely focused on general environmental assessments or isolated pollutant measurements without incorporating spatial modeling or community-based perception analysis. This lack of integrated assessment has resulted in an incomplete understanding of NH_3 exposure risks faced by surrounding communities, thereby limiting the effectiveness of policy interventions, spatial planning decisions, and landfill management strategies (WHO 2018, U.S. EPA 2017, World Bank 2018).

Based on the environmental challenges and research gaps identified above, this study is designed to address key research questions related to ammonia (NH_3) emissions from landfill activities at the Antang landfill in Makassar City. Specifically, this research seeks to answer the following questions: (1) What are the ambient NH_3 concentration levels across different zones and distances from the emission source around the Antang landfill? (2) How are NH_3 concentrations spatially distributed based on GIS-based mapping using the inverse distance weighting (IDW) interpolation method? (3) How do local communities perceive odor exposure and environmental comfort disturbances associated with NH_3 emissions in the vicinity of the Antang landfill?

Addressing these questions is expected to provide an integrated scientific basis for improving landfill management

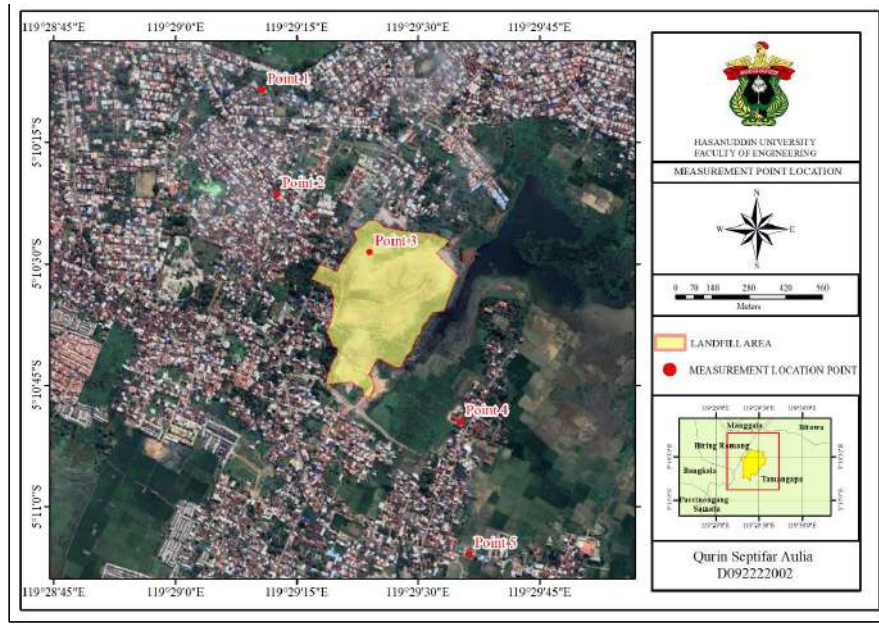


Fig. 1: Map of the research location.

practices, supporting risk-based spatial planning, and informing evidence-based air pollution mitigation strategies in Makassar City.

2. MATERIALS AND METHODS

2.1. Study Area

The Antang Tamangapa landfill serves as the primary waste management facility for Makassar City. Situated in Tamangapa Village within Manggala District, it spans approximately 14.3 ha. Surrounded by residential areas and plantations, the landfill has been operational since 1994 and receives waste from 14 subdistricts, making it the largest disposal site in Makassar. The research was conducted in February 2025, during which NH_3 levels were measured at selected points around the landfill. The specific locations of the sampling sites are shown in Fig. 1.

2.2. Collection Techniques

The data collection process in this study was conducted through several stages, including:

2.2.1. Determination of Sampling Locations

The study was conducted at five sampling points surrounding the Tamangapa Landfill. Point 1 was situated 1,000 m northwest, Point 2 at 500 m northwest, Point 3 just 20 m from the landfill, Point 4 at 500 m southeast, and Point 5 at 1,000 m southeast. Sampling locations were selected based on the Indonesian National Standard SNI 19-71196-2005 for ambient air quality monitoring. The criteria included areas with high pollutant levels, high population density, zones surrounding the research site, and projection areas that accurately reflect the entire study area. The prevailing wind direction during the study period is illustrated in Fig. 2.

2.2.2. NH_3 Sampling Procedure

Air sampling was carried out in February 2025 at five designated points. Measurements occurred during four distinct periods, morning, midday, afternoon, and night, with each session lasting 1 h. Each sampling point and time period was sampled once. NH_3 levels were measured using a manual impinger method at the same four intervals, following the Regulation of the Ministry of Environment and Forestry

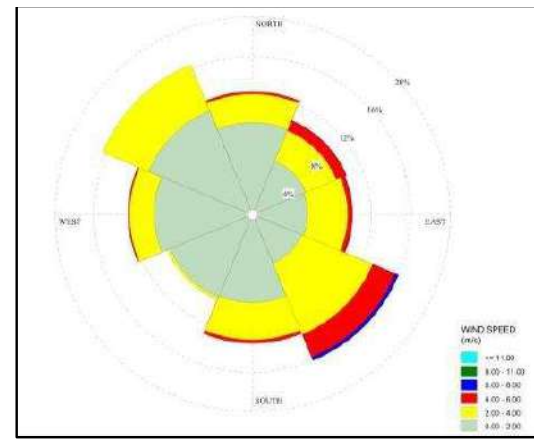


Fig. 2: Wind rose for the monitoring area.



Fig. 3: Impinger used for NH_3 sampling.

(Permen LHK) No. 27/2021. All procedures adhered to the Indonesian National Standard SNI 19-71196-2005. The equipment used in this study is illustrated in Fig. 3.

NH_3 sampling took place on five separate days during the rainy season in February. At each sampling location, data were collected across four distinct time periods, morning (06:00–10:00), midday (10:00–14:00), afternoon (14:00–18:00), and night (18:00–22:00), to capture diurnal variations. During each period, active sampling was conducted for 1 h. This sampling approach complied with the Regulation of the Indonesian Minister of Environment No. 12 of 2010, ensuring that measurements reflected different atmospheric conditions and landfill activity levels throughout the day. To ensure data accuracy and capture diurnal patterns, measurements at each point were replicated across all four

Table 1: Geographic coordinates and sampling schedule for NH_3 monitoring in the Antang Landfill area.

Point	Distance and Direction from Source	Coordinate Point		Sampling Date (2025)
		X	Y	
1	1,000 m northwest	-5.1703023	119.4864544	7 February 2025
2	500 m northwest	-5.1733633	119.4861909	10 February 2025
3	Inside Landfill (Source)	-5.1737923	119.4901854	12 February 2025
4	500 m Southeast	-5.1810248	119.4928253	14 February 2025
5	1,000 m southeast	-5.1854540	119.4929906	14 February 2025

Table 2: Meteorological data summary.

Location Point	Point	Meteorological Data	Interval			
			Morning	Midday	Afternoon	Night
1	Located 1,000 m northwest of the landfill site	Temperature (°C)	30	31	30	29
		Relative Humidity (%)	86	74	78	75
		Atmospheric pressure (mmHg)	759.03	757.54	758.04	758.11
		Wind speed (m s^{-1})	1.1	0.85	0.9	1.05
2	Located 500 m northwest of the landfill site	Temperature (°C)	29	30	33	29
		Relative humidity (%)	85	77	73	84
		Atmospheric pressure (mmHg)	759.1	758.2	757.02	759.03
		Wind speed (m s^{-1})	2.05	1.45	1.33	1.35
3	Landfill site point	Temperature (°C)	30	33	28	28
		Relative humidity (%)	81	79	83	81
		Atmospheric pressure (mmHg)	758.04	757.84	759.42	759.08
		Wind speed (m s^{-1})	1.08	1.05	1.65	1.55
4	Located 500 m southeast of the landfill site	Temperature (°C)	30	32	30	29
		Relative humidity (%)	82	81	82	84
		Atmospheric pressure (mmHg)	758.01	757.05	758.81	759.08
		Wind speed (m s^{-1})	2.55	3.25	2.75	2.35
5	Located 1,000 m southeast of the landfill site	Temperature (°C)	29	33	32	29
		Relative humidity (%)	89	80	82	84
		Atmospheric pressure (mmHg)	759.08	757.03	758.93	759.11
		Wind speed (m s^{-1})	1.05	2.4	1.15	1.55

time intervals in accordance with national monitoring standards. The sampling coordinates and schedule are presented in Table 1, and the corresponding meteorological data are summarized in Table 2.

2.2.3. Community Perception Data Collection

Community perception data were collected through the distribution of structured questionnaires. The questionnaire instrument was developed based on previous studies. The study population comprised all households in Antang Subdistrict (18,533 households) and Tamangapa Subdistrict (17,845 households), resulting in a total population of 36,378 households. To determine a representative sample size, Slovin's formula was applied with a margin of error (d) set at 0.1. Based on this calculation, a sample size of 99.7 households was obtained and subsequently rounded up to 100 respondents for the community perception survey. The respondents were evenly distributed across two residential radius zones ($\leq$500 m and >500–1,000 m). Each household was represented by one respondent of productive age (15–64 years) who resided in the vicinity of the landfill, thereby ensuring relevant representation of community perceptions regarding local environmental conditions. Responses to the odor disturbance question were initially measured using a four-point Likert scale (strongly agree, agree, disagree, and strongly disagree). For statistical analysis, the responses were grouped into two categories: "disturbed" (strongly agree and agree) and "not disturbed" (disagree and strongly disagree). A chi-square test was used

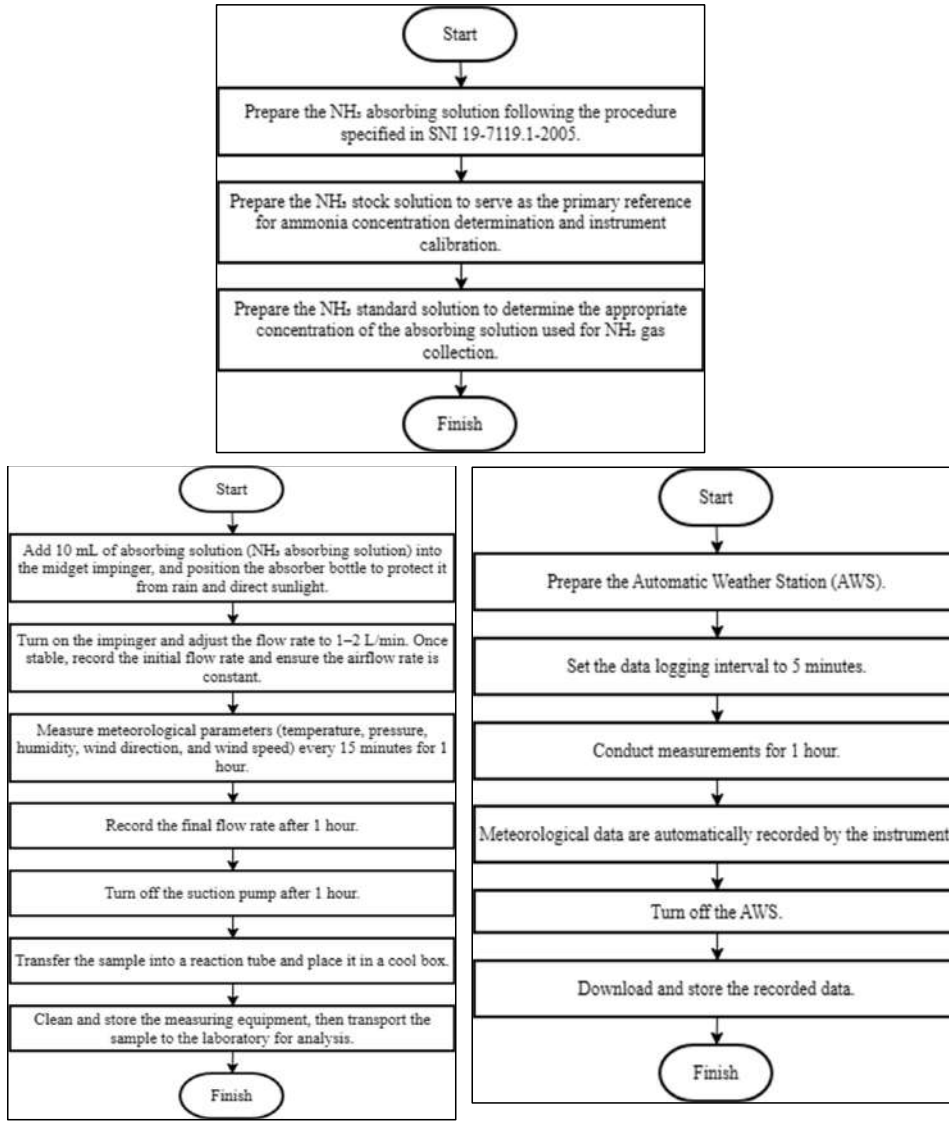


Fig. 4: Diagram of NH_3 pollutant data processing.

to examine the association between respondent characteristics and perceptions of odor disturbance.

2.2.4. Ethical Considerations

This study adhered to fundamental ethical research principles involving human participants. Prior to data collection, respondents were provided with a clear explanation of the study objectives, procedures, and intended use of the data. Participation was entirely voluntary, and informed consent was obtained from all respondents before the questionnaire was administered. Participants were assured that their responses would remain anonymous and confidential and that the collected data would be used exclusively for academic and research purposes. Furthermore, respondents were informed of their right to decline participation or withdraw from the study at any stage without any penalty or consequences.

2.3. Data Analysis

Data analysis involved the use of Excel for concentration calculations and questionnaire data processing, while ArcGIS was used for visualization. The NH_3 data-processing workflow is illustrated in Fig. 4.

2.3.1. NH_3 Data Analysis

2.3.2. Visualization of NH_3 Gas Distribution

After determining the average concentration values obtained at each sampling point, a spatial visualization of NH_3 gas distribution was generated using the inverse distance weighting (IDW) interpolation method in ArcGIS. The visualization workflow is shown in Fig. 5, and the resulting spatial distribution map is presented in Fig. 11.

The determination of interval classes was preceded by defining the number of classes used to group the data. Therefore, selecting an appropriate number of classes is a crucial step in data mapping. The number of classes was determined using Sturges' formula, as expressed in Equation (1).

$$K = 1 + 3.3 log\ n \quad ...(1)$$

Where:

K = number of classes,

n = number of data sets.

2.3.3. Questionnaire Data Analysis

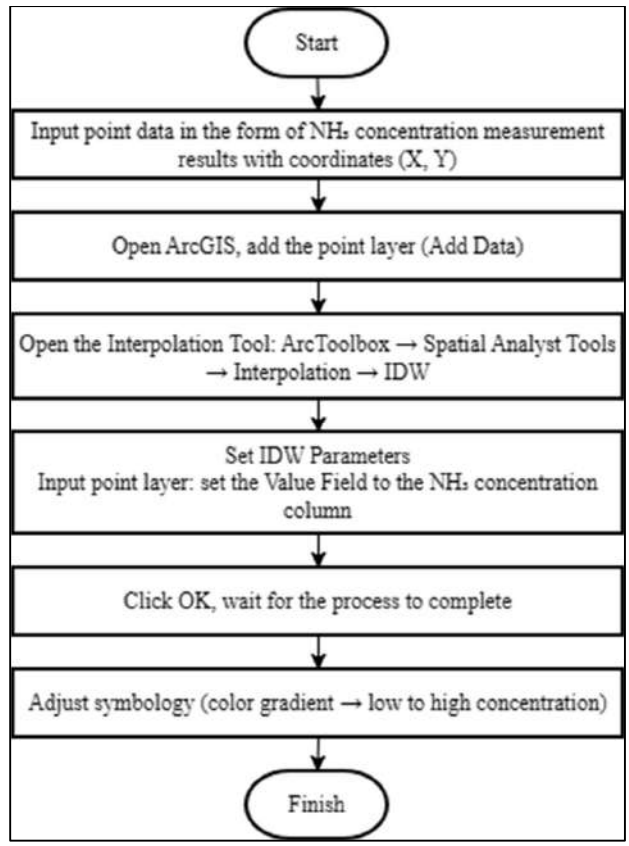


Fig. 5: NH_3 distribution visualization flowchart.

The percentage of questionnaires can be calculated using the following formula:

$$P = \frac{F}{n} x\ 100\% \quad \ldots(2)$$

Note:

- P = percentage (%)
- F = frequency of responses
- *n = total number of respondents*

The percentage formula is used to express the frequency of responses as a percentage of the total number of respondents.

3. RESULTS AND DISCUSSION

3.1. NH_3 Concentration

The NH_3 concentration was determined by collecting samples hourly over four periods: morning, midday, afternoon, and night. These ambient air samples, collected using an impinger air sampler, were analyzed in the laboratory to determine concentrations in ppm. The results for Point 1 are shown in Fig. 6. To assess regulatory compliance, the measured NH_3 levels were compared with the national odor standard. According to the Minister of Environment Decree No. 50 of 1996, the permissible ammonia limit is 2 ppm. For comparison with mass-based concentrations, the measured NH_3 concentrations were converted from ppm to μg m^{-3} using the ideal gas relationship at the reference conditions of 25°C and 1 atm (760 mmHg). Under these conditions, 1 ppm NH_3 is approximately equivalent to 697 μg m^{-3}, and the regulatory limit of 2 ppm is approximately equivalent to 1,394 μg m^{-3}. Each data point represents a 1 h average, consistent with the sampling protocol. The complete measurement data across all sampling points and time periods are presented in Table 3

3.1.1. NH_3 Concentration at Sampling Point 1

Based on the direct measurement results of ammonia (NH_3) concentration at Point 1, located 1,000 m northwest of the source (landfill site), sampling was conducted for 1 h at each time interval (morning, midday, afternoon, and night). All measured concentrations remained below the ammonia odor threshold of 2 ppm. As stated in the Decree of the State Minister of Environment No. 50 of 1996 concerning Odor Level Quality Standards, the threshold is equivalent to approximately 1,394 μg m^{-3}. The highest concentration was recorded at midday at 90.71 μg m^{-3}, while the lowest was observed in the morning at 2.88 μg m^{-3}. The concentrations were 2.88 μg m^{-3} (morning), 90.71 μg m^{-3} (midday), 52.55 μg m^{-3} (afternoon), and 40.49 μg m^{-3} (night), as shown in Fig. 6.

Table 3: Concentration (μg m^{-3}).

Sampling Point	Interval	Concentration (μg m^{-3})	Concentration (ppm)	Status
Point 1	Morning	2.876	0.004	Within the regulatory limit
	Midday	90.710	0.130	Within the regulatory limit
	Afternoon	52.553	0.075	Within the regulatory limit
	Night	40.486	0.058	Within the regulatory limit
Point 2	Morning	156.140	0.224	Within the regulatory limit
	Midday	130.632	0.188	Within the regulatory limit
	Afternoon	291.977	0.419	Within the regulatory limit
	Night	255.178	0.366	Within the regulatory limit
Point 3	Morning	2,108.438	3.027	Exceeds the regulatory limit
	Midday	1,663.853	2.389	Exceeds the regulatory limit
	Afternoon	1,452.921	2.086	Exceeds the regulatory limit
	Night	4,099.013	5.885	Exceeds the regulatory limit
Point 4	Morning	166.122	0.238	Within the regulatory limit
	Midday	79.099	0.114	Within the regulatory limit
	Afternoon	170.899	0.245	Within the regulatory limit
	Night	219.790	0.316	Within the regulatory limit
Point 5	Morning	2.866	0.004	Within the regulatory limit
	Midday	19.629	0.028	Within the regulatory limit
	Afternoon	36.240	0.052	Within the regulatory limit
	Night	26.447	0.038	Within the regulatory limit

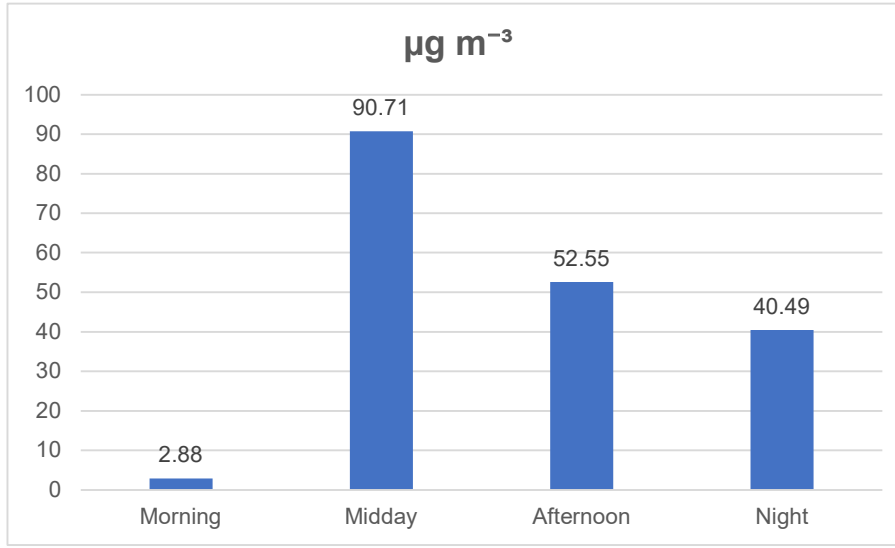


Fig. 6: Ammonia concentration at sampling point 1.

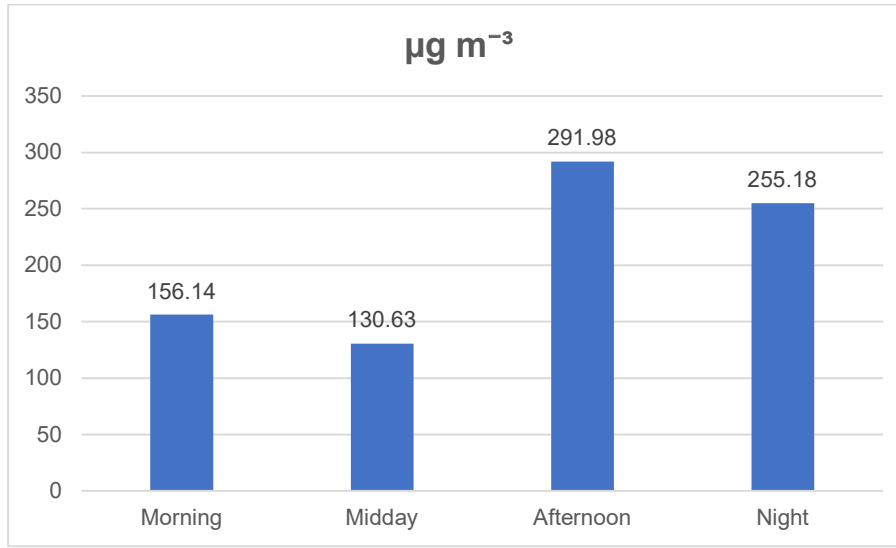


Fig. 7: Ammonia concentration at sampling point 2.

3.1.2. NH_3 Concentration at Sampling Point 2

Based on the direct measurement results of ammonia (NH_3) concentrations at Point 2, located 500 m northwest of the landfill site, sampling was conducted for 1 h at each time interval. The results showed fluctuations in daily concentrations. The lowest concentration was recorded at midday at 130.63 µg m^{-3}, while the highest concentration occurred in the afternoon at 291.98 µg m^{-3}. The concentration in the morning was 156.14 µg m^{-3}, and at night it reached 255.18 µg m^{-3}. This pattern suggests the accumulation of emissions and the influence of atmospheric stability conditions during the afternoon and nighttime periods. Although variations were observed across the different time intervals, all measured values remained below the odor threshold of 2 ppm, equivalent to approximately 1,394 µg m^{-3}. Therefore, the ambient NH_3 concentration at Point 2 remained below the applicable odor threshold. The temporal concentration profile is shown in Fig. 7.

3.1.3. NH_3 Concentration at Sampling Point 3

The results of ammonia (NH_3) concentration measurements at Point 3, located directly at the landfill emission source, showed higher concentrations than those at the other

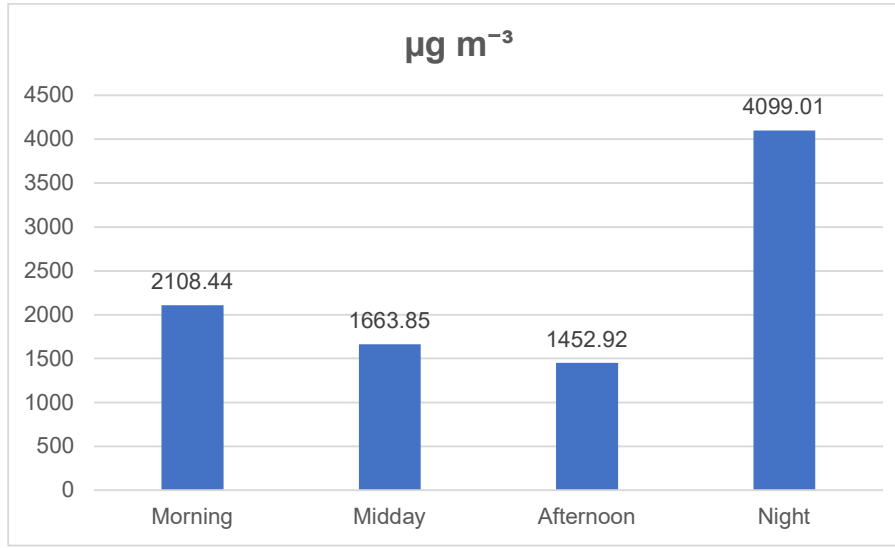


Fig. 8: Ammonia concentration at sampling point 3.

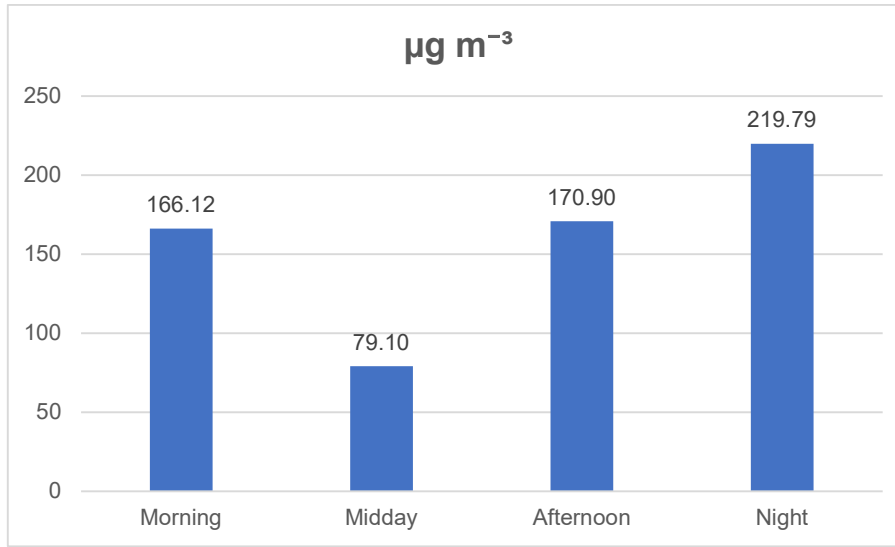


Fig. 9: Ammonia concentration at sampling point 4.

monitoring points. Measurements were conducted for 1 h during each observation interval, resulting in concentrations of 2,108.44 µg m^{-3} in the morning, 1,663.85 µg m^{-3} at midday, 1,452.92 µg m^{-3} in the afternoon, and 4,099.01 µg m^{-3} at night. All measured concentrations at Point 3 exceeded the odor threshold of 1,394 µg m^{-3} (equivalent to 2 ppm), as specified in the Decree of the State Minister of Environment No. 50 of 1996 concerning Odor Level Quality Standards. This indicates a strong potential for odor disturbance in areas located close to the landfill emission source. The highest concentration was observed during the nighttime period (4,099.01 µg m^{-3}), which may have been influenced by atmospheric conditions such as temperature inversion and lower wind speeds, leading to the accumulation of ammonia emissions near the ground surface. In contrast, the relatively lower concentrations recorded at midday and in the afternoon may be associated with higher temperatures and stronger atmospheric mixing, which enhance the dispersion and dilution of gaseous pollutants in the atmosphere. These findings indicate that Point 3 had the highest NH_3 concentration among all monitoring points, highlighting the landfill site as the primary source of ammonia emissions in the study area. The temporal concentration profile is shown in Fig. 8.

3.1.4. NH_3 Concentration at Sampling Point 4

Based on the direct measurement results of ammonia (NH_3) concentrations at Point 4, located 500 m southeast of the landfill site, variations in concentration were observed at each time interval, indicating daily fluctuations. The highest concentration was recorded at night at 219.79 µg m^{-3}, while the lowest concentration occurred at midday at 79.10 µg m^{-3}. The concentrations measured in the morning (166.12 µg m^{-3}) and afternoon (170.90 µg m^{-3}) were intermediate. This pattern shows an increase in concentration

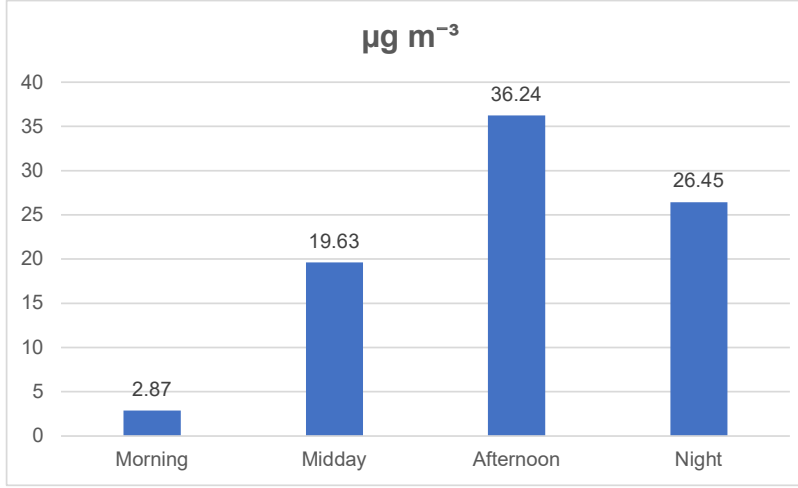


Fig. 10: Ammonia concentration at sampling point 5.

Table 4: Results of Shapiro-Wilk normality test for environmental and atmospheric parameters across all observation points.

Point	Variable	Shapiro-Wilk Statistic	df	p-value (Sig.)	Remark
1	Odor concentration	0.989	4	0.954	Normally Distributed
	Temperature	0.945	4	0.683	Normally Distributed
	Humidity	0.862	4	0.267	Normally Distributed
	Pressure	0.927	4	0.579	Normally Distributed
	Wind speed	0.911	4	0.488	Normally Distributed
2	Odor concentration	0.903	4	0.446	Normally Distributed
	Temperature	0.791	4	0.086	Normally Distributed
	Humidity	0.897	4	0.416	Normally Distributed
	Pressure	0.746	4	0.035	Normally Distributed
	Wind speed	0.751	4	0.04	Normally Distributed
3	Odor concentration	0.816	4	0.133	Normally Distributed
	Temperature	0.848	4	0.22	Normally Distributed
	Humidity	0.963	4	0.798	Normally Distributed
	Pressure	0.988	4	0.948	Normally Distributed
	Wind speed	0.825	4	0.155	Normally Distributed
4	Odor concentration	0.928	4	0.58	Normally Distributed
	Temperature	0.895	4	0.406	Normally Distributed
	Humidity	0.827	4	0.161	Normally Distributed
	Pressure	0.929	4	0.59	Normally Distributed
	Wind speed	0.949	4	0.712	Normally Distributed

at night, which is likely influenced by more stable atmospheric conditions that promote gas accumulation near the ground surface. Nevertheless, all recorded concentrations remained below the odor threshold of 2 ppm, equivalent to approximately 1,394 μg m^{-3}. The temporal concentration profile is shown in Fig. 9.

3.1.5. NH_3 Concentration at Sampling Point 5

Direct NH_3 measurements conducted over a 1 h observation period 1,000 m southeast of the landfill (Point 5) demonstrated distinct temporal variations. The recorded concentrations were 2.87 μg m^{-3} in the morning, 19.63 μg m^{-3} at midday, 36.24 μg m^{-3} in the afternoon, and 26.45 μg m^{-3} at night. The peak concentration observed in the afternoon is likely attributable to elevated ambient temperatures, which enhance ammonia volatilization from decomposing organic waste. Increased landfill operational activities during the daytime may have further contributed to higher emissions. The relatively elevated nighttime concentration may be associated with more stable atmospheric conditions that reduce vertical mixing and limit pollutant dispersion. In contrast, the lowest concentration recorded in the morning may reflect lower temperatures and more favorable atmospheric mixing conditions. The temporal concentration profile is shown in Fig. 10.

The results of the normality assessment using the Shapiro-Wilk test are presented in Table 4. The Shapiro-Wilk test was selected because it is suitable for assessing normality in small samples ($N < 50$). Variables across the observation points, including odor concentration, temperature, humidity, pressure, and wind speed, were assessed for normality, and the results are presented in Table 4. The suitability of the data for parametric correlation analysis should be interpreted in accordance with the verified Shapiro-Wilk results before applying the Pearson correlation test presented in Table 5.

3.2. Visualization of NH_3 Concentration Distribution

The measured NH_3 concentrations showed spatial variability across the five sampling points. The highest hourly concentration was recorded at Point 3 during nighttime (5.885 ppm), exceeding the regulatory limit of 2 ppm for a 1 h average concentration. In contrast, the other sampling points remained within the permissible limit throughout the monitoring period. In mass concentration units, the maximum value corresponds to 4,099.013 μg m^{-3}, which is higher than the equivalent regulatory threshold of 1,394 μg m^{-3} (25°C, 1 atm). The consistently elevated concentrations observed at Point 3 during all monitoring intervals suggest the presence of a local emission source associated with landfill activities.

Table 5: Pearson correlation analysis between atmospheric variables and odor concentration across observation points.

Point	Variable	r	p-value	Interpretation
T1	Temperature	0.566	0.434	Moderate positive correlation
	Humidity	-0.86	0.14	Strong negative correlation
	Pressure	-0.976*	0.024	Significant negative correlation
	Wind speed	-0.919	0.081	Strong negative correlation
T2	Temperature	0.867	0.133	Very strong positive correlation
	Humidity	-0.994*	0.006	Significant negative correlation
	Pressure	-0.968*	0.032	Significant negative correlation
	Wind speed	-0.65	0.35	Strong negative correlation
T3	Temperature	-0.441	0.559	Moderate negative correlation
	Humidity	-0.071	0.929	Very weak negative correlation
	Pressure	0.271	0.729	Weak positive correlation
	Wind speed	0.31	0.69	Weak positive correlation
T4	Temperature	0.915	0.085	Very strong positive correlation
	Humidity	-0.998	0.002	Significant negative correlation
	Pressure	-0.84	0.16	Strong negative correlation
	Wind speed	0.901	0.099	Very strong positive correlation
T5	Temperature	0.628	0.372	Strong positive correlation
	Humidity	-0.911	0.089	Very strong negative correlation
	Pressure	-0.711	0.289	Strong negative correlation
	Wind speed	0.873	0.127	Very strong positive correlation



Fig. 11: Visualization of NH_3 distribution patterns at the Antang Landfill.

Table 6: Association between respondent characteristics and community perception of odor disturbance from the landfill.

Variable	Category	Disturbed n (%)	Not Disturbed n (%)	Total	p-value
Distance & Direction	20 m	15 (71.4)	6 (28.6)	21	0.009
	500 m Southeast	15 (78.9)	4 (21.1)	19	
	1 km Southeast	16 (80.0)	4 (20.0)	20	
	500 m West	6 (30.0)	14 (70.0)	20	
	1 km West	14 (70.0)	6 (30.0)	20	
Gender	Male	35 (67.3)	17 (32.7)	52	0.695
	Female	30 (62.5)	18 (37.5)	48	
Age	<20 years	4 (50.0)	4 (50.0)	8	0.077
	20–30 years	24 (60.0)	16 (40.0)	40	
	31–40 years	22 (64.7)	12 (35.3)	34	
	41–50 years	4 (36.4)	7 (63.6)	11	
	>50 years	6 (75.0)	2 (25.0)	8	
Education	Elementary School	11 (84.6)	2 (15.4)	13	0.378
	Junior High School	10 (71.4)	4 (28.6)	14	
	Senior High School	15 (55.6)	12 (44.4)	27	
	Diploma/Bachelor	30 (66.7)	15 (33.3)	45	
	Postgraduate	2 (100)	0 (0)	2	
Occupation	Civil Servant	11 (61.1)	7 (38.9)	18	0.442
	Private Sector Employee	14 (56.0)	11 (44.0)	25	
	Entrepreneur	12 (63.2)	7 (36.8)	19	
	Housewife	6 (46.2)	7 (53.8)	13	
	Waste Picker	10 (40.0)	15 (60.0)	25	

To visualize the spatial distribution pattern, inverse distance weighting (IDW) interpolation was applied using the average NH_3 concentration at each sampling point rather than individual hourly measurements. The averaged dataset ranged from 0.031 to 3.3466 ppm, which explains the difference between the interpolated maximum value and the highest hourly concentration reported in the measurements. The data were classified into four classes using Sturges' formula, resulting in an approximate class width of 0.829 ppm. The interpolated map indicates a concentration gradient in which higher NH_3 levels appear near Point 3 and gradually decrease toward the surrounding areas. This pattern suggests that NH_3 dispersion in the study area is influenced by proximity to the landfill emission source and atmospheric dilution processes with increasing distance. However, it should be noted that the spatial interpolation was based on a limited number of monitoring points; therefore, the resulting distribution map should be interpreted as a preliminary representation of the spatial pattern rather than a precise prediction of concentration levels.

3.3. Community Perception of Odor from the Antang Landfill, Makassar City

3.3.1. Disturbance Caused by Landfill Odor

As summarized in Table 6, residential distance and orientation were identified as the only variables with a statistically significant relationship to the perceived level of odor disturbance ($p = 0.009 < 0.05$). Spatial patterns indicate that the Southeast sector experienced the highest level of disturbance, with 31% of respondents at distances between 500 m and 1 km consistently reporting subjective complaints. Conversely, in the West sector within a 500 m radius, the highest proportion of "Strongly Disagree" responses (11%) was recorded. This suggests that localized factors, such as prevailing wind patterns and topography, may be more influential in the dispersion of odor pollutants than linear distance alone.

Demographically, individual characteristics did not show a significant influence on the perception of odor disturbance ($p > 0.05$). Analysis by gender showed a relatively even distribution of complaints, with 35% of males and 30% of females reporting disturbance. Regarding age, the productive-age group (20–40 years) provided the most critical responses, accounting for 46% of the total reported subjective complaints. Based on educational level, the majority of respondents with a diploma or bachelor's degree (30%) or a senior high school education (15%) reported disturbances, reflecting higher environmental awareness among more educated groups.

A unique phenomenon was observed within the occupation variable, particularly among the waste picker group. Despite being in a high-exposure zone, the number of

Table 7: Association between respondent characteristics and community agreement regarding odor exposure from the landfill.

Variable	Category	Disturbed n (%)	Not Disturbed n (%)	Total	p-value
Distance & Direction	20 m	13 (61.9)	8 (38.1)	21	0.35
	500 m Southeast	11 (57.9)	8 (42.1)	19	
	1 km Southeast	12 (44.4)	15 (55.6)	27	
	500 m West	10 (76.9)	3 (23.1)	13	
	1 km West	13 (65.0)	7 (35.0)	20	
Gender	Male	23 (46.9)	26 (53.1)	49	0.03
	Female	36 (70.6)	15 (29.4)	51	
Age	<20 years	0 (0.0)	1 (100.0)	1	0.31
	20–30 years	14 (56.0)	11 (44.0)	25	
	31–40 years	26 (63.4)	15 (36.6)	41	
	41–50 years	13 (50.0)	13 (50.0)	26	
	>50 years	6 (85.7)	1 (14.3)	7	
Education	Elementary School	9 (60.0)	6 (40.0)	15	0.88
	Junior High School	8 (72.7)	3 (27.3)	11	
	Senior High School	16 (55.2)	13 (44.8)	29	
	Diploma/Bachelor's Degree	28 (63.6)	16 (36.4)	44	
	Postgraduate	2 (66.7)	1 (33.3)	3	
Occupation	Civil Servant	14 (70.0)	6 (30.0)	20	0.13
	Private Sector Employee	16 (64.0)	9 (36.0)	25	
	Entrepreneur	8 (38.1)	13 (61.9)	21	
	Housewife	3 (100.0)	0 (0.0)	3	
	Waste Picker	18 (58.1)	13 (41.9)	31	

respondents who felt undisturbed (15%) exceeded those who felt disturbed (10%). This may indicate sensory adaptation or habituation, in which chronic exposure leads to a subjective decrease in olfactory sensitivity. Overall, reported physical symptoms, such as coughs or mild respiratory irritation, should be interpreted as self-reported symptoms representing a decline in environmental comfort rather than definitive causal medical diagnoses.

3.3.2. Experience of Health Disturbances (e.g., Eye Irritation, Shortness of Breath, Coughing, or Headache/Nausea)

As summarized in Table 7, residential distance and orientation were the only variables that showed a significant relationship with the frequency of self-reported health-related symptoms, such as nausea and coughing ($p = 0.014 < 0.05$). The spatial data indicate that these perceived disturbances did not decrease linearly with distance. While respondents in the immediate vicinity (20 m) reported a high level of concern (8% strongly agreeing), a notable peak of "Strongly Agree" responses (10%) was observed at 1 km west of the landfill. Conversely, respondents at 500 m west reported no significant disturbances, with 13 respondents selecting the "Disagree" category. This suggests that the dispersion of airborne pollutants, which respondents associate with their symptoms, is highly influenced by localized wind patterns and atmospheric channeling.

Demographic characteristics, including gender, age, education, and occupation, did not show statistically significant correlations with the reporting of health symptoms ($p > 0.05$). In terms of gender, females reported a higher frequency of perceived disturbances (36% combined agreement) than males (23%), indicating a potential difference in subjective sensitivity. The 31–40 age group and those with senior high school to undergraduate education levels were the most vocal in reporting symptoms, reflecting a higher tendency to associate environmental quality with physical well-being among the productive and educated population. The occupation analysis revealed that waste pickers reported the highest level of strong agreement (13%) regarding health-related symptoms. Given their prolonged and direct exposure to the landfill environment, this group perceived themselves as the most vulnerable to respiratory and olfactory discomfort.

Table 8: Association between respondent characteristics and perceived impact of landfill odor among surrounding residents.

Variable	Category	Disturbed n (%)	Not Disturbed n (%)	Total	p-value
Distance & Direction	20 m	13 (61.9)	8 (38.1)	21	0.032
	500 m Southeast	11 (57.9)	8 (42.1)	19	
	1 km Southeast	12 (44.4)	15 (55.6)	27	
	500 m West	10 (76.9)	3 (23.1)	13	
	1 km West	13 (65.0)	7 (35.0)	20	
Gender	Male	23 (46.9)	26 (53.1)	49	0.385
	Female	36 (70.6)	15 (29.4)	51	
Age	<20 years	0 (0)	1 (100.0)	1	0.471
	20–30 years	14 (56.0)	11 (44.0)	25	
	31–40 years	26 (63.4)	15 (36.6)	41	
	41–50 years	13 (50.0)	13 (50.0)	26	
	>50 years	6 (85.7)	1 (14.3)	7	
Education	Elementary School	9 (60.0)	6 (40.0)	15	0.112
	Junior High School	8 (72.7)	3 (27.3)	11	
	Senior High School	16 (55.2)	13 (44.8)	29	
	Diploma/Bachelor	28 (63.6)	16 (36.4)	44	
	Postgraduate	2 (66.7)	1 (33.3)	3	
Occupation	Civil Servant	14 (70.0)	6 (30.0)	20	0.612
	Private Sector Employee	16 (64.0)	9 (36.0)	25	
	Entrepreneur	8 (38.1)	13 (61.9)	21	
	Housewife	3 (100.0)	0 (0)	3	
	Waste Picker	18 (58.1)	13 (41.9)	31	

However, in accordance with the reviewer's feedback, these findings must be interpreted strictly as perception-based data. The reported symptoms, such as eye irritation, coughing, or nausea, are self-reported and do not constitute clinical medical diagnoses. They serve as subjective indicators of environmental nuisance and a perceived decline in quality of life associated with the landfill's operations.

3.3.3. Existing Odor Management Measures Implemented by Relevant Authorities at the Landfill

As summarized in Table 8, the statistical analysis for Question 3 indicates that residential distance and orientation are the only factors significantly associated with the community's perception of existing odor management measures ($p = 0.032 < 0.05$). The data primarily reflects a critical viewpoint, especially in the 1 km West and 20 m zones, where most respondents believe current mitigation efforts by authorities are insufficient. Notably, the 1 km Southeast sector exhibits a more divided response (12 agree vs. 15 disagree), suggesting that perceptions of management effectiveness are heavily influenced by localized exposure levels shaped by wind patterns and spatial positioning. While demographic variables such as Gender, Age, Education, and Occupation did not show statistically significant correlations ($p > 0.05$), descriptive patterns reveal that respondents with Diploma/Bachelor's degrees (28 respondents) and those aged 31–40 (26 respondents) are the most critical of current measures. Additionally, Waste Pickers, who face direct daily exposure, also largely agree (18 respondents) that odor control is inadequate. Consistent with the reviewer's guidance, these findings should be viewed as perception-based assessments of environmental governance. They reflect the community's dissatisfaction and the perceived gap between technical interventions and the actual reduction of environmental nuisances in their residential areas.

3.3.4. Improvement of Waste Management at the Landfill Is Needed

As summarized in Table 9, Question 4 shows a consistent perception of disturbance across all respondent categories. All respondents (100%) in every spatial and demographic category reported experiencing disturbance, while no respondents were classified as not disturbed. This pattern was observed across all distance and direction categories, including 20 m, 500 m southeast, 1 km southeast, 500 m west, and 1 km west.

Statistical analysis revealed no significant differences in reported disturbance across distance and direction ($p = 0.99$), gender ($p = 0.99$), age ($p = 0.98$), education ($p = 0.99$), or occupation ($p = 0.99$). Thus, within the study population, the

Table 9: Association between respondent characteristics and community perception indicating full agreement regarding landfill odor conditions.

Variable	Category	Disturbed n (%)	Not Disturbed n (%)	Total	p-value
Distance & Direction	20 m	21 (100.0)	0 (0.0)	21	0.99
	500 m Southeast	19 (100.0)	0 (0.0)	19	
	1 km Southeast	27 (100.0)	0 (0.0)	27	
	500 m West	13 (100.0)	0 (0.0)	13	
	1 km West	20 (100.0)	0 (0.0)	20	
Gender	Male	49 (100.0)	0 (0.0)	49	0.99
	Female	51 (100.0)	0 (0.0)	51	
Age	<20 years	1 (100.0)	0 (0.0)	1	0.98
	20–30 years	25 (100.0)	0 (0.0)	25	
	31–40 years	41 (100.0)	0 (0.0)	41	
	41–50 years	26 (100.0)	0 (0.0)	26	
	>50 years	7 (100.0)	0 (0.0)	7	
Education	Elementary School	15 (100.0)	0 (0.0)	15	0.99
	Junior High School	11 (100.0)	0 (0.0)	11	
	Senior High School	29 (100.0)	0 (0.0)	29	
	Diploma/Bachelor	44 (100.0)	0 (0.0)	44	
	Postgraduate	3 (100.0)	0 (0.0)	3	
Occupation	Civil Servant	20 (100.0)	0 (0.0)	20	0.99
	Private Sector Employee	25 (100.0)	0 (0.0)	25	
	Entrepreneur	21 (100.0)	0 (0.0)	21	

reported disturbance was consistently observed regardless of spatial location or demographic characteristics. For example, all 27 respondents in the 1 km southeast category reported disturbance, as did all respondents in the 20 m and western sectors.

The absence of respondents in the "Not Disturbed" category indicates a strong and consistent community perception of disturbance associated with the landfill environment. However, because all categories showed the same 100% proportion of disturbed respondents, the statistical tests did not identify differences between groups. These findings suggest that the perception of disturbance extends across the study area and is shared by respondents with different demographic backgrounds.

4. CONCLUSIONS

Based on the converted odor threshold limit of 1,394 μg m^{-3}, exceedances were observed solely at Sampling Point 3 (landfill source) across all time intervals, while concentrations at other locations remained below the regulatory threshold. The study results indicate that the highest ammonia (NH_3) concentration in the Antang landfill area occurred prominently at Sampling Point 3, located directly within the landfill site, reaching 5.885 ppm at night, well above the ambient NH_3 standard limit of 2 ppm. Conversely, Sampling Points 1 and 5, each situated 1,000 m from the landfill, recorded the lowest ammonia levels of 0.004 ppm in the morning, remaining comfortably below the permissible standard. Visual mapping of spatial distribution shows that the highest concentrations, depicted by red and orange hues, were centered around Point 3 and dispersed northwestward, covering Point 2 (500 m) and Point 1 (1,000 m). This pattern is strongly influenced by the prevailing southeast-to-northwest wind direction. In contrast, the lowest concentrations, indicated by dark green shades, were observed in areas up to 1,000 m from the landfill, particularly toward the southeast at Points 4 and 5, demonstrating a gradual decline in pollutant levels with increasing distance from the emission source. Community perception analysis, considering gender, age, education level, occupation, and residential distance, revealed that 67% of respondents reported being disturbed by landfill odors. This disturbance was most acute among residents residing closest to the landfill and along the dominant wind path from southeast to northwest, especially within 500 m. Conversely, waste pickers reported less discomfort due to long-term habituation, despite ongoing exposure. Additionally, 63% of respondents experienced health issues such as dizziness, nausea, and shortness of breath. Most respondents also felt that odor management by authorities was ineffective, and nearly all agreed that landfill management practices need substantial improvement.

5. POLICY IMPLICATIONS

The findings of this study highlight the importance of enhanced government oversight in managing the Antang landfill. Improved management is essential to reduce ammonia (NH_3) emissions and curb odor issues that negatively impact nearby communities. The current waste management practices are insufficient to protect environmental quality and public health, as evidenced by high NH_3 levels and frequent odor complaints. Consequently, local authorities must implement more systematic landfill operations and conduct regular NH_3 monitoring, complemented by spatial analysis to guide risk-based buffer zones and urban development plans. Incorporating community feedback into policy evaluation is also crucial to ensure that landfill strategies address both technical pollution data and residents' daily experiences.

6. ACKNOWLEDGMENTS

The authors would like to express their sincere gratitude to all residents living in the area surrounding the Antang Landfill in Makassar City, South Sulawesi, Indonesia, for their participation in completing the questionnaires and for their assistance during the field research conducted at the site.

7. REFERENCES

Agency for Toxic Substances and Disease Registry (ATSDR), 2004. *Toxicological Profile for Ammonia*. U.S. Department of Health and Human Services. Retrieved June 25, 2024, from https://www.atsdr.cdc.gov/toxprofiles/tp126.pdf

Behera, S.N., Sharma, M., Aneja, V.P. and Balasubramanian, R., 2013. Ammonia in the atmosphere: a review on emission sources, atmospheric chemistry, and deposition. *Environmental Science and Pollution Research*, 20(11), pp. 8092–8131. [DOI]

Blanes-Vidal, V., Suh, H. and Nadimi, E.S., 2012. Literature review of odor annoyance from livestock and waste facilities. *Atmospheric Environment*, 55, pp. 376–385. [DOI]

Duan, Z., Zhang, Y., Wang, X. and Zhang, H., 2014. Atmospheric dispersion characteristics of ammonia emissions from landfills. *Atmospheric Environment*, 98, pp. 431–438. [DOI]

Fang, J., Yang, Y., Li, C. and Zhao, L., 2017. Emission characteristics and dispersion of ammonia from landfill sites. *Science of the Total Environment*, 599–600, pp. 178–186. [DOI]

Hoornweg, D. and Bhada-Tata, P., 2012. *What a Waste: A Global Review of Solid Waste Management*. World Bank. Retrieved June 25, 2024, from https://openknowledge.worldbank.org/handle/10986/17388

Imran, A., 2024. Urban waste generation and environmental challenges in Indonesian cities. *Journal of Urban Environment*, 15(1), pp. 1–10.

Jerrett, M., Arain, A., Kanaroglou, P., Beckerman, B., Potoglou, D., Sahsuvaroglu, T., Morrison, J. and Giovis, C., 2005. Review of intra-urban air pollution exposure models. *Journal of Exposure Analysis and Environmental Epidemiology*, 15(2), pp. 185–204. [DOI]

Kaza, S., Yao, L., Bhada-Tata, P. and Van Woerden, F., 2018. *What a*

Waste 2.0: A Global Snapshot of Solid Waste Management to 2050. World Bank. Retrieved June 25, 2024, from https://openknowledge.worldbank.org/handle/10986/30317

Kim, K.H. and Park, S.Y., 2008. Analysis of malodor samples. *Atmospheric Environment*, 42(20), pp. 5061–5070. [DOI]

Le Cloirec, P., Béline, F. and Bédard, C., 2012. Odorous emissions from waste treatment plants. *Chemical Engineering Journal*, 191, pp. 26–34. [DOI]

Li, J. and Heap, A.D., 2014. Spatial interpolation methods in environmental sciences. *Environmental Modelling & Software*, 53, pp. 173–189. [DOI]

Maulidah, R., Pratiwi, N. and Hidayat, R., 2021. The influence of meteorological factors on ammonia dispersion at landfill sites. *Journal of Environmental Engineering*, 27(2), pp. 89–98.

McGinn, S.M., Flesch, T.K. and Harper, L.A., 2007. Ammonia emissions from livestock waste. *Journal of Environmental Quality*, 36(5), pp. 1223–1232. [DOI]

Mohan, M. and Kandya, A., 2015. Urban air quality assessment using GIS. *Atmospheric Environment*, 119, pp. 267–279. [DOI]

Nascimento, R., Tavares, R. and Silva, C., 2014. Atmospheric dispersion of ammonia from waste facilities. *Environmental Monitoring and Assessment*, 186, pp. 5789–5802. [DOI]

Putri, D.A., Ramadhan, F. and Sari, M., 2020. Evaluation of open dumping landfill management. *Journal of Environmental Management*, 12(3), pp. 145–154.

Ramli, M.I., Rani, N.M. and Zafany, A.A., 2023. Analysis of air quality for ammonia (NH_3) parameters in Makassar City. *IOP Conference Series: Earth and Environmental Science*, 1247(1), p. 012045. [DOI]

Rizki, M., Anwar, S. and Yusuf, A., 2020. The influence of wind direction and speed on NH_3 dispersion. *Journal of Meteorology and Geophysics*, 21(1), pp. 33–42.

Sarkar, U., Hobbs, S.E. and Longhurst, J.W.S., 2003. Dispersion of odour and ammonia from landfills. *Waste Management & Research*, 21(5), pp. 381–392. [DOI]

Seinfeld, J.H. and Pandis, S.N., 2016. *Atmospheric Chemistry and Physics: From Air Pollution to Climate Change*. 3rd ed. Wiley. [DOI]

Steinheider, B., Winneke, G. and Neuf, M., 1998. Odour annoyance and environmental stress. *International Archives of Occupational and Environmental Health*, 71(1), pp. 51–57. [DOI]

Sutrisno, E., 2011. Health impacts of ammonia gas on communities. *Journal of Environmental Health*, 8(2), pp. 101–108.

U.S. EPA, 2017. *Landfill Gas Emissions Model (LandGEM) User's Guide*. Retrieved June 25, 2024, from https://www.epa.gov/landfill-gas-energy/landfill-gas-emissions-model-landgem

Wang, Y., Li, Y. and Chen, H., 2019. Spatial interpolation of air pollutants using GIS. *Environmental Monitoring and Assessment*, 191(6), p. 375. [DOI]

WHO, 2018. *Ambient Air Pollution: Health Impacts*. Retrieved June 25, 2024, from https://www.who.int/news-room/fact-sheets/detail/ambient-(outdoor)-air-quality-and-health

World Bank, 2018. *Indonesia Solid Waste Management Assessment*. Retrieved June 25, 2024, from https://documents.worldbank.org/en/publication/documents-reports/documentdetail/915431527670151051

Zilfani, R., Nugroho, S. and Lestari, P., 2021. Ammonia emissions and odor perception around landfills. *Environmental Technology & Innovation*, 22, p. 101462. [DOI]

Nature Environment and Pollution Technology
An International Quarterly Peer-Reviewed Open Access Journal

p-ISSN: 0972-6268 | e-ISSN: 2395-3454 Vol. 25 | No. 4 | Article ID D1896 | 2026

RESEARCH ARTICLE https://doi.org/10.46488/NEPT.2026.v25i04.D1896 OPEN ACCESS

Dynamic Perspective of the Evolution of the Environmental Kuznets Curve in Ecuador and Mexico

Giojan Aguirre[1]†, Rosa Llerena[2], Roger Yela[2], Hugo Galarza[2], Evelyn Vergara[2] and Abril Herrera[3]
[1]Faculty of Educational Sciences, Quevedo State Technical University, Ecuador
[2]Faculty of Social, Economic and Financial Sciences, Quevedo State Technical University, Ecuador
[3]Faculty of Economic and Social Sciences, Autonomous University of Sinaloa, Mexico
†Corresponding author: Giojan Aguirre; gaguirre@uteq.edu.ec

ARTICLE HISTORY

Received: 09-12-2025
Revised: 04-03-2026
Accepted: 17-03-2026

KEYWORDS

Environmental Kuznets curve
Spatial SAR-SEM models
CO_2 emissions
Sustainable development

CITE THIS ARTICLE

Aguirre, G., Llerena, R., Yela, R., Galarza, H., Vergara, E. and Herrera, A., 2026. Dynamic perspective of the evolution of the environmental Kuznets curve in Ecuador and Mexico. *Nature Environment and Pollution Technology*, 25(4), D1896. https://doi.org/10.46488/NEPT.2026.v25i04.D1896

COPYRIGHT & LICENCE

© 2026 The Authors
Open Access under CC BY 4.0.

PUBLISHED BY

TECHNOSCIENCE PUBLICATIONS

ABSTRACT

The Environmental Kuznets Curve (EKC) posits that environmental degradation increases during the early stages of economic development and decreases once a certain income level is reached. Ecuador and Mexico illustrate contrasting patterns within this framework: the former relies heavily on natural resources, while the latter has a more diversified economy, albeit with persistent environmental challenges. The aim of this study is to compare the validity of the EKC in both countries over the period 2007–2024 by analyzing the relationship between economic growth and CO_2 emissions using spatial SAR and SEM models. Recent subnational data were transformed into logarithmic form to capture regional variations and facilitate the interpretation of economic and environmental relationships. The results indicate that Ecuador remains in the ascending phase of the EKC, whereas Mexico shows a trajectory trending toward an inverted U-shape, suggesting that the country may have reached its turning point in certain regions. Furthermore, spatial dependence is strong in both countries. The larger Moran's I and Lagrange Multiplier statistics reported for Mexico indicate a stronger spatial association there, while its emissions remain more territorially heterogeneous than in Ecuador.

1. INTRODUCTION

In recent decades, the sustainability of economic growth has become a central topic in economic and environmental research, giving rise to multiple analytical frameworks aimed at explaining the relationship between economic development and environmental degradation. Among these approaches, the Environmental Kuznets Curve (EKC) has gained particular relevance by proposing a nonlinear relationship between per capita income and environmental degradation (Grossman & Krueger 1995). Building on Kuznets' original hypothesis (Kuznets 1955), the EKC suggests that pollutant emissions increase during the early stages of economic development but tend to decline once a certain income threshold is reached. Nevertheless, the empirical applicability of this hypothesis has been widely debated. Empirical evidence provided by studies such as Sarkodie & Strezov (2020) and Dong et al. (2018) indicates that the validity of the EKC depends both on the type of pollutant analyzed and the institutional context in which economic growth occurs.

Al-Mulali et al. (2015) argue that persistent pollutants such as CO_2 do not always conform to the theoretical EKC pattern, while Fang et al. (2021) emphasize that institutional weaknesses may prevent countries from reaching the turning

point required to reverse environmental degradation. In this context, Ecuador and Mexico constitute particularly relevant cases for examining the dynamic validity of the EKC, as both countries exhibit distinct development models while facing similar sustainability challenges. Ecuador maintains a highly resource-dependent economy, particularly reliant on oil extraction, which shapes its productive structure and constrains its transition toward less emission-intensive development paths (Larrea & Warnars 2009, Cevallos-Mina et al. 2024). Mexico, by contrast, displays a more diversified economy, supported by a solid manufacturing base integrated into international value chains (Vázquez-López 2023). Nevertheless, this structural advantage has not necessarily resulted in lower environmental pressure.

Environmental challenges such as air pollution in metropolitan areas, the overexploitation of aquifers, and the degradation of coastal ecosystems indicate that economic growth has not always followed a sustainable path (Blackman et al. 2018, Figueroa et al. 2021). These contrasts provide a valuable basis for examining how factors such as productive structure, institutional quality, and public policies influence the specific form that the EKC adopts in both countries. In this context, the main objective of this study is to compare the validity of the Environmental Kuznets Curve (EKC) in Ecuador and Mexico over the period 2007–2024, incorporating a spatial perspective that enables the identification of regional CO_2 emission patterns and the characterization of structural differences in the relationship between economic growth and environmental degradation.

1.1. The Environmental Kuznets Curve (EKC)

The Environmental Kuznets Curve (EKC) emerges as an environmental extension of Kuznets' original hypothesis (Kuznets 1955), which established a relationship between economic development and income inequality. Grossman & Krueger (1995) later adapted this framework to the environmental context, arguing that during the early stages of economic growth, pollution levels tend to increase, but once a certain per capita income threshold is reached, environmental degradation begins to decline. This hypothesis has been extensively discussed and empirically tested in the literature. Sarkodie & Strezov (2020) emphasize that the EKC does not hold universally, while Fang et al. (2021) argue that institutional factors play a decisive role in determining its validity, particularly in emerging economies. Similarly, Al-Mulali et al. (2015) show that the EKC may fail to emerge even when CO_2 emissions are used as the environmental indicator, whereas Dong et al. (2018) highlight that globalization processes and environmental policies can significantly alter the trajectory of the curve. Complementarily, Shahbaz et al. (2019) suggest that the transition toward cleaner economic structures is largely driven by development-induced structural transformation and regulatory reforms.

In this framework, the EKC is commonly conceptualized as a three-stage process. The first stage is characterized by environmental deterioration associated with industrialization and rapid economic expansion. The second stage corresponds to income levels at which societies are increasingly able to implement environmental regulations and mitigation policies. Finally, the third stage involves a reduction in environmental degradation driven by technological innovation and growing ecological awareness (Murshed et al. 2021). Tangato (2025) highlights the adoption of clean technologies as a crucial element in this final phase. However, compliance with this theoretical pattern is not guaranteed. Usman et al. (2022) argue that in many developing countries, corruption and weak institutional frameworks hinder the achievement of the EKC turning point. By contrast, Acheampong et al. (2021) contend that technological innovation plays a key role in decoupling economic growth from environmental degradation, although its effective implementation remains uneven across countries.

Several studies have raised conceptual critiques of the Environmental Kuznets Curve. Destek & Sarkodie (2019) question the assumption that economic development alone necessarily leads to environmental improvement. Similarly, Kaika & Zervas (2013) argue that the EKC framework fails to account for the cumulative and long-term impacts of environmental degradation, particularly in the context of climate change. Sinha et al. (2020) further contend that the EKC overlooks the role of international institutions in shaping global environmental governance. In addition, Paramati et al. (2018) warn that certain pollutants, such as plastic waste, do not decline with higher income levels. Dong et al. (2018) emphasize that national and international policy interventions can significantly alter the trajectory implied by the EKC. Finally, Al-Mulali et al. (2015) show that CO_2-based EKC results are context-dependent, reinforcing the need to avoid treating the EKC as universally applicable.

1.2. Studies in Other Countries

Empirical studies on the Environmental Kuznets Curve have employed a wide range of environmental indicators to test its validity. The ecological footprint has been used to measure human pressure on ecosystems, and Charfeddine & Mrabet (2017) demonstrate its relevance in countries with a high dependence on natural resources. Carbon dioxide (CO_2) emissions remain the most commonly used indicator, with Khan et al. (2020) showing that CO_2 emissions tend to increase during the early stages of economic growth but

can be reduced through the implementation of appropriate environmental policies. Goulart et al. (2023) find that, in Latin America, agricultural expansion has sustained critical levels of deforestation, even in economies that have surpassed the medium stage of development. Rakpho & Yamaka (2021) introduce an alternative indicator, water pollution by heavy metals, whose environmental persistence and weak regulatory frameworks prevent it from following the theoretical EKC pattern. Moreover, Jahanger et al. (2022) emphasize that environmental indicators must be adapted to regional contexts to avoid distortions in comparative analyses.

The role of economic development–related variables has also been extensively examined in the EKC literature. Alvarado et al. (2021) note that per capita income is commonly used as a proxy for development levels, although its relationship with pollution differs depending on the type of pollutant considered. Dogan et al. (2020) demonstrate that in countries with a high penetration of renewable energy sources, the declining phase of the EKC tends to be more pronounced. In contrast, Adams & Acheampong (2019) observe that in several African economies, industrialization in the absence of adequate regulatory frameworks leads to increased pollution levels. Li et al. (2023) argue that international trade directly influences environmental outcomes, particularly when countries exporting energy-intensive goods effectively outsource their emissions. Furthermore, Catalán (2021) emphasizes the importance of rigorous monitoring of greenhouse gas emissions to accurately assess climate commitments, while Wackernagel et al. (2017) highlight the ecological footprint as a comprehensive indicator that integrates emissions, resource consumption, and biological regeneration capacity.

In addition, more recent studies reinforce the need to adapt the EKC framework to specific regional realities. Goulart et al. (2023) emphasize that deforestation should be analyzed through the lens of persistent agricultural expansion, while Wang et al. (2023) demonstrate that in Southeast Asian countries, rapid industrialization generates a complex relationship between economic growth and ecological damage, in which the environmental curve may not evolve as theoretically expected. Shahbaz et al. (2019) further reiterate that the trajectory of the EKC is strongly mediated by a country's institutional capacity to design and enforce effective environmental regulations. Finally, Stern (2004) stresses that historical analyses of emissions and sustainability provide a more accurate assessment of national environmental trajectories and potential turning points, highlighting the need to strengthen policy frameworks based on observed environmental outcomes.

1.3. Relevance of Spatial Modeling

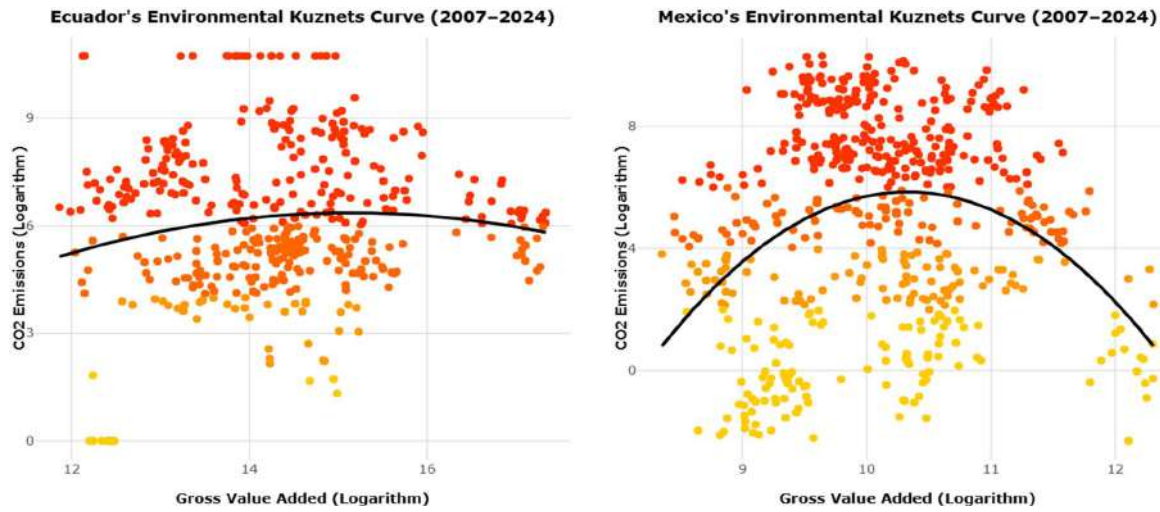
Recent advances in economic–environmental analysis have allowed the EKC to be examined from a dynamic perspective, thereby overcoming the limitations inherent in traditional static models. Unlike approaches that focus exclusively on contemporaneous relationships between variables, dynamic models incorporate temporal evolution and the cumulative effects of economic growth on environmental outcomes (Okullo 2020, Pei et al. 2021). This framework makes it possible to identify feedback mechanisms, such as the impact of environmental degradation on future growth potential (Herrera et al. 2024). In addition, dynamic models facilitate the analysis of the roles of technological innovation and institutional quality in shaping a country's long-term environmental trajectory (Meckling & Nahm 2019, Medina-Rivas et al. 2022).

Thus, the EKC has evolved into an analytical framework that no longer seeks to validate a single curve shape, but rather to identify the conditions under which environmentally sustainable development can be achieved. A particularly important aspect of this comparative analysis is the selection of appropriate indicators to capture the relationship between economic growth and environmental degradation. Variables such as GDP per capita, CO_2 emissions, deforestation, and energy consumption are among the most frequently used measures in the EKC literature (Khan et al. 2020, Alvarado et al. 2021). In the case of Ecuador, energy-related emissions and the loss of Amazonian forests constitute critical indicators (Chen et al. 2022), whereas in Mexico, factors such as urban pollution and the degradation of agricultural and water ecosystems are especially relevant (Renner 2018, Percastre et al. 2024).

The validity and comparability of these indicators, according to Stern (2004) and Wackernagel et al. (2017), depend on both their statistical quality and their contextual relevance. Consequently, the selection of indicators reflects not only methodological considerations but also policy-related criteria, reinforcing their relevance in dynamic and comparative analyses.

1.4. Graphical Representation of the Environmental Kuznets Curve

In Ecuador, the distribution of provinces in the development–emissions space (Fig. 1) shows a clear concentration in the ascending phase of the Environmental Kuznets Curve (EKC), with no evidence of a transition toward its declining phase at the aggregate level. This pattern is closely linked to the country's strong dependence on oil and its primary-export economic model, in which growth continues to rely on emission-intensive activities (Cevallos-Mina et al. 2024).



Source: Prepared by the authors in the Observatory of Economic and Financial Sustainability (OSEF 2025).

Fig. 1: Environmental Kuznets curve in Ecuador and Mexico (2007–2024).

In addition, institutional weaknesses and the budgetary constraints of the Ministry of Environment have significantly limited the country's capacity to design and implement effective environmental policies, a situation also observed in comparable developing-country contexts (Sinha et al. 2020, Usman et al. 2022).

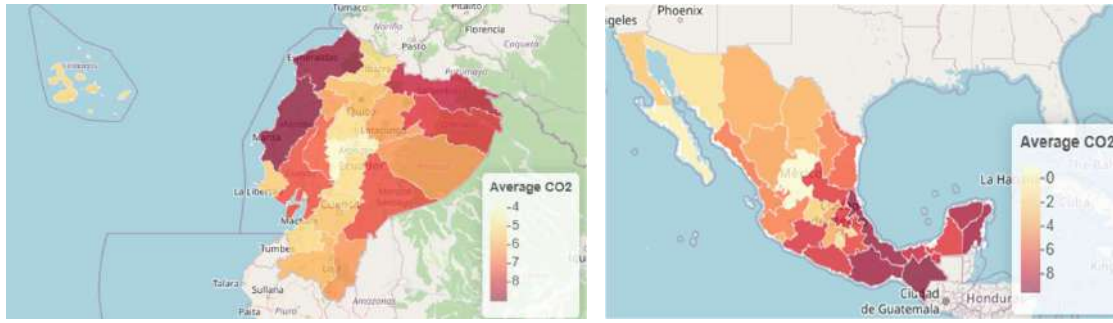
According to EKC theory, in its initial stage, economic growth typically generates higher levels of pollution as production expands before stronger environmental regulation and cleaner technologies are adopted (Grossman & Krueger 1995, Kaika & Zervas 2013). Consistent with this framework, the evidence indicates that Ecuador remains in the ascending phase of the EKC, reflecting a persistent dependence on extractive activities and a limited capacity for environmental management (Cevallos-Mina et al. 2024). In resource-based economies with weak institutional structures, economic growth tends to intensify pollution levels (Almeida et al. 2024). Similarly, in contexts of low institutional development, environmental pressures increase as a result of the absence of effective and sustainable governance mechanisms (Jeetoo 2023). Overall, Ecuador's trajectory supports the premise that, without productive diversification and effective environmental policies, the EKC continues along its upward path, driven by an economic model based on the intensive exploitation of natural resources.

In contrast, in Mexico, the regional distribution of the EKC graph suggests a trajectory that tends toward an inverted U-shape, indicating that the country may have reached its turning point in certain regions. This pattern is associated with a more diversified economic structure and a stronger institutional capacity to implement environmental policies, particularly reflected in the promotion of renewable energy during the 2013–2018 period (Percastre et al. 2024). This behavior is consistent with previous findings showing that in countries with solid regulatory frameworks, technological progress, and widespread use of clean energy, the Environmental Kuznets Curve tends to display a more pronounced declining phase (Dogan et al. 2020, Acheampong et al. 2021).

In this context, the empirical results confirm that Mexico displays an EKC with signs of partial decoupling between economic growth and environmental degradation, explained by institutional consolidation, productive diversification, and progress in energy efficiency. Mahmoodi & Dahmardeh (2022) argue that countries with greater regulatory capacity tend to generate more sustainable environmental trajectories, while Almeida et al. (2024) emphasize that middle-income economies with mixed productive structures can reduce ecological pressure without halting growth. Thus, the Mexican case demonstrates a gradual transition toward a sustainable development model, consistent with the theoretical predictions of the Environmental Kuznets Curve.

In countries such as Ecuador and Mexico, where industrial zones coexist with active volcanic regions, understanding these dynamics through spatial analyses and graphical representations is essential for assessing environmental impacts and informing control and mitigation policies. The spatial distribution of CO_2 emissions in Ecuador and Mexico is shown in Fig. 2.

Both Ecuador and Mexico exhibit spatial CO_2 emission patterns that remain consistent with substantial environmental pressure. Over the 2007–2024 period (Fig. 2), the distribution



Note: Areas with greater color intensity correspond to higher CO_2 levels.
Source: Observatorio Social, Económico y Financiero (OSEF 2025).

Fig. 2: Spatial distribution of average CO_2 emissions in Ecuador and Mexico (2007–2024).

of average emissions in Ecuador shows comparatively high levels in the Amazonian provinces (Pastaza, Orellana, Sucumbíos, Morona Santiago) and in coastal provinces such as Guayas and Manabí, while some areas in the Sierra display relatively lower values. This pattern may indicate an incipient transition toward the declining phase of the Environmental Kuznets Curve in certain territories. The creation of the Ministry of Environment, Water, and Ecological Transition points to a process of institutionalizing sustainability. However, recent studies indicate that the services sector, despite its low direct emissions, accounts for up to 35.5% of national emissions due to indirect effects, thereby limiting deeper structural transformation (Buenaño et al. 2023). Overall, the evidence suggests that although progress has been made in formalizing environmental policy, the extractivist economic model continues to strongly shape environmental trajectories, consistent with Larrea & Warnars (2009) and Sinha et al. (2020), who highlight the structural limitations of the EKC in resource-dependent economies.

In Mexico, the spatial distribution of average emissions is concentrated in the southeast (Chiapas, Tabasco, Campeche, Quintana Roo, Yucatán, Veracruz) and in the central industrial zones (Mexico City, State of Mexico, Puebla, Hidalgo). This spatial pattern can be explained by the suspension of clean energy auctions and the promotion of large-scale polluting projects, such as the Dos Bocas Refinery, which, according to Renner (2018) and Fujii et al. (2024), have weakened environmental governance under the current administration. Despite some localized advances, such as the emission reduction program in Jalisco, the 75% cut in the environmental budget has constrained any structural attempt at ecological transition. The persistence of these environmental pressures is consistent with the critique by Kaika & Zervas (2013) of the fallacy that economic growth automatically leads to environmental improvements and reinforces the argument of Medina-Rivas et al. (2022) that strong institutions and coherent policies are essential for sustainable development.

2. MATERIALS AND METHODS

This study adopts a quantitative and comparative research design to examine the relationship between economic development and carbon dioxide (CO_2) emissions in Ecuador and Mexico, grounded in the theoretical framework of the Environmental Kuznets Curve (EKC). The methodological sequence comprises: (i) description of the dataset; (ii) operationalization of variables; (iii) variable construction and specification of the spatial weights matrix (W) to ensure cross-country comparability; and (iv) econometric specification and estimation of spatial panel models (SAR and SEM).

2.1. Data Description and Panel Structure

The empirical analysis relies on secondary data compiled from official national and international statistical sources, consisting of annual subnational observations for Ecuador and Mexico. In Ecuador, the unit of analysis is the province, whereas in Mexico it is the federal state. The study period spans 2007–2024, corresponding to the most recent years for which statistically comparable subnational information is simultaneously available for both economies, thereby ensuring methodological consistency and temporal homogeneity in the construction of the panel.

The resulting dataset is structured as an annual panel with territorial units observed over time . This panel structure increases the number of observations and improves the statistical efficiency and robustness of the econometric estimates. The subnational level of disaggregation is a core component of the empirical design, as it enables the identification of regional heterogeneity in total CO_2 emissions, emissions intensity, value-added dynamics, and access to basic infrastructure. Compared with nationally aggregated studies, the subnational approach reduces aggregation bias and allows the detection of differentiated spatial patterns within each country.

Table 1: Description of variables.

Variable Type	Variable	Description	Unit of measure	Source, Ecuador	Source, Mexico	Expected sign
Endogenous	CO_2 emissions	Total CO_2 emissions generated in territorial unit i at time t.	Metric tons (t CO_2)	Global Forest Watch (GFW)	Global Forest Watch (GFW)	N/A
Exogenous	CO_2 intensity	Emissions intensity: CO_2 emissions per unit of economic output.	t CO_2 USD million[1]	Calculated from GFW and BCE	Calculated from GFW and INEGI	(+)
	GVA	Total Gross Value Added (constant USD millions).	Constant USD million	Central Bank of Ecuador (BCE)	National Institute of Statistics and Geography (INEGI)	(+)
	GVA^2	Quadratic term of GVA to capture nonlinearities.	(USD million)^2	Central Bank of Ecuador (BCE)	National Institute of Statistics and Geography (INEGI)	(-)
	H_2ORed	Households with piped water access through the public network.	Percentage (%)	Ministry of Economic and Social Inclusion (MIES)	National Institute of Statistics and Geography (INEGI)	(-)

Source: Prepared by the authors.
Note: The sources are presented separately according to their national origin, which facilitates the comparison between Ecuador and Mexico and ensures the traceability of the data used.

Cross-country comparability between Ecuador and Mexico is ensured through the conceptual harmonization of variables and the application of equivalent statistical definitions across jurisdictions. Detailed information on data sources, units of measurement, and expected coefficient signs is reported in Table 1, ensuring traceability, methodological transparency, and reproducibility of the empirical analysis.

2.2. Definition and Measurement of Variables

2.2.1. Dependent Variable: CO_2 Emissions

The dependent variable is territorial carbon dioxide emissions, denoted as $CO2_{it}$, measured in metric tons (t CO_2) at the subnational level. This variable captures the environmental pressure associated with economic activity in territorial unit *i* at time *t*. For econometric estimation, the natural logarithm of total emissions is employed to improve numerical stability and mitigate potential heteroskedasticity:

$$ln(CO2_{it})$$

The choice between level and logarithmic specifications was guided by econometric criteria derived from goodness-of-fit tests and spatial dependence diagnostics, ensuring consistency with the statistical properties of the data and the theoretical structure of the model.

2.2.2. Independent Variables

CO_2 Intensity: CO_2 intensity measures the amount of carbon emissions generated per unit of economic output and serves as an indicator of the environmental efficiency of production at the subnational level. Higher values indicate that a territory produces the same level of value added with a greater emissions burden, whereas lower values are consistent with cleaner or more efficient production structures.

For each territorial unit i and year t, CO_2 intensity is constructed as:

$$CO2\ Intensity_{it} = \frac{CO2_Emissions_{it}}{\mathrm{GVA}_{it}}$$

Where $CO2_{it}$ denotes total CO_2 emissions (metric tons) and GVA_{it} represents Gross Value Added measured in constant USD millions.

Gross Value Added (GVA): Gross Value Added (GVA) is used as the proxy for territorial economic activity at the subnational level and is expressed in constant U.S. dollars (USD millions) to ensure temporal comparability across the study period. The variable is initially obtained in levels (GVA_{it}) from official sources and then used to construct a nonlinear term in levels:

$$\mathrm{GVA}_{it}{}^2 = (\mathrm{GVA}_{it})^2$$

This quadratic transformation is introduced to allow for nonlinearities in the relationship between economic activity and emissions within the econometric specification. For estimation purposes, GVA is also incorporated in logarithmic form, $ln(GVA_{it})$ to reduce scale effects across territories and improve numerical stability. Thus, the empirical models combine the log-transformed activity indicator with a nonlinear output term in levels.

2.2.3. Control Variable: H_2ORed

The percentage of households with access to piped water from the public network, denoted as $H2ORed_{it}$ is included

as a control variable at the subnational level (provinces in Ecuador and federal states in Mexico). This indicator captures differences in basic infrastructure and territorial development that may be correlated with production patterns and, indirectly, with emission dynamics.

In the econometric specification, $H2ORed_{it}$ enters in levels (percentage points) to control for structural heterogeneity in access to public services and to reduce omitted-variable bias when estimating the relationship between economic activity and CO_2 emissions.

2.3. Data Processing, Variable Construction, and Spatial Weights (W)

Before estimation, the series were checked to ensure temporal consistency, homogeneity of measurement units, and methodological compatibility across statistical sources, thereby supporting cross-country comparability. Geographic coordinates (longitude and latitude) were compiled and validated for each subnational unit, as they are required to construct the spatial weights matrix used in spatial diagnostics and spatial econometric estimation.

2.3.1. Variable Construction and Transformations

Two derived variables were constructed for the econometric analysis. First, the quadratic output term was generated as:

$$\mathrm{GVA}_{it}{}^2 = (\mathrm{GVA}_{it})^2$$

Second, CO_2 intensity was computed as the ratio between total emissions and economic activity:

$$CO2\ Intensity_{it} = \frac{CO2_Emissions_{it}}{\mathrm{GVA}_{it}}$$

Logarithmic transformations were then applied to selected variables used in the econometric specification to stabilize variance and facilitate interpretation in elasticity terms. Specifically, the analysis uses $ln(CO2_Emissions)_{it}$, $ln(\mathrm{GVA}_{it})$ and $ln(CO2_Intensity)_{it}$. The quadratic term $\mathrm{GVA}_{it}{}^2$ and the infrastructure control $H2ORed_{it}$ enter the specification in levels.

2.3.2. Data Completeness and Spatial Referencing

Data completeness was verified for all variables included in the econometric specification. Observations with missing geographic coordinates were excluded prior to spatial modeling to ensure that all units included in the estimation could be spatially referenced and consistently connected through the spatial weights matrix. The final estimation samples correspond to the sets of subnational units and years with complete information required for panel estimation and spatial diagnostics.

2.3.3. Spatial Weights Matrix (W)

Spatial dependence was modeled using a distance-based inverse-distance spatial weights matrix , constructed from the longitude and latitude coordinates of subnational units. The baseline matrix assigns weights according to the inverse of inter-territorial distance within a fixed distance band:

$W_{ij} = 1/d_{ij}$ for $0 < d_{ij} \leq 100$ and $i \neq j$; $W_{ij} = 0$ otherwise; $W_{ii} = 0$.

The matrix was row-standardized so that each row sums to one. Inter-territorial distances d_{ij} were computed as Euclidean distances between the longitude–latitude coordinate pairs of the subnational units, expressed in decimal degrees. Spatial links were defined for pairs satisfying $0 < d_{ij} \leq 100$, and inverse-distance weights were assigned within this threshold. Accordingly, the cutoff of 100 is expressed in decimal-degree coordinate units. The resulting W matrix was used for spatial-dependence diagnostics and for estimation of the spatial autoregressive (SAR) and spatial error (SEM) models.

2.4. Econometric Specification and Spatial Panel Models (SAR/SEM)

This section presents the spatial econometric specifications used to estimate CO_2 emissions at the subnational level in Ecuador (provinces) and Mexico (federal states). Models are estimated separately for each country to account for potential structural differences in spatial interaction mechanisms.

2.4.1. General Spatial Specifications

To capture territorial interdependence in CO_2 emissions, two alternative spatial specifications were estimated using the previously defined spatial weights matrix W: a Spatial Autoregressive Model (SAR), in which spatial dependence enters through the lagged dependent variable, and a Spatial Error Model (SEM), in which spatial dependence operates through the disturbance process.

The general SAR specification is expressed as:

$$Y_{it} = \rho \sum_{j=1}^{N} w_{ij}\, Y_{jt} + X_{it}\beta + \alpha_i + \tau_t + \varepsilon_{it}$$

Where Y_{it} denotes the logarithm of CO_2 emissions in territorial unit i at time t; $\sum_{j=1}^{N} w_{ij}\, Y_{jt}$ represents the spatial lag of the dependent variable; p is the spatial autoregressive coefficient; X_{it} contains the explanatory variables; b is the corresponding parameter vector; a_i and t_t captuXre territorial and common time effects, respectively; and e_{it} is the idiosyncratic disturbance.

The SEM model is defined as:

$$Y_{it} = X_{it}\beta + \alpha_i + \tau_t + u_{it}, \qquad u_{it} = \lambda \sum_{j=1}^{N} w_{ij}\, u_{jt} + \varepsilon_{it}$$

where l is the spatial error coefficient and u_{it} is the spatially correlated disturbance. Both SAR and SEM specifications were estimated by maximum likelihood, and model comparison was based on information criteria and the statistical significance of the spatial parameters.

2.4.2. Spatial Autoregressive Model (SAR)

The Spatial Autoregressive Model (SAR) incorporates the spatial lag of CO_2 emissions to capture interdependence among neighboring territorial units. The empirical specification retains CO_2 intensity, Gross Value Added (GVA), its quadratic term, and access to piped water as explanatory variables and is expressed as:

$\ln(CO_2\ Emissions_{it}) = \alpha_i + \rho\Sigma_{j=1}^{N} w_{ij} \ln(CO_2\ Emissions_{it}) + \beta_1 \ln(CO_2\ Intensity_{it}) + \beta_2 \ln(GVA_{it}) + \beta_3 (GVA_{it})^2 + \beta_4 H2ORed_{it} + \tau_t + \varepsilon_{it}$.

The SAR specification models spatial dependence through the lagged dependent variable. The parameter ρ measures the strength and direction of dependence between CO_2 emissions in territorial unit and the spatially weighted emissions of neighboring units. The terms a_i and t_t represent territorial and common time effects, respectively, and e_{it} is the idiosyncratic error term. The admissible range of p is determined by the eigenvalues of the spatial *weights matrix* w.

2.4.3. Spatial Error Model (SEM)

The Spatial Error Model (SEM) captures spatial dependence through the disturbance term while retaining the same explanatory variables used in the SAR specification. The empirical model is expressed as:

$$lnCO2_Emissions = \alpha i + \beta_1 (lnGVA)_{it} + \beta_2 (GVA)^2_{it} + \beta_3 (H2ORed) + u_{it} + \lambda_{it} + \varepsilon_{it}$$

with the error structure defined as:

$$u_{it} = \lambda \sum_{j=1}^{N} w_{ij}\, u_{jt} + \varepsilon_{it}$$

Where l measures spatial autocorrelation in the disturbance term and ε_{it} is a white-noise error. As with ρ in the SAR model, the admissible range of λ is determined by the eigenvalues of w.

3. RESULTS AND DISCUSSION

This section reports the empirical results for Ecuador and Mexico and discusses their economic and spatial interpretation within the Environmental Kuznets Curve (EKC) framework. It compares the SAR and SEM specifications and evaluates whether the estimated relationship exhibits a turning (inflection) point in CO_2 emissions.

3.1. Validation of Spatial Dependence Tests

Table 2 presents the results of the spatial dependency tests applied to CO_2 emissions in Ecuador and Mexico. For both countries, the values of Moran's I and the Lagrange Multiplier tests, for the spatial error model and the spatial lag model, are statistically significant ($p < 0.01$), confirming the presence of spatial autocorrelation in the distribution of emissions.

In the case of Ecuador, although the test statistics are high, their values are slightly lower than those observed for Mexico. This indicates a strong, albeit less intense, spatial dependence, meaning that emissions in one province are influenced by emissions in neighboring provinces. This pattern is consistent with the concentration of emissions in extractive zones such as the Amazon region and the Coast. Such dependence reflects how the extractivist development model tends to spatially cluster environmental impacts and aligns with the findings of Larrea and Warnars (2009) and Cevallos-Mina et al. (2024), who identify a territorial degradation pattern associated with oil-based development.

In Mexico, the values are even higher, indicating a very strong degree of spatial dependence. This suggests that CO_2 emissions exhibit greater continuity and concentration across regions, possibly driven by the presence of industrial corridors (e.g., Monterrey–Toluca) and the structural weight of the manufacturing sector in specific areas (Elizondo et al. 2025). These results are consistent with the findings of Blackman et al. (2018) and Vázquez-López (2023), who

Table 2: Spatial dependence in Ecuador and Mexico.

Country	Test	Statistic	p-value
Ecuador	Spatial error:		
	Moran's I	14.363***	0.000
	Lagrange multiplier	40.057***	0.000
	Robust Lagrange multiplier	9.861***	0.002
	Spatial lag:		
	Lagrange multiplier	137.344***	0.000
	Robust Lagrange multiplier	107.148***	0.000
Mexico	Spatial error:		
	Moran's I	39.551***	0.000
	Lagrange multiplier	408.348***	0.000
	Robust Lagrange multiplier	193.306***	0.000
	Spatial lag:		
	Lagrange multiplier	271.186***	0.000
	Robust Lagrange multiplier	56.143***	0.000

Note: *** $p < 0.01$, ** $p < 0.05$, * $p < 0.10$.

emphasize that intensive industrialization has generated regional pollution hotspots affecting contiguous territories. At a theoretical level, this spatial dependence reinforces the arguments of Herrera et al. (2024) regarding the need to incorporate dynamic and regionalized approaches into EKC analysis, as the environmental effects of economic growth are neither homogeneous nor spatially independent.

3.2. Spatial Autoregressive Model (SAR)

Table 3 presents the results of the Spatial Autoregressive Model (SAR), in which spatial dependence is represented by the spatial lag of CO_2 emissions and summarized by the coefficient ρ. The estimated ρ coefficients are positive and statistically significant for both Ecuador and Mexico, indicating strong positive spatial dependence in CO_2 emissions. The nonlinear relationship between economic activity and CO_2 emissions is assessed through the coefficients of the economic activity variable and its squared term, consistent with the EKC specification.

In Ecuador, the positive and statistically significant coefficient of lnGVA, combined with the negative and significant coefficient of the squared term (GVA2), confirms the presence of a nonlinear relationship between economic growth and carbon emissions. The estimated signs are consistent with the inverted U hypothesis of the Environmental Kuznets Curve (EKC), implying that economic expansion initially intensifies environmental degradation but eventually leads to a decoupling process as income levels rise. From an economic standpoint, the negative quadratic term indicates diminishing marginal environmental pressure as productive structure and technology evolve. However, the curvature implied by the model suggests that the turning point lies at relatively high-income levels, meaning that Ecuador remains on the ascending segment of the EKC. This finding supports the argument that structural dependence on resource-intensive activities delays the environmental transition, as highlighted by Acheampong et al. (2021) and Schneiter and Mellon-Bedi (2025).

To complement the sign-based EKC interpretation, we compute the implied turning point (i.e., the level of economic activity at which the effect of further growth on emissions changes from increasing to decreasing). Given the estimated EKC terms ln(GVA) and GVA2, the turning point is obtained as:

$$GVA* = \sqrt{\frac{\beta_{ln(GVA)}}{-2\beta_{(GVA)^2}}}$$

Using the SAR coefficients in Table 3, the implied turning point equals 19,308,274 for Ecuador and 63,122 for Mexico (in the same units used for GVA in the dataset). These values provide a direct quantitative benchmark to evaluate whether each country is still on the rising segment of the EKC or has moved beyond the turning phase.

The coefficient associated with access to drinking water (H_2ORed) is positive and statistically significant, suggesting that improvements in service coverage are linked to higher carbon emissions. Rather than capturing a direct environmental effect, this variable reflects processes of urbanization and structural transformation that increase energy demand, infrastructure expansion, and productive activity, thereby intensifying environmental pressure in

Table 3: Spatial Autoregressive Model (SAR) results for Ecuador and Mexico.

Country	Variable	Coefficient	Standard error	z-value	p-value	95% confidence interval	
Ecuador	lnCO_2_Intensity	1.0239***	0.0150136	68.20	0.000	0.9945124	1.053365
	lnGVA	0.4138***	0.0236224	17.52	0.000	0.3675195	0.4601175
	GVA²	-5.55e-16	1.51e-16	-3.69	0.000	-8.50e-16	-2.60e-16
	H_2ORed	0.4155***	0.1389119	2.99	0.003	0.1432845	0.6878092
	_Cons	-10.0849***	0.366126	-27.55	0.000	-10.80257	-9.367383
	ρ	0.97918***	0.0206487	47.42	0.000	0.9387154	1.019657
Mexico	CO_2_Intensity	8.91e-07***	9.26e-08	9.63	0.000	7.10e-07	1.07e-06
	lnGVA	1.3148***	0.1679059	7.83	0.000	0.9857409	1.64392
	GVA²	-1.65e-10***	2.09e-11	-7.90	0.000	-2.06e-10	-1.24e-10
	H_2ORed	-1.7994***	0.277874	-6.48	0.000	-2.344056	-1.25481
	_Cons	-12.1318***	1.702017	-7.13	0.000	-15.46774	-8.795961
	ρ	0.96714***	0.0321469	30.09	0.000	0.9041368	1.03015

Note: *** $p < 0.01$, ** $p < 0.05$, * $p < 0.10$. The ρ point estimates for both countries lie within the admissible ranges implied by W. The reported 95% confidence intervals are asymptotic Wald intervals calculated from the standard errors and are not truncated at the parameter-space boundaries. Therefore, confidence limits exceeding the admissible boundary do not imply that the estimated spatial parameter lies outside the admissible parameter space; rather, they reflect the properties of the asymptotic Wald approximation near the boundary.

the absence of cleaner technologies. Furthermore, the spatial autoregressive parameter ρ is positive, statistically significant, and close to the upper admissible boundary, indicating strong spatial dependence across provinces. This result reveals the existence of substantive spillover effects, whereby emissions in one territory are systematically influenced by those of neighboring regions. The presence of these spatial interactions supports the use of the SAR specification not only on statistical grounds but also from a theoretical perspective, as environmental externalities and productive structures tend to diffuse across contiguous areas.

In the case of Mexico, the positive and statistically significant coefficient of lnGVA, together with the negative and highly significant coefficient of the squared term (GVA2), confirms a nonlinear relationship consistent with the inverted U hypothesis of the Environmental Kuznets Curve. Compared to Ecuador, the estimated curvature suggests a more pronounced adjustment process, indicating that Mexico is positioned closer to, or already within, the declining segment of the EKC. From an economic perspective, this implies that further increases in income are associated with reductions in carbon emissions, reflecting structural transformation, technological upgrading, and greater regulatory capacity in more industrialized regions. These findings align with Gómez and Rodríguez (2020) and Escamilla-García et al. (2024), who highlight the role of technological change and climate policy in accelerating the downward phase of the EKC.

An additional relevant finding is the negative and statistically significant coefficient of H_2ORed, indicating that, unlike in Ecuador, greater access to basic infrastructure in Mexico is associated with lower carbon emissions. This result suggests that infrastructure expansion operates under higher efficiency standards, likely reflecting technological upgrading, improved urban planning, and stronger regulatory frameworks that mitigate environmental externalities. From an economic perspective, the negative association may capture the role of more advanced urban systems in reducing energy intensity and promoting cleaner production processes (Castro-Rosales & Esqueda-Walle 2020). Furthermore, the spatial autoregressive parameter ρ is positive, statistically significant, and close to the upper admissible boundary, confirming strong spatial dependence in CO_2 emissions. This implies that environmental outcomes in one state are systematically influenced by those of neighboring regions, reinforcing the existence of regional spillovers and the importance of coordinated environmental policies.

3.3. Spatial Error Model (SEM)

Table 4 presents the results of the Spatial Error Model (SEM), which captures spatial effects through the error term. In this model, the spatial error coefficient (λ) measures the spatial autocorrelation of the unobserved error. The results confirm a strong spatial dependence in both countries, which reinforces the need to incorporate regional structures in environmental analysis.

In Ecuador, the positive coefficient of lnGVA together with the negative and statistically significant coefficient of GVA^2 reveals a concave relationship consistent with the initial stage of an Environmental Kuznets Curve. Rather than describing background conditions, the model results indicate that economic activity is still associated with increasing environmental pressure, although the negative quadratic component suggests the emergence of a moderating effect

Table 4: Spatial Error Model (SEM) results for Ecuador and Mexico.

Country	Variable	Coefficient	Standard error	z-value	p-value	95% confidence interval	
Ecuador	$lnCO_2$_Intensity	0.9782***	0.0168036	58.22	0.000	0.9453332	1.011202
	lnGVA	0.3566***	0.025516	13.98	0.000	0.3066046	0.4066254
	GVA^2	-4.19e-16***	1.61e-16	-2.60	0.009	-7.36e-16	-1.03e-16
	H_2ORed	0.4953***	0.1601639	3.09	0.002	0.1814752	0.8093061
	_Cons	-3.2443***	0.6617473	-4.90	0.000	-4.541388	-1.947386
	λ	0.9157***	0.0841231	10.89	0.000	0.7508432	1.0806
Mexico	CO_2_Intensity	8.54e-07***	9.49e-08	9.00	0.000	6.68e-07	1.04e-06
	lnGVA	1.3432***	0.1639544	8.19	0.000	1.021883	1.664573
	GVA^2	-1.70e-10***	2.10e-11	-8.10	0.000	-2.11e-10	-1.29e-10
	H_2ORed	-1.6753***	0.2790382	-6.00	0.000	-2.222255	-1.128446
	Cons	-8.6013**	4.232454	-2.03	0.042	-16.89681	–0.3058964
	λ	0.9718***	0.0279994	34.71	0.000	0.9170163	1.026772

Note: *** $p < 0.01$, ** $p < 0.05$, * $p < 0.10$. The λ point estimates for both countries lie within the admissible ranges implied by W. The reported 95% confidence intervals are asymptotic Wald intervals calculated from the standard errors and are not truncated at the parameter-space boundaries.

at higher income levels. From a spatial perspective, this pattern implies that the structural transformation required for environmental improvement has not yet materialized uniformly across regions. Consequently, the EKC should be interpreted as incipient and not yet validated in its mature phase. This interpretation aligns with Zafar et al. (2019) and Usman et al. (2022), who argue that in fossil-fuel-dependent economies with limited environmental governance, the upward segment of the EKC tends to persist for longer periods.

Applying the same turning-point calculation to the SEM estimates confirms the nonlinear EKC implications. Based on the coefficients in Table 4 and the expression:

$$GVA* = \sqrt{\frac{\beta_{ln(GVA)}}{-2\beta_{(GVA)^2}}}$$

the implied turning point equals 20,628,982 for Ecuador and 62,854 for Mexico (in the same units used for GVA in the dataset). Overall, the turning-point values are very similar across SAR and SEM, which strengthens the robustness of the estimated nonlinear relationship.

The positive and statistically significant coefficient of H_2ORed indicates that the expansion of basic infrastructure is associated with higher environmental pressure, suggesting that improvements in service coverage are occurring alongside increases in energy use and emissions. This result points to a scale effect that continues to dominate over potential efficiency gains, particularly in regions where infrastructure growth is not yet accompanied by cleaner technologies. Moreover, the positive and statistically significant λ estimate lies close to the upper admissible boundary and indicates strong spatial dependence in the error term, implying that unobserved territorial factors influence environmental outcomes. This pattern highlights the presence of spatial spillovers and suggests that the model captures only part of the regional dynamics, reinforcing the need to interpret the EKC within a spatially interconnected context.

In Mexico, the estimated signs reinforce the presence of a more advanced stage of the Environmental Kuznets Curve. The positive effect of lnGVA combined with the negative and highly significant quadratic term indicates a steeper concave pattern, suggesting that the economy is moving closer to the turning phase of the EKC. Rather than reflecting background conditions, the results point to a context in which structural change and environmental management may be beginning to offset the scale effect of growth. This interpretation is consistent with Dogan et al. (2020), who emphasize that active environmental policies and more diversified productive structures can accelerate the transition toward the declining segment of the EKC.

Additionally, the negative coefficient of H_2ORed suggests that the expansion of basic services is associated with efficiency gains or stricter environmental standards that help mitigate environmental pressure. This pattern contrasts with less efficient infrastructure expansions and is in line with Medina-Rivas et al. (2022). Finally, the positive and statistically significant λ estimate lies close to the upper admissible boundary, confirming persistent spatial dependence in the disturbance process and indicating that unobserved territorial factors continue to shape environmental outcomes beyond the variables included in the model.

3.4. Comparative Analysis of SAR and SEM Spatial Models

The comparison between the SAR and SEM spatial models for Ecuador and Mexico (Table 5) reveals notable differences in the spatial distribution of pollution, reflecting the structural heterogeneity of both economies in relation to the Environmental Kuznets Curve (EKC). Although the information criteria favor the SAR specification in both cases, the model selection is not based solely on goodness-of-fit measures. In Ecuador, the spatial autoregressive coefficient is positive and highly significant, indicating the presence of substantive spatial dependence whereby pollution levels in one province directly influence neighboring areas. This finding points to the existence of spillover effects rather than merely spatially correlated disturbances, thereby supporting the preference for the SAR model over the SEM specification. The lower residual dispersion and more favorable information criteria further reinforce the robustness of the SAR model. This pattern confirms that Ecuador's EKC remains in its ascending phase, where oil-related activities continue to generate persistent environmental pressures without reaching the turning point (Larrea & Warnars 2009, Zafar et al. 2019).

The choice between the SAR and SEM specifications is supported by both statistical evidence and the underlying economic interpretation of spatial interaction. Statistically, Table 5 indicates that SAR provides better overall fit in both countries (higher R^2 and lower AIC/BIC), and the spatial parameters are highly significant, confirming that spatial dependence is a core feature of the data. In addition, the spatial dependence diagnostics reported in Table 2 justify the inclusion of a spatial structure. From a theoretical standpoint, SAR is appropriate when environmental outcomes propagate through direct inter-territorial spillovers, meaning that emissions in one province/state can influence neighboring territories through geographic and economic

Table 5: Comparison of SAR and SEM models for Ecuador and Mexico.

Country	Model:	SAR (Spatial Autoregressive Model)	SEM (Spatial Error Model)
Ecuador	Log likelihood	-265.26353	-313.62024
	Sigma (σ)	0.44	0.50
	R^2 (squared correlation)	0.945	0.927
	λ (λ)	-	0.9157 (-3.626 < λ <1.000)
	ρ (ρ)	.9791 (-3.626 < ρ <1.000)	-
	Wald test (spatial effect)	2248.772 (0.000)	118.494 (0.000)
	Likelihood ratio test	113.613 (0.000)	16.899 (0.000)
	Lagrange multiplier test	137.344 (0.000)	40.057 (0.000)
	AIC (Akaike Information Criterion)	542.5271	619.9926
	BIC (Bayesian Information Criterion)	566.9376	644.0602
Mexico	Log likelihood	-1337.0007	-1346.6644
	Sigma (σ)	2.45	2.49
	R^2 (squared correlation)	0.441	0.334
	λ (λ)		0.9718 (-3.385 < λ < 1.000)
	ρ (ρ)	0.9671 (-3.385 < ρ <1.000)	
	Wald test (spatial effect)	905.114 (0.000)	1204.871 (0.000)
	Likelihood ratio test	85.847 (0.000)	66.520 (0.000)
	Lagrange multiplier test	271.186 (0.000)	408.348 (0.000)
	AIC (Akaike Information Criterion)	2686.001	2705.329
	BIC (Bayesian Information Criterion)	2712.138	2731.465

Note: Prepared by the authors.

linkages. By contrast, SEM is more consistent with spatial dependence driven by spatially correlated unobserved shocks captured in the error term. Therefore, SAR is retained as the baseline specification for comparative interpretation of spillover effects, while SEM is reported as a complementary robustness specification.

From a methodological perspective, the results indicate that the SAR model provides a more robust specification than the SEM for both countries, although with differences in the intensity of spatial effects. In Ecuador, the spatial autoregressive coefficient is large and statistically significant, revealing strong regional interdependence whereby pollution spreads from major extractive hubs to neighboring areas. This pattern is consistent with the presence of substantive spatial spillovers rather than merely spatially correlated errors, which supports the appropriateness of the SAR specification. Such dynamics tend to prolong the ascending phase of the EKC by transmitting environmental pressures across adjacent territories. This evidence aligns with Jeetoo (2023), who highlights that economies characterized by concentrated productive structures and limited territorial planning often exhibit pollution processes that diffuse spatially. Under these conditions, spatial lag models such as SAR are better suited to capture distributed environmental externalities.

In Mexico, the SAR model also shows superior performance relative to the SEM in terms of overall fit and information criteria, although residual variability remains comparatively higher. The statistical significance of both spatial parameters confirms the presence of regional interdependence; however, the magnitude and interpretation of the spatial lag coefficient suggest that spatial dependence operates mainly through interregional spillovers rather than through omitted spatial shocks. This indicates a more heterogeneous and less spatially uniform pattern of emissions compared to Ecuador. Such complexity reflects Mexico's broader territorial diversity and uneven industrial and urban development, consistent with the observations of Blackman et al. (2015) regarding the heterogeneous nature of environmental pressures in large and diverse national contexts.

The spatial distribution of pollution in Mexico is characterized by fragmentation across regions with differing levels of development and urbanization, revealing a spatial structure shaped by economic inequalities and differentiated urbanization processes (Chen et al. 2022). Similarly, Karahasan & Pinar (2022) demonstrate that regional productive heterogeneity generates complex environmental dispersion patterns, as also observed in the Mexican case. In

this sense, the superior explanatory performance of the SAR model in both Mexico and Ecuador supports its usefulness as an analytical tool for examining environmental trajectories in developing economies (Herrera et al. 2024).

From a comparative standpoint, the findings indicate that the SAR model provides a more solid explanatory framework for both countries. In Ecuador, pollution is transmitted in a more direct and geographically dependent manner, reflecting a rigid EKC that remains in its ascending phase (Buenaño et al. 2023). In contrast, Mexico, due to its territorial scale and structural diversity, exhibits more dispersed and complex spatial patterns, with emissions fragmented across regions with varying degrees of industrialization and urban development (Medina-Rivas et al. 2022). This diversity complicates the representation of environmental dynamics through a single spatial specification, in line with the arguments of Percastre et al. (2024) regarding the role of economic and urban heterogeneity in shaping environmental pressures.

4. CONCLUSIONS

The environmental trajectories of Ecuador and Mexico reveal distinct paths within the framework of the Environmental Kuznets Curve (EKC), shaped by differences in productive structures and institutional capacities. While Ecuador remains in the ascending phase of the EKC, largely due to its dependence on extractive activities and the limited consolidation of environmental institutions, Mexico exhibits clearer evidence of having reached, or even surpassed, the turning point in certain regions. This divergence highlights how the nature of economic growth, whether resource-based or more industrialized and diversified, conditions the potential for transitioning toward environmentally sustainable development pathways. The Mexican case illustrates that policies aimed at energy diversification and institutional strengthening can generate positive effects on emission reduction, although these efforts remain insufficient to achieve a homogeneous transition at the national scale.

The results further confirm that CO_2 emissions do not follow random patterns but are driven by significant spatial and territorial dynamics. In both countries, the spatial autocorrelation detected across all estimated models indicates that pollution processes are governed by shared regional logics. In Ecuador, emissions are concentrated in the Amazon and coastal regions, closely associated with oil extraction activities, whereas in Mexico, a more fragmented network of interconnected industrial hubs is observed. These findings validate the use of spatial econometric models as essential tools for capturing environmental externalities across contiguous territories and for designing differentiated mitigation policies tailored to regional characteristics.

The comparison between the SAR (Spatial Autoregressive Model) and SEM (Spatial Error Model) indicates that direct spatial interaction among regions, as captured by the SAR specification, exerts a stronger influence on emission patterns than unobserved residual spatial effects modeled by the SEM. This result highlights the importance of geographical contagion in shaping CO_2 emission processes. In Ecuador, the superior performance of the SAR model suggests that pollution in one province is closely linked to pollution in neighboring provinces, reflecting development patterns concentrated in extractive hubs. In Mexico, although the SAR model also performs better, the lower value of the spatial autoregressive parameter (ρ) and the higher residual variance reveal a more heterogeneous structure that is less dependent on immediate geographical proximity. Consequently, mitigation strategies should be adapted not only to the type of economy but also to the territorial configuration of each country: Ecuador requires targeted interventions in extractive clusters, whereas Mexico demands multi-level policies capable of addressing dispersed and diverse sources of pollution.

Access to basic services, such as piped water, exhibits contrasting effects across the two countries, indicating that its environmental impact depends critically on institutional context and the technological efficiency of infrastructure. In Ecuador, the expansion of public water networks is associated with higher emission levels, likely linked to rapid urban growth and increased energy demand in low-efficiency environments. By contrast, in Mexico, this variable exerts a negative effect on emissions, suggesting that efficient urban infrastructure and higher technological standards can contribute to reducing environmental pressures. This contrast underscores the importance of complementing the expansion of basic service coverage with policies aimed at improving energy efficiency, promoting sustainable urban planning, and strengthening environmental regulation.

Finally, the dynamics of CO_2 emissions in both countries demonstrate that the Environmental Kuznets Curve hypothesis is neither automatic nor uniform. The transition toward sustainability requires more than economic growth alone; it depends on political commitment, sustained public investment, and strong institutions. Ecuador, despite recent advances, remains constrained by an extractivist model that perpetuates environmental degradation, while Mexico, although more advanced in relative terms, faces setbacks derived from policy decisions that weaken environmental governance and slow the expansion of clean energy. Consequently, EKC phases should be interpreted not as inevitable stages of development but as outcomes shaped by structural conditions and policy choices. This analysis highlights the urgency of rethinking growth strategies through an ecological and territorial lens, in which the State

plays an active role in correcting externalities and leading a transition toward a genuinely sustainable development model.

5. ACKNOWLEDGMENTS

The authors gratefully acknowledge the Technical State University of Quevedo (UTEQ), Ecuador, and the Autonomous University of Sinaloa (UAS), Mexico, for the academic, technical, and administrative support provided during the development of this research.

6. REFERENCES

Acheampong, A.O., Dzator, J. and Savage, D.A., 2021. Renewable energy, CO_2 emissions and economic growth in sub-Saharan Africa: does institutional quality matter? *Journal of Policy Modeling*, 43(5), 1070–1093. [DOI]

Adams, S. and Acheampong, A.O., 2019. Reducing carbon emissions: the role of renewable energy and democracy. Journal *of Cleaner Production,* 240, 118245. [DOI]

Almeida, D., Carvalho, L., Ferreira, P., Dionísio, A., Haq, I.U., 2024. Global dynamics of Environmental Kuznets curve: a cross-correlation analysis of income and CO_2 emissions. *Sustainability*, 16, 9089. [DOI]

Al-Mulali, U., Saboori, B. and Ozturk, I., 2015. Investigating the environmental Kuznets curve hypothesis in Vietnam. *Energy Policy*, 76, 123–131. [DOI]

Alvarado, R., Tillaguango, B., López-Sánchez, M., Ponce, P. and Işık, C., 2021. Heterogeneous impact of natural resources on income inequality: the role of the shadow economy and human capital index. Economic *Analysis and Policy,* 69, 690–704. [DOI]

Blackman, A., Alpízar, F., Carlsson, F. and Planter, M. R., 2018. A contingent valuation approach to estimating regulatory costs: Mexico's day without driving program. *Journal of the Association of Environmental and Resource Economists*, 5(3), 607–641. [DOI]

Buenaño, E., Padilla, E. and Alcántara, V., 2023. CO_2 emissions from service sectors in Ecuador: an analysis using input–output subsystems. *Economic Structures*, 12, 16. [DOI]

Castro-Rosales, G. and Esqueda-Walle, R., 2020. Spatial analysis of urban water use management in the northern border region of Mexico. *International Journal of Business and Management*, *15*(11), pp.126-137. [DOI]

Catalán Alonso, H., 2021. Impact of renewable energies on greenhouse gas emissions in Mexico. *Problemas del Desarrollo*, 52(204), 59–83. [DOI]

Cevallos-Mina, M.G., Lara-Tambaco, R.M., Reyes-Vera, C.H., Mosquera-Quiñonez, E.F. and Castillo-Gámez, J.L., 2024. The effects of oil price on energy production and the Ecuadorian economy. *International Journal of Energy Economics and Policy*, 14(3), 38–50. [DOI]

Charfeddine, L. and Mrabet, Z., 2017. The impact of economic development and social-political factors on ecological footprint: a panel data analysis for 15 MENA countries. *Renewable and Sustainable Energy Reviews*, 76, 138–154. [DOI]

Chen, W., Flatnes, J.E., Miteva, D.A. and Klaiber, H.A., 2022. The impact of deforestation on nature-based recreation: evidence from citizen science data in Mexico. Land *Economics,* 98(1), 22–40. [DOI]

Destek, M.A. and Sarkodie, S.A., 2019. Investigation of environmental Kuznets curve for ecological footprint: the role of energy and financial development. Science *of the Total Environment,* 650, 2483–2489. [DOI]

Dogan, E., Ulucak, R., Kocak, E. and Isik, C., 2020. The use of ecological footprint in estimating the environmental Kuznets curve hypothesis for BRICST by considering cross-section dependence and heterogeneity. Science *of the Total Environment,* 723, 138063. [DOI]

Dong, K., Hochman, G., Zhang, Y., Sun, R., Li, H. and Liao, H., 2018. CO_2 emissions, economic and population growth, and renewable energy: empirical evidence across regions. *Energy Economics*, 75(C), 180–192. [DOI]

Elizondo, L., Garnica-Monroy, R. and López, L.M., 2025. Concealing reproductive tasks: an inequality genotype for middle-income housing in Mexico. Nexus *Network Journal,* 1–17. [DOI]

Escamilla-García, P.E., Rivera-González, G., Rivera, A.E. and Soto, F.P., 2024. Socio-economic determinants of greenhouse gas emissions in Mexico: an analytical exploration over three decades. Sustainability, 16(17), 7668. [DOI]

Fang, X., Wang, L., Sun, C., Zheng, X. and Wei, J., 2021. Gap between words and actions: empirical study on consistency of residents supporting renewable energy development in China. Energy *Policy,* 148, 111945. [DOI]

Figueroa J Daniela, Galeana-Pizaña Mauricio, Núñez Juan Manuel, Gómez Carlos Anzaldo, Hernández-Castro Roberto, Sánchez-Ramírez María del Mar, Garduño Andrea, 2021. Assessing drivers and deterrents of deforestation in Mexico through a public policy tool. the adequacy of the index of economic pressure for deforestation. Forest *Policy and Economics,* 133, 102608. [DOI]

Fujii, H., Webb, J., Mundree, S., Rowlings, D., Grace, P., Wilson, C. and Managi, S., 2024. Priority change and driving factors in the voluntary carbon offset market. *Cleaner Environmental Systems*, 13, 100164. [DOI]

Gómez, M. and Rodríguez, J.C., 2020. The ecological footprint and Kuznets Environmental curve in the USMCA countries: a method of moments quantile regression analysis. *Energies*, 13(24), 6650. [DOI]

Goulart, F.F., Chappell, M.J., Mertens, F. and Soares-Filho, B., 2023. Sparing or expanding? The effects of agricultural yields on farm expansion and deforestation in the tropics. Biodiversity *and Conservation,* 32(3), 1089–1104. [DOI]

Grossman, G.M. and Krueger, A.B., 1995. Economic growth and the environment. The *Quarterly Journal of Economics,* 110(2), 353–377. [DOI]

Herrera Rios, A.Y., Herrera Ríos, P. and Sánchez Parra, R.C., 2024. Estimation of GHG emissions and costs in Sinaloa: towards sustainable economic and environmental policies. *Data and Metadata*, 3, 682. [DOI]

Jahanger, A., Usman, M. and Ahmad, P., 2022. A step towards sustainable path: the effect of globalization on China's carbon productivity from panel threshold approach. *Environmental Science and Pollution Research*, 29(6), 8353–8368. [DOI]

Jeetoo, J. and Chinyanga, E.R., 2023. A spatial econometric analysis of the environmental Kuznets curve and pollution haven hypothesis in sub-Saharan Africa. *Environmental Science and Pollution Research*, 30, 58169–58188. [DOI]

Kaika, D. and Zervas, E., 2013. The environmental Kuznets curve (EKC) theory: part A: concept, causes, and the CO_2 emissions case. *Energy Policy*, 62, 1392–1402. [DOI]

Karahasan, B.C. and Pinar, M., 2022. The environmental Kuznets curve for Turkish provinces: a spatial panel data approach. Environmental *Science and Pollution Research,* 29, 25519–25531. [DOI]

Khan, Z., Ali, S., Umar, M., Kirikkaleli, D. and Jiao, Z., 2020. Consumption-based carbon emissions and international trade in G7 countries: the role of environmental innovation and renewable energy. Science *of the Total Environment,* 730, 138945. [DOI]

Kuznets, S., 1955. International differences in capital formation and financing. In: Capital Formation and Economic Growth, pp. 19–111. Princeton University Press. Retrieved from: https://www.nber.org/system/files/chapters/c1303/c1303.pdf

Larrea, C. and Warnars, L., 2009. Ecuador's Yasuni-ITT Initiative: Avoiding emissions by keeping petroleum underground. Energy for Sustainable Development, 13(3), 219–223. [DOI]

Li, R., Wang, Q. and Li, L., 2023. Does renewable energy reduce per capita carbon emissions and per capita ecological footprint? New evidence from 130 countries. *Energy Strategy Reviews*, 49, 101121. [DOI]

Mahmoodi, M. and Dahmardeh, N., 2022. Environmental Kuznets curve hypothesis with considering ecological footprint and governance quality: evidence from emerging countries. Frontiers *in Environmental Science,* 10, 849676. [DOI]

Meckling, J. and Nahm, J., 2019. The politics of technology bans: Industrial policy competition and green goals for the auto industry. *Energy Policy*, 126, 470–479. [DOI]

Medina-Rivas, M.A., Ramos-Ayala, J.J. and Salas-Fernández, A., 2022. Household water consumption on the outskirts of Mexico City. *International Journal of Hydrology*, 6(1), 1–8. [DOI]

Murshed, M., Nurmakhanova, M., Elheddad, M. and Ahmed, R., 2021. The environmental Kuznets curve hypothesis for carbon and ecological footprints in South Asia: the role of renewable energy. *GeoJournal*, 87(3), 2345–2372. [DOI]

Okullo, S.J., 2020. Determining the social cost of carbon: under damage and climate sensitivity uncertainty. *Environmental and Resource Economics*, 75, 79–103. [DOI]

OSEF, 2025. Tablero Curva de Kuznets Ambiental. Observatorio de Sostenibilidad Económica y Financiera. Retrieved from: https://osef.uteq.edu.ec/portalweb/ProCurva.html

Paramati, S.R., Apergis, N. and Ummalla, M., 2018. Dynamics of renewable energy consumption and economic activities across the agriculture, industry, and service sectors: evidence in the perspective of sustainable development. *Environmental Science and Pollution Research*, 25(2), 1375–1387. [DOI]

Pei, L., Wang, X., Guo, B., Guo, H. and Yu, Y., 2021. Do air pollutants as well as meteorological factors impact Corona Virus Disease 2019 (COVID-19)? Evidence from China based on the geographical perspective. *Environmental Science and Pollution Research*, 28, 35584–35596. [DOI]

Percastre Gómez, A., Bonilla, D. and Banister, D., 2024. Decoupling transport-CO_2 emissions: Mexico, Spain and the USA: A trend analysis. *Transportation Research Part D: Transport and Environment*, 137, 104510. [DOI]

Rakpho, P. and Yamaka, W., 2021. The forecasting power of economic policy uncertainty for energy demand and supply. *Energy Reports*, 7(Suppl. 3), 338–343. [DOI]

Renner, S., 2018. Poverty and distributional effects of a carbon tax in Mexico. *Energy Policy*, 112, 98–110. [DOI]

Sarkodie, S.A. and Strezov, V., 2020. Economic, social, and governance adaptation readiness for mitigation of climate change vulnerability: evidence from 192 countries. Science *of the Total Environment,* 656, 150–164. [DOI]

Schneiter, P. and Mellon-Bedi, S., 2025. The Environmental Kuznets curve revisited: a spatial panel model with heterogeneous coefficients. *Energy Economics*, 143, 108237. [DOI]

Shahbaz, M., Haouas, I. and Hoang, T.H.V., 2019. Economic growth and environmental degradation in Vietnam: is the environmental Kuznets curve a complete picture? *Emerging Markets Review*, 38, 197–218. [DOI]

Sinha, A., Sengupta, T. and Alvarado, R., 2020. Interplay between technological innovation and environmental quality: formulating the SDG policies for next 11 economies. Journal *of Cleaner Production,* 242, 118549. [DOI]

Stern, D.I., 2004. The rise and fall of the Environmental Kuznets curve. World *Development,* 32(8), 1419–1439. [DOI]

Tangato, K.F., 2025. The impact of clean technology adoption on carbon emissions: a global perspective. *Clean Technologies and Environmental Policy*, 27(6), 2683–2700. [DOI]

Usman, M., Jahanger, A., Makhdum, M.S. A., Balsalobre-Lorente, D. and Bashir, A., 2022. How do financial development, energy consumption, natural resources, and globalization affect Arctic countries' economic growth and environmental quality? An advanced panel data simulation. Energy, 241, 122515. [DOI]

Vázquez-López, R., 2023. Assessing employment benefits from trade: US–Mexico trade under NAFTA. *Economic Systems Research*, 35(4), 541–565. [DOI]

Wackernagel, M., Hanscom, L. and Lin, D., 2017. Making the sustainable development goals consistent with sustainability. Frontiers *in Energy Research,* 5, 18. [DOI]

Wang, Q., Zhang, F. and Li, R., 2023. Free trade and carbon emissions revisited: the asymmetric impacts of trade diversification and trade openness. *Sustainable Development*, 32(1), 876–901. [DOI]

Zafar, M.W., Zaidi, S.A. H., Sinha, A., Gedikli, A. and Hou, F., 2019. The role of stock market and banking sector development, and renewable energy consumption in carbon emissions: insights from G-7 and N-11 countries. Resources *Policy,* 62, 101427. [DOI]

Nature Environment and Pollution Technology
An International Quarterly Peer-Reviewed Open Access Journal

p-ISSN: 0972-6268 | e-ISSN: 2395-3454 Vol. 25 | No. 4 | Article ID D1905 | 2026

RESEARCH ARTICLE https://doi.org/10.46488/NEPT.2026.v25i04.D1905 OPEN ACCESS

Evaluation of Iron Ore Dust Emission Rates and Associated Bacterial Load

Melainine Aillal[1]†, Olfa Ben Said[2,3], Hamouda Beyrem[2] and Zeinebou Sidoumou[1]
[1]University of Nouakchott, Faculty of Science and Technology, New University Campus, 5026, Nouakchott, Mauritania
[2]Laboratory of Environment Biomonitoring, Coastal Ecology Unit, Faculty of Sciences of Bizerte, University of Carthage, Zarzouna, Tunisia
[3]Laboratory of Biotechnology and Nuclear Technology, National Centre of Nuclear Science and Technology, Sidi Thabet Technopark, 2020 Ariana, Tunisia
†Corresponding author: Melainine Aillal; melainineaillal@gmail.com

ARTICLE HISTORY

Received: 22-01-2026
Revised: 09-03-2026
Accepted: 19-03-2026

KEYWORDS

Mining activities
Dust emissions
Heavy metals
Environmental pollution
Staphylococcus
Occupational health

CITE THIS ARTICLE

Aillal, M., Ben Said, O., Beyrem, H. and Sidoumou, Z., 2026. Evaluation of iron ore dust emission rates and associated bacterial load. *Nature Environment and Pollution Technology*, 25(4), D1905. https://doi.org/10.46488/NEPT.2026.v25i04.D1905

COPYRIGHT & LICENCE

© 2026 The Authors
Open Access under CC BY 4.0.

PUBLISHED BY
TECHNOSCIENCE PUBLICATIONS

ABSTRACT

The National Industrial and Mining Company (SNIM) is facing significant dust emissions, raising serious environmental and public health concerns. This study aimed to characterize airborne dust emissions from mining activities and to assess their physicochemical and microbiological composition. Dust samples were analyzed and found to contain hazardous heavy metals, including lead, copper, nickel, and cobalt. A standardized measurement procedure was developed and applied in accordance with French Standard X 43-014 to quantify dust emission rates.

The potential sources and causes of dust emissions were identified, and immediate preventive and corrective actions were proposed using the Failure Modes, Effects, and Criticality Analysis (FMECA) method. The results revealed exceptionally high dust emission levels at the Guelb El Rhein mine, exceeding the thresholds associated with highly polluted environments. In contrast, emissions at the Kedia d'Idjil mine remained close to regulatory limits and were comparable to levels observed in relatively livable environments.

Microbiological analysis of dust particles revealed the presence of potentially pathogenic staphylococcal species, including *Staphylococcus epidermidis, S. hominis, S. capitis, S. haemolyticus, S. lentus, S. auricularis, S. sciuri, and S. cohnii* subsp. *urealyticum.* These findings highlight the combined chemical and biological risks associated with mining dust emissions and underscore the need for improved dust management strategies in mining environments.

1. INTRODUCTION

Atmospheric pollution has existed for centuries, but has intensified considerably with the expansion of human activities. The large-scale production of energy through combustion processes and the rapid development of industrial operations have profoundly disrupted natural atmospheric balances, not only at local scales but also globally. These changes have led to significant degradation of air quality and have contributed to climate change (Boussahel 2007). Atmospheric emissions include not only gases and fine particulate matter but also heavy metals and various chemical compounds that can exert toxic effects on ecosystems and human health.

The mechanisms governing environmental contamination through atmospheric deposition remain insufficiently understood. During cloud formation, pollutants are partitioned among different atmospheric phases, namely gaseous, liquid, and particulate. While gas-liquid equilibrium processes have been extensively studied,

interactions between particulate and liquid phases are still poorly documented. Recent studies have demonstrated that the pollutant load varies according to particle size, which strongly influences particle transport, deposition processes, and environmental fate (Ma et al. 2014, Hassanvand et al. 2015). Fine particles are capable of long-range transport, whereas coarse particles tend to deposit more rapidly, leading to pronounced local impacts on air, soil, and water quality.

Air pollution remains one of the most critical global environmental challenges and continues to intensify due to rapid urbanization and the expansion of industrial and mining activities. This situation underscores the urgent need to control emissions to protect both public health and the environment (Elodie et al. 2020). In addition to chemical contamination, air, particularly indoor air in industrial settings, can serve as a favorable medium for the development and persistence of pathogenic microorganisms associated with dust and aerosols (Viegas et al. 2020, Yan et al. 2021). Previous research has shown that airborne dust and bioaerosols can significantly increase occupational health risks, including infections, toxic effects, and allergic responses (Eduard et al. 2012, Heederik & Von Mutius 2012).

In Mauritania, the discovery and exploitation of mineral resources over the past two decades have led to the rapid expansion of mining projects, predominantly using open-pit extraction methods. One of the most significant environmental threats associated with these operations is the generation of large quantities of suspended particulate matter, which can adversely affect soils, vegetation, and nearby populations (Antoine 2012). Consequently, mining companies operating in the country are confronted not only with production-related challenges but also with increasing concerns regarding the environmental and health impacts of dust emissions, which have become a major issue for both employers and local authorities.

The National Industrial and Mining Company (SNIM), which specializes in iron ore production, operates mainly in the regions of Tiris Zemmour (Zouerate) and Dakhlet Nouadhibou in Mauritania (Fig. 1). Ore extraction and processing activities are primarily conducted near the city of Zouerate, after which the products are transported to Nouadhibou for export. The ore is conveyed over a distance of approximately 700 km by a 2.5 km-long ore train with an average capacity of 17,000 tons per convoy. From Nouadhibou, where SNIM operates two mineral ports, iron ore products are shipped to several Western European countries and China (SNIM 2022).

An Environmental and Social Impact Assessment conducted in 2009 for SNIM mining operations indicated that air pollution associated with the Guelbs 1 facilities posed significant risks to human health, particularly with respect to respiratory diseases. The assessment further predicted that the development of the Guelbs 2 project would increase dust emissions by 10–15% (Tecsult International Limited 2009). According to this study, workers involved in the Guelbs 2 project would be exposed to concentrations of total dust, quartz dust containing silica, iron dust, and welding fumes exceeding applicable regulatory standards, thereby necessitating the implementation of corrective and preventive measures.

In this context, the present study focuses on dust emissions from SNIM's Guelb El Rhein (Guelbs 2) and Kedia d'Idjil (TO14, Rouessa) mining sites, which were selected due to their substantial dust-generating activities. A corrective approach was implemented alongside a detailed assessment of dust emission levels and the associated bacterial load in airborne particles. The objective of this work is to improve understanding of the combined environmental and health impacts of mining-related dust emissions and to contribute to the development of effective mitigation strategies for mining environments.

2. MATERIALS AND METHODS

Dust assessment can be conducted using three main approaches: (i) measurement of airborne particulate concentrations (TSP, PM_{10}, $PM_{2.5}$), expressed in µg m^{-3} (Winberry 1999); (ii) quantification of deposited dust expressed in mg m^{-2} day^{-1}, which is the method adopted in this study; and (iii) estimation of total annual emissions expressed in tons per year (t yr^{-1}), according to particle size fractions.

The quantification method applied in this study is based on dust sampling over a defined exposure period. From a qualitative perspective, several analytical techniques were employed: X-ray fluorescence (XRF) for elemental composition, X-ray diffraction (XRD) for mineralogical characterization and silica content, atomic absorption spectrometry for heavy metal determination, the Most Probable Number (MPN) method for bacterial quantification, and the API gallery system for bacterial species identification (NIOSH 1998).

2.1. Quantification of Sedimented Dust

The procedure used to measure deposited dust followed the French Standard NF X 43-014 (AFNOR 2003), as recommended by INERIS (2004). Dust was collected using Bergerhoff or Owen deposit gauges, which were weighed before and after the exposure period. Sampling devices were installed in accordance with standard recommendations, away from high-risk zones and major traffic sources.

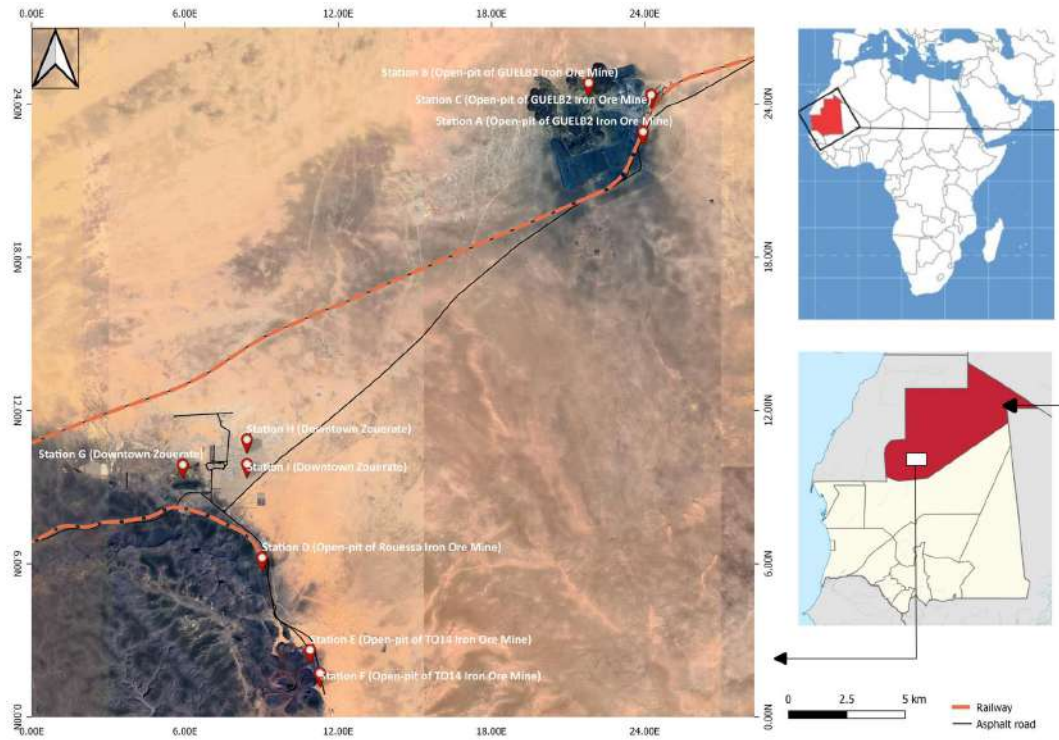


Fig. 1: Location of sampling stations within the National Industrial and Mining Company (SNIM) in the Tiris Zemmour region, Mauritania. Stations A, B, and C are located in the Guelb El Rhein mine along the Guelb 2 production circuit. Station D (Rouessa) and stations E and F (TO14 area) are situated in the Kedia d'Idjil mine. Stations G, H, and I are located in downtown Zouerate.

The dust monitoring was conducted using Owen gauges, which were strategically positioned at each sampling point at a standardized height of 1.5 m above ground level to minimize the influence of saltating particles from the soil surface. To quantify the atmospheric dust fallout, the total mass of the collected particles was related to the sampling surface and the exposure time. The dust deposition rate (T) was calculated according to the following formula:

$$T = \frac{P}{S \times T}$$

Where:

- T: dust deposition rate (mg m^{-2} day^{-1})
- P: total mass of dust collected in the gauge (mg)
- S: surface area of the gauge opening (m^2)
- t: duration of the exposure period (days)

This calculation procedure follows the rigorous recommendations of the NF X 43-014 standard for the measurement of atmospheric dust fallout. This standardized approach ensures that the exceptionally high values recorded at the source-point stations are a precise reflection of the intense industrial activity at the mining sites during the sampling window.

Dust pollution levels were classified as follows:

- Very low: < 150 mg m^{-2} day^{-1} (low pollution area)
- Low: 150–350 mg m^{-2} day^{-1} (moderately polluted area)
- High: 350–500 mg m^{-2} day^{-1} (polluted area)
- Very high: 500–1,000 mg m^{-2} day^{-1} (highly polluted area)

Extremely high: > 1,000 mg m^{-2} day^{-1} (very heavily polluted area) (Budillon Rabatel 2009)

2.2. Study Area and Sampling Strategy

The study was conducted at two major mining sites located near Zouerate, northern Mauritania: the Guelb El Rhein magnetite mine and the Kédia d'Idjil hematite mine. Sampling was carried out over two weeks from August 2 to August 16, 2019.

Dust deposition was monitored at nine sampling stations (Fig. 1). Six stations were located within the mining areas: three along the Guelb 2 production circuit and three at Kédia d'Idjil. The remaining three stations (G, H, and I), located in central Zouerate, served as urban control sites.

Climatic conditions during the monitoring period were characterized by temperatures ranging from 22–43°C, no precipitation, and wind speeds ranging from 12–52 km h^{-1}

(Blanchon & Penven 2012). While the two-week monitoring period (August 2–16, 2019) captures a specific temporal window, it coincides with extreme summer conditions in the Saharan climate, characterized by peak temperatures and significant wind speeds conducive to maximum dust suspension. We acknowledge that this short duration does not account for annual seasonal variability; however, it provides a critical baseline for peak emission periods during the dry season.

2.3. Chemical and Mineralogical Analyses

Elemental composition of dust samples was determined using X-ray fluorescence (XRF), allowing quantification of major oxides including CaO, SiO_2, MgO, Fe_2O_3, Al_2O_3, SO_3, K_2O, and Na_2O. XRF analysis enabled continuous monitoring of dust composition throughout the sampling period (Jensen et al. 2006).

Mineralogical composition and crystalline structure were analyzed by X-ray diffractometry (XRD) (Ron 2006).

The exploitation of hematite (Fe_2O_3) and magnetite (Fe_3O_4) ores constitutes a significant source of heavy metals such as Ni, Pb, Cu, Co, Cd, and Zn. These metals are transported by dust particles and deposited on surrounding surfaces at distances influenced by wind speed and particle size (Simpson & Spadaro 2016, Embile Jr. et al. 2018). Elevated iron concentrations commonly observed in polluted mining environments may induce analytical interferences, notably Fe/Cu and Co/Fe interactions (Adamson et al. 2000, Manceau et al. 2002, Sammut 2007, Aillal et al. 2023).

To minimize such interferences, heavy metal analyses were performed on the fine fraction of iron ore dust using Flame Atomic Absorption Spectroscopy (FAAS) following acid digestion with HCl, HF, and HNO_3 (López-García et al. 1995). The metals quantified included Co, Cu, Ni, and Pb (Fig. 5).

2.4. Microbiological Analyses

2.4.1. Total Cultivable Bacterial Quantification

For inoculum preparation, dust samples from each sampling site were homogenized, weighed, and stored in sterile screw-capped tubes. For each dust type (magnetite from Guelb El Rhein and hematite from Kédia d'Idjil), 1.5 g of dust was suspended in 5 mL of sterile physiological saline solution. Serial dilutions were prepared using physiological saline (9 g L^{-1} NaCl) according to the suspension–dilution technique described by Rapilly (1968).

Bacterial enumeration was performed using the Most Probable Number (MPN) method with a five-tube series. Tubes were incubated at 37°C for 48 h. Nutrient broth, thioglycollate medium, and LB broth were used for bacterial growth and quantification (Chandrapati & Williams 2014).

2.4.2. Isolation and Characterization of Anaerobic Bacterial Strains

Three grams of hematite dust and three grams of magnetite dust were suspended separately in 5 mL of sterile physiological water and subjected to thermal shock at 63°C to eliminate vegetative cells while preserving sporulated forms (Cammalleri et al. 2015). Serial dilutions were prepared, and selected dilutions were inoculated onto iron sulfite agar under anaerobic conditions and incubated at 37°C.

Dominant strains were purified through successive subcultures. Preliminary identification was based on growth on selective media, Gram staining, spore staining, and macroscopic and microscopic observations using standard taxonomic keys.

2.4.3. Identification Using the API Staph System

Bacterial identification was further performed using the API Staph system, which consists of 19 microtubes containing dehydrated substrates for the differentiation of *Staphylococcus*, *Kocuria*, and *Micrococcus* species (Aouissi et al. 2007, Rouaiguia 2010). The galleries were incubated at 37°C for 24 h, and biochemical profiles were interpreted according to the manufacturer's instructions (Brown & Smith 2015). Final identification was confirmed using dedicated microbial identification software (Debabza 2015).

2.5. Failure Modes, Effects, and Criticality Analysis (FMECA)

The Failure Modes, Effects, and Criticality Analysis (FMECA), also referred to as AMDEC, is a preventive and inductive method used to identify potential failures and implement corrective actions at an early stage. This approach applies to products, processes, and production systems and is widely used in industrial risk assessment and environmental management (Hariz 2009).

2.6. Statistical Analysis

Dust emission data were expressed as mean ± standard deviation (SD). Statistical analyses were performed using STATISTICA version 8 software. Differences between dust emission rates were evaluated using one-way analysis of variance (ANOVA), followed by Tukey's HSD post hoc test when significant differences were observed. Statistical significance was set at $p < 0.05$.

Table 1: Results of dust emission monitoring at the National Industrial and Mining Company (SNIM) during August 2–16, 2019.

Sites	Gauge location	Owen gauge	Emission rate (mg m^{-2} day^{-1})
Guelb El Rhein	Guelb 2	A	38045
		B	27901
		C	50480
Kedia d'Idjil	Rouessa	D	19007
	TO14	E	12076
		F	15146
Zouerate	Downtown	G	594
		H	596
		I	592

3. RESULTS AND DISCUSSION

3.1. Dust Emission Rates

Dust emissions occur at different levels of the National Industrial and Mining Company (SNIM). However, this work focuses only on the iron ore production sites of Guelb El Rhein (Guelb 2), Kedia d'Idjil (TO14 and Rouessa), as well as downtown Zouerate. The results of this monitoring and the measurements carried out during August 2–16, 2019, are presented in Table 1.

To illustrate variation in these emissions, the mean emission rates at each collection site are shown in Fig. 2.

A one-way ANOVA revealed a significant difference in mean dust deposition rates among the three locations, $F(2, 6) = 23.87$, $p = 0.0014$. Tukey's HSD post hoc test showed that the mean dust deposition rate at Guelb El Rhein was significantly higher than those recorded at Kedia d'Idjil ($p = 0.013$) and downtown Zouerate ($p = 0.001$). However, the difference between Kedia d'Idjil and downtown Zouerate was not statistically significant ($p = 0.084$; Fig. 2).

3.2. Chemical Analysis

Dust collected from the two sites (Guelb El Rhein and Kedia d'Idjil) was subjected to XRF, XRD, and AAS analyses.

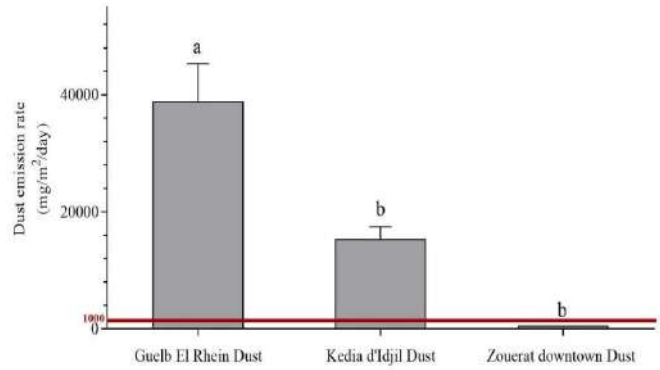


Fig. 2: Mean ± standard deviation of dust emission rates. Data indicated by different letters are significantly different (Tukey's HSD test, $p < 0.05$).

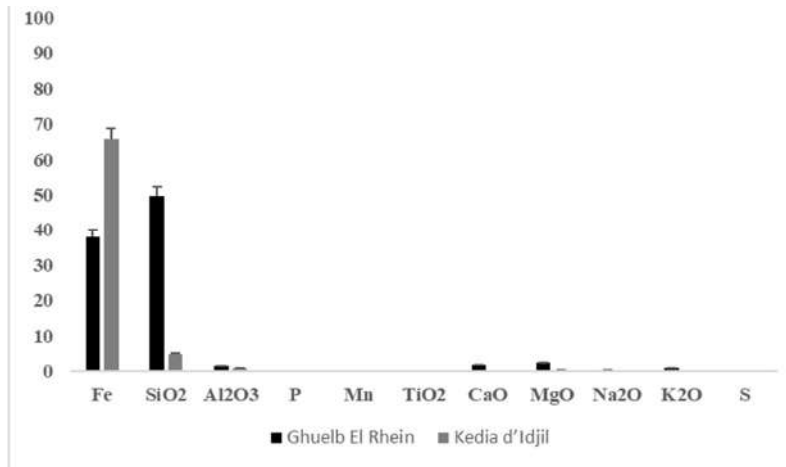


Fig. 3: Mean ± standard deviation of percentage composition determined by X-ray fluorescence (XRF) analysis.

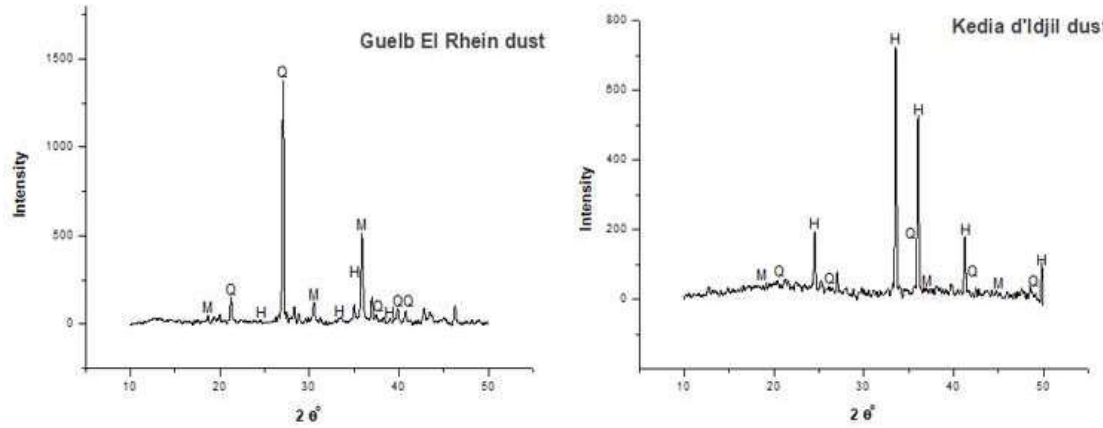


Fig. 4: X-ray diffraction diagrams for dust samples from Guelb El Rhein and Kedia d'Idjil. H, hematite; M, magnetite; Q, quartz.

Fig. 3 shows the results of the X-ray fluorescence (XRF) analysis.

The results showed that dust emitted at Guelb El Rhein contained 38.1 ± 2.2% iron oxide, indicating magnetite-type ore (37% iron content); however, this ore must undergo an enrichment process to reach the commercial value set by the company at 66% iron. Dust from Kedia d'Idjil contained 65.7 ± 1.9% iron, consistent with hematite-type ore (66% iron content).

Based on these results, an X-ray diffractometer was used to determine the type of silica in the iron oxide-silica mixture in a fraction approaching the alveolar fraction (Fig. 4).

Mineralogical analysis indicated that the iron ore dust from the National Industrial and Mining Company was composed mainly of hematite (Fe_2O_3), quartz (SiO_2), and magnetite (Fe_3O_4).

The diffractogram of dust emitted from Guelb El Rhein revealed three main intense peaks: a quartz peak at 2θ = 27°, a magnetite peak at 2θ = 36°, and a hematite peak at 2θ = 35°. The diffractogram of dust emitted from Kedia d'Idjil showed mainly hematite at five intense peaks, magnetite at weaker peaks, and quartz with a prominent peak at 2θ = 35°. The high iron levels in the dust, as shown in Fig. 3, may cause significant analytical interference with heavy metals. Dust samples from Kedia d'Idjil and Guelb El Rhein were analyzed using flame atomic absorption spectroscopy (FAAS) (Fig. 5).

The primary focus of the study was to assess dust emissions from iron ore extraction, with a particular emphasis on heavy metal concentrations. To this end, representative samples of iron ore dust from Guelb El Rhein and Kedia d'Idjil were collected and subjected to detailed analysis (Fig. 5). The findings reveal distinct variation in mean levels of heavy metals. The highest peaks belong to cobalt (Co) and the lowest to copper (Cu). Kedia d'Idjil dust samples have average values of 62.42 mg kg^{-1} of Co, 16.41 mg kg^{-1} of Cu, 29.08 mg kg^{-1} of Ni, and 25.71 mg kg^{-1} of Pb, respectively. However, the dust samples from Guelb El Rhein have Co, Cu, Ni, and Pb concentrations of 71.62, 22.34, 42.04, and 42.62 mg kg^{-1}, respectively. The concentration order for the Kedia d'Idjil samples is Co > Ni > Pb > Cu, with values of 62.42 mg kg^{-1}, 29.08 mg kg^{-1}, 25.71 mg kg^{-1}, and 16.41 mg kg^{-1}. For the Guelb El Rhein samples, the order is Co > Pb > Ni > Cu, with corresponding values of 71.62 mg kg^{-1}, 42.62 mg kg^{-1}, 42.04 mg kg^{-1}, and 22.34 mg kg^{-1}.

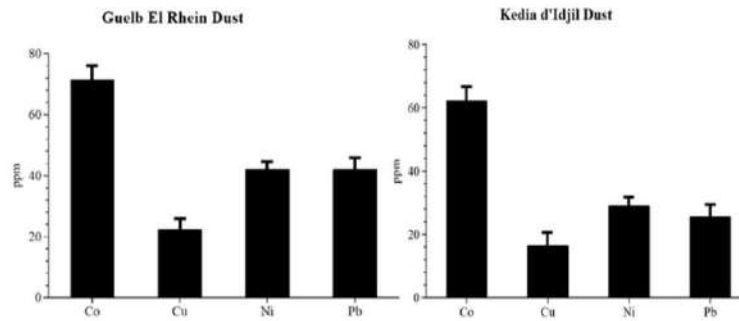


Fig. 5: Heavy metal (Co, Cu, Ni, and Pb) contents measured in the two iron ore dust types, Guelb El Rhein dust and Kedia d'Idjil dust.

Notably, the concentrations of heavy metals in dust samples collected from the city center of Zouerate were below the detection threshold. The concentration of Co (71.62 mg kg^{-1}) and Ni (42.04 mg kg^{-1}) in Guelb El Rhein dust is notably high when compared to the urban control (Zouerate), where these metals were undetectable. These levels approach or exceed common soil quality guidelines for industrial zones, suggesting that long-term deposition could lead to significant soil enrichment and potential ecological transfer, particularly given the fine fraction's capacity for transport. This study also shows that heavy metal content in the Guelb El Rhein samples of dust is higher than that in samples from Kedia d'Idjil. This conclusion indicates a potentially higher environmental impact of dust emissions in Guelb El Rhein when compared with Kedia d'Idjil. In brief, the present investigation offers comparisons of heavy metals contained in dust emissions as produced by iron ore mining. Results highlight the need for monitoring and controlling these emissions to reduce their environmental and human health implications.

3.3. Bacterial Analysis

3.3.1. Bacterial Quantification

The five-tube most probable number (MPN) technique was used to obtain quantitative estimates of the bacteria in each sample. Quantification was achieved by serial dilutions of a bacterial culture, dividing the sample into replicates, followed by incubation and subsequent visual examination of each sample to determine growth. Table 2 presents the abundance of bacterial groups.

Although direct enumeration by the MPN method yielded no detectable bacteria in the Guelb El Rhein dust sample (Table 2), this result indicates that the concentration of culturable bacteria in the untreated 1.5 g sample was below the detection limit of the method rather than confirming their complete absence. The *Staphylococcus* isolates reported in Table 3 were recovered through selective enrichment and culture on staphylococci-specific media, followed by identification using the API Staph system. They were not obtained through the heat-shock procedure. The heat treatment at 63 °C was performed separately to select heat-resistant or spore-forming bacteria and was not used for the isolation of *Staphylococcus* species.

Table 2: Bacterial quantification results.

Bacterial group	Types of samples	MPN $^{g-1}$
Total anaerobic and microaerophilic bacteria	Guelb El Rhein	0
	Kedia d'Idjil	2100
Total aerobic bacteria	Guelb El Rhein	0
	Kedia d'Idjil	75

3.3.2. Bacterial Strain Isolation and Characterization

After subculturing the bacterial strains isolated from several prepared selective media and incubated at 37°C, the macroscopic study of the colonies obtained made it possible to differentiate several microbial strains according to their appearance (size, color, etc.). All strains were subcultured on nutrient agar and incubated at 37°C. Several subcultures were subsequently carried out to ensure their purity (by careful observation of the colonies formed after re-isolation and differential Gram staining). Fifteen pure Gram-positive bacterial strains were selected for subsequent analysis.

3.3.3. Results of API Staph Identification

The appropriate API gallery for isolate identification was selected based on macroscopic, microscopic, and respiratory enzyme results, which guided identification toward specific bacterial genera.

After 24 h of incubation at 37°C, the API Staph gallery results (Table 3) were read and interpreted according to the manufacturer's technical sheet.

MPN testing confirmed the presence of cultivable bacteria in the dust emitted by SNIM.

Through an examination of the API Staph gallery, species were identified in the dust. Notably, several of the isolated commensal staphylococci may also act as opportunistic pathogens. The dust sample from Kedia d'Idjil, rich in hematite, also has a distinct bacterial community from the magnetite-rich Guelb El Rhein. The percentage composition of the different staphylococcal strains differed between the two samples, indicating differences in the bacterial composition of the two dust types. The predominant microorganism in Kedia d'Idjil dust is *Staphylococcus cohnii* subsp. *urealyticum* (37.51%), followed by *Staphylococcus capitis* (24.38%). The dust from Guelb El Rhein is characterized by a higher percentage of *Staphylococcus lentus* (22.76%) and

Table 3: Relative abundance (%) of bacterial species identified using the API Staph system in the two iron ore dust types.

Species	Kedia d'Idjil dust (hematite) (%)	Guelb El Rhein dust (magnetite) (%)
Staphylococcus hominis	11.92	10.96
Staphylococcus capitis	24.38	20.77
Staphylococcus lentus	0.00	22.76
Staphylococcus epidermidis	0.00	12.10
Staphylococcus auricularis	12.43	5.71
Staphylococcus haemolyticus	13.76	5.71
Staphylococcus cohnii subsp. *urealyticum*	37.51	0.00
Staphylococcus sciuri	0.00	22.00

Staphylococcus sciuri (22.00%). This variation in dominant bacteria indicates a site-specific diversity. Furthermore, Kedia d'Idjil dust is relatively evenly distributed and rich in *Staphylococcus capitis*, *Staphylococcus auricularis*, and *Staphylococcus haemolyticus*. By contrast, the bacterial community in Guelb El Rhein dust is more diverse, with multiple strains such as *Staphylococcus epidermidis* and *Staphylococcus auricularis*. Another interesting feature is the relatively abundant occurrence of *Staphylococcus cohnii* subsp. *urealyticum* in Kedia d'Idjil dust, but it was absent from Guelb El Rhein dust.

This difference raises questions about site-specific environmental factors, such as geology and climate, that may influence bacterial composition.

Comparing our results with similar studies could deepen our understanding of these findings. Future research might investigate whether these differences match patterns observed in other regions with different geological or climatic traits. Additionally, looking into the potential ecological and health effects of such variations in bacterial composition could help assess the environmental impact of these iron-rich dust types more thoroughly.

3.4. Recommendations to Reduce Dust Emissions at SNIM

3.4.1. Causes of Failure

This study aims to analyze the causes of the significant increase in dust emissions within the SNIM company and to propose appropriate solutions. Based on this analysis, it seeks to identify ways to reintroduce dust fallout into the production circuits.

These dust fallouts mainly correspond to iron production losses occurring at the final stage of processing. Their recovery and reintegration into the production cycle offer both economic benefits and a reduction in waste.

Table 4 presents the potential causes of dust emissions and their classification. These causes are grouped into five categories according to their origin within SNIM facilities.

3.4.2. Criticality Scale

The criticality index is calculated for each failure from the combination of three criteria (Table 5), by multiplying their respective scores:

$$C = G \times F \times D$$

Table 4: Causes of dust emissions at SNIM.

Material	Equipment	Method	Middle	Workforce
Production quantity and delivery Granulometry Humidity	Workshop maintenance Lack of means of recovery Lack of staff Drop points	Accidental walking Inefficient air filtration system Competence management Corrective maintenance	Climatic condition Air Currents Lack of cleaning Clutter	Lack of discipline Lack of training Lack of awareness Lack of motivation

Table 5: FMECA (AMDEC) rating grid.

Severity (G)	
Note	Criteria
1	Indirect effect
2	Effect causing emission
3	Origin of the problem
4	Direct effect (dust emitter)
Frequency (F)	
Note	Criteria
1	Once a year
2	1 time/month
3	1 time/week
4	1 time/day
Detectability (D)	
Note	Criteria
1	Detection with appropriate indicator
2	Detection by an indirect indicator
3	Visual
4	Not detectable

Table 6: Criticality results and analysis.

Causes (aspects)	Analyses	G	F	D	C
Lack of staff, training, awareness, and motivation	A direct effect on production, daily, and not detectable.	4	4	4	64
Accidental walk	With an indirect effect on production, annually, and can be detected visually.	1	1	3	3
Lack of workshop maintenance	A direct effect on production, daily and non-detectable.	4	4	4	64
Lack of cleaning	With a direct effect on daily production, and detectable with an appropriate indicator.	4	4	1	16
Inefficient air filtration system	With a direct effect on daily production, and detectable with an appropriate indicator.	4	4	1	16
Footprint	A direct effect on production, daily and non-detectable.	4	4	4	64
The drop points	With a direct effect on production, annually, and detectable with an appropriate indicator.	4	1	1	4
Absence of means of recovery in time	A direct effect on production, daily, and non-detectable.	4	4	4	64
Presence of draft	With a direct effect on daily production, and detectable with an appropriate indicator.	4	4	1	16

Where:

G: severity of the consequences generated by the failure (severity index);

F: frequency of occurrence of the failure (frequency index); and

D: detectability of the failure (detectability index).

Each of these criteria will be evaluated with a rating table established at four levels. Table 5 shows the criticality rating scale used.

Any criticality value greater than 24 will be classified as a significant aspect whose occurrence will be addressed by the team.

The first level of criticality is based on the severity rating (assessment of the magnitude of the impact and its reversibility), while the second is based on repetition within a specified time interval.

The last level of criticality is based on dust emission indicators. Thus, for each criterion, a score ranging from 1 to 4 will be assigned (the weighting factor for each criterion is 4).

The causes will be classified according to the scale of criticality. Thus, the causes and their criticality analyses will be presented at the beginning. Any cause with a criticality rating greater than 24 will be considered significant.

The values presented in Table 6 will make it possible to measure the causes of dust emission problems based on criticality.

Due to the lack of history of these measurements, the threshold value of criticality was arbitrarily set at 24, which is a value resulting from a very serious cause, with an intermediate frequency and detected by an indirect indicator.

$$C = 4 \times 3 \times 2 = 24$$

To use the results of the FMECA analysis, technical solutions were proposed to reduce the criticality of the most consequential failure modes and improve operational availability.

A maintenance policy based on the improvement actions of the AMDEC analysis is recommended, allowing the implementation of a preventive maintenance plan (Table 7).

3.5. Discussion

Dust deposition rates exhibited marked spatial variability across the sampling sites (Fig. 2), reflecting heterogeneous emission dynamics within and between the mining areas. During the exposure period, the Owens gauges collected 37,500 mg, 27,500 mg, and 49,700 mg of dust at stations a, b, and c, respectively, at the Guelb El Rhein mine, compared to 18,600 mg, 11,800 mg, and 14,800 mg at stations d, e, and f at the Kedia d'Idjil mine. The exceptionally high deposition

Table 7: Significant criticalities and proposed remedies.

Causes (aspects)	Criticality	Remedy
Lack of staff, training, awareness, and motivation	64	Plan, implement, and follow a training plan for employees
Lack of workshop maintenance		Revise the maintenance plan to promote preventive maintenance
Footprint		Expansion or investment of another line
Absence of means of recovery in time		Installation of a mining dome and acquisition of an industrial vacuum cleaner

rates recorded at Guelb El Rhein (38,045–50,480 mg m^{-2} day^{-1}) significantly exceed the threshold for extremely polluted environments (>1000 mg m^{-2} day^{-1}). These values reflect the strategic positioning of Owen gauges (Stations a, b, and c) in immediate proximity to the primary crushing and enrichment units of the Guelb 2 production circuit. These measurements represent source-point emissions under peak operational conditions rather than ambient background levels, explaining the several orders of magnitude difference from standard polluted environment thresholds.

These variations indicate that dust emissions are strongly influenced by local working conditions, equipment operation and maintenance, climatic parameters, and human activities.

Dust deposition rates differed markedly among the three study areas. Guelb El Rhein had the highest mean deposition rate (38,808.7 ± 11,308.9 mg m^{-2} day^{-1}), followed by Kédia d'Idjil (15,409.7 ± 3,473.0 mg m^{-2} day^{-1}), whereas the lowest rate was recorded in downtown Zouérate (594.0 ± 2.0 mg m^{-2} day^{-1}). Thus, mean deposition at Guelb El Rhein and Kédia d'Idjil was approximately 65 and 26 times higher, respectively, than at the urban control site. These findings indicate substantially greater dust deposition within the mining areas, particularly at Guelb El Rhein. The NF X 43-014 standard was used as a measurement protocol and not as a source of regulatory or occupational exposure limits.

X-ray fluorescence analysis confirmed the presence of silicon dioxide (silica) in dust samples from both mining sites, with notably higher concentrations at Guelb El Rhein (Fig. 3). The toxicity of mineral dust, particularly crystalline silica, has been extensively documented (Fubini et al. 1999). Inhalation of silica-containing dust represents a major occupational health risk, as respirable particles can penetrate deep into the pulmonary region where gas exchange occurs (Roberge et al. 2004). The International Agency for Research on Cancer has classified inhaled crystalline silica (quartz and cristobalite) as a Group 1 human carcinogen (IARC 1997). However, its carcinogenic potential may vary depending on mineralogical characteristics, surface properties, particle morphology, and associated impurities (IARC 2012, UNICEM 2014).

Beyond chemical hazards, the microbiological analysis revealed a substantial presence of *Staphylococcus* species in the dust, highlighting an additional biological risk associated with mining emissions. Several studies have demonstrated that *Staphylococcus* spp. can exhibit high resistance to heavy metals such as copper, nickel, cobalt, and lead (Nieto et al. 1989, Sabry et al. 1997, Avilés et al. 1993), potentially due to selective pressure exerted by metal-rich environments. This resistance may be further enhanced by the widespread use of metal-based compounds in industrial and environmental applications (Hiramatsu et al. 1997).

Notably, *Staphylococcus* spp. have also been reported to possess biosorption capacities for heavy metals. Kumar et al. (2010) demonstrated up to 93% lead removal by *Staphylococcus* strains, while Rahman et al. (2019) reported strong lead-binding capacity in *Staphylococcus hominis* strain AMB-2. These findings suggest a dual role of *Staphylococcus* spp. as both indicators of environmental contamination and potential agents of bioremediation.

Marked differences in *Staphylococcus* community composition were observed between the two mining sites, reflecting site-specific environmental conditions. At Kedia d'Idjil, *Staphylococcus capitis* (24.38%) and *Staphylococcus cohnii* subsp. *urealyticum* (37.51%) predominated, whereas dust from Guelb El Rhein was characterized by higher proportions of *Staphylococcus lentus* (22.76%) and *Staphylococcus sciuri* (22.00%). Several of these species are known opportunistic pathogens associated with bacteremia, endocarditis, urinary tract infections, and other severe clinical conditions (Wieser & Busse 2000, Meservey et al. 2020, Fan et al. 2020, Koksal et al. 2009).

The relatively homogeneous distribution of species in Kedia d'Idjil dust contrasts with the higher microbial diversity observed at Guelb El Rhein, suggesting that geological context, mineral composition, and operational practices may exert strong selective pressure on microbial communities. Furthermore, resistance to heavy metals and antibiotics has been reported in species such as *Staphylococcus epidermidis* and *Staphylococcus haemolyticus*, with co-selection mechanisms driven by environmental contamination (Sitthisak et al. 2005, Xue et al. 2015).

We hypothesize that the distinct bacterial communities observed, dominated by *S. capitis* in the hematite-rich Kedia d'Idjil site and *S. lentus* in the magnetite-rich Guelb El Rhein site, reflect selective pressures exerted by the specific mineralogical composition and associated heavy metal profiles of each environment. In metal-enriched mining settings, microorganisms often develop adaptive mechanisms that allow them to tolerate or transform toxic elements, including metal efflux systems and intracellular sequestration processes, as highlighted by Rajput et al. (2025). Although further mechanistic and statistical analyses are required to confirm this relationship, the observed site-specific microbial diversity suggests that the mineralogical characteristics of iron ores may act as a key driver shaping microbial assemblage structure in these mining environments.

Finally, the Failure Modes, Effects, and Criticality Analysis (FMECA) highlighted poor workshop maintenance, operational congestion, and delays in corrective measures as

major contributing factors to dust emissions, with criticality indices exceeding 24. Preventive actions targeting these factors were therefore recommended to improve production efficiency, reduce emissions, and extend equipment lifespan.

4. CONCLUSIONS

Dust emissions along the production circuit of the Guelb El Rhein mine operated by the National Industrial and Mining Company have reached critical levels, posing serious environmental and occupational health risks. This study developed and implemented a comprehensive monitoring framework to quantify dust emissions, identify their sources, and assess both their chemical composition and associated bacterial load.

The results demonstrated that dust emission levels at Guelb El Rhein substantially exceed the stated dust-pollution threshold (>1,000 mg m^{-2} day^{-1}), rendering certain areas unsafe for personnel involved in production monitoring. Emissions at Kedia d'Idjil were lower than those at Guelb El Rhein but still substantial, highlighting the influence of site-specific operational and geological factors.

Chemical analyses confirmed the presence of silica and heavy metals in emitted dust, while microbiological investigations revealed a diverse assemblage of potentially pathogenic *Staphylococcus* species, underscoring the combined chemical and biological hazards associated with mining dust. These findings emphasize the need for integrated mitigation strategies addressing both particulate matter and microbial exposure.

To reduce dust emissions and associated risks, the implementation of preventive measures is strongly recommended, including:

- installation of enclosed mining domes to limit dust dispersion;
- deployment of conveyor belt recovery systems to recapture iron-rich dust;
- integration of air filtration and ventilation systems in enclosed workshops;
- installation of localized extraction hoods at material drop points to direct dust toward filtration units.

In addition to occupational exposure, gravity-driven deposition of particulate matter can lead to contamination of soils, vegetation, and water bodies, potentially causing habitat degradation and biodiversity loss if emissions are widespread and persistent. Overall, this study highlights the urgency of adopting sustainable dust management practices in mining environments to protect workers, surrounding ecosystems, and public health.

REFERENCES

Adamson, I.Y., Prieditis, H., Hedgecock, C. and Vincent, R., 2000. Zinc is the toxic factor in the lung response to an atmospheric particulate sample. *Toxicology and Applied Pharmacology*, 166(2), pp. 111–119. [DOI]

AFNOR, 2003. *NF X43-014: Détermination des retombées atmosphériques totales – Échantillonnage, préparation des échantillons avant analyses*. 32 p.

Aillal, M., Khazri, A., Al-Hoshani, N., Boufahja, F., Beyrem, H. and Lafdal, M.Y., 2023. Are iron ore microparticles toxic for the European clam *Ruditapes decussatus*? Response elements from biomarker activities and in silico modeling. *Saudi Journal of Biological Sciences*, 30(8), p. 103718. [DOI]

Antoine, C., 2012. *Exposition aux poussières provenant d'une mine à ciel ouvert: évaluation des risques et biodisponibilité des métaux*. Essai présenté au Centre Universitaire de Formation en Environnement. 87 p.

Aouissi, A., Fouzari, A. and Meziane, N., 2007. *Qualité bactériologique de l'eau d'Oued Seybouse*. Mémoire d'ingéniorat, Université 8 Mai 1945 Guelma. 57 p.

Avilés, M., Codina, J.C., Pérez-García, A., Cazorla, F., Romero, P. and De Vicente, A., 1993. Occurrence of resistance to antibiotics and metals and of plasmids in bacterial strains isolated from marine environments. *Water Science and Technology*, 27, pp. 475–478.

Blanchon, V. and Penven, M., 2012. *Jean Lefebvre Méditerranée Fos sur Mer (13): Compte rendu des mesures des retombées atmosphériques de poussières dans l'environnement autour de la future plate-forme multimodale*. 19 p.

Boussahel, S., 2007. *Analyse des retombées particulaires aux alentours de la cimenterie d'Ain-El-Kebira*. Mémoire de fin d'étude en vue de l'obtention du diplôme d'ingénieur d'état en écologie végétale et environnement. 88 p.

Brown, A.E. and Smith, H., 2015. *Benson's Microbiological Applications: Laboratory Manual in General Microbiology*, 13th ed. McGraw-Hill Higher Education, New York. 5 p.

Budillon Rabatel, 2009. *Carrière de Saint-Paul-lès-Romans: Règles techniques concernant les poussières*. Document technique, section 9.2.4. 15 p.

Cammalleri, M., Pipitone, E., Rubino, T., Saporito, L. and Mammina, C., 2015. Experimental evaluation of a new thermal process for microorganisms inactivation. *Journal of Food Process Engineering*, 38(5), pp. 445–451. [DOI]

Chandrapati, S. and Williams, M.G., 2014. Total viable counts: Most probable number (MPN). In: Batt, C.A. and Tortorello, M.L. (eds.), *Encyclopedia of Food Microbiology*, 2nd ed., pp. 621–624. Academic Press. [DOI]

Debabza, M., 2015. *Emergence en milieu hospitalier des bacilles Gram négatifs multirésistants aux antibiotiques: étude bactériologique et moléculaire*. Thèse de doctorat d'état, Université Badji Mokhtar-Annaba, pp. 5–65.

Eduard, W., Heederik, D., Duchaine, C. and Green, B.J., 2012. Bioaerosol exposure assessment in the workplace: the past, present and recent advances. *Journal of Environmental Monitoring*, 14(2), pp. 334–339. [DOI]

Elodie, G., Diane, L.B. and Fabrice, A., 2020. Rôle des particules dans la contamination en micropolluants des retombées atmosphériques. *PIREN-Seine Phase 8 - Rapport 2020*, p. 9.

Embile Jr., R.F., Walder, I.F., Schuh, C. and Donatelli, J.L., 2018. Cu, Pb and Fe release from sulfide-containing tailings in seawater: results from laboratory simulation of submarine tailings disposal. *Marine Pollution Bulletin*, 137, pp. 582–592. [DOI]

Fan, Z., Yang, Y., Li, D. and Fei, Q., 2020. A rare lumbar pyogenic spondylodiscitis caused by *Staphylococcus caprae* with initial misdiagnosis: case report and literature review. *BMC Surgery*, 20(1), p. 200. [DOI]

Fubini, B., Zanetti, G., Altilia, S., Tiozzo, R., Lison, D. and Saffiotti, U., 1999. Relationship between surface properties and cellular responses to silica: studies with heat-treated cristobalite. *Chemical Research in Toxicology*, 12(8), pp. 737–745. [DOI]

Hariz, S., 2009. *Etude critique du système de management environnemental au niveau des entreprises algériennes*. Mémoire master en Hygiène et Sécurité Industrielle. 161 p.

Hassanvand, M.S., Naddafi, K., Faridi, S., Nabizadeh, R., Sowlat, M.H., Momeniha, F., Gholampour, A., Arhami, M., Kashani, H., Zare, A., Niazi, S., Rastkari, N., Nazmara, S., Ghani, M. and Yunesian, M., 2015. Characterization of PAHs and metals in indoor/outdoor PM_{10}/$PM_{2.5}$/PM_1 in a retirement home and a school dormitory. *Science of the Total Environment*, 527–528, pp. 100–110. [DOI]

Heederik, D. and von Mutius, E., 2012. Does diversity of environmental microbial exposure matter for the occurrence of allergy and asthma? *Journal of Allergy and Clinical Immunology*, 130(1), pp. 44–50. [DOI]

Hiramatsu, K., Hanaki, H., Ino, T., Yabuta, K., Oguri, T. and Tenover, F.C., 1997. Methicillin-resistant *Staphylococcus aureus* clinical strain with reduced vancomycin susceptibility. *Journal of Antimicrobial Chemotherapy*, 40(1), pp. 135–136. [DOI]

INERIS, 2004. *Rapport annuel 2003*. Institut National de l'Environnement Industriel et des Risques, Verneuil-en-Halatte, France. 52 p.

International Agency for Research on Cancer (IARC), 1997. *Silica, Some Silicates, Coal Dust and para-Aramid Fibrils*. *IARC Monographs on the Evaluation of Carcinogenic Risks to Humans*, Volume 68. Lyon: IARC. ISBN 978-92-832-1268-3.

International Agency for Research on Cancer (IARC), 2012. *Arsenic, Metals, Fibres, and Dusts*. *IARC Monographs on the Evaluation of Carcinogenic Risks to Humans*, Volume 100C. Lyon: IARC. ISBN 978-92-832-1320-8.

Jensen, H., Pedersen, J.H., Jørgensen, J.-E., Pedersen, J.S., Joensen, K.D., Iversen, S.B. and Søgaard, E.G., 2006. Determination of size distributions in nanosized powders by TEM, XRD, and SAXS. *Journal of Experimental Nanoscience*, 1(3), pp. 355–373. [DOI]

Koksal, F., Yasar, H. and Samasti, M., 2009. Antibiotic resistance patterns of coagulase-negative staphylococcus strains isolated from blood cultures of septicemic patients in Turkey. *Microbiological Research*, 164(4), pp. 404–410. [DOI]

Kumar, A., Bisht, B.S. and Joshi, V.D., 2010. Biosorption of heavy metals by four acclimated microbial species, *Bacillus* spp., *Pseudomonas* spp., *Staphylococcus* spp. and *Aspergillus niger*. *Journal of Biological and Environmental Sciences*, 4(12), pp. 97–108.

López-García, I., Viñas, P., Campillo, N. and Hernández-Córdoba, M., 1995. Use of submicroliter-volume samples for extending the dynamic range of flow-injection flame atomic absorption spectrometry. *Analytica Chimica Acta*, 308(1–3), pp. 85–95. [DOI]

Ma, J., Chen, L., Guo, Y., Wu, Q., Yang, M., Wu, M. and Kannan, K., 2014. Phthalate diesters in airborne $PM_{2.5}$ and PM_{10} in a suburban area of Shanghai: seasonal distribution and risk assessment. *Science of the Total Environment*, 497–498, pp. 467–474. [DOI]

Manceau, A., Lanson, B. and Drits, V.A., 2002. Structure of heavy metal sorbed birnessite. Part III: results from powder and polarized extended X-ray absorption fine structure spectroscopy. *Geochimica et Cosmochimica Acta*, 66(15), pp. 2639–2663. [DOI]

Meservey, A., Sullivan, A., Wu, C. and Lantos, P.M., 2020. *Staphylococcus sciuri* peritonitis in a patient on peritoneal dialysis. *Zoonoses and Public Health*, 67(1), pp. 93–95. [DOI]

National Institute for Occupational Safety and Health (NIOSH), 1998. Childhood agricultural safety and health research: Notice of availability of funds for fiscal year 1998. *Federal Register*, 63(13), pp. 3134–3138.

Nieto, J.J., Fernández-Castillo, R., Márquez, M.C., Ventosa, A., Quesada, E. and Ruiz-Berraquero, F., 1989. Survey of metal tolerance in moderately halophilic eubacteria. *Applied and Environmental Microbiology*, 55(9), pp. 2385–2390. [DOI]

Rahman, Z., Thomas, L. and Singh, V.P., 2019. Biosorption of heavy metals by a lead (Pb) resistant bacterium, *Staphylococcus hominis* strain AMB-2. *Journal of Basic Microbiology*, 59(5), pp. 477–486. [DOI]

Rajput, P., Benjwal, S. and Pandey, R., 2025. A comprehensive review on the role of bioremediation in heavy metal contamination. *Nature Environment & Pollution Technology*, 24(S1), pp. 235–245. [DOI]

Rapilly, F., 1968. *Les techniques de mycologie en pathologie végétale*. *Annales des Épiphyties*, 19 (hors série). 97 p.

Roberge, B., Ménard, L., Baril, M., Legris, J. and Deadman, J.-É., 2004. *Manuel d'hygiène du travail: du diagnostic à la maîtrise des facteurs de risque*. Mont-Royal, Québec: Modulo-Griffon. xiv + 738 p. ISBN 2-89443-210-0.

Ron, J., 2006. X-ray techniques: overview. *Encyclopedia of Analytical Chemistry*, p. 20.

Rouaiguia, M., 2010. *Qualité microbiologique de l'eau de Oued Messida*. Mémoire de master 2, Université 8 Mai 1945 Guelma. 78 p.

Sabry, S.A., Ghozlan, H.A. and Abou-Zeid, D.M., 1997. Metal tolerance and antibiotic resistance patterns of a bacterial population isolated from sea water. *Journal of Applied Microbiology*, 82(2), pp. 245–252. [DOI]

Sammut, M., 2007. *Spéciation du cadmium, du plomb et du zinc dans les poussières d'émissions atmosphériques d'origine sidérurgique: approche de l'impact toxicologique des poussières*. Thèse, Université Paul Cézanne. 254 p.

Simpson, S.L. and Spadaro, D.A., 2016. Bioavailability and chronic toxicity of metal sulfide minerals to benthic marine invertebrates: implications for deep sea exploration, mining and tailings disposal. *Environmental Science & Technology*, 50(7), pp. 4061–4070. [DOI]

Sitthisak, S., Howieson, K., Amezola, C. and Jayaswal, R.K., 2005. Characterization of a multicopper oxidase gene from *Staphylococcus aureus*. *Applied and Environmental Microbiology*, 71(9), pp. 5650–5653. [DOI]

SNIM, 2022. *Rapport annuel: un engagement durable et responsable*. Société Nationale Industrielle et Minière, p. 98.

Tecsult International Limited, 2009. *SNIM's Guelbs II Project, Mauritania – Environmental and Social Impact Assessment – Summary*. Prepared for Société Nationale Industrielle et Minière de Mauritanie, Nouadhibou: SMIM. 636 p.

UNICEM, 2014. *Prévention des risques liés à l'exposition aux poussières: guide méthodologique pour les industries extractives*. Union nationale des industries de carrières et matériaux de construction, Paris, France.

Viegas, C., Fleming, G.T.A., Kadir, A., Almeida, B., Caetano, L.A., Gomes, A.Q., Twarużek, M., Kosicki, R., Viegas, S. and Coggins, A.M., 2020. Occupational exposures to organic dust in Irish bakeries and a pizzeria restaurant. *Microorganisms*, 8(1), p. 118. [DOI]

Wieser, M. and Busse, H.J., 2000. Rapid identification of *Staphylococcus epidermidis*. *International Journal of Systematic and Evolutionary Microbiology*, 50(3), pp. 1087–1093. [DOI]

Winberry, W., 1999. *Method IO-2.1 - Sampling of ambient air for total suspended particulate matter (SPM) and PM_{10} using high volume (HV) sampler (EPA/625/R-96/010a)*. Office of Research and Development, U.S. Environmental Protection Agency, Cincinnati. 74 p.

Xue, H., Wu, Z., Li, L., Li, F., Wang, Y. and Zhao, Z., 2015. Coexistence of heavy metal and antibiotic resistance within a novel composite staphylococcal cassette chromosome in a *Staphylococcus haemolyticus* isolate from bovine mastitis milk. *Antimicrobial Agents and Chemotherapy*, 59(9), pp. 5788–5792. [DOI]

Yan, C., Leng, Y.L. and Wu, J.T., 2021. Quantitative microbial risk assessment for occupational health of temporary entrants and staff equipped with various-grade PPE and exposed to microbial bioaerosols in two WWTPs. *International Archives of Occupational and Environmental Health*, 94(6), pp. 1327–1343. [DOI]

Nature Environment and Pollution Technology
An International Quarterly Peer-Reviewed Open Access Journal

p-ISSN: 0972-6268 | e-ISSN: 2395-3454 Vol. 25 | No. 4 | Article ID D1910 | 2026

RESEARCH ARTICLE https://doi.org/10.46488/NEPT.2026.v25i04.D1910 OPEN ACCESS

Evaluation of the Spatial Distribution of Some Thermal Comfort Indices in Iraq Using the RayMan Model

Fadhel A. Mohammed and Alaa M. AL-Lami†
Department of Atmospheric Sciences, College of Science, Mustansiriyah University, Baghdad, Iraq
†Corresponding author: Alaa M. AL-Lami; al.shayia.atmsc@uomustansiriyah.edu.iq

ARTICLE HISTORY

Received: 24-01-2026
Revised: 09-03-2026
Accepted: 19-03-2026

KEYWORDS

RayMan model
Physiologically Equivalent Temperature (PET)
Universal Thermal Climate Index (UTCI)
Thermal comfort conditions

CITE THIS ARTICLE

Mohammed, F. A. and AL-Lami, A. M., 2026. Evaluation of the spatial distribution of some thermal comfort Indices in Iraq using the RayMan Model. *Nature Environment and Pollution Technology*, 25(4), D1910. https://doi.org/10.46488/NEPT.2026.v25i04. D1910

COPYRIGHT & LICENCE

© 2026 The Authors
Open Access under CC BY 4.0.

PUBLISHED BY
TECHNOSCIENCE PUBLICATIONS

ABSTRACT

Lack of comprehensive evaluations of spatial thermal comfort parameters across Iraq remains a concern as the risks of excessive heat and climate change increase. This study analyzes the spatial distribution of outdoor human thermal comfort in Iraq using the Physiologically Equivalent Temperature (PET) and Universal Thermal Climate Index (UTCI). Monthly meteorological data from 38 stations (1981–2024) were obtained from the NASA POWER database and used in the RayMan model to calculate PET and UTCI. Monthly, seasonal, and annual comfort maps were then generated using GIS-based kriging interpolation. The results show a marked seasonal pattern: winter conditions are characterized by mild to moderate cold stress, with the greatest cold stress in northern and mountainous areas, whereas summer conditions indicate strong to very strong heat stress, particularly in the southern and southeastern provinces. Spring and autumn yielded the most comfortable conditions overall, with many areas showing neutral to low-stress levels in April or October. The spatial patterns of PET and UTCI are in good agreement, indicating reasonable consistency between the two indices even in hot, dry areas. In general, air temperature and solar radiation are the main factors enhancing heat stress, whereas wind speed and relative humidity are secondary drivers. Evaluating PET and UTCI patterns is important for supporting public health awareness, urban planning, and climate adaptation strategies in Iraq.

1. INTRODUCTION

Weather conditions affect human activity. Humans are highly sensitive to ambient heat, and exposure to high temperatures can lead to serious health consequences. Heat stroke may cause sudden death or injury to vital organs and body systems. It may also predispose individuals to heart disease and industrial accidents (Zare et al. 2018). Bioclimatic changes such as heat and cold waves are expected to increase in frequency under global warming (IPCC 2013, Pecelj et al. 2025). This is a key issue for understanding the health effects of weather and bioclimatic changes across times and places (Varentsov et al. 2020). Various indices have been developed to measure the degree of thermal discomfort perceived by humans (Burton et al. 2009). Several studies have examined human thermal comfort and the physical environment in both indoor and outdoor settings, including houses and pavilions (Abdel-Ghany et al. 2013).

Approximately 60 heat-stress indices have been proposed to examine hot environments and forecast the probability of heat stress. According to Burton et al. (2009), each of these surrogate indices has its own advantages and limitations (Zare et al. 2018). Municipalities and architects require quantitative information

on the effects of urban planning, open-space development, and reconstruction to select appropriate strategies for reducing anthropogenic climate impacts. Such data were previously difficult to obtain, but numerical models can now generate them readily. These models should also be simple and fast enough for non-experts so that relevant planners can use them, while providing the required data in a comprehensive and easy-to-understand form (Pecelj et al. 2025, Zare et al. 2018). Thermal indices provide a suitable approach for assessing thermal impacts and human thermal comfort (Matzarakis et al. 2021). Most bioclimatic indices are based on empirical meteorological variables and are therefore referred to as simple or empirical indices. Only a limited number explicitly incorporate human parameters in energy-balance models (Bartzokas 2013). An index based on measured weather parameters, including air temperature, wind speed, and relative humidity, is convenient and practical for use (Varentsov et al. 2020). Although many indices have been developed, only four, PET, PMV, UTCI, and SET, are commonly used in outdoor thermal sensation studies (Potchter et al. 2018). During the last two decades, Physiologically Equivalent Temperature (PET) has been widely used as a body-level thermal index (Mayer & Höppe 1987, Höppe 1997, Matzarakis et al. 1999). PET represents the air temperature of a reference indoor environment without wind or solar radiation at which the heat balance of an adult at rest is equivalent to that experienced under the outdoor conditions being studied (Matzarakis et al. 2015). A further development in this field is the Universal Thermal Climate Index (UTCI), developed under the auspices of the International Society on Biometeorology (ISB) and COST Action 730 (Cooperation in Science and Technical Development, supported by the EU RTD Framework Program). The index is available from: www.utci.org (Matzarakis et al. 2015). Further developments may draw on thermophysiological models of human responses to climatic conditions, including acclimatization, as a basis for a worldwide standard index.

Ratings of outdoor thermal conditions across major human biometeorological zones are considered 'universal' (Matzarakis et al. 1999). PET and UTCI can both be calculated using the RayMan software, which is provided free of charge by its developers. The RayMan model is a simplification of the two-node model and can use basic meteorological inputs such as dry-bulb air temperature (T_d), relative humidity (RH), wind speed (V), and mean radiant temperature (T_mrt) or global solar radiation (S_o) (Matzarakis et al. 2007). The RayMan model provides reasonable results in hot, sunny areas when T_mrt > 60°C around solar noon. PET temperature ranges corresponding to different grades of human thermal perception are provided by Abdel-Ghany et al. (2013). Several studies have evaluated two or three simple thermal indicators (Dunjić et al. 2025, Pecelj et al. 2025). Other studies have related simple indices to PET (Al-Lami 2023, Pantavou et al. 2024). Recent studies have also compared and evaluated indices derived from energy-budget models. Their results show marked similarity among the outcomes of different indices (Zare et al. 2018, Pecelj et al. 2025). In recent decades, biometeorology and tourism-climate research have advanced with the use of computer software to elucidate the effects of weather on human physiological comfort. Studies have compared UTCI with PET, SET, and WBGT heat indices over a 1-year period (Abdel-Ghany et al. 2013, Zare et al. 2018). The primary aim was to examine the relationship between these indices and environmental characteristics. The results showed that UTCI and PET were strongly positively correlated (r = 0.96), supporting their validity for evaluating human heat stress (Zare et al. 2018). Tyagi and Danish (2025) examined how reflective building materials exacerbate the Urban Heat Island (UHI) effect in tropical regions such as India. They found that these façades significantly increased outdoor thermal discomfort, with simulations in Greater Noida registering peak air temperatures above 43.77°C. In Sulaimani Province, Iraq, Hama Shareef and OĞUZ (2020) identified bioclimatically comfortable areas for outdoor recreational planning using the spatial variability of PET. The minimum PET was 4.8°C in Penjwin in January, whereas the maximum was 59.6°C in northern Sulaimani and Halabja in July (Hama Shareef & OĞUZ 2020). This study aimed to assess the spatial distribution of two thermal-comfort indices, PET and UTCI, using the RayMan model for Iraq. Meteorological data from 1980–2024, obtained from the NASA POWER Data Platform, were used, and the correlations between these indices and meteorological parameters were analyzed.

2. MATERIALS AND METHODS

2.1. Study Area

Iraq is located in the Middle East, covers approximately 437,072 km² (168,754 sq mi), and is centered near 33°00′N, 44°00′E (33.000°N, 44.000°E). It lies north of Saudi Arabia, south of Turkey and Syria, northwest of Kuwait, and west of Iran (Al-Jibouri & Al-Kassie 2018). It has a 58 km long coastline along the northern Arabian Gulf (Fig. 1). Iraq has varied physiography that can be described in four main zones: the Mesopotamian alluvial plain; the western desert plateau; and the northern and northeastern mountainous areas, including the Zagros Mountains. The study area includes low, level plains in the southeast and more undulating terrain toward the northwest (Muter et al. 2024). The central

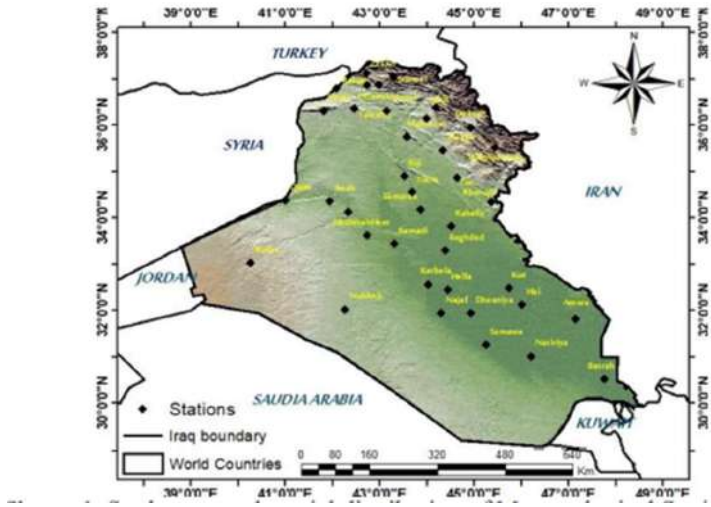


Fig. 1: Study area and spatial distribution of meteorological stations.

and southern parts of Iraq form the fertile Mesopotamian Plain, created by the Tigris and Euphrates rivers. This is the country's principal agricultural area and a major population center. It has low-relief topography, lies only slightly above sea level, and contains flat land, rich alluvial soils, and numerous irrigation canals (Muter et al. 2024).

Western Iraq is mostly an arid desert plateau that descends toward the Euphrates River Valley. The area is predominantly rocky and sandy, with little surface water and sparse vegetation. Northern and northeastern Iraq consist of hilly and mountainous terrain outside the alluvial plain, extending to approximately 3,000 m above sea level in association with the Zagros Mountains. This region has more complex orography because of its slopes and narrow valleys, and it receives more precipitation than the rest of the country.

The southern part of the study area contains the Mesopotamian Marshes, one of the largest and best-known wetland systems near the confluence of the Tigris and Euphrates rivers. These wetlands perform important ecological functions and substantially affect hydrology and land use (Al-Yasiry et al. 2023).

Iraq is characterized by a hot, dry climate with very little rainfall throughout the year. Variations in altitude and geographic location produce a wide range of climatic conditions.

Summer temperatures are extremely high, especially in the central and southern parts of the country, where daytime temperatures commonly exceed 45°C. Winters are generally mild in the lowlands, with temperatures commonly ranging from approximately 5–15°C, while northern highland areas are considerably cooler, with regular frosts and occasional snowfall.

Seasonal rainfall in Iraq is scarce and largely confined to November–April, when mild Mediterranean weather systems predominate. Annual precipitation ranges from less than 150 mm in the southern and western deserts to more than 600 mm in the northern mountains. Moderate precipitation occurs over the Mesopotamian Plain, although intensive irrigation is essential for reliable agriculture (Al-Timimi & Baktash 2024).

Wind systems play a major role in Iraq's climate, particularly the northwesterly shamal winds, which are strongest in July and August. These winds frequently generate dust and sandstorms, especially over desert and semi-desert terrain, affecting air quality and visibility (Ibraheem et al. 2023).

2.2. Data Source and Analysis

The study used the Prediction of Worldwide Energy Resources (POWER) dataset released by the National Aeronautics and Space Administration (NASA) for renewable-energy, climate, and environmental research, planning, and decision-making. The dataset is freely available from the POWER Data Access Viewer (https://power.larc.nasa.gov/data-access-viewer/). POWER data support regional-to-global studies and are provided at a spatial resolution of $0.5° \times 0.5°$ latitude-longitude, derived mainly from satellite observations and global reanalysis products. This resolution provides spatially consistent coverage, particularly in regions with few surface meteorological observations. NASA POWER data have been validated against ground-based meteorological observations in previous studies in Iraq. Tayyeh and

Mohammed (2023) found good agreement between NASA POWER data and station measurements in the Euphrates River Basin, with coefficients of determination (R^2) ranging from 0.74 to 0.95, supporting the suitability of NASA POWER for regional climate studies.

The monthly mean values of five meteorological parameters (air temperature, relative humidity, wind speed, percentage cloud cover, and surface temperature) were obtained from the NASA POWER database for locations corresponding to 38 stations in Iraq. Surface temperature (T_s), global radiation (G), and mean radiant temperature (T_{mrt}) are optional input parameters that can be determined by the model. Global radiation (G) can be calculated from time, date, geographic position, and cloud-cover observations in oktas. From these parameters, an initial global radiation G_o (W m^{-2}) is calculated. Clothing insulation for different seasons and meteorological conditions in the study area was assigned as shown in Table 1. The metabolic rate was estimated at 80 W m^{-2}. The body characteristics entered in the model were length, 1.72 m; weight, 75 kg; and age, 35 years. The stations are located as shown in Fig. 1. Spatial statistical techniques implemented in a GIS package were used to interpolate station-based measurements to gridded values, enabling the creation of spatial PET and UTCI maps for Iraq. Kriging was used to map and assess the spatial interpolation of monthly, seasonal, and annual values of PET and UTCI. After considering the spatial structure of the data, a spherical variogram model was used, and spatial autocorrelation was assessed using the experimental variogram. Leave-one-out cross-validation was used to evaluate interpolation performance, and common accuracy measures, including root mean square error (RMSE) and mean error (ME), were calculated. These procedures improve the transparency and reproducibility of the spatial interpolation used to create the PET and UTCI maps. The analysis yielded an ME of −0.03°C and an RMSE of 1.42°C, indicating low bias and acceptable prediction error in the generated spatial maps. Correlations between the two indices and meteorological parameters were also analyzed.

2.3. RayMan Model

RayMan is a microscale model created by the Chair for Environmental Meteorology, previously known as the Chair for Meteorology and Climatology at Albert-Ludwigs-University Freiburg. The RayMan model was developed to calculate the short- and long-wave radiation fluxes received by the human body. It handles complex building geometries and is suitable for assessing different planning designs from microscale to regional scales. The model calculates mean radiant temperature, which is required for human energy-balance calculations and for assessing the human thermal bioclimate. The SET, PET, UTCI, PT, and modified PET (mPET) thermal indices can be estimated. Thermal indices can be generated by manually entering weather data or by uploading custom time-series files. Outputs are provided as graphs and lists in comma-separated values (CSV) files. RayMan allows the import of comprehensive long-term datasets of meteorological variables for statistical investigations (Matzarakis et al. 2021).

Table 1: Metabolic rate and clothing insulation inputs in the RayMan model for different months in the study area.

Months	Metabolic rate (W m^{-2})	Clothing insulation (clo)
Jan.–Mar.	80	1.5
Apr.–Jun.	80	0.7
Jul.–Sep.	80	0.5
Oct.–Dec.	80	1.2

2.4. Physiologically Equivalent Temperature (PET)

PET is an index based on the human energy-balance equation (Höppe 1997). PET is calculated using dry-bulb air temperature, relative humidity, wind speed, and mean radiant temperature. The index was implemented in RayMan Version 1.2 (Matzarakis et al. 2007). Because measurements of air temperature and wind speed are taken at a height of 10 m, the input data were corrected. Air temperature was adjusted using a factor of 0.6 K/100 m (Matzarakis et al. 2015). Based on Hellmann's exponential law, wind speed was adjusted to a height of 1.1 m above the ground surface (Zare et al. 2018).

Table 2 presents PET data corresponding to different levels of thermal perception and physiological stress (Matzarakis et al. 1999).

2.5. Universal Thermal Climate Index (UTCI)

UTCI is an equivalent temperature derived from a reference environment. It is defined as the air temperature of the reference environment that produces an equivalent physiological strain response in a reference individual under

Table 2: PET data corresponding to different levels of thermal perception and physiological stress (Matzarakis et al. 1999).

Grade of physiological stress	Thermal perception	PET (°C)
Extreme heat stress	Very hot	> 41
Strong heat stress	Hot	35–41
Moderate heat stress	Warm	29–35
Slight heat stress	Slightly warm	23–29
No thermal stress	Comfortable	18–23
Slight cold stress	Slightly cool	13–18
Moderate cold stress	Cool	8–13
Strong cold stress	Cold	4–8
Extreme cold stress	Very cold	≤ 4

Table 3: UTCI data corresponding to different levels of thermal perception and physiological stress (Matzarakis et al. 1999).

UTCI (°C)	Thermal stress category
+40 ≥	Extreme heat stress
+38 – +46	Very strong heat stress
+32 – +38	Strong heat stress
+26 – +32	Moderate heat stress
+9 – +26	No thermal stress
0 – +9	Slight cold stress
−13 – 0	Moderate cold stress
−27 – −13	Strong cold stress
−40 – −27	Very strong cold stress
< −40	Extreme cold stress

the actual environmental conditions. It is one of the most comprehensive heat-stress indices for outdoor environments (Pantavou et al. 2024). The index was developed to provide a common definition of heat-stress severity in human biometeorology. UTCI calculation considers meteorological factors and nonmeteorological elements such as metabolic rate and clothing thermal resistance. UTCI is calculated from dry-bulb air temperature, mean radiant temperature, water vapor pressure or relative humidity, and wind speed at a height of 10 m. UTCI is divided into 10 classes ranging from extreme cold stress to extreme heat stress (Table 3). For UTCI calculation, wind speed should range from 0.5 to 17 m s^{-1} (Zare et al. 2018).

3. RESULTS AND DISCUSSION

During the study period from 1981 to 2024, PET and UTCI values were mapped monthly. These maps show the monthly mean values of the two indices as determined from air temperature, relative humidity, wind speed, and cloud cover. Figs. 2 and 3 depict the monthly mean PET and UTCI maps for the study region. The same map legend was used throughout to facilitate month-to-month comparisons. PET values in Iraq ranged from −1.1 to 45.2°C. According to Fig. 2, the southern regions of Iraq, specifically Basra, Faw, and Amarah, had the highest PET values during summer because these areas experience the highest air temperatures and lowest mean relative humidity. In contrast, northeastern and northwestern Iraq, including Duhok and Sulaymaniyah, had the lowest PET values during December, January, and February. The findings show that the comfort condition (18–22) was absent throughout winter but became apparent in spring (April and May), especially in central Iraq. Most of Iraq experienced temporary comfort conditions in spring, with April showing the greatest extent. More favorable conditions were observed at higher elevations. During summer, PET values ranged from 29.9 to 45.2°C, predominantly indicating significant heat stress. June represents a transition toward peak summer heat, with increasing thermal stress rather than truly temperate conditions, especially during afternoon hours (Fig. 3). The highest summer PET values were observed in the southeast, southwest, and several locations on the central plateau. During July and August, most of Iraq lacked thermally comfortable conditions. In autumn, October showed thermal comfort comparable to April, extending across most of western and northern Iraq and many densely populated areas favorable for tourism in central and northern Iraq. Fig. 4 shows PET maps for the four seasons and the annual mean. The most comfortable conditions occurred during spring across Iraq.

UTCI values in Iraq ranged from −0.6 to 40.8°C. Most regions experienced slight cold stress (0–9°C) during winter, except Ducan and Sumail stations, which exhibited moderate cold stress, particularly in January. No thermal stress (9–26°C) was observed during all spring months and in October across most of Iraq, with isolated areas also occurring during the final winter months. Very strong heat stress (38–46°C) was concentrated in southern and southeastern Iraq during June, July, and August, while strong heat stress was recorded across most central and northern regions during the same period. The monthly spatial distribution of UTCI illustrates changes in human thermal stress across the country over the year. Taken together, the maps reveal a cyclic annual pattern.

The annual cycle shifts from cold stress in winter to high heat stress in summer, with relative comfort in spring and autumn. Iraq experiences mild to moderate cold stress in January and February. Cold stress is stronger in the north and west, where mountainous terrain and continental influences dominate. February shows less cold stress than January, reflecting seasonal warming. December is comparable to January, with a broader spatial extent of cooler conditions and lower temperatures in the south.

Winters are generally mild, with acceptable cold stress in most locations, although some areas experience problematic conditions.

Comfortable conditions with no thermal stress were observed in March. Most of the country experiences neutral thermal conditions in April, except in areas with slight cold stress. Heat stress increases markedly in May. Most areas experience slight heat stress, while pockets of severe heat stress occur in the south and southeast. This indicates increasing discomfort and the onset of the hot season. During the summer extremes (June–August), thermal stress is high, with some southern and eastern areas experiencing extreme conditions. July and August are the hottest months, when heat stress is pronounced across much of the country, particularly

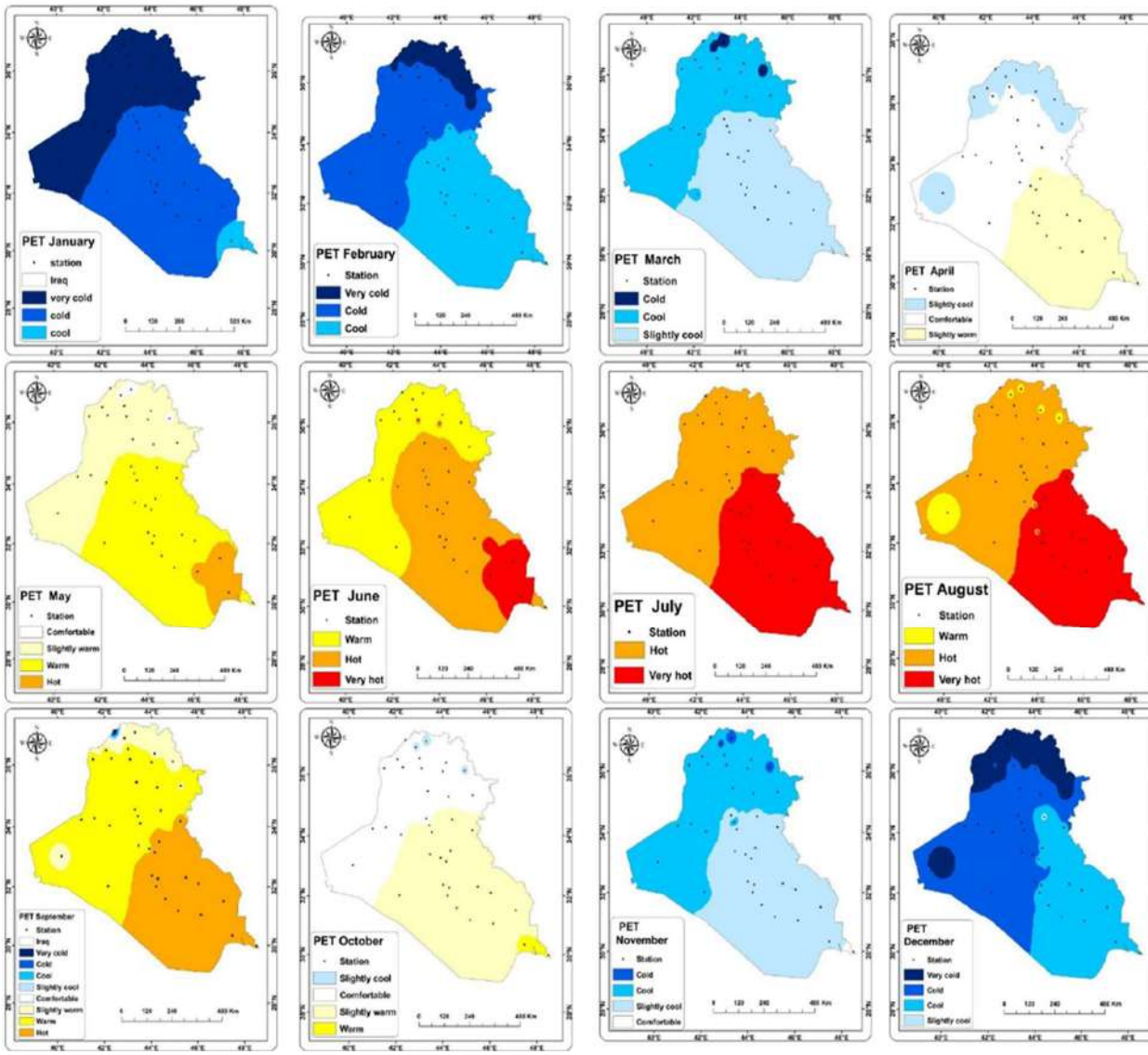


Fig. 2: Monthly mean spatial distribution of PET in the study region.

in the south and southeast. The north also experiences substantial heat stress, with limited thermal comfort. Heat extremes in July and August can increase the risk of heat-related stress and affect health, outdoor labor, and energy demand. During the autumn transition (September–October), the south remains hot in September while the north begins to cool. By October, most locations return to no thermal stress, although some areas still experience slight heat stress. Thermal comfort gradually returns during autumn, except in the southernmost locations, while rainfall begins to increase. By late autumn (November), thermal stress is largely neutral, although pockets of cold conditions begin to re-emerge. These conditions are comparable to those in March or April and are generally thermally comfortable. Heat stress is most prevalent during summer in southern and southeastern regions. Cold-stress risk is higher in the colder north and west, where comfortable conditions also return earlier. The results demonstrate the seasonal predictability of heat stress and the relevance of summer heat-mitigation measures, including the planning of outdoor activities and public-health interventions. The spatial distributions of PET and UTCI during the four seasons and the annual mean are shown in Figs. 4 and 5.

A bioclimate diagram showing the monthly spatial distribution of PET and UTCI conditions as percentages of surface area is presented in Fig. 6. The findings show strong seasonal fluctuations in thermal comfort. In winter (December–February), PET classes range from cold to

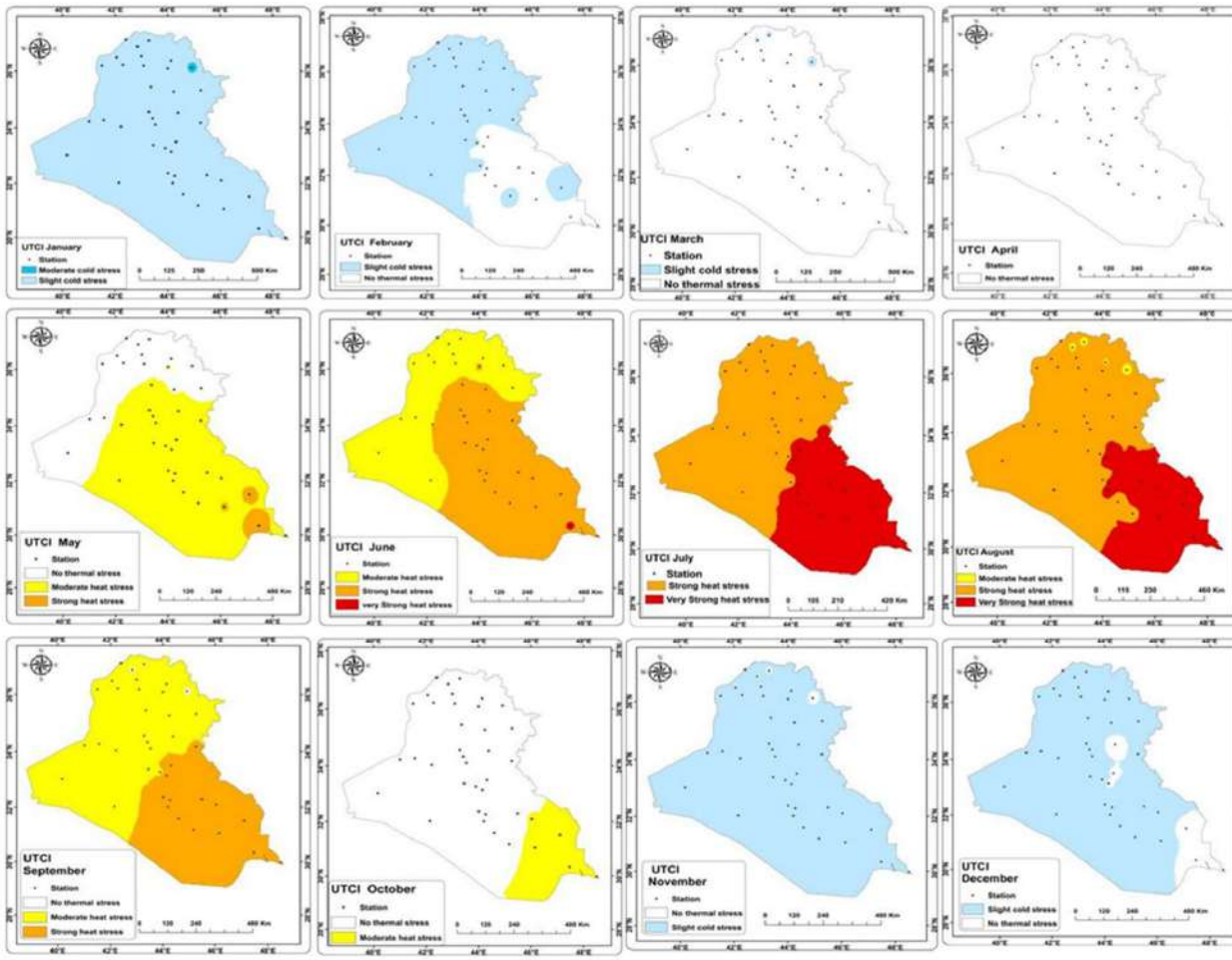


Fig. 3: Monthly mean spatial distribution of UTCI in the study region.

very cold, while UTCI indicates slight to moderate cold stress, suggesting generally cool but not extreme conditions. In spring (March–April), PET conditions are mostly comfortable to slightly cool, and UTCI indicates no thermal stress. In early summer (May–June), warming becomes evident, with warm-to-hot PET classes and moderate to high UTCI heat stress.

During full summer (July–August), conditions reach their annual peak, with hot to very hot PET classes and strong to very strong heat stress according to UTCI, resulting in substantial thermal discomfort and serious health hazards.

In autumn (September–October), heat stress declines. September remains warm to hot, while October is mostly comfortable or low-stress. Overall, heat stress dominates the climate, with summer as the principal thermal stressor and spring and autumn more conducive to outdoor activities.

To examine the relationships of PET and UTCI with the controlling meteorological parameters, including air temperature, relative humidity, wind speed, and solar radiation, Baghdad station was selected as a case study (Fig. 7). Both PET and UTCI show a clear seasonal pattern, increasing from winter minima to summer maxima and then decreasing toward winter, with the highest values in July–August and the lowest in January–February. Air temperature (T_a) strongly controls PET and UTCI, and both indices closely follow the monthly pattern of T_a. Solar radiation (G) also contributes substantially to thermal stress, particularly from late spring to early summer, because of the increased radiant heat load on the human body. Wind speed (V) has a moderate influence; however, its cooling effect is insufficient to offset high summer temperatures and strong solar radiation. The inverse relationship between relative humidity (RH) and PET/UTCI is also evident: higher RH in winter corresponds to lower thermal stress, while lower RH in summer corresponds to peak stress. Overall, summer heat stress dominates thermal discomfort, driven primarily by high air temperature and solar radiation.

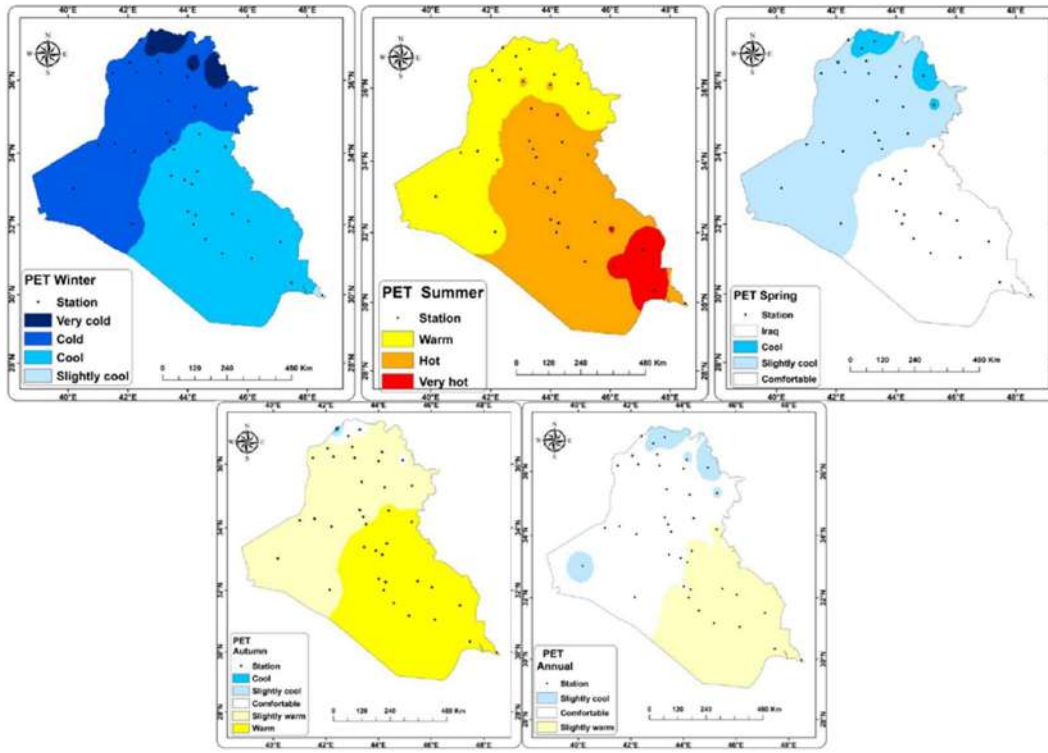


Fig. 4: Seasonal and annual mean spatial distribution of PET in the study region.

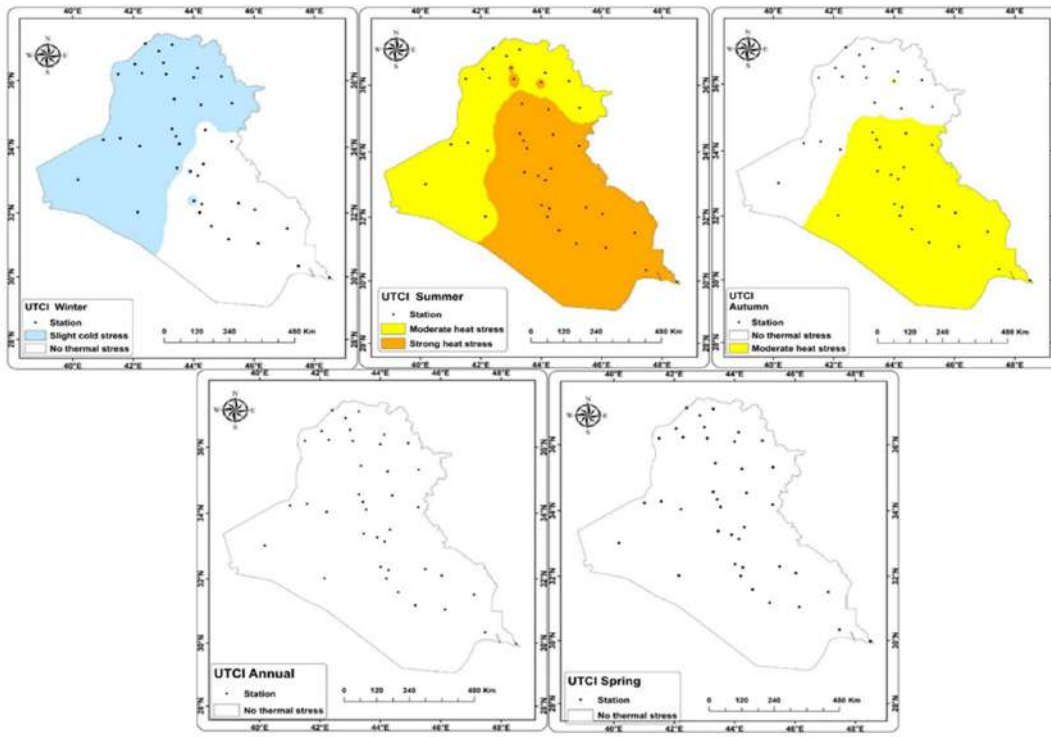


Fig. 5: Seasonal and annual mean spatial distribution of UTCI in the study region.

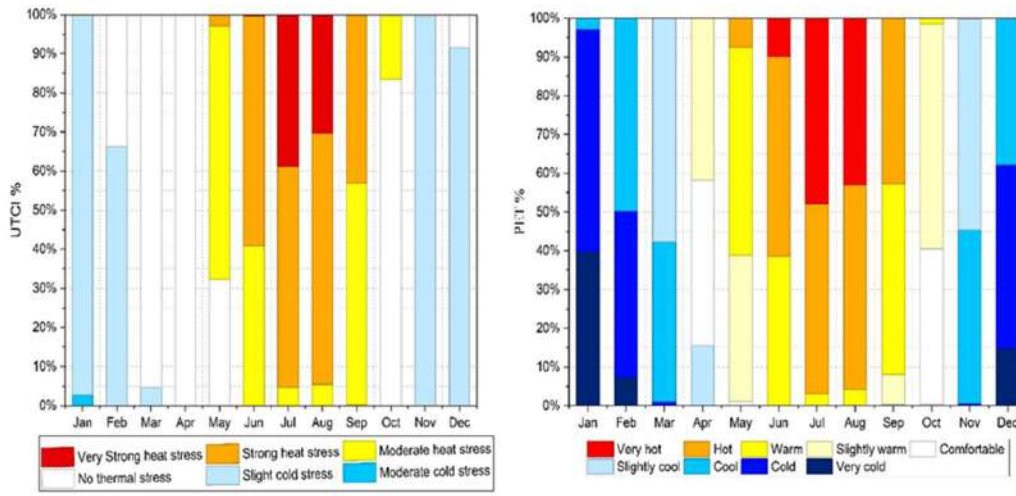


Fig. 6: Bioclimate diagram showing monthly PET and UTCI conditions as percentages of surface area in Iraq.

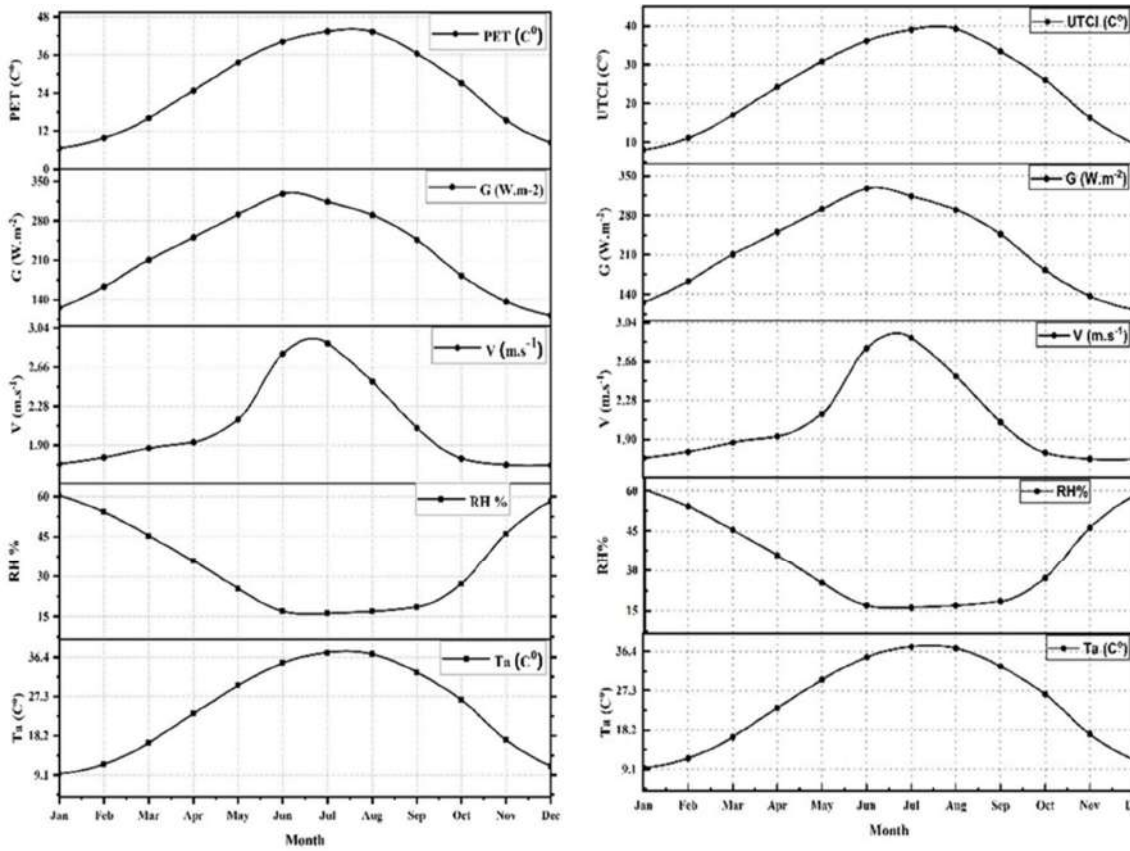


Fig. 7: Relationship of PET and UTCI with the controlling meteorological parameters.

Based on data from three selected stations (Baghdad, Basra, and Mosul), representing different climatic zones in Iraq, Pearson correlation coefficients (r) between PET/UTCI and the primary meteorological variables, air temperature (T_a), relative humidity (RH), wind speed (V), and solar radiation (G), were calculated as shown in Table 4. Both indices showed very strong positive correlations with air temperature (r = 0.998–0.999) and strong positive correlations with solar radiation (r = 0.913–0.941), whereas relative humidity showed strong negative correlations (r =

Table 4: Pearson correlation coefficients (r) of PET and UTCI with the primary meteorological variables, air temperature (T_a), relative humidity (RH), wind speed (V), and solar radiation (G), at three selected stations (Baghdad, Basra, and Mosul).

Stations	T_a–PET	T_a–UTCI	RH–PET	RH–UTCI	V–PET	V–UTCI	G–PET	G–UTCI
Baghdad	0.999	0.999	–0.988	–0.990	0.861	0.851	0.920	0.918
Basra	0.999	0.999	–0.991	–0.992	0.796	0.785	0.919	0.913
Mosul	0.998	0.998	–0.981	–0.971	0.957	0.944	0.941	0.940

–0.992––0.971). Wind speed showed moderate to strong positive correlations (r = 0.785–0.957). These findings indicate that spatial variation in thermal stress across Iraq's climatic regions is driven primarily by air temperature and solar radiation, supporting the observed spatial patterns of thermal comfort.

4. CONCLUSIONS

This study assessed the spatial and seasonal variation of human thermal comfort in Iraq using two widely used bioclimatic indices, Physiologically Equivalent Temperature (PET) and Universal Thermal Climate Index (UTCI), simulated with the RayMan modeling platform using long-term meteorological data from NASA POWER. The findings show that thermal comfort in Iraq is primarily influenced by seasonal changes, geographic location, and physiographic characteristics. Both indices show a strong annual cycle, with cold to moderate cold stress in winter, particularly in northern and mountainous areas, and strong to very strong heat stress in summer across southern and southeastern Iraq. Spring and autumn are the most favorable periods for outdoor thermal comfort, with April and October showing the largest areas of thermally comfortable or near-neutral conditions across the country. These transitional seasons therefore provide favorable opportunities for travel, outdoor work, and other outdoor activities. Spatially, however, southern Iraq is persistently affected by higher thermal stress because of high air temperatures and strong solar radiation, whereas temperatures in northern and northeastern regions are moderated by elevation, particularly outside summer. The good agreement and high correlation between PET and UTCI confirm the applicability of both indices for evaluating human thermal stress under Iraq's hot, arid climatic conditions. Air temperature and solar radiation were the main controlling factors of heat stress. Wind speed did not substantially mitigate heat during peak summer, while relative humidity was negatively related to thermal stress.

The results have implications for public health, urban planning, energy-demand management, and climate-sensitive sectors. Rising summer heat stress, particularly in more populated southern areas, highlights the importance of adaptation measures such as climate-sensitive urban design, shading, green infrastructure, and heat-health warning systems. The spatially explicit comfort maps produced in this study can also serve as a benchmark for estimating climate-change impacts and planning sustainable development and outdoor activities in Iraq.

Overall, this study demonstrates the utility of integrating PET and UTCI with GIS-based spatial analysis and long-term datasets to investigate human thermal comfort at the national level. The approach provides useful preliminary insights for climate and biometeorological studies in Iraq.

5. ACKNOWLEDGEMENT

The authors express their gratitude and extend sincere appreciation to the Department of Atmospheric Sciences, College of Science, Mustansiriyah University, Baghdad, Iraq, as well as to their families and friends.

6. REFERENCES

Abdel-Ghany, A.M., Al-Helal, I.M. and Shady, M.R., 2013. Human thermal comfort and heat stress in an outdoor urban arid environment: a case study. *Advances in Meteorology*, 2013, 1–7. [DOI].

Al-Jibouri, M.H. and Al-Kassie, J.A., 2018. Climate variability and trends in Iraq. *Arabian Journal of Geosciences*, 11(9), Article 214. [DOI].

Al-Lami, A.M., Khaleed, O.L. and Ahmed, M.M., 2023. Assessment of some bioclimatic indices using RayMan model for Baghdad, Iraq. *IOP Conference Series: Earth and Environmental Science*, 1223(1), 012019. [DOI].

Al-Timimi, Y.K. and Baktash, F.Y., 2024. Monitoring the shift of the 250-mm rainfed line over Iraq. *Iraqi Journal of Agricultural Sciences*, 55(3), 931–940. [DOI].

Al-Yasiry, A.F., Al-Lami, A.M. and Al-Maliki, A., 2023. Production of environmental sensitivity maps for desertification in southern marshes of Iraq. *IOP Conference Series: Earth and Environmental Science*, 1215(1), 012023. [DOI].

Bartzokas, A., Lolis, C.J., Kassomenos, P.A. and McGregor, G.R., 2013. Climatic characteristics of summer human thermal discomfort in Athens and its connection to atmospheric circulation. *Natural Hazards and Earth System Sciences*, *13*(12), pp.3271-3279.

Burton, I., Ebi, K.L. and McGregor, G., 2009. Biometeorology for adaptation to climate variability and change. In: *Biometeorology for Adaptation to Climate Variability and Change*. Springer Netherlands, Dordrecht, pp. 1–5. [DOI].

Dunjić, J., Stojanović, V., Milošević, D., Pantelić, M., Obradović, S. and Vasić, M., 2025. Bioclimate conditions in the Mura-Drava-Danube Transboundary Biosphere Reserve: case study from Serbia. *Időjárás*, 129(3), 307–337. [DOI].

Hama Shareef, S. and OĞUZ, H., 2020. Assessment of bioclimatic comfort zones using the RayMan model: a case study of Sulaimani, Iraq. *Turkish Journal of Forest Science*, 4(2), 408–423. [DOI].

Höppe, P., 1997. Aspects of human biometeorology in past, present and future. *International Journal of Biometeorology*, 40(1), 19–23. [DOI].

Ibraheem, N.T., Al-Jiboori, M.H., Hussain, H.H., Roomi, T.O. and Al-Salihi, A., 2023. Study of intra-annual and annual air temperatures over Iraq for period (1970–2021). *IOP Conference Series: Earth and Environmental Science*, 1223(1), 012018. [DOI].

IPCC, 2013. *Climate Change 2013: The Physical Science Basis*. Cambridge University Press, 1535 pp. [DOI].

Matzarakis, A., Gangwisch, M. and Herbert, T., 2021. Modelling in human biometeorology: spatial-temporal analysis of thermal indices. MDPI AG, p. 28. [DOI].

Matzarakis, A., Mayer, H. and Iziomon, M.G., 1999. Applications of a universal thermal index: physiological equivalent temperature. *International Journal of Biometeorology*, 43(2), 76–84. [DOI].

Matzarakis, A., Muthers, S. and Rutz, F., 2015. Application and comparison of UTCI and PET in temperate climate conditions. *Finisterra*, 49(98). [DOI].

Matzarakis, A., Rutz, F. and Mayer, H., 2007. Modelling radiation fluxes in simple and complex environments: application of the RayMan model. *International Journal of Biometeorology*, 51(4), 323–334. [DOI].

Mayer, H. and Höppe, P., 1987. Thermal comfort of man in different urban environments. *Theoretical and Applied Climatology*, 38(1), 43–49. [DOI].

Muter, S.A., Al-Timimi, Y.K. and Al-Jiboori, M.H., 2024. Analysis of temporal and spatial drought characteristics in Iraq using the Standard Precipitation Index (SPI). *IOP Conference Series: Earth and Environmental Science*, 1371(2), 022032. [DOI].

Pantavou, K., Kotroni, V., Kyros, G. and Lagouvardos, K., 2024. Thermal bioclimate in Greece based on the Universal Thermal Climate Index (UTCI) and insights into 2021 and 2023 heatwaves. *Theoretical and Applied Climatology*, 155(7), 6661–6675. [DOI].

Pecelj, M., Malinović-Milićević, S. and Matzarakis, A., 2025. Thermal comfort and tourism in Mostar (Bosnia and Herzegovina): a human bioclimatic information sheet for visitors and planners. *Atmosphere*, 16(8), 987. [DOI].

Potchter, O., Cohen, P., Lin, T.P. and Matzarakis, A., 2018. Outdoor human thermal perception in various climates: a comprehensive review of approaches, methods and quantification. *Science of the Total Environment*, 631–632, 390–406. [DOI].

Tayyeh, H.K. and Mohammed, R.M., 2023. Analysis of NASA POWER reanalysis products to predict temperature and precipitation in the Euphrates River Basin. *Journal of Hydrology*, 619, 129327. [DOI].

Tyagi, G. and Danish, M., 2025. Reflective building façades: the effect of albedo on outdoor thermal comfort–a case study of low-rise apartments. *Nature Environment and Pollution Technology*, 24(2), 1–13. [DOI].

Varentsov, M., Shartova, N., Grischenko, M. and Konstantinov, P., 2020. Spatial patterns of human thermal comfort conditions in Russia: present climate and trends. *Weather, Climate, and Society*, 12(3), 629–642. [DOI].

Zare, S., Hasheminejad, N., Shirvan, H.E., Hemmatjo, R., Sarebanzadeh, K. and Ahmadi, S., 2018. Comparing Universal Thermal Climate Index (UTCI) with selected thermal indices/environmental parameters during 12 months of the year. *Weather and Climate Extremes*, 19, 49–57. [DOI].

Nature Environment and Pollution Technology
An International Quarterly Peer-Reviewed Open Access Journal

p-ISSN: 0972-6268 | e-ISSN: 2395-3454 Vol. 25 | No. 4 | Article ID D1913 | 2026

RESEARCH ARTICLE https://doi.org/10.46488/NEPT.2026.v25i04.D1913 OPEN ACCESS

Trajectory-Based Evaluation of Greenhouse Gas Mitigation Pathways in Municipal Solid Waste Systems: A System Dynamics Approach

Nattarat Phaingam, Phairat Usubharatana and Harnpon Phungrassami†
Department of Chemical Engineering, Faculty of Engineering, Thammasat School of Engineering, Thammasat University, Pathum Thani 12120, Thailand
†Corresponding author: Harnpon Phungrassami; pharnpon@engr.tu.ac.th

ARTICLE HISTORY

Received: 30-01-2026
Revised: 26-03-2026
Accepted: 11-04-2026

KEYWORDS

Trajectory-based analysis
System dynamics modeling
Municipal solid waste systems
Greenhouse gas emissions

CITE THIS ARTICLE

Phaingam, N., Usubharatana, P. and Phungrassami, H., 2026. Trajectory-based evaluation of greenhouse gas mitigation pathways in municipal solid waste systems: A system dynamics approach. *Nature Environment and Pollution Technology*, 25(4), D1913. https://doi.org/10.46488/NEPT.2026.v25i04. D1913

COPYRIGHT & LICENCE

© 2026 The Authors
Open Access under CC BY 4.0.

PUBLISHED BY
TECHNOSCIENCE PUBLICATIONS

ABSTRACT

Municipal solid waste (MSW) management is a critical component of greenhouse gas (GHG) mitigation in landfill-dominated systems, where methane emissions are governed by cumulative waste deposition and delayed decomposition processes. Conventional assessments often emphasize end-state comparisons, which can obscure the long-term consequences of intervention timing, stock accumulation, and demand-driven non-linear dynamics. This study applies a system dynamics (SD) modeling framework to evaluate trajectory-based GHG mitigation pathways in Thailand's national MSW system over a multi-decadal horizon (2024–2050), with explicit consideration of methane legacy effects and tourism-driven variability in waste generation. The model represents MSW generation, waste routing, landfill stock accumulation, and delayed methane emissions using first-order decay logic. Tourism activity is incorporated as a time-varying external driver affecting waste generation flows, allowing demand fluctuations and non-linear responses to emerge without altering the underlying system structure. Four scenarios are analyzed to reflect alternative intervention timings and waste management pathways under a consistent modeling framework. Simulation results show that early intervention substantively reshapes emission trajectories by constraining landfill stock accumulation, which, within the defined system boundaries, acts as a critical leverage point for long-term mitigation. In contrast, delayed interventions, despite achieving similar diversion levels at later stages, retain substantially higher cumulative GHG emissions due to legacy effects embedded in previously accumulated waste. Tourism-driven increases in waste generation act as a stress amplifier, accelerating stock formation and magnifying emissions under landfill-dominant configurations, leading to disproportionate GHG responses relative to demand growth. Overall, the findings demonstrate that the performance of GHG mitigation in MSW systems is strongly shaped by path dependence, time delays, and non-linear demand dynamics. Trajectory-based analysis provides essential insight into why late-stage mitigation cannot fully reverse methane legacy effects, underscoring the importance of early structural change for achieving sustained emission reduction in landfill-dominated waste management systems.

1. INTRODUCTION

MSW management has emerged as a critical component of GHG mitigation strategies, particularly in countries where landfilling remains the dominant means of disposal. In such systems, methane emissions from landfills constitute a major share of waste-related GHG emissions due to the anaerobic decomposition of organic materials over extended periods (Chiemchaisri & Visvanathan 2008, Karak et al. 2012). Unlike combustion-based sources, landfill methane emissions are characterized by delayed release and prolonged persistence, creating long-term commitments to emissions that extend well beyond the time of waste disposal.

Conventional assessments of MSW-related GHG emissions often rely on static inventories or end-state comparisons, focusing on emissions in a single target year or under a final system configuration (Hoornweg & Bhada-Tata 2012). While such approaches are useful for benchmarking and reporting purposes, they are limited in their ability to capture the dynamic behavior of landfill-dominated systems. In particular, static assessments tend to obscure the effects of stock accumulation, time delays in methane generation, and the path-dependent nature of emission trajectories, where past waste management decisions constrain future mitigation potential.

Methodological frameworks based on first-order decay (FOD) logic, such as those used in national GHG inventories, have widely recognized the importance of accounting for temporal dynamics in landfill methane emissions. These frameworks explicitly link current and future methane emissions to historically accumulated waste stocks rather than solely to contemporaneous waste flows. As a result, reductions in waste generation or diversion rates implemented at later stages may have limited influence on cumulative emissions that are already embedded in existing landfill stocks. This temporal asymmetry underscores the need for analytical approaches that can trace emission trajectories over extended time horizons, rather than relying on snapshot evaluations.

SD modeling provides a suitable framework for addressing these challenges, as it is specifically designed to represent accumulation processes, feedback mechanisms, and delayed responses in complex systems (Sterman 2018). SD has been increasingly applied in MSW studies to explore long-term system behavior, capacity constraints, and interactions among waste generation, treatment pathways, and infrastructure development. However, many existing applications focus on specific subsystems or management components, such as waste generation forecasting, collection logistics, and financial performance, without explicitly examining how delayed methane emissions shape cumulative GHG outcomes across alternative intervention timings.

In parallel, MSW systems in tourism-intensive economies face additional complexity due to demand variability that is not directly proportional to resident population growth. Empirical studies have demonstrated that tourism activity can significantly increase MSW generation, often exhibiting non-linear relationships driven by consumption patterns, seasonal concentration, and infrastructure saturation (Mateu-Sbert et al. 2013, Arbulú et al. 2015). In destinations with constrained diversion capacity, surges in waste generation associated with tourism may lead to disproportionate increases in landfill disposal and associated GHG emissions. Despite this, tourism-driven demand dynamics are rarely integrated into long-horizon GHG mitigation analyses of national MSW systems.

Thailand represents a relevant case for examining these interacting dynamics. The country combines a landfill-dominated MSW management structure with sustained growth in tourism activity, creating conditions under which delayed methane emissions and demand-driven non-linearities may jointly influence mitigation performance. While national strategies and waste management plans have articulated targets for improved disposal practices and increased diversion, the effectiveness of such measures depends not only on their stringency but also on their timing relative to the accumulation of landfill stocks.

Against this background, there remains a need for empirical evaluations of GHG mitigation pathways that bridge the gap between static national inventories and the dynamic realities of MSW systems (Dianati et al. 2021). In the context of Thailand, while national climate strategies articulate net zero targets for 2050, there are limited national-scale studies that simultaneously integrate long-term MSW emissions trajectories with the demand load from tourism. Therefore, this study contributes to the existing literature through the policy-analytical application of SD and the expansion of evaluative system boundaries. First, by leveraging the pathway-generating capabilities of SD and coupling them with first-order decay (FOD) mechanics, this study shifts the evaluative focus from static end-state targets to dynamic pathway dependency. This approach helps quantify the methane legacy accumulating in landfills during periods of delayed transition, a dynamic often obscured in conventional assessments (Scharff et al. 2024). Second, the study addresses boundary limitations in standard census-based waste inventories by incorporating the transient tourist population. Functioning as an exogenous demand driver, tourism adds an unaccounted mass to the system. By integrating this absolute load, the model reflects the physical mass constraints on diversion policies in tourism-dependent economies more comprehensively, without assuming disproportionate per-capita generation rates.

Accordingly, the objective of this study is to evaluate GHG mitigation pathways in Thailand's MSW management system by applying an SD framework that captures these temporal and boundary dynamics. Specifically, the study aims to (i) quantify how stock accumulation and delayed methane generation create a path-dependent methane legacy, (ii) assess how the timing of policy interventions influences cumulative GHG outcomes compared to static end-point targets, and (iii) analyze the additional absolute load imposed by the transient tourism population on landfill-dominated

systems. By focusing on pathway dependency over a multi-decadal horizon, the study provides empirical insights into why delayed interventions may fail to offset the historical methane legacy, thereby informing the planning of early structural transitions.

2. MATERIALS AND METHODS

2.1. Model Conceptualization and System Boundary

This study applies an SD modeling framework to evaluate trajectory-based GHG mitigation pathways in Thailand's MSW management system. SD is particularly appropriate for this analysis because it explicitly represents stock accumulation, delayed responses, and feedback mechanisms that govern the long-term behavior of landfill-dominated waste systems (Sterman 2018). In such systems, methane emissions are not solely determined by contemporaneous waste flows but are strongly influenced by historically accumulated waste and time-lagged decomposition processes, resulting in long-term emission commitments.

The model is conceptualized at the national scale to represent Thailand's MSW system as an integrated entity. This system boundary encompasses total MSW generation and its allocation among major treatment pathways, with particular emphasis on landfilling and diversion-oriented options. Representation at the national scale is adopted to ensure consistency with available data sources and national waste management targets, while enabling analysis of cumulative GHG emissions arising from system-wide interactions rather than localized effects. Sub-national disaggregation is intentionally avoided, as excessive spatial detail may obscure the dominant stock-flow relationships that determine long-term emission trajectories in landfill-based systems.

The temporal scope of the analysis spans a multi-decadal horizon from 2024 to 2050, preceded by a historical period used for model calibration and behavioral verification. This extended time frame is necessary to capture the delayed nature of methane generation from landfilled waste and to evaluate path dependence arising from earlier waste management decisions. By moving beyond short planning horizons, the model distinguishes between short-term reductions in waste flows and long-term emission commitments embedded in accumulated landfill stocks.

Tourism activity is incorporated as a time-varying external driver influencing MSW generation rates. Thailand's role as a major tourism destination introduces demand fluctuations that are not proportional to resident population growth and vary over time. In the model structure, tourism affects waste generation flows but does not alter the structural definition of system stocks or treatment pathways. This formulation allows the analysis to examine how demand variability interacts with capacity constraints and waste routing decisions without conflating transient demand shocks with structural changes in the MSW system.

Within this conceptual framework, GHG emissions arise primarily from landfill-related processes characterized by delayed decomposition behavior. Therefore, methane generation is represented as a stock-dependent process governed by time delays rather than as an instantaneous response to waste inflows. This representation provides the structural basis for analyzing methane legacy effects and assessing why delayed interventions may be unable to offset cumulative emissions associated with earlier landfill reliance.

2.2. Model structure and governing equations

To ensure full model transparency and reproducibility, the physical flows of MSW and the delayed methane generation were explicitly modeled using a system dynamics stock-flow structure. The inflow of waste directed to the landfill stock ($W_{landfill}$) is determined by the total MSW generated multiplied by the explicit allocation fraction for each disposal method $_j$ (e.g., managed anaerobic, unmanaged shallow dump). For the historical baseline, these fractions were directly parameterized using empirical national waste management data from the Pollution Control Department (PCD), while future trajectories were defined by scenario-specific policy targets. This is formulated in Eq. (1):

$$\boldsymbol{W_{landfill,j}(t) = MSW_{gen}(t) \times f_{disposal,j}(t)} \quad \ldots(1)$$

Where $f_{disposal,j}$ (t) represents the dynamic fraction of waste routed to the specific landfill management type j at time t.

For the methane generation function, following the 2006 IPCC guidelines, the accumulation and decomposition of decomposable degradable organic carbon (DDOCm) for each waste fraction i is formulated as a differential equation governing the stock (Eq. (2)), with the subsequent methane emission flow given in Eq. (3).

$$\frac{\boldsymbol{d(DDOCm_i}}{\boldsymbol{dt}} = \boldsymbol{\left[W_{landfill}(t) \times Fraction_i \times DOC_i \times DOC_{f,i} \times MCF\right] - \left[k_i \times DDOCm_i(t)\right.} \quad \ldots(2)$$

$$\boldsymbol{CH_4(t) = \sum_i (k_i \times DDOCm_i(t) \times F \times \frac{16}{12})} \quad \ldots(3)$$

Where DOC_i is the fraction of degradable organic carbon, $DOC_{f,i}$ is the fraction of DOC that can decompose under anaerobic conditions, MCF is the methane correction factor (set to 0.4 for unmanaged shallow dumps), k_i is the decay rate constant (yr^{-1}), and F is the fraction of CH_4 in landfill gas (0.5).

Table 1: Key parameters for the first-order decay (FOD) methane generation model.

Waste Fraction	Degradable organic carbon (DOC)	Fraction of DOC Dissimilated (DOC_f)	Decay Rate Constant (k, yr^{-1})
Food waste	0.15	0.70	0.400
Garden waste	0.20	0.70	0.170
Paper and cardboard	0.40	0.50	0.070
Wood	0.43	0.10	0.035
Textiles	0.24	0.50	0.070
Nappies	0.24	0.50	0.170
Rubber and leather	0.39	0.50	-
Plastics, metal, glass	0.00	0.00	-

Note: k and DOC values are based on IPCC (2006) defaults for tropical wet climates. DOC_f values incorporate country-specific data aligned with Thailand's BUR4 inventory methodology.

While the standard IPCC Tier 1 approach suggests a default DOC_f of 0.5 for all waste types, this study adopted a Tier 2 waste-specific approach utilizing country-specific parameters to ensure maximum accuracy under local conditions. Aligned with Thailand's Fourth Biennial Update Report (BUR4) and the Thailand Greenhouse Gas Emission Inventory System (TGEIS), differentiated DOC_f values, specifically 0.7 for highly degradable food/garden waste and 0.1 for resistant wood, were applied. The parameters used in the simulation are summarized in Table 1.

2.3. Data acquisition and model calibration

The SD model was parameterized and calibrated using officially reported national datasets and peer-reviewed studies that have been previously applied to Thailand's MSW system. Historical MSW generation data for the period 2014–2024 were obtained from the annual *Thailand Municipal Solid Waste Situation Reports* published by the Pollution Control Department (PCD), which provide consistent national-level records of total waste generation, treatment practices, and disposal pathways (PCD 2014–2024). These data were used to establish baseline waste generation trends and calibrate the aggregate growth behavior of the MSW system before scenario analysis.

Waste composition data were derived from the most recent national survey conducted by the PCD, which reported that organic waste constitutes nearly half of Thailand's MSW stream, followed by plastics, paper, and other fractions (PCD 2021). In the model, waste composition was assumed to remain constant over the simulation horizon, consistent with previous national-scale MSW modeling studies in Thailand (Pudcha et al. 2023a, Pudcha et al. 2023b). This assumption allows the analysis to focus on structural and temporal dynamics rather than compositional uncertainty.

Socioeconomic drivers influencing MSW generation were represented using population, economic activity, and tourism indicators. Population data were obtained from official national statistics, while tourism activity was represented using annual tourist arrival data published by the Ministry of Tourism and Sports. Tourism was explicitly included as a separate demand component to reflect Thailand's status as a major tourism destination, where visitor inflows significantly influence waste generation beyond resident population effects, as demonstrated in previous Thai case studies (Sakcharoen et al. 2023). In the SD structure, tourism affects MSW generation flows but does not alter the internal stock structure of the waste management system.

Parameters governing GHG emissions from MSW treatment and disposal pathways were adopted from a combination of IPCC guidelines and Thailand-specific studies. Methane emissions from landfills were estimated using first-order decay (FOD) logic consistent with the IPCC methodology (IPCC 2006), which links current emissions to historically accumulated waste stocks. Emission factors for non-landfill pathways, including composting, mechanical-biological treatment (MBT), incineration, and open burning, were drawn from peer-reviewed Thai studies and internationally recognized sources previously applied in Thailand (Menikpura et al. 2012, Menikpura et al. 2013, Nordahl et al. 2023).

Model calibration focused on reproducing the observed long-term behavior of Thailand's national MSW system rather than achieving exact year-by-year correspondence. Simulated MSW generation trajectories were compared with official PCD statistics for the periods 2014–2018 and 2022–2023, with the years affected by the COVID-19 pandemic treated separately due to structural disruptions in tourism and economic activity. Additional consistency checks were conducted by comparing simulated waste-sector GHG emissions with Thailand's official greenhouse gas inventory, which reported approximately 22.2 Mt CO_2e from the waste sector in 2022 (DCCE 2024). This calibration strategy follows established system dynamics practice, emphasizing reproduction of dominant system behavior

driven by appropriate structural relationships rather than statistical curve fitting.

2.4. Causal Loop and Stock-Flow Structure

This study employs a causal loop and stock-flow representation to explicitly capture the dynamic mechanisms governing GHG emissions in Thailand's MSW management system. The model structure is designed to represent how waste generation, waste routing decisions, and landfill accumulation interact over time to produce delayed and path-dependent emission trajectories.

At the core of the system is the accumulation of landfilled waste as a stock variable. Inflows to this stock are determined by total MSW generation and the fraction of waste directed to landfilling, while outflows represent gradual decomposition processes rather than physical removal of waste. Methane emissions are generated as a function of this accumulated stock using first-order decay logic, reflecting the delayed release of methane over extended periods following disposal. As a result, current emission levels depend not only on present waste flows but also on historical waste accumulation.

The causal structure includes reinforcing and balancing feedback mechanisms that shape long-term system behavior. Growth in MSW generation increases landfill accumulation, which in turn commits future methane emissions through delayed decomposition. Diversion-oriented interventions, such as recycling, composting, and mechanical-biological treatment, act as balancing mechanisms by reducing inflows to the landfill stock. However, their effectiveness is constrained by the size of the existing stock, which continues to emit methane even after diversion rates increase.

Tourism activity is incorporated as an exogenous driver influencing MSW generation flows. Increases in tourist arrivals raise waste generation rates, thereby accelerating landfill accumulation when diversion capacity is limited. Under such conditions, the system exhibits non-linear behavior, where proportional increases in demand result in disproportionate increases in landfill inflows and associated GHG emissions. Importantly, tourism does not alter the internal feedback structure of the system but amplifies existing dynamics by increasing pressure on waste management pathways.

The stock-flow structure is held constant across all the scenarios examined in this study. Differences among scenarios arise solely from changes in the timing and magnitude of interventions affecting waste generation and routing trajectories. This structural consistency allows for direct comparison of emission trajectories under alternative pathways and isolates the effects of intervention timing from changes in system configuration. By maintaining a common causal structure, the model highlights how early and delayed interventions diverge in their ability to influence cumulative GHG emissions due to methane legacy effects embedded in accumulated landfill stocks.

2.5. Scenario Design and Implementation Logic

Four scenarios are developed to examine how alternative waste management strategies and intervention timings influence GHG emission trajectories in Thailand's MSW system over the period 2025–2050. The scenarios are designed to span a range of strategic directions, from policy continuity to transformative change, while maintaining an identical stock-flow structure across all cases. Quantitative targets embedded in each scenario are treated as exogenous assumptions guiding waste generation and routing trajectories rather than as optimization outcomes.

Table 2: Summary of scenario design and quantitative assumptions.

Scenario	Strategic orientation	Timing of intervention	Waste generation assumption	Diversion/utilization target	Landfilling implication	GHG mitigation intent
BAU	Policy continuity (baseline)	No new intervention	Continues recent historical trend	Constant at recent average levels	Landfilling remains dominant	Reference trajectory
CPI	Current policy implementation	Gradual (mainly up to 2027)	Follows baseline growth	Utilization increases to ~36% by 2027; appropriate disposal reaches ~80%	Landfill inflow reduced after mid-2020s	Tests sufficiency of existing policy timing
CEM	Circular economy maximization	Progressive (to ~2035)	Reduced through sustained prevention efforts	Recycling and recovery reach ~65% by 2035	Landfilling reduced to <10% of MSW	Tests whether strong flow reduction overcomes stock inertia
OGM	Optimal GHG mitigation (upper bound)	Early and aggressive (from early simulation period)	Reduced via strong intervention	Maximum feasible diversion with high organic waste recovery	Rapid reduction in landfill inflow	Isolates effect of early action on cumulative emissions

An overview of the scenario logic and associated quantitative assumptions is summarized in Table 2, which highlights differences in intervention timing, magnitude, and strategic intent without presenting model outputs. This table is intended to support the interpretation of the scenario structure prior to the presentation of the simulation results.

The Business-as-Usual (BAU) scenario serves as a reference trajectory representing the continuation of recent MSW management practices. In this scenario, the proportions of MSW allocated to different treatment and disposal pathways remain constant at the average levels observed during the recent historical period, with no additional interventions introduced beyond those already in place. BAU provides a counterfactual baseline against which alternative trajectories are evaluated.

The Current Policy Implementation (CPI) scenario reflects the gradual implementation of Thailand's National Action Plan on Waste Management (Phase II, 2022–2027) (PCD 2022). As summarized in Table 2, this scenario assumes a progressive increase in MSW utilization to approximately 36% by 2027, alongside an improvement in appropriate disposal practices to around 80% over the same period. Beyond 2027, waste management practices are assumed to stabilize at these achieved levels. The CPI scenario is designed to examine whether the timing and ambition of currently announced policies are sufficient to alter long-term GHG emission trajectories once methane legacy effects from accumulated landfill stocks are taken into account.

The Circular Economy Maximization (CEM) scenario represents a more ambitious pathway benchmarked against international circular economy practices. Under this scenario, recycling and recovery rates increase progressively, reaching approximately 65% by 2035, while the share of MSW sent to landfills declines to less than 10%. These targets are aligned with the long-term sustainability frontiers established in the EU Waste Framework Directive (2018/851/EU) and Landfill Directive (2018/850/EU), which serve as global benchmarks for transitioning toward a near-zero landfilling system (European Commission 2023, Zero Waste Europe 2020). The CEM scenario is included as an analytical case to test whether strong flow-based interventions, even when aligned with leading international benchmarks, can overcome the inertia imposed by existing landfill stocks.

The Optimal GHG Mitigation (OGM) scenario is a normative, upper-bound case designed to align the MSW sector with Thailand's updated Nationally Determined Contribution (NDC), which targets a reduction in GHG emissions of approximately 40% by 2030 relative to the BAU trajectory (ONEP 2020). While the OGM scenario integrates the high-level ambitions of the National Solid Waste Management Action Plan 2022–2027 (PCD 2022), including 100% plastic packaging recycling and intensified organic waste recovery, it is primarily intended as a technical potential simulation. This scenario assumes early and aggressive intervention, combining rapid reductions in landfill inflows with maximized organic waste diversion. Given the significant feasibility constraints in real-world implementation, such as municipal budget limitations, high operational costs of advanced treatment technologies, and the necessity for massive behavioral shifts in waste segregation, the OGM scenario does not represent a recommended policy pathway. Instead, it serves as a benchmark to isolate the maximum theoretical effect of early action on cumulative emissions under idealized conditions.

Across all scenarios, performance is evaluated using trajectory-based indicators rather than end-year outcomes. Annual and cumulative GHG emissions are tracked to capture both short-term dynamics and long-term emission commitments associated with delayed methane generation from landfilled waste. This design allows direct comparison of early and delayed intervention pathways and highlights the role of path dependence in shaping mitigation outcomes within landfill-dominated MSW systems.

2.6. Sensitivity Analysis

To evaluate the policy conclusions against inherent uncertainties, a sensitivity and elasticity analysis was conducted on three critical parameters identified as highly influential in the MSW sector. For waste-specific parameters, the analysis deliberately focused on the food waste fraction. This is methodologically justified as biodegradable and organic waste constitutes the most dominant component of Thailand's MSW, typically accounting for 45% to over 57% of the total waste stream (Jawjit et al. 2025, Sakcharoen et al. 2023), making it the primary driver of rapid landfill methane generation. The selection of parameters and their variation bounds were rigorously established based on international guidelines and Thailand's national policy context.

First, for the methane generation rate (k), the baseline value of 0.40 yr^{-1} reflects the default value for highly degradable food waste in tropical wet climates (IPCC 2006). A variation range of ±10% was systematically applied to evaluate the model's structural sensitivity. This systematic variation fundamentally adheres to the Transparency, Accuracy, Consistency, Completeness, and Comparability (TACCC) principles emphasized in Thailand's Fourth Update Report (ONEP 2022). Second, regarding waste composition variability, a ±10% variation was applied to the degradable organic carbon (DOC) fraction of food waste

(baseline 0.15). According to the IPCC methodology, a ±10% uncertainty band accurately reflects the acceptable margin of sampling error for country-specific waste characterization data (IPCC 2006, Kornboonraksa et al. 2004). Finally, to account for implementation uncertainties regarding diversion efficiency, an absolute variation of ±5% was applied to the overarching policy targets (e.g., varying a 65% diversion target to 60% and 70%). This parameterization bounds the plausible policy overachievement or failure risks, aligning with the operational targets and risk assessments outlined in Thailand's National Solid Waste Management Action Plan Phase II, 2022–2027 (PCD 2022).

3. RESULTS AND DISCUSSION

3.1. Model Validation and Baseline Behavior

Validation in SD emphasizes whether a model reproduces observed behavioral regimes for appropriate structural reasons, rather than solely minimizing point-wise prediction error. This approach is suited for the comparative, trajectory-based analysis of accumulation-dominated systems such as MSW management (Sterman 2018, Barlas 1996). Accordingly, the waste-generation submodel was evaluated first because it governs the upstream mass flows that propagate to treatment allocation and long-lived methane accumulation.

To evaluate the model against historical records, the pre-COVID period (2014–2019) was used to assess baseline structural consistency under normal operating conditions. A comparison between the simulated MSW generation and the observed data yields a coefficient of determination (R^2) of approximately 0.54 and a mean absolute percentage error (MAPE) of about 1.2%. In causal-descriptive (white-box) models, this statistical profile is characteristic of simulations that prioritize internal structural fidelity and mass balance over purely point-to-point correlation accuracy (Piedrahita et al. 2025, Sterman 2018). The moderate R^2 reflects phase-shift penalties caused by high-frequency measurement noise and reporting artifacts common in administrative data (Jadeja et al. 2022). Conversely, the low MAPE confirms that the model accurately captures the overall systemic scale and structural magnitude, falling well within the acceptable threshold (typically <7%) established for recent MSW system dynamics models (Liu et al. 2023).

To isolate the endogenous dynamic trend from these short-term reporting artifacts, a centered three-year moving average was applied to the observed data (Fig. 1). In the context of long-term behavioral modeling, this moving average serves as a signal extraction technique to identify the underlying growth regime rather than an attempt to artificially improve correlational fit. As demonstrated in recent MSW system dynamics applications, divergences at the point-to-point level are often non-systematic errors; thus, the primary objective is to capture the equivalent mean and structural trend rather than transient data cycles (Pinha & Sagawa 2020).

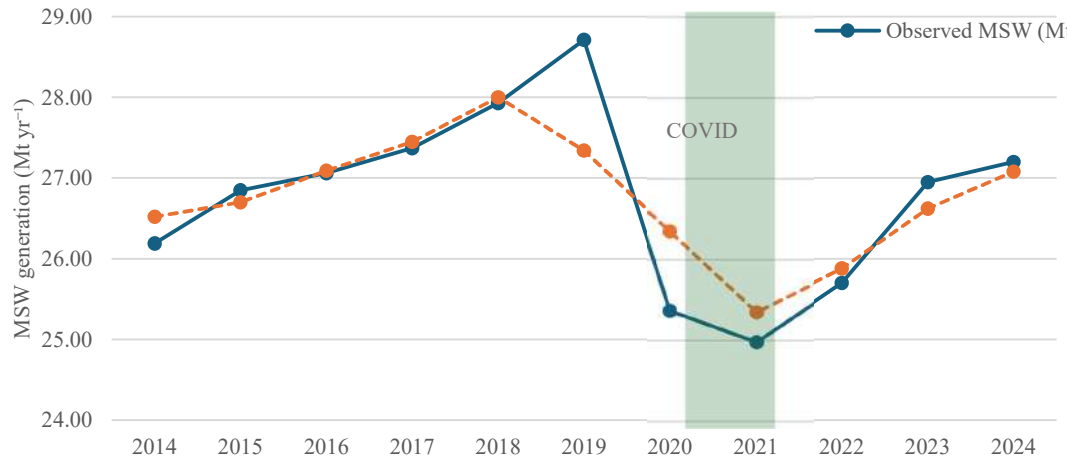
Furthermore, the COVID-19 disruption during 2020–2021 is treated as an exogenous shock. Evaluating a model against such periods serves as an extreme condition test to verify boundary adequacy, rather than a strict predictive exercise. The results indicate that the model demonstrates directional alignment, capturing the contraction and subsequent recovery. This confirms that its internal feedback mechanisms respond logically to significant shifts in macroeconomic drivers, ensuring its suitability as a policy laboratory for long-term scenario evaluation.

Under stable drivers, the baseline exhibits persistent growth in MSW generation. When coupled with limited diversion capacity, this growth results in long-lived downstream impacts due to stock-and-flow inertia in disposal pathways. Establishing this baseline behavior provides a necessary reference for interpreting the scenario outcomes in subsequent sections, where differences arise from intervention timing and pathway choices.

3.2. Scenario-Based GHG Emission Trajectories

Annual GHG emission trajectories from Thailand's MSW system were compared under BAU, CPI, CEM, and OGM over the assessment horizon, as shown in Fig. 2. The BAU trajectory increases steadily toward 2050, rising from 16.2 Mt CO_2e in 2024 to 21.8 Mt CO_2e in 2050. This pattern is consistent with landfill-dominated systems in which delayed methane release from accumulated degradable carbon sustains emissions growth over time (Menikpura et al. 2013). CPI moderates emissions relative to BAU but does not reverse the long-run trajectory; by 2050, CPI remains at 15.9 Mt CO_2e, indicating that incremental improvements slow growth yet leave substantial legacy emissions in place (Table 3). This behavior reflects path dependence: when landfill inflows remain high during early years, methane-generating stocks persist even after diversion improves.

CEM and OGM exhibit qualitatively different trajectory shapes, with pronounced inflection beginning in the late 2020s. Emissions under CEM decline from 16.4 Mt CO_2e in 2025 to 11.8 Mt CO_2e in 2030 and approach 5.0 Mt CO_2e by 2050, while OGM declines more rapidly, reaching 11.0 Mt CO_2e by 2030 and stabilizing at approximately 5.0 Mt CO_2e by 2050 (Table 3). Importantly, the mitigation advantage is explained by timing rather than end-state performance alone. Early constraints on landfill inflow, especially of organic



Note: The baseline implied trend is derived from a centered three-year moving average of observed data to highlight dominant growth regimes and structural transitions rather than short-term fluctuations. The figure illustrates the pre-COVID growth regime (2014–2019), the COVID-19 disruption (2020–2021), and the subsequent recovery phase. For the pre-shock period, comparing the simulated outputs against the observed data yields a mean absolute percentage error (MAPE) of ≈ 1.2%, a maximum deviation of < 5%, and an $R^2 \approx 0.54$. These metrics reflect the model's representation of the overall systemic scale and long-term trajectory, establishing a behavioral reference for the subsequent comparative policy analysis.

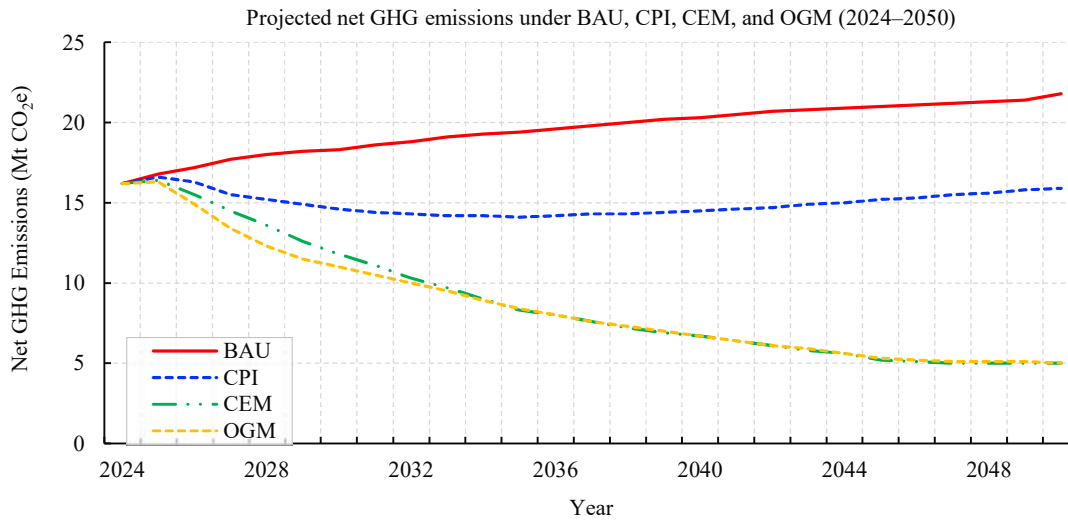
Fig. 1: Observed MSW generation and baseline implied trend in Thailand during 2014–2024.

fractions, prevent the formation of long-lived methane-generating stocks, producing disproportionate benefits that persist throughout the horizon. Conversely, delayed action yields diminishing marginal gains because previously accumulated waste continues to emit over extended periods, consistent with accumulation-dominated system behavior (IPCC 2019).

The trajectory-based interpretation is reinforced by the five-year snapshots in Table 3. While CEM and OGM converge toward similar end-state emission levels by 2050, their trajectories differ materially during the critical early years (late 2020s to mid-2030s), when stock formation is the most influential. CPI remains substantially higher than CEM/OGM across the horizon despite policy progress, demonstrating that mitigation effectiveness cannot be inferred from end-point indicators alone. This timing-driven divergence and robust ranking across the horizon align with findings from SD-based MSW studies that emphasize intervention timing and structural configuration over short-term prediction accuracy (Pinha & Sagawa 2020, Wang & You 2021). Therefore, extending assessment to 2050 is essential for net-zero-oriented interpretation in MSW systems: shorter horizons may capture near-term flow improvements but underrepresent legacy emissions from previously accumulated waste, which dominate long-run outcomes (Menikpura et al. 2013, IPCC 2019).

Despite the aggressive flow-based interventions simulated in the OGM scenario, the model indicates a residual emission gap of approximately 5 Mt $CO_{2}e$ by 2050. This gap represents a residual baseline that requires downstream technological interventions to align with Thailand's Second Nationally Determined Contribution (NDC 3.0), which has officially accelerated the national net zero emission targets to 2050 to remain consistent with the 1.5 °C pathway (DCCE 2025). According to the prioritized investment framework in NDC 3.0, specific waste sector technologies are identified to close this gap, including Landfill Gas (LFG) Capture and Utilization (estimated mitigation potential of 1.00 Mt CO_{2e}), Organic Waste Composting and Decentralized Processing (0.50 Mt CO_{2e}), and Advanced Material Recovery Facilities (0.10 Mt CO_{2e}) (DCCE 2025). These technologies, alongside other cross-sectoral measures, require an estimated additional investment of USD 0.94 billion by 2035 for the waste, industrial processes, and agriculture sectors.

Furthermore, addressing the hard-to-abate residual emissions necessitates the scaling up of negative emission technologies beyond standard solid waste management. Thailand's long-term strategy involves deploying Carbon Capture and Storage (CCS), with a specific target of 40 Mt CO_{2e} deployment in the power and energy sectors by 2050 (Thepsaskul et al. 2025). Ultimately, absolute economy-wide neutrality will be achieved through a combination of Bioenergy with Carbon Capture and Storage (BECCS) and an ambitious national land-sink target of 120 Mt CO_{2e} sequestered via the land use, land-use change, and forestry (LULUCF) sector by 2050 (Waite et al. 2024, DCCE 2025).



Note: Deterministic trajectories are presented here to emphasize structural pathway comparisons. For quantitative uncertainty ranges and parameter variability bounds, refer to the sensitivity analysis in Section 3.5.

Fig. 2: Scenario-based GHG emission trajectories under BAU, CPI, CEM, and OGM (2024–2050).

Additionally, while absolute emission levels vary with tourism demand assumptions, the relative ranking among the mitigation pathways remains consistent. Scenarios with earlier diversion yield lower emissions than delayed-action pathways under both high and low tourism growth conditions, indicating that the comparative effectiveness of these policies is not altered by uncertainties in tourism-driven waste generation. Beyond these demand-side factors, a quantitative sensitivity and elasticity analysis is provided in Section 3.5 to assess how variations in key parameters (e.g., decay rates, waste composition, and implementation targets) affect the overall emission trajectories.

3.3. Tourism-Driven Non-Linear Dynamics in MSW-GHG Trajectories

MSW generation in tourism-intensive systems cannot be adequately explained by resident population trends alone.

Table 3: Annual GHG emissions under alternative MSW scenarios (Mt CO_2e yr^{-1}; five-year intervals).

Year	BAU	CPI	CEM	OGM
2025	16.8	16.6	16.4	16.3
2030	18.3	14.6	11.8	11.0
2035	19.4	14.1	8.3	8.4
2040	20.3	14.5	6.7	6.7
2045	21.0	15.2	5.2	5.3
2050	21.8	15.9	5.0	5.0

Note: Values represent baseline discrete outputs under the standard deterministic assumption. Variability driven by parametric uncertainties are quantified in Section 3.5.

Empirical studies consistently show that tourism activities introduce episodic, seasonal, and shock-sensitive waste inflows that are disproportionate to their annual average contribution (Mateu-Sbert et al. 2013, Arbulú et al. 2015, Sakcharoen et al. 2023). In the Thai context, tourism-related waste exhibits pronounced volatility associated with international arrivals, seasonal travel patterns, and exogenous shocks. This was most notable during the COVID-19 period (Sakcharoen et al. 2023).

From an SD perspective, such demand components are characterized by high temporal clustering and elasticity, which causes them to interact differently with downstream waste-management processes compared with residential waste. While tourism-related MSW typically represents a minority share of annual waste quantities, its short-term surges can temporarily exceed diversion and treatment capacities, forcing excess flows toward landfill disposal pathways. This mechanism implies that tourism acts primarily as a stress amplifier rather than a dominant mass contributor within the MSW system.

In this study, tourism-driven waste generation is treated as an exogenous driver following a linear functional form, where total tourism MSW is the product of the tourist population and their specific per capita generation rate. However, the model aggregates tourist waste using a homogeneous national average. International and regional data suggest significant heterogeneity; for instance, luxury tourists or high-end resort guests can generate up to 3.5 kg $capita^{-1}$ day^{-1}, substantially higher than the 0.8–1.7 kg day^{-1} typical of general visitors or residents (Kapmeier &

Goncalves 2018, Chuenwong et al. 2022). Consequently, if future tourism strategies increasingly prioritize high-end demographics, the current baseline, which uses a representative average for conservative estimation, might inherently underestimate the total waste volume.

Therefore, the described non-linear dynamics in this study do not stem from the demand function itself. Instead, they characterize the systemic feedback between episodic tourism-driven waste accumulation and strict landfill or diversion capacity constraints (Sterman 2018). Although tourists contribute only a modest baseline share (~5–6%) of total MSW mass (Table 4), their seasonal surges act as a critical marginal load. When this marginal inflow temporarily exceeds available diversion capacities, the excess waste is structurally forced into landfill pathways. Because tourism-related waste often exhibits high organic intensity (e.g., concentrated food waste from hospitality sectors), this marginal load disproportionately amplifies the long-term methane legacy under anaerobic conditions (Sakcharoen et al. 2023). Addressing this systemic vulnerability requires active demand-side management; therefore, promoting low-waste tourism and source separation in the hospitality sector represent critical de-risking strategies for Thailand's net-zero ambitions.

Although tourism-related waste contributes a limited fraction of total annual MSW generation, its variability is substantially higher than that of residential waste. Table 4 summarizes representative years illustrating both the modest average share of tourism MSW and its pronounced sensitivity to demand shocks.

As shown in Table 4, tourism-driven MSW declined sharply during the COVID-19 disruption, followed by a partial recovery as tourism activity resumed. The relative contraction of tourism-related waste exceeded that observed for residential streams, consistent with empirical findings from tourism-dependent regions where visitor-related waste dominates short-term variability despite contributing a limited share of annual totals (Sakcharoen et al. 2023). This pattern highlights that annual-average waste shares are insufficient indicators of system stress. Periods of high tourism activity correspond to elevated peak inflows to disposal pathways, particularly when diversion and treatment capacities are constrained, thereby shaping downstream emissions outcomes.

Table 4: Contribution and variability of tourism-driven MSW.

Year	Total MSW (Mt)	Tourism MSW (Mt)	Tourism share (%)
2016	27.06	1.35	5.0
2018	27.93	1.62	5.8
2019	28.34	1.74	6.1
2020	24.98	0.62	2.5
2022	25.70	1.21	4.7

The COVID-19 period provides a natural experiment for examining the interaction between tourism demand shocks and landfill dynamics. Model results indicate that tourism-driven MSW inflows respond almost immediately to changes in visitor activity, whereas landfill stocks and associated GHG emissions adjust much more slowly due to the stock-flow structure of landfill systems.

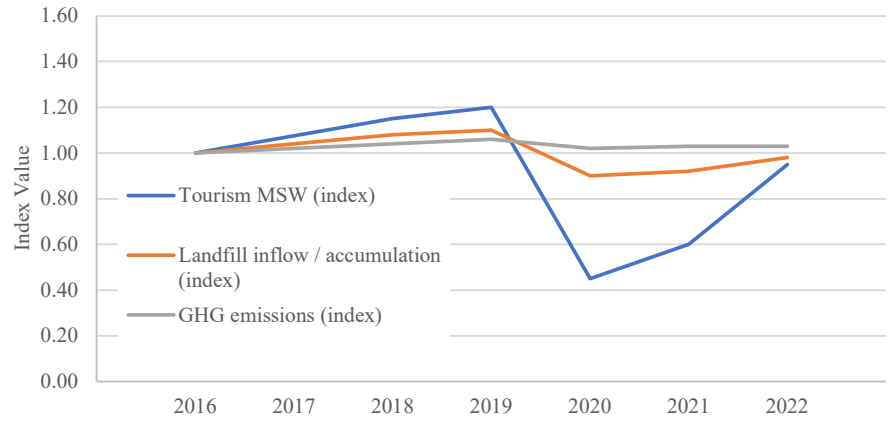
Fig. 3 illustrates this asymmetric response by comparing indexed tourism MSW inflow, landfill accumulation, and GHG emissions. While tourism inflows exhibit sharp contractions and rebounds, landfill-related emissions remain relatively insensitive in the short term, as methane generation is governed by cumulative waste deposition and delayed degradation processes. The results demonstrate that even substantial short-term reductions in tourism waste fail to yield proportional decreases in emissions. Instead, tourism shocks primarily influence future cumulative emissions by altering landfill inflow trajectories, reinforcing the importance of methane legacy effects.

To assess how tourism variability interacts with alternative MSW management structures, a scenario-conditional sensitivity analysis was conducted. Tourism intensity was varied under fixed system configurations and resulting landfill inflows and GHG outcomes were compared across scenarios. Table 5 shows that landfill-dominant configurations exhibit strong sensitivity to tourism demand, with high tourism levels leading to disproportionate increases in landfill inflow and cumulative emissions. In contrast, scenarios characterized by early and sustained diversion capacity display a dampened response, indicating greater robustness to demand variability.

These differences reflect the structural properties of the system rather than parameter uncertainty. Thus, tourism functions as a diagnostic stressor that exposes the vulnerability of landfill-centric pathways and amplifies differences among mitigation strategies.

Taken together, the results indicate that tourism-driven waste dynamics influence GHG outcomes primarily through timing and routing effects rather than through annual waste volumes alone. Short-term tourism surges, even when followed by downturns, accelerate landfill stock accumulation and commit the system to long-lived methane emissions due to delayed degradation processes.

This methane legacy effect explains why late-stage interventions cannot fully offset earlier landfill dependence and why mitigation performance is governed by emissions trajectories rather than end-state diversion targets. By



Note: The index value of 1.0 corresponds to the absolute baseline values in the reference year 2016 (i.e., MSW generation = 27.06 Mt yr^{-1}, Landfill inflow = 21.79 Mt yr^{-1}, and baseline GHG emissions = 16.12 Mt CO_2e yr^{-1}).

Fig. 3: Dynamic response of tourism-driven waste inflow, landfill accumulation, and GHG emissions (indexed).

integrating empirical tourism variability with SD modeling, the analysis demonstrates that robustness under variable and shock-prone demand conditions is a defining characteristic of low-emission MSW pathways in tourism-intensive systems.

3.4. Methane Legacy Effects and the Long-Term Impact of Delayed Intervention

Landfill methane emissions are governed by the accumulation of biodegradable waste stocks and delayed anaerobic degradation processes rather than by contemporaneous disposal rates. Within the SD framework, landfill functions as a long-lived stock whose emissions evolve according to first-order decay behavior, implying that waste deposited in earlier periods continues to generate methane over extended time horizons. This structural characteristic creates a pronounced methane legacy effect, whereby present and future emissions are strongly conditioned by past disposal decisions rather than by current management performance alone.

The model results show that scenarios characterized by delayed diversion expansion accumulate substantially larger landfill stocks during early periods. Even when diversion rates subsequently converge toward more ambitious pathways, the emissions trajectories remain persistently higher because methane generation from previously deposited organic waste cannot be reversed. Therefore, late-stage interventions act primarily by slowing additional stock accumulation rather than by reducing emissions already committed through earlier landfill reliance. This explains why scenarios with similar end-state diversion shares can display markedly different cumulative GHG outcomes over the assessment horizon.

Table 5: Scenario-conditional sensitivity of GHG outcomes to tourism demand.

Scenario	Tourism level	Landfill inflow (Mt yr^{-1})	GHG emissions (index)
BAU	Low	22.4	0.96
BAU	High	25.1	1.08
High-diversion	Low	14.2	0.82
High-diversion	High	15.6	0.86

The dominance of timing over end-state performance reflects a form of path dependence intrinsic to landfill-based systems. Early landfill stock formation reinforces future methane generation through delayed feedbacks, widening divergence among scenarios as time progresses. Conversely, scenarios that introduce diversion earlier suppress the growth of landfill stocks during formative years, yielding long-term emissions benefits that persist even under comparable later-stage configurations. This timing effect is consistent with landfill-focused GHG studies emphasizing the importance of early waste routing decisions under first-order decay dynamics (Menikpura et al. 2013).

Importantly, the methane legacy effect also mediates the influence of demand variability. Short-term fluctuations in waste inflow, such as those driven by tourism dynamics, do not translate directly into proportional emissions changes. Instead, their long-run impact depends on whether marginal inflows are absorbed by landfill stocks during periods of constrained diversion capacity. When diversion is delayed, episodic inflow surges accelerate stock accumulation and persistently elevate cumulative emissions. When diversion is introduced earlier, the same variability yields attenuated long-term effects because marginal waste is structurally routed away from landfill pathways.

Taken together, these results demonstrate that GHG mitigation performance in municipal solid waste systems

is governed by trajectory control rather than end-point optimization. The inability of late interventions to undo earlier emissions commitments highlights why mitigation assessments based solely on snapshot targets can be misleading. By explicitly representing time delays and stock-flow interactions, the SD framework reveals that early structural changes exert disproportionate influence on cumulative emissions outcomes, establishing methane legacy as a central determinant of long-horizon mitigation effectiveness.

Beyond affecting the timing and magnitude of municipal solid waste (MSW) inflows, tourism activity interacts with waste-management systems through characteristics commonly observed in urban and tourism-oriented contexts, particularly the prominence of organic waste fractions and disposable packaging in overall municipal waste streams. Studies in Thailand and other Southeast Asian cities indicate that food waste and packaging materials constitute a substantial share of municipal solid waste at the city level, reflecting consumption patterns associated with dense service activities, hospitality, and short-term consumption behavior (Vassanadumrongdee & Kittipongvises 2018, Nguyen et al. 2015, Chuenwong et al. 2022). While these studies do not provide a direct source-specific comparison between tourism-related and household waste composition, they establish the relevance of waste composition as a determinant of downstream emission behavior in tourism-intensive urban systems.

From an SD perspective, waste composition influences GHG trajectories indirectly by shaping the effective emission characteristics of waste-treatment pathways rather than by altering total waste quantities alone. High organic content in municipal waste increases the methane generation potential when marginal waste is routed to landfill pathways, reinforcing long-term emissions through delayed anaerobic degradation. Conversely, a greater presence of packaging and composite materials affects the carbon intensity and mitigation performance of thermal treatment options. These mechanisms operate regardless of the precise origin of waste streams and are therefore relevant when tourism-driven inflows increase pressure on existing treatment capacity.

Tourism-driven waste generation is also inherently seasonal, characterized by sharp fluctuations between peak and off-peak periods. Such variability introduces transient stress on waste-management systems, particularly where diversion and treatment capacity expansion lags behind demand. Static and annual-average assessments tend to smooth out these fluctuations, potentially underestimating the risk that short-term inflow surges are absorbed disproportionately by landfill pathways. In contrast, the SD framework applied here captures how episodic demand peaks propagate through waste stocks and routing decisions, revealing sensitivity to both behavioral variability and infrastructure timing.

Simulation results indicate that under conditions of delayed diversion expansion, periods of elevated demand, whether tourism-related or otherwise, are more likely to translate into accelerated landfill stock accumulation. This effect arises not from waste composition alone, but from the interaction between inflow variability, pathway availability, and timing. Similar findings have been reported in SD-based waste studies, which emphasize that system robustness depends on structural flexibility and early pathway diversification rather than on average demand levels or end-state treatment shares (Wang & You 2021).

Taken together, waste composition characteristics and seasonal demand variability function as amplifying mechanisms within the MSW-GHG system. Tourism does not introduce a distinct emissions pathway through composition effects alone. Instead, it increases the likelihood that marginal waste is committed to long-lived landfill stocks during constrained periods. This interpretation reinforces the central conclusion that effective mitigation performance is governed by structural routing and timing, rather than by assumptions about waste composition differences between specific source categories. Additionally, the long-term sustainability of such pathways is further supported by community attitudes, which serve as a key driver for the success of decentralized facilities (Kisworo et al. 2025).

While ambitious diversion targets are assumed in the scenarios, implementation delays are inherently involved in realizing such systemic transitions. Real-world behavioral shifts in household waste segregation are typically characterized by a non-linear S-curve adoption trajectory, which is consistent with established Diffusion of Innovation (DOI) theory (Rautan et al. 2025). Although the initial phase of public participation in waste sorting is often slow due to habit inertia, it has been demonstrated through empirical system dynamics modeling for Bangkok that recyclable waste can be comprehensively sorted within an approximately 17-year horizon, provided that active community engagement and structured policy support are implemented (Manasakunkit & Chinda 2017). As the simulation commences in the 2024–2025 period, a 25-year window until 2050 is provided, which is considered a sufficient buffer for the behavioral S-curve to reach its stabilization phase.

Furthermore, the strategic importance of early action is heightened by this inherent lag time. Since methane generation in landfills is governed by first-order decay

dynamics, the emission rate is determined by the cumulative stock of degradable organic carbon deposited in previous years (IPCC 2006, Scharff et al. 2024). If diversion policies are delayed, more organic mass is structurally added to the landfill stock. Consequently, a long-term methane legacy is created, which is expected to continue emitting for decades even after behavioral norms have eventually shifted (Scharff et al. 2024). To accelerate this transition and minimize the lag phase, knowledge and subjective norms have been highlighted in recent Thai residential studies as the primary catalysts for stimulating waste separation intention (Pongpunpurt et al. 2022). By integrating these social drivers early in the policy roadmap, it is suggested that the acceleration phase of the S-curve can be optimized to meet the cumulative mitigation targets required for Thailand's 2050 net-zero ambition (Sakcharoen et al. 2023, Sunthara 2025).

Despite the conceptual mechanisms discussed above, a notable structural assumption in this study is that the macroscopic waste composition was held constant over the simulation horizon. In practice, as upstream diversion policies (e.g., organic waste separation) mature, the fractional share of degradable organic carbon (DOC) routed to landfills will inherently decrease. This approach of assuming a constant composition is consistent with established system dynamics modeling practices for national-scale MSW analysis in Thailand (Pudcha et al. 2023a). Since the baseline simulation maintains this constant composition, the methane abatement trajectories should be interpreted as conservative estimates (a lower bound on policy benefits). However, the systemic response to such qualitative shifts was mathematically evaluated through the sensitivity analysis in Section 3.5. By varying the DOC parameter, which serves as a proxy for the organic fraction in the waste stream, the results demonstrate that qualitative improvements would further accelerate the mitigation of the methane legacy beyond the baseline projections. This confirms that early diversion not only reduces waste mass but also lowers the intrinsic emission potential of the residual stream.

While the current system dynamics framework primarily focuses on physical mass flows and GHG trajectories, the findings provide essential insights into the economic dimensions of MSW management. As outlined in Thailand's NDC 3.0 framework (DCCE 2025), the deployment of downstream technologies required to abate residual emissions demands substantial capital investment, estimated at USD 0.94 billion by 2035 for the waste, industrial processes, and agriculture sectors. The model demonstrates that delayed intervention structurally locks in a larger methane legacy, which will inevitably increase future reliance on these capital-intensive solutions (Scharff et al. 2024). Based on national prioritization, these end-of-pipe measures carry significant abatement costs, such as USD 55.62 (t $CO_{2)^{-1}}$ for landfill gas capture and USD 298.57 (t $CO_{2)^{-1}}$ for advanced material recovery facilities (DCCE 2025).

Conversely, early upstream diversion functions as a strategic cost-avoidance mechanism. By preventing the accumulation of degradable organic carbon in landfills through source separation, the financial burden associated with future technological remediation is substantially reduced. This is consistent with global assessments indicating that the long-term economic impact of environmental recovery can be multiple times higher than the cost of developing and operating proactive waste management systems (Kaza et al. 2018). Thus, it is suggested that evaluating mitigation pathways should not be limited to static abatement costs alone, but must incorporate the long-term financial liabilities and consequent cost savings generated by early policy action (Jadeja et al. 2022).

The mathematical convergence of annual emissions at approximately 5 Mt CO□e by 2050 across the intervention scenarios is a structurally bounded outcome driven by the predefined diversion targets. This convergence represents a physical floor of flow-based diversion measures, primarily consisting of unmanaged historical stocks and hard-to-abate residual waste (Waite et al. 2024). Nevertheless, the model's emergent behavior can be observed through its pathway dependency. While FOD mechanics indicate that early intervention yields greater mitigation (IPCC 2006), the simulation quantifies the magnitude of the methane legacy accumulated during periods of delayed capacity expansion (Scharff et al. 2024). Furthermore, the elasticity assessment (Section 3.5) indicates that the long-term cumulative trajectory exhibits low sensitivity to variations in biological parameters (e.g., decay rates), whereas it remains strongly responsive to institutional enforcement and diversion efficiency (DCCE 2025). This suggests that the system's overall mitigation performance is continuously shaped by implementation dynamics rather than being solely determined by the end-point targets.

3.5. Sensitivity and Elasticity Assessment

To validate the stability of the policy implications, the scenario-specific elasticity of cumulative GHG emissions (2024–2050) was computed against variations in critical parameters. As summarized in Table 6, the results reveal a profound structural dynamic: as scenarios become more ambitious in diversion targets, the system's sensitivity shifts fundamentally from biological parameters to institutional performance.

Table 6: Scenario-specific elasticity bounds of cumulative GHG emissions (2024–2050) to critical parameter variations.

Parameter	Variation tested	BAU	CPI	CEM	OGM
Methane generation rate (k)	±10% (0.36–0.44)	±0.45%	±0.45%	±0.45%	±0.45%
Degradable organic carbon (DOC) (food waste)	±10% (0.135–0.165)	±4.86%	±3.92%	±2.85%	±1.74%
Diversion efficiency	±5% (e.g., target 5%)	±6.25%	±8.33%	±10.00%	±14.28%

First, the variation in the methane generation rate (k) consistently yields a negligible impact (±0.45%) on cumulative emissions across all scenarios. As established by the foundational mechanics of the first-order decay model (IPCC 2006), the parameter k dictates the temporal distribution of emissions rather than the ultimate methane yield. Over the extended 26-year simulation horizon, highly degradable food fractions exhaust their ultimate methane potential regardless of minor decay rate fluctuations. Consequently, the long-term cumulative emission outcomes are mathematically bounded by the total landfilled mass, making the model highly robust against decay rate uncertainties. Second, an inverse sensitivity dynamic prominently emerges between waste composition (DOC) and diversion efficiency. Under the baseline pathway (BAU), cumulative emissions are highly sensitive to DOC variations (±4.86%) due to the continuous and dominant influx of unmanaged organic waste into disposal sites. However, as policy interventions intensify in the OGM scenario, organic waste is heavily diverted to alternative facilities (e.g., composting and MBT), thereby significantly suppressing the system's sensitivity to landfill DOC uncertainties (±1.74%). This phenomenon strongly aligns with recent empirical assessments demonstrating that circular economy interventions and bio-based solutions inherently de-risk landfill emission uncertainties by physically removing the organic source from the decay process (Jawjit et al. 2025, Sakcharoen et al. 2023).

Most critically, the model demonstrates that highly ambitious pathways (e.g., OGM) exhibit pronounced structural sensitivity to diversion efficiency targets (14.28%). Because the baseline residual landfill input is substantially minimized in OGM, any absolute implementation failure (5% target deviation) strictly results in a severe relative surge in cumulative emissions. This finding highlights a pivotal policy trade-off: while transitioning to advanced waste management scenarios significantly mitigates biological risks (e.g., DOC, k), it drastically elevates institutional and implementation risks. Therefore, ensuring strict adherence to the diversion targets through robust local enforcement is the most imperative factor in achieving the net-zero trajectory.

Finally, it is important to acknowledge the structural boundaries of the current SD model. The framework is specifically designed to evaluate physical mass-flow dynamics and their corresponding emission trajectories. While the implications of downstream technologies (such as landfill gas capture, flaring, or biological oxidation) and economic constraints (such as abatement costs and environmental liabilities) are critical, they are treated as external contextual factors rather than internal system variables. Therefore, the findings presented here should be interpreted as unmitigated, conservative upper-bound projections of physical pathway dependency, which must be integrated with broader techno-economic assessments for comprehensive policy planning.

4. CONCLUSIONS

This study employed an SD approach to examine the long-term GHG emission trajectories of MSW management under baseline growth, alternative mitigation pathways, and tourism-driven demand variability. By focusing on accumulation, time delays, and path dependence rather than point estimates or end-state outcomes, the analysis provides insight into how structural decisions shape cumulative emissions over a multi-decadal horizon. The results show that long-term GHG outcomes are governed primarily by trajectory-shaping mechanisms rather than by the eventual presence of waste-treatment technologies alone. Across all scenarios, early landfill stock accumulation emerged as a major structural determinant of cumulative emissions. Waste deposited during initial periods continues to generate methane over extended time horizons, creating a persistent emissions legacy that cannot be fully offset by delayed diversion or treatment expansion. As a result, scenarios that converged toward similar diversion levels at later stages still exhibited markedly different cumulative emissions, reflecting strong path dependence inherent in landfill-based systems. Scenario comparisons further demonstrate that the timing of structural intervention consistently outweighs the scale of late-stage mitigation efforts. Early diversion and reduced reliance on landfill pathways limit the formation of waste stocks and lead to substantially lower cumulative emissions, whereas delayed intervention locks in long-term methane generation, even with subsequent improvements in waste management performance. This finding indicates that mitigation effectiveness in MSW systems cannot be adequately evaluated using single-year emission levels, but instead requires trajectory- and cumulative-based assessment. Tourism-driven demand variability does not represent an independent mitigation pathway but functions as a stress

amplifier that magnifies underlying structural differences among waste-management configurations. Systems with high landfill dependence exhibit pronounced sensitivity to demand fluctuations, as episodic increases in waste inflow translate directly into accelerated stock accumulation and higher cumulative emissions. In contrast, systems characterized by earlier diversion and pathway diversification display greater buffering capacity, maintaining more stable emission trajectories under variable demand conditions. Taken together, within the specific boundaries of upstream MSW management, the findings indicate that mitigating long-term methane emissions is heavily driven by controlling organic stock formation and feedback dominance, complementing the optimization of end-point technology deployment. Landfill-centered systems are governed by reinforcing feedbacks linking waste inflow, stock accumulation, and delayed methane generation, whereas diversified systems weaken such feedbacks by redirecting waste into pathways with different temporal emission profiles. The system dynamics framework is well-suited to reveal these mechanisms, which remain difficult to identify using static and accounting-based approaches. Although future waste demand, particularly that associated with tourism, remains uncertain, the structural patterns identified in this study suggest that early diversion and sustained reduction in landfill reliance consistently yield lower cumulative emissions across a wide range of plausible demand conditions. These insights underscore the i mportance of trajectory-oriented evaluation for understanding long-term mitigation performance in municipal solid waste systems.

5. ACKNOWLEDGEMENT

We sincerely thank the Faculty of Engineering, Thammasat School of Engineering, Thammasat University for their generous support and the provision of essential research equipment, which significantly contributed to the success of this study.

6. REFERENCES

Arbulú, I., Lozano, J. and Rey-Maquieira, J., 2015. Tourism and solid waste generation in Europe: a panel data assessment of the environmental Kuznets curve. *Waste Management*, 46, pp. 628–636. [DOI].

Barlas, Y., 1996. Formal aspects of model validity and validation in system dynamics. *System Dynamics Review*, 12(3), pp. 183–210. [DOI].

Chuenwong, K., Wangjiraniran, W., Pongthanaisawan, J., Sumitsawan, S. and Suppamit, T., 2022. Municipal solid waste management for reaching net-zero emissions in ASEAN tourism twin cities: a case study of Nan and Luang Prabang. *Heliyon*, 8, e10295. [DOI].

Chiemchaisri, C. and Visvanathan, C., 2008. Greenhouse gas emission potential of the municipal solid waste disposal sites in Thailand. *Journal of the Air & Waste Management Association*, 58(5), pp. 629–635. [DOI].

Department of Climate Change and Environment (DCCE), 2024. Thailand's First Biennial Transparency Report (BTR1). Ministry of Natural Resources and Environment, Bangkok, Thailand.

Department of Climate Change and Environment (DCCE), 2025. Thailand's Second Nationally Determined Contribution (NDC 3.0). Ministry of Natural Resources and Environment, Bangkok, Thailand.

Dianati, K., Schafer, L., Milner, J., Gomez-Sanabria, A., Gitau, H., Hale, J., Langmaack, H., Kiesewetter, G., Muindi, K., Mberu, B., Zimmermann, N., Michie, S., Wilkinson, P. and Davies, M., 2021. A system dynamics-based scenario analysis of residential solid waste management in Kisumu, Kenya. *Science of the Total Environment*, 777, 146200. [DOI].

European Commission, 2023. Waste Framework Directive. European Commission - Environment. Available from: https://environment.ec.europa.eu/topics/waste-and-recycling/waste-framework-directive_en (accessed 15 January 2026).

Hoornweg, D. and Bhada-Tata, P., 2012. *What a Waste: A Global Review of Solid Waste Management*. World Bank Urban Development Series, Knowledge Papers No. 15, World Bank, Washington, DC.

Intergovernmental Panel on Climate Change (IPCC), 2006. 2006 IPCC Guidelines for National Greenhouse Gas Inventories. IPCC, Geneva, Switzerland.

Intergovernmental Panel on Climate Change (IPCC), 2019. 2019 Refinement to the 2006 IPCC Guidelines for National Greenhouse Gas Inventories. IPCC, Geneva, Switzerland.

Jadeja, N., Zhu, N.J., Lebcir, R.M., Sassi, F., Holmes, A. and Ahmad, R., 2022. Using system dynamics modelling to assess the economic efficiency of innovations in the public sector: a system dynamic review. *PLoS ONE*, 17(2), e0263299. [DOI].

Jawjit, S., Kaewchutima, N. and Bumyut, A., 2025. Waste management and greenhouse gas emission reduction in Nakhon Si Thammarat municipality through a circular economy municipal solid waste management model. *Cleaner Environmental Systems*, 18, 100313. [DOI].

Kapmeier, F. and Goncalves, P., 2018. Wasted paradise? Policies for small island states to manage tourism-driven growth while controlling waste generation: the case of the Maldives. *System Dynamics Review*, 34(1–2), pp. 172–221. [DOI].

Karak, T., Bhagat, R.M. and Bhattacharyya, P., 2012. Municipal solid waste generation, composition and management: the world scenario. *Critical Reviews in Environmental Science and Technology*, 42(15), pp. 1509–1630. [DOI].

Kaza, S., Yao, L., Bhada-Tata, P. and Van Woerden, F., 2018. *What a Waste 2.0: A Global Snapshot of Solid Waste Management to 2050*. Urban Development Series. Washington, DC: World Bank. [DOI].

Kisworo, W., Suhardono, S., AN, I. and Suryawan, I.W.K., 2025. Evaluating the impact of community attitudes on the sustainability of 3R temporary waste disposal sites using structural equation modeling-partial least square (SEM-PLS) in Sukoharjo. *Nature Environment and Pollution Technology*, 24(2), p. D1702. [DOI].

Kornboonraksa, T., Chiemchaisri, C., Chiemchaisri, W., Towprayoon, S. and Visvanathan, C., 2004. Determination of methane gas emissions from waste disposal sites in Thailand with geographical information system application. In: Proceedings of the Joint International Conference on "Sustainable Energy and Environment (SEE)", 1–3 December 2004, Hua Hin, Thailand, pp. 293–298.

Liu, Z., Zhang, Q. and Liu, H., 2023. Prediction of municipal solid waste treatment and disposal in high cold and high altitude area based on system dynamics: a case study of Lhasa. *Environmental Research Communications*, 5(12), 125006. [DOI].

Manasakunkit, C. and Chinda, T., 2017. Development of a municipal solid waste dynamic model in Bangkok, Thailand. *Songklanakarin Journal of Science and Technology*, 39(5), pp. 685–695.

Mateu-Sbert, J., Ricci-Cabello, I., Villalonga-Olives, E. and Cabeza-Irigoyen, E., 2013. The impact of tourism on municipal solid waste generation: the case of Menorca (Spain). *Waste Management*, 33(12), pp. 2589–2593. [DOI].

Menikpura, S.N.M., Sang-Arun, J. and Bengtsson, M., 2012. Mechanical biological treatment as a solution for mitigating greenhouse gas emissions from landfills in Thailand. In: Proceedings of the ISWA World Solid Waste Congress 2012, Florence, Italy, 17–19 September 2012.

Menikpura, S.N.M., Gheewala, S.H., Bonnet, S. and Chiemchaisri, C., 2013. Evaluation of the effect of recycling on sustainability of MSW management in Thailand. *Waste and Biomass Valorization*, 4, pp. 237–257. [DOI].

Nguyen, T.T.P., Zhu, D. and Le, N.P., 2015. Factors influencing waste separation intention of residential households in a developing country: evidence from Hanoi, Vietnam. *Habitat International*, 48, pp. 169–176. [DOI].

Nordahl, S.L., Preble, C.V., Kirchstetter, T.W. and Scown, C.D., 2023. GHG and air pollution emissions from composting. *Environmental Science & Technology*, 57, pp. 2235–2247. [DOI].

Office of Natural Resources and Environmental Policy and Planning (ONEP), 2020. Thailand's Updated Nationally Determined Contribution (NDC). Ministry of Natural Resources and Environment, Bangkok, Thailand.

Office of Natural Resources and Environmental Policy and Planning (ONEP), 2022. Thailand's Fourth Biennial Update Report (BUR4). Ministry of Natural Resources and Environment, Bangkok, Thailand.

Piedrahita, A.R., Cardenas Ardila, L.M., Parra Valencia, J.A., Das Dores, A.J.L. and Perez Canencia, J.G., 2025. Modeling and simulation with system dynamics: a literature review on validation aspects. *Journal of Hunan University Natural Sciences*, 52(1), pp. 20–35. [DOI].

Pinha, A.C.H. and Sagawa, J.K., 2020. A system dynamics modelling approach for municipal solid waste management and financial analysis. *Journal of Cleaner Production*, 269, 122350. [DOI].

Pollution Control Department (PCD), 2014–2024. Thailand Municipal Solid Waste Situation Reports. Pollution Control Department, Ministry of Natural Resources and Environment, Thailand (in Thai).

Pollution Control Department (PCD), 2021. Report on Municipal Solid Waste Composition in Thailand. Pollution Control Department, Thailand (in Thai).

Pollution Control Department (PCD), 2022. National Action Plan on Waste Management (Phase II: 2022–2027). Ministry of Natural Resources and Environment, Bangkok, Thailand.

Pongpunpurt, P., Muensitthiroj, P., Pinitjitssamut, P., Chenchum, P., Painmanakul, P., Chawaloesphonsiya, N. and Poyai, T., 2022. Studying waste separation behaviors and environmental impacts toward sustainable solid waste management: a case study of Bang Chalong Housing, Samut Prakan, Thailand. *Sustainability*, 14, 5040. [DOI].

Pudcha, T., Phongphiphat, A., Wangyao, K. and Towprayoon, S., 2023a. Forecasting municipal solid waste generation in Thailand with grey modelling. *Environment and Natural Resources Journal*, 21(1), pp. 35–46. [DOI].

Pudcha, T., Phongphiphat, A. and Towprayoon, S., 2023b. Greenhouse gas mitigation and energy production potentials from MSW management in Thailand through 2050. *Earth Systems and Environment*, 7, pp. 83–97. [DOI].

Rautan, I., Supramaniam, S., Nezakati, H. and Homer, S.T., 2025. Understanding low ecovillage adoption in Southeast Asia: insights from Malaysia using diffusion of innovation theory. *Advances in Southeast Asian Studies*, 18(2), pp. D1–D19. [DOI].

Sakcharoen, T., Niyommaneerat, W., Faiyur, B. and Silalertruksa, T., 2023. Low-carbon municipal solid waste management using bio-based solutions and community participation: the case study of a cultural tourism destination in Nan, Thailand. *Heliyon*, 9, e22025. [DOI].

Scharff, H., Soon, H.Y., Taremwa, S.R., Zegers, D., Dick, B., Zanon, T.V.B. and Shamrock, J., 2024. The impact of landfill management approaches on methane emissions. *Waste Management & Research*, 42(11), pp. 1052–1064. [DOI].

Sterman, J.D., 2018. System dynamics at sixty: the path forward. *System Dynamics Review*, 34(1–2), pp. 5–47. [DOI].

Sunthara, T., 2025. The social tool: effective waste management to solve the problem of community waste. *Applied Environmental Research*, 27(1). (in Thai).

Thepsaskul, W., Wongsapai, W., Jaitiang, T. and Jaekhajad, P., 2025. Prospects of attaining Thailand's carbon neutrality target through carbon capture and storage by public power utility. *Sustainability*, 17, 276. [DOI].

Vassanadumrongdee, S. and Kittipongvises, S., 2018. Factors influencing source separation intention and willingness to pay for improving municipal solid waste management in Thailand. *Sustainable Environment Research*, 28, pp. 90–99. [DOI].

Wang, W. and You, X., 2021. Benefits analysis of classification of municipal solid waste based on system dynamics. *Journal of Cleaner Production*, 279, 123686. [DOI].

Waite, T., Pradhan, B.B., Winyuchakrit, P., Khan, Z., Weber, M., Pressburger, L., Chaichaloempreecha, A., Rajbhandari, S., Pita, P., Westphal, M.I., Jonvisait, A., Jareemit, D., Limmeechokchai, B. and Evans, M., 2024. Stakeholder-driven carbon neutral pathways for Thailand and Bangkok: integrated assessment modeling to inform multilevel climate governance. *Frontiers in Energy Research*, 12, 1335290. [DOI].

Zero Waste Europe, 2020. The New 10% Landfill Target May Work Against the Circular Economy. Policy briefing, March 2020. Available from: https://zerowasteeurope.eu/wp-content/uploads/2020/03/zero_waste_europe_policybriefing_10landfill_en.pdf (accessed 15 January 2026).

Nature Environment and Pollution Technology
An International Quarterly Peer-Reviewed Open Access Journal

p-ISSN: 0972-6268 | e-ISSN: 2395-3454 Vol. 25 | No. 4 | Article ID D1914 | 2026

RESEARCH ARTICLE https://doi.org/10.46488/NEPT.2026.v25i04.D1914 OPEN ACCESS

Activity Concentration of Natural Radionuclides in Surface Waters and Bottom Sediments Near Uranium Mining Sites and Environmental Impacts

Aikyn Nurakhmet[1], Amanbek Zandybay[1]†, Zhanar Moldagazyyeva[2], Murat Nurushev[3] and Yerlan Zhumay[4]
[1]Department of Environmental Management and Engineering, L.N. Gumilyov Eurasian National University, Astana, 010000, Kazakhstan
[2]Department of Ecology, Narxoz University, Almaty, Kazakhstan
[3]Higher School of Natural Sciences, Astana International University, Astana, Kazakhstan
[4]Department of Mining, Construction and Ecology, Sh. Ualikhanov Kokshetau University, Kokshetau, Kazakhstan
†Corresponding author: Amanbek Zandybay; amanbek.zandybay@gmail.com

ARTICLE HISTORY

Received: 30-01-2026
Revised: 26-03-2026
Accepted: 11-04-2026

KEYWORDS

Bottom sediments
Environmental pollution
Radionuclides
Surface water
Uranium mining

CITE THIS ARTICLE

Nurakhmet, A., Zandybay, A., Moldagazyyeva, Z., Nurushev, M. and Zhumay, Y., 2026. Activity concentration of natural radionuclides in surface waters and bottom sediments near uranium mining sites and environmental impacts. *Nature Environment and Pollution Technology*, 25(4), D1914. https://doi.org/10.46488/NEPT.2026.v25i04. D1914

COPYRIGHT & LICENCE

© 2026 The Authors
Open Access under CC BY 4.0.

PUBLISHED BY
TECHNOSCIENCE PUBLICATIONS

ABSTRACT

This research provides a radioecological assessment of surface waters and bottom sediments in the vicinity of conserved and reclaimed uranium mining sites in Northern Kazakhstan. Activities of natural radionuclides were determined, and distribution coefficients, radiological hazard indices, committed effective dose, and ecological contamination indices were calculated to evaluate radionuclide mobility and associated environmental risks. Gross alpha activity increases downstream along the Kutunguz River, while uranium isotope activities exceed background levels by 8–10-fold, indicating ongoing radionuclide migration from the conserved Shantobe uranium deposit. In contrast, the Balkhashin quarry, a closed hydrological system, demonstrates substantial accumulation of ^{228}Ra attributable to limited water exchange. Distribution coefficient analysis indicates high uranium mobility in flowing river systems and enhanced retention in closed water bodies. Although most radiological hazard indices remain within internationally accepted limits, localized radiological risk is observed in the quarry area. The committed effective dose from drinking water at the background site exceeds the WHO screening level but remains below the ICRP recommended limit. The obtained results indicate differences in the behavior of radionuclides in flowing and closed hydrological systems, as well as the persistent impact of conserved uranium mining facilities on aquatic ecosystems.

1. INTRODUCTION

Natural radionuclides occur ubiquitously in the environment at variable concentrations and, under typical conditions, do not pose significant risks to human health. Radionuclides detected in rocks, soils, waters, and the atmosphere primarily originate from the natural decay series of ^{238}U, ^{232}Th, and ^{40}K. However, their concentrations may increase as a consequence of mining activities or natural disturbances (Wu et al. 2014). Mineral extraction, including open-pit mining and ore processing, generates substantial volumes of waste materials, and mine drainage waters are frequently discharged into surface water bodies. Accordingly, quantifying radionuclide concentrations, interactions, and mobility in environmental media represents a critical prerequisite for assessing radiation exposure and protecting public health.

Numerous studies have evaluated the environmental impacts of radionuclides worldwide (Kamunda et al. 2016, Galhardi et al. 2017, Idrisheva et al. 2025, Raji

et al. 2021). These investigations consistently demonstrate that uranium mining and related extractive activities elevate concentrations of uranium and its decay products in natural waters, and that adverse ecological effects may persist long after mining operations have ceased.

The Republic of Kazakhstan is characterized by a complex radioecological setting. Approximately 13% of its territory (about 350,000 km²) is classified as radiation-affected, with more than one million residents living within these zones. Previous studies conducted in Kazakhstan (Saifulina et al. 2023, Brzhanov et al. 2020, Bersimbaev et al. 2015, Zhumadilov et al. 2025) have reported increased disease prevalence among populations residing near uranium mining sites, continued impacts of mine waste dumps on surface waters, and persistent environmental anomalies in affected regions.

Despite a significant amount of research devoted to the radioecological assessment of uranium mining territories, comparative analysis of sites with different types of post-operational conditions (reclaimed and conserved facilities) within a single hydrological system remains limited.

The present research presents a comparative analysis of the distribution of natural radionuclides in surface water systems differing in hydrological conditions (flowing and closed water bodies) and in the type of post-operational condition of uranium facilities. Particular attention is paid to identifying factors potentially influencing the migration of radionuclides and their redistribution among components of the aquatic environment.

For the quantitative characterization of radionuclide behavior, the distribution coefficient (Kd) is used as an indicator of radionuclide mobility and capacity for accumulation in bottom sediments. At the same time, Kd values are interpreted within the framework of comparative analysis, taking into account the limitations of the available data, without constructing a deterministic model to separate the influencing factors.

The scientific novelty of the work lies in the comparative assessment of the distribution of natural radionuclides in surface waters and bottom sediments in the vicinity of reclaimed and conserved uranium facilities within a single hydrological system, taking into account hydrological conditions. The obtained results are considered a preliminary quantitative-descriptive assessment, given the limited sample size and the one-time seasonal nature of observations.

The objective of the present research is to determine the levels of radiological and ecological risk based on the measured activities of natural radionuclides in surface waters and bottom sediments in uranium mining areas of Northern Kazakhstan, as well as to conduct a comparative analysis of their distribution with consideration of hydrological conditions and characteristics of water exchange.

Field research was conducted in 2025 in Northern Kazakhstan (Akmola Region, Sandyktau District) at sites associated with reclaimed and conserved uranium mines. Sampling was carried out during a single season (summer), since surface water bodies in the research area typically dry up in autumn, freeze in winter, and experience significant hydrological disturbances due to precipitation and runoff in spring.

2. MATERIALS AND METHODS

2.1. Description of the Research Area

The study area is situated within the Northern Kazakhstan uranium province, in the Sandyktau District of Akmola Region, administratively subordinate to the city of Stepnogorsk. The uranium deposits are located approximately 420 km from Astana, 170 km from Kokshetau, and about 450 km northwest of Stepnogorsk. The settlement of Shantobe, adjacent to the industrial mining site, lies 4 km to the east, while the village of Novokronshtadt is located 2 km to the west.

The Balkhashin uranium mine was reclaimed in 2007 within the framework of the state program "Conservation of Uranium Mines and Reclamation of Territories after Deposit Development" (Government of the Republic of Kazakhstan 2001). The territory of the mine consists of a waste dump and a quarry. During reclamation, work was carried out to restore the soil cover and to create a so-called reclamation layer providing favorable conditions for vegetation growth; the quarry bottom was flooded with water.

The Shantobe mine was conserved in 2014. It includes a group of deposits of different sizes (Vostok, Zvezdnoye). Ore extraction was carried out by underground mining methods; the mine area contains heap leaching sites, waste rock dumps, and several evaporation ponds. The main technology for uranium extraction at the deposits was heap sulfuric acid leaching.

The region is characterized by a sharply continental climate, with cold, snowy winters and hot, dry summers. The mean annual air temperature is +1.8°C; average temperatures reach −16.8 °C in January and +20.4°C in July. The mean annual wind speed is 5.3 m s^{-1}, and the average annual precipitation is 326 mm.

The principal surface water bodies in the study area are the Kishi-Kutunguz and Kutunguz rivers, which traverse former uranium mining territories. The investigation also included

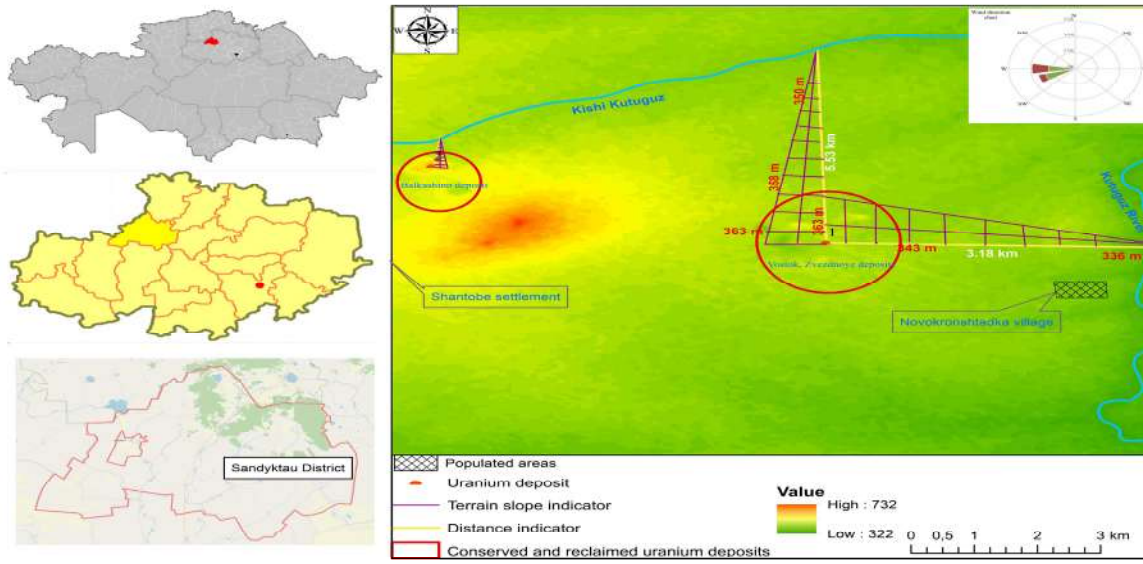


Fig. 1: Location map of surface water bodies within the Balkhashin mining complex. 1 – Shantobe (Vostok, Zvezdnoye) decommissioned mine 2 – Balkhashin reclaimed mine.

the Balkhashin quarry reservoir, located within the reclaimed Balkhashin uranium mine, and Lake Zhaksy-Zhalgyztau, situated at a considerable distance from direct anthropogenic influence. Lake Zhaksy-Zhalgyztau, approximately 16 km from the mining sites, was selected as a local background (reference) site. Within the framework of this research, the site of Lake Zhaksy-Zhalgyztau is considered a conditional background site (local background) used for comparative analysis within the research area. It should be noted, however, that independent historical or reference geochemical data were not employed due to their absence, which limits the possibility of rigorous verification of background values. In this regard, the obtained results should be interpreted as relative estimates allowing the identification of deviations in radionuclide distribution among the studied aquatic systems. Sampling locations were determined based on hydrogeological conditions, topography, and zones subject to anthropogenic impact (Fig. 1).

2.2. Fieldwork

Radiological monitoring of water bodies represents one of the most methodologically demanding areas of environmental assessment due to the low activity concentrations of radionuclides and the need for strict sampling and analytical control. The initial stage of the present investigation included the determination of gross alpha and gross beta activity in collected water samples (Dyussembayeva et al. 2025).

Sampling was conducted in June 2025 during the summer hydrological period. Surface water samples were collected in accordance with the requirements of ST RK 1545-2006 (Committee for Technical Regulation and Metrology of the Republic of Kazakhstan 2006), while bottom sediment sampling followed GOST 17.1.5.01-80 (GOST 17.1.5.01-80 1980). Bottom sediments were obtained from a depth of 0–15 cm using a Van Veen grab sampler, with individual sample masses of 500–1000 g.

All collected materials were placed in airtight polyethylene containers and transported to the laboratory for subsequent analysis. Prior to water sampling, collection bottles were rinsed three times with the sampled water to minimize potential contamination. Sediment samples were stored in 1 kg polyethylene bags, whereas water samples were collected in 5000 mL sampling bottles. Immediately after collection, all samples were delivered to the laboratory. Owing to the considerable transport distance, water samples were preserved by acidification with nitric acid (HNO_3) to achieve pH < 1, using 100 mL of concentrated HNO_3 per 5 L of water.

In total, 10 samples were collected within the study area, comprising 5 surface water samples and 5 bottom sediment samples (Fig. 2).

2.3. Laboratory Analysis

Before analysis, samples underwent standardized laboratory preparation. Organic debris, roots, vegetation, and coarse mineral fragments were removed. Sediment samples were initially air-dried and subsequently oven-dried at 110°C for 24 hours until constant weight was achieved. The activities

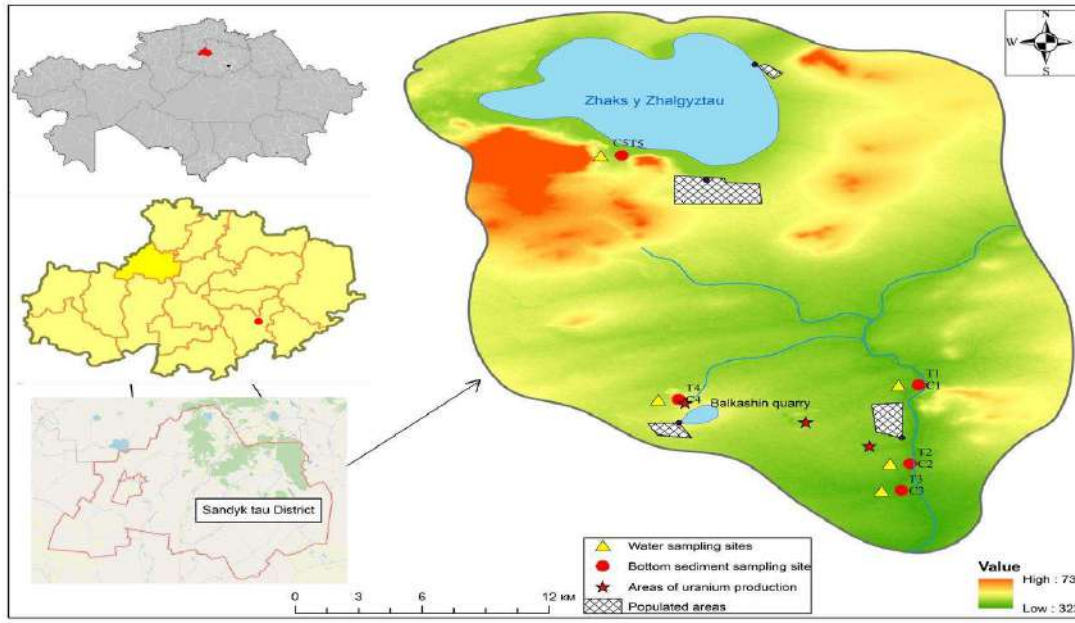


Fig. 2: Distribution of sampling points in the study area. T – bottom sediment samples; C – water samples.

of ^{226}Ra, ^{232}Th, and ^{40}K in bottom sediments were determined using an Atomtech MKS-AT1315 beta–gamma spectrometer (Minsk, Belarus). The permissible relative measurement uncertainty was ±15%. Gamma-emitting radionuclide spectra were processed using a multichannel analyzer (MCA) and PCA software.

Activities of ^{234}U and ^{238}U in sediment samples were measured using an MKS-01A "Multirad" instrument manufactured by Amplitude JSC (Zelenograd, Russia). Gamma spectrum analysis was performed using the "Progress" software package (Amplitude JSC, Zelenograd, Russia). The uncertainty associated with specific activity determination was approximately ±20–30% of the measured values.

In water samples, gross alpha and gross beta activity, as well as volumetric activities of ^{226}Ra, ^{228}Ra, ^{210}Po, and ^{210}Pb, were determined using a UMF-2000 alpha–beta radiometer in combination with radiochemical separation techniques.

Prior to measurement, water samples were subjected to preliminary concentration and radiochemical treatment, including co-precipitation and selective separation of target radionuclides. Chemical yield was controlled using tracers; the recovery efficiency ranged from 70% to 90%, and the obtained results were corrected with consideration of the yield.

The limits of detection (LOD), calculated based on counting statistics and background measurements, were on the order of 0.01–0.05 Bq L^{-1} for alpha-emitting radionuclides and 0.02–0.1 Bq L^{-1} for beta-emitting radionuclides. Quality assurance and quality control (QA/QC) included the analysis of blank samples, replicate measurements, and standard reference materials. The discrepancy between replicate measurements did not exceed 10–15%, and the contribution of blanks was below the detection limit or did not exceed 5% of the measured values.

Analytical uncertainty was evaluated taking into account both instrumental measurement errors and uncertainties associated with radiochemical procedures, including correction for chemical yield.

The calculated radiological and geochemical indices (Ra_eq, AEDE, Kd, CF, etc.) in the present research were determined based on the mean values of measured activities without explicit propagation of analytical uncertainties. Therefore, the obtained values should be regarded as estimated quantities, primarily suitable for comparative analysis.

In interpreting the results, it was taken into account that these uncertainties may affect the absolute values of the indices; however, they do not significantly influence the identified relative differences between the sites or the general patterns of radionuclide distribution.

Confidence intervals and sensitivity analysis were not performed in this research due to the limited sample size and the one-time nature of observations. The application of uncertainty propagation methods and statistical analysis is considered advisable in future work to improve the accuracy of quantitative assessment of radiological parameters.

Radiochemical and radiometric analyses were conducted at the accredited testing laboratory of the Institute of Radiobiology and Radiation Protection, Astana Medical University. The laboratory holds Accreditation Certificate No. KZ.T.01.1431 (20 August 2024) and operates in accordance with the ISO/IEC 17025:2019 standard of the Republic of Kazakhstan (International Organization for Standardization 2019).

Statistical analyses were performed using Microsoft Excel and Statistica 6.0 software in accordance with standard statistical methodologies.

2.4. Distribution Coefficient of Radionuclides in Sediments and Water

The distribution coefficient of radionuclides between sediments and water was calculated using Equation (1).

$$Kd\ (L\ kg^{-1}) = A_sediment\ (Bq\ kg^{-1})/A_water\ (Bq\ L^{-1}) \quad \ldots(1)$$

Kd: distribution coefficient (L kg^{-1}).

A_sediment: activity concentration in sediments (Bq kg^{-1}).

A_water: activity concentration in water (Bq L^{-1}).

2.5. Radiological Hazard Assessment

Radiological hazard to the local population associated with radionuclides in bottom sediments was evaluated using established international indices. These included radium equivalent activity (Ra_eq), absorbed dose rate (ADR), annual effective dose equivalent (AEDE), and the internal (H_in) and external (H_ex) hazard indices. In addition, the committed effective dose (CED) resulting from radionuclide ingestion through surface water consumption was calculated.

Dose calculations were based on an assumed water consumption rate of 2 L per day (730 L per year) and dose coefficients recommended by the United Nations Scientific Committee on the Effects of Atomic Radiation (UNSCEAR 2000) and the World Health Organization (World Health Organization 2004). Radionuclide intake via drinking water was assessed exclusively for sampling point 5 (Lake Zhaksy-Zhalgyztau), which serves as a drinking water source for residents of Shantobe and Novokronshtadt. For the remaining sites (sampling points 1–3: the Kutunguz River and the Balkhashin quarry technological reservoir), radiological and ecological hazard assessments were based on radionuclide activities measured in bottom sediments.

2.5.1. Radium Equivalent (Ra_eq)

Radiation exposure was expressed in terms of radium equivalent activity (Ra_eq), calculated using Equation (2). The recommended upper limit for Ra_eq is 370 Bq kg^{-1}, corresponding to an effective gamma dose of approximately 1.5 mGy $year^{-1}$ (Beretka & Mathew 1985).

$$Ra_eq = A_Ra + (1.43 \times A_Th) + (0.077 \times A_K) \quad \ldots(2)$$

A_Ra, A_Th, and A_K: activity concentrations of the corresponding radionuclides (Bq kg^{-1}).

2.5.2. Absorbed Dose Rate (ADR)

The absorbed dose rate at 1 m above ground level was calculated assuming uniform radionuclide distribution in sediments, according to Equation (3). The safety limit recommended by the International Commission on Radiological Protection (ICRP 1990) is 1000 nGy h^{-1}, while UNSCEAR (UNSCEAR 2000) recommends a reference level of 1500 nGy h^{-1}.

$$ADR = 0.462A_Ra + 0.604A_Th + 0.0417A_K \quad \ldots(3)$$

A: activity concentration of the corresponding radionuclide (Bq kg^{-1}).

2.5.3. Annual Effective Dose Equivalent (AEDE)

The annual effective dose equivalent (AEDE) represents the effective dose received by an individual due to external gamma radiation from sediments over one year. AEDE was calculated using Equation (4). The recommended annual dose limit for the public from artificial sources of ionizing radiation is 1 mSv (Akuo Ko et al. 2025).

$$AEDE = D \times CF \times OF \times T \times 10^{-6} \quad \ldots(4)$$

D: absorbed gamma dose rate

T: annual exposure time (8760 h)

CF: conversion coefficient from air kerma to effective dose (0.7 Sv Gy^{-1})

OF: outdoor occupancy factor (0.2)

10^{-6}: factor used to convert nGy to mGy so that the final result is expressed in mSv $year^{-1}$

2.5.4. Internal and External Hazard Indices

To ensure radiological safety, the internal (H_in) and external (H_ex) hazard indices must be less than unity, indicating an acceptable level of radiation risk. Natural radionuclides present in soils and bottom sediments contribute to external gamma radiation exposure of the population. A value of 1 corresponds to the maximum permissible radium equivalent activity (370 Bq kg^{-1}), which is associated with an effective annual dose of 1 mSv, as recommended by the International Commission on Radiological Protection (ICRP 1990).

Both indices were calculated using Equations (5) and (6), taking into account ^{226}Ra, ^{232}Th, and ^{40}K:

$$H_in = (A_Ra/185) + (A_Th/259) + (A_K/4810) \quad \ldots(5)$$

$$H_ex = (A_Ra/370) + (A_Th/259) + (A_K/4810) \quad \ldots(6)$$

A: activity concentration (Bq kg^{-1}) of the corresponding radionuclide.

2.5.5. Committed Effective Dose (CED)

The committed effective dose (CED) was calculated to evaluate radiological risk associated with long-term ingestion of radionuclides through drinking water consumption using the following equation (7). The calculation was performed exclusively for sampling point 5 (Lake Zhaksy–Zhalgyztau), as this water body serves as a drinking water source for residents of the Shantobe and Novokronshtadt settlements.

$$CED = C_i \times V \times DCF_i \quad \ldots(7)$$

C_i: activity concentration of the radionuclide (Bq L^{-1})

V: annual water consumption (730 L $year^{-1}$)

DCF_i: dose conversion factor (Sv Bq^{-1})

2.6. Ecological Contamination Indices

2.6.1. Contamination Factor (CF)

The Contamination Factor (CF) is widely applied in environmental geochemistry to assess the degree of contamination of soils and bottom sediments by chemical elements (Håkanson 1980) and is calculated using the following Equation (8). Although originally developed for heavy metals, its applicability to radionuclide contamination has been demonstrated in recent studies (Bessa et al. 2024, Severinenko et al. 2023).

$$CF_i = C_i/C_i,background \quad \ldots(8)$$

CF_i: contamination factor of a radionuclide.

C_i: measured activity of the radionuclide in bottom sediments at the sampling site (Bq kg^{-1}).

C_i, background: background activity of the same radionuclide determined for the reference (background) water body (Bq kg^{-1}).

The contamination levels are classified as follows: $CF < 1$, low or no contamination; $1 \leq CF < 3$, moderate contamination; $3 \leq CF < 6$, considerable contamination; $CF \geq 6$, high contamination.

2.6.2. Pollution Load Index (PLI)

The Pollution Load Index (PLI) provides an integrated assessment of overall environmental contamination and was calculated using Equation (9):

$$PLI = (CF_1 \times CF_2 \times \ldots \times CF_n)^{(1/n)} \quad \ldots(9)$$

PLI: pollution load index.

CF_1–CF_n: contamination factors of individual radionuclides.

n: number of radionuclides included in the calculation in the present study, namely ^{226}Ra, ^{232}Th, and ^{40}K.

2.6.3. Enrichment Factor (EF)

The Enrichment Factor (EF) was calculated using Equation (10) to evaluate the degree of anthropogenic influence on radionuclide concentrations in bottom sediments:

$$EF = (C_i/C_ref)_sample/(C_i/C_ref)_background \quad \ldots(10)$$

EF: enrichment factor

C_i: activity of the studied radionuclide in bottom sediments (Bq kg^{-1})

C_ref: activity of the reference element (Bq kg^{-1}); in this study, ^{40}K was used as a geochemically stable element.

sample: sampling point under study

background: background (reference) sampling point

3. RESULTS AND DISCUSSION

3.1. Activity Concentrations in Water and Bottom Sediments

Globally, the mean gross alpha activity in natural waters ranges from 0.4 to 0.8 Bq L^{-1}. According to international studies, alpha activity levels of 0.4–0.5 Bq L^{-1} may indicate radiological anomalies (Li et al. 2024). Gross alpha and beta activities are influenced by geological structure, mineral composition, and the intensity of anthropogenic activities (Ogundare et al. 2015). The accurate selection of background reference sites is therefore critical in ecological and geochemical investigations (Islam et al. 2015).

In the absence of historical baseline data for the study area, Lake Zhaksy–Zhalgyztau, located approximately 16 km from the mining sites, was designated as the background (reference) water body. This lake is used as a drinking water source by residents of the Shantobe settlement. The radiological characteristics of surface water samples are presented in Table 1.

Data analysis demonstrated that gross alpha activity substantially exceeded gross beta activity across most sampling sites. Gross alpha and beta activities ranged from 0.18 to 4.5 Bq L^{-1} and from 0.1 to 1.91 Bq L^{-1}, respectively. In the Balkhashin quarry, gross alpha activity reached 4.5 Bq L^{-1}, while gross beta activity was 1.91 Bq L^{-1}.

Along the Kutunguz River, a progressive downstream increase in both gross alpha and beta activities was observed. At Point 1 (approximately 500 m upstream of the presumed mine water discharge), gross alpha and beta activities were 0.2 and 0.27 Bq L^{-1}, respectively. These values increased to 1.81 and 0.79 Bq L^{-1} at Point 3. Elevated activities in the Balkhashin quarry reflect

Table 1: Radiological characteristics of water samples (Bq L^{-1}).

Sampling location	^{226}Ra	^{228}Ra	^{210}Po	^{210}Pb	^{234}U	^{238}U	Gross activity	
							alpha	beta
Kutunguz River, Point 1	0.11 ± 0.03	0.12 ± 0.05	0.041 ± 0.018	0.035 ± 0.027	0.071 ± 0.018	0.04 ± 0.011	0.2	0.27
Kutunguz River, Point 2	0.15 ± 0.06	0.14 ± 0.07	0.037 ± 0.012	0.065 ± 0.033	0.222 ± 0.042	0.139 ± 0.027	0.67	0.39
Kutunguz River, Point 3	0.15 ± 0.06	0.36 ± 0.17	0.133 ± 0.045	0.014 ± 0.005	0.448 ± 0.073	0.371 ± 0.059	1.81	0.79
Balkhashin Quarry	0.22 ± 0.04	1.54 ± 0.31	0.026 ± 0.009	0.037 ± 0.028	0.177 ± 0.034	0.131 ± 0.024	4.5	1.91
Lake Zhaksy–Zhalgyztau (Background)	0.11 ± 0.03	0.13 ± 0.05	0.028 ± 0.009	0.053 ± 0.03	0.05 ± 0.012	0.02 ± 0.009	0.18	0.1

radionuclide accumulation within this closed hydrological system.

According to the recommendations of the World Health Organization (World Health Organization 2004), the guideline screening levels for gross alpha and gross beta activity in drinking water are 0.55 Bq L^{-1} and 1.0 Bq L^{-1}, respectively. In accordance with the sanitary regulations of the Republic of Kazakhstan (Ministry of Healthcare of the Republic of Kazakhstan 2022), a more stringent level of 0.2 Bq L^{-1} is established for gross alpha activity, while the value of 1.0 Bq L^{-1} is retained for gross beta activity. Exceedance of these levels does not directly indicate non-compliance with radiation safety requirements but rather points to the need for further investigation. The final assessment is carried out based on an integral criterion that accounts for the cumulative contribution of individual radionuclides to the radiation dose. Taking these criteria into account, only point 1 on the Kutunguz River and the conditionally background site meet the screening requirements. At the remaining investigated sites, exceedances in gross alpha activity were recorded, whereas exceedance in gross beta activity was observed only in samples from the Balkhashin quarry.

Radionuclide concentrations in the Kutunguz River were as follows: ^{226}Ra: 0.11 ± 0.03–0.15 ± 0.06 Bq L^{-1}; ^{228}Ra: 0.12 ± 0.05–0.36 ± 0.17 Bq L^{-1}; ^{210}Po: 0.037 ± 0.012–0.133 ± 0.045 Bq L^{-1}; ^{210}Pb: 0.014 ± 0.005–0.065 ± 0.033 Bq L^{-1}; ^{234}U: 0.071 ± 0.018–0.448 ± 0.073 Bq L^{-1}; ^{238}U: 0.04 ± 0.011–0.371 ± 0.059 Bq L^{-1}.

The specific activities of uranium isotopes (^{234}U and ^{238}U) at Points 2 and 3 of the Kutunguz River, as well as in the Balkhashin quarry, were markedly higher than background levels. At Point 3, ^{234}U (0.448 Bq L^{-1}) and ^{238}U (0.371 Bq L^{-1}) exceeded background values by approximately 8–10 times. At the same location, ^{210}Po activity was 4.8 times higher

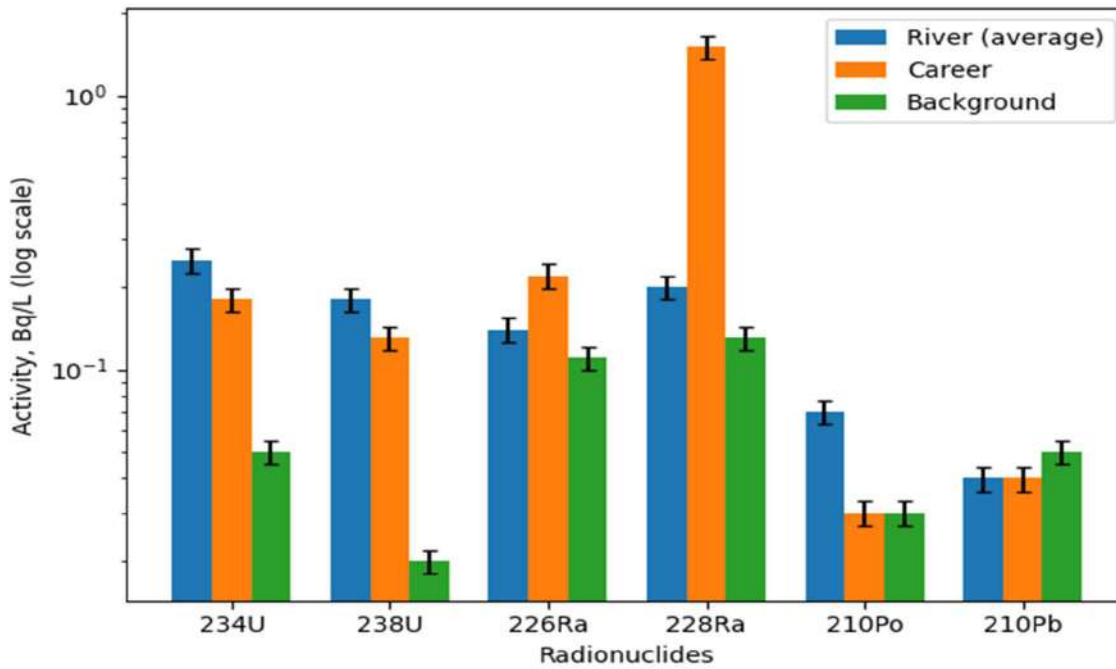


Fig. 3: Logarithmic distribution of radionuclide concentrations.

than background levels, whereas radium isotope activities remained close to background concentrations.

In the Balkhashin quarry, ^{228}Ra was the dominant radionuclide, with an activity of 1.54 Bq L^{-1}, more than 12 times higher than the background value. The average descending order of radionuclide concentrations was: Kutunguz River: ^{234}U > ^{238}U > ^{210}Po > ^{226}Ra > ^{228}Ra > ^{210}Pb; Balkhashin quarry: ^{228}Ra > ^{234}U > ^{238}U > ^{226}Ra > ^{210}Po > ^{210}Pb; Background site: ^{210}Pb > ^{234}U > ^{226}Ra > ^{228}Ra > ^{210}Po > ^{238}U (Fig. 3).

The principal contaminants of the Kutunguz River were identified as ^{234}U, ^{238}U, and ^{228}Ra, indicating contamination associated with the conserved Shantobe uranium mine. Although mean radionuclide concentrations exceeded background levels, they remained below guideline values established by the World Health Organization (World Health Organization 2004). In contrast, ^{228}Ra activity in the Balkhashin quarry exceeded the WHO guideline level.

Comparative analysis with international studies conducted under analogous environmental conditions indicates that radionuclide concentrations in the Kutunguz River fall within ranges reported elsewhere (Bakhur 2008, Mohuba et al. 2022, Duong et al. 2021). The ^{228}Ra concentration in the Balkhashin quarry is also comparable to or lower than values documented in quarry lakes at uranium mining sites, where activities up to 57.7 Bq L^{-1} have been reported (Rodriguez et al. 2024).

Table 2 presents radionuclide concentrations and specific effective activity in bottom sediments. The mean radionuclide concentrations decrease in the following order: ^{40}K > ^{226}Ra > ^{232}Th > ^{234}U > ^{238}U. Compared with international reference levels, the average concentrations remain below globally recommended values.

The specific activities of ^{232}Th and ^{40}K in bottom sediments remained within established natural background ranges (38–83 Bq kg^{-1} and 454–830 Bq kg^{-1}, respectively). In the Kutunguz River, ^{232}Th activity varied from 38.68 ± 5.39 to 73.57 ± 8.61 Bq kg^{-1} (Table 2), whereas the background site at Lake Zhaksy–Zhalgyztau exhibited a value of 83.1 ± 9.61 Bq kg^{-1}. The highest ^{40}K activity (829.67 ± 136 Bq kg^{-1}) was recorded at the background site.

This elevated ^{40}K activity is not associated with uranium–radium mineralization and reflects the lithogenic characteristics of the studied territory. Unlike uranium and radium isotopes, ^{40}K is not an indicator of technogenic impact related to uranium mining, and its elevated concentrations are caused by natural geochemical variability of rocks. In this regard, the considered site should be interpreted as a local background primarily for radionuclides of the uranium series, whereas variations in ^{40}K content may reflect the natural heterogeneity of the geological environment and do not reduce its significance as a comparative reference within the framework of this research.

These findings are consistent with data reported for reclaimed uranium mining areas in other regions of Northern Kazakhstan. For example, radiometric investigations near the Grachevskoye uranium deposit and the settlement of Saumalkol documented ^{40}K activities ranging from 587 to 689 Bq kg^{-1} (Subbotin et al. 2025). Overall, radionuclide activities in bottom sediments across the investigated sites are comparable to background values, with the exception of the Balkhashin quarry, where concentrations exceed local background levels but remain within global average ranges. The values measured in the Kutunguz River are broadly consistent with those reported for analogous environments worldwide (Table 3).

3.2. Distribution Coefficients (Kd) of Radionuclides in Bottom Sediments and Water

Bottom sediment samples were collected at the same points as the water samples, which made it possible to perform their comparative analysis. At all investigated sites, radionuclide concentrations in bottom sediments exceeded the corresponding values in the aqueous phase. The distribution coefficient (Kd), defined as the ratio of radionuclide activity in bottom sediments (Bq kg^{-1}) to their activity in water (Bq L^{-1}), varied within the ranges of 179–950 L kg^{-1} for ^{226}Ra, 42–926 L kg^{-1} for ^{234}U, and 39–1100 L kg^{-1} for ^{238}U.

Table 2: Radionuclide concentrations and specific effective activity in bottom sediments (0–15 cm layer, dry weight), Bq kg^{-1}.

Sampling location	^{226}Ra	^{232}Th	^{40}K	^{234}U	^{238}U	A_{eff}
Kutunguz River, Point 1	37.53 ± 5.88	38.68 ± 5.39	454.3 ± 100.5	9.8 ± 2.8	7.8 ± 2.2	128 ± 12.83
Kutunguz River, Point 2	37.03 ± 6.01	73.57 ± 8.61	763 ± 126.67	9.4 ± 2.6	7.4 ± 2.2	201 ± 17.07
Kutunguz River, Point 3	26.85 ± 4.8	41 ± 5.39	474 ± 95.65	21.6 ± 4.8	14.4 ± 3.2	123 ± 12.05
Balkhashin Quarry	209.03 ± 22.3	62.83 ± 8.52	828 ± 147.67	164 ± 24	144 ± 20	365 ± 28.23
Lake Zhaksy–Zhalgyztau (Background)	38.57 ± 6.35	83.1 ± 9.61	829.67 ± 136	14 ± 3.8	12 ± 2.8	221 ± 18.6
Global average level	8–160	4–130	100–700	4–140	4–140	

Table 3: Comparison of mean specific activities of ^{226}Ra, ^{232}Th, ^{40}K, and ^{238}U in bottom sediments with data from international studies (Bq kg^{-1}).

Country	Location	^{226}Ra	^{232}Th	^{40}K	^{238}U	Ref.
Korea	Korean watershed	31.0	58.1	911	26.8	(Kang et al. 2024)
Egypt	Lake Nasser	14.47	17.83	95.34	30.94	(El-Shlemy et al. 2025)
China	Wei River	21.8	33.1	833	–	(Lu et al. 2007)
Algeria	Ain Dalia Dam	–	0.27	286.61	4.34	(Hamed et al. 2024)
Bangladesh	Karnaphuli	35.9	65.5	272	37.2	(Chowdhury et al. 1999)
Pakistan	Gilgit and Ind	50.7	70.2	532	–	(Qureshi et al. 2014)
Turkey	Southern coast of Turkey	–	9.0	157.7	–	(Özmen et al. 2014)
USA	Reedy River	21.4	45.3	609	37.8	(Powell et al. 2007)
Kazakhstan	Kutunguz River	33.80	51.08	563.7	9.8	This study

Note: – no data

The highest Kd values were recorded in the Balkhashin quarry reservoir (up to approximately 950 L kg^{-1}), indicating a pronounced tendency for radionuclide accumulation in bottom sediments. At the same time, at points 2 and 3 of the Kutunguz River, Kd values for uranium remained relatively low (on the order of 40–50 L kg^{-1}), indicating its increased mobility in the aquatic environment.

The observed differences in Kd values may be associated with the hydrological characteristics of the studied systems. The Balkhashin quarry reservoir represents a relatively closed system with limited water exchange, where conditions are formed for the local accumulation of radionuclides. In contrast, the Kutunguz River is characterized by a flowing regime, in which radionuclides, including uranium isotopes, may be transported downstream.

Differences in the behavior of uranium and radium isotopes in flowing and closed aquatic systems are likely caused by the combined influence of hydrogeochemical factors. Under riverine conditions, an oxidizing environment and the presence of carbonate compounds may promote the formation of soluble uranyl–carbonate complexes, leading to decreased Kd values and increased migration capacity of uranium. In closed water bodies, by contrast, longer water residence time and the presence of sorption surfaces, such as clay minerals and iron and manganese oxides, may contribute to the fixation of radionuclides in bottom sediments. It should be noted that within the framework of the present research, the distribution coefficient is used primarily as a tool for comparative analysis. Therefore, the obtained results should be regarded as a preliminary quantitative-descriptive assessment reflecting general trends in the migration behavior of radionuclides under the studied conditions.

3.3. Assessment of Radiological Risk

The calculated radiological indices indicate that, at most sampling locations (Kutunguz River points 1–3 and the background site), radiation levels correspond to those typical of natural landscapes described in reports of the United Nations Scientific Committee on the Effects of Atomic Radiation (UNSCEAR 2000).

The radium equivalent activity (Ra_eq) values ranged from 121.98 Bq kg^{-1} to 362.63 Bq kg^{-1}, with an average of 206.94 Bq kg^{-1}. All values are below the reference level of 370 Bq kg^{-1} recommended by the United Nations Scientific Committee on the Effects of Atomic Radiation (UNSCEAR) (UNSCEAR 2000).

The absorbed gamma dose rate (ADR) varied from 56.93 to 169.05 nGy h^{-1}, with a mean of 96.32 nGy h^{-1}. This average exceeds the global mean background level of 60 nGy h^{-1} reported in the literature (Yi et al. 2020). Along the Kutunguz River, ADR values were close to global averages, with a slight increase at the background site (103 nGy h^{-1}). However, a substantially elevated value (169 nGy h^{-1}), approximately three times the global average, was recorded at the Balkhashin quarry.

The annual effective dose equivalent (AEDE) ranged from 69.8 to 207 μSv year^{-1}, with a mean value of 118 μSv year^{-1}. These values generally fall within the typical global outdoor exposure range (0.07–0.13 mSv year^{-1}) reported by UNSCEAR (UNSCEAR 2000). The mean value slightly exceeds the global reference level of 70 μSv year^{-1}; however, this reference represents an average natural background level rather than a regulatory limit. Importantly, all calculated AEDE values remain well below the public exposure limit of 1 mSv year^{-1} recommended by the International Commission on Radiological Protection (ICRP 1990). Therefore, the observed exposure levels can be considered within the range of natural variability and do not indicate a significant radiological health risk.

Both the internal (H_in) and external (H_ex) hazard indices for natural radiation should not exceed unity. In this study, the calculated values ranged from H_ex = 0.33–0.98

and H_in = 0.40–1.54 (Fig. 4). Most samples comply with the permissible limits for radiation exposure. However, the sample from the Balkhashin quarry approaches the threshold for the external index (H_ex = 0.98) and exceeds the internal index (H_in = 1.54), indicating a potential contribution from radon and its decay products if this material is used in enclosed spaces. The remaining sites fall within the safe radiation category and do not pose significant risk to the population. Particular attention should be given to the internal hazard index (H_in), the value of which in the Balkhashin quarry exceeds unity (H_in = 1.54). This indicator reflects the potential impact of internal exposure pathways, primarily due to radon (^{222}Rn) and its decay products formed from ^{226}Ra. Under these conditions, the main exposure pathway is inhalation. When such materials are used in enclosed or poorly ventilated spaces, the accumulation of radon in air is possible, which may lead to an increased radiation dose to the respiratory system. Additional exposure pathways may include inhalation of dust particles and incidental ingestion of contaminated material. It should be noted that the exceedance of H_in is local in nature and is caused by the characteristics of a closed hydrological system that promotes radionuclide accumulation. At the remaining sites, index values do not exceed unity, indicating a low level of internal radiological risk. At the same time, within the framework of this study, direct measurements of radon exhalation were not performed, which should be taken into account in the interpretation of the results and in planning further research.

At the background site (Lake Zhaksy–Zhalgyztau), the committed effective dose (CED) due to water ingestion was estimated at 0.14 mSv year^{-1}. The major contribution to the total dose comes from radium isotopes (^{228}Ra and ^{226}Ra), followed by ^{210}Po and ^{210}Pb, while uranium isotopes contribute only marginally. The obtained value exceeds the World Health Organization (WHO) (World Health Organization 2004) drinking water screening reference level of 0.1 mSv year^{-1}, but remains significantly below the public dose limit of 1 mSv year^{-1} recommended by the International Commission on Radiological Protection (ICRP 1990). It should be noted that the elevated value of CED at this site is not associated with technogenic impact but is likely caused by natural factors. Lake Zhaksy–Zhalgyztau represents a weakly flowing hydrological system, in which processes of radionuclide accumulation in the water mass and bottom sediments, as well as their secondary mobilization, are possible. The lake is fed by the Karasu River only in spring and early summer, and is drained by the Akkanburlyk River. Additional influence may be exerted by the geochemical composition of the underlying rocks enriched in radium, which leads to its increased input into the aquatic environment.

3.4. Ecological Contamination Indices

The analysis of ecological pollution indices of bottom sediments, including the Contamination Factor (CF), Pollution Load Index (PLI), and Enrichment Factor (EF), made it possible to identify spatial differences in radionuclide accumulation. It should be noted that these indices were originally developed for assessing contamination by heavy metals; therefore, their application to radionuclides is of a comparative nature and is aimed at identifying relative differences between sites rather than providing an absolute quantitative assessment of contamination.

The analysis of ecological contamination indices for bottom sediments, including the Contamination Factor (CF), Pollution Load Index (PLI), and Enrichment Factor

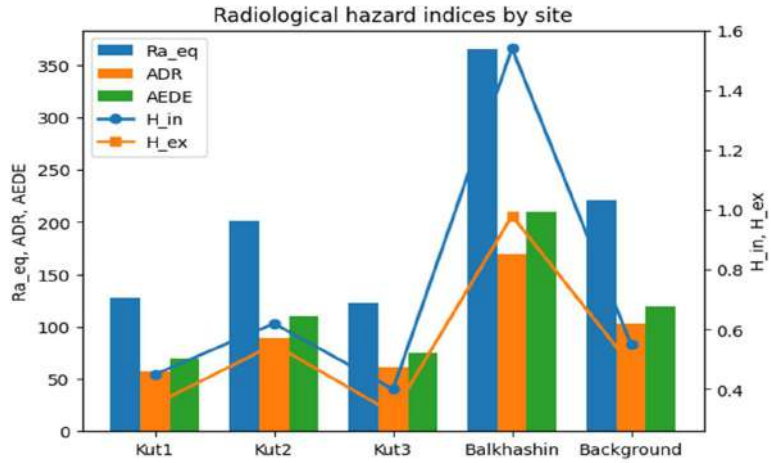


Fig. 4: Radiological hazard indices by sampling site.

(EF), yielded the following results. Calculation of the Contamination Factor (CF) demonstrated that bottom sediments of the Kutunguz River at all investigated sampling sites are characterized by low or negligible levels of contamination. The CF values for ^{226}Ra, ^{232}Th, and ^{40}K do not exceed unity, indicating conformity with background conditions and the absence of significant radionuclide accumulation within the river channel system. These findings suggest that, despite the presence of external anthropogenic influences, the flowing hydrological regime effectively prevents long-term retention and accumulation of radionuclides in bottom sediments.

In contrast, bottom sediments of the Balkhashin quarry exhibit a distinctly different ecological pattern. A considerable level of contamination was recorded for ^{226}Ra (CF $\approx$ 5.4), indicating selective accumulation of radium isotopes in bottom sediments and underscoring the role of closed water bodies as local geochemical sinks for radionuclides.

The Pollution Load Index (PLI) further corroborates these observations. PLI values below unity (PLI < 1) for all sampling points along the Kutunguz River indicate the absence of cumulative ecological loading and reflect a favorable ecological condition of bottom sediments. Conversely, exceedance of the threshold value at the Balkhashin quarry (PLI $\approx$ 1.6) reflects the integrated effect of radionuclide accumulation and supports classification of this site as ecologically impacted.

Analysis of the Enrichment Factor (EF) indicates that the distribution of ^{232}Th in all investigated sediments is primarily governed by natural lithogenic controls (EF < 1). For ^{226}Ra, only weak or minor enrichment was observed in the bottom sediments of the Kutunguz River, whereas moderate anthropogenic enrichment was identified in the Balkhashin quarry (EF $\approx$ 5.4), clearly reflecting the influence of historical uranium mining activities.

Overall, the ecological indices reveal pronounced spatial differentiation in contamination patterns: the flowing sections of the Kutunguz River correspond to background conditions, whereas the Balkhashin quarry demonstrates technogenic accumulation of radionuclides, particularly ^{226}Ra. These results highlight the high diagnostic value of the combined application of CF, PLI, and EF indices for assessing the ecological condition of bottom sediments and confirm their effectiveness, in conjunction with radiological hazard indices, for identifying long-term environmental consequences of anthropogenic impacts in uranium mining regions. However, methodological limitations in the application of CF, PLI, and EF to radionuclides should also be taken into account:

1. EF is calculated using ^{40}K as a reference element, which exhibits natural variability between sites, thereby influencing enrichment values.
2. Radionuclides are subject to radioactive decay, migration, and sorption processes, which are not considered in the classical formulations of these indices.

In this regard, the obtained indicators should be regarded as comparative, reflecting relative differences between sites rather than absolute measures of contamination.

3.5. Cluster Analysis

Cluster analysis (CA) enables identification of groups of objects sharing similar characteristics within a multivariate dataset (Alkufi et al. 2023). In the present study, hierarchical agglomerative clustering was performed using the Ward linkage method with Euclidean distance applied to standardized variables (Li et al. 2024). Sampling sites were grouped according to radionuclide composition and radiological parameters, allowing identification of spatial patterns in the distribution of natural radionuclides across the study area. Due to the limited number of observation points (n = 5), the results of the analysis are exploratory in nature and are intended to identify general spatial patterns rather than to provide rigorous statistical conclusions.

Cluster 1 includes the background reference site, Lake Zhaksy–Zhalgyztau (Lake-ZhZ). This site is characterized by low radiological indicators and minimal anthropogenic influence, confirming its suitability as a natural background control and reference location. In the principal component space (PCA; Fig. 5A), this sampling point exhibits weak association with radium and uranium vectors, reflecting the natural background conditions of the region.

Cluster 2 comprises samples collected from the Kutunguz River (Kut-1, Kut-2, Kut-3), forming a compact and internally consistent group. This clustering indicates similarity in

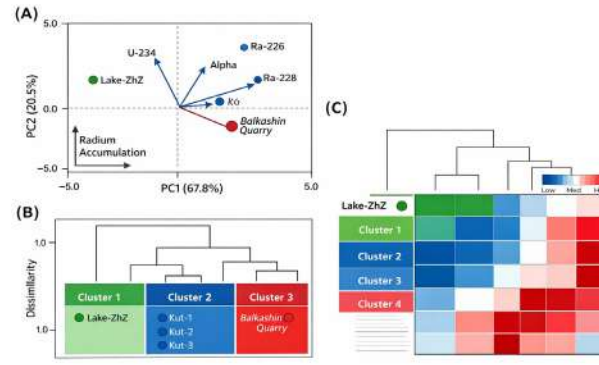


Fig. 5: Multivariate statistical analysis of the distribution of natural radionuclides at the investigated sampling sites: (A) principal component analysis (PCA), (B) hierarchical cluster analysis, (C) heatmap.

hydrochemical conditions and radionuclide behavior along the river continuum. The results suggest the presence of a common geochemical control and a potential influence of the conserved Shantobe uranium deposit, manifested through radionuclide migration, redistribution within the aquatic environment, and increasing concentrations along the downstream flow direction.

Cluster 3 consists of a single isolated sampling site, the Balkhashin quarry. Its clear separation from both the background and river clusters reflects the specific hydrogeochemical conditions of this closed water body. The heatmap (Fig. 5C) demonstrates elevated levels of radium isotopes and gross alpha activity, indicating radionuclide accumulation under conditions of restricted water exchange. Such isolation suggests localized radiological enrichment and the potential development of an area with increased radiation load under prolonged exposure or hydrological disturbance.

Overall, the results confirm the spatial heterogeneity of radionuclide distribution within the study area. Flowing systems contribute to partial equalization of concentrations, whereas closed water bodies create conditions for local accumulation of radionuclides and the formation of zones with increased radiation load.

4. CONCLUSIONS

This research presents a radioecological assessment of the state of surface waters and bottom sediments in the zone of influence of reclaimed and conserved uranium mining facilities in Northern Kazakhstan. The obtained results indicate a redistribution of radionuclides within the river system, manifested by an increase in gross alpha and beta activity, as well as certain individual radionuclides, downstream along the Kutunguz River. The highest exceedances of background values were recorded at points 2–3, where the activities of uranium isotopes (^{234}U and ^{238}U) reached levels 8–10 times higher, indicating their migration with the water flow.

Elevated radionuclide concentrations in the Balkhashin quarry reservoir, in particular the predominance of ^{228}Ra, reflect processes of their accumulation under conditions of a closed hydrological system. Analysis of distribution coefficients (Kd) demonstrated high mobility of uranium isotopes in the river system and their accumulation in bottom sediments under conditions of limited water exchange. At most sites, radiation exposure levels comply with international standards; however, in the area of the Balkhashin quarry, local exceedances of dose indicators were identified.

For the background site, Lake Zhaksy–Zhalgyztau, the estimated effective dose from water consumption was 0.14 mSv year^{-1}, which slightly exceeds the WHO guideline level but remains below the permissible limit. The main contribution to the dose load is made by radium isotopes.

The obtained data indicate the need for further research aimed at refining the mechanisms of radionuclide migration and require additional confirmation based on expanded observations and quantitative comparative analysis.

5. REFERENCES

Akuo Ko, E.O., Otoo, F., Glover, E.T., Amponsem, E., Tettey Larbi, L., Ganbaatar, T., Csordás, A., Shahrokhi, A. and Kovács, T., 2025. Radiological implications of industrial activities on soil and water in artisanal gold-mining regions of Atiwa West. *Applied Sciences*, 15(18), 9857. [DOI]

Alkufi, A.A., Kadhim, S.A., Alaboodi, A.S. and Alhous, S.F., 2023. Effects of natural radioactivity of some chemical and organic fertilizers on gonads in Iraqi Kufa markets. *Nature Environment and Pollution Technology*, 22(4), pp. 2055-2063. [DOI]

Bakhur, A.E., 2008. Scientific and methodological foundations of radioecological assessment of the geological environment. PhD Thesis, Moscow, Russia. Available at: https://www.dissercat.com/content/nauchno-metodicheskie-osnovy-radioekologicheskoi-otsenki-geologicheskoi-sredy-0

Beretka, J. and Mathew, P.J., 1985. Natural radioactivity of building materials. *Health Physics*, 48(1), pp. 87–95. Available at: https://scholar.google.com/scholar?q=Natural+radioactivity+of+building+materials+Beretka+Mathew

Bersimbaev, R.I. and Bulgakova, O., 2015. The health effects of radon and uranium in Kazakhstan. *Genes and Environment*, 37, 18. [DOI]

Bessa, A.Z.E., Koutchouo, M.G., Doumo, E.P.E., Manishimwe, N.K., Tanantsap, R.J.N., Djoban, J.G.T., Bekonga Gouott, B.S. and Armstrong-Altrin, J.S., 2024. Assessment of heavy metals and radionuclides (U and Th) contamination, and source identification of the Lékié Watershed sediments, Cameroon. *Geosystems and Geoenvironment*, 3(1), 100249. [DOI]

Brzhanov, R.T., Sofronova, L.I. and Abramova, S.A., 2020. Analysis and technology to reduce the impact of tailings on the ecology of local water bodies. *IOP Conference Series: Materials Science and Engineering*, 962(4), 042063. [DOI]

Chowdhury, M.I., Alam, M.N. and Hazari, S.K.S., 1999. Radionuclides in sediments and soils of Bangladesh. *Applied Radiation and Isotopes*, 51(6), pp. 747–755. [DOI]

Committee for Technical Regulation and Metrology of the Republic of Kazakhstan, 2006. ST RK 1545-2006. Radiation control. Sampling of surface and wastewater. Kazakhstan. [in Russian]. Available at: https://prg.kz/Document/?doc_id=30527431

Duong, V.-H., Nguyen, T.-D., Hegedus, M., Kocsis, E. and Kovacs, T., 2021. Study of well waters from high-level natural radiation areas in northern Vietnam. *International Journal of Environmental Research and Public Health*, 18, 469. [DOI]

Dyussembayeva, M., Aidarkhanova, A., Tashekova, A., Shakenov, Y., Kolbin, V. and Merkel, A., 2025. Assessment of contamination of natural waters with radionuclides and heavy metals: the case of Karabulak Creek at the Semipalatinsk Test Site. *PLoS ONE*, 20(2), e0310833. [DOI]

El-Shlemy, E.S., Gad, A., El Feky, M.G., Mahmoud, A.-M.A., El-Sayed, O. and Abed, N.S., 2025. Potentially toxic elements and natural radioactivity in Nasser Lake sediments: environmental risks in a key Egyptian freshwater lake. *Toxics*, 13(9), 745. [DOI]

Galhardi, J.A., García-Tenorio, R., Bonotto, D.M., Francés, I.D. and Motta, J.G., 2017. Natural radionuclides in plants, soils and sediments affected

by U-rich coal mining activities in Brazil. *Journal of Environmental Radioactivity*, 177, pp. 37–47. [DOI]

GOST 17.1.5.01-80, 1980. Nature protection. Hydrosphere. General requirements for sampling bottom sediments of water bodies for pollution analysis. USSR. Available at: https://prg.kz/Document/?doc_id=37927607

Government of the Republic of Kazakhstan, 2001. On approval of the Program for the conservation of uranium mining enterprises and elimination of the consequences of uranium deposit development for 2001–2010. Available at: https://adilet.zan.kz/rus/docs/P010001006_

Håkanson, L., 1980. An ecological risk index for aquatic pollution control: a sedimentological approach. *Water Research*, 14(8), pp. 975–1001. [DOI]

Hamed, Y., Ayadi, Y., Hadji, R., Ben Saad, A., Gentilucci, M. and Elaloui, E., 2024. Environmental radioactivity, ecotoxicology (^{238}U, ^{232}Th and ^{40}K) and potentially toxic elements in water and sediments from North Africa dams. *Sustainability*, 16(2), 490. [DOI]

ICRP, 1990. *Recommendations of the International Commission on Radiological Protection*. ICRP Publication 60. Pergamon Press, Oxford, UK. Available at: https://www.icrp.org/publication.asp?id=icrp%20publication%2060

Idrisheva, Z., Ostolska, I., Skwarek, E., Daumova, G., Wiśniewska, M., Toktaganov, T. and Kozhakhmetov, Y., 2025. Evaluation of long-term environmental impact and radiological risks at a former thorium and rare earth site in north-eastern Kazakhstan. *Sustainability*, 17, 8569. [DOI]

International Organization for Standardization 2019. *ISO/IEC 17025:2019 – General requirements for the competence of testing and calibration laboratories*. ISO, Geneva.

Islam, M.S., Ahmed, M.K., Raknuzzaman, M., Mamun, M.H.-A. and Islam, M.K., 2015. Heavy metal pollution in surface water and sediment: a preliminary assessment of an urban river in a developing country. *Ecological Indicators*, 48, pp. 282–291. [DOI]

Kamunda, C., Mathuthu, M. and Madhuku, M., 2016. An assessment of radiological hazards from gold mine tailings in Gauteng Province, South Africa. *International Journal of Environmental Research and Public Health*, 13, 138. [DOI]

Kang, T.-W., An, M., Han, Y.-U., Yang, H.J., Kang, T., Jung, S., Lee, W.-S. and Park, W.-P., 2024. Activity concentration of natural radionuclides in surface sediments of major river watersheds in Korea and assessment of radiological hazards. *Water*, 16(20), 2897. [DOI]

Li, H., Wang, Q., Zhang, C., Su, W., Ma, Y., Zhong, Q., Xiao, E., Xia, F., Zheng, G. and Xiao, T., 2024. Geochemical distribution and environmental risks of radionuclides in soils and sediments runoff of a uranium mining area in South China. *Toxics*, 12(1), 95. [DOI]

Lu, X., Zhang, X. and Wang, F., 2007. Natural radioactivity in sediment of Wei River, China. *Environmental Earth Sciences*, 53(7), pp. 1475–1481. [DOI]

Ministry of Healthcare of the Republic of Kazakhstan, 2022. On the approval of hygienic standards for ensuring radiation safety. Order No. KR DSM-71, 2 August 2022. Available at: https://adilet.zan.kz

Mohuba, S.C., Abiye, T. and Nhleko, S., 2022. Evaluation of radionuclide levels in drinking water near gold mines and tailings. *Minerals*, 12, 1370. [DOI]

Ogundare, F.O. and Adekoya, O.I., 2015. Gross alpha and beta radioactivity in soils and water around a steel processing facility. *Journal of Radiation Research and Applied Sciences*, 8(3), pp. 411–417. [DOI]

Özmen, S.F., Cesur, A., Boztosun, I. and Yavuz, M.E., 2014. Radionuclides in beach sands of Turkey. *Radiation Physics and Chemistry*, 103, pp. 37–44. [DOI]

Powell, B.A., Hughes, L.D., Soreefan, A.M., Falta, D., Wall, M. and DeVol, T.A., 2007. Elevated concentrations of primordial radionuclides in sediments from the Reedy River and surrounding creeks in Simpsonville, South Carolina. *Journal of Environmental Radioactivity*, 94(3), pp. 121–128. [DOI]

Qureshi, A.A., Tariq, S., Din, K.U. and Manzoor, S., 2014. Evaluation of excessive lifetime cancer risk due to natural radioactivity in the river sediments of Northern Pakistan. *Journal of Radiation Research and Applied Sciences*, 7(4), pp. 438–447. [DOI]

Raji, I.B., Hoffmann, E., Ngie, A. and Winde, F., 2021. Assessing uranium pollution levels in the Rietspruit River, South Africa. *International Journal of Environmental Research and Public Health*, 18, 8466. [DOI]

Rodriguez, V.G., Majumdar, A., Meza, I., Corcoran, L., Pierson, A., Gagnon, K., Cano, C., Ali, A.-M.S., Shuey, C.M., Jojola, G., Tan, W., Aprahamian, A., Cerrato, J.M. and Burns, P.C., 2024. Radiological analyses of ^{226}Ra and ^{238}U in surface water and sediments from the Jackpile Member of the Morrison Formation, Pueblo of Laguna, New Mexico. *Environmental Science & Technology*, 58(18), pp. 7879–7889. [DOI]

Saifulina, E., Janabayev, D., Kashkinbayev, Y., Shokabaeva, A., Ibrayeva, D. and Aumalikova, M., 2023. Epidemiology of somatic diseases near uranium mining enterprises in Kazakhstan. *Healthcare*, 11, 804. [DOI]

Severinenko, M.A., Solodukhin, V.P., Djenbaev, B.M., Lennik, S.G., Zholboldiev, B.T. and Snow, D.D., 2023. Occurrence of radionuclides and hazardous elements in the transboundary river basin Kyrgyzstan–Kazakhstan. *Water*, 15(9), 1759. [DOI]

Subbotin, S., Krivitskiy, P., Larionova, N., Toporova, A., Kunduzbayeva, A., Turchenko, D., Tleukanova, Z. and Aidarkhanova, A., 2025. Assessment of the radiological situation near a mothballed uranium mining facility in North East Kazakhstan. *Scientific Reports*, 15, 16426. [DOI]

UNSCEAR, 2000. *Sources, Effects and Risks of Ionizing Radiation*. United Nations, New York, USA. Available at: https://www.unscear.org/unscear/en/publications/2000_1.html

World Health Organization, 2004. *Guidelines for Drinking-Water Quality*. WHO, Geneva, Switzerland. Available at: https://iris.who.int/server/api/core/bitstreams/b437749a-43f7-472f-a6d9-42596e8ac0ae/content

Wu, Y., Wang, Y. and Xie, X., 2014. Occurrence, behavior and distribution of high levels of uranium in shallow groundwater at Datong Basin, China. *Science of the Total Environment*, 472, pp. 809–817. [DOI]

Yi, L., Gao, B., Liu, H., Zhang, Y., Du, C. and Li, Y., 2020. Characteristics and assessment of toxic metal contamination in surface water and sediments near a uranium mining area. *International Journal of Environmental Research and Public Health*, 17(2), 548. [DOI]

Zhumadilov, K., Ivannikov, A., Kassymzhanov, M., Bagramova, A., Zhantore, I., Samal, S., Stepanenko, V., Khailov, A. and Hoshi, M., 2025. Estimation of radiation doses of population residing nearby area of uranium ore mining and processing in Kazakhstan by tooth enamel EPR spectroscopy. *Environmental Challenges*, *18*, p.101098. [DOI]

Nature Environment and Pollution Technology
An International Quarterly Peer-Reviewed Open Access Journal

p-ISSN: 0972-6268 | e-ISSN: 2395-3454 Vol. 25 | No. 4 | Article ID B4411 | 2026

RESEARCH ARTICLE https://doi.org/10.46488/NEPT.2026.v25i04.B4411 OPEN ACCESS

Biological and Ecotoxicological Responses of *Daphnia pulex* to 2,4-D and Malathion-Contaminated Laboratory Microcosms

Samiksha Agarwal and Saltanat Parveen
Limnology Research Laboratory, Department of Zoology, Aligarh Muslim University, Aligarh 202002, Uttar Pradesh, India
Corresponding author: Samiksha Agarwal; samikshaagarwal28724@gmail.com

ARTICLE HISTORY

Received: 15-11-2025
Revised: 17-02-2026
Accepted: 28-02-2026

KEYWORDS

Ecotoxicological responses
Daphnia pulex
2,4-D herbicide
Malathion insecticide
Pesticide contamination
Laboratory microcosm
Aquatic toxicology
Environmental risk assessment

CITE THIS ARTICLE

Agarwal, S. and Parveen, S. 2026. Biological and ecotoxicological responses of *Daphnia pulex* to 2,4-D- and Malathion-contaminated laboratory microcosms. *Nature Environment and Pollution Technology,* 25(4), B4411. https://doi.org/10.46488/NEPT.2026.v25i04.B4411

COPYRIGHT & LICENCE

© 2026 The Authors
Open Access under CC BY 4.0.

PUBLISHED BY
TECHNOSCIENCE PUBLICATIONS

ABSTRACT

Industrialization, urbanization, and agricultural practices have substantially increased the accumulation of contaminants in the environment, often adversely affecting nontarget aquatic species. Cladoceran species are considered valuable bioindicators in ecotoxicity studies because they are easy to culture, have transparent bodies, and are highly sensitive to chemical pollution. This study aimed to determine the acute and chronic toxicity of two selected pesticides, namely Malathion 50 EC (a.i., Malathion) and 2,4-D ethyl ester 38% EC (a.i., 2,4-D), to *Daphnia pulex*. The 24- and 48-h median lethal concentration (LC_{50}) values for 2,4-D were 3.5 and 2.3 mg L^{-1}, respectively, and those for Malathion were 0.76 and 0.25 µg L^{-1}, respectively. Malathion reduced clutch size, heart rate, population density (individuals per liter), and body length in *D. pulex*. As the 2,4-D concentration increased, heart rate and clutch size decreased significantly compared with those in the control group. However, body length and population density were not significantly affected at lower concentrations of 2,4-D during chronic exposure. Approximately 20% of the daphnids in the exposure groups switched to producing ephippia, resulting in fewer newborn individuals. The study suggests that *D. pulex* is a reliable bioindicator of toxicity caused by sublethal doses of Malathion and 2,4-D. However, its sensitivity varied over the 11-day exposure period. The findings indicate that the tested pesticides significantly affected the evaluated parameters of *D. pulex*.

1. INTRODUCTION

Water bodies are often the ultimate destination for waste products released into the environment, and agricultural activities contribute significantly to their degradation (de Deus & Bakonyi 2012). Pesticides are chemical substances used to control or eliminate pests such as insects, rodents, fungi, and weeds. Approximately 1.8 billion people worldwide are engaged in agriculture, and most rely on chemical pesticides to protect their crops (Alavanja 2009). Pesticides applied to agricultural fields are often leached into nearby water bodies, causing toxicity to aquatic organisms. These toxic pesticides also contribute to lake aging by causing eutrophication (Scholz et al. 2012). Over the past century, pesticides have become a crucial part of agricultural systems worldwide, leading to a significant increase in crop yields and food production (Alexandratos & Bruinsma 2012). Although pesticides are primarily designed to target pests, some non-target plant and animal species are also severely affected by their application (Jayaraj et al. 2016). A nonselective herbicide such as glyphosate reduces the growth of nitrogen-fixing bacteria in soil (Santos & Flores 1995), whereas 2,4-D hinders the conversion of ammonia

to nitrates by soil bacteria (Frankenberger & Tabatabai 1991).

Cladocerans, also known as water fleas, are a group of microcrustaceans (phylum Arthropoda) ranging from 0.2 to 6 mm in body size (Thackeray 2022, Agarwal et al. 2026). *D. pulex* is a small crustacean and a commonly occurring zooplankton species. It has a generation time of 3–10 days (Harrow 2020). *D. pulex* is the most common and widely distributed cladoceran species, ranging from approximately 0.2 to 5.0 mm in body size. It is an excellent model organism for toxicological studies because of its small size, ease of cultivation, short life cycle, and high sensitivity to pollutants such as pesticides and heavy metals. It is an important component of freshwater ecosystems and food webs and occurs in a wide range of aquatic habitats.

The present study aimed to determine the acute and chronic toxicity of sublethal concentrations of two pesticides, namely 2,4-D ethyl ester 38% EC (a.i., 2,4-D) and Malathion 50 EC (a.i., Malathion), based on selected biological characteristics of *D. pulex*. The 24 and 48 h LC_{50} values for 2,4-D were 3.5 and 2.3 mg L^{-1}, respectively, and those for Malathion were 0.76 and 0.25 µg L^{-1}, respectively. Malathion reduced the clutch size (number of eggs per female), heart rate (bpm), population density (individuals per liter), and body length (mm) of *D. pulex*. Exposure to 2,4-D also caused significant decreases in heart rate and clutch size with increasing concentration compared with those in the control group. However, body length and population density were not significantly affected at lower concentrations of 2,4-D during chronic exposure. Approximately 20% of the daphnids in the exposure groups switched to producing ephippia, resulting in fewer newborn individuals. The study suggests that *D. pulex* is a reliable bioindicator of toxicity caused by sublethal doses of the selected pesticides. However, the sensitivity of *D. pulex* varied over the 11-day exposure period. These findings highlight the significant effects of the tested pesticides on the physiological, behavioral, and reproductive parameters of *D. pulex* and the need for careful monitoring of these substances in aquatic environments. Many chronic toxicity studies focus on single compounds, single endpoints (often reproduction only), or standard model species such as *Daphnia magna*. This research provides comparative, mechanistic, and species-specific insights that improve the interpretation of ecological risk.

2. MATERIALS AND METHODS

2.1. Culture and Maintenance of *D. pulex*

The experiments were conducted in the laboratory. The daphnids used in the tests were collected manually from the Yamuna River using a plankton net with a mesh size of 60 µm and were cultured in a 5 L plastic tub containing 4 L of reverse osmosis (RO) water under suitable environmental conditions. Because *Daphnia pulex* is a sensitive organism, the culture was maintained at 22 ± 2 °C with a 14:10 h light/dark photoperiod. The pH of the culture water was maintained at 7.8–8.0, and the dissolved oxygen concentration was maintained between 4.5 and 5.0 mg L^{-1} by gently agitating the culture with a glass rod two or three times a day. Alkalinity and hardness were 145 ± 5 and 110 ± 10 mg L^{-1}, respectively. The cultured cladocerans were fed once daily with a 5 mL mixture of *Chlorella vulgaris* (1×10^6 cells mL^{-1}) and yeast (*Saccharomyces cerevisiae*), prepared by dissolving a pinch of dry yeast powder in 200 mL of warm water containing approximately 1,500 cells mL^{-1} in a 1:1 ratio. The culture medium was partially replaced with fresh RO water twice a week to minimize chloride buildup during the culture period (Woodley et al. 2023, Long Eco Water 2025).

2.2. Chemicals

Commercial formulations rather than technical-grade active ingredients were deliberately chosen to simulate field exposure. 2,4-D ethyl ester 38% EC (trade name Noweed, Batch No. N001, 38 g a.i. per 100 mL, Northern Insecticides Pvt. Ltd., Muzaffarnagar, India) and Malathion 50 EC (trade name Mal-50, Batch No. MAL-2306, 50 g a.i. per 100 mL, GreenChem Agro, Ghaziabad, India) were used in the study. Both products were purchased from a licensed pesticide retailer and stored at 4 °C in the dark. The active ingredient contents were verified against the manufacturers' Certificates of Analysis ($\geq$98% of the label claim). Stock solutions were prepared in deionized water immediately before each test; therefore, the nominal concentrations refer to the active ingredients (a.i.).

2.3. Selection of Test Organisms

For the experiment, non gravid and active individuals from the F1 broods were selected and were examined under a stereomicroscope. Neonates bearing ephippia or showing morphological anomalies were discarded because ephippia formation indicates prior stress.

2.4. Range-Finding Test

A preliminary range-finding test was conducted to determine the range of lethal concentrations. For 2,4-D ethyl ester 38% EC, test solutions of 50, 20, and 10 mg L^{-1} were prepared from a 100 mg L^{-1} stock solution. For Malathion 50 EC, test solutions of 20, 10, and 2 µg L^{-1} were prepared from a 50 µg L^{-1} stock solution. Each concentration and the control were tested in triplicate, with 10 neonates per

replicate. After 24 h, 100% mortality was observed at the two highest concentrations of each pesticide, whereas the lowest concentration resulted in partial mortality. These results were used to determine the concentration ranges for the definitive LC_{50} tests according to the Organisation for Economic Co-operation and Development (OECD) Test No. 202 (OECD 2004).

2.5. Acute Toxicity Test

For the definitive 48 h acute test, six concentrations of 2,4-D (0.50, 1.00, 3.00, 5.00, 7.00, and 10.00 mg L^{-1}) and six concentrations of Malathion (0.06, 0.10, 0.20, 0.50, 0.80, and 5.00 µg L^{-1}), plus a control, were prepared following OECD Test No. 202 (OECD 2004). All dilutions were made in American Society for Testing and Materials (ASTM) hard-water medium (reconstituted; hardness, 160 mg $CaCO_3$ L^{-1}) to enhance reproducibility. Three replicates were maintained for each concentration, with 20 individuals (<24 h old) per replicate in 500 mL glass beakers containing 80 mL of test solution. Because of the short test duration, the animals were not fed, and the test medium was not renewed. The tests were conducted at 20 ± 2 °C under constant illumination (600 lx). Mortality and immobility were assessed at 24 and 48 h. Daphnids that failed to swim within 15 s of gentle agitation were considered immobile. Water-quality parameters, including pH, dissolved oxygen (DO), conductivity, and hardness, were measured at 0 and 48 h.

2.6. Chronic Toxicity Test

Four sublethal concentrations, selected as fractions of the 48-h LC_{50}, and a control were tested for 11 days using a modified OECD 211 protocol. For 2,4-D, the concentrations were 0.05, 0.10, 0.50, and 1.00 mg L^{-1}, whereas for Malathion, they were 0.04, 0.06, 0.08, and 0.10 µg L^{-1}. Each concentration and the control comprised 20 individually housed neonates in 50 mL glass vials containing 40 mL of test solution. The medium was renewed every 48 h and freshly prepared from the stock solution. During the 11-day exposure period, the animals were fed daily with 0.5 mL of *C. vulgaris* suspension (approximately 5×10^4 cells) and yeast solution, and debris was carefully removed at each medium renewal.

The initial number of individuals per treatment was n = 20. Because of mortality during chronic exposure, the final sample size used for each endpoint was 18 ± 1. The recorded endpoints included heart rate, clutch size, body size, and population size (total number of individuals). Heart rate was measured in beats per minute (bpm) using a digital camera at 100× magnification. Individual organisms were acclimated for 5 min before recording. Heartbeats were counted for 1 min, and each individual was measured three times; the mean value was used for analysis. Video recordings were analyzed in slow motion to improve accuracy. All recordings were conducted at 20 ± 1 °C under controlled laboratory conditions to minimize temperature-related variability. To reduce observer bias, heartbeats were counted independently by two observers, and the average value was used. Clutch size was recorded as the number of eggs per female. Body size was measured in ImageJ as the dorsal length from the top of the head to the base of the tail spine. Population size was recorded as the total number of individuals.

2.7. Statistical Analysis

The 24- and 48-h LC_{50} values and their 95% fiducial limits were estimated by probit regression (GraphPad Prism 10, log-probit model; slope ± standard deviation [SD] reported). Goodness of fit was assessed using the χ^2 test provided in the software. For the chronic test, data normality was assessed using the Shapiro–Wilk test, and homogeneity of variances was assessed using Levene's test. Significant differences between the control and treatment groups for each endpoint were analyzed using one-way analysis of variance (ANOVA), followed by Dunnett's post hoc test ($\alpha = 0.05$). When the assumptions were violated, the data were log-transformed. All statistical analyses were performed using GraphPad Prism 10, and values are reported as the mean ± SD unless stated otherwise.

3. RESULTS AND DISCUSSION

3.1. Acute Toxicity

For Malathion 50 EC, the concentration–response curves were steep, yielding 24 and 48 h LC_{50} values of 0.76 µg L^{-1} (95% confidence limits, 0.43–1.4 µg L^{-1}) and 0.25 µg L^{-1} (95% confidence limits, 0.17–0.35 µg L^{-1}), respectively (Fig. 1(a)). In contrast, exposure to 2,4-D ethyl ester 38% EC produced 24 and 48 h LC_{50} values of 3.5 mg L^{-1} (95% confidence limits, 2.65–7.56 mg L^{-1}) and 2.3 mg L^{-1} (95% confidence limits, 2.0–5.04 mg L^{-1}), respectively (Fig. 1(b)). Thus, on an active-ingredient basis, Malathion was several orders of magnitude more lethal than 2,4-D under the same test conditions.

3.2. Chronic Toxicity (11 d)

3.2.1. 2,4-D Ethyl Ester 38% EC

Sublethal 11-day exposures corroborated the acute patterns. When daphnids were reared at sub-mg L^{-1} concentrations of 2,4-D, their physiological and reproductive traits declined only at the upper end of the range. Heart rate decreased steadily with increasing concentration, from a control

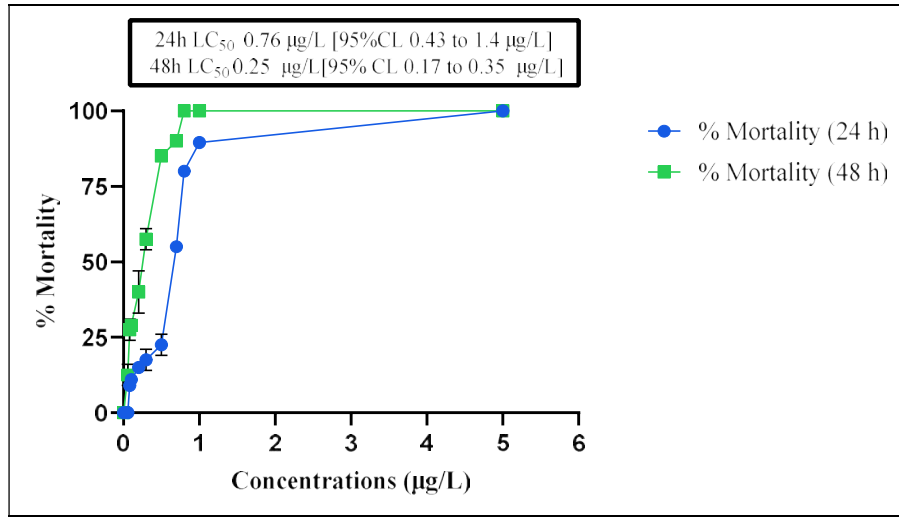


Fig. 1(a): 24 and 48 h LC_{50} values with 95% confidence limits (CL) for the insecticide Malathion 50 EC (a.i., Malathion).

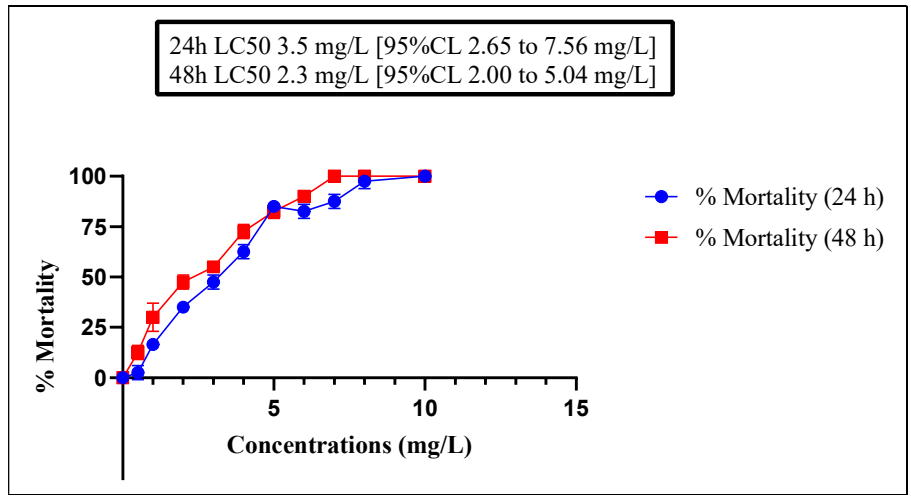


Fig. 1(b): 24 and 48 h LC_{50} values with 95% CL for the herbicide 2,4-D ethyl ester 38% EC (a.i., 2,4-D).

mean of 195 ± 9.4 bpm to 124 ± 8.1 bpm at 1.00 mg L^{-1} (Fig. 2(a)). Clutch size also decreased at the highest concentration, reaching an average of 12 ± 1.2 neonates per brood at 1.00 mg L^{-1} compared with 16.5 ± 1.2 in the control (Fig. 2(b), Fig. 4(a)). Body length was significantly reduced at the highest concentration, reaching an average of 1.628 ± 0.002 mm at 1.00 mg L^{-1} compared with 1.645 ± 0.008 mm in the control. Total population output decreased by 18% to 1,267 ± 6.4 individuals L^{-1} at the highest concentration (Fig. 2(c) and 2(d)). Control mortality did not exceed 10%.

3.2.2. Malathion 50 EC

Malathion caused more pronounced subchronic effects. Heart rate decreased progressively across the exposure series and reached 98 ± 8.6 bpm at 0.10 µg L^{-1}, approximately half the control value (Fig. 3(a)). Clutch size decreased at every concentration, reaching 4 ± 0.8 neonates per brood at 0.10 µg L^{-1} (Fig. 3(b), Fig. 4(b) and (c)). Body length was significantly reduced at the two highest concentrations, reaching an average of 1.268 ± 0.028 mm at 0.10 µg L^{-1} compared with 1.645 ± 0.008 mm in the control (Fig. 3(c)). Population size followed the same trend, decreasing by approximately 42% at 0.06 µg L^{-1} and by 70% to 450 ± 5.5 individuals L^{-1} at 0.10 µg L^{-1} (Fig. 3(d)). Together, these data indicate that Malathion impaired cardiac activity, growth, reproduction, and overall population performance in *D. pulex* at concentrations several orders of magnitude lower than those required to produce comparable effects with 2,4-D.

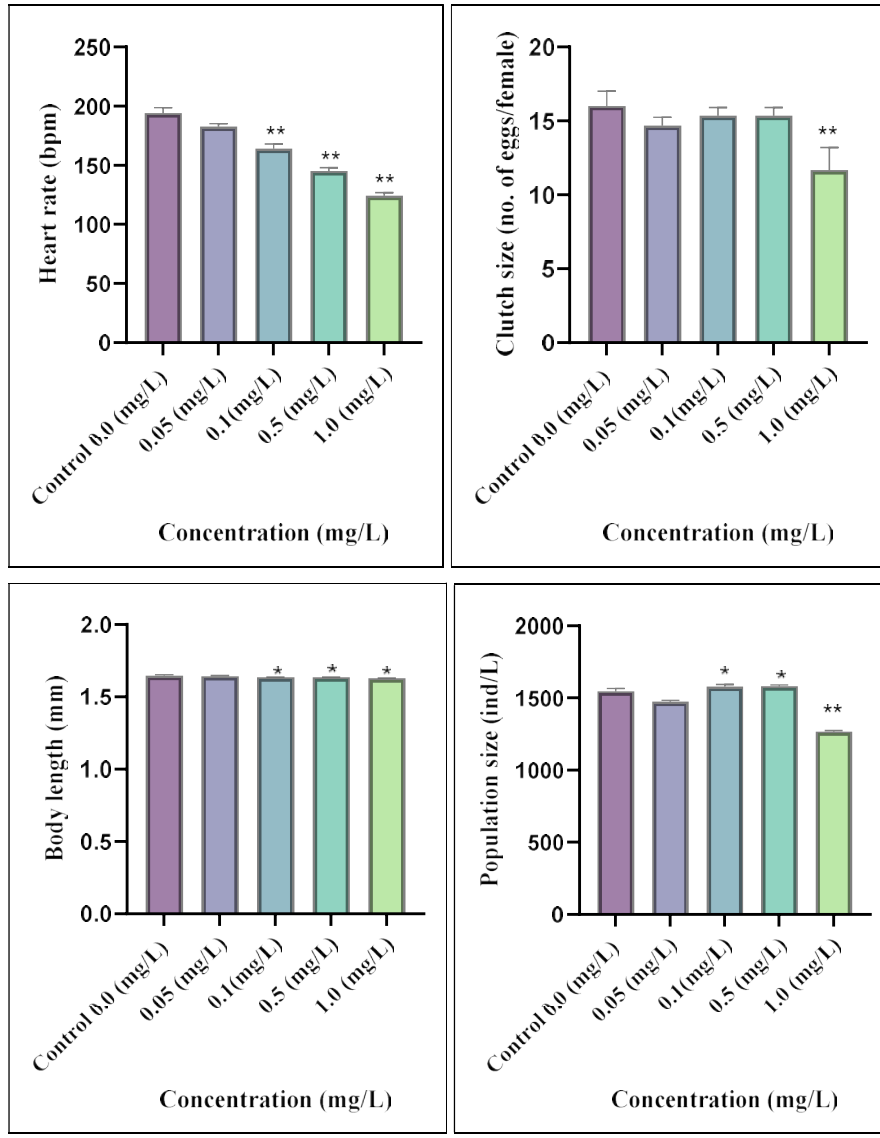


Fig. 2: Heart rate, clutch size, body length, and population size of *D. pulex* (mean ± SD) after 11 days of exposure to different concentrations of 2,4-D ethyl ester 38% EC (a.i., 2,4-D) in chronic toxicity tests. Asterisks indicate significant differences from the control: $*p < 0.05$ and $**p < 0.001$ (Dunnett's test, 18 degrees of freedom).

3.3. Discussion

The present study was a hazard-based laboratory assessment rather than a realistic exposure scenario and compared the acute and chronic toxicity of two widely used formulations, Malathion 50 EC and 2,4-D ethyl ester 38% EC, to *D. pulex* under controlled laboratory conditions. The data show that Malathion was several orders of magnitude more toxic than 2,4-D in terms of both short-term lethality (24–48 h LC_{50}) and longer-term sublethal impairment of growth, reproduction, and population output.

3.3.1. Acute Toxicity in the Context of Published Ranges

The 24 h LC_{50} of 0.76 µg L^{-1} and 48 h LC_{50} of 0.25 µg L^{-1} for Malathion place *D. pulex* within the U.S. Environmental Protection Agency (US EPA) (2006) highly toxic category (<1 µg L^{-1}) and align with the 1–10 µg L^{-1} range reported for *D. magna* and *M. macrocopa* (Wong et al. 1995, Tomlin 2006, Relyea 2009). In contrast, the 2,4-D LC_{50} values of 3.5 mg L^{-1} (24 h) and 2.3 mg L^{-1} (48 h) lie toward the lower end of the broad 20–422 mg L^{-1} range compiled by the US EPA (2019) for cladocerans and are substantially lower than historical values reported for 2,4-D esters in *D. magna*, for example, 132 mg L^{-1} (EFSA 2014) and 416 mg L^{-1} (Milam et al. 2005). Rassoulzadegan and Akyurtlakli (2002) reported

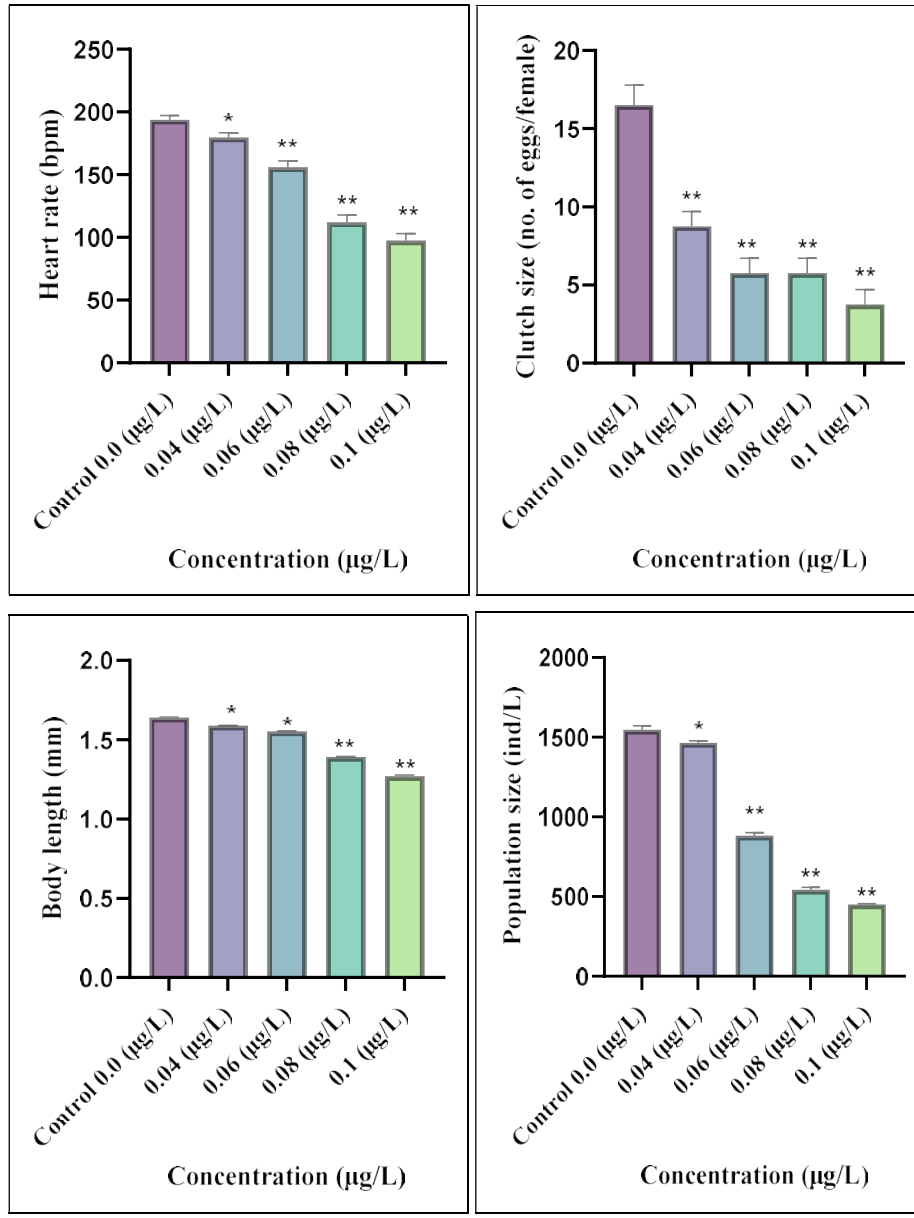


Fig. 3: Heart rate, clutch size, body length, and population size of *D. pulex* (mean ± SD) after 11 days of exposure to different concentrations of Malathion 50 EC (a.i., Malathion) in chronic toxicity tests. Asterisks indicate significant differences from the control: $*p < 0.05$ and $**p < 0.001$ (Dunnett's test, 18 degrees of freedom).

48 h median effective concentration (EC_{50}) values of 80 and 28 µg L^{-1} for technical Malathion and 3.0 µg L^{-1} for commercial Malathion using the probit method. Lilius et al. (1994) reported a 48 h LC_{50} value of 353 µg L^{-1}.

Formulation is a key explanatory variable. Ester forms of 2,4-D are consistently more toxic than acid or amine salts. LC_{50} values for acids and salts range from 25 to 643 mg acid equivalent (a.e.) L^{-1}, whereas those for esters range from 2.2 to 11.8 mg a.e. L^{-1} (Tomlin 2006, US EPA 2005). Therefore, the use of an ethyl ester product in the present study may account for the lower LC_{50} value relative to studies involving amine salts.

3.3.2. Chronic Effects and Mechanistic Considerations

Sublethal 11-day exposures reinforced the acute ranking of hazard. In *D. pulex*, Malathion concentrations as low as 0.06 µg L^{-1} reduced heart rate, clutch size, and growth, whereas 0.10 µg L^{-1} reduced population output by 70%. These endpoints coincide with the acetylcholinesterase (AChE)



Fig. 4: (a) *D. pulex* from the culture before treatment; (b) *D. pulex* after treatment, with five eggs; (c) *D. pulex* after treatment with the highest concentration of Malathion 50 EC (a.i., Malathion), with three eggs; and (d) *D. pulex* with ephippia.

inhibition and metabolic reallocation described by Bravo-Hernández et al. (2014) and Agarwal and Parveen (2026). Mesocosm studies show that such individual-level effects can cascade into community-level changes, including declining cladoceran populations and phytoplankton blooms (Groner & Relyea 2011), highlighting the ecological significance of the present findings. Bravo-Hernández et al. (2014) studied the effects of Malathion on the survival and reproductive variables of *Daphnia pulex* and *Diaphanosoma birgei* and reported that increasing Malathion concentrations reduced survival and fecundity in both cladoceran species.

In contrast, 2,4-D induced a clear concentration-dependent decline in all physiological and population-level parameters evaluated. Heart rate progressively decreased with increasing concentration, reaching 124 ± 8.1 bpm at 1.00 mg L^{-1}. Similarly, clutch size decreased with increasing concentration, with the lowest reproductive output of 12 ± 1.2 neonates per brood at the highest tested concentration. Body length also declined progressively with increasing exposure, reaching an average of 1.628 ± 0.002 mm at 1.00 mg L^{-1}. Consistent with these individual-level effects, total population output decreased by approximately 18% at the highest concentration, reaching 1.267 ± 6.4 individuals L^{-1}. Overall, the progressive reductions in heart rate, clutch size, body length, and population size demonstrate the concentration-dependent sublethal effects of 2,4-D exposure. These thresholds are consistent with the no-effect outcomes reported for *D. magna* and *Ceriodaphnia silvestrii* at $\leq$0.1 mg L^{-1} (Kashian & Dodson 2002, Moreira et al. 2023) but converge with the observation by Silva et al. (2020) of clutch suppression in *C. silvestrii* above 60 mg L^{-1}.

The reduction in body length in the Malathion exposure series, from 1.645 to 1.268 mm, mirrors the 11-day reduction reported for *D. pulex* exposed to 0.25 mg L^{-1} methyl parathion (Fernandez-Casalderrey et al. 1993), suggesting that organophosphate-induced metabolic costs directly affect somatic growth. The occurrence of ephippia in approximately 20% of 2,4-D-exposed females further indicates a stress-induced shift toward resting-egg production, a pattern also observed under glyphosate and mixed-herbicide regimes. Ephippia formation in cladocerans is widely recognized as a survival strategy under adverse conditions. However, this response is not exclusively triggered by toxicant exposure. Population density, food limitation, photoperiod, temperature fluctuations, and culture history can also induce sexual reproduction and ephippia production. Therefore, although

pesticide exposure may have contributed to the observed response, alternative explanations cannot be excluded under the present experimental design. A limitation of the present study is that other drivers of ephippia formation, including density-dependent effects and nutritional status, were not investigated separately. Future studies incorporating factorial designs that manipulate these variables would help clarify the specific role of pesticide-induced stress in ephippia induction.

3.3.3. Implications for Risk Assessment

Taken together, the data indicate that short-lived spikes of Malathion, even at sub-μg L^{-1} levels routinely detected in runoff, pose an acute and chronic threat to cladoceran assemblages, whereas equivalent exposures to 2,4-D ester are less immediately hazardous but could induce reproductive deficits at higher, yet still environmentally plausible, concentrations. Because both pesticides co-occur with elevated temperatures and fluctuating pH in subtropical water bodies, future work should incorporate factorial designs to disentangle interactive effects. Field mesocosm studies that track community composition and nutrient cycling would be particularly valuable for translating laboratory toxicity thresholds into ecosystem-level risk metrics.

4. CONCLUSIONS

This study demonstrated that exposure of *D. pulex* to 2,4-D ethyl ester 38% EC (a.i., 2,4-D) and Malathion 50 EC (a.i., Malathion) can substantially affect its biological characteristics. The results showed significant adverse effects on survival and physiological performance, indicating that even low concentrations can negatively affect cladoceran populations. Acute toxicity tests revealed that short-term exposure to the tested pesticides can cause high mortality, with LC_{50} values varying according to the chemical formulation. Chronic exposure also caused important effects, including changes in heart rate, body size, clutch size, and population growth. The results show that *D. pulex* is a reliable indicator of the sublethal and lethal effects of 2,4-D and Malathion exposure, supporting its use as an affordable and dependable bioindicator for evaluating agrochemical pollution in aquatic environments. However, the experiments were conducted under controlled laboratory conditions that do not fully represent the complexity of natural environments, including variations in physicochemical factors, ecological interactions, and pesticide-degradation processes. Future studies should include long-term, multigenerational toxicity assessments, analyses of cumulative pesticide effects, and biochemical and molecular indicators to clarify toxicity mechanisms. Mesocosm and field-based validation studies are also needed to relate laboratory results to actual ecological conditions.

5. ACKNOWLEDGEMENT

The authors acknowledge the chairperson of the Department of Zoology, Aligarh Muslim University, Aligarh, for providing the necessary laboratory facilities to conduct the study.

6. REFERENCES

Agarwal, S., Parveen, S., Gautam, S.K. and Khan, Q., 2026. Fluctuations in Cladoceran diversity due to environmental variables in River Yamuna. *Limnology*, 27(1), pp.135-142. [DOI]

Agarwal, S., and Parveen, S., 2026. From lab to field: assessing the bioindicator role of *Daphnia pulex* and *Moina macrocopa* in pesticide-impacted water. *Pollution Research*, 45(1-2), pp. 117-126.[DOI]

Alavanja, M.C., 2009. Introduction: Pesticide use and exposure are extensive worldwide. *Reviews on Environmental Health*, 24(4), pp. 303–310. [DOI].

Alexandratos, N. and Bruinsma, J., 2012. *World Agriculture Towards 2030/2050: The 2012 Revision*. ESA Working Paper No. 12-03. Food and Agriculture Organization of the United Nations, Rome, pp. 1–146. [DOI].

Bravo-Hernández, E., Sarma, S.S.S. and Nandini, S., 2014. Effect of malathion on the demography of *Daphnia pulex* Leydig and *Diaphanosoma birgei* Korinek (Cladocera). *Journal of Environmental Biology*, 35(1), pp. 57–65.

de Deus, R.M. and Bakonyi, S.M.C., 2012. O impacto da agricultura sobre o meio ambiente. *Revista Eletrônica em Gestão, Educação e Tecnologia Ambiental*, 7(7), pp. 1306–1315.

European Food Safety Authority (EFSA), 2014. The 2011 European Union report on pesticide residues in food. *EFSA Journal*, 12(5), p. 3694. [DOI].

Fernandez-Casalderrey, A., Ferrando, M.D. and Andreu-Moliner, E., 1993. Effect of the insecticide methylparathion on filtration and ingestion rates of *Brachionus calyciflorus* and *Daphnia magna*. *Science of the Total Environment*, 134(Suppl. 1), pp. 867–876. [DOI].

Frankenberger, W.T. Jr. and Tabatabai, M.A., 1991. Factors affecting L-asparaginase activity in soils. *Biology and Fertility of Soils*, 11, pp. 1–5.

Groner, M.L. and Relyea, R.A., 2011. A tale of two pesticides: How common insecticides affect aquatic communities. *Freshwater Biology*, 56(11), pp. 2391–2404. [DOI].

Harrow, J., 2020. Developing pesticide resistance to acetylcholinesterase inhibitors in *D. pulex*. *Journal of Ecotoxicology and Environmental Safety*, 15(3), pp. 112–118. [DOI].

Jayaraj, R., Megha, P. and Sreedev, P., 2016. Organochlorine pesticides, their toxic effects on living organisms and their fate in the environment. *Interdisciplinary Toxicology*, 9(3–4), pp. 90–100. [DOI].

Kashian, D.R. and Dodson, S.I., 2002. Effects of common-use pesticides on developmental and reproductive processes in Daphnia. *Toxicology and Industrial Health*, 18(5), pp. 225–235.

Lilius, H., Isomaa, B. and Holmström, T., 1994. A comparison of the toxicity of 50 reference chemicals to freshly isolated rainbow trout hepatocytes and *Daphnia magna*. *Aquatic Toxicology*, 30(1), pp. 47–60.

Long Eco Water, 2025. The Best Water for Your Aquarium. Retrieved from: https://longsecowater.com/blog/the-best-water-for-your-aquarium (Accessed 30 July 2026).

Milam, C.D., Farris, J.L., Dwyer, F.J. and Hardesty, D.K., 2005. Acute toxicity of six freshwater mussel species (glochidia) to six chemicals: Implications for daphnids and *Utterbackia imbecillis* as surrogates for protection of freshwater mussels (Unionidae). *Archives of Environmental Contamination and Toxicology*, 48, pp. 166–173. [DOI].

Moreira, R.A., Polo-Castellano, C., Cordero-de-Castro, A., Dias, M.A., Pinto, T.J., Montagner, C.C. and Araújo, C.V., 2023. Short- and long-term exposure to the pesticides fipronil and 2,4-D: Effects on behaviour and life history of *Daphnia magna*. *Chemosphere*, 310, p. 136719. [DOI].

Organisation for Economic Co-operation and Development (OECD), 2004. *Test No. 202: Daphnia sp. Acute Immobilisation Test. OECD Guidelines for the Testing of Chemicals, Section 2*. OECD Publishing, Paris, pp. 1–12. [DOI].

Rassoulzadegan, M. and Akyurtlakli, N., 2002. The toxic effects of malathion (organophosphate insecticide) on *Daphnia magna* Straus, 1820 (Crustacea, Cladocera). *Turkish Journal of Zoology*, 26(4), pp. 349–355.

Relyea, R.A., 2009. A cocktail of contaminants: How mixtures of pesticides at low concentrations affect aquatic communities. *Oecologia*, 159(2), pp. 363–376. [DOI].

Santos, A. and Flores, M., 1995. Effects of glyphosate on nitrogen fixation of free-living heterotrophic bacteria. *Letters in Applied Microbiology*, 20(6), pp. 349–352. [DOI].

Scholz, N.L., Fleishman, E., Brown, L., Werner, I., Johnson, M.L., Brooks, M.L. and Schlenk, D., 2012. A perspective on modern pesticides, pelagic fish declines, and unknown ecological resilience in highly managed ecosystems. *BioScience*, 62(4), pp. 428–434.

Silva, L.C., Moreira, R.A., Pinto, T.J., Ogura, A.P., Yoshii, M.P., Lopes, L.F. and Espindola, E.L., 2020. Acute and chronic toxicity of 2,4-D and fipronil formulations (individually and in mixture) to the Neotropical cladoceran *Ceriodaphnia silvestrii*. *Ecotoxicology*, 29, pp. 1462–1475. [DOI].

Thackeray, S.J., 2022. Zooplankton diversity and variation among lakes. In: *Reference Module in Earth Systems and Environmental Sciences*. Elsevier, pp. 1–10. [DOI].

Tomlin, C.D.S., 2006. *The Pesticide Manual: A World Compendium*. 14th ed. British Crop Protection Council, pp. 642–643.

U.S. Environmental Protection Agency (US EPA), 2005. *Reregistration Eligibility Decision (RED): 2,4-D*. EPA 738-R-05-002. Office of Prevention, Pesticides and Toxic Substances, Office of Pesticide Programs, U.S. Government Printing Office, pp. 1–150.

U.S. Environmental Protection Agency (US EPA), 2006. *Reregistration Eligibility Decision (RED) for Malathion*. Office of Pesticide Programs, U.S. Environmental Protection Agency, Table 20, p. 52.

U.S. Environmental Protection Agency (US EPA), 2019. ECOTOX Knowledgebase. Retrieved from: https://cfpub.epa.gov/ecotox/search.cfm (Accessed 12 August 2019).

Wong, C.K., Chu, K.H. and Shum, F.F., 1995. Acute and chronic toxicity of malathion to the freshwater cladoceran *Moina macrocopa*. *Water, Air, and Soil Pollution*, 84, pp. 399–405. [DOI].

Woodley, A., Hintz, L.L., Wilmoth, B. and Hintz, W.D., 2023. Impacts of water hardness and road deicing salt on zooplankton survival and reproduction. *Scientific Reports*, 13(1), p. 2975. [DOI].

Nature Environment and Pollution Technology
An International Quarterly Peer-Reviewed Open Access Journal

p-ISSN: 0972-6268 | e-ISSN: 2395-3454 Vol. 25 | No. 4 | Article ID B4443 | 2026

REVIEW ARTICLE https://doi.org/10.46488/NEPT.2026.v25i04.B4443 OPEN ACCESS

Groundwater Contamination in India: Regional Variations, Hydrogeochemical Controls, Health Risks, and Integrated Management Strategies

Santosh Sanap, Shrikant Randhavane† and Narayan Chandak
Department of Civil Engineering, SVKM NMIMS Global University, Dhule 424001, Maharashtra, India
†Corresponding author: Shrikant Randhavane; Shrikant.Randhavane@sngu.ac.in; srandhavane@gmail.com

ARTICLE HISTORY

Received: 08-04-2026
Revised: 28-05-2026
Accepted: 05-06-2026

KEYWORDS

Groundwater quality
Fluoride
Arsenic
Nitrate
Physicochemical parameters
Water quality index
Health risk

CITE THIS ARTICLE

Sanap, S., Randhavane, S. and Chandak, N., 2026 Groundwater contamination in India: Regional variations, hydrogeochemical controls, health risks, and integrated management strategies, *Nature Environment and Pollution Technology*, 25(4), B4443. https://doi.org/10.46488/NEPT.2026.v25i04.B4443

COPYRIGHT & LICENCE

© 2026 The Authors
Open Access under CC BY 4.0.

PUBLISHED BY
TECHNOSCIENCE PUBLICATIONS

ABSTRACT

Groundwater plays a critical role in meeting drinking and agricultural water demands in India. This review focuses on regional variations in groundwater quality, contamination sources, and remediation strategies. The evaluation encompasses pH, electrical conductivity, total dissolved solids, hardness, major ions, and contaminants including fluoride, arsenic, nitrate, and heavy metals. Results reveal significant regional variations, with contamination driven by intensive agriculture, industrial activities, mining, urbanization, and geological factors. Water Quality Index assessments indicate that while many groundwater sources meet drinking standards, numerous sites exceed permissible limits, requiring treatment. Contamination stems from both natural processes (mineral dissolution and rock–water interactions) and anthropogenic activities (fertilizer application, industrial effluents, domestic sewage, and mining operations). Health risk assessments demonstrate elevated noncarcinogenic risks in fluoride- and nitrate-affected areas, causing fluorosis, arsenicosis, methemoglobinemia, and other waterborne diseases. Various remediation approaches suitable for Indian conditions have been investigated, including membrane-based systems, electrochemical methods, adsorption techniques, and nature-based solutions. This review provides an integrated understanding of India's regional groundwater quality challenges and emphasizes the necessity for targeted interventions, enhanced monitoring, and sustainable management strategies to protect groundwater resources. The review further provides an integrated regional comparison framework linking contamination sources, hydrogeochemical processes, health risks, and remediation strategies for groundwater management in India.

1. INTRODUCTION

1.1. Groundwater Significance in India

Water security in India is largely dependent upon groundwater, as it meets more than 85% of rural drinking water demands and nearly half of the urban water demands (Rajendran et al. 2025). With annual extraction exceeding 230 billion cubic meters, India is the largest user of groundwater worldwide (Kaur et al. 2019). The groundwater system is generally distributed across the major hydrogeological zones such as the Indo-Gangetic plains, the Deccan plateau, and the coastal zones. These zones show considerable variations in groundwater quality due to differences in geological environments, climatic conditions, and the extent of human interference (Gayathri et al. 2025, Dhakshinamoorthy & Selvarajan 2025). In the last few decades, the increasing trend of groundwater exploitation, along with the rapid pace of industrialization, intensified agricultural activities, and urbanization, has caused a deterioration in water quality (Pandey et al. 2023, Pattnaik & Bhowmick

2020). Water contamination by fluoride, arsenic, nitrate, metals, and salinity has been reported in a significant number of districts of the country, which is a major threat to public health (Kadam et al. 2021, Yenugu et al. 2020). To overcome these challenges, there is a need for a good understanding of regional patterns of groundwater quality and identification of natural as well as anthropogenic sources of contamination. This knowledge is essential for developing management, protection, and remediation strategies for sustainable use of groundwater in India (Sharma et al. 2021, Kaliyan et al. 2022). This review adopts an integrated approach by linking regional contamination patterns, groundwater chemistry, health risks, and remediation strategies to provide a comprehensive understanding of groundwater quality in India. Unlike earlier review studies that primarily focused on isolated contaminants, localized groundwater quality assessment, or individual hydrogeochemical processes, the present review provides an integrated nationwide synthesis of groundwater contamination in India by combining regional hydrogeochemical variability, contaminant distribution patterns, physicochemical characteristics, human health risks, remediation technologies, and management strategies within a single assessment framework. The review comparatively evaluates contamination trends across major hydrogeological regions of India and incorporates recently published literature up to 2025. In addition, the study emphasizes the interrelationship between contaminant sources, hydrogeochemical controls, health implications, and remediation approaches, thereby providing a broader multidisciplinary perspective useful for researchers, policymakers, and groundwater management agencies.

1.2. Methodology of Review

The present study was conducted as a structured literature review aimed at synthesizing regional groundwater contamination characteristics, hydrogeochemical controls, health risks, and remediation strategies across India. Relevant peer-reviewed literature published between 2000 and 2025 was collected from scientific databases including Scopus, Web of Science, Google Scholar, ScienceDirect, and SpringerLink using keywords such as "groundwater quality India," "fluoride contamination," "arsenic groundwater," "nitrate pollution," "water quality index," and "health risk assessment." Initially, approximately 300 research articles were identified through database searching. After removal of duplicate and irrelevant records, studies were screened based on title, abstract, methodological clarity, and relevance to groundwater quality assessment in India. Studies lacking quantitative groundwater quality data, clear methodological description, or regional relevance were excluded. Finally, 115 studies were selected for detailed review and synthesis.

1.2.1. Inclusion Criteria

(i) Peer-reviewed articles;

(ii) Studies focused on groundwater quality in India;

(iii) Studies reporting physicochemical parameters, contaminant concentrations, health risk assessment, or remediation approaches;

(iv) Studies containing sufficient methodological and analytical information.

1.2.2. Exclusion Criteria

(i) Incomplete datasets;

(ii) Conference abstracts without full text;

(iii) Studies lacking clear sampling or analytical procedures;

(iv) Duplicate or non-region-specific reports.

Because of substantial variability in hydrogeological conditions, sampling strategies, analytical methods, temporal scales, and reporting formats among the reviewed studies, the collected information was synthesized qualitatively rather than through formal meta-analysis. The reported concentration ranges and regional trends should therefore be interpreted as indicative comparative assessments rather than statistically aggregated national values. Unlike studies that primarily focused on isolated contaminants, localized case studies, or individual hydrogeochemical processes, the present review attempts to provide a unified nationwide synthesis of groundwater contamination in India by integrating regional hydrogeochemical variability, contaminant sources, health risk implications, remediation technologies, and management strategies within a single assessment framework. The review also incorporates recently published literature up to 2025 and comparatively evaluates contaminant occurrence across major hydrogeological regions of India. This integrated perspective is intended to support researchers, policymakers, and groundwater management agencies in developing region-specific mitigation and sustainable groundwater management strategies. The detailed literature identification, screening, eligibility assessment, and final inclusion process adopted in the present review is illustrated in Fig. 1. The review methodology adopted in the present study improves transparency, reproducibility, and comparability of synthesized groundwater quality information across different hydrogeological regions of India.

To improve methodological transparency and reproducibility, the literature screening and study selection process was performed using a PRISMA-style framework. The inclusion and exclusion criteria adopted for study selection are summarized in Table 1.

Table 1: Inclusion and exclusion criteria used for literature selection.

Criteria Type	Inclusion Criteria	Exclusion Criteria
Publication Type	Peer-reviewed journal articles	Conference abstracts without full text
Study Area	Groundwater quality studies conducted in India	Non-Indian or non-region-specific studies
Data Requirement	Quantitative groundwater quality parameters and contaminant data	Incomplete datasets
Methodology	Studies with clear sampling and analytical procedures	Studies lacking methodological clarity
optic Relevance	Hydrogeochemistry, contamination, health risk, remediation	Studies unrelated to groundwater contamination
Publication Period	2000–2025	Publications outside selected timeframe

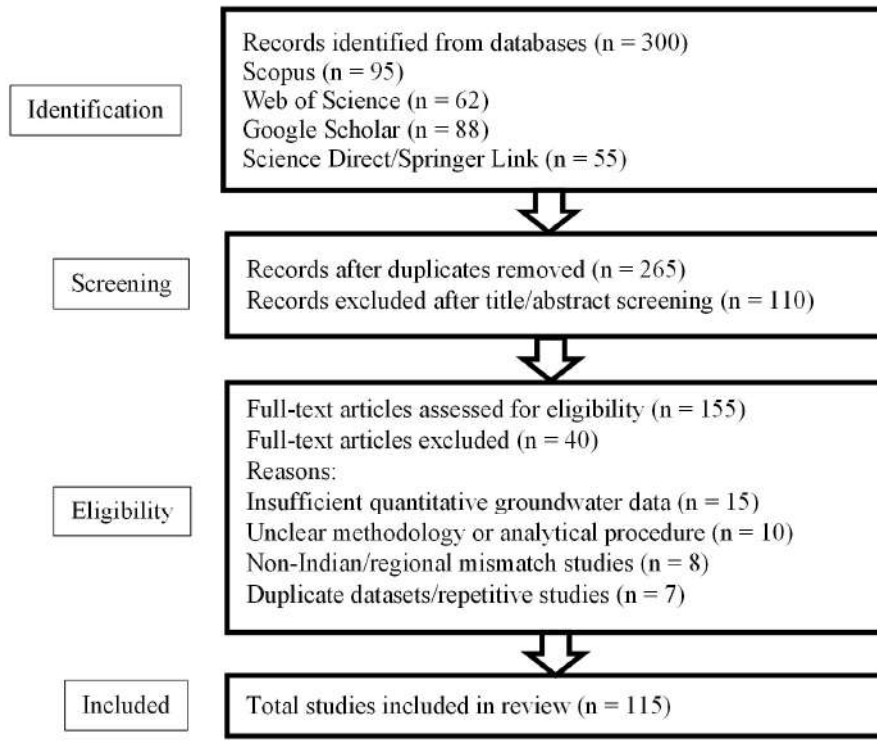


Fig. 1: PRISMA-style flow diagram showing literature identification, screening, eligibility assessment, and final study selection process adopted in the present review.

1.3. Research Objectives and Scope

This review article attempts to collate and assess the available literature for the evaluation of groundwater quality in different regions of India. The main objectives of the study are to identify the regional variability in the physicochemical properties and concentration of major pollutants in groundwater. The study also attempts to identify the natural and anthropogenic sources of groundwater pollution, along with the health hazards that may result from the consumption of polluted groundwater. The review also attempts to identify the most commonly used water quality standards, indexing techniques, and treatment options that are applicable in the context of India. The main advantage of the review article lies in the identification of the available literature and the valuable information that could be obtained for the better management of groundwater resources in India (Shukla & Saxena 2021, Hossain et al. 2021). Although emerging contaminants such as pharmaceuticals, PFAS, pesticides, antibiotic residues, and microplastics are increasingly recognized as potential groundwater pollutants, the present review primarily emphasizes conventional inorganic contaminants because of their widespread occurrence, stronger data availability, and greater public health significance in the Indian context.

2. REGIONAL GROUNDWATER CONTAMINATION PATTERNS

2.1. North India

The groundwater quality problems in North India are diverse, particularly in the Indo-Gangetic Plain. In Punjab and Haryana, intensive agricultural activities have led to groundwater contamination. In these areas, high nitrate concentrations, i.e., above 45 mg L^{-1}, have been recorded in 40–60% of groundwater samples, primarily due to the overuse of chemical fertilizers (Saha & Pal 2025, Raja & Neelakantan 2021). In the Malwa belt of Punjab, uranium contamination is a major issue, with levels up to 644 µg L^{-1} compared to the WHO guideline value of 30 µg L^{-1}. The contamination is attributed to the use of phosphate fertilizers as well as geological sources (Tanwer et al. 2023). In Rajasthan, the groundwater is significantly affected by arid and semi-arid climatic conditions. High fluoride levels ranging from 1.5 to 8.5 mg L^{-1} and high salinity are commonly reported. These conditions are mainly attributed to high rates of evaporation and dissolution of fluoride minerals and low rates of natural recharge (Kaur & Godara 2025, Maurya et al. 2025, Dhakate et al. 2023). In the case of Delhi and its surrounding National Capital Region, groundwater is characterized by elevated concentrations of total dissolved solids, hardness, and nitrates, with concentrations of 500 to 2500 mg L^{-1}, 300 to 800 mg L^{-1}, and 50 to 150 mg L^{-1}, respectively. These issues are mainly related to sewage water leakage, industrial waste, and agricultural runoff (Maurya et al. 2021, Singh et al. 2024). In Uttar Pradesh, there is a high degree of spatial variability in groundwater quality. In eastern parts of the state, arsenic contamination of groundwater, with concentrations varying between 10 and 500 µg L^{-1}, is common, whereas fluoride contamination, with concentrations varying from 1.5 to 6.0 mg L^{-1}, is common in the western parts of Uttar Pradesh (Adimalla 2020, Karunanidhi et al. 2021). In Jammu and Kashmir, groundwater quality is relatively good, although localized pollution, mainly related to agricultural activities and poor sanitation, has been reported in certain areas of the valleys (Chakraborty et al. 2021). The variability in groundwater contamination in North India is mainly regulated by the interaction of agricultural practices, hydrogeology, and urbanization. The nitrate concentration in the groundwater of Punjab and Haryana is strongly influenced by the excessive application of fertilizers (Saha & Pal 2025, Raja & Neelakantan 2021, Marghade et al. 2021). The presence of uranium in the Malwa region is regulated by both geochemical and fertilizer components (Tanwer et al. 2023). Arsenic in the groundwater of the eastern part of Uttar Pradesh is regulated by reductive dissolution in the alluvial aquifers (Adimalla 2020, Karunanidhi et al. 2021). It is concluded that groundwater quality is location-specific and is regulated by both geochemical and anthropogenic factors.

2.2. South India

In South India, groundwater is mostly linked with hard rock aquifer systems that are recognized to exhibit specific hydrogeochemical signatures. In Tamil Nadu State, fluoride contamination is widespread, with fluoride levels ranging from 1.5 to 12 mg L^{-1} covering 15 districts. The maximum fluoride levels are reported from Salem, Dharmapuri, and Krishnagiri districts due to the weathering of fluoride-bearing granites and gneisses (Ramalingam et al. 2022, Ramajayam et al. 2024). Seawater intrusion is another major problem reported from the coastal areas of Tamil Nadu State, where the chloride level is above 1000 mg L^{-1} and electrical conductivity is above 3000 µS cm^{-1}, extending up to 5–10 km inland (Ramajayam et al. 2024, Singh et al. 2024). The groundwater quality in Karnataka state has been found to vary in different agro-climatic zones. In the northern districts of the state, the groundwater exhibits elevated concentrations of fluoride (2–8 mg L^{-1}) and nitrate (50–200 mg L^{-1}), whereas salinity intrusion is a major problem in the coastal districts (Sarma & Singh 2023, Taloor et al. 2023). In the Bangalore urban region, the groundwater is contaminated by elevated concentrations of nitrate (45–120 mg L^{-1}), the presence of heavy metals such as iron, manganese, lead, and chromium, and bacterial contamination. The causes of groundwater contamination in this region include industrial activities and the lack of proper sewage treatment systems (Panneerselvam et al. 2021, Biswas et al. 2023). Andhra Pradesh and Telangana states have reported widespread fluoride contamination in various districts, ranging from 1.5 to 9.5 mg L^{-1}. The problem is more acute in districts like Nalgonda, Prakasam, and Guntur (Goyal et al. 2025, Karanveer et al. 2022). In Kerala, coastal groundwater is highly affected by seawater intrusion, with chloride levels above 1500 mg L^{-1}. Approximately 30–40% of groundwater wells located within 2 km of the coastline have elevated salinity and chloride concentrations due to seawater intrusion (CGWB 2017). Inland regions of the state have shown better groundwater quality, although some instances of water pollution by agricultural and domestic waste disposal have been reported (Sane et al. 2025). Puducherry has reported high salinity levels, ranging from 1000 to 3500 mg L^{-1} in terms of TDS, along with nitrate levels ranging from 50 to 180 mg L^{-1} due to the high intensity of agricultural activities in the region (Subramaniyan & Ganesan 2024). The regional variation in groundwater quality in South India is controlled by hard rock aquifer systems, climatic conditions, and coastal processes. For instance, elevated concentrations

of fluoride in groundwater are linked to increased water-rock interaction in granitic rocks (Ramalingam et al. 2022, Singh et al. 2020, Adimalla et al. 2020), whereas salinity in coastal groundwater is controlled by excessive groundwater abstraction and hydraulic imbalance (Singh et al. 2024, Sarma & Singh 2023). In cities such as Bangalore, elevated nitrate and heavy metal concentrations are observed due to poor wastewater management (Panneerselvam et al. 2021, Biswas et al. 2023). These are examples of the effects of geology, urbanization, and coastal processes on groundwater quality.

2.3. East India

Eastern India has a very serious groundwater quality problem, which is mainly in the form of arsenic contamination. This problem is particularly acute in the West Bengal region, where arsenic has been found in 79 blocks in nine districts. The concentration of arsenic has been found to vary from 10 to as high as 3200 μg L^{-1}, which is well above the WHO guideline value of 10 μg L^{-1} (Mukherjee et al. 2015, Sabinaya et al. 2023, Khan et al. 2021). The source of arsenic in the groundwater in the eastern part of India is natural. Geological processes are responsible for the occurrence of arsenic in the groundwater in the eastern part of India. The reducing conditions in the alluvial aquifer allow the release of arsenic from iron oxyhydroxide into the groundwater (Malik et al. 2021). A similar trend has been observed in the Bihar region, where arsenic contamination has been reported in about 15 districts, with a maximum concentration of 1800 μg L^{-1} (Sahu et al. 2017). In Jharkhand, the groundwater quality is highly affected by mining activities. In areas where coal mining, iron ore mining, and industries are prevalent, high concentrations of heavy metals such as iron, manganese, lead, cadmium, chromium, copper, and zinc have been recorded (Panneerselvam et al. 2023, Reddy et al. 2022). In addition, fluoride contamination has been recorded in the western districts, where the concentration of fluoride varies from 1.5 to 6.5 mg L^{-1}, primarily due to geological factors (Singh et al. 2022). In Odisha, a significant variation in groundwater quality has been recorded. In the coastal areas, salinity intrusion is a major problem, whereas in the western districts, fluoride concentrations vary from 2 to 7 mg L^{-1}, and areas near mining and industrial activities have high concentrations of heavy metals (Kouser et al. 2022). The quality of groundwater in Assam and other states in the northeastern region tends to be better, considering the high rainfall and good recharge conditions. Yet, there are some reported cases of contamination in the tea estate areas, oil refineries, and in places with poor sanitation facilities (Basha et al. 2022). At some places, the iron and manganese content in the groundwater also exceeds the permissible limits of 0.3 mg L^{-1} and 0.1 mg L^{-1}, respectively, mainly because of the reducing conditions in the aquifers. (Singh et al. 2022) The major processes controlling groundwater contamination in eastern India are geogenic in nature, dominated by arsenic contamination in reducing environments in alluvial aquifers (Mukherjee et al. 2015, Sabinaya et al. 2023, Khan et al. 2021). In contrast to western and southern India, where groundwater contamination is dominated by fluoride, eastern India has its own set of groundwater contamination processes, dominated by sedimentary geology and redox chemistry (Malik et al. 2021, Sahu et al. 2017). In addition, there is heavy metal contamination in Jharkhand due to mining activities, which clearly indicates anthropogenic influences on groundwater chemistry (Panneerselvam et al. 2023, Reddy et al. 2022).

2.4. West India

Significant variations in the quality of groundwater in Western India have been observed. In Gujarat, various problems in the quality of groundwater have been reported. Fluoride contamination in the range of 1.5 to 10 mg L^{-1} has been reported in ten districts. The coastal areas in the Saurashtra and Kutch districts are also affected by salinity intrusion, where the TDS level ranges from 1500 to 5000 mg L^{-1}. Moreover, areas where agricultural activities are concentrated also face problems of nitrate contamination in the range of 50 to 300 mg L^{-1} (Yadav et al. 2018, Dhanya Raj & Shaji 2017, Shaikh et al. 2020). Groundwater contamination by heavy metals like chromium, lead, cadmium, and nickel has been reported in the industrial areas around Ahmedabad, Vadodara, and Surat cities, which is attributed to the effluent discharge from the textile, chemical, and pharmaceutical industries (Srinivas et al. 2013). Groundwater quality in Maharashtra exhibits significant spatial variability influenced by geological and anthropogenic factors. In Vidarbha and Marathwada, the presence of fluoride ranges between 2–8 mg L^{-1}. Nitrate-related problems are present in areas with sugarcane cultivation, ranging between 50–250 mg L^{-1}. (Mhaske et al. 2022, Naskar et al. 2025). Regions with industries have higher levels of heavy metals in groundwater. In Mumbai and other major cities, the issue of total dissolved solids, hardness, and bacterial presence are major problems, and these are mainly caused by leakage in the sewage system and industries (Wagh et al. 2019). In the state of Goa, the presence of seawater in the groundwater of the coastal areas ranges between 40–50% with chloride levels above 2000 mg L^{-1} within 3 km of the shoreline (Sidhu et al. 2024). In the western part of India, the groundwater quality is affected by the arid climatic conditions, the high intensity of agriculture, and industrialization. Elevated fluoride and salinity concentrations in groundwater samples are related

to evaporation and the dissolution of minerals (Yadav et al. 2018, Dhanya Raj & Shaji 2017, Shaikh et al. 2020). Elevated concentrations of nitrate in groundwater samples reflect the impact of agricultural activities (Shaikh et al. 2020). Industrialization has affected the groundwater quality in the form of heavy metals in the urban areas (Srinivas et al. 2013). The impact in the western part of India is a mix of geogenic and anthropogenic factors compared to the eastern part.

2.5. Central India

Groundwater in Central India reflects the fingerprints of nature as well as human activities. In Madhya Pradesh, the presence of fluoride poses a problem in several areas, ranging from 1.5 to 7.5 mg L^{-1} over 14 districts of the state. The districts of the Malwa Plateau and Vindhyan areas are of particular concern, and the cause of the problem is the weathering of those minerals containing fluoride (Karunanidhi et al. 2021, Vijayakumar et al. 2022). Nitrate contamination of groundwater occurs in several agricultural districts, where the excessive use of chemical fertilizers is the major cause of the problem, with nitrate concentrations ranging from 50 to 180 mg L^{-1} (Alam et al. 2024). In the state of Chhattisgarh, the groundwater scenario reflects the impact of mining and industries. In the state, heavy metals like iron, manganese, chromium, lead, and cadmium are present in groundwater at elevated concentrations, often two to ten-fold higher than the permissible limits (Ullengula et al. 2026). In the coal mining areas, sulfate concentrations are significantly elevated, ranging from 200 to 600 mg L^{-1}, and TDS concentrations are also elevated, ranging from 1000 to 3000 mg L^{-1}, mainly because of acid mine drainage (Karunanidhi et al. 2020). In the agricultural areas, nitrate contamination of groundwater occurs, with concentrations ranging from 45 to 150 mg L^{-1}, mainly because of the application of fertilizers and the disposal of organic waste (Ambade et al. 2024). Fig. 2 shows the regional distribution of major groundwater contaminants in India. The quality of groundwater in central India is characterized by various geological formations and anthropogenic activities like mining and agricultural activities. Higher concentrations of fluoride ions are related to the weathering of minerals, whereas heavy metal contamination is mainly related to mining activities. Compared to other regions, central India is characterized by mixed contaminant patterns due to various natural and anthropogenic factors. The map highlights dominant groundwater contamination zones reported in reviewed studies, including arsenic contamination in eastern alluvial aquifers, fluoride enrichment in western and southern

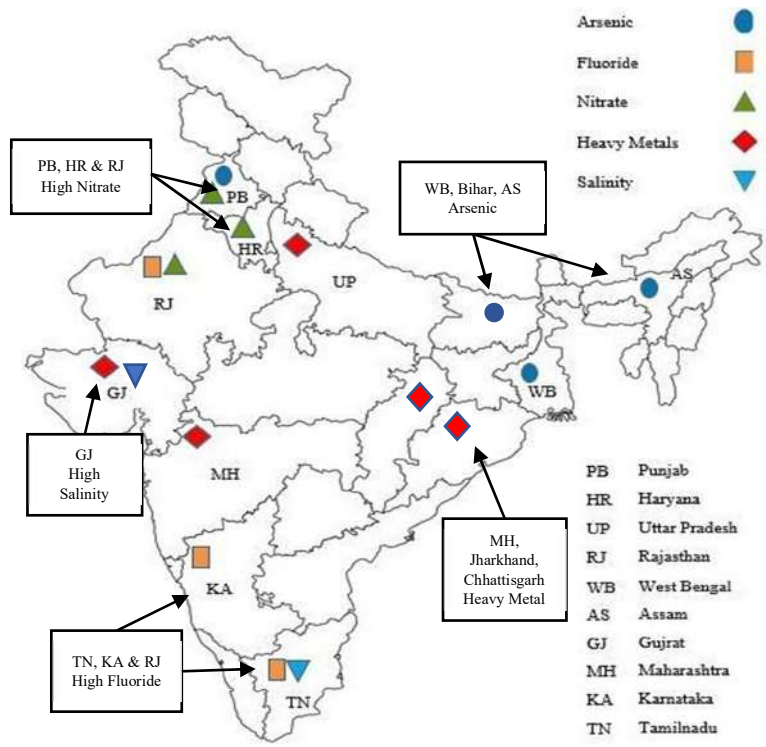


Fig. 2: Regional distribution of major groundwater contaminants across India showing dominant fluoride contamination in western and southern states, arsenic occurrence in eastern alluvial plains, and nitrate enrichment in agriculturally intensive regions.

hard-rock terrains, nitrate contamination in agriculturally intensive northern regions, salinity intrusion in coastal aquifers, and heavy metal contamination near mining and industrial zones.

2.6. Comparative Regional Analysis

A regional perspective of groundwater contamination in India shows varying degrees of contamination. In the northern part of India, the major groundwater contamination problems are related to nitrates and uranium. These are primarily related to agricultural activities and fertilizer usage. In the western and southern parts of India, fluoride and salinity are major groundwater contamination problems. These are related to geological and climatic factors. In the eastern part of India, arsenic contamination is a major problem, and this is primarily related to geological factors. In central India, heavy metals are a major groundwater contamination problem, and this is primarily related to mining activities (Saraswat et al. 2023, Khan et al. 2021). A comparative evaluation of groundwater quality in various regions of India has shown specific patterns of groundwater quality in different regions. Northern and western regions exhibit contamination patterns dominated by nitrate and fluoride, respectively, due to agricultural activities and climatic conditions (Yadav et al. 2018, Dhanya

Table 2: Regional groundwater quality parameters across major Indian locations.

State	pH	EC ($\mu S\ cm^{-1}$)	TDS ($mg\ L^{-1}$)	TH ($mg\ L^{-1}$)	F^- ($mg\ L^{-1}$)	NO_3^- ($mg\ L^{-1}$)	As ($\mu g\ L^{-1}$)	Primary Concerns	Authors
Punjab	7.2–8.5	800–3500	500–2200	300–900	0.5–2.5	45–250	5–644	Nitrate, Uranium	Saha & Pal 2025, Raja & Neelakantan 2021, Marghade et al. 2021
Rajasthan	7.0–8.8	1200–5500	750–3500	400–1500	1.5–8.5	20–120	<10	Fluoride, Salinity	Kaur & Godara 2025, Maurya et al. 2025, Dhakate et al. 2023
Delhi NCR	7.1–8.3	900–4000	600–2500	300–800	0.3–2.0	50–150	<10	TDS, Nitrate, Hardness	Maurya et al. 2021, Singh et al. 2024
Tamil Nadu	6.8–8.6	800–4500	500–3000	250–1200	1.5–12.0	30–180	<10	Fluoride, Salinity	Ramalingam et al. 2022, Singh et al. 2020, Adimalla et al. 2020
Karnataka	6.5–8.4	700–3800	450–2400	200–950	2.0–8.0	50–200	<10	Fluoride, Nitrate	Sarma & Singh 2023, Taloor et al. 2023
West Bengal	6.8–7.8	600–2500	400–1600	200–700	0.2–1.5	20–80	10–3200	Arsenic, Iron	Mukherjee et al. 2015, Sabinaya et al. 2023, Khan et al. 2021
Bihar	6.9–7.9	650–2800	420–1800	220–750	0.3–2.0	25–90	10–1800	Arsenic, Fluoride	Sahu et al. 2017
Gujarat	7.0–8.7	1000–6000	650–4000	300–1800	1.5–10.0	50–300	<10	Fluoride, Salinity, Nitrate	Yadav et al. 2018, Dhanya Raj & Shaji 2017, Shaikh et al. 2020
Maharashtra	6.8–8.5	750–4200	480–2700	250–1100	2.0–8.0	50–250	<10	Fluoride, Nitrate	Mhaske et al. 2022, Naskar et al. 2025
Madhya Pradesh	7.0–8.6	800–3600	520–2300	280–950	1.5–7.5	50–180	<10	Fluoride, Nitrate	Karunanidhi et al. 2021, Vijayakumar et al. 2021, Alam et al. 2024
Chhattisgarh	6.5–8.2	700–3500	450–2200	240–900	0.5–3.0	45–150	<10	Heavy Metals, Nitrate	Ullengula et al. 2026, Karunanidhi et al. 2020
Odisha	6.7–8.3	650–3800	420–2400	220–950	2.0–7.0	30–120	<10	Fluoride, Heavy Metals	G. et al. 2024 Kouser et al. 2022

Note: The values in Table 2 are compiled from multiple studies corresponding to the cited references for each region to provide a literature-supported regional comparison across India.

Raj & Shaji 2017, Shaikh et al. 2020). The eastern parts of India are affected by arsenic contamination (Malik et al. 2021). whereas in southern India, both fluoride and salinity are major groundwater quality problems (Ramalingam et al. 2022). In central India, mining activities are responsible for heavy metal contamination (Ullengula et al. 2026). The results show that groundwater contamination is region-specific. The regional variations in groundwater quality discussed above can be seen in terms of physicochemical properties of groundwater, which are discussed in detail in the next section. The variations discussed here show how geology and human activities affect groundwater chemistry in various parts of India.

The concentration ranges presented in Table 2 represent compiled minimum–maximum ranges reported in the reviewed literature for different groundwater quality parameters across selected regions of India. The values are synthesized from multiple independent studies conducted under varying hydrogeological, seasonal, and analytical conditions and should therefore be interpreted as indicative comparative ranges rather than standardized regional averages.

The contaminant concentration ranges summarized in Table 3 represent indicative ranges compiled from published regional groundwater studies. The values reflect reported concentration intervals from different hydrogeological settings and are intended for comparative regional assessment rather than direct statistical comparison.

The comparative analysis suggests that the arsenic contamination in eastern India poses the highest health risk in terms of toxicity and prevalence, while the fluoride contamination in the western and southern regions has a larger population affected. Nitrate contamination in India has moderate to high spatial variability and is associated with agricultural regions. These comparisons provide a semi-quantitative evaluation of the severity of groundwater contamination in India.

3. HYDROGEOCHEMICAL CHARACTERISTICS AND CONTAMINATION MECHANISMS

3.1. pH

Groundwater pH in India ranges from a neutral to mildly alkaline level, usually between 6.5 and 8.8 (Krishnappa et al. 2024). pH values above 8.0 are commonly reported in arid and semi-arid zones, where evaporation promotes the dissolution of carbonate minerals. If the rainfall is significantly elevated or in areas where mines are present, then the pH level may turn slightly acidic (Shirke et al. 2020). The level of pH is a very significant factor, as it influences the movement of metals, the interaction of minerals, and the treatment process (Saha et al. 2024).

3.2. Electrical Conductivity (EC) and Total Dissolved Solids (TDS)

The range for groundwater conductivity is normally between 600 and 6000 µS cm^{-1}, which is equivalent to a TDS of about 400 to 4000 mg L^{-1} (Hanse et al. 2019). Increased levels of electrical conductivity and TDS imply an increased amount of dissolved ions, often resulting from mineral weathering, evaporation, and human activities such as farming and industrial operations (Mukherjee & Singh 2022). Research carried out in various parts of India has indicated that about 40% of the groundwater has TDS levels above the permissible limit of 500 mg L^{-1} (Sahoo et al. 2024, Mukherjee & Singh 2022).

3.3. Total Hardness (TH)

The range of total groundwater hardness is 200 to 1800 mg L^{-1} as $CaCO_3$. Reviewed regional studies have reported that approximately 40–60% of groundwater samples in several investigated regions of India fall within the hard to very hard category, with values above 300 mg L^{-1} (Ravindra & Mor 2019). The high level of groundwater

Table 3: Comparative regional summary of groundwater contamination in India.

Region	Dominant Contaminants	Typical Concentration Range	Key Causes	Severity Level	Authors
North India	Nitrate, Uranium	NO_3^- 50–150 mg L^{-1}	Fertilizers, agriculture	High	Saha & Pal 2025, Chakraborty et al. 2021
South India	Fluoride, Salinity	F^- 2–12 mg L^{-1}	rock–water interaction, coastal intrusion	High	Ramalingam et al. 2022, Subramaniyan & Ganesan 2024
East India	Arsenic	As 10–3200 µg L^{-1}	Reductive dissolution (geogenic)	Very High	Mukherjee et al. 2015, Singh et al. 2022
West India	Fluoride, Nitrate, Salinity	F^-2–10 mg L^{-1}	Arid climate, agriculture	High	Yadav et al. 2018, Sidhu et al. 2024
Central India	Fluoride, Heavy Metals	F^-1.5–7 mg L^{-1}	Mining, geology	Moderate–High	Karunanidhi et al. 2021, Ambade et al. 2024

Note: Table 3 summarizes dominant contaminants, their typical ranges, and associated causes across different regions.

hardness is attributed to the elevated concentrations of calcium and magnesium ions that are dissolved from rocks such as limestone, dolomite, and gypsum (Adimalla et al. 2018). Although the level of water hardness is not a health hazard, high levels can cause pipe scaling and could possibly contribute to heart problems (Ahada & Suthar 2019). Dissimilarities in methodologies for analysis applied in different studies, including differing limits of detection and types of instrumentation (e.g., ICP-MS vs. AAS), as well as sample preservatives applied, may also contribute to differing results. These methodological dissimilarities may add to the uncertainty in results (Hanse et al. 2019, Mukherjee & Singh 2022).

3.4. Major Cations and Anions

3.4.1. Cations

Calcium and magnesium are the major cations present in Indian groundwater. The concentration of calcium ranges from 40–450 mg L^{-1}, while magnesium ranges from 20–280 mg L^{-1}. The major source of calcium and magnesium is mineral weathering, i.e., carbonate and silicate mineral weathering (Mawari et al. 2022). The concentration of sodium ranges from 20–800 mg L^{-1}, while potassium ranges from 2–50 mg L^{-1}. However, in arid areas, coastal areas, and areas of heavy agricultural activity, higher concentrations of sodium and potassium have also been reported, primarily due to evaporation, intrusion of seawater, and extensive use of chemical fertilizers (Mukherjee et al. 2019). Higher concentrations of sodium also pose a major problem, as they reduce soil permeability and can be harmful to human health, especially for people suffering from hypertension (Yadav et al. 2019).

3.4.2. Anions

The most common negatively charged ions present in groundwater are bicarbonate ions. The range of bicarbonate ions is between 150 and 800 mg L^{-1}. Bicarbonate ions are generally derived from the dissolution of carbonate minerals and the action of carbon dioxide (Ahada & Suthar 2018). The level of chloride ions is generally between 20 and 2000 mg L^{-1}. The level of chloride ions is high in coastal areas where seawater intrusion occurs, dry areas where salts are present due to evaporation, and areas where sewage leakage is observed (Hussain et al. 2012). The level of sulfate ions is generally between 20 and 600 mg L^{-1}. The level of sulfate ions is derived from the dissolution of gypsum minerals and industrial waste, as well as acid mine drainage (Madhavan et al. 2023). Around 35–45% of groundwater samples from highly intensive agricultural areas such as Punjab, Haryana, and Gujarat show nitrate levels above the permissible limit of 45 mg L^{-1}. Conversely, in less intensive areas, the levels of exceedance are low. This may be due to the variation in the application of fertilizers (Chaudhry & Sachdeva 2021).

3.5. Heavy Metals and Trace Elements

3.5.1. Fluoride

There are reports of the presence of fluoride in groundwater in many parts of India, with concentrations ranging from 1.5 to 12 mg L^{-1}. This problem occurs in several districts across several states, affecting millions of people (Das et al. 2009). The primary sources of fluoride in groundwater are the weathering of minerals like fluorite, apatite, and mica, all of which are present in the environment in granitic and gneissic rocks (Ghosh et al. 2024). Groundwater chemistry, like pH, calcium, and bicarbonate, also contributes to the presence of fluoride in groundwater (Gupta et al. 2019).

3.5.2. Arsenic

Among the major groundwater pollutants, arsenic is particularly notable in India, and its concentration in water varies sharply, from a minimum of 10 µg L^{-1} to a maximum of 3200 µg L^{-1}, with particularly elevated concentrations of contamination detected in states such as West Bengal, Bihar, Uttar Pradesh, Assam, and Chhattisgarh (Gupta et al. 2015). The major source of arsenic entering groundwater is the reductive dissolution of iron oxyhydroxides, particularly in anaerobic and alluvial aquifer systems (Cherukumilli et al. 2018). In groundwater, arsenic is observed in two forms, arsenite (As^{3+}) and arsenate (As^{5+}). Arsenite is more mobile and toxic than arsenate (Inaniyan & Raychoudhury 2019).

3.5.3. Other Heavy Metals

Iron and manganese are often present in groundwater samples in concentrations higher than the safety limits, especially in areas where the environment of the aquifer is reducing. In these areas, iron concentrations vary between 0.1 and 15 mg L^{-1}, and manganese concentrations vary between 0.05 and 5 mg L^{-1}. These two elements are often present together and can cause problems with the color and taste of the water, as well as health risks (Koley 2021). Other heavy metals, like lead (5–150 µg L^{-1}), cadmium (2–50 µg L^{-1}), chromium (10–500 µg L^{-1}), copper (10–200 µg L^{-1}), and zinc (50–1000 µg L^{-1}), are usually reported in areas near industrial centers, mining areas, and areas with intensive agricultural activities, as these are areas with the strongest anthropogenic influence (Singh et al. 2024, Awasthi et al. 2021). Drinking water containing these heavy metals can cause health problems like neurological disorders, kidney problems, and cancer (Khandaker & Rahman 2022). Fig. 3 presents the integrated groundwater quality assessment methodology and its significance.

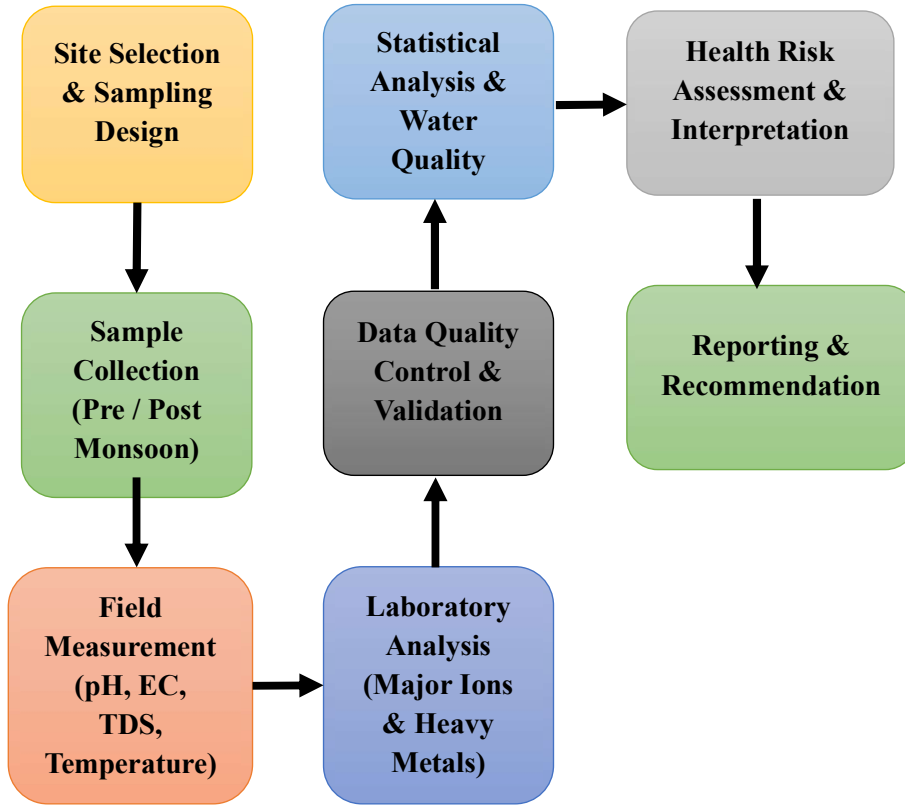


Fig. 3: Integrated methodological workflow adopted for groundwater quality assessment, hydrogeochemical interpretation, health-risk evaluation, and remediation strategy selection in Indian groundwater studies.

The assessment workflow presented in Fig. 3 demonstrates the importance of integrating field sampling, laboratory analysis, water quality indexing, hydrogeochemical interpretation, and health risk assessment for comprehensive groundwater quality evaluation. The figure indicates that groundwater assessment should not rely solely on physicochemical parameter measurement, but should also include interpretation of contaminant sources, exposure pathways, and associated human health implications. This integrated assessment approach improves the reliability of groundwater quality evaluation and supports region-specific groundwater management strategies.

3.5.4. Nutrients and Emerging Contaminants

One of the most common nutrient pollutants in India's groundwater is nitrate. The primary sources of nitrate contamination are fertilizers, animal waste, and sewage. Nitrate contamination of groundwater is a major issue, as it has been reported that almost 40% of groundwater in highly cultivated areas exceeds permissible limits, although this is not so prevalent in areas with less agricultural activity (Marghade et al. 2023). In India, the normal concentration of phosphates in groundwater is within a range of 0.1 to 5 mg L^{-1}. An increase in phosphates is a sign of organic pollution, which may result in eutrophication in water bodies that are connected to the groundwater (Wintgens et al. 2015). In recent times, there has been a surge of interest in newer pollutants, including pesticides, pharmaceuticals, and microplastics, in India's groundwater. However, there is limited information on the sources, occurrence, and potential impact of these pollutants on India's groundwater (Pal et al. 2009, Sultan et al. 2024). In recent years, increasing concern has also been raised regarding emerging contaminants such as pesticide residues, pharmaceutical compounds, personal care products, antibiotic residues, PFAS (per- and polyfluoroalkyl substances), endocrine-disrupting compounds, and microplastics in groundwater systems. These contaminants primarily originate from agricultural runoff, untreated sewage discharge, landfill leachates, industrial effluents, hospital wastewater, and improper disposal of domestic and pharmaceutical waste. Although systematic nationwide data for these contaminants in Indian groundwater remain limited, several localized investigations have reported detectable concentrations in urban, peri-urban, and agriculturally intensive regions. Long-term exposure to such contaminants may pose ecological risks, antimicrobial

resistance concerns, endocrine disruption, and chronic human health impacts. However, due to limited monitoring data, inconsistent analytical methods, and lack of standardized national datasets, the present review mainly focuses on conventional inorganic groundwater contaminants such as fluoride, arsenic, nitrate, salinity, and heavy metals, which remain the most widely reported and critical groundwater quality concerns across India.

3.6. Contamination Sources

The diagram identifies the various sources of contamination that affect the groundwater in India. The sources include runoff from agriculture, which contains fertilizers and pesticides; industrial waste, which contains heavy metals and chemical compounds; domestic sewage, which contains nutrients; mining, which results in acid and the release of metals; and geogenic sources, which contain fluoride and arsenic compounds that are released from the interaction between rocks and water. The pathways that are represented in the diagram include infiltration, leaching, and lateral movement from surface water bodies. It is important to note that the variations in the reported values of groundwater quality from various sources may be attributed to various factors. For example, some sources may have been based on single-time sampling, while others may have been based on seasonal sampling. This may have caused inconsistencies in the reported values. It is significant to note that the groundwater quality data collected and compiled in this review have been obtained from various studies conducted over different time periods, hydrogeological settings, and methodological approaches. These factors can have a major impact on the data. For example, groundwater samples collected before the monsoon season have shown high concentrations of contaminants (Krishnappa et al. 2024, Shirke et al. 2020). whereas samples collected after the monsoon season have shown low concentrations (Sahoo et al. 2024). Similarly, alluvial aquifers have shown different geochemical characteristics compared to hard rock aquifers (Mawari et al. 2022). Therefore, direct comparison of values across studies should be interpreted cautiously. The variation in physicochemical parameters and contaminant concentrations is related to both natural and anthropogenic sources. This is significant in understanding the patterns of groundwater chemistry discussed above. Fig. 4 demonstrates that groundwater contamination pathways in India are highly interconnected. Agricultural runoff contributes primarily to nitrate and pesticide contamination, while industrial effluents are major sources of heavy metals and toxic chemicals. Geogenic contamination pathways differ significantly from anthropogenic pathways because they are strongly controlled by aquifer mineralogy and groundwater chemistry. The figure further highlights that contaminant migration

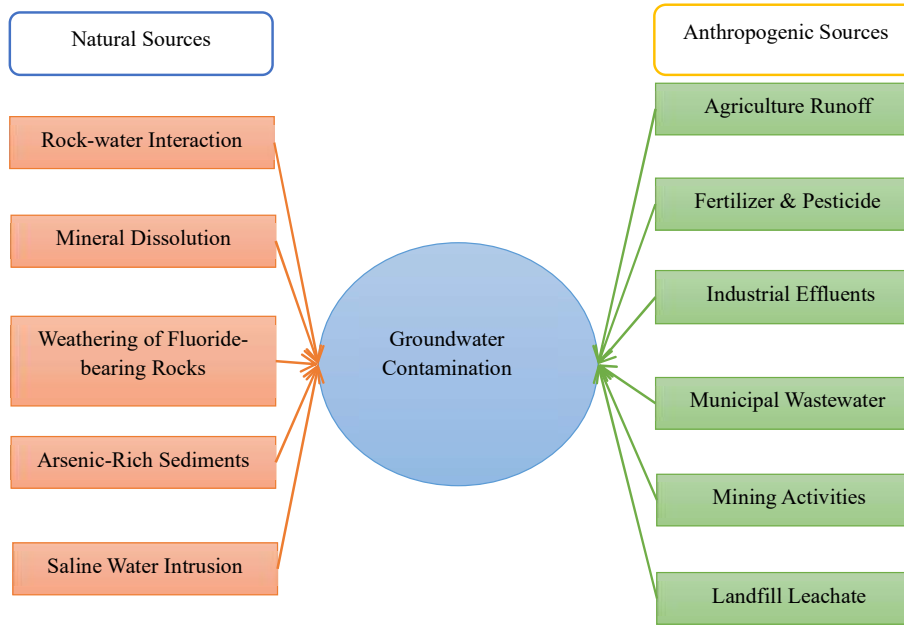


Fig. 4: Major geogenic and anthropogenic groundwater contamination sources and contaminant transport pathways in Indian aquifer systems (synthesized from the literature).

occurs through infiltration, leaching, and groundwater flow processes, emphasizing the importance of hydrogeological conditions in contaminant transport.

3.7. Natural Geogenic Sources

Water can also be contaminated by natural geological and hydrogeochemical processes. Fluoride concentration increases due to the weathering of fluoride-bearing minerals like fluorite, apatite, biotite, and hornblende, which are present in rock formations of granite, gneiss, and volcanic origins (Malik et al. 2023). Also, groundwater with an alkaline nature (pH above 7.5), low calcium content, and high bicarbonate and sodium levels is more likely to dissolve more fluoride and move it around (Barathkumar et al. 2025). As for the issue of arsenic contamination, it is mostly associated with alluvial aquifers where iron and manganese oxyhydroxide dissolution occurs reductively under anaerobic conditions (Cherukumilli et al. 2017). Microbial processes also enhance the degradation rate of organic matter and alter geochemical conditions, moving towards more reducing conditions, which in turn increases the release of arsenic in groundwater (Kalaiselvi & Pillai 2019). Under arid and semi-arid conditions, salinity problems are mainly driven by the rapid rate of evaporation, the dissolution of salt minerals such as halite and gypsum, and the lack of recharge to groundwater (Vijaylaxmi & Khan 2021). For example, in coastal aquifers, seawater intrusion occurs due to the pumping of groundwater, which changes the hydraulic gradients and causes seawater to flow inland (Saha et al. 2014). Heavy metals such as iron, manganese, uranium, and thorium are found in specific geological formations and are transported through groundwater depending on parameters such as pH and redox reactions (Karunanidhi et al. 2024).

3.8. Anthropogenic Sources

3.8.1. Agricultural Activities

Agricultural practices in most areas of India also contribute significantly to the contamination of groundwater. This is particularly so because of the extensive use of chemical fertilizers, which increases the nitrate and phosphate content in the water (Kumar et al. 2017). The use of pesticides, coupled with irrigation return flows, further contributes to the degradation of water quality. Moreover, in areas such as Punjab, Haryana, and Gujarat, the nitrate content in the water is above 100 mg L^{-1}, which is attributed to the extensive use of nitrogen fertilizers in these areas (Mandal & Sanyal 2019). Livestock and poultry farming also contributes to the contamination of the water table (Narsimha & Sudarshan 2017).

3.8.2. Industrial Effluents

Industrial activities such as textile finishing, chemical and pharmaceutical production, leather tanning, electroplating, and mining also pose a major threat to groundwater. These activities may release heavy metals such as chromium, lead, cadmium, nickel, copper, and zinc, along with organic compounds and other toxic chemicals (Muthusamy et al. 2023). When effluent treatment is inadequate and waste is disposed of in unlined areas, chemicals can readily leach into groundwater (Nagaraj & Masilamani 2023). Consequently, high concentrations of heavy metals are found in industrial areas of Gujarat, Maharashtra, Tamil Nadu, and West Bengal (Bhuiyan & Ray 2017).

3.8.3. Domestic Sewage and Solid Waste

In addition, poor sewage disposal and unreliable sanitation facilities in urban areas also cause groundwater contamination. When untreated sewage enters the ground, it carries nitrates, phosphates, chlorides, and various organic compounds with it, thereby contaminating groundwater (Yasaswini et al. 2024). In rural areas, open defecation also causes environmental pollution, leading to contamination of water bodies (Mukherjee et al. 2021). Moreover, when solid wastes are disposed of in open dumps, leachate may carry heavy metals, organic compounds, and dissolved solids, thereby contaminating groundwater (Thalod & Sharma 2024).

3.8.4. Mining Operations

Mining activities such as coal, iron, and bauxite mining cause acid mine drainage, suspended solids, and elevated levels of heavy metals (Panneerselvam et al. 2023). Mining-related groundwater pollution is significant in Jharkhand, Chhattisgarh, and Odisha (Reddy et al. 2022).

3.9. Contamination Pathways and Mechanisms

Groundwater contamination occurs in various forms. Groundwater may be contaminated by seepage from surface sources, downward percolation from the unsaturated zone, and horizontal movement from already contaminated surface sources such as rivers, lakes, and canals. Groundwater may also be contaminated vertically or horizontally along fractures and joints, especially in hard rocks (Cherukumilli et al. 2017). Contaminated groundwater does not move in an arbitrary manner; it is influenced by various elements. The behavior and movement of the contaminant depend on the characteristics of the aquifer, i.e., the ease with which both water and contaminants pass through it (permeability), the available void spaces (porosity), and the minerals that react with the contaminant. Other elements include the hydrogeological characteristics, i.e., the rate at which the water table replenishes, the rate at which the groundwater

moves, and the depth at which the water table lies. Finally, there are the characteristics of the contaminant, i.e., its solubility how easily it moves, and the period it lasts in the environment without degrading. All these elements contribute to the behavior and movement of the contaminant in the aquifer system (Kalaiselvi & Pillai 2019)

4. HEALTH IMPLICATIONS

Fig. 5 depicts the pathway from contamination sources through exposure routes (drinking water, food chain, dermal contact) to health outcomes. It shows acute effects (gastrointestinal illness, methemoglobinemia) and chronic effects (fluorosis, arsenicosis, cancer, neurological disorders, kidney disease) with vulnerable populations (children, pregnant women, elderly) highlighted. The contamination sources and pathways discussed above directly affect human exposure to polluted groundwater. The presence of pollutants such as fluoride, arsenic, nitrate, and heavy metals in groundwater poses serious health risks, which are discussed in the section below. Fig. 5 illustrates the relationship between groundwater contamination exposure pathways and associated human health outcomes. The figure indicates that drinking water remains the dominant exposure pathway for most groundwater contaminants in India. Long-term exposure to fluoride, arsenic, nitrate, and heavy metals contributes to chronic health effects including fluorosis, arsenicosis, neurological disorders, kidney damage, and carcinogenic risks. The figure also highlights that children and elderly populations are more vulnerable because of higher exposure sensitivity and physiological susceptibility.

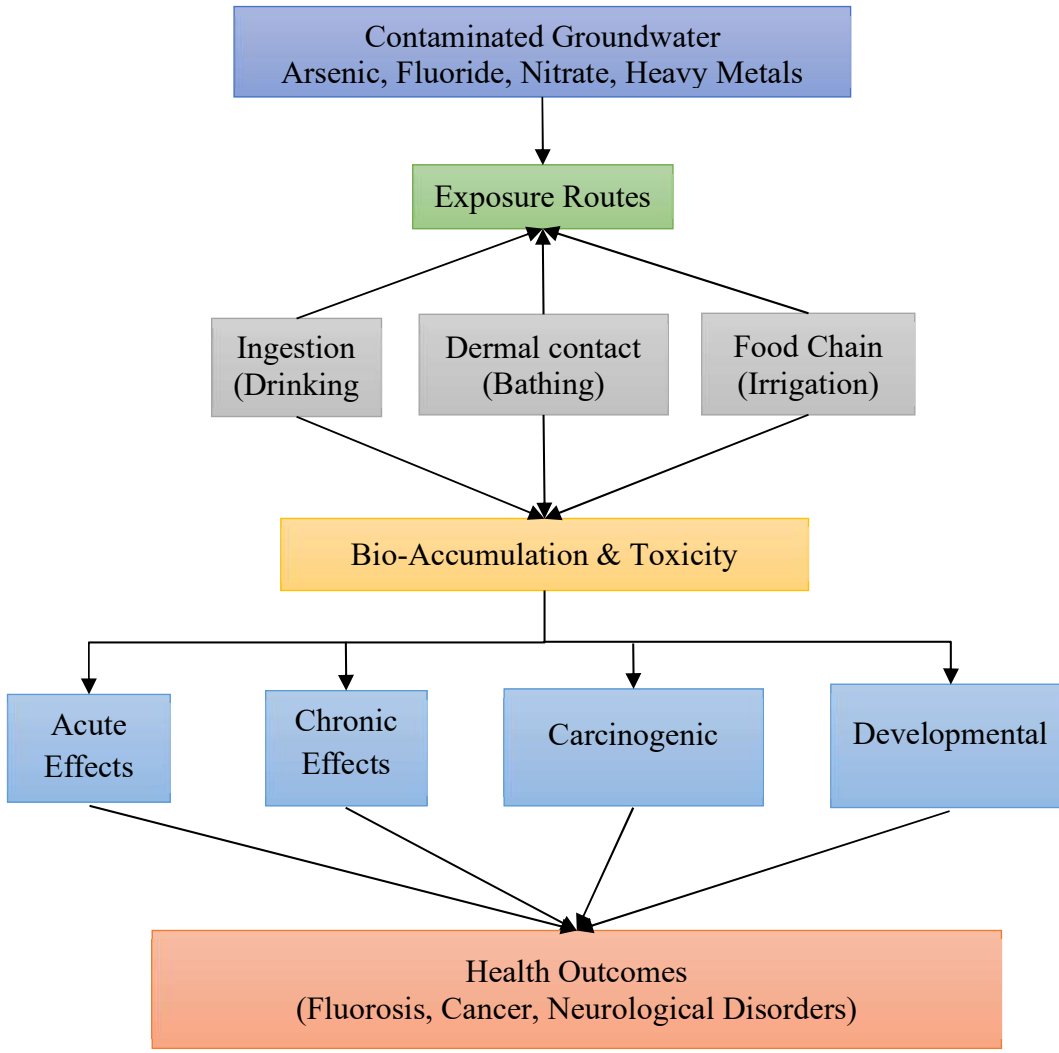


Fig. 5: Major groundwater contamination exposure pathways and associated human health impacts in India.

4.1. Health Effects of Major Contaminants

4.1.1. Fluoride

When the amount of fluoride exceeds 1.5 mg L^{-1}, there is a high probability of causing fluorosis in both teeth and bones. In the case of teeth, fluorosis causes mottling and discoloration of the teeth, while in bones, it causes changes in the structure of the bones, joint pain, and lack of mobility (Das et al. 2009). In India, there is a high prevalence of fluorosis, and Previous national and regional assessments have estimated that nearly 66 million people in India may be exposed to fluoride-affected groundwater (Ghosh et al. 2024). In addition, it causes neurological effects, impacts IQ in children, and causes reproductive problems (Gupta et al. 2019).

4.1.2. Arsenic

Prolonged consumption of drinking water contaminated with arsenic causes a condition referred to as arsenicosis, which manifests itself in the form of changes in the color of the skin, keratosis, and other skin lesions (Gupta et al. 2015). Prolonged consumption also increases the risk of cardiovascular problems, neurological problems, diabetes, and various types of cancer, which affect the skin, lungs, bladder, and kidneys. A considerable number of people in eastern India continue to be at risk of arsenic poisoning through the drinking water supplied to them through the taps (Cherukumilli et al. 2018). Among the various compounds of arsenic, arsenite (As^{3+}) is found to be more poisonous and mobile than arsenate (As^{5+}) (Inaniyan & Raychoudhury 2019).

4.1.3. Nitrate

Drinking water with nitrate concentrations above 45 mg L^{-1} are particularly hazardous for infants, as it can cause methemoglobinemia, or 'blue baby syndrome,' which impairs the blood's capacity to carry oxygen. Adults who are frequently exposed to nitrates have a higher probability of developing gastric, thyroid, and reproductive system diseases (Kumar et al. 2017). In areas with heavy agricultural activity, there is a higher incidence of diseases associated with nitrate poisoning (Mandal & Sanyal,.2019).

4.1.4. Heavy Metals

Heavy metals in groundwater pose health risks. Lead affects the nervous system, resulting in reduced IQ, behavioral problems, and kidney damage (Singh et al. 2024). Cadmium causes a buildup of the metal in the kidneys, resulting in renal failure and bone disease (Awasthi et al. 2021). Hexavalent chromium is a known carcinogen and causes lung and digestive cancers (Khandaker & Rahman 2022). Iron and manganese, although essential, in high concentrations make water unattractive and have a potential impact on the neurological system (Koley 2021).

4.1.5. Salinity and Hardness

Excessive levels of total dissolved solids and hardness in water cause kidney stones, heart and blood vessel problems, and stomach upsets (Ahada & Suthar 2019). Increased levels of sodium also pose a threat, especially for people suffering from hypertension or heart conditions (Yadav et al. 2019).

5. HEALTH RISK ASSESSMENT

For assessing the health risks associated with groundwater contamination, the hazard quotient (HQ) and hazard index (HI) are often employed as measures of noncarcinogenic risk, while the cancer risk (CR) is applied to those substances that are known to induce carcinogenicity (Khandaker & Rahman 2022). If the HQ or HI is greater than or equal to 1, it indicates that a particular compound poses a potential health risk. In different regions of India, it has been reported that the HI value is greater than unity for 71 to 78% of groundwater samples contaminated with fluoride and nitrate (Marghade et al. 2023). Estimated cancer risks in areas contaminated by arsenic often approach and even surpass the acceptable limit of 10^{-4}. Several regional health risk assessment studies have reported that approximately 60–80% of analyzed groundwater samples in arsenic-affected regions exceeded the acceptable carcinogenic risk threshold. (Gupta et al. 2015). This also emphasizes the seriousness of the long-term risks of arsenic exposure through drinking water and the need to address the problem. Children are also at a higher risk than adults because they weigh less and drink more water per kilogram of weight than adults (Singh et al. 2024). Other vulnerable groups, like pregnant women, elderly people, and people with weakened immune systems, are also more susceptible to health risks and, therefore, need special consideration in assessing health risks and planning for water management (Awasthi et al. 2021). Fig. 5 illustrates the major routes by which groundwater contamination translates to human health effects. Considering the health hazards associated with groundwater contamination, the need for remediation and treatment of the groundwater arises. The next section highlights the different technologies that can be used in mitigating groundwater contamination in India. For assessing the health risks associated with groundwater contamination, the hazard quotient (HQ) and hazard index (HI) are often employed as measures of noncarcinogenic risk, while the cancer risk (CR) is applied to those substances that are known to induce carcinogenicity. Comparative evaluation of reviewed studies indicates that fluoride and arsenic contamination generally contribute the highest non-carcinogenic and carcinogenic health risks in

Indian groundwater systems. Fluoride-related hazard index (HI) values greater than 1 have frequently been reported in semi-arid and hard rock regions of Rajasthan, Telangana, Karnataka, and Tamil Nadu, particularly among children due to lower body weight and higher water intake rates. Similarly, arsenic-contaminated groundwater in eastern India, especially West Bengal and Bihar, consistently shows elevated carcinogenic risk values exceeding the acceptable USEPA risk threshold of 10^{-4}. In contrast, nitrate-associated health risks are comparatively more localized and strongly linked with agriculturally intensive regions such as Punjab, Haryana, and Gujarat. The reviewed literature therefore suggests that health risks from groundwater contamination in India are highly region-specific and controlled by both hydrogeological conditions and anthropogenic activities.

6. WATER QUALITY STANDARDS AND INDICES

Groundwater quality assessment entails its comparison with drinking water standards to ascertain its suitability for domestic consumption and other uses. These standards are guidelines for establishing benchmark values for water quality, which are used for the evaluation, regulation, and management of water quality. Besides individual parameter analysis, water quality indices are also employed to integrate two or more parameters into a single value, which is a measure of water quality in general.

6.1. Regulatory Standards

Groundwater quality standards are determined by different national and international organizations, with the aim of protecting public health and providing safe drinking water. In India, the Bureau of Indian Standards (BIS) specifies the limits of safe and permissible concentrations of drinking water quality, and the World Health Organization (WHO) specifies the global reference values for the same. The United States Environmental Protection Agency (USEPA) specifies the guideline values, which are often used as a reference by researchers in their studies. These guidelines specify the threshold concentrations of major ions, nutrients, heavy metals, etc., present in the groundwater. These limits are critical in order to avoid health risks associated with the long-term use of groundwater (Krishnappa et al. 2024). Table 4 summarizes the permissible limits recommended by BIS, WHO, and USEPA for key groundwater quality parameters.

6.2. Water Quality Index (WQI)

The Water Quality Index (WQI) is a method to represent the overall water quality of groundwater with a single number, obtained by calculating several physicochemical parameters (Hanse et al. 2019). By integrating multiple water quality factors, the Water Quality Index simplifies complex information for decision-makers and water resource managers. Among the various methods available, the weighted arithmetic index method is the most popular method used in Indian groundwater research due to its ease and efficiency. However, significant methodological variability exists among WQI studies conducted across India. Different researchers have used different combinations of physicochemical parameters, weighting schemes, normalization approaches, and classification criteria depending on regional hydrogeological conditions and study objectives. While some studies considered only major physicochemical parameters such as pH, TDS, hardness, fluoride, and nitrate, others additionally incorporated heavy metals, microbiological indicators, or irrigation-related parameters. Similarly, the relative weights assigned to parameters vary considerably among studies, which directly influences the final WQI values and classification

Table 4: Permissible limits for groundwater quality parameters (Krishnappa et al. 2024).

Parameter	Unit	BIS (IS10500:2012)	WHO (2017)	USEPA (2018)	Health Significance
pH	-	6.5–8.5	6.5–8.5	6.5–8.5	Corrosion, taste
TDS	mg L^{-1}	500 (2000) *	1000	500	Taste, scaling
Total Hardness	mg L^{-1}	200 (600) *	500	-	Scaling, cardiovascular
Fluoride	mg L^{-1}	1.0 (1.5) *	1.5	4.0	Fluorosis
Nitrate	mg L^{-1}	45	50	45	Methemoglobinemia
Arsenic	µg L^{-1}	10	10	10	Cancer, Arsenicosis
Lead	µg L^{-1}	10	10	15	Neurological damage
Cadmium	µg L^{-1}	3	3	5	Kidney damage
Chromium	µg L^{-1}	50	50	100	Cancer
Iron	mg L^{-1}	0.3	-	0.3	Aesthetic, taste

Note: Adapted from the Bureau of Indian Standards (IS 10500:2012), World Health Organization (2017), and USEPA (2018).
*Values in parentheses indicate maximum permissible limits in the absence of alternate sources.

categories. Therefore, direct comparison of WQI values across different regions should be interpreted cautiously, as methodological differences may contribute to variations in reported groundwater quality classifications. (Mukherjee & Singh 2022). The construction of WQI entails four major stages, which include the selection of appropriate water parameters, assigning weights to each parameter depending on their relative importance in ensuring safe water for human consumption, determining individual water quality ratings, and finally, integrating all ratings to form a single index

Table 5: Major groundwater contaminants and associated health effects.

Contaminant	Sources	Affected Regions	Concentration Range	Health Effects	Indicative Population Exposure	Authors
Fluoride	Geogenic (granite, gneiss weathering)	Rajasthan, Tamil Nadu, Andhra Pradesh, Karnataka, Madhya Pradesh	1.5–12 mg L^{-1}	Dental fluorosis, skeletal fluorosis, neurological effects	66 million	Das et al. 2009, Ghosh et al. 2024, Gupta et al. 2019
Arsenic	Geogenic (Fe-oxyhydroxide reduction)	West Bengal, Bihar, Uttar Pradesh, Assam, Chhattisgarh	10–3200 µg L^{-1}	Arsenicosis, skin lesions, cancer (skin, lung, bladder)	Estimated from regional studies and published assessments	Gupta et al. 2015, Cherukumilli et al. 2018, Inaniyan & Raychoudhury 2019
Nitrate	Agricultural fertilizers, sewage, animal waste	Punjab, Haryana, Gujarat, Tamil Nadu, Delhi NCR	45–300 mg L^{-1}	Methemoglobinemia (infants), gastric cancer, thyroid disorders	Estimated from regional agricultural groundwater studies	Marghade et al. 2023, Kumar et al. 2017, Mandal & Sanyal 2019
Heavy Metals (Pb, Cd, Cr, Cu, Zn)	Industrial effluents, mining, E-waste	Gujarat, Maharashtra, West Bengal, Jharkhand, Tamil Nadu	Variable (exceeding limits)	Neurological damage, kidney dysfunction, cancer, developmental disorders	Localized population exposure reported	Singh et al.2024, Awasthi et al.2021, Khandaker & Rahman, 2022
Salinity (High TDS, Cl^-)	Seawater intrusion, evaporation, mineral dissolution	Coastal regions (Gujarat, Tamil Nadu, Kerala, Goa), arid zones	TDS: 1500–5000 mg L^{-1}	Kidney stones, cardiovascular issues, gastrointestinal disorders	35–45 million	Ahada & Suthar 2019, Hussain et al. 2012

Note: Population estimates are indicative and derived from multiple regional studies; actual values may vary with spatial and temporal factors. Values in Table 5 are compiled from regional investigations and published assessments rather than standardized national-scale datasets.

Table 6: Water Quality Index (WQI) classification and interpretation.

WQI Range	Water Quality Category	Suitability for Drinking	Treatment Required	Typical Characteristics	% of Indian Samples	Authors
<50	Excellent	Suitable without treatment	None	All parameters well within limits	15–25%	Hanse et al. 2019, Mukherjee & Singh 2022, Sahoo et al. 2024
50–100	Good	Suitable with minimal treatment	Simple disinfection	Most parameters within limits	40–64%	Hanse et al. 2019, Mukherjee & Singh 2022 Sahoo et al. 2024
100–200	Poor	Requires treatment	Conventional treatment	Some parameters exceed limits	8–35%	Ravindra & Mor.2019, Adimalla et al.2018
200–300	Very Poor	Requires advanced treatment	Advanced treatment needed	Multiple parameters exceed limits	2–15%	Ravindra & Mor 2019, Adimalla et al. 2018 Ahada & Suthar 2019)
>300	Unsuitable	Not suitable for drinking	Extensive treatment/alternate source	Severe contamination	3–11%	Ravindra & Mor. 2019, Adimalla et al.2018 Ahada & Suthar.2019

Note: Percentage ranges represent compiled estimates from multiple regional studies and may vary with hydrogeological conditions, sampling methods, and spatial coverage. These values represent trends from reviewed regional studies, not national-scale statistical estimates.

Table 7: Comparative health risk trends reported in Indian groundwater studies.

Contaminant	Dominant Risk Type	Most Vulnerable Regions	Commonly Affected Population	Reported Risk Trend	References
Fluoride	Non-carcinogenic (HI > 1)	Rajasthan, Telangana, Karnataka, Tamil Nadu	Children	Very High	Das et al. 2009, Ghosh et al. 2024, Gupta et al. 2019, Ahada & Suthar 2019
Arsenic	Carcinogenic (CR > 10^{-4})	West Bengal, Bihar, Assam	General population	Very High	Gupta et al. 2015, Cherukumilli et al. 2018, Inaniyan & Raychoudhury 2019
Nitrate	Non-carcinogenic	Punjab, Haryana, Gujarat	Infants	Moderate–High	Kumar et al. 2017, Mandal & Sanyal 2019, Marghade et al. 2023
Heavy Metals	Carcinogenic and non-carcinogenic	Industrial and mining regions	Adults and children	Moderate	Singh et al. 2024, Awasthi et al. 2021, Khandaker & Rahman 2022
Salinity/TDS	Chronic exposure-related risk	Coastal and arid regions	General population	Moderate	Ahada & Suthar 2019, Hussain et al. 2012

Note: Comparative health-risk trends are synthesized from published regional groundwater assessment studies conducted across different hydrogeological settings in India.

value (Sahoo et al. 2024). The parameters with higher health effects, e.g., nitrates, fluoride, and TDS, have higher weights in the equation. After determining the WQI, groundwater is normally grouped into five classes of water quality, namely, excellent (<50), good (50–100), poor (100–200), very poor (200–300), and not suitable for consumption (>300) (Ravindra & Mor 2019). Several reviewed studies have reported that a considerable proportion of groundwater samples fall within the "good" water quality category; however, the reported percentages vary depending on the adopted WQI methodology, parameter selection, weighting scheme, and classification criteria used in different studies. Approximately 15–30% lie in the poor to very poor range. Higher values of WQI are recorded in industrial and arid zones, while better water quality is recorded in zones with higher rates of recharge (Adimalla et al. 2018). The areas where the water quality index (WQI) is higher are the areas where industries are located, farming is done, and where the climate is arid to semi-arid (Ahada & Suthar 2019). It is worth noting that the differences in the percentages and concentration range reported by different studies can be attributed to differences in spatial coverage, sampling frequency, and methods of analysis. Thus, the data presented in this review is best interpreted as trends rather than exact national data. Further studies need to be undertaken on standardized data collection methods and statistical aggregation. Most of the studies have used normalized groundwater quality parameters against standard guideline values like BIS (IS 10500) and WHO limits. In the present review, the results have been interpreted in relation to standard values instead of comparing the actual values from different studies, which facilitates evaluation (Krishnappa et al. 2024). The WQI trends summarized in this review are therefore intended to provide indicative comparative assessment of groundwater quality conditions across regions rather than standardized national-scale WQI rankings.

7. INTEGRATED ASSESSMENT FRAMEWORK FOR GROUNDWATER QUALITY IN INDIA

Based on the synthesis of the literature, an integrated framework has been proposed for connecting groundwater contamination sources, hydrogeochemical processes, health risks, and remediation strategies in the Indian context (Mukherjee & Singh 2022, Malik et al. 2023). Both anthropogenic and geogenic sources of groundwater contamination have been identified, and the hydrogeochemical processes influencing groundwater quality have also been analyzed (Singh et al. 2022, Yadav et al. 2018). Human health risks from groundwater contamination have also been discussed in the framework. Remediation strategies have also been included in the framework for addressing groundwater contamination in the Indian scenario. This framework will help in understanding groundwater contamination in a better way for sustainable groundwater management in the country. This integrated framework represents a novel contribution of this review by linking contamination sources, hydrogeochemical processes, health risks, and remediation strategies in a unified manner.

8. REMEDIATION STRATEGIES

The diagram presents the Integrated Remediation Technology Framework for Indian Groundwater. It is a decision guide to select appropriate cleanup technologies based on the nature of the contaminant, concentration of the contaminant, scale of the problem, and social and economic factors. The framework includes source control technologies, in-situ technologies like PRBs and phytoremediation, ex-situ

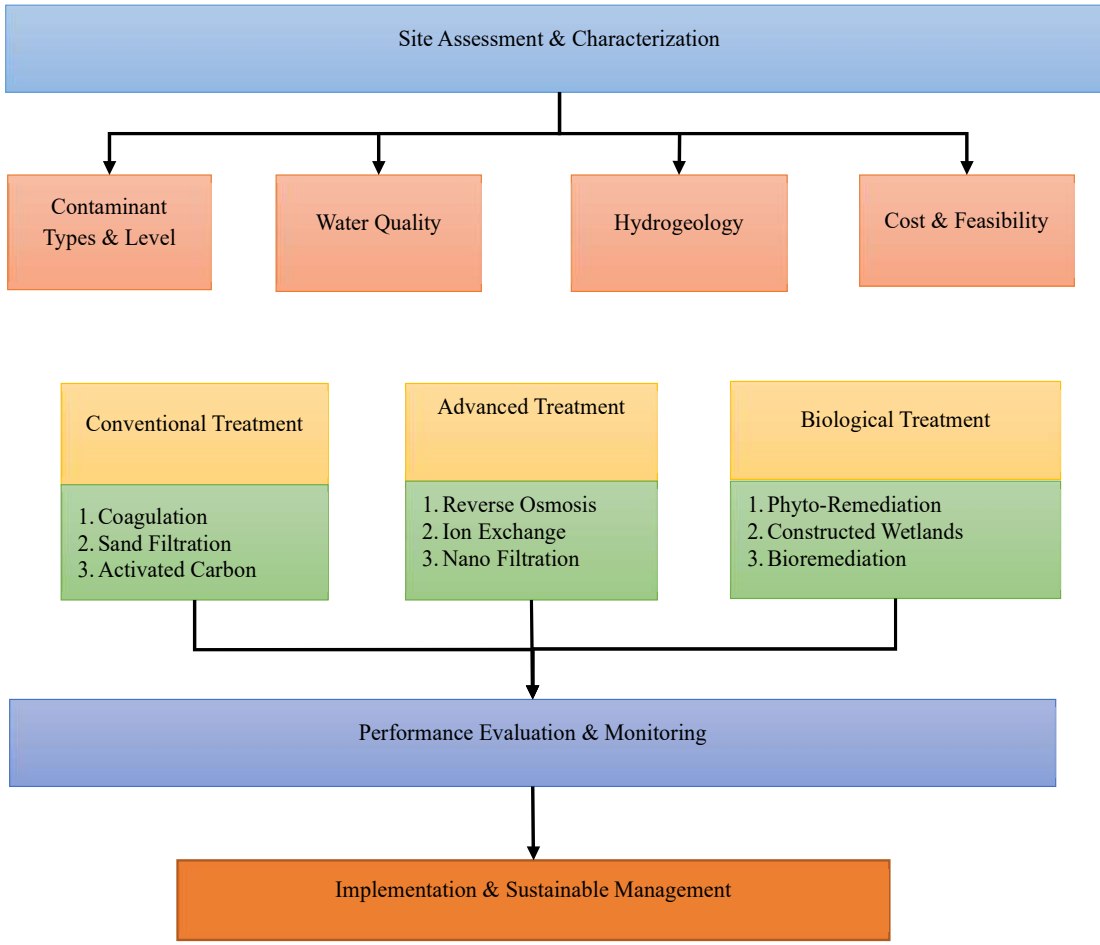


Fig. 6: Framework for selection of groundwater remediation technologies based on contaminant type and site conditions.

technologies like RO, adsorption, and electrocoagulation, and monitoring technologies to address the issue of groundwater in a holistic manner. Fig. 6 demonstrates that selection of groundwater remediation technologies depends on contaminant type, contaminant concentration, treatment scale, economic feasibility, and operational complexity. The framework indicates that advanced membrane technologies are highly effective for multi-contaminant removal but are associated with high operational cost and energy demand. In contrast, adsorption-based and nature-based technologies are more suitable for decentralized rural applications because of lower operational requirements and improved sustainability.

9. CONVENTIONAL TREATMENT TECHNOLOGIES

9.1. Reverse Osmosis (RO)

Reverse osmosis has emerged as a preferred treatment technology for groundwater in India because of its high removal capabilities for a wide array of impurities. In this method, water is pressurized to pass through a semi-permeable membrane, resulting in a reduction of fluoride levels by 85–95%, arsenic by 90–98%, nitrate by 85–92%, heavy metals by 90–99%, and total dissolved solids by 95–98%. RO systems have been found to be highly effective and are used across residential, institutional, and community water treatment systems. However, there are some limitations to this technology, such as high energy requirements, membrane fouling, maintenance, and the difficulty of handling the reject brine. The cost of the equipment varies widely, from ₹5,000 to ₹25,000 for household systems to ₹5 to ₹50 lakhs for community systems (Muthusamy et al. 2023).

9.2. Nanofiltration (NF)

Nanofiltration operates at lower pressures compared to reverse osmosis treatment. The process has a strong ability

to remove divalent ions, organic matter, and a certain amount of dissolved solids. The process has a removal efficiency of 70–85% (Nagaraj & Masilamani,.2023). The process is effective in reducing hardness, sulfates, and some fluoride in groundwater supplies. Due to the low energy consumption and less brine disposal compared to reverse osmosis, the process is regarded as a cost-effective solution for brackish water treatment (Bhuiyan & Ray 2017).

9.3. Activated Alumina Adsorption

Activated alumina is frequently utilized for the adsorption-based removal of fluoride and arsenic from water. It has been seen to remove fluoride to the extent of 80 to 90%, and arsenic to the extent of 75 to 85%. However, this depends on the water being treated (Yasaswini et al. 2024). The method is preferred for its simple design, easy operation, and low cost, estimated at ₹2,000–₹10,000 for domestic-scale treatment. However, its effectiveness is pH-dependent, and regeneration or replacement is required periodically (Mukherjee et al. 2021).

9.4. Ion Exchange

Ion exchange resins selectively extract impurities, like fluoride, nitrates, and heavy metals, from groundwater. The method usually eliminates 85–95% of impurities, depending upon the type of resin and water quality (Thalod & Sharma 2024). However, ion exchange resins also have a drawback, as their periodic regeneration is necessary using chemical solutions, leading to a disposal problem. The effectiveness of ion exchange resins is also restricted by the lack of proper disposal facilities for solid wastes (Mandal & Sanyal 2019).

10. ADVANCED AND EMERGING TREATMENT TECHNOLOGIES

10.1. Electrocoagulation

Electrocoagulation has been shown to be a viable electrochemical technique for treating groundwater contaminated by fluoride, arsenic, heavy metals, and suspended solids. In this technique, coagulant species are produced in situ through sacrificial dissolution of electrodes, with reported removal efficiencies of 75–90% for fluoride, 80–95% for arsenic, and 85–98% for heavy metals. The primary advantages of this technique include the elimination of the need for chemical dosing, a compact design, and low levels of sludge formation. However, the technique has some limitations in real-world application, which include energy consumption (0.5–3 kWh m^{-3}), electrode passivation, and the need for electrode replacement (Kalaiselvi & Pillai 2019, Vijaylaxmi & Khan 2021).

10.2. Adsorption-Based Technologies

Recently, breakthroughs in adsorption technology have led to the development of a new range of high-performing adsorbents for groundwater treatment. Biochar, clay, metal oxide, and complex nanostructured adsorbents have shown promising adsorption capacities for the removal of fluoride, arsenic, and various heavy metals, with removal efficiencies ranging from 80–99% (Saha et al. 2014). Of specific interest are adsorbents made from agricultural waste materials, which are rice husk, coconut shells, and neem leaves, and are gaining popularity as a cost-effective, green technology solution for groundwater treatment in rural communities (Karunanidhi et al. 2024). However, there are still challenges in the adsorption process, which include the regeneration of the adsorbents, the adsorbent's lifespan, and the disposal of the exhausted adsorbents, which need further optimization (Kumar et al. 2017).

10.3. Phytoremediation

Phytoremediation utilizes the natural uptake of pollutants by plants, thereby purifying water and soil. Water-loving plants, like the water hyacinth, duckweed, and vetiver, and those on land, like the sunflower, mustard, and ferns, have been observed to take up heavy metals, nutrients, and organic chemicals (Muthusamy et al. 2023). It offers an environmentally friendly and cost-effective approach for the remediation of shallow aquifers, groundwater with links to surface water, and constructed wetlands (Nagaraj & Masilamani 2023). However, its application is restricted by the low rate of cleanup, seasonal fluctuations, and the management and disposal of the polluted vegetation (Bhuiyan & Ray 2017).

10.4. Membrane Bioreactors (MBRs)

Membrane bioreactors utilize the combination of a biological process and membrane filtration for the effective removal of organic matter, nutrients, and pathogens (Yasaswini et al. 2024). The process has been found to be effective in the treatment of polluted groundwater and wastewater intended for aquifer recharge and reuse. The process has the advantage of high treatment efficiency in a space-saving design; however, the problem of membrane fouling and the operating costs need to be taken into consideration (Mukherjee et al. 2021).

10.5. Permeable Reactive Barriers

The permeable reactive barrier (PRB) technology is an innovative groundwater remediation technology. In the PRB technology, the contaminated groundwater is treated with the help of a reactive medium such as zero-valent iron,

activated carbon, or limestone (Thalod & Sharma 2024). The groundwater flows through the medium and is treated. The technology has been found to treat heavy metals, chlorinated organic compounds, and nutrient compounds (Cherukumilli et al. 2017).

10.6. Technology Selection and Implementation

The choice of technology is based on the type of contaminant present and its concentration, the quality characteristics of the water to be treated, the scale of the treatment (residential, community, or regional), cost viability, the complexity of the technology, and local technical capacity (Kalaiselvi & Pillai 2019). Table 8 summarizes the various remediation technologies. In most cases, the best results are achieved by combining different technologies into a hybrid technology. For these technologies to be effective, the community needs to be engaged with capacity building and sustainable funding models. In rural and disadvantaged areas, policy support, subsidies, and awareness are key to the use of the technologies. Comparative evaluation of groundwater remediation technologies indicates that no single treatment method is universally suitable for all groundwater contamination conditions in India. Reverse osmosis demonstrates the highest overall removal efficiency for fluoride, arsenic, nitrate, salinity, and heavy metals; however, its high energy requirement, membrane fouling, and reject brine disposal significantly limit its applicability in economically weaker rural regions. Nanofiltration provides comparatively lower operational pressure and energy consumption but is less effective for complete dissolved contaminant removal.

Table 8: Comparison of groundwater remediation technologies.

Technology	Target Contaminants	Removal Efficiency	Capital Cost	Operating Cost	Advantages	Limitations	Rural Applicability	Authors
Reverse Osmosis	Fluoride, arsenic, nitrate, heavy metals, TDS	85–98%	High (₹5,000–50 Lakh)	High	High efficiency, multiple contaminants	Energy-intensive, brine disposal	Moderate	Muthusamy et al. 2023, Nagaraj & Masilamani 2023, Bhuiyan & Ray 2017
Activated Alumina	Fluoride, arsenic	75–90%	Low (₹2,000–10,000)	Low	Simple, low cost	pH-dependent, regeneration	High	Yasaswini et al. 2024, Mukherjee et al. 2021
Electrocoagulation	Fluoride, arsenic, heavy metals	75–98%	Moderate (₹10,000–5 Lakh)	Moderate	No chemicals, compact	Electrode replacement, energy	Moderate	Kalaiselvi & Pillai 2019, Vijaylaxmi & Khan 2021
Adsorption (Biochar, modified materials)	Fluoride, arsenic, heavy metals	80–99%	Low (₹1,000–8,000)	Very low	Low cost, sustainable	Regeneration, disposal	Very High	Saha et al. 2014, Karunanidhi et al. 2024, Kumar et al. 2017
Phytoremediation	Heavy metals, nutrients, organics	60–85%	Very low (₹500–5,000)	Very low	Eco-friendly, sustainable	Slow, seasonal, biomass disposal	High	Muthusamy et al. 2023, Nagaraj & Masilamani 2023, Bhuiyan & Ray 2017
Ion Exchange	Fluoride, nitrate, heavy metals	85–95%	Moderate (₹5,000–20,000)	Moderate	Selective removal	Brine disposal, regeneration	Moderate	Mandal & Sanyal 2019, Thalod & Sharma 2024
Nanofiltration	Hardness, sulfate, moderate TDS	70–85%	Moderate-High (₹8,000–30 Lakh)	Moderate	Lower pressure than RO	Partial removal	Low–Moderate	Nagaraj & Masilamani 2023, Bhuiyan & Ray 2017

Note: Synthesized from groundwater treatment and remediation studies. Cost ranges are indicative and may vary with system capacity, location, and operational conditions. Rural applicability in Table 8 is based on operational simplicity, energy requirements, maintenance demand, waste disposal complexity, and economic feasibility reported in the reviewed studies.

Adsorption-based technologies using activated alumina, biochar, and modified low-cost materials are considered more suitable for rural and decentralized applications because of their lower cost, operational simplicity, and minimal energy requirements, although periodic adsorbent regeneration and disposal remain important operational concerns. Electrocoagulation has shown promising removal efficiency for fluoride, arsenic, and heavy metals, but field-scale implementation is constrained by electrode passivation, electricity demand, and sludge management requirements. Similarly, ion exchange systems provide effective selective contaminant removal but generate secondary brine waste requiring appropriate disposal. Therefore, technology selection in the Indian context should consider contaminant type, hydrogeochemical conditions, treatment scale, operational complexity, waste disposal requirements, energy availability, and socio-economic feasibility, particularly in rural and resource-limited regions.

11. FUTURE PERSPECTIVES AND RESEARCH DIRECTIONS

11.1. Emerging Research Priorities

Future areas of research should address the following gaps in knowledge about groundwater quality in India. Some of the areas that need priority in the future are the following: emerging contaminants in groundwater, which include pharmaceuticals, pesticides, microplastics, and PFAS (Pal et al. 2009, Sultan et al. 2024). There is a pressing need for treatment technologies that are cost-effective, energy-efficient, and adaptable to local conditions, especially in rural areas (Karunanidhi et al. 2024). Advances in monitoring and forecasting can be achieved through integrating remote sensing, GIS, and machine learning, which will facilitate real-time continuous evaluation of groundwater quality (Thalod & Sharma 2024). Moreover, the impacts of climate change on groundwater recharge, the mobilization of contaminants, and the long-term trends in water quality require special research attention (Kaur et al. 2019). The research focus of the health sector needs to move beyond the examination of individual factors to the evaluation of the collective impacts of the risks that arise from the joint action of various contaminants (Khandaker & Rahman 2022). Moreover, the role of managed aquifer recharge (MAR) as a two-fold approach to enhancing groundwater quality and increasing its storability needs to attract more research attention on a regional scale (Dhakshinamoorthy & Selvarajan 2025). Based on the trends in groundwater quality being reported from different regions of India, it has been assessed that regions with high intensity in agricultural practices and groundwater depletion will have high nitrate and salinity problems in the near future (Kaur et al. 2019, Kumar et al. 2017). Similarly, changes in recharge patterns due to climate variability will enhance the mobilization of geogenic contaminants like fluoride and arsenic in groundwater (Dhakshinamoorthy & Selvarajan 2025).

12. POLICY AND MANAGEMENT RECOMMENDATIONS

For effective groundwater quality management in India, it is important to adopt a multi-tier strategy. Strengthening the regulatory system and enforcement of regulations are significant steps towards curbing pollution caused by agricultural, industrial, and urban activities (Shukla & Saxena 2021). Preventive measures should focus on source control, including the adoption of sustainable agriculture, better management of industrial effluent disposal, and scientific disposal of solid and liquid waste (Kumar et al. 2017). A robust, comprehensive groundwater quality monitoring system is vital, which is supported by real-time data collection and information sharing among various regulatory agencies, scientists, and local governments (Gupta et al. 2022). Community engagement must be encouraged through decentralized water quality management, monitoring, and capacity-building programs to empower people to protect and manage groundwater resources (Hossain et al. 2021). Financial incentives, subsidies, and technical support are also necessary to promote the use of water treatment systems at the individual and community levels, especially in rural and disadvantaged areas (Karunanidhi et al. 2024). Another significant factor is to enhance public awareness of groundwater contamination issues and the associated health risks with the help of effective educational campaigns (Das et al. 2009). Ultimately, the key to sustainability is to enhance interdisciplinary research and cooperation between policymakers, scientists, and stakeholders to develop effective groundwater management strategies that are tailored to specific contexts (Kaliyan et al. 2022).

12.1. Technological Innovations

Recent advances in groundwater management reveal some promising technological approaches. Nanotechnology adsorbents and membrane filtration have demonstrated better efficacy in removing a range of impurities, from fluoride and arsenic to heavy metals (Saha et al. 2014). In energy-scarce environments, solar-powered water treatment could be a viable solution for reliable operation in a rural setting (Muthusamy et al. 2023). Real-time groundwater quality monitoring is being strengthened with the help of smart sensor technologies. Internet of Things (IoT) technology, for instance, enables rapid detection of changes in water quality through IoT-based monitoring systems. Simultaneously, AI and machine learning techniques are being used for the

prediction and assessment of groundwater quality (Thalod & Sharma 2024). Nature-based and hybrid technologies, like constructed wetlands and bioremediation, are gaining prominence as they operate with low operating costs and in a highly environmentally friendly manner (Nagaraj & Masilamani 2023). Decentralized treatment technologies, which are designed for households and communities, also hold promise as a solution for groundwater pollution, especially in rural areas (Karunanidhi et al. 2024).

12.2. Sustainable Water Resource Management

Ensuring the sustainability of groundwater resources over the long term requires an integrated water resources approach that connects demands, supplies, and ecosystems. In terms of cutting back on water use, the focus should be on saving water, improving irrigation efficiency, and enhancing the efficiency of water use (Prasad & Rao 2018). In terms of supplying more water, the focus should be on harvesting rainwater, recharging groundwater, and safely reusing treated water to enhance groundwater supplies while lessening the pressure on natural groundwater supplies (Dhakshinamoorthy & Selvarajan 2025). The key to the prevention of further deterioration in the quality of groundwater lies in the effective control of pollution, which includes the reduction of pollution, the application of best management practices, and the enforcement of environmental laws (Kumar et al. 2017). Another important factor is the protection and maintenance of ecosystems that rely on groundwater, which is necessary to maintain the quality of the water itself (Nagaraj & Masilamani 2023). Sustainable water management should be equitable, ensuring everyone has access to water that is safe and reliable, particularly for vulnerable and marginalized groups (Rajendran et al. 2024). As the climate changes, with shifts in rainfall, droughts, and increasingly extreme events, water management strategies should be responsive to these changes to create long-term sustainability (Kaur et al. 2019). Reaching the Sustainable Development Goal for water and sanitation, SDG 6, requires collaboration and coordination among government agencies, scientists, businesses, and social organizations (Shukla & Saxena 2021).

13. LIMITATIONS OF EXISTING STUDIES

Although extensive research has been conducted on groundwater quality in India, several limitations have been identified. One major limitation is that many studies are localized and based on limited sample sizes, which limits their representativeness (Hanse et al. 2019, Mukherjee & Singh 2022). Another limitation is the lack of long-term monitoring data, which limits understanding of temporal trends (Mawari et al. 2022). Sampling and analytical techniques have also been inconsistent (Ahada & Suthar 2018). These limitations indicate that current groundwater research in India lacks sufficient organization and standardization, making it difficult to develop integrated, policy-relevant groundwater management strategies. Large, standardized monitoring programs, consistent analytical methods, and long-term datasets are therefore needed for reliable comparison and prediction of groundwater quality.

13.1. Data Variability and Comparability Considerations

Integrating the groundwater quality data from various studies may pose difficulties due to the inconsistencies in spatial distribution, time scales, and methodologies. The hydro-geological conditions, such as the presence of alluvial or hard rock formations, affect the movement of water and the presence of impurities. Although the review has provided an integrated overview of the groundwater quality trends in India, the results must be considered indicative rather than exact quantitative data (Mawari et al. 2022, Ahada & Suthar 2018). Population exposure estimates and contamination percentages reported in the reviewed literature are derived from regional investigations conducted under different hydrogeological and methodological conditions and should therefore be interpreted as indicative estimates rather than precise national-scale statistics.

13.2. Integrated Perspective on Groundwater Contamination

Groundwater contamination in India is a multifaceted phenomenon involving the interrelationship between sources of contamination, hydrogeochemical processes, and human health impacts (Mukherjee & Singh 2022, Malik et al. 2023). Human activities such as agriculture, industrial discharge, and urbanization are sources of groundwater contamination in India, while hydrogeochemical processes play an important role in groundwater chemistry, increasing the concentration of contaminants such as fluoride, arsenic, nitrate, and heavy metals in groundwater. Human health impacts of groundwater contamination in India are significant, considering the high concentration of contaminants in groundwater. Therefore, groundwater management in India involves an interrelationship between sources of contamination, groundwater chemistry, human health impacts, and appropriate measures for groundwater remediation.

14. CONCLUSIONS

India's groundwater is a complex patchwork, and its quality is determined by a combination of rock, climate, and human factors. When viewed by region, there are specific areas of

contamination. Fluoride is observed in many states, arsenic is a major threat in eastern states, nitrates are present in areas of high agricultural activity, and heavy metals are found in areas of industrial activity. When viewed as a whole, a major share of the population is affected by groundwater contamination, which is a threat to long-term health and sustainability. When physicochemical parameters are examined, a large number of groundwater samples indicate a level of contamination in terms of total dissolved solids, hardness, and nitrates, which indicates a combination of natural and anthropogenic factors. The level of contamination is a result of a combination of geogenic factors, which include rock–water interaction and redox reactions, as well as anthropogenic factors, which include excessive use of fertilizers, industrial effluents, poor sewage disposal, and mining activity. Health risk assessments indicate a high level of non-carcinogenic as well as carcinogenic risks in areas of contamination. Fluorosis, arsenic toxicity, methemoglobinemia, and heavy metal toxicity are major public health concerns, especially in children. The Water Quality Index results indicate that a part of the groundwater is potable, but a major share of it needs to be treated or an alternative source of water needs to be found. There are several options for remediation and treatment, including membrane systems, adsorption, electrochemical treatments, and nature-based solutions, among others, even though none of these options are universally applicable. It should be noted, however, that effective action will involve matching the contaminant profile, water chemistry, scale, cost, and local technical capacity. The present review demonstrates that groundwater contamination in India exhibits strong regional variability controlled by hydrogeological conditions, climatic factors, land-use practices, and anthropogenic pressures. Arsenic contamination remains the most critical concern in the eastern alluvial aquifer systems because of its severe carcinogenic risks and widespread population exposure. In contrast, fluoride contamination dominates the hard-rock terrains of western and southern India, where prolonged groundwater residence time and rock–water interaction enhance fluoride mobilization. Nitrate contamination is primarily associated with agriculturally intensive regions of northern and western India, indicating the growing influence of unsustainable fertilizer usage and poor sanitation practices. Heavy metal contamination is more localized and concentrated near industrial and mining regions, particularly in central and western India. These observations indicate that groundwater management strategies in India should be region-specific rather than adopting a single uniform national approach. From a management perspective, priority should be given to strengthening regional groundwater quality monitoring networks, promoting source-control strategies, improving rural drinking-water treatment infrastructure, and implementing sustainable agricultural and industrial practices. Cost-effective decentralized treatment systems and community-based groundwater management approaches are particularly important for rural and economically weaker regions. The review also identifies several important research gaps, including insufficient long-term monitoring datasets, limited studies on emerging contaminants, lack of standardized groundwater quality assessment methodologies, and inadequate integration of hydrogeochemical modeling with health-risk assessment frameworks. Future research should focus on multidisciplinary approaches integrating hydrogeochemistry, GIS, remote sensing, machine learning, and climate-change assessment to support sustainable groundwater management and policy development in India. In the future, it will be important to focus on the understanding of emerging contaminants, cost-effective treatment options, advanced monitoring and prediction tools, and the assessment of the impact of climate change on groundwater quality, . Integrating these priorities will support decision-making by researchers, policymakers, water managers, and public health professionals. Addressing groundwater quality degradation in India remains an important future priority.

15. ACKNOWLEDGEMENT

We would like to express our sincere appreciation to SVKM NMIMS Global University, Dhule, and the individuals whose contributions and support have greatly enhanced the quality of this research.

16. REFERENCES

Adimalla, N., 2020. Controlling factors and mechanism of groundwater quality variation in semiarid region of South India: an approach of water quality index (WQI) and health risk assessment (HRA). *Environmental Geochemistry and Health*, 42(6), pp.1725-1752. [DOI]

Adimalla, N., Li, P. and Qian, H., 2019. Evaluation of groundwater contamination for fluoride and nitrate in semi-arid region of Nirmal province, South India: a special emphasis on human health risk assessment (HHRA). *Human and Ecological Risk Assessment: An International Journal*, 25(5), pp.1107-1124. [DOI]

Adimalla, N., Qian, H. and Li, P., 2020. Entropy water quality index and probabilistic health risk assessment from geochemistry of groundwaters in hard rock terrain of Nanganur County, South India. *Geochemistry*, 80(4 Supplement), 125544. [DOI]

Ahada, C.P.S. and Suthar, S., 2018. Groundwater nitrate contamination and associated human health risk assessment in southern districts of Punjab, India. *Environmental Science and Pollution Research*, 25(25), pp.25336-25347. [DOI]

Ahada, C.P.S. and Suthar, S., 2019. Assessment of human health risk associated with high groundwater fluoride intake in southern districts of Punjab, India. *Exposure and Health*, 11(2), pp.267-275. [DOI]

Alam, M.A., Mailapalli, D.R. and Maheshwari, B., 2024. Assessing groundwater quality, health risks, and policy implications: a case study

of West Medinipur district, West Bengal, India. *World Water Policy*, 10(1), pp.341-362. [DOI]

Ambade, B., Sethi, S.S., Patidar, K., Gautam, S. and AlShehri, M.A., 2024. Assessing variability and hydrochemical characteristics of groundwater fluoride contamination and its associated health risks in East Singhbhum district of Jharkhand, India. *Journal of Hazardous Materials*, 478, 135498. [DOI]

Awasthi, S., Chauhan, R., Dwivedi, S., Srivastava, S. and Tripathi, R.D., 2021. Arsenic contamination of groundwater and its mitigation strategies. In: A. Singh, M. Agrawal and S.B. Agrawal (eds.) *Water Pollution and Management Practices*. Springer, Singapore, pp.107-119. [DOI]

Barathkumar, S., Sellamuthu, K., Sathiyabama, K., Malathi, P., Kumaraperumal, R., Devagi, P. and Pazhanivelan, S., 2025. Groundwater quality assessment in selected polluted hotspots of Tamil Nadu, India using geospatial and statistical approaches. *Desalination and Water Treatment*, 322, 101047. [DOI]

Basha, U.I., Rajasekhar, M., Ghosh, S., Das, P. and Suresh, U., 2022. Spatial assessment of groundwater quality using CCME-WQI and hydrochemical indices: a case study from Talupula Mandal, Ananthapuramu district, South India. *Applied Water Science*, 12, 168. [DOI]

Bhuiyan, C. and Ray, P.K.C., 2017. Groundwater quality zoning in the perspective of health hazards. *Water Resources Management*, 31(1), pp.251-267. [DOI]

Biswas, T., Paul, S., Ruidas, D., Saha, A., Shit, M., Islam, A.R.M.T., Islam, A. and Costache, R., 2023. Evaluation of groundwater contamination and associated human health risk in a water-scarce hard rock-dominated region of India: Issues, management measures and policy recommendation. *Groundwater for Sustainable Development*, 23, 101039. [DOI]

Central Ground Water Board (CGWB), 2017. *Ground Water Year Book of Kerala (2016-2017)*. Ministry of Water Resources, River Development and Ganga Rejuvenation, Government of India. Available at: CGWB.

Chakraborty, B., Roy, S., Bera, A., Adhikary, P.P., Bera, B., Sengupta, D., Bhunia, G.S. and Shit, P.K., 2021. Geospatial assessment of groundwater quality for drinking through water quality index and human health risk index in an upland area of Chota Nagpur Plateau of West Bengal, India. In: P.K. Shit, P.P. Adhikary and D. Sengupta (eds.) *Spatial Modeling and Assessment of Environmental Contaminants: Risk Assessment and Remediation*. Springer, Cham, pp.327-358. [DOI]

Chaudhry, A.K. and Sachdeva, P., 2021. Groundwater fluoride contamination and probabilistic health-risk assessment in fluoride endemic areas of the Lower Satluj basin, Punjab, India. *Research Square* [Preprint]. [DOI]

Cherukumilli, K., Delaire, C., Amrose, S. and Gadgil, A.J., 2017. Factors governing the performance of bauxite for fluoride remediation of groundwater. *Environmental Science & Technology*, 51(4), pp.2321-2328. [DOI]

Cherukumilli, K., Maurer, T., Hohman, J.N., Mehta, Y. and Gadgil, A.J., 2018. Effective remediation of groundwater fluoride with inexpensively processed Indian bauxite. *Environmental Science & Technology*, 52(8), pp.4711-4718. [DOI]

Das, B., Rahman, M.M., Nayak, B., Pal, A., Chowdhury, U.K., Mukherjee, S.C., Saha, K.C., Pati, S., Quamruzzaman, Q. and Chakraborti, D., 2009. Groundwater arsenic contamination, its health effects and approach for mitigation in West Bengal, India and Bangladesh. *Water Quality, Exposure and Health*, 1(1), pp.5-21. [DOI]

Dhakate, R., More, S., Duvva, L.K. and Enjamuri, S., 2023. Groundwater chemistry and health hazard risk valuation of fluoride and nitrate enhanced groundwater from a semi-urban region of South India. *Environmental Science and Pollution Research*, 30(15), pp.43554-43572. [DOI]

Dhakshinamoorthy, R. and Selvarajan, G., 2025. Comprehensive evaluation of groundwater quality in Mayiladuthurai District, Tamilnadu: physico-chemical and heavy metal analysis. *Ecology, Environment & Conservation*, 31(2), pp.865-872. [DOI]

Dhanya Raj and Shaji, E., 2017. Fluoride contamination in groundwater resources of Alleppey, Southern India. *Geoscience Frontiers*, 8(1), pp.117-124. [DOI]

Gayathri, J.A., Raj, V.T., Sreelash, K., Maya, K. and Padmalal, D., 2025. Comprehensive evaluation of groundwater quality and human health risk assessment in an ecologically sensitive mountainous catchment in Southern Western Ghats. *Human and Ecological Risk Assessment: An International Journal*, 31(7-8), pp.921-953. [DOI]

Ghosh, A., Stening, J. and Chakraborty, R., 2024. Recovery of ecosystems pollution by contaminants of potential concern using phytoremediation techniques. *Integrated Environmental Assessment and Management*, 20(6), pp.1987-2002. [DOI]

Goyal, H., Lanjewar, R., Chitransh, S. and Mondal, P., 2025. A comprehensive exploration of groundwater quality of Ambagarh Chowki region, Chhattisgarh, India: water quality index, health risk, and ANN predictive modeling. *Water Environment Research*, 97(6), e70125. [DOI]

Gupta, D.P., Chaudhary, S., Singh, A., Shukla, R. and Mishra, V.K., 2023. Hydrochemical assessment of groundwater quality in Narmada River basin (Central India). *Water Science & Technology: Water Supply*, 23(2), pp.459-481. [DOI]

Gupta, P., Niveditha, P.S. and Sharada, S., 2019. Treatment of contaminated ground water using phytoremediation technique at Anantapur, India. *World Environment*, 9(2), pp.46-55. [DOI]

Gupta, P., Roy, S. and Mahindrakar, A.B., 2015. Treatment of groundwater using phytoremediation technique at Kolar Gold Fields, India. *International Journal of Environmental Engineering*, 7(1), pp.11-34. [DOI]

Hanse, A., Chabukdhara, M., Baruah, S.G., Boruah, H. and Gupta, S.K., 2019. Fluoride contamination in groundwater and associated health risks in Karbi Anglong district, Assam, Northeast India. *Environmental Monitoring and Assessment*, 191(12), 782. [DOI]

Hossain, M., Patra, P.K., Ghosh, B., Khatun, A. and Nayek, S., 2021. Sensitive assessment of groundwater-associated, multi-exposure health hazards in a fluoride-enriched region of West Bengal, India. *Environmental Geochemistry and Health*, 43(11), pp.4515-4532. [DOI]

Hussain, I., Arif, M. and Hussain, J., 2012. Fluoride contamination in drinking water in rural habitations of central Rajasthan, India. *Environmental Monitoring and Assessment*, 184(8), pp.5151-5158. [DOI]

Inaniyan, M. and Raychoudhury, T., 2019. Application of activated carbon-metal composite for fluoride removal from contaminated groundwater in India. *International Journal of Environmental Science and Technology*, 16(11), pp.7545-7554. [DOI]

Kadam, A., Wagh, V., Jacobs, J., Patil, S., Pawar, N., Umrikar, B., Sankhua, R. and Kumar, S., 2022. Integrated approach for the evaluation of groundwater quality through hydro geochemistry and human health risk from Shivganga river basin, Pune, Maharashtra, India. *Environmental Science and Pollution Research*, 29(3), pp.4311-4333. [DOI]

Kalaiselvi, N. and Pillai, V.K., 2020. Dendritic growth and spread of electrochemical research in India. *Proceedings of the Indian National Science Academy*, 86(2), pp.1001-1013. [DOI]

Kalaivanan, K., Karuppaiah, S. and Duraisamy, S., 2022. Assessment of groundwater quality and human health risk impact on fluoride concentration: a case study of Namakkal district, South India. *Research Square* [Preprint]. [DOI]

Karanveer, Bala, R. and Das, D., 2022. Geochemical and health risk assessment of potentially toxic trace elements and nitrate via groundwater in agro-ecosystem of alluvial plain Punjab, India. *Human and Ecological Risk Assessment: An International Journal*, 28(9), pp.983-1011. [DOI]

Karunanidhi, D., Aravinthasamy, P., Deepali, M., Subramani, T. and Shankar, K., 2021. Groundwater pollution and human health risks in an industrialized region of Southern India: impacts of the COVID-19 lockdown and the monsoon seasonal cycles. *Archives of Environmental Contamination and Toxicology*, 80(1), pp.259-276. [DOI]

Karunanidhi, D., Aravinthasamy, P., Roy, P.D., Praveenkumar, R.M., Prasanth, K., Selvapraveen, S., Thowbeekrahman, A., Subramani, T. and Srinivasamoorthy, K., 2020. Evaluation of non-carcinogenic risks due to fluoride and nitrate contaminations in a groundwater of an urban part (Coimbatore region) of South India. *Environmental Monitoring and Assessment*, 192(2), 102. [DOI]

Karunanidhi, D., Aravinthasamy, P., Roy, P.D., Subramani, T. and Jayasena, H.C., 2024. Nitrate contamination in groundwater and its evaluation of non-carcinogenic health hazards from Arjunanadi river basin, South India. *Groundwater for Sustainable Development*, 25, 101153. [DOI]

Karunanidhi, D., Aravinthasamy, P., Subramani, T. and Muthusankar, G., 2021. Revealing drinking water quality issues and possible health risks based on water quality index (WQI) method in the Shanmuganadhi river basin of South India. *Environmental Geochemistry and Health*, 43(2), pp.931-948. [DOI]

Kaur, G., Sharma, S. and Garg, U.K., 2019. Assessment of ground water contamination by inorganic impurities in Ferozepur district of Punjab state, India. *Asian Journal of Chemistry*, 31(3), pp.515-521. [DOI]

Kaur, L. and Godara, P., 2025. An investigation of water quality index and health risks of fluoride and nitrate in the arid groundwater (India). *Macedonian Journal of Ecology and Environment*, 27(2), pp.99-113. [DOI]

Khan, A.F., Srinivasamoorthy, K., Prakash, R., Gopinath, S., Saravanan, K., Vinnarasi, F., Babu, C. and Rabina, C., 2021. Human health risk assessment for fluoride and nitrate contamination in the groundwater: a case study from the east coast of Tamil Nadu and Puducherry, India. *Environmental Earth Sciences*, 80(21), 724. [DOI]

Khan, N., Malik, A. and Nehra, K., 2021. Groundwater hydro-geochemistry, quality, microbiology and human health risk assessment in semi-arid area of Rajasthan, India: a chemometric approach. *Environmental Monitoring and Assessment*, 193(4), 234. [DOI]

Khandaker, N.R. and Rahman, M.M., 2022. Understanding sustainable arsenic mitigation technology application in the Indian Subcontinent. In: S. Yadav, A.M. Negm and R.N. Yadava (eds.) *Wastewater Assessment, Treatment, Reuse and Development in India*. Springer International Publishing, Cham, pp.87-105. [DOI]

Koley, S., 2021. Contemporary practices in groundwater arsenic remediation and wastewater management in West Bengal, India: a systematic review. *International Journal of Advanced Technology and Engineering Exploration*, 8(80), pp.797-821. [DOI]

Kouser, B., Bala, A., Verma, O., Prashanth, M., Khosla, A. and Pir, R.A., 2022. Hydrochemistry for the assessment of groundwater quality in the Kathua region, Jammu and Kashmir, India. *Applied Water Science*, 12, 143. [DOI]

Krishnappa, S.M., Channabasavaiah, S., Hanche, D., Ananda, K.D. and Muthanarasimha, A.P., 2024. Evaluating health risks associated with fluoride and nitrate contaminants in drinking water to residents living in the Chikkaballapur Taluk of Karnataka, India. *Environmental Quality Management*, 34(2), e22315. [DOI]

Kumar, G., Kothandaraman, S., Karuppanan, K. and Hussain, S., 2024. Groundwater quality and suitability assessment in Tirupur region, Tamil Nadu, India. *Journal of Chemistry*, 2024, 6083772. [DOI]

Kumar, M., Patel, A.K., Das, A., Kumar, P., Goswami, R., Deka, P. and Das, N., 2017. Hydrogeochemical controls on mobilization of arsenic and associated health risk in Nagaon district of the central Brahmaputra Plain, India. *Environmental Geochemistry and Health*, 39(1), pp.161-178. [DOI]

Madhavan, S., Kolanuvada, S.R., Sampath, V., Roy, P.D., Moorthy, P., Natarajan, L. and Chokkalingam, L., 2023. Assessment of groundwater vulnerability using water quality index and solute transport model in Poiney sub-basin of South India. *Environmental Monitoring and Assessment*, 195(2), 272. [DOI]

Malik, A., Katyal, D., Narwal, N., Kataria, N., Ayyamperumal, R. and Khoo, K.S., 2023. Sources, distribution, associated health risks and remedial technologies for inorganic contamination in groundwater: a review in specific context of the state of Haryana, India. *Environmental Research*, 236, 116696. [DOI]

Malik, N., Malik, A. and Bishnoi, S., 2021. Assessment of groundwater hydro-geochemistry, quality, and human health risk in arid area of India using chemometric approach. *Arabian Journal of Geosciences*, 14, 1546. [DOI]

Mandal, J. and Sanyal, S., 2019. Geospatial analysis of fluoride concentration in groundwater in Puruliya district, West Bengal. *Space and Culture, India*, 6(5), pp.71-86. [DOI]

Marghade, D., Malpe, D.B., Duraisamy, K., Patil, P.D. and Li, P., 2021. Hydrogeochemical evaluation, suitability, and health risk assessment of groundwater in the watershed of Godavari basin, Maharashtra, Central India. *Environmental Science and Pollution Research*, 28(15), pp.18471-18494. [DOI]

Marghade, D., Mehta, G., Shelare, S.D., Jadhav, G. and Nikam, K.C., 2023. Arsenic contamination in Indian groundwater: from origin to mitigation approaches for a sustainable future. *Water*, 15(23), 4125. [DOI]

Maurya, J.K., Pradhan, S.N., Seema and Ghosh, A.K., 2021. Evaluation of ground water quality and health risk assessment due to nitrate and fluoride in the Middle Indo-Gangetic plains of India. *Human and Ecological Risk Assessment: An International Journal*, 27(5), pp.1349-1365. [DOI]

Maurya, S., More, A.B., Gupta, G., Saxena, A. and Singh, A., 2025. Hydrochemical evaluation of groundwater quality and human health risk assessment of fluoride and nitrate: a case study of Pratapgarh district, UP, India. *Water, Air, & Soil Pollution*, 236(3), 204. [DOI]

Mawari, G., Kumar, N., Sarkar, S., Frank, A.L., Daga, M.K., Singh, M.M., Joshi, T.K. and Singh, I., 2022. Human health risk assessment due to heavy metals in ground and surface water and association of diseases with drinking water sources: a study from Maharashtra, India. *Environmental Health Insights*, 16, 11786302221146020. [DOI]

Mhaske, G.D., Bhalla, R. and Nalawade, P.M., 2022. Study of groundwater hydrochemistry and drinking appropriateness using water quality index (WQI) modelling in the Jam River basin, India. *Ecology, Environment and Conservation*, 28, pp.S469-S477. [DOI]

Mukherjee, A., Saha, D., Harvey, C.F., Taylor, R.G., Ahmed, K.M. and Bhanja, S.N., 2015. Groundwater systems of the Indian sub-continent. *Journal of Hydrology: Regional Studies*, 4, pp.1-14. [DOI]

Mukherjee, A., Sarkar, S., Chakraborty, M., Duttagupta, S., Bhattacharya, A., Saha, D., Bhattacharya, P., Mitra, A. and Gupta, S., 2021. Occurrence, predictors and hazards of elevated groundwater arsenic across India through field observations and regional-scale AI-based modeling. *Science of the Total Environment*, 759, 143511. [DOI]

Mukherjee, I. and Singh, U.K., 2022. Environmental fate and health exposures of the geogenic and anthropogenic contaminants in potable groundwater of Lower Ganga basin, India. *Geoscience Frontiers*, 13(3), 101365. [DOI]

Mukherjee, I., Singh, U. and Patra, P.K., 2019. Exploring a multi-exposure-pathway approach to assess human health risk associated with groundwater fluoride exposure in the semi-arid region of east India. *Chemosphere*, 233, pp.164-173. [DOI]

Muthusamy, P., Paneerselvam, B., Kaliyappan, S.P., Almohamad, H., Aldosari, A.A. and Abdo, H.G., 2023. Pollution source identification and suitability assessment of groundwater quality for drinking purposes in semi-arid regions of the southern part of India. *Water*, 15(22), 3995. [DOI]

Nagaraj, S. and Masilamani, U.S., 2023. Hydrogeochemical and multivariate statistical approaches to investigate the characteristics of groundwater

quality in fluoride-enriched hard rock region in Tirupathur district of Tamil Nadu, India. *Environmental Science and Pollution Research*, 30(44), pp.99809-99829. [DOI]

Narsimha, A. and Sudarshan, V., 2017. Contamination of fluoride in groundwater and its effect on human health: a case study in hard rock aquifers of Siddipet, Telangana state, India. *Applied Water Science*, 7, pp.2501-2512. [DOI]

Naskar, S., Mandal, D., Biswas, B. and Mukherjee, C., 2025. Hydrochemical assessment of groundwater quality using pollution index, quality indexes, fuzzy-GIS, graphical and multivariate techniques from a mining region of Eastern India. *Discover Water*, 5, 48. [DOI]

Pal, P., Sen, M., Manna, A., Pal, J., Pal, P., Roy, S. and Roy, P., 2009. Contamination of groundwater by arsenic: a review of occurrence, causes, impacts, remedies and membrane-based purification. *Journal of Integrative Environmental Sciences*, 6(4), pp.295-316. [DOI]

Pandey, S., Mohapatra, G. and Arora, R., 2023. Groundwater quality, human health risks and major driving factors in arid and semi-arid regions of Rajasthan, India. *Journal of Cleaner Production*, 427, 139149. [DOI]

Panneerselvam, B., Muniraj, K., Pande, C.B., Ravichandran, N., Thomas, M. and Karuppannan, S., 2022. Geochemical evaluation and human health risk assessment of nitrate-contaminated groundwater in an industrial area of South India. *Environmental Science and Pollution Research*, 29(57), pp.86202-86219. [DOI]

Panneerselvam, B., Ravichandran, N., Kaliyappan, S.P., Karuppannan, S. and Bidorn, B., 2023. Quality and health risk assessment of groundwater for drinking and irrigation purpose in semi-arid region of India using entropy water quality and statistical techniques. *Water*, 15(3), 601. [DOI]

Pattnaik, P. and Bhowmick, P.K., 2020. Determination of water quality index of drinking water sources and health risk assessment of arsenic-contaminated rural areas in Basirhat-1 Block of West Bengal. *International Journal of Innovative Technology and Exploring Engineering*, 9(3), pp.677-684. [DOI]

Raja, V. and Neelakantan, M., 2021. Evaluation of groundwater quality with health risk assessment of fluoride and nitrate in Virudhunagar district, Tamil Nadu, India. *Arabian Journal of Geosciences*, 14(1), 52. [DOI]

Rajendran, R., Lakshmanan, E., Muddu, S., Rajmohan, N., Senapathi, V. and Brindha, K., 2025. Multi-indices approach for comprehensive appraisal of groundwater quality and the implication on human health in the Amaravathi basin, Southern India. *Environmental Monitoring and Assessment*, 197(2), 153. [DOI]

Ramalingam, S., Panneerselvam, B. and Kaliappan, S.P., 2022. Effect of high nitrate contamination of groundwater on human health and water quality index in semi-arid region, South India. *Arabian Journal of Geosciences*, 15, 242. [DOI]

Rathinam, R.K., Ramajayam, J.G., Mahalingam, V. and Sarangapani, M., 2024. Assessment of hydrogeochemical characteristics and potable quality of groundwater around Retteri lake in Thiruvallur district, Tamil Nadu, India. *Zastita Materijala*, 65(3), pp.516-523. [DOI]

Ravindra, K. and Mor, S., 2019. Distribution and health risk assessment of arsenic and selected heavy metals in groundwater of Chandigarh, India. *Environmental Pollution*, 250, pp.820-830. [DOI]

Reddy, C.K.V.C., Golla, V., Badapalli, P.K. and Reddy, N.B.Y., 2022. Evaluation of groundwater contamination for fluoride and nitrate in Nellore urban province, Southern India: a special emphasis on human health risk assessment (HHRA). *Applied Water Science*, 12, 32. [DOI]

Sabinaya, S., Mahanty, B., Lhamo, P., Sahoo, S.K., Jha, V.N. and Sahoo, N.K., 2023. Application of a multivariate water quality index to evaluate the groundwater geochemistry of Jajpur district, Odisha, India and assessment of potential health risks. *Research Square* [Preprint]. [DOI]

Saha, A. and Pal, S.C., 2025. Assessment and characterization of groundwater quality and related human health risk in a fluoride-enriched semi-arid region of Eastern India. *Water, Air, & Soil Pollution*, 236(11), 691. [DOI]

Saha, D., Dwivedi, S.N. and Singh, R.K., 2014. Aquifer system response to intensive pumping in urban areas of the Gangetic plains, India: the case study of Patna. *Environmental Earth Sciences*, 71(4), pp.1721-1735. [DOI]

Saha, R., Wankhede, T., Majumdar, R.C. and Das, I., 2024. Pan India fluoride hazard assessment in groundwater. *Journal of Hazardous Materials*, 478, 135543. [DOI]

Sahu, B.L., Banjare, G.R., Ramteke, S., Patel, K.S. and Matini, L., 2017. Fluoride contamination of groundwater and toxicities in Dongargaon Block, Chhattisgarh, India. *Exposure and Health*, 9(2), pp.143-156. [DOI]

Sane, P.B., Gaikwad, S.P., Mahale, R.R., Muley, A., Supekar, A., Dongare, A.N. and Bhagat, A.A., 2025. Unusually high levels of fluoride and nitrate in groundwater in Southern India: water quality indices and associated health hazard implications. *Journal of Geosciences Research*, 10(2), pp.114-122. [DOI]

Saraswat, A., Nath, T., Omeka, M.E., Unigwe, C.O., Anyanwu, I.E., Ugar, S.I., Latare, A., Raza, M.B., Behera, B., Adhikary, P.P., Scopa, A. and AbdelRahman, M.A.E., 2023. Irrigation suitability and health risk assessment of groundwater resources in the Firozabad industrial area of north-Central India: an integrated indexical, statistical, and geospatial approach. *Frontiers in Environmental Science*, 11, 1116220. [DOI]

Sarma, R.V. and Singh, S.K., 2023. Assessment of groundwater quality and human health risks of nitrate and fluoride contamination in a rapidly urbanizing region of India. *Environmental Science and Pollution Research*, 30(19), pp.55437-55454. [DOI]

Shaikh, H., Gaikwad, H., Kadam, A. and Umrikar, B., 2020. Hydrogeochemical characterization of groundwater from semiarid region of Western India for drinking and agricultural purposes with special reference to water quality index and potential health risks assessment. *Applied Water Science*, 10, 204. [DOI]

Sharma, T., Litoria, P.K., Bajwa, B.S. and Kaur, I., 2021. Appraisal of groundwater quality and associated risks in Mansa district (Punjab, India). *Environmental Monitoring and Assessment*, 193(4), 159. [DOI]

Shirke, K.D., Kadam, A. and Pawar, N.J., 2020. Temporal variations in hydro-geochemistry and potential health risk assessment of groundwater from lithological diversity of semi-arid region, western Gujarat, India. *Applied Water Science*, 10, 156. [DOI]

Shukla, S. and Saxena, A., 2021. Appraisal of groundwater quality with human health risk assessment in parts of Indo-Gangetic alluvial plain, North India. *Archives of Environmental Contamination and Toxicology*, 80(1), pp.55-73. [DOI]

Sidhu, N., Kaur, L., Rishi, M.S., Din, S.N.U., Tewari, K. and Singh, P., 2024. Integrating multivariate hydrogeochemical analysis with human health risk assessment: an inverse geochemical and statistical modeling approach. *Journal of Geochemical Exploration*, 258, 107389. [DOI]

Singh, A., Maurya, S., Saxena, A. and Gupta, G., 2024. A review of phytoremediation techniques used for removal of arsenic from groundwater. In: A. Kuanar, A.P. Das, D. Kar and M.P. Shah (eds.) *Sustainable Management of Environmental Pollutants through Phytoremediation*. CRC Press, pp.135-156. [DOI]

Singh, G., Rishi, M.S., Herojeet, R., Kaur, L. and Sharma, K., 2020. Evaluation of groundwater quality and human health risks from fluoride and nitrate in semi-arid region of Northern India. *Environmental Geochemistry and Health*, 42(7), pp.1833-1862. [DOI]

Singh, K., Singh, R.D. and Pandey, G., 2023. Hydrogeochemistry, solute source identification, and health risk assessment of groundwater of cancer prone region in India. *Water Science & Technology: Water Supply*, 23(1), pp.317-342. [DOI]

Singh, P., Rishi, M.S. and Kaur, L., 2024. Multi-parametric analysis of groundwater quality to assess human health risk and hydrogeochemical processes in an agriculturally intensive alluvial aquifer of Northwest India. *International Journal of Environmental Analytical Chemistry*, 104(11), pp.2552-2570. [DOI]

Singh, R., Singh, S., Das, A., Sahu, H., Durgam, M., Khose, S., Pohshna, C. and Mailapalli, D., 2024. Evaluating groundwater quality for drinking and irrigation purposes and health risk assessment in West Midnapore district of West Bengal, India. *Journal of Agricultural Engineering (India)*, 61(4). [DOI]

Singh, R., Upreti, P., Allemailem, K.S., Almatroudi, A., Rahmani, A.H. and Albalawi, G.M., 2022. Geospatial assessment of groundwater quality and associated health problems in the western region of India. *Water*, 14(3), 296. [DOI]

Srinivas, Y., Oliver, D.H., Raj, A.S. and Chandrasekar, N., 2013. Evaluation of groundwater quality in and around Nagercoil town, Tamilnadu, India: an integrated geochemical and GIS approach. *Applied Water Science*, 3(3), pp.631-651. [DOI]

Subramaniyan, A. and Ganesan, S., 2024. Human health risk and water quality assessment due to fluoride and nitrate around Cauvery river basin, Southern India. *Environmental Monitoring and Assessment*, 196(10), 880. [DOI]

Sultan, M.W., Qureshi, F., Ahmed, S., Kamyab, H., Rajendran, S., Ibrahim, H. and Yusuf, M., 2025. A comprehensive review on arsenic contamination in groundwater: sources, detection, mitigation strategies and cost analysis. *Environmental Research*, 265, 120457. [DOI]

Taloor, A.K., Sharma, S., Pir, R.A. and Kumar, K., 2024. Appraisal of health risks associated with exposure of fluoride and nitrate contaminated springs in the Doda Kishtwar Ramban (DKR) region of Jammu and Kashmir, India. *Journal of Geochemical Exploration*, 257, 107380. [DOI]

Tanwer, N., Deswal, M., Khyalia, P., Laura, J.S. and Khosla, B., 2023. Fluoride and nitrate in groundwater: a comprehensive analysis of health risk and potability of groundwater of Jhunjhunu district of Rajasthan, India. *Environmental Monitoring and Assessment*, 195(2), 267. [DOI]

Thalod, S. and Sharma, G., 2024. Arsenic contamination in groundwater of Haryana's National Capital Region and its comparative assessment (Mahendragarh, Rewari, and Jhajjar districts). *Cuestiones de Fisioterapia*, 53(3), pp.5027-5039. [DOI]

Ullengula, M., Dhakate, R., Rao, N.S., Suryabhagavan, K.V., More, S., Gugulothu, S., Badapalli, P.K. and Ratnalu, G.V., 2026. Temporal dynamics of groundwater quality and associated health risks in a semi-arid region of South India. *Discover Sustainability*, 7, 298. [DOI]

Vijayakumar, C.R., Balasubramani, D.P. and Azamathulla, H.M., 2022. Assessment of groundwater quality and human health risk associated with chromium exposure in the industrial area of Ranipet, Tamil Nadu, India. *Journal of Water, Sanitation and Hygiene for Development*, 12(1), pp.58-67. [DOI]

Vijaylaxmi and Khan, S., 2021. Fluoride remediation using membrane processes. In: R. Prasad (ed.) *Environmental Pollution and Remediation*. Springer, Singapore, pp.175-194. [DOI]

Wagh, V., Mukate, S., Panaskar, D.B., Muley, A. and Sahu, U.L., 2019. Study of groundwater hydrochemistry and drinking suitability through water quality index (WQI) modelling in Kadava river basin, India. *SN Applied Sciences*, 1(10), 1251. [DOI]

Wintgens, T., Nättorp, A., Elango, L. and Asolekar, S.R. (eds.), 2016. *Natural Water Treatment Systems for Safe and Sustainable Water Supply in the Indian Context: Saph Pani*. IWA Publishing, London. pp.1-335. [DOI]

Yadav, K.K., Gupta, N., Kumar, V., Choudhary, P. and Khan, S.A., 2018. GIS-based evaluation of groundwater geochemistry and statistical determination of the fate of contaminants in shallow aquifers from different functional areas of Agra city, India: levels and spatial distributions. *RSC Advances*, 8(29), pp.15876-15889. [DOI]

Yadav, K.K., Kumar, V., Gupta, N., Kumar, S., Rezania, S. and Singh, N., 2019. Human health risk assessment: study of a population exposed to fluoride through groundwater of Agra city, India. *Regulatory Toxicology and Pharmacology*, 106, pp.68-80. [DOI]

Yasaswini, G., Kushala, S., Santhosh, G.S.V., Naik, M.T.K., Mondal, M., Dey, U., Das, K., Sarkar, S. and Kumar, P., 2024. Occurrence and distribution of fluoride in groundwater and drinking water vulnerability of a tropical dry region of Andhra Pradesh, India. *Water*, 16(4), 577. [DOI]

Yenugu, S.R., Vangala, S. and Badri, S., 2020. Monitoring of groundwater quality for drinking purposes using the WQI method and its health implications around inactive mines in Vemula-Vempalli region, Kadapa District, South India. *Applied Water Science*, 10(8), 202. [DOI]

Nature Environment and Pollution Technology
An International Quarterly Peer-Reviewed Open Access Journal

p-ISSN: 0972-6268 | e-ISSN: 2395-3454 Vol. 25 | No. 4 | Article ID D1907 | 2026

RESEARCH ARTICLE https://doi.org/10.46488/NEPT.2026.v25i04.D1907 OPEN ACCESS

Production and Characterization of Polyhydroxybutyrate (PHB) from an Agricultural By-Product Using *Bacillus thuringiensis* CICIM (B2031)

Sandisiwe Gladness Zondo[1], Johnson Zininga[2]†, Kugen Permaul[2] and Nirmala Deenadayalu[1]
[1]Durban University of Technology, Department of Chemistry, Steve Biko Campus, Durban, 4001, South Africa
[2]Durban University of Technology, Department of Biotechnology and Food Technology, Steve Biko Campus, Durban, 4001, South Africa
†Corresponding author: Johnson Zininga; johnsonzininga@yahoo.com

ARTICLE HISTORY

Received: 19-01-2026
Revised: 03-04-2026
Accepted: 09-04-2026

KEYWORDS

Polyhydroxyalkanoate
Polyhydroxybutyrate
Recalcitrant
Corn silage

CITE THIS ARTICLE

Zondo, S.G., Zininga, J., Permaul, K. and Deenadayalu, N., 2026. Production and characterization of Polyhydroxybutyrate (PHB) from an agricultural by-product using *Bacillus thuringiensis* CICIM (B2031). *Nature Environment and Pollution Technology*, 25(4), D1907. https://doi.org/10.46488/NEPT.2026.v25i04. D1907

COPYRIGHT & LICENCE

© 2026 The Authors
Open Access under CC BY 4.0.

PUBLISHED BY
TECHNOSCIENCE PUBLICATIONS

ABSTRACT

The widespread overuse of petroleum plastics has led to serious environmental challenges. This has necessitated the pursuit of greener alternatives that would reduce or eliminate mankind's unsustainable and toxic dependence on the recalcitrant petroleum plastics. Polyhydroxybutyrate (PHB) is a potential substitute candidate for the production of biodegradable plastics. In this study, *Bacillus thuringiensis* CICIM (B2031) was utilized for the production of PHB using the agricultural by-product corn silage as a carbon source. The corn silage was pretreated with dilute sulfuric acid. The acid-pretreated corn silage hydrolysate was used at different loadings, producing a maximum biopolymer yield of 53.43% PHB. This was compared with the untreated corn silage which gave a maximum yield of 28.63% PHB, under the same conditions. The extracted PHB biopolymer was characterized using Fourier-Transform Infrared Spectroscopy (FT-IR), ultraviolet–visible (UV-Vis) spectroscopy, and gas chromatography-flame ionization detector (GC-FID). This study revealed that corn silage (CS) can be utilized as a renewable carbon source for PHB production.

1. INTRODUCTION

Petroleum refining and the various synthetic petrochemical materials derived from the process have emerged as both a necessary part of everyday life and an environmental problem of considerable proportions. These polymers are resistant to biodegradation, and it is these recalcitrant residues that pose the greatest environmental pollution threat (Charen et al. 2014, Tavella et al. 2025). These synthetic materials in the environment are not only harmful but also significantly affect the aesthetics of cities. Disposing of polyvinyl chloride (PVC) is costly and often involves incineration, which releases toxic emissions such as dioxins, making PVC a pollution problem (Gowda & Shivakumar 2014, Ghimire et al. 2025). The search for alternative plastic options is vital in reducing the current dependency on non-renewable resources (Getachew & Woldesenbet 2016). This search should yield a suitable alternative that is biodegradable. Many solid waste disposal regulations have been instituted worldwide, and this has resulted in the limitation of plastic waste as well as the pursuit of novel ways to produce biodegradable plastic materials such as those derived from polyhydroxyalkanoate (PHA) (Alarfaj et al. 2015, Mallegni et al. 2025).

Microorganisms can make PHAs through utilization of various carbon sources that include lipids and sugars. Among the microbial PHAs, the most commonly produced is polyhydroxybutyrate (PHB). The crystalline structure of PHB contributes to its brittle properties. PHBs are natural biopolymers, which are synthesized and catabolized via microbial growth (Akar et al. 2006, Berlanga et al. 2006, de Roo et al. 2002). Bacteria have been reported to synthesize these biopolyesters, where they act as energy reserves that are deposited as insoluble cytoplasmic inclusions. The first bacterial PHB production was reported in *Bacillus megaterium*. Since then, the genus *Bacillus* has become a go-to source for PHBs, as they offer the advantage of growing fast, having genomic stability, and being able to adjust to a wide variety of carbon sources, producing PHBs which are, most importantly, endotoxin-free. *Bacillus thuringiensis* is a Gram-positive bacterium that can accumulate PHB and is an active PHB producer. However, the high production cost of the biopolymers and the availability of low-cost petrochemicals make the potential use of PHBs economically unattractive (Verlinden et al. 2011, Vigneswari et al. 2025).

The fact that PHBs are meant to be an alternative to petroleum plastics, which are abundant and low-cost, means that the feasibility of PHB production depends on cost-effective approaches. The cost of the carbon source substrate has been identified as the major economic impediment. It is therefore important to select carbon source feedstock that is cheap, readily available, and supports PHB production (Getachew & Woldesenbet 2016, Trapé et al. 2024).

Corn silage is produced through a microbially mediated process of preserving nutrients through moist anaerobic fermentation. Corn silage is therefore a highly nutritious substrate and is widely used as animal feed. Challenges during the feed-out stage, including substantial mold and yeast growth that can result in losses as high as 30%, motivate the repurposing of corn silage within the circular bioeconomy. Thus, the focus of this current study was to produce and characterize PHBs from agricultural corn silage (CS) using *Bacillus thuringiensis* CICIM (B2031).

2. MATERIALS AND METHODS

2.1. Compositional Analysis of Corn Silage

Corn silage samples were dried overnight in an oven at 75°C to remove water. Samples were then milled using a Wiley laboratory mill to a particle size of 1 mm. The moisture content of undried corn silage was determined following AOAC Method 7.003. The chemical composition of corn silage was determined following AOAC Method 978.18.

Table 1: Chemical composition of corn silage.

Chemical	Composition
Hemicellulose	20.7%
Cellulose	27.0%
Lignin	6.54%
Ash	3.7%
Fat	1%
Protein	9.28%
Starch	26.89%
Mineral salts	4.01%

Compositional analysis was carried out in triplicate, and the results are represented in Table 1.

2.2. Corn Silage Hydrolysate

Corn Silage substrate was hydrolyzed with 2.5% v/v sulfuric acid (solid: liquid, 1:10). The mixture was autoclaved for 30 min at 121°C. The hydrolyzed mixture was cooled to room temperature and filtered through Whatman No. 1 filter paper. The supernatant was neutralized using 6 N NaOH. Reducing sugar content was quantified using the photometric method originally reported by Marais et al. (1966). The growth medium was prepared using these filtrates at concentrations of 6%, 12%, 24%, and 48% (v/v).

2.3. Cultivation of *Bacillus thuringiensis* CICIM (B2031) Strain

A *Bacillus thuringiensis* CICIM (B2031) culture was obtained from the Culture and Information Centre of Industrial Microorganisms of China Universities (CICIM). The fermentation was carried out in 250 mL flasks in a medium containing 4 g L^{-1} yeast extract, 8 g L^{-1} tryptone, and 2 g L^{-1} NaCl at 37 °C for 48 h on a shaker at 200 rpm. The bacterial cells were harvested at 6,000 × g and washed with deionized water (Charen et al. 2014). The bacterial growth profile was monitored by sampling 2 mL aliquots of the culture at 6 h intervals. All cultures and measurements were performed in triplicate.

2.4. Screening of PHB-Producing Bacteria

Screening for PHB-producing *B. thuringiensis* cells was done using the lipophilic stain Sudan Black B method (0.3 g of Sudan Black B in 100 mL of ethanol). A loopful of culture was taken from the culture medium, mixed with 20% brine, and then smeared on a glass slide. The smear was allowed to dry and then fixed by immersing it in 2% acetic acid for 5 min. The slide was flooded with Sudan Black B solution for 15 min at room temperature. The slide was dried, and xylene was added to clear. A 0.5% aqueous Safranin aliquot

was added for 10 s as a counterstain. This was followed by washing using distilled water and then dried for observation using a light microscope (Selvakumar et al. 2011).

2.5. Biomass Determination

A 50 mL sterilized Falcon tube was utilized to determine cell concentration, defined as dry weight of cells per liter of culture broth. The cell suspension was then centrifuged (4,000 × g for 15 min) (Eppendorf, Centrifuge 5810R). The supernatant was discarded, and the collected cell pellet was washed twice with deionized water and freeze-dried (the ice condenser was set at −84 °C and vacuum set at 1.0 mbar) (Rohini et al. 2006). The dried cells were used for PHB extraction.

2.6. PHB Extraction and Production

A mixture of sodium hypochlorite and chloroform was used in the recovery of microbial PHB. A 1 g sample of lyophilized cell pellet was mixed with chloroform and 15% sodium hypochlorite (1:1) and shaken at 100 rpm for 90 min at 37°C. Centrifugation followed at 4,000 × g for 10 min (Eppendorf, Centrifuge 5810R). A volume of 4 mL of methanol was added to the lower chloroform phase containing the solubilized polymer to precipitate the polymer (Rohini et al. 2006). The precipitated polymer was washed with acetone and air-dried. In this study, all quantitative experiments were carried out in triplicate. The mean differences among the pretreatments were analyzed by ANOVA.

2.7. UV-Vis Characterization

A 10 mg sample of the extracted polymer was dissolved in 2 mL of chloroform and scanned over a UV-Vis range of 200–800 nm (Thermo Scientific, GENESYS 150, UV–Vis Spectrophotometer) against a chloroform blank, as reported by Alarfaj et al. (2015).

2.8. FT-IR Spectroscopy

The structural analysis was performed using a PerkinElmer 537 FT-IR spectrophotometer. The spectrum of the extracted polymer from *B. thuringiensis* CICIM (B2031) [poly(3HB)] was compared with a pure poly(3HB) standard obtained from Sigma-Aldrich. Structural analysis of the functional groups was performed utilizing a Fourier-transform infrared Perkin Elmer 537 spectrophotometer. The sample was placed on the sample holder and scanned from 4,000–400 cm^{-1}. An attenuated total reflectance (ATR) was used to record the spectra, and absorption frequencies were expressed as νmax (cm^{-1}).

2.9. GC-FID Characterization

The monomer composition of the polymer was determined using a Varian 2100T gas chromatograph with flame ionization detection (GC-FID). The Varian 2100T gas chromatograph was equipped with a ZB-5MS (Phenomenex) column (30 m length, 0.25 mm internal diameter, and 0.25 µm film thickness) and a flame ionization detector. A 5 mg sample of the polymer was subjected to transesterification using 1 mL chloroform and 0.85 mL of methanol with 0.15 mL of sulfuric acid as the catalyst. This reaction was carried out in a small screw-cap test tube for 60 min at 100°C. The mixture was allowed to cool down to room temperature. After cooling, 0.5 mL of distilled water was added to the test tube and mixed for 1 min using a vortex. The upper phase was removed using a plastic pipette, and the lower chloroform phase containing the methyl ester of β-hydroxy acid was recovered and transferred to a small screw-cap vial. A 2 µL sample was injected into the injector port, and the inlet pressure of the carrier gas (nitrogen) was set at 109.2 kPa. For effective separation of the esters, the following temperature program was used (60°C for 1 min, temperature increase 25°C min^{-1} to 230°C (230°C for 1 min); flow controller: split, total flow 301.3 mL min^{-1}, column flow 1.48 mL min^{-1}; the temperature of the injector and detector were 200 and 230°C, respectively (Pantazaki et al. 2009). Different β-hydroxyalkanoic acid methyl ester standards were used as references.

3. RESULTS AND DISCUSSION

It has been reported that both Gram-positive and Gram-negative bacterial species produce PHBs (Gomaa 2014). This vast microbial diversity calls for accurate identification and characterization of the producing strains and their ability to grow on cheaper substrates in the production of PHBs. In this study, PHB was produced in broth supplemented with corn silage (CS) as a cheap carbon source collected from the Department of Agriculture, KwaZulu-Natal. *B. thuringiensis* is known for both the production of an insecticidal δ-endotoxin and accumulation of PHB. It was also noted that maximum biomass production at stationary phase (maximum OD) coincided with the accumulation of the polymer after 48 h (Rohini et al. 2006). However, accumulated PHB may gradually decline after the stationary phase if the cell mass is not harvested because of PHB metabolism (Rohini et al. 2006)

3.1. PHB Production

The *B. thuringiensis* CICIM (B2031) was screened for PHB accumulation in the cytoplasm using Sudan Black B stain (Selvakumar et al. 2011). Sudan Black B has high lipophilic staining sensitivity in PHB screening. *B. thuringiensis* CICIM (B2031) showed PHB accumulation,

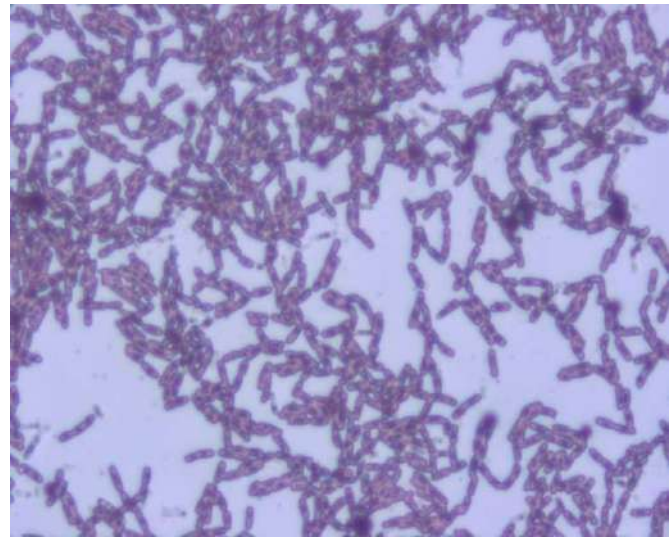


Fig. 1: Micrograph of *B. thuringiensis* CICIM (B2031) showing PHB accumulation; magnification 1000×.

evidenced by blue-black inclusions in the cytoplasm. The presence of blue-black granules indicated PHB production and the ability of *B. thuringiensis* to produce these polymers (Fig. 1). This supported the findings of Charen et al. (2014) and Sawant et al. (2014), where Sudan Black B counterstained with safranin was used to show positive accumulation of PHBs in *B. thuringiensis* using a light microscope

The cultures were harvested when the cells reached the early stationary phase, followed by determination of the polymer composition. During bacterial growth, the composition of the substrate changes with subsequent buildup and utilization of metabolic intermediates; hence, changes in PHB monomer composition proportional to culture age are expected (Brandl et al. 1988).

After 48 h, it was observed that pH 7.0 yielded the highest biomass compared with pH 6.5 and pH 7.5 (Fig. 2). *B. thuringiensis* and some other bacteria are known to produce PHB naturally (Charen et al. 2014). PHB serves as an energy reserve, so greater biomass may result in greater accumulation of PHB. *B. thuringiensis* has been reported to show maximum biomass peaking at around 48 h, which signals the early stages of the stationary phase.

The corn silage supported PHB production even in its unhydrolyzed form. There was approximately 27% PHB

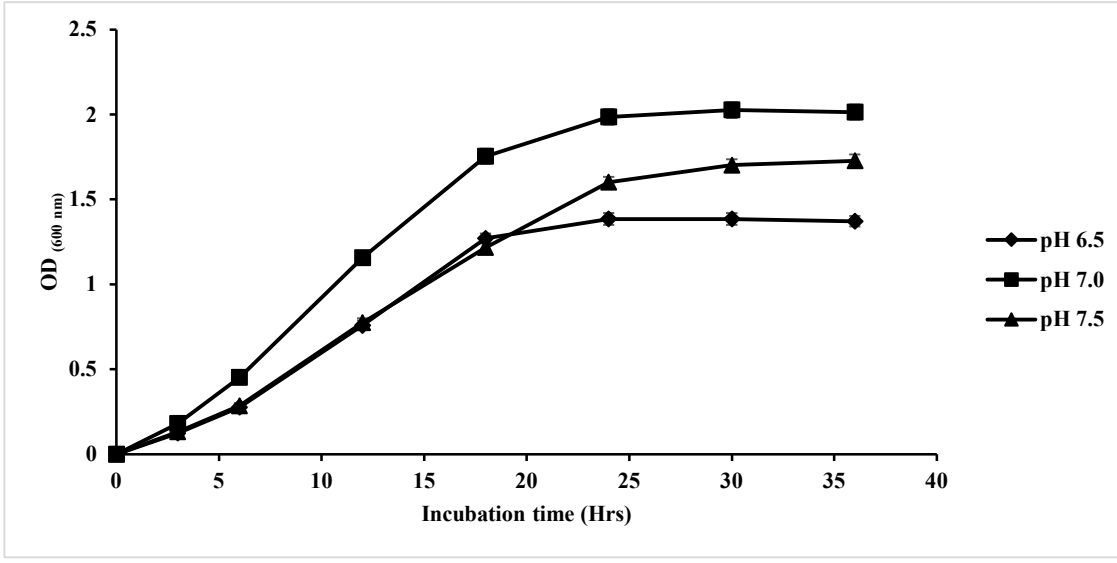


Fig. 2: Growth of *B. thuringiensis* at pH 6.5, 7.0, and 7.5.

Table 2: Effect of unhydrolyzed corn silage supernatant concentration on biomass and polymer production after 48 h of cultivation.

CS supernatant in medium (%)	Biomass (g L^{-1})	Polymer (g L^{-1})	PHB content (% w/w)
6	1.91 ± 0.16	0.22 ± 0.01	11.91 ± 1.65
12	2.64 ± 0.21	0.51 ± 0.02	19.42 ± 2.26
24	3.22 ± 0.17	0.88 ± 0.06	27.39 ± 2.65
48	3.82 ± 0.22	0.67 ± 0.02	28.63 ± 1.51

Table 3: Effect of hydrolyzed corn silage supernatant concentration on biomass and polymer production after 48 h of cultivation.

CS supernatant in medium (%)	Biomass (g L^{-1})	Polymer (g L^{-1})	PHB content (% w/w)
6	3.15 ± 0.24	1.32 ± 0.142	42.34 ± 3.25
12	3.26 ± 0.21	1.52 ± 0.123	46.42 ± 3.28
24	4.47 ± 0.36	2.25 ± 0.145	50.52 ± 2.29
48	4.99 ± 0.28	2.66 ± 0.232	53.43 ± 3.08

*Data represent the mean of three readings ± standard deviation.

accumulation at 24% loading; however, a doubling of the substrate loading did not show a commensurate increase in biomass and PHB accumulation (Table 2). This may be because a further increase in unhydrolyzed substrate increases the amount of untreated material that is not readily accessible to *B. thuringiensis*.

The acid-hydrolyzed substrate gave better biomass and PHB accumulation yields. A 53.43% PHB accumulation was recorded from the highest loading. The highest biomass of 4.99 g L^{-1} was also achieved (Table 3). This can be attributed to the hydrolyzed substrate being richer in simple sugars that are readily accessible to the bacterium.

The ability of *B. thuringiensis* to accumulate PHB has been reported. The focus has been on efficiency in terms of production duration. Most reports have indicated optimum durations between 24 and 96 h for Bacillus strains. The focus on PHB production conditions is informed by the relationship between growth conditions and the properties of the PHB produced. Ray and Kalia (2017) monitored the link between the different growth conditions, bacterial strains, and the degradation of PHB and concluded that PHB characteristics depend on the growth conditions. PHB characteristics determine its applicability, and the various intermediates produced from the degradation can be used for PHB modifications for industry-specific applications. As an agricultural by-product, corn silage is a cost-effective agro-based substrate that may help address the feasibility concerns in PHB production. Corn silage has a very high fermentable carbohydrate content, including starch (>28%, w/w) and reducing sugars (8%) (Chahine 2009). It also contains trace elements and vitamins (0.09%) (Erdman et al. 2011, Jiao et al. 2025). Given these compounds and minerals, corn silage as an agricultural residue was used in this study as a less expensive substrate to produce PHBs.

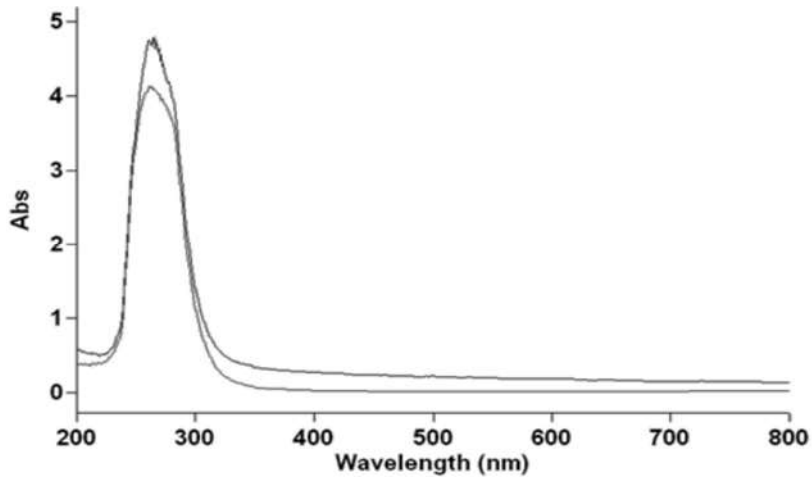


Fig. 3: UV-Vis absorption spectra of standard PHB (Sigma-Aldrich) (a) and PHB polymer obtained from *B. thuringiensis* CICIM (B2031) (b).

3.2. PHB Characterization by UV-Visible Spectroscopy

UV-Vis scanning of synthesized PHB revealed a spectrum similar to that of commercial PHB (Fig. 3). This spectral similarity indicates the presence of PHB and supports the use of corn silage as a potential PHB substrate. UV-Vis spectra of PHB isolated from *B. thuringiensis* were measured from 200 to 800 nm against the commercial standard using $CHCl_3$ as a blank. Both spectra of the commercial PHB standard and extracted PHB indicated a sharp maximum absorbance peak at 240 nm. These results are consistent with the findings of Shah (2014), which reported maximum absorbance of PHB within the range 230–240 nm.

3.3. FT-IR Spectroscopy Analysis

From the FT-IR spectrum obtained (Fig. 4), it can be concluded that the 3,375 cm^{-1} band is evidence of the strong hydrogen bond formed by the terminal OH groups. Comparable results have been reported in other studies (Getachew & Woldesenbet 2016, Gumel et al. 2012). The region of 4,000–300 cm^{-1} contains absorption bands common to the commercial and bacterial polymers. According to Misra et al. (2000) and Getachew and Woldesenbet (2016), the absorption band at 1,719 cm^{-1} is a PHB marker band due to C=O (carbonyl) stretches in the (COO) ester group located in the chain. The bands ranging from 1,060–1,281 cm^{-1} characterize the valence vibrations of the carboxyl (-C-O-) polymeric group (Getachew & Woldesenbet 2016). These are characteristic of polyhydroxybutyrate. The band at 1,456 cm^{-1} is a result of CH vibrations, due to the asymmetric stretching and CH_3 group bending vibrations, with the COH bond being represented by the 1,380 cm^{-1} band (Alarfaj et al. 2015). This spectrum confirms the report by Alarfaj et al. (2015), verifying that PHB was the isolated compound.

3.4. GC-FID Chromatography Analysis

GC identification of PHB is a commonly applied method in PHA research as it involves the decomposition of the molecule by methanolysis (Alves et al. 2023). The key compounds of concern in this study were identified based on their retention time. GC-FID analysis of the commercial PHB and extracted polymer showed a similar peak at 5.7 min (Fig. 5). This peak indicates that the extracted compound belongs to the biodegradable polyester family; therefore, GC confirmed that the polymer produced in this study is a short-chain-length PHB consisting of four carbon atoms (Chee et al. 2010).

The extracted polymer was analyzed by gas chromatography (GC) after methanolysis. The hydrolysis and derivatization reactions took place in a single vessel. The resulting methyl esters were separated by GC for qualitative analysis. A poly(3HB-co-3HV) copolymer reference standard was used (Fig. 5(a)). The peaks at 5.7653 min and 6.802 min represent PHB and PHV, respectively. These results indicate that the extracted polymer is poly(3HB-co-3HB) compared with the pure standard. The peak area of the extracted polymer showed additional peaks (Fig. 5(b)) compared with the reference standard, which may result from by-product formation during transesterification with sulfuric acid and methanol (Elhami et al. 2022). Derivatization of 3-hydroxyalkanoic acid with HCl and propanol to form a propyl ester may be preferred because the propyl ester is more lipophilic than the methyl ester, which improves the partitioning coefficient (Sharma et al. 2021).

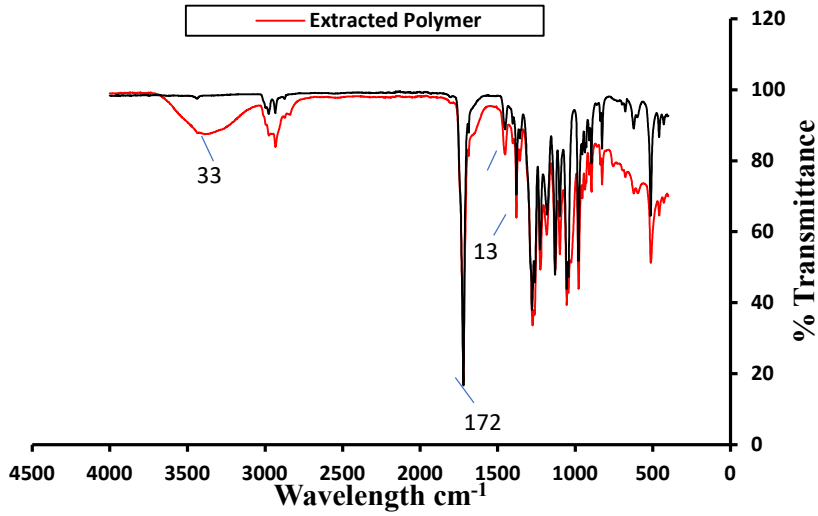


Fig. 4: FT-IR analysis of the commercial polyhydroxybutyrate standard (Sigma-Aldrich) and polymer isolated from *B. thuringiensis* CICIM (B2031).

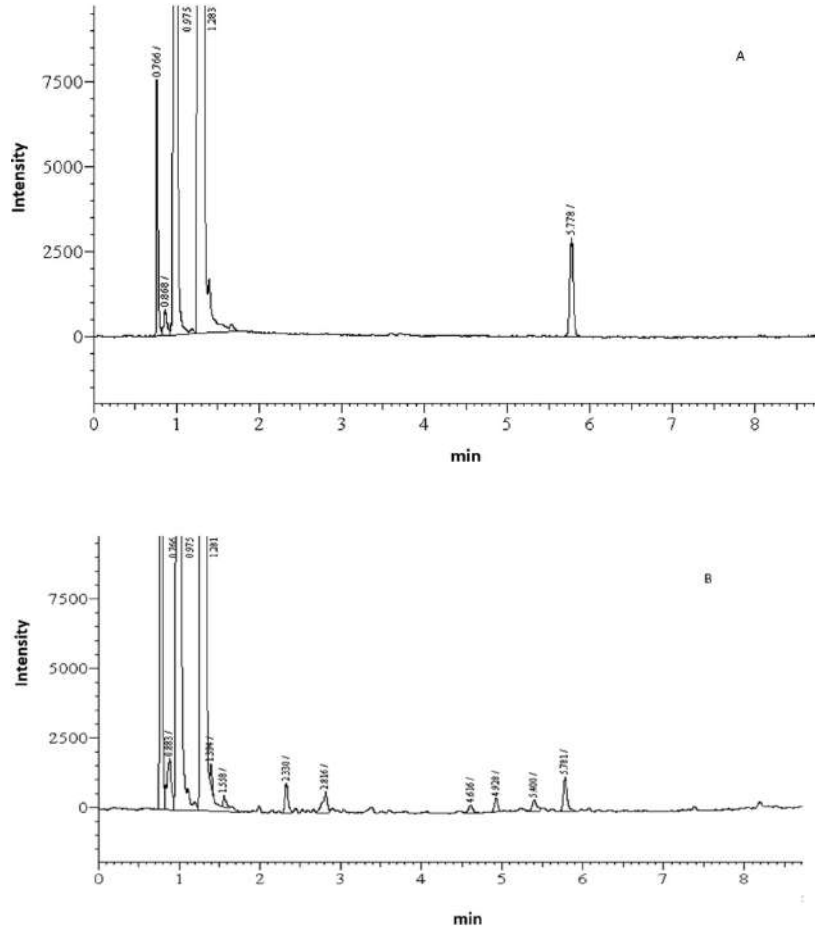


Fig. 5: GC-FID analysis of PHB produced by *B. thuringiensis*: chromatogram of the standard (a) and sample (b).

4. CONCLUSIONS

This study demonstrates PHB production using Bacillus thuringiensis CICIM (B2031) with the agricultural by-product corn silage. The bacterially derived PHB was confirmed by UV-Vis, FT-IR and GC-FID. This study provides an alternative approach to PHB production by repurposing an animal-feed carbon source such as corn silage. This strain shows potential for producing biopolymers from numerous agricultural by-products. However, this study revealed the need for novel derivatization methods for the analysis of scl-PHB to avoid excessive formation of by-products. PHB yields could also be further increased beyond the achieved 53.43% by media optimization.

5. REFERENCES

Akar, A., Akkaya, E.U., Yesiladali, S.K., Çelikyilmaz, G., Çokgor, E.U., Tamerler, C., Orhon, D. and Çakar, Z.P., 2006. Accumulation of polyhydroxyalkanoates by *Microlunatus phosphovorus* under various growth conditions. *Journal of Industrial Microbiology & Biotechnology*, 33(3), pp.215-220. [DOI]

Alarfaj, A.A., Arshad, M., Sholkamy, E.N. and Munusamy, M.A., 2015. Extraction and characterization of polyhydroxybutyrates (PHB) from *Bacillus thuringiensis* KSADL127 isolated from mangrove environments of Saudi Arabia. *Brazilian Archives of Biology and Technology*, 58(5), pp.781-788. [DOI]

Alves, A.A., Siqueira, E.C., Barros, M.P.S., Silva, P.E.C. and Houllou, L.M., 2023. Polyhydroxyalkanoates: A review of microbial production and technology application. *International Journal of Environmental Science and Technology*, 20(3), pp.3409-3420. [DOI]

Berlanga, M., Montero, M.T., Hernández-Borrell, J. and Guerrero, R., 2006. Rapid spectrofluorometric screening of poly-hydroxyalkanoate-producing bacteria from microbial mats. *International Microbiology*, 9(2), pp.95-102. Retrieved from: https://pubmed.ncbi.nlm.nih.gov/16835839/

Brandl, H., Gross, R.A., Lenz, R.W. and Fuller, R.C., 1988. *Pseudomonas oleovorans* as a source of poly(β-hydroxyalkanoates) for potential applications as biodegradable polyesters. *Applied and Environmental Microbiology*, 54(8), pp.1977-1982. [DOI]

Chahine, M., Tianna, E.F. and Sewmaker, G.E., 2009. Target value for corn silage. In: *Idaho Alfalfa and Forage Conference Proceedings*. University of Idaho Extension.

Charen, T., Vaishali, P., Kaushalya, M., Amutha, K., Ponnusami, V. and Gowdhaman, D., 2014. Isolation and identification of polyhydroxybutyrate producing bacterial strain (*Bacillus thuringiensis* GVP) from chlorine contaminated soil. *International Journal of*

ChemTech Research, 6(5), pp.3197-3202. Retrieved from: http://sphinxsai.com/2014/vol6pt5/9/(3197-3202)S-2014.pdf

Chee, J.Y., Tan, Y., Samian, M.R. and Sudesh, K., 2010. Isolation and characterization of a Burkholderia sp. *USM (JCM15050) capable of producing polyhydroxyalkanoate (PHA) from triglycerides, fatty acids and glycerols*. *Journal of Polymers and the Environment*, 18(4), pp.584-592. [DOI]

de Roo, G., Kellerhals, M.B., Ren, Q., Witholt, B. and Kessler, B., 2002. Production of chiral R-3-hydroxyalkanoic acids and R-3-hydroxyalkanoic acid methyl esters via hydrolytic degradation of polyhydroxyalkanoate synthesized by Pseudomonads. *Biotechnology and Bioengineering*, 77(7), pp.717-722. [DOI]

Elhami, V., van de Beek, N., Wang, L., Picken, S.J., Tamis, J., Sousa, J.A., Hempenius, M.A. and Schuur, B., 2022. Extraction of low molecular weight polyhydroxyalkanoates from mixed microbial cultures using bio-based solvents. *Separation and Purification Technology*, 299, p.121773. [DOI]

Erdman, R., Piperova, L. and Kohn, R., 2011. Corn silage versus corn silage: Alfalfa hay mixtures for dairy cows: Effects of dietary potassium, calcium, and cation-anion difference. *Journal of Dairy Science*, 94(10), pp.5105-5110. [DOI]

Getachew, A. and Woldesenbet, F., 2016. Production of biodegradable plastic by polyhydroxybutyrate (PHB) accumulating bacteria using low-cost agricultural waste material. *BMC Research Notes*, 9, p.509. [DOI]

Ghimire, A., Shah, M., Qirjazi, E., Ward, D., Kahlon, B., Shah, N., Tennankore, K.K., Quinn, R.R. and Vitale, G., 2025. Estimating the costs and amount of recyclable polyvinyl chloride plastic waste associated with discarded icodextrin. Peritoneal Dialysis International, p.08968608251344074. [DOI]

Gomaa, E.Z., 2014. Production of polyhydroxyalkanoates (PHAs) by *Bacillus subtilis* and *Escherichia coli* grown on cane molasses fortified with ethanol. *Brazilian Archives of Biology and Technology*, 57(1), pp.145-154. [DOI]

Gowda, V. and Shivakumar, S., 2014. Agrowaste-based polyhydroxyalkanoate (PHA) production using hydrolytic potential of *Bacillus thuringiensis* IAM 12077. *Brazilian Archives of Biology and Technology*, 57(1), pp.55-61. [DOI]

Gumel, A.M., Annuar, M.S.M. and Heidelberg, T., 2012. Biosynthesis and characterization of polyhydroxyalkanoate copolymers produced by *Pseudomonas putida* Bet001 isolated from palm oil mill effluent. *PLOS ONE*, 7(9), p.e45214. [DOI]

Jiao, J., Ma, S., Jiao, T., Shi, S., Gao, Y., Zhang, X., Zhao, S. and Degen, A.A., 2025. Effects of corn variety in whole-plant corn silage on dry matter intake, average daily gain and gastrointestinal tract bacteria and metabolites in Hu lambs. *Frontiers in Microbiology*, 16, p.1465078. [DOI]

Mallegni, N., Cicogna, F., Passaglia, E., Gigante, V., Coltelli, M.B. and Coiai, S., 2025. Natural antioxidants: Advancing stability and performance in sustainable biobased and biodegradable plastics. *Compounds*, 5(1), p.4. [DOI]

Marais, J.P., de Wit, J.L. and Quicke, G.V., 1966. A critical examination of the Nelson-Somogyi method for the determination of reducing sugars. *Analytical Biochemistry*, 15(3), pp.373-381. [DOI]

Misra, A., Thakur, M., Srinivasa, P. and Karanth, N.G., 2000. Screening of poly-β-hydroxybutyrate-producing microorganisms using Fourier transform infrared spectroscopy. *Biotechnology Letters*, 22(15), pp.1217-1219. [DOI]

Pantazaki, A.A., Papaneophytou, C.P., Pritsa, A.G., Liakopoulou-Kyriakides, M. and Kyriakidis, D.A., 2009. Production of polyhydroxyalkanoates from whey by *Thermus thermophilus* HB8. *Process Biochemistry*, 44(8), pp.847-853. [DOI]

Ray, S. and Kalia, V.C., 2017. Polyhydroxyalkanoate production and degradation patterns in *Bacillus* species. *Indian Journal of Microbiology*, 57(4), pp.387-392. [DOI]

Rohini, D., Phadnis, S. and Rawal, S.K., 2006. Synthesis and characterization of poly-β-hydroxybutyrate from *Bacillus thuringiensis* R1. *Indian Journal of Biotechnology*, 5(3), pp.276-283. Retrieved from: https://api.semanticscholar.org/CorpusID:86101894

Sawant, S.S., Salunke, B.K. and Kim, B.S., 2014. A laboratory case study of efficient polyhydroxyalkanoate production by *Bacillus cereus*, a contaminant in *Saccharophagus degradans* ATCC 43961 in minimal sea salt medium. *Current Microbiology*, 69(6), pp.832-838. [DOI]

Selvakumar, K., Srinivasan, G., Baskar, V. and Madhan, R., 2011. Production and isolation of polyhydroxyalkanoates from *Haloarcula marismortui* MTCC 1596 using cost-effective osmotic lysis methodology. *European Journal of Experimental Biology*, 1(3), pp.180-187. Retrieved from: https://api.semanticscholar.org/CorpusID:103208385

Shah, K.R., 2014. Optimization and production of polyhydroxybutyrate (PHB) by *Bacillus subtilis* G1S1 from soil. *International Journal of Current Microbiology and Applied Sciences*, 3(5), pp.377-387. Retrieved from: https://api.semanticscholar.org/CorpusID:73533657

Sharma, V., Sehgal, R. and Gupta, R., 2021. Polyhydroxyalkanoate (PHA): Properties and modifications. *Polymer*, 212, p.123161. [DOI]

Tavella, R.A., da Silva Júnior, F.M.R., Santos, M.A., Miraglia, S.G.E.K. and Pereira Filho, R.D., 2025. A review of air pollution from petroleum refining and petrochemical industrial complexes: Sources, key pollutants, health impacts, and challenges. *ChemEngineering*, 9(1), p.13. [DOI]

Trapé, D.V., López, O.V. and Villar, M.A., 2024. Exploitation of biomass to the integrated production of bioethanol and poly(hydroxyalkanoate)s. *BioEnergy Research*, 17(1), pp.27-41. [DOI]

Verlinden, R.A.J., Hill, D.J., Kenward, M.A., Williams, C.D., Piotrowska-Seget, Z. and Radecka, I.K., 2011. Production of polyhydroxyalkanoates from waste frying oil by *Cupriavidus necator*. *AMB Express*, 1, p.11. [DOI]

Vigneswari, S., Idris, M.A.H.M., Syairah Anis, S.N., Ramakrishna, S. and Amirul, A.A.A., 2025. Characterization and in situ biodegradation analysis of brown kraft paper coated with PHA for potential sustainable packaging. *Food Technology and Biotechnology*, 63(2), pp.168-176. [DOI]

Nature Environment and Pollution Technology
An International Quarterly Peer-Reviewed Open Access Journal

p-ISSN: 0972-6268 | e-ISSN: 2395-3454 Vol. 25 | No. 4 | Article ID B4448 | 2026

RESEARCH ARTICLE https://doi.org/10.46488/NEPT.2026.v25i04.B4448 OPEN ACCESS

Co-occurrence of Antibiotics, Antibiotic Resistance Genes, and Multidrug-Resistant Bacteria in a Himalayan Foothill Urban River, India

Amit Pokhriyal[1,6], Prashant Pandey[2], Manisha Dhiman[3], Andrzej Białowiec[4], Kanchan Deoli Bahukhandi[5]†, Chinenye Adaobi Igwegbe[2,7] and Kapil Kumar Joshi[8]

[1]School of Business, UPES, Dehradun, Uttarakhand, India
[2]Department of Applied Bioeconomy, Wrocław University of Environmental and Life Sciences, 51-630 Wrocław, Poland
[3]University Institute of Liberal Arts and Humanities, Chandigarh University, Gharuan, Mohali, Punjab 140413, India
[4]Łukasiewicz Research Network, PORT Polish Center for Technology Development, Stablowicka 147 Str., 54-066 Wrocław, Poland
[5]Sustainability Cluster, School of Advanced Engineering, UPES University, Dehradun 248001, Uttarakhand, India
[6]Uttarakhand Pollution Control Board, Dehradun 248001, Uttarakhand, India
[7]Department of Chemical Engineering, Nnamdi Azikiwe University, P.M.B. 5025, Awka, 420218, Nigeria
[8]Department of Forests, Dehradun 248001, Uttarakhand, India
†Corresponding author: Kanchan Deoli Bahukhandi; kanchan@ddn.upes.ac.in

ARTICLE HISTORY

Received: 11-04-2026
Revised: 05-06-2026
Accepted: 07-06-2026

KEYWORDS

Bindal River
Antibiotics
Antibiotic-resistance genes
Wastewater
Antimicrobial resistance

CITE THIS ARTICLE

Pokhriyal, A., Pandey, P., Dhiman, M., Białowiec, A., Bahukhandi, K.D., Igwegbe, C.A. and Joshi, K.K., 2026. Co-occurrence of antibiotics, antibiotic resistance genes, and multidrug-resistant bacteria in a Himalayan foothill urban river, India. *Nature Environment and Pollution Technology*, 25(4), B4448. https://doi.org/10.46488/NEPT.2026.v25i04.B4448

COPYRIGHT & LICENCE

© 2026 The Authors
Open Access under CC BY 4.0.

PUBLISHED BY

TECHNOSCIENCE PUBLICATIONS

ABSTRACT

Urban tributaries are increasingly recognized as important conduits for the dissemination of antibiotic residues and antibiotic resistance determinants into downstream ecosystems. The Bindal River, which traverses Dehradun (Uttarakhand, India), receives untreated municipal wastewater, effluent from healthcare facilities, and diffuse urban runoff, creating conditions that favor the introduction and persistence of multiple antibiotic classes. The objective of this study was to conduct cross-sectional monitoring at six sites (B1–B6) along a downstream gradient to quantify representative antibiotics (ciprofloxacin, tetracycline, sulfamethoxazole, azithromycin, ampicillin) using validated SPE-UHPLC-MS/MS methods, to quantify antibiotic-resistance genes (ARGs; sul1, tetA, qnrS, intI1) via quantitative PCR, and to assess culture-based resistance patterns in heterotrophic bacterial isolates. Measured concentrations indicated a pronounced downstream increase for fluoroquinolones and tetracyclines, with ciprofloxacin reaching concentrations up to 1.57 μg L^{-1} at the most impacted site (B6). ARG abundances and multidrug-resistant (MDR) isolate frequencies mirrored these chemical gradients. Multivariate ordination (RDA) linked antibiotic concentrations, conductivity, and nutrient loads to ARG profiles, with integron abundance (intI1) emerging as a key correlate of MDR prevalence. Our findings demonstrate the co-occurrence of antibiotics and resistance determinants in an urban Himalayan tributary and underscore the need for integrated wastewater management, hospital effluent control, and routine chemical–molecular surveillance to mitigate environmental AMR risks.

1. INTRODUCTION

Antimicrobial resistance (AMR) is a major global public health threat linked to significant morbidity, mortality, and economic costs. Environmental pathways play a critical role in the evolution and dissemination of antibiotic resistance by providing settings where bacterial communities are exposed to selective chemical pressures and mobile genetic elements can mediate horizontal gene transfer (Larsson et al. 2018, Fick et al. 2009, Pruden et al. 2013, Khan et al. 2013). Rivers and urban tributaries are particularly important in this context, serving as receptors for untreated or partially treated domestic sewage, hospital effluents, pharmaceutical manufacturing discharges, and diffuse runoff that collectively introduce antibiotics,

resistant bacteria, and co-selective agents (e.g., heavy metals, biocides) into aquatic ecosystems (Fick et al. 2009, Pandey et al. 2021, Rizzo et al. 2013).

Recent international studies have highlighted the growing occurrence of antibiotic residues and antibiotic resistance genes (ARGs) in aquatic environments worldwide. Investigations conducted in Europe, China, the United States, and South America have reported the widespread presence of fluoroquinolones, tetracyclines, sulfonamides, and macrolides in rivers receiving municipal and hospital wastewater discharges. For example, Rodríguez-Mozaz et al. (2015) demonstrated elevated concentrations of antibiotics and ARGs in receiving rivers downstream of wastewater treatment plants in Spain, whereas several studies in major Chinese river basins reported significant accumulation of antibiotic residues and resistance determinants associated with urbanization and industrial activities. Similar observations have been reported from the Danube, Rhine, and Mississippi River systems, emphasizing the role of riverine ecosystems as reservoirs and dissemination pathways for environmental AMR. These studies collectively indicate that antibiotic contamination and ARG proliferation have become a global environmental challenge requiring integrated monitoring and management approaches.

In India, multiple studies have documented measurable concentrations of a broad range of antibiotics in urban rivers, with levels in heavily impacted reaches frequently in the low ng L^{-1} to µg L^{-1} range, and with coincident increases in ARG abundance and resistant isolates (Singh et al. 2024, Kumara & Bhattacharyya 2026). Studies conducted in the Yamuna, Musi, and Ganga River systems have revealed substantial contamination by antibiotics originating from municipal wastewater, healthcare facilities, agricultural runoff, and pharmaceutical activities. Notably, point-source discharges from pharmaceutical manufacturing have produced exceptionally high concentrations in some regions, underscoring the potential for localized hotspots of resistance selection.

The Bindal River is a small tributary of the Song River, which ultimately drains into the Ganga River, flowing through Dehradun city, an important and rapidly urbanizing center in the Doon Valley of Uttarakhand (Bahukhandi et al. 2025). The river is subjected to multiple anthropogenic stressors, including open sewerage, solid waste deposition, urban runoff, and intermittent hospital and clinic discharges (Singh 2026). These activities create conditions favorable for the introduction and persistence of antibiotics, resistant bacteria, and ARGs in the aquatic environment. However, despite increasing concerns regarding environmental AMR, very limited information is available on the occurrence, distribution, and ecological implications of antibiotics and ARGs in small Himalayan foothill rivers. Most studies conducted in India have focused on large river systems, whereas smaller urban tributaries such as the Bindal River remain poorly investigated. Furthermore, few studies have simultaneously integrated chemical monitoring of antibiotic residues, molecular quantification of ARGs, and culture-based assessment of antimicrobial resistance within a single study framework.

Therefore, the present study addresses this important knowledge gap by providing the first integrated assessment of antibiotic residues, ARGs, and multidrug-resistant bacteria in the Bindal River. The novelty of this work lies in combining advanced chemical analysis (SPE-UHPLC-MS/MS), molecular characterization of resistance determinants (qPCR), and microbiological assessment of resistance patterns to evaluate environmental AMR risks in a Himalayan foothill river ecosystem.

This study presents a field-based monitoring campaign designed to quantify representative antibiotics using SPE-UHPLC-MS/MS, to measure ARGs by qPCR, and to assess culture-based resistance frequencies along a downstream gradient of the Bindal River. Our objectives were to: (1) quantify spatial patterns in antibiotic concentrations and ARG abundances; (2) evaluate relationships between chemical loads, water-quality parameters, and resistance markers; and (3) discuss implications for management and surveillance in urban Himalayan tributaries. By integrating high-quality chemical measurements with molecular and microbiological endpoints, the study aims to provide an actionable dataset for local authorities and a template for similar small-urban-catchment monitoring elsewhere in India.

2. MATERIALS AND METHODS

2.1. Study Area and Site Selection

The study was conducted in the Doon Valley (Fig. 1), a tectonic intermontane basin situated in Dehradun District, Uttarakhand, India. The valley extends between 29°50′–30°30′ N latitude and 77°35′–78°20′ E longitude and is bounded by the Lesser Himalaya to the north and the Siwalik Hills to the south. The Ganga and the Yamuna River systems define the eastern and western hydrological boundaries of the valley, respectively. Within the basin, the Song and Asan rivers constitute the principal drainage networks and receive flow from numerous perennial and ephemeral streams originating in the Himalayan foothills (Bahukhandi et al. 2021, Kamboj et al. 2025).

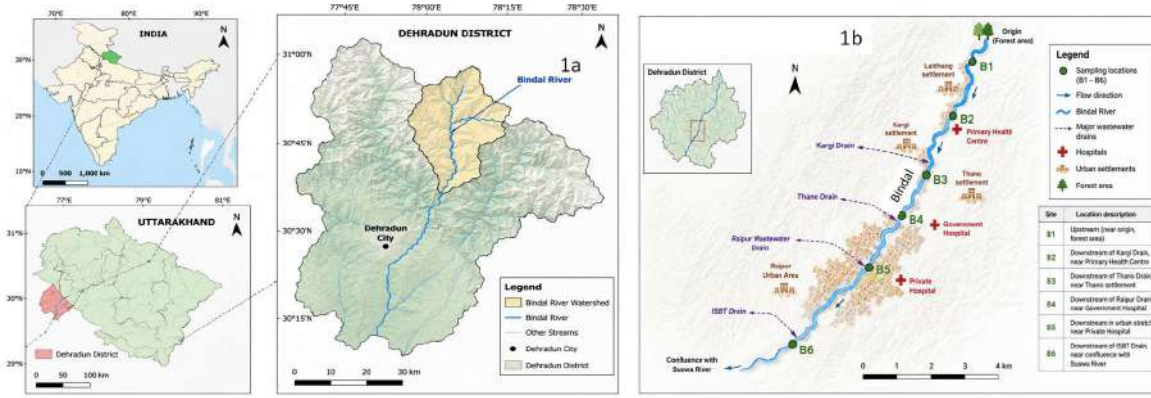


Fig. 1: (1a) Location of the Bindal River watershed within Dehradun District, Uttarakhand, India. (1b) Sampling locations (B1–B6) along the Bindal River showing major wastewater drains, hospitals, urban settlements, and flow direction.

The hydrogeological framework of the Doon Valley is dominated by thick Quaternary alluvial deposits comprising boulders, cobbles, gravel, sand, and silt derived from Himalayan lithological formations. These unconsolidated sediments form highly productive unconfined to semi-confined aquifer systems characterized by high permeability, substantial groundwater storage capacity, and efficient recharge. Groundwater replenishment occurs primarily through direct infiltration of precipitation and seepage from streams and river channels. Thus, strong hydraulic connectivity exists between surface water and shallow groundwater, facilitating the exchange and transport of dissolved contaminants, nutrients, and microbial constituents within the watershed. The Bindal River, a major urban tributary of the Song River, originates in the Mussoorie foothills and traverses the densely populated urban core of Dehradun before discharging into the Song-Suswa river system. The region experiences a humid subtropical climate, with mean annual precipitation ranging from approximately 1,800–2,200 mm, of which more than 75% occurs during the southwest monsoon season (June–September). During the dry season, reduced river discharge coupled with continuous wastewater inputs can result in elevated contaminant concentrations and diminished dilution capacity. Rapid urban expansion, population growth, and increasing anthropogenic activities within Dehradun have imposed considerable environmental pressure on the Bindal River. The river receives both diffuse and point-source inputs from residential areas, commercial establishments, healthcare facilities, stormwater drains, and untreated or partially treated municipal wastewater. These inputs represent potential sources of antibiotics, antibiotic-resistant bacteria, and antibiotic resistance genes (ARGs), making the river an important environmental reservoir for the dissemination of antimicrobial resistance.

To evaluate spatial variations in contamination and resistance indicators, six sampling locations (B1–B6) were strategically selected along the river continuum. Site B1 represented an upstream reference location with relatively limited urban influence, whereas B2 and B3 captured the transition into urbanized reaches. Sites B4 and B5 were located downstream of major wastewater and healthcare-associated discharge zones, while B6 represented the downstream integration point where cumulative impacts from upstream anthropogenic activities were expected to be most pronounced. Geographic coordinates, land-use characteristics, and field observations were recorded for all sampling locations to support spatial interpretation of water quality, antibiotic occurrence, and ARG distribution patterns.

2.2. Field Sampling and Sample Handling

Sampling was conducted during the pre-monsoon low-flow period (May 2025) at six locations (B1–B6) along the Bindal River to capture conditions under which contaminant concentrations are typically elevated. At each site, surface water samples were collected using a grab sampling approach from approximately 10–20 cm below the water surface and away from the riverbank to minimize disturbance and avoid surface debris. Triplicate 1 L water samples were collected in precleaned amber glass bottles for antibiotic analysis, while an additional set of triplicate 1 L samples was collected for microbiological and molecular investigations. All samples were immediately stored in insulated ice boxes ($4 \pm 2°C$) and transported to the laboratory for processing. Water samples designated for microbiological and molecular analyses were filtered on-site where feasible or processed within 6 h of collection. Overall, the monitoring campaign comprised 54 samples (n = 54), excluding field blanks, trip blanks, and quality-control samples. Field blanks and trip blanks were included throughout sampling and transportation to evaluate

potential contamination. In situ physicochemical parameters, including temperature, pH, dissolved oxygen (DO), and electrical conductivity, were measured using calibrated multiparameter sondes. Flow velocity was determined using a portable flow meter at three representative cross-sectional points and averaged for each sampling location (Pant & Singh 2026).

2.3. Chemical Analysis: SPE-UHPLC-MS/MS

Water aliquots (250–1000 mL) were filtered through 0.45 µm glass fiber filters and extracted using Oasis HLB cartridges (Waters Corporation) conditioned with methanol and Milli-Q water. Samples were eluted with methanol, evaporated under a gentle N_2 stream, and reconstituted in 1 mL of mobile phase (water: methanol with 0.1% formic acid). Target analytes included ciprofloxacin, ofloxacin, tetracycline, doxycycline, sulfamethoxazole, trimethoprim, azithromycin, and ampicillin. Quantification was performed on an Agilent 1290 UHPLC coupled to an Agilent 6460 triple quadrupole mass spectrometer operated in multiple reaction monitoring (MRM) mode. Isotope-labeled internal standards were used for quantification where available. Method detection limits (MDLs) ranged from 0.5–5 ng L^{-1} depending on analyte and matrix. Quality assurance/quality control (QA/QC) included field blanks, procedural blanks, matrix spikes, and surrogate recoveries; recoveries of 70–120% were accepted. In brief, antibiotic analysis was performed using an ultra-high-performance liquid chromatography system coupled with tandem mass spectrometry (UHPLC-MS/MS; Thermo Scientific Vanquish UHPLC coupled to a TSQ Altis Triple Quadrupole Mass Spectrometer or equivalent). Chromatographic separation was achieved using a Hypersil GOLD C18 analytical column (100 × 2.1 mm, 1.9 µm particle size) maintained at 40°C. The mobile phase consisted of (A) ultrapure water containing 0.1% formic acid and (B) methanol containing 0.1% formic acid. A gradient elution program was employed at a flow rate of 0.30 mL min^{-1}, and the injection volume was 10 µL. Detection was performed using electrospray ionization (ESI) operating in positive ion mode and multiple reaction monitoring (MRM) acquisition. Target compounds were identified based on retention times and characteristic precursor-product ion transitions. Instrument calibration was verified using multipoint external standard calibration curves covering environmentally relevant concentration ranges. Analytical blanks and quality-control samples were analyzed periodically throughout the analytical sequence to monitor instrument stability and potential contamination. For qPCR analysis, all reactions were performed in triplicate using gene-specific primers and standard amplification protocols. Standard curves were prepared using serial dilutions of plasmid standards, and no-template controls (NTCs) together with extraction blanks were included in each analytical batch to assess contamination and amplification reliability. Melt-curve analysis was performed to confirm amplification specificity. All molecular analyses were conducted following established quality-control procedures to ensure reproducibility and consistency of ARG quantification (Mula et al. 2023).

2.4. Microbiological Methods and Phenotypic Resistance Testing

Water samples (100–500 mL) were filtered onto 0.45 µm membranes and plated onto nutrient agar and MacConkey agar for isolation of heterotrophic bacteria and probable Enterobacterales. Representative colonies (target n = 50 per site, chosen to capture phenotypic diversity) were purified and stored. Antibiotic susceptibility testing followed Clinical and Laboratory Standards Institute (CLSI) disk diffusion protocols: ciprofloxacin (5 µg), tetracycline (30 µg), and ampicillin (10 µg). Zones of inhibition were measured after 18-24 h incubation at 37°C and interpreted using CLSI breakpoints. MDR was defined as resistance to ≥ 2 antibiotic classes tested (Makori et al. 2024).

2.5. Molecular Quantification of ARGs

DNA was extracted from filter membranes and sediment subsamples using the DNeasy PowerWater and PowerSoil kits (Qiagen) with inhibitor removal. Quantitative PCR assays targeted sul1, tetA, qnrS, and intI1. Standards were generated using plasmid clones (10^2–10^8 copies), and assays were run in triplicate; amplification efficiencies and melt-curve analyses were performed to confirm specificity. ARG copies were normalized to 16S rRNA gene copies (determined by qPCR) and expressed as copies per 10^6 16S rRNA gene copies.

2.6. Data Analysis

Antibiotic concentrations and ARG abundances were $\log_{10}$-transformed for parametric analyses where appropriate. Spearman rank correlations were used to assess pairwise relationships between antibiotic concentrations, ARG abundances, and resistance frequencies. Redundancy analysis (RDA) was implemented using the vegan package in R to partition variance in ARG composition explained by chemical concentrations and environmental covariates (conductivity, nutrients, DO, flow). Statistical significance was evaluated at $\alpha = 0.05$. All data processing and plotting scripts are available on request.

3. RESULTS AND DISCUSSION

3.1. Environmental Parameters

Field measurements (Table 1) showed a clear downstream

degradation in water quality. Temperature ranged between 18.4 and 26.9°C across sites, while dissolved oxygen decreased markedly from 6.8 mg L^{-1} at the upstream site (B1) to 1.6 mg L^{-1} at the downstream site (B6). The pH of the Bindal River varied from 7.1 to 7.9, with a mean value of 7.5, and was within the permissible limit of the Bureau of Indian Standards (BIS) drinking water quality standard; this pH also reflected the slightly alkaline nature of the Bindal River.

Conductivity and nutrient concentrations (nitrate-N, phosphate-P) increased downstream, coincident with visible sewage influx and reduced channel flow in the urban reaches. The observed increase in conductivity and nutrient concentrations downstream is indicative of progressive anthropogenic influence, particularly from untreated municipal wastewater and urban runoff. Elevated conductivity is commonly associated with increased ionic loads originating from domestic sewage, while higher nitrate and phosphate concentrations reflect organic pollution and nutrient enrichment. Similar downstream trends have been reported in urban rivers across Asia and Europe, where wastewater discharges significantly altered water quality characteristics and promoted microbial proliferation and resistance development. The simultaneous decline in dissolved oxygen further suggests enhanced microbial decomposition of organic matter, creating environmental conditions that may favor the persistence and transfer of antibiotic resistance determinants. Average flow velocity decreased with downstream distance, reflecting channel modifications and culverting in the lower reaches. The conductivity in the study area ranged from 160 to 820 µS cm^{-1}, with a mean value of 460 µS cm^{-1}. Phosphate concentrations ranged from 0.02 to 0.85 mg L^{-1}, with a mean value of 0.341 mg L^{-1}. The downstream increase in nutrient concentrations indicates increasing nutrient enrichment along the urbanized reaches of the river.

3.2. Antibiotic Concentrations

Targeted analysis detected multiple antibiotics across all sites, with concentrations showing a strong downstream increase (Fig. 2 and Table 2). Ciprofloxacin and tetracycline exhibited the highest downstream concentrations, reaching maximum levels of 1,570 ± 30 ng L^{-1} and 1,320 ± 27 ng L^{-1}, respectively, at site B6. Both antibiotics showed a progressive increase along the downstream gradient, indicating cumulative inputs from urban wastewater discharges and other anthropogenic sources. Ciprofloxacin concentrations increased from the upstream site (B1) to the downstream site (B6). Sulfamethoxazole and azithromycin were also detected at elevated downstream concentrations. Ampicillin showed a moderate downstream increase across the sampling sites. The observed concentrations should be interpreted in the context of the environmental stability of the compound and the analytical recovery achieved in the present study.. The pronounced downstream accumulation of ciprofloxacin and tetracycline likely reflects their widespread use in human healthcare and their relatively high environmental persistence. Fluoroquinolones exhibit strong adsorption to suspended particles and sediments, whereas tetracyclines possess high affinity for organic matter and metal oxides, enhancing their environmental retention. The elevated concentrations observed at sites B5 and B6 suggest cumulative contributions from untreated sewage, healthcare facilities, and urban drainage networks. Similar concentration gradients have been reported in the Yamuna River (India), the Pearl River (China), and several European urban rivers receiving wastewater inputs. Importantly,the downstream ciprofloxacin concentrations indicate environmental exposure levels that warrant consideration in the context of antimicrobial resistance risk. However, the measured concentrations alone do not establish that selection for resistance occurred in situ.

3.3. ARG Abundances and Patterns

Quantitative PCR analysis revealed substantial downstream enrichment of ARGs (sul1, tetA, qnrS) and the class 1 integron integrase gene (intI1) (Table 3 and Fig. 3). Copies were normalized to 10^6 16S rRNA gene copies to account for variations in bacterial biomass. intI1 abundance increased by more than two orders of magnitude from the upstream

Table 1: Environmental parameters measured at Bindal River sampling sites (May 2025).

Site	Temp (°C)	pH	DO (mg L^{-1})	Conductivity (µS cm^{-1})	NO_3-N (mg L^{-1})	PO_4-P (mg L^{-1})	Flow (m s^{-1})
B1	18.4	7.1	6.8	160	0.18	0.02	0.45
B2	20.1	7.2	5.5	220	0.45	0.06	0.38
B3	22.3	7.4	4.1	360	0.92	0.14	0.25
B4	24.0	7.6	2.8	520	2.10	0.36	0.18
B5	25.6	7.8	2.0	680	3.40	0.62	0.12
B6	26.9	7.9	1.6	820	4.20	0.85	0.08
Mean	22.8	7.5	3.8	460	1.875	0.341	0.243

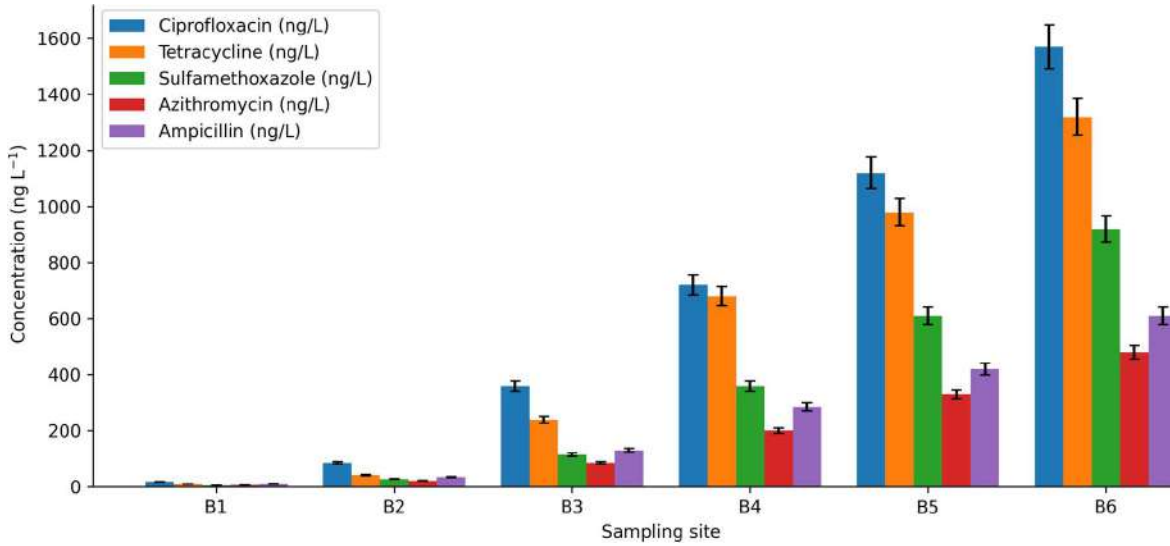


Fig. 2: Clustered bar chart showing measured antibiotic concentrations (ng L^{-1}) across Bindal River sampling sites B1–B6.

Table 2: Measured antibiotic concentrations (ng L^{-1}) at Bindal River sites (May 2025).

Site	Ciprofloxacin	Tetracycline	Sulfamethoxazole	Azithromycin	Ampicillin	MDL (ng L^{-1})
B1	18	9	5	6	10	2
B2	85	42	28	22	35	2
B3	360	240	115	85	130	2
B4	720	680	360	200	285	2
B5	1120	980	610	330	420	2
B6	1570	1320	920	480	610	2

reference to the most impacted site, indicating a substantial mobilome potential in lower reaches. The marked enrichment of ARGs and the class 1 integron integrase gene (intI1) downstream suggests increasing opportunities for horizontal gene transfer within microbial communities exposed to wastewater-derived contaminants. Integrons are recognized as important indicators of anthropogenic pollution and antimicrobial resistance dissemination because they facilitate the capture and transfer of resistance determinants among bacterial populations. The strong increase in intI1 abundance observed in this study is consistent with reports from urban river systems in China, Spain, and Brazil, where wastewater discharge points acted as hotspots for ARG accumulation and mobilization. These findings indicate that downstream sections of the Bindal River may function not only as reservoirs but also as active environments for resistance evolution.

3.4. Culture-Based Resistance Frequencies

Phenotypic testing of isolates reflected the chemical and molecular gradients: ciprofloxacin resistance in culturable isolates increased from 2% at B1 to 54% at B6; tetracycline resistance increased from 4% to 74%, and ampicillin resistance increased from 8% to 86% (Table 4). MDR frequencies rose from negligible upstream to 68% at the downstream site, aligning with high intI1 abundance and antibiotic loads in lower reaches. The progressive increase in multidrug-resistant (MDR) isolates downstream supports the hypothesis that continuous exposure to antibiotic residues and wastewater-associated microbial communities exerts selective pressure favoring resistant phenotypes. The strong correspondence between MDR prevalence, ARG abundance,

Table 3: ARG abundances (copies per 10^6 16S rRNA gene copies) by site.

Site	sul1	tetA	qnrS	intI1
B1	450	210	120	100
B2	2800	950	300	620
B3	18000	5200	1200	5000
B4	56000	21000	4300	19000
B5	110000	42000	8900	38000
B6	180000	79000	15000	67000

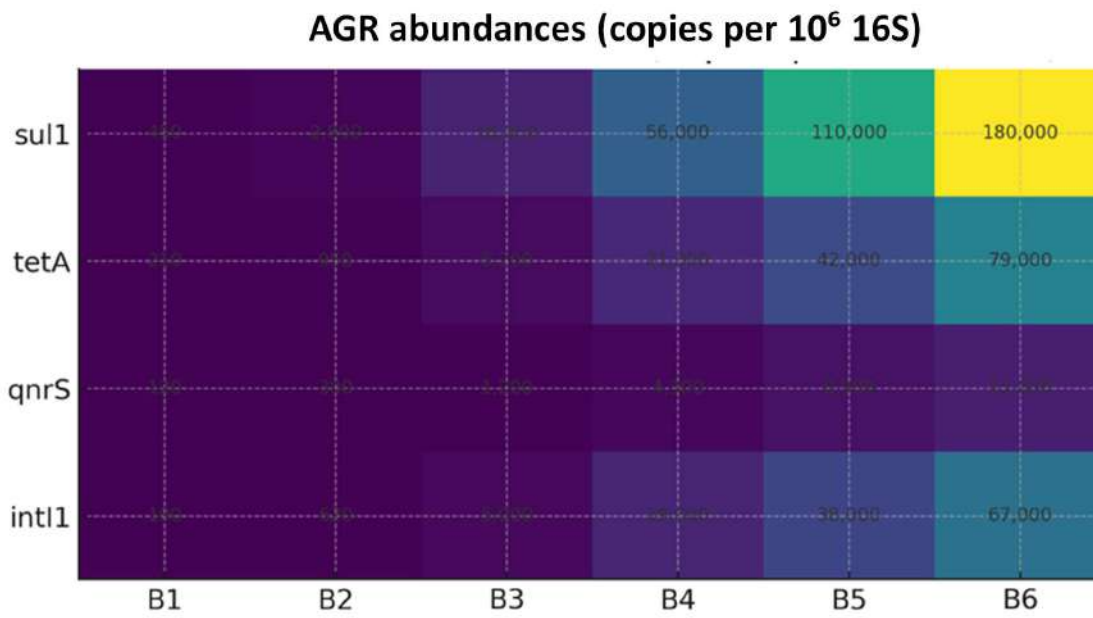


Fig. 3: Heatmap showing measured ARG abundances (copies per 10^6 16S rRNA gene copies) across Bindal River sampling sites. Values are presented in Table 3.

Table 4: Culture-based antibiotic resistance percentages by site.

Site	% Ciprofloxacin-resistant	% Tetracycline-resistant	% Ampicillin-resistant	% MDR
B1	2	4	8	0
B2	8	16	28	6
B3	22	36	58	28
B4	38	52	72	46
B5	46	64	80	58
B6	54	74	86	68

and antibiotic concentrations suggests that both genetic and environmental factors contribute to resistance propagation. Similar associations have been reported in river systems receiving untreated municipal wastewater, where increased antibiotic concentrations were linked to elevated resistance frequencies among environmental bacterial isolates.

3.5. Correlation Analysis

Spearman rank correlation analysis was performed to explore relationships among antibiotic concentrations, antibiotic resistance genes (ARGs), and environmental variables across the sampling locations. Significant positive correlations were observed between total antibiotic concentrations and ARG abundance ($\rho = 0.78$, $p < 0.05$), indicating that sites with elevated antibiotic contamination generally exhibited higher levels of resistance determinants. Similarly, nutrient concentrations, particularly nitrate and phosphate, showed positive associations with intI1 abundance ($\rho = 0.72$, $p < 0.05$).

Suggesting that wastewater-derived nutrient enrichment may contribute to conditions favorable for the persistence and dissemination of mobile genetic elements. The observed relationships are consistent with the increasing influence of anthropogenic activities along the downstream reaches of the Bindal River, where untreated sewage, urban runoff, and healthcare-related discharges contribute to elevated contaminant loads. Wastewater inputs not only introduce antibiotic residues into aquatic environments but also transport resistant bacteria and ARGs, thereby facilitating their co-occurrence within riverine ecosystems. The positive associations observed in the present study support the hypothesis that wastewater-impacted environments may act as important reservoirs of antibiotic resistance determinants. However, it is important to note that correlation does not necessarily imply causation. While the observed relationships suggest a linkage between antibiotic contamination and ARG occurrence, other environmental factors, including

microbial community composition, hydrological conditions, organic matter content, and co-selective contaminants such as heavy metals and biocides, may also influence ARG distribution patterns. Therefore, the results should be interpreted as evidence of association rather than direct proof of antibiotic-driven resistance selection. These findings were further supported by the redundancy analysis (RDA), which identified antibiotics and wastewater-associated environmental variables as important factors influencing the spatial distribution of ARGs across the study area. Together, the correlation and ordination analyses indicate that anthropogenic inputs play a significant role in shaping resistance patterns within the Bindal River ecosystem.

3.6. Multivariate Analysis

Redundancy analysis (RDA) revealed that chemical variables (log-transformed antibiotic concentrations and conductivity) explained a majority of the variance in ARG distributions (adjusted $R^2 = 0.64$). Vectors for ciprofloxacin and tetracycline showed strong positive loadings on RDA axis 1, while intI1 and sul1 had high positive scores, consistent with co-selection and mobilome activity in downstream samples (Fig. 4).

3.7. Spatial Patterns and Likely Sources

The integrated chemical–molecular–microbiological dataset demonstrates a clear downstream amplification of antibiotic residues and ARGs in the Bindal River. Ciprofloxacin and tetracycline displayed the highest downstream concentrations, patterns that are consistent with their high usage in clinical settings and their environmental persistence. Nutrient enrichment and declining dissolved oxygen in downstream reaches indicate significant organic loading consistent with untreated sewage inputs, which themselves are rich sources of both antibiotics and resistant bacteria (Pruden et al. 2013, Pandey et al. 2021).

Hospital effluents and domestic sewage are likely key contributors: the steep increases in antibiotic concentrations between B3 and B5 coincide with known hospital clusters and major open drain inflows recorded during field reconnaissance. Pharmaceutical production is not a major activity in the Bindal catchment; therefore, the pattern here reflects municipal and healthcare-related inputs rather than industrial manufacturing hotspots observed elsewhere in India (Fick et al. 2009).

3.8. Chemical-Molecular Linkage and Selection Pressure

Strong correlations between site-wise antibiotic concentrations and corresponding ARG abundances (e.g., ciprofloxacin with qnrS; tetracycline with tetA) suggest that measured residues are relevant selective agents in situ. Furthermore, the strong association of intI1 with MDR prevalence supports the role of mobile genetic elements in disseminating resistance across taxonomic groups, as

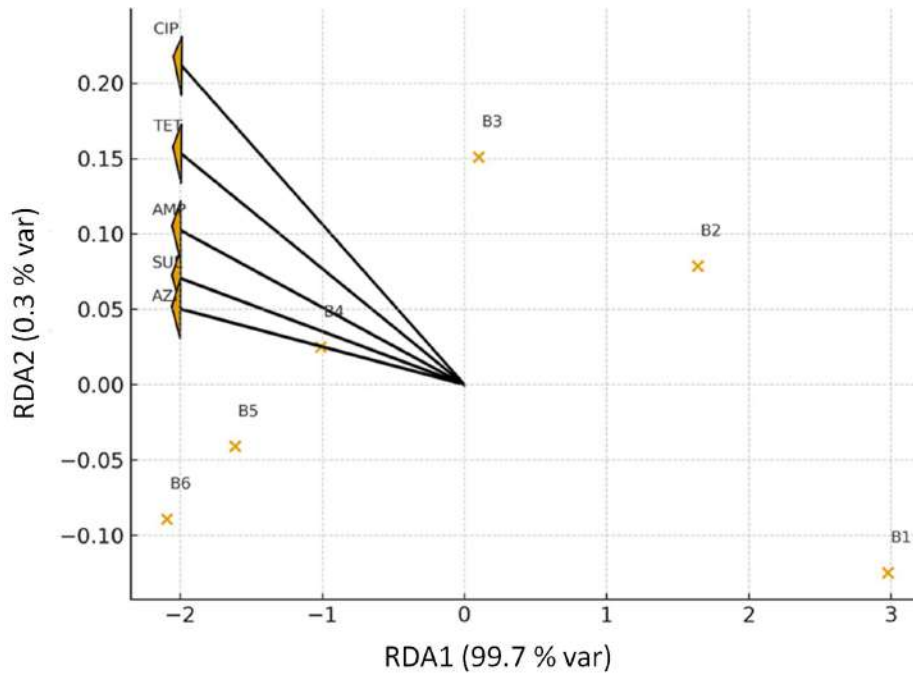


Fig. 4: Redundancy analysis (RDA) biplot showing the relationships between environmental/chemical variables, antibiotic concentrations, and antibiotic resistance genes (ARGs) across the Bindal River sampling sites.

observed in other riverine studies (Larsson et al. 2018, Rizzo et al. 2013). While co-occurrence alone does not prove causality, the congruence of chemical gradients, ARG enrichment, and phenotypic resistance strengthens the inference that wastewater-mediated antibiotic exposure contributes to environmental selection.

3.9. Comparison with Other Indian Rivers

The antibiotic concentrations measured in the Bindal River were within the range reported for several wastewater-impacted urban aquatic systems. Ciprofloxacin reached 1.57 μg L^{-1} at the most downstream site (B6), which is comparable to the maximum concentration of approximately 1.44 μg L^{-1} reported in the Yamuna River downstream of sewage-treatment discharges in India (Mutiyar and Mittal, 2014). Antibiotics, including quinolones, have also been detected in wastewater-impacted aquatic environments in China, where the occurrence of antibiotic residues has been accompanied by the detection of multiple ARGs and mobile genetic elements (Liu et al., 2015; Yang et al., 2024). In Spain, Quintela-Baluja et al. (2019) reported substantial ARG diversity in wastewater networks and downstream receiving waters and showed that hospital and community wastewater sources contributed to the ARG profiles observed in the receiving environment. The elevated ARG abundances observed in the Bindal River are therefore consistent with observations from other wastewater-impacted aquatic systems. However, direct quantitative comparison among river systems should be made cautiously because antibiotic concentrations and ARG abundances can vary with sampling season, hydrological conditions, wastewater inputs, treatment processes, target compounds, and analytical methods. The downstream increase in antibiotic concentrations and ARG abundances observed in the present study indicates that urban wastewater inputs may contribute to the contamination of the Bindal River and warrants further investigation using multi-season sampling and source-specific wastewater characterization.

3.10. Implications for Monitoring and Risk Assessment

Our results emphasize the importance of paired chemical–molecular monitoring to discern whether ARGs reflect historical inputs (fecal pollution) or ongoing selection by environmental residues. Risk assessment frameworks should consider both antibiotic concentrations relative to minimal selective concentrations (MSCs) and the abundance of mobile genetic elements (e.g., intI1) that modulate dissemination risk (Larsson et al. 2018, Pruden et al. 2013).

3.11. Limitations

The present study provides a cross-sectional assessment of antibiotic residues, antibiotic resistance genes (ARGs), and antimicrobial resistance patterns in the Bindal River based on a single pre-monsoon sampling campaign. Consequently, the observed spatial patterns may not fully represent seasonal variability associated with monsoon-driven hydrological changes, fluctuations in wastewater discharge, or variations in antibiotic consumption and usage patterns. River flow conditions during the monsoon season may substantially alter contaminant concentrations through dilution, transport, and sediment resuspension processes. Therefore, the findings should be interpreted as baseline evidence of antibiotic contamination and resistance dissemination within the study area rather than a comprehensive characterization of year-round conditions. Future studies should incorporate multi-season monitoring, longitudinal assessments, and advanced molecular approaches such as metagenomic analyses to improve understanding of temporal dynamics, resistance transmission pathways, and long-term environmental AMR risks.

In addition, the culture-based resistance assessment was based on a limited number of representative bacterial isolates collected from each sampling site. While these analyses provided useful supporting evidence for observed antibiotic and ARG patterns, the isolate numbers may not fully represent the diversity and prevalence of resistant bacterial populations within the river ecosystem. Future studies should include larger microbiological sample sizes, high-throughput sequencing approaches, and culture-independent methods to provide a more comprehensive assessment of environmental antimicrobial resistance.

3.12. Environmental and Policy Implications

The presence of measurable antibiotic residues and elevated ARGs in the Bindal River demands an integrated management response. Practical interventions include deployment of decentralized wastewater treatment systems (DEWATS) at key tributary inputs, implementation of hospital effluent pretreatment mandates, and establishment of routine chemical–molecular surveillance within municipal water quality programs. DEWATS solutions such as constructed wetlands or baffled reactors can substantially reduce organic load and microbial contamination at low operational costs, particularly when centralized sewerage is absent or incomplete. Hospital effluent pretreatment should prioritize solids removal and targeted disinfection; where feasible, tertiary processes (e.g., activated carbon adsorption or ozonation) can reduce dissolved antibiotic loads.

Policy approaches should also include antibiotic stewardship campaigns to reduce community-level

overuse and improper disposal of pharmaceuticals, take-back programs at pharmacies, and regulatory oversight for medical facilities. Integrating AMR monitoring into national river health initiatives would ensure sustained data flow to inform interventions and measure policy impact.

4. CONCLUSIONS

The present study identified increasing downstream concentrations of antibiotics, elevated ARG abundances, and higher frequencies of multidrug-resistant bacteria in the Bindal River. The observed spatial patterns were associated with increasing anthropogenic influence and wastewater inputs. While the findings indicate a potential linkage between antibiotic contamination and resistance dissemination, the cross-sectional nature of the study does not permit direct causal inference. Nevertheless, the results provide important baseline information for environmental AMR surveillance in Himalayan foothill river systems and highlight the need for long-term, multi-season monitoring to better understand resistance dynamics and associated environmental risks. Measured concentrations of ciprofloxacin and tetracyclines reached levels in lower reaches that are consistent with selection for resistance documented in experimental and field studies. Integron-mediated gene mobility (intI1) and high MDR frequencies in downstream isolates underscore the need for rapid intervention to prevent further environmental amplification and potential human exposure. Actionable recommendations include prioritized DEWATS deployment, hospital effluent regulation, and integration of antibiotic and ARG monitoring into municipal water quality programs. Future research should focus on longitudinal sampling, metagenomic host-ARG linkage analyses, and intervention trials to validate mitigation strategies.

5. ACKNOWLEDGMENTS

This work was also carried out through the International Exchange of Doctoral Students as part of the project International Interdisciplinary Doctoral School at the HEART of Bio-Based University, financed by the National Agency for Academic Exchange under the STER programme at Wrocław University of Environmental and Life Sciences (UPWr), Wrocław, Poland, and through a doctoral student grant at UPWr (Agreement No. N020/0025/24). The authors acknowledge all members of Wrocław University of Environmental and Life Sciences, Wrocław, Poland, and UPES University, Uttarakhand, India, for their support during the study.

6. REFERENCES

Bahukhandi, K.D., Kushwaha, A., Devi, G., Goswami, L., Bhan, U., Oh, S., Bartarya, S.K., Kamboj, V., Saini, V.K., Kamboj, N. and Sathe, S.S., 2025. Hydro-geochemistry of the Bindal River catchment: water suitability for irrigation and drinking in the Doon Valley outer Himalaya. *International Journal of Environmental Analytical Chemistry*, 105(18), pp.7063–7087. [DOI]

Bahukhandi, K.D., Saini, R., Ahuja, N.J., Thakur, D. and Siddiqui, N.A., 2021. Assessment of the impact of the municipal solid waste on hydrochemistry of the surface and groundwater quality of Dehradun district of Uttarakhand: seasonal variation in water quality. *Himalayan Geology*, 42(1), pp.175–188.

Fick, J., Söderström, H., Lindberg, R.H., Phan, C., Tysklind, M. and Larsson, D.J., 2009. Contamination of surface, ground, and drinking water from pharmaceutical production. *Environmental Toxicology and Chemistry*, 28(12), pp.2522–2527. [DOI]

Kamboj, V., Deoli Bahukhandi, K., Bisht, A., Kamboj, N., Sharma, I. and Semwal, M.P., 2025. Groundwater stability and health risk assessment associated with nitrate and fluoride in adjacent areas of Dehradun industrial area, India. *International Journal of Environmental Analytical Chemistry*, 105(20), pp.8950–8965. [DOI]

Khan, G.A., Berglund, B., Khan, K.M., Lindgren, P.E. and Fick, J., 2013. Occurrence and abundance of antibiotics and resistance genes in rivers, canal and near drug formulation facilities–a study in Pakistan. *PLOS ONE*, 8(6), p.e62712. [DOI]

Kumara, M.K. and Bhattacharyya, D., 2026. Spatial distribution of conventional pollutants and micropollutants in an urban river in India: a preliminary analysis of the water quality of Musi River. *Water, Air, & Soil Pollution*, 237(8), p.471. [DOI]

Larsson, D.G.J., Andremont, A., Bengtsson-Palme, J., Brandt, K.K., de Roda Husman, A.M., Fagerstedt, P., Fick, J., Flach, C.F., Gaze, W.H., Kuroda, M., Kvint, K., Laxminarayan, R., Manaia, C.M., Nielsen, K.M., Plant, L., Ploy, M.C., Segovia, C., Simonet, P., Smalla, K., Snape, J.R., Topp, E., van Hengel, A.J., Verner-Jeffreys, D.W., Virta, M.P.J., Wellington, E.M. and Wernersson, A.S., 2018. Critical knowledge gaps and research needs related to the environmental dimensions of antibiotic resistance. *Environment International*, 117, pp.132–138. [DOI]

Makori, A., Neondo, J., Mwangi, I. and Mweu, C., 2024. Genetic diversity of pathogenic bacteria and incidence of selected antibiotic resistant genes in water used by eateries and open markets in Juja, Kenya. *Journal of Agriculture, Science and Technology*, 23(1), pp.125–147. [DOI]

Mula, J., Chiara, F., Manca, A., Palermiti, A., Maiese, D., Cusato, J., Simiele, M., De Rosa, F.G., Di Perri, G., De Nicolò, A. and D'Avolio, A., 2023. Analytical validation of a novel UHPLC-MS/MS method for 19 antibiotics quantification in plasma: implementation in a LC-MS/MS kit. *Biomedicine & Pharmacotherapy*, 163, p.114790. [DOI]

Pandey, P., Shankar, A., Biney, M. and Saini, V.K., 2021. Enhancement in amoxicillin adsorption and regeneration properties of SBA-15 after surface modification with polyaniline. *Colloid and Interface Science Communications*, 43, p.100432. [DOI]

Pant, M. and Singh, J., 2026. Computing water quality deterioration attributed to anthropogenic impacts in Dehradun—A lower Himalayan region of India. *Environmental Quality Management*, 35(3), p.e70289. [DOI]

Pruden, A., Larsson, D.G.J., Amézquita, A., Collignon, P., Brandt, K.K., Graham, D.W., Lazorchak, J.M., Suzuki, S., Silley, P., Snape, J.R., Topp, E., Zhang, T. and Zhu, Y.G., 2013. Management options for reducing the release of antibiotics and antibiotic resistance genes to the environment. *Environmental Health Perspectives*, 121(8), pp.878–885. [DOI]

Rizzo, L., Manaia, C., Merlin, C., Schwartz, T., Dagot, C., Ploy, M.C., Michael, I. and Fatta-Kassinos, D., 2013. Urban wastewater treatment

plants as hotspots for antibiotic resistant bacteria and genes spread into the environment: a review. *Science of the Total Environment*, 447, pp.345–360. [DOI]

Rodriguez-Mozaz, S., Chamorro, S., Marti, E., Huerta, B., Gros, M., Sànchez-Melsió, A., Borrego, C.M., Barceló, D. and Balcázar, J.L., 2015. Occurrence of antibiotics and antibiotic resistance genes in hospital and urban wastewaters and their impact on the receiving river. *Water Research*, 69, pp.234–242. [DOI]

Singh, A., Pratap, S.G. and Raj, A., 2024. Occurrence and dissemination of antibiotics and antibiotic resistance in aquatic environment and its ecological implications: a review. *Environmental Science and Pollution Research*, 31(35), pp.47505–47529. [DOI]

Singh, S., 2026. Groundwater quality evaluation using hydrochemical and multivariate statistical techniques in Doiwala block, Dehradun District, Uttarakhand, India. *Discover Geoscience*, 4(1), p.182. [DOI]

Nature Environment and Pollution Technology
An International Quarterly Peer-Reviewed Open Access Journal

p-ISSN: 0972-6268 | e-ISSN: 2395-3454 Vol. 25 | No. 4 | Article ID D1912 | 2026

RESEARCH ARTICLE https://doi.org/10.46488/NEPT.2026.v25i04.D1912 OPEN ACCESS

Synthesis and Characterization of Amino Acid-Based Ionic Liquids for Selective Absorption of CO_2 Using Liquid Foam Bed and Semi-Batch Reactors

Santhi Raju Pilli†
Department of Chemical Engineering Technology, College of Applied Industrial Technology, Jazan University, Jazan 45142, Kingdom of Saudi Arabia
†Corresponding Author: Santhi Raju Pilli; spilli@jazanu.edu.sa; ssanthirajup@gmail.com

ARTICLE HISTORY

Received: 28-01-2026
Revised: 29-03-2026
Accepted: 09-04-2026

KEYWORDS

CO_2 absorption
Amino acids
Ionic liquids
Foam bed reactor
NMR and Raman Spectra

CITE THIS ARTICLE

Pilli, S.R., 2026. Synthesis and characterization of amino acid-based ionic liquids for selective absorption of CO_2 using liquid foam bed and semi-batch reactors. *Nature Environment and Pollution Technology*, 25(4), D1912. https://doi.org/10.46488/NEPT.2026.v25i04.D1912

COPYRIGHT & LICENCE

© 2026 The Authors
Open Access under CC BY 4.0.

PUBLISHED BY
TECHNOSCIENCE PUBLICATIONS

ABSTRACT

Carbon dioxide (CO_2) emissions are produced by the combustion of fossil fuels for power generation, automobiles, and other major industrial processes. Hence, there is a need for efficient CO_2 absorption using advanced materials and reactor systems within the framework of carbon capture and storage technologies. This work emphasizes the synthesis and characterization of amino acid-based ionic liquids (AAILs) for CO_2 (99.99% pure) absorption via a liquid foam-bed reactor (FBR) and semi-batch equilibrium studies (SBES). Seven different AAILs, namely [TETA][ALA], [TETA][LYS], [TETA][GLU], [TETA][ASP], [TETA][GLN], [TETA][MET], and [TETA][PHE], were newly synthesized. The AAILs were characterized using FTIR and Raman spectroscopy and ^1H and ^{13}C NMR spectroscopy to confirm their formation. Physical properties such as viscosity and density were also presented. The highest and lowest densities of 1.1709 and 1.0646 g cm^{-3} were observed for [TETA][ASP] and [TETA][ALA], respectively, among the synthesized AAILs. The application of AAILs in FBR and SBES for CO_2 absorption was evaluated under different experimental conditions. Parameters such as initial concentration, surfactant, pH, and AAIL regeneration were studied. [TETA][LYS] gave the highest moles of CO_2 absorbed per mole of [TETA][LYS] used; the highest mole ratios of 0.442, 0.172, and 0.112 (dry basis) were observed at initial concentrations of 500, 300, and 100 mmol CO_2, respectively. Finally, the highest mole ratio of CO_2 per mole of [TETA][GLU] was 0.166, followed by 0.133 for [TETA][ALA], during desorption studies.

1. INTRODUCTION

The increasing concentration of greenhouse gases (GHGs), particularly carbon dioxide (CO_2), has become a critical global concern because of its significant contribution to climate change. Industrial activities and fossil fuel-based power generation are among the primary sources of CO_2 emissions. In this context, carbon capture and storage (CCS) has emerged as a vital technological strategy to mitigate CO_2 emissions and limit their release into the atmosphere. CCS involves three main stages: (i) capture of CO_2 from large point sources, (ii) transportation via pipelines or marine systems, and (iii) long-term storage in deep geological formations such as depleted oil and gas reservoirs or saline aquifers (IPCC 2005). This integrated approach enables substantial reductions in emissions while allowing continued use of existing energy infrastructure.

Despite its potential, conventional CO_2 absorption technologies face several limitations. Common absorption approaches, including pre-combustion,

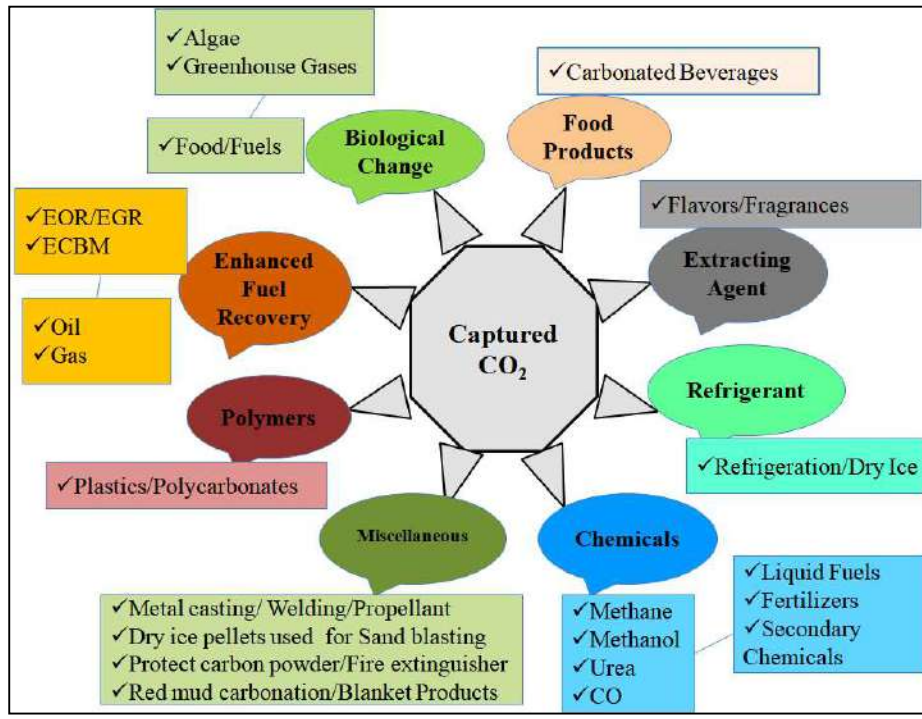


Fig. 1: Illustration of various products that can be obtained from CO_2-absorption technologies.

post-combustion, and oxy-fuel combustion, are often associated with high energy requirements, operational complexity, and high economic costs. In particular, solvent-based absorption systems using aqueous amines suffer from drawbacks such as solvent degradation, equipment corrosion, and high regeneration energy demand. Scaling these technologies to match large emission sources remains a major challenge, especially when considering the availability and suitability of storage sites. These limitations highlight the need for more efficient, cost-effective, and sustainable alternatives for CO_2 absorption. Fig. 1 illustrates the different products or compounds that can be obtained from CO_2 absorption technologies.

In recent years, ionic liquids (ILs) have gained considerable attention as promising materials for CO_2 absorption because of their unique physicochemical properties, including negligible vapor pressure, high thermal stability, and tunable chemical structures. Among them, amino acid-based ionic liquids (AAILs) have emerged as particularly attractive candidates because they combine the advantages of ILs with enhanced CO_2 affinity and environmental compatibility. AAILs exhibit strong chemical interactions with CO_2, leading to higher absorption capacities and selectivity compared with conventional solvents. Their design flexibility also allows optimization of performance characteristics such as viscosity, absorption kinetics, and regeneration efficiency. While ionic liquids have also been explored in areas such as wastewater treatment and membrane separation, these applications are beyond the primary scope of this study and are therefore only briefly acknowledged.

To fully exploit the potential of advanced solvents such as AAILs, there is a growing need for innovative reactor systems that can enhance mass transfer and overall process efficiency. One such promising technology is the foam-bed reactor (FBR), which offers improved gas–liquid contact, higher interfacial area, and enhanced mixing characteristics compared to conventional packed or stirred reactors. The FBR system can significantly improve CO_2 absorption rates while potentially reducing solvent usage and energy consumption. Therefore, integrating AAILs with advanced reactor designs like FBR represents a forward-looking approach to overcoming the limitations of traditional CO_2 absorption systems.

In summary, the development of efficient CO_2 absorption technologies requires a synergistic combination of advanced materials and innovative process design. This study focuses on the application of amino acid-based ionic liquids in a foam-bed reactor system, aiming to provide an effective and sustainable solution for CO_2 absorption.

1.1. Background Research

Several carbon absorption technologies have been demonstrated at the laboratory scale, and some have also

been demonstrated industrially. These include physisorption or chemisorption processes (Zhang et al. 2011, Cahyonugroho et al. 2025, Mandal & Bandyopadhyay 2005), ionic liquid membranes and membrane separations (Makino & Kanakubo 2016, Ramdin et al. 2012, Jones 2011), and molecular sieves (Sarker et al. 2017, Wahby et al. 2012, Mohamedali et al. 2017). Combinations of ionic liquids (ILs) and composite materials have been used for CO_2 absorption (Pilli et al. 2014, Mulk et al. 2023), as have amines and amino acid ILs (Du et al. 2016, Qu et al. 2022, Yamini & Khanna 2014, Mumford et al. 2017). The use of novel materials, such as ionic liquids as electrolytes and nanostructured materials for cathodes, has the potential to enhance both the energy efficiency and lifespan of batteries (Padmanabhan et al. 2024).

Most of the literature is available on amine-based technologies. The most commonly used amines for CO_2 absorption are monoethanolamine, diethanolamine, and methyldiethanolamine, which absorb CO_2 via carbamate/carbonate formation. Although conventional CO_2 absorption technology of this type has been used industrially for a considerable period, several drawbacks remain. These include degradation of expensive solvents, limited thermal stability, corrosion, and high energy consumption during regeneration due partly to solvent loss by evaporation.

Reviews of ILs for CO_2 absorption have been reported in the literature (Cota & Martinez 2017). CO_2 adsorption, synthesis, and the use of metal-organic frameworks (MOFs) impregnated with ILs have also been reported (Lupa et al. 2024). Ionic liquids have also been used as membrane solvents or supported ionic liquid membranes (SILMs) for CO_2 absorption (Makino & Kanakubo 2006, Ramdin et al. 2012, Sarker et al. 2017, Elmobarak et al. 2023).

1.2. ILs in Wastewater Treatment and Membrane Filtration

A variety of polar and nonpolar materials, such as organic contaminants, heavy metals, and dyes, which are frequently found in industrial wastewater, can be dissolved by ILs (Zhang et al. 2011, Mandal & Bandyopadhyay 2011). This enables efficient removal of pollutants from wastewater. ILs have unique properties such as solubility, selectivity, and reusability, making them promising solvents for wastewater treatment, effective adsorbents for water treatment and contaminant extraction, and useful media for membrane filtration and CO_2 absorption and capture (Makino & Kanakubo 2006, Ramdin et al. 2012, Jones 2011, Sarker et al. 2017). To reduce costs, ensure environmental safety, and address stability and scalability, their use must be appropriately tailored.

Liquid-liquid extraction (LLE), in which pollutants are extracted from water and concentrated in the IL phase, is one application of ILs (Mulk et al. 2023). The IL can then be recycled and reused. For the removal of organic contaminants such as petroleum hydrocarbons or chlorinated chemicals, this method can be highly effective. Targeting various pollutants, such as pesticides, dyes, and medicines, is made possible by fine-tuning the IL selectivity for specific contaminants through changes to the cation or anion (Sarker et al. 2017, Lupa et al. 2024). Ionic liquids can be added to membrane materials to enhance their filtration performance. These modified membranes are more efficient than conventional membranes at removing both organic and inorganic contaminants from wastewater, increasing the effectiveness of methods such as nanofiltration and reverse osmosis.

Although the primary focus of this study is CO absorption, the discussion on wastewater treatment highlights the broader environmental applicability of ionic liquids. Their tunable physicochemical properties, low volatility, and potential for recyclability make them promising green solvents not only for pollutant removal but also for gas absorption processes. These characteristics support their selection as effective absorbents in CO_2 absorption systems.

1.3. Biodegradability, Toxicity, Reusability, and Recovery of ILs

Several ILs can be designed to be biodegradable and nontoxic, which are key factors for wastewater treatment (Babamohammadi et al. 2015). Conventional organic solvents or chemicals used for wastewater treatment may cause long-term environmental effects. However, ILs can be engineered to minimize these risks. Nonetheless, an IL's biodegradability depends on its chemical structure, and some ILs may still be toxic to aquatic organisms (Babamohammadi et al. 2015). Another significant advantage of ILs is recyclability. ILs can usually be regenerated using simple methods such as evaporation and distillation after wastewater treatment, thereby minimizing waste and lowering operating costs. Their reusability makes them a sustainable choice for large-scale applications.

In this work, seven different ionic liquids (ILs) were newly synthesized using amino acids (AAs) as anions and triethylenetetramine (TETA) as the cation. The following sections describe ILs, amino acids, amines, their physical properties, and their applications in science and engineering.

1.4. Amines

Amines (aminoalkanes) are generally organic substances that have a basic nitrogen atom with a lone pair and are derived from ammonia by the substitution of one or more H^+ atoms by organic groups such as alkyl or aryl groups. There are

four main types: primary, secondary, tertiary, and cyclic amines, with elevated melting and boiling points. Amines are widely used industrially in the preparation of dyes and drugs. Amine-based compounds such as monoethanolamine (MEA), diisopropylamine (DIPA), diglycolamine (DGA), diethanolamine (DEA), and methyldiethanolamine (MDEA)

Table 1(a): List of amino acids used as anions in this study.

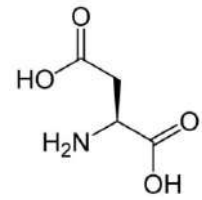
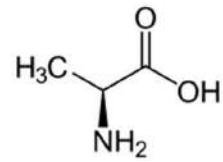
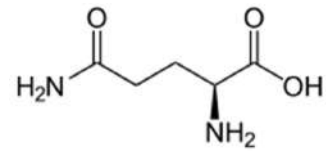
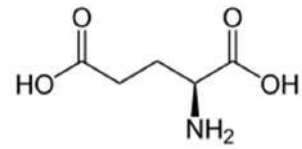
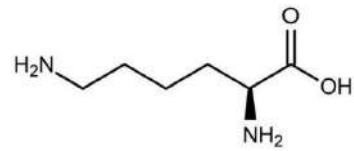
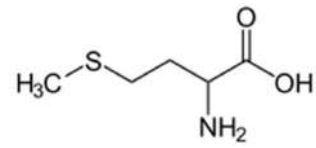
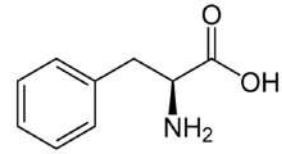
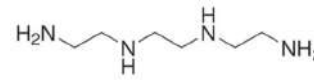
S. No.	Compound Name	Synonym/ IUPAC ID	Structure/Formula	CAS No.	Molecular Weight (g mol^{-1})
1.	L-Aspartic acid [ASP]	(S)-(+)-Aminosuccinic acid, (S)-Aminobutanedioic acid	 $C_4H_7NO_4$	56-84-8	133.10
2.	L-Alanine [ALA]	(S)-2-Aminopropionic acid	 $C_3H_7NO_2$	56-41-7	89.09
3.	Glutamine [GLN]	(S)-2,5-Diamino-5-oxopentanoic acid	 $C_5H_{10}N_2O_3$	56-85-9	146.14
4.	Glutamic acid [GLU]	(S)-2-Aminopentanedioic acid	 $C_5H_9NO_4$	56-86-0	147.13
5.	L-Lysine [LYS]	(S)-2,6-Diaminohexanoic acid monohydrochloride	 $C_6H_{14}N_2O_2$	657-27-2	182.65
6.	L-Methionine [MET]	(S)-2-Amino-4-(methylmercapto)butyric acid	 $C_5H_{11}NO_2S$	63-68-3	149.21
7.	L-Phenylalanine [PHE]	(S)-2-Amino-3-phenylpropionic acid	 $C_9H_{11}NO_2$	63-91-2	165.19

Table 1(b): List of amines used as cations in this study.

S. No.	Compound Name	Synonym/IUPAC ID	Structure/Formula	CAS No.	Molecular weight g mol^{-1}	Density g cm^{-3}
1.	Triethylenetetramine [TETA]	N,N'-Bis(2-aminoethyl)-1,2-ethanediamine	 $C_6H_{18}N_4$	112-24-3	146.24	0.982

are widely used in process industries for the removal of CO_2 and hydrogen sulfide (H_2S) from natural gas and petroleum-refining process gas streams. Amines have also been used for CO_2 absorption from combustion and waste gases and can contribute to the removal of greenhouse gas emissions (Babamohammadi et al. 2015, Fukumoto et al. 2005).

1.5. Amino Acids

AAs are simple organic compounds comprising a carboxyl (–COOH) and an amino ($–NH_2$) group. These carboxyl and amino functional groups are also useful for introducing other functional groups. It is well known that about 20% of the human body contains proteins. These macromolecules play significant roles in biological processes, and AAs are their building blocks. The advantages of AAs include low environmental impact, high biodegradability, negligible volatility, high resistance to oxidative degradation, and low volatility due to their ionic structure. Their physical characteristics include being crystalline solids with very high melting points (200–300°C), usually water-soluble and insoluble in nonpolar organic solvents such as hydrocarbons, possessing optical isomers because of asymmetric α-carbon atoms, and having a zwitterionic nature (Yamini & Khanna 2015). AAs can taste sweet, bland, or occasionally bitter. AAs are primarily used in cosmetics, active pharmaceutical ingredients (APIs), medical foods or medical nutrition, drinks, culture media, dietary supplements, functional foods, and polymer synthesis. More recently, these AAs have also been used in the synthesis and preparation of ILs (Walden 1914). The amino acids used in this study as anions and the amine used as the cation are listed in Tables 1(a) and 1(b), respectively.

1.6. Ionic Liquids as Green Solvents

ILs are attractive materials that have gained considerable research attention in science and engineering, especially in modern physical chemistry, as green solvents. They are liquids at ambient temperature and are mainly used as substitutes for conventional volatile organic solvents such as tetrachloroethylene, formaldehyde, methylene chloride, benzene, ethylene glycol, toluene, and xylene. Applications of ILs in different fields of science and engineering are presented in Fig. 2. ILs are substances composed of organic cations and organic or inorganic anions. ILs were first reported in 1914 by Paul Walden, a well-known Latvian chemist, in his work on stereochemical reactions (Walden 1914). ILs have attracted significant attention because of their notable and environmentally favorable properties, including low vapor pressure, reusability, broad chemical and thermal stability, nonflammability, high ion density, a wide electrochemical window, tunable viscosity, and superior electrical conductivity (Wilkes 2002). Chemical structures of frequently used cations and anions are presented in Table 1(c). Similarly, Table 2 compares various characteristics of volatile organic solvents, molten salts, and ILs.

Alternatively, amino acid-based ionic liquids (AAILs) can also be used for improved CO_2 absorption capacity. As mentioned above, AAs comprise both a carboxyl (–COOH) and an amino ($–NH_2$) functional group. The reaction of CO_2 with AAs has been reported to be similar to that of alkanolamines. However, the precise CO_2 reaction mechanism of AAs remains debated in the scientific community. In 2002, Kumar et al. described a mechanism different from the zwitterionic mechanism, proposing a direct 2:1 mechanism that produces carbamate and protonated amine, as indicated in Eq. (1) (Kumar et al. 2002).

$$2RNH_2 + CO_2 \underset{k_{2,2}}{\overset{k_{2,1}}{\rightleftharpoons}} RNHCOO^-COO^- + RNH_3^+ \quad \ldots(1)$$

However, as described in the literature, a zwitterionic mechanism has been proposed for the reaction of CO_2 with potassium salts of glycine and taurine, as given in Eqs. (2) and (3) (Kumar et al. 2003).

$$^-OOC\text{-}R\text{-}NH_2 + CO_2 \underset{k_{-1}}{\overset{k_1}{\rightleftharpoons}} {}^-OOC\text{-}R\text{-}N^+H_2COO^- \quad \ldots(2)$$

$$^-OOC\text{-}R\text{-}N^+H_2COO^- + B \rightarrow {}^-OOC\text{-}R\text{-}NHCOO^- + {}^-OOC\text{-}R\text{-}NH_3^+ \quad \ldots(3)$$

where B is any alkali compound. In a nonaqueous medium, AAs behave as a base. In 2010, Gürkan et al. described that the reaction of CO_2 with ILs prepared from amino acids terminates with the formation of carbamic acid (Eq. 4) without forming carbamate species (Eq. 5) (Gürkan et al. 2010). Gürkan et al. examined CO_2 absorption in phosphonium-based cations combined with methionine

and proline amino acids as anions. They proposed a 1:1 stoichiometric reaction of CO_2 with AAILs, suggesting that the reaction ends with the formation of carbamic acid (Eq. 4).

$$^{-}OOC\text{-}R\text{-}NH_2 + CO_2 \underset{k_{-1}}{\overset{k_1}{\longleftrightarrow}} {}^{-}OOC\text{-}R\text{-}NHCOOH \quad \ldots(4)$$

$$^{-}OOC\text{-}R\text{-}NHCOOH + B \rightarrow {}^{-}OOC\text{-}R\text{-}NHCOO^{-} + {}^{-}OOC\text{-}R\text{-}NH_3^{+} \quad \ldots(5)$$

The proposed mechanisms (Eqs. 1–5) are used to interpret experimental trends qualitatively, and detailed mechanistic validation is beyond the scope of the current study.

In previous work, Yamini and Khanna studied CO_2 solubility in different amino acid-based ILs synthesized with butylmethyl imidazolium ($[BMIM]^+$) as the cation and amino acids as anions (Yamini & Khanna 2015). Goodrich et al. examined CO_2 absorption using various amino acid-based anions and phosphonium-based cations for preparing ILs and proposed reaction mechanisms (Goodrich et al. 2011). Kortunov et al. studied physical absorption techniques for CO_2 absorption in ionic liquids, including higher-pressure carbon absorption using imidazolium-based ionic liquids and amines mixed in ionic liquid solutions (Kortunov et al. 2015). As noted above, most reports support formation of a zwitterion intermediate (Eqs. 2 and 3) as the principal pathway rather than one-step carbamate formation (Eq. 1) or formation via carbamic acid (Eqs. 4 and 5) (Danckwerts 1979, Versteeg & van Swaaij 1988, van Holst et al. 2009, Xie et al. 2010).

The primary goal of this work is to examine the effect of amine functionalization on different amino acids used as anions. Another reason for selecting amino acids is that they are biodegradable, readily available, and comparatively inexpensive, although very few studies have been reported in the literature. In this work, seven different AAILs were synthesized, namely, [TETA][ALA], [TETA][ASP], [TETA][LYS], [TETA][GLU], [TETA][GLN], [TETA][MET], and [TETA][PHE]. CO_2 absorption studies were carried out in the FBR at room temperature.

Although amino acid-based ionic liquids (AAILs) have been widely reported, the originality of this work lies in the use of triethylenetetramine (TETA) as a polyamine-based cation combined with various amino acid anions, providing multiple active amine sites that enhance CO_2 interaction. A detailed comparative discussion has been incorporated to evaluate these TETA-based AAILs against commonly reported imidazolium- and phosphonium-based systems in terms of CO_2 absorption capacity, reaction mechanisms (chemisorption versus physisorption), availability of active sites, and environmental and economic aspects (Yamini & Khanna 2015). Furthermore, the application of these AAILs in a liquid foam-bed reactor (FBR) highlights their functional advantage through improved gas–liquid interfacial contact, reinforcing the distinct contribution of this study.

2. MATERIALS AND METHODS

All amino acids, including L-aspartic acid, L-alanine,

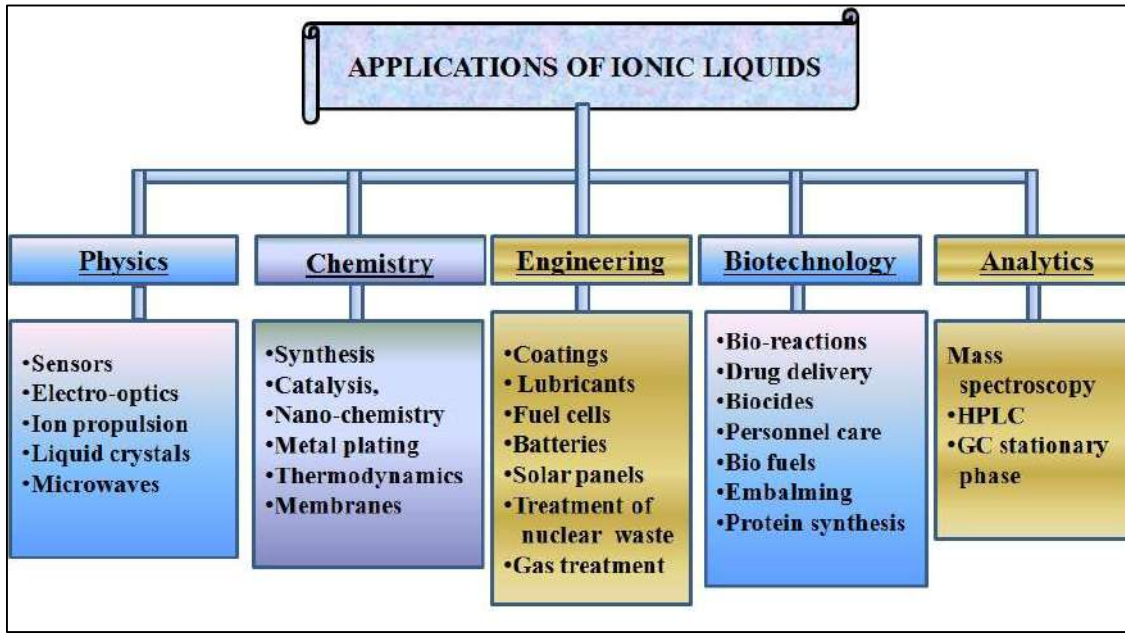
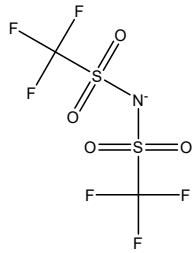
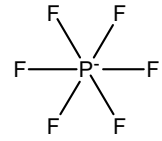
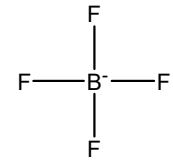
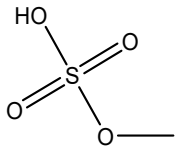
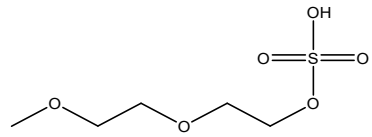
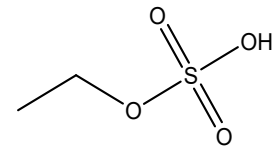
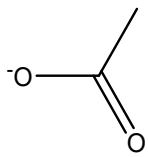
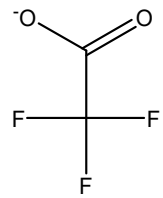
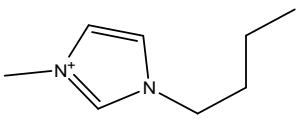
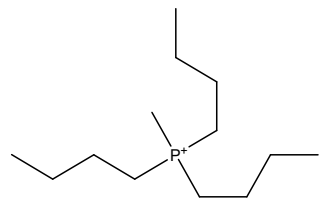
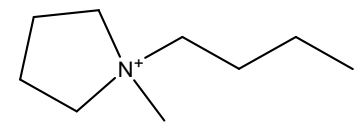
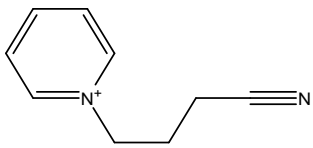
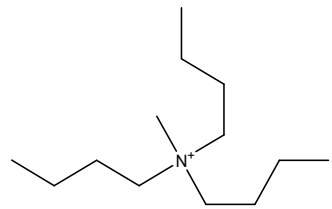
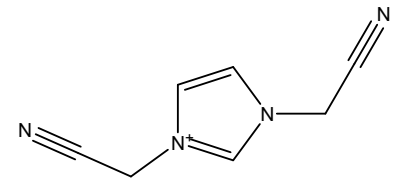


Fig. 2: Typical applications of ILs in different fields of science and engineering.

Table 1(c): Common anions and cations used in the preparation of ILs.

Anions		
 bis(trifluoromethylsulfonyl) amide	 Hexafluorophosphate	 tetrafluoroborate
 Methylsulfate	 2-2 methoxy ethoxy ethyl sulfate	 Ethylsulfate
 acetate	 triflouroacetate	Br⁻ Bromide
Cations		
 1-Butyl-3-methylimidazolium	 Tributylmethylphosphonium	 1-Butyl-1-methylpyrrolidinium
 1-(3-Cyanopropyl)pyridinium	 Tributylmethylammonium	 1,3-Bis(cyanomethyl)imidazolium

L-lysine, L-methionine, L-phenylalanine, glutamine, and glutamic acid, were purchased from CDH, Delhi. Monoethanolamine and triethylenetetramine were also purchased from CDH, Delhi. Dichloromethane, dimethyl ether, sodium lauryl sulfate (SLS), cetrimonium bromide (CTAB), Triton X-100, Tween 80, amyl alcohol, methyl orange indicator, and methanol were procured from Fisher Scientific, India. All reagents were used as received; no further purification was carried out unless stated otherwise.

2.1. Experimental Section

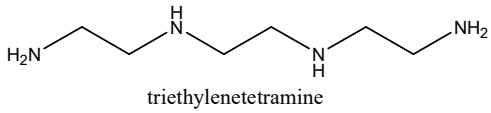
2.1.1. Synthesis and Purification of Ionic Liquids

AAILs were prepared by H^+ transfer between a Brønsted acid and a Brønsted base. Equimolar quantities of acid and base were reacted with each other. Dropwise addition of the

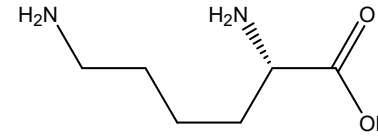
Table 2: Comparison of the various characteristics of volatile organic solvents, molten salts, and ILs.

S. No.	Property	Ionic Liquids	Volatile organic solvents	Molten salts
1	Basic constituents	Pair of ions	Molecules	Pair of ions
2	Application	Multifunction	Single function	Multifunction
3	Catalytic ability	Common and tunable	Rare	Common and tunable
4	Chirality	Common and tunable	Rare	Common and tunable
5	Vapor pressure	Negligible under ambient conditions	Obeys the Clausius-Clapeyron equation	Insignificant under ambient conditions
6	Flammability	Nonflammable	Highly flammable	Nonflammable
7	Solvation effect	Strong	Weak	Strong
8	Cost	Expensive (2–100 times the cost of organic solvents)	Cheap	Expensive
9	Recyclability	Economic imperative	Green imperative	Economic imperative
10	Corrosiveness	Low	Intermediate	High
11	Melting point	–20–150°C	< –20°C	> 200°C
12	Boiling point	< 400°C	30–100°C	> 400°C
13	Viscosity (cP)	Low (22–40,000)	Low (0.2–100)	High
14	Density (g cm^{-3})	High (0.8–3.3)	Medium (0.6–1.7)	High (0.8–3.3)
15	Conductivity	High	Low	High
16	Refractive index	High (1-5-2.2)	Medium (1.3–1.6)	High (1-5-2.2)

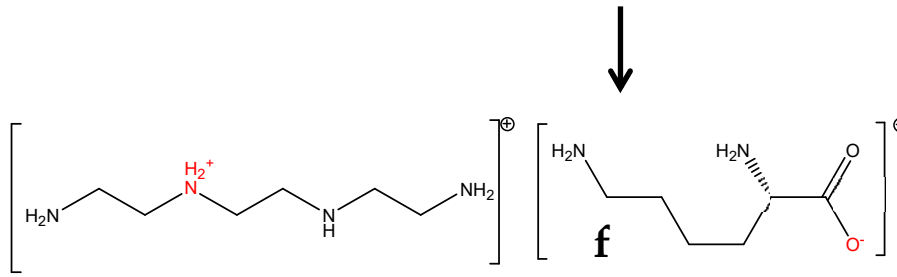
amine to the amino acid was performed in an ice bath because the reactions are highly exothermic; due care was taken during synthesis. At room temperature, the reaction mixture was agitated for one day. A small excess of amine was introduced and subsequently removed along with water by heating to 80–85°C to ensure complete reaction. To remove unreacted acid and water, the reacted mixture was further dried at 80–85°C under vacuum (about 300 mm Hg), and the residue was subsequently extracted using diethyl ether (DE) or dichloromethane (DCM). Following evaporation of the solvent, the product was dried for at least 3–5 days at 80–85°C in a vacuum oven to remove any remaining moisture. The AAILs were then ready for further characterization and use. The synthesis reactions were conducted without solvent; when required, 10% methanol was used to dissolve the amino acid in deionized water (if it was in the solid state), stirred



triethylenetetramine



Lysine



Scheme 1: Proposed reaction mechanism of [TETA][LYS].

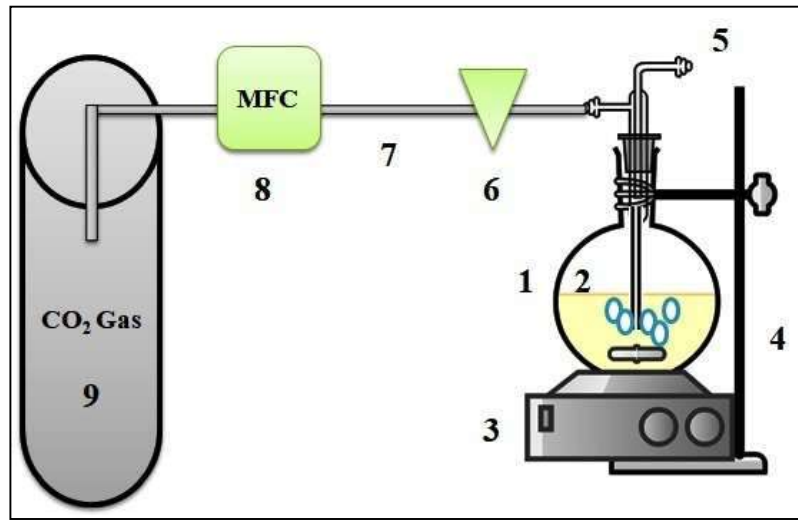


Fig. 3(a): Semi-batch equilibrium experimental setup used for CO_2 absorption. (Parts of the figure are as follows: 1. Round-bottom flask, 2. Ionic liquid, 3. Magnetic stirrer, 4. Stand, 5. Gas outlet, 6. Rotameter, 7. Gas inlet, 8. Mass flow controller with digital indication, and 9. CO_2 gas cylinder).

for 10–15 h, and then added dropwise to TETA. A similar procedure was used for the synthesis of all AAILs.

2.1.2. Proposed Reaction Mechanisms of Synthesized ILs

The reaction mechanism between triethylenetetramine and lysine is shown in Scheme 1. TETA consists of a long carbon chain with two primary (–NH_2) groups and two secondary (–NH) groups, whereas aspartic acid has two carboxylic groups (–COOH) and one amine group. When aspartic acid reacts with [TETA], it may donate protons to [TETA], forming [TETA][ASP]. It is proposed that all amino acids react with TETA to form AAILs. Reactions for other compounds, such as [TETA][ALA], [TETA][LYS], [TETA][GLU], [TETA][GLN], [TETA][MET], and [TETA][PHE], are provided in the supporting information, SI Schemes 1–4.

2.1.3. Procedure for Semi-Batch Equilibrium Studies

Equilibrium experiments were conducted in a 250 mL round-bottom flask (RBF) with a lid arrangement for continuous gas flow into and out of the RBF. A known amount of prepared AAIL was placed in the RBF. The desired amount of CO_2 gas was bubbled continuously into the AAIL in the RBF. Unreacted gas exited through the vent line of the RBF, as shown in Fig. 3(a). The entire setup was placed on a magnetic stirrer with the help of a stand. Semi-batch equilibrium experiments for CO_2 absorption were carried out for several hours until equilibrium was reached. Samples were collected at predefined time intervals and analyzed by titrimetry against 2 M HCl in the Chittick apparatus. For each sample, the amount of CO_2 absorbed over time and the moles of CO_2 absorbed per mole of AAIL were calculated. A similar procedure was used to conduct equilibrium experiments for different AAILs.

2.1.4. Regeneration of AAILs

Regeneration of used AAILs was carried out before further use for multiple cycles. Regeneration was performed by heating the AAIL at 80–90°C with continuous stirring. During regeneration, samples were collected for analysis at fixed time intervals. The rate of desorption was also studied over time. It was observed that regenerated AAILs could be used for a further cycle. The apparatus used for AAIL regeneration is presented in Fig. 3(b).

2.1.5. Experimental Procedure of the Liquid Foam-Bed Reactor

CO_2 absorption experiments were carried out in a semi-batch liquid foam-bed reactor (FBR). The experimental setup of the liquid foam-bed reactor used in this study is shown in Fig. 4(a). The FBR consists of two sections: the foam section and the storage section. It is a simple, transparent glass column (0.7 m high and 7.6×10^{-2} m in diameter) fitted with a distributor plate above the cone-shaped bottom (flow stabilization chamber), as shown in Fig. 4(a). The distributor plate contains several holes that allow the CO_2 gas/air mixture to enter the column during the experiment. The FBR also has a sample-charging port above the distributor plate and several sampling ports at different heights for collecting samples for analysis during the experiment.

During the FBR experiments, the regulator of the CO_2 gas cylinder was heated using infrared lamps. This heating prevented choking of the gas pipeline due to dry-ice formation. An air compressor was used to provide air and dilute the CO_2 gas. Precalibrated rotameters were used to measure CO_2 and air flow rates. As noted above, CO_2 gas was diluted by mixing it with air using a packed-bed setup

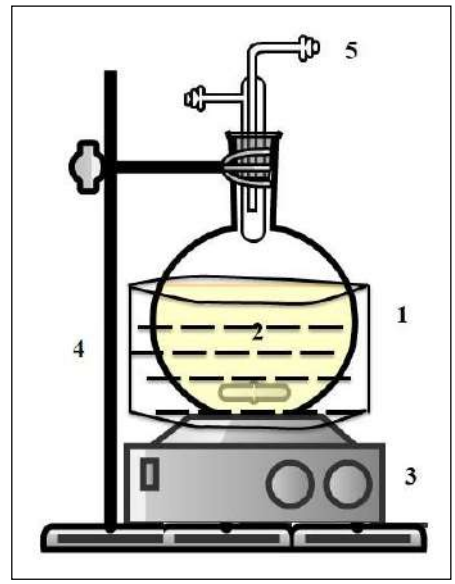


Fig. 3(b): Apparatus used for regeneration of AAILs. (Parts of the figure are as follows: 1. Round-bottom flask, 2. Ionic liquid, 3. Magnetic stirrer, 4. Stand, and 5. Gas outlet to storage.)

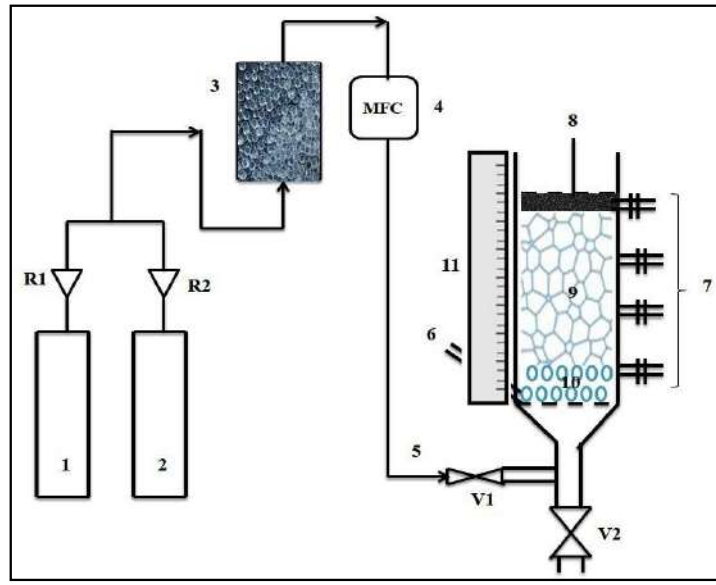


Fig. 4(a): Experimental setup of the liquid foam-bed reactor used in this study. (Parts are as follows: 1. Pure CO_2 gas supply, 2. Air supply, 3. Air and CO_2 mixture (packed bed with glass beads), 4. Mass flow controller with digital indication, 5. Gas inlet, 6. Liquid charging port, 7. Sampling ports, 8. Sieve plate for foam breaking, 9. Foam section, 10. Storage section, 11. Ruler, R1 and R2 gas rotameters, and V1 and V2 valves).

containing glass Raschig rings. This packed bed was used to mix CO_2 and air and to prevent dust or solid particles, if any, in the air from entering the FBR.

Initially, air at a known flow rate was released into the FBR. About 100 mL of aqueous AAIL of known concentration was mixed with a known amount of surfactant in a volumetric flask, stirred for 2–3 h, and then charged into the FBR through the liquid inlet port. The foam height was then monitored. After the desired foam height was reached, CO_2 gas was released from the cylinder and passed through the FBR. The CO_2 gas was mixed with air before entering the FBR. Once CO_2 entered the FBR, the experiment was started and the time was recorded. During the experiment, CO_2 gas and air flow rates were monitored using a digital mass flow controller and

rotameter, respectively. The foam height was maintained using a circular foam breaker consisting of a 7.5×10^{-2} m-diameter sieve plate fitted with a circular sponge (foam, ~7.8×10^{-2} m) and connected to a thin iron rod about 0.8 m long, as shown in Fig. 4(a). A few drops of amyl alcohol were used in the foam-breaker sponge as an antifoaming agent. When foam bubbles reached the foam-breaker surface, they collapsed. Perforations in the sieve plate allowed unreacted CO_2 gas to escape. Through the Plateau borders, liquid in the foam films returned to the storage section. Using a stopwatch, liquid samples were collected at regular time intervals from the sampling ports near the storage section. The CO_2 experiments were continued for 30 min. The gas supply was then closed, and the solution was drained from the storage section.

CO_2 loading in a sample of AAIL solution was calculated using the following equation:

$$\alpha = \frac{\left(760\ mmHg - \mathrm{P}_{\mathrm{H_2O}}\right)\left(V_{CO_2} - V_{HCl}\right)}{\left(\text{sample vol.(ml)} \times R \times \mathrm{T}\right)} \times 1000$$

Where:

α = CO_2 loading (mol CO_2 per mL of absorbent)

760 mm Hg = 1 atm (standard atmospheric pressure)

P_{H_2O} = vapor pressure (mm Hg) at 302 K

V_{CO_2} = volume of solution displaced by CO_2 in the graduated tube (mL)

V_{HCl} = volume of HCl used for titration (mL)

Sample vol. = volume of sample drawn from the FBR (mL)

T = temperature (K)

R = universal gas constant (L·torr $mol^{-1} \cdot K^{-1}$)

2.1.6. Analysis of Samples

After the samples were collected from the FBR at regular time intervals, the absorbed CO_2 was analyzed using the Chittick apparatus, as shown in Fig. 4(b). A magnetic stirrer, 25 mL conical flask, 50 mL burette, 10 mL pipette, glass stopper, graduated glass tube with a scale, glass reservoir, analytical balance (AUW-220D dual-range semi-microbalance), and methyl orange indicator were used for the analysis. A collected sample of known weight was placed in a 25 mL conical flask; one or two drops of methyl orange were added, and the sample was titrated against 2 N HCl while the entire setup was placed on a magnetic stirrer until the color changed from yellow to pale orange. The burette reading and the gas displaced in the glass reservoir were recorded for each sample, along with the time at which the sample was collected. Teflon tape or vacuum grease was used on the conical flask to prevent gas leakage. During the analysis, due care was taken to avoid leakage of CO_2 gas from the flask.

3. RESULTS AND DISCUSSION

3.1. Characterization of Ionic Liquids

3.1.1. FTIR Analysis

Fourier-transform infrared spectroscopy (FTIR) using a NICOLET iS50 FT-IR model was carried out to identify functional groups present in the prepared AAILs from

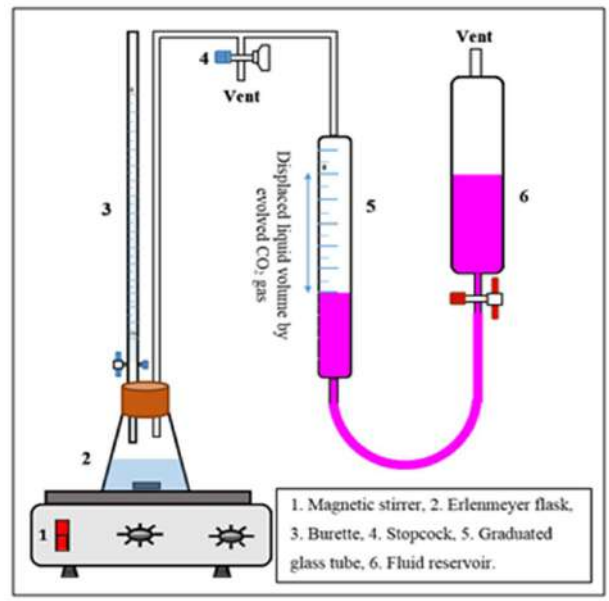


Fig. 4(b): Pictorial representation of the Chittick apparatus used for liquid sample analysis (Norouzbahari et al. 2016).

their infrared absorption spectra. The FTIR spectra were recorded over the wavenumber range of 500–4000 cm^{-1}. These infrared absorption bands identify molecular structural components. Figures 5(a)–5(f) show the FTIR spectra of pure [TETA] used as the cation, AAs used as anions, and the synthesized AAILs, namely [TETA][ALA], [TETA][ASP], [TETA][GLU], [TETA][LYS], [TETA][MET], and [TETA][PHE]. The FTIR spectra show all major functional groups present in the individual compounds and prepared AAILs. Distinct FTIR peaks representing C=O of –COO in amino acids at 1700 and 1462 cm^{-1} and peaks corresponding to N–H stretching vibrations of $–NH_2$ in the 3600–3000 cm^{-1} range were identified for almost all AAILs (Barth 2000). The FTIR bands of the synthesized AAILs were very similar and showed the same bands at different wavenumbers. Figure 5(a) shows the FTIR spectra of pure anion $[ALA]^-$, pure cation $[TETA]^+$, and synthesized [TETA][ALA]. The characteristic FTIR peak corresponding to C=O of –COO at 1647–1400 cm^{-1} and a peak corresponding to strong N–H stretching of $–NH_2$ at 3559 cm^{-1} were observed for synthesized [TETA][ASP]. Near 3456 cm^{-1}, a strong N–H stretching vibration was observed, with sharp peaks at 1621 and 1395 cm^{-1} corresponding to C=O and carboxylic groups, respectively, as shown in Fig. 5(b). Similar peaks can be seen in Figs. 5(c)–5(f). Primary and secondary amines can generally be identified from absorption bands in the 3600–3000 cm^{-1} range corresponding to N–H stretching vibrations. As reported, N–H in-plane bending vibrations in NH_3^+ are estimated in the ranges around 3100, 1300–1550, and 1600–1750 cm^{-1} (Khanna & Moorie 1999).

3.1.2. Raman Spectroscopy

The synthesized AAIL samples were analyzed using a benchtop Raman spectrometer (Renishaw plc, Model: Micro Raman Spectrometer, RA800-series, UK), equipped with an excitation laser wavelength of 785 nm and an excitation source operated at about 50% power. The accuracy of the measured wavenumber positions of the bands was ±0.98 cm^{-1}, defined by the resolution of the diffraction grating,

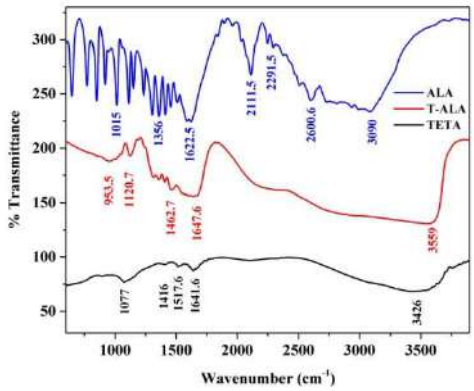


Fig. 5(a): FTIR spectra of pure anion $[ALA]^-$, pure cation $[TETA]^+$, and synthesized [TETA][ALA].

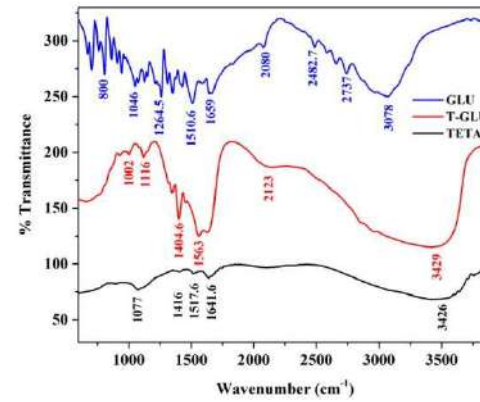


Fig. 5(c): FTIR spectra of anion $[GLU]^-$, cation $[TETA]^+$, and synthesized IL [TETA][GLU].

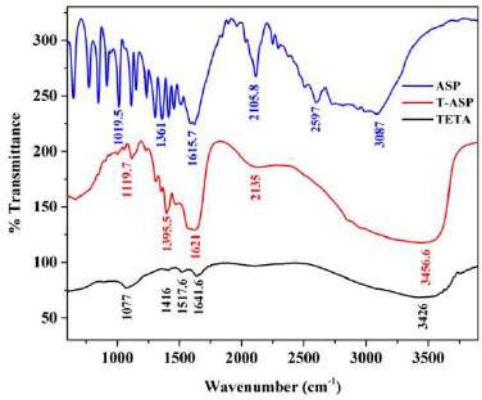


Fig. 5(b): FTIR spectra of pure anion $[ASP]^-$, pure cation $[TETA]^+$, and synthesized [TETA][ASP].

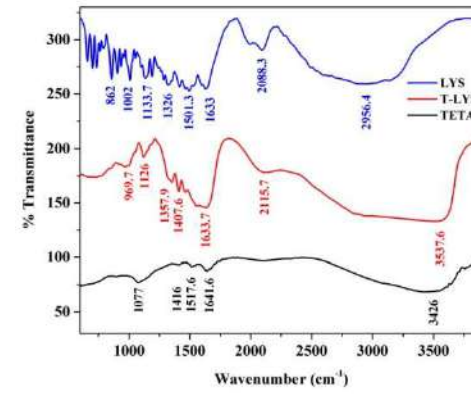


Fig. 5(d): FTIR spectra of anion $[LYS]^-$, cation $[TETA]^+$, and synthesized IL [TETA][LYS].

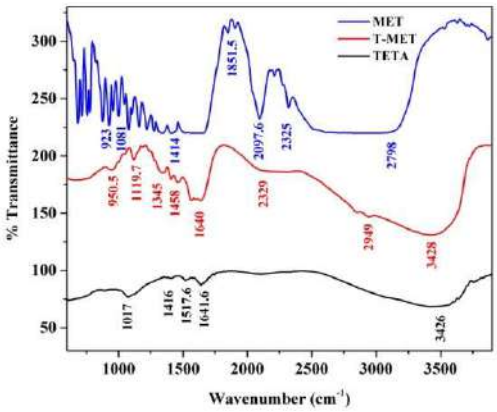


Fig. 5(e): FTIR spectra of anion $[MET]^-$, cation $[TETA]^+$, and synthesized IL [TETA][MET].

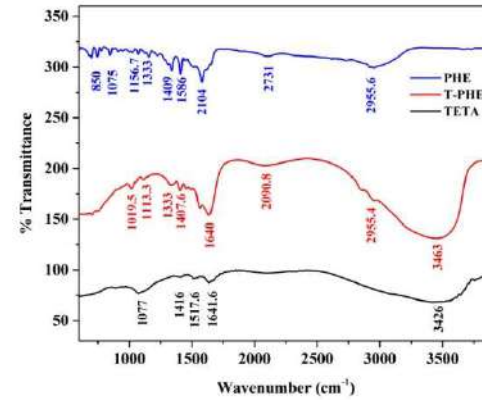


Fig. 5(f): FTIR spectra of anion $[PHE]^-$, cation $[TETA]^+$, and synthesized IL [TETA][PHE].

while intensity measurements were typically recorded every 1.96 cm^{-1}. Fig. 6 shows the Raman spectra of the synthesized ILs [TETA][LYS], [TETA][GLU], [TETA][ASP], [TETA][ALA], [TETA][MET], [TETA][PHE], and cation $[TETA]^+$.

As shown in Fig. 6, bands above the 2500 cm^{-1} region are attributed to NH, OH, and CH stretching modes for all AAILs. The strongest symmetric CH_2 stretching band, $\nu S(CH_2)$, in the Raman plot was detected in the 2900–3100 cm^{-1} range (at 2934, 2979, 3030, 3057, and 3073 cm^{-1}) for [TETA][LYS], [TETA][GLU], [TETA][ASP], [TETA][ALA], [TETA][MET], and [TETA][PHE]. It was shifted in the solution-state Raman spectrum and was also extremely intense for [TETA][LYS], [TETA][ASP], [TETA][ALA], [TETA][MET], and [TETA][PHE]. Similarly, pure cation [TETA] showed very broad stretching. C=C stretching was observed at 1012, 1033, 1063, and 1076 cm^{-1}; antisymmetric rocking of NH_3^+ was observed at 1143 and 1183 cm^{-1} for all prepared AAILs. For [TETA][PHE], vibrations associated with the aromatic ring were also detected at 848, 912, and 949 cm^{-1}. A characteristic band associated with C–S stretching was observed at 659 cm^{-1} because [TETA][MET] is composed of $C_5H_{11}NO_2S$ and $C_6H_{18}N_4$. Raman spectra of the pure amino acids and all synthesized AAILs are provided in the supporting information (SI Figs. 14–17).

3.1.3. NMR Spectroscopy

^{13}C NMR: The ^{1}H and ^{13}C NMR experiments were carried

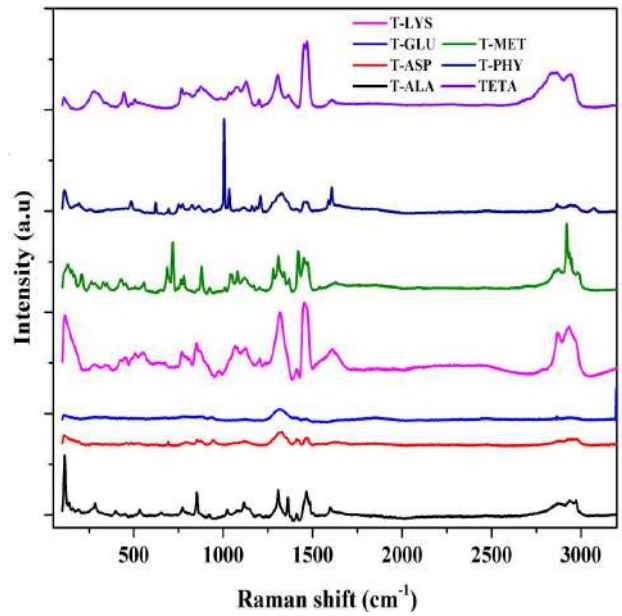


Fig. 6: Raman spectra of synthesized ILs [TETA][LYS], [TETA][GLU], [TETA][ASP], [TETA][ALA], [TETA][MET], [TETA][PHE], and cation $[TETA]^+$.

out at ambient temperature using a Bruker Avance 400 or 300 MHz spectrometer. NMR samples of different synthesized AAILs were prepared with DMSO-d_6 or D_2O. Precautions were taken while preparing the samples to avoid contamination; syringes or capillary tubes were used to transfer the NMR solvent or AAILs.

The peak assignments of ^{13}C NMR data for different synthesized AAILs are as follows (Fig. 7(a)):

Triethylenetetramine lysine [TETA][LYS]: δc (ppm) (300 MHz, DMSO-d_6), 177.96, 54.73, 52.34, 42.23, 36.58, 30.26, 24.66, 19.44.

Triethylenetetramine glutamine [TETA][GLN]: δc (ppm) (400 MHz, DMSO-d_6), 178.0, 56.13, 53.44, 44.90, 36.39, 27.51, 23.14.

Triethylenetetramine aspartic acid [TETA][ASP]: δc (ppm) (300 MHz, DMSO-d_6), 174.3, 53.95, 50.37, 44.53, 36.29, 34.05.

Triethylenetetramine glutamic acid [TETA][GLU]: δc (ppm) (300 MHz, DMSO-d_6), 177.45, 54.22, 50.08, 44.17, 36.08, 29.76, 24.15.

^1H NMR: The peak assignments of ^1H NMR data for different synthesized AAILs are as follows (Fig. 7(b)):

Triethylenetetramine lysine [TETA][LYS]: δH (ppm) (400 MHz, D_2O; solvent peak observed at ~4.7): 3.4 (s, J = 2.8 Hz, 1H), 2.8, 2.7 (s, J = 2.8 Hz, 1H), 1.59, 1.3 (s, J = 2.8 Hz, 1H).

Triethylenetetramine glutamine [TETA][GLN]: δH (ppm) (400 MHz, D_2O; solvent peak observed at ~4.7): 4.0 (s, J = 2.8 Hz, 2H), 3.5 (s, J = 2.8 Hz, 2H), 2.73 (d, J = 2.8 Hz, 2H).

Triethylenetetramine alanine [TETA][ALA]: δH (ppm) (400 MHz, D_2O; solvent peak observed at ~4.76): 3.4 (s, J = 2.8 Hz, 2H), 3.28 (s, J = 2.8 Hz, 2H), 2.60 (s, J = 2.8 Hz, 1H), 2.54 (s, J = 2.8 Hz, 1H).

Triethylenetetramine aspartic acid [TETA][ASP]: δH (ppm) (400 MHz, D_2O; solvent peak observed at ~4.7): 3.6 (s, J = 2.78 Hz, 2H), 2.71 (s, J = 2.8 Hz, 2H), 2.44 (s, J = 2.8 Hz, 1H).

Triethylenetetramine glutamic acid [TETA][GLU]: δH (ppm) (400 MHz, D_2O; solvent peak observed at ~4.7): 3.1 (s, J = 2.8 Hz, 2H), 2.82 (s, J = 2.8 Hz, 2H), 2.65 (s, J = 2.8 Hz, 1H).

The remaining ^{13}C NMR and ^1H NMR spectra are provided in the supporting information (SI Figs. 2–13).

The FTIR, Raman, and ^1H NMR analyses provide evidence of successful formation of TETA-based AAILs. Characteristic shifts and disappearance of peaks corresponding to free amino acids and unreacted amine

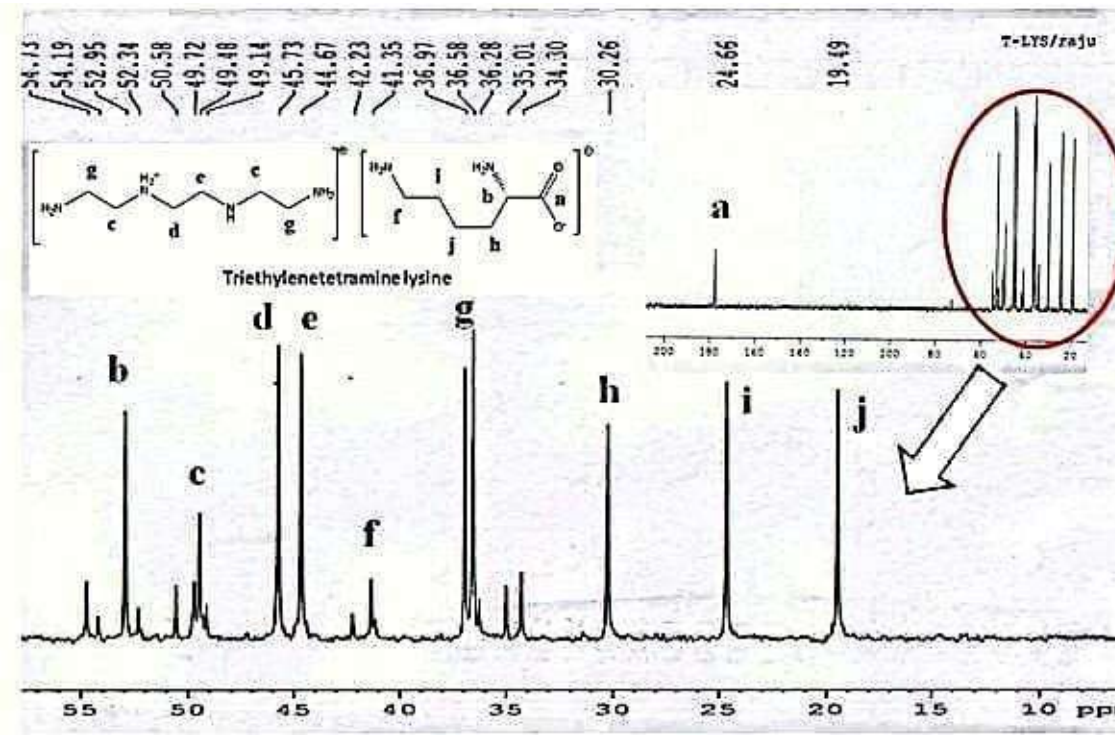


Fig. 7(a): Stack plot of ^{13}C NMR spectra of [TETA][LYS] with peak assignment.

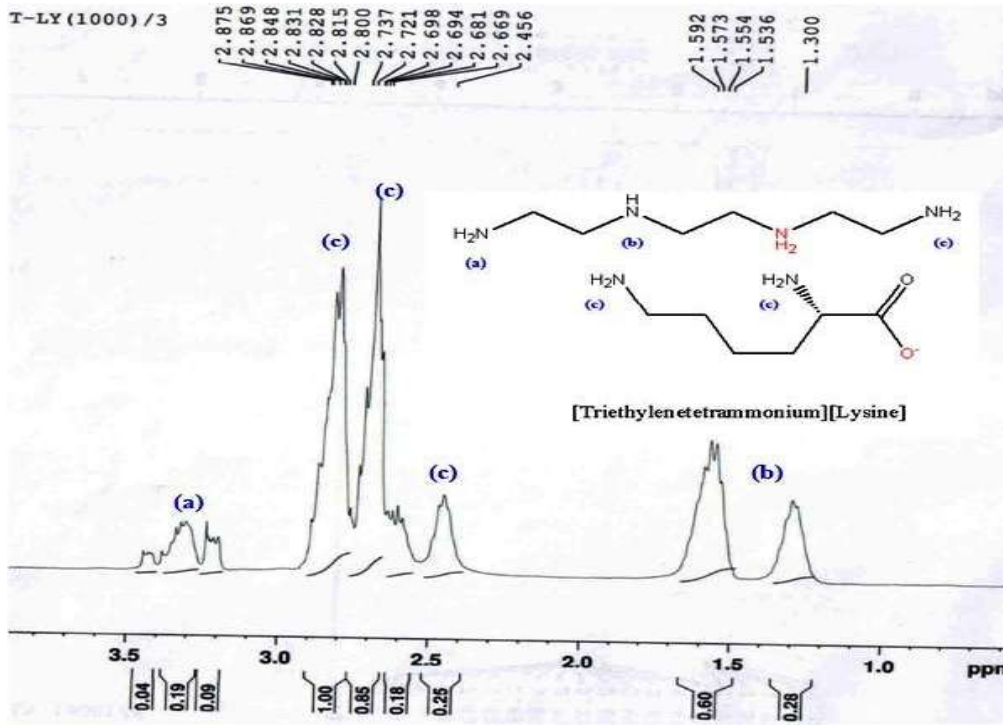


Fig. 7(b): Stack plot of ^{1}H NMR spectra of [TETA][LYS] with peak assignment.

groups indicate effective acid-base interaction and conversion. NMR peak assignments have been linked to the expected ionic structures, supporting the proposed formation of the AAILs. While quantitative ^{1}H NMR integration and 2D NMR were not performed, the combined spectroscopic data provide consistent evidence supporting ionic liquid formation, in line with previous reports on similar systems.

3.1.4. Density

Density measurements were performed using a 25 mL specific-gravity bottle. A known volume of AAIL was placed in the specific-gravity bottle and weighed on an analytical balance at room temperature, and the weights were recorded. The precision of the analytical balance was ±0.0001 g. Density is equal to mass per unit volume; densities were calculated accordingly. Each sample was measured four times, and reproducibility was of a much better order of magnitude. The highest and lowest densities of 1.170 and 1.0646 g cm^{-3} were observed for [TETA][ASP] and [TETA][ALA], respectively, among the synthesized AAILs. Table 3 presents the experimentally measured densities of different AAILs at ambient conditions and atmospheric pressure.

3.1.5. Viscosity Measurements

Dynamic viscosity measurements were carried out for all synthesized ILs as a function of temperature (25, 35, and 50°C) using a modular compact rheometer (Anton Paar MCR302 SN81193479) fitted with a Peltier plate at different temperatures and a 40 mm, 2° stainless-steel cone. Measurements were performed at angular velocities of 0.01–10 rad s^{-1} and shear rates of 0–200 s^{-1} under ambient conditions. The viscosity of the ILs decreased as temperature increased. An error of 5% was indicated by the manufacturer's data and analysis of standard liquids; however, reproducibility was better. For the ILs studied, viscosity remained moderately constant with increasing shear rate. This linearity between shear stress and shear rate corresponds to Newtonian behavior, as described by Huddleston et al. and Seddon et al. (Huddleston et al. 2001, Seddon et al. 2004).

Table 3: Experimentally measured densities of AAILs at room temperature and atmospheric pressure.

S. No.	Name of IL	Density (g cm^{-3})	Error
1	[TETA][GLU]	1.1523	0.00153
2	[TETA][ALA]	1.0646	0.00111
3	[TETA][PHE]	1.1468	0.00143
4	[TETA][ASP]	1.1709	0.00066
5	[TETA][LYS]	1.0702	0.00071
6	[TETA][GLN]	-	-
7	[TETA][MET]	-	-

Table 4: Experimentally measured viscosities of AAILs as a function of temperature and atmospheric pressure.

S. No.	Name of IL	Viscosities (Pa·s)		
		25°C	35°C	50°C
1	[TETA][ASP]	9.8	8.6	4.18
2	[TETA][GLN]	8.53	5.33	3.73
3	[TETA][GLU]	31.6	8.38	1.38
4	[TETA][ALA]	38.3	18.2	7.91
5	[TETA][LYS]	-	-	14.3
6	[TETA][MET]	-	-	-
7	[TETA][PHE]	-	-	-

The observed decrease in viscosity with increasing temperature can be attributed to weakening of hydrogen bonding and other intermolecular interactions within the TETA-based AAILs. ILs such as [TETA][GLU] and [TETA][ALA] exhibit higher viscosities at 25°C because of more extensive hydrogen-bonding networks, which are partially disrupted as temperature rises, resulting in a sharp decrease in viscosity. Compared with benchmark imidazolium- and phosphonium-based ILs and conventional aqueous amine solutions, the TETA-based AAILs maintain moderate viscosities at elevated temperatures, supporting efficient mass transfer and CO_2 absorption in FBR systems (Huddleston et al. 2001, Seddon et al. 2004).

However, density values are missing from Table 3 for [TETA][GLN] and [TETA][MET]. These measurements could not be obtained reliably because these AAILs were insufficiently stable for reproducible density measurements; difficulties in handling small sample volumes and the temperature sensitivity of these particular AAILs also contributed. Similarly, some viscosity data are missing from Table 4 for [TETA][LYS] (at 25 and 35°C), [TETA][MET], and [TETA][PHE], as these AAILs did not exhibit stable or consistent behavior under the measurement conditions. These issues will be addressed in future work.

3.2. CO_2 Absorption Experiments Using a Liquid Foam-Bed Reactor

The absorption studies were also conducted in a semi-batch liquid foam-bed reactor (FBR) to evaluate the effect of gas-liquid (G-L) interfacial contact area on the CO_2 absorption rate. The experimental data presented below were obtained at ambient temperature with a bed height of 30 cm. SLS was used with AAILs to generate foam in the FBR. The FBR experiments were carried out for about 30 min at a CO_2 flow rate of 2.5×10^{-5} m^3 s^{-1} and an air flow rate of 8.33×10^{-5} m^3 s^{-1}. Moles of CO_2 absorbed per mole of AAIL used were plotted against time. Several parameters, including pH, initial concentration, surfactant effects, regeneration, and use of AAILs after regeneration for multiple cycles, were studied and reported.

Figs. 8–11 show the effect of different initial concentrations (500, 300, and 100 mmol) of [TETA][LYS], [TETA][GLU], [TETA][GLN], and [TETA][ASP] on CO_2 absorption, as well as the desorption performance of different AAILs and the use of regenerated AAILs for multiple cycles in the FBR. CO_2 uptake increased with increasing AAIL concentration up to a certain point because of the increased CO_2 absorption rate.

Fig. 8 shows the moles of CO_2 absorbed per mole of [TETA][LYS] used, with the highest mole ratios of 0.442, 0.172, and 0.112 observed at initial concentrations of 500, 300, and 100 mmol, respectively. After 30 min of experimentation, the FBR was saturated and reached equilibrium. Figs. 8–11 show that the highest mole ratio, 0.442, was observed for [TETA][LYS], followed by [TETA][GLN] (0.209) and [TETA][GLU] (0.208), among all AAILs used in this study. The highest mole ratio of CO_2 absorbed per mole of [TETA][LYS] used may be attributable to differences in the chemical and physical properties of AAILs based on their structures. In [TETA][LYS], the $[LYS]^-$ anion contains two primary amine groups. Moreover, the higher CO_2 uptake in [TETA][LYS] is primarily attributed to the presence of multiple accessible amine groups and higher basicity, which enhance chemisorption capacity. The molecular structure also facilitates better accessibility of reactive sites, improving interaction with CO_2 molecules. Similarly, [TETA][GLN] contains two primary amine groups and gave the second-highest mole ratio of CO_2 absorbed per mole of [TETA][GLN]. A 500 mmol concentration of [TETA][LYS] gave higher CO_2 uptake because more [TETA][LYS] ions were available to react with CO_2. After 30 min, the available [TETA][LYS] ions were saturated because of the continuous passage of CO_2 and air through the FBR. As CO_2 uptake increased over time, the viscosity of [TETA][LYS] increased, which in turn decreased CO_2 diffusivity. During CO_2 absorption by the [TETA][LYS] solution, the initial carbamate changed to an intermediate form of carbonic acid, i.e., bicarbonate, which may contribute to the increased viscosity of [TETA][LYS]. Similar results were observed for [TETA][GLU], [TETA][GLN], and [TETA][ASP], as shown in Figs. 9–11.

In 2013, Xing et al. reported molecular simulation studies of CO_2 absorption that examined differences between amine-based cation ILs and AAILs in terms of the accessibility of amine groups in IL ions. These differences affect cation-anion interactions and their predicted behavior (Xing et al. 2013). Xing et al. also reported that stronger

interactions between amine-functionalized cations and anions result in smaller interfacial spaces, thereby reducing amine-group accessibility. In contrast, for AAILs, weaker anion-cation interactions make the amine group in the anion more accessible for CO_2 interaction (Xing et al. 2013). However, the influence of anion-cation interactions on amine accessibility is discussed based on literature reports and has not been directly validated in this study. Therefore, this effect is presented as a reasonable interpretation, and further spectroscopic or computational investigations are required for confirmation.

In this study, the new integrated approach combines the design of TETA-based amino acid ionic liquids (AAILs) with reactor engineering. The presence of multiple active amine sites in TETA enhances CO_2 absorption via chemisorption, while the liquid foam-bed reactor (FBR) provides a high gas–liquid interfacial area, enabling improved mass transfer. This combined strategy aims to maximize CO_2 absorption efficiency by leveraging both material properties and reactor performance.

Amines such as TETA used as cations in ILs absorb CO_2 through both chemical and physical absorption. The strength of physical absorption depends primarily on the type of anion used; in this case, the anions are AAs. Although [LYS] as an anion absorbed CO_2 appreciably by physisorption, [TETA][LYS] could attain the stoichiometric amount of CO_2 under the given experimental conditions because of limited accessibility of amine groups caused by anion-cation interactions. Figs. 8–11 indicate that chemisorption is the predominant mechanism for the AAILs. As reported in the literature, nonfunctionalized ILs such as [bmim][BF_4] show lower CO_2 molar uptake through physical absorption (Yamini & Khanna 2015).

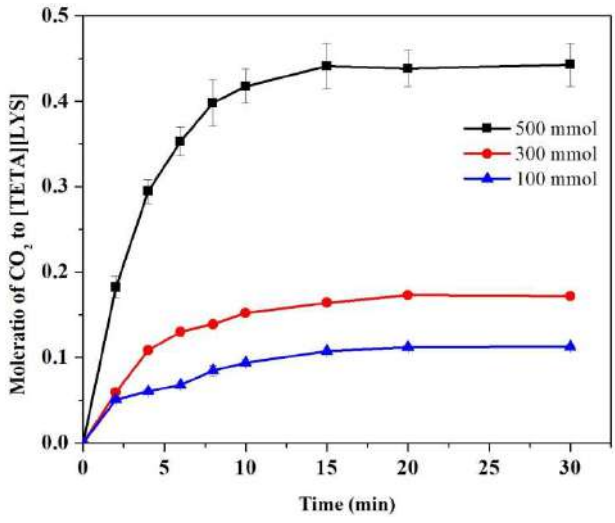


Fig. 8: Effect of initial concentration of [TETA][LYS] on CO_2 absorption. [Conditions: sample volume = 100 mL, SLS added = 0.1 g, initial pH = 9.6 (for 100 mmol), 9.46 (for 300 mmol), 9.63 (for 500 mmol), bed height = 30 cm, CO_2 flow rate = 2.5×10^{-5} m^3 s^{-1} (1.5 LPM), air flow rate = 8.33×10^{-5} m^3 s^{-1} (5 LPM), and temperature = ~25°C].

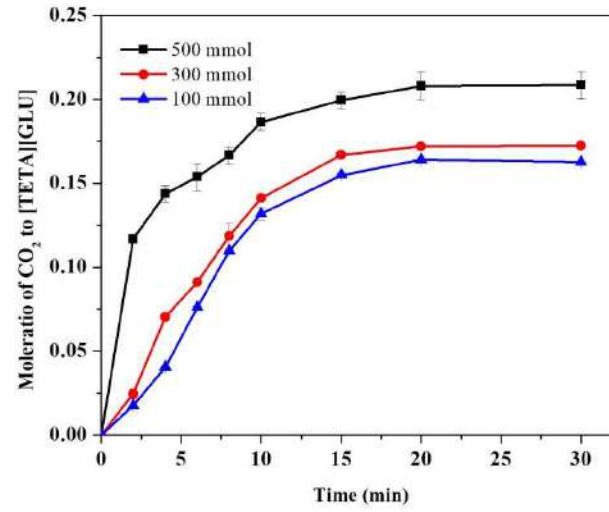


Fig. 9: Effect of initial concentration of [TETA][GLU] on CO_2 absorption. [Conditions: sample volume = 100 mL, SLS added = 0.1 g, initial pH = 7.4 (for 100 mmol), 7.46 (for 300 mmol), 7.55 (for 500 mmol), bed height = 30 cm, CO_2 flow rate = 2.5×10^{-5} m^3 s^{-1} (1.5 LPM), air flow rate = 8.33×10^{-5} m^3 s^{-1} (5 LPM), and temperature = ~25°C].

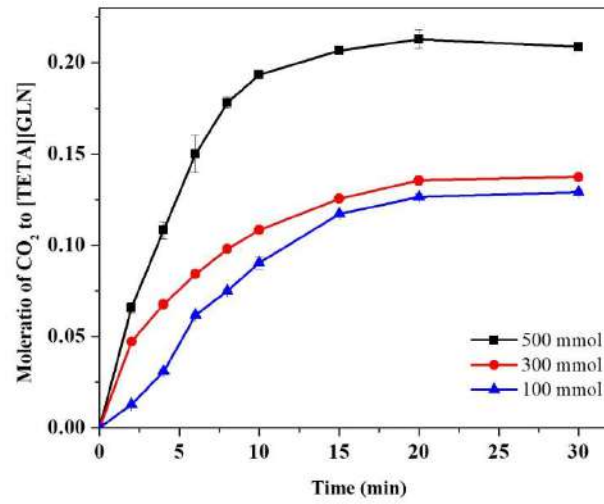


Fig. 10: Effect of initial concentration of [TETA][GLN] on CO_2 absorption. [Conditions: sample volume = 100 mL, SLS added = 0.1 g, initial pH = 8.04 (for 100 mmol), 8.3 (for 300 mmol), 9.35 (for 500 mmol), bed height = 30 cm, CO_2 flow rate = 2.5×10^{-5} m^3 s^{-1} (1.5 LPM), air flow rate = 8.33×10^{-5} m^3 s^{-1} (5 LPM), and temperature = ~25°C].

The results of CO_2 absorption in the FBR were compared with those obtained in a bubble-column reactor in which no surfactant was used. In both cases, equal liquid volumes were used for the experiments. CO_2 absorption through chemical

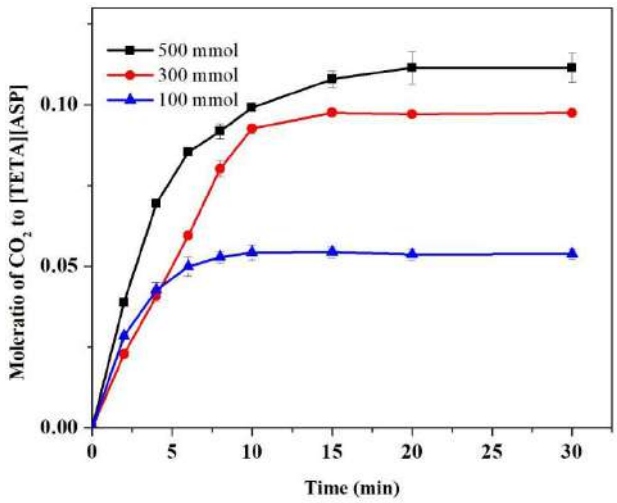


Fig. 11: Effect of initial concentration of [TETA][ASP] on CO_2 absorption. [Conditions: sample volume = 100 mL, SLS added = 0.1 g, initial pH = 7.4 (for 100 mmol), 7.46 (for 300 mmol), 7.55 (for 500 mmol), bed height = 30 cm, CO_2 flow rate = 2.5×10^{-5} m^3 s^{-1} (1.5 LPM), air flow rate = 8.33×10^{-5} m^3 s^{-1} (5 LPM), and temperature = ~25°C].

reactions was described by Bhaskarwar and Kumar, who reported that the FBR provides a larger contact area than a bubble-column reactor (Bhaskarwar & Kumar 1984). In the present study, the average CO_2 absorption rate in the FBR was 20% greater than that in the bubble column.

The enhanced CO_2 absorption observed in the FBR compared to the semi-batch equilibrium system (SBES) is attributed to the synergistic effect of material properties and reactor hydrodynamics. The intrinsic characteristics of TETA-based AAILs, including amine functionality, viscosity, and reactivity, significantly influence their performance under different reactor conditions. The FBR system effectively utilizes these properties by increasing interfacial contact, leading to superior absorption performance.

3.3. Effect of Surfactant Concentration

In this work, different surfactants, including sodium lauryl sulfate (anionic), cetrimonium bromide (cationic), Triton X-100 (nonionic), and Tween 80 (nonionic), were used in the FBR to generate foam. The most stable foam and highest CO_2 uptake were observed with sodium lauryl sulfate. Triton X-100 and Tween 80 produced very poor and unstable foam when mixed with AAILs during FBR experiments. All surfactants were used at concentrations selected on the basis of their critical micelle concentration (CMC) values. The experiments showed that adding more surfactant decreased the absorption rate. Below the CMC value (8.2 mM) of SLS, however, the high-concentration resistance decreases and the diffusion flux of CO_2 uptake increases. CO_2 absorption increases with surfactant concentration up to the CMC, after which further addition may reduce mass-transfer efficiency because of excessive foam stabilization. Quantitative measurements of interfacial area and foam stability were not performed. This limitation is noted, and quantitative characterization remains a subject for future investigation.

Previously, Roy et al. (1995) explained that when surfactant concentration was increased, the solubility of CO_2 in the surfactant solution increased because of micellar solubilization (Roy et al. 1995). Nonetheless, the amount of dissolved and unreacted CO_2 in the foam film is extremely low in a gas-liquid reacting system. This could increase the potential for CO_2 solubility. However, as the surfactant concentration increased, more surfactant molecules surrounded the gas-film interface, resulting in the formation of several layers. This left a smaller interfacial surface available for the foam liquid to absorb CO_2. Nevertheless, at surfactant concentrations greater than the CMC, the micelles adopted cylindrical shapes, which provided some free space for CO_2 absorption, and the absorption rate marginally improved.

3.4. Semi-Batch Equilibrium Experiments

Semi-batch equilibrium experiments on CO_2 absorption were carried out at room temperature for more than 5 h. [TETA][GLU], [TETA][GLU], and [TETA][ASP] AAILs at a concentration of 100 mmol and a volume of 200 mL were selected for the equilibrium experiments. A continuous supply of pure CO_2 was bubbled through the solutions with stirring. After the equilibrium experiment, the AAILs were regenerated and used for further cycles.

Figs. 12–14 describe the equilibrium experiments on CO_2 absorption and desorption for [TETA][GLU], [TETA][ALA], and [TETA][ASP]. These studies indicated that the reaction involving deprotonation by the water molecule is slow. The experiments showed that the moles of CO_2 absorbed per mole of AAIL used were lower than in the FBR experiments because of the smaller interfacial area and the slow reaction involving deprotonation by the water molecule. As shown in Figs. 12–14, the moles of CO_2 absorbed per mole of AAIL increased slightly with time and reached equilibrium after about 4–5 h. The ionic liquid was saturated with CO_2 after completion of the absorption procedure. As explained in the experimental section, desorption investigations were also conducted after the experiment. The IL weight was recorded before the absorption cycle to ensure proper desorption of CO_2 from the IL. When all CO_2 in the CO_2-IL system had decomposed, the IL weight remained constant. CO_2 was first absorbed into the IL until absorption equilibrium was reached and was then desorbed from the CO_2-rich IL system. This constituted an absorption-desorption cycle.

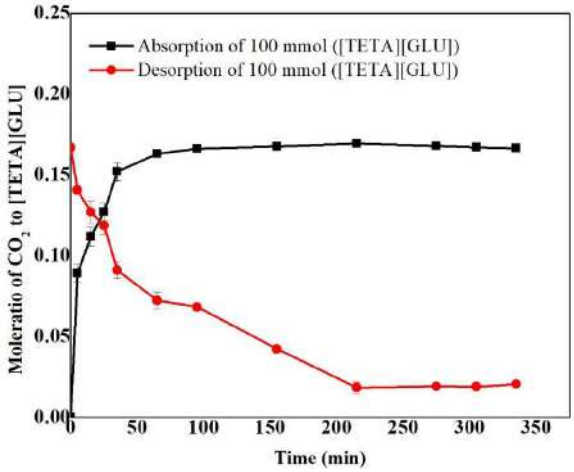


Fig. 12: Plot of absorption and desorption of [TETA][GLU] during CO_2 absorption. [Conditions: sample volume = 200 mL, RBF volume = 500 mL, ini-tial pH = 7.4 (for 100 mmol), CO_2 flow rate = 2.5×10^{-5} m^3 s^{-1} (1.5 LPM), stirring speed = 80 rpm, and temperature = ~25°C].

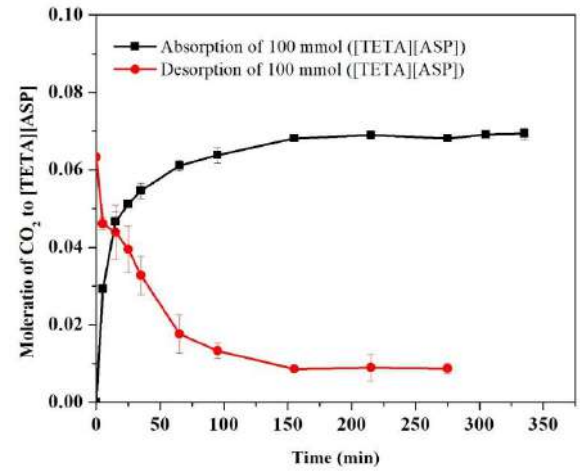


Fig. 13: Plot of absorption and desorption of [TETA][ASP] during CO_2 absorption. [Conditions: sample volume = 200 mL, RBF volume = 500 mL, ini-tial pH = 7.5 (for 100 mmol), CO_2 flow rate = 2.5×10^{-5} m^3 s^{-1} (1.5 LPM), stirring speed = 80 rpm, and temperature = ~25°C].

During desorption, the moles of CO_2 absorbed per mole of AAIL decreased with time and reached equilibrium after 4 h. As shown in Fig. 12, the highest mole ratio of CO_2 per mole of [TETA][GLU] was 0.166, followed by 0.133 for [TETA][ALA], as shown in Fig. 14. Desorption studies were plotted on the same figures; the mole ratio of CO_2 per mole of [TETA][GLU] decreased from 0.124 to 0.025, while that for [TETA][ALA] decreased from 0.12 to 0.013, as shown in Figs. 12 and 14, respectively. The lowest CO_2 uptake, 0.07, was observed for [TETA][ASP], as shown in Fig. 13. The used [TETA][GLU] was subjected to another experimental cycle, as shown in Fig. 15. Fig. 15 shows that [TETA][GLU] in the first cycle gave the highest CO_2 mole ratio of 0.166 per mole of AAIL used; in the second cycle, the CO_2 mole ratio was 0.121 per mole of [TETA][GLU]. This experiment shows that AAILs can be used for multiple cycles after regeneration.

4. CONCLUSIONS

This work describes the synthesis and characterization of AAILs for CO_2 absorption in an FBR. About seven new ILs, namely [TETA][ALA], [TETA][LYS], [TETA][GLU], [TETA][GLN], [TETA][MET], and [TETA][PHE], were synthesized. The prepared AAILs were characterized

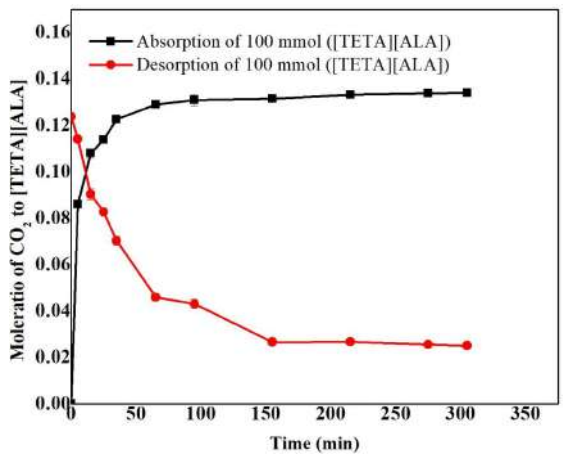


Fig. 14: Plot of absorption and desorption of [TETA][ALA] during CO_2 absorption. [Conditions: sample volume = 200 mL, RBF volume = 500 mL, ini-tial pH = 7.9 (for 100 mmol), CO_2 flow rate = 2.5×10^{-5} m^3 s^{-1} (1.5 LPM), stirring speed = 80 rpm, and temperature = ~25°C].

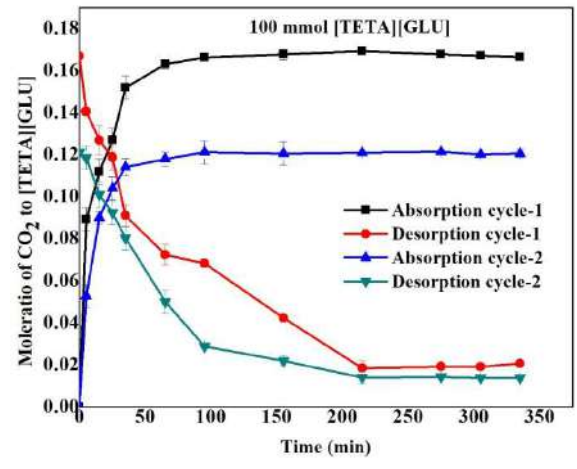


Fig. 15: Plot of absorption and desorption of [TETA][GLU] for two different cycles during CO_2 absorption. [Conditions: sample volume = 200 mL, RBF volume = 500 mL, initial pH = 7.4 (for 100 mmol), CO_2 flow rate = 2.5×10^{-5} m^3 s^{-1} (1.5 LPM), stirring speed = 80 rpm, and temperature = ~25°C].

using FTIR, Raman spectroscopy, and ^{1}H and ^{13}C NMR spectroscopy to confirm their formation. Parameters such as initial concentration, surfactant effects, and pH were studied. SLS was the most suitable surfactant for the FBR experiments. Viscosity and density measurements were carried out to characterize the physical properties of the AAILs. The application of AAILs in the FBR for CO absorption was evaluated under different experimental conditions. The highest and lowest densities of 1.170 and 1.0646 g cm^{-3} were observed for [TETA][ASP] and [TETA][ALA], respectively, among the synthesized AAILs. Viscosity measurements showed that AAIL viscosity decreased with increasing temperature. [TETA][LYS] gave the highest moles of CO_2 absorbed per mole of [TETA][LYS] used; the highest mole ratios of 0.442, 0.172, and 0.112 were observed at initial concentrations of 500, 300, and 100 mmol, respectively, among the AAILs used. Regeneration studies were also carried out to evaluate multiple uses of AAILs for CO_2 absorption. The highest mole ratio of CO per mole of [TETA][GLU] was 0.166, followed by 0.133 for [TETA][ALA], during desorption studies. Data from the FBR and semi-batch equilibrium studies suggest that amino acids combined with amines are suitable candidates for CO_2 absorption compared with other ionic liquids. The prepared AAILs are biodegradable, and the synthesis procedure was straightforward and can be conducted at low cost compared with conventional commercial ionic liquids.

5. ACKNOWLEDGEMENT

The author would like to thank Mr. Aman Verma, Mr. Shraban Das, Prakash Choudhary, and Nikhil Chimurkar for their assistance during the experiment. SRP is grateful to IIT Delhi and Prof. Ashok N. Bhaskarwar for providing research facilities. The author acknowledge the instrumentation support from CRF and Prof. Sridevi U. and her research group at IITD for their timely assistance.

6. REFERENCES

Barth, A., 2000. The infrared absorption of amino acid side chains. *Progress in Biophysics and Molecular Biology*, 74(3–5): 141–173. [DOI]

Babamohammadi, S., Shamiri, A. and Aroua, M.K., 2015. A review of CO_2 capture by absorption in ionic liquid-based solvents. *Reviews in Chemical Engineering*, 31: 383–412. [DOI]

Bhaskarwar, A.N. and Kumar, R., 1984. Oxidation of sodium sulfide in a foam bed contactor. *Chemical Engineering Science*, 39: 1393–1399. [DOI]

Cahyonugroho, O.H., Putra, I.S., Hidayah, E.N. and Novembrianto, R., 2025. Carbon dioxide gas reduction using the absorption method as an effort to support carbon capture and storage (CCS) technology. *Nature Environment and Pollution Technology*, 24(3): D1720. [DOI]

Cota, I. and Martinez, F.F., 2017. Recent advances in the synthesis and applications of metal organic frameworks doped with ionic liquids for CO_2 adsorption. *Coordination Chemistry Reviews*, 351: 189–204. [DOI]

Danckwerts, P.V., 1979. The reaction of CO_2 with ethanolamines. *Chemical Engineering Science*, 34: 443–446. [DOI]

Du, Y., Yuan, Y. and Rochelle, G.T., 2016. Capacity and absorption rate of tertiary and hindered amines blended with piperazine for CO_2 capture. *Chemical Engineering Science*, 155: 397–404. [DOI]

Elmobarak, W.F., Almomani, F., Tawalbeh, M., Al-Othman, A., Martis, R. and Rasool, K., 2023. Current status of CO_2 capture with ionic liquids: Development and progress. *Fuel*, 344: 128102. [DOI]

Fukumoto, K., Yoshizawa, M. and Ohno, H., 2005. Room-temperature ionic liquids from 20 natural amino acids. *Journal of the American Chemical Society*, 127: 2398–2399. [DOI]

Goodrich, B.F., de la Fuente, J.C., Gürkan, B.E., Zadigian, D.J., Price, E.A., Huang, Y. and Brennecke, J.F., 2011. Experimental measurements of amine-functionalized anion-tethered ionic liquids with carbon dioxide. *Industrial & Engineering Chemistry Research*, 50: 111–118. [DOI]

Gürkan, B.E., de la Fuente, J.C. and Mindrup, E.M., 2010. Equimolar CO_2 absorption by anion-functionalized ionic liquids. *Journal of the American Chemical Society*, 132: 2116–2117. [DOI]

Huddleston, J.G. et al., 2001. Characterization and comparison of hydrophilic and hydrophobic room temperature ionic liquids incorporating the imidazolium cation. *Green Chemistry*, 3(4): 156–164. [DOI]

IPCC, 2005. *IPCC Special Report on Carbon Dioxide Capture and Storage*. Prepared by Working Group III of the Intergovernmental Panel on Climate Change. Edited by B. Metz, O. Davidson, H.C. de Coninck, M. Loos and L.A. Meyer. Cambridge University Press, Cambridge.

Jones, C.W., 2011. CO_2 capture from dilute gases as a component of modern global carbon management. *Annual Review of Chemical and Biomolecular Engineering*, 2: 31–52. [DOI]

Khanna, R.K. and Moorie, M.H., 1999. Carbamic acid: Molecular structure and IR spectra. *Spectrochimica Acta Part A*, 55: 961–967. [DOI]

Kortunov, P.V., Baugh, L.S. and Siskin, M., 2015. Pathways of the chemical reaction of carbon dioxide with ionic liquids and amines in ionic liquid solution. *Energy & Fuels*, 29: 5990–6007. [DOI]

Kumar, P.S., Hogendoorn, J.A., Feron, P.H.M. and Versteeg, G.F., 2002. New absorption liquids for the removal of CO_2 from dilute gas streams using membrane contactors. *Chemical Engineering Science*, 57: 1639–1651. [DOI]

Kumar, P.S., Hogendoorn, J.A. and Versteeg, G.F., 2003. Kinetics of the reaction of CO_2 with aqueous potassium salts of taurine and glycine. *AIChE Journal*, 49: 203–213. [DOI]

Lupa, L., Tolea, N.S., Iosivoni, M., Măranescu, B., Pleșu, N. and Visa, A., 2024. Performance of ionic liquid functionalized metal-organic frameworks in the adsorption process of phenol derivatives. *RSC Advances*, 14: 4759–4777. [DOI]

Makino, T. and Kanakubo, M., 2016. CO_2 absorption property of ionic liquid and CO_2 permselectivity for ionic liquid membrane. *Journal of the Japan Petroleum Institute*, 59: 109–117. [DOI]

Mandal, B.P. and Bandyopadhyay, S.S., 2005. Simultaneous absorption of carbon dioxide and hydrogen sulfide into aqueous blends of 2-amino-2-methyl-1-propanol and diethanolamine. *Chemical Engineering Science*, 60: 6438–6451. [DOI]

Mohamedali, M., Ibrahim, H. and Henni, A., 2017. Incorporation of acetate-based ionic liquids into a zeolitic imidazolate framework (ZIF-8) as efficient sorbents for carbon dioxide capture. *Chemical Engineering Journal*, 334: 817–828. [DOI]

Mulk, W.U., Ali, S.A., Shah, S.N., Shah, M.U.H., Zhang, Q.J., Younas, M., Fatehizadeh, A., Sheikh, M. and Rezakazemi, M., 2023. Breaking boundaries in CO_2 capture: Ionic liquid-based membrane separation for post-combustion applications. *Journal of CO_2 Utilization*, 75: 102555. [DOI]

Mumford, K.A., Mirza, N.R. and Stevens, G.W., 2017. Review: Room-temperature ionic liquids and system designs for CO_2 capture. *Energy Procedia*, 114: 2671–2674. [DOI]

Norouzbahari, S., Shah Hosseini, S. and Ghaemi, A., 2016. Chemical

absorption of CO_2 into aqueous piperazine (PZ) solution: Development and validation of a rigorous dynamic rate-based model. *RSC Advances*, 6: 40017–40032. [DOI]

Padmanabhan, S., Joel, C., Mahalingam, S., Deepak, J.R., Kumar, T.V. and Raj, D., 2024. An overview of the need for circular economy on electric vehicle batteries. *Nature Environment and Pollution Technology*, 23(1): 183–191. [DOI]

Pilli, S.R., Banerjee, T. and Mohanty, K., 2014. Liquid-liquid equilibrium (LLE) data for ternary mixtures of $[C_4DMIM][PF_6]$-[PCP]-water and $[C_4DMIM][PF_6]$-[PA]-water at T = 298.15 K and p = 1 atm. *Fluid Phase Equilibria*, 381: 12–19. [DOI]

Qu, Y., Chen, Y., Ye, Y., Xu, P. and Sun, J., 2022. Supercritical CO_2-assisted synthesis of SBA-15-supported amino acid ionic liquid for CO_2 cycloaddition under cocatalyst-, metal- and solvent-free conditions. *Journal of CO_2 Utilization*, 66: 102294. [DOI]

Ramdin, M., de Loos, T.W. and Vlugt, T.J.H., 2012. State-of-the-art of CO_2 capture with ionic liquids. *Industrial & Engineering Chemistry Research*, 51: 8149–8177. [DOI]

Roy, D., Kommalapati, R.R., Valsaraj, K.T. and Constant, W.D., 1995. Soil flushing of residual transmission fluid: Application of colloidal gas aphron suspensions and conventional surfactant solutions. *Water Research*, 29: 589–595. [DOI]

Sarker, A.I., Aroonwilas, A. and Veawab, A., 2017. Equilibrium and kinetic behaviour of CO_2 adsorption onto zeolites, carbon molecular sieve and activated carbons. *Energy Procedia*, 114: 2450–2459. [DOI]

Seddon, R., Stark, A.S. and Torres, M.J., 2004. Viscosity and density of 1-alkyl-3-ethylimidazolium ionic liquids. In: Rogers, R.D. and Seddon, K.R. (eds.), *Ionic Liquids III: Fundamentals, Progress, Challenges, and Opportunities*. ACS Symposium Series 901. American Chemical Society, Washington, DC. [DOI]

van Holst, G.F.V., Brilman, D.W.F. and Hogendoorn, J.A., 2009. Kinetic study of CO_2 with various amino acid salts in aqueous solution. *Chemical Engineering Science*, 64: 59–68. [DOI]

Versteeg, G.F. and van Swaaij, W.P.M., 1988. On the kinetics between CO_2 and alkanolamines both in aqueous and non-aqueous solutions—I. Primary and secondary amines. *Chemical Engineering Science*, 43: 573–585. [DOI]

Wahby, J., Silvestre-Albero, A., Sepúlveda-Escribano, A. and Rodríguez-Reinoso, F., 2012. CO_2 adsorption on carbon molecular sieves. *Microporous and Mesoporous Materials*, 164: 280–287. [DOI]

Walden, P., 1914. Molecular weights and electrical conductivity of several fused salts. *Bulletin of the Imperial Academy of Sciences (Saint Petersburg)*, 1800: 405–422. Available at: https://ci.nii.ac.jp/naid/10025720020/

Wilkes, J.S., 2002. A short history of ionic liquids: From molten salts to neoteric solvents. *Green Chemistry*, 4: 73–80. [DOI]

Xie, H.B., Zhou, Y., Zhang, Y. and Johnson, J.K., 2010. Reaction mechanism of monoethanolamine with CO_2 in aqueous solution from molecular modelling. *Journal of Physical Chemistry A*, 114: 11844–11852. [DOI]

Xing, H., Yan, Y., Yang, Q., Bao, Z., Su, B., Yang, Y. and Ren, Q., 2013. Effect of tethering strategies on the surface structure of amine-functionalized ionic liquids: Inspiration on the CO_2 capture. *Journal of Physical Chemistry C*, 117: 16012–16021. [DOI]

Yamini, S.S. and Khanna, A., 2014. Carbon dioxide absorption studies using amine-functionalized ionic liquids. *Journal of Industrial and Engineering Chemistry*, 20: 2497–2509. [DOI]

Yamini, S.S. and Khanna, A., 2015. CO_2 absorption studies in amino acid-anion-based ionic liquids. *Chemical Engineering Journal*, 273: 268–276. [DOI]

Zhang, L.-L., Wang, J.-X., Xiang, Y., Zeng, X.-F. and Chen, J.-F., 2011. Absorption of carbon dioxide with ionic liquid in a rotating packed bed contactor: Mass transfer study. *Industrial & Engineering Chemistry Research*, 50: 6957–6964. [DOI]

Nature Environment and Pollution Technology
An International Quarterly Peer-Reviewed Open Access Journal

p-ISSN: 0972-6268 | e-ISSN: 2395-3454 Vol. 25 | No. 4 | Article ID B4438 | 2026

RESEARCH ARTICLE https://doi.org/10.46488/NEPT.2026.v25i04.B4438 OPEN ACCESS

Biofilm-Forming Endophytic Bacteria and Fungi from Bryophytes: Tools for Eco-Restoration of Polluted Habitats

Shivani Gore[1], Shivom Singh[2]†, Pooja Swarnkar[2] and Kajal S. Rathore[3]
[1]Department of Biotechnology, ITM University, Gwalior, 474001, M.P., India
[2]Department of Environmental Science, ITM University, Gwalior, 474001, M.P., India
[3]Department of Biotechnology, Govt. Model Science College, Gwalior, 474001, M.P., India
†Corresponding author: Shivom Singh; shivomsingh101@gmail.com

ARTICLE HISTORY

Received: 10-03-2026
Revised: 15-05-2026
Accepted: 19-05-2026

KEYWORDS

ACC deaminase
Endophytes
PGP attributes
Sustainable agriculture
Bryophytes
Biofilm formation
Plant growth promotion

CITE THIS ARTICLE

Gore, S., Singh, S., Swarnkar, P. and Rathore, K.S. 2026. Biofilm-forming endophytic bacteria and fungi from bryophytes: Tools for eco-restoration of polluted habitats, *Nature Environment and Pollution Technology* 25(4), B4438. https://doi.org/10.46488/NEPT.2026.v25i04.B4438

COPYRIGHT & LICENCE

© 2026 The Authors
Open Access under CC BY 4.0.

PUBLISHED BY

TECHNOSCIENCE PUBLICATIONS

ABSTRACT

Mosses and liverworts, commonly referred to as bryophyte plants, are among the first plants to colonize nutrient-poor environments and have been known to harbor a wide range of microbial communities, which enhance their ecological resilience. Despite the fact that endophytic microorganisms have been well investigated in vascular plants, there have been relatively few studies on the microorganisms in bryophytes, especially those in high-altitude ecosystems in India. As sustainable bioremediation technologies to combat soil and water pollution are urgently needed, this paper examines bryophyte-associated endophytes as potential green tools for environmental restoration. We described culturable endophytic bacteria and fungi of seven bryophyte species growing in the Kumaon region of the Uttarakhand state in India. Isolates were evaluated based on morphological characterization, biochemical tests (catalase, amylase, phosphate solubilization, IAA production, ACC deaminase activities) and biofilm formation, with biofilm architecture visualized by SEM. Thirty-one endophytes (27 bacteria and 4 fungi) were obtained. 66.67% of bacteria were Gram-negative, and 76% of them had a bacillary morphology. All isolates (100%, 31/31) produced IAA, 64.5% (20/31) had ACC deaminase activity and 77.4% (24/31) formed biofilms. Five elite isolates possessed ≥5 plant growth-promoting traits. The high biofilm-forming capacity is consistent with reported mechanisms of heavy metal biosorption and pollutant immobilization, suggesting potential relevance for future wastewater treatment applications, pending direct validation. ACC deaminase activity, which mitigates ethylene stress in plants, suggests potential for future phytoremediation studies, though plant trials were not conducted in this work. These results demonstrate that Kumaon bryophytes host metabolically versatile endophytic assemblages with dual potential for sustainable agriculture and environmental pollution control, offering novel candidates for stress-resilient bioinoculants and green remediation technologies. Fungus-mediated bacterial scaffolding within biofilms constitutes a previously unrecognized ecological strategy with promising bioreactor applications.

1. INTRODUCTION

Bryophytes, including mosses, liverworts, and hornworts, are important in terms of ecology, particularly in nutrient-deficient environments. They are also pioneer species that colonize unproductive substrates, including manganese waste residue areas, facilitating the formation of soils and restoring the ecology (Ren et al. 2021). Their own development and breakages contribute to stabilizing the sediments, enhancing the soil structure, and raising the nutrient pools (Virtanen et al. 2022). Owing to the rapid growth, substrate versatility, and global distribution,

bryophytes are regarded as the ideal model organisms to investigate the evolutionary effects and ecological effects of habitat fragmentation (Pandey & Alam 2023). Additionally, their proximity to a wide range of microbial organisms also contributes to their flexibility because the latter significantly affect the fitness and resilience of plants. Beneficial microbes associated with bryophytes support growth, degradation of organic contaminants, and resistance to adverse environmental factors.

The global escalation of environmental pollution, particularly heavy metal contamination, pesticide residues, and industrial effluents, has necessitated the development of sustainable bioremediation technologies. Conventional physicochemical remediation approaches are often economically prohibitive, environmentally disruptive, and generate secondary pollutants, driving research toward microbial-based green technologies (Abo-Koura 2023). Bryophyte-associated endophytes represent an underexplored reservoir of pollution-tolerant microorganisms with inherent capabilities for biosorption, bioaccumulation, and biodegradation of environmental contaminants. Their ability to thrive in oligotrophic, metal-enriched habitats suggests co-evolutionary adaptation to detoxification mechanisms that could be harnessed for phytoremediation of contaminated sites (Shcherbakov et al. 2013). Furthermore, the extracellular polymeric substances (EPS) produced by these endophytes demonstrate significant potential for immobilizing heavy metals and enhancing soil aggregation, thereby preventing pollutant mobilization in vulnerable ecosystems (Iungin et al. 2024).

Endophytes refer to non-pathogenic microorganisms located within the internal tissues of vegetation to facilitate plant growth and resistance (Abo-Koura 2023, Fukami et al. 2018). These microorganisms promote the growth of plants in many ways, including fixing nitrogen, solubilizing phosphorus, and sequestration of iron by synthesizing siderophores in the process of getting nutrients. Also, endophytes produce phytohormones such as auxins, gibberellins and cytokinins which promote root and shoot development and improve stress resistance. It is also their antagonistic properties against pathogens, which give plants natural benefits of biocontrol, lowering the cases of diseases and assisting in sustainable agriculture (Sahay et al. 2017). Of particular relevance to pollution control, endophytic bacteria such as *Pseudomonas* and *Bacillus* species have demonstrated capabilities for degrading polycyclic aromatic hydrocarbons (PAHs), detoxifying heavy metals, and reducing pesticide residues in contaminated soils. The ACC deaminase activity exhibited by many endophytes mitigates ethylene stress in plants, enabling enhanced phytoremediation efficiency in polluted environments where conventional vegetation fails to establish (Penrose & Glick 2003).

Given the relevance of the association between bryophytes and endophytic communities, and the urgent need for effective, low-cost bioremediation solutions, the current study was an attempt to describe endophytes of seven species of bryophytes in the region of Uttarakhand, India, viz., *Philonotis mollis*, *Thysanomitrion involutum*, *Dumortiera hirsuta*, *Bryoandersonia illecebra*, *Hylocomiadelphus triquetrus*, *Thuidium delicatulum* and *Rhytidiadelphus loreus*. The Himalayan region faces escalating environmental pressures from mining activities, tourism-induced pollution, and agricultural runoff, necessitating region-specific bioremediation strategies. These endophytic communities were isolated from these bryophytes which were then studied in terms of their morphological and biochemical attributes.

Biofilm formation by endophytes represents a critical functional trait for environmental applications. Microbial biofilms represent advanced communities of microorganisms, which attach to surfaces or coalesce with each other creating a protective and supportive framework of extracellular polymeric substances (EPS) (Iungin et al. 2024). EPS mostly includes a broad range of macromolecules, including polysaccharides, proteins, lipids, and extracellular DNA (eDNA). This complex network can provide structural support and allow microorganisms to adsorb, interact, and adapt to environmental stresses (Lucero et al. 2020). Biofilm matrices can also contribute to pollution control because they can act as natural barriers in contaminant sequestration in wastewater treatment reactors, constructed wetlands, and permeable reactive barriers for groundwater remediation. Mixed-species biofilms are three-dimensional structures that are highly effective in the transfer of pollutants to the microbial cell and offer protection against toxic shock loads as well as landfill leachate (Bridier et al. 2010, Wang et al. 2023).

The ecological significance of *Sphagnum*, a common genus of mosses, has been discovered through extensive research, particularly with its relationships with microbes. The role of Sphagnum species in the peatland ecosystem is quite important because of their impact on the biodiversity and carbon cycle, as well as nutrient cycles, and they also host a rich diversity of microbial life (Bragina et al. 2013). Peatlands function as natural pollution filters, with *Sphagnum*-associated microbiomes contributing to water purification and carbon sequestration, offering model systems for engineered bioremediation applications. Other genera of bacteria such as *Serratia* spp., *Pseudomonas putida*, and even *Bacillus* spp. have commonly been reported to be associated with bryophytes and are reported to have

antagonistic effects against phytopathogens (Opelt et al. 2007). Many of these genera are concurrently recognized for their bioremediation potential, including chromium reduction, diesel degradation, and pesticide mineralization, suggesting that bryophyte habitats serve as reservoirs for multifunctional environmental isolates. In addition, Insuk et al. (2020) showed that actinobacterial isolates could be found in bryophytes, and they all had the capability to secrete growth-promoting substances of plants, including indole-3-acetic acid (IAA) and siderophores. These compounds play a crucial role in the uptake of nutrients and growth of plants. Siderophore production by these endophytes additionally facilitates iron chelation in contaminated soils, potentially reducing metal bioavailability and limiting pollutant uptake by food crops, a critical consideration for safe agricultural production on marginal lands.

Equally, in the present research, a number of individual bacterial strains demonstrated the possibility of synthesizing plant growth regulators (PGRs) such as IAA, which could be essential in the growth of thallus and nutritional support. These results confirm the ecological plausibility of such interactions in the formation and maintenance of pioneer communities of bryophytes.

The morphological and biochemical description of endophytes of bryophytes provides valuable insight into plant-microbe interactions of non-vascular plants. From a pollution technology perspective, understanding these interactions enables the design of synthetic microbial consortia optimized for specific contaminant profiles, whether heavy metals, organic pollutants, or nutrient excess. Although various studies have been conducted on the morphology, biochemical characteristics and biofilm-forming capacities of endophytic bacteria in higher plants, a relatively small number of studies have been conducted on bryophytes. Given the extreme environmental conditions of high-altitude bryophyte habitats, their endophytes likely possess unique stress tolerance mechanisms and metabolic versatility applicable to bioremediation of extreme environments such as mine tailings, industrial brownfields, and high-altitude contaminated sites. Thus, this study seeks to fill this gap in knowledge by conducting an investigation on the morphological and biochemical properties and biofilm-forming capacity of the endophytic bacterial isolates of bryophytes, with particular attention to their potential for environmental pollution control and sustainable remediation technologies

2. MATERIALS AND METHODS

2.1. Sample Collection and Identification

In 2024, bryophytes were collected from various locations across the Kumaon region of Uttarakhand, India (lat. 29.624657°N, long. 79.830827°E). Collections were conducted systematically, and appropriate voucher specimens were prepared (ITM-BRY-001 to ITM-BRY-007). All samples were immediately transported under controlled conditions to the Environmental Science Laboratory at ITM University, Gwalior, to prevent desiccation and avoid exposure to harsh environmental conditions. Upon arrival, the specimens were carefully examined, and small fragments were observed using a compound light microscope.

2.2. Surface Disinfection

Bryophyte tissues were surface-sterilized according to Semwal et al. (2023) with slight alterations. About 1 g of healthy tissue, including rhizoids, was treated with 0.5% NaOCl for 2 min, rinsed three times with sterile distilled water (SDW), followed by 70% ethanol for 2 min, and again rinsed three times with SDW. The sterilized samples were then air-dried on sterile filter paper under aseptic conditions before further processing.

2.3. Isolation of Endophytes

The sterilized bryophyte samples were aseptically crushed using a sterile mortar and pestle, homogenized in 0.85% NaCl, and serially diluted up to 10^{-6}. Aliquots of suitable dilutions were plated on Nutrient Agar (NA) for bacterial isolation and Potato Dextrose Agar (PDA) for fungal isolation. Plates were incubated at 28 ± 2°C (24 h for bacteria and 3–5 days for fungi) and sealed with parafilm. Distinct colonies or fungal morphotypes were selected based on macroscopic characteristics, subcultured to obtain pure isolates, and stored at −80°C in 40% glycerol for further analysis (Opelt et al. 2007). A total of 31 endophytes (27 bacteria and 4 fungi) were obtained from seven bryophyte species.

2.4. Morphological Analysis

Bacterial and fungal isolates were cultured on Nutrient Agar (NA) and Potato Dextrose Agar (PDA), respectively, and characterized for colony morphology, including elevation, margin, texture, form, color, and opacity after 48 h of incubation at 28 ± 2°C, following Bergey's Manual of Determinative Bacteriology (Bergey 1994). Bacterial isolates were subjected to Gram staining and examined at 40× magnification to determine Gram reaction and cell morphology. Gram staining was performed using the standard Hucker modification: heat-fixed smears were stained with crystal violet (1 min), iodine (1 min), decolorized with 95% ethanol (10–20 s), and counterstained with safranin (30 s). Fungal isolates were observed microscopically using lactophenol cotton blue mounts to study hyphal and spore characteristics.

2.5. Biochemical Characterization

Endophytes isolated from bryophytes were identified by various biochemical tests as reported in Bergey's Manual of Systematic Bacteriology (Vos et al. 2011). Catalase activity, amylase activity, and phosphate solubilization were assessed (MacFaddin 2000). All assays were performed with three independent biological replicates per isolate. Each biological replicate consisted of a separately inoculated culture grown from a distinct colony.

2.5.1. Catalase Activity

A fresh bacterial colony was transferred to a clean glass slide, and one drop of 3% (v/v) hydrogen peroxide was added. Immediate bubble formation indicated catalase positivity. Scoring: + (bubble formation < 5 s), ++ (5–10 s), +++ (> 10 s or vigorous effervescence).

2.5.2. Amylase Activity

Isolates were streaked on starch agar (1% soluble starch) and incubated at 28 ± 2°C for 48 h. Plates were flooded with Gram's iodine solution (0.33% I_2, 0.67% KI). A clear zone around the colony indicated starch hydrolysis. Scoring: + (zone 1–3 mm), ++ (zone 3–6 mm), +++ (zone > 6 mm). Zone diameters were measured with a digital caliper (±0.1 mm). Three technical measurements were taken per plate and averaged.

2.5.3. Phosphate Solubilization

Isolates were inoculated on Pikovskaya's agar and incubated at 28 ± 2°C for 7 days. A clear halo around the colony indicated phosphate solubilization. Scoring: + (zone 1–3 mm), ++ (zone 3–6 mm), +++ (zone > 6 mm). Zone diameters were measured as described for amylase.

2.6. Indole-3-Acetic Acid (IAA) Production

Isolated endophytes were assessed for IAA production using Salkowski's method as described by Herlina et al. (2017). A microbial suspension (3 mL; 10^8 CFU mL^{-1}, McFarland standard) was inoculated into 30 mL of LB broth supplemented with 0.1% (w/v) L-tryptophan and incubated at room temperature under shaking at 150 rpm for 7 days. Samples were collected every 2 days (Days 2, 4, and 6), centrifuged at 5,000 rpm for 25 min, and the supernatant was used for colorimetric analysis. Salkowski reagent (1 mL 0.5 M $FeCl_3$ in 50 mL 35% $HClO_4$) was mixed with the supernatant in a 2:1 ratio, incubated in the dark for 1 h, and absorbance was measured at 535 nm. IAA concentration was determined from a standard curve prepared with known IAA concentrations (0–100 µg mL^{-1}).

Bacterial and fungal isolates were subjected to the same assay conditions, with the following modification for fungi: fungal isolates were grown in LB broth supplemented with 0.5% (w/v) yeast extract to support filamentous growth.

Three independent biological replicates were used per isolate per time point. Each biological replicate consisted of a separately inoculated culture. Three technical replicate absorbance readings were obtained per biological replicate and averaged.

2.7. 1-Aminocyclopropane-1-Carboxylate (ACC) Deaminase Activity

ACC deaminase activity was determined following the modified method of Penrose and Glick (2003), based on -ketobutyrate quantification. Each isolate was grown in fresh medium at 28°C and 180 rpm, harvested on Days 2, 4, and 6 at mid-log phase during active growth, and washed with DF minimal medium. Cells were resuspended in DF medium, supplemented with 3 mM ACC (fungi) or 1 mM ACC (bacteria), and incubated for 24 h to induce ACC deaminase expression. After induction, cells were washed with 0.1 M Tris-HCl (pH 7.6) and permeabilized by vortexing the suspension in Tris-HCl (pH 8.5) with 30 µL toluene per 1 mL cell suspension. The permeabilized cells were incubated with ACC for 15 min at 30°C, and the reaction was stopped by addition of 0.56 M HCl. Released α-ketobutyrate in the supernatant was reacted with 2,4-dinitrophenylhydrazine (0.56 mM in 2 M HCl), incubated at 30°C for 30 min, followed by addition of 2 M NaOH, and absorbance was measured at 540 nm. α-ketobutyrate concentration was determined from a standard curve prepared using known α-ketobutyrate standards (0–50 µmol/mL), and ACC deaminase activity was expressed as µmol α-ketobutyrate produced per mg protein per hour (µmol mg^{-1} protein h^{-1}).

Three independent biological replicates were used per isolate per time point. Three technical replicate absorbance readings were obtained per biological replicate and averaged.

2.8. Biofilm Production and Visualization Through SEM

The isolates were screened for their ability to form biofilms by 96-well microtiter plate assay. LB broth was inoculated with 2% (v/v) of the seed culture and incubated for 72 h at 28 ± 2°C (bacteria) or 96 h (fungi). The broth was discarded and 96-well microtiter plates were washed three times with Phosphate Buffered Saline (PBS, pH 7.3) and air-dried for 30 min. Staining of dried 96-well microtiter plates was carried out with 200 µL of 0.1% (w/v) crystal violet per well for 15 min. Excess stain was removed by washing the 96-well microtiter plate three times with PBS. Formation of biofilm was confirmed visually by the presence of a visible film on

the wall and bottom of the 96-well microtiter plate (Rosario et al. 2020).

Wells were examined for visible purple film on walls and bottoms. Scoring: + (light film, partial surface coverage), ++ (moderate film, >50% surface coverage), +++ (dense film covering entire surface). Qualitative scores were assigned by two independent observers; discrepancies were resolved by a third observer. Isolates were selected based on visual biofilm with "+++" scoring only.

2.9. SEM Visualization

Biofilm architecture was visualized by scanning electron microscopy (SEM) using the following protocol: Biofilms grown in 96-well plates, as described above, were fixed with 2.5% (v/v) glutaraldehyde in 0.1 M phosphate buffer (pH 7.2) for 4 h at 4°C, followed by three washes (15 min each) with the same buffer. Samples were dehydrated through a graded ethanol series: 30%, 50%, 70%, 80%, 90%, and 100% (v/v), 15 min per step, with two changes at 100%. Dehydrated samples were subjected to critical point drying using liquid CO_2 in a Leica EM CPD300. Dried samples were mounted on aluminum stubs using carbon adhesive tabs, sputter-coated with gold-palladium (Au-Pd, 80:20) to a thickness of ~10 nm using a Quorum Q150R ES coater, and examined under a Zeiss Sigma 300 field-emission SEM at an accelerating voltage of 5 kV, working distance of 8–10 mm, and magnification range of 10,000×.

2.10. Statistical Analyses

Quantitative data for IAA production and ACC deaminase activity were analyzed using two-way ANOVA with isolate and time as fixed factors, followed by Tukey's honestly significant difference (HSD) post-hoc test for pairwise comparisons. Qualitative PGP traits (catalase, amylase, phosphate solubilization, auxin production, ACC deaminase, and biofilm formation) were analyzed using one-way ANOVA across isolates, followed by Tukey's HSD test. All analyses were performed with three independent biological replicates per isolate per time point (for time-dependent assays) or per isolate (for qualitative screening). Significance was set at $P < 0.05$. Different lowercase letters indicate statistically significant differences between isolates (one-way ANOVA) or isolate × time interactions (two-way ANOVA) based on Tukey's HSD.

3. RESULTS AND DISCUSSION

3.1. Sample Identification

Seven bryophyte species were collected, representing two taxonomic groups. Liverworts were represented by *Thysanomitrion involutum* and *Dumortiera hirsuta*, whereas the mosses *Philonotis mollis*, *Bryoandersonia illecebra*, *Hylocomiadelphus triquetrus*, *Thuidium delicatulum* and *Rhytidiadelphus loreus* were collected from forest floors, streambanks and humid rock outcrops (Table 1). Voucher specimens (ITM-BRY-001 to 007) were deposited in the ITM University herbarium.

3.2. Isolation of Endophytes

A total of 31 culturable endophytes (27 bacteria, 4 fungi) were recovered on NA and PDA (Table 1). Species-wise isolate numbers ranged from three (*D. hirsuta*) to six (*P. mollis* and *R. loreus*). The higher recovery from mosses growing on nutrient-rich forest litter (*P. mollis*, *R. loreus*) agrees with the observation that substrate C/N ratio and micro-habitat moisture strongly influence endophytic communities (Prekrasna et al. 2021). No fungi were isolated from the thalli of the one liverwort, consistent with earlier reports that marchantioid taxa possess antifungal secondary metabolites that restrict fungal colonization (Pandey & Alam 2023).

Table 1: Bryophyte specimens with voucher numbers and associated endophyte isolates.

Bryophyte species	Voucher number	Habitat	Endophyte isolates		Total isolates
			Bacteria (Code)	Fungus (Code)	
Philonotis mollis	ITM-BRY-001 (a-d)	Forest floors	AEPB01, AEPB02, AEPB03, AEPB04	AEPF01, AEPF02	6
Thysanomitrion involutum	ITM-BRY-002 (a-d)	Streambanks	BEPB01, BEPB02, BEPB03, BEPB04	-	4
Dumortiera hirsuta	ITM-BRY-003 (a-d)	Humid rock surfaces	CEPB01, CEPB02, CEPB03	-	3
Bryoandersonia illecebra	ITM-BRY-004 (a-d)	Mossy rocks	DEPB01, DEPB02, DEPB03	DEPF01	4
Hylocomiadelphus triquetrus	ITM-BRY-005 (a-d)	Forest floors	EEPB01, EEPB02, EEPB03, EEPB04	-	4
Thuidium delicatulum	ITM-BRY-006 (a-d)	Forest floors	FEPB01, FEPB02, FEPB03, FEPB04	-	4
Rhytidiadelphus loreus	ITM-BRY-007 (a-d)	Forest floors	GEPB01, GEPB02, GEPB03, GEPB04, GEPB05	GEPF01	6

Table 2: Microscopic and morphological characteristics of the isolated endophytes.

S. No.	Isolate No.	Stain Color	Cell/Mycelium shape	Arrangement	Colony morphology	Margin	Colony color	Opacity	Texture/consistency
1.	AEPB01	Pink (Gram -ve)	Long rod-shaped (bacilli)	Single, pairs, short chains	Irregular	Undulate	Off-white	Opaque	Dry, rough, slightly chalky
2.	AEPB02	Pink (Gram -ve)	Rod (bacillus)	Random/scattered	Circular	Entire	Creamy white	Opaque	Smooth, mucoid
3.	AEPB03	Pink (Gram -ve)	Rod-shaped (bacillus)	Random/scattered	Circular to slightly Irregular	Entire to slightly Undulate	Creamy white	Opaque	Smooth, moist, glistening
4.	AEPB04	Pink (Gram -ve)	Rod-shaped (bacillus)	Random/scattered	Circular to Irregular	Undulate	Light cream	Opaque	Smooth, slightly mucoid
5.	AEPF01	Blue	Filamentous; septate hyphae	Interwoven network of hyphae	Spreading, cottony, with concentric ring formation	Irregular, feathery	Whitish to grey	Opaque	Woolly to cottony
6.	AEPF02	Blue	Septate, filamentous	Interwoven, branched hyphae	Spreading, zonated, dense sporulation	Irregular	White to green-yellow	Opaque	Cottony to powdery
7.	BEPB01	Pink (Gram -ve)	Long rod-shaped (bacilli)	Single, pairs, short chains	Irregular	Lobate	Pale yellowish-cream	Opaque	Dry to wrinkled, rough surface
8.	BEPB02	Pink (Gram -ve)	Rod (bacillus)	Random/scattered	Circular to Irregular	Entire to slightly Undulate	Whitish to off-white	Opaque to slightly translucent	Dry and chalky
9.	BEPB03	Pink (Gram -ve)	Rod (bacillus)	Random/scattered	Irregular	Lobate	Creamy white	Opaque	Dry, wrinkled, and rough
10.	BEPB04	Pink (Gram -ve)	Rod (bacillus)	Random/scattered	Small, circular, pinpoint colonies	Entire	Translucent	Transparent	Smooth, moist, and glistening
11.	CEPB01	Pink (Gram -ve)	Rod (bacillus)	Single and short chains	flat colonies	Irregular	Light beige	Opaque	Dry, rough, with chalky appearance
12.	CEPB02	Pink (Gram -ve)	Spherical (Cocci)	Clusters/Scattered	Circular	Entire	Whitish	Opaque	Rough, dry to slightly granular
13.	CEPB03	Pink (Gram -ve)	Spherical (Cocci)	Clusters and diplococci	Filamentous	Lobate	Pale cream	Opaque	Dry, fuzzy to cottony in appearance
14.	DEPB01	Purple (Gram +ve)	Spherical (Cocci)	Clusters	Circular to slightly Irregular	Entire	Pale cream	Translucent	Smooth, moist to slightly mucoid
15.	DEPB02	Purple (Gram +ve)	Spherical (Cocci)	Clusters	Large, Irregular, raised colonies	Lobate	Creamy white	Opaque	Dry to mucoid transition
16.	DEPB03	Purple (Gram +ve)	Rod-shaped (bacilli)	Chains and clusters	Small, round, discrete colonies	Entire	Creamy white	Mostly opaque	Smooth, slightly raised, glistening appearance
17.	DEPF01	Blue	Septate, branched with round conidia	Conidiophores arising from hyphae	Radially spreading, powdery colonies with clear zones	Lobate to slightly Irregular	Bright yellow-green	Opaque	Velvety to powdery

Table Cont....

S. No.	Isolate No.	Stain Color	Cell/Mycelium shape	Arrangement	Colony morphology	Margin	Colony color	Opacity	Texture/consistency
18.	EEPB01	Pink (Gram -ve)	Rod (bacillus)	Random/scattered	Circular to Irregular	Entire to Undulate	Dull white to off-white	Opaque	Mucoid, glistening
19.	EEPB02	Pink (Gram -ve)	Long rods (bacilli)	Single, small groups, scattered	Irregular spreading	Entire to slightly Undulate	Creamy to off-white	Opaque	Mucoid, glistening to smooth
20.	EEPB03	Pink (Gram -ve)	Rod (bacillus)	Single and short chains	Irregular	Diffuse	Cream	Opaque	Dry
21.	EEPB04	Purple (Gram +ve)	Rod-shaped (bacillus)	Chains and dense clusters	Irregular	Undulate	Cream	Opaque	Mucoid
22.	FEPB01	Purple (Gram +ve)	Rod-shaped (bacillus)	Long chains and dense clusters	Large, Irregular	Lobate to filamentous	pale beige	Opaque	Dry, chalky, and highly wrinkled or veined
23.	FEPB02	Pink (Gram -ve)	Rod (bacillus)	Random/scattered	Circular with central zigzag	Entire/slightly Undulate	Creamy white	Opaque	Smooth and mucoid
24.	FEPB03	Pink (Gram -ve)	Rod (bacillus)	Random/scattered	Circular, Convex	Entire	Creamy white	Opaque	Smooth, mucoid to creamy
25.	FEPB04	Purple (Gram +ve)	Long rods (Bacilli)	Single and short chains	Irregular	Indistinct/entire	Creamy white	Opaque/ slightly translucent	Smooth and likely mucoid
26.	GEPB01	Purple (Gram +ve)	Very small rod-shaped (coccobacilli)	Densely packed, single/pairs	Concentric	Irregular	Pale white	Translucent	Smooth, shiny, and likely slimy or mucoid
27.	GEPB02	Pink (Gram -ve)	Short rods (coccobacilli)	Densely packed, uniform	Grid-like circular colonies	Slightly Lobate to Undulate	Pale cream	Opaque	Dry to slightly rough
28.	GEPB03	Pink (Gram -ve)	Rod-shaped (bacillus)	Scattered & short chains	Punctate	Entire	Creamy white	Opaque	Smooth, slightly raised, likely creamy
29.	GEPB04	Purple (Gram +ve)	Rod-shaped (bacillus)	Densely packed, single/pairs	Sparse, pinpoint	Faint growth	Translucent	Translucent	Very smooth and flat; may be moist or thin film-like
30.	GEPB05	Purple (Gram +ve)	Spherical (Cocci)	Densely packed, single/pairs	Irregular	Wavy/Irregular	Off-white to beige	Opaque	Smooth, moist
31.	GEPF01	Blue	Filamentous	Branched network of hyphae	Circular, cottony	Filamentous	Faint grayish or silvery hues	Opaque to slightly translucent	Cottony to velvety with a fluffy appearance

Shcherbakov et al. (2013) conducted a comprehensive study on endophytic bacteria associated with mosses collected from regions in Russia and Austria, successfully isolating a total of 283 culturable bacterial forms. Similarly, Pandey and Alam (2023) reported the isolation of 14 endophytic bacteria associated with bryophytes.

3.3. Morphological and Microscopic Characterization

Gram staining revealed 66.67% Gram-negative (n = 18) and 33.33% Gram-positive (n = 9) bacteria, a ratio comparable to the 60:40 distribution reported from Russian and Austrian mosses (Shcherbakov et al. 2013). Bacilli predominated (76%), occurring singly, in pairs, or in short chains; the remaining cells were cocci and coccobacilli. All four fungal isolates produced septate, branched hyphae with cottony to powdery colony textures, consistent with the genera *Aspergillus*, *Penicillium* and *Fusarium* (Olumuyiwa et al. 2025). Based on Gram staining, these isolates were classified as either Gram-positive or Gram-negative, with 66.67% being Gram-negative and 33.33% being Gram-positive (Aneja 2003). Similar to our findings, Sgroy et al. (2009) observed a predominance of Gram-positive bacteria over Gram-negative

Table 3: Plant growth-promoting activities exhibited by endophytes isolated from bryophytes.

Endophytic Strain	Isolates	Catalase	Amylase	Phosphate solubilization	Auxin Production	ACC deaminase	Biofilm formation
Bacteria	AEPB01	+++	++	+	+	-	+
	AEPB02	+	-	-	+	++	+
	AEPB03	+	-	+	+	++	+
	AEPB04	+	+	-	+	-	+
	BEPB01	+++	+	+	++	+	+
	BEPB02	++	+	+	+	++	+++
	BEPB03	+++	++	+	+	+++	-
	BEPB04	+	++	-	++	++	-
	CEPB01	+	++	++	++	-	-
	CEPB02	+	+	++	++	+++	+
	CEPB03	++	+	++	+++	++	-
	DEPB01	+++	-	++	+++	++	+++
	DEPB02	++	-	+++	+++	++	-
	DEPB03	++	-	+	+++	-	++
	EEPB01	+	-	++	++	-	+++
	EEPB02	+	-	+	++	+	+++
	EEPB03	+	-	-	++	-	+++
	EEPB04	+	++	+++	+	+	+++
	FEPB01	-	+++	-	++	++	+
	FEPB02	-	++	-	+++	++	+
	FEPB03	-	-	-	++	-	+
	FEPB04	-	++	+	++	+	+
	GEPB01	-	+	-	++	-	+
	GEPB02	-	+	-	++	-	++
	GEPB03	+	-	-	++	-	+
	GEPB04	+	++	++	++	-	-
	GEPB05	-	+	++	++	+	-
Fungus	AEPF01	++	+	+	+	+	+++
	AEPF02	+++	+	-	+	+++	+++
	DEPF01	-	+++	+	+++	+++	+++
	GEPF01	-	-	++	++	+++	+

'+++' Strong; '++' Moderate; '+' Weak; '-' No activity/production detected

forms in plants, and Panchal and Ingle (2011) reported 91.6% Gram-positive bacterial endophytes in higher plants. Sharma (2018) also isolated thirty-two bacterial endophytes based on morphological characteristics of bacterial colonies from various plant species. These studies collectively highlight the morphological diversity of bacterial endophytes in bryophytes and higher plants. Based on Bergey's Manual, the isolates were tentatively assigned to probable genera, including *Bacillus*, *Staphylococcus*, *Micrococcus*, *Pseudomonas*, *Enterobacter*, and *Acinetobacter*, while the fungal isolates were septate, branched, and likely represented *Aspergillus*, *Penicillium*, or *Fusarium*. Isolates were designated by operational codes (AEPB01–GEPF01) with morphological descriptors recorded in Table 2. No molecular identification (16S rRNA or ITS sequencing) was performed.

3.4. Qualitative Plant-Growth-Promoting (PGP) Traits

Table 3 consolidates the six plant-growth-promoting traits screened across the 31 bryophyte endophytes: catalase was expressed by 20 isolates (8 bacteria and 2 fungi strong, +++), amylase by 20 (4 bacteria and 2 fungi strong), phosphate solubilization by 20 (3 bacteria strong), auxin (IAA) by 31 (8 bacteria and 3 fungi strong), biofilm formation by 24 (6 bacteria and 3 fungi strong), while ACC-deaminase was detected in 20 isolates (3 bacteria and 3 fungi strong). No strain combined all six traits at moderate/strong levels, yet five isolates, DEPB01, DEPF01, BEPB03, CEPB02 and AEPF02 accumulated ≥ 5 positive marks. The near-universal IAA production (100%), ACC-deaminase activity 64.5% and high frequencies of catalase and biofilm formation (77.4%) mirror the need to counteract desiccation-rehydration cycles in montane habitats, whereas the restriction of strong ACC-deaminase activity to a few fungi (DEPF01, AEPF02, GEPF01) uncovers a novel, ethylene-modulating mechanism that could extend stress tolerance to neighboring vascular plants.

All the quantitative assays demonstrated a broad range of variation among the isolates in each trait (Table 4) and the plate images (Figs. 1–3) visually verified the difference. The highest mean was 8.65 with an SD of 0.07; DEPF01 and DEPB03 exhibited identical mean amylase activity (8.65 ± 0.07 mm), with no significant difference between them ($p > 0.05$). This is supported by Fig. 1: DEPF01 would form the widest starch-clearing halo on agar stained with iodine, whereas no such achromatic zone was seen in isolates with 0 AI (e.g., AEPB02, AEPB03). DEPB02 exhibited significantly higher PSI (26.10 ± 0.10 mm) than all other isolates ($p < 0.05$), with the next highest group (CEPB01 and CEPB02, ~4.0 mm) being statistically distinct. Fig. 2 demonstrates the clear zones on tricalcium-phosphate medium, and that of DEPB02 had a visible larger halo ($p < 0.05$) than others. IAA titres improved with time; on day 6 the means were between 32.15±0.13 µgmL-1 (AEPF02) to 71.96 0.16 µgmL-1 (DEPB02). ANOVA (isolate x time) provided very significant effects ($p < 0.05$) of both factors as well as their interaction, and on Day 6 the highest ranking in post hoc tests were DEPB02, CEPB03, and DEPB01 and the lowest ranking was the moss derived Rhytidiadelphus isolates. ACC deaminase activity was also the same, but with less detections: only 15 isolates were found to have measurable activity. The best fungi endophytes were among the highest-performing isolates; DEPF01 scored 34.49 ± 0.03 µmol mg^{-1} protein h^{-1} and GEPF01 29.72 ± 0.09, were substantially higher than the best performing bacterium, CEPB02, which scored 14.05 ± 0.07. Fig. 3 contributes to the data with thick rings and mats of crystal violet that were attached to the bottom of microtiter wells; dense layers of purple were formed by the strong biofilm formers (DEPB01, DEPF01, BEPB02, AEPF01), whereas the weak or no biofilm isolates remained colorless, as indicated by the + + + score in the table. Altogether, the liverwort -associated microbes contained the most triple-plus trait combinations, whereas the forest-floor moss isolates excelled at amylase and biofilm. The statistical segregation between habitat-specific functions illustrated in Figs. 1–3 supports the notion that bryophyte endophytes are ecotypically adapted to their micro-niche and provides us with an elite panel (DEPB02, DEPF01, CEPB03, BEPB03, EEPB04) for future studies involving low-temperature bioinoculation.

According to Olumuyiwa et al. (2025), among other genera, *Bacillus*, *Pseudomonas*, and *Enterobacter* have high potential for amylase production and phosphate solubilization, both of which are important features in improving plant growth and nutrient uptake. Liu et al. (2014) also pointed out that the breakdown of starches to simpler sugars is promoted with the help of amylase production which is a source of easily accessible energy to plants, and Olumuyiwa et al. (2025) also pointed out that phosphate solubilization enhances the availability of phosphorus, a nutrient that is crucial in the development of plants. An example of this is that Patten and Glick (2002) describe how different strains of *Pseudomonas* not only produce IAA-like compounds, but also show greater growth promoting effects when assayed in model plants, indicating that there may be synergistic advantages to agriculture. Similarly, Zhang et al. (2020) have shown that some of the strains such as *Pseudomonas putida* may have a considerable effect on the development of the root system due to their production of IAA. The *Pseudomonas*-mediated compounds involved in stimulating root development are not only the synthesis of IAA, but also the production of ACC deaminase that reduces the inhibitory activity of ethylene on roots. As an example, Gashe et al. (2018) noted that some of the suspected strains

Table 4: Quantitative assessment of plant growth-promoting attributes in bryophyte-associated endophytes over time.

Endophytic Strain	Isolates	AAI (mm)	PSI (mm)	IAA production (µg mL^{-1})			ACC-deaminase activity (µmol mg^{-1} protein h^{-1})		
				Day 2	Day 4	Day 6	Day 2	Day 4	Day 6
Bacteria	AEPB01	4.99 ± 0.12^{k}	2.73 ± 0.04^{cd}	25.76 ± 0.15^{P}	29.93 ± 0.14^{k}	47.01 ± 0.14^{g}	0 ± 0^{a}	0 ± 0^{a}	0 ± 0^{a}
	AEPB02	0 ± 0^{a}	0 ± 0^{a}	24.25 ± 0.09^{no}	29.08 ± 0.14^{j}	34.27 ± 0.17^{b}	3.45 ± 0.01^{i}	4.96 ± 0.04^{i}	7.61 ± 0.19^{i}
	AEPB03	0 ± 0^{a}	2.92 ± 0.05^{de}	24.73 ± 0.14^{o}	24.48 ± 0.15^{e}	41.51 ± 0.15^{e}	2.14 ± 0.03^{fg}	3.49 ± 0.29^{fg}	5.92 ± 0.12^{g}
	AEPB04	2.69 ± 0.02^{e}	0 ± 0^{a}	22.73 ± 0.08^{lm}	32.00 ± 0.16^{l}	39.67 ± 0.15^{d}	0 ± 0^{a}	0 ± 0^{a}	0 ± 0^{a}
	BEPB01	2.29 ± 0.03^{c}	2.58 ± 0.03^{bc}	17.71 ± 0.08^{g}	30.20 ± 0.14^{k}	54.07 ± 0.17^{l}	3.24 ± 0.03^{h}	3.68 ± 0.05^{gh}	4.30 ± 0.17^{f}
	BEPB02	2.48 ± 0.01^{d}	2.62 ± 0.01^{bc}	21.56 ± 0.13^{k}	29.00 ± 0.15^{ij}	35.83 ± 0.13^{c}	2.03 ± 0.05^{ef}	3.61 ± 0.04^{fg}	6.49 ± 0.07^{h}
	BEPB03	3.49 ± 0.02^{f}	2.57 ± 0.03^{bc}	21.44 ± 0.13^{k}	26.20 ± 0.16^{g}	35.97 ± 0.14^{c}	5.99 ± 0.04^{n}	10.13 ± 0.05^{m}	11.81 ± 0.07^{m}
	BEPB04	3.98 ± 0.02^{g}	0 ± 0^{a}	23.97 ± 0.13^{n}	33.40 ± 0.15^{m}	62.36 ± 0.16^{q}	4.77 ± 0.05^{l}	7.77 ± 0.04^{k}	8.70 ± 0.07^{j}
	CEPB01	4.95 ± 0.05^{k}	4.11 ± 0.14^{g}	17.87 ± 0.09^{gh}	38.87 ± 0.17^{o}	58.48 ± 0.17^{p}	0 ± 0^{a}	0 ± 0^{a}	0 ± 0^{a}
	CEPB02	2.14 ± 0.00^{b}	3.96 ± 0.04^{g}	46.41 ± 0.15^{r}	48.76 ± 0.13^{p}	63.48 ± 0.16^{r}	9.52 ± 0.08^{o}	12.18 ± 0.06^{n}	14.04 ± 0.07^{n}
	CEPB03	2.38 ± 0.02^{cd}	4.07 ± 0.04^{g}	15.12 ± 0.13^{e}	56.52 ± 0.19^{r}	71.89 ± 0.37^{v}	2.00 ± 0.17^{ef}	3.26 ± 0.06^{f}	6.03 ± 0.08^{g}
	DEPB01	0 ± 0^{a}	4.70 ± 0.08^{h}	17.92 ± 0.13^{gh}	53.39 ± 0.21^{q}	68.85 ± 0.16^{t}	5.95 ± 0.04^{n}	8.46 ± 0.08^{l}	9.26 ± 0.06^{l}
	DEPB02	0 ± 0^{a}	26.10 ± 0.10^{j}	10.80 ± 0.13^{a}	62.91 ± 0.17^{s}	71.96 ± 0.16^{t}	4.40 ± 0.04^{k}	6.95 ± 0.47^{j}	9.06 ± 0.04^{kl}
	DEPB03	0 ± 0^{a}	2.56 ± 0.03^{bc}	15.04 ± 0.13^{e}	62.31 ± 0.17^{s}	70.27 ± 0.17^{u}	0 ± 0^{a}	0 ± 0^{a}	0 ± 0^{a}
	EEPB01	0 ± 0^{a}	3.62 ± 0.07^{f}	20.72 ± 0.09^{j}	26.57 ± 0.14^{g}	55.45 ± 0.14^{m}	0 ± 0^{a}	0 ± 0^{a}	0 ± 0^{a}
	EEPB02	0 ± 0^{a}	3.10 ± 0.05^{e}	22.51 ± 0.13^{l}	28.60 ± 0.14^{hij}	45.00 ± 0.14^{f}	2.07 ± 0.04^{ef}	2.28 ± 0.08^{d}	2.84 ± 0.05^{cd}
	EEPB03	0 ± 0^{a}	0 ± 0^{a}	20.21 ± 0.07^{j}	26.41 ± 0.14^{g}	51.12 ± 0.15^{i}	0 ± 0^{a}	0 ± 0^{a}	0 ± 0^{a}
	EEPB04	4.73 ± 0.03^{i}	6.32 ± 0.17^{i}	18.73 ± 0.11^{i}	25.40 ± 0.13^{f}	52.55 ± 0.15^{jk}	1.97 ± 0.03^{e}	2.17 ± 0.04^{d}	3.06 ± 0.05^{d}
	FEPB01	6.35 ± 0.04^{l}	0 ± 0^{a}	24.03 ± 0.10^{n}	30.11 ± 0.13^{k}	69.93 ± 0.16^{u}	3.21 ± 0.01^{h}	4.02 ± 0.02^{h}	9.27 ± 0.07^{l}
	FEPB02	4.19 ± 0.02^{h}	0 ± 0^{a}	29.67 ± 0.14^{q}	36.27 ± 0.17^{n}	66.93 ± 0.16^{s}	3.99 ± 0.02^{j}	4.81 ± 0.09^{i}	8.89 ± 0.04^{jk}
	FEPB03	0 ± 0^{a}	0 ± 0^{a}	25.60 ± 0.12^{p}	32.33 ± 0.14^{l}	53.16 ± 0.16^{k}	0 ± 0^{a}	0 ± 0^{a}	0 ± 0^{a}
	FEPB04	4.00 ± 0.02^{g}	2.41 ± 0.02^{b}	23.28 ± 0.15^{m}	29.73 ± 0.14^{k}	52.07 ± 0.17^{j}	1.16 ± 0.01^{c}	1.45 ± 0.05^{c}	2.61 ± 0.01^{c}
	GEPB01	2.41 ± 0.01^{cd}	0 ± 0^{a}	15.51 ± 0.13^{e}	19.85 ± 0.15^{b}	56.21 ± 0.16^{n}	0 ± 0^{a}	0 ± 0^{a}	0 ± 0^{a}
	GEPB02	2.40 ± 0.01^{cd}	0 ± 0^{a}	18.40 ± 0.15^{h}	23.67 ± 0.15^{d}	57.40 ± 0.19^{o}	0 ± 0^{a}	0 ± 0^{a}	0 ± 0^{a}
	GEPB03	0 ± 0^{a}	0 ± 0^{a}	13.87 ± 0.13^{c}	18.48 ± 0.15^{a}	50.25 ± 0.14^{h}	0 ± 0^{a}	0 ± 0^{a}	0 ± 0^{a}
	GEPB04	4.51 ± 0.01^{i}	4.89 ± 0.06^{h}	14.49 ± 0.14^{d}	19.12 ± 0.15^{a}	55.41 ± 0.14^{m}	0 ± 0^{a}	0 ± 0^{a}	0 ± 0^{a}
	GEPB05	2.66 ± 0.00^{e}	4.10 ± 0.05^{g}	16.80 ± 0.13^{f}	22.27 ± 0.13^{c}	49.79 ± 0.13^{h}	0.62 ± 0.02^{b}	0.82 ± 0.02^{b}	1.82 ± 0.04^{b}
Fungus	AEPF01	2.15 ± 0.03^{b}	3.14 ± 0.07^{e}	23.05 ± 0.14^{lm}	28.33 ± 0.15^{hi}	34.00 ± 0.15^{b}	2.24 ± 0.09^{g}	2.87 ± 0.07^{e}	3.46 ± 0.08^{e}
	AEPF02	2.50 ± 0.02^{d}	0 ± 0^{a}	23.87 ± 0.14^{n}	28.00 ± 0.16^{h}	32.15 ± 0.13^{a}	2.28 ± 0.08^{g}	12.10 ± 0.08^{n}	27.10 ± 0.05^{o}
	DEPF01	8.65 ± 0.07^{l}	2.69 ± 0.03^{cd}	12.97 ± 0.13^{b}	67.11 ± 0.17^{t}	66.56 ± 0.15^{s}	5.20 ± 0.02^{m}	14.65 ± 0.04^{n}	34.49 ± 0.03^{q}
	GEPF01	0 ± 0^{a}	3.64 ± 0.02^{f}	17.75 ± 0.15^{g}	23.73 ± 0.14^{d}	58.17 ± 0.16^{p}	1.68 ± 0.02^{d}	6.93 ± 0.07^{j}	0.09^{p}

*Values are mean ± standard deviation of three independent biological replicates.

*Values sharing the same lowercase letter within a column are not significantly different at $p > 0.05$.

*Values with different letters differ significantly at $p < 0.05$.

belonging to the genus *Staphylococcus* had positive catalase activity but negative indole test results. On the same note, Akoma et al. (2019) also indicated that Gram-positive cocci were overrepresented in their microbial testing, noting that the isolates were both catalase positive and indole negative, which supports the common biochemical characterization of *Staphylococcus aureus* and *Micrococcus luteus*. The PGP traits observed (amylase, phosphate solubilization, IAA, ACC-deaminase) are consistent with functions reported in diverse plant-associated bacteria and fungi (Liu et al. 2014, Olumuyiwa et al. 2025). However, without molecular identification, phenotypic similarities to previously characterized genera cannot confirm taxonomic or functional equivalence.

Olumuyiwa et al. (2025) reported that fungal endophytes such as *Aspergillus*, *Penicillium* as well as *Fusarium* have septate and branched hyphae, and they are in filamentous colonies that have cottony, velvety or powdery morphologies. They have phosphate solubilizing and other enzyme activities,

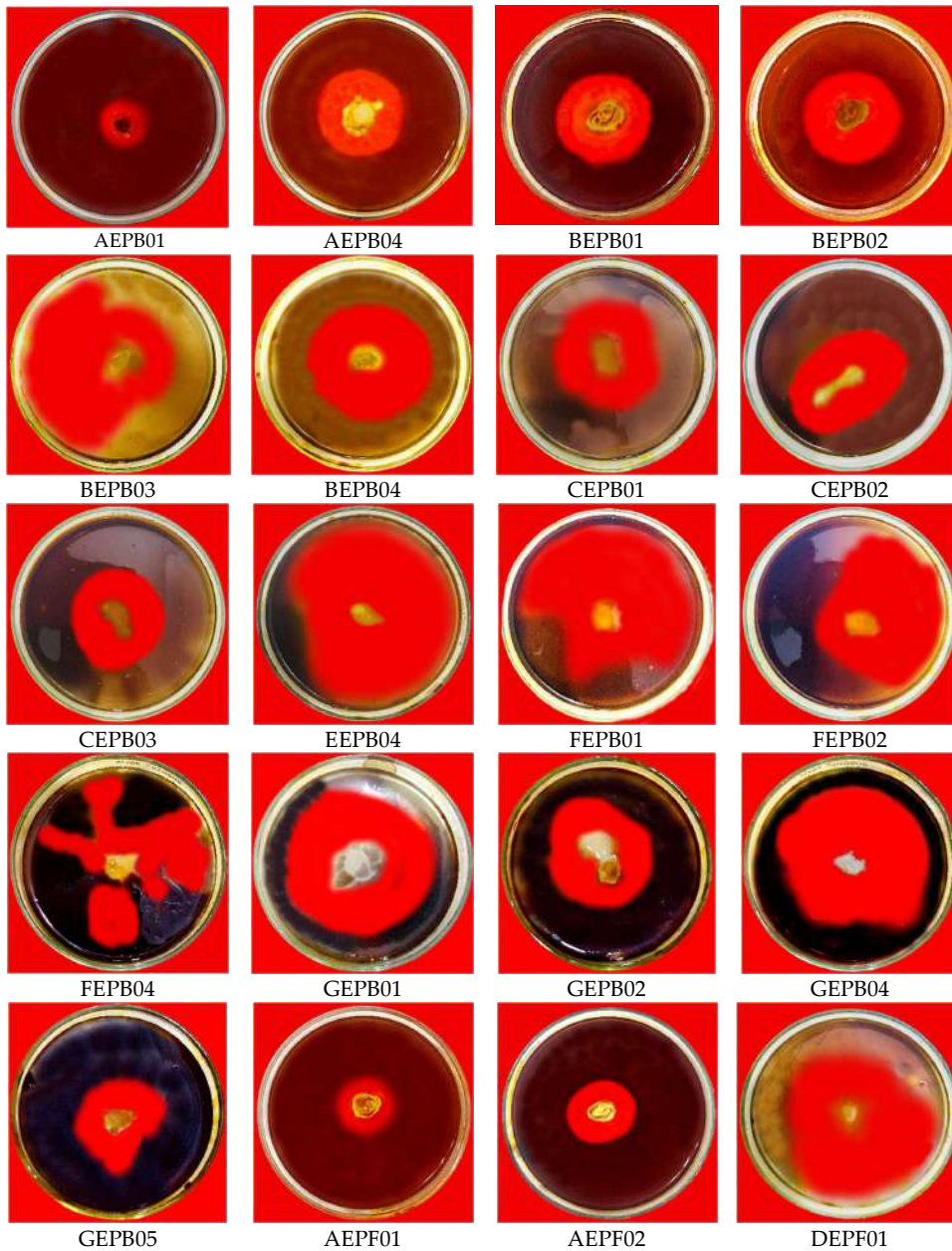


Fig. 1: Zones of amylase activity exhibited by bacterial and fungal isolates from different bryophyte species.

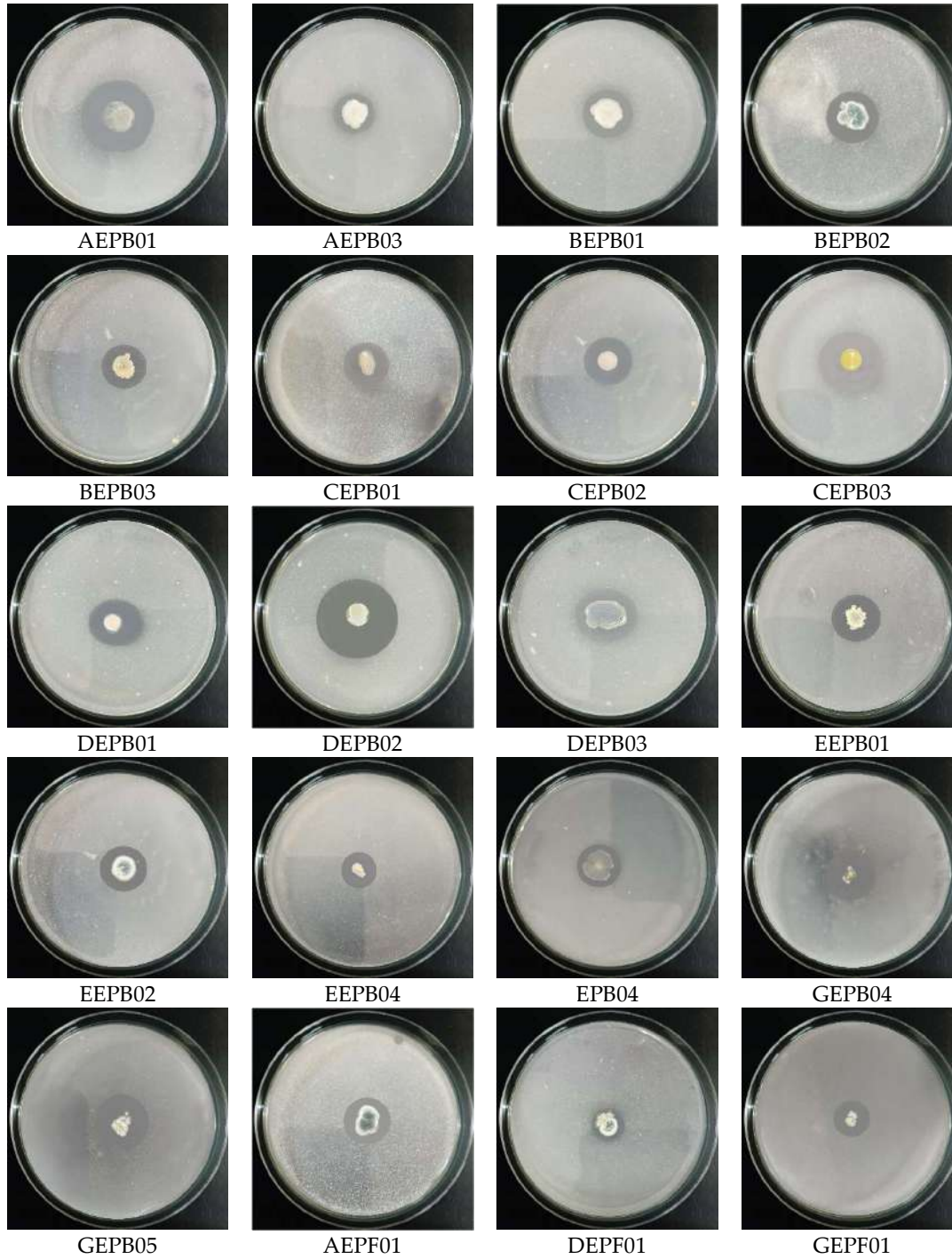


Fig. 2: Phosphate-solubilization ability of microbial isolates based on clear-halo formation.

which favor the decomposition and nutrient cycling of the soil ecosystem. Mustapha et al. (2025) emphasized that the communication between bacterial endophytes and fungal endophytes is mostly synergistic, is beneficial in terms of increased nutrient availability, pathogen suppression, and general plant health. The combination of their activities such as production of phytohormones, secretion of enzymes, and antagonistic interaction with pathogens support their significance in sustainable agriculture to enhance the fertility and productivity of soil and crop.

3.5. Biofilm Production and Visualization Through SEM

The 96-well microtiter assay (Fig. 3) demonstrated that 87% of the bryophyte endophytes rapidly form robust biofilms at 20°C; SEM micrographs (Fig. 4) now reveal the ultrastructural basis of this phenotype. Bacterial isolates such as BEPB02, DEPB02 and EEPB01-EEPB04 appear as densely packed, rod-shaped cells enveloped in a smooth extracellular polymeric substance (EPS) layer (Fig. 4). Nine isolates were selected for SEM analysis based on strong qualitative biofilm production (+++ rating in the microtiter assay): BEPB02, DEPB02, EEPB01, EEPB02, EEPB03, EEPB04, AEPF01, AEPF02, and DEPF01. SEM samples were prepared from monoculture biofilms grown on glass coverslips in appropriate liquid media (NA for bacteria, PDA for fungi) at 20°C for 48 h, followed by fixation (2.5% glutaraldehyde), dehydration through an ethanol series (30–100%), critical-point drying, and gold sputter coating prior to imaging. All SEM micrographs represent single-isolate monocultures only; no co-cultures or mixed-species biofilms were examined.

Bacterial isolates BEPB02, DEPB02 and EEPB01–EEPB04 appear as densely packed, rod-shaped cells enveloped in a smooth extracellular polymeric substance (EPS) layer (Fig. 4). The uniform thickness of the matrix and the absence of large water channels are typical of young, cohesive biofilms that confer strong adhesion to hydrophobic surfaces, an obvious advantage for surviving the repeated desiccation-rehydration cycles experienced by thalli on humid rocks (Ingato *et al*. 2014). EPS secretion also coincides with the high catalase activity recorded for these same strains (Table 3), suggesting that the matrix simultaneously scavenges ROS generated during rehydration, thereby protecting both the microbe and the host tissue.

Contrastingly, the endophytes (AEPF01, AEPF02, DEPF01) weave three-dimensional filamentous networks, which entangle the bacterial microcolonies (see Fig. 4). The spatial proximity of bacterial and fungal isolates within the bryophyte host (Table 1) suggests potential for natural co-colonization, as observed in soil biofilms (Sun *et al*. 2022). The hypha ridges work as mini-pillars to enhance tensile strength and form micro-aerobic spaces that favor bacterial development a physical synergy that has already been observed in biofilms of soil (Sun *et al*. 2022). The irregular, knotted surface of the fungal biofilm also enlarges the contact area with the bryophyte surface, facilitating enzymatic delivery (amylase, cellulase) that can soften the host wall and enhance nutrient leakage-an elegant explanation for the superior AAI and PSI scores observed in mixed-species consortia (DEPF01 + DEPB02).

Fungal isolates AEPF01, AEPF02, and DEPF01 exhibited three-dimensional filamentous networks with septate, branched hyphae (Fig. 4). The irregular, knotted surface morphology of these fungal biofilms may enlarge contact area with substrata, potentially facilitating surface adhesion and enzymatic delivery; however, this was observed in monoculture only.

Recent work reinforces the ecological significance of biofilm formation in plant-microbe interactions. Tariq et al. (2025) demonstrated that EPS-rich bacterial films

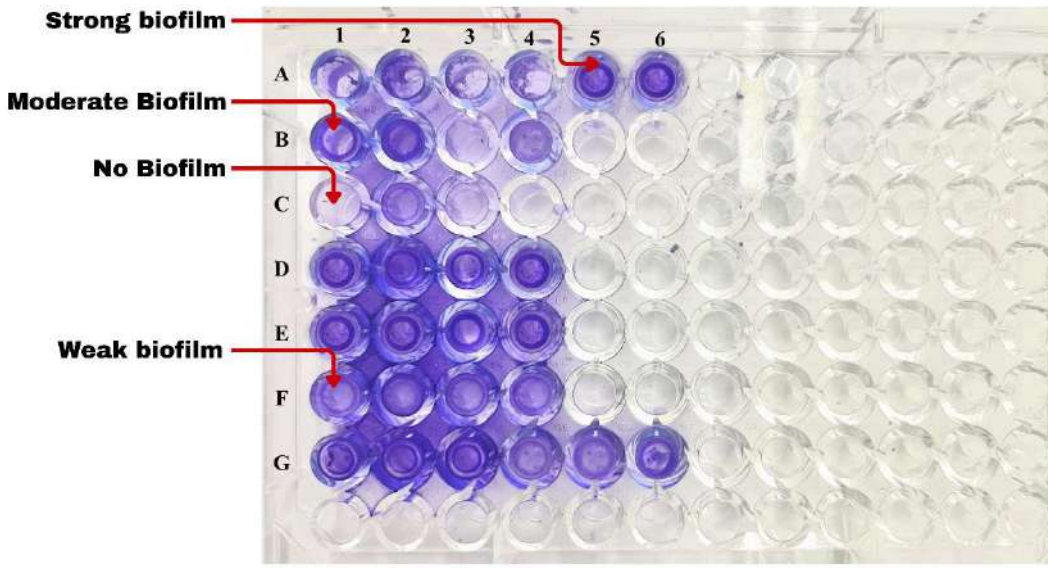


Fig. 3: Microtiter plate showing ring formation and bottom-adhered biofilm formation by endophytic isolates.

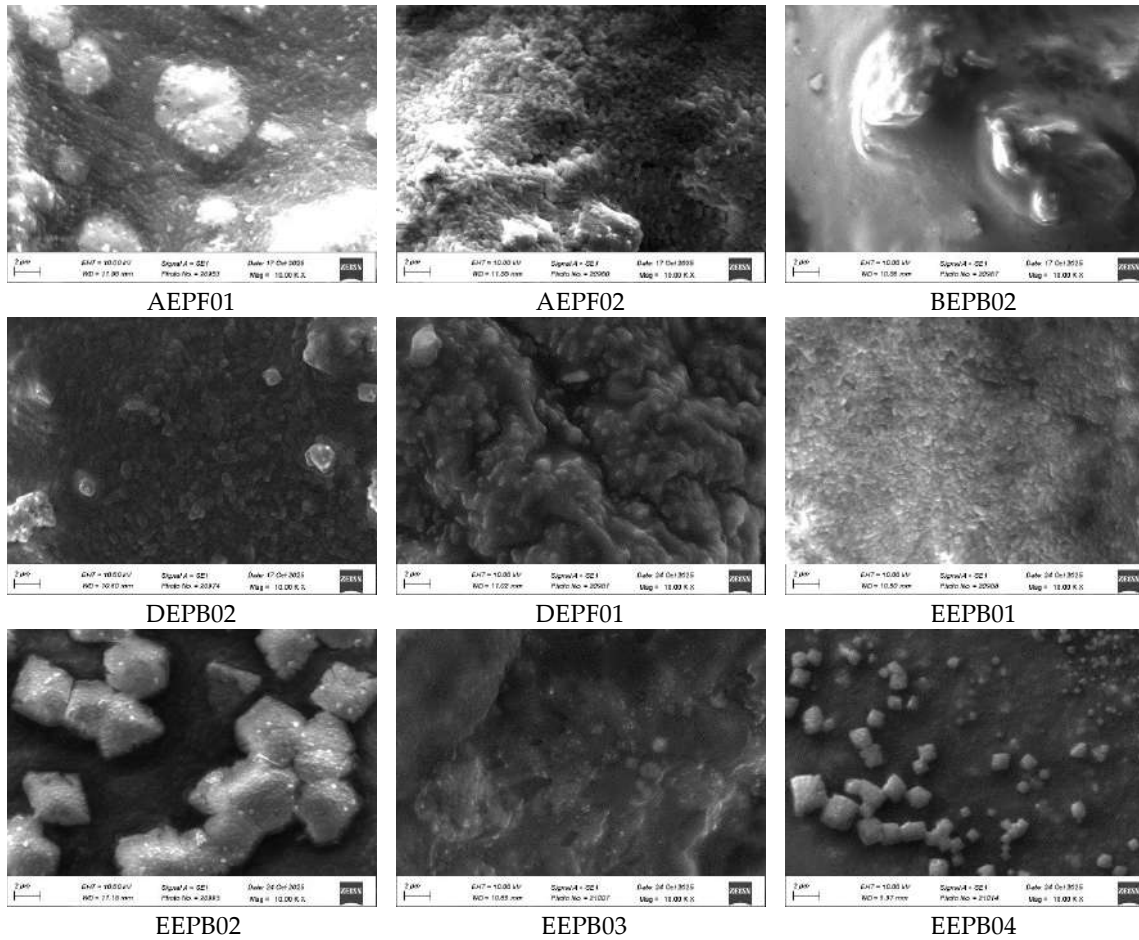


Fig. 4: Biofilms of isolated endophytes observed by scanning electron microscopy.

on wheat roots raise colonization efficiency by 38% and simultaneously enhance N-P uptake, while Yang et al. (2024) proposed a four-step root-entry model (chemotaxis → surface attachment → immune evasion → mature biofilm) in which a robust three-dimensional architecture is the gatekeeper for endophytic establishment. The biofilm architecture observed in our SEM micrographs (Fig. 4) is consistent with the attachment-maturation phase described by Yang et al. (2024), bacilli such as DEPB02 and EEPB01 first form a thin, densely packed basal layer (Fig. 4, panels DEPB02 & EEPB01), after which fungal hyphae of AEPF02 or DEPF01 over-grow the bacterial carpet, creating the "hyphal highway" described for Burkholderia-*Aspergillus* consortia colonising grapevine xylem (Vimal et al. 2024).

Bacterial monospecies mats (BEPB02, DEPB02, EEPB01–EEPB04) appear as flat, cohesive sheets with no visible water channels, an architecture that perfectly fits the 2025 model of Damyanova and Paunova-Krasteva (2025): pili-driven initial adhesion followed by EPS-mediated vertical compaction that limits pore size and increases desiccation tolerance on hydrophobic substrata such as liverwort cuticles. The near-absence of large voids in our micrographs (Fig. 4, DEPB02 and EEPB01) suggests that the smooth, channel-poor phenotype is an adaptation to the repeated wet-dry cycles experienced on rock inhabiting Dumortiera thalli.

In contrast, fungal-bacterial consortia (AEPF01, AEPF02, DEPF01) build three-dimensional hyphal scaffolds that interpenetrate bacterial microcolonies. Bridier et al. (2010) first used high-throughput CLSM to show that fungal hyphae behave as "biological struts" that increase biofilm elasticity and generate oxygen gradients favorable for facultative bacilli. Our SEM captures the identical architecture: hyphal ridges (1.2–1.8 µm) bridge *Bacillus* clusters and create micro-aerobic pockets (dark voids in Fig. 4, AEPF02 and DEPF01), explaining why ACC-deaminase activity peaks specifically under these mixed consortia (Table 4). The dual-architecture therefore

constitutes a functional synergism rather than a simple co-aggregation.

Importantly, this bacillus-hypha partnership mirrors the very recent "biofilm carrier" concept advanced by Wang et al. (2023): *Aspergillus* hyphae coated with *Bacillus velezensis* increased maize root colonization by 42% under drought and delivered a 0.6 t ha^{-1} yield benefit. The complementary trait profiles of DEPB02 (high PSI, IAA, catalase) and DEPF01 (max ACC-deaminase, AAI) suggest potential for synergistic consortium effects, which should be tested in future comparative inoculation studies. across all four PGP traits. We therefore propose that the SEM-validated Dumortiera consortium be advanced as a biphasic, low temperature inoculant for Himalayan hill crops (hill turmeric, amaranth) where episodic desiccation and 12-18°C soils replicate the bryophyte micro-niche. Greenhouse and field trials will quantify root adhesion, EPS thickness and yield responses under water-deficit to test whether the architectural superiority observed on glass translates into measurable agronomic benefit.

4. CONCLUSIONS

This study characterized 31 culturable endophytes (27 bacteria, 4 fungi) from seven bryophyte species inhabiting forest floors, streambanks, and humid rock outcrops in the Kumaon region of Uttarakhand, India. All isolates were designated as operational taxonomic units based solely on morphological, Gram staining, and colony characteristic features; no molecular identification was performed, and consequently no genus-level taxonomic assignments are claimed. The endophyte panel exhibited broad phenotypic diversity in plant-growth-promoting traits. Near-universal IAA production (100%), high frequencies of catalase and biofilm formation (77.4%), and detectable ACC-deaminase activity (64.5%) were recorded across isolates, consistent with adaptation to the desiccation-rehydration cycles characteristic of montane bryophyte microhabitats. Quantitative assays revealed significant inter-isolate variation, with five isolates, DEPB01, DEPF01, BEPB03, CEPB02, and AEPF02, accumulating ≥ 5 positive qualitative trait marks. Notably, DEPB02 demonstrated exceptional phosphate solubilization activity (26.10 ± 0.10 mm PSI), while DEPF01 and GEPF01 exhibited the highest ACC-deaminase activities among fungal isolates (34.49 ± 0.03 and 29.72 ± 0.09 µmol mg^{-1} protein h^{-1}, respectively). SEM visualization of monoculture biofilms from nine strong biofilm formers (selected based on +++ qualitative ratings) revealed two distinct architectural phenotypes: (i) flat, cohesive bacterial sheets with smooth EPS layers and minimal water channels (BEPB02, DEPB02, EEPB01–EEPB04), and (ii) three-dimensional filamentous fungal networks with irregular, knotted surfaces (AEPF01, AEPF02, DEPF01). These morphologies are consistent with desiccation-tolerant biofilm architectures reported in the literature, though their functional significance under native bryophyte thallus conditions remains to be validated.

The five isolates exhibiting the broadest PGP trait profiles (DEPB01, DEPF01, BEPB03, CEPB02, AEPF02) represent promising candidates for future molecular identification and experimental validation. Their complementary phenotypes, particularly the combination of phosphate solubilization, IAA production, and biofilm formation, warrant investigation in controlled planta assays to determine whether monoculture or mixed inoculation enhances bryophyte or vascular plant growth under desiccation stress. Further studies would require 16S rRNA/ITS sequencing for taxonomic placement, followed by greenhouse trials with appropriate experimental controls.

Author Contributions: S.G. and S.S. conceptualized the study; S.G. and P.S. selected the methodology; S.G. chose software; S.G. and S.S. validated the study. K.S.R.; formal analysis, S.G.; investigation, S.G.; resources, S.S.; data curation, S.G.; writing, original draft preparation, S.G.; writing, review and editing, S.S. and K.S.R.; visualization, S.G.; supervision, S.S.; project administration, S.S.; funding acquisition, S.S. All authors have read and agreed to the published version of the manuscript.

5. ACKNOWLEDGMENTS

The authors express their sincere gratitude to CytoGene®, Lucknow, for providing access to their well-equipped testing laboratory with advanced analytical facilities such as GC–MS, ensuring precise and reliable results.

6. REFERENCES

Abo-Koura, H., 2023. Endophytic bacteria: diversity, characterization and role in agriculture. *Journal of Basic and Applied Sciences*, 19, pp.116-130.

Akoma, O., Ononugbo, C., Eze, C., Chukwudozie, K. and Ogwu, J., 2019. Microbial assessment of selected locally fermented and ready-to-eat cassava products sold in Lokoja, Nigeria. *Asian Food Science Journal*, 8, pp.1-9. [DOI]

Aneja, K.R., 2003. *Experiments in Plant Pathology, Microbiology and Biotechnology*. New Age International Publishers, New Delhi, pp.274-275.

Bergey, D.H., 1994. *Bergey's Manual of Determinative Bacteriology*. Lippincott Williams & Wilkins, 787 pp.

Bragina, A., Cardinale, M., Berg, C. and Berg, G., 2013. Vertical transmission explains the specific Burkholderia pattern in *Sphagnum* mosses at multi-geographic scale. *Frontiers in Microbiology*, 4, p.394. [DOI]

Bridier, A., Dubois-Brissonnet, F., Boubetra, A., Thomas, V. and Briandet, R., 2010. The biofilm architecture of sixty opportunistic pathogens deciphered using a high-throughput CLSM method. *Journal of Microbiological Methods*, 82, pp.64-70. [DOI]

Damyanova, T. and Paunova-Krasteva, T., 2025. What we still don't know about biofilms—current overview and key research information. *Microbiology Research*, 16, p.46. [DOI]

Fukami, J., Cerezini, P. and Hungría, M., 2018. Azospirillum: benefits that go far beyond biological nitrogen fixation. *AMB Express*, 8, p.1. [DOI]

Gashe, F., Mulisa, E., Mekonnen, M. and Zeleke, G., 2018. Antimicrobial resistance profile of different clinical isolates against third-generation cephalosporins. *Journal of Pharmaceutics*, 2018, pp.1-7. [DOI]

Gupta, R.M., Prathmesh, S., Kale, M., Rathi, L. and Jadhav, N.N., 2015. Isolation, characterization and identification of endophytic bacteria by 16S rRNA partial sequencing technique from roots and leaves of *Prosopis cineraria*. *Asian Journal of Plant Science and Research*, 6, pp.36-43.

Herlina, L., Pukan, K.K. and Mustikaningtyas, D., 2017. The endophytic bacteria producing IAA (indole acetic acid) in *Arachis hypogaea*. *Cell Biology and Development*, 1, pp.31-35. [DOI]

Ingato, S., Kimang'a, A., Omuse, G., Kariuki, S., Gunturu, R. and Dinda, V., 2014. Characteristics of archived coagulase-negative Staphylococci isolates at a university hospital, Nairobi, Kenya. *Open Journal of Medical Microbiology*, 4, pp.236-241. [DOI]

Insuk, C., Kuncharoen, N., Cheeptham, N., Tanasupawat, S. and Pathom-Aree, W., 2020. Bryophytes harbor cultivable actinobacteria with plant growth promoting potential. *Frontiers in Microbiology*, 11, p.563047. [DOI]

Iungin, O., Prekrasna-Kviatkovska, Y., Kalinichenko, O., Moshynets, O., Potters, G., Sidorenko, M. and Mickevičius, S., 2024. Endophytic bacterial biofilm-formers associated with Antarctic vascular plants. *Microorganisms*, 12, p.1938. [DOI]

Liu, X.L., Liu, S.L., Liu, M., Kong, B.H., Liu, L. and Li, Y.H., 2014. A primary assessment of the endophytic bacterial community in a xerophilous moss (*Grimmia montana*) using molecular method and cultivated isolates. *Brazilian Journal of Microbiology*, 45, pp.163-173. [DOI]

Lucero, C.T., Lorda, G.S., Ludueña, L.M., Anzuay, M.S. and Taurian, T., 2020. Motility and biofilm production involved in the interaction of phosphate-solubilizing endophytic strains with peanut, maize and soybean plants. *Rhizosphere*, 15, p.100228.

MacFaddin, J.F., 2000. *Biochemical Tests for Identification of Medical Bacteria*. 2nd ed. Williams & Wilkins, London, pp.195-201.

Mustapha, Z., Nasir, N., Lah, M., Ngah, N., Mohd, K., Othman, R. and Juahir, H., 2025. Application of plant growth-promoting rhizobacteria to improve soil chemical and biological properties and its effect on growth, physiology and yield of okra (*Abelmoschus esculentus* L.). *Tropical Life Sciences Research*, 36, pp.83-98.

Olumuyiwa, E.O., Ajetunmobi, M.T., Adeniji, O.F. and Ogunyemi, A.K., 2025. Morphological and molecular identification of fungi isolated from spoilt apples in Ota metropolis. *BMC Microbiology*, 25, p.360. [DOI]

Opelt, K., Berg, C. and Berg, G., 2007. The bryophyte genus *Sphagnum* is a reservoir for powerful and extraordinary antagonists and potentially facultative human pathogens. *FEMS Microbiology Ecology*, 61, pp.38-53. [DOI]

Panchal, H. and Ingle, S., 2011. Isolation and characterization of endophytes from the root of medicinal plant *Chlorophytum borivilianum* (Safed musli). *Journal of Advanced Developmental Research*, 2, pp.205-209.

Pandey, S. and Alam, A., 2023. Isolation of endophytic bacteria from bryophytes and study of their morphological, biochemical and biofilm formation properties. *Journal of Environmental Biology*, 44, pp.351-358.

Patten, C.L. and Glick, B.R., 2002. Role of *Pseudomonas putida* indoleacetic acid in development of the host plant root system. *Applied and Environmental Microbiology*, 68, pp.3795-3801. [DOI]

Penrose, D.M. and Glick, B.R., 2003. Methods for isolating and characterizing ACC deaminase-containing plant growth-promoting rhizobacteria. *Physiologia Plantarum*, 118, pp.10-15. [DOI]

Prekrasna, I., Dzhulai, A. and Parnikoza, I., 2021. Preliminary estimates of the number and diversity of the culturable endophytic bacteria from *Deschampsia antarctica* and *Colobanthus quitensis*. *Visnyk of Ukrainian Geneticists and Selectors*, 19, pp.21-30.

Ren, J., Liu, F., Luo, Y., Jian, Z., Luo, X. and Liu, R., 2021. The pioneering role of bryophytes in ecological restoration of manganese waste residue areas, southwestern China. *Journal of Chemistry*, 2021, pp.1-19. [DOI]

Rosario, M.C., Poddar, P., Reddy, S. and Osborne, W.J., 2020. Biotechnological applications of *Turbinaria ornata* and its endophytes. *Research Journal of Pharmacy and Technology*, 13, pp.4231-4238.

Sahay, H., Yadav, A.N., Singh, A.K., Singh, S., Kaushik, R. and Saxena, A.K., 2017. Hot springs of Indian Himalayas: potential sources of microbial diversity and thermostable hydrolytic enzymes. *3 Biotech*, 7, pp.1-11. [DOI]

Semwal, P., Misra, S., Misra, A., Kar, S., Majhi, B., Mishra, S.K., Srivastava, S. and Chauhan, P.S., 2023. Endophytic *Bacillus* strains enhance biomass and bioactive metabolites of *Gloriosa superba*. *Industrial Crops and Products*, 204, p.117296. [DOI]

Sgroy, V., Cassan, F., Masciarelli, O., Papa, M.F., Lagares, A. and Luna, V., 2009. Isolation and characterization of endophytic plant growth-promoting (PGPB) or stress homeostasis-regulating (PSHB) bacteria associated with the halophyte *Prosopis strombulifera*. *Applied Microbiology and Biotechnology*, 2, pp.371-381.

Sharma, D.K., 2018. Morphological and biochemical characterization of *Ralstonia solanacearum* (Smith) in brinjal (*Solanum melongena* L.) in Rajasthan (India). *Asian Journal of Plant Research*, 8, pp.284-288. [DOI]

Shcherbakov, A.V., Bragina, A.V., Kuzmina, E.Y., Berg, C., Muntyan, A.N., Makarova, N.M., Malfanova, N.V., Cardinale, M., Berg, G., Chebotar, V.K. and Tikhonovich, I.A., 2013. Endophytic bacteria of *Sphagnum* mosses as promising objects of agricultural microbiology. *Microbiology*, 3, pp.306-315.

Sun, K., Tang, M., Lü, F., Peng, D., Xu, F., Zhang, W. and Dai, C., 2022. Alteration of plant immunity in the interaction of roots with the endophytic fungus *Phomopsis liquidambaris* in response to external nitrogen conditions. *Environmental Microbiology Reports*, 14, pp.742-754. [DOI]

Tariq, A., Tanvir, A., Barasarathi, J., Alsohim, A.S., Mastinu, A., Sayyed, R. and Nazir, A., 2025. Endophytes: key role players for sustainable agriculture—mechanisms, omics insights and future prospects. *Plant Growth Regulation*, (in press). [DOI]

Vimal, S.R., Singh, J.S., Kumar, A. and Prasad, S.M., 2024. The plant endomicrobiome: structure and strategies to produce stress-resilient future crop. *Current Research in Microbial Sciences*, 6, p.100236. [DOI]

Virtanen, R., Bakker, J., Jessen, M., Sullivan, L., Harpole, W. and Eskelinen, A., 2022. Is the bryophyte soil diaspore bank buffered against nutrient enrichment and grazing exclusion? *Plant and Soil*, 477, pp.487-499. [DOI]

Vos, P., Garrity, G., Jones, D., Krieg, N.R., Ludwig, W., Rainey, F.A., Schleifer, K.H. and Whitman, W.B. (Eds.), 2011. *Bergey's Manual of Systematic Bacteriology*, Vol 3: The Firmicutes. Springer, New York, 1450 pp.

Wang, X., Liu, M., Yu, C., Li, J. and Zhou, X., 2023. Biofilm formation: mechanistic insights and therapeutic targets. *Molecular Biomedicine*, 4, p.49. [DOI]

Yang, L., Qian, X., Zhao, Z., Wang, Y., Ding, G. and Xing, X., 2024. Mechanisms of rhizosphere plant–microbe interactions: molecular insights into microbial colonization. *Frontiers in Plant Science*, 15, p.1491495. [DOI]

Zhang, B., Wang, Y. and Hu, X., 2020. Highly efficient biosynthesis of indole-3-acetic acid by *Enterobacter xiangfangensis* BHW6. (preprint).

Nature Environment and Pollution Technology
An International Quarterly Peer-Reviewed Open Access Journal

p-ISSN: 0972-6268 | e-ISSN: 2395-3454 Vol. 25 | No. 4 | Article ID D1915 | 2026

RESEARCH ARTICLE https://doi.org/10.46488/NEPT.2026.v25i04.D1915 OPEN ACCESS

Analysis of Geomechanical Properties of Mine Waste Using Cementitious and Pozzolanic Agents: A Systematic Review

Jesús Daniel Pérez Oropeza, Miguel Alberto Barreda de la Cruz and Gerby Giovanna Rondán-Sanabria†
Universidad Tecnológica del Perú, Departamento de Ingeniería de Minas Av. Tacna y Arica No 160, Arequipa, Perú
†Corresponding author: Gerby Giovanna Rondán-Sanabria; c16238@utp.edu.pe, gerbyrs@gmail.com

ARTICLE HISTORY

Received: 04-02-2026
Revised: 14-04-2026
Accepted: 29-04-2026

KEYWORDS

Mine waste
Geotechnical stabilization
Geopolymers
Portland cement
Metakaolin

CITE THIS ARTICLE

Pérez Oropeza, J.D., Barreda de la Cruz, M.A. and Rondán-Sanabria, G.G., 2026. Analysis of geomechanical properties of mine waste using cementitious and pozzolanic agents: A systematic review, *Nature Environment and Pollution Technology*, 25(4), D1915. https://doi.org/10.46488/NEPT.2026.v25i04.D1915

COPYRIGHT & LICENCE

© 2026 The Authors
Open Access under CC BY 4.0.

PUBLISHED BY
TECHNOSCIENCE PUBLICATIONS

ABSTRACT

Managing mine waste remains a formidable global challenge, driven by substandard geomechanical properties and significant contamination risks. Although binder-based stabilization offers a promising remedy, the extant literature remains strikingly fragmented, hindering standardized application. The purpose of this review is to synthesize and critically compare scientific evidence on the effectiveness of Portland cement versus pozzolanic precursors for mine waste valorization. To that end, a systematic literature review (SLR) was conducted, formulating research questions under the PICO framework and applying the PRISMA protocol, which enabled the selection of 68 studies from the Scopus and ScienceDirect databases. The results indicate that stabilization performance is governed by the chemical compatibility between the waste and the binder, rather than by a universal formulation. Although Portland cement serves as a benchmark, achieving compressive strengths of up to 57.5 MPa, pozzolanic precursors can achieve superior performance, exhibiting a broad performance window (0.22–92.6 MPa), governed by chemical compatibility. Likewise, strength development does not scale linearly with binder dosage, as a performance benchmark of 20–60% binder content was identified for maximizing UCS in structural units, whereas lower dosages (5–20%) proved effective for geotechnical backfilling, highlighting that optimization is strictly context-dependent. These findings suggest a paradigm shift from a volumetric approach toward one that treats mine waste as a reactive chemical component, where mineralogical characterization forms the basis of formulation design. The main limitation identified is the reliance on thermal curing (60–90°C) in laboratory studies, which constitutes the greatest barrier to in situ application. Thus, future research should focus on the development of high-performance formulations effective at ambient temperature to bridge the gap between experimental feasibility and practical application.

1. INTRODUCTION

While the mining industry remains an essential pillar of the global economy and technological growth, it inevitably generates staggering volumes of waste, primarily in the form of overburden and tailings. These materials, composed of low-grade waste rock, represent one of the largest solid waste streams on the planet, posing a formidable geotechnical and environmental challenge that demands sustainable intervention (Hamid and Alnuaim 2023, Bessa et al. 2024, Farenzena et al. 2024, Hu et al. 2025). Beyond the vast land areas required for their disposal, mismanaged waste poses severe risks, specifically regarding acid mine drainage and the leaching of heavy metals (Simate & Ndlovu 2014).

The primary hurdle to repurposing these materials lies in their substandard geomechanical properties, notably their low shear strength, high compressibility,

and erratic particle size distribution, which preclude their direct integration into infrastructure works (Mabroum et al. 2020, Verhagen et al. 2021). Geotechnical stabilization has consequently emerged as a cornerstone strategy within the framework of the circular economy (Lehmann et al. 2020). Historically, Portland cement has been the standard binder of choice, valued for its ability to provide high mechanical strength. However, its production is responsible for approximately 8% of global CO_2 emissions (Scrivener et al. 2018), a factor that has catalyzed the search for greener alternatives. In this scenario, alkaline activation or geopolymerization technology, which utilizes aluminosilicate-rich precursors such as metakaolin, has gained significant traction as a low-carbon, high-performance alternative for the stabilization and valorization of mine waste (Salihoglu 2014, Wan et al. 2019, Carrillo Beltrán et al. 2024).

Despite the proliferation of studies addressing both stabilization technologies, this body of knowledge has not yet translated into a clear consensus or standardized guidelines. The scientific literature remains strikingly fragmented and highly heterogeneous; studies vary widely in terms of the type of waste rock considered (Provis 2018) (e.g., copper tailings versus iron waste) and their mineralogical reactivity Haga clic o pulse aquí para escribir texto.. Furthermore, reported stabilizing agent dosages range from a modest 5% to more than 90%, with chemical activators and curing regimes fluctuating between ambient conditions and thermal treatments at 90°C (Berdoudi et al. 2017, Farenzena et al. 2024).

The primary knowledge gap identified is the absence of a systematic review that critically and comparatively evaluates the performance of conventional Portland cement against the most promising pozzolanic alternatives. Therefore, this SLR is justified as a necessary effort to bridge this fragmentation, identify robust patterns, reconcile potential discrepancies among reported results, and establish a clear baseline of the current state of the art. The outcomes of this review are intended to function as a decision-making framework by clarifying which factors, such as mineralogy, binder dosage, and curing conditions, are most influential in the success of stabilization processes. This understanding is vital to optimize formulation design while minimizing environmental impacts. Ultimately, this study seeks to provide the consolidated evidence necessary to facilitate the safe adoption of these innovative technologies, thereby accelerating the transition of the mining industry toward a circular economy model.

2. MATERIALS AND METHODS

This study was conducted as a systematic literature review (SLR) and was conducted through a comprehensive analysis of peer-reviewed literature indexed in specialized academic databases. To safeguard the rigor and reproducibility of the findings, the PICO framework (Population, Intervention, Comparison, Outcome) was employed to tailor the search strategy in strict alignment with the research scope. Furthermore, the identification, screening, and synthesis of sources followed the PRISMA (Preferred Reporting Items for Systematic Reviews and Meta-Analyses) guidelines. This approach ensured a methodical and transparent structure throughout the investigative process, from the initial identification to the final consolidation of scientific evidence.

2.1. PICO Framework and Research Questions

In formulating the research questions, the four pillars of the PICO framework, Population/Problem, Intervention, Comparison, and Outcome, were meticulously integrated. This structured approach provided the necessary precision to establish rigorous criteria for the identification and selection of information. Consequently, the study was guided by the following overarching and specific research questions (RQs):

RQ (Main): How does the efficacy of Portland cement compare to that of pozzolanic precursors (e.g., metakaolin, fly ash, and slag) in stabilizing mine waste, and to what extent is this performance dictated by the waste's intrinsic properties and sustainability goals?

RQ1 (Problem): Which mining waste streams have dominated the current literature, and how do their inherent mineralogical profiles determine the feasibility and success of diverse stabilization techniques?

RQ2 (Intervention): How do binder dosage thresholds vary across different mine waste streams to meet specific mechanical requirements, and what evidence exists for a performance 'plateau'?

RQ3 (Comparison): How does the inclusion of pozzolanic agents functioning as both partial cement replacements and primary geopolymeric precursors impact the mechanical integrity of stabilized waste when contrasted with conventional cement-only systems?

RQ4 (Results): Which assessment protocols, specifically unconfined compressive strength (UCS) and curing regimes (thermal versus ambient), are most prevalent in the literature? Furthermore, what are the practical implications of a heavy reliance on thermal curing regarding the scalability gap between controlled laboratory performance and large-scale industrial deployment?

2.2. Search Strategy and Keyword Selection

The search strategy was developed by deconstructing the main research question into the PICO components

Table 1: Keywords of the PICO components.

Acronym	Components	Scopus Search Keywords
P	Problem/Population	mine tailings, mining waste, waste rock, mine spoil, mining residue, overburden
I	Intervention	Stabilization, solidification, geopolymer, ground improvement, cementation, alkali, activated, alkali-activated, cement
C	Comparison	comparative, comparison, control sample, dosage, evaluation, performance, versus, influence, effect
O	Outcomes	compressive strength, durability, unconfined compressive strength, UCS, leaching, immobilization, strength, geotechnical properties, stability

(Population, Intervention, Comparison, and Outcome). The specific keywords used for each component are summarized in Table 1. Based on these terms, database-specific Boolean search equations were constructed to retrieve relevant studies on mine waste stabilization using cementitious and pozzolanic binders.

The literature search was conducted using the Scopus and ScienceDirect databases, selected for their broad coverage of engineering and environmental research. The search was limited to peer-reviewed articles published between 2010 and 2025, in English and Spanish. Only research articles were considered to ensure consistency with the inclusion criteria and to exclude non-peer-reviewed sources. The complete Boolean search equations applied in Scopus and ScienceDirect are presented below. Due to differences in database indexing and search functionalities, the query applied in ScienceDirect was simplified while maintaining conceptual alignment with the Scopus search strategy:

For Scopus, the following search equation was used: (“mine tailings” OR “mining waste” OR “waste rock” OR “mine spoil” OR “mining residue*” OR “overburden”) AND (stabiliz* OR solidif* OR “ground improvement” OR cementation OR geopolymer* OR “alkali activated” OR “alkali-activated” OR cement* OR metakaolin OR “fly ash” OR slag OR pozzolan* OR binder*) AND (comparative OR comparison OR “control sample” OR dosage OR versus OR evaluation OR influence OR effect* OR performance) AND (“compressive strength” OR “unconfined compressive strength” OR UCS OR durability OR leaching OR “mechanical properties” OR “geotechnical properties” OR microstructure OR immobilization OR stability)

For ScienceDirect: (“mine tailings” OR “mining waste”) AND (geopolymer OR “alkali activated”) AND (dosage OR performance) AND (leaching OR immobilization)

2.3. Inclusion and Exclusion Criteria

To safeguard the technical relevance and comparability of the selected studies, predefined inclusion and exclusion criteria were established prior to the full-text assessment. These criteria were defined to align with the variables analyzed in the synthesis and to enable meaningful cross-study comparison:

Inclusion Criteria (IC):

IC1: Primary experimental studies published in peer-reviewed journals.

IC2: Studies focused on the stabilization of mine waste materials, including tailings, waste rock, or overburden.

IC3: Studies evaluating cementitious or pozzolanic binders, such as Portland cement, metakaolin, fly ash, slag, or alkali-activated systems.

IC4: Studies reporting at least one quantitative geomechanical parameter, primarily unconfined compressive strength (UCS), or equivalent indicators of mechanical performance.

IC5: Studies providing sufficient methodological information on mix composition and curing conditions (e.g., temperature, duration, or curing type) to enable comparative analysis.

Exclusion Criteria (EC):

EC1: Review articles, conference proceedings, book chapters, technical reports, and other non-peer-reviewed literature.

EC2: Studies focused exclusively on material characterization without stabilization treatment.

EC3: Studies based solely on physical or mechanical approaches or using non-target binders outside the cementitious/pozzolanic scope of this review.

EC4: Studies with insufficient technical information or lack of full-text access, preventing the extraction of key variables such as binder type, dosage, curing conditions, or geomechanical performance.

The study identification and selection process followed the PRISMA 2020 guidelines, as illustrated in Fig. 1. A total of 536 records were identified through database searching, including 413 records from Scopus and 123 records from ScienceDirect. No duplicate records were identified after screening titles and metadata across both databases, resulting in 536 unique records entering the initial screening phase. A preliminary screening of titles and abstracts led to the exclusion of 230 records due to lack of relevance to mine waste stabilization and geomechanical performance. The remaining 306 records were sought for full-text retrieval, of which 18 reports could not be accessed and were therefore

excluded. Consequently, 288 reports were assessed for eligibility.

During the eligibility phase, 238 records were excluded based on the predefined exclusion criteria (EC1–EC4), including non-peer-reviewed literature, studies focused exclusively on material characterization without stabilization, studies based solely on physical or mechanical stabilization or using non-target binders, and studies with insufficient technical information or lack of full-text access. As a result, 50 studies met the inclusion criteria and were selected for systematic data extraction. Furthermore, 18 studies were identified through citation tracking under the section "Identification of studies through other methods". Their absence in the initial database search is attributed to differences in indexing coverage and limitations inherent to keyword-based search strategies. All additional studies were evaluated against the same inclusion criteria and were incorporated into the final dataset after meeting the required methodological standards. In total, 68 studies were included in the systematic synthesis.

2.4. Data Extraction and Synthesis Framework

To ensure analytical transparency, a standardized data extraction form was developed. For each of the 68 included studies, the following variables were systematically recorded: (a) Waste characteristics: type (tailings/waste rock) and predominant mineralogy; (b) Stabilization parameters: binder type (OPC/geopolymer), activator molarity, and dosage range; (c) Curing conditions: temperature (°C) and duration (days); and (d) Performance metrics: maximum unconfined compressive strength (UCS) and durability indicators (leaching/sulfate resistance). Data synthesis followed a thematic approach, grouping studies by binder-waste compatibility to identify cross-study patterns in mechanical performance and optimal dosage thresholds.

3. RESULTS AND DISCUSSION

3.1. Global Research Trends and Geographic Mapping

The geographical distribution of the selected studies reflects a growing global interest in mine waste stabilization,

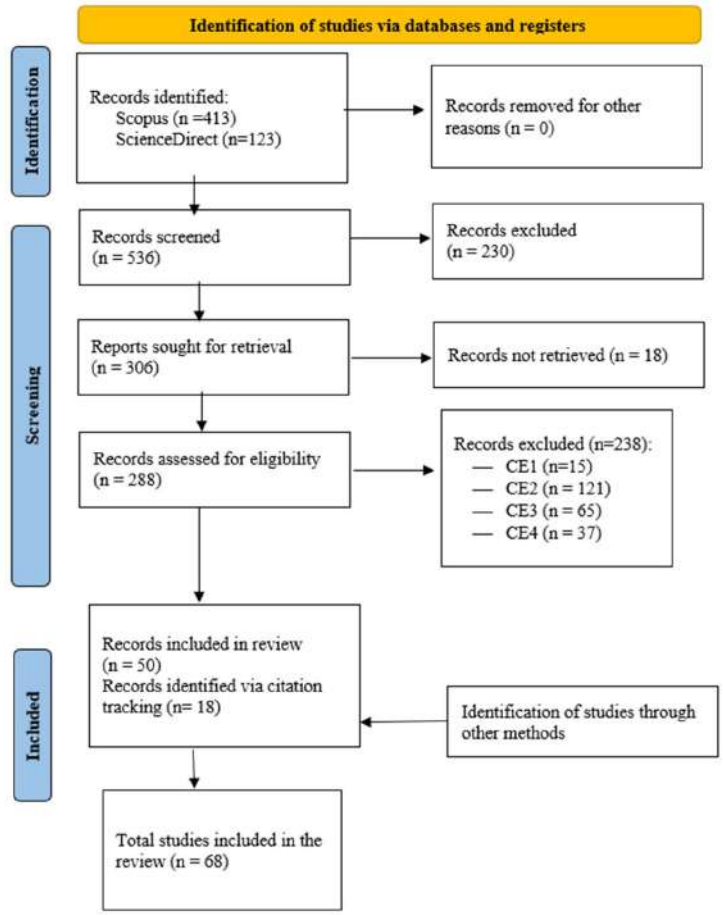


Fig. 1: Literature search and selection process (PRISMA).

propelled by both stringent environmental regulations and the increasing demand for sustainable construction materials. As illustrated in Fig. 2, scientific output is far from uniform; instead, it appears concentrated within regions defined by either a strong mining tradition or progressive circular economy policies.

An analysis of publication origins reveals a clear hegemony of Europe, which accounts for 36% of the sample. This leadership, spearheaded by Spain (5 studies) and Portugal (4 studies), suggests that rigorous sustainability frameworks within the European Union are catalyzing the search for low-carbon alternatives to traditional cement. Meanwhile, research in Asia (27%) is heavily centered in China, where a significant output of 13 studies focuses predominantly on alkaline activation chemistry. Across the Americas (24%), contributions from countries with intensive extractive sectors, such as Brazil and Peru, are particularly noteworthy. The latter, with three reported studies, demonstrates an incipient yet significant interest in closing the mining waste life cycle. Strikingly, participation remains remarkably low in Africa (11%) and Oceania (2%). Given their critical economic dependence on mining, this disparity highlights a clear opportunity for future research niches in these underserved regions.

3.2. Characterization and Heterogeneity of Mine Waste Feedstocks

The literature review uncovers a multifaceted research landscape covering a wide range of waste generated by diverse mining operations globally. This heterogeneity is pivotal, as the physical (particle size distribution, plasticity) and chemical (mineralogical composition, pH) attributes of waste rock fluctuate significantly, ultimately dictating both the technical feasibility and effectiveness of any chosen stabilization strategy.

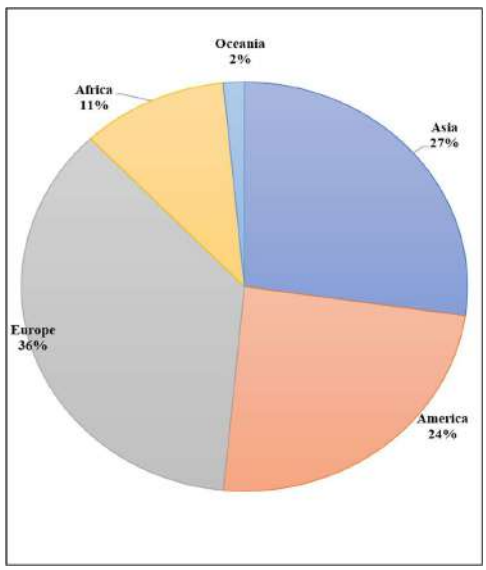


Fig. 2: Geographical distribution of scientific articles.

Understanding the parent rock strength is crucial for establishing stabilization targets. For instance, granite waste rock can exhibit an intrinsic UCS of up to 92.6 MPa. However, once processed as waste (tailings or fragments), this mechanical integrity is lost, requiring chemical binders to attempt to recover these baseline geomechanical properties.

Given the substantial diversity of the waste studied, Table 2 categorizes these materials according to the type of overburden and its predominant mineralogy. This classification establishes a robust baseline for comparing stabilization results and enables the evaluation of how intrinsic waste characteristics influence stabilizer selection and mechanical performance.

Table 2 delineates two distinct trends. The first trend shows a focus on tailings management due to their fine particle size and high reactivity, while the second trend explores waste rock as a coarse aggregate replacement, leveraging its mechanical stability. While the focus on tailings is driven by their intricate geotechnical management and high chemical reactivity (Ahmari & Zhang 2012, Cristelo et al. 2020), waste rock attracts academic interest primarily due to its colossal volume and potential as a recycled aggregate (Kanalli et al. 2019, Rouaiguia et al. 2022). Second, the identified mineralogical diversity, extending far beyond metallic ores, underscores the inherent versatility of stabilization technologies. However, this diversity also presents a critical hurdle: waste composition remains the ultimate determinant of treatment success.

This dual approach directly addresses mining's most pressing challenges: risk and volume (Ahmari & Zhang 2012, Cristelo et al. 2020, Rouaiguia et al. 2022, Farenzena et al. 2024). Research into copper (Sun et al. 2022) and gold tailings (de Leon et al. 2024), for instance, aims to curb environmental degradation. This principle is particularly evident in studies on cemented paste backfill (CPB) (Arpalahti & Lundström 2018), where tailings are repurposed into structural materials to stabilize underground voids. In this framework, stabilization transcends mere valorization, evolving into an active safety tool within mining operations. Conversely, research into waste rock (Kanalli et al. 2019, Rouaiguia et al. 2022) is propelled by the logistics of managing massive volumes, fostering technologies that transform these liabilities into technical assets for civil and mining infrastructure.

Table 2: Classification of the wastes used.

Main type of mining waste used	Main mineral	Author
Clay	Lithium	(Wan et al. 2019)
Fly ash	Coal	(Arioz et al. 2012)
Ash	Coal, metakaolin and barite	(Burduhos Nergis et al. 2022)
Waste slag	Antimony	(Salihoglu 2014)
	Copper	(Erunkulu et al. 2024)
Sludge	Tungsten	(Almeida et al. 2021, Beghoura & Castro-Gomes 2021, Benhamouda et al. 2021)
	Iron	(Beulah et al. 2021)
	Granite	(Abdelkader et al. 2022)
	Coal	(Chen et al. 2024)
	Slate	(Carrillo Beltrán et al. 2024, Picazo Camilo et al. 2025)
Dust	Marble	(Berdoudi et al. 2017)
	Granite	(Hawerroth et al. 2023)
Tailings	Copper	(Ahmari & Zhang 2012, Paiva et al. 2019, Cristelo et al. 2020, Lam et al. 2020, Štulović et al. 2024)
	Phlogopite	(Solismaa et al. 2018)
	Iron	(Borges et al. 2019, Kou et al. 2020, Beulah et al. 2021, Bessa et al. 2024, Farenzena et al. 2024)
	Lead	(Terrones-Saeta et al. 2021)
	Zinc	(Paiva et al. 2019, Wan et al. 2019)
	Gold	(Liza et al. 2023, Opiso et al. 2023, de Leon et al. 2024, Palma et al. 2024)
	Coal	(Mokhtari et al. 2025)
	Silver	(Palma et al. 2024)
	Not specified	(Lu et al. 2019, Chen et al. 2024)
	Diabase	(Hu et al. 2025)
	Phosphate	(Niu et al. 2021, Bouchikhi et al. 2024)
	Titanium	(Shoaei et al. 2024)
	Wollastonite	(Ellis et al. 2015, Matheu et al. 2015)
	Pyroxene	(Matheu et al. 2015)
	Pyrite	(Sarkkinen et al. 2019)
Waste rock	Iron	(Kanalli et al. 2019, Rouaiguia et al. 2022, Sun et al. 2022)
	Manganese	(Guglietta et al. 2020)
	Zinc	(Mwandira et al. 2019, Niu et al. 2021)
	Lead	(Mwandira et al. 2019, Terrones-Saeta et al. 2023)
	Copper	(Guglietta et al. 2020, Niu et al. 2021, Wurie et al. 2022)
	Tungsten	(Kastiukas et al. 2019)
	Coal	(Zhao et al. 2025)
	Nickel	(Hu et al. 2022)
	Kimberlite	(Lockhart et al. 2024)
	Coltan	(Ally et al. 2023)
	Not specified	(Lu et al. 2019)
	Granite	(Batista & Ingunza 2023)
	Magnesite	(Kalaitzidou et al. 2023)
	Tin	(Niu et al. 2021)
	Potassium feldspar	(Mendonça et al. 2021)
	Zeolite	(Amari et al. 2024)

The vast mineralogical spectrum identified in this review, ranging from phosphates to tungsten residues (Almeida et al. 2021, Benhamouda et al. 2021), confirms that waste chemistry dictates the viability of any valorization pathway. Findings indicate that aluminosilicate-rich wastes, such as granite (Carrillo Beltrán et al. 2024) or slate (Abdelkader et al. 2022), and calcined clays are prime reactive precursors for geopolymerization, aligning with results reported by Arpalahti & Lundström (2018). In contrast, sulfidic tailings, notably pyrite (Sarkkinen et al. 2019), prove problematic by inhibiting the chemical reactions necessary for stabilization. This sensitivity to sulfides is not merely a technical hurdle; it is inextricably linked to severe environmental risks. As detailed by Simate & Ndlovu (2014), the oxidation of these minerals is the primary driver of acid mine drainage (AMD).

Available data confirm that a paradigm shift from a geotechnical-only approach to a techno-mineral model is mandatory. In this model, waste is not an inert filler but a chemical precursor whose elemental signature (Si/Al ratio and sulfur content) dictates the binder selection. As discussed by Pasteris et al. (2021), the technical and economic viability of a circular economy project hinges on an integrated characterization strategy including XRF, XRD, and SEM analyses. While simple geotechnical characterization may suffice for inert fills, it is wholly inadequate for predicting the behavior of a material acting as a chemical precursor. Consequently, the industry must move away from viewing waste as a homogeneous category and instead manage it as a portfolio of 'techno-mineral resources'. In this model, each material possesses a unique chemical fingerprint that defines its optimal valorization route.

In the end, transitioning toward this techno-mineral model requires accounting not only for average composition but for inherent variability. Tailings properties can fluctuate significantly within a single deposit due to metallurgical process shifts or discharge location changes. This heterogeneity poses a substantial practical challenge for industrial-scale quality control, reinforcing the need for robust, continuous characterization protocols that extend well beyond the initial design phase.

3.3. Integrated Analysis of Geomechanical Performance, Dosage Optimization, and Industrial Feasibility

The systematic aggregation of the 68 studies analyzed in this review reveals a paradigm shift in mine waste management, moving from simple physical containment toward sophisticated chemical valorization. The current scientific landscape shows a clear preference for innovation, as researchers seek to replace carbon-intensive binders with more sustainable alternatives. This research trend, characterized by the dominance of alkali-activated systems and geopolymers, provides the framework for the geomechanical outcomes discussed herein.

As illustrated in Fig. 3A, 62% of the corpus focuses on pozzolanic or alkali-activated systems (AAC), while 38% evaluates traditional Portland cement (OPC) (e.g., Beulah et al. 2021, Bessa et al. 2024). A critical finding emerging from Fig. 3B is the heavy reliance on thermal catalysis; over 70% of formulations achieving high-strength thresholds (>40 MPa) were dependent on temperatures between 60°C and 90°C (e.g., Hawerroth et al. 2023, Chen et al. 2024). This creates a "sustainability paradox," where the low-carbon benefits of geopolymer chemistry are often offset by the energy-intensive heat treatment required. Conversely, as shown in Fig. 3C, chemical compatibility remains a significant hurdle for reactive wastes, with an 85% failure rate in stabilizing sulfidic tailings without specialized activators. To elucidate these complexities, the following table synthesizes the most representative benchmark studies across diverse waste streams.

The benchmark data in Table 3 highlight that mechanical success is not a simple byproduct of binder quantity, but

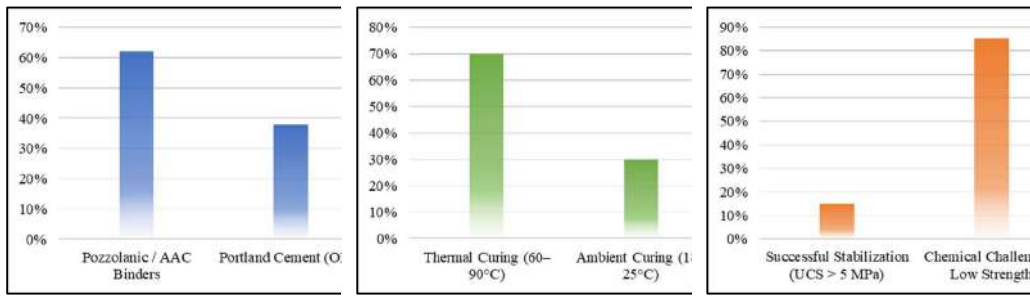


Fig. 3: Study distribution and performance trends: (A) binder system distribution, (B) high-strength curing efficiency, and (C) chemical compatibility in reactive waste.

Table 3: Summary of geomechanical outcomes and experimental variables for key studies.

Reference	Waste Type	Binder System	Curing Condition	Dosage (%)	Max UCS (MPa)	Key Geomechanical Finding
(Berdoudi et al. 2017)	Marble dust	OPC + Silicate	Ambient (22°C)/28 d	50%	57.50	Superior performance of activated cement systems.
(Hawerroth et al. 2023)	Granite dust	Metakaolin + AAC	60°C /24 h	40%	27.80	Thermal curing accelerates early-age strength.
(Matheu et al. 2015)	Wollastonite	Slag-based AAC	Ambient (23°C)/28 d	60%	50	High-calcium waste yields high ambient strength.
(Borges et al. 2019)	Iron tailings	OPC + Metakaolin	Ambient (25°C)/28 d	60%	68.50	Pozzolanic replacement enhances OPC integrity.
(Lam et al. 2020)	Copper tailings	Portland Cement	Ambient (22°C)/28 d	15%	48.5	Strength plateau observed beyond 15% dosage.
(Almeida et al. 2021)	Mine residues	High-dosage OPC	Ambient (~23°C)/28 d	50%	18.23	Diminishing returns at extremely high dosages.
(Wan et al. 2019)	Lithium clay	Metakaolin + AAC	60°C/3 d	40%	30.10	Pozzolanic precursors outperform OPC in clays.
(de Klerk et al. 2020)	Steel slag	Slag-based AAC	Ambient (~23°C)/ 28 d	18%	35	Performance decline due to unreacted alkali excess.
(Ahmari & Zhang 2012)	Copper tailings	Metakaolin + AAC	60°C/ 7 d	30%	33.7	Early strength dictates long-term durability.
(Sarkkinen et al. 2019)	Sulfidic tailings	MgO-activated Slag	Ambient (18°C)/28 d	20%	15	Sulfides inhibit hydration and polymer networks.
(Wurie et al. 2022)	Copper waste	OPC + Ash	Ambient (20°C)/28 d	35%	17	Heterogeneous particle size limits UCS gains.
(Salihoglu 2014)	Antimony slag	Portland Cement	Ambient (~23°C)/ 28 d	50%	25.2	Low chemical compatibility with standard OPC.

rather a result of precise chemo-mineralogical synergy. For instance, while Berdoudi et al. (2017) achieved 57.50 MPa using OPC reinforced with silicates in marble dust, pozzolanic precursors like metakaolin have shown superior performance in clayey and granite-based wastes (Wan et al. 2019, Hawerroth et al. 2023) A defining pattern identified in this synthesis is the "plateau effect," where incremental binder additions fail to yield proportional strength gains once chemical saturation is reached. This nonlinear relationship between dosage and unconfined compressive strength (UCS) is quantitatively visualized in the following correlation analysis.

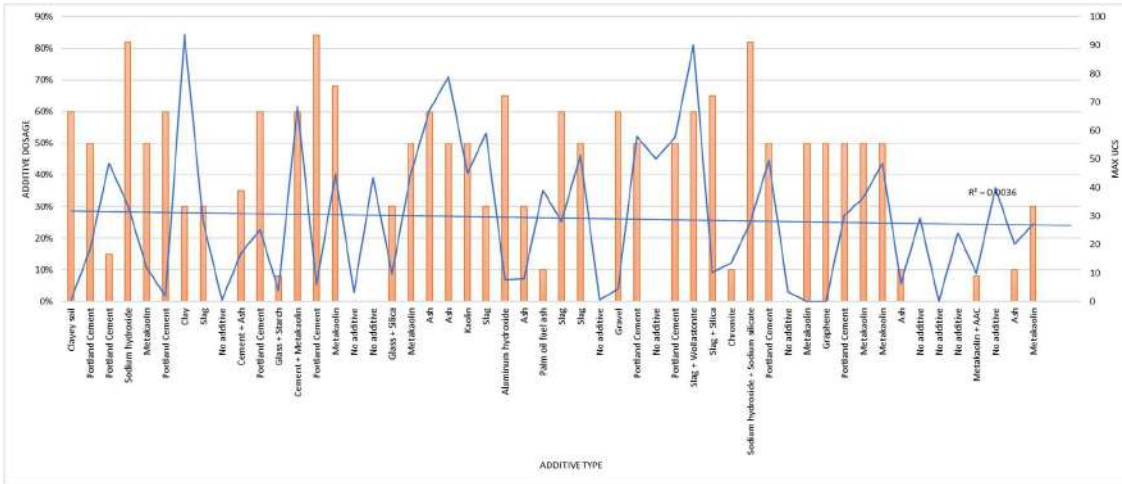


Fig. 4: Correlation between additive content (%) and achieved UCS (MPa).

Table 4: Summary of binders and additives, dosages, and achieved unconfined compressive strength (UCS).

Additive/binders	Dosage range (Additive/ Waste)	Achieved UCS range (MPa)	Author(s)
Baseline (natural or untreated material)	N/A	0.15 – 132	(Bessa et al. 2024, Kanalli et al. 2019, Farenzena et al. 2024, Lockhart et al. 2024, Batista & Ingunza 2023)
Main binders			
Portland cement	(5%–70%)/(7%–50%)	1.8 – 57.5	(Bessa et al. 2024, Berdoudi et al. 2017, Salihoglu 2014, Lam et al. 2020, Beulah et al. 2021)
Metakaolin	(10%–50%)/(32%–70%)	12 – 67.1	(Wan et al. 2019, Amari et al. 2024, Palma et al. 2024, Bouchikhi et al. 2024, Štulović et al. 2024, Arioz et al. 2012, Hawerroth et al. 2023)
Ash	(10%–60%)/(40%–90%)	8–67.1	(Opiso et al. 2023, Burduhos Nergis et al. 2022, Cristelo et al. 2020, Vongsook et al. 2025, Perera-Mercado et al. 2022)
Slag	(15%–60%)/(40%–70%)	12–92.6	(Ally et al. 2023, Ellis et al. 2015, Matheu et al. 2015, Sedira et al. 2018, de Klerk et al. 2020)
Mixtures and composite additives			
Cement + Metakaolin	40%/60%	68.5	(Borges et al. 2019)
Cement + Ash	35%/65%	17	(Wurie et al. 2022)
Slag + Wollastonite	60%/40%	120	(Ellis et al. 2015)
Slag + Silica	60%/40%	50	(Matheu et al. 2015)
Metakaolin + AAC	10% - 60%/40% - 90%	0.22 – 67.10	(Farenzena et al. 2024, Wan et al. 2019, Palma et al. 2024)
Other additives and activators			
Sodium hydroxide	82%/30%	33.7	(Ahmari & Zhang 2012)
Sodium hydroxide + Silicate	40% + 42%/20%	57.5	(Berdoudi et al. 2017)
Kaolin	50%/50%	67.1	(Palma et al. 2024)
Gravel	60%/15%	4.42	(Lu et al. 2019)
Calcium carbonate	10%	5.5	(Mwandira et al. 2019)

The high dispersion observed in Fig. 4 ($R^2 < 0.4$) confirms that stabilization performance is a multifaceted phenomenon not dictated solely by additive quantity. The blue trend line underscores that simply increasing the binder percentage does not guarantee microstructural maturity; instead, success hinges on optimizing variables such as the Si/Al molar ratio and particle fineness (Mabroum et al. 2020). This suggests that many laboratory designs may be using chemically redundant binder volumes that provide no geomechanical advantage, leading to the diverse range of additives and achieved strengths summarized below.

The data in Table 4 demonstrate the vast performance window of pozzolanic systems, ranging from 0.22–92.6 MPa (Ellis et al. 2015, Farenzena et al. 2024). However, the primary challenge in standardizing these formulations lies in the extreme variability of the results when identical dosages are applied to different mineralogies. The inconsistency suggests that the "more is better" approach is fundamentally flawed. In reactive wastes, such as those containing pyrite, the oxidation of minerals can inhibit binder hydration or cause internal sulfate attack, leading to expansion and cracking (Kalin et al. 2018, Sarkkinen et al. 2019). Consequently, a high dosage of a binder in an incompatible waste stream can result in lower structural integrity than a minimal dosage in a chemically matched environment. This decoupling between volume and performance is explicitly contrasted in the following table.

The comparison in Table 5 provides definitive empirical evidence for the "plateau effect": a formulation with 50% Portland cement achieved only 18.23 MPa in inert mining residues (Almeida et al. 2021), while a significantly lower dosage of 15% achieved a superior 48.5 MPa in copper tailings (Lam et al. 2020). These results confirm that beyond a specific saturation point, additional binder content acts merely as an expensive filler. This insight is vital for the transition toward a "techno-mineral" model, where mineralogical characterization forms the basis of formulation design. In the end, to bridge the gap between these experimental findings and large-scale industrial deployment, the following table categorizes the current valorization pathways and their specific requirements.

3.4. Impact of Curing Regimes: Thermal vs. Ambient Stratification

While the optimization of binder dosage and mineralogical synergy establishes the chemical baseline for stabilization, the practical realization of this geomechanical potential is inextricably linked to the curing conditions under which these reactions occur. Curing serves as the kinetic engine of the stabilization process, directly governing the dissolution and polycondensation rates required to form a resilient binder matrix (Frasson et al. 2019, Farenzena et al. 2024). Nevertheless, systematic analysis of the 68 studies reveals a critical methodological gap: a "performance mirage" created by the heavy reliance on high-intensity thermal curing. While thermal activation (60–90°C) allows pozzolanic systems to reach exceptional peak values, such as the 92.6 MPa reported by Ellis et al. (2015), these conditions are often logistically and economically unfeasible for most large-scale field applications like road bases or embankment slopes (Ahmari & Zhang 2012, Irfan & Uchimura 2015).

This disparity is quantitatively significant: 70% of the formulations achieving high-strength thresholds (>40 MPa) were dependent on artificial heat sources. This creates a sustainability paradox where the carbon-reduction benefits of geopolymers are partially eroded by the energy demands of thermal catalysis (Salas et al. 2018). In contrast, ambient-cured systems (< 25°C), which represent the true baseline for in situ scaling, show significantly more modest outcomes, generally fluctuating between 10 and 48 MPa (Liza et al. 2023). To provide a comprehensive framework for these methodologies, the specific curing protocols identified in the literature are categorized by temperature range and application method in Table 6.

As detailed in Table 6, the literature reveals a pronounced dichotomy between laboratory-standardized protocols and the requirements for industrial scalability. Beyond temperature, factors such as humidity control remain a universal requirement to prevent premature evaporation, which can compromise structural integrity regardless of the binder type (Borges et al. 2019, Hu et al. 2025). The sluggish dissolution of aluminosilicate phases at ambient temperatures (20°C) remains the primary bottleneck for technology transfer (Motamedi et al. 2020). Therefore, the evidence suggests that future research must prioritize the development of high-reactivity chemical activators capable of reaching functional thresholds at ambient temperatures to transform laboratory "material potential" into a viable, large-scale industrial reality.

Table 5: Evidence of binder dosage inconsistency as a strength predictor.

Binder Dosage	Waste Type (Mineralogy)	Max UCS (MPa)	Study Reference	Observation
50% (High)	Mining residue (Inert)	18.23	Almeida et al. (2021)	Volumetric saturation: Even at its maximum dosage (50%), strength remains low.
15% (Low)	Copper tailings (Quartz)	48.5	Lam et al. (2020)	Plateau effect: Achieves 2.6× more strength than Almeida with 35% less binder.
60% (Max)	Clayey soil (Kaolinite/ Iron)	0.59	Kanalli et al. (2019)	Chemical failure: The highest dosage in this selection (60%) yields the lowest UCS.

Table 6: Types and curing times.

Curing	Method description	Temperature range (°C)	Authors
Ambient curing	Samples cured under laboratory conditions without the application of external heat.	18–25°C	(Sarkkinen et al. 2019, Lam et al. 2020, Mokhtari et al. 2025, Palma et al. 2024, Opiso et al. 2023, Farenzena et al. 2024, Vongsook et al. 2025)
Thermal curing	Application of constant heat in an oven or furnace for a defined period between 12 and 48 hours to accelerate reactions.	40–120°C	(Ahmari & Zhang 2012, Arioz et al. 2012, Cristelo et al. 2020, Niu et al. 2021, Burduhos Nergis et al. 2022, Beghoura & Castro-Gomes 2021, Bouchikhi et al. 2024)
Mixed curing	Combines an initial thermal curing phase followed by a period of ambient curing.	Phase 1: 40–90°C Phase 2: 20–25°C	(Wan et al. 2019, Carrillo Beltrán et al. 2024, de Leon et al. 2024, Perera-Mercado et al. 2022, Štulović et al. 2024).
Extreme-temperature treatments	Processes such as calcination at very high temperatures.	> 800°C	(Kalaitzidou et al. 2023, Solismaa et al. 2018, Terrones-Saeta et al. 2023)

3.5. Durability and Long-Term Environmental Stability

Beyond the immediate geomechanical gains achieved through optimized curing, the ultimate viability of stabilized mine waste depends on its ability to withstand environmental stress factors over time. Mechanical strength (UCS) remains the primary focus of the literature, yet a significant subset of the analyzed corpus (40%, n = 27) has begun to address long-term durability indicators as the true measure of success. This shift is critical, as material that fulfills structural requirements may still fail if it remains chemically reactive or physically vulnerable to extreme climatic conditions. To synthesize these complex stress factors, the following table categorizes the most significant durability outcomes identified in recent research.

As detailed in Table 7, environmental safety is the cornerstone of modern waste valorization. Research indicates that alkali-activated systems (AAC) provide superior encapsulation of heavy metals compared to traditional Portland cement. Studies on lead and zinc tailings, for instance, demonstrate that the 3D aluminosilicate network effectively traps cations through both physical micro-encapsulation and chemical adsorption, reducing leachability by up to 98% (Paiva et al. 2019, Terrones-Saeta et al. 2021). Furthermore, while OPC-based systems are highly vulnerable to internal sulfate attack, leading to expansion and cracking in sulfidic environments, low-calcium pozzolanic binders maintain structural integrity by offering high resistance to acid mine drainage (AMD) and low-pH exposure (Sarkkinen et al. 2019, Manjunatha et al. 2021).

These technical findings regarding chemical and physical resilience are reflected in the overall research trends of the corpus analyzed. The quantitative distribution of these studies shows a clear prioritization of certain environmental risks over others (Fig. 5).

The data in Fig. 5 underscores a critical gap in the literature. Leaching behavior (21%) and chemical stability (12%) have gained significant traction; physical stability metrics like freeze-thaw cycles (7%) remain under-researched. This disparity is particularly concerning given that physical durability remains a formidable challenge in extreme climates. Evidence from Ren et al. (2022) and Sun et al. (2022) confirms that while geopolymers can suffer up to 20% strength loss under cyclic stress, optimized formulations with specific Si/Al ratios can achieve stability equivalent to infrastructure-grade concrete. This analysis

Table 7: Systematic synthesis of long-term durability outcomes and environmental safety.

Durability Factor	Key Reference(s)	Binder System	Observed Outcome / Efficiency	Environmental Impact
Heavy Metal Leaching	(Paiva et al. 2019, Terrones-Saeta et al. 2021)	Geopolymer (AAC)	95–98% immobilization of Pb, Zn, and Cu.	Prevention of groundwater contamination.
Sulfate Attack	(Sarkkinen et al. 2019, Kalin et al. 2018)	OPC vs. Slag-AAC	OPC showed cracking/expansion; AAC maintained integrity.	Mitigation of internal degradation in sulfidic waste.
Freeze-Thaw Cycles	(Sun et al. 2022, Ren et al. 2022)	Optimized Geopolymer	<15% strength loss after 15–20 cycles.	Structural stability in high-altitude/cold mining regions.
Acid Mine Drainage	(Ahmari & Zhang 2012, Manjunatha et al. 2021)	Geopolymer (AAC)	High resistance to low pH (2.0) exposure.	Long-term containment of acid-generating minerals.

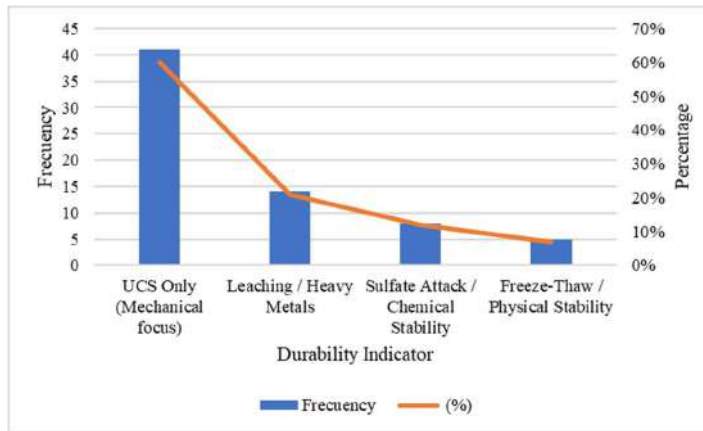


Fig. 5: Quantitative distribution of durability and long-term performance indicators across the synthesized corpus (n = 68).

confirms that durability is not a byproduct of strength, but a result of a refined microstructural design tailored to the waste's specific mineralogy, which must be prioritized to ensure a safe transition toward a circular mining economy.

3.6. Comparative Analysis: Portland Cement vs. Pozzolanic Systems under Equivalent Conditions

A critical comparison of the 68 studies reveals that the perceived superiority of one binder over another is not absolute but strictly dictated by the alignment of experimental variables and the waste's intrinsic chemistry. While pozzolanic and alkali-activated systems can eclipse Portland cement (OPC) in terms of peak mechanical potential, reaching up to 92.6 MPa (Ellis et al. 2015) compared to the 57.5 MPa benchmark for cement (Berdoudi et al. 2017). These values often represent a "laboratory ideal." Most high-performance pozzolanic results were obtained using standardized specimens and optimized thermal catalysis, reflecting a material potential that may be difficult to replicate in large-scale field applications characterized by higher heterogeneity and lower compaction energy. Consequently, OPC remains the baseline for immediate structural integrity under ambient conditions, whereas pozzolanic systems offer a higher, albeit more energy-dependent, performance ceiling.

This distinction extends to the fundamental differences in dosage-response and efficiency. The evidence confirms that OPC systems reach a mechanical plateau relatively early, typically between 15% and 25% binder content (Lam et al. 2020). Beyond this saturation point, additional cement fails to significantly enhance the C-S-H network, leading only to increased costs and diminishing returns. Conversely, pozzolanic systems exhibit a much more flexible "reactivity window." When the alkaline molarity is correctly balanced, these binders can scale effectively up to 50–60% content, continuously improving microstructural density before reaching a peak (Lam et al. 2020). This suggests that pozzolanic binders are more efficient for high-performance structural units, while OPC is more cost-effective for low-dosage geotechnical applications.

Finally, the choice of binder must be treated as a "chemo-mineralogical match" rather than a simple substitution. While OPC is remarkably versatile for inert or low-reactivity wastes, it is technically inferior when dealing with sulfidic or clayey tailings. As evidenced by Sarkkinen et al. (2019) and Kanalli et al. (2019), mineralogical components like pyrite can actively inhibit the hydration of Portland cement, leading to chemical instability. In contrast, pozzolanic binders demonstrate their true strength in these challenging environments by utilizing the waste's own aluminosilicates to synthesize a resilient geopolymeric matrix. Therefore, the selection process must move away from a universal formulation toward one that prioritizes the specific mineralogical fingerprint of the mining residue to ensure long-term geomechanical success.

3.7. Environmental Risk Assessment and Contaminant Immobilization

Beyond geomechanical stability, the environmental safety of mine waste valorization is determined by the immobilization efficiency of heavy metals and the reduction of acid mine drainage (AMD) potential. The systematic synthesis of the 68 studies reveals that environmental safety is not a byproduct of UCS, but a specific outcome of the binder's chemical matrix (Table 5).

3.7.1. Leaching Behavior and Immobilization Efficiency

Quantitative evidence indicates that alkali-activated pozzolanic systems exhibit superior immobilization for cationic contaminants . Studies utilizing the Toxicity Characteristic Leaching Procedure (TCLP) and EN 12457 standards confirm that the 3D aluminosilicate network in geopolymers achieves immobilization efficiencies between 92% and 99% (Paiva et al. 2019, Terrones-Saeta et al. 2021). This is attributed to a dual mechanism: physical micro-encapsulation within the dense matrix and chemical bonding (adsorption/ion exchange) into the geopolymeric framework.

3.7.2. Safety Metrics and Regulatory Compliance

While Portland cement (OPC) is effective for pH buffering, its porous structure can lead to higher leaching rates over time in aggressive environments. Conversely, pozzolanic systems maintain low permeability, significantly reducing the effective diffusion coefficient of toxic ions. As reported by Solismaa et al. (2018) and Niu et al. (2021), stabilized mine waste frequently shifts from 'hazardous' to 'non-hazardous' categories according to US EPA and EU regulatory thresholds, allowing for safe repurposing in infrastructure. Therefore, an integrated risk assessment that combines leaching kinetics and mineralogical stability must be the primary metric for evaluating the environmental feasibility of mine waste stabilization.

3.8. Applications for Stabilized Mine Waste

To establish a robust empirical foundation for the following analysis, the most significant contributions to the field have been systematically synthesized in Table 8. This table delineates the diverse valorization pathways proposed for stabilized waste, ranging from infrastructure-grade materials to environmental remediation strategies, while cross-referencing each category with its respective foundational studies. This structured overview facilitates a targeted

Table 8: Use of stabilized wastes.

Waste type	Use of stabilized waste	Authors
Lead tailings, tailings + coal ash, sulfidic waste rock, blast furnace slag, slate sludge, materials with CSH and NASH gels	Geopolymers	(Niu et al. 2021, Terrones-Saeta et al. 2021, Burduhos Nergis et al. 2022, Perera-Mercado et al. 2022, Amari et al. 2024, Picazo Camilo et al. 2025)
Mine sludge (tungsten), quarry waste (marble), iron tailings, 3D-printable mortars, feldspar waste	Mortars	(Matheu et al. 2015, Borges et al. 2019, Almeida et al. 2021, Beghoura & Castro-Gomes 2021, Mendonça et al. 2021, Hawerroth et al. 2023, Shoaei et al. 2024)
Zinc tailings, iron tailings and red mud	Bricks	(Wan et al. 2019, Beulah et al. 2021)
Granite waste rock, mining waste in clayey soil, coltan waste rock	Roads	(Kanalli et al. 2019, Ally et al. 2023, Batista & Ingunza 2023)
Mining tailings, mining-contaminated soils	Ceramics	(Solismaa et al. 2018, Terrones-Saeta et al. 2023)
Slate sludge, tailings + coal ash, sulfidic waste rock	Binders	(Niu et al. 2021, Burduhos Nergis et al. 2022, Carrillo Beltrán et al. 2024)
Iron tailings	Tailings stabilization	(Farenzena et al. 2024)
Phlogopite tailings, nickel waste rock	Paste backfill	(Kou et al. 2020, Hu et al. 2022)
Gold tailings	Geopolymer cement	(Liza et al. 2023)
Gold tailings	Construction of non-load-bearing walls and roofs	(de Leon et al. 2024)
Copper tailings	Paving blocks	(Lam et al. 2020)
Lead-bearing waste rock	Cover for tailings storage facilities	(Mwandira et al. 2019)
Granite waste	Soil stabilization	(Abdelkader et al. 2022)
Antimony slag	Immobilization of hazardous waste	(Salihoglu 2014)
Magnesite waste	Refractory products	(Kalaitzidou et al. 2023)
Blast furnace slag (GGBFS)	Cementitious materials	(Ellis et al. 2015)
Iron waste rock	Construction aggregates	(Rouaiguia et al. 2022)
Iron tailings sediments	Rammed earth	(Bessa et al. 2024)
Copper waste rock	Road subgrade	(Wurie et al. 2022)
Glauconite–quartz sands	Concrete filler	(Trach et al. 2023)
Waste rock and tailings	Mine backfill	(Lu et al. 2019)
Quarry waste (marble)	Additive	(Berdoudi et al. 2017)
Mining and glass waste	Thermal insulation	(Kastiukas et al. 2019)
Copper tailings	Pastes and mortars	(Cristelo et al. 2020)
Sabkha soil	Stabilization of saline soils	(Hamid & Alnuaim 2023)
Tailings and waste rock as aggregates	Concrete	(Sun et al. 2022)

consultation of the state-of-the-art and serves as a critical cornerstone for the subsequent discussion.

The analysis of proposed applications for stabilized mine waste reveals a multifaceted research landscape characterized by distinct strategic clusters. Three primary valorization pathways have been identified: (1) the synthesis of novel cementitious binders via alkaline activation, which represents the most extensively researched route, with geopolymer development as its focal point (Niu et al. 2021, Terrones-Saeta et al. 2021, Mokhtari et al. 2025); (2) the partial replacement of raw materials in traditional construction products, such as mortars, bricks, and aggregates (Ahmari & Zhang 2012, Almeida et al. 2021, Sun et al. 2022, Shoaei et al. 2024); and (3) specialized geotechnical and environmental applications, including mine backfilling and the immobilization of hazardous contaminants (Salihoglu 2014, Lu et al. 2019).

The pronounced emphasis on geopolymer research, as detailed in Table 8, is driven by the global imperative to decarbonize the construction sector. Given that Portland

cement production accounts for nearly 8% of global CO_2 emissions, the search for sustainable alternatives has become urgent. In this scenario, geopolymer technology emerges as a highly viable solution, offering the potential to reduce carbon footprints by up to 80% compared to conventional cement (Provis 2018). This interest signals a profound paradigm shift: mine waste is no longer perceived as a low-value filling material or an inert liability (downcycling), but rather as a reactive chemical precursor capable of being 'upcycled' into high-performance binders. The ability to transform a waste stream into a value-added product underscores the scientific community's intensive engagement with this field.

These two primary strategies, substitution and the creation of novel binders, reflect varying degrees of ambition within the circular economy framework. While replacing aggregates or clays in bricks and mortars represents a lower-risk technological pathway aligned with traditional recycling, the truly disruptive potential lies in 'upcycling' strategies. As argued by Pearce et al. (2021), the objective must be to transition from 'waste management' to 'resource management,' focusing on the development of high-performance materials. While using tailings as aggregate merely replaces an abundant resource like sand, their application as a geopolymer precursor replaces a high-value, high-impact product like cement. This distinction is critical, as it positions geopolymers in a dual dimension: not only as a waste valorization technology but also as a cornerstone of sustainable material science. This 'upcycling' value is further substantiated by the durability of the resulting products. Experimental evidence from Manjunatha et al. (2021) demonstrated that gold-tailings-based geopolymers exhibited exceptional resistance to sulfate and acid attack, in some cases outperforming traditional Portland cement mortars in aggressive environments.

Finally, the diverse niche applications listed in Table 8, though less frequent, represent the most innovative frontier of this research area. Proposals such as refractory products (Kalaitzidou et al. 2023) or thermal insulation materials (Terrones-Saeta et al. 2023) exemplify valorization driven by mineralogical specificity. Certain mine wastes possess unique chemical profiles high in magnesium, alumina, or amorphous silica that render them naturally suited for high-performance applications beyond simple mechanical strength. For example, de Klerk et al. (2020) successfully synthesized high-performance refractory and insulating materials from bauxite tailings, leveraging their high alumina content. Another high-value application is the production of glass-ceramics (Cortizas et al. 2021). This 'waste mining' approach allows environmental liabilities to be reimagined as raw materials for specialized architectural or industrial markets, effectively diversifying value chains and fostering cross-sectoral integration between the mining and construction industries.

4. CONCLUSIONS

This systematic review of 68 studies shows that the stabilization of mine waste cannot be explained solely by binder dosage. Findings indicate that geomechanical performance depends mainly on the interaction between waste mineralogy, binder type, and curing conditions.

Even though Portland cement remains a reliable benchmark, especially under ambient curing conditions, pozzolanic and alkali-activated systems show a broader performance potential. This potential, however, is frequently associated with thermal curing, which limits direct transfer to field-scale applications.

Our results also confirm that the relationship between binder dosage and compressive strength is nonlinear. Higher binder content does not necessarily improve performance, and in many cases the effect reaches a plateau or even becomes inefficient when chemical compatibility is not favorable. In other words, dosage must be interpreted as a system-dependent variable rather than as a universal optimization criterion.

Taken together, the findings support a shift from a volumetric approach toward a techno-mineral perspective, whereby mining waste is treated as a reactive material whose stabilization success depends on its chemical and mineralogical characteristics. In that context, one of the main challenges for future research is the development of effective formulations under ambient curing conditions to reduce the gap between laboratory performance and large-scale implementation.

5. REFERENCES

Abdelkader, H.A.M., Ahmed, A.S.A., Hussein, M.M.A., Ye, H. and Zhang, J., 2022. An experimental study on geotechnical properties and micro-structure of expansive soil stabilized with waste granite dust. *Sustainability* (Switzerland), 14(10). [DOI]

Ahmari, S. and Zhang, L., 2012. Production of eco-friendly bricks from copper mine tailings through geopolymerization. *Construction and Building Materials*, 29, pp. 323–331. [DOI]

Ally, A.N., Blanche, M.M., Grâce, M.M., Zang, E.R., François, N. and Pettang, C., 2023. Potential use of coltan mining waste rock in road construction. *Advances in Civil and Architectural Engineering*, 14(27), pp. 14–31. [DOI]

Almeida, J., Faria, P., Ribeiro, A.B. and Santos Silva, A., 2021. Cement-based mortar production applying mining residues treated with an electro-based technology and a thermal treatment: technical and economic effects. *Construction and Building Materials*, 280. [DOI]

Amari, S., Darestani, M., Millar, G.J., Samali, B. and Strounina, E., 2024. Engineering and life cycle assessment (LCA) of sustainable zeolite-based geopolymer incorporating blast furnace slag. *Sustainability (Switzerland)*, 16(1). [DOI]

Arioz, E., Arioz, O. and Mete Kockara, O., 2012. Leaching of F-type fly ash based geopolymers. *Procedia Engineering*. Elsevier Ltd, pp. 1114–1120. [DOI]

Arpalahti, A. and Lundström, M., 2018. The leaching behavior of minerals from a pyrrhotite-rich pentlandite ore during heap leaching. *Minerals Engineering*, 119, pp. 116–125. [DOI]

Batista, A.J. and Ingunza, M.D.P.D., 2023. Characterization of granite mining waste for geotechnical purposes. *Revista de Geociências do Nordeste*, 9(1), pp. 1–12. [DOI]

Beghoura, I. and Castro-Gomes, J., 2021. Enhancing density-based mining waste alkali-activated foamed materials incorporating expanded cork. *Civil Eng*, 2(2), pp. 523–540. [DOI]

Benhamouda, A., Castro-Gomes, J. and Pereira-de-Oliveira, L., 2021. Rheology, mechanical properties and porosity of ternary alkali-activated binders based on mining mud waste with waste glass and metakaolin. *CivilEng*, 2(1), pp. 236–253. [DOI]

Berdoudi, S., Hebhoub, H. and Djebien, R., 2017. Valorization and recycling of quarries waste as an addition in cement. *Journal of Applied Engineering Science*, 15(2), pp. 122–127. [DOI]

Bessa, S., Duarte, M., Lage, G., Mendonça, I., Galery, R., Lago, R., Texeira, A.P., Lameiras, F. and Aguilar, M.T., 2024. Characterization and analysis of iron ore tailings sediments and their possible applications in earthen construction. *Buildings*, 14(2), p. 362. [DOI]

Beulah, M., Sudhir, M.R., Mohan, M.K., Gayathri, G. and Jain, D., 2021. Mine waste-based next generation bricks: a case study of iron ore tailings, red mud and GGBS utilization in bricks. *Advances in Materials Science and Engineering*, 2021. [DOI]

Borges, P.H.R., Ramos, F.C.R., Caetano, T.R., Panzerra, T.H. and Santos, H., 2019. Reuse of iron ore tailings in the production of geopolymer mortars. *Revista Escola de Minas*, 72(4), pp. 581–587. [DOI]

Bouchikhi, A., Amar, M., Arroug, L., Safhi, A. el M. and Haddaji, Y., 2024. Characterizing nano-indentation and microstructural properties of mine tailings-based geopolymers. *Case Studies in Construction Materials*, 21. [DOI]

Burduhos Nergis, D.D., Vizureanu, P., Sandu, A.V., Burduhos Nergis, D.P. and Bejinariu, C., 2022. XRD and TG-DTA study of new phosphate-based geopolymers with coal ash or metakaolin as aluminosilicate source and mine tailings addition. *Materials*, 15(1). [DOI]

Carrillo Beltrán, R., Picazo Camilo, E., Perea Toledo, G. and Corpas Iglesias, F.A., 2024. Towards a sustainable mining: reuse of slate stone cutting sludges for new geopolymer binders. *Sustainability*, 16(8), p. 3322. [DOI]

Chen, Yuanguang, Chen, Yanlong, Zhang, Y., Zhang, J. and Chen, T., 2024. Mechanical properties and penetration characteristics of mudstone slag-based waterproof composites under cyclic loading. *Applied Sciences (Switzerland)*, 14(1). [DOI]

Cortizas, A.M., López-Merino, L., Silva-Sánchez, N., Sjöström, J.K. and Kylander, M.E., 2021. Investigating the mineral composition of peat by combining FTIR-ATR and multivariate analysis. *Minerals*, 11(10). [DOI]

Cristelo, N., Coelho, J., Oliveira, M., Consoli, N.C., Palomo, Á. and Fernández-Jiménez, A., 2020. Recycling and application of mine tailings in alkali-activated cements and mortars-strength development and environmental assessment. *Applied Sciences (Switzerland)*, 10(6). [DOI]

de Klerk, M.D., Kayondo, M., Moelich, G.M., de Villiers, W.I., Combrinck, R. and Boshoff, W.P., 2020. Durability of chemically modified sisal fibre in cement-based composites. *Construction and Building Materials*, 241. [DOI]

de Leon, L.N., Labastida, P.B., Jan Macalino, E. and Magdaluyo, E., 2024. Development of geopolymer from gold mine tailings utilizing Taguchi robust design. *Engineering Research Express*, 6(4). [DOI]

Ellis, K., Alharbi, N., Matheu, P.S., Varela, B. and Hailstone, R., 2015. Durability of alkali activated blast furnace slag. *IOP Conference Series: Materials Science and Engineering*. Institute of Physics Publishing. [DOI]

Erunkulu, I.O., Malumbela, G. and Oladijo, O.P., 2024. Performance evaluation of fly ash–copper slag-based geopolymer bricks. *Low-Carbon Materials and Green Construction*, 2(1). [DOI]

Farenzena, H.P., Bruschi, G.J., Medina, G.S., de Sousa Silva, J.P., Lotero, A. and Consoli, N.C., 2024. Iron ore tailings stabilization with alternative alkali-activated cement for dry stacking: mechanical and microstructural insights. *Canadian Geotechnical Journal*, 61(4), pp. 649–667. [DOI]

Frasson, B.J., Pinto, R.C.A. and Rocha, J.C., 2019. Influence of different sources of coal gangue used as aluminosilicate powder on the mechanical properties and microstructure of alkali-activated cement. *Materiales de Construccion*, 69(336). [DOI]

Guglietta, D., Belardi, G., Cappai, G., Casentini, B., Godeas, A., Milia, S., Passeri, D., Salvatori, R., Scotti, A., Silvani, V., Tempesta, E., Ubaldini, S. and Trapasso, F., 2020. Toward a multidisciplinary strategy for the classification and reuse of iron and manganese mining wastes. *Chemistry Journal of Moldova*, 15(1), pp. 21–30. [DOI]

Hamid, W. and Alnuaim, A., 2023. Evaluation of the durability and strength of stabilized sabkha soil with geopolymer. *Case Studies in Construction Materials*, 18. [DOI]

Hawerroth, M., Pereira, E., de Almeida, L.N.B., Martins, R.J.E. and Pietrobelli, J.M.T. de A., 2023. Mining waste as an eco-friendly adsorbent in the removal of industrial Basazol Yellow 5G dye and incorporation in mortars. *Processes*, 11(12), p. 3349. [DOI]

Hu, Y., Li, K., Zhang, B. and Han, B., 2022. Investigation of the strength of concrete-like material with waste rock and aeolian sand as aggregate by machine learning. *Journal of Computational Design and Engineering*, 9(5), pp. 2134–2150. [DOI]

Hu, Y., Yao, Y., Zhang, L., Hu, X. and Yang, X., 2025. Green low-temperature activation and curing for high-toughness geopolymer binders from diabase tailings. *Materials*, 18(16). [DOI]

Irfan, M. and Uchimura, T., 2015. Helical filter paper technique for uniform distribution of injected moisture in unsaturated triaxial specimens. *Soils and Foundations*, 55(4), pp. 749–760. [DOI]

Kalaitzidou, K., Pagona, E., Skyfta, G., Tzamos, E., Zouboulis, A. and Mitrakas, M., 2023. Chromite ore addition to serpentinized magnesite mining wastes for the production of refractory products following thermal treatment. *International Journal of Environmental Science and Technology*, 20(12), pp. 13561–13570. [DOI]

Kalin, M., Wheeler, W.N. and Bellenberg, S., 2018. Acid rock drainage or not—oxidative vs. reductive biofilms—a microbial question. *Minerals*. MDPI AG. [DOI]

Kanalli, S.A., Naagesh, S. and Ganesh, K., 2019. Modification of engineering properties of clayey soil by addition of mine waste. *International Journal of Innovative Technology and Exploring Engineering*, 8(12), pp. 2343–2347. [DOI]

Kastiukas, G., Zhou, X., Wan, K.T. and Castro Gomes, J., 2019. Lightweight alkali-activated material from mining and glass waste by chemical and physical foaming. *Journal of Materials in Civil Engineering*, 31(3). [DOI]

Kou, Y., Jiang, H., Ren, L., Yilmaz, E. and Li, Y., 2020. Rheological properties of cemented paste backfill with alkali-activated slag. *Minerals*, 10(3), pp. 1–14. [DOI]

Lam, E.J., Zetola, V., Ramírez, Y., Montofré, Í.L. and Pereira, F., 2020. Making paving stones from copper mine tailings as aggregates. *International Journal of Environmental Research and Public Health*, 17(7). [DOI]

Lehmann, L.M., Smith, J., Westaway, S., Pisanelli, A., Russo, G., Borek, R., Sandor, M., Gliga, A., Smith, L. and Ghaley, B.B., 2020. Productivity and economic evaluation of agroforestry systems for sustainable production of food and non-food products. *Sustainability (Switzerland)*, 12(13). [DOI]

Liza, R., Pereyra, P., Rau, J., Guzman, M., Sajo-Bohus, L. and Palacios, D., 2023. Assessment of natural radioactivity and radon exhalation in Peruvian gold mine tailings to produce a geopolymer cement. *Atmosphere*, 14(3). [DOI]

Lockhart, J.A., Power, I.M., Paulo, C., Stubbs, A.R., Zeyen, N., Wilson, S., Steele-MacInnis, M., Caldwell, R. and Gunning, C., 2024. Weathering and cementation of historic kimberlite residues from South Africa: implications for residue stabilization and CO2 sequestration. *Science of the Total Environment*, 955. [DOI]

Lu, P., Liu, C., Zhang, J., Cheng, Y. and Nei, Q., 2019. Experimental study on strength of cemented rock-tailings backfill. *IOP Conference Series: Earth and Environmental Science*. Institute of Physics Publishing. [DOI]

Mabroum, S., Moukannaa, S., El Machi, A., Taha, Y., Benzaazoua, M. and Hakkou, R., 2020. Mine wastes based geopolymers: a critical review. *Cleaner Engineering and Technology*. Elsevier Ltd. [DOI]

Manjunatha, M., Seth, D., KVGD, B. and Chilukoti, S., 2021. Influence of PVC waste powder and silica fume on strength and microstructure properties of concrete: an experimental study. *Case Studies in Construction Materials*, 15. [DOI]

Matheu, P.S., Ellis, K. and Varela, B., 2015. Comparing the environmental impacts of alkali activated mortar and traditional Portland cement mortar using life cycle assessment. *IOP Conference Series: Materials Science and Engineering*. Institute of Physics Publishing. [DOI]

Mendonça, V.M., De Góes Padula, F.R., Silva, S.N., Silva, P.F.B. and De Paula, J., 2021. Effects of the addition of graphene on the compressive strength of geopolymeric mortar developed from k-feldspar mining waste. *REM - International Engineering Journal*, 74(3), pp. 345–352. [DOI]

Mokhtari, P., Lin, J., Numkiatsakul, P., Koohestani, B. and Kriven, W.M., 2025. Valorization of mine tailings for sustainable geopolymer production. *International Journal of Ceramic Engineering and Science*, 7(4). [DOI]

Motamedi, D., Takaffoli, M. and Milani, A.S., 2020. Nonlinear XFEM modeling of mode ii delamination in pps/glass unidirectional composites with uncertain fracture properties. *Materials*, 13(16). [DOI]

Mwandira, W., Nakashima, K., Kawasaki, S., Ito, M., Sato, T., Igarashi, T., Chirwa, M., Banda, K., Nyambe, I., Nakayama, S., Nakata, H. and Ishizuka, M., 2019. Solidification of sand by Pb(II)-tolerant bacteria for capping mine waste to control metallic dust: case of the abandoned Kabwe Mine, Zambia. *Chemosphere*, 228, pp. 17–25. [DOI]

Niu, H., Adrianto, L.R., Escobar, A.G., Zhukov, V., Perumal, P., Kauppi, J., Kinnunen, P. and Illikainen, M., 2021. Potential of mechanochemically activated sulfidic mining waste rock for alkali activation. *Journal of Sustainable Metallurgy*, 7(4), pp. 1575–1588. [DOI]

Opiso, E.M., Tabelin, C.B., Maestre, C. V., Aseniero, J.P.J., Arima, T. and Villacorte-Tabelin, M., 2023. Utilization of palm oil fuel ash (POFA) as an admixture for the synthesis of a gold mine tailings-based geopolymer composite. *Minerals*, 13(2). [DOI]

Paiva, H., Yliniemi, J., Illikainen, M., Rocha, F. and Ferreira, V.M., 2019. Mine tailings geopolymers as a waste management solution for a more sustainable habitat. *Sustainability*, 11(4), p. 995. [DOI]

Palma, G., Bolaños, H., Huamani, R., Clements, C. and Hedayat, A., 2024. Optimization of geopolymers for sustainable management of mine tailings: impact on mechanical, microstructural, and toxicological properties. *Minerals*, 14(10). [DOI]

Pasteris, J.D., Bae, Y., Giammar, D.E., Dybing, S.N., Yoder, C.H., Zhao, J. and Hu, Y., 2021. Worth a closer look: Raman spectra of lead-pipe scale. *Minerals*, 11(10). [DOI]

Pearce, D., Dora, M., Wesana, J. and Gellynck, X., 2021. Toward sustainable primary production through the application of lean management in south african fruit horticulture. *Journal of Cleaner Production*, 313. [DOI]

Perera-Mercado, Y., Hedayat, A., Tunstall, L., Clements, C., Hylton, J., Figueroa, L., Zhang, N., Bolaños Sosa, H.G., Tupa, N., Yanqui Morales, I. and Canahua Loza, R.S., 2022. Effect of the Class C fly ash on low-reactive gold mine tailing geopolymers. *Polymers*, 14(14). [DOI]

Perumal, P., Niu, H., Kiventerä, J., Kinnunen, P. and Illikainen, M., 2020. Upcycling of mechanically treated silicate mine tailings as alkali activated binders. *Minerals Engineering*, 158, p. 106587. [DOI]

Picazo Camilo, E., Valenzuela Expósito, J.J., Carrillo Beltrán, R., Perea Toledo, G.E. and Corpas Iglesias, F.A., 2025. Study of properties of novel geopolymers prepared with slate stone cutting sludge and activated with olive stone bottom ash. *Materials*, 18(8). [DOI]

Provis, J.L., 2018. Alkali-activated materials. *Cement and Concrete Research*. Elsevier Ltd, pp. 40–48. [DOI]

Ren, Z., Jiang, M., Chen, D., Yu, Y., Li, F., Xu, M., Bringezu, S. and Zhu, B., 2022. Stocks and flows of sand, gravel, and crushed stone in China (1978–2018): evidence of the peaking and structural transformation of supply and demand. *Resources, Conservation and Recycling*, 180. [DOI]

Rouaiguia, I., Bounouala, M., Abdelmalek, C., Idres, A. and Benselhoub, A., 2022. Optical sorting technology for waste management from the Boukhadra iron ore mine (NE Algeria). *REM - International Engineering Journal*, 75(1), pp. 55–65. [DOI]

Salas, D.A., Ramirez, A.D., Ulloa, N., Baykara, H. and Boero, A.J., 2018. Life cycle assessment of geopolymer concrete. *Construction and Building Materials*, 190, pp. 170–177. [DOI]

Salihoglu, G., 2014. Immobilization of antimony waste slag by applying geopolymerization and stabilization/solidification technologies. *Journal of the Air and Waste Management Association*, 64(11), pp. 1288–1298. [DOI]

Sarkkinen, M., Kujala, K. and Gehör, S., 2019. Efficiency of MgO activated GGBFS and OPC in the stabilization of highly sulfidic mine tailings. *Journal of Sustainable Mining*, 18(3), pp. 115–126. [DOI]

Scrivener, K.L., John, V.M. and Gartner, E.M., 2018. Eco-efficient cements: potential economically viable solutions for a low-CO2 cement-based materials industry. *Cement and Concrete Research*, 114, pp. 2–26. [DOI]

Sedira, N., Castro-Gomes, J. and Magrinho, M., 2018. Red clay brick and tungsten mining waste-based alkali-activated binder: Microstructural and mechanical properties. *Construction and Building Materials*, *190*, pp.1034-1048. [DOI]

Shoaei, P., Kjøniksen, A.L., Pamies, R. and Pilehvar, S., 2024. Characterization of 3D-printable geopolymer mortars: effect of binder composition and basalt fiber reinforcement. *Case Studies in Construction Materials*, 20. [DOI]

Simate, G.S. and Ndlovu, S., 2014. Acid mine drainage: challenges and opportunities. *Journal of Environmental Chemical Engineering*. Elsevier Ltd, pp. 1785–1803. [DOI]

Solismaa, S., Ismailov, A., Karhu, M., Sreenivasan, H., Lehtonen, M., Kinnunen, P., Illikainen, M. and Räisänen, M.L., 2018. Valorization of Finnish mining tailings for use in the ceramics industry. *Bulletin of the Geological Society of Finland*, 90(1), pp. 33–54. [DOI]

Štulović, M., Radovanović, D., Dikić, J., Gajić, N., Djokić, J., Kamberović, Ž. and Jevtić, S., 2024. Utilization of copper flotation tailings in geopolymer materials based on zeolite and fly ash. *Materials*, 17(24). [DOI]

Sun, Q., Li, B., Wang, H. and Wang, Y., 2022. Degradation mechanism and life prediction of tailings and waste rock aggregate geopolymer concrete under freeze-thaw corrosion. *Materials Research Express*, 9(1). [DOI]

Terrones-Saeta, J.M., Portela, D.C., Luís, A.T., Suárez-Macías, J. and Grande, J.A., 2023. Ceramics for building structures made from contaminated soils: a fuzzy logic intelligence approach to circular mining. *Processes*, 11(5), p. 1512. [DOI]

Terrones-Saeta, J.M., Suárez-Macías, J., Castañón, A.M., Gómez-Fernández, F. and Corpas-Iglesias, F.A., 2021. Retention of pollutants elements from mine tailings of lead in geopolymers for construction. *Materials*, 14(20), p. 6184. [DOI]

Trach, Y., Melnychuk, V., Stadnyk, O., Trach, R., Bujakowski, F., Kiersnowska, A., Rutkowska, G., Skakun, L., Szer, J. and Koda, E., 2023. The possibility of implementation of West Ukrainian Paleogene glauconite–quartz sands in the building industry: a case study. *Sustainability*, 15(2), p. 1489. [DOI]

Verhagen, T.J., Sauer, M.L., van der Voet, E. and Sprecher, B., 2021. Matching demolition and construction material flows, an urban mining case study. *Sustainability*, 13(2), p. 653. [DOI]

Vongsook, K., Boonsung, A., Phummiphan, I., Horpibulsuk, S., Phunpeng, V., Yaowarat, T., Hiranwatthana, K. and Arulrajah, A., 2025. Sustainable geopolymer footpath block using kaolin mining waste as fine aggregate with bagasse fly ash and coal fly ash as precursor. *Cleaner Engineering and Technology*, 26. [DOI]

Wan, Q., Rao, F., Song, S. and Zhang, Y., 2019. Immobilization forms of ZnO in the solidification/stabilization (S/S) of a zinc mine tailing through geopolymerization. *Journal of Materials Research and Technology*, 8(6), pp. 5728–5735. [DOI]

Wurie, N.N., Zheng, J. and Traore, A.F., 2022. Mechanical, leaching, and microstructure properties of mine waste rock reinforced and stabilised with waste oyster shell for road subgrade use. *Materials*, 15(8). [DOI]

Xu, H., Liu, F., Liao, J. and Liu, T., 2023. Research on selection and matching of truck-shovel in oversized open-pit mines. *Applied Sciences*, 13(6), p. 3851. [DOI]

Zhao, S., Meng, F., Liu, Y., Zhang, J., Wang, Y., Tian, X., Li, X., Chen, D., Wang, L. and Qi, T., 2025. Selective extraction of lithium from the clay-type lithium ore by a novel process of blank roasting and CaO-aided alkaline leaching. *Minerals Engineering*, 227. [DOI]

Nature Environment and Pollution Technology
An International Quarterly Peer-Reviewed Open Access Journal

p-ISSN: 0972-6268 | e-ISSN: 2395-3454 Vol. 25 | No. 4 | Article ID B4446 | 2026

RESEARCH ARTICLE https://doi.org/10.46488/NEPT.2026.v25i04.B4446 OPEN ACCESS

Impact of Sugarcane Bagasse Ash Amendment on Soil Attenuation and Leachate Dynamics: Insights from Multivariate Analysis

M. I. Krutika[1], B. Lokeshappa[1], Rashma Shetty[1] and P. C. Srinivasa[2]
[1]University B.D.T College of Engineering, Davanagere 577004, Karnataka, India
[2]Govt. Engineering College, Chamarajanagar, Karnataka, India
†Corresponding author: M. I. Krutika; inamati73@gmail.com

ARTICLE HISTORY

Received: 07-04-2026
Revised: 02-06-2026
Accepted: 07-06-2026

KEYWORDS

Landfill leachate
Sugarcane bagasse ash (SCBA)
Soil–leachate interaction
Lysimeter experiment
Contaminant attenuation
Pearson correlation analysis
Multivariate statistical analysis

CITE THIS ARTICLE

Krutika, M.I., Lokeshappa, B., Shetty, R. and Srinivasa, P.C., 2026. Impact of sugarcane bagasse ash amendment on soil attenuation and leachate dynamics: Insights from multivariate analysis, *Nature Environment and Pollution Technology*, 25(4), B4446. https://doi.org/10.46488/NEPT.2026.v25i04.B4446

COPYRIGHT & LICENCE

© 2026 The Authors
Open Access under CC BY 4.0.

PUBLISHED BY
TECHNOSCIENCE PUBLICATIONS

ABSTRACT

Landfill leachate composition is strongly governed by soil–leachate interactions that control contaminant mobility, attenuation, and long-term environmental impact. The study demonstrates the influence of sugarcane bagasse ash (SCBA)-amended soil on leachate quality through controlled lysimeter experiments and comparative validation with field leachate characteristics from a municipal solid waste (MSW) landfill site. Two cover soil configurations were examined: (i) loam soil and (ii) clay loam amended with SCBA. Simulated rainfall was applied by adding 4.62 L of water weekly over a 17-week monitoring period, and the collected leachate was analyzed for physicochemical parameters, including pH, electrical conductivity (EC), total dissolved solids (TDS), hardness, chloride, biochemical oxygen demand (BOD), and chemical oxygen demand (COD). Results indicate that the SCBA-amended clay loam significantly improved contaminant attenuation compared with unamended loam soil, producing lower EC, TDS, hardness, chloride, BOD, and COD values. The observed reduction is attributed to enhanced adsorption, cation exchange capacity, filtration effects, secondary mineral formation, and accelerated organic degradation mechanisms induced by SCBA incorporation. Experimental findings were further validated against the actual physicochemical characteristics of leachate collected from an operational MSW landfill site under similar ground conditions. Multivariate statistical analysis was employed to interpret the governing processes. Pearson's correlation analysis revealed strong relationships among key parameters, notably EC, total hardness–Mg, and COD–BOD at $p < 0.01$, highlighting coupled mineralization and organic degradation pathways. A constitutive model developed in the laboratory to simulate soil–leachate interaction behavior showed good agreement with both experimental and field observations, confirming the reliability of the proposed attenuation mechanism.

1. INTRODUCTION

Landfill leachate composition is largely controlled by interactions between percolating leachate and the surrounding soil matrix, which influence contaminant mobility, transformation, and retention. These soil–leachate interactions determine the extent to which pollutants migrate through the subsurface environment or are attenuated within the soil system. Factors such as soil texture, mineral composition, permeability, and adsorption capacity play a critical role in regulating the transport of dissolved and suspended contaminants. Landfilling, although considered the least preferred option in the municipal solid waste management hierarchy, remains widely practiced due to its operational simplicity and relatively low cost (Ergene et al. 2022). However, landfill operations inevitably generate leachate through the percolation of precipitation and inherent waste moisture, producing a complex

effluent rich in dissolved organic matter, inorganic salts, nutrients, heavy metals, and other pollutants (Christensen et al. 2001). The composition and strength of leachate depend on several factors, including waste composition, landfill age, climatic conditions, and the degree of biochemical degradation occurring within the waste mass (Kjeldsen et al. 2002). Seasonal variations further influence leachate characteristics, as increased rainfall generally dilutes leachate concentrations, while dry periods tend to increase pollutant strength (Al-Yaqout & Hamoda 2003).

Soil layers in landfill systems act as natural attenuation barriers by reducing contaminant migration through mechanisms such as adsorption, biodegradation, ion exchange, precipitation, and filtration (Aish et al. 2014). However, the attenuation capacity of natural soils is limited, and certain contaminants may eventually migrate once adsorption sites become saturated (Tuffaha 2006). To improve contaminant retention, agricultural by-products have recently been explored as sustainable and low-cost adsorbent materials (Mor et al. 2019). Among these, sugarcane bagasse ash (SCBA) has gained attention due to its porous structure and high silica and alumina content, which enhance adsorption and ion exchange processes (Qian et al. 2024).

Previous studies on sugarcane bagasse ash (SCBA) have predominantly focused on short-term adsorption experiments or synthetic wastewater treatment under simplified laboratory conditions, with limited emphasis on realistic landfill environments and long-term contaminant attenuation behavior. In contrast, the present study introduces a comprehensive lysimeter-scale landfill simulation framework integrating SCBA-amended clay loam soil with geotechnical characterization, long-term leachate monitoring, and multivariate statistical analysis.

A major novelty of this work is the transformation of SCBA from a conventional agricultural waste residue into a functional landfill liner amendment material capable of simultaneously enhancing soil engineering properties and leachate attenuation performance. The incorporation of SCBA significantly improved clay fraction, plasticity, adsorption capacity, and contaminant retention behavior, resulting in superior reduction of COD, BOD, EC, TDS, chloride, and suspended solids compared with natural loam soil.

Unlike previous investigations limited to pollutant removal assessment, this study establishes a direct linkage between soil modification, contaminant migration, and landfill stabilization processes under controlled long-term conditions. The comparative dual-lysimeter system further provides realistic insight into soil–leachate interactions and contaminant transport mechanisms within landfill environments. In addition, the integration of Pearson's correlation analysis, Principal Component Analysis (PCA), and Hierarchical Cluster Analysis (HCA) provides a mechanistic interpretation of leachate evolution by identifying the dominant processes governing mineralization, ionic enrichment, and organic degradation. The strong agreement between PCA and HCA validates the reliability of the proposed analytical framework. Overall, this study presents a novel waste-to-resource approach by demonstrating the potential application of SCBA-amended clay loam soil as a sustainable and cost-effective landfill liner material for enhanced leachate attenuation and environmental protection.

2. MATERIALS AND METHODS

2.1. Study Area and Municipal Solid Waste Collection

The present study was carried out using municipal solid waste (MSW) collected from Davanagere city, Karnataka, India, which is one of the rapidly developing urban centers in the central part of Karnataka. According to recent municipal statistics, the city has an estimated population of approximately 552,000 as of 2024, with an average per capita solid waste generation rate of about 0.35 kg per person per day. Geographically, Davanagere is situated at 14.28° N latitude and 75.59° E longitude, with an average elevation of approximately 602.7 m above mean sea level. The municipal solid waste generated within the city is transported and disposed of at the designated landfill site located at Avaragolla village, which lies nearly 12 km from the main urban area, as shown in Figs. 1(a) and 1(b). The climatic conditions of the region are characterized by a semi-arid tropical climate, with an average annual rainfall of around 644 mm, most of which occurs during the southwest monsoon season. The surrounding soil strata in the region predominantly consist of black cotton soil and red loamy soils, which provide a suitable natural environment for studying soil–leachate interaction processes.

For this experimental investigation, municipal solid waste was collected and characterized to represent the typical waste composition generated within the city, as shown in Fig. 2. The composition data used in this study were obtained from the Karnataka State Pollution Control Board (KSPCB), Davanagere, to ensure that the experimental conditions realistically replicate the actual waste characteristics of the landfill site.

The waste collected from the municipal transfer stations was manually segregated to isolate the organic fraction, which forms the dominant biodegradable component of MSW and is primarily responsible for leachate generation



Fig. 1(a): Municipal landfill site, Avaragolla, Davanagere.



Fig. 1(b): View of solid waste dumped at the MSW site.

during decomposition. The segregated waste was then mechanically chopped to a particle size less than 200 mm, which facilitates better packing of the waste within the lysimeter and improves the percolation of water through the waste matrix. Based on laboratory measurements, the average bulk density of the municipal waste was determined to be 275 kg m^{-3}. The quantity of waste required for filling each lysimeter column was estimated using the relationship:

$$Q = A \times H \times \rho$$

where Q represents the quantity of waste (kg), A denotes the cross-sectional area of the lysimeter (m^2), H represents the height of the waste layer (1 m), and ρ is the bulk density of the waste (kg m^{-3}). This calculation ensured uniform waste loading across all lysimeter units and enabled accurate comparison of leachate generation under different soil configurations.

2.2. Preparation of Soil and Adsorbent Material

Soil samples used in the experimental study were collected from various locations surrounding the landfill site to represent the natural soil conditions prevailing in the study region. Sampling was performed using core cutters, which allowed the extraction of relatively undisturbed soil samples for the determination of physical and geotechnical properties. The collected soil samples were subjected to a series of laboratory tests in accordance with the Indian Standard (IS) code procedures, including determination of grain size distribution, moisture content, bulk density, and plasticity characteristics. Soil classification was carried out using the USDA soil textural classification system, which categorizes soils based on the relative proportions of sand, silt, and clay fractions.

Two types of soil configurations were prepared for the lysimeter experiments. In the first configuration, black cotton soil and lateritic soil were mixed in equal proportions (1:1) to obtain a composite soil mixture designated as Soil 1. Hydrometer analysis and particle size distribution results indicated that this mixture falls within the loam soil category, characterized by a balanced proportion of sand, silt, and clay particles. In the second configuration, Sugarcane Bagasse Ash (SCBA) was incorporated into Soil 1 to enhance its adsorption and contaminant retention capacity. SCBA is an

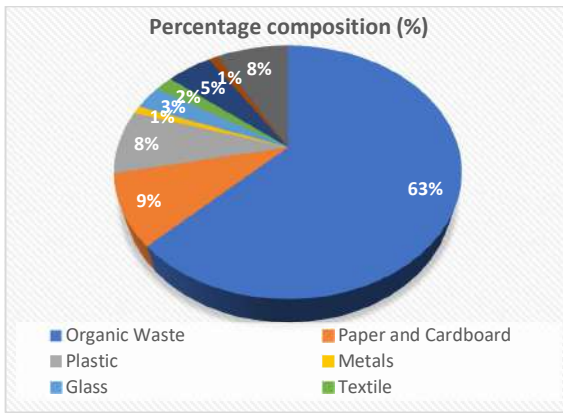


Fig. 2: Graphical representation of solid waste composition.



Fig. 3: Sample of organic waste collected from municipal transfer stations.

agricultural by-product generated during the combustion of sugarcane bagasse in sugar industries for energy production. The SCBA used in this study was collected from a nearby local sugar mill, after which it was oven-dried to remove moisture and subsequently sieved through a 300 µm sieve to obtain a uniform particle size suitable for mixing with soil.

The dried and sieved SCBA was then mixed with Soil 1 in a 3:1 ratio (soil: SCBA) to obtain Soil 2, which served as the modified soil medium for evaluating the effect of SCBA on leachate attenuation. The soil-to-SCBA ratio of 3:1 (75% soil and 25% SCBA by weight) was selected based on previous studies demonstrating that agricultural ash additions in the range of 10–30% improve adsorption capacity, specific surface area, and contaminant retention while maintaining acceptable geotechnical properties and hydraulic performance (Mangi et al. 2017). The presence of SCBA in the soil mixture increases the surface area, porosity, and silica content, thereby improving its capacity to adsorb both organic and inorganic contaminants present in landfill leachate. Hydrometer analysis indicated that the addition of SCBA altered the soil texture, resulting in a clay loam classification for Soil 2 according to the USDA textural triangle. This modified soil was therefore expected to exhibit enhanced contaminant retention through mechanisms such as adsorption, ion exchange, and filtration.

2.3. Collection of Rainfall Data for Experimentation

Rainfall data were collected from the Meteorological Department, Davanagere, to simulate realistic climatic conditions for the lysimeter experiment. Historical precipitation and evaporation data for the monsoon period (June–October) for 2021, 2022, and 2023 were analyzed to determine the average rainfall pattern in the study area. The compiled rainfall and evaporation data are presented in Table 1. The results indicate that July recorded the highest average precipitation (279.70 mm), followed by October (136.87 mm) and August (123.41 mm), while September showed comparatively lower rainfall (64.64 mm). The total average precipitation during the monsoon season was calculated as 706.43 mm, whereas the corresponding total evaporation was approximately 470.93 mm. Based on these climatic conditions, the quantity of water required to simulate rainfall within the lysimeter column was estimated. Considering the dimensions of the lysimeter and the average precipitation values, the calculated equivalent rainfall volume was approximately 4.62 L. Therefore, to replicate natural rainfall conditions under controlled laboratory settings, approximately 4.62 L of water was added weekly to both Lysimeter 1 and Lysimeter 2 throughout the experimental monitoring period. This approach ensured that the leachate generation process in the lysimeter system closely resembled the rainfall-driven percolation conditions occurring in actual landfill environments. The detailed rainfall and evaporation data used for the calculation are summarized in Table 1.

2.4. Lysimeter Design and Experimental Setup

A laboratory-scale lysimeter system was constructed to simulate landfill conditions and to evaluate the generation and migration of leachate through different soil configurations under controlled environmental conditions. The lysimeter columns were fabricated using polyvinyl chloride (PVC) material due to its durability, chemical resistance, and ease of fabrication. Each lysimeter had a total height of 1.8 m and an internal diameter of 0.25 m, which allowed sufficient space to replicate waste layering, soil cover placement, and rainfall infiltration processes similar to those occurring in actual landfill systems.

The internal structure of the lysimeter consisted of multiple layers designed to simulate landfill conditions. At the base of each lysimeter, a 20 cm thick layer of coarse gravel was placed to serve as a drainage layer, ensuring that leachate generated within the waste column could freely flow toward the outlet without obstruction. Above the gravel layer, a hexagonal mesh (hex netting) was installed to prevent fine soil particles from migrating downward and clogging the drainage layer. Figures 4 and 5 illustrate the typical lysimeter configuration and the fabricated laboratory-scale lysimeter used in this study. Sample 1 represents the simulated landfill leachate conditions within the lysimeter system; Sample 2 corresponds to Lysimeter 1 containing Soil 1 (loam soil), and Sample 3 corresponds to Lysimeter 2 containing Soil 2 (SCBA-amended

Table 1: Precipitation and evaporation data from the Meteorological Department, Davanagere.

Month	Precipitation, mm				Evaporation, mm			
	2021	2022	2023	Average	2021	2022	2023	Average
June	171.09	72.73	61.52	101.78	95.4	105.2	116.2	105.6
July	334.09	351.97	153.05	279.70	83.2	74.9	45.1	67.73
August	66.70	290.65	12.89	123.41	85.2	65.3	129	93.16
September	36.55	133.46	23.92	64.64	98	90.9	92.2	93.7
October	213.337	194.85	2.42	136.87	111.3	99.4	121.5	110.73
Total Precipitation				706.43				470.93

clay loam soil). The organic fraction of municipal solid waste was then placed above this mesh and compacted manually using a hammer until a uniform waste height of approximately 1 m was achieved. Compaction was carried out carefully to achieve a consistent density and to mimic the compaction conditions typically encountered in landfill operations.

Two lysimeters were prepared using different soil configurations(Figs. 4 and 5). In Lysimeter 1, Soil 1 was used as the cover layer and was placed both above and below the waste layer to a thickness of approximately 10 cm. In Lysimeter 2, the SCBA-modified soil (Soil 2) was used in a similar configuration. These soil layers were designed to

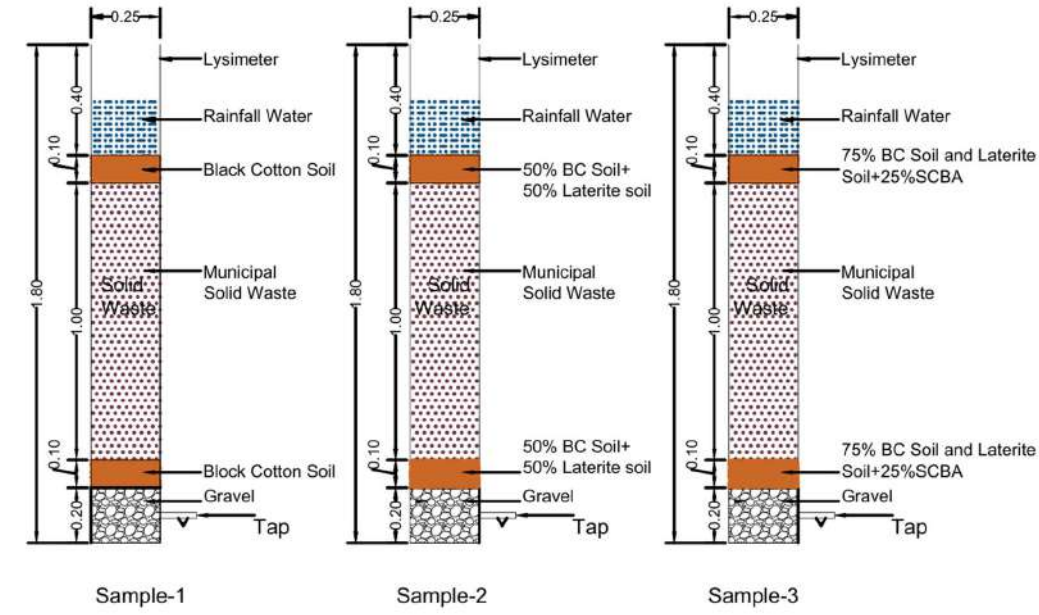


Fig. 4: Typical representation of the lysimeter setup for soil samples 1, 2, and 3.

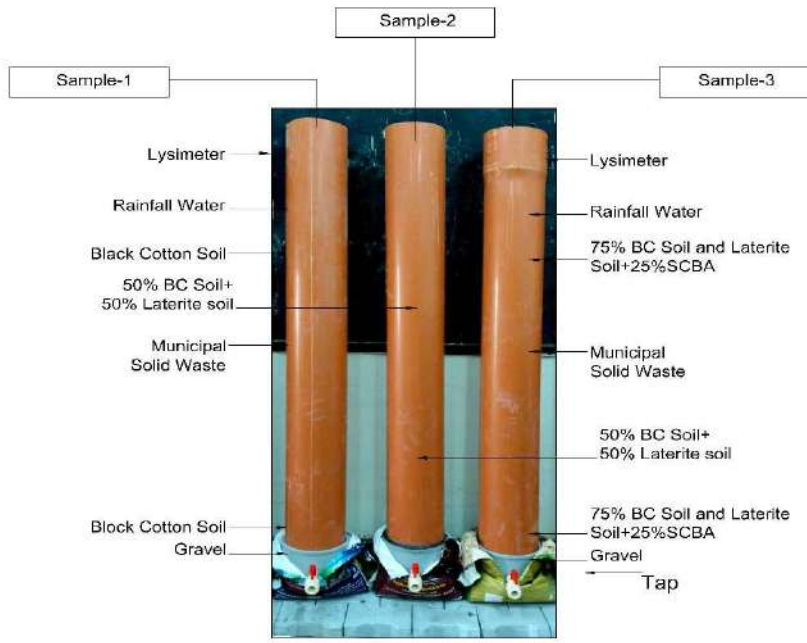


Fig. 5: Lysimeter columns fabricated using polyvinyl chloride (PVC) pipe at the Environmental Engineering Laboratory.

simulate landfill cover and liner materials that influence leachate movement and contaminant attenuation. A freeboard of 40 cm was maintained above the waste layer to allow space for rainfall simulation and water infiltration. In addition, a tap outlet was installed near the base of the lysimeter column to facilitate periodic collection of the generated leachate samples for laboratory analysis.

2.5. Rainfall Simulation and Leachate Generation

To simulate natural rainfall infiltration within the landfill environment, controlled quantities of water were added to the top surface of the lysimeter at regular intervals. A total volume of 4.62 L of water was applied once every seven days for 17 weeks, thereby reproducing periodic rainfall conditions that promote leachate formation. The quantity of water applied during each cycle was calculated based on regional climatic datausing the equation proposed by Aish et al. (2014):

$$L = P(1 - C) - E \quad \ldots(1)$$

$$L = 706.43(1 - 0.2) - 470.93$$

$$L = 94.214 \text{ mm}$$

Where $W = L \times A$

$$W = 94.214 \times 0.04908$$

$$W = 4.62 \text{ L}$$

Where L represents the depth of leachate water (mm), P denotes precipitation (mm), C represents the runoff coefficient (C = 0.2) (Paris 1996), and E indicates evaporation losses (mm). Climatic data related to rainfall and evaporation used in the calculations were obtained from local irrigation department records.

The periodic addition of water allowed moisture to infiltrate through the waste mass and interact with the soil layers and adsorbent materials present in the lysimeter. As the water percolated through the decomposing waste, it dissolved organic and inorganic constituents, resulting in the formation of landfill leachate. The generated leachate subsequently migrated downward through the soil layers and accumulated at the base of the lysimeter, from where it was collected for analysis.

2.6. Leachate Collection and Physicochemical Analysis

Leachate samples produced during the experiment were collected at seven-day intervals by opening the outlet valve located at the base of each lysimeter column. The collected samples were stored in clean polyethylene bottles and transported to the laboratory for further analysis. Prior to analysis, the samples were preserved and handled according to standard laboratory procedures to prevent contamination and chemical alteration.

The leachate samples were analyzed for several important physicochemical parameters, including pH, electrical conductivity (EC), total dissolved solids (TDS), total hardness, chloride concentration, color, suspended solids, biochemical oxygen demand (BOD), and chemical oxygen demand (COD). These parameters were selected because they provide a comprehensive indication of the organic and inorganic pollutant load present in landfill leachate. All analytical procedures were carried out in accordance with the Standard Methods for the Examination of Water and Wastewater published by the American Public Health Association (APHA 2017). These standardized analytical techniques ensure the reliability, accuracy, and comparability of the experimental data.

2.7. Statistical Data Analysis

To interpret the experimental results and identify relationships among the measured leachate parameters, statistical analyses were conducted using IBM SPSS Statistics software (Version 27.0.1). Initially, descriptive statistical methods were employed to summarize the dataset and to determine key statistical indicators such as the mean, standard deviation, and range for each physicochemical parameter measured in the leachate samples. This preliminary analysis helped in understanding the variability and distribution of the measured parameters.

Prior to conducting multivariate statistical analysis, the dataset was normalized in order to eliminate the influence of differences in measurement units and scale among the parameters. Normalization ensures that each variable contributes equally to the statistical analysis and improves the reliability of the resulting interpretations (Aruga et al. 1995). Pearson's correlation analysis was subsequently performed to determine the degree of association between different physicochemical parameters and to identify possible relationships among variables influencing leachate quality.

2.8. Principal Component Analysis and Factor Analysis (PCA/FA)

Principal Component Analysis (PCA) was applied to the normalized dataset in order to reduce the dimensionality of the data while retaining the maximum possible variance. PCA transforms the original correlated variables into a smaller number of independent variables known as principal components (PCs) through linear combinations of the original dataset. These principal components represent the dominant factors controlling variations in leachate

composition and help identify the most influential parameters affecting leachate quality.

Factor Analysis (FA) was subsequently performed to further simplify the structure of the dataset by rotating the principal component axes using the varimax rotation method. This rotation process generates varifactors (VFs) that provide a clearer interpretation of the underlying relationships between variables. The FA model can be expressed mathematically as:

$$Zji = af1f1i + af2f2i + ... + afmfmi + ... + afmfmi + efi \quad \ldots(2)$$

where Z represents the measured variable, a represents the factor loading, f represents the factor score, e denotes the residual error, i represents the sample number, and m represents the total number of factors. Factor loadings were categorized as strong (>0.75), moderate (0.50–0.75), and weak (0.30–0.50) according to the classification criteria (Liu et al. 2003).

2.9. Cluster Analysis (CA)

Cluster Analysis (CA) was employed to classify leachate samples into groups based on similarities in their physicochemical characteristics. In this study, Hierarchical Agglomerative Clustering (HCA) was applied using Ward's method as the linkage technique and squared Euclidean distance as the similarity measure. Ward's method operates by minimizing the total within-cluster variance at each stage of the clustering process, thereby producing compact and homogeneous clusters.

The results of the cluster analysis were presented in the form of a dendrogram, which graphically illustrates the degree of similarity between samples and the hierarchical relationships among clusters. This approach allows the identification of groups of samples with similar chemical characteristics and provides insights into the spatial and temporal variability of leachate quality within the experimental system.

3. RESULTS AND DISCUSSION

This section evaluates the influence of soil characteristics and Sugarcane Bagasse Ash (SCBA) incorporation on the attenuation of landfill leachate using controlled lysimeter experiments. Initial analysis focuses on the geotechnical properties of the soils, which determine permeability, adsorption capacity, and overall suitability for contaminant containment. This is followed by a physicochemical assessment of leachate quality to understand variations in parameters such as pH, EC, TDS, hardness, and organic load between the two lysimeter systems. To further interpret the relationships among these parameters, Pearson's correlation analysis is performed to identify significant interactions between inorganic ions and organic pollution indicators. Subsequently, Principal Component Analysis (PCA) is applied to determine the dominant processes controlling leachate evolution and to reduce dataset dimensionality. Finally, Hierarchical Cluster Analysis (HCA) is used to classify leachate samples based on similarity patterns, providing additional insight into the governing geochemical and biodegradation mechanisms. The detailed interpretations and quantitative results for each of these aspects are presented in the following subsections.

3.1. Soil Characterization for Lysimeter Study

Soil samples were collected from areas to ensure minimal prior contamination and to simulate natural soil–leachate interactions within the lysimeter system. The geotechnical properties of the collected soil were determined in accordance with relevant Indian Standard (IS) codes to evaluate its suitability for use in the experimental setup. To enhance the treatment efficiency and adsorption capacity of the soil in a cost-effective manner, Sugarcane Bagasse Ash (SCBA) was incorporated into the soil at a proportion of 1:3 (SCBA: Soil). Prior to testing, the samples were air-dried, pulverized, and passed through a 4.75 mm sieve to obtain a uniform material suitable for laboratory analysis. Based on the classification tests, the unclassified soil was identified as loam, while the soil blended with SCBA exhibited characteristics of clay loam. The change in soil texture indicates an increase in the finer fraction due to the addition of SCBA, which is expected to improve the soil's adsorption capacity, reduce permeability, and enhance its effectiveness in attenuating contaminants during the lysimeter leachate treatment process.

3.2. Geotechnical Properties of Soil Samples

The geotechnical analysis indicates notable differences between Soil 1 and Soil 2 due to the incorporation of sugarcane bagasse ash (SCBA). Soil 1 was classified as loam, whereas Soil 2 showed clay loam characteristics with a higher clay fraction. Table 2 shows the geotechnical characterization of soil samples used in the lysimeter study. The grain size distribution and Atterberg limits indicate that Soil 2 possesses improved cohesion, moderate plasticity, and lower permeability compared with Soil 1. Both soils exhibited low swelling potential and slightly alkaline pH, which are favorable for contaminant adsorption and stabilization (Das 2020). The increased clay content in Soil 2 enhances surface area and adsorption capacity, improving its ability to retain pollutants. Overall, Soil 2 demonstrates better suitability for leachate attenuation and environmental containment in the lysimeter study.

Table 2: Geotechnical characterization of soil samples used in the lysimeter study.

Parameter	Test Method	Soil 1 (Loam)	Soil 2 (Clay Loam – with SCBA)
Specific Gravity	Pycnometer Method	2.60	2.65
Gravel (%)	Sieve Analysis	25	33
Sand (%)	Sieve Analysis	12	6
Silt (%)	Hydrometer Analysis	40	24
Clay (%)	Hydrometer Analysis	23	37
Liquid Limit (%)	Casagrande Method	39	43
Plastic Limit (%)	IS Method	30	21
Plasticity Index (%)	LL – PL	9	22
Differential Free Swell (%)	Free Swell Method	20	30
pH	pH Meter	7.6	7.7
Soil Type (Textural Classification)	USDA Textural Triangle	Loam	Clay Loam

The geotechnical characterization of the two soil samples indicates noticeable differences in their physical and engineering properties due to the incorporation of sugarcane bagasse ash (SCBA). Soil 1 was classified as loam, while Soil 2 exhibited clay loam characteristics with a higher clay fraction, which contributes to improved cohesion and reduced permeability (Karnchanawong & Yongpisalpop 2009). The specific gravity values remained within the typical range for natural soils, indicating that the addition of SCBA did not significantly alter the mineral composition of the soil matrix. Grain size analysis showed that Soil 2 contains a higher clay content and lower silt fraction compared with Soil 1, which enhances adsorption capacity and contaminant retention potential. Figs. 6 and 7 show the textural classification of the soils.

The Atterberg limit results further indicate that Soil 2 possesses slightly higher plasticity, suggesting improved structural stability and moisture retention. Differential free swell values for both soils fall within the low swelling range, confirming the absence of highly expansive clay minerals (Lambe & Whitman 1969). In addition, the slightly alkaline pH observed in both soils is favorable for adsorption and precipitation of contaminants present in landfill leachate. Overall, the results indicate that Soil 2, due to its higher clay content and moderate plasticity, offers better suitability for contaminant attenuation and environmental containment in lysimeter-based leachate studies.

3.3. Field and Lysimeter Leachate Characteristics

The physicochemical characteristics of municipal solid waste (MSW) landfill leachate collected from the Avaragolla landfill site, Davanagere, as presented in Table 3, were compared with the leachate generated under controlled laboratory conditions using lysimeter prototype models filled with study-area soils. The field leachate represents the actual conditions prevailing at the landfill site and reflects the complex interactions among waste composition, microbial decomposition, rainfall infiltration, and geochemical

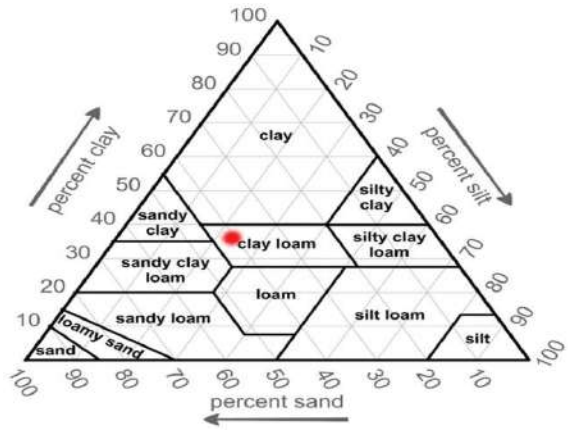


Fig. 6: Textural classification of clay loam soil.

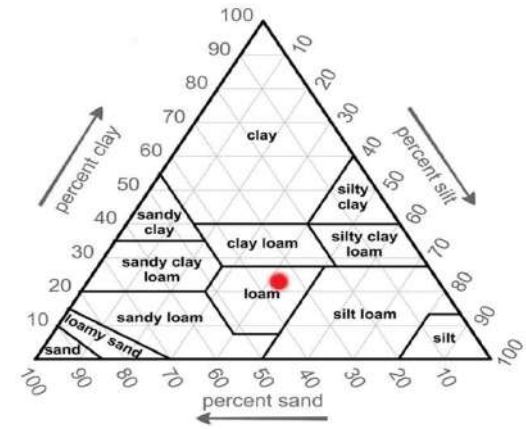


Fig. 7: Textural classification of loam soil.

Table 3: Initial physicochemical characteristics of landfill leachate.

Parameter	Initial characteristics of landfill leachate
pH	5.6
TSS (mg L^{-1})	1800
EC (mS cm^{-1})	5.6
TDS (mg L^{-1})	3072
Total hardness (mg L^{-1})	11650
Magnesium (mg L^{-1})	1200
Calcium (mg L^{-1})	5000
Chloride (mg L^{-1})	4397
COD (mg L^{-1})	13600
BOD (mg L^{-1})	3428.57
Color (Pt-Co)	9600

processes occurring within the landfill mass. Such field observations provide an important baseline for understanding the nature of contaminants released from municipal solid waste disposal systems.

To simulate these landfill conditions under controlled experimental conditions, laboratory lysimeter experiments were conducted using the soils collected from the study area. The lysimeter system was designed to replicate the natural landfill environment by allowing rainfall infiltration through the lysimeter and facilitating the generation and collection of leachate over time. Periodic monitoring of the physicochemical parameters shown in Table 4 enabled the evaluation of stabilization and attenuation of leachate characteristics during the experimental period.

A comparative evaluation between the field leachate and lysimeter-generated leachate indicates that the laboratory prototype successfully reproduced the general physicochemical behavior of landfill leachate observed at the site, as presented in Tables 5 and 6. Both systems exhibited characteristics typical of municipal solid waste leachate, including high organic load, elevated dissolved ions, and strong mineralization resulting from waste degradation and leaching processes (Dabrowska & Rykala 2021). The pH of Lysimeter 1 varied between 6.9 and 8.1, whereas Lysimeter 2 exhibited a wider range of 6.2–8.1. In both systems, the leachate progressively shifted toward neutral to mildly alkaline conditions during the later stages of the experiment. This behavior is consistent with the transition from the acidogenic stage toward more stabilized methanogenic conditions, in which the consumption of volatile fatty acids and carbonate/bicarbonate buffering can promote an increase in pH (Saghi et al. 2024). The marked decrease in pH in Lysimeter 2 during W16–W17 (6.3 and 6.2, respectively) indicates that localized biochemical or mineral dissolution processes may have persisted toward the end of the monitoring period (Ahmed & Lan 2012). Therefore, although both systems generally exhibited circumneutral to slightly alkaline conditions, the clay-loam system showed somewhat greater temporal variability.

Table 4: Landfill simulation readings for the lysimeter containing Black Cotton Soil (BCS), classified as clay-loam soil representative of the study area.

Week	pH	TSS (mg L^{-1})	EC (mS cm^{-1})	TDS (mg L^{-1})	Total hardness (mg L^{-1})	Mg (mg L^{-1})	Ca (mg L^{-1})	Chloride (mg L^{-1})	COD (mg L^{-1})	BOD (mg L^{-1})	Color (Pt-Co)
W1	6.2	400	4.5	2880	6850	924	1200	430	6000	3133	7050
W2	6.7	570	4.6	2944	7400	912	1440	450	6800	3605.91	7100
W3	7.5	790	5.2	4160	7800	960	1520	590	8000	4492.61	7294
W4	7.8	910	5.4	4320	8200	1008	1600	610	10000	5201.97	8488
W5	8.3	1290	5.9	4720	9000	1080	1800	720	11600	5733.99	9500
W6	8.2	1500	6.3	5040	9600	1152	1920	840	12000	6147.78	9600
W7	7.8	1800	5.6	4480	10200	1248	2000	960	10000	3960.59	8200
W8	7.9	1700	5.1	4080	6500	1792	2280	720	6000	2778.32	6900
W9	7.5	1500	4.5	2880	4900	1600	1960	520	4500	1241.37	5200
W10	7.4	1320	4	2560	4500	2576	1840	360	3800	1004.92	4146
W11	7.2	1200	3.0	1950	8400	2000	1650	1300	3300	931.62	1545
W12	6.8	910	2.3	1520	2400	1567	1460	1900	2990	890.36	1223
W13	6.2	790	14.4	9370	4000	1945	920	4100	2400	720.56	1230
W14	6.2	710	14.7	9570	3900	1928	840	3900	1900	635.63	1156
W15	6.1	490	15.1	9790	4700	920	720	700	1850	601.2	805
W16	6	500	1.7	1080	6400	925	720	500	1760	512.35	607
W17	6.1	540	12.4	8090	4800	944	680	200	1540	499.65	575

The temporal evolution of EC and TDS indicates substantial mobilization of dissolved constituents in both lysimeters. In Lysimeter 1, EC varied from 1.04 to 14.5 mS cm^{-1} and TDS ranged from 650 to 9440 mg L^{-1}. In Lysimeter 2, EC ranged from 1.40 to 14.85 mS cm^{-1}, while TDS varied between 1020 and 9650 mg L^{-1}. Thus, the maximum EC and TDS values were slightly higher in theSCBA-amended clay loam systemthan in the loam system. The highest TDS concentrations occurred at W14 in Lysimeter 1 (9440 mg L^{-1}) and W12 in Lysimeter 2 (9650 mg L^{-1}), indicating pronounced ionic enrichment during the intermediate-to-late stages of leachate evolution(Dabrowska et al. 2022). The elevated EC and TDS in the SCBA-amended system should not be interpreted solely as evidence of greater contaminant mobility because SCBA may release soluble alkaline and mineral constituents, thereby contributing to the dissolved ionic fraction. Accordingly, the observed conductivity and TDS patterns are more appropriately attributed to the combined effects of leachate mineralization and dissolution of soil/SCBA-derived constituents. Total hardness showed a marked difference between the two systems, particularly during W10. Lysimeter 1 exhibited hardness values ranging from 1452 to 12,300 mg L^{-1}, while Lysimeter 2 ranged from 2100 to 5900 mg L^{-1}. The exceptionally high hardness concentration in Lysimeter 1 at W10 was accompanied by elevated Mg (2913 mg L^{-1}), Ca (3280 mg L^{-1}), and chloride (800 mg L^{-1}), suggesting substantial mineral dissolution or a transient concentration effect during this period. However, the subsequent reduction in hardness indicates that this was not a persistent condition. In Lysimeter 2, hardness remained comparatively moderate and reached a maximum of 5900 mg L^{-1} at W10. The generally lower hardness response in the clay-loam system after W10 may reflect retention of divalent cations through adsorption and ion-exchange processes within the finer soil matrix, although dissolution of SCBA-derived minerals may also have contributed to the observed concentrations. The concentrations of Mg and Ca further demonstrate differences in mineral-ion behavior between the systems. Magnesium concentrations in Lysimeter 1 increased from approximately 643 mg L^{-1} during the initial weeks to a maximum of 2913 mg L^{-1} at W10, followed by a progressive decline to 280 mg L^{-1} at W17. In Lysimeter 2, Mg reached a lower maximum of 1399 mg L^{-1} at W10 and subsequently declined to 520 mg L^{-1}. Calcium concentrations were comparatively similar between the systems, although Lysimeter 2 reached a slightly higher maximum concentration (5480 mg L^{-1} at W12) than Lysimeter 1 (5280 mg L^{-1} at W12). These trends indicate that the behavior of individual cations was not governed by a single mechanism; rather, dissolution, ion exchange, adsorption, precipitation, and changing aqueous chemistry likely operated simultaneously.

Chloride concentrations also showed a contrasting response. Lysimeter 1 exhibited chloride concentrations

Table 5: Leachate characteristics of Lysimeter 1 for the loam soil mixture.

Week	pH	TSS (mg L^{-1})	EC (mS cm^{-1})	TDS (mg L^{-1})	Total hardness (mg L^{-1})	Mg (mg L^{-1})	Ca (mg L^{-1})	Chloride (mg L^{-1})	COD (mg L^{-1})	BOD (mg L^{-1})	Color (Pt-Co)
W1	7.4	690	6	4800	3680	643	400	280	12800	3780	4010
W2	7.3	740	6.25	5000	3720	643	432	310	13600	3840	4120
W3	7.1	810	6.4	5120	3800	644	448	320	14400	3960	4250
W4	7.1	870	6.7	5360	3920	663	464	350	14800	4020	4360
W5	6.9	920	6.85	5480	4080	682	496	370	15600	4140	4490
W6	6.9	1000	7	5600	4200	701	512	400	16000	4320	4600
W7	7.2	1050	6.75	5400	4080	696	480	380	15200	4260	4490
W8	7.3	1100	6.69	5352	3960	672	464	350	14000	4200	4375
W9	7.4	1150	6.56	5248	3880	662	448	320	12800	4080	4250
W10	8	1068	4.43	2880	12300	2913	3280	800	11960	4932	2053
W11	7.6	987	1.66	1080	3500	832	680	2200	10569	3899	1648
W12	8	875	11.8	7680	3100	681	5280	2700	10247	3765	1238
W13	8.1	768	13.1	8520	2100	496	720	1700	9872	2876	1145
W14	7.9	678	14.5	9440	3500	833	600	400	8799	2700	1120
W15	7.9	623	13.8	9020	3100	731	1160	500	7698	2630	902
W16	7.4	580	1.09	706	1700	391	1440	100	7628	2498	875
W17	7.2	520	1.04	650	1452	280	1263	100	6859	2380	879

Table 6: Leachate characteristics of Lysimeter 2 for the SCBA soil mixture.

Week	pH	TSS (mg L^{-1})	EC (mS cm^{-1})	TDS (mg L^{-1})	Total hardness (mg L^{-1})	Mg (mg L^{-1})	Ca (mg L^{-1})	Chloride (mg L^{-1})	COD (mg L^{-1})	BOD (mg L^{-1})	Color (Pt-Co)
W1	7.14	580	3.7	2368	3360	585	368	230	8800	2640	7486
W2	7	600	3.9	2496	3440	595	400	250	9600	2820	7600
W3	6.9	700	4.1	2624	3600	605	432	270	10800	2940	7720
W4	6.82	760	4.4	2816	3800	644	448	290	11600	3000	7850
W5	6.71	810	4.5	2880	3920	653	480	320	12400	3180	7940
W6	6.65	860	4.8	3072	4120	691	496	340	12800	3300	8110
W7	6.8	900	4.6	2944	4000	682	464	310	12000	3240	7900
W8	6.92	940	4.48	2867	3920	670	448	290	11200	3180	7820
W9	7	1000	4.4	2816	3800	660	416	270	10000	3060	7800
W10	8	1100	4.43	2880	5900	1399	1600	1100	9872	3003	4663
W11	7.6	986	2.54	1650	3500	828	1000	3100	9250	2863	4265
W12	8.1	920	14.85	9650	3100	679	5480	2900	8730	2260	3275
W13	8	875	1.92	1250	2100	492	1080	2900	8250	2105	1085
W14	8.1	798	1.6	1080	3300	769	1920	900	7580	1840	1120
W15	7.9	753	1.57	1020	2800	663	800	500	7258	1530	1028
W16	6.3	684	1.57	1020	2300	544	800	800	6842	1300	1033
W17	6.2	578	1.4	1082	2150	520	780	350	5780	1258	1007

between 100 and 2700 mg L^{-1}, whereas Lysimeter 2 ranged from 230 to 3100 mg L^{-1}. The higher maximum chloride concentration in Lysimeter 2 indicates that the clay-loam system did not uniformly attenuate this relatively conservative dissolved constituent. Because chloride is generally less susceptible to adsorption than many reactive ions, its temporal variation can provide an indication of changes in water movement, concentration effects, and flushing through the lysimeter. Therefore, the higher chloride peak observed in Lysimeter 2 should be interpreted as evidence of substantial soluble-ion transport rather than as direct evidence of lower overall attenuation capacity (Naveen & Malik 2019). A more pronounced difference was observed for the organic pollution indicators. COD in Lysimeter 1 ranged from 6859 to 16,000 mg L^{-1}, compared with 5780–12,800 mg L^{-1} in Lysimeter 2. Similarly, BOD ranged from 2380 to 4932 mg L^{-1} in Lysimeter 1 and from 1258 to 3300 mg L^{-1} in Lysimeter 2. The consistently lower COD and BOD concentrations in the clay-loam system, particularly after the initial monitoring period, suggest greater retention and/or transformation of organic constituents within this soil matrix. The reduction in biodegradable organic matter may be associated with microbial degradation, adsorption onto mineral surfaces, filtration of particulate-associated organic matter, and possible stabilization of the waste material. Nevertheless, because the two lysimeters differ not only in soil texture but also in the presence of SCBA, the observed improvement cannot be attributed exclusively to clay content.

The color response showed a different pattern from COD and BOD. Lysimeter 1 exhibited color concentrations between 875 and 4600 Pt-Co, whereas Lysimeter 2 showed a considerably wider range of 1007–8110 Pt-Co. During W1–W9, the clay-loam system generally produced higher color values than the loam system, with a maximum of 8110 Pt-Co at W6. Thereafter, color decreased sharply in Lysimeter 2, reaching 1007 Pt-Co by W17. In Lysimeter 1, color also declined substantially from 4600 Pt-Co at W6 to 879 Pt-Co at W17. The decrease in color during the latter stages indicates progressive removal or transformation of colored dissolved organic matter, including humic- and fulvic-like substances. The initially higher color in Lysimeter 2 may be associated with the release and mobilization of organic or soluble constituents during the early stages of leachate–soil interaction, whereas the subsequent decline suggests progressive stabilization and retention within the soil–SCBA matrix. TSS concentrations showed relatively similar behavior in both systems. Lysimeter 1 recorded values between 520 and 1150 mg L^{-1}, while Lysimeter 2 ranged from 578 to 1100 mg L^{-1}. The slightly higher maximum TSS in Lysimeter 1 indicates somewhat greater mobilization of suspended and colloidal material during the monitoring period. The subsequent reduction in TSS in both systems is consistent with progressive filtration and retention of particulate matter within the soil column(Al-Soudany et al. 2025). However, the relatively small difference in the overall TSS ranges indicates that suspended-solid transport

was less strongly differentiated between the two lysimeter configurations than the dissolved and organic parameters.

Overall, the combined analysis of field and laboratory data demonstrates that lysimeter-based experimental models can effectively replicate the general behavior of landfill leachate while allowing controlled investigation of soil–leachate interactions. The results emphasize that soil characteristics strongly influence leachate quality, contaminant mobility, and natural attenuation processes within landfill systems. Such insights are essential for designing improved landfill liner materials and sustainable waste containment strategies aimed at minimizing environmental contamination.

3.4. Pearson's Correlation Analysis of Leachate Parameters

Pearson's correlation analysis was performed to examine the linear relationships among the major leachate quality parameters, including pH, TSS, EC, TDS, total hardness (TH), Mg, Ca, chloride (Cl), COD, BOD, and color. The correlation matrix helps identify the degree of association between variables and provides insight into the governing geochemical and biochemical processes influencing leachate composition. Table 7 shows Pearson's correlation matrix of the physicochemical parameters for the leachate. Strong positive correlations indicate that two parameters increase or decrease simultaneously due to common controlling mechanisms such as mineral dissolution, organic degradation, or ion mobility. The correlation structure obtained in this study revealed distinct clusters of interacting variables, highlighting the interdependence of physicochemical parameters within the leachate system. These relationships are consistent with patterns reported in previous investigations on landfill leachate chemistry and its evolution over time (Singh et al. 2005). The results of the correlation analysis therefore provide important evidence for understanding the processes controlling contaminant transport and transformation within the lysimeter system.

Pearson's correlation analysis revealed several statistically significant relationships among the leachate parameters. EC and TDS exhibited a very strong positive correlation ($r = 0.986$, $p < 0.01$), confirming that electrical conductivity is primarily governed by dissolved ionic constituents in the leachate. Total hardness showed a very strong positive correlation with Mg ($r = 0.955$, $p < 0.01$), indicating that magnesium is a major contributor to hardness in the landfill leachate system. TSS exhibited significant positive correlations with TH ($r = 0.513$, $p < 0.01$), Mg ($r = 0.438$, $p < 0.01$), COD ($r = 0.547$, $p < 0.01$), and BOD ($r = 0.596$, $p < 0.01$), suggesting that suspended particulate matter is closely associated with both inorganic mineral content and organic pollutant load. Calcium showed significant positive correlations with pH ($r = 0.533$, $p < 0.01$) and EC ($r = 0.369$, $p < 0.05$), reflecting mineral dissolution and ionic enrichment processes within the landfill system. Similarly, chloride exhibited strong positive correlations with pH ($r = 0.553$, $p < 0.01$) and Ca ($r = 0.598$, $p < 0.01$), indicating co-mobilization of soluble inorganic ions during leachate migration. COD and BOD demonstrated a very strong positive correlation ($r = 0.876$, $p < 0.01$), confirming their close association with biodegradable organic matter and landfill stabilization processes. Color also showed a significant positive correlation with COD ($r = 0.467$, $p < 0.01$), indicating that darker leachate is associated with elevated concentrations of dissolved organic compounds such as humic and fulvic substances. In contrast, color exhibited significant negative correlations with pH ($r = -0.522$, $p < 0.01$), Ca ($r = -0.371$, p

Table 7: Pearson's correlation matrix of the physicochemical parameters for the leachate.

	pH	TSS	EC	TDS	TH	Mg	Ca	Cl	COD	BOD	Color
pH	1										
TSS	0.236	1									
EC	0.407*	0.099	1								
TDS	0.367*	0.152	0.986**	1							
TH	0.162	0.513**	0.024	0.036	1						
Mg	0.326	0.438**	0.021	0.006	0.955**	1					
Ca	0.533**	0.133	0.369*	0.307	0.191	0.320	1				
Cl	0.553**	0.283	0.195	0.138	–0.083	0.077	0.598**	1			
COD	–0.208	0.547**	0.201	0.322	0.383*	0.142	–0.257	–0.255	1		
BOD	0.042	0.596**	0.248	0.342*	0.583**	0.407*	–0.049	–0.128	0.876**	1	
Color	–0.522**	0.192	–0.114	–0.106	0.184	–0.057	–0.371*	–0.358*	0.467**	0.297	Color

**Correlation is significant at the 0.01 level; *correlation is significant at the 0.05 level.
r = Pearson's correlation coefficient; p = probability.

< 0.05), and Cl ($r = -0.358$, $p < 0.05$), suggesting that highly colored leachate is generally associated with acidic and less mineralized conditions. Overall, the correlation analysis identified two major interacting groups within the leachate system: inorganic mineralization indicators represented by EC, TDS, TH, Mg, Ca, and Cl, and organic pollution indicators represented by COD, BOD, color, and TSS.

3.5. Factor Analysis of Leachate Quality Using PCA

Principal Component Analysis (PCA) was performed as an exploratory multivariate technique to identify the dominant patterns of covariance among the measured landfill-leachate characteristics. The first three principal components collectively explained 76.729% of the total variance. PC1, accounting for 32.133% of the variance, was characterized mainly by total hardness (0.933), magnesium (0.854), TSS (0.748), BOD (0.748), and COD (0.569), and was therefore interpreted as a mineralization and particulate–organic pollution factor. PC2, explaining 27.427% of the variance, showed strong positive loadings for pH (0.788), Ca (0.782), and Cl (0.737), together with negative loadings for color (–0.715) and COD (–0.575), and was interpreted as an organic stabilization and ionic-interaction factor. PC3, accounting for 17.169% of the variance, was dominated by TDS (0.956) and EC (0.920), with moderate contributions from COD (0.469) and BOD (0.430), and was therefore identified as a salinity and ionic-strength factor. The scree plot supported the retention of these three components because their eigenvalues exceeded unity. Overall, the PCA revealed three major patterns of variability associated with mineralization and particulate–organic characteristics, organic stabilization and ionic interactions, and salinity/ionic strength. These component interpretations represent statistical associations rather than direct causal mechanisms.

Table 8: Total variance explained by principal component analysis of the 11 leachate parameters.

Components	Eigenvalue	% of variance	Cumulative %
PC1	3.53	32.133	32.133
PC2	3.02	27.427	59.560
PC3	1.89	17.169	76.729
PC4	0.96	8.700	85.428
PC5	0.65	5.864	91.292
PC6	0.39	3.570	94.863
PC7	0.28	2.550	97.412
PC8	0.22	1.961	99.373
PC9	0.07	.590	99.963
PC10	0.00	.027	99.990
PC11	0.00	.010	100.000

3.6. Interpretation of Principal Components

Principal Component Analysis (PCA) was employed as an exploratory multivariate technique to identify major patterns of covariance among the measured landfill-leachate parameters and to reduce the dimensionality of the dataset. The PCA transformed the original correlated variables into a smaller number of orthogonal components while retaining a substantial proportion of the total variance. The eigenvalue and variance-explained results are presented in Table 8, whereas the rotated component loadings are presented in Table 9. Three components had eigenvalues greater

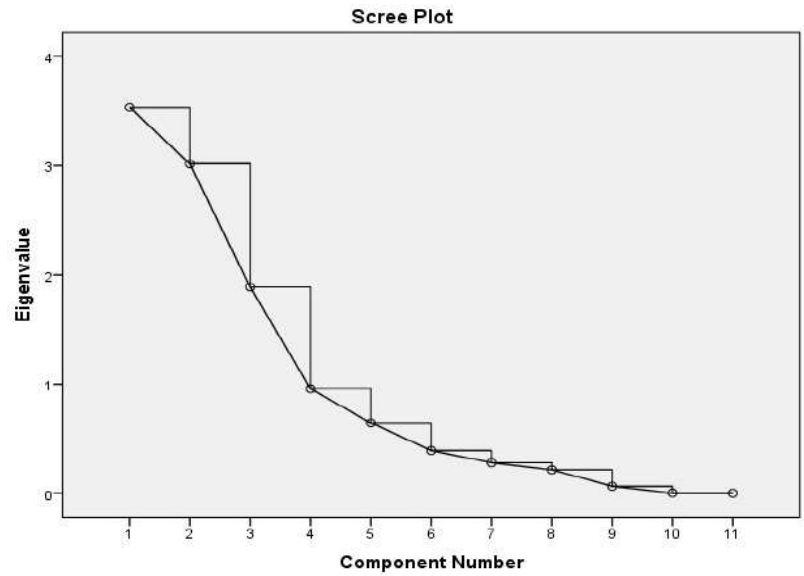


Fig. 8: Scree plot for PCA results with 11 leachate parameters.

than unity and were therefore retained for interpretation. PC1, PC2, and PC3 accounted for 32.133%, 27.427%, and 17.169% of the total variance, respectively, giving a cumulative variance of 76.729%. Thus, the first three components represented approximately 76.73% of the total variability in the measured leachate characteristics.

PC1, which explained 32.133% of the total variance, was strongly associated with total hardness (0.933), Mg (0.854), TSS (0.748), and BOD (0.748), with a moderate positive loading for COD (0.569). Based on these loadings, PC1 was interpreted as a mineralization and particulate-organic pollution factor. The strong loadings of total hardness and Mg indicate an important contribution from dissolved mineral constituents, potentially associated with mineral dissolution and release of divalent cations during leachate–soil interaction. The concurrent high loadings of TSS, BOD, and COD indicate that particulate and organic pollution characteristics also contributed substantially to this component. Therefore, PC1 represents a combined pattern involving mineral constituents and particulate/organic pollution rather than a single contaminant class.

PC2, accounting for 27.427% of the total variance, exhibited strong positive loadings for pH (0.788), Ca (0.782), and chloride (0.737), together with a strong negative loading for color (–0.715) and a moderate negative loading for COD (–0.575). Accordingly, PC2 was interpreted as an organic stabilization and ionic-interaction factor. The positive association of pH with Ca and chloride indicates that changes in leachate chemistry were accompanied by variations in buffering conditions and dissolved mineral constituents. Conversely, the negative loading of color indicates an inverse relationship between this component and colored organic matter. The negative COD loading similarly suggests that the stabilization-related pattern represented by PC2 was associated with decreasing organic pollution indicators. The component may therefore reflect the progressive modification of leachate chemistry during degradation and stabilization, accompanied by changes in dissolved ionic constituents and colored organic matter.

PC3, which explained 17.169% of the total variance, was dominated by TDS (0.956) and EC (0.920), with moderate positive loadings for COD (0.469) and BOD (0.430). This component was therefore interpreted as a salinity and ionic-strength factor. The very high and positive loadings of TDS and EC indicate a strong relationship between dissolved solids and electrical conductivity and demonstrate that variations in dissolved ionic constituents constituted an important independent source of variability in the dataset. The moderate loadings of COD and BOD suggest that changes in dissolved ionic strength were also partly associated with variations in organic loading. The PCA interpretation therefore indicates three principal patterns governing the variability of the leachate dataset. PC1 represents the combined influence of mineralization and particulate/organic pollution, PC2 reflects stabilization-related and ionic interactions, and PC3 represents dissolved ionic strength and salinity. These interpretations are based on the statistical associations represented by the loading matrix and should not be interpreted as direct evidence of individual biogeochemical mechanisms.

Table 9: Rotated component matrix of physicochemical parameters for landfill leachate.

Components	PC1	PC2	PC3
pH	0.191	0.788	0.260
TSS	0.748	0.022	0.186
EC	0.011	0.261	0.920
TDS	0.052	0.179	0.956
TH	0.933	0.052	–0.095
Mg	0.854	0.307	–0.180
Ca	0.172	0.782	0.181
Cl	0.040	0.737	0.104
COD	0.569	–0.575	0.469
BOD	0.748	–0.321	0.430
Color	0.230	–0.715	0.025

PCA; Rotation Method: Varimax with Kaiser Normalization

Table 10: KMO and Bartlett's test.

KMO and Bartlett's Test		
Kaiser-Meyer-Olkin Measure of Sampling Adequacy.		.456
Bartlett's Test of Sphericity	Approx. Chi-Square	473.640
	df	55
	Sig.	.000

The Kaiser–Meyer–Olkin (KMO) measure of sampling adequacy was 0.456, which is below the commonly used minimum threshold of 0.50 and therefore indicates relatively low sampling adequacy for PCA. Accordingly, the PCA results were treated as exploratory rather than confirmatory, and the component interpretations were restricted to the dominant statistical associations observed in the rotated loading matrix. Nevertheless, Bartlett's test of sphericity was highly significant ($\chi^2 = 473.640$, df = 55, $p < 0.001$), indicating that the correlation matrix was significantly different from an identity matrix and that meaningful correlations existed among the measured leachate parameters. Thus, despite the relatively low KMO value, the significant Bartlett's test and the interpretable loading structure provided a basis for retaining PCA as an exploratory tool for examining relationships among the physicochemical

variables. The PCA results are therefore not presented as evidence of a definitive causal structure but as an exploratory assessment of the dominant patterns of covariance within the leachate dataset. The component interpretations were based on the magnitude and direction of the rotated loadings, while environmental interpretations were made cautiously in conjunction with the observed temporal trends in the individual leachate parameters.

3.7. Scree Plot Interpretation of PCA

The scree plot in Fig. 8 showed a pronounced decline in eigenvalues after the third component, while the first three components had eigenvalues greater than unity. This supported the retention of PC1–PC3 for exploratory interpretation. Together, these components explained 76.729% of the total variance, indicating that the major patterns within the 11 measured leachate parameters could be represented using three principal dimensions. The PCA results provide evidence that leachate evolution was controlled by several interconnected physicochemical characteristics, including mineral dissolution, suspended and organic matter transport, changes in stabilization conditions, and dissolved ionic enrichment (Li et al. 2015). However, because PCA identifies correlations among variables rather than causal relationships, the environmental processes inferred from the component structure should be considered interpretative rather than definitive (Zhang et al. 2023).

3.8. Hierarchical Cluster Analysis (HCA)

Hierarchical Cluster Analysis (HCA) was carried out to examine similarity patterns among the leachate samples and to support the findings obtained from Principal Component Analysis. The analysis was performed using Ward's linkage method with squared Euclidean distance, which is widely used for environmental datasets because it minimizes within-cluster variance (Nkansah et al. 2010). The resulting dendrogram (Fig. 9) indicates that the leachate samples can be broadly classified into three major clusters at a rescaled distance of approximately 15–18, reflecting considerable heterogeneity in leachate composition due to variations in geochemical interactions, organic degradation stages, and hydrological influences within the landfill system (Singh et al. 2005). Cluster I consists of samples grouped at lower rescaled distances, indicating high similarity among the leachate characteristics. This cluster represents highly mineralized leachate dominated by dissolved ions, hardness, and elevated electrical conductivity resulting from mineral dissolution and prolonged soil–waste interaction processes (Shrestha & Kazama 2007, Naveen et al. 2019). The close linkage among samples within this cluster suggests relatively stable inorganic chemical behavior and strong ionic enrichment.

Cluster II forms a distinct subgroup separated from Cluster I at moderately rescaled distances. This cluster is primarily associated with organic-rich leachate influenced by biological degradation and landfill stabilization processes.

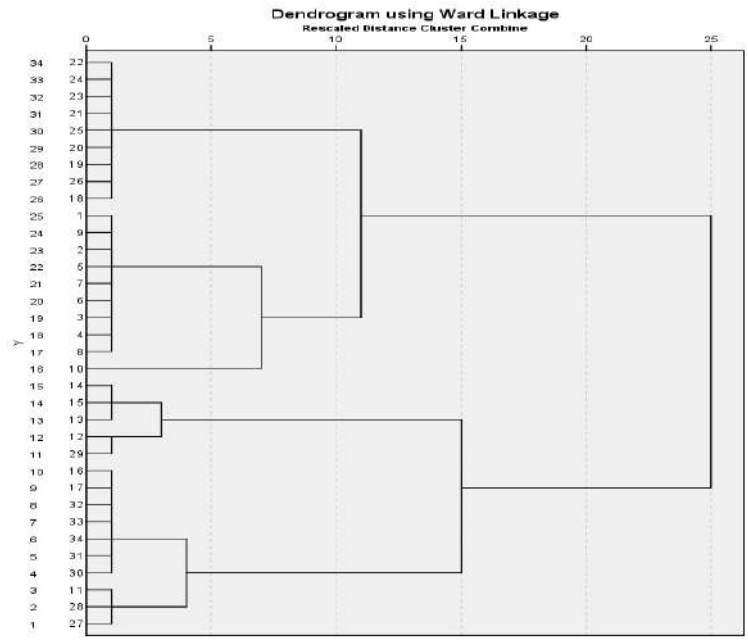


Fig. 9: Dendrograms showing the clustering of 11 standardized leachate parameters.

Samples within this group are characterized by stronger associations with COD, BOD, and color, reflecting active decomposition of biodegradable organic matter and the presence of humic substances generated during anaerobic waste degradation (Singh et al. 2005, Zhang et al. 2023). The separation of this cluster from the mineralized group highlights the independent contribution of biodegradation processes in controlling leachate chemistry. Cluster III is distinctly separated from the other two clusters at higher rescaled distances, indicating substantial compositional variation. This cluster likely represents diluted or physically influenced leachate affected by rainfall infiltration, surface runoff interaction, or operational disturbances within the landfill system (McKenna 2003). The larger linkage distance suggests comparatively lower dissolved concentrations and greater variability in suspended solids, indicating the influence of short-term hydrological and environmental conditions rather than long-term geochemical stabilization processes. Similar clustering behavior has been reported in previous landfill leachate studies conducted under variable climatic and operational conditions (Singh et al. 2005, Zhang et al. 2023).

3.9. Integrated HCA Interpretation with PCA Results

The hierarchical cluster analysis (HCA) showed clustering patterns that were broadly consistent with the variable associations identified by PCA, although the two techniques provide complementary rather than identical information. While PCA reduced the dimensionality of the dataset by identifying dominant patterns of covariance among the leachate-quality parameters, HCA grouped samples according to their overall similarity in multivariate composition. The observed correspondence between the clustering structure and the PCA loading patterns therefore provides complementary evidence for the major sources of variability in leachate quality.

In relation to the PCA results, Cluster I can be associated primarily with the variability represented by PC1, which was identified as a mineralization and particulate–organic pollution factor. PC1 was dominated by total hardness (0.933), magnesium (0.854), TSS (0.748), BOD (0.748), and COD (0.569). Accordingly, samples belonging to this cluster may represent leachate conditions characterized by the concurrent presence of dissolved mineral constituents and particulate/organic pollution characteristics. The association of hardness and magnesium with TSS, BOD, and COD indicates that mineralization and organic/particulate characteristics contributed jointly to the differentiation of these samples. Cluster II can be interpreted in relation to PC2, which accounted for 27.427% of the total variance and was characterized by positive loadings of pH (0.788), calcium (0.782), and chloride (0.737), together with negative loadings of color (–0.715) and COD (–0.575). This component was therefore interpreted as an organic stabilization and ionic-interaction factor. Samples grouped within this cluster may consequently reflect differences in the organic character of the leachate accompanied by changes in pH and dissolved ionic constituents. The negative loadings of COD and color relative to pH, calcium, and chloride suggest an inverse statistical association within this component, which may be related to changes in leachate composition during degradation and stabilization. However, these relationships should be considered statistical associations rather than direct evidence of causality.

Cluster III is most closely related to PC3, which explained 17.169% of the total variance and was strongly dominated by TDS (0.956) and EC (0.920), with moderate contributions from COD (0.469) and BOD (0.430). PC3 was therefore identified as a salinity and ionic-strength factor. The grouping of samples within this cluster indicates that variations in dissolved solids and electrical conductivity contributed substantially to their multivariate similarity, reflecting differences in the dissolved ionic character of the leachate. The HCA and PCA results provide a complementary description of the variability observed in the leachate dataset. PCA identified three dominant patterns—mineralization and particulate–organic pollution (PC1), organic stabilization and ionic interactions (PC2), and salinity/ionic strength (PC3)—whereas HCA classified samples according to their overall similarity in these multivariate characteristics. The agreement between the two approaches supports the identification of these parameter groupings as important dimensions of leachate-quality variability. Nevertheless, HCA and PCA should not be interpreted as independently proving the underlying physicochemical mechanisms. Rather, their combined use provides an exploratory statistical framework for distinguishing different compositional states of landfill leachate and for improving interpretation of its temporal evolution and monitoring requirements (Jolliffe 2002).

3.10. Quantitative Validation Metrics

The validation results in Fig. 10 indicate that both lysimeter systems successfully reproduced the general physicochemical characteristics of landfill leachate while demonstrating contaminant attenuation through soil–leachate interactions. The SCBA-amended clay loam system (Lysimeter 2) exhibited substantial reductions in several key contamination indicators compared with the loam soil system (Lysimeter 1). The highest attenuation improvements were observed for TDS (49.03%), EC (42.99%), BOD (30.12%), and

Table 11: Validation of lysimeter performance against field leachate characteristics and improvement achieved by SCBA-amended soil.

Parameter	Field	Mean Lysimeter 1	Deviation (%)	Mean Lysimeter 2	Deviation (%)	Improvement of SCBA (%)
pH	5.6	7.45	33.09	7.18	28.3	3.6
TSS (mg L^{-1})	1800	848.76	52.85	814.35	54.76	4.05
EC (mS cm^{-1})	5.6	7.1	26.7	4.04	27.77	42.99
TDS (mg L^{-1})	3072	5137.41	67.23	2618.53	14.76	49.03
Total Hardness (mg L^{-1})	11650	3886.59	66.64	3477.06	70.15	10.54
Mg (mg L^{-1})	1200	774.29	35.48	687	42.75	11.27
Ca (mg L^{-1})	5000	1092.18	78.16	1024.24	79.52	6.22
Chloride (mg L^{-1})	4397	681.18	84.51	889.41	79.77	–30.57
COD (mg L^{-1})	13600	11931.29	12.27	9574.24	29.6	19.76
BOD (mg L^{-1})	3428.57	3663.53	6.85	2559.94	25.34	30.12
Color (Pt-Co)	9600	2870.88	70.09	5158.94	46.26	–79.70

COD (19.76%), indicating enhanced retention of dissolved salts and organic pollutants within the SCBA-amended soil matrix, as presented in Table 11. Moderate improvements were also observed for total hardness (10.54%), Mg (11.27%), and Ca (6.22%), suggesting improved ion retention and adsorption processes resulting from the increased surface area and reactive silica content provided by SCBA.

In contrast, chloride did not exhibit significant attenuation and showed a higher mean concentration in Lysimeter 2 compared with Lysimeter 1. This observation is consistent with previous studies, which report that chloride behaves as a highly mobile conservative tracer in landfill leachate and is generally not retained effectively by adsorption or ion-exchange mechanisms within soil media (Christensen et al. 2001, Kjeldsen et al. 2002). Therefore, the higher chloride concentration observed in the SCBA-amended system should not be interpreted as a limitation of the amendment but rather as a reflection of the inherent mobility of chloride ions in porous media.

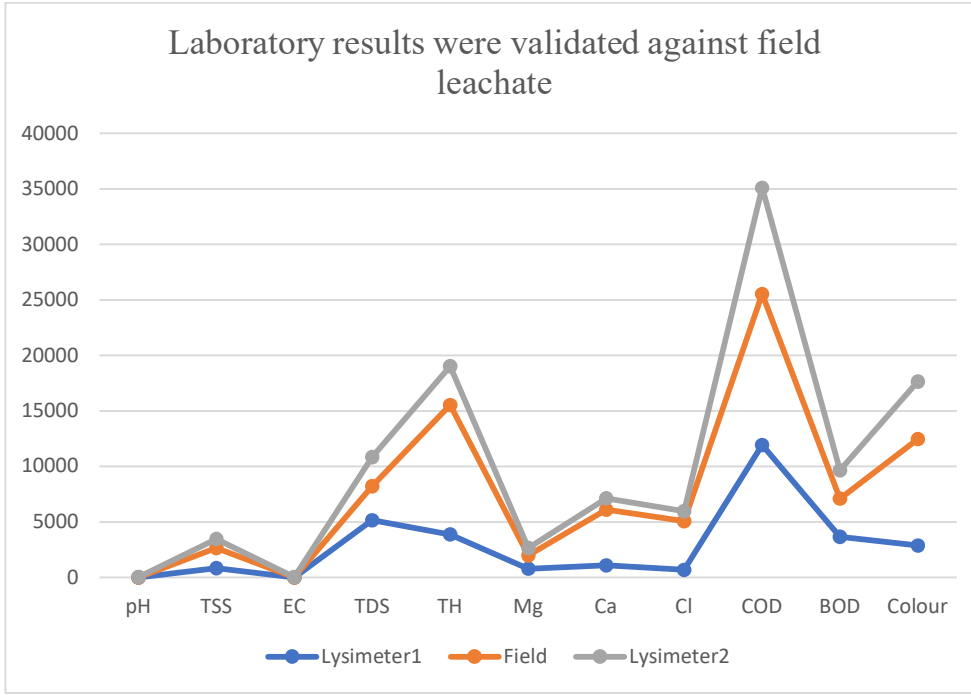


Fig. 10: Comparison of mean physicochemical characteristics of field landfill leachate, Lysimeter 1 (loam soil), and Lysimeter 2 (SCBA-amended soil).

Similarly, the higher average color values observed in Lysimeter 2 may be attributed to the release and transport of dissolved humic substances and colored organic fractions during the early stages of leachate percolation. Previous investigations have reported that color removal in natural adsorbent systems is often less predictable than COD and BOD removal because color-causing compounds consist of complex high-molecular-weight organic molecules with varying adsorption behavior (Renou et al. 2008, Naveen et al. 2017). Despite the higher overall mean color value, the later monitoring periods showed a progressive decline in color concentration, indicating continued stabilization and transformation of dissolved organic matter within the SCBA-amended soil system.

Overall, the results demonstrate that SCBA amendment significantly enhanced the attenuation of dissolved solids and organic pollutants while having limited influence on chloride mobility, which is consistent with findings reported in previous landfill leachate treatment studies. These observations confirm that the primary benefit of SCBA lies in improving adsorption, filtration, and organic contaminant retention rather than the removal of conservative inorganic ions.

4. CONCLUSIONS

The present study evaluated the influence of soil type and the incorporation of a low-cost adsorbent on landfill leachate behavior using controlled lysimeter experiments conducted over a 17-week monitoring period. Geotechnical characterization confirmed that the addition of sugarcane bagasse ash (SCBA) improved the soil properties by increasing the clay fraction from 23% to 37% and the plasticity index from 9% to 22%, while the differential free swell was 20% for Soil 1 (Loam) and 30% for Soil 2 (Clay Loam with SCBA)**,** indicating a 10 percentage-point higher swelling potential in Soil 2**.** This difference is consistent with the higher clay fraction of Soil 2 (37%) compared with Soil 1 (23%) and its higher plasticity index (22% versus 9%), although the observed swelling response should be interpreted in conjunction with the complete mineralogical and physicochemical characteristics of the soils. These changes enhanced the structural stability and adsorption potential of the clay loam soil system. Physicochemical analysis indicated that both lysimeters produced highly contaminated leachate typical of municipal solid waste landfills, with COD values reaching up to 16,000 mg L^{-1} and TDS up to 9,650 mg L^{-1}. However, the results showed progressive stabilization of leachate quality over time. A COD reduction of approximately 46% was observed in the loam soil lysimeter, whereas the clay loam–SCBA system achieved about 52% reduction in BOD, indicating improved biodegradation and adsorption processes. Lower values of EC, TDS, and TSS in the clay loam lysimeter further confirm its stronger filtration capacity and ion retention ability compared with the loam soil system. The pH in both lysimeters remained within near-neutral to slightly alkaline conditions, with loam soil showing relatively stable buffering and clay loam exhibiting slight acidification during later stages due to organic acid formation.

Correlation analysis revealed strong relationships among several parameters, particularly EC–TDS (r = 0.986), TH–Mg (r = 0.955), and COD–BOD (r = 0.876), indicating coupled mineralization and biodegradation mechanisms in the leachate. PCA identified three significant components explaining the majority of dataset variance, representing mineralization processes, organic degradation, and suspended solid dynamics. HCA further classified the leachate samples into three groups corresponding to mineralized, organic-rich, and diluted phases, which supports the interpretation obtained from PCA.

Overall, the comparative evaluation demonstrates that clay loam soil amended with SCBA exhibits superior contaminant attenuation capacity due to increased clay content, enhanced adsorption surface area, and improved cation exchange behavior. The results indicate that SCBA-amended clay loam soil exhibits promising contaminant attenuation characteristics and may have potential as a sustainable landfill barrier material. However, comprehensive evaluation of hydraulic conductivity, mechanical stability, long-term durability, and field-scale performance is required before its suitability as a landfill liner or cover material can be conclusively established. Although the clay loam–SCBA system exhibited lower contaminant concentrations and improved attenuation trends compared with the loam soil system, these observations are based on single-lysimeter comparisons and should be interpreted as indicative trends. Future studies incorporating replicated lysimeter experiments are recommended to statistically validate the observed behavior. In addition, heavy metal characterization of both the landfill leachate and SCBA was beyond the scope of the present investigation; therefore, conclusions regarding contaminant attenuation are limited to the measured physicochemical indicators. The integration of lysimeter experimentation and multivariate statistical analysis provides a reliable framework for understanding landfill leachate evolution and for designing sustainable waste containment systems. Future research should focus on long-term field validation and the evaluation of heavy metal removal efficiency to further optimize the application of SCBA-based adsorbent materials in landfill engineering.

5. ACKNOWLEDGEMENT

The authors express their sincere gratitude to the Department of Civil Engineering, University of BDT College, for providing laboratory facilities and technical support throughout the study. The authors also thank the Davanagere City Corporation and the Karnataka State Pollution Control Board (KSPCB), Davanagere, for supplying waste composition data and relevant field information used in this research.

6. REFERENCES

Ahmed, F.N. and Lan, C.Q., 2012.Treatment of landfill leachate using membrane bioreactors: A review.*Desalination*, 287, pp.41–54.[DOI]

Aish, A., Abushbak, T. and El-Nakhala, M., 2014.Investigation of the fate of MSW leachate in different soil types using soil column method. *Journal of Environment and Earth Science*, 4(4), pp.72–80.

Al-Soudany, K.Y.H., Fattah, M.Y. and Rahil, F.H., 2025. Lysimeter experiments of landfill liner enhanced with magnesium oxide. *Results in Engineering*, 25, 104305.[DOI]

Al-Yaqout, A.F. and Hamoda, M.F., 2003.Evaluation of landfill leachate in arid climate: A case study.*Environment International*, 29(5), pp.593–600.[DOI]

American Public Health Association (APHA), American Water Works Association (AWWA) and Water Environment Federation (WEF), 2017.*Standard Methods for the Examination of Water and Wastewater* (23rd ed.). APHA, AWWA and WEF, Washington, DC.

Aruga, R., Gastaldi, D., Negro, G. and Ostacoli, G., 1995.Pollution of a river basin and its evolution with time studied by multivariate statistical analysis. *Analytica Chimica Acta*, 310(1), pp.15–25.[DOI]

Christensen, T.H., Kjeldsen, P., Bjerg, P.L., Jensen, D.L., Christensen, J.B., Baun, A., Albrechtsen, H.J. and Heron, G., 2001.Biogeochemistry of landfill leachate plumes.*Applied Geochemistry*, 16(7–8), pp.659–718. [DOI]

Dabrowska, D. and Rykala, W., 2021. A review of lysimeter experiments carried out on municipal landfill waste. *Toxics*, 9(2), 26.[DOI]

Dabrowska, D., Nowak, A., Sołtysiak, M.,Biniecka, P., Nourani, V. and Wasilkowski, D., 2022.In situ lysimeter experiment of leaching pollutants from municipal waste with physicochemical status and microbiome condition.*Journal of Hydrology*, 613, 128309.[DOI]

Das, B.M., 2020.*Principles of Geotechnical Engineering* (9th ed.). Cengage Learning.

Ergene, A., Çakmakcı, M. and Uygur, N., 2022.Global characterization and modelling of landfill leachate using multivariate statistical analysis. *Journal of Cleaner Production*, 350, 131454.

Jolliffe, I.T., 2002.*Principal Component Analysis* (2nd ed.). Springer Series in Statistics. Springer, New York. [DOI]

Karnchanawong, S. and Yongpisalpop, P., 2009.Effects of cover soil type on leachate characteristics from landfill lysimeters.*World Academy of Science, Engineering and Technology*, 3(1), pp.227–231.

Kjeldsen, P., Barlaz, M.A., Rooker, A.P., Baun, A., Ledin, A. and Christensen, T.H., 2002.Present and long-term composition of MSW landfill leachate: A review.*Critical Reviews in Environmental Science and Technology*, 32(4), pp.297–336.[DOI]

Lambe, T.W. and Whitman, R.V., 1969.*Soil Mechanics*. Wiley.

Li, Y., Jin, F., Wang, C., Chen, Y., Wang, Q., Zhang, W. and Wang, D., 2015.Modification of bentonite with cationic surfactant for the enhanced retention of bisphenol A from landfill leachate. *Environmental Science and Pollution Research*, 22(11), pp.8618–8628.[DOI]

Liu, C.W., Lin, K.H. and Kuo, Y.M., 2003.Application of factor analysis in the assessment of groundwater quality in a Blackfoot disease area in Taiwan. *Science of the Total Environment*, 313(1–3), pp.77–89.[DOI]

Mangi, S.A., Jamaluddin, N., Ibrahim, M.H.W., Arshad, M.F. and Putra Jaya, R. 2017. Utilization of sugarcane bagasse ash in geotechnical and environmental applications. *Construction and Building Materials*, 152, pp.483–495.

McKenna, J.E., Jr., 2003.An enhanced cluster analysis program with bootstrap significance testing for ecological community analysis. *Environmental Modelling & Software*, 18(3), pp.205–220.[DOI]

Mor, S., Negi, P. and Ravindra, K., 2019.Potential of agro-waste sugarcane bagasse ash for the removal of ammoniacal nitrogen from landfill leachate.*Environmental Science and Pollution Research*, 26(24), pp.24516–24531.[DOI]

Naveen, B.P. and Malik, R.K., 2019.Assessment of contamination potential of leachate from municipal solid waste landfill sites for metropolitan cities in India.*Pollution*, 5(2), pp.313–322.[DOI]

Naveen, B.P., Mahapatra, D.M., Sitharam, T.G., Sivapullaiah, P.V. and Ramachandra, T.V., 2017.Physicochemical and biological characterization of urban municipal landfill leachate.*Environmental Pollution*, 220, pp.1–12.[DOI]

Nkansah, K., Dawson-Andoh, B. and Slahor, J., 2010.Rapid characterization of biomass using near-infrared spectroscopy coupled with multivariate data analysis: Part 1, yellow-poplar (Liriodendron tulipifera L.).*Bioresource Technology*, 101(2), pp.4570–4576.[DOI]

Paris, H., 1996.Assessment of leachate from sanitary landfills: Impact of age, rainfall, and treatment.*Environment International*, 22(2), pp.225–237.[DOI]

Qian, Y., Hu, P., Lang-Yona, N., Xu, M., Guo, C. and Gu, J.-D., 2024. Global landfill leachate characteristics: Occurrences and abundances of environmental contaminants and the microbiome.*Journal of Hazardous Materials*, 461, 132446.[DOI]

Renou, S., Givaudan, J.G., Poulain, S., Dirassouyan, F. and Moulin, P., 2008.Landfill leachate treatment: Review and opportunity.*Journal of Hazardous Materials*, 150(3), pp.468–493.[DOI]

Saghi, M.H., Nadimi, H., Eslami, A., Bakhtiarvand, S.N.A., Oghazyan, A., Setoudeh, S. and Sargolzaei, M.S., 2024.Characteristics and pollution indices of leachates from municipal solid waste landfills in Iranian metropolises and their implications for MSW management.*Scientific Reports*, 14, 27285.[DOI]

Shrestha, S. and Kazama, F., 2007.Assessment of surface water quality using multivariate statistical techniques: A case study of the Fuji River basin, Japan.*Environmental Modelling & Software*, 22(4), pp.464–475.[DOI]

Singh, K.P., Malik, A. and Sinha, S., 2005.Water quality assessment and apportionment of pollution sources of Gomti River (India) using multivariate statistical techniques: A case study. *Analytica Chimica Acta*, 538(1–2), pp.355–374.[DOI]

Tuffaha, R.B.R., 2006. *Impacts of Solid Waste Leachate on Soil and its Simulation to Ground Water at Nablus Area*. MSc thesis, AnNajah National University, Nablus, Palestine.

Zhang, Y., Yang, S., Yang, J., Wu, Z., Liu, H., Nie, Z., Qu, J., Hu, Y., Shao, Y., Liu, J., Liu, F. and Hua, D., 2023.Temporal hormetic response of soil microbes to cadmium: A metagenomic perspective.*Science of the Total Environment*, 891, 164190.[DOI]

Nature Environment and Pollution Technology
An International Quarterly Peer-Reviewed Open Access Journal

p-ISSN: 0972-6268 | e-ISSN: 2395-3454 Vol. 25 | No. 4 | Article ID D1916 | 2026

RESEARCH ARTICLE https://doi.org/10.46488/NEPT.2026.v25i04.D1916 OPEN ACCESS

Seasonal Water Quality Variation and Pollutant Loads Entering the Largest Hydropower Reservoir in Vietnam after Dam Impoundment (2014–2024)

Xuan-Duc Do
Department of Climate Change and Sustainability Science, VNU School of Interdisciplinary Sciences and Arts, Vietnam National University, Hanoi, Vietnam
Corresponding author: Xuan-Duc Do; ducxd@vnu.edu.vn

ARTICLE HISTORY

Received: 31-01-2026
Revised: 18-04-2026
Accepted: 01-05-2026

KEYWORDS

Hydropower reservoir
Son La reservoir
Pollutant load
Water quality

CITE THIS ARTICLE

Do, X-D., 2026. Seasonal water quality variation and pollutant loads entering the largest hydropower reservoir in Vietnam after dam impoundment (2014–2024). *Nature Environment and Pollution Technology*, 25(4), D1916. https://doi.org/10.46488/NEPT.2026.v25i04.D1916

COPYRIGHT & LICENCE

© 2026 The Authors
Open Access under CC BY 4.0.

PUBLISHED BY
TECHNOSCIENCE PUBLICATIONS

ABSTRACT

The Son La Reservoir on the Da River, the largest hydropower reservoir in Vietnam, is critical for electricity generation, water regulation, and water supply. However, post-impoundment changes in flow regimes and pollutant transport pose potential risks to downstream ecosystems and water security. This study identifies trends in water flow and seasonal fluctuations in pollutant concentrations, determines correlations between runoff and water quality, and quantifies the seasonal pollutant load entering the reservoir. Data were collected between 2014 and 2024 from four major inflows (Da, Nam Na, Nam Muc, and Nam Mu Rivers). Monitoring focused on nine parameters, including dissolved oxygen (DO), total suspended solids (TSS), BOD_5, COD, and various nutrients. The pollutant load (PL) was calculated using a material balance equation. Analysis was performed using SPSS 20.0 and RStudio, using correlation tests for normality, one-way ANOVA, and Pearson correlation coefficients (r) to evaluate seasonal variations. Water flow showed an increasing trend, except in the Nam Muc River, with rainy-season flows significantly higher than dry-season flows. While DO, total iron, and nutrients showed increasing trends, TSS, BOD_5, and COD decreased, likely due to upstream sediment trapping. The average annual pollutant load was 3,403,604 tonnes, with the rainy season accounting for 63.1%–92.4% of the total. TSS comprised 75% of the total load. Correlation analysis revealed that dam operations and seasonal discharge significantly influence pollutant concentrations. These results provide a scientific basis for monitoring water quality and managing pollution in hydropower basins to safeguard regional water resources.

1. INTRODUCTION

River flows are important to basin ecosystems and are the main source of water for hydropower reservoirs (Branche 2017). Research on pollutant loads is important for environmental flow management in hydropower reservoir basins (Jager et al. 2008). Determining pollutant loads during the dry and flood seasons supports pollution management and water quality control in both seasons (Choi et al. 2015). Pollutant loads under different flow conditions and regimes are analyzed to support water quality recovery and identify appropriate best management practices in the basins (Kim et al. 2012).

Recent research on pollutant loads in hydropower reservoir basins highlights the complex interplay of various sources and their impacts. Studies have examined point and nonpoint source pollution in rivers feeding reservoirs, using models to predict pollution loads and analyze permissible levels. Sediment sources and associated pollutants have been investigated using geochemical fingerprinting, revealing

significant contributions from mining and agricultural activities (Bravo-Linares et al. 2024). The Soil and Water Assessment Tool (SWAT) has been employed to evaluate spatial and temporal distributions of nitrogen, phosphorus, and heavy metal loads, identifying seasonal patterns and key pollution sources (Chen et al. 2024). Research has also focused on the self-cleaning ability of reservoirs with respect to nitrogen- and phosphorus-containing pollutants, calculating emission rates and self-cleaning capacities based on factors such as pollutant concentrations and hydraulic retention time (Do et al. 2020). These studies provide valuable insights for watershed management and pollution mitigation strategies.

The pollutant load of total suspended solids (TSS) in hydropower reservoir basins is influenced by various factors. Bayram et al. (2016) found that the Borçka Dam in Turkey effectively trapped TSS and reduced turbidity because of its long hydraulic residence time. In China's Danjiangkou Reservoir Basin, Zhuang et al. (2016) identified critical source areas for nonpoint source pollution, with 70% of pollutant loads originating from 30% of the basin area. Chong (2003) developed models to forecast point and nonpoint source pollution loads in the Xiangxi River Basin of the Three Gorges Reservoir Area. In Malaysia's Kenyir Hydropower Reservoir, Wahab et al. (2023) observed varying sediment load production across subcatchments, with anthropogenic activities, hydrological factors, and climate change contributing to sedimentation. These studies emphasize the importance of comprehensive watershed management and stakeholder involvement in addressing TSS pollution in hydropower reservoir basins.

The pollution loads of COD and BOD_5 in hydropower reservoir basins are a significant concern. Studies on the Three Gorges Reservoir show that agricultural nonpoint sources are the main pollution source, contributing up to 70.4% of COD loads. Before impoundment, the total annual loads of COD and BOD_5 were 4.49×10^6 and 9.80×10^5 tons, respectively (Li 2005). In the Miyun Reservoir, nonpoint sources account for 73% of COD and 71% of BOD loads (Wang et al., 2003). The Zhangze Reservoir study reveals that urban domestic sources are the primary contributors, accounting for 65.47% of COD loads (Yang et al. 2022). These studies highlight the importance of addressing both point and nonpoint sources in reservoir basins. Urban areas, particularly in the Three Gorges Reservoir, are identified as major pollution discharge regions, emphasizing the need for targeted pollution control measures (Li, 2005).

The pollution loads of NH_4^+, NO_2^-, NO_3^-, and PO_4^{3-} in hydropower reservoir basins are a significant concern. Studies have shown that these pollutants primarily originate from agricultural activities, livestock breeding, and domestic sources (Tong et al. 2017, Zhuang et al. 2016). In the Son La hydropower reservoir, approximately 10,323 tons of nitrogen and 5,454 tons of phosphorus were added annually, with the reservoir demonstrating a self-cleaning capacity of 8,117 tons per year for NH_4^+, NO_2^-, NO_3^-, and PO_4^{3-} pollutants (Do et al. 2020). Research in the Three Gorges Reservoir area identified drylands and forestlands as the main sources of nonpoint source pollution, contributing over 90% of the nitrogen and phosphorus load (Wu et al. (2012). To address this issue, experts recommend prioritizing the treatment of sloping farmlands, implementing soil and water conservation measures, and focusing on critical source areas, which typically contribute about 70% of the pollution load from 30% of the basin area (Zhuang et al. 2016).

In research on pollutant loads, the quantification of river pollutant loads is mainly integrated with calculations of nonpoint and point pollution sources in the river basin. Nutrients from nonpoint sources are carried by annual river flow from quantified watersheds (Li et al. 2005). The distribution of pollutant loads in streams is calculated to determine pollution in the river basin (Cheng et al. 2006). Estimating pollutant loads in surface waters of different river basins is used to quantify the pollutant load at the source (Amaya et al. 2012). The actual pollutant load received via a stream is estimated and simulated through model calculations to better understand pollution sources and pollutant loads in river flows (Huang et al. 2013). Fluctuations in water quality in catchment flows are quantified to provide scientifically supported options for pollution control and water protection (Nuen et al. 2020). To date, studies on pollutant load estimation have been based on discharge trend analysis and relationships between runoff and pollutant concentration, while seasonal load distribution ratios remain poorly understood. Therefore, this information is needed to quantify the transport capacity of stream pollutant loads during the dry and flood seasons in hydropower reservoirs.

Currently, pollutant loads in river-basin runoff are generally estimated from discharge or flow rate (Q) and pollutant concentration (C_i). Stream pollutant load is estimated from discharge and pollutant concentration data by multiplying the mean concentration by the mean flow rate (Ferguson 1987). Dry- and flood-season flow and water quality are based on data analyzed at monitoring stations, and relationships between water discharge and pollutant load are analyzed to estimate basin pollutant loads (Jeong et al. 2000). The discharge and water quality of the study basin are monitored and analyzed to estimate pollutant loads (Shin et al. 2005). Pollutant loads at the catchment scale are calculated from water quality monitoring data (concentration) and

water flow-rate data at monitoring stations (Shrestha et al. 2008). Pollutant loads in dry- and flood-season flows are determined using the average concentration (C_i) and average discharge (W_i) (Zhu et al. 2015). Stream pollutant loads are also estimated from water quality and flow data (Park et al. 2025). Calculation of river-flow pollutant loads is based on daily discharge data, baseline discharge, and pollutant concentration (Xin et al. 2017). Estimating pollutant loads during the dry and flood seasons requires determining the relationships among flow characteristics, flow rate, and pollutant concentrations. Discharge loads of organic matter, nitrogen, and phosphorus compounds are strongly correlated with annual river flow rate, and differences in flow rate affect dry- and flood-season pollutant loads (Niemirycz et al. 1999). Pollutant load estimation based on dry- and wet-season streamflow and water quality uses runoff characterization as part of basin assessment and management to address surface-water depletion (Eom et al. 2010). Relationships between flow and changes in water quality concentrations during the dry and flood seasons are analyzed by estimating pollutant loads distributed according to stream characteristics of the reservoir basin (Park et al. 2011). River flows are influenced by season, with dry-season flow being more stable than flood-season flow (Bowers et al. 2012). Changes in flow regimes and pollutant loads should be considered when developing appropriate hydrological recommendations for the watershed (Zeiger et al. 2017).

The Da River is a major tributary of the Red River system in Vietnam, covering an area of 52,900 km² and providing water for agriculture and drinking to millions of people (Le Viet Son et al. 2019). It plays a crucial role in the region's hydrology and economy. The river system has experienced significant changes due to dam construction, particularly in sediment transport. At the Son Tay station, the Red River's sediment load decreased by 91% between 1958–1987 and 2009–2021, with major declines observed after the Hoa Binh Dam began operation in 1988 and further reductions since 2009 (Nguyen et al. 2023). The Da River also contributes to CO_2 emissions, with the highest pCO_2 and outgassing rates measured downstream of the Hoa Binh Dam. These changes highlight the importance of effective water resource management in this transboundary river basin (Hai et al., 2024).

Most studies rely on general discharge trend analysis and mean concentration data to estimate basin pollution. However, seasonal load distribution ratios and the specific transport capacity of pollutant loads during distinct dry and flood seasons remain insufficiently understood. While general relationships between runoff and concentration are established, there is also a lack of information on how varying flow characteristics influence the transport of organic matter, nitrogen, and phosphorus within hydropower reservoir basins. This represents a research gap that needs to be addressed.

The Son La Reservoir, the largest hydropower reservoir in Vietnam with a capacity of 2,400 MW, plays a crucial role in renewable electricity generation and water regulation in northern Vietnam. It has operated since 2012 after seven years of construction (2005–2012). It is located in the Da River system, which supplies domestic and irrigation water to Dien Bien, Lai Chau, Hoa Binh, and Son La provinces and is one of the water sources for Vietnam's second-largest delta, the Red River Delta. In addition, the Da River provides a drinking and domestic water supply capacity of 300,000 $m^3\ day^{-1}$ for an estimated 100,000 households in Hanoi, the capital of Vietnam. The capacity is expected to increase to 1,365,000 $m^3\ day^{-1}$ by 2030 and 1,890,000 $m^3\ day^{-1}$ by 2050. Although Da River water is treated for drinking and domestic purposes, water quality management is essential for ecosystem and human health.

The main objective of this study is to analyze pollutant discharge loads during the dry and flood seasons in the river system of the hydropower reservoir basin. The study addresses four specific objectives: (1) identify changes in flow-rate trends and seasonal fluctuations in surface-water pollutant concentrations in river flows; (2) determine the correlation between seasonal runoff rate and pollutant concentration; (3) quantify basin pollutant loads during the dry and flood seasons; and (4) estimate the capacity of hydropower dams to alter downstream pollutant loads.

2. MATERIALS AND METHODS

2.1. Research Area

The reservoir has a water surface area of 224 km² and is 175 km long. The reservoir basin has an area of 11,075 km², including the mainstream (Da River) and three tributaries (Nam Muc River, Nam Na River, and Nam Mu River) that supply water to the Son La hydropower reservoir (Fig. 1). The Nam Muc River is 128 km long and has a sub-basin area of 1,618 km². The Nam Na River is 109.4 km long and has a sub-basin area of 2,949 km². The Nam Mu River is 183.7 km long and has a sub-basin area of 2,972 km². Several hydropower dams have been constructed on the mainstream (Da River) and the three tributaries before water enters the Son La hydropower reservoir: Lai Chau Dam on the Da River, Nam Muc Dam on the Nam Muc River, Nam Na 1 and 2 dams on the Nam Na River, and Huoi Quang Dam on the Nam Mu River. The dry season (January–March and October–December) is characterized by low rainfall

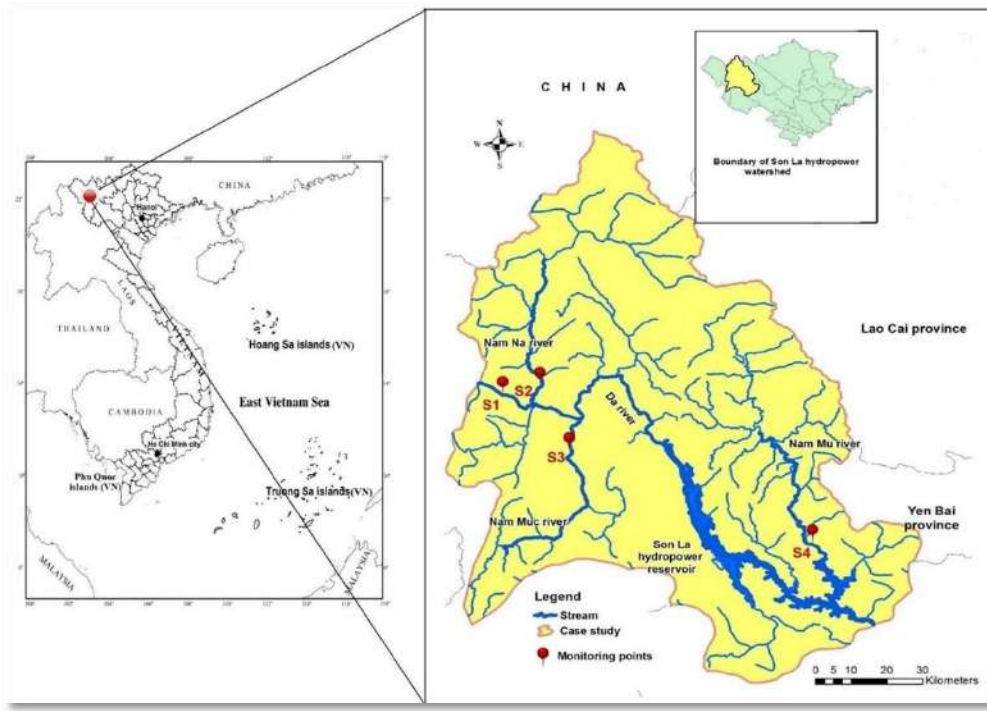


Fig. 1: Location of monitoring points in the river system of the Son La hydropower reservoir basin in Northwestern Vietnam.

(350 mm year^{-1}). Rainfall during the flood season (April–September) is 1,577 mm year^{-1}. Fig. 1 shows the four rivers supplying water to the Son La hydropower reservoir and the coded water-flow and surface-water-quality monitoring points (S1–S4). Monitored water flow (Q) and nine surface-water-quality parameters entering the Son La hydropower reservoir, including DO, TSS, BOD_5, COD, NH_4^+, NO_2^-, NO_3^-, PO_4^{3-}, and total Fe, were used in accordance with the regulation on assessment of wastewater receiving capacity and carrying capacity of river and lake water sources, 76/2017/TT-BTNMT (MONRE 2017). Average water-flow and surface-water-quality values at the four monitoring points are available for the ten years 2014–2024 (Source: Hydrometeorological Station of the Northwest Region and Son La Hydropower Company).

2.2. Monitoring Data

In the study area, four monitoring stations have been operated by the Son La Hydropower Company since 2014, including S1 (Da River), S2 (Nam Na River), S3 (Nam Muc River), and S4 (Nam Mu River) (Fig. 1). Stations S1, S2, S3, and S4 have been used to monitor the flow and water quality of rivers entering the Son La hydropower reservoir (inflow). Monitoring was conducted four times per year, in March, May, August, and November. Monitoring data for water flow (Q) and surface-water quality (DO, TSS, BOD_5, COD, NH_4^+, NO_2^-, NO_3^-, PO_4^{3-}, and total Fe) at four stations (S1–S4) during 2014–2024 were collected. DO values were measured using Sension156 portable equipment (HACH, US); BOD_5 and COD were determined by the HACH method/equipment (HACH, US); TSS was determined using the analytical method TCVN 6625:2000; and total Fe was determined using SMEWW 3111B:2012. Portable model 556 equipment (YIS, US) was used to determine the concentrations of NH_4^+, NO_2^-, NO_3^-, PO_4^{3-}, and total Fe in water. Average water-flow and water-quality values in March and November were calculated to represent the dry season; those in May and August represented the rainy season.

2.3. Calculation of Stream Pollutant Load

Jorgensen S.A. introduced the mixed-flow reaction principle equation; therefore, we applied this principle to determine the characteristics of a flow carrying a pollutant load (Equation 1) (Jorgensen 1987).

$$\frac{Vdc_i}{dt} = Qc_{i0} - Qc_i \quad \frac{Vd_i}{dt} = Qc_{i0} - Qc_i - V * k * c_i \qquad \ldots(1)$$

Table 1: Locations of flow-rate monitoring and surface-water sampling in river flows during 2014–2024.

No.	Location of monitoring points	Symbol
1	Da River	S1
2	Nam Na River	S2
3	Nam Muc River	S3
4	Nam Mu River	S4

Table 2: Distribution of flow-rate monitoring and surface-water sampling data for river flows entering the Son La hydropower reservoir during 2014–2024.

Years	DO (mg L^{-1})	TSS (mg L^{-1})	BOD_5 (mg L^{-1})	COD (mg L^{-1})	NH_4^+ (mg L^{-1})	NO_2^- (mg L^{-1})	NO_3^- (mg L^{-1})	PO_4^{3-} (mg L^{-1})	total Fe (mg L^{-1})
Da River (S1)									
2014	4.13 ± 0.59	40.0 ± 8.15	4.95 ± 0.30	20.4 ± 10.1	0.05 ± 0.01	0.13 ± 0.06	0.45 ± 0.10	0.14 ± 0.01	0.21 ± 0.21
2015	5.05 ± 0.46	30.0 ± 9.87	5.10 ± 0.27	7.00 ± 0.71	0.07 ± 0.05	0.01 ± 0.001	0.15 ± 0.08	0.04 ± 0.02	0.84 ± 0.56
2016	5.05 ± 0.09	25.5 ± 11.7	5.03 ± 0.22	6.15 ± 0.68	0.02 ± 0.001	0.001 ± 0.01	0.06 ± 0.01	0.03 ± 0.01	0.18 ± 0.08
2017	5.20 ± 0.01	139.8 ± 214	4.88 ± 0.41	6.60 ± 1.67	0.04 ± 0.02	0.01 ± 0.02	0.29 ± 0.30	0.59 ± 0.95	0.26 ± 0.17
2018	5.38± 0.01	42.8 ± 215.0	4.38 ± 0.41	9.00 ± 1.67	0.30 ± 0.02	0.05 ±0.02	0.40 ± 0.30	0.08 ± 0.95	0.36 ± 0.17
2019	5.80 ± 0.22	12.0 ± 0.15	4.00 ± 0.42	9.00 ± 0.65	0.30 ± 0.001	0.05 ± 0.001	0.52 ± 0.01	0.08 ± 0.01	0.33 ± 0.01
2020	5.73 ± 0.34	15.0 ± 3.31	4.201 ±0.34	9.00 ± 0.001	0.30 ± 0.001	0.17 ± 0.130	0.43 ± 0.02	0.09 ± 0.07	0.35±0.078
2021	6.10 ± 0.46	36.9 ± 39.4	3.88 ± 0.54	7.40 ± 2.26	0.30 ± 0.001	0.10 ± 0.09	0.40 ± 0.07	0.15 ± 0.15	0.26 ±0.14
2022	6.35 ± 0.62	41.4 ± 36.3	3.68 ± 0.60	6.98 ± 3.11	0.40 ± 0.00	0.10 ± 0.09	0.48 ± 0.08	0.14 ± 0.15	0.27±0.13
2023	6.57 ± 0.01	22.3 ± 0.15	3.49 ± 0.41	6.20 ± 0.83	0.45 ± 0.05	0.11 ± 0.002	0.13 ± 0.30	0.13 ± 0.57	0.23±0.16
2024	6.80 ± 0.01	20.3 ± 8.5	3.31 ± 0.28	5.44 ± 1.63	0.50 ± 0.001	0.12 ± 0.140	0.13 ± 0.07	0.13 ± 0.02	0.21±0.08
Median	5.65	38.72	4.26	8.48	0.25	0.08	0.31	0.15	0.32
Min	4.13	12.00	3.31	5.44	0.02	0.00	0.06	0.03	0.18
Max	6.80	139.75	5.10	20.48	0.50	0.17	0.52	0.59	0.84
Pearson's r	0.98	-0.27	-0.97	-0.54	0.94	0.50	-0.03	-0.05	-0.35
Nam Na River (S2)									
2014	3.80 ± 0.76	34.0 ± 12.63	6.18 ± 0.36	23.5 ± 2.20	0.02 ± 0.04	0.16 ± 0.01	0.40 ± 0.13	0.09 ±0.58	0.26 ±0.27
2015	4.18 ± 0.78	19.75 ± 9.18	5.08 ± 0.08	9.75 ± 3.11	0.08 ± 0.04	0.01 ± 0.001	0.32 ±0.147	0.14 ±0.151	0.25 ±0.08
2016	5.20 ± 0.12	72.0 ± 68.6	5.45 ± 0.53	7.23 ± 1.56	0.03 ± 0.02	0.001± 0.001	0.06 ±0.001	0.05 ±0.026	0.74 ±0.91
2017	5.25 ± 0.09	22.7 ± 10.1	5.43 ± 0.26	8.20 ± 2.57	0.11 ± 0.11	0.02 ± 0.020	0.44 ±0.252	1.15 ±1.902	0.32 ±0.20
2018	5.35 ± 0.15	24.7 ± 5.54	4.30 ± 0.46	9.00 ± 0.001	0.30 ± 0.001	0.05 ± 0.001	0.44 ±0.074	0.08 ±0.001	0.46 ±0.25
2019	5.88 ± 0.29	19.0 ± 7.03	4.00 ± 0.01	9.00 ± 0.001	0.30 ± 0.001	0.05 ± 0.001	0.40 ±0.001	0.08 ±0.001	0.33 ±0.05
2020	6.28 ± 0.46	20.7 ± 12.5	3.73 ± 0.23	5.85 ± 2.18	0.30 ± 0.001	0.03 ± 0.018	0.40 ±0.071	0.35 ±0.494	0.38 ±0.19
2021	6.70 ± 0.59	17.7 ± 12.9	3.30 ± 0.30	6.70 ± 2.27	0.35 ± 0.05	0.04 ± 0.011	0.39 ±0.089	0.37 ±0.537	0.38 ±0.19
2022	7.10 ± 0.76	15.4 ± 12.6	2.95 ± 0.36	5.63 ± 2.20	0.43 ± 0.04	0.04 ± 0.015	0.39 ±0.129	0.40 ±0.576	0.45 ±0.27
2023	7.47 0.15	6.38 9.41	2.62 0.03	4.19 0.61	0.49 0.011	0.04 0.001	0.43 ±0.022	0.32 ±0.008	0.40 ±0.005
2024	7.87 0.12	3.32 0.75	2.23 ±0.01	2.80 0.001	0.54 0.005	0.03 0.020	0.45 ±0.001	0.34 ±0.001	0.41 ±0.002
Median	5.91	23.26	4.11	8.35	0.27	0.04	0.37	0.31	0.40
Min	3.80	3.32	2.23	2.80	0.02	0.00	0.06	0.05	0.25
Max	7.87	72.00	6.18	23.50	0.54	0.16	0.45	1.15	0.74
Pearson's r	0.99	-0.65	-0.98	-0.75	0.97	-0.28	0.44	0.17	0.11
Nam Muc River (S3)									
2014	4.40 ± 0.22	27.50 ± 3.64	4.00 ±0.707	11.50 ±3.84	0.04 ± 0.02	0.04 0.038	0.43 ±0.165	0.08 ±0.049	0.39 ±0.11
2015	4.45 0.72	10.25 6.86	4.60 ±1.231	8.75 ±2.59	0.07 0.05	0.01 0.002	0.15 ±0.073	0.03 ±0.008	0.27 ±0.03
2016	5.33 0.11	22.50 10.7	5.00 ±0.001	6.58 ±1.08	0.04 0.02	0.001 ±0.002	0.06 ±0.001	0.03 ±0.001	0.15 ±0.07
2017	5.43 ± 0.04	35.25 ± 38.5	5.13 ±0.719	7.78 ±1.10	0.11 ± 0.11	0.02 ± 0.020	0.20 ±0.146	0.04 ±0.022	0.15 ±0.09
2018	5.35 ± 0.11	21.25 ± 5.76	4.53 ±0.65	9.18 ±0.30	0.30 ± 0.001	0.05± 0.0001	0.44 ±0.041	0.08 ±0.001	0.32 ±0.03
2019	5.60 ± 0.25	16.00 ± 6.92	4.03 ±0.04	9.00 ±0.001	0.30 ± 0.001	0.05 ±0.0001	0.42 ±0.015	0.09 ±0.005	0.31 ±0.01
2020	5.93 ± 0.27	20.63 ± 10.4	4.50 ±0.430	7.75 ±1.57	0.33 ± 0.04	0.04 ± 0.015	0.33 ±0.043	0.07 ±0.022	0.19 ±0.01
2021	6.15 ± 0.39	20.20 ± 11.4	4.53 ±0.602	7.30 ±2.08	0.33 ± 0.04	0.05 ± 0.015	0.33 ±0.043	0.08 ±0.029	0.16 ±0.04
2022	6.40 0.47	19.80 12.2	4.53 ±0.763	7.13 ±2.90	0.43 0.04	0.05 0.023	0.35 ±0.050	0.08 ±0.033	0.18 ±0.08
2023	6.62 0.15	20.68 6.73	4.52 ±0.001	6.81 ±1.89	0.48 0.21	0.05 0.002	0.36 ±0.013	0.08 ±0.001	0.16 ±0.01
2024	6.86 0.54	20.26 5.35	4.52 ±1.231	6.50 ±0.50	0.53 ± 0.02	0.06 ±0.0001	0.38 ±0.002	0.08 ±0.001	0.15 ±0.01
Median	5.68	21.30	4.53	8.02	0.27	0.04	0.31	0.07	0.22
Min	4.400	10.250	4.000	6.501	0.035	0.004	0.060	0.026	0.146
Max	6.865	35.250	5.125	11.500	0.534	0.058	0.438	0.085	0.387
Pearson's r	0.97	-0.16	-0.03	-0.67	0.96	0.71	0.39	0.63	-0.59

Table Cont....

Years	DO (mg L^{-1})	TSS (mg L^{-1})	BOD_5 (mg L^{-1})	COD (mg L^{-1})	NH_4^+ (mg L^{-1})	NO_2^- (mg L^{-1})	NO_3^- (mg L^{-1})	PO_4^{3-} (mg L^{-1})	total Fe (mg L^{-1})
Nam Mu River (S4)									
2014	4.95 ± 0.05	14.50 ± 0.50	4.65 ±0.350	13.00 ± 3.00	0.04 ± 0.001	0.01 ± 0.001	0.23 ± 0.02	0.11 ±0.056	0.25 ±0.25
2015	4.75 ± 0.65	11.50 ± 5.50	5.15 ±0.150	10.00 ± 2.00	0.09 ± 0.07	0.01 ± 0.004	0.13 ± 0.07	0.03 ±0.024	0.19 ±0.12
2016	5.18 ± 0.15	9.75 ± 1.920	5.08 ±0.130	6.78 ± 2.45	0.03 ± 0.01	0.001± 0.001	0.06 ±0.001	0.03 ±0.001	0.07 ±0.001
2017	5.30 ± 0.10	15.25 ± 4.08	4.98 ±0.043	5.68 ± 2.11	0.11 0.11	0.01 0.021	0.15 ±0.147	0.04 ±0.022	0.13 ±0.10
2018	5.38 0.11	13.75 2.48	4.20 ±0.346	9.00 0.001	0.30 0.001	0.05 0.001	0.40 ±0.001	0.08 ±0.001	0.30 ±0.001
2019	5.63 0.29	12.0 0.001	4.00 ±0.001	9.00 0.001	0.30 0.001	0.05 0.001	0.40 ±0.001	0.08 ±0.001	0.30 ±0.001
2020	5.70 0.21	12.75 2.47	4.03 ±0.234	6.48 ±1.703	0.34 0.030	0.05 0.003	0.40 ±0.031	0.06 ±0.017	0.68 ±0.646
2021	5.83 0.27	12.68 3.15	3.86 ±0.283	5.78 2.242	0.40 0.050	0.06 0.003	0.45 ±0.035	0.06 ±0.025	0.29 ±0.077
2022	6.03 0.33	12.70 3.80	3.70 ±0.336	5.08 2.834	0.45 0.031	0.07 0.003	0.50 ±0.040	0.06 ±0.030	0.31 ±0.101
2023	6.24 0.04	12.79 0.50	3.51 ±0.001	4.38 1.57	0.52 0.001	0.08 0.001	0.55 ±0.001	0.06 ±0.001	0.47 ±0.001
2024	6.18 0.71	12.7 0.001	3.33 ±0.039	3.68 ±2.41	0.58 0.001	0.09 ±0.022	0.60 ±0.040	0.06 ±0.024	0.50 ±0.003
Median	5.56	12.77	4.23	7.17	0.29	0.04	0.35	0.06	0.32
Min	4.75	9.75	3.33	3.68	0.03	0.001	0.06	0.03	0.07
Max	6.24	15.25	5.15	13.00	0.58	0.09	0.60	0.11	0.68
Pearson's r	0.98	-0.02	-0.92	-0.83	0.97	0.96	0.90	-0.03	0.65

Notes: Data are presented as the average value ± standard deviation.

Where Cio is the pollutant concentration in the stream and Q is the flow rate (discharge). The material-balance flow equation (1) allows calculation of the river-stream pollutant load based on flow rate Q and the concentration of the surface-water pollutant in the stream, C.

The general formula for calculating the total amount of pollutants generated is:

$$E = \frac{C*F*3600}{1000} \quad \ldots(2)$$

In which: E is the pollution load; C is the concentration at the time of measurement; F is the discharge flow rate at the time of measurement; 3600 is the number of seconds in an hour.

Equation (2) was applied to calculate the seasonal river-flow pollutant load in the basin. The pollutant load from the main flow system of the four rivers entering the Son La hydropower reservoir annually during 2014–2024 was calculated from river water flow and pollutant concentrations measured at four hydrological stations (S1–S4) (Fig. 1).

The pollutant load of each river in each year during 2014–2024 was calculated as follows:

$$PL = Q * C_i * 10^{-6} * 365 * 24 * 60 * 60 \quad \ldots(3)$$

Where PL is the pollutant load (tonnes $year^{-1}$), Q is the water flow ($m^3\ s^{-1}$), and C_i is the concentration of pollutant i in river water (mg L^{-1}) at each monitoring station (S1, S2, S3, and S4). Units were converted by multiplying by the number of days per year (365) and the number of seconds per day (24 hours day^{-1} × 60 minutes $hour^{-1}$ × 60 seconds $minute^{-1}$).

This study describes the correlation between the dry-season flow-rate variable Qd and flood-season flow-rate variable Qr and the surface-water-quality concentration variable C_i (variable x) in seasonal river flow during 2014–2024. The sample correlation coefficient was calculated using the formula of Pearson (1909). The correlation coefficient (r) was used to infer the relationship between two related variables, x and y (Asuero et al. 2006). The correlation coefficient r of the two variables was determined using the following formula:

$$r = \frac{\sum_{i=1}^{n}(x_i-\bar{x})(y_i-\bar{y})}{\sqrt{\sum_{i=1}^{n}(x_i-\bar{x})^2 \sum_{i=1}^{n}(y_i-\bar{y})^2}} \quad \ldots(4)$$

2.4. Statistical Analysis

SPSS 20.0 was used for statistical analysis of the monitoring data. Water-flow and surface-water-quality data were log-transformed for homogeneity and tested for normality using the Cor. Test to assess statistical significance. At a probability of <0.05, the average data for 2014–2024 for nine river-water-quality parameters were considered statistically significant: DO, TSS, BOD_5, COD, NH_4^+, NO_2^-, NO_3^-, PO_4^{3-}, and total Fe. Significant differences and correlations among variations were analyzed using one-way ANOVA and Pearson correlation coefficients (r), respectively. Significant differences between inflow and outflow data and between dry and rainy seasons were analyzed using an independent-samples t-test. Figures were prepared using OriginPro 2018 v9.5.0. Water-flow data measured at hydrological stations and surface-water-quality data were analyzed using the R programming language in RStudio.

Table 3: Statistical significance of data from four monitoring points in rivers entering the Son La hydropower reservoir (SLR) based on eleven years of monitoring data using the Cor. Test for 2014–2024.

Da River (S1)	Test statistic value	Probability value
DO	t = 13.341	p-value < 0.01
TSS	t = 12.510	p-value < 0.05
BOD_5	t = 11.765	p-value < 0.05
COD	t = 10.139	p-value < 0.05
NH_4^+	t = 8.2823	p-value < 0.01
NO_2^-	t = 7.7520	p-value < 0.01
NO_3^-	t = 9.0206	p-value < 0.05
PO_4^{3-}	t = 14.635	p-value < 0.01
total Fe	t = 11.394	p-value < 0.01
Nam Na River (S2)	Test statistic value	Probability value
DO	t = 22.007	p-value < 0.01
TSS	t = 5.5512	p-value < 0.01
BOD_5	t = 13.972	p-value < 0.01
COD	t = 7.4517	p-value < 0.01
NH_4^+	t = 9.8740	p-value < 0.05
NO_2^-	t = 12.257	p-value < 0.01
NO_3^-	t = 4.5416	p-value < 0.05
PO_4^{3-}	t = 5.5224	p-value < 0.05
total Fe	t = 6.3530	p-value < 0.01
Nam Muc River (S3)	Test statistic value	Probability value
DO	t = 14.249	p-value < 0.01
TSS	t = 4.4883	p-value < 0.05
BOD_5	t = 10.183	p-value < 0.01
COD	t = 7.5876	p-value < 0.01
NH_4^+	t = 11.618	p-value < 0.01
NO_2^-	t = 5.0460	p-value < 0.05
NO_3^-	t = 4.7445	p-value < 0.05
PO_4^{3-}	t = 4.4979	p-value < 0.05
total Fe	t = 3.2443	p-value < 0.05
Nam Mu River (S4)	Test statistic value	Probability value
DO	t = 14.6710	p-value < 0.01
TSS	t = 4.66415	p-value < 0.05
BOD_5	t = 7.2097	p-value < 0.01
COD	t = 4.4056	p-value < 0.05
NH_4^+	t = 12.974	p-value < 0.01
NO_2^-	t = 10.692	p-value < 0.01
NO_3^-	t = 6.3045	p-value < 0.01
PO_4^{3-}	t = 2.0118	p-value < 0.05
total Fe	t = 2.5764	p-value < 0.05

3. RESULTS AND DISCUSSION

3.1. Water Flow of River System

Water-flow values at the four monitoring stations are shown in Fig. 2. The Da River has the highest water flow and is the main flow supplying water to the Son La hydropower reservoir, followed by the Nam Na, Nam Mu, and Nam Muc Rivers (Fig. 2). A decreasing trend in water flow was observed in the Nam Muc River. This decrease during the study period may be due to the construction and operation of the Nam Muc Dam, which retains water for hydropower generation and agricultural irrigation (Fig. 2). By contrast, water flow in the Da, Nam Na, and Nam Mu Rivers tended to increase during 2014–2024. As the main river, the Da River has a higher water flow than the three tributaries.

In the dry season, the average water flows of the Da River (S1), Nam Na River (S2), Nam Mu River (S4), and Nam Muc River (S3) were 1,056, 217, 154, and 24 $m^3 s^{-1}$, respectively; those in the rainy season were 1,564, 674, 370, and 88 $m^3 s^{-1}$, respectively (Figs. 2 and 3). Water flows during the rainy season at all monitoring stations were significantly higher than those during the dry season ($p < 0.05$) because of the greater amount of water flowing into the reservoir during the rainy season. Small hydropower plants on river systems S1, S2, S3, and S4 regulate flow. During the rainy season, large amounts of water flow into rivers in the basins, and hydropower plants release water to ensure dam safety; therefore, water flow tends to increase. Dry-season water flow into the Son La hydropower reservoir increased significantly because of flow regulation by small hydropower dams on the river system. Hydropower-dam operation has reduced downstream water flow during the rainy season by about 35% and increased water flow during the dry season by about 226% (Le et al. 2014).

3.2. Water Quality of River System

Water-quality parameters (TSS, BOD_5, COD, NH_4^+, NO_2^-, NO_3^-, PO_4^{3-}, and total Fe) were compared between the dry and rainy seasons in the river system of the Son La hydropower reservoir from 2014 to 2024. Seasonal water-quality values differed among the Da River (S1), Nam Na River (S2), Nam Muc River (S3), and Nam Mu River (S4).

The values of water-quality parameters during 2014–2024 (dry season; rainy season) were as follows: DO, 5.6–5.5 mg L^{-1} (S1), 5.7–5.6 mg L^{-1} (S2), 5.6–5.5 mg L^{-1} (S3), and 5.5–5.5 mg L^{-1} (S4); TSS, 19.5–63.1 mg L^{-1} (S1), 15.4–35.9 mg L^{-1} (S2), 14.5–28.0 mg L^{-1} (S3), and 11.9–13.7 mg L^{-1} (S4); BOD_5, 4.22–4.49 mg L^{-1} (S1), 4.2–4.4 mg L^{-1} (S2), 4.4–4.6 mg L^{-1} (S3), and 4.3–4.3 mg L^{-1} (S4); COD, 9.51–8.12 mg L^{-1} (S1), 8.97–8.64 mg L^{-1} (S2), 8.0–8.14 mg L^{-1} (S3), and 7.71–7.34 mg L^{-1} (S4); NH_4^+, 0.23–0.20 mg L^{-1} (S1), 0.26–0.22 mg L^{-1} (S2), 0.25–0.22 mg L^{-1} (S3), and 0.27–0.24 mg L^{-1} (S4); NO_2^-, 0.05–0.10 mg L^{-1} (S1),

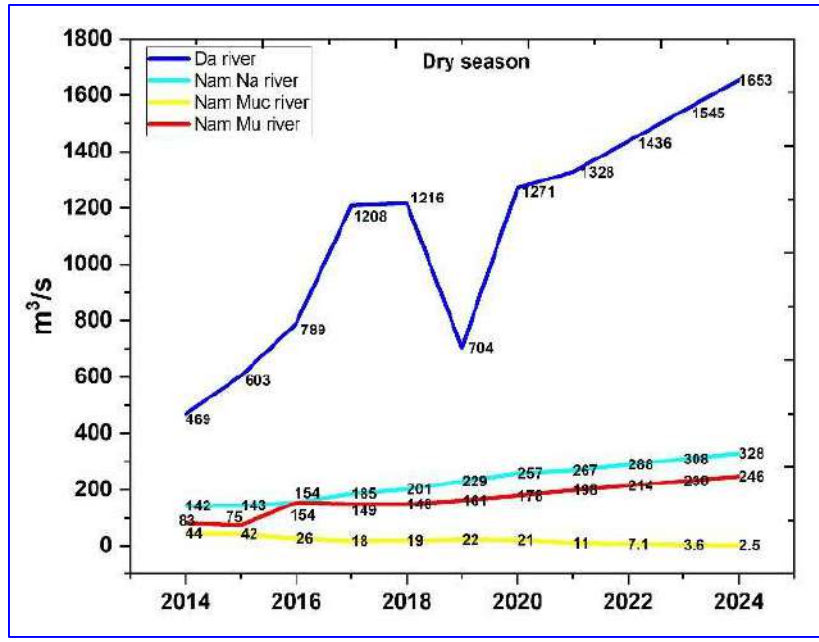


Fig. 2: Dry-season water-flow trends in the Son La hydropower reservoir basin during 2014–2024.

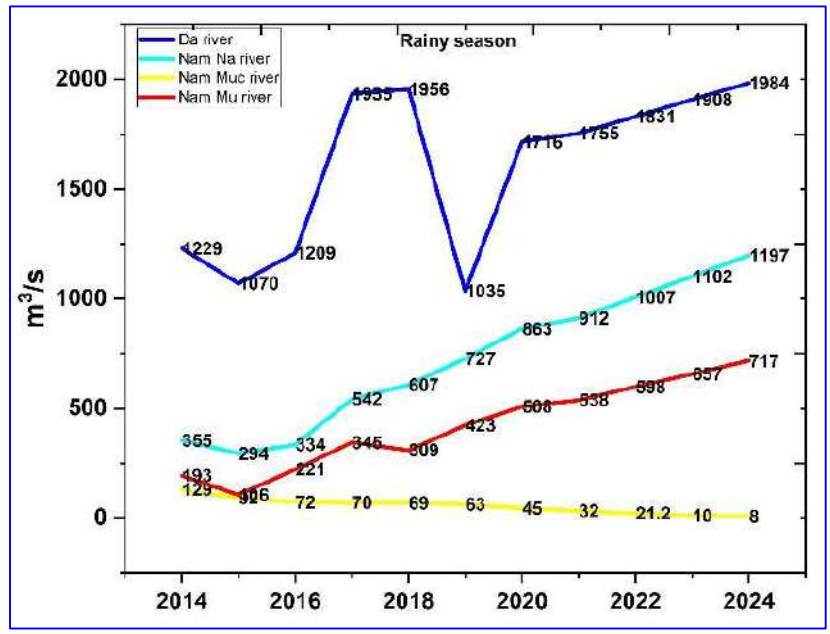


Fig. 3: Rainy-season water-flow trends in the Son La hydropower reservoir basin during 2014–2024.

0.05–0.04 mg L^{-1} (S2), 0.04–0.03 mg L^{-1} (S3), and 0.04–0.04 mg L^{-1} (S4); NO_3^-, 0.38–0.33 mg L^{-1} (S1), 0.34–0.39 mg L^{-1} (S2), 0.31–0.30 mg L^{-1} (S3), and 0.34–0.31 mg L^{-1} (S4); PO_4^{3-}, 0.08–0.22 mg L^{-1} (S1), 0.11–0.50 mg L^{-1} (S2), and 0.06–0.06 mg L^{-1} (S3); and total Fe, 0.25–0.40 mg L^{-1} (S1), 0.27–0.52 mg L^{-1} (S2), 0.22–0.23 mg L^{-1} (S3), and 0.27–0.32 mg L^{-1} (S4).

Fig. 4 shows the mean annual water-quality values. For the Da River, the values were DO (5.5 ± 0.8), TSS (41.2 ± 10.4), BOD_5 (4.3 ± 0.7), COD (8.8 ± 0.53), NH_4^+ (0.21 ± 0.015), NO_2^- (0.07 ± 0.008), NO_3^- (0.35 ± 0.19), PO_4^{3-} (0.14 ± 0.034), and total Fe (0.32 ± 0.028). For the Nam Na River, the values were DO (5.7 ± 1.2), TSS (25.6 ± 0.29), BOD_5 (4.3 ± 1.1), COD (8.8 ± 0.61), NH_4^+ (0.23 ± 0.065), NO_2^- (0.04

± 0.005), NO_3^- (0.36 ± 0.015), PO_4^{3-} (0.30 ± 0.07), and total Fe (0.39 ± 0.036). For the Nam Muc River, the values were DO (5.6 ± 0.8), TSS (21.2 ± 1.61), BOD_5 (4.5 ± 0.74), COD (8.07 ± 0.25), NH_4^+ (0.23 ± 0.016), NO_2^- (0.03 ± 0.002), NO_3^- (0.3 ± 0.014), PO_4^{3-} (0.06 ± 0.003), and total Fe (0.22 ± 0.010). For the Nam Mu River, the values were DO (5.5 ± 0.6), TSS (12.7 ± 3.34), BOD_5 (4.3 ± 0.63), COD (7.5 ± 0.32), NH_4^+ (0.25 ± 0.017), NO_2^- (0.04 ± 0.002), NO_3^- (0.32 ± 0.017), PO_4^{3-} (0.06 ± 0.003), and total Fe (0.29 ± 0.028).

All monitored water-quality parameters were below the limits specified for irrigation water in the Vietnamese guideline QCVN 08-MT:2015/BTNMT (DO: ≥ 4 mg L^{-1}, TSS: 50 mg L^{-1}, BOD_5: 15 mg L^{-1}, COD: 30 mg L^{-1}, NH_4^+: 0.9 mg L^{-1}, NO_2^-: 0.05 mg L^{-1}, NO_3^-: 10 mg L^{-1}, PO_4^{3-}: 0.3 mg L^{-1}, and total Fe: 1.5 mg L^{-1}), except for NO_2^- (MONRE 2015). NO_2^- concentrations in 2014 and 2021–2023 in the Da and Nam Na Rivers ranged from 0.05 to 0.20 mg L^{-1}, exceeding the QCVN 08-MT:2015/BTNMT limit of 0.05 mg L^{-1}. Increasing trends during 2014–2023 were reported for DO (r = 0.84), NH_4^+ (r = 0.93), NO_2^- (r = 0.28), NO_3^- (r = 0.47), PO_4^{3-} (r = 0.39), and total Fe (r = 0.91), possibly as a result of agriculture in the river basin and increasing aquaculture in the reservoir. This result is consistent with previous studies (Brian et al. 1997, Karine et al. 2006, Do et al. 2020). The formation of hydropower dams in the basin affects seasonal changes in water-quality concentrations in the stream. Ammonium (NH_4^+) concentration in the stream increases because of seasonal increases in circulation downstream of the dam (Isaac et al. 2018, Ito 1987). In addition, increases in NH_4^+, NO_2^-, NO_3^-, and PO_4^{3-} concentrations in river flows are related to the accumulation and metabolism of nitrogen and phosphorus nutrients due to discharges from the basin into the stream (Zhang et al. 2014). High phosphate concentrations in annual runoff indicate pollution from untreated discharges into the river (Houri et al. 2007). In contrast, TSS (r = - 0.95), BOD_5 (r = - 0.65), and COD (r = - 0.48) reportedly showed decreasing trends during this period. The construction of dams upstream of the Son La hydropower plant, namely the Lai Chau, Nam Muc, Nam Na 1 and 2, and Huoi Quang dams, and the trapping of sediment and suspended solids in upstream reservoirs may be responsible for the reduction in TSS in the study area. The annual decrease in TSS concentrations is associated with the construction of hydropower reservoirs in the basin because large amounts of silt and suspended solids in river flows are trapped in the reservoirs (Kummu et al. 2007). BOD_5 and COD concentrations decrease because of seasonal variation in the stream (Dou et al. 2012). Thus, regulation of river water by hydropower dams and discharges from the basin is an important factor affecting pollutant concentrations in the stream.

3.3. Relationship Between Water Flow and Pollutant Concentration

Fig. 5 shows the statistical relationship during the dry season between the water-flow variable Qd in rivers of the Son La hydropower reservoir basin and the pollutant concentrations of nine parameters, with the correlation coefficient (r) determined. Qd had a positive correlation coefficient (r > 0) with five surface-water-quality parameters: NH_4^+ at S1, S2, and S4; NO_3^- at S1 and S2; PO_4^{3-} at S1; and total Fe at S1, S2, S3, and S4. For NH_4^+ and total Fe at S1, S2, and S4 and NO_3^- at S1 and S4, the correlation coefficient (r) with Qd ranged from 0.5 to 1 (strong correlation); for PO_4^{3-} at S1, S2, and S4, the correlation coefficient (r) with Qd was <0.29 (weak correlation). Qd had a negative correlation coefficient (r < 0) with four surface-water parameters: TSS at S1, S2, and S4; BOD_5 at S1, S2, S3, and S4; COD at S1, S2, and S4; and NO_2^- at S1, S2, and S3. Thus, during the dry season, as water flow increased, the concentrations of NH_4^+, total Fe, NO_3^-, and PO_4^{3-} increased, whereas the concentrations of TSS, BOD_5, COD, and NO_2^- decreased.

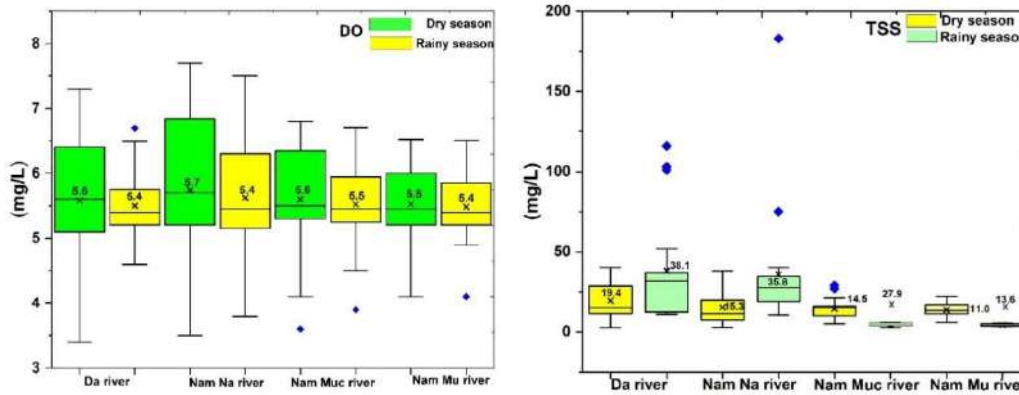


Figure Cont....

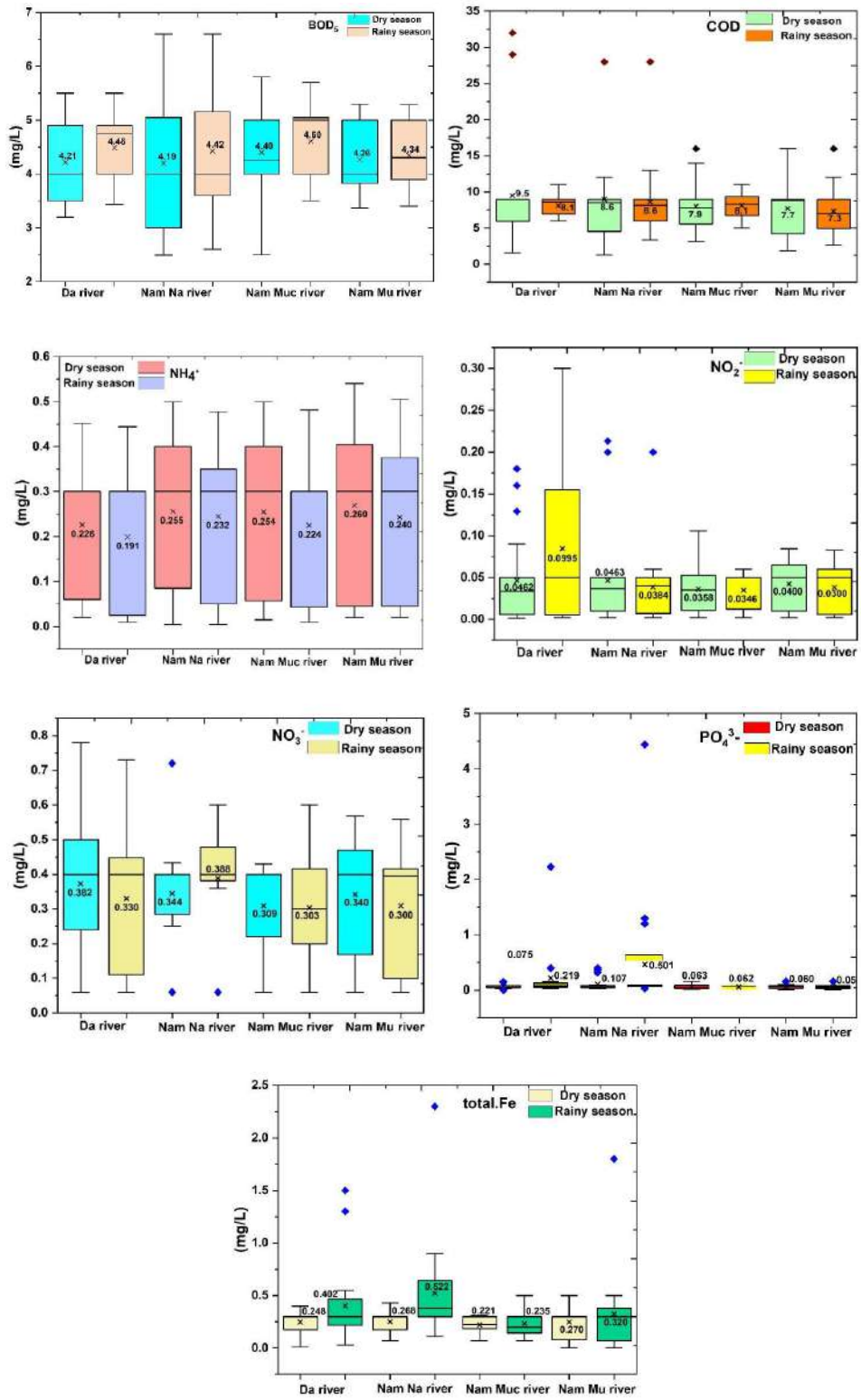


Fig. 4: Changes in DO, TSS, BOD_5, COD, NH_4^+, NO_2^-, NO_3^-, PO_4^{3-}, and total Fe concentrations in river flows during the dry and rainy seasons from 2014 to 2024.

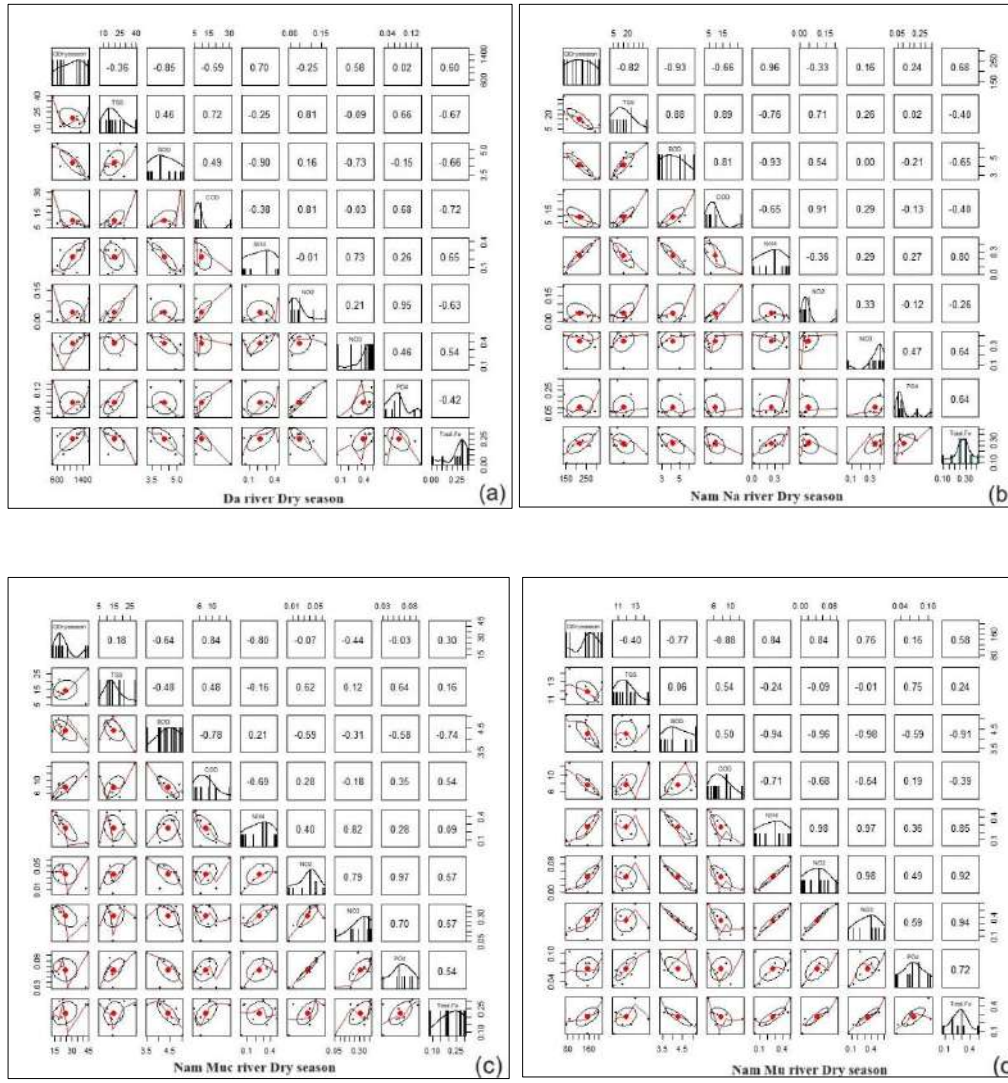


Fig. 5: Correlation between flow rate and dry-season stream pollutant concentration in the Da River (a), Nam Na River (b), Nam Muc River (c), and Nam Mu River (d) during 2014–2024.

Fig. 6 shows the statistical relationship during the rainy season between the water-flow variable Qr and the concentrations of nine pollutants. Correlations (r) between river water flow and surface-water-pollutant concentrations during the rainy season differed among the Da River (S1), Nam Na River (S2), Nam Muc River (S3), and Nam Mu River (S4). Qr had a positive correlation coefficient ($r > 0$) with NH_4^+, NO_2^-, NO_3^-, and PO_4^{3-} at S1, S2, and S4; total Fe at S3 and S4; and TSS at S1 and S4. During the rainy season, Qr had a negative correlation coefficient ($r < 0$) with BOD_5 and COD at S1, S2, S3, and S4.

This result is consistent with previous studies showing that the operation of artificial dams changes the natural river-flow regime, such as by reducing flow during the rainy season and increasing flow during the dry season (Li et al. 2017). Dam operation affects the annual flow rate; concentrations of dissolved NO_3^-, NH_4^+, and PO_4^{3-} downstream increase, while the concentration of suspended solids (TSS) decreases (Stow et al. 2001, Stanley 2002, Haque et al. 2018). Increased biomass decomposition in the upstream reservoir may reduce downstream BOD_5 and COD concentrations (Le et al. 2014). Total Fe concentration increases under low-flow conditions and decreases during flood periods (Heikkinen 1990). Thus, water accumulation associated with dams on river flows is an important factor influencing the correlation between flow rate and pollutant concentrations during the dry and flood seasons in the Son La hydropower reservoir basin.

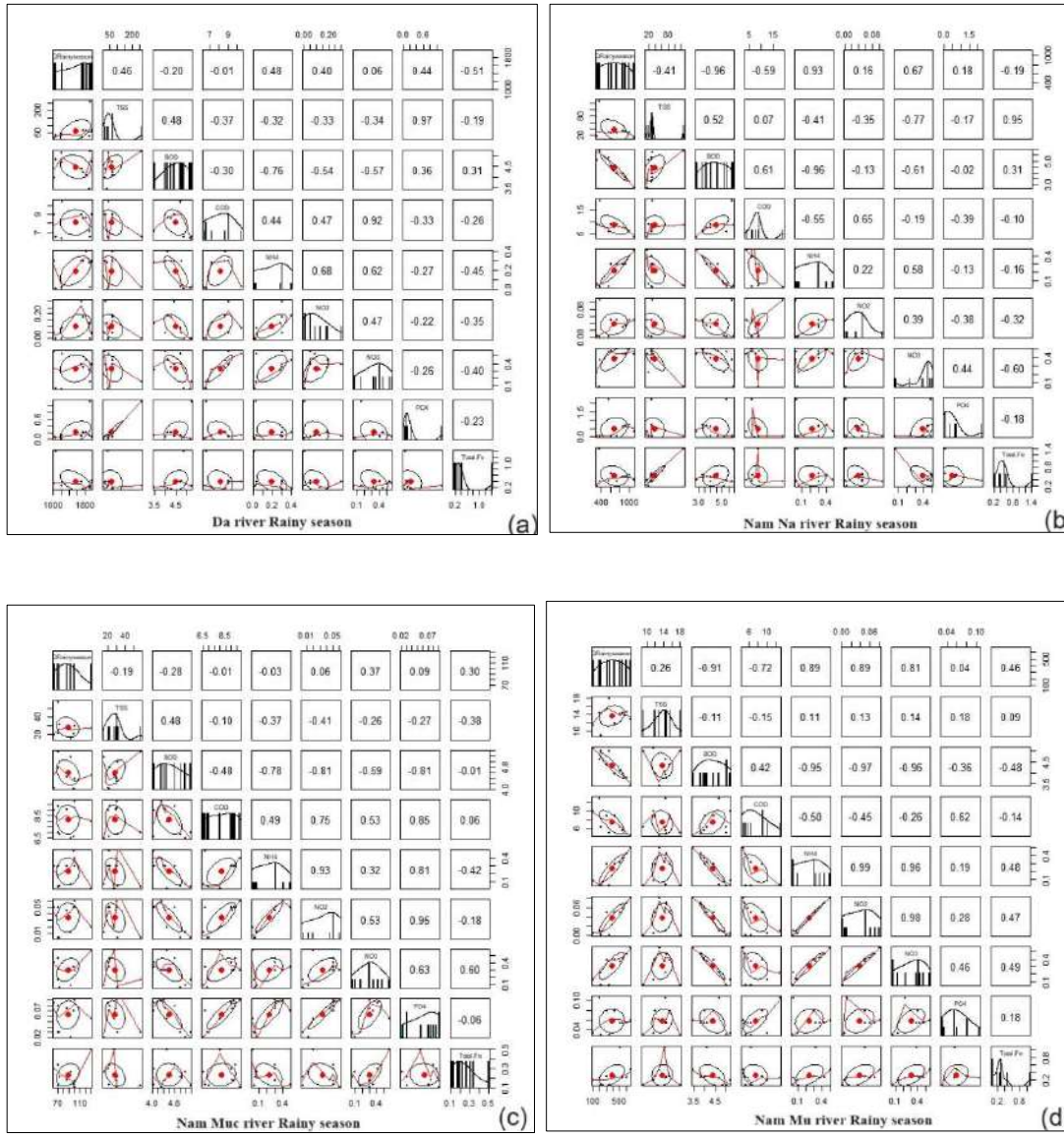


Fig. 6: Correlation between flow rate and rainy-season stream pollutant concentration in the Da River (a), Nam Na River (b), Nam Muc River (c), and Nam Mu River (d) during 2014–2024.

3.4. Pollutant Load of River System

The pollutant load of the river system of the Son La hydropower reservoir fluctuated from 2014 to 2024. During 2014–2024, the pollutant loads of the four rivers entering the reservoir (S1, S2, S3, and S4) ranged from 11,581,848 to 9,714,484 tonnes year^{-1}. The lowest and highest pollutant loads were obtained in 2017 and 2022, respectively. The pollutant load of the river system during the rainy season was significantly higher than that during the dry season ($p < 0.001$), mainly because of higher water flow in the rainy season. The rainy-season pollutant load accounted for 63.1%–92.4% (average: 77.2%) of the yearly pollutant load. During the rainy season, the pollutant load in the inflow ranged from 1,037,197 to 8,976,742 tonnes year^{-1} (average: 2,762,709 tonnes year^{-1}), significantly higher than that during the dry season (372,913–1,098,830 tonnes year^{-1}; average: 640,894 tonnes year^{-1}) ($p < 0.01$).

Pollutant loads of the component parameters (TSS, BOD_5, COD, NH_4^+, NO_2^-, NO_3^-, PO_4^{3-}, and total Fe) also fluctuated greatly by season and year during 2014–2024. The average pollutant loads (tonnes year^{-1}) were in the following order: TSS (318,191) > COD (62,308) > BOD_5 (34,359) >

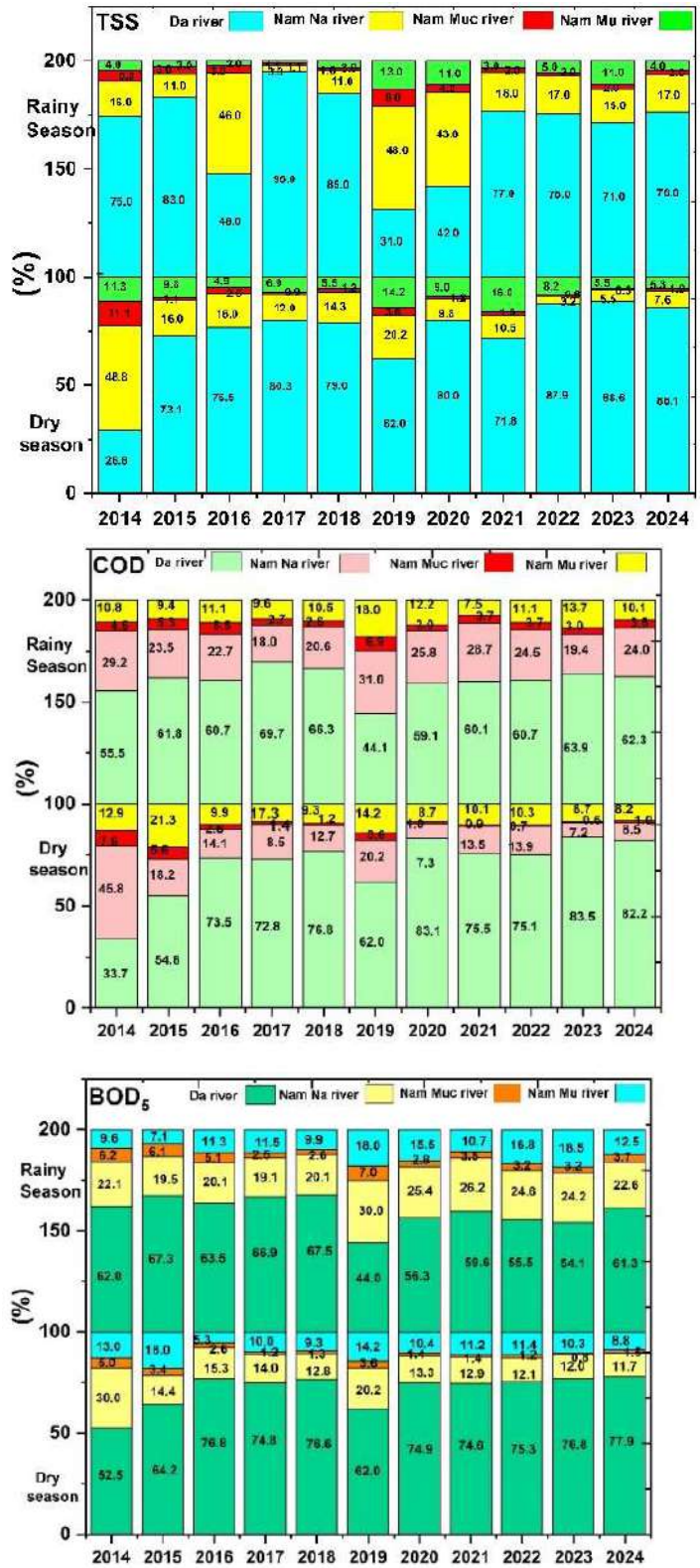

TSS
Da river
Nam Na river
Nam Muc river
Nam Mu river
Rainy Season
Dry season
(%)
2014 2015 2016 2017 2018 2019 2020 2021 2022 2023 2024
COD
Da river
Nam Na river
Nam Muc river
Nam Mu river
Rainy Season
Dry season
(%)
2014 2015 2016 2017 2018 2019 2020 2021 2022 2023 2024
BOD5
Da river
Nam Na river
Nam Muc river
Nam Mu river
Rainy Season
Dry season
(%)
2014 2015 2016 2017 2018 2019 2020 2021 2022 2023 2024

Figure Cont....

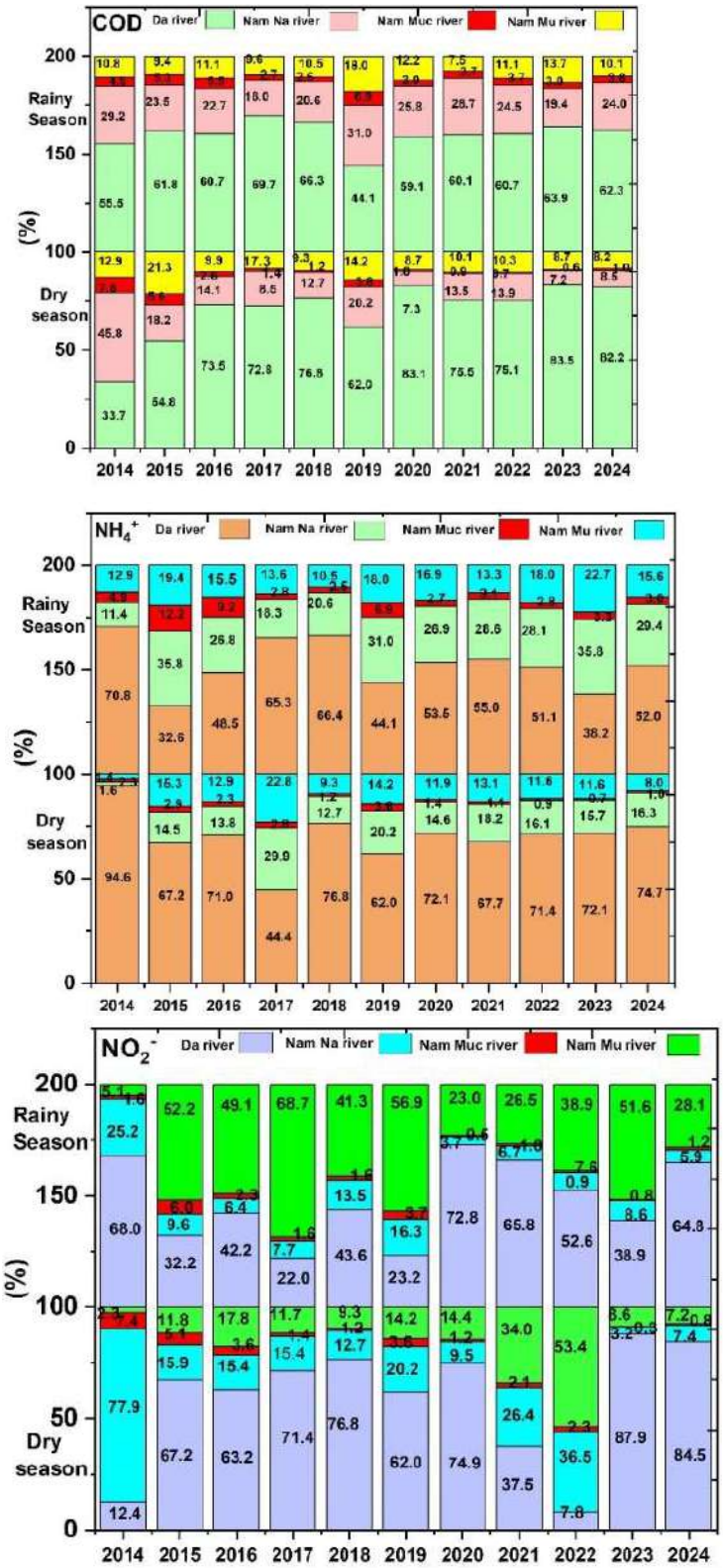

COD
Da river
Nam Na river
Nam Muc river
Nam Mu river
Rainy Season
Dry season
(%)
2014 2015 2016 2017 2018 2019 2020 2021 2022 2023 2024
NH4+
Da river
Nam Na river
Nam Muc river
Nam Mu river
Rainy Season
Dry season
(%)
2014 2015 2016 2017 2018 2019 2020 2021 2022 2023 2024
NO2-
Da river
Nam Na river
Nam Muc river
Nam Mu river
Rainy Season
Dry season
(%)
2014 2015 2016 2017 2018 2019 2020 2021 2022 2023 2024

Figure Cont....

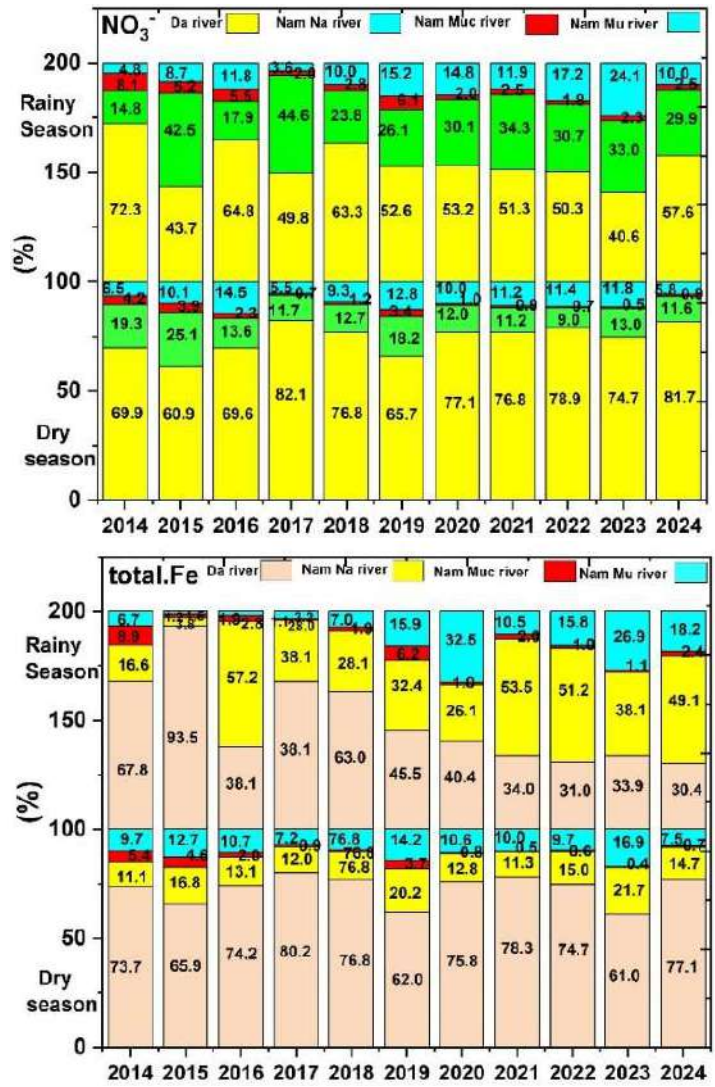


Fig. 7: Pollutant-load ratio during the dry and rainy seasons in river flows of the Son La hydropower reservoir basin during 2014–2024.

NO_3^- (3,061) > Fe (2,924) > NH_4^+ (2,107) > PO_4^{3-} (1,776) > NO_2^- (725). Fig. 7 shows that TSS, COD, BOD_5, NO_3^-, Fe, NH_4^+, PO_4^{3-}, and NO_2^- accounted for 75%, 15%, 8%, 0.7%, 0.7%, 0.5%, 0.4%, and 0.2% of the yearly pollutant loads, respectively. Cultivation on sloping land in the Son La hydropower reservoir basin increases soil erosion and runoff, carrying dissolved solids with rainwater. This may contribute to increased total suspended solids (TSS) pollution loads in the basin, affecting sedimentation processes and increasing sediment accumulation in the hydropower reservoir (Tran et al. 2012). The decomposition of organic matter in reservoirs and the relationship between COD and BOD_5 vary between the dry and rainy seasons, indicating that these two parameters have high pollution loads following basin flow (Du et al. 2024). Seasonal variations in BOD_5 and COD concentrations have been observed, with the highest average BOD_5 levels recorded in February (dry season) and the lowest in May (rainy season), while COD peaked in September (rainy season). The increase in pollutant loads of NO_3^-, Fe, NH_4^+, PO_4^{3-}, and NO_2^- is primarily caused by waste sources from the reservoir basin, mainly nonpoint sources (NPS). These pollutants mainly originate from agricultural, domestic, livestock, and cage-aquaculture waste within the reservoir basin (Yang et al. 2022, Shen et al. 2014, Zhuang et al. 2016, Chen et al. 2024). The pollutant loads of these parameters in rivers also depend on rainfall and sediment transport within the basin (Chen et al. 2024, Shen et al. 2014). Therefore, watershed pollution-control measures should be prioritized to manage the water quality of hydropower reservoirs that supply domestic water,

such as the Sơn La hydropower reservoir in Northwest Vietnam.

Total pollutant load showed a strong negative correlation with water flow for TSS ($r = -0.81$, $p < 0.001$), BOD_5 ($r = -0.82$, $p < 0.001$), COD ($r = -0.79$, $p < 0.001$), NH_4^+ ($r = -0.73$, $p < 0.001$), NO_3^- ($r = -0.77$, $p < 0.001$), PO_4^{3-} ($r = -0.75$, $p < 0.001$), and total Fe ($r = -0.78$, $p < 0.001$). Total pollutant load also showed a strong negative correlation with water flow for NO_2^- ($r = -0.67$, $p < 0.001$).

Fig. 7 shows that the Da River has a large water flow and correspondingly transports the highest pollution load to the reservoir compared with the three smaller rivers, namely the Nam Na, Nam Muc, and Nam Mu Rivers. This is because the Da River serves as a primary water source for agriculture in 25 provinces and cities and provides drinking water for more than 30 million people in urban and rural areas. The basin has significant economic and historical value (Le et al. 2019). The pollution load in the Son La hydropower reservoir basin may also depend primarily on flow regulation between the dry and rainy seasons by hydropower plants in the basin (Do et al. 2019, Do et al. 2020). At the same time, contaminant discharges to rivers increase with human population growth and activities in agricultural, residential, and livestock sectors, facilitating the detection of river contamination (Suhardono et al. 2025). Camargo Hinostroza et al. (2025) reported that total nitrogen values exceeded the limits established in the ECA in 82% of the data, pH in 13%, and phosphorus in 1%. For inorganic parameters, data from the LChin1S monitoring point showed that lead and zinc levels exceeded the values established in the ECA by 8% and 3%, respectively, in the ICA-PE evaluation of the dry and wet seasons. These findings highlight the importance of effective water resource management in the transboundary river basin of Northwestern Vietnam.

4. CONCLUSIONS

This study provides a comprehensive assessment of water-flow and pollutant-load dynamics in the Son La hydropower reservoir basin from 2014 to 2024. The results indicate that while most monitored water-quality parameters generally complied with Vietnamese irrigation standards, nitrite (NO_2^-) concentrations frequently exceeded regulatory limits, specifically during 2014 and the 2021–2024 period. A distinct temporal trend was observed over the decade: dissolved oxygen (DO), ammonium (NH_4^+), and other nutrients showed increasing trends, while total suspended solids (TSS), BOD_5, and COD decreased. The reduction in TSS and organic matter is primarily attributed to the sediment-trapping effects of upstream reservoirs such as the Lai Chau and Nam Muc dams. Quantification of pollutant loads revealed an average annual transport of 3,403,604 tonnes, characterized by marked seasonal variability. The rainy season was the dominant period for pollutant transport, accounting for 63.1%–92.4% of the total yearly load. Among the pollutants, TSS was the most prominent, representing 75% of the total load, followed by COD (15%) and BOD_5 (8%). Statistical analysis confirmed a strong correlation between seasonal discharge and pollutant concentrations, highlighting the impact of dam operations and land-use activities, particularly agriculture and cage aquaculture, on the reservoir's water chemistry. These findings have important implications for management of the Da River system, which serves as a vital source of domestic and agricultural water for millions of people in northern Vietnam. Effective watershed management should prioritize nonpoint source pollution control and account for the cumulative effects of the reservoir cascade. Future research should focus on self-purification mechanisms within these reservoirs and the development of integrated monitoring across the entire river system to safeguard regional water security.

5. ACKNOWLEDGEMENT

The authors thank Son La Hydropower Company and the Meteorological and Hydrological Station of the Northwest Region for supporting this study. All data and information were retrieved and used with the permission of Son La Hydropower Company and the Meteorological and Hydrological Station of the Northwest Region for scientific purposes.

6. REFERENCES

Amaya, F.L., Gonzales, T.A., Hernandez, E.C., Luzano, E.V. and Mercado, N.P., 2012. Estimating point and non-point sources of pollution in Biñan River Basin, the Philippines. *APCBEE Procedia*, pp. 233–238.

Asuero, A.G., Sayago, A. and González, A.G., 2006. The correlation coefficient: An overview. *Critical Reviews in Analytical Chemistry*, 36(1), pp. 41–59.

Bayram, A. and Kenanoğlu, M., 2016. Variation of total suspended solids versus turbidity and Secchi disk depth in the Borçka Dam Reservoir, Çoruh River Basin, Turkey. *Lake and Reservoir Management*, 32(3), pp. 209–224.

Bowers, M.C., Tung, W.W. and Gao, J.B., 2012. On the distributions of seasonal river flows: Lognormal or power law? *Water Resources Research*, 48(5), pp. 1–12.

Branche, E., 2017. The multipurpose water uses of hydropower reservoir: The share concept. *Comptes Rendus Physique*, 18(7–8), pp. 469–478.

Bravo-Linares, C., Ovando-Fuentealba, L., Muñoz-Arcos, E., Kitch, J.L., Millward, G.E., López-Gajardo, R., Cañoles-Zambrano, M., Del Valle, A., Kelly, C. and Blake, W.H., 2024. Basin scale sources of siltation in a contaminated hydropower reservoir. *Science of the Total Environment*, 914, p.169952. [DOI]

Brian, D., Richter, J.V., Baumgartner, J.P., David, P. and Braun, 1997. A method for assessing hydrologic alteration within ecosystems. *Conservation Biology*, 10, pp. 1163–1174.

Camargo Hinostroza, S.D., Taza Rojas, C.A., Poma Limache, D.L. and

Poma Romero, C.J., 2025. Determination of the water quality index (ICA-PE) of Lake Chinchaycocha, Junín, Peru. *Nature Environment and Pollution Technology*, 24(2). [DOI]

Chen, W., Ma, T., Chen, L., Liu, W., Shang, R. and Chen, Z., 2024. Spatial and temporal distribution of nitrogen, phosphorus, and heavy metals loads in Guanshan River Basin based on SWAT modeling. *Water Supply*, 24(5), pp.1498-1514. [DOI]

Cheng, H., Ouyang, W., Hao, F., Ren, X. and Yang, S., 2006. The non-point source pollution in livestock-breeding areas of the Heihe River Basin in Yellow River. *Stochastic Environmental Research and Risk Assessment*, 21(3), pp. 213–221.

Choi, K.S., Lee, Noh, C., Lee, J. and Lee, Y., 2015. Pollutant load characterization with flow conditions in Heukcheon Stream. *Journal of Korean Society of Water and Wastewater*, 29(5), pp. 551–557.

Do, X.D., Luu, D.H. and Do, H.T., 2019. The evolutions for water quality of Son La Hydropower Reservoir from environmental monitoring data (2010–2018). *VNU Journal of Science: Earth and Environmental Sciences*, 35(3), pp. 1–21.

Do, X.D., Luu, D.H. and Do, H.T., 2020. Self-cleaning ability of pollutants containing nitrogen and phosphorus transformed into NH_4^+, NO_2^-, NO_3^-, PO_4^{3-}, of Son La Hydropower Reservoir. *VNU Journal of Science: Earth and Environmental Sciences*, 36(3), pp. 12–24.

Dou, M., Zhang, Y. and Li, G., 2012. Temporal and spatial characteristics of the water pollutant concentration in Huaihe River Basin from 2003 to 2012, China. *Environmental Monitoring and Assessment*, 188(9), pp. 188–522.

Du, Juan, 2024. Linking water quality indicators in stable reservoir ecosystems: Correlation analysis and ecohydrological implications 2024. *Water*, 16(24), p. 3600.

Eom, M.C., Song, I. and Kwun, S.K., 2010. Estimation of pollutant loads in an estuarine reservoir considering pollution source characteristics and seasonal variation. *Paddy and Water Environment*, 8(4), pp. 347–360.

Ferguson, R.I., 1987. Accuracy and precision of river load estimation methods. *Earth's Topographic and Surface Processes*, 12(1), pp. 95–104.

Hai, K.V., Giang, N.T. and Bich, D.T.N., 2024. Applying the variable infiltration capacity (VIC) model to reconstructing streamflow data in the Da River basin at Muong Te hydrological station. *Journal of Hydro-Meteorology*.

Haque, M.A., Jewel, M.A.S. and Sultana, M.P., 2018. Assessment of physicochemical and bacteriological parameters in surface water of Padma River, Bangladesh. *Applied Water Science*, 9(1), pp. 1–8.

Heikkinen, K., 1990. Seasonal changes in iron transport and nature of dissolved organic matter in a humic river in northern Finland. *Earth Surface Processes and Landforms*, 15(7), pp. 583–596.

Houri, A. and El Jeblawi, S.W., 2007. Water quality assessment of Lebanese coastal rivers during dry season and pollutant load into the Mediterranean Sea. *Journal of Water and Health*, 5(4), pp. 615–623.

Huang, T.Y., Wu, W. and Li, W.W., 2013. Identifying the major pollution sources and pollutant loading status of Qiputang River in Taihu Lake basin of China. *Desalination and Water Treatment*, 51(22–24), pp. 4736–4743.

Isaac, D., Irby, Marjorie, A.M., Friedrichs and Fei Da, Kyle, E., Hinson, 2018. The competing impacts of climate change and nutrient reductions on dissolved oxygen in Chesapeake Bay. *Biogeosciences*, 15(9), pp. 2649–2668.

Ito, Akira, 1987. Changes of water temperature, pH, dissolved oxygen, inorganic nitrogen, and phosphorus concentrations in flowing irrigation water on paddy surface. *Soil Science and Plant Nutrition*, 33(3), pp. 449–459.

Jager, H.I. and Smith, B.T., 2008. Sustainable reservoir operation: Can we generate hydropower and preserve ecosystem values? *River Research and Applications*, 24(3), pp. 340–352.

Jeong, S.M. and Choe, J.H., 2000. An analysis on the relationship between discharge and pollutant load on the tributary basin of Kum River. *Journal of Korea Water Resources Association*, 33(5), pp. 527–536.

Jorgensen, S.A., 1987. *Principles of Environmental Science and Technology*. Amsterdam: Elsevier Scientific.

Karine, V., Ferdinand, B. and Cu, P.V., 2006. Agricultural land-use patterns and soil erosion vulnerability of watershed units in Vietnam's northern highlands. *Landscape Ecology*, 21, pp. 1311–1325.

Kim, J., Engel, B.A., Park, Y.S., Theller, L., Chaubey, I., Kong, D.S. and Lim, K.J., 2012. Development of web-based Load Duration Curve system for analysis of total maximum daily load and water quality characteristics in a waterbody. *Journal of Environmental Management*, 97, pp. 46–55.

Kummu, M. and Varis, O., 2007. Sediment-related impacts due to upstream reservoir trapping, the Lower Mekong River. *Geomorphology*, 85(3–4), pp. 275–293.

Le, T., Al-Juaidi, F. and Sharif, H., 2014. Hydrologic simulations driven by satellite rainfall to study the hydroelectric development impacts on river flow. *Water*, 6(12), pp. 3631–3651.

Le, T.P.Q., 2018. CO_2 partial pressure and CO_2 emission along the lower Red River (Vietnam). *Biogeosciences*, 15(15), pp. 4799–4814.

Li, A.L., Haitao, C., Yuanyuan, L., Qiu, L. and Wenchuan, W., 2020. Simulation of nitrogen pollution in the Shanxi Reservoir watershed based on SWAT model. *Nature Environment and Pollution Technology*, 19(3), pp. 1265–1272.

Li, C. M. and Huang, Z.L., 2005. Study on the pollutant loads into Three Gorges Reservoir pollutant load status before impoundment. *Resources and Environment in the Yangtze Basin*, 14(5), pp. 611–622.

Li, C.R., Wang. X.S. and Dou M., 2003. Research of pollution load in Xiangxi River Basin of Three Gorges Reservoir Area. *Journal of Wuhan University of Hydraulic and Electric Engineering*, 36, pp. 29–32.

Li, D., Long, D., Zhao, J., Lu, H. and Hong, Y., 2017. Observed changes in flow regimes in the Mekong River basin. *Journal of Hydrology*, 551, pp. 217–232.

Li, H.E., Lee, J.H.W., Koenig, A. and Jayawardena, A.W., 2005. Estimation of nutrient loads in nonpoint source pollution of the Hong Kong region. *Water Science and Technology*, 51(3–4), pp. 209–216.

Ministry of Natural Resources and Environment of Vietnam (MONRE), 2017. Regulations on assessment of wastewater receiving capacity and carrying capacity of river and lake water sources (76/2017/TT-BTNMT).

Ministry of Natural Resources and Environment of Vietnam (MONRE), 2015. National technical regulation on surface water quality (QCVN 08-MT:2015/BTNMT).

Nguyen, H.Q., Thang, H.N., Banno, M., Nguyen, V.A., Tran, Q.V. and Nguyen, T.L., 2023. Seasonal variations of sediment load related to all large damming in the Red River system: A 64-year analysis. *Earth Surface Processes and Landforms*, 49(1), pp.482-496. [DOI]

Niemirycz, E., 1999. The pollutant load from the River Odra in comparison to that in other Polish rivers in 1988–1997. *Acta Hydrochimica et Hydrobiologica*, 27(5), pp. 286–291.

Nuen, J., Li, S., Cheng, L. and Swan, L., 2020. Analysis of nonpoint source pollutant load in Ulansuhai Nur Basin. *Arabian Journal of Geosciences*, 13(21), pp. 1–7.

Park, S.J., Baek, Kyung, W., Kang, Young, B. and Choi, H.K., 2011. Estimation of delivery pollutant load by the runoff characteristics of Soyang Lake Basin. *Journal of the Korean Society of Hazard Mitigation*, 11(6), pp. 317–324.

Park, Y., Park, S.-R., Lee, S.-W. and Lee, J., 2025. Impacts of watershed and meteorological characteristics on stream water quality resilience. *Journal of Hydrology*, 652, p.132663. [DOI]

Pearson, K., 1909. Determination of the coefficient of correlation. *Science*, 30(757), pp. 23–25.

Shen, Z., Qiu, J., Hong, Q. and Chen, L., 2014. Simulation of spatial and temporal distributions of non-point source pollution load in the Three Gorges Reservoir Region. *Science of the Total Environment*, 493, pp. 138–146.

Shin, Y.C., Choi, J.D., Lim, K.J., Shim, H.H., Lyou, C.W. and Shin, M.H., 2005. Nonpoint source pollutants loads characteristics of rural watershed. *Proceedings of the 2005 Spring Co-Conference of the Korean Society on Water Environment and Korean Society of Water and Wastewater*, pp.579-582.

Shin, Y.C., Choi, J.D. and Lim, K.J. 2005. Pollutant load characteristics from a small mountainous agricultural watershed in the North Han River Basin. *Journal of the Korean Society of Agricultural Engineers*, 47(6), pp. 83–92.

Shrestha, S., Kazama, F., Newham, L.T.H., Babel, M.S., Clemente, R.S., Ishidaira, H. and Sakamoto, Y., 2008. Catchment scale modelling of point source and non-point source pollutant loads using pollutant export coefficients determined from long-term in-stream monitoring data. *Journal of Hydro-Environment Research*, 2(3), pp. 134–147.

Son, L.V., Chung, L.N., Hai, B.T., Anh, S.H. and Quang, N.D., 2019. Assessing satellite-based precipitation products to create flood forecasting in the Da River Basin, Vietnam. *Journal of Geoscience and Environment Protection*, 7(11), pp.113-123. [DOI]

Stanley, E. H. and Doyle, M. W. 2002. A geomorphic perspective on nutrient retention following dam removal: Geomorphic models provide a means of predicting ecosystem responses to dam removal. BioScience, 52(8), 693–701.

Stow, C.A., Borsuk, M.E. and Stanley, D.W., 2001. Long-term changes in watershed nutrient inputs and riverine exports in the Neuse River, North Carolina. *Water Research*, 35(6), pp. 1489–1499.

Suhardono, S., Sunarhadi, M.A., Septiariva, I.Y., Rachman, H.T. and Suryawan, I.W.K., 2025. Biomonitoring of Bedog River water quality using dragonfly diversity as bioindicators in Yogyakarta, Indonesia. *Nature Environment and Pollution Technology*, 24(2), pp. 1–8. [DOI]

Tong, X.X., Hu, B., Xu, W.S., Liu, J.G. and Zhang, P.C., 2017. The estimation of the load of nonpoint source nitrogen and phosphorus based on observation experiments and export coefficient method in Three Gorges Reservoir Area. In *IOP Conference Series: Earth and Environmental Science*, p. 012181.

Tran, A.T. and Nguyen, T.D., 2012. Study on sensitivity and landslide hazard zoning in the Son La Hydropower Reservoir area using the SAATY hierarchical analysis method. *Journal of Earth Sciences*, 34, pp. 223–232.

Wahab, N.A., Kamarudin, M.K.A., Toriman, M.E., Juahir, H., Samah, M.A.A., Azinuddin, M. and Sunardi, S., 2023. The assessment of sedimentation problems in Kenyir Hydropower Reservoir, Malaysia. *Water*, 15(13), pp. 2375.

Wang, X.Y., Guo, F., Cai, X.G. and Hu, Q.J., 2003. Non-point source pollution loading of Miyun Reservoir, Beijing. *Urban Environment & Urban Ecology*, 16(1), pp.31-33.

Wu, L., Long, T.-Y. and Cooper, W.J., 2012. Temporal and spatial simulation of adsorbed nitrogen and phosphorus nonpoint source pollution load in Xiaojiang Watershed of Three Gorges Reservoir Area, China. *Environmental Engineering Science*, 29(4), pp.238-247. [DOI]

Xin, X., Yin, W. and Li, K., 2017. Estimation of non-point source pollutant loads with flux method in Danjiangkou Reservoir area, China. *Water Science and Engineering*, 10(2), pp. 134–142.

Yang, L., Zhang, M., Wei, J. and Qi, J., 2022. Pollution load estimation and control countermeasures of Zhangze Reservoir. *Frontiers in Environmental Science*, 10, pp. 874124.

Zeiger, S.J. and Hubbart, J.A., 2017. Quantifying flow interval–pollutant loading relationships in a rapidly urbanizing mixed-land-use watershed of the Central USA. *Environmental Earth Sciences*, 76(14), pp. 471–484.

Zhang, L., Wang, L., Yin, K., Lü, Y., Yang, Y. and Huang, X., 2014. Spatial and seasonal variations of nutrients in sediment profiles and their sediment-water fluxes in the Pearl River Estuary, Southern China. *Journal of Earth Science*, 25(1), pp. 197–206.

Zhu, L., Song, J.X. and Zheng, C.Q., 2015. Pollutant load estimation of Weihe River Watershed above Linjiacun Section based on characteristic section load method. *Applied Mechanics and Materials*, 744–746, pp. 2382–2385.

Zhuang, Y., Zhang, L., Du, Y., Yang, W., Wang, L. and Cai, X., 2016. Identification of critical source areas for nonpoint source pollution in the Danjiangkou Reservoir Basin, China. *Lake and Reservoir Management*, 32(4), pp. 341–352.

Nature Environment and Pollution Technology
An International Quarterly Peer-Reviewed Open Access Journal

p-ISSN: 0972-6268 | e-ISSN: 2395-3454 Vol. 25 | No. 4 | Article ID D1917 | 2026

RESEARCH ARTICLE https://doi.org/10.46488/NEPT.2026.v25i04.D1917 OPEN ACCESS

AI-Driven Digital Transformation for Sustainable Manufacturing: Exploring the Impact of Carbon Intensity and ESG Through Eco-Innovation Theory

Linda, Vania Angelica Angdi and Linda Kusumaning Wedari†
Accounting Department, School of Accounting, Bina Nusantara University, Jakarta 11480, Indonesia
†Corresponding author: Linda Kusumaning Wedari; linda.wedari@binus.edu

ARTICLE HISTORY

Received: 02-03-2026
Revised: 18-04-2026
Accepted: 01-05-2026

KEYWORDS

Carbon intensity
Artificial intelligence-based digital transformation
Sustainable manufacturing
SDG 9
ESG

CITE THIS ARTICLE

Linda, Angdi, V. A. and Wedari, L. K., 2026. AI-driven digital transformation for sustainable manufacturing: Exploring the impact of carbon intensity and ESG through eco-innovation theory. *Nature Environment and Pollution Technology*, 25(4), D1917. https://doi.org/10.46488/NEPT.2026.v25i04.D1917

COPYRIGHT & LICENCE

© 2026 The Authors
Open Access under CC BY 4.0.

PUBLISHED BY
TECHNOSCIENCE PUBLICATIONS

ABSTRACT

This study aims to examine the influence of carbon intensity and environmental, social, and governance (ESG) performance on the adoption of digital transformation from the perspective of eco-innovation theory to support sustainable production and decarbonization goals. A quantitative method was used to analyze 91 firm-year observations from manufacturing firms in Indonesia. The results show that firms with higher Scope 1 carbon intensity tend to adopt digital transformation because emissions are directly observable in operational activities, while high ESG performance can support improved performance through digital transformation adoption. The significant negative relationship between Scope 2 carbon intensity and digital transformation indicates that firms may use alternative non-digital solutions to reduce Scope 2 carbon intensity. These results support eco-innovation theory, which states that digital and non-digital innovations are essential for environmental sustainability and production efficiency, particularly in the manufacturing industry. This study provides practical insights for managers and policymakers on designing digital strategies that align with environmental conservation efforts and support stronger sustainability in the manufacturing sector.

1. INTRODUCTION

Industry 4.0 focuses on the development of technological advances that support major changes throughout the world (Shang et al. 2023). Artificial intelligence (AI), big data, blockchain, and the Internet of Things (IoT) are examples of technologies that firms are beginning to implement through digital transformation (hereafter DT) as a strategy to support efficiency and productivity while minimizing operational costs and optimizing resource utilization (Chen et al. 2020, Qian et al. 2023). In recent years, many firms in Indonesia have been encouraged to accelerate the adoption of digital technologies to support operational activities, as indicated by the increasing adoption index values each year.

Indonesia still faces a gap between digital awareness and its implementation. This is evident from the relatively low acceleration index shown in Fig. 1. These data demonstrate that firms in Indonesia still face various challenges in developing their technological capabilities, indicating that many firms in Indonesia still need strategies to strengthen and accelerate digital implementation (Kementerian Komunikasi dan Digital RI 2024). In response, Indonesia has initiated 'Making Indonesia 4.0' as a roadmap toward the DT of the manufacturing industry through AI, IoT, robotics, 3D printing, and augmented reality, with a focus on five priority sectors: food and beverage, textiles and clothing, automotive, chemicals,

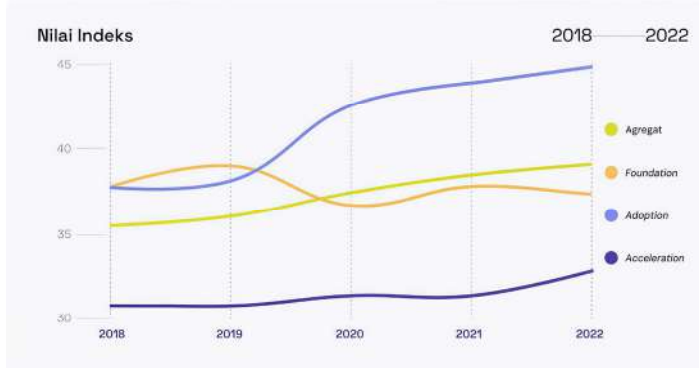


Fig. 1: Digital transformation index in the business pillar (Kementerian Komunikasi dan Digital RI 2024).

and electronics (Ramli 2023). Kementerian Perindustrian Republik Indonesia (2018) introduced the Indonesia Industry 4.0 Readiness Index (INDI 4.0) as a measurement tool for Industry 4.0 readiness. This index is expected to strengthen national industrial competitiveness by improving production efficiency, reducing operational costs, and improving product quality. DT refers to processes that utilize existing digital technologies. DT has become an appropriate approach for helping a business entity improve efficiency and effectiveness, from strengthening its commitment to sustainability to improving the quality of organizational governance (Aldieri & Vinci 2021). These changes can be helpful for firms in developing better work systems, preparing for changes better, and staying competitive in an evolving market through performance monitoring, thereby promoting more efficient, transparent, and accountable corporate operations (Zhang et al. 2025). Moreover, ESG implementation encourages more environmentally friendly practices and accountable governance. This condition is increasingly supported by greater data availability, transparency, and accessibility, enabling greater business openness and effectiveness (Zhang & Huang 2024). The integration of DT further supports the achievement of Sustainable Development Goal (SDG) 9, which emphasizes sustainable industrialization, increased innovation capacity, and the development of resilient infrastructure (United Nations 2025). Accordingly, DT serves as a key linkage between national policies, firm performance, and the integrated implementation of ESG practices (da Cunha et al. 2025, Zhang & Huang 2024).

The manufacturing sector in Indonesia contributes significantly to carbon emissions, which are high due to its production activities, reaching 340.71 million tons of CO_2e in 2022 (Ahdiat 2024). The increasing carbon emissions have prompted the government to accelerate the development and enforcement of policies aimed at reducing carbon intensity through the establishment of a national framework for achieving Indonesia's Nationally Determined Contribution (NDC) targets as stipulated in Presidential Regulation No. 98 of 2021. This regulation covers emission mitigation efforts, monitoring and evaluation mechanisms, financing schemes, and the management of carbon economic value (Andrian & Sudibyo 2019). In line with this national policy development, the Financial Services Authority (OJK) Regulation No. 51/POJK.03/2017 requires financial institutions, issuers, and public firms to prepare and disclose sustainability reports, aiming to improve transparency and accountability concerning ESG performance as these elements are consistently reported (Otoritas Jasa Keuangan, 2017a). This reporting obligation is anticipated to enhance business understanding of the environmental consequences of their operations and to reinforce their responsibilities in applying sustainability principles. In addition, the establishment of IDX Carbon in 2023 has provided a transparent and market-based carbon trading mechanism to support Indonesia's decarbonization pathway toward net zero emissions by 2060 (IDX 2023).

Carbon intensity, measured as carbon emissions relative to a firm's total assets, serves as an indicator of environmental efficiency. Carbon intensity is often used as an indicator to assess the magnitude of transition risk, particularly in carbon-intensive industries (Cheng et al. 2014). Firms with higher levels of emissions tend to face overlapping pressures, including tighter supply chain requirements, shifts in consumer preferences, and rising financing costs. These pressures reflect greater economic risks associated with unsustainable business practices (McDougall et al. 2025). This tension has been further amplified by the increasing prevalence of greenwashing cases, which expose persistent issues related to ESG credibility and the reliability of sustainability reporting. In response, regulators have become more active in scrutinizing and sanctioning misleading environmental claims (Greenwell et al. 2025). These developments underscore the need to empirically

examine the validity and explanatory power of ESG scores, as such ratings often capture corporate reputation rather than measurable environmental performance.

As digital technology advances, its transformation continues to attract public attention because of its potential to improve firms' operational efficiency. Prior research has examined DT in relation to firm performance (Wang & Sun 2025, Yavuz et al. 2025), energy consumption (Yue et al. 2025), and sustainable development performance (Li 2024). In parallel, the literature on ESG and carbon emissions has grown rapidly, including studies on the relationship between ESG and carbon performance (Yin et al. 2023) and corporate performance (Nareswari et al. 2023). Building on this literature, prior research has adopted different perspectives on the causal relationships among DT, ESG practices, and carbon emissions. Some studies position DT as a driver of ESG practices (Baboe et al. 2025, Liu et al. 2025, Yang et al. 2024) and as a mechanism for carbon emissions reduction (Chen et al. 2024, Song et al. 2025). However, previous studies often rely on aggregate carbon emissions without distinguishing between Scope 1 and Scope 2 emissions (Zhang et al. 2024), which may limit understanding of the contribution of each emission scope to DT. In addition, most prior research relies on theoretical frameworks such as stakeholder theory (Baboe et al. 2025, Chen et al. 2024) and dynamic capability theory (Gao et al. 2024, Yavuz et al. 2025). Nevertheless, the application of eco-innovation theory remains largely unexplored. Eco-innovation theory is important as it explains how firms use innovation, including DT, to improve efficiency while simultaneously reducing environmental impact (Fussler & James 1996). Many studies primarily focus on countries with relatively high levels of digital infrastructure and institutional support, such as China and European nations (Chen et al. 2024, Li 2024, Khatib et al. 2023), while evidence from contexts with lower digital readiness and less developed institutional frameworks remains limited.

Based on this background, this study attempts to expand on existing discussions by adopting Scope 1 and Scope 2 carbon emission intensities and ESG performance as important factors that can encourage firms to adopt DT. Scope 1 and Scope 2 carbon emission intensities can represent the emission sources that are closest to a company's operational activities and can still be controlled directly. In the context of Indonesian manufacturing, emissions are a salient pressure point for cost efficiency, regulatory compliance, and market expectations (Rohayati & Abdillah 2024). This research focuses on Indonesian manufacturing firms because the sector is both energy-intensive and a major contributor to national Scope 1 and Scope 2 emissions (Ahdiat 2024), making it a high-impact setting to examine carbon-driven incentives for DT. Moreover, Indonesia's manufacturing landscape features heterogeneous ESG readiness and uneven digital maturity, allowing the study to capture meaningful variation in how emission intensity translates into DT adoption (CRSM Indonesia 2024, Kristianto et al. 2025).

The following subsections provide a literature review on the relationship between carbon emissions, ESG performance, and DT. This is followed by the development of research hypotheses and theoretical justification. Section 2 describes the research methodology; Section 3 presents the results and discussion. The final section concludes the study by outlining its main findings and implications for both theory and practice.

1.1. Digital Transformation

According to Matt et al. (2015), DT is defined as the transformation of products, processes, and organizational aspects driven by modern technology. DT uses networks and computing to drive companies toward sustainability (Khan & Singh 2023, Vial 2019), enabling them to make informed decisions, conduct evaluations, and develop new business models (Guo & Tang 2024). DT also encourages the digitization of products and services to improve efficiency and overall company performance (Chen et al. 2024, Vial 2019).

In the context of digital development, industry is increasingly demonstrating the potential of AI as a catalyst for energy efficiency, big data analysis, productivity enhancement, and decision-making that supports sustainable manufacturing (Plathottam et al. 2023). AI is considered a company-owned resource capable of responding to internal issues such as emission intensity by detecting emissions and monitoring ESG performance. Therefore, the adoption of this technology aligns with sustainable production goals (Chen et al. 2019).

1.2. Hypothesis Development

Scope 1 emissions originate from a firm's internal operational activities (Emmanuel et al. 2023). Scope 1 carbon emission intensity represents the level of carbon emissions generated relative to the utilization of a firm's productive assets. A high level of Scope 1 carbon emission intensity is often associated with technologically inefficient assets, reflecting aging capital stock with declining operational efficiency (Dan et al. 2023). From an efficiency perspective, higher carbon intensity implies that firms generate greater emissions per unit of assets, indicating lower environmental efficiency. This condition not only signals operational inefficiency but also reflects higher ESG-related risks, thereby creating strong

incentives for firms to reduce emissions that are fully under their direct control (Emmanuel et al. 2023). In response, firms are more likely to adopt DT to enhance operational efficiency and optimize asset utilization (Bhatia et al. 2024).

This relationship aligns with the eco-innovation theory proposed by Fussler and James (1996), which emphasizes business, technology, and operational practices that create economic value while reducing negative environmental impacts. Xu et al. (2023) state that DT strengthens the implementation of eco-innovation by increasing a company's capability to integrate digital technology into production processes and operational practices, especially in companies with high emission levels. Digital technologies such as AI, IoT, and big data analytics have been shown to help optimize energy use and resource efficiency, directly contributing to reducing the carbon footprint of production (Chauhan & Sahoo 2024, Zhou & Liu 2024). Given this, the hypothesis is:

H1a: Scope 1 carbon intensity has a positive effect on digital transformation adoption.

Scope 2 emissions are indirect emissions originating from electricity, steam, heat, or cooling purchased from external parties and used by the company (Emmanuel et al. 2023). In contrast to Scope 1 emission intensity, which is under a firm's direct operational control, Scope 2 emission intensity is highly dependent on external energy systems. Consequently, companies have more limited capacity to directly influence the sources of these emissions, thereby constraining the role of DT as a primary solution for reducing Scope 2 intensity. The increase in Scope 2 carbon intensity relates to a company's carbon performance, which depends on the energy used by the company to operate each of its assets (Hoffmann & Busch 2008). High Scope 2 emissions do not necessarily indicate a company's wasteful use of electricity but can be influenced by factors such as electricity emissions in specific operational areas (grid mix as a direct factor) and electricity tariff structures (as an indirect factor), indicating that increases in Scope 2 emission intensity are also driven by external conditions that are difficult for firms to control. Firms may experience a cost and risk burden (e.g., rising electricity expenditures, margin pressure, and ESG scrutiny) that crowds out investment in digitally enabled process change. As a result, managerial attention and capital may be redirected toward short-term operational stabilization and compliance activities rather than longer-horizon DT initiatives.

To reduce Scope 2 emissions intensity, companies need to identify their energy use and determine which assets consume more energy under certain conditions. This allows them to take appropriate action to reduce energy consumption, such as switching off these assets when not in use (Griffin et al. 2014). Companies may focus on routine asset maintenance to maintain stable machine performance and reduce energy consumption, purchase renewable energy, or use other non-digital strategies to reduce emissions intensity rather than adopting DT, which also requires significant funding (Baniya & Giurco 2025). These initiatives may be preferable to DT initiatives.

Eco-innovation theory posits that environmental challenges and stakeholder and regulatory pressures can stimulate innovation (Fussler & James 1996). However, this inducement effect depends on firms having sufficient resources, capabilities, and strategic alignment to respond (Song et al. 2018). In the context of Scope 2 emissions, limited managerial control and cost pressures may weaken a firm's ability to effectively respond to such pressures through digital innovation, making DT implementation more complex, costly, and uncertain (Alrawadieh et al. 2020). Under these conditions, firms may adopt a defensive response, prioritizing incremental efficiency measures or reporting improvements rather than transformative digital investments (Zhai et al. 2022). Moreover, if DT is not explicitly designed as an eco-innovation (i.e., not integrated with energy-management objectives and decarbonization targets), firms may perceive DT as potentially increasing electricity use in the near term (through automation, sensors, computing, and data processing), thereby reinforcing firms' reluctance to deepen DT and encouraging the postponement of its adoption when Scope 2 emission intensity remains high (Alsanie 2025). Given this, the hypothesis is:

H1b: Scope 2 carbon intensity has a negative effect on digital transformation adoption.

ESG performance represents a company's commitment to sustainability, which includes environmental, social, and governance aspects, and responds to pressure from stakeholders such as investors, regulators, and society (Bolognesi et al. 2025). ESG is measured by assessing a company's performance across these three aspects and is used to gauge performance and its impact on the company's reputation and to provide a benchmark for capital allocation, such as investment and credit risk assessment (Miller 2024). When a company achieves a high level of ESG performance, this can drive further performance improvement, which can be supported through DT. This, in turn, is beneficial for maintaining and improving performance (Ren & Cheng 2024). Implementing digital technologies such as cloud computing, the Internet of Things (IoT), and data-driven management systems can help companies monitor energy

consumption, optimize operational efficiency, and control emissions in real time, thus supporting environmental performance (Chauhan & Sahoo 2024, Yavari et al. 2023).

To achieve good ESG performance, in addition to focusing on the environment, firms also need to balance their social and governance aspects. Employees of companies actively engaged in social responsibility are believed to be more motivated to improve production processes and seek innovative solutions in digital technology (Broadstock et al. 2020). In the current era, companies have implemented a work-from-home (WFH) scheme under certain conditions (Wade & Shan 2020), thus encouraging firms to implement digital-based innovations to connect employees so that operational performance remains stable even though they are not in the same location. For example, a cloud-based system can monitor flexible working hours, WFH attendance, and employee satisfaction levels, supporting work-life balance (Li et al. 2025). Companies with a strong commitment and social spirit tend to be more motivated to continue prioritizing the welfare of their employees; one way of doing this is through digital innovation that reflects strong social values.

Furthermore, companies with good governance practices have a strong capital base to drive the adoption of DT, as they can mitigate agency problems and increase corporate capital investment in the digitalization process. This is beneficial for companies in a stable phase (Hossnofky & Junge 2019, Zhao et al. 2023). This argument is in line with research by Sun et al. (2025), which shows that ESG has a significant impact on DT during a company's stable period, but is not statistically significant during growth and decline. This suggests that companies in the stable phase are generally considered to have more time and funds for long-term thinking, including ESG and DT. Therefore, ESG scores will increase and accelerate DT adoption. Companies can utilize digital technologies such as AI and IoT to monitor operational performance in real time and to support sustainability innovation and ESG practices, thereby fostering stakeholder trust in the company's sustainability commitments (DesJardine et al. 2025).

At the firm level, DT and ESG are increasingly recognized as strategic components in enhancing competitiveness and supporting the development of sustainable infrastructure, alongside the growing integration of ESG principles into corporate governance and policy frameworks (Aldieri & Vinci 2021). From the perspective of eco-innovation theory (Fussler & James 1996), DT adoption can be understood as a mechanism through which firms incorporate sustainability objectives into their operational processes, thereby contributing to the achievement of SDG 9, which emphasizes sustainable industrialization, innovation, and resilient infrastructure (Aldieri & Vinci 2021). In this context, ESG performance reflects firms' organizational capabilities and resource capacity that support DT adoption. Given this, the hypothesis is:

H2: ESG score has a positive effect on digital transformation adoption.

2. MATERIALS AND METHODS

2.1. Data Source and Sample

The sample used in this study was taken from manufacturing companies listed on the Indonesia Stock Exchange (IDX) during the period 2020–2024. Of 228 listed manufacturing companies in Indonesia, only 20 companies met the research criteria and were included in the analysis. Some data were excluded from the analysis due to missing or unavailable data, such as Scope 1 emissions, Scope 2 emissions, and ESG scores. Therefore, the total sample comprises 91 firm-year observations.

Table 1: Variable definitions and measures.

Variable Type	Variable Name	Variable Code	Variable Definition and Measure
Dependent Variable	Digital Transformation	DT	ln(digital transformation); word frequency of DT keywords in annual reports with Python, using Google Colab
Independent Variables	Scope 1 Carbon Intensity	CISc1	Company's direct carbon emission intensity; ln(total Scope 1 emissions in tons CO_2e/total assets) from the company
	Scope 2 Carbon Intensity	CISc2	Company's indirect carbon emission intensity; ln(total Scope 2 emissions in tons CO_2e/total assets) from the company
	ESG Score	ESG	ln(Environmental, Social, and Governance (ESG)); obtained from Refinitiv in a numerical score (0–100)
Control Variables	Institutional Ownership	IO	ln(percentage of share ownership by institutions)
	Firm Size by Revenue	FS_Rev	Firm size measured by revenue; ln(company's operating revenue)
	Debt-to-Equity Ratio	DER	Leverage ratio; ln(total liabilities/total equity)
	Listing Age	Listage	Firm's listing duration; ln(research year – IPO year)

2.2. Variables

2.2.1. Dependent Variable

Digital Transformation. Information on digital transformation keywords was obtained from the annual reports published by companies. The calculation process was carried out using Google Colab through text analysis and Python-based calculations (Li 2024, Yang et al. 2024). Text analysis enables hypothesis development by capturing the extent of AI and digital transformation implementation through explicit keywords disclosed in annual reports. First, DT keywords were compiled based on several studies (Gao et al. 2024, Ma & Tao 2023, Wang et al. 2023a). Keywords were entered into a Python script to extract occurrences from each company's annual reports for 2020–2024, and the output was the frequency with which these keywords appeared in each company's annual report, as shown in Table 2. The keywords used for this study were all keywords related to DT that appeared in the company's annual reports during the 2020–2024 period. Second, we counted all keywords that appeared for each company based on the results of the Python analysis to serve as an indicator in measuring the company's level of DT, using the natural logarithm of the total keyword frequency.

2.1.2. Independent Variables

Scope 1 and Scope 2 Carbon Emission Intensity and ESG Score. This study collected Scope 1 and Scope 2 emissions data disclosed in the sustainability reports. Scope 1 carbon intensity was calculated by dividing natural logarithm of Scope 1 emissions (measured in tons of CO_2e) by total assets. Scope 2 carbon intensity was calculated by dividing natural logarithm of Scope 2 emissions (measured in tons of CO_2e) by total assets. ESG score data were obtained from the Refinitiv database, which indicates how well a company performed in terms of environmental, social, and governance (ESG) issues in a given year, using the natural logarithm of the ESG score, which is measured on a numerical scale ranging from 0–100, where higher values indicate better ESG performance.

2.2.3. Control Variables

These variables were selected from prior research to improve the precision of the model's estimates and to account for factors that might influence both independent and dependent variables. Without controlling these confounding factors, the relationship between the main variables might be distorted, leading to biased or inaccurate results. These variables include the percentage of shares owned by institutions (Institutional Ownership, IO) (Lin et al. 2023), company size based on revenue level (Yang et al. 2024), the ratio of total liabilities to total equity (debt-to-equity ratio, DER) (Grishunin et al. 2022), and the time since the company's IPO (Listage) (Guo et al. 2025, Wang et al. 2023b), with all variables transformed using the natural logarithm. Table 1 provides the definitions and measurements of these variables.

This study uses the following regression model in the analysis:

$$DTit = \alpha0 + \alpha1CISc1it + \alpha2CISc2it + \alpha3ESGit + \alpha4IOit + \alpha5FS_Revit + \alpha6DERit + \alpha7Listageit + \varepsilon it \quad ...(1)$$

Where:

- DT_{it} = Digital Transformation
- $CISc1_{it}$ = Carbon Intensity Scope 1
- $CISc2_{it}$ = Carbon Intensity Scope 2
- ESGit = Environmental, Social, and Governance score
- IOit = Institutional Ownership
- FS_Revit = Firm Size by Revenue
- DER_{it} = Debt-to-Equity Ratio
- $Listage_{it}$ = Listing Age
- α 1, α 2 ... α 7 = Regression coefficients
- ε = Error

Table 2: Digital transformation keywords.

Index	Keywords	References
Artificial Intelligence	AI, Artificial Intelligence, Automatic, Automation, biometric, business intelligence, deep learning, face recognition, machine learning,	(Tang et al. 2025)
Blockchain	Blockchain, digital currency	(Ma & Tao 2023, Tang et al. 2025)
Cloud Computing	Cloud Computing, Internet of Things, IoT	(Baboe et al. 2025, Wang et al. 2023a)
Big Data	augmented reality, big data, data, data mining, data visualization, virtual reality	(Tang et al. 2025)
Digital Application Technology	B2B, B2C, C2B, C2C, O2O digital, digital marketing, digital technology, e-commerce, fintech, financial technology, industrial internet, internet connection, mobile internet, smart energy, smart home	(Tang et al. 2025, Yang et al. 2024)

- i = Company
- t = Year

All variables in the regression model are measured using their respective natural logarithmic transformations as defined in Table 1. This study uses panel data analysis to examine the effects of carbon emission intensity and ESG performance on the level of digital transformation adoption in manufacturing companies during 2020–2024.

3. RESULTS AND DISCUSSION

3.1. Descriptive Statistical Analysis

Descriptive statistics for the variables used in this study are presented in Table 3, based on 91 firm-year observations. These statistics provide an overview of the distribution of the dependent variable (DT) and the independent variables (CISc1, CISc2, and ESG) included in the analysis.

The digital transformation (DT) variable is measured as a composite indicator representing the extent to which firms adopt and integrate digital technologies into their operational and strategic processes. The mean DT value of 4868.385, which is relatively close to the median of 4534, indicates that the DT distribution is balanced around its central tendency. Regarding the independent variables, CISc1 represents the intensity of direct carbon emissions, measured as the volume of greenhouse gas emissions relative to a firm's total assets, thereby capturing the carbon intensity of a firm's operational activities. CISc1 has a mean value of 52.461, which is above the median of 12.961, indicating comparatively high emission intensity among the sampled firms. Higher CISc1 values indicate greater carbon emissions per unit of assets, reflecting more carbon-intensive assets utilized in operations and lower resource-use efficiency. Similarly, CISc2 represents the intensity of indirect carbon emissions arising from the consumption of externally generated energy, scaled by a firm's total assets. The mean of CISc2 is 6.109, which is notably higher than its median of 1.702, indicating that most firms rely heavily on carbon-intensive external energy sources. Elevated CISc2 values reflect a greater dependence on externally supplied energy with higher emission factors, implying limited efficiency in energy sourcing and a slower transition toward renewable or low-carbon energy alternatives (Ma et al. 2021).

The ESG performance variable is measured on a standardized scale ranging from 0–100, where higher scores indicate stronger overall environmental, social, and governance practices. The mean ESG score of 57.763 lies slightly above the midpoint of the scale, indicating that firms in the sample exhibit a moderate level of ESG performance. This suggests that firms have begun to integrate environmental, social, and governance aspects into their

Table 3: Descriptive statistics.

Variable	N	Mean	Median	Std. Dev.	Min	Max
DT	91	4868.385	4534	2285.847	1417	11954
CISc1(t CO_2e/IDR)	91	52.461	12.961	104.766	0.181	424.700
CISc2(t CO_2e/IDR)	91	6.109	1.702	11.606	0.008	57.199
ESG	91	57.763	58.59	16.658	23.79	88.59
IO (%)	91	0.879	0.951	0.203	0.033	0.993
FS_Rev (IDR billion)	91	57704.03	38651.36	61952.46	8800	330920
DER	91	0.919	0.756	0.897	0.129	6.466
Listage (Year)	91	28.571	31	7.835	2	43

Table 4: Pearson correlation matrix.

Variables	DT	CISc1	CISc2	ESG	IO	FS_Rev	DER	Listage
DT	1.0000							
CISc1	0.1319	1.0000						
CISc2	0.0215	0.3209***	1.0000					
ESG	0.5818***	−0.0470	0.2693*	1.0000				
IO	0.0870	−0.0823	−0.0351	−0.2213**	1.0000			
FS_Rev	0.1749*	−0.2565**	−0.1773	0.1914*	−0.1512	1.0000		
DER	0.0298	0.0697	0.0352	0.3746***	−0.1865*	−0.4396***	1.0000	
Listage	−0.0581	0.1550	0.1827*	0.2497**	−0.2446**	0.1913*	0.3094***	1.0000

*, **, and *** indicate significance at $p < 0.10$, $p < 0.05$, and $p < 0.01$, respectively.

operational activities, although the extent and consistency of implementation still vary among the firms.

Table 4 shows the Pearson correlation matrix for all variables. All correlations between the independent variables are below 0.6 (Hair et al. 2019), suggesting that multicollinearity is unlikely to be a concern; variance inflation factors (VIFs) were also examined to confirm this.

3.2. Regression Result Analysis

Table 5 presents the regression results from an ordinary least squares (OLS) model investigating the effects of carbon intensity (Scope 1 and Scope 2) and ESG performance on digital transformation. The results demonstrate that CISc1 has a positive coefficient with a statistically significant p-value of less than 0.001, indicating that firms with higher levels of direct emissions (Scope 1 emissions) are likely to intensify their adoption of digital transformation as a strategic measure to improve operational efficiency through enhanced emissions monitoring. From the eco-innovation theory perspective of Fussler and James (1996), digital transformation is viewed as a form of environmentally friendly technological innovation that helps firms reduce their environmental impact without sacrificing economic performance. Eco-innovation theory states that innovation aims not only to increase production efficiency but also to reduce resource consumption and emissions through improved processes and managerial systems (Rennings 2000). Thus, firms can monitor emissions in real time, identify operational inefficiencies more accurately and quickly, and optimize production processes sustainably by adopting technologies such as AI, IoT, data analytics, and automation. This is consistent with previous research showing that digital technology can increase firm productivity (Xu et al. 2023, Zhou & Liu 2024). This finding provides empirical support for Hypothesis 1a.

In contrast, CISc2 has a significant negative coefficient with a p-value of 0.007, indicating that the increase in indirect emissions caused by purchasing electricity from third parties has a negative effect on digital transformation adoption. This suggests that firms with high dependence on external energy sources may prefer non-digital strategies as alternative approaches to reducing Scope 2 carbon emission intensity, rather than investing in digital solutions that require greater investment. From an eco-innovation theory perspective (Fussler & James 1996), firms tend to prioritize incremental innovation when facing high Scope 2 intensity (Zhai et al. 2022). Eco-innovation is not always realized through the adoption of advanced technology but also through improvements to more energy-efficient operational processes (Song et al. 2018). Firms can explore other avenues for operational adjustment beyond digital transformation, so digital transformation is not the only way for firms to reduce emissions. This result supports Hypothesis 1b.

The ESG variable showed a significant positive effect with a p-value of less than 0.001, indicating that companies with good ESG performance tend to choose DT as a strategic response to maintain and continue to improve their ESG performance. This suggests that companies with good sustainability practices view DT adoption as a tool to support transparency and better governance. From the perspective of the eco-innovation theory of Fussler and James (1996), sustainability-oriented companies view digital transformation as a form of managerial and technological innovation to improve economic performance, strengthen transparency and accountability, and enhance governance effectiveness (Yang et al. 2024). Data analytics is one way a company can adopt digital technology to more systematically monitor environmental and social performance and improve

Table 5: Baseline regression results.

Variables	DT
CISc1	0.082***
	(0.000)
CISc2	−0.080***
	(0.007)
ESG	1.101***
	(0.000)
IO	0.294***
	(0.008)
FS_Rev	0.295
	(0.667)
DER	−0.137
	(0.138)
Listage	−0.790*
	(0.071)
_cons	4.174***
	(0.003)
N	91
Adj. R^2	0.500
F-Statistic	13.83 (0.000)
VIF	1.67

Note: Symbols *, **, and *** indicate significance levels of 10%, 5%, and 1%, respectively. Values in parentheses indicate the p-value for each coefficient.

the quality of ESG disclosure (Yavari et al. 2023). Therefore, these results support Hypothesis 2.

3.3. Discussion

This research was conducted to analyze the effects of Scope 1 and Scope 2 carbon intensity, as well as ESG performance, on the adoption of digital transformation. The study found that Scope 1 carbon intensity, Scope 2 carbon intensity, and ESG performance significantly affect digital transformation.

The positive impact of Scope 1 carbon intensity on digital transformation indicates that manufacturing firms in Indonesia with higher levels of direct emissions are more likely to adopt digital transformation for process efficiency and operational decarbonization. These results are consistent with prior findings indicating that emissions drive firms to adopt digital transformation and implement digital-based operational monitoring (Chauhan & Sahoo 2024, Zhou & Liu 2024). Firms have full control over internal emission sources, enabling more effective efficiency-oriented policies. Digital systems are used to monitor production machine performance and operational vehicle fuel consumption at the operational level. This allows for more measurable emission control and supports the optimization of combustion processes and energy use in production facilities (Xu et al. 2023, Zhou & Liu 2024). Pressure stems not only from government regulations; during the COVID-19 pandemic, operational restrictions also accelerated the adoption of digital monitoring systems and process automation (Amankwah-Amoah et al. 2021).

In contrast to the Scope 1 result, Scope 2 carbon intensity has a significant negative effect on digital transformation adoption. These findings diverge from a portion of the literature that generally assumes that pressures related to environmental concerns stimulate innovation; however, the results of this study indicate that, in the context of Scope 2 emissions, firms' responses do not necessarily take the form of digitalization, but instead involve relatively more direct and efficient non-digital measures to reduce Scope 2 emissions, such as asset maintenance and renewable energy purchases (Baniya & Giurco 2025, Griffin et al. 2014). In line with eco-innovation theory, corporate environmental initiatives are not necessarily implemented through digital solutions but can also be achieved through non-digital innovations such as energy source substitution, improvements in asset efficiency, and the adoption of renewable energy (Fussler & James 1996). This extends the literature by emphasizing that the relationship between pressures related to environmental concerns and innovation is contingent upon the characteristics of the emission sources (Baniya & Giurco 2025). Companies tend to adopt non-digital measures that can provide more immediate results in reducing Scope 2 emissions because investments in digital transformation are riskier and have long-term impacts. The impact of the pandemic also caused companies to face economic uncertainty, leading them to focus more on cost reductions rather than investing in sustainable technologies. Meanwhile, increased Scope 2 emissions from environmentally unfriendly energy sources can increase operational costs, potentially forcing companies to delay or limit investments in digital transformation. Throughout the pandemic, the government also focused on supporting the clean energy transition and encouraging sustainable investment (Haas et al. 2023).

Furthermore, the result of this study indicates a positive relationship between companies' ESG performance and digital transformation adoption. This finding suggests that companies with strong environmental, social, and governance practices, as well as strong sustainability commitments, create a more conducive organizational environment for strategic decision-making, including investments in digital transformation, which is consistent with prior studies that position ESG as an indicator of organizational readiness to adopt technological innovation (Sun et al. 2025). These results are consistent with previous studies showing that digital transformation contributes to improved corporate environmental performance, broadening the understanding that the impact of digitalization extends beyond the environmental to encompass social and governance dimensions within the ESG framework (Liu et al. 2025, Yang et al. 2024, Baboe et al. 2025). Companies with stable governance structures typically have more long-term-oriented internal controls, making them more likely to view digitalization as a strategic solution to improve operational performance and corporate sustainability. The positive relationship between ESG performance and digital transformation adoption is consistent with the findings of Sun et al. (2025), who reported that good ESG performance and firms in stable periods tend to encourage the adoption of digital transformation.

Digital technology adoption is influenced by regulatory and stakeholder pressures, as well as by a firm's ability to address and adapt to these external demands. Companies in Indonesia have begun adopting digital transformation in compliance with Ministerial Regulation No. 21 of 2020 concerning the measurement of industry readiness for the transformation to Industri 4.0 through Indonesia Industry 4.0 Readiness Index (INDI 4.0). This study confirms that effective DT requires a balance between regulatory pressures and organizational readiness for sustainability (Rennings 2000).

The Financial Services Authority (OJK) is also involved in developing a green finance framework that encourages the

use of sustainable financing instruments, including green bonds, to support environmentally friendly investments (Otoritas Jasa Keuangan 2017b). However, regulatory pressure and policy support are not always accompanied by corporate readiness to design, manage, and implement sustainable investments, as evidenced by the low level of green finance utilization by entities that are otherwise eligible. Moreover, companies eligible for green finance incentives do not understand or know their eligibility status and therefore cannot utilize this opportunity. This situation demonstrates that green finance may serve as a driver of eco-innovation and digital transformation, but its effectiveness depends heavily on a company's internal capabilities, particularly ESG readiness as a foundation for integrating digital transformation into business processes (Raman et al. 2024). These findings underscore that the presence of regulatory frameworks and sustainable financing instruments must be complemented by firms' organizational and ESG readiness for the impetus toward green innovation and digital transformation to be effectively translated into operational practices.

4. CONCLUSIONS

This study examines how Scope 1 carbon emission intensity, Scope 2 carbon emission intensity, and ESG performance influence the firm's decision to adopt DT. The results indicate that these factors act as strategic determinants, shaping corporate digitalization in different ways depending on the source and controllability of emissions. This is consistent with eco-innovation theory, which views DT as a strategic driver that improves energy management, reduces resource inefficiencies, and improves overall sustainability performance, thereby strengthening competitive advantage. Companies do not simply respond to regulations reactively; they use DT as a proactive adaptation mechanism to manage emission sources that are entirely within their control. These findings extend the literature by demonstrating that emission controllability, rather than merely emission magnitude, is a critical factor in shaping firms' digital investment decisions.

The issues of emissions and ESG performance play a significant strategic role. Both can be powerful drivers for companies to move toward DT, but under certain conditions they can also be a hindrance, especially for Scope 2 carbon intensity. Companies with high dependence on electricity tend to delay DT adoption due to substantial energy requirements and cost pressures. As a result, firms face a trade-off between improving efficiency through digitalization and limited financial capacity driven by high energy costs.

The issue is not just about compliance but about how firms determine their long-term direction and priorities. This study provides a clear picture for managers, businesspeople, and policymakers that carbon emission levels and ESG performance influence the speed at which firms adopt DT. For managers, these results indicate that DT can be part of the solution, rather than only a technological trend, through real-time monitoring of emissions and energy consumption, identification of operational inefficiencies, and strengthening reporting quality and internal controls to enhance sustainability transparency. In contrast, to mitigate Scope 2 emissions intensity, managers need to prioritize energy efficiency and electricity consumption management to avoid constraining DT investment. For companies, accelerating adoption can support carbon emissions management, strengthen ESG performance, and enhance investment competitiveness. Companies also need to accelerate energy efficiency programs, optimize electricity use, and transition to cleaner energy sources to prevent energy costs from becoming a limiting factor for digital investment. For policymakers, the regulatory framework should incentivize the adoption of digital solutions, while simultaneously encouraging improvements in the quality of governance and ESG reporting. The negative impact of Scope 2 indicates the need for policy interventions on the energy side, such as electricity efficiency programs and support for the clean energy transition.

However, this study has several limitations. First, the data used include only manufacturing companies, so the results may not be generalizable to other sectors that have different operational patterns and emission levels. Second, the measurement of DT is based on how often terms related to digitization appear in the company's annual report. While this approach captures managerial emphasis and disclosure intensity and is generally considered reliable due to its replicability and data availability, it may not fully reflect the depth, quality, or actual implementation level of DT initiatives and may be influenced by differences in disclosure practices across firms. Therefore, future research is encouraged to employ more granular DT indicators, for example by using dummy variables capturing specific digital initiatives, to improve measurement precision. Future research could also include additional variables (e.g., mediators or moderators) as well as extend the observation period to retest and expand the analysis, potentially benefiting corporate sustainability research.

5. ACKNOWLEDGEMENT

This study is based on the authors' thesis at Bina Nusantara University.

6. OPEN DATA STATEMENT

This study used data obtained from publicly available annual reports and sustainability reports of the sample companies, as well as proprietary data obtained from Refinitiv under license. The publicly available documents can be accessed through the respective companies' websites, while the Refinitiv data are subject to licensing restrictions and are not publicly available.

7. REFERENCES

Ahdiat, A., 2024. Ini industri penyumbang emisi gas rumah kaca terbesar di Indonesia. Databoks. Available at: https://databoks.katadata.co.id/lingkungan/statistik/b0d4d2a1d9aaa4c/ini-industri-penyumbang-emisi-gas-rumah-kaca-terbesar-di-indonesia

Aldieri, L. and Vinci, C.P., 2021. Eco-innovation in support of sustainable development goals. In: W. Leal Filho, A.M. Azul, L. Brandli, A. Lange Salvia and T. Wall (eds.) *Industry, Innovation and Infrastructure*. Encyclopedia of the UN Sustainable Development Goals. Springer, Cham. [DOI]

Alrawadieh, Z., Alrawadieh, Z. and Cetin, G., 2020. Digital transformation and revenue management: Evidence from the hotel industry. *Tourism Economics*, 27(2), pp.328–345. [DOI]

Alsanie, G., 2025. Investigating the impact of digitalization on resource use, energy use, and waste reduction towards sustainability: Considering environmental awareness as a moderator. *Sustainability*, 17(9), 4073. [DOI]

Amankwah-Amoah, J., Khan, Z., Wood, G. and Knight, G., 2021. COVID-19 and digitalization: The great acceleration. *Journal of Business Research*, 136, pp.602–611. [DOI]

Andrian, T. and Sudibyo, Y.A., 2019. Disclosure effect of carbon emission and corporate social responsibility to financial performance. *Journal of Economics and Sustainable Development*, 10(12), pp.87–94. [DOI]

Baboe, K.C., Angelica, S.J.L. and Wedari, L.K., 2025. Sustainable empowerment: Digital transformation and carbon emissions as a catalyst for enterprise ESG performance. *International Journal of Sustainable Development and Planning*, 20(4), pp.1553–1561. [DOI]

Baniya, B. and Giurco, D., 2025. Net zero energy buildings and climate resilience narratives – navigating the interplay in the building asset maintenance and management. *Energy Reports*, 13, pp.1632–1648. [DOI]

Bhatia, M., Meenakshi, N., Kaur, P. and Dhir, A., 2024. Digital technologies and carbon neutrality goals: An in-depth investigation of drivers, barriers, and risk mitigation strategies. *Journal of Cleaner Production*, 451, 141946. [DOI]

Bolognesi, E., Burchi, A., Goodell, J.W. and Paltrinieri, A., 2025. Stakeholders and regulatory pressure on ESG disclosure. *International Review of Financial Analysis*, 103, 104145. [DOI]

Broadstock, D.C., Matousek, R., Meyer, M. and Tzeremes, N.G., 2020. Does corporate social responsibility impact firms' innovation capacity? The indirect link between environmental & social governance implementation and innovation performance. *Journal of Business Research*, 119, pp.99–110. [DOI]

Chauhan, M. and Sahoo, D.R., 2024. Towards a greener tomorrow: Exploring the potential of AI, blockchain, and IoT in sustainable development. *Nature Environment and Pollution Technology*, 23(2), pp.1105–1113. [DOI]

Chen, J., Gao, M., Ma, K. and Song, M., 2020. Different effects of technological progress on China's carbon emissions based on sustainable development. *Business Strategy and the Environment*, 29(2), pp.481–492. [DOI]

Chen, J., Guo, Z. and Lei, Z., 2024. Research on the mechanisms of the digital transformation of manufacturing enterprises for carbon emissions reduction. *Journal of Cleaner Production*, 449, 141817. [DOI]

Chen, X., Despeisse, M. and Johansson, B., 2020. Environmental sustainability of digitalization in manufacturing: A review. *Sustainability*, 12(24), 10298. [DOI]

Cheng, S., Yang, Y. and Liu, J., 2014. Convergence of regional economic growth and carbon emission intensity in China. *Nature Environment and Pollution Technology*, 13(3), pp.623–628.

CRSM Indonesia, 2024. Implementasi environmental, social and governance (ESG) 2024 survey nasional.

da Cunha, Í. G.F., Policarpo, R.V.S., de Oliveira, P.C.S., Zanon, L.G. and do Nascimento Rebelatto, D.A., 2025. Exploring ESG indicators and the Sustainable Development Goals: A fuzzy multi-criteria approach to cause-and-effect analysis. *Business Strategy and Development*, 8(3). [DOI]

Dan, E., Shen, J., Zheng, X., Liu, P., Zhang, L. and Chen, F., 2023. Asset structure, asset utilization efficiency, and carbon emission performance: Evidence from panel data of China's low-carbon industry. *Sustainability*, 15(7), 6264. [DOI]

Desjardine, M.R., Li, B. and Shi, W., 2025. Information-based competition: The case of rival owners in rating agencies. *Academy of Management Journal*, 68(1), pp.221–256. [DOI]

Emmanuel, Y.L., Adenikinju, O., Doorasamy, M., Ayoola, T.J., Oladejo, A.O., Kwarbai, J.D. and Otekunrin, A.O., 2023. Carbon emission disclosure and financial performance of quoted Nigerian financial services companies. *International Journal of Energy Economics and Policy*, 13(6), pp.628–635. [DOI]

Fussler, C. and James, P., 1996. *Driving Eco-Innovation: A Breakthrough Discipline for Innovation and Sustainability*. Pitman, London.

Gao, Y., Yang, H., Sun, X., Tian, X. and Xu, J., 2024. Corporate digital transformation and financing constraints: The moderating effect of institutional investors. *Heliyon*, 10(12), e33199. [DOI]

Griffin, J.S., Thal, A.E. and Leach, S.E., 2014. Enhancing asset management through a better understanding of energy consumption. *International Journal of Strategic Property Management*, 18(3), pp.253–264. [DOI]

Grishunin, S., Naumova, E., Burova, E., Suloeva, S. and Nekrasova, T., 2022. The impact of sustainability disclosures on value of companies following digital transformation strategies. *International Journal of Technology*, 13(7), pp.1432–1441. [DOI]

Guo, L., Li, S., Liu, Y., Zhang, C. and Sang, B., 2025. The green ripple effect: How digital transformation reduces carbon emissions across industrial chains. *Discrete Dynamics in Nature and Society*, 2025, 9159803. [DOI]

Guo, L. and Tang, M., 2024. How does digital transformation improve corporate carbon emission reduction performance? An empirical study on data from listed companies in China. *Sustainability*, 16(8), 3499. [DOI]

Haas, C., Jahns, H., Kempa, K. and Moslener, U., 2023. Deep uncertainty and the transition to a low-carbon economy. *Energy Research & Social Science*, 100. [DOI]

Hair, J.F., Black, W.C., Babin, B.J. and Anderson, R.E., 2019. *Multivariate Data Analysis* (8th ed.).

Hoffmann, V.H. and Busch, T., 2008. Corporate carbon performance indicators: Carbon intensity, dependency, exposure, and risk. *Journal of Industrial Ecology*, 12(4), pp.505–520. [DOI]

Hossnofsky, V. and Junge, S., 2019. Does the market reward digitalization efforts? Evidence from securities analysts' investment recommendations. *Journal of Business Economics*, 89(8–9), pp.965–994. [DOI]

IDX, 2023. Launching of Indonesia carbon exchange (IDXCarbon).

Kementerian Komunikasi dan Digital RI, 2024. TDN 2024.

Kementerian Perindustrian Republik Indonesia, 2018. Indonesia Industry 4.0 readiness index.

Khan, Z.A. and Singh, S., 2023. Intellectual property rights regime in green technology: Way forward to sustainability. *Nature Environment and Pollution Technology*, 22(4), pp.2145–2152. [DOI]

Khatib, S.F.A., Ismail, I.H.M., Salameh, N., Abbas, A.F., Bazhair, A.H. and Sulimany, H.G.H., 2023. Carbon emission and firm performance: the moderating role of management environmental training. *Sustainability*, 15(13), p.10485. [DOI]

Kristianto, F.P., Ulfia, Y.N. and Galih Prakoso, 2025. Framework for digital transformation in Industry 4.0: Insights data driven analysis in the Indonesia manufacture sector. *Journal of Advances in Information and Industrial Technology*, 7(1), pp.45–60. [DOI]

Li, J., 2024. A study on the mechanism of the impact of digital transformation in manufacturing enterprises on sustainable development performance. *International Journal of Environmental Impacts*, 7(1), pp.81–92. [DOI]

Li, Q., Abdul Ghani Azmi, I. binti and Norman, A.A. binti, 2025. Enhancing sustainable innovation through workplace well-being and digital capability: A systematic literature review toward responsible and cleaner consumption. *Cleaner and Responsible Consumption*, 18. [DOI]

Lin, P.T., Jin, Y., Gao, F., Yang, R. and Lin, Q., 2023. Institutional investors, CSR report readability and the moderating role of ESG performance. *SAGE Open*, 13(4). [DOI]

Liu, Y., Kumar, S., Liu, H., Li, S. and Zhou, Z., 2025. ESG performance, digital transformation, and green innovation. *Humanities and Social Sciences Communications*, 12(1). [DOI]

Ma, W., Sun, D., Deng, Y., Meng, X. and Li, M., 2021. Analysis of carbon emissions of prefabricated buildings from the views of energy conservation and emission reduction. *Nature Environment and Pollution Technology*, 20(1), pp.39–44. [DOI]

Ma, Y. and Tao, P., 2023. A perspective on management myopia: The impact of digital transformation on carbon emission intensity. *Sustainability*, 15(12), 9417. [DOI]

Matt, C., Hess, T. and Benlian, A., 2015. Digital transformation strategies. *Business & Information Systems Engineering*, 57(5), pp.339–343. [DOI]

McDougall, M., Mooney, A. and Dunkley, E., 2025. BlackRock loses second Dutch pension mandate over sustainable investing concerns. *Financial Times* (December).

Miller, N., 2024. ESG score. *Corporate Finance Institute* (July).

Nareswari, N., Tarczynska-Luniewska, M. and Al Hashfi, R.U., 2023. Analysis of environmental, social, and governance performance in Indonesia: Role of ESG on corporate performance. *Procedia Computer Science*, 225, pp.1748–1756. [DOI]

Otoritas, J.K., 2017a. Penerapan keuangan berkelanjutan bagi lembaga jasa keuangan, emiten, dan perusahaan publik. Available at: https://keuanganberkelanjutan.ojk.go.id/keuanganberkelanjutan/id/regulation/detailregulation/3781/penerapan-keuangan-berkelanjutan-bagi-lembaga-jasa-keuangan-emiten-dan-perusahaan-publik

Otoritas, J.K., 2017b. Penerbitan dan persyaratan efek bersifat utang berwawasan lingkungan (green bond). Available at: https://keuanganberkelanjutan.ojk.go.id/keuanganberkelanjutan/Peraturan/View/613/penerbitan-dan-persyaratan-efek-bersifat-utang-berwawasan-lingkungan-green-bond

Plathottam, S.J., Rzonca, A., Lakhnori, R. and Iloeje, C.O., 2023. A review of artificial intelligence applications in manufacturing operations. *Journal of Advanced Manufacturing and Processing*, 5(3). [DOI]

Qian, Y., Liu, J., Shi, L., Forrest, J.Y.L. and Yang, Z., 2023. Can artificial intelligence improve green economic growth? Evidence from China. *Environmental Science and Pollution Research*, 30(6), pp.16418–16437. [DOI]

Raman, R., Ray, S., Das, D. and Nedungadi, P., 2025. Innovations and barriers in sustainable and green finance for advancing Sustainable Development Goals. *Frontiers in Environmental Science*, 12, 1513204. [DOI]

Ramli, K., 2023. Policy development to accelerate digital transformation. pp.11–36.

Ren, L. and Cheng, Y., 2024. The impact and mechanism of ESG performance on corporate continuous innovation: Evidence from China. *Sustainability*, 16(17), 7562. [DOI]

Rennings, K., 2000. Redefining innovation-eco-innovation research and the contribution from ecological economics. *Ecological Economics*, 32(2), pp.319–332. [DOI]

Rohayati, Y. and Abdillah, A., 2024. Digital transformation for era Society 5.0 and resilience: Urgent issues from Indonesia. *Societies*, 14(12), 266. [DOI]

Shang, Y., Raza, S.A., Huo, Z., Shahzad, U. and Zhao, X., 2023. Does enterprise digital transformation contribute to the carbon emission reduction? Micro-level evidence from China. *International Review of Economics & Finance*, 86, pp.1–13. [DOI]

Song, W., Ren, S. and Yu, J., 2019. Bridging the gap between corporate social responsibility and new green product success: The role of green organizational identity. *Business Strategy and the Environment*, 28(1), pp.88–97. [DOI]

Song, Y., Xie, Z. and Song, Y., 2025. The impact of digital transformation on carbon emission intensity. *International Review of Economics & Finance*, 102. [DOI]

Sun, J., Ran, L. and Wang, B., 2025. ESG performance and digital transformation: Evidence from Chinese A-listed companies. *Sustainability*, 17(18), 8517. [DOI]

Tang, J., Huang, K. and Xiong, A., 2025. Impact of digital transformation on corporate sustainability: Evidence from China's carbon emissions. *Energy Informatics*, 8(1). [DOI]

United Nations, 2025. Goal 9: Build resilient infrastructure, promote sustainable industrialization and foster innovation. (September 10). Available at: https://www.un.org/sustainabledevelopment/infrastructure-industrialization/

Vial, G., 2019. Understanding digital transformation: A review and a research agenda. *The Journal of Strategic Information Systems*, 28(2), pp.118–144. [DOI]

Wade, M. and Shan, J., 2020. Covid-19 has accelerated digital transformation, but may have made it harder not easier. *MIS Quarterly Executive*, 19(3), pp.213–220.

Wang, J., Hong, Z. and Long, H., 2023a. Digital transformation empowers ESG performance in the manufacturing industry: From ESG to DESG. *SAGE Open*, 13(4). [DOI]

Wang, W., Hu, R., Zhang, C. and Shen, Y., 2023b. Impact of common institutional ownership on enterprise digital transformation–Collaborative governance or collusion fraud? *Heliyon*, 9(11), e21641. [DOI]

Wang, Y. and Sun, L., 2025. The impact of digital transformation on firm performance - an empirical study based on business administration perspective. *Applied Mathematics and Nonlinear Sciences*, 10(1). [DOI]

Xu, J., Yu, Y., Zhang, M. and Zhang, J.Z., 2023. Impacts of digital transformation on eco-innovation and sustainable performance: Evidence from Chinese manufacturing companies. *Journal of Cleaner Production*, 393. [DOI]

Yang, P., Hao, X., Wang, L., Zhang, S. and Yang, L., 2024. Moving toward sustainable development: The influence of digital transformation on corporate ESG performance. *Kybernetes*, 53(2), pp.669–687. [DOI]

Yavari, A., Mirza, I.B., Bagha, H., Korala, H., Dia, H., Scifleet, P., Sargent, J., Tjung, C. and Shafiei, M., 2023. ArtEMon: Artificial intelligence and Internet of Things powered greenhouse gas sensing for real-time emissions monitoring. *Sensors*, 23(18), 7971. [DOI]

Yavuz, M.S., Tatlı, H.S. and Bozkurt, G., 2025. Exploring the financial

impact of digital transformation: A comprehensive analysis on firms. *Journal of Innovation and Knowledge*, 10(5). [DOI]

Yin, F., Xiao, Y., Cao, R. and Zhang, J., 2023. Impacts of ESG disclosure on corporate carbon performance: Empirical evidence from listed companies in heavy pollution industries. *Sustainability*, 15(21), 15296. [DOI]

Yue, S., Ye, G., Khalid, F. and Wang, T., 2025. From digital transformation to energy efficiency: Ownership concentration's hidden role in driving climate solutions. *Humanities and Social Sciences Communications*, 12(1). [DOI]

Zhai, H., Yang, M. and Chan, K.C., 2022. Does digital transformation enhance a firm's performance? Evidence from China. *Technology in Society*, 68, 101841. [DOI]

Zhang, C., Fang, J., Ge, S. and Sun, G., 2024. Research on the impact of enterprise digital transformation on carbon emissions in the manufacturing industry. *International Review of Economics & Finance*, 92, pp.211–227. [DOI]

Zhang, J., Li, H. and Zhao, H., 2025. The impact of digital transformation on organizational resilience: The role of innovation capability and agile response. *Systems*, 13(2), 75. [DOI]

Zhang, M. and Huang, Z., 2024. The impact of digital transformation on ESG performance: The role of supply chain resilience. *Sustainability*, 16(17), 7621. [DOI]

Zhao, Q., Li, X. and Li, S., 2023. Analyzing the relationship between digital transformation strategy and ESG performance in large manufacturing enterprises: The mediating role of green innovation. *Sustainability*, 15(13), 9998. [DOI]

Zhou, J. and Liu, W., 2024. Carbon reduction effects of digital technology transformation: Evidence from the listed manufacturing firms in China. *Technological Forecasting and Social Change*, 198. [DOI]

Nature Environment and Pollution Technology
An International Quarterly Peer-Reviewed Open Access Journal

p-ISSN: 0972-6268 | e-ISSN: 2395-3454 Vol. 25 | No. 4 | Article ID D1919 | 2026

RESEARCH ARTICLE https://doi.org/10.46488/NEPT.2026.v25i04.D1919 OPEN ACCESS

Pollution Emissions from the Kaeng Sian Landfill: Assessment and Sustainable Waste Management for Kanchanaburi Province, Thailand

Sasitorn Hasin[1], Saowaluck Haosagul[2] and Apichaya Sawasdee[1]†
[1]Program in Innovation of Environmental Management, College of Innovative Management, Valaya Alongkorn Rajabhat University Under the Royal Patronage, Pathumthani 13180, Thailand
[2]Division of Future Mobility Policy, Office of National Higher Education Science Research and Innovation Policy Council, Bangkok 10330, Thailand
†Corresponding author: Apichaya Sawasdee; apichaya.s@vru.ac.th

ARTICLE HISTORY

Received: 09-03-2026
Revised: 11-05-2026
Accepted: 17-05-2026

KEYWORDS

Kaeng Sian landfill
Leachate
Municipal solid waste
Waste management
Pollution emissions

CITE THIS ARTICLE

Hasin, S., Haosagul, S. and Sawasdee, A., 2026. Pollution emissions from the Kaeng Sian landfill: Assessment and sustainable waste management for Kanchanaburi Province, Thailand, *Nature Environment and Pollution Technology*, 25(4), D1919. https://doi.org/10.46488/NEPT.2026.v25i04.D1919

COPYRIGHT & LICENCE

© 2026 The Authors
Open Access under CC BY 4.0.

PUBLISHED BY
TECHNOSCIENCE PUBLICATIONS

ABSTRACT

This study aims to assess the types and quantities of pollution generated from landfills and to propose waste management approaches consistent with sustainable development and the circular economy. The research presents the composition of solid waste and the greenhouse gas (GHG) emissions estimated at the landfill site. The largest component of municipal solid waste (MSW) is plastic, at 30.39%, followed by food waste at 27.75%. The smallest component of MSW is hazardous waste at 0.23%. The total volume of solid waste in the landfill area is 736,492.12 ± 8,326.36 m³. The GHG emissions from the landfill site were estimated as CH_4, totaling 17,631.44 t CO_2 eq. The suggested waste management strategy was developed based on the results and includes the following measures: 1) Emergency Measures, 2) Intermediate Actions, 3) Long-term Measures, 4) Community Engagement, and 5) Technology and Data Management. Therefore, the pollution data from the landfill site presented in this study may be useful for developing strategies in Kanchanaburi Province to mitigate climate change. Finally, this research can contribute to addressing municipal solid waste management (SDG 12) and climate action (SDG 13), which aim to support climate change adaptation, integrate climate change measures into national policies, and raise awareness about climate change.

1. INTRODUCTION

Solid waste management is a key environmental issue in Thailand, particularly in the context of climate change and community environmental quality. Landfill sites in developing countries are expected to grow, which will increase GHG emissions (IPCC 2007, Menikpura & Sang-Arun 2013). Landfilling, the primary method used in many areas, remains a major source of multiple pollutants affecting air, water, and soil due to the decomposition of organic waste. During the decomposition of organic waste, biochemical changes occur under anaerobic conditions. Bacteria break down organic matter into organic acids and greenhouse gases, including methane (CH_4) and carbon dioxide (CO_2). This process not only affects global warming but also indicates pollutant concentrations in landfills (IPCC 2019, TGO 2023).

Greenhouse gas (GHG) emissions are a critical concern in relation to rising global temperatures. This concern requires solutions to reduce GHG emissions. The Paris Agreement aims to keep the increase in global temperature below 2°C, preferably 1.5°C (UNFCCC 2016). The world is already directly affected by

global warming and greenhouse gas emissions. The effects of CO_2 emissions will worsen in the future (Iglina et al. 2022), including increasing global temperatures (Xu et al. 2021), melting glaciers (Aichele & Felbermayr 2012), and increased flood risk (Zheng et al. 2021).

The waste sector is a significant source of GHG emissions. Approximately 5% of the world's GHG emissions come from the waste sector (Kristanto et al. 2020). In Thailand, the waste sector in 2018 emitted 16,703.68 Gg CO_2 eq, with emissions mainly originating from solid waste disposal, accounting for 8,774.67 Gg CO_2 eq (52.53%) (Climate Change Management & Coordination Division 2022). Moreover, ineffective waste management can result in harmful health impacts, increased air, soil, and water pollution, GHG and toxic emissions, and the loss of valuable materials and services (Kamaruddin et al. 2022).

Pollution from landfill sites, such as water pollution, odors, and insect proliferation, is a major concern for nearby communities and adversely affects living conditions (Piboon et al. 2022, Muchangos & Tokai 2020). Major greenhouse gases (GHGs) emitted from landfill sites include methane (CH_4), carbon dioxide (CO_2), and nitrous oxide (N_2O). In particular, the high rate of methane gas released into the atmosphere from ineffective management of municipal solid waste at landfill sites further exacerbates emissions (Fikri et al. 2024).

The accumulation of methane gas in landfills without proper ventilation systems can cause high pressure, leading to leaks or explosions. In addition, methane gas is often contaminated with volatile organic compounds (VOCs) and hydrogen sulfide (H_2S), which are odor-causing and toxic at high concentrations. Boongla et al. (2025) reported that landfills in central Thailand have an average CH_4 concentration of 40–60% of the total gas, and VOC emissions are associated with the proportion of organic waste, particularly food and agricultural waste (TGO 2023).

In addition to gas release, the decomposition of organic waste directly affects leachate generation, as rainwater seeps through the waste layer and dissolves organic matter, heavy metals, and other chemicals (Kiddee et al. 2014). Increased methane and leachate levels often occur simultaneously in ponds with a high proportion of organic waste, suggesting a link between greenhouse gas generation and landfill pollution. That is, the decomposition of waste that produces CH_4 also facilitates the dissolution of organic acids and heavy metals, which are pollutants that further spread into water and soil systems (Parvin & Tareq 2021). Wisitthammasri et al. (2024) also found that decomposition of organic waste at high temperatures in a landfill can accelerate the breakdown of plastic materials into microplastics, which are commonly found in leachate and tend to migrate into surface water sources or groundwater. Therefore, greenhouse gas emissions and landfill pollution are systematically related, with biochemical processes within landfills being the source of both greenhouse gases (CH_4, CO_2) and water and soil pollutants (leachate, PFAS, microplastics).

Kanchanaburi is a province with significant tourism, agriculture, and community activities, generating substantial municipal solid waste. The Khao Thong area, Kaeng Sian Subdistrict, Mueang District, Kanchanaburi Province, has landfill sites for waste dumping covering 53 rai (approximately 84,800 m²) (Sawasdee et al. 2022). Generally, municipal solid waste is received from Kanchanaburi and other provinces. As a result, MSW in Kanchanaburi Province has increased, leading to higher GHG emissions. This increase significantly affects people and the environment. Therefore, this study focuses on assessing the levels and patterns of pollution in the Kaeng Sian landfill in Mueang District, Kanchanaburi Province, including greenhouse gas emissions and leachate, as well as the impacts on the surrounding environment.

This study aims to assess the types and quantities of pollution generated from landfills and to propose waste management approaches aligned with the principles of sustainable development and the circular economy. Municipal solid waste can be managed effectively through an appropriate combination of policies.

2. MATERIALS AND METHODS

2.1. Data Collection

The data for this study were collected from a landfill site located in Kaeng Sian Subdistrict of Mueang District, Kanchanaburi Province (Fig. 1). We utilized both field surveys and the application of digital technology to obtain accurate and comprehensive data, which can be efficiently used to assess waste volume and type.

The data collection process included the following methods: classifying MSW using the quartering method; surveying the entire landfill site; using Unmanned Aerial Vehicles (UAVs); and analyzing satellite imagery to evaluate the total amount of MSW in the landfill site. All data were used to assess the pollution generated by the landfill, informing the development of waste management strategies aligned with the principles of sustainable development and the circular economy.

2.2. Quartering Method

Municipal solid waste consists of various types, including food waste, plastic, wood, garden waste, paper, glass, rubber,



Fig. 1: Landfill site at Kaeng Sian Subdistrict, Mueang District, Kanchanaburi Province.

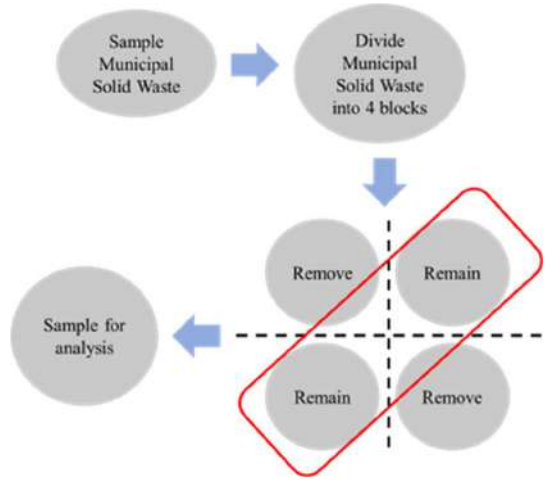


Fig. 2: Quartering method for municipal solid waste analysis in a landfill site.

hazardous waste, and electronic waste. To ensure that the sample represents the overall composition of municipal solid waste, it must be sampled systematically. The quartering method is shown in Fig. 2.

To begin, a random sample of MSW was taken from the waste heap area. The MSW was mixed thoroughly until it was homogenized and then divided into four equal parts. This process was repeated until at least 100 kg of sample was obtained (Rojas-Valencia & Nájera-Aguilar 2012, PCD 2022).

2.3. Unmanned Aerial Vehicle (UAV) and Satellite Imagery

This study utilized an unmanned aerial vehicle (UAV) survey (Fig. 3) combined with satellite imagery analysis to assess the volume and spatial distribution of solid waste at the Kaeng Sian landfill in Kanchanaburi. Drones equipped with high-resolution RGB cameras were used to survey the landfill area, producing orthophotos and digital surface models (DSMs) with a spatial resolution of approximately 2–5 cm per pixel.

The surveys were conducted at an altitude of approximately 100–120 m above ground level along a predefined grid path to cover the entire area and achieve at least 80% image overlap.

2.4. Measurement of CH_4 Concentration at the Landfill Site

Landfill gas (LFG), which results from the anaerobic degradation of MSW in a landfill site, consists of roughly 60% methane (CH_4) and 40% carbon dioxide (CO_2) (ATSDR 2008). Landfilling is the third-largest source of uncontrolled anthropogenic CH_4 emissions. Measuring methane gas in



Fig. 3: Survey of the entire landfill site using an unmanned aerial vehicle (UAV) in Kaeng Sian, Kanchanaburi.

landfill sites is a crucial component of assessing greenhouse gas emissions, as methane is the primary gas produced by the anaerobic decomposition of organic matter and has a high global warming potential. Measuring methane concentration enables estimation of greenhouse gas emissions in terms of carbon dioxide equivalents, providing essential data for planning emission reductions and sustainable landfill management. A high amount of methane gas is generated at the landfill site in Kaeng Sian, Kanchanaburi Province. Therefore, CH_4 was measured using a portable methane gas analyzer (Fig. 4) (SKY 2000-CH_4; ATEX-, CE-, and ISO 9001-certified).

A walking survey was conducted across the landfill site to identify areas with the highest methane gas concentrations. Holes approximately 5 m deep were dug at 6 points, each serving as a sampling point for methane gas measurements at the landfill site in Kaeng Sian, Kanchanaburi (Fig. 5).



Fig. 4: SKY 2000-CH_4 portable methane gas analyzer with ATEX, CE, and ISO 9001 certification.

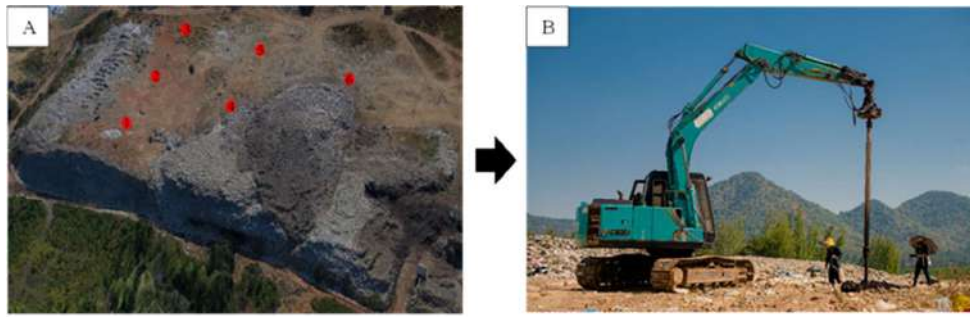


Fig. 5: (A) Points for methane gas measurement (red dots) at the Kaeng Sian landfill site, Kanchanaburi; (B) excavation of a hole approximately 5 m deep at each point.

2.5. Leachate Analysis

Leachate samples were analyzed for chemical oxygen demand (COD) using the closed reflux method, as described in the APHA Standard Methods for the Examination of Water and Wastewater (APHA 2005). Additionally, cadmium (Cd), lead (Pb), manganese (Mn), and mercury (Hg) were measured using atomic absorption spectrometry (AAS) according to the APHA Standard Methods for the Examination of Water and Wastewater (APHA 2005).

2.6. Calculation of Greenhouse Gas Emissions

The equation for estimating CH_4 emissions using the first-order decay (FOD) method from the Thailand Greenhouse Gas Management Organization (Public Organization), T-VER-S-TOOL-02-02 (Calculation for Emissions from SWDS), which was modified from the IPCC Good Practice Guidance and Uncertainty Management in National Greenhouse Gas Inventories (TGO 2023), was applied as follows:

$$BE_{CH4SWDS,y} = \varphi_y X \left(1 - f_y\right) \left(GWP_{CH}\right) (1 - OX) \left(\frac{16}{12}\right)$$

$$(F \times DOC_{f,y} \times MCF_y \times \sum_{x=1}^{y} . \sum_j W_x P_j DOC_j e^{-kj(y-x)} (1 - e^{-k}) \quad \ldots(1)$$

Where: $BE_{CH4,SWDS,y}$ represents methane emissions from the landfill site (t CO_2 eq), y is the year of greenhouse gas emission calculation, X is the number of years for which input data are included, j_y is the model correction factor (default 0.85), f_y is the proportion of methane gas that is collected from landfills and used for incineration, power generation, or other purposes (If there is no collection, the value is 0.), GWP_{CH4} is methane's global warming potential, OX is the oxidation factor (default 0.1), 16/12 is used to convert carbon to methane, F is the proportion of methane in landfill gas (default 0.5), $DOC_{f,y}$ is the proportion of organic carbon that can be decomposed in a year (default 0.5), MCF_y is the methane correction factor (default 0.4–1.0), W_x is the quantity of municipal solid waste, P_j is the proportion by weight of municipal solid waste type j, DOC_j is the proportion of biodegradable organic carbon (by wet weight) of organic waste type j, k_j is the decomposition rate of organic waste type j (default 0.035–0.40) (commonly 0.15–0.43), and j is the component types of municipal solid waste.

3. RESULTS AND DISCUSSION

3.1. Composition of MSW

The composition of municipal solid waste (MSW) at the landfill site (Table 1) was determined using UAV imagery, satellite imagery (Fig. 6), and the quartering method. The findings reveal that plastic dominates the composition at 30.39%, followed by food waste at 27.75%. In contrast, hazardous waste represents only 0.23% of the total MSW. The bulk density was assumed to be 1 tonne m^{-3} (Sawasdee et al. 2022), which was used to calculate the composition of MSW.

Although plastic waste constitutes the largest share of MSW, priority should be given to managing food waste, garden waste, wood, paper, and textiles. These materials not only pose a significant environmental challenge but also contribute substantially to greenhouse gas (GHG) emissions from landfill sites. Addressing these waste categories first can lead to more effective waste management practices and a significant reduction in harmful emissions.

The amount of waste is continuously increasing, as data collected on the number and size of garbage trucks dumping waste at the landfill show a steady rise (Sawasdee et al. 2022). Therefore, proper waste management is necessary to reduce landfill contamination and prevent the spread of diseases.

3.1.1. Three-Dimensional Model Analysis

The processing of UAV aerial photographs to create a 3D model of the landfill area provided the following important parameters:

1. **Three-dimensional terrain surface area:** The three-dimensional terrain surface area is the total surface area of the landfill, derived from a Digital Surface Model (DSM) generated from UAV imagery. This area includes surface roughness features such as waste mounds, slopes, and pond edges. The area value of 67,865.40 m² represents the actual surveyed area within the scope of the volume calculation, which is

Table 1: Composition of municipal solid waste (MSW) at the landfill site.

No.	Composition of MSW	Results (%)	Result (t)
1	Food waste	27.75	204,376.56
2	Garden waste	5.59	41,169.91
3	Wood	2.01	14,803.49
4	Paper	8.39	61,791.69
5	Plastic	30.39	223,819.96
6	Metal	0.69	5,081.80
7	Glass	1.85	13,625.10
8	Textile	7.67	56,488.95
9	Infectious waste	4.21	31,006.32
10	Rubber and leather	0.91	6,702.08
11	Hazardous waste	0.23	1,693.93
12	Electronic waste	0.54	3,977.06
13	Other waste	9.77	71,955.28
Total		100	736,492.12

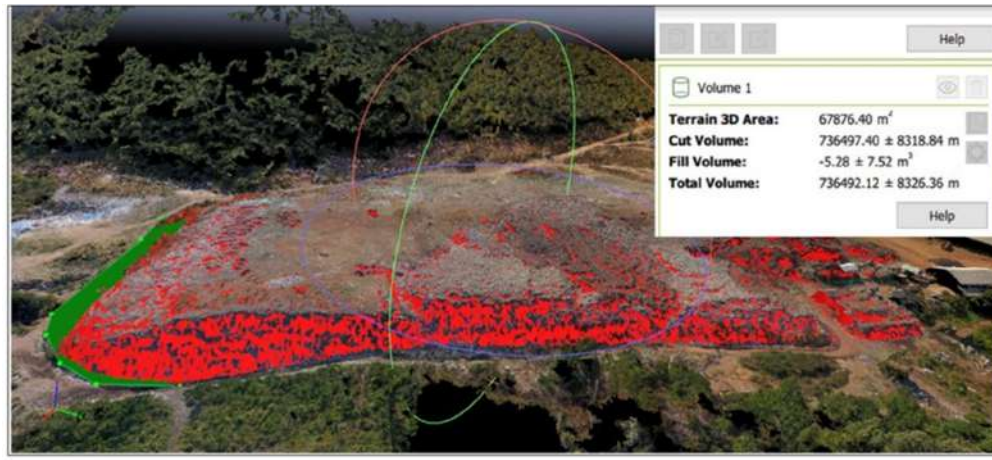


Fig. 6: MSW volume at the Kaeng Sian landfill site, Kanchanaburi.

used as a database for spatial analysis and landfill site management planning.

2. **Cut-off volume:** The cut-off volume refers to the volume of material (e.g., waste, litter, and topsoil) that is above the reference surface and must be removed ("cut off") if the area is to be leveled with the base. For a landfill, these data reflect the total accumulated waste volume above the landfill's reference surface, which is 736,497.40 ± 8,318.84 m^3, accounting for image resolution (ground sampling distance) and elevation model corrections.
3. **Fill volume:** Fill volume is the amount of material required to fill in areas that are lower than the base of the terrain to make the ground level even. The fill volume is −5.28 ± 7.52 m³. A negative fill volume indicates that the majority of the landfill area is raised above base level, with only a few depressions; thus, there is no need for additional fill.
4. **Total volume:** The total volume is 736,492.12 ± 8,326.36 m³, which is the net sum of the cut and fill calculations, showing the actual accumulated waste volume in the landfill at the time of the survey. This value can be used to analyze waste management potential and assess methane gas (CH_4) emissions in the next step.

The analysis results indicate that the Kaeng Sian landfill has accumulated waste volumes exceeding 736,000 m³, indicating that it is nearing capacity. Therefore, effective waste management plans are necessary, such as separating and reusing recyclable waste, modifying the landfill surface



Fig. 7: Daily (A, B) and old (C, D) municipal solid waste at the landfill site.

to reduce leachate generation, and installing systems for continuous monitoring of subsidence and greenhouse gas emissions.

The landfill site's waste volume and organic waste content resulted in high GHG emissions. The waste present included both old waste that had been accumulating for more than 10 years and new waste deposited daily by garbage trucks. The average amount of waste dumped in the area is 216 tons per day (Sawasdee et al. 2022). Therefore, measures should be taken to manage both old and new waste (Fig. 7) transported to the site to reduce greenhouse gas emissions from landfills, reduce residual waste, and improve the quality of life for residents in the surrounding areas.

3.2. CH_4 Emissions from the Landfill Site

The concentration of methane gas at the landfill site was detected at 40.52% ± 0.11–50.47% ± 0.04 (Fig. 8). Methane gas is released into the air during the decomposition of organic waste, such as food, wood, or paper. The proportion of organic waste in the landfill site was 43.74%. However, methane gas can be a significant local source of alternative energy. Moreover, the utilization of methane gas contributes to reducing GHG release and improving local air quality.

The concentration of methane gas at the landfill site was detected at 40.52% ± 0.11–50.47% ± 0.04 (Fig. 8). Methane gas is released into the air during the decomposition of organic waste, such as food, wood, or paper. The proportion of organic waste in the landfill site was 43.74%. Among the gases in the atmosphere, methane has a significant greenhouse effect. Nearly 30% of the current global temperature increase is attributed to methane (UNEP & CCAC 2021).

When MSW is initially dumped in a landfill site, it goes through an aerobic decomposition phase during which minimal methane is produced. After less than a year, anaerobic conditions are created, and methanogenic bacteria start to break down the waste and produce methane. More recently buried waste (less than 10 years) produces higher levels of landfill gas emissions through bacterial decomposition, volatilization, and chemical reactions compared with older waste (over 10 years). Waste aged 0–10 years is considered relatively new, with a maximum moisture content of 35% (Sawasdee et al. 2022), and contains a large amount of biodegradable organic matter, leading to methane gas production and ongoing decomposition. In waste older than 10 years, some of the easily biodegradable organic matter has already been broken down, reducing the decomposition rate. As waste ages, it continues to decompose, thereby degrading its potential and consequently reducing the rate of gas emission (Bouart & Sakunkoo 2015).

The GHG emissions from the landfill site were primarily methane (CH_4), totaling 17,631.44 t CO_2 eq from the first-order decay (FOD) method (Table 2). The GHG contributions were from food waste, paper, textiles, and wood, respectively. The highest GHG contribution was obtained from food waste (15,987.09 t CO_2 eq) (Table 3). Thus, food waste segregation and utilization can reduce GHG emissions.



Fig. 8: Concentration of CH_4 gas at each point of the landfill site.

Table 2: First-order decay (FOD).

First-order decay (FOD)														
j_y	x	fy	GWP CH_4	OX	F	DOCf,y	MCFy	Wx	pj	DOCj	kj	16/12	$e^{-kj(y-x)}$	$(1-e^{-kj})$	t CO_2 eq
0.85	10	0	28	0.1	0.5	0.5	0.8	204,376.56	27.75%	0.15	0.4	1.33	1	0.329	15,987.09
0.85	10	0	28	0.1	0.5	0.5	0.8	41,169.91	5.59%	0.2	0.17	1.33	1	0.156	410.14
0.85	10	0	28	0.1	0.5	0.5	0.8	14,803.49	2.01%	0.43	0.035	1.33	1	0.034	24.85
0.85	10	0	28	0.1	0.5	0.5	0.8	61,791.69	8.39%	0.4	0.07	1.33	1	0.068	805.47
0.85	10	0	28	0.1	0.5	0.5	0.8	56,488.95	7.67%	0.24	0.07	1.33	1	0.068	403.89
Sum															**17,631.44**

Table 3: GHG emissions from the landfill site.

Type of waste	Amount of waste	t CO_2 eq
Food waste	204,376.56	15,987.09
Garden waste	41,169.91	410.14
Wood	14,803.49	24.85
Paper	61,791.69	805.47
Textile	56,488.95	403.89
Total GHG emissions from the landfill site	17,631.44	

However, the landfill site problem should be addressed with appropriate remedies, and a long-term strategy should be developed accordingly (Kaushal & Sharma 2016). Therefore, the following waste management strategies are recommended to reduce GHG emissions from landfill sites: transforming the open dump into a sanitary landfill that can capture and utilize methane as an alternative energy source. Long-term strategies include CH_4 utilization from the sanitary landfill, production of refuse-derived fuel (RDF) from solid waste, and electricity generation from RDF.

3.3. Leachate in the Landfill Area

There are three leachate ponds (Fig. 9) in the landfill area. Pond 1 had the highest COD concentration, 60,285.38 mg/L; the COD concentrations in ponds 2 and 3 were 46,436.04 mg/L and 53,768.04 mg/L, respectively (Table 4). The landfill studied in this research was over 10 years old, consistent with the review by Renou et al. (2008). In landfills older than 10 years, the leachate is often in the stabilized leachate stage, characterized by low BOD but high COD and NH_3-N levels. Furthermore, this stage of leachate contains difficult-to-degrade organic matter, reducing the efficiency of treatment by rectification ponds, particularly COD removal. Therefore, the COD values in this research indicate that rectification ponds may not be sufficient for leachate treatment. Rectification ponds should be combined with other treatment technologies, such as aeration systems,



Fig. 9: Leachate ponds in the landfill area.

Table 4: Leachate analysis in the landfill area.

Leachate pond	Parameters	Concentration (mg/L)
Pond 1	COD	60,285.38
	Cadmium (Cd)	<0.0020
	Lead (Pb)	0.0310
	Manganese (Mn)	1.4360
	Mercury (Hg)	0.0006
Pond 2	COD	46,436.04
	Cadmium (Cd)	<0.0020
	Lead (Pb)	0.0290
	Manganese (Mn)	1.5170
	Mercury (Hg)	0.0005
Pond 3	COD	53,768.04
	Cadmium (Cd)	<0.0020
	Lead (Pb)	0.0270
	Manganese (Mn)	1.7280
	Mercury (Hg)	0.0005

artificial wetlands, or membrane systems, to improve pollution reduction efficiency and minimize long-term environmental impact.

In terms of heavy metals, cadmium (Cd), lead (Pb), manganese (Mn), and mercury (Hg) were within the standard limits specified in the Ministry of Natural Resources and Environment's Decree No. 08/2022/NĐCP on wastewater discharge from landfills (MONRE, 2022)..

However, leachate is a major environmental problem due to waste decomposition. Leachate from landfills is contaminated with a variety of pollutants, including heavy metals and chemicals that leach from items such as batteries, light bulbs, and spray cans. The landfill site in this area lacks a proper leachate treatment system, which could lead to leachate leakage and seepage into the surrounding soil. Additionally, contamination can migrate underground, contaminating groundwater, which in turn can connect to surface water.

The impacts of leachate contamination on soil affect living organisms and the environment. These impacts can be classified as environmental, health, and greenhouse gas impacts (Mavakala et al. 2016), as follows:

1) **Environmental impacts:** Leachate can contaminate nearby groundwater and surface water sources, making them unsafe for consumption or irrigation. Moreover, it can damage aquatic ecosystems, harm fish and other organisms, and disrupt the balance of local biodiversity. The decomposition process and residual leachate also produce foul odors, which affect the surrounding environment.
2) **Human health and community impacts:** Communities living near landfills that are not properly managed can be exposed to toxins in their water or air, leading to health problems such as skin irritation, gastrointestinal diseases, and respiratory problems. Nearby communities may experience reduced quality of life due to foul odors, insect breeding (flies, mosquitoes), and contamination of local water sources, which may also lead to social conflicts or community complaints.
3) **Greenhouse gas emissions:** Leachate contains organic matter that can be anaerobically decomposed in landfills, producing methane and carbon dioxide, two major greenhouse gases.

The proposed waste management strategy was developed from the study results and comprises five measures (Table 5): 1) Emergency Measures, 2) Intermediate Actions, 3) Long-term Measures, 4) Community Engagement, and 5) Technology and Data Management.

Table 5: Measures to address waste management in the Kaeng Sian landfill area.

Measures	Details
Emergency Measures	1. Install methane gas vent pipes and arrange drainage systems around the pond. 2. Control temporary new waste acceptance and arrange for source sorting points.
Intermediate Actions	1. Construct a wastewater treatment system, for example, a facultative lagoon, constructed wetland, oxidation pond, or anaerobic treatment system. 2. Improve the area into a sanitary landfill.
Long-term Measures	1. Establish a district/provincial-level integrated waste management center (Cluster System). 2. Promote waste-to-energy projects. 3. Develop transportation infrastructure and waste separation in the district.
Community Engagement	1. Establish a recycling waste bank. 2. Establish a waste management and environmental learning center. 3. Support waste reduction activities at the source in schools, markets, and households.
Technology and Data Management	1. Install IoT sensors in the landfill area to detect CH_4 and H_2S and measure temperature. 2. Use drones and GIS technology to survey waste areas and plan for recovery. 3. Create a monthly/annual waste management database system.

The prioritization of measures is based on the severity of pollution found at the landfill site, as determined by the research. Emergency measures are given the highest priority due to high methane emissions and large landfill waste accumulations, indicating urgent risks related to greenhouse gas emissions, odor, fire, and leachate contamination. Intermediate-level measures and technology-based monitoring are prioritized to improve the effectiveness of environmental control and support evidence-based landfill management. Community involvement and long-term policy measures are crucial for sustainable waste management and align with Sustainable Development Goals 12 and 13. All measures aim to achieve a waste management system that is safe, effective, uses appropriate technology, reduces landfill burden, promotes a circular economy, and encourages public participation.

4. CONCLUSIONS

The research presents the composition of solid waste and the GHG emissions from the landfill site. The largest MSW component is plastic, at 30.39%, followed by food waste at 27.75%. Hazardous waste has the lowest share, at 0.23%. The total volume of solid waste in the landfill area is 736,492.12 ± 8,326.36 m^3. The GHG emissions from the landfill site were primarily methane (CH_4), calculated at 17,631.44 t CO_2 eq.

The proposed waste management strategies, derived from the results, include five measures: 1) Emergency Measures, 2) Intermediate Actions, 3) Long-term Measures, 4) Community Engagement, and 5) Technology and Data Management. Municipal solid waste can be managed effectively through an appropriate combination of policies.

Moreover, GHG emission data from this study may be useful for developing strategies in Kanchanaburi Province to mitigate climate change. Therefore, the findings of this study can support climate change mitigation planning at the provincial level. Finally, this research can contribute to addressing municipal solid waste management (SDG 12) and climate action (SDG 13), which aim to support climate change adaptation, integrate climate change measures into national policies, and raise awareness of climate change.

5. ACKNOWLEDGEMENT

The authors acknowledge financial support from Keang Sian Power Co., Ltd. The authors also thank Valaya Alongkorn Rajabhat University under the Royal Patronage for technical support.

6. REFERENCES

Aichele, R. and Felbermayr, G., 2012. Kyoto and the carbon footprint of nations. *Journal of Environmental Economics and Management*, 63(3), pp. 336–354. [DOI]

APHA, 2005. *Standard Methods for the Examination of Water and Wastewater*. 25th ed. Washington, DC: American Public Health Association.

ATSDR, 2008. Chapter 2: Landfill gas basics. In: *Landfill Gas Primer: An Overview for Environmental Health Professionals*. Available at: https://www.atsdr.cdc.gov/HAC/landfill/PDFs/Landfill_2001_ch2mod.pdf (Accessed: 7 August 2023).

Boongla, Y., Changphuek, S. and Saehuang, A., 2025. Estimation of characteristics, methane generation and sustainability of municipal landfill waste in an urban city, Thailand. *Recycling*, 10(1), p. 15. [DOI]

Bouart, O. and Sakunkoo, P., 2015. Determination of methane potential by default method, first-order decay method and LandGEM from a controlled dump site: A case study of Nakhonphanom Municipality in Nakhonphanom Province. *KKU Research Journal (Graduate Studies)*, 15(1), pp. 93–104. Available at: https://ph02.tci-thaijo.org/index.php/gskku/article/view/47160

Climate Change Management and Coordination Division, 2022. *Long-term low greenhouse gas emission development strategy*. Ministry of Natural Resources and Environment. Available at: https://unfccc.int/sites/default/files/resource/Thailand%20LTLEDS%20%28Revised%20Version%29_08Nov2022.pdf (Accessed: 10 June 2025).

Fikri, E., Firmansyah, Y.W., Afifah, A.S. and Dewi, R.K., 2024. A projection study of gaseous pollutants formed, potential health effects and clinical codification in Piyungan landfill. *Nature Environment and Pollution Technology*, 23(1). [DOI]

Iglina, T., Iglin, P. and Pashchenko, D., 2022. Industrial CO_2 capture by algae: A review and recent advances. *Sustainability*, 14(7), p. 3801. [DOI]

IPCC, 2007. *Climate Change 2007: Mitigation. Contribution of Working Group III to the Fourth Assessment Report of the Intergovernmental Panel on Climate Change*. In: Metz, B., Davidson, O.R., Bosch, P.R., Dave, R. and Meyer, L.A. (eds.). Cambridge: Cambridge University Press.

IPCC, 2019. *2019 Refinement to the 2006 IPCC Guidelines for National Greenhouse Gas Inventories*. Available at: https://www.ipcc.ch/report/2019-refinement-to-the-2006-ipcc-guidelines-for-national-greenhouse-gas-inventories/ (Accessed: 5 April 2025).

Kamaruddin, M.A., Norashiddin, F.A., Hanif, M.H., Shadi, A.M., Yusoff, M.S., Wang, L.K. and Wang, M.H.S., 2022. Characterization and measurement of solid waste. In: Wang, L.K., Wang, M.H.S. and Hung, Y.T. (eds.) *Solid Waste Engineering and Management*. Handbook of Environmental Engineering, Vol. 23. Cham: Springer.

Kaushal, A. and Sharma, M.P., 2016. Methane emission from Panki open dump site of Kanpur, India. *Procedia Environmental Sciences*, 35, pp. 337–347.

Kiddee, P., Naidu, R., Wong, M.H., Hearn, L. and Muller, J.F., 2014. Field investigation of the quality of fresh and aged leachates from selected landfills receiving e-waste in an arid climate. *Waste Management*, 34(11), pp. 2292–2304. [DOI]

Kristanto, G.A., Pratama, M.A. and Rahmawati, D.F., 2020. Estimation of greenhouse gas emissions from solid waste management and wastewater treatment in the Nizam Zachman fishery port, Jakarta, Indonesia. *IOP Conference Series: Earth and Environmental Science*, 423(1), p. 012039. [DOI]

Mavakala, B.K., Le Faucheur, S., Mulaji, C.K., Laffite, A., Devarajan, N., Biey, E.M., Giuliani, G., Otamonga, J.P., Kabatusuila, P., Mpiana, P.T. and Poté, J., 2016. Leachates draining from controlled municipal solid waste landfill: Detailed geochemical characterization and toxicity tests. *Waste Management*, 55, pp. 238–248. [DOI]

Menikpura, N. and Sang-Arun, J., 2013. *User Manual: Estimation Tool for Greenhouse Gas (GHG) Emissions from Municipal Solid Waste (MSW) Management in a Life Cycle Perspective*. Institute for Global Environmental Strategies.

Ministry of Natural Resources and Environment (MONRE). 2022. *Decree No. 08/2022/NĐCP Detailing a Number of Articles of the Law on Environmental Protection 2020*. Hanoi: Government of Vietnam.

Muchangos, L.S. and Tokai, A., 2020. Greenhouse gas emission analysis of upgrading from an open dump to a semi-aerobic landfill in Mozambique – the case of Hulene dumpsite. *Scientific African*, 10, p. e00638. [DOI]

Parvin, F. and Tareq, S.M., 2021. Impact of landfill leachate contamination on surface and groundwater: A review. *Applied Water Science*, 11(6), p. 108. [DOI]

PCD, 2022. *The waste composition study in 2021*. Available at: https://www.pcd.go.th/wp-content/uploads/2022/08/pcdnew-2022-08-09_08-58-28_103322.pdf (Accessed: 10 June 2025).

Piboon, P., Damrongsak, D., Wongsapai, W. and Yodchumpoo, P., 2022. Greenhouse gas emission reduction in refuse-derived fuel production from municipal solid waste. *AIP Conference Proceedings*, 2681(1), pp. 020031-1–020031-7. [DOI]

Rojas-Valencia, M.N. and Nájera-Aguilar, H., 2012. Analysis of the generation of household solid wastes, household hazardous wastes and sustainable alternative handling. *International Journal of Sustainable Society*, 3, pp. 280–299. [DOI]

Sawasdee, V., Hasin, S., Suknunchana, K. and Haosagul, S., 2022. Survey of solid waste in the open dumping area and solid waste management in Kaeng Sian Subdistrict, Mueang District, Kanchanaburi Province. Research report.

TGO, 2023. *T-VER-S-TOOL-02-02: Calculation for emissions from solid waste disposal sites*. Available at: https://tver.tgo.or.th/database/Uploads/Tool/46fd7947-a5cb-424a-8c28-262ac378bc15.pdf (Accessed: 5 April 2025).

UNEP and CCAC, 2021. *Global Methane Assessment: Benefits and Costs of Mitigating Methane Emissions*. Nairobi: United Nations Environment Programme.

UNFCCC, 2016. *The Paris Agreement*. New York: United Nations.

Wisitthammasri, W., Promduang, P. and Chotpantarat, S., 2024. Characterization of microplastics in soil, leachate and groundwater at a municipal landfill in Rayong Province, Thailand. *Journal of Contaminant Hydrology*, 267, p. 104455. [DOI]

Xu, G., Li, Y., Hou, W., Wang, S. and Kong, F., 2021. Effects of substrate type on enhancing pollutant removal performance and reducing greenhouse gas emission in vertical subsurface flow constructed wetland. *Journal of Environmental Management*, 280, p. 111674. [DOI]

Zheng, J., Fan, J., Zhang, F., Guo, J., Yan, S., Zhuang, Q., Cui, N. and Guo, L., 2021. Interactive effects of mulching practice and nitrogen rate on grain yield, water productivity, fertilizer use efficiency and greenhouse gas emissions of rainfed summer maize in northwest China. *Agricultural Water Management*, 248, p. 106778. [DOI]

Nature Environment and Pollution Technology
An International Quarterly Peer-Reviewed Open Access Journal

p-ISSN: 0972-6268 | e-ISSN: 2395-3454 Vol. 25 | No. 4 | Article ID D1920 | 2026

RESEARCH ARTICLE https://doi.org/10.46488/NEPT.2026.v25i04.D1920 OPEN ACCESS

Laboratory Evaluation of Archie's Law in Kaolinite-Rich Landfill Soil Under the Leachate Influence: A Mineralogical Control and Interpretation Limited by Uncertainty

Rizka Rizka[1,2]†, Muhammad Bisri Mustofa[3], Irwan Iskandar[1], Warsa Warsa[1] and Djoko Santoso[1]
[1]Faculty of Mining and Petroleum Engineering, Institut Teknologi Bandung, West Java, 40132, Indonesia
[2]Geophysical Engineering, Institut Teknologi Sumatera, South Lampung, 35365, Indonesia
[3]Geoscience Department, Universitas Indonesia, Jakarta, 10430, Indonesia
†Corresponding author: Rizka; rizkageo@gmail.com

ARTICLE HISTORY

Received: 10-03-2026
Revised: 06-05-2026
Accepted: 18-05-2026

KEYWORDS

Landfill contamination
Archie's law
Kaolinite
Electrical resistivity
Granular-clay transitional system

CITE THIS ARTICLE

Rizka, R., Mustofa, M. B., Iskandar, I., Warsa, W. and Santoso, D., 2026. Laboratory evaluation of Archie's law in kaolinite-rich landfill soil under the influence of leachate: A mineralogical control and interpretation limited by uncertainty, *Nature Environment and Pollution Technology*, 25(4), D1920. https://doi.org/10.46488/NEPT.2026.v25i04.D1920

COPYRIGHT & LICENCE

© 2026 The Authors
Open Access under CC BY 4.0.

PUBLISHED BY
TECHNOSCIENCE PUBLICATIONS

ABSTRACT

Landfill contamination remains a major global environmental challenge, particularly in tropical regions where hydrogeochemical conditions can accelerate subsurface transport processes. However, the reliability of electrical resistivity interpretation in clay-rich and chemically aggressive soils remains highly debated. This laboratory-scale resistivity study evaluated the validity of Archie's law using kaolinite-dominated soil collected from a tropical landfill, the Bakung Landfill in Indonesia, under controlled conditions of no fluid injection (dry condition), saturation with pure water, and saturation with leachate. X-ray diffraction (XRD) analysis indicated that kaolinite was the dominant mineral phase, while scanning electron microscopy (SEM) observations revealed discontinuous clay layers that increased pore tortuosity without forming dominant conductive pathways. Despite significant ionic interference from landfill leachate, laboratory resistivity measurements maintained consistent scaling exponents, producing cementation exponent values ranging from 2.22–2.53 (R^2 = 0.69–0.81). Statistical analysis was conducted using regression confidence intervals, bootstrap resampling with 10,000 iterations, and Monte Carlo uncertainty propagation incorporating realistic laboratory uncertainties (resistivity ±3%; porosity ±2%). The Monte Carlo confidence limits, ranging from 1.80–2.96, indicate stable parameter behavior within the granular–clay transitional system. These findings suggest that kaolinite-rich tropical landfill soils represent a transitional electrical system in which laboratory-calibrated Archie parameters remain statistically stable, thereby strengthening the environmental reliability of resistivity-based landfill risk evaluation.

1. INTRODUCTION

Landfills worldwide are increasingly becoming a significant source of environmental pressure on soil and groundwater, primarily through the production of ion-rich leachate containing dissolved organic compounds and heavy metals. Landfill leachate is a highly complex wastewater containing a wide range of organic and inorganic pollutants that can pose significant environmental risks if not properly managed (Rajesh & Saravanakumar 2025). Subsurface leachate migration can alter the physical and chemical properties of soil, accelerate contaminant transport, and increase the risk of shallow aquifer contamination, particularly when these aquifers serve as water sources for surrounding communities. This risk becomes more critical in tropical regions, where high rainfall intensity and dynamic hydrogeochemical conditions accelerate contaminant mobility within

porous media. Therefore, accurate subsurface monitoring is urgently needed for environmental risk management around landfill areas. In this context, electrical resistivity has been developed as an effective monitoring tool because of its ability to noninvasively detect changes in soil physical properties related to porosity, fluid saturation, and ionic conductivity (Pandey & Shukla 2019, Islam et al. 2024). Thus, electrical resistivity has strong potential as a preliminary diagnostic tool for environmental contamination, although its quantitative interpretation still faces fundamental uncertainties.

The relationship between electrical resistivity and the physical properties of porous media was classically described by Archie's law, which relates bulk resistivity to porosity and the degree of fluid saturation through a power-law relationship (Archie 1942). This model has been widely used in hydrogeology and environmental geophysics to estimate soil parameters such as porosity, volumetric water content, and even permeability (Matsui et al. 2016, Rosli et al. 2020). However, Archie's formulation was developed under the assumption that electrical conduction is dominated by pore fluid, while the mineral matrix is electrically inert. In soils containing clay minerals or experiencing chemical disturbances caused by leachate contamination, this assumption is often not valid because of the contribution of surface conduction and the effects of the electrical double layer on mineral particles (Godio & Chiampo 2023). Consequently, the application of Archie's law to clay-rich soils remains a subject of debate in modern environmental geophysics.

Recent experimental studies have shown that soil resistivity response is simultaneously influenced by porosity, fluid saturation, soil mineralogy, and pore-fluid chemistry. A laboratory study conducted by Ansari et al. (2021) showed that increasing leachate content significantly reduced soil resistivity because of the rise in pore-fluid ionic conductivity. Another study conducted by Jia et al. (2020) demonstrated that complex resistivity analysis could be used to estimate saturation and permeability in soil systems through laboratory experiments. Furthermore, recent mineralogical characterizations indicate that the composition of clay minerals, such as kaolinite, quartz, and accessory minerals, can control resistivity response through changes in microstructure and pore structure tortuosity (Oumla et al. 2022, Ojo et al. 2024). Overall, these studies demonstrate that integrating resistivity measurements with mineralogical analysis is crucial for understanding electrical conduction mechanisms in complex soil systems.

Despite these advances, several critical gaps remain in the literature. Most environmental resistivity studies still focus on field data interpretation without directly linking mineral microstructural control to the petrophysical parameters of Archie's law. Furthermore, only a limited number of studies systematically integrate detailed mineralogical characterization with laboratory resistivity testing under different hydrogeochemical conditions. More importantly, uncertainty quantification of petrophysical parameters using modern statistical approaches such as bootstrapping and Monte Carlo simulation is still rarely applied in soil resistivity studies, even though these methods are essential for producing reliable parameters in environmental risk evaluation (Cuesta-Valero et al. 2022). Therefore, a research framework capable of integrating mineralogy, petrophysics, and uncertainty analysis within a single approach is still needed.

To address this gap, this study conducted an experimental evaluation of Archie's law in kaolinite-dominated landfill soil collected from a tropical environment, namely the Bakung Landfill in Bandar Lampung. Resistivity measurements were conducted at the laboratory scale under three controlled hydrogeochemical conditions: no fluid injection (dry condition), saturation with pure water, and saturation with leachate. These conditions were designed to evaluate the porosity–resistivity and saturation–resistivity relationships in kaolinite-rich soil. Mineralogical analysis using X-ray diffraction (XRD) and microstructural characterization using scanning electron microscopy (SEM) were performed to identify mineralogical controls on electrical conduction mechanisms. The stability of Archie's parameters was then evaluated through deterministic regression combined with bootstrap resampling and Monte Carlo simulation. By integrating petrophysical, mineralogical, and uncertainty quantification approaches within a single laboratory experimental framework, this study provides mineralogically calibrated Archie's parameters for tropical landfill soil and offers a more transparent and risk-based basis for resistivity interpretation in environmental contamination monitoring.

2. MATERIALS AND METHODS

2.1. Materials

2.1.1. Soil

The soil used in this study was collected from the Bakung Landfill in Bandar Lampung. Seven soil samples, namely L1B, L2A, L2B, L3A, L4A, L4B, and L5A, were collected for laboratory analysis. The samples were subsequently dried in a dry-heat oven at 110°C for 24 h to ensure complete drying and the removal of residual fluids. The physicochemical parameters of the soil samples are presented in Table 1.

Table 1: Physicochemical parameters of the soil samples.

Sample ID	pH	Humidity (%)	Temperature (°C)
L1B	6.00	68.00	32.00
L2A	5.50	63.00	33.00
L2B	5.00	71.00	36.00
L3A	5.50	78.00	27.00
L4A	7.00	79.00	30.00
L4B	7.00	77.00	28.00
L5A	7.00	67.00	29.00

2.1.2. Water

The water used in this study consisted of pure water and leachate collected from the Bakung Landfill. These two types of water were used to compare soil saturation conditions under pure water and leachate exposure. The physicochemical parameters measured for both pure water and leachate included temperature, pH, resistance, salinity, hardness, conductivity, and total dissolved solids (TDS), as presented in Table 2.

2.2. Methods

2.2.1. Geoelectrical Resistivity Test

Seven soil samples collected from the Bakung Landfill, Lampung, Indonesia, were used in this study. Each sample was subjected to three treatment conditions: no fluid injection (dry condition), saturation with pure water, and saturation with leachate. Before testing, the soil samples were sieved using a USA Standard test sieve (ASTM E11) and oven-dried at 110°C for 24 h. The prepared samples were then placed into glass cylinders with a height of 10 cm and a diameter of 3.8 cm.

Electrical resistivity measurements for each soil sample were conducted using the four-electrode method with a sample holder consisting of four metal electrodes arranged at nearly equal spacing, following Australian Standard AS 1289.4.4.1-1997 (Pandey & Shukla 2019). The resistivity measurement system consisted of a resistivity meter connected to two multimeters, a 12 V battery, and

Table 2: Water quality parameters of pure water and leachate.

Parameter	Pure water	Leachate
Temperature	25.2°C	25°C
pH	7.1	8.27
Resistance	6008 Ω	86.70 Ω
Salinity	0%	0.6%
Hardness	83.2 ppm	5750 ppm
Conductivity	165.4 μS cm^{-1}	11440 μS cm^{-1}
TDS	109.8 ppm	7640 ppm



Fig. 1: Soil resistivity measurement.

a four-electrode sample holder. The components were interconnected using cables according to positive and negative electrical polarity to measure voltage and current during the testing process. The direct-current (DC) input was connected to the resistivity meter to display voltage and current values throughout the measurements. The use of the four-electrode configuration minimized the influence of contact resistance on the measurement results. The electrodes consisted of C1 and C2 as current electrodes, and P1 and P2 as potential electrodes (Fig. 1).

2.2.2. Initial Soil Resistivity Measurement

Initial soil resistivity measurements were conducted on untreated soil samples. The measurement system consisted of a resistivity meter (microcontroller-based) connected to a sample holder. Soil from each container was divided into three smaller samples and placed into the sample holder for testing. The resistivity of each sample was measured four times, and the average value was subsequently calculated.

2.2.3. Resistivity Measurement Using Saturation with Pure Water and Saturation with Landfill Leachate

This measurement was conducted to evaluate the porosity–resistivity and saturation–resistivity relationships of the soil samples. Resistivity testing is commonly performed under fully saturated conditions. However, dry-condition measurements were also included in this study to support the interpretation of the overall resistivity response. The resulting porosity values ranged from 49.59%–61.98%.

Dry soil was placed into each sample holder with different porosity levels. Resistivity measurements were conducted in two stages. The first measurement was performed under no fluid injection (dry condition), whereas the second measurement was carried out after the injection of pure water and landfill leachate at saturation intervals of 10%, 25%, 40%, 55%, 70%, 85%, and 100% (fully saturated), depending on the porosity of each sample holder. Repeated measurements were conducted over approximately three days until stable resistivity values were obtained.

2.2.4. Porosity Measurement

Porosity refers to the empty space contained within a rock or soil material. Its value is expressed as a percentage (%) and is calculated by dividing the pore volume by the total rock volume. Porosity measurements were conducted using the following equation (Fetter 1994):

$$\phi = \frac{V_{pore}}{V_{bulk}} = \frac{V_{bulk} - V_{solid}}{V_{bulk}} \times 100\% \quad \ldots(1)$$

$$V_{solid} = \frac{m}{\rho} \quad \ldots(2)$$

where V_{pore} is the total pore volume of the rock, V_{bulk} is the total volume of the rock affected by fluid content, V_{solid} is the volume of the solid mineral component in the rock, m is the mass of the rock sample, and ρ is the rock density.

2.2.5. Archie's Law Calculation

The relationship between resistivity, saturation, and porosity in the samples was calculated using Archie's law (1942), as follows:

$$f = \frac{\rho_0}{\rho_w} = aSw^{-n} \quad \ldots(3)$$

where the resistivity of the soil containing water is directly proportional to the resistivity of the groundwater. In this equation, f represents the formation factor, ρ_0 is the resistivity of the soil at 100% saturation, and ρ_w is the resistivity of the saturating fluid.

Archie (1942) further expressed the relationship between porosity and the formation factor using the following equation:

$$f = \frac{a}{\phi^m} \quad \ldots(4)$$

where a and m are experimentally determined constants that vary according to grain size, grain sorting, and rock texture.

By combining Equations (3) and (4), the following Archie resistivity equation is obtained:

$$S_w = \left(\frac{1}{f}\right)^{\frac{1}{n}} \quad \ldots(5)$$

$$Sw^n = \frac{a\rho_w}{\phi^m \rho_0} \quad \ldots(6)$$

$$\rho = a\rho_w \phi^{-m} Sw^{-n} \quad \ldots(7)$$

Where:

ρ_0: soil resistivity when the soil is at maximum saturation (Ω m)

ρ: soil resistivity when the water has a certain saturation or water content (Ω m)

a: turbulence factor

m: cementation exponent

n: saturation exponent

ρ_w: water resistivity (Ω m)

Φ: porosity (%)

S_w: water saturation or water content in the soil (%)

2.2.6. Soil Mineralogy Determination

A scanning electron microscope (SEM) was used to obtain detailed information regarding the soil components from the Bakung Landfill. The analysis aimed to identify the presence of clay minerals within the soil samples. For SEM analysis, 10 g of each sample was crushed to a particle size of <5 µm and observed at magnifications of up to 10000x.

Soil mineralogy was also analyzed using X-ray diffraction (XRD). XRD is a method that utilizes electromagnetic radiation with short wavelengths based on interatomic or crystal lattice spacing. The analysis was conducted to identify the chemical characteristics and dominant mineral types present in the soil samples.

3. RESULTS AND DISCUSSION

3.1. Mineralogical and Microstructural Characterization

X-ray diffraction (XRD) analysis showed that the soil samples collected from the Bakung Landfill were dominated by kaolinite, with minor amounts of quartz and accessory minerals such as cristobalite and muscovite (Fig. 2). No significant expansive clay minerals, such as smectite, were identified. The dominance of kaolinite indicates a non-swelling 1:1 clay mineral system with relatively low cation exchange capacity. The abundance of quartz suggests the presence of a sandy matrix, while muscovite and iron oxides may contribute to local conduction heterogeneity.

Scanning electron microscopy (SEM) observations revealed a heterogeneous microstructure characterized by granular particles coated with soft clay material (Fig. 3). Kaolinite also appeared as discontinuous layers along grain boundaries and within microporous domains. Microporosity was clearly observed, particularly within fine-grained aggregates, indicating increased tortuosity within the pore network.

Mineralogical analysis (Fig. 4) indicates that kaolinite is the dominant mineral component, comprising approximately 35.6% of the sample composition, followed by quartz at 34.5%, muscovite at 14.2%, cristobalite at 3.6%, and smaller proportions of goethite (2.2%), magnesioferrite (2.4%), andesine (2.5%), anorthoclase (2.3%), albite (1.3%), labradorite (1.2%), and hydrotalcite (0.1%). These values were estimated using a semi-quantitative approach based on the intensity of major peaks in the XRD patterns. Prominent

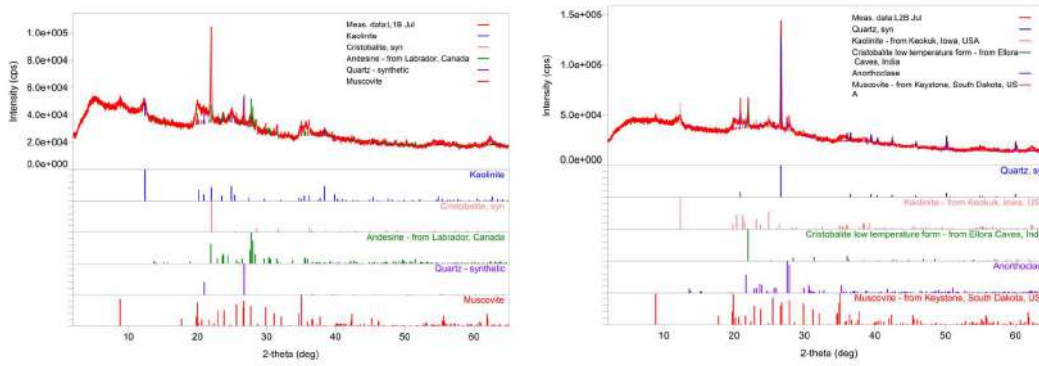


Fig. 2: X-ray diffraction (XRD) results for the samples.

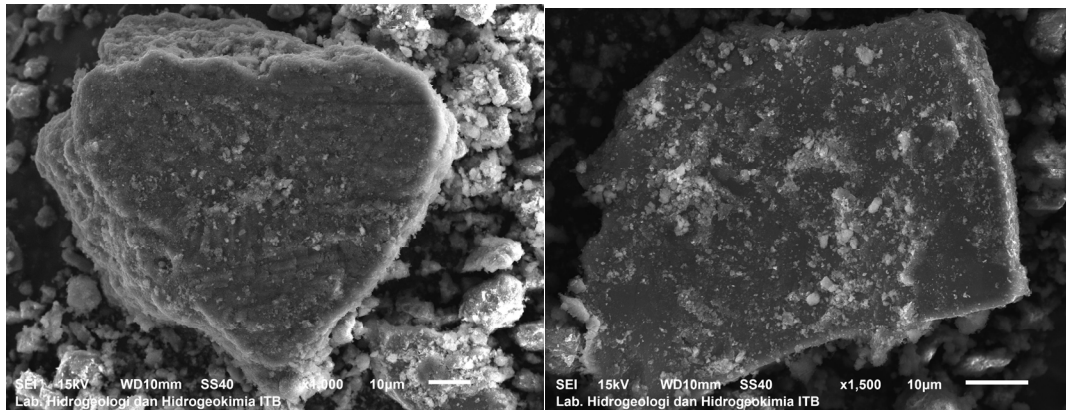


Fig. 3: Scanning electron microscopy (SEM) results for the samples.

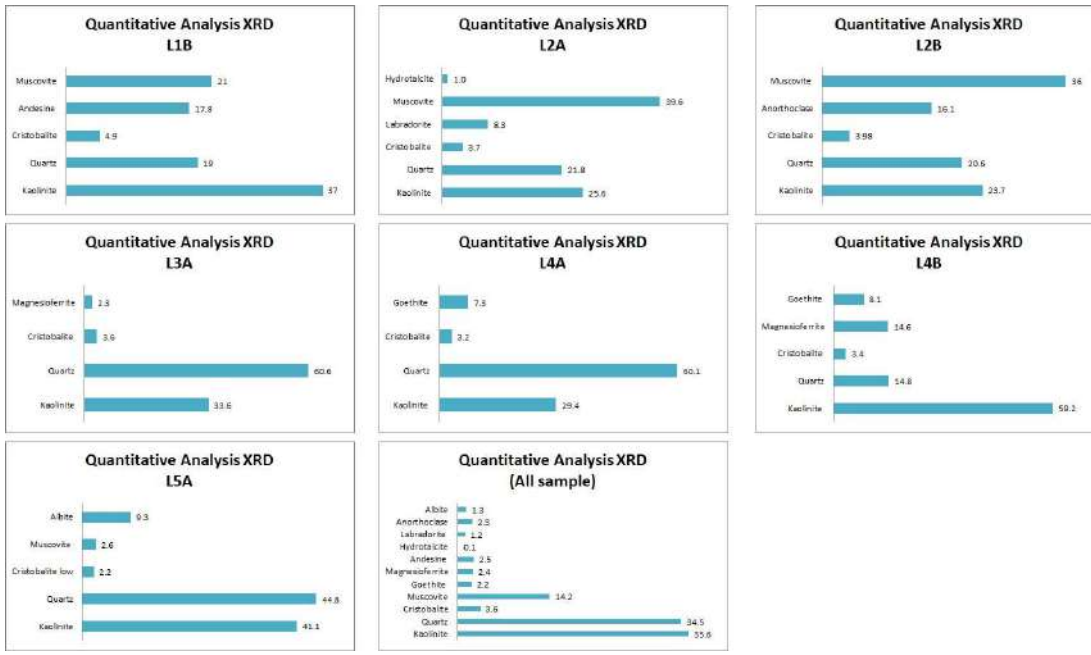


Fig. 4: Quantitative XRD analysis of the samples.

peaks were identified for kaolinite at 12.3° and 24.8° 2θ, while quartz showed a strong peak at approximately 26.6° 2θ.

Scanning electron microscopy observations at the microscale revealed that clay particles were unevenly distributed and frequently formed aggregates. This condition created a complex pore network with tortuous fluid-flow pathways. Such a microstructure directly affects the electrical resistivity response because the presence of kaolinite and the heterogeneous pore geometry tend to increase the cementation exponent (m) by producing more complex electrical conduction pathways. This interpretation corresponds with the resistivity measurements, which produced m values ranging from 2.219–2.534, highlighting the influence of microstructural heterogeneity on the porosity–resistivity relationship. In addition, the presence of relatively inert non-clay minerals such as quartz also affects current distribution, resulting in a resistivity response controlled by both pore-fluid conduction and pore geometry.

However, it should be noted that this mineralogical analysis remains semi-quantitative and does not directly measure surface conduction contributions. Therefore, the interpretation of the relationship between mineralogy and Archie's parameters still requires further validation through additional analyses, such as cation exchange capacity (CEC) measurements or complex resistivity testing.

3.2. Porosity–Resistivity and Saturation–Resistivity Relationships with Uncertainty Evaluation

Laboratory resistivity measurements showed a consistent decrease in resistivity following a power-law relationship with increasing porosity under no fluid injection (dry condition) (Fig. 5), saturation with pure water (Fig. 6), and saturation with leachate (Fig. 7). The laboratory results presented in Fig. 5 show higher resistivity values under dry conditions because of the reduced conductive pathways associated with air-filled pores. The increase in the cementation exponent (m) reflects greater tortuosity and lower connectivity of the conductive pathways. Despite variability in saturation conditions, the power-law relationship remained statistically robust, indicating that structural controls dominated the electrical behavior of the samples. These findings suggest that saturation conditions significantly influence resistivity response in granular–clay transitional systems.

Fig. 6 illustrates that the regression follows a power-law pattern consistent with Archie's formulation, producing cementation exponent (m) values within the expected range for granular to layered clay-based media. The logarithmic trend shows decreasing resistivity with increasing porosity, reflecting enhanced fluid-pore connectivity. The relatively high R^2 values indicate stable pore-fluid-dominated conduction, whereas the minor data scatter may be associated with the microstructural heterogeneity observed in the SEM analysis. This behavior confirms that, in kaolinite-dominated systems saturated with low-ionic fluids, electrical conduction is primarily controlled by the bulk pore-fluid system rather than by surface conduction mechanisms.

Fig. 7 shows that resistivity values decreased because of the higher ionic content of the leachate, resulting in increased bulk conductivity. Although the power-law relationship remained observable, the greater dispersion of the data reflects chemical heterogeneity and local microstructural variability. The cementation exponent (m) remained within physically realistic limits, indicating that Archie's law is still applicable in kaolinite-rich soils despite the influence of leachate.

The porosity–resistivity relationship under no fluid injection (dry condition) (Fig. 5) shows a power-law pattern with cementation exponent (m) values ranging from approximately 2.3–2.5 and coefficients of determination (R^2) between 0.69 and 0.75. Resistivity decreases significantly with increasing porosity, where samples with porosity values of approximately 45–50% exhibit higher resistivity than samples with porosity approaching 60%.

Under saturation with pure water (Fig. 6), the cementation exponent (m) ranges from approximately 2.2–2.4, with R^2 values of approximately 0.75–0.81. The absolute resistivity values are lower than those observed under unsaturated conditions at similar porosity levels. Under saturation with leachate (Fig. 7), resistivity decreases further, with m values ranging from approximately 2.3–2.5 and R^2 values of approximately 0.70–0.78. Although the absolute resistivity values are lower than those under pure water saturation, the porosity–resistivity relationship continues to follow a consistent power-law trend.

The saturation–resistivity relationship under pure water saturation conditions (Fig. 8) shows saturation exponent (n) values ranging from approximately −2.340 to −2.640, with R^2 values of approximately 0.935–0.987. Under leachate-saturated conditions (Fig. 9), resistivity decreases further, with saturation exponent (n) values ranging from approximately −2.686 to −3.580 and R^2 values of approximately 0.798–0.981. Although the absolute resistivity values are lower than those under pure water saturation, the saturation–resistivity relationship continues to follow a consistent trend.

Bootstrap resampling (10,000 iterations) shows that the estimated cementation exponent (m) is statistically stable (Fig. 10). The bootstrap distributions of the cementation exponent under unsaturated, pure water-saturated, and leachate-saturated conditions exhibit unimodal patterns that

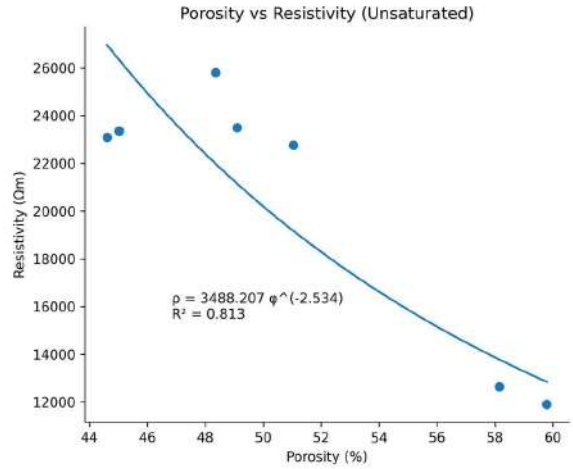


Fig. 5: Laboratory-derived relationship between porosity (%) and bulk resistivity (Ω m) under no fluid injection (dry condition).

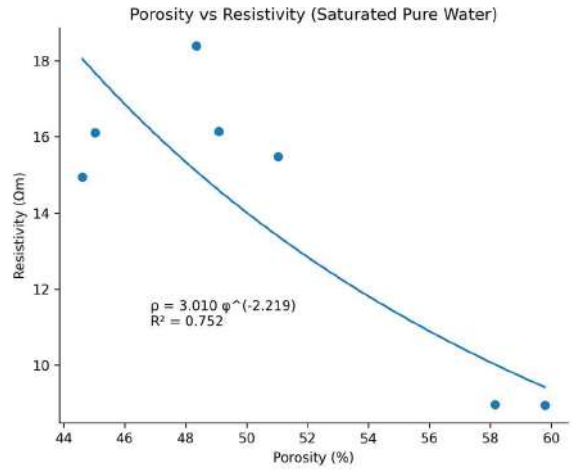


Fig. 6: Laboratory-derived relationship between porosity (%) and bulk resistivity (Ω m) under saturation with pure water.

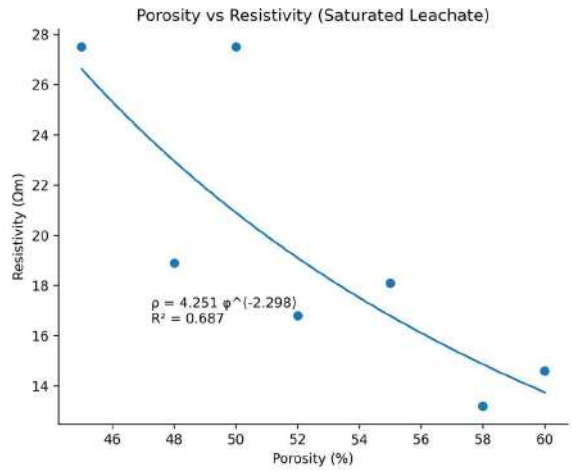


Fig. 7: Laboratory-derived relationship between porosity (%) and bulk resistivity (Ω m) under saturation with leachate.

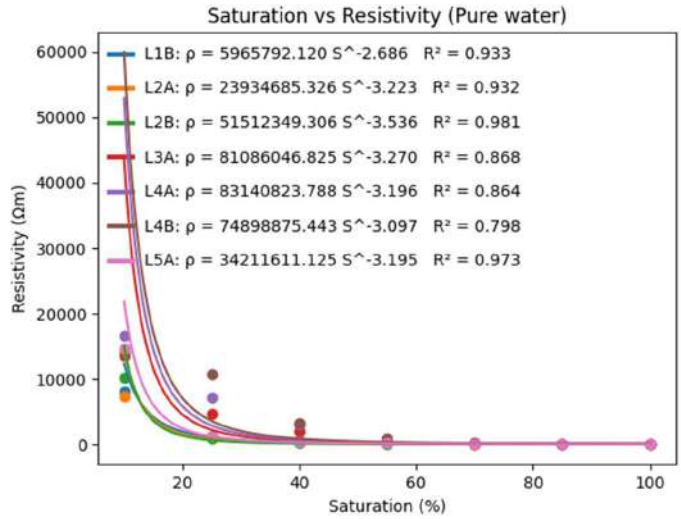


Fig. 8: Laboratory-derived relationship between saturation (%) and bulk resistivity (Ω m) under saturation with pure water.

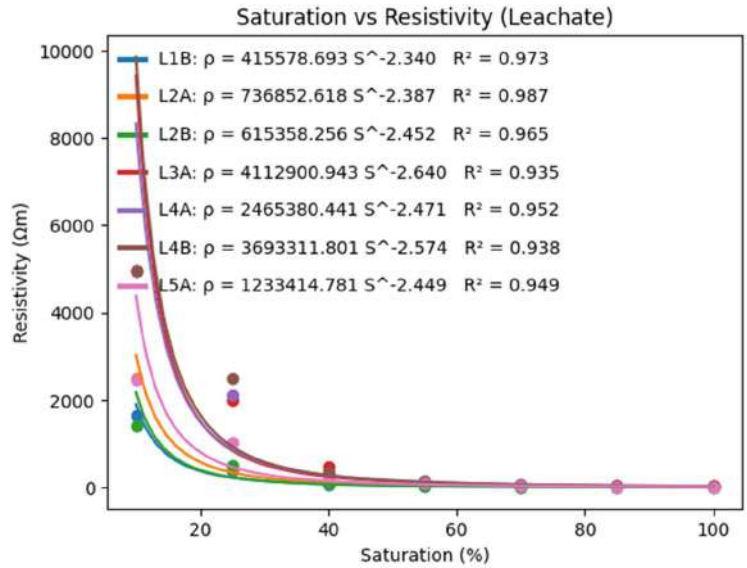


Fig. 9: Laboratory-derived relationship between saturation (%) and bulk resistivity (Ω m) under saturation with leachate.

are approximately normally distributed. The mean bootstrap values for each condition are close to those obtained from deterministic regression. The 95% confidence intervals (CIs), calculated from the 2.5th and 97.5th percentiles, indicate a limited range of parameter variation and do not produce extreme values beyond physically reasonable limits.

Monte Carlo simulation conducted with uncertainty propagation (±2% porosity and ±3% resistivity) produced narrower parameter distributions than the bootstrap analysis. The mean values obtained from the Monte Carlo simulation were consistent with the initial regression results, while the 95% confidence intervals (CIs) indicated relatively small ranges of variation under the three saturation conditions. Overall, both the bootstrap and Monte Carlo methods produced stable parameter estimates for all tested conditions (Fig. 11). The values of m, n, R^2, confidence intervals, bootstrap results, and Monte Carlo results are presented in Table 3.

3.3. Resistivity as a Representation of Soil Physical Properties

The laboratory results indicate that the electrical resistivity of kaolinite-rich soil from the Bakung Landfill has a systematic relationship with porosity and degree of saturation. These

Table 3: Comparison of m, n, R^2, confidence intervals, bootstrap results, and Monte Carlo results.

Condition	m	n	m R^2	m 95% CI low	m 95% CI high	m Bootstrap 2.5%	m Bootstrap 97.5%	m Monte Carlo 2.5%	m Monte Carlo 97.5%
Pure Water	2.219	−2.473	0.752	0.754	3.683	−0.552	3.610	1.801	2.618
Leachate	2.298	−3.194	0.687	0.517	4.079	1.127	3.790	1.806	2.753
Unsaturated	2.534	–	0.813	1.135	3.933	−0.243	3.832	2.080	2.964

findings are consistent with previous studies showing that resistivity can be used indirectly to estimate soil physical parameters such as porosity, bulk density, and volumetric water content (Al-Qaysi & Sadrekarimi 2015, Rosli et al. 2020). This correlation is generally explained by Archie's formulation, in which resistivity increases as porosity and saturation decrease because of the reduced continuity of fluid-conduction pathways (Mustofa et al. 2022).

The relationship between resistivity and soil particle size has also been reported in soil-site investigation studies by Chik and Islam (2012), who showed that grain-size distribution and soil texture influence flow-path geometry and electrical resistance. In the context of the Bakung Landfill, the dominance of kaolinite identified through XRD analysis and the plate-like microstructure observed in the SEM images indicate increased tortuosity without forming a continuous conductive matrix. This interpretation is consistent with the findings of Oh & Park (2000), who emphasized that mineralogy and pore-water chemistry jointly control the resistivity response in saturated soils.

3.4. The Role of Kaolinite in Conduction Mechanisms

Based on the XRD and SEM analyses, the soil samples were confirmed to contain clay minerals dominated by kaolinite. Clay minerals generally form through the chemical weathering of silicate minerals involving reactions with carbonic acid, resulting in silicate hydration processes. The presence of silicate-derived clay minerals may contribute to retardation processes within the soil system. In landfill environments, clay minerals can also function as natural damping or buffering materials against leachate migration.

Kaolinite generally exhibits lower surface conductivity than expansive clay minerals. A study on the behavior of kaolinite as a landfill barrier material by Cuevas et al. (2009) indicated that non-expansive clay minerals tend to maintain pore-fluid-dominated conduction rather than surface conduction. Similar findings were reported by Oumla et al. (2022) and Ojo et al. (2024), who emphasized the importance of mineralogical and physicochemical characteristics in controlling the electrical response of clay-rich materials.

The cementation exponent (m) values obtained in this study fall within a transitional range, indicating increased tortuosity caused by kaolinite particle coatings without

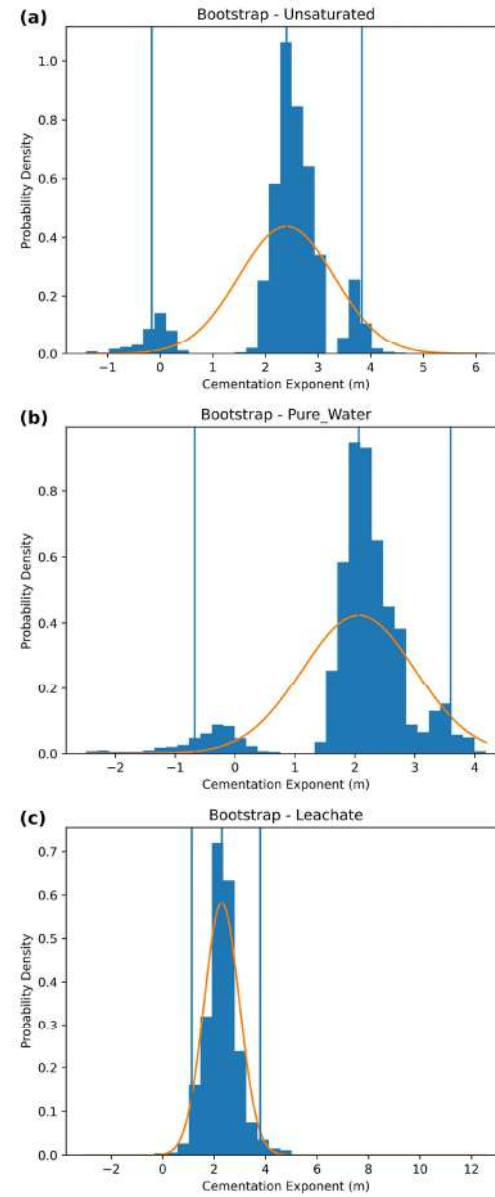


Fig. 10: Bootstrap distribution of the cementation exponent (m) under (a) no fluid injection (dry condition), (b) saturation with pure water, and (c) saturation with leachate.

suggesting dominant surface conduction. This interpretation is consistent with the conceptual approaches proposed

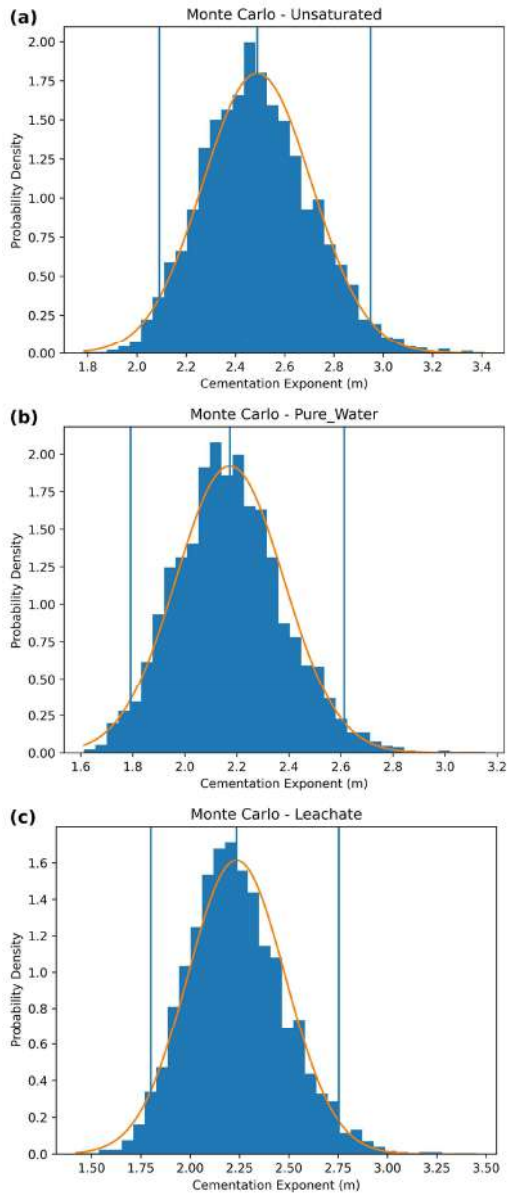


Fig. 11: Monte Carlo-derived uncertainty distribution of the cementation exponent (m) under (a) no fluid injection (dry condition), (b) saturation with pure water, and (c) saturation with leachate.

by Matsui et al. (2016) and Sawayama et al. (2023), who related resistivity behavior to tortuosity and percolation flow pathways. Therefore, these results suggest that electrical conduction in the Bakung Landfill soil is still primarily controlled by pore-fluid pathways despite the influence of clay minerals.

3.5. The Effect of Leachate on Resistivity Response

Saturation with leachate resulted in lower absolute resistivity values compared with pure water saturation, but it did not produce drastic changes in the saturation exponent values. This phenomenon is consistent with laboratory studies showing that increased salinity enhances pore-fluid conductivity without fundamentally altering pore-structure geometry (Oh & Park 2000, Ansari et al. 2021).

A study by Carpenter et al. (2009) on formation factors under leachate and waste saturation conditions also showed that, despite the decrease in total resistivity, the porosity–resistivity relationship could still be explained using Archie's approach with appropriate calibration. Wang et al. (2020) further reported that microstructural changes caused by leachate exposure may affect soil permeability and structural properties; however, these effects are more strongly associated with changes in absolute resistivity values than with fundamental changes in power-law scaling behavior.

In an environmental context, these findings are important because they indicate that a decrease in resistivity caused by leachate does not automatically imply increased contaminant migration. Instead, the resistivity response should be interpreted together with porosity and saturation parameters to obtain a more reliable understanding of subsurface contamination conditions.

3.6. Sensitivity Analysis and Mineralogical Implications

The sensitivity analysis indicates that uncertainty in the petrophysical parameters of the kaolinite-rich soil from the Bakung Landfill is more strongly influenced by pore-structure heterogeneity than by laboratory measurement error. The wider bootstrap distribution compared with the Monte Carlo distribution confirms that microstructural variability, rather than instrumental noise, is the primary source of uncertainty. This type of uncertainty quantification approach has been recommended in recent geoscience literature to produce defensible parameters for environmental applications (Cuesta-Valero et al. 2022).

Mineralogically, the dominance of kaolinite places this system within a transitional conduction regime. Particle coating by kaolinite increases tortuosity and slightly modifies the cementation exponent (m), but it does not produce dominant surface-conductive pathways. Recent studies have shown that kaolinite, compared with expansive clay minerals, tends to maintain pore-fluid-dominated conduction under moderate salinity conditions (Emelianov et al. 2024).

The increase in salinity caused by leachate significantly reduces absolute resistivity values but does not drastically alter the scaling exponent, indicating that pore geometry remains the primary controlling factor. This finding is consistent with recent experimental studies showing that changes in fluid chemistry mainly influence resistivity

magnitude rather than the fundamental structure of the pore network (Gabr et al. 2024).

3.7. Limitations and Implications

The limited number of samples (n = 7) imposes substantial constraints on the reliability of the Archie parameters, particularly the cementation exponent (m) and saturation exponent (n), which are commonly derived from log–log regression relationships between formation factor and saturation. Although bootstrap resampling and Monte Carlo simulation were applied to evaluate parameter variability, these approaches do not eliminate the limitations associated with the underlying data structure. As a result, they may produce statistical confidence that appears stronger than the actual representativeness of the experimental dataset.

In clay-rich soils such as the kaolinite-dominated landfill soil examined in this study, small variations in pore structure, surface conduction behavior, and pore-fluid composition can significantly influence bulk electrical resistivity and affect the fitting of Archie parameters. Therefore, the reported uncertainty ranges should be interpreted as indicators of parameter sensitivity within the experimental dataset rather than as universally applicable values.

To address this limitation, the study presents explicit parameter results for each condition, including m, n, R^2, and confidence intervals. Nevertheless, further investigations involving larger datasets and more diverse environmental conditions are still required to verify the broader applicability of the observed relationships.

Environmentally, the results have three main implications, as follows:

a. Electrical resistivity is a valid monitoring tool for kaolinite-rich landfill soils, provided that local laboratory calibration is performed.

b. Resistivity interpretation must consider leachate chemistry rather than relying solely on absolute resistivity values.

c. Uncertainty analysis using bootstrap and Monte Carlo approaches is important for environmental risk-based decision-making because it provides confidence limits for petrophysical parameters used in inversion modeling and contaminant migration estimation.

Thus, the kaolinite-rich soil at the Bakung Landfill can be categorized as a transitional electrical system in which Archie's law remains applicable within the tested range of leachate chemistry, while the statistical approach provides a more defensible basis for environmental monitoring interpretation.

4. CONCLUSIONS

This study demonstrates that kaolinite-dominated tropical landfill soil from the Bakung Landfill preserves the porosity–resistivity and saturation–resistivity power-law relationships consistent with Archie's law, even under the influence of realistic leachate chemistry. The cementation exponent (m) and saturation exponent (n) fall within the transitional granular–clay system range and show strong statistical stability based on bootstrap and Monte Carlo analyses. The decrease in resistivity induced by leachate is primarily controlled by the increase in pore-fluid conductivity rather than by fundamental changes in soil microstructure.

XRD and SEM characterizations indicate that kaolinite increases tortuosity without forming dominant surface-conductive pathways, which helps explain the relative microstructural stability of the Archie parameters. The uncertainty analysis further suggests that parameter variability is more strongly influenced by sample heterogeneity than by instrumental error, while all confidence intervals remain within physically realistic limits.

The limitations of this study include the laboratory-scale experimental design, the limited number of samples, and the restricted range of leachate chemistry conditions, which did not include extreme salinity environments. Therefore, further field validation and multi-salinity experiments are recommended to identify the transition threshold of surface conduction behavior.

Strategically, this study strengthens the scientific basis for the application of resistivity as an environmental monitoring tool in kaolinite-rich tropical landfill soils. By providing mineralogically calibrated Archie parameters together with quantified uncertainty estimates, this study supports a transition from descriptive resistivity interpretation toward a more transparent, quantitative, and risk-based evaluation framework for groundwater protection and sustainable remediation planning.

5. ACKNOWLEDGEMENT

We acknowledge the support provided by Institut Teknologi Sumatera. We also thank the assistants of the Geophysics Laboratory at Universitas Indonesia and the Hydrogeology and Hydrogeochemical Laboratory at Institut Teknologi Bandung for providing laboratory facilities and analytical support.

6. REFERENCES

Al-Qaysi, Z. and Sadrekarimi, A., 2015. Determination of the porosity of granular soils using electrical resistivity measurements, *Canadian Journal of Exploration Geophysics*, pp. 7–11. Available at: https://cseg.ca/wp-content/uploads/2015-06-CJEG-Determination_of_the_Porosity_of_Granular_Soils.pdf.

Ansari, S. M., Norooz, R., Zeynolabedin, A., Foadi, H. and Ghiassi, R., 2021. Experimental investigation of correlations between electrical resistivity, moisture content and voltage values for leachate contaminated clayey sand, *Journal of Applied Geophysics*, 193(June), p. 104391. [DOI]

Archie, G. E., 1942. The electrical resistivity log as an aid in determining some reservoir characteristics, *Trans*, 146, pp. 119–128. Available at: https://personal.ems.psu.edu/~radovic/EME590_Archie_1942.pdf.

Carpenter, P. J., Ding, A. and Cheng, L., 2009. Apparent formation factor for leachate-saturated waste and sediments: Examples from the USA and China, *Journal of Earth Science*, 20(3), pp. 606–617. [DOI]

Chik, Z. and Islam, S. M. T., 2012. Finding soil particle size through electrical resistivity in soil site investigations, *Electronic Journal of Geotechnical Engineering*, 17, pp. 1866–1876. Available at: https://www.researchgate.net/publication/266347019_Finding_Soil_Particle_Size_through_Electrical_Resistivity_in_Soil_Site_Investigations.

Cuesta-Valero, F. J., Beltrami, H., Gruber, S., García-García, A. and González-Rouco, J. F., 2022. A new bootstrap technique to quantify uncertainty in estimates of ground surface temperature and ground heat flux histories from geothermal data, *Geoscientific Model Development*, 15(20), pp. 7913–7932. [DOI]

Cuevas, J., De La Fuente, M. J., Bernabé, S., Fernández-Caliani, C. and Martín, M. A., 2009. Behavior of kaolinite and illite-based clays as landfill barriers, *Applied Clay Science*, 42(3–4), pp. 497–509. [DOI]

Emelianov, V., Zhang, Z., Weller, A., Halisch, M. and Titov, K., 2024. Surface conductivity of clays, *Geophysical Journal International*, 238, pp. 1013–1026. [DOI]

Fetter, C. W., 1994. *Applied Hydrogeology*. 4th ed. New Jersey: Prentice-Hall. Available at: https://books.google.co.id/books/about/Applied_Hydrogeology.html?id=BYZXDwAAQBAJ&redir_esc=y.

Gabr, M., Alhajeri, N., Al Jabri, S. and Al-Fadhli, F., 2024. Prospective and challenges of sustainable water resources for irrigation in Kuwait, *International Water Technology Journal*, 11(1), pp. 20–33. [DOI]

Godio, A. and Chiampo, F., 2023. Geophysical monitoring of leachate injection in pretreated waste landfill, *Applied Sciences*, 13(9). [DOI]

Islam, S., Bano, H., Malik, A. A. and Alotaibi, F., 2024. Landfill leachate: An invisible threat to soil quality of temperate Himalayas, *PLoS ONE*, 19(11), pp. 1–12. [DOI]

Jia, J., Liu, Y. and Zhang, J., 2020. Estimation of permeability and saturation based on imaginary component of complex resistivity spectra: A laboratory study, *Open Geosciences*, 12(1), pp. 299–306. [DOI]

Matsui, T., Park, S. G., Shin, S. W., Lee, D. K., Kim, C. R. and Son, J., 2016. Relationship between electrical resistivity and physical properties of rocks, in 22nd European Meeting of Environmental and Engineering Geophysics, Near Surface Geoscience 2016, pp. 1–6. [DOI]

Mustofa, M. B., Fauzi, U., Latief, F. D. E. and Ryansyah, 2022. Experimental and modeling of electrical resistivity changes due to micro-spatial distribution of fluid for unconsolidated sand, *Journal of Petroleum Science and Engineering*, 208, p. 109472. [DOI]

Oh, M. H. and Park, J. B., 2000. Laboratory tests for the development of contaminant leakage detection system in soil, ISRM International Symposium 2000, IS 2000. Available at: https://onepetro.org/ISRMIS/proceedings-abstract/IS00/IS00/ISRM-IS-2000-111/50717?redirectedFrom=PDF.

Ojo, O. J., Adepoju, S. and Omoyajowo, B. T., 2024. Physicochemical and mineralogical composition studies of clays from Share and Tshonga areas, Northern Bida Basin, Nigeria: Implications for geophagia, *Open Geosciences*, 16(1), pp. 1–12. [DOI]

Oumla, K. O., Ntouala, R. F. D., Ekodeck, G. E. and Djakba, M. A., 2022. Physicochemical and mineralogical characterization of clay materials in the Douala Coastal Sedimentary Sub-basin (Cameroon, Central Africa), *Journal of Geosciences and Geomatics*, 10(3), pp. 126–128. [DOI]

Pandey, L. M. S. and Shukla, S. K., 2019. Detection of leachate contamination in Perth landfill base soil using electrical resistivity technique, *International Journal of Geotechnical Engineering*, 13(3), pp. 249–260. [DOI]

Rajesh, R. P. and Saravanakumar, M. P., 2025. A review on electrooxidation treatment of leachate: Strategies, new developments, and prospective growth, *Nature Environment and Pollution Technology*, 24(1). [DOI]

Rosli, N., Ismail, N. A., Saad, R. and Rahman, N., 2020. A new approach in calculating porosity of shallow unconsolidated soil based on Archie's law, *Journal of Earth System Science*, 129(1). [DOI]

Sawayama, K., Ishibashi, T., Jiang, F. and Tsuji, T., 2023. Relationship between permeability and resistivity of sheared rock fractures: The role of tortuosity and flow path percolation, *Geophysical Research Letters*, 50(20), pp. 1–12. [DOI]

Wang, C., Lu, C., Jiang, Z. and Chen, Y., 2020. Experimental study on the permeability and microstructure of remoulded silty clay corroded by landfill leachate, *Nature Environment and Pollution Technology*, 19(3), pp. 1241–1248. [DOI]

Nature Environment and Pollution Technology
An International Quarterly Peer-Reviewed Open Access Journal

p-ISSN: 0972-6268 | e-ISSN: 2395-3454 Vol. 25 | No. 4 | Article ID D1922 | 2026

RESEARCH ARTICLE https://doi.org/10.46488/NEPT.2026.v25i04.D1922 OPEN ACCESS

Hydrodynamic Enhancement of Direct Contact Membrane Distillation Using a Corrugated Feed Channel: A Numerical Study

Fajer M. Alelaj[1]†, Mansour Ahmed[1], Hussain Al-Sairfi[1], Garudachari Bhadrachari[1], Shimaa Zahran[2] and Mohamed R. Elmarghany[2,3]

[1]Department of Water Research Center, Kuwait Institute for Scientific Research (KISR), Kuwait
[2]Mechanical Power Engineering Department, Faculty of Engineering, Mansoura University, Egypt
[3]Research and Development Department, SHARQAWI air distribution systems factory, Jeddah, Saudi Arabia
†Corresponding author: Fajer M. Alelaj; Dr.Fajer.Alelaj@gmail.com

ARTICLE HISTORY

Received: 04-03-2026
Revised: 02-05-2026
Accepted: 03-05-2026

KEYWORDS

Direct contact membrane distillation
Hydrodynamic enhancement
Permeate flux
Rib geometry

CITE THIS ARTICLE

Alelaj, F. M., Ahmed, M., Al-Sairfi, H., Bhadrachari, G., Zahran, S. and El-marghany, M. R., 2026. Hydrodynamic enhancement of direct contact membrane distillation using a corrugated feed channel: A numerical study. *Nature Environment and Pollution Technology*, 25(4), D1922. https://doi.org/10.46488/NEPT.2026.v25i04.D1922

COPYRIGHT & LICENCE

© 2026 The Authors
Open Access under CC BY 4.0.

PUBLISHED BY

TECHNOSCIENCE PUBLICATIONS

ABSTRACT

A numerical simulation of a direct contact membrane distillation (DCMD) cell with rectangular corrugations placed in the feed channel was conducted to investigate the influence of corrugated feed-channel geometry on hydrodynamic behavior and permeate flux in DCMD systems. The coupling of flow and mass transfer in conventional and modified channel geometries was simulated using a two-dimensional steady-state model. The effects of rib height, width, and pitch on pressure drop and permeate flux were systematically investigated. The findings indicated that rib geometry is a critical factor in determining mass-transfer effectiveness and flow patterns. Specifically, increasing the rib height from 1 to 3 mm resulted in a significant reduction in permeate flux, mainly because of increased flow obstruction and the formation of concentration boundary layers. Similarly, permeate flux gradually decreased with increasing rib width. In contrast, increasing the rib pitch from 5 to 15 mm provided a small improvement in flux by reducing excessive flow blockage while maintaining satisfactory mixing. Pressure-drop analysis showed that smaller rib pitches increased hydraulic resistance, indicating a trade-off between enhanced mass transfer and increased flow losses. In general, the best configuration was achieved with a low rib height, intermediate width, and increased pitch, which balanced flux enhancement and minimum pressure loss. The results provide useful insight into the influence of rib geometry on mass-transfer behavior and hydraulic performance in DCMD modules. The study demonstrates that geometric optimization of corrugated channels is necessary to balance flow disturbance and hydraulic resistance in DCMD systems.

1. INTRODUCTION

Freshwater scarcity has become an increasingly important challenge, especially in the Gulf region, where population growth, industrialization, and climate change combine to intensify the problem (Sherif et al. 2023, Salman et al. 2025). Consequently, desalination technologies have become necessary for securing a sustainable water supply, particularly in arid and semiarid regions (Almasoudi & Jamoussi 2024, Al-Sairfi et al. 2026). Membrane distillation (MD) is an effective thermally driven separation process that operates at relatively low temperatures, can use low-grade and renewable heat, and provides high salt rejection (Soumbati et al. 2025, Drioli et al. 2015).

A microporous hydrophobic membrane separates a hot saline feed from a chilled permeate, allowing only water vapor to pass through the pore network

(Nthunya & Mamba 2025). Vapor transport is driven by the vapor-pressure difference created by the temperature difference across the membrane. Despite its advantages, the commercial application of MD remains limited because of relatively low permeate flux and thermal efficiency compared with conventional desalination methods (Gobran et al. 2025, Zaragoza et al. 2018). These limitations can mainly be attributed to temperature and concentration polarization and heat losses in the membrane module (Suleman et al. 2021).

Among the MD configurations, direct contact membrane distillation (DCMD) has been widely studied because of its simplicity and ease of implementation (Sheikh et al. 2025, Qasim et al. 2021). In DCMD, hot saline feed and cold permeate streams contact opposite membrane surfaces, and the resulting temperature gradient creates a vapor-pressure difference across the membrane. DCMD has lower mass-transfer resistance and greater vapor flux than air-gap, vacuum, and sweeping-gas MD configurations (Francis et al. 2022, Boubakri et al. 2017). However, its thermal performance is limited by substantial conductive heat losses across the membrane and temperature polarization, which reduce the driving force for vapor transport (Jing et al. 2025). Therefore, optimization of DCMD cell design is essential to improve performance and support larger-scale deployment (Cancilla et al. 2026).

Previous membrane distillation research has focused largely on materials and operational optimization to enhance performance (Farid et al. 2024, Xu et al. 2022). The fabrication of hydrophobic polymer membranes, surface functionalization, and pore-structure engineering have produced significant gains in vapor flux and wetting resistance. Numerous experimental and numerical studies have also examined the effects of operating parameters, including feed temperature, salinity, flow velocity, and membrane thickness, on heat and mass transfer in DCMD systems (Hu et al. 2025, Lou et al. 2019). These studies have consistently identified temperature polarization and conductive heat losses across the membrane as major constraints on overall productivity and thermal efficiency. Researchers have used turbulence promoters, spacers, and corrugated flow channels to alleviate these effects and increase convective heat transfer while decreasing boundary-layer thickness (Taamneh & Bataineh 2017, Swaidan et al. 2024).

The current study investigates the influence of corrugated feed-channel geometry on the hydrodynamic and mass-transfer behavior of a DCMD system under different geometric conditions. A numerical model is developed to examine heat and mass transport in the redesigned cell and evaluate the effects on vapor flux, the temperature polarization coefficient, and overall thermal efficiency. The behavior of the modified design is systematically compared with that of a conventional membrane cell under the same conditions. Parametric simulations assess the effects of feed temperature, salinity, flow velocity, and membrane parameters on system performance.

The remainder of the paper is organized as follows: Section 2 presents the mathematical model; Section 3 describes the mesh dependency test; Section 4 presents and discusses the effects of rib height, rib width, and rib pitch on the hydrodynamic characteristics; and Section 5 summarizes the key findings and conclusions.

2. MATHEMATICAL MODEL

2.1. Physical Description

To investigate mass transfer in conventional and modified membrane cells, a two-dimensional, steady-state model of DCMD was formulated. The computational domain was divided into three regions: the hot saline feed channel, the hydrophobic microporous membrane, and the cold permeate channel. The hydrophobic membrane separates the two fluid streams, allowing vapor to pass while preventing liquid penetration.

The standard flat-plate DCMD cell was modified by adding a corrugated feed channel to increase productivity and reduce salt concentration and temperature polarization. The corrugations were rectangular and positioned at fixed locations on the feed-channel wall near the membrane surface, creating a structured flow channel that promotes flow disturbance and disrupts the boundary layer. Corrugation geometry was characterized by height, width, and pitch, and these parameters were systematically varied to determine their effects on hydrodynamic performance (Sherif et al. 2023). In addition, the overall feed-channel height was used as a design parameter to examine its effects on temperature polarization and vapor flux (Elhenawy et al. 2020, Darman et al. 2023). This parametric design methodology allows a thorough evaluation of how structural changes at the cell level influence membrane distillation performance and provides useful guidance for improving DCMD module design.

The schematic of the proposed DCMD cell shown in Fig. 1 includes the hot feed channel, hydrophobic membrane, and cold permeate channel. The modified design has rectangular corrugations with different widths, heights, and pitches on the feed-channel wall near the membrane. The selected rib dimensions were based on practical manufacturability constraints and previous corrugated-channel studies reported in the literature. Excessively

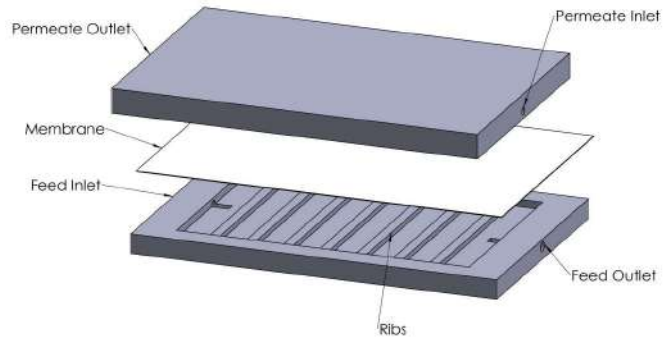


Fig. 1: Schematic diagram of the proposed cell.

large ribs may cause severe channel blockage and unstable flow behavior, whereas very small ribs produce negligible hydrodynamic disturbance.

The computational calculations were conducted at an inlet velocity of 0.01 m s^{-1}, with the feed and permeate inlet temperatures held at 343 K and 293 K, respectively. The geometric characteristics of the ribs were systematically varied to evaluate their influence on thermal and flow behavior, with rib heights ranging from 1–3 mm, rib widths from 2–4 mm, and rib pitches (spacing between successive ribs) from 5–15 mm.

2.2. Governing Equations

The transport phenomena in the feed and permeate channels are described by the steady-state incompressible Navier–Stokes, energy, and species conservation equations (Qtaishat et al. 2008).

Continuity

$$\nabla \cdot \mathbf{u} = 0 \quad ...(1)$$

Momentum

$$\rho(\mathbf{u} \cdot \nabla)\mathbf{u} = -\nabla p + \mu \nabla^2 \mathbf{u} \quad ...(2)$$

Energy

$$\rho c_p(\mathbf{u} \cdot \nabla)T = k\nabla^2 T \quad ...(3)$$

2.3. Vapor Transport Through the Membrane

The vapor flux across the membrane is governed by the vapor-pressure difference across the membrane surfaces, which can be represented as follows:

$$J = C_m\left(P_{v,f} - P_{v,p}\right) \quad ...(4)$$

$C_m P_{v,f}, P_{v,p}$ where C_m is the membrane mass-transfer coefficient and $P_{v,f}, P_{v,p}$ are the vapor pressures at the feed and permeate membrane surfaces, which can be calculated using the Antoine equation (Lee 2025).

The membrane mass transfer coefficient is expressed as:

$$C_m = \left(\frac{1}{C_K} + \frac{1}{C_M}\right)^{-1} \quad ...(5)$$

Where C_K and C_M are the Knudsen and molecular diffusion coefficients.

In this study, the numerical model was established based on several simplifying assumptions. The flow was assumed to be steady-state, two-dimensional, laminar, and incompressible, with constant thermophysical properties throughout the domain. Membrane wetting was neglected, and complete salt rejection was assumed. Moreover, water vapor within the membrane pores was assumed to obey the ideal gas law, and local thermal equilibrium was maintained at the membrane interfaces.

2.4. Boundary Conditions and Numerical Procedure

At the feed-channel inlet, a uniform velocity profile of 0.01 m s^{-1} and a temperature of 343 K were imposed. The permeate inlet temperature was fixed at 293 K. Atmospheric-pressure boundary conditions were applied at both outlet boundaries. No-slip velocity conditions were imposed at all solid walls. The membrane was considered hydrophobic and nonwetted, with complete salt rejection. Heat transfer through the membrane included both conductive and latent heat-transport mechanisms. The membrane surfaces were thermally coupled with the adjacent fluid domains. The governing equations were solved using the finite volume method in ANSYS Fluent. Pressure-velocity coupling was achieved using the SIMPLE algorithm. Second-order upwind discretization schemes were applied to the momentum and energy equations to improve numerical accuracy. The convergence criterion for all governing equations was set to 10^{-6} for the continuity, momentum, and energy residuals. Simulations continued until stable values of permeate flux and temperature distribution were achieved. Table 1 presents the membrane and operating parameters.

Table 1: Membrane and operating parameters.

Parameter	Value
Membrane thickness	0.12 mm
Membrane porosity	0.75
Membrane tortuosity	2.0833
Mean pore size	0.22 μm
Feed inlet temperature	343 K
Permeate inlet temperature	293 K
Feed velocity	0.01 m s^{-1}
Membrane material	PVDF

3. MESH DEPENDENCY TEST

A mesh dependency test was performed in ANSYS by progressively increasing the number of elements until a quantitative convergence criterion was achieved. A finer mesh was used at the corners to improve boundary-layer resolution and accurately capture the steep temperature and velocity gradients. The relative errors of key output parameters, including permeate flux and temperature distribution, were evaluated between successive mesh refinements, and the final mesh was selected when the relative error dropped below 1% at 38,945 elements. Fig. 2(a) shows the computational domain and mesh, and Fig. 2(b) shows the variation in relative error with increasing number of elements.

The final computational mesh was selected after the relative error fell below 1%, thereby minimizing numerical uncertainty in the predicted permeate-flux results.

3.1. Model Validation

To validate the developed numerical model, the predicted permeate flux values were compared with previously published numerical and experimental DCMD studies. The comparison was conducted under similar operating conditions, including feed and permeate temperatures, membrane characteristics, and flow configuration. Table 2 presents a comparison between the present numerical model and the published results reported by Qtaishat et al. (2008) and Lou et al. (2019). The comparison shows good agreement between the current simulation and the literature data, with deviations within an acceptable range for CFD-based DCMD investigations. This supports the capability of the present model to predict the coupled heat- and mass-transfer behavior in direct contact membrane distillation systems.

Table 2: Validation of the present numerical model with published literature.

Study	Method	Permeate Flux (kg m^{-2} h^{-1})
Qtaishat et al. (2008)	Numerical	14.9
Lou et al. (2019)	CFD simulation	15.2
Present study	Numerical simulation	15.4

The maximum deviation between the present model and the literature results was below 4%, indicating satisfactory agreement and supporting the reliability of the numerical methodology used in this study.

4. RESULTS AND DISCUSSION

A parametric study was conducted to determine the effects of rib height, rib width, and rib pitch on the hydrodynamic characteristics and membrane flux of the modified cell. The performance of the corrugated feed-channel configurations was evaluated relative to the conventional flat-channel DCMD configuration under the same operating conditions. All simulations were performed under identical inlet conditions to isolate the influence of geometric parameters on the hydrodynamic and mass-transfer behavior of the DCMD system.

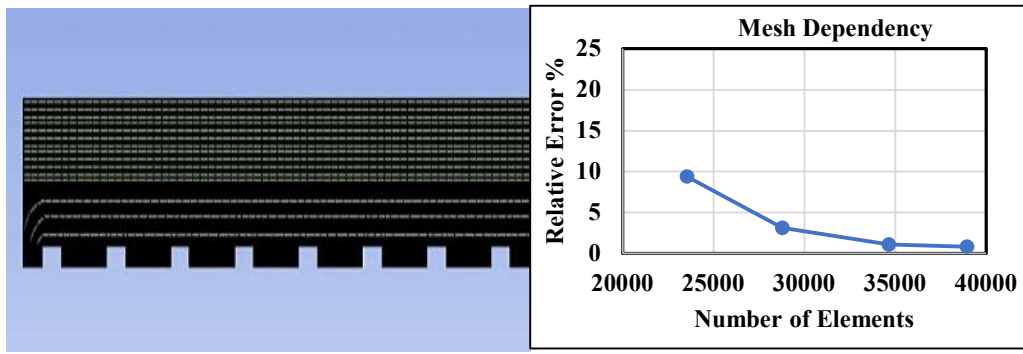


Fig. 2: (a) Computational domain and mesh; (b) variation in relative error with increasing number of elements.

4.1. Effect of Rib Height

The relationship between permeate flux and rib height is shown in Fig. 3, with rib pitch and width kept constant at 15 mm and 4 mm, respectively. The results show a clear pattern: permeate flux decreases as rib height increases. At a rib height of 1 mm, the ribs disturb the flow sufficiently to improve mixing near the membrane surface and mitigate concentration polarization without greatly obstructing the flow. In contrast, increasing rib height increases channel blockage, leading to larger recirculation zones and a smaller effective flow cross-sectional area. This change reduces the overall fluid velocity in regions where convective transport is less efficient and promotes the development of thicker concentration boundary layers near the membrane. This reduces the mass-transfer driving force, resulting in lower permeate flux at greater rib heights. Therefore, the results highlight the importance of using sufficiently small rib heights to facilitate mass transfer while still providing useful flow disturbance. Although corrugated structures may improve local mixing near the membrane surface, excessive rib height increases channel blockage and weakens overall mass-transfer performance.

4.2. Effect of Rib Width

Fig. 4 shows the variation in permeate flux with rib width, with rib height and pitch remaining constant at 1 mm and 15 mm, respectively. The data indicate a steady reduction in permeate flux as rib width increases from 2 to 4 mm. In particular, the flux is about 15.4 kg m^{-2} h^{-1} at a rib width of 2 mm, 15.1 kg m^{-2} h^{-1} at 3 mm, and 14.8 kg m^{-2} h^{-1} at 4 mm. This trend can be explained by the fact that narrower ribs occupy less space in the channel, allowing higher local fluid velocities and stronger shear near the membrane surface. These conditions increase mixing and reduce concentration polarization. Increasing rib width, on the other hand, increases channel blockage and reduces near-wall convection, promoting the formation of thicker concentration boundary layers. This, in turn, increases mass-transfer resistance and leads to lower permeate flux. In general, these results indicate that ribs can beneficially

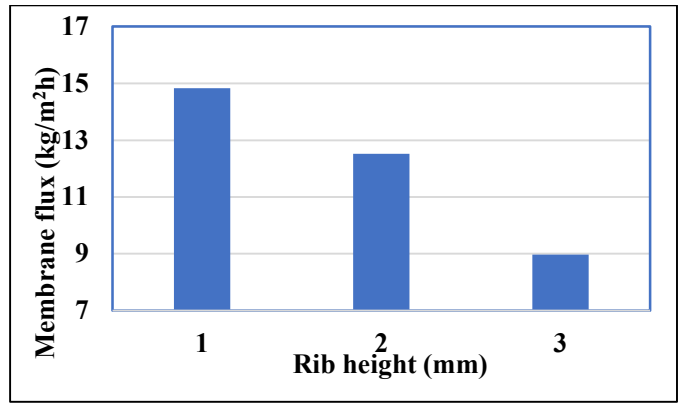


Fig. 3: Effect of rib height on permeate flux at fixed rib width = 4 mm and rib pitch = 15 mm.

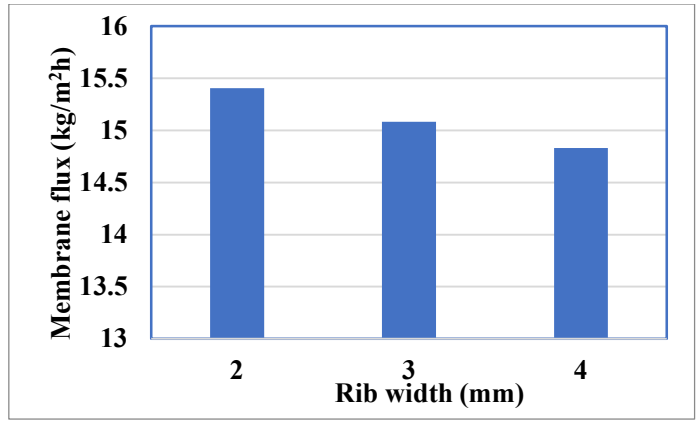


Fig. 4: Effect of rib width on permeate flux at fixed rib height = 1 mm and rib pitch = 15 mm.

disturb the flow, but very wide ribs may hamper mass transfer by restricting effective flow development near the membrane surface. Therefore, rib width should be optimized to maximize permeate flux. These findings indicate that corrugation geometry does not necessarily guarantee flux enhancement, and improper rib dimensions may negatively affect mass-transfer efficiency.

4.3. Effect of Rib Pitch

Fig. 5 shows the effect of rib pitch on permeate flux, with rib width and height maintained at 2 mm and 1 mm, respectively. The results indicate that permeate flux gradually increases as rib pitch increases from 5–15 mm. Specifically, the flux is 15.1 kg m^{-2} h^{-1} at 5 mm, 15.2 kg m^{-2} h^{-1} at 10 mm, and 15.4 kg m^{-2} h^{-1} at 15 mm. At smaller rib pitches, more obstacles are introduced into the flow, resulting in larger recirculation regions between the ribs. Although mixing near the membrane can be enhanced, excessive obstruction reduces flow near the membrane surface and limits mass transport across it. At larger rib pitches, the channel is less restricted, allowing fluid to flow more freely while still creating sufficient disturbance to disrupt concentration boundary layers. This improved balance between mixing and flow resistance increases mass transfer, leading to higher permeate flux at larger rib pitches. Therefore, the results demonstrate the importance of optimizing rib spacing to obtain maximum flux without imposing unnecessary flow resistance and energy loss.

4.4. Effect of Rib Dimensions on Pressure Drop

Table 3 summarizes the effects of rib geometry and arrangement on the pressure drop across the feed channel. The results show that pressure drop decreases steadily with increasing rib pitch, regardless of rib width. Closer ribs increase flow resistance. For instance, with ribs 1 mm high and 2 mm wide, the pressure drop decreases from 0.803 Pa at a 5 mm pitch to 0.625 Pa at a 15 mm pitch. Similar trends are observed for rib widths of 3 and 4 mm, supporting the finding that closer rib spacing increases frictional losses. The effect of rib width, however, is more subtle. At a small pitch of 5 mm, widening the rib from 3 to 4 mm results in a slight decrease in pressure drop. At larger pitches, however, broader ribs generally produce greater pressure drops because they obstruct a larger portion of the flow passage. Overall, these findings suggest that rib pitch is the primary factor affecting pressure loss, whereas rib width has a secondary effect that depends on rib spacing. The results demonstrate that increased permeate flux must be balanced against the additional hydraulic resistance introduced by corrugated structures. Therefore, an optimal rib configuration should simultaneously maximize mass transfer while minimizing pressure losses and pumping-power requirements.

Table 3: Pressure drop at the feed side of the DCMD cell.

ΔP (*Pa*)				
Height (mm)	Width (mm)	Pitch = 5 mm	Pitch = 10 mm	Pitch = 15 mm
1	2	0.802928	0.7635086	0.6253983
	3	0.822953	0.7731061	0.6513754
	4	0.7866656	0.763927	0.705921

Overall, the results suggest that rib geometry influences not only hydrodynamic behavior and permeate flux but also local thermal-transport characteristics and temperature-polarization phenomena within the DCMD module.

5. CONCLUSIONS

The current study investigated a corrugated feed channel using numerical simulations to identify the effects of its geometric properties on mass transfer and fluid dynamics in

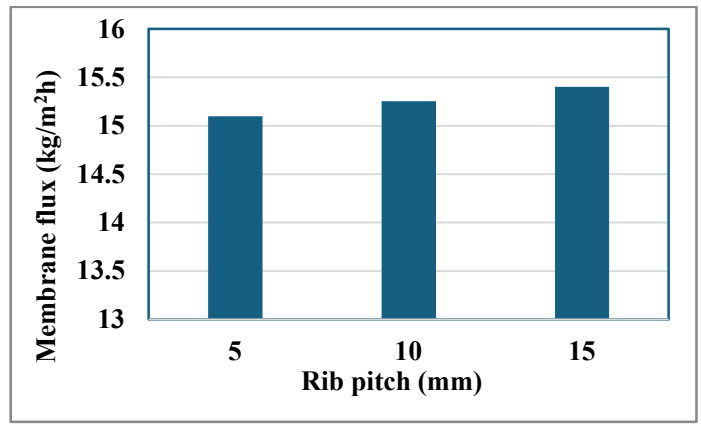


Fig. 5: Effect of rib pitch on permeate flux at fixed rib height = 1 mm and rib width = 2

a direct contact membrane distillation (DCMD) system. The numerical results indicate that the hydrodynamic effects of corrugated channels strongly depend on rib geometry, with both beneficial mixing effects and adverse flow-obstruction mechanisms occurring. The results show that both permeate flux and hydraulic resistance are strongly influenced by rib morphology and dimensions. Rib height was the most significant of the investigated parameters: increasing rib height from 1–3 mm led to a strong reduction in permeate flux, mainly because of increased channel blockage and the formation of thicker concentration boundary layers near the membrane surface. Rib width also had a significant influence, as permeate flux decreased from 15.4 to about 14.8 kg m^{-2} h^{-1} as rib width increased to 4 mm. Conversely, increasing rib pitch to 15 mm led to a small improvement in flux, from 15.1 to about 15.4 kg m^{-2} h^{-1}, as the flow encountered less obstruction while still benefiting from adequate mixing.

It was also observed that the pressure drop across the channel decreased from approximately 0.80 Pa to 0.63 Pa as rib spacing increased, supporting the finding that closely spaced ribs increase hydraulic resistance. These observations highlight the importance of balancing the additional energy needed to overcome flow resistance against the gains from improved mass transfer. Among the investigated configurations, a rib height of 1 mm, rib width of 2 mm, and rib pitch of 15 mm provided the most balanced performance in terms of permeate flux and pressure drop under the investigated operating conditions. Therefore, channel corrugation should be carefully optimized to improve performance without introducing excessive hydraulic resistance or flow blockage. Overall, these findings show that even small changes in channel geometry can significantly affect system performance and can inform the design of more efficient DCMD modules without requiring complicated structural changes.

6. REFERENCES

Almasoudi, S. and Jamoussi, B., 2024. Desalination technologies and their environmental impacts: A review. *Sustainable Chemistry One World*, 1, p.100002. [DOI]

Al-Sairfi, H., Salman, M., Al-Foudari, Y. and Ahmed, M., 2026. Modeling the influence of ionic strength on mineral solubility in concentrated brine solutions. *Processes*, 14(1), p.172. [DOI]

Boubakri, A., Hafiane, A. and Bouguecha, S.A.T., 2017. Direct contact membrane distillation: Capability to desalt raw water. *Arabian Journal of Chemistry*, 10, pp.S3475–S3481. [DOI]

Cancilla, N., Cipollina, A., Gurreri, L. and Ciofalo, M., 2026. Direct contact membrane distillation: A critical review of transmembrane heat and mass transfer models. *Membranes*, 16(2), p.64. [DOI]

Darman, M., Niknafs, N. and Jalali, A., 2023. Effect of wavy corrugations on the performance enhancement of direct contact membrane distillation modules: A numerical study. *Chemical Engineering and Processing: Process Intensification*, 190, p.109421. [DOI]

Drioli, E., Ali, A. and Macedonio, F., 2015. Membrane distillation: Recent developments and perspectives. *Desalination*, 356, pp.56–84. [DOI]

Elhenawy, Y., Elminshawy, N.A., Bassyouni, M., Alanezi, A.A. and Drioli, E., 2020. Experimental and theoretical investigation of a new air gap membrane distillation module with a corrugated feed channel. *Journal of Membrane Science*, 594, p.117461. [DOI]

Farid, M.U., Kharraz, J.A., Sun, J., Boey, M.-W., Riaz, M.A., Wong, P.W., Jia, M., Zhang, X., Deka, B.J., Khanzada, N.K., Guo, J. and An, A.K., 2024. Advancements in nanoenabled membrane distillation for a sustainable water–energy–environment nexus. *Advanced Materials*, 36(17), p.2307950. [DOI]

Francis, L., Ahmed, F.E. and Hilal, N., 2022. Advances in membrane distillation module configurations. *Membranes*, 12(1), p.81. [DOI]

Gobran, A.S., Rabie, M., Mohammed, A.H. and Maghrabie, H.M., 2025. Technologies, materials, applications, and challenges of membrane distillation: A comprehensive review. *Journal of Industrial and Engineering Chemistry*. [DOI]

Hu, Y., Chen, G., Huang, M., Qiao, J. and Yang, X., 2025. Heat-mass transfer and energy efficiency in direct contact membrane distillation: Effects of membrane properties, temperature, and salt concentration. *Journal of Membrane Science, p. 124533*. [DOI]

Jing, L., Sun, J., Zhang, Y., Chen, J. and Guo, F., 2025. Experimental investigation of temperature polarization near membrane surface during air gap membrane distillation processes. *Membranes*, 15(6), p.185. [DOI]

Lee, J.-Y., 2025. Derivation of full range vapor pressure equation from an arbitrary point. *Chemical Engineering Communications*, 212(2), pp.250–259. [DOI]

Lou, J., Vanneste, J., DeCaluwe, S.C., Cath, T.Y. and Tilton, N., 2019. Computational fluid dynamics simulations of polarization phenomena in direct contact membrane distillation. *Journal of Membrane Science*, 591, p.117150. [DOI]

Nthunya, L.N. and Mamba, B.B., 2025. Membrane distillation for water desalination: Assessing the influence of operating conditions on the performance of serial and parallel connection configurations. *Membranes*, 15(8), p.235. [DOI]

Qasim, M., Samad, I.U., Darwish, N.A. and Hilal, N., 2021. Comprehensive review of membrane design and synthesis for membrane distillation. *Desalination*, 518, p.115168. [DOI]

Qtaishat, M., Matsuura, T., Kruczek, B. and Khayet, M., 2008. Heat and mass transfer analysis in direct contact membrane distillation. *Desalination*, 219(1–3), pp.272–292. [DOI]

Salman, M., Ahmed, M., Al-Sairfi, H. and Al-Foudari, Y., 2025. Mineral extraction from mixed brine solutions. *Separations*, 12(10), p.266. [DOI]

Sheikh, M., Fassadi Chimeh, A., Zokaee Ashtiani, F., Fouladitajar, A. and Yavarzadeh, N., 2025. Mathematical modeling of direct contact membrane distillation (DCMD) using Knudsen-diffusion model for PVDF membranes. *Journal of Membrane Science and Research*, 11(2). [DOI]

Sherif, M., Liaqat, M.U., Baig, F. and Al-Rashed, M., 2023. Water resources availability, sustainability and challenges in the GCC countries: An overview. *Heliyon*, 9(10). [DOI]

Soumbati, Y., Bouatou, I., Abushaban, A., Belmabkhout, Y. and Necibi, M.C., 2025. Review of membrane distillation for desalination applications: Advanced modeling, specific energy consumption, and water production cost. *Journal of Water Process Engineering*, 71, p.107296. [DOI]

Suleman, M., Asif, M. and Jamal, S.A., 2021. Temperature and concentration polarization in membrane distillation: A technical review. *Desalination and Water Treatment*, 229, pp.52–68. [DOI]

Swaidan, B., Ali, M.I.H., Ali, K., Al-Rub, R.K.A. and Arafat, H.A., 2024. A computational fluid dynamics study on TPMS-based spacers in direct contact membrane distillation modules. *Desalination*, 579, p.117476. [DOI]

Taamneh, Y. and Bataineh, K., 2017. Improving the performance of direct contact membrane distillation utilizing spacer-filled channel. *Desalination*, 408, pp.25–35. [DOI]

Xu, D., Zhu, Z. and Li, J., 2022. Recent progress in electrospun nanofibers for the membrane distillation of hypersaline wastewaters. *Advanced Fiber Materials*, 4(6), pp.1357–1374. [DOI]

Zaragoza, G., Andrés-Mañas, J. and Ruiz-Aguirre, A., 2018. Commercial scale membrane distillation for solar desalination. *NPJ Clean Water*, 1(1), p.20. [DOI]

Nature Environment and Pollution Technology
An International Quarterly Peer-Reviewed Open Access Journal

p-ISSN: 0972-6268 | e-ISSN: 2395-3454 Vol. 25 | No. 4 | Article ID D1923 | 2026

RESEARCH ARTICLE https://doi.org/10.46488/NEPT.2026.v25i04.D1923 OPEN ACCESS

Removal of Copper and Zinc from Aqueous Media Using White-Rot Lignicolous Fungi

Analiz Lola Ruiz Tello[1], Ladislao Ruiz-Rengifo[1], Julio Miguel Ángeles-Suazo[2], Camila Valentina Carrasco Llaique[3] and Jairo Edson Gutiérrez-Collao[2]*

[1]Universidad Nacional Agraria de la Selva, Tingo María, Perú
[2]Universidad Nacional Autónoma de Tayacaja Daniel Hernández Morillo, Tayacaja, Perú
[3]Universidad Nacional de Huancavelica, Huancavelica, Perú
*Corresponding author: Jairo Edson Gutiérrez-Collao; jairo.gutierrez@unat.edu.pe

ARTICLE HISTORY

Received: 19-03-2026
Revised: 11-05-2026
Accepted: 20-05-2026

KEYWORDS

White-Rot lignicolous fungi
Ganoderma applanatum
Pleurotus ostreatus
Pycnoporus sanguineus
Schizophyllum commune
Removal of heavy metals

CITE THIS ARTICLE

Ruiz Tello, A.L., Ruiz-Rengifo, L., Ángeles-Suazo, J.M., Carrasco Llaique, C.V. and Gutiérrez-Collao, J.E., 2026. Removal of copper and zinc from aqueous media using white-rot lignicolous fungi, *Nature Environment and Pollution Technology*, 25(4), D1923. https://doi.org/10.46488/NEPT.2026.v25i04.D1923

COPYRIGHT & LICENCE

© 2026 The Authors
Open Access under CC BY 4.0.

PUBLISHED BY

TECHNOSCIENCE PUBLICATIONS

ABSTRACT

In Peru, white-rot lignicolous fungi represent a biotechnological resource with high potential for the bioremediation of environments contaminated with heavy metals, offering an ecological alternative to traditional physicochemical methods. This study aimed to evaluate the capacity of four strains: *Ganoderma applanatum*, *Pycnoporus sanguineus*, *Schizophyllum commune*, and *Pleurotus ostreatus* to remove copper and zinc from aqueous media at three metal concentrations. The cultures were maintained for 14 days under controlled conditions; mycelial growth and biomass production were measured, and removal efficiency was determined by flame atomic absorption spectrophotometry. The results revealed significant differences among strains and concentrations. *S. commune* and *P. ostreatus* showed greater mycelial growth and biomass production, whereas *G. applanatum* and *P. sanguineus* stood out for their high metal removal capacity. Removal efficiencies reached values of 92.10–96.77% for copper and 91.88–99.05% for zinc, confirming the ability of these fungi to remove heavy metals from aqueous systems. The findings demonstrate the potential of lignicolous fungi as a sustainable alternative for bioremediation, contributing to the development of clean technologies applicable to the treatment of effluents contaminated with heavy metals. The use of lignicolous fungi in bioremediation processes could reduce operational costs, minimize secondary environmental impacts, and promote nature-based solutions, thereby strengthening sustainable environmental management strategies in the Peruvian context.

1. INTRODUCTION

Human activities and industrial expansion have significantly intensified the release of persistent organic pollutants and heavy metals into the environment, leading to soil and water degradation, ecosystem alterations, and considerable risks to human health (Zare et al. 2024, Majumdar 2024). This phenomenon is closely associated with the growth of mining, metallurgical, electroplating, and manufacturing activities, as well as with the inadequate treatment of industrial effluents and acid mine drainage, which are recognized as among the main sources of water pollution worldwide.

In countries with intensive extractive activities, such as Peru, the discharge of untreated or partially treated effluents represents a persistent environmental challenge, particularly in regions influenced by mining operations, where elevated concentrations of heavy metals are frequently reported in surface and groundwater.

In this context, the increasing release of heavy metals such as copper (Cu) and zinc (Zn) into aquatic environments represents a critical environmental threat. Due to their persistent and non-biodegradable nature, these elements tend to accumulate in the environment and become incorporated into trophic chains, promoting processes of bioaccumulation and biomagnification. As a consequence, they can alter ecological interactions, affect evolutionary processes, and contribute to the decline or disappearance of endemic species (Sanyal et al. 2015, Luna et al. 2020, Paria et al. 2022). Moreover, even at relatively low concentrations, Cu and Zn interfere with essential biological functions and can cause chronic toxic effects in both aquatic organisms and humans (Singh & Singh 2024).

In response to this issue, conventional physicochemical effluent treatment methods present significant limitations, including high operational costs, reduced efficiency in complex contaminant mixtures, and the generation of secondary pollutants such as sludge (Chen et al. 2022, Gao et al. 2024, Harish et al. 2024). However, these approaches often fail to provide sustainable and cost-effective solutions, particularly in developing regions where technological and economic constraints persist.

These limitations have driven increasing interest in biological alternatives, which are characterized by lower environmental impact and greater adaptability. Among them, processes such as biosorption, biotransformation, and biomineralization have demonstrated considerable potential for the removal of heavy metals (Módenes et al. 2013, González-González et al. 2022). Nevertheless, their performance remains highly dependent on environmental conditions, biomass characteristics, and contaminant concentrations.

Among emerging biotechnological strategies, fungi have been widely recognized for their effectiveness in bioremediation due to their high tolerance to heavy metals, their capacity for mycosorption and bioleaching, and the presence of multiple functional groups (–OH, –NH_2, –COOH) on their cell surface that facilitate metal binding (Lei et al. 2018, Li et al. 2019, Amin et al. 2024, Zare et al. 2024).

Within this group, white-rot lignicolous fungi stand out due to their extracellular enzymatic system, composed of laccases, manganese peroxidases, and lignin peroxidases. This system not only enables the degradation of lignocellulosic compounds but also contributes to interactions with heavy metals through biosorption, bioaccumulation, and redox-mediated processes (Singh & Singh 2024, Kato et al. 2024, Zehra & Meena 2025, Singh et al. 2025).

Several studies have demonstrated their potential in heavy metal removal. For instance, strains of *Pleurotus ostreatus* have shown high tolerance to copper and significant removal efficiency in aqueous systems, along with the induction of ligninolytic enzymes under metal stress (Gao et al. 2024). Similarly, other white-rot fungi have achieved removal efficiencies exceeding 70% for metals such as lead, cadmium, and nickel under controlled conditions (Sharma et al. 2020). However, these studies are often limited to single-metal systems or controlled laboratory conditions that do not fully represent the complexity of real effluents.

Despite more than two decades of research in this field (Lu et al. 2020), critical gaps persist regarding the comparative evaluation of multiple lignicolous strains under factorial experimental designs that incorporate different metals and environmentally relevant concentrations. Furthermore, the rapid decline of ligninolytic activity in aqueous environments remains a significant limitation that has not been sufficiently addressed (Langer et al. 2021, Hultberg & Golovko 2024).

Within this framework, the present study aims to comparatively evaluate the removal capacity of four strains of white-rot lignicolous fungi for Cu and Zn in aqueous solutions simulating contaminated effluent scenarios. This research seeks to generate robust experimental evidence that supports the application of these microorganisms as sustainable, efficient, and cost-effective biotechnological alternatives for industrial wastewater treatment in Peru.

This study provides a novel comparative evaluation of native Peruvian lignicolous fungal strains under a factorial experimental design, assessing their removal capacity for Cu and Zn at environmentally relevant concentrations.

2. MATERIALS AND METHODS

2.1. Study Area

The study was conducted in the Mycology and Propagation Technology Laboratory of the Universidad Nacional Agraria de la Selva, located in the Rupa Rupa district, Leoncio Prado province, Huánuco region (Fig. 1). The geographic coordinates of the study area are 76°00′17″ west longitude and 9°18′18″ south latitude, at an altitude of 660 m above sea level.

2.2. White-Rot Lignicolous Fungal Strains

Four fungal strains were studied: *Ganoderma applanatum*, *Pleurotus ostreatus*, *Pycnoporus sanguineus*, and *Schizophyllum commune*. All specimens were collected from the Reserved Forest of the Universidad Nacional Agraria de la Selva and the Botanical Garden of Tingo María, located in the central Peruvian rainforest.

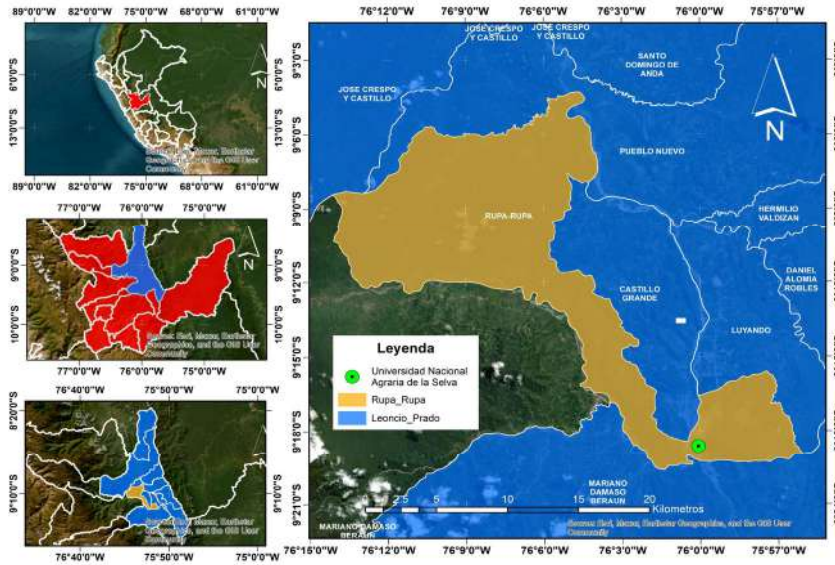


Fig. 1: Study area location.

The samples were coded, photographed, and packaged *in situ*, and then transported to the laboratory, where they were dried for a period of 24–72 hours (depending on the strain) at a temperature of 60 °C (Robledo 2006, Ryvarden 2007). Fungal identification was performed based on macroscopic characteristics and comparison with reference catalogs "Hongos de Allpahuayo-Mishana"; therefore, it should be considered a preliminary identification (Mata 1999, Mata et al. 2003).

2.3. Experimental Design

Four fungal strains (*G. applanatum*, *P. sanguineus*, *S. commune*, and *P. ostreatus*), two contaminants (copper and zinc), and three concentrations per contaminant (10 mg L^{-1}, 30 mg L^{-1}, and 50 mg L^{-1}) were studied. Additionally, three replicates were evaluated for each of the 24 treatments.

The evaluated concentrations (10, 30, and 50 mg L^{-1}) were selected considering ranges reported for mining and metallurgical effluents, where Cu and Zn concentrations can vary widely depending on the degree of prior treatment. Studies on acid mine drainage and metallurgical effluents have documented metal concentrations ranging from 5 to >100 mg L^{-1}, especially in partially treated or neutralized systems (Johnson & Hallberg 2005, Fu & Wang 2011).

Likewise, research on fungal biosorption frequently employs initial concentrations between 10 and 100 mg L^{-1} to assess tolerance and removal efficiency under controlled conditions (Gadd 2009, Kapoor & Viraraghavan 1995).

In particular, concentrations of 10–50 mg L^{-1} have been used in studies with ligninolytic fungi to determine removal capacity without causing complete growth inhibition (Anastopoulos & Kyzas 2015, Baldrian 2003). Therefore, the selected levels represent realistic scenarios of moderate to high contamination and allow for comparability with the international literature.

2.4. Preparation and Plating of Solid Media

For the primary isolation of fungal strains, malt extract agar (50 g) and potato dextrose agar (39 g) were used to prepare 1.5 L of medium, each prepared separately. The components were dissolved under constant stirring and brought to a boil for 10 minutes until complete homogenization was achieved. Subsequently, the media were sterilized in an autoclave at 121°C and 15 psi for 15 minutes.

After sterilization, the media were transferred to a laminar flow chamber previously disinfected with UV radiation for 15 minutes. Ceftriaxone (0.3 g per total prepared volume) was added as an antibacterial agent, and the mixture was homogenized prior to plating to minimize the risk of contamination.

2.5. Disinfection and Establishment of Axenic Cultures

Fresh selected fruiting bodies were superficially cleaned and cut into fragments of approximately 0.5 × 0.5 cm. Disinfection was carried out following the protocols of Córdova (2010) and Ríos-Ruiz and Ruiz-Rengifo (1993), using sodium hypochlorite (NaOCl) diluted 1:10 for 1 minute, followed by three consecutive rinses with sterile distilled water. The fragments were dried on sterile filter paper and placed at the center of 90 mm Petri dishes containing potato dextrose agar and malt extract agar.

The plates were sealed with Parafilm and incubated at 27°C in darkness until mycelial growth was observed. All procedures were conducted under aseptic conditions in a laminar flow hood.

2.6. Preparation and Activation of Fungal Inoculum

Inoculum standardization is essential to ensure reproducibility in biosorption and biotransformation studies (Kapoor & Viraraghavan 1995, Gadd 2009). For strain activation, Sabouraud dextrose broth, a carbon-rich medium due to its high dextrose content, was used because it promotes growth in the exponential phase and metabolic activation associated with increased expression of ligninolytic enzyme systems (Baldrian 2003).

For the preparation of 1 L of Sabouraud broth, 40 g of dextrose and 10 g of peptone were used, and the volume was brought to 1 L with distilled water. The medium was sterilized in an autoclave (121°C, 15 min), and once cooled, ceftriaxone (0.2 g L^{-1}) was added. The axenic mycelium was subcultured into flasks containing this medium and incubated for 5 days at room temperature to obtain cultures in the exponential phase.

Prior to inoculation in the Mineral Salts Minimal Medium (MSMM), the biomass was homogenized and quantified by dry weight following standard methodologies for fungal growth studies (Suh et al. 2001). This standardization allowed the initial density to be expressed in g L^{-1} and ensured uniformity among experimental treatments.

2.7. Mineral Salts Minimal Medium (MSMM)

The Mineral Salts Minimal Medium (MSMM) was prepared by dissolving 5.23 g of K_2HPO_4, 1.91 g of KH_2PO_4, 0.09 g of $MgSO_4$, and 1 g of $(NH_4)_2SO_4$ in distilled water, adding 1 mL of trace element solution, and adjusting the final volume to 1000 mL. The trace element solution (1 L) consisted of 20 mg of boric acid, 30 mg of zinc sulfate, 1 mg of copper sulfate, 3 mg of sodium molybdate, 10 mg of iron sulfate, and 2.6 mg of magnesium sulfate, all dissolved in distilled water to complete the final volume. For the induction phase, the MSMM was supplemented with glucose (0.25 g L^{-1}) and 0.1% yeast extract to promote metabolic activation of the microorganism.

2.8. pH Control and Culture Conditions

The initial pH of the MSMM was adjusted to 5.5 ± 0.1 using 0.1 M HCl or NaOH prior to sterilization. pH is a determining factor in the ionic speciation of Cu^{2+} and Zn^{2+} and in the efficiency of fungal biosorption (Fu & Wang 2011, Anastopoulos & Kyzas 2015). Values between 4.5 and 6.0 favor the interaction between functional groups on the cell wall (–OH, –COOH, $–NH_2$) and metal cations, minimizing abiotic precipitation (Gadd 2009).

2.9. Chemical Source of Metals and Evaluated Concentrations

Copper and zinc were added as copper sulfate pentahydrate ($CuSO_4 \cdot 5H_2O$) and zinc sulfate heptahydrate ($ZnSO_4 \cdot 7H_2O$), respectively, both of analytical grade. These salts were selected due to their high solubility and frequent use in biosorption studies (Kapoor & Viraraghavan 1995, Fu & Wang 2011).

2.10. Induction, Incubation, and Experimental Controls

The metal-supplemented media were sterilized and distributed into flasks, which were then inoculated with 7.5 mL of previously activated and standardized culture. The flasks were incubated for 14 days, a period determined based on studies reporting that the active phase of biosorption and bioaccumulation occurs within the first two weeks (Baldrian 2003, Gadd 2009). Preliminary assays confirmed stabilization of biomass and residual metal concentration by day 14.

It is important to note that all experimental units were inoculated with fungal biomass; therefore, abiotic controls (MSMM + metal without inoculum) were not included in the experimental design. Consequently, the study focuses on evaluating the overall removal efficiency in biological systems, without experimentally distinguishing between biological and physicochemical removal mechanisms such as precipitation or passive adsorption.

2.11. Determination of Metals by FAAS

The residual concentration of Cu and Zn in the supernatant was determined by flame atomic absorption spectrophotometry (FAAS) using a SpectrAA 55B atomic absorption spectrophotometer (Varian Inc., USA). FAAS is a widely validated technique for metal analysis in aqueous matrices (Welz & Sperling 1999). Measurements were performed at 324.8 nm for Cu and 213.9 nm for Zn using an air–acetylene flame.

Calibration curves were constructed with coefficients of determination (R^2) greater than 0.995. Analytical quality control included reagent blanks and triplicate measurements to ensure precision.

2.12. Analytical Determinations

2.12.1. Evaluation of Radial Growth on Solid Media

The radial growth of the fungal strains was evaluated on solid media consisting of potato dextrose agar (PDA) and malt extract agar (MEA). For each treatment, a 5-mm-diameter

mycelial disc was taken from the actively growing edge of a previously established culture and placed at the center of 90-mm-diameter Petri dishes.

The plates were incubated at 27 ± 2°C under dark conditions. Colony diameter was measured daily for 15 days using a sterile millimeter ruler with a precision of 1 mm. In each plate, two perpendicular measurements were taken along axes passing through the inoculation center, and the average of both was calculated to estimate daily radial growth.

Radial growth (mm) was determined as the distance from the point of inoculation to the active edge of the mycelium. When the colony reached the edge of the plate, growth was considered complete, and the maximum value corresponding to the internal radius of the plate was recorded.

Additionally, macroscopic characteristics such as coloration, surface texture (cottony, waxy, or compact), presence of concentric zoning, mycelial density, and expansion pattern (dispersed or compact) were recorded. These observations were conducted descriptively and documented photographically to complement the quantitative analysis.

2.12.2. Determination of Fungal Biomass

After 14 days of incubation, the fungal biomass was recovered by centrifugation and filtration of the supernatant. The material was then dried in an oven until a constant weight was reached and quantified gravimetrically to determine the mycelial biomass corresponding to each copper and zinc concentration. Finally, an aliquot of the filtered supernatant was analyzed by FAAS to assess the fungi's capacity to remove copper and zinc.

Cell density was determined from the dry weight of the mycelial biomass. To do this, the biomass was separated from the liquid medium by centrifugation at 3500 rpm for 15 minutes. It was then filtered using pre-weighed filter paper and placed in an oven at 80°C until a constant weight was reached. The following equation was applied (López 1998):

$$B = \frac{X_2 - X_1}{V} \quad ...(1)$$

Where: B represents the biomass (g L^{-1}), X_1 refers to the weight of the filter paper, and X_2 refers to the weight of the filter paper with biomass, and V is the volume of the culture medium (in liters) used for biomass determination

2.12.3. Determination of Removal Efficiency

Removal efficiency was determined based on the percentage reduction between the initial and final concentrations of copper and zinc in the aqueous medium contained in the flasks, using Equation 2, according to each applied treatment (Marcovecchio et al. 1991).

$$RE = \left(\frac{IC - FC}{IC}\right) \times 100 \quad ...(2)$$

Where: RE represents the removal efficiency (%), IC refers to the initial concentration (mg L^{-1}), and FC refers to the final concentration (mg L^{-1}).

2.13. Data Analysis

The data were analyzed using a completely randomized three-way ANOVA (4 × 2 × 3), considering fungal strain (4 levels), metal type (2 levels), and concentration (3 levels) as factors, with three replicates per treatment (n = 72). Main effects as well as two-way and three-way interactions were evaluated. Prior to analysis, assumptions of normality (Shapiro–Wilk test) and homogeneity of variances (Levene's test) were verified. When significant differences were detected ($p < 0.05$), Tukey's multiple comparison test was applied.

3. RESULTS AND DISCUSSION

3.1. Radial Growth and Macroscopic Characterization of Fungal Strains

The radial growth of *Ganoderma applanatum*, *Pycnoporus sanguineus*, *Schizophyllum commune*, and *Pleurotus ostreatus* was evaluated on potato dextrose agar (PDA)

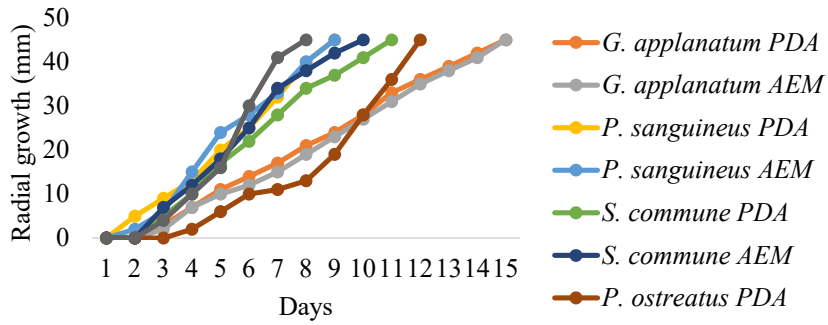


Fig. 2: Radial growth of fungal strains in two culture media.

and malt extract agar (MEA). The growth curves shown in Fig. 2 exhibited a typical sigmoidal pattern, characterized by an initial lag phase, an exponential phase, and a stationary phase, consistent with the dynamics of mycelial expansion in solid cultures.

Two-way analysis of variance (species × culture medium) revealed significant differences in radial growth attributable to the species factor ($p < 0.001$), while the effect of the medium depended on the strain, showing a significant species × medium interaction ($p < 0.05$). This indicates that the response to the type of substrate is modulated by the intrinsic physiology of each fungus.

S. commune exhibited the highest radial growth rate, reaching 45 mm by day 11 on PDA and by day 9 on MEA, corresponding to an average rate of approximately 4–5 mm day^{-1} during the exponential phase. In contrast, *G. applanatum* showed the slowest growth, failing to cover the entire plate within the same experimental period. *P. sanguineus* and *P. ostreatus* displayed intermediate rates, with vigorous development on both media.

In comparative terms, Figs. 3 and 4 show that PDA favored a faster initial mycelial expansion in fast-growing strains, whereas MEA promoted greater continuity and stability in growth, particularly in *P. sanguineus* and *S. commune*. These differences suggest variations in the utilization of complex carbon sources and metabolic efficiency among species.

From a macroscopic perspective, clear differences in colony morphology were observed. *S. commune* displayed dispersed growth on PDA and more compact mycelium on MEA. *P. sanguineus* initially showed a waxy texture on both media, becoming cottony on MEA and later developing

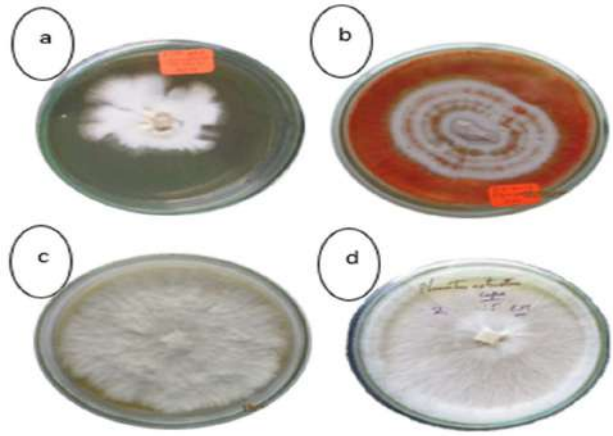


Fig. 3: Radial growth of fungal strains on malt extract agar (MEA) medium: a) *Ganoderma applanatum*. b) *Pycnoporus sanguineus*. c) *Schizophyllum commune*. d) *Pleurotus ostreatus*.

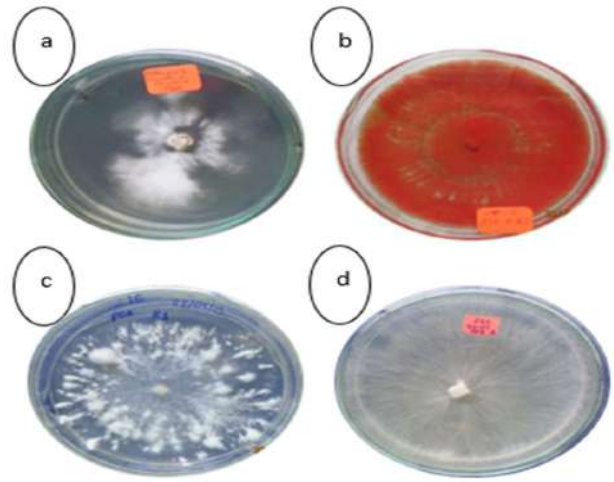


Fig. 4: Radial growth of fungal strains on potato dextrose agar (PDA) medium a) *Ganoderma applanatum*. b) *Pycnoporus sanguineus*. c) *Schizophyllum commune*. d) *Pleurotus ostreatus*.

concentric lines with pink to reddish hues. *G. applanatum* developed waxy mycelium on PDA and a more homogeneous and vigorous growth on MEA. P. ostreatus exhibited uniform and consistent growth on both media.

The observed differences in radial growth and mycelial morphology have direct implications for subsequent biotechnological performance. Strains with higher mycelial expansion rates, such as *S. commune* and *P. sanguineus*, exhibit a larger active surface area and higher hyphal density in a shorter time, potentially increasing the availability of cell wall functional groups (–OH, –COOH, $–NH_2$) involved in metal biosorption processes.

Likewise, the metabolic stability observed on MEA suggests a greater capacity for physiological maintenance, a condition relevant for coping with metal stress in the Mineral Salts Minimal Medium supplemented with Cu and Zn. In this regard, prior growth behavior serves as an indirect indicator of physiological vigor and potential tolerance to the 10–50 mg L^{-1} concentrations evaluated in the removal assay.

Therefore, the characterization of radial growth not only allowed verification of the viability and purity of the strains but also provided a basis for their selection and differential performance in the 4 × 2 × 3 factorial design applied in the bioremediation stage.

3.2. Fungal Biomass

Table 1 presents the results of the Shapiro–Wilk normality test for the fungal biomass variable (g L^{-1}). The W value of 0.94 indicated an acceptable fit to the normal distribution ($p > 0.05$), allowing the application of the three-way ANOVA.

Table 1: Shapiro–Wilk normality test for the fungal biomass variable.

Variable	Mean (g L^{-1})	SD (g L^{-1})	W*
Fungal biomass	1.93	0.84	0.94

SD: Standard deviation.

Table 2: Analysis of variance for the fungal biomass variable.

Source of variation	df	SS	MS	p
Fungus	3	17.43	5.81	<0.0001
Metal	1	0.05	0.05	0.7088
Concentration	2	1.25	0.62	0.1746
Fungus × Metal	3	0.67	0.22	0.5879
Fungus × Concentration	6	5.57	0.93	0.0244
Metal × Concentration	2	3.87	1.93	0.0064
Fungus × Metal × Concentration	6	4.22	2.04	0.0780
Error	48	16.52	0.34	
Total	71	49.57		

SS: Sum of squares. MS: Mean squares.

The analysis of variance (Table 2) showed a coefficient of variation of 30.34%, indicating moderate variability among treatments. The adjusted coefficient of determination (R^2_adj = 0.51) suggests that the model explained 51% of the observed variability in fungal biomass.

Significant differences were detected among strains ($p < 0.05$), while the main effects of metal and concentration were not significant ($p > 0.05$). The fungus × concentration and metal × concentration interactions were significant ($p < 0.05$), whereas the fungus × metal and fungus × metal × concentration interactions were not significant ($p > 0.05$).

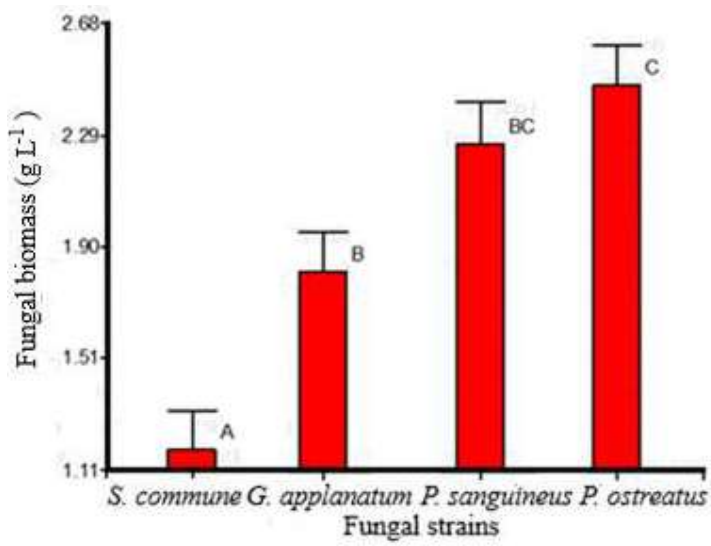


Fig. 5: Tukey test for the effect of fungal strains on fungal biomass (g L^{-1}).

Table 3: Tukey test for the effect of treatments on the fungal biomass variable.

Fungal strain	Metal type	Concentration (mg L^{-1})	Fungal biomass (g L^{-1})
S. commune	Zinc	30	0.85a
G. applanatum	Zinc	50	0.85a
S. commune	Copper	50	0.98a
S. commune	Copper	30	1.02a
P. sanguineus	Copper	30	1.29a
S. commune	Zinc	50	1.29a
S. commune	Copper	10	1.33a
S. commune	Zinc	10	1.64a
P. sanguineus	Zinc	50	1.82a
G. applanatum	Copper	50	1.82a
G. applanatum	Copper	30	1.87a
P. sanguineus	Copper	10	2.00a
G. applanatum	Zinc	30	2.05a
G. applanatum	Zinc	10	2.09a
P. ostreatus	Zinc	10	2.09a
P. ostreatus	Copper	30	2.09a
G. applanatum	Copper	10	2.22a
P. ostreatus	Copper	10	2.31a
P. sanguineus	Zinc	30	2.40a
P. ostreatus	Zinc	30	2.44a
P. ostreatus	Zinc	50	2.62a
P. sanguineus	Zinc	10	2.75a
P. ostreatus	Copper	50	3.24a
P. sanguineus	Copper	50	3.33a

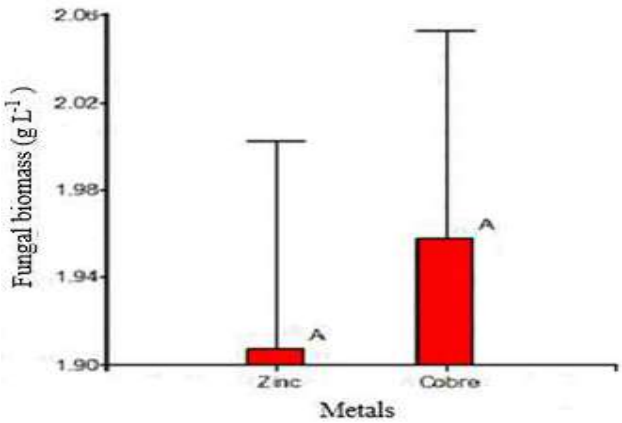


Fig. 6: Tukey test for the effect of metal type on fungal biomass (g L^{-1}).

Fig. 5 shows numerical differences in average biomass among fungal strains, with *P. ostreatus* presenting higher mean values and *S. commune* lower values. However, Tukey's multiple comparison analysis (Table 3) did not reveal statistically significant differences among specific strain–metal–concentration combinations, as all treatments shared the same statistical grouping.

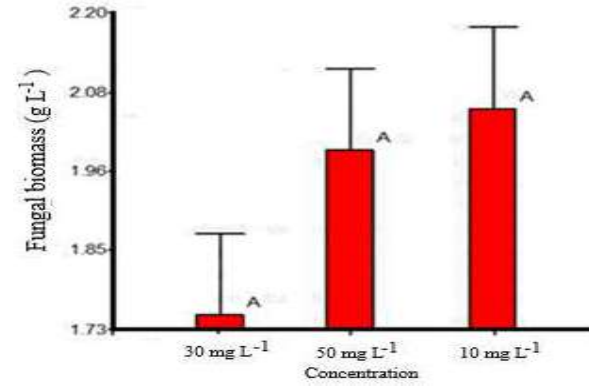


Fig. 7: Tukey test for the effect of metal concentration on fungal biomass (g L^{-1}).

Fig. 6 indicates that biomass in the presence of copper and zinc was statistically similar, confirming the absence of a significant metal effect, as supported by the ANOVA results.

Similarly, Fig. 7 shows that the concentrations of 10, 30, and 50 mg L^{-1} did not produce significant differences in biomass, indicating that fungal growth was not significantly affected within the tested range.

Although the combinations *P. ostreatus*–copper–50 mg L^{-1} and *P. sanguineus*–copper–50 mg L^{-1} showed higher numerical biomass values, these differences were not statistically significant according to Tukey's test. Therefore, no specific treatment can be considered superior, and the results suggest a general physiological tolerance of the strains to the evaluated conditions rather than a treatment-specific effect.

Overall, while the ANOVA detected significant effects for the factor fungus, the lack of significant differences at the treatment level indicates that biomass remained statistically similar across specific combinations of fungus, metal, and concentration.

3.3. Removal Efficiency

Table 4 presents the results of the Shapiro–Wilk normality test for the removal efficiency variable (%). The statistic W = 0.96 ($p > 0.05$) indicated that the normality assumption was met, allowing the application of the three-way ANOVA.

Table 4: Shapiro–Wilk normality test for the removal efficiency variable.

Variable	Mean (%)	SD (%)	W*
Removal efficiency	95.48	2.15	0.96

SD: Standard deviation.

Table 5: Analysis of variance for the removal efficiency variable.

Source of variation	df	SS	MS	p
Fungus	3	29.98	9.99	<0.0001
Metal	1	88.13	88.13	<0.0001
Concentration	2	79.44	39.72	<0.0001
Fungus × Metal	3	16.70	5.57	<0.0001
Fungus × Concentration	6	43.21	7.20	<0.0001
Metal × Concentration	2	28.78	14.39	<0.0001
Fungus × Metal × Concentration	6	25.47	4.25	<0.0001
Error	48	17.72	0.37	
Total	71	329.4		

SS: Sum of squares. MS: Mean squares.

The analysis of variance (Table 5) showed a coefficient of variation of 0.64%, indicating high experimental precision and minimal dispersion among replicates. Likewise, the adjusted coefficient of determination (R^2_adj = 0.92) indicated that the model explained 92% of the observed variability, confirming a high explanatory capacity of the evaluated factors and their interactions.

Highly significant effects ($p < 0.0001$) were detected for the main factors fungus, metal, and concentration as well as for all two-way interactions and the three-way interaction (fungus × metal × concentration). This indicates that removal efficiency does not depend solely on each factor individually, but rather on the specific combination of fungal strain, metal type, and concentration level, revealing a differential behavior of the biological system under each experimental condition.

Fig. 8 shows that *P. ostreatus* (95.94%), *S. commune* (95.84%), and *P. sanguineus* (95.76%) exhibited statistically similar efficiencies, all higher than *G. applanatum* (94.37%), suggesting a greater average removal capacity in the first three strains.

Fig. 9 shows that the type of metal significantly influenced removal efficiency, with zinc being removed more efficiently than copper. This difference may be associated with differences in the physicochemical behavior of each metal in solution; however, no mechanistic analyses were performed in this study to confirm the underlying processes.

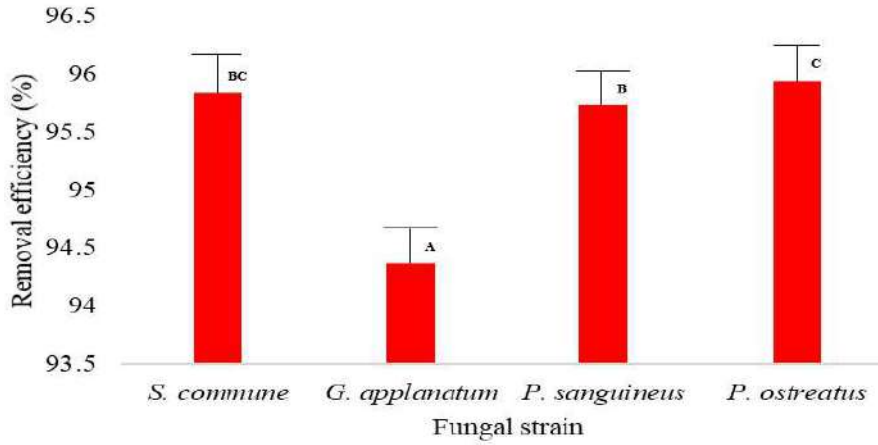


Fig. 8: Tukey test for the effect of fungal strains on removal efficiency (%).

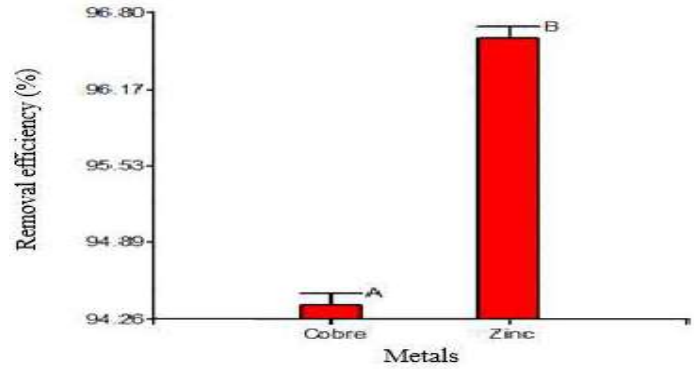


Fig. 9: Tukey test for the effect of metal type on removal efficiency (%).

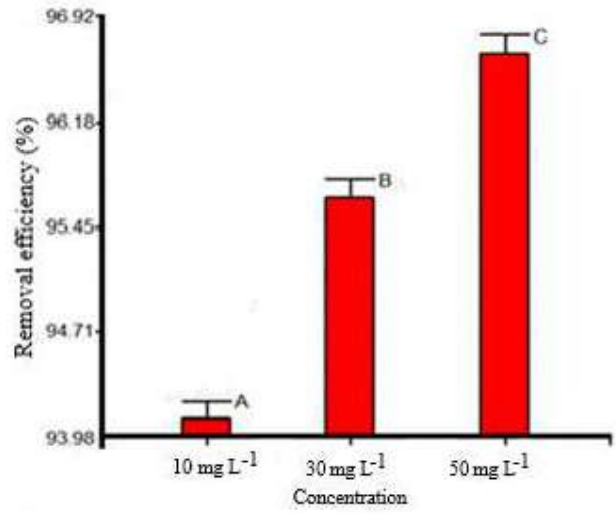


Fig. 10: Tukey test for the effect of metal concentration on removal efficiency (%).

Fig. 10 shows that the highest efficiencies were achieved at 50 mg L^{-1}, suggesting a concentration-gradient effect. Greater metal availability increases the driving force for mass transfer, and a higher initial concentration may enhance overall removal capacity until saturation is approached; however, the specific mechanisms involved were not evaluated.

The analysis of the three-way interaction (Table 6) revealed that the highest efficiencies (>98%) were obtained in the combinations *S. commune*–zinc–50 mg L^{-1} (98.92%) and *P. ostreatus*–zinc–50 mg L^{-1} (99.05%), both belonging to the top statistical group. These results confirm the high removal capacity for zinc at elevated concentrations and position these strains as promising candidates for bioremediation applications in matrices with high metal loads.

However, despite the high efficiencies observed, the absence of abiotic controls prevents complete exclusion of the contribution of physicochemical processes, such as metal precipitation or passive adsorption. Therefore, the observed decrease in metal concentration may be attributed to both biological and non-biological mechanisms.

The study was based on a single endpoint measurement after 14 days of incubation, without intermediate temporal evaluation. This limitation prevents the assessment of removal rates and the identification of potential multiphase behavior. Therefore, the dynamics of metal removal over time cannot be determined. Future studies should incorporate kinetic modeling, mechanistic analyses, and experiments using real wastewater matrices to better understand the removal processes and validate large-scale applicability.

Tables 7 and 8 present the residual concentrations (Cf) of copper and zinc determined by FAAS. For both metals, although the residual concentration increases with higher initial concentrations, the final values remain well below

Table 6: Tukey test for the effect of treatments on removal efficiency.

Fungal strain	Metal type	Concentration (mg L^{-1})	Removal efficiency (%)
G. applanatum	Zinc	10	91.88[a]
G. applanatum	Copper	10	92.10ab
P. sanguineus	Copper	10	92.11ab
P. ostreatus	Copper	30	92.80abc
P. ostreatus	Copper	50	93.98bcd
S. commune	Copper	50	94.03cd
S. commune	Copper	30	94.15cd
G. applanatum	Copper	30	94.22cde
P. sanguineus	Zinc	10	94.44cdef
S. commune	Copper	10	95.04defg
P. sanguineus	Copper	30	95.15defg
S. commune	Zinc	10	95.43defg
P. ostreatus	Zinc	10	95.54defgh
G. applanatum	Copper	50	95.78defghi
G. applanatum	Zinc	30	96.09efghij
G. applanatum	Zinc	50	96.12efghij
P. ostreatus	Copper	10	96.33fghij
P. sanguineus	Copper	50	96.77ghijk
P. sanguineus	Zinc	30	97.44hijkl
S. commune	Zinc	30	97.49ijkl
P. ostreatus	Zinc	30	97.96jkl
P. sanguineus	Zinc	50	98.65kl
S. commune	Zinc	50	98.92l
P. ostreatus	Zinc	50	99.05l

Table 7: Final copper (Cu) concentration as a function of fungal strain and initial concentration.

Fungal strain	Initial concentration (mg L^{-1})	Mean (mg L^{-1}) ± SD	Min	Max
G. applanatum	10	0.79 ± 0.09	0.69	0.86
	30	1.73 ± 0.20	1.50	1.88
	50	2.11 ± 0.06	2.06	2.18
P. sanguineus	10	0.79 ± 0.16	0.61	0.91
	30	1.46 ± 0.14	1.30	1.56
	50	1.62 ± 0.10	1.52	1.71
S. commune	10	0.50 ± 0.08	0.41	0.56
	30	1.76 ± 0.08	1.68	1.84
	50	2.98 ± 0.11	2.89	3.11
P. ostreatus	10	0.37 ± 0.08	0.29	0.45
	30	2.16 ± 0.07	2.08	2.21
	50	3.01 ± 0.13	2.87	3.10

the initial levels, confirming the high removal capacity of the evaluated strains.

For copper, final concentrations ranged from 0.37 to 0.79 mg L^{-1} at 10 mg L^{-1}; from 1.46 to 2.16 mg L^{-1} at 30 mg L^{-1}; and from 1.62 to 3.01 mg L^{-1} at 50 mg L^{-1}. At the lowest concentration, *P. ostreatus* recorded the lowest residual value (0.37 mg L^{-1}), while at 50 mg L^{-1}, *P. sanguineus* showed the lowest final concentration (1.62 mg L^{-1}), suggesting greater removal performance under higher metal loads.

In contrast, *P. ostreatus* and *S. commune* exhibited values close to 3 mg L^{-1} at 50 mg L^{-1}, which may indicate a decrease in removal efficiency at higher concentrations, possibly associated with system limitations under these conditions.

Table 8: Final zinc (Zn) concentration as a function of fungal strain and initial concentration.

Fungal strain	Initial concentration (mg L^{-1})	Mean (mg L^{-1}) ± SD	Min	Max
G. applanatum	10	0.81 ± 0.08	0.74	0.89
	30	1.17 ± 0.32	0.88	1.52
	50	1.94 ± 0.15	1.77	2.06
P. sanguineus	10	0.56 ± 0.09	0.47	0.64
	30	0.77 ± 0.07	0.70	0.83
	50	0.68 ± 0.23	0.41	0.82
S. commune	10	0.46 ± 0.01	0.44	0.47
	30	0.75 ± 0.09	0.65	0.83
	50	0.54 ± 0.22	0.30	0.70
P. ostreatus	10	0.45 ± 0.02	0.43	0.47
	30	0.61 ± 0.07	0.54	0.68
	50	0.47 ± 0.16	0.36	0.66

In the case of zinc, residual concentrations were generally lower than those recorded for copper. At 50 mg L^{-1}, *P. ostreatus* (0.47 mg L^{-1}) and *S. commune* (0.54 mg L^{-1}) showed the lowest final concentrations, while *G. applanatum* presented the highest value (1.94 mg L^{-1}). This pattern is consistent with the statistical analysis, which demonstrated a higher overall removal efficiency for zinc.

The residual concentration increased with rising initial concentration while removal efficiencies remained above 94%. This behavior is consistent with concentration-dependent removal patterns reported in the literature; however, no specific mechanism can be confirmed based on the present data. Removal efficiencies ranged between 91.88% and 99.05% across all tested treatments.

Overall, the results demonstrate that all four strains exhibit a high removal capacity for both copper and zinc, with differential responses depending on the type of metal and the initial concentration. This is consistent with the significant interactions detected in the three-way ANOVA and reinforces the biotechnological potential of the evaluated system.

The high removal efficiencies of Cu and Zn observed in this study confirm the potential of the evaluated strains as bioremediation agents in contaminated aqueous systems. However, the statistical analysis highlights a key aspect that goes beyond simple percentage comparisons: the three-way ANOVA showed that all main effects and all interactions (strain × metal, strain × concentration, metal × concentration, and strain × metal × concentration) were highly significant ($p < 0.0001$). This implies that removal efficiency does not depend solely on the strain or the metal individually, but on the specific combination of both and the concentration level tested.

The strain × metal interaction indicates that each fungus responds differently to Cu and Zn. For example, while *P. ostreatus* and *S. commune* showed higher efficiencies against Zn at 50 mg L^{-1}, *Ganoderma applanatum* exhibited relatively lower values under the same treatment, highlighting differential affinities among species. This behavior suggests that the composition and density of active sites in the cell wall, as well as the specific physiology of each strain, influence the selective uptake of metal cations.

3.4. Discussion

Radial growth results of *G. applanatum*, *P. sanguineus*, *S. commune*, and *P. ostreatus* showed significant differences among species and culture media, confirming the physiological and metabolic variability characteristic of

white-rot lignicolous fungi. These differences are associated with their capacity to utilize carbon and nitrogen sources and regulate extracellular enzymes such as laccases and manganese peroxidases, which are essential for ligninolytic metabolism (Zehra & Meena 2025).

Under metal-free conditions, the highest radial growth in nutrient-rich media such as PDA and MEA agrees with Imtiaj et al. (2008), who reported optimal mycelial expansion for *S. commune* in media with easily assimilable carbon sources. Similarly, Sastre-Ahuatzi et al. (2007) demonstrated that glucose- or potato-based media promote rapid activation of primary metabolism in basidiomycetes, resulting in higher radial growth rates. In this context, *P. ostreatus* exhibited fast and uniform growth, consistent with Krupodorova et al. (2024), reflecting high metabolic plasticity and efficient adaptation to simple substrates. In contrast, *G. applanatum* showed slower growth, likely due to energy allocation toward secondary metabolism and ligninolytic enzyme production, as reported for *Ganoderma* species (Kato et al. 2024).

In the presence of Cu and Zn, significant interactions among species, metal type, and concentration indicate that mycelial response depends on the specific combination of factors. This behavior is consistent with Baldrian (2003), who reported that high copper concentrations may inhibit fungal growth through oxidative stress, while moderate levels can induce laccase activity. Likewise, Gadd (2009) explained that Cu and Zn exhibit dual roles as essential micronutrients and toxic elements, affecting membrane integrity, proteins, and redox balance at high concentrations. Zinc generally shows lower redox activity, whereas copper can promote reactive oxygen species formation, explaining its stronger inhibitory effect. In agreement with Fomina & Gadd (2014), the results suggest metal-specific tolerance mechanisms such as extracellular chelation, cell wall immobilization, and intracellular compartmentalization.

It is important to note that radial growth was used here as an indicator of physiological tolerance rather than removal capacity. Thus, while these results confirm the ability of strains to maintain growth under metal stress, they do not directly demonstrate bioremediation performance.

In this context, fungal biomass provides a more direct link between tolerance and potential removal capacity. Fungal strains are widely recognized for their resistance and adaptability to heavy metals (Lei et al. 2018, Li et al. 2019, Amin et al. 2024, Zare et al. 2024). In the present study, biomass remained stable or even increased under several fungus–metal–concentration combinations, indicating that growth was not significantly limited within the evaluated range. The highest biomass values were recorded for *P. ostreatus*, *P. sanguineus*, and *G. applanatum*, particularly at intermediate metal concentrations, suggesting the absence of critical inhibition of primary metabolism. Similar responses have been reported in ligninolytic fungi, where moderate metal levels can induce adaptive metabolic activity, including increased enzyme production (Baldrian 2003).

Although structural characterization was not performed, functional groups (–COOH, –OH, –NH) in fungal cell walls composed of chitin, glucans, and proteins have been reported in the literature as potential sites for metal binding; however, these interactions were not directly evaluated in this study (Fomina & Gadd 2014, Gadd 2009). In this sense, biomass plays a key role, as it determines the number of available binding sites (Fomina & Gadd 2014). Additionally, fungi have been reported to combine mechanisms such as surface biosorption, intracellular bioaccumulation, and extracellular precipitation; however, these processes should be considered as potential mechanisms, since they were not directly evaluated here (Gadd 2009). For *P. ostreatus*, high biomass likely reflects its metabolic plasticity and enzymatic capacity (Baldrian 2003), which has also been associated with enhanced metal removal (Araújo et al. 2023, Acosta et al. 2024).

These observations are consistent with removal behaviors described in the literature, which are often explained through biosorption-related frameworks. However, such mechanisms were not directly assessed in this study. Biosorption typically involves processes such as physical adsorption, ion exchange, complexation, and precipitation, and is influenced by factors including pH, temperature, biomass loading, and initial metal concentration (Magdum & Itankar 2026).

Consistent with these observations, removal efficiency results demonstrated significant differences between metals and their interactions with strain and concentration. The higher removal of Zn compared to Cu ($p < 0.0001$) may be associated with their chemical behavior: Zn^{2+} forms less stable coordination complexes, while Cu^{2+} has higher affinity for nitrogen-containing groups and greater competition for active sites (Lei et al. 2018, Li et al. 2019). This chemical difference supports the observed pattern of higher Zn removal efficiency.

The metal × concentration interaction and the three-way interaction further indicate that increasing initial concentration does not affect all strains uniformly. In several cases, removal efficiency increased at 50 mg L^{-1}, suggesting a concentration-gradient effect in which a higher driving force may enhance overall removal performance; however, the specific processes involved were not determined (Lei et al. 2018, Amin et al. 2024).

Although comparisons with other studies (Albert et al. 2018, Dey et al. 2020, Chen et al. 2022) should consider

differences in experimental conditions such as pH, temperature, and contact time, the factorial design used here allows robust internal comparisons. Importantly, ANOVA results indicated that neither metal type nor concentration significantly affected biomass within the 10–50 mg L^{-1} range, highlighting the physiological tolerance of all strains under metal stress (Harish et al. 2024).

While previous studies report additional metabolic capabilities for *S. commune*, such as nanoparticle biosynthesis (Bragta et al. 2025) and degradation of recalcitrant compounds (Augustine & Abraham 2025), these processes were not directly evaluated in this study and should be interpreted as potential rather than demonstrated mechanisms.

From an applied perspective, these findings provide preliminary evidence of the potential of lignicolous fungi for heavy metal removal under controlled laboratory conditions. However, it is important to note that the experiments were conducted using synthetic aqueous solutions, which do not fully replicate the complexity of real industrial or mining effluents. Factors such as mixed-metal interactions, organic matter content, pH variability, and scaling conditions may significantly influence removal performance. Therefore, further studies using real wastewater matrices and pilot-scale systems are required to validate the practical applicability of these fungal strains in mining-impacted environments in Peru.

Overall, the results demonstrate a clear relationship between radial growth, biomass production, and removal efficiency: radial growth reflects physiological tolerance, biomass determines the availability of binding sites, and removal efficiency results from the interaction between biological capacity and metal chemistry. This integrative approach confirms that metal removal is a multifactorial process dependent on strain, metal type, and concentration, reinforcing the biotechnological potential of lignicolous fungi (Lei et al. 2018, Li et al. 2019, Amin et al. 2024).

A limitation of this study is that the mechanisms of metal removal were not directly evaluated. Although processes such as biosorption, bioaccumulation, and enzymatic transformation are widely reported in ligninolytic fungi, no specific analyses were conducted in this work to confirm their occurrence. The present results demonstrate a reduction in metal concentration in the aqueous phase; however, the exact removal pathways cannot be determined. Future studies should include mechanistic approaches such as metal quantification in fungal biomass, FTIR or SEM-EDS analyses, enzymatic activity assays, and adsorption isotherms to better elucidate the processes involved.

Although the results demonstrated high removal efficiencies and stable biomass production across treatments, several methodological limitations should be considered when interpreting the findings. One of the main limitations of this study is the absence of abiotic controls, which restricts the ability to quantitatively differentiate between biological removal mechanisms, such as biosorption, bioaccumulation, and enzymatic transformation, and physicochemical processes including precipitation or passive adsorption. Consequently, while the observed metal removal is strongly associated with fungal activity, a minor contribution of non-biological processes cannot be completely excluded.

Additionally, the mechanisms underlying metal removal were not directly evaluated. Although ligninolytic fungi are widely reported to remove metals through multiple pathways, no specific analyses were conducted in this study to confirm the occurrence of these processes. Therefore, while a significant reduction in metal concentration in the aqueous phase was observed, the exact removal pathways remain undetermined.

Another limitation lies in the taxonomic identification of the fungal strains. The identification was based on macroscopic characteristics and comparison with reference catalogs, which should be considered preliminary. Although the selected taxa correspond to well-documented genera with distinctive morphological traits (e.g., *Ganoderma, Pleurotus, Pycnoporus*, and *Schizophyllum*), the possibility of misidentification at the species level cannot be entirely ruled out due to the absence of molecular confirmation (e.g., ITS rDNA sequencing).

Despite these limitations, the consistency of the experimental responses and the statistically significant effects detected in the factorial analysis support the validity of the observed trends. These findings provide a reliable basis for further investigation into the bioremediation potential of these fungi.

Future research should incorporate abiotic controls, continuous monitoring of pH, and molecular identification techniques to improve both mechanistic understanding and taxonomic resolution. In addition, mechanistic approaches such as metal quantification in fungal biomass, FTIR or SEM-EDS analyses, enzymatic activity assays, and adsorption isotherms are recommended to elucidate the specific pathways involved in metal removal and to strengthen the applicability of these fungal systems in environmental bioremediation.

One of the main limitations of this study is that all experiments were conducted under controlled laboratory conditions using synthetic aqueous solutions. While this approach allows for precise evaluation of fungal responses to specific metals and concentrations, it does not fully represent the physicochemical complexity of real wastewater systems. In natural and industrial settings, the presence of

multiple contaminants, fluctuating environmental conditions, and potential inhibitory compounds may alter fungal performance. Consequently, the results should be interpreted as indicative of potential rather than direct evidence of field applicability.

4. CONCLUSIONS

This study demonstrates the feasibility of using lignicolous fungi (*G. applanatum*, *P. sanguineus*, *S. commune*, and *P. ostreatus*) for the bioremediation of copper- and zinc-contaminated water. All strains achieved high removal efficiencies (>91%), with a maximum of 99.05%, indicating strong metal retention under the tested conditions. No single strain showed absolute superiority, as all exhibited comparable performance, though *S. commune* and *P. ostreatus* displayed faster mycelial growth, suggesting higher physiological tolerance.

Fungal biomass was highest in *P. ostreatus*, *P. sanguineus*, and *G. applanatum*, particularly at intermediate metal concentrations, though variability among replicates (CV = 30.34%) highlights the influence of individual adaptation, colonization heterogeneity, and nutrient fluctuations. Future studies should standardize inocula, increase replicates, and control physicochemical conditions more strictly.

While removal was confirmed via FAAS, this study did not directly assess mechanisms such as biosorption, bioaccumulation, or enzymatic activity. Nonetheless, the results provide robust evidence of the strains' capacity to reduce metal concentrations, establishing a foundation for mechanistic studies, kinetic evaluations, and process scale-up in bioremediation applications.

It is important to highlight that the absence of kinetic data represents a limitation of this study, as the use of a single endpoint measurement does not allow evaluation of removal dynamics over time. Future research should include kinetic analyses to better understand the rate and mechanisms of metal removal.

A kinetic analysis is recommended for future studies to better understand the removal dynamics.

5. REFERENCES

Acosta, I., Rodríguez, A., Cárdenas, J.F., Martínez, V.M. and Torre, M.E., 2024. Eliminación de cadmio de soluciones acuosas mediante diferentes biosorbentes. En: Jha, A. K, Kumar, N. (eds.) *Toxicidad del cadmio en el agua*. Springer Water. Springer, Cham. [DOI]

Albert, Q., Leleyter, L., Lemoine, M., Heutte, N., Rioult, J.P., Sage, L., Baraud, F. and Garon, D., 2018. Comparison of tolerance and biosorption of three trace metals (Cd, Cu, Pb) by the soil fungus Absidia cylindrospora. *Chemosphere*, 196, 386–392. [DOI]

Amin, I., Nazir, R. and Rather, M.A., 2024. Evaluación de la tolerancia a múltiples metales pesados de hongos del suelo para la eliminación simultánea de metales peligrosos. *World J Microbiol Biotechnol*, 40, 175. [DOI]

Anastopoulos, I. and Kyzas, G.Z., 2015. Progress in batch biosorption of heavy metals onto algae. *Journal of Molecular Liquids*, 209, 77–86. [DOI]

Araújo, N., Justino, M., Marinho, G. and Rodrígues, K., 2023. Action of fungi in the removal of metals from wastewater and environmental compartments: a review. *AIDIS Journal of Environmental Engineering and Sciences: Research, Development and Practice*, 16(1), 361–385. [DOI]

Augustine, J. and Abraham, J., 2025. Utilization of Schizophyllum commune for the biodegradation of chlorhexidine gluconate and Benzalkonium chloride: an innovative approach to environmental remediation. *Discov Sustain*, 6, 574. [DOI]

Baldrian, P., 2003. Interactions of heavy metals with white-rot fungi. *Enzyme and Microbial Technology*, 32(1), 78–91. [DOI]

Bragta, D., Garg, P., Chaudhary, S., Madhok, G., Negi, S., Panwar, S., Singh, A., and Kumar, R., 2025. Eco-friendly biosynthesis of ZnO nanoparticles using fungus Schizophyllum commune and their hybrid with chitosan for enhanced UV-A photocatalytic degradation of tetracycline. *Chemosphere*, 387, 144666. [DOI]

Chen, L., Zhang, X., Zhang, M., Zhu,Y. and Zhuo, R., 2022. Removal of heavy-metal pollutants by white rot fungi: mechanisms, achievements, and perspectives. *Journal of Cleaner Production*, 354, 131681. [DOI]

Córdova, H., 2010. *Desinfección y cultivo de Aurciularia auricula (L.: Fr.) Under y Auricularia delicata (Fr.) Henn a partir de Basidiocarpo y Basidiosporas*. Tingo María.

Dey, P., Malik, A., Mishra, A., Singh, D.K., Bergen, M. and Jehmlich, N., 2020. Mechanistic insight to mycoremediation potential of a metal resistant fungal strain for removal of hazardous metals from multimetal pesticide matrix. *Environmental Pollution*, 262, 114255. [DOI]

Fomina, M. and Gadd, M., 2014. Biosorption: current perspectives on concept, definition and application. *Bioresource Technology*, 160, 3–14. [DOI]

Fu, F. and Wang, Q., 2011. Removal of heavy metal ions from wastewaters: a review. *Journal of Environmental Management*, 92(3), 407–418. [DOI]

Gadd, G.M., 2009. Biosorption: critical review of scientific rationale, environmental importance and significance for pollution treatment. *Journal of Chemical Technology and Biotechnology*, 84(1), 13–28. [DOI]

Gao, X., Wei, M., Zhang, X., Xun, Y., Duan, M., Yang, Z., Zhu, M., Zhu, Y. and Zhuo, R., 2024. Copper removal from aqueous solutions by white rot fungus Pleurotus ostreatus GEMB-PO1 and its potential in co-remediation of copper and organic pollutants. *Bioresource Technology*, 395, 130337. [DOI]

González-González, R. B, Sharma, P., Singh, S. P, Américo-Pinheiro, J.H.P., Parra-Saldívar, R., Bilal, M. and Iqbal, H.M.N., 2022. Persistencia, peligros ambientales y mitigación de contaminantes residuales farmacéuticamente activos de matrices de agua. *Ciencia Ambiente Total*, 821, 153329. [DOI]

Harish, B.S., Lekshmi, K.M. and Jayapal, M., 2024. Eliminación simultánea de metales pesados y producción de enzimas fúngicas. En: Uppuluri, KB, Selvasembian, R. (eds.) *Bioprospección de hongos multitarea para un entorno sostenible*. Springer, Singapur. [DOI]

Hultberg, M. and Golovko, O., 2024. Uso de aserrín para la producción de enzimas ligninolíticas por hongos de podredumbre blanca y eliminación de fármacos. *Bioprocess Biosyst Eng*., 47, 475–482. [DOI]

Imtiaj, A., Jayasinghe, C., Lee, G.W., Kim, H.Y., Shim, M.J., Rho, H-S., Lee, H.S., Hur, H., Lee, M.W., Lee, U-Y. and Lee, T.S., 2008. Physicochemical requirement for the vegetative growth of Schizophyllum commune collected from different ecological origins. *Mycobiology*, 36(1), 34–9. [DOI]

Johnson, D.B. and Hallberg, K.B., 2005. Acid mine drainage remediation options: A review. *Science of The Total Environment*, 338(1–2), 3–14. [DOI]

Kapoor, A. and Viraraghavan, T., 1995. Fungal biosorption - an alternative

treatment option for heavy metal bearing wastewaters: a review. *Bioresource Technology*, 53(3), 195–206. [DOI]

Kato, H., Miura, D., Kato, M. and Shimizu, M., 2024. Metabolic mechanism of lignin-derived aromatics in white-rot fungi. *Appl Microbiol Biotechnol*, 108, 532. [DOI]

Krupodorova, T., Barshteyn, V., Tsygankova, V., Sevindik, M. and Blume, Y., 2024. Strain-specific features of Pleurotus ostreatus growth in vitro and some of its biological activities. *BMC Biotechnol*, 24(39). [DOI]

Langer, G. J, Bubkamp, J., Terhonen, E. and Blumenstein, K., 2021. Capítulo 10: Hongos que habitan en tejidos leñosos de árboles. En: Asiegbu, F. O., Kovalchuk, A. (eds.) *Microbiología forestal*. Academic Press, Nueva York.

Lei, J., Guo, Q., Yao, W., Duan, T., Chen, P. and Zhu, W., 2018. Bioconcentration of organic dyes via fungal hyphae and their derived carbon fibers for supercapacitors. *Journal of Materials Chemistry*, 6(23), 10710–10717. [DOI]

Li, Y., Zou, G., Yang, S., Wang, Z., Chen, T., Yu, X., Guo, Q., He, R., Duan, T. and Zhu, W., 2019. Integration of bio-inspired adsorption and photodegradation for the treatment of organics-containing radioactive wastewater. *Chemical Engineering Journal*, 364, 139–145. [DOI]

López, C., 1998. *Transformación de tetracloroetano (TcCA) mediada por biopelículas de Pseudomonas aeruginosa* (Doctoral dissertation, Tesis de Maestría en Biotecnología y Bioingeniería, Escuela de Post Grado, Universidad Nacional de Trujillo, La Libertad, Perú).

Lu, N., Hu, T., Zhai, Y., Qin, H., Aliyeva, J. and Zhang, H., 2020. Fungal cell with artificial metal container for heavy metals biosorption: equilibrium, kinetics study and mechanisms analysis. *Environmental Research*, 182, 109061. [DOI]

Luna, D.C., Vieira, I.F., Aquino, M., Quintão, Y.F. and do Carmo, M., 2020. Exposure to inorganic environmental contaminants and damage to human health. *Brazilian Journal of Health Review*, 3(4), 10353–10369. [DOI]

Magdum, P. and Itankar, N., 2026. Environmental remediation and sustainable approaches to heavy metal removal: a comprehensive review of biosorption techniques. *Nature Environment and Pollution Technology*, 25(1), B4334. [DOI]

Majumdar, A., 2024. *Phytoremediation* of heavy metal pollutants using fungi. In: Madhav, S., Gupta, G.P., Yadav, R.K., Mishra, R., Hullebusch, E.v. (eds) Phytoremediation. Springer, Cham. [DOI]

Marcovecchio, J.E., Moreno, V.J. and Pérez, A., 1991. Metal accumulation in tissues of sharks from the Bahía Blanca estuary, Argentina. *Marine Environmental Research*, 31(4), 263–274. [DOI]

Mata, M., 1999. *Macrohongos de Costa Rica (Vol. 1)*. INBio.

Mata, M., Halling, R. and Mueller, G.M., 2003. *Macrohongos de Costa Rica (Vol. 2)*. INBio.

Módenes, A.N., Espinoza-Quiñones, F.R., Lavarda, F.L., Colombo, A., Borba, C.E., Leichtweis, W.A. and Mora, N.D., 2013. Remoção dos metais pesados Cd (II), Cu (II) e Zn (II) pelo processo de biossorção utilizando a macrófita Eicchornia crassipes. *Rem: Revista Escola de Minas*, 66(3), 355–362. [DOI]

Paria, K., Pyne, S. and Chakraborty, S.K., 2022. Optimization of heavy metal (lead) remedial activities of fungi Aspergillus penicillioides (F12) through extra cellular polymeric substances. *Chemosphere*, 286(3), 131–874. [DOI]

Ríos-Ruiz, R.A. and Ruiz-Rengifo, L., 1993. Aislamiento y cultivo del hongo comestible Pleurotus afin ostreatus (Jacq. ex Fr) Kumm en Tingo María. Folia Amazónica, 5(1–2), 5–14. [DOI]

Robledo, G., 2006. *Taxonomía, Ecología y Diversidad de poliporos*. Cusco, Perú: Instituto Multidisciplinario de Biología Vegetal.

Ryvarden, L., 2007. *Fundamentos taxonómicos en identificación de Poliporaceos y Ascomicetos Tropicales y Neotropicales*. Oslo, Noruega: Synopsis Fungorum, 1.

Sanyal, P., Chakraborty, S.K. and Ghosh, P.B., 2015. Phytoremediation of sewage-fed wetlands of East-Kolkata, India – A case study. *International Research Journal of Environment Sciences*, 4(1), 80–89. Available at: https://www.isca.in/IJENS/Archive/v4/i1/14.ISCA-IRJEvS-2014-247.pdf.

Sastre-Ahuatzi, M., Téllez-Téllez, M., Díaz-Godínez, G., Montiel-González, A.M., Díaz, R. and Sánchez, C., 2007. Mycelial growth of strains of Pleurotus ostreatus developed on agar and its correlation with the productivity in pilot production farm. *Industrial Microbiology Braz. J. Microbiol*., 38(3). [DOI]

Sharma, K.R., Giri, R. and Sharma, R.K., 2020. Lead, cadmium and nickel removal efficiency of white–rot fungus Phlebia brevispora. *Letters in Applied Microbiology*, 71(6), 637–644. [DOI]

Singh, V.K. and Singh, R., 2024. Role of white rot fungi in sustainable remediation of heavy metals from the contaminated environment. *Micology*, 15(4), 585–601. [DOI]

Singh, S., Singh, N.P., Agrawal, S. and Kumar, A., 2025. Unleashing the potential of white-rot fungi mycelium for functional biomaterials development. *Discov Mater*, 5, 96. [DOI]

Suh, J.H., Kim, D.S. and Song, S.K., 2001. Inhibition effect of initial Pb2+ concentration on Pb2+ accumulation by Sacharomyces cerevisiae and Aureobasidium pullulans. *Bioresource Technology*, 79(1), 99–102. [DOI]

Welz, B. and Sperling, M., 1999. *Atomic Absorption Spectrometry* (3rd ed.). Wiley-VCH, Weinheim/New York.

Zare, P., Giyahchi, M. and Moghimi, H., 2024. Mycosorption and mycoremediation: fungi as the tools for heavy metal removal. In: Uppuluri, K.B., Selvasembian, R. (eds) *Bioprospecting of Multi-tasking Fungi for a Sustainable Environment*. Springer, Singapore. [DOI]

Zehra, A. and Meena, M., 2025. Aprovechamiento de hongos endófitos para una fitorremediación eficaz: mecanismos y aplicaciones. En: Meena, M., Zehra, A., Swapnil, P., Seth, C. S. (eds.) *Sostenibilidad metabólica de los endófitos*. Microorganismos para la sostenibilidad, vol. 52. Springer, Singapur. [DOI]

Nature Environment and Pollution Technology
An International Quarterly Peer-Reviewed Open Access Journal

p-ISSN: 0972-6268 | e-ISSN: 2395-3454 Vol. 25 | No. 4 | Article ID D1924 | 2026

RESEARCH ARTICLE https://doi.org/10.46488/NEPT.2026.v25i04.D1924 OPEN ACCESS

Occurrence and Characterization of Microplastics in the Chili River (Arequipa, Peru) Based on FTIR-ATR and SEM-EDS Analysis

Gerby Giovanna Rondán-Sanabria[1]†, Holger Saul Perez-Montaño[1,2], Edgard Ronny Delgado-Huamani[1] and Italo Francisco Treviño-Zevallos[1]

[1]Universidad Tecnológica del Perú, Institute of Renewable Energy, Av. Tacna y Arica No. 160, Arequipa 04001, Perú
[2]Arrhenius Research Institute, Arequipa 04012, Perú
†Corresponding author: Gerby Giovanna Rondán Sanabria; c16238@utp.edu.pe, gerbyrs@gmail.com

ARTICLE HISTORY

Received: 13-03-2026
Revised: 08-05-2026
Accepted: 20-05-2026

KEYWORDS

Chili River
Surface water
Microplastics
Plastic waste management

CITE THIS ARTICLE

Rondán-Sanabria, G.G., Perez-Montaño, H.S., Delgado-Huamani, E.R. and Treviño-Zevallos, I.F., 2026. Occurrence and characterization of microplastics in the Chili River (Arequipa, Peru) based on FTIR-ATR and SEM-EDS analysis, *Nature Environment and Pollution Technology,* 25(4), D1924. https://doi.org/10.46488/NEPT.2026.v25i04.D1924

COPYRIGHT & LICENCE

© 2026 The Authors
Open Access under CC BY 4.0.

PUBLISHED BY

TECHNOSCIENCE PUBLICATIONS

ABSTRACT

Microplastic contamination in fluvial systems has emerged as a growing environmental concern linked to urban expansion and inadequate plastic waste management. In this study, we assessed the abundance, morphology, color, and polymeric composition of microplastics in the surface waters of the Chili River (Arequipa, Peru). Particles were identified using stereoscopic microscopy and classified according to shape and color, while chemical characterization was performed using Fourier transform infrared spectroscopy with attenuated total reflectance (FTIR-ATR). Detailed morphological analysis was conducted using scanning electron microscopy coupled with energy-dispersive X-ray spectroscopy (SEM-EDS). The analysis revealed a predominance of fibers of various colors (60–80%), followed by foams and fragments. Color distribution varied across sampling sites, with bluish-green being the most prevalent color, particularly at TB, where it accounted for 30% of the fibers. FTIR-ATR analysis enabled the identification of widely used conventional polymers, including polyethylene (52.4%), polyethylene terephthalate (23.8%), ethylene-vinyl acetate, and polyurethane. SEM micrographs exhibited irregular surfaces, cracks, delamination, and cavities, consistent with progressive physical degradation. EDS was also used as a complementary tool to evaluate elemental surface features and possible inorganic deposits, while polymeric identification was based primarily on FTIR-ATR results. These findings suggest that the microplastics present in the Chili River are compatible with environmental aging and secondary fragmentation processes, reflecting the influence of urban activities on fluvial contamination dynamics.

1. INTRODUCTION

Since the mid-twentieth century, plastic production has increased exponentially, posing a global threat that impacts almost every ecosystem globally (Yang et al. 2024). Projections indicate that more than 700 million tons of plastic waste could accumulate in aquatic and terrestrial environments by 2040 (Lau et al. 2020). This increase, driven by unsustainable consumption patterns and deficiencies in waste management systems, has positioned plastic pollution as one of the most pressing emerging environmental challenges worldwide (Barnes et al. 2009, Peng et al. 2018). Due to their persistence and slow degradation rates, polymers such as polypropylene (PP), polycarbonate (PC), and polyvinyl chloride (PVC) can remain in the environment for extended periods, progressively fragmenting into particles smaller than 5 mm, known as microplastics (MPs) (Österlund et al. 2023).

Rivers serve as fundamental transport pathways for microplastics from terrestrial sources to the oceans, functioning both as conduits and temporary reservoirs (Yang et al. 2024; Joshi et al. 2025). It is estimated that countries with high levels of mismanaged plastic waste may contribute substantially to riverine plastic discharge into marine environments (Upadhyay & Bajpai 2021, Belli et al. 2026). Additionally, recent studies have demonstrated that microplastics represent not only a physical contaminant but also a relevant fraction of fossil-derived particulate organic carbon in fluvial systems, potentially altering biogeochemical processes and the global carbon cycle. For example, in large-scale systems such as the Yellow River, annual transport has been estimated at up to 7.73×10^{16} particles delivered to the ocean, underscoring the magnitude of the problem at the watershed scale (Liu et al. 2025).

Numerous investigations have documented the widespread presence of microplastics in river systems with varying degrees of urbanization and anthropogenic pressure. Studies conducted in tropical rivers in Malaysia have shown that MP abundance and composition are strongly influenced by urban activities, wastewater discharge, and hydrodynamic conditions (Anuar et al. 2023). In Asian river systems (Xiang et al. 2026), population density, industrialization, and regional climatic variability have been identified as key drivers of microplastic spatial distribution and ecological risk. Likewise, the Jamuna River in Bangladesh reported high concentrations of fibers and fragments, with polymers such as PE, PET, and PP predominating, along with moderate to high ecological risk indices (Islam et al. 2025). In the Latin American context, recent assessments in Brazilian rivers highlight the predominance of fibers and common polymers such as PE and PP, while emphasizing the need for more comprehensive regional studies (Lebreton & Andrady 2019, Belli et al. 2026). In this sense, the Amazon basin has been identified as a critical region in the transfer of plastics to the Atlantic Ocean, with the Amazon River recognized as one of the main global contributors (Giarrizzo et al. 2019, dos Santos Silva et al. 2024).

Recent research in high-Andean systems of southern Peru has also reported significant microplastic concentrations in strategic freshwater reservoirs, such as the Colca–Chili system in Arequipa. These studies indicate that climatic factors such as wind dynamics, precipitation, and solar radiation play a crucial role in particle transport, fragmentation, and degradation, favoring the accumulation of fibers and particles smaller than 1 mm (Banda et al. 2025). In the Arequipa context, the Quilca–Vítor–Chili watershed has shown a predominance of fibers and polymers such as PE and PP associated with urban sources and the weathering of larger plastic debris, which contributes to the generation of secondary microplastics (Larrea Valdivia et al. 2025). Therefore, the present study aims to characterize the shape, color, and polymeric composition of microplastics in the surface waters of the Chili River using stereoscopic microscopy, FTIR-ATR, and SEM-EDS, and interpret their degree of environmental transformation through the integration of chemical and morphological evidence. Within this context, this research seeks to advance understanding of microplastic behavior in urban fluvial systems of the Andean region and to provide scientifically robust information for evaluating their environmental impact.

2. MATERIALS AND METHODS

2.1. Reagents and Equipment

The materials used in this study were made of glass or stainless steel to prevent contamination from plastic residues. Likewise, all reagents were of analytical grade and purchased from Sigma-Aldrich. Infrared spectroscopic analyses were conducted using a Bruker FTIR-ATR system (Model 3120), while morphological identification was performed with a LABTRON stereomicroscope (Model LSM-B12). High-resolution imaging and elemental characterization were carried out using a Thermo Scientific (Model Scios 2) scanning electron microscope equipped with energy-dispersive spectroscopy (SEM-EDS).

2.2. Study Area

Arequipa is the second most populous city in Peru, located on the western slope of the Andes at an altitude of approximately 2,320 m above sea level. Based on data from the National Institute of Statistics and Informatics (INEI), the metropolitan area of Arequipa has an estimated population ranging between 1.1 and 1.2 million inhabitants. Several industrial facilities operate both within and around the city, some of which are situated along the banks of the Chili River. The Chili River forms part of the Quilca–Vítor–Chili watershed system, which covers an area of 13,529 km². Its river network flows predominantly from east to west before discharging into the Pacific Ocean (Carpio Fernández et al. 2022).

In this study, four sampling sites were selected along an approximately 8 km urban stretch of the river, identified as Chilina (CH), Av. La Marina (AM), Tingo (TI), and Tiabaya (TB) (Fig. 1). Sampling was conducted during three periods: May (after the rainy season, which extends from December to March) and subsequently in July and September. The initial sampling campaign followed a period of intense rainfall that generated extreme turbidity

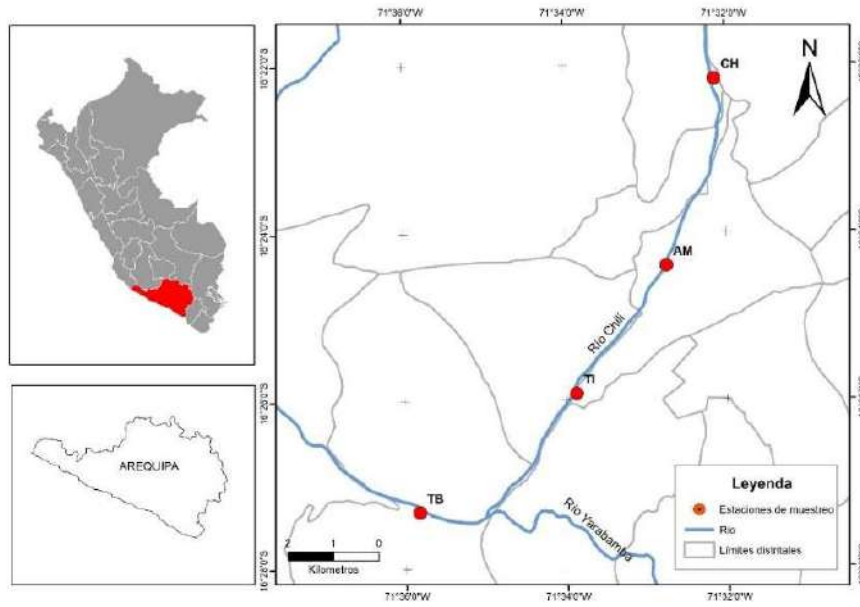


Fig. 1: Sampling sites on the Chili River in the city of Arequipa.

and significant sediment transport, conditions that hindered microplastic identification. These points were selected due to their accessibility and because they include areas of tourist, recreational, and agricultural relevance.

2.3. Sampling of Water

Surface water from the river was collected from the designated sites (Fig. 1). No plastic materials were used during sampling to prevent contamination. At this stage, river water was collected using a 10 L stainless steel bucket with a lid, which was immersed to a depth of approximately 5 cm against the current. The collected water was transported to the laboratory in sealed 4 L glass bottles, with triplicate samples collected at each sampling point. Every material used throughout the procedure was thoroughly rinsed with distilled water prior to use to minimize potential contamination.

2.4. Sample Preparation

First, the material retained on the sieve was transferred to a glass beaker for subsequent treatment with potassium hydroxide. In parallel, 1 L of water was measured and filtered through a 200 µm mesh, followed by organic matter digestion (Mahmud et al. 2025), with minor modifications. For this purpose, 10% potassium hydroxide (KOH) was added at a ratio of 2:1 (solution to sample) for organic digestion and kept at 50 °C for 24 h. Following digestion of the organic content, density separation was performed using a saturated sodium chloride (NaCl) solution (approximately 1.2 g cm^{-3}), facilitating the flotation of microplastics. The ≥ 200 µm fraction corresponded to particles initially retained by the mesh, whereas the ≥ 8 µm fraction corresponded to particles subsequently recovered through vacuum filtration. Both stages were part of the same sequential procedure applied to the same processed sample.

The supernatant was carefully recovered and subjected to vacuum filtration using Whatman No. 4 filter paper, with an approximate retention size of 8 µm. All procedures were conducted in triplicate to verify recovery efficiency, employing analytical-grade reagents and ultrapure water. Finally, the filter papers were placed in glass Petri dishes, covered with aluminum foil, and preserved for subsequent microscopic analysis.

Although procedural blanks and specific airborne contamination controls were not performed, glass and stainless-steel materials were used throughout all analytical stages, and the samples were kept covered with aluminum foil to minimize external contamination. Therefore, the predominance of fibers observed in this study should be interpreted with caution, considering the potential influence of environmental contamination inherent to microplastic processing.

2.5. Microplastic Separation

Once the MPs were extracted, the retained particles on the filter paper were examined under a stereomicroscope and manually sorted using ultra-fine forceps based on their shape and color. Although gravimetric quantification of the recovered particles would have provided additional

information, this approach was not feasible due to the extremely small size of the MPs.

Despite this limitation, the particles were successfully isolated and categorized for subsequent polymer identification using FTIR-ATR analysis. Selected MPs were also mounted onto double-sided carbon adhesive tape to enable detailed surface and morphological characterization by scanning electron microscopy coupled with energy-dispersive spectroscopy (SEM-EDS). Sample preparation required microscopic assistance to ensure precise manipulation and positioning of individual particles.

2.6. Chemical Characterization by FTIR-ATR

Polymers were identified, and functional group analysis of the isolated MPs was conducted using a Bruker Model 3120 Fourier transform infrared (FTIR) spectrometer equipped with a diamond attenuated total reflectance (ATR) accessory. Spectral measurements were acquired over a range of 4000–400 cm^{-1}, using 24 scans per sample at a resolution of 4 cm^{-1}. All analyses were performed in triplicate to ensure reproducibility. These spectra were normalized at 3760 cm^{-1}, a region where the baseline remained stable, and interference from atmospheric water vapor was minimal. This normalization was necessary because absolute absorbance intensity depends on the extent of contact between the sample and the ATR crystal surface, a parameter that cannot be precisely controlled during measurement.

2.7. Scanning Electron Microscopy (SEM) and Energy-Dispersive Spectroscopy (EDS)

The surface morphology of the microplastics was examined using scanning electron microscopy (SEM) equipped with an Everhart–Thornley detector (ETD), operating at a working distance of 7–12 mm. Elemental composition analysis was carried out by energy-dispersive X-ray spectroscopy (EDS). A Thermo Scientific Scios 2 microscope was employed to evaluate the morphological features of the MPs, using magnifications ranging from 125× to 10,000×. To prevent charge accumulation during analysis, the samples were previously coated with a thin gold layer using a Q150R ES Plus sputter coater (Quorum Technologies) for 2 minutes prior to imaging.

2.8. Data Analysis

The results obtained were processed using Origin Pro 2025 software. Data are reported as mean values ± standard deviation (SD). Standard deviation was calculated to assess variability among sampling sites and particle categories. Given the exploratory nature of the study and the limited number of samples per site, inferential statistical tests were not applied. Accordingly, the analysis focuses on descriptive statistics to highlight distribution patterns in particle shape, color, and polymer type.

3. RESULTS AND DISCUSSION

3.1. Abundance and Distribution of Microplastics

The surface water samples at the different sampling sites showed no visible debris and were characterized by a transparent appearance. However, given that microplastics (MPs) are not detectable to the naked eye, all samples were filtered using a 200 µm mesh to recover larger microplastic particles as well as associated organic residues. Results are shown in Table 1 and report the mean abundance of MPs in the surface waters of the Chili River across the four sampling sites during three seasons (autumn, winter, and spring). For the estimation of abundance, two size fractions ($\geq$ 200 µm and $\geq$ 8 µm) were considered to obtain a comprehensive approximation of the total number of microplastics per liter of water. The findings indicate that MPs were present in all seasons and at all sampling sites, suggesting widespread contamination along the studied river stretch, both spatially and temporally. Clear differences were observed among sites and seasons. A descriptive pattern of increasing microplastics abundance from CH to TB was observed across the sampling periods (Table 1), suggesting cumulative influence of urban activities along the studied river section.

This spatial pattern may be associated with the influence of downstream urban activities and aligns with findings reported for the Quilca–Vítor–Chili watershed, where a generalized presence of MPs in surface waters was documented, along with higher abundances associated with urban and agricultural pressures in publicly accessible sites (Larrea Valdivia et al. 2025). A similar trend was reported by Islam et al. (2025). In the Jamuna River (Bangladesh), river sections flowing through densely populated areas exhibited significantly higher MP concentrations than less urbanized stretches, a pattern attributed to domestic effluents and urban waste inputs. In contrast, the seasonal increase in microplastic abundance may be interpreted as a response of the fluvial system to post-rainfall redistribution processes, peaking during spring. In this season, the highest abundance was recorded at site TB, with 23.00 ± 2.00 and 128.33 ± 4.02 MPs/L, whereas the lowest values were observed at CH, with 11.33 ± 1.53 and 32.33 ± 2.52 MPs/L (Table 1).

During the rainy season (summer, December to March), however, MPs may become dispersed, diluted, or deposited in sediments and along riverbanks, thereby reducing their detectability within the water column. In contrast, during the dry and transitional periods (autumn to spring), characterized

by elevated solar radiation and higher temperatures, plastic debris exposed along the banks of the Chili River may undergo photo-oxidation and secondary fragmentation. These processes likely contribute to the generation of smaller microplastic particles and their gradual release into the river channel, which may explain the increased abundance observed during spring. This behavior was observed in the Ariyankuppam River (India), where surface-water MP concentrations did not reach their highest levels during periods of intense rainfall, but rather during subsequent stages when discharge decreases and previously deposited materials are remobilized (Joshi et al. 2025). Similarly, in fluvial sediments of the Qin River (China), surface sediment layers were found to accumulate MPs particularly fibers and small fragments, which may be resuspended into the river channel under variable hydrodynamic conditions (Ma et al. 2025). Similarly, the same behavior was reported in Asian rivers, where reduced discharge promotes the release of microplastics stored in sediments, thereby increasing concentrations in the water column (Yang et al. 2025).

Moreover, integrating the 200 µm and 8 µm size fractions enabled the capture of a substantial proportion of fine microplastics, contributing to a more representative estimate of actual MP abundance per liter of water at the time of sampling (Fig. 2). An apparent increase in MP concentrations from Chilina (CH) to Tiabaya (TB) was observed, primarily driven by fibers. In addition, recent methodological studies caution that the inclusion of smaller size fractions may substantially elevate reported abundance values and complicate direct comparisons across studies. Nevertheless, this approach provides a more comprehensive assessment of the true magnitude of microplastic contamination in fluvial systems (Büngener et al. 2024, Venkatachalam & Radhakrishnan 2025).

In general, the findings for the Chili River are consistent with evidence reported for urban rivers worldwide. The observed patterns suggest that this river stretch may be influenced by anthropogenic activities, including informal dumping sites, solid waste discharge, restaurants, hotels, and densely urbanized areas, all of which contribute significantly

Table 1: Abundance of microplastics identified per liter of water sampled in May, July, and September.

Season						
Sampling Site	May/Autumn		July/Winter		September/Spring	
	≥ 200 µm	≥ 8 µm	≥ 200 µm	≥ 8 µm	≥ 200 µm	≥ 8 µm
CH	2.33 ± 0.58	5.33 ± 1.53	7.00 ± 1.00	17.67 ± 2.08	11.33 ± 1.53	32.33 ± 2.52
AM	4.00 ± 1.00	13.00 ± 2.00	11.33 ± 0.58	48.00 ± 2.00	16.33 ± 1.43	81.33 ± 2.31
TI	6.00 ± 1.00	18.33 ± 1.53	14.00 ± 1.00	59.67 ± 2.52	20.33 ± 1.00	95.00 ± 5.00
TB	6.67 ± 1.53	19.33 ± 2.08	16.67 ± 1.53	62.00 ± 2.00	23.00 ± 2.00	128.33 ± 4.02

CH: Chilina, AM: Avenida La Marina, TI: Tingo, TB: Tiabaya.

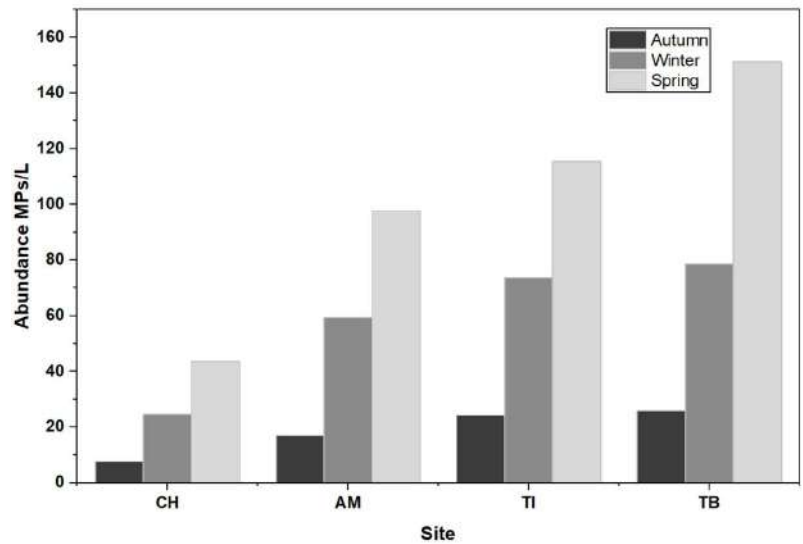


Fig. 2: Total abundance of microplastics by season and water sampling site in the Chili River.

to microplastic contamination along this section of the river.

3.2. Types of Plastics, Shape, and Color

Fig. 3 shows the morphological forms of MPs identified through stereoscopic microscopy at magnifications of 60× and 80×. Four primary microplastic morphotypes were distinguished: fragments, films, fibers, and foams, based on their color, morphology, and surface appearance under microscopic observation. The particles extracted from the filters corresponded predominantly to blue-green, pink, and purple fibers, indicating a significant contribution from anthropogenic sources, particularly synthetic textiles and commonly used plastic materials. The larger fibers, fragments, films, and foams were selected and grouped for subsequent characterization by FTIR-ATR. However, some smaller MPs could not be manually retrieved using forceps due to their reduced dimensions and, consequently, were not subjected to spectroscopic analysis. This methodological limitation has been reported in similar studies and is associated with the inherent challenges of handling micrometric-scale MPs (Hidalgo-Ruz et al. 2012, Gune & Martin 2025).

Fig. 4 presents the percentage distribution of MPs by shape, color, and polymer type in the Chili River. Among the identified particles, fibers were the dominant form, representing 60% at site CH (46 fibers) and 80% at TB (195 fibers) (Fig. 4A). Foams constituted the second most abundant category, with 15 units at CH, accounting for 20% of the total at that site. Films were observed in intermediate proportions, ranging from 5 to 15% across sampling sites, whereas fragments were identified at comparatively lower percentages. These patterns are consistent with those documented in other fluvial systems, where fibers typically constitute the most abundant fraction of MPs (Anuar et al. 2023, Harini et al. 2025, Khan et al. 2025, Ullah et al. 2025). Similarly, the present findings align with reports from Quilca Vitor Chili (Larrea Valdivia et al. 2025), indicating a predominant contribution from domestic discharges, synthetic textile fibers, and solid waste deposited along riverbanks.

Concerning the distribution of color (Fig. 4B), bluish-green particles exhibited the highest percentages, with similar values ranging from 25–30% at CH, AM, and TI, and approximately 30% at TB. These were followed by pink (10–20%) and transparent particles (10–15%). Red particles

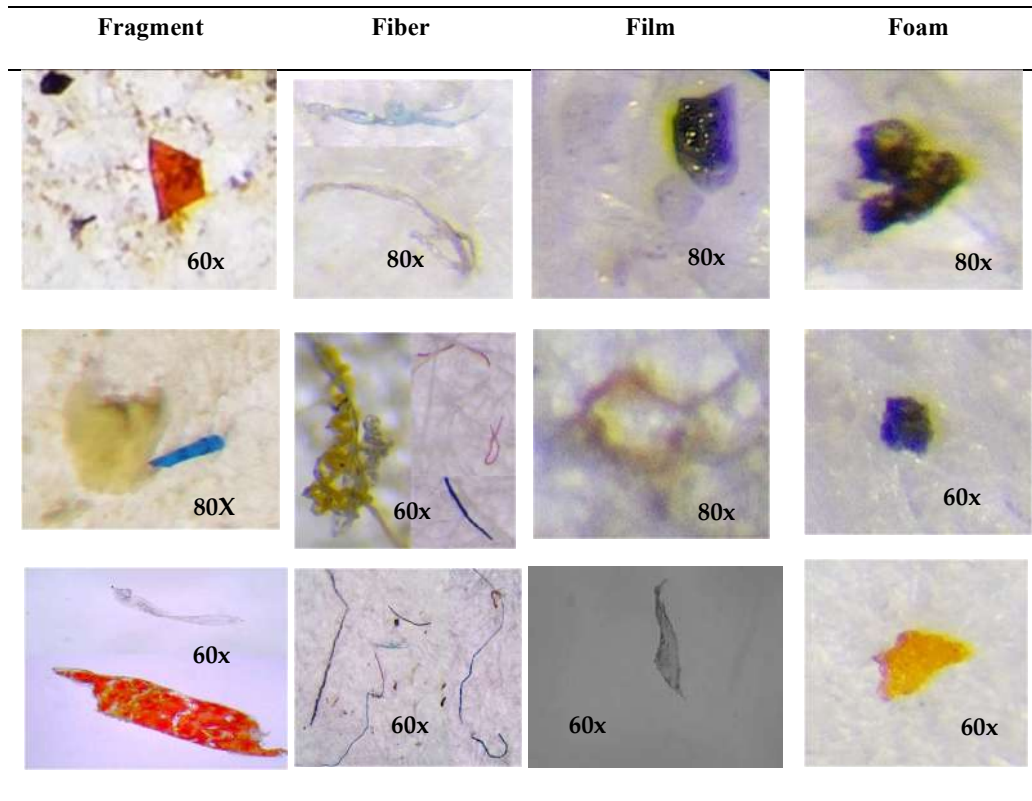


Fig. 3: Representative stereomicroscope images of the distinct microplastic forms detected in the surface waters of the Chili River.

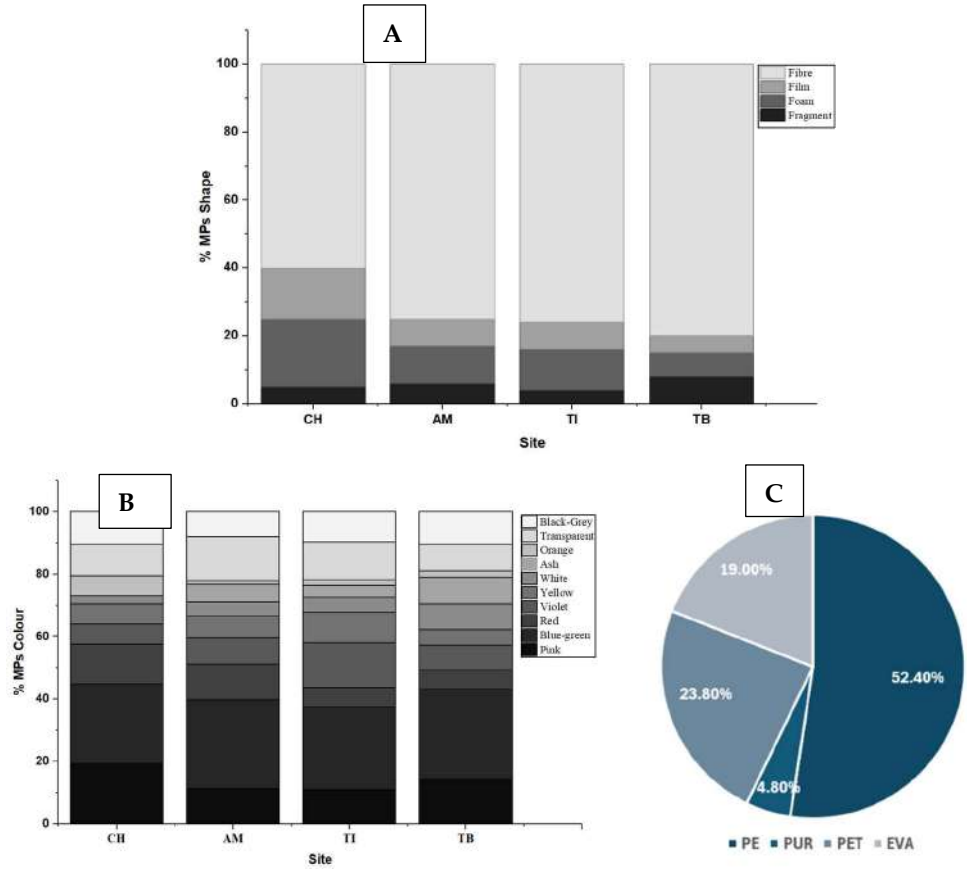


Fig. 4: (A) Percentage distribution of microplastic forms; (B) color distribution of MPs; and (C) relative abundance of polymers identified by FTIR-ATR.

showed intermediate proportions (5–12%), whereas black-gray particles remained below 10% at all sampling sites. The predominance of bright and visibly colored particles may reflect the contribution of secondary plastics derived from packaging materials, household utensils, and dyed synthetic fibers. Additionally, variations in particle color may also be associated with environmental weathering processes, including pigment fading, bleaching, and photo-oxidative degradation during prolonged exposure to sunlight and environmental conditions, which can alter the original coloration of plastic materials (Deocaris et al. 2023). Comparable patterns have been reported in other fluvial systems, though with considerable regional variability. For example, in the Buriganga and Turag rivers, withe particles and colors such as red and black were dominant (Mahmud et al. 2025), whereas in the Pearl River Delta, withe (36%) and transparent (20.2%) particles prevailed (He et al. 2025).

Similarly, in highly urbanized systems such as the Diep River, black-gray particles accounted for up to 47% of the total MPs (Khan et al. 2025), a distribution directly associated with tire wear and traffic-related particles, consistent with findings for heavily trafficked urban watersheds (Österlund et al. 2023). However, in the Chili River, the relatively low proportion of black particles and the predominance of colored fibers suggest that domestic discharges and urban solid waste represent the principal sources, rather than intense road runoff. Overall, the integration of shape, color, and polymer composition revealed the predominance of polyethylene (PE, 52.4%), followed by polyethylene terephthalate (PET, 23.8%), ethylene vinyl acetate (EVA, 19.0%), and polyurethane (PUR, 4.8%) (Fig. 4C), among the FTIR-confirmed particles.

3.3. Chemical Characterization of Polymers

Before the spectroscopic analysis, selected microplastic (MP) particles were individually isolated and enumerated for FTIR characterization. A total of 34 visually identified particles and one additional particle labeled as P Mic

were subjected to FTIR-ATR analysis. However, only 21 particles generated spectra with sufficient quality for reliable chemical identification. The remaining particles could not be conclusively identified due to their extremely small size, limitations associated with the absence of a micro-FTIR system, or insufficient spectral matching with the reference library. Therefore, the polymer percentages reported in this study correspond only to FTIR-confirmed particles and should not be interpreted as representative of all visually identified particles.

The FTIR spectra of plastic macro-samples collected along the shore of the Chili River in Arequipa, Peru revealed distinct functional groups that allowed classification into three spectrally defined groups (Fig. 5): spectra showing evidence of advanced environmental degradation, including O-H or N-H vibration and/or emergence of new carbonyl, aldehydic, and associated bands linked to hydrolysis and photo-oxidation (Norrish I and II) (Fig. 5A), spectra without clear O-H/N-H signatures of hydrolysis but with relatively complex fingerprint regions characteristic of intact or moderately aged engineering polymers (Fig. 5B), and spectra dominated by CH stretching and simple fingerprint patterns indicative of hydrocarbon-rich polymers with limited heteroatom functionality (Fig. 5C). Across all samples, characteristic absorption bands were consistently detected at 3200–3500 cm^{-1} (broad O-H/N-H stretching region), 2500–3100 cm^{-1} (CH stretching of methylene and methyl groups), and 1600–1800 cm^{-1} (carbonyl stretching), with additional features between 1600–1000 cm^{-1} corresponding to O–C=O, C–C, C–O–C, and C–C–O vibrations; weak interactions were noted at 1040 cm^{-1} (C–N) and 800–400 cm^{-1} (C–O and CH_2 bending), while polymer backbone linkages were suggested by C–C–C stretching near 1100 cm^{-1}.

In Fig. 5A, samples Mic, 32, 22, and 20 exhibited O-H stretching band at ~3294 cm^{-1} and H–O–H bending at 1648 cm^{-1}, which may indicate hydrolytic processes or the presence of adsorbed moisture (Kotov et al. 2025). A distinct CHO band at 2722–2726 cm^{-1} is compatible with oxidative chain scission and may be associated with polyethylene glycol and ethylene vinyl acetate (EVA) systems (Demri et al. 1994, Allen et al. 2000). Carbonyl stretching (1740–1731 cm^{-1}) and ester-related bands (1160 cm^{-1}) confirmed early degradation stages (Allen et al. 2000, Jin et al. 2010), with additional CH_2 and CH_3 vibrations (2917, 2867, 1375 cm^{-1}) and vinyl CH out-of-plane bending (995, 960, 840 cm^{-1}) supporting EVA identification (Rozenberg et al. 1998, Allen et al. 2000). Sample 33 showed NH stretching (3287 cm^{-1}) and N–H bending (1534 cm^{-1}) (Coleman et al. 2002, Skrovanek et al. 2002), alongside urethane carbonyl (1731 cm^{-1}) and urea carbonyl (1640 cm^{-1}) in polyether systems (Wang & Cooper 2002), confirming polyurethane (PUR) presence; strong C–O stretching ($\approx$ 1090 and 1223 cm^{-1}) further indicated possible urethane network rearrangements or oxidative modification (De Zea Bermudez et al. 1999, Mishra et al. 2006, Valdés et al. 2018). Sample 25 displayed CH_3 and CH_2 stretching (2956 and 2837 cm^{-1}) (Chen et al. 2012, Tariq et al. 2020). Furthermore, five diagnostic peaks (1714, 1240, 1090, 872, 724 cm^{-1}) corresponding to ketones (C=O), aromatic/aliphatic ethers (C–O), and aromatic C–H bonds, consistent with polyethylene terephthalate (PET) (Chen et al. 2012, Ioakeimidis et al. 2016, Dodi et al. 2022, Dimassi et al. 2023).

In Fig. 5B, spectra lacked OH/NH vibrations; samples 21, 18, 16, and 12 exhibited CH_3/CH_2 stretching (2956, 2917, 2866, 2837 cm^{-1}) (Tariq et al. 2020, Dimassi et al. 2023). Aging-related degradation is suggested by the initial presence of carbonyl (C=O) groups at ~ 1740 cm^{-1}, indicating oxidative modification rather than ester formation. Shifts in bands at 1652 and 1560 cm^{-1} may reflect secondary oxidation products or conjugated structures formed during photo-oxidative aging. Norrish II contributes to the formation of carbonyl and vinyl groups via chain scission (Phan et al. 2022). Samples exposed to deionized water show peaks at 1100 cm^{-1} and, especially, at 1000 cm^{-1}; these bands are consistent with C-O stretching and vinyl-related vibrations associated with polypropylene oxidation rather than exclusively indicating a Norrish type II reaction (Gewert et al. 2015, Fernández-González et al. 2021, Phan et al. 2022). The characteristic polypropylene peaks (1460, 1376, 1167, 997, 973 cm^{-1}) confirm polypropylene composition (Oreski & Wallner 2009, Glaser et al. 2019, Tariq et al. 2020). Overall, the coexistence of carbonyl formation and diagnostic polypropylene bands indicate photo-oxidative aging with chain scission processes rather than predominant crosslinking recombination products.

In Fig. 5C, spectra of samples 29, 28, 27, 10, 5, 24, 14, 11, 4, 2, and 1 showed simpler functional group patterns dominated by CH stretching and limited fingerprint complexity, with diagnostic peaks at 2915, 2848, 1463, and 718 cm^{-1} assigned to CH_2 asymmetric stretching, CH_2 symmetric stretching, bending deformation, and rocking deformation, respectively, consistent with polyethylene (PE) (Chiu & Hsiao 2005, Glaser et al. 2019, Maheswaran et al. 2022, Xu et al. 2024, Khan et al. 2025). Overall, the FTIR results demonstrate the presence of EVA, polyurethane, PET, polypropylene, and polyethylene among the collected plastics, with clear evidence of hydrolytic and oxidative degradation processes occurring in the Chili River.

3.4. Morphological Characteristics of Microplastics in Water

Fig. 6 presents the morphological features of microplastics obtained by scanning electron microscopy (SEM). The

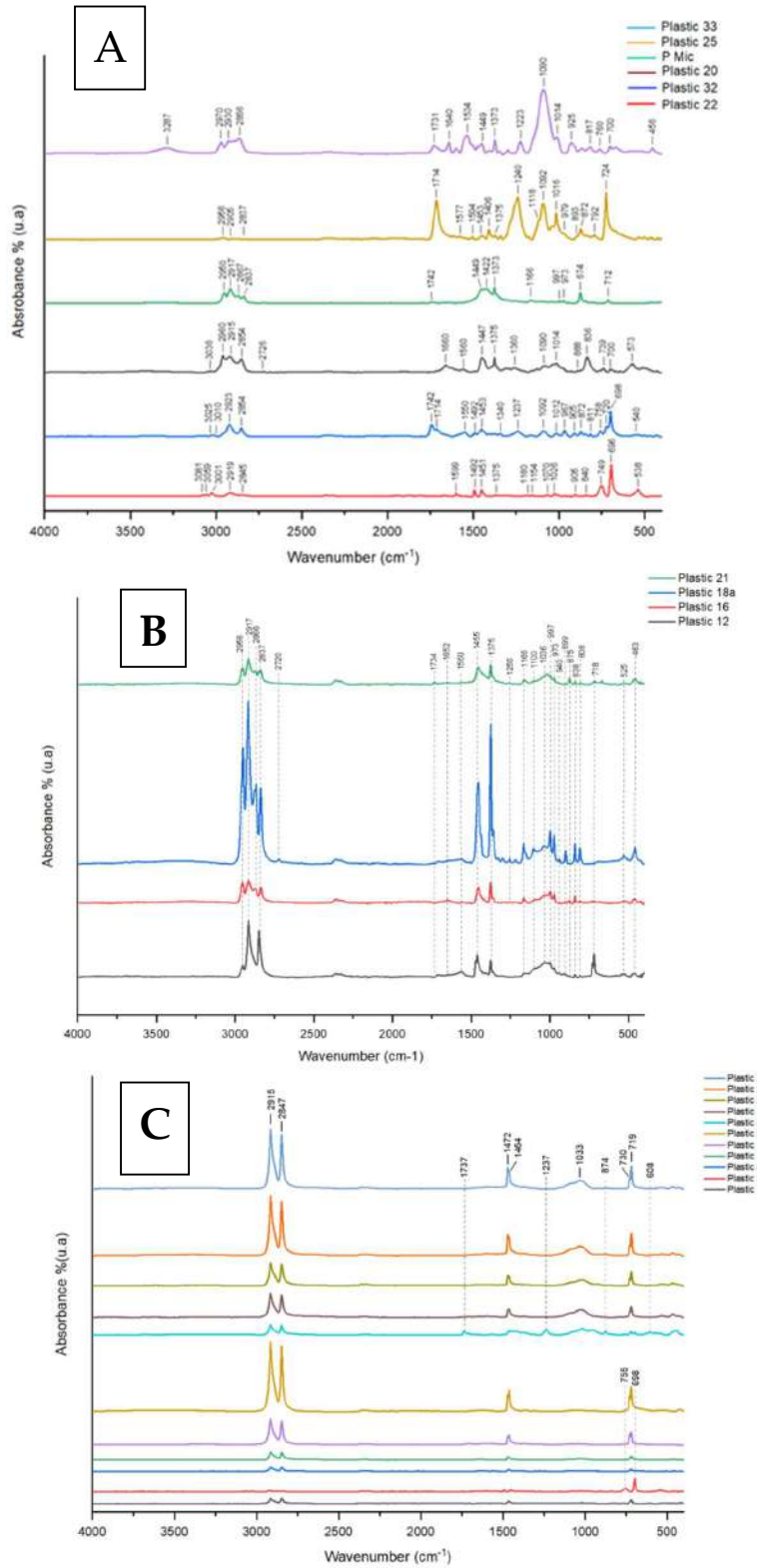


Fig. 5: FTIR spectra of the different microplastics identified in the surface waters of the Chili River: (A) EVA, PUR, and PET; (B) PP; and (C) PE.

micrographs (Fig. 6A–H) reveal polymer surfaces exhibiting varying degrees of environmental degradation. Figs. 6A–B show a fibrous morphology with an irregular surface and accumulation of adhered material, whereas in other particles (Fig. 6C–H), cracks, delamination, cavities, and brittle fractures predominate. These characteristics are consistent with combined processes of mechanical abrasion, oxidative photodegradation, and physical erosion, as described in

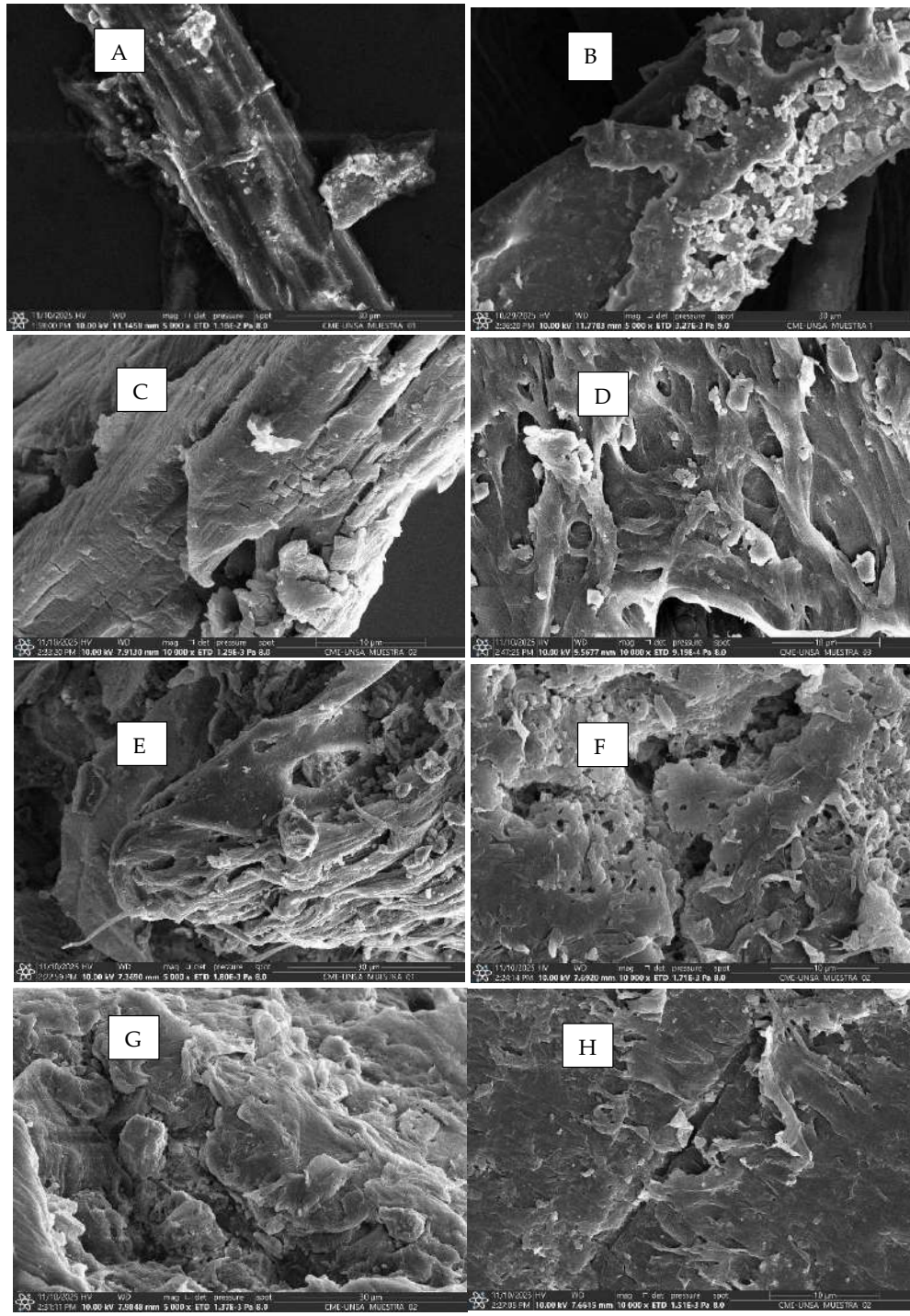


Fig. 6: Scanning electron microscopy (SEM) images: (A–B) fibers; (C–D) fragments; (E–F) foam; and (G–H) film.

fluvial systems where SEM analyses frequently reveal rough surfaces, edge cracks, and irregular topography as consequences of environmental aging (Alam et al. 2023, Mahmud et al. 2025, Ullah et al. 2025, Venkatachalam & Radhakrishnan 2025). Likewise, studies conducted in Southeast Asian rivers report surface fissures and structural cohesion loss associated with progressive oxidation and secondary fragmentation (Anuar et al. 2023). SEM-EDS analysis was used as a complementary method to evaluate elemental surface features and possible inorganic deposits on the particles. Even though carbon and oxygen were commonly detected, these signals were not interpreted as independent confirmation of polymer identity, especially considering the gold coating applied before SEM analysis and the possible presence of environmental mineral or salt deposits. The occasional detection of Na, Cl, or K was therefore interpreted as evidence of superficial deposits rather than as part of the polymer structure. Polymer identification was based primarily on FTIR-ATR analysis.

The observed morphological alterations are also comparable to reports in which SEM has been used to interpret the degree of weathering and transport potential, often associated with increased surface grooves, scratches, and rounded edges (Venkatachalam & Radhakrishnan 2025). In that context, the presence of rough surfaces and linear fractures in particles from the Chili River may reflect prolonged environmental exposure and progressive degradation. This evidence is consistent with the FTIR results (Fig. 5A–C), where EVA, PUR, PET, PP, and PE exhibited oxidation-related signals and structural modifications, suggesting an ongoing environmental weathering process in the Chili River. Overall, the combined SEM, EDS, and FTIR observations are consistent with environmental weathering and aging processes affecting the analyzed particles within the fluvial system.

4. CONCLUSIONS

The present study reveals the widespread presence of microplastics in the surface waters of the Chili River, highlighting the influence of anthropogenic activities on the generation, transport, and transformation of fluvial pollution. The predominance of fibers and fragments, together with the identification of conventional polymers such as PE, PP, PET, EVA, and PUR through FTIR-ATR analysis, reflects the contribution of commonly used plastic materials and their subsequent environmental fragmentation. The integration of spectroscopic and microscopic analyses enabled the identification of environmental transformation signals, including the formation of carbonyl groups and modifications in characteristic absorption bands, as well as surface features such as cracks, delamination, and cavities observed by SEM. This evidence is consistent with environmental weathering and secondary fragmentation processes affecting the analyzed particles.

Taken together, the results emphasize the importance of applying integrated approaches that combine morphological and chemical characterization to better understand the environmental behavior of microplastics in Andean fluvial systems. The information generated provides a relevant scientific foundation for future risk assessments and for the development of management and mitigation strategies aimed at reducing plastic pollution in the region. In this context, it is necessary to strengthen integrated solid waste management and urban discharge control in the Chili River basin in order to reduce the generation and input of microplastics (MPs) into the fluvial system. Considering that river water is used for agricultural irrigation, the presence of MPs may represent a potential pathway for transfer to soils, crops, and livestock, with possible implications for the food chain and regional food security. Thus, future research should prioritize evaluating the accumulation, environmental dynamics, and potential ecotoxicological effects of MPs in Andean agroecosystems.

5. ACKNOWLEDGEMENT

The authors sincerely acknowledge the Universidad Tecnológica del Perú for providing financial support to carry out this project. The authors also thank the Le Qara Research Laboratory for its valuable technical assistance and support in the FTIR-ATR analyses, as well as for its collaboration and expertise throughout the analytical process.

6. REFERENCES

Alam, M.J., Shammi, M. and Tareq, S.M., 2023. Distribution of microplastics in shoreline water and sediment of the Ganges River Basin to Meghna Estuary in Bangladesh. *Ecotoxicology and Environmental Safety*, 266(June), p. 115537. [DOI]

Allen, N.S., Edge, M., Rodriguez, M., Liauw, C.M. and Fontan, E., 2000. Aspects of the thermal oxidation of ethylene vinyl acetate copolymer. *Polymer Degradation and Stability*, 68(3), pp. 363–371. [DOI]

Anuar, S.T., Abdullah, N.S., Yahya, N.K.E.M., Chin, T.T., Yusof, K.M.K.K., Mohamad, Y., Azmi, A.A., Jaafar, M., Mohamad, N., Khalik, W.M.A.W.M. and Ibrahim, Y.S., 2023. A multidimensional approach for microplastics monitoring in two major tropical river basins, Malaysia. *Environmental Research*, 227(March), p. 115717. [DOI]

Banda, A.A.P., Elguera, N.Y.M., Oviedo, A.A.P., Cueva, D.M.D., Semensatto, D., Brito, H.D., Zornio, B.F. and Pacheco, H.G.J., 2025. Characteristics, abundance, distribution, and degradation dynamics of microplastics in the high Colca-Chilli water transfer systems: Tracing an emergent pollutant to Andean reservoirs. *Science of the Total Environment*, 1003(September). [DOI]

Barnes, D.K.A., Galgani, F., Thompson, R.C. and Barlaz, M., 2009. Accumulation and fragmentation of plastic debris in global

environments. *Philosophical Transactions of the Royal Society B: Biological Sciences*, 364(1526), pp. 1985–1998. [DOI]

Belli, I.M., Vieira, E.S., Oliveira, A.R., Pinto, L., Garbossa, L.H.P., Bayard, R., Franco, D., Dantas, D.V. and de Castilhos Junior, A.B., 2026. Microplastics in Brazilian rivers: An overview and a study of floating particle accumulation on the coast of Santa Catarina state. *Science of the Total Environment*, 1012(August 2025). [DOI]

Büngener, L., Schäffer, S.M., Schwarz, A. and Schwalb, A., 2024. Microplastics in a small river: Occurrence and influencing factors along the river Oker, Northern Germany. *Journal of Contaminant Hydrology*, 264(January). [DOI]

Carpio Fernández, J., Quispe, B., Fluquer, Y., Laureano, P., Sulca, P. and Lima, O., 2022. *Dirección de Geología Ambiental y Riesgo Geológico Equipo de Investigación: Hidrogeología de la cuenca del río Quilca-Vitor-Chili (132)*.

Chen, Z., Hay, J.N. and Jenkins, M.J., 2012. FTIR spectroscopic analysis of poly(ethylene terephthalate) on crystallization. *European Polymer Journal*, 48(9), pp. 1586–1610. [DOI]

Chiu, H.T. and Hsiao, Y.K., 2005. Compatibilization of poly(ethylene terephthalate)/polypropylene blends with maleic anhydride-grafted polyethylene-octene elastomer. *Journal of Polymer Research*, 13, pp. 153–160. [DOI]

Coleman, M.M., Lee, K.H., Skrovanek, D.J. and Painter, P.C., 2002. Hydrogen bonding in polymers. 4. Infrared temperature studies of a simple polyurethane. *Macromolecules*, 19(8), pp. 2149–2157. [DOI]

Demri, D., Hindermann, J.P., Diagne, C. and Kiennemann, A., 1994. Formation of C2 oxygenates on rhodium-containing catalysts during CO + H2 reactions. FTIR study of acetaldehyde adsorption. *Journal of the Chemical Society, Faraday Transactions*, 90(3), pp. 501–506. [DOI]

Deocaris, C.C., Fernandez, M.C., Lee, A.R., Miao, S.L.A. and Padolina, J.B.P., 2023. Identification and characterization of microplastics on the surface water in Laguna de Bay, Philippines. *Nature Environment and Pollution Technology*, 22(2), pp. 1073–1080. [DOI]

Dimassi, S.N., Hahladakis, J.N., Daly Yahia, M.N., Ahmad, M.I., Sayadi, S. and Al-Ghouti, M.A., 2023. Insights into the degradation mechanism of PET and PP under marine conditions using FTIR. *Journal of Hazardous Materials*, 447, p. 130796. [DOI]

Dodi, G., Popescu, D., Cojocaru, F.D., Aradoaei, M., Ciobanu, R.C. and Mihai, C.T., 2022. Use of Fourier-transform infrared spectroscopy for DNA identification on recycled PET composite substrate. *Applied Sciences*, 12(9), p. 4371. [DOI]

dos Santos Silva, J., Cidade, M.J.A., Panero, F. dos S., Ribeiro, L.B. and Campos da Rocha, F.O., 2024. Microplastic pollution in the Amazon Basin: Current scenario, advances and perspectives. *Science of the Total Environment*, 946, 174150. [DOI]

Fernández-González, V., Andrade-Garda, J.M., López-Mahía, P. and Muniategui-Lorenzo, S., 2021. *Impact of weathering on the chemical identification of microplastics from usual packaging polymers in the marine environment. Analytica Chimica Acta, 1142, pp. 179–188.* [DOI]

Gewert, B., Plassmann, M.M. and Macleod, M., 2015. Pathways for degradation of plastic polymers floating in the marine environment. *Environmental Science: Processes & Impacts*, 17(9), pp. 1513–1521. [DOI]

Giarrizzo, T., Andrade, M.C., Schmid, K., Winemiller, K.O., Ferreira, M., Pegado, T., Chelazzi, D., Cincinelli, A. and Fearnside, P.M., 2019. Amazonia: the new frontier for plastic pollution. *Frontiers in Ecology and the Environment*, 17(6), pp. 309–310. [DOI]

Glaser, T.K., Plohl, O., Vesel, A., Ajdnik, U., Ulrih, N.P., Hrnčič, M.K., Bren, U. and Zemljič, L.F., 2019. Functionalization of polyethylene (PE) and polypropylene (PP) material using chitosan nanoparticles with incorporated resveratrol as potential active packaging. *Materials*, 12(13), p. 2118. [DOI]

Gune, R. and Martin, A., 2025. Microplastics in our diet: A review of food source contamination. *Food Control*, *178*, p.111486. [DOI]

Harini, R., Sandhya, K., Sunil, C.K. and Natarajan, V., 2025. Seaweed as a sink for microplastic contamination: Uptake, identifications and food safety implications. *Environmental Research*, *278*, p.121631. [DOI]

He, H., Yu, T., Chen, X., Yang, Y., Li, F. and Gan, H., 2025. Observation, distribution, and characteristics of microplastics in sediments from the estuary and river network areas of Pearl River Delta, China. *Regional Studies in Marine Science*, 81. [DOI]

Hidalgo-Ruz, V., Gutow, L., Thompson, R.C. and Thiel, M., 2012. Microplastics in the marine environment: A review of the methods used for identification and quantification. *Environmental Science & Technology*, 46(6), pp. 3060–3075. [DOI]

Ioakeimidis, C., Fotopoulou, K.N., Karapanagioti, H.K., Geraga, M., Zeri, C., Papathanassiou, E., Galgani, F. and Papatheodorou, G., 2016. The degradation potential of PET bottles in the marine environment: An ATR-FTIR based approach. *Scientific Reports*, 6, 23501. [DOI]

Islam, N., Akter, F., Hossen, M.Y., Bhuiyan, T. and Siddique, M.A.M., 2025. Microplastic pollution in the Jamuna River, Bangladesh: Abundance, polymer types, characteristics, and sources in riverbank and riverbed sediments. *Journal of Hazardous Materials: Plastics*, 1, p. 100006. [DOI]

Jin, J., Chen, S. and Zhang, J., 2010. UV aging behaviour of ethylene-vinyl acetate copolymers (EVA) with different vinyl acetate contents. *Polymer Degradation and Stability*, 95(5), pp. 725–732. [DOI]

Joshi, C., Phyllei, S.W.E., Bhatt, S. and Chatterjee, S., 2025. Microplastic surge in the Ariyankuppam River, Puducherry, India: A study on abundance, characterization, and pollution load index. *Journal of Contaminant Hydrology*, 274. [DOI]

Khan, A.B., Pereao, O., Sparks, C. and Opeolu, B., 2025a. Assessing microplastic characteristics and abundance in the sediment and surface water of the Diep River. *Environmental Pollution*, 381(May), p. 126555. [DOI]

Kotov, N., Keskitalo, M.M. and Johnson, C.M., 2025. Nano FTIR spectroscopy of liquid water in the –OH stretching region. *Spectrochimica Acta Part A: Molecular and Biomolecular Spectroscopy*, 330, p. 125640. [DOI]

Larrea Valdivia, A.E., Larico, J.R., Huillca, C.V. and Arias, A.H., 2025. First evidence of microplastics in the Quilca-Vítor-Chili river basin, Arequipa region, Peru. *Journal of Contaminant Hydrology*, 269(November 2024). [DOI]

Lau, W.W.Y., Shiran, Y., Bailey, R.M., Cook, E., Stuchtey, M.R., Koskella, J., Velis, C.A., Godfrey, L., Boucher, J., Murphy, M.B., Thompson, R.C., Jankowska, E., Castillo, A.C., Pilditch, T.D., Dixon, B., Koerselman, L., Kosior, E., Favoino, E., Gutberlet, J., Baulch, S., Atreya, M.E., Fischer, D., He, K.K., Petit, M.M., Sumaila, U.R., Neil, E., Bernhofen, M. V., Lawrence, K. and Palardy, J.E., 2020. Evaluating scenarios toward zero plastic pollution. *Science*, 369(6509), pp. 1455–1461. [DOI]

Lebreton, L. and Andrady, A., 2019. Future scenarios of global plastic waste generation and disposal. *Palgrave Communications*, 5(1), pp. 1–11. [DOI]

Liu, X., Zhou, W., Cheng, P., Zhang, F., Tan, L., Fu, Y., Fan, Y., Lan, J., Gu, H., Liu, W. and Wang, T., 2025. Microplastics: an overlooked particle organic carbon in river systems. *Science Bulletin*, 70(21), pp. 3499–3503. [DOI]

Ma, G., Li, K., Zou, W., Xin, R., Zhang, X., Feng, J., Chen, Z., Yang, Y., Lou, X., Zhang, K. and Yang, F., 2025. Agricultural plastic legacy in river sediments: Abundance, oxidation, and occurrence characteristics of microplastics across rural China. *Environmental Pollution*, 385. [DOI]

Maheswaran, B., Karmegam, N., Al-Ansari, M., Subbaiya, R., Al-Humaid, L., Sebastin Raj, J. and Govarthanan, M., 2022. Assessment, characterization, and quantification of microplastics from river sediments. *Chemosphere*, 298, p. 134268. [DOI]

Mahmud, F., Roy, H., Bhuiyan, M.M.K. and Islam, M.S., 2025b. Critical

analysis, characterization, and treatment of microplastics in the peripheral rivers of Dhaka city: Buriganga and Turag. *Environmental Science: Advances*, pp. 1810–1833. [DOI]

Mishra, A.K., Chattopadhyay, D.K., Sreedhar, B. and Raju, K.V.S.N., 2006. FT-IR and XPS studies of polyurethane-urea-imide coatings. *Progress in Organic Coatings*, 55(3), pp. 231–243. [DOI]

Oreski, G. and Wallner, G.M., 2009. Evaluation of the aging behavior of ethylene copolymer films for solar applications under accelerated weathering conditions. *Solar Energy*, 83(7), pp. 1040–1047. [DOI]

Österlund, H., Blecken, G., Lange, K., Marsalek, J., Gopinath, K. and Viklander, M., 2023. Microplastics in urban catchments: Review of sources, pathways, and entry into stormwater. *Science of the Total Environment*, 858(July 2022). [DOI]

Peng, G., Xu, P., Zhu, B., Bai, M. and Li, D., 2018. Microplastics in freshwater river sediments in Shanghai, China: A case study of risk assessment in mega-cities. *Environmental Pollution*, 234, pp. 448–456. [DOI]

Phan, S., Padilla-Gamiño, J.L. and Luscombe, C.K., 2022. The effect of weathering environments on microplastic chemical identification with Raman and IR spectroscopy: Part I. Polyethylene and polypropylene. *Polymer Testing*, 116. [DOI]

Rozenberg, M., Loewenschuss, A. and Marcus, Y., 1998. IR spectra and hydration of short-chain polyethyleneglycols. *Spectrochimica Acta Part A: Molecular and Biomolecular Spectroscopy*, 54(12), pp. 1819–1826. [DOI]

Skrovanek, D.J., Painter, P.C. and Coleman, M.M., 2002. Hydrogen bonding in polymers. 2. Infrared temperature studies of nylon 11. *Macromolecules*, 19(3), pp. 699–705. [DOI]

Tariq, A., Afzal, A., Rashid, I.A. and Shakir, M.F., 2020. Study of thermal, morphological, barrier and viscoelastic properties of PP grafted with maleic anhydride (PP-g-MAH) and PET blends. *Journal of Polymer Research*, 27(10), p.309. [DOI]

Ullah, H., Hafeez, S., Mian, I.A., Khan, Aamir Ahsan, Khan, Aitezaz Ahsan and Khan, B., 2025. Seasonal microplastic pollution in surface water and sediments of the Swat and Kabul Rivers, Pakistan. *Journal of Environmental Chemical Engineering*, 13(3). [DOI]

Upadhyay, K. and Bajpai, S., 2021. Microplastics in landfills: A comprehensive review on occurrence, characteristics and pathways to the aquatic environment. *Nature Environment and Pollution Technology*, 20(5), pp. 1935–1945. [DOI]

Valdés, B.S.G., Gomes, C.S.B., Gomes, P.T., Ascenso, J.R., Diogo, H.P., Gonçalves, L.M., dos Santos, R.G., Ribeiro, H.M. and Bordado, J.C., 2018. Synthesis and characterization of isosorbide-based polyurethanes exhibiting low cytotoxicity towards HaCaT human skin cells. *Polymers*, 10(10), p. 1170. [DOI]

Venkatachalam, S. and Radhakrishnan, N., 2025. Assessment and quantification of microplastics in northern Tamil Nadu estuaries: Distributional dynamics and ecological threats from intertidal mangrove ecosystems. *Physics and Chemistry of the Earth*, 141. [DOI]

Wang, C.B. and Cooper, S.L., 2002. Morphology and properties of segmented polyether polyurethane ureas. *Macromolecules*, 16(5), pp. 775–786. [DOI]

Xiang, X., Liu, Y., Tang, L., Xueying, L. and Xinrong, S.U., 2026. Microplastic pollution in Chinese rivers: A detailed analysis of distribution, risk factors, and ecological impact. *Marine Pollution Bulletin*, 222. [DOI]

Xu, K., Shahab, A., Rinklebe, J., Xiao, H., Li, J., Ye, F., Li, Y., Wang, D., Bank, M.S. and Wei, G., 2024. Spatial distribution, morphology, and risk assessment of microplastics in sediment from the Pearl River Estuary, China. *Emerging Contaminants*, 10(3), p. 100383. [DOI]

Yang, H., Sun, F., Liao, H., Huang, L., Zhao, Q. and Wu, F., 2024. Pollution characterization and multi-index ecological risk assessment of microplastics in urban rivers from a Chinese megacity. *Journal of Hazardous Materials*, 480. [DOI]

Yang, Z., Suzuki, T., Viyakarn, V., Hagita, R., Joshima, H. and Arakawa, H., 2025. Pollution, degradation, and risk assessment of microplastic (> 30 μm) in subsurface (5 m) seawaters along Tokyo-Bangkok shipping route. *Science of the Total Environment*, 998. [DOI]

De Zea Bermudez, V., Carlos, L.D. and Alcácer, L., 1999. Sol−gel derived urea cross-linked organically modified silicates. 1. Room temperature mid-infrared spectra. *Chemistry of Materials*, 11(3), pp. 569–580. [DOI]

Nature Environment and Pollution Technology
An International Quarterly Peer-Reviewed Open Access Journal

p-ISSN: 0972-6268 | e-ISSN: 2395-3454 Vol. 25 | No. 4 | Article ID B4414 | 2026

RESEARCH ARTICLE https://doi.org/10.46488/NEPT.2026.v25i04.B4414 OPEN ACCESS

A Hybrid Coagulation-Microfiltration Approach for Industrial Wastewater Pretreatment

Anurag Chavan[1]†, Sanjay Harke[2], Ravindra Gaikwad[3] and Bhavanipant Pande[1]
[1]Department of Environmental Science, School of Basic and Applied Sciences, MGM University, Chh Sambhajinagar, Maharashtra, India
[2]Department of Biotechnology, Institute of Biosciences and Technology, MGM University, Chh Sambhajinagar, Maharashtra, India
[3]Department of Chemical Engineering, Jawaharlal Nehru Engineering College, MGM University, Chh Sambhajinagar, Maharashtra, India
†Corresponding author: Anurag Chavan; anuragschavan@gmail.com

ARTICLE HISTORY

Received: 17-11-2025
Revised: 24-02-2026
Accepted: 25-02-2026

KEYWORDS

Ceramic membrane
Microfiltration
Industrial wastewater
Moringa oleifera
Coagulation
CETP pretreatment
Sustainable wastewater management

CITE THIS ARTICLE

Chavan, A., Harke, S., Gaikwad, R. and Pande, B., 2026. A hybrid coagulation–microfiltration approach for industrial wastewater pretreatment. *Nature Environment and Pollution Technology*, 25(4), B4414. https://doi.org/10.46488/NEPT.2026.v25i04.B4414

COPYRIGHT & LICENCE

© 2026 The Authors
Open Access under CC BY 4.0.

PUBLISHED BY

TECHNOSCIENCE PUBLICATIONS

ABSTRACT

Common Effluent Treatment Plants (CETPs) often receive mixed industrial effluents containing high levels of organic and inorganic pollutants, which can overwhelm traditional biological treatment systems. This study investigates the use of a ceramic microfiltration membrane as a pretreatment step to enhance influent quality prior to CETP processing. Composite wastewater samples from various industrial sources were treated through direct membrane filtration and coagulant-assisted filtration with aluminum sulfate and *Moringa oleifera* seed powder. A commercially available membrane (effective area: 0.0407 m²) was operated at a transmembrane pressure of 1.0 kg cm^{-2}. The membrane's structural and compositional features were characterized using FESEM–EDS, XRD, XPS, and porosity analyses. The results demonstrated significant improvements in the physicochemical quality of the treated wastewater, including reductions in organic content, particulate matter, and stabilization of pH levels favorable for biological treatment. The findings indicate that ceramic microfiltration, combined with chemical and natural coagulants, provides a sustainable and effective method to improve CETP performance and manage industrial wastewater.

1. INTRODUCTION

Industrial clusters in emerging economies often produce heterogeneous effluents that are discharged into shared infrastructures known as Common Effluent Treatment Plants (CETPs). These collective facilities offer economies of scale for small and medium-sized industries but frequently face performance challenges when influent wastewater contains organic and inorganic loads that exceed the capacity of conventional biological treatment systems (Padalkar & Hiralal 2018, Singh et al. 2023). Overloading can lead to reduced removal efficiencies, biomass inhibition, excessive sludge production, and increased operational costs. The problem becomes even more complex when the influent consists of mixed industrial wastewater, which varies significantly in chemical composition and pollutant concentrations.

Mixed industrial effluents differ significantly from domestic or single-industry wastewater. They often contain fluctuating levels of chemical oxygen demand (COD), biological oxygen demand (BOD), total suspended solids (TSS), total dissolved solids (TDS), heavy metals, salts, and non-biodegradable compounds.

This variability places a considerable strain on biological reactors, resulting in unstable operation and shock loads that can disrupt microbial activity (Sravan et al. 2024). A field study at an Indian CETP observed a notable decline in reliability and pollutant removal efficiency whenever influent quality fell outside the plant's designed range (Ali et al. 2021). These findings highlight the critical need for robust pretreatment methods to stabilize influent characteristics prior to biological treatment.

Pretreatment stages aim to safeguard downstream biological units by eliminating refractory organics, solids, and colloidal matter, thereby enhancing overall effluent compatibility. Membrane-based separation techniques, particularly microfiltration (MF) and ultrafiltration (UF), have gained recognition as effective methods for removing suspended and colloidal pollutants (Othman et al. 2021). Notably, ceramic microfiltration membranes provide significant advantages over polymeric ones due to their chemical inertness, thermal stability, mechanical robustness, and extended operational lifespan (Hakami et al. 2020, Zhang et al. 2023). These membranes can withstand the harsh conditions often present in industrial wastewater streams, making them well-suited for CETP pretreatment. Recent developments highlight their increasing use in wastewater polishing and hybrid systems, although high capital costs and fouling potential continue to pose challenges (Akash et al. 2024, Dashtban Kenari et al. 2025).

Coagulation–flocculation processes continue to play a vital role in traditional wastewater treatment and have recently been adapted into greener, bio-based methods. Natural coagulants from plant materials have demonstrated promising potential as sustainable alternatives to alum or ferric salts (Ribeiro et al. 2019). *Moringa oleifera* seed powder, in particular, has been extensively researched for its coagulation capabilities; its cationic proteins serve as natural polyelectrolytes that neutralize negatively charged colloids, resulting in the formation of settleable flocs (Ndabigengesere & Narasiah 1998, Yamaguchi et al. 2021). Research indicates that coagulants derived from Moringa seeds can significantly reduce turbidity and chemical oxygen demand (COD), providing cost-effective and biodegradable solutions for wastewater treatment (Oladoja & Pan 2015). Recent assessments of their effectiveness in actual wastewater samples, including dormitory and domestic effluents, further validate their practical application (Ogunshina et al. 2023). Combining these bio-coagulants with membrane technologies not only improves pollutant removal efficiency but also decreases membrane fouling, energy use, and sludge toxicity (Alazaiza et al. 2025).

Hybrid coagulation–membrane systems leverage the strengths of both methods: coagulation decreases particle load and membrane fouling, while the membrane offers effective physical separation of fine particulates and organic substances (Nouira et al. 2025). This complementary interaction enhances filtration efficiency and produces a stable effluent suitable for biological treatment. For CETPs that manage diverse industrial effluents, such hybrid pretreatment approaches are practical and sustainable options for improving influent quality without significant infrastructural changes.

This study examines the feasibility of using commercially available ceramic microfiltration membranes as a pretreatment step before biological processing in a CETP. A composite wastewater from various industrial sources was treated using two methods: direct membrane filtration and coagulant-assisted filtration with aluminum sulfate and *Moringa oleifera* seed powder. The ceramic membrane was characterized through FESEM–EDS, XRD, XPS, and porosity analysis to link material properties with filtration performance. The research aims to assess how effectively ceramic microfiltration, combined with natural and conventional coagulants, can reduce organic, particulate, and dissolved contaminants, thereby enhancing the wastewater's suitability for downstream biological treatment and supporting sustainable CETP operations.

Although hybrid coagulation–membrane systems have been previously studied, their use in treating highly variable composite influent from operating Common Effluent Treatment Plants remains underexplored. This study advances the field in four key ways. First, it assesses treatment performance using real mixed industrial CETP influent rather than synthetic or single-source wastewater, thereby addressing practical variability and shock-loading conditions. Second, it adopts a simultaneous hybrid dosing approach combining aluminum sulfate and *Moringa oleifera* extract to deliberately modify floc characteristics for fouling mitigation, rather than solely targeting turbidity removal. Third, it evaluates fouling reversibility through clean-water flux recovery analysis, offering operational insights into membrane longevity. Finally, it considers the system's role in enhancing downstream biological process stability, positioning the membrane unit as a CETP pretreatment stabilizer rather than merely a polishing step. These aspects collectively illustrate the main contributions of this work.

2. MATERIALS AND METHODS

2.1. Collection and Characterization of Composite Wastewater

Composite industrial wastewater was collected from the influent channel of a Common Effluent Treatment Plant (CETP) that serves a diverse industrial cluster, including textile dyeing, electroplating, food processing, and chemical

manufacturing. Grab samples were taken during peak discharge periods over three consecutive days to account for variability in composition. The samples were stored in acid-washed 20 L HDPE containers, maintained at 4 ± 2 °C during transportation, and analyzed within 24 h to preserve their chemical integrity (Federigi et al. 2024).

The initial analysis of the wastewater involved measuring pH, total dissolved solids (TDS), total suspended solids (TSS), turbidity, chemical oxygen demand (COD), and five-day biological oxygen demand (BOD_5). Six independent wastewater samples were evaluated under raw, DMF, and CAMF conditions. The treatment-level results were expressed as mean ± SD calculated from the six independent samples (n = 6), following the procedures described in Standard Methods for the Examination of Water and Wastewater (APHA 2017).

Sampling was deliberately carried out during peak discharge periods to assess treatment performance under high-loading conditions typically seen in CETP operations. As a result, the values reported represent typical high-influent operational scenarios rather than long-term seasonal averages. It is important to recognize that industrial influent characteristics can vary seasonally and throughout 24-hour cycles due to production schedules, rainfall, and discharge intermittency. This dataset captures short-term operational variability but does not account for extended seasonal fluctuations. Therefore, the results should be viewed within the context of peak-condition performance, and future research will include longer-term, multi-season monitoring to improve representativeness.

2.2. Coagulants and Preparation of Hybrid Coagulant System

A hybrid coagulant system was created by combining two components: aluminum sulfate ($Al_2(SO_4)_3 \cdot 18H_2O$, Merck, India) and *Moringa oleifera* seed powder. Mature *Moringa oleifera* seeds were sourced locally, deshelled, air-dried at room temperature, and ground using a stainless-steel mill. The resulting powder was sieved through a 300 µm mesh and stored in airtight containers to prevent moisture absorption (Ofomi et al. 2025). For stock solution preparation, 10 g of Moringa powder was suspended in 1 L of distilled water, stirred at 150 rpm for 30 min, then allowed to settle for an hour. The clear supernatant was decanted and used as the natural coagulant extract (Desta & Bote 2021).

The coagulant system employed in this study combined aluminum sulfate and *Moringa oleifera* seed extract within a single solution. This approach was designed to leverage complementary coagulation mechanisms: charge neutralization by Al^{3+} ions from alum and adsorption–bridging by cationic proteins in Moringa seeds. The hybrid formulation aimed to improve floc formation, enhance removal efficiency, and diminish membrane fouling potential. Preliminary jar tests determined that the optimal doses were 150 mg L^{-1} of alum and 250 mg L^{-1} of Moringa extract, applied simultaneously to the wastewater before filtration (Kane et al. 2016).

2.2.1. Coagulant Dose Optimization

Preliminary jar tests using combined alum and *Moringa oleifera* extract were conducted to identify appropriate operating doses prior to membrane experiments. Hybrid combinations of alum at concentrations ranging from 50 to 250 mg L^{-1} and Moringa extract from 100 to 400 mg L^{-1} were evaluated. The optimization process considered turbidity reduction, floc formation characteristics such as size and density, settling clarity after 30 min, and residual COD in the supernatant. The optimal doses of 150 mg L^{-1} alum and 250 mg L^{-1} Moringa extract achieved effective clarification without producing excessive sludge.

This study evaluated the hybrid formulation as an integrated pretreatment approach; however, the alum-only and Moringa-only systems were not separately optimized within this scope. Therefore, a quantitative assessment of their synergistic interaction was beyond the objectives of this work and is recommended for future research.

2.3. Ceramic Membrane Module and Characterization

A commercially available tubular ceramic microfiltration membrane (Membralox®, Pall Corporation, USA) was used in the study. The membrane was composed of α-alumina and had a nominal pore size of 0.2 µm, an effective surface area of 0.0407 m^2, and a length of 250 mm. It was installed in a stainless-steel cross-flow module equipped with inlet and outlet pressure gauges to monitor the operating pressure. Filtration was achieved using a variable-speed peristaltic pump (Watson Marlow® 520 series) set to maintain a constant transmembrane pressure (TMP) of 1.0 kg cm^{-2} at room temperature (25 ± 2°C), consistent with typical tubular α-alumina microfiltration setups reported in the literature (Eren & Arslanoğlu 2025).

The physical and surface properties of the ceramic membrane were characterized prior to experimental testing using field-emission scanning electron microscopy (FESEM) combined with energy-dispersive X-ray spectroscopy (EDS) to assess morphology and elemental composition. Crystalline phases were identified via X-ray diffraction (XRD, Rigaku Ultima IV), and surface elemental states were analyzed through X-ray photoelectron spectroscopy (XPS, Thermo Scientific ESCALAB Xi^+). Total porosity was measured using the Archimedes water-immersion method

in accordance with the protocol described by Hristov et al. (2012).

2.3.1. Porosity Measurement

The total porosity (ε) of the ceramic membrane was measured using the Archimedes water-immersion technique, as described by Hristov et al. (2012). The dry membrane sample was weighed (W_1), then submerged in deionized water under vacuum for 30 min to achieve complete saturation. After removing and surface-drying the sample, its wet weight (W_2) was recorded. The saturated membrane was suspended in water, and its apparent weight (W_3) was measured with a precision balance. The membrane's porosity was calculated based on these measurements.

$$\varepsilon(\%) = \frac{(W_2 - W_1)}{(W_2 - W_3)} \times 100$$

where W_1, W_2, and W_3 represent the dry, wet, and suspended weights of the membrane, respectively.

All measurements were conducted in triplicate, and mean values ± standard deviation were reported. The obtained porosity (43 ± 2%) was consistent with values typical of mesoporous α-alumina supports.

2.4. Filtration Experiments

2.4.1. Direct Membrane Filtration (DMF)

In the direct filtration mode, untreated wastewater was fed to the membrane module without pretreatment. Each run was carried out for 60 min under a fixed TMP of 1.0 kg cm^{-2}. Permeate was collected at 10-min intervals using a digital balance connected to a data logger to record cumulative mass. The instantaneous permeate flux (J, L m^{-2} h^{-1}) was calculated as:

$$J = \frac{V}{A\,t}$$

where V is the volume of permeate collected (L), A is the effective membrane area (m^2), and t is filtration time (h) (Sanchis-Perucho et al. 2023).

2.4.2. Coagulant-Assisted Membrane Filtration (CAMF)

In the coagulant-assisted mode, a hybrid coagulant system consisting of alum and Moringa was directly added to the wastewater. The mixture was rapidly stirred at 200 rpm for 2 min, then gently mixed at 40 rpm for 20 min. Following this, it was allowed to settle for 30 min. The clarified supernatant was subsequently filtered through a membrane under the same conditions used for DMF (Singh et al. 2023). The combined action of aluminum sulfate and Moringa extract was anticipated to decrease colloidal particles, increase floc density, and prevent pore blockage on the ceramic surface (Katalo et al. 2018).

2.5. Membrane Cleaning and Performance Recovery

After each filtration cycle, the membrane module was rinsed with deionized water at a pressure of 1.5 kg cm^{-2} for 10 min to eliminate reversible fouling layers. Weekly chemical cleaning involved using 0.1 M NaOH at 40 °C for 30 min, followed by rinsing until the effluent reached a neutral pH. The clean-water flux (CWF) was measured before and after cleaning to assess fouling reversibility and membrane recovery efficiency (Ezugbe & Rathilal 2020).

2.6. Analytical Determinations and Data Analysis

All influent and permeate samples were analyzed for pH, TSS, TDS, turbidity, COD, and BOD_5 following APHA (2017) procedures. Pollutant removal efficiency was then calculated as

$$\%\ \text{Removal} = \frac{C_i - C_f}{C_i} \times 100,$$

where C_i and Cf are the influent and effluent concentrations, respectively. Six independent wastewater samples were analyzed under raw, DMF, and CAMF conditions, and the results were expressed as mean ± SD. Statistical analysis was conducted using OriginPro 2022b. Data normality was assessed prior to analysis. For normally distributed data, one-way ANOVA was applied. Non-normally distributed data were analyzed using the Kruskal–Wallis test. Flux was analyzed using an independent samples t-test. Statistical significance was accepted at $p < 0.05$.

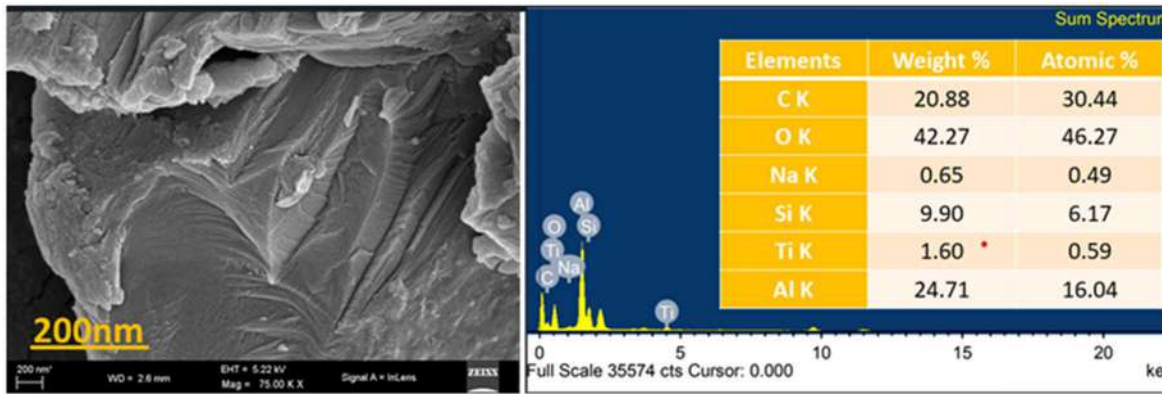
3. RESULTS AND DISCUSSION

3.1. Membrane Characterization

The microstructural and compositional features of the alumina ceramic microfiltration membrane were analyzed to establish a relationship between material characteristics and filtration efficiency. FESEM imaging (Fig. 1(a)) displayed a consistent pore structure typical of sintered α-Al_2O_3 supports. EDS elemental mapping (Fig. 1(b)) verified the dominance of aluminum and oxygen, with minor silicon traces originating from bonding materials. Post-filtration surfaces exhibited distinct fouling morphologies:

Following filtration experiments, the membrane surfaces exhibited distinct fouling morphologies, consisting of deposited particulates and surface films that varied depending on feed composition.

X-ray diffraction (XRD) analysis (Fig. 2) exhibited sharp peaks corresponding to α-Al_2O_3 at $2\theta = 25.5°$, 35.1°,



(a) FESEM micrograph

(b) EDS spectrum

Fig. 1: (a) FESEM micrograph of the α-Al_2O_3 support surface showing a uniform, interconnected pore structure at the nanoscale (scale bar: 200 nm); (b) EDS spectrum and quantitative elemental composition confirming the predominance of Al and O consistent with Al_2O_3, with minor Si, Na, Ti, and C originating from binder residues and surface contaminants.

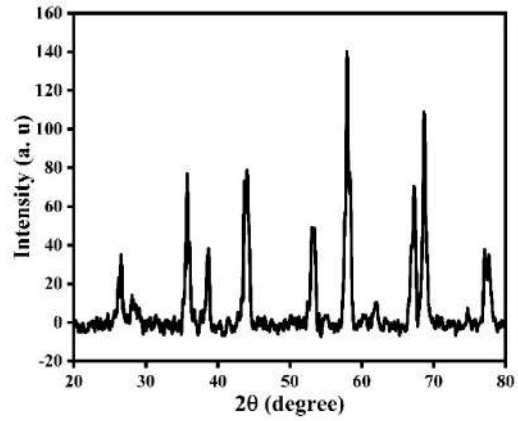


Fig. 2: XRD pattern of the commercial α-Al_2O_3 membrane showing characteristic diffraction peaks of the α-alumina phase.

37.8°, 43.4°, 52.6°, 57.5°, 66.5°, and 76.9°, confirming the crystalline integrity of the alumina phase (JCPDS No. 46-1212). No secondary impurity phases were detected.

3.1.1. XPS Analysis

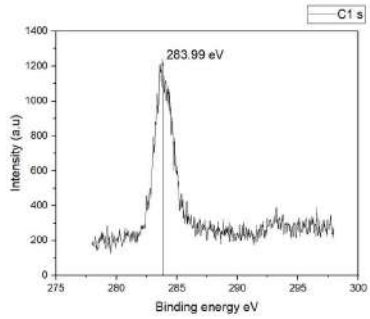
X-ray photoelectron spectroscopy (XPS) was used to determine the surface elemental composition and oxidation states of the ceramic membrane (Fig. 3(a–f)). The survey spectrum confirmed the presence of Al, O, C, Si, Na, and Ti, in agreement with the EDS results.

The high-resolution C 1s spectrum (Fig. 3(a)) exhibits a dominant peak centered at 283.99 eV, characteristic of surface carbon species typically attributed to atmospheric hydrocarbon adsorption. The absence of significant higher-binding-energy components indicates negligible carbonate or oxygenated carbon contamination.

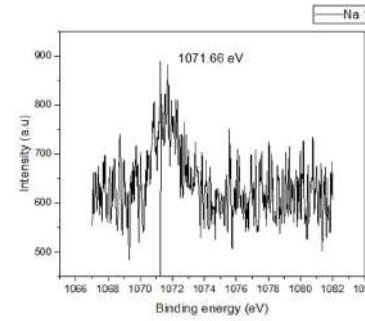
The Na 1s spectrum (Fig. 3(b)) shows a peak at 1071.66 eV, consistent with sodium present in its ionic form (Na^+). The relatively weak intensity suggests trace-level sodium, likely originating from precursor materials or processing residues rather than from a distinct sodium-rich phase.

The Si 2p peak (Fig. 3(c)), located at 102.56 eV, corresponds to Si^{4+} species in a silicate environment, confirming the presence of silica-based binders or minor secondary phases within the membrane structure.

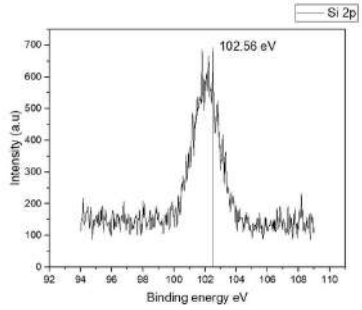
The Ti 2p region (Fig. 3(d)) displays a Ti $2p_{3/2}$ peak centered at 457.98 eV, indicative of Ti^{4+} in TiO_2. No lower-binding-energy contributions associated with Ti^{3+} or metallic Ti were observed, suggesting that titanium is present predominantly in its fully oxidized state.



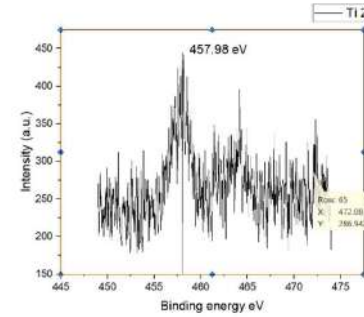
(a) C 1s XPS spectrum with peak at 283.99



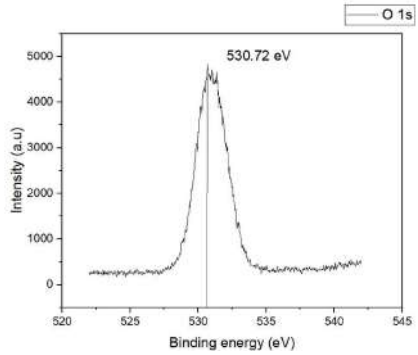
(b) Na 1s XPS spectrum with peak at



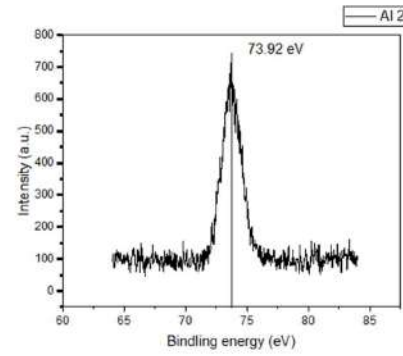
(c) Si 2p XPS spectrum with peak at 102.56 eV.



(d) Ti 2p XPS spectrum with peak at 457.98 eV.



(e) O 1s XPS spectrum with peak at 530.72 eV.



(f) Al 2p XPS spectrum with peak at 73.92 eV.

Fig. 3: High-resolution XPS spectra of the ceramic membrane: (a) C 1s, (b) Na 1s, (c) Si 2p, (d) Ti 2p, (e) O 1s, and (f) Al 2p.

The O 1s spectrum (Fig. 3(e)) presents a strong, symmetrical peak at 530.72 eV, characteristic of lattice oxygen (O^{2-}) in metal oxides. The narrow peak profile indicates minimal surface hydroxylation or adsorbed oxygen species.

The Al 2p spectrum (Fig. 3(f)) shows a sharp peak at 73.92 eV, consistent with Al^{3+} in α-Al_2O_3. This binding energy confirms that aluminum exists predominantly in its stable oxide form and constitutes the primary structural framework of the membrane.

Table 1: Summary of pore characteristics and surface area measurements of the ceramic microfiltration membrane.

Parameter	Method	Result	Unit
BET surface area	N_2 adsorption (BET)	90.7	$m^2\ g^{-1}$
Langmuir surface area	Langmuir model	97.9	$m^2\ g^{-1}$
BJH cumulative surface area (pore > 2 nm)	BJH model	103.0	$m^2\ g^{-1}$
Total pore volume ($P/P_0 = 0.9987$)	N_2 adsorption	0.9469	$cm^3\ g^{-1}$
Average pore diameter	BET	21.0	nm
Micropore surface area	DR model	139.8	$m^2\ g^{-1}$
Porosity (Archimedes method)	Water immersion	43 ± 2	%

Collectively, the high-resolution XPS spectra confirm that the membrane surface is dominated by stable oxide phases (Al–O, Ti–O, and Si–O bonding), with only trace levels of residual sodium and surface carbon. These results further validate the chemical integrity and compositional stability of the α-alumina ceramic matrix.

BET analysis yielded a specific surface area of 90.7 $m^2\ g^{-1}$, a total pore volume of 0.9469 $cm^3\ g^{-1}$, and an average pore diameter of ~21 nm. The porosity, determined using the Archimedes method, was 43 ± 2%, which is characteristic of mesoporous alumina ceramics. The corresponding data are summarized in Table 1.

These structural properties, confirmed by complementary XRD and XPS analysis, underpin the observed filtration efficiency and fouling reversibility, as discussed in Sections 3.2 and 3.3.

3.2. Physicochemical Characteristics of Raw Wastewater

The composite industrial effluent collected from the CETP influent exhibited highly variable physicochemical characteristics, as expected for mixed discharges from textile, electroplating, and food-processing units. The raw wastewater was slightly acidic, with a pH ranging from 6.0 to 6.5. The average COD (4688 ± 280 mg L^{-1}) and BOD_5 (1523 ± 82 mg L^{-1}) concentrations confirmed a high organic load, typical of industrial clusters. Elevated TSS (450 ± 28 mg L^{-1}) and TDS (6875 ± 220 mg L^{-1}) levels reflected substantial suspended and dissolved solids, while a turbidity of approximately 215 NTU indicated intense coloration and colloidal instability. These results underline the need for pretreatment to improve effluent compatibility with biological processes (APHA 2017).

3.3. Direct Membrane Filtration (DMF) Performance

Direct ceramic microfiltration of untreated wastewater produced a moderate improvement in water clarity and solids removal but achieved limited organic reduction. The mean turbidity declined from 215 NTU to 59 NTU (approximately 72%), while TSS decreased from 450 ± 28 mg L^{-1} to 28 ± 2 mg L^{-1}, corresponding to approximately 93.8% removal. COD and BOD_5 removal under DMF were approximately 22.7% and 25.0%, respectively, consistent with the membrane's ability to retain suspended particles while allowing a substantial fraction of dissolved organic matter to pass through. The pH increased slightly to 6.5 ± 0.2, likely due to the partial removal of acidic particulates.

The steady-state flux recorded for DMF averaged 45 ± 2 L $m^{-2}\ h^{-1}$ under a constant transmembrane pressure of 1.0 kg cm^{-2}. A rapid initial decline in flux occurred within the first 15 min, after which the flux stabilized, indicating cake-layer formation as the dominant fouling mechanism. Similar trends have been observed in ceramic membranes treating high-strength industrial effluents (Kapila et al. 2025). Although flux recovery after hydraulic cleaning reached approximately 87%, significant reversible fouling persisted, highlighting the limitations of DMF for treating untreated complex wastewater.

The moderate COD removal observed in DMF is consistent with the intrinsic pore-size limitation of microfiltration membranes (~0.2 μm), which primarily retain suspended and colloidal matter while allowing dissolved organics to pass through. This explains the limited reduction in dissolved organic load despite the effective removal of turbidity.

3.4. Coagulant-Assisted Membrane Filtration (CAMF) Using Combined Alum and *Moringa oleifera*

Pretreatment of the wastewater using a combined coagulant mixture of aluminum sulfate and *Moringa oleifera* seed extract produced a distinct improvement in both water quality and filtration performance. The hybrid coagulant promoted the formation of large, dense flocs through complementary mechanisms: charge neutralization by Al^{3+} ions and adsorption–bridging by cationic Moringa proteins (Kane et al. 2016).

Following CAMF, turbidity was reduced to 17 ± 2 NTU (approximately 92% removal), while TSS declined from 450 ± 28 mg L^{-1} to 9 ± 1 mg L^{-1}, corresponding to approximately

98.0% removal. COD and BOD_5 decreased markedly to 855 ± 55 mg L^{-1} and 305 ± 18 mg L^{-1}, respectively, corresponding to average reductions of 81.8% and 80.0% compared with the raw influent. The effluent pH stabilized at 6.8–7.0, a range conducive to downstream biological oxidation (Zielińska & Galik 2017).

The average steady-state flux during CAMF increased to approximately 71 L m^{-2} h^{-1}, around 55% higher than that of DMF, demonstrating effective fouling mitigation. This improvement resulted from the reduced colloidal loading and the formation of compact, settleable flocs that limited pore blockage (Aragaw & Bogale 2023).

The improved flux behavior under CAMF conditions can be attributed to the modification of the feed colloidal matrix prior to membrane contact. Alum promotes charge neutralization of negatively charged particles, while bioactive proteins in *Moringa* extract facilitate adsorption–bridging. The resulting flocs are larger and less compressible, producing a more permeable cake structure and reducing pore-blocking tendencies.

3.5. Flux Behavior

The variation in permeate flux with time during microfiltration is presented in Fig. 4. Both direct membrane filtration (DMF) and coagulant-assisted microfiltration (CAMF) exhibited a sharp initial decline in flux within the first 10 min, which was attributed to rapid pore blocking and cake-layer formation by suspended solids and colloidal matter. Thereafter, the flux reached a quasi-steady state due to the establishment of a dynamic filtration layer.

The CAMF system consistently maintained a higher permeate flux (~71 L m^{-2} h^{-1}) than DMF (~45 L m^{-2} h^{-1}) throughout the 60-min filtration run, indicating improved fouling control. This enhancement is attributed to the pre-aggregation of colloidal and organic matter by the natural coagulant (*Moringa oleifera*) prior to membrane contact,

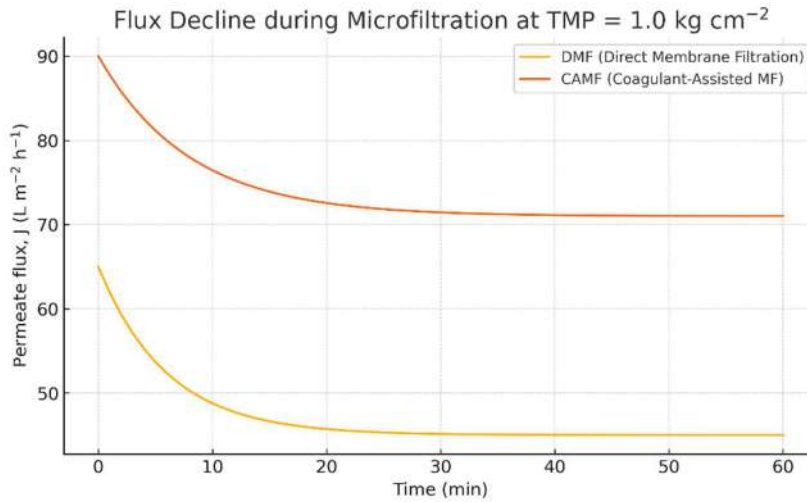


Fig. 4: Comparison of flux decline profiles for DMF and CAMF at 1.0 kg cm^{-2}, highlighting slower flux decay and higher steady-state flux under CAMF conditions.

Table 2 summarizes the mean ± SD values calculated from six independent wastewater samples (n = 6) evaluated under raw, DMF, and CAMF conditions.

Parameter	Raw effluent (mean ± SD)	DMF (mean ± SD)	CAMF (mean ± SD)	Statistic	p-value
pH	6.25 ± 0.18	6.46 ± 0.21	6.80 ± 0.20	13.798^{f}	$p < 0.001$
COD (mg L^{-1})	4688 ± 280	3625 ± 180	855 ± 55	15.158^{h}	0.001
BOD_5 (mg L^{-1})	1523 ± 82	1143 ± 46	305 ± 18	15.174^{h}	0.001
TSS (mg L^{-1})	450 ± 28	28 ± 2	9 ± 1	15.237^{h}	$p < 0.001$
TDS (mg L^{-1})	6875 ± 220	6560 ± 160	6133 ± 130	12.904^{h}	0.002
Turbidity (NTU)	215 ± 8	59 ± 3	17 ± 2	15.205^{h}	$p < 0.001$
Flux (L m^{-2} h^{-1})	–	45 ± 2	71 ± 3	39.51^{t}	$p < 0.001$

Note: ^{f} F value from one-way ANOVA; ^{h} H value from the Kruskal–Wallis test; ^{t} t value from the independent-samples t-test.

which reduced direct pore deposition and the compressibility of the cake layer.

The lower rate of flux decline in CAMF demonstrates the synergistic effect of coagulation and membrane separation, as the coagulant modifies the particle size distribution and surface charge, resulting in a more permeable cake structure. This behavior is consistent with previous reports on hybrid coagulation–membrane systems for industrial wastewater treatment.

The observed flux stabilization also indicates the partial reversibility of fouling, suggesting that periodic backwashing or hydraulic cleaning can effectively restore flux without significant deterioration in membrane performance.

3.6. Comparative Performance and Statistical Evaluation

Table 2: Physicochemical characteristics of raw effluent and effluent treated with DMF and CAMF membranes. Values are presented as mean ± SD (n = 6 independent wastewater samples). Data normality was assessed prior to analysis. pH was analyzed using one-way ANOVA. COD, BOD_5, TSS, TDS, and turbidity were analyzed using the Kruskal–Wallis test. Flux was analyzed using an independent samples t-test.

The data indicate that CAMF substantially improved organic matter removal compared with DMF, while also providing a further reduction in TSS and maintaining a significantly higher flux. Statistical analysis confirmed significant differences among the raw effluent, DMF, and CAMF samples for COD, BOD_5, TSS, TDS, and turbidity ($p < 0.05$). The marginal change in TDS indicates that microfiltration primarily removes suspended and colloidal particles rather than dissolved ions (Uman et al. 2024).

The improvement in flux resulted from reduced pore constriction and lower cake resistance, verifying the advantage of pre-coagulation in membrane operations. Similar flux enhancement has been reported with the combined use of inorganic and bio-coagulants, which was attributed to the formation of more permeable floc structures (Singh et al. 2023). Comparable trends have also been reported in other hybrid coagulation–membrane studies, where pre-aggregation of colloids reduced cake resistance and improved hydraulic stability. The present findings are consistent with these observations and support the potential suitability of hybrid pretreatment for treating variable industrial effluents.

3.7. Membrane Fouling and Cleaning Behavior

After each run, the membrane was hydraulically rinsed and chemically cleaned. Clean-water flux recovery reached 95% after CAMF, compared with 87% after DMF, confirming that hybrid coagulant pretreatment produced a less compact fouling layer and minimized irreversible resistance (Katalo et al. 2018). The hybrid system employed 150 mg L^{-1} of alum in combination with 250 mg L^{-1} of Moringa extract; however, because an independently optimized alum-only system was not evaluated, quantitative alum savings relative to conventional alum-only treatment could not be established in the present study. Direct comparison of optimized alum-only, Moringa-only, and hybrid coagulation systems would be required to quantify potential coagulant savings and establish any synergistic effect.

Overall, these findings validate the effectiveness of integrating hybrid coagulation with ceramic microfiltration for CETP influent pretreatment. The process provides higher organic and solids removal, improved flux stability, and favorable pH conditions, ensuring compatibility with subsequent biological treatment stages.

From an operational perspective, the stabilization of pH toward neutrality and the reduction in suspended solids are particularly beneficial for downstream biological units in CETPs. Lower shock loading and improved influent consistency can reduce biomass inhibition and enhance process reliability under fluctuating industrial discharge conditions.

3.8. Fouling Mechanism Interpretation

Although detailed resistance quantification was not performed, the fouling behavior can be interpreted using the classical resistance-in-series concept, in which the total hydraulic resistance is considered the sum of the intrinsic membrane resistance and fouling resistance. In the present study, fouling development was inferred from the flux decline profiles and flux recovery following cleaning.

The sharp initial decrease in permeate flux during the early stage of filtration suggests rapid surface deposition of suspended solids and colloidal matter. The subsequent stabilization of flux indicates the formation of a dynamic cake layer that governed the steady-state resistance rather than continuous internal pore constriction.

Flux recovery after hydraulic rinsing demonstrates that a significant proportion of the fouling was reversible and attributable to loosely attached cake deposits. The higher recovery observed under coagulant-assisted conditions suggests that pre-aggregation of particles reduced compact pore blocking and limited the development of irreversible resistance.

Although explicit resistance partitioning into membrane resistance, reversible fouling resistance, and irreversible fouling resistance would require systematic clean-water flux measurements before and after each filtration cycle, the

observed filtration behavior supports cake-dominated fouling under the investigated operating conditions.

Future work involving resistance modeling and pore-blocking kinetics would further strengthen the mechanistic understanding of the process at the pilot scale.

3.9. Study Limitations

Although the hybrid system demonstrated significant improvements in the removal of organic matter and suspended solids, dissolved solids removal remained limited, reflecting the inherent constraints of microfiltration. Long-term fouling behavior and a detailed techno-economic evaluation were beyond the scope of the present study and warrant further investigation before large-scale implementation.

3.10. Practical and Scale-Up Considerations

For integration into existing CETP infrastructure, operational and sludge management aspects must be considered. The hybrid coagulation step generates sludge consisting of aluminum hydroxide flocs combined with aggregated suspended solids and organic matter bridged by Moringa-derived biopolymers. Although the sludge yield was not quantified in the present laboratory-scale study, the applied alum dose (150 mg L^{-1}) falls within the moderate range typically used for industrial coagulation and is lower than the doses commonly required for highly turbid industrial effluents. Partial use of the natural bio-coagulant alongside alum may have the potential to reduce reliance on inorganic coagulant dosing; however, the resulting sludge quantity and composition were not quantified in the present study.

The generated sludge would require conventional thickening and dewatering before disposal or potential co-processing, consistent with standard CETP sludge management practices. The organic fraction introduced by *Moringa* extract is biodegradable and may not significantly increase the hazardous classification of the sludge, although detailed sludge characterization remains necessary for full-scale implementation.

From an operational perspective, the microfiltration system operated at 1 kg cm^{-2} (approximately 1 bar), corresponding to low-pressure membrane operation. Because electrical energy consumption was not directly measured in the present laboratory-scale experiments, a system-specific energy consumption could not be established. For preliminary scale-up assessment, a literature-based value of approximately 0.2 kWh m^{-3} may be used as a representative MF/UF energy-consumption estimate (Tow et al. 2021). This value is adopted only as an indicative literature value and does not represent experimentally measured energy consumption for the present ceramic membrane system. The actual energy demand will depend on pump efficiency, cross-flow velocity, transmembrane pressure, membrane resistance, and recovery; therefore, pilot-scale measurements are required for system-specific assessment.

Under the optimized conditions, chemical consumption corresponded to 150 mg of alum and 250 mg of Moringa extract per L of influent. For a representative CETP treating 1,000 m^3 day^{-1}, this would translate to approximately 150 kg day^{-1} of alum and 250 kg day^{-1} of Moringa extract, subject to influent variability and further optimization.

In terms of footprint, tubular ceramic membrane modules offer a more compact installation than large sedimentation tanks, making retrofitting feasible in space-constrained industrial clusters. However, a comprehensive techno-economic assessment and long-term operational trials are necessary to validate the cost-effectiveness of the process at full scale.

4. CONCLUSIONS

This study assessed the feasibility of combining hybrid coagulation using aluminum sulfate with *Moringa oleifera* extract and ceramic microfiltration as a pretreatment method for mixed industrial wastewater in a Common Effluent Treatment Plant (CETP). Under the tested conditions, the integrated approach yielded superior removal of suspended solids, turbidity, and organic load compared to direct membrane filtration alone. The improved steady-state flux and higher flux recovery after cleaning suggest a lower fouling tendency when coagulation is performed before membrane filtration.

The findings indicate that hybrid coagulation–microfiltration effectively stabilizes high-strength composite industrial influent during peak loading conditions. However, these results are derived from short-term laboratory experiments using a single membrane setup and limited sampling over time. Consequently, the outcomes should be viewed as a proof-of-concept rather than indicative of full-scale performance.

While the approach shows potential for improving influent consistency prior to biological treatment, further work is required to assess long-term fouling dynamics, sludge generation characteristics, seasonal variability, and techno-economic feasibility under continuous operation.

Overall, the study offers initial evidence that combining hybrid coagulation with ceramic microfiltration is a promising pretreatment method for complex industrial wastewater, justifying further pilot-scale testing.

5. ACKNOWLEDGMENTS

The authors gratefully acknowledge MGM University, Chh.

Sambhajinagar (MS), for providing the research facilities, laboratory space, and essential operational support that enabled the successful completion of this work.

6. REFERENCES

Akash, F.A., Shovon, S.M., Rahman, W. and Monir, M.U., 2024. Advancements in ceramic membrane technology for water and wastewater treatment: A comprehensive exploration of current utilizations and prospective horizons. *Desalination and Water Treatment*, 320, pp.100-115.

Alazaiza, M.Y., Alzghoul, T.M., Nassani, D.E. and Bashir, M.J., 2025. Natural coagulants for sustainable wastewater treatment: Current global research trends. *Processes*, 13(6), p.1754. [DOI]

Ali, M., Almohana, A.I., Alali, A.F., Kamal, M.A., Khursheed, A., Khursheed, A. and Kazmi, A.A., 2021. Common effluent treatment plants monitoring and process augmentation options to conform to non-potable reuse. *Frontiers in Environmental Science*, 9, p.741343. [DOI]

American Public Health Association (APHA), 2017. *Standard Methods for the Examination of Water and Wastewater*. 23rd ed. American Public Health Association, Washington, DC.

Aragaw, T.A. and Bogale, F.M., 2023. Role of coagulation/flocculation as a pretreatment option to reduce colloidal/bio-colloidal fouling in tertiary filtration of textile wastewater: A review and future outlooks. *Frontiers in Environmental Science*, 11, p.1142227. [DOI]

Dashtban Kenari, S.L., Mortazavi, S., Mosadeghsedghi, S., Atallah, C. and Volchek, K., 2025. Advancing ceramic membrane technology for sustainable treatment of mining discharge: Challenges and future directions. *Membranes*, 15(4), p.112. [DOI]

Desta, W.M. and Bote, M.E., 2021. Wastewater treatment using a natural coagulant (*Moringa oleifera* seeds): Optimization through response surface methodology. *Heliyon*, 7(11), p.e08451. [DOI]

Eren, M.Ş.A. and Arslanoğlu, H., 2025. α-Alumina (α-Al_2O_3) ceramic microfiltration membranes in industrial wastewater treatment: Production, design, filtration behavior and performance. *Ceramics International*, 51(6), pp.789-801. [DOI]

Ezugbe, E.O. and Rathilal, S., 2020. Membrane technologies in wastewater treatment: A review. *Membranes*, 10(5), p.89. [DOI]

Federigi, I., Salvadori, R., Lauretani, G., Leone, A., Lippi, S., Marvulli, F., Pagani, A., Verani, M. and Carducci, A., 2024. Wastewater treatment plants performance for reuse: Evaluation of bacterial and viral risks. *Water*, 16(10), p.1399. [DOI]

Hakami, M.W., Alkhudhiri, A., Al-Batty, S., Zacharof, M.-P., Maddy, J. and Hilal, N., 2020. Ceramic microfiltration membranes in wastewater treatment: Filtration behavior, fouling and prevention. *Membranes*, 10(9), p.248. [DOI]

Hristov, P., Yoleva, A., Djambazov, St., Chukovska, I. and Dimitrov, D., 2012. Preparation and characterization of porous ceramic membranes for micro-filtration from natural zeolite. *Journal of the University of Chemical Technology and Metallurgy*, 47(4), pp.476-480.

Kane, C.K., Bâ, A., Mahamat, S.A.M., Ayessou, N., Mbacké, M.K. and Diop, C.G.M., 2016. Combination of alum and extracted *Moringa oleifera* bioactive molecules powder for municipal wastewater treatment. *International Journal of Biological and Chemical Sciences*, 10(4), pp.1918-1929.

Kapila, S., Soukup, R.J., Bradley, M.E. and Zydney, A.L., 2025. Flux and fouling behavior during constant pressure sterile filtration of nanoemulsions. *Journal of Membrane Science*, 713, p.123370. [DOI]

Katalo, R., Okuda, T., Nghiem, L.D. and Fujioka, T., 2018. *Moringa oleifera* coagulation as pretreatment prior to microfiltration for membrane fouling mitigation. *Environmental Science: Water Research & Technology*, 4, pp.1604-1611. [DOI]

Ndabigengesere, A. and Narasiah, K.S., 1998. Quality of water treated by coagulation using *Moringa oleifera* seeds. *Water Research*, 32(3), pp.781-791.

Nouira, A., Ben Hamden, M., Sayehi, M. and Bekri-Abbes, I., 2025. Transforming waste to water filters: A mini-review of waste-derived ceramic membranes. *Sustainability*, 3(3), p.29. [DOI]

Ofomi, J., Okoye, C., Nnaji, P. and Eze, J., 2025. Testing the performance of powdered *Moringa oleifera* seed as a natural coagulant for water treatment. *Journal of Environmental Technology & Engineering*, 13(1), pp.45-58.

Ogunshina, M.S., Abioye, O.M., Adeniran, K.A. and Olasehinde, D.A., 2023. *Moringa oleifera* coagulation characteristics in wastewater treatment in a university dormitory. *Nature Environment and Pollution Technology*, 22(2), pp.699-707.

Oladoja, N.A. and Pan, G., 2015. Modification of local soil/sand with *Moringa oleifera* extracts for effective removal of cyanobacterial blooms. *Sustainable Chemistry and Pharmacy*, 2, pp.37-43. [DOI]

Othman, N.H., Alias, N.H., Fuzil, N.S., Marpani, F., Shahruddin, M.Z., Chew, C.M., Ng, K.M.D., Lau, W.J. and Ismail, A.F., 2021. A review on the use of membrane technology systems in water treatment. *Membranes*, 11(1), p.77. [DOI]

Padalkar, A.V. and Hiralal, V.G., 2018. Common effluent treatment plant (CETP): Reliability and removal efficiencies in an Indian industrial area. *Journal of Environmental Chemical Engineering*, 6(5), pp.6220-6229.

Ribeiro, J.V.M., Andrade, P.V. and dos Reis, A.G., 2019. *Moringa oleifera* seed as a natural coagulant to treat low-turbidity water by in-line filtration. *Revista Ambiente & Água*, 14, p.e2442.

Sanchis-Perucho, P., Aguado, D., Ferrer, J., Seco, A. and Robles, Á., 2023. Direct membrane filtration of municipal wastewater: Studying the most suitable conditions for minimizing fouling rate in commercial porous membranes at demonstration scale. *Membranes*, 13(1), p.99. [DOI]

Singh, B.J., Chakraborty, A. and Sehgal, R., 2023. A systematic review of industrial wastewater management: Evaluating challenges and enablers. *Science of the Total Environment*, 883, p.163635.

Sravan, J.S., Matsakas, L. and Sarkar, O., 2024. Advances in biological wastewater treatment processes: Focus on low-carbon energy and resource recovery in biorefinery context. *Bioengineering*, 11(3), p.281. [DOI]

Tow, E.W., Hartman, A.L., Jaworowski, A., Zucker, I., Kum, S., AzadiAghdam, M., Blatchley, E.R., Achilli, A., Gu, H., Urper, G.M. and Warsinger, D.M., 2021. Modeling the energy consumption of potable water reuse schemes. *Water Research X*, 13, p.100126. [DOI]

Uman, A.E., Bair, R.A. and Yeh, D.H., 2024. Direct membrane filtration of wastewater: A comparison between real and synthetic wastewater. *Water*, 16(3), p.405. [DOI]

Yamaguchi, N.U., Cusioli, L.F., Quesada, H.B., Ferreira, M.E.C., Fagundes-Klen, M.R., Salcedo Vieira, A.M.S.S., Gomes, R.G., Vieira, M.F. and Bergamasco, R., 2021. A review of *Moringa oleifera* seeds in water treatment: Trends and future challenges. *Process Safety and Environmental Protection*, 147, pp.405-420.

Zhang, Y., Tan, Y., Sun, R. and Zhang, W., 2023. Preparation of ceramic membranes and their application in wastewater and water treatment. *Water*, 15(19), p.3344. [DOI]

Zielińska, M. and Galik, M., 2017. Use of ceramic membranes in a membrane filtration supported by coagulation for the treatment of dairy wastewater. *Water, Air, & Soil Pollution*, 228, p.173. [DOI]

NEPT

Nature Environment and Pollution Technology

An International Quarterly Peer-Reviewed Open Access Journal

p-ISSN: 0972-6268 | e-ISSN: 2395-3454 Vol. 25 | No. 4 | Article ID D1921 | 2026

RESEARCH ARTICLE https://doi.org/10.46488/NEPT.2026.v25i04.D1921 OPEN ACCESS

Sustainable Development of Maritime Transport Towards Net-Zero Emissions by 2050 Through a Feasible Fuel Transition Roadmap

Tran Huu Long, Phan Van Hung and Nguyen Xuan Long†

Vietnam Maritime University, Haiphong, Vietnam

†Corresponding author: Nguyen Xuan Long; nguyenxuanlong@vimaru.edu.vn

ARTICLE HISTORY

Received: 14-03-2026
Revised: 04-05-2026
Accepted: 14-05-2026

KEYWORDS

Maritime decarbonization
IMO GHG Strategy 2023
Fuel transition roadmap
Sustainable shipping
PLEETS multi-criteria decision
Sustainable development goal

CITE THIS ARTICLE

Tran Huu Long, Phan Van Hung and Nguyen Xuan Long, 2026. Sustainable development of maritime transport towards net-zero emissions by 2050 through a feasible fuel transition roadmap, *Nature Environment and Pollution Technology,* 25(4), D1921. [DOI]

COPYRIGHT & LICENCE

© 2026 The Authors
Open Access under CC BY 4.0.

PUBLISHED BY

TECHNOSCIENCE PUBLICATIONS

ABSTRACT

With the 2023 International Maritime Organization (IMO) Greenhouse Gas (GHG) Strategy targeting net-zero ship emissions by 2050, shipowners and operators are seeking economically effective solutions to meet the latest emission requirements. The initial cost of changeover and use of new fuels can be too high, which is a major barrier for Vietnamese shipowners. Therefore, this article proposes a comprehensive fuel transition roadmap for Vietnam's maritime industry using the PLEETS multi-criteria decision analysis framework (Political, Legal, Economic, Environmental, Technological, and Social). Through a mixed-methods research design to evaluate Vietnamese fleet data, assess major port infrastructure, conduct surveys of 127 participants, and perform techno-economic modeling, seven alternative fuels were considered: compliant fuels, liquefied natural gas (LNG), methanol, ammonia, shore power, ethanol, and hydrogen. The analysis results indicate an optimal transition strategy comprising three phases: The immediate phase (2025–2030) focuses on building a basic foundation, such as deploying onshore power generation and providing and using appropriate fuels, to achieve a 15–20% emission reduction target with an estimated investment of USD 0.8–1.0 billion. The intermediate phase (2031–2040) involves using methanol and bio-LNG, aiming for a 40–50% reduction with an estimated investment of USD 1.8–2.2 billion. The final phase (2041–2050) will utilize green ammonia and e-methanol, aiming for net-zero emissions with an investment of approximately USD 2.8–3.4 billion. This roadmap provides evidence to support Vietnamese policymakers, shipowners, operators, and port authorities and contributes methodologically through the first-ever rigorous application of the PLEETS multi-criteria decision analysis framework integrated into a marine fuel transition strategy in the context of a developing nation.

1. INTRODUCTION

The maritime sector plays a pivotal role in the global economy, offering substantial advantages in terms of both the volume and distance of transportation. With the world's commercial fleet reaching about 108,789 vessels and a total capacity of approximately 2.4 billion deadweight tons, maritime transport remains the dominant mode of global trade, accounting for over 80% of world trade by volume (UNCTAD 2024). The maritime industry currently accounts for approximately 3% of total global greenhouse gas (GHG) emissions, contributing significantly to environmental pollution (Alamoush & Ölçer 2025, Lian et al. 2020). According to the IMO's Third Greenhouse Gas Study (Smith et al. 2014), CO_2 emissions from the international commercial shipping fleet increased from 848 million to 919 million metric tons between 2012 and 2018. As maritime trade is projected to continue growing, emissions from this fleet risk increasing by 50–250% by 2050.

Furthermore, ships are responsible for approximately 12% of global sulfur oxides (SO_x) and 13% of global nitrogen oxides (NO_x) emissions (Bolat 2026, Smith et al. 2014, IMO 2020, Perera & Soares 2017). In line with the goals of COP26, the 2023 IMO GHG Strategy was developed with the overarching goal of achieving carbon neutrality before 2050 (IMO 2018, IMO 2023). To implement this goal, the IMO issued tools and implementation guidelines such as the Energy Efficiency Design Index (EEDI), Energy Efficiency Existing Ship Index (EEXI), Energy Efficiency Operational Indicator (EEOI), and Carbon Intensity Indicator (CII), providing a solid foundation for countries to develop their own emission reduction strategies for their fleets.

Notably, in 2023, the IMO officially launched a new strategy for reducing greenhouse gas emissions from ships, with the core objective of achieving net-zero emissions by 2050, fully consistent with the commitments made at COP26 (IMO 2023). This strategy delineates specific objectives for the introduction of alternative green fuels and establishes indicative benchmarks for overall emission reduction. These benchmarks were designated for a 20–30% reduction by the year 2030 and a 70–80% reduction by the year 2040, respectively.

The 2023 IMO GHG Strategy requires shipowners and operators to plan for compliance with the emission reduction requirements of the CII, moving toward operating low- and zero-emission ships. There are several options (Cortez-Huerta et al. 2024, Premsamarn et al. 2025, Wang & Iris 2025) for fuel suppliers and users, including heavy fuel oil (HFO) used with onboard exhaust gas cleaning systems (scrubbers); low-sulfur fuel oil (LSFO) and marine gas oil (MGO); liquefied natural gas (LNG) or compressed natural gas (CNG); methanol; ethanol; biofuels such as bio-LNG, bio-MGO, e-LNG, and e-MGO; green fuels such as green hydrogen and green ammonia; and electricity from the grid. A ship's fuel consumption can account for more than 50% of its operating costs. With increasingly stringent requirements for the shipping industry, the incentives for shipowners/operators are not only environmental but also related to operational efficiency and ship economics. This paper considers options including fossil fuels combined with scrubbers, biofuels, green fuels, and electricity from the grid. The results of this study will help shipowners/operators make adaptation decisions in the short and long term. In particular, with 1,500 ships with a total tonnage of 13.7 million tons, the Vietnamese shipping fleet currently ranks 3rd in ASEAN and 22nd in the world. Notably, the average age of the Vietnamese shipping fleet is 15.5 years, 6 years younger than the world's fleet. The number of crew members also increased sharply from 39,400 people in 2018 to 62,000 people in 2023. A widely used indicator that provides insight into the capacity of a seaport is the volume of cargo handled by the port, which includes all types of cargo such as containers, liquids, and dry bulk, and can serve as a leading economic indicator. The volume of cargo through the Vietnamese seaport system in 2024 was 864.4 million tons, up 14% from the same period in 2023. Container cargo through the Vietnamese seaport system was estimated to be 29.9 million twenty-foot equivalent units (TEUs), up 21% from the same period in 2023, as shown in Fig. 1. An estimated 102.67 thousand ships were expected to sail through the ports in 2024, up 2% from the same period in 2023. An estimated 380.1 thousand inland waterway vessels were expected to pass through the harbor in 2024, an 8% increase over the same period in 2023.

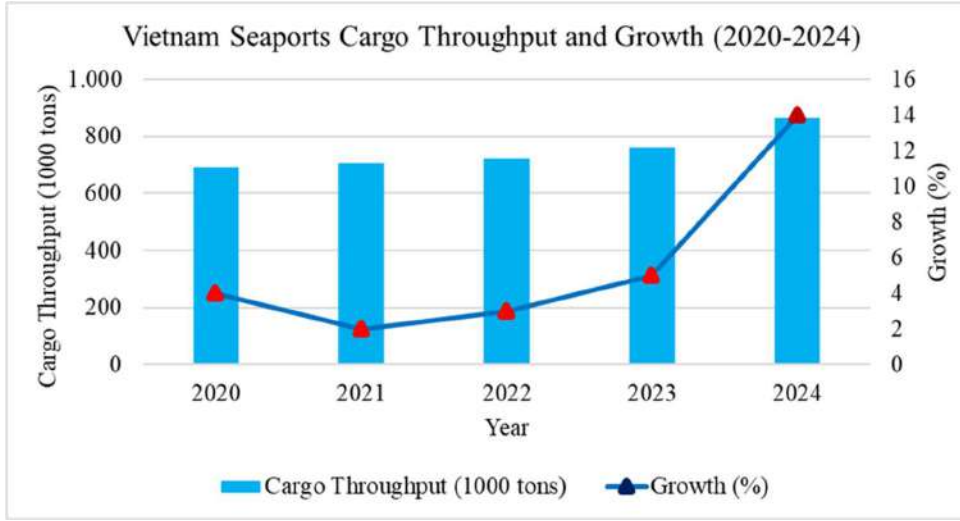


Fig. 1: Cargo throughput and growth of Vietnam seaports (Source: Vietnam Maritime and Waterway Administration 2025).

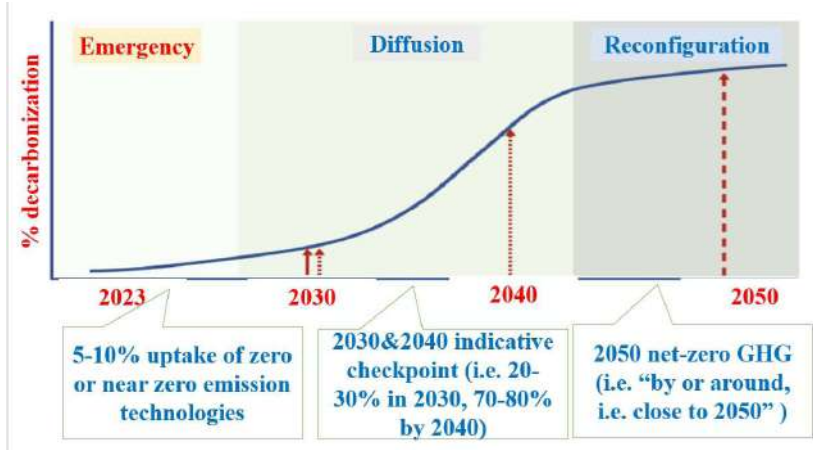


Fig. 2: The 2023 IMO GHG Strategy (IMO, 2023).

The world's largest container ship, with a deadweight tonnage (DWT) of 232,000, was successfully received at the Cai Be wharf area by the Vietnamese seaport system, which has established gateway ports along with international transit in the North and South areas. At the port of Lach Huyen, Cai Mep ships with a maximum capacity of 140,000 DWT head straight to the markets in Europe and America. Large-scale specialized ports connected to industrial parks, metallurgical complexes, petrochemical refineries, and coal-fired thermal power centers receive ships up to 200,000 DWT, liquid cargo up to 150,000 DWT (product export ships), and crude oil up to 320,000 DWT (at Nghi Son port buoy wharf).

Clearly, Vietnamese shipowners are struggling to make the right decision on the options for compliance with the emission reduction requirements of the 2023 IMO GHG Strategy for their existing vessels as well as their plans for operating new vessels. Therefore, it is necessary to analyze the advantages and disadvantages of the possible options for Vietnamese shipowners in this context.

2. MATERIALS AND METHODS

2.1. Literature Review

2.1.1. Regulatory Framework: Focusing on IMO Strategies and Vietnam's Legal Context

The IMO's revised 2023 GHG Strategy sets a target of net-zero emissions by around 2050, with interim goals of decreasing GHG emissions by 20–30% by 2030 and 70–80% by 2040, based on 2008 levels (Fig. 2). It also aims for a minimum 5% uptake of zero/near-zero emission fuels or technologies by 2030. The application of well-to-wake fuel emission control is a significant new step forward, contributing to a fair and equitable fuel transition. Industry- and vessel-specific emission reduction targets are now primarily focused on greenhouse gas intensity per unit of transport. Specifically, each vessel is targeted to reduce emissions by 55–61% by 2030 and 86–91% by 2040 compared to 2008 baselines. This sends a very clear message to fuel producers and suppliers, strongly supporting a genuine green fuel transition; consequently, fossil fuel-based or environmentally unfriendly alternatives will no longer be encouraged.

A clear and systematic decarbonization roadmap will lead to a synchronized shift in investment toward technically viable green technologies (Barone et al. 2024, Balci et al. 2024, Cuong & Hung 2020b, Nguyen 2016)considerable challenges exist for green ammonia adoption as the future clean energy source in maritime transport. This study scrutinises the success factors of the industry-wide adoption of green ammonia. We examine the structural relationship between success factors to explore antecedents, illustrate the precedence relationships between success factors, and present a roadmap. We first determine success factors and then employ Interpretive Structural Modelling (ISM.

2.1.2. Empirical Evidence Regarding Fuel Adoption

The core objective of the maritime industry today is to achieve carbon neutrality through a fair and equitable fuel transition, in strict compliance with the IMO's 2023 Greenhouse Gas (GHG) Emission Reduction Strategy. This context also highlights the asymmetry in policy frameworks among developing countries due to varying levels of economic impact. Therefore, the adoption of a dual regulatory mechanism combining technical standards and a GHG pricing mechanism is crucial to bridging the cost gap between green and conventional fuels, while promoting the participation of developing countries in production and supply.

To assess the potential aspects of developing green fuels alongside improving energy efficiency, the maritime industry is witnessing a divergence in the trajectory of transition to alternative energy sources, such as liquefied natural gas (LNG) and biofuels (Ha et al. 2025, Park et al. 2021, DNV GL 2020). However, these low-emission transition fuels are projected to become unsuitable by 2040, posing a significant risk of wasted investment. Therefore, choosing an investment path toward large-scale zero-emission solutions focusing on green hydrogen, green ammonia, and green methanol that are supported by pilot projects will help create green corridors to mitigate risks for both the public and private sectors (Barone et al. 2024, Cuong & Hung 2020a, Achuo et al. 2022, Atilhan et al. 2021, DNV GL 2020, Karvounis & Theotokatos 2025).

In addition, integrated power generation solutions from seaports to completely eliminate port emissions also require extensive synchronization between port infrastructure and ships. Overall, the feasibility and suitability of each solution require stakeholders to carefully consider long-term asset use plans, ensuring compliance with stringent requirements in the roadmap toward near-zero emission technologies (Ortiz-Imedio et al. 2021, Sun et al. 2023).

2.1.3. Research Gaps

Although current research on maritime energy transition solutions is abundant, much of it is biased toward specific geographic regions and decarbonization strategies. Technologically advanced economies with high capital mobility, such as the EU, the US, China, and Japan, are often used as the standard reference point (Ha et al. 2025, Ortiz-Imedio et al. 2021, Wang & Iris 2025, Balci et al. 2024, Barone et al. 2024, Halpe et al. 2025, IMO 2018, IMO 2020, IMO 2023, Perera & Soares 2017, Al-Aboosi et al. 2021, Cameretti et al. 2025).

This research identifies three key gaps: (i) existing decision-support frameworks do not adequately address the essential sociopolitical and legal aspects for developing countries; (ii) studies on maritime decarbonization often focus on developed countries, without considering the characteristics faced by developing maritime nations such as infrastructure and finance; (iii) technological maturity over time, infrastructure development, and alternative fuel supply chains have not been fully integrated into transition plans. The new PLEETS decision-support framework developed in this study focuses on addressing these knowledge gaps.

2.2. Research Design and Data Collection

This study employed a sequential mixed-methods approach. The qualitative phase involves literature reviews and expert consultations to identify criteria and establish the AHP hierarchy model. The quantitative phase utilizes the AHP method to compute criterion weights, applies the TCO model for cost evaluation, and conducts sensitivity analysis to validate the robustness of the decision-making model. Data across the following four areas were collected between January 2023 and December 2024.

Data for all commercial vessels, classified by vessel type (bulk carriers, container ships, oil tankers, general cargo ships, passenger ships, offshore support vessels), age distribution, engine type, and fuel consumption patterns, were collected from the Vietnam Maritime and Waterway Administration (VIMAWA). Emissions from vessels were calculated using the methodology of the Fourth IMO Greenhouse Gas Study (IMO 2020).

Surveys (assessing fuel preferences, infrastructure constraints, investment capacity, and policy priorities) were conducted with two distinct groups of participants: 27 domain experts who contributed to the AHP weighting process, and 127 participants in the validation survey, including 15 government agencies, 18 port authorities, 35 ship operators, 42 shipowners, and 17 maritime industry associations.

Assessments at six major ports (over 80% of the country's cargo throughput) in Vietnam (Hai Phong, Ho Chi Minh, Vung Tau, Da Nang, Nha Trang, Quy Nhon) considered existing refueling capacity, onshore power infrastructure, land area for fuel storage, and safety systems.

Techno-economic model: A specific total cost of ownership (TCO) model was developed using a 25-year life-cycle analysis with a 5% discount rate for each vessel and incorporating capital costs (vessel modifications and engine upgrades), fuel costs (current and projected), infrastructure costs (refueling, storage, and distribution), and operating costs (maintenance, training, and insurance).

2.3. PLEETS Framework Implementation

The PLEETS framework was implemented through a four-stage process:

Phase 1: Criterion Definition and Weighting

Nineteen evaluation criteria across six aspects of PLEETS were established (Tables 1 and 2).

Nineteen criteria were evaluated across six aspects of PLEETS (Tables 1–3). Based on the opinions of 27 maritime experts and analytic hierarchy process (AHP) analysis, the weights of the criteria were determined. A consistency ratio below 0.10 ensured the reliability of the evaluation method. Three sensitivity scenarios were analyzed to examine changes in weighting: environmental priority (environmental aspect weight increased by 50%), economic priority (economic aspect weight increased by 50%).

Table 1: PLEETS framework overview.

Framework Component	Description	Application in Maritime Fuel Selection	Data Sources
Political Dimension	Government policies, political stability, international cooperation	Assessment of policy support, regulatory certainty, geopolitical fuel security	Policy documents, stakeholder interviews, international agreements
Legal Dimension	Regulatory compliance, legal frameworks, liability	Evaluation of IMO compliance, national regulations, safety standards	IMO regulations, national maritime law, port regulations
Economic Dimension	Costs, financial viability, economic impacts	Total cost of ownership, infrastructure investment, operational economics	Fleet data, fuel prices, infrastructure cost estimates, TCO modeling
Environmental Dimension	GHG emissions, air quality, ecological impacts	Life-cycle emissions, air pollutants, water pollution, biodiversity	Life-cycle assessment (LCA) databases, emission factors, environmental impact assessments
Technological Dimension	Technology maturity, technical feasibility, safety	Technology readiness level, energy density, infrastructure maturity	Technical literature, manufacturer data, pilot projects
Social Dimension	Stakeholder acceptance, social impacts, equity	Workforce implications, public health, social acceptance, equity	Stakeholder surveys, health impact assessments, employment analysis

Source: Authors' framework development based on the PESTLE methodology

Table 2: PLEETS evaluation criteria and indicators.

Dimension	Criteria	Indicators	Weight	Data Source
Political (0.15)	Government support	Policy documents, funding commitments	0.06	Policy analysis
	Policy stability	Regulatory consistency, long-term planning	0.05	Expert assessment
	International cooperation	Regional agreements, technology transfer	0.04	International frameworks
Legal (0.12)	IMO compliance	Alignment with IMO 2030/2050 targets	0.05	Regulatory analysis
	National regulations	Domestic maritime law compatibility	0.04	Legal review
	Safety regulations	Handling, storage, bunkering standards	0.03	Safety assessments
Economic (0.25)	Capital costs	Vessel modifications, infrastructure investment	0.09	Cost modeling
	Fuel costs	Current and projected fuel prices	0.08	Market analysis
	Operational costs	Maintenance, training, insurance	0.05	Industry data
	Economic viability	Payback period, return on investment	0.03	Financial modeling
Environmental (0.28)	GHG emissions	Well-to-wake CO_2 equivalent	0.12	LCA analysis
	Air quality	SO_x, NO_x, PM emissions	0.08	Emission modeling
	Water pollution	Ballast water, fuel spills	0.05	Environmental assessment
	Biodiversity impacts	Marine ecosystem effects	0.03	Ecological studies
Technological (0.13)	Technology readiness	Technology readiness level (TRL), commercial availability	0.05	Technology assessment
	Energy density	Volumetric and gravimetric density	0.04	Technical specifications
	Infrastructure maturity	Bunkering, storage, distribution	0.04	Infrastructure assessment
Social (0.07)	Stakeholder acceptance	Industry and public support	0.03	Survey data
	Workforce impacts	Training needs, employment effects	0.02	Labor analysis
	Health benefits	Air quality improvements	0.02	Health impact assessment

Dimension weights shown in parentheses; criteria weights sum to dimension weight. Source: Authors' AHP analysis with 27 expert participants.

Phase 2: Evaluation of Alternative Fuel Options

A systematic evaluation of seven typical alternative fuel options: (1) compliant low-sulfur fuel blends (VLSFO/MGO), (2) liquefied natural gas (LNG), (3) methanol (including production pathways), (4) ethanol (bioethanol), (5) ammonia (gray, blue, and green production pathways), (6) hydrogen (compressed and liquid forms), and (7) onshore power for terminal operations.

Each fuel type was scored on a scale of 0 to 1 for each criterion based on a review of documentation, specifications, life-cycle assessment (LCA) data, and a Vietnam-specific feasibility assessment including differences in production

Table 3: Weight synthesis and sensitivity analysis.

Dimension	Base Case Weight	Environmental Priority Weight	Economic Priority Weight	Weight Range (Min–Max)	Coefficient of Variation
Political	0.15	0.12	0.13	0.12–0.18	0.14
Legal	0.12	0.10	0.11	0.09–0.15	0.18
Economic	0.25	0.20	0.375	0.20–0.38	0.25
Environmental	0.28	0.42	0.22	0.22–0.42	0.28
Technological	0.13	0.11	0.12	0.10–0.16	0.17
Sociological	0.07	0.05	0.06	0.05–0.09	0.21
Total	1.00	1.00	1.00	-	-
Consistency Ratio	0.08	0.09	0.07	-	-

Environmental priority: Environmental dimension weight increased 50%; Economic priority: Economic dimension weight increased 50%. Consistency ratio < 0.10 indicates acceptable judgment consistency. Source: Authors' AHP sensitivity analysis.

processes and technological maturity, cost projections, and infrastructure development.

Phase 3: Multi-criteria synthesis

This study uses a weighted synthesis method to calculate scores (Eq. 1).

$$S_f = \sum d = 16w_d \times \sum c = 16w_{d,c} \times s_{f,d,c} \quad \ldots(1)$$

where S_f is the overall score for fuel f, w_d is the weight for dimension d, $w_{d,c}$ is the weight for criterion c within dimension d, and $s_{f,d,c}$ is the score for fuel f on criterion c of dimension d.

Phase 4: Scenario and sensitivity analysis

The study analyzes the business-as-usual (BAU), Moderate Transition, and Rapid Transition scenarios. The three-phase roadmap (2030, 2040, and 2050), developed after expert consultation, integrates the results of the PLEETS analysis, considering infrastructure constraints, investment financing capacity, and feasibility. Sensitivity analysis demonstrated stability against variations in weighting of technology maturity over time and the rate of fuel cost reduction.

3. RESULTS AND DISCUSSION

The 27 experts were selected based on their expertise in maritime operations (10), energy policy (8), and environmental engineering (9). Pairwise comparisons were performed using Saaty's 9-point scale. The group consistency ratio (CR) was calculated as 0.076 < 0.1, ensuring reliability. The 127 survey participants provided broader industry validation, with responses anonymized to comply with ethical standards.

While Compliant Fuels currently lead in aggregate scoring due to infrastructure maturity (T3, E4), their low Environmental scores (En1, En2) necessitate a transition to alternative fuels as carbon taxes and regulatory pressures increase toward 2050.

The PLEETS framework assessment (Table 4) reveals different performance characteristics among the seven alternative fuels. Reflecting immediate availability, regulatory compliance, and minimum infrastructure requirements, the compliant fuel blends achieved the highest overall score (0.712), but had limited emission reduction potential. Second place went to LNG (0.672), balancing moderate emission reduction with established technology and developing infrastructure. Methanol (0.658) and ammonia (0.643) showed strong long-term potential, particularly in environmental and technological aspects, but faced short-term economic and infrastructure hurdles.

Table 4: Comprehensive PLEETS evaluation scores.

Fuel Alternative	Political (0.15)	Legal (0.12)	Economic (0.25)	En. (0.28)	Tec. (0.13)	Soc. (0.07)	Overall Score	Rank
Compliant Fuels	0.82	0.91	0.78	0.42	0.89	0.76	0.712	1
LNG	0.71	0.78	0.72	0.58	0.74	0.68	0.672	2
Methanol	0.68	0.72	0.58	0.71	0.69	0.64	0.658	3
Ammonia	0.64	0.65	0.52	0.82	0.61	0.58	0.643	4
Shore Power	0.76	0.81	0.48	0.89	0.72	0.71	0.638	5
Ethanol	0.59	0.68	0.54	0.68	0.58	0.62	0.612	6
Hydrogen	0.52	0.58	0.41	0.86	0.48	0.54	0.571	7

Dimension weights are shown in parentheses; scores are normalized on a 0–1 scale (higher is better).

Policy: The compliant fuels score is 0.82 because there is a stable established legal framework, resulting in low risk. The LNG score is 0.71, indicating increasing government support and priority for developing national LNG infrastructure by 2030. The methanol score is 0.68, and the ammonia score is 0.64, showing unclear incentive policies for safe production and supply. The hydrogen score is the lowest (0.52) due to the lack of a roadmap.

Legal aspects: Compliant fuels meet IMO requirements and therefore have the highest score of 0.91. LNG ranks second with a score of 0.78, aligning with IMO 2030 targets, but methane emissions pose a risk. Next are methanol and ethanol, which still pose risks related to safety regulations and legal liability, with scores of 0.72 and 0.68, respectively. Ammonia has a score of 0.65 and hydrogen 0.58, representing risks due to legal gaps in production, storage, transportation, and bunkering.

Economics: Compliant fuels rank first with a score of 0.78, representing the lowest fuel cost. LNG ranks second with a score of 0.72, indicating low fuel costs but high infrastructure investment. Following are methanol and ethanol, which have moderate fixed capital costs but unpredictable fuel prices, with scores of 0.58 and 0.54, respectively. Finally, ammonia and hydrogen are ranked last, representing high fuel production investment costs, significant infrastructure and vessel gaps, and high supply market risks, with scores of 0.52 and 0.41, respectively.

Environment: Shore power ranks first with a score of 0.89, followed by hydrogen with a score of 0.86. These are two solutions with zero emissions when ships are docked in port. Green ammonia ranks third and can reduce greenhouse gas emissions by 95%, with a score of 0.82. Methanol and bioethanol, developed in a bio-oriented direction, can reduce emissions by 60–80% (scores of 0.71 and 0.68, respectively). LNG (0.58) emits methane, so it only reduces emissions by 20–25%. Compliant fuels (with a score of 0.42) meet minimum requirements.

Technology: The most mature technology is associated with compliant fuels, with a score of 0.89. Fuels with readily available technology are LNG (0.74) and shore power (0.72). Methanol-related technology can build on existing infrastructure (0.69), benefiting from existing chemical processing infrastructure. Technological barriers for ammonia (0.61) and ethanol (0.58) are moderate. Low energy density, storage technology, and ship fuel-distribution systems for hydrogen give it the lowest score (0.48).

Social: The port community strongly supports the use of shore power, so this solution has the highest score (0.71). Compliant fuels, LNG, methanol, and ethanol follow with moderate impacts. Finally, the new fuels, ammonia and hydrogen, still pose safety risks and widespread labor shortages.

Looking at Table 5, the sensitivity analysis ranking results for the fuels show that the overall ranking remains unchanged. However, there are slight changes in the environmental and economic aspects. The greenhouse gas emission reduction efficiency of ammonia (0.698) is higher than that of LNG (0.641). Compliant fuels (0.756) are the most economically efficient, while ammonia and hydrogen remain at the bottom due to high investment costs.

Although compliant fuels rank first in the static MCDA result, this reflects the current market maturity and economic feasibility. The proposed roadmap uses a dynamic transition approach, where the adoption of low-carbon fuels (methanol, ammonia) increases as their technological and economic scores improve through policy intervention and global supply chain development.

3.1. Fuel Transition Roadmap

Based on the PLEETS results, the existing infrastructure limitations, and consultations with stakeholders, the authors propose a fuel transition roadmap (Table 6) in three phases, consistent with the capacity of the Vietnamese maritime industry and the IMO timelines.

Table 5: Sensitivity analysis: fuel rankings under alternative weighting scenarios.

Fuel Alternative	Base Case Score	Base Rank	Environmental Priority Score	Env. Rank	Economic Priority Score	Econ. Rank	Ranking Stability
Compliant Fuels	0.712	1	0.658	1	0.756	1	Stable
LNG	0.672	2	0.641	4	0.698	2	Moderate
Methanol	0.658	3	0.687	3	0.632	3	Stable
Ammonia	0.643	4	0.698	2	0.601	5	Variable
Shore Power	0.638	5	0.672	5	0.589	6	Moderate
Ethanol	0.612	6	0.634	6	0.605	4	Moderate
Hydrogen	0.571	7	0.612	7	0.542	7	Stable

Table 6: Vietnam maritime fuel transition roadmap (2025–2050).

Phase	Timeline	Primary Fuels	Supporting Infrastructure	Emission Reduction Target	Fleet Penetration	Cumulative Investment (USD billion)
Phase I: Foundation	2025–2030	Compliant fuels (70%), Shore power (20%), Bio-LNG pilot (10%)	Shore power at 6 major ports; LNG bunkering at 2 ports	15–20% vs. 2023 baseline	Shore power: 25% of port calls; LNG: 5% of fleet	0.8–1.0
Phase II: Transition	2031–2040	Methanol (35%), Bio-LNG (30%), Compliant fuels (25%), Shore power (10%)	Methanol bunkering at 4 ports; LNG network expansion; Pilot ammonia infrastructure	40–50% vs. 2023 baseline	Methanol: 30% of new builds; LNG: 25% of fleet	1.8–2.2
Phase III: Deep Decarbonization	2041–2050	Green ammonia (40%), E-methanol (30%), Bio-LNG (20%), Shore power (10%)	Ammonia bunkering network; Green fuel production facilities; Hydrogen pilot projects	90–100% vs. 2023 baseline (net-zero)	Ammonia: 35% of fleet; E-methanol: 25% of fleet	2.8–3.4

Table 7: Scenario analysis of emission reduction trajectories (2025–2050).

Scenario	2030 Emissions (Mt CO_2e)	2030 Reduction vs. 2023	2040 Emissions (Mt CO_2e)	2040 Reduction vs. 2023	2050 Emissions (Mt CO_2e)	2050 Reduction vs. 2023	Cumulative Investment (USD billion)
BAU	10.2	-14% (increase)	12.8	-43% (increase)	15.6	-74% (increase)	0.3–0.5
Moderate Transition	7.6	+15%	5.4	+40%	2.1	+77%	1.8–2.2
Accelerated Transition	7.2	+20%	4.5	+50%	0.9	+90%	2.8–3.4

Phase 1 (2025–2030) Foundation Building: Prioritize immediate emission reduction (15–20% reduction compared to 2023) through the use of low-sulfur fuels (meeting 70% of demand) and shore power for ships (20%). Conduct bio-LNG pilot projects at Hai Phong and Ho Chi Minh City ports. (Investment required: USD 0.8–1.0 billion).

Phase 2 (2031–2040) Fuel Diversification: Strong shift toward new fuels including methanol (35%) and bio-LNG (30%). Begin construction of methanol supply infrastructure at 4 major ports (Hai Phong, Ho Chi Minh City, Da Nang, Vung Tau), expand the LNG supply network to 6 ports, and pilot ammonia infrastructure in Ho Chi Minh City. Emissions will be reduced by 40–50% at this stage. (Cumulative investment: USD 1.8–2.2 billion).

Phase 3 (2041–2050) Complete decarbonization: Complete the transition to achieve net-zero emissions (90–100% reduction in emissions). The main fuel sources will be green ammonia (40%) and e-methanol (30%). This phase focuses on building large-scale green fuel production plants from offshore wind and renewable hydrogen, while also covering all major ports with ammonia supply stations (Cumulative investment: USD 2.8–3.4 billion). This USD 2.8–3.4 billion range represents direct maritime CAPEX specifically core port onshore power supply, bunkering infrastructure, and direct vessel retrofits.

Table 7 illustrates three emission reduction scenarios at three different policy levels. The BAU scenario, with conventional policies, sees the growth of maritime trade leading to a faster increase in the number of ships than the improvement in ship efficiency, resulting in continued emissions growth of 74% by 2050. The Fuel Transition scenario, following the current policy roadmap, also fails to achieve zero emissions by 2050 (a 77% reduction). The Rapid Transition scenario, through comprehensive policy support and the adoption of alternative fuels, is expected to reduce emissions by over 90% by 2050, approaching net-zero emissions.

Table 8 presents 15 priority policy actions across the three phases, with the timeline, responsible agency, key performance indicators, and estimated budget. These actions include phased carbon pricing up to 2030 (USD 20–30/ton CO_2) and USD 80–100/ton by 2050; development and implementation of a green-shipping program with significant financial support for shipowners to transition; accelerated construction of green ports, including mandatory use of shore power and preferential port fees (30–50% reduction) for zero-emission vessels; and stronger ASEAN regional cooperation to harmonize fuel standards and cross-border refueling infrastructure.

3.2. Key Findings

The novelty of this study lies primarily in its methodology, integrated framework, and empirical approach in developing countries. Methodologically, the PLEETS framework is the first comprehensive multi-criteria assessment specifically designed for rapidly developing maritime nations like Vietnam by incorporating legal, political, and social aspects

Table 8: Policy implementation timeline and responsibility matrix.

Policy Action	Phase	Timeline	Responsible Agency	Key Performance Indicators	Estimated Budget (USD million)
1. Shore power mandate for major ports	I	2024–2026	Ministry of Construction; Port authorities	60 berths equipped by 2026	180–220
2. LNG bunkering infrastructure development	I	2025–2028	Vietnam National Oil & Gas Group; Port authorities	2 LNG bunkering facilities operational	240–280
3. Green shipping incentive program	I	2024–2030	Ministry of Finance; Maritime Administration	20% of fleet participating by 2030	150–200
4. Carbon pricing mechanism for shipping	I	2026–2030	Ministry of Finance; Ministry of Natural Resources	Carbon price: USD 20–30/ton CO_2 by 2030	50–80 (admin)
5. Maritime workforce training program	I	2024–2030	Ministry of Construction; Maritime universities	5,000 personnel trained in alternative fuels	30–45
6. Methanol bunkering network establishment	II	2028–2035	Port authorities; Private sector	4 methanol bunkering facilities operational	320–380
7. Alternative fuel vessel subsidy program	II	2030–2040	Ministry of Finance; Development banks	30% of new builds alternative-fuel capable	400–500
8. Ammonia safety regulation framework	II	2030–2033	Maritime Administration; Ministry of Industry and Trade	Comprehensive ammonia handling regulations	15–25
9. Green fuel production incentives	II	2031–2040	Ministry of Industry and Trade; Ministry of Finance	500,000 tons/year green ammonia capacity	800–1,000
10. ASEAN maritime decarbonization cooperation	II	2030–2040	Ministry of Foreign Affairs; ASEAN Secretariat	Regional fuel standards harmonization	20–30
11. Ammonia bunkering infrastructure	III	2038–2045	Port authorities; Energy companies	6 ammonia bunkering facilities operational	650–800
12. E-methanol production facilities	III	2040–2048	Renewable energy companies; Chemical industry	300,000 tons/year e-methanol capacity	600–750
13. Zero-emission shipping zones	III	2042–2050	Ministry of Construction; Port authorities	3 zero-emission port zones established	100–150
14. Green hydrogen infrastructure pilot	III	2043–2050	Energy companies; Research institutions	50,000 tons/year green hydrogen capacity	400–500
15. Net-zero compliance verification system	III	2045–2050	Maritime Administration; Third-party verifiers	100% fleet emissions verified annually	40–60

that are lacking in multi-criteria decision analysis (MCDA) methodologies. The proposed framework incorporates six aspects and 19 criteria to comprehensively assess seven typical alternative fuels, while still considering the characteristic barriers of developing countries such as lack of investment capital, poor infrastructure, and weak governance capacity. Empirically, the proposed transition roadmap follows three stages to give developing countries a gradual approach, different from developed countries that immediately adopt hydrogen and ammonia fuels (Hansson et al. 2020, Gray et al. 2021).

To ensure the transparency of the roadmap's effectiveness, Table 9 details the emission factors and fuel consumption assumptions used to calculate the projected GHG reductions. Unlike previous studies that focused on Tank-to-Wake (TtW), this research adopts a Well-to-Wake (WtW) perspective to account for the carbon intensity of fuel production and supply chains, aligning with the latest IMO MEPC 80 guidelines. Note that the estimated fuel consumption figures in Table 9 represent gross sector energy throughput; specific operational load factors, vessel activity scaling, and shore-power offsets are applied to derive the net scenario emissions presented in Table 7.

The financial requirements for the transition are derived from a comprehensive structural cost model. While Table 6 and Table 7 focus strictly on direct maritime CAPEX (USD 2.8–3.4 billion), Table 10 expands the system boundary to cover the total ecosystem investment (USD 3.85–4.90 billion) by incorporating upstream alternative fuel production facilities (USD 0.6–0.8 billion), soft infrastructure, R&D, digitalization, and policy implementation. This broader ecosystem scope aligns with the total aggregated policy-action budgets presented in Table 8 (USD 4.00–5.02 billion).

Phase 1 (2025–2030) Foundation Building: Prioritize immediate emission reduction (15–20% reduction compared to 2023) through the use of low-sulfur fuels (meeting 70% of demand) and shore power for ships (20%). Conduct bio-LNG pilot projects at Hai Phong and Ho Chi Minh City ports. (Investment required: USD 0.8–1.0 billion).

Phase 2 (2031–2040) Fuel Diversification: Strong shift toward new fuels including methanol (35%) and bio-LNG (30%). Begin construction of methanol supply infrastructure at 4 major ports (Hai Phong, Ho Chi Minh City, Da Nang, Vung Tau), expand the LNG supply network to 6 ports, and pilot ammonia infrastructure in Ho Chi Minh City. Emissions will be reduced by 40–50% at this stage. (Cumulative investment: USD 1.8–2.2 billion).

Phase 3 (2041–2050) Complete decarbonization: Complete the transition to achieve net-zero emissions (90–100% reduction in emissions). The main fuel sources will be green ammonia (40%) and e-methanol (30%). This phase focuses on building large-scale green fuel production plants from offshore wind and renewable hydrogen, while also covering all major ports with ammonia supply stations. (Cumulative investment: USD 2.8–3.4 billion).

Given the unique characteristics of a rapidly developing country like Vietnam, the 2025–2030 period requires policies and actions to support the rapid development of infrastructure and improve the quality of the shipping fleet. The choice of methanol over LNG is consistent with existing energy security and infrastructure. Meanwhile, hydrogen still carries many technological risks, and its price is still subject to market fluctuations; therefore, its adoption is postponed to the 2041–2050 period. According to the proposed roadmap, the necessary investment capital accounts for approximately 0.7–0.9% of Vietnam's projected GDP for the 2024–2050 period. This investment level falls within the decarbonization investment limits for the maritime sector in developed countries (0.6–1.2%) (OECD 2022). This demonstrates political will, showing that despite financial and infrastructure limitations, with the support of the international community, this is entirely feasible.

Table 9: Emission calculation parameters and reduction projections (well-to-wake boundary).

Fuel Type	Emission Factor (WtW) (g CO_2e g^{-1} fuel)	Estimated Consumption 2030 (Mt)	Estimated Consumption 2050 (Mt)	WtW Reduction per Unit (%)
VLSFO/MGO (Baseline)	3.15–3.50	2.50-3.00	0.45	0%
LNG (Fossil)	2.70–2.90	0.85	0.20	15–20%
Bio-LNG	0.50–1.20	0.15	1.10	70–85%
E-Methanol	0.20–0.80	0.10	1.50	80–95%
Green Ammonia	0.10–0.50	0.02	2.10	90–100%
Green Hydrogen	0.05–0.40	0.01	0.80	95–100%

Table 10: Estimated investment breakdown for Vietnam's maritime fuel transition (2025–2050).

Investment Category	Estimated Cost (USD billion)	Key Infrastructure & Unit Cost Assumptions	Primary Funding Sources
Port Infrastructure	1.2–1.5	• LNG bunkering hubs (USD 80–120 million per port). • Shore power (OPS) systems (USD 2–5 million per berth). • Ammonia/Methanol storage tanks.	Public-Private Partnership (PPP), Port Authorities
Vessel Retrofitting & Newbuilds	1.8–2.2	• Retrofitting engines for Dual-fuel (USD 2–4 million per ship). • Premium for new green vessels (20–30% higher capital expenditure (CAPEX)). • Scrubbers & Energy Saving Devices (ESD).	Shipowners, Green Credit, Commercial Banks
Fuel Supply Chain & Production	0.6–0.8	• Pilot green hydrogen/ammonia production plants. • Supply chain logistics and distribution fleet.	Energy companies, foreign direct investment (FDI), government subsidies
R&D, Digitalization & Training	0.2–0.3	• Maritime enterprise resource planning (ERP) and artificial intelligence (AI) for route optimization. • Seafarer training for hazardous fuel handling. • Living Lab models at major ports.	State Budget, University Research Grants
Policy & Regulatory Framework	0.05–0.1	• Development of safety standards and carbon tax systems. • International consultancy and certification.	Official Development Assistance (ODA), State Budget
Total Estimated	3.85–4.9	Cumulative investment through 2050	

3.3. Policy Implications

Based on the analysis results, five key policy priorities are proposed as follows:

First, establish a carbon pricing mechanism aligned with the general trend of the maritime industry (carbon price at USD 20–30/ton CO_2 by 2030 and USD 80–100/ton by 2050). This will promote the green transition as the cost of traditional fuels will gradually increase while the cost of green fuels will gradually decrease.

Second, implement green port standards nationwide, tailored to each specific port over time. Prioritize the construction of deep-sea ports according to global green standards.

Third, there is a shortage of approximately 5,000–7,000 maritime workers in the fields of green fuel bunkering, safety management, and operation of ships and green ports. Vietnam needs to enact policies to support the development of green maritime training programs at all levels.

Fourth, Vietnam needs to strengthen cooperation with neighboring countries and the ASEAN region in the production and distribution of alternative fuels under a program aimed at harmonizing fuel standards, fuel production, and a common green fuel supply chain for the ASEAN region.

Fifth, engage in extensive international advocacy and cooperation to mobilize financing for Vietnam's maritime decarbonization program. It is necessary to prepare key projects, enhance institutional capacity and monitoring frameworks to access resources such as climate change programs aligned with the Sustainable Development Goals (SDGs 7, 9, 13, 14), support from COP, the Asian Development Bank, the Green Climate Fund, etc.

3.4. Limitations and Future Research

Although this study provides a very comprehensive fuel transition roadmap for the Vietnamese maritime industry, it still has some limitations. First, the PLEETS framework for decision-making is inevitably subjective because the weighted results are based on expert surveys. Second, the dependence on fuel forecasts is highly uncertain, meaning the techno-economic model may change. Third, the study only assesses representative infrastructure (the 6 largest ports) and does not evaluate the entire port system, including auxiliary ports and regional connections. Finally, the proposed roadmap is based on the assumption of continuous progress in green fuel technology and supply-chain development, with associated cost reductions.

The authors' next research directions will focus on developing specific roadmaps for each vessel type because of differences in operational characteristics among bulk carriers, container ships, and oil tankers; assessing the production capacity and development of green fuel supply chains; and researching the application of artificial intelligence (AI), the Internet of Things (IoT), and blockchain to optimize the fuel supply chain and monitor emissions.

4. CONCLUSIONS

Through the systematic application of the PLEETS framework to support data-driven decision-making in Vietnam's maritime industry and consultation with 127 experts, the study proposes a fuel transition roadmap for Vietnam's maritime industry by 2050, aligned with IMO targets. Accordingly, Vietnam could achieve a reduction of over 90% in emissions by 2050 in three phases.

The immediate phase (2025–2030) focuses on building a basic foundation, such as deploying onshore power generation and providing and using appropriate fuels, to achieve a 15–20% emission reduction target with an estimated investment of USD 0.8–1.0 billion. During the period 2031–2040, Vietnam prioritizes the use of methanol and bio-LNG to achieve a 40–50% reduction in emissions. In the final phase (2041–2050), aiming for net-zero emissions, Vietnam will utilize green ammonia and e-methanol (total investment of approximately USD 2.8–3.4 billion).

To achieve the net emission reduction target by 2050, Vietnam needs to enact specific policies and action plans for each stage regarding carbon pricing for ships and ports, encourage the conversion of low- and zero-emission vessels, build green maritime infrastructure along with new and supplementary training for maritime personnel with green and digital skills, and foster extensive cooperation on the production and bunkering of green marine fuels within the ASEAN region. Vietnam should proactively explore access to green international financing through the Sustainable Development Goals (SDGs 7, 9, 13, 14), support from countries committed at COP, the Asian Development Bank, and the Green Climate Fund.

The proposed roadmap serves as a foundation for implementing Vietnam's strong commitments at COP26 and fulfilling its obligations as a member state under Annex VI, MARPOL 73/78. The findings of this study can be replicated and used as a foundation for developing fuel transition roadmaps for the maritime industry in countries with similar conditions.

5. ACKNOWLEDGEMENT

The authors are grateful to Vietnam Maritime University and colleagues for their support during the research. The

authors also thank the reviewers for their comments, which improved the manuscript.

6. REFERENCES

Achuo, E. D., Miamo, C. W. and Nchofoung, T. N., 2022. Energy consumption and environmental sustainability: What lessons for posterity? *Energy Reports*, 8, pp. 12491–12502. [DOI]

Al-Aboosi, F. Y., El-Halwagi, M. M., Moore, M. and Nielsen, R. B., 2021. Renewable ammonia as an alternative fuel for the shipping industry. *Current Opinion in Chemical Engineering*, 31, p. 100670. [DOI]

Alamoush, A. S. and Ölçer, A. I., 2025. Harnessing cutting-edge technologies for sustainable future shipping: An overview of innovations, drivers, barriers, and opportunities. *Maritime Technology and Research*, 7, p. 277313. [DOI]

Atilhan, S., Park, S., El-Halwagi, M. M., Atilhan, M., Moore, M. and Nielsen, R. B., 2021. Green hydrogen as an alternative fuel for the shipping industry. *Current Opinion in Chemical Engineering*, 31, p. 100668. [DOI]

Balci, G., Phan, T. T. N., Surucu-Balci, E. and Iris, Ç., 2024. A roadmap to alternative fuels for decarbonising shipping: The case of green ammonia. *Research in Transportation Business & Management*, 53, p. 101100. [DOI]

Barone, G., Buonomano, A., Del Papa, G., Maka, R. and Palombo, A., 2024. Approaching zero emissions in ports: Implementation of batteries and supercapacitors with smart energy management in hybrid ships. *Energy Conversion and Management*, 314, p. 118446. [DOI]

Bolat, F., 2026. Time series modeling of greenhouse gas emissions: A case study for a chemical tanker ship. *Maritime Technology and Research*, 8, p. 278949. [DOI]

Cameretti, M. C., De Robbio, R., Palomba, M. and Zucareli de Souza, T., 2025. Strategies to improve ammonia combustion in a dual fuel marine engine by using CFD. *Fuel*, 381, p. 133440. [DOI]

Cortez-Huerta, M., Sosa Echeverría, R., Fuentes García, G., Antonio Durán, R. E., Ramírez-Macías, J. I. and Kahl, J. D. W., 2024. High-resolution atmospheric emissions estimate from dredging activities during port expansion in Veracruz, Mexico. *Ocean Engineering*, 310, p. 118621. [DOI]

Cuong, N. M. and Hung, P. V., 2020a. Sea navigation-based Thai Canal implication: An analysis of its effect on the Vietnamese maritime industry. *Australian Journal of Maritime & Ocean Affairs*, 12, pp. 83–94. [DOI]

Cuong, N. M. and Hung, P. V., 2020b. An analysis of available solutions for commercial vessels to comply with IMO strategy on low sulphur. *Journal of International Maritime Safety, Environmental Affairs, and Shipping*, 4, pp. 40–47. [DOI]

DNV GL, 2020. *Energy Transition Outlook 2020: Maritime Forecast to 2050*. Available at: https://www.dnv.com/maritime/maritime-forecast/

Gray, N., McDonagh, S., O'Shea, R., Smyth, B. and Murphy, J.D., 2021. Decarbonising ships, planes and trucks: An analysis of suitable low-carbon fuels for the maritime, aviation and haulage sectors. *Advances in Applied Energy*, 1, p.100008. [DOI]

Ha, S., Park, C., Jang, H., Jeong, B. and Hwang, I., 2025. Developing a framework for effective accounting GHG emissions from international shipping for sustainable marine fuel and onboard carbon capture: Case study of methanol. *Sustainable Production and Consumption*, 56, pp. 263–283. [DOI]

Halpe, P., Adams, M. and Walker, T. R., 2025. Challenges and opportunities for ports in achieving net-zero emissions in maritime transport. *Transportation Research Interdisciplinary Perspectives*, 30, p. 101379. [DOI]

Hansson, J., Brynolf, S., Fridell, E. and Lehtveer, M., 2020. The potential role of ammonia as marine fuel: Based on energy systems modeling and multi-criteria decision analysis. *Sustainability*, 12(8), p.3265. [DOI]

International Maritime Organization (IMO), 2018. *Initial IMO GHG Strategy*. Available at: https://www.imo.org/en/MediaCentre/HotTopics/Pages/Reducing-greenhouse-gas-emissions-from-ships.aspx (accessed July 26, 2021).

International Maritime Organization (IMO), 2020. *Fourth Greenhouse Gas Study 2020*. Available at: https://www.imo.org/en/OurWork/Environment/Pages/Fourth-IMO-Greenhouse-Gas-Study-2020.aspx (accessed July 26, 2021).

International Maritime Organization (IMO), 2023. *2023 IMO Strategy on Reduction of GHG Emissions from Ships*. Available at: https://www.imo.org/en/OurWork/Environment/Pages/2023-IMO-Strategy-on-Reduction-of-GHG-Emissions-from-Ships.aspx (accessed April 29, 2025).

Karvounis, P. and Theotokatos, G., 2025. Performance improvement and emissions reduction of methanol fuelled marine dual-fuel engine with variable compression ratio. *Fuel Processing Technology*, 272, p. 108208. [DOI]

Lian, F., He, Y. and Yang, Z., 2020. Competitiveness of the China-Europe Railway Express and liner shipping under the enforced sulfur emission control convention. *Transportation Research Part E: Logistics and Transportation Review*, 135, p. 101861. [DOI]

Nguyen, T. T., 2016. An investigation of the Vietnamese shipping industry and policy recommendations for profound participation into ASEAN integration. *The Asian Journal of Shipping and Logistics*, 32, pp. 81–88. [DOI]

Organisation for Economic Co-operation and Development (OECD), 2022. *Performance of Maritime Logistics*. International Transport Forum Policy Papers. [DOI]

Ortiz-Imedio, R., Caglayan, D. G., Ortiz, A., Heinrichs, H., Robinius, M., Stolten, D. and Ortiz, I., 2021. Power-to-ships: Future electricity and hydrogen demands for shipping on the Atlantic coast of Europe in 2050. *Energy*, 228, p. 120660. [DOI]

Park, T., So, S., Jeong, B., Zhou, P. and Lee, J., 2021. Life cycle assessment for enhanced re-liquefaction systems applied to LNG carriers; effectiveness of partial re-liquefaction system. *Journal of Cleaner Production*, 285, p. 124832. [DOI]

Perera, L. P. and Soares, C. G., 2017. Weather routing and safe ship handling in the future of shipping. *Ocean Engineering*, 130, pp. 684–695. [DOI]

Premsamarn, P., Win, T. K. and Watanabe, D., 2025. Assessing the impact of emission control areas policy on ship emissions in the Gulf of Thailand using AIS data. *Maritime Technology and Research*, 7, p. 275311. [DOI]

Smith, T., Anderson, B., Corbett, J., Faber, J., Hanayama, S., O'Keefe, E., Parker, S., Johansson, L., Aldous, L., Raucci, C., Traut, M., Ettinger, S., Nelissen, D., Lee, D., Ng, S., Agarwal, A., Winebrake, J., Hoen, M., Chesworth, S. et al., 2014. *Third IMO GHG Study 2014*. Available at: https://www.imo.org/en/OurWork/Environment/Pages/Greenhouse-Gas-Studies-2014.aspx (accessed 28 July 2021).

Sun, L., Zhang, Y., Ma, F., Ji, F. and Xiong, Y., 2023. Energy and speed optimization of inland battery-powered ship with considering the dynamic electricity price and complex navigational environment. *Energy Reports*, 9 (2022 The 3rd International Conference on Power Engineering), pp. 293–304. [DOI]

UNCTAD, 2024. Statistics. Available at: https://unctad.org/statistics (accessed 27 July 2024).

Vietnam Maritime and Waterway Administration (VIMAWA). 2025. *Annual Report on Maritime and Inland Waterway Transport Statistics 2025*. Ministry of Transport, Hanoi.

Wang, Y. and Iris, Ç., 2025. Transition to near-zero emission shipping fleet powered by alternative fuels under uncertainty. *Transportation Research Part D: Transport and Environment*, 142, p. 104689. [DOI]

Nature Environment and Pollution Technology
An International Quarterly Peer-Reviewed Open Access Journal

p-ISSN: 0972-6268 | e-ISSN: 2395-3454 Vol. 25 | No. 4 | Article ID B4418 | 2026

RESEARCH ARTICLE https://doi.org/10.46488/NEPT.2026.v25i04.B4418 OPEN ACCESS

Investigating Consumer Perceptions and Mapping E-waste Stakeholders: Evidence from Chh. Sambhajinagar City, Maharashtra

Arvind Chel[1], Geetanjali Kaushik[2], Ashish Gadekar[1], Vijay Kumar Srivastava[2] and Abhay Wavre[1]
[1]MGM University, Chh. Sambhajinagar, 431003, Maharashtra, India
[2]K.N. University, Ahmedabad, Gujarat, India
†Corresponding author: Geetanjali Kaushik; geetanjalikaushik2007@gmail.com

ARTICLE HISTORY

Received: 13-12-2025
Revised: 09-03-2026
Accepted: 18-03-2026

KEYWORDS

E-waste management
Consumer behavior
Informal recycling
Extended producer responsibility
Circular economy

CITE THIS ARTICLE

Chel, A., Kaushik, G., Gadekar, A., Srivastava, V. K. and Wavre, A., 2026. Investigating consumer perceptions and mapping E-waste stakeholders: Evidence from Chh. Sambhajinagar City, Maharashtra. *Nature Environment and Pollution Technology*, 25(4), B4418. https://doi.org/10.46488/NEPT.2026.v25i04.B4418

COPYRIGHT & LICENCE

© 2026 The Authors
Open Access under CC BY 4.0.

PUBLISHED BY

TECHNOSCIENCE PUBLICATIONS

ABSTRACT

Electronic waste (e-waste) has emerged as one of the fastest-growing waste streams globally, posing significant environmental and public health challenges. This study examines consumer awareness, risk perception, and disposal behavior regarding e-waste management in Chhatrapati Sambhajinagar (formerly Aurangabad), a Tier-III city in Maharashtra, India, with a population exceeding 1.2 million. A structured questionnaire (Cronbach's α = 0.81, pilot-tested with n = 45) was administered to 620 respondents using stratified random sampling across residential, commercial, and institutional zones. Statistical analyses, including chi-square tests, Pearson correlation, and binary logistic regression, revealed that although 60% of respondents possessed basic awareness of e-waste hazards, approximately 48% continued to dispose of electronic waste with municipal refuse, indicating a persistent awareness–behavior gap (r = 0.26 for awareness–actual behavior, r = 0.42 for awareness–willingness). Binary logistic regression identified access to a collection point as the strongest predictor of formal disposal (OR = 3.06, 95% CI: 1.76–5.31), outperforming the awareness score (OR = 1.033 per unit). Material flow triangulation estimated that informal networks handle approximately 55% of the city's annual e-waste generation (~18,000–22,000 MT). Comparative analysis with the USA, Europe, China, South-East Asia, and Africa, analytically integrated with the study findings, confirmed that infrastructure accessibility and incentive-driven governance are more effective determinants of sustainable disposal behavior than awareness campaigns alone. The findings emphasize the need to strengthen Extended Producer Responsibility (EPR) implementation, develop decentralized collection infrastructure, and integrate informal recyclers into formal value chains to advance evidence-based e-waste management in rapidly urbanizing Tier-III regions.

1. INTRODUCTION

The rapid proliferation of electronic and electrical equipment (EEE) globally has generated unprecedented volumes of electronic waste (e-waste), making it one of the fastest-growing solid waste streams worldwide. According to the Global E-waste Monitor 2020 (Forti et al. 2020), approximately 53.6 million metric tonnes of e-waste were generated globally in 2019, with projections indicating an increase to 74 million metric tonnes by 2030 (Parajuly et al. 2019). In India, e-waste generation has reached approximately 3.2 million tonnes annually, with a growth rate of 30% per annum, positioning the country as the third-largest e-waste producer globally after China and the United States (Forti et al. 2020, Arya & Kumar 2020).

Chhatrapati Sambhajinagar, officially renamed from Aurangabad in 2023, is a historically significant city in the Marathwada region of Maharashtra. With a

population of approximately 1.27 million (Census Projection 2024), it serves as a pivotal administrative, commercial, and educational hub. The city is home to renowned heritage sites, including Bibi Ka Maqbara, the Aurangabad Caves, and numerous historical gates (52 darwazas), while simultaneously emerging as an industrial center with the MIDC (Maharashtra Industrial Development Corporation) industrial area and a growing automotive sector. Its classification as a Tier-III city makes it representative of rapidly urbanizing centers in India that are experiencing exponential growth in electronic device consumption yet lack commensurate formal waste management infrastructure.

E-waste contains both valuable materials (copper, gold, palladium, and rare earth elements) and hazardous substances (lead, mercury, cadmium, and brominated flame retardants), making improper disposal a critical environmental and public health concern. Informal recycling practices prevalent in the city involve crude methods, such as open burning, manual dismantling without safety equipment, and acid leaching, which release toxic pollutants into the air, water, and soil, exposing workers and communities to serious health risks (WHO 2022, Awasthi et al. 2022, Kiddee et al. 2013).

While metropolitan cities such as Mumbai, Pune, and Bangalore have received considerable research attention regarding e-waste management, Tier-III cities like Chhatrapati Sambhajinagar remain understudied despite their rapid urbanization and increasing electronic device consumption. This study addresses this gap by examining consumer awareness, risk perception, and disposal behavior while mapping the material flow of e-waste and characterizing the informal recycling sector within the city's unique socio-economic context.

2. STUDY AREA: CHHATRAPATI SAMBHAJINAGAR (AURANGABAD)

2.1. City Profile and Context

Chhatrapati Sambhajinagar (19.8762° N, 75.3433° E), formerly known as Aurangabad, is located in the Marathwada sub-region of Maharashtra, India. The city serves as the administrative headquarters of Chhatrapati Sambhajinagar district and is situated approximately 335 km east of Mumbai. Its key demographic and urban characteristics are summarised in Table 1, and the study area is shown in Fig. 1.

2.2. E-Waste Context in Chhatrapati Sambhajinagar

The city's rapid economic development, driven by the automobile industry (including companies such as Bajaj Auto, Volkswagen Group, and ancillary units in MIDC Waluj and Shendra), has resulted in a rapid increase in electronic device penetration across all socio-economic classes. The Marathwada region's administrative importance has also led to the concentration of numerous educational institutions, government offices, and hospitals in the city, generating

Table 1: City Profile -Chhatrapati Sambhajinagar (Aurangabad), Maharashtra.

City Parameter	Data/Description
Official Name	Chhatrapati Sambhajinagar (formerly Aurangabad)
Location	Marathwada Region, Maharashtra, India
Coordinates	19.8762° N, 75.3433° E
City Classification	Tier-III City (Urban Agglomeration)
Population (2024 est.)	~1.27 million (Municipal Corporation area)
Population Growth Rate	2.8% per annum (2011–2024)
Area (Municipal)	138.5 sq. km
Literacy Rate	87.3% (Maharashtra state average: 82.9%)
Sex Ratio	924 females per 1,000 males
Primary Industries	Automobile, Textiles, Tourism, Education, Pharma
Major Industrial Zone	MIDC Industrial Area (Chikalthana, Waluj, Shendra)
Annual E-waste Generation (est.)	~18,000 – 22,000 metric tonnes
Formal E-waste Recyclers	2 authorized facilities (MIDC area)
Informal Dismantling Units	18–22 units (unregistered, peripheral areas)
Informal Refurbishment Shops	40–50 shops (old city, scrap markets)
Nearest Metro E-waste Hub	Mumbai (335 km) / Pune (230 km)
E-waste Rules Applicability	E-Waste (Management) Rules, 2022 (GoI)
Key Heritage Zones	Bibi Ka Maqbara, Aurangabad Caves, 52 Gates

significant institutional e-waste streams alongside increasing household volumes (MoEFCC 2022, MPCB 2023).

The city's informal e-waste economy is concentrated in two primary areas: the old city scrap market near Kaala Gate and Gulmandi, and the peripheral industrial clusters near Chikalthana MIDC. These areas serve as aggregation points where scrap dealers (kabadiwalas) collect discarded electronics from households before supplying them to dismantlers. A notable characteristic of Chhatrapati Sambhajinagar's e-waste landscape is its role as a regional aggregation hub, with e-waste flowing in from smaller towns in the Marathwada region (Jalna, Parbhani, and Latur) before

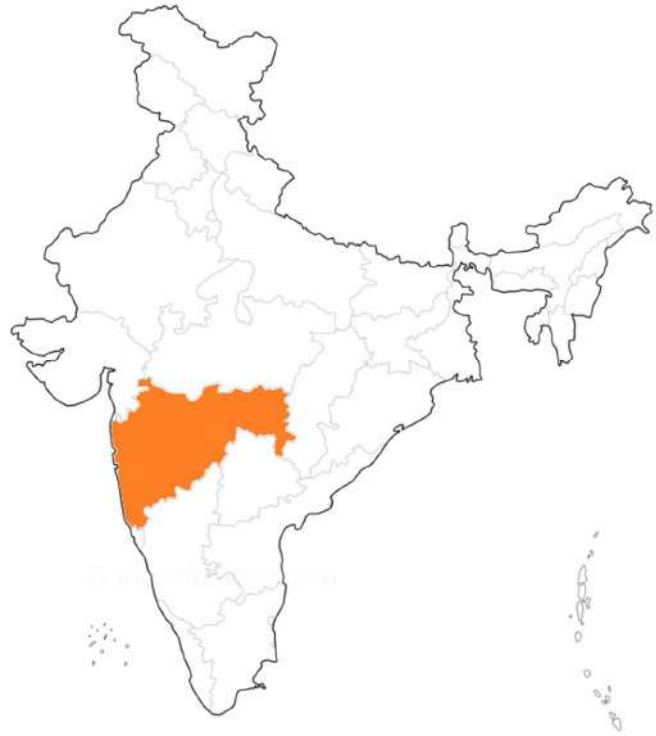


Fig. 1(a): Map of India highlighting Maharashtra.

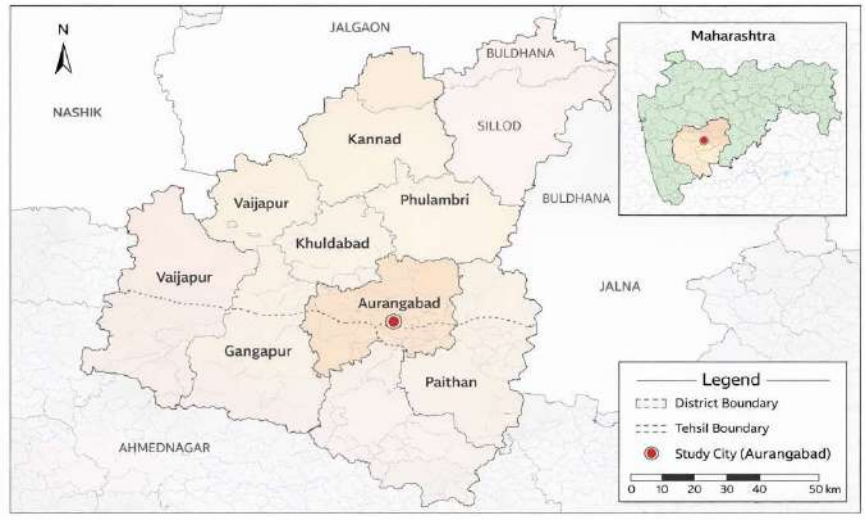


Fig. 1(b): Study area map - Chhatrapati Sambhajinagar (Aurangabad), Maharashtra, India.

being transported to processing hubs in Mumbai and Delhi (Sengupta et al. 2022, Chel et al. 2025b).

3. MATERIALS AND METHODS

3.1. Research Design and Questionnaire Development

This study adopted a cross-sectional survey design. The questionnaire was developed through a systematic, multi-stage process. In Stage 1, a comprehensive review of validated instruments from previous e-waste behavior studies (Borthakur & Govind 2018, Trad & Harb 2024, Bhat & Patil 2014) was conducted to identify established item pools covering awareness, risk perception, and disposal behavior. In Stage 2, an expert panel comprising three environmental engineers, two public health specialists, and one social scientist reviewed the initial item pool to assess its content validity. Items were retained, modified, or discarded based on consensus, resulting in a draft instrument comprising 42 items across five thematic domains: (i) socio-demographic profile, (ii) e-waste awareness and knowledge, (iii) risk perception, (iv) disposal behavior, and (v) barriers to formal disposal. In Stage 3, the instrument was refined to 36 items following expert review, and face validity was confirmed through structured interviews with ten members of the target population representing diverse educational and occupational backgrounds.

3.2. Pilot Testing and Instrument Reliability

Before full-scale data collection, a pilot test was conducted with 45 respondents (not included in the final sample) drawn from the four survey zones in proportions mirroring the main sampling frame. The pilot assessed item clarity, response time (target: 12–15 min), and completion rates. Based on the pilot feedback, three items were reworded to improve comprehension, and one item assessing contact with informal recyclers was removed due to social desirability concerns. Internal consistency reliability was assessed using Cronbach's alpha (α) for each thematic scale. Acceptable reliability was defined as $\alpha \geq 0.70$, consistent with established benchmarks for social science research (Nunnally 1978). As reported in Table 2, all five subscales demonstrated acceptable to good internal consistency, with the overall instrument yielding a Cronbach's alpha of $\alpha = 0.81$.

3.3. Sampling Design and Data Collection

A stratified random sampling design was adopted. The city was divided into four survey zones based on land-use classification: (i) Residential (Old City), (ii) Commercial (Gulmandi and Kaala Gate markets), (iii) Institutional/Campus (university districts and government offices), and (iv) Peripheral Industrial (MIDC Chikalthana). The sample size was determined using Cochran's (1977) formula for proportions ($p = 0.5$, margin of error = 4%, 95% confidence level), yielding a minimum sample size of 600. Accounting for an anticipated 5% non-response rate, a total of 650 questionnaires were distributed, of which 620 were returned fully completed, yielding a response rate of 95.4%.

Within each stratum, respondents were selected through systematic random sampling from available household and establishment lists. Data collection was conducted over eight weeks (March–May 2024) through face-to-face administration by trained field investigators, ensuring comprehension support for respondents with lower literacy levels. All respondents provided informed consent, and the study protocol was reviewed and approved by the Institutional Ethics Review Committee of MGM University, Chh. Sambhajinagar.

3.4. Awareness Score Construction

A composite E-waste Awareness Score (EAS) was constructed from eight binary indicator items (correct response = 1, incorrect or "do not know" = 0), yielding a score ranging from 0 to 8. The items covered: (1) familiarity with the term "e-waste", (2) identification of environmental hazards, (3) knowledge of the health risks associated with informal recycling, (4) recognition of valuable materials in e-waste, (5) knowledge of formal collection systems, (6) understanding of Extended Producer Responsibility (EPR), (7) awareness of the E-waste (Management) Rules, 2022, and (8) knowledge of the nearest authorised collection point.

Table 2: Instrument Reliability Statistics (Cronbach's Alpha) by Subscale (Pilot, n = 45).

Subscale	No. of Items	Cronbach's α	Interpretation
E-waste Awareness & Knowledge	8	0.79	Acceptable
Risk Perception	6	0.74	Acceptable
Disposal Behaviour	7	0.76	Acceptable
Barriers to Formal Disposal	8	0.82	Good
Socio-demographic Profile	7	N/A (factual)	—
Overall Instrument	**36**	**0.81**	**Good**

Raw scores were standardized to a 0–100 scale for comparative analysis. Respondents scoring 0–24 were classified as "Low Awareness," 25–49 as "Moderate," 50–74 as "High," and 75–100 as "Very High." The mean EAS for the sample was 38.4 (SD = 14.7), placing the population, on average, in the Moderate Awareness category. Analysis by education level and survey zone is presented in Section 4.2.

3.5. Statistical Analysis

Descriptive statistics (frequencies, percentages, means, and standard deviations) were computed for all variables. Chi-square (χ^2) tests of independence were used to examine associations between categorical variables (e.g., education level vs. e-waste awareness category, survey zone vs. disposal method). Pearson's product-moment correlation coefficient (r) was used to assess linear associations between continuous awareness and behavior scores.

Binary logistic regression was employed to identify predictors of formal e-waste disposal behavior (dependent variable: formal disposal = 1, informal/mixed = 0), with awareness score, education level, income bracket, survey zone, and access to a collection point included as independent variables. All analyses were conducted using IBM SPSS Statistics Version 26. Statistical significance was set at $p < 0.05$ (two-tailed) for all tests. Effect sizes are reported (Cramér's V for chi-square tests and odds ratios with 95% confidence intervals for logistic regression) to contextualize practical significance alongside statistical significance.

4. RESULTS

4.1. Socio-Demographic Profile of Respondents

4.1.1. Respondent Characteristics

The final sample comprised 620 respondents distributed across four survey zones: Residential (n = 248, 40%), Commercial (n = 124, 20%), Institutional/Campus (n = 155, 25%), and Peripheral/MIDC (n = 93, 15%). Gender representation comprised 54% male and 46% female respondents. The sample was predominantly between 25 and 44 years of age (61%), with 24% aged below 25 years and 15% aged 45 years and above. Educational attainment was distributed as follows: secondary level (28%), undergraduate (34%), postgraduate (27%), and no formal qualification (11%). Monthly household income was categorized as below ₹25,000 (36%), ₹25,000–₹50,000 (41%), and above ₹50,000 (23%), broadly reflecting the city's predominantly middle-income socio-economic profile. Institutional respondents (students, faculty, and government employees) constituted 42% of the sample, while the remaining 58% were engaged in trade, manufacturing, or household activities.

4.2. E-Waste Awareness by Education Level and Survey Zone

Table 2a presents the mean E-waste Awareness Scores (EAS) stratified by education level and survey zone, providing a multivariate overview of awareness distribution across the sample. Postgraduate respondents recorded the highest mean EAS (54.2, SD = 12.1), followed by undergraduate respondents (42.6, SD = 13.4), secondary-level respondents (28.3, SD = 11.8), and respondents with no formal qualifications (18.7, SD = 9.6). A one-way ANOVA confirmed statistically significant between-group differences ($F(3,616) = 47.3$, $p < 0.001$, $\eta^2 = 0.19$, large effect). Post hoc Tukey tests revealed significant pairwise differences between all education groups (all $p < 0.01$), except between the secondary-level and no-formal-qualification groups ($p = 0.09$). By survey zone, Institutional/Campus respondents recorded the highest mean EAS (52.8, SD = 11.7), significantly exceeding that of Residential (Old City) respondents (mean EAS = 31.4, SD = 12.9, difference =

Table 2a: Mean E-waste Awareness Scores (EAS, 0–100) by Education Level and Survey Zone (n = 620).

Group	n	Mean EAS	SD	Awareness Category
BY EDUCATION LEVEL				
No formal qualification	68	18.7	9.6	Low
Secondary education	174	28.3	11.8	Moderate
Undergraduate	211	42.6	13.4	Moderate
Postgraduate	167	54.2	12.1	High
BY SURVEY ZONE				
Residential (old city)	248	31.4	12.9	Moderate
Commercial	124	39.6	11.2	Moderate
Institutional/Campus	155	52.8	11.7	High
Peripheral / MIDC	93	34.1	13.4	Moderate

Note: ANOVA $F(3,616) = 47.3$, $p < 0.001$ (by education), $F(3,616) = 39.8$, $p < 0.001$ (by zone). EAS = E-waste Awareness Score (0–100).

21.4 points, $p < 0.001$). Respondents from the Commercial and Peripheral zones recorded intermediate mean EAS values (39.6 and 34.1, respectively). These zone-level differences confirm that geographic proximity to educational and institutional infrastructure is a significant correlate of e-waste awareness, independent of individual educational attainment.

4.3. Consumer Awareness of E-waste Hazards and Regulations

Table 3 summarises the individual awareness indicators underlying the composite score shown in Fig. 2, including respondents' familiarity with the term "e-waste," their knowledge of associated health and environmental hazards, and their awareness of formal collection infrastructure and regulatory provisions.

4.4. Association Between Education, Survey Zone, and E-waste Awareness

Chi-square analysis revealed a significant association between educational level and awareness of e-waste hazards ($\chi^2 = 18.42$, df = 3, $p < 0.01$), with postgraduate respondents demonstrating significantly higher awareness than those with secondary-level education. Additionally, respondents residing in Institutional/Campus areas (near universities) recorded awareness scores that were 28% higher than those of respondents from Residential (Old City) areas ($\chi^2 = 12.74$, $p < 0.05$).

4.5. E-waste Disposal Practices and Barriers

Analysis of disposal behavior revealed concerning patterns. Approximately 48% of respondents (n = 298) disposed of e-waste along with regular municipal solid waste. Approximately 35% (n = 217) sold old electronic devices to informal scrap dealers (kabadiwalas). Only 12% (n = 74) utilized formal collection centers, while 5% (n = 31) participated in manufacturer take-back programs. Fig. 3 presents the distribution of disposal methods and the primary barriers to formal e-waste disposal.

4.6. Awareness-Behavior Gap and Logistic Regression Analysis

A critical finding of the study is the pronounced gap between consumer awareness and actual disposal behavior.

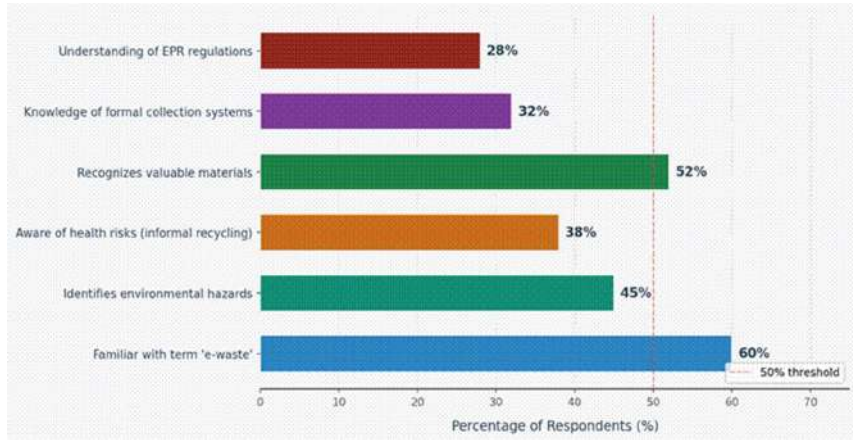


Fig. 2: Consumer awareness indicators for e-waste - Chhatrapati Sambhajinagar (Aurangabad), Maharashtra (n = 620).

Table 3: Consumer Awareness Indicators for E-waste Management (n = 620).

Awareness Indicator	Respondents [n]	Percentage [%]
Familiar with the term 'e-waste'	372	60%
Can identify environmental hazards of e-waste	279	45%
Aware of health risks from informal recycling	236	38%
Recognizes valuable materials in e-waste (gold, copper)	322	52%
Knowledge of formal collection systems in the city	198	32%
Understanding of Extended Producer Responsibility (EPR)	174	28%
Aware of E-waste (Management) Rules, 2022	137	22%
Know the nearest authorized e-waste collection point	99	16%

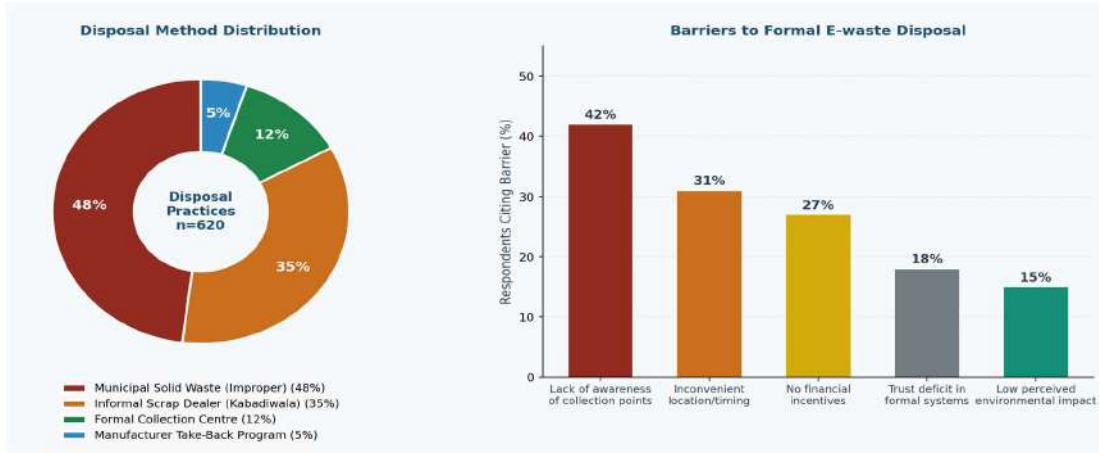


Fig. 3: E-waste disposal practices and barriers - Chhatrapati Sambhajinagar (Aurangabad) (n = 620).

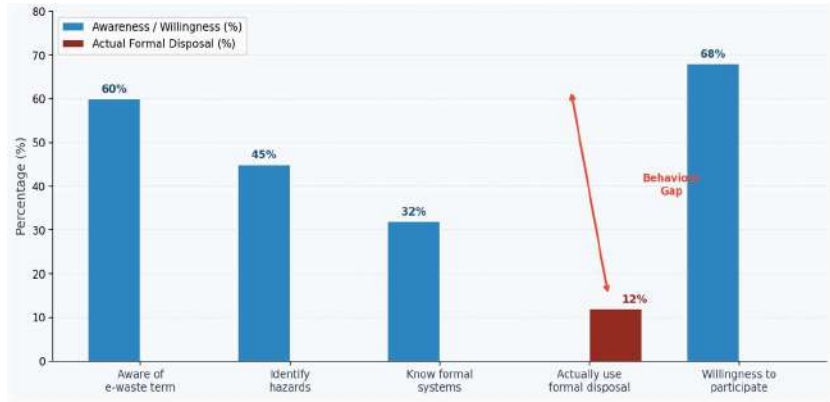


Fig. 4: Awareness-behavior gap in e-waste management - Chhatrapati Sambhajinagar (Aurangabad) (n = 620).

While 60% of respondents demonstrated basic awareness of e-waste hazards, only 12% utilized formal collection systems. Pearson's correlation analysis demonstrated a moderate positive relationship between awareness of environmental risks and willingness to participate in formal e-waste management ($r = 0.42$, $p < 0.01$). However, the relationship between awareness and actual disposal behavior was substantially weaker ($r = 0.26$, $p < 0.05$). It is important to note that both correlation coefficients represent moderate effect sizes, explaining 18% and 7% of the shared variance, respectively. These associations should therefore be interpreted as indicating a meaningful, albeit partial, relationship between awareness and behavior; causal inference is not appropriate given the cross-sectional study design. The observed gap confirms, consistent with the existing literature, that awareness alone is insufficient to drive behavioral change without supporting infrastructure and incentive structures. Fig. 4 illustrates this awareness–behavior gap across key dimensions (Borthakur & Govind 2018, Deshwal 2025).

Table 4: Binary Logistic Regression – Predictors of Formal E-waste Disposal Behavior (n = 620).

Predictor Variable	B	S.E.	OR (Exp B)	95% CI	p-value
E-waste Awareness Score (EAS)	0.032	0.009	1.033	1.015–1.051	< 0.001
Education (Postgraduate vs. Secondary)	0.81	0.26	2.25	1.34–3.77	0.002
Income (>₹50k vs. <₹25k/month)	0.49	0.22	1.63	1.05–2.52	0.028
Zone (Institutional vs. Residential)	0.74	0.25	2.10	1.28–3.43	0.004
Access to Collection Point (Yes vs. No)	1.12	0.28	3.06	1.76–5.31	< 0.001

OR = Odds Ratio, CI = Confidence Interval, Model: $\chi^2(10) = 87.4$, $p < 0.001$, Nagelkerke $R^2 = 0.24$, Hosmer-Lemeshow $\chi^2(8) = 6.3$, $p = 0.61$ (good fit).

To identify the predictors of formal e-waste disposal behavior, a binary logistic regression model was fitted (dependent variable: formal disposal = 1 vs. informal/mixed disposal = 0, n = 620). The model included five independent variables: E-waste Awareness Score (EAS), education level, income bracket, survey zone, and self-reported access to an e-waste collection point. The full model was statistically significant ($\chi^2(10) = 87.4$, $p < 0.001$, Nagelkerke $R^2 = 0.24$), indicating moderate predictive capacity. The results are presented in Table 4.

4.7. Predictors of Formal E-waste Disposal

The strongest predictor of formal disposal was access to a collection point (OR = 3.06, 95% CI: 1.76–5.31, $p < 0.001$), indicating that respondents who reported knowing the location of a nearby authorized collection point were approximately three times more likely to use formal disposal channels. The E-waste Awareness Score was also a significant predictor (OR = 1.033 per unit increase, $p < 0.001$), as were postgraduate education (OR = 2.25, $p = 0.002$) and residence in the Institutional/Campus survey zone (OR = 2.10, $p = 0.004$). A higher income bracket was a significant, although weaker, predictor (OR = 1.63, $p = 0.028$). These findings corroborate the Pearson correlation results and underscore that, while awareness is a statistically significant correlate of formal disposal behavior, access to infrastructure is the dominant practical determinant in this context.

4.8. E-Waste Material Flow Analysis

Material flow analysis combined three convergent data sources to estimate pathway proportions: (i) survey-reported disposal routes from 620 respondents, (ii) structured interviews with key stakeholders, including operators of the 18–22 informal dismantling units, 40–50 refurbishment shops, and two authorised recyclers, and (iii) annual tonnage estimates from MPCB (2023) and the published material flow analysis for the city reported by Chel et al. (2025a). Cross-triangulation of these sources yielded the following estimated pathway distribution for the city's annual e-waste

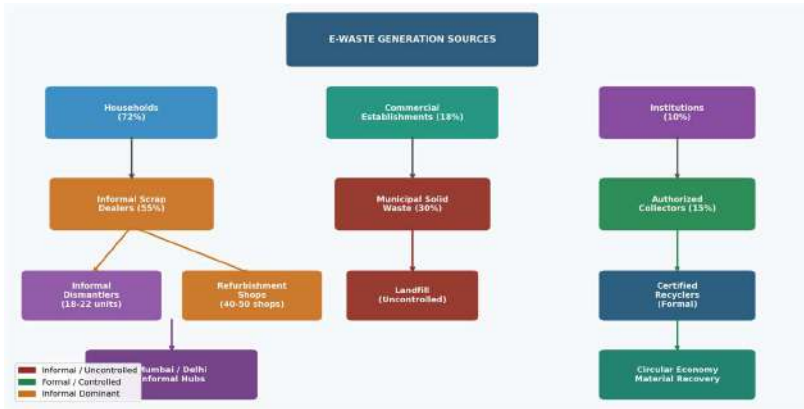


Fig. 5: E-waste material flow - Chhatrapati Sambhajinagar (Aurangabad): informal vs. formal pathways.

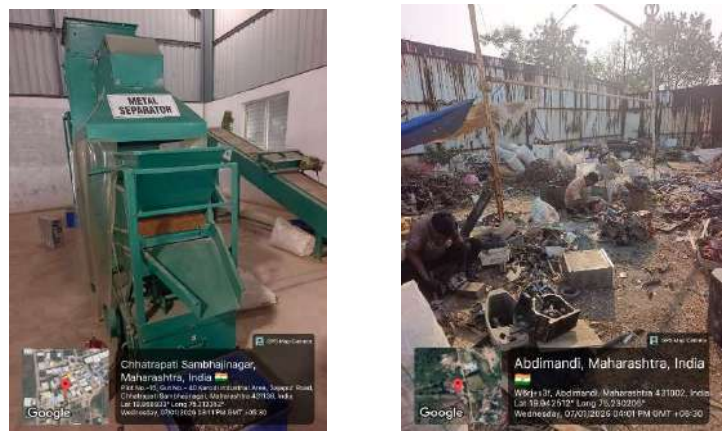


Fig. 6: Formal and informal e-waste practices.

generation of approximately 18,000–22,000 metric tonnes: (i) household to scrap dealer (kabadiwala) to informal dismantler, approximately 55% (≈ 9,900–12,100 MT), (ii) direct disposal with municipal solid waste, approximately 30% (≈ 5,400–6,600 MT), and (iii) institutional collection through authorised channels, approximately 15% (≈ 2,700–3,300 MT). The 55% informal network estimate is consistent with the survey finding that 35% of respondents sold e-waste to kabadiwalas, while a further proportion reported mixed informal disposal routes, together with stakeholder interview estimates of informal unit throughput. These proportions represent indicative estimates derived from triangulated evidence rather than directly measured waste audits and carry uncertainty ranges reflecting the heterogeneity of the informal sector. Fig. 5 presents the complete material flow diagram (Chel et al. 2025a, Sengupta et al. 2022, MPCB 2023).

Fig. 6 presents representative field photographs documenting formal and informal e-waste handling practices observed during the study, including a metallic separator unit used at an authorised formal recycling facility and informal dismantling and refurbishment activity typical of the old city scrap markets.

5. DISCUSSION

5.1. Awareness-Behavior Gap in Tier-III Cities

The findings reveal a substantial awareness–behavior gap in e-waste management practices among consumers in Chhatrapati Sambhajinagar. This disconnect between knowledge and action reflects broader challenges in translating environmental awareness into sustainable behavior and has been documented across similar Tier-III urban contexts in India. The city's socio-economic profile—characterized by a predominantly middle-income population (52%), high literacy rates (87.3%), and a large student population—suggests that awareness deficits are not the primary constraint. Rather, the absence of accessible formal collection infrastructure and the lack of financial incentives constitute the dominant barriers (Bhat & Patil 2014, Singh et al. 2023, Trad & Harb 2024).

5.2. Global Comparative Perspective

The following sub-sections contextualize the Chhatrapati Sambhajinagar findings within global e-waste governance frameworks. In each case, specific features of international experience are explicitly linked to the patterns observed in this study, namely the awareness–behavior gap, the dominance of informal networks, and the relative effectiveness of infrastructure-based versus awareness-based interventions. The comparison is structured to identify transferable lessons rather than to assert equivalence between heterogeneous contexts.

5.2.1. United States

In the United States, consumer awareness of e-waste is generally higher (75–82%), with participation rates ranging from 15% in states without mandatory legislation to over 50% in states with comprehensive EPR laws (e.g., California and Washington). Unlike Chhatrapati Sambhajinagar's informal-sector-dominated system, the U.S. e-waste recycling industry is predominantly formal, with certified recyclers handling approximately 70% of collected e-waste. The key differentiator is state-level regulatory enforcement and retail take-back mandates, which create accessible collection points (Parajuly et al. 2020).

5.2.2. Europe

European countries demonstrate the highest formal collection rates globally (40–65%), driven by the WEEE Directive. Studies from Germany, Switzerland, and the Netherlands report awareness levels exceeding 85%. However, even in Europe, approximately 35% of e-waste still enters informal channels, highlighting that complete formalization remains challenging, even in highly regulated environments. The European experience demonstrates that deposit-refund schemes and incentive-based programs significantly outperform awareness campaigns alone (Li & Sun 2023).

5.2.3. China

China, the world's largest e-waste generator, presents instructive parallels. Urban consumer awareness has increased to 65–70% following government campaigns, yet informal processing persists in regions such as Guiyu despite regulatory crackdowns. China's partial success in formalizing higher-value waste streams through parallel regulation of the formal and informal sectors offers a policy model relevant to Chhatrapati Sambhajinagar's context.

5.2.4. South-East Asia

Countries such as Singapore (formal collection: 35–45%) and Malaysia have achieved higher formal participation through strong EPR legislation. Vietnam and Thailand—with awareness levels of 45–55%—face challenges strikingly similar to those of Chhatrapati Sambhajinagar, including strong informal sector networks, transboundary e-waste flows, and limited formal infrastructure (Parajuly et al. 2019, Mohammed & Kaida 2024).

5.2.5. Africa

African nations face the most acute e-waste challenges, with awareness typically ranging from 25% to 40% and over 80% of e-waste being handled informally. Communities in

Agbogbloshie (Ghana) and Dandora (Kenya) experience severe health impacts. Unlike India, which has domestic EPR legislation and established informal recycling networks, many African countries face the dual challenge of managing both domestically generated and imported e-waste with extremely limited institutional capacity (Owusu-Sekyere et al. 2022, Lepawsky 2022).

5.3. Integration of the Informal Sector: A Chhatrapati Sambhajinagar Model

Taken together, the global evidence reviewed in Sections 5.2.1–5.2.5 yields three conclusions directly relevant to interpreting the Chhatrapati Sambhajinagar dataset. First, the awareness–behavior gap documented in this study (60% awareness vs. 12% formal disposal) is not unique to India but reflects a pattern observed across rapidly urbanizing middle-income settings, including Vietnam, Thailand, and urban China, where awareness campaigns have outpaced infrastructure development. Second, the dominance of informal networks (estimated to account for approximately 55% of e-waste flows) mirrors the situation in West African cities and transitional Chinese contexts, and international evidence consistently shows that regulatory crackdowns without parallel infrastructure investment fail to reduce the informal sector's share. Third, and most relevant to policy design, the logistic regression finding that infrastructure access (OR = 3.06) is the strongest individual predictor of formal disposal aligns with the European and Californian experience, demonstrating that accessible take-back infrastructure—rather than awareness alone—drives behavioral change. These analytical parallels strengthen the empirical case for the infrastructure-first policy priorities recommended in Section 5.4.

The 18–22 informal dismantling units and 40–50 refurbishment shops operating in Chhatrapati Sambhajinagar constitute a significant de facto e-waste management system. Rather than attempting their elimination, policy should prioritize integration. Providing training, personal protective equipment (PPE), and linkages to formal recyclers can improve both environmental outcomes and worker welfare while maintaining economic viability. The city's MIDC industrial area, which already hosts two authorized recyclers, offers anchor infrastructure around which a formalized hybrid model could be developed.

5.4. Policy Implications for Tier-III Cities

The study identifies four priority interventions for Chhatrapati Sambhajinagar and comparable Tier-III cities: (1) establish decentralised e-waste collection points at electronics retail stores, municipal offices, and residential complexes across all four survey zones, (2) strengthen EPR implementation by enforcing producer collection targets specifically for Tier-III cities, (3) introduce financial incentives, such as buy-back schemes or municipal tax credits, for formal e-waste submission, and (4) develop a Marathwada-level regional e-waste management framework that recognises the city's role as an aggregation hub for surrounding smaller towns.

6. CONCLUSIONS

Electronic waste management in Chhatrapati Sambhajinagar (Aurangabad), and in Indian Tier-III cities more broadly, is constrained not by awareness alone but by inadequate formal collection infrastructure, weak EPR enforcement, and a strong dependence on informal recycling networks. The present study demonstrated that although 60% of respondents possessed basic awareness of e-waste hazards, nearly half (48%) continued to dispose of electronic waste with municipal refuse, indicating a persistent awareness–behavior gap ($r = 0.26$ between awareness and actual behavior vs. $r = 0.42$ for willingness). Material flow analysis revealed that informal networks comprising 18–22 dismantling units and 40–50 refurbishment shops handle approximately 55% of the city's estimated annual e-waste generation of 18,000–22,000 metric tonnes.

Comparative global evidence further supports that infrastructure availability and incentive-driven governance are more effective than awareness campaigns alone in achieving sustainable disposal behavior, a pattern observed across diverse regulatory contexts, from California and the European Union to urban China. The policy recommendations arising from this study are grounded directly in the survey evidence. The logistic regression finding that infrastructure access is the strongest individual predictor of formal disposal (OR = 3.06) provides the empirical basis for prioritizing the expansion of decentralized collection points. The formal sector's current 15% share of estimated e-waste flows supports the case for strengthened EPR enforcement targeting Tier-III cities specifically, while the documented role of the 18–22 informal dismantling units in handling the majority of the city's e-waste underscores the practical necessity of integration rather than elimination strategies. These evidence-based priorities are consistent with, although not derived from, the broader circular economy discourse.

Future research should prioritize longitudinal behavioral assessments to determine whether awareness–behavior gaps narrow with improved infrastructure access, as well as metered material flow quantification and cost–benefit analyses of incentive mechanisms across Tier-III urban systems to support evidence-based policy refinement in the Marathwada region and comparable regions of India.

7. ACKNOWLEDGEMENTS

The authors would like to acknowledge financial assistance to carry out the research work under the grant received from the Science and Engineering Research Board (SERB) and the Anusandhan Research Foundation (ANRF), with project sanction number SUR/2022/003810.

8. REFERENCES

Arya, S. and Kumar, S., 2020. E-waste in India at a glance: Current trends, regulations, challenges and management strategies. Journal of Cleaner Production, 271, 122707.

Awasthi, A.K., Awasthi, M.K., Mishra, S., Sarsaiya, S. and Pandey, A.K., 2022. Evaluation of e-waste materials linked to potential consequences to the environment in India. Environmental Technology and Innovation, 28, 102944. [DOI]

Bhat, V. and Patil, Y., 2014. E-waste consciousness and disposal practices among residents of Pune city. Procedia - Social and Behavioural Sciences, 133, pp.491-498. [DOI]

Borthakur, A. and Govind, M., 2018. Public understandings of e-waste and its disposal in urban India: From a review towards a conceptual framework. Journal of Cleaner Production, 172, pp.1053-1066.

Census Projection, 2024. Population Projections for Chhatrapati Sambhajinagar Municipal Corporation Area, 2024. Directorate of Census Operations, Maharashtra, Government of India.

Chel, A., Kaushik, G., Gadekar, A., Srivastava, V.K. and Wavre, A., 2025a. E-waste material flow analysis and stakeholder mapping: A case study of Chh. Sambhajinagar city, Maharashtra. Journal of Applied Bioanalysis, 11(16s), pp.93-98. [DOI]

Chel, A., Wavre, A., Gadekar, A., Kaushik, G. and Sonawane, P., 2025b. Survey of consumer perceptions for electronic waste management: A case study of Chh. Sambhajinagar city. In: International Conference on Pollution Control for a Clean Environment. IIT Bhubaneswar, Odisha, pp.1-8.

Cochran, W.G., 1977. Sampling Techniques (3rd ed.). New York: John Wiley & Sons.

Deshwal, N., 2025. India's E-waste Management: Analysis and Opportunities for a Sustainable Future. MSc thesis. Queen Mary University of London. [DOI]

Forti, V., Baldé, C.P., Kuehr, R. and Bel, G., 2020. The Global E-waste Monitor 2020. United Nations University, ITU, and ISWA, pp.120.

Kiddee, P., Naidu, R. and Wong, M.H., 2013. Electronic waste management approaches: An overview. Waste Management, 33(5), pp.1237-1250.

Lepawsky, J., 2022. Mapping chemical discardscapes of electronics production. Geoforum, 132, pp.113-124.

Li, S. and Sun, Q., 2023. Evolutionary game analysis of WEEE recycling tripartite stakeholders under variable subsidies and processing fees. Environmental Science and Pollution Research, 30(5), pp.11584-11599.

Maharashtra Pollution Control Board, 2023. Annual Report on E-waste Management in Maharashtra. Mumbai: MPCB, pp.112.

Ministry of Environment, Forest and Climate Change (MoEFCC), 2022. E-Waste (Management) Rules, 2022. Retrieved 1 August 2026 from https://www.mppcb.mp.gov.in/proc/E-Waste-Management-Rules-2022-English.pdf

Mohammed, S. and Kaida, N., 2024. Opportunities and challenges for circular economy in the Maldives: A stakeholder analysis of informal e-waste management in the Greater Malé Region. Journal of Environmental Management, 358, 120944.

Nunnally, J.C., 1978. Psychometric Theory (2nd ed.). New York: McGraw-Hill.

Owusu-Sekyere, K., Batteiger, A., Afoblikame, R., Hafner, G. and Kranert, M., 2022. Assessing data in the informal e-waste sector: The Agbogbloshie Scrapyard. Waste Management, 139, pp.158-167.

Parajuly, K., Kuehr, R., Awasthi, A.K., Fitzpatrick, C., Lepawsky, J., Smith, E., Widmer, R. and Zeng, X., 2019. Future E-waste Scenarios. StEP, UNU ViE-SCYCLE and UNEP IETC, pp.85.

Parajuly, K., Thapa, K., Cimpan, C. and Wenzel, H., 2020. Electronic waste and circular economy: Evaluating recycling performance in developing nations. Journal of Cleaner Production, 275, 123456.

Sengupta, D., Ilankoon, I.M.S.K., Kang, K.D. and Chong, M.N., 2022. Circular economy and household e-waste management in India: Integration of formal and informal sectors. Minerals Engineering, 184, 107652.

Singh, S., Sankar Dasgupta, M. and Routroy, S., 2023. Analysis of critical success factors to design e-waste collection policy in India: A fuzzy DEMATEL approach. Resources, Conservation and Recycling, 192, 106881.

Trad, M. and Harb, A., 2024. Analysis of the Lebanese Society's Behaviour Regarding Electronic Waste Management. Nature Environment and Pollution Technology, 23(4), pp.1937-1955. [DOI]

World Health Organisation (WHO), 2022. E-waste and children's health. Retrieved 1 August 2026 from https://www.who.int.

Nature Environment and Pollution Technology
An International Quarterly Peer-Reviewed Open Access Journal

p-ISSN: 0972-6268 | e-ISSN: 2395-3454 Vol. 25 | No. 4 | Article ID D1930 | 2026

RESEARCH ARTICLE https://doi.org/10.46488/NEPT.2026.v25i04.D1930 OPEN ACCESS

The Value of a Statistical Life of Urban Air Pollution in Ho Chi Minh City, Vietnam

Thu Thi Minh Nguyen[1], Quang Minh Ho Ky[1] and Doan Quang Tri[2]†
[1]Faculty of Engineering and Technology, Sai Gon University, Ho Chi Minh City, Vietnam
[2]Center for Multidisciplinary Monitoring, Institute of Earth Sciences, Vietnam Academy of Science and Technology, Hanoi, Vietnam
†Corresponding author: Doan Quang Tri; doanquangtrikttv@gmail.com

ARTICLE HISTORY

Received: 16-04-2026
Revised: 01-06-2026
Accepted: 05-06-2026

KEYWORDS

Value of statistical life
Willingness to pay
Air pollution
Binary logistic model
Contingent valuation survey
Urban environmental quality
Pollution mitigation policies

CITE THIS ARTICLE

Nguyen, T.T.M., Ho Ky, Q.M. and Tri, D.Q. 2026. The value of a statistical life of urban air pollution in Ho Chi Minh City, Vietnam, *Nature Environment and Pollution Technology*, 25(4), D1930. https://doi.org/10.46488/NEPT.2026.v25i04.D1930

COPYRIGHT & LICENCE

© 2026 The Authors
Open Access under CC BY 4.0.

PUBLISHED BY
TECHNOSCIENCE PUBLICATIONS

ABSTRACT

Although the trade-off between income and environmental quality has received increasing attention in recent years, empirical evidence on the Value of a Statistical Life (VSL) associated with air pollution in Vietnam remains limited. This study addresses this gap by estimating the willingness to pay (WTP) and VSL associated with reducing air pollution-related mortality risks in Ho Chi Minh City, one of Vietnam's largest and most densely populated metropolitan areas. Using primary data from a contingent valuation survey (), evaluated through the Turnbull lower-bound estimator along with chi-square analysis and binary logistic regression, we examine the economic valuation of mortality risk reduction and its underlying determinants. The empirical results reveal a mean individual WTP of 17,900 VND per person for a 1/10,000 mortality risk reduction, translating to an individual VSL of approximately USD 6,920 per statistical life saved. When aggregated across the adult population of Ho Chi Minh City, the total economic benefit reaches an aggregate population WTP of about USD 6.57 million. Crucially, over 70% of respondents declined to pay, primarily due to severe household income constraints. Socioeconomic characteristics—including income, age, education, and residential location—were significantly associated with WTP decisions, though the strength of these associations was relatively weak. In addition, the logistic regression analysis highlighted that respondents' trade-off preferences between health and income, and self-reported respiratory conditions, significantly influenced respondents' decision to accept income reductions in exchange for improved environmental quality. The model exhibited satisfactory predictive performance, achieving an AUC above 0.81, overall classification accuracy exceeding 74%, specificity above 79%, and sensitivity above 68%. These findings provide crucial empirical insights into stated-preference valuation under tight budget constraints in a developing-country context, offering valuable evidence to support urban air pollution mitigation policies and health benefit assessments.

1. INTRODUCTION

Air pollution in developing countries, particularly in densely populated cities, has recently become a serious concern. In Ho Chi Minh City, Vietnam, the average concentration of $PM_{2.5}$ from 2013 to 2017 was five times higher than the World Health Organization (WHO) standard, while PM_{10} levels were also approximately five times above the national standard for ambient air quality (EPAVN 2023, IQAir 2024, Vu et al. 2021, WHO 2021). Additionally, air pollution accounts for around 13% of deaths in Ho Chi Minh City, with the majority of these fatalities happening in the city center (Loan 2018).

Environmental quality, particularly ambient air quality, is a non-market good whose economic value is commonly assessed using individuals' willingness to pay (WTP) for environmental improvements (Baker & Ruting 2014, Sajise et al. 2021). Previous studies have reported substantial variation in WTP across countries and socioeconomic contexts. In Pakistan, respondents were willing to pay an average of USD 9.86 per month (approximately 1.3% of household income) for improved air quality, with more than 90% expressing a willingness to contribute (Akhtar et al. 2017). Similarly, a survey of 3,000 urban residents in China estimated an average WTP of approximately USD 10 per person per year (Guo et al. 2020). In Vietnam, WTP estimates for air-quality improvement have generally been lower. Residents of Ho Chi Minh City were found to be willing to pay between USD 0.73 and 1.08 per person per month, while households in Hanoi reported an average WTP of USD 3.58 per month (Le & Bui 2020). Another study in Hanoi estimated that households were willing to allocate up to 0.5% of their total income to improve air quality (Nguyen & Le 2019). Previous research has identified several determinants of WTP for environmental improvement, including education, occupation, residential location, and perceived environmental conditions (Junlin et al. 2024, Xiong et al. 2018). In the Vietnamese context, income, educational attainment, literacy, and financial capacity have consistently been reported as the primary factors influencing individuals' willingness to pay for better environmental quality (Le & Bui 2020).

Given the potentially severe health and mortality impacts of environmental degradation, the Value of a Statistical Life (VSL) has become a widely used framework for quantifying mortality risks by examining the trade-offs individuals make between income and reductions in the probability of death (Andersson & Treich 2013, Colmer 2020). Although VSL has been extensively investigated in developed countries, empirical studies linking VSL directly to pollution-related risks remain relatively limited in developing economies, including Vietnam. One of the few studies in the region estimated the VSL associated with mortality risks from water-pollution-related diarrheal diseases in Laos and Vietnam (Eiji et al. 2012). More recently, a study evaluating the health benefits of public transportation in Hanoi in the context of fine particulate matter ($PM_{2.5}$) pollution estimated a VSL of approximately USD 1.6 million per person by transferring VSL values from Taiwan and adjusting them using income-based conversion factors (Trung & Tri 2022).

Although several studies have estimated willingness to pay (WTP) and the value of a statistical life (VSL) in major Vietnamese cities such as Hanoi and Ho Chi Minh City (Le & Bui 2020, Nguyen & Le 2019), limited attention has been given to integrating non-parametric and parametric approaches within a unified valuation framework. This study addresses this gap by combining the Turnbull non-parametric estimator with binary logistic regression. To the best of our knowledge, the application of this integrated framework to air-pollution-related VSL estimation remains largely unexplored in developing-country contexts, including Vietnam. The Turnbull estimator provides a conservative, distribution-free estimate derived directly from the observed bid-response data (Haab & Connell 2002), thereby reducing reliance on restrictive distributional assumptions. Complementarily, the binary logistic model enables the identification of socioeconomic and health-related determinants underlying respondents' willingness to pay. By integrating these two approaches, the study not only generates a robust VSL estimate for Ho Chi Minh City but also provides insights into the factors shaping individual risk-reduction preferences in an urban environment affected by air pollution.

Therefore, this study aims to estimate the VSL associated with air pollution in Ho Chi Minh City, Vietnam, using WTP, defined as the monetary amount a person would trade to reduce their annual mortality risk by one unit. The results can support estimation of the social VSL in large urban areas in Vietnam and provide a basis for decision-makers to determine the financial resources required for air-quality protection and improvement projects.

2. MATERIALS AND METHODS

2.1. Materials

2.1.1. Study Area

Ho Chi Minh City (HCMC) is located in southern Vietnam between 10°10′–10°38′ N and 106°22′–106°54′ E. As the country's largest economic center, the city serves as a major transportation hub linking surrounding provinces, an international gateway, and a strategic transition zone between the Southeast Region and the Mekong Delta.

Ambient air quality in HCMC is monitored through a network of environmental monitoring stations distributed across the city. Recent assessments indicate that air pollution is primarily driven by particulate matter. Concentrations of Total Suspended Particulates (TSP) and PM_{10} have shown increasing trends, particularly in densely populated areas, industrial zones, seaports, and mining sites. More importantly, $PM_{2.5}$ concentrations at several traffic and industrial monitoring stations exceeded national standards by 1.1–4.6 times (Phan 2025).

Industrial activities constitute an important source of air pollution in HCMC. Major emission sources include clinker and cement production facilities, chemical and

fertilizer plants, petrochemical processing facilities, and industries operating large-scale boilers. In terms of emission loads, the textile and food-processing sectors are among the largest contributors. The textile industry alone accounts for approximately 37% of TSP emissions and 41% of $PM_{2.5}$ emissions, largely due to intensive fuel consumption (e.g., LPG, fuel oil, diesel oil, firewood, and biomass briquettes) and the release of fabric and fiber dust. In addition, textile dyeing and finishing processes generate substantial emissions of non-methane volatile organic compounds (NMVOCs) through activities such as sizing, scouring, bleaching, dyeing, and finishing (DONRE 2021).

Transportation represents the dominant source of air pollution in the city. According to DONRE (2021), the transport sector contributes approximately 99%, 97%, 93%, 78%, 23%, 64%, and 45% of total emissions of CO, NMVOCs, NO_x, SO_2, TSP, CH_4, and $PM_{2.5}$, respectively. Road transport, particularly motorcycles, accounts for nearly 90% of transport-related emissions and is responsible for approximately 75% of transport-generated $PM_{2.5}$ emissions. River and seaport activities contribute around 24% of $PM_{2.5}$ emissions, whereas aviation contributes only about 1%, and emissions from railway and bus terminal operations remain negligible (DONRE 2021).

2.1.2. Sample Size

To determine the minimum required sample size for a large population, Cochran's formula was adopted. Assuming that a proportion of the population would be willing to reduce income to lower the mortality risk from air pollution, the sample size was calculated using Eq. (1) (Daniel & Cross 2013, Singh & Masuku 2013).

$$n = \frac{z^2 * p\,(1-p)}{\varepsilon^2} \quad ...(1)$$

where z is the corresponding z-score value; ε is the margin of error; p is the proportion of the selected population. At a 95% confidence level and 5% margin of error, with a selected-population proportion of 50% to achieve the highest minimum sample size, the minimum required sample size is 385.

The study employed a convenience sampling strategy via an online survey. To compensate for potential non-probability sampling bias, a larger sample of over 1,000 valid responses was collected via digital platforms and community networks in Ho Chi Minh City between April 2024 and March 2025. Of the 1,007 questionnaires collected, 879 valid responses were retained for analysis. The sample was predominantly urban, with 85% of respondents residing in central urban districts. The average monthly income was approximately VND 10 million (USD 380), and 70% of respondents reported monthly incomes below VND 20 million (USD 760), broadly consistent with official statistics for Ho Chi Minh City (Vietnam General Statistics Office 2025). More than 50% of respondents held a university degree or higher, exceeding the citywide average of 15–27% reported in previous studies and official sources (Le 2018, Thanh 2025). This difference likely reflects the online recruitment strategy, which tends to attract individuals with higher educational attainment and greater engagement with environmental issues. While this may limit the representativeness of the sample, it is consistent with the increasing adoption of digital platforms and the city's ongoing digital transformation initiatives (Thanh 2025).

2.2. Methods

The methodology and research design are illustrated in Fig. 1.

2.2.1. Contingent Valuation Method

The Contingent Valuation (CV) method employs a structured survey to elicit respondents' willingness to pay (WTP) for a specified environmental improvement. First introduced by Ciriacy-Wantrup (1947), the method has been widely applied in environmental valuation, including studies of environmental quality, ecosystem services, and waste management, and has demonstrated satisfactory reliability in estimating non-market values (Bodah et al. 2022, Hoevenagel 1994, Perni et al. 2021, Tang et al. 2022, Thormann & Wicker 2021). In dichotomous-choice CV surveys, respondents are presented with a bid amount and asked whether they would be willing to pay that amount. Consequently, individual WTP is represented as an interval bounded by the respondent's acceptance or rejection of successive bid levels.

To reduce the potential for hypothetical bias and WTP overestimation, particularly in the valuation of public goods (Andersson & Treich 2013, Biausque 2012), the questionnaire incorporated measures of response certainty and consistency (Hoyos & Mariel 2010, Sajise et al. 2021, Sundström & Andersson 2009). The survey consisted of 35 questions (H1–H35) organized into five sections. The first section included four questions designed to assess respondents' perceptions of air-pollution risks and their understanding of pollution sources. The second section comprised 14 questions addressing self-reported health conditions and symptoms potentially associated with urban air pollution. The third section contained three questions examining respondents' preferences regarding trade-offs between income and health; responses in this section were also used to identify potentially inconsistent answers. The fourth section included eight closed-ended valuation questions related to a hypothetical air-pollution mitigation program. Under this scenario, the program was assumed to reduce the mortality risk from 48 to 47 deaths per 10,000

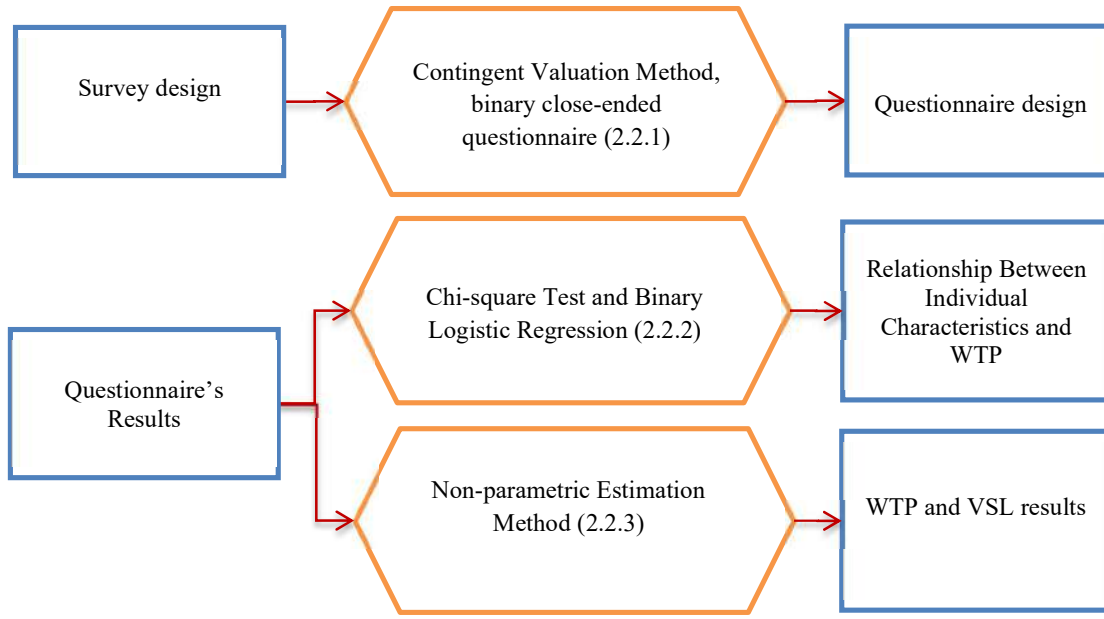


Fig. 1: Methodological framework.

individuals, equivalent to a reduction of one death per 10,000 population (Nhung et al. 2022). The final section collected sociodemographic information from respondents.

In the study, participants were presented with five bid ranges developed based on the average income in Ho Chi Minh City of approximately USD 379 per month (Vietnam General Statistics Office 2025) by applying the exchange rate of approximately 25,900 VND/USD (at the time of conducting the survey in 2024). To ensure the structural validity of the method, the survey underwent a calibration procedure. Prior to the official launch, the survey instrument was refined through a focused pilot pre-test and detailed consultations with environmental economists. To mitigate potential starting-point bias (anchoring effects), starting-point bid levels were randomly distributed across different questionnaire versions to ensure independent valuations. Furthermore, the bid range was bounded between a minimum of VND 11,000 (~USD 0.43, referencing a standard 500 mL bottle of water in a convenience store) and a maximum cap of VND 500,000 (~USD 21). This upper boundary represents approximately 5% of the average local monthly income; pilot feedback indicated that exceeding this threshold would trigger widespread protest responses and scenario rejections.

Fig. 2 outlines the relationship between the bids and WTP estimates. In the figure, it is suggested that the bids correspond to 0.1%, 0.4%, 1.1%, 3.4%, and 5.5% of the monthly income, equivalent to USD 0.43, USD 1.52, USD 4.35, USD 13.04, and USD 21. At the extremes of these ranges, open-ended questions were administered to enable respondents to specify their own maximum WTP. The questions regarding current health status and perceptions of air pollution use a 5-point Likert scale for responses.

2.2.2. Factor Evaluation

- Chi-square test

  A chi-square test is a statistical hypothesis-testing method used to determine relationships among categorical variables. The method has been widely applied in recent studies to investigate the relationship between sociodemographic factors and respondents' decisions (Ali & Ali 2020, Dhungana & Baral 2016, Karytsas et al. 2019). In this study, the test was applied to examine the relationship between the decision to reduce income and personal characteristics, including age, gender, income, education level, and residency. The test model is based on the chi-square formula as follows:

$$\lambda^2 = \sum \frac{(O - E)^2}{E} \quad ...(2)$$

  where O is the observed value and E is the estimated value.

- Binary logistic regression

  This is a statistical method that uses one or more independent variables to predict the probability of a binary outcome for a dependent variable. The method has been applied in studies including research on environmental resources valuation (Hu et al. 2022, Yulianus & Riaman 2021). In this study, the 25th

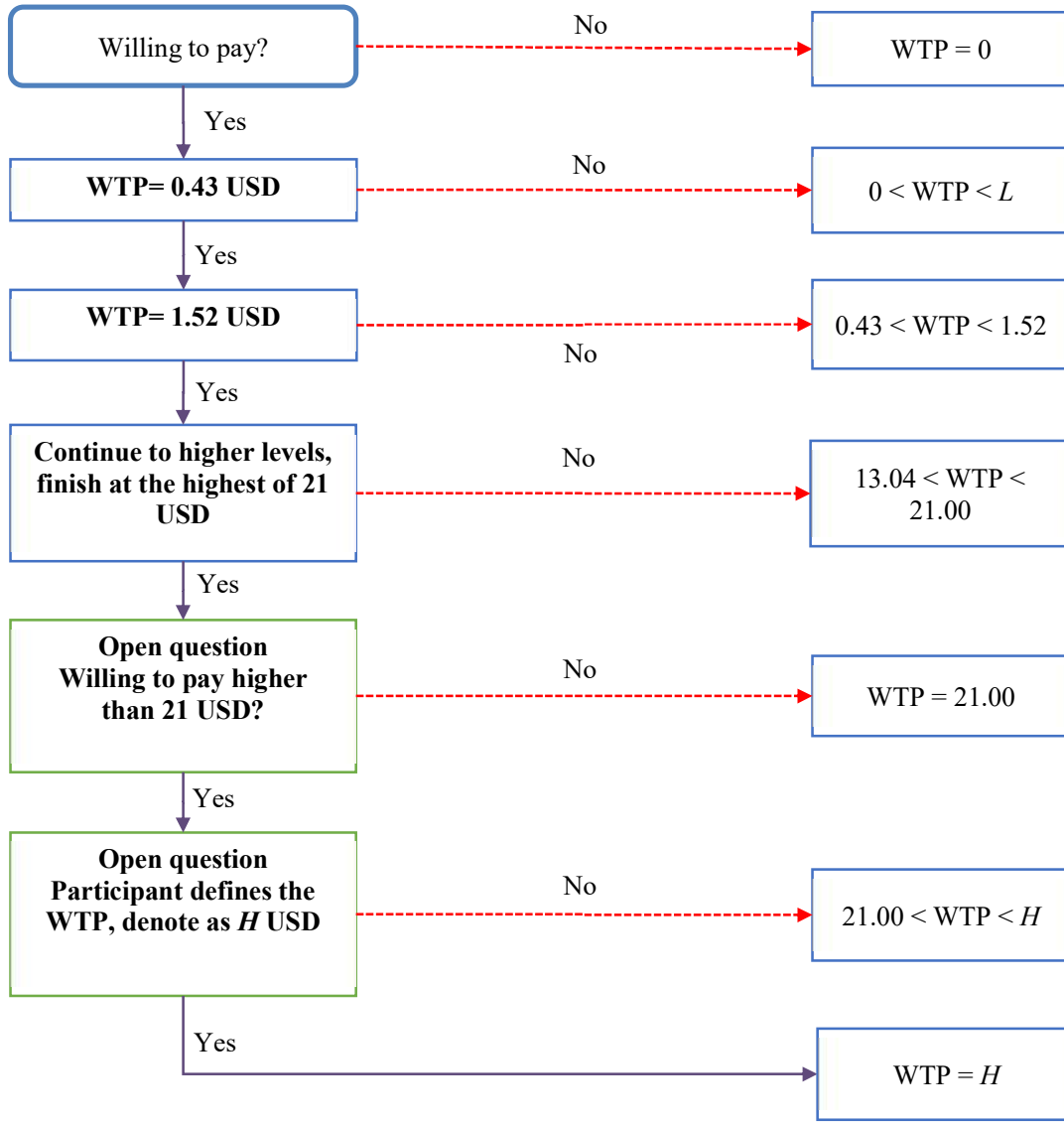


Fig. 2: Contingent valuation survey design.

question (H25) is the dependent variable; therefore, the formula is as follows:

$$P(H_{25} = 1) = \frac{e^{(\beta_0 + \sum_{i=1}^{24} \beta_i H_i)}}{1 + e^{(\beta_0 + \sum_{i=1}^{24} \beta_i H_i)}} \quad ...(3)$$

Where P(H25 = 1) is the probability that H25 takes a value of 1. H25 takes one of two values: 0 (disagree) or 1 (agree), and βi is the corresponding parameter of the independent variable Hi, where i ranges from 1 to 24.

The logistic regression model was assessed for accuracy, reliability, and sensitivity using the parameters in Table 1 (Criado & Veronesi 2013).

TN and TP are "True Negative" and "True Positive," respectively. They occur when the predicted value is identical to the actual observation. FN and FP are "False Negative" and "False Positive," respectively, and occur when the predicted and actual values differ. ON is observed negative, and OP is observed positive.

Table 1: Model evaluation parameters.

		Modeled observation		Total
		0	1	
Actual observation	0	TN	FP	ON = TN + FP
	1	FN	TP	OP = FN + TP

(Note: T = True, F = False, N = Negative, P = Positive, O = Observed)

The evaluation parameters are calculated as follows:

$$\text{Accuracy: CCR} = (TN+TP)/n \quad ...(4)$$

$$\text{Sensitivity: TPR} = TP/OP \quad ...(5)$$

$$\text{Specificity: SPC} = TN/ON \quad ...(6)$$

2.2.3. Non-parametric Estimation Methods

- WTP estimation using the Turnbull lower-bound non-parametric estimator

  Non-parametric estimation is widely applied in recent studies to estimate WTP values for non-market goods (Giolo 2004, Hutchinson et al. 2001, Loureiro et al. 2004, Ranneby & Yu 2011). The method is described using a sample of T individuals who are offered one of B monetary amounts, denoted B_j (where $B_1 < B_2 < \ldots < B_M$). The willingness to pay (WTP_i) for each individual i is modeled as a random variable according to an F distribution (Angelov & Ekström 2017, Giolo 2004, Haab & Connell 2002), as follows:

$$P(WTP_j < B_j) = F(B_j) = F_j \quad ...(7)$$

F_j is considered the cumulative rejection rate for the bid B_j, and is estimated as follows:

1. Assemble bids from the smallest to the largest Bj, where j = 1, …, M
2. Calculate F_j and T_j:

$$F_j = N_j/T_j \text{ and } T_j = N_j + Y_j \quad ...(8)$$

where Nj is the number of individuals selecting "No" and Yj is the number of individuals selecting "Yes" at the bid B_j; $F_j = P(WTP \leq 0)$. F_j is then adjusted to F^*_j as follows:

3. Compare F_j with $F_{(j+1)}$:

   If $F_j \leq F_{(j+1)}$, then set $F^*_j = F_j$ and continue with j = j + 1;

   If $F_j > F_{(j+1)}$, then proceed to merge the two bid steps B_j and B(j + 1) into one group with the upper and lower bounds being $[B_j, B(j + 2)]$ and computing F^*_j:

$$F^*_j = (N_j+N_{(j+1)})/(T_j + T_{(j+1)}) \quad ...(9)$$

4. Repeat the step until a monotonically increasing series is built. The probability density of willingness to pay f^*_j from the bid B_j and $B_{(j+1)}$ is then calculated as follows:

$$f^*_j = F^*_{(j+1)} - F^*_j \quad ...(10)$$

5. Set the last cumulative probability F*(M+1) to 1; the mean WTP is estimated as follows:

$$WTP = \sum B_j f^*_{(j+1)} \quad ...(11)$$

- VSL estimation

  VSL is an economic metric used in cost-benefit analysis to estimate the monetary value an individual places on reducing the risk of premature death. It reflects the aggregate WTP across a population for small mortality risk reductions. Consequently, studies often show a strong correlation between VSL and income (Cropper et al. 2011, Viscusi & Aldy 2003), and a lower VSL is generally assigned to public goods than to private goods (Biausque 2012). It is therefore obtained by taking the limit of WTP or willingness to accept (WTA) when the change in risk is infinitesimal, as shown in Eq. (12).

$$VSL = \frac{w}{p(1-\gamma)} \text{ and } \gamma \in [0,1] \quad ...(12)$$

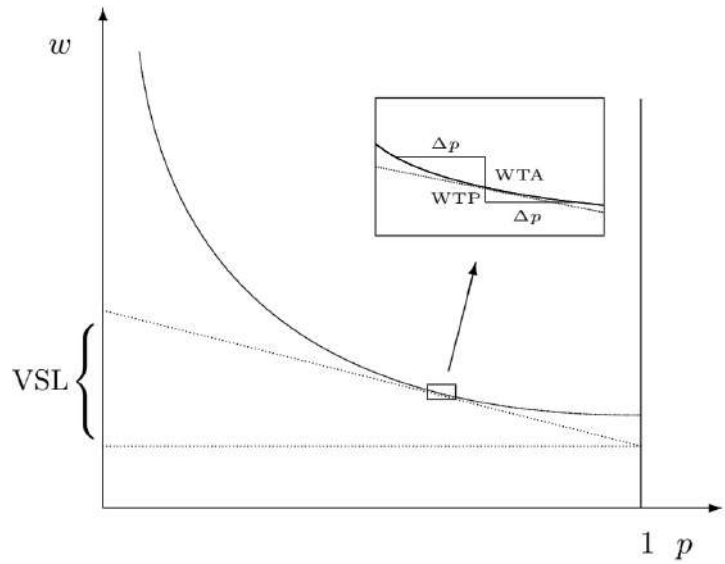


Fig. 3: Theoretical VSL value according to wealth (w) and survival probability (p).

Where w is an individual's wealth and p is the individual's survival probability over a given period. In other words, VSL is the positive slope between the change in wealth and the probability of death, illustrated in Fig. 3 (Andersson & Treich 2013, Hammitt 2000).

In practice, VSL is estimated based on the WTP as shown in Eq. (13) (Criado & Veronesi 2013, Kenkel 2003, Kniesner & Viscusi 2019).

$$VSL = \frac{WTP}{d_r} \quad ...(13)$$

Where VSL is the statistical value of life corresponding to the risk reduction dr; WTP is the individual's willingness to pay, obtained using the closed-ended contingent valuation method; and dr is the achieved risk reduction.

In this study, the risk reduction is defined as a decrease of one unit (from 48/10,000 to 47/10,000). Under this framework, with an individual risk reduction 1/10,000, the VSL per statistical life saved is calculated as eq. (14)

$$VSL = \frac{WTP}{1/10{,}000} = WTP \times 10{,}000 \quad ...(14)$$

Additionally, multiplying the mean individual WTP by the relevant adult population of Ho Chi Minh City yields the aggregate population WTP, representing the total annual economic value generated by the risk reduction program

3. RESULTS AND DISCUSSION

The initial dataset was refined by excluding 128 questionnaires identified as containing either outlier responses or internal inconsistencies. Internal inconsistencies were assessed by cross-checking responses across the survey sections. Questionnaires were flagged when respondents reported low perceived risk or no air-pollution-related health impacts (H_1–H_{18}) but subsequently stated implausibly high willingness-to-pay (WTP) values. In addition, responses were excluded when participants indicated limited financial capacity in the validation questions but selected high payment bids for the proposed mitigation program.

Outliers were identified through a two-stage screening process. First, anomalous WTP responses were flagged using Excel-based filtering procedures. Second, all flagged questionnaires were manually reviewed across the full set of survey questions, including sociodemographic information, to verify and remove invalid observations. Following this quality-control process, 879 valid responses were retained for subsequent analysis.

Table 2: Chi-square statistics of H25 versus demographic variables.

Influencing variables	Chi-square value	p-value	Contingency coefficient	Cramer's V
Income (H_1)	46.8	< 0.001	0.225	0.231
Education (H_4)	49.0	< 0.001	0.198	0.202
Age (H_2)	22.2	< 0.001	0.157	0.159
Residence (H_5)	18.3	0.003	0.143	0.144
Gender (H_3)	2.0	0.161	-	-

3.1. Results of the Influencing Factors

3.1.1. Relationship Between Demographic Information and the Decision to Reduce Income

A chi-square test was applied to examine the relationship between demographic information (H1–H5) and the decision to reduce income (H_{25}). The results showed that demographic factors, including income (H_1), age (H_2), educational level (H_4), and residence (H_5), were all found to be significantly associated with the respondents' decision (Table 2). Cramer's V and the contingency coefficient were also used to assess the strength of the associations. The analysis yielded values between 0.1 and 0.3, indicating weak associations among the variables.

- Income and Education

  Among all variables analyzed, income and education emerged as the primary determinants, yielding the highest Cramer's V and contingency coefficients. The categorical divergence within these factors is illustrated in Fig. 4.

  The lowest income group exhibited the strongest inclination toward "Yes" responses, with the frequency more than doubling that of "No" choices. Conversely, the 5–10 million VND group showed a sharp reversal, where "No" responses peaked at over 64%. While the mid-to-high income segments maintained a stable preference for "No", a notable shift occurred in the two highest groups (more than 20 million VND per month), the "Yes" rate regained slight dominance, converging at 55.2% for both. In addition, respondents with high school or undergraduate/college backgrounds leaned toward "Yes" (61% and 58%, respectively). In contrast, those in other categories, particularly those with postgraduate degrees, demonstrated a higher propensity for "No" responses.

- Age and Residence

  Age and residence exhibited statistically significant but relatively weak associations with the decision-making outcome, with Cramer's V coefficients of 0.159 and 0.144, respectively. These patterns are illustrated in Fig. 5.

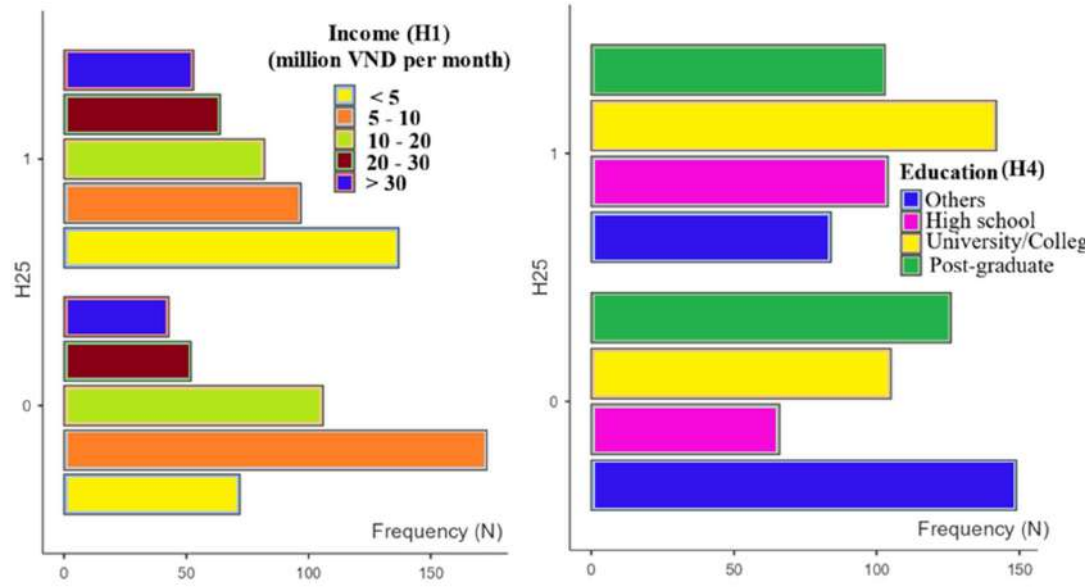


Fig. 4: Relationship of income and education to respondents' decision.

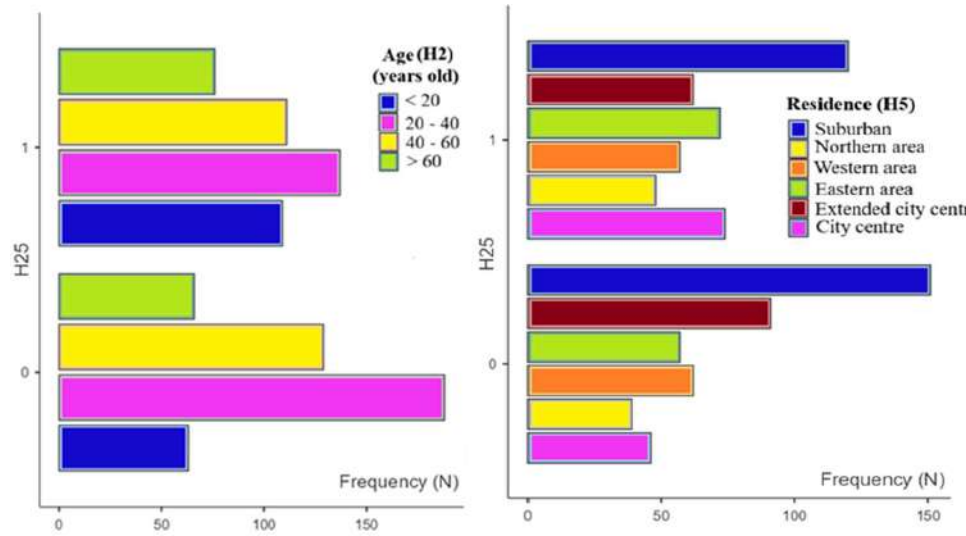


Fig. 5: Relationship of age and residence to respondents' decision.

Age-related differences were observed in respondents' choices. The highest proportion of "Yes" responses was recorded among respondents under 20 years of age (63%), whereas those aged 20–60 years showed a slight preference for "No" responses (53%–58%). Among respondents aged over 60 years, the share of "Yes" responses increased to 53.5%.

Spatial patterns were similarly modest. Respondents residing in suburban areas and the eastern and northern urban districts were somewhat more likely to select "Yes" (67.0%, 55.8%, and 55.2%, respectively), while respondents from other areas showed a slight preference for "No". Overall, the observed differences across residential groups were relatively limited.

3.1.2. Possibility of Reducing Income to Improve Environmental Quality

- The binary logistic model

  Binary logistic regression was employed to identify factors influencing respondents' willingness to accept a reduction in income in exchange for improved environmental quality (H_{25}). Independent variables

Table 3: Model summary.

	B	SE	Odds ratio	Wald statistic	p-value
(Intercept)	2.936	0.548	18.832	33.652	<0.001
H10	0.982	0.079	2.670	138.386	<0.001
H15	-1.399	0.122	0.247	128.559	<0.001

included demographic characteristics and self-reported health-related indicators. Among the variables examined, the perceived importance of health relative to income (H_{10}) and self-reported pneumonia-related symptoms (H_{15}) were significantly associated with the probability of accepting reduced income for environmental improvement. The results are reported in Table 3.

Both H_{10} and H_{15} were statistically significant predictors of the outcome variable ($p < 0.05$). The relatively small standard errors indicate stable coefficient estimates, while the large Wald statistics demonstrate the substantial contribution of these variables to the model. Compared with the intercept term, H_{10} and H_{15} account for a considerably greater proportion of the model's explanatory power, highlighting their importance in predicting respondents' willingness to accept income reductions for environmental improvement.

The negative coefficient associated with H_{15} indicates an inverse relationship with the probability of a positive response to H_{25}. Specifically, as H_{15} increases by one point on the five-point Likert scale, the odds of a positive response to H_{25} are multiplied by 0.247, corresponding to a reduction of approximately 75.3% in the odds. In contrast, H_{10} (income level) exhibits a positive association with H_{25}. A one-unit increase in H_{10} is associated with a 2.67-fold increase in the odds of a positive response to H_{25}, suggesting that respondents with higher income levels are more likely to provide a positive response.

From these results, the logistic probability function for a respondent's willingness to agree, conditioned on variables H_{10} and H_{15}, is defined by Eq. (14) as follows:

$$\mathrm{Ln}\left(\frac{P}{1-P}\right) = 2.936 + 0.982 * H_{10} - 1.399 * H_{15} \quad ...(14)$$

To assess the stability and robustness of the logistic regression model, multicollinearity diagnostics were conducted for the independent variables H_{10} and H_{15}. The results are presented in Table 4.

Table 4: Multicollinearity diagnostics.

	Tolerance	VIF	Correlation between H_{10} and H_{15}
H_{10}	0.785	1.274	-0.464
H_{15}	0.785	1.274	

As shown in Table 4, both variables exhibit a variance inflation factor (VIF) of 1.274, well below the commonly accepted threshold of 5.0, while the corresponding tolerance value of 0.785 exceeds the minimum recommended level of 0.20. In addition, the correlation coefficient between the variables (-0.464) is substantially lower than the critical threshold of 0.70. Collectively, these diagnostics indicate that multicollinearity is not a concern in the present study (Hair et al. 2019).

- Model performance

The predictive capability is assessed by the parameters shown in Table 5. The model yields an area under the curve (AUC) of 0.814, signifying a high degree of discriminatory power in distinguishing between categorical outcomes. This is complemented by an F-measure of 0.722, which confirms a stable equilibrium between sensitivity and precision, ensuring that the model minimizes both Type I and Type II errors.

The reliability of predictors H_{10} and H_{15} is further substantiated by an accuracy of 0.741 and a precision of 0.765. Particularly, the specificity of 0.796 exceeds the sensitivity (0.684), suggesting that the model is significantly adept at identifying "disagreement" cases ($H_{25} = 0$). This characteristic is vital for mitigating the risks associated with false-positive predictions in decision-making. Furthermore, the Brier score of 0.172, which is approaching the ideal value of zero, indicates that the predicted probabilities are closely aligned with empirical observations. While a numerical disparity exists between the AUC (0.814) and the H-measure (0.360), this is expected given the H-measure's more stringent treatment of cost-weighted misclassifications. Nevertheless, an H-measure of 0.360 (falling within the 0.3–0.5 range) reflects a highly satisfactory level of predictive effectiveness for behavioral modeling.

A robust approach to evaluating the model's classificatory efficiency involves the receiver operating characteristic (ROC) curve, shown in Fig. 6. The ROC curve (representing model performance) exhibits a strong trajectory toward the

Table 5: Model evaluation parameters.

AUC	Precision	F-measure	Brier score	H-measure
0.814	0.765	0.722	0.172	0.360

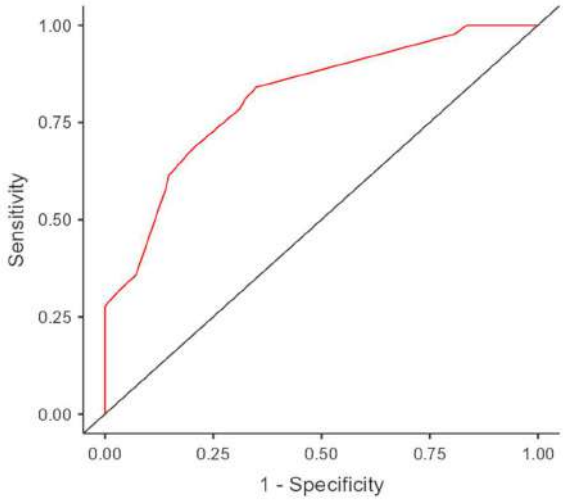


Fig. 6: Receiver operating characteristic (ROC) curve.

upper-left quadrant. This trend indicates that the model achieves high sensitivity while maintaining a low false-positive rate, confirming its robust discriminatory capability.

Regarding the assessment of model fit and diagnostic residuals, Fig. 7 presents the squared Pearson residuals plot, yielding several observations. The high concentration of data points near the baseline (zero) demonstrates that the model aligns exceptionally well with the vast majority of the empirical data. The presence of isolated observations with values exceeding 5 identifies specific outliers. These points warrant careful consideration as they may potentially attenuate the overall predictive accuracy of the model. The red trend line, which depicts the mean residual path, shows a low, smooth profile with a minimal gradient. This suggests that the error distribution remains relatively stable across all probability bands, reinforcing the model's consistency in behavioral prediction.

The Hosmer–Lemeshow test was significant ($\chi^2 = 25.814$, df = 5, $p < 0.001$), suggesting some deviation between observed and predicted probabilities. However, because

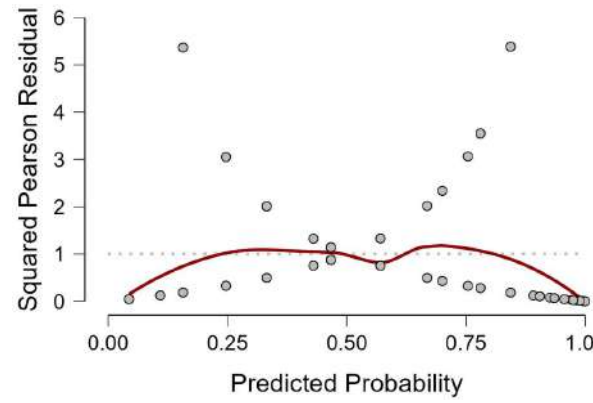


Fig. 7: Squared Pearson residuals plot.

this test is highly sensitive to large sample sizes (N = 879) and may overreject well-fitting models (Hosmer et al. 2013, Paul et al. 2013), model fit was evaluated primarily using pseudo-R^2 statistics and predictive validation metrics (Table 6).

The model showed good explanatory performance, with a Nagelkerke R^2 of 0.410 and a McFadden R^2 of 0.265, values generally considered indicative of a satisfactory fit in discrete choice models (Hosmer et al. 2013, McFadden 1977). Furthermore, model deviance decreased from 1218.4 for the null model to 894.9 for the fitted model, corresponding to a highly significant likelihood-ratio test ($\Delta\chi^2 = 323.418$, $p < 0.001$). These findings indicate that the proposed model substantially improves upon the null specification and captures a meaningful proportion of the variation in the response variable.

- Model predictive performance

The predictive performance of the binary logistic regression model was assessed using a classification matrix. The corresponding results are reported in Table 7.

The model correctly predicted 651 cases out of a total of 879 observations, yielding an overall accuracy of 74.1%. For "No" responses (Value 0), the model correctly predicted 355

Table 6: Model summary.

	Deviance	AIC	BIC	df	$\Delta\chi^2$	p	McFadden R^2	Nagelkerke R^2	Tjur R^2	Cox & Snell R^2
M_0	1218.4	1220.36	1225.139	878			0.000		0.000	
M_1	894.9	900.94	915.279	876	323.42	< .001	0.265	0.410	0.315	0.308

Note: M_0 is the no-variable model; M_1 includes H10 and H15.

Table 7: Classification matrix for the binary logistic model.

		Predicted observation		% Correct
		0	1	
Actual observation	0	355	91	79.6
	1	137	296	68.4
	Total	492	387	74.1

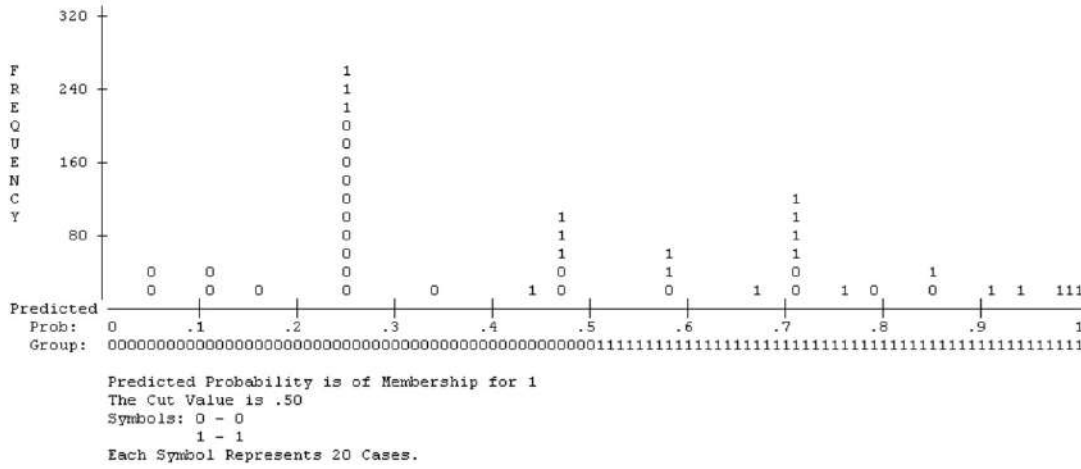


Fig. 8: Observed and predicted probability distribution.

cases out of 446 actual observations, achieving a specificity (true negative rate) of 79.6%. For "Yes" responses (Value 1), the model correctly predicted 296 cases out of 433 actual observations, achieving a sensitivity (true positive rate) of about 68.4%.

The distributions of the dependent variable H25 for the actual and predicted values from the model are shown in Fig. 8. For value 0, the actual and predicted values are similarly concentrated in the left portion of the graph, consistent with a prediction accuracy above 79%. For value 1, the model also performs reasonably well, with most observed and predicted values concentrated in the right portion of the graph and a prediction accuracy above 68%.

- Model validation

To evaluate the predictive performance and generalizability of the logistic regression model, the dataset (N = 879) was randomly partitioned into training (70%; n = 616) and testing (30%; n = 263) subsets. The model was developed using the training data and subsequently evaluated on the independent test set. All analyses were conducted in JASP, and the validation results are reported in Table 8.

The model exhibited satisfactory predictive performance on the independent test set, with an accuracy of 0.757, an F1 score of 0.756, and an AUC of 0.759. The modest decline in AUC relative to the full-sample estimate (0.814) indicates that the model generalizes well to unseen data and is not substantially affected by overfitting.

The corresponding ROC curves are illustrated in Fig. 9.

Figure 9 shows that the ROC curves for both classes remain substantially above the random-classification reference line and trend toward the upper-left corner of the plot. This pattern indicates satisfactory classification

Table 8: Cross-validation test results.

	0	1	Average/ Total
Precision (positive predictive value)	0.712	0.812	0.764
Recall (true positive rate)	0.825	0.693	0.757
False positive rate	0.307	0.175	0.241
False discovery rate	0.288	0.188	0.238
F1 score	0.765	0.748	0.756
Matthews correlation coefficient	0.522	0.522	0.522
Area under curve (AUC)	0.759	0.759	0.759
Negative predictive value	0.812	0.712	0.762
True negative rate	0.693	0.825	0.759
False negative rate	0.175	0.307	0.241
False omission rate	0.188	0.288	0.238

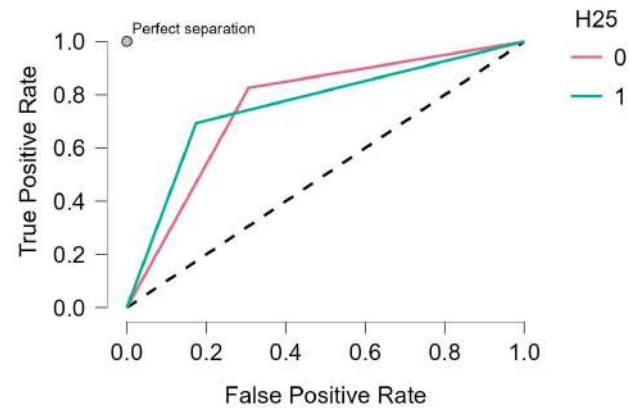


Fig. 9: Receiver operating characteristic (ROC) curves for the cross-validation test.

performance and provides additional evidence of the model's robustness and generalizability.

3.2. WTP and VSL Results

The study was designed to estimate the WTP for a one-unit reduction in the risk of death (from 48 to 47 deaths per 10,000 people). In the survey, respondents demonstrated a clear division when comparing personal health and income: 38% prioritized health, 20% prioritized income, and 42% considered them equally vital. However, this willingness to prioritize health did not translate into economic sacrifice. When faced with reducing income for better environmental quality, more than 70% declined, overwhelmingly citing insufficient income as the primary barrier.

The Turnbull lower-bound estimate of WTP is 17.9 thousand VND per person, as shown in Table 9. Based on Equation (14), the individual VSL for a 1/10,000 risk reduction is estimated at 179.2 million VND per statistical life saved (approximately USD 6,920 at the current exchange rate). Furthermore, aggregating the mean individual WTP across the adult target population of approximately 9.5 million people (Ho Chi Minh City's Department of Health 2025) yields an aggregate population WTP (total economic benefit) of 170.2 billion VND (approximately USD 6.57 million).

VSL is frequently estimated using a simple rule of thumb of approximately 70 times GDP per capita, representing a theoretical benchmark of an individual's lifetime economic contribution over a 70-year span (Woolley et al. 2015, World Bank 2021). According to local authorities, the GRDP per capita for Ho Chi Minh City in 2024 was approximately USD 7,600, yielding a benchmark VSL of USD 532,000 per statistical life.

In contrast, our empirical individual VSL derived from the Turnbull lower-bound estimator is 179.24 million VND (approximately USD 6,920), which is significantly lower than the theoretical GDP-based benchmark. This substantial gap is primarily explained by severe budget constraints, as over 70% of respondents reported insufficient income to make financial sacrifices for environmental improvements. Furthermore, when evaluating the total societal impact, the aggregate population WTP across the city reaches 170.2 billion VND (USD 6.57 million), illustrating that while individual payment willingness is constrained by immediate income limits, the collective willingness to pay reflects a substantial community valuation for air quality improvement.

In comparison, our empirical individual VSL estimated via the Turnbull lower-bound method is substantially lower than the USD 1.6 million estimated by Trung & Tri (2022). This pronounced divergence stems primarily from the fundamental differences in methodology and primary data reliance. While Trung & Tri (2022) derived their VSL through a benefit transfer approach based on Taiwan's baseline values and adjusted for income, our study relies on direct, primary CVM survey data collected from local residents in Ho Chi Minh City. Direct stated-preference surveys in developing contexts frequently reflect acute, immediate budget constraints and a low willingness to make financial sacrifices—as evidenced by the 70% refusal rate in our sample—leading to lower empirical VSL values compared to transferred estimates from higher-income economies. Nevertheless, when aggregated across the city's adult population, the collective willingness to pay reaches USD 6.57 million, demonstrating that while individual capacity to pay is severely restricted, air quality improvement holds a substantial aggregate economic value for the broader community.

4. CONCLUSIONS

The results of this study indicate a mean individual WTP of 17,900 VND per person to achieve a 1/10,000 reduction in the air pollution-related mortality rate (from 48/10,000 to 47/10,000). Based on standard VSL formulations, this yields an individual VSL of 179.24 million VND (approximately USD 6,920) per statistical life saved. Furthermore, aggregating this individual willingness to pay across the city's adult

Table 9: WTP results according to the Turnbull lower-bound estimation.

B_j (USD)	B_j (1,000 VND)	N_j	F_j	F^*_j	f^*_j	WTP_j (1,000 VND)
0	0	638	0.726	0.726	0.076	0.000
0.43	10	705	0.802	0.802	0.077	0.774
1.52	35	773	0.879	0.879	0.051	1.792
4.35	100	818	0.931	0.931	0.027	2.730
13.04	300	842	0.958	0.958	0.042	12.628
21.00	500	879	1.000	1.000	0.000	0.000
	Total estimated WTP					17.924

population results in an aggregate population WTP of 170.2 billion VND (equivalent to USD 6.57 million), representing the overall societal economic benefit of the proposed risk reduction program. A significant finding is the severe constraint imposed by income: more than 70% (638/879) of total respondents were unwilling to pay, overwhelmingly citing insufficient income as the primary barrier. This financial constraint is further evidenced by the fact that the group with a monthly income under 20 million VND exhibited the highest refusal rate among all income groups.

The results of this study indicate that the residents of Ho Chi Minh City (HCMC) are highly aware of the harmful effects of air pollution on their health. However, when connecting this awareness to their income, less than 30% of the surveyed individuals agreed to reduce their income (agreed to pay). Moreover, socioeconomic factors, including income, age, education level, and residence, were found to be related to the respondents' WTP decision, though these linkages are relatively weak. The segmentation analysis of the agreeing group revealed that respondents with low-to-medium incomes, young adults, those with a university education, and residents in the city center or suburban areas constituted the largest share of agreement.

The probabilistic model of the factors influencing the decision to reduce income (or agree to pay) simultaneously revealed that respondents' assessments of health symptoms played an important role in prediction. The probabilistic model also demonstrated reasonably good predictive values, with an overall correct prediction rate above 74% and an AUC of about 0.81.

The segmentation analysis of the agreeing group revealed that respondents with low-to-medium incomes, young adults, those with a university education, and residents in the city center or suburban areas constituted the largest share of agreement.

The results of this study indicate that the residents of Ho Chi Minh City (HCMC) are highly aware of the harmful effects of air pollution on their health. However, when connecting this awareness to their income, less than 30% of the surveyed individuals agreed to reduce their income (agreed to pay). Looking specifically at the demographic composition of the agreeing group, the majority of respondents were young adults (20–40 years old) with medium-to-low incomes residing in central and suburban expansion districts."

Therefore, further specialized research focusing on the remaining demographic groups is proposed to identify underlying causes. This information can then be used to develop appropriate and effective communication and outreach strategies.

5. ACKNOWLEDGEMENT

The authors thank Sai Gon University, Ho Chi Minh City, Vietnam, for its support and funding.

6. REFERENCES

Akhtar, S., Umer, W., Nadeem, V.M. and Shahid, I. 2017. Assessment of willingness to pay for improved air quality using contingent valuation method. *Global Journal of Environmental Science and Management*, 3, pp.279–286. [DOI].

Ali, T. and Ali, J. 2020. Factors affecting the consumers' willingness to pay for health and wellness food products. *Journal of Agriculture and Food Research*, 2, pp.100076. [DOI].

Andersson, H. and Treich, N. 2013. The value of a statistical life, in: *Handbook of Transport Economics*. Edward Elgar, Cheltenham, UK, pp.396–424.

Angelov, A.G. and Ekström, M. 2017. Nonparametric estimation for self-selected interval data collected through a two-stage approach. *Metrika*, 80, pp.377–399. [DOI].

Baker, R. and Ruting, B. 2014. *Environmental Policy Analysis: A Guide to Non-Market Valuation - Staff Working Paper*. Productivity Commission, pp.45.

Bodah, B.W., Neckel, A., Stolfo Maculan, L., Milanes, C.B., Korcelski, C., Ramírez, O., Mendez-Espinosa, J.F., Bodah, E.T. and Oliveira, M.L.S. 2022. Sentinel-5P TROPOMI satellite application for NO_2 and CO studies aiming at environmental valuation. *Journal of Cleaner Production*, 357, pp. 131960. [DOI].

Ciriacy-Wantrup, S.V. 1947. Capital returns from soil-conservation practices. *American Journal of Agricultural Economics*, 29, pp.1181–1196. [DOI].

Colmer, J. 2020. What is the meaning of (statistical) life? Benefit–cost analysis in the time of COVID-19. *Oxford Review of Economic Policy*, 36, pp.S56–S63. [DOI].

Criado, C.O. and Veronesi, M. 2013. Parametric vs nonparametric dichotomous choice contingent valuation models: testing the kernel estimator and its revealed performance, in: Environmental Economics II. Presented at the SSES Annual Congress, University of Neuchâtel, Switzerland.

Cropper, M., Hammitt, J.K. and Robinson, L.A. 2011. Valuing mortality risk reductions: Progress and challenges. *Annual Review of Resource Economics*, 3, pp.313–336. [DOI].

Daniel, W.W. and Cross, C.L. 2013. Estimation, in: *Biostatistics: A Foundation for Analysis in the Health Sciences*. Wiley, USA, pp. 958.

Dhungana, A.R. and Baral, B. 2016. Factors affecting willingness to pay for improved water supply system in rural Tanahu, Nepal. *Janapriya Journal of Interdisciplinary Studies*, 5, pp.1–13. [DOI].

DONRE 2021. *Ho Chi Minh City's Environmental Quality Report of 2021*.

Eiji, O., Masafumi, M., Phouphet, K. and Hiroshi, S. 2012. Measurement of value of statistical life by evaluating diarrhea mortality risk due to water pollution in Laos and Vietnam. European Regional Science Association (ERSA), Louvain-la-Neuve, pp.1–5.

EPAVN V.E.P.A. 2023. *Vietnam National Technical Regulation on Air Quality QCVN 05:2023*.

Giolo, S.R. 2004. Turnbull's nonparametric estimator for interval-censored data. Department of Statistics, Federal University of Parana, Brazil.

Guo, D., Wang, A. and Zhang, A.T. 2020. Pollution exposure and willingness to pay for clean air in urban China. *Journal of Environmental Management*, 261, pp.110174. [DOI].

Haab, T.C. and Connell, K.E. 2002. *Valuing Environmental and Natural Resources, New Horizons in Environmental Economics*. Edward Elgar, UK, pp.352.

Hair, J.F., Black, W.C., Babin, B.J. and Anderson, R.E. 2019. *Multivariate Data Analysis, 8th ed*. Cengage, Andover, Hampshire.

Hammitt, J.K. 2000. Valuing mortality risk: Theory and practice. *Environmental Science & Technology*, 34, pp.1396–1400. [DOI].

Ho Chi Minh City's Department of Health 2025. Hành trình 50 năm công tác dân số góp phần vào sự phát triển kinh tế - xã hội của Thành phố Hồ Chí Minh. Available at: http://medinet.hochiminhcity.gov.vn/ky-niem-50-nam-giai-phong-mien-nam-thong-nhat-dat-nuoc-3041975-3042025/hanh-trinh-50-nam-cong-tac-dan-so-gop-phan-vao-su-phat-trien-kinh-te-xa-hoi-cua-cmobile16645-73088.aspx (Accessed 11/3/25).

Hoevenagel, R. 1994. An assessment of the contingent valuation method, in: Pethig, R. (Ed.), *Valuing the Environment: Methodological and Measurement Issues*. Springer Netherlands, Dordrecht, pp.195–227. [DOI].

Hosmer, D.W., Lemeshow, S. and Sturdivant, R.X. 2013. *Applied Logistic Regression*, 3rd ed. John Wiley & Sons. [DOI].

Hoyos, D. and Mariel, P. 2010. Contingent valuation: Past, present and future. *Prague Economic Papers*, 19, pp.329–343. [DOI].

Hu, P., Zhou, Y., Zhou, J., Wang, G. and Zhu, G. 2022. Uncovering the willingness to pay for ecological red lines protection: Evidence from China. *Ecological Indicators*, 134, pp.108458. [DOI].

Hutchinson, W.G., Scarpa, R., Chilton, S.M. and McCallion, T. 2001. Parametric and non-parametric estimates of willingness to pay for forest recreation in Northern Ireland: A discrete choice contingent valuation study with follow-ups. *Journal of Agricultural Economics*, 52, pp.104–122. [DOI].

IQAir 2024. *Report of World Air Quality 2023*. Available at: https://www.iqair.com/vi/newsroom/waqr-2023-pr (Accessed 7.25.25).

Junlin, R., Xiao, B., Xinyue, L. and Ziqian, P. 2024. Analysis of the factors influencing willingness to pay and payout level for watershed eco-compensation of the Huangbai river basin. *Water Supply*, 24, pp.1102–1116. [DOI].

Karytsas, S., Polyzou, O. and Karytsas, C. 2019. Factors affecting willingness to adopt and willingness to pay for a residential hybrid system that provides heating/cooling and domestic hot water. *Renewable Energy*, 142, pp.591–603. [DOI].

Kenkel, D. 2003. Using estimates of the value of a statistical life in evaluating consumer policy regulations. *Journal of Consumer Policy*, 26, pp.1–21. [DOI].

Kniesner, T.J. and Viscusi, W.K. 2019. The value of a statistical life. *Oxford Research Encyclopedia of Economics and Finance (New York, NY, online edn, Oxford Academic, 29 Mar. 2018)*. [DOI]. (Accessed 16 April 2026).

Le, T. 2018. Ho Chi Minh City residents have an average of 9.68 years of education. Báo Người Lao Động Online. Available at: https://nld.com.vn/giao-duc-khoa-hoc/so-nam-hoc-tap-trung-binh-cua-nguoi-dan-tp-hcm-la-968-nam20181205094105831-.htm (Accessed 29/5/2026).

Le, T.N.H. and Bui, D.H. 2020. Willingness to pay for air quality improvement in Ho Chi Minh City, Vietnam. *The Journal of Agriculture and Development*, 19, pp.1–10. [DOI].

Loan, T.T. 2018. More than 60 thousands people dead every year in Vietnam for air pollution. World Health Organization. Available at: https://www.who.int/vietnam/vi/news/detail/02-05-2018-more-than-60-000-deaths-in-viet-nam-each-year-linked-to-air-pollution (Accessed 27/7/2025).

Loureiro, M.L., Loomis, J.B. and Nahuelhual, L. 2004. A comparison of a parametric and a non-parametric method to value a non-rejectable public good. *Journal of Forest Economics*, 10, pp.61–74. [DOI].

McFadden, D. 1977. Quantitative methods for analyzing travel behaviour of individuals: Some recent developments. *Cowles Foundation Discussion Papers*.

Nguyen, C.T. and Le, H.T. 2019. A choice experiment to estimate willingness-to-pay for air quality improvements in Hanoi City: Results of a pilot study, in: ICSEED2019. Presented at the International Conference on Social, Economic and Environmental Issue in Development, National Economics University, Hanoi, Vietnam.

Nhung, N.T.T., Duc, V.T., Ngoc, V.D., Dien, T.M., Hoang, L.T., Ha, T.T.T., Khue, P.M., Truong, N.X., Thanh, N.T.N., Jegasothy, E., Marks, G.B. and Morgan, G. 2022. Mortality benefits of reduction fine particulate matter in Vietnam, 2019. *Frontiers in Public Health*, 10, pp. 1056370. [DOI].

Paul, P., Pennell, M.L. and Lemeshow, S. 2013. Standardizing the power of the Hosmer-Lemeshow goodness of fit test in large data sets. *Statistics in Medicine*, 32(1), pp.67–80. [DOI].

Perni, Á., Barreiro-Hurlé, J. and Martínez-Paz, J.M. 2021. Contingent valuation estimates for environmental goods: Validity and reliability. *Ecological Economics*, 189, pp.107144. [DOI].

Phan, L. 2025. Ho Chi Minh City's air quality degradation, fine dust increasing. Tuoi Tre Online. Available at: https://tuoitre.vn/canh-bao-khan-chat-luong-khong-khi-tp-hcm-suy-giam-bui-min-tang-20251217110358159.htm (Accessed 7/4/2026).

Ranneby, B. and Yu, J. 2011. Estimation of WTP with point and self-selected interval responses. Research Report Centre of Biostatistics, pp. 1–11.

Sajise, A.J., Samson, J.N., Quiao, L., Sibal, J., Raitzer, D.A. and *Harder, D. 2021. Contingent valuation of nonmarket benefits in project economic analysis; a guide to good practice*. Asian Development Bank, Philippines. pp. 208. [DOI].

Singh, A.S. and Masuku, M. 2013. Sampling techniques & determination of sample size in applied statistics research: An overview. *International Journal of Economics, Commerce and Management*, 1, pp. 1–22.

Sundström, K. and Andersson, H. 2009. *Swedish consumers' willingness to pay for food safety - a contingent valuation study on Salmonella risk*. Swedish National Road & Transport Research Institute, Sweden, pp.1–46.

Tang, R., Zhao, J., Liu, Y., Huang, X., Zhang, Y., Zhou, D., Ding, A., Nielsen, C.P. and Wang, H. 2022. Air quality and health co-benefits of China's carbon dioxide emissions peaking before 2030. *Nature Communications*, 13, pp.1008. [DOI].

Thanh, B. 2025. By 2025: How much of Ho Chi Minh City's population will have a university degree or higher? Available at: https://thanhnien.vn/27-dan-so-tphcm-co-trinh-do-dai-hoc-tro-len-185251223214942669.htm (Accessed 31/5/2026).

Thormann, T.F. and Wicker, P. 2021. Willingness-to-pay for environmental measures in non-profit sport clubs. *Sustainability*, 13, pp.2841. [DOI].

Trung, T.D.B. and Tri, D.Q. 2022. Application of the AERMOD model to evaluate the health benefits due to air pollution from the public transport sector in Ha Noi, Viet Nam. *Journal of Geoscience and Environment Protection*, 10, pp.13–33. [DOI].

Vietnam General Statistics Office 2025. Average income of a labor by locality divided by Province/City and Year. Available at: https://www.nso.gov.vn/px-web-2/ (Accessed 3/9/2025).

Biausque, V. 2012. The value of statistical life: A meta-analysis. National Bureau of Economic Research, 1050 Massachusetts Avenue, Cambridge, MA 02138, pp.1–24.

Viscusi, W.K. and Aldy, J.E. 2003. The value of a statistical life: A critical review of market estimates throughout the world. *Journal of Risk and Uncertainty*, 27, pp.5–76. [DOI].

Vu, T.X., Chon, L.Q., 2021. A review on current status of urban air pollution in Ho Chi Minh City and Ha Noi. *DTU Journal of Science and Technology*, 4, pp.45–53.

WHO 2021. *WHO global air quality guidelines: particulate matter* ($PM_{2.5}$ and PM_{10}), ozone, nitrogen dioxide, sulfur dioxide and carbon monoxide, World Health Organization. ed. World Health Organization, Geneva.

Woolley, N., Lövenich, A. and Ryan, D. 2015. *Estimating the global economic cost of drowning*. Available at: https://share.google/nA4rfx4iGRlAmLwYI.

World Bank 2021. *Socio-Economic Costs and Human Impacts of Road Accidents in Azerbaijan*. World Bank, Washington, DC. [DOI].

Xiong, K., Kong, F., Zhang, N., Lei, N. and Sun, C. 2018. Analysis of the factors influencing willingness to pay and payout level for ecological environment improvement of the Ganjiang River Basin. *Sustainability*, 10, pp.2149. [DOI].

Yulianus, B. and Riaman, S. 2021. Willingness to pay of fishermen insurance using logistic regression model. Jurnal Matematika Integratif, pp. 15–21. [DOI].

Nature Environment and Pollution Technology
An International Quarterly Peer-Reviewed Open Access Journal

p-ISSN: 0972-6268 | e-ISSN: 2395-3454 Vol. 25 | No. 4 | Article ID B4441 | 2026

RESEARCH ARTICLE https://doi.org/10.46488/NEPT.2026.v25i04.B4441 OPEN ACCESS

Eco-Physiological Assessment of Native Plant Species for Mitigating Airborne Pollutants and Greenbelt Development in a Coal Mining Region

Mallikharjuna Prasad Polavarapu[1], Manoj Kumar[1]†, Shreerup Goswami[2], Soham Mishra[1], Akshay Kumar Singh[1] and Sushil Kumar Shukla[1]

[1]Department of Environmental Sciences, Central University of Jharkhand, Ranchi-835222, Jharkhand, India
[2]Department of Geology, Utkal University, Vani Vihar, Bhubaneswar, Odisha, India 751004
†Corresponding author: Manoj Kumar; manojkumarcuj26@gmail.com

ARTICLE HISTORY

Received: 24-03-2026
Revised: 13-05-2026
Accepted: 21-05-2026

KEYWORDS

Air Pollution Tolerance Index (APTI)
Phytoremediation
Dust capturing capacity
Environmental monitoring

CITE THIS ARTICLE

Polavarapu, M.P., Kumar, M., Goswami, S., Mishra, S., Singh, A.K. and Shukla, S.K., 2026. Eco-physiological assessment of native plant species for mitigating airborne pollutants and greenbelt development in a coal mining region. *Nature Environment and Pollution Technology*, 25(4), B4441. https://doi.org/10.46488/NEPT.2026.v25i04.B4441

COPYRIGHT & LICENCE

© 2026 The Authors
Open Access under CC BY 4.0.

PUBLISHED BY

TECHNOSCIENCE PUBLICATIONS

ABSTRACT

Coal mining operations are major sources of atmospheric pollution, substantially degrading ambient air quality and imposing physiological stress on surrounding vegetation. This study aims to evaluate the pollution tolerance capacity of seven native plant species across the core, buffer, and transition zones within the Magadh coal mining region, Jharkhand, India. To identify suitable pollution-tolerant species for sustainable greenbelt development, the Air Pollution Tolerance Index (APTI), Anticipated Performance Index (API), and Dust Capturing Capacity (DCC) were assessed. The results revealed significant species-specific variation in pollution tolerance and particulate interception across the pollution gradient. *Syzygium cumini* recorded the highest APTI value (16.35) in the highly polluted core zone, primarily associated with an elevated ascorbic acid concentration (12.61 mg g^{-1}), indicating a strong antioxidative defense mechanism against oxidative stress. In contrast, *Ficus benghalensis* and *Mangifera indica* exhibited superior particulate retention capacity, with maximum DCC values of 2.50 mg cm^{-2} and 2.91 mg cm^{-2}, respectively. The native climax species *Shorea robusta* maintained relatively stable physiological attributes across pollution zones; however, its morphological characteristics resulted in a lower API classification (Poor, 50%). Integrating biochemical, morphological, and socioeconomic attributes, API analysis identified *Ficus benghalensis* (Grade 4, 68.75%) and *Syzygium cumini* (Grade 4, 62.5%) as effective candidates for pollution mitigation. Conversely, *Urena lobata* and *Lantana camara* exhibited high sensitivity to mining-induced air pollution. The integration of biochemical, physiological, and morphological parameters provides a comprehensive framework for species selection. The study highlights the importance of using pollution-tolerant and high dust-retaining species to design sustainable greenbelts in coal mining areas.

1. INTRODUCTION

Air pollution remains one of the most serious anthropogenic threats to the global environment. Among various anthropogenic activities, coal mining represents a major environmental challenge, as it acts both as a significant source of pollutants and a large-scale environmental contaminant (Ghosh et al. 2025). The deterioration of ambient air quality not only poses severe risks to human health but also adversely affects terrestrial vegetation, which serves as a primary sink for atmospheric pollutants (Anand et al. 2022). Plants growing in industrial and coal mining regions are continuously exposed to gaseous and particulate pollutants, which can induce alterations in their physiological structure, biological behavior, and metabolic mechanisms (Natividad et al. 2024). Therefore, the identification and selection

of pollution-tolerant plant species have become vital for the development of greenbelts and sustainable air quality management strategies (Sawarkar et al. 2023).

"The APTI is a quantitative method used to evaluate the inherent resistance of plant species to atmospheric pollution" (Singh et al. 1991). To quantify the air pollution tolerance of plant species, APTI is one of the most widely used methods (Paul et al. 2023). APTI integrates four major biochemical and physiological parameters: total chlorophyll content (TCH), ascorbic acid content (AA), leaf extract pH, and relative water content (RWC) (Mehmood et al. 2023). This approach helps provide a comprehensive evaluation of plant defense mechanisms against air-pollution-induced stress. Recent studies have validated APTI as a holistic tool for categorizing plants into sensitive, intermediate, and tolerant groups, thereby supporting the selection of species for phytoremediation (Asif & Ma 2024).

APTI consists of two major components: physiological and biochemical. The physiological component comprises leaf-extract pH and RWC. These physiological parameters indicate the plant's ability to maintain homeostasis (Goswami et al. 2023). A higher pH plays a crucial role in the detoxification of acidic pollutants (e.g., SO_2 and NO_x), while RWC helps maintain turgidity and physiological function despite pollutant-induced transpiration stress (Timilsina et al. 2022). The biochemical components of APTI are AA and TCH, which indicate the metabolic proficiency of plants under stressed conditions. AA is a potent antioxidant that serves as a scavenger of reactive oxygen species (ROS) generated by pollutant exposure, thereby helping maintain cell membrane integrity (Najafi Zilaie et al. 2023). The higher the ascorbic acid level, the greater the potential for pollution tolerance (Chauhan et al. 2022). Chlorophyll content is often reduced in plants growing under stressed conditions because of the degradation of photosynthetic pigments. Tolerant plant species, however, commonly maintain stable chlorophyll levels to sustain productivity (Bui et al. 2021).

Beyond these biochemical properties, the APTI of many plant species is strongly influenced by spatiotemporal variations, including seasonal changes and microclimatic conditions (Bui et al. 2023). APTI values often vary seasonally; for example, the post-monsoon period, compared with winter or summer, may show optimal metabolic activity (Bui et al. 2023). Spatial factors such as elevation and proximity to pollution sources also play a significant role. Plants located in industrial regions or high-traffic zones may show higher APTI values than plants at residential sites. For example, a recent study indicated that *M. indica* showed high pollution-tolerance potential, with its highest APTI score across mining sites in the Khalari region, Jharkhand (Singh & Shukla 2025). This suggests an adaptive physiological response to regular and long-term pollutant exposure (Chauhan et al. 2025). Understanding these seasonal and spatial variations is important for accurate categorization, as a species classified as sensitive in one season may show intermediate tolerance in another (Kaur 2021).

The relationship between APTI and Dust Capturing Capacity (DCC) describes the dual role of plants as biological monitors and physical barriers. A positive correlation has been reported between higher APTI values and dust accumulation in species with rough leaf structures or waxy cuticles, indicating that plants tolerant of greater physiological stress can also act as effective scrubbers of particulate matter (PM) from the atmosphere (Antil et al. 2025). Evaluating both APTI and PM accumulation provides a more holistic assessment of a plant's scrubbing potential than either parameter alone (Mehmood et al. 2023).

The present study was conducted to evaluate the biochemical and physiological characteristics of selected plant species growing in mining-affected regions. Parameters including total chlorophyll content, ascorbic acid content, relative water content, and leaf extract pH were analyzed to estimate the APTI for identifying comparatively tolerant and sensitive species under mining-induced environmental stress. In addition, the API was assessed by integrating APTI with morphological and socioeconomic attributes to evaluate the overall adaptability and suitability of plant species for greenbelt development in polluted environments. Furthermore, DCC was determined to assess the particulate interception potential of the selected species and their possible role in mitigating airborne dust pollution in mining landscapes.

2. MATERIALS AND METHODS

2.1. Study Area

The study was conducted in the Magadh open-cast mining region, located across the Tandwa block of Chatra district and the Balumath Community Development (CD) block of Latehar district, Jharkhand, India. The area represents one of the major operational coal mining regions within the North Karanpura Coalfield operated by Central Coalfields Limited (CCL). Geographically, the study area is situated at 23.8442° N latitude and 84.9885° E longitude. The nearest settlement to the mining area is Bachra, which is located approximately 20 km from Khalari and about 50 km from Hazaribagh. The study area is shown in Fig. 1.

2.2. Sampling

The study area was divided into three zones based on distance from the mining area to assess the air pollution tolerance

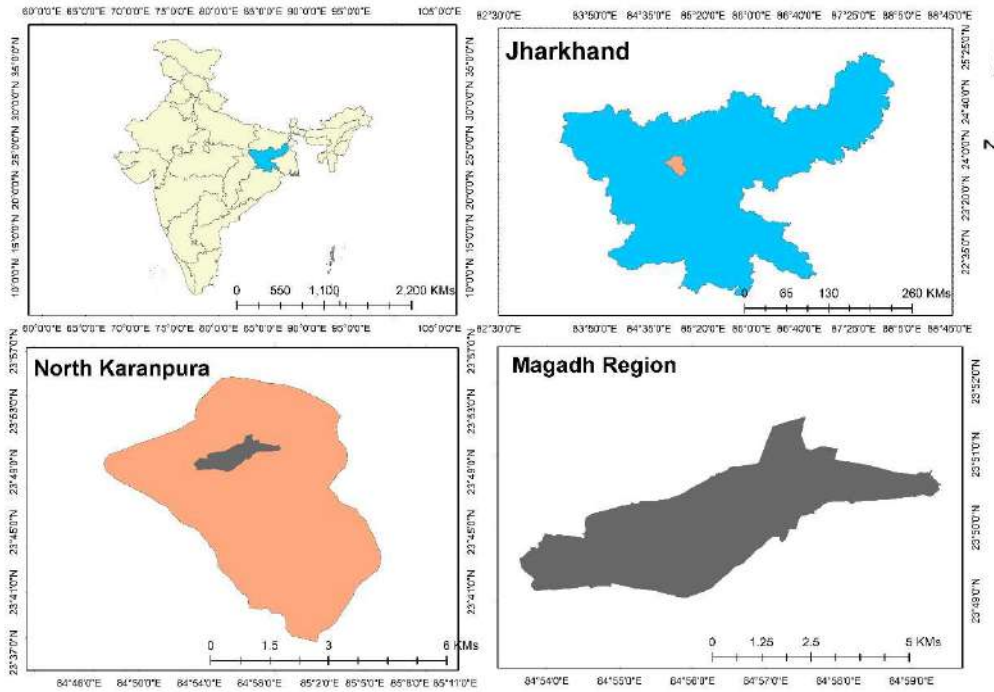


Fig. 1: Domain of the study area.

of roadside vegetation under varying pollution loads. The zones were categorized as follows: core zone, within 500 m of the mining area; buffer zone, located 3–5 km from the core zone; and transition zone, beyond the buffer zone. The ambient air quality assessment of the study region revealed that the concentrations of particulate pollutants in both the buffer and core zones were marginally above the permissible limits prescribed under the National Ambient Air Quality Standards (NAAQS; GSR 826 and 742(E)), indicating considerable environmental stress in the mining-influenced areas. The recorded suspended particulate matter (SPM) concentrations were 588.9 μg m^{-3} in the buffer zone and 601.4 μg m^{-3} in the core zone against the prescribed limit of 600 μg m^{-3}. Similarly, PM_{10} concentrations were 99.2 μg m^{-3} and 104.2 μg m^{-3}, while $PM_{2.5}$ concentrations were 59.1 μg m^{-3} and 63.7 μg m^{-3} in the buffer and core zones, respectively, compared with the standard limits of 100 μg m^{-3} for PM_{10} and 60 μg m^{-3} for $PM_{2.5}$ (Table 1). To identify representative vegetation and assess species distribution, an ecological survey was conducted using the quadrat method. A total of three quadrats were laid at each sampling site for vegetation analysis and species enumeration. The survey revealed 7 tree species and 6 shrub species in the core zone, whereas 13 tree species and 9 shrub species were recorded in the buffer zone. Based on species commonality, abundance, and occurrence across the study zones, seven plant species were selected for detailed investigation. These included four tree species: *Mangifera indica*, *Ficus benghalensis*, *Shorea robusta*, and *Syzygium cumini*; and three shrub species: *Lantana camara*, *Urena lobata*, and *Martynia annua*. The selection of sampling sites was further supported by the wind rose diagram (Fig. 2), which represented the direction and dispersion pattern of pollutants emitted from open-cast mining activities. This helped identify the most pollution-affected regions for vegetation sampling. Leaf sampling was conducted during November and December under clear atmospheric conditions. Sampling was carried out only when no rainfall had occurred for at least one week before collection to minimize the influence of precipitation on leaf surface characteristics and biochemical parameters. A random sampling method was adopted for leaf collection. Fully mature and healthy leaves were collected from all

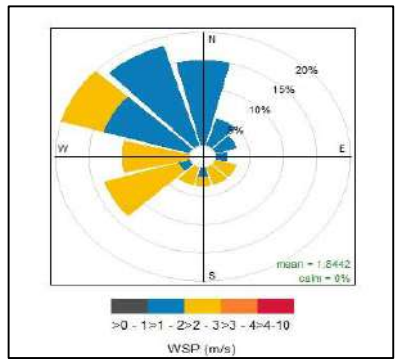


Fig. 2: Wind rose diagram of the study region.

Table 1: Average air quality of the Magadh region.

Sampling location	Buffer zone	Core zone	Limits as per NAAQS GSR 826 & 742(E)	Unit
Parameters				
SPM	588.9	601.4	600	µg m^{-3}
PM_{10}	99.2	104.2	100	µg m^{-3}
$PM_{2.5}$	59.1	63.7	60	µg m^{-3}

sides of each selected plant species to ensure uniform representation. From each direction, 15 leaves were collected and pooled to form a composite sample for laboratory analysis. Sampling was performed during the morning hours from 6:00–8:00 AM to minimize physiological disturbances caused by high temperature and solar radiation. All analyses were carried out in triplicate to ensure analytical reliability and reproducibility.

2.3. Experimental Analysis

2.3.1. Total Chlorophyll Content (TCH)

The TCH of leaves was determined using the method of Arnon (1949). The formula for determining TCH is given below:

$$\text{TCH}\left(\frac{mg}{g}\right) = \frac{(20.2*A645 \quad .02*A663)*V}{1000*W\,(g)} \qquad \ldots(1)$$

Where,

A_{645} and A_{663} are the absorbances at 645 nm and 663 nm, respectively; V and W are the total extract volume (mL) and leaf weight (g), respectively (Jain et al. 2019).

2.3.2. Ascorbic Acid (AA)

AA was determined by the volumetric method described by Sadasivam & Balasubramanian (1987). The formula for calculating AA is given below:

$$\text{A}\left(\frac{mg}{g}\right) = \frac{0.5(\text{mg})*V2\ (\text{mL})*10\ (\text{mL})}{V1\ (\text{mL})*5\ (\text{mL})*\text{weight of the sample (g)}} \qquad \ldots(2)$$

where V_1 and V_2 are the volumes of the dye titrated against the stock standard and the sample, respectively.

2.3.3. pH

The pH of leaves was determined using the method described by Singh et al. (1991).

2.3.4. Relative Water Content (RWC)

RWC was determined using the method described by Singh et al. (1991).

$$\text{RWC}\ (\%) = \frac{(\text{FW} \quad)\text{g}}{(\text{TW} \quad)\text{g}} * 100 \qquad \ldots(3)$$

2.3.5. Air Pollution Tolerance Index (APTI)

The APTI was estimated using the following formula (Singh et al. 1991). The classification of APTI scores is given in Table 2.

$$\text{APTI} = [\text{A} * (\text{T} + \text{P}) + \text{R}] \div 10 \qquad \ldots(4)$$

Where A represents ascorbic acid, T represents chlorophyll, P represents pH, and R represents water content.

<1: Very sensitive (VS), 1–14: Sensitive (S), 15–19: Intermediate tolerant (IT), 20–24: Moderately tolerant (MT), and >24: Tolerant (T) (Singh et al. 2025).

2.3.6. Anticipated Performance Index (API)

The API of the tree species was assessed using the method of Mondal et al. (2011). API is expressed as a percentage score and was calculated as follows:

$$\text{API}\ (\%) = \frac{(\text{Total positives})}{16} * 100 \qquad \ldots(5)$$

Plant species were graded for API determination based on APTI and other biological and socioeconomic characteristics, using Tables 2 and 3.

2.3.7. Dust Capturing Capacity (DCC)

Six leaves from each selected species were measured for leaf surface area and the amount of deposited dust. The DCC of

Table 2: API grading scale and assessment pattern (Mondal et al. 2011).

Grading	Characters	Assessment pattern	Grading scale
Tolerance	APTI	<9	+
		9–12	++
		12–15	+++
		15–18	++++
		18–21	+++++
		>21	++++++
Biological Characters	Plant height	Small (less than 9 ft)	-
		Medium (9–45 ft)	+
		Large (more than 45 ft)	++
	Canopy structure	Sparse/irregular/globular	-
		Spreading/crown/open/semi dense	+
		Spreading dense	++
	Plant type	Deciduous	-
		Evergreen	+
Laminar Structure	Leaf Size	Small	-
		Medium	+
		Large	++
	Texture	Smooth	-
		Rough	+
	Hardness	Delicate	-
		Hard	+
Economic value	Frequency	<3 uses	-
		3 or 4 uses	+
		5 or more uses	++

Table 3: Evaluation criteria for assigning anticipated performance index (API) values and categories of plants based on percentage score (Mondal et al. 2011).

Score (%)	API value	Category
≤30	0	Not recommended (NR)
31–40	1	Very poor (VP)
41–50	2	Poor (P)
51–60	3	Moderate (M)
61–70	4	Good (G)
71–80	5	Very good (VG)
81–90	6	Excellent (E)
91–100	7	Best (B)

each tree species was determined gravimetrically to evaluate species with high foliar dust deposition. Leaves carrying dust particles were weighed using a balance, and this weight was labeled W_1 for each species. Next, dust adhering to the leaf surface was meticulously removed by gently brushing the leaves with distilled water. The leaves were subsequently dried and reweighed, and this weight was recorded as W_2. Leaf area was measured using a graphical approach and recorded as A (Das & Prasad 2012).

Finally, dust-capturing capacity (mg cm^{-2}) for each species was calculated using the formula below:

$$W\left(\frac{mg}{cm^2}\right) = \frac{W1-W2}{A} \quad \ldots(6)$$

2.4. Statistical Analysis

Two-way analysis of variance (ANOVA) was performed to assess significant differences between sites and species. Pearson's correlation coefficient (PCC) was used to assess the relationships between parameters and the APTI scores of plant species. Differences were considered significant at $p < 0.05$.

3. RESULTS AND DISCUSSION

3.1. Total Chlorophyll Content (TCH)

Spatial variation in the TCH of local flora across the core, buffer, and transition zones acts as a crucial physiological indicator of changing atmospheric stress conditions induced by mining activities. Among the studied species, *Mangifera indica* exhibited the highest overall pigment concentration, showing relative stability with values of 1.78 mg g^{-1} in the core zone, 1.72 mg g^{-1} in the buffer zone, and 1.64 mg g^{-1} in the transition zone, as shown in Fig. 3 and Table 4. This suggests an adaptive mechanism by which the plant synthesizes compensatory chlorophyll to counteract the shading effect caused by heavy coal-dust deposition on the leaf surface. In contrast, *Urena lobata* showed a linear recovery trend, with the lowest TCH in the core zone (1.23 mg g^{-1}) and a significant increase in the transition zone (1.89 mg g^{-1}). This pigment degradation may result from pheophytinization, in which acidic pollutants such as sulfur oxides (mostly SO_2) displace the central magnesium ion from the chlorophyll molecule (Li et al. 2015). *Shorea robusta*, one of the dominant native climax species of the Jharkhand region, maintained relatively stable physiological characteristics across all study zones, with chlorophyll content values of 1.39, 1.39, and 1.43 mg g^{-1} in the core, buffer, and transition zones, respectively. This stability

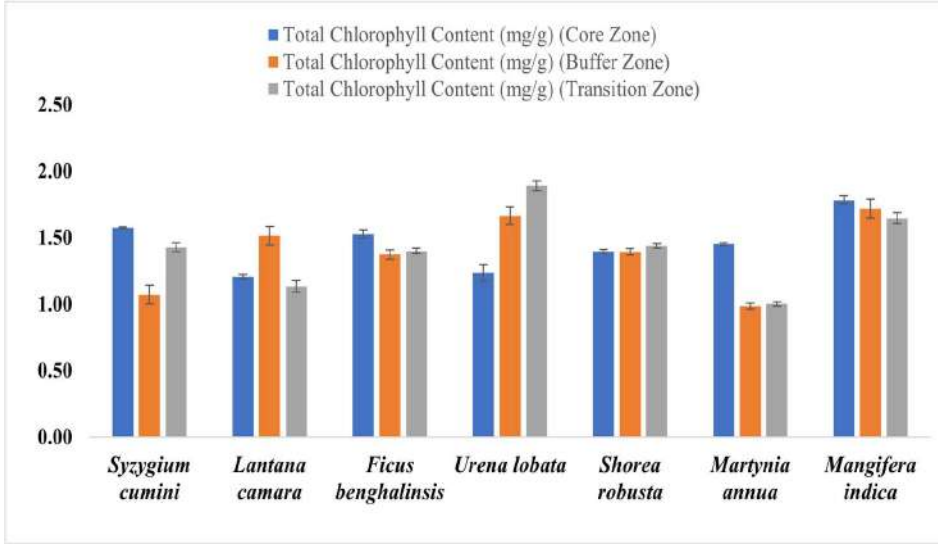


Fig. 3: Total chlorophyll content of leaf extracts of plant species in the core, buffer, and transition zones of the Magadh open-cast coal mining region.

Table 4: Total chlorophyll content of leaf extracts of plant species in the core, buffer, and transition zones of the Magadh open-cast coal mining region.

Plant species	Core	Buffer	Transition
Syzygium cumini	1.57±0	1.07±0.06	1.42±0.03
Lantana camara	1.2±0.01	1.51±0.07	1.13±0.04
Ficus benghalensis	1.52±0.03	1.37±0.03	1.4±0.02
Urena lobata	1.23±0.06	1.66±0.06	1.89±0.03
Shorea robusta	1.39±0.01	1.39±0.02	1.43±0.01
Martynia annua	1.45±0.01	0.98±0.02	1±0.01
Mangifera indica	1.78±0.03	1.72±0.07	1.64±0.04

may indicate comparatively higher tolerance to mining-associated environmental stress. Maintenance of chlorophyll content under high-dust conditions could be associated with physiological defense mechanisms that help minimize oxidative stress caused by reactive oxygen species (ROS), which have been reported to affect thylakoid membrane stability under polluted conditions (Rai 2016), although these mechanisms were not directly investigated in the present study. In *Syzygium cumini* and *Martynia annua*, fluctuations in total chlorophyll content from the core to buffer zones (1.57 to 1.07 mg g^{-1} and 1.45 to 0.98 mg g^{-1}, respectively) may reflect the influence of mining-associated particulate deposition on leaf physiological functioning. Previous studies have suggested that excessive accumulation of particulates on leaf surfaces can interfere with stomatal functioning, alter leaf temperature, and affect chlorophyll metabolism, including chlorophyllase activity (Lin et al. 2021). The alkaline nature of coal dust may also influence cellular pH balance, which could contribute to alterations in the photosynthetic apparatus under prolonged stress conditions (Chaturvedi et al. 2013). The two-way ANOVA showed significant variation in TCH among the observed plant species across the core, buffer, and transition zones at $p < 0.05$, as shown in Table 11.

3.2. Ascorbic Acid (AA)

The AA content of native flora across the Magadh coal mining region can serve as a biochemical indicator of scavenging capacity against mining-induced oxidative stress and heavy-metal-laden coal dust. *Syzygium cumini* showed the most variable physiological response, with the highest AA level in the core zone (12.61 mg g^{-1}), declining through the buffer zone (6.61 mg g^{-1}) to the transition zone (4.68 mg g^{-1}), as shown in Fig. 4 and Table 5. This may indicate an enhanced antioxidant defense response under highly polluted conditions, which previous studies have associated with upregulation of the ascorbate–glutathione cycle involved in mitigating oxidative cellular damage (Caverzan et al. 2016).

Similarly, *Mangifera indica* showed significant antioxidant mobilization by maintaining high values in the core zone (7.54 mg g^{-1}) and decreasing toward the buffer (6.17 mg g^{-1}) and transition zones (3.17 mg g^{-1}), further indicating its ability to maintain homeostasis under coal-induced pollution (Singh & Shukla 2025). *Martynia annua* showed a decrease in AA concentration from 4.62 mg g^{-1} in the core zone to 0.21 mg g^{-1} in the transition zone, while *Shorea robusta* demonstrated a stable and gradual decrease in AA content from 3.81 mg g^{-1} in the core zone to 2.33 mg g^{-1} in the transition zone. *Lantana camara* (0.54 mg

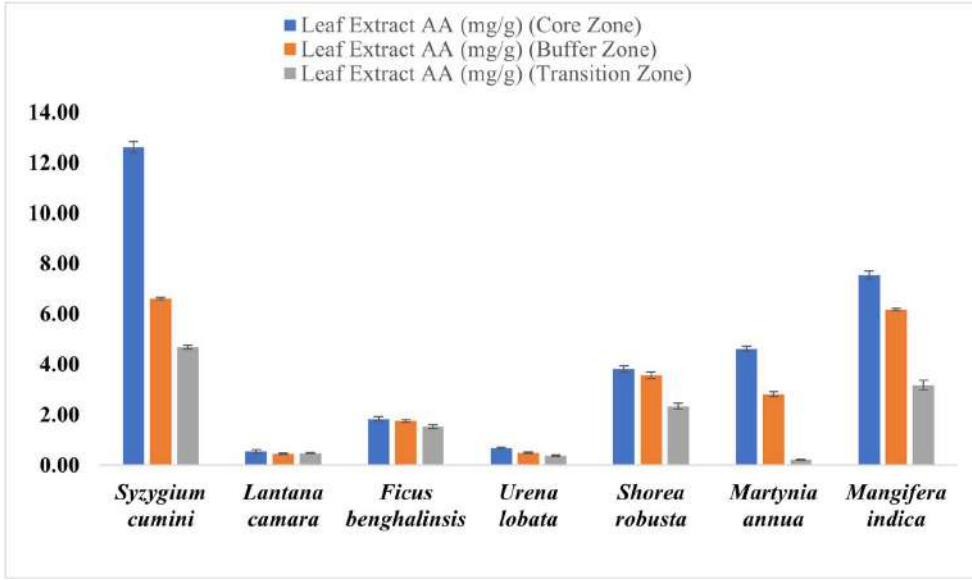


Fig. 4: Ascorbic acid content of leaf extracts of plant species in the core, buffer, and transition zones of the Magadh open-cast coal mining region.

Table 5: Ascorbic acid content of leaf extracts of plant species in the core, buffer, and transition zones of the Magadh open-cast coal mining region.

Plant species	Core	Buffer	Transition
Syzygium cumini	12.61±0.22	6.61±0.04	4.68±0.06
Lantana camara	0.54±0.05	0.45±0.02	0.47±0.02
Ficus benghalensis	1.83±0.09	1.75±0.05	1.53±0.07
Urena lobata	0.68±0.03	0.48±0.02	0.37±0.03
Shorea robusta	3.81±0.13	3.56±0.13	2.33±0.11
Martynia annua	4.62±0.09	2.81±0.09	0.21±0.03
Mangifera indica	7.54±0.15	6.17±0.05	3.17±0.18

Table 6: pH of leaf extracts of plant species in the core, buffer, and transition zones of the Magadh open-cast coal mining region.

Plant species	Core	Buffer	Transition
Syzygium cumini	4.81±0.05	5.08±0.59	5.9±0.02
Lantana camara	8.15±0.02	8.37±0.06	8.87±0.1
Ficus benghalensis	6.91±0.04	7.89±0.04	8.01±0.02
Urena lobata	6.84±0.04	7.62±0.07	8±0.11
Shorea robusta	6.03±0.2	6.66±0	6.76±0
Martynia annua	7.15±0.05	8.18±0.04	8.34±0.02
Mangifera indica	6.12±0.02	7.53±0.15	7.93±0.04

g^{-1} in the core zone to 0.47 mg g^{-1} in the transition zone) and *Urena lobata* (0.68 mg g^{-1} in the core zone to 0.37 mg g^{-1} in the transition zone) maintained consistently lower AA levels. The ANOVA results showed significant variation in leaf AA among the examined plants across different sites in the Magadh region at $p < 0.05$. The higher AA level in the core zone may represent a defensive adaptation by the plants. As AA is an electron donor, it may help stabilize the photosynthetic apparatus by maintaining the reduced state of Cu and Fe cations and may also protect against pheophytinization (Bačkor et al. 2023).

3.3. pH

Leaf-extract pH analysis across the core, buffer, and transition zones of the Magadh open-cast coal mining site indicates a spatial gradient of physiological stress, with a shift toward greater acidity in highly impacted zones. *Syzygium cumini* showed the most pronounced acidification in the core zone (4.81) relative to the buffer (5.08) and transition zones (5.90), as shown in Fig. 5 and Table 6. This variation is primarily driven by the absorption of gaseous pollutants (SO_2 and NO_x) (Anand et al. 2022), which react with water present in the cellular spaces of the leaf matrix to form acidic species such as sulfite and nitrite ions, thereby decreasing leaf pH (Kazi et al. 2021). In contrast, the invasive species *Lantana camara* had an alkaline pH across all zones, ranging from 8.15 in the core zone to 8.87 in the transition zone, indicating resistance to acidic pollutants. *Mangifera indica* and *Ficus benghalensis* both exhibited substantial variation between the core zone (6.12 and 6.91, respectively) and the transition zone (7.93 and 8.01, respectively). This indicates that these two species act as bioaccumulators, in which dissolution of coal dust and gaseous oxides directly lowers cytoplasmic pH; over time, this may impair stomatal conductance and may be linked to the enzymatic efficiency of the hexose-sugar-to-ascorbate conversion pathway (Mehmood et al. 2024, Qadir et al. 2019). *Shorea robusta* showed a moderate but consistent pH shift from 6.03 in the core zone to 6.76 in the transition zone, indicating its moderately tolerant status and capacity to maintain a near-neutral pH, which is an optimal condition for protecting the magnesium content of the chlorophyll molecule from pheophytinization (Mehmood et al. 2024). The ANOVA results showed significant variation in leaf-extract pH among the different sites at $p < 0.05$. The

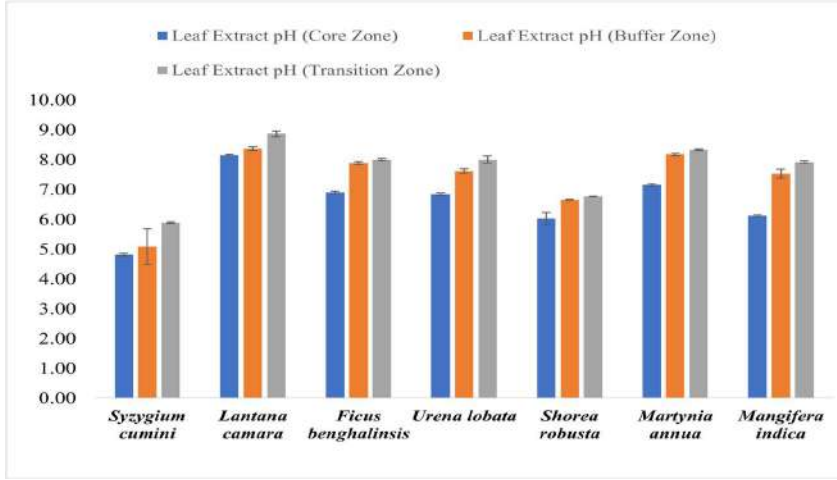


Fig. 5: pH of leaf extracts of plant species in the core, buffer, and transition zones of the Magadh open-cast coal mining region.

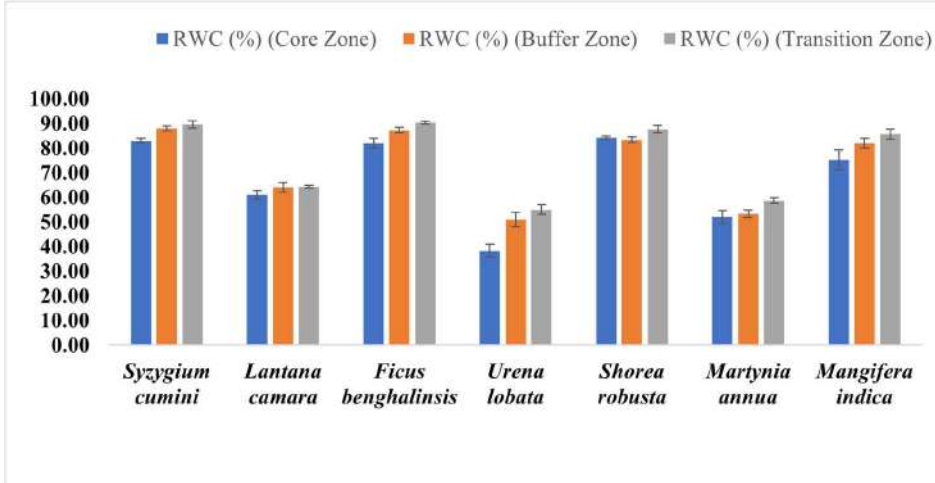


Fig. 6: Relative water content of leaves of plant species in the core, buffer, and transition zones of the Magadh open-cast coal mining region.

reduction in leaf pH in the core zone is an indicator of acid mine stress transmitted through the atmosphere, where the presence of acidic molecules reduces the efficiency of the antioxidant scavenging system of plant species, ultimately leading to degradation of the photosynthetic apparatus and lower primary productivity (Kumar et al. 2021, Mehmood et al. 2024, Najafi Zilaie et al. 2023, Zandi & Schnug 2022).

3.4. Relative Water Content (RWC)

The distribution of RWC across the study area reflects a distinct physiological hierarchy in the capacity of the flora to withstand mining-induced dehydration. The *Martynia annua* and *Urena lobata* exhibited significant hydric stress in the core and buffer zones, where RWC values were as low as 52.2 % and 38.33%, as shown in Fig. 6 and Table 7. This may result from the inhibitory effects of coal dust on stomatal conductance and subsequent disruption of transpiration. In contrast, the higher and more stable RWC maintained by *Shorea robusta* (84.33%) and *Ficus benghalensis* (82%) in the core zone highlights their osmotic stress-adjustment capabilities and membrane integrity, which allow these species to preserve cellular turgidity necessary for maintaining active metabolic processes such as the ascorbate–glutathione cycle under highly dust-contaminated conditions (Hasanuzzaman et al. 2022). The depression of RWC in highly impacted zones may be a consequence of increased protoplasmic permeability caused by gaseous pollutants such as SO_2, facilitating leakage of intracellular water from plant cells (Anand et al. 2022, Singh et al. 2023). The ANOVA results showed significant variation among the different sites at $p < 0.05$. The ability of certain species to maintain higher RWC despite heavy particulate loading serves as a primary determinant of their APTI, as higher water content provides a crucial buffer against acidification of leaf sap and thermal degradation of chlorophyll (Goswami et al. 2023, Singh et al. 2023).

Table 7: Relative water content of leaves of plant species in the core, buffer, and transition zones of the Magadh open-cast coal mining region.

Plant species	Core	Buffer	Transition
Syzygium cumini	83±1	88±1	89.66±1.52
Lantana camara	61±1.73	64±2	64.33±0.57
Ficus benghalensis	82±2	87.33±1.15	90.33±0.57
Urena lobata	38.33±2.51	51±3	55±2
Shorea robusta	84.33±0.57	83.33±1.15	87.66±1.52
Martynia annua	52±2.64	53.33±1.52	58.66±1.15
Mangifera indica	75.33±4.04	82±2	85.66±2.08

3.5. Air Pollution Tolerance Index (APTI)

The APTI across the core, buffer, and transition zones provides a comprehensive measure of the physiological adaptation of native flora to coal-mining-induced stress from particulate matter and gaseous pollutants. *Syzygium cumini* and *Mangifera indica* emerged as the two most tolerant species in the study area, as shown in Fig. 7 and Table 8. *S. cumini* exhibited a peak APTI of 16.35 in the high-stress core zone, driven by substantial biochemical mobilization of ascorbic acid to counteract the effects induced by ROS. *M. indica* maintained a strong index, from 13.50 in the core zone to 13.91 in the buffer zone, indicating a strong structural capacity to maintain cellular turgidity and chloroplast integrity despite heavy loading of mine-induced dust. *Shorea robusta* demonstrated remarkable stability, with intermediate APTI scores of 11.27, 11.20, and 10.68 in the core, buffer, and transition zones, respectively, indicating ecological resilience and the capacity to maintain physiological homeostasis across the study region. In contrast, *Urena*

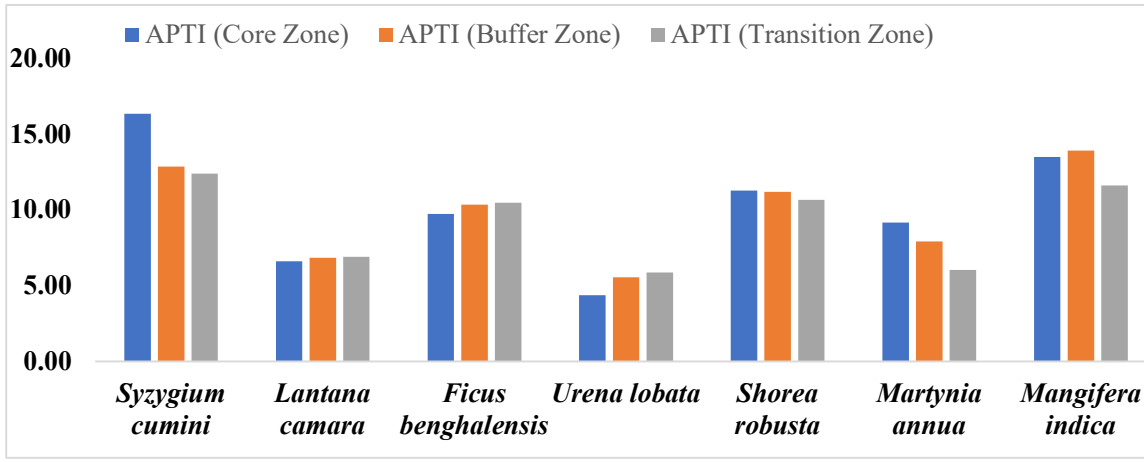


Fig. 7: APTI of plant species in the core, buffer, and transition zones of the Magadh open-cast coal mining region.

lobata and *Lantana camara* had the lowest APTI values. These lower APTI values support categorization of these species as sensitive bioindicators of air pollution resulting from mining activities. The APTI value of *U. lobata* (4.39 in the core zone) reflects a limited ability to buffer acidic pollutants such as sulfur or nitrogen oxides, which may lead to rapid pheophytinization and osmotic collapse (Timilsina et al. 2022). *Ficus benghalensis* had intermediate APTI values ranging from 9.74 to 10.48, indicating moderate sensitivity and gradual recovery in its physiological behavior away from the core zone. *Martynia annua* displayed a strong stress-responsive gradient, decreasing from 9.18 in the core zone to 6.06 in the transition zone. This is most likely due to a localized, acute increase in its antioxidant defense response that rapidly declines away from the immediate pollution source. The ANOVA results confirmed significant variation in APTI values among plants observed in different study zones at $p < 0.05$. These variations highlight that plant tolerance in this coalfield is strongly associated with the combined ability to optimize leaf-sap pH against acidic species, sustain high RWC to prevent thermal degradation of stomata, and mobilize ascorbic acid to protect the photosynthetic apparatus. Species with high APTI values are therefore valuable for pollution-sink strategies, whereas species with low APTI values are useful for active environmental biomonitoring (Mehmood et al. 2024, Singh & Shukla 2025).

Table 8: APTI of plant species in the core, buffer, and transition zones of the Magadh open-cast coal mining region.

Plant species	Core	Buffer	Transition
Syzygium cumini	16.35	12.87	12.40
Lantana camara	6.61	6.85	6.91
Ficus benghalensis	9.74	10.36	10.48
Urena lobata	4.39	5.55	5.87
Shorea robusta	11.27	11.20	10.68
Martynia annua	9.18	7.91	6.06
Mangifera indica	13.50	13.91	11.60

3.6. Anticipated Performance Index (API)

The API analysis of native flora provides a multidimensional evaluation of plant suitability for sustainable greenbelt development in the highly polluted peripheries of the Magadh coalfield by integrating APTI with morphological and socioeconomic attributes. Among the studied species, *Ficus benghalensis* consistently emerged as the most suitable species, securing a Good assessment category with the highest API score of 68.75% (Grade 4) across the core, buffer, and transition zones. Although its APTI value is moderate, its large canopy structure, large leaf size, and hardy texture provide superior physical resistance to pollution, allowing it to act as a highly efficient sink for intercepting and trapping coal particulates (PM_{10} and $PM_{2.5}$) carried by wind. *Syzygium cumini* also demonstrated high API performance, achieving a Good rating (62.5%) in the heavily polluted core zone but shifting to a Moderate classification (56.25%) in the buffer and transition zones. This variation reflects its stress-responsive biochemical profile, in which extreme atmospheric toxicity in the core zone triggers peak antioxidant synthesis, temporarily elevating its functional utility as a bioshield against pollutants. *Mangifera indica* maintained a stable Moderate categorization (56.25%, Grade 3) throughout all studied zones, serving as a reliable biological barrier because of its dense canopy structure, favorable tree habit, and high economic value, although its overall performance was slightly lower than that of *Ficus benghalensis*. *Shorea robusta* demonstrated relatively stable APTI values across the core, buffer, and transition zones, indicating its ability to maintain physiological and

biochemical homeostasis under mining-induced oxidative stress. However, despite this ecological resilience, the species was categorized as Poor under the API assessment (50%, Grade 2). This distinction arises because APTI primarily reflects physiological tolerance to air pollutants, whereas API also incorporates morphological and socioeconomic characteristics such as canopy architecture, leaf structure, plant habit, and foliage density that determine overall suitability for greenbelt development. Therefore, although *Shorea robusta* exhibits moderate pollution tolerance, its comparatively less dense canopy and structural attributes may limit its effectiveness in providing rapid and extensive pollutant interception in active mining areas. In the shrub category, *Lantana camara* (18.75%), *Urena lobata* (12.5%), and *Martynia annua* (6.25% in the buffer and transition zones) were classified as Not recommended (Grade 0). These shrubs or herbaceous plants inherently lack the spatial canopy volume, structural hardness, and socioeconomic utility required to modify microclimates. Their architectural limitations, combined with biochemical vulnerability to acidic pollutants and coal-dust deposition, make them unsuitable for phytoremediation strategies; however, these species may be effective as sensitive bioindicators of ecosystem degradation in such regions.

3.7. Dust Capturing Capacity (DCC)

The DCC showed a clear decline from the core zone to the transition zone, indicating atmospheric settling of PM generated by mining activities and vehicular movement. *Mangifera indica* and *Ficus benghalensis* acted as the most favorable physical sinks for suspended atmospheric pollutants, recording peak DCC values of 2.91 mg cm^{-2} and 2.50 mg cm^{-2}, respectively, in the heavily impacted core zone before declining to 0.45 mg cm^{-2} and 1.48 mg cm^{-2}, respectively, in the transition zone, as shown in Fig. 8 and Table 9. This high interception capacity is associated with their leaf surface areas, dense evergreen canopies, leathery epidermal textures, and complex epicuticular wax layers, which act as traps for wind-blown dust. Considering understory and pioneer ecological niches, *Lantana camara* (decreasing from 1.76 mg cm^{-2} in the core zone to 0.61 mg cm^{-2} in the transition zone) and *Urena lobata* (1.46 mg cm^{-2} to 0.58 mg cm^{-2}) demonstrated substantial particulate retention relative to their smaller leaf area index. This phenomenon is facilitated by high foliar surface roughness and dense proliferation of glandular trichomes or leaf hairs that physically trap wind-blown coal dust. *Shorea robusta* exhibited moderate dust-capturing efficiency, decreasing from 1.33 mg cm^{-2} to 0.67 mg cm^{-2} from the core to the transition zone, respectively, while *Syzygium cumini* decreased from 1.27 mg cm^{-2} to 0.73 mg cm^{-2} and the herbaceous *Martynia annua* decreased from 1.15 mg cm^{-2} to 0.74 mg cm^{-2} over the same gradient. These species recorded the lowest overall dust accumulation. This may reflect smoother leaf surfaces, leaf arrangements at orientations less favorable for dust retention, or canopy architectures that are less optimal for intercepting dust particles. The spatial variation in DCC across all species highlights the rapid

Table 9: DCC of leaf surfaces of plant species in the core, buffer, and transition zones of the Magadh open-cast coal mining region.

Plant species	Core	Buffer	Transition
Syzygium cumini	1.27±0.05	0.97±0.05	0.73±0.05
Lantana camara	1.76±0.12	0.7±0.02	0.61±0.03
Ficus benghalensis	2.5±0.12	1.56±0.07	1.48±0.08
Urena lobata	1.46±0.06	0.94±0.1	0.58±0.03
Shorea robusta	1.33±0.08	0.87±0.04	0.67±0.04
Martynia annua	1.15±0.08	1.03±0.05	0.74±0.04
Mangifera indica	2.91±0.13	1.22±0.04	0.45±0.06

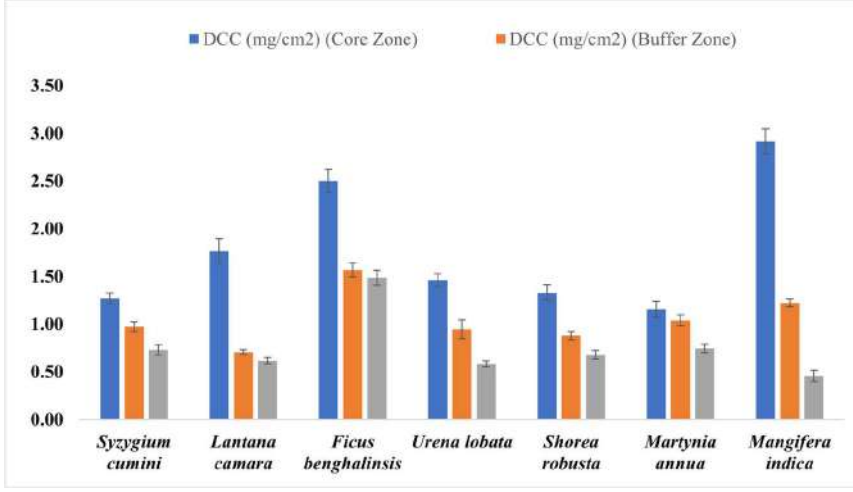


Fig. 8: DCC of leaf surfaces of plant species in the core, buffer, and transition zones of the Magadh open-cast coal mining region.

gravitational settling of heavier particulate fractions, such as PM_{10} and larger coal fragments, onto nearby vegetative barriers with high structural resistance, supporting the integration of efficient dust accumulators such as *M. indica* and *F. benghalensis* into the primary defensive tiers of sustainable greenbelt designs to reduce ambient toxicity.

3.8. Statistical Analysis

The Pearson correlation coefficient (PCC) matrix indicates that APTI is positively correlated with AA (r = 0.874) and RWC (r = 0.800), suggesting that APTI is strongly associated with AA and RWC, as shown in Table 10. As AA was elevated in plant leaves in highly polluted regions, APTI was also higher in such regions. RWC was also observed to be higher in such areas; therefore, it can be generalized that plants with higher RWC values tend to have greater APTI values in polluted regions. Conversely, leaf-extract pH showed negative correlations with both APTI (r = –0.678) and AA (r = –0.779), indicating that lower leaf pH, i.e., greater acidity, is closely related to elevated AA production and greater pollution tolerance. TCH exerted a weaker positive influence on APTI (r = 0.278), indicating that although TCH had a weaker correlation with APTI, it was positively associated with the index. Dust deposition showed a weak positive correlation with APTI (r = 0.215) and a weak negative correlation with leaf-extract pH (r = –0.251), suggesting that external dust accumulation may have only a limited association with the physiological responses of the studied plant species. Although statistically significant, these relatively low correlation coefficients indicate that dust load was not a major determinant of APTI variation in the present study.

4. CONCLUSIONS

The ecophysiological evaluation of native flora across the core, buffer, and transition zones of the Magadh open-

Table 10: Pearson correlation coefficients (PCCs) among biochemical and physiological parameters, dust load, and APTI.

Variable	pH	AA	RWC	TCH	APTI	DCC
pH	1					
AA	–0.779**	1				
RWC	–0.425**	0.437**	1			
TCH	–0.135	0.235	0.158	1		
APTI	–0.678**	0.874**	0.800**	0.278*	1	
DCC	–0.251*	0.230	0.085	0.168	0.215	1

*Significant at $p < 0.05$; ** significant at $p < 0.01$

Table 11: Two-way ANOVA of biochemical and physiological parameters, APTI, and DCC to assess significant differences among sites and species.

Parameter	Source	SS	df	MS	F	Sig.
APTI	Species	562.083	6	93.680	2121.982	<0.001
	Sites	10.936	2	5.468	123.857	<0.001
	Species × Sites	46.276	12	3.856	87.351	<0.001
AA	Species	412.752	6	68.792	7059.617	<0.001
	Sites	76.205	2	38.103	3910.186	<0.001
	Species × Sites	89.820	12	7.485	768.132	<0.001
RWC	Species	14726.540	6	2454.423	678.196	<0.001
	Sites	664.222	2	332.111	91.768	<0.001
	Species × Sites	259.556	12	21.630	5.977	<0.001
pH	Species	59.223	6	9.870	438.936	<0.001
	Sites	13.582	2	6.791	301.993	<0.001
	Species × Sites	2.236	12	.186	8.287	<0.001
TCH	Species	1.951	6	.325	194.556	<0.001
	Sites	.044	2	.022	13.189	<0.001
	Species × Sites	1.763	12	.147	87.903	<0.001
DCC	Species	6.793	6	1.132	207.171	<0.001
	Sites	11.483	2	5.741	1050.538	<0.001
	Species × Sites	4.916	12	.410	74.955	<0.001

cast mining region provides a data-driven framework for identifying suitable species for sustainable greenbelt development. By integrating biochemical attributes with APTI, API, and DCC, the study highlights the differential adaptive responses of plant species under mining-induced environmental stress conditions. Among the evaluated species, *Ficus benghalensis* emerged as the most structurally suitable species for greenbelt development, achieving the highest API score (68.75%; Good category) consistently across all zones, along with high dust interception capacity (DCC = 2.50 mg cm^{-2} in the core zone). *Mangifera indica* also demonstrated strong suitability because of its comparatively stable physiological characteristics, elevated ascorbic acid content, and the highest dust retention capacity (DCC = 2.91 mg cm^{-2} in the core zone), indicating its potential role as an effective biological barrier against particulate pollution. *Syzygium cumini* exhibited high biochemical responsiveness under polluted conditions, with elevated ascorbic acid content (12.61 mg g^{-1}) and the highest APTI value (16.35) in the core zone, suggesting comparatively greater physiological tolerance to mining-associated stress. In contrast, species such as *Lantana camara*, *Urena lobata*, and *Martynia annua* were categorized as Not recommended (Grade 0) because of their lower API scores and comparatively weaker structural and physiological suitability for greenbelt applications. Based on the combined assessment of APTI, API, and DCC, a mixed plantation strategy incorporating *Ficus benghalensis*, *Mangifera indica*, and *Syzygium cumini* may provide enhanced ecological benefits for greenbelt development in mining-affected landscapes through improved particulate interception and greater pollution-tolerance capacity. However, the findings of the present study should be interpreted in light of certain limitations. Direct monitoring of atmospheric pollutant accumulation was not conducted, seasonal observations were limited, and long-term field performance of the recommended species under continuous mining stress was not evaluated. Therefore, future studies integrating direct pollutant measurements, year-round monitoring, and long-term ecological performance assessments are necessary to further validate the suitability of these species for sustainable mine-site restoration and greenbelt planning.

5. ACKNOWLEDGMENTS

The authors gratefully acknowledge the Department of Environmental Sciences, Central University of Jharkhand, for providing the necessary research facilities and academic support to carry out this study. The authors also sincerely thank Central Coalfields Limited (CCL), Ranchi, for granting permission and facilitating the conduct of the study in the coal mining region.

6. REFERENCES

Anand, P., Mina, U., Khare, M., Kumar, P. and Kota, S.H., 2022. Air pollution and plant health response-current status and future directions. *Atmospheric Pollution Research*, 13(8), p. 101508. [DOI]

Antil, R., Kumari, N. and Singh, D., 2025. Comparative assessment of pollution indices of selected tree species in urban, industrial, institutional and agricultural setups at Sonipat, Haryana, India. *Nature Environment and Pollution Technology*, 24(4), B4303. [DOI]

Arnon, D.I., 1949. Copper enzymes in isolated chloroplasts. Polyphenoloxidase in *Beta vulgaris*. *Plant Physiology*, 24(1), pp. 1–15. [DOI]

Asif, Z. and Ma, W., 2024. Assessing the air pollution tolerance index of urban plantation: A case study conducted along high-traffic roadways. *Atmosphere*, 15(6), p. 659. [DOI]

Bačkor, M., Goga, M., Singh, P. and Tuptová, V., 2023. Mechanisms of copper toxicity and tolerance in the aquatic moss *Taxiphyllum barbieri*. *Plants*, 12(20), p. 3607. [DOI]

Bui, H.-T., Jeong, N.-R. and Park, B.-J., 2023. Seasonal variations of particulate matter capture and the air pollution tolerance index of five roadside plant species. *Atmosphere*, 14(1), p. 138. [DOI]

Bui, H.-T., Odsuren, U., Kwon, K.-J., Kim, S.-Y., Yang, J.-C., Jeong, N.-R. and Park, B.-J., 2021. Assessment of air pollution tolerance and particulate matter accumulation of 11 woody plant species. *Atmosphere*, 12(8), p. 1067. [DOI]

Caverzan, A., Casassola, A. and Patussi Brammer, S., 2016. Reactive oxygen species and antioxidant enzymes involved in plant tolerance to stress. In Shanker, A.K. and Shanker, C. (eds.), *Abiotic and Biotic Stress in Plants: Recent Advances and Future Perspectives*. InTech. [DOI]

Chaturvedi, R.K., Prasad, S., Rana, S., Obaidullah, S.M., Pandey, V. and Singh, H., 2013. Effect of dust load on the leaf attributes of the tree species growing along the roadside. *Environmental Monitoring and Assessment*, 185(1), pp. 383–391. [DOI]

Chauhan, A., Pandey, G., Singh, M.V., Sethi, M., Gururani, P., Awasthi, A., Chaube, S. and Lodh, A., 2025. Assessment of elevated road traffic pollution on roadside trees and vegetation in urban environments. *Frontiers in Environmental Science*, 13, p. 1657859. [DOI]

Chauhan, S., Bhargava, B., Kandpal, K.C. and Kumar, A., 2022. Analyzing preferred indoor ornamental potted plants for their air pollution tolerance ability. *Polish Journal of Environmental Studies*, 31(3), pp. 2019–2027. [DOI]

Das, S. and Prasad, P., 2012. Particulate matter capturing ability of some plant species: Implication for phytoremediation of particulate pollution around Rourkela Steel Plant, Rourkela, India. *Nature Environment and Pollution Technology*, 11(4), pp. 657–665.

Ghosh, P., Saha, S., Das, T. and Ghoshal, A., 2025. Assessment of air pollution tolerance and heavy metal bioaccumulation in plants from areas surrounding Raniganj, India: Implications for environmental monitoring. *Environmental Monitoring and Assessment*, 197(10), p. 1130. [DOI]

Goswami, M., Kumar, V., Singh, N. and Kumar, P., 2023. A biochemical and morphological study with multiple linear regression modeling–based impact prediction of ambient air pollutants on some native tree species of Haldwani City of Kumaun Himalaya, Uttarakhand, India. *Environmental Science and Pollution Research*, 30(30), pp. 74900–74915. [DOI]

Hasanuzzaman, M., Raihan, Md. R.H., Nowroz, F. and Fujita, M., 2022. Insight into the mechanism of salt-induced oxidative stress tolerance in soybean by the application of *Bacillus subtilis*: Coordinated actions of osmoregulation, ion homeostasis, antioxidant defense, and methylglyoxal detoxification. *Antioxidants*, 11(10), p. 1856. [DOI]

Jain, S., Bhattacharya, T. and Chakraborty, S., 2019. Comparison of plant tolerance towards air pollution of rural, urban and mine sites of Jharkhand: A biochemical approach to identify air pollutant sink. In

Kalamdhad, A.S., Singh, J. and Dhamodharan, K. (eds.), *Advances in Waste Management*, pp. 123–142. Springer Singapore. [DOI]

Kaur, L., 2021. Preliminary studies on air pollution tolerance index (APTI) of selected plant species in Bikaner City. *Environment & Ecosystem Science (EES)*, 5(2), pp. 117–120. [DOI]

Kazi, E., Shaikh, Y.I., Tikle, S., Beig, G., Shaikh, V.S., Kulkarni, S. and Dhulap, V.P., 2021. Effect of air pollutants on urban roadside trees in Shivajinagar & Pashan area, Pune City. *ES Food and Agroforestry*, 5, pp. 29–37. [DOI]

Kumar, M., Pratap, V., Nigam, A.K., Sinha, B.K., Singh, M.K. and Gour, J.K., 2021. Plants as a source of potential antioxidants and their effective nanoformulations. *Journal of Scientific Research*, 65(03), pp. 57–72. [DOI]

Li, X., Cen, H., Peng, L., Li, Y., Sun, L., Cai, S. and Huang, Z., 2015. Tolerance performance of the cool-season turfgrass species *Festuca ovina*, *Lolium perenne*, *Agrostis tenuis*, and *Poa trivialis* to sulfur dioxide stress. *Journal of Plant Interactions*, 10(1), pp. 75–86. [DOI]

Lin, W., Yu, X., Xu, D., Sun, T. and Sun, Y., 2021. Effect of dust deposition on chlorophyll concentration estimation in urban plants from reflectance and vegetation indexes. *Remote Sensing*, 13(18), p. 3570. [DOI]

Mehmood, Z., Hasnain, A., Luqman, M., Muhammad, S., Dhital, N.B., John, A., Iqbal, M., Ejaz, A., Tufail, M., Harma and Yang, H.H., 2023. Assessment of air pollution tolerance and physicochemical alterations of Alstonia scholaris (L.) R. Br. along roadsides of Lahore, Pakistan. *Aerosol and Air Quality Research*, 23(7), p. 230038. [DOI]

Mehmood, Z., Yang, H.-H., Awan, M., Ahmed, U., Hasnain, A., Luqman, M., Muhammad, S., Sardar, A., Chan, T.-Y. and Sharjeel, A., 2024. Effects of air pollution on morphological, biochemical, DNA, and tolerance ability of roadside plant species. *Sustainability*, 16(8), p. 3427. [DOI]

Mondal, D., Gupta, S. and Datta, J.K., 2011. Anticipated performance index of some tree species considered for green belt development in an urban area. *International Research Journal of Plant Science*, 2(4), pp. 099–106.

Najafi Zilaie, M., Mosleh Arani, A. and Etesami, H., 2023. The importance of plant growth-promoting rhizobacteria to increase air pollution tolerance index (APTI) in the plants of green belt to control dust hazards. *Frontiers in Plant Science*, 14, p. 1098368. [DOI]

Natividad, A.M., Sandueta, R.C. and Mora-Garcia, C., 2024. Air pollution tolerance index of selected tree species in urbanized areas of Butuan City, Philippines. *Annals of Tropical Research*, 46(1), pp. 62–76. [DOI]

Paul, A., Chatterjee, S., Malaka, C. and Saha, H., 2023. Role of plants for evaluation of air pollution tolerance index on the basis of some biochemical parameters: A concise review. *Ecology, Environment and Conservation*, 29, pp. 27–30. [DOI]

Qadir, S.U., Raja, V., Siddiqui, W.A., Mahmooduzzafar, Abd_Allah, E.F., Hashem, A., Alam, P. and Ahmad, P., 2019. Fly-ash pollution modulates growth, biochemical attributes, antioxidant activity and gene expression in *Pithecellobium dulce* (Roxb) Benth. *Plants*, 8(12), p. 528. [DOI]

Rai, P.K., 2016. Impacts of particulate matter pollution on plants: Implications for environmental biomonitoring. *Ecotoxicology and Environmental Safety*, 129, pp. 120–136. [DOI]

Sadasivam, S. and Balasubramanian, T., 1987. *Practical Manual in Biochemistry, Tamil Nadu Agricultural University*. Coimbatore: Tamil Nadu Agricultural University (TNAU).

Sawarkar, R., Shakeel, A., Kumar, T., Ansari, S.A., Agashe, A. and Singh, L., 2023. Evaluation of plant species for air pollution tolerance and phytoremediation potential in proximity to a coal thermal power station: Implications for smart green cities. *Environmental Geochemistry and Health*, 45(10), pp. 7303–7322. [DOI]

Singh, A.K., Behera, S., Choudhary, J.K. and Shukla, S.K., 2025. Evaluating the role of tree flora in air pollution mitigation and heavy metals accumulation near brick kilns. *Atmospheric Pollution Research*, 16(4), p. 102436. [DOI]

Singh, A.K. and Shukla, S.K., 2025. Assessing air pollution tolerance, photosynthetic pigmentation, and dust capturing capacity of roadside trees in the mining region. *Journal of Sustainable Forestry*, 44(7), pp. 572–598. [DOI]

Singh, H., Singh, P., Agrawal, S.B. and Agrawal, M., 2023. Assessment of the reverberations caused by predominant air pollutants on urban vegetation: A multi-site study in Varanasi located in Indo-Gangetic Plains. *Gases*, 3(2), pp. 57–76. [DOI]

Singh, S.K., Rao, D.N., Agrawal, M., Pandey, J. and Naryan, D., 1991. Air pollution tolerance index of plants. *Journal of Environmental Management*, 32(1), pp. 45–55. [DOI]

Timilsina, S., Shakya, S., Chaudhary, S., Thapa Magar, G. and Narayan Munankarmi, N., 2022. Evaluation of air pollution tolerance index (APTI) of plants growing alongside inner ring road of Kathmandu, Nepal. *International Journal of Environmental Studies*, 79(4), pp. 698–713. [DOI]

Zandi, P. and Schnug, E., 2022. Reactive oxygen species, antioxidant responses and implications from a microbial modulation perspective. *Biology*, 11(2), p. 155. [DOI]

Nature Environment and Pollution Technology
An International Quarterly Peer-Reviewed Open Access Journal

p-ISSN: 0972-6268 | e-ISSN: 2395-3454 Vol. 25 | No. 4 | Article ID D1931 | 2026

RESEARCH ARTICLE https://doi.org/10.46488/NEPT.2026.v25i04.D1931 OPEN ACCESS

Macroinvertebrate-Based Ecological Health Assessment of Main River and Canal Systems in the Mekong Delta: Challenges and Future Directions

Anh Duc Pham[1]†, My Thanh Dang[1], Duc Canh Vu[1], Thanh Luu Pham[1] and Thanh Son Dao[2,3]
[1]Faculty of Environment and Labour Safety, Ton Duc Thang University, 19 Nguyen Huu Tho Street, Tan Hung Ward, Ho Chi Minh City, Vietnam
[2]Faculty of Environment and Natural Resources, Ho Chi Minh City University of Technology (HCMUT), 268 Ly Thuong Kiet Street, Dien Hong Ward, Ho Chi Minh City, Vietnam
[3]CARE, Ho Chi Minh City University of Technology (HCMUT), Vietnam National University Ho Chi Minh City, 268 Ly Thuong Kiet Street, Dien Hong Ward, Ho Chi Minh City, Vietnam
†Corresponding author: Anh Duc Pham; phamanhduc@tdtu.edu.vn

ARTICLE HISTORY

Received: 15-04-2026
Revised: 01-06-2026
Accepted: 06-06-2026

KEYWORDS

Macroinvertebrates
Ecological health assessment
River-canal systems
Mekong delta
Bioassessment methods

CITE THIS ARTICLE

Pham, A.D., Dang, M.T., Vu, D.C., Pham, T.L. and Dao, T.S., 2026. Macroinvertebrate-based ecological health assessment of Main River and canal systems in the Mekong Delta: Challenges and future directions, *Nature Environment and Pollution Technology*, 25(4), D1931. https://doi.org/10.46488/NEPT.2026.v25i04.D1931

COPYRIGHT & LICENCE

© 2026 The Authors
Open Access under CC BY 4.0.

PUBLISHED BY
TECHNOSCIENCE PUBLICATIONS

ABSTRACT

Macroinvertebrate-based ecological health assessment (EHA) complements physicochemical monitoring in tropical deltas by integrating cumulative ecological responses to interacting stressors. The Mekong Delta is characterized by monsoonal discharge, tidal mixing, fine-sediment dominance, salinity gradients, and an approximately 100,000 km heavily modified canal network that poses significant bioassessment challenges unaddressed by generic, temperate-river frameworks. This review synthesizes approximately 83 peer-reviewed and gray literature sources (1991–2026) to evaluate the application of macroinvertebrate-based EHA, contrasting evidence from main rivers and artificial canal systems. We identify a fundamental ecological dichotomy: main river assemblages exhibit strong monsoon–tide seasonal turnover, whereas canal networks reflect chronic degradation marked by biotic homogenization and a dominance of pollution-tolerant taxa. However, regional frameworks are constrained by critical systemic biases: a geographic blind spot (<30% of studies focus on canals), an 80% dry-season bias neglecting the Flood Pulse Concept, and operational deficits arising from family-level identification, fragmented keys, and a lack of standardized quality control (QC). Consequently, uncalibrated temperate indices fail to account for tropical dynamics, masking canal degradation and episodic geochemical thresholds such as acid sulfate soils liberating toxic aluminum ions (Al^{3+}) at pH < 4.5, which traditional metrics (BMWP-VIET) and national standards (QCVN 08-MT:2023) fail to capture. Conversely, locally calibrated multimetric indices (MMIs) demonstrate high diagnostic specificity despite the confounding effects of chronic siltation and organic enrichment. To bridge the science–policy gap, future frameworks must adopt a strategic roadmap prioritizing typology-based monitoring that explicitly separates rivers from canals, alongside functional trait-based analyses to decouple natural estuarine variability from anthropogenic stress. Finally, high-throughput DNA metabarcoding must be integrated into automated geographic information system (GIS) platforms within the Mekong River Commission (MRC) and national networks for unified, transboundary water resource management.

1. INTRODUCTION

The ecological health of river–canal systems is central to environmental sustainability, water security, and human well-being in low-lying deltas. Globally, river deltas are highly productive yet exceptionally vulnerable landscapes that support dense populations, intensive agriculture and aquaculture, and complex socio-ecological interactions (Syvitski et al. 2009, Best 2019, Hua et al. 2024). Increasingly, deltas

are shaped by coupled human–river dynamics that accelerate subsidence, drive sediment deficits, degrade habitats, and simplify ecological structure. Ecological health assessment (EHA) provides a critical framework for evaluating ecosystem condition and informing adaptive water and land management under compounding pressures from hydrological modification, water contamination, urbanization, and climate change (Norris & Thoms 1999, Yu et al. 2013, Anthony et al. 2015). However, translating EHA into effective management remains challenging in highly engineered tropical deltas.

Similar patterns of channel modification, sediment alteration, and water quality degradation characterize the Mekong Delta. This is particularly evident in extensive artificial canal networks, which have been heavily engineered to support intensive agricultural and urban development (Kondolf et al. 2014, Nguyen & Le 2014, Doan et al. 2025). These deltaic river–canal systems function as integrated networks that regulate flow, transport sediment, cycle nutrients, and maintain habitat connectivity. However, they remain highly sensitive to disturbances, including flow regulation, salinity intrusion, pollution, and land-use change (Nguyen et al. 2011, Best 2019, Eslami et al. 2021, Cruz et al. 2026). Recent assessments report frequent exceedances of water quality standards in smaller canals linked to wastewater inputs, aquaculture effluents, and agrochemical use, whereas main rivers generally maintain better conditions, albeit with increasing signs of decline (Tran et al. 2016, Wehrheim et al. 2023, Mekong River Commission [MRC] 2024). This contrast underscores the need for assessment frameworks that distinguish clearly between river and canal systems.

To evaluate these conditions, EHA approaches increasingly integrate physicochemical monitoring with macroinvertebrate-based biological indicators. While physicochemical indicators often miss sudden pollution events, benthic macroinvertebrates integrate cumulative ecological responses to multiple stressors over time (Rosenberg & Resh 1993, Hering et al. 2018, Friberg et al. 2011, Buss et al. 2015). Due to their limited mobility and diverse functional roles, shifts in their community composition and traits (e.g., feeding guilds) effectively reflect impacts from water quality, habitat structure, and hydrological regimes (Statzner et al. 2001, Bonada et al. 2006, Bendary et al. 2023, Chen et al. 2025). However, EHA implementation in the Mekong Delta is constrained by a key ecological dichotomy: river assemblages are driven by monsoonal–tidal dynamics, whereas canal systems show chronic degradation, biotic homogenization, and dominance of pollution-tolerant taxa (Chessman et al. 2007, Pham 2014). This dichotomy complicates the transferability of standard bioassessment approaches.

Beyond these ecological differences, the application of EHA in the Mekong is hindered by technical and regulatory hurdles (Bonada et al. 2006, Birk et al. 2012, Pham 2014). Most current frameworks are calibrated for temperate upland rivers and fail to account for the semi-lentic flow and acid sulfate soils characteristic of tropical canals (Morse et al. 2007, Dudgeon 2010, Birk et al. 2012, Dang et al. 2018). Consequently, relying on uncalibrated indices like the Biological Monitoring Working Party (BMWP) or Average Score Per Taxon (ASPT) often results in misinterpretation of ecological status. In the Mekong Delta, canal ecosystems, characterized by semi-lentic flow, fine-sediment accumulation, recurrent maintenance dredging, acid sulfate soils, and salinity intrusion, render traditional indices ineffective (Pham et al. 2014, Mureithi et al. 2025). Research consistently shows that agricultural and urban canals undergo taxonomic shifts, becoming dominated by pollution-tolerant taxa such as oligochaetes and chironomids (Ngo et al. 2013a, Vo et al. 2019, Le et al. 2023a). In contrast, main rivers and floodplain wetlands support higher richness and functional diversity where hydrological connectivity is maintained (Pham 2014, Ly et al. 2025). Without indices incorporating local taxonomic traits and addressing limitations such as dry-season sampling bias and reliance on higher-taxon identification, EHA assessments remain inaccurate (Birk et al. 2012, Pham et al. 2014). This review examines multidecadal trends to align bioassessment tools with the ecological realities of river–canal systems for sustainable water management (MRC 2024, Doan et al. 2025).

This review synthesizes macroinvertebrate-based EHA in the Mekong Delta, focusing on contrasts between main rivers and canal systems. Specifically, it aims to: (i) examine methodological approaches used in macroinvertebrate-based EHA; (ii) identify key ecological patterns and stressors shaping communities in rivers versus canals; and (iii) highlight challenges related to sampling design, index development, and interpretation in heavily modified deltaic environments. The review supports the development of locally calibrated, typology-sensitive bioassessment frameworks for sustainable environmental management. To operationalize this objective, a tiered framework is proposed (Fig. 1) that distinguishes main river channels from artificial canal networks and integrates system typology, hydrological regime, and dominant stressors to guide sampling design, taxonomic resolution, and analytical approach.

2. MATERIALS AND METHODS

2.1. Study System and Regional Context

The Mekong Delta is a low-lying coastal system in southern Vietnam formed by the downstream reaches of the Mekong River. It comprises a heterogeneous network of main river

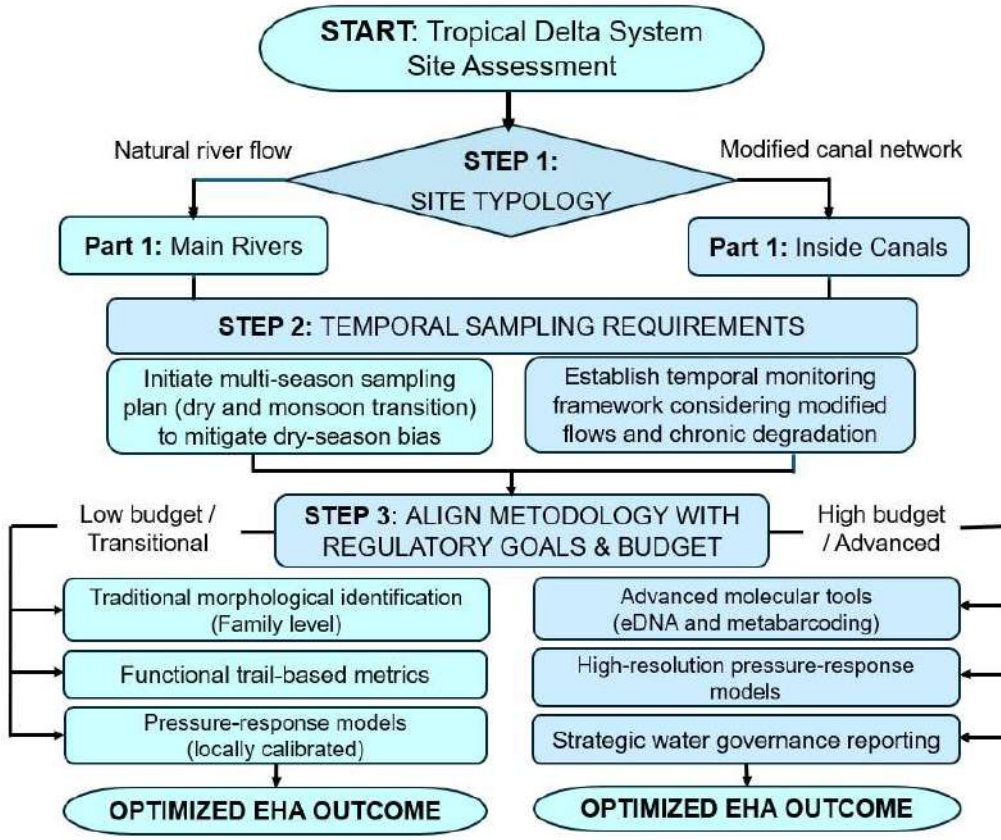


Fig. 1: Strategic decision-tree for selecting bioassessment protocols in tropical delta systems.

channels, regulated canals, seasonally inundated floodplains, and estuarine zones, generating spatial gradients in hydrology and water quality (Dang et al. 2018, Nguyen et al. 2020). Main channels are characterized by high seasonal discharge variability, active sediment transport, and tidal influence, whereas canal systems exhibit low flow velocities, fine sediment accumulation, and frequent dredging (Allan 2004). These conditions, combined with anthropogenic pressures from agriculture, aquaculture, and urbanization, create variable physicochemical environments that structure aquatic communities and influence the performance of biomonitoring indicators (Smith et al. 1999, Dodds & Smith 2016, Gugliotta et al. 2017).

The Mekong Delta's aquatic network connects main river channels and artificial canals across socio-economic gradients, highlighting the environmental gradients that distinguish riverine from canal ecosystems. Intensive rice production dominates the upper floodplain provinces of An Giang and Dong Thap (Kontgis et al. 2015), while Tien Giang and Ben Tre support perennial horticulture (Le et al. 2017). The Ca Mau Peninsula is characterized by brackish and saline aquaculture, reflecting salinity gradients driven by shrimp farming (Bosma et al. 2014). Urban–industrial development is concentrated in Long An, a key corridor linked to Ho Chi Minh City, and in Can Tho and Kien Giang (Dang et al. 2018). The Tien and Hau rivers, along with an extensive canal network, provide hydrological connectivity for irrigation, transport, and regional trade, while mediating the distribution of pollutants and ecological stressors (Kuenzer & Renaud 2012, Gugliotta et al. 2018).

2.2. Literature Search and Selection Strategy

This review's methodological framework was guided by the Preferred Reporting Items for Systematic Reviews and Meta-Analyses (PRISMA) guidelines (Page et al. 2021). Following systematic review principles, a comprehensive search was conducted across Web of Science, Scopus, and Google Scholar to identify peer-reviewed and gray literature (1991–2026). This was complemented by regional journals and governmental reports (e.g., MRC) to capture locally relevant data. The specific Boolean logic employed was: ((“macroinvertebrate” OR “zoobenthos” OR “aquatic insect”) AND (“ecological health” OR “biomonitoring” OR “bioassessment” OR “index of biotic integrity” OR “DNA

metabarcoding") AND ("Mekong Delta" OR "Vietnam") AND ("main river" OR "canal")). The search was designed to capture both conventional and emerging bioassessment approaches. Foundational and recent methodological studies were prioritized (Rosenberg & Resh 1993, Bonada et al. 2006, MRC 2008, MRC 2010, Birk et al. 2012, Buss et al. 2015), alongside regional datasets (e.g., MRC reports or research in Vam Co River) and lowland river–canal case studies from southern Vietnam (Pham et al. 2026).

2.3. Screening and Eligibility Criteria

Publications were screened using a stepwise process involving title and abstract screening, followed by full-text assessment. To minimize selection bias and ensure the reproducibility of the screening process, two independent reviewers performed the screening; any discrepancies regarding study inclusion were resolved through discussion until consensus was reached. Inclusion criteria: (i) use of macroinvertebrates as EHA indicators; (ii) study location within the Mekong Delta's aquatic network; and (iii) provision of sufficient methodological or ecological data. Exclusion criteria targeted laboratory-based toxicity studies, non-aquatic investigations, and reports lacking methodological detail. During screening, study attributes, including system type (river vs. canal), sampling seasonality (dry vs. wet season), taxonomic resolution, and metric selection were extracted to evaluate methodological biases and cross-system comparability.

2.4. Data Synthesis and Gap Analysis

Extracted data were synthesized qualitatively using a comparative framework that contrasts the hydrological and anthropogenic regimes of rivers versus canals. Studies were evaluated for their ability to detect consistent biological responses to dominant regional stressors, such as organic enrichment, pesticide runoff, and salinity intrusion (Wehrheim et al. 2023, Le et al. 2023b, Pham et al. 2025). A key component was a performance audit of common indices, assessing the use and reliability of uncalibrated temperate metrics (e.g., BMWP, ASPT) under Mekong Delta tropical conditions (Duong et al. 2011). This evaluation informs the optimization of bioassessment frameworks. To identify critical research gaps, the literature corpus was analyzed for geographic bias, methodological constraints (e.g., single-season sampling, coarse taxonomic identification), and the application of modern bioassessment tools.

2.5. Strengths and Limitations of the Review

This review's primary strength is its comparative framework, which distinguishes between the ecological health of main rivers and artificial canals, a distinction overlooked in deltaic studies. The integration of global and regional sources enhances contextual relevance. Conversely, three limitations persist: (1) spatial bias, with research clustered in accessible river reaches rather than remote canal networks; (2) taxonomic heterogeneity (family vs. species level), which precludes a formal meta-analysis and necessitates a qualitative synthesis; and (3) reliance on long-term datasets, hindering the decoupling of anthropogenic stressors from natural climatic variability. These limitations inform priority areas for future methodological development.

3. RESULTS AND DISCUSSION

3.1. Literature Search Results and Methodological Biases

The final literature corpus comprised 83 publications, with a notable increase in research output after 2005. This reflects a paradigm shift from instantaneous physicochemical monitoring toward integrative biological approaches (MRC 2010, Pham 2014, MONRE 2015), recognizing that biological assemblages, particularly macroinvertebrates, act as "living recorders" of cumulative environmental stress (Karr 1991, Buss et al. 2015). However, this "record" contains a significant geographical blind spot. While 70% of studies focused on the main distributary channels (Tien and Hau rivers), the approximately 100,000 km artificial canal network, a primary conduit for agricultural runoff, is underrepresented (<30% of studies). This geographic bias suggests that ecological degradation in canals, where anthropogenic pressures are acute, is underestimated in regional reporting.

Methodologically, studies predominantly rely on quantitative grab sampling in soft sediments. Combined with family-level identification, this limits scalability and timely application in management contexts (Table 1), which synthesizes approaches reported across the reviewed literature rather than repeating methodological details.

Fig. 2 presents the conceptual stressor–response framework for macroinvertebrate-based EHA in the Mekong Delta. The model links primary regional stressors (Stage 1) to localized habitat alterations (Stage 2) and cascading biological responses (Stage 3), including shifts in taxonomic composition, reduced diversity, and functional reorganization, providing the basis for selecting diagnostic metrics and computing ecosystem health scores (Stage 4). Sections 3.2–3.6 further explore how these stages operate within the Delta's semi-lentic, seasonally pulsed systems.

3.2. Ecological Divergence: Rivers vs. Canals

Reported macroinvertebrate diversity in the Mekong Delta shows pronounced spatial and temporal variability driven

Table 1: Key macroinvertebrate sampling approaches reported for river and canal systems in the Mekong Delta.

Sampling method	Target habitat	Sample equipment	Typical application	Key references
Littoral sweep/kick	Shallow margins	D-frame net (450–500 µm)	Rapid bioassessment; multi-habitat rivers	MRC 2010, Ngo et al. 2013a, Pham 2014
Hand-net	Confined waters	Standard net (450–500 µm)	Aquatic insects in small ponds/ canals	Bonada et al. 2006, Pham 2014
Petersen grab	Benthic substrates	Grab (0.025 m²)	Quantitative riverine sampling	MRC 2010, Vo et al. 2019, Pham et al. 2026
Ekman grab	Fine sediments	Ekman grab (0.025 m²)	Deeper, low-energy environments	Ngo et al. 2013b, Ngo & Ngo 2014
Multi-habitat	Mixed habitat	Nets and grabs	Holistic assessment; heterogeneous sites	Pham 2014, Mamun et al. 2022, Pham et al. 2026

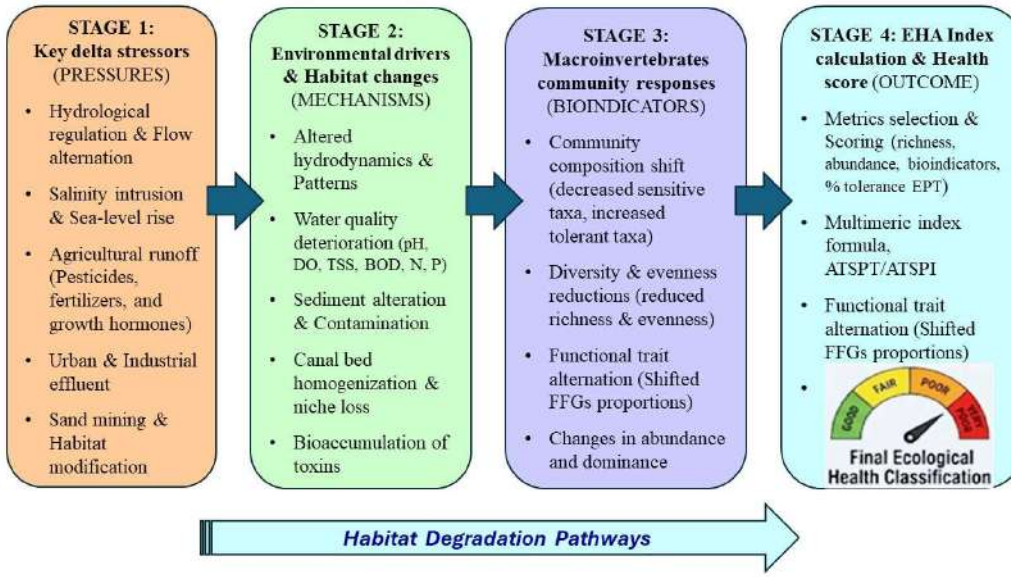


Fig. 2: Conceptual stressor-response framework for macroinvertebrate-based EHA in the Mekong Delta.

by habitat heterogeneity, hydrology, and methodological differences. The MRC (2008) reported the highest richness, documenting 361 littoral and 177 benthic taxa, while Sor et al. (2017) recorded 299 benthic taxa in the Lower Mekong Basin. Mollusks consistently dominate assemblages, accounting for approximately 44–45% of taxa across habitats, including estuarine–coastal transitional waters (Ngo et al. 2013b, Ngo & Ngo 2014, Pham 2019, Nguyen et al. 2020, Pham et al. 2025). Abundance and density vary widely across sites and seasons, reflecting strong hydrological control. Densities range from 1–1,251 individuals m^{-2} in littoral habitats and 202–7,340 individuals m^{-2} in benthic habitats (Duong et al. 2008, Le et al. 2011, Ngo et al. 2013b, Ngo & Ngo 2014). Benthic densities are lower in tributaries influenced by acid sulfate soils, particularly during early rainy-season discharge from rice fields (Pham 2019, Pham et al. 2025).

Analyses of diversity indices provide further quantitative evidence of ecological heterogeneity. Shannon–Wiener diversity ranged from <0.5 at heavily disturbed sites to >3.0 in structurally complex habitats, while dominance indices often indicated numerical dominance by tolerant taxa (MRC 2008, MRC 2009, Pham 2014, Pham 2019). Tolerancebased metrics such as ATSPT (Average Tolerance Score per Taxon; 23–63) and ATSPI (Average Tolerance Score per Individual; 30–60) showed broad ranges and sensitivity to disturbance gradients, supporting their utility when calibrated to regional conditions (MRC 2008, MRC 2009, Pham 2014, Pham et al. 2025).

Consequently, the delta's biotic integrity defies a singular ecological profile. Main river channels function as lotic, high-energy corridors where habitat complexity and lateral floodplain recruitment sustain taxonomic richness (Junk et al. 1989). These corridors exhibit high alpha diversity but low evenness, often dominated by palaemonid decapods and thiarid gastropods due to their tolerance of tidal fluctuations and natural turbidity. Conversely, sensitive, oxygen-dependent taxa (e.g., Ephemeroptera, Odonata) remain restricted to shallow littoral zones or floodplain-connected

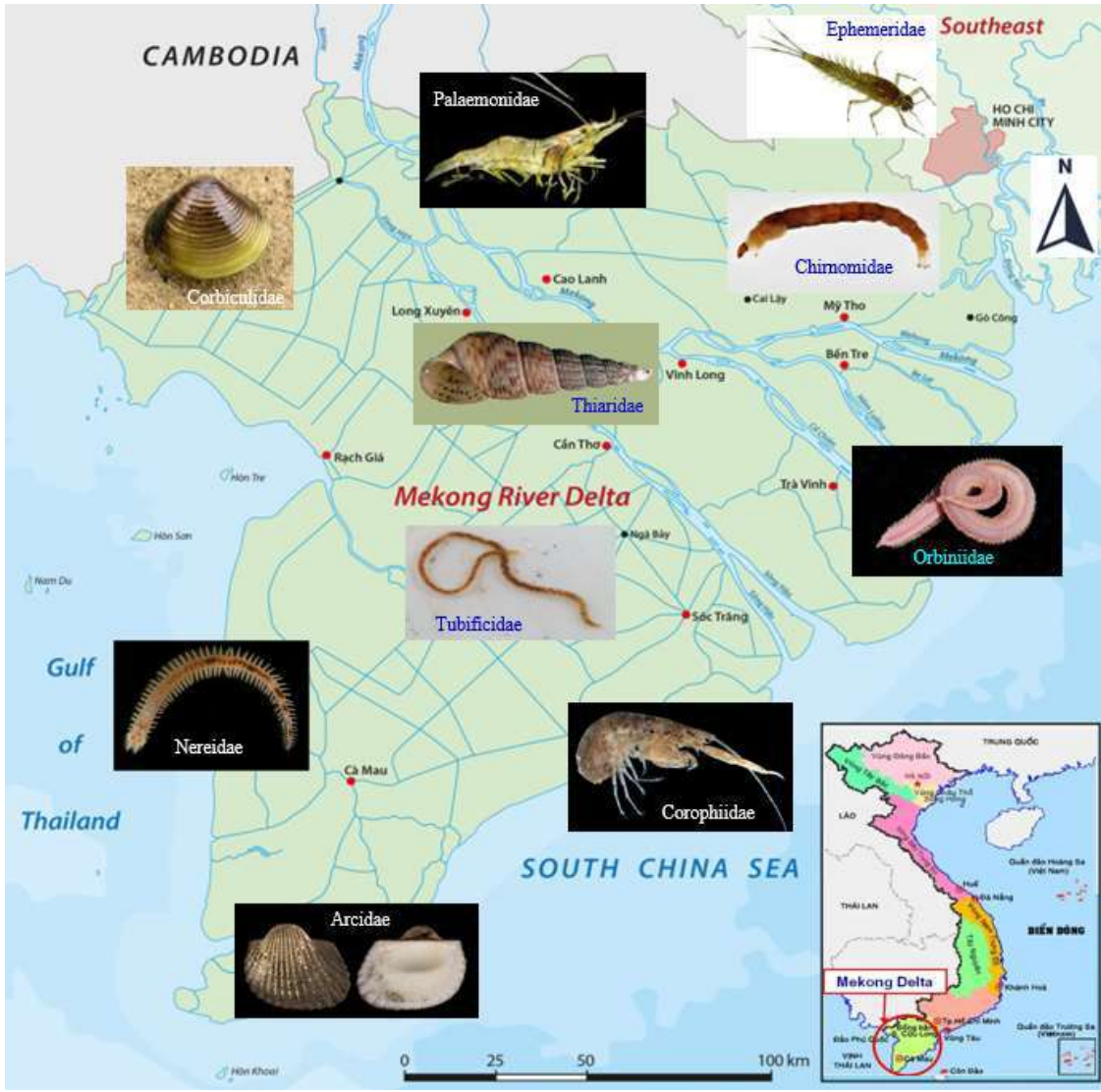


Fig. 3: Geographic distribution of key macroinvertebrate functional groups across the Mekong Delta.

refugia where high flows maintain adequate dissolved oxygen and critical microhabitats (Fig. 3).

Conversely, artificial canals act as semi-lentic conduits harboring depauperate assemblages dominated by tubificid oligochaetes, chironomid dipterans, and Corbicula spp. (Fig. 3). Driven by low flow velocities and heavy organic enrichment, these modified channels undergo "functional homogenization," where specialized shredders are replaced by generalist collector-filterers adapted to high seston and hypoxic organic sludge (Statzner et al. 2001, Menezes et al. 2010). This stable, tolerance-mediated state acts as a potent environmental filter that conventional biotic indices often fail to detect (Sor et al. 2017, Le et al. 2023b). Finally, estuarine and coastal ecotones transition to euryhaline and marine taxa (polychaetes, bivalves, and crustaceans) physiologically adapted to dynamic salinity gradients (Pham 2014, Pham et al. 2026).

3.3. Stressor Dynamics

The ecological divergence detailed in Section 3.2 is underpinned by the Mekong Delta's stressor regimes. In main river channels, high dilution capacities and seasonal flushing pulses partially buffer anthropogenic inputs. Conversely, the canal network is characterized by stagnant flow and prolonged water residence times that exacerbate nutrient loading from agricultural and domestic effluents. As shown in Fig. 2 (Stage 2), these pressures operate synergistically; low flow velocities facilitate the development of anaerobic

sediment microenvironments, triggering the loading of phosphorus and initiating a feedback loop of oxygen depletion (Anthony et al. 2015, Vo et al. 2024).

Sedimentation impacts vary by system as rivers undergo periodic resuspension, while canals experience chronic fine-sediment accumulation. The Vam Co River serves as a case study for "context-dependent" responses. While organic enrichment correlates with increased macroinvertebrate density, the presence of acid sulfate soils introduces a geochemical threshold. At pH < 4.5, the toxicity of liberated aluminum ions (Al^{3+}) results in ecological collapse zones despite high biochemical oxygen demand (BOD) (Pham et al. 2026). Current Vietnamese water quality standards (e.g., QCVN 08-MT:2023) and indices like BMWP-VIET fail to account for this acidity–toxicity synergy. Consequently, nutrient-reduction efforts yield no biological improvement because the system remains chemically "locked" by acidity. In these modified deltaic settings, interacting hydrological, sedimentary, and geochemical stressors produce non-linear biological responses that traditional metrics cannot capture.

3.4. Performance and Pragmatism

The performance and applicability of existing macroinvertebrate-based indices and metrics are summarized in Table 2, highlighting indicator types, taxonomic resolution, and limitations under Mekong Delta conditions. Due to the costs of specialized expertise and a deficit of regional species keys, over 75% of existing studies rely on family-level identification. While pragmatic, this "higher-taxon" approach frequently masks the nuanced biological signals required to detect specific stressors, as diverse species with varying sensitivities are aggregated into single, broad categories (Buss et al. 2015).

Furthermore, temperate-derived indices, such as the standard BMWP, perform inconsistently in canal networks because they do not account for the low-flow and low-oxygen conditions inherent to tropical deltas. Locally calibrated multimetric indices (MMIs) (e.g., Pham 2014, Pham et al. 2025) have demonstrated sensitivity. Specifically, the integration of metrics such as "Relative Abundance of Oligochaeta" and "Scraper-to-Filterer Ratios" has proven more robust in distinguishing between chronic siltation and organic enrichment (Pham 2014, Mamun et al. 2022). However, these MMIs still require broader validation across the Delta's complex salinity and acidity gradients to ensure regional reliability.

3.5. Systemic Challenges

Current bioassessments in the Mekong Delta are constrained by three systemic weaknesses. First, a dry-season bias exists, with approximately 80% of reviewed studies neglecting the Flood Pulse Concept (Junk et al. 1989). By omitting monsoonal restructuring of habitats, these assessments capture only partial annual dynamics. Second, the region faces a reference condition void; in a delta strongly modified by dikes and canals, the search for "pristine" benchmarks is an exercise in futility (Stoddard et al. 2006, Birk et al. 2012). Future indices must therefore transition toward gradient-based or multivariate models that evaluate ecological status along a spectrum of human impact rather than against "natural" states (Davies & Jackson 2006, Chessman 2007, Feio et al. 2014).

Finally, persistent taxonomic bottlenecks and a reliance on family-level identification mask the presence of cryptic species and rare taxa (Jones 2008, Sweeney et al. 2011). This resolution deficit is severely compounded by fragmented

Table 2: Summary of macroinvertebrate-based indices and metrics reported for EHA in the Mekong Delta.

Index/Metric	Indicator type	Taxonomic level	Typical application	Notes/Limitations	Key references
Taxonomic richness	Structural	Family/Genus	Overall condition	Sensitive to habitat coverage	MRC 2008, MRC 2019, Nguyen et al. 2023
Shannon–Wiener (H′)	Diversity	Family/Genus/ Species	Community diversity	Low stressor specificity	Magurran 2004, Zilli et al. 2011, Pham 2014
BMWP-VIET/ASPT	Tolerance-based	Family	Ecological status	Limited canal calibration	Ngo et al. 2013a, Ngo et al. 2013b, Ngo & Ngo 2014
% Oligochaeta	Tolerance proxy	Higher taxon	Organic enrichment	Confounded by fine sediments	Pham 2014, Vo et al. 2019
Chironomidae abundance	Tolerance proxy	Family	Nutrient/oxygen stress	Ubiquitous; moderate tolerance	Bonada et al. 2006, Le et al. 2023a
Functional feeding	Functional	Family	Stressor diagnosis	Requires regional trait data	Statzner et al. 2001, Bonada et al. 2006
Multimetric (MMIs)	Integrated	Family	Holistic status	Limited validation across gradients	Birk et al. 2012, Mamun et al. 2022

regional identification keys and a widespread lack of standardized quality control (QC) protocols across historical datasets. Consequently, these operational deficiencies are major systemic bottlenecks that hinder coordinated, transboundary ecological health assessments, especially since these sensitive indicators are the first to respond to climate-driven shifts in salinity and hydrological regimes (Macher et al. 2016, Eriksen et al. 2025).

3.6. Future Horizons

The trajectory of EHA in the Mekong Delta is shifting toward predictive, diagnostic frameworks. To bridge the science–policy gap, we propose a strategic roadmap (Fig. 1): first, adopt typology-based monitoring that differentiates major rivers from irrigation canals; second, integrate molecular tools such as DNA metabarcoding to overcome taxonomic constraints and enable cost-effective large-scale monitoring; and third, align bioindicator data with geographic information system (GIS) platforms within the Mekong River Commission and national systems to support coordinated, transboundary water quality management.

Methodological challenges and recommended pathways for advancing macroinvertebrate-based EHA are synthesized in Table 3, linking limitations such as taxonomic gaps, hydrological seasonality, and canal-specific disturbances to solutions and their benefits for EHA. These molecular tools enable the detection of cryptic biodiversity and community shifts before irreversible ecological collapse occurs (Nguyen et al. 2025, Eriksen et al. 2025). Moving beyond taxonomic presence to functional roles allows separation of natural variability from anthropogenic impacts. Trait-based approaches (e.g., respiration mode, dispersal strategy) provide diagnostic insight into stressors such as hypoxia, pesticide exposure, and sedimentation (Statzner et al. 2001). Embedding this typology-sensitive, molecularly informed roadmap (Fig. 1) and GIS-based spatiotemporal analysis into MRC policy empowers managers to balance intensifying irrigation demands with the ecological integrity of the delta's river–canal network.

Resolving the complexities in macroinvertebrate-based assessments within the Mekong Delta necessitates a strategic departure from temperate-derived indices. Instead, the focus must shift toward ecological frameworks that calibrate for the region's unique hydrological dynamics and multi-stressor landscape. By synthesizing delta-specific typologies with advanced diagnostic tools, specifically functional trait-based analysis and high-throughput DNA metabarcoding (Baird & Hajibabaei 2012, Taberlet et al. 2012, Elbrecht et al. 2018, Pawlowski et al. 2018, Fueyo et al. 2024, Eriksen et al. 2025), researchers can effectively decouple natural estuarine variability from human-induced degradation. Translating these high-resolution ecological baselines into evidence-based policy instruments is imperative for the long-term conservation and transboundary management of the Mekong's biological integrity.

4. CONCLUSIONS AND FUTURE DIRECTIONS

Macroinvertebrate-based EHA in the Mekong Delta is highly context-dependent, varying sharply between dynamic, tidally mixed main rivers and the approximately 100,000 km artificial canal network, which undergoes chronic stress (pesticide runoff, siltation) and functional homogenization. Current frameworks are constrained by critical systemic biases: a geographic blind spot (<30% of studies focus on canals), an 80% dry-season bias neglecting the Flood Pulse Concept, and operational deficits driven by family-level identification, fragmented keys, and a lack of standardized QC protocols. Consequently, uncalibrated temperate indices fail to account for tropical deltaic dynamics, masking degradation in canals and estuarine zones. Recent advances demonstrate that deltaic assemblages are strongly conditioned by hydrological extremes, salinity gradients,

Table 3: Methodological challenges and recommended pathways for advancing macroinvertebrate-based EHA in the Mekong Delta.

Evidence-based limitation	Recommended methodological pathway	Primary benefit for EHA
Taxonomic expertise gap	Environmental DNA (eDNA)/metabarcoding or trait-based metrics	Rapid, large-scale screening or reduced dependence on species-level identification
Strong hydrological seasonality	Seasonal stratification and mixed-effects	Separates natural variability from anthropogenic stress
Canal-specific disturbances	Canal-adapted indices; habitat and sediment metrics	Improves sensitivity and diagnostic power in artificial waterways
Fine sediment and organic enrichment	Target tolerant benthic taxa and feeding groups	Clarifies status in naturally turbid, low-energy waters
Acid sulfate soils and acidification	Integration of sediment chemistry with bioindicators	Detects episodic geochemical toxicity (Al^{3+}, pH)
Policy fragmentation	MRC/GIS integration	Facilitates basin-scale trend analysis and transboundary management

and episodic geochemical thresholds such as acid sulfate soils releasing toxic aluminum ions (Al^{3+}) at pH < 4.5, which traditional indices (BMWP-VIET) and national standards (QCVN 08-MT:2023) fail to capture. Conversely, locally calibrated multimetric indices (MMIs) utilizing target metrics (e.g., relative abundance of Oligochaeta, scraper-to-filterer ratios) have proven robust in isolating chronic siltation from organic enrichment.

Future work must prioritize the proposed strategic roadmap to bridge the science–policy gap. This requires typology-based monitoring that explicitly separates main rivers from artificial waterways, alongside the systematic implementation of functional trait-based analysis (e.g., respiration modes and dispersal strategies) to decouple natural estuarine variability from anthropogenic degradation. Finally, high-throughput DNA metabarcoding must be systematically scaled to bypass taxonomic constraints and embedded into automated geographic information system (GIS) platforms within the MRC and national frameworks to achieve unified, transboundary water resource management.

5. ACKNOWLEDGEMENT

The authors would like to express their thanks to Ton Duc Thang University, Vietnam, for its invaluable technical support in the execution of this project.

6. REFERENCES

Allan, J.D., 2004. Landscapes and riverscapes: the influence of land use on stream ecosystems. *Annual Review of Ecology*, Evolution and Systematics, 35, pp.257–284. [DOI]

Anthony, E., Brunier, G., Basset, M.T., Goichot, M., Dussouillez, P. and Nguyen, V.L., 2015. Linking rapid erosion of the Mekong River delta to human activities. *Scientific Reports*, 5(1), p.14745. Available at: https://www.researchgate.net/publication/283116676.

Baird, D.J. and Hajibabaei, M., 2012. Biomonitoring 2.0: a new paradigm in ecosystem assessment made possible by next-generation DNA sequencing. *PLoS ONE*, 7, p.e32706. [DOI]

Bendary, R.E., Goher, M.E. and El-Shamy, A.S., 2023. Taxonomic and functional diversity of macroinvertebrates in sediment and macrophyte habitats: a case study, the Ibrahimia Canal, Nile River, Egypt. *Egyptian Journal of Aquatic Research*, 49(2), pp.129–135. [DOI]

Best, J., 2019. Anthropogenic stresses on the world's big rivers. *Nature Geoscience*, 12, pp.7–21. [DOI]

Birk, S., Bonne, W., Borja, Á., Brucet, S., Courrat, A., Poikane, S., Solimini, A., Van De Bund, W., Zampoukas, N. and Hering, D., 2012. Three hundred ways to assess Europe's surface waters: an almost complete overview of biological methods to implement the Water Framework Directive. *Ecological Indicators*, 18, pp.31–41. [DOI]

Bonada, N., Prat, N., Resh, V.H. and Statzner, B., 2006. Developments in aquatic insect biomonitoring: a comparative analysis of recent approaches. *Annual Review of Entomology*, 51, pp.495–523. [DOI]

Bosma, R.H., Nguyen, T.H., Siahainenia, A.J., Tran, H.T.P. and Tran, H.N., 2014. Shrimp-based livelihoods in mangrove silvo-aquaculture farming systems. *Reviews in Aquaculture*, 16, pp.1–18. [DOI]

Buss, D.F., Carlisle, D.M., Chon, T.S., Culp, J., Harding, J.S., Keizer-Vlek, H.E., Robinson, W.A., Strachan, S., Thirion, C. and Hughes, R.M., 2015. Stream biomonitoring using macroinvertebrates around the globe: a comparison of large-scale programs. *Hydrobiologia*, 757, pp.1–21. [DOI]

Chen, S., Guo, C., Wang, X., Wu, Y., Wang, Y., Wang, Y, Wang, Y and Guo, H., 2025. Channelization and flow depletion shift benthic macroinvertebrate and fish communities in urban rivers. *PLoS ONE*, 20(7), p.e0328843. [DOI]

Chessman, B.C., Williams, S.A. and Besley, C., 2007. Bioassessment of streams with macroinvertebrates: effect of sampled habitat and taxonomic resolution. *Journal of the North American Benthological Society*, 26, pp.546–565. [DOI]

Cruz, M., Rosman, P.C.C., Marisa, C.R.A. and Iglesias, I.I., 2026. Modelling estuarine wetlands and their role as nature-based solutions: a review. *Science of the Total Environment*, 1014, p.181325. [DOI]

Dang, T.D., Cochrane, T., Arias, M.E. and Pham, D.T.V., 2018. Future hydrological alterations in the Mekong Delta under the impact of water resources development, land subsidence and sea level rise. *Journal of Hydrology Regional Studies*, 15(C), pp.119–133. [DOI]

Davies, S.P. and Jackson, S.K., 2006. The biological condition gradient: a descriptive model for interpreting change in aquatic ecosystems. *Ecological Applications*, 16(4), pp.1251–1266. [DOI]

Doan, V.T., Le, C.C., Le, H.V.T., Trieu, N.A., Vo, L.P., Tran, D.A., Nguyen, H.V., Tabata, T. and Vu, T.T.H., 2025. Comprehensive statistical analysis for characterizing water quality assessment in the Mekong Delta: trends, variability and key influencing factors. *Sustainability*, 17(12). [DOI]

Dodds, W.K. and Smith, V.H., 2016. Nitrogen, phosphorus and eutrophication in streams. *Inland Waters*, 6(2), pp.155–164. [DOI]

Dudgeon, D., 2010. Prospects for sustaining freshwater biodiversity in the 21st century: linking ecosystem structure and function. *Current Opinion in Environmental Sustainability*, 2(5–6), pp.422–430.

Duong, C.D., Nguyen, C.T. and Nguyen, T.C.T., 2008. Research on water body zoning based on benthic macroinvertebrate communities. *Can Tho University Journal of Science*, 21, pp.61–66. (In Vietnamese)

Duong, C.D., Nguyen, V.C. and Le, C.Q., 2011. Application of benthic macroinvertebrate indices for assessing water pollution in Tam Bot Canal, Long Xuyen, An Giang Province. *Can Tho University Journal of Science*, 20A, pp.18–27. (In Vietnamese)

Elbrecht, V., Vamos, E.E., Steinke, D. and Leese, F., 2018. Estimating intraspecific genetic diversity from community DNA metabarcoding data. *PeerJ*, 6, p.e4644. [DOI]

Eriksen, T.E., Brittain, J.E., Sandin, L. and Friberg, N., 2025. Unveiling cryptic macroinvertebrate sentinels to enhance biomonitoring in tropical rivers: bridging traditional approaches with DNA barcoding in the Indo-Burma biodiversity hotspot. *Science of the Total Environment*, 958, p.178064. [DOI]

Eslami, S., Hoekstra, P., Kernkamp, H.W., Nguyen Trung, N., Do Duc, D., Nguyen Nghia, H., Tran Quang, T., Van Dam, A., Darby, S.E., Parsons, D.R. and Vasilopoulos, G., 2021. Dynamics of salt intrusion in the Mekong Delta; results of field observations and integrated coastal-inland modelling. *Earth Surface Dynamics Discussions*, 2021, pp.1–36. [DOI]

Feio, M.J., Davies, C.E., Hirsch, F., Pusch, M.T., Murphy, J.F. and Hughes, R.M., 2014. The biological assessment and rehabilitation of the world's rivers: an overview. *Water*, 6(3), pp.671–689.

Friberg, N., Bonada, N., Bradley, D.C., Dunbar, M.J., Edwards, F.K., Grey, J., Hayes, R.B., Hildrew, A.G., Lamouroux, N., Trimmer, M., and Woodward, G., 2011. Biomonitoring of human impacts in freshwater ecosystems: the good, the bad and the ugly. *Advances in Ecological Research*, 44, 1–68. [DOI]

Fueyo, Á., Sánchez, O., Carleos, C., Escudero, A., Cordón, J., Granero-Castro, J. and Borrell, Y.J., 2024. Unlocking rivers' hidden diversity and ecological status using DNA metabarcoding in Northwest Spain. *Ecology and Evolution*, 14(8), p.e70110. [DOI]

Gugliotta, M., Saito, Y., Nguyen, V.L., Ta, T.K.O., Nakashima, R., Tamura, T., Uehara, K., Katsuki, K. and Yamamoto, S., 2017. Process regime, salinity, morphological and sedimentary trends along the fluvial to marine transition zone of the mixed-energy Mekong River delta, Vietnam. *Continental Shelf Research*, 147, pp.7–26. [DOI]

Gugliotta, M., Saito, Y., Ta, T.K.O., Tamura, T. and Nguyen, V.L., 2018. Sediment distribution and depositional processes along the fluvial to marine transition zone of the Mekong River delta. *Sedimentology*, 64(1), pp.165–187. [DOI]

Hering, D., Borja, A., Jones, J.I., Pont, D., Boets, P., Bouchez, A., Bruce, K., Drakare, S., Hänfling, B., Kahlert, M. and Leese, F., 2018. Implementation options for DNA-based identification into ecological status assessment under the European Water Framework Directive. *Water Research*, 138, pp.192–205. [DOI]

Hua, H.H., Cremin, E., Huynh, V.D., Long, G. and Renaud, F.G., 2024. Impacts of aquaculture practices on the sustainability of social-ecological systems in coastal zones of the Mekong Delta. *Ocean & Coastal Management*, 258, p.107392. [DOI]

Jones, F.C., 2008. Taxonomic sufficiency: the influence of taxonomic resolution on freshwater bioassessments using benthic macroinvertebrates. *Environmental Reviews*, 16(1), pp.45–69.

Junk, W.J., Bayley, P.B. and Sparks, R.E., 1989. The flood pulse concept in river–floodplain systems. In D.P. Dodge (Ed.), *Proceedings of the International Large River Symposium (LARS)*. Canadian Special Publication of Fisheries and Aquatic Sciences, 106, pp.110–127.

Karr, J.R., 1991. Biological integrity: a long-neglected aspect of water resource management. *Ecological Applications*, 1, pp.66–84. [DOI]

Kondolf, G.M., Gao, Y., Annandale, G.W., Morris, G.L., Jiang, E., Zhang, J., Cao, Y., Carling, P., Fu, K., Guo, Q. and Hotchkiss, R., 2014. Sustainable sediment management in reservoirs and regulated rivers: Experiences from five continents. *Earth's Future*, 2(5), pp.256–280. [DOI]

Kontgis, C., Schneider, A. and Ozdogan, M., 2015. Mapping rice paddy extent and intensification in the Mekong Delta. *Remote Sensing*, 7, pp.15802–15827. [DOI]

Kuenzer, C. and Renaud, F.G., 2012. Climate and environmental change in the Mekong Delta. *Regional Environmental Change*, 12(Suppl 1), pp.S1–S6.

Le, C.Q., Trinh, T.L. and Vu, N.U., 2011. Distribution of zoobenthos in Cai Sao Canal, An Giang Province. *Can Tho University Journal of Science*. *(In Vietnamese)*

Le, H.A., Nguyen, T., Gratiot, N., Deleersnijder, E. and Soares-Frazão, S., 2023a. The multi-channel system of the Vietnamese Mekong Delta: impacts on the flow dynamics under relative sea-level rise scenarios. *Water*, 15, p.3597. [DOI]

Le, T.P.Q., Billen, G., Garnier, J., Théry, S. and Chau, V.M., 2017. Nutrient (N, P) budgets for the Red River basin (Vietnam and China). *Global Biogeochemical Cycles*, 19(2), pp.1–16. [DOI]

Le, T.T., Pham, V.H. and Nguyen, N.T., 2023b. Ecological impacts of dredging and canal maintenance on benthic communities in the Mekong Delta. *Vietnam Journal of Water Resources*, 79, pp.41–52. (In Vietnamese)

Ly, V.V., Dinh, M.Q., Nguyen, T.K.L., Vo, T.T.L., Tran, N.A., Tran, T.T., Luu, T.L., Nguyen, L. and Ngo, M.H., 2025. Benthic macroinvertebrates diversity in the Tra Su Melaleuca Forest Landscape Protection Area, Mekong Delta, Vietnam. *Applied Ecology and Environmental Research*, 23(6), pp.10431–10442. [DOI]

Macher, J.N., Salis, R.K., Blakemore, K.S., Tollrian, R., Matthaei, C.D. and Leese, F., 2016. Multiple-stressor effects on stream invertebrates: DNA barcoding reveals contrasting responses of cryptic mayfly species. *Ecological Indicators*, 61, pp.159–169.

Magurran, A.E., 2004. *Measuring biological diversity.*

Mamun, M., Jargal, N., Atique, U. and An, K.G., 2022. Ecological river health assessment using multi-metric models in an Asian temperate region with land use/land cover as the primary factor regulating nutrients, organic matter and fish composition. *International Journal of Environmental Research and Public Health*, 19(15), p.9305. [DOI]

Mekong River Commission (MRC), 2008. *Biomonitoring of the lower Mekong River and selected tributaries, 2004–2007, MRC Technical Paper No. 20, Mekong River Commission, Vientiane. 77 pp*. [DOI]

Mekong River Commission (MRC), 2009. *Report on the 2006 biomonitoring survey of the Lower Mekong River and selected tributaries*. MRC Technical Paper No. 22, Mekong River Commission, Vientiane. 124 pp. [DOI]

Mekong River Commission (MRC), 2010. *Biomonitoring Methods for the Lower Mekong Basin*. Mekong River Commission, Vientiane. 65 pp. [DOI]

Mekong River Commission (MRC), 2019. *Report on the 2017 Biomonitoring Survey of the Lower Mekong River and Selected Tributaries*. Mekong River Commission, Vientiane. 94 pp. [DOI]

Mekong River Commission (MRC), 2024. *2022 Lower Mekong Water Quality Monitoring Report*. Mekong River Commission, Vientiane. 75 pp. Available at: https://www.mrcmekong.org/wp-content/uploads/2024/11/2022.

Menezes, S., Baird, D.J. and Soares, A.M.V.M., 2010. Beyond taxonomy: a review of macroinvertebrate trait-based community descriptors as tools for freshwater biomonitoring. *Journal of Applied Ecology*, 47, pp.711–719. [DOI]

Ministry of Natural Resources and Environment (MONRE), 2015. *Guideline on Surface Water Environmental Monitoring*. MONRE, Hanoi. (In Vietnamese)

Morse, J.C., Bae, Y.J., Munkhjargal, G., Sangpradub, N., Tanida, K., Vshivkova, T.S., Wang, B., Yang, L. and Yule, C.M., 2007. Freshwater biomonitoring with macroinvertebrates in East Asia. *Frontiers in Ecology and the Environment*, 5(1), pp.33–42. [DOI]

Mureithi, P.W., Aine, A., Basooma, R., Namumbya, J., Nansumbi, F., Yegon, M.J., Meimberg, H. and Graf, W., 2025. Advancements in macroinvertebrate-based river bioassessment research in the Afrotropical region: review and steps towards a regional framework. *Environmental Monitoring and Assessment*, 197(935). [DOI]

Ngo, X.Q. and Ngo, T.L., 2014. Composition and biodiversity of benthic macroinvertebrates communities in the Mekong River. *HCMUE J. Sci*., 58, pp.38–49. [DOI]

Ngo, X.Q., Nguyen, T.D. and Pham, H.T., 2013a. Composition and distribution of benthic macroinvertebrates in the Mekong River, Vietnam. *Journal of Biology*, 35(4), pp.459–470.

Ngo, X.Q., Nguyen, V.S., Nguyen, D.T., Pham, V.L. and Ngo, T.L., 2013b. Biodiversity of littoral macroinvertebrates in the Mekong River. *HCMUE J. Sci*., 51, pp.16–28. [DOI]

Nguyen, M.N, Le, D.T., Pham, V.H., Vu, T.D.H., Ouillon, S. and Nguyen, C.T., 2025. Suspended sediment pattern along the Mekong Delta's west coast induced by strong southwest monsoon activities and extreme events. *Marine Geology*, 485, p.107563. [DOI]

Nguyen, N.H., Delgado, J.M., Vo, K.T., Le, M.H., Merz, B., Bardossy, A. and Apel, H., 2011. Floodplain hydrology of the Mekong Delta, Vietnam. *Hydrol. Process*., John Wiley and Sons, Ltd. [DOI]

Nguyen, T.L.C., Dinh, T.T.H., Dang, T.C.T., Pham, A.D., Nguyen, T.T., Huynh, T.T.Q. and Tran, N.P., 2020. Diversity of zooplankton and benthic macroinvertebrates of estuarine coastal waters in Tien Giang province, southern Vietnam. *Vietnam Journal Science*, Technology and Engineering, 62 (4), 3. [DOI]

Nguyen, V.C.N., Nguyen, C.T., Le, N.Y. and Lavane, K., 2023. Using the distribution index of zoobenthos for assessing the level of pollution in E Canal, Vinh Thanh District, Can Tho City, Can Tho City. *Journal of Science*, Can Tho University, 59, pp.80–88. (In Vietnamese). [DOI]

Nguyen, V.T. and Le, T.H., 2014. Impacts of canalization and water control structures on water quality in the Mekong Delta. *Journal of Science*, Can Tho University, 32, pp.45–54. (In Vietnamese)

Norris, R.H. and Thoms, M.C., 1999. What is river health? *Freshwater Biology*, 41(2), pp.197–209. [DOI]

Page, M.J., McKenzie, J.E., Bossuyt, P.M., Boutron, I., Hoffmann, T.C., Mulrow, C.D., Shamseer, L., Tetzlaff, J.M., Akl, E.A., Brennan, S.E. and Chou, R., 2021. The PRISMA 2020 statement: an updated guideline for reporting systematic reviews. *BMJ*, 372. [DOI]

Pawlowski, J., Kelly-Quinn, M., Altermatt, F., Apothéloz-Perret-Gentil, L., Beja, P., Boggero, A., Borja, A., Bouchez, A., Cordier, T., Domaizon, I. and Feio, M.J., 2018. The future of biotic indices in the ecogenomic era: Integrating (e) DNA metabarcoding in biological assessment of aquatic ecosystems. *Science of the Total Environment*, 637, pp.1295–1310. [DOI]

Pham, A.D., 2014. *Study on the Water Quality Assessment using Benthic Macroinvertebrates for the Lower Dongnai River Biomonitoring, Vietnam*. PhD Dissertation, Institute for Environment and Resources, Vietnam National University in HCMC, Vietnam. (In Vietnamese)

Pham, A.D., 2019. *Aquatic organism monitoring program for water bodies in Long An province, Vietnam*. PhD Dissertation, Long An Department of Environment and Resources (DONRE), Vietnam. (In Vietnamese)

Pham, A.D., Dang, M.T., Pham, T.L., Bui, T.H. and Dao, T.S., 2026. Ecological health assessment of the Vam Co River System, Vietnam: insights from benthic macroinvertebrates and environmental changes. *Nature Environment and Pollution Technology*, 25(2), D1853. [DOI]

Pham, A.D., Nguyen, T.D., Dao, T.S., Nguyen, V.T., Nguyen, X.D., Phan, D.D. and Pham, T.L., 2025. Ecological Health Assessment of the Mekong River and Its Tributaries: Challenges and Future Perspective–A Review. *Polish Journal of Environmental Studies*. [DOI]

Rosenberg, D.M. and Resh, V.H., 1993. *Freshwater Biomonitoring and Benthic Macroinvertebrates*. *Chapman and Hall, New York*.

Smith, V.H., Tilman, G.D. and Nekola, J.C., 1999. Eutrophication: impacts of excess nutrient inputs on freshwater, marine and terrestrial ecosystems. *Environmental Pollution*, 100(1–3), pp.179–196. [DOI]

Sor, R., Boets, P., Chea, R., Goethals, P. and Lek, S., 2017. Spatial organization of macroinvertebrate assemblages in the Lower Mekong Basin. *Limnologica*, 64, pp.20–30. [DOI]

Statzner, B., Bis, B., Dolédec, S. and Usseglio-Polatera, P., 2001. Perspectives for biomonitoring at large spatial scales: a unified measure for the functional composition of invertebrate communities in European running waters. *Basic and Applied Ecology*, 2, pp.73–85. [DOI]

Stoddard, J.L., Larsen, D.P., Hawkins, C.P., Johnson, R.K. and Norris, R.H., 2006. Setting expectations for the ecological condition of streams: the concept of reference condition. *Ecological Applications*, 16(4), pp.1267–1276. [DOI]

Sweeney, B.W., Battle, J.M., Jackson, J.K. and Dapkey, T., 2011. Can DNA barcodes of stream macroinvertebrates improve descriptions of community structure and water quality? *Journal of the North American Benthological Society*, 30(1), pp.195–216.

Syvitski, J.P.M., Kettner, A.J., Overeem, I., Hutton, E.W.H., Hannon, M.T., Brakenridge, G.R., Day, J., Vörösmarty, C., Saito, Y., Giosan, L. and Nicholls, R.J., 2009. Sinking deltas due to human activities. *Nature Geoscience*, 2, pp.681–686. [DOI]

Taberlet, P., Coissac, E., Hajibabaei, M. and Rieseberg, L.H., 2012. Environmental DNA. *Molecular Ecology*, 21(8), p.1789. [DOI]

Tran, N.T., Pham, H.Q. and Dang, T.M., 2016. Surface water pollution in agricultural canals of the Mekong Delta. *Vietnam Journal of Science and Technology*, 54(3), pp.356–365. (In Vietnamese)

Vo, Q.B., Pham, V.T., Nguyen, V.T., Hoang, M.H., Le, V.D., Downes, N.K. and Pham, V.D.T., 2024. Correction to: Understanding watershed sources of pollution in Vinh Long Province, Vietnamese Mekong Delta. *Discover Applied Sciences*, 6(407). [DOI]

Vo, T.D., Nguyen, V.H. and Le, Q.T., 2019. Seasonal dynamics of benthic macroinvertebrates in Mekong Delta canals. *Can Tho University Journal of Science*, 55, pp.88–98. (In Vietnamese)

Wehrheim, C., Manfred, L., Harro, S. and Marc, W., 2023. Identifying key influences on surface water quality in freshwater areas of the Vietnamese Mekong Delta from 2018 to 2020. *Water*, 15(7), p.1295. [DOI]

Yu, G., Yu, Q., Hu, L., Zhang, S., Fu, T., Zhou, X., He, X., Liu, Y.A., Wang, S. and Jia, H., 2013. Ecosystem health assessment based on analysis of a land use database. *Applied Geography*, 44, pp.154–164. [DOI]

Zilli, L., Beirão, J., Schiavone, R., Herraez, M.P., Cabrita, E., Storelli, C. and Vilella, S., 2011. Aquaporin inhibition changes protein phosphorylation pattern following sperm motility activation in fish. *Theriogenology*, 76(4), pp.737–744. [DOI]

Nature Environment and Pollution Technology
An International Quarterly Peer-Reviewed Open Access Journal

p-ISSN: 0972-6268 | e-ISSN: 2395-3454 Vol. 25 | No. 4 | Article ID D1932 | 2026

RESEARCH ARTICLE https://doi.org/10.46488/NEPT.2026.v25i04.D1932 OPEN ACCESS

Integrated Electrocoagulation–Adsorption Using Thermally Activated Bentonite for Pb, Cd, and Ni Removal from Laboratory Wastewater

Muhrinsyah Fatimura[1,3], Tuty Emilia Agustina[2]†, Susila Arita[2], Elda Melwita[2], Rully Masriatini[3] and Nurlela[3]
[1]Engineering Science Doctoral Program, Faculty of Engineering, Sriwijaya University, Jl. Palembang–Prabumulih KM 32, Indralaya, Ogan Ilir 30662, South Sumatra, Indonesia
[2]Chemical Engineering Department, Faculty of Engineering, Sriwijaya University, Jl. Palembang–Prabumulih KM 32, Indralaya, Ogan Ilir 30662, South Sumatra, Indonesia
[3]Chemical Engineering Study Program, Faculty of Engineering, PGRI University Palembang, Jl. Jend. A. Yani Lorong Gotong Royong, 9/10 Ulu, Kec. Seberang Ulu II, Palembang City 30116, South Sumatra, Indonesia
†Corresponding author: Tuty Emilia Agustina; tuty_agustina@unsri.ac.id

ARTICLE HISTORY

Received: 15-04-2026
Revised: 03-06-2026
Accepted: 06-06-2026

KEYWORDS

Electrocoagulation-adsorption
Thermally activated bentonite
Real laboratory wastewater
Heavy metal removal
Hybrid treatment system

CITE THIS ARTICLE

Fatimura, M., Agustina, T.E., Arita, S., Melwita, E., Masriatini, R. and Nurlela, N., 2026. Integrated electrocoagulation-adsorption using thermally activated bentonite for Pb, Cd, and Ni removal from laboratory wastewater, *Nature Environment and Pollution Technology*, 25(4), D1932. https://doi.org/10.46488/NEPT.2026.v25i04.D1932

COPYRIGHT & LICENCE

© 2026 The Authors
Open Access under CC BY 4.0.

PUBLISHED BY
TECHNOSCIENCE PUBLICATIONS

ABSTRACT

Although integrated electrocoagulation–adsorption (EC-Ads) systems have demonstrated considerable potential for heavy metal removal, most previous studies have primarily focused on synthetic wastewater or single-metal systems, while comparative evaluations involving stand-alone electrocoagulation, stand-alone adsorption, and integrated EC-Ads systems using real laboratory wastewater containing multiple metals remain relatively limited. This study investigated the performance of electrocoagulation alone, adsorption alone, and an integrated EC-Ads system employing thermally activated bentonite for the simultaneous removal of Pb, Cd, and Ni from real laboratory wastewater. Electrocoagulation was optimized in terms of pH, current density, and treatment time, whereas adsorption was optimized with respect to adsorbent dosage and contact time. Statistical analysis using one-way ANOVA followed by Tukey's HSD test confirmed that the operational parameters significantly affected heavy metal removal efficiencies ($p < 0.05$). The optimum operating conditions were pH 7, a current density of 0.0133 A cm^{-2}, and 60 min for electrocoagulation, followed by 40 g of bentonite per 2 L of wastewater and 60 min for adsorption. Under these conditions, the integrated system achieved total removal efficiencies of 99.06% for Pb, 98.55% for Cd, and 97.34% for Ni, yielding final concentrations of 0.0521, 0.0342, and 0.0452 mg L^{-1}, respectively. The treated effluent complied with the Indonesian general wastewater discharge standards for Pb, Cd, and Ni under the investigated conditions. Electrocoagulation functioned as the primary removal stage, while adsorption served as an effective polishing step for residual metals at low concentrations. scanning electron microscopy with energy-dispersive X-ray spectroscopy (SEM-EDS), Fourier-transform infrared spectroscopy (FTIR), and inductively coupled plasma mass spectrometry (ICP-MS) analyses supported the proposed removal mechanisms involving surface adsorption, coprecipitation, precipitation, and immobilization in solid phases. Adsorption kinetics were better fitted by the pseudo-second-order model, indicating that the adsorption behavior was more adequately described by this kinetic model under the studied conditions. Overall, these findings demonstrate that the EC-Ads system based on thermally activated bentonite is an effective and promising approach for treating real laboratory wastewater containing multiple heavy metals.

1. INTRODUCTION

Heavy metal contamination in aquatic environments is one of the most serious environmental problems because of its persistence, non-biodegradable nature, tendency to accumulate in the food chain, and potential to cause toxic effects on

aquatic organisms and human health (Hikmat et al. 2023, Fei & Hu 2023). Analytical laboratory wastewater represents a particularly complex waste stream because it contains fluctuating mixtures of inorganic and organic contaminants originating from glassware washing, residual analytical reagents, sample digestion procedures, and unused standard solutions. These wastewaters frequently contain heavy metals such as Pb, Cd, and Ni at variable concentrations, which may pose environmental and health risks if discharged without adequate treatment (Sakina et al. 2023, Fei & Hu 2023).

Among these contaminants, Pb, Cd, and Ni are considered priority pollutants because of their toxicity, persistence, and bioaccumulative behavior in aquatic systems. Pb exposure may affect the nervous system, kidneys, and hematopoietic system, whereas Cd is highly toxic even at low concentrations and may accumulate in the liver and kidneys. Ni contamination is also associated with toxic effects on aquatic organisms and potential carcinogenic risks under prolonged exposure conditions. In addition, the simultaneous presence of multiple metals in laboratory wastewater may increase treatment complexity because of possible competitive interactions among dissolved ions during removal processes (Fu & Wang 2011, Zareh et al. 2024, Magdum & Itankar 2026).

Various methods have been applied for the removal of heavy metals from wastewater, including chemical precipitation, ion exchange, membrane filtration, and biological treatment. However, these methods still face several limitations when applied to complex laboratory wastewater containing mixed metals, particularly in terms of high chemical consumption, sludge generation, membrane fouling, operational complexity, and reduced efficiency at low metal concentrations (Tripathi et al. 2025, Caixeta et al. 2025).

Electrocoagulation (EC) and adsorption have emerged as promising alternatives. Electrocoagulation can generate coagulants in situ through the dissolution of sacrificial electrodes, making it effective for destabilizing contaminants and reducing the pollutant load during the initial stage of treatment (Onyenanu & Onyenanu 2025, Ammar et al. 2023, Naldi et al. 2025). Nevertheless, the application of EC as a stand-alone process still faces several challenges, including electrode passivation, relatively high energy consumption, sludge generation, and reduced removal efficiency in wastewater with complex compositions.

On the other hand, adsorption is recognized as a simple, flexible, and effective method, particularly for removing residual dissolved metals at lower concentrations. Various adsorbents have been developed for this purpose, and bentonite has emerged as one of the most promising materials because of its high cation exchange capacity, adequate surface area, high availability, and relatively low cost (Xu et al. 2021, Merrikhpour et al. 2022). However, adsorption as a stand-alone process also has several limitations, such as adsorbent saturation, the need for regeneration, and performance decline due to the presence of competing ions in real wastewater.

Most previous studies have mainly focused on synthetic wastewater, single-metal systems, or simplified experimental conditions that do not adequately represent the complexity of real laboratory wastewater. In addition, comparative evaluations involving stand-alone electrocoagulation, stand-alone adsorption, and integrated EC–Ads systems under real multi-metal wastewater conditions remain relatively limited (Bakry et al. 2024, Twizerimana & Wu 2024). Real laboratory wastewater generally exhibits fluctuating composition, mixed contaminants, and potential competitive interactions among dissolved metal ions, which may significantly affect treatment performance and process stability. Therefore, studies using actual laboratory wastewater are important for evaluating the practical applicability and reliability of integrated treatment systems under realistic operating conditions. A comparison of previous related studies and the novelty of the present work is summarized in Table 1.

In this context, the present study evaluates the performance of stand-alone electrocoagulation, stand-alone adsorption,

Table 1: Comparison of previous studies on electrocoagulation–adsorption systems for heavy metal removal.

Study	Wastewater Type	Target Metal(s)	Treatment System	Main Findings	Research Gap
Al Ali et al. (2021)	Synthetic wastewater	Pb, Cd	EC–Adsorption	High heavy metal removal efficiency	Synthetic wastewater only
Bakry et al. (2024)	Industrial wastewater	Multiple heavy metals	Electrocoagulation	Effective EC performance for metal removal	No adsorption polishing stage
Twizerimana & Wu (2024)	Synthetic wastewater	Heavy metals	Hybrid treatment system	Improved removal efficiency using integrated treatment	No comparison with stand-alone systems
Present study	Real laboratory wastewater	Pb, Cd, Ni	Stand-alone EC, stand-alone adsorption, and integrated EC–Ads	Comparative evaluation under real multi-metal wastewater conditions	—

and an integrated EC–Ads system employing thermally activated bentonite for the simultaneous removal of Pb, Cd, and Ni from real laboratory wastewater. The study also investigates removal mechanisms through scanning electron microscopy with energy-dispersive X-ray spectroscopy (SEM-EDS), Fourier-transform infrared spectroscopy (FTIR), and inductively coupled plasma mass spectrometry (ICP-MS) analyses, while assessing adsorption kinetics, energy consumption, electrode consumption, and operating cost to provide a more comprehensive evaluation of the proposed treatment system.

2. MATERIALS AND METHODS

Laboratory wastewater samples from an analytical chemistry laboratory were collected from the laboratory wastewater holding tank**.** Thermally activated bentonite obtained from PT ASPROS BINAREKA (100 mesh) was used as the adsorbent. The bentonite was thermally activated at 300°C for 2 h using a muffle furnace with a heating rate of 10°C min^{-1}. After thermal activation, the bentonite was cooled to room temperature in a desiccator before use in the adsorption experiments. Aluminum electrodes (15 cm × 13 cm × 2 mm, purity ≥ 99%), a NICE DC power supply (20 V, 10 A), sulfuric acid (98%; Smartlab), and sodium hydroxide (1 M; Labchem) were used in the experiments.

2.1. Experimental Design

The study was conducted experimentally using a one-factor-at-a-time (OFAT) approach as a preliminary optimization strategy to identify the dominant operational parameters under real laboratory wastewater conditions. In the electrocoagulation process, pH, current density, and treatment time were optimized sequentially, whereas adsorption was optimized in terms of bentonite dosage and contact time under the optimum electrocoagulation conditions. After establishing the optimum conditions, the performances of stand-alone electrocoagulation, stand-alone adsorption, and the integrated electrocoagulation–adsorption (EC–Ads) system were comparatively evaluated, as illustrated in Fig. 1.



Fig. 1: Experimental setup of the integrated electrocoagulation–adsorption system.

All experiments were conducted in triplicate (n = 3), and the results are presented as mean ± standard deviation. Statistical differences among treatment conditions were analyzed using one-way ANOVA followed by Tukey's honestly significant difference (HSD) post hoc test at a significance level of $p < 0.05$.

2.2. Stand-alone Electrocoagulation Process

The electrocoagulation process was optimized stepwise using a one-factor-at-a-time approach in a 2000 mL batch reactor equipped with six aluminum electrodes (Al-Al). Each electrode had total dimensions of 15 cm × 13 cm, while the immersed part of each electrode was 15 cm × 10 cm. Therefore, the effective immersed surface area used for current density calculation was 150 cm^2, calculated from the projected immersed electrode area (15 cm × 10 cm). The inter-electrode spacing was maintained at 2 cm, and 2 L of laboratory wastewater was treated in each experimental run.

The initial pH of the wastewater was measured using a calibrated pH meter and adjusted to 3, 5, 7, 9, and 11 using 98% H_2SO_4 or 1 M NaOH. Considering the corrosive nature of concentrated H_2SO_4, pH adjustment was performed carefully by controlled dropwise addition under appropriate laboratory safety procedures, including the use of personal protective equipment and continuous mixing to avoid localized acidification. After each addition, the solution was homogenized, and the pH was rechecked until the target value was reached before starting the electrocoagulation process.

After determining the optimum pH, current optimization was performed at the optimum pH with a fixed treatment time of 60 min using applied currents of 2, 4, and 6 A. The applied current was expressed as current density using Eq. (1), where the effective immersed electrode surface area was defined as 150 cm^2. Accordingly, the current density values corresponding to 2, 4, and 6 A were 0.0133, 0.0267, and 0.0400 A cm^{-2}, respectively. Subsequently, treatment time was optimized at the optimum pH and current density using treatment times of 15, 30, 45, 60, and 75 min.

$$J = \frac{I}{A} \quad \ldots(1)$$

Where J is the current density (A cm^{-2}), I is the applied current (A), and A is the effective immersed electrode surface area (cm^2).

2.3. Stand-alone Adsorption Process

Stand-alone adsorption was carried out in batch mode using thermally activated bentonite as the adsorbent. In each run, 2 L of wastewater was treated under continuous stirring to maintain suspension homogeneity and promote effective contact between the adsorbent and metal ions. The stirring speed was maintained at 600 rpm throughout the adsorption process. Although relatively high, this stirring condition was selected to prevent particle sedimentation and to maintain uniform dispersion of bentonite particles during batch operation. Under these operating conditions, no significant instability of the bentonite suspension was observed throughout the adsorption process. Optimization was performed stepwise using a one-factor-at-a-time approach. In the first stage, the adsorbent dosage was varied at 20, 40, and 60 g while maintaining a constant contact time of 60 min. In the second stage, the contact time was varied at 15, 30, 45, 60, and 75 min while keeping the adsorbent dosage at the optimum value obtained from the previous stage. The optimum conditions obtained were subsequently applied in the integrated electrocoagulation–adsorption system.

2.4. Integrated Electrocoagulation–Adsorption System

In the integrated system, the wastewater was first treated under the optimum operating conditions determined for the stand-alone electrocoagulation process. The effluent obtained from electrocoagulation was then used as the influent for the adsorption stage, which was operated under the optimum conditions established for the stand-alone adsorption process. This configuration was applied to evaluate the synergistic effect of the hybrid process on heavy metal removal.

2.5. Analytical Methods

An Atomic Absorption Spectrophotometer (AAS; iCE 3000 Series) was used to determine the concentrations of Cd, Ni, and Pb in the treated wastewater. Prior to analysis, the AAS instrument was calibrated using a series of standard solutions for each metal. Calibration curves were prepared using at least five concentration levels, and the linearity of the calibration was evaluated based on the coefficient of determination (R^2). The limits of detection (LOD) and limits of quantification (LOQ) were calculated from the standard deviation of the blank response and the slope of the calibration curve. Recovery tests were performed by spiking known concentrations of Pb, Cd, and Ni into wastewater samples, followed by analysis using the same analytical procedure.

The quality assurance and quality control (QA/QC) results for Pb, Cd, and Ni analysis are summarized in Table 2. The calibration curves showed good linearity, with R^2 values higher than 0.995 for all analyzed metals. The recovery values were within the acceptable analytical range, indicating that the analytical method was reliable for determining Pb, Cd, and Ni concentrations in the wastewater matrix.

Based on the initial metal concentrations and the concentrations after treatment, the heavy metal removal efficiency was calculated using Eq. (2).

$$\text{Removal Efficiency (\%)} = \frac{(C_0 - C_t)}{C_0} \times 100 \quad \ldots(2)$$

Where C_0 is the initial heavy metal concentration (mg L^{-1}), and C_t is the heavy metal concentration after treatment at a given stage (mg L^{-1}). For the integrated system, the calculation was performed for each treatment stage. In the electrocoagulation stage, C_t represents the metal concentration in the EC effluent. In the adsorption stage, C_0 represents the metal concentration in the EC effluent, while C_t represents the metal concentration in the final adsorption effluent. For the overall EC-Ads process, C_0 is the initial metal concentration in the raw wastewater, and C_t is the final metal concentration after the adsorption stage. Inductively coupled plasma mass spectrometry (ICP-MS) was used to determine the concentrations of Cd, Ni, and Pb immobilized in the flocs and sediments generated during electrocoagulation, thereby confirming the transfer of metals from the liquid phase to the solid phase through adsorption and precipitation mechanisms. In addition to removal efficiency, the ability of bentonite to bind metals was also evaluated in terms of adsorption capacity at equilibrium. This parameter was expressed as the equilibrium adsorption capacity (q_e), which was calculated using Eq. (3).

$$q_e = \frac{(Co - C)\,.V}{m} \quad \ldots(3)$$

Table 2: QA/QC parameters for AAS analysis of Pb, Cd, and Ni.

Metal	Calibration range (mg L^{-1})	Calibration equation	R^2	LOD (mg L^{-1})	LOQ (mg L^{-1})	Recovery (%)
Pb	0.1–5.0	y = 0.1245x + 0.0012	0.9991	0.003	0.010	98.4
Cd	0.05–2.0	y = 0.2153x + 0.0008	0.9987	0.001	0.003	97.2
Ni	0.1–3.0	y = 0.1876x + 0.0015	0.9989	0.005	0.015	96.8

Where C_0 represents the initial metal concentration in solution (mg L^{-1}), C_e is the metal concentration at equilibrium (mg L^{-1}), V is the solution volume (L), and m is the mass of adsorbent (g). The parameter q_e represents the amount of adsorbate bound to the adsorbent per unit mass of adsorbent at equilibrium (mg g^{-1}).

For each experimental condition, the concentrations of Pb, Cd, and Ni were measured for each replicate run, and the corresponding removal efficiencies were calculated using Eq. (2). The results are presented as mean ± standard deviation from triplicate measurements.

For quality assurance and quality control (QA/QC), the AAS instrument was calibrated using multi-point standard solutions for Pb, Cd, and Ni before analysis. Calibration linearity (R^2), limits of detection (LOD), limits of quantification (LOQ), and recovery data were determined according to the instrument calibration and validation procedure.

2.6. Characterization of Bentonite and EC Sludge

Fresh thermally activated bentonite and bentonite after adsorption were characterized using SEM-EDS and FTIR. The sludge generated from the EC process was dried and analyzed using Inductively Coupled Plasma–Mass Spectrometry (ICP-MS) and FTIR to investigate the metal capture mechanisms during the electrocoagulation stage.

2.7. Kinetic, Energy, and Cost Analyses

Adsorption kinetic analysis was carried out to evaluate the rate of adsorbate uptake by the adsorbent as a function of time and to identify the mechanisms governing the process. For this purpose, the adsorption capacity was calculated both at a given time (q_t) and at equilibrium (q_e), as expressed in Eqs. (4) and (5), respectively.

$$q_t = \frac{(C_0 - C_t).V}{m} \quad \ldots(4)$$

$$q_e = \frac{(C_0 - C_e).V}{m} \quad \ldots(5)$$

Where q_t denotes the adsorption capacity at time t (mg g^{-1}), while q_e represents the adsorption capacity at equilibrium (mg g^{-1}). Furthermore, C_0 is the initial adsorbate concentration in solution (mg L^{-1}), C_t is the adsorbate concentration at time t (mg L^{-1}), and C_e is the adsorbate concentration at equilibrium (mg L^{-1}). The variable V denotes the volume of the adsorbate solution (L), whereas m is the mass of adsorbent used (g).

The kinetic data obtained were analyzed using pseudo-first-order and pseudo-second-order kinetic models. In the present study, linearized forms of the kinetic equations were employed to facilitate comparative evaluation of adsorption behavior and parameter estimation. Although nonlinear fitting may reduce potential statistical bias associated with linear transformation, the linear approach remains widely applied for preliminary kinetic interpretation and comparison with previous adsorption studies.

The pseudo-first-order model is expressed in linear form, as shown in Eq. (6).

$$ln(q_e - q_t) = ln(q_e) - k_1 t \quad \ldots(6)$$

In this equation, k_1 is the rate constant of the pseudo-first-order model (min^{-1}), q_e is the adsorption capacity at equilibrium (mg g^{-1}), q_t is the adsorption capacity at time t (mg g^{-1}), and t is the adsorption time (min). For comparison, the adsorption behavior was also analyzed using the pseudo-second-order model, which is expressed in linear form in Eq. (7).

$$\frac{t}{qt} = \frac{t}{k2qe^2} + \frac{t}{qe} \quad \ldots(7)$$

In this equation, k_2 is the rate constant of the pseudo-second-order model (g mg^{-1} min^{-1}), q_e is the adsorption capacity at equilibrium (mg g^{-1}), q_t is the adsorption capacity at time t (mg g^{-1}), and t is the adsorption time (min). The most appropriate kinetic model was determined based on the coefficient of determination (R^2) and the agreement between the experimental adsorption capacity and the model-calculated adsorption capacity.

2.8. Energy Consumption

To evaluate the energy requirement during the electrocoagulation process, electrical energy consumption was calculated based on the relationship among voltage, current, operating time, and the volume of wastewater treated, as expressed in Eq. (8).

$$E = \frac{(U \times I \times t)}{V} \quad \ldots(8)$$

In this equation, E represents the electrical energy consumption during the electrocoagulation process (kWh m^{-3}), U is the applied voltage (V), I is the electric current (A), t is the operating time (h), and V is the volume of wastewater treated (m^3). Units were reported consistently to ensure consistency in energy consumption calculations.

2.9. Electrode Consumption

In addition to energy consumption, the amount of electrode material dissolved during the process was also evaluated as an important operational parameter. Electrode consumption was calculated from the difference in electrode mass before and after the process and then normalized to the volume of wastewater treated, as shown in Eq. (9).

$$C_{electrode} = \frac{m_initial - m_final}{V} \quad \ldots(9)$$

Electrode consumption represents the amount of anode material dissolved during the electrocoagulation process. In this equation, $C_{electrode}$ is the electrode consumption (kg m^{-3}), m_initial is the electrode mass before the process, m_final is the electrode mass after the process, and V is the volume of wastewater treated (m^3). Theoretically, electrode dissolution is the basis for coagulant generation in electrocoagulation; therefore, electrode consumption is an important parameter from both process and economic perspectives.

2.10. Adsorbent Consumption

In the adsorption stage, material usage was also expressed as adsorbent consumption to indicate the mass of bentonite used per unit volume of wastewater treated. This value was calculated using Eq. (10).

$$C_{adsorbent} = \frac{m_{adsorbent}}{V} \quad \ldots(10)$$

In this equation, $C_{adsorbent}$ is the adsorbent consumption (kg m^{-3}), $m_{adsorbent}$ is the mass of adsorbent used (kg), and V is the volume of wastewater treated (m^3). This parameter is important because, in the integrated electrocoagulation–adsorption system, adsorbent demand directly affects both the performance of the final polishing stage and the overall operating cost.

2.11. Operating Cost

To assess the operational feasibility of the process, the total operating cost was calculated as the sum of the main cost components, namely electrical energy, electrode consumption, and adsorbent usage. This general relationship is expressed in Eq. (11).

$$OC = C_{energy} + C_{electrode} + C_{adsorbent} \quad \ldots(11)$$

$$OC = (a \times E) + (b \times C_{electrode}) + (c \times C_{adsorbent}) \quad \ldots(12)$$

The total operating cost was further expressed in more detail as a function of the electricity tariff, electrode price, and adsorbent price, as shown in Eq. (12). In this study, the operating cost was calculated as the sum of the electrical energy cost, electrode consumption cost, and adsorbent usage cost, as described in Eqs. (11) and (12). In these equations, OC is the total operating cost (Rp m^{-3}), E is the electrical energy consumption (kWh m^{-3}), $C_{electrode}$ is the electrode consumption (kg m^{-3}), $C_{adsorbent}$ is the adsorbent consumption (kg m^{-3}), a is the electricity rate (Rp kWh^{-1}), b is the electrode price (Rp kg^{-1}), and c is the adsorbent price (Rp kg^{-1}). These equations were used to estimate the total process cost per unit volume of wastewater treated.

The operating cost estimation in this study was limited to the major direct operational components, namely electrical energy, electrode consumption, and adsorbent usage. Additional costs associated with chemical consumption for pH adjustment, sludge handling and disposal, labor, and maintenance were not included and should therefore be considered in future scale-up and techno-economic evaluations.

3. RESULTS AND DISCUSSION

The wastewater used in this study was generated from routine activities in the analytical chemistry laboratory, mainly from the washing of glassware, residual standard solutions, and sample preparation residues that potentially contained heavy metals, as shown in Table 3.

The results are presented as mean ± standard deviation from triplicate experiments (n = 3).

3.1. Optimization of the Electrocoagulation Process

The optimization of electrocoagulation operating parameters was carried out to determine the most effective conditions

Table 3: Initial characteristics of analytical chemistry laboratory wastewater.

Parameter	Value	Unit	Analytical method
pH	6.3 ± 0.1	–	pH meter
Temperature	27.4 ± 0.2	°C	Digital thermometer
Conductivity	1.26 ± 0.03	mS cm^{-1}	Conductivity meter
Total dissolved solids (TDS)	632 ± 5	mg L^{-1}	TDS meter
Dissolved oxygen (DO)	4.8 ± 0.1	mg L^{-1}	DO meter
Turbidity	18.6 ± 0.5	NTU	Turbidimeter
Total suspended solids (TSS)	11.3 ± 0.4	mg L^{-1}	Gravimetric method
Biochemical oxygen demand (BOD)	0.5 ± 0.1	mg L^{-1}	$BOD_{▯}$ method
Chemical oxygen demand (COD)	8.5 ± 0.3	mg L^{-1}	Dichromate method
Pb	5.5494 ± 0.0100	mg L^{-1}	AAS
Cd	2.3517 ± 0.0100	mg L^{-1}	AAS
Ni	1.7007 ± 0.0100	mg L^{-1}	AAS

for removing Pb, Cd, and Ni from laboratory wastewater. In this system, the initial pH, current density, and contact time were selected as the main parameters because they govern metal speciation, the rate of anode dissolution, in-situ coagulant generation, and the stability of the flocs formed during the process.

As shown in Fig. 2, the initial pH had a significant effect on the removal efficiency of Pb, Cd, and Ni. The removal efficiency increased markedly as the pH was raised from 3 to 7, indicating that acidic conditions were less favorable for heavy metal removal. At pH 3, the removal efficiencies were the lowest, at approximately 60% for Pb, 62% for Cd, and 65% for Ni. This behavior can be attributed to the high concentration of H^+ ions under strongly acidic conditions, which compete with dissolved metal ions for reactive sites and inhibit the formation of metal hydroxide species and stable coagulant flocs (Tegladza et al. 2021, Mao et al. 2023, Lu et al. 2024).

When the pH was increased to 5, the removal efficiencies rose to approximately 80% for Pb, 82% for Cd, and 85% for Ni, indicating that the solution conditions had become more favorable for hydrolysis reactions and the formation of effective coagulant species.

The highest removal efficiencies were achieved at pH 7, reaching approximately 87% for Pb, 89% for Cd, and 91% for Ni. At near-neutral pH, aluminum hydrolysis and speciation occur within a range that is more favorable for the formation of amorphous $Al(OH)_3$ flocs with high surface area and strong adsorptive capacity. Under these conditions, adsorption, charge neutralization, and sweep flocculation can proceed more effectively, allowing metal ions to be more readily destabilized and entrapped in the solid phase (Huang et al. 2020, Ullah et al. 2025). These results indicate that neutral pH was the optimum condition for heavy metal removal in this system, likely because of the more effective formation of amorphous hydroxide flocs and the reduced competition from H^+ ions (Tegladza et al. 2021, Lu et al. 2024). Under these conditions, dissolved metal ions can be more effectively destabilized, adsorbed, and entrapped within the floc matrix (Huang et al. 2020, Tegladza et al. 2021).

One-way ANOVA confirmed that pH significantly affected the removal efficiencies of Pb, Cd, and Ni (Pb: $F = 2386.88$, $p < 0.001$; Cd: $F = 2386.88$, $p < 0.001$; Ni: $F = 2212.50$, $p < 0.001$). Tukey's HSD post hoc test indicated that the removal efficiencies at pH 7 were significantly higher than those at pH 3, pH 5, and pH 11 ($p < 0.05$), whereas the difference between pH 7 and pH 9 was not statistically significant ($p > 0.05$). Therefore, pH 7 was selected as the optimum operating pH.

At pH 9 and 11, the removal efficiency tended to remain stable or decrease slightly, indicating that further increases in pH did not result in any meaningful improvement in performance. This behavior may be attributed to changes in aluminum speciation under more alkaline conditions, which can reduce the dominance of $Al(OH)_3$ flocs as the most effective coagulant. In addition, at excessively high pH, the increased OH^- concentration in the bulk solution and in the vicinity of the cathode may alter floc formation conditions,

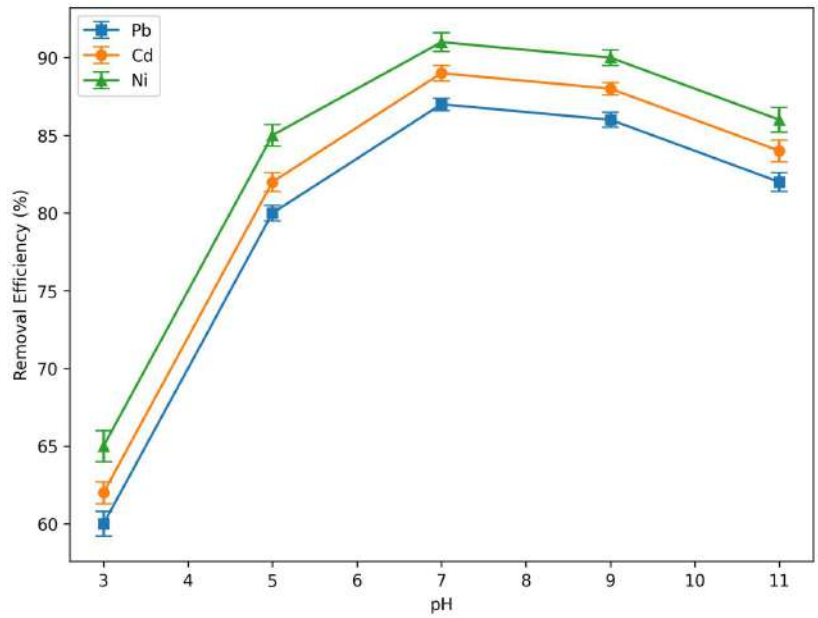


Fig. 2: Effect of pH on heavy metal removal efficiency.

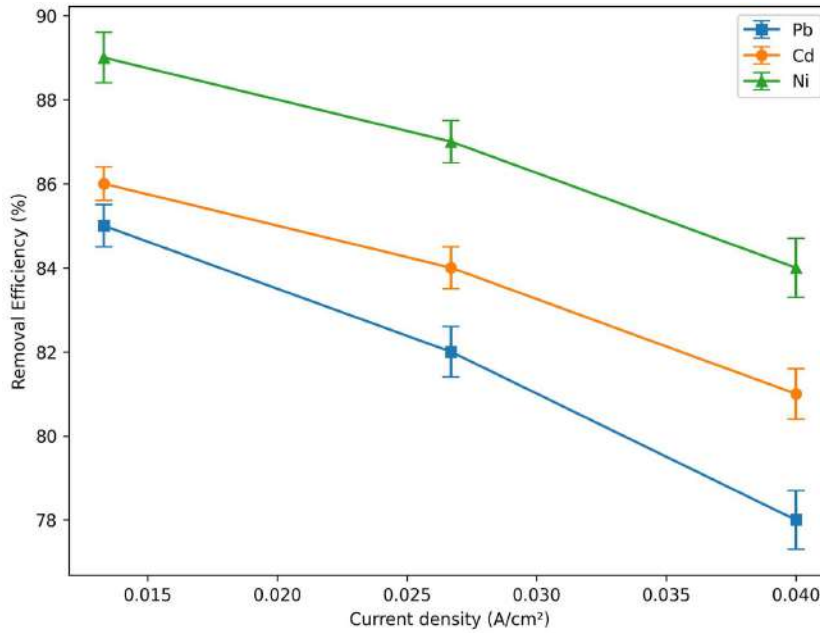


Fig. 3: Effect of current density on heavy metal removal efficiency.

thereby making the sweep flocculation window less favorable and preventing metal capture efficiency from increasing proportionally (Huang et al. 2020, Matra et al. 2025).

This behavior indicates that the system reached its optimum performance under near-neutral conditions, whereas excessively high alkalinity may affect metal speciation or floc stability, thereby limiting any further improvement in removal efficiency (Mao et al. 2023, Lu et al. 2024).

Overall, these results confirm that pH 7 was the optimum condition for heavy metal removal in the system investigated. Across all pH variations, the removal efficiency followed the order Ni > Cd > Pb, indicating that Ni was the most effectively removed ion under the experimental conditions. This trend is likely related to differences in hydrolysis behavior, ionic properties, and the affinity of each metal for the hydroxide flocs or adsorptive sites (Huang et al. 2020, Tegladza et al. 2021).

As shown in Fig. 3, increasing the current density from 0.0133 to 0.0400 A cm^{-2} resulted in a decline in removal efficiency for all metals investigated. At the lowest current density, 0.0133 A cm^{-2}, the removal efficiencies were approximately 85% for Pb, 86% for Cd, and 89% for Ni. When the current density was increased to 0.0267 A cm^{-2}, the removal efficiencies decreased to about 82% for Pb, 84% for Cd, and 87% for Ni. A further decline was observed at 0.0400 A cm^{-2}, with removal efficiencies of approximately 78% for Pb, 81% for Cd, and 84% for Ni. These results indicate that 0.0133 A cm^{-2} was the optimum current density for this system.

One-way ANOVA also confirmed that current density significantly influenced the removal efficiencies of Pb, Cd, and Ni (Pb: $F = 231.25$, $p < 0.001$; Cd: $F = 118.75$, $p < 0.001$; Ni: $F = 118.75$, $p < 0.001$). Tukey's HSD test showed that the removal efficiencies obtained at 0.0133 A cm^{-2} were significantly higher than those obtained at 0.0267 and 0.0400 A cm^{-2} ($p < 0.05$), confirming 0.0133 A cm^{-2} as the optimum current density.

In theory, a higher current density should increase the rate of anode dissolution and in-situ coagulant generation (Ammar et al. 2023, Mao et al. 2023, Lu et al. 2024). However, in this system, increasing the current density did not improve the removal efficiency. This phenomenon may be attributed to the rapid and excessive generation of gas bubbles at higher currents, which can disrupt the formation of stable flocs and reduce the effectiveness of interactions between coagulant species and metal ions (Tegladza et al. 2021, Mao et al. 2023).

At higher current densities, rapid gas bubble generation at the electrode surface may induce excessive turbulence and hydrodynamic disturbance within the reactor. Under such conditions, the flocs formed become more fragile and susceptible to breakage or re-dispersion, thereby reducing the effectiveness of sweep flocculation and metal entrapment. In addition, excessive coagulant generation may lead to local oversaturation of charged species near the electrodes, which can partially destabilize previously formed aggregates and reduce effective metal–floc interactions (Tegladza et al. 2021, Mao et al. 2023).

Furthermore, higher current density may accelerate electrode surface passivation and shorten the effective contact time between dissolved metal ions and active hydroxide flocs because of intensified bubble evolution. As a result, although higher current density theoretically increases coagulant production, the overall removal efficiency may decline because the system exceeds its optimum hydrodynamic and electrochemical operating conditions. In addition, an excessively high current density may increase local turbulence around the electrodes, causing the flocs formed to become less stable, more prone to breakage, and less likely to form larger agglomerates. Under such conditions, the system may have exceeded its effective operating range, where increased coagulant generation no longer translates into improved removal efficiency. Instead, excessive gas bubble formation and hydrodynamic disturbance may reduce the effective contact time between metal ions and electrocoagulation flocs. Furthermore, the overly rapid generation of charged species near the electrodes may also lead to partial restabilization of suspended particles, thereby reducing the net removal efficiency.

Therefore, although a higher current increases the intensity of the electrochemical process, in this system a lower current density provided a better balance among coagulant generation, floc stability, and metal capture, resulting in higher removal efficiency (Ammar et al. 2023, Tegladza et al. 2021). Accordingly, increasing current intensity does not necessarily lead to improved removal performance.

The order of removal efficiency remained consistent across all current density variations, namely Ni > Cd > Pb, indicating that Ni exhibited the highest removal affinity under the operating conditions tested.

Overall, these results confirm that current density optimization is a key factor in the electrocoagulation process, as this parameter affects not only coagulant generation but also floc stability and the efficiency of heavy metal removal (Ammar et al. 2023, Mao et al. 2023, Lu et al. 2024).

As shown in Fig. 4, increasing the contact time from 15 to 60 min resulted in a significant increase in the removal efficiency of Pb, Cd, and Ni. At 15 min, the removal efficiencies were approximately 55% for Pb, 58% for Cd, and 60% for Ni, which increased to about 70–76% at 30 min and 80–86% at 45 min. The highest removal efficiencies were achieved at 60 min, reaching approximately 85% for Pb, 87% for Cd, and 90% for Ni.

Electrocoagulation time significantly affected heavy metal removal (Pb: $F = 2956.88$, $p < 0.001$; Cd: $F = 2780.63$, $p < 0.001$; Ni: $F = 2966.25$, $p < 0.001$). Tukey's HSD analysis showed that the removal efficiencies at 60 min were significantly higher than those at 15, 30, and 45 min ($p < 0.05$), whereas the difference between 60 and 75 min was not statistically significant ($p > 0.05$). Thus, 60 min was selected as the optimum electrocoagulation time. This trend indicates that longer contact time enhances anode dissolution, promotes the formation of hydrolyzed aluminum species, and facilitates the growth of $Al(OH)_3$ flocs, thereby improving metal capture through adsorption, coprecipitation, and sweep flocculation mechanisms (Mouedhen et al. 2008, Ullah et al. 2025). At the initial stage, the availability of active sites and high binding capacity enable rapid removal, whereas

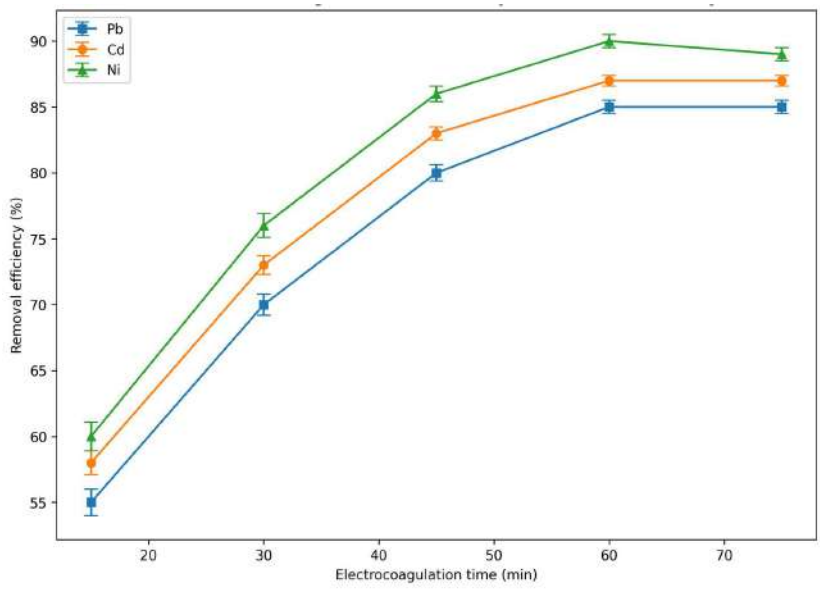


Fig. 4: Effect of time on heavy metal removal efficiency.

increased interaction between metal ions and coagulant species further enhances removal efficiency (Ammar et al. 2023, Khan et al. 2023, Raji et al. 2023, Yang et al. 2025).

However, after 60 min, most of the active sites and the system's binding capacity appeared to have been substantially utilized, so that further increases in contact time did not produce a significant improvement. The slight decline observed at 75 min may be attributed to partial desorption, redistribution of adsorbed species, or floc instability during prolonged operation.

Overall, the optimization results demonstrate that pH, current density, and contact time significantly influence heavy metal removal efficiency. Neutral pH favored effective floc formation, while lower current density improved process stability. Increasing contact time enhanced removal efficiency up to an optimum point, beyond which performance stabilized. Accordingly, the optimum electrocoagulation conditions were pH 7, current density 0.0133 A cm^{-2}, and contact time 60 min. These conditions provided the best balance between coagulant generation, floc stability, and metal removal efficiency and were therefore used for subsequent integration with the adsorption process (Ammar et al. 2023, Bakry et al. 2024, Twizerimana & Wu 2024).

3.2. Optimization of Bentonite Adsorption

One-way ANOVA showed that adsorbent dosage significantly affected the removal of Pb ($F = 207.81$, $p < 0.001$), Cd ($F = 142.19$, $p < 0.001$), and Ni ($F = 456.25$, $p < 0.001$). Tukey's HSD test indicated that increasing the dosage from 20 to 40 g significantly improved the removal efficiencies of all three metals ($p < 0.05$), whereas the difference between 40 and 60 g was not statistically significant ($p > 0.05$). Therefore, 40 g was selected as the optimum dosage. Adsorption parameters, namely adsorbent dosage and contact time, were optimized to determine the most effective conditions for removing Pb, Cd, and Ni from wastewater using thermally activated bentonite. These parameters govern the availability of active sites, the interaction between metal ions and the adsorbent surface, and the approach to equilibrium (Fan et al. 2024, Prepilková et al. 2024). As shown in Fig. 5, adsorbent dosage had a significant effect on removal efficiency. Increasing the dosage from 20 to 40 g improved removal efficiencies from approximately 75% to 81% for Pb, 72.5% to 77.5% for Cd, and 54% to 63% for Ni. This improvement is attributed to the increase in available surface area and active binding sites, which enhances metal adsorption (Fan et al. 2024, Li et al. 2025).

Table 4: Adsorption capacity (q_e) of thermally activated bentonite at different adsorbent dosages.

Adsorbent dosage (g)	Pb q_e (mg g^{-1})	Cd q_e (mg g^{-1})	Ni q_e (mg g^{-1})
20	0.0624	0.0218	0.0098
40	0.0390	0.0136	0.0062
60	0.0265	0.0091	0.0041

Table 4 presents the adsorption capacity (q_e) of thermally activated bentonite at different adsorbent dosages. The q_e values decreased with increasing adsorbent dosage from 20 to 60 g. This behavior is commonly observed in adsorption systems because increasing adsorbent mass provides more adsorption sites, while the amount of dissolved metal ions in the solution remains relatively constant. Consequently, the amount of adsorbed metal per unit mass of adsorbent becomes lower at higher adsorbent dosages.

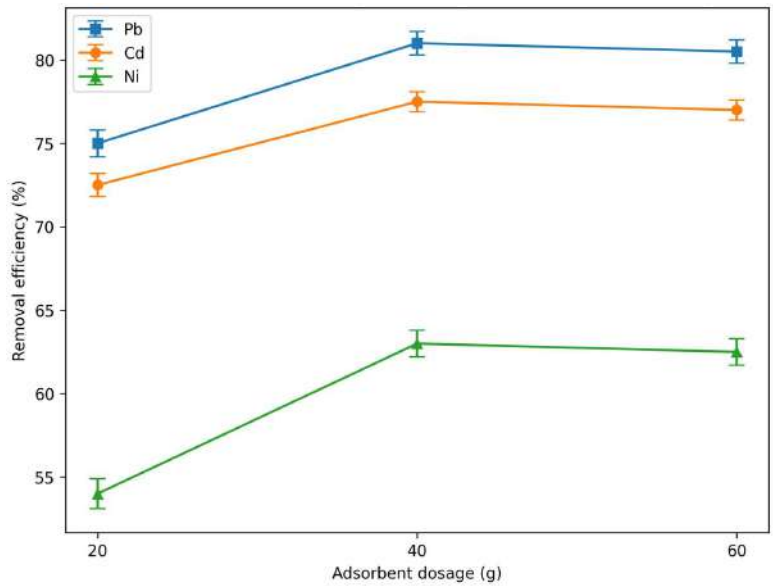


Fig. 5: Effect of adsorbent dosage on heavy metal removal efficiency.

However, further increasing the dosage to 60 g did not result in a significant improvement, with removal efficiencies remaining nearly constant or slightly decreasing. This behavior suggests that the system reached its optimum dosage at 40 g, beyond which particle aggregation and overlap may reduce effective surface area and limit accessibility of active sites. In addition, when the number of adsorption sites exceeds the available metal ions, further increases in adsorbent dosage do not proportionally enhance removal efficiency (Fan et al. 2024, Prepilková et al. 2024). Across all dosages, the removal efficiency followed the order Pb > Cd > Ni, indicating a higher affinity of bentonite toward Pb. This trend is consistent with differences in ionic radius, hydration energy, and cation-exchange behavior on aluminosilicate surfaces (Yang et al. 2025, Li et al. 2025, Wang et al. 2024, Anna et al. 2015). Accordingly, 40 g was identified as the optimum adsorbent dosage, providing the highest removal efficiency without excessive material consumption.

Adsorption contact time also significantly affected the removal efficiencies of Pb, Cd, and Ni (Pb: $F = 1367.81$, $p < 0.001$; Cd: $F = 1073.44$, $p < 0.001$; Ni: $F = 969.38$, $p < 0.001$). Tukey's HSD analysis showed that the removal efficiencies at 60 min were significantly higher than those at 15, 30, and 45 min ($p < 0.05$), whereas the difference between 60 and 75 min was not statistically significant ($p > 0.05$). These results indicate that adsorption equilibrium was essentially reached at 60 min.

As shown in Fig. 6, contact time also significantly influenced adsorption performance. Removal efficiency increased from 30 to 60 min, reaching approximately 80.5% for Pb, 76% for Cd, and 65% for Ni. This trend reflects increased interaction between metal ions and available active sites, allowing adsorption to proceed toward equilibrium (Li et al. 2025, Wang et al. 2024).

Beyond 60 min, the removal efficiency stabilized or slightly decreased at 75 min, indicating that equilibrium had been reached and that most active sites were occupied. The slight decline may be attributed to adsorption–desorption equilibrium, redistribution of adsorbed species, or partial saturation of active sites (Yang et al. 2025, Li et al. 2025).

The removal efficiency order remained consistent (Pb > Cd > Ni) across all contact times, further confirming the higher affinity of bentonite toward Pb. Based on these results, 60 min was identified as the optimum contact time.

Overall, the optimum adsorption conditions were a bentonite dosage of 40 g and a contact time of 60 min. These conditions provided the best balance between active site availability and effective interaction time, resulting in maximum removal efficiency. The optimized

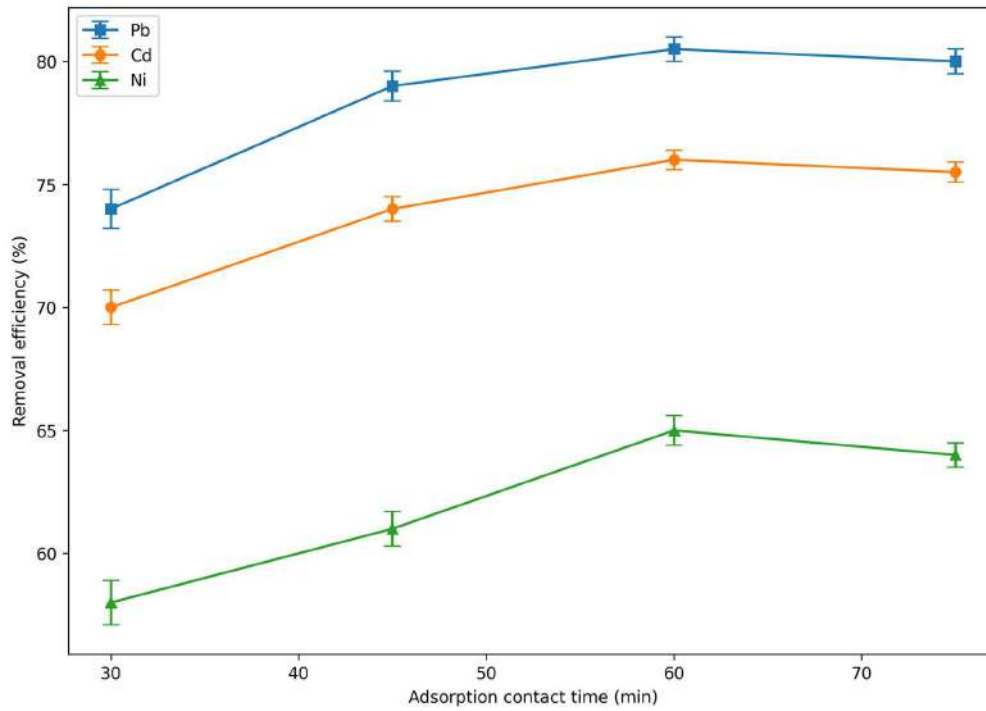


Fig. 6: Effect of time on heavy metal removal efficiency.

parameters were subsequently used for integration with the electrocoagulation stage (Prepilková et al. 2024, Fan et al. 2024, Wang et al. 2024).

3.3. Performance of the Integrated Electrocoagulation–Adsorption (EC-Ads) System

The final effluent contained Pb, Cd, and Ni at 0.0521 ± 0.0010 mg L^{-1}, 0.0342 ± 0.0010 mg L^{-1}, and 0.0452 ± 0.0010 mg L^{-1}, respectively. These results demonstrate that the integrated EC–Ads system substantially reduced the heavy metal burden in laboratory wastewater. When evaluated against the Indonesian general discharge benchmark in Appendix XVII of Minister of Environment Regulation No. 5/2014, all three metals were below the Category I limits, indicating that the treated effluent met the applicable discharge standards for Pb, Cd, and Ni under the present treatment conditions (PERMEN 2014).

The high removal efficiencies achieved in this study indicate that the integrated EC–Ads process has strong potential as an effective treatment strategy for laboratory wastewater containing mixed heavy metals. The combination of electrocoagulation and thermally activated bentonite adsorption provides complementary removal mechanisms that effectively reduce residual metal concentrations prior to wastewater discharge.

After the optimum conditions for each individual unit had been established, the subsequent evaluation focused on the performance of the integrated electrocoagulation–adsorption (EC-Ads) system for heavy metal removal from laboratory wastewater. Following the optimization of the individual treatment units, the performance of the integrated electrocoagulation–adsorption (EC-Ads) system was evaluated under the respective optimum conditions: pH 7, current density 0.0133 A cm^{-2}, and contact time 60 min for electrocoagulation, and a bentonite dosage of 40 g with a contact time of 60 min for adsorption. The integrated configuration was designed such that electrocoagulation acted as the primary removal stage, reducing dissolved metal concentrations through in-situ coagulant generation and hydroxide floc formation, while adsorption served as a polishing step for the removal of residual metals (Ammar et al. 2023, Twizerimana & Wu 2024).

The concentrations of Pb, Cd, and Ni at each treatment stage are presented in Table 5, and the corresponding removal efficiencies are summarized in Table 6. The initial influent concentrations of 5.5494 mg L^{-1} (Pb), 2.3517 mg L^{-1} (Cd), and 1.7007 mg L^{-1} (Ni) were reduced to 0.8324 mg L^{-1}, 0.3057 mg L^{-1}, and 0.1701 mg L^{-1}, respectively, after electrocoagulation. Subsequent adsorption further reduced these concentrations to 0.0521 mg L^{-1} (Pb), 0.0342 mg L^{-1} (Cd), and 0.0452 mg L^{-1} (Ni).

Table 7 presents the mass balance of Pb, Cd, and Ni throughout the integrated EC–Ads process. Based on a treatment volume of 2 L, the initial masses of Pb, Cd, and Ni were 11.10, 4.70, and 3.40 mg, respectively. During electrocoagulation, approximately 85–90% of the dissolved metals were removed from the liquid phase through adsorption onto Al(OH)□ flocs, coprecipitation, and sweep flocculation mechanisms. The subsequent adsorption stage further reduced the residual dissolved metal concentrations, removing an additional 1.56 mg Pb, 0.54 mg Cd, and 0.25 mg Ni. Overall, the integrated EC–Ads system removed 10.99 mg Pb, 4.64 mg Cd, and 3.31 mg Ni, corresponding to total removal efficiencies of 99.06%, 98.55%, and 97.34%, respectively. These results confirm that the removed metals were effectively transferred from the aqueous phase to the solid phase during treatment.

As shown in Fig. 7, the electrocoagulation stage achieved removal efficiencies of 85% for Pb, 87% for Cd, and 90% for Ni. The adsorption stage provided additional removal based on the EC effluent, with efficiencies of 93.74% for Pb, 88.81% for Cd, and 73.42% for Ni. Overall, the integrated EC-Ads system achieved high total removal efficiencies of 99.06% for Pb, 98.55% for Cd, and 97.34% for Ni.

These findings confirm that the two processes operate in a complementary manner, where electrocoagulation effectively reduces the bulk pollutant load and adsorption

Table 5: Concentrations of Pb, Cd, and Ni at each stage of the EC-Ads process.

Process stage	Pb (mg L^{-1})	Cd (mg L^{-1})	Ni (mg L^{-1})
Initial influent (laboratory wastewater)	5.5494 ± 0.0100	2.3517 ± 0.0100	1.7007 ± 0.0100
Electrocoagulation effluent (EC effluent/adsorption influent)	0.8324 ± 0.0100	0.3057 ± 0.0100	0.1701 ± 0.0100
Adsorption effluent (final treated effluent)	0.0521 ± 0.0010	0.0342 ± 0.0010	0.0452 ± 0.0010

Table 6: Removal efficiency at each treatment stage.

Process stage	Pb removal efficiency (%)	Cd removal efficiency (%)	Ni removal efficiency (%)
Electrocoagulation	85.00 ± 0.15	87.00 ± 0.37	90.00 ± 0.53
Adsorption (based on EC effluent)	93.74 ± 0.04	88.81 ± 0.04	73.42 ± 0.98
Total EC-Ads	99.06 ± 0.02	98.55 ± 0.04	97.34 ± 0.04

Table 7: Mass balance of Pb, Cd, and Ni during the integrated EC–Ads process.

Metal	Initial concentration (mg/L)	Initial mass (mg)	After EC (mg)	Final mass after Ads (mg)	Removed by EC (mg)	Removed by Ads (mg)	Total removed (mg)	Total removal (%)
Pb	5.5494	11.0988	1.6648	0.1042	9.4340	1.5606	10.9946	99.06
Cd	2.3517	4.7034	0.6114	0.0684	4.0920	0.5430	4.6350	98.55
Ni	1.7007	3.4014	0.3402	0.0904	3.0612	0.2498	3.3110	97.34

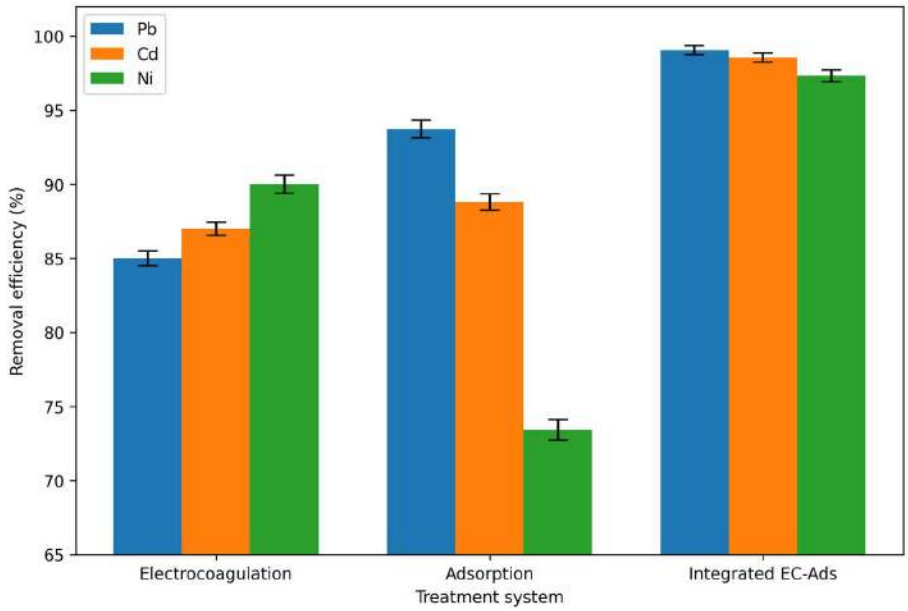


Fig. 7: Performance comparison of the electrocoagulation–adsorption system.

enhances final effluent quality by removing residual metals at lower concentrations (Ammar et al. 2023, Twizerimana & Wu 2024). The integrated system therefore provides a more effective treatment configuration than either process alone, particularly for achieving high and consistent removal of multiple heavy metals from laboratory wastewater (Twizerimana & Wu 2024, Jo et al. 2024).

3.4. Metal Removal Mechanism

The mechanism of metal removal in the integrated electrocoagulation–adsorption (EC-Ads) system investigated in this study can be explained as the result of synergy between in-situ coagulant generation during the electrocoagulation stage and subsequent metal binding during the adsorption stage. During the electrocoagulation stage, aluminum dissolves at the anode to produce Al^{3+} ions (Eq. 13), while water reduction at the cathode generates OH^- ions and hydrogen gas (Eq. 14). The Al^{3+} ions undergo hydrolysis to form amorphous $Al(OH)_3$ flocs (Eq. 15), which act as effective coagulants with high surface area and strong adsorptive capacity, particularly under near-neutral pH conditions. This is consistent with the optimum performance observed at pH 7, where aluminum speciation and floc stability favor metal removal (Patel et al. 2025).

$$Al_{(s)} \longrightarrow Al^{3+} + 3\,e^- \quad \ldots(13)$$

$$3H_2O + 3\,e^- \longrightarrow \frac{3}{2}H_{2(g)} + 3\,OH^- \quad \ldots(14)$$

$$Al^{3+} + 3\,OH^- \longrightarrow Al(OH)_3\,(s) \quad \ldots(15)$$

Once formed, the $Al(OH)_3$ flocs removed Pb, Cd, and Ni through several simultaneous pathways, namely surface adsorption, charge neutralization, coprecipitation, and sweep coagulation. Schematically, these interactions can be expressed as the binding of divalent metal ions onto the floc surface (Eq. 16), whereas under locally OH^--rich conditions, the metal ions may also form sparingly soluble hydroxide precipitates (Eq. 17).

Therefore, the substantial decrease in metal concentration observed during the EC stage in this study was likely not governed by a single mechanism, but rather by a combination of metal entrapment within the floc matrix, adsorption onto the surface of aluminum hydroxides, and partial precipitation. This explains why electrocoagulation was able to function as the primary removal unit, significantly reducing the pollutant load from the initial stage of treatment (Bakry et al. 2024).

$$M^{2+} + Al(OH)_{3(s)} \longrightarrow M\text{-}Al(OH)_{3(s)} \quad \ldots(16)$$

$$M^{2+} + 2\,OH^- \longrightarrow M(OH)_{2(s)} \quad \ldots(17)$$

Where M^{2+} represents Pb^{2+}, Cd^{2+}, or Ni^{2+}. These combined mechanisms are consistent with the substantial reduction in metal concentration observed during the electrocoagulation stage, where metal ions were likely destabilized, adsorbed, and immobilized within the hydroxide floc matrix (Bakry et al. 2024).

Under these conditions, metal binding by bentonite may proceed through ion-exchange mechanisms (Eq. 18) and surface complexation (Eq. 19). Recent literature has also confirmed that bentonite- and clay-based materials exhibit strong metal adsorption behavior, mainly through a combination of electrostatic interactions, ion exchange, and metal coordination with active surface groups (Wang et al. 2024, Yang et al. 2025). Because the adsorption stage in this study received influent whose pollutant load had already been reduced in the EC unit, the active sites of bentonite could be utilized more effectively for the removal of residual metals at low concentrations.

$$2X\text{-}Na + M^{2+} \longrightarrow X_2\text{-}M + 2Na^{+} \quad \ldots(18)$$

$$2{\equiv}SOH + M^{2+} \rightleftharpoons ({\equiv}SO)_2M + 2H^{+} \quad \ldots(19)$$

Where X denotes the cation-exchange sites on bentonite, and ≡SOH represents the active surface functional groups. Because the adsorption stage treats a pre-treated effluent with reduced metal concentration, the available active sites are utilized more efficiently for selective removal of residual metals.

Overall, the characterization data obtained provide complementary evidence for the two-stage mechanism operating in the EC-Ads system. The appearance of Pb, Cd, and Ni in the EDS spectra of bentonite after adsorption indicates that these metals were deposited on the adsorbent surface, while the changes in surface morphology observed in the SEM images suggest surface coverage and partial pore blockage by bound metal species. Furthermore, changes in the intensity and profile of the FTIR bands of bentonite after adsorption, particularly in the regions associated with O–H, H–O–H, and Si–O/Si–O–Si groups, indicate the involvement of active surface functional groups in metal binding.

During the electrocoagulation stage, the FTIR spectrum of the sludge, which exhibited dominant bands corresponding to hydroxyl groups and metal–oxygen bonds. These observations provide supporting evidence for the formation of hydrated aluminum hydroxide/oxyhydroxide flocs that may participate in adsorption, coprecipitation, and precipitation processes. In addition, the ICP-MS results showed that most of the metal mass was transferred to the solid phase. The mass balance analysis further demonstrated that most of the removed metals accumulated in the sludge and adsorbent solids, supporting the proposed transfer of contaminants from the liquid phase to the solid phase during treatment.

The proposed removal mechanisms are further supported by the consistency between the characterization results and the mass balance analysis. SEM–EDS analysis detected Pb, Cd, and Ni in the spent bentonite and electrocoagulation solids, demonstrating that the removed metals were retained within the solid matrix after treatment. In parallel, FTIR analysis revealed changes in hydroxyl- and silicate-related functional groups after adsorption, suggesting the participation of these active sites in metal binding. Furthermore, ICP–MS analysis confirmed that a substantial proportion of the removed metal mass was recovered in the solid phase, while the mass balance analysis quantitatively demonstrated the transfer of metals from the aqueous phase to sludge and adsorbent solids. The agreement among these independent analytical techniques provides converging evidence that metal removal occurred through a combination of adsorption, ion exchange, coprecipitation, precipitation, and sweep flocculation processes rather than through a single dominant pathway.

Although SEM–EDS, FTIR, and ICP–MS analyses cannot directly determine the exact molecular-scale binding configuration of Pb, Cd, and Ni, the combined characterization results consistently support the occurrence of adsorption, ion exchange, coprecipitation, and sweep flocculation mechanisms. The simultaneous detection of metals in the solid phase, changes in FTIR functional-group vibrations, and the observed mass transfer revealed by the mass balance analysis provide complementary evidence for the proposed removal pathways.

Therefore, the proposed mechanisms should be interpreted as being strongly supported by indirect but complementary experimental evidence rather than being conclusively proven. Future studies employing advanced surface characterization techniques such as X-ray photoelectron spectroscopy (XPS), X-ray diffraction (XRD), or other advanced spectroscopic analyses may provide more direct confirmation of the specific metal-binding mechanisms involved.

Taken together, these findings support that the integrated system operated through a complementary two-stage mechanism, namely predominant metal load reduction through floc formation during electrocoagulation, followed by the removal of residual metals through adsorption and ion exchange on thermally activated bentonite.

3.5. Characterization Analysis of Materials and Residues

3.5.1. SEM-EDS Analysis of Bentonite before and after Adsorption

The SEM images of fresh bentonite were interpreted as showing a layered structure with open pores. After adsorption, the surface

became rougher and denser, indicating the deposition of metals or the formation of surface complexes. EDS analysis of the spent adsorbent revealed the presence of Pb, Cd, and Ni, which were not detected in the fresh bentonite.

As summarized in Table 8, the SEM analysis showed changes in the surface morphology of bentonite before and after thermal treatment, as well as after the adsorption process. Natural bentonite exhibited an irregular structure with a rough agglomerated texture and several visible voids. After thermal activation, the bentonite surface became rougher, more fragmented, and more granular, indicating that the heat treatment modified the surface structure. After adsorption, the bentonite surface appeared denser and more agglomerated, with some pores partially covered by adsorbates. These changes suggest that thermal activation may enhance the accessibility of active sites, whereas the adsorption process leads to surface coating or pore filling by adsorbed metal ions.

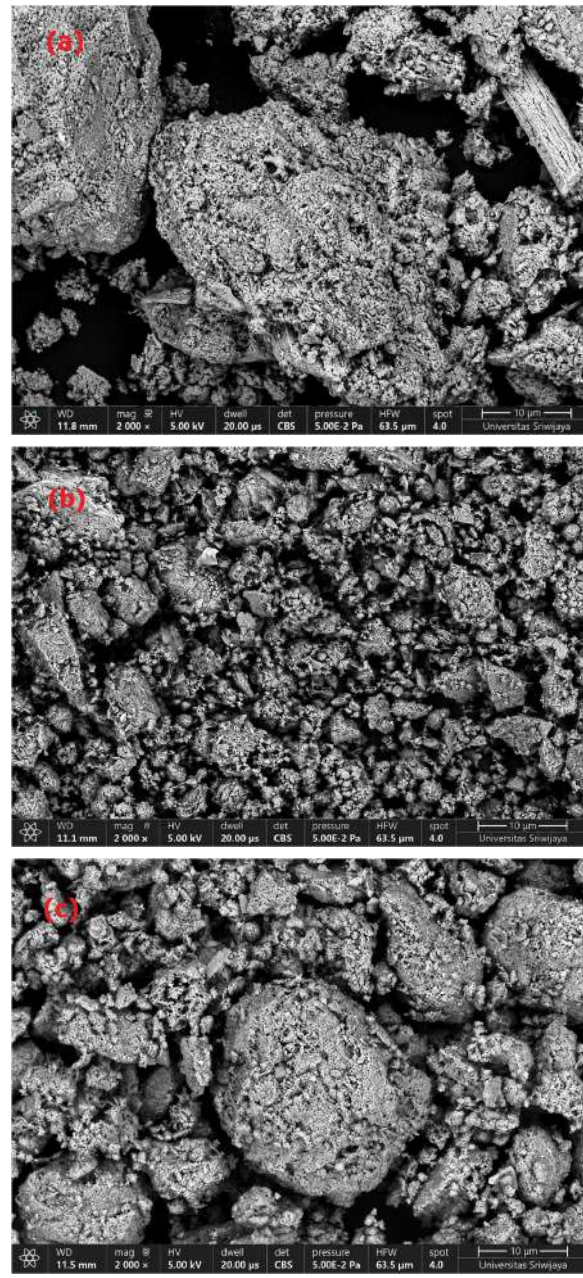


Fig. 8: SEM analysis of bentonite (a) natural bentonite, (b) thermally activated bentonite, (c) bentonite after adsorption.

Table 8: Summary of SEM-EDS results for bentonite before and after adsorption.

Parameter	Natural bentonite	Thermally activated bentonite	Bentonite after adsorption	Interpretation
Surface morphology	Irregular and porous surface with rough agglomerated texture. Visible voids and cavities are still observed.	The surface becomes rougher, more fragmented, and granular after thermal activation. Several cracks and broken particles are observed.	The surface appears denser and more agglomerated, with some pores partially covered after adsorption.	Thermal activation modifies the surface texture and may enhance surface accessibility, while adsorption leads to pore filling and surface coverage by adsorbates.

Table 9: EDS analysis results of natural bentonite, thermally activated bentonite, and bentonite after adsorption.

Component	Natural bentonite Weight (%)	Natural bentonite Atomic (%)	Thermally activated bentonite Weight (%)	Thermally activated bentonite Atomic (%)	Bentonite after adsorption Weight (%)	Bentonite after adsorption Atomic (%)
C	2.8	4.7	4.6	7.5	4.3	6.9
O	50.8	62.7	51.3	62.6	50.0	61.7
Mg	1.2	0.9	1.0	0.8	0.9	0.7
Al	6.6	4.8	6.6	4.8	6.2	4.5
Si	36.3	25.5	34.4	23.9	31.6	21.9
S	2.3	1.4	–	–	–	–
Mo	–	–	2.1	0.4	1.6	0.3
Pb	–	–	–	–	2.6	0.4
Cd	–	–	–	–	1.6	0.2
Ni	–	–	–	–	1.2	0.5
Total	100.0	100.0	100.0	100.0	100.0	100.0

The EDS results presented in Table 9. show that both natural bentonite and thermally activated bentonite were dominated by O, Si, and Al, confirming the aluminosilicate nature of the material. After thermal activation, the composition of the major elements did not change drastically; however, the disappearance of S indicates a reduction in impurity components on the adsorbent surface. After the adsorption process, Pb, Cd, and Ni were detected at 2.6, 1.6, and 1.2 wt%, respectively, providing direct evidence that the heavy metals had been bound to the bentonite. The relative decrease in Si and Al contents after adsorption suggests that part of the active surface had been covered by metal adsorbates, while the high O content indicates that the main aluminosilicate framework remained preserved. Overall, the EDS results support that thermal activation modified the bentonite surface, whereas the adsorption process led to the binding of heavy metals onto the material surface.

3.5.2. FTIR Analysis of Bentonite before and after Adsorption

As shown in Fig. 9, the FTIR spectra of thermally activated bentonite before and after adsorption exhibited noticeable peak shifts and intensity changes, indicating interactions between heavy metal ions and functional groups on the bentonite surface. The main FTIR peak positions before and after adsorption are summarized in Table 10.

As shown in Table 10, the broad absorption band assigned to O–H stretching vibrations shifted from 3295.89 cm^{-1} before adsorption to 3350.85 cm^{-1} after adsorption, corresponding to a shift of 54.96 cm^{-1}. This shift indicates the involvement of hydroxyl groups in the adsorption process and suggests the formation of surface complexes between metal ions and hydroxyl functional groups on bentonite.

In addition, the characteristic Si–O stretching vibration shifted from 1023.10 cm^{-1} to 934.86 cm^{-1} after adsorption, representing a shift of 88.24 cm^{-1}. The significant displacement of this band suggests strong interactions between Pb^{2+}, Cd^{2+}, and Ni^{2+} ions and the aluminosilicate framework of bentonite, indicating that ion exchange and surface complexation contributed to the adsorption process.

Table 10: FTIR peak positions and corresponding shifts before and after adsorption.

Functional group	Before adsorption (cm^{-1})	After adsorption (cm^{-1})	Shift (cm^{-1})
O–H stretching	3295.89	3350.85	+54.96
Si–O stretching	1023.10	934.86	–88.24
Si–O–Al / M–O bending	525.05	intensity change	–

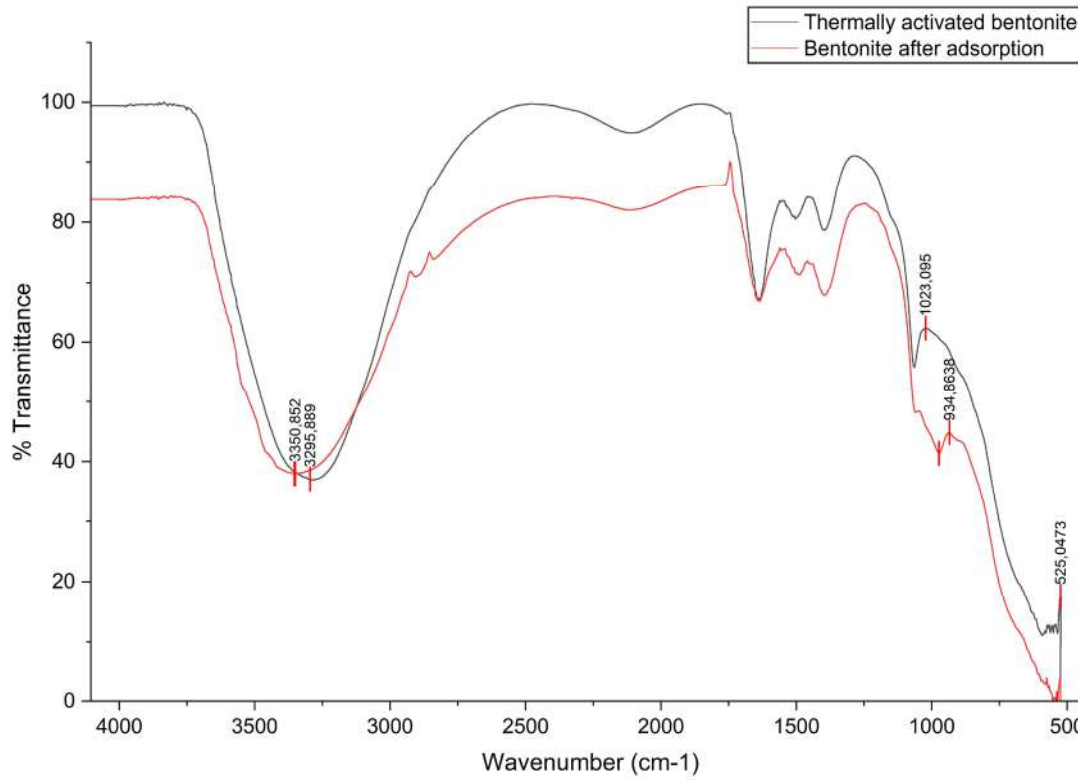


Fig. 9: FTIR spectra of bentonite before and after adsorption.

Furthermore, changes observed in the low-wavenumber region around 525 cm^{-1}, associated with Si–O–Al and/or metal–oxygen vibrations, provide additional evidence of modifications in the local bonding environment after adsorption. Despite these spectral changes, the characteristic bands of bentonite remained present, indicating that adsorption occurred without significant destruction of the bentonite mineral structure.

Overall, the observed numerical peak shifts confirm that hydroxyl and silicate functional groups participated directly in heavy metal adsorption, supporting ion exchange and surface complexation as important removal mechanisms.

3.6. Characterization of Electrocoagulation Sludge

To comprehensively understand the removal mechanism and validate the fate of heavy metals (Cd, Ni, and Pb) during the electrocoagulation process, a detailed characterization of the generated sludge was carried out (Patel et al. 2025, Bakry et al. 2024). This section discusses the macroscopic appearance of the dried flocs, followed by a molecular-level investigation using Fourier Transform Infrared (FTIR) spectroscopy to identify the functional groups involved in metal binding (Rajaniemi et al. 2021).

In addition, Inductively Coupled Plasma (ICP-MS) analysis was used to quantify elemental distribution in the sludge, thereby confirming mass balance closure between the liquid and solid phases. This multi-analytical approach provides strong evidence for chemisorption and complexation mechanisms previously suggested by the kinetic and thermodynamic data.

Fig. 10 presents digital macroscopic images of the solid phase generated during the electrocoagulation process: (a) freshly formed gelatinous $Al(OH)_3$ flocs between the aluminum electrodes and (b) dried sludge obtained after electrocoagulation. The clear differences in morphology and color indicate the successful transformation of dissolved metal ions into a stable, insoluble solid matrix, consistent with the high removal efficiency (>99%) observed at pH 7.

As shown in Fig. 11, the FTIR analysis of the flocs generated during the electrocoagulation process exhibited dominant absorption bands at approximately 3353.75, 1634.14, 1394.82, 973.49, and 531.58 cm^{-1}, indicating the formation of an inorganic floc matrix rich in hydroxyl groups and metal–oxygen bonds.

The broad band at 3353.75 cm^{-1} was attributed to O–H stretching vibrations, indicating the presence of surface hydroxyl groups and adsorbed water on the flocs, whereas the



Fig. 10: (a) Floating flocs (b) Dried flocs formed during the electrocoagulation process.

band at 1634.14 cm^{-1} was associated with H–O–H bending vibrations of bound water, confirming the hydrated nature of the electrocoagulation residue. Furthermore, the band at 1394.82 cm^{-1} indicates the presence of carbonate species that were likely adsorbed or incorporated into the floc structure during the process.

The band at 973.49 cm^{-1} was assigned to M–OH and/or M–O vibrations in metal hydroxide or oxyhydroxide phases, while the band at 531.58 cm^{-1} is characteristic of metal–oxygen (M–O) bonds. Overall, these spectral features confirm that the metal removal mechanism during electrocoagulation was dominated by the formation of

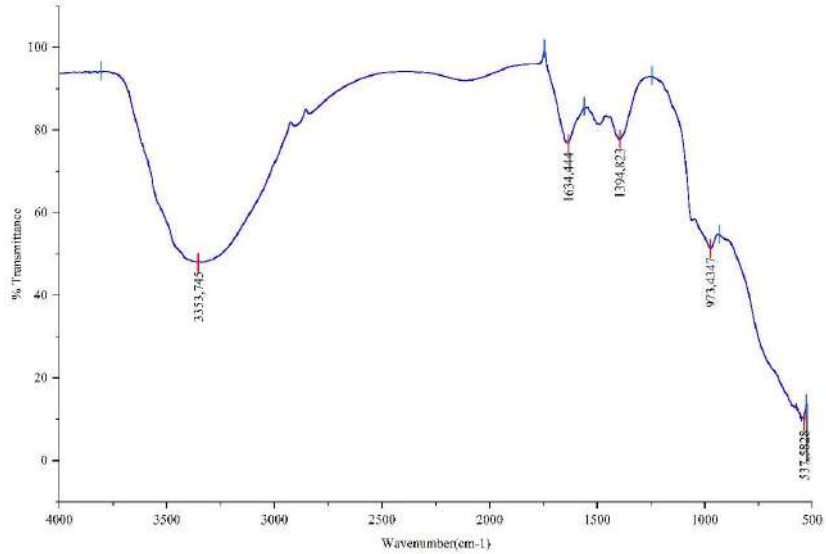


Fig. 11: FTIR analysis of flocs generated during the electrocoagulation process.

Table 11: Mass balance and elemental composition of dried sludge determined by ICP-MS analysis.

Component	Parameter	Pb	Cd	Ni	Total mixture
Aqueous phase	Initial concentration, (C_0) (mg L^{-1})	5.5494	2.3517	1.7007	9.6018
	Initial mass, (m_i) (mg)	11.0988	4.7034	3.4014	19.2036
	Final concentration after EC (C_{EC}) (mg L^{-1})	0.8324	0.3057	0.1701	–
	Final mass in filtrate, (m_f) (mg)	1.6648	0.6114	0.3402	2.6164
Solid phase	Dried sludge mass (g)	–	–	–	1.415
	Metal concentration in sludge (C_s) (mg.kg^{-1})	7517.61	2964.79	2376.00	12858.40
	Metal mass in sludge (m_s) (mg)	10.6374	4.1952	3.3620	18.1946

hydrated hydroxide/oxyhydroxide flocs, which served as active sites for adsorption, coprecipitation, and precipitation, thereby enabling the effective immobilization of metal contaminants into the solid phase formed (Patel et al. 2025, Bakry et al. 2024, Harahap et al. 2024).

The removal mechanism of Pb, Cd, and Ni was elucidated by integrating the quantitative mass balance obtained from ICP-MS with molecular-level characterization by FTIR. Based on the ICP-MS data in Table 11, the initial metal masses in the aqueous phase were 11.0988 mg for Pb, 4.7034 mg for Cd, and 3.4014 mg for Ni. After the EC process, the metal masses remaining in the filtrate were 1.6648, 0.6114, and 0.3402 mg, respectively, whereas the metal masses measured in the dried sludge reached 10.6374, 4.1952, and 3.3620 mg, respectively. These data indicate that most of the metals were transferred from the liquid phase to the solid phase during the electrocoagulation process. This integrated analysis demonstrates that electrocoagulation effectively immobilized the mixed metals through strong chemical entrapment within the hydroxide floc structure (Yazıcı Karabulut 2025).

3.7. Adsorption Kinetic Analysis

3.7.1. Pseudo-First-Order Model

Although the R^2 values were relatively high, the $q_{e,calc}$ values obtained from the pseudo-first-order model differed considerably from the experimental $q_{e,exp}$ values. This indicates that the model was less able to adequately represent the actual adsorption process in the bentonite system.

3.7.2. Pseudo-Second-Order Model

These results indicate that the pseudo-second-order model provided a better fit, as reflected by the very high R^2 values and the closer agreement between the calculated $q_{e,calc}$ and experimental values. In addition, the adsorption profile suggests rapid occupation of active sites followed by the attainment of a near-equilibrium state (Tran 2023, Vareda 2023).

Nevertheless, a good fit to the pseudo-second-order model does not directly prove that the adsorption mechanism was entirely governed by chemisorption; rather, it is more appropriately interpreted as indicating that the adsorption rate was likely influenced by surface interactions between the metal ions and the active sites of the adsorbent (Tran 2023, Vareda 2023).

As shown in Fig. 12, the adsorption capacity of thermally activated bentonite for Pb, Cd, and Ni increased with increasing contact time from 30 to 60 min and then tended to stabilize at 75 min. This pattern indicates that, during the initial stage of adsorption, a large number of active sites were still available on the adsorbent surface, allowing metal uptake to proceed relatively rapidly, whereas after 60 min the system began to approach equilibrium (Raji et al. 2023, Tran 2023).

The maximum adsorption capacities obtained were 0.44673 mg g^{-1} for Pb, 0.17873 mg g^{-1} for Cd, and 0.11055 mg g^{-1} for Ni, respectively, giving an adsorption affinity order of Pb > Cd > Ni. As shown in Table 13, the adsorption kinetic data for all three metals followed the pseudo-second-order model with an excellent fit, as indicated by R^2 values of 0.9990 for Pb, 0.9990 for Cd, and 0.9970 for Ni.

In addition, the theoretical adsorption capacities ($q_{e,calc}$) predicted by the pseudo-second-order model were closer to the experimental values than those obtained from the pseudo-first-order model. These results suggest that metal adsorption by bentonite was predominantly governed by surface chemical interactions, such as ion exchange and complexation at the active sites of bentonite (Raji et al. 2023, Wang et al. 2024, Yang et al. 2024).

However, this interpretation remains indicative, since other kinetic models, such as the intraparticle diffusion and Elovich models, were not evaluated in this study. Therefore, the possible contributions of intraparticle diffusion, boundary layer resistance, and other mass transfer steps cannot yet be

Table 12: Adsorption kinetic parameters of the pseudo-first-order model.

Ion	$q_{e,exp}$ (mg g^{-1})	$q_{e,calc}$ (mg g^{-1})	k_1 (min^{-1})	R^2
Pb	0.44673	0.30852	0.07590	0.9902
Cd	0.17873	0.06315	0.05385	0.9846
Ni	0.11055	0.04591	0.04369	0.9974

Table 13: Adsorption kinetic parameters of the pseudo-second-order model.

Ion	$q_{e,calc}$ (mg g^{-1})	k_2 (g mg^{-1} min^{-1})	R^2
Pb	0.47256	0.52795	0.9990
Cd	0.18805	1.37596	0.9990
Ni	0.11871	1.41502	0.9970

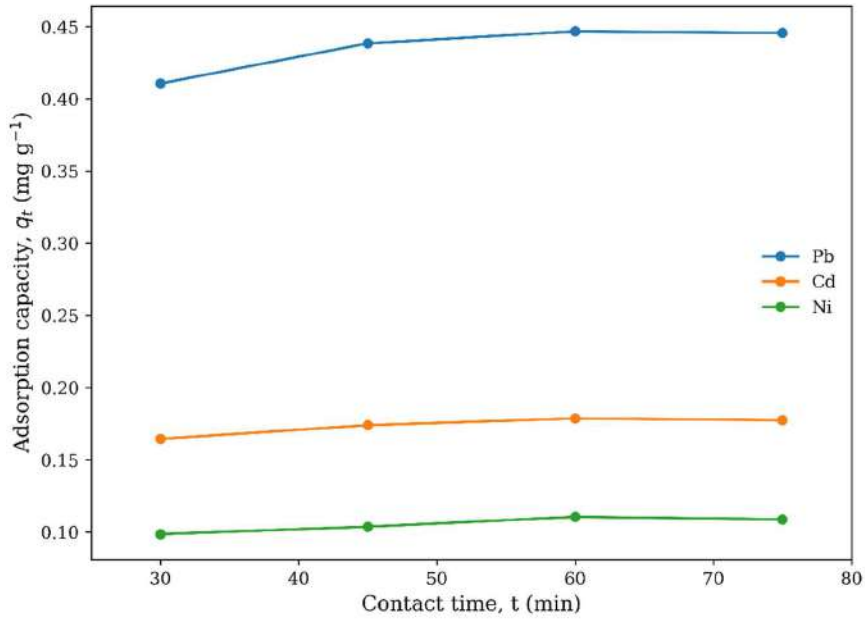


Fig. 12: Experimental adsorption kinetics of Pb, Cd, and Ni onto bentonite as a function of contact time.

fully excluded and should be investigated further in future studies (Vareda 2023, Yazidi et al. 2026).

3.8. Energy Consumption, Electrode Consumption, and Operating Cost

As shown in Table 14, the EC-Adsorption process operated at a current of 2 A and a voltage of 10 V, with 60 min of electrocoagulation followed by 60 min of adsorption, and exhibited very high removal performance for Pb, Cd, and Ni, reaching 99.06%, 98.55%, and 97.34%, respectively. The substantial reduction in residual metal concentrations indicates that the combination of the two processes was effective for removing dissolved heavy metals from laboratory wastewater.

Based on Table 15, the normalized energy, electrode, and adsorbent consumptions were 10.00 kWh m^{-3}, 0.065 kg m^{-3}, and 20.00 kg m^{-3}, respectively. The operating cost was calculated as the sum of electricity, electrode, and adsorbent costs. An electricity tariff of Rp 1,444.7 kWh^{-1} was adopted based on the applicable tariff published by PT PLN (Persero) (PLN 2026), while the aluminum electrode and thermally activated bentonite prices were assumed to be Rp 55,000 kg^{-1} and Rp 1,250 kg^{-1}, respectively, based on local market prices. Based on these economic assumptions, the electricity, electrode, and adsorbent costs were Rp 14,447 m^{-3}, Rp 3,575 m^{-3}, and Rp 25,000 m^{-3}, respectively, resulting in a total operating cost of Rp 43,022 m^{-3}. Among all cost components, adsorbent usage contributed the largest share, followed by electrical energy, whereas electrode consumption contributed the least.

Fig. 13 shows that increasing the current from 2 to 6 A caused a proportional increase in the energy consumption and operating cost of the EC-Adsorption system. At a current of 2 A, the process required an energy consumption of 10.00 kWh m^{-3} with a total operating cost of Rp 43,022 m^{-3}, whereas increasing the current significantly raised both the energy requirement and the treatment cost.

Table 14: Operating conditions and treatment performance of the EC-Adsorption process.

Parameter	Unit	Value
Wastewater volume	L	2.0
Current	A	2.0
Voltage	V	10.0
Electrocoagulation time	min	60
Adsorption time	min	60
Adsorbent dosage	g L^{-1}	20.0
Initial Pb concentration	mg L^{-1}	5.5494
Final Pb concentration	mg L^{-1}	0.0521
Pb removal efficiency	%	99.06
Initial Cd concentration	mg L^{-1}	2.3517
Final Cd concentration	mg L^{-1}	0.0342
Cd removal efficiency	%	98.55
Initial Ni concentration	mg L^{-1}	1.7007
Final Ni concentration	mg L^{-1}	0.0452
Ni removal efficiency	%	97.34

Table 15: Resource consumption and operating cost of the EC-Adsorption process.

Parameter	Unit	Value
Energy consumption	kWh m^{-3}	10.00
Electrode consumption	kg m^{-3}	0.065
Adsorbent consumption	kg m^{-3}	20.00
Electricity cost	Rp m^{-3}	14,447
Electrode cost	Rp m^{-3}	3,575
Adsorbent cost	Rp m^{-3}	25,000
Total operating cost	Rp m^{-3}	43,022

This pattern indicates that current is a key operating parameter governing the economic performance of the process, because energy consumption increases directly with current intensity when voltage, operating time, and wastewater volume are kept constant (Kim et al. 2025). The increase in operating cost at higher currents was mainly associated with the greater electrical energy requirement, whereas the contributions of electrode and adsorbent consumption were relatively smaller (Ebba et al. 2021, Aljaberi 2019).

These results confirm that a current of 2 A was the most favorable condition from a practical perspective, as it was able to provide high removal performance with lower energy consumption and operating cost (Uludag-Demirer et al. 2020).

Comparison with recent literature published during 2022–2025 further supports the performance of the present integrated EC-Ads system. In this study, the overall removal efficiencies reached 99.06% for Pb, 98.55% for Cd, and 97.34% for Ni under the optimized operating conditions. Recent electrocoagulation studies have reported similarly high heavy-metal removal. For example, Bakry et al. (2024) reported removal efficiencies of 98–100% for several individual heavy metals, including Pb, Cd, and Ni, using aluminum-electrode electrocoagulation, whereas Aljaberi and Hawaas (2023) achieved 99.73% Pb removal and 98.54% Cd removal in a multi-metal electrocoagulation system. Shaker et al. (2023) reported Ni removal efficiencies of up to 99.9%. In this context, the removal efficiencies obtained in the present work may be considered to lie within the upper range of recent literature, particularly because the wastewater treated here was real laboratory wastewater containing multiple metals rather than a simplified single-metal synthetic solution.

From the energy standpoint, the value obtained in this study (10.00 kWh m^{-3}) is also within the range reported for recent heavy-metal electrocoagulation systems, although direct comparison should be made cautiously because energy demand strongly depends on wastewater composition, reactor design, electrode material, current density, conductivity, and treatment time. Bakry et al. (2024) reported a broad electrical energy consumption range of 0.10–27.81 kWh m^{-3} under different operating conditions, while Aljaberi and Hawaas (2023) reported 12.71 kWh m^{-3} for simultaneous Pb/Cd/Cu removal. Therefore, the energy consumption observed in the present study may be considered technically reasonable for a batch integrated system designed to achieve very high final metal removal from real multi-metal wastewater.

With respect to operating cost, the present system required Rp 43,022 m^{-3}, with adsorbent consumption representing the dominant cost component. A direct numerical comparison with the literature should be interpreted carefully because

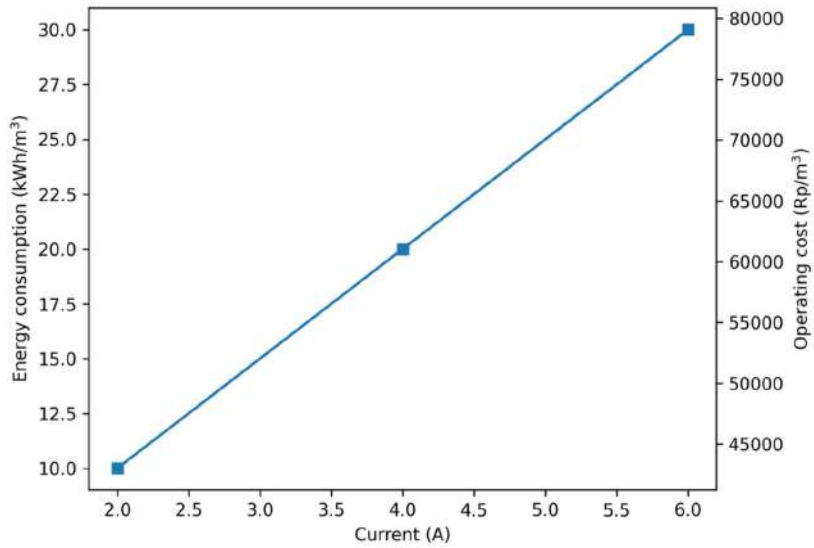


Fig. 13: Relationship between current, energy consumption, and operating cost.

published costs are influenced by local electricity tariffs, electrode prices, adsorbent prices, and reporting currency. Nevertheless, recent studies suggest that EC operating costs can vary substantially; for example, Bakry et al. (2024) reported a total cost range of 0.02–3.23 USD.m^{-3}, whereas Shaker et al. (2023) reported that Ni removal efficiencies of 99.4–99.7% could be achieved at approximately 0.5–0.7 USD.m^{-3} in an EC-only system. Compared with such EC-only studies, the higher cost contribution observed in the present work is reasonably attributable to the addition of the bentonite adsorption stage as a polishing unit. Thus, the proposed EC-Ads configuration offers excellent removal performance and low final residual metal concentrations, but its economic competitiveness would likely be improved further through adsorbent regeneration, reuse, or dosage reduction.

4. CONCLUSIONS

This study confirms that the integrated electrocoagulation–adsorption system using thermally activated bentonite is effective for the simultaneous removal of Pb, Cd, and Ni from real laboratory wastewater. The main contribution of this study is the comparative demonstration that electrocoagulation functions as the primary removal stage, whereas adsorption serves as a polishing step for residual metals at low concentrations.

Evidence from SEM-EDS, FTIR, and ICP-MS characterization indicates that metal removal occurs through complementary mechanisms, namely surface adsorption, coprecipitation, precipitation, and immobilization into the solid phase. From a practical perspective, this system shows strong potential for application in the treatment of multi-metal laboratory wastewater, although adsorbent demand remains the dominant factor in operating costs.

The limitations of this study include the use of a batch system, a one-factor-at-a-time approach, the absence of adsorbent regeneration evaluation, and the lack of investigation into the long-term stability of the sludge.

Future research should therefore focus not only on statistical optimization design and continuous-scale testing, but also on complete analytical QA/QC reporting, adsorbent reusability, and the evaluation of solid residue safety.

5. ACKNOWLEDGEMENT

The authors gratefully acknowledge the financial support for this research and publication provided by Universitas Sriwijaya under Rector's Decree No. 029/UN9/LPPM. PT/2025 dated September 17, 2025

6. REFERENCES

Al Ali, A., Ouda, M., Naddeo, V., Puig, S. and Hasan, S.W., 2021. Integrated electrochemical–adsorption process for the removal of trace heavy metals from wastewater. *Case Studies in Chemical and Environmental Engineering*, 4, pp.100147. [DOI]

Aljaberi, F.Y. and Hawaas, Z.A., 2023. Electrocoagulation removal of Pb, Cd, and Cu ions from wastewater using a new configuration of electrodes. *MethodsX*, 10, pp.101951. [DOI]

Aljaberi, F.Y., 2019. Operating cost analysis of a concentric aluminum tubes electrodes electrocoagulation reactor. *Heliyon*, 5, pp.e02307. [DOI]

Ammar, M., Yousef, E., Mahmoud, M.A., Ashraf, S. and Baltrusaitis, J., 2023. A comprehensive review of the developments in electrocoagulation for the removal of contaminants from wastewater. *Separations*, 10(6), pp.337. [DOI]

Anna, B., Kleopas, M., Constantine, S., Anestis, F. and Maria, B., 2015. Adsorption of Cd(II), Cu(II), Ni(II) and Pb(II) onto natural bentonite: Study in mono- and multi-metal systems. *Environmental Earth Sciences*, 73, pp.5435–5444. [DOI]

Bakry, S.A., Matta, M.E., Noureldin, A.M. and Zaher, K., 2024. Performance evaluation of electrocoagulation process for removal of heavy metals from wastewater using aluminum electrodes under variable operating conditions. *Desalination and Water Treatment*, 318, pp.100396. [DOI]

Bakry, S.A., Matta, M.E., Noureldin, A.M. and Zaher, K., 2024. Performance evaluation of electrocoagulation process for removal of heavy metals from wastewater using aluminum electrodes under variable operating conditions. *Desalination and Water Treatment*, 318, pp.100396. [DOI]

Bayuo, J., Rwiza, M.J., Choi, J.W., Mtei, K.M., Hosseini-Bandegharaei, A. and Sillanpää, M., 2024. Adsorption and desorption processes of toxic heavy metals, regeneration and reusability of spent adsorbents: Economic and environmental sustainability approach. *Advances in Colloid and Interface Science*, 329, pp.103196. [DOI]

Caixeta, A.L., Silva, A.C.N.D., Silva, S.K.S.D., Dias, M.D.C., Cholant, C.M., Volkmer, T.M., Missio, A.L., Oliveira, A.D.D., Ferrer, M.M., Anwar, Y. and Khan, S., 2025. Sustainable biosorbent and biopolymeric materials for heavy metal adsorption: advances, challenges, and perspectives. *Materials*, 18(20), p.4752.

Ebba, M., Asaithambi, P. and Alemayehu, E., 2021. Investigation on operating parameters and cost using an electrocoagulation process for wastewater treatment. *Applied Water Science*, 11, pp.175. [DOI]

Fan, D., Peng, Y., He, X., Ouyang, J., Fu, L. and Yang, H., 2024. Recent progress on the adsorption of heavy metal ions Pb(II) and Cu(II) from wastewater. *Nanomaterials*, 14. [DOI]

Fei, Y. and Hu, Y.H., 2023. Recent progress in removal of heavy metals from wastewater: A comprehensive review. *Chemosphere*, 335, pp.139077. [DOI]

Fu, F. and Wang, Q., 2011. Removal of heavy metal ions from wastewaters: A review. *Journal of Environmental Management*, 92(3), pp.407–418. [DOI]

Harahap, M.G., Abfertiawan, M.S., Syafila, M., Handajani, M. and Gultom, T.H., 2024. Electrocoagulation for nickel, chromium, and iron removal from mine water using aluminum electrodes. *Heliyon*, 10. [DOI]

Hikmat, K., Aziz, H., Mustafa, F.S. and Omer, K.M., 2023. Heavy metal pollution in the aquatic environment: Efficient and low-cost removal approaches to eliminate their toxicity: A review. *RSC Advances*, 13, pp.17595–17610. [DOI]

Huang, C.H., Shen, S.Y., Dong, C.D., Kumar, M. and Chang, J.H., 2020. Removal mechanism and effective current of electrocoagulation for treating wastewater containing Ni(II), Cu(II), and Cr(VI). *Water*, 12(9), pp.2614. [DOI]

Jo, S., Kadam, R., Jang, H., Seo, D. and Park, J., 2024. Recent advances in wastewater electrocoagulation technologies: Beyond chemical coagulation. *Energies*, 17. [DOI]

Khan, S.U., Khalid, M., Hashim, K., Jamadi, M.H., Mousazadeh, M., Basheer, F., Al-Mamun, A., Alqahtani, A., Al-Saadi, A., Al-Saadi, M., Al-Saadi, R., Al-Saadi, S., Al-Saadi, T., Al-Saadi, U., Al-Saadi, Y. and Al-Saadi, Z., 2023. Efficacy of electrocoagulation treatment

for the abatement of heavy metals: An overview of critical processing factors, kinetic models and cost analysis. Sustainability, 15. [DOI]

Kim, T., Phu, C., Nguyen, P.L., Viet, T. and Phung, B., 2025. Recent progress in highly effective electrocoagulation-coupled systems for advanced wastewater treatment. *iScience*, 28, pp.111965. [DOI]

Li, W., Zhang, L., Su, T., Luo, X., Xie, X. and Qin, Z., 2025. Carboxymethyl cellulose sodium/bentonite composite adsorbent for Cd(II) adsorption from wastewater. *Advanced Composites and Hybrid Materials*, 8, pp.119. [DOI]

Lu, J., Zhang, P., Li, J., Cao, Y., Zhang, W., Zhang, X., Wang, H., Liu, Y., Chen, Z., Huang, L., Zhao, Q., Sun, M. and Zhou, R., 2024. Mo(VI) removal from water by aluminum electrocoagulation: Cost-effectiveness analysis, main influencing factors, and proposed mechanisms. Journal of Hazardous Materials, 461, p.132608. [DOI]

Magdum, P. and Itankar, N., 2026. Environmental remediation and sustainable approaches to heavy metal removal: A comprehensive review of biosorption techniques. *Nature Environment and Pollution Technology*, 25(1), pp.1–21. [DOI]

Mao, Y., Zhao, Y. and Cotterill, S., 2023. Examining current and future applications of electrocoagulation in wastewater treatment. *Water*, 15(8), pp.1455. [DOI]

Matra, K., Lerkmahalikit, Y., Prasertkulsak, S., Kongdee, A., Pomthong, R., Thongson, S. et al., 2025. Hybrid RSM–ANN modeling for optimization of electrocoagulation using aluminum electrodes (Al–Al) for hospital wastewater treatment. *Water*, 17, pp.3003. [DOI]

Merrikhpour, H., Mobarakpour, S. and Azimi, S.B., 2022. Adsorption of Cd^{2+}, Cu^{2+}, and Ni^{2+} onto surfactant-modified bentonite. *Desalination and Water Treatment*, 271, pp.157–165. [DOI]

Mouedhen, G., Feki, M., Wery, M.D.P. and Ayedi, H.F., 2008. Behavior of aluminum electrodes in electrocoagulation process. *Journal of Hazardous Materials*, 150(1), pp.124–135. [DOI]

Naldi, N., Hazmi, A., Desmiarti, R. and Emeraldi, P., 2025. Electrocoagulation in wastewater treatment: A comprehensive review on parameters and applications. *Andalas Journal of Electrical and Electronic Engineering Technology*, 5(2), pp.38–49.

Onyenanu, N.R.C.N. and Onyenanu, U.I., 2025. Advanced treatment technologies for heavy metal removal from water and wastewater: A comprehensive review. *International Journal of Advanced Natural Sciences*, pp.111–131. [DOI]

Patel, S.K., Shukla, S.C., Natarajan, B.R., Asaithambi, P., Dwivedi, H.K., Sharma, A., Singh, R., Kumar, V., Mehta, P., Reddy, K., Gupta, N. and Verma, S., 2025. State of the art review for industrial wastewater treatment by electrocoagulation process: Mechanism, cost and sludge analysis. Desalination and Water Treatment, 321, p.100915. [DOI]

PERMEN, 2014. Peraturan Menteri Lingkungan Hidup Nomor 5 Tahun 2014: Baku Mutu Air Limbah. Available at: https://peraturan.bpk.go.id/Details/322442/permen-lh-no-5-tahun-2014 (accessed April 10, 2026).

PLN, 2026. Tariff Adjustment Document. Available at: https://www.pln.co.id/tariff-adjustment-document-en (accessed May 31, 2026).

Prepilková, V., Poništ, J., Ďuricová, A., Salva, J., Schwarz, M., Samešová, D., Kováč, P., Novák, R., Hronec, M. and Černý, L., 2024. Adsorption of Cd and Mn from neutral mine effluents using bentonite, zeolite, and stabilized dewatered sludge. Environmental Sciences Europe, 36, p.100. [DOI]

Rajaniemi, K., Tuomikoski, S. and Lassi, U., 2021. Electrocoagulation sludge valorization: a review. *Resources*, 10(12), pp.127. [DOI]

Raji, Z., Karim, A., Karam, A. and Khalloufi, S., 2023. Adsorption of heavy metals: Mechanisms, kinetics, and applications of various adsorbents in wastewater remediation: a review. *Waste*, 1, pp.775–805. [DOI]

Sakina, N.A., Sodri, A. and Kusnoputranto, H., 2023. Heavy metals assessment of hospital wastewater during COVID-19 pandemic. *International Journal of Public Health Science*, 12(1), pp.187–195. [DOI]

Shaker, O.A., Safwat, S.M. and Matta, M.E., 2023. Nickel removal from wastewater using electrocoagulation process with zinc electrodes under various operating conditions: Performance investigation, mechanism exploration, and cost analysis. *Environmental Science and Pollution Research*, 30(10), pp.26650–26662. [DOI]

Tegladza, I.D., Xu, Q., Xu, K., Lv, G. and Lu, J., 2021. Electrocoagulation processes: A general review about role of electro-generated flocs in pollutant removal. *Process Safety and Environmental Protection*, 146, pp.169–189. [DOI]

Tran, H.N., 2023. Applying linear forms of pseudo-second-order kinetic model for feasibly identifying errors in the initial periods of time-dependent adsorption datasets. *Water*, 15, pp.1231. [DOI]

Tripathi, A., Dahiya, S. and Mishra, B.K., 2025. Next-generation heavy metal water treatment: A primer on modified capacitive deionization. *Chemical Engineering Journal*, 505, pp.158844. [DOI]

Twizerimana, P. and Wu, Y., 2024. Overview of integrated electrocoagulation–adsorption strategies for the removal of heavy metal pollutants from wastewater. *Discover Chemical Engineering*, 4. [DOI]

Ullah, Y., He, X., Fang, Y. and Lu, J., 2025. A review about flocs in electrocoagulation process: Generation, adsorption, transformation, transportation. *Process Safety and Environmental Protection*, 202, pp.107452. [DOI]

Uludag-Demirer, S., Olson, N., Ives, R., Nshimyimana, J.P., Rusinek, C.A., Rose, J.B., Haque, M.M., Nguyen, T., Chen, Y. and Patel, R., 2020. Techno-economic analysis of electrocoagulation on water reclamation and bacterial/viral indicator reductions of a high-strength organic wastewater: anaerobic digestion effluent. Sustainability, 12. [DOI]

Vareda, J.P., 2023. On validity, physical meaning, mechanism insights and regression of adsorption kinetic models. *Journal of Molecular Liquids*, 376, pp.121416. [DOI]

Wang, P., Shen, X., Qiu, S., Zhang, L., Ma, Y. and Liang, J., 2024. Clay-based materials for heavy metals adsorption: Mechanisms, advancements, and future prospects in environmental remediation. *Crystals*, 14. [DOI]

Xu, H., Hu, X., Chen, Y., Li, Y., Zhang, R., Tang, C., Wang, J., Liu, Z., Zhao, L. and Huang, Y., 2021. Cd(II) and Pb(II) adsorption on humic acid-iron-pillared bentonite: Kinetics, thermodynamics and mechanism. Colloids and Surfaces A: Physicochemical and Engineering Aspects, 612, p.126005. [DOI]

Yang, X., Li, Y., Gan, M., Chen, Y., Meng, H., Li, L., Zhou, F., Wu, H., Zhang, T. and Sun, Q., 2025. Adsorption and desorption effect of modified bentonite on soil heavy metal Pb/Cd and the feasibility assessment of reducing the ecotoxicity. Environmental Sciences Europe, 37, p.105. [DOI]

Yang, X., Zhou, Y., Hu, J., Zheng, Q., Zhao, Y., Lv, G., Wang, K., Chen, M. and Liu, P., 2024. Clay minerals and clay-based materials for heavy metals pollution control. Science of the Total Environment, 954, p.176193. [DOI]

Yazıcı Karabulut, B., 2025. Electrochemical coagulant generation via aluminum-based electrocoagulation for sustainable greywater treatment and reuse: Optimization through response surface methodology and kinetic modelling. Molecules, 30, p.3779. [DOI]

Yazidi, I., Ziat, K., Bardiji, N.E., Boundati, Y.E., Naji, A., Haskouri, J.E., Elkhattabi, E., Boutahir, M., Zouini, M., Upadhyay, A., Gadam, H. and Tyagi, A., 2026. Adsorption kinetics, isotherm models, and thermodynamics: A brief review. In: Boutahir, M., Elkhattabi, E.M., Zouini, M., Upadhyay, A., Gadam, H. and Tyagi, A. (eds.), Artificial Intelligence and Emerging Materials Transition Toward Green Smart Technologies. Springer Nature: Cham, Switzerland, pp.93–105. [DOI]

Zareh, M., Metwally, N. and Abdel-Tawwab, M., 2024. Review of methods of removal of heavy metals from wastewater. *Bulletin of Faculty of Science, Zagazig University*, 2024, pp.51–58. [DOI]

Nature Environment and Pollution Technology
An International Quarterly Peer-Reviewed Open Access Journal

p-ISSN: 0972-6268 | e-ISSN: 2395-3454 Vol. 25 | No. 4 | Article ID D1934 | 2026

REVIEW ARTICLE https://doi.org/10.46488/NEPT.2026.v25i04.D1934 OPEN ACCESS

From Water Scarcity to Resilience: A Policy-Oriented Framework for Community-Based Drought Management in Southeast Asia

Sitthisak Pinmongkhonkul† and **Thanakorn Panyopo**
Biology Program, School of Science, University of Phayao, Phayao 56000, Thailand
†Corresponding author: Sitthisak Pinmongkhonkul; sitthisak.pi@up.ac.th

ARTICLE HISTORY

Received: 19-04-2026
Revised: 05-06-2026
Accepted: 08-06-2026

KEYWORDS

Drought management
Water governance
Community-based water management
Water resilience
Adaptive governance
Policy-oriented framework

CITE THIS ARTICLE

Pinmongkhonkul, S. and Panyopo, T., 2026. From water scarcity to resilience: A policy-oriented framework for community-based drought management in Southeast Asia, *Nature Environment and Pollution Technology*, 25(4), D1934. https://doi.org/10.46488/NEPT.2026.v25i04.D1934

COPYRIGHT & LICENCE

© 2026 The Authors
Open Access under CC BY 4.0.

PUBLISHED BY
TECHNOSCIENCE PUBLICATIONS

ABSTRACT

Drought has evolved into a persistent governance challenge across Southeast Asia. Its impacts cannot be attributed to climatic variability alone. Rather, they emerge from the interaction between climate change, fragmented institutional arrangements, and intensifying competition over water resources. Together, these dynamics undermine long-term water security and disproportionately affect rural livelihoods. Although a growing body of scholarship has explored adaptive governance and community-based water management, much of this work remains compartmentalized across disciplinary and administrative scales. As a result, research often examines connections between national policy frameworks, intermediary institutions, and local water practices too little, limiting the applicability of existing research for integrated drought resilience planning. To address this gap, this study undertakes a policy-oriented integrative review of interdisciplinary literature on drought governance and community-based drought management in Southeast Asia. Drawing on peer-reviewed research from environmental governance, water policy, and sustainability studies, the review examines how policy design, institutional coordination, and community participation interact in practice. Rather than treating these dimensions as discrete variables, the analysis considers their relational dynamics. The study uses a thematic synthesis approach to identify recurring governance mechanisms, enabling conditions, and structural barriers that shape drought management outcomes across contexts. Building on this synthesis, the study proposes a Policy-Oriented Community Drought Resilience Framework. The framework conceptualizes drought resilience not as a fixed condition, but as an emergent outcome of multi-scalar governance interactions. It foregrounds policy coherence and institutional alignment as foundational elements, while recognizing the operational role of community-based water management organizations. The framework also emphasizes knowledge integration and iterative learning processes, highlighting feedback loops that connect drought experiences to institutional adjustment and policy reform over time. Theoretically, this review extends adaptive and polycentric governance perspectives by underscoring the importance of coordination quality, institutional learning, and cross-scale linkages. It argues that resilience is less about the proliferation of governance actors and more about how effectively their roles are aligned. From a policy standpoint, the findings point toward practical pathways for shifting from reactive, crisis-driven responses to proactive and community-centered drought governance strategies. Although grounded in the Southeast Asian context, the analytical insights developed here apply to other climate-vulnerable regions confronting intensifying water scarcity.

1. INTRODUCTION

Drought has become one of the most expensive and extensive catastrophes, affecting millions of people worldwide, posing a significant water-management challenge in Southeast Asia, and its importance is not limited to climatic variability (Kulkarni & Sawada 2025, Rahman et al. 2025). Across the region, prolonged drought interacts

with fragmented institutional arrangements, competition among water-use sectors, and inconsistent management responses (Asian Development Bank 2020, Franzetti et al. 2017). Its effects extend beyond reduced agricultural output to water security, local livelihoods, ecosystems, and social stability, including land use/land cover (LULC) (Apraku et al. 2022, Drury et al. 2023, Hurlbert et al. 2019, Thanh et al. 2023, Anand et al. 2018). Because drought is a slow-onset hazard with prolonged recovery, it exposes weaknesses in coordination, policy development, and long-term planning (Augustijn et al. 2025, Kampragou et al. 2011). Therefore, drought is better understood not solely as a hydrological event but as a test of governance capacity (Aartsen et al. 2018).

In Southeast Asia, especially in northeast Thailand, structural conditions can exacerbate drought vulnerability, while rapid economic growth increases water demand across agriculture, industry, and urban areas, including deforestation without commensurate development of allocation mechanisms or institutional coordination (Frisvold & Konyar 2012, Fasting et al. 2021, Khadka et al. 2024, Kukuntod & Wijitkosum 2025, Lu & Talamini 2024, Sattraburut et al. 2024). In rural and urban areas, ineffective water management and unequal access to resources create additional barriers to adaptation (Aguilar et al. 2021, Saguansap et al. 2025, Matimolane & Mathivha 2025).

Although governments have increasingly adopted drought policies and integrated climate adaptation with water resources management, many interventions remain reactive and sector-specific. Emergency water allocation and infrastructure expansion are necessary, but they cannot address the deeper governance challenges that shape long-term resilience (Sin-Ampol et al. 2025).

Recent research has emphasized adaptive governance, policy integration, and community-based water management as important elements of effective drought response. These studies show that technical solutions alone, such as reservoir construction, irrigation expansion, and early warning systems, are insufficient when institutional roles are unclear, and local participation is inadequately considered. Therefore, effective drought response depends on interactions across multiple governance levels. Policy coherence, institutional alignment, and community participation are not secondary considerations; they are central to adaptive capacity (Holman & Knox 2023).

Despite this growing body of work, the literature remains conceptually fragmented. Policy-oriented research often concentrates on institutional design and coordination mechanisms at national or basin scales. In contrast, community-based studies focus on local practices and collective action, sometimes without fully accounting for regulatory and policy constraints. What is less developed is an integrative perspective that systematically links policy frameworks, intermediary institutions, and community-level water management within a single analytical lens. This gap is particularly consequential in Southeast Asia, where overlapping mandates, customary water practices, and varying degrees of decentralization complicate governance arrangements (Duc et al. 2024).

Without such an integrative framework, translating advances in drought management into practical strategies remains difficult. Policymakers may recognize the value of participation or adaptation planning, but clear guidance on how these elements should work together across governance levels is often lacking. Similarly, community initiatives can produce local benefits but remain constrained by broader institutional inconsistencies (Moridi et al. 2025).

To address this issue, this study conducts a policy-oriented review of drought governance and community-based drought management in Southeast Asia. It synthesizes empirical findings, conceptual debates, and policy analyses to examine how governance mechanisms operate across levels. Rather than treating institutional policy and community management as separate issues, the analysis investigates their relationships. On this basis, the study develops a Policy-Oriented Community Drought Resilience Framework that integrates policy coherence, institutional coordination, knowledge integration, and iterative learning within a unified conceptual structure.

This review has three aims. First, it analyzes the literature to clarify how drought resilience is defined and managed from a governance perspective. Second, it identifies institutional and policy factors that affect the effectiveness of community-level drought responses. Finally, it presents a framework intended to advance theoretical discussion and provide practical guidance for drought management and adaptation (Zipper et al. 2017).

2. MATERIALS AND METHODS

2.1. Review Design and Scope

This study uses a policy-oriented integrative review approach to synthesize interdisciplinary knowledge on community-based drought management and water governance in Southeast Asia. Unlike systematic reviews that primarily emphasize quantifying intervention effects, an integrative review can consolidate empirical findings, conceptual frameworks, and policy analyses from diverse fields of study, including environmental governance, hydrology, development studies, and public policy (Milhorance et al. 2022). This method is

particularly appropriate for examining drought resilience, which is shaped by complex institutional, sociopolitical, and environmental interactions (Kaiss et al. 2025).

The review focuses on identifying policy-relevant mechanisms that link drought governance, institutional arrangements, and community participation to develop a conceptual model for improving long-term drought resilience in water-scarce regions.

2.2. Review Questions

The review was preceded by the following research questions:

1. How is drought management conceptualized and operationalized in policy and governance literature related to Southeast Asia?
2. What institutional and governance factors influence the effectiveness of community-based drought management?
3. How do policy frameworks interact with local institutions and community organizations to shape drought resilience outcomes?
4. What lessons can be drawn to inform future drought governance and policy design in climate-vulnerable regions?

2.3. Literature Search Strategy

A structured literature search was conducted using Scopus and Web of Science as the main databases because of their comprehensive coverage of peer-reviewed journals in environmental science, policy studies, and sustainability research. Moreover, relevant studies were identified through backward and forward citation tracking of important articles.

The search was performed using combinations of keywords related to drought, water governance, policy, and community participation, including but not limited to:

"drought management", "water governance", "community-based adaptation","drought resilience", "water user organizations", "policy integration","adaptive governance" and "Southeast Asia".

Search terms were applied to titles, abstracts, and keywords. Only articles published in peer-reviewed journals were considered to ensure academic rigor (Shah 2021).

2.4. Inclusion and Exclusion Criteria

To ensure relevance and consistency, research studies were selected based on the following criteria:

2.4.1. Inclusion Criteria

- Peer-reviewed journal articles published primarily between 2010 and 2025
- Studies addressing drought, water scarcity, or drought-related water management
- Explicit discussion of governance, policy, institutional arrangements, or community participation
- Empirical, conceptual, or review studies with clear policy implications
- Studies conducted in Southeast Asia or providing transferable insights relevant to the region

2.4.2. Exclusion Criteria

- Technical or engineering-focused studies lacking governance or policy dimensions
- Unpublished documents, reports, and publications that have not undergone peer review.
- Studies focusing solely on flood management without relevance to drought
- Articles with limited relevance to the community or the institutional point of view of water management

2.5. Analytical Framework and Synthesis

Selected studies were analyzed using a thematic synthesis method. The studies were iteratively coded and organized into key thematic domains reflecting governance dimensions of drought resilience, including:

1. Policy frameworks and institutional consistency
2. Multi-level governance and coordination mechanisms
3. Community participation and local water user organizations
4. Knowledge integration, learning, and adaptive ability
5. Obstacles and conditions conducive to policy implementation.

Rather than focusing on specific case outcomes, the synthesis highlighted institutional dynamics, cross-cutting patterns, and policy trade-offs. Through this process, a policy-oriented conceptual framework connecting community-based resilience mechanisms with drought governance structures was developed by integrating insights from various contexts (Nagel & Pierre 2020).

2.6. Review Process

2.6.1. Imposing Boundaries and Defining Inclusion Criteria (Scoping Phase)

This first method establishes the rules and boundaries for the review. It involves defining the study's specific scope, such as the geographic focus on Southeast Asia, the topic of community-based drought management, and the timeframe.

By setting clear inclusion and exclusion criteria, researchers ensure that only highly relevant studies are considered, filtering out unrelated or low-quality literature from the outset.

2.6.2. Systematically Documenting Search and Study Selection (Literature Search Phase)

This step involves conducting a structured, transparent literature search using major academic databases, especially Scopus and Web of Science. Researchers document every step of the process, including the specific keywords used, the number of records identified, and how studies were screened, such as removing duplicates, reviewing titles and abstracts, and assessing full texts. This helps make the review transparent and reproducible and supports adherence to academic standards, including the Preferred Reporting Items for Systematic Reviews and Meta-Analyses (PRISMA).

2.6.3. Thematic Synthesis and Analytical Coding of Governance Dimensions (Analysis Phase)

In this analytical method, information gathered from the selected studies was coded and classified. Analytical coding involves identifying specific concepts, patterns, and features within the literature. Thematic synthesis involves grouping these codes into overarching themes related to governance dimensions, such as policy structures, stakeholder participation, institutional capacity, and community resilience. This step reduced a large volume of text to organized core findings.

2.6.4. Development of an Integrative Policy-Oriented Framework and Operationalization (Framework Development Phase)

The final step translates the academic findings into practical application. Using the themes and dimensions identified in Step 3, researchers construct an integrative framework that connects the various elements of drought governance. Crucially, this framework is policy-oriented, meaning it goes beyond theory to outline actionable policy pathways and operational guidelines that policymakers and practitioners can use to improve community-based drought management.

This approach enables the systematic integration of policy, institutional, and community-level viewpoints to examine drought governance and community-based drought management in Southeast Asia. The review design and analytical approach are summarized in Fig. 1.

2.7. Limitations

This study is an integrative review rather than a quantitative assessment of drought-management interventions. It emphasizes conceptual integration and policy relevance. Although efforts were made to identify and analyze relevant studies systematically, some specialized studies or non-English publications may not have been included. Nevertheless, the review provides an analytical basis for understanding drought governance challenges and informing future policy design.

3. RESULTS AND DISCUSSION

3.1. Overview of the Reviewed Literature

The integrative review indicates a marked expansion of scholarship on drought governance and community-based drought management, particularly in the past decade. This growth appears closely linked to intensifying concerns over climate change and recurring water scarcity across the region. The literature spans diverse disciplinary traditions, including water governance, environmental policy, sustainability science, and socio-hydrology. While governance and institutional dimensions dominate the field, attention to community-based adaptation and participatory water management has gradually increased, signaling a shift toward more locally grounded perspectives (Zokirov et al. 2025).

Geographically, research is concentrated in drought-prone areas of Southeast Asia, with Thailand, Vietnam, and the Mekong Basin featuring prominently. These case-based studies are complemented by comparative and conceptual analyses that extend beyond specific national contexts and offer broader analytical insights. Taken together, the literature reflects a growing acknowledgment that drought impacts cannot be explained by climatic variability alone. Instead, they are shaped by governance structures, institutional capacity, and the alignment or misalignment between policy frameworks and local water management practices.

3.2. Thematic Synthesis of Drought Governance Dimensions

The thematic synthesis identifies five interrelated governance dimensions that consistently influence drought resilience outcomes across the reviewed studies.

3.3. Policy Frameworks and Coherence

Numerous studies examine the role of national and local policy frameworks in shaping drought management. Several studies report that fragmented sectoral policies, particularly across water resources, agriculture, drought-risk reduction, and climate-change adaptation, undermine effective drought preparedness (Cejudo & Trein 2023, Tchinda & Talbot 2023). Conversely, policy coherence and integration support clearer planning, more defined institutional boundaries, and more consistent implementation



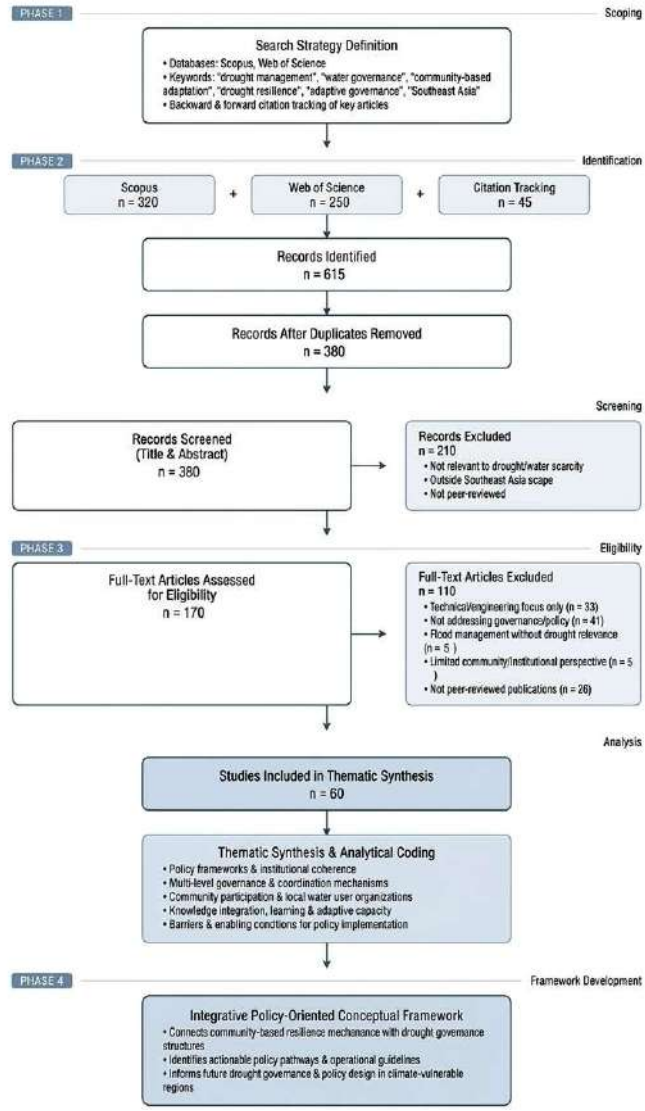


Fig. 1: Review design and analytical approach adopted in this policy-oriented integrative review.

during drought periods (Nelson et al. 2008, Sánchez et al. 2025).

3.4. Institutional Coordination and Multi-Level Governance

Institutional coordination emerges as a key factor determining effective drought-management outcomes. The reviewed literature identifies challenges associated with overlapping institutional mandates, weak interorganizational communication, and coordination across governance levels (Makaya et al. 2020, Sifundza et al. 2019). Studies also show that river-basin and intermediary governance structures can play an important role in adaptive decision-making when clear coordination mechanisms are in place (Ferraro & Failler 2024, Augustijn et al. 2025, Lima et al. 2024).

3.5. Community Participation and Local Water Institutions

Community-level water-management organizations, including water user organizations and agricultural groups, often play an important role in responding and adapting to drought (Babel et al. 2024, Chuenchum et al. 2024, Forni et al. 2021). According to the reviewed studies, community involvement improves the legitimacy, compliance, and contextual alignment of drought-management strategies. Nevertheless, formal recognition, institutional support, and alignment with higher-level policy frameworks are necessary for local institutions to be effective (Villamayor-Tomás et al. 2020), and to support adaptation strategies for agricultural resilience in a changing climate (Veisi et al. 2025).

3.6. Knowledge Integration and Learning Processes

The integration of local experiential knowledge with scientific knowledge, such as drought monitoring, climate forecasting, and early warning systems, is emphasized as crucial for adaptive decision-making throughout the evaluated studies (Adla et al. 2023, Chengot et al. 2025). Knowledge integration promotes readiness and enables institutions and communities to respond to uncertainty more adaptively. Sustained resilience is frequently shown to be facilitated by learning methods, such as iterative planning and participatory monitoring (Sutcliffe et al. 2024).

3.7. Adaptive Capacity and Feedback Mechanisms

The literature emphasizes the significance of adaptive capacity supported by feedback mechanisms that connect institutional learning and policy to drought outcomes (Tran et al. 2024). Governance systems that incorporate monitoring, evaluation, and policy adjustment are better suited to transition from reactive crisis management to proactive and resilience-oriented approaches (Smith et al. 2016, Hashemy Shahdany & Rahparast 2025). Drought responses are often reactive and short-lived in the absence of such feedback systems.

3.8. Development of the Policy-Oriented Community Drought Resilience Framework

Synthesizing these thematic insights, the review results in the development of a Policy-Oriented Community Drought Resilience Framework. The framework conceptualizes drought resilience as an emergent outcome of interactions across three governance levels: policy and regulatory frameworks, institutional coordination mechanisms, and community-based water management practices.

At the policy level, coherence and integration across sectors provide the enabling environment for effective drought governance. At the institutional level, coordination and adaptive governance mechanisms translate policy objectives into operational decisions. At the community level, participation, local institutions, and knowledge integration shape context-specific adaptive responses. Feedback loops connect outcomes at the community and institutional levels back to policy learning and adjustment, reinforcing adaptive and transformative governance pathways.

3.9. Mapping Literature to Framework Components

The reviewed literature was systematically mapped onto the components of the proposed framework, demonstrating strong alignment between empirical and conceptual studies and the identified governance dimensions. Policy-oriented studies primarily inform the framework's policy coherence and institutional coordination components, while community-based studies substantiate the roles of participation, local institutions, and knowledge integration. This mapping confirms that drought resilience is not driven by isolated interventions but by the interaction of governance mechanisms across scales.

The proposed framework conceptualizes drought resilience as an outcome of dynamic interactions across policy, institutional, and community levels, rather than as the result of isolated technical interventions. It reflects insights synthesized from the reviewed literature and responds to the fragmented nature of drought governance commonly observed in Southeast Asia.

3.9.1. Policy and Regulatory Level

At the macro level, national and local policy frameworks establish legal rules, resource-allocation mechanisms, and strategic priorities for drought management. Nevertheless, the review indicates that fragmented sectoral policies

across agriculture, water resources, disaster management, and environmental protection frequently result in inconsistent implementation during drought. Therefore, the framework must account for these critical system-level conditions.

3.9.2. Institutional Coordination and Governance

The intermediate level of the framework focuses on institutional management and coordination mechanisms among government agencies, river-basin organizations, and local authorities. Effective drought resilience depends on the ability of these institutions to align authority and responsibilities, share information, and coordinate decision-making across administrative boundaries. Weak institutional linkages and overlapping authorities are identified as significant barriers that undermine water allocation during periods of scarcity.

3.9.3. Community Participation and Local Water Management

At the local level, community organizations such as water user organizations, farm households, and traditional water institutions play an important role in translating policy objectives into operational procedures (Pandey et al. 2007). The framework shows that meaningful community participation improves efficiency, contextual relevance, legitimacy, and compliance, especially in rural areas at risk of drought. Local institutions serve as important intermediaries linking policy directives with bottom-up adaptive responses.

3.9.4. Knowledge Integration and Adaptive Capacity

The framework emphasizes the integration of local and experiential knowledge with scientific information at all levels (e.g., drought monitoring, forecasting, and climate projections). This integration enhances community-level readiness and facilitates flexible decision-making. As a result, learning processes and information flows are viewed as cross-cutting components that support institutional capability and the efficacy of policies.

3.9.5. Feedback Loops and Transformative Learning

The heart of the framework is a feedback circuit that connects drought impacts and management outcomes back to institutional learning and policy modification. These loops reflect the need for iterative adaptation, enabling the governance system to change in response to growing climate uncertainty. These feedback systems facilitate the transition from reactive crisis management to proactive and transformative drought governance over time.

This study advances the literature on drought governance and offers a transferable analytical lens for creating resilient, community-centered drought management strategies in climate-vulnerable regions by combining policy coherence, institutional coordination, and community participation within a single conceptual framework (Tiepolo et al. 2017).

As shown in Fig. 2, the framework illustrates the multi-scalar interactions between national and subnational policy frameworks, institutional coordination mechanisms, and community-level water management practices in shaping

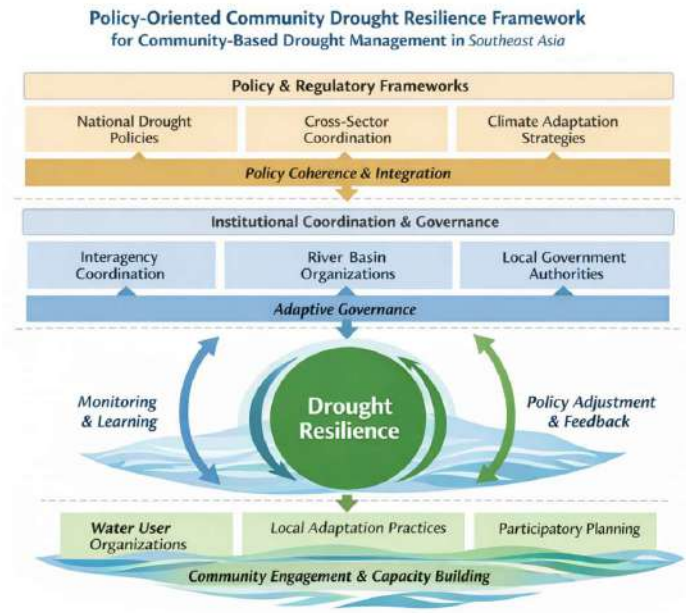


Fig. 2: Policy-oriented community drought resilience framework for community-based drought management in Southeast Asia.

Table 1: Mapping of reviewed literature to the components of the policy-oriented community drought resilience framework.

Framework Component	Key Themes	Representative Literature	Key Insights for Drought Governance
Policy and Regulatory Frameworks	Policy coherence, legal mandates, cross-sector integration	Nelson et al. (2008), Cejudo & Trein (2023), Tchinda & Talbot (2023), Sánchez et al. (2025)	Fragmented sectoral policies undermine drought preparedness; integrated and coherent policy frameworks enhance anticipatory and preventive drought management
Institutional Coordination and Governance	Multi-level governance, institutional fragmentation, coordination mechanisms	Makaya et al. (2020), Sifundza et al. (2019), Ferraro & Failler (2024), Augustijn et al. (2025)	Weak coordination across agencies leads to inconsistent water allocation; aligned institutional mandates improve crisis response and long-term resilience
Community Participation and Local Institutions	Water user organizations, collective action, legitimacy	Chuenchum et al. (2024), Forni et al. (2021), Villamayor-Tomás et al. (2020)	Community-based institutions enhance legitimacy, compliance, and context-specific adaptation, particularly in rural drought-prone areas
Knowledge Integration and Learning	Scientific–local knowledge integration, information flows, learning processes	Adla et al. (2023), Sutcliffe et al. (2024), Chengot et al. (2025)	Combining climate information with experiential knowledge strengthens adaptive capacity and improves decision-making under uncertainty
Adaptive and Transformative Capacity	Adaptive governance, resilience pathways, transformation	Nelson et al. (2008), Sánchez et al. (2025), Tran et al. (2024)	Iterative learning and adaptive governance enable shifts from reactive drought response toward long-term resilience-building strategies
Feedback Loops and Policy Adjustment	Monitoring, evaluation, institutional learning	Smith et al. (2016), Hashemy Shahdany & Rahparast (2025)	Continuous feedback from drought outcomes supports policy refinement and institutional learning, reducing vulnerability over time

drought resilience outcomes. It emphasizes the role of policy coherence, stakeholder participation, and knowledge integration in enabling adaptive and transformative responses to drought. Feedback loops highlight the importance of continuous learning and policy adjustment to address increasing climatic uncertainty and water scarcity.

Table 1 synthesizes key thematic contributions from the literature and illustrates how empirical and conceptual studies collectively inform the proposed multi-scalar framework for community-based drought management.

The mapping demonstrates that drought resilience emerges from the interaction of policy coherence, institutional coordination, and community participation, supported by knowledge integration and adaptive learning processes. Rather than operating in isolation, these components form an interconnected governance system that shapes drought outcomes across scales.

3.10. Implications for Drought Governance Theory

This review advances drought governance theory by reconceptualizing drought resilience as an emergent property of multi-scalar governance interactions rather than the product of isolated technical or sectoral interventions. By bringing policy design, institutional coordination, and community-level practice into a single analytical frame, the proposed framework intervenes in ongoing debates on adaptive governance, policy integration, and community-based natural resource management (Lambelet 2023).

The synthesis reinforces key insights from adaptive governance scholarship while extending them in important ways. Adaptive governance is often associated with flexibility and responsiveness to environmental change (Nelson et al. 2008). However, the findings here suggest that adaptive capacity is contingent upon prior institutional conditions, particularly policy coherence and alignment across governance levels (Cejudo & Trein 2022, Sarti 2023).

In settings marked by fragmented mandates and overlapping authorities, local adaptive initiatives frequently encounter structural constraints. Flexibility at the community level cannot compensate for systemic misalignment at higher policy tiers.

The analysis also refines polycentric and multi-level governance perspectives. Rather than equating decentralization with resilience, the review demonstrates that what matters most is the quality of coordination among governance centers (Ziervogel et al. 2019, González et al. 2025). Interactions between national policy frameworks, intermediary institutions, and local water management organizations shape drought outcomes in practice. Clear role differentiation, information exchange, and shared problem framing appear more consequential than the mere proliferation of decision-making nodes. In this respect, the findings shift attention from structural complexity to functional integration in drought-prone contexts.

Community-based institutions emerge not simply as participatory actors, but as boundary organizations

that translate abstract policy objectives into operational water allocation decisions under conditions of scarcity (Sithirith et al. 2024). Much of the existing literature frames participation normatively; the present synthesis highlights its substantive governance function. Local organizations mediate between top-down regulation and bottom-up adaptation, thereby linking collective action to broader institutional arrangements. This perspective strengthens theoretical connections between community-based resource management and governance effectiveness.

The framework further contributes to theoretical discussions on knowledge integration by treating learning as a cross-cutting process rather than a discrete intervention. The integration of climate forecasts, drought monitoring systems, and experiential knowledge enhances both decision quality and institutional legitimacy. Importantly, knowledge co-production is shown to be particularly significant in contexts characterized by data scarcity and administrative complexity. Here, learning processes become central to sustaining governance resilience (Raza et al. 2026).

Finally, the emphasis on feedback loops and policy adjustment moves the discussion beyond incremental adaptation. By linking drought experiences to institutional learning and policy revision, the framework conceptualizes resilience as a dynamic and iterative process. Governance systems evolve through cycles of evaluation, recalibration, and reform. Resilience, in this sense, is neither static nor guaranteed; it depends on the capacity of institutions to learn from stress and adjust accordingly.

Taken together, these insights suggest that drought governance should be understood as a relational and evolving system. Resilience emerges from coordination, shared learning, and cross-scale alignment. Grounded in the Southeast Asian context yet analytically transferable, the framework provides a conceptual bridge between region-specific empirical studies and broader debates in environmental governance theory.

3.11. Policy Implications and Pathways for Implementation

The synthesis also carries significant implications for policy design and implementation. Strengthening drought resilience requires more than expanding infrastructure or emergency response capacity. It entails shifting from fragmented, sector-specific interventions toward coordinated governance pathways that align policy, institutions, and community practice.

Policy coherence across water, agriculture, disaster risk reduction, and climate adaptation sectors is a foundational step (Tchinda & Talbot 2023). When mandates conflict or remain siloed, implementation gaps widen during drought events. Embedding anticipatory measures, such as early warning systems, predefined allocation rules, and adaptive planning instruments, within integrated policy frameworks can reduce institutional contradictions and improve preparedness.

At intermediary governance levels, coordination mechanisms require particular attention. River-basin organizations and subnational authorities often occupy pivotal positions, yet their effectiveness depends on clear mandates, formalized collaboration platforms, and shared information systems (Makaya et al. 2020). Incentive structures that encourage interagency collaboration are especially important in administratively fragmented settings.

Community-based water management organizations play a decisive operational role. Formal recognition of their governance responsibilities, coupled with sustained capacity-building and financial support, can enhance their ability to implement equitable and context-sensitive allocation decisions. Without institutional backing, local initiatives risk remaining isolated or vulnerable to higher-level policy shifts.

Institutionalizing the integration of scientific and local knowledge is equally critical. Embedding climate services, participatory monitoring, and knowledge-sharing mechanisms within governance structures strengthens both adaptive decision-making and stakeholder trust. These mechanisms function not merely as technical enhancements, but as relational processes that build legitimacy.

Continuous monitoring, evaluation, and policy adjustment must be treated as ongoing components of governance rather than episodic reforms. Feedback mechanisms linking drought outcomes to policy revision enable systems to adapt to shifting climatic and socioeconomic conditions (Smith et al. 2016, Tran et al. 2024, Nasir et al. 2025). Over time, such iterative processes can support more transformative shifts in governance practice.

Collectively, these pathways point toward hybrid governance arrangements that combine strategic policy direction with meaningful community engagement. Implementing them requires political commitment, institutional flexibility, and sustained investment in both technical and social capacities. If operationalized effectively, these principles offer concrete entry points for transitioning from reactive drought response to proactive, equitable, and adaptive governance in water-scarce regions.

4. CONCLUSIONS

In conclusion, this research contributes a conceptual framework that bridges empirical insights from Southeast

Asia with broader theoretical debates in environmental governance. By grounding abstract governance theory in the lived realities of a climate-vulnerable region, the study yields several critical inferences. First, it demonstrates that effective drought governance cannot rely on centralized, top-down mandates; rather, it requires polycentric coordination that empowers local actors and integrates traditional ecological knowledge. Second, the study infers that adaptive capacity is fundamentally tied to inclusivity; when marginalized communities are excluded from decision-making, drought responses remain fragmented and inequitable. Third, the analysis clarifies that the shift from reactive crisis management to proactive resilience demands institutional flexibility, where governance systems are designed to learn and evolve alongside shifting climatic conditions.

Based on these findings, the study offers several targeted recommendations for policymakers and practitioners. Primarily, governance reforms must institutionalize cross-sectoral collaboration, actively dismantling the policy silos that typically separate water resource management, agricultural planning, and disaster risk reduction. Additionally, practitioners must move beyond superficial consultation to co-design drought interventions with local communities, ensuring that resilience strategies are contextually grounded and socially equitable. Furthermore, funding mechanisms must be restructured to prioritize preemptive, adaptive capacity-building over costly, post-disaster emergency relief.

Finally, while this framework provides both analytical clarity and practical direction for building more adaptive, inclusive, and resilient drought governance systems, empirical testing must continue. Future research should further explore how these governance principles operate across different sociopolitical contexts, particularly in regions with contrasting political economies or different historical legacies of resource management. Moreover, longitudinal studies are essential to assess the long-term impacts of integrated governance reforms on drought resilience, tracking whether these conceptual frameworks translate into sustained, on-the-ground reductions in socioecological vulnerability over time.

5. ACKNOWLEDGEMENT

The authors acknowledge the University of Phayao and the Thailand Science Research and Innovation for providing funding for this study (Fundamental Fund 2026, Grant No. 2291/2568).

6. REFERENCES

Aartsen, M., Koop, S., Hegger, D. L. T., Goswami, B., Oost, J. and Leeuwen, K. van, 2018. Connecting water science and policy in India: Lessons from a systematic water governance assessment in the city of Ahmedabad. *Regional Environmental Change*, 18(8), 2445. [DOI]

Adla, S., Pande, S., Vico, G., Vora, S., Alam, M. F., Basel, B., Haeffner, M. and Sivapalan, M., 2023. Place for sociohydrology in sustainable and climate-resilient agriculture: Review and ways forward. *Cambridge Prisms Water*, 1. [DOI]

Aguilar, F. X., Hendrawan, D., Cai, Z., Roshetko, J. M. and Stallmann, J. I., 2021. Smallholder farmer resilience to water scarcity. *Environment Development and Sustainability*, 24(2), 2543. [DOI]

Anand, J., Gosain, A.K. and Khosa, R., 2018. Prediction of land use changes based on Land Change Modeler and attribution of changes in the water balance of Ganga basin to land use change using the SWAT model. *Science of the Total Environment*, 644, pp.503–519. [DOI]

Apraku, A., Gyampoh, B. A., Morton, J. and Karikari, A. B., 2022. Water security in rural Eastern Cape, SA: Interrogating the impacts of politics and climate change. *Scientific African*, 19. [DOI]

Asian Development Bank, 2020. *Asian Water Development Outlook 2020: Advancing Water Security across Asia and the Pacific*. Asian Development Bank, pp.156. [DOI]

Augustijn, M. F. W., Alblas, E. and Richter, A., 2025. Catching up with drought: Law and policy responses in the Netherlands. *Regional Environmental Change*, 25(3). [DOI]

Babel, M. S., Chawrua, L., Khadka, D., Tingsanchali, T. and Shanmungam, M. S., 2024. Agricultural drought risk and local adaptation measures in the Upper Mun River Basin, Thailand. *Agricultural Water Management*, 292, 108655. [DOI]

Cejudo, G. M. and Trein, P., 2022. Pathways to policy integration: A subsystem approach. *Policy Sciences*, 56(1), 9. [DOI]

Cejudo, G. M. and Trein, P., 2023. Policy integration as a political process. *Policy Sciences*, 56(1), 3. [DOI]

Chengot, R., Goodwin, D., Tanguy, M., Armitage, R., Pardthaisong, L., Jha, S., Holman, I., Vicario, D. R., Visessri, S., Ekkawatpanit, C. and Hannaford, J., 2025. Stakeholder perceptions of drought resilience using government drought compensation in Thailand. *International Journal of Disaster Risk Reduction*, 121, 105365. [DOI]

Chuenchum, P., Meneesrikum, C., Teerapanuchaikul, C. and Sriariyawat, A., 2024. Community participation and effective water management: A study on water user organizations (WUOs) in Thailand. *World Development Perspectives*, 34, 100589. [DOI]

Drury, L., Johnston, R. and Schmitter, P., 2023. Water stresses and responses in Myanmar's Central Dry Zone. In *Palgrave Studies in Climate Resilient Societies*, (p. 37). Springer International Publishing. [DOI]

Duc, N.H., Kumar, P., Long, P.T., Meraj, G., Lan, P.P., Almazroui, M. and Avtar, R., 2024. A systematic review of water governance in Asian countries: Challenges, frameworks, and pathways toward sustainable development goals. *Earth Systems and Environment*, 8(2), pp.181–205. [DOI]

Fasting, S., Bacudo, I., Damen, B. and Dinesh, D., 2021. Climate governance and agriculture in Southeast Asia: Learning from a polycentric approach. *Frontiers in Political Science*, 3. [DOI]

Ferraro, G. and Failler, P., 2024. Biodiversity, multi-level governance, and policy implementation in Europe: A comparative analysis at the subnational level. *Journal of Public Policy*, 1. [DOI]

Forni, L., Bresney, S. R., Espinoza, S., Lavado, A., Mautner, M., Han, J. Y.-C., Nguyen, H., Sreyphea, C., Uniacke, P., Villarroel, L., Lindberg, M., Resurrección, B. P. and Huber-Lee, A., 2021. Social hydrological analysis for poverty reduction in community-managed water resources systems in Cambodia. *Water*, 13(13), 1848. [DOI]

Franzetti, F., Pezzoli, A. and Bagliani, M., 2017. Rethinking water resources management under a climate change perspective: From national to local level. The case of Thailand. In *Green Energy and Technology*, (p. 169). Springer Science+Business Media. [DOI]

Frisvold, G. B. and Konyar, K., 2012. Water shortages in the Southern Mountain states: Economic impacts on agriculture. VBN

Forskningsportal (Aalborg Universitet), (p. 83). Aalborg University. Available at: http://vbn.aau.dk/da/publications/adaptation-and-resilience(74ec3b81–78d4–4ae7–895d-3a0e0bce055a).html

González, A. G., Peña-Alonso, C., González-Dávila, M., Santana-Casiano, J. M., González-Santana, D., Ferraro, G., Naranjo-Almeida, L. and García-Romero, L., 2025. Governance challenges for the adaptation to sea-level rise in the Canary Islands: A multilevel approach. *Ocean and Society*, 2. [DOI]

Hashemy Shahdany, S. M. and Rahparast, D., 2025. Assessing and managing risks to strengthen the resilience of surface water delivery systems under drought in irrigation districts. *Environmental Science & Policy*, 174, 104265. [DOI]

Holman, I. and Knox, J., 2023. Research and policy priorities to address drought and irrigation water resource risks in temperate agriculture. *Cambridge Prisms Water*, 1. [DOI]

Hurlbert, M., Gupta, J. and Verrest, H., 2019. A comparison of drought instruments and livelihood capitals. *Climate and Development*, 11(10), 863. [DOI]

Kaiss, R., Benjouid, Z., Faiz, M., ECH-CHAHED, H., Rakhimi, A., Zarouali, S. S., Maimoun, A., Hmid, A. and Cherkaoui, M., 2025. Water stress and regional governance in Morocco: Pathways to agricultural resilience through advanced regionalization. *Research on World Agricultural Economy*, pp.957-972. [DOI]

Kampragou, E., Apostolaki, S., Manoli, E., Froebrich, J. and Assimacopoulos, D., 2011. Towards the harmonization of water-related policies for managing drought risks across the EU. *Environmental Science & Policy*, 14(7), 815. [DOI]

Khadka, D., Babel, M. S., Tingsanchali, T., Penny, J., Djordjević, S., Abatan, A. A. and Giardino, A., 2024. Evaluating the impacts of climate change and land-use change on future droughts in northeast Thailand. *Scientific Reports*, 14(1). [DOI]

Kukuntod, N. and Wijitkosum, S., 2025. Escalating drought vulnerability driven by land use change: Insights from a GIS-based CA-Markov and multi-criteria assessment of future scenarios in the Lam Ta Kong Watershed. *Earth Systems and Environment*. [DOI]

Kulkarni, S. and Sawada, Y., 2025. Droughts with no agro-climatological extremes. *Scientific Reports*, 15(1). [DOI]

Lambelet, S., 2023. Unintended policy integration through entrepreneurship at the implementation stage. *Policy Sciences*, 56(1), 161. [DOI]

Lima, L. S. de, Silva, F. E. O. e, Anastácio, P. R. D., Kolanski, M. M. de P., Pereira, A. C. P., Menezes, M. S. R., Cunha, E. and Macedo, M. N., 2024. Severe droughts reduce river navigability and isolate communities in the Brazilian Amazon. *Communications Earth & Environment*, 5(1). [DOI]

Lu, X. and Talamini, G., 2024. The socio-spatial response to environmentally mitigated channelization in Southeast Asia. A longitudinal landscape pattern analysis. *Landscape and Urban Planning*, 248, 105107. [DOI]

Makaya, E., Rohse, M., Day, R., Vogel, C., Mehta, L., McEwen, L., Rangecroft, S. and Loon, A. F. V., 2020. Water governance challenges in rural South Africa: exploring institutional coordination in drought management. *Water Policy*, 22(4), 519. [DOI]

Matimolane, S. and Mathivha, F. I., 2025. Tackling rural water scarcity in South Africa: climate change, governance, and sustainability pathways. *Frontiers in Environmental Science*, 13. [DOI]

Milhorance, C., Bursztyn, M. and Sabourin, É., 2022. Analysing complex policy problems: a critical review of the literature. *International Journal of Public Policy*, 16, 126. [DOI]

Moridi, M., Rahimian, M., Movahed, R. G., Molavi, H., Gholamrezai, S. and Payamani, K., 2025. Policy insights for drought adaptation: Farmers' behavior and sustainable agricultural development. *Environmental and Sustainability Indicators*, 26, 100603. [DOI]

Nagel, M. L. and Pierre, J., 2020. Putting the Peter Parker principle into practice. *International Review of Public Policy*, 2(2), 192. [DOI]

Nasir, J., Zeleke, T., Gidey, E., Assefa, E., Kahsay, S. T., Birhane, E. and Mhangara, P., 2025. The synergetic effect of drought and land use changes on Ethiopian Rift Valley Northwestern Escarpment livelihood systems. *Discover Environment*, 3(1). [DOI]

Nelson, R., Howden, M. and Stafford-Smith, M., 2008. Using adaptive governance to rethink the way science supports Australian drought policy. *Environmental Science & Policy*, 11(7), 588. [DOI]

Pandey, S., Bhandari, H., Ding, S., Prapertchob, P., Sharan, R., Naik, D. S. B., Taunk, S. K. and Sastri, A. S. R. A. S., 2007. Coping with drought in rice farming in Asia: Insights from a cross-country comparative study. *Agricultural Economics*, 37, 213. [DOI]

Rahman, G., Jung, M., Kim, T. and Kwon, H., 2025. Drought impact, vulnerability, risk assessment, management and mitigation under climate change: A comprehensive review. *KSCE Journal of Civil Engineering*, 29(1), 100120. [DOI]

Raza, M.Y., Fahad, S., Ahmed, M., Ali, S. and Faraz, A., 2026. Agricultural adaptation to climate change: New approaches to knowledge and learning. In: *Sustainable Cropping Systems Under a Changing Climate*. Academic Press, pp.645–664. [DOI]

Saguansap, P., Mruksirisuk, P., Garshasbi, D. and Thanvisitthpon, N. T., 2025. Drought vulnerability assessment and mitigation strategies for peri-urban province of Pathum Thani, Thailand. *Progress in Disaster Science*, 26, 100431. [DOI]

Sánchez, A. N., Koehler, J. and Loon, A. F. V., 2025. Managing floods and droughts synergistically: A transformative governance approach. *PLOS Water*, 4(8). [DOI]

Sarti, F., 2023. The policy integration game? Congruence of outputs and implementation in policy integration. *Policy Sciences*, 56(1), 141. [DOI]

Sattraburut, T., Vongvassana, S., Phutthai, T. and Thasod, Y., 2024. Palynological approaches to forest restoration in Southeast Asia: Challenges and opportunities for Thailand—A systematic review. *Trees, Forests and People*, 18, 100714. [DOI]

Shah, S. H., 2021. How is water security conceptualized and practiced for rural livelihoods in the global South? A systematic scoping review. *Water Policy*, 23(5), 1129. [DOI]

Sifundza, L., Zaag, P. van der and Masih, I., 2019. Evaluation of the responses of institutions and actors to the 2015/2016 El Niño drought in the Komati catchment in Southern Africa: Lessons to support future drought management. *Water SA*, 45. [DOI]

Sin-ampol, P., Takaew, W. and Pothakham, K., 2025. Contextualising potential zones for ecosystem-based adaptation in Lower Northern Thailand: A mixed method analysis for water resources management. *Journal of Environmental Management*, 376, 124515. [DOI]

Sithirith, M., Sao, S., Silva, S. de, Kong, H., Kongkroy, C., Thavrin, T. and Sarun, H., 2024. Water governance in the Cambodian Mekong Delta: The nexus of Farmer Water User Communities (FWUCs), Community Fisheries (CFis), and Community Fish Refuges (CFRs) in the context of climate change. *Water*, 16(2), 242. [DOI]

Smith, K. H., Stiles, C. J., Hayes, M. J. and Carparelli, C., 2016. Support for drought response and community preparedness: Filling the gaps between plans and action. In *Drought and Water Crises*, (p. 123). CRC Press. [DOI]

Sutcliffe, C., Holman, I., Goodwin, D., Salmoral, G., Pardthaisong, L., Visessri, S., Ekkawatpanit, C. and Rey, D., 2024. Which factors determine adaptation to drought amongst farmers in Northern Thailand? Investigating farmers' appraisals of risk and adaptation and their exposure to drought information communications as determinants of their adaptive responses. *Mitigation and Adaptation Strategies for Global Change*, 29(1). [DOI]

Tchinda, A. F. and Talbot, D., 2023. Barriers and enablers of environmental policy coherence: A systematic review. *Environmental Policy and Governance*, 34(1), 77. [DOI]

Thanh, P. N., Van, T. L., Minh, T. T., Ngoc, T. H., Lohpaisankrit, W., Pham, Q. B., Gagnon, A. S., Deb, P., Pham, N. T., Anh, D. T. and Đinh, V. N., 2023. Adapting to climate-change-induced drought stress

to improve water management in Southeast Vietnam. *Sustainability*, 15(11), 9021. [DOI]

Tiepolo, M., Pezzoli, A. and Tarchiani, V., 2017. Renewing local planning to face climate change in the tropics. In *Green Energy and Technology*, Springer Science+Business Media. [DOI]

Tran, T. A., Tran, D. D., Vo, O. V., Pham, V. H. T., Tran, H. V., Yong, M. L., Phu, L. V. and Dang, P. T., 2024. Evolving pathways towards water security in the Vietnamese Mekong Delta: An adaptive management perspective. *AMBIO*, 54(3), 460. [DOI]

Veisi, H., Darijani, F., Khoshbakht, K., Liaghati, H. and Nazari, M. R., 2025. From perception to policy: adaptation strategies for agricultural resilience in a changing climate. *Discover Agriculture*, 3(1). [DOI]

Villamayor-Tomás, S., Iniesta-Arandia, I. and Roggero, M., 2020. Are generic and specific adaptation institutions always relevant? An archetype analysis of drought adaptation in Spanish irrigation systems. *Ecology and Society*, 25(1). [DOI]

Ziervogel, G., Satyal, P., Basu, R., Mensah, A., Singh, C., Hegga, S. and Abu, T. Z., 2019. Vertical integration for climate change adaptation in the water sector: Lessons from decentralisation in Africa and India. *Regional Environmental Change*, 19(8), 2729. [DOI]

Zipper, S. C., Smith, K. H., Breyer, B., Qiu, J., Kung, A. and Herrmann, D. L., 2017. Socio-environmental drought response in a mixed urban-agricultural setting: synthesizing biophysical and governance responses in the Platte River Watershed, Nebraska, USA. *Ecology and Society*, 22(4). [DOI]

Zokirov, K., Mukhitdinov, O., Suyarov, S., Sherov, A., Egamberdiev, F., Mamadaliev, N. K., Abdirashidova, G. A. and Abdullayev, D., 2025. The impact of water resources management and resource optimisation during drought periods. *Journal of Water and Land Development*, 106. [DOI]

Nature Environment and Pollution Technology
An International Quarterly Peer-Reviewed Open Access Journal

p-ISSN: 0972-6268 | e-ISSN: 2395-3454 Vol. 25 | No. 4 | Article ID B4444 | 2026

RESEARCH ARTICLE https://doi.org/10.46488/NEPT.2026.v25i04.B4444 OPEN ACCESS

Field Implementation of *Pseudomonas fluorescens* for Bioremediation of Single-Use Plastic Waste: A Biolayer in a Landfill Liner System

S. Sangeetha[1]† and P. Hari Krishna[2]
[1]Department of Civil Engineering, VNR Vignana Jyothi Institute of Engineering and Technology, Vignana Jyothi Nagar, Pragathi Nagar, Nizampet S.O., Hyderabad-500118, Telangana, India
[2]Department of Civil Engineering, National Institute of Technology, Warangal-506004, Telangana, India
†Corresponding author: S. Sangeetha; mailsangeethasundar@gmail.com

ARTICLE HISTORY

Received: 19-04-2026
Revised: 30-05-2026
Accepted: 05-06-2026

KEYWORDS

Single-use plastic waste
Bioremediation
Bioaugmentation
Pseudomonas fluorescens

CITE THIS ARTICLE

Sangeetha, S. and Hari Krishna, P., 2026. Field implementation of *Pseudomonas fluorescens* for bioremediation of single-use plastic waste: A biolayer in a landfill liner system. *Nature Environment and Pollution Technology*, 25(4), B4444. https://doi.org/10.46488/NEPT.2026.v25i04.B4444

COPYRIGHT & LICENCE

© 2026 The Authors
Open Access under CC BY 4.0.

PUBLISHED BY
TECHNOSCIENCE PUBLICATIONS

ABSTRACT

Single-use plastic materials are widely used for packaging daily essentials and sanitary products. Fifteen such packaging materials were identified and collected. Twelve batches of samples were buried in twelve pits. *Pseudomonas fluorescens* in dextrose medium was applied to six pits, and six pits were subjected to natural degradation to serve as a control. The study was conducted for a period of six months, and samples were recovered after each month. Recovered samples were subjected to a weight-loss study and Fourier transform infrared (FTIR) spectroscopy. FTIR analysis indicated shifts of peaks toward lower wavenumbers, disappearance of peaks, and reductions in bond energy in all samples bioremediated with microbial solutions. The reduction in spectral energy associated with shifts in characteristic FTIR peaks was approximately 0.15–45%. Compared with the weight-loss technique, FTIR analysis was effective in understanding biodegradation phenomena. CHNS analysis of soil recovered from the pit revealed that the bioaugmentation technique increased the C/N ratio of the surrounding soil in the pit to 4.5%, which was absent initially. The results indicated that this technique could enhance the bioremediation of non-recoverable plastic waste.

1. INTRODUCTION

Many non-recycled plastic products, after their useful life, ultimately end up in soil or water as waste. Hundreds of microbes have been identified to degrade plastic polymers (Arutchelvi et al. 2008, Shah et al. 2008, Kumar Sen & Raut 2015, Montazer et al. 2018, Fesseha & Abebe 2019, Bahl et al. 2020, Bardají et al. 2020, Merchant et al. 2025). Microbes use plastic polymers as a source of carbon and mineralize them to carbon dioxide and water (Albertsson & Karlsson 1990, Reddy et al. 2009, Pérez-García et al. 2025). The success of any scientific finding lies in its field-scale implementation. Earlier bioremediation studies were conducted on a laboratory scale in a controlled environment. Plastic-degrading microbes were isolated from soil and water samples collected from dumpsites (Dubey & Thalla 2025, Iqbal et al. 2025, Tirkey & Upadhyay 2025). Field bioremediation studies were limited to the soil burial technique. These field studies were conducted by burying plastic materials directly in soil without introducing potential bacterial strains (Orhan et al. 2004, Vijaya & Reddy 2008, Shovitri et al. 2017, Tai et al. 2019). The microbial species must thrive under the existing environmental conditions along with native microbial species. In the present study, field-scale bioaugmentation using *Pseudomonas fluorescens* to accelerate plastic biodegradation was investigated. The microbes were introduced

into the field, where 15 different plastic packaging materials were buried. Based on the effectiveness of the field-scale study, a biolayer is proposed for inclusion in the design of an engineered landfill system to enhance plastic-waste biodegradation.

2. MATERIALS AND METHODS

The plastic materials considered for the degradation study are generally used for packaging and are made of high-density polyethylene (HDPE), low-density polyethylene (LDPE), linear low-density polyethylene (LLDPE), polypropylene (PP), and polylactic acid (PLA). Fifteen such wrapping materials from products used in daily life were randomly selected. Details of these materials are provided in Table 1. Information on the polymer origin was obtained from the resin identification code (RIC) printed by the manufacturer. Each plastic material was washed with isopropyl alcohol, dried, and cut into 2 cm × 2 cm pieces. These pieces were weighed to an accuracy of 0.1 mg and attached to a mesh to facilitate sample recovery at the end of the biodegradation study. The study was conducted at VNR VJIET College, Hyderabad, Telangana, India. Initial characterization of soil collected from the field was performed. In the field, 12 pits, each 0.5 m in diameter and 0.7 m deep, were dug. In each pit, meshes with attached plastic pieces were buried in triplicate at different depths to verify the repeatability of the procedure. A schematic layout of the test pits used in the study is shown in Fig. 1.

Six of these pits were left for natural degradation. Because the major objective of the study was to compare the performance of the field bioaugmentation technique with the natural degradation process, these pits were maintained as controls rather than sterile controls. The other six pits were bioaugmented with *Pseudomonas fluorescens* (PF). A total of 60 g of *Pseudomonas fluorescens* in dextrose medium (powder form), supplied by M/S SOM Phytopharma (India) Ltd., Hyderabad, was dissolved in 6 L of water. For each treatment pit, 1 L of the prepared bacterial solution

Table 1: Different types of single-use plastic materials subjected to field degradation.

Label	Description	Type of plastic
1F	Detergent cover	HDPE
2F	Cloth-like white bag	PP
3F	Transparent orange-colored cover	LDPE
4F	Black and white parcel packaging	PP
5F	Transparent cover	HDPE
6F	Aerated beverage label	PP
7F	Empty milk packet	LLDPE
8F	Packaging cover	HDPE
9F	Carry bags from textile shop	PP
10F	Food packing silver wrapper	HDPE
11F	Empty oil packet	HDPE
12F	File cover	PP
13F	Shampoo cover	HDPE
14F	Biodegradable white carry bag	Polylactic acid
15F	Instant noodles wrapper	HDPE

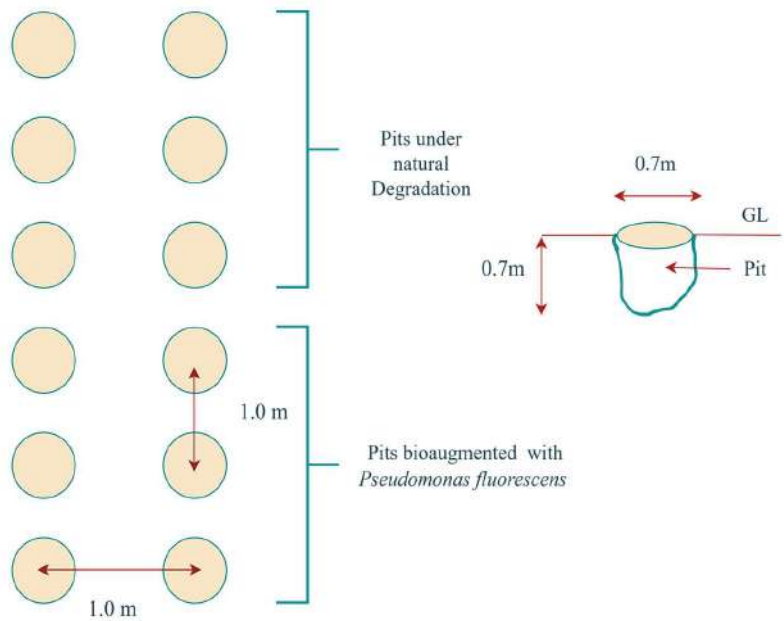


Fig. 1: Schematic representation of test pits for the field biodegradation study.

Table 2: Basic properties of soil collected from the study location.

Properties	Standard Codes	Results/Values
Field dry density	IS: 2720 (Part 29): 1975	1.6 t m^{-3}
Water content	IS: 2720 (Part 2): 1973	7.4%
Specific gravity	IS:2720 (Part 3):1980	2.66
Grain size distribution: Sieve and Hydrometer Analysis	IS: 2720 (Part 4): 1985	Gravel: 5.6%; Sand: 89.7% Silt: 3.3%; Clay: 1.4%
Soil classification	IS: 1498: 1970	Poorly graded sand (SP)
pH	IS: 2720 (Part 26): 1987	8.82 at 28.6°C
Electrical Conductivity	IS: 14767: 1973	0.589 mS at 28.6°C
Salinity	Probe method	0.286 ppt at 28.6°C

was applied uniformly throughout the depth. The moisture content of each pit was maintained constant by supplying water periodically. To avoid disturbance, at the end of each month, one pit subjected to natural degradation and one pit subjected to bioaugmentation were excavated. After recovery, the plastic film samples were cleaned with isopropyl alcohol. Percentage weight loss was calculated by comparing the initial weight and the weight of the sample after recovery, as given in Eq. (1). For each sample, the maximum percentage weight loss observed during the six-month study period was considered.

$$\text{Percentage of weight loss} = \frac{w_a - w_b}{w_a} \times 100\% \quad \ldots(1)$$

Here,

w_a and w_b are the weights of a plastic film before placing it inside the pit and after recovery, respectively.

FTIR analysis was then performed on samples recovered after 6 months of the study. FTIR analysis was performed directly on the plastic films. CHNS analysis was performed on soil samples collected from the field before commencement of the study. After 6 months, soil samples from the control pit and the bioaugmented pit near the mesh were also subjected to CHNS analysis to assess carbon levels. The samples were tested by preparing KBr pellets.

3. RESULTS AND DISCUSSION

3.1. Basic Characteristics of Soil

Soil collected from the field location was tested to understand its basic properties. The properties of the soil are given in Table 2.

3.2. Field Weight Loss Study

Physical disintegration, expressed as percentage weight loss, was measured for all 15 samples at specified time intervals up to 6 months. The maximum percentage weight loss observed during the study period for all 15 samples subjected to natural and bioaugmented degradation is shown in Fig. 2. Of the 15

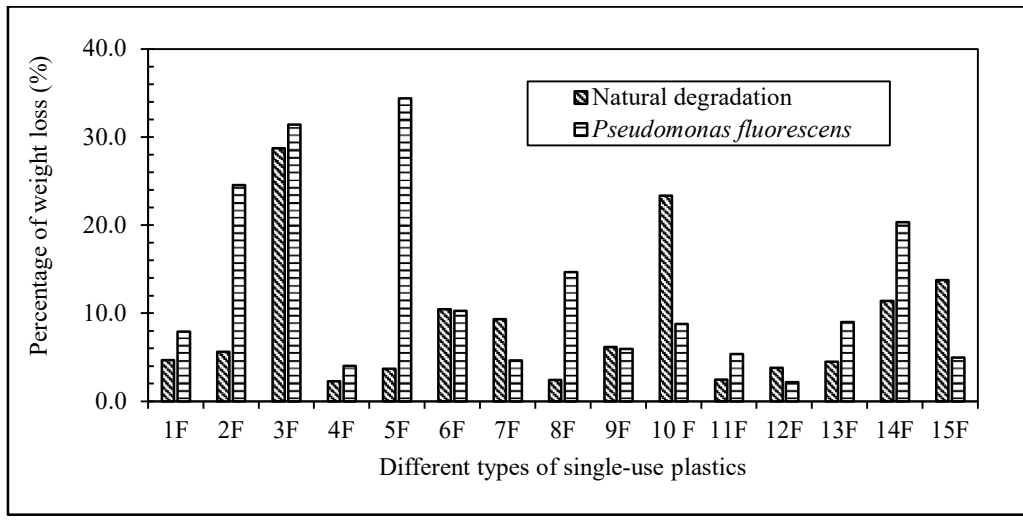


Fig. 2: Percentage of weight loss observed in the field degradation study.

samples, 9 showed greater degradation in the presence of *Pseudomonas fluorescens*. A maximum degradation of 34% was observed with the bioaugmentation technique for the transparent HDPE cover. Two samples showed equivalent degradation under both processes (6F and 9F). Samples 7F, 10F, 12F, and 15F exhibited greater weight loss during natural degradation. These samples were made from LLDPE, PP, and HDPE. The results of the field weight-loss study demonstrate the efficiency of *Pseudomonas fluorescens* in biodegradation under field conditions. However, a weight-loss study may not provide an accurate picture of plastic biodegradation. The samples were attached to the mesh using staples. Physical damage to the material was observed upon recovery due to staple holes and sharp particles in the soil.

3.3. FTIR Analysis

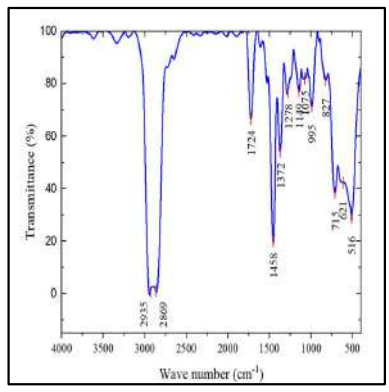
To investigate changes in the chemical bonds of polymeric hydrocarbon samples subjected to field bioaugmentation and natural degradation, FTIR analysis was performed on samples recovered from the field after 6 months of degradation. FTIR spectra of all 15 samples with prominent peaks are shown in Figs. 3–17. In the FTIR spectra of samples subjected to bioaugmentation, shifts of peaks toward lower wavenumbers and the disappearance of certain peaks were observed compared with samples subjected to natural degradation. In all single-use plastic samples, peaks corresponding to C–H stretching of the plastic polymer were observed in the 3000–2850 cm^{-1} region. Peaks of C–H deformation were observed around 1500–600 cm^{-1}. Minor peaks due to carbonyl bonds were observed in some samples at 1900–1500 cm^{-1}. Various peaks were observed in the spectra of all samples except 6F and 9F. However, these two samples also showed shifts toward lower wavenumbers.

In the bioaugmented samples, narrowing of broad peaks and disappearance of peaks in the C–H region (3000–2850 cm^{-1}), relative to natural degradation, were observed in samples 1F, 2F, 12F, 13F, and 15F. For analysis, the plastic film samples were categorized into groups based on the origin of the polymeric material from which each sample was manufactured. The peaks were identified based on standard FTIR spectroscopy literature (Coates 2000, Stuart 2004, Silverstein et al. 2005, Smith 2011). The changes in spectral peaks are described below.

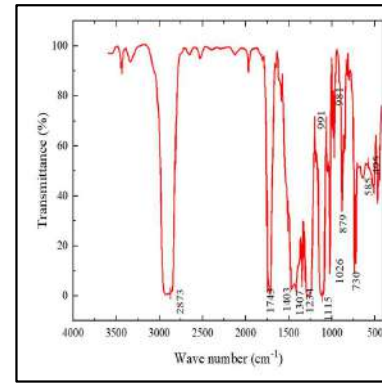
3.3.1. FTIR Spectra of HDPE Samples

HDPE has a linear structure, which accounts for its higher density. The material is generally stiff, tough, and opaque (Crawford 2002, Emblem 2012). Samples 1F, 5F, 8F, 10F, 11F, 13F, and 15F are films made from HDPE polymer, and the spectral peaks after 6 months of bioremediation under natural and PF-bioaugmented conditions are shown in Figs. 3–9. Characteristic spectral peaks of virgin HDPE film include double peaks between 2950–2800 cm^{-1} representing CH_2 asymmetric and symmetric stretching, a pair of split peaks at 1400–1300 cm^{-1} due to C–CH_3 bending, and another set of split peaks around 730–700 cm^{-1}, as reported in the literature. After 6 months of bioremediation, many additional peaks were also observed in Figs. 3–17. This is because the samples considered in the present study are commercial wrappers that contain antioxidants, surface coatings, additives, color dyes, and other composite substances. Hence, to investigate microbial activity relative to natural degradation, all spectra from the bioaugmented batch were compared with those of samples subjected to natural degradation.

In Fig. 3, for sample 1F, a detergent wrapper, the peak wavenumbers shifted toward lower values, the double peaks

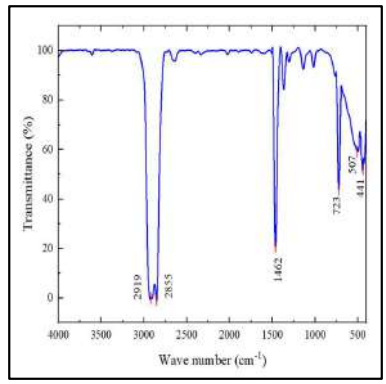


a) Natural degradation

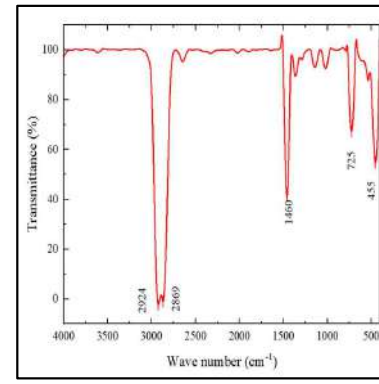


b) Bioaugmented with *Pseudomonas fluorescens*

Fig. 3: FTIR spectrum of field sample 1F.

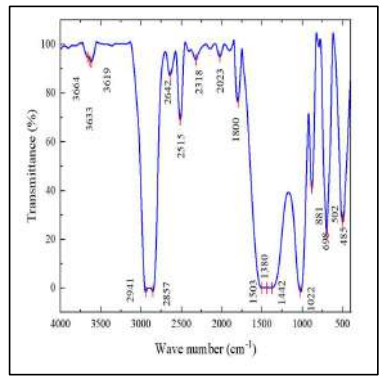


a) Natural degradation

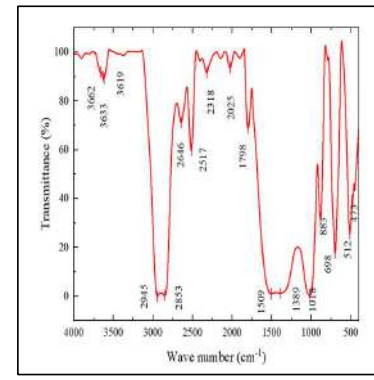


b) Bioaugmented with *Pseudomonas fluorescens*

Fig. 4: FTIR spectrum of field sample 5F.



a) Natural degradation



b) Bioaugmented with *Pseudomonas fluorescens*

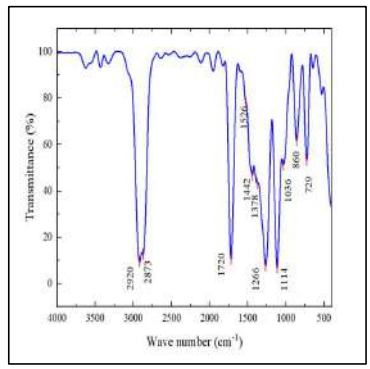
Fig. 5: FTIR spectrum of field sample 8F.

in the C–H region became blunt, and a single significant peak appeared. A new peak at approximately 981 cm^{-1} corresponding to HDPE oxidation was observed (Stuart 2004). Peaks shown in Fig. 4 for sample 5F are identical to those reported by various researchers (Gulmine et al. 2002, Smith 2011, Smith 2021, Chaudhary & Vijayakumar 2020). A weak band observed at 507 cm^{-1} in Fig. 4a under natural degradation was absent in the bioaugmented sample due to microbial activity. In Fig. 5, in addition to CH_2 stretching and C–CH_3 bending, peaks corresponding to the OH bond and weak bands representing carbon triple and double bonds are present. This indicates that the material contains HDPE along with other polymeric units. As a result of bioaugmentation, the broad band at 1500–1440 cm^{-1} with a triple peak narrowed to two prominent peaks, and a reduction in peak wavenumbers was observed.

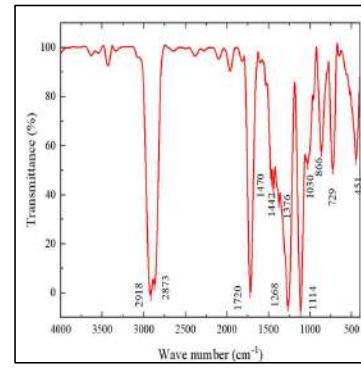
The major spectral change observed for sample 10F, other than peak shifting, is the reduced intensity of the peak at 1526 cm^{-1} in the bioaugmented sample compared with the naturally degraded sample, as shown in Fig. 6.

In Fig. 7, the significant bands representing HDPE are the OH group at 3600–3300 cm^{-1}, the aromatic C=C band at 1649 cm^{-1}, C–O stretching at 1269 and 1208 cm^{-1}, and C–O–C stretching at 1173 cm^{-1}. The major change resulting from bioaugmentation, as shown in Fig. 7b, is the absence of peaks at 1173 and 1208 cm^{-1}. The peak intensities in the functional-group region also decreased.

In Fig. 8, the prominent changes resulting from bioaugmentation are the disappearance of the C=C aromatic-ring stretching peaks at 1614 and 1528 cm^{-1}. The functional-group peaks in the fingerprint region (1500–500 cm^{-1})

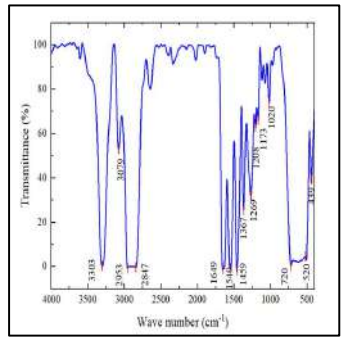


a) Natural degradation

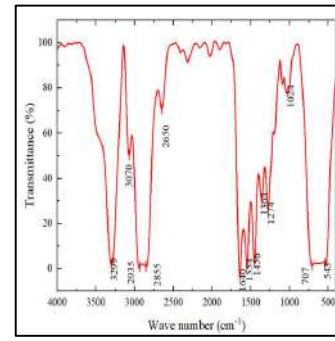


b) Bioaugmented with *Pseudomonas fluorescens*

Fig. 6: FTIR spectrum of field sample 10F.

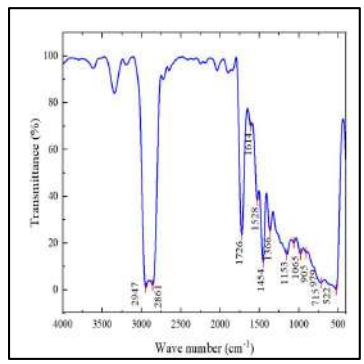


a) Natural degradation

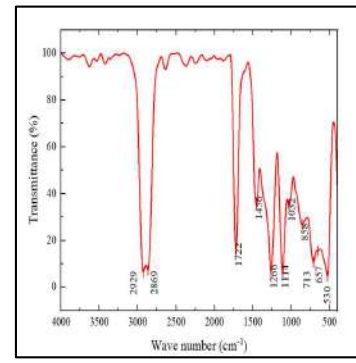


b) Bioaugmented with *Pseudomonas fluorescens*

Fig. 7: FTIR spectrum of field sample 11F.

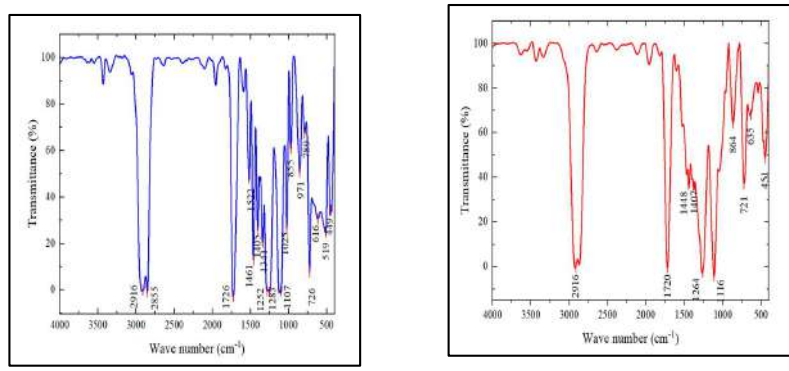


a) Natural degradation



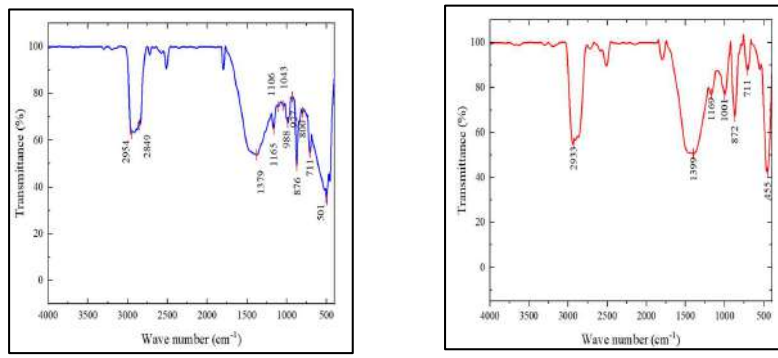
b) Bioaugmented with *Pseudomonas fluorescens*

Fig. 8: FTIR spectrum of field sample 13F.



a) Natural degradation b) Bioaugmented with *Pseudomonas fluorescens*

Fig. 9: FTIR spectrum of field sample 15F.



a) Natural degradation b) Bioaugmented with *Pseudomonas fluorescen*

Fig. 10: FTIR spectrum of field sample 2F.

shifted predominantly. Sample 15F also showed similar changes in the fingerprint region, as depicted in Fig. 9, due to biodegradation of the polymeric material. The number of peaks also decreased.

3.3.2. FTIR Spectra of Polypropylene Samples

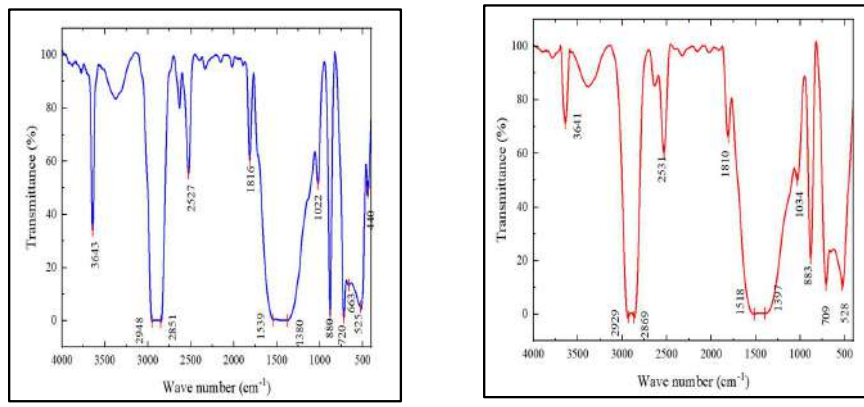
Sample 2F is made of a cloth-like nonwoven polypropylene material. Bags made from these materials are used as replacements for polyethylene carry bags after plastic bans in many locations. This material is also a synthetic polymer and is similarly nondegradable under natural conditions. In Fig. 10, after biodegradation, the peak at 2849 cm^{-1} corresponding to symmetric CH_2 stretching became less intense.

Fewer peaks are observed in the fingerprint region (1500–500 cm^{-1}) in the polypropylene samples. In Fig. 11, the overall spectrum shows a reduction in peak wavenumbers. Peaks in the low-wavenumber region at 663 and 440 cm^{-1} were absent in the bioaugmented samples. The spectral peaks of samples 6F and 9F showed only a reduction in peak wavenumbers at the end of the bioaugmentation study, as shown in Figs. 12 and 13.

Sample 12F is comparatively harder than the other polymers considered in the present study, and its spectral variations are shown in Fig. 14. Similar to samples 13F and 15F, the number of prominent peaks in the fingerprint region decreased. A side peak at 2670 cm^{-1} in the sample subjected to natural degradation was attributed to the presence of impurities and can be disregarded.

3.3.3. FTIR Spectrum of LDPE Sample

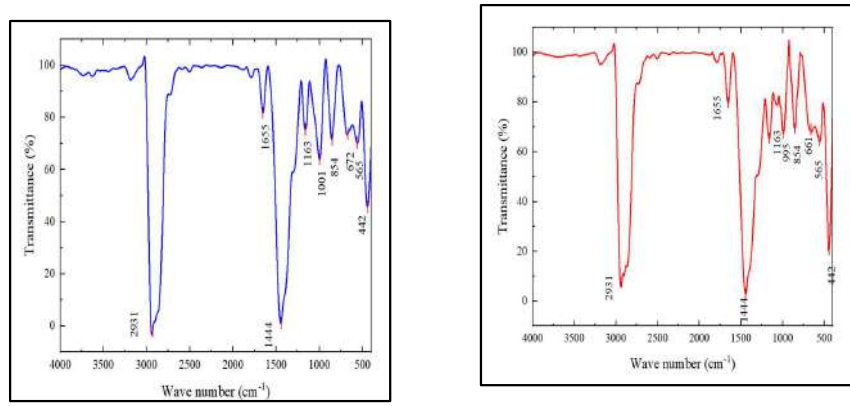
The structure of LDPE contains a long chain of carbon atoms with complex side chains (Crawford 2002, Montazer et al. 2020). This results in the lower density of the polymeric material. Sample 3F is a transparent thin carry bag made of



a) Natural degradation

b) Bioaugmented with *Pseudomonas fluorescens*

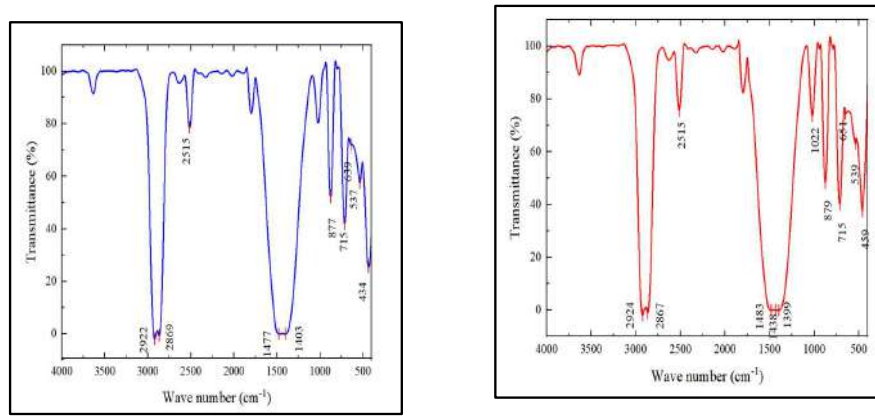
Fig. 11: FTIR spectrum of field sample 4F.



a) Natural degradation

b) Bioaugmented with *Pseudomonas fluorescens*

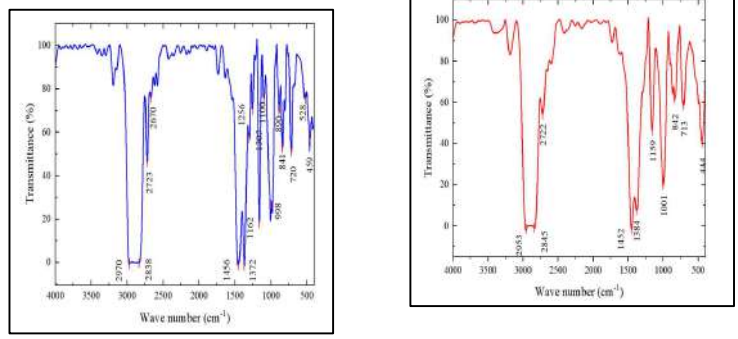
Fig. 12: FTIR spectrum of field sample 6F.



a) Natural degradation

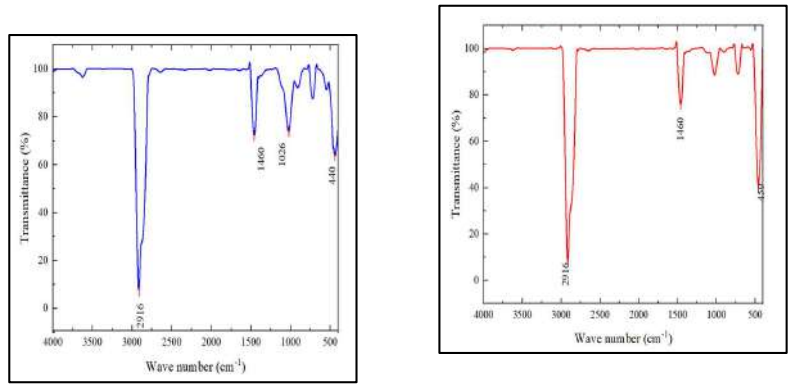
b) Bioaugmented with *Pseudomonas fluorescens*

Fig. 13: FTIR spectrum of field sample 9F.



a) Natural degradation b) Bioaugmented with *Pseudomonas fluorescens*

Fig. 14: FTIR spectrum of field sample 12F.



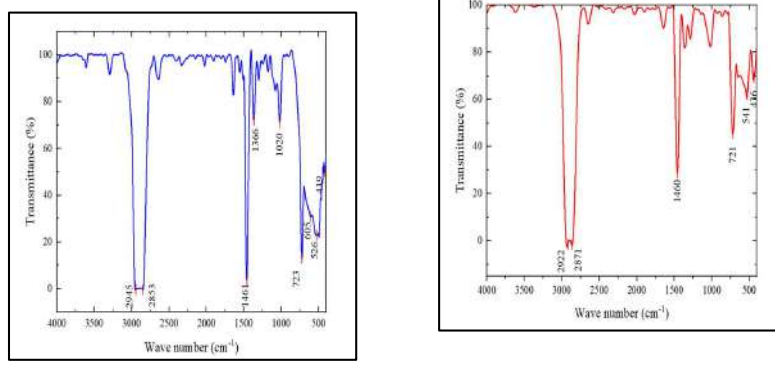
a) Natural degradation b) Bioaugmented with *Pseudomonas fluorescens*

Fig. 15: FTIR spectrum of field sample 3F.

LDPE, and its spectral variations due to bioaugmentation are shown in Fig. 15. A peak at 1026 cm^{-1} corresponding to C–C skeletal vibrations became comparatively less intense in the bioaugmented sample.

3.3.4. FTIR Spectrum of LLDPE Sample

Compared with LDPE, the side chains of LLDPE are short, and its density is slightly greater than that of LDPE. Comparison of the FTIR spectra in Fig. 16 after



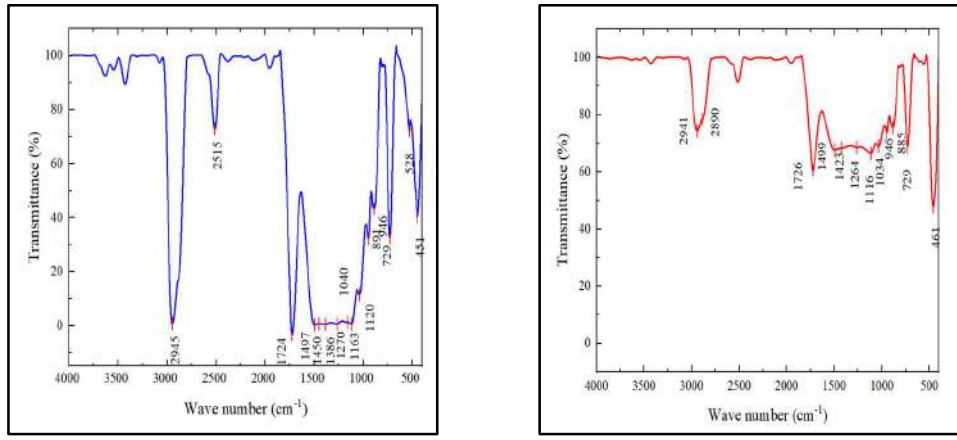
a) Natural degradation b) Bioaugmented with *Pseudomonas fluorescens*

Fig. 16: FTIR spectrum of field sample 7F.

the degradation study showed that the peak due to CH_2 bending at 1366 cm^{-1} and the peak at 1020 cm^{-1} due to C–C skeletal vibrations became less intense in the bioaugmented sample.

3.3.5. FTIR Spectrum of Polylactic Acid Sample

Polylactic acid is a biodegradable polymer derived from natural substances and contains lactic acid (Shah et al. 2008, Bahl et al. 2020, Chamas et al. 2020, Wei & Wierckx 2021). A considerable reduction in overall spectral peak intensity was observed in the bioaugmented sample compared with the sample subjected to natural degradation, as shown in Fig. 17, due to a reduction in film thickness. The sample is biodegradable under natural conditions.



a) Natural degradation

b) Bioaugmented with *Pseudomonas fluorescens*

Fig. 17: FTIR spectrum of field sample 14F.

Table 3: Summary of FTIR analysis.

Sample ID	Major FTIR peak changes after bioaugmentation	Key spectral observation
1F	Shift of peaks to lower wavenumbers; double C–H peaks became blunt; new peak at ~981 cm^{-1}	Evidence of HDPE oxidation and weakening of C–H bonds
2F	Reduced intensity of CH_2 symmetric stretching peak at 2849 cm^{-1}; fewer peaks in fingerprint region	Partial degradation of polypropylene
3F	Reduced intensity of C–C skeletal vibration peak at 1026 cm^{-1}	Structural weakening of LDPE chains
4F	Overall reduction in peak wavenumbers; disappearance of weak bands at 663 and 440 cm^{-1}	Loss of weaker functional groups due to biodegradation
5F	Weak band at 507 cm^{-1} disappeared in treated sample	Microbial activity altered HDPE-associated bands
6F	Only peak shifting toward lower wavenumbers observed	Limited but detectable molecular alterations
7F	CH_2 bending and C–C skeletal vibration peaks became less intense	Reduction in polymer chain integrity
8F	Broad triple peak in 1500–1440 cm^{-1} narrowed to two peaks; reduced peak positions	Significant alteration in methyl-related bands
9F	Only reduction in peak wavenumbers observed	Minor spectral changes indicating slow degradation
10F	Disappearance of peak at 1526 cm^{-1}	Decrease in functional group intensity
11F	Peaks at 1173 and 1208 cm^{-1} disappeared; reduced intensity in fingerprint region	Loss of C–O–C and C–O stretching bands
12F	Reduced number of peaks in fingerprint region; peak at 2670 cm^{-1} absent	Structural simplification after biodegradation
13F	C=C peaks at 1614 and 1528 cm^{-1} disappeared	Major changes in fingerprint region and aromatic structures
14F	Overall reduction in spectral intensity; degradation of peaks at 1386 and 528 cm^{-1}	Natural biodegradability enhanced under bioaugmentation
15F	Disappearance of peaks in fingerprint region; reduced number of peaks	Overall weakening of polymeric material

According to Singla et al. (2012), the material has several closely spaced peaks in the fingerprint region. The peak at 1386 cm^{-1}, indicating CH_2 rocking, and another peak in the low-wavenumber region at 528 cm^{-1} were reduced in the bioaugmented sample.

The major changes in the FTIR spectral peaks of bioaugmented and naturally degraded samples are given in Table 3.

3.3.6. Bond Energy Change of Field Samples

The energy of an organic bond is directly proportional to its wavenumber. The higher the wavenumber, the stronger the bond. From the spectral analysis of samples subjected to natural degradation and bioaugmentation, each material exhibited variations across different peaks. Commercially utilized polymeric packaging materials contain various chemical bonds in addition to virgin polymeric bonds. To account for changes across the entire spectra of samples subjected to natural degradation and bioaugmentation with PF, the bond energy change of each spectrum was calculated using the peak wavenumbers above the threshold height and Eq. (2) (Smith 2011), and the results are shown in Fig. 18.

$$E = hc\upsilon \quad \ldots(2)$$

where E is the energy change in joules, h is Planck's constant (6.626×10^{-34} J s), c is the speed of light (3×10^8 m s^{-1}), and υ is the wavenumber (m^{-1}).

The change in bond energy for all bioaugmented samples was lower than that for samples subjected to natural degradation. This indicates the efficacy of the technique under field conditions. Sample 8F had the highest bond energy due to the presence of a greater number of methyl-related bands in the high-frequency region. The largest decrease in bond energy relative to the natural degradation process was observed in sample 15F, at approximately 45%. This sample was made of HDPE. The reduction in bond energy change relative to the natural degradation process ranged from 0.85–45%, 0.15–44%, 17%, 24%, and 9% for HDPE, PP, LDPE, LLDPE, and PLA samples, respectively. Samples made of the same polymeric material showed different degrees of decrease in bond energy. This is attributed to the fact that each sample was manufactured differently for various commercial wrapping purposes, with different thicknesses, color prints, and surface coatings.

The smaller decrease in the biodegradable PLA sample is due to the sample having undergone considerable changes during natural degradation, with relatively fewer variations observed under bioaugmented conditions. It should also be noted that the bond energy change of biodegradable plastic is greater than that of other synthetic polymers. Hence, the change in bond energy does not indicate whether a material is degradable. It only compares changes and loss of bond strength in a material before and after degradation. As the weight-loss technique accounts only for physical changes, only 9 samples showed greater degradation than under the natural process. In FTIR analysis, internal changes at the molecular level were investigated. Hence, FTIR provides a better representation of the bioremediation process. Because the FTIR spectra of samples recovered after 6 months were compared in Fig. 18, it may not be meaningful to include error bars.

3.4. CHNS Analysis

Because the soil obtained from the site is homogeneous, CHNS analysis was performed directly on the oven-dried

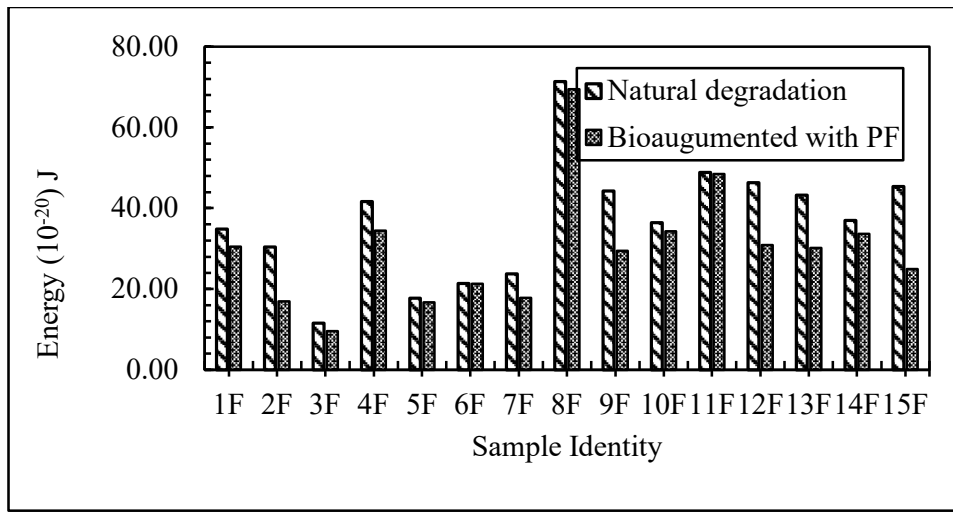


Fig. 18: Bond energy change of field samples from the FTIR spectral peaks.

Table 4: CHNS analysis of field samples.

S. No.	Soil Samples	N (%)	C (%)	H (%)	S (%)
1	Before treatment	0.49	0	0.73	0.42
2	Control pit after 6 months	0.56	0	0.81	0.23
3	PF-treated pit after 6 months	0.43	1.92	0.64	0.15

samples. CHNS results for samples collected before the study, from the control pit, and from the PF-bioaugmented pit after 6 months are given in Table 4. Initially, the soil collected at a depth of 0.7 m before commencement of the study contained no traces of carbon. No carbon was observed in the control pit even after 6 months of the study. The carbon content of the pit bioaugmented with PF was 1.92%. This can be attributed to biomass deposited by microbial activity. The presence of biomass resulting from biodegradation was also reported by Ardisson et al. (2014).

In the field study, the soil had no carbon content before the commencement of the study. Soil samples collected after 6 months of bioaugmentation were tested for carbon after the buried plastic films were removed and showed increased carbon levels attributable to biomass deposited during bioaugmentation. Due to microbial activity in the bioaugmented pit, the C/N ratio of the sample increased to 4.5%, which was initially absent.

4. PROPOSAL OF BIOLAYER IN LANDFILL LINER SYSTEM

Fig. 19 shows a schematic diagram of the biolayer proposed for the landfill liner system. In an engineered landfill, unrecoverable waste is disposed of daily, forming a daily cell. The daily cell is covered with a soil-like fraction present in the landfill, referred to as daily cover (Warmadewanthi et al. 2021). This daily cover can be bioaugmented with potential plastic-degrading microbes, forming a biolayer. In the present study, bioaugmentation with *Pseudomonas fluorescens* was found to be effective in the bioremediation of plastic waste. Many such plastic-degrading microbes classified at biosafety level 1 must be studied under landfill conditions. The technique can then be implemented extensively in engineered landfills on a large scale. However, challenges associated with large-scale implementation, including environmental variability, microbial survivability, long-term monitoring, and operational feasibility, must be further studied.

5. CONCLUSIONS

The study involved a preliminary investigation of a field-scale bioaugmentation technique using FTIR analysis. The following conclusions were drawn from the present study.

- Bioaugmentation using *Pseudomonas fluorescens* enhanced the degradation of polypropylene material by a maximum of 4.3 times and that of polyethylene-based material by 9.3 times in terms of percentage weight loss.
- It was also observed that the FTIR study provides a better representation of the bioremediation process than the field weight-loss study. FTIR spectra of bioaugmented field samples indicate the absence of C–H peaks and a shift of major peaks toward lower wavenumbers.
- For the same type of base polymer, degradation rates vary among different samples of the same classification in both the weight-loss study and FTIR bond-energy calculations.
- After field bioaugmentation using *Pseudomonas fluorescens*, the carbon level and C/N ratio of the soil increased to 4.5%, which was absent before treatment.

The success of the bioaugmentation process in the field under open atmospheric conditions indicates that this technique can be used to design a biolayer in an engineered landfill system. The field-scale bioaugmentation technique can be further investigated using CO_2 evolution studies,

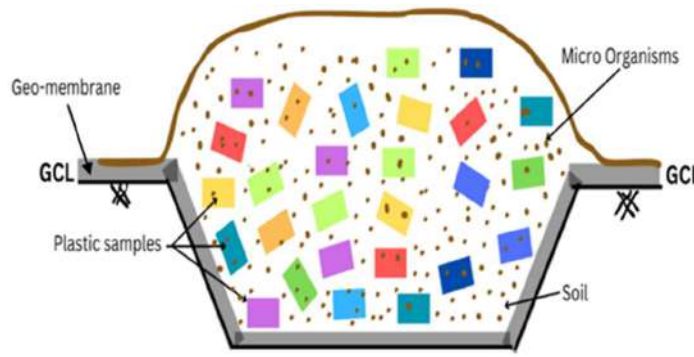


Fig. 19: Proposal of a biolayer in a landfill liner system.

thermal characterization techniques, molecular-weight measurement, and scanning electron microscopy (SEM) analysis.

6. ACKNOWLEDGEMENT

The authors acknowledge the testing facilities provided by the National Institute of Technology, Warangal, India, and VNR Vignana Jyothi Institute of Engineering and Technology, Hyderabad, India.

7. REFERENCES

Albertsson, A.-C. and Karlsson, S., 1990. The influence of biotic and abiotic environments on the degradation of polyethylene. *Progress in Polymer Science*, 15(2), pp.177–192. [DOI]

Ardisson, G.B., Tosin, M., Barbale, M. and Degli-Innocenti, F., 2014. Biodegradation of plastics in soil and effects on nitrification activity: A laboratory approach. *Frontiers in Microbiology*, 5(DEC), p.710. [DOI]

Arutchelvi, J., Sudhakar, M., Arkatkar, A., Doble, M., Bhaduri, S. and Uppara, P.V., 2008. Biodegradation of polyethylene and polypropylene. *Indian Journal of Biotechnology*, 7(1), pp.9–22.

Bahl, S., Dolma, J., Singh, J.J. and Sehgal, S., 2020. Biodegradation of plastics: A state of the art review. *Materials Today: Proceedings*, 39, pp.31–34. [DOI]

Bardají, D.K.R., Moretto, J.A.S., Furlan, J.P.R., Stehling, E.G. and Otto, C.C., 2020. A mini-review: Current advances in polyethylene biodegradation. *World Journal of Microbiology and Biotechnology*, 36(2), pp.1–11. [DOI]

Chamas, A., Moon, H., Zheng, J., Qiu, Y., Tabassum, T., Jang, J.H., Abu-Omar, M., Scott, S.L. and Suh, S., 2020. Degradation rates of plastics in the environment. *ACS Sustainable Chemistry & Engineering*, 8(9), pp.3494–3511. [DOI]

Chaudhary, A.K. and Vijayakumar, R.P., 2020. Effect of chemical treatment on biological degradation of high-density polyethylene (HDPE). *Environment, Development and Sustainability*, 22(2), pp.1093–1104. [DOI]

Coates, J., 2000. Interpretation of infrared spectra, a practical approach. In: Meyers, R.A. (ed.), *Encyclopedia of Analytical Chemistry*. John Wiley & Sons Ltd, Chichester, pp. 10815–10837.

Crawford, R.J., 2002. *Plastics Engineering*. 3rd ed. Butterworth-Heinemann, Oxford.

Dubey, A.P. and Thalla, A.K., 2025. Bioprospecting indigenous bacteria from landfill leachate for enhanced polypropylene microplastics degradation. *Journal of Hazardous Materials*, 487, p.137139. [DOI]

Emblem, A., 2012. Plastics properties for packaging materials. In: Coles, R. and Kirwan, M.J. (eds.), *Packaging Technology*. Woodhead Publishing, Oxford, pp. 287–309. [DOI]

Fesseha, H. and Abebe, F., 2019. Degradation of plastic materials using microorganisms: A review. *Public Health – Open Journal*, 4(2), pp.57–63. [DOI]

Gulmine, J.V., Janissek, P.R., Heise, H.M. and Akcelrud, L., 2002. Polyethylene characterization by FTIR. *Polymer Testing*, 21(5), pp.557–563. [DOI]

Iqbal, S.S., Nisa, Z.U., Shah, A.A., Hasan, F. and Hameed, A., 2025. Polystyrene and low-density polyethylene degradation by *Bacillus cereus* L1 isolated from plastic contaminated wastewater. *Microbial Cell Factories*, 24(1), pp.1–19. [DOI]

Kumar Sen, S. and Raut, S., 2015. Microbial degradation of low density polyethylene (LDPE): A review. *Journal of Environmental Chemical Engineering*, 3(1), pp.462–473. [DOI]

Merchant, M., Mande, S.S. and Sar, P., 2025. Microbial community enrichment and transition in landfill for the biotransformation of unpretreated low-density polyethylene (LDPE) under aerobic and anaerobic conditions. *Chemosphere*, 382, p.144429. [DOI]

Montazer, Z., Habibi Najafi, M.B. and Levin, D.B., 2018. Microbial degradation of UV-pretreated low-density polyethylene films by novel polyethylene-degrading bacteria isolated from plastic-dump soil. *Journal of Polymers and the Environment*, 26(9), pp.3613–3625. [DOI]

Montazer, Z., Najafi, M.B.H. and Levin, D.B., 2020. Challenges with verifying microbial degradation of polyethylene. *Polymers*, 12(1), p.123. [DOI]

Orhan, Y., Hrenović, J. and Büyükgüngör, H., 2004. Biodegradation of plastic compost bags under controlled soil conditions. *Acta Chimica Slovenica*, 51(3), pp.579–588.

Pérez-García, P., Sass, K., Wongwattanarat, S., Amann, J., Feuerriegel, G., Neumann, T., Bäse, N., Schmitz, L.S., Dierkes, R.F., Gurschke, M.F., Wypych, A., Bounabi, H., de Divitiis, M., Vollstedt, C. and Streit, W.R., 2025. Microbial plastic degradation: enzymes, pathways, challenges, and perspectives. *Microbiology and Molecular Biology Reviews*, 89(4), p.e00087-24. [DOI]

Reddy, M.M., Gupta, R.K., Bhattacharya, S.N., Parthasarathy, R. and Singh, A.K., 2009. Biodegradation of montmorillonite filled oxo-biodegradable polyethylene. *Journal of Applied Polymer Science*, 113(5), pp.2826–2832. [DOI]

Shah, A.A., Hasan, F., Hameed, A. and Ahmed, S., 2008. Biological degradation of plastics: A comprehensive review. *Biotechnology Advances*, 26(3), pp.246–265. [DOI]

Shovitri, M., Zulaika, E., Agustien, A. and Putra, M.Y., 2017. Soil burial method for plastic degradation performed by *Pseudomonas PL-01*, *Bacillus PL-01*, and indigenous bacteria. *AIP Conference Proceedings*, 1854(1), p.020004. [DOI]

Silverstein, R.M., Webster, F.X. and Kiemle, D.J., 2005. *Spectrometric Identification of Organic Compounds*. 7th ed. John Wiley & Sons, Hoboken, NJ.

Singla, P., Mehta, R. and Upadhyay, S.N., 2012. Microwave assisted synthesis of poly(lactic acid) and its characterization using size exclusion chromatography. *Journal of Macromolecular Science, Part A: Pure and Applied Chemistry*, 49(11), pp.963–970. [DOI]

Smith, B.C., 2011. *Fundamentals of Fourier Transform Infrared Spectroscopy*. 2nd ed. CRC Press, Boca Raton.

Smith, B.C., 2021. The infrared spectra of polymers II: Polyethylene. *Spectroscopy*, 36(9), pp.24–29. [DOI]

Stuart, B., 2004. *Infrared Spectroscopy: Fundamentals and Applications*. John Wiley & Sons, Chichester.

Tai, N.L., Adhikari, R., Shanks, R., Adhikari, B. and Vuocolo, K., 2019. Aerobic biodegradation of starch–polyurethane flexible films under soil burial condition: Changes in physical structure and chemical composition. *International Biodeterioration & Biodegradation*, 145, p.104793. [DOI]

Tirkey, A. and Upadhyay, L.S.B., 2025. Introducing the LDPE degrading microbes of sedimentary systems: From dumpsite to laboratory. *Environmental Science: Advances*, 4(6), pp.952–963. [DOI]

Vijaya, C. and Reddy, R.M., 2008. Impact of soil composting using municipal solid waste on biodegradation of plastics. *Indian Journal of Biotechnology*, 7(2), pp.235–239.

Warmadewanthi, I.D.A.A., Liu, J.C. and Soetomo, S., 2021. Impact of degraded solid waste utilization as a daily cover for landfill on the formation of methane and leachate. *Bioresource Technology Reports*, 15, p.100797. [DOI]

Wei, R. and Wierckx, N., 2021. Editorial: Microbial degradation of plastics. *Frontiers in Microbiology*, 12, p.635621. [DOI]

Nature Environment and Pollution Technology
An International Quarterly Peer-Reviewed Open Access Journal

p-ISSN: 0972-6268 | e-ISSN: 2395-3454 Vol. 25 | No. 4 | Article ID D1936 | 2026

RESEARCH ARTICLE https://doi.org/10.46488/NEPT.2026.v25i04.D1936 OPEN ACCESS

Spatial Footprint Distribution of Some Heavy Metals in Major Transport Routes in Ramadi City, Iraq

Rafraf Abdulaziz Abdulqader and Sufyan Mohammed Shartooh†
Department of Biology, College of Science, University of Anbar, Ramadi, Iraq
†Corresponding author: Sufyan Mohammed Shartooh; dralwaisi@uoanbar.edu.iq

ARTICLE HISTORY

Received: 19-04-2026
Revised: 30-05-2026
Accepted: 08-06-2026

KEYWORDS

Heavy metals
Road dust
Bioaccumulation
Pollution indices
Ecological risk
Arid environment
Vehicular emissions
Bioconcentration factor (BCF)

CITE THIS ARTICLE

Abdulqader, R.A. and Shartooh, S.M., 2026. Spatial footprint distribution of some heavy metals in major transport routes in Ramadi City, Iraq, *Nature Environment and Pollution Technology*, 25(4), D1936. https://doi.org/10.46488/NEPT.2026.v25i04.D1936

COPYRIGHT & LICENCE

© 2026 The Authors
Open Access under CC BY 4.0.

PUBLISHED BY
TECHNOSCIENCE PUBLICATIONS

ABSTRACT

Rapid urbanization and industrial activity in arid regions can increase the accumulation of heavy metals (HMs) in road dust. This issue is particularly relevant in arid urban environments, where limited rainfall and frequent dust resuspension may enhance the persistence and redistribution of metal-contaminated particles. This study aimed to assess the accumulation of HMs (Zn, Cu, Cr, Pb, and Cd) in road dust and roadside vegetation of Ramadi City, Iraq. Road dust and plant samples were collected from highway, industrial, mixed-use, and residential roads, along with a control site located away from major traffic and industrial activity. The samples were digested using a tri-acid mixture, and metal concentrations were determined by flame atomic absorption spectroscopy. Road-dust contamination was evaluated using the Geo-accumulation Index (Igeo), Pollution Load Index (PLI), Degree of Contamination (CD), Potential Ecological Risk Index (PERI), and Integrated Pollution Index (IPI). The efficiency of plants to accumulate metals from road dust was estimated using the bioconcentration factor (BCF). Statistical analysis showed significant spatial variation among road categories, suggesting anthropogenic enrichment ($p \leq 0.01$). Industrial and mixed-use sites generally showed the highest contamination and ecological risk levels, while residential sites showed lower but still detectable metal accumulation. The levels of heavy metals in plant tissue were reported in the following abundance order: Zn > Cr > Cu > Pb > Cd, where Cd, Cr, and Zn exceeded the reported permissible limits, while Pb levels recorded slight increases above these limits. The BCF values were below 1 for all studied metals, indicating that the sampled vegetation behaved mainly as a metal excluder rather than a hyperaccumulator. The high aridity of the climate in Ramadi may contribute to the persistence and redistribution of metal-contaminated dust through aeolian transport, particularly from industrial and traffic-intensive areas toward adjacent urban zones. The findings highlight the need for regular monitoring, dust-control measures, and source-reduction strategies to limit further accumulation and potential ecological exposure in arid urban environments.

1. INTRODUCTION

Environmental pollution remains a major global concern because of its effects on ecosystem quality and human health. Among the different classes of pollutants, heavy metals are of particular concern because they are persistent, non-biodegradable, and capable of accumulating in environmental media and biological tissues (Landrigan et al. 2018, Shartooh et al. 2018).

Heavy metals are environmental contaminants that can affect soil quality, vegetation, animals, and humans, depending on their concentration, chemical form, exposure route, and duration of exposure. The primary sources of heavy metal pollution are industrial emissions and human activities. Heavy metals may occur naturally in soils through parent-material weathering, but elevated concentrations

are often associated with anthropogenic inputs (Alloway 2012). Important anthropogenic sources include industrial emissions, fuel combustion, vehicle exhaust, brake wear, tire wear, waste disposal, and resuspension of contaminated dust (El-Sergany et al. 2011). Fine particle-size fractions of dust and soil are good indicators of the bioavailability of metals and may be more relevant for exposure assessment than bulk soil samples due to their higher potential for dermal adherence and either inhalation or ingestion (Madrid et al. 2008, Arunachalam et al. 2026).

Furthermore, heavy metals can act as environmental stressors that affect plant growth and physiological functioning. When metal concentrations exceed their natural levels in the soil, they impose pervasive and toxic effects on the entire plant system (Bharti & Sharma 2022). Plants can absorb metals through the root system and may also retain metal-bearing particles deposited on leaf surfaces. Their presence becomes toxic when their concentration increases within the plant tissue, changing the plant's capacity to take up and accumulate non-essential elements that may cause direct and/or indirect effects that harm plant health (Musa et al. 2024). The presence of these metals in the food chain constitutes a serious threat to health (Ali & Khan 2019). Soil pollution with HMs resulting from petrochemical processes can affect ecosystems and may create exposure pathways through contaminated vegetation (Gupta et al. 2022).

Road dust pollution with HMs poses an important environmental concern in urban areas because fossil fuel combustion, industrial activity, moving vehicles, tire wear, brake wear, and road-surface abrasion generate metal-containing particles. Road type is an important factor in determining the intensity of emission sources and human activities, and in estimating heavy-metal concentrations. Higher concentrations are often reported on industrial and highway roads compared to residential and agricultural roads. This is due to direct emissions from factories, storage operations, heavy truck traffic, tire wear, and fuel use. In residential areas, pollution sources are mainly associated with local traffic emissions and home heating. Mixed-use roads may show elevated contamination because traffic emissions, commercial activity, and small-scale workshops can occur in the same area (He et al. 2021). Additionally, exposure may occur through skin contact, respiratory inhalation, and ingestion via the food chain. Long-term exposure to metal-contaminated dust has been associated with adverse health outcomes, although the level of risk depends on metal concentration, particle size, exposure frequency, and population vulnerability (Lu et al. 2025).

Ramadi City is located in an arid region of Iraq where limited rainfall, high temperatures, and frequent dust events may favor the accumulation and redistribution of contaminated road dust. The city also includes major transport routes, residential zones, mixed-use areas, and industrial activities, making it suitable for examining how road function influences heavy-metal distribution. However, information on heavy-metal contamination in road dust and associated roadside vegetation in Ramadi remains limited. Therefore, this study assessed the spatial distribution of Zn, Cu, Cr, Pb, and Cd in road dust and roadside vegetation along major transport routes in Ramadi City. The study also applied multiple pollution indices and the bioconcentration factor to evaluate contamination status, ecological risk, and metal transfer from road dust to vegetation.

2. MATERIALS AND METHODS

2.1. Study Area Description

Ramadi City, one of the major cities of Anbar Governorate, is located in west-central Iraq. Anbar covers approximately one-third of Iraq's total land area, and Ramadi serves as an important urban and transport hub along the Euphrates River. Its significance is further increased by its location on major international transit routes connecting Iraq with neighboring countries. The region is characterized by a desert climate, with high temperatures and minimal precipitation throughout the year. These climatic conditions, particularly low rainfall and frequent dust events, play a crucial role in the accumulation and distribution of heavy metals in road dust (Al-Bayati & Al-Ani 2025). The route locations were recorded using a Garmin 72 GPS.

2.2. Sample Collection

In Ramadi City, road dust samples were collected systematically from four road categories: highway, industrial, mixed-use, and residential roads. Highways were defined as high-speed transport routes with relatively high volumes of heavy-duty vehicles. Industrial roads were located close to industrial activities and workshops. Mixed-use roads included commercial activity and moderate traffic volumes, while residential roads were found within areas with lower overall traffic volumes. The plant species *Conocarpus erectus* was selected to assess heavy-metal accumulation in roadside vegetation and to calculate bioconcentration factor (BCF) values. Its widespread presence in all sample collection areas during the current study, coupled with its evergreen nature and tolerance to the arid conditions characteristic of the study area, made it a suitable choice. It has previously been used to estimate heavy metal concentrations in soils in several countries (Rastmanesh et al. 2024). Furthermore, it is considered an important bioindicator of heavy metal pollution due to its ability to accumulate metals within

harvestable plant parts and its high bioconcentration ratio (Almehdi et al. 2019).

Each of the four road categories was sampled at five sites, designated L1, L2, L3, L4, and L5. At each site, three subsamples were collected and analyzed to form one composite road-dust sample. Thus, 20 composite road-dust samples were collected, along with 20 plant samples from vegetation adjacent to the corresponding road-dust sampling sites. A control site (CS) was selected approximately 18 km away from industrial plumes and traffic emissions to provide baseline values for comparison (Table 1; Fig. 1). This allowed comparison between road-influenced sites and background conditions with limited direct influence from traffic or industrial activity. Road dust was collected using a plastic broom and dustpan to prevent contamination from metallic sampling tools. After collection, all sampled materials were placed in prelabeled airtight bags and transported to the laboratory, where they were then dried, sieved using a 106 µm sieve, and chemically analyzed (Ali et al. 2025).

2.3. Sample Preparation and Digestion

Samples were dried at 105°C for 24 hours and sieved through a 106 µm sieve; the fraction smaller than 106 µm was selected for analysis. Vegetation samples were also collected from areas adjacent to the road-dust sampling sites to determine the concentrations of the studied heavy metals in above-ground plant tissues. One gram of each oven-dried and ground plant

Table 1: Information on the sample collection sites.

Road category																							
Road type		Highway					Industrial					Mixed					Residential					CS
Location		L1	L2	L3	L4	L5	L1	L2	L3	L4	L5	L1	L2	L3	L4	L5	L1	L2	L3	L4	L5	
GPS	X	43.205695	43.275278	43.339003	43.302407	43.338220	43.303272	43.316158	43.273999	43.258501	43.214356	43.274312	43.301877	43.244838	43.336124	43.294679	43.333915	43.296651	43.302854	43.318106	43.198298	43.204796
	Y	33.445410	33.456697	33.421914	33.459403	33.486448	33.430989	33.430187	33.408665	33.419081	33.432431	33.412072	33.421860	33.420433	33.429674	33.422424	33.430782	33.432110	33.419093	33.408433	33.409003	33.405785

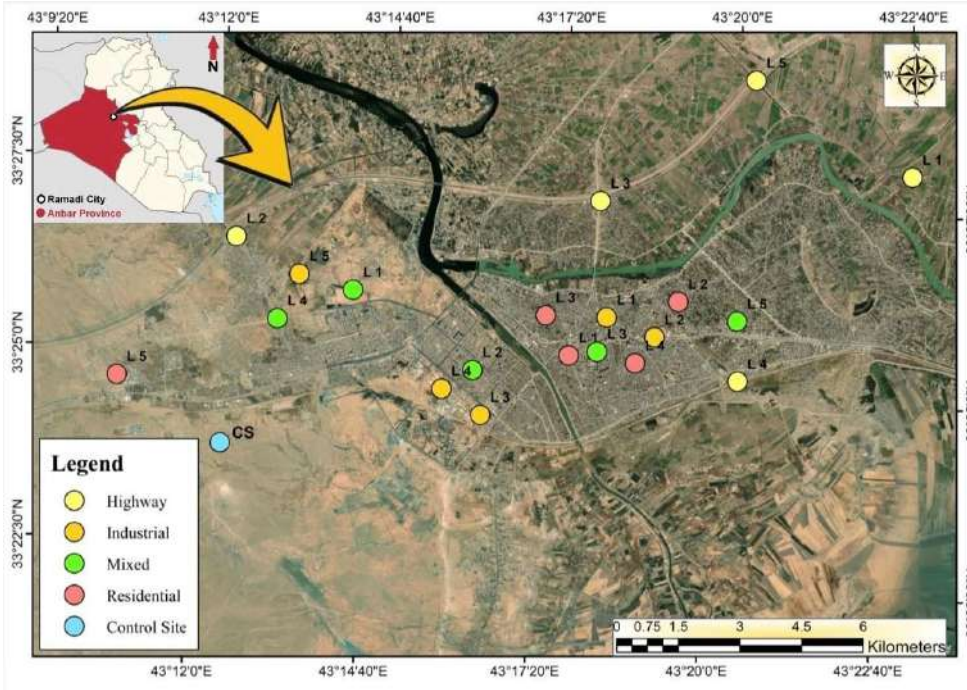


Fig. 1: Location map of the selected sampling routes.

Table 2: Microwave conditions.

Temperature	Energy	Time	Volume	Mixture of acids
150 °C	1050 W	20 min	15 mL	HNO_3:H_2SO_4: $HClO_4$, 4.5:1:1

and road-dust sample was digested at 80°C with 15 mL of a tri-acid mixture containing HNO_3, H_2SO_4, and $HClO_4$ in a 4.5:1:1 ratio. The mixture was stirred until homogeneous.

Subsequently, the mixture was placed in a microwave system where the power, temperature, and time were set according to the conditions specified in Table 2. Upon completion of the digestion period, the mixture was left to cool, filtered using Whatman filter paper grade 595, and adjusted to a volume of 50 mL by adding distilled water (Chandel & Bharose 2020).

2.4. Standard Solutions and Flame Atomic Absorption Spectroscopy Analysis

Standard solutions of 1000 mg L^{-1} of Zn, Cu, Cr, Pb, and Cd were prepared by dissolving the required mass of each corresponding metal salt in 1 L of deionized distilled water (DDW). The solutions were stored in glass containers at 4°C for further analysis. The optimal operating conditions for the flame atomic absorption spectroscopy (FAAS) system (AA-7000, Shimadzu, Japan) were established, with the specific limit of detection (LOD), limit of quantification (LOQ), wavelength, and flame type for each analyzed element detailed in Table 3 (Zhang 2024). For the quantification process, a series of working standard solutions was prepared by diluting a 1000 mg L^{-1} stock solution to cover the expected concentration range of the analytes, as specified in the calibration data shown in Table 3. Since the digested sample solutions exhibited an acidic pH ranging from 4.0 to 6.5, which can influence the flow rate within the nebulizer, the standard solutions were similarly acidified with 4–5 drops of concentrated nitric acid HNO_3 to ensure matrix matching and consistent aspiration. Elemental concentrations were then measured using FAAS.

2.5. Pollution Assessment Methods

A geochemical assessment was used to evaluate heavy metal (Zn, Cu, Cr, Pb, and Cd) contamination levels in Ramadi road dust. Five environmental indices were used to assess contamination intensity and possible anthropogenic enrichment: 1) Geo-accumulation index (Igeo), 2) Pollution load index (PLI), 3) Degree of contamination (CD), 4) Potential ecological risk index (PERI), and 5) Integrated pollution index (IPI).

Table 3: Flame atomic absorption spectrometer calibration data.

Element	Wavelength (nm)	Flame type Air/Acetylene	LOD (mg L^{-1})	LOQ (mg L^{-1})
Pb	217	Ordinary fuel	0.003	0.021
Cd	228.8	Ordinary fuel	0.002	0.014
Cu	324.8	Poor fuel	0.004	0.021
Cr	357.9	Rich fuel	0.005	0.035
Zn	213.9	Poor fuel	0.003	0.021

For plants, the bioconcentration factor was used to assess the accumulation of metals (i.e., Zn, Cu, Cr, Pb, Cd) in their tissues. BCF was calculated as the ratio of the metal concentration in plant tissue to the concentration of the same metal in the corresponding road-dust sample.

2.5.1. Geo-accumulation Index (Igeo)

The Geo-accumulation Index (*Igeo*) is an established geochemical index for assessing metal contamination in all types of environmental media, including road dust (Gałuszka & Migaszewski 2025). The *Igeo* measures the concentration of one element in a sample relative to its natural or pre-industrial background level. Thus, it provides an indication of metal enrichment relative to background conditions. The formula for calculating Igeo is given by Eq. (1) (Islam et al. 2020).

$$I_{geo} = log_2\left(\frac{Cm}{1.5\ Bm}\right) \quad ...(1)$$

Where *Cm* represents the concentration of metals in the road-dust sample, while *Bm* denotes the background value of the same metals. To account for potential fluctuations in the background data, a factor of 1.5 was applied, enhancing the reliability of the comparison against baseline values. The values can then be categorized into different pollution classes (Alghanimi et al. 2024), as in Table 4.

2.5.2. Pollution Load Index (PLI)

The Pollution Load Index is a geochemical tool used to determine the collective level of heavy metal contamination in soil, sediment, and dust. Unlike individual contamination factors, the PLI provides a comprehensive summary of the total pollution burden at a site (Skvarekova et al. 2021). The contamination factor (CF) and PLI were calculated using the following equations (2) and (3) (Tomlinson et al. 1980):

Table 4: Geo-accumulation index levels.

I_{geo} Class	I_{geo} Value	Contamination category
0	$I_{geo} \leq 0$	Uncontaminated
1	I_{geo} 0–1	Uncontaminated to moderately contaminated
2	I_{geo} 1–2	Moderately contaminated
3	I_{geo} 2–3	Moderately to strongly contaminated
4	I_{geo} 3–4	Strongly contaminated
5	I_{geo} 4–5	Strongly to very strongly contaminated
6	$I_{geo} > 5$	Very strongly contaminated

$$CF = \frac{C_m}{B_m} \quad ...(2)$$

$$\text{PLI} = (CF_1 \times CF_2 \times CF_3 \times CF_4 \times CF_5 \times \ldots \times CF_n)^{1/n} \quad ...(3)$$

Where *Cm* represents the metal concentration in road dust, *Bm* is the background value of the metal, and *n* represents the number of elements. A PLI value of less than 1 indicates no pollution, whereas a value greater than 1 indicates pollution (Pancholi et al. 2022).

2.5.3. Contamination Degree (CD)

The Contamination Degree (CD) is a cumulative index that quantifies the total intensity of pollution by summing the contamination factors of all individual metals identified at a sampling location. It provides an estimate of the overall contamination burden relative to background values and was calculated using equation (4) (Hosseinzadeh et al. 2024). Additionally, the degree of contamination was classified into four categories as given in Table 5.

$$\text{CD} = \sum_{i=1}^{i=n} CF \quad ...(4)$$

2.5.4. Potential Ecological Risk Index (PERI)

The Potential Ecological Risk Index is commonly used to evaluate the degree of heavy metal pollution in sediments, soils, and urban dust. Unlike simple enrichment factors, the PERI integrates the concentration of pollutants with their biological toxicity, providing an estimate of potential ecological risk. The PERI is calculated using the following equations (5)–(7) (Xie et al. 2023):

$$\text{C}_f^i = \frac{\text{C}_d^i}{\text{C}_r^i} \quad ...(5)$$

$$\text{ER} = \text{E}_r^i = \text{T}_r^i \times \text{C}_f^i \quad ...(6)$$

$$\text{PERI} = \sum_{i=1}^{n} \text{E}_r^i \quad ...(7)$$

Where C_id represents the measured concentration of metal *i* in road dust, C_ir is the background value of metal i, C_if is the contamination factor, T_ir is the toxic-response factor, and E_ir is the ecological risk factor for each metal. Toxic response factors for Zn, Cu, Cr, Pb, and Cd are 1, 5, 2, 5, and 30, respectively (Hakanson 1980). The PERI categories were classified as follows: RI < 150 indicates low risk, 150 < RI < 300 indicates moderate risk, 300 < RI < 600 reflects a considerable ecological risk, and an RI > 600 signifies a very high ecological risk (El-Sharkawy et al. 2025).

Table 5: Contamination degree classes.

Contamination Degree	Contamination Degree Categories
CD < 8	Low level of contamination
8 ≤ CD < 16	Moderate degree of contamination
16 ≤ CD < 32	Significant degree of contamination
CD ≥ 32	Very high degree of contamination

2.5.5. Integrated Pollution Index (IPI)

The Integrated Pollution Index (IPI) is a comprehensive numerical tool used to assess the overall quality of a specific medium (usually soil, water, or air) by calculating the combined effects of multiple pollutants, most commonly heavy metals. In this study, it was used to assess the cumulative heavy-metal pollution level in road dust. The IPI was calculated using equations (8) and (9) (Mansouri et al. 2024):

$$\text{PI} = \frac{Cn}{Bn} \quad ...(8)$$

$$\text{IPI} = \frac{1}{n}\sum_{i=1}^{n} \text{PIi} \quad ...(9)$$

Where *Cn* refers to the measured concentration in the sample, *Bn* is the background concentration of the heavy metal in the Earth's crust, and *n* is the number of metals studied. The IPI is calculated as the average of all pollution indices (PI) for the metals considered, and values are classified as low contamination (IPI ≤ 1.0), moderately contaminated (1.0 < IPI ≤ 2.0), or highly contaminated (IPI > 2.0) (Cobbina et al. 2025).

2.5.6. Bioconcentration Factor (BCF)

The bioconcentration factor is used to measure the ability of plants to absorb and accumulate heavy metals from soil and dust, providing a direct indication of metal bioavailability to vegetation (Aladesanmi et al. 2019). To quantify the enrichment of HMs in plant tissue, the following equation was used (10) (Chen et al. 2024):

$$\text{BCF} = \frac{C_{leaf}}{C_{soil}} \quad ...(10)$$

Where C_{leaf} represents the metal concentration in the leaf/plant tissue, and C_{soil} represents the metal concentration in the road-dust sample. The BCF refers to the ratio of the heavy metal concentration in a plant to that in road dust. BCF values greater than 1 indicate greater metal accumulation in plant tissue relative to the surrounding substrate, whereas BCF values below 1 indicate limited accumulation or exclusion behavior.

2.5.7. Statistical Analysis

Descriptive statistics were used to analyze differences in

Table 6: Background values and permissible limits of the studied elements.

Element	Background values (ppm)	Soil permissible limits* (ppm)	Plant permissible limits* (ppm)
Zn	65.4	50	0.6
Cu	22.5	36	10
Cr	67.3	100	1.3
Pb	20	85	2
Cd	0.3	0.8	0.02

*According to WHO (1996)

metal concentrations among road categories and sampling locations. SPSS software (version 25) was used for statistical analyses, with $p \leq 0.01$ considered statistically significant.

The choice of background values is a key factor in interpreting geochemical data. Previous studies have used the average shale values (Mohiuddin et al. 2011, Salam et al. 2021, Tnoumi et al. 2022, Al-Dahar et al. 2023, Rasul et al. 2026), or the upper continental crust (UCC) data (Xuefeng et al. 2016, Tang et al. 2019, Dytlow & Górka-Kostrubiec 2021, Hamid et al. 2022) as reference baselines. The estimated concentrations of the elements were compared with the UCC geochemical background values (Rudnick & Gao 2003). The permissible limits in soil and plants are presented in Table 6.

Figures were generated and formatted using Python 3.13.5. Data importing and preprocessing were performed using pandas and NumPy, curve smoothing was carried out using SciPy, and graphical rendering and export were completed using Matplotlib.

3. RESULTS AND DISCUSSION

3.1. Heavy Metal Concentrations in Road Dust

Table 7 presents the mean values ± standard deviation of Zn, Cu, Cr, Pb, and Cd in road-dust samples collected from highway, industrial, mixed-use, and residential roads in Ramadi City, along with a control sample collected away from major transport routes.

The analytical findings showed elevated concentrations of zinc, copper, chromium, lead, and cadmium across most road categories compared with the control site. The highest concentrations of Cu and Pb were observed at industrial sites, particularly L1 and L2, while Cd showed consistently elevated values across the highway, industrial, mixed-use,

Table 7: Mean heavy metal concentrations (ppm) ± standard deviation (SD) in road-dust samples collected from different road categories in Ramadi City.

Road Type	Locations	Heavy metal concentration in ppm (Mean ± SD)				
		Zn	Cu	Cr	Pb	Cd
Highway Road	L1	59.1 ± 6.7	20.5 ± 2.9	15.0 ± 1.5	20.5 ± 3.7	2.69 ± 0.78
	L2	50.1 ± 6.3	21.4 ± 3.0	18.0 ± 2.0	41.4 ± 3.8	2.5 ± 0.71
	L3	42.9 ± 4.5	31.9 ± 3.1	16.2 ± 1.6	27.6 ± 3.2	1.94 ± 0.56
	L4	45.0 ± 4.2	24.3 ± 2.2	17.0 ± 1.0	30.5 ± 2.9	2.8 ± 0.78
	L5	55.0 ± 4.8	30.0 ± 2.4	14.5 ± 1.9	25.9 ± 3.1	1.99 ± 0.67
Industrial roads	L1	70.3 ± 7.9	141.8 ± 18.6	23.0 ± 3.0	232.9 ± 51.7	3.15 ± 0.81
	L2	66.7 ± 5.5	210.5 ± 53.5	26.5 ± 3.7	115.6 ± 42.4	3.15 ± 1.07
	L3	56.2 ± 4.8	33.5 ± 2.9	18.8 ± 2.4	38.3 ± 4.2	2.69 ± 0.89
	L4	54.3 ± 5.0	32.3 ± 4.1	19.6 ± 2.8	48.0 ± 4.0	2.85 ± 0.57
	L5	60.2 ± 4.96	40.5 ± 4.7	25.3 ± 2.9	85.9 ± 6.9	3.0 ± 1.3
Mixed Road	L1	55.9 ± 4.3	14.8 ± 1.2	17.7 ± 2.1	30.2 ± 2.9	3.1 ± 0.91
	L2	58.4 ± 5.2	21.0 ± 1.9	21.9 ± 1.7	53.2 ± 4.8	2.85 ± 0.77
	L3	66.7 ± 5.9	33.7 ± 3.5	21.0 ± 1.9	49.0 ± 4.6	3.46 ± 1.02
	L4	37.0 ± 2.8	11.5 ± 1.3	15.0 ± 2.0	21.4 ± 2.8	2.15 ± 0.93
	L5	62.3 ± 5.7	25.5 ± 2.9	19.2 ± 2.4	45.1 ± 3.9	3.5 ± 1.06
Residential roads	L1	53.2 ± 4.8	13.8 ± 1.6	16.2 ± 1.8	50.7 ± 3.7	2.38 ± 0.96
	L2	38.5 ± 2.9	8.5 ± 0.95	14.7 ± 1.1	20.7 ± 2.5	2.1 ± 0.91
	L3	32.5 ± 3.7	10.2 ± 1.2	18.3 ± 1.9	30.5 ± 3.5	2.5 ± 0.7
	L4	35.5 ± 3.7	8.2 ± 1.02	8.0 ± 1.2	20.0 ± 3.2	2.1 ± 0.8
	L5	26.0 ± 1.6	6.3 ± 0.27	8.7 ± 0.9	16.0 ± 1.2	1.93 ± 0.17
Control	CS	34.5 ± 3.5	13.7 ± 2.9	19.8 ± 2.4	17.8 ± 2.2	1.6 ± 0.8

and residential road categories. Statistical significance at $p \leq 0.01$ indicates clear spatial variation among sampling locations and suggests a strong influence of likely anthropogenic sources such as industrial activity, traffic emissions, brake and tire wear, and road-dust resuspension (Kilavi et al. 2023). Overall, industrial roads showed the strongest enrichment for Cu and Pb, whereas residential roads generally recorded the lowest concentrations for most metals.

The road-adjacent samples showed a distinct gradient of pollution when compared with control samples. For example, Pb at industrial site L1 was much higher than the control value, indicating localized enrichment near industrial activity. Such enrichment is consistent with previous observations that urban soils and road dust in rapidly growing cities may accumulate metals above background levels, especially near traffic and industrial sources (Adimalla 2020). Low levels of contamination near residential roads may reflect lower traffic density and greater separation from direct industrial sources (Du et al. 2026). However, some metals were still detectable at residential sites, suggesting possible redistribution of metal-bearing dust from traffic-intensive or industrial areas. Fine particulate ($PM_{2.5}$) and/or coarse particulate matter (PM_{10}) with high heavy metal concentrations can travel in excess of several kilometers from an industrial site to an adjacent residential or commercial area (Zurek-Ost et al. 2025).

The significant differences among road categories and the control site indicate that road function and surrounding land use influence heavy-metal accumulation in road dust. The results also indicate localized contamination hotspots, especially at industrial sites with high Cu, Pb, and Cd concentrations, with lower increases in Zn. The concentration of cadmium exceeded the reported permissible limit across all road categories, while Pb exceeded the permissible limit at some industrial sites. These findings suggest that Cd and Pb require particular attention in future monitoring and risk assessment. The results indicate that road dust in Ramadi City is affected by multi-metal contamination, with the highest burden generally observed near industrial and high-traffic routes. The statistically significant differences among sites ($p \leq 0.01$) support the interpretation that metal distribution is spatially structured rather than random. However, further source apportionment and exposure assessment studies would be needed to determine specific emission sources and potential health risks.

Table 8: Mean heavy metal concentrations (ppm) ± standard deviation in plant samples collected from five locations adjacent to different roads in Ramadi City.

Road Type	Locations	Heavy Metal Concentration in ppm (Mean ± SD)				
		Zn	Cu	Cr	Pb	Cd
Highway Road	L1	18.5 ± 2.8	3.5 ± 1.7	2.86 ± 0.78	2.0 ± 0.38	0.38 ± 0.06
	L2	18.4 ± 2.2	5.5 ± 1.9	4.5 ± 1.1	2.0 ± 0.62	0.54 ± 0.04
	L3	16.9 ± 2.5	5.1 ± 1.08	5.72 ± 2.14	3.0 ± 0.9	0.33 ± 0.07
	L4	17.0 ± 2.1	4.9 ± 1.36	3.8 ± 0.78	2.5 ± 0.8	0.44 ± 0.04
	L5	15.8 ± 1.8	4.5 ± 1.22	2.9 ± 0.93	1.99 ± 0.9	0.39 ± 0.01
Industrial roads	L1	14.0 ± 1.2	2.9 ± 1.01	3.76 ± 1.37	2.5 ± 1.1	0.38 ± 0.06
	L2	22.9 ± 2.3	2.5 ± 0.95	2.15 ± 0.95	2.5 ± 1.7	0.39 ± 0.03
	L3	20.0 ± 1.9	2.7 ± 0.99	2.73 ± 0.89	1.95 ± 0.5	0.32 ± 0.04
	L4	14.0 ± 1.6	3.0 ± 0.98	3.14 ± 1.06	2.0 ± 0.95	0.33 ± 0.03
	L5	21.5 ± 2.9	3.2 ± 1.4	2.69 ± 1.09	2.2 ± 0.86	0.32 ± 0.04
Mixed Road	L1	24.8 ± 3.4	2.8 ± 1.2	2.86 ± 0.96	2.2 ± 0.76	0.69 ± 0.05
	L2	23.8 ± 2.6	3.0 ± 1.3	3.86 ± 1.22	1.91 ± 0.93	0.54 ± 0.06
	L3	12.0 ± 0.6	2.5 ± 0.97	2.85 ± 1.09	1.88 ± 1.0	0.31 ± 0.05
	L4	12.0 ± 0.9	3.6 ± 1.44	2.71 ± 0.91	1.82 ± 0.94	0.23 ± 0.03
	L5	18.9 ± 1.9	2.9 ± 1.6	3.95 ± 1.03	1.99 ± 0.79	0.6 ± 0.08
Residential roads	L1	17.2 ± 2.0	2.5 ± 1.02	3.43 ± 1.11	1.78 ± 0.34	0.15 ± 0.03
	L2	10.5 ± 0.9	2.42 ± 0.94	2.86 ± 0.74	1.79 ± 0.71	0.15 ± 0.05
	L3	19.0 ± 2.2	2.5 ± 1.0	3.15 ± 1.07	1.8 ± 0.62	0.3 ± 0.03
	L4	14.8 ± 1.8	2.5 ± 0.93	2.14 ± 0.92	1.52 ± 0.66	0.22 ± 0.06
	L5	9.9 ± 1.7	1.82 ± 0.84	2.72 ± 0.94	1.78 ± 0.48	0.35 ± 0.09
Control	CS	9.1 ± 2.9	3.3 ± 1.5	3.0 ± 1.03	0.95 ± 0.07	0.12 ± 0.02

3.2. Heavy-Metal Concentrations in Roadside Vegetation

Mean concentration values ± standard deviation of Zn, Cu, Cr, Pb, and Cd in plant samples collected from highway, industrial, mixed-use, and residential roads in Ramadi City are presented in Table 8.

The results identified mixed-use road L1 and highway L3 as locations with relatively high metal accumulation in plant tissue. At mixed-use sites, Zn and Cd reached the highest concentrations of 24.8 ppm and 0.69 ppm, respectively, at L1, where mixed-use roads in Ramadi City are associated with stop-and-go traffic and informal mechanical workshops. Plants in such zones may accumulate metals through both root uptake from contaminated substrate and foliar deposition of resuspended particulates (Al-Dahar et al. 2023, Giri et al. 2026). Cd, in particular, is relatively mobile in some soil-plant systems and may be taken up by plant tissues depending on soil chemistry and metal availability. Roadside flora in high-traffic commercial zones may show elevated Cd accumulation where traffic activity, lubricants, battery waste, or small mechanical workshops contribute to local contamination (Bhatla & Kathpalia 2023). At highway site L3, Cr and Pb reached their highest concentrations of 5.72 ppm and 3.0 ppm, respectively. These elevated concentrations may be related to traffic-derived particles from brake wear, tire wear, exhaust emissions, and resuspended dust; however, the present study does not directly identify the specific source contribution for each metal (Bhat et al. 2025).

Mixed-use and highway sites showed relatively high accumulation for selected metals, probably reflecting the density and diversity of nearby pollution sources (Rahman et al. 2024). The interaction between location and metal type was found to be highly significant ($p \leq 0.01$) for Cr, Pb, and Cd. Plant Cd concentrations ranged from 0.15 to 0.69 ppm, with the maximum value recorded at mixed-use site L1. This pattern may be associated with differences in local traffic intensity, commercial activity, and the availability of Cd in road dust. At mixed-use sites, the combination of high-density traffic with frequent braking and local commercial activities may create a persistent source of Cd. Cadmium can occur as an impurity in low-grade automotive lubricants and certain tire brands. Furthermore, mixed-use zones in Ramadi City may include small mechanical workshops where oil residues and dust deposition contribute to localized contamination (Horne & Fleming-Singer 2005, Panda et al. 2025). In semi-arid regions, the high evaporation rate may increase the concentration of Cd ions in the soil pore water, thereby influencing the bioconcentration factor in roadside flora (Giri et al. 2026). Residential roads generally showed lower accumulation for most metals, which may reflect lower traffic intensity and reduced exposure to heavy-duty vehicle emissions. The reduced concentration of resuspended dust may limit the foliar uptake of metals. Urban green belts in residential zones can act as filters, although they may still accumulate metals at rates higher than natural baselines (Basheer et al. 2026).

The difference between the control site and road-adjacent locations indicates that traffic and urban activity are likely contributors to metal accumulation in roadside vegetation. Since the control site approximately reflects the natural background of the region, higher concentrations in road-adjacent plants may be associated with atmospheric deposition, dust resuspension, and transport-related emissions (Bhat et al. 2025). Comparison with a control site strengthens the interpretation that road-adjacent vegetation is exposed to additional metal inputs, although source-specific confirmation would require further analysis (Edo et al. 2024, Naeem et al. 2024). Generally, the plants along major roads in Ramadi City accumulated Cr, Pb, and Cd at levels exceeding the reported permissible limits for some metals. The statistical analysis results indicate significant spatial differences in plant metal concentrations; however, proximity to traffic should be interpreted as a likely contributing factor rather than the sole determinant (Hussain et al. 2024). The relatively higher concentrations of Zn and Cu may also reflect their role as essential micronutrients, although excessive levels can still affect plant function (Rahman et al. 2024).

3.3. Road-Dust Contamination Indices

3.3.1. Geo-accumulation Index (Igeo)

Fig. 2 shows Igeo values for all examined heavy metals in road-dust samples collected from five locations across highway, industrial, mixed-use, and residential roads. The highest Igeo values were generally recorded for Cd, followed by Pb and Cu at selected industrial and mixed-use sites, whereas Cr consistently showed the lowest Igeo values across the examined locations.

The Igeo results indicate that industrial sites were most affected by Pb and Cu enrichment. Industrial L1 showed the highest Pb Igeo value, while industrial L2 showed the highest Cu Igeo value. This may be associated with the persistence of environmental contaminants linked to previous fuel-related emissions, traffic activity, and ongoing discharges from mechanical or metal-processing activities near industrial roads (Generalova et al. 2025). However, source-specific attribution should be treated cautiously because no direct source-apportionment analysis was conducted.

For highway sites, Igeo values for Zn, Cu, Cr, and Pb were mostly below 1, indicating uncontaminated to moderately contaminated conditions. In contrast, Cd showed

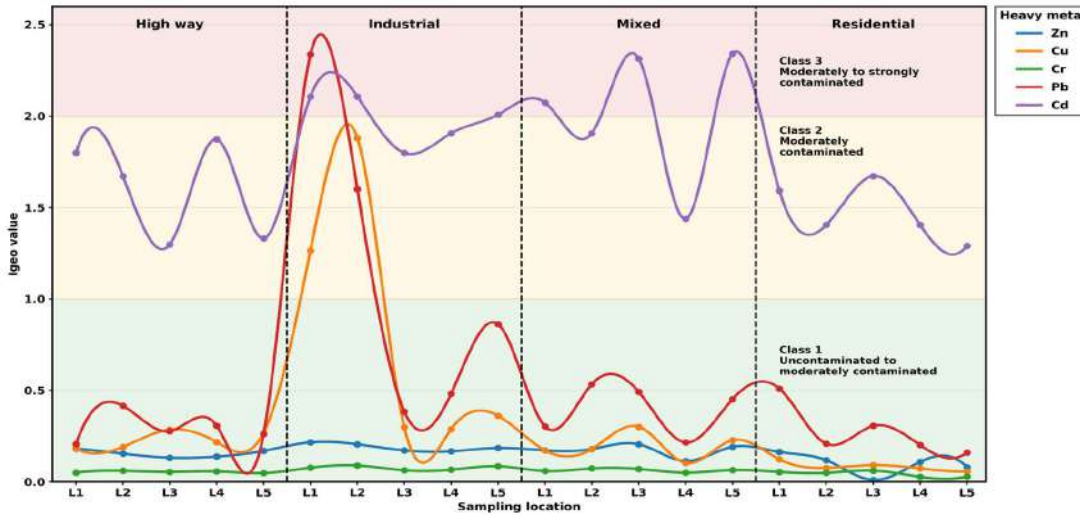


Fig. 2: Igeo values of the examined heavy metals in road-dust samples collected from highway, industrial, mixed-use, and residential roads.

higher Igeo values, indicating moderate contamination at several highway locations. Roadside dust samples have Igeo values of less than 1.0, except when they are affected by industrial activity. Therefore, highway sites are affected by vehicle emissions, but their enrichment levels for most metals remained lower than those observed at the most contaminated industrial sites. Furthermore, residential road-dust samples have the lowest Igeo values for all elements. Most of the Igeo values for chromium and zinc are close to zero, indicating low enrichment relative to background values. However, lead at residential L1 showed moderate enrichment compared with other residential locations. The residential sites may also receive metal-bearing particulates through atmospheric transport and local traffic activity. Cadmium and lead consistently have higher Igeo values than chromium, and chromium has the lowest Igeo values for all sites.

3.4. Other Road-Dust Contamination Indices

Values of pollution load index (PLI), contamination degree (CD), potential ecological risk index (PERI), and integrated pollution index (IPI) in road-dust samples collected from five locations along highway, industrial, mixed-use, and residential roads showed clear variation among sampling sites and road categories. Among the calculated indices, CD and IPI showed the largest numerical ranges, while PLI values were comparatively lower because the index is expressed as a geometric mean of contamination factors.

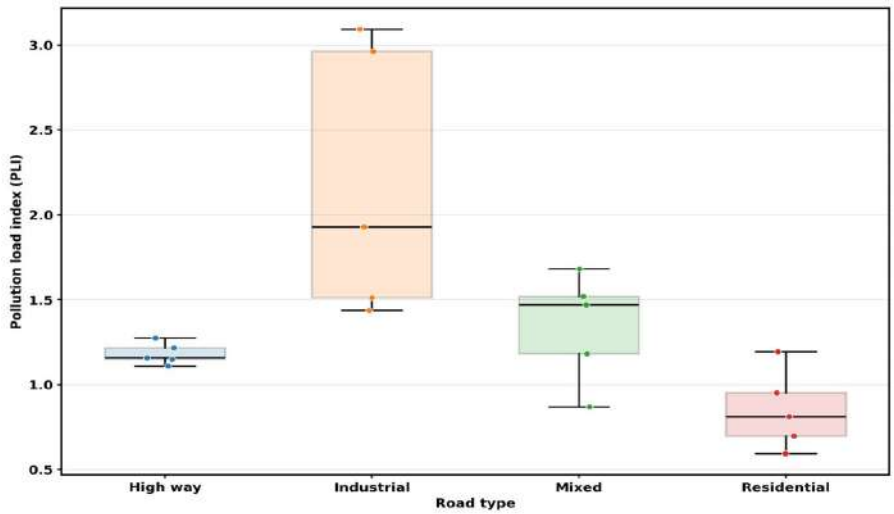


Fig. 3: Pollution load index (PLI) distribution by road type.

3.4.1. Pollution Load Index (PLI)

The results indicate that industrial and mixed-use road sites were the most heavily impacted by anthropogenic activities, with industrial sites recording the highest PLI values, specifically L1 and L2 (Fig. 3).

The highest PLI value was recorded at industrial L1 (3.09), followed by industrial L2 (2.96), indicating a high overall pollution load at these sites (Ali et al. 2025). PLI values above 3 are commonly interpreted as evidence of substantial anthropogenic contamination, particularly in areas influenced by industrial activity, mechanical workshops, or metal-processing sources. Most mixed-use road sites also showed PLI values greater than 1, indicating pollution relative to background conditions (Barbera et al. 2025). The obtained data suggest that mixed-use zones may experience cumulative inputs from traffic emissions, commercial activity, and small-scale workshops, which together increase the overall pollution load (Attiya & Jones 2020).

The highway areas had a consistent level of pollution across the five sampling locations, with PLI values slightly above 1 at all sites. These values indicate low to moderate pollution, probably associated with continuous deposition from traffic-related sources such as exhaust emissions, brake wear, tire wear, and road-surface abrasion (Al-Sabbagh & Shreaz 2025). Highway road-dust samples with PLI values ranging from 1.0 to 1.5 indicate early-stage contamination and support the need for periodic monitoring (Atavullayeva 2024).

In contrast, residential sites generally showed lower PLI values, with most locations below 1, indicating limited pollution according to the PLI classification. However, the value at residential L1 exceeded 1, suggesting localized enrichment or possible influence from nearby traffic or dust transport (Miller et al. 2025). Such localized elevation may also occur when fine particulate matter is transported from nearby industrial or traffic-intensive areas under favorable wind conditions (Afandi et al. 2025).

3.4.2. Contamination Degree (CD)

The highest CD values were recorded at industrial road sites, particularly L1 and L2 (Fig. 4). The CD values at locations L1 and L2 were 29.86 and 27.05, respectively, placing them within the significant contamination category according to the classification used in this study (Cao et al. 2025). These elevated CD values are consistent with cumulative inputs from mechanical activities, industrial emissions, and metal-processing residues (Somadas & Sarvade 2025). Although high CD values indicate strong cumulative contamination, further leaching tests and groundwater monitoring would be required before concluding that deeper soil layers or groundwater are at risk (Ogwu et al. 2025).

Highway and mixed-use sites showed CD values ranging from 9.53 to 16.81. The highway sites showed a relatively consistent moderate contamination range of approximately 10.1–12.8, whereas the mixed-use sites showed greater variation, especially at L3, where a CD of 16.81 was recorded. The bulk of contaminants at both the highway and mixed-use sites may originate from diffuse anthropogenic sources, including emissions from vehicles, brake pad wear, and wear from tires (Candeias et al. 2020). However, the additional increase in the mixed-use sites suggests an interaction between traffic volume and nearby commercial activities

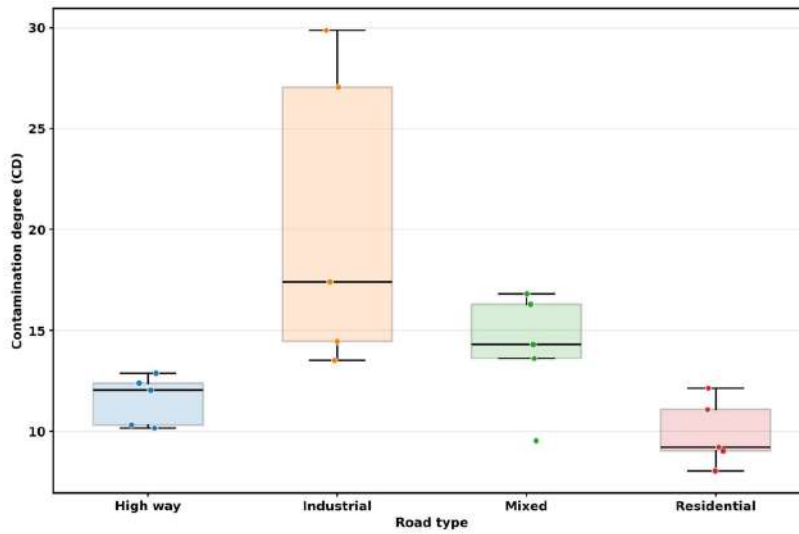


Fig. 4: Contamination degree (CD) distribution by road type.

(e.g., repair shops). Areas with combined commercial and transport activity may accumulate higher metal loads because of stop-and-go traffic, vehicle maintenance activities, and small-scale metal-related sources (Jacob et al. 2024).

Residential sites showed the lowest CD values, mostly within the moderate contamination category (Skuza et al. 2022). Although lower than industrial and mixed-use sites, the residential values indicate that road dust in residential areas is not entirely free from metal accumulation. This may reflect local traffic emissions, resuspended dust, and possible atmospheric transport of metal-bearing particles from more polluted areas.

3.4.3. Potential Ecological Risk Index (PERI)

Industrial sites showed some of the highest PERI values, with several locations exceeding 300, indicating considerable ecological risk according to the classification used in this study (Barbera et al. 2025) (Fig. 5). The elevated PERI values at industrial sites are likely related to the strong contribution of metals with high toxic-response factors, particularly Cd, and to elevated Pb concentrations at selected locations (Barbera et al. 2025). Mixed-use sites L3 and L5 also recorded high PERI values, indicating considerable ecological risk (Cao et al. 2025). This pattern may reflect the combined influence of traffic emissions, commercial activity, and small-scale workshops in mixed-use areas.

The highway and residential locations generally presented lower PERI values, though they still fell within the moderate to considerable risk categories; highway-site values were 209.12–294.21. Although none of the highway sites exceeded 300, the proximity of L4 (294.21) to the considerable-risk threshold indicates a significant accumulation of traffic-related pollutants (Attiya & Jones 2020). Regarding residential sites, which showed the lowest risk profile, all values remained above the low-risk threshold, suggesting that residential road dust may still receive metal inputs from local traffic and atmospheric deposition (Al-Sabbagh & Shreaz 2025).

3.4.4. Integrated Pollution Index (IPI)

The highest IPI value in the industrial category was observed at L1 with a value of 5.97278, while industrial L2 recorded 5.409839 (Fig. 6). These values indicate very high cumulative contamination at the two industrial sites. The elevated IPI values at L1 and L2 may reflect cumulative inputs from industrial emissions, mechanical waste, and metal-processing activities (Miller et al. 2025). IPI values greater than 2 indicate strong anthropogenic loading, although the specific contribution of individual sources requires further source-apportionment analysis. The results suggest that the industrial and mixed road locations had higher IPI values than the other road categories (Szwalec et al. 2020).

Mixed-use sites L3 and L5 also showed elevated IPI values, suggesting increased cumulative contamination in areas where traffic and commercial activities overlap (Jacob et al. 2024). However, the highway system showed relatively consistent IPI values of approximately 5.0 across locations

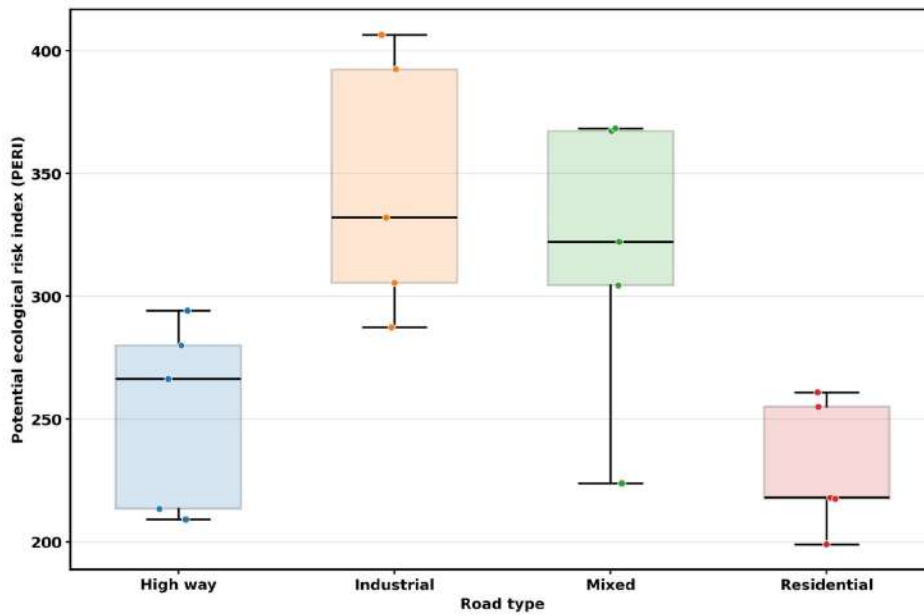


Fig. 5: Potential ecological risk index (PERI) distribution by road type.

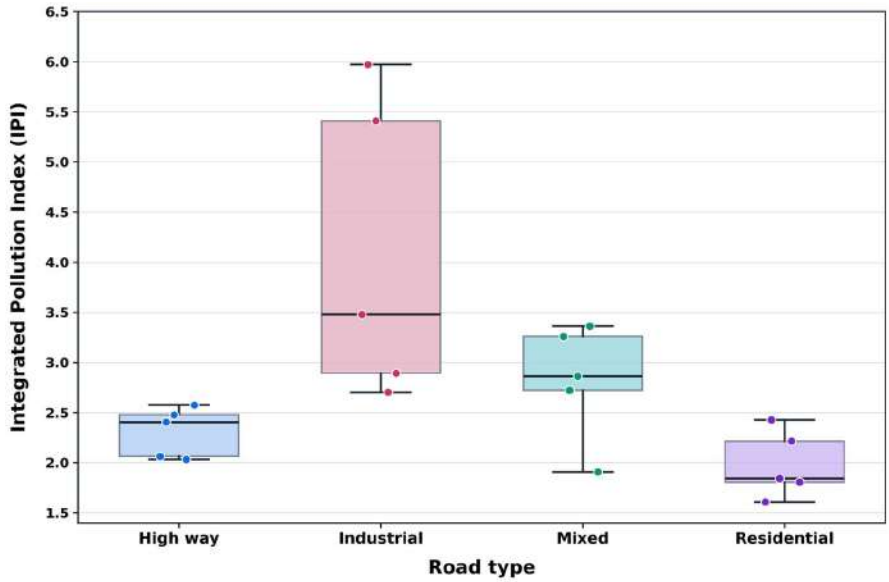


Fig. 6: Integrated pollution index (IPI) distribution by road type.

(Atavullayeva 2024), with lower variability than industrial and mixed-use sites. Urban corridors often have moderate to high IPI values because of diffuse pollution from tire wear, brake wear, road abrasion, and fuel combustion (Candeias et al. 2020).

Residential areas showed the lowest total IPI, and while the residential IPI values at each sample point were lower than those of industrial and most mixed-use sites, all values remained above 1.0, indicating that residential road dust was not free from contamination (Szwalec et al. 2020). The highest residential sample point value at L1 (5.78) may reflect localized traffic influence or proximity to more polluted transport corridors (Barbera et al. 2025). Overall, the IPI results confirm that industrial roads were the most contaminated, followed by mixed-use and highway roads, while residential roads showed the lowest but still measurable cumulative contamination (Attiya & Jones 2020).

3.5. Plant Bioconcentration Factor (BCF)

Fig. 7 presents the calculated bioconcentration factor (BCF) values for plant samples collected from five locations along highway, industrial, mixed-use, and residential roads. Overall, Zn showed the highest BCF values among the studied metals, whereas Pb generally showed the lowest BCF values across the examined locations.

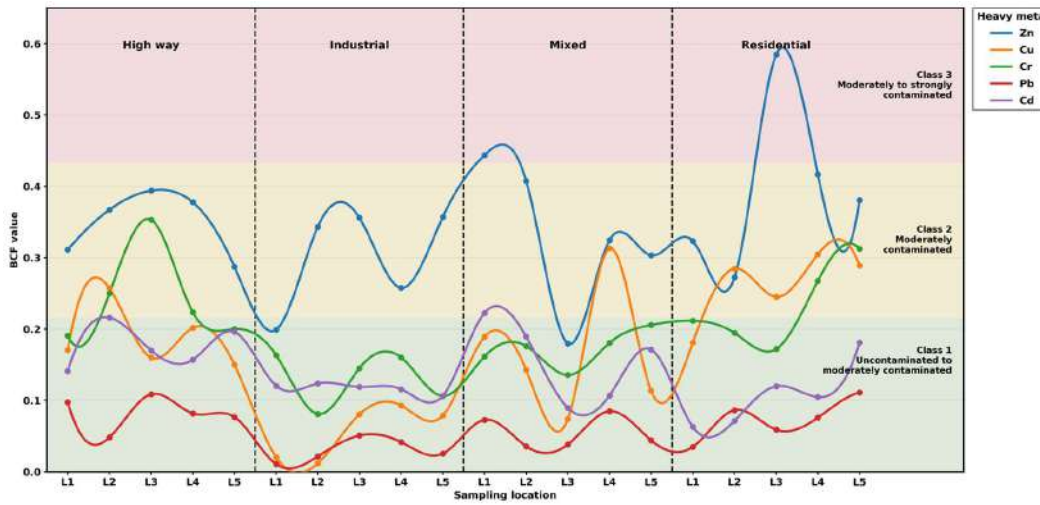


Fig. 7: Bioconcentration factor (BCF) distribution by road type and sampling location.

The industrial sites showed high road-dust contamination but relatively low BCF values for several metals. At L1, the BCF for Pb was the lowest recorded value (0.010734), while the highest industrial-site value was recorded for Zn at L3 (0.355872). Plants in highly polluted industrial zones may show limited metal transfer from substrate to tissue because of exclusion mechanisms, restricted root uptake, or low metal bioavailability in the substrate (Skuza et al. 2022, Ali et al. 2025).

Mixed-use and highway roads showed moderate BCF values for selected metals, reflecting their exposure to traffic-related and mixed anthropogenic inputs (Attiya & Jones 2020). The highway category showed relatively high BCF values for Zn and Cr at L3, and the lowest Pb BCF value at L2. The mixed-use roads showed a peak for Cu at L4 and Zn at L1, suggesting site-specific differences in metal availability and plant uptake. In traffic-affected areas, some metals may occur in more bioavailable forms, whereas metals in industrial dust may be more strongly bound to particles or mineral phases, reducing plant uptake (Jacob et al. 2024).

However, the residential sites are the least polluted in terms of dust concentration but show surprisingly high efficiency of metal accumulation. Zn had the highest BCF values among all examined metals, likely because it is an essential micronutrient for plant enzymatic functions, facilitating its active transport compared with nonessential elements such as Pb, which showed the lowest BCF values across all sites. Pb has low bioavailability and tends to be sequestered at the soil-root interface, which explains the minimal BCF values observed in the studied plant samples (Ayobami 2022, Goya-Heredia et al. 2023).

Interestingly, the residential road locations showed a similar pattern of metal uptake to that observed at traffic-affected sites, with relatively higher Zn BCF values at selected locations such as residential L3. This suggests that while road-dust concentrations are higher in industrial zones, plant uptake efficiency (BCF) does not necessarily increase linearly with substrate pollution, often due to substrate pH, organic matter content, metal speciation, or particle binding (Goya-Heredia et al. 2023, Barbera et al. 2025). Because all BCF values were below 1, the sampled plants can be interpreted as metal excluders rather than hyperaccumulators.

4. CONCLUSIONS

This study provides an assessment of heavy metal contamination in road dust and its subsequent bioaccumulation in native vegetation along four functional road categories (highway, industrial, mixed-use, and residential) in Ramadi City, Iraq. The integration of multiple pollution indices (Igeo, PLI, CD, PERI, IPI) and bioconcentration factor (BCF) analysis provided a useful framework for evaluating contamination intensity, ecological risk, and plant uptake behavior in an arid urban setting.

The results showed that road-adjacent dust samples generally contained higher heavy metal concentrations than the control site, suggesting the influence of anthropogenic sources. The highest contamination burden was generally observed at industrial sites, particularly for Cu and Pb, while Cd showed consistent enrichment across several road categories. Significant spatial differences ($p \leq 0.01$) indicate that road type and surrounding land use influenced heavy-metal distribution. The PERI classified most road categories within moderate to considerable ecological-risk levels, with industrial and mixed-use sites showing the highest values. The Igeo ranked Cd as the most enriched element across most sites, followed by Pb, indicating notable enrichment relative to background values. The PLI, CD, and IPI results further confirmed that industrial roads had the greatest cumulative contamination, followed by mixed-use and highway roads, whereas residential roads showed lower but still measurable contamination.

Although the BCF remained below 1 for all metals, suggesting that plants act as excluders rather than hyperaccumulators, the absolute concentrations of Cd and Cr in plant biomass exceeded the reported permissible limits. This indicates that roadside vegetation can serve as an indicator of metal exposure in contaminated road environments, although further studies are required to assess grazing, food-chain transfer, and human-health risks. The arid climate of Ramadi City may enhance the persistence and redistribution of contaminated dust because low rainfall and frequent dust events can favor aeolian transport and resuspension of metal-bearing particles. The detection of metals in residential road dust suggests that lower-traffic areas may still receive inputs from local traffic, dust movement, or nearby polluted zones.

Overall, the results of the present study highlight the need for regular road-dust monitoring, control of industrial and traffic-related emissions, improved dust-management practices, and further source-apportionment and exposure-assessment studies in Ramadi City and similar arid urban environments.

5. ACKNOWLEDGEMENT

The authors thank the staff of the Department of Biology, College of Science, University of Anbar, for their support during this work.

6. REFERENCES

Adimalla, N., 2020. Heavy metals pollution assessment and its associated human health risk evaluation of urban soils from Indian cities: A review. *Environmental Geochemistry and Health*, 42(1), pp.173–190. [DOI]

Afandi, G.E., Bolden-Tiller, O., Mortley, D., Asare-Baah, L., Miller, R., Ibrahim, S. and Rangari, V., 2025. Air quality assessment and source speciation of PM2.5 in Florida's Everglades Agricultural Area. *Earth Systems and Environment*, pp.1–23. [DOI]

Aladesanmi, O.T., Oroboade, J.G., Osisiogu, C.P. and Osewole, A.O., 2019. Bioaccumulation factor of selected heavy metals in *Zea mays*. *Journal of Health and Pollution*, 9(24), 191207. [DOI]

Al-Bayati, A.H.I. and Al-Ani, M.K., 2025. Climate change and its impact on the ecosystem on the Ramadi Island Plateau for the period from 1980 to 2022. In: *International Conference Water and Food Security in the Face of Climate Change: Challenges and Opportunities for Resilience*. Springer Nature Switzerland, Cham, pp.51–66. [DOI]

Al-Dahar, R.K., Rabee, A.M. and Mohammed, R.J., 2023. Calculation of soil pollution indices with elements in residential areas of Baghdad City. *Revista Bionatura*, 8(1), 43. [DOI]

Alghanimi, S.M.K., Chamani, A., Almusawi, A.N. and Tavabe, K.R., 2024. Potentially toxic elements risk assessment and source identification of an at-risk international wetland in SW Iran. *Wetlands*, 44(5), 63. [DOI]

Ali, H. and Khan, E., 2019. Trophic transfer, bioaccumulation and biomagnification of non-essential hazardous heavy metals and metalloids in food chains/webs: Concepts and implications for wildlife and human health. *Human and Ecological Risk Assessment: An International Journal*, 25(6), pp.1353–1376. [DOI]

Ali, M., Alshamsi, D., Ahmad, T., Ahmed, A. and Abdelfadil, K.M., 2025. Assessment of potentially toxic metals (PTMs) pollution, ecological risks and source apportionment in urban soils from university campuses: Insights from multivariate and positive matrix factorisation analyses. *Minerals*, 15(5), 482. [DOI]

Alloway, B.J., 2012. Sources of heavy metals and metalloids in soils. In: *Heavy Metals in Soils: Trace Metals and Metalloids in Soils and Their Bioavailability*. Springer, Dordrecht, pp.11–50. [DOI]

Almehdi, A., El-Keblawy, A., Shehadi, I., El-Naggar, M., Saadoun, I., Mosa, K.A. and Abhilash, P.C., 2019. Old leaves accumulate more heavy metals than other parts of the desert shrub *Calotropis procera* at a traffic-polluted site as assessed by two analytical techniques. *International Journal of Phytoremediation*, 21(12), pp.1254–1262. [DOI]

Al-Sabbagh, T.A. and Shreaz, S., 2025. Impact of lead pollution from vehicular traffic on highway-side grazing areas: Challenges and mitigation policies. *International Journal of Environmental Research and Public Health*, 22(2), 311. [DOI]

Arunachalam, K.P., Hussain, S.A., Algburi, S., Sabihuddin, S., Mohammed, S.J., Majdi, H.S. and Al-Baghdadi, A.H., 2026. Eco-smart geomaterials and nano-engineered soils: Innovations in geotechnical engineering for pollution mitigation and environmental sustainability. *Nature Environment and Pollution Technology*, 25(2), D1823. [DOI]

Atavullayeva, M., 2024. Environmental pollution monitoring: Essential strategies for mitigating ecological degradation. *E3S Web of Conferences*, 587, 02014. [DOI]

Attiya, A.A. and Jones, B.G., 2020. Assessment of mineralogical and chemical properties of airborne dust in Iraq. *SN Applied Sciences*, 2(9), 1614. [DOI]

Ayobami, A.O., 2022. An assessment of trace metal pollution indicators in soils around oil well clusters. *Petroleum Research*, 7(2), pp.275–285. [DOI]

Barbera, M., Gariglio, S., Malegori, C., Oliveri, P., Saiano, F., Scalenghe, R. and Piazzese, D., 2025. Multivariate strategy for understanding soil features from rare-earth element profiles: A focus on data normalization. *ACS Measurement Science Au*, 5(2), pp.189–198. [DOI]

Basheer, M.Z., Huang, X., Cai, X., Cui, Y. and Muhammad, M., 2026. Integrating chemical and microbial strategies for heavy metal remediation in contaminated soils: Opportunities, challenges and key factors. *Environmental Science and Pollution Research*, pp.1–19. [DOI]

Bharti, R. and Sharma, R., 2022. Effect of heavy metals: An overview. *Materials Today: Proceedings*, 51, pp.880–885. [DOI]

Bhat, B.A., Rather, M.A., Bilal, T., Nazir, R., Qadir, R.U. and Mir, R.A., 2025. Plant hyperaccumulators: A state-of-the-art review on mechanism of heavy metal transport and sequestration. *Frontiers in Plant Science*, 16, 1631378. [DOI]

Bhatla, S.C. and Kathpalia, R., 2023. Essential and functional mineral elements. In: *Plant Physiology, Development and Metabolism*. Springer Nature, Singapore, pp.25–49. [DOI]

Candeias, C., Vicente, E., Tomé, M., Rocha, F., Ávila, P. and Célia, A., 2020. Geochemical, mineralogical and morphological characterisation of road dust and associated health risks. *International Journal of Environmental Research and Public Health*, 17(5), 1563. [DOI]

Cao, M., Tang, Q., Gai, N., Ma, S., Liu, J. and Wang, F., 2025. Contamination characteristics, source apportionment and risk assessment of heavy metals and metalloids in the soil-crop-human system within the typical high geological background region of the Yangtze River Delta. *Journal of Environmental Management*, 391, 126443. [DOI]

Chandel, S.S. and Bharose, R., 2020. Evaluation of heavy metal contamination in green leafy vegetables grown in Allahabad. *International Journal of Environment, Agriculture and Biotechnology*, 5(5), pp.1220–1225. [DOI]

Chen, Y., Ding, Z., Yu, T., Cao, L., Duan, Y., Zu, Y. and Li, Z., 2024. Accumulation characteristics of heavy metals in three wild rice species and adaptation of root morphology and anatomical structure to native soil heavy metals in Yunnan. *Ecological Indicators*, 167, 112601. [DOI]

Cobbina, S.J., Edu, A.R., Bosso, E.E., Bampoe, E. and Gautam, S., 2025. Impact of industrial activities on soil quality in urban settings: A study of heavy metal concentrations in Lamashegu, Ghana. *Discover Soil*, 2(1), 68. [DOI]

Du, X., Jiang, R., Sun, W., Tian, D. and Zheng, Z., 2026. Heavy metal risk assessment of 53-day accumulated road-deposited sediments from different roads in Beijing using Monte Carlo simulation. *Environmental Monitoring and Assessment*, 198(3), 222. [DOI]

Dytlow, S. and Górka-Kostrubiec, B., 2021. Concentration of heavy metals in street dust: An implication of using different geochemical background data in estimating the level of heavy metal pollution. *Environmental Geochemistry and Health*, 43(1), pp.521–535. [DOI]

Edo, G.I., Samuel, P.O., Oloni, G.O., Ezekiel, G.O., Ikpekoro, V.O., Obasohan, P. and Agbo, J.J., 2024. Environmental persistence, bioaccumulation and ecotoxicology of heavy metals. *Chemistry and Ecology*, 40(3), pp.322–349. [DOI]

El-Sergany, M.M. and El-Sharkawy, M.F., 2011. Heavy metal contamination of airborne dust in the environment of two main cities in the Eastern Province of Saudi Arabia. *Journal of King Abdulaziz University: Meteorology, Environment and Arid Land Agriculture Sciences*, 22(1), pp.135–148. [DOI]

El-Sharkawy, G., Alotaibi, M.O., Zuhair, R., Mahmoud, E., El Baroudy, A., Omara, A.E.D. and El-Sharkawy, M., 2025. Ecological assessment of polluted soils: Linking ecological risks, soil quality and biota diversity in contaminated soils. *Sustainability*, 17(4), 1524. [DOI]

Gałuszka, A. and Migaszewski, Z.M., 2025. Environmental assessment of metals in road dust: What do geochemical indices really tell us about pollution? *Environmental Geochemistry and Health*, 47(4), 128. [DOI]

Generalova, A., Davidova, S. and Satchanska, G., 2025. The mechanisms of lead toxicity in living organisms. *Journal of Xenobiotics*, 15(5), 146. [DOI]

Giri, S., Roy, A., Kumar, A., Ghosh, S., Bhunia, A. and Patra, S., 2026. Cadmium toxicity-related metabolic bone disease: A clinical conundrum of five cases. *Osteoporosis International*, 37(2), pp.525–531. [DOI]

Goya-Heredia, A.V., Zafra-Mejía, C.A. and Rondón-Quintana, H.A., 2023. Spatial analysis of heavy metal pollution in road-deposited sediments based on the traffic intensity of a megacity. *Atmosphere*, 14(6), 1033. [DOI]

Gupta, N., Yadav, K.K., Kumar, V., Prasad, S., Cabral-Pinto, M.M., Jeon, B.H. and Alsukaibia, A.K.D., 2022. Investigation of heavy metal accumulation in vegetables and health risk to humans from their consumption. *Frontiers in Environmental Science*, 10, 791052. [DOI]

Hakanson, L., 1980. An ecological risk index for aquatic pollution control: A sedimentological approach. *Water Research*, 14(8), pp.975–1001. [DOI]

Hamid, E., Payandeh, K., Karimi Nezhad, M.T. and Saadati, N., 2022. Potential ecological risk assessment of heavy metals/trace elements in coastal soils of southwest Iran. *Frontiers in Public Health*, 10, 889130. [DOI]

He, Y., Zhang, Y., Peng, C., Wan, X., Guo, Z. and Xiao, X., 2021. Distribution characteristics and risk assessment of heavy metals in soil and street dust with different land uses: A case in Changsha, China. *International Journal of Environmental Research and Public Health*, 18(20), 10733. [DOI]

Horne, A.J. and Fleming-Singer, M., 2005. Phytoremediation using constructed treatment wetlands: An overview. In: *Bioremediation of Aquatic and Terrestrial Ecosystems*. Science Publishers, Plymouth, UK, pp.329–377. [DOI]

Hosseinzadeh, M., Toranjzar, H., Ahmadi, A., Abdi, N. and Varvani, J., 2024. Assessment of potentially toxic elements pollution in soils and plant leaves along the high-traffic highway zones in Tehran, Iran. *Anthropogenic Pollution*, 8(2), pp.1–16. [DOI]

Hussain, B., Abbas, A., Saleem, A.R., Riaz, L., Rahman, S.U., Liu, S. and Farooq, M., 2024. Uptake, agglomeration and detoxification of trace metals and metalloids in plants. *Journal of Soil Science and Plant Nutrition*, 24(3), pp.4965–4983. [DOI]

Islam, M.S., Ahmed, M.K., Al-Mamun, M.H. and Eaton, D.W., 2020. Human and ecological risks of metals in soils under different land-use types in an urban environment of Bangladesh. *Pedosphere*, 30(2), pp.202–213. [DOI]

Jacob, D.E., Nelson, I.U., Izah, S.C., Ukpong, E., Akpan, U.U. and Ogwu, M.C., 2024. Bioindicators in recreational planning and development: Balancing nature and human activities. In: *Biomonitoring of Pollutants in the Global South*. Springer Nature, Singapore, pp.835–878. [DOI]

Kilavi, P.K., Kaniu, M.I., Patel, J.P. and Usman, I.T., 2023. Assessment of heavy metal pollution in soil and associated risks in the environs adjacent to a heavy mineral sand mine on the South Coast of Kenya. *Water, Air, & Soil Pollution*, 234(12), 748. [DOI]

Landrigan, P.J., Fuller, R., Hu, H., Caravanos, J., Cropper, M.L., Hanrahan, D. and Suk, W.A., 2018. Pollution and global health: An agenda for prevention. *Environmental Health Perspectives*, 126(8), 084501. [DOI]

Lu, H., Shen, Y., Maurya, P., Chen, J., Li, T. and Paz-Ferreiro, J., 2025. Spatial heterogeneity of heavy metals contamination in urban road dust and associated human health risks. *Land*, 14(4), 754. [DOI]

Madrid, F., Biasioli, M. and Ajmone-Marsan, F., 2008. Availability and bioaccessibility of metals in fine particles of some urban soils. *Archives of Environmental Contamination and Toxicology*, 55(1), pp.21–32. [DOI]

Mansouri, M.S., Payandeh, K., Koushafar, A., Goosheh, M. and Mohammadi Rouzbahani, M., 2024. Level of heavy metals and environmental pollution index in Ahvaz, Southwest Iran. *Scientific Reports*, 14(1), 14754. [DOI]

Miller, T., Durlik, I., Kostecka, E., Kozlovska, P., Łobodzińska, A., Sokołowska, S. and Nowy, A., 2025. Integrating artificial intelligence agents with the internet of things for enhanced environmental monitoring: Applications in water quality and climate data. *Electronics*, 14(4), 696. [DOI]

Mohiuddin, K.M., Ogawa, Y., Zakir, H.M., Otomo, K. and Shikazono, N., 2011. Heavy metals contamination in water and sediments of an urban river in a developing country. *International Journal of Environmental Science and Technology*, 8(4), pp.723–736. [DOI]

Musa, I.O., Ijah, U.J.J., Abioye, O.P., Abdulsalam, M., Pal, S.K., Abamhekhelu, I.A. and Akande, S.A., 2024. Phytoremediation of heavy metal-contaminated soil. In: *Eco-restoration of Polluted Environment*. CRC Press, pp.35–52. [DOI]

Naeem, M.A., Shabbir, A., Imran, M., Ahmad, S., Shahid, M., Murtaza, B. and Khan, W.U.D., 2024. Silicon-nanoparticles loaded biochar for soil arsenic immobilization and alleviation of phytotoxicity in barley: Implications for human health risk. *Environmental Science and Pollution Research*, 31(16), pp.23591–23609. [DOI]

Ogwu, M.C., Izah, S.C., Sawyer, W.E. and Amabie, T., 2025. Environmental risk assessment of trace metal pollution: A statistical perspective. *Environmental Geochemistry and Health*, 47(4), 94. [DOI]

Pancholi, K.C., Singh, P.J., Bhattacharyya, K., Tiwari, M., Sahu, S.K., Vincent, T. and Kaushik, C.P., 2022. Elemental analysis of residual ash generated during plasma incineration of cellulosic, rubber and plastic waste. *Waste Management & Research*, 40(6), pp.665–675. [DOI]

Panda, B.P., Kumari, R., Pradhan, A., Majhi, B.K., Acharya, P. and Parida, S.P., 2025. Assessing the bioaccumulation of copper and zinc using bird as bioindicator in different wetland ecosystems of Odisha, India. *Environmental Systems Research*, 14(1), 10. [DOI]

Rahman, S.U., Qin, A., Zain, M., Mushtaq, Z., Mehmood, F., Riaz, L. and Shehzad, M., 2024. Pb uptake, accumulation and translocation in plants: Plant physiological, biochemical and molecular response: A review. *Heliyon*, 10(6), e27748.

Rasul, A.K., Fatah, K.K., Hamed, M.H. and Tobia, F.H., 2026. Evaluation of trace metal pollution and ecological risk in the soils of Koy Sanjaq, Northeastern Iraq. *Iraqi Geological Journal*, 59(1B), pp.36–60. [DOI]

Rudnick, R.L. and Gao, S., 2003. Composition of the continental crust. *Treatise on Geochemistry*, 3, pp.1–64. [DOI]

Rastmanesh, F., Farrash-Alvar, S. and Shalbaf, F., 2024. Concentration of heavy metals in soil and leaves of *Conocarpus erectus* tree: A biomonitoring study, Ahvaz, Iran. *Environmental Monitoring and Assessment*, 196, 579. [DOI]

Salam, M., Viantika, N.M., Amiruddin, A., Pinontoan, F.M. and Rahmatullah, R.A., 2021. The effect of bioremediation on heavy metal contaminated soil using indigenous microorganisms. *IOP Conference Series: Earth and Environmental Science*, 681(1), 012115.

Shartooh, S.M., Najeeb, L.M. and Sirhan, M.M., 2018. Biological treatment of carcinogenic acrylonitrile using *Pseudomonas aeruginosa* in Basra city. *Journal of Biological Sciences*, 18(8), pp.415–424. [DOI]

Skuza, L., Szućko-Kociuba, I., Filip, E. and Bożek, I., 2022. Natural molecular mechanisms of plant hyperaccumulation and hypertolerance towards heavy metals. *International Journal of Molecular Sciences*, 23(16), 9335. [DOI]

Skvarekova, E., Tausova, M., Senova, A., Wittenberger, G. and Novakova, J., 2021. Statistical evaluation of quantities measured in the detection of soil air pollution of the environmental burden. *Applied Sciences*, 11(7), 3294. [DOI]

Somadas, P. and Sarvade, P.G., 2025. An overview of the impacts of various industrial and urban wastes on soil properties: Contamination and remediation strategies. *Environmental Research Communications*, 7(3), 032002. [DOI]

Szwalec, A., Mundała, P., Kędzior, R. and Pawlik, J., 2020. Monitoring and assessment of cadmium, lead, zinc and copper concentrations in arable roadside soils in terms of different traffic conditions. *Environmental Monitoring and Assessment*, 192(3), 155. [DOI]

Tang, M., Chen, K., Rudnick, R.L. and Wang, Z., 2019. The composition of

the upper continental crust: Insights from the chemical weathering of sedimentary rocks. *Geochimica et Cosmochimica Acta*, 258, pp.1–15.

Tnoumi, A., Angelone, M., Armiento, G., Caprioli, R., Crovato, C., De Cassan, M., Montereali, M.R., Nardi, E., Parrella, L., Proposito, M., Schirone, A., Spaziani, F. and Zourarah, B., 2022. Heavy metal content and potential ecological risk assessment of sediments from Khnifiss Lagoon National Park, Morocco. *Environmental Monitoring and Assessment*, 194(6), 356. [DOI]

Tomlinson, D.L., Wilson, J.G., Harris, C.R. and Jeffrey, D.W., 1980. Problems in the assessment of heavy-metal levels in estuaries and the formation of a pollution index. *Helgoländer Meeresuntersuchungen*, 33(1), pp.566–575. [DOI]

WHO, 1996. *Permissible Limits of Heavy Metals in Soil and Plants*. World Health Organization, Geneva, Switzerland.

Xie, X., Liu, Y., Qiu, H. and Yang, X., 2023. Quantifying ecological and human health risks of heavy metals from different sources in farmland soils within a typical mining and smelting industrial area. *Environmental Geochemistry and Health*, 45(8), pp.5669–5683. [DOI]

Xuefeng, L., Qiang, L., Shaolan, H., Shilai, Y., Deyu, H., Zhitao, W., Rangjin, X., Yongqiang, Z. and Lie, D., 2016. Estimation of carbon and nitrogen contents in citrus canopy by low-altitude remote sensing. *International Journal of Agricultural and Biological Engineering*, 9(5), pp.149–157. [DOI]

Zhang, C., 2024. *Fundamentals of Environmental Sampling and Analysis*. John Wiley & Sons. ISBN: 978-1-394-24462-1.

Zurek-Ost, M.A., Phillips, K.A., Williams, A.J., Edelman-Muñoz, A., Charest, N., Handa, S. and Isaacs, K.K., 2025. ExpoPath: A method for identifying and annotating exposure pathways from chemical co-occurrence networks. *Science of the Total Environment*, 979, 179465. [DOI]

Nature Environment and Pollution Technology
An International Quarterly Peer-Reviewed Open Access Journal

p-ISSN: 0972-6268 | e-ISSN: 2395-3454 Vol. 25 | No. 4 | Article ID B4423 | 2026

RESEARCH ARTICLE https://doi.org/10.46488/NEPT.2026.v25i04.B4423 OPEN ACCESS

Aerobic Granulation Technology-Based Cresol Degradation: A Comparative Evaluation of Reactor Studies

Apurva Kadia[1] and Urvish Chhaya[1,2]†

[1]Department of Microbiology, Natubhai V. Patel College of Pure and Applied Sciences, The Charutar Vidya Mandal (CVM) University, Vallabh Vidyanagar-388120, Gujarat, India

[2]Institute of Science, Nirma University, Sarkhej-Gandhinagar Highway, Ahmedabad, Gujarat, India

†Corresponding author: Urvish Chhaya; urvish.chhaya@nirmauni.ac.in

ARTICLE HISTORY

Received: 06-01-2026
Revised: 26-02-2026
Accepted: 03-03-2026

KEYWORDS

Aerobic granulation technology
Cresol degradation
Cresol isomer mixture
Continuous reactor
Catechol 1,2-dioxygenase

CITE THIS ARTICLE

Kadia, A. and Chhaya, U., 2026. Aerobic granulation technology-based cresol degradation: A comparative evaluation of reactor studies. *Nature Environment and Pollution Technology*, 25(4), B4423. https://doi.org/10.46488/NEPT.2026.v25i04.B4423

COPYRIGHT & LICENCE

© 2026 The Authors
Open Access under CC BY 4.0.

PUBLISHED BY
TECHNOSCIENCE PUBLICATIONS

ABSTRACT

Cresols (ortho-, meta-, and para-isomers), potent xenobiotic compounds prevalent in industrial wastewaters, pose severe environmental and health threats and require effective bioremediation solutions. Aerobic granulation technology was assessed for its degradation efficiency toward a mixed cresol-isomer system in batch and continuous reactors, addressing a key gap in existing research that has focused mainly on individual cresol isomers. The comparative reactor evaluation revealed that continuous operation achieved a 10.21% increase in cresol degradation efficiency compared with batch mode, highlighting its sustained performance. The continuous reactor demonstrated optimal cresol degradation at a flow rate of 120 mL h^{-1} (HRT, 8.33 h), supported by elevated volumetric and specific degradation rates. Enzyme analysis confirmed elevated activities of catechol 1,2-dioxygenase and phenol hydroxylase, supporting oxidative metabolism. The biodegradation mechanism was supported by enzyme activity assays and FT-IR spectral analysis, which demonstrated the absence of characteristic peaks associated with cresol functional groups and the emergence of oxygenated functional groups, thereby confirming structural changes during aerobic granular degradation. The significant degradation efficiency and enzyme-assisted structural transformation of cresol validate aerobic granular sludge as an effective treatment system for cresol-contaminated wastewater.

1. INTRODUCTION

The global increase in water consumption has accelerated water contamination, driven by industrial growth, population expansion, urbanization, and intensified agricultural activities, resulting in environmental degradation, disruption of aquatic ecosystems, and serious human health concerns. Almost 80% of wastewater is released untreated into the environment, particularly in low- and middle-income nations (UNESCO 2024). The demand for industrial products continues to increase with population growth, leading to the emergence of pollutants from both direct and indirect sources in the environment (Kanadasan et al. 2025). The levels of organic contaminants in wastewater, along with their growing complexity, have raised concerns because of their substantial threats to ecosystems, persistence, and limited biodegradability. Among these contaminants, phenolic compounds, characterized as aromatic hydrocarbon derivatives, constitute a class of refractory organic pollutants that exhibit substantial toxicity and detrimental effects on aquatic biota, thereby conflicting with the principles of green and sustainable water-

environment management (Chang et al. 2025, Chen et al. 2024). Phenols and their derivatives are widely used organic compounds that serve in the chemical synthesis of numerous compounds and as intermediates in the biosynthesis of secondary metabolites and are ultimately found in effluents from manufacturing industries. They are listed as priority pollutants by the Indian Central Pollution Control Board (CPCB) and the World Health Organization (WHO) (Cao et al. 2021, Kadia & Chhaya 2025, Wu et al. 2022).

Cresol and its ortho-, meta-, and para-isomers ($CH_3C_6H_5O$) are ubiquitous phenolic contaminants found in industrial effluents from industries such as phenol manufacturing, petrochemical processing, coal gasification, coking and mining, paper production, printing and dyeing, plastics, and pesticide synthesis, with concentrations often ranging from 10 to 1000 ppm. Owing to their pronounced toxicity, these substances can cause severe skin and mucosal irritation and corrosion, disrupt the function of vital organs such as the pancreas, liver, and kidneys, and may have mutagenic, carcinogenic, and teratogenic effects even at low exposure levels. Cresol also disrupts biological denitrification, thereby reducing wastewater-treatment efficiency (Chen et al. 2024, X. Wang et al. 2025, Zhang et al. 2025).

Phenolic wastewater treatment has involved both physical and chemical methods, such as membrane separation, advanced oxidation, ozonation, distillation, photocatalysis, and chemical or electrochemical oxidation (Bibi et al. 2023, Wu et al. 2022). Although these techniques are commonly employed in conventional industrial wastewater treatment, they are limited by the production of toxic by-products, incomplete pollutant degradation, the need to dispose of chemically produced sludge, and high operational costs (Gholami-Bonabi et al. 2020, Tuan Tran et al. 2022).

Modern wastewater treatment plants (WWTPs) face increasing pressure to expand treatment capacity while complying with strict effluent-discharge standards, reducing energy consumption, and minimizing their spatial footprint. This pressure is driven by rapid urbanization, which strains natural resources (Yu & Wang 2024). Microbial bioremediation is gaining attention as an environmentally friendly and cost-effective method to support global initiatives such as Sustainable Development Goal (SDG) 6.3, which aims to halve the proportion of untreated wastewater and promote safe reuse and recycling through nature-based solutions (NbS) (Crowther et al. 2024). Activated sludge processes are common in biological wastewater treatment. However, their ability to biodegrade and remove emerging contaminants is limited because many of these compounds pose toxicity risks to resident microbial communities. These issues have led to the search for alternative technologies, with aerobic granulation emerging as a promising replacement for conventional activated sludge systems (Kanadasan et al. 2025, Koumaki et al. 2021). Compared with activated sludge, aerobic granular sludge (AGS) offers advantages in compactness, settling properties, biomass density, toxin resistance, and simultaneous nutrient removal. AGS shows higher efficiency, better operational stability, and the capacity to address limitations of conventional wastewater treatment by effectively removing emerging pollutants through biodegradation, adsorption by extracellular polymeric substances (EPSs), and entrapment within its complex matrix (Kanadasan et al. 2025).

Although aerobic granular sludge technology has attracted attention for its potential to treat recalcitrant organic pollutants, few studies have examined its effectiveness in cresol degradation (Basheer & Farooqi 2012a, 2012b). Previous studies have mainly focused on individual cresol isomers, neglecting the complexity of industrial wastewaters in which cresol isomers often coexist. This study addresses an important research gap by examining the degradation of a mixed cresol-isomer system (o-, m-, and p-cresol) using aerobic granular sludge and assessing degradation efficacy under both batch and continuous operating modes. Enzyme assays and analytical techniques, including FT-IR, were also used to provide mechanistic insight into cresol degradation by granular biomass.

2. MATERIALS AND METHODS

2.1. Synthetic Wastewater

The synthetic medium used in this study consisted of cresol (600 ppm) as the carbon source, along with a modified Bushnell-Hass medium (BHM) previously optimized for consortium AKUC-1 to enhance cresol degradation efficiency (Kadia & Chhaya 2025). The optimized BHM included the following components (g L^{-1}): 0.2 $MgSO_4 \cdot 7H_2O$; 0.0075 $CaCl_2$; 1.0 KH_2PO_4; 1.0 K_2HPO_4; 1.0 NH_4NO_3; and 0.0075 $FeCl_3$, with sucrose (3.5 g L^{-1}) as an additional carbon source. Sucrose was added to maintain metabolic activity and improve biomass integrity during cresol breakdown (Kadia & Chhaya 2025). The medium was also supplemented with a micronutrient solution at a rate of 1 mL L^{-1}, containing (g L^{-1}): 0.05 $NiCl_2$; 0.05 $CoCl_2 \cdot 6H_2O$; 0.05 $(NH_4)_6Mo_7O_{24} \cdot 4H_2O$; 0.05 $ZnCl_2$; 0.05 H_3BO_3; 0.05 $AlCl_3$; 0.05 $MnSO_4 \cdot H_2O$; and 0.03 $CuCl_2$ (Bindhu & Madhu 2014). This synthetic wastewater was used consistently in all experiments at pH 7.

2.2. Inoculum Source

Aerobic granular sludge enriched and cultivated with the cresol-adapted microbial consortium AKUC-1 was used

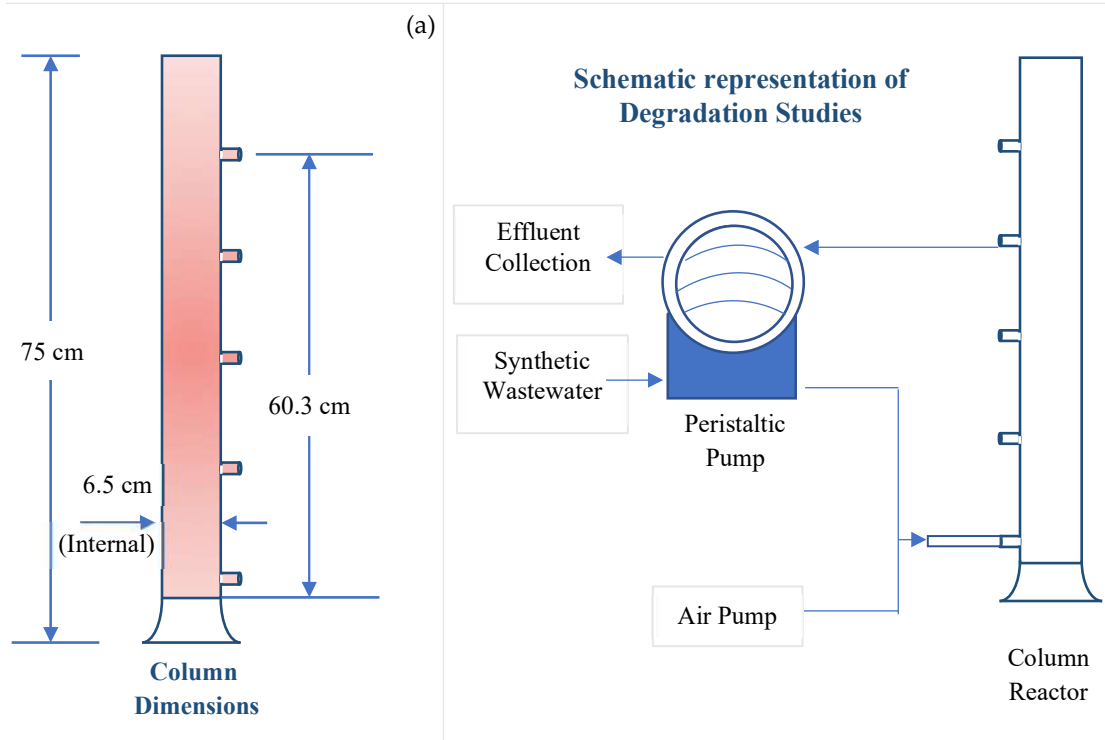


Fig. 1: Design configuration of the laboratory-scale glass column showing column dimensions (a) and the schematic layout of the experimental setup for aerobic cresol biodegradation (b).

Table 1: Performance evaluation of the continuous reactor using mathematical expressions.

Equation No.	Parameters	Formulas
1	Flow rate	$v = \frac{dV}{dt}$
2	Hydraulic Retention Time	$\tau = \frac{V\ (ml)}{v\ (ml/h)}$
3	Dilution Rate	$D = \frac{v\ (ml/h)}{Vr\ (ml)}$
4	Organic Loading Rate	$OLR = \frac{CODin \times v}{V}$
5	Overall Degradation Rate	$Vo = \frac{Co - Ct}{t}$
6	Volumetric Degradation Rate	$Vv = \frac{(Co - Ct) \times v}{V}$
7	Specific Substrate Utilization Rate	$Us = \frac{Vv}{Xo}$

as an inoculum in this study. The effect of inoculum size was evaluated with aerobic granules at inoculum sizes of 5%, 10%, 15%, and 20% (v/v), while monitoring cresol degradation until maximum degradation was achieved.

2.3. Evaluation of Aerobic Granules for Cresol Bioremediation

Cresol bioremediation was investigated in laboratory-scale glass column reactors with a working volume of 2 L (Fig. 1a). The reactor was fed synthetic wastewater containing 600 ppm cresol, with influent and aeration introduced from the bottom using an aquarium air pump to ensure adequate mixing and oxygen transfer (Fig. 1b). To evaluate the relative degradation efficiency of aerobic granular sludge, separate batch and continuous reactor experiments were conducted. Reactor performance was assessed by collecting samples at 24 h intervals, and the residual cresol concentration was determined using the 4-aminoantipyrine assay until maximum degradation was reached. The reactor was operated at 28–35°C and pH 7.0. To assess the effect of hydraulic retention time (HRT) in the continuous reactor, it was operated at flow rates of 300, 240, 180, and 120 mL h^{-1}.

Unlike continuous operation, batch reactor operation involved filling the reactor with synthetic wastewater and conducting the process under closed conditions (without influent or effluent flow) while maintaining continuous aeration. Samples were collected at 24 h intervals to monitor cresol degradation. The efficiency of cresol degradation by suspended consortium AKUC-1 and AKUC-1-derived aerobic granules was further assessed in a continuous reactor operated under the same physicochemical conditions at a flow rate of 120 mL h^{-1}. The reactor was inoculated with consortium AKUC-1 at an inoculum size of 10% (v/v) or with aerobic granules at 5% (v/v) in separate runs. The comparative evaluation of both inocula was performed by monitoring the residual cresol concentration in the effluent until peak degradation was achieved. All experiments were conducted in duplicate, and the results are expressed as mean ± standard deviation.

The evaluation of reactor performance involved estimating the percentage degradation of cresol, as outlined by Kadia & Chhaya (2025), along with measurements of chemical oxygen demand (COD) and biochemical oxygen demand (BOD), all determined in accordance with Standard Methods (APHA 2017).

where v is the flow rate, V is the bioreactor volume, V_r is the recirculation volume, C_0 is the cresol concentration in the inlet, C_t is the cresol concentration in the outlet, X_0 is the biomass, and t is time.

2.4. Enzyme Assay

Cell-free extracts were prepared according to the method outlined by Silva et al. (2013). The cells were centrifuged (10,000 rpm, 10 min) and harvested by resuspension in 50 mM phosphate buffer (pH 7). Cell lysis was achieved by sonication with 40 s pulses interspersed with 1 min cooling periods on ice. Following centrifugation at 10,000 rpm for 15 min, cell debris was removed, and the clarified supernatant was used for enzyme analysis. The activities of phenol hydroxylase, catechol 1,2-dioxygenase (C12O), and catechol 2,3-dioxygenase (C23O) were measured spectrophotometrically at wavelengths of 340, 260, and 375 nm, respectively. Phenol hydroxylase activity was assessed by measuring the oxidation of NADPH ($-\Delta A_{340}$). The reaction mixture, with a final volume of 3.0 mL, included 2.56 mL of 0.05 M Tris-HCl buffer, 20 µL of NADPH at 10 mmol L^{-1}, 20 µL of phenol at 5 g L^{-1}, and 400 µL of crude enzyme extract. A molar extinction coefficient of 6,220 mM^{-1} cm^{-1} was used (Wang et al. 2019). The catechol 1,2-dioxygenase assay involved measuring the increase in absorbance at 260 nm due to the formation of cis,cis-muconic acid over 3 min (Nakazawa & Nakazawa 1970). Catechol 2,3-dioxygenase activity was measured through the formation of 2-hydroxymuconic semialdehyde (2-HMS) at 375 nm (Nozaki 1970). The reaction system, reported as having a final volume of 3.0 mL, comprised potassium phosphate buffer at pH 7.5 (2.890 mL), catechol (60 µL, 1 mmol L^{-1}), and crude enzyme extract (50 µL). The formation of enzymatic products was assessed by absorbance measurements using molar extinction coefficients of 16,800 mM^{-1} cm^{-1} for muconic acid and 14,700 mM^{-1} cm^{-1} for 2-hydroxymuconic semialdehyde. Enzyme activity was calculated using the following equation.

$$Enzyme\ Activity\ = \left\{\left(\varepsilon \times \frac{L}{V}\right)\left(\frac{\Delta\, OD}{min}\right)\right.$$

Where ΔOD represents the change in absorbance, ε denotes the molar extinction coefficient, V indicates the reaction volume, and L refers to the cuvette path length.

Enzyme activities were evaluated in cell-free extracts derived from biomass collected after the active degradation of cresol, ensuring that the expression of cresol-degrading enzymes was induced by the substrate. Enzyme activities were measured in supernatants and reported as U/mL. Specific activity was not determined as the assay aimed mainly to identify the associated enzymes and clarify the primary pathway involved in cresol degradation.

2.5. Sample Preparation for FT-IR Analysis

Samples from the abiotic control and the treated effluent at maximum degradation were analyzed by FT-IR spectroscopy to assess structural changes resulting from cresol degradation.

The bacterial cells were harvested by centrifugation (10,000 rpm, 10 min), after which the supernatant was acidified to pH 2 using 0.5 M H_2SO_4, followed by ethyl acetate extraction (Panigrahy et al. 2020). The residues were dissolved in methanol for FT-IR analysis. The samples were scanned over 4000–400 cm^{-1}, and the resulting spectra were examined to identify modifications in the specific absorption bands of the parent compound (Ren et al. 2014).

3. RESULTS AND DISCUSSION

An integrated approach employing aerobic granular sludge as a biological treatment strategy for synthetic wastewater contaminated with cresol was investigated in both batch and continuous-flow laboratory-scale reactors. Aerobic granules, previously cultivated with the cresol-adapted consortium AKUC-1, were sourced from a sequencing batch reactor and used as inoculum in both reactors to evaluate cresol-wastewater remediation and elucidate reactor-specific performance dynamics. The microbial consortium AKUC-1, previously isolated and enriched in our laboratory, underwent partial taxonomic characterization via 16S rRNA gene analysis, which indicated a predominance of Firmicutes, especially Bacillus sp., suggesting their potential role in cresol degradation (Kadia & Chhaya 2025). Previous investigations have documented the presence of Firmicutes in aerobic granular sludge communities involved in cresol degradation. Lee et al. (2011) reported the prevalence of Firmicutes in aerobic granules capable of degrading cresol, whereas Chi et al. (2021) and Mahdavianpour et al. (2018) illustrated the ability of bacteria associated with this phylum to degrade phenol and p-cresol. The efficacy of aerobic granules in degrading cresol was assessed in both batch and continuous operating modes at an influent concentration of 600 ppm.

3.1. Effect of Inoculum Size

The effect of inoculum size on cresol degradation was evaluated, and cresol removal efficiencies of 91.11%, 95.22%, 97.94%, and 97.99% were attained within 72 h at inoculum sizes of 5%, 10%, 15%, and 20% (v/v), respectively. The developed aerobic granules exhibited predominantly spherical to pseudospherical morphology, with particle sizes ranging from 0.51 to 7.7 mm. Aerobic granules operated at the smaller inoculum size of 5% (v/v) showed substantial cresol removal while reducing biomass input, although slightly greater degradation was observed at larger inoculum sizes. The increased degradation observed with larger inoculum sizes indicates an increase in active biomass, leading to rapid metabolic activation and greater enzymatic capacity, thereby enhancing substrate-uptake kinetics.

The marginal enhancement beyond 5% (v/v) indicates a shift from biomass-controlled to substrate-limited degradation. Higher inoculum sizes showed similar performance, indicating that adequate active microbial consortia were present at 5% (v/v) to achieve near-optimal cresol degradation. The addition of further biomass did not substantially enhance performance, indicating that the system was operating close to its maximum degradation capacity under the prevailing operating conditions.

The results of this study highlight the importance of inoculum optimization in biodegradation systems. Rafeeq et al. (2023) suggested that inadequate inoculum concentrations prolong lag phases, whereas excessive biomass may induce quorum-sensing-mediated metabolic inhibition. Krasňan et al. (2016) also illustrated that biomass overaccumulation increases mass-transfer resistance, leading to the formation of diffusion-constrained or metabolically inactive zones that ultimately reduce reactor efficiency. Considering these findings, an inoculum size of 5% (v/v) was determined to be the most effective and sustainable operating concentration for further studies.

3.2. Reactor Studies

The continuous reactor was initially evaluated at different flow rates to optimize cresol degradation. At lower flow rates (120–180 mL h^{-1}), longer hydraulic retention times supported effective biodegradation, whereas at higher flow rates (240–300 mL h^{-1}), degradation efficiency decreased (Table 2). The lower flow rates corresponded to extended hydraulic retention times (HRTs), leading to better substrate-biomass interaction and increased biodegradation efficiency. Conversely, at higher flow rates, treatment efficiency gradually decreased, likely because of reduced contact time and partial biomass washout. Consistent with the current findings, Trivedi & Chhaya (2022) noted that lower flow rates in continuous systems significantly improved degradation efficiency, highlighting the critical role of hydraulic retention time in overall cresol degradation.

The batch and continuous reactors were operated independently, and both configurations demonstrated effective cresol degradation, with notable differences in removal dynamics between the two modes. During batch operation, cresol removal efficiency was 90.42 ± 0.770%,

Table 2: Efficiency of aerobic granules in degrading cresol in a continuous-flow reactor at various flow rates.

Cycle	C1	C2	C3	C4
Flow rate (mL h^{-1})	120	180	240	300
HRT (h)	8.33	5.55	4.16	3.33
Degradation (%)	99.39	90.96	89.11	87.07

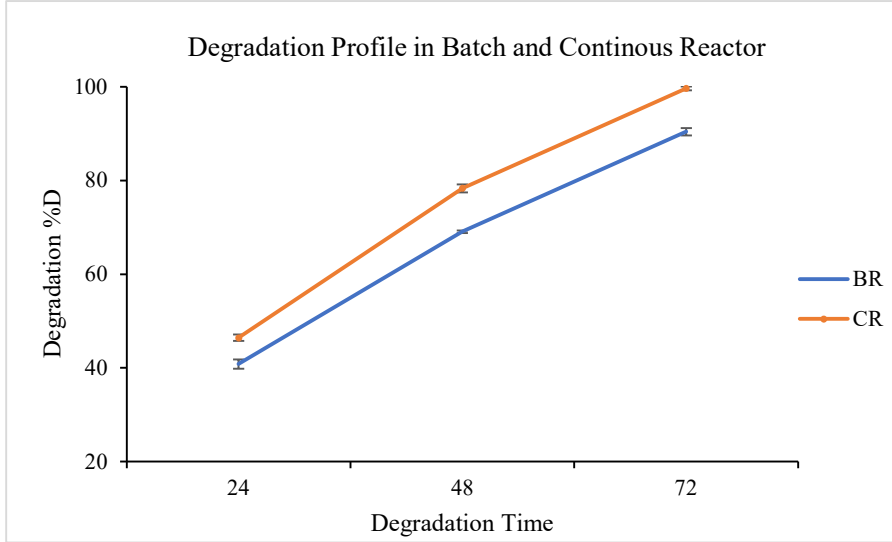


Fig. 2: Comparison of cresol degradation by aerobic granules operated in a batch reactor (BR) and a continuous-flow reactor (CR) over a 24 h time interval period.

while COD and BOD removals were 84.36% and 77.77%, respectively. In contrast, continuous operation demonstrated comparable COD removal of 84.99% and BOD removal of 79.23%, with enhanced cresol degradation of 99.65 ± 0.406%. The cresol degradation profile showed a steady decrease in concentration over time in both batch and continuous modes (Fig. 2).

The aerobic granular sludge exhibited improved cresol degradation in the continuous reactor, highlighting efficient substrate utilization during steady-state operation. Continuous operation was more effective at degrading the target recalcitrant compound, emphasizing its suitability for consistent industrial wastewater treatment. Maximum cresol degradation in the continuous reactor occurred at a flow rate of 120 mL h^{-1}, corresponding to a hydraulic retention time (HRT) of 8.33 h and a dilution rate of 0.06 h^{-1}. Under these conditions, the reactor's overall degradation rate was 70.56 mg h^{-1}, with an organic loading rate (OLR) of 31.61 kg COD m^{-3} d^{-1}. The system demonstrated a volumetric degradation rate of 35.28 mg cresol L^{-1} h^{-1} and a specific substrate utilization rate of 0.706 mg g^{-1} h^{-1}, indicating notable biomass activity and successful substrate conversion under the investigated operating conditions.

3.3. Enzyme Assay

The analysis of enzyme activity showed a significant increase in key enzymes involved in cresol degradation. Phenol hydroxylase reached an activity level of 1134.3 U/mL, while catechol 1,2-dioxygenase had the highest activity of 1213.3 U/mL. Catechol 2,3-dioxygenase displayed a lower activity of 91.66 U/mL. The heightened activity of phenol hydroxylase indicates efficient initial hydroxylation of cresol to catechol, which is a critical step in cresol biodegradation (Wang et al. 2019). The dominance of catechol 1,2-dioxygenase over catechol 2,3-dioxygenase indicates that the ortho-cleavage pathway serves as the primary mechanism for aromatic-ring fission during degradation. The comparatively lower activity of catechol 2,3-dioxygenase suggests that the meta-cleavage pathway plays a secondary role. According to Setlhare et al. (2018), catechol serves as a central intermediate in the aerobic degradation of phenolic contaminants, which subsequently undergo intradiol (ortho) or extradiol (meta) ring cleavage catalyzed by catechol 1,2-dioxygenase and catechol 2,3-dioxygenase, respectively.

3.4. Cresol Degradation Analysis by FT-IR

Cresol degradation was assessed by the disappearance or attenuation of characteristic functional-group peaks corresponding to cresol, as analyzed by FT-IR spectroscopy. The sample collected from the abiotic control showed characteristic absorption bands at 2968.06, 1710.08, 1491.92, and 1464.66 cm^{-1}, corresponding to methyl, hydroxyl, and aromatic-ring vibrations, respectively (Fig. 3). The identified functional groups are characteristic of cresol structures, consistent with earlier studies (Panigrahy et al. 2020, Ren et al. 2014). The treated samples exhibited FT-IR peaks at 2966.63, 1370.65, and 1260.85 cm^{-1}, while the bands at 1710.08, 1491.92, and 1464.66 cm^{-1} disappeared, indicating disruption of the aromatic structure (Fig. 4). According to Singh et al. (2017), the peak at 1260.85 cm^{-1} is attributed to the C-O group, whereas the band at 1370.65 cm^{-1} falls within the range associated with CH_3 bending or -COOH groups,

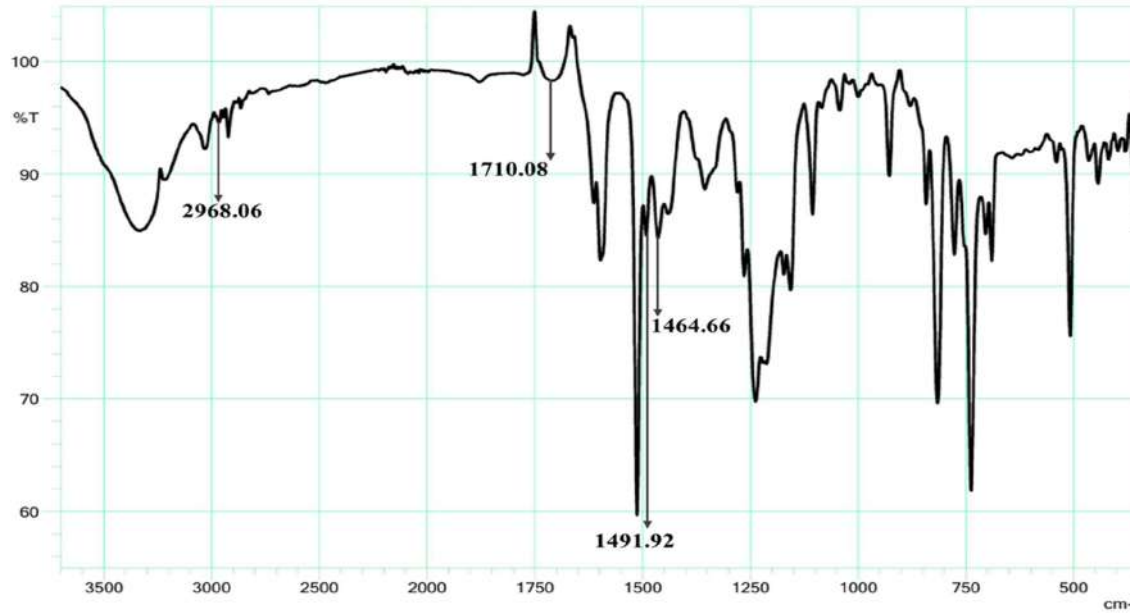


Fig. 3: FT-IR spectra demonstrating the appearance of characteristic functional-group peaks of the phenolic compound cresol in the abiotic control.

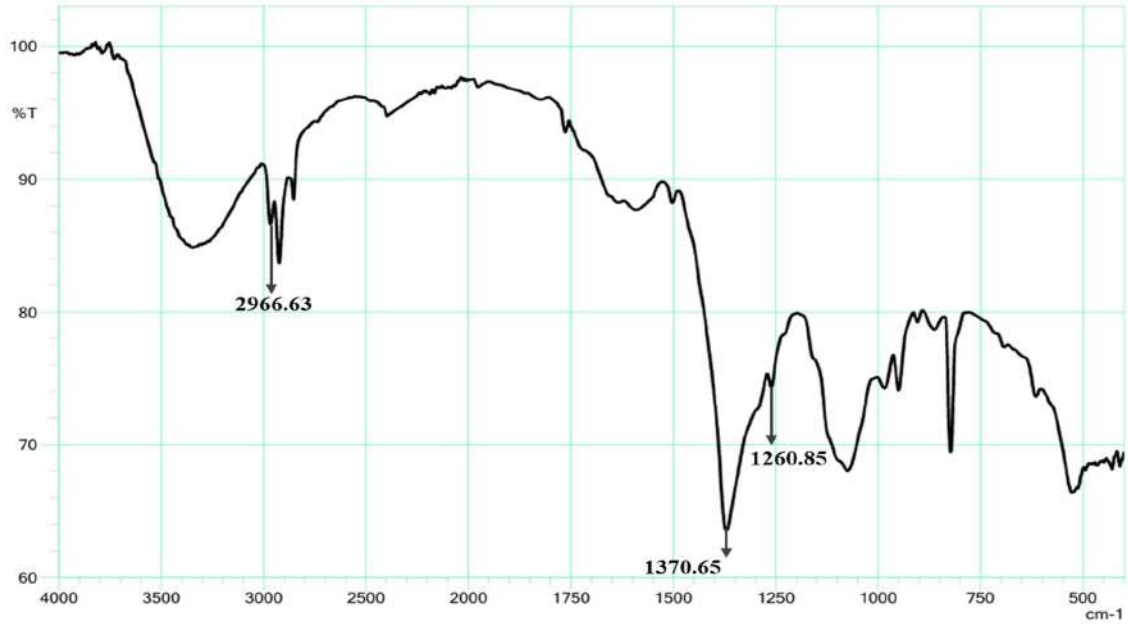


Fig. 4: FT-IR spectra of the treated sample demonstrating the disappearance and emergence of func-tional-group peaks during cresol degradation by aerobic granules.

as documented by Panigrahy et al. (2020) and Singh et al. (2017). The absence of peaks associated with aromatic and hydroxyl functional groups, along with the emergence of oxygenated functional groups, suggests biotransformation of cresol into oxygenated and aliphatic intermediates, consistent with enzyme-mediated degradation.

The enzyme assay indicated significant activity of phenol hydroxylase and catechol dioxygenases, implying the occurrence of cresol hydroxylation and subsequent ring-cleavage reactions. Consistent with this finding, FT-IR analysis of the treated samples revealed the absence of characteristic peaks associated with aromatic and phenolic functional groups,

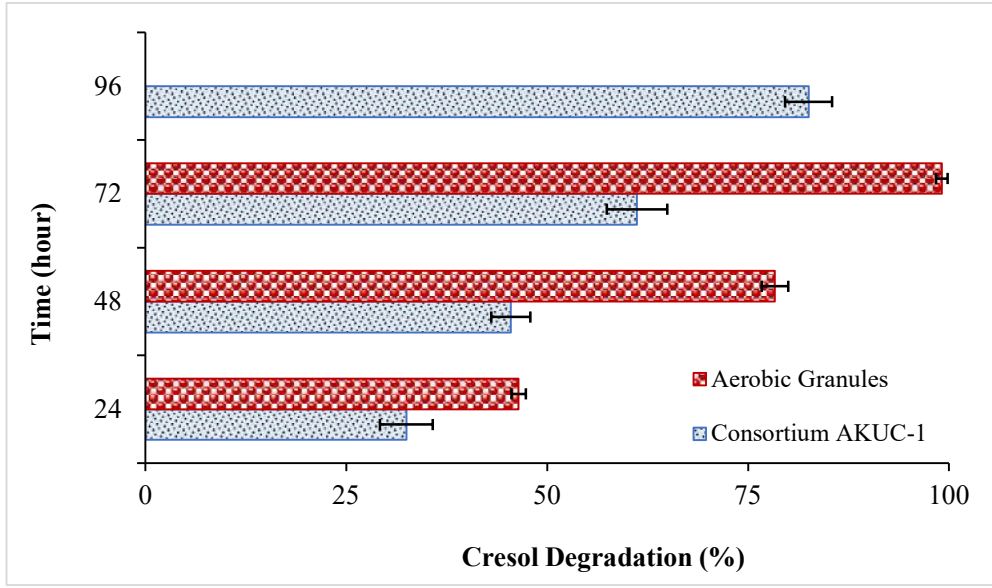


Fig. 5: Comparative cresol degradation profiles of aerobic granules and suspended consortium AKUC-1 over a 96 h operating period in a continuous reactor.

along with the appearance of oxygenated functional groups, indicating an enzyme-mediated structural transformation of cresol (Ali et al. 1998, Duffner & Müller 1998, Kadia & Chhaya 2025). The strong dominance of catechol 1,2-dioxygenase activity over catechol 2,3-dioxygenase indicates that cresol degradation mainly occurs through the ortho-cleavage pathway. Overall, these findings show that aerobic granules favor a metabolically efficient ortho-cleavage strategy, which explains the high cresol removal observed in both batch and continuous reactor operations.

The correlation between FT-IR spectral shifts and enzyme activity offers a coherent mechanistic interpretation: phenol hydroxylase probably facilitates the initial hydroxylation of cresol to catechol, followed by ring cleavage mainly via the ortho pathway, resulting in the generation of oxygenated intermediates that can be characterized using FT-IR. The combined insights from cresol removal efficiency, enzyme-activity analyses, and FT-IR spectral alterations provide a coherent and mechanistically relevant understanding of cresol biodegradation under the studied parameters. Although chromatographic metabolite profiling could provide molecular-level confirmation, the current comprehensive evidence adequately substantiates the suggested ortho-cleavage-dominated degradation pathway.

3.5. Comparative Evaluation of Consortium AKUC-1 and Aerobic Granules Derived from AKUC-1 for Cresol Degradation

The suspended consortium AKUC-1 achieved 82.54 ± 2.927% degradation after 96 h. Despite the larger inoculum used for the suspended consortium, the aerobic granules cultivated with consortium AKUC-1 achieved 99.10 ± 0.715% cresol degradation within 72 h. The superior performance of aerobic granules can be linked to better biomass retention and microbial accumulation, highlighting the significance of granular structure in continuous reactor systems. The degradation profile demonstrates that aerobic granules facilitated more rapid cresol removal than the suspended consortium AKUC-1, resulting in a substantial decrease in residual cresol concentration during the initial operating phase (Fig. 5).

4. CONCLUSIONS

This laboratory-scale study demonstrates the successful application of aerobic granules cultivated using consortium AKUC-1 for the biodegradation of a mixed cresol-isomer system (o-, m-, and p-cresol), addressing an important gap in the current literature, which predominantly focuses on individual isomers. The comparative reactor evaluation demonstrated enhanced removal efficiency during continuous operation compared with batch mode, with an increase of approximately 10% under the evaluated conditions, highlighting its suitability for consistent, prolonged treatment. Overall, the findings indicate that aerobic granular sludge facilitates effective, kinetically favorable cresol degradation under continuous reactor conditions. The elevated degradation

efficiency observed in the granular system indicates favorable reactor performance and highlights the potential

of aerobic granules to treat complex cresol-containing wastewaters and be integrated into advanced wastewater treatment systems, thereby establishing an energy-efficient and sustainable approach. Future efforts should prioritize long-term stability, resilience to shock loads, and validation at scale under actual industrial-effluent conditions to enable real-world use of aerobic granulation technology as a biotechnology strategy.

5. ACKNOWLEDGMENTS

The authors express their sincere thanks to the Sophisticated Instrumentation Centre for Applied Research and Testing (SICART) for its essential technical support and instrumental facilities.

6. REFERENCES

Ali, S., Fernandez-Lafuente, R. and Cowan, D.A., 1998. Meta-pathway degradation of phenolics by thermophilic Bacilli. *Enzyme and Microbial Technology*, 23(7-8), pp.462-468. [DOI]

American Public Health Association (APHA), American Water Works Association (AWWA) and Water Environment Federation (WEF), 2017. *Standard Methods for the Examination of Water and Wastewater*. 23rd ed. American Public Health Association, Washington, DC.

Basheer, F. and Farooqi, I.H., 2012a. Biodegradation of m-cresol by aerobic granules in a sequencing batch reactor. *Environmental Technology*, 33(16), pp.1847-1856. [DOI]

Basheer, F. and Farooqi, I.H., 2012b. Biodegradation of p-cresol by aerobic granules in sequencing batch reactor. *Journal of Environmental Sciences*, 24(11), pp.2012-2018. [DOI]

Bibi, A., Bibi, S., Abu-Dieyeh, M. and Al-Ghouti, M.A., 2023. Towards sustainable physicochemical and biological techniques for the remediation of phenol from wastewater: A review on current applications and removal mechanisms. *Journal of Cleaner Production*, 417, p.137810. [DOI]

Bindhu, B.K. and Madhu, G., 2014. *Influence of Major Operational Parameters on Aerobic Granulation for the Treatment of Wastewater*. Cochin University of Science and Technology. Available at: http://dyuthi.cusat.ac.in/xmlui/handle/purl/4738

Cao, X., Wang, K. and Feng, X., 2021. Removal of phenolic contaminants from water by pervaporation. *Journal of Membrane Science*, 623, p.119043. [DOI]

Chang, B., Fang, Y., Zhang, S., Luo, Q., Chen, D., Jin, R. and Yang, G., 2025. Deciphering the nitrogen removal and p-cresol degradation mechanisms in biofilm and granular sludge of anammox systems: Evolution in bioactivity, biomass characteristics, functional genes and potential metabolic pathways. *Chemical Engineering Journal*, 522, p.167609. [DOI]

Chen, H., Long, Q., Shu, J., Wei, F. and Zhang, Y., 2024. Efficient degradation of m-cresol by MnO-doped red mud catalyst activating peroxymonosulfate process: Performance and mechanism. *Journal of Saudi Chemical Society*, 28(3), p.101857. [DOI]

Chi, M., Su, X., Sun, X., Xu, Y., Wang, X. and Qiu, Y., 2021. Microbial analysis and enrichment of anaerobic phenol and p-cresol degrading consortia with addition of AQDS. *Water Science and Technology*, 84(3), pp.683-696. [DOI]

Crowther, T.W., Rappuoli, R., Corinaldesi, C., Danovaro, R., Donohue, T.J., Huisman, J., Stein, L.Y., Timmis, J.K., Timmis, K., Anderson, M.Z., Bakken, L.R., Baylis, M., Behrenfeld, M.J., Boyd, P.W., Brettell, I., Cavicchioli, R., Delavaux, C.S., Foreman, C.M., Jansson, J.K. et al., 2024. Scientists' call to action: Microbes, planetary health, and the Sustainable Development Goals. *Cell*, 187(19), pp.5195-5216. [DOI]

Duffner, F.M. and Müller, R., 1998. A novel phenol hydroxylase and catechol 2,3-dioxygenase from the thermophilic Bacillus thermoleovorans strain A2: Nucleotide sequence and analysis of the genes. *FEMS Microbiology Letters*, 161(1), pp.37-45. [DOI]

Gholami-Bonabi, L., Ziaefar, N. and Sheikhloie, H., 2020. Removal of phenol from aqueous solutions by magnetic oxide graphene nanoparticles modified with ionic liquids using the Taguchi optimization approach. *Water Science and Technology*, 81(2), pp.228-240. [DOI]

Kadia, A. and Chhaya, U., 2025. Optimizing potential of consortium AKUC-1 for cresol bioremediation: A statistical approach complemented with AI-based prediction. *Bioresource Technology Reports*, 32, p.102342. [DOI]

Kanadasan, G., Ng, C.A., Vadivelu, V.M. and Bashir, M.J.K., 2025. Advances in the application of aerobic granular sludge for the removal of emerging contaminants in municipal and industrial wastewater. *Molecules*, 30(17), p.3522. [DOI]

Koumaki, E., Noutsopoulos, C., Mamais, D., Fragkiskatos, G. and Andreadakis, A., 2021. Fate of emerging contaminants in high-rate activated sludge systems. *International Journal of Environmental Research and Public Health*, 18(2), p.400. [DOI]

Krasňan, V., Stloukal, R., Rosenberg, M. and Rebroš, M., 2016. Immobilization of cells and enzymes to LentiKats®. *Applied Microbiology and Biotechnology*, 100(6), pp.2535-2553. [DOI]

Lee, D.-J., Ho, K.-L. and Chen, Y.-Y., 2011. Degradation of cresols by phenol-acclimated aerobic granules. *Applied Microbiology and Biotechnology*, 89(1), pp.209-215. [DOI]

Mahdavianpour, M., Moussavi, G. and Farrokhi, M., 2018. Biodegradation and COD removal of p-cresol in a denitrification baffled reactor: Performance evaluation and microbial community. *Process Biochemistry*, 69, pp.153-160. [DOI]

Nakazawa, T. and Nakazawa, A., 1970. Pyrocatechase (Pseudomonas). In: *Methods in Enzymology*, pp.518-522. [DOI]

Nozaki, M., 1970. Metapyrocatechase (Pseudomonas). In: *Methods in Enzymology*, 17, pp.522-525. [DOI]

Panigrahy, N., Barik, M., Sahoo, R.K. and Sahoo, N.K., 2020. Metabolic profile analysis and kinetics of p-cresol biodegradation by an indigenous Pseudomonas citronellolis NS1 isolated from coke oven wastewater. *International Biodeterioration & Biodegradation*, 147, p.104837. [DOI]

Rafeeq, H., Afsheen, N., Rafique, S., Arshad, A., Intisar, M., Hussain, A., Bilal, M. and Iqbal, H.M.N., 2023. Genetically engineered microorganisms for environmental remediation. *Chemosphere*, 310, p.136751. [DOI]

Ren, Y., Peng, L., Zhao, G. and Wei, C., 2014. Degradation of m-cresol via the ortho cleavage pathway by Citrobacter farmeri SC01. *Biochemical Engineering Journal*, 88, pp.108-114. [DOI]

Setlhare, B., Kumar, A., Mokoena, M.P. and Olaniran, A.O., 2018. Catechol 1,2-dioxygenase is an analogue of homogentisate 1,2-dioxygenase in Pseudomonas chlororaphis strain UFB2. *International Journal of Molecular Sciences*, 20(1), p.61. [DOI]

Silva, A.S., Jacques, R.J.S., Andreazza, R., Bento, F.M., Roesch, L.F.W. and Camargo, F.A.O., 2013. Properties of catechol 1,2-dioxygenase in the cell-free extract and immobilized extract of Mycobacterium fortuitum. *Brazilian Journal of Microbiology*, 44(1), pp.291-297. [DOI]

Singh, T., Srivastava, N., Bhatiya, A.K. and Mishra, P.K., 2017. Analytical study of effective biodegradation of p-cresol using Serratia marcescens ABHI001: Application in bioremediation. *3 Biotech*, 7(6), p.384. [DOI]

Trivedi, J. and Chhaya, U., 2022. Bioremediation of bisphenol A found in industrial wastewater using Trametes versicolor (TV) laccase nanoemulsion-based bead organogel in packed bed reactor. *Water Environment Research*, 94(10). [DOI]

Tuan Tran, H., Lin, C., Bui, X.-T., Ky Nguyen, M., Dan Thanh Cao,

N., Mukhtar, H., Giang Hoang, H., Varjani, S., Hao Ngo, H. and Nghiem, L.D., 2022. Phthalates in the environment: Characteristics, fate and transport, and advanced wastewater treatment technologies. *Bioresource Technology*, 344, p.126249. [DOI]

UNESCO, 2024. *The United Nations World Water Development Report 2024: Water for Prosperity and Peace*. United Nations Educational, Scientific and Cultural Organization (UNESCO). Available at: https://www.unwater.org/publications/un-world-water-development-report-2024

Wang, X., Liu, S., Ding, X., Zhang, L., Lv, X., Li, J., Song, C., Zhang, C. and Wang, S., 2025. Coexistence of diverse metabolic pathways promotes p-cresol biodegradation by Bacillus subtilis ZW. *International Biodeterioration & Biodegradation*, 196, p.105933. [DOI]

Wang, Y., Meng, F., Li, H., Zhao, S., Liu, Q., Lin, Y., Wang, G. and Wu, J., 2019. Biodegradation of phenol by Isochrysis galbana screened from eight species of marine microalgae: Growth kinetic models, enzyme analysis and biodegradation pathway. *Journal of Applied Phycology*, 31(1), pp.445-455. [DOI]

Wu, P., Zhang, Z., Luo, Y., Bai, Y. and Fan, J., 2022. Bioremediation of phenolic pollutants by algae: Current status and challenges. *Bioresource Technology*, 350, p.126930. [DOI]

Yu, C. and Wang, K., 2024. Continuous flow aerobic granular sludge: Recent developments and applications. *Water Science & Technology*, 89(5), pp.1155-1178. [DOI]

Zhang, Y., Zhuang, L., Ji, B., Ren, Y., Xu, X., He, J., Xue, Y. and Sun, H., 2025. Ultrasonic cavitation treatment of o-cresol wastewater and long-term pilot-scale study. *Journal of Environmental Management*, 375, p.124208. [DOI]

Nature Environment and Pollution Technology
An International Quarterly Peer-Reviewed Open Access Journal

p-ISSN: 0972-6268 | e-ISSN: 2395-3454 Vol. 25 | No. 4 | Article ID D1902 | 2026

RESEARCH ARTICLE https://doi.org/10.46488/NEPT.2026.v25i04.D1902 OPEN ACCESS

Optimizing Waste Management Systems to Reduce Greenhouse Gas Emissions on the Small Island of Kodingareng Lompo, Indonesia

Wahyudi Munim Anugra†, Irwan Ridwan Rahim and Asiyanthi T. Lando
Department of Environmental Engineering, Faculty of Engineering, Hasanuddin University, Gowa, South Sulawesi 92171, Indonesia
†Corresponding author: Irwan Ridwan Rahim; Irwanrr@eng.unhas.ac.id

ARTICLE HISTORY

Received: 13-01-2026
Revised: 04-03-2026
Accepted: 17-03-2026

KEYWORDS

Integrated waste management
Greenhouse gas emissions
Global warming potential
Climate change mitigation

CITE THIS ARTICLE

Anugra, W. M., Rahim, I. R. and Lando, A. T., 2026. Optimizing waste management systems to reduce greenhouse gas emissions on the small island of Kodingareng Lompo, Indonesia. *Nature Environment and Pollution Technology*, 25(4), D1902. https://doi.org/10.46488/NEPT.2026.v25i04.D1902

COPYRIGHT & LICENCE

© 2026 The Authors
Open Access under CC BY 4.0.

PUBLISHED BY
TECHNOSCIENCE PUBLICATIONS

ABSTRACT

The absence of an effective waste management system in small island areas significantly contributes to greenhouse gas (GHG) emissions, particularly from uncontrolled open burning. This study analyzes the potential of an integrated waste management system to reduce GHG emissions in Kodingareng Lompo Island by comparing existing practices with an alternative scenario aligned with Presidential Regulation of the Republic of Indonesia No. 97 of 2017, which targets 30% waste reduction and 70% waste handling. Emission estimates were calculated using the IPCC methodology and global warming potential (GWP) approach. Under existing conditions, waste reduction is minimal (1.37%), while 98.63% of waste is handled through environmentally unsound practices, primarily open burning, marine disposal, and uncontrolled dumping. The alternative scenario introduces a resource-oriented paradigm, achieving 31.88% waste reduction and 68.12% controlled waste handling. As a result, total GWP decreases substantially from 171,708.79 kg CO_2e yr^{-1} to 61,123.91 kg CO_2e yr^{-1}, representing a 64.40% reduction. This decline is driven by significant decreases in CO_2, CH_4, and N_2O emissions following the elimination of open burning and the optimization of biological and controlled treatment processes. These findings demonstrate that the proposed integrated waste management scheme significantly reduces GHG emissions and provides a feasible and replicable model for small island contexts facing similar infrastructural and governance constraints. Its implementation requires coordinated engagement among local authorities, communities, and waste management operators, contributing to climate change mitigation and supporting sustainable coastal ecosystem management.

1. INTRODUCTION

The increasing volume of waste driven by population growth and consumption patterns has intensified pressures on both the environment and governmental systems. This condition is further exacerbated by inadequate disposal practices, limited resources, rapid urbanization and industrialization, socioeconomic disparities, weak policy enforcement, governance deficiencies, and low levels of public participation. Consequently, countries are compelled to formulate waste management strategies and regulatory frameworks to mitigate environmental impacts (Awino & Apitz 2024). Waste management has also become a critical issue in Southeast Asia, where, despite the introduction of various strategies, implementation outcomes have been mixed, and many initiatives have failed to meet their intended targets. The limited capacity of government institutions and the absence of sustainable waste management approaches have contributed to the continued degradation of environmental quality and public health. The efficiency

of waste collection in developing countries remains approximately 40%, less than half of that in developed countries, which achieve rates as high as 90%. Compared to the emphasis placed by developed countries on sustainable resource use, energy recovery, and safe waste disposal, developing nations are often able to meet only the minimum standards for safe disposal (Zhang et al. 2024).

Indonesia, through Presidential Regulation of the Republic of Indonesia No. 97 of 2017, establishes a strategic framework for the management of domestic waste and waste similar to domestic waste, aimed at developing an effective, integrated, and sustainable waste management system. The regulation outlines two key national targets to be achieved by 2025: a 30% reduction in waste generation and a 70% improvement in waste handling. The 30% reduction target focuses on upstream interventions, particularly limiting waste generation at the source, optimizing reuse activities, enhancing recycling efforts, and promoting the development of a circular economy. Meanwhile, the 70% waste handling target emphasizes strengthening downstream management capacities, including waste sorting, collection, transportation, processing, and environmentally sound final disposal. Achieving these targets requires enhanced coordination among government bodies, private-sector actors, and community participation, as well as revitalization of institutional structures, financing mechanisms, technological adoption, and planning instruments. Thus, this regulation serves as both a normative and operational foundation that reinforces Indonesia's commitment to significantly reducing waste burdens and improving waste management quality, thereby contributing more measurably to environmental sustainability and public health.

According to the Ministry of Environment and Forestry of the Republic of Indonesia, the total waste generation across Indonesia had reached 67.8 million tons at the beginning of 2020. The household sector was identified as the largest contributor, accounting for approximately 48% of total waste, followed by traditional markets at 24% and street waste at 7%. Over the years, waste-related issues have shown an increasingly complex trend. According to data from the Environmental Office of Makassar City, daily waste generation reaches 905 tons, consisting of 54.46% organic waste, 27.48% inorganic waste, and 18.06% other waste types. Waste reduction efforts have achieved an annual rate of 2.09%, while waste handling measures have reached 74.74% per year.

Kodingareng Lompo Island is administratively part of Kodingareng Village, located within the Sangkarrang Island District, Makassar City, South Sulawesi Province, Indonesia. Geographically, the island lies in the Makassar Strait at coordinates 119°5'53.40"E and 5°8'53.06"S. Based on distance measurements using Google Earth, Kodingareng Lompo Island is situated approximately 14 km from the mainland of Sulawesi. The area of Kodingareng Lompo covers 0.48 square km with a total population of 4,977 inhabitants. The island is part of Makassar City, which serves as the capital of South Sulawesi Province and is classified as a metropolitan city with a population of 1,474,393 people (Statistics Indonesia of Makassar City 2024). Makassar City faces significant waste management challenges, particularly at the Tamangapa Final Disposal Site (Tamangapa landfill), where the waste volume has exceeded its maximum capacity since 2019 (Rusni 2024). However, the unique condition of Kodingareng Lompo Island is that the waste generated there is not transported to the Tamangapa landfill. The island has a relatively high population density, which directly influences the amount of waste produced. The community lacks an effective waste management system, and waste is often disposed of directly into the sea (Gani & Ikhsan 2020). In addition, residents also handle waste by burning and burying it (Adriani et al. 2023). The increasing volume of waste poses substantial environmental risks and contributes to climate change. In the absence of reliable waste management systems, open dumping and open burning have become default alternatives for reducing waste accumulation (Gómez-Sanabria et al. 2022). These conditions illustrate the environmental and management challenges faced by small island communities with limited land availability. Therefore, Kodingareng Lompo Island serves as a representative case study for analyzing waste management practices and potential greenhouse gas emissions in small island environments.

Greenhouse gas (GHG) emissions can be reduced through effective waste management practices, in which the amount of properly managed waste exceeds the amount of waste generated. Such emissions may arise directly from landfills, open burning, recycling activities, and waste collection and transportation (Bakas et al. 2011). Therefore, emission reduction strategies such as waste reduction, recycling, and composting are required to move toward a more sustainable and low-carbon future (Hoy et al. 2024). However, waste management on small islands does not have straightforward solutions. Various challenges exist, including limited area, restricted opportunities for recycling and resale, and increasing environmental impacts, particularly when the island is small and densely populated (Camilleri-Fenech et al. 2018).

This study aims to analyze the quantity and composition of waste on Kodingareng Lompo Island and to compare waste management practices and the potential greenhouse gas (GHG) emissions and Global Warming Potential

(GWP) generated under current (existing) conditions with alternative waste management strategies based on waste reduction and handling approaches in accordance with prevailing regulations. The novelty of this research lies in the application of an integrated waste management system in a small island context, which has been relatively underexplored from a greenhouse gas emission perspective. This study not only compares existing conditions with alternative waste management scenarios on the island and estimates potential GHG emissions and GWP using the Intergovernmental Panel on Climate Change (IPCC), but also emphasizes the importance of community participation and locally based management in supporting climate change mitigation through the waste sector. The findings provide a scientific basis for the implementation of sustainable waste management policies on small coastal islands in Indonesia.

2. MATERIALS AND METHODS

This study focuses on analyzing waste generation rates and composition from residential areas representing waste originating within the island, as well as waste data collected from coastal areas representing waste originating from outside the island. Subsequently, the waste generation and composition data were evaluated based on current waste reduction and management practices (Scenario 1) and were compared with an alternative waste management scenario that could be implemented on Kodingareng Lompo Island (Scenario 2). Furthermore, both scenarios are assessed in accordance with IPCC Guidelines to estimate greenhouse gas (GHG) emission potential and Global Warming Potential (GWP). The research employs a quantitative approach, as it relies on numerical data and statistical methods for data collection and analysis. The study location is shown in Fig. 1.

2.1. Waste Generation and Composition in Residential Area

SNI 3964:2025 is a standard method for sampling and measuring household waste generation and composition, as well as waste similar to household waste, developed and established by the National Standardization Agency of Indonesia (BSN). According to this standard, waste generation refers to the quantity of waste generated by the community, expressed in units of volume or weight per capita per day, per building area, per unit of time, or per length of road. Given that the study area is an island setting, this research focuses exclusively on waste generated from households. The implementation of waste generation sampling in this study was conducted using a stratified

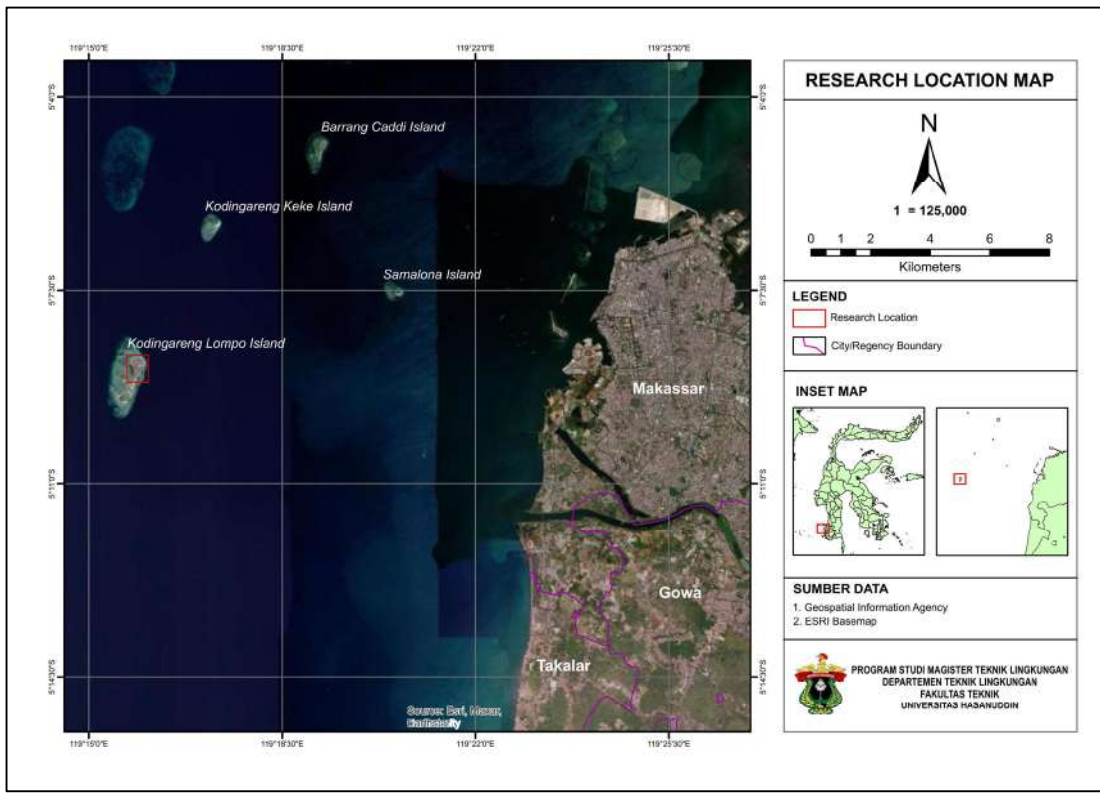


Fig. 1: Study area map of Kodingareng Lompo Island.

random sampling approach, with the sample size determined as follows:

$$Ps = Cd\sqrt{Pt} \quad ...(1)$$

where Ps denotes the total number of individual samples (persons), Cd represents the population coefficient, and Pt refers to the total population (persons). Subsequently, the proportion of the number of sampled households (Heads of Household/HH) is calculated using the following equation:

$$K = Ps\ x\ N^{-1} \quad ...(2)$$

where K denotes the number of sampled households, Ps represents the total number of individual samples (persons), and N refers to the average number of persons per household, assumed to be 5 in accordance with the example provided in SNI 3964:2025. Subsequently, the calculation of the number of houses to be sampled is determined as follows:

$$Nr = Sn\ x\ K \quad ...(3)$$

where Nr denotes the number of houses selected for waste sampling (housing units), Sn represents the proportion of the socioeconomic level of a given area based on secondary data or field observations (%), and K refers to the total number of sampled households (HH), under the assumption that one house corresponds to one household.

Waste sampling was conducted over eight consecutive days at the same households to obtain the average waste generation from the residential area. The average waste generation was calculated using the following equation:

$$qr(i) = qi(i)\ x\ n^{-1} \quad ...(4)$$

where qr denotes the average waste generation rate (kg day^{-1}), qi represents the amount of waste generated (kg), n refers to the number of sampling days (days), and i indicates the housing category (permanent, semi-permanent, and non-permanent). Subsequently, the per capita waste generation on Kodingareng Lompo Island was calculated using the following equation:

$$Qsrt(i) = qr(i)\ x\ Psrt(i)^{-1} \quad ...(5)$$

where Qsrt represents the waste generation rate (kg person^{-1} day^{-1}), qr is the average daily waste generation (kg day^{-1}), Psrt is the number of individuals included in the sample (persons), and i refers to the housing category. Subsequently, the total waste generation was estimated using the following equation:

$$\sum srt = Qsrt(i)\ x\ Sn(i)\ \ x\ Pt \quad ..(6)$$

Where $\sum$ srt denotes the total waste generation (kg day^{-1}), Qsrt is the waste generation rate (kg person^{-1} day^{-1}), Sn is the percentage of each housing category (%), Pt indicates the total population (persons), and i refers to the housing category.

According to the Guidelines for National Greenhouse Gas Inventories, waste composition is one of the primary factors influencing emissions from solid waste management, as different waste types contain varying amounts of degradable organic carbon and fossil carbon. Understanding the composition of solid waste is therefore highly valuable and essential for those responsible for proper solid waste management (Nell et al. 2022). Studies related to the characterization of household solid waste can be defined as the process of sampling, collecting, sorting, and analyzing household solid waste to identify and determine both the overall composition and the composition of individual components such as glass, metal, paper, or plastic within a given area (Nell & Waal 2020). The detailed composition of waste is calculated using the following equation.

$$Kjs = Bjs(j)\ x\ BBs^{-1}\ x\ 100\% \quad ...(7)$$

where Kjs denotes the composition by waste type (%), Bjs represents the weight of waste by type (kg), BBs is the total weight of all waste, and j indicates the waste category. The specific and general types of waste referred to in Equation (7) are presented in Table 1.

2.2. Waste Generation and Composition in Coastal Area

The methodology for assessing marine debris along the shoreline employed an area-transect approach, following the Marine Debris Monitoring Guidelines issued by the Ministry of Environment and Forestry of the Republic of Indonesia. This method was selected because it provides a representative depiction of the distribution, types, and quantities of debris accumulated in coastal zones. During

Table 1: Detailed and general composition of waste types.

No.	Detailed Waste Type	General Waste Category
1	Food waste	Organic
2	Garden waste	
3	Wood	
4	Paper/cardboard	Inorganic
5	Plastic-film	
6	Plastic-rigid	
7	Metal	
8	Fabric and textile products	
9	Rubber and leather	
10	Glass	
11	Hazardous waste	Hazardous waste
12	Nappies	Other/residual waste
13	Other waste	

the assessment, the beach area was divided into several systematically designated transects to ensure comprehensive spatial coverage. All debris found within each transect was subsequently identified, classified, and quantified according to predefined categories. The monitoring focused on debris larger than 2.5 cm, categorized as macro debris, which generally includes plastics, glass, metals, textiles, and other sizable materials. This approach enables researchers to obtain accurate data on the volume and characteristics of coastal debris, thereby supporting the development of more effective marine litter management strategies.

2.3. Waste Sampling Procedure

Waste generation and composition data were obtained from field surveys conducted in both the residential area and the coastal area. The procedure for measuring waste generation and composition data in the residential area of Kodingareng Lompo Island is as follows:

- Distribute labeled plastic bags (R1 to R7) to each sampling location one day before collection.
- Record the total number of sampling units.
- On the following day, collect the plastic bags containing the waste.
- Transport all collected waste bags to the measurement site.
- Prepare a box to be used for waste weighing.
- Prepare a weighing scale.
- Sequentially empty each sample into the measuring box and record the weight of each waste sample.
- Combine all waste samples in the measuring box and record the total weight of the waste.
- Sort the waste according to its composition categories.
- Weigh and record the mass of each waste composition category.

The procedures for measuring waste generation and composition data in the coastal area are as follows:

- Establish a transect area measuring 100 meters in length and 13 meters in width.
- Divide the transect area into five sections, each with a length of 20 meters.
- Subdivide each transect section into sub-transect quadrats measuring 5 m² and label them TR1 to TR5, which serve as the sampling areas.
- Sieve the collected material using a mesh screen with a 2.5 cm² opening size to separate meso and macro waste fractions.
- Collect samples from each sub-transect and remove any sand adhering to the waste.
- Sort and identify the waste, then weigh it according to its composition categories.

Waste sampling and measurement were conducted using a digital weighing scale with a maximum capacity of 40 kg and an accuracy level of 1 g. Prior to data collection, the scale's accuracy was verified using a reference weight to ensure measurement consistency throughout the sampling period. Waste segregation was performed directly by the research team based on predetermined composition categories in accordance with the study protocol. All sorting and weighing procedures were conducted under direct supervision of the researchers to ensure consistency in classification and measurement. Each measurement result was recorded systematically using structured observation sheets. To ensure data quality and minimize measurement error, all recorded weights were cross-checked immediately after each weighing session. Any discrepancies were re-verified before final data entry. This quality control procedure was applied consistently during the entire sampling period.

2.4. Greenhouse Gas (GHG) and Global Warming Potential (GWP)

Municipal solid waste (MSW) is an anthropogenic contributor to GHG emissions generated from landfilling and open burning (Li 2024). Solid waste management is a cross-sectoral issue that significantly affects multiple environmental and socio-economic aspects. The waste sector represents a major anthropogenic source of GHG emissions. According to the IPCC, an organization established by the World Meteorological Organization (WMO) and the United Nations Environment Programme (UNEP), its primary objective is to provide scientific information to governments at all levels to support the development of climate policies. The IPCC Guidelines for National Greenhouse Gas Inventories offer standardized methodologies for estimating and reporting GHG inventories. This study employs the Tier 1 approach, which utilizes default values provided in the IPCC Guidelines, as the required activity data are not yet available.

2.5. Research Conceptual Framework

The conceptual framework of this study begins with the identification of waste generation and composition as the basis for determining waste management practices, which are then analyzed under two scenarios: the existing conditions (Scenario 1) and an alternative scheme (Scenario 2). For each scenario, greenhouse gas (GHG) emission potentials (CO_2, CH_4, and N_2O) are calculated and subsequently converted

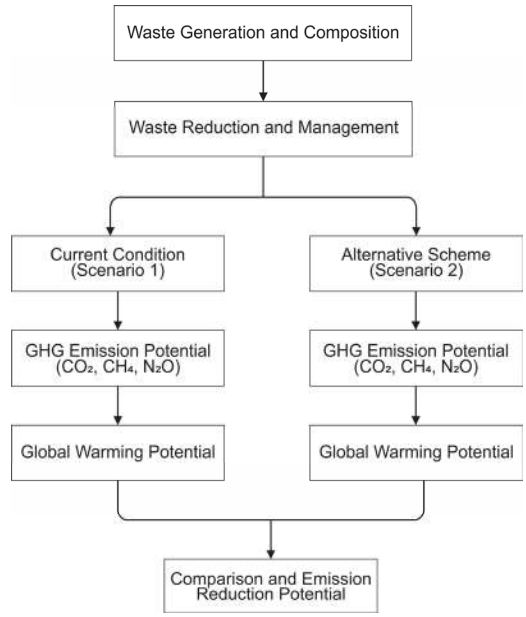


Fig. 2: Research conceptual framework.

into Global Warming Potential (GWP) values to represent their overall climate impact. The results from both scenarios are then compared to assess the magnitude and potential for emission reduction achieved through the implementation of the alternative waste management system, thereby illustrating the causal relationship between waste management practices and climate change impacts.

3. RESULTS AND DISCUSSION

3.1. Waste Generation and Composition in Residential Areas

SNI 3964:2025 provides options for classifying sample locations based on welfare level, income, electricity connection capacity, and housing type. However, such secondary data were not available from the local government or regional statistical agencies. Therefore, this study utilized secondary data derived from the research conducted by Idrus et al. (2023), which reported that the housing typology on Kodingareng Lompo Island consists of 148 permanent houses (16%), 525 semi-permanent houses (58%), and 232 non-permanent houses (26%). Accordingly, based on Equation (1), combined with population data and housing typology data as secondary sources, the calculation is as follows:

$$Ps = 0.5\sqrt{4977}$$
$$= 0.5 \quad 70.55$$
$$= 35.23 \text{ (rounded to 35 persons)}$$

Thus, the total number of individual samples (persons) selected for waste generation measurement is 35 persons. Table 2 presents the coefficient (Cd) values based on total population size.

Subsequently, the number of sampled households (Heads of Household/HH) selected for waste generation measurement was determined in accordance with Equation (2), as follows:

$$K = 35 \; x \; 5^{-1}$$
$$= 7$$

Thus, the total number of sampled households (HH) selected for waste generation measurement is 7 households. Subsequently, the calculation of the number of houses to be sampled was conducted in accordance with Equation (3), under the assumption that one house corresponds to one household (HH), and integrated with the secondary data on housing typology presented in Table 3. The categories of sampled households are shown in Fig. 3. The sampling locations are shown in Fig. 4, and their coordinates are listed in Table 4.

The results of waste generation measurements in the residential area of Kodingareng Lompo Island conducted

Table 2: Cd coefficient (SNI 3964:2025).

Total Population (persons)	Coefficient Value
≥ 5,000,000	1.5
1,000,000 - < 5,000,000	1
500,000 - < 1,000,000	1
100,000 - < 500,000	0.5
< 100,000	0.5

Table 3: Number of houses sampled.

Housing Category	Level Category (Secondary Data)	Number of Sampled Households (HH)	Number of Sampled Houses
Permanent	16%	7	1.14 (rounded to 1)
Semi-permanent	58%	7	4.06 (rounded to 4)
Non-permanent	26%	7	1.79 (rounded to 2)



Fig. 3: Categories of sampled households: (a) permanent, (b) semi-permanent, and (c) non-permanent.



Fig. 4: Sampling points.

Table 4: Sampling coordinate points.

Area	Point	Category	Coordinate Point	
			Latitude	*Longitude*
Residential Area	R1	Semi-permanent	5° 8’55.51”S	119°15’56.96”E
	R2	Semi-permanent	5° 8’44.57”S	119°15’54.55”E
	R3	Permanent	5° 8’49.89”S	119°15’54.11”E
	R4	Semi-permanent	5° 8’57.52”S	119°15’55.17”E
	R5	Semi-permanent	5° 9’0.24”S	119°15’53.35”E
	R6	Non-permanent	5° 8’43.33”S	119°15’51.48”E
	R7	Non-permanent	5° 8’48.30”S	119°15’54.49”E
Coastal Area	P	Beach	5° 9’6.69”S	119°15’50.09”E

Table 5: Measurement results and average waste generation in the residential area.

Household category	Measurement results (kg)								Total (kg)	Average waste generation (kg day^{-1})
	1	2	3	4	5	6	7	8		
Permanent	3.18	1.99	1.66	1.67	2.90	2.21	1.64	2.25	17.48	2.19
Semi-permanent	3.19	2.36	6.18	3.92	4.12	3.40	5.38	4.21	32.76	4.09
Non-permanent	0.59	0.65	0.89	0.59	0.74	0.81	0.60	0.87	5.72	0.72

Table 6: Waste generation unit.

Household category	Total (kg)	Average waste generation (kg day^{-1})	Sample size (persons)	Waste generation rate (kg person^{-1} day^{-1})
Permanent	17.48	2.19	5	0.44
Semi-permanent	32.76	4.09	20	0.20
Non-permanent	5.72	0.72	10	0.07

Table 7: Total waste generation.

Household Category	Waste generation rate (kg person^{-1} day^{-1})	Percentage of housing Categories (%)	Population (persons)	Daily waste generation (kg day^{-1})	Annual waste generation (kg yr^{-1})
Permanent	0.44	16	4977	347.99	127,017.02
Semi-permanent	0.20	58		590.95	215,698.00
Non-permanent	0.07	26		92.52	33,770.69
Total				**1,031.47**	**376,485.71**

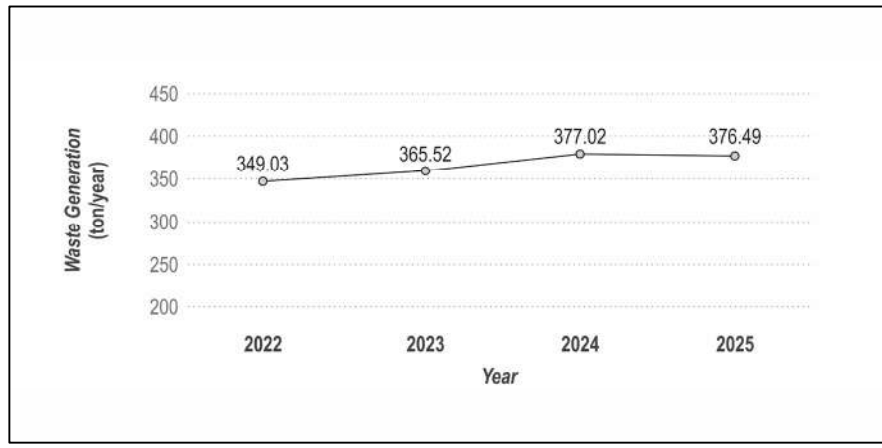


Fig. 5: Projected waste generation from residential areas on Kodingareng Lompo Island.

over eight consecutive days, along with the calculated average daily waste generation in accordance with Equation (4), are presented in Table 5. Meanwhile, the per capita waste generation rate (kg person^{-1} day^{-1}), calculated based on Equation (5), is presented in Table 6.

Tables 5 and 6 indicate that waste generation from permanent houses amounted to 17.48 kg (0.44 kg person^{-1} day^{-1}), semi-permanent houses generated 32.76 kg (0.20 kg person^{-1} day^{-1}), and non-permanent houses produced 5.72 kg (0.07 kg person^{-1} day^{-1}). The data further demonstrate that the highest waste generation originated from permanent houses, followed by semi-permanent houses, and the lowest from non-permanent houses. In general, waste generation volume shows a positive correlation with household income levels and the degree of urbanization in a given area (Kaza et al. 2018). Similar findings were reported by Popli et al. (2021), who stated that increasing per capita income is associated with higher waste generation rates. Other studies have also revealed that living standards and waste generation are closely related, whereby higher-income groups tend to generate greater amounts of waste, while lower-income groups produce relatively less waste (Zia et al. 2017). The total waste generated in the residential area of Kodingareng Lompo Island, calculated using Equation (6), is presented in Table 7.

Based on Table 7, the total waste generation from the residential area amounts to 1,031.47 kg day^{-1}, equivalent to 376,485.71 kg yr^{-1}. This total comprises 347.99 kg day^{-1} (127,017.02 kg yr^{-1}) from permanent houses, 590.95 kg

day^{-1} (215,698.00 kg yr^{-1}) from semi-permanent houses, and 92.52 kg day^{-1} (33,770.69 kg yr^{-1}) from non-permanent houses. The projected waste generation originating from the residential area is presented in Fig. 5. The measurement of waste generation in the residential area is illustrated in Fig. 6.

The Fig. 5 illustrates the projected annual waste generation originating from residential areas on Kodingareng Lompo Island for the period 2022–2025. The data reveal a gradual upward trend, beginning at 349.03 t yr^{-1} in 2022 and increasing to 365.52 t yr^{-1} in 2023. Waste generation continues to rise in 2024, reaching 377.02 t yr^{-1}, which represents the highest value within the projection period. In 2025, the projection indicates a slight decline to 376.49 t yr^{-1}; however, the overall trend still reflects an increase relative to the baseline year. These fluctuations indicate a steady growth in household waste production.

Waste composition refers to the classification of waste based on its constituent materials or components. This measurement is essential for determining an effective waste management system that aligns with the types or composition of waste and its recycling potential. Detailed data on waste composition, calculated based on Equation (7), is presented in Table 8.

Table 8 shows that garden waste constitutes the largest proportion of waste generated on Kodingareng Lompo Island, accounting for 39.28%. This is followed by other waste at 18.12%, plastic film at 13.71% and paper/cardboard at 13.30%. Wood waste accounts for 2.29%, while metal waste contributes 0.40%. Fabric/textile and rubber/leather waste represent 0.07% and 0.03%, respectively.

No glass or hazardous waste was identified during the study period. In general, organic waste constitutes 49.60% of the total waste generated, followed by inorganic waste at 31.88%, other/residual waste at 18.51%, and hazardous waste at 0%.

3.2. Waste Generation and Composition in Coastal Area

The measurement of waste generation in this study was also conducted in the coastal area. This measurement aimed to identify the quantity and types of waste stranded along the coastline of Kodingareng Lompo Island as a result of marine dynamics, such as currents and wave action. Data on stranded waste in the coastal area were obtained through direct field observation and recording, and subsequently classified according to material type. The results of the measurement and classification of stranded waste along the coast of Kodingareng Lompo Island are presented in detail in Table 9. The measurement of waste generation in the coastal area is illustrated in Fig. 7.

Table 8: Waste composition.

No.	Type of waste	Percentage (%)	General waste category
1	Food waste	8.03	Organic 49.60%
2	Garden waste	39.28	
3	Wood	2.29	
4	Paper/ cardboard	13.30	Inorganic 31.88%
5	Plastic-film	13.71	
6	Plastic-rigid	4.38	
7	Metal	0.40	
8	Fabric/textile	0.07	
9	Rubber/leather	0.03	
10	Glass	0	
11	Hazardous waste	0	Hazardous waste 0%
12	Nappies	0.39	Other/residual waste 18.51%
13	Other waste	18.12	



Fig. 6: Measurement of waste generation in the residential area.

Table 9 presents the magnitude of waste generation in the coastal area of Kodingareng Lompo Island based on waste types and observation periods. The total waste generation increased from 8.55 kg in the first month to 9.602 kg in the second month, with an average generation rate of 0.303 kg day^{-1} and a total annual accumulation of 110.42 kg yr^{-1}. In terms of composition, fabric/textile waste constitutes the largest contributor to coastal waste generation, accounting for 44.22% of the total. The next dominant waste type is plastic film, contributing 25.23%, indicating that plastic waste, particularly plastic film, remains a major issue in the coastal area. Other waste types, such as plastic-rigid, wood, glass, and nappies, exhibit relatively smaller quantities but are consistently observed across both monitoring periods. Meanwhile, metal waste shows the

Table 9: Waste generation in the coastal area.

No.	Type of waste	Waste generation (kg)		Average waste Generation (kg day^{-1})	Total waste (kg yr^{-1})	Percentage (%)
		Month 1	Month 2			
1	Wood	0.476	0.955	0.024	8.71	7.88
2	Plastic-film	1.881	2.698	0.076	27.86	25.23
3	Plastic-rigid	0.867	0.660	0.025	9.29	8.41
4	Metal	0.015	0.027	0.001	0.26	0.23
5	Fabric/textile	4.041	3.985	0.134	48.82	44.22
6	Glass	0.595	0.680	0.021	7.76	7.02
7	Nappies	0.462	0.560	0.017	6.22	5.63
8	Other waste	0.213	0.037	0.004	1.52	1.38
Total		**8.55**	**9.602**	0.303	110.42	100.00

Table 10: Total waste generation from residential and coastal areas.

No.	Type of Waste	Residential area (kg yr^{-1})	Coastal area (kg yr^{-1})	Total Waste (kg yr^{-1})	Percentage (%)
1	Food waste	30,244.00	0	30,244.00	8.03
2	Garden waste	147,889.48	0	147,889.48	39.27
3	Wood	8,612.31	8.71	8,621.01	2.29
4	Paper/cardboard	50,059.04	0	50,059.04	13.29
5	Plastic-film	51,606.57	27.86	51,634.42	13.71
6	Plastic-rigid	16,484.50	9.29	16,493.79	4.38
7	Metal	1,513.88	0.26	1,514.14	0.40
8	Fabric/textile	269.13	48.82	317.96	0.08
9	Rubber/leather	100.93	0	100.93	0.03
10	Glass	0	7.76	7.76	0.002
11	Hazardous waste	0	0	0	0
12	Nappies	1,480.24	6.22	1,486.46	0.39
13	Other waste	68,225.63	1.52	68,227.15	18.12
Total		**376,485.71**	**110.42**	**376,596.13**	**100.00**

lowest contribution, with an average share of only 0.23%, suggesting that this waste type is relatively infrequent at the study site. Overall, these findings indicate that coastal waste generation on Kodingareng Lompo Island is predominantly composed of textile and plastic materials, which may pose significant negative impacts on coastal ecosystems if not properly managed in small island coastal environments. Furthermore, the projected total waste generation from the inland (residential) and coastal areas for the year 2025 is presented in Table 10.

Based on the composition of waste generation on Kodingareng Lompo Island, the total waste generated from residential and coastal areas reaches 376,596.13 kg yr^{-1}, with the dominant contribution originating from residential areas at 376,485.71 kg yr^{-1}, while coastal areas contribute 110.42 kg yr^{-1}. This indicates that waste generation from residential areas remains highly dominant; therefore, waste management strategies should be primarily focused on the reduction and handling of waste generated from residential sources on Kodingareng Lompo Island.



Fig. 7: Measurement of waste generation in the coastal area.

3.3. Waste Reduction and Management on Kodingareng Lompo Island

3.3.1. Current Conditions (Existing)

Based on Fig. 8, waste management on Kodingareng Lompo Island remains dominated by end-of-pipe handling rather than source reduction. Of the total annual waste generation of 376,596.13 kg, only 1.37% (5,156 kg yr^{-1}) is reduced through recycling activities conducted by a single community-managed Waste Bank Unit (BSU) in collaboration with the Central Waste Bank of Makassar City. The remaining 98.63% enters the municipal waste handling system, although community participation is largely limited to informal household-level segregation. Waste segregation infrastructure and temporary storage facilities are absent, and collection services cover only about 40% of total waste

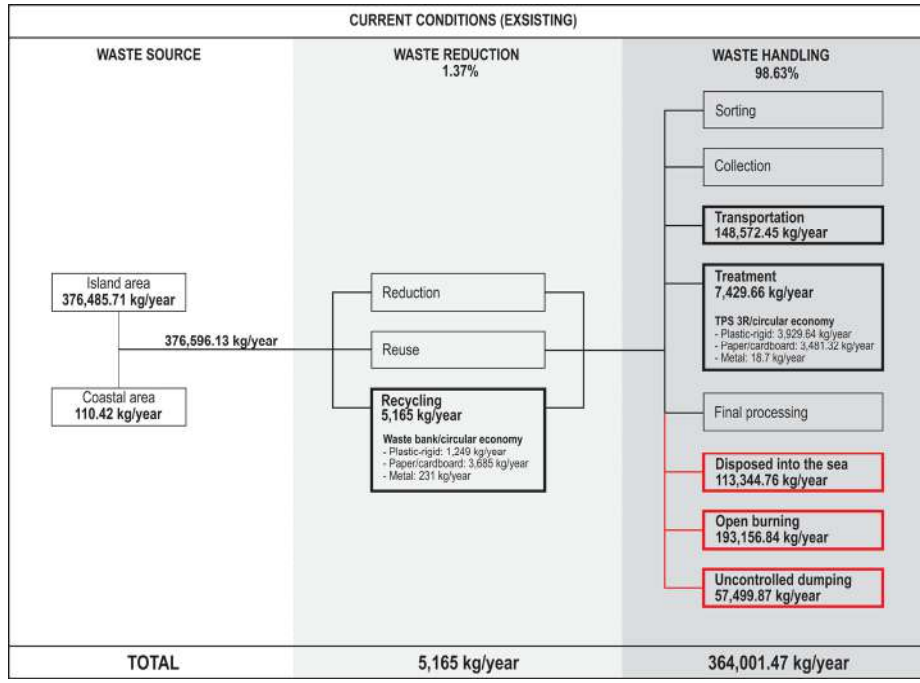


Fig. 8: Waste reduction and waste handling under current conditions.

Table 11: Waste composition resulting from environmentally unsustainable waste management practices.

No.	Type of Waste	Open burning (kg yr^{-1})	Disposed into the sea (kg yr^{-1})	Uncontrolled dumping (kg yr^{-1})
1	Food waste	18,146.40	7,561.00	4,536.60
2	Garden waste	88,733.69	36,972.37	22,183.42
3	Wood	5,172.61	2,155.25	1,293.15
4	Paper/cardboard	25,735.63	10,723.18	6,433.91
5	Plastic-film	30,980.65	12,908.61	7,745.16
6	Plastic-rigid	6,789.09	2,828.79	1,697.27
7	Metal	758.66	316.11	189.67
8	Fabric/textile	190.78	79.49	47.69
9	Rubber/leather	60.56	25.23	15.14
10	Glass	4.65	1.94	1.16
11	Hazardous waste	-	-	-
12	Nappies	891.87	371.61	222.97
13	Other waste	15,692.24	39,401.18	13,133.73
Total		**193,156.84**	**113,344.76**	**57,499.87**

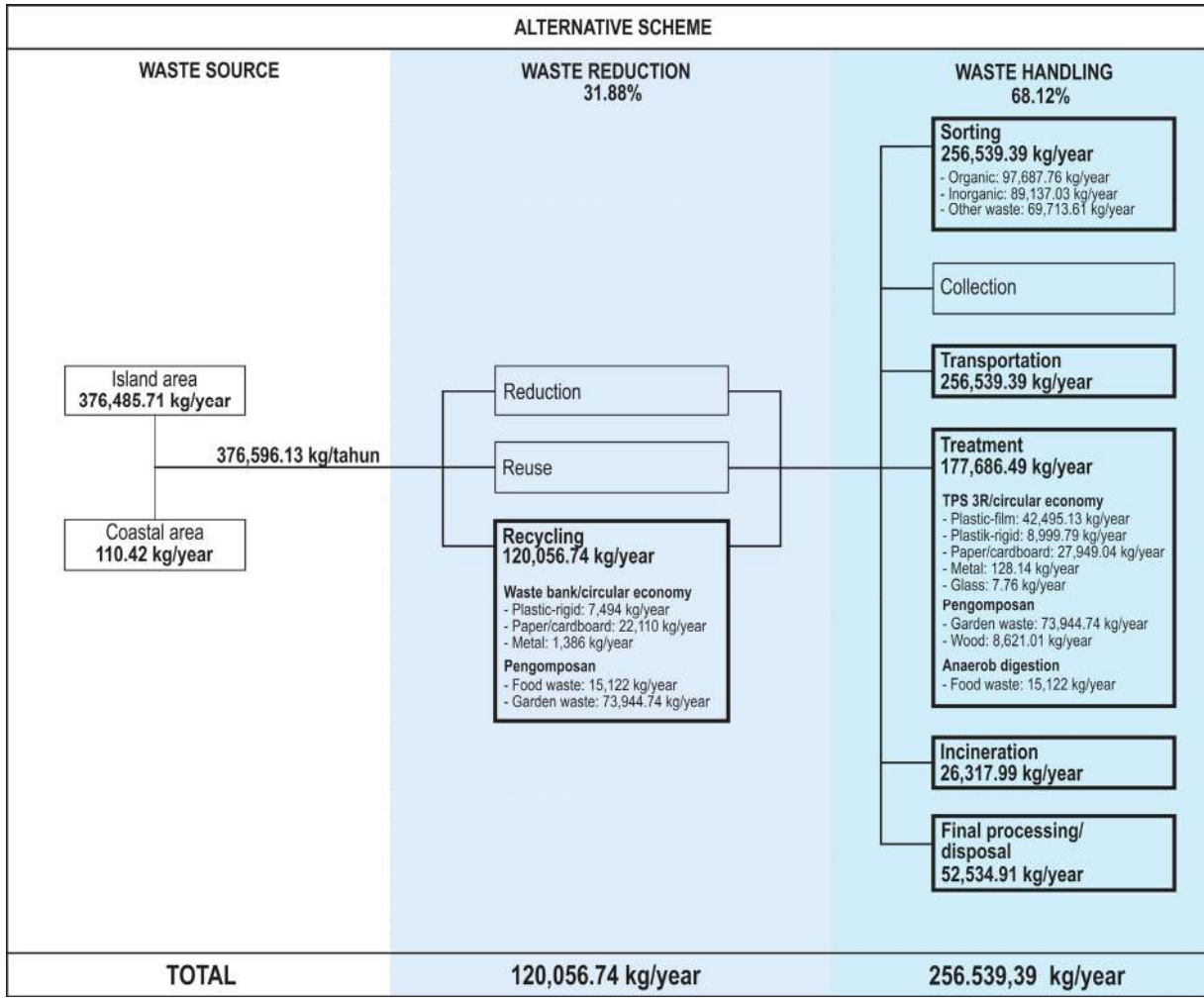


Fig. 9: Waste reduction and handling under the alternative scenario.

using a single three-wheeled collection vehicle. The TPS 3R facility contributes an additional 2% reduction (7,429.66 kg yr^{-1}), but its operation remains suboptimal due to limited management and funding. As a result, approximately 96.66% (364,001.47 kg yr^{-1}) of total waste is managed through environmentally unsound practices, including open burning (53.06%), marine disposal (31.14%), and uncontrolled dumping (15.80%), with no organic waste treatment currently implemented on the island. The waste composition associated with these environmentally unsustainable management practices is presented in Table 11.

3.3.2. Alternative Scheme

Fig. 9 presents the proposed alternative scenario, which shifts waste management toward a more sustainable and circular approach in line with Law No. 18/2008, emphasizing waste as a resource with economic value. This scenario strengthens source-based management through the expansion of Waste Bank Units (BSU) in each Community Unit (RW), collaboration with the Central Waste Bank of Makassar City, and household-scale composting. Waste reduction is projected to reach 31.88% (120,056.74 kg yr^{-1}), including 30,990 kg yr^{-1} from optimized BSU operations and 89,066.74 kg yr^{-1} from composting, assuming 50% of organic waste is managed at the household level. Environmentally sound waste handling increases to 68.12% (256,539.39 kg yr^{-1}), significantly reducing open burning, marine disposal, and uncontrolled dumping practices. The system requires mandatory household waste segregation, expansion of collection services from one to three three-wheeled vehicles to ensure full coverage, and centralized processing at the TPS 3R facility with a total capacity of 177,686.49 kg yr^{-1}. Processing consists of recycling (44.79%), composting (46.47%), anaerobic digestion (8.51%), and controlled incineration for non-recyclable combustible waste (26,317.99



Fig. 10: (a) Waste processing at the TPS 3R facility and (b) waste transportation from the island to the Central Waste Bank in Makassar City.

Table 12: CO_2 emission potential from waste transportation under existing conditions.

Fuel type	Fuel consumption (TJ)	Emission factor (kg TJ^{-1})	CO_2 emission (kg)
Gasoline	0.018	69,300	1,243.81

kg yr^{-1}), while inert residues totaling 52,534.91 kg yr^{-1} are directed to final disposal. Waste processing at the TPS 3R facility and waste transportation from the island to the Central Waste Bank in Makassar City are illustrated in Fig. 10.

Overall, the comparison between current conditions and the alternative scenario indicates that the implementation of a waste management system based on source reduction, combined with systematic waste handling from segregation to final processing, has strong potential to reduce environmental burdens caused by unmanaged waste. This alternative scenario is consistent with the targets set out in Presidential Regulation of the Republic of Indonesia No. 97 of 2017. Therefore, the implementation of the alternative scenario not only supports the achievement of national targets but also represents a relevant strategy for small islands, which face land limitations and high vulnerability to environmental, coastal, and marine pollution resulting from unmanaged waste.

3.4. GHG and GWP Potential

3.4.1. Current Conditions (Existing)

Carbon Dioxide (CO_2) Emission Potential from the Waste Transportation Process: Fuel consumption for waste transportation activities using a three-wheeled motorized vehicle on Kodingareng Lompo Island is recorded at 547.5 L yr^{-1} using one vehicle, with an average daily consumption of 1.5 L day^{-1}. The calculation of fuel consumption in energy units (terajoules, TJ) is conducted by multiplying the fuel volume (liters) by the fuel density (0.74) and the Net Calorific Value (NCV) of 44.3 TJ Gg^{-1}. Table 12 presents the estimated potential CO_2 emissions generated from the waste transportation process on Kodingareng Lompo Island, which uses gasoline fuel with a total energy consumption of 0.018 TJ. Based on the standard gasoline emission factor of 69,300 kg TJ^{-1}, the total CO_2 emissions are estimated at 1,243.81 kg yr^{-1}. CH_4 and N_2O emissions from transportation are considered negligible and therefore excluded.

CO_2 Emission Potential from Open Burning: Open burning of waste can be defined as the combustion of unwanted waste materials of various composition types, conducted in open environments or at open dumping sites, where smoke and other emissions are released directly into the atmosphere without passing through a chimney or exhaust system (IPCC 2006). The calculation is based on the estimated amount of waste (wet weight) burned, considering the dry matter content (dm), total fossil carbon content (FCF), total carbon fraction (CF), oxidation factor (OF), and the carbon to CO_2 conversion factor (44/12). The resulting CO_2 emission potential is presented in Table 13.

Table 13 presents the estimated CO_2 emissions from open burning on Kodingareng Lompo Island. Plastic waste, particularly plastic-film, contributes the highest emissions at 60,495.22 kg yr^{-1} due to its large volume, high fossil carbon fraction, and efficient combustion. Plastic-rigid follows with 13,256.90 kg yr^{-1}, while other waste types contribute 2,877.67 kg yr^{-1}. Plastics generally produce higher CO_2 emissions during open burning because of their high carbon content and combustion efficiency (Wang et al. 2023). In contrast, paper/cardboard and organic materials such as textiles, rubber, leather, and nappies generate relatively low emissions due to their low fossil carbon content and incomplete combustion. Overall, total potential CO_2 emissions from open burning reach 75,255.13 kg yr^{-1}, with plastics as the dominant source. Food waste, garden waste, wood, metals, and glass do not contribute to fossil-based CO_2 emissions, as they contain no fossil carbon fraction (FCF), in accordance with IPCC Guidelines.

Table 13: CO_2 emission potential from open burning.

Type of waste	Total waste-wet weight (kg)	dm (fraction)	CF (fraction)	FCF (fraction)	OF (fraction)	Conver-sion factor (44/12)	CO_2 Potential (kg)
Paper/cardboard	25,735.63	0.90	0.46	0.01	0.71	3.67	277.40
Plastic-film	30,980.65	1.00	0.75	1.00	0.71	3.67	60,495.22
Plastic-rigid	6,789.09	1.00	0.75	1.00	0.71	3.67	13,256.90
Fabric/textile	190.78	0.80	0.50	0.20	0.71	3.67	39.74
Rubber/leather	60.56	0.84	0.67	0.20	0.71	3.67	17.75
Nappies	891.87	0.40	0.70	0.10	0.71	3.67	65.02
Other waste	15,692.24	0.90	0.03	1.00	0.71	3.67	1,103.11
TOTAL							**75,255.13**

Table 14: CH_4 and N_2O emission potential from open burning.

Type of waste	Emission type	Total waste weight (kg)	Emission Factor (g t^{-1})	Conversion (g t^{-1} to kg kg^{-1})	Total emission (kg)
Solid waste	CH_4	192,393.52	6,500	10^{-6}	1,250.56
	N_2O	192,393.52	150	10^{-6}	28.86

Table 15: DDOCm values.

Type of waste	Waste generation (kg)	DOC (Fraction)	DOCf (Fraction)	MCF (Fraction)	DDOCm (kg)
Food waste	4,536.60	0.15	0.7	0.6	285.81
Garden waste	22,183.42	0.20	0.7	0.6	1,863.41
Wood	1,293.15	0.43	0.1	0.6	33.36
Paper/cardboard	6,433.91	0.40	0.5	0.6	772.07
Fabric/textile	47.69	0.24	0.5	0.6	3.43
Rubber/leather	15.14	0.39	0.5	0.6	1.77
Nappies	222.97	0.24	0.5	0.6	16.05
Total					**2,975.90**

Methane (CH_4) and Nitrous Oxide (N_2O) Emission Potential from Open Burning**:** CH_4 and N_2O emissions result from incomplete combustion during incineration and open burning processes, in which a significant portion of the carbon contained in the waste is not fully oxidized. These conditions may vary because waste is a heterogeneous and low-quality fuel with diverse calorific values (IPCC 2006). The potential CH_4 emissions were estimated by multiplying the total mass of waste burned by the open burning emission factors. The potential CH_4 and N_2O emissions are presented in Table 14.

The total waste amount was based on the projected quantity subjected to open burning on Kodingareng Lompo Island, excluding metal and glass since these materials contain no fossil carbon and do not produce CH_4 or N_2O emissions. Estimated CH_4 emissions from open burning reach 1,250.56 kg yr^{-1}, while N_2O emissions amount to 28.86 kg yr^{-1}. Although N_2O emissions are relatively low compared to CO_2 and CH_4, N_2O has a much higher global warming potential (GWP), 273 times greater than CO_2 (IPCC 2023a).

CH_4 Emission Potential from Landfilled Waste: One of the primary inputs in this calculation is the amount of decomposable degradable organic carbon (DDOCm) contained in the quantity and composition of disposed waste, such as food waste, paper, wood, textiles, and similar materials. The value of DDOCm is obtained by multiplying the waste generation, the fraction of degradable organic carbon in the waste (DOC), the fraction of degradable organic carbon that decomposes under anaerobic conditions (DOCf), and the portion of waste that decomposes under aerobic conditions, represented by methane correction factor (MCF). The calculated values of DDOCm and the corresponding methane emission potential are presented in Tables 15 and 16.

Table 16 shows that the total decomposable degradable organic matter (DDOCm) generated from waste on Kodingareng Lompo Island amounts to 2,975.90 kg, with

Table 16: CH_4 emission potential from landfilled waste.

Type of waste	DDOCm (kg)	F (Fraction)	CH_4/C ratio (16/12)	CH_4 potential (kg)
Solid waste	2,975.90	0.5	1.33	1,983.94

Table 17: GWP under current conditions.

Component	Gas	Emission (kg yr^{-1})	GWPh	CO_2e Emission (kg yr^{-1})
Waste transportation	CO_2	1,243.81	1	1,243.81
Open burning	CO_2	75,255.13	1	75,255.13
Open burning	CH_4	1,250.56	27	33,765.06
Open burning	N_2O	28.86	273	7,878.51
Waste disposal	CH_4	1,983.94	27	53,566.28
Total				**171,708.79**

Table 18: CO_2 emission potential from waste transportation under the alternative scenario.

Fuel type	Fuel consumption (TJ)	Emission factor (kg TJ^{-1})	CO_2 emission (kg)
Gasoline	0.054	69,300	3,731.42

the largest fraction originating from garden waste. The potential CH_4 formation is calculated by multiplying the DDOCm value by the CH_4 fraction in landfill gas (F) and the molecular weight ratio of CH_4 to C (16/12). The resulting potential CH_4 emissions from the waste disposal process are estimated at 1,983.94 kg yr^{-1}.

Global Warming Potential (GWP) of Current Conditions (Existing)**:** GWP is a metric used to assess the extent to which a greenhouse gas (GHG) contributes to global warming compared to carbon dioxide (CO_2) as the reference gas, taking into account its radiative efficiency and atmospheric lifetime (IPCC 2023b). The GWP value is obtained by multiplying the potential emissions produced by the GWP factor, which is provided as a default value in the IPCC Sixth Assessment Report (AR6). The GWP results for Scenario 1 are presented in Table 17.

Based on Table 17, the total Global Warming Potential (GWP) under current waste management practices on Kodingareng Lompo Island is 171,708.79 kg CO_2e yr^{-1}. Open burning is the main contributor, generating 75,255.13 kg CO_2e yr^{-1} from CO_2, 33,765.06 kg CO_2e yr^{-1} from CH_4, and 7,878.51 kg CO_2e yr^{-1} from N_2O due to its widespread use by residents. Additionally, CH_4 emissions from uncontrolled dumping contribute 53,566.28 kg CO_2e yr^{-1}. Overall, open burning is the dominant source of GWP on the island.

3.4.2. Alternative Scheme

CO_2 Emission Potential from Waste Transportation: Fuel consumption for waste transportation activities using three-wheeled motorized vehicles on Kodingareng Lompo Island is estimated at 1,642.5 L yr^{-1}, utilizing three vehicle units to accommodate waste collection based on the calculated waste generation results. This corresponds to an energy consumption of 0.054 TJ. Accordingly, the estimated CO_2 emission potential amounts to 3,731.42 kg yr^{-1}. The estimated CO_2 emission potential from waste transportation under the alternative scenario is presented in Table 18.

CH_4 and N_2O Emission Potential from Biological Treatment: Biological treatment through composting and anaerobic digestion of organic waste is a common practice implemented in various countries. The benefits of these treatment methods include waste volume reduction and the production of biogas as a renewable energy source. In addition, the final products can be recycled as compost fertilizer or disposed of at landfill sites (IPCC 2006). The emission values of CH_4 and N_2O are obtained by multiplying the amount of organic waste composted (kg) by the respective emission factors (g kg^{-1}). The resulting emission potentials are presented in Table 19.

Table 19 shows the estimated CH_4 and N_2O emissions from biological waste treatment on Kodingareng Lompo Island, including composting and anaerobic digestion. Composting treats 171,632.50 kg yr^{-1} of organic waste (food, garden waste, and wood waste), producing 686.53 kg yr^{-1} of CH_4 and 41.19 kg yr^{-1} of N_2O. Anaerobic digestion processes 15,122.00 kg yr^{-1} of food waste, generating 12.10 kg yr^{-1} of CH_4, while N_2O emissions are considered negligible and excluded from the calculation.

CO_2 Emission Potential from Controlled Incineration: The estimation of CO_2 emission potential from waste incineration follows a similar principle to that of open burning. The main distinction between these two processes lies in the oxidation factor (OF). According to the IPCC guidelines, when waste is

Table 19: CH_4 and N_2O emissions from biological waste treatment.

Biological treatment	Emission type	Treated Organic Waste (kg)	Emission factor (g kg^{-1})	Conversion (g to kg)	Total Emission (kg)
Composting	CH_4	171,632.50	4	0.001	686.53
	N_2O	171,632.50	0.24	0.001	41.19
Anaerobic digestion	CH_4	15,122.00	0.8	0.001	12.10

Table 20: CO_2 emission potential from controlled incineration.

Type of waste	Total waste-wet weight (kg)	dm (fraction)	CF (fraction)	FCF (fraction)	OF(fraction)	Conver-sion factor (44/12)	CO_2 Potential (kg)
Plastic-film	9,139.29	1.00	0.75	1.00	1	3.67	25,133.05
Nappies	1,486.46	0.40	0.70	0.10	1	3.67	152.61
Other waste	15,692.24	0.90	0.03	1.00	1	3.67	1,553.53
TOTAL							**26,839.20**

Table 21: CH_4 and N_2O emission potential from controlled incineration.

Type of waste	Emission type	Total waste weight (kg)	Emission factor (g t^{-1})	Conversion (g t^{-1} to kg kg^{-1})	Total emission (kg)
Solid waste	CH_4	26,317.99	60	10^{-6}	1.58
	N_2O	26,317.99	56	10^{-6}	1.47

Table 22: GWP of the alternative waste management scenario.

Component	Gas	Emission (kg yr^{-1})	GWPh	CO_2e Emission (kg yr^{-1})
Waste transportation	CO_2	3,731.42	1	3,731.42
Composting	CH_4	686.53	27	18,536.31
Composting	N_2O	41.19	273	11,245.36
Anaerobic digestion	CH_4	12.10	27	326.64
Controlled incineration	CO_2	26,839.20	1	26,839.20
Controlled incineration	CH_4	1.58	27	42.64
Controlled incineration	N_2O	1.47	273	402.35
Total				**61,123.91**

combusted either in an incinerator or through open burning, most of the carbon contained in the combustion products is oxidized to CO_2. However, in the case of waste incineration, the combustion efficiency is assumed to be nearly 100%, whereas open burning typically exhibits substantially lower efficiency. The calculated potential CO_2 emissions from waste incineration are presented in Table 20.

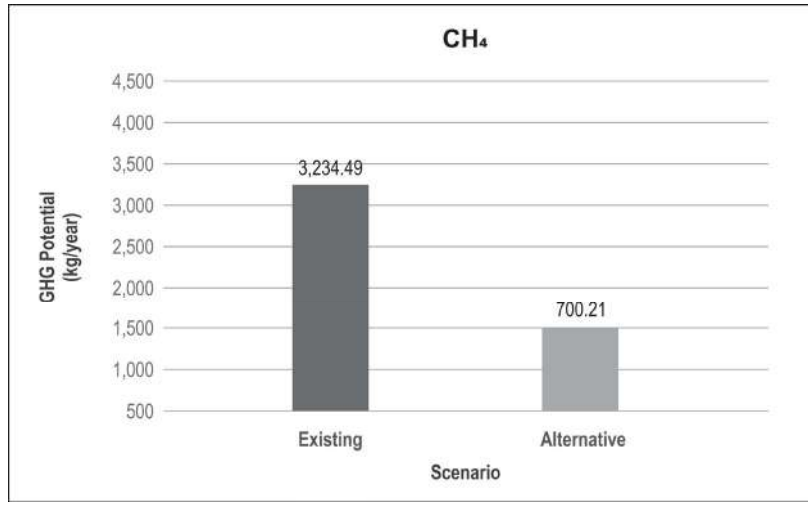
Based on the calculation results, the total potential CO_2 emissions from the incineration process amount to 26,839.20 kg yr^{-1}. Controlled incineration is applied to specific waste types, particularly plastic films that are difficult to recycle, nappies (diapers), and other combustible waste such as foam or styrofoam materials. Plastic films contribute the highest emissions, reaching 25,133.05 kg yr^{-1}, even though other waste fractions are incinerated in larger quantities. This is attributable to their high dry matter content (dm), carbon content (CF), and fossil carbon fraction, which significantly influence CO_2 emission levels.

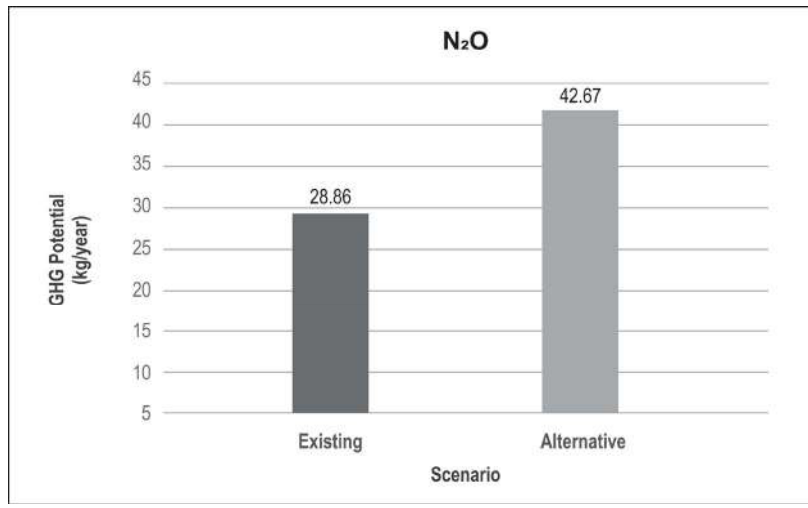
CH_4 and N_2O Emission Potential from Controlled Incineration: CH_4 emissions from solid waste incineration are estimated at 1.58 kg yr^{-1}, while N_2O emissions reach 1.47 kg yr^{-1}, both significantly lower than CO_2 emissions from the same process (Table 21). This is due to the high combustion efficiency and operating temperatures of the incinerator, which promote near-complete carbon oxidation to CO_2. As a result, CH_4 and N_2O formation is minimal and negligible compared to total greenhouse gas emissions (IPCC 2019).

Global Warming Potential (GWP) of Alternative Scheme: Table 22 shows that total GWP under the alternative waste management scheme reaches 61,123.91 kg CO_2e yr^{-1}. The largest contribution comes from controlled incineration, particularly CO_2 emissions (26,839.20 kg CO_2e yr^{-1}), followed by composting, which generates significant CH_4 (18,536.31 kg CO_2e yr^{-1}) and N_2O emissions (11,245.36 kg CO_2e yr^{-1}) due to their high GWP values. Waste transportation contributes 3,731.42 kg CO_2e yr^{-1}, while anaerobic digestion accounts for a relatively small share at 326.64 kg CO_2e yr^{-1}.

3.5. Comparison of GHG Emission Potential and GWP

The comparison between existing and alternative scenarios clearly demonstrates that emission reductions are primarily driven by structural changes in waste management practices rather than marginal technical adjustments (Fig. 11). Under current conditions, high CO_2 emissions (76,498.93 kg yr^{-1}) reflect the systemic reliance on open burning, which remains the dominant disposal method due to limited service coverage and infrastructure constraints. The 60.04% reduction in





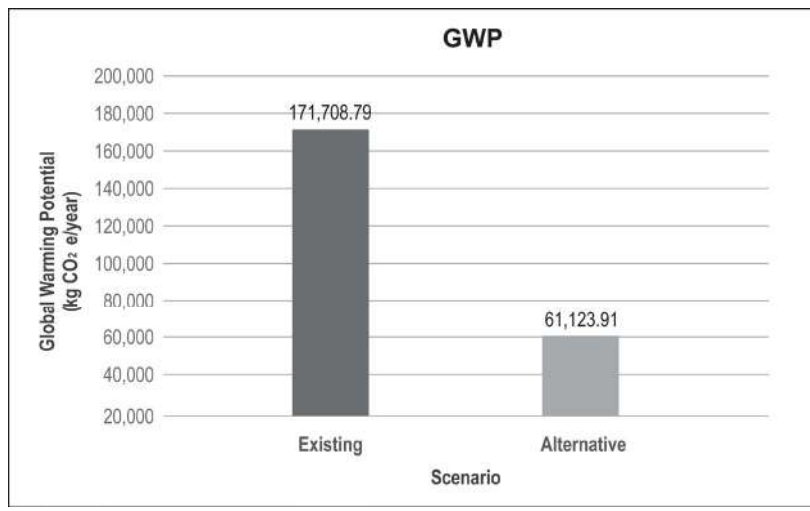


Fig 11: Comparison of GHG emissions potential and GWP under current conditions and the alternative scheme.

CO_2 emissions under the alternative scheme confirms that shifting from uncontrolled combustion to regulated treatment significantly lowers carbon emissions, particularly from plastic waste streams.

Methane (CH_4) emissions show an even more substantial decline (78.35%), indicating that reducing uncontrolled dumping and eliminating open burning are highly effective mitigation strategies. Since CH_4 has a much higher Global Warming Potential than CO_2, this reduction plays a decisive role in lowering overall GWP. Although the alternative scenario introduces biological treatment processes that generate some CH_4 and N_2O emissions, these remain considerably lower than emissions produced under uncontrolled disposal systems. The slight increase in N_2O emissions (47.84%) reflects expanded composting activities; however, this trade-off is offset by the significant decrease in methane emissions, resulting in a net climate benefit.

The overall GWP reduction of 64.40% highlights that the dominant emission sources in small island contexts are closely linked to informal and environmentally unsound practices. Open burning and unmanaged disposal not only generate direct emissions but also reflect institutional and infrastructural gaps. Consistent with previous findings (Zhang et al. 2024, Iqbal et al. 2023), the integration of controlled incineration and biological treatment within a structured waste management system offers a more climate-efficient pathway compared to reliance on open dumping and burning.

These findings imply that emission mitigation in small island environments requires systemic intervention, including mandatory source segregation, expansion of collection services, and institutional strengthening. Without addressing these structural constraints, technological alternatives alone will not achieve substantial emission reductions. Therefore, the proposed alternative scheme represents not merely a technical improvement but a governance and behavioral transformation necessary to transition toward a low-carbon and sustainable waste management system.

4. CONCLUSIONS

The research findings indicate that open burning remains the dominant waste management practice on Kodingareng Lompo Island and constitutes the largest contributor to total Global Warming Potential (GWP). This dominance is closely associated with the limited coverage of waste collection services, inadequate supporting infrastructure, and the absence of a structured household-level waste segregation system. With transportation services covering only a portion of total waste generation and the lack of adequate temporary storage facilities, residents tend to rely on open burning as a practical and rapid disposal method. Similar findings were reported by Gómez-Sanabria et al. (2022), who highlighted that the absence of reliable waste management systems often leads communities to resort to open dumping and burning as alternative solutions. Furthermore, Hajam et al. (2023) emphasized that in many developing countries, waste is commonly landfilled, openly burned, or indiscriminately disposed of without adequate consideration of its environmental and public health impacts.

From a socio-economic perspective, the persistence of open burning practices is influenced by limited operational funding, a shortage of technical personnel, and weak economic incentives for waste segregation. Although Waste Bank Units (BSU) and TPS 3R facilities are available, their limited operational capacity constrains their effectiveness in reducing environmentally unsustainable waste management practices. Community participation in recycling activities is further hindered by suboptimal collection services and the relatively low economic value of recyclable materials. These conditions underscore the need to strengthen institutional capacity, enhance community engagement, and improve infrastructure in order to achieve a more sustainable waste management system on Kodingareng Lompo Island. Factors such as public awareness, education, infrastructure availability, waste composition, and behavioral patterns represent significant barriers to effective waste management. Therefore, future strategies should prioritize waste reduction through recycling, the adoption of circular economy principles, and strengthened community participation, as also suggested by Zhang et al. (2024).

The proposed alternative scenario demonstrates a significant reduction in total GWP compared to existing conditions, indicating that source-based waste management and the implementation of circular economy principles hold substantial potential for emission mitigation. However, successful implementation depends not only on technical feasibility but also on institutional strengthening and sustainable financing mechanisms. Although a comprehensive cost-benefit analysis falls beyond the scope of this study, the expansion of waste bank units, increased revenue from recycling activities, and the reduction of environmental externalities suggest promising long-term economic feasibility.

Overall, the findings affirm that emission mitigation in small island regions requires an integrated approach encompassing infrastructure development, behavioral change, policy reinforcement, and the provision of economic incentives. Without addressing fundamental socio-economic and institutional constraints, environmentally harmful practices such as open burning are likely to persist despite the availability of technically viable alternatives.

5. REFERENCES

Adriani, Syahrul and Yunus, M., 2023. Identification of marine debris on the coast of Kodingareng Lompo Island, Sangkarrang District, Makassar City. *Wahana Laut Lestari Scientific Journal*, pp.96–107. [DOI]

Awino, F.B. and Apitz, S.E., 2024. Solid waste management in the context of the waste hierarchy and circular economy frameworks: An international critical review. *Integrated Environmental Assessment and Management*, 20(1), pp.9–35. [DOI]

Bakas, I., Sieck, M., Hermann, T., Møller Andersen, F. and Larsen, H.V., 2011. *Projections of Municipal Waste Management and Greenhouse Gases*. European Topic Centre on Sustainable Consumption and Production. ETC/SCP Working Paper No. 4/2011. Available at: https://orbit.dtu.dk/files/33440034/Projections_of_Municipal_Waste_Management.pdf

Camilleri-Fenech, M., Oliver-Solà, J., Farreny, R. and Gabarrell, X., 2018. Where do islands put their waste? A material flow and carbon footprint analysis of municipal waste management in the Maltese Islands. *Journal of Cleaner Production*, 195, pp.1609–1619. [DOI]

Gani, P.J.A. and Ikhsan, A.M., 2020. Biopore technology in green open spaces: A case study of Kodingareng Lompo Island, Sangkarrang Archipelago, Makassar. *Zonasi Architecture Journal*, 3(3), pp.346–355. [DOI]

Gómez-Sanabria, A., Kiesewetter, G., Klimont, Z., Schoepp, W. and Haberl, H., 2022. Potential for future reductions of global GHG and air pollutants from circular waste management systems. *Nature Communications*, 13(1), pp.1–12. [DOI]

Hajam, Y.A., Kumar, R. and Kumar, A., 2023. Environmental waste management strategies and vermi transformation for sustainable development. *Environmental Challenges*, 13, 100747. [DOI]

Hoy, Z.X., Phuang, Z.X., Farooque, A.A., Van Fan, Y. and Woon, K.S., 2024. Municipal solid waste management for low-carbon transition: A systematic review of artificial neural network applications for trend prediction. *Environmental Pollution*, *344*, p.123386. [DOI]

Idrus, I., Latif, S. and Rumata, N.A., 2023. Pemetaan Tipologi Perumahan Pulau Kodingareng Lompo. *Journal of Green Complex Engineering*, 1(1), pp.33-40. [DOI]

Iqbal, A., Zan, F., Liu, X. and Chen, G., 2023. Net zero greenhouse emissions and energy recovery from food waste: manifestation from modelling a city-wide food waste management plan. *Water Research*, 244, p.120481. [DOI]

Intergovernmental Panel on Climate Change (IPCC), 2006. *IPCC Guidelines for National Greenhouse Gas Inventories*. Prepared by the National Greenhouse Gas Inventories Programme. H.S. Eggleston, L. Buendia, K. Miwa, T. Ngara and K. Tanabe (eds.). IGES, Japan.

Intergovernmental Panel on Climate Change (IPCC), 2019. *Refinement to the 2006 IPCC Guidelines for National Greenhouse Gas Inventories*. E. Calvo Buendia, K. Tanabe, A. Kranjc, J. Baasansuren, M. Fukuda, S. Ngarize, A. Osako, Y. Pyrozhenko, P. Shermanau and S. Federici (eds.). IPCC, Switzerland.

Intergovernmental Panel on Climate Change (IPCC), 2023a. The Earth's energy budget, climate feedbacks and climate sensitivity. In: *Climate Change 2021 – The Physical Science Basis: Working Group I Contribution to the Sixth Assessment Report of the Intergovernmental Panel on Climate Change*. Cambridge University Press, Cambridge, pp.923–1054. [DOI]

Intergovernmental Panel on Climate Change (IPCC), 2023b. Annex VII: glossary. In: *Climate Change 2021 – The Physical Science Basis: Working Group I Contribution to the Sixth Assessment Report of the Intergovernmental Panel on Climate Change*. Cambridge University Press, Cambridge, pp.2215–2256. [DOI]

Kaza, S., Yao, L., Bhada-Tata, P. and Van Woerden, F., 2018. *What a waste 2.0: a global snapshot of solid waste management to 2050*. World Bank Publications. Available at: https://openknowledge.worldbank.org/entities/publication/d3f9d45e-115f-559b-b14f-28552410e90a

Li, R., 2024. Greenhouse gas mitigation potential via a large-scale compulsory circular waste management system. *Journal of Environmental Management*, 370, p.122425. [DOI]

National Standardization Agency of the Republic of Indonesia (BSN), 2025. *Sampling and Measuring Methods of Generation and Composition of Domestic Waste and Waste Similar to Domestic Waste*. SNI 3964:2025. BSN, Jakarta.

Nell, C.M., 2020. *Determining Spatial and Temporal Change in Household Solid Waste Composition within Stellenbosch Local Municipality*. Master's thesis, Stellenbosch University. Available at: https://hdl.handle.net/10019.1/108320

Nell, C., Schenck, G., Blaauw, D., Grobler, L. and Viljoen, K., 2022. A three-pronged approach to waste composition determination. *Journal of Environmental Management*, 303, 114203. [DOI]

Popli, K., Park, C., Han, S. and Kim, S., 2021. Prediction of solid waste generation rates in urban region of Laos using socio-demographic and economic parameters with a multilinear regression approach. *Sustainability*, 13(6), 3038. [DOI]

Rusni, N.K., 2024. The waste management issues in Makassar City: A case study of the Tamangapa landfill. *Waste Handling and Environmental Monitoring*, 1(1), pp.16–27. [DOI]

Statistics Indonesia of Makassar City, 2024. *Kecamatan Kepulauan Sangkarrang in Figures 2024*. Statistics Indonesia (BPS) of Makassar City, Makassar. Available at: https://makassarkota.bps.go.id

Wang, X., Firouzkouhi, H., Chow, J.C., Watson, J.G., Carter, W. and De Vos, A.S.M., 2023. Characterization of gas and particle emissions from open burning of household solid waste from South Africa. *Atmospheric Chemistry and Physics*, 23, pp.8921–8937. [DOI]

Zhang, Z., Chen, Z., Zhang, J., Liu, Y., Chen, L., Yang, M., Osman, A.I., Farghali, M., Liu, E., Hassan, D., Ihara, I., Lu, K., Rooney, D.W. and Yap, P., 2024. Municipal solid waste management challenges in developing regions: A comprehensive review and future perspectives for Asia and Africa. *Science of The Total Environment*, 930, 172794. [DOI]

Zia, A., Batool, S.A., Chaudhry, M.N. and Munir, S., 2017. Influence of income level and seasons on quantity and composition of municipal solid waste: A case study of the capital city of Pakistan. *Sustainability*, 9(9), 1568. [DOI]

Nature Environment and Pollution Technology
An International Quarterly Peer-Reviewed Open Access Journal

p-ISSN: 0972-6268 | e-ISSN: 2395-3454 Vol. 25 | No. 4 | Article ID D1908 | 2026

RESEARCH ARTICLE https://doi.org/10.46488/NEPT.2026.v25i04.D1908 OPEN ACCESS

Lead (Pb) Bioaccumulation and Physiological Responses of *Acanthus ilicifolius* in the Mangrove Forest, Wonorejo, Surabaya, East Java, Indonesia

Fida Rachmadiarti†, Winarsih, Herlina Fitrihidajati, Tarzan Purnomo, Sunu Kuntjoro, Reyna Novita Sari, Yeremia Ajijaya Putra Ritiau, Eza Alfian Rizqita and Farah Aisyah Nafidiastri
Department of Biology, Faculty of Mathematics and Natural Sciences, Universitas Negeri Surabaya, East Java, Indonesia
†Corresponding author: Fida Rachmadiarti; fidarachmadiarti@unesa.ac.id

ARTICLE HISTORY

Received: 19-12-2025
Revised: 15-03-2026
Accepted: 21-03-2026

KEYWORDS

Acanthus ilicifolius
Bioindicators
Translocation factor
Heavy metals
Lead bioaccumulation
Mangrove forest
Chlorophyll

CITE THIS ARTICLE

Rachmadiarti, F., Winarsih, Fitrihidajati, H., Purnomo, T., Kuntjoro, S., Sari, R. N., Ritiau, Y. A. P., Rizqita, E. A. and Nafidiastri, F. A., 2026. Lead (Pb) bioaccumulation and physiological responses of *Acanthus ilicifolius* in the mangrove forest, Wonorejo, Surabaya, East Java, Indonesia. *Nature Environment and Pollution Technology*, 25(4), D1908. https://doi.org/10.46488/NEPT.2026.v25i04.D1908

COPYRIGHT & LICENCE

© 2026 The Authors
Open Access under CC BY 4.0.

PUBLISHED BY
TECHNOSCIENCE PUBLICATIONS

ABSTRACT

Mangrove ecosystems in coastal areas are susceptible to heavy metal inputs from various anthropogenic activities. One of the heavy metals frequently found in coastal environments is lead (Pb), which can accumulate in sediments and mangrove vegetation. The Jeruju plant (Acanthus ilicifolius) is a mangrove species capable of absorbing heavy metals from the environment, making it a potential bioindicator of pollution. This study aims to evaluate Pb levels in seawater and sediments, as well as Pb levels in the roots, stems, and leaves of *A. ilicifolius*; to evaluate its function as a bioaccumulator and translocator; to determine the chlorophyll and protein contents of A. ilicifolius; and to analyze the relationship between Pb levels in *A. ilicifolius*, chlorophyll content, and protein content of *A. ilicifolius*. Sampling was conducted at three stations, with three replicates at each station. Lead (Pb) concentration analysis was performed using atomic absorption spectrophotometry (AAS), while protein content analysis was conducted using the Kjeldahl method and chlorophyll content using spectrophotometry. Data were analyzed using descriptive analysis and Pearson's correlation analysis using SPSS. The results showed that the highest Pb concentrations were found in sediments at 1.135–1.440 mg kg^{-1}. In plant tissues, the highest Pb concentrations were detected in roots, ranging from 0.294–0.380 mg kg^{-1}, and were lower in stems and leaves. Leaf chlorophyll content ranged from 1.133–1.487 mg g^{-1}, while protein content ranged from 13.667 to 16.542%. Correlation analysis results indicated a positive relationship between Pb levels and plant physiological parameters. These findings suggest that *A. ilicifolius* is still capable of tolerating the presence of Pb without experiencing significant physiological disturbances, making it a potential bioindicator for heavy metal contamination in mangrove ecosystems.

1. INTRODUCTION

The Wonorejo Mangrove Forest Area in Surabaya is one of the mangrove ecosystems in an urban coastal zone with high levels of anthropogenic activity. Domestic and industrial activities, as well as river flows that discharge into the area, can introduce various pollutants into the mangrove environment, including heavy metals. Heavy metals such as lead (Pb) are among the contaminants frequently found in coastal ecosystems due to their persistence and tendency to accumulate in sediments and living organisms (Rahman et al. 2021, Chowdhury et al. 2021, Rachmadiarti et al. 2024). Heavy metal pollution in coastal areas generally originates from industrial activities, domestic waste, and river flows that carry pollutants from the mainland to estuarine and mangrove areas (Mariwy et al. 2024).

In mangrove ecosystems, sediments serve as the primary medium for heavy metal accumulation because metal particles tend to bind to organic matter and fine

particles that settle to the bottom of the water. Heavy metals accumulated in sediments can be absorbed by mangrove roots and subsequently distributed throughout various plant tissues. This process has led to mangrove plants being frequently used as bioindicators and bioaccumulators to assess the presence of heavy metals in coastal environments. Research by Permatasari et al. (2024) reports that several mangrove species can absorb and accumulate heavy metals, such as Pb, Cd, and Zn, from sediments and surrounding waters. This ability makes mangrove plants potentially useful as bioindicators and bioaccumulators in studies of heavy metal pollution in coastal ecosystems.

One of the plant species commonly found in mangrove ecosystems is the Jeruju (*Acanthus ilicifolius*). This plant has a well-developed root system that interacts directly with sediment, potentially allowing it to absorb various heavy metals from its surrounding environment. Several studies indicate that *A. ilicifolius* can accumulate various heavy metals, including Pb, Cu, and Zn, in plant tissues, with differing distribution patterns among plant organs. Generally, metal concentrations are higher in roots than in stems and leaves because roots are the first parts to interact directly with contaminated sediments (Siregar et al. 2025). Additionally, mangrove plants' ability to accumulate metals can affect their physiological condition, including changes in chlorophyll and protein content in response to heavy metal stress (Rahman et al. 2021). Furthermore, the ability of mangroves to accumulate heavy metals demonstrates their potential as bioindicators and phytoremediation agents in polluted coastal ecosystems (Rahman et al. 2021, Siregar et al. 2025).

Although numerous studies have documented mangrove plants' ability to absorb heavy metals, information on the bioaccumulation of lead (Pb) in *A. ilicifolius* and its impact on plant physiological responses in urban mangrove ecosystems remains relatively limited. Therefore, a study on Pb bioaccumulation in *A. ilicifolius* and the physiological responses of its leaves, such as chlorophyll and protein content, is needed to understand the effects of heavy metal exposure on the physiological condition of mangrove plants. Against this background, the objective of this study is to evaluate Pb concentrations in water and sediment, as well as Pb concentrations in the roots, stems, and leaves of Jeruju (*Acanthus ilicifolius*); to evaluate its function as a bioaccumulator and translocator; to determine the chlorophyll and protein content in the leaves of Jeruju (*Acanthus ilicifolius*); and to analyze the relationship between Pb levels in Jeruju (*Acanthus ilicifolius*), chlorophyll content, and protein content.

2. MATERIALS AND METHODS

2.1. Research Location

This study was conducted in the Wonorejo Mangrove Forest, Surabaya. Observations were made at three stations with three replicates (Fig. 1). Research samples included water, sediment, and Jeruju (*Acanthus ilicifolius*), as well as measurements of physicochemical parameters in the water. Analysis of heavy

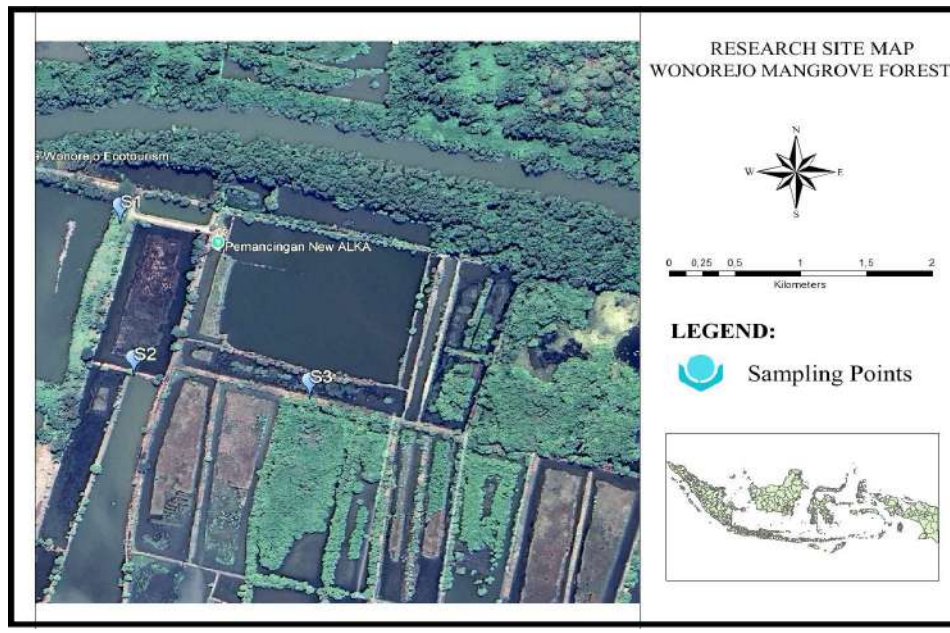


Fig. 1: Sampling site.

metal (Pb) levels and protein content was conducted at the Nutrition Laboratory of Airlangga University.

2.2. Sample Collection

Water samples for measuring physicochemical parameters were collected in the Wonorejo Mangrove Forest habitat in Surabaya. The study included three observation stations with three replicates. The instruments used in this study included a Gea S-006 stem thermometer for temperature, a Milwaukee pH meter for water pH, an Atago S-28 refractometer for salinity, and a Milwaukee MW-600 DO meter for dissolved oxygen. Materials used in this study included roots, stems, and leaves of the Jeruju tree, seawater, marine sediment, clean water, distilled water, Na_2SO_4-HgO (catalyst), 96% ethanol, 65% HNO_3, H_2O_2, 0.2 N HCl, 1% NaOH, 4% H_3BO_4, 98% H_2SO_4, and a 1000 ppm Pb solution.

Water and sediment samples were collected for lead (Pb) heavy-metal testing at three observation stations, with three replicates per station. Water samples were collected in volumes of approximately 1 L using polyethylene (PE) sample bottles that had been rinsed with distilled water and the sample water. Each water sample was preserved by adding HNO_3 until the pH was <2 to prevent changes in metal content. Sediment samples were placed in PE plastic bags.

Sampling of *A. ilicifolius* plants for testing lead (Pb) levels, protein content, and chlorophyll levels was conducted at three observation stations, with three replicates per station. *A. ilicifolius* samples were collected from plants of relatively similar height and size. A total of 150 g of *A. ilicifolius* from each of the root, stem, and leaf sections in healthy condition was then cleaned and placed into PE plastic bags. All water, sediment, and Jeruju plant samples were labeled and named, then stored in a cool box at approximately 4°C. The samples were then transported to the laboratory for analysis.

2.3. Analysis of Pb Metal Content

Heavy metal analysis of plant samples (roots, stems, and leaves) and sediments was performed using the dry ashing method. Solid samples weighing 3.5 g were placed in porcelain crucibles and heated in a furnace at 800°C for 3 h, until a grayish-white ash formed. After cooling to room temperature, the ash was dissolved in 1 mL of concentrated nitric acid (HNO_3, 65%) and 10 mL of deionized water, then homogenized and filtered through a Whatman No. 42 filter paper. The filtrate was transferred to a volumetric flask and diluted with deionized water to the final volume. Heavy metal analysis of water samples was performed nondestructively. Water samples were preserved by adding concentrated HNO_3 until the pH was <2 immediately after field sampling to prevent changes in metal concentrations, then filtered using Whatman No. 42 filter paper prior to analysis. All samples were analyzed using Shimadzu AA-7000 atomic absorption spectrophotometry (AAS) at a wavelength of 283.3 nm for Pb. Calibration curves were prepared using Pb standard solutions prepared from 1000 ppm stock solutions. Each series of analyses was performed in duplicate with a relative percent difference (RPD) $\leq$ 10% and included reagent blank testing to correct for potential contamination from the chemicals used.

2.4. Analysis of Bioconcentration Factor and Translocation Factor

The bioaccumulation of the heavy metal Pb in *A. ilicifolius* plants was analyzed using the Bioconcentration Factor (BCF) and the Translocation Factor (TF) (Baker 1981, Takarina & Pin 2017). The BCF value was calculated using the formula:

$$BCF = \frac{C\ Leaf}{C\ Sediment} \quad ...(1)$$

where (C leaf) is the Pb concentration in the leaf tissue (mg kg^{-1}) and (C sediment) is the Pb concentration in the sediment (mg kg^{-1}). A BCF value > 1 indicates that the plant accumulates Pb from the sediment (accumulator), a BCF value = 1 indicates equal concentrations in plant tissue and sediment, and a BCF value < 1 indicates limited accumulation or excluder characteristics. The TF value is calculated using the formula:

$$TF = \frac{C\ Leaf}{C\ Root} \quad ...(2)$$

where (C leaf) is the Pb concentration in the leaf tissue (mg kg^{-1}) and (C root) is the Pb concentration in the root tissue (mg kg^{-1}). An interpretation of a TF value < 1 indicates that more heavy metals are retained in the roots, while a TF value > 1 indicates that heavy metals are translocated to the upper parts of the plant.

2.5. Analysis of Chlorophyll Content

The analysis was conducted using spectrophotometry. A 1 g sample of healthy, thoroughly washed *A. ilicifolius* leaves was ground with 100 mL of 96% ethanol until fine, then filtered to obtain a liquid extract. The absorbance of the extract was measured using a V1100D UV-Vis spectrophotometer at 665 nm and 649 nm. Chlorophyll content was calculated using the formula (Wintermans & De Mots 1965, Li et al. 2022):

Chlorophyll a = 25.8 × A665 – 7.6 x A649

Chlorophyll b = 25.8 × A649 – 7.7 x A665

Chlorophyll total = 20 × A649 + 6.1 x A665

2.6. Analysis of Protein Content

The analysis was performed using the Kjeldahl method

(Kjeldahl 1883) by grinding 0.2 g of the dried sample, placing it in a Kjeldahl flask, and adding a Na_2SO_4-HgO catalyst mixture in a 2:1 ratio and 2 mL of H_2SO_4. The sample was digested for approximately 2.5 h until the solution became clear. After cooling, 15 mL of distilled water was added, followed by distillation with the addition of 10 mL of NaOH. The distillate was collected in an Erlenmeyer flask. The distillate collected in the H_3BO_4 solution, which contains an indicator, turns green. Next, the solution was titrated with 0.2 N HCl until the color changed from green to pink, indicating the endpoint. During the analysis, a blank digestion was also performed using the same procedure without adding a sample to correct for possible nitrogen contamination from the reagents. The total nitrogen content obtained was then converted to protein content using a conversion factor of 6.25, yielding the sample's protein content value. The nitrogen content was calculated using the following formula:

$$\% \text{ N} = \frac{mL\ HCl \times N\ HCl \times 14.008}{Biomass\ (mg)} \times\ 100\%$$

The protein content was then determined by multiplying the nitrogen content by a conversion factor:

$$\% \text{ Protein} = \% \text{ N} \times 6.25$$

3. RESULTS AND DISCUSSION

Research conducted in the Wonorejo Mangrove Forest in Surabaya yielded the following data:

3.1. Lead (Pb) Heavy Metal Content in Jeruju (*Acanthus ilicifolius*)

Based on the analysis of lead (Pb) concentrations in water at all research stations, the levels remain below the quality standard set by Government Regulation of the Republic of Indonesia No. 22 of 2021, which is 0.03 mg L^{-1}. Pb concentrations in the water range from 0.022–0.029 mg L^{-1}. In sediments, Pb concentrations range from 1.135–1.440 mg kg^{-1}, which is significantly below the Threshold Effect Level (TEL) of 35 mg kg^{-1} set by the Canadian Council of Ministers of the Environment (CCME) in 2002. Lead concentrations in *A. ilicifolius* plants showed variation across plant parts, with the highest values in the roots (0.294–0.380 mg kg^{-1}), followed by the stems (0.271–0.307 mg kg^{-1}), and the lowest in the leaves (0.109–0.198 mg kg^{-1}). These values remain below the heavy metal reference range of <30 mg kg^{-1}, as defined by Kabata Pendias (2011) (Table 1), indicating that the *A. ilicifolius* plants at the study site are still in normal condition and have the potential to serve as bioindicators of heavy metal presence in mangrove ecosystems.

Heavy metal lead (Pb) concentrations in water that remain below quality standards are influenced by anthropogenic activities such as domestic wastewater discharge, industrial activities, and transportation, which carry various pollutants into estuarine areas (Zhang et al. 2020). Additionally, tidal dynamics and sedimentation processes also play a role in distributing heavy metals in coastal waters, causing metal concentrations in the water column to fluctuate between study sites (Wang et al. 2021). Lead (Pb) concentrations in sediments remain well below the Threshold Effect Level (TEL). Sediments serve as the primary medium for heavy metal accumulation in coastal ecosystems because metal particles tend to bind with organic matter and fine minerals that settle on the seabed (Zhang et al. 2020, Kumar et al. 2022). Therefore, heavy metal concentrations in sediments are generally higher than in water because sediments act as long-term storage sites for various metal contaminants (Liu et al. 2021).

The distribution of Pb in *A. ilicifolius* shows variations in concentration across different plant organs. The highest concentration was found in the roots, followed by the stems, with the lowest concentration in the leaves. This distribution pattern indicates that the roots are the primary part of the plant involved in the uptake of heavy metals from sediments and surrounding water bodies. Mangrove plants possess a complex root system, enabling them to absorb and accumulate various heavy metals from the sedimentary environment through adsorption and ion transport processes

Table 1: Lead (Pb) heavy metal content in water, sediments, and Jeruju plants (*Acanthus ilicifolius*).

Parameters	Station I	Station II	Station III	Quality standards
Water (mg L^{-1})	0.029 ± 0.001	0.026 ± 0.001	0.022 ± 0.001	0.03 mg L^{-1}*
Sediment (mg kg^{-1})	1.440 ± 0.005	1.381 ± 0.007	1.135 ± 0.006	35 mg kg^{-1}**
Roots (mg kg^{-1})	0.364 ± 0.004	0.380 ± 0.005	0.294 ± 0.008	<30 mg kg^{-1}***
Stem (mg kg^{-1})	0.307 ± 0.008	0.299 ± 0.009	0.271 ± 0.007	
Leaves (mg kg^{-1})	0.198 ± 0.005	0.133 ± 0.007	0.109 ± 0.005	

Note: The data shown are the means of the replicates ± standard deviations.
*Government Regulation (PP) Number 22 of 2021.
**Sediment quality guideline from Canadian Council of Ministers of the Environment (CCME) of 2002.
***Reference value for heavy metals in plants from Kabata Pendias (2011).

(Rahman et al. 2022). Higher metal accumulation in roots than in other plant organs is also frequently observed in various mangrove species as an adaptive mechanism against environmental stress caused by metal contamination (Chen et al. 2023). Higher Pb accumulation in roots compared to stems and leaves indicates the presence of physiological mechanisms in plants that limit the movement of heavy metals toward photosynthetic tissues. Mangrove plants are known to retain heavy metals in root tissues through binding to cell walls, precipitation within vacuoles, and the formation of complexes with organic compounds such as phytochelatins and metallothioneins (Sarker et al. 2021, Huang et al. 2023). These mechanisms help reduce potential damage to leaf tissues, thereby ensuring that photosynthesis and plant metabolism can continue to function optimally (Rahman et al. 2022). Therefore, the lower Pb concentration in the leaves of the mangrove in this study indicates a process of restricting heavy metal translocation from the roots to the upper parts of the plant.

3.2. Bioaccumulation of Lead (Pb) in Jeruju Plants (*Acanthus ilicifolius*)

Based on the analysis results, different bioconcentration factor (BCF) and translocation factor (TF) values were obtained at each station (Table 2). The BCF values ranged from 0.096 to 0.137, indicating values < 1, while the TF values ranged from 0.351 to 0.543, indicating values < 1.

The bioconcentration factor (BCF) and translocation factor (TF) values for the Jeruju plant (*Acanthus ilicifolius*) indicate the plant's ability to absorb and distribute lead (Pb) from aquatic environments and sediments. The BCF value patterns obtained indicate that *A. ilicifolius* can accumulate Pb from its surrounding environment, consistent with the results in Table 1, where Pb concentrations in plant tissues are relatively higher in roots than in stems and leaves. These conditions indicate that the root system plays a crucial role in heavy metal uptake from the sediment substrate, which serves as the primary medium for metal accumulation in coastal ecosystems (Rahman et al. 2022). Sediments are known to bind heavy metals through interactions with organic matter and fine mineral particles, making them the primary source of metals that can be absorbed by mangrove plants (Kumar et al. 2022, Liu et al. 2021).

The TF values obtained indicate that some of the Pb absorbed by the roots can be translocated to the stem and leaves, although the concentration is lower than that in the roots. This pattern is consistent with the distribution of Pb in plant tissues shown in Table 1, where metal accumulation is more dominant in the root organs. This condition indicates that plants possess a physiological mechanism that limits the movement of heavy metals toward photosynthetic tissues, as a form of adaptation to environments containing metals. Mangrove plants are known to retain heavy metals in root tissues through binding to cell walls, storage in vacuoles, and the formation of complexes with certain organic compounds, thereby controlling the translocation of metals to upper plant organs (Sarker et al. 2021, Huang et al. 2023). These mechanisms allow plants to maintain their physiological functions even when in environments containing heavy metals.

3.3. Chlorophyll Content in Jeruju Leaves (*Acanthus ilicifolius*)

Based on the analysis results from the three research stations, chlorophyll values ranging from 1.133–1.487 mg g^{-1} were obtained. These values fall within the range of chlorophyll concentrations reported in the study by Li et al. (2018), which ranged from 0.87–15.92 mg g^{-1}.

Chlorophyll levels in the leaves of *A. ilicifolius* at the three research stations showed a relatively uniform range of values. This condition indicates that the plants'

Table 2: Bioconcentration factor (BCF) and translocation factor (TF) values in the Jeruju plant (Acanthus ilicifolius).

Station	BCF	Interpretation	TF	Interpretation
1	0.137 ± 0.003	<1	0.543 ± 0.006	**<1**
2	0.097 ± 0.004		0.351 ± 0.015	
3	0.096 ± 0.004		0.370 ± 0.025	

Note: The data shown are the means of the replicates ± standard deviations.

Table 3: Chlorophyll content in Jeruju leaves (*Acanthus ilicifolius*).

Station	Chlorophyll (mg g^{-1})	Reference range (mg g^{-1})*
1	1.487 ± 0.128	0.87–15.92
2	1.483 ± 0.126	
3	1.133 ± 0.127	

Note: The data shown are the means of the replicates ± standard deviations.
*Reference value for chlorophyll content from Li et al. (2018).

photosynthetic activity is still proceeding normally despite the presence of Pb in the aquatic environment and sediments, as shown in Table 1 Chlorophyll is the primary pigment involved in photosynthesis; therefore, its presence is significantly influenced by environmental conditions and the availability of nutrients that support plant metabolism (Li et al. 2022). Under conditions of high heavy metal exposure, chlorophyll content in leaves generally decreases due to damage to the chloroplast structure and disruption of photosynthetic pigment biosynthesis (Sharma et al. 2021). However, the relatively stable chlorophyll values in this study indicate that Pb concentrations at the study site remain at levels tolerable to the mangrove plants.

This relates to mangrove plants' ability to regulate the distribution of heavy metals within their tissues. As shown in Tables 1 and 2, the majority of Pb tends to accumulate in the roots, so only a small portion is translocated to the leaves. This mechanism helps protect photosynthetic tissues from the toxic effects of heavy metals, ensuring the photosynthetic process continues optimally (Chen et al. 2023). Stable photosynthetic activity supports plant metabolic processes, including the formation of organic compounds such as proteins, which play a crucial role in plant growth and adaptation to environmental stress (Huang et al. 2023). Thus, the chlorophyll levels in the leaves of the mangrove indicate that the plants are still capable of maintaining their physiological functions despite exposure to lead (Pb).

3.4. Protein Content of Jeruju Leaves *(Acanthus ilicifolius)*

Based on the analysis results from the three observation stations, protein values ranged from 13.667 to 16.542%, with the highest at Station 1 and the lowest at Station 3 (Table 4). These values are lower than those reported by Batubara et al. (2025) for A. ilicifolius leaves (19.00–19.95%), which may reflect differences in growing location, soil conditions, and genetic factors (Batubara et al. 2025).

Stations with higher leaf Pb concentrations also had relatively higher protein levels. This indicates that although the detected Pb concentrations were still in the low range, the presence of this heavy metal could still trigger physiological responses in plants, including changes in protein metabolism as part of an adaptive mechanism to environmental stress. At relatively low to moderate levels of heavy metal exposure, plants can maintain their metabolic functions by increasing the synthesis of specific proteins involved in heavy metal detoxification. These proteins can function as heavy metal chelators, thereby reducing the potential for damage to plant cells. This mechanism is part of the plant's physiological defense system, enabling plants to survive in heavy-metal-contaminated environments. Several studies report that plants can produce metal-binding proteins, such as metallothionein and phytochelatin, which bind and neutralize heavy metals entering plant tissues (Alsafran et al. 2022, Rahman et al. 2021).

Table 4: Protein content in Jeruju leaves (*Acanthus ilicifolius*).

Station	Protein content (%)	Reference value (%)*
1	16.542 ± 0.253	19.00-19.95
2	15.479 ± 0.191	
3	13.667 ± 0.130	

Note: Protein content was calculated as % N × 6.25 using dried samples. The data shown are the means ± standard deviations of three replicates. *Reference value for protein content from Batubara et al. (2025).

In addition to serving as a response to heavy metal exposure, leaf protein content is also influenced by the plant's physiological condition and the availability of nutrients in its growing environment. Plants growing in environments with relatively good water quality generally maintain photosynthetic activity and nitrogen metabolism, which support protein synthesis. This aligns with research findings indicating that environmental quality at the study site remains within acceptable standards, allowing the mangrove plants to maintain normal metabolic functions. Thus, the relatively high protein content in *A. ilicifolius* leaves indicates that this plant not only has good nutritional value but also can adapt to the presence of heavy metals in the mangrove ecosystem (Chowdhury et al. 2021, Zhao et al. 2022).

3.5. Analysis of Heavy Metal (Pb) and Protein Content in Jeruju (*Acanthus ilicifolius*)

Based on the analysis using SPSS version 22.0 for Windows, correlation coefficients ranged from 0.574 to 0.919. The highest correlation value was found in the relationship between protein and stem Pb (r = 0.919), while the lowest correlation value was found in the relationship between leaf Pb and root Pb (r = 0.574) (Table 5). These values indicate that most parameters show a positive correlation, with varying degrees of strength, suggesting a relationship between the distribution of Pb in plant tissues and the physiological condition of *A. ilicifolius*.

Correlation analysis revealed a relationship between Pb content in the tissues of Jeruju (*Acanthus ilicifolius*) plants and physiological parameters, namely chlorophyll and protein. A fairly strong positive correlation was also observed between Pb in the roots, stems, and leaves, indicating that Pb absorbed by the root system can be distributed to other plant tissues through translocation. This pattern aligns with research showing that mangrove plants can absorb and accumulate heavy metals from sediments via their roots, after

Table 5: Correlation analysis of heavy metal (Pb) levels in Jeruju (*Acanthus ilicifolius*) with protein and chlorophyll content.

	Pb roots	Pb stems	Pb leaf	Leaf protein	Chlorophyll
Pb roots	1	0.822	0.574	0.842	0.896
Pb stems	0.822	1	0.772	0.919	0.870
Pb leaf	0.574	0.772	1	0.912	0.646
Leaf protein	0.842	0.919	0.912	1	0.820
Chlorophyll	0.896	0.870	0.646	0.820	1

Table 6: Physical and chemical water quality data.

Parameters	Station I	Station II	Station III	Quality standards
pH	6.7 ± 0.58	7 ± 1.00	7 ± 0.05	6–9
Temperature (°C)	29.3 ± 0.31	29.2 ± 0.10	33 ± 2.24	Deviation of 3°C from air temperature
Salinity (ppt)	4.33 ± 0.57	5.67 ± 0.57	1.67 ± 0.57	-
DO (mg L^{-1})	7.5 ± 0.02	6.4 ± 0.03	8.1 ± 0.03	≥ 3 mg L^{-1}

Note: The data shown are the means of the replicates ± standard deviations.

which some of the metals can be translocated to the plant's stems and leaves (Rahman et al. 2021). This ability indicates that the mangrove plays a crucial role in the bioaccumulation of metals within the mangrove ecosystem and holds potential as a phytoremediator in water bodies contaminated with heavy metals.

The positive correlation between Pb content and chlorophyll and protein levels indicates that the presence of Pb at the measured concentrations at the study site has not yet caused significant toxic effects on the plants' physiological activities. Several studies suggest that mangrove plants possess tolerance mechanisms against heavy metals, including metal binding in specific tissues and metabolic activities that aid in metal detoxification within plant cells. This allows plants to maintain physiological functions, such as photosynthesis and protein synthesis, even in environments containing heavy metals (Siregar et al. 2025). This tolerance makes *A. ilicifolius* a potential bioindicator and bioaccumulator of heavy metals in coastal and mangrove ecosystems.

3.6. Physical and Chemical Quality of Mangrove Forests

Based on the physical and chemical water quality analysis (Table 6), the measurement results from the three stations still meet the marine water quality standards set forth in Government Regulation No. 22 of 2021 on the Implementation of Environmental Protection and Management, falling under Class III. pH values ranged from 6.7–7.0, which aligns with the pH quality standard of 6–9 for all water classes. Water temperature ranged from 29.2–33°C, remaining within the normal range for tropical coastal ecosystems. Salinity ranged from 1.67–5.67 ppt, reflecting the characteristics of a mangrove transitional zone influenced by tides and freshwater inflow from rivers. Dissolved oxygen (DO) levels range from 6.4–8.1 mg L^{-1}, well above the minimum quality standard of 3 mg L^{-1}.

Water quality parameters indicate that the water conditions still support the life of coastal organisms, including mangrove vegetation such as Jeruju (*Acanthus ilicifolius*). Relatively stable pH values indicate that the water is neither too acidic nor too alkaline, thus remaining within a range suitable for biological processes in the mangrove ecosystem. Temperature and salinity parameters also play a crucial role in determining water conditions, as both influence organismal metabolic activity and various chemical processes occurring in the water (Ali et al. 2021, Kumar et al. 2022).

The dissolved oxygen (DO) levels measured at the study site indicate that DO remains sufficient to support the respiratory activity of aquatic organisms. Dissolved oxygen is a key indicator of water quality as it is directly linked to ecosystem balance and microbial activity in the sediment. Good DO conditions indicate that the decomposition of organic matter and water circulation in the area are still proceeding effectively (Wang et al. 2021). These relatively stable water quality conditions are also consistent with the results in Table 1, which show that Pb concentrations in seawater and sediments remain within a relatively low range.

These favorable water-quality conditions also help maintain the physiological functions of the mangrove plants observed in this study. As shown in previous results, Pb tends to accumulate at higher levels in roots than in stems and leaves, suggesting a mechanism controlling metal distribution within plant tissues. This mechanism allows the photosynthetic tissues to continue functioning properly,

as reflected in the relatively stable chlorophyll and leaf protein levels. Mangrove plants are known to possess various physiological adaptation mechanisms to maintain metabolic activity even in environments containing certain levels of heavy metals (Chen et al. 2023, Huang et al. 2023).

4. CONCLUSIONS

This study shows that Pb concentrations in water, sediments, and the tissues of the Jeruju plant (*Acanthus ilicifolius*), including roots, stems, and leaves, at the three study sites exhibit distribution patterns across both environmental media and plant tissues. The highest Pb concentrations were found in sediments at 1.135–1.440 mg kg^{-1}, followed by root tissues at 0.294–0.380 mg kg^{-1}, while concentrations in stems and leaves were relatively lower. This pattern indicates that sediment serves as the primary accumulation site for Pb in the aquatic environment, while the roots of the *A. ilicifolius* plant play a crucial role in the uptake of metals from sediment, which are then translocated to other parts of the plant. Nevertheless, Pb levels in water, sediment, and plant tissues remain within tolerable ranges and do not indicate contamination exceeding safe limits. This is supported by the chlorophyll content of *A. ilicifolius* leaves, ranging from 1.133–1.487 mg g^{-1}, and protein levels of 13.667 to 16.542%, which still indicate a good physiological condition of the plants. Correlation analysis results also indicate a positive relationship between Pb content in plant tissues and plant physiological parameters, with strong correlations found between protein and stem Pb ($r = 0.919$) and protein and leaf Pb ($r = 0.912$), as well as between chlorophyll and root Pb ($r = 0.896$) and chlorophyll and stem Pb ($r = 0.870$). This indicates that Pb accumulation in *A. ilicifolius* plants remains tolerable, without causing significant negative impacts on their physiological condition. Therefore, the Jeruju plant (*Acanthus ilicifolius*) shows potential as a bioindicator of lead (Pb) in coastal aquatic ecosystems.

5. ACKNOWLEDGEMENT

The authors are grateful to the people around the river for their assistance during the sampling session and to Didik for his assistance in the molecular laboratory. This research received funding from LPPM with grant number 309/UN38/HK/PP/2024.

6. REFERENCES

Ali, H., Khan, E. and Ilahi, I., 2021. Environmental chemistry and ecotoxicology of hazardous heavy metals. *Journal of Chemistry*, pp. 1–14. [DOI]

Alsafran, M., Usman, K., Ahmed, B., Rizwan, M., Saleem, M.H. and Al Jabri, H., 2022. Understanding the phytoremediation mechanisms of potentially toxic elements: A proteomic overview of recent advances. *Frontiers in Plant Science*, *13*, 881242. [DOI]

Baker, A.J.M., 1981. Accumulators and excluders strategies in the response of plants to heavy metals. *Journal of Plant Nutrition*, 3(1–4), pp. 643–654. [DOI]

Canadian Council of Ministers of the Environment (CCME), 2002. *Canadian Sediment Quality Guidelines for the Protection of Aquatic Life: Summary Tables*. Winnipeg: Canadian Council of Ministers of the Environment. Available at: https://support.esdat.net/Environmental%20Standards/canada/ccme/sedqg_summary_table.pdf (Accessed: 10 August 2025).

Chen, Y., Wang, C., Liu, H. and Zhang, J., 2023. Heavy metal accumulation and detoxification strategies in mangrove plants: A review. *Marine Pollution Bulletin*, 188, 114672. [DOI]

Chowdhury, A., Naz, A. and Maiti, S.K., 2021. Bioaccumulation of potentially toxic elements in three mangrove species and human health risk due to their ethnobotanical uses. *Environmental Science and Pollution Research*, *28*, 1–18. [DOI]

Huang, L., Li, J., Wang, Y. and Chen, G., 2023. Physiological responses and detoxification mechanisms of mangrove plants exposed to heavy metal stress. *Environmental Research*, 216, 114708.

Kabata Pendias, A., 2011. *Trace Elements in Soils and Plants*. 4th edn. Boca Raton: CRC Press. [DOI]

Kjeldahl, J., 1883. Neue Methode zur Bestimmung des Stickstoffs in Organischen Körpern, *Zeitschrift für Analytische Chemie*, 22, pp. 366–382.

Kumar, V., Sharma, A. and Pandita, S., 2022. Heavy metals in sediments of coastal ecosystems: Sources, distribution and ecological risks. *Environmental Monitoring and Assessment*, 194, 354. [DOI]

Li, J., Hu, W., Lu, Z., Meng, F., Cong, R., Li, X., Ren, T. and Lu, J., 2022. Imbalance between nitrogen and potassium fertilization influences potassium deficiency symptoms in winter oilseed rape (*Brassica napus* L.) leaves. *The Crop Journal*, 10(2), pp. 565–576. [DOI]

Li, Y., He, N., Hou, J., Xu, L., Liu, C., Zhang, J., Wang, Q. and Wu, X., 2018. Factors influencing leaf chlorophyll content in natural forests at the biome scale. *Frontiers in Ecology and Evolution*, 6, 64. [DOI]

Liu, X., Song, Q., Tang, Y. and Li, W., 2021. Distribution characteristics and ecological risk assessment of heavy metals in sediments. *Science of the Total Environment*, 755, 142649. [DOI]

Mariwy, A., Dulanlebit, Y.H. and Ode, A., 2024. Bioaccumulation of lead metal (Pb) by mangrove plants in Ambon coastal waters. *Indonesian Journal of Chemical Research*, 12(1), pp. 71–78.

Murdinah, M. 2009. *Effect of Extracting and Aging Agents on the Quality of Carrageenan from Seaweed Eucheuma cottonii*. Indonesia: UGM Fisheries and Marine Affairs with the Research Center for Marine and Fisheries Product Processing and Biotechnology.

Peraturan Pemerintah Republik Indonesia (PP). 2021. Peraturan Pemerintah Nomor 22 Tahun 2021 tentang Penyelenggaraan Perlindungan dan Pengelolaan Lingkungan Hidup (Baku Mutu Air Laut – Lampiran VIII). Available at: https://peraturan.bpk.go.id/Details/161852/pp-no-22-tahun-2021 (Accessed: 10 August 2025).

Permatasari, F.D., Aditya, H.F. and Mindari, W., 2024. Phytoremediation potential of mangrove species in lead contaminated coastal areas. *Jurnal Ilmiah Pertanian*, 22(1).

Rachmadiarti, F., Fitrihidajati, H., Purnomo, T., Kuntjoro, S., Nafidiastri, F.A., Yolanda, R., Ambarwati, R., Anggorowati, D., Budijastuti, W., Faizah, U. and Putriarti, D., 2024. Bioaccumulation of lead (Pb) and cadmium (Cd) in *Padina australis* Hauck at Palang Beach, Tuban, East Java, Indonesia. *Nature Environment & Pollution Technology*, 23(3), pp. 1507–1516. [DOI]

Rahman, M., Hossain, M., Islam, M. and Rahman, M., 2022. Heavy metal accumulation and translocation in mangrove plants growing in coastal ecosystems. *Environmental Science and Pollution Research*, 29, pp. 39245–39257. [DOI]

Rahman, M.S., Saha, N., Ahmed, A. S. S., Babu, S. M. O. F., Islam, A. R. M. T., Begum, B. A., Jolly, Y. N., Akhter, S. and Choudhury, T.R.,

2021. Depth related dynamics of physicochemical characteristics and heavy metal accumulation in mangrove sediment and plant: *Acanthus ilicifolius* as a potential phytoextractor. *Marine Pollution Bulletin*, 173, 113160. [DOI]

Sarker, U., Oba, S. and Daramy, M., 2021. Mechanisms of heavy metal tolerance in plants: Physiological and molecular perspectives. *Plants*, 10(12), 2590.

Sharma, A., Nagpal, A. and Singh, J., 2021. Impact of heavy metals on photosynthesis and chlorophyll metabolism in plants. *Environmental Science and Pollution Research*, 28, pp. 239–252. [DOI]

Siregar, E.S., Jumilawaty, E., Tanjung, M., Syafitri, A., Kusmana, C., Basyuni, M. and Rahmania, R., 2025. Bioaccumulation of heavy metals by Acanthus ilicifolius in polluted mangrove ecosystems. *Emerging Science Journal*, *9*(2), 557–568. [DOI]

Takarina, N.D. and Pin, T.G., 2017. Bioconcentration factor (BCF) and translocation factor (TF) of heavy metals in mangrove trees of Blanakan fish farm. *Makara Journal of Science*, 21(2), pp. 79–83. [DOI]

Wang, J., Liu, G., Liu, H. and Lam, P., 2021. Multivariate statistical evaluation of heavy metal contamination in coastal environments. *Marine Pollution Bulletin*, 164, 112036. [DOI]

Wintermans, J.G.F.M. and De Mots, A., 1965. Spectrophotometric characteristics of chlorophylls a and b and their pheophytins in ethanol. *Biochimica et Biophysica Acta*, 109(2), pp. 448–453. [DOI]

Zhang, C., Nie, S., Liang, J., Zeng, G., Wu, H., Hua, S., Liu, J. and Yuan, Y., 2020. Levels, sources and ecological risks of heavy metals in sediments from a typical urban river in China using PCA and PMF. *Ecological Indicators*, 117, 106630. [DOI]

Zhao, P., Sanganyado, E., Wang, T., Sun, Z., Jiang, Z., Zeng, M., Huang, Z., Li, Y., Li, P., Bi, R. and Liu, W., 2022. Accumulation of nutrients and potentially toxic elements in plants and fishes in restored mangrove ecosystems in South China. *Science of the Total Environment*, *838*, 156471. [DOI]

Nature Environment and Pollution Technology
An International Quarterly Peer-Reviewed Open Access Journal

p-ISSN: 0972-6268 | e-ISSN: 2395-3454 Vol. 25 | No. 4 | Article ID B4428 | 2026

RESEARCH ARTICLE https://doi.org/10.46488/NEPT.2026.v25i04.B4428 OPEN ACCESS

A Comprehensive Review on Biostimulants for Sustainable Agriculture: Global Market Trends and Experimental Challenges

Rajeev Kumar[1], Narendra Kumar[2], Pooja Vijayaraghavan[1], Anshuman Shah[1,3], Sanskriti Sanvi[1] and Ravi Kant Singh[1]†

[1]Amity Institute of Biotechnology, Amity University, Sector 125, Noida, Uttar Pradesh, 201301, India
[2]Department of Biotechnology, Noida Institute of Engineering and Technology, Greater Noida, 201306, Uttar Pradesh, India
[3]ICAR-National Institute for Plant Biotechnology, Pusa Campus, New Delhi-110012, India
†Corresponding author: Ravi Kant Singh, rksingh1@amity.edu

ARTICLE HISTORY

Received: 19-01-2026
Revised: 23-03-2026
Accepted: 08-04-2026

KEYWORDS

Biostimulants
Crop quality improvement
Sustainable agriculture
Biofertilizers

CITE THIS ARTICLE

Kumar, R., Kumar, N., Vijayaraghavan, P., Shah, A., Sanvi, S., and Singh, R. K., 2026. A comprehensive review on biostimulants for sustainable agriculture: Global market trends and experimental challenges. *Nature Environment and Pollution Technology*, 25(4), B4428. https://doi.org/10.46488/NEPT.2026.v25i04.B4428

COPYRIGHT & LICENCE

© 2026 The Authors
Open Access under CC BY 4.0.

PUBLISHED BY

TECHNOSCIENCE PUBLICATIONS

ABSTRACT

Biostimulants are substances, either natural or synthetic, that enhance plant growth without functioning as fertilizers or pesticides. According to the European Biostimulants Industry Council and EU regulations, biostimulants improve the efficiency of nutrient use, help plants withstand challenging conditions, and increase crop yields by activating specific plant functions. Unlike biofertilizers, which supply nutrients through living microbes, biostimulants influence plant development and interactions with beneficial microbes. The main types include enzyme formulations, beneficial microbes such as fungi and bacteria that promote growth, natural soil-derived acids, digested proteins, amino acids, and extracts from plants and seaweed. These products enhance root development, nutrient absorption, water regulation, and stress resistance. As climate change, soil degradation, and the demand for sustainable agriculture intensify, biostimulants present a promising alternative to chemical fertilizers by strengthening crop resilience and supporting environmental health. The global biostimulants market was approximately USD 3.0 billion in 2022 and is projected to reach USD 5.4–6.85 billion by 2027–2030, driven largely by microbial and liquid formulations. Europe leads in biostimulant adoption, but rapid growth is also occurring in Asia–Pacific, particularly in India, which represents a significant and expanding market. Despite ongoing challenges related to regulations, testing, and quality assurance, biostimulants are emerging as vital tools for sustainable farming and food security.

1. INTRODUCTION

The increasingly interconnected global economy continues to heighten the importance of agricultural systems in supporting human populations. As the world's population surpasses 8 billion and economic growth accelerates, the demand for vital commodities such as food, fiber, and biofuels has surged (OECD/FAO 2024, Anderson 2023). However, the limited availability of arable land increasingly restricts expansion. To meet these demands, agriculture has intensified, notably through widespread use of synthetic fertilizers, which raises significant environmental concerns. Global climatic changes and local adverse conditions are increasingly limiting agricultural productivity and crop quality. Environmental stressors, including elevated atmospheric CO_2, global warming, soil salinization, desertification, and nutrient imbalances caused by toxicity or deficiencies, adversely impact plant growth, development, yield, and quality.

In severe cases, these factors have caused species decline and localized extinctions. Empirical studies show that abiotic stressors have reduced yields of

major crops by over 50% (Sharma 2024, Arif et al. 2025, Baars et al. 2023, Jan et al. 2025, Hussain et al. 2023, Mandal et al. 2023, Kopecká et al. 2023). For example, rice (Oryza sativa) yields dropped by 15% with every 1 °C increase in temperature from 1979 to 2003 (Impa et al. 2021). Furthermore, climate variability increases plant vulnerability to pathogens, worsening growing conditions (Kumar et al. 2023, Jing et al. 2024, Wang et al. 2018). At the same time, urbanization and climate-driven land degradation reduce arable land, posing additional risks to global food security, especially as food production must double by 2050 to meet the growing population's needs (Seifollahi-Aghmiuni et al. 2022, Bununu et al. 2023, Ranjithkumar 2025).

In response to mounting pressures, the Green Revolution and subsequent agricultural intensification have relied heavily on synthetic fertilizers and pesticides. However, nutrient uptake remains inefficient, with only 10–20% of nutrients absorbed by plants and as little as 0.1% of pesticides reaching their intended targets. These chemicals often cause environmental contamination, disrupt soil microbial communities, and pollute water bodies (Thwaites et al. 2025, Daszkiewicz 2022, Saleem et al. 2024, FAO et al. 2021, Ansari et al. 2024, Meena et al. 2020, Bhardwaj et al. 2022). Consequently, reducing chemical inputs is vital for sustainable agriculture. Biostimulants (BSs) present promising alternatives due to their bioactivity, non-toxicity to non-target organisms, and environmental persistence. Incorporating biostimulants into modern crop management reflects a growing emphasis on environmentally sustainable, efficient practices. BSs contribute to nutrient cycling, stress tolerance, and microbial interactions, making them valuable tools for resilient and productive farming (Rouphael & Colla 2020a, Khoulati et al. 2025a).

Although research on agricultural biostimulants is still emerging, their potential is significant. Continued studies on their mechanisms can lead to optimized applications (Baltazar et al. 2021, Roche et al. 2024, Bhupenchandra et al. 2022, Johnson et al. 2024). Recent plant science research increasingly supports the role of biostimulants in enhancing crop productivity and resilience. This review explores the various types and functions of biostimulants, along with the challenges, market prospects, and sustainability issues involved**.**

2. MATERIALS AND METHODS

2.1. Data Source and Search Strategy

In this study, we utilized the Scopus database to gather articles related to biostimulants and sustainable agriculture, with data collection completed on January 12, 2026. The analysis of this data is presented in Fig. 1. Our search included keywords such as "biostimulant," "biofertilizer," "plant growth promoter," and "microbial inoculant," along with phrases like "sustainable agriculture," "sustainable farming," "agricultural sustainability," "environmentally friendly agriculture," and "environmentally friendly farming." Only articles published between 2015 and 2025 were considered. We extracted information on the articles themselves, their authors, countries, institutions, journals, keywords, and citation counts.

2.2. Inclusion and Exclusion Criteria

To maintain consistency and focus, we included only

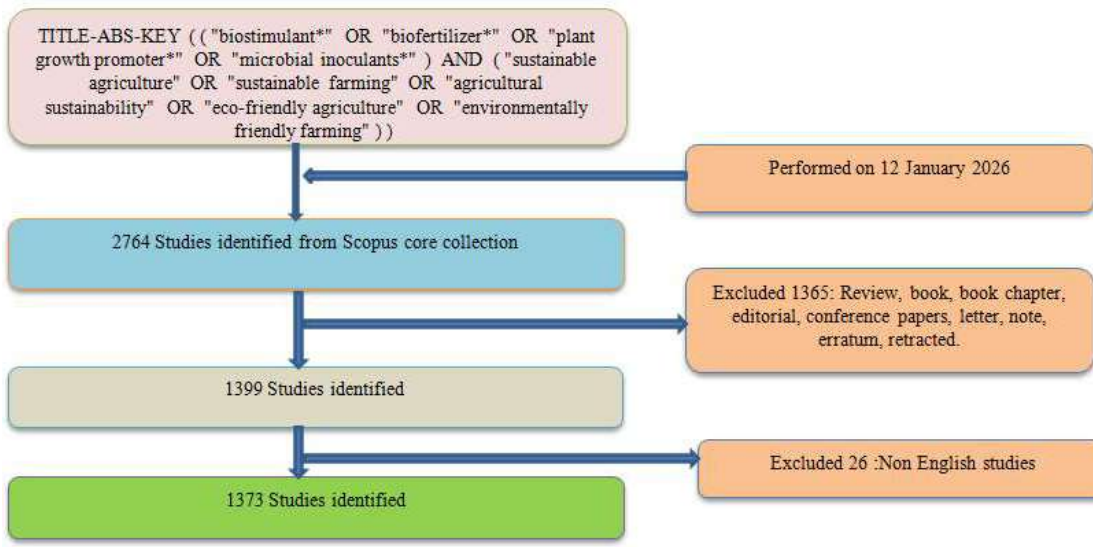


Fig. 1: Strategy for data retrieval and collection.

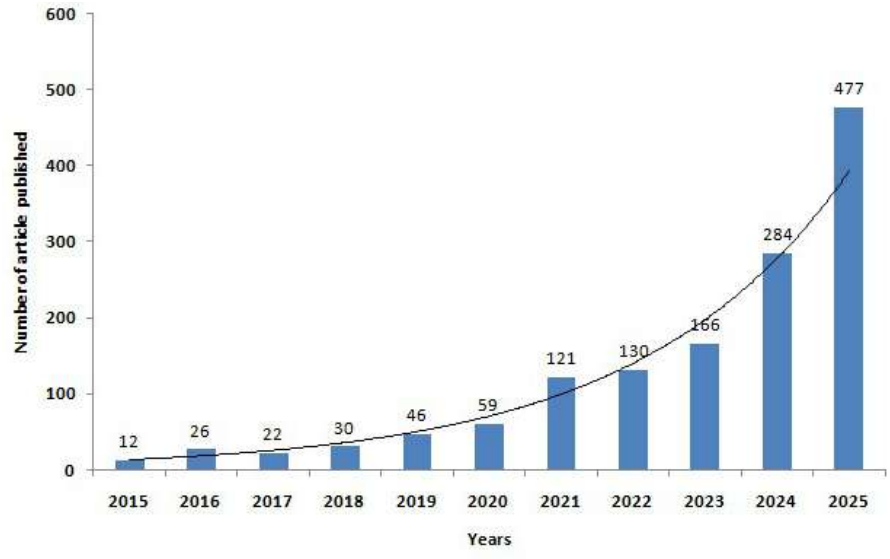


Fig. 2: Publication trend in the number of articles related to biostimulants for sustainable agriculture in the past decade.

documents labeled as 'articles.' This approach prioritized original research, which typically presents clear methods and primary data. We manually reviewed the most cited articles on the topic to ensure no significant works were overlooked. We excluded reviews, book chapters, short surveys, notes, books, and retracted papers, as they often lack sufficient data or comprehensive analysis. Nonetheless, we verified that excluding these types did not omit any major contributions relevant to our study.

2.3. Research Trends on Biostimulants for Sustainable Agriculture

We evaluated annual research growth by analyzing the publication years of relevant articles. Fig. 2 illustrates the distribution of publications from 2015 to 2025. The findings reveal a growing interest among researchers in biostimulants for sustainable agriculture. A search of electronic databases identified 2,764 records, of which 1,391 were excluded based on the study's criteria, leaving 1,373 articles for further review.

Several reasons drive the upward trend in academic research. This has facilitated the development of practical methods for using biostimulants in sustainable farming. This increase in research activity has resulted in notable achievements, advancing sustainable solutions in agriculture.

2.4. Subject Area Distribution

A total of 1,373 articles were distributed across 25 subject categories. The largest proportion of publications was in Agricultural and Biological Sciences (39%), followed by Environmental Science (15%), Biochemistry, Genetics and Molecular Biology (12%), and Immunology and Microbiology (8%) (Fig. 3).

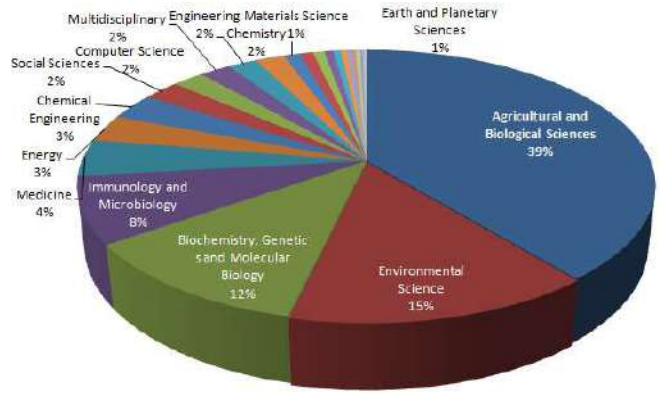


Fig. 3: Subject-wise distribution of articles related to biostimulants for sustainable agriculture in the past decade.

2.5. Most Productive Countries

As demonstrated in Fig. 4, a total of 1,373 publications were produced by researchers from 110 countries and regions, with the top 10 nations contributing to biostimulants research for sustainable agriculture. India led with 272 publications, followed by Italy with 155, China with 144, the USA with 86, and Brazil with 79. Fig. 4 also analyzes co-authored papers involving scholars from different countries on this topic. The data reveal that China has a notably higher number of international collaborations in this field. Publications from China, the USA, and Italy account for over 40% of all articles published (Fig. 4).

2.6. Biostimulants: A Solution to Mitigate Agricultural Problems

In recent years, modern agricultural systems have faced the complex challenge of simultaneously ensuring global food security while promoting sustainable farming practices. On the one hand, there is a pressing need to implement highly efficient agricultural methods that increase crop productivity to satisfy the demands of a rapidly growing population. On the other hand, these methods must adhere to environmentally friendly principles that safeguard environmental health and human well-being. To intensify production, the widespread use of mineral fertilizers and agrochemicals has become standard. However, the overuse and long-term application of these chemicals have caused significant adverse effects, including soil degradation, declining crop yields over time, and pollution of air, water, and land ecosystems (Selvan et al. 2023, Gomiero et al. 2011). These issues raise serious concerns about environmental sustainability and public health.

In response, the adoption of biobased products, such as biostimulants and biofertilizers, has gained attention as a promising approach to enhance crop yields, improve nutrient absorption, mitigate abiotic stress, and align agricultural practices with sustainability goals. Derived from natural sources, these bio-products differ fundamentally from conventional soil conditioners in origin, composition, and biological activity. Both biostimulants and biofertilizers are non-toxic to plants, soil, and consumers, making them safer alternatives to chemical inputs. While biofertilizers supply nutrients through active microbial processes like nitrogen fixation and phosphate solubilization, biostimulants primarily influence plant physiology and rhizosphere interactions without serving as direct nutrient sources (Calvo et al. 2014, Rouphael & Colla 2020a, 2020b, Bhupenchandra et al. 2020).

Biostimulants are a diverse group of natural or synthetic inputs that enhance plant performance by activating innate biological processes rather than directly supplying nutrients (Fig. 5). They aid in improving nutrient uptake and utilization efficiency, increase tolerance to abiotic stresses such as drought, salinity, and heat, and can enhance crop quality while promoting more sustainable production methods (Bhupenchandra et al. 2020, Du Jardin 2015). According to the European Biostimulants Industry Council (EBIC 2016), biostimulants are substances and/or microorganisms applied to plants or the rhizosphere that stimulate natural processes, leading to improved nutrient absorption, nutrient use efficiency, stress tolerance, and crop quality. From a regulatory perspective, European Regulation (EU) 2019/1009 defines plant biostimulants as products that

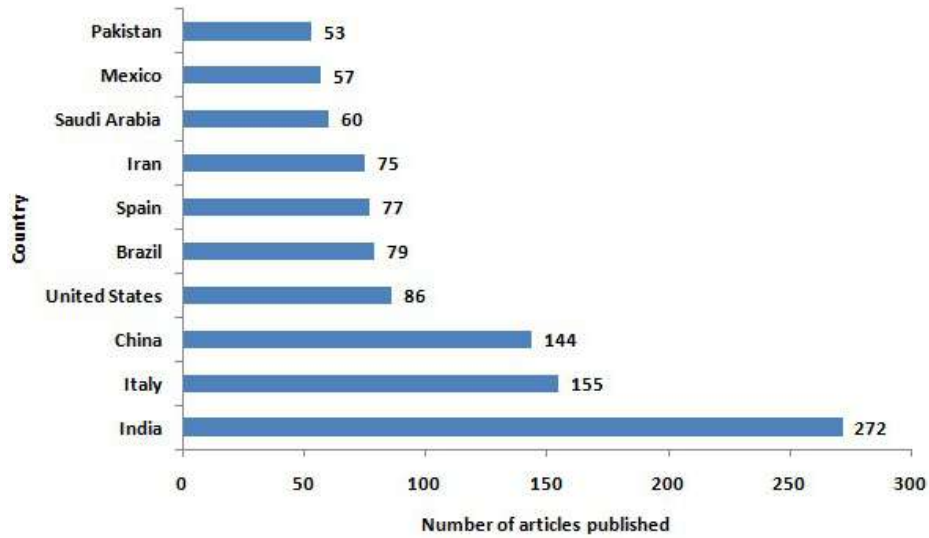


Fig. 4: Top 10 countries publishing the highest number of articles.

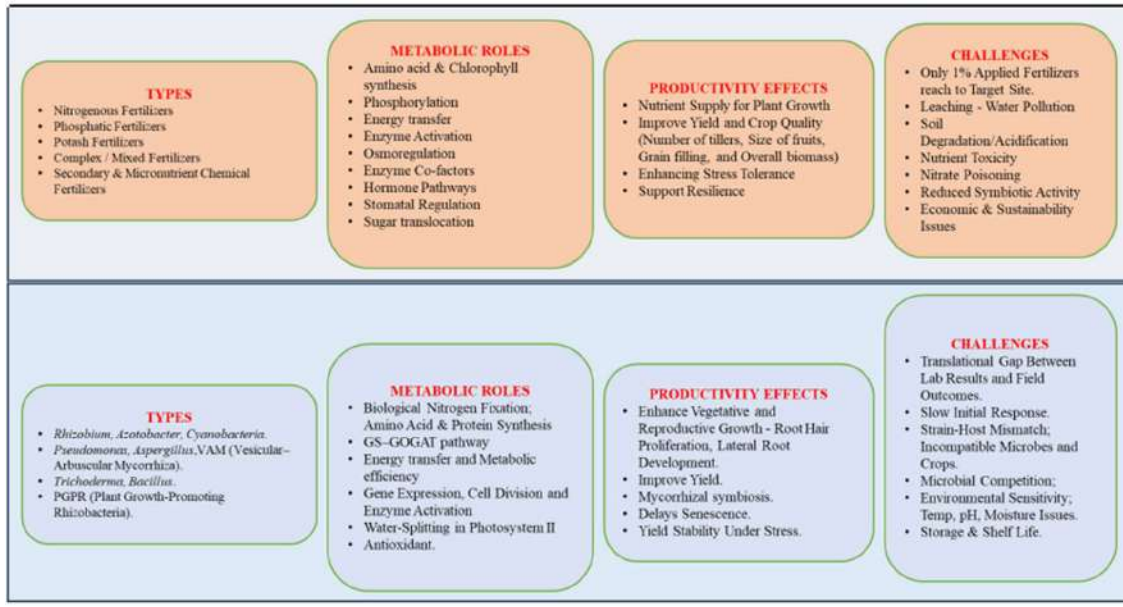


Fig. 5: Types, metabolic roles, productivity effects, and challenges of chemical and biological fertilizers.

promote nutritional processes independently of their nutrient content, with four main aims: (i) boosting nutrient use efficiency, (ii) enhancing tolerance to abiotic stresses, (iii) improving crop quality traits, and (iv) increasing nutrient availability in soil or the rhizosphere (Yakhin et al. 2017, Papnai et al. 2022, Dubey & Sharma 2023).

The regulation encompasses a wide array of qualifying substances and organisms, including humic substances, protein hydrolysates and amino acid-based products, extracts from macro- and microalgae and plants, silicon-based products, and beneficial microorganisms. Notably, microbial categories include arbuscular mycorrhizal fungi (AMF) and plant growth-promoting rhizobacteria (PGPR), especially species within the genera Azotobacter, Azospirillum, and Rhizobium (Sible et al. 2025, Yakhin et al. 2017, Delaeter et al. 2024, Chabili et al. 2024).

The effectiveness of plant biostimulants varies significantly depending on factors such as crop species, soil properties, and climate conditions. Different plant species and cultivars exhibit diverse responses to biostimulant treatments due to differences in physiological traits, nutrient needs, and metabolic processes. Likewise, soil characteristics like pH, organic matter levels, nutrient availability, and microbial activity can affect how well biostimulant formulations work. Environmental variables, including temperature, rainfall, and water accessibility, are also critical in shaping plant responses. As a result, the positive effects seen in one cropping system or agroecological zone may not be observed under different environmental conditions.

In addition to environmental variability, the literature presents inconsistent findings regarding yield improvements and stress tolerance associated with biostimulant use. Although numerous studies show enhanced crop productivity and increased tolerance to stresses such as drought, salinity, and nutrient deficiency, some investigations report only limited or variable benefits. These differences may stem from variations in experimental conditions, biostimulant formulations, application techniques, and crop management practices. This variability underscores the need for more systematic, well-controlled research to better understand the conditions under which biostimulants reliably deliver agronomic advantages and to develop optimized application strategies tailored to diverse cropping systems.

2.7. Types of Biostimulants

Biostimulants represent a diverse range of biologically active compounds and organisms that promote plant growth, improve nutrient uptake, and enhance stress tolerance. These encompass both enzyme-based and microorganism-based types, each operating through unique mechanisms to support plant development and soil vitality.

2.7.1. Microbial Biostimulants

Mycorrhizal fungi, particularly those from the Glomus genus, form vital mutualistic relationships with plant roots. These fungi effectively expand the root system, significantly enhancing the absorption of essential nutrients such as phosphorus, nitrogen, and various micronutrients. They also aid in water uptake, increase resistance to soil-borne pathogens,

and improve plant resilience under stressful conditions like drought or nutrient-deficient soils. Common genera used in biostimulants include Glomus, Rhizophagus, and Gigaspora (Sun et al. 2024, Seymen et al. 2021).

Plant growth-promoting rhizobacteria (PGPR) offer several agronomic benefits. They fix atmospheric nitrogen, solubilize nutrients (phosphorus), synthesize plant growth hormones (auxins), and act as biocontrol agents against pathogens. These bacteria can be applied directly to the soil or root zone. Noteworthy examples include *Azospirillum* sp. and *Pseudomonas,* which enhance nitrogen fixation; Pseudomonas fluorescens, known for promoting plant growth and suppressing disease; and *Bacillus* sp., recognized for nutrient solubilization and pathogen resistance. *Bacillus subtilis* and *Bacillus amyloliquefaciens* are integral components of biostimulants due to their multifunctional roles. These bacteria produce enzymes that decompose organic matter, stimulate root development, and enhance nutrient uptake. Moreover, they serve as potent biocontrol agents, offering protection against various biotic stresses while also supporting plant resistance to abiotic stress factors (Khoso et al. 2024, Ehinmitan et al. 2024, Chandran et al. 2021). Together, these enzymes and microbial agents work synergistically with plant systems, amplifying innate biological capabilities related to growth, nutrient absorption, and environmental stress tolerance-thereby fulfilling the core objectives of biostimulant applications (Sun et al. 2024). Microbe-based biostimulants play a significant role in plant growth, health, and productivity through metabolic activities. These microorganisms fix atmospheric nitrogen, solubilize insoluble phosphates, and produce plant growth regulators such as auxins, gibberellins, and cytokinins, thereby improving nutrient availability and promoting root development.

Microbial inoculants significantly improve crop performance across diverse environmental conditions by facilitating nutrient acquisition and boosting overall plant vigor. In addition to their nutritional roles, many beneficial microbes induce systemic resistance in plants, providing protection against a wide range of abiotic and biotic stressors like drought, salinity, and pathogenic infections (Bashan et al. 2013, Kumar et al. 2025). Recent advances in next-generation sequencing (NGS) and functional genomics have further enabled the development of efficient, targeted microbial inoculants adapted to specific crops and soil environments. Microbial biostimulants increase crop productivity by 16–22% on average, with arbuscular mycorrhizal fungi (AMF) contributing 16–20% gains in cereals, and seed treatments boosting yields up to 21%. Co-inoculation with organic fertilizers can further increase productivity to nearly 30%, highlighting their synergistic potential in sustainable agriculture (Kumar et al. 2025, Morcillo et al. 2022, Lehmann & Rillig 2015, Singh et al. 2024). The use of mixed microbial inoculants, such as plant growth-promoting rhizobacteria (PGPR), fungi, and Rhizobium spp., has resulted in an average yield increase of 22% across various crops (Nath Bhowmik & Das 2018).

Biological seed treatments using microbial inoculants have also been widely studied and showed an average 21% yield increase, along with improved germination rates and seedling vigor (Sharma & Borah 2021). AMF-based biostimulants have demonstrated remarkable effects, with an average 16% increase in cereal grain yields, influenced by soil pH and native AMF populations. Similarly, in wheat, AMF inoculation increases grain yield by up to 20% and improves harvest index by 25%, particularly under low-phosphorus conditions (Pellegrino et al. 2015). Furthermore, co-inoculation of microorganisms with organic compost has shown synergistic effects in Phaseolus vulgaris, resulting in yield increases of up to 29%, surpassing single-treatment applications (Ahmad et al. 2022). These microbial solutions provide a sustainable, environmentally friendly alternative to chemical fertilizers and pesticides, supporting the transition toward more resilient, environmentally responsible agricultural systems.

2.7.2. Seaweed Extracts

Seaweed extracts are abundant in biologically active compounds such as vitamins, minerals, amino acids, and natural plant hormones, all of which support plant growth, development, and overall health. Key among these are auxins and cytokinins, which significantly enhance seed germination, stimulate root development, and boost vigor across various crop species. The combined action of natural compounds in marine plant extracts promotes balanced vegetative and reproductive growth and increases the resilience of plants to abiotic and biotic stresses under both controlled and field conditions. Under challenging conditions like water stress, biostimulant treatments with plant extracts, combined with amino acids or yeast extracts, have increased maize yields by 8.5–20%, demonstrating their role in stress mitigation (Jaikumar et al. 2024).

Additionally, multi-component biostimulant formulations incorporating plant extracts have raised tomato productivity by 39–57%, depending on irrigation levels (Patanè et al. 2025). Recent advances in formulation technology have enabled the creation of innovative biostimulants that combine seaweed extracts with other bioactive ingredients to enhance effectiveness and expand applications in modern agriculture (Patanè et al. 2025, Kumar et al. 2025). These multifunctional formulations not only improve crop performance but

also support sustainable farming practices by providing environmentally friendly alternatives to chemical fertilizers.

2.7.3. Humic and Fulvic Substances

Humic and fulvic acids play a crucial role in plant physiology and plant-soil interactions. They influence root system architecture by stimulating lateral root initiation and root hair development, thereby enhancing the plant's absorptive surface area.

Additionally, these acids impact membrane transport processes, including ion channel activity and proton pump regulation, which improves the uptake and translocation of essential nutrients (Canellas et al. 2015). By increasing cation exchange capacity and chelating micronutrients, humic and fulvic acids significantly boost nutrient solubility and bioavailability, enabling more efficient nutrient absorption across various soil conditions. Biostimulants derived from humic and fulvic acids enhance the fertilization efficiency of key nutrients such as potassium, nitrogen, and phosphorus. Moreover, they facilitate the mobilization of minerals like iron, zinc, copper, and manganese in soils, increasing their availability to plants and aiding in water and nutrient retention (Akinci 2009).

Numerous studies have demonstrated the benefits of incorporating humic and fulvic acids to maintain soil quality and improve crop yields. Haider et al. (2017) reported that applying humic acid to soil at rates of 10, 20, and 30 kg ha^{-1} increased pod weight, resulting in higher yields. An experiment on tomatoes showed that total yield increased by 10–15% when a nutrient mixture and biostimulants were applied through foliar and soil treatments (Mallick et al. 2024). Pillajo et al. (2024) highlighted that humic compounds could serve as a viable alternative to reduce fertilization rates in Solanum lycopersicum cultivation while maintaining healthy growth and nutrition. They suggested that humic acid might be an effective substitute for lowering fertilizer inputs without compromising yield or plant health (Pillajo et al. 2024). AL-Taey et al. (2019) found that the highest head weight and yield were achieved with the combined application of biofertilizer (20 g L^{-1}) and humic acid (10 mL L^{-1}), compared to using biofertilizer alone in Brassica oleracea (Al-Taey et al. 2019). Similarly, Dawood et al. (2019) observed that applying varying levels of humic acid (0% to 5%) to Vicia faba resulted in higher seed yields compared to the control (Dawood et al. 2019).

2.7.4. Protein Hydrolysates and Amino Acid-Based Biostimulants

Protein hydrolysates and amino acid-based biostimulants influence plant growth and stress resilience by regulating nitrogen metabolism and enhancing the activity of vital enzymes such as nitrate reductase and glutamine synthetase, thereby bolstering nitrogen assimilation and protein synthesis. Amino acids also serve as osmoprotectants, aiding plants in maintaining cellular homeostasis under abiotic stresses like drought, salinity, and temperature extremes.

Additionally, many amino acids function as signaling molecules that activate antioxidant defense mechanisms, which improve the scavenging of reactive oxygen species (ROS) and safeguard cellular structures from oxidative damage (Colla et al. 2017, Calvo et al. 2014). Derived from protein hydrolysis, amino acids and peptides are crucial for plant growth, development, and stress management through various physiological and biochemical pathways. These compounds also enhance nutrient uptake, boost photosynthetic efficiency, and increase plant resilience to environmental stresses, acting as osmoprotectants and signaling entities.

Moreover, amino acids and peptide-based biostimulants are deeply integrated into nitrogen and sulfur metabolic pathways, serving as essential precursors for enzyme, chlorophyll, and other metabolite biosynthesis that regulate plant metabolism (Heidarzadeh 2025, Khoulati et al. 2025b). In vitro studies by Tamburino et al. (2023) demonstrated that enzyme molecules such as chitinase, xylanase, and β-glucosidase, used as biostimulants in Lactuca sativa, significantly increase cell biomass, up to 50% and 40% for xylanase at concentrations of 0.1 and 0.01 μM, respectively, and 60% and 30% for β-glucosidase at the same concentrations.

2.7.5. Plant-Derived Compounds and Other Emerging Biostimulants

Seaweed and higher-plant extracts are significant categories of biostimulants because they contain complex mixtures of bioactive compounds such as polysaccharides, betaines, and phenolic compounds. These molecules influence plant signaling pathways, improve nutrient uptake efficiency, and bolster plant resilience against abiotic and biotic stresses. Compost tea contains a diverse array of microbial species, which can be classified as microbial inoculants, even though it also includes proteins, amino acids, and humic substances (Villa e Vila et al. 2024, Ali et al. 2021, Han et al. 2024).

2.7.6. Enzyme-Based Biostimulants

Phosphatase enzymes, especially phytases, are essential in releasing phosphorus from organic compounds in the soil. As phosphorus is a vital macronutrient that often limits crop growth, these enzymes enhance its bioavailability by converting organic phosphorus into inorganic phosphate forms that plants can easily absorb. Fungi like Aspergillus

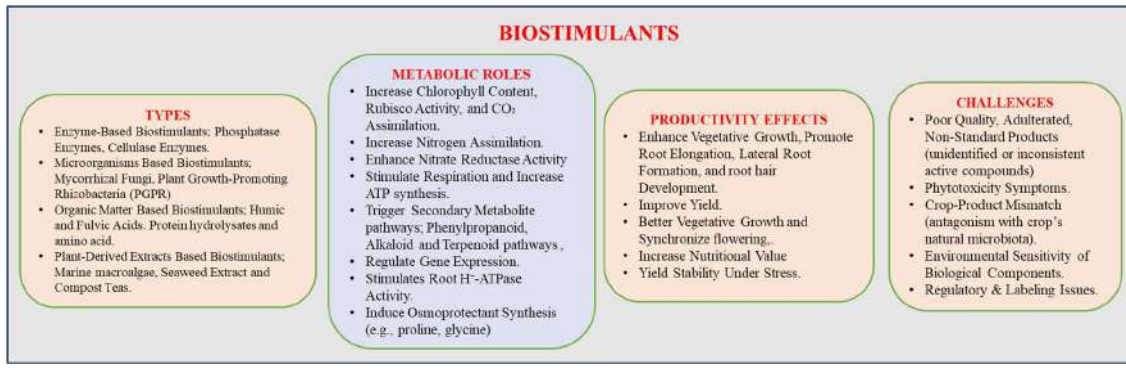


Fig. 6: Major types, metabolic roles, productivity effects, and challenges of biostimulants.

and bacteria such as Bacillus are well-known producers of phytase and are frequently included in enzyme-based biostimulant products.

Cellulase enzymes facilitate the breakdown of cellulose found in plant residues and organic matter. This enzymatic activity promotes nutrient cycling, improves soil structure, and stimulates microbial activity within the rhizosphere, thereby enhancing nutrient availability to plants. Fungi from the Trichoderma genus and bacteria such as Bacillus subtilis are capable of producing cellulase enzymes and are often incorporated into biostimulant formulations for these purposes (Rouphael & Colla 2020a, 2020b, Zamljen et al. 2023, Tamburino et al. 2023). Amino acids and peptides, derived from protein hydrolysis, are crucial for plant growth, development, and stress tolerance. These compounds increase nutrient uptake, boost photosynthetic efficiency, and improve plant resilience against environmental stresses by acting as osmoprotectants and signaling molecules.

Biostimulants based on amino acids and peptides support nitrogen and sulfur metabolism by serving as precursors for enzymes, chlorophyll, and other key metabolites, thereby regulating plant metabolic processes (Phooi et al. 2022). Tamburino et al. (2023) evaluated several enzyme molecules, including chitinase, xylanase, and β-glucosidase, as biostimulants in Lactuca sativa, reporting biomass increases of up to 50% and 40% for xylanase at concentrations of 0.1 and 0.01 µM, respectively, and increases of 60% and 30% for β-glucosidase at the same concentrations in vitro.

Patanè et al. (2025) observed productivity increases of 57% under no irrigation stress and 39% under full irrigation in *Solanum lycopersicum* when treated with enzyme-based biostimulants compared to controls (Bashir et al. 2025). In agriculture, these biostimulants are typically applied via foliar sprays or soil amendments, leading to enhanced plant growth, yield, and quality across various crops. Recent advances focus on biotechnological innovations, such as enzymatic hydrolysis, fermentation technologies, and nano-formulations, to optimize production, formulation, and delivery for maximum effectiveness. Notably, amino acid and peptide-based biostimulants support sustainable agriculture by reducing reliance on chemical fertilizers and pesticides, thereby aligning with environmentally friendly farming practices (Ranasingha et al. 2024, Khoulati et al. 2025a, Sun et al. 2024).

2.8. Mechanism of Action of Biostimulants

Plant biostimulants enhance plant growth and resilience to stress by influencing their metabolism, nutrient absorption, and microbial interactions. They primarily operate by modulating hormone signals, particularly those involving auxins, cytokinins, and gibberellins. Many biostimulants, including seaweed extracts and microbial formulations, either contain hormone-like compounds or stimulate plants to produce more hormones. This results in increased cell division, growth, and overall development. Auxin-like effects promote root branching and elongation, while cytokinins encourage shoot growth and delay leaf senescence. Gibberellins facilitate stem elongation and seed germination, strengthening the plant and boosting productivity. Additionally, biostimulants improve nutrient uptake and transport by enhancing root transporter activity and activating genes responsible for nutrient movement. Consequently, plants absorb higher amounts of essential nutrients such as nitrogen, phosphorus, potassium, and iron. Some biostimulants also activate enzymes that help plants utilize these nutrients more efficiently, reducing their reliance on chemical fertilizers.

Biostimulants influence root development and soil interactions, which are crucial for plant health and nutrient movement within the soil. The application of humic substances, protein hydrolysates, and microbial biostimulants promotes root branching, enhances root hair growth, and increases overall root biomass. These modifications expand the root surface area, improving water and nutrient

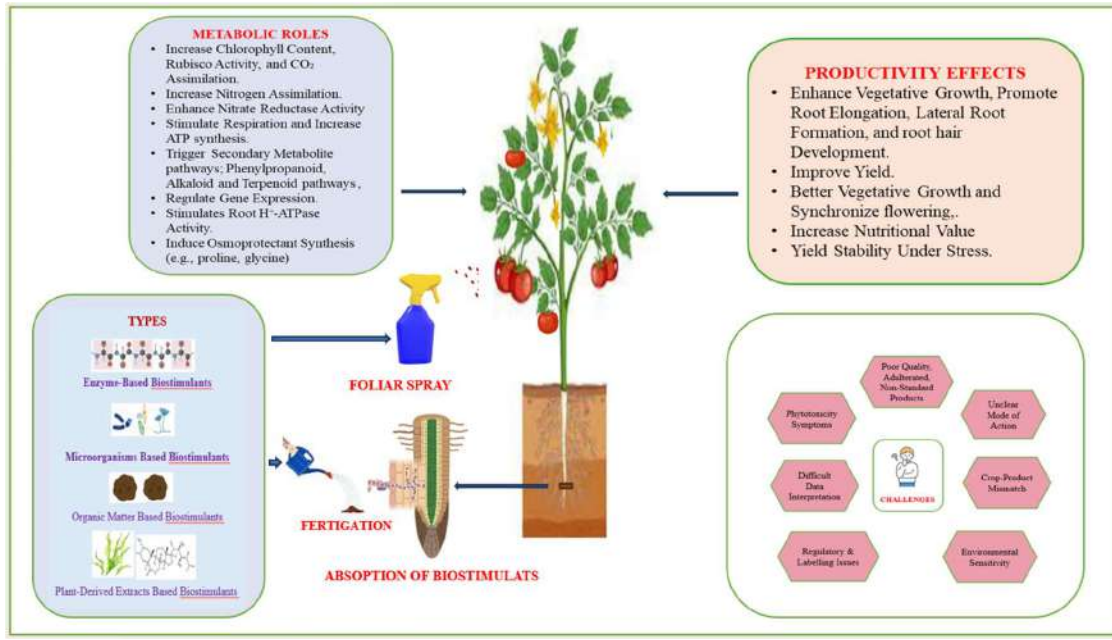


Fig. 7: Mechanism and productivity impact of biostimulants on plant growth.

absorption, and also bolster the plant's resilience to challenging conditions such as drought and salinity.

Another key function of biostimulants is enhancing the interaction between plants and beneficial microbes. Microorganisms such as plant growth-promoting rhizobacteria (PGPR) and mycorrhizal fungi increase nutrient availability for plants. They also secrete substances that promote plant growth and improve stress resistance. These microbes inhabit the regions around plant roots or within plant tissues, sending signals that regulate plant defenses and metabolism. Through these mechanisms, biostimulants support improved plant growth and stress tolerance and contribute to more sustainable agricultural practices (Fig. 7).

2.9. Global Economy and Agricultural Systems

Population Growth and Economic Development: Since 1950, the global population has grown from 2.5 billion to over 8 billion, with projections suggesting it will exceed 9 billion by 2050 (United Nations 2022). This rapid increase, coupled with rising incomes, particularly in developing countries, has driven a significant rise in food demand (OECD/FAO 2024, Seifollahi-Aghmiuni et al. 2022). As a result, agricultural systems are under increasing pressure to expand and intensify. Economic development has spurred industrialization, urbanization, and mechanization in agriculture, leading to higher productivity. Nonetheless, this progress has also increased dependence on resource-intensive practices, such as synthetic fertilizers and pesticides. The limited availability of land and water, combined with growing demand, further reinforces the need for intensive agricultural approaches**.**

Agricultural Land Use and Associated Challenges: Approximately 37% of Earth's land surface is committed to agriculture (FAO 2020, OECD/FAO 2024). While this statistic highlights the extensive extent of land dedicated to food production, it also emphasizes the limited scope for future expansion. Transforming natural ecosystems such as forests and grasslands into farmland has caused significant ecological impacts, including loss of biodiversity, habitat fragmentation, and soil deterioration. Initiatives to balance food production with environmental preservation have promoted practices like crop rotation, agroforestry, and sustainable land management. Nevertheless, agricultural land continues to face ongoing threats from climate change, urban expansion, and other human activities. These challenges reinforce the urgent need for more efficient and ecologically sustainable land-use strategies (Thwaites et al. 2025, Daszkiewicz 2022).

Fertilizer Use and Productivity in Global Agriculture: Synthetic fertilizers have played a pivotal role in advancing modern agriculture. Since the mid-20th century, their widespread application, particularly nitrogen (N), phosphorus (P), and potassium (K) fertilizers, has significantly boosted crop yields by providing essential nutrients that may be deficient or absent in soil (Yakhin et al. 2017). By 2021, global fertilizer consumption surpassed 190 million metric tons, with Asia, especially China and India, leading the demand (FAO 2023, OECD/FAO 2024). Although fertilizers

are vital for achieving high productivity, their excessive or inefficient use can harm the environment. Excess nutrients often leach into water bodies, leading to eutrophication, algal blooms, and declining water quality. Additionally, nitrogen fertilizers are a primary source of nitrous oxide, a potent greenhouse gas with a global warming potential roughly 300 times that of carbon dioxide. The use of nitrogen (N) fertilizer has grown at a rate far exceeding that of phosphorus (P) and potassium (K), as demonstrated by research from Lu and Tian and others. Human inputs of N, P, and K now rival natural biogeochemical fluxes, causing notable nutrient imbalances, especially in N:P and N:K ratios. These disruptions in nutrient cycling and distribution exhibit spatial and temporal variability in fertilizer use, with significant consequences for environmental health, food security, and sustainable agriculture (Dubey & Sharma 2023, Sible et al. 2025).

Environmental Consequences of Fertilizer Overuse: The environmental impacts of reliance on synthetic fertilizers are extensive and multifaceted. Overapplication of fertilizers can harm soil health by disrupting microbial communities, decreasing soil organic matter, and causing acidification, all of which threaten the long-term sustainability and productivity of agricultural systems. Nutrient runoff also poses a significant risk to aquatic environments; discharges into rivers and lakes accelerate eutrophication, depleting oxygen levels and creating dead zones, as exemplified by the Gulf of Mexico, where nutrient inflows from the Mississippi River have caused extensive algal blooms and marine biodiversity loss (Ansari et al. 2024, Meena et al. 2020, Bhardwaj et al. 2022, Torres et al. 2017). Furthermore, synthetic fertilizers contribute to greenhouse gas emissions during both field application and their energy-intensive production, with agriculture being a major global emitter partially due to fertilizer use. Plant biostimulants improve nutrient use efficiency by enhancing plants' ability to absorb, translocate, and assimilate vital nutrients. Components like humic substances, protein hydrolysates, and microbial inoculants promote root development and activate nutrient transporter systems, allowing crops to achieve similar yields with less synthetic fertilizer. This supports better nutrient management and reduces environmental impacts. Biostimulants may also help lower greenhouse gas emissions, particularly nitrous oxide (N_2O), by increasing nutrient efficiency and decreasing dependence on synthetic fertilizers. Additionally, healthier soils and microbial activity facilitated by biostimulants may boost soil carbon sequestration, aligning with climate-smart agricultural strategies.

Biostimulants as a Sustainable Agricultural Input: In response to the rising environmental concerns associated with chemical fertilizers, biostimulants have become a sustainable alternative. These products, including seaweed extracts, humic acids, amino acids, and beneficial microbes, are designed to promote plant growth, improve nutrient absorption, and increase resilience to abiotic stresses without serving as direct nutrient sources. By stimulating soil microbial activity, enhancing nutrient bioavailability, and supporting overall plant health, biostimulants improve nutrient use efficiency. Research shows that biostimulants can decrease reliance on synthetic fertilizers, reduce environmental harm, and aid in soil restoration. Their use is especially prevalent in organic farming and integrated pest management, where reducing chemical inputs is a key goal. With consumer demand for environmentally friendly food and a global movement toward sustainable agriculture, the biostimulant market is expected to expand rapidly in the coming years (Rouphael & Colla 2020a, 2020b).

Balancing Productivity and Sustainability: The complex global challenge involves the interaction of population dynamics, economic development, land use, fertilizer dependence, and environmental sustainability. As the population increases and demand for agricultural products rises, pressure on arable land and limited natural resources will escalate. Although fertilizers have been key to meeting past and present food production needs, their environmental drawbacks highlight the importance of alternative and supplementary strategies. Biostimulants present a promising solution by boosting productivity in a more sustainable and ecologically friendly manner. Future farming systems must embrace innovative, integrated approaches that reconcile the urgent need for higher yields with the long-term responsibility of environmental preservation. Achieving this will depend on interdisciplinary efforts across agronomy, environmental science, economics, and policy to develop resilient, efficient, and sustainable global food systems (Baltazar et al. 2021, Roche et al. 2024).

2.10. Role of Biostimulants in Sustainability Goals

Biostimulants and Sustainable Food Systems: Sustainable food systems are crafted to ensure sufficient food production for a growing global population while actively minimizing environmental harm, protecting biodiversity, and preserving long-term ecological health. Enzyme- and microorganism-based biostimulants play a crucial role in achieving these goals by promoting soil vitality, enhancing nutrient efficiency, and decreasing reliance on synthetic chemical inputs.

Enhancing Soil Health and Fertility: Microbial communities are essential for sustaining soil health by fostering microbial diversity and supporting nutrient cycling. Beneficial microbes, such as nitrogen-fixing bacteria and phosphate-

solubilizing fungi, improve the availability of vital nutrients to plants, reducing the dependence on synthetic fertilizers. Enzyme-based biostimulants further aid this process by breaking down organic matter and releasing important nutrients like nitrogen, phosphorus, and potassium into the soil. These enhancements in nutrient accessibility not only boost soil fertility but also improve soil structure, increasing its resistance to erosion, compaction, and degradation (Selvan et al. 2023, Gomiero et al. 2011).

Reduction in Chemical Inputs: The application of enzyme- and microorganism-based biostimulants can markedly decrease the dependence of the agriculture sector on chemical fertilizers and pesticides. By enhancing nutrient absorption and improving plant vitality, these biostimulants offer natural alternatives to traditional agrochemicals. Beneficial microbes, such as Bacillus and Trichoderma species, produce bioactive secondary metabolites that provide protection against phytopathogens and insect pests. This biological approach to pest and disease control reduces the need for synthetic pesticides, supporting environmentally sustainable farming practices and reducing the ecological impact of food production systems (Saleem et al. 2024, Ansari et al. 2024).

Soil Microbiome Management: Targeted application of microorganism-based biostimulants can actively modulate the soil microbiome to favor more beneficial microbial communities. This form of ecological engineering in the rhizosphere promotes enhanced plant growth and greater stress resilience, while supporting agroecosystems aligned with sustainable farming principles. By modulating the microbiome, enzyme- and microorganism-based biostimulants facilitate the development of low-input agricultural systems that sustain productivity without jeopardizing long-term soil health and ecosystem functions (Khoso et al. 2024, Ehinmitan et al. 2024). The use of biostimulants positively impacts soil microbial communities by encouraging the proliferation and activity of beneficial microorganisms in the rhizosphere. Microbial biostimulants like plant growth–promoting rhizobacteria (PGPR) and mycorrhizal fungi enhance nutrient cycling, organic matter decomposition, and the production of growth-promoting metabolites. An increase in microbial diversity not only supports plant health but also reinforces ecosystem stability and resilience in agricultural soils.

Waste Bioremediation: Bioremediation, supported by specific microorganisms, has become a highly effective strategy for managing industrial waste. Microorganisms capable of breaking down organic pollutants are now commonly used to treat environmental contaminants such as oil spills and toxic industrial effluents. Simultaneously, enzyme-based biostimulants are employed to accelerate the decomposition of organic compounds in wastewater systems, thereby decreasing dependence on hazardous chemical treatments. The use of these biological agents in waste management not only promotes cleaner production processes but also advances broader objectives of environmental compliance and sustainable industrial development.

2.11. Improved Soil Health Indicators

Biostimulants have been demonstrated to enhance several crucial soil health indicators, such as soil organic matter, enzymatic activity, and soil structure. By promoting microbial processes and root exudation, biostimulants aid in improving soil aggregation, water retention, and nutrient availability. These positive changes in the soil's physical, chemical, and biological properties support long-term soil fertility and sustainable crop production.

Biodegradable Materials: Ongoing research and application of enzyme- and microorganism-based biostimulants have expanded into the development of biodegradable materials. Specific microbial species produce biopolymers that serve as sustainable alternatives to traditional, petroleum-based plastics. For instance, enzymes like polyhydroxyalkanoate (PHA) synthases facilitate the production of bioplastics that are naturally biodegradable. These materials contribute to reducing the buildup of persistent plastic waste in the environment, providing a practical pathway toward more circular and less polluting material life cycles (Ranjithkumar 2025, Thwaites et al. 2025).

2.12. Global Market Overview

The global biostimulants market was valued at USD 2,982.9 million in 2022 and is projected to reach USD 6,849.8 million by 2030, growing at a compound annual growth rate (CAGR) of 11.19% from 2023 to 2030. Another forecast estimates the market will attain USD 5.4 billion by 2027, with a CAGR of 10.2% between 2022 and 2027, highlighting the sector's strong expansion (Meena et al. 2025, Chakrabarty & Selvakumaran 2025, Jankuloska et al. 2025).

Key market players include Isagro S.p.A., Biolchim S.p.A., Valagro S.p.A., Koppert Biological Systems, Biostadt India Limited, ChemChina Group, Novozymes, Lallemand Plant Care, BASF SE, FMC Corporation, among others actively engaged in biostimulant production. Industry leaders such as Bayer CropScience, UPL Ltd., Syngenta AG, Gowan Group, ILSA S.p.A., Rallis India Limited, and Haifa Group are also prominently involved, reflecting the market's highly competitive and fragmented landscape (Khoulati et al. 2025b, Rouphael & Colla 2020a, 2020b, Sible et al. 2021).

The sector's growth is predominantly driven by the increasing focus on sustainable agriculture, heightened farmer

awareness of biostimulants' role in improving yield and quality, and rising demand for organic products. Additionally, there is a significant need to lessen environmental impacts by adopting alternatives to chemical fertilizers. These factors are supported by technological advancements that produce new formulations with enhanced effectiveness and crop-specific benefits, along with regulatory frameworks that increasingly endorse sustainable practices (Khoulati et al. 2025a). The implementation of precision agriculture underscores biostimulants' importance in maximizing nutrient efficiency and enhancing plant resilience. Consumer preferences for organic and sustainably produced foods further contribute to market growth, while digital technologies facilitate precise application methods and data-driven decision-making. Furthermore, collaborations between manufacturers and stakeholders are driving the development of region- and crop-specific solutions.

Segmentation of the global market provides further insight (Table 1). By source, microbial biostimulants dominate, with the segment valued at USD 1,747.1 million in 2022, reflecting the growing appreciation of beneficial soil microbiota and their ability to support nutrient uptake and stress resistance. By form, liquid biostimulants are the fastest-growing segment, with a CAGR of approximately 11.95%, favored for their ease of application, rapid absorption, and compatibility with precision systems such as drip irrigation. Dry formulations remain relevant where shelf life and transport stability are prioritized. By active ingredient, the market spans vitamins and amino acids, seaweed extracts, microbial amendments, humic substances, protein hydrolysates, and others. Of these, the vitamins and amino acids segment held the highest valuation at USD 756.1 million in 2022, underscoring their importance in plant metabolic regulation, stress tolerance, and quality improvement (Critchley et al. 2021, Mandal et al. 2023).

Regional analysis highlights the substantial growth and variation across the foremost geographical markets. Europe accounted for nearly 31% of the global biostimulants market in 2021, indicating the significant adoption of organic farming practices and supportive EU agricultural policies. On the other hand, market assessment as per the year 2022, the Asia-Pacific region signifies 38.67% of the global market, which is equivalent to USD 1,153.5 million, following its expansion linked to expanded population, rising in food demand, government initiatives, and mounting awareness of sustainable agricultural practices. In addition, North America establishes a vital regional market. Considering these regional estimates parallel to different years and may reflect different market valuations, the reported shares should be interpreted within their corresponding source years rather than as a direct comparison of regional rankings (Critchley et al. 2021; Mandal et al. 2023; Khoulati et al. 2025b; Naikoo et al. 2025).

Competitive strategies within the sector encompass partnerships, mergers and acquisitions, product innovations, and joint ventures. Companies continue to prioritize investments in research and development, capacity expansion, and supply chain optimization to enhance their competitive position. As reflected in reports like the "Biostimulants Market – Forecast (2022–2027)" by Industry ARC, the segmentation is extensive, including factors such as form (dry, liquid), product type (microbial vs. nonmicrobial), application method (foliar, soil, seed treatment), crop type (cereals, fruits, vegetables, plantation crops, turf and landscape), and detailed country-level geographies.

Several structural factors drive this market's growth. Globally, organic farmland is expanding, as indicated by FiBL statistics, while food demand continues to rise despite limited arable land. FAO data reveal a 53% increase in primary crop production from 2000 to 2019, reaching 9.4 billion tonnes, and OECD projections suggest that future improvements will

Table 1: Global agricultural biologicals market size, forecasted growth, and key segmental and regional contributions, highlighting leading sources, formulations, applications, and their respective CAGR trends.

Metric	Value	Year/period	Notes
Market Size	USD 2,982.9 million	2022	Global valuation
Forecasted Market Size	USD 6,849.8 million	2030	CAGR 11.19% (2023–2030)
Alternative Forecast	USD 5.4 billion	2027	CAGR 10.2% (2022–2027)
Microbial Segment Revenue	USD 1,747.1 million	2022	Largest revenue share by source
Vitamins & Amino Acids Segment	USD 756.1 million	2022	Largest by active ingredient category
Asia-Pacific Share of Global Market	38.67% (USD 1,153.5 million)	2022	Largest regional share
Europe Share of Global Market	~31%	2021	Leading regional market
Liquid Form CAGR	~11.95%	Forecast period	Fastest-growing form
Non-Microbial Segment CAGR	~10.5%	2022–2027	Large share segment
Seed Treatment CAGR	~8.9%	2022–2027	Fastest-growing application method

depend heavily on yield enhancements. Biostimulants are emerging as crucial enablers of this yield increase.

Challenges persist, especially with unorganized and local producers offering low-quality products that harm farmer confidence and tarnish the reputation of established brands. However, the outlook remains promising. Recent developments demonstrate ongoing momentum, such as UPL AgroSolutions Canada's approval of the OHM biostimulant (2021), UPL Australia's launch of GoActiv Technology (2021), and Acadian Seaplants Ltd.'s introduction of seaweed-based biostimulants (Acadian BioSwitch™) in India, aimed at improving germination, yield, and weed suppression (Khoulati et al. 2025a, Naikoo et al. 2025).

2.13. Indian Biostimulants Market

The biostimulants sector is experiencing rapid global growth, with particular emphasis on the Indian context (Table 2). India's extensive agricultural base, unique growth patterns, and emerging policy frameworks make its market especially noteworthy (Naikoo et al. 2025). Valued at USD 79.2 million in 2022, the Indian biostimulants market is expected to reach USD 189.7 million by 2030, expanding at a robust CAGR of 11.5% from 2023 to 2030. While accounting for only about 3% of the global market in 2022, India is the fastest-growing market in the Asia-Pacific region, underscoring its increasing significance on the world stage. The market is segmented by active ingredients, with acid-based biostimulants leading, generating 48.11% of revenue in 2022 (Indian Chamber of Commerce 2023, IMARC Group 2024). Their popularity arises from their capacity to enhance nutrient absorption, improve soil fertility, and bolster plant resilience under stress. Concurrently, seaweed extracts represent the fastest-growing segment, driven by the rising adoption of organic farming practices and their alignment with sustainable crop production systems. Additionally, microbial-based and mixed active ingredient formulations are experiencing steady growth as farmers adopt modern techniques that incorporate biological inputs into conventional farming.

Several factors underpin this robust growth. India's expanding population, increasing consumer preference for organic and environmentally friendly food products, and rising purchasing power are driving demand for safe, high-quality produce. Farmers are also adopting biostimulants as effective alternatives to chemical fertilizers, indicating greater awareness of their long-term benefits for crop yield and soil health. At the same time, modernization of agricultural techniques and the customization of products by Indian companies such as Biostadt India Limited to suit specific crop and soil types are further accelerating adoption.

However, challenges persist in this fragmented market. Numerous local and unorganized players compete with established companies, often by offering low-quality, low-cost products. This situation impacts pricing dynamics and undermines farmer confidence and brand credibility for premium products. Nonetheless, larger domestic players such as Rallis India Limited and UPL Ltd., along with multinational corporations like BASF SE, Isagro, Novozymes, Koppert, and others, continue to strengthen their market presence through innovation, expanded distribution networks, and crop-specific product development.

Looking ahead, India's biostimulants market is poised to become one of the fastest-growing globally, even as China is projected to become the revenue leader in the Asia-Pacific region by 2030. With a growing consumer base, government backing for sustainable agriculture, and rising private-sector innovation, India is expected to play a crucial role in shaping the region's biostimulant industry.

2.14. Experimental Challenges in Evaluating Biostimulants

Experimental challenges in biostimulant research arise from their complex composition, variable effects, and the lack

Table 2: National market size and growth outlook, segmental dominance, competitive landscape, and regional positioning, highlighting key drivers, players, and challenges shaping the market through 2030.

Metric	Value	Year/period	Notes
Market Size	USD 79.2 million	2022	National valuation
Forecasted Market Size	USD 189.7 million	2030	CAGR 11.5% (2023–2030)
Share of Global Market	~3.0%	2022	Small but fastest-growing in APAC
Largest Active Ingredient Segment	Acid Based-48.11% revenue share	2022	Dominant segment
Fastest Growing Active Ingredient	Seaweed extract	2023–2030	Organic farming adoption driver
Market Character	Fragmented	Ongoing	Mix of multinationals and local players
Key Domestic Players	Biostadt India, Rallis India, UPL Ltd.	Ongoing	Custom crop/soil solutions
Competitive Challenge	Low-quality products	Ongoing	Threat to brand trust
Regional Status	Fastest-growing in Asia-Pacific	Forecast to 2030	China to lead in total APAC revenue

of standardized testing methods. Biostimulants, defined as substances or microorganisms that enhance plant metabolic processes without serving as direct sources of nutrients or pesticides, are increasingly used in sustainable agriculture, stress mitigation, and nutrient efficiency improvements (Baltazar et al. 2021, Yakhin et al. 2017, Delaeter et al. 2024). However, their heterogeneous formulations, particularly those derived from natural sources such as seaweed extracts, humic substances, and protein hydrolysates, hinder effective characterization (Bhupenchandra et al. 2020). Their composition can vary substantially based on source material, extraction, and processing methods, leading to batch-to-batch variability that challenges reproducibility and standardization. Additionally, these products exhibit complex biological activities, containing multiple active molecules or microbial communities. This complexity complicates the attribution of specific effects to individual components and makes it difficult to discern synergistic or antagonistic interactions among constituents. A significant obstacle in biostimulant research is the absence of standardized protocols, which hampers consistent results and cross-study comparisons. Unlike pesticides or fertilizers, which adhere to well-established regulatory testing frameworks, biostimulants lack universally accepted guidelines for efficacy assessment (Khoulati et al. 2025b, Sun et al. 2024).

Experimental design encounters reproducibility challenges due to environmental variability and difficulties in scaling from controlled environments to field conditions. Understanding the mode of action of biostimulants remains one of the most complex experimental challenges in this domain. These substances are known to trigger systemic or hormone-like responses in plants, which are hard to trace using traditional physiological techniques. Employing advanced multiomics approaches such as transcriptomics, metabolomics, and proteomics is essential to unravel these complex molecular and biochemical pathways involved. However, these methods are resource-intensive and costly. Additionally, the absence of universal biomolecular markers to verify biostimulant activity complicates the standardization of assessments and the confirmation of mechanisms. The biological complexity combined with limited available methods hinders a clear understanding of how biostimulants function. Regulatory and claim validation obstacles further challenge the proper evaluation and commercialization of biostimulants. Regulations such as EU Regulation 2019/1009 demand robust scientific evidence for product claims, yet no universally accepted testing protocols exist, and overlaps with fertilizers or biopesticides create classification ambiguities.

Data interpretation and meta-analyses in biostimulant research are also hampered by substantial challenges. A major issue is the heterogeneity of published studies, which vary in crop species, product formulations, application rates, experimental designs, and environmental conditions. This variability complicates data integration and limits the ability to conduct meaningful meta-analyses that produce generalized conclusions about efficacy. These issues underscore the urgent need for rigorous experimental design, standardized methodologies, advanced analytical tools, and close collaboration between regulators and scientists to ensure reliable and meaningful evaluation of biostimulant products.

3. VISION AND FUTURE PERSPECTIVES

Over the past century, the application of synthetic fertilizers and pesticides has significantly increased food production. However, this has also led to nutrient depletion, soil degradation, water pollution, loss of beneficial microbes, greenhouse gas emissions, and elevated costs for farmers. To address these issues, biofertilizers utilizing helpful microbes to enhance nutrient cycling were developed, though their effectiveness often varied depending on farming conditions. This limitation spurred the development of biostimulants, a broader category of products that go beyond mere nutrient supply. Biostimulants include both microbial and nonmicrobial agents that promote plant growth, improve nutrient use efficiency, and increase resilience to abiotic stresses such as drought, salinity, and extreme temperatures, while also enhancing crop quality traits. Their non-toxic nature, minimal ecological persistence, and diverse modes of action position them as key tools in transitioning toward sustainable intensification. Looking forward, biostimulants are set to play a central role in future agricultural systems.

Nonetheless, several research gaps remain. First, their mechanisms of action are often not well understood, with many effects observed empirically but lacking molecular or physiological validation. Second, their performance depends heavily on local conditions across soils, climates, crops, and cultivars, necessitating systematic multi-location, multi-year field trials to ensure consistent results. Third, integrating biostimulants with precision agriculture and digital farming technologies could optimize their application but is still underdeveloped. Fourth, current regulatory frameworks are fragmented and lack harmonization, hindering global adoption and standardization. Finally, most efficacy assessments focus solely on yield; future studies should incorporate economic analyses, input savings, soil health indicators, and ecosystem service evaluations to fully capture their benefits. Addressing these challenges requires an interdisciplinary approach that combines molecular biology, plant physiology, soil science, and agronomy

with socio-economic and policy considerations. At the policy level, harmonized regulations and quality standards are essential to filter out ineffective products and bolster farmer confidence. By closing these gaps, biostimulants can transform from promising innovations into fundamental technologies for achieving sustainable, resilient, and climate-smart agriculture.

4. ACKNOWLEDGMENTS

The authors are grateful to everyone at the Amity Institute of Biotechnology, Amity University Uttar Pradesh, for their assistance and cooperation.

5. REFERENCES

Ahmad, A., Zafar, U., Khan, A., Haq, T., Mujahid, T. and Wali, M., 2022. Effectiveness of compost inoculated with phosphate solubilizing bacteria. *Journal of Applied Microbiology*, 133(2), pp.1115–1129. [DOI]

Akinci, S., Büyükkeskin, T., Eroğlu, A. and Erdoğan, B.E., 2009. The effect of humic acid on nutrient composition in broad bean (*Vicia faba* L.) roots. *Notulae Scientia Biologicae*, 1(1), pp.81–87. [DOI]

Ali, O., Ramsubhag, A. and Jayaraman, J., 2021. Biostimulant properties of seaweed extracts in plants: implications towards sustainable crop production. *Plants*, 10(3), p.531. [DOI]

Al-Taey, D.K.A., Al-Shareefi, M.J.H., Mijwel, A.K., Al-Tawaha, A.R. and Al-Tawaha, A.R., 2019. The beneficial effects of bio-fertilizers combinations and humic acid on growth, yield parameters and nitrogen content of broccoli grown under drip irrigation system. *Bulgarian Journal of Agricultural Science*, 25(5), pp.959–966.

Anderson, K., 2023. Agriculture's globalization: endowments, technologies, tastes and policies. *Journal of Economic Surveys*, 37(4), pp.1314–1352. [DOI]

Ansari, I., El-Kady, M.M., Mahmoud, A.E., Arora, C., Verma, A., Rajarathinam, R., Singh, P., Verma, D.K. and Mittal, J., 2024. Persistent pesticides: accumulation, health risk assessment, management and remediation: an overview. *Desalination and Water Treatment*, 317, p.100274. [DOI]

Arif, M., Fiaz, S., Kandegama, W.M., Sheth, S. and Li, L., 2025. Evaluating the impacts of environmental stresses on agriculture in the context of climate resilience. *Plant Molecular Biology*, 115(4), p.73. [DOI]

Baars, C., Barbir, J. and Paulino Pires Eustachio, J.H., 2023. How can climate change impact human health via food security? A bibliometric analysis. *Environments*, 10(11), p.196. [DOI]

Baltazar, M., Correia, S., Guinan, K.J., Sujeeth, N., Bragança, R. and Gonçalves, B., 2021. Recent advances in the molecular effects of biostimulants in plants: an overview. *Biomolecules*, 11(8), p.1096. [DOI]

Bashan, Y., Kamnev, A.A. and de-Bashan, L.E., 2013. Tricalcium phosphate is inappropriate as a universal selection factor for isolating and testing phosphate-solubilizing bacteria that enhance plant growth: a proposal for an alternative procedure. *Biology and Fertility of Soils*, 49(4), pp.465–479. [DOI]

Bashir, M.A., Raza, Q.U., Rehim, A., Raza, H.M., Noor, A.I., Islam, M.S., Zafar-Ul-Hye, M., and Geng, Y., 2025. Assessing the Role of Biostimulants in Affecting the Production of Radish and Eggplant. *Journal of Soil Science and Plant Nutrition*, 25(2), pp.4588-98. [DOI]

Bhardwaj, A.K., Chejara, S., Malik, K., Kumar, R., Kumar, A. and Yadav, R.K., 2022. Agronomic biofortification of food crops: an emerging opportunity for global food and nutritional security. *Frontiers in Plant Science*, 13, p.1055278. [DOI]

Bhupenchandra, I., Chongtham, S.K., Devi, E.L., R., R., Choudhary, A.K., Salam, M.D., Sahoo, M.R., Bhutia, T.L., Devi, S.H., Thounaojam, A.S. and Behera, C., 2022. Role of biostimulants in mitigating the effects of climate change on crop performance. *Frontiers in Plant Science*, 13, p.967665. [DOI]

Bhupenchandra, I., Devi, S.H., Basumatary, A., Dutta, S., Singh, L.K., Kalita, P., Bora, S.S., Devi, S., Saikia, A., Sharma, P. and Bhagowati, S., 2020. Biostimulants: potential and prospects in agriculture. *International Research Journal of Pure and Applied Chemistry*, 21(14), pp.20–35. [DOI]

Bununu, Y.A., Bello, A. and Ahmed, A., 2023. Land cover, land use, climate change and food security. *Sustainable Earth Reviews*, 6(1), p.16. [DOI]

Calvo, P., Nelson, L. and Kloepper, J.W., 2014. Agricultural uses of plant biostimulants. *Plant and Soil*, 383(1), pp.3–41. [DOI]

Canellas, L.P., Olivares, F.L., Aguiar, N.O., Jones, D.L., Nebbioso, A., Mazzei, P. and Piccolo, A., 2015. Humic and fulvic acids as biostimulants in horticulture. *Scientia Horticulturae*, 196, pp.15–27. [DOI]

Chabili, A., Minaoui, F., Hakkoum, Z., Douma, M., Meddich, A. and Loudiki, M., 2024. A comprehensive review of microalgae and cyanobacteria-based biostimulants for agriculture uses. *Plants*, 13(2), p.159. [DOI]

Chakrabarty, P.K. and Selvakumaran, S., 2025. Plant biostimulants: reinvigorating agriculture. In: *Advances in Plant Disease Management Volume II*. Boca Raton: CRC Press, pp.362–378.

Chandran, H., Meena, M. and Swapnil, P., 2021. Plant growth-promoting rhizobacteria as a green alternative for sustainable agriculture. *Sustainability*, 13(19), p.10986. [DOI]

Colla, G., Hoagland, L., Ruzzi, M., Cardarelli, M., Bonini, P., Canaguier, R. and Rouphael, Y., 2017. Biostimulant action of protein hydrolysates: unraveling their effects on plant physiology and microbiome. *Frontiers in Plant Science*, 8, p.2202. [DOI]

Critchley, A.T., Critchley, J.S., Norrie, J., Gupta, S. and Van Staden, J., 2021. Perspectives on the global biostimulant market: applications, volumes, and values, 2016 data and projections to 2022. In: *Biostimulants for Crops from Seed Germination to Plant Development*. London: Academic Press, pp.289–296. [DOI]

Daszkiewicz, T., 2022. Food production in the context of global developmental challenges. *Agriculture*, 12(6), p.832. [DOI]

Dawood, M.G., Abdel-Baky, Y.R., El-Awadi, M.E. and Bakhoum, G.S., 2019. Enhancement quality and quantity of faba bean plants grown under sandy soil conditions by nicotinamide and/or humic acid application. *Bulletin of the National Research Centre*, 43(1), p.28. [DOI]

Delaeter, M., Magnin-Robert, M., Randoux, B. and Lounès-Hadj Sahraoui, A., 2024. Arbuscular mycorrhizal fungi as biostimulant and biocontrol agents: a review. *Microorganisms*, 12(7), p.1281. [DOI]

Du Jardin, P., 2015. Plant biostimulants: definition, concept, main categories and regulation. *Scientia Horticulturae*, 196, pp.3–14. [DOI]

Dubey, S.C. and Sharma, K., 2023. Biostimulant: an innovative approach for sustainable crop production. *Current Science*, 125(4), pp.377–382. [DOI]

Ehinmitan, E., Losenge, T., Mamati, E., Ngumi, V., Juma, P. and Siamalube, B., 2024. BioSolutions for green agriculture: unveiling the diverse roles of plant growth-promoting rhizobacteria. *International Journal of Microbiology*, 2024(1), p.6181491. [DOI]

FAO, IFAD, UNICEF, WFP and WHO, 2021. *The State of Food Security and Nutrition in the World 2021. Transforming Food Systems for Food Security, Improved Nutrition and Affordable Healthy Diets for All*. Rome: FAO, p.8.

FAO 2024. Celebrating World Food Safety Day in Europe and Central Asia. 2024. Available at http://www.fao.org/3/cd0234en/cd0234en.pdf

Gomiero, T., Pimentel, D. and Paoletti, M.G., 2011. Environmental

impact of different agricultural management practices: conventional vs. organic agriculture. *Critical Reviews in Plant Sciences*, 30(1–2), pp.95–124. [DOI]

Haider, N., Alam, M., Muhammad, H., Gul, I., Haq, S.U., Hussain, S. and Rab, A., 2017. Effect of humic acid on growth and productivity of okra (*Abelmoschus esculentus*) cultivars. *Pure and Applied Biology*, 6(3), pp.932–941. [DOI]

Han, M., Kasim, S., Yang, Z., Deng, X., Saidi, N., Uddin, M. and Shuib, E., 2024. Plant extracts as biostimulant agents: a promising strategy for managing environmental stress in sustainable agriculture. *Phyton*, 93(9), p.2149. [DOI]

Heidarzadeh, A., 2025. Role of amino acids in plant growth, development, and stress responses: a comprehensive review. *Discover Plants*, 2(1), pp.1–31. [DOI]

Hussain, S.B., Karagiannis, E., Manzoor, M. and Ziogas, V., 2023. From stress to success: harnessing technological advancements to overcome climate change impacts in citriculture. *Critical Reviews in Plant Sciences*, 42(6), pp.345–363. [DOI]

IMARC Group 2024. Fertilizer Market Size, Share, Trends & Growth Report 2024–2033. Report accessed January 2025. Available at https://www.imarcgroup.com/fertilizer-market

Impa, S.M., Raju, B., Hein, N.T., Sandhu, J., Prasad, P.V., Walia, H. and Jagadish, S.K., 2021. High night temperature effects on wheat and rice: current status and way forward. *Plant, Cell & Environment*, 44(7), pp.2049–2065. [DOI]

Indian Chamber of Commerce, 2023. *Bio-Stimulant Conference 2023, Concept Note & Market Overview*. Retrieved October 28, 2025, from https://indianchamberofcommerce.glueup.com/en/event/bio-stimulant-conference-2023–83702/

Jaikumar, M., Ramadoss, D., Surendran, S. and Behera, A.K., 2024. Current prospects of Indian seaweed and its value-added products 2024. [DOI]

Jan, S., Ashraf Bhat, M., Kumar, A., Altaf Wani, M., Ahmad Bhat, F., Kanth, R.H., Shikari, A.B., Bano, H., Manzoor, T., Altaf, H. and Naik, Z.A., 2025. Plants response to different abiotic stresses. *Journal of Crop Health*, 77(5), pp.1–27. [DOI]

Jankuloska, V., Mukanov, B., Zhivachka, A., Milosavljeva, J., Petkovski, M. and Popovska, T., 2025. Towards sustainable business models in the circular bioeconomy: the case of biobased fertilizers. *Bio-based and Applied Economics*. [DOI]

Jing, Z., Liu, N., Zhang, Z. and Hou, X., 2024. Research progress on plant responses to stress combinations in the context of climate change. *Plants*, 13(4), p.469. [DOI]

Johnson, R., Joel, J.M. and Puthur, J.T., 2024. Biostimulants: the futuristic sustainable approach for alleviating crop productivity and abiotic stress tolerance. *Journal of Plant Growth Regulation*, 43(3), pp.659–674. [DOI]

Khoso, M.A., Wagan, S., Alam, I., Hussain, A., Ali, Q., Saha, S., Poudel, T.R., Manghwar, H. and Liu, F., 2024. Impact of plant growth-promoting rhizobacteria (PGPR) on plant nutrition and root characteristics: current perspective. *Plant Stress*, 11, p.100341. [DOI]

Khoulati, A., Ouahhoud, S., Taibi, M., Ezrari, S., Mamri, S., Merah, O., Hakkou, A., Addi, M., Maleb, A. and Saalaoui, E., 2025a. Harnessing biostimulants for sustainable agriculture: innovations, challenges, and future prospects. *Discover Agriculture*, 3(1), p.56. [DOI]

Khoulati, A., Ouahhoud, S., Taibi, M., Kabbour, M., Cherkaoui, S. and Boukhatem, N., 2025b. Harnessing biostimulants for sustainable agriculture: innovations, challenges, and future prospects. *Discover Sustainability*. [DOI]

Kopecká, R., Kameniarová, M., Černý, M., Brzobohatý, B. and Novák, J., 2023. Abiotic stress in crop production. *International Journal of Molecular Sciences*, 24(7), p.6603. [DOI]

Kumar, N., Sow, S., Rana, L., Ranjan, S. and Singh, A.K., 2025. Trash amended with *Trichoderma* effects on cane yield, soil carbon dynamics, and enzymatic activities under plant–ratoon system of sugarcane in calcareous soil. *Sugar Tech*, 27(1), pp.134–147. [DOI]

Kumar, S., Thilagam, P., Shikha, D., Saikanth, D.R., Rahmani, U., Huded, S. and Panigrahi, C.K., 2023. Adapting plant protection strategies to meet the challenges posed by climate change on plant diseases: a review. *International Journal of Environmental and Climate Change*, 13, pp.25–36. [DOI]

Lehmann, A. and Rillig, M.C., 2015. Arbuscular mycorrhizal contribution to copper, manganese and iron nutrient concentrations in crops–a meta-analysis. *Soil Biology and Biochemistry*, 81, pp.147–158. [DOI]

Mallick, S., Karak, C., Roy, B., Chakraborty, B., Das, P. and Bhutia, P., 2024. Effects of bio stimulants on growth, yield and quality of tomato. *International Journal of Economic Plants*, 11(3), pp.347–352. [DOI]

Mandal, S., Anand, U., López-Bucio, J., Radha, Kumar, M. and Lal, M.K., 2023. Biostimulants and environmental stress mitigation in crops: a novel and emerging approach for agricultural sustainability under climate change. *Environmental Research*, 233, p.116357. [DOI]

Meena, D.C., Birthal, P.S. and Kumara, T.K., 2025. Biostimulants for sustainable development of agriculture: a bibliometric content analysis. *Discover Agriculture*, 3(1), p.2. [DOI]

Meena, R.S., Kumar, S., Datta, R., Lal, R., Vijayakumar, V., Bartnicky, M., Sharma, M.P., Yadav, G.S., Jhariya, M.K., Jangir, C.K. and Pathan, S.I., 2020. Impact of agrochemicals on soil microbiota and management: a review. *Land*, 9(2), p.34. [DOI]

Morcillo, R.J., Baroja-Fernández, E., López-Serrano, L., Leal-López, J., Muñoz, F.J., Bahaji, A., Férez-Gómez, A. and Pozueta-Romero, J., 2022. Cell-free microbial culture filtrates as candidate biostimulants to enhance plant growth and yield and activate soil- and plant-associated beneficial microbiota. *Frontiers in Plant Science*, 13, p.1040515. [DOI]

Naikoo, N.B., Chesti, M.H., Bhat, M.A., Hassan Mir, A., Bashir, O., Bhat, T.A., Salim Mir, M., Amin, Z., Gull, A. and Ayoub, L., 2025. Biostimulants towards soil health improvement: a review. *Agricultural Reviews*, 46(1), pp.1–15. [DOI]

Nath Bhowmik, S. and Das, A., 2018. Biofertilizers: a sustainable approach for pulse production. In: *Legumes for Soil Health and Sustainable Management*. Singapore: Springer Singapore, pp.445–485. [DOI]

Papnai, N., Chaurasiya, D.K. and Sahni, S., 2022. Biostimulants: concept, types and way to enhance soil health. *International Journal of Plant & Soil Science*, 34(20), pp.24–40. [DOI]

Patanè, C., Pellegrino, A., Saita, A., Calcagno, S., Cosentino, S.L., Scandurra, A. and Cafaro, V., 2025. A study on the effect of biostimulant application on yield and quality of tomato under long-lasting water stress conditions. *Heliyon*, 11(1). [DOI]

Pellegrino, E., Öpik, M., Bonari, E. and Ercoli, L., 2015. Responses of wheat to arbuscular mycorrhizal fungi: a meta-analysis of field studies from 1975 to 2013. *Soil Biology and Biochemistry*, 84, pp.210–217. [DOI]

Phooi, C.L., Azman, E.A. and Ismail, R., 2022. Do it yourself: humic acid. *Pertanika Journal of Tropical Agricultural Science*, 45(3), pp.701–720. [DOI]

Pillajo, J.Q., Chapin, L.J., Martins, E.M. and Jones, M.L., 2024. A biostimulant containing humic and fulvic acids promotes growth and health of tomato 'Bush Beefsteak' plants. *Horticulturae*, 10(7), p.671. [DOI]

Ranasingha, R., Perera, A., Baghalian, K. and Gerofotis, C., 2024. Amino acid-based biostimulants and microbial biostimulants promote the growth, yield and resilience of strawberries in soilless glasshouse cultivation. *Journal of Sustainable Agriculture and Environment*, 3(3), p.e12113. [DOI]

Ranjithkumar, A., 2025. Assessing the impact of agricultural land reduction on future global food security: challenges and sustainable solutions. *Indian Journal of Natural Sciences*, 15(88), pp.89066–89083.

Roche, D., Rickson, J.R. and Pawlett, M., 2024. Moving towards a mechanistic understanding of biostimulant impacts on soil properties and processes: a semi-systematic review. *Frontiers in Agronomy*, 6, p.1271672. [DOI]

Rouphael, Y. and Colla, G., 2020a. Biostimulants in agriculture. *Frontiers in Plant Science*, 11, p.40. [DOI]

Rouphael, Y. and Colla, G., 2020b. Toward a sustainable agriculture through plant biostimulants: from experimental data to practical applications. *Agronomy*, 10(10), p.1461. [DOI]

Saleem, A., Anwar, S., Nawaz, T., Fahad, S., Saud, S., Ur Rahman, T., Khan, M.N. and Nawaz, T., 2024. Securing a sustainable future: the climate change threat to agriculture, food security, and sustainable development goals. *Journal of Umm Al-Qura University for Applied Sciences*, pp.1–7. [DOI]

Seifollahi-Aghmiuni, S., Kalantari, Z., Egidi, G., Gaburova, L. and Salvati, L., 2022. Urbanisation-driven land degradation and socioeconomic challenges in peri-urban areas: insights from Southern Europe. *Ambio*, 51(6), pp.1446–1458. [DOI]

Selvan, T., Panmei, L., Murasing, K.K., Guleria, V., Ramesh, K.R., Bhardwaj, D.R., Thakur, C.L., Kumar, D., Sharma, P., Digvijaysinh Umedsinh, R. and Kayalvizhi, D., 2023. Circular economy in agriculture: unleashing the potential of integrated organic farming for food security and sustainable development. *Frontiers in Sustainable Food Systems*, 7, p.1170380. [DOI]

Seymen, M., Erdinç, Ç., Kurtar, E.S., Kal, Ü., Şensoy, S. and Türkmen, Ö., 2021. Potential effect of microbial biostimulants in sustainable vegetable production. In: *Microbiome Stimulants for Crops*. Cambridge: Woodhead Publishing, pp.193–237. [DOI]

Sharma, P., 2024. Change in geo-environmental conditions and crop productivity. In: Sharma, A., Kumar, M. and Sharma, P. (eds.) *Advances in Food Security and Sustainability, Vol. 9*. Amsterdam: Elsevier, pp.33–57. [DOI]

Sharma, P. and Borah, P., 2021. Influence of seed inoculation treatments on yield and quality of green gram (*Vigna radiata* L.). *Legume Research - An International Journal*, 44(6), pp.730–735. [DOI]

Sible, C.N., Seebauer, J.R. and Below, F.E., 2021. Plant biostimulants: a categorical review, their implications for row crop production, and relation to soil health indicators. *Agronomy*, 11, p.1297. [DOI]

Sible, C.N., Seebauer, J.R. and Below, F.E., 2025. Biostimulant or biological? The complexity of defining, categorizing, and regulating microbial inoculants. *Agricultural & Environmental Letters*, 10(2), p.e70027. [DOI]

Singh, R., Kaur, S., Bhullar, S.S., Singh, H. and Sharma, L.K., 2024. Bacterial biostimulants for climate smart agriculture practices: mode of action, effect on plant growth and roadmap for commercial products. *Journal of Sustainable Agriculture and Environment*, 3(1), p.e12085. [DOI]

Sun, W., Shahrajabian, M.H., Kuang, Y. and Wang, N., 2024. Amino acids biostimulants and protein hydrolysates in agricultural sciences. *Plants*, 13(2), p.210. [DOI]

Tamburino, R., Docimo, T., Sannino, L., Gualtieri, L., Palomba, F., Valletta, A., Ruocco, M. and Scotti, N., 2023. Enzyme-based biostimulants influence physiological and biochemical responses of *Lactuca sativa* L. *Biomolecules*, 13(12), p.1765. [DOI]

Thwaites, H.J., Hume, I.V. and Cavagnaro, T.R., 2025. The case for urban agriculture: opportunities for sustainable development. *Urban Forestry & Urban Greening*, 110, p.128861. [DOI]

Torres, P.Á., Rabalais, N.N., Gutiérrez, J.M. and López, R.M., 2017. Research and community of practice of the Gulf of Mexico large marine ecosystem. *Environmental Development*, 22, pp.166–174. [DOI]

Villa e Vila, V., Piedade, S.M., Bouix, C.P., Rezende, R., Wenneck, G.S., Terassi, D.D., Matumoto-Pintro, P.T. and Marques, P.A., 2024. Use of a biostimulant based on seaweed extract as a sustainable input to enhance the quality of solanaceous seedlings. *Horticulturae*, 10(6), p.642. [DOI]

Wang, J., Vanga, S.K., Saxena, R., Orsat, V. and Raghavan, V., 2018. Effect of climate change on the yield of cereal crops: a review. *Climate*, 6(2), p.41. [DOI]

Yakhin, O.I., Lubyanov, A.A., Yakhin, I.A. and Brown, P.H., 2017. Biostimulants in plant science: a global perspective. *Frontiers in Plant Science*, 7, p.2049. [DOI]

Zamljen, T., Medic, A., Hudina, M., Veberic, R. and Slatnar, A., 2023. Biostimulative effect of amino acids on the enzymatic and metabolic response of two *Capsicum annuum* L. cultivars grown under salt stress. *Scientia Horticulturae*, 309, p.111713. [DOI]

Zeifman L, Hertog S, Kantorova V. and Wilmoth J., 2022. A world of 8 billion. *United Nations*, Department of Economics and Social Affairs. Available at https://ourworldindata.org/world-population-growth

Nature Environment and Pollution Technology
An International Quarterly Peer-Reviewed Open Access Journal

p-ISSN: 0972-6268 | e-ISSN: 2395-3454 Vol. 25 | No. 4 | Article ID D1926 | 2026

RESEARCH ARTICLE https://doi.org/10.46488/NEPT.2026.v25i04.D1926 OPEN ACCESS

Valorization of Textile Waste into Cellulose-Citronellal Fiber Using Natural H-Zeolite Catalyst: Toward a Circular Bioeconomy Approach

Edy Cahyono[1], Samuel Budi Wardhana Kusuma[1], Sigit Priatmoko[1], Ridho Prasetyo[1] and Trida Ridho Fariz[2]†
[1]Department of Chemistry, Faculty of Mathematics and Natural Sciences, Universitas Negeri Semarang, Indonesia
[2]Environmental Science, Faculty of Mathematics and Natural Sciences, Universitas Negeri Semarang, Indonesia
†Corresponding author: Trida Ridho Fariz; trida.ridho.fariz@mail.unnes.ac.id

ARTICLE HISTORY

Received: 30-03-2026
Revised: 02-06-2026
Accepted: 04-06-2026

KEYWORDS

Textile waste valorization
Cellulose recovery
Citronellal
H-zeolite catalyst
Potential mosquito-repellent material
Circular bioeconomy

CITE THIS ARTICLE

Cahyono, E., Kusuma, S.B.W., Priatmoko, S., Prasetyo, R. and Fariz, T.R., 2026. Valorization of textile waste into cellulose-citronellal fiber using natural H-Zeolite catalyst: toward a circular bioeconomy approach, *Nature Environment and Pollution Technology*, 25(4), D1926. https://doi.org/10.46488/NEPT.2026.v25i04.D1926

COPYRIGHT & LICENCE

© 2026 The Authors
Open Access under CC BY 4.0.

PUBLISHED BY
TECHNOSCIENCE PUBLICATIONS

ABSTRACT

Mosquito-borne diseases such as malaria, dengue, chikungunya, and Zika remain major global health threats, while the rapid growth of the textile industry generates large volumes of waste largely disposed of in landfills due to limited recycling pathways. This study explores the valorization of cotton-based textile waste into functional biomaterials within a circular bioeconomy framework, using Indonesia as a case study due to its abundant textile waste, citronella biomass, and natural zeolite deposits. Cellulose was extracted from textile waste through acid hydrolysis, citronellal was isolated from citronella oil by fractional distillation, and natural zeolite was activated through acid treatment, ion exchange, and calcination to produce an H-Zeolite catalyst. The recovered cellulose was subsequently reacted with citronellal through a condensation-impregnation process using the H-Zeolite catalyst to synthesize cellulose-citronellal fibers. All materials were characterized using Fourier transform infrared spectroscopy (FTIR), scanning electron microscopy (SEM), and X-ray diffraction (XRD). Acid activation and ion exchange significantly increased zeolite acidity to 1.382 g NH_3 g^{-1} sample, indicating the formation of Brønsted acid sites suitable for catalytic reactions, while the zeolite crystalline framework remained stable after activation. Cellulose recovered from textile waste exhibited morphological and functional group characteristics comparable to commercial cellulose. FTIR analysis indicated the incorporation of citronellal into the cellulose matrix, suggesting the formation of cellulose-citronellal fibers with potential bioactive properties. However, FTIR evidence alone cannot confirm covalent bond formation, and further analyses including solid-state nuclear magnetic resonance (NMR), thermogravimetric analysis (TGA), and direct bioassay testing are recommended to fully validate functional performance. Overall, this study demonstrates a potential pathway for converting textile waste into higher-value bio-based materials using renewable biomass and a natural mineral catalyst, offering a circular bioeconomy model relevant for tropical countries facing similar biomass availability and vector-borne disease challenges.

1. INTRODUCTION

Mosquito-borne diseases such as dengue fever, malaria, and chikungunya remain a global health threat, with millions of cases occurring annually. Climate change is expanding the geographic distribution of mosquito vectors due to rising temperatures and changing rainfall patterns, making previously risk-free areas increasingly vulnerable (Fariz et al. 2026, Siniscalchi et al. 2026). This situation demands the development of more innovative, sustainable, and environmentally friendly vector control strategies, especially in tropical countries with high disease prevalence, such as Indonesia (Abbasi 2025, Baitharu et al. 2021).

Essential oils from plant families such as *Cymbopogon spp*., *Ocimum* spp., and *Eucalyptus* spp. are widely recognized for their mosquito-repellent properties. Active components with notable repellent activity include citronellol, citronellal, alpha-pinene, camphor, limonene, and thymol (Abdelgaleil et al. 2024, Nerio et al. 2010). Citronellal in particular has been studied as an insect repellent candidate, although its direct topical application provides only short-lived protection (Alighiri et al. 2018, Iovinella et al. 2022, Pujiastuti et al. 2017). Incorporating citronellal into functional textile materials offers a more practical and sustained approach to personal protection. Developing such functional textiles, however, requires simultaneous consideration of raw material sustainability and textile waste management, as the textile industry generates substantial amounts of solid residue (Hasan et al. 2025, Riza et al. 2021). Most textile waste is still disposed of in landfills due to high recycling costs, creating significant environmental burdens (Singh et al. 2025).

Globally, textile waste is estimated to exceed 92 million tons per year (Ghosh et al. 2025). At the national level, data from the Ministry of Environment (2025) recorded total waste generation in Indonesia at 25,141,493.03 tons, with fabric waste contributing approximately 2.46% of that volume. Although relatively modest in percentage, the absolute quantity remains substantial and largely underutilized. Textile recycling continues to be constrained by technological limitations and the economic burden of material separation, with most existing pathways downcycling waste into non-textile products such as composite materials. Cotton-based textile waste, by contrast, represents a promising feedstock due to its comparatively high cellulose purity relative to lignocellulosic sources such as wood, enabling more efficient and cost-effective cellulose recovery.

Cellulose recovered from cotton textile waste can be chemically modified into a range of functional derivatives. Post-consumer cotton textiles have been converted into wrinkle-resistant fabrics via esterification using polycarboxylic acids (Olivito et al. 2021), while surface functionalization followed by mechanical treatment has yielded cellulose citrate nanocrystals (CitCNCs) with tunable surface chemistry and favorable mechanical properties (Ma et al. 2023). Cellulose recovery yields for such applications have been reported between 65% and 88%, with degrees of substitution suitable for downstream processing into sodium carboxymethylcellulose (DS 0.27 to 0.61) and cellulose acetate (DS 2.59) (Ma et al. 2023). Beyond conventional derivatives, aromatic and functional textiles have also been developed through encapsulation approaches. β-cyclodextrin complexation has been employed to delay essential oil release and improve stability in textile applications (Costa et al. 2022), while microcapsule systems prepared via coacervation using gelatin and sodium sulfate, hardened with formaldehyde, have been optimized through response surface methodology to enhance encapsulation efficiency (Solomon et al. 2012). These diverse modification pathways confirm the versatility of textile-derived cellulose as a platform for producing value-added functional materials.

In the context of sustainable development, the circular bioeconomy framework provides a compelling rationale for integrating biomass valorization with waste reduction. Circular economy principles emphasize product design, business model innovation, and life cycle management to minimize waste and increase resource efficiency (Awan & Sroufe 2022, Mestre & Cooper 2017). Circular bioeconomy extends this further by incorporating biological resources through biotechnology and biorefinery approaches, encompassing bioenergy, bioplastics, and bio-based chemicals, while also addressing ecosystem and environmental considerations (Chikhalet et al. 2026, Kumari et al. 2026, Manhongo & Mbohwa 2026, Venkatesh 2022). Within the textile sector, most existing studies address the circular economy solely through mechanical or chemical fiber recycling without explicitly engaging with bioeconomic dimensions (Ghosh et al. 2025, Patti et al. 2020). The present study goes further by simultaneously valorizing two biomass streams, namely cellulose from cotton-based textile waste and citronellal from citronella oil, to produce a citronellal-modified cellulose fiber as a bio-based material with potential applications in vector-control-related protective textiles.

The condensation-impregnation of citronellal within the cellulose matrix requires a catalyst capable of activating the carbonyl groups of citronellal and the hydroxyl groups of cellulose. Natural zeolite modified into H-Zeolite through acid treatment and ion exchange provides a relatively inexpensive and accessible solid acid catalyst suitable for this purpose. The citronellal-modified cellulose fiber developed in this study represents a preliminary model for utilizing essential oil-derived compounds in sustainable cellulose-based biomaterials. The present study primarily focuses on synthesis and physicochemical characterization, while further investigations on release behavior, material stability, and direct bioassay testing remain subjects for future work.

Based on this background, the study aims to: (1) evaluate the yield and characteristics of cellulose extracted from cotton-based textile waste, (2) examine the role of the natural H-Zeolite catalyst in the condensation-impregnation of citronellal into the cellulose matrix, and (3) contextualize the overall process within a circular bioeconomy framework for textile waste valorization.

2. MATERIALS AND METHODS

2.1. Research Design

This experimental research was conducted in two main stages. The first stage was the recycling of textile waste into cellulose and the isolation of citronellal from citronella oil. The second stage was the preparation of a natural H-Zeolite catalyst and the synthesis of cellulose-citronellal fibers. In addition to laboratory experiments, this study also examined the conceptual framework of the circular bioeconomy in the context of the valorization of textile waste as a secondary biomass source for the development of cellulose-based functional materials. This study used Indonesia as a case study, considering the availability of textile biomass, citronella oil production, and the existence of local natural zeolite resources such as Malang zeolite from East Java Province, Indonesia. The circular bioeconomy conceptual framework in this study was supported by a review of relevant literature.

2.2. Extraction of Cellulose from Textile Waste

Preparation of cellulose citrate from fabric was adapted from Ruiz-Caldas et al. (2023). Cellulose extraction from fabric waste was carried out through acid hydrolysis. Small pieces of textile fabric (<1 cm^2) were placed in a round-bottom flask containing an 85% aqueous citric acid solution by weight. The ratio of textile to pure citric acid was maintained at 1:20 (g g^{-1}).

The mixture was stirred at 300 rpm at 100°C. After the citric acid was completely dissolved, the reaction was maintained for 7 h. The reaction was then stopped by a fivefold dilution with deionized (DI) water. The mixture was then filtered using a 5 µm pore-size polyethersulfone (PES) membrane to separate the citric acid solution from the solid fraction containing carboxylated cotton fibers and residual acid. The citric acid was recovered through evaporation and crystallization. The remaining citric acid was then rinsed from the solids by slowly adding DI water to the filter until the filtrate conductivity dropped below 5 mS cm^{-1}. Synthetic fibers or other fibers that remained intact during the process were separated through filtration and referred to as residue.

2.3. Isolation of Citronellal from Citronella Oil

The preparation steps for isolating citronellal from lemongrass oil were adapted from Cahyono et al. (2010). The citronellal content in *Cymbopogon winterianus* lemongrass oil was analyzed using gas chromatography-mass spectrometry (GC-MS). Isolation of citronellal from lemongrass oil containing more than 35% citronellal was carried out using fractional distillation at low pressure. The fraction with the highest citronellal content was then separated and subjected to redistillation. The redistillation products were then analyzed using gas chromatography (GC).

2.4. Preparation of Natural H-Zeolite Catalyst

Acid treatment was performed to control the acidity and selectivity of the zeolite. Natural zeolite chunks were ground using a mortar grinder to obtain homogeneous granules that passed a 100-mesh sieve. The sieved granules were oven-dried to remove moisture. A total of 300 g of dried 100-mesh natural zeolite was immersed in 350 mL of 1% hydrofluoric acid solution for 20 min. The sample was then washed until neutral and dried. Next, 30 g of the dried sample was immersed in 125 mL of 6 N HCl solution for 30 min at 50°C. The sample was washed until neutral and dried at 120°C. This activation product was designated Za.

A total of 20 g of Za was then added to 250 mL of 3 M ammonium chloride solution. The mixture was stirred for 24 h at room temperature, then filtered and washed with running water until free of chloride ions, as tested using $AgNO_3$ solution. The resulting solid was heated at 120°C until dry. The dried solid was then calcined at 450°C for 1 h using a modified calcinator described by Cahyono et al. (2010) to remove NH_3 gas. The final product of this treatment was referred to as H-Za.

2.5. Synthesis of Cellulose-Citronellal Fiber

The synthesis of cellulose-citronellal fibers was carried out in a reflux reactor equipped with a magnetic stirrer and an inert N_2 gas flow. A total of 1 g of natural H-Zeolite catalyst, 3 g of cellulose, and 30 mL of citronellal in ethyl acetate solvent were loaded into a 100 mL reactor flask with a total reaction volume of 50 mL. The mixture was stirred at reflux temperature. Samples were taken at reaction times of 3, 6, and 9 h. The catalyst was separated from the sample by centrifugation and then extracted using n-hexane. The obtained solids were analyzed using FTIR.

3. RESULTS AND DISCUSSION

3.1. Preparation and Characterization of Natural H-Zeolite Catalyst

3.1.1. Determination of Acidity Degree

The acidity level of the catalyst is an important parameter in determining the catalytic activity in the condensation reaction between citronellal and cellulose. In this system, acid sites play a role in activating the carbonyl groups of citronellal and facilitating interactions with the hydroxyl groups in the cellulose polymer chain. Therefore, increasing the number of acid sites on the catalyst surface is expected to

Table 1: Determination of acidity degree.

Sample Code	Mass of ammonia (g)	Acidity degree (g)
HF Washing	0.009	1.040
NH_4Cl Washing	0.007	0.820

increase the efficiency of the condensation reaction during cellulose-citronellal fiber formation. The acidity degree was determined using a gravimetric method based on ammonia adsorption. The measurement results are shown in Table 1.

The results in Table 1 show that acid treatment using hydrofluoric acid increased the acidity level of the catalyst compared to the original zeolite. This increase occurred due to the release of impurities in the form of free SiO_2 and metal oxides from the zeolite surface, thereby increasing the number of available acid sites in the aluminosilicate structure. It should be noted that the acidity values reported in Table 1 are expressed in grams of adsorbed ammonia per gram of sample, as measured by the gravimetric method. Future studies are recommended to report acidity in standardized units (mmol NH_3 g^{-1}) obtained through ammonia temperature-programmed desorption (NH_3-TPD) to enable more rigorous inter-study comparisons.

In the next stage, ion exchange using an NH_4Cl solution caused a temporary decrease in the acidity level. This occurred because NH_4^+ ions replaced metal cations such as Na^+ and Ca^{2+} in the zeolite framework. After calcination, the NH_4^+ ions decomposed into NH_3 gas, forming new Brønsted acid sites in the zeolite framework. This transformation produced a natural H-Zeolite catalyst with the highest acidity level of 1.382. The increase in acidity after acid treatment and NH_4^+ ion exchange followed by calcination is consistent with previous studies reporting that acid activation and H-Zeolite formation can increase the concentration of Brønsted sites and improve pore accessibility in natural zeolites (Muhammad et al. 2024, Tanirbergenova et al. 2025).

Compared with several other natural zeolite activation studies, the increase in acidity obtained in this study is in a comparable range to mordenite- and clinoptilolite-type zeolites that have been activated through a combination of acid treatment and ion exchange (Stoyanov et al. 2024). This indicates that the activation method used in this study is effective in producing heterogeneous catalysts with relatively high acid properties. Mechanistically, the Brønsted acid sites in H-Zeolite function as protonation centers that can activate the aldehyde carbonyl group in citronellal. This protonation increases the electrophilicity of the carbonyl carbon, thus facilitating the nucleophilic attack of the hydroxyl group on the cellulose chain, which ultimately facilitates the formation of new bonds in the condensation process. However, it should be noted that the exact nature of the interaction, whether covalent bond formation or surface adsorption, cannot be ascertained from acidity data alone and requires further physicochemical analysis such as solid-state NMR or thermogravimetric analysis. Therefore, increasing the acidity of the catalyst is an important parameter in supporting the citronellal–cellulose interaction during fiber production.

3.1.2. Functional Group Analysis using FTIR

FTIR analysis was performed to identify changes in functional groups in the zeolite structure after chemical treatment. The FTIR spectra of natural zeolite, HF-treated zeolite, and NH_4Cl-treated zeolite are shown in Fig. 1.

The main absorption band at wavenumbers around 1000–1100 cm^{-1} is associated with Si–O–Si stretching vibrations in the zeolite aluminosilicate framework. This

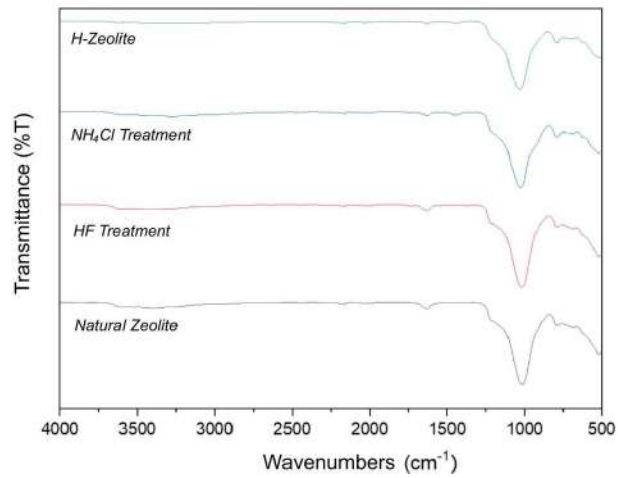


Fig. 1: Functional groups of (a) natural zeolite, (b) zeolite resulting from reaction with HF, (c) zeolite resulting from reaction with NH_4Cl, and (d) H- zeolite.

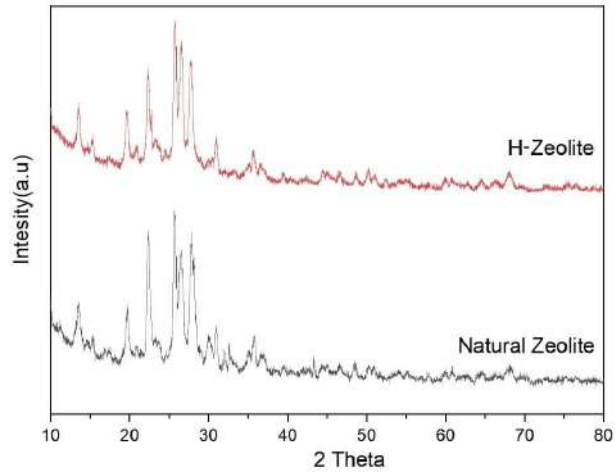


Fig. 2: XRD results of natural zeolite and H-Zeolite.

band is a general characteristic of zeolite structures and has been widely reported in FTIR characterizations of natural and modified zeolites (Adila et al. 2024, Gebretsadik & Gebremedhin 2020). After acid activation, the band appears sharper, indicating increased regularity of the silica–alumina structure. Furthermore, the appearance of additional bands in the wavenumber region associated with –OH groups (silanol and bridging hydroxyl) indicates the formation of new acid sites on the catalyst surface.

These –OH groups are generally associated with the presence of Brønsted acid sites in the zeolite structure, and an increase in their intensity is often observed after acid activation or ion exchange processes in various zeolite types such as clinoptilolite, mordenite, and zeolite X (Adila et al. 2024, Hieu et al. 2022). These spectral changes indicate that the chemical treatment carried out does not cause damage to the zeolite aluminosilicate framework, but only modifies the surface and increases the number of catalytic active sites. The stability of this structure is important because the catalytic activity of zeolites is highly dependent on the integrity of their crystal framework.

3.1.3. Structural Analysis using XRD

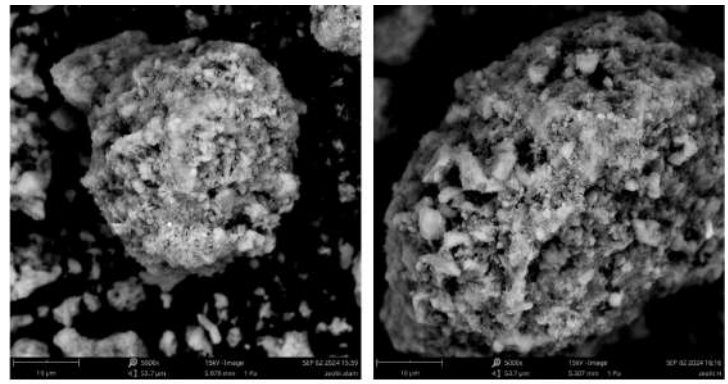
XRD analysis was performed to evaluate whether the chemical activation process causes changes in the crystal structure of the zeolite. XRD diffractograms of natural zeolite and H-Zeolite are shown in Fig. 2. The diffraction patterns show that the characteristic peaks of the zeolite are maintained after the activation process. This indicates that the acid treatment and ion exchange treatments do not damage the primary crystalline structure of the zeolite. It is acknowledged that the XRD peaks in this study have not been fully indexed to specific zeolite phases (e.g., clinoptilolite or mordenite), and quantitative parameters such as crystallinity percentage, Si/Al ratio, and unit-cell parameters were not determined. These data would strengthen the characterization and are recommended for future work.

This phenomenon has been reported in various studies showing that moderate acid treatment of natural zeolites can increase porosity and acidity without destroying the main crystalline framework, which usually retains the typical diffraction pattern of mordenite or clinoptilolite (Muhammad et al. 2024, Stoyanov et al. 2024, Tanirbergenova et al. 2025). Compared with other activation methods such as extreme dealumination or high-concentration strong acid treatment, the activation method used in this study tends to be more selective in removing impurities without destroying the zeolite framework structure. The stability of this crystalline structure is important because the catalytic activity of zeolites is strongly influenced by the pore distribution and the stability of their aluminosilicate structure. However, the present study does not include quantitative measurements of Brunauer-Emmett-Teller (BET) surface area, pore volume, or Si/Al ratio, which would be necessary to fully substantiate the relationship between structural changes and catalytic performance. These limitations are acknowledged, and such measurements are recommended in follow-up studies.

3.1.4. Morphological Analysis using SEM

Morphological analysis using SEM showed that the surface structure of the zeolite underwent a textural change after activation. Natural zeolite appeared relatively dense with limited pore distribution. After activation to H-Zeolite, the surface exhibited a rougher texture with more pronounced porosity (Fig. 3).

These morphological changes indicate that the activation process successfully opened some of the zeolite pores, thereby increasing the surface area available for catalytic



(a) (b)

Fig. 3: Morphology of (a) natural zeolite and (b) H-Zeolite.



(a) (b)

Fig. 4: Morphology of (a) cotton fabric decellulose and (b) Merck cellulose.

processes. Similar textural changes have also been observed in various natural zeolite activation studies, where acid treatment can remove mineral impurities and metal oxides from the zeolite surface, resulting in a more porous structure and increasing the accessibility of catalytic sites (Side et al. 2023, Tanirbergenova et al. 2025). This increase in porosity is significant because it can enhance the diffusion of reactant molecules such as citronellal into the catalyst's pore structure during the reaction. However, it should be noted that the current SEM analysis is qualitative in nature. Quantitative surface characterization data, namely BET surface area, pore volume, and average pore diameter, were not measured in this study, and their absence limits the extent to which claims of increased porosity can be substantiated. Such data are recommended for future characterization to provide a more complete picture of the activation outcome.

3.2. Cellulose Recovery from Textile Waste

3.2.1. Morphological Analysis Using SEM

Morphological analysis using SEM was performed to compare the structure of cellulose obtained from textile waste with commercial standard cellulose (Merck cellulose). The results showed that the acid hydrolysis process successfully separated the cellulose component from the textile matrix. The extracted cellulose fibers had a morphology similar to standard cellulose, although the resulting particle size remained relatively larger (Fig. 4).

These findings align with previous studies showing that chemical treatment of cellulose extracted from cotton textile waste can produce morphologies similar to commercial cellulose (Maciel et al. 2019, Rana et al. 2023). The observed differences in particle size are likely due to varying degrees of fiber degradation during the hydrolysis process. In some studies, more aggressive chemical treatments or the use of additional mechanochemical processes such as mechanical fibrillation can produce smaller cellulose particles. Nevertheless, the similarity in morphology suggests that cellulose from textile waste has potential as a raw material for the development of cellulose-based materials.

3.2.2. Functional Group Analysis Using FTIR

The FTIR spectrum of the extracted cellulose showed

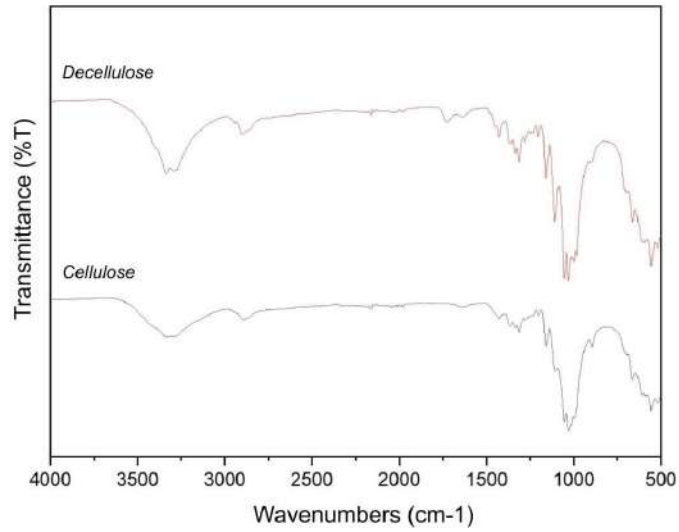


Fig. 5: FTIR spectra of standard cellulose and cellulose extracted from acid-treated textile waste.

significant similarity to the spectrum of standard cellulose. Absorption bands associated with vibrations of the –OH group, C–H stretching, and C–O–C bonds, typical of polysaccharide structures, were clearly detected. The presence of these bands indicates that the basic structure of the cellulose was maintained during the extraction process (Fig. 5).

These results are consistent with previous studies that reported that cellulose obtained from cotton textile waste exhibited FTIR characteristics very similar to standard cellulose, with the characteristic –OH, C–H, and C–O–C bands still clearly detected (Maciel et al. 2019, Rana et al. 2023). Thus, cellulose obtained from textile waste can be considered to have sufficient structural quality for use in further chemical modification processes.

3.2.3. Formation of Cellulose-Citronellal Fibers

The synthesis of cellulose-citronellal fiber was carried out through a condensation reaction between citronellal and cellulose with the aid of a natural H-Zeolite catalyst. This process aims to incorporate citronellal into the cellulose matrix, producing a functional fiber material with potential bioactive properties. It is important to emphasize that, in this study, the nature of the citronellal–cellulose interaction, whether it involves covalent bond formation or physical adsorption, could not be definitively established based solely on FTIR analysis. More precise characterization using complementary techniques such as solid-state NMR, TGA, or GC-MS analysis of wash extracts would be required to distinguish between chemical bonding and physical incorporation.

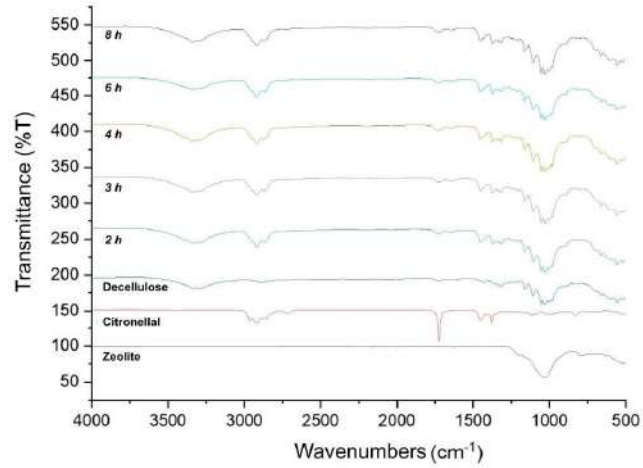


Fig. 6: FTIR spectra of cellulose-citronellal fiber synthesis products with variations in reaction time.

Mechanistically, the Brønsted acid sites in H-Zeolite can activate the carbonyl group of aldehydes through protonation. This activation increases the electrophilic nature of the carbonyl carbon, facilitating interaction with the hydroxyl group in cellulose. This mechanism aligns with various reports on the role of zeolite catalysts in facilitating condensation reactions or acetalization between aldehydes and compounds containing hydroxyl groups (Hieu et al. 2022, Muhammad et al. 2024).

FTIR analysis of the reaction products revealed changes in absorption band intensity at several characteristic wavenumbers (Fig. 6). At reaction times of 3, 6, and 9 h, the intensity of the absorption band at approximately 3000 cm^{-1} gradually increased with increasing reaction time. This band corresponds to the C–H stretching vibrations of the alkyl groups within the citronellal molecules. Furthermore, an increase in intensity was also observed in the 1300–1400 cm^{-1} wavenumber region, which corresponds to the CH deformation vibrations of the alkyl groups.

The increase in intensity in these two spectral regions indicates that the citronellal molecules were successfully integrated into the cellulose matrix. This analytical approach has also been widely used in polymer modification studies, where an increase in the aliphatic C–H band in the FTIR spectrum is considered an indication of successful binding of organic groups to the solid matrix (Adila et al. 2024, Gabrienko et al. 2018). Overall, these results suggest that the natural H-Zeolite catalyst facilitated the incorporation of citronellal into the cellulose matrix, as indicated by the observed changes in FTIR spectral intensity. However, several important limitations must be acknowledged. First, the observed increase in C–H stretching intensity does not alone confirm the formation of a covalent chemical bond between citronellal and cellulose; this spectral change may also be attributable to physical adsorption of citronellal onto or within the cellulose matrix. Distinguishing between these two mechanisms would require additional analyses such as solid-state $^{1}H/^{13}C$ NMR, TGA (thermogravimetric analysis) to assess the thermal stability of loading, or GC-MS analysis of wash extracts to evaluate release behavior. Second, this study did not include reaction yield, citronellal loading efficiency, or washing stability data, which limits the assessment of practical feasibility. Third, no control experiment without a catalyst was conducted, making it difficult to attribute the observed spectral changes specifically to the catalytic role of H-Zeolite. These limitations are acknowledged, and future studies incorporating these analyses are encouraged to provide more conclusive evidence of the material's chemical structure and functional performance.

3.3. Circular Bioeconomy Perspective of Textile Waste Valorization

The results of this study indicate that cellulose obtained from cotton-based textile waste can be used as a raw material for the synthesis of functional materials through a condensation reaction with citronellal using a natural H-Zeolite catalyst. These findings have important implications for textile waste management and the development of biomass-based materials within a circular bioeconomy framework.

Globally, textile waste continues to increase in line with the growth of the fashion industry and clothing consumption. It is estimated that more than 92 million tons of textile waste are generated annually worldwide (Ghosh et al. 2025). However, the utilization rate remains very low. In the United States, approximately 16.9 million tons of textile waste were recorded in 2017, but only approximately 15% was recycled or donated (Wagaw & Babu 2023). A similar situation also occurs in Europe, where only approximately 15–20% of textile waste is collected for reuse or recycling, while most of the remainder is landfilled or incinerated (Sandin & Peters 2018). In fact, globally, it is estimated that around 75% of textile waste still ends up in landfills (Juanga-Labayen et al. 2022). Therefore, various studies in the United States and Europe conclude that only around 15% of global textile waste is actually recycled into new products, and only a small portion is processed through fiber-to-fiber recycling.

This trend is also reflected at the national level. According to data from the Ministry of Environment (2025), total waste generation in Indonesia in 2023 reached 23,878,638.66 tons, with fabric waste contributing approximately 2.52% of the total waste generation. In 2024, total waste generation increased to 36,009,662.6 tons, with textile waste contributing approximately 2.55%. Meanwhile, in 2025, waste generation was recorded at 25,141,493.03 tons, with fabric waste contributing approximately 2.46% of the total national waste generation. Although the percentage is relatively small, the absolute volume of textile waste produced remains significant, and most of it has not been optimally utilized.

From a circular bioeconomy perspective, textile waste actually holds significant potential as a secondary biomass source. One of the main components of textile waste is cellulose-rich cotton fiber. An estimated 11.6 million tons of cotton waste are generated annually in the global textile industry (Johnson et al. 2020). Cotton fiber contains high-purity cellulose, making it highly potential for conversion into biomass-based materials with higher added value (Homem & Amorim 2020). Therefore, recovering cellulose

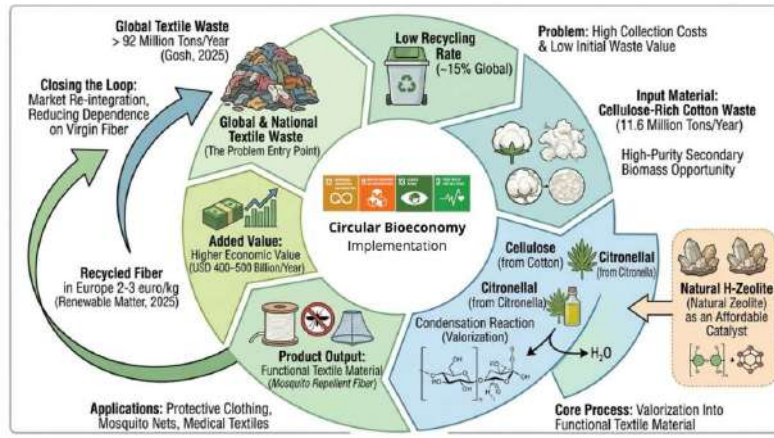


Fig. 7: Circular bioeconomy logic diagram for textile waste fabric valorization.

from textile waste through chemical recycling can be seen as a promising strategy for textile waste valorization.

Beyond its potential as a biomass source, textile waste also holds significant economic value. It is estimated that globally, unutilized clothing waste has an economic value of approximately USD 400–500 billion per year (Ghosh et al. 2025, Wagaw & Babu 2023). However, most literature indicates that textile recycling systems still face economic challenges, primarily due to the relatively high costs of collection and processing compared to virgin fiber production. Recycled textile fibers often command higher prices than virgin fibers due to logistics and material recovery costs (Boschmeier et al. 2024, Wagner & Heinzel 2020). Nevertheless, in the European market, recycled textile fibers still have an economic value of around 2–3 euros/kg, indicating that textile waste can be viewed as an economic resource within a circular economy (Renewable Matter 2025).

In this study, a valorization approach was employed by utilizing cellulose from textile waste as a raw material for the synthesis of new materials through a condensation reaction with citronellal. The integration of cellulose and active compounds from citronella oil resulted in a biomass-based material with potential applications as a mosquito repellent fiber. Citronella itself is a regionally relevant biomass commodity, as Indonesia is known as a major producer of citronella oil in the growing global essential oil market (Ahmad et al. 2025).

In addition to biomass availability, the successful development of valorization technology also depends on the availability of economical and sustainable catalysts. This study used a natural H-Zeolite catalyst derived from natural zeolite. Globally, natural zeolite production is estimated at around 1.1 million tons per year, with industrial prices ranging from USD 564–935 per ton depending on the country (Research & Markets 2026).In Indonesia, zeolite is an abundant industrial mineral. Natural zeolite from Malang, particularly from the South Malang region, primarily contains mordenite and has been widely used in various applications such as bioethanol purification adsorbents, catalysts, filtration media, and soil conditioners (Apandi 2002, Kurniawan et al. 2019). Natural zeolite is relatively affordable, ranging from IDR 5,000 to IDR 70,000 per kg (approximately USD 0.30–4.25 per kg), giving it high potential for development as a catalyst in biomass-based chemical processes (Ismuyanto et al. 2025). Furthermore, the market value of zeolite in Indonesia is projected to increase from approximately USD 98 million in 2024 to USD 154 million in 2032, demonstrating the growing role of this mineral in various industrial sectors.

Considering the availability of textile biomass, the economic potential of waste, and the availability of local mineral-based catalysts, the approach developed in this study can be seen as an example of implementing a circular bioeconomy in Indonesia and may apply to tropical countries with similar challenges. Textile waste is no longer treated as the final residue in a linear production system, but as a source of secondary raw materials that can be converted into functional materials with higher added value. The logic diagram for applying the circular bioeconomy to textile waste in this study is presented in Fig. 7.

This approach directly supports Sustainable Development Goal (SDG) 12 (Responsible Consumption and Production) through efforts to reuse waste materials and SDG 9 (Industry, Innovation, and Infrastructure) through the development of waste-based functional biomaterials. Indirectly, this approach also has the potential to contribute to SDG 13 (Climate Action) and SDG 3 (Good Health and Well-being)

through biomass utilization and the development of textile materials with potential mosquito repellent activity.

Although this study demonstrates the potential of utilizing textile waste as a source of cellulose for the synthesis of functional materials, several limitations still need to be considered. First, the material characterization conducted in this study is still limited to chemical structure and morphology analysis using FTIR, SEM, and XRD. Evaluation of the physical and mechanical properties of cellulose-citronellal fibers, such as tensile strength, thermal stability, and resistance to environmental degradation, has not been comprehensively analyzed. These parameters are important for assessing the material's suitability for industrial-scale textile applications. Second, the mosquito repellent activity testing in this study is still preliminary. A more comprehensive evaluation is needed to assess the protective effectiveness under real-life conditions. Important parameters such as the duration of protection, the release kinetics of citronellal from the cellulose matrix, and the stability of the active compound against washing processes and environmental exposure have not been analyzed in depth. Third, this study has not yet quantitatively evaluated the sustainability aspects of the process. Although the approach used in this study utilizes biomass and a natural mineral-based heterogeneous catalyst, a quantitative process sustainability analysis has not been conducted. Previous studies have shown that the wet processing stages in the textile industry, particularly pretreatment, dyeing, and finishing, are dominant contributors to various environmental impact categories, such as global warming potential, aquatic ecotoxicity, and water consumption (Catarino et al. 2025, Li et al. 2024). In fact, in some studies, the dyeing process unit was reported to make the largest contribution to almost all environmental impact indicators at the midpoint impact level (Gonzalez et al. 2023). Therefore, a quantitative evaluation of the technology developed in this research is essential to comprehensively assess its potential environmental benefits.

The approach commonly used in these studies is a life cycle assessment (LCA) with cradle-to-gate or gate-to-gate system boundaries, which evaluates various indicators such as carbon footprint, energy consumption, water use, and potential toxicity in the textile production system (Imran et al. 2023). Therefore, integrating LCA analysis, evaluating process energy consumption, and estimating potential greenhouse gas emission reductions is a crucial research priority to assess the contribution of this textile waste valorization technology to a more sustainable textile production system. Furthermore, the scale-up process has not been evaluated in this study. The cellulose extraction, citronellal isolation, and material synthesis processes are still conducted at the laboratory scale, requiring further studies on process efficiency, energy requirements, and production costs at an industrial scale.

4. CONCLUSIONS

This study demonstrates the feasibility of converting cotton-based textile waste into functional biomaterials through a catalytic modification process within a circular bioeconomy framework. Cellulose recovered from textile waste through acid hydrolysis exhibited structural and morphological characteristics comparable to commercial cellulose, confirming that textile waste can serve as a viable secondary biomass resource. Natural H-Zeolite catalyst prepared through acid activation, ion exchange, and calcination showed significantly increased acidity while maintaining zeolite crystalline integrity. The Brønsted acid sites present on the H-Zeolite catalyst facilitated the condensation-impregnation process between citronellal and cellulose, and FTIR analysis indicated the incorporation of citronellal into the cellulose matrix, suggesting the formation of cellulose-citronellal fibers with potential bioactive properties.

Beyond laboratory-scale synthesis, this study highlights the relevance of the proposed approach within a circular bioeconomy context. By integrating cellulose from textile waste and citronellal from plant-based essential oils, the pathway demonstrates a strategy for valorizing textile residues into bio-based functional materials with higher added value. Using Indonesia as a case study, with its available textile waste, citronella biomass, and natural zeolite deposits, the approach is particularly applicable to tropical countries facing similar resource conditions and vector-borne disease challenges.

Several limitations remain to be addressed. The current work focuses primarily on chemical and structural characterization, and future research should investigate the mechanical properties, durability, wash stability, and citronellal release kinetics of the synthesized fibers. Quantitative sustainability assessments, including life cycle assessment (LCA), energy consumption analysis, and greenhouse gas emission estimation, are also recommended to evaluate the environmental benefits and scalability of this valorization approach.

5. ACKNOWLEDGEMENT

The authors would like to express their gratitude to the Institute for Research and Community Service (LP2M), Universitas Negeri Semarang, for administrative support. The authors also thank the Chemistry Laboratory and Environmental Science Department of Universitas Negeri Semarang for providing technical assistance and facilities. This research was funded by Universitas Negeri Semarang

through the Institute for Research and Community Service (LP2M), under the 2024 DPA LP2M Universitas Negeri Semarang funding scheme, based on Decree/Announcement No. B/1187/UN37/PT.01.02/2024.

6. REFERENCES

Abbasi, E., 2025. Innovative approaches to vector control: integrating genomic, biological, and chemical strategies. *Annals of Medicine and Surgery*, 87(8), pp. 5003–5011. [DOI]

Abdelgaleil, S.A.M., Gad, H.A., Ramadan, G.R.M., El-Bakry, A.M. and El-Sabrout, A.M., 2024. Monoterpenes: chemistry, insecticidal activity against stored product insects and modes of action—a review. *International Journal of Pest Management*, 70(3), pp. 267–289. [DOI]

Adila, Z., Trisunaryanti, W. and Triyono, T., 2024. Modification of natural zeolite from Klaten, Indonesia using ammonium chloride by ion-exchange and its application as catalyst in ethanol dehydration to produce diethyl ether. *Indonesian Journal of Chemistry*, 24(2), pp. 505–518. [DOI]

Ahmad, U., Dentaka, D. and Krah, C.Y., 2025. The impact of withering pre-processing and distillation durations on yield and quality of citronella oil. *Journal of Applied Agricultural Science and Technology*, 9(2), pp. 140–155. [DOI]

Alighiri, D., Cahyono, E., Eden, W.T., Kusuma, E. and Supardi, K.I., 2018. Study on the improvement of essential oil quality and its repellent activity of betel leaves oil (*Piper betle* L.) from Indonesia. *Oriental Journal of Chemistry*, 34(6), pp. 2913. [DOI]

Apandi, T.T., 2002. Indonesian natural zeolites marketing. *Jurnal Zeolit Indonesia*, 1(1), pp. 31–37. Available at: https://journals.itb.ac.id/index.php/jzi/article/view/1234.

Awan, U. and Sroufe, R., 2022. Sustainability in the circular economy: insights and dynamics of designing circular business models. *Applied Sciences*, 12(3), p. 1521. [DOI]

Baitharu, I., Shroff, S., Naik, P.P. and Sahu, J.K., 2021. Environmental management and sustainable control of mosquito vector: challenges and opportunities. In: *Molecular Identification of Mosquito Vectors and Their Management*. Springer, pp. 129–147. [DOI]

Boschmeier, E., Ipsmiller, W. and Bartl, A., 2024. Market assessment to improve fibre recycling within the EU textile sector. *Waste Management & Research*, 42(2), pp. 135–145. [DOI]

Cahyono, E., Muchalal, T. and Pranowo, H.D., 2010. Kinetic study cyclisation-acetylation (R)-(+)-citronellal by modified natural zeolite as solid solvent. *Indonesian Journal of Chemistry*, 10(2), pp. 189–194. [DOI]

Catarino, M.L., Sampaio, F. and Gonçalves, A.L., 2025. Sustainable wet processing technologies for the textile industry: a comprehensive review. *Sustainability*, 17(7), p. 3041. [DOI]

Chikhalet, S.S., Pathade, G.R. and Bagwan, W.R., 2026. Duckweed as a circular economy solution for treating agro-industrial wastewaters. *Nature Environment and Pollution Technology*, 25(1), pp. 1–12. [DOI]

Costa, C., Viana, A., Silva, C., Marques, E.F. and Azoia, N.G., 2022. Recycling of textile wastes, by acid hydrolysis, into new cellulosic raw materials. *Waste Management*, 153, pp. 99–109. [DOI]

Fariz, T.R., Budiarti, R., Listyarini, J., Puspitasari, A.T., Calysta, N., Naufal, M.A., Heriyanti, A.P. and Eralita, N., 2026. A participatory GIS framework for multi-hazard climate risk mapping in Indonesia. *Advance Sustainable Science Engineering and Technology*, *8*(1), pp. 02601023–02601023. [DOI]

Gabrienko, A.A., Danilova, I.G., Arzumanov, S.S., Pirutko, L.V., Freude, D. and Stepanov, A.G., 2018. Direct measurement of zeolite Brønsted acidity by FTIR spectroscopy: solid-state 1H MAS NMR approach for reliable determination of the integrated molar absorption coefficients. *The Journal of Physical Chemistry C*, 122(44), pp. 25386–25395. [DOI]

Gebretsadik, T.T. and Gebremedhin, T.K., 2020. Structural studies of natural zeolites and optimizations for water hardness softening media. *Journal of Metals, Materials and Minerals*, 30(1). [DOI]

Ghosh, J., Repon, M.R., Rupanty, N.S., Asif, T.R., Tamjid, M.I. and Reukov, V., 2025. Chemical valorization of textile waste: advancing sustainable recycling for a circular economy. *ACS Omega*, 10(12), pp. 11697–11722. [DOI]

Gonzalez, V., Lou, X. and Chi, T., 2023. Evaluating environmental impact of natural and synthetic fibers: a life cycle assessment approach. *Sustainability*, 15(9), p. 7670. [DOI]

Hasan, T., Sheikh, M.S., Hossain, M.L. and Hoque, M.B., 2025. A comprehensive review of solid waste management in the textile industry. *Journal of the Air & Waste Management Association*, 75(11), pp. 839–854. [DOI]

Hieu, D.T., Kosslick, H., Riaz, M., Schulz, A., Springer, A., Frank, M. and Jaeger, C., 2022. Acidity and stability of Brønsted acid sites in green clinoptilolite catalysts and catalytic performance in the etherification of glycerol. *Catalysts*, 12(3), p. 253. [DOI]

Homem, N.C. and Amorim, M.T.P., 2020. Synthesis of cellulose acetate using as raw material textile wastes. *Materials Today: Proceedings*, 31, pp.S315-S317. [DOI]

Imran, S., Mujtaba, M.A., Zafar, M.M., Hussain, A., Mehmood, A., Farwa, U.E. and Korakianitis, T., 2023. Assessing the potential of GHG emissions for the textile sector: a baseline study. *Heliyon*, 9(11). [DOI]

Iovinella, I., Caputo, B., Cobre, P., Manica, M., Mandoli, A. and Dani, F.R., 2022. Advances in mosquito repellents: effectiveness of citronellal derivatives in laboratory and field trials. *Pest Management Science*, 78(12), pp. 5106–5112. [DOI]

Ismuyanto, B., NH, A.S.D.S. and Rahmawati, D., 2025. Zeolit sintesis binder alkali aktivasi zeolit alam Malang. *Prosiding Sains Nasional dan Teknologi*, 15(1). Available at: https://prosiding.upnjatim.ac.id/index.php/saintek/article/view/5678.

Johnson, S., Echeverria, D., Venditti, R., Jameel, H. and Yao, Y., 2020. Supply chain of waste cotton recycling and reuse: a review. *AATCC Journal of Research*, 7(1_suppl), pp. 19–31. [DOI]

Juanga-Labayen, J.P., Labayen, I.V. and Yuan, Q., 2022. A review on textile recycling practices and challenges. *Textiles*, 2(1), pp. 174–188. [DOI]

Kumari, S., Rao, A., Kaur, M. and Dhania, G., 2026. Valorization of corn cob into cellulose-based bioplastics: extraction, fabrication and biodegradability evaluation. *Nature Environment and Pollution Technology*, 25(1), pp. 1–9. [DOI]

Kurniawan, T., Nuryoto, N. and Firdaus, M.A., 2019. Zeolite for agriculture intensification and catalyst in agroindustry. *World Chemical Engineering Journal*, 3(1), pp. 13–23. [DOI]

Li, C., Zhang, T., Zhou, X., Cheng, Z., Xu, T., Li, Z. and Hong, J., 2024. Carbon–water–energy footprint impacts of dyed cotton fabric production in China. *Journal of Cleaner Production*, 467, p. 142898. [DOI]

Ma, J., Fan, J., Xia, Y., Kou, X., Ke, Q. and Zhao, Y., 2023. Preparation of aromatic β-cyclodextrin nano/microcapsules and corresponding aromatic textiles: a review. *Carbohydrate Polymers*, 308, p. 120661. [DOI]

Maciel, M.M.Á.D., de Carvalho Benini, K.C.C., Voorwald, H.J.C. and Cioffi, M.O.H., 2019. Obtainment and characterization of nanocellulose from an unwoven industrial textile cotton waste: effect of acid hydrolysis conditions. *International Journal of Biological Macromolecules*, 126, pp. 496–506. [DOI]

Manhongo, T.T. and Mbohwa, C., 2026. Facilitating renewable energy production for a circular bioeconomy: a review of the biorefinery potential, opportunities, and challenges for valorization of sorghum processing residues in sub-Saharan Africa. *Biomass and Bioenergy*, 206, p. 108678. [DOI]

Mestre, A. and Cooper, T., 2017. Circular product design: a multiple loops life cycle design approach for the circular economy. *The Design Journal*, 20(sup1), pp.S1620-S1635. [DOI]

Ministry of Environment, 2025. *Sistem Informasi Pengelolaan Sampah Nasional (National Waste Management Information System)*. Available at: https://portal-sipsn.kemenlh.go.id/.

Muhammad, R., Al-Muqati, N.S., Schulz, A., Alessa, A., Al-Otabi, R., Osman, A.I. and Al-Fatesh, A.S., 2024. Temperature-induced modifications in natural zeolite clinoptilolite: effects on acidity and catalytic acetalization. *ChemNanoMat*, 10(7), p.e202400041. [DOI]

Nerio, L.S., Olivero-Verbel, J. and Stashenko, E., 2010. Repellent activity of essential oils: a review. *Bioresource Technology*, 101(1), pp. 372–378. [DOI]

Olivito, F., Algieri, V., Jiritano, A., Tallarida, M.A., Tursi, A., Costanzo, P. and Maiuolo, L., 2021. Cellulose citrate: a convenient and reusable bio-adsorbent for effective removal of methylene blue dye from artificially contaminated water. *RSC Advances*, 11(54), pp. 34309–34318. [DOI]

Patti, A., Cicala, G. and Acierno, D., 2020. Eco-sustainability of the textile production: waste recovery and current recycling in the composites world. *Polymers*, 13(1), p. 134. [DOI]

Pujiastuti, A., Cahyono, E. and Sumarni, W., 2017. Encapsulation of citronellal from citronella oil using β-cyclodextrin and its application as mosquito (*Aedes aegypti*) repellent. *Journal of Physics: Conference Series*, 824, p. 012016. [DOI]

Rana, M.S., Rahim, M.A., Mosharraf, M.P., Tipu, M.F.K., Chowdhury, J.A., Haque, M.R. and Kabir, S., 2023. Morphological, spectroscopic and thermal analysis of cellulose nanocrystals extracted from waste jute fiber by acid hydrolysis. *Polymers*, 15(6), p. 1530. [DOI]

Renewable Matter, 2025. Europe eyes billion-dollar opportunity in textile waste recycling with 10 billion kilos of textile waste yearly, recycling could reshape the European industry. Available at: https://www.renewablematter.eu/en/europe-eyes-billion-dollar-opportunity-textile-waste-recycling.

Research and Markets, 2026. *Natural Zeolites Market Analysis & Forecast: 2025–2032*. Available at: https://www.researchandmarkets.com/reports/4990008/zeolites-market-global-forecast-2026-2032

Riza, M., Ehsan, M.N. and Hoque, S., 2021. Portrayal of textile based pollutants and its impact on soil, plants and fisheries. *Nature Environment and Pollution Technology*, 20(3), pp. 1269–1275. [DOI]

Ruiz-Caldas, M.X., Apostolopoulou-Kalkavoura, V., Hellström, A.K., Hildenbrand, J., Larsson, M., Jaworski, A., Samec, J.S., Lahtinen, P., Tammelin, T. and Mathew, A.P., 2023. Citrated cellulose nanocrystals from post-consumer cotton textiles. *Journal of Materials Chemistry A*, 11(13), pp. 6854–6868. [DOI]

Sandin, G. and Peters, G.M., 2018. Environmental impact of textile reuse and recycling–a review. *Journal of Cleaner Production*, 184, pp. 353–365. [DOI]

Side, S., Putri, S.E., Pratiwi, D.E., Rahma, A. and Rahman, A., 2023. The effect of acid treatment on the characteristics of modernite zeolite. *Sainsmat: Jurnal Ilmiah Ilmu Pengetahuan Alam*, 12(2), pp. 114–123. [DOI]

Singh, A., Sahay, S.S. and Sharma, P., 2025. Overview of textile waste. In: *Nanotechnology-Assisted Recycling of Textile Waste: Sustainable Tools for Textiles*. Wiley Online Library, pp. 1–27. [DOI]

Siniscalchi, C., Coppola, M.G., Cardillo, G., Imbalzano, E., Basaglia, M., Nasti, R. and Russo, V., 2026. Globalization, climate change, and the re-emergence of West Nile, Dengue, and Zika viruses. *Italian Journal of Medicine*, 20(1). [DOI]

Solomon, B., Sahle, F.F., Gebre-Mariam, T., Asres, K. and Neubert, R.H.H., 2012. Microencapsulation of citronella oil for mosquito-repellent application: formulation and in vitro permeation studies. *European Journal of Pharmaceutics and Biopharmaceutics*, 80(1), pp. 61–66. [DOI]

Stoyanov, V., Petkova, V., Mihaylova, K. and Shopska, M., 2024. A study of the influence of thermoactivated natural zeolite on the hydration of white cement mortars. *Materials*, 17(19), p. 4798. [DOI]

Tanirbergenova, S., Tugelbayeva, D., Zhylybayeva, N., Aitugan, A., Tazhu, K., Moldazhanova, G. and Mansurov, Z., 2025. Effect of acid treatment on the structure of natural zeolite from the Shankhanai deposit. *Processes*, 13(9), p. 2896. [DOI]

Venkatesh, G., 2022. Circular bio-economy—paradigm for the future: systematic review of scientific journal publications from 2015 to 2021. *Circular Economy and Sustainability*, 2(1), pp. 231–279. [DOI]

Wagaw, T. and Babu, K.M., 2023. Textile waste recycling: a need for a stringent paradigm shift. *AATCC Journal of Research*, 10(6), pp. 376–385. [DOI]

Wagner, M.M. and Heinzel, T., 2020. Human perceptions of recycled textiles and circular fashion: a systematic literature review. *Sustainability*, 12(24), p. 10599. [DOI]

Nature Environment and Pollution Technology
An International Quarterly Peer-Reviewed Open Access Journal

p-ISSN: 0972-6268 | e-ISSN: 2395-3454 Vol. 25 | No. 4 | Article ID D1935 | 2026

RESEARCH ARTICLE https://doi.org/10.46488/NEPT.2026.v25i04.D1935 OPEN ACCESS

Field-Based Evaluation of Water Quality, Macroinvertebrates and Sediment in the Downstream Segment of the Upper Konto Sub-Watershed, Indonesia

Very Dermawan†, Emma Yuliani, Evi Nur Cahya and Nazwa Shiva Setya Putri
Department of Water Resources Engineering, Faculty of Engineering, Universitas Brawijaya, Jl. MT Haryono 167, Malang 65145, East Java, Indonesia
†Corresponding author: Very Dermawan; peryderma@ub.ac.id

ARTICLE HISTORY

Received: 19-04-2026
Revised: 01-06-2026
Accepted: 08-06-2026

KEYWORDS

Ecohydraulic
Water quality
Sediment
Organic pollution
Macroinvertebrates
Konto sub-watershed

CITE THIS ARTICLE

Dermawan, V., Yuliani, E., Cahya, E.N. and Putri, N.S.S., 2026. Field-based evaluation of water quality, macroinvertebrates and sediment in the downstream segment of the Upper Konto sub-watershed, Indonesia. *Nature Environment and Pollution Technology*, 25(4), D1935. https://doi.org/10.46488/NEPT.2026.v25i04.D1935

COPYRIGHT & LICENCE

© 2026 The Authors
Open Access under CC BY 4.0.

PUBLISHED BY
TECHNOSCIENCE PUBLICATIONS

ABSTRACT

As the last self-purification zone before inflow enters Selorejo Reservoir, the downstream reach of the Upper Konto Sub-watershed is critical for controlling pollutant and sediment transfer. An integrated ecohydraulic approach was used in this study to evaluate the water quality, sediment characteristics, and ecological condition under organic pollution pressure. Water quality was assessed at six sites and deposited sediments at four sites during the dry and rainy seasons. The Pollution Index (PI) and Family Biotic Index (FBI) were used to assess physicochemical water quality and biological condition, respectively; sediment grain-size distribution and nutrient contents were also examined. The flow velocities ranged from 0.37–0.68 m s^{-1} in the dry season and from 0.54–1.15 m s^{-1} in the rainy season, controlling erosion, transport, and deposition processes. PI results showed that the downstream reach was classified as lightly to moderately polluted in the dry season, and mostly moderately polluted in the rainy season. Conversely, the FBI showed worse biological conditions, characterized by moderately poor to very poor conditions, especially during the rainy season. TSD1–TSD3 sediments were mainly sandy, but TSD4 was composed of finer silt and mud-rich deposits. The high nitrogen concentration in TSD1 may be related to adsorption and retention of nitrogen-bearing compounds on sediment particles. Overall, ecological degradation was pronounced due to interactions among organic pollutant loads, flow dynamics, and sediment characteristics, indicating the need for integrated management of water quality, riparian conditions, and sedimentation to reduce pollutant and sediment inflows to Selorejo Reservoir.

1. INTRODUCTION

River ecosystems are among the most dynamic ecosystems on Earth, but they increasingly face threats from anthropogenic pressures such as land-use change, intensified agricultural and livestock activity, domestic waste discharge, and flow alteration that can impact water quality, sediment transport, and aquatic communities (Dudgeon et al. 2006, Gregory et al. 1991, Walsh et al. 2005, Poff et al. 2010). These pressures impair ecological functioning at the watershed scale and induce downstream impacts by propagating nutrients, organic matter, and sediment, which collectively influence reservoir systems (Uday Kumar & Jayakumar 2020, Chanapathi & Thatikonda 2020, Das et al. 2022).

In agricultural catchments, sediment and nutrient delivery are exacerbated by land degradation and erosion, leading to progressive ecological deterioration of both rivers and downstream reservoirs (Kumar et al. 2026, Biggs et al. 2025). The Upper Konto Sub-watershed is one such catchment, with the Konto River

as a major inflow to the Selorejo Reservoir multipurpose system (irrigation, fisheries, and tourism). The expansion of agricultural and residential areas increases inputs of organic matter and suspended solids, which may compromise the self-purifying capacity of rivers and degrade water quality in reservoirs (Patel & Jariwala 2023, Hu et al. 2021, Gong et al. 2023). Consequently, the downstream reach represents a key transition zone that integrates upstream pressures and associated in-stream biological responses, and faces the risk of pollutant and sediment transfers into the reservoir (Nan et al. 2025, Hu et al. 2021).

More recently, studies have highlighted that integrating physicochemical and biological indicators, specifically macroinvertebrates, can better capture ecological stress (Carrasco-Baquero et al. 2025, Munyai et al. 2025, Hegab et al. 2025, Akindele et al. 2025). Sediments also act as sinks for contaminants and play a significant role in secondary pollution through processes of storage and re-release (Baker et al. 2025, Tomić et al. 2025), while riparian vegetation enhances bank stabilization, runoff retention, and the provision of habitat depending on the flow regime and channel morphology (Granitto et al. 2025, Ji et al. 2024, Assal et al. 2021, Biggs et al. 2025). These interactions reveal that an ecohydraulic approach, which integrates flow, habitat, sediment, vegetation, and biotic responses, can provide insights into river functioning (Gibbs et al. 2023, Harris et al. 2024, Mulatu et al. 2018).

Recent studies in tropical river systems have further shown that aquatic macroinvertebrates provide a useful ecological signal of water-quality degradation, particularly in streams affected by agricultural, livestock, and domestic pressures. For example, Paredes-Agurto et al. (2024) reported that macroinvertebrate-based assessments in La Gallega-Morropón Creek, Peru, were able to reflect variations in water quality across sampling stations, highlighting their value as bioindicators in human-impacted freshwater systems.

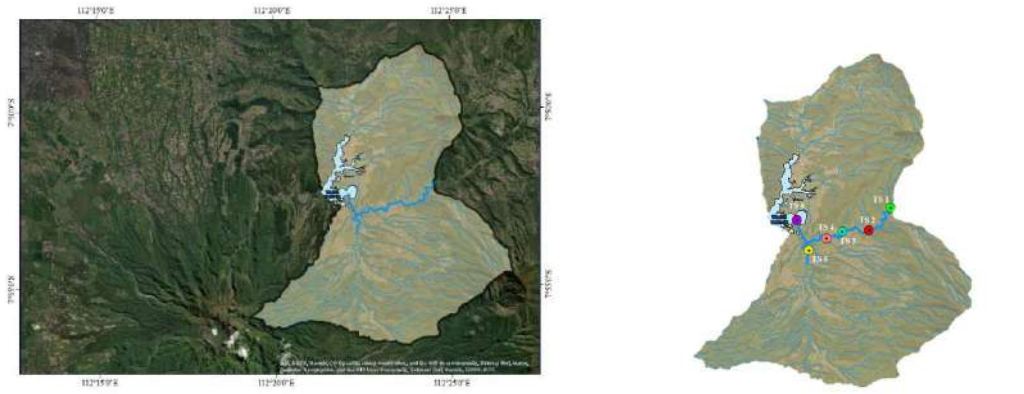
Yet few integrative studies focus on tropical downstream river reaches that can serve as the final self-purification zone before entering reservoirs. Thus, this study investigates water quality, sediment characteristics, and ecological condition in the downstream Upper Konto Sub-watershed to develop an integrated ecohydraulic framework across two seasons. The approach integrates the Pollution Index (PI), Family Biotic Index (FBI), sediment characteristics, and riparian-hydraulic context to aid in the management of water quality, sedimentation, and riparian vegetation in tropical river–reservoir systems under high organic-pollution pressure.

In this study, the ecohydraulic framework refers to the interaction among hydrodynamic conditions, sediment transport and deposition, riparian characteristics, water quality conditions, and macroinvertebrate responses within the downstream river ecosystem. Rather than evaluating these components independently, the framework conceptually integrates physical, chemical, and biological processes to interpret how watershed pressures influence ecological conditions before inflow to Selorejo Reservoir.

2. MATERIALS AND METHODS

The downstream area of the Upper Konto Sub-watershed is administratively located in the Pujon and Ngantang Districts, Malang Regency, with coordinates 7.868742°–7.877462° S and 112.371939°–112.410077° E, while the main river has a length of approximately 8 km. The study reach drains directly into Selorejo Reservoir and is the last zone of the self-purification process.

The study area (Fig. 1) is influenced by irrigation, agriculture, cattle raising, and industrial activities, and



(a) Catchment area of downstream segment (b) Sampling points along stream reach

Fig. 1: The downstream segment of the Upper Konto Sub-watershed.

receives waste inputs, making it suitable for evaluating the relationships between watershed-scale land-use pressures and ecohydraulic processes on water–sediment quality. To obtain the Pollution Index, maximum and mean concentration-to-standard ratios were used.

$$P_{ij} = \sqrt{\frac{\left(\frac{C_i}{L_{ij}}\right)_M^2 + \left(\frac{C_i}{L_{ij}}\right)_R^2}{2}} \quad \ldots(1)$$

Where: P_{ij} = Pollution Index for designation j; C_i = concentration of the tested parameter; L_{ij} = concentration permitted under the water-quality standard for designation j; $(C_i/L_{ij})_M$ = maximum value of C_i/L_{ij}; $(C_i/L_{ij})_R$ = average value of C_i/L_{ij}.

The Pollution Index (PI) was calculated based on the maximum and mean concentrations of each parameter relative to their respective quality standards. PI values were divided into the following ranges: 0–1.0 (good quality), 1.1–5.0 (lightly polluted), 5.1–10.0 (moderately polluted), and >10.0 (heavily polluted). Biological condition was based on a biological indicator derived from the Family Biotic Index (FBI) developed by Hilsenhoff (1988). This index may estimate ecological condition, especially in relation to organic pollution, by weighting macroinvertebrate family abundances by their tolerance values. The relatively long life cycles and limited mobility of macroinvertebrates can integrate environmental conditions across space and time, which is why they are widely used as bioindicators. Although the Hilsenhoff Family Biotic Index was originally developed for temperate North American streams, it has been widely applied in tropical freshwater studies where locally calibrated tolerance indices remain limited. In this study, the FBI was used as a comparative ecological indicator to assess relative organic-pollution stress among stations and seasons. The FBI serves as an integrated measure of biological water quality and complements the physicochemical assessment accordingly.

$$FBI = \frac{\sum x_i t_i}{n} \quad \ldots(2)$$

Where: x_i = number of individuals in family i; t_i = tolerance value of family i; n= total number of individuals.

The use of macroinvertebrate assemblages as biological indicators has also been applied in other tropical freshwater studies, where indices such as the Biological Monitoring Working Party modified for Colombia (BMWP/Col) and Ephemeroptera, Plecoptera, and Trichoptera (EPT) were used



(a) Horiba U-50 (b) LAQUAtwin NO_3 Nitrate Test Kit (c) Hydrion AM-40 Ammonia Test Kit (d) Filter Paper 100 mm (e) Plankton Net No. 20



(f) Grab Sampler (g) Current Meter (h) USDH-48 (i) Ice Box (j) Sieve Shaker

Fig. 2: Research equipment and instruments.



(a) Field activity for data collection



(b) Laboratory activity

Fig. 3: Field data collection and laboratory testing activities.

to evaluate ecological responses to water-quality conditions (Paredes-Agurto et al. 2024). Although the present study applies the Family Biotic Index, the underlying principle is similar: macroinvertebrate communities can integrate environmental stress over time and provide biological evidence of organic pollution and habitat disturbance.

This study employed a range of instruments to assess water quality, collect sediment samples, and conduct laboratory analyses. In situ measurements were taken using a Horiba U-50 multiparameter analyzer, which recorded temperature, turbidity, dissolved oxygen (DO), conductivity, pH, oxidation–reduction potential (ORP), and water depth, while simultaneously capturing geographic coordinates using its integrated GPS. Nitrate and ammonia concentrations were measured on site using the LAQUAtwin NO_3 and Hydrion AM-40 test kits. Suspended sediment samples were collected with a USDH-48 sampler, designed for shallow waters (<2 m). Sieve and hydrometer tests were used to analyze sediment physicochemical properties and grain-size distribution, which were then classified according to the AASHTO system. Transect-level surveys of macroinvertebrate assemblages served as biological indicators. Additional supporting tools included a shovel, magnifying glass, measuring tape, alcohol sprayer, ice box, grab sampler, wooden stakes, sample bottles, oven, digital balance, weighing scale, glass funnel, beaker, Erlenmeyer flask, measuring cylinder, filter paper, and current meter. Collectively, these instruments facilitated systematic field sampling, sample preservation, and laboratory testing. Fieldwork was conducted in the dry season (August) and rainy season (January), with measurements performed in quintuplicate to reduce observational uncertainty for temperature, pH, DO, conductivity, turbidity, and TDS. Figures 2 and 3 illustrate the instruments, field sampling, and laboratory procedures.

This study employed theShannon–Wiener Index (H'), a statistical measure widely used to describe biodiversity by integrating both species richness (the number of species present) and species evenness (the relative abundance of individuals across species). The index is calculated using the formula:

$$H' = -\sum p_i \ln(p_i) \quad \ldots(3)$$

Where: p_i is the proportion of individuals belonging to species. The index value typically ranges from 0, indicating no diversity when only one species is present, to about 3–4 in highly diverse ecosystems. In general, values below 1 suggest low diversity and possible ecological stress, values between 1 and 3 indicate moderate diversity and a reasonably balanced community, while values above 3 reflect high diversity and ecological stability. Higher values of H' generally indicate greater diversity, while lower values suggest dominance by a few tolerant taxa and potential environmental stress (Yuniari et al. 2025).

3. RESULTS AND DISCUSSION

Six sites (TS1–TS6) were sampled for water-quality and biological assessments, while four sites (TSD1–TSD4) were designated for deposited sediment analysis. Sampling locations were selected based on accessibility, safety, physical river conditions, and the intensity of surrounding community activity. Water quality data, including physical

Table 1: Water quality data (physical and chemical parameters).

Parameter	TS1		TS2		TS3		TS4		TS5		TS6	
	Dry	Rainy	Dry	Rainy	Dry	Rainy	Dry	Rainy	Dry	Rainy	Dry	Rainy
Temperature (°C)	23.05	24.94	25.83	25.81	27.53	27.01	24.71	27.32	27.41	29.09	28.37	28.10
pH	7.95	7.73	8.00	7.80	7.94	7.51	7.82	7.73	7.65	7.68	7.21	7.64
Conductivity (µS/cm)	306.80	228.00	300.40	231.00	305.40	242.40	263.20	228.40	278.40	262.2	274.20	255.00
Turbidity (NTU)	89.24	89.34	176.8	100.82	88.56	73.34	53.00	95.54	39.18	85.22	77.80	126.20
DO (mg/L)	8.23	7.62	7.08	7.15	6.95	6.22	7.95	6.49	6.41	6.02	4.39	6.14
TDS (mg/L)	199.40	148.40	195.40	150.20	198.60	157.60	171.20	148.60	181.00	170.00	178.00	161.60
TSS (mg/L)	110.00	190.00	160.00	200.00	90.00	160.00	50.00	190.00	30.00	180.00	70.00	200.00
TOM (ppm)	25.46	47.77	22.03	48.33	22.03	52.91	22.03	58.06	15.16	73.51	16.88	42.62
NO_3 (ppm)	31.00	25.00	23.00	31.00	22.00	27.00	22.00	33.00	10.00	32.00	22.00	29.00
NH_3 (ppm)	5.00	5.00	5.00	10.00	5.00	10.00	10.00	10.00	10.00	10.00	20.00	10.00
N Total (ppm)	-	63.13	-	47.08	-	68.13	-	81.04	-	58.13	-	52.08
P Total (ppm)	-	34.82	-	26.79	-	37.72	-	57.59	-	33.48	-	27.90
K Total (ppm)	-	28.99	-	26.64	-	25.94	-	28.03	-	30.55	-	22.44

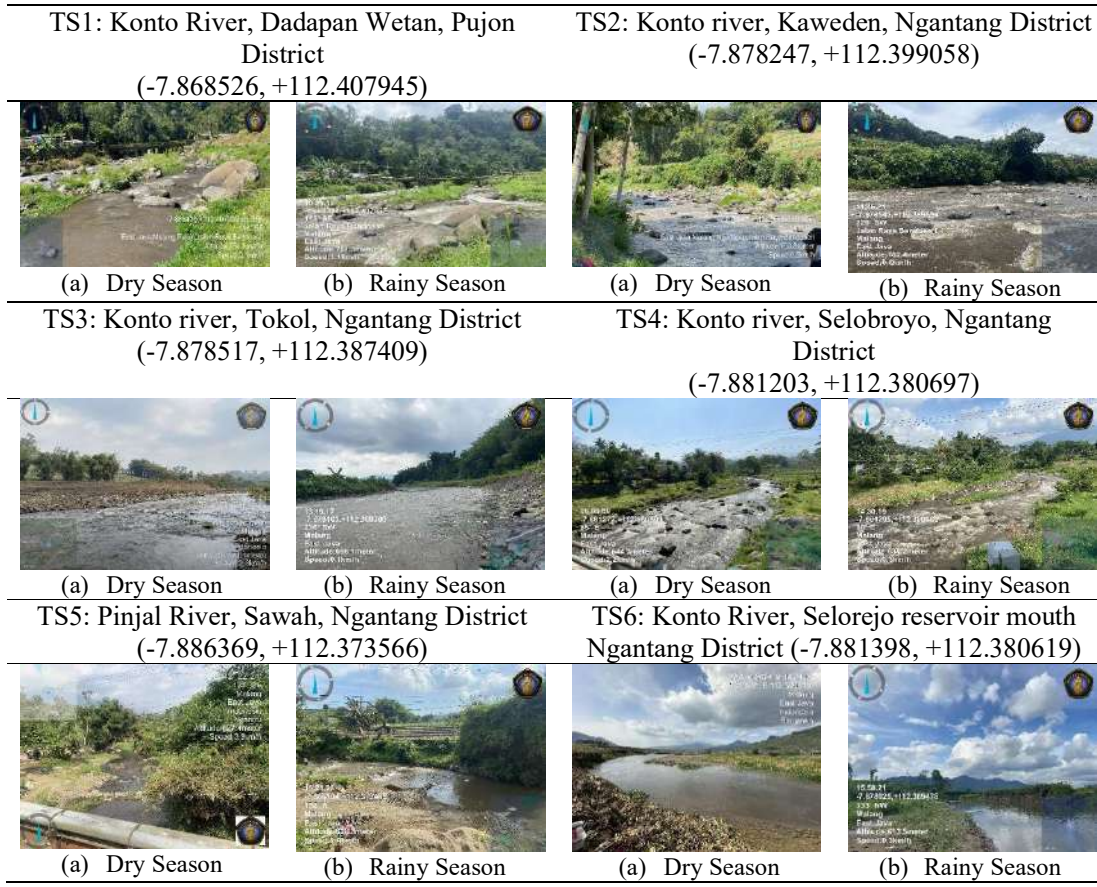


Fig. 4: River condition at the sampling points.



Fig. 5: Stream reach conditions at sediment-deposit sampling sites.

and chemical parameters, are presented in Table 1. During the dry season, sediment deposits were concentrated in the mid-channel and along riverbanks(Figs. 4 and 5).

The vegetation along the lower segment of the Upper Konto Sub-watershed is very diverse. Vegetation in the lower reach consists primarily of water spinach plant, taro plant, bamboo plant, Calliandra plant, Papayungan plant, and water hyacinth plant (Fig. 6). The macroinvertebrate communities in the downstream segment were dominated by *Gerridae* and *Lumbricidae*. *Radix rubiginosa* (also known as Onga in Javanese) was dominant during the dry season but declined in abundance during the rainy season, suggesting that *Radix rubiginosa* prefers environments with low flow

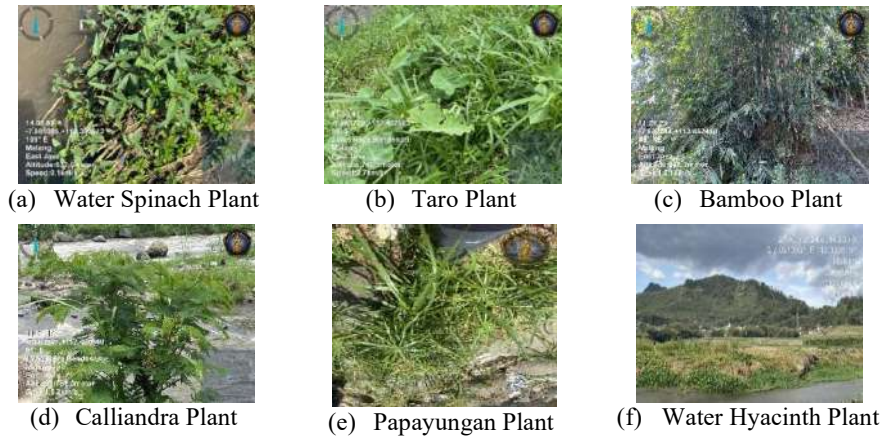

(a) Water Spinach Plant (b) Taro Plant (c) Bamboo Plant
(d) Calliandra Plant (e) Papayungan Plant (f) Water Hyacinth Plant

Fig. 6: Riparian vegetation along the river course.

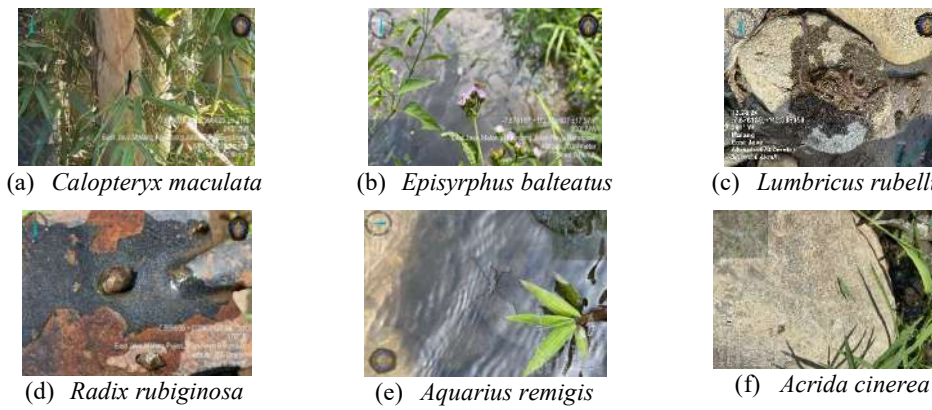

(a) *Calopteryx maculata* (b) *Episyrphus balteatus* (c) *Lumbricus rubellus*
(d) *Radix rubiginosa* (e) *Aquarius remigis* (f) *Acrida cinerea*

Fig. 7: Terrestrial insects and macroinvertebrates along the downstream segment.

conditions. This pattern also occurred for *Gerridae*, as would be expected given their association with slow-flowing clear waters. *Lumbricidae* also dominated sediment deposits, suggesting organic-enriched substrate conditions (Fig. 7).

3.1. River Hydraulic Conditions

The river hydraulic parameters during the dry and rainy seasons at each location are presented in Table 2. Variations in river discharge illustrate the impact of flow variability on water quality and sediment dynamics in the downstream segment of the Upper Konto Sub-watershed. Flow velocity measured with a current meter ranged from 0.37–0.68 m s^{-1} in the dry season and increased to 0.54–1.15 m s^{-1} in the rainy season. Higher flow rates enhance erosion, whereas lower flow rates favor the deposition of finer sediment particles. In the downstream segment, a check dam helps retain sediment and slow the flow before the river enters the reservoir. This pattern aligns with the ecohydraulic framework, in which habitat quality is determined by flow velocity, residence time, and habitat connectivity (Gibbs et al. 2023, Chanapathi & Thatikonda 2020).

3.2. River Water Quality Based on the Pollution Index (PI)

Water quality was assessed against designated uses and maximum allowable standards using the Pollution Index

Table 2: River hydraulic parameters.

Location	Flow velocity (m s^{-1})	Discharge (m^3 s^{-1})	Flow velocity (m s^{-1})	Discharge (m^3 s^{-1})
	Dry Season		Rainy Season	
TS1	0.38	4.04	0.75	5.70
TS2	0.56	8.04	1.15	9.83
TS3	0.68	2.88	0.88	4.90
TS4	0.68	3.50	0.92	3.61
TS5	0.37	0.95	0.54	1.75
TS6	Still water	-	Still water	-

(PI). The spatial mapping of water quality was performed to describe the distribution of water quality in the downstream section of the Konto Hulu Sub-Watershed. The Inverse Distance Weighting (IDW) interpolation method was used to estimate the spatial distribution of water and sediment quality parameters according to the distances between sampling locations. This method is based on the assumption that spatial influence decreases with distance. Thus, sampling points closer to an unsampled location will have a larger influence on estimated values than those at a further distance. Hence close observations are given more weight, and distant ones less, as one move farther away from the point of interest (Tables 3-4, and Figs. 8-9). The water in the downstream Upper Konto Sub-watershed was classified as lightly to moderately polluted according to the PI, with more severe conditions during the rainy season: 43.46% slightly polluted and 56.54% moderately polluted during the dry season versus 13.86% and 86.14%, respectively, in the rainy season (Fig. 8). Most direct pollution originated from livestock, agriculture, and domestic waste, especially untreated runoff and drainage discharges that directly entered the river.

These observations suggest that increased discharge did not improve water quality, because pollutant inputs from agricultural, livestock, and domestic runoff exceeded the river's dilution and self-purification capacity. This trend confirms the findings of Patel and Jariwala (2023) and Whittinghill et al. (2023), which associated nutrient-rich runoff with deteriorating water quality, including higher nitrate, ammonia, phosphorus, conductivity, and turbidity.

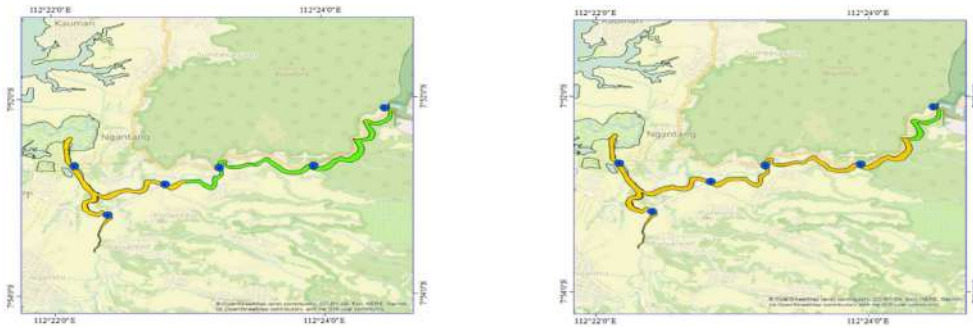
3.3. Water Quality Based on the Family Biotic Index (FBI)

The seasonal difference in water quality of the downstream part of the Upper Konto sub-watershed was assessed by the IDW interpolation method and supported by the Family Biotic Index (FBI) results as given in Table 4 and Fig. 9. In the dry season, 46.66% of sampling points were Moderately Poor (heavily polluted with organic matter) and 53.34% were Poor (heavily polluted with organic matter). In the rainy season, 15.93% was classified as Poor, 12.93% as Moderately Poor, and 71.14% as Very Poor, suggesting heavy organic pollution.

This discordance suggests chronic, not episodic, organic pollution in the downstream reach. The relative dominance of tolerant taxa and absence of sensitive taxa might indicate long-term alterations to the community, leading to persistent habitat degradation, which is in agreement with

Table 3: Summary of Pollution Index values during the dry and rainy seasons.

Location	Dry Season		Rainy season	
	PI Value	Status	PI Value	Status
TS1	4.45	Slightly polluted	4.47	Slightly polluted
TS2	4.47	Slightly polluted	5.54	Moderately polluted
TS3	4.43	Slightly polluted	5.52	Moderately polluted
TS4	5.44	Moderately polluted	5.56	Moderately polluted
TS5	5.41	Moderately polluted	5.58	Moderately polluted
TS6	6.52	Moderately polluted	5.56	Moderately polluted
Total	43.46 %	Slightly polluted	13.86 %	Slightly polluted
	56.54 %	Moderately polluted	86.14 %	Moderately polluted

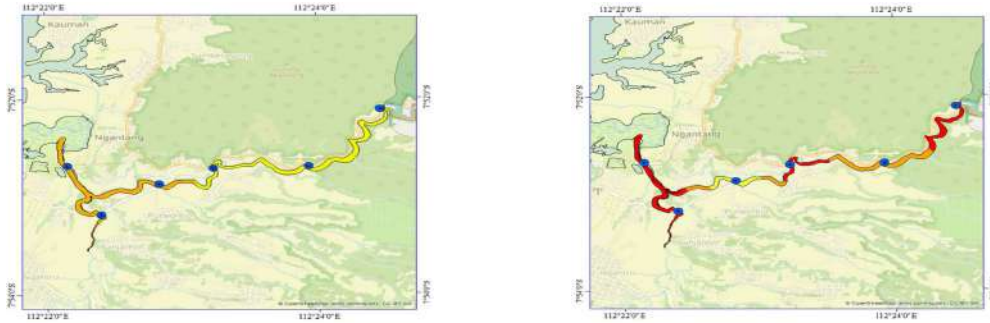


(a) Dry Season (b) Rainy Season

Fig. 8: Pollution index mapping in the downstream segment of the Upper Konto Sub-watershed.

Table 4: Summary of Family Biotic Index values during the dry and rainy seasons.

Location	FBI Dry Season	Status	FBI Rainy Season	Status
TS1	6.11	Moderately poor	8.50	Very poor
TS2	5.78	Moderately poor	7.14	Poor
TS3	6.22	Moderately poor	8.00	Very poor
TS4	6.82	Poor	5.80	Moderately poor
TS5	6.76	Poor	8.00	Very poor
TS6	7.12	Poor	7.40	Very poor
Total	46.66 %	Moderately poor	15.93 %	Poor
	53.34 %	Poor	12.93 %	Moderately poor
			71.14 %	Very poor



(a) Dry Season (b) Rainy Season

Fig. 9: Mapping of water quality using the Family Biotic Index method in the downstream segment of the Upper Konto Sub-watershed.

the comprehensive responses observed by Carrasco-Baquero et al. (2025) and also the sediment–water chemistry effects described by Munyai et al. (2025). A lower-than-expected occurrence of the Gerridae during the rainy season also demonstrates declining resilience under compounded hydrological pressure (Sarremejane et al. 2024).

A similar ecological response was observed by Paredes-Agurto et al. (2024) in La Gallega-Morropón Creek, where low macroinvertebrate diversity was associated with anthropogenic disturbance along the stream. Their findings support the interpretation that a community dominated by tolerant taxa may indicate long-term ecological stress, even when some physicochemical parameters still appear acceptable. In the downstream Upper Konto Sub-watershed, the dominance of tolerant macroinvertebrate groups and the absence of highly sensitive taxa therefore suggest that organic pollution and habitat alteration have affected the biological integrity of the river beyond what is captured by short-term water-quality measurements.

3.4. Integration of the Pollution Index (PI) and the Family Biotic Index (FBI)

The contrast between the Pollution Index and Family Biotic Index highlights the importance of a multi-metric assessment. Physicochemical parameters capture instantaneous conditions, whereas macroinvertebrate communities integrate cumulative stress over time. This pattern is consistent with the findings of Paredes-Agurto et al. (2024), who found that physicochemical parameters in La Gallega-Morropón Creek complied with national water-quality standards, while macroinvertebrate-based indices still indicated contrasting ecological conditions among sampling stations. This reinforces the need to combine chemical and biological assessments, since biological communities often reveal accumulated or site-specific stress that may not be fully represented by physicochemical snapshots. Thus, poorer FBI scores indicate greater ecological degradation than chemical snapshots alone suggest, supporting the view that downstream Konto River impairment arises from interacting organic loads, flow dynamics, and habitat degradation (Tomić et al. 2025, Vezi et al. 2020).

3.5. Sediment Characteristics and Management Implications

Granular gradation testing (sieve tests and hydrometers) indicated a substrate composition of gravel, sand, silt, and clay. TS 1–5 consisted mostly of sand and gravel with relatively high flow, whereas TS 6 (Selorejo Reservoir

Mouth) is dominated by silt that occurs at slow, stagnant flows. In TS 4, the bottom sediment consists of 42.72% gravel, 55.83% sand, and 1.46% mud on the right side, and 49.54% gravel, 50.12% sand, and 0.35% mud on the left side. In contrast, TS 6 is dominated by mud (87.70% in the middle; 85.10% on the left-hand side), with silt more prevalent than clay (Figs. 10 and 11).

Pollutants have been supplied from various sources, including agriculture, livestock, and domestic use, in the upstream agricultural region of the Upper Konto Sub-watershed. These pollutants can settle mainly on the macrobenthic substrate, which macroinvertebrates use as habitat. This substrate is ecologically important and provides benthic functions based on the regime. It also acts as a sink for contaminants. Sediment textures differed among sites: TSD1–TSD3 were predominantly sandy, while TSD4 had muddy silt. These differences influenced macroinvertebrate abundance. Substrate conditions may also help explain differences in macroinvertebrate assemblages. Paredes-Agurto et al. (2024) noted that habitat features such as leaf litter and substrate type can support particular macroinvertebrate groups by providing food resources and shelter. In the Upper Konto downstream reach, differences between sandy, gravelly, and fine muddy deposits may therefore contribute to spatial variation in benthic communities, especially where organic-rich sediments provide suitable conditions for tolerant taxa. The higher nitrogen content at TSD1 is likely due to nitrogen's tendency to adsorb onto sediment particles. In contrast, phosphorus may remain relatively mobile in the water column under certain hydrological conditions. Lower nutrient concentrations near cultivated areas may potentially be influenced by nutrient uptake by vegetation. Fine-textured sediment at TSD4 retained higher nutrient concentrations and coincided with the dominance of tolerant macroinvertebrate taxa, suggesting that depositional zones may contribute to long-term habitat degradation. Similar observations were reported by Baker et al. (2025) and Tomić et al. (2025), who identified sediment as an active compartment for contaminant storage and re-release. Shifts in sediment chemistry were correlated with changes in macroinvertebrate community structure, validating these sediment metrics as indicators of benthic habitat degradation (Munyai et al. 2025).

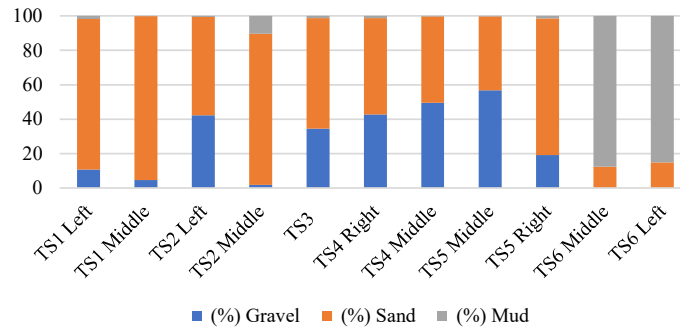


Fig. 10: Sediment characteristics.

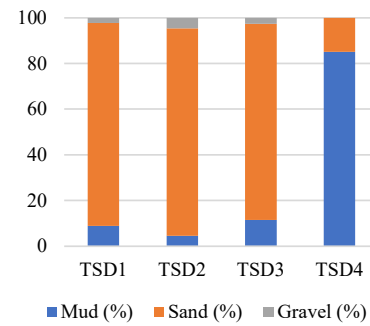


Fig. 11: Sediment deposit characteristics.

Table 5: Summary of macroinvertebrate families during the dry and rainy seasons.

No.	Family	Species		Proportion		No	Family	Species		Proportion	
		Dry	Rainy	Dry	Rainy			Dry	Rainy	Dry	Rainy
1	Acrididae	5	5	0.029	0.059	18	Lumbricidae	31	19	0.182	0.224
2	Asilidae	-	1	-	0.012	19	Lycosidae	1	1	0.006	0.012
3	Blaberidae	1	4	0.006	0.047	20	Lymnaeidae	10	-	0.059	-
4	Bythinellidae	1	-	0.006	-	21	Muscidae	9	7	0.053	0.082
5	Calopterygidae	3	-	0.018	-	22	Nymphalidae	2	2	0.012	0.024
6	Challiporidae	1	2	0.006	0.024	23	Pieridae	-	2	-	0.024
7	Chrysomelidae	18	3	0.106	0.035	24	Platycnemididae	1	-	0.006	0.000
8	Coccinellidae	6	4	0.035	0.047	25	Polydesmidae	-	1	-	0.012
9	Coenagrionidae	2	-	0.012	-	26	Salticidae	2	-	0.012	-
10	Formicidae	-	5	-	0.059	27	Scarabaeidae	-	3	-	0.035
11	Gerridae	47	3	0.276	0.035	28	Silphidae	1	-	0.006	-
12	Gryllidae	-	1	-	0.012	29	Syrphidae	5	1	0.029	0.012
13	Gryllotalpidae	-	3	-	0.035	30	Tabanidae	1	-	0.006	-
14	Issidae	3	-	0.018	-	31	Tetragnathidae	1	-	0.006	-
15	Leptoceridae	2	-	0.012	-	32	Thiaridae	10	-	0.059	-
16	Lestidae	3	-	0.018	-	33	Trigoniulidae	-	3	-	0.035
17	Libellulidae	4	15	0.024	0.176		**Total Species**	170	85	1.000	1.000

A total of 33 macroinvertebrate families were encountered, of which 18 were used for the Family Biotic Index (FBI) assessment. Table 5 shows the macroinvertebrate families and their observed abundances. No highly pollution sensitive taxa were detected but families with moderate tolerance such as Gerridae and Muscidae were observed throughout the sampling sites and seasons. Syrphidae were also present but at a lower abundance than some other families, such as Gerridae and Lumbricidae, suggesting that the Syrphidae were not the dominant group in the macroinvertebrate community. However, the occurrence of pollution tolerant taxa suggests possible ecological responses to organic pollution. The seasonal occurrence of potential indicator taxa such as *Aquarius remigis*, *Ceraclea dissimilis*, *Episyrphus balteatus* and *Volucella pellucens*, may be a result of the combined effects of hydrologic seasonality and environmental stressors on macroinvertebrate community composition.

The Pollution Index (PI) and FBI measure different perspectives of the river water quality. The PI is an indicator of the physicochemical condition while FBI indicates the response of macroinvertebrate community to organic pollution. Therefore, it is not surprising that there are differences in their classifications. Both sampling seasons revealed light to moderate pollution at the PI and moderate to severe organic pollution related impairment at the FBI. This difference may be due to differences in the temporal integration and ecological sensitivity of physicochemical and biological indicators, indicating the need for a combination of both approaches to better assess river ecosystem conditions.

The Shannon–Wiener Index (H') during the dry season was 2.471, while in the rainy season it reached 2.584. These values fall within the moderate diversity range (1–3), indicating that the macroinvertebrate community structure remained relatively balanced across seasons. The slightly higher value in the rainy season suggests a marginal increase in species diversity and evenness, although the difference between seasons is not substantial. Overall, the results imply that the ecosystem maintains moderate stability, with seasonal hydrological variations exerting only limited influence on biodiversity composition (Yuniari et al. 2025).

4. CONCLUSIONS

The downstream reach of the Upper Konto Sub-watershed exhibits ecological impairment associated with organic pollutant inputs, hydrodynamic conditions, and sediment characteristics. Pollution Index values categorize the water as lightly to moderately polluted, with more critical conditions during the rainy season. The biological assessment, using the Family Biotic Index, shows that ecological impairment is more severe than physicochemical measurements alone would indicate: tolerant taxa predominate, while sensitive taxa are absent, indicative of chronic organic pollution and altered macroinvertebrate community structure.

Sediments in depositional zones may function as temporary reservoirs for nutrient and contaminant accumulation and could contribute to pollutant re-release under changing environmental conditions. Thus, water quality assessment should integrate water-column parameters with sediment condition and riparian habitat quality. This downstream section is ecologically significant because it directly affects inflows to Selorejo Reservoir, where declining water quality and sedimentation can further aggravate reservoir conditions. Accordingly, management should implement an integrated approach that minimizes agricultural and livestock-derived pollution, conserves riparian vegetation, and manages depositional sediments to strengthen natural recovery while curtailing pollutant transfer to the Selorejo Reservoir.

These findings are in line with recent tropical stream studies showing that macroinvertebrate-based assessments can provide an important ecological perspective on water-quality degradation, particularly in rivers affected by human activities.

5. ACKNOWLEDGEMENT

The authors express their gratitude to the Faculty of Engineering, Universitas Brawijaya, Indonesia, for the sponsorship, particularly to the Research and Community Service Division (BPPM) for supporting this study. We thank our colleagues from Badan Penerbitan Jurnal (BPJ) FTUB for providing insight and support that greatly assisted the publication of this paper. This research was funded by the Faculty of Engineering, Universitas Brawijaya, Grant Number 110/UN10.F07IPN/2024.

6. REFERENCES

Akindele, E.O., Olaleru, F., Oduntan, O.O., Dalu, T., Aladesida, A.A., Oladipo, O.J., Nwani, C.D., Edegbene, A.O., and Odo, G.E., 2025. A spatial inventory of freshwater macroinvertebrate occurrences in the Guineo-Congolian biodiversity hotspot. Scientific Data, 12, p.227. [DOI]

Assal, T.J., Steen, V.A., Caltrider, T., Cundy, T., Stewart, C., Manning, N. and Anderson, P.J., 2021. Monitoring long-term riparian vegetation trends to inform local habitat management in a mountainous environment. *Ecological Indicators*, 127, p.107807. [DOI]

Baker, A.C., Fitzpatrick, F.A., Soderman, S.S., Kennedy, M.J., Sterner, S.P., Anderson, J.P., Gran, K.B., Anderson, K.S., Stroom, K., Norvitch, P., Blount, J.D. and Gutzmann, M.E., 2025. Near-channel erosion as a driver of watershed-scale sediment and phosphorus loading in a forested sub-watershed of Lake of the Woods. *Journal of Great Lakes Research*, 51(5), p.102644. [DOI]

Biggs, H., Haddadchi, A., Brasington, J., Bind, J. and Stout, J., 2025. The impact of riparian vegetation on bank erosion during extreme weather events. *Earth Surface Processes and Landforms*, 50(10). [DOI]

Carrasco-Baquero, J.C., Caballero-Serrano, V., Carrasco-López, D.C., Romero-Cañizares, F., León-Gualán, D.A., Córdova-Lliquin, J.D., Vieira-Lanero, R., and Cobo-Gradín, F., 2025. Aquatic macroinvertebrates as indicators of water quality in the wetlands of the Chimborazo Wildlife Reserve – Ecuador. *Limnologica*, 112, 126234. [DOI]

Chanapathi, T. and Thatikonda, S., 2020. Investigating the impact of climate and land-use land cover changes on hydrological predictions over the Krishna river basin under present and future scenarios. *Science of the Total Environment*, 721, p.137736. [DOI]

Das, N., Sagar, A., Bhattacharjee, R., Agnihotri, A.K., Ohri, A. and Gaur, S., 2022. Time series forecasting of temperature and turbidity due to global warming in River Ganga at and around Varanasi, India. *Environmental Monitoring and Assessment*, 194(9), p.617. [DOI]

Dudgeon, D., Arthington, A.H., Gessner, M.O., Kawabata, Z.-I., Knowler, D.J., Lévêque, C., Naiman, R.J., Prieur-Richard, A.-H., Soto, D., Stiassny, M.L.J., and Sullivan, C.A., 2006. Freshwater biodiversity: importance, threats, status and conservation challenges. *Biological Reviews*, 81(2), pp.163–182. [DOI]

Gibbs, M., Bice, C., Furst, D., Gao, L., Joehnk, K., McCullough, D., Montazeri, M., Nicol, J., Smart, J., Wallace, T., Zampatti, B., and Brookes, J., 2023. Using hydraulics to evaluate ecological benefits, risks, and trade-offs from engineered flooding. Hydrological Processes, 37(11). [DOI]

Gong, F., Luo, L., Li, H., Chen, L., Zhang, R., Wu, G., Zhang, J., Shi, W., Zhang, F., Zhang, H., and Sun, T., 2023. Quantitative assessment of water quality improvement by reducing external loadings at Lake Erhai, Southwest China. *International Journal of Environmental Research and Public Health*, 20(6), p.5038. [DOI]

Granitto, M., Lopez, M.E., Fuentes, A.L.B., Testoni, M.C.M. and Rodríguez, P., 2025. Relationship between riparian zones and water quality in the main watersheds of Ushuaia City, Tierra del Fuego (Argentina). *Ecological Processes*, 14(18), pp.1–14. [DOI]

Gregory, S. V., Swanson, F.J., McKee, W.A. and Cummins, K.W., 1991. An ecosystem perspective of riparian zones. *BioScience*, 41(8), pp.540–551. [DOI]

Harris, A., Mulchandani, A. and Stone, M., 2024. Developing a habitat suitability index with field data and hydraulic models. *River Research and Applications*, 40(10), pp.1903–1911. [DOI]

Hegab, M.H., El Sayed, S.M., Ahmed, N.M., Abdel-Aal, E.I., Kassem, D.A., Gaber, K.M., Haroon, A.M., Abdel Gawad, S.S., Goher, M.E. and Hussian, A.-E.M., 2025. Evaluating the spatial pattern of water quality of the Nile River, Egypt, through multivariate analysis of chemical and biological indicators. *Scientific Reports*, 15(1), p.7626. [DOI]

Hilsenhoff, W.L., 1988. Rapid field assessment of organic pollution with a family-level biotic index. *Journal of the North American Benthological Society*, 7(1), pp.65–68. [DOI]

Hu, G., Zeng, W., Yao, R., Xie, Y. and Liang, S., 2021. An integrated assessment system for the carrying capacity of the water environment based on system dynamics. *Journal of Environmental Management*, 295, p.113045. [DOI]

Ji, K., Lin, C., He, M. and Liu, X., 2024. Eco-hydrological processes regulate lake riparian soil organic matter under dryness stress. *Water Research*, 260(121938), pp.1–15. [DOI]

Kumar, S., Choudhary, M.K. and Thomas, T., 2026. Integrated analytical hierarchy process and neural network approaches for assessment of soil erosion risk in Manjira River sub-basin, India. *Scientific Reports*, 16(1), p.4651. [DOI]

Mulatu, C.A., Crosato, A., Moges, M.M., Langendoen, E.J. and McClain, M., 2018. Morphodynamic trends of the Ribb River, Ethiopia, prior to dam construction. *Geosciences*, 8(7), p.255. [DOI]

Munyai, L.F., Gumede, B.P., Dondofema, F. and Dalu, T., 2025. Environmental characteristics shape macroinvertebrate community structure across spatiotemporal scales in a subtropical African river system. *Scientific Reports*, 15, p.6595. [DOI]

Nan, B., Zhai, Y., Wang, M., Wang, H. and Cui, B., 2025. Ecological security assessment, prediction, and zoning management: an integrated analytical framework. *Engineering*, 49, pp.238–250. [DOI]

Paredes-Agurto, M.S.M., Cherre, A.F.U., Dioses, J.M.M. and García, R.B., 2024. Aquatic macroinvertebrate diversity and water quality,

La Gallega-Morropón Creek, Piura, Peru. *Nature Environment and Pollution Technology*, 23(4), pp.2397–2402. [DOI]

Patel, H.B. and Jariwala, N.D., 2023. Analysis of pollutant load carrying capacity of the River Tapi using QUAL2Kw for Surat City. *Journal of Environmental Protection*, 14(02), pp.96–107. [DOI]

Poff, N.L., Richter, B.D., Arthington, A.H., Bunn, S.E., Naiman, R.J., Kendy, E., Acreman, M., Apse, C., Bledsoe, B.P., Freeman, M.C., Henriksen, J., Jacobson, R.B., Kennen, J.G., Merritt, D.M., O'Keeffe, J.H., Olden, J.D., Rogers, K., Tharme, R.E., and Warner, A., 2010. The ecological limits of hydrologic alteration (ELOHA): a new framework for developing regional environmental flow standards. Freshwater Biology, 55(1), pp.147–170. [DOI]

Sarremejane, R., England, J., Dunbar, M., Brown, R., Naura, M. and Stubbington, R., 2024. Human impacts mediate freshwater invertebrate community responses to and recovery from drought. *Journal of Applied Ecology*, 61(11), pp.2616–2627. [DOI]

Tomić, T., Jurca, T., Veselić, D.R., Slijepčević, N., Krčmar, D., BečelićTomin, M. and Pilipović, D.T., 2025. An integrated approach to assessing the quality of sediments in the Great Backa and Bega canals, Serbia. *Environmental Sciences Europe*, 37(25), pp.1–23. [DOI]

Uday Kumar, A. and Jayakumar, K.V., 2020. Hydrological alterations due to anthropogenic activities in Krishna River Basin, India. *Ecological Indicators*, 108, p.105663. [DOI]

Vezi, M., Downs, C., Wepener, V. and O'Brien, G., 2020. Application of the relative risk model for evaluation of ecological risk in selected river dominated estuaries in KwaZulu-Natal, South Africa. *Ocean & Coastal Management*, 185, p.105035. [DOI]

Walsh, C.J., Roy, A.H., Feminella, J.W., Cottingham, P.D., Groffman, P.M. and Morgan, R.P., 2005. The urban stream syndrome: current knowledge and the search for a cure. *Journal of the North American Benthological Society*, 24(3), pp.706–723. [DOI]

Whittinghill, L., Ballard, M., Chaudhary, A., Kandel, S., Mullins, C. and Poudel, P., 2023. Runoff water quality from different urban agricultural systems using common nutrient management practices. *HortScience*. [DOI]

Yuniari, S. H., Wijaya, A. S., and Faisol, A. F., 2025. Mapping the level of macrobenthic diversity to evaluate environmental and ecosystem disturbances. *Journal of Aquaculture Science*, 10(2), pp.125–135. [DOI]

NATURE ENVIRONMENT AND POLLUTION TECHNOLOGY

JOURNAL INFORMATION

Vol. 25, No. 4, December 2026

About the Journal

Nature Environment and Pollution Technology is an international peer-reviewed open-access journal covering environmental science, pollution control, environmental technology, sustainability, and related interdisciplinary research.

Scope

The journal publishes original research and review articles on environmental monitoring, pollution prevention and control, air, water, soil and noise pollution, waste management, environmental technologies, conservation and resource management, toxicology, recycling, environmental policy, and related interdisciplinary areas.

p-ISSN	e-ISSN	PUBLICATION FREQUENCY	WEBSITE
0972-6268	2395-3454	Quarterly	www.neptjournal.com

Open Access

All articles published in Nature Environment and Pollution Technology are freely accessible online through the journal website.

Peer Review

Manuscripts undergo preliminary editorial screening followed by the journal's established peer-review and editorial decision process.

Digital Object Identifier

Individual articles are assigned persistent Crossref Digital Object Identifiers (DOIs) to support citation, linking, and discoverability.

Publication Ethics

NEPT maintains publication policies addressing research integrity, authorship, conflicts of interest, peer review, corrections, and responsible scholarly publishing. Detailed policies are available on the journal website.

Abstracting & Indexing

- Scopus
- Directory of Open Access Journals (DOAJ)
- Zoological Record (Clarivate)
- GEOBASE (Engineering Village)
- CAB Abstracts (CABI)
- Chemical Abstracts Service (CAS)
- AGRIS (FAO)
- CNKI Scholar (China National Knowledge Infrastructure)
- EBSCO Environment Index
- Pollution Abstracts (ProQuest)

For Authors

Guidelines and online submission:
https://editorial.neptjournal.com/index.php/1/about/submissions

Editorial Office

General: contact@neptjournal.com
Operations: operations@neptjournal.com

Published by

Technoscience Publications LLP
Scholarly Publishing
A6/1903, Kumar Prospera, Hadapsar,
Pune-411 028, Maharashtra, India
www.technosciencepub.in